PUBLICATIONS OF GODDARD SPACE FLIGHT CENTER 1963

Volume II
SPACE TECHNOLOGY

For sale by the Superintendent of Documents, U.S. Government Printing Office
Washington, D.C., 20402 – Price $7.00

FOREWORD

This publication is a collection of articles, papers, talks, and reports generated by the scientific and engineering staff of Goddard Space Flight Center in the year 1963. Many of these articles were originally published in scientific or engineering Journals or as official NASA technical publications, while others are documents of a more informal nature. All are reprinted here as nearly verbatim as typography and format will permit.

The articles are grouped into broad subject categories, but no detailed subdivision has been made. Within each category, the articles are arranged alphabetically by author. An overall author index is given in the back of the volume. A special Acknowledgments section is also included, which lists the various journals and other non-NASA publications from which particular articles have been taken.

The years 1963 and 1964 are being published as whole-year issues, and the resulting size dictates the use of two volumes; the first volume is titled Space Sciences, the second Space Technology. It is anticipated, however, that future issues will be quarterly single volumes.

Page intentionally left blank

CONTENTS

Page

FOREWORD iii

I. PROJECTS AND PROGRAMS

THE NATIONAL AERONAUTICS AND SPACE ADMINISTRATION TOPSIDE SOUNDER PROGRAM, *by* L. J. BLUMLE, R. J. FITZENREITER, *and* J. E. JACKSON 1

THE ORBITING SOLAR OBSERVATORY SPACECRAFT, *by* F. P. DOLDER, O. E. BARTOE, R. C. MERCURE, Jr., R. H. GABLEHOUSE, and J. C. LINDSAY 16

STEREO PHOTOGRAPHY OF THE ECHO II BALLOONS NUMBER 9, 11, AND 13, *by* S. H. GENATT 22

GROUND OPERATION EQUIPMENT FOR THE ORBITING ASTRONOMICAL OBSERVATORY, *by* E. J. HABIB, A. G. FERRIS, H. W. COOPER, *and* R. L. MCCONAUGHY 32

EXPLORATION OF THE ATMOSPHERE OF VENUS BY A SIMPLE CAPSULE, *by* R. A. HANEL 48

THE ORBITING GEOPHYSICAL OBSERVATORIES, *by* G. H. LUDWIG 62

OPERATIONS WITH AN EXPERIMENTAL SATELLITE, *by* D. G. MAZUR 93

RELAY, *by* S. METZGER *and* R. H. PICKARD 105

RELAY I SPACECRAFT PERFORMANCE, *by* R. H. PICKARD 111

RELAY, AN EXPERIMENTAL SATELLITE FOR TV AND MULTICHANNEL TELEPHONY COMMUNICATION, *by* R. H. PICKARD, S. ROTH, *and* J. KIESLING 122

TIROS OPERATIONS, *by* E. F. POWERS 141

TIROS ACHIEVEMENTS, *by* R. M. RADOS 146

THE ORBITING GEOPHYSICAL OBSERVATORIES, *by* W. E. SCULL 149

ARIEL I, THE FIRST INTERNATIONAL SATELLITE 160

II. SPACECRAFT AND SUBSYSTEMS

SATELLITE ATTITUDE DETERMINATION: DIGITAL SENSING AND ON-BOARD PROCESSING, *by* J. S. ALBUS *and* D. H. SCHAEFER 221

A SMALL MULTIPURPOSE ROCKET PAYLOAD FOR IONOSPHERIC STUDIES, *by* S. J. BAUER *and* J. E. JACKSON 230

TELEMETRY DATA PROCESSING FOR THE ECCENTRIC ORBITING GEOPHYSICAL OBSERVATORY SATELLITE, *by* R. COATES, C. CREVELING, E. HABIB, M. MAHONEY, *and* C. STOUT 242

MATHEMATICAL ANALYSIS FOR THE ORIENTATION AND CONTROL OF THE ORBITING ASTRONOMICAL OBSERVATORY SATELLITE, *by* P. B. DAVENPORT 251

A PRECISION ENDLESS-LOOP MAGNETIC TAPE RECORDER FOR SPACE APPLICATIONS, *by* R. C. FALWELL, K. W. STARK, *and* A. F. WHITE 260

ANALYTICAL THEORY OF THE STRETCH YO-YO FOR DE-SPIN OF SATELLITES, *by* J. V. FEDOR 272

THE MRIR-PCM TELEMETRY SYSTEM—A PRACTICAL EXAMPLE OF MICROELECTRONIC LOGIC DESIGN, *by* P. M. FEINBERG 283

FINE POINTING CONTROL FOR THE ORBITING ASTRONOMICAL OBSERVATORY (OAO), *by* G. E. GRAHAM 294

ADVANCED EARTH SENSOR DESIGN CONSIDERATIONS, *by* B. K. LUNDE 299

RELIABILITY VERSUS ACCURACY TRADEOFFS, *by* B. K. LUNDE 302

A RELIABLE EARTH SENSOR FOR ATTITUDE SENSING, *by* B. K. LUNDE 307

ANALYSIS OF THE DYNAMIC TESTS OF THE STRETCH YO-YO DESPIN SYSTEM, *by* W. R. MENTZER 313

Page

A METHOD TO OPTIMIZE THE SOLAR CELL POWER SUPPLY FOR INTERPLANETARY SPACECRAFT, *by* G. B. NICHOLS 326
A MAGNETIC CORE VOLTAGE-TO-FREQUENCY CONVERTER, *by* S. PAULL 336
CHARACTERISTICS OF PASSIVE COMMUNICATION SATELLITES WITH LAMBERTIAN SURFACES, *by* H. P. RAABE 346
DATA STORAGE FOR METEOROLOGICAL SATELLITES, *by* M. I. SCHNEEBAUM *and* R. A. STAMPFL 357
A MEDIUM-DATA-RATE DIGITAL TELEMETRY SYSTEM, *by* M. R. TOWNSEND, P. M. FEINBERG, *and* J. G. LESKO, Jr 363
THE SOLAR POWER SUPPLY SYSTEM FOR THE ORBITING ASTRONOMICAL OBSERVATORIES, *by* C. J. WENZINGER *and* H. CARLETON 369
A LINEARIZED ANALYSIS AND DESIGN OF AN AUTOMATIC BALANCING SYSTEM FOR THE THREE-AXIS AIR BEARING TABLE, *by* F. ZAJAC *and* D. SMALL 379

III. VEHICLE TECHNOLOGY

AN APPROXIMATION METHOD FOR DETERMINATION OF PROPULSION REQUIREMENTS ASSOCIATED WITH LOW THRUST COPLANAR ORBITAL TRANSFER IN A CENTRAL FORCE FIELD UNDER NEGLIGIBLE EXTERNAL PERTURBATIONS, *by* K. I. DUCK 391
VEHICLE TECHNOLOGY CONSIDERATIONS FOR A SOLAR PROBE, *by* J. A. FOSCHETTI 402
FLIGHT VIBRATION DATA FROM THE DELTA 9 LAUNCH VEHICLE, *by* L. A. WILLIAMS 409

IV. SOUNDING ROCKETS

ROCKET SOUNDINGS IN THE MESOSPHERE, *by* W. NORDBERG 425
THE ROCKET-GRENADE EXPERIMENT, *by* W. NORDBERG *and* W. SMITH 443
INVESTIGATION OF HF AND VHF ROCKET-BORNE SHROUD ANTENNAS, *by* G. H. SPAID *and* J. R. HAGEMEYER 464

V. SENSORS

A POSSIBLE METHOD OF CORRECTING LOW FREQUENCY RADIO OBSERVATIONS FOR IONOSPHERIC ABSORPTION, *by* L. W. BROWN 475
A SCINTILLATION COUNTER TELESCOPE FOR CHARGE AND MASS IDENTIFICATION OF PRIMARY COSMIC RAYS, *by* D. A. BRYANT, G. H. LUDWIG, *and* F. B. MCDONALD 491
FINE SUN TRACKER FOR ADVANCED ORBITING SOLAR OBSERVATORY, *by* C. CANTOR 497
DELINEATION OF TRACKS OF HEAVY COSMIC RAYS AND NUCLEAR PROCESSES WITHIN LARGE SILVER CHLORIDE CRYSTALS, *by* C. B. CHILDS *and* L. M. SLIFKIN 506
SPECTRALLY SELECTIVE PHOTODETECTORS FOR THE MIDDLE AND VACUUM ULTRAVIOLET, *by* L. DUNKELMAN, W. B. FOWLER, *and* J. P. HENNES 513
ULTRAVIOLET PHOTODETECTORS, *by* L. DUNKELMAN 522
MIDDLE ULTRAVIOLET PHOTOELECTRIC DETECTION TECHNIQUES, *by* L. DUNKELMAN, J. P. HENNES, *and* W. B. FOWLER 532
FAILURE PROBLEM WITH A RHENIUM MASS SPECTROMETER FILAMENT AND ITS SOLUTION, *by* A. G. EUBANKS *and* H. E. FRANKEL 542
AN ATTITUDE CONTROL SYSTEM FOR THE ADVANCED ORBITING SOLAR OBSERVATORY, *by* P. G. FAHLSTROM 546
EXPERIMENTS FROM A SMALL PROBE WHICH ENTERS THE ATMOSPHERE OF MARS, *by* R. A. HANEL, L. E. RICHTMYER, R. A. STAMPFL, *and* W. G. STROUD 549
PHYSICAL MEASUREMENTS FROM METEOROLOGICAL SATELLITES, *by* R. A. HANEL *and* D. Q. WARK 563
IMAGE CONSTRUCTION FOR CONCAVE GRATINGS AT GRAZING INCIDENCE, BY RAY TRACING, *by* S. O. KASTNER, *and* W. M. NEUPERT 569

Page

A DETECTOR-ANALYZER FOR STUDYING THE INTERPLANETARY PLASMA, *by* K. W. OGILVIE, N. MCILWRAITH, H. J. ZWALLY, *and* T. D. WILKERSON 575
ATMOSPHERIC SAMPLING INSTRUMENTATION, *by* N. W. SPENCER 583
A MASS SPECTROMETER FOR AN AERONOMY SATELLITE, *by* N. W. SPENCER *and* C. A. REBER 587
THE AUTOMATIC PICTURE TRANSMISSION (APT) TV CAMERA SYSTEM FOR METEOROLOGICAL SATELLITES, *by* R. A. STAMPFL *and* W. G. STROUD 590
A VACUUM ULTRAVIOLET PHOTOIONIZATION DETECTOR, *by* A. K. STOBER, R. SCOLNIK, *and* J. P. HENNES 599
ULTRAVIOLET OPTICAL PROPERTIES OF DIAMOND, *by* W. C. WALKER *and* J. OSANTOWSKI 605
THE ULTRAVIOLET REFLECTION SPECTRUM OF CADMIUM SULFIDE, *by* W. C. WALKER *and* J. OSANTOWSKI 611
THE IMPEDANCE OF AN ELECTRICALLY SHORT ANTENNA IN THE IONOSPHERE, *by* H. A. WHALE 613
ION SHEATH EFFECTS NEAR ANTENNAS RADIATING WITHIN THE IONOSPHERE, *by* H. A. WHALE 618
THE SOUTHERN SKY SURVEY PAYLOAD, *by* R. M. WINDSOR 626

VI. ENVIRONMENTAL TESTING

SINUSOIDAL VIBRATION TESTING OF NONLINEAR SPACECRAFT STRUCTURES, *by* W. F. BANGS 639
THE PURPOSES OF ENVIRONMENTAL TESTING FOR SCIENTIFIC SATELLITES, *by* J. H. BOECKEL 646
ENVIRONMENTAL TENSILE TESTING OF NYLON PARACHUTE MATERIALS, *by* J. A. FARKAS 684
MECHANICAL IMPEDANCE STUDY OF THE X–259 ROCKET MOTOR, *by* R. G. HARTENSTEIN *and* W. G. ELSEN 693
A SURVEY OF LARGE SPACE CHAMBERS, *by* R. T. HOLLINGSWORTH 706
POWER TRANSISTOR COOLING IN A SPACE ENVIRONMENT, *by* J. E. A. JOHN *and* J. J. HILLIARD 713
ACHIEVING SATELLITE RELIABILITY THROUGH ENVIRONMENTAL TESTS, *by* J. C. NEW 722
A THEORETICAL BASIS FOR MECHANICAL IMPEDANCE SIMULATION IN SHOCK AND VIBRATION TESTING OF ONE-DIMENSIONAL SYSTEMS, *by* F. J. ON *and* R. O. BELSHEIM 762
FLIGHT SHOCK AND VIBRATION DATA OF THE ECHO A–12 APPLICATION VERTICAL TESTS [AVT–1 AND AVT–2], *by* W. B. TERENIAK *and* S. A. CLEVENSON 776
THE MERCURY-XENON ARC AND THE CARBON ARC AS SOURCES OF SOLAR SIMULATION, *by* M. P. THEKAEKARA 791
EXPERIENCE IN THERMAL-VACUUM TESTING EARTH SATELLITES AT GODDARD SPACE FLIGHT CENTER, *by* A. R. TIMMINS *and* K. L. ROSETTE 799

VII. TRACKING SYSTEMS

MINITRACK CALIBRATION SYSTEM, *by* J. H. BERBERT, J. D. OOSTERHOUT, P. D. ENGELS, *and* E. J. HABIB 811
REAL-TIME AUTOMATIC DIGITAL OPTICAL TRACKER, *by* W. J. CARRION 818
NASA PRECISION MULTI-MODE MOUNT, *by* W. J. CARRION *and* E. Y. LEE 821
DIGITAL TELEVISION SCANNING SYSTEM, *by* L. O. CAUDILL 826
DEVELOPMENT OF A RANGE AND RANGE RATE SPACECRAFT TRACKING SYSTEM, *by* E. J. HABIB, G. C. KRONMILLER, JR., P. D. ENGELS, *and* H. J. FRANKS, JR 832

Page

MOTS—THE MINITRACK OPTICAL TRACKING SYSTEM, *by* D. W. HARRIS, J. H. BERBERT, E. J. HABIB, *and* B. W. MCKENDREE 869
PULSED-LASER RANGING, *by* T. S. JOHNSON 876
THE S–66 LASER TRACKING EXPERIMENT, *by* H. H. PLOTKIN 880
CHARACTERISTICS OF THE X–Y ANTENNA MOUNT FOR DATA ACQUISITION, *by* A. J. ROLINSKI, D. J. CARLSON, *and* R. J. COATES 885
PRELIMINARY REPORT ON THE SINGLE STATION DOPPLER-INTERFEROMETER ROCKET TRACKING TECHNIQUE, *by* J. C. SEDDON 893
THE RANGE AND RANGE RATE SYSTEM AND DATA ANALYSIS FOR SYNCOM 1 (1963 4A), *by* H. W. SHAFFER, W. D. KAHN, W. J. BODIN, JR., G. C. KRONMILLER, JR., P. D. ENGELS, *and* E. J. HABIB 913
A SYSTEM FOR RE-ENTRY TRACKING OF THE APOLLO SPACECRAFT, *by* V. SIMAS 925

VIII. GENERAL

EARTH REFLECTED SOLAR RADIATION INCIDENT UPON AN ARBITRARILY ORIENTED SPINNING FLAT PLATE, *by* F. G. CUNNINGHAM 937
POWER INPUT TO A SMALL FLAT PLATE FROM A DIFFUSELY RADIATING SPHERE WITH APPLICATION TO EARTH SATELLITES: THE SPINNING PLATE, *by* F. G. CUNNINGHAM 965
ON THE TEMPERATURE DEPENDENCE OF THE BREAKDOWN FIELD OF $BaTiO_3$, *by* P. H. FANG 980
THE EFFECT OF SOLAR RADIATION PRESSURE ON THE SPIN OF EXPLORER XII, *by* J. V. FEDOR 982
CONSERVATIVE TORQUES AND MOMENTS OF INERTIA INVOLVED IN THE DESIGN OF A LABORATORY MODEL SOLAR ARRAY WITH VARIABLE PADDLE-ARM ORIENTATION, *by* S. G. MCCARRON 991
A FINITE DIFFERENCE SOLUTION FOR THE TRANSVERSE VIBRATION OF A RECTANGULAR PLATE WITH INTERNAL VISCOUS DAMPING SUPPORTED AT A FINITE NUMBER OF POINTS UNDER GENERAL BOUNDARY CONDITIONS, *by* C. A. WAGNER 1001
ACKNOWLEDGMENT OF NON-NASA PUBLICATIONS 1025
AUTHOR INDEX 1027

I. PROJECTS AND PROGRAMS

THE NATIONAL AERONAUTICS AND SPACE ADMINISTRATION TOPSIDE SOUNDER PROGRAM*

L. J. BLUMLE, R. J. FITZENREITER, J. E. JACKSON
Goddard Space Flight Center

The NASA Topside Sounder Program is reviewed with particular emphasis upon the fixed-frequency topside sounder satellite which is scheduled for 1963. A rocket test conducted on June 24, 1961, as part of this project established the feasibility of the topside sounding technique and revealed many of the unique phenomena associated with it. A comparison of the design of the *fixed*-frequency topside sounder with that of the Alouette (1963 $\beta\alpha$), the recent Canadian *swept*-frequency topside sounder, reveals the complementary features of their scientific objectives and the basic differences in the technologies employed. Although the common goal of the two experiments is to improve our knowledge of the detailed structure of the upper ionosphere, the differences in approach have resulted in the development of separate data analysis techniques.

INTRODUCTION

A topside sounder is a satellite version of instrumentation used extensively on the ground for routine observations of the ionosphere. The conventional equipment used for such ground-based soundings of the ionosphere is basically a low-frequency radar. If a radar is operated with a carrier frequency of a few megacycles, echoes are received from the ionosphere; the electron density at the reflection level is determined from the carrier frequency, and the altitude at which reflection takes place is indicated by the signal's round trip propagation time. Changing the radar carrier frequency results in reflections occurring at different density levels, and a complete altitude profile of electron density can be derived up to the altitude of *maximum* electron density. This altitude can vary from about 250 km to 400 km or more, depending upon the latitude and upon the sun-spot number (Reference 1). The level of maximum electron density separates the "bottomside" and the "topside" of the ionosphere.

The vertical radio sounding technique has been used for about 30 years and until the advent of space research it was the main tool for ionospheric investigations. Ground-based observations have revealed the broad features of the structure and behavior of the bottomside ionosphere, e.g., the daily and seasonal variations and the strong controlling effect of the 11-year sunspot cycle, the differences between the polar, temperate, and equatorial regions of the ionosphere, and the influence of the geomagnetic field. Many other ionospheric peculiarities such as sporadic E, spread-F, and the seasonal and equatorial anomalies were also discovered from these ground-based studies. Although these phenomena are quite well documented, their detailed mechanisms are far from being completely understood. Nevertheless these early ground-based observations have stimulated considerable theoretical study of the fundamental phenomena occurring in the ionosphere; and the resulting body of knowledge has provided an excellent starting point for ionospheric investigations utilizing space technology.

*Based on a talk presented at the American Astronautical Society/American Association for the Advancement of Science meeting at Philadelphia, Pa., Dec. 27, 1962.

INVESTIGATIONS OF THE TOPSIDE IONOSPHERE

Before 1958 little was known about the upper or topside ionosphere, except that it was relatively heavily ionized. Radar signals reflected from the moon (References 2 and 3) had shown that the total electron content in the topside was about three times that in the bottomside. Direct exploration of the upper ionosphere began in 1958 when *high altitude space vehicles* became available. It should be noted, however, that the development of a ground-based method for topside studies also began in 1958. This method, known as the incoherent backscatter technique (Reference 4), is now used systematically for observations over a few geographic locations (References 5 and 6). The NASA space science program, organized during the latter part of 1958 and the beginning of 1959, emphasized the investigation of the topside ionosphere by providing for four different groups of experiments. The four basic approaches are illustrated in Figure 1.

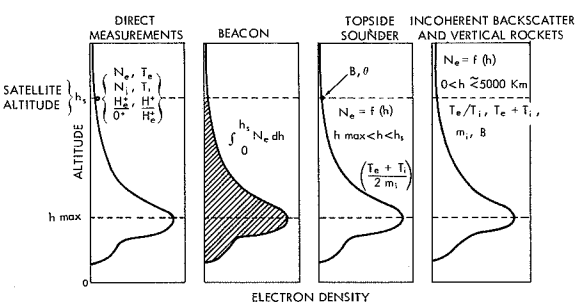

FIGURE 1.—Four types of ionospheric experiment.

Direct measurements provide a detailed picture of the ionosphere in the immediate vicinity of the spacecraft. Typical parameters which can be obtained are electron and ion densities N_e and N_i, electron and ion temperatures T_e and T_i, and ionic composition. Explorer VIII (1960 $\xi 1$) and Ariel I (1962 $\sigma 1$) were both direct measurement satellites. Explorer VIII was one of two space projects credited with the experimental discovery of an ionized helium belt which, during the daytime, envelops the earth at altitudes ranging from 1000 to 2500 km (Reference 7). Sputnik III (1958 $\delta 2$) and Explorer VIII together showed that atomic oxygen was the major ionic constituent of the topside ionosphere below 1000 km. Electron temperatures measured by Explorer VIII were found to vary between 1000°K at night and 1800°K in the daytime. These results were subsequently confirmed and extended by Ariel I, which contained improved versions of the Explorer VIII experiments (Reference 8).

The *beacon* satellite provides transmissions of radio signals at frequencies high enough to penetrate the ionosphere, but low enough to be influenced by the ionosphere (Reference 9). Beacon observations yield the total electron content $\int_0^h s\ N_e\ dh$ below the satellite and provide some information about irregularities. This type of satellite is ideal for international participation, since independent observers all over the world can obtain information about the ionosphere, with relatively simple radio receivers.

It will be sufficient to note at this point that with the *topside sounder* technique it is possible to obtain a complete topside profile up to the satellite, and also to obtain additional local parameters such as the intensity β and the direction θ of the earth's magnetic field.

High-altitude *vertical rocket soundings* have been primarily useful for obtaining typical topside electron density profiles. One of the most accurate topside profiles ever obtained is shown in Figure 2. The smoothness of this

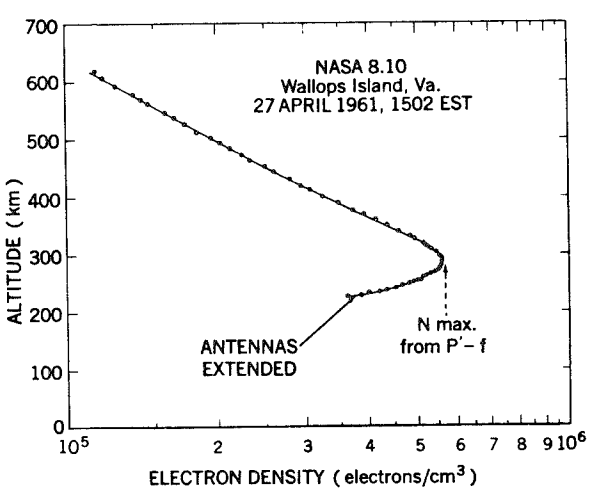

FIGURE 2.—Vertical rocket electron-density profile obtained by a vertical rocket.

curve and the exponential decay of the density with altitude suggest that for the particular location and time of the measurement, the ion-electron gas in the topside ionosphere behaved very much like a neutral gas (Reference 10). In other words, the density distribution seemed to be controlled by gravity, temperature, and mass. In the case of an ion-electron gas, the temperature is the average of the electron and ion temperature. Similarly the effective mass is the mean electron-ion mass, which is essentially half of the ion mass. The electron density profile shown in Figure 3 reveals a change in ion composition at an altitude of about 1000 km, and it provides supporting evidence that the transition was one from 0^+ to He^+ as shown by the solid curve rather than 0^+ to H^+ as shown by the dashed curve (Reference 11).

From these experimental data the model of the quiet topside ionosphere at middle latitudes shown in Figure 4 was derived, which indicates the three regions where 0^+, He^+, and H^+ are respectively predominant (Reference 12). Experimental observations (References 11, 13, and 7), as well as theoretical considerations (Reference 14) show that the altitude distribution of the three major ionic constituents is controlled by the topside temperature in the manner illustrated by Figure 5. The 3-to-1 range of temperatures shown in Figure 5 illustrates the range of values which might be expected during a complete sunspot cycle. A typical diurnal temperature variation is generally less than 2-to-1.

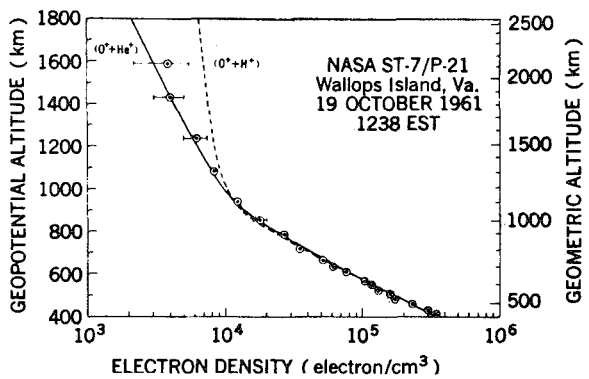

FIGURE 3.—Experimental electron-density profile indicating a change in ionic composition at about 1,000 kilometers.

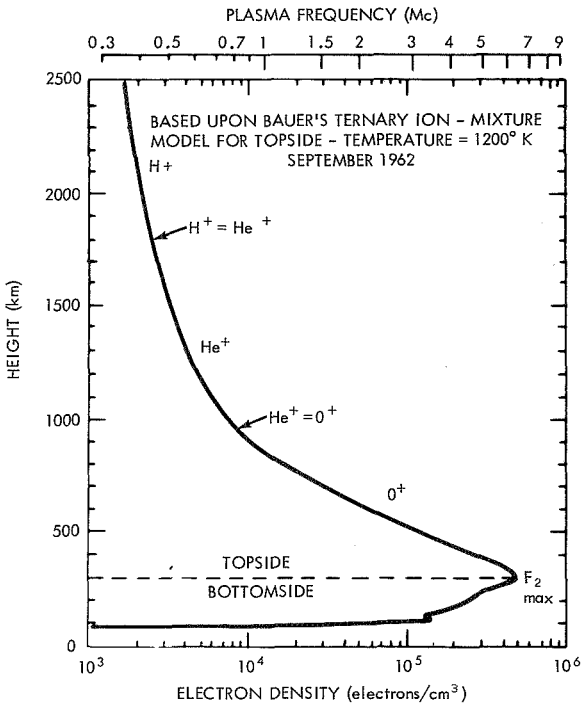

FIGURE 4.—Theoretical average daytime ionsphere.

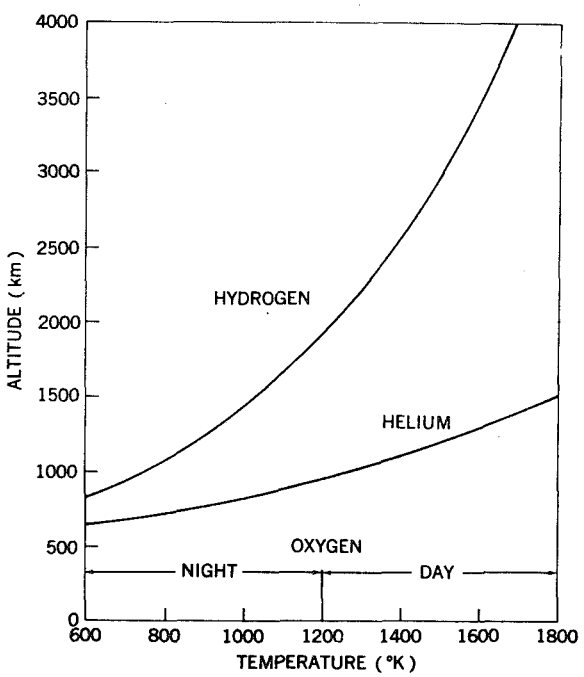

Figure 5.—Principal ionic constituents as a function of altitude and temperature.

RADIO SOUNDINGS OF THE IONOSPHERE

Perhaps the most sophisticated method used for ionospheric investigation is the topside sounding technique, an extension of the method used so successfully in ground-based (or bottomside) sounders. It may be helpful first to describe briefly the conventional vertical technique.

The sounding equipment used is basically a low-frequency radar system in which the carrier frequency is swept periodically from about 1 Mc to about 20 Mc. The transmitted signals reflect from the ionosphere when they reach an electron density given by

$$N=\frac{f^2}{80.6}, \tag{1}$$

where N is the electron density per cm^3 and f is frequency in kc.

Since ionospheric densities increase almost monotonically up to about 300 or 400 km, echoes are obtained from increasingly higher altitudes as the frequency is increased from 1 to 20 Mc. Actually, it is only under very rare conditions that the maximum electron density is large enough to reflect 20 Mc; and in practice there is a maximum frequency (less than 20 Mc) for which a reflection can be obtained.

The instrumentation measures the round-trip time for the pulsed signal and plots this quantity as a function of the sounding frequency. The result is a record such as the one shown in Figure 6. The time scale is actually calibrated in terms of altitude, i.e., the travel time is converted to an equivalent distance based upon the free-space propagation velocity. Since the velocities in an ionized medium are less than free-space velocities, the altitudes so obtained are greater by a factor which is a function of the electron-density profile, the frequency used, and, to a lesser extent, the magnetic field of the earth. In view of the distortion in the height scale, this presentation is called a P'-f (or h'-f) record, i.e., a record of *apparent path lengths*, or *virtual heights*, versus *frequency*. A subsequent analysis, which takes these effects into consideration, can be performed to convert the P'-f record to electron density versus altitude.

Multiple echoes can also be seen in Figure 6 corresponding to two round trips between the ground and the ionosphere. Additional features which can be noted in Figure 7 (a redrawn version of Fig. 6) include the presence of two traces, corresponding to the ordinary and extraordinary modes of propagation which are due to the presence of the earth's magnetic field. These two modes have different propagation and reflection properties.

The frequency at which reflection occurs for the ordinary mode is

$$f_0=10^{-3}\sqrt{81N_e}\ \text{Mc}, \tag{2}$$

where N_e is the electron density in electrons/cm^3. For the extraordinary mode, the reflection condition is

$$f_x=\frac{f_H+\sqrt{4f_0^2+f_H^2}}{2}\ \text{Mc}, \tag{3}$$

where $f_H=2.8H$ Mc and H is the earth's magnetic field in gauss. There is also the Z mode, usually seen only at high latitudes and not apparent in Figures 6 and 7; for this mode, the reflection condition is

$$f_z=\frac{-f_H+\sqrt{4f_0^2+f_H^2}}{2}\ \text{Mc}. \tag{4}$$

If $f_0>>f_H$, the approximations

$$f_x\approx f_0+\frac{f_H}{2},$$

$$f_z\approx f_0-\frac{f_H}{2}$$

may be used.

The formula relating the virtual height h' and the actual height h at which reflection occurs is

$$h'=\int_0^h\left(\mu+f\frac{\partial\mu}{\partial f}\right)dh, \tag{5}$$

where μ, the phase refractive index, is a function of the electron density N_e, the sounding frequency f, the geomagnetic field H, the magnetic

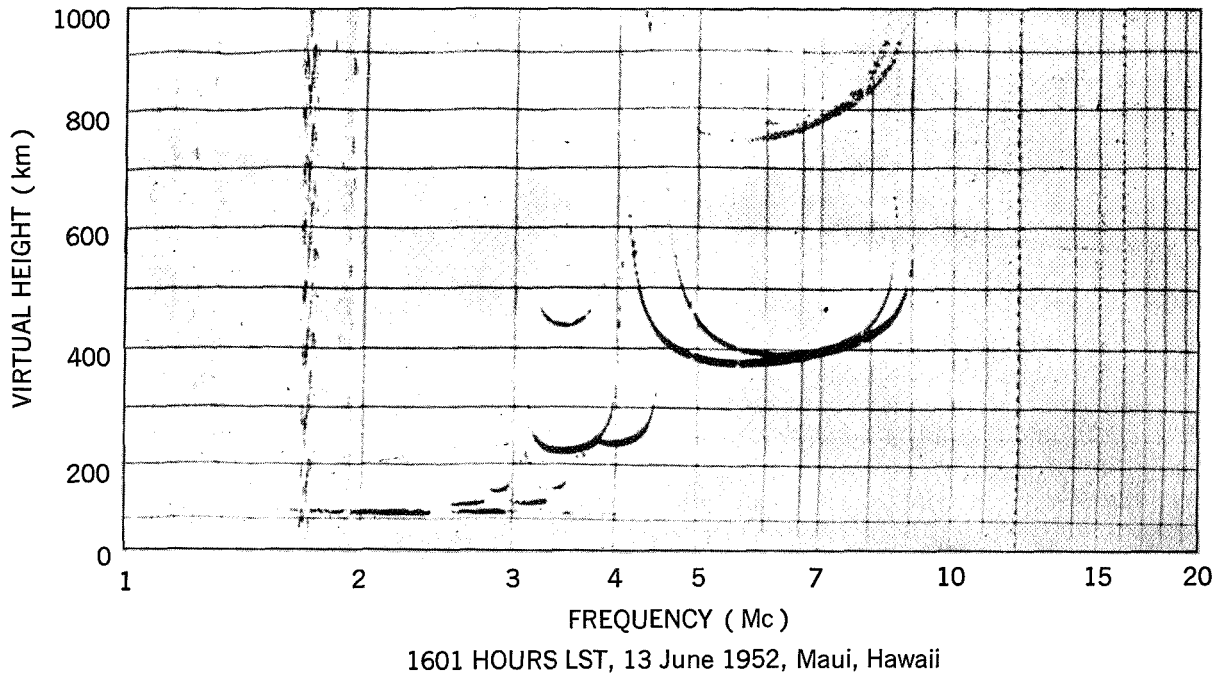

FIGURE 6.—Typical bottomside sounding.

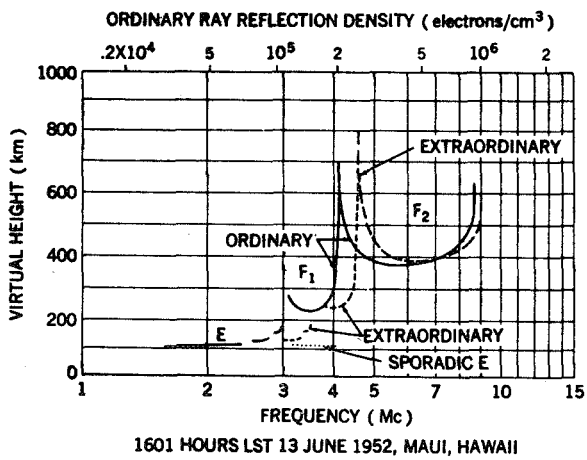

FIGURE 7.—Typical virtual height record (traced from iongram).

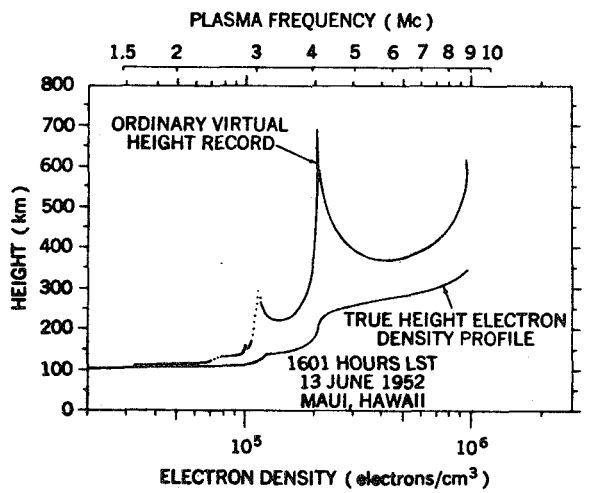

FIGURE 8.—Reduced true height electron density profile from bottomside sounding.

dip angle θ_H, and, only in the lowest portion of the ionosphere, the electronic collision frequency ν. The data analysis which involves the solution of this integral equation is most readily done by electronic computers. The result of such an analysis performed on the ionogram shown earlier is illustrated in Figure 8. It is seen that apparent heights and true heights differ quite substantially.

NASA TOPSIDE SOUNDER PROGRAM

Early in 1958, consideration of satellite-borne topside sounding experiments began simultaneously in several United States, Canadian, and European groups. A proposal from the Canadian Defence Research Telecommunication Establishment (DRTE) came to NASA

at the end of 1958. NASA was pleased to accept DRTE's cooperation on the Topside Sounder Program, and it was agreed that this scientific undertaking would be a joint Canadian-United States effort with the Canadians responsible for designing and manufacturing the complete satellite and NASA for launching and overall program direction. This topside sounder effort, began in Canada early in 1959. Since its successful launching the spacecraft has been known as the ALOUETTE (1962 $\beta\alpha$).

Concurrently, NASA had requested that the Central Radio Propagation Laboratory (CRPL) of the National Bureau of Standards conduct feasibility studies and recommend immediate and long-range approaches for this area of research. (CRPL had also proposed a topside sounding experiment in mid 1958.) In June 1959, a CRPL study report recommended the fixed-frequency system as a first-generation experiment and suggested that DRTE be encouraged to develop its swept-frequency system as a second-generation experiment. The latter of these recommendations was, in fact, a concurrence by CRPL with the decision already reached between NASA and DRTE. Then, NASA and CRPL discussed the development of the fixed-frequency system as a parallel effort, in view of its complementary features. The design of a U.S. fixed-frequency topside sounder experiment began at the Airborne Instruments Laboratory (AIL) in May 1960 under the scientific supervision of CRPL. The swept- and fixed-frequency sounder projects were conducted as a single program under NASA technical direction. Figure 9 is a chart of the responsibility and data distribution for the program.

The telemetry stations for both the swept-frequency and fixed-frequency sounders are shown in Figure 10. The area bounded by the dotted line is the region within which both satellites will be higher than 15 degrees above the horizon for one or more telemetry stations. The entire unshaded area indicates the horizon-to-horizon coverage provided by these stations. It is seen that *each* station can provide data over an area comparable to that of the United States.

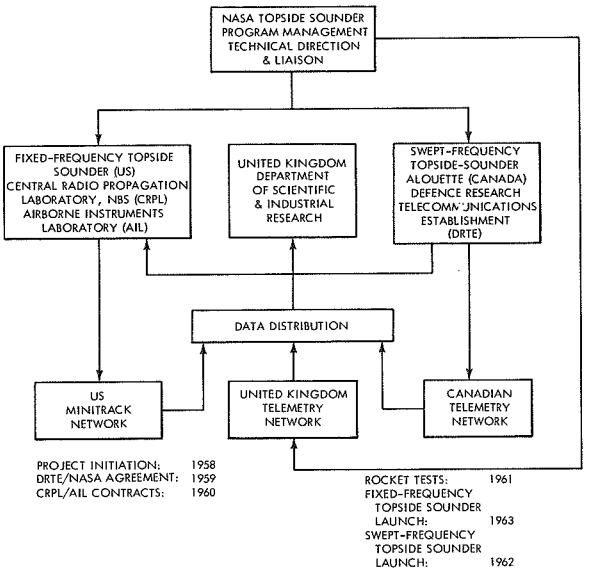

FIGURE 9.—The NASA Topside Sounder Program.

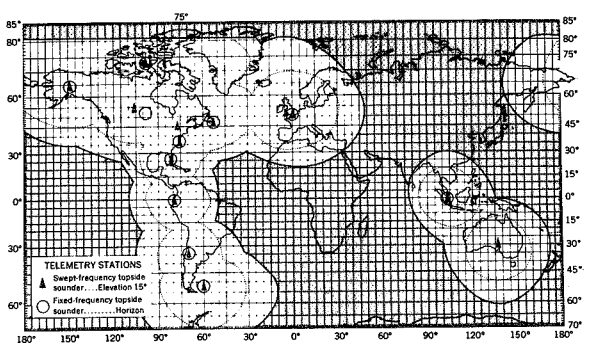

FIGURE 10.—Telemetry coverage for the Topside Sounder Program based on a 1,000-km, 80° inclination orbit.

Although the two experiments are similar in objective and techniques, the emphasis and instrumentation used in the two experiments are quite different. The Canadian experiment was intended primarily to investigate the polar, arctic, and auroral effects which produce very complex ionospheric conditions over Canada. For that purpose DRTE has established telemetry stations at Resolute Bay, Northwest Territories; Prince Albert, Saskatchewan; and Ottawa, Ontario. The U.S. experimenters, however, will emphasize the study of meridional cross-sections through the ionosphere, using United States and Canadian telemetry stations

along the 75°W meridian. The United Kingdom also operates telemetry stations in the South Atlantic; at Winkfield, England; and at Singapore.

The U.S. topside sounder experiment is illustrated in Figure 11, which shows that downward soundings will be made with six fixed-frequencies (f_1, . . ., f_6). Reflection points for a typical daytime electron density distribution are indicated on the figure, as they would be obtained both from the fixed-frequency topside sounder satellite and from a ground-based sounding station. It is seen that a complete profile can be obtained by simultaneous use of bottomside and topside soundings. Because only six fixed frequencies are used, a complete sounding can be performed in a very short time (0.1 second) corresponding to less than 1 kilometer of horizontal motion of the satellite. Thus, each sounding is performed essentially at a fixed location.

In view of its fast profile acquisition rate, this system is very well suited for determining horizontal irregularities in the ionosphere. However, it provides the vertical structure with only limited resolution. In the Canadian experiment the frequency is swept continuously from 0.5 to 11.5 Mc and a much higher resolution in depth is achieved; but a complete sweep requires about 12 seconds, during which the satellite travels nearly 90 km horizontally. Thus, the swept-frequency soundings provide very accurate profiles where the ionosphere is horizontally stratified; but they are subject to errors due to horizontal gradients in the ionospheric structure.

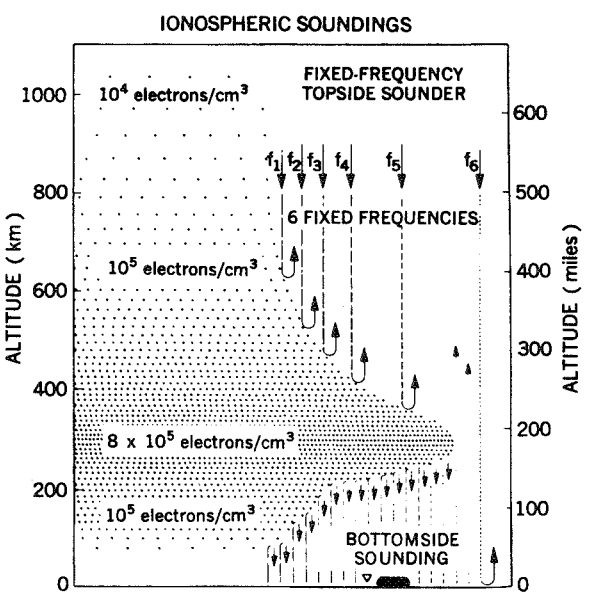

FIGURE 11.—The U.S. topside sounder experiment.

ROCKET TESTS CONDUCTED IN THE FIXED-FREQUENCY TOPSIDE SOUNDER PROGRAM

Since previous rocket experimentation provides no precedent for the Topside Sounder Program, an important part of the CRPL–AIL effort has been the rocket testing of a simplified topside sounder. The original plan called for only a single daytime firing to a height of about 1000 km during undisturbed ionospheric conditions. But in June 1960, it was decided that it would be scientifically inadvisable to adjust the parameters of the satellite topside sounders on that basis alone: A nighttime firing under disturbed conditions was deemed highly desirable. The final plan, therefore, included a second rocket test to study topside reflection characteristics at a time when spread-F echoes, indicative of disturbed ionospheric conditions, were being observed on bottomside soundings. In the planning of the Canadian experiment the prevalence of spread-F echoes in polar and arctic regions gave considerable importance to knowing the degree to which topside echoes will be degraded during this condition. Since spread-F is regularly observed in the equatorial region, the results of the tests were also useful in planning the U.S. experiment.

The daytime test (Reference 15) and the nighttime test (Reference 16) were both conducted successfully and the results were presented at the Eight Annual National Meeting of the American Astronautical Society in January 1962 (Reference 17). The success of these two experiments was most important to the program, since they demonstrated the feasibility of the topside sounder technique. In both flights the maximum altitude was about 1000 km, which corresponded to the planned altitude for both satellites. Figure 12, a

portion of the record taken near the apogee of the daytime flight, shows strong echoes at 4.07 Mc and 5.97 Mc, the two frequencies chosen for that test. This result showed that the power level planned for the sounding transmitter was adequate and that proper design parameters had been used for the instrumentation. The night test subsequently revealed, however, that under spread-F conditions the strength of the received echoes could be enhanced by as much as two orders of magnitude. This required modification of the satellite receiver design to protect against saturation. A most important discovery resulting from these rocket tests was the fact that unusual effects occur when the sounder frequency is the same as one of the local plasma resonances. These effects, which are shown in Figure 13 for daytime tests, occured as the sounder passed through the three reflection levels—the ordinary, extra-ordinary, and Z levels—for each of the two frequencies. When one of these conditions is encountered, the sounder provides not only the local electron density, but also the local geomagnetic field. These phenomena have since been observed regularly on the swept-frequency topside sounder ionograms.

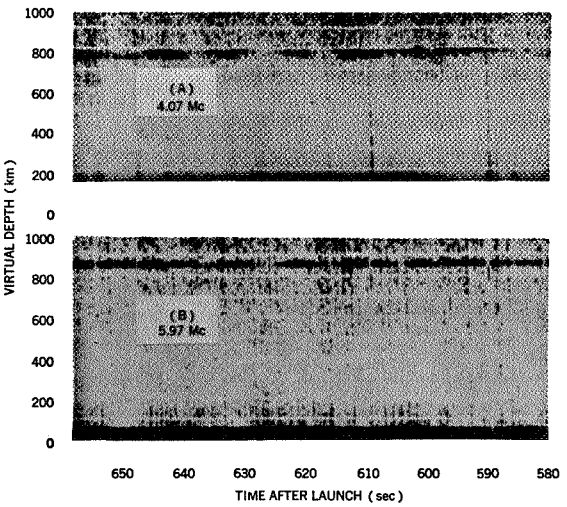

FIGURE 12.—Expanded record of the apogee portion of the daytime rocket test.

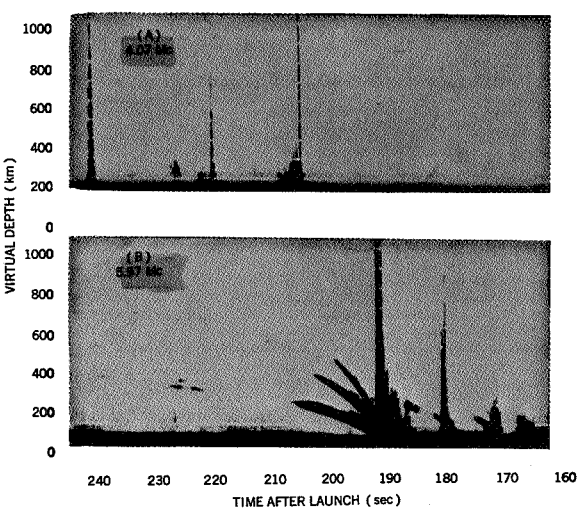

FIGURE 13.—Plasma resonances observed on the daytime rocket tests.

ENGINEERING DESIGNS OF THE CANADIAN AND U.S. TOPSIDE SOUNDERS

Both topside sounder satellites consist basically of a pulsed transmitter and a receiver tuned to the transmitter wave frequency to obtain the echo returns from the ionosphere. The receiver's output is telemetered to the ground via a 2-watt transmitter operating in the 136 Mc band. Both satellites operate only when commanded from a telemetry station. They then obtain telemeter data for a 10-minute period and turn off automatically after this interval to avoid discharging the storage batteries. Solar cells charging nickel-cadmium storage batteries provide the power for both spacecraft: No active temperature controls are used on either.

The two spacecraft employ different techniques of obtaining ionospheric data: The wave frequency of the swept-frequency transmitter is continuously varied from 0.5 Mc to 11.5 Mc at a rate of about 1 Mc/sec. The fixed-frequency sounder transmits at six fixed frequencies: 2.85, 3.72, 4.60, 5.47, 6.82, and 8.57 Mc.* The pulse repetition rates for both sounders is 66 pulses/sec; therefore, both spacecraft acquire data points at the same rate. The telemetry video format has been designed so that the telemetry acquisition and

*These frequencies were changed to 1.5, 2.0, 2.85, 3.72, 5.47, and 7.22 Mc subsequent to the presentation of this paper.

data processing equipment are nearly identical for both spacecraft. Completely transistorized electronics were used in both satellites, and both were designed to have useful lifetimes of about 1 year.

The choice of sounding frequencies is limited by two important quantities. Since any frequency greater than the critical frequency f_0F_2 of the F region of the ionosphere will penetrate through to the ground, the expected maximum value of f_0F_2 sets the upper frequency limit. The lower frequency limit is set by the efficiency of the sounding antenna, which decreases rapidly for an antenna that is small compared to a wavelength. However, for the fixed-frequency topside sounder, it was also convenient to choose frequencies which could be grouped into pairs with equal differences, so that each pair can use the same receiver intermediate frequency. This led initially to the following three pairs of nominal frequencies: 3 and 5 Mc; 4 and 6 Mc; and 8 and 10 Mc; the two frequencies in each pair differing by 2 Mc, the receiver intermediate frequency. Actually, because the launching was postponed to a later date in the solar cycle, the frequencies were revised downward to 2.85 and 3.72 Mc; 4.60 and 5.47 Mc; and 6.82 and 8.57 Mc.* Figures 14 and 15 illustrate the latitude ranges over which

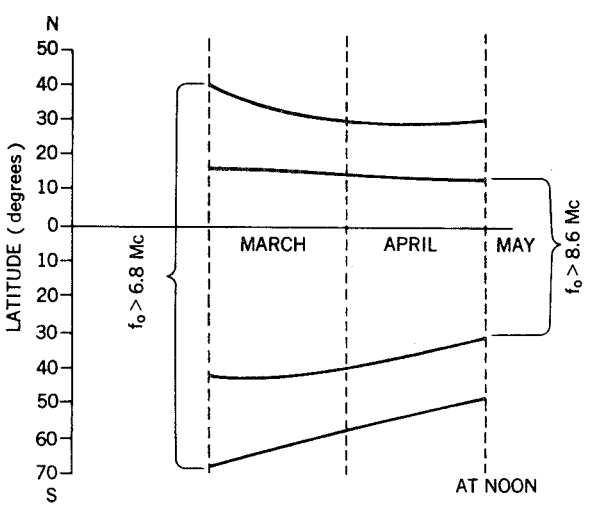

FIGURE 14.—Predicted latitudes at which the critical frequency at noon will exceed 6.8 and 8.6 Mc for the period of March to May 1963.

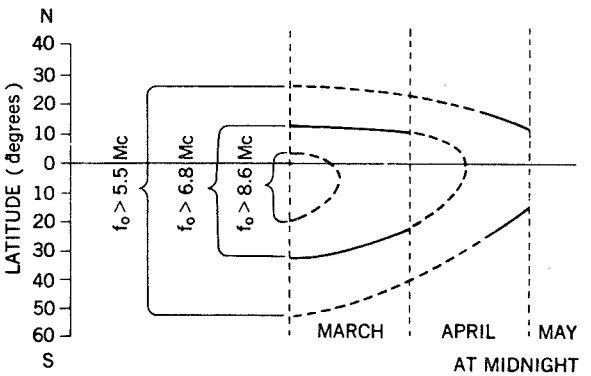

FIGURE 15.—Predicted latitudes at which the critical frequency at midnight will exceed 5.5, 6.8, and 8.6 Mc for the period of March to May 1963.

the critical frequencies of the F region are expected to exceed the fixed sounding frequencies at noon and midnight for March, April, and May 1963. Although predictions for the later months of 1963 are not yet available, the usefulness of the fixed-frequency topside sounder satellite for profile determination will probably decrease somewhat during the summer and increase again during the following winter.

The important mechanical and electrical characteristics of both spacecraft are summarized in Table 1.

SOLAR CELL DEGRADATION

A very important environmental condition which seriously affects the design and operational life of the topside sounder satellites was created by the recent high altitude nuclear tests, which produced a belt of high energy electrons similar to the natural Van Allen radiation belts. These electrons cause a degradation in the efficiency of the solar cells from which the topside sounder satellites derive their electrical power: Figure 16 shows the predicted and observed solar cell degradation for the swept-frequency topside sounder satellite. It is of interest to note that most of the degradation in the performance of an experiment with an operational lifetime of 1 year occurs within the first 40 days. On the basis of these observations, the anticipated daily

TABLE 1.—*Characteristics of the Swept-Frequency and Fixed-Frequency Topside Sounder Satellites*

Characteristic	Swept-frequency topside sounder	Fixed-frequency topside sounder
Mechanical:		
Shape	Oblate spheroid	Truncated cone.
Diameter	42 inches	20 inches.
Height	34 inches	32½ inches.
Weight	319 pounds	95 pounds.
Sounding antenna type	2 crossed dipoles 150 feet tip-to-tip 75 feet tip-to-tip	3 crossed dipoles. 62 feet tip-to-tip.
Telemetry antenna type	Turnstile	Turnstile.
Number of solar cells	6480	2400.
Storage battery type	Nickel-cadmium	Nickel-cadmium.
Electrical:		
Sounding frequency	0.45 to 11.5 Mc	2.85, 3.72, 4.60, 5.47, 6.82, and 8.57 Mc.
Pulse width	100μsec	100μsec.
Pulse repetition rate	67/sec	67/sec.
2-watt telemetry transmitter frequency.	136.089 Mc	136.350 Mc.
Orbit	80° inclination, 1000 km circular	80° inclination, 1000 km circular.
Launch vehicle	Thor-Agena B	Scout.

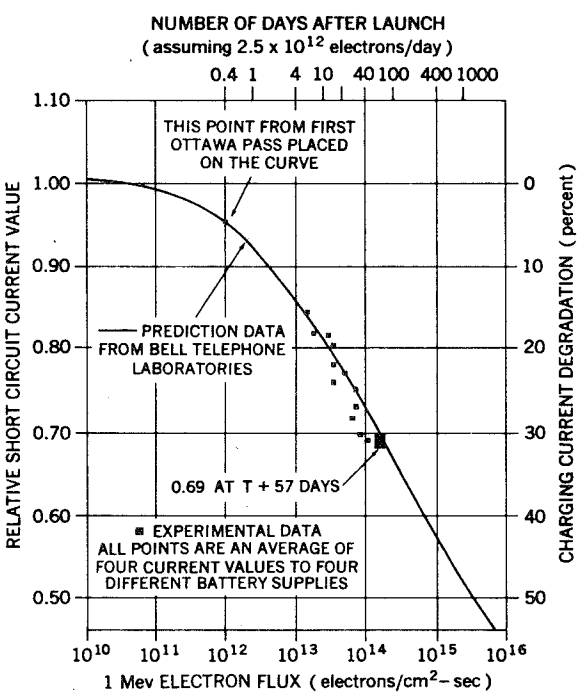

FIGURE 16.—Solar charging current degradation for the swept-frequency topside sounder satellite.

operation of the fixed-frequency topside sounder satellite will be as indicated in Table 2.

TABLE 2.—*Predicted Daily Operation of the Fixed-Frequency Topside Sounder Satellite Based Upon Anticipated Solar Cell Degradation*

Months after launch	Hours of sounding per day (including 1 hour at night)	Percent of orbit in sunlight
0	5.3	100–65
1	3.5	65
2	4.5	100
3	4.4	100
4 to 12	[1] 1.8 to 3.2	[2] 65–100

[1] Minimum and maximum range of sunlight.
[2] Minimum and maximum range of percent of orbit in sunlight.

EXPERIMENTAL OBJECTIVES AND DATA ANALYSIS

The swept-frequency topside sounder satellite is unquestionably more sophisticated than the fixed-frequency version of the topside sounder. This has resulted in a much larger and heavier spacecraft requiring a bigger and more expensive launch vehicle. The fixed-frequency topside sounder approach might therefore be more

suitable for space applications where size and weight are at a premium, e.g., the initial exploration of the planetary ionospheres. However, there are considerations other than those involving weight, size, and relative complexity. A more important difference is the fact that the swept-frequency topside sounder ionograms are better for studying one group of ionospheric problems, fixed-frequency topside sounder ionograms for studying another group.

The swept-frequency topside sounder sweeps at a rate of 1 Mc/sec. The time interval over which reflections are received is about 5 to 10 seconds, depending upon the value of the maximum electron density; and the sweep is repeated every 18 seconds. This means that one sounding is made while the satellite moves 35 to 70 km horizontally, and that there is a distance between successive soundings of 130 km. Since a continuous virtual-depth curve is obtained by the swept-frequency technique, this method is best suited for deriving accurate and complete true height profiles, provided that the vertical-distribution remains unchanged over the horizontal distance corresponding to a complete sweep. This condition is generally satisfied at middle latitudes under quiet ionospheric conditions. From these profiles, electron-ion temperatures and ionic constituents may be obtained.

On the other hand, the fixed-frequency topside sounder makes a sounding in depth in $\frac{1}{10}$ second, during which time the satellite moves less than 1 km along its orbit. Thus, the fixed-frequency topside sounder ionograms correspond more nearly to the instantaneous vertical electron density distribution beneath the satellite. Since there will be no more than 12 data points (6 ordinary and 6 extraordinary echoes) on each fixed-frequency topside sounder ionogram, the resolution in depth will be limited. However, such resolution is not the primary purpose of the fixed-frequency experiment: it is designed to study the structure of horizontal electron-density gradients and localized irregularities 100 km or less in horizontal extent.

To facilitate these studies, the fixed-frequency topside sounder data are displayed as virtual-depth contours for each sounding frequency, which is related to the electron density at the reflection point by the reflection conditions (Equations 2 through 4). Figure 17 illustrates the virtual depth as a function of frequency, obtained from two consecutive swept-frequency topside sounder ionograms (solid curves) and possible virtual-depth contours for the fixed-frequency topside sounder sounding frequencies (dotted contours). This picture illustrates the difference in the data point distributions. It should be pointed out that these two types of data presentations are identical to those used to study the ionosphere from the ground: pulsed soundings at fixed frequencies ($h'-t$) and soundings at swept frequencies ($h'-f$). The advantage of the fixed-frequency techniques is that it can resolve small scale gradients in electron density. For example, Figure 17 shows a localized region of enhanced density; and it is possible to ascertain the altitude, size, and density of this small irregularity. Another type of irregularity known to exist in the ionosphere is a geomagnetic field-aligned irregularity that is most likely associated with the spread-F phenomenon. An example of arctic spread-F is shown in the two ionograms of Figure 18: one of these shows spread-F as seen in a swept-frequency topside sounder ionogram; the other shows spread-F in a conventional bottomside sounding.

There may be two quite different kinds of field-alined irregularities in the F region, which give rise to two different kinds of spread-F. This theory is based on inferences from bottomside soundings, rocket tests of the fixed-frequency topside sounder, and swept-frequency topside sounder ionograms. The first kind of irregularity consists of columns of *excess* ionization ($+\Delta N_e$), and spread-F from these is due to scattering of radio waves which impinge normally to the axis of the columns. The second kind consists of columns *deficient* in ionization ($-\Delta N_e$), and spread-F in this case is due to ducting of radio waves within the columns (Reference 18). The two types of irregularities occur at both high and low latitudes. Much of the complication of spread-

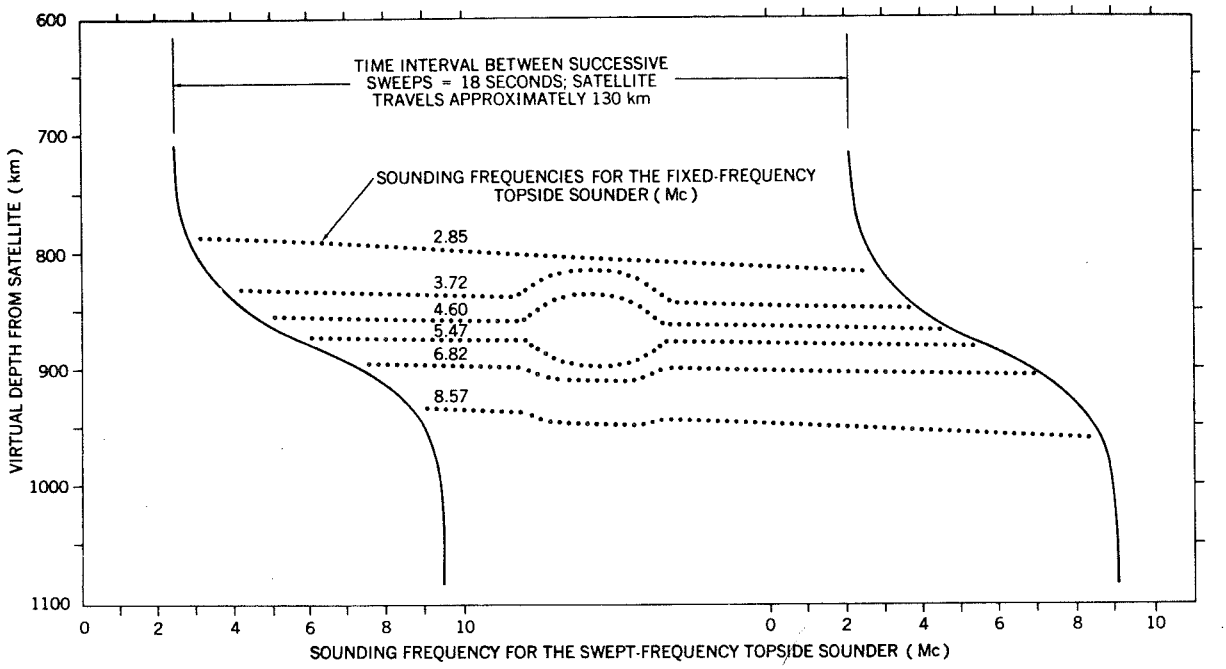

FIGURE 17.—Swept-frequency topside sounder ionograms and simulated fixed-frequency topside sounder data. (Simulated topside sounder data showing successive swept-frequency topside sounder ionograms (solid curves. complemented by fixed-frequency topside sounder virtual-height contours of constant electron density (dotted curves). The number of dots per curve represents one-third of the number of data points. The bulge in the dotted curves indicated presence of localized region of enhanced electron density.

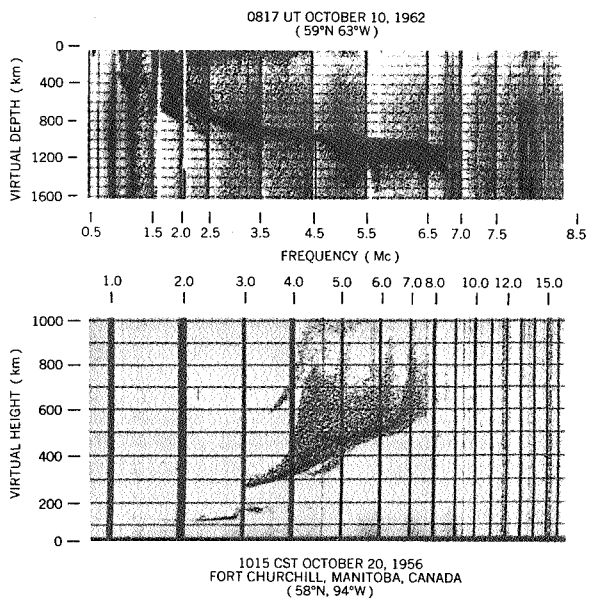

FIGURE 18.—Arctic spread-F.

F may be due to the varying intensity and geometrical arrangement of these two types of irregularities.

Because the diameter of these irregularities can be as small as a kilometer or less, swept-frequency soundings do not resolve individual irregularities. The fixed-frequency method, on the other hand, should help clarify the nature of these irregularities, particularly the ducting types, since it will resolve their size, spacing, length, and relation to the latitude and degree of magnetic disturbance, etc. Also, an indication of the magnitude of $\Delta N_e/N_e$ can be obtained from the relative efficiency of ducting on the several fixed frequencies. The need for resolving such horizontal gradients can be seen from Figure 19 (Reference 19) which illustrates the equatorial anomaly: contours of constant electron density along the 75th West meridian reveal very pronounced horizontal gradients in the equatorial regions.

TRUE HEIGHT ANALYSIS

The virtual depth measured at a particular sounding frequency is proportional to the total round-trip time of the transmitted signal.

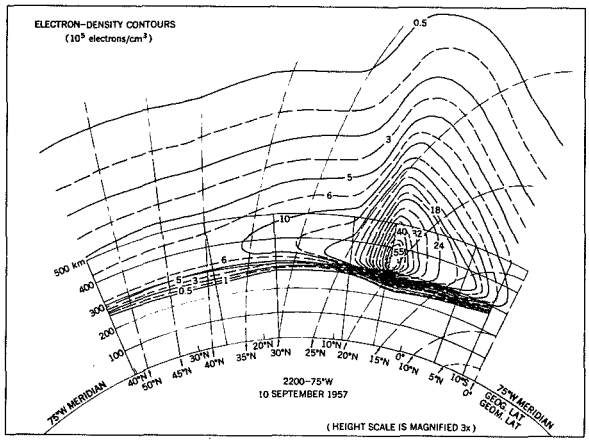

FIGURE 19.—The equatorial anomaly.

If the virtual depths are known as a function of frequency, it is possible to derive the true heights of reflections. The heart of any program of analysis lies in the integral of Equation 5 which must be inverted and solved for the true heighth. One important difference between the existing methods of data reduction is the number of data points required for the analysis. This difference poses no problem in reducing the continuous swept-frequency topside sounder ionograms, and most methods may be applied with proper modifications. However, some are not well suited for analyzing the fixed-frequency topside sounder data, since there will be a maximum of 12 data points for each ionogram. Even though a maximum of only 12 points can be determined on a true height profile, these points should be enough to define some important ionospheric parameters such as scale height and the latitudinal distribution of ionization. The analysis of the fixed-frequency sounding data will be facilitated by what is already known from the swept-frequency topside sounder data. Fixed-frequency sounding data are being simulated at GSFC and CRPL by choosing virtual depths at the six planned sounding frequencies from swept-frequency topside sounder ionograms, and various methods of analysis are being tested. For example, a lamination method which assumed linear (or exponential) distribution of ionization between data points has been applied at GSFC to these simulated data and compared with the results of a complete analysis of swept-frequency topside sounder ionograms. With this assumption the integral (Equation 5) can be inverted to obtain the true height profile by a method due to Jackson (Reference 20). The true heights so obtained can differ by as much as 50 km from a true height analysis of the swept-frequency topside sounder ionogram. However, the slopes of the profiles and hence the corresponding scale heights are in good agreement. This approach is currently being pursued further at GSFC.

A more sophisticated method under investigation at CRPL and GSFC that lends itself particularly well to the planned fixed-frequency data point distribution is a method which assumes the true height profile can be represented by a polynomial. Upon subsitution into the integral it is possible to derive a matrix set of coefficients which, when multiplied by observed virtual depths, yield the true heights (References 21 and 22).

CONCLUSION

The success of the NASA program of topside ionosphere studies is evidenced by the considerable amount of knowledge obtained from Explorer VIII, Ariel I, and high altitude rocket soundings. Perhaps the most spectacular of these accomplishments to date has been the Canadian swept-frequency topside sounder, Alouette (References 22 through 36), which will probably yield more data about the upper ionosphere electron density distribution than all the other programs combined. Other important aspects of ionospheric structure hitherto relatively unexplored will be studied synoptically with the launching of the United States fixed-frequency topside sounder satellite in 1963.

What remains to be obtained is a better understanding of the solar control of the earth's upper ionosphere. These sun-earth relationships should be investigated over a period extending from the minimum to the maximum of solar activity. To accomplish this objective it is planned to combine the best features of the various ionospheric satellite experiments in a single ionospheric monitoring satellite.

REFERENCES

1. WRIGHT, J. W., "Dependence of the Ionospheric F Region on the Solar Cycle," *Nature*, 194 (4827): 461–462, May 5, 1962.
2. EVANS, J. V., "The Electron Content of the Ionosphere," *J. Atmospheric and Terrestrial Phys.* 11(*cf*): 259–271, 1957.
3. BAUER, S. J., and DANIELS, F. B., "Ionospheric Parameters Deduced from the Faraday Rotation of Lunar Radio Reflections," *J. Geophys. Res.* 63(2): 439–442, June 1958.
4. GORDON, W. E., "Incoherent Scattering of Radio Waves by Free Electrons with Applications to Space Exploration by Radar," *Proc. IRE*, 46(11): 1824–1829, November 1958.
5. BOWLES, K. L., "Incoherent Scattering by Free Electrons as a Technique for Studying the Ionosphere and Exosphere: Some Observations and Theoretical Considerations," *J. Res. Nat. Bur. Stand.* 65D(1): 1–14, January–February 1961.
6. EVANS, J. V., "Diurnal Variation of the Temperature of the F Region," *J. Geophys. Res.* 67(12): 4914–4920, November 1962.
7. BOURDEAU, R. E., WHIPPLE, E. C., Jr., DONLEY, J. L., and BAUER, S. J., "Experimental Evidence for the Presence of Helium Ions Based on Explorer VIII Satellite Data," *J. Geophys. Res.* 67(2): 467–476, February 1962.
8. WILLMORE, A. P., BOYD, R. L. F., and BOWEN, P. J., "Some Preliminary Results of the Plasma Probe Experiments on the Ariel Satellite," *Proc. of the Conf. on the Ionosphere*, London, 1962.
9. SWENSON, G. W., Jr., "The Utilization of Ionosphere Beacon Satellites," presented at the COSPAR meeting, Washington, May 1962. NASA Technical Note D–1669, 1963.
10. JACKSON, J. E., and BAUER, S. J., "Rocket Measurement of a Daytime Electron-Density Profile up to 620 Kilometers," *J. Geophys. Res.* 66(9): 3055–3057, September 1961.
11. BAUER, S. J., and JACKSON, J. E., "Rocket Measurement of the Electron-Density Distribution in the Topside Ionosphere," *J. Geophys. Res.* 67(4): 1675–1677, April 1962.
12. BAUER, S. J., "On the Structure of the Topside Ionosphere," *J. Atmospheric Sci.* 19(3): 276–278 May 1962.
13. HANSON, W. B., "Upper Atmosphere Helium Ions," *J. Geophys. Res.* 67(1): 183–188, January 1962.
14. BAUER, S. J., "Helium Ion Belt in the Upper Atmosphere," *Nature*, vol. 197, January 1963.
15. KNECHT, R. W., VAN ZANDT, T. E., and RUSSELL S., "First Pulsed Radio Soundings of the Topside of the Ionosphere," *J. Geophys. Res.* 66(9): 3078–3081, September 1961.
16. KNECHT, R. W., and RUSSELL, S., "Pulsed Radio Soundings of the Topside of the Ionosphere in the Presence of Spread F, "*J. Geophys. Res.* 67(3): 1178–1182, March 1962.
17. JACKSON, J. E., KNECHT, R. W., and RUSSELL, S., "First Results in the NASA Topside Sounder Satellite Program" NASA Technical Note D–1538, Sept. 1962 (appeared also in Advances in the Astronautical Sciences, vol. 11, 1962).
18. VAN ZANDT, T. E., CALVERT, W., KNECHT, R. W., and GOE, G. B., "Evidence for Field Aligned Ionization Irregularities Between 200 and 1000 Km Above the Earth's Surface," presented at the COSPAR meeting, Washington, May 1962.
19. WRIGHT, J. W., "Note on the Quiet Day Vertical Cross Section of the Ionosphere Along 75 °W Geógraphic Meridian," *J. Geophys. Res.* 64(10): 1631–1634, 1959.
20. JACKSON, J. E., "A New Method for Obtaining Electron-Density Profiles from P'-f Records," *J. Geophys. Res.* 61(1): 107–127, March 1956.
21. TITHERIDGE, J. E., "A New Method for the Analysis of h' (f) Records," *J. Atmospheric and Terrestrial Phys.* 21(1): 1–12, April 1961.
22. KNECHT. R, W., VAN ZANDT, T. E., and WATTS, J. M., "The Ionospheric Topside Sounder Program March 15, 1960, to January 21, 1961," NBS Report no. 6740, February 1, 1961.
23. CHAPMAN, J. H., "Topside Sounding of the Ionosphere," *Advances in the Astronautical Sciences*, vol. 12, 1962.
24. PETRIE, L. E., "Top-Side Spread Echoes," *Can. J. Phys.* 41(1): 194–195, January 1963.
25. WARREN, E. S., "Sweep-Frequency Radio Soundings of the Top-Side of the Ionosphere," *Can. J. Phys.* 40: 1692, 1962.
26. WARREN, E. S., "Perturbation of the Local Electron Density by Alouette Satellite," *Can. J. Phys.* 41(1): 188–189, January 1963.
27. HAGG, E. L., "A Preliminary Study of the Electron Density at 1000 Kilometers," *Can. J. Phys.* 41(1): 195–199, January 1963.
28. NELMS, G. L., "Scale Heights of the Upper Ionosphere from Top-Side Soundings," *Can. J. Phys.* 41(1): 202–206, January 1963.
29. WARREN, E. S., "Some Preliminary Results of Sounding the Topside of the Ionosphere by Radio Pulses from a Satellite," of *Nature*, Letter to Editor.
30. MULDREW, D. B., "The Relationship of F-Layer Critical Frequencies to the Intensity of the Outer Van Allen Belt," *Can. J. Phys.* 41(1): 199–202, January 1963.
31. LOCKWOOD, G. E. K., "Plasma and Cyclotron Spike Phenomena Observed on Top-Side Ionograms," *Can. J. Phys.* 41(1): 190–194, January 1963.

32. MAR, J., "Meteoroid Impact on the Topside Sounder Satellite," *Can. Aero. and Space J.* 8(9): 237–240, November 1962.
33. WARREN, H. R., and MAR, J., "Structural and Thermal Design of the Topside Sounder Satellite," *Can. Aero. and Space J.* 8(7): 161–169, September 1962.
34. LOCKWOOD, G. E. K., and PETRIE, L. E., "Low Latitude Field Aligned Ionization Observed by the Alouette Topside Sounder," *J. Planetary and Space Sciences*, in press.
35. KING, J. W., "Preliminary Studies of the Upper Ionosphere Deduced from Topside Sounder Data," *Nature*, in press.
36. KNECHT, R. W., and VAN ZANDT, T. E., "Some Early Results from the Ionosphere Topside Sounder Satellite," *Nature*, in press.

THE ORBITING SOLAR OBSERVATORY SPACECRAFT

F. P. DOLDER, O. E. BARTOE, R. C. MERCURE, JR., AND R. H. GABLEHOUSE

Ball Brothers Research Corp.

AND

J. C. LINDSAY

Goddard Space Flight Center

The first Orbiting Solar Observatory (1962 ζ1) was launched March 7, 1962, at 1606 UT from the Atlantic Missile Range, Cape Canaveral, Florida. This spacecraft was designed to point approximately 75 pounds of instruments at the sun with an accuracy of about 1 minute of arc. An additional 100 pounds of instruments are carried in a spinning section of the satellite which sweeps across the sun every 2 seconds. The total weight of the spacecraft is 458.3 pounds. In orbit, it is 92 inches in diameter and 37 inches in height. It carries data recording equipment that can store 90 minutes of data. Upon ground command, these data are played back over the spacecraft's transmission system in 5 minutes. The spacecraft is in an almost perfect 300-nautical-mile circular orbit inclined 32.8 degrees to the equator, and has worked perfectly since injection into orbit; at the present writing it has completed over 1,000 orbits. The pointing system has functioned with an accuracy of approximately 2 minutes in azimuth angle and 2.5 minutes in elevation. The temperature inside the satellite has stabilized to 5°C; and excellent radio transmission has been received.

INTRODUCTION

Since the development of the high-altitude sounding rocket it has been possible for scientists to observe the sun from outside the main portion of the earth's atmosphere; however, sounding rockets allow only a fleeting glimpse of the sun and extended observations have not been possible. With the advent of the earth orbiting satellite, it was quickly recognized that long-term unimpeded solar observation was possible. One of the early programs initiated by NASA was the development of an Orbiting Solar Observatory to furnish an observing platform for solar studies. On March 7, 1962, at 1606 UT, OSO I (1962 ζ1) was launched from the Atlantic Missile Range by a Thor-Delta-vehicle.

The OSO I spacecraft was designed to point approximately 75 pounds of instruments at the sun with an accuracy of about 1 minute of arc. An additional 1,000 pounds of instruments are carried in a spinning section of the satellite and sweep across the sun every 2 seconds.

The total weight of the spacecraft is 458.3 pounds; with the arms extended (Fig. 1) it is 92

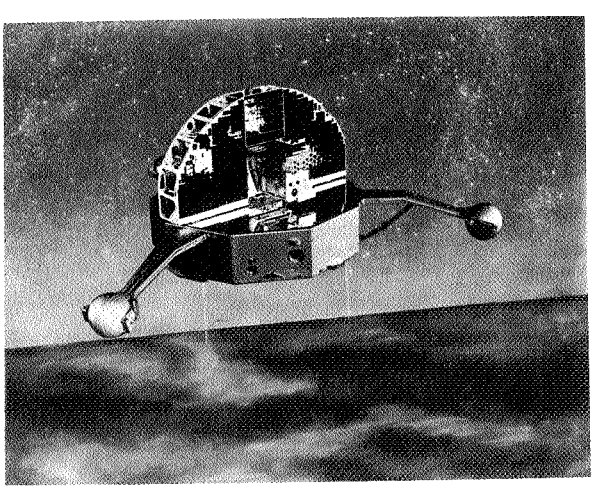

FIGURE 1.—Rear view of the first Orbiting Solar Observatory (OSO I).

inches in diameter, 37 inches in height, and consists of two portions—the "wheel," the lower nine-sided cylinder with three arms attached; and the "sail," the fan-shaped structure mounted above the wheel, which carries the pointed instruments and the solar cell array. The sail is attached to the wheel by a shaft running through the wheel; the wheel is free to rotate with respect to the sail.

In order to provide attitude stability, the wheel is kept spinning at 30 rpm. This spin rate is measured by optical rate sensors and is controlled to within ± 5 percent by reaction jets (Fig. 2) which use compressed N^2 gas.

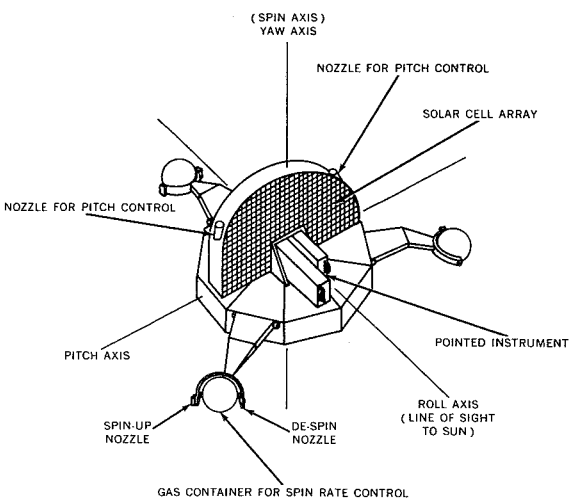

FIGURE 2.—Attitude axes of the Orbiting Solar Observatory.

(The N^2 gas supply carried by the spacecraft is calculated to at least 6 months.) The angular momentum of the spinning wheel produces great gyroscopic rigidity and the spin axis tends to remain fixed in inertial space. Although there are various disturbing torques which tend to precess the satellite, the precession rate is less than a degree per day. The angle between the solar vector and the spin axis is measured by optical error detectors; whenever the angle exceeds 3 degrees, a second set of reaction jets is used to precess the satellite until the pitch error is corrected. The spacecraft is free to precess in roll about the solar vector, but this rate is small.

The sail is free to rotate about the spin axis and is controlled by optical error sensors so that, during the sunlit portion of the orbit, the plane of the sail is perpendicular to the solar vector; this is accomplished by a servo motor on the sail's shaft which drives against the wheel (the azimuth servo). The accuracy of this alignment is 1 to 2 minutes of arc. In the center of the sail is a gimbal which is free to move in pitch with respect to the sail. The pointed experiments are carried in this gimbal. A second servo motor (the elevation servo), on the gimbal shift, is optically controlled to align the instruments to the sun, again with an accuracy of 1 to 2 minutes of arc. The servo systems derive their error signals from two sets of photoelectric sensors: one set mounted on the pointed instruments, and the second on the sail. The set mounted on the instruments senses the angles between the direction in which the instruments are pointing and the sun, producing a current output proportional to these angles; these detectors have limited fields of view but can measure angles of less than 1 minute. The set mounted on the sail is used to control the sail so that it is pointed at the sun within a few degrees. When this has been done, control is switched to the instrument detectors which will have the sun in their field of view. During the dark portion of each orbit, the servo systems are automatically turned off by a photoelectric switch; the sail is then allowed to spin with the wheel.

Each time the satellite passes from the dark to the sunlit portion of the orbit, the photoelectric switch turns on the servo systems. The azimuth servo stops the sail and alines it so that the solar vector is normal to the plane of the sail. This is done under the control of the error detectors mounted on the sail. When the error detectors which are mounted on the instrument have the sun in their field of view, control is switched from the sail detectors to the instrument detectors. These detectors then control both the azimuth and elevation servos and aline the instruments accurately to the sun. This acquisition cycle takes approximately 45 seconds.

The azimuth and elevation servo systems are designed to use a total power of less than 4 watts (including the power used to drive the motors). This is accomplished by driving the azimuth and elevation motors with a pulse-width modulated power amplifier. The motors are driven by pulses which are always of maximum drive voltage but whose width varies depending upon the torque level required from the motor. This scheme eliminates power losses in the power transistors controlling the motors, since they are either saturated or cut off.

Low power consumption also requires that all bearings, motor brushes, and slip rings have very low friction. This presents a problem, since these components would ordinarily be sealed to protect them from the space environment; however, sealing results in too high a friction level and hence in higher power requirements. To overcome this, all slip rings, motor brushes, and bearings are operated exposed to the space environment. One of the most significant achievements during the OSO I development was the perfecting of treatments for these components which allow them to operate when exposed to the low pressure of the space environment for extended periods of time and still maintain acceptably low friction levels. The treatments have no out gassing products which might contaminate the scientific experiments.

EXPERIMENTS

The pointed instrument gimbal can carry 75 pounds of experiments in a space 38 x 8 x 8 inches. The OSO I spacecraft carries two pointed instruments which have a combined weight of 65.5 pounds. One is a 20.5-pound X-ray spectrometer which covers the spectral range from 30 to 400A. The second instrument, which weighs 45 pounds, consists of several different experiments: solar X-ray (20 to 100 kev and 1 to 8A) monitoring experiments, a gamma ray (0.510 Mev) monitoring experiment, an interplanetary dust particle experiment, and an experiment designed to monitor the aging of the photoelectric error sensors used in the spacecraft's servo system.

There are nine wedge-shaped compartments in the wheel. Of these, five are normally available for scientific instruments; a total weight of about 100 pounds can be accommodated. The other four compartments in the wheel are for the spacecraft's control, telemetry, data storage, and command systems; in OSO I, a sixth experiment shares one of these four compartments. The six experiments were furnished by the Goddard Space Flight Center and Ames Research Center of NASA, the University of Rochester, the University of California, and the University of Minnesota. The locations of these experimental packages and a brief description of each are shown in Figure 3. The total weight of the six wheel experiments in OSO I is 113 pounds.

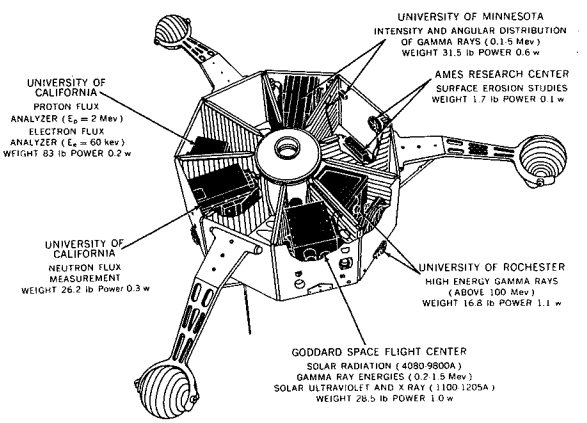

FIGURE 3.—Experiments in the OSO I wheel.

Since the wheel spins at 30 rpm and its spin axis is normal to the solar vector, each experiment in the wheel sweeps the sun every 2 seconds. Also, the spacecraft slowly rolls about the solar vector because of external torques and hence, over a period of time, each wheel experiment will be able to scan the entire celestial sphere. This is extremely useful for experiments that are intended to survey the sky or to compare the radiations and emissions of the sun with those from other regions of space.

The OSO I solar cell array delivers approximately 30 watts of power at 20 volts to the spacecraft during the time it is oriented to the sun. This power is used to operate the control

system, telemetry, and experiments during the day, and to charge the nickel-cadmium batteries. During the dark period, the telemetry and wheel experiments operate from the storage batteries. Of the 30 watts, approximately 15 are used by the control and telemetry systems and 13 by the experiments; this allows 2 watts as a safety margin.

The telemetry system is FM–FM and has eight channels; six channels are assigned to the scientific experiments, one is used for monitoring the spacecraft's operation, and one is used for a reference oscillator. Each experimenter is assigned a channel. The output of each experiment is conditioned to 0 to 5 volts and is used to deviate a subcarrier oscillator. The outputs of the eight subcarrier oscillators are combined and then recorded by a magnetic tape recorder in the spacecraft that can record for 90 minutes. The reference oscillator referred to above is used for wow and flutter compensation of the tape recorder. Upon command from the ground, the tape can be played back in 5 minutes. When the tape is played back, the recorder output modulates a high power (1.75 watts) FM transmitter. In the record mode, data are being stored on tape and the signals are also used to modulate a low power (250-milliwatt) transmitter so that real-time information is available. Each part of the telemetry system—subcarrier oscillators, tape recorders, and transmitters—is duplexed in the spacecraft; the spares can be substituted by ground command if the unit in operation fails.

Because of the increased speed of playback, the information rate into the tape recorder is limited. A total of 17.5 cps (square wave) of information bandwidth is available to the experimeters. On OSO-I, this was divided as shown in Table I. Even with these seemingly small data rates, a large amount of data is being collected by the experiments on OSO I.

The OSO I is equipped with a tone-type command system capable of accepting 10 commands which are used to initiate playback from the tape recorder, to interchange parts of the telemetry system, and to turn either all the wheel experiments or all the pointed experiments on or off. These last two commands are incorporated so that if too much power is being used or if the power supply is not developing the proper amount of power, the experiments can be turned off to allow the batteries to be charged and then turned on again.

TABLE 1.—*Telemetry Allocations for OSO I*

Experiment	Bandwidth
Goddard X-ray spectrometer	6
Goddard gamma ray experiment	4
University of California proton, electron, and neutron experiment	3
University of Rochester gamma ray experiment	2
Goddard gamma ray, X-ray, and interplanetary dust experiment	1.5
University of Minnesota gamma ray experiment	1
Spacecraft monitoring channel	1

The spacecraft's temperature is controlled passively by means of the absorptivity/emissivity ratio of the surface. This is done by either covering the various surfaces with paint having the proper ratio, or by highly polishing the surfaces. In order to find the correct ratio, a detailed mathematical analysis was made and the effects of changing the surface characteristics of the spacecraft were simulated on a digital computer.

SPACECRAFT PERFORMANCE

The actual performance of OSO I has been most gratifying. The spacecraft is in an almost perfect 300-nautical-mile circular orbit, inclined 32.85 degrees to the equator; the period is 96.15 minutes. At the time of injection, the spacecraft acquired the sun, and all control systems and experiments worked perfectly. At the present writing, the spacecraft has completed over 1,000 orbits and a preliminary analysis has shown all spacecraft systems and all experiments to be functioning properly.

The pointing accuracy in azimuth (about the spin axis) has ranged from 0.5 to 1.8 minutes of arc. The power required to drive the azimuth motor is approximately 3 watts, slightly more than was expected. Figure 4 shows the ob-

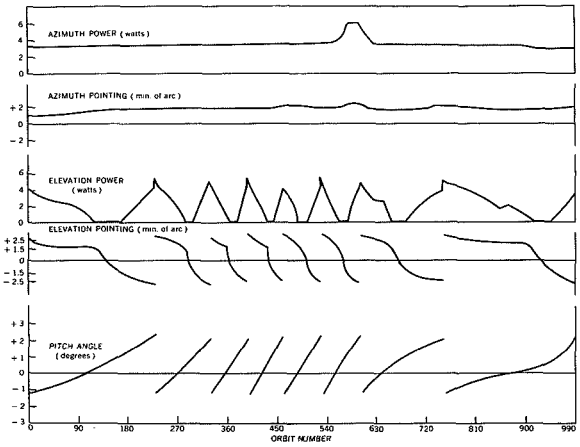

FIGURE 4.—OSO I azimuth error angles.

served azimuth error angle and the azimuth drive power.

The elevation error has ranged as high as 2.5 minutes of arc and the elevation drive power has been as high as 4 watts. This is also slightly higher than was anticipated, and is attributed to excessive torque on the instruments from two flexible electric cables from the instruments to the spacecraft's sail. These cables are colder than was anticipated and it is believed that they have become stiffer. Figure 4 shows the pitch angle of the spacecraft and the variation of the elevation error angle and drive power with time.

The rate of consumption of N_2 gas used to control the pitch angle and the spin rate is quite low. The spacecraft was injected into orbit with a pitch angle of about 3.5 degrees. The pitch control system corrected this to -1.0 degree, as it was designed to do, immediately after injection. No additional pitch gas was used until orbit 233, when again the pitch angle had increased to the allowable limit of 3 degrees. This amounted to a precession of about 0.25 degree per day. A third pitch correction was made during orbit 329. Between orbits 233 and 329, the precession rate averaged 0.67 degree per day. The rate of change of the pitch angle is expected to vary with time, since it is a function of the angle between the spin axis and the plane of the ecliptic. When the spin axis is normal to the ecliptic plane, there is no change in pitch attitude as the earth goes around the sun. When the spin axis is contained in the ecliptic plane the pitch, if not corrected, will change about 1 degree per day because of the earth's motion around the sun. With the observed rate of N_2 gas exhaustion, the gas supply should last more than six months.

The solar power supply appears to be working very well. The nickel-cadmium batteries are being properly charged and their voltage ranges from 20.4 volts at the end of the day to 18.5 volts at the end of the night. This voltage swing is as expected and indicates that the batteries are not being severely discharged during the night. The solar cell array is running slightly cooler than was expected, increasing the solar cell output by between 1 and 2 watts; therefore, the batteries are being kept well charged. Inside the wheel the temperature is 5°C, which compares very well with the design temperature, and is essentially constant throughout the orbit. The temperature excursions of the outer panels of the wheel do not exceed 12°C throughout the orbit. Thirty orbits were required to reach temperature equilibrium. The highest temperature reached on the solar cell array during the day is 60°C and at night the cell cools down to −38°C. The solar cell panel's rate of change of temperature as the spacecraft enters the sunlight is about 7 degrees per minute. A temperature monitor inside the Goddard x-ray spectrometer indicates a temperature of about 7°C with only about ±1 degree change over the orbit.

The FM-FM telemetry system of the spacecraft has been most satisfactory. The signals received at the ground stations during tape recorder playback have been strong and clean. A record of a data transmission received at the Fort Myers, Fla., station compares favorably with one made in the laboratory during spacecraft checkout. It is possible to receive real-time data transmissions from the spacecraft in Boulder, Colo. The signal is sufficiently good that information concerning the operation of the spacecraft and the experiments is routinely being gathered at Boulder.

The OSO I command system is functioning properly but has been found quite susceptible

to spurious commands. This was not unexpected, since the same type of trouble occurred with the Explorer XI (1961 ν1) which has the same command system. Because of this possibility, the commands were structured so that nothing catastrophic to the spacecraft could occur if the command system did accept spurious commands. This difficulty has been an annoyance but has not compromised the spacecraft's operation.

SUMMARY

In summary, the OSO I was designed to provide a stabilized observing platform above the earth's atmosphere from which scientific observations of the sun and space could be performed. It is the first of a series of orbiting observatories which will progressively become more sophisticated, versatile, and useful. Operating experience with the OSO I has already given an observing time equivalent to that which would require nearly 10,000 Aerobee-Hi sounding rocket flights, at a fraction of the cost of such a rocket program. The first Orbiting Solar Observatory has successfully performed its mission and has ushered in a new era in astronomy and astrophysics.

STEREO PHOTOGRAPHY OF THE ECHO II BALLOONS NUMBER 9, 11, AND 13

SOL H. GENATT
Goddard Space Flight Center

A description is given of the equipment and technique used to determine the deviation from sphericity of the skin of three Echo II balloon satellites at varying skin pressures. Diagrams and photographs illustrate the instrumental setup and the results of the stereophotography.

1. REQUIREMENTS OF PROJECT

The Echo Project presented the Optical Systems Branch with certain requirements when the Branch was asked to participate in the test inflations of the 135-foot-diameter Echo II balloon satellites at Lakehurst, N.J. These requirements were as follows:

(*a*) Areas on the balloon surface were to be photographed in stereo fashion for the purpose of measuring irregularities in surface contour. The accuracy required was $\pm 1/16$ inch.

(*b*) The number of areas on each balloon photographed were 3 in number and the center of each was located approximately 10 to 11 degrees south of the Equator of the balloons.

(*c*) The size of each area to be photographed was to be approximately 10 feet along a parallel of latitude at the center of the area and at least 6 to 7 feet along the central meridian.

(*d*) x, y, z, coordinates of points along a parallel of latitude passing near the center of the area were required. These points were to be approximately three inches apart on the surface of the balloon while the coordinates were to be referred to a mean established datum plane. Accuracy of the coordinates was to be held to $\pm 1/16$ inch.

(*e*) A topographic contouring was required covering each of the photographed areas. The contour lines were to be spaced one-eighth inch apart with an accuracy as mentioned in 1(*a*).

(*f*) All the above work was to be performed at each of several different skin pressures to which each balloon was to be inflated and at a relaxed state at each of the pressures.

(*g*) The resultant data was to be presented in two forms.

(1) Contour lines representing each photographed area were to be shown on charts at a scale of approximately one-fifth the original size.

(2) Profile coordinate measurements were to be presented both in the form of a listing and superimposed upon a separate profile chart.

2. PHOTOGRAPHIC EQUIPMENT USED IN TEST INFLATIONS

The cameras selected to perform the stereo photography were the Wild RC8 cameras with the 6-inch Aviogon lenses. These cameras were selected on the basis of being the most suited for this application, both from an optical viewpoint and from a reduction capability standpoint. Picture size is 9 x 9 inches.

As normally used in aircraft, the cameras take a series of vertical photographs of objects on the ground. In this type of work, the distances between cameras and objects are considered to be infinity as far as the lens system is concerned. At Lakehurst, N.J., the distance between cameras and balloon surfaces were to be on the order of 13 feet. In order to record images on the balloon surface in sharp detail in the focal plane, the cameras had to be modified by increasing slightly the distance between the optical system and the emulsion side of the film. The task of modification was performed by the Wild Heerbrugg Company's office in Port Washington, N.Y. New calibrated focal lengths for the two cameras were as follows: 158.13mm and 159.83mm.

Superimposed on each frame taken by the cameras is the following data:

(*a*) Fiducial marks in each corner of the frame.
(*b*) The setting of a level bubble.
(*c*) The picture face of a timing clock.
(*d*) An altimeter reading.
(*e*) A camera number identification.
(*f*) The focal length of the camera.
(*g*) A counter number to identify a particular frame.

The film used in the cameras for the test was DuPont, Cronar, High Contrast, Fine Grain, Type 140. It had an ASA rating of 64 and came packaged in 200-foot rolls, 9½ inches wide.

Auxiliary Equipment Used in Photography

In the dirigible hangar at Lakehurst, N.J., where the tests were held, a special scaffolding was constructed to support the two cameras plus the operating personnel (Fig. 1). The top of the scaffolding consisted of three connected parts. Each part which was to be a separate camera station was a level plywood platform measuring approximately 8 by 16 feet. Looking down upon the camera stations from above, they presented the appearance as in Figure 2.

During the tests, the balloon was to be suspended from the ceiling of the hangar with its polar axis vertical and its south pole 6 feet above the floor of the hangar.

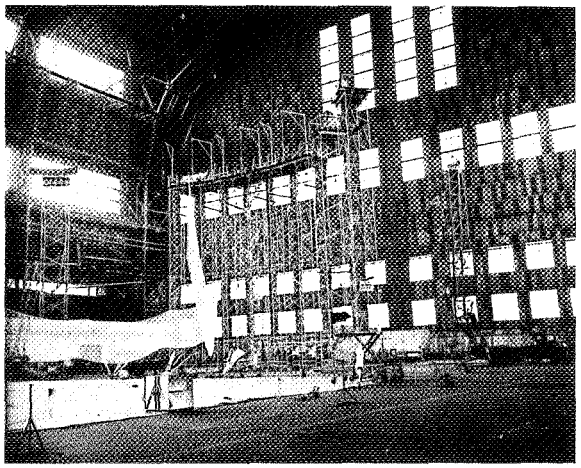

FIGURE 1

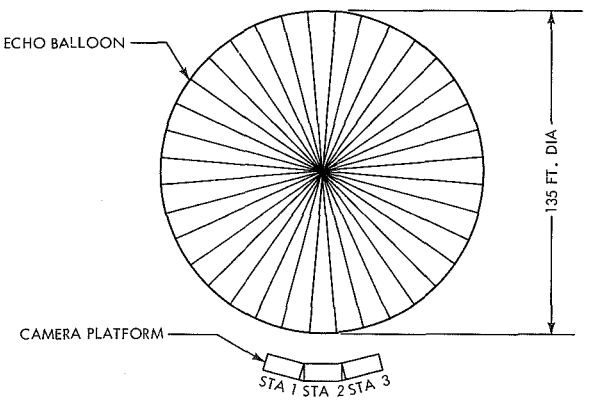

FIGURE 2

As mentioned earlier, the RC8 cameras are normally used suspended vertically with their lens cones pointing straight down. In the tests at Lakehurst, they were to be employed with their lens cones elevated above the horizontal so that they looked perpendicularly at an area on the balloons 10°–11° below the equator (Fig. 3). This necessitated designing and constructing large, portable, aluminum dollies to hold the cameras pointing rigidly in the desired direction and with the ability to move freely in any direction.

Each dolly supported its camera so that the focal plane was approximately 2 feet above the bottoms of the wheels of the dolly. A scaffolding was built with platforms approximately 56 feet above the floor of the hangar. The

764-173 O—65——3

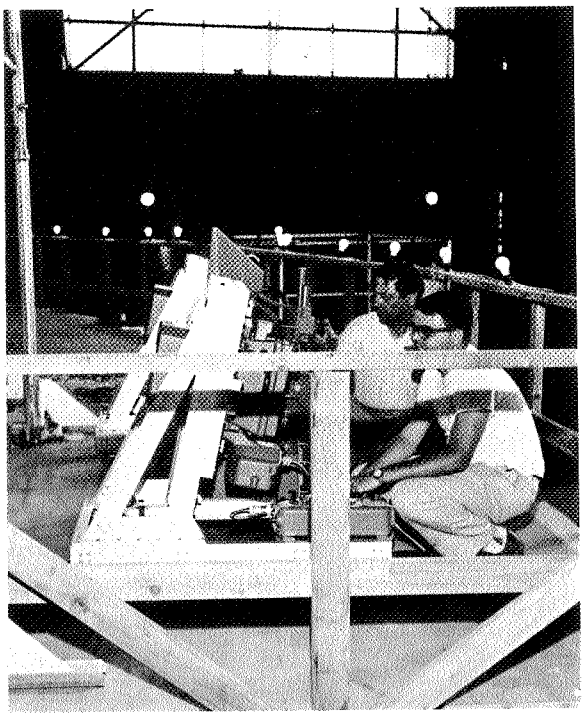

FIGURE 3

dollies moved upon this platform and the geometry of the situation was as represented by Figure 4.

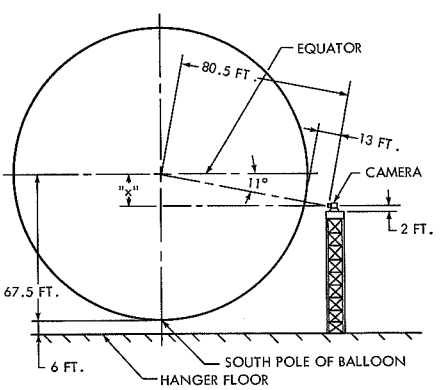

FIGURE 4

RC8 cameras with Aviogon lenses are normally used under what photogrammetrists refer to as a 0.6 base/height ratio. This means that the horizontal distance between the two cameras, exposure stations is usually 60 percent of the vertical distance between the midpoint of the stations, and the ground. Since the Wild Co. modified the cameras to photograph in sharp detail objects 12.9 feet from the cameras, the distance between the two cameras approximated 7.74 feet. It was found in practice that the tolerance on the 12.9 feet for sharp detail was ± 5 inches.

The Aviogon f/5.6 lens used in the cameras has a field of view of 90°. Spaced 7.74 feet apart, the cameras photographed an area that was common to both of 10.8 feet along a parallel of latitude and 18 feet along a central meridan as seen in Figure 5.

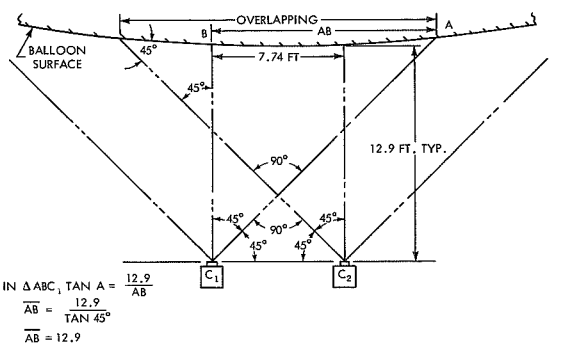

FIGURE 5

If the cameras had been mounted so that they were both in a vertical plane instead of in a horizontal plane, then the area common to both would have been rotated 90° and the two measurements quoted would have been reversed as far as meridians and parallels go.

When all the equipment necessary to take the photographs had been assembled at a camera station, the layout as seen from above was as diagramed in Figure 6. Included in the equipment were the following items:

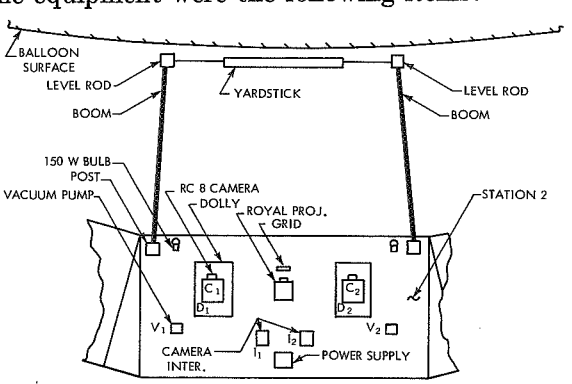

FIGURE 6

(*a*) A Royal Projector machine which projected upon the surface of the balloon the Army Map Service "Distorted Surface Pattern," which consisted of approximately 5,000 irregularly spaced dots. This grid was upon a 10-inch-square piece of glass (positive). During use, the bulb in the projector was operated at 130 volts.

(*b*) Camera vacuum pumps which provided suction behind the focal plane frame so that the film laid perfectly flat while the exposure was made.

(*c*) Camera intervalometer or control boxes which governed the exposure times of the shutters and permitted either manual or automatic operation of the cameras. In use, the exposure times averaged $\frac{1}{10}$ second and the exposures were all taken manually with one operator attending each camera.

(*d*) Two surveyors leveling rods, each four meters long, were suspended approximately 4–5 inches from the surface of the balloon. The marks on each rod faced the camera stations and were used to introduce vertical control into the resulting photographs. Both rods were held by booms extending out from posts in the corners of the camera stations. A yardstick was suspended between the two meter sticks to introduce horizontal control into the photography (Fig. 7).

(*e*) It was found that when the photography was performed at night, auxiliary lighting upon the surface of the balloon was required to light up the dot images. This was provided by two 150-watt spotlight bulbs connected to the front of each station. During daylight photography, these bulbs were unnecessary as windows in the hangar walls allowed in sufficient sunlight to illuminate the dot images plus the photographed area.

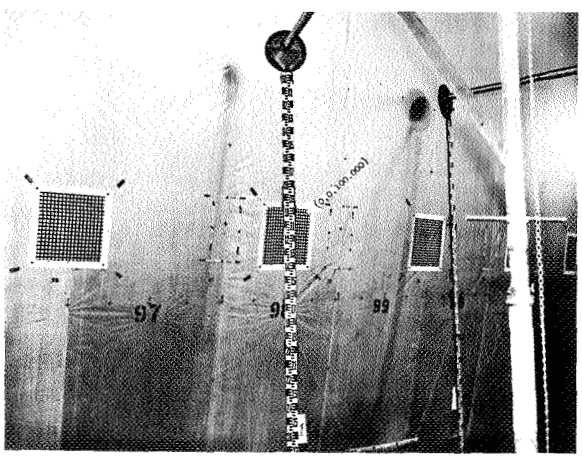

FIGURE 7

3. PROCEDURES, PRIOR, DURING, AND FOLLOWING EACH TEST INFLATION

Echo balloons Nos. 9 and 11 were each photographed at four different skin pressures, including a relaxed condition at each pressure before they each burst. Balloon No. 13 was photographed at one additional higher skin pressure than the other two before it burst.

The procedure followed at each camera station prior to the first test was as follows:

(*a*) A thin, flat, glass plate was inserted into the focal plane of each camera. The sides of the two dollies were then set parallel to each other and the camera centers separated by 7.74 feet.

(*b*) Previous to (*a*), the balloon had been stationed in its position, which it was to occupy during the tests.

(*c*) The projector was then switched on throwing the grid pattern upon the balloon surface.

(*d*) Images of the balloon surface with the dot pattern upon it plus the meter rod markings were then examined on the glass surface in the focal plane with high power eyepieces. This inspection determined the best placing of the cameras on the platforms to give sharp detailed images. At the same time, the illumination was adjusted to minimize "hot spots" or local reflections of the bulbs' light from the skin surface and to achieve nearly uniform lighting over the entire photographed area.

(*e*) Black paint marks were then laid on the plywood platform around each of the four wheels of each dolly to insure replacing the cameras in correct position after they had been moved from one station to another.

(*f*) Exposures at each camera were taken manually by the two operators who watched each other so that the two members of the pair of photos were taken within one-quarter second of each other. In this ¼-second interval, there was no noticeable movement of the balloon proper to cause distortion in the resulting photography.

(*g*) A total of five exposures at each camera station at each skin pressure were taken. This was done so that a choice could be had in deciding which pair of photos should be reduced. Because the balloon moved slightly in most cases between exposures, this safeguard was taken to insure at least one sharply focused pair. As it turned out, at least three or four pairs in each set of five were in sharp focus.

(*h*) After all testing at the various pressures had been completed, the film was processed in the photo labs of the Navy at the Lakehurst Facility. It was developed in DK50 solution with an extended developing time. After developing, a portable air drier was used to dry the film.

(*i*) Approximately 3 hours after developing had begun, the film was ready to inspect. A standard light table was used here with a low power eyepiece. First, the film roll from one camera was inspected for clarity of detail and the best of the five frames was selected at each station for each pressure. Next, the roll from the other camera was inspected and the corresponding photo to complete the pair was indicated with markings and notations in the border of the frame. These markings enabled the personnel at the U.S. Army Map Service to know which pair of photos at each pressure level was to be reduced.

4. REDUCTION OF PHOTOS

When the pairs of successful photographs arrived at the U.S. Army Map Service, they were put through a standard reduction process. This was the process normally followed with aerial photography from which contour mapping of various areas was desired. It consisted of first making for each pair of photos to be reduced a pair of diapositives. In this process, the detail on the photographic negatives is printed onto a super-flat glass plate, 0.250 inch thick and of the same outer dimensions as the negative. The process is characterized by introducing in the transfer the minimum possible dimensional change and at the same time the sharpest detail. It is the process preferred for all high-order mapping tasks.

The transfer for the film took place in a Wild U3–A Modified Diapositive Printer machine (Fig. 8). This machine which is essentially a

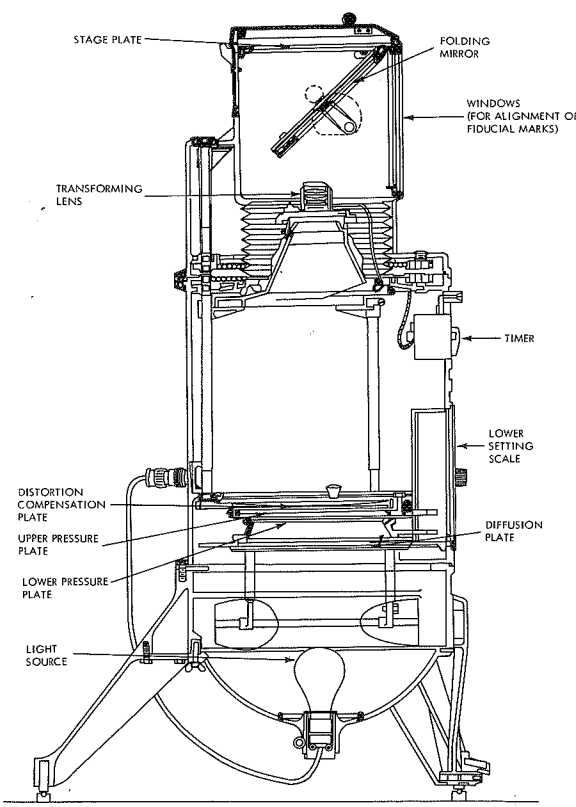

FIGURE 8

reducing camera of the highest precision was created in order to make it possible in photogrammetric practice for photographs from all usual surveying cameras to be used in any desired plotting machine. The printer allows the negatives to be transformed in such a manner that the dimensions and focal lengths of the diapositives produced correspond to the ranges and optical-geometrical requirements of the plotting machines which are later used to contour the photographs.

Additional functions performed by the above plotter are distortion compensation, addition of the principal point, and automatic dodging.

(*a*) By the employment of distortion compensating plates to account for any distortion introduced in the original photography, the optical system of the printer introduces a calculated distortion such that the resultant distortion of camera, printer, and plotter combined is zero.

(*b*) The principal point of the photograph appears as a small cross or circle on the diapositive as a result of the operator alining the fiducial marks appearing on the film with collimating lines in the printer before an exposure is made.

(*c*) In order to tone down hard contrasts when printing, the U3–A has a built-in automatic electronic contrasting or dodging Cintel unit. This device makes it possible to even up the image density across the entire plate and eases the task of the operator who examines the plates for contouring by eliminating practically all glare on the plates.

5. STEREOSCOPIC PARALLAX

In order to understand how the projection plotters used in photogrammetry permit contouring to be accomplished, it may be well to illustrate how the elevation of a single point on a pair of stereoscopic films is determined. The reason for this is that the stereoplanigraph machine when properly set up and oriented and made parallax free, accomplishes automatically and continuously what an operator performs in the measurement of a single point. The following paragraphs are from "Manual of Photogrammetry" by the American Society of Photogrammetry.

One may define stereoscopic parallax as a measurable linear distance composed of line segments on each of two photographs of the same object taken from different camera stations. It is a linear element that is associated with the distances from the camera stations to the object, the separation of the camera stations, and the focal lengths of the cameras. Difference in parallax, or parallax difference, is caused by the difference in the distances from two objects to the pair of camera stations. Parallax difference in vertical aerial photographs is directly related to the relief displacements on the two photographs. Parallax difference is the principal cause of the perception of depth obtained by looking at one of a pair of photographs with each eye. Parallax difference is the element that is used to determine elevations of objects and to draw contour lines with aerial photographs by means of stereoscopic instruments.

In Figure 9, two truly vertical photographs of equal focal length f are shown a distance $00'=B$ apart and at an altitude H above a horizontal reference plane. An object A has an elevation h and images of A occur at a on the left photograph and at a' on the right one. An x-axis is adopted on each photograph parallel to $00'$, and n and n' are both the principal points and nadir points of the respective photographs. The ordinates aa_1 and $a'a'_1$ are perpendicular to the x-axis. Triangle $00'A_1$ is in the vertical plane that contains the two perspective centers (camera stations). AA_1 is perpendicular to plane $00'A_1$, and the elevation of A_1 is also h. The absolute stereoscopic

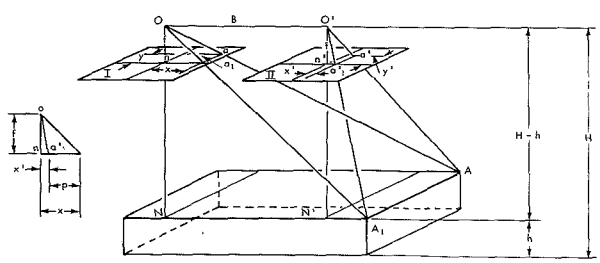

FIGURE 9

parallax of A is defined as the algebraic difference of the abscissas na_1 and $n'a'_1$.

$$p=x-x'$$

The elements are illustrated graphically in the smaller figure which is composed of triangle $0a_1n$ of the left photograph and triangle $0'a_1n'$ of the right one. From similar triangles we have,

$$\frac{p}{f}=\frac{B}{H-h} \tag{1}$$

$$h=H-\frac{Bf}{p} \tag{2}$$

The foregoing equations serve principally to define stereoscopic parallax but parallax difference is used to determine elevations. Differentiating the above formulae, we get,

$$\Delta h=\frac{\Delta p(H-h_1)}{p_1+\Delta p}$$

$$\Delta p=\frac{\Delta h p_1}{(H-h_1)}-\Delta h$$

h_1 is the elevation of the lower of two objects, and p_1 is the parallax the lower point according to equation (1).

In the photogrammetry performed for the Echo II photography, the values of f were known to the nearest ten microns, while B was kept within ± 1 inch of a measured value. H approximated 12.9 feet ± 5 inches, while p was measured to the nearest micron on each diapositive. For determining linear and vertical scale in the diapositives, a knowledge of the above values of f, B, and H was used in addition to the markings of the meter rods and yardstick superimposed on the balloon surface. For balloons 9 and 11, an additional feature used to obtain scale values was the almost constant length of a gore distance along the 11° parallel. For balloon No. 13, markings in the form of small crosses placed on the balloon surface shortly after construction of the balloon, provided linear and horizontal scales. These markings were spaced across the area to be photographed at a distance of every 3 inches in both a parallel of latitude direction and a longitude direction. They were placed in this manner because of the experience gained in the reduction of balloons 9 and 11 which preceded 13. This one step greatly eased the problems of the operator in determining scale on the photographs and would be a recommended procedure in any future similar work.

The plotting machine used to reduce all the photography was the Zeiss C–8 Stereoplanograph (Fig. 10). This machine, which is considered to be the most precise stereoscopic plotting instrument built, is designed to do contouring at an interval of 1/1250, or it has a C-factor capability of 1/1250. Experience at A.M.S. has shown that it can accurately contour at a C-factor of 1/1500.

In the United States, vertical error in mapping is commonly expressed as a C-factor, this being the ratio of contour interval to flying height at which 90 percent of all points are accurate to within one-half the contour interval, and all points are accurate to within one contour interval. In the stereophotography performed at Lakehurst, the flying height equivalent was approximately 13 feet or 156 inches. Since the C-factor used at A.M.S. in this job was 1/1500, we can determine the minimum contour interval that the planograph is capable of accurately handling by,

$$\frac{\text{Flying height}}{C\text{-factor}}=\text{Contour interval}$$

or

$$\frac{\text{Flying height}}{\text{Contour interval}}=C\text{-factor}$$

or

$$\frac{156}{\text{C.I.}}=1500$$

$$\text{Contour interval}\cong 1/10 \text{ inch.}$$

Since the contour interval requirement presented by the Echo Project was for it to be ⅛ inch and the stereoplanograph used to do the contouring had the proven capability of doing accurate contouring at 1/10-inch intervals, at the distances used in the Echo Project, all reduction was being performed well within the capabilities of the instrument.

Quoting again from the "Manual of Photogrammetry," "the basic idea of the stereoplanograph is a reversal of the process employed in making the photographs. In photography, the rays of light from the landscape produce pic-

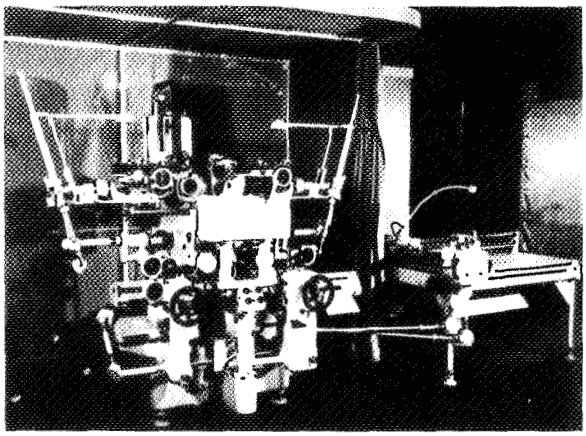

FIGURE 10

tures in the camera, whereas in the stereoplanograph they are reversed and pass from the picture to the outside through lenses to form a model of the landscape. The cone of light rays originally entering the camera are reprojected in two projectors in the instrument so as to recover the conditions existing in nature at the time of the original exposures. The light rays from the projectors intersect in space to form a spacial model. This spacial model is viewed stereoscopically through a binocular optical system containing floating or measuring marks with which measurements can be made. The measuring marks are moved relative to the projectors and the model by means of a three-dimensional cross-slide system, and the movements in the plane representing the ground plan are transferred to the coordinatograph machine where the compilation of all measurements is made."

For the x, y, z, profile measurements across each area of the balloon photographed at each station, the origin of the coordinate system was always taken to be a corner of a grid pattern on the balloon surface in the photographed area (Fig. 7). This corner was always given the coordinates of (0,0,100.000) and was the point to which all z coordinates were referred.

After setting the machine on this point, a new setting was inserted into the machine for a z coordinate of 100.125 inches. The operator then looking into the machine no longer saw the floating dot mark tangent to the balloon surface but instead saw it either embedded inside the balloon or suspended in space above it. By turning handwheels, he could then bring back or move the floating dot so that it was tangent to the balloon surface at all points which had z values ⅛ inch greater than the previous setting. As he did this, a contour line of ⅛-inch interval was automatically drawn out on the coordinatograph machine at the desired scale.

Figure 11 shows a profile measurement obtained at a relaxed condition of a 4800 p.s.i. inflation pressure. These pressures are along the surface and not perpendicular to it. The figures printed along the profile indicate in inches the z coordinate of the center of the small crosses imprinted on the balloon surface and running along a parallel of latitude. The values are with regard to a point chosen near the edge of the profile and arbitrarily given a z value of 0.00.

Figures 12 and 13 show the contouring of the same area on the balloon surface at two different pressures; namely, 4,800 p.s.i. and 7,400 p.s.i., both at relaxed conditions. As the pressure increased from the smaller to the larger value,

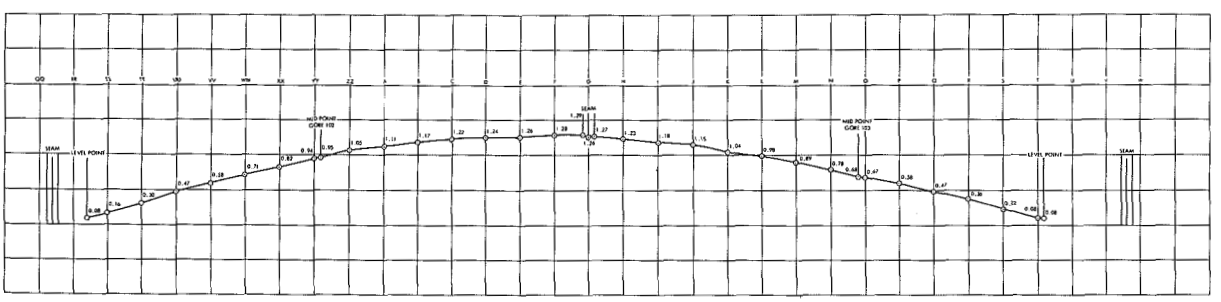

FIGURE 11

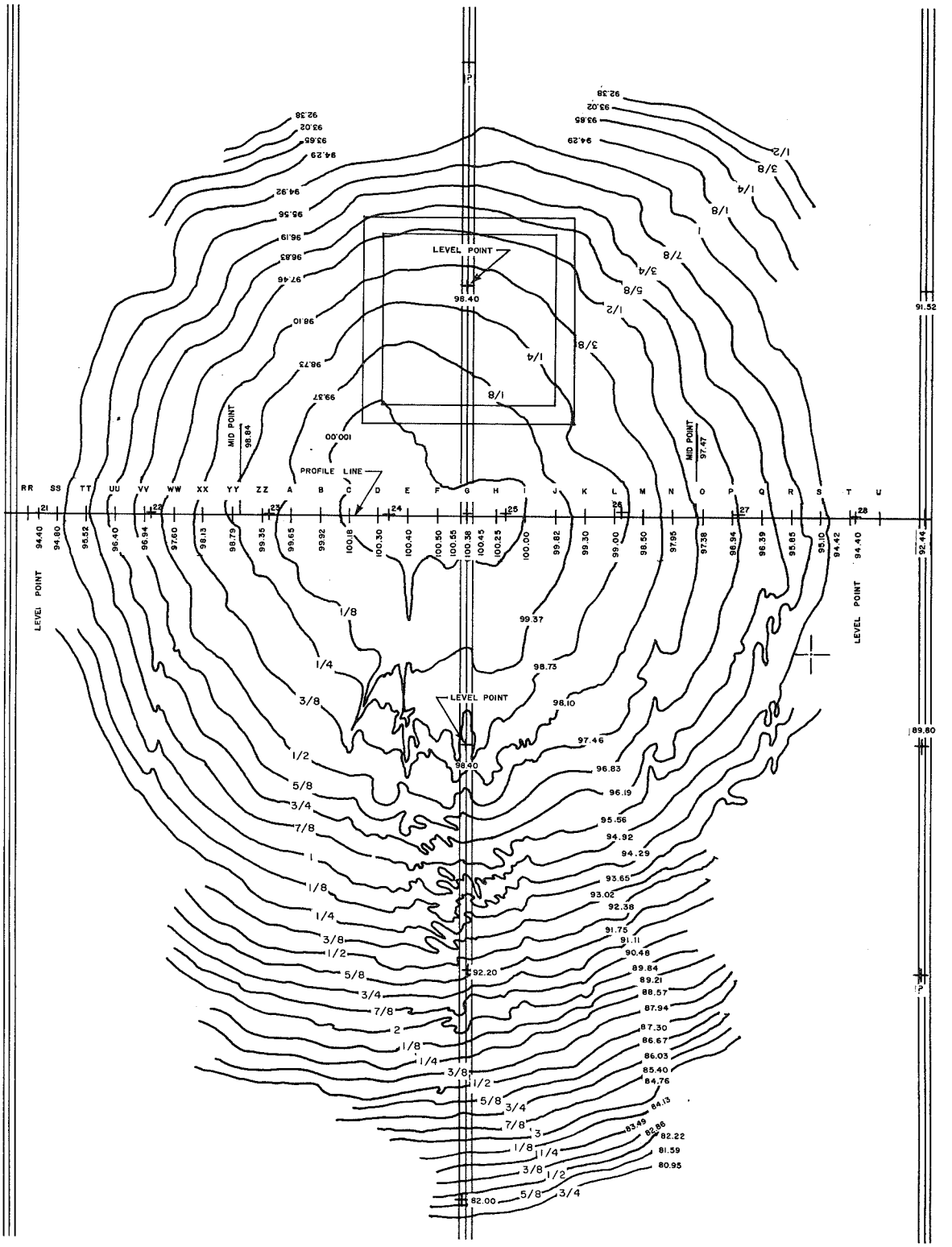
LEVEL POINT
98.40
MID POINT
98.84
MID POINT
97.47
PROFILE LINE
RR SS TT UU VV WW XX YY ZZ A B C D E F G H J K L M N O P Q R S T U
LEVEL POINT
LEVEL POINT
LEVEL POINT
92.20
82.00
91.52
89.80
92.44

FIGURE 12

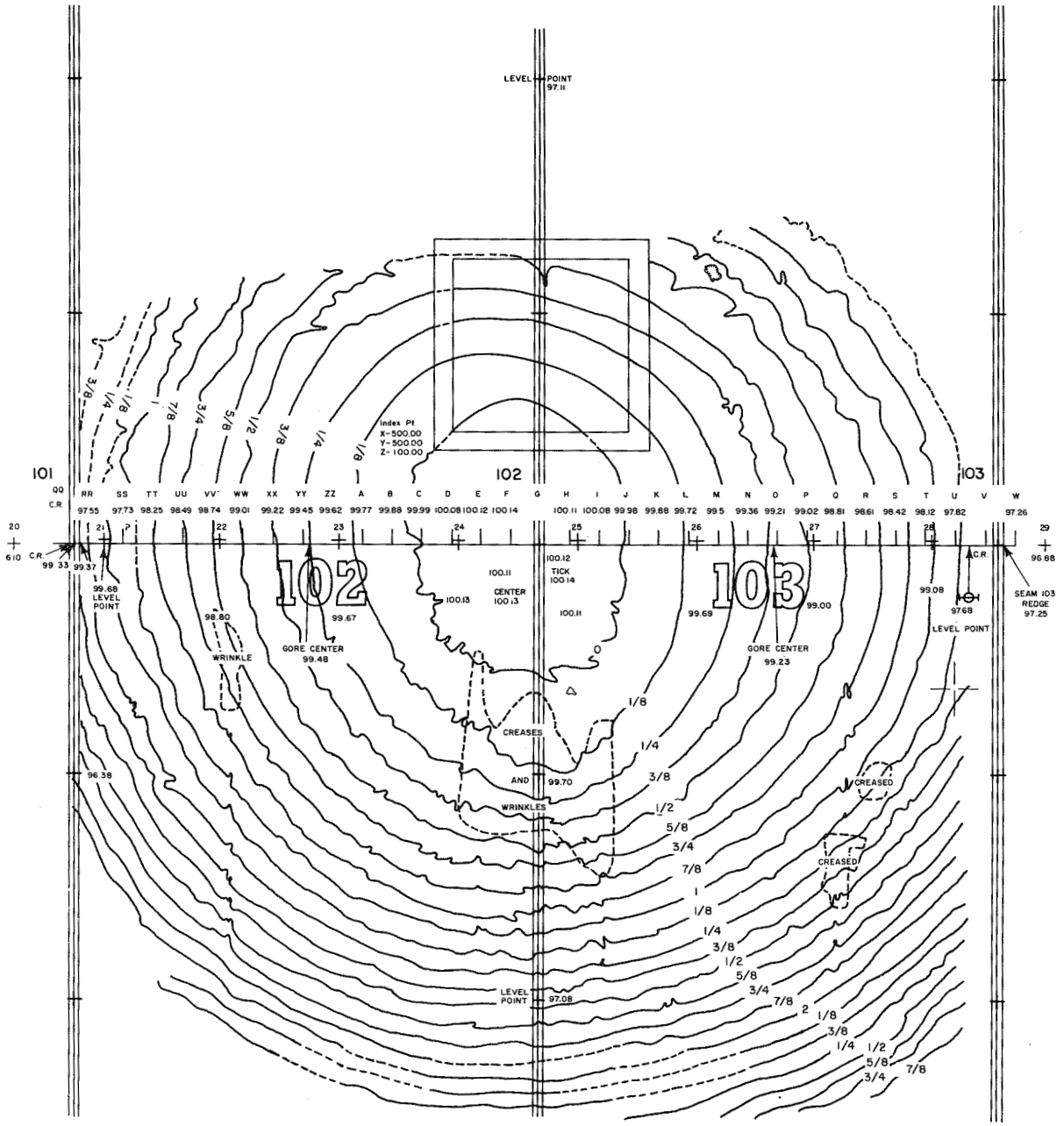

FIGURE 13

it is evident how many of the wrinkles disappeared from the skin surface and how a more spherical shape developed.

ACKNOWLEDGMENTS

The author wishes to thank the U.S. Geological Survey and the U.S. Naval Bureau of Weapons for their respective loans, each of a Wild RC–8 camera to the Goddard Space Flight Center for this test; also the Messrs. R. W. Underwood, L. L. Vance, H. L. Currie, and D. E. Leonardo of the U.S. Army Map Service for their assistance in obtaining and processing the photography at Lakehurst, N.J.

GROUND OPERATION EQUIPMENT FOR THE ORBITING ASTRONOMICAL OBSERVATORY*

E. J. HABIB AND A. G. FERRIS

Goddard Space Flight Center

H. W. COOPER

Westinghouse Electric Corp., Air Arm Division

R. L. McCONAUGHY

Grumman Aircraft Engineering Corp.

The Orbiting Astronomical Observatory (OAO) is a precisely stabilized satellite capable of being pointed to an accuracy of a fraction of a second of arc and designed for a useful orbiting lifetime in excess of one year. The OAO will be controlled by ground operation equipment at remote control stations; this equipment will transmit operating commands which have been verified on an operational simulator that includes a large-scale digital computer. Suitable safeguards are incorporated to prevent irreversible commands from being transmitted to the satellite. An auxiliary real-time control mode is provided by connecting one remote control station by microwave link to a Central Control Station which will be located at Goddard Space Flight Center. The Central Control Station control and display equipment provides a quick-look capability for evaluating the spacecraft status by means of a printer and novel "index card" type display system. The operational philosophy of the proposed design and the unique features are applicable not only to the control of the OAO but to other future controlled scientific satellites.

INTRODUCTION

The Orbiting Astronomical Observatory (OAO) is one of a new class of scientific satellites under the cognizance of the Goddard Space Flight Center (GSFC) of the National Aeronautics and Space Administration (NASA). The spacecraft will provide a highly stable and precisely orientable reference for the payload: It will also furnish all the communications, data processing, and power to reorient the observatory, to command the payload, and to store and transmit scientific data to ground stations.

This report presents the ground operation and control aspects of the OAO system. Descriptions of certain of the key portions of the spacecraft system, the operating philosophy, and the experiments carried in the payload are presented to aid in the understanding of the Ground Operations Equipment (GOE) requirements. However, the emphasis in this report is on the Ground Operation Equipment.

*Presented at the Institute of the Aerospace Sciences National Tracking and Command of Aerospace Vehicles Symposium, San Francisco, Feb. 19, 1962.

THE OAO SYSTEM AND EXPERIMENTS

Figure 1 shows the OAO as it will appear in orbit. The central structure is 10 feet in length and 7 feet in diameter; with the paddles extended it will be approximately 21 feet wide. It will weigh 2,600 pounds and will carry 1,000 pounds of experimental equipment (for a total weight of 3,600 pounds). The flap on top serves two purposes: it is a shutter to protect the telescope optics which will be damaged if the OAO points within a few degrees of the sun, and it is a sun shade to maintain the isothermal environment which will be degraded if the OAO points even within

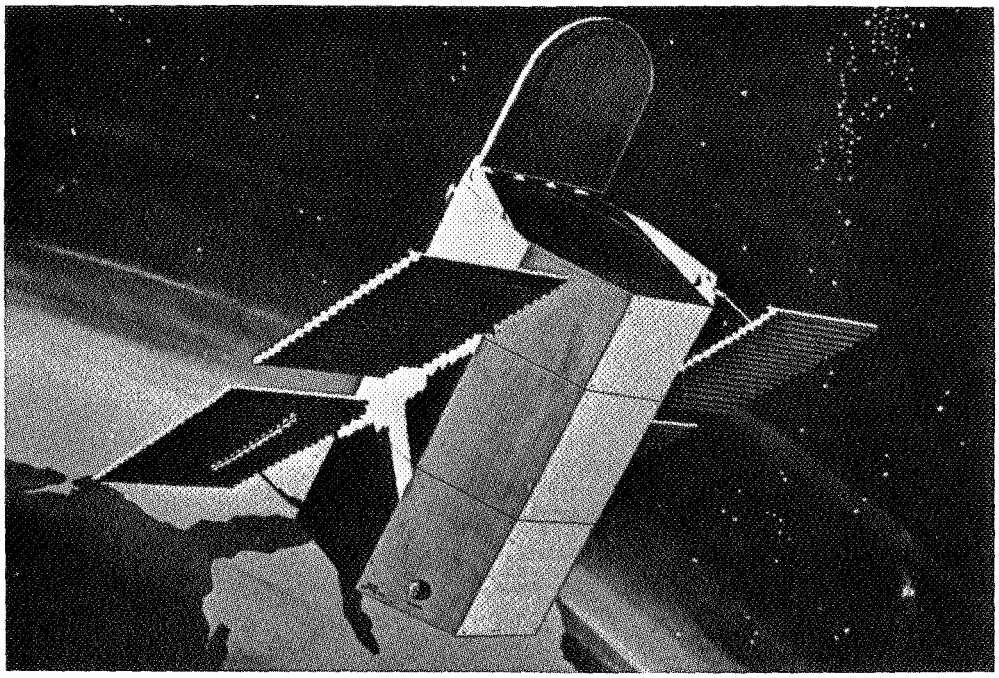

FIGURE 1.—The OAO in orbit.

45 degrees of the sun. With the spacecraft oriented as shown, sunlight arriving from the left side is converted to approximately 1 kilowatt of electrical power. The mean temperature in the equipment bays is maintained at 18 ± 36°C, while the temperature in the central tube will be isothermal within 10°C of any design temperature between 0°C and −30°C.

The OAO will be placed in a 32-degree orbit at an altitude of 400 to 600 statute miles. In this orbit, the period per circuit of the earth is about 100 minutes and the OAO is within view of a ground station a maximum of 12 minutes. The three remote stations which will be located (Fig. 2) at Rosman, N.C., Quito, Ecuador, and Santiago, Chile. These locations were selected to provide one contact per orbit with a minimum duration of 5 minutes.

The OAO differs from all previous satellites in that it is an orbiting ground controlled scientific laboratory and it is the first to allow extremely precise pointing of the sensors. The control problem is quite difficult. Whereas in prior earth-viewing satellites the means of stabilizing or of procuring a stabilization reference have been simple—either spin stabilization or stabilization to the earth's vertical with infrared sensors tracking the earth's edge—in the OAO the stabilization to an arbitrary direction in space will be by reference provided by six star trackers. The complexity of the star tracking arrangement requires more sophistication in the ground operation equipment than was required for the previous satellites.

The spacecraft operates in four principal modes: first, the initial orientation and stabilization mode; second, the calibration mode; third, the operational mode; and fourth, the backup, or trouble shooting mode, which is used when there appears to be trouble in the spacecraft subsystems.

The OAO is designed to stabilize automatically in three axes after being placed in orbit and then to aline its optical axis toward a specified area of sky on the basis of information entered in the spacecraft memory before launch. The maneuvers executed by the spacecraft to accomplish this initial orientation and stabilization are described in Appendix A. During this mode, the Ground Operation Equipment monitors the status of these maneu-

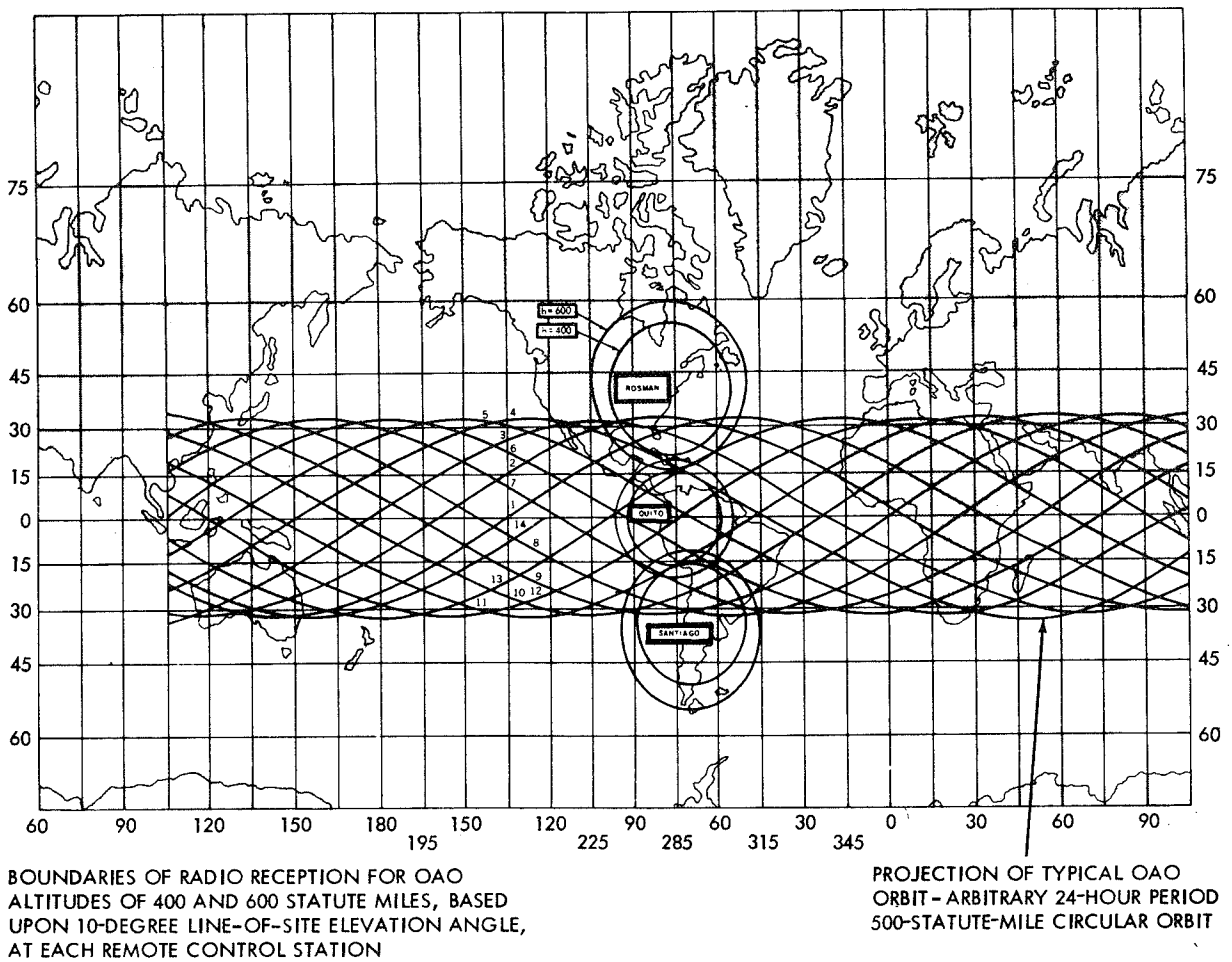

FIGURE 2.—Locations of the remote control stations.

vers and provides a means for assisting in the event of any malfunctions. This mode may take up to three orbits.

In the calibration mode, the OAO's optical devices are calibrated with respect to one another so that the effects of any distortion or inaccuracies which may have been introduced during launch are eliminated.

The major portion of the satellite life will be in the operational mode, gathering data and transmitting these data to the ground control stations.

The backup mode allows the Central Control Station to command the spacecraft in real time through the North Carolina station which is linked to the Central Control Station by microwave.

Figure 3 is a functional diagram of the major elements of the OAO system. In essence, the control equipment on the OAO points the telescope which secures the scientific information; the communications equipment relays these data to the ground stations where they are recorded. The readings are mailed to the Data Reduction Facility for processing. The scientific data are then distributed to the person conducting the experiment.

The primary experiments for the first three observatory systems are all concerned with stellar astronomy in the ultraviolet range (1000A to 3000A). The OAO–I will carry two prime experiments complementary in their use of the spacecraft systems: (1) a mapping study of the celestial sphere in four ultraviolet ranges (as

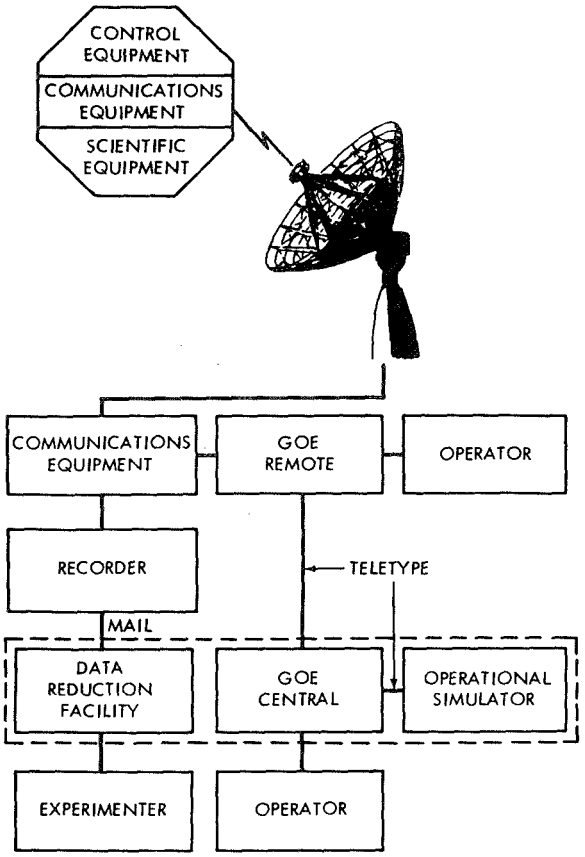

FIGURE 3.—Functional diagram of the OAO system.

shown in Fig. 4) under the direction of Dr. Fred Whipple of the Smithsonian Astrophysical Observatory, and (2) a broadband photometry study of individual stars and nebulae using the equipment shown in Figure 5 which will be developed by the University of Wisconsin team headed by Dr. Arthur Code. The sky mapping experiment will use primarily picture transmission in real time, while the star and nebulae study data will be stored and read out on command. In these experiments, the spacecraft controls must aim the roll (or main optical) axis of the satellite at specific portions of the sky with accuracies approaching 20 seconds of arc. Although this is not the ultimate desired accuracy of 0.1 second of arc (corresponding to a displacement of 0.03 inch at a distance of 1 mile), it is near the limit obtainable without using error signals taken from the experimenter's optics.

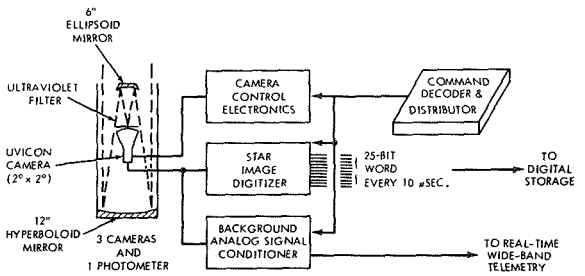

FIGURE 4.—The OAO–I sky mapping experiment: plan to photograph 70 percent of the sky in 6 months in four ultraviolet color bands—2900A to 2300A, 2900A to 1600A, 1600A to 1300A, 1600A to 1200A.

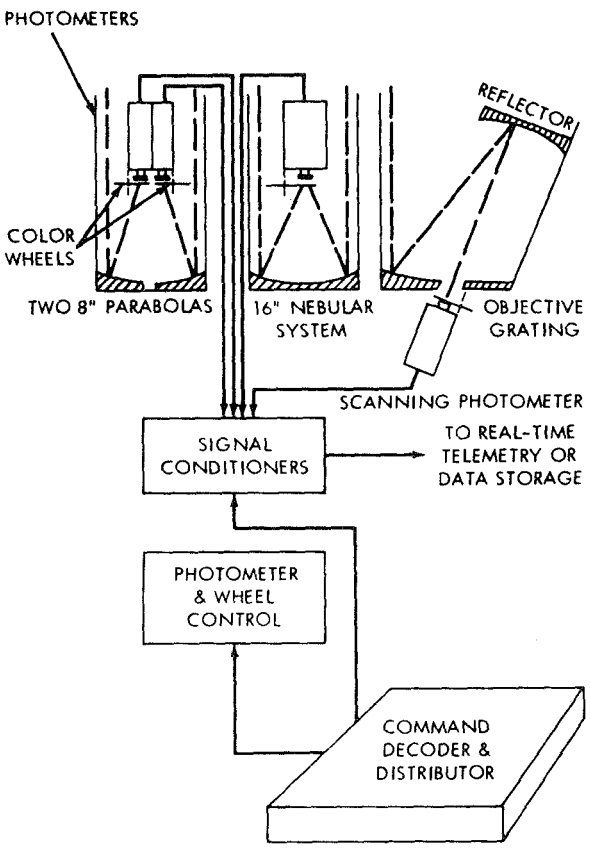

FIGURE 5.—The OAO–I stellar energy experiment: determination of ultraviolet stellar energy distribution in the spectral region from 3000A to 800A.

The OAO–II will contain an absolute spectrophometry experiment designed by a GSFC team headed by Dr. James Milligan. The optical system will employ a 36-inch primary mirror and will use both the spacecraft's

coarse and fine control capabilities, However, the experiment is designed to obtain useful data even if the fine control system does not operate. Data from this experiment will be stored and read out on command.

The experiment on the OAO–III is concerned primarily with determining the absorption features of the interstellar medium. This experiment will be directed by Princeton University under the direction of Dr. Lyman Spitzer and will require maximum performance from the optical and thermal systems and a control accuracy of 0.1 second of arc. The OAO–IV and later spacecraft in this series probably will be used for studies of the sun and planets, in addition to a limited amount of payload capacity for small secondary experiments.

In order to accomplish the satellite mission and to secure and transmit the data required by the experiments, the spacecraft requires electronic equipment as shown in the block diagram of Figure 6. The essential features of the spacecraft electronic system are: a precision clock; a core memory data storage system; a TV system for attitude verification; and data processing and communications equipment in the form of transmitters, encoders, receivers, command memory, etc.

The OAO communications include command operation on 148 megacycles and telemetry on 136 and 400 megacycles as shown in the portion of Figure 7 marked "Remote Control Station." The 400-mc receiver is operated at 300-kc IF band width and the narrow-band signal is received on 136 Mc with a 10-kc IF band width. The 300-kc band width is necessary for transmitting the slow-scan television image. The stable nature ot the image allows slow-scan techniques with adequate resolution. The Pulse Code Modulation (PCM) data can be transmitted on either the narrow-band

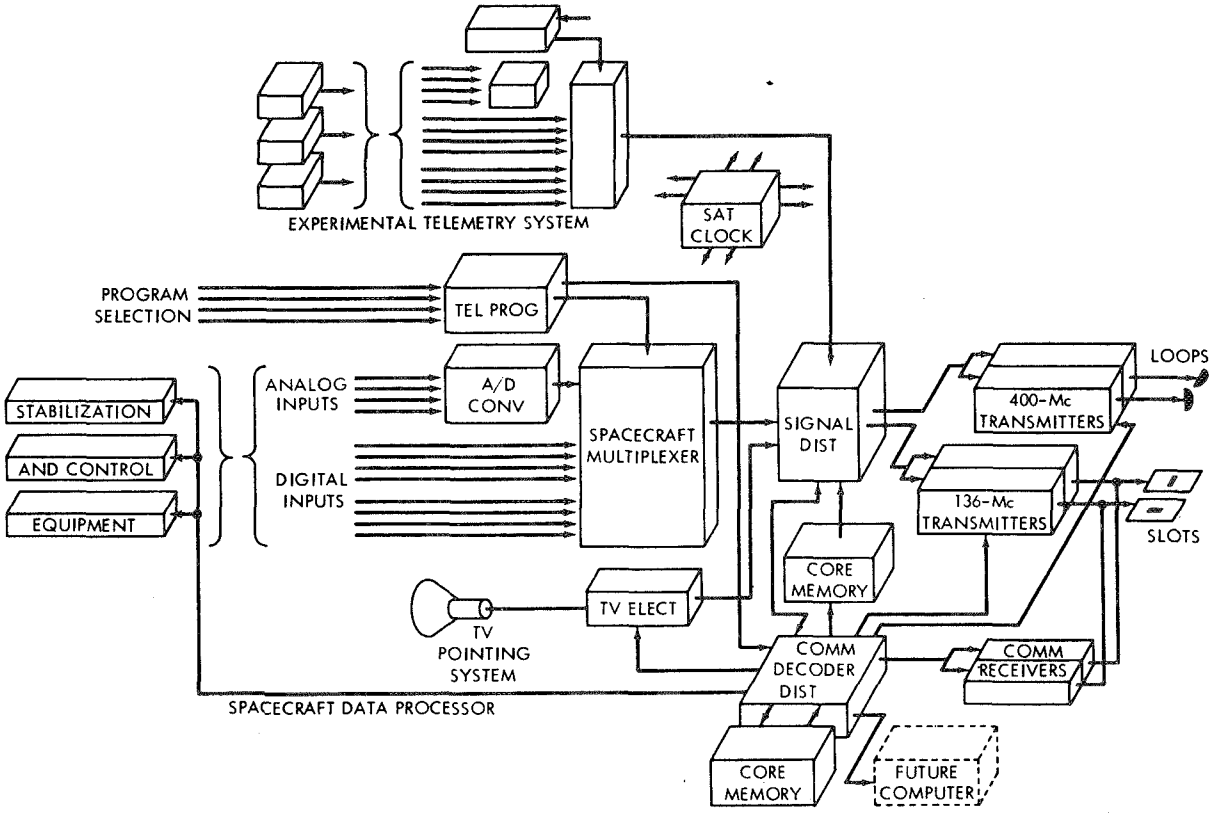

FIGURE 6.—The electronics of the OAO.

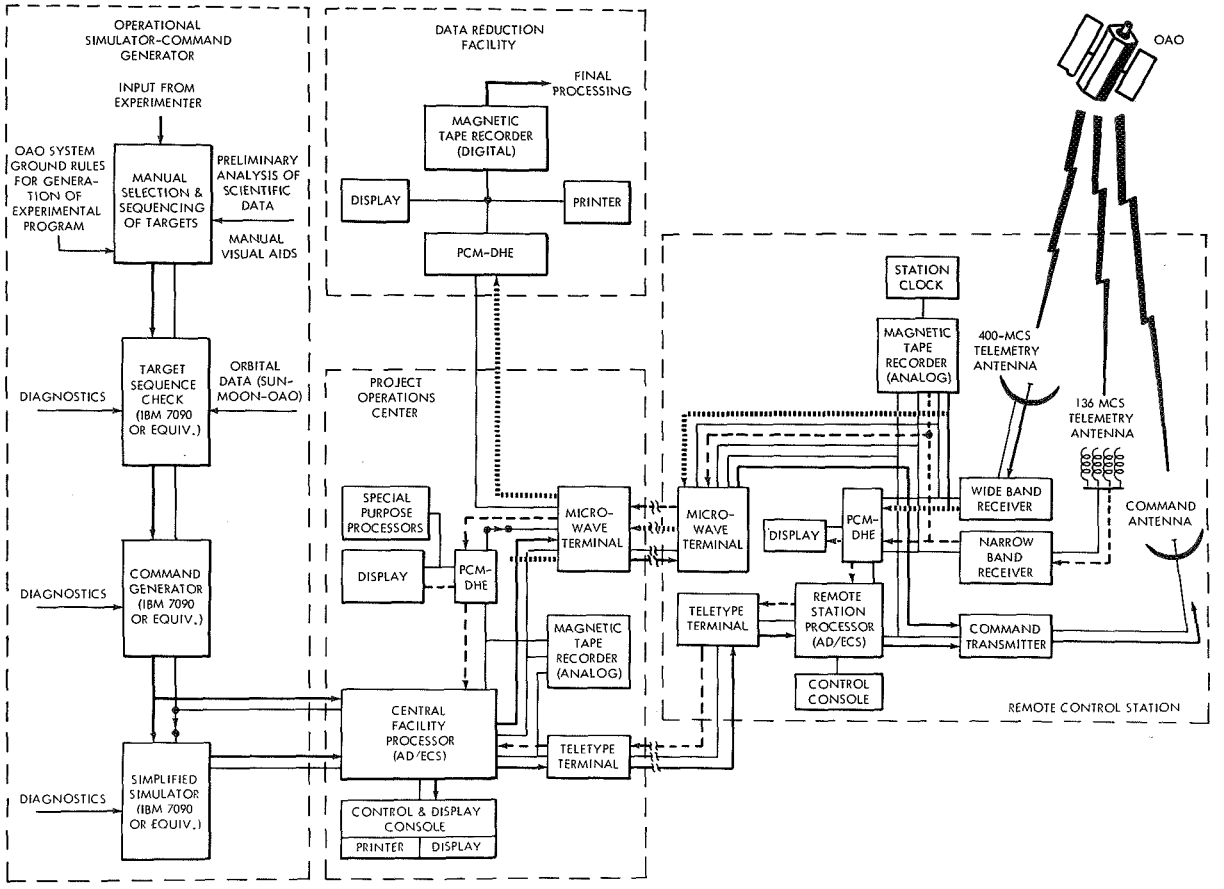

FIGURE 7.—The OAO ground operation equipment.

or the wide-band links if malfunctions occur in the spacecraft communications.

High-power ground transmitters and high-gain ground antenna systems are used to increase the signal-to-noise ratio. In addition, because of the extreme importance of transmitting correct commands to the spacecraft, the commands and their complements are transmitted, and compared in the spacecraft while they are retransmitted to the remote control station for further comparison.

GROUND OPERATION COMPLEX

Figure 7 is a block diagram of the OAO Ground Operation Equipment complex. Table 1 lists the system elements and functions. The operational simulator-command generator establishes the feasibility of the commands which the experimenter requires. These commands are verified on a large-scale digital computer which introduces orbital and astronomical data and spacecraft conditions as well as other constraints on the operation. Upon verification, these commands are passed to the Project Operations Center. The commands are then sent by teletype or by microwave to the remote control station which actually communicates with the satellite.

In addition to a radio beacon which is used for tracking, three radio links are used to communicate with the OAO. The remote control stations are all identical in their functions and equipment. They normally only secure data from the satellite and transmit predetermined commands to the satellite. However, in case of emergency or if desired, the GSFC Central Control Station can assume real-time control of satellite operations through the North

Carolina station. This is done by direct microwave connection. The predetermined commands are originated and checked at GSFC and are transmitted to the remote control stations by teletype at least a day in advance of their use.

The two telemeter links transmit to the remote control stations all the data available in the OAO; these data are recorded on magnetic tape at the remote control stations. Tapes containing scientific or experimental data are mailed to the Data Reduction Facility at the Central Control Station for processing for the experimenter. Data indicating the status of the spacecraft and the experiment are processed by the remote control station—first, to determine whether the satellite is in a satisfactory state to accept commands for the next orbit, and, second, to prepare the data for transmission to the Central Control Station where it may be analyzed and used to update predictions of the OAO behavior.

The essential functions of the Ground Operation Equipment—message distribution, data processing, signal distribution logic, displays, controls, and command modulators—are diagrammed in Figure 8.

The equipment described here will be common to all OAO spacecraft, and portions of it may be used for other future scientific satellites. It monitors the condition of the spacecraft and subsystems and generates the commands necessary to accomplish the scientific experiments and, if possible, to correct any malfunctions that may occur in the satellite.

Remote Control Stations

The data processing function at each of the remote control stations is handled by a general-purpose computer of intermediate capacity, the General Mills AD/ECS–37a. This equipment is used in conjunction with a display and control console which provides the operator link to the system (Figs. 9, 10, and 11). Figure 12 shows the data flow in the normal mode of operation. The control console and the computer at the remote control station

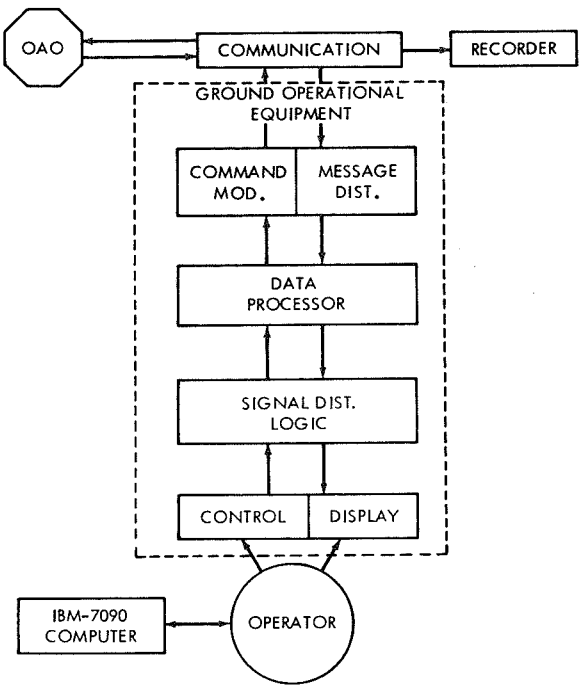

FIGURE 8.—Functional diagram of the ground operation equipment.

(block diagram shown in Fig. 13) implements the operating functions which are:

1. Receive commands, predicted status, and instructions from the Central Control Station and store these in AD/ECS–37a computer.
2. Set the Estimated Time Arrival display per instructions from the Central Control Station.
3. Perform precontact checkout of station equipment.
4. Monitor the beacon signal for the OAO contact.
5. Interrogate the spacecraft when station time agrees with Estimated Time of Arrival and beacon signals exceeds threshold.
6. Verify commands.
7. Receive current status data, check parity, and check with predicted status.
8. If status check fails, transmit hold commands and notify the Central Control Station.

TABLE 1.—*System Elements and Functions*

Element	Operational simulator-command generator	Project operations center	Data reduction facility	Remote station
Equipment	IBM 7090 peripheral equipment.	Communications terminal equipment. PCM–DHE. Display and control console. General Mills. AD/ECS–37a.	PCM–DHE. On-off line printer. Off-line plotter. Small computer. Large computer.	RF Equipment. PCM–DHE. Display and control console (limited). General Mills. AD/ECS–37a.
Functions	Command Generator Simulator diagnostics.	Duplicate remote control station capability. Display scientific data (limited).	Decomm-sort-catalog scientific data. Quick-look at scientific data. Final Format-output data complete. Status data time history by parameter.	Command Transmission. Status compare. Command Verification. Format conversion and check. Decomm and conversion for display. Scientific Data decomm and display (limited). Signal routing.
Inputs	Orbital data. Star catalog. Sequence of targets. Status data-spacecraft and experiments.	Punched paper tape from remote control stations. Predicted status from operational simulator. Command from command generator.	Magnetic tape from remote control stations. Punched paper tape from project operations center. Direction and requirements from experiments.	Punched paper tape from project operations center. RF (NB & WB) from spacecraft.
Outputs	Commands. Predicted status. Diagnostics. Ground rules for experimenters.	Punched paper tape to remote control stations. Direct digital to microwave link. Magnetic tape to IBM 7090.	Status data-time history. Experimenters data package.	Commands to spacecraft. Punched paper tape to project operations center. Go, no-go to spacecraft system.

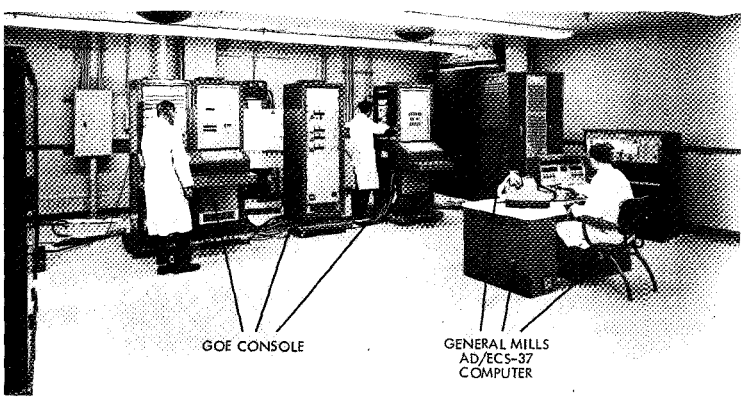

FIGURE 9.—Ground operation equipment at a typical remote control station.

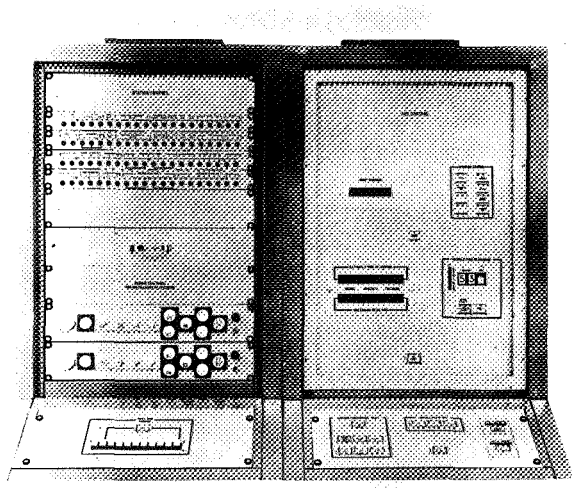

FIGURE 10.—Remote control station operating panel—station control/GOE control.

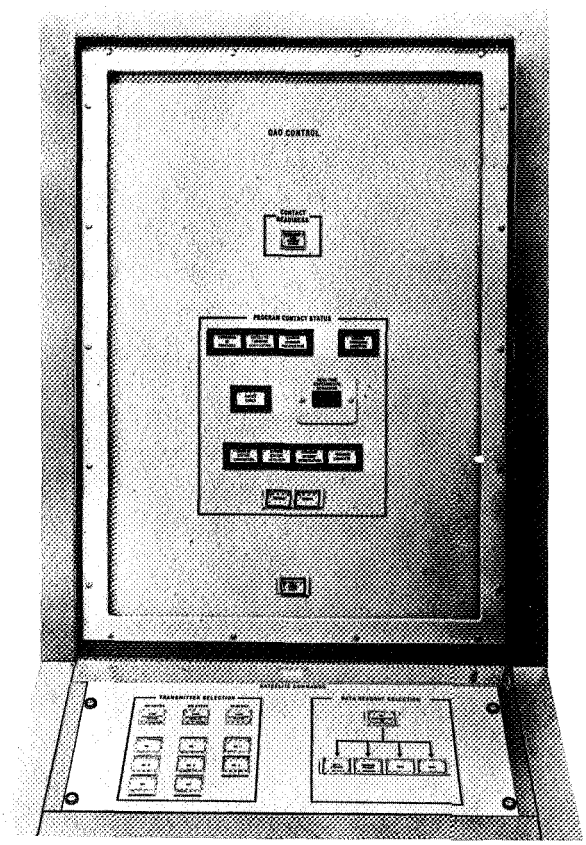

FIGURE 11.—Remote control station operating panel—OAO control.

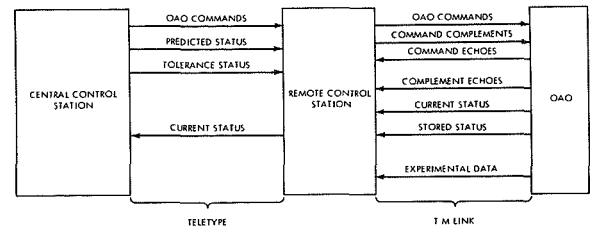

FIGURE 12.—Data flow in the normal mode of operation.

9. If status check passes, transmit and verify additional commands.
10. Record all commands transmitted and all data received.
11. Display results of command-verify, parity, and status checks.
12. Display Greenwich Mean Time, Estimated Time of Arrival, and contact time remaining.
13. Convert status data TWX format and transmit to the Central Control Station.
14. Send magnetic-tape recording to the Central Control Station.

The remote control station operator may select the satellite transmitters and beacons which he wishes to use and the type of data to be transmitted from the satellite. The OAO control portion of the console provides this capability (Figure 11). Control over the physical motions of the satellite is limited to preprogrammed commands for future execution or a "hold" command to sustain it in an unchanged condition.

The rest of the console provides control of the ground station and equipment (Fig. 10). The station status is a simple go, no-go signal which indicates the readiness of particular pieces of equipment. The system functional test controls initiate actions which establish the operating readiness of the Ground Operation Equipment. The mode selector control on the North Carolina station can transfer control to the Central Control Station via the microwave link.

Central Control Station

The foundation of the OAO ground operations is a large-scale computer which keeps track of astronomical and orbital motions, which maintains an up-to-date status of the observatory,

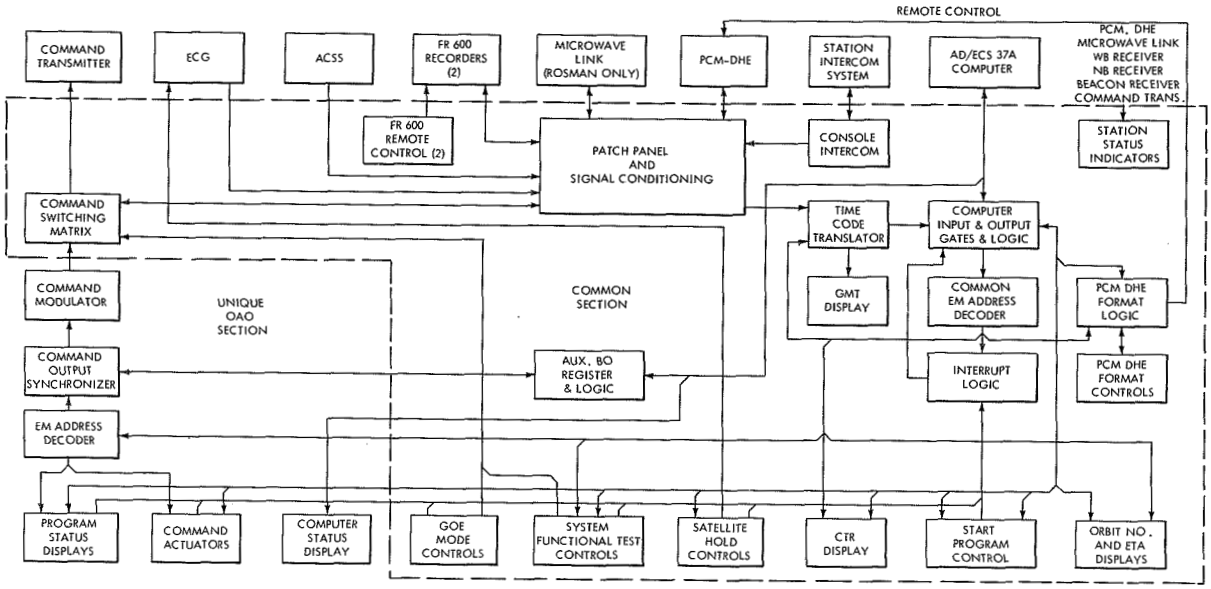

FIGURE 13.—Block diagram of the remote control station control console.

and which accepts programmed operational and performance constraints of the OAO system. In addition to the large-scale computer the equipment in the Central Control Station is the same as that at the remote control stations with certain display and control portions augmented. The Central Control Station console consists of six relay racks of equipment. The three units shown in Figure 14 combined with two units similar to those shown in Figure 10 and a power supply unit make up the console.

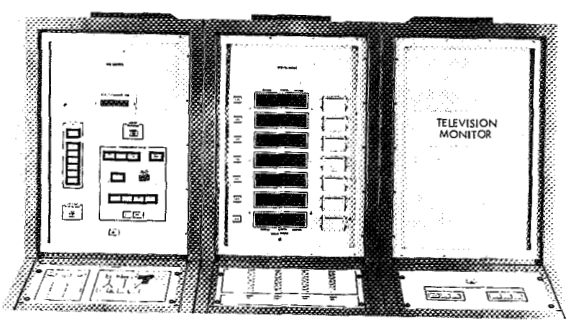

FIGURE 14.—Central Control Station—OAO control/display.

Figure 15 is a block diagram of the Central Control Station equipment not including the large scale digital computer.

The functions of the Central Control Station are:

1. Generate commands, predicted status values, contact times, and instructions.
2. Convert commands and other data to TWX format and transmit to remote control stations.
3. Generate and store alternate program for quick takeover.
4. Receive the previous OAO contact data from the remote control stations and convert these data to IBM 7090 format.
5. Display status data.
6. Enter data and experimenter's instructions into a large-scale digital computer for evaluation and use in generating commands for the next contact.
7. Display Greenwich Mean Time, satellite equivalent time, estimated time of arrival, and contact time remaining.

By using the information from the satellite and the desired sequence of astronomical observations, the computer generates commands in spacecraft language, predicts the state of the spacecraft at the start of each ground contact, and establishes tolerances within which the prediction is valid. The tolerances established for the go, no-go evaluation must account for

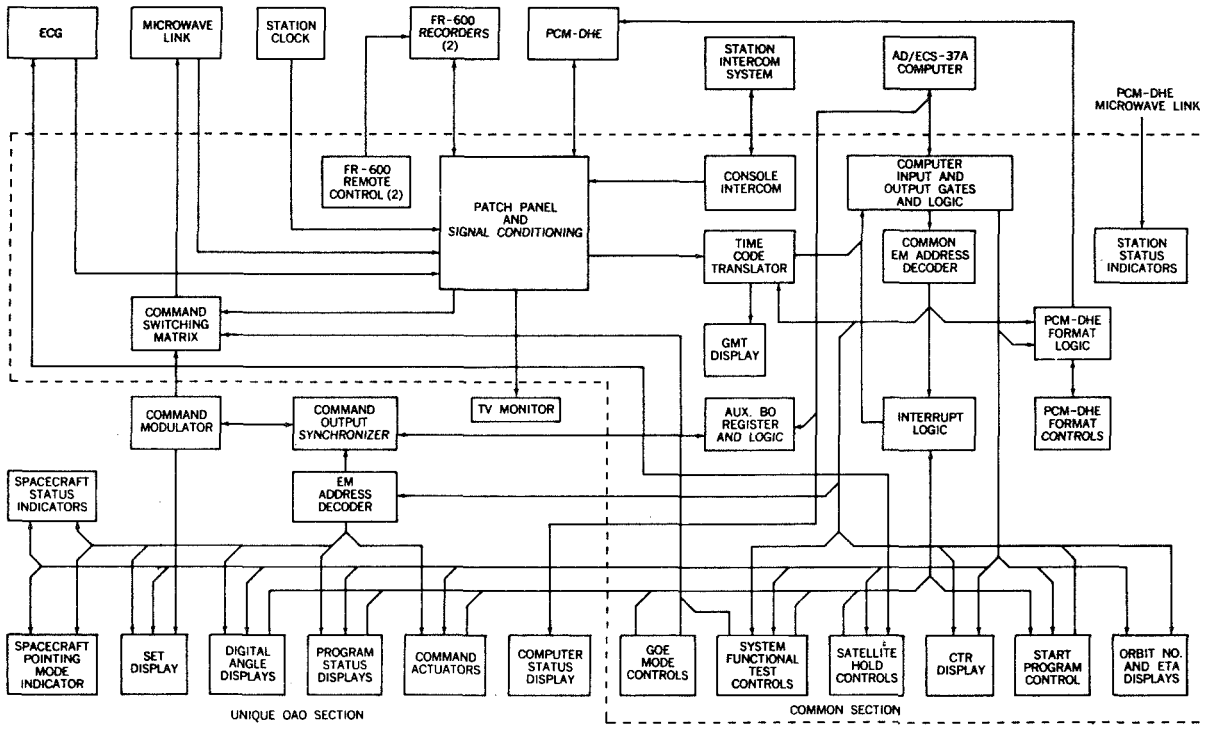

FIGURE 15.—Block diagram of the Central Control Station equipment.

the accuracy with which the forecast is made, the accuracy with which the quantity can be measured, and the importance of the quantity to the successful performance of the OAO. During the one contact per orbit, lasting from 5 to 12 minutes, data must be read from the memory on the spacecraft and new instructions stored in the command memory of the spacecraft. The design problem of the ground operation equipment is basically how most efficiently to transfer information from a multiplicity of sensors in the spacecraft to the human operator on the ground, how to assist him in making decisions, and how best to redirect the necessary controlling actions to the spacecraft subsystem.

Although the Central Control Station communicates only with the satellite in real time via the North Carolina remote station by microwave link, considerably more data are displayed here than are displayed at the remote control stations.

The Central Control Station equipment enables the operator to examine the data received from 294 analog measurements within the satellite. In addition to the analog status items, there are 192 bilevel status items. These items provide information on equipment components whose status is characterized by one of two states, for example, on-off or open-close. Another 25 items provide, in decimal form, angular data and time from the satellite. The angular data is called up from the AD/ECS–37a computer using a plastic index card with a title in English which provides a positive means of identifying the display status item. Holes in the card actuate a set of microswitches (Fig. 16) which provide coding for entry of the command to the computer, which, in turn, calls up the desired information from the computer memory. For a permanent record of all channels, a printer is used.

The optimum amount of information which the operator can read and act upon would require an extensive human factors study. However, the amount of information presented upon the control and display panels at the Central Control Station has been determined by

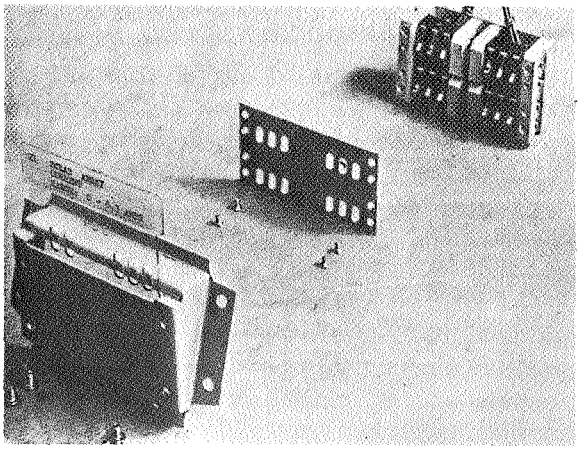

FIGURE 16.—Selector switch assembly.

a human factors analysis to be well within the capability of the average operator.

As a means of verifying the orientation of the OAO, a television camera with a field of view approximately 8 degrees square is boresighted along the optical axis of the spacecraft. With a 1-second frame period and the available communications band width, a resolution of 350 lines is possible. The ground based television monitor, provided at the Central Control Station only, can be used for coarse verification of the pointing data derived from the star tracker gimbal angles. The spacecraft camera, operating in the visible spectrum, is entirely separate from ultraviolet-sensitive cameras provided as part of the experiment.

DESCRIPTION OF OPERATION

Satellite Commands

The most important task of the Ground Operation Equipment is to generate and transmit commands to the spacecraft. The commands transmitted to the satellite consist of seven basic types in either a real-time command mode or a stored command mode. The commands and their codes are given in Table 2.

The gimbal angle commands are commands to the star trackers, while the attitude change commands control the OAO's coarse momentum wheels directly for changing attitude. Each command consists of two 32-bit words. The first word classifies the command and addresses the proper channel for coding and the second word is the command itself. Figure 17 shows the formats for the control and gimbal angle commands which are typical of command formats. Note that the control command format permits 156 [=12×13] bilevel commands.

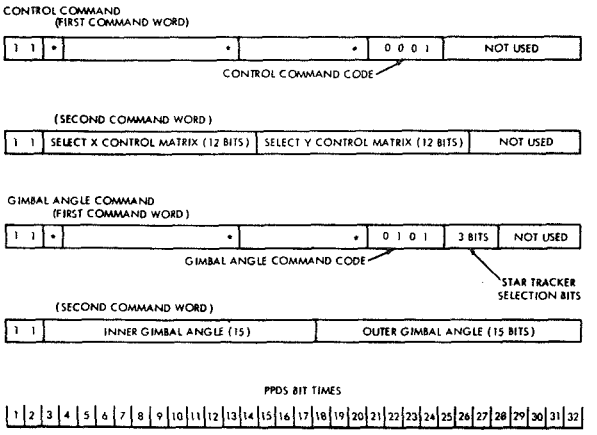

FIGURE 17.—The OAO command format. Variable bit configurations are indicated by asterisks.

TABLE 2.—*Satellite Commands and Their Codes*

Command	Code
Control	100
Data handling	011
Address transfer	001
Attitude change	010
Experimenter's	110
Gimbal angle	101
Ground synchronization	000

The commmands transmitted to the OAO from the remote stations are in a PCM NRZ format at a 1-kilobit rate. The data transmitted consist of the command words and their complements to provide error checking. The complement form simplifies the on-board command verification. While verification is being accomplished by the electronic equipment in the satellite, the commands and their complements are echoed (retransmitted) to the ground where the ground operation equipment compares the echo from the satellite with the

original transmitted command to ensure that they have been properly received. A real-time command will be executed immediately upon on-board verification and is independent of ground verification.

An alarm is generated and transmitted by the OAO when the complement is not verified on board. Receipt of the alarm causes the Ground Operation Equipment to inhibit transmission of the commands to the OAO. The command message is then retransmitted, beginnning with the command that failed, or beginning with a preceding command. Similar action occurs if the command echo is not verified.

Typical Contact With the OAO

Contact with the OAO is established at predicted time of contact or when the beacon Automatic Gain Control level indicates that the OAO is in range. The operator initiates a start command to cause the data processor, under control of a stored program, to issue the commands necessary to cause a readout of current status from the OAO. Necessary gating signals are sent to the PCM data-handling equipment to define the format and word size for proper signal flow in and from the PCM data-handling equipment.

The computer program causes current and predicted status to be compared word by word. In the comparison, the limits of predicted status are extracted from storage an item at a time and the difference between limits and actual values for that parameter are computed and evaluated. If one or more items are out of tolerance, the computer causes the spacecraft to be reinterrogated and recompares status. This cycle is repeated until the predicted and current status are compared successfully, or until a fixed number of cycles have been executed. If the former, the computer activates the Current Status Comparison indicator to GO (GREEN) and proceeds to the next subroutine. If the comparison is unsuccessful, the computer activates the Current Status Comparison indicator to NO GO (RED) and activates either the Recycle or Manual switch indicator to an AMBER state. The Recycle indicator is activated if the computer program indicates that it is possible to repeat the sequence without running out of time for the rest of the contact operations. If time is so short that the automatic program cannot continue, the computer gives the operator irrevocable manual control of the contact and activates the Manual switch indicator to AMBER.

The Recycle and Manual switch indicators are used in the same fashion at all critical points in the contact operations shown by the program status indicators. The next subroutine, command transmission and verification, routes commands in the sequence defined by the Central Control Station. The complement of each command word is transmitted immediately following the command word proper as previously described.

Command output synchronizer logic converts the command message to serial form and accomplishes the synchronization and format conversions. The bit-rate synchronizing signal is initiated by computer control and after a delay (3 to 10 milliseconds) determined by the computer subroutine, the command message is initiated. The spacecraft data processing subsystem compares the command word with its complement and also retransmits the command and complement to the remote control station. If the complement check in the spacecraft fails, the spacecraft transmits an alarm in lieu of echoing the command. A gating signal routes the commands through the PCM data handling equipment into the computer where the echoed command is compared with the transmitted command as described previously.

Receipt of the alarm signal initiates a subroutine that will determine which specific command word failed, reset the spacecraft verification logic, and start a new transmission at the command where the error occurred. If this command is transmitted and verified, the process continues until the message is completed or a subsequent error is detected. If a fixed number of repeat cycles has been executed on a given command and an error persists, the Command Memory Verification light goes red

and the program halts until the operator either: (1) Recycles, (2) switches in redundant communication links and then Recycles, or (3) takes manual control. When the Command Memory Verification light shows red or no-go, the operator can base his decision of which alternate to pursue by reference to the Satellite Command Verification, Ground Command Verification, and Parity Check lights which indicate the source of the no-go condition.

When the computer has successfully transmitted, received acknowledgment, of and verified the assigned command message, it will proceed with the next subroutine which may consist of a number of real time experiments. The manually switched commands may be employed as necessary by the station operator in either the Recycle or Manual condition discussed previously.

When the computer has successfully transmitted, received acknowledgment of, and verified the assigned command message, it will either halt or proceed with the next subrouting, depending on the state of the Proceed/Halt switch. The manually switched commands may be employed as necessary by the station operator when the Manual light is on.

After the contact is completed, the computer is directed to transcribe the actual status data received from the spacecraft to teletype format and to punch a paper tape containing these data. The information on the tape is transmitted to the Central Control Station via teletype. All data received from the OAO (including stored status), all commands transmitted to the OAO, Greenwich Mean Time from the station clock, and an appropriate voice commentary by the OAO operator are recorded on magnetic tape. In certain cases of failure, the Central Control Station may request that stored status (data gathered during the previous orbit and stored on board) be teletyped back to eliminate the delay encountered in mailing the magnetic tape.

CONCLUSION

The Ground Operation Equipment which has been described and discussed will achieve reliable system operation: First, by forecasting the spacecraft performance on an operational simulator—a large-capacity digital computer at the Central Control Station—and establishing tolerances. Second, minimizing human error by using a medium-capacity digital computer as part of the Ground Operation Equipment to compare status data received from the satellite with the forecast status. Third, minimizing human error by displaying a minimum of information to the remote control station operator and minimizing the number of commands that he must or can transmit to the satellite using his own judgment.

A complete satus data print out is used in the Central Control Station as a rapid, error-proof means of displaying the greater amount of intelligence available there. With this greater intelligence, emergency control over the satellite may be exercised in a real-time mode. Even here the philosophy is to use this capability as a backup or abnormal operating technique and to rely on the fundamental preprogramed operational philosophy.

These techniques are new and are fundamental to the success of a precision scientific satellite, such as the OAO, and should find wide application in future satellite and spacecraft upon verification by the OAO program.

Appendix A

INITIAL STABILIZATION

Immediately after injection of the satellite into orbit, the orientation may be random and there will probably be a residual motion caused by the separation mechanism. There are four steps to accomplish stabilization:

First, the motion is stopped and an initial orientation is established. Three orthogonally mounted rate gyros, eight coarse and eight fine sun sensors accomplish this. The rate gyros detect the motion of the satellite about all axes and, by operating gas jets, bring the spacecraft to a near standstill. Simultaneously, the sun sensors locate the sun with respect to the satellite and their signals, also by operating the gas jets, rotate the satellite so that the optical axis is aligned with the sun.

Since the sun, in effect, rotates about an inertially stabilized satellite at 1 degree per day, the next step is to produce a nonrotating celestial reference in the satellite. This is performed by six highly accurate star trackers gimbaled with respect to the pitch, roll, and yaw axes. The angles of the star trackers with respect to the satellite axis, properly transformed, indicate the pointing of the satellite optical axis.

Before launch six reference stars are chosen, and for that particular day, the angles of these stars with respect to a line connecting the earth and sun are computed. The star trackers are then erected to coincide with these predetermined angles.

The second phase is then initiated by slowly rotating the satellite about the roll axis. At a particular roll angle, the star trackers will produce a star presence signal simultaneously. Since the earth may be occulting some of the stars, a minimum of four simultaneous signals is preferred, although this may be reduced to two on ground command. Once this has occurred, the primary satellite control system, consisting of momentum wheels is switched from the sun sensors to the star trackers for its error signals.

This provides the initial celestial reference but the optical axis still points at the sun.

The next step is to aim at a desired target star. To accomplish this, the satellite carries core-storage command memory of 256 30-bit words, a star-tracker gimbal-angle digital logic, an analog coordinate transformer, and a system clock.

After the central control station has determined that the initial reference has been acquired, predetermined commands are authorized for transmission to the OAO to reorient the OAO. New gimbal angles for the star trackers replace the initial set. The large inertia wheels are commanded to rotate through a specified number of revolutions, thus turning the spacecraft through a predetermined angle. While moving to this new position, a star tracker may reach its gimbal limit, but this will have been anticipated on the ground and the star tracker's gimbals will have been commanded to another guide star, again by the output from command memory, before reorientation occurs. On reaching the new orientation, the star tracker error signals are connected to the small inertia wheels to maintain attitude.

Alternatively, by using the satellite and its tracking star trackers as a reference, an error signal can be generated to move a star tracker to acquire a new guide star. By driving either

the satellite or the star trackers, a reference in space is continually maintained while moving the satellite to any orientation, subject to the restriction that pointing the optical axis at the sun is not permitted. As a safety measure, the sun shutter automatically closes if the optical axis approaches within 45 degrees of the sun.

Summarizing, the initial stabilization routine is—

1. Initial rate stabilization and solar orientation.
2. Roll search, for preselected guide stars.
3. Celestial orientation.
4. Celestial pointing and holding.

EXPLORATION OF THE ATMOSPHERE OF VENUS BY A SIMPLE CAPSULE

RUDOLF A. HANEL
Goddard Space Flight Center

The exploration of the planet Venus by probes which penetrate the atmosphere will allow direct measurements of very important physical parameters. Early probes must be restricted to a few simple instruments but, carefully chosen, they will yield a truly remarkable increase of knowledge. These results will then pave the way for more sophisticated instruments, to be considered as second and third generation. The main target of the early experiments should be the structure and composition of the atmosphere. Accordingly, pressure, temperature, and density will be measured as well as the nitrogen, carbon dioxide, argon, water vapor, and cloud content. Simple methods to determine these parameters are discussed.

LIST OF SYMBOLS

A	cross-sectional area
C_D	aerodynamic drag coefficient
C_p	specified heat at constant pressures
C_v	specified heat at constant volume
c	velocity of sound
g	gravitational force on Venus
H	scale height
h	height
M	molecular weight
m	mass
p	pressure
R	gas constant
T	temperature
t	time
u	descent velocity of probe
z	acoustical impedance
Γ_{ad}	adiabatic lapse rate
Γ_{obs}	observed lapse rate
γ	specific heat ratio
ρ	density

INTRODUCTION

Earthbound observations of reflected, refracted, and emitted radiation in several regions of the electromagnetic spectrum have been the principal source of information about the planet Venus. Only recently, after the successful adventure of Mariner II (1962 $\alpha\rho 1$), have other data, such as the absence of a strong magnetic field, become available.

Large and complicated instruments serve the earthbound astronomer and he can, within reason, repeat his experiment or observation as often as he desires. However, surface observations suffer from the small solid angle which the planet subtends and from the interference of the Earth's atmosphere. In spite of these limitations remarkable results have been achieved. These results have been summarized by Moore, Urey, and Kuiper (References 1–3), and more recently by Kellogg and Sagan, de Vaucouleurs, Kuiper and Middlehurst, Öpik (References 4–7) and others.

The most important sources of data about Venus can be classified according to the technique and the part of the electromagnetic spectrum used, under one or more of the following headings:

1. General astronomical data—mass, size, oribital parameters, etc.
2. Planetary photometry—albedo at various wavelengths, cloud markings, etc.
3. Polarization studies (References 8–10).

4. Near infrared spectroscopy (References 11–17).
5. Far infrared radiometry and spectroscopy (References 18–24).
6. Occultation method (Reference 25).
7. Radar and microwave radiometry (References 26–31).
8. Mariner II measurements.

MODELS OF VENUS

On the bases of theoretical considerations and the experimental evidence just listed (or some part of it), attempts have been made to generate a consistent picture of the atmosphere and surface of Venus. Each attempt usually culminates in a "model" which matches at least a few and hopefully all of the experimental data. These models allow extrapolation to facts which are inaccessible by direct measurements from Earth. It is characteristic of the state of knowledge about Venus that the number of atmospheric models almost exceeds the number of experimental facts. Only a few recent models, those discussed by Kellogg and Sagan (Reference 4), will be mentioned here.

The Greenhouse Model

The radiometric temperature ($\approx 600°K$) in the microwave region is believed to be the temperature of the surface of Venus (Reference 32). An atmosphere fairly transparent in the region of solar radiation but opaque in the region of thermal radiation provides the energy-tapping or greenhouse effect. A fairly high amount of water vapor should exist below the clouds, but this has not been confirmed by recent microwave data. The surface pressure would be much higher than on earth, presumably 2 to 5 atmospheres; a more recent estimate yields even 50 atm. (Reference 33).

The Aeolospheric Model

Öpik (Reference 34) also accepts the high temperature in the microwave region as coming from the surface. However, here the high temperature is maintained by friction among grinding particles in the atmosphere. A very dusty atmosphere effectively isolates the surface from solar radiation as well as from thermal cooling. This model seems to be the most reasonable one, but its agreement with certain theories, such as the general circulation theory, has yet to be substantiated.

The Ionospheric Model

In contrast with the previously mentioned models, the ionospheric model explains the high microwave temperature by emission from a very dense ionosphere. This model, almost discarded a year ago, temporarily achieved new support from measurements indicating the absence of a magnetic field (Mariner II) and from the discovery of an apparent correlation between Venus radar data and solar flux in the 20 cm region (Reference 35). However, tentative information on limb darkening, determined by the microwave radiometer on Mariner II, seems to rule out this model.

Other Models

In addition to the above-mentioned models much has been published that at times contains implicit statements equivalent to particular models. Only a few of the writers need be mentioned: de Vaucouleurs, Chamberlain and Kuiper, Sinton and Strong, Barrett, Kaplan, and Mintz (References 5, 15, 24, 36, 37, and 38).

In spite of these efforts the atmosphere of Venus remains a puzzle. Basic parameters such as surface pressure are uncertain to approximately 2 orders of magnitude—the value for pressure varies from 0.3 atm. for the ionospheric model to perhaps 50 atm. for the greenhouse model (Reference 33); the relative abundance of CO_2 is quoted as high as 80 percent (Reference 7) and as low as 4 percent (Reference 16) and de Vaucouleurs quotes seven different suggestions for the composition of the visible clouds, some more likely than others (Reference 5). Even the orientation of the axis of rotation and the rotation rate are uncertain. Estimates of the latter range from 10 to 225 days and there is evidence for both direct and retrograde rotation.

In summary, the experimental data about Venus are not only limited but inconsistent as well. It seems that observations from the surface of the earth will yield further results. For example, better estimates of the CO_2 con-

centration are expected from near infrared spectroscopy and much can be learned with more powerful radar instruments. More promising still are the high-altitude baloon-borne spectroscopic experiments planned by Schwarzschild (Princeton University), which will elevate fairly elaborate equipment above much of the earth's atmosphere. But, in general, earthbound methods have been well explored.

Another means of obtaining information is from flyby platforms. Although these will completely overcome the limitations imposed by the Earth's atmosphere and will "magnify" the planet by passing rather close to it, they will do so at the expense of the information rate in the telemetering link. In addition, it is likely that only simple instruments will be flown within the next decade.

DIRECT EXPLORATION OF THE ATMOSPHERE OF VENUS

All the techniques discussed so far, earthbound and balloon-borne instruments and flyby spacecraft, have one basic limitation in common—they have to infer many physical parameters from observations at a distance. Although, in theory it is possible to derive pressure, temperature, and composition from spectroscopic measurements taken outside an atmosphere, without knowledge of the altitude distribution and the nature of the reflecting layers, these spectroscopic data are subject to misinterpretation. Certain crude assumptions can be made and may be justified as first attempts to solve the puzzle, but a final settlement of the physical and chemical states of the atmosphere and its circulation, as well as planetary surface properties, can be obtained much more easily and more accurately by *in situ* measurements performed by a probe which penetrates the atmosphere of Venus. The basic parameters (pressure, temperature, and composition) which describe an atmosphere could be measured directly with very simple and reliable instruments, and would not have to be extracted from difficult spectral observations.

By studying the parameters which should be determined with an entry probe and the engineering problems involved, it becomes apparent that possible *in situ* experiments and instruments may be divided into three classes: (I) elementary, (II) advanced, and (III) furture, or those which are reasonable within 5, 10, and 20 years.

Class I

This group is considered the first generation of experiments capable of making measurements within the atmosphere of Venus. The total weight of all sensors, including their electronics, can be set at about 5 kg. The total payload includes communication components, batteries, and structure, and will weigh roughly 50 kg; an information rate of 1 bit per second will suffice. The primary goal of the experiments is a basic and general understanding of the atmosphere, and pressure, temperature, and density profiles are essential for this. As much as possible should be learned about the composition of the atmosphere, including the altitude distribution and the particle composition of the clouds. A small number of simple experiments should be more than sufficient to show which model atmosphere is correct, and in fact will allow a more definitive model to be established. It can be visualized that this kind of payload not only will be used for the first two or four attempts but also will supplement more complicated missions in the future. For early attempts the heat shield must be overdesigned; later, however, better data on the atmospheric composition will permit reduction of the heat shield weight and a corresponding increase in payload weight. Overall weight and size should stay fairly constant, but succeeding experiments could vary and be made more specific. Also, early versions of the classII experiments may even be flown on later class I vehicles.

Class II

Obviously, the detailed planning of this vehicle and its experiments will be strongly influenced by the results of the class I experiments. The main purposes of this investiga-

tion will be to refine the atmospheric profiles determined by class I probes and to obtain information about the surface. Thus, successful landing on the surface is required. The sensors can have a weight up to 25 kg, and the total weight of the capsule including transmitter and power supply (possibly nuclear) will be about 200 kg. Transmission rates of 16 bits per second and greater can be expected for direct transmissions.

Mass spectrometers will determine trace elements and refine estimates of the atmospheric constituents. The composition of clouds and the size distribution, polarization, and scattering properties of particles will also be determined. In addition, a radar altimeter will provide more accurate altitude determinations; it will allow a fast descent through most of the atmosphere and the deployment of a parachute just before impact. Such a mission will avoid excessive heating in the lower atmosphere during descent if the lower atmosphere should be as hot as 600°K. Survival at the surface for as long as several hours is also feasible with insulating techniques and heat dissipation through phase conversion. The nature of the surface, wind speed, barometric fluctuations, radioactivity, precise measurements of surface gravity, and other data can then be determined.

Class III

This system is the most advanced exploration system visualized, short of manned exploration. It will utilize microscopes and television cameras. Chemical analysis of surface material, determinations of the rotation rate of Venus (by gyros), refinement of ionospheric and atmospheric data, and even subsurface exploration can be carried out. In addition, constant-level balloons drifting in the atmosphere of Venus with long-life batteries could help to determine wind speed and the circulation patterns. The specific design of the class III mission must rest so much on the results of the earlier missions that a further discussion of class III experiments becomes purely academic.

PHYSICAL PARAMETERS

Before considering specific instruments and techniques applicable to an early class I probe, a brief discussion of the physical parameters to be measured is in order. The conclusions which can be drawn from a set of measurements will be developed with the use of the information diagram shown in Figure 1.

It is appropriate to mention here that the purpose of this paper is to describe a set of experiments that would be suitable for early Venus entry capsules, and that it is not addressed to any particular mission or program. The descriptions merely represent preliminary models and, although presented in the indicative mood for ease of expression, should not be interpreted as representing a final selection of experiments for a specific Venus mission.

On the left side of Figure 1 are listed particular physical parameters to be measured, specifically the atmospheric pressure, temperature, velocity of sound, acoustical impedance of the gas, CO_2 and water vapor concentrations, and presence of clouds. For all these, the time of observation must also be accurately known. The individual sensors measure quantities which lead to the determination of secondary parameters as indicated by arrows and the symbols in the rectangular blocks. The following are pertinent equations:

$$\rho_1=\frac{C_D A}{2g^3 m}\left(\frac{\Delta p}{\Delta t}\right)^2, \qquad M_1=\frac{C_D ART}{2g^3 mp}\left(\frac{\Delta p}{\Delta t}\right)^2, \qquad h_1=\int_t^{t0}\left(\frac{2mg}{\rho C_D A}\right)^{1/2} dt,$$

$$\rho_2=\frac{zT_3}{cT}, \qquad M_2=\frac{zRT}{cp}, \qquad h_2=\int_p^{p0}\frac{dp}{\rho g},$$

$$\gamma=\frac{C_p}{C_v}, \qquad \Gamma_{ad}=\frac{-g(h)}{C_p}, \qquad H=\frac{RT}{Mg}.$$

T_3 is the temperature of the tube used for the acoustic experiment. Certain parameters, such as the density, can also be determined independently by different methods. One of the methods for determining the density needs only an accurate pressure vs. time relation. The mass m of the descending body and its aerodynamic drag coefficient C_D must be known. Because of the uncertainties in the amount of ablation material lost during the entry phase, this technique clearly requires dropping the heat shield before the sequence of measurements begins. Another method, based on the acoustical properties of the atmosphere, yields a more accurate density estimate.

Whenever possible, attempts have been made to determine important parameters by more than one method, the second being an independent method if feasible. Altitude, density, and mean molecular weight are determined by totally or at least partially independent means. Fundamental parameters such as temperature and pressure must be recorded by duplicate instruments. The carbon dioxide concentration is determined directly by a specific sensor and also indirectly from the ratio of nitrogen to carbon dioxide to argon. This is significant; if the two CO_2 determinations agree, the hypothesis assumed in the acoustical determination of the N_2:CO_2:A ratio (that N_2, CO_2, and A are the major constituents of the Venus atmosphere) is proven.

The duplicate and independent determination of important parameters provides a number of advantages considered essential for scientific exploration:

1. Close agreement between the results of independent experiments gives confidence in the measurements.
2. Error analysis on two independent experiments can improve the accuracy to which a quantity can be determined.
3. Since the number of relations which exist between the measured parameters is greater than the number of parameters, the system is overdetermined and the loss of a sensor is not as catastrophic as it is in a system which is not overdetermined.

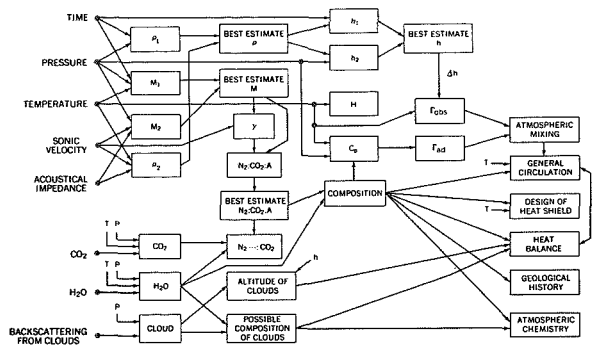

FIGURE 1.—Some of the physical parameters of the planet Venus and its atmosphere that can be derived from a small number of sensors making *in situ* measurements.

The information flow diagram further shows how information from the sensors contributes to an understanding of the general circulation in the atmosphere, the mixing in the layers below and above the clouds, and the heat budget and thermal structure in the atmosphere below the clouds. Atmospheric chemistry, photodissociation theory, and surface chemistry can be used to improve and extend knowledge about Venus. A knowledge of the existence of clouds at a certain pressure and temperature and a knowledge of the phase diagrams of possible chemical substances will rule out certain cloud hypotheses and may help to determine the composition of the clouds.

It should be pointed out that the flow diagram (Fig. 1) is by no means complete. Many more conclusions can be drawn from these simple experiments. The flow diagram shows only what is derived from the sensors in the probe. Although existing knowledge also has to be fed into this pattern, it has been omitted from Figure 1 to avoid needless complication. The main purpose here is to show the great amount of information that can be derived from a rather small number of carefully chosen but basically simple experiments. As will be shown later, the instruments do not contain moving parts which require lubrication; so the calibration (if not a built-in property of the instrument) can be maintained during the long journey in space as well as during the rather severe entry phase. A detailed description of possible experiments follows.

PRESSURE

It is proposed to measure the ambient pressure during the descent phase, after the capsule has reached a descent speed below Mach 1. Individual potentiometer-type pressure gauges with ranges of 0.7, 7, and 70 atm. will be used in an arrangement which provides complete redundancy. The units will have an accuracy of ±2 percent even after a 140°C baking period of 24 hours or more.

Pressure data are used in the determination of the density, altitude, mean molecular weight, and composition of the atmosphere. One method of determining the density and mean molecular weight uses primarily the pressure data and therefore will be discussed under this heading. For other cases when the pressure is used in conjunction with other information the particular technique will be described in a separate section.

A capsule descending in a planetary atmosphere reaches terminal velocity very quickly, and gravitational and aerodynamic forces then balance each other:

$$mg=\tfrac{1}{2}C_D A\rho u^2.$$

Because of the uncertainties in the loss of ablation material during the entry phase, it is clear that the heat shield must be dropped; otherwise, the descending mass m and the drag coefficient C_T will not be known accurately enough. From the hydrostatic relation

$$\frac{dp}{p}=-\frac{dh}{H}$$

and (neglecting any vertical wind component)

$$u=\frac{dh}{dt},$$

the density can be found:

$$\rho=\frac{C_D A}{2g^3 m}\left(\frac{dp}{dt}\right)^2.$$

Since $\overline{M}=\rho RT/p$, the mean molecular weight is

$$\overline{M}=\frac{C_D ART}{2g^3 mp}\left(\frac{dp}{dt}\right)^2$$

From the mean molecular weight an estimate of the CO_2 content can be obtained; $\overline{M}=28$ for N_2 only and $\overline{M}=44$ for CO_2 only.

To indicate the advantages and the shortcomings of this method, an estimate of the expected accuracy will be made. The probable error in the determination of the CO_2 content of the Cytherean atmosphere is calculated under the following assumptions:

1. The atmosphere consists mainly of N_2 and CO_2.
2. The probable error in the temperature measurement is ±2 percent between 180° and 330°K.
3. The factor $C_D A$ has been determined carefully in the Earth's atmosphere, and the value is correct for Venus to within ±2 percent.
4. The pressure is measured to ±2 percent full range but readings are taken at only half range, resulting in a probable error in p of ±4 percent.
5. The mass of the descending assembly (capsule plus parachute, without heat shield) is known to better than ±0.5 percent.
6. The gravitational constant of Venus is known to ±1 percent.
7. The differential dp/dt can be derived from a series of pressure and time readings; and smoothing techniques yield about the same accuracy as the pressure measurement: ±4 percent.

The probable error (root mean square) in the mean molecular mass $\overline{M}$ is then about ±7 percent, which corresponds to a probable error in the CO_2 content of ±15 percent for $\overline{M}=35$. By making somewhat more optimistic assumptions (which may become severe for actual instruments), the probable error can be lowered to perhaps ±10 percent but this will be difficult to achieve.

Clearly, this technique is not the most accurate one: but it is readily available since pressure, temperature, and time will certainly be measured with an early probe. Although a ±10-percent accuracy in CO_2 concentration is not too impressive, the technique is capable of distinguishing between a low, medium, or high CO_2 content in the atmosphere of Venus.

TEMPERATURE

It is proposed to measure the ambient gas temperature during the descent phase, after the capsule has reached Mach 1. The temperature sensors will be platinum resistance elements with temperature ranges from 150° to 750°K and 180° to 330°K. The first range is intended to give the overall temperature profile down to the surface. The second range is intended primarily to provide a higher accuracy in the vicinity of the visible cloud layers, since accurate temperature values will be very important in identifying the cloud composition.

The temperature reading will have a probable error of about ±2 percent, ocrresponding to ±12°K for the 150° to 750°K range and ±3°K for the smaller temperature range. The errors quoted include aerodynamic heating and calibration errors, and errors introduced in amplifying and quantizing the information in the capsule for transmission. The temperature data are used in the determination of many other physical parameters; for example, determination of the molecular weight, scale height, density lapse rate, and composition requires the value of the ambient gas tempreature directly or in correction terms.

MOLECULAR MASS, DENSITY, AND SPECIFIC HEAT RATIO

The experiment for finding the values for the molecular mass, density, and specific heat ratio has been discussed previously for a Mars mission (Reference 39). The instrumentation will be identical for Venus except for minor changes, such as reduction of the microphone spacing to accommodate a wider dynamic range. $\overline{M}$, ρ, and the mean specific heat ratio $\bar{\gamma}=C_p/C_v$ will be determined by acoustical means. The velocity of sound in a gas c is a function of T, M, and $\bar{\gamma}$, and is given by $c^2=\bar{\gamma}RT/\overline{M}$, where R is the gas constant. This well-known relation has been used in the past in various techniques to measure the temperature of the Earth's atmosphere, where $\overline{M}$ and $\bar{\gamma}$ were accurately known. It is proposed to reverse this method and bring a volume of the atmosphere of Venus into a thermostatically controlled tube where the temperature is known accurately and to determine $\overline{M}/\bar{\gamma}$ by measuring the velocity of sound through the medium in the tube. Simultaneously, the acoustical impedance of the gas in the tube will be measured, and division of the acoustical impedance by the speed of sound will yield ρ_1, the density of the gas in the tube. From ρ_1 the density of the ambient gas is

$$\rho=\frac{\rho_1 T_3}{T_1},$$

where T_3 denotes the temperature of the thermostatically controlled tube and T_1 the ambient gas temperature measured by the resistance thermometer. From the ambient gas density and temperature, the mean molecular mass is found by applying the gas law

$$\overline{M}=\frac{\rho RT}{p},$$

where p is measured by the pressure experiment. Since $\overline{M}/\bar{\gamma}$ has been given by the velocity measurement, $\bar{\gamma}$ can now be determined.

In Figure 2, a mixture of the three gases N_2, CO_2, and A is shown. It is generally accepted that these gases are probably the major constituents of the atmosphere of Venus. The $\overline{M}/\bar{\gamma}$ point of an arbitrary mixture of these gases must fall within the triangle formed by the CO_2, N_2, and A points. According to present estimates, the possible amounts of water vapor, oxygen, and other gases are too small to contribute appreciably to $\overline{M}$. Curves of constant sound velocity c^2 are straight lines through the origin. The relative abundances of the respective components in the three-gas mixture are completely determined by the measurements of c and $\overline{M}$.

The CO_2 concentration found by the acoustical method is not as accurate as the one derived by optical means, which will be described below, but is a good independent check. Also, as mentioned above, agreement between the optical and the acoustical CO_2 determination is a conclusive test of the hypothesis that the atmosphere consists mainly of nitrogen, carbon dioxide, and argon.

The proposed technique (Fig. 3) is to measure the velocity of sound through the gas in a spiral

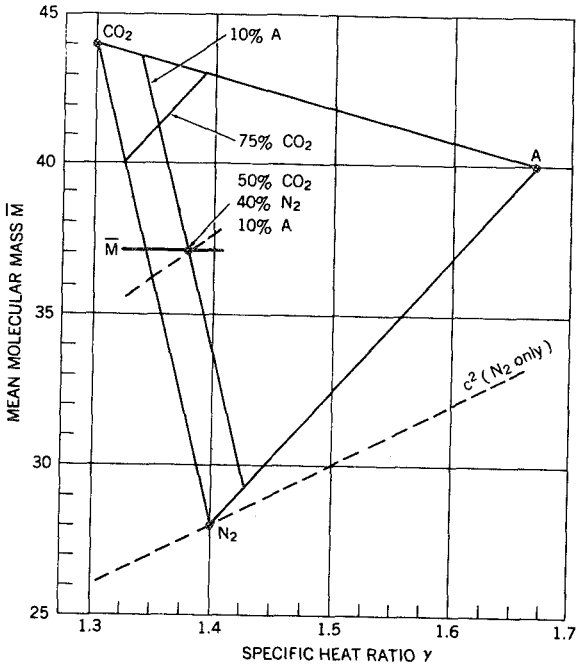

FIGURE 2.—A particular mixture of nitrogen, carbon dioxide, and argon corresponding to a unique position on a diagram of mean molecular mass versus the specific heat ratio. The measurement of two independent parameters such as molecular mass (solid horizontal line) and velocity of sound (dashed diagonal line) determines the abundance of the three gases in the mixture.

tube about 2 m in length and 1 cm in diameter. For ease in illustration Figure 3 shows a linear arrangement of this tube. At one end of the tube a generator drives a small sonic transducer at a constant frequency of about 4 kc. Two identical condenser microphones are placed along the tube with a nominal 4 wavelength separation. Both microphones resonate above 10 kc and form part of the wall of the tube. The test tube is extended beyond the second microphone and is acoustically terminated by damping material and rough wall surfaces to avoid reflections and standing waves in the tube. Since the two microphones and their amplifiers are identical, their phase shifts cancel each other. The phase shift as measured by the phase comparator is determined only by the wavelength of sound in the medium and, since the generator frequency is constant, by the velocity of sound in the gas.

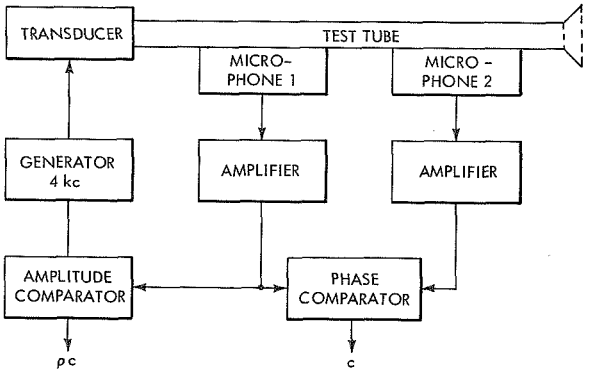

FIGURE 3.—Block diagram of the acoustic experiment. The phase comparator gives the velocity of sound in the gas and the amplitude comparator yields the density and mean molecular mass using, in addition, temperature information derived by other sensors.

In addition to the determination of the speed of sound, the instrument is capable of measuring the density of the gas in the tube. The mechanical and electrical impedance of the sound generator are chosen so that the velocity of the diaphragm is essentially independent of the acoustic radiation impedance of the tube. Under these conditions the sound pressure developed in the air contained in the tube is proportional to the acoustical impedance. Since the microphone used responds to sound pressure, the electrical signal generated by the microphone is proportional to the acoustic impedance of the gaseous medium. This constant of proportionality, which also contains the transducer sensitivity, can easily be determined by calibration in an N_2 atmosphere over a nominal pressure range.

The accuracy requirements imposed on the speed of sound determination can be judged by considering the values shown in Table 1. A controlled gas temperature of 320°K was assumed. The first and last rows represent what are presently considered to be the boundaries for the composition of the Cytherean atmosphere. The instrument is designed to cover the range from about 290 to 365 m/sec. The two microphones, 4 wavelengths apart, register phase differences between 0 and 360 degrees over the 75 m/sec change in velocity. A ±1-percent accuracy in the phase measure-

TABLE 1.—*Velocity of Sound for Various Possible Atmospheres of Venus*

Gas	Velocity of sound (m/sec)
100% N_2	364
95% N_2+5% A	362
95% N_2+5% CO_2	358
80% N_2+10% CO_2+10% A	349
10% N_2+80% CO_2+10% A	292

ment yields the velocity of sound to ±0.75 m/sec, giving an overall accuracy of ±0.25 percent.

Calculation of the velocity of sound in Table 1 was based on the ideal gas law. It is more accurate to use Vander Waals' equation, and it can be shown that this may affect the fourth significant figure in the velocity term. Furthermore, the specific heat of gases shows a frequency dependence in the vicinity of molecular relaxation frequencies. This condition is especially true for CO_2 at low pressures and is one of the reasons why a relatively low operating frequency was chosen for the experiment. Because of these conditions, calibration of the instrument will be performed in an artificial atmosphere for a number of N_2:CO_2:A ratios.

Figure 4 shows a breadboard apparatus used to experimentally check the method of obtaining the mean molecular weight and density of unknown gas mixtures by acoustic means. Condenser microphone cartridges are used at the two smaller holes to measure phase and amplitude. The electronic breadboard converts the acoustic phase angle between the microphones to an analog voltage. The velocity of sound in various media has been measured to an accuracy of ±0.1 percent with this instrument.

CO_2 CONCENTRATION

Measurement of this quantity is of critical importance for problems such as atmospheric

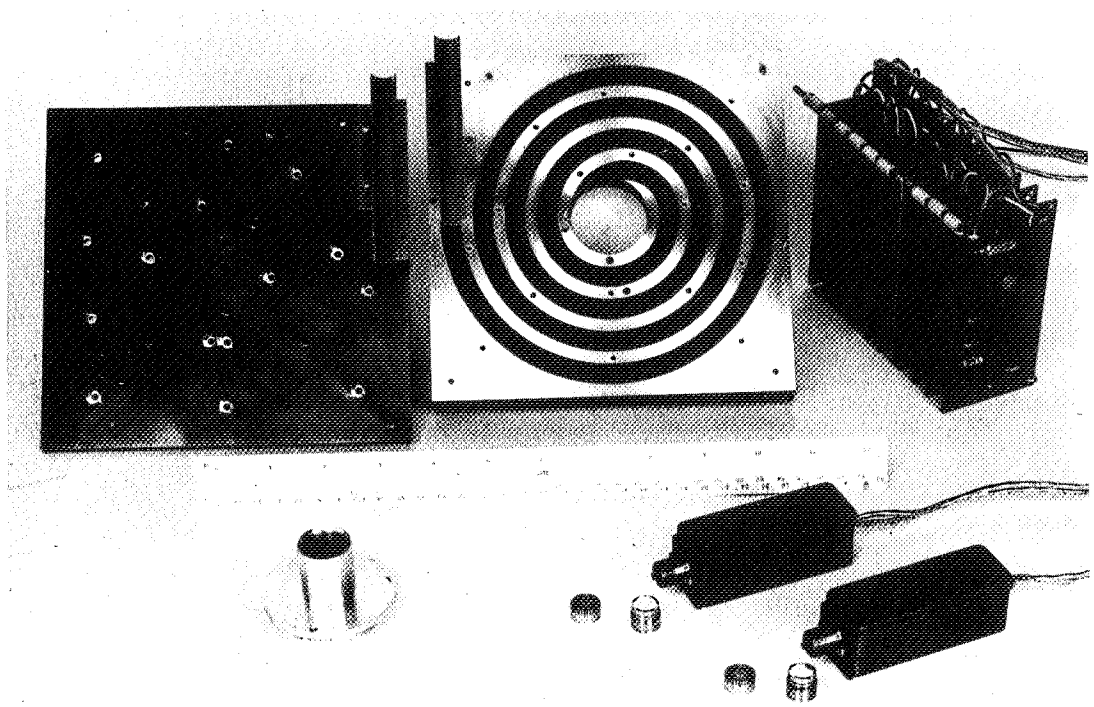

FIGURE 4.—A breadboard model to verify the feasibility of the acoustic experiment. An aluminum block with a spiral sound path houses the driver in the center; condenser microphones are inserted into threaded holes which are visible in the spiral grooves.

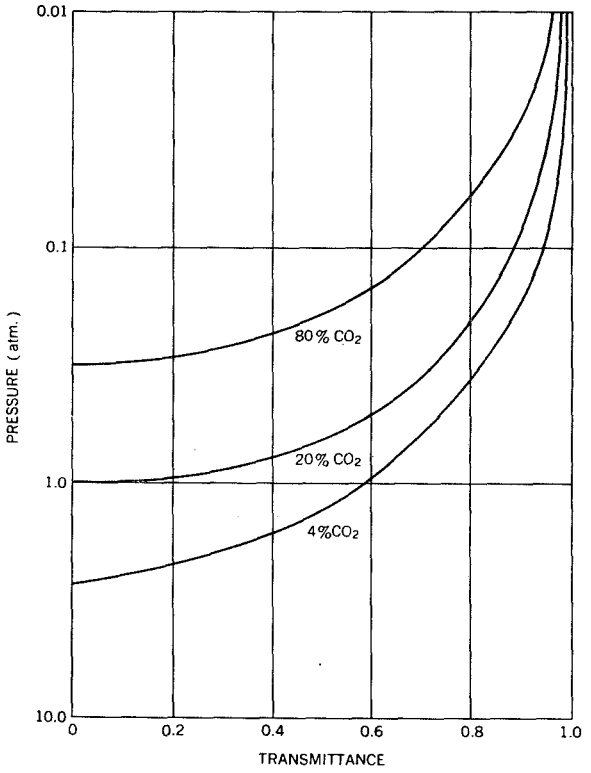

FIGURE 5.—Transmittance versus ambient gas pressure for a 1 cm path length in the 4.25μ CO_1 band. Calculations have been made for a 0.2μ bandwidth and various CO_2 concentrations. The rapid increase in pressure is due not only to the rise in the amount of gas in the fixed path length but also to an increase in the absorption coefficient (pressure broadening effect).

heat balance and the efficient design of planetary entry capsules. A specific experiment, based on the absorption of radiation from an infrared source over a known path length in a strong absorption band, will accurately determine the CO_2 content. Measurements will be taken at constant time intervals during the descent phase. Calculations on the expected absorption have been made using the laboratory data of Howard, Burch, and Williams (Reference 40). For the pressure range of most interest ($0.01<p<10$ atm.) a separation of a few centimeters between the source and detector will be used. In Figures 5 and 6 the results are shown for the 2.7μ band with a 10 cm path length and for the 4.25μ band with a 1 cm path length.

From the instrumental point of view, the 2.7μ band is more desirable. Although some overlapping water vapor bands have to be considered, it can be shown that a high moisture content (which has never been detected in spectroscopic data of Venus from Earth) would cause only negligible absorption and would, therefore, not interfere with the determination of CO_2 in this band. Hence, a 0.2μ band centered at 2.7μ and one at 4.25μ are considered.

It can be seen from Figures 5 and 6 that for a particular pressure, 0.3 to 1 atm. for example, the transmittance depends very much on the relative CO_2 content, becoming more sensitive for smaller CO_2 concentrations. The instrument used is essentially self-calibrating, since the transmittance is almost unity at low pressures (very high in the atmosphere) and becomes practically zero after a descent ot several pressure scale heights. This allows accurate measurement independent of moderate changes of detector sensitivity.

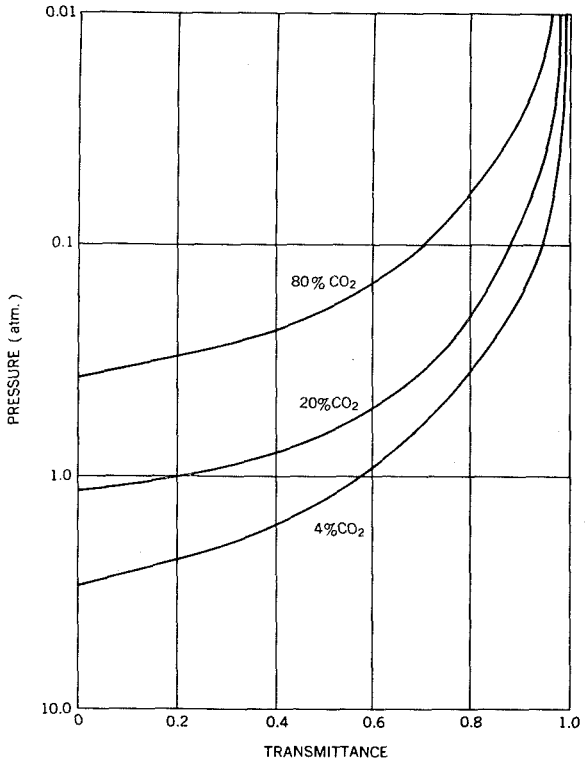

FIGURE 6.—Transmittance versus pressure for a 0.2μ bandwidth at the 2.7μ CO_2 absorption band and with a 10 cm path length.

Solar radiation cannot be considered as a source of radiation for two reasons: First, a landing on the dark side of Venus is most likely for an early (minimum energy) trajectory, and also direct transmission to Earth will probably be necessary. Second, clouds would interfere with direct absorption methods. A light source on board was considered most suitable. A small linear filament can be made to survive the entry shock, but temperatures in the 800°–1000°K range are required after the deceleration phase. The filament will be heated by a pulsed current producing an alternating component in the infrared flux. This scheme completely avoids a mechanical chopper and, therefore, moving parts. The effective modulation of the source which can be achieved is very high even for a relatively small change in the black body temperature of the filament (Fig. 7).

The detector will be a thermopile evaporated on a solid low-heat-capacity material. This detector is sensitive enough and lends itself well to a rugged construction capable of operating over a wide range of ambient temperatures.

H_2O CONTENT

Water vapor as well as CO_2 could act as an important constituent to generate a greenhouse effect. Water vapor has never been conclusively detected by spectroscopic or radar techniques from Earth; it is desirable to confirm whether or not it is in the Venus atmosphere by *in situ* experiments. However, a spectroscopic detection method on a capsule similar to the one described for CO_2, even one using the same infrared source, is not very practical The strongest water vapor absorption band, centered at 6.3μ, is much weaker than the 4.2μ CO_2 band and, although water droplets or ice clouds would require a saturated atmosphere in their vicinity, the water vapor concentration—even at 100 percent relative humidity—is rather small. Therefore, practical absorption path lengths are in the meter, rather than centimeter, range.

For early missions, humidity sensitive elements based on the change of resistance in a tungsten oxide element are more practical

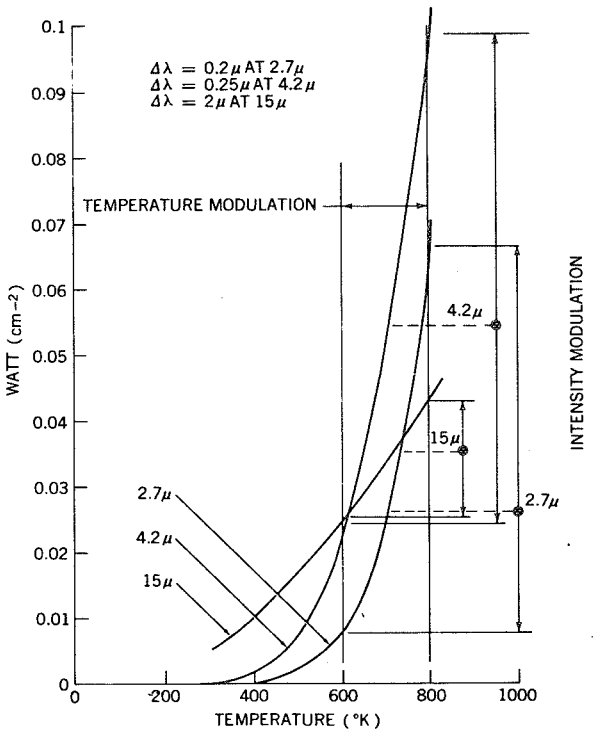

FIGURE 7.—Comparison of available energy and modulation efficiency of the source as a junction of equivalent black body temperature. For a 700° K black body, the 4.2μ region yields the strongest signal and the 2.7μ region the highest intensity modulation. Temperature modulation of ±100° K is assumed.

than any other. Such elements are commercially available. The sensor is cleaned by heating it to cherry red, and sterilization by heat is therefore easy. Very low values of relative humidity are more difficult to measure since the resistance elements now available reach impedances on the order of $10^9\Omega$, compared with the 0.5 MΩ needed for 100 percent relative humidity.

CLOUD DETECTION BY SCATTERING

Scattering experiments can determine the particle size, density, and even the refractive index and therefore the composition of particles in a cloud. But, even without phase angle and polarization studies, very useful information can be gained by simple techniques since the ability to detect the presence or absence of clouds, as

the capsule descends in the atmosphere, can yield important conclusions. For instance, a low relative humidity, detected by the tungsten oxide detector described above, and the presence of clouds clearly would rule out water or ice clouds. The pressure, temperature, and concentration measured by the capsule can be used to plot a curve on the phase diagram of a possible cloud substance (Fig. 8). Substances which are the candidates for cloud particles include formaldehyde, dust, salt, ammonium nitrate, polymers of carbon suboxide, certain organic compounds (malonic or oxalic acid), nitrogen peroxides, and water. Some of these have a low probability on the basis of present knowledge and more will be eliminated by the study of phase diagrams and pressure, temperature, and cloud occurrence data which will be obtained from Venus probes.

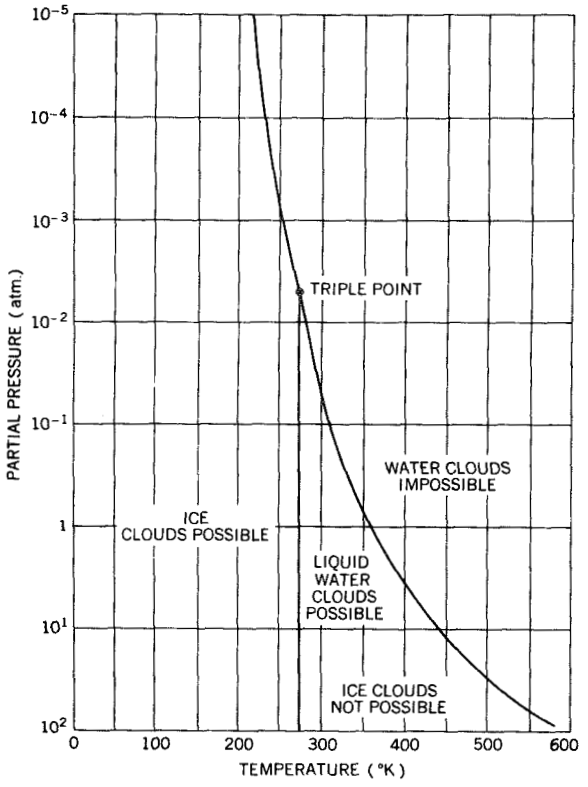

FIGURE 8.—Phase diagram of water. By using this and partial pressure, and temperature data derived from the sensors, it may be possible to rule out the existence of liquid water or ice clouds. Similar diagrams for other constituents are also available.

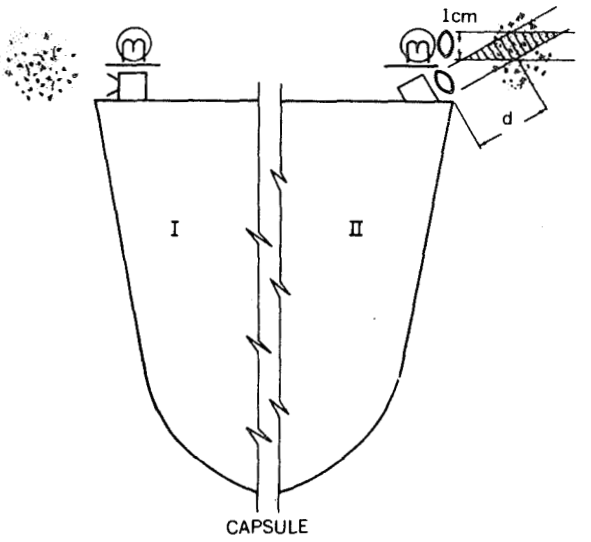

FIGURE 9.—Schematic view of two cloud detectors. Each consists of a modulated light source and a receiver. Version I operates within a large solid angle, and version II uses optical elements to separate the sensitive detection area from the immediate vicinity of the capsule.

The simple experiment proposed here will detect clouds and give an estimate on their particle density. Again, since the scattering experiment must work on the planet's dark side, must have its own light source. Two arrangements have been considered, both of which depend on the backscattering of light from cloud particles. The first one consists simply of a modulated light source and a detector without lenses, shielded from each other. The second method employs lenses to separate the cloud-detection area from the capsule (Fig. 9). The first has the advantages of simplicity and higher sensitivity whereas the second has the advantage of separating the detection area from the vicinity of the capsule. The detector can be simply a diffused-junction silicon diode (solar cell) operated in the photovoltaic mode. The light source can be designed for a power consumption below 3 watts and still yield a sufficient signal-to-noise ratio of 100 to 1.

The spectral response of silicon cells peaks at about 8500A. These cells can be made very rugged and should easily withstand sterilization temperatures. The source may be a simple tungsten lamp or a pulsed arc of the

TABLE 2.—*Proposed Experiments*

Parameter	Value or method
Pressure (aneroid potentiometer).	0–0.7, 0–7, and 0–70 atm. or logarithmic response.
Temperature (platinum resistance thermometer).	150°–750°K; 180°–330°K.
Acoustic experiment	100 mb–10 atm., 290–365 m/sec.
CO_2 experiment	Tungsten source; 4.2μ.
H_2O experiment	Platinum oxide detector.
Scattering experiment	Source on board, visible light.
Total weight of experiments.	12 lb.
Total power consumption	15 watts.

xenon type—the spectral characteristic of the silicon type is especially favorable for a tungsten source.

CONCLUSIONS

A summary of the experiments and their weight and power consumption, excluding structure and information-handling electronics (analog-to-digital converter, storage memory, transmitter, etc.), is given in Table 2.

ACKNOWLEDGMENTS

The author wishes to acknowledge Mr. J. Ainsworth for his contributions to the pressure and temperature experiment; Mr. F. Bartko and Dr. D. Harris for calculations regarding the absorption and scattering experiments; and Mr. M. Strange for designing the electronic circuits of the acoustic experiment.

REFERENCES

1. MOORE, P., "The Planet Venus," New York: Macmillan Co., 1957.
2. UREY, H. C., "The Atmospheres of the Planets," in: *Handbuch der Physik*, ed. by S. Flugge, 52: 363–418, Berlin: Springer-Verlag, 1959.
3. KUIPER, G. P., ed., "Atmospheres of the Earth and Planets," Chicago: University of Chicago Press, 1952.
4. KELLOGG, W. W., and SAGAN, C., "The Atmospheres of Mars and Venus," Washington, D.C. Nat. Acad. Sci.-Nat. Res. Coun. Publ. 944, 1962.
5. DE VAUCOULEURS, G., "Reconnaissance of the Near Planets—A Survey of Planetary Problems in the Space Age," Air Force Office of Scientific Research, Washington, D.C., AFOSR-DRA-61-1, November 1961.
6. KUIPER, G. P., and MIDDLEHURST, B. M., "Planets and Satellites," Chicago: University of Chicago Press, 1961.
7. ÖPIK, E. J., "Atmosphere and Surface Properties of Mars and Venus," Ch. VI in: *Progress in the Astronautical Sciences: Vol. 1*, ed. by J. F. Singer, New York: Interscience Publ. Co., 1962.
8. LYOT, B., "Recherches sur la polarisation de la lumiere des planetes et de quelques substances terrestres," *Ann. Obs. Meudon* VIII, fasc. I, 1–61.
9. DOLLFUS, A., "Polarization Studies of Planets," in: *Planets and Satellites*, ed., by G. P. Kuiper and B. M. Middlehurst, Chicago: University of Chicago Press, 1961, pp. 343–349.
10. GEHRELS, T., and TESKA, T. M., "The Wavelength Dependence of Polarization," *Appl. Optics* 2(1): 67–77, January 1963.
11. ADAMS, W. S., and DUNHAM, T., JR., "Absorption Bands in the Infra-Red Spectrum of Venus," *Publ. Astron. Soc. Pac.* 44(260): 243–245, August 1932.
12. ADEL, A., "Temperature of Venus," *Astrophys. J.* 86: 337–339, October 1937.
13. KUIPER, G. P., "Infrared Spectra of Planets," *Astrophys. J.* 106(2): 251–254, September 1947.
14. DUNHAM, T., JR., "Spectroscopic Observations of the Planets at Mount Wilson," in: *The Atmospheres of the Earth and Planets*, ed. by G. P. Kuiper, Chicago: University of Chicago Press, 1952, pp. 288–305.
15. CHAMBERLAIN, J. W., and KUIPER, G. P., "Rotational Temperature and Phase Variation of the Carbon Dioxide Bands of Venus," *Astrophys. J.* 124(2): 399–405.
16. SPINRAD, H., "Spectroscopic Temperature and Pressure Measurements in the Venus Atmosphere," *Pub. Astron. Soc. Pac.* 74(438): 187–201, June 1962.
17. KUIPER, G. P., "Infrared Spectra of Stars and Planets, I: Photometry of the Infrared Spectrum of Venus, 1–2.5 microns," No. 15 in *Communications of the Lunar and Planetary Laboratory I* No. 14–16, Univ. of Arizona Press, Oct. 26, 1962.
18. COBLENTZ, W. W., and LAMPLAND, C. O., "Radiometric Measurements on Mars," *Publ. Astron. Soc. Pac.* 36(213): 272–274, October 1924.
19. COBLENTZ, W. W., and LAMPLAND, C. O., "Some Measurements of the Spectral Components of Planetary Radiation and Planetary Temperatures," *J. Frank. Inst.* 199: 785–841, June 1925, and 200: 103–126, July 1925.
20. COBLENTZ, W. W., and LAMPLAND, C. O., "Further Radiometric Measurements of Mars," Nat. Bur. Stand. Sci. Paper 553, pp. 237–276, 1927.

21. PETTIT, E., and NICHOLSON, S. B., "Measurements of the Radiation from the Planet Mercury," *Publ. Astron. Soc. Pac.* 35(206): 194–198, August 1923.
22. PETTIT, E., and NICHOLSON, S. B., "Lunar Radiation and Temperatures," *Astrophys. J.* 71(2): 102–135, March 1930.
23. PETTIT, E., and NICHOLSON, S. B., "Radiation from the Planet Mercury," *Astrophys. J.* 83(2): 84–102, March 1936.
24. SINTON, W. M., and STRONG, J., "Radiometric Observations of Venus," *Astrophys. J.* 131(2): 470–490, March 1960.
25. MENZEL, D. H., and de VAUCOULEURS, G., "Results from the Occulation of Regulus by Venus, July 7, 1959," *Astronom. J.* 65(6): 351, August 1960.
26. MAYER, C. H., MCCULLOUGH, T. P., and SLOANAKER, R. M., "Observations of Venus at 3.15-cm Wave Length," *Astrophys. J.* 127(1): 1–10, January 1958.
27. MAYER, C. H., MCCULLOUGH, T. P., and SLOANAKER, R. M., "Measurements of Planetary Radiation at Centimeter Wavelengths," *Proc. IRE* 46(1): 260–266, January 1958.
28. MAYER, C. H., MCCULLOUGH, T. P., and SLOANAKER, R. M., "Observations of Mars and Jupiter at a Wave Length of 3.15 cm," *Astrophys. J.* 127(1): 11–16, January 1958.
29. ALSOP, L. E., GIORDMAINE, J. A., ET AL., "Observations Using a Maser Radiometer at 3-cm Wavelength," *Astronom. J.* 63(8): 301, September 1958.
30. GIBSON, J. E., and MCEWAN, R. J., "Observations of Venus at 8.6 mm Wavelength," in: *Paris Symposium on Radio Astronomy, 1958,* ed. by R. N. Bracewell, Stanford: Stanford University Press.
31. KUZMIN, A. D., and SALOMONOVICH, A. E., "Radio Emissions from Venus in the 8 mm Bandwidth," *Astron. Zhur.* 37(2): 297–300, March–April 1960.
32. SAGAN, C., "The Radiation Balance of Venus," Calif. Inst. Tech. JPL Tech. Rept. No. 32–34, Sept. 15, 1960.
33. SAGAN, C., "Structure of the Lower Atmosphere of Venus," *Icarus* 1(2): 151–169, 1962.
34. ÖPIK, E. J., "The Aeolosphere and Atmosphere of Venus," *J. Geophys. Res.* 66(9): 2807–2819, September 1961.
35. PRIESTER, W., ROEMER, M., and SCHMIDT-KALER, T., "Apparent Relation Between Solar Activity and the 440 Mc/s Radar Distance of Venus," *Nature* 196(4853): 464–465, November 3, 1962.
36. BARRETT, A. H., "Microwave Absorption and Emission in the Atmosphere of Venus," *Astrophys. J.* 133(1): 281–293, January 1961.
37. KAPLAN, L. D., "A New Interpretation of the Structure and CO_2 Content of the Venus Atmosphere," *Planet. Space Sci.* 8(1): 23–29, October 1961.
38. MINTZ, Y., "Temperature and Circulation of the Venus Atmosphere," *Planet. Space Sci.* 5(2): 141–152, June 1961.
39. HANEL, R. A., RICHTMYER, L. E., ET AL., "Experiments from a Small Probe Which Enters The Atmosphere of Mars," NASA Technical Note D–1899, to be published.
40. HOWARD, J. N., BURCH, D. L., and WILLIAMS, D., "Near-Infrared Transmission Through Synthetic Atmospheres," Geophys. Res. Paper No. 40, AFCRC–TR–55–213, Bedford, Mass., November 1955.

THE ORBITING GEOPHYSICAL OBSERVATORIES

GEORGE H. LUDWIG
Goddard Space Flight Center

The Orbiting Geophysical Observatories and the supporting ground checkout equipment, data acquisition and tracking stations and data processing equipment are designed to conduct large numbers of diverse experiments in space. Measurements will be made within the earth's atmosphere, ionosphere, exosphere, magnetosphere, and in cislunar space to obtain a better understanding of earth-sun relationships and of the earth as a planet. Configured to meet scientific requirements, the observatories include six booms to support detectors away from disturbances generated in the main body. Five degrees of freedom allow the orientation of experiments relative to three references—the earth, the sun, and the orbital plane. Power, thermal control, and data handling subsystems provide for the proper operation of the experiments and telemetry of the data. Ground stations receive these data, which are then processed into a form suitable for use by the experimenters. The systems have been designed to make available a standard spacecraft and support equipment which can be used repeatedly to carry large numbers of easily integrated experiments in a wide variety of orbits.

INTRODUCTION

During the 5 years since the launching of the first artificial earth satellite, the satellite systems have passed through a rapid evolutionary process. For investigations in the space sciences, two principal satellite types are now in use. The first is the relatively small satellite which includes the Explorer series, the Vanguard series, the State University of Iowa Injun series, the Naval Research Laboratory Lofti and Solar Radiation series, and the international program Ariel and Alouette series. These spacecraft, in general, contain sets of directly related experiments, usually provided by a small number of laboratories or, in a few cases, a single laboratory. The second type is the comparatively large orbiting observatory. Three observatory series are now in use or planned, the Orbiting Solar Observatory (OSO), the Orbiting Geophysical Observatory (OGO) which is described in this paper, and the Orbiting Astronomical Observatory (OAO). These standard spacecraft are designed to carry large numbers of easlly installed experiments of a somewhat more diverse nature.

The Small, Explorer Type Satellites

The first of the Explorer type satellites were necessarily quite lightweight and simple because of the limitations of the launch vehicles and the desire for reliability in a new technology. As larger launch vehicles such as the Delta become available, the weight and size of these spacecraft increased. And as we have become more experienced, the complexity of the spacecraft has tended to increase to provide a greater amount of information from each launching. We may expect to see a continuation of the use of the Explorer type of satellite, since it will continue to have several advantages over the larger and more complex observatories. These advantages may be summarized:

1. Some experiments may require satellite orbits into which the larger observatories cannot be placed due to launch vehicle limitations. Or a sufficiently large number of experiments may not require a particular orbit to warrant the use of an observatory.
2. The experiments may require a different spatial orientation than is contemplated

for any of the larger observatories. For example, a spin stabilized satellite may be more suitable for certain experiments which need to rapidly scan on the celestial sphere. Magnetic field orientation may be preferred for certain groups of charged-particle experiments.

3. Some classes of very sensitive experiments may require small satellites to avoid contamination or interference from the satellite structure, power and electronic subsystems, or other experiments.
4. It is possible to launch a small satellite with a very short lead time for the high priority investigation of new phenomena. At the present time this is feasible only under exceptional circumstances. An example is the launching of Explorer XV for the investigation of the high flux of geomagnetically trapped particles injected by the Starfish high altitude nuclear explosion in the summer of 1962.
5. During the early phases of the observatory program the reliability of the small satellites may be higher than that of the observatories. This advantage may disappear later because the larger weight capability of the observatories permits the inclusion of a higher degree of redundancy, and because the repeated use of the standard observatory designs should lead to a continuous increase in reliability. This point is speculative at this time, since only one observatory has been launched (OSO–1). Interestingly, its operating lifetime has been longer than the average lifetimes of the recent Explorer type satellites.
6. A number of experimenters feel that the small satellite with its simple telemetry system and spin or magnetic field stabilization offers them a more nearly ideal tool for research and university student training, in that they are able to retain more direct control over their own investigations. The organizational structure is simpler for the smaller satellite programs, and less effort is required for liaison with other groups and for the planning of the operational aspects such as the prelaunch testing and data processing. This is correct at the present time. Whether it will continue to be true when the observatory programs have progressed further remains to be seen.

The Observatories

The small satellites, as a rule, have tended to be highly integrated mechanically, thermally, and electrically in order to take full advantage of the launch vehicle capability; i.e., they were built as tightly knit, homogeneous assemblies. To illustrate, it was necessary to almost completely disassemble the Explorer I and Pioneer IV spacecraft in order to change the batteries. This situation has steadily improved with the availability of the Delta launch vehicle, and the internal satellite systems have tended to become separated into more easily changeable subassemblies. But a moderately high degree of electronic system integration is still employed. This means that the spacecraft will continue to be essentially one-mission systems in the sense that extensive redesign of the subsystems will be necessary to accommodate each new set of experiments.

As the larger launching vehicles such as the Thor-Agena and Atlas-Agena have become available, it has become possible to launch heavier experiments and larger numbers of small experiments. In addition, it has become possible to increase the capabilities of the data handling, power, and thermal subsystems to allow greater flexibility. And solar, earth, and inertial reference attitude control systems have become feasible. It has become possible to establish well defined, standard, electrical and mechanical interfaces between the experiments and the various spacecraft subsystems. Thus, the concept of a family of standard observatories has evolved. These spacecraft are standard in the sense that they present a well defined set of interfaces to the experiments and are highly flexible in order to accommodate many types of experiments. It should not be

necessary to design and develop a new spacecraft for each mission, instead a spacecraft design can be used repeatedly with only minor modifications to carry different combinations of experiments on successive missions.

The advantages of the standard observatory concept, in addition to those discussed above, include the following:

1. Large numbers of directly and indirectly related experiments can be performed concurrently to study the correlations between several phenomena at given positions in space. For example, with the OGO it will be possible to study simultaneously the relationships between solar events, the solar plasma, the earth's trapped radiation belts, the earth's magnetic field, and the atmospheric structure.
2. Alternately, a few heavy or bulky instruments can be launched to perform more extensive, complex, or detailed observations. The OGO will be able to carry a single large, earth oriented experiment weighing more than 68 kg.
3. The electrical, mechanical, and thermal interfaces between the experiments and spacecraft subsystems are well defined and will remain essentially fixed from mission to mission. It should be possible to avoid difficulties encountered in previous projects when the experiments and spacecraft were developed concurrently without benefit of previously existing definitions of the interfaces between them. The subsystems have been designed with enough flexibility so that they should not seriously limit the evolution of experiment technology for some time.
4. The system reliability should be ultimately improved by the repeated use and stepwise improvement of a basic design, and by the fact that the larger weight allotment will permit a higher degree of redundancy.
5. Continued use of a standard spacecraft design should lead to higher operating efficiency through the continuous evolution and use of a ground data acquisition and tracking station network, data processing equipment, and operating procedures. The use of the larger spacecraft will reduce the total operational load since a given number of experiments will be carried on a smaller number of spacecraft.
6. In spite of the rather high initial development cost of the observatories, the ultimate cost of orbiting a given weight of experiments should be lower than if they were carried on a greater number of small satellites, since the development of a new spacecraft for each new mission will be avoided.

THE OGO PROJECT

The Orbiting Geophysical Observatory project includes the development and use of the experiments and spacecraft which make up the observatory, the ground checkout equipment, the complex of ground receiving and tracking stations, and the data processing equipment. It is a part of the NASA space sciences long range program. The NASA Headquarters and the Goddard Space Flight Center, located at Greenbelt, Md., share the responsibility for the original formulation of the concept and the statement of the general objectives. The management of the project is a responsibility of the Goddard Space Flight Center. The project manager is responsible to the director of the center in the carrying out of this responsibility. The project scientist works very closely with the manager to ensure that the scientific objectives are met. He serves as the main scientific contact with the experimenters and monitors the development of the spacecraft and data handling systems so that the requirements of the experimenters can best be met. The ground systems manager also works directly with the project manager to ensure that the tracking, data acquisition, and data processing needs will be met.

Once the experiments for each launching are selected by NASA Headquarters, contracts are written by Goddard for the financial support of the experimenter's efforts. The experi-

menters are furnished with necessary technical information to enable them to design their instruments, to plan for their integration and testing, and for data processing after launch. Beyond this, the experimenters retain the responsibility for delivering to Goddard finished experiments which will meet their initial objectives and which will survive the environmental tests.

The experimenters also retain primary responsibility for the processing and analysis of the data obtained from their experiments. They will receive digital computer tapes containing the raw data in cleaned and sorted but otherwise unprocessed form from their own experiments and the necessary housekeeping and timing information. A different set of tapes will contain the orbit and observatory orientation information. The experimenters arrange for their own computer programing, processing, tabulation, analysis, etc. in keeping with the belief that the typical investigator prefers to retain direct control over this phase of the operation.

Orbits and experiments have been chosen for the first two OGO missions. The first observatory, designated OGO–A and sometimes referred to as the Eccentric Orbiting Geophysical Observatory (EGO) will be launched by an Atlas-Agena B in mid 1964 from the Atlantic Missile Range into a highly eccentric orbit having initial perigee and apogee heights of 280 and 110,000 km above the earth, respectively, and an initial orbital inclination of approximately 31 degrees. The second will be launched into a near-polar orbit in late 1964, and is known as the OGO–B or Polar Orbiting Geophysical Observatory (POGO). The launching will occur with a Thor-Agena from the Pacific Missile Range. The POGO orbit will have perigee and apogee heights of 250 and 920 km above the earth.

DESCRIPTION OF THE SPACECRAFT

The Orbiting Geophysical Observatory consists of two parts, the experiments and the spacecraft. The spacecraft is being designed and built by the Space Technology Laboratories, Inc. of Redondo Beach, Calif. It consists of a basic structure to support and enclose the experiments and other assemblies, an attitude stabilization subsystem, and power data handling, communications, and thermal control subsystems for servicing the experiments. The weight of the spacecraft is approximately 394 kg, and it is designed to accommodate about 76 kg of experiments, making a total observatory weight of about 470 kg.

Configuration

The external configuration of the deployed observatory is shown in the drawing of Figure 1. The central box structure measures 1.70 m long by 0.78 m high by 0.81 m wide. Its size was chosen to provide a large internal volume to accommodate an assortment of large or irregularly shaped experiments in addition to the spacecraft subsystem components. It was limited, however, by the requirement that it fit within the standard nose fairing for the Agena rocket. The action of the attitude control system causes one of the 0.81 m by 1.70 m faces of the main body to face the earth at all times. Experiments which require earth orientation are mounted on this face, and those requiring orientation away from the earth are located on the opposite side.

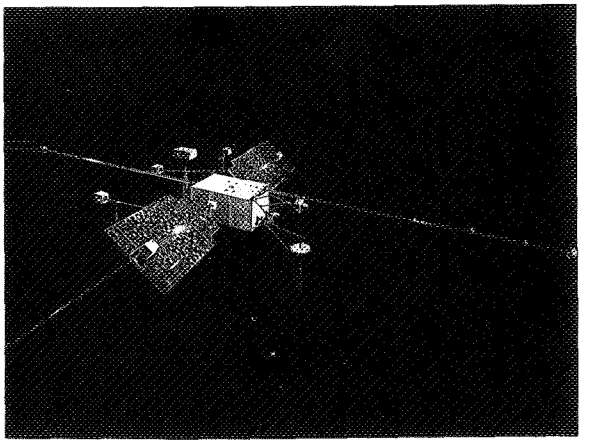

FIGURE 1.—The Orbiting Geophysical Observatory. The distance from tip to tip of the long booms is about 17.7 m. The distance between ends of the solar panels is about 6.0 m. The appendages are configured for the first flight.

The solar panels which provide the electrical power for the observatory are mounted on a shaft which passes through the main body. The attitude control system orients the silicon solar cells mounted on these panels toward the sun by controlling the rotation of the main body about the earth-observatory axis and by controlling the rotation of the solar panels about their shaft axis. Enclosures located on each solar panel contain experiments requiring a fixed orientation with respect to the sun. The orientation of the solar panels toward the sun results in the orientation, at right angles to the observatory-sun line, of the two main body faces through which the shaft passes. Thus, these two faces are never illuminated by the sun, and are used to radiate excess heat from the observatory.

A pair of experiment containers is located on another shaft which rotates about the observatory-earth axis. This rotation is controlled by the attitude control system so that the detector axes fall in the orbital plane. Thus, the angle between the detector axes and the observatory velocity vector will be simply related to the true anomaly. This angle will always be zero at apogee and perigee, and throughout the entire orbit if the orbit is circular. Experiments designed to investigate the characteristics of particles whose velocities are not large compared with the velocity of the spacecraft will be located in these containers.

Booms extending from the ends of the main body support experiments at some distance from the central assemblies. They are intended for detectors whose measurements might be affected by disturbances generated in the main body and solar panels. For example, the magnetometer sensors are located at the ends of long booms so the magnetic fields at the sensors produced by ferromagnetic materials and electric currents in the spacecraft are smaller than the interplanetary magnetic fields which are being investigated. Isolation is also necessary for investigations of portions of the electromagnetic wave spectrum, experiments sensitive to the outgassing from the main body, and experiments which cannot tolerate the proximity of appreciable mass. Two long booms approximately 6.5 m and 6.3 m in length and four short booms each approximately 1.3 m in length, are included, as indicated in Figure 1. The distance from the tip of the near boom to the tip of the loop on the far boom in Figure 1 is approximately 17.7 m.

Some of the antennas for the communications system are also supported on these booms. And the high gain antenna for the wideband digital data transmitter is supported by an additional boom so that it will not obstruct the view of experiments mounted in the main body. Two more booms provide large moments for the cold gas jets which apply torques to the observatory main body to help control its orientation.

The observatory is designed to fold into a launch configuration which will fit within the 1.65 m outside diameter nose fairing. The structural design model of the folded OGO is shown in Figure 2. The various appendages can be seen folded and supported against the main body in their launch positions. After injection into orbit, pneumatically actuated latches release all the appendages, and they are driven to the open positions by spiral springs located in the hinge joints. Levers and detents rigidly lock the joints in the open position.

Structure

The basic structure of the main body can be seen in Figure 3. The panels which form the sides are made of lightweight corrugated aluminum sandwich sheets to give the required stiffness, thermal conductivity, and ease of attaching assemblies. Four longerons in the corners of the spacecraft together with the four vertical side panels absorb the acceleration loads during launch and transmit them to the four supports at the bottom of the main body. The loads are carried from these four legs to the upper ring of the Agena by the four inverted Vees of the interstage structure as shown in Figure 2. The observatory is held to the Agena during launch by a tension band with four shoes which clamp the four supporting feet to the interstage structure. Upon receipt of the separation signal from the Agena following injection, explosive actuators release the tension band and coil springs located at each of the four

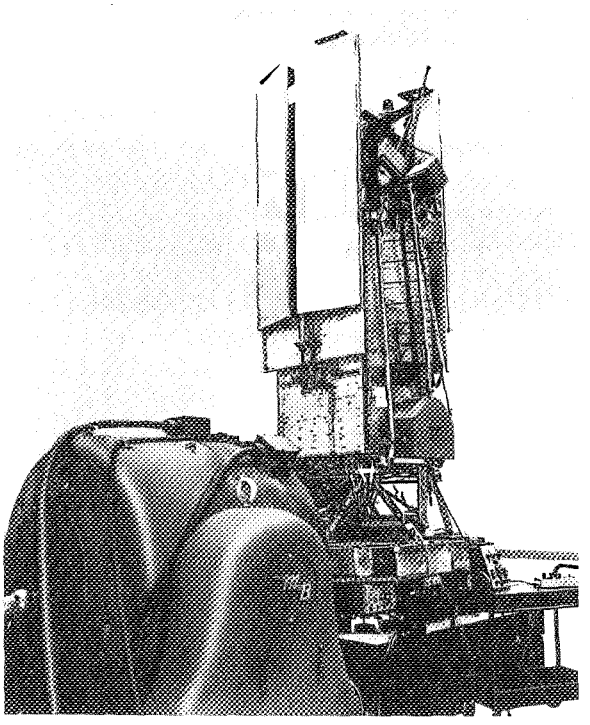

FIGURE 2.—The Observatory in its folded configuration. The structural design model with generalized appendage experiment containers is mounted on the vibration table for one of the two transverse vibration tests. Only a few of the thermal control louvers are mounted, and none of the solar cells are in place. The main body is mounted on the adapter by which it will be attached to the Agena rocket. (Photo courtesy of Space Technology Laboratories.)

feet impart a separation velocity of approximately 1.5 m sec.$^{-1}$. The spring tensions are carefully matched so that the angular velocity imparted to the observatory upon separating is less than 1 degree per second.

The two sides of the main body through which the solar array shaft passes are designed to serve as efficient radiators of heat. The panels are covered with a grid of louvers whose positions are thermostatically controlled to vary the exposure of the radiating surfaces.

The other two side panels are hinged in sections to provide easy access to the interior. These doors are securely closed in flight by fasteners around their peripheries. Additional rigidity is given to the main body structure by removable internal braces, the solar array shaft assembly, and an intercostal structure attached to the thermal radiating panels.

Spacecraft system internal assemblies are attached to the two thermal radiating panels, the intercostal structure, and the lower door sections. A large volume inside the main body is reserved for experiments. The shape and size of this region provides great flexibility for accommodating a large variety of experiment configurations. One possible arrangement is shown in Figure 3. For convenience in planning the experiment locations, the upper two-thirds of each door is divided into 15 basic modular areas, each measuring 20.32 cm square. The lower nine squares on each door are clear to depths of 20.32 cm behind the door. The upper six squares are clear all the way through the body. Each experimenter having an assembly in the main body is assigned an integral number of these squares. He may use a portion of each modular area, the entire area, or he can utilize several squares for a single assembly. Since the upper portion of the main body is completely unobstructed, large experiments can be located in that region.

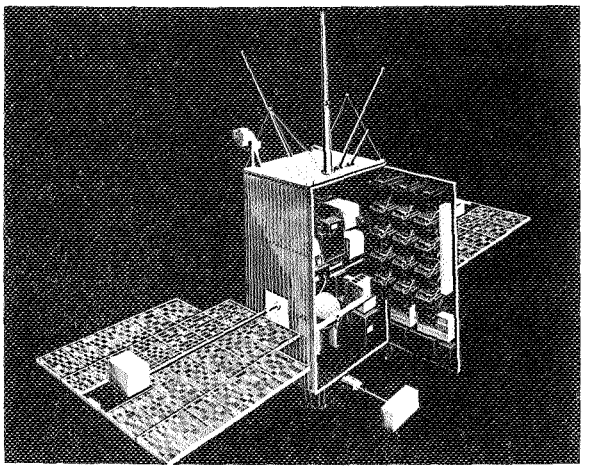

FIGURE 3.—The main body with one of its two doors open. Experiments are mounted on the upper two-thirds of this door and the corresponding door on the opposite side. Subassemblies for the servicing subsystems are mounted inside the main body. Many of the appendages are not shown and the experiment containers are different from those which will actually be used. The length of the main body is 1.7 m.

A single experiment as large as 61.0 by 40.6 by 76.2 cm can be accommodated.

The OGO structure is strong enough to support 227 kg in addition to the 470 kg basic observatory. This growth potential will be used when larger launch vehicles become available to accommodate a larger experiment load. Included in the growth potential is the capability of carrying and separating in orbit a 135-kg auxiliary satellite to perform experiments requiring an especially undisturbed environment or to perform mother-daughter experiments where the large separation between this small satellite and the main observatory will be useful.

Each solar array panel consists of a lightweight aluminum framework to which the solar cell modules are attached. Figure 4 shows one of the panels with its solar cell module plates

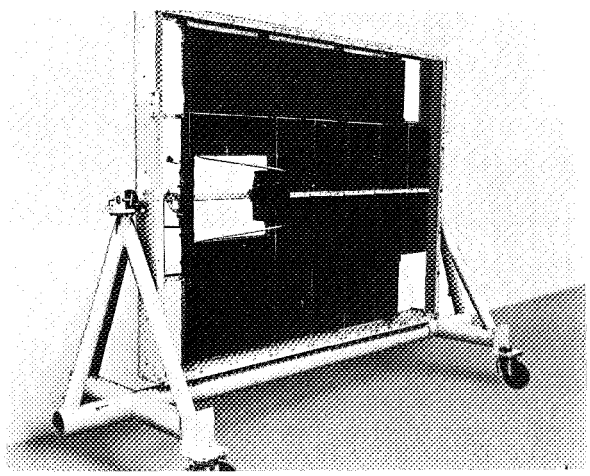

FIGURE 4.—One of the two solar array panels in its handling fixture. Each of the 144 moduleplates contains 112 gridded P–N junction silicon cells. (Photo courtesy of Space Technology Laboratories.)

attached. The 144 module plates can be removed independently to simplify replacement of cells which may fail during the observatory testing program. The panel is fastened to the solar array shaft by hinge.

The orbital plane experiment containers are supported by a trussed structure at one end of the main body. These containers, their supporting shafts, and their cylindrical drive assembly can be seen on the lower end of the observatory in Figure 2.

The booms are made of lightweight aluminum tubing. They are hinged at the main body end so they can be folded for launch. The two long booms each consist of three short sections which fold against the main body in the launch configuration. Electrical cables to the experiments in the containers are routed through the booms. The fittings for attaching the containers to the ends of the booms and those for attaching the booms to the main body are made of thermally and electrically insulating fiberglass. The thermal insulation is necessary to prevent heat loss through the booms from the temperature controlled boom containers and the main body. The electrical insulation permits control of the boom potentials by experiments designed to study thermal energy charged particles.

Standard mounting fittings permit the easy attachment of the solar, orbit plane, and boom experiment containers. These fittings define the mechanical interfaces between the experiments and the spacecraft. The appendage container designs are tailored to the needs of the experiments in order to utilize the somewhat limited weight capabilities at these positions most efficiently. The structure is designed to support 7.17 kg at each solar experiment container attachment point, 7.35 kg at each orbit plane experiment container attachment point, and 3.27 kg at each boom experiment attachment point.

For the attitude control system to operate properly, it is necessary that the principal axes of the complete observatory be properly positioned. This is done by careful distribution of the experiment mass in the observatory and by adjustment of the long boom positions. Swivel joints and adjusting screws at the bases of these booms permit adjustment over a range of approximately 10 degrees in two planes.

The release of gases from the observatory is controlled to minimize interference to experiments designed to study the characteristics of the atmosphere. The attitude control system gas jets are directed away from all experiment enclosures. Small volumes such as the tubular booms are freely vented to prevent the trans-

port of gases from one position in the orbit to another. Large volumes such as the main body and appendage experiment containers are vented away from all experiment mounting positions. Especial care is taken to avoid venting gas toward the orbital plane experiment containers, since the atmospheric structure experiments are usually located there.

Thermal Control

The thermal control subsystem has been designed to maintain the temperatures of all assemblies located within the main body of the spacecraft within the limits of 5° C to 35° C. Since the orientation of the main body with respect to the sun is variable, and since the satellite may spend periods as long as 2 hours in the earth's shadow, it was necessary to use an active thermal control system. Use of an active system also makes it easier to accommodate large variations in experiment power dissipation and in the sizes of sensor openings through the external surfaces.

Thermal input to the spacecraft from the sun and earth is reduced to a very low value by the use of an efficient radiation shield, and the thermal radiation from the body is controlled by the use of variable-area radiation panels. The radiation shield, consisting of multiple layers of aluminized mylar, covers all areas of the main body which may be exposed to the sun. The two sides of the main body through which the solar panel shaft passes and the end of the main body at which the orbit plane experiments are located are never exposed to the sun, due to the action of the attitude control system. These three surfaces are efficient heat radiators and are covered with thermal insulation louvers to control their exposure. Each louver is positioned by a bimetallic spring which senses the temperature of the radiating panel. When the temperature of the radiating panels rise, the louvers open to allow the radiation of more heat. The construction of one of the thermal control panels can be seen in Figure 5 which shows the radiating surface, the louvers, and the bimetallic elements. Calculations indicate that the temperature of the main body will not lower significantly in the earth's shadow as long as normal operating electrical power is dissipated.

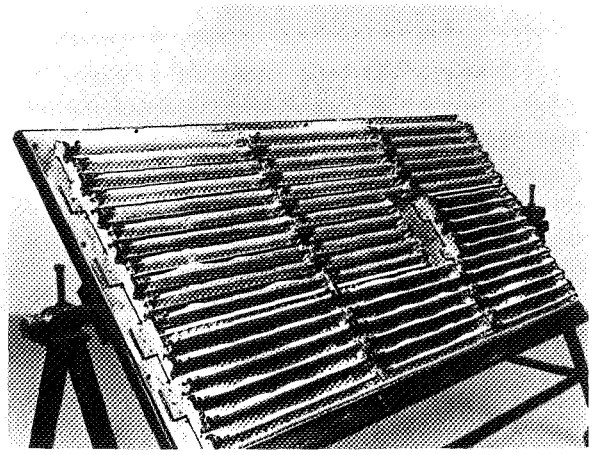

FIGURE 5.—One of the louvered thermal control panels. The louvers are individually controlled by bimetallic thermostats which sense the temperature of the high emissivity radiation panel underneath. (Photo courtesy of Space Technology Laboratories.)

Thermal control of the appendage experiment containers is obtained by the use of a combination of thermal radiation shields, radiation surfaces, and electrical heating. The containers are thermally insulated from their mountings. The radiation area sizes and locations are chosen to provide a proper heat balance during periods of maximum energy input. Electrical heaters in the containers supply additional energy during long eclipses or when the experiment power is turned off. With this system, the temperatures of experiment assemblies within the appendage containers will normally be between 0° C and 40° C.

Experiment sensors that protrude through the radiation barriers on either the main body or the appendage containers present special thermal problems. They must be designed so the solar energy flux of about 1400 W/m^2 does not cause excessive heating of the sensors, and the thermal radiation when the sensors are not illuminated by the sun does not cause excessive cooling. In some cases it is necessary to allow greater temperature excursions of sensors having large openings.

The solar array presents a particularly difficult thermal design problem. Only about 10.5

percent of the 10,000 watts of solar energy incident on the two solar panels is converted into electrical energy. Most of the rest is radiated from the rear surfaces of the panels. A potassium silicate compound having a high infrared emissivity and a low visual and U.V. absorptivity is used on these back surfaces to keep the solar cell temperatures below approximately 85° C when fully illuminated. It is necessary to keep the solar cell temperatures above −140° C during eclipse to avoid damage to the cells by thermal stresses. This is accomplished by making the beryllium solar cell substrates thick enough to provide sufficient thermal mass to prevent cooling below −140° C after 2 hours in darkness.

The solar cell energy spectral response peaks in the blue region. The red region of the solar spectrum, which contributes thermal energy without contributing to the electric power generation, is rejected by an electrodeposited optical coating applied to 0.15-mm-thick glass slides which cover the solar cells. These glass slides also provide a limited measure of protection from charged particle radiation and micrometeoroid damage.

Power Supply

The power supply subsystem consists of a solar energy converter, a chemical battery, a charge regulator and power distribution equipment. The solar energy converter consists of 32,256 gridded P–N junction silicon cells, each having an effective area of 1.9 cm^2 and a solar energy conversion efficiency in space of 10.5 percent. The individual cells are mounted in groups of 112 on beryllium plates or substrates, as shown in Figure 4. Beryllium is used because of its light weight and because its coefficient of thermal expansion is similar to that of the silicon cells. The cells on the 7 by 16 cell modules are wired in series-parallel. One hundred and forty-four of these modules are attached to each of the two solar panels. The complete array can supply an initial total electrical power of approximately 650 watts. Allowances for losses due to light transmission through the glass cover slides, orientation errors and errors in measurement and cell matching result in an initial effective available power of approximately 490 watts at 29.5 volts. Degradation during the 1 year operating period due to damage from charged particle radiation and micrometeoroid bombardment may reduce the power output to approximately 300 watts. Of this, 50 watts average power is reserved for operation of the experiments. The rest is used by the attitude control, thermal control, data handling, and communications systems.

Two nickel-cadmium battery packs, each of 12 ampere-hours capacity, provide electrical power to the observatory during eclipse and assist in gross regulation of the power bus voltage. Each battery consists of 22 prismatic cells and weighs about 15 kg. The two batteries are mounted directly on the two radiating faces of the main body to prevent excessive battery temperatures. Half of each battery pack is electrically connected in series with half of the other pack to equalize the heat dissipated from the two packs between the two radiating panels. The size of the battery has been selected so that the depth of discharge during the two hour EGO eclipse will be limited to 75 percent. When the spacecraft is placed in a near-earth orbit, with more frequent, 35 minutes eclispes, the discharge depth will be limited to 25 percent. A silver-cadmium battery is also being developed for use on later observatories. This battery is non-magnetic, and therefore more compatible with the magnetic field experiments. It is also expected to have a somewhat higher efficiency in terms of stored energy per unit mass.

Charge control equipment regulates the charging of the chemical batteries by the solar arrays. Two regulators maintain a preset charge current to the two batteries by shunting the unneeded portion of the array output current through power transistors. These transistors are mounted on heat sinks at the outboard ends of the arrays. One of several preset charge current rates can be chosen by ground command to fit the sunlight-eclipse ratio and power load conditions. Sensors reduce the charge rate to a trickle charge when the chemical battery is fully

charged or when its temperature exceeds 35° C. If the battery temperature exceeds 52° C due to battery failure, a relay transfers operation to the remaining battery. Should both batteries fail, the solar array will furnish power directly to the electrical power bus.

The batteries are connected directly to the primary 28 volt bus which provides power for the attitude control system, command receiver, and data handling systems. A secondary bus, connected to the primary bus through an undervoltage cutoff relay, provides power to the experiments and the rest of the communications system. The undervoltage cutoff relay disconnects the secondary bus whenever the voltage falls below 23.5 volts. This is not expected to occur unless there is excessive damage to the solar array, unless orientation is lost, or unless there is an excessive power drain. The undervoltage relay is reset by ground command.

The power bus upper voltage limit is set at 33.5 volts by the charge control equipment. Therefore, experiments must be capable of operating over the range of input voltage from 23.5 to 33.5 volts. Experiments and spacecraft systems which require other voltages or better regulation employ converters and regulators. The converters employing chopping circuits for their operation are synchronized at frequencies of 2461 cps or 7384 cps to minimize interference to experiments designed to investigate the VLF portion of the electro-magnetic wave spectrum. Motors in the attitude control system are operated from a 400 cps power inverter.

Attitude Control

The OGO has five degrees of freedom; rotation of the main body about each of its three principal axes, rotation of the solar array with respect to the main body, and rotation of the orbit plane experiments with respect to the main body. The attitude control system controls those motions to meet the orientation requirements of the experiments, solar array, thermal radiating surfaces, and directional antenna. The rotations of the main body about the longitudinal (pitch) axis and about the solar array (roll) axis are controlled so that one of the main body experiment mounting surfaces and the directional antenna are directed toward the center of the earth with an accuracy of ± 2 degrees. The rotation of the main body about the satellite-earth (yaw) axis and the rotation of the solar array about its shaft axis are controlled so that the solar array and the solar experiments are directed toward the sun, and the two main body thermal control side panels are alined perpendicular to the sun line. The sun pointing accuracies are normally ± 5 degrees. The rotation of the orbit plane experiments with respect to the main body about their mounting axis (parallel to the body yaw axis) is controlled so that these experiments are always directed in the plane of the orbit with an accuracy of ± 5 degrees whenever the main body angular rate about an axis normal to the plane of the orbit is greater than about 1.1 degrees per minute. Near apogee of a highly eccentric orbit this angular rate is lower, and the orbit plane orientation error may become much larger.

The operation of the attitude control system can be seen with the use of the simplified functional diagram in Figure 6. This diagram shows the system in its normal mode of operation. The earth horizon is detected by infrared

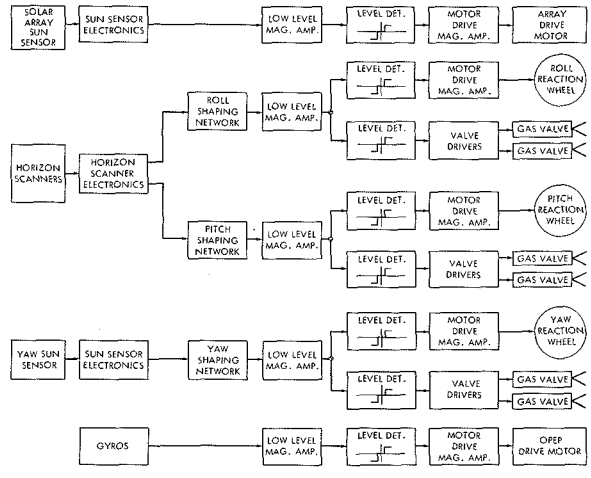

FIGURE 6.—Simplified functional diagram of the OGO attitude control subsystem. The system is shown in its normal control mode. The configuration is somewhat different for the launch and acquisition modes as described in the text.

edge-sensing scanners. Horizon scanner logic circuits determine the earth's center over the entire range of satellite-earth distance from 280 km to greater than 17 earth radii, where the angle subtended by the earth ranges from about 150 degrees to about 6 degrees. The sun subtends too small an angle to be accepted as a tracking source. The error signals produced by the scanner logic are amplified and applied to motors which drive the roll and pitch inertia wheels. The reactions to the angular acceleration of these wheels produce torques which rotate the observatory to reduce the earth orientation errors. The reaction wheel servo systems have central dead-bands, so that no power is applied to the drive motors until the errors exceed 0.4 degree. These same error signals are applied in parallel to argon gas jets, with somewhat wider dead-bands. Thus the cold gas jets are used only when large errors occur due to the non-symmetric buildup of main body external torques from unbalanced aerodynamic forces, magnetic field interactions, solar radiation pressure, and the gravity gradient. The torques needed to satisfy the orientation requirements are very nearly periodic over one orbit, and can be supplied by the reaction wheels alone. Thus, the gas jets are not expected to operate oftener than about once per orbit. This low duty cycle for the use of the gas jets and the use of argon gas rather than a gas having a lower atomic weight are necessary to avoid interference with the experiments which will measure the atmospheric composition.

The direction to the sun is sensed by silicon P–N junction cells generally similar to the solar cells used for power generation. They are used in pairs, with baffles between the two cells of each pair. The difference in the outputs from the cells in each pair are a measure of the error. Coarse and fine sensors are included for use during sun acquisition and normal operation respectively. The error signals from the yaw sun sensor control a reaction wheel-cold gas jet system nearly identical to the pitch system. And a drive motor rotates the array to keep that sensor error signal within its deadband. An additional output from the fine sun sensors indicates whether or not they are illuminated by the sun. A "sun absent" indication switches control to the coarse sensors, and yaw and array torques are again produced as soon as the coarse sensors are illuminated. Thus, the system is inactive as long as the observatory is in eclipse, but reacquires the sun rapidly upon emerging from the earth's shadow.

The position of the orbit plane experiment package (OPEP) is controlled by a functionally independent control loop. It utilizes a single degree-of-freedom position gyroscope operating in a gyrocompassing mode. Its angular momentum vector is perpendicular to the local vertical (earth-observatory line) and therefore to the axis of rotation of the OPEP. The angular momentum vector is fixed with respect to the OPEP and rotates with it. As the observatory makes each orbit around the earth, it makes one complete rotation about a line perpendicular to the orbit plane. If the gyro angular momentum vector is also alined normal to the orbit plane, then no rotation of this vector occurs, the OPEP's are properly positioned, and no error signal is developed. Whenever the gyro angular momentum vector is not normal to the orbit plane, the rotation of a component of the angular momentum vector with the observatory produces an error signal which acts through a servo system similar to the solar array system to reposition the gyro and OPEP so that the angular momentum vector is again normal to the orbit plane.

The control system has three modes of operation, launch, acquisition, and normal control. The launch mode, in which the control system is made inactive, is maintained until after the appendages have been deployed following separation from the Agena vehicle. At that time, the system is switched into the first phase of the acquisition mode by ground command or by the observatory sequencing equipment. In the first phase of the acquisition mode the solar array is rotated so that the solar cells face in the direction away from the OPEP end of the main body. When this position has been reached, the array is held fixed with respect to the main body and the system enters the sun acquisition phase. The observatory is rotated about its

yaw and roll axes to acquire the sun by the use of the error signals generated by the solar sensors. In addition, an angular rate about the pitch (longitudinal) axis of about one-half degree per second is initiated under control of a pitch rate gyro. Sun acquisition normally requires 10 minutes or less. The earth search phase of acquisition is initiated by a 70-minute timer. During earth search the solar array continues to point toward the sun, and the main body rotates, first about the pitch axis and then about the roll axis, until the horizon scanner is locked onto the earth. Because of the small pitch rate introduced in phase two, and because of the geometry of the orbits, earth acquisition is obtained within one orbital period. When earth acquisition is indicated by the horizon scanners, the system switches into the normal mode of operation. The system is switched into the acquisition mode again by ground command or when two or more of the four horizon scanners are not tracking.

Data Handling and Telemetry

The spacecraft data handling and telemetry subsystem is designed to process, store, and telemeter experiment and spacecraft data, and to generate timing signals for use by the experiments and the spacecraft subsystems.

The major elements of the data handling and telemetry subsystem are shown in the block diagram of Figure 7. It is a high-capacity digital and analog system designed to condition, multiplex, store, and transmit data from the experiments and spacecraft subsystems to the ground receiving stations.

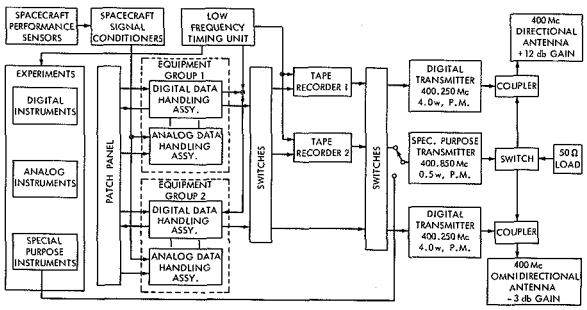

FIGURE 7.—Functional diagram of the OGO data handling and transmission subsystem.

Its design was based upon the requirement that the simplest practicable interface exist between the experiments and the data system. An additional consideration was the fact that the data system design will have to accommodate a wide variety of experiments having, in many cases, requirements which were completely unknown at the time the data system was designed. Three forms of data from experiments can be accommodated, frequency division multiplexed data to the special purpose telemetry system, time division multiplexed analog data to the analog-to-digital converter and digital telemetry system, and time division multiplexed digital data directly to the digital telemetry system.

The interface wiring from a special purpose or analog experiment output to the data system consists of a single line. The requirements are simply specified in that the output of the experiment must remain within the zero-to-5-volt range and must have a sufficiently low output impedance so the measuring accuracy will not be unduly affected by the input impedance of the data system.

The digital data interface allows many different types of digital experiments to be flown without requiring modification to the data system. All signal conditioning is performed within the experiments. Two types of synchronizing lines carry signals from the data system to the experiments to control their presentation of data over the digital data output lines. One type of synchronizing line provides bit pulses; the other provides word pulses for each data multiplexer input. Thus, the experimenter has complete freedom to divide his particular word or group of words as he desires.

Special-Purpose Telemetry

The frequency division multiplexed special purpose system is a wide-band telemetry system for use by experiments which are incompatible with the time sharing, or sampling, feature of the digital system. The special purpose system can accept five input signals lying within the frequency range of 300 cps to 100 kc and with amplitudes not exceeding 5.0

volts peak-to-peak. These signals are added in a combiner, and the composite signal amplitude is controlled by an automatic gain control circuit. The composite signal phase modulates a 400.850 Mc $\pm$ 0.003 percent transmitter having a power output of 0.5 watt. The transmitter normally radiates continuously, but can be turned off and on by ground command.

The signals from the experiments which are to be telemetered by the special purpose system may be of any form, as long as all frequency components fall within the 300 cps to 100 kc band. Frequency, phase, or amplitude modulation of the signals is permissible. It is necessary that the characteristics of the five signals be chosen so they can be separated without interference after reception on the ground. For this reason, it is usually recommended that standard IRIG frequency-modulated subcarrier oscillators be used in the experiment instrumentation whenever possible.

It should be noted that the special purpose data are not stored in the spacecraft. Thus, these data are recovered only when real-time telemetry is being received by the ground station.

Digital Data Processing

Data from most of the experiments are sampled, digitized, stored, and telemetered by the wideband digital data system. As shown in Figure 7, it consists of timing assemblies to provide timing for experiments and all electronic subsystems, a patch panel to facilitate connection of the experiments to the data system, data handling assemblies for sequentially sampling all data inputs and converting analog data to binary form, tape recorders for storing the binary data, and transmitters and antennas for data transmission.

The data handling system is designed to permit the greatest possible flexibility in the design of experiments. Experiments whose sensors produce basically analog signals, such as current, voltage or resistance, employ signal conditioning equipment to present analog voltages in the range zero to 5 volts with low source impedances to the data system, where they are converted to digital form. On the other hand, experiment sensors such as Geiger-Müller counters, etc., which produce outputs which are fundamentally digital in nature, employ digital techniques to process and condition the data. The data are presented to the data system in serial binary form in synchronism with pulses obtained from the data system.

All experiment data outputs are routed to the data-handling system through a patch panel. This patch panel contains terminals for all experiment outputs, data system inputs, and data timing signals. The telemetry format is assembled by interconnecting these terminals. The use of the patch panel provides easy initial formating and allows last minute changes in the format without affecting the other equipment in the spacecraft or the electrical cables.

Two redundant data-handling equipment groups are employed to sample the many input lines sequentially and for conversion of the voltage analog signals into binary form. Normally, one equipment group provides an output to one of the two digital transmitters for real-time transmission, while the other provides an output to one of the two redundant tape recorders for storage. The roles of the two equipment groups can be reversed in the event of a partial system failure. A conceptual block diagram of one of the two equipment groups is shown in Figure 8. Although the analog and digital inputs are gated in separate sub-

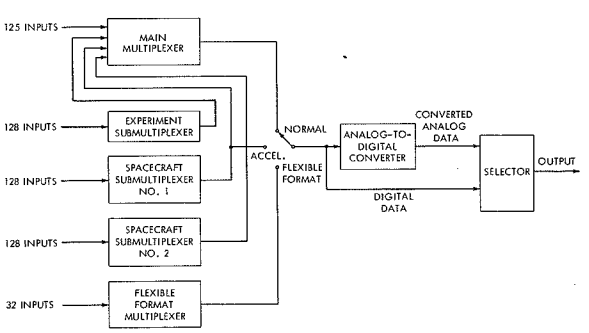

FIGURE 8.—Block diagram of one of the two identical data handling equipment groups. The selector selects the converted analog data line whenever analog inputs are sampled, and the digital data line whenever digital inputs are sampled. This figure is intended to give a functional picture of the system. The system is actually synthesized in a somewhat different manner.

assemblies in practice, the operation is the same as though there were five time-division multiplexers. Each multiplexer is functionally equivalent to a multiple position rotary switch. The main multiplexer sequentially samples 128 inputs. Three of these inputs are outputs from the three submultiplexers, each of which in turn samples 128 inputs. Each submultiplexer advances one position whenever the main multiplexer advances 128 positions, or one complete rotation. Thus the main multiplexer is used for rapidly varying data, while the submultiplexers are useful for sampling more slowly varying data.

Spacecraft submultiplexer Number one can be operated at the main multiplexer rate when the data from its inputs are needed more frequently as, for example, during appendage deployment and initial attitude acquisition. In this event, subcommutator number one provides data directly to the transmitter or tape recorder, and the inputs to the other multiplexes are not processed.

A flexible format multiplexer can be substituted for the other multiplexes on command. This device permits the time division multiplexing of 32 different data lines in 32 different sampling formats, as selected by ground command. It is provided for use when a few experiments require high sampling rates for relatively short periods of time.

Each multiplexer contains both analog and digital gates, appropriately interspersed. When ever an analog gate is turned on the analog voltage is converted by the eight-bit analog-to-digital converter. But when a digital gate is turned on, the serial binary data bypass the converter.

The pulse code modulated (PCM) data from the data handling equipment groups are in the form of a non-return to zero (NRZ) Manchester code in which binary zeros are represented by "01" and ones by "10." This code provides at least one level transition for every bit regardless of the bit pattern to aid in bit synchronization during ground data processing.

The largest element in the digital data format is a *sequence*, consisting of one cycling of the three submultiplexers and, thus, 128 cyclings of the main multiplexer. Each cycle of the main multiplexer, or *frames* results in the processing of 128 words, or input *samples*. Each word consists of nine binary *bits*. Thus, one sequence includes one submultiplexer cycle, 128 main multiplexer cycles or frames, 16,384 words, and 147,456 binary bits. The data-handling bit rates can be set by ground command at 1,000, 8,000, or 64,000 bits per second for the EGO missions, or at 4,000, 16,000, or 64,000 bits per second for the POGO missions. Tape recordings in the observatory is always done at 1,000, or 4,000 bits per second, and tape recorder readout occurs at 64,000 or 128,000 bits per second for EGO and POGO respectively Real-time digital telemetry can occur at any of the bit rates, depending on the requirements of the experiments. These format specifications and bit rates result in the sampling of each of the 128 inputs to the main multiplexer 0.8681, 3.472, 6.944, 13.89, or 55.55 times per second and of each of the 384 inputs to the three submultiplexers every 147.5, 36.86, 18.43, 9.216, or 2.304 seconds, depending on whether the 1-, 4-, 8-, 16-, or 64-kilobit rate is in use.

Additional signals are available to the experiments. These include power, power converter 2,461 cps synchronization, motor 400 cps synchronization, ground commands, and timing at 0.01, 0.1, 1, 10, 100, 1,000 pulses per second. Timing pulses corresponding to the sampling times of many of the digital inputs are provided to assist the experimenters in programing the data conditioning within their experiments. To assist the experimenter in determining the data handling system operating conditions, additional signals indicate whether real-time data are being transmitted, the real-time bit rate, and the equipment group which is feeding the data storage system.

Digital Data Storage

Two identical redundant tape recorders store the digital data so that continuous data can be recovered from the observatory by a small number of ground receiving stations. Each of the recorders has a storage capacity of 43.2 million binary bits. The recording bit rate is either 1,000 or 4,000 binary bits per second, depending on the mission; thus, the recorders

can record for 12 or 3 hours respectively. The two recorders can store sequentially to provide times up to 24 or 6 hours between readouts. Readout of one recorder can occur while data are being stored on the other to provide continuous coverage. Readout times for the two cases are 11.25 and 5.625 minutes, respectively, per recorder. The recorder tapes are reversed for readout, resulting in time reversal of these data. Time is reversed again during processing on the ground to place it in its original order.

Digital Data Telemetry

The digital outputs of either of the two data-handling equipment groups or either of the two tape recorders are telemetered on ground command by either of the transmitters. Complete command-controlled across-strapping provisions allow the full use of the extensive parallel redundancy to increase the reliability of the data-handling system.

One of the two digital wideband transmitters is energized upon receipt of a ground command. The telemetry system is automatically turned off by a timer approximately 23 minutes after loss of the command carrier. One of the transmitters feeds the omnidirectional antenna, which has a gain of -3 decibels in the earthward hemisphere relative to isotropic radiation and is circularly polarized. The other digital transmitter drives the directional antenna which has a gain of $+12$db, a half-power beam width of less than 40 degrees, and is circularly polarized. Normally the transmitter driving the directional antenna will be used when the transmission distance is greater than about three earth radii. When the observatory is near the earth the omnidirectional antenna, with its greater beam width, will be used. It is not possible to operate both digital transmitters simultaneously, but one digital transmitter and the special purpose transmitter may transmit concurrently. If both digital transmitters should fail, or if a lower transmitter power is desired, then the digital data can be transmitted by the special purpose transmitter. The special purpose transmitter feeds either the directional or the omnidirectional antenna through a command-operated coaxial switch and two 400-Mc coupler networks located in the antenna feed lines.

The power outputs of the digital wideband transmitters are four watts. The 400.250 Mc ± 0.003 percent carriers are bi-phase modulated by the PCM data. The angle between the two phases is adjusted to leave approximately 10 percent of the radiated power at the carrier frequency. This simplifies lock-on and tracking of the carrier by the ground receivers.

Observatory Synchronization and Timing

A central timing system provides high accuracy timing and synchronization for the entire observatory. The basic timing sources are two redundant 256-kc crystal oscillators having long-term stabilities of one part in 10^5 per year and short-term stabilities of one part in 10^6 per hour. Only one oscillator is used at a time so that all timing is derived from a single source. Countdown circuits produce signals for synchronizing the data handling assemblies and the tape recorders, for time reference in the experiments and for synchronizing all power converters to minimize interference to VLF experiments. An additional register generates observatory accumulated time, which is recorded and telemetered with all digital data to serve as a basic data-time reference.

Ground Command Reception

Two redundant AM command receivers operating at approximately 120 Mc, are fed from dipole omnidirectional antennas, as shown in Figure 9. The dipoles are crossed in a single assembly, thus providing polarization-diversity reception. The receivers have 33.15 Mc and 7.3 Mc IF frequencies and IF bandwidths of 40 kc. The bandwidths of the audio sections are 11 kc. The basic receiver noise figures are 4 db. With an antenna noise temperature of 1000° K, the command noise power is -121 dbm. The receivers are set to unsquelch at -115 dbm and, at the same point, relays operate to indicate the presence of an RF carrier. Each receiver contains two AGC loops to permit operation over a wide range in signal strengths.

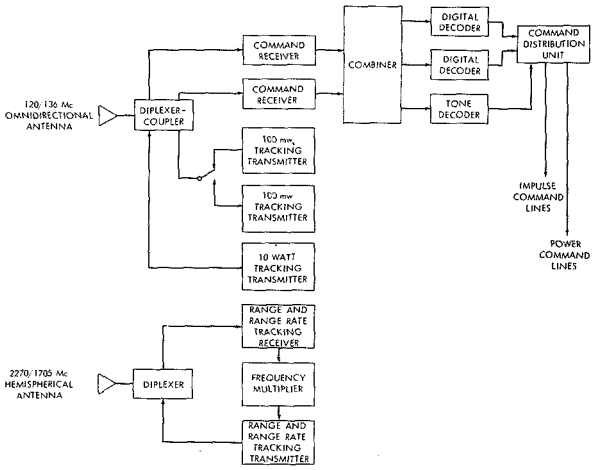

FIGURE 9.—Functional diagram of the OGO command and tracking subsystems.

The outputs of the two command receivers feed, in a parallel redundant fashion, two digital decoders and a single tone decoder. The squelch or failure detection circuits in the receivers maintain the input to the decoders at a constant level, regardless of the number of receivers which are operating.

The digital decoders permit the reception and proper routing of 254 independent commands. They operate on a frequency shift keying (FSK) signal where one frequency represents a binary "0" and a second represents a "1." Each digital decoder can be addressed separately, but the output from a single decoder provides complete digital command capability. Outputs from the digital decoder operate relays arrayed in a 16 by 16 matrix. Two types of relay are used, power command and impulse command. Of the 254 commands, 104 are utilized to control the data handling, communications, power, attitude control, and thermal systems and to initiate deployment of the appendages. The other 150 commands are reserved for the experiments. Fifty power relays, requiring separate on and off commands, provide electrical power to the various experiments. And 50 impulse relays provide grounding of 50 control lines for approximately 50 milliseconds following execution of the proper commands.

The digital command words contain 24 binary bits. The first bit is always "1" to provide synchronization. The next three bits contain the satellite and decoder addresses. The next two bits designate the mode of operation of the decoder, while the next eight bits contain the command itself and select the proper relay in the command distribution unit. The complement to the two mode bits and eight command bits is retransmitted as a parity check. If the parity check succeeds, a command execute signal is generated to energize the proper command relay, and command execution is indicated in the telemetered data.

A few of the most important commands can be received as tone commands and decoded in the relatively simple and highly reliable tone decoder. This sequential tone command system permits reception of real time digital data from the observatory at secondary receiving stations without requiring that they have the somewhat complex digital command generator. In addition, this simple tone command system permits limited operation of the observatory and recovery of data in the event of failure of the digital command system.

Observatory Tracking Equipment

Orbits of most previous satellites have been determined by the use of the Worldwide Satellite network, formerly known as the Minitrack network. This network of tracking stations and the necessary computational techniques are well established, and will be used in the OGO program. This system will be supplemented by a range and range-rate system which is expected to permit the more accurate computation of the orbit parameters in a shorter time, especially in the case of the highly eccentric orbit in which the satellite spends a large fraction of its time at large distances from the earth and the angular rates are very low.

The observatory tracking system components are indicated in Figure 9. Three 136.00 ± 0.41 Mc beacon transmitters will provide a continuous tracking signal for the ground stations. One of the two redundant low power (100 mw) transmitters operates continuously except when

the high-power (10 watt) transmitter is energized. The high power transmitter, utilized only on missions with apogee distances greater than approximately two earth radii, is controlled by a timer which turns the transmitter off 45 seconds after it is energized.

The beacon transmitters use the same crossed dipole omnidirectional antenna as the command receivers. A diplexer-coupler provides the necessary isolation between the beacon transmitters and the receivers. For beacon transmission the antenna polarization is circular.

The completely independent range and range-rate system utilizes a diplexed antenna, receiver, frequency multiplier, and transmitter. Signals at frequencies of approximately 2270 and 2271 Mc are received from two ground stations simutaneously, converted, and retransmitted as 1.4 and 3.2 Mc sidebands on a 1705.000 Mc carrier. The received signals are phase modulated by range tones at frequencies of (500 kc, 100 kc, or 20 kc), 4 kc, 800 cps, and (160 cps, 32 cps, or 8 cps). The ground stations determine the range of the observatory by comparing the phases of the transmitted and received modulating frequencies. The range-rate is ascertained by measuring the doppler shifts of the RF signals. The use of two ground tracking stations simultaneously permits high accuracy trilateration of the observatory.

The overall goal of the tracking program is to be able to determine for the experimenters the position of the observatory at all times within a sphere of uncertainty having a radius of 1 km or less at radial distances of less than 1000 km and of 100 km at radial distances of 17 earth radii.

THE OGO EXPERIMENTS

Experiments for the Orbiting Geophyiscal Observatories are selected by the Office of Space Sciences, NASA Headquarters, Washington, D.C., from those proposed by research groups in universities, industry, NASA laboratories, and other Government agencies. Many of the experiments are the result of initial technical development supported by NASA as a part of its advanced development program. Selection of experiments has been completed for the first EGO and POGO launches. Lists of these experiments, the principal investigators, and their institutions are included in Tables 1 and 2. More complete technical descriptions of these experiments will be published from time to time by the experimenters.

OGO ORBITS

The Orbiting Geophysical Observatories can be placed in a number of different orbits, depending on the needs of the experiments. The minimum perigee height is set by the requirement that the atmospheric drag must be small enough to insure a 1-year lifetime. The maximum apogee height is limited at the present time to about 18 earth radii (geocentric) for a 31-degree inclination by the capabilities of presently available launch vehicles. As larger launch vehicles become available, missions with apogee at lunar distances will require only minor adjustments of some of the subsystem parameters. The orbital inclination is limited by the launch site and range instrumentation locations. The Atlantic Missile Range at Cape Canaveral, Fla., is located at a geographic latitude of about 28.5 degrees. Thus, orbital inclinations between 28.5 and approximately 50 degrees are achievable without overflying inhabited land masses during the initial trajectories. Lower orbital inclinations are possible only by altering the course of the vehicle after liftoff or by launching from a lower latitude. Higher inclination orbits, including Polar orbits, are possible by launching from the Pacific Missile Range at Lompoc, Calif.

The planned nominal orbital parameters for the EGO orbit are listed in Table 3. This orbit was chosen to cause the observatory to traverse the high intensity radiation belts for a study of their characteristics throughout the entire trapping region, and to make atmospheric, exospheric, ionospheric, and magnetospheric measurements from near the nearth to interplanetary space. Especially interesting is the possibility of studying the shape of the boundary of the magnetosphere and of the plasma shock front presumed to exist on the sunward side of the

TABLE 1.—*Experiments for OGO–A (EGO–1)*

Experimenter	Experiment	Detector
K. A. Anderson, Univ. Calif.	Solar proton flux, 10–90 Mev, energy and variations.	Scintillation counter.
J. H. Wolfe, Amer. Res. Ctr.	Solar plasma flux, energy and direction.	Electrostatic analyzer.
H. J. Bridge, Mass. Inst. of Tech.	Solar plasma flux, energy and direction.	Faraday cup.
T. L. Cline and E. W. Hones, Goddard Space Flt. Ctr. and Inst. for Defense Anal.	Search for positrons and solar gamma ray flux and spectrum.	Scintillation counters.
L. R. Davis, Goddard Space Flt. Ctr.	Geomagnetically trapped electron and proton flux, energy and direction.	Phosphor scintillation counter.
F. B. McDonald and G. H. Ludwig, Goddard Space Flt. Ctr.	Galactic and solar cosmic ray flux, charge and energy.	dE/dx vs. E scintillation telescope.
J. A. Simpson, Univ. Chicago	Galactic and solar cosmic ray flux, charge and energy.	dE/dx vs. E and range detector.
J. A. Van Allen, State Univ. Iowa	Geomagnetically trapped electron and proton flux and energy.	Omnidirectional Geiger counters and solid state detector.
J. R. Winckler and R. L. Arnoldy, Univ. Minn.	Geomagnetically trapped electron energy and flux, and total ionization.	Magnetic electron spectrometer and ion chamber.
R. S. Lawrence, National Bureau of Standards.	Electron density by RF propagation, 40 and 360 Mc.	Radio transmitter.
R. Sagalyn, A. F. Cambridge Res. Lab.	Thermal charged particle density, energy, and composition.	Spherical ion and electron trap.
E. C. Whipple, Goddard Space Flt. Ctr.	Thermal charged particle density, energy and composition.	Planar ion and electron trap.
H. A. Taylor, Goddard Space Flt. Ctr.	Atmospheric composition, 1–48 amu.	Bennett RF mass spectrometer.
J. P. Heppner, Goddard Space Flt. Ctr.	Magnetic field strength and direction.	Rubidium-vapor and flux-gate magnetometer.
E. J. Smith, Jet Propulsion Lab.	Magnetic field low frequency variations, 0.01–1000 cps.	Triaxial search coil magnetometer.
W. M. Alexander, Goddard Space Flt. Ctr.	Micron dust particle velocity and mass.	Time-of-flight and momentum detectors.
F. T. Haddock, Univ. Mich.	Solar and Jovian radio-noise burst frequency spectrum, 2–4 Mc.	Radio receiver.
R. A. Helliwell, Stanford Univ.	VLF terrestrial noise, solar particle emissions, and cosmic noise frequency distribution and strength, 0.2–100 kc.	VLF receiver.
P. M. Mange, Naval Res. Lab.	Geocoronal Lyman-alpha intensity and location of scattering layer.	Lyman-alpha ion chambers.
C. L. Wolff, K. L. Hallam, and S. P. Wyatt, Goddard Space Flt. Ctr. and Univ. Ill.	Gegenschein intensity and location.	Gegenschein scanning photometer.

TABLE 2.—*Experiments for OGO–C (POGO–1)*

Experimenter	Experiment	Detector
R. A. Hoffman, L. R. Davis, A. Konradi, J. M. Williamson, Goddard Space Flt. Ctr.	Low-energy trapped radiations; elecrons, 10–100 kev; protons, 100 kev–4.5 Mev.	Phosphor scintillation counter.
H. V. Neher and H. Anderson, Cal. Inst. of Tech. and Jet Propulsion Lab.	Total ionization over polar regions	Ionization chamber.
J. A. Simpson, Univ. Chicago	0.3–30 Mev nucleons	Scintillation telescope.
J. A. Van Allen, Univ. Iowa	Net downflux of corpuscular radiation in auroral zones and over polar caps.	Geiger counters.
W. R. Webber, Univ. Minn	Energy spectrum and charged-particle composition of galactic and solar cosmic rays.	Scintillation Čerenkov detector.
R. E. Bourdeau, Goddard Space Flt. Ctr.	Ionospheric charged particles	Planar retarding potential analyzer.
L. M. Jones and E. J. Schaefer, Univ. Mich.	Neutral-particle and ion measurements: 0–6 amu and 0–40 amu.	Paul massenfilter mass spectrometer.
G. P. Newton, Goddard Space Flt. Ctr.	Neutral-particle density	Bayard-Alpert density gage.
H. A. Taylor and H. C. Brinton, Goddard Space Flt. Ctr.	Atmospheric composition 1–45 amu	Bennett RF mass spectrometer.
W. M. Alexander, C. W. McCracken, O. E. Berg, L. Secretan, Goddard Space Flt. Ctr.	Micrometeorites: mass, velocity, charge.	Time-of-flight and momentum detector.
J. P. Heppner, H. R. Boroson, J. C. Cain, Goddard Space Flt. Ctr.	World Magnetic Survey	Rubidium-vapor magnetometer.
R. E. Holzer and E. J. Smith, Univ. Calif. at L.A. and Jet Propulsion Lab.	Magnetic field fluctuations, 1–1000 cps.	Triaxial search coil magnetometer
F. T. Haddock, Univ. Mich	Radio-astronomy measurements of galactic emission at 2.5 and 3.0 Mc/s.	Radio receiver.
R. A. Helliwell, Stanford Univ	VLF measurements at 0.2–100 kc	VLF receiver.
M. G. Morgan and T. Laaspere, Dartmouth Col.	VLF emissions and whistlers between 0.5 and 10 kc/s.	VLF receiver.
C. A. Barth and L. Wallace, Jet Propulsion Lab. and Yerkes Observatory.	Measurements of airglow; 1100 Å to 3400 Å.	Ebert UV spectrometer.
J. Blamont and E. I. Reed, Univ. Paris and Goddard Space Flt. Ctr.	Airglow in the UV and at 3914 Å, 5577 Å and 6300 Å.	Photometers.
H. E. Hinteregger	Solar emission in the 200–1600 Å region.	Scanning spectrometer.
R. W. Kreplin, T. A. Chubb, and H. Friedman, Naval Res. Lab.	Solar X-ray emissions in the 0.5–3 Å, 2–8 Å, 8–16 Å, and 44–60 Å bands.	Ionization chambers.
P. M. Mange, T. A. Chubb, and H. Friedman, Naval Res. Lab.	Lyman-alpha and far UV airglow between 1230 Å and 1350 Å.	Ionization chambers.

TABLE 3.—*Nominal Initial Orbital Parameters*

Parameter	EGO–1	POGO–1
Semi-major axis	62,450 km	6,970 km
Eccentricity	0.8934	0.04830
Inclination	30.8 deg.	90 deg.
Argument of perigee	−45.8 deg.	−73.8 deg.
Rt. ascension of ascending node.	144.5 deg.	−19.4 deg.
Period	43.143 hr.	1.609 hr.
Injection geodetic latitude.	−20.4 deg.	−17.1 deg.
Injection longitude	111.9 deg.	47.1 deg.

boundary. A number of interplanetary experiments are also included, since the observatory will spend long periods of time beyond the magnetosphere.

The characteristics of this orbit can be seen with the use of several graphs. For the purposes of most of the orbit calculations the middle of the fourth quarter or 2000 UT on 15 November 1963 was used as a launch time. Adjustments will be necessary when the exact date and time are chosen but these data are representative for that era. Figure 10 indicates the geocentric radial distance and true anomaly as a function of time for the initial orbit. True anomaly is the perigee, earth center, observatory angle. The percentage of time that the observatory will spend within a specified range in height can easily be ascertained from this graph.

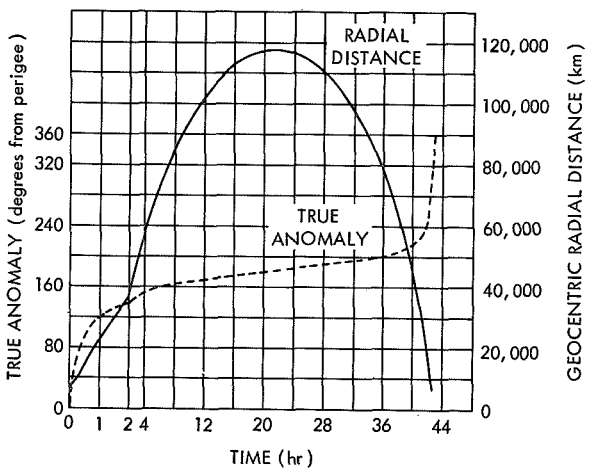

FIGURE 10.—True anomaly and geocentric radial distance for the EGO orbit. The time spent within any range in radial distance can easily be determined. The observatory will spend about 75 percent of its time beyond the magnetosphere when apogee is generally toward the sun.

The region in geomagnetic space through which the observatory will pass during its first month in orbit is indicated in Figure 11. The orbit is shown projected on a meridian plane whose coordinates are geocentric radial distance and geomagnetic latitude. The first orbit is plotted to indicate the general form of the orbits. The bands span 22.8 degrees in latitude (twice the angle between the geomagnetic and geographic equatorial planes), and the satellite ranges between plus and minus $(i+11.4)$ degrees in latitude where i is the orbital inclination. For this particular EGO orbit i increases from its initial value of 30.8 degrees to 42.2 degrees by the end of one year due to orbital perturbations induced by the gravitational fields of the sun and moon. This coupling also causes the perigee height to increase from 277 km to 3164 km by the end of the year. These orbital perturbations depend strongly on the time of launch.

The lines-of-sight of experiments looking away from the earth will trace a simple path on the celestial sphere, as shown in Figure 12.

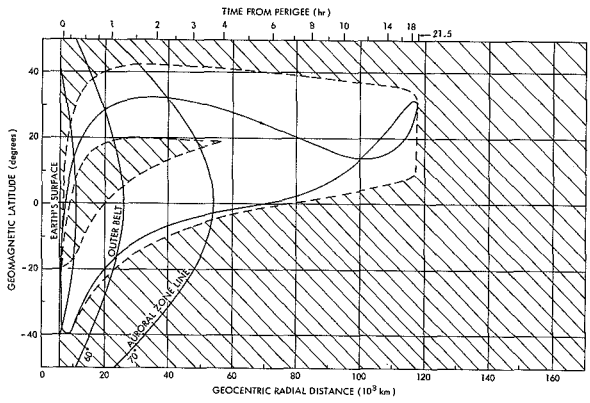

FIGURE 11.—Nominal geomagnetic coordinate limits for the first month of the EGO orbit. The first complete orbit is indicated by the heavy line. The center of the inner proton radiation belt is located just inside the 40 degree magnetic field line, while the outer belt is centered just inside the 60-degree field line.

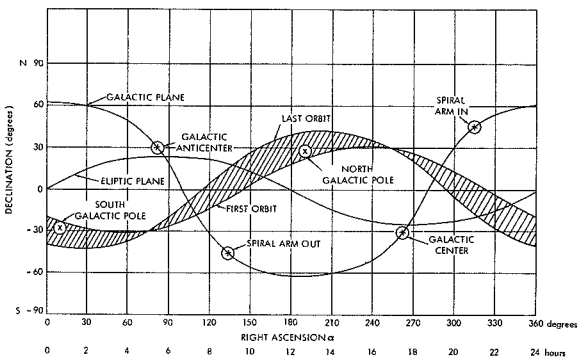

FIGURE 12.—Projection of the lines of sight of detectors looking away from the earth and toward the sun on the celestial sphere. The detectors looking away from the earth trace one path around the sphere during each orbit. The shaded area indicates the region covered as the orbit precesses during one year. The detectors observing the sun trace one path around the celestial sphere during one year along the path marked ecliptic plane. The manner in which these paths change for different launch times is described in the text.

Paths are shown for the initial orbit and for the last orbit in the first year. The shaded area is the region which contains all paths occurring throughout the first year after the launch. The path changes phase throughout the year because of the precession of the right ascension of the ascending node from 144 degrees initially to 115 degrees after 1 year. The path extends to a higher declination because of the increase in orbital inclination mentioned before. Changes in launch time and date result in the shifting of the phase of the paths shown.

The path of the sun, and therefore the path of the line-of-sight of experiments looking toward the sun throughout the 1-year period, is also shown in Figure 12. On 21 March the sun is located at zero degrees right ascension and zero degrees declination and proceeds along the path marked ecliptic plane at the approximate rate of 0.98 degree per day.

The approximate orbital parameters for the first POGO are also listed in Table 3. This orbit will allow the observation of many phenomena directly over the polar and auroral regions, and the determination of the variations of these phenomena over the complete range in latitude.

For each mission the time of launch, and therefore the location of the orbit in space, must be chosen to satisfy a number of limiting conditions. These launch window restraints include the following:

1. For a high eccentricity orbit such as the EGO orbit, the gravitational coupling of the observatory with the sun and the moon is significant, resulting in a continuous change of all orbital parameters including the perigee height. The observatory must be launched so the perigee height will not drop below approximately 230 km not during its first year so it will not lose its energy due to aerodynamic drag and plunge into the earth.
2. The maximum time per orbit that the observatory lies within the earth's shadow must not exceed 2 hours during the one year operating period. For longer eclipse times the temperature of the solar array would drop to below $-140°$C and damage would result to the solar-cell mountings due to stresses produced by unequal thermal contractions of different materials.
3. During the launch, deployment, and initial acquisition sequences, the sun must not directly illuminate the louvered thermal control surfaces for extended periods of time.
4. The experiments may impose additional restraints. For example, it may be desirable to specify an initial value for the angle between the line of apsides and the earth-sun line.

These restraints require that very extensive orbital calculations be made to select a suitable launch date and time. These studies may indicate the need for modification of certain restraints to permit a launching in the desired season. To illustrate, it was necessary to include a timer in the observatory to delay the beginning of the attitude control acquisition cycle, to permit orbital injection in the earth's shadow.

PRELAUNCH OPERATIONS

Between the times that the experiment fabrication is completed and the observatory is launched into orbit, it is necessary to electrically check and environmentally test the experiments, integrate them into the spacecraft, calibrate the experiments, check for interference, environmentally test the complete observatory, ship the observatory to the launch site, and conduct the launch site operation. These steps are necessary to insure that the experiments and spacecraft operate properly as an integrated unit, that they are properly calibrated, and that they will have a reasonable probability of surviving the conditions imposed imposed by the launch and space environments. These steps are expected to require approximately 7 months, at least for the first few observatories.

The OGO testing philosophy attaches great importance to the complete testing of assemblies before they are integrated into the observatory to detect most of the design and production errors and early component failures. Environmental tests of the completely integrated observatory are also made, primarily to uncover design and fabrication errors in the interconnection of assemblies and the mechanical attachment of the assemblies to the spacecraft structure, to disclose problems which result from interactions between assemblies, and to detect additional early component failures.

Electrical, Mechanical, Thermal, and Magnetic Testing of Experiments

Whenever a new experiment assembly is designed for use in the OGO program, the first flight-quality unit, usually referred to as the prototype unit, is subjected to a set of electrical and environmental design qualification tests to ensure that the mechanical, electrical, and thermal designs have a sufficiently large margin of safety. A safety factor of 1.5 is usually required for all mechanical conditions, and all assemblies are tested over a temperature range 20° C greater than anticipated in orbit. After the design has been qualified, at least two units, a flight unit and spare flight unit, are built for each launch attempt. These units are subjected to a set of flight acceptance tests at levels equal to those expected during the actual launch and operation in orbit. These tests are intended primarily to disclose poor workmanship and to induce early component failures.

Electrical Tests

Each experimenter is required to furnish ground checkout equipment with his experiment instrumentation. Generally this equipment is built in two parts. The first is a sensor exciter which provides an input to the basic sensor or detector. It may be very simple, such as a radioactive source for checking GM counters, or somewhat more complex, as a precision variable low-current source for calibrating the input electrometer circuits of ion collectors. Its function is to produce a predictable non-zero output of the detectors so that an end-to-end check of the operation of the instruments can be made periodically throughout the testing program, and to facilitate detailed calibration of the experiments.

The second part of the ground checkout equipment is used for more extensive testing and calibration of the instruments. This experiment test set is capable of operating the experiment independently of the spacecraft, and is used by the experimenter whenever he wishes to check, calibrate, or find difficulties in his instruments. It may include some or all of these provisions:

a. The ground checkout equipment may provide all signals to the experiment which are normally obtained from the spacecraft in flight, such as bit pulses, word pulses, switch, mode and bit rate signals, timing pulses, command and synchronizing signals, and DC power, in order to operate the experiment instrumentation independently of all other equipment.
b. It may have a means for accepting data from the experiment and displaying them.
c. It may be capable of monitoring a number of test parameters, such as internal voltages, waveforms, and event occurrences.

d. It may provide calibration inputs, for example, a means for substituting pulses of known characteristics at some internal point in the instrumentation.

e. Control inputs may be provided. An example is the relaxation of coincidence requirements in an energetic particles directional telescope to facilitate ground checkout by particles from a radioactive source having energies too low to penetrate both detectors.

The sensor exciter will be used throughout the observatory integration, testing, and prelaunch operations to check for proper operation of the experiments. The experiment test set will not normally be used after the experiments are mounted in the spacecraft except for detailed experiment calibration, interference detection, and troubleshooting in the event of a failure during the testing program.

Upon delivery to Goddard, the experiments are connected to a spacecraft electrical simulator. This equipment presents an electrical interface to the experiments which is nearly identical to that presented by the spacecraft. It is capable of providing bit, word, switch, mode, bit-rate, timing, command, and power synchronization signals and electrical power to the experiments and of accepting and processing data from experiments, either singly, or in groups of any size up to the full complement for a particular mission. Provisions are included to vary critical parameters, such as the supply voltage, pulse amplitudes, etc., to ensure that the electrical performance of the experiments is nonmarginal.

The spacecraft simulator is shown in block diagram form in Figure 13. It contains a low frequency timing assembly, digital data handling assembly, and analog data handling assembly electrically identical to those used in the spacecraft. The analog data handling assembly is also mechanically identical to the one used in the spacecraft because the distributed capacitances and lead lengths are somewhat critical in this assembly. The spacecraft simulator contains additional assemblies for performance monitoring purposes and to provide signals which are not derived from the data handling assemblies.

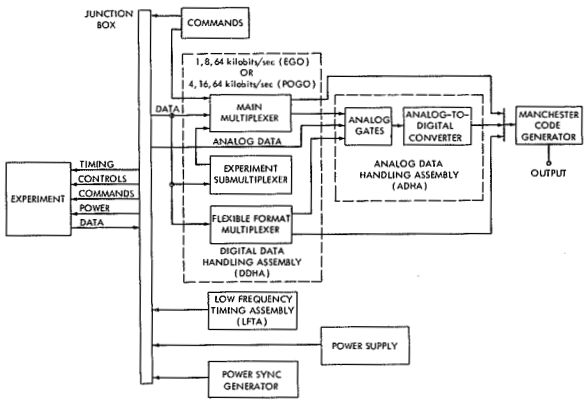

FIGURE 13.—The spacecraft simulator for checking the operation of experiments whenever they are not mounted in the spacecraft.

The method of using the spacecraft simulator for experimental testing is shown in Figure 14. The experimenters' sensor exciters and test sets are used to stimulate the detectors and to monitor and control the experiments as before. The spacecraft simulator provides the necessary driving signals to the experiments and accepts their data. The PCM ground station demultiplexes the data. A number of display devices, including a multiple pen analog recorder, a multichannel optical oscillograph, a bar oscilloscope, and a digital printer are included as a part of the ground station. A medium size digital computer (Scientific Data Systems model 910) is included as a part of the experiment checkout system for use when more complex sorting, rapid access storage, computation, and output of data is desired. This com-

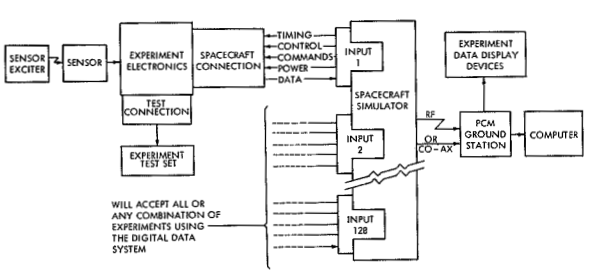

FIGURE 14.—The use of the experimenter's test equipment, spacecraft simulator, PCM demultiplexing equipment, and computer in checking and calibrating OGO experiments.

puter has a core storage capacity of 4,000 24-bit words, and a priority interrupt feature which allows the computer to accept data from several sources and to operate on several programs concurrently. Thus, completely independent processing programs can be run on several different experiments at the same time.

A number of these electrical test systems have been or are being assembled for location at the experimental electrical, mechanical, and thermal test areas, the observatory integration and test areas, and the launch sites. The principal purposes of the systems are:

a. For use by experimenters to check the operation of breadboarded developmental experiments. The earlier an experiment is tested on a realistic interface, the easier it is to make the necessary corrections.
b. To check the electrical performance of flight quality experiment assemblies as soon as they are completed to detect design or fabrication errors.
c. For use by the experimenters in calibrating their instruments.
d. For use by the experimenters in locating difficulties in their instruments after failures have occurred. Whenever improper operation of any experiment assembly located in the spacecraft is detected, the experiment is removed from the spacecraft for analysis with the use of the simulator or experimenters' checkout equipment and is returned to the spacecraft after it has been repaired.
e. Data from the observatory will also be processed by the PCM ground station and computer to assist in the checking of experiments when they are mounted and operated in the spacecraft. Thus, the same data processing programs and procedures can be used for observing the operation of the experiments throughout the entire program.

Mechanical Tests

The prototype and flight experiment and spacecraft assemblies, and the complete observatories, are subjected to series of mechanical environmental tests to detect design and fabrication errors in both components and assemblies. In general, the test levels are equal to *1.5 times* the maximum expected launch conditions for the *prototype* assemblies and observatory and are *equal* to the expected launch conditions for the *flight* assemblies and observatories. The tests are as follows:

a. Measurements are made of the critical dimensions of the assemblies and the locations of mounting provisions, detector openings, etc., to make sure that they will fit into the spacecraft. The weights and centers of gravity are measured.
b. A leak test is given to assemblies which are hermetically sealed. Geiger Müller counters, ionization chambers, electrometer tubes, etc., are considered self-checking and are exempted from this test.
c. A humidity test is given to prototype assemblies and the prototype observatories. The test conditions are 95 percent relative humidity at a temperature of 30 degrees centigrade for 24 hours. Only survival of the exposure is required. Instuments which might be permanently damaged by the exposure may be exempted from the test if precautions are taken to prevent the exposure of those assemblies throughout the program.
d. Vibration tests are given to all assemblies and to the complete observatories. A photograph of the structural design model observatory mounted on a vibration table for one of the transverse axis tests is shown in Figure 2. The vibration tests include both sinusoidal swept frequency and random motion tests in the frequency range 10 cps to 2000 cps. The expected sinusoidal vibration level for experiment assemblies varies, depending on the location within the observatory, reaching a value of 9.3 g RMS at certain frequencies and locations. The expected random motion vibration level is 11.3 g RMS with an equal power distribution in the frequency range 20 cps to 2000 cps.

e. A linear acceleration test is given to the prototype observatory by the use of a centrifuge. The maximum expected acceleration is 9 g.

Thermal Tests

The experiment thermal tests determine whether the instrumentation operates properly throughout the range of temperatures expected in orbit, that heat produced within the assemblies can be carried away in the absence of a convective atmosphere, and that the solar inputs to portions of the detectors exposed to the sun will not create excessive thermal gradients. The complete observatory is given thermal tests for these same reasons and, in addition, to check the operation of the active spacecraft thermal control subsystems. Experiment assemblies which are located in the spacecraft main body are expected to experience temperatures in the range from 5° C to 35° C, while those located in appendages must operate over the range from 0° C to 45° C. The flight assemblies are tested at these levels, while the prototype assemblies are tested over ranges which are 20° C greater.

A test in a thermal-vacuum chamber determines the ability of the experiments to operate without the benefit of convective heat transfer at temperature extremes for extended periods of time. Assemblies in which detectors are exposed through thermally significant openings in the spacecraft thermal radiation shield are given solar simulation tests. For this test the assemblies are located inside a vacuum chamber, the chamber wall temperature and experiment mounting plate temperature are controlled, and an arc light provides a simulated solar input.

Magnetic Field Tests

The very sensitive magnetometer experiments impose a requirement that the magnetic fields produced by the spacecraft and other experiments be extremely low. Electrical current paths are arranged to produce a very low stray field. Nonmagnetic materials are used wherever possible, but some are necessary for motors, relays, etc. It is necessary that these magnetic circuits be very efficient to minimize the stray fields. To ensure that these measures have been effective, the magnetic fields of each assembly and the complete observatory are measured. The permanent, magnetically induced, and electrically induced steady state fields are measured at present. It may be necessary in the future to add measurements of the AC fields of devices employing power transformers and rotating components.

Integration of Experiments Into the Spacecraft and Experiment Calibration

Upon completion of the fabrication and testing of the spacecraft assemblies, they are installed in the spacecraft structure. In general, the integration is done one subsystem at a time, and operational tests are made as each assembly is installed. Test vans have been built to assist in the integration of the OGO observatory and in its checkout throughout the observatory testing program and during the launch operation. The interior of one of these vans is shown in Figure 15. It is capable of supplying numerous controlling signals to the subsystems and displaying data from the subsystems so the operators can verify the proper operation of the spacecraft.

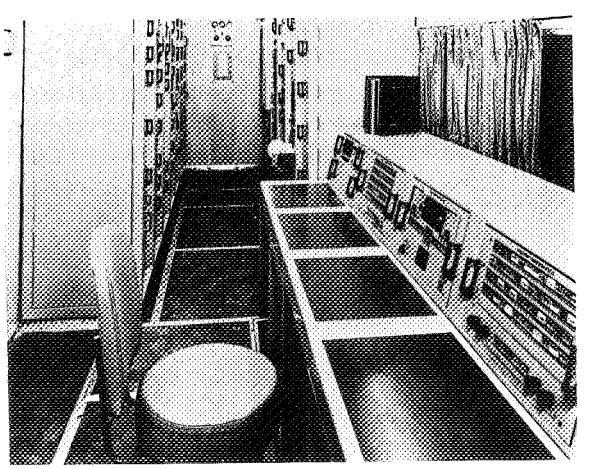

FIGURE 15.—The interior of the spacecraft system test van. The operator's console is at the left, and the rest of the equipment is mounted in the racks at the rear. The van contains a complete telemetry and ground command station, and semiautomatic test equipment to perform rapid tests on the spacecraft subsystems. (Photo courtesy of Space Technology Laboratories.)

After the spacecraft subsystems are completely integrated and subsystem interference tests have been made, the integration of the experiments is started. One at a time they are mounted in the spacecraft, electrically connected, and their operation is checked through the spacecraft data handling system. They are then operated in groups and, finally, all together to check for interference between experiments and between the spacecraft subsystems and experiments.

Following the complete integration of the observatory the experiments are calibrated, and the observatory environmental testing is begun.

During the various phases of the environmental testing program, the complete observatory is given an Integrated System Test (IST) with the use of the test van. A long series of checks is automatically sequenced by the van operator, and the data from the data handling system are compared with preset limits. The test continues automatically as long as the data remain within the predicted limits. If an out-of-tolerance condition occurs, an indication of the nature of the condition is given to the van operator, and the automatic sequence stops until the operator initiates further action. Several thousand checks are necessary to completely verify the condition of the observatory. Checks of the experiments may be included in the automatic test sequence whenever possible. If it is not possible to make the checkout of some of the experiments semiautomatic, they will be checked out manually. Even with the use of the automatic checkout equipment, a complete IST is expected to require several days.

At several points in the observatory environmental test sequence periods of time are set aside for extensive calibration and checkout of the experiments by the experimenters. An additional period is reserved for this purpose just prior to shipment of the flight observatories to the launch site. A shorter period is reserved for calibration at the launch site during the final observatory checkout in the hangar. During these periods, the experimenters will have exclusive access to the observatory for tests of their choice, to give them the best possible chance of knowing the detailed characteristics of their instruments when mounted on the spacecraft.

Launch Site Operations

The observatory will be shipped to the launch site with the appendages, solar panels, and certain critical components removed. Upon arrival in the preparation hangar at the launch site another integrated systems test will be performed to ensure that the observatory was not damaged in transit. The observatory will be completely assembled, aligned, weighed, its center of gravity determined, and it will be mechanically and electrically checked. It will be carried to the launch pad in the folded configuration for mating with the launch vehicle. An abbreviated IST will be performed in this position, and the shroud will be installed over the observatory. Following additional testing, the observatory will be ready for launch.

DATA ACQUISITION, TRACKING, AND DATA PROCESSING

An earth satellite the size of the OGO is capable of producing an extremely large quantity of data. If the first observatory operates properly for the entire one year period, it will provide approximately 2×10^8 nine-bit measurements. Since the data are of no value unless they can be analyzed selectively and efficiently by the experimenters, a great deal of attention has been given to the development of a ground support complex which will give each experimenter the data he needs in an easily usable form as rapidly as possible.

This ground station system, indicated in Figure 16, includes networks of data acquisition and satellite tracking stations, a control center, a quick-look facility, and a data processing line. The data from the spacecraft are tape recorded at the data acquisition stations, and the tapes are mailed to the OGO Control Center located at Goddard. The Minitrack and range and range-rate tracking stations forward tracking data by teletype to the Control Center where they are used for computation of the orbital parameters. Command instructions are transmitted to the observatory from the data acquisition stations

764-173 O—65——7

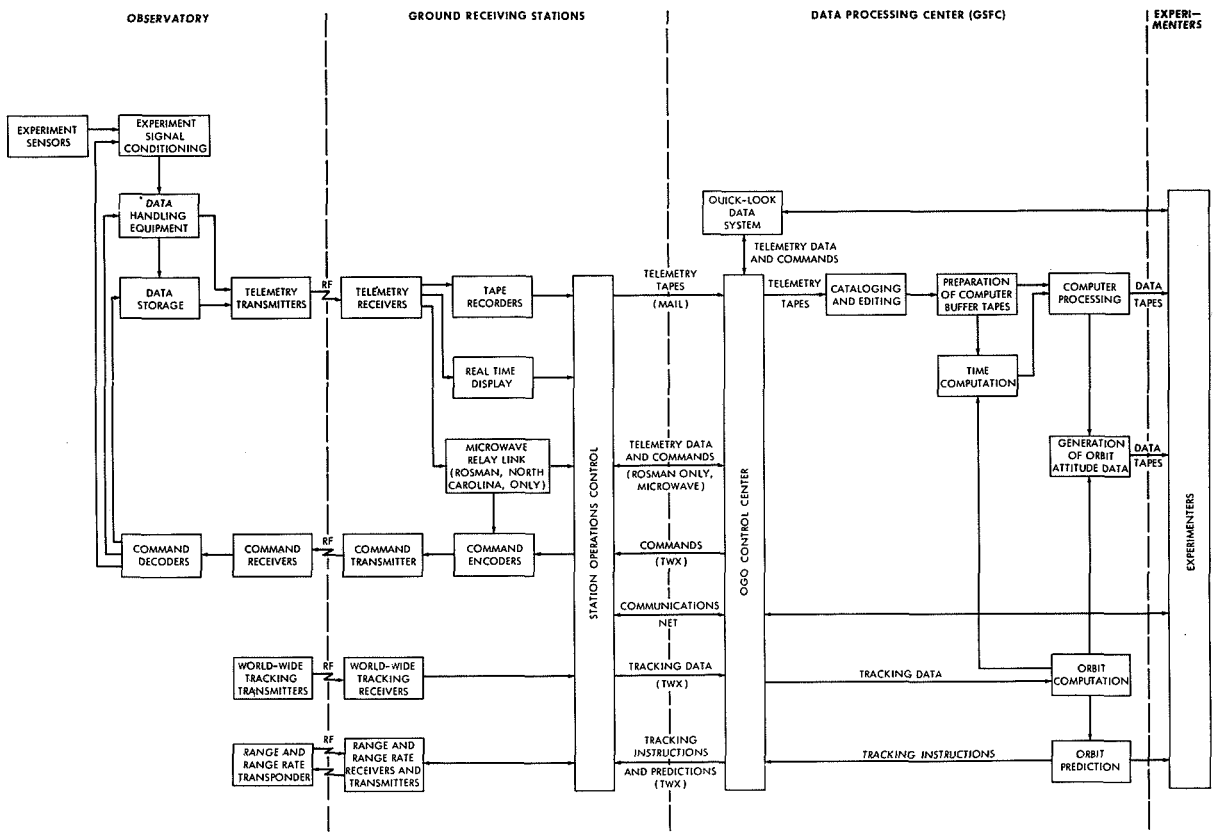

FIGURE 16.—A flow chart for operation of the OGO in orbit.

after being generated there or received from the Control Center.

Telemetry data from one of the data acquisition stations located in Rosman, North Carolina are relayed directly to Goddard by means of a wideband microwave relay link. These real-time data are processed at the OGO Control Center for quicklook purposes when the ability to react rapidly to conditions on the observatory is necessary.

The data recorded at from all acquisition stations is processed by the OGO Production Processing Line. At the completion of this processing, individual digital computer tapes are produced for each experimenter which contain the data from his own experiment, timing information, observatory housekeeping parameters (spacecraft temperatures, voltages, etc.), and orbital data. The experimenters will receive two sets of tapes, one containing data telemetered from the observatory and timing information, and the other containing the orbital data and timing information. The merging of these data by use of the common timing information will be done by the experimenters as a part of their more complete data analysis. This procedure will avoid delaying the telemetry data processing until the final orbit is determined, and will permit easier updating of data tapes if this is necessary.

The production data processing is primarily a sorting operation, providing the experimenters with raw data as telemetered from their instruments. All calibrations, corrections, coordinate transformations, etc. will be computed by the experimenters as a part of their data analysis, so that they may maintain close supervision over these operations.

Data Acquisition

Data acquisition for both the EGO and POGO will be accomplished by primary and

secondary stations which will have the capability of receiving and recording both the digital and special purpose telemetry at the maximum data rates. The signals will be demodulated and recorded on magnetic tapes, which will be forwarded to Goddard for processing.

The distinctions between the primary and secondary stations are in the sizes of the receiving antennas and the capability for local data processing. The primary stations have 26 m diameter parabolic antennas and PCM data-handling equipment to permit limited decommutation and data display for use in controlling the observatory subsystems. The secondary stations have 12 m diameter parabolic antennas and no decommutation equipment. Primary stations are located at Rosman (North Carolina) and at Fairbanks (Alaska) and secondary stations are located at Johannesburg (South Africa) and Quito (Ecuador). These four stations provide EGO orbital coverage about 95 percent of the time, and about 11 percent POGO orbital coverage. Of course, the on-board tape recorders afford 100 percent coverage for digital data at the lower data bit rates.

Tracking

The Worldwide Satellite (Minitrack) network will track the OGO's by use of the RF interferometer technique. This is an angle measuring system whose accuracy is expected to be marginal for the EGO mission since that observatory spends a large fraction of its time at large distances from the earth. Minitrack stations are located at Antofagasta (Chile), Blossom Point (Md.), College (Alaska), East Grand Forks (Minn.), Fort Myers (Fla.), Johannesburg (South Africa), Lima (Peru), Goldstone (Calif.), Saint Johns (Newfoundland), Quito (Ecuador), Santiago (Chile), Woomera (Australia), and Winkfield (England). A range and range-rate (two-way Doppler) system will also be used to permit a much more accurate and rapid orbit determination. Range and range-rate stations are located at Carnarvon (Australia), Johannesburg (South Africa), and Rosman (N.C.).

Tracking data from both types of station will be sent via teletype to Goddard where they will be used for orbit calculations. The orbital information will be furnished to the experimenters and to all ground receiving stations to permit them to properly direct their antennas toward the observatory.

The Quick-Look Data System

The Quick-Look Data System, consisting of the Rosman primary data acquisition station, the Rosman-Goddard microwave relay link, and the OGO Control Center at Goddard, will permit the display of telemetered data at Goddard on a real-time basis, and the immediate transmission of responding commands to the observatory. The microwave relay link has adequate bandwidth to relay both the digital and special purpose telemetry to Goddard simultaneously. The return link can relay digital or tone commands.

The arrangement of the OGO Control Center is shown in Figure 17. Incoming digital data are routed to the PCM decommutation equipment which preconditions the signals, detects synchronization, and formats the data for direct entry into the computer. The computer is a Scientific Data Systems model 920, generally similar to the ones used for checkout of the experiments before launch.

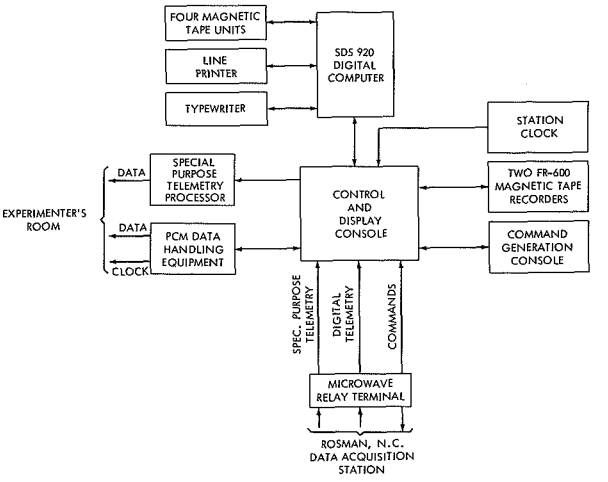

FIGURE 17.—Functional diagram of the OGO control center located at the Goddard Space Flight Center. showing details of the quick-look data system.

A number of uses of the Quick-Look Data System are planned:

Spacecraft Status Checks

The appropriate program is selected and read into the computer memory. The program causes the computer to select the telemetry words containing spacecraft instrumentation data. Each data word is compared with predefined upper and lower limits to determine if its value is within the range of acceptability. In addition, the data word is converted into its true value (in terms of engineering units) so it can be printed out in a form intelligible to station personnel. A printout of all out-of-tolerance data for each spacecraft subsystem can be obtained upon request (a pushbutton on the control and display console) by the station operator. A printout of all data is available from a 300-per-minute line printer. This printer will be kept on file as a permanent record of spacecraft performance.

Experiment Data Processing

The computer can be programed to perform routine status checks on experiments in much the same manner that they are performed on spacecraft systems. In addition, programs or sets of programs for each experiment aboard the spacecraft will permit a quick look at experiment data for the purpose of evaluating current performance, for calibration, and for monitoring the occurrence of especially significant events when a quick command response may be desired.

Use of Experimenter's Special Data Processing Equipment

The composite special-purpose telemetry signal will be available in an experimenter's room near the Control Center. An experimenter can locate his own special equipment there to process his data in any manner he may desire.

Command Initiation

The computer can be programed to initiate selected commands through the command console in response to specified results of the status checks. Alternatively, commands can be initiated manually. The commands are routed through the microwave link to the command transmitter at the Rosman station and thence, to the observatory. Commands can also be relayed through the other data acquisition stations by teletype.

Data Recording

Two magnetic tape recorders record the incoming telemetry signals, ground time (GMT) and housekeeping data. The recorded data may be played back into the Quick-Look Data System after a real-time pass has been completed, to provide the opportunity to investigate, in greater detail, the nature of unusual events which may have occurred during the real-time pass.

Production Data Processing

The Production Data Processing System converts data from the data acquisition station magnetic recording tapes into a form which is easily used by the experimenters, as shown in Figure 18. This processing operation is divided into four phases:

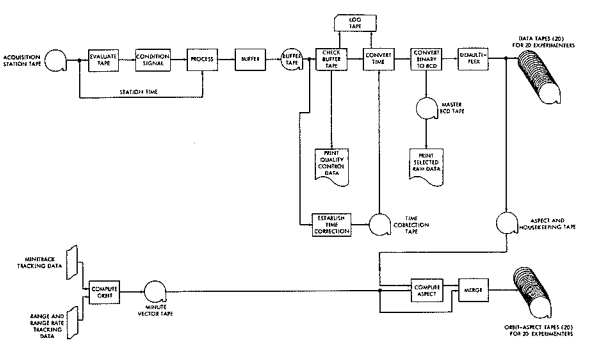

FIGURE 18.—Flow chart for the processing of OGO data and computation of the orbits.

Phase I—Production of Computer-Compatible Buffer Tapes

Depending upon the location of the data-acquisition station, shipment of tapes from the station to Goddard may take from 2 days to 2 weeks. Upon receipt, the tapes will be logged and the contents of the tape will be examined to permit a quick feedback to the data acquisition stations for rapid correction in the

event of equipment malfunction or the use of incorrect procedures.

The tapes will be handled differently, depending on the bit rate in use and whether the data are real-time or on-board recorded, so that the buffer tape created as an end result of the Phase I operation will contain the data in a uniform format. For the first few weeks after launch, tapes will be processed in the order in which they are received; after that, they will be processed chronologically.

The primary functions of the signal conditioner are to establish bit synchronization and to reconstruct the data in a noise-free form. The data processor establishes frame and submultiplexer sequence synchronization. It also combines the data with the acquisition station time.

Phase II—Generation of the Individual Experimenters' Tapes

This operation will use a digital computer whose ultimate outputs will be demultiplexed experimenter data tapes and an aspect-housekeeping tape. The computer will also ascertain whether the data quality has deteriorated in the satellite, during telemetry, or in the Phase I operation.

The task of correlating universal time and the data will be performed during the time-conversion portion of Phase II. A time-correction tape, generated as a part of the Phase III operation, will contain a lookup table listing universal time as a function of the contents of the spacecraft time word register. In order to associate a particular data frame with the proper time, it will be necessary to examine the contents of the telemetered time words, look up the corresponding universal time on the time-conversion tape, and insert this value in the time field. This scheme will provide an ultimate accuracy of about 6 milliseconds.

A master BCD (binary coded decimal) tape containing all data will be generated for further use by the processing personnel on an off-line basis.

The demultiplexing routine is programmed to place only the information needed by each individual experimenter on his digital data tape.

The processing of the Special-Purpose Telemetry is tailored to the detailed requirements of the experimenters who use it. In general, copies of the demodulated signal tapes are furnished to the experimenter who is then responsible for further processing.

Phase III—Production of Time Conversion Information

The Phase III operation will result in the generation of a time-correction tape which will permit the conversion of spacecraft time to corrected universal time. The spacecraft time contained on the real-time telemetry tapes and the acquisition-station tape will be compared on a routine basis. Propagation delays in transmitting data from the satellite to the stations (about 0.4 sec. from EGO apogee) and from the standard time station WWV to the receiving stations (0.058 sec. for Woomera, Australia) will be taken into account, as well as any time variations and discontinuities, if they exist, of the basic spacecraft clock. Data time can be determined with an accuracy of about 1 second if the available numbers are used and no additional computations are performed. Six-millisecond accuracy is possible by performing a timing interpolation.

Phase IV—Generation of the Orbit-Attitude Tapes

An orbit tape obtained from the standard orbital parameter computation and the aspect housekeeping tape serve as inputs to this phase. The output orbit-attitude tapes contain a block of information for each minute of the observatory lifetime. Included on these output tapes are time, satellite position and velocity, the location of the subsatellite point on the earth's surface, the ideal observatory orientation computed on the basis of the orbital information only, and the actual orientation computed with the knowledge of the attitude control subsystem error angles and array angles.

CONCLUSION

The Orbiting Geophysical Observatory program includes the development and use of a large standard spacecraft, the necessary testing and calibration equipment and techniques, the

data acquisition and tracking ground station networks, and the data processing system, and provides support for the development of experiments and the analysis of the data. Thus, it provides a suitable working environment for the experiments in space, and delivers data to the experimenters in a form suitable for entry into a computer for analysis. These facilities will allow scientists to perform large numbers of geophysical experiments in a variety of possible orbits for extended periods of time. The scientists retain the full responsibility for the development and preparation of the experiment instrumentation and for the analysis and publication of the data from their experiments. It is hoped that this observatory concept will be of great value in the investigation of phenomena in space.

BIBLIOGRAPHY

DAVIS, R. B., and WIGGINS, E. T.: 1962, "Automation for Spacecraft Ground Support Equipment," *Proc. Inst. Soc. of America* 8, 33.

GLASER, P. F.: 1962, "The Orbiting Geophysical Observatory Communications and Data Handling Subsystems," *Proc. of the 1962 National Telemetering Conference* 2, 3–3.

LUDWIG, G. H., and SCULL, W. E.: 1962, "The Orbiting Geophysical Observatory—New Tool for Space Research," *Astronautics* 7, 24.

SCULL, W. E., and LUDWIG, G. H.: 1962, "The Orbiting Geophysical Observatories," *Proc. Inst. Radio Engrs.* 50, 2287.

STAMBLER, I.: 1963, "The OGO Satellites," *Space Aeronautics* 39, 70.

OPERATIONS WITH AN EXPERIMENTAL SATELLITE

D. G. MAZUR

Goddard Space Flight Center

The operational aspects of an engineering type experimental satellite are considered in light of the techniques and procedures employed and experience gained in the successful in-orbit operation of the RELAY communication satellite.

Requirements for satellite command and real-time telemetry data reduction and evaluation are emphasized and the actual system employed for RELAY is described. Real-time checkout and evaluation of the satellite's wideband communication subsystem is similarly discussed. The manner in which these capabilities were employed is illustrated with specific examples given.

Need for a central operational control point is considered with specific emphasis on communication satellites. The operations center for RELAY is described and its functions detailed. The operational support communications, such as teletype, telephone and video monitor links, required to perform effective control of the satellite through the test and control station and coordination of the complex of ground stations is illustrated. Specific capabilities and potentialities of this center are detailed.

In addition, the procedure required to assure an effective schedule of experiments is given. The required monthly, weekly and daily plans for scheduling communication experiments and station participation are discussed and their relative importance explained.

OPERATIONS WITH AN EXPERIMENTAL SATELLITE

In the design of an experimental satellite system, the operational considerations are sometimes compromised or perhaps ignored to some degree. There is always interest in designing, building, and launching new satellites, but once in orbit the job is considered complete. The operations phase is left to some obscure group to turn on the telemetry system occasionally to gather data to be mailed to some location for automatic processing and storage for subsequent analysis at a later date. These are the procedures which often characterize satellites which are strictly scientific in nature. The operational considerations for an experimental satellite system such as RELAY are more critical in that because of power requirements it is necessary to monitor telemetry during each orbit pass that the wideband transponder is used. Additionally, the complex task of scheduling and conducting communications experiments with several different participating countries require full time attention. Some of these aspects as they relate to Project RELAY are discussed below.

Project RELAY is an experimental communication satellite program whose purpose is to demonstrate the feasibility of wideband and narrowband communications between Europe, South America, and the United States using a low-altitude repeater earth satellite. This system is comprised of the orbiting satellite, the participating communication stations in the United States and other countries, two GSFC control and test stations, and an operations center. Figure 1 is a simplified block diagram of the RELAY system.

The external configuration of the RELAY spacecraft is that of an octagonal cylinder topped by an octagonal truncated cone. The cylindrical portion is 29.22 inches in diameter and 16.45 inches high. The truncated cone portion is 15.25 inches high and is shaped to conform to the shape of the Delta launch vehicle low drag nose fairing. With the exception of the upper and lower surfaces the entire spacecraft is covered with solar cells.

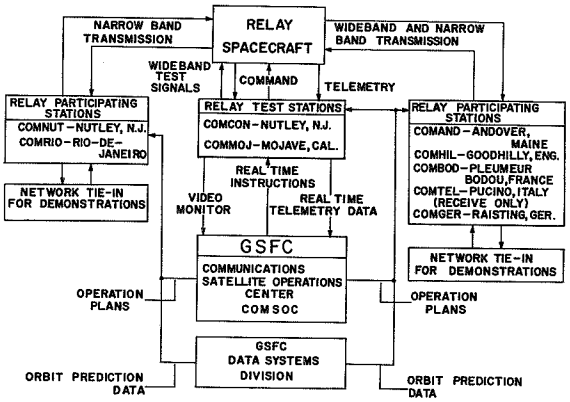

FIGURE 1.—Relay system block diagram.

The wideband communication antenna is mounted on a boom which extends 19 inches above the truncated portion of the spacecraft. Figure 2 shows the external view of the spacecraft. The spacecraft was designed to support a total of 100 minutes per day of the wideband communication subsystems operation. This total operating time was to be accumulated on three or four successful orbit passes and since the orbit has a period of three hours, this operation would be covered over a period of approximately 12 hours per day. RELAY satellite also carries a radiation experiment package to determine the effects of radiation on solid state devices, in particular, solar cells, and to evaluate these effects in terms of lifetime of possible usage in future communications satellites. Thirty different solar cells are being tested in this experiment along with several diodes. Figure 3 is a cutaway diagram showing basic features of the spacecraft.

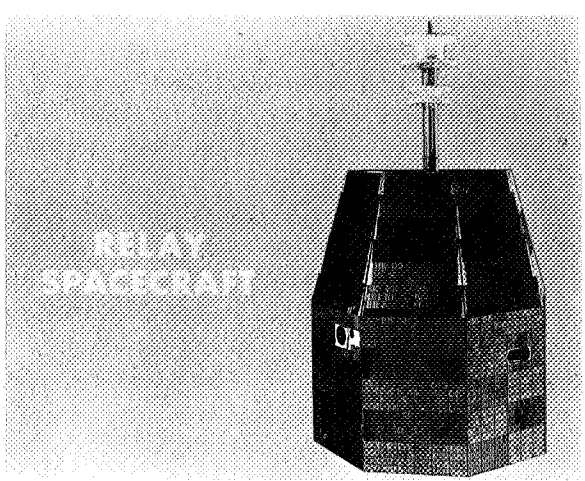

FIGURE 2.—External view of spacecraft.

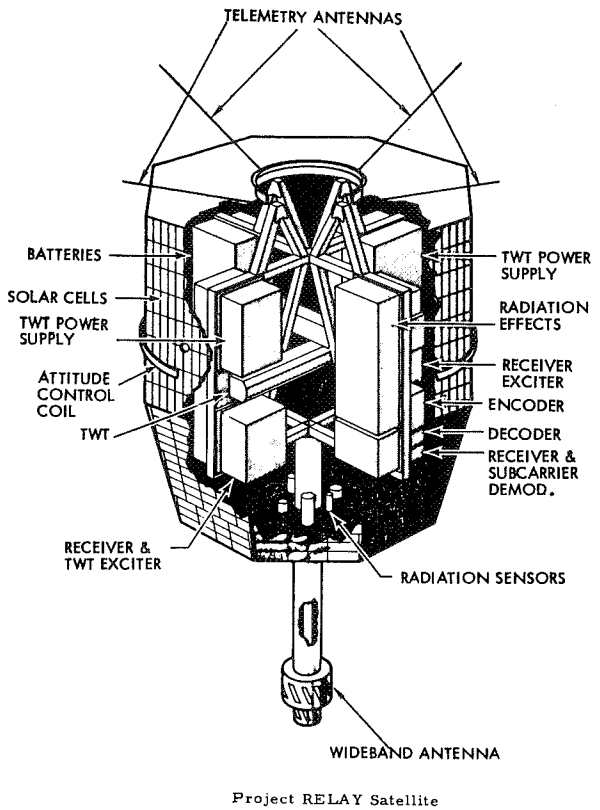

FIGURE 3.—Cutaway view of spacecraft.

RELAY I was successfully launched on December 13, 1962, in a nearly precise nominal orbit. Figure 4 gives a table of RELAY orbital characteristics along with the nominal values that were expected.

The participating stations consist of the American Telephone & Telegraph station at Andover, Maine (COMAND); the International Telephone & Telegraph station at Nutley, N.J. (COMNUT); British Post Office station, Goonhilly Downs, Cornwall, England (COMHIL); C.N.E.T. station, Pleumeur-Bodou, France (COMBOD); Telespazio, Fucino, Italy (COMTEL); and Radional at Rio de Janeiro, Brazil (COMRIO). The Deutsche Bundespost of Germany is completing a station at Raisting, Germany, which will be operational in mid-1964. The Japanese Government is also par-

RELAY Orbit Characteristics

Item	Nominal	Actual
Height of Apogee	3999.48 nm	4020.70 nm
Height of Perigee	699.92 nm	712.13 nm
Period	184.36 min	185.09 min
Eccentricity	0.28475	0.28462
Inclination	47.766°	47.496°
Right Ascension of Ascending Node (injection)	217.22°	218.74°
Argument of Perigee (injection)	176.426°	177.5°
Nodal Rate	-1.2845°/day	-1.2779°/day
Perigee Rate	1.2030°/day	1.2123°/day

FIGURE 4.—Relay orbit characteristics.

ticipating in the program and will have a station with receiving capability in the latter part of 1963. The Andover, Maine, and Pleumeur-Bodou, France, ground stations are very similar and employ a 60-foot horn for wideband and narrowband transmissions and reception, and can either auto- rack or be used in a program track mode. Figure 5 depicts the Andover Horn with the radome removed. The Goonhilly, England, site employs an 85-foot parabolic reflector which does not have auto-track capability and tracks by means of program drive tapes. Figure 6 is a picture of the Goonhilly Antenna. Goonhilly is also used for both wideband and narrowband communi-

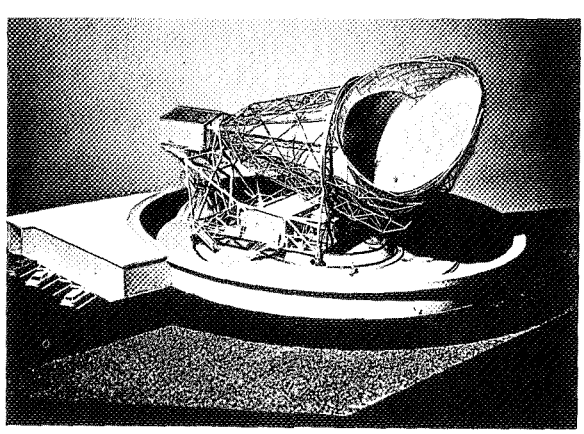

FIGURE 5.—Andover horn antenna.

cations. The Fucino, Italy, site does not yet have the capability of transmitting and is only used for wideband and narrowband reception. The ITT station at Nutley, N.J., and the Rio de Janeiro sites are primarily narrowband stations and are used extensively for two-way

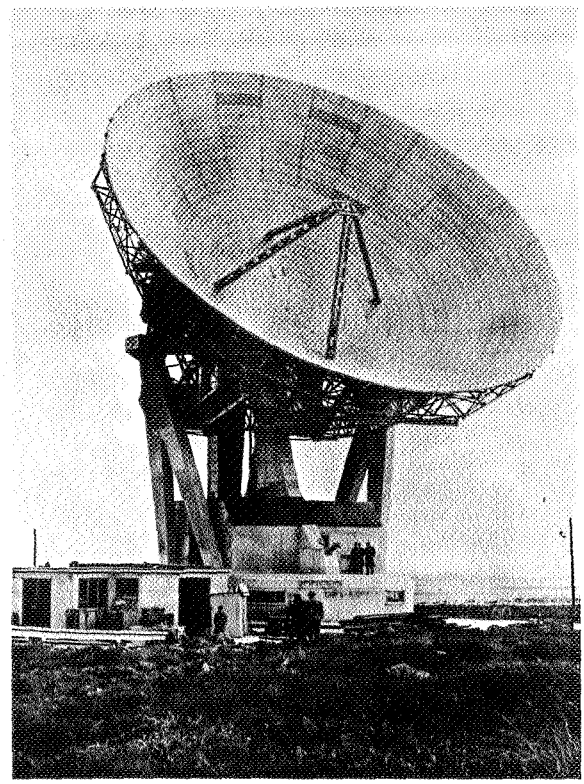

FIGURE 6.—Goonhilly antenna.

narrowband communication experiments between the United States and South America. Figure 7 is a picture of the Rio station.

The two GSFC control and test stations are located at Nutley, N.J , and Mojave, Calif. The Nutley site shares the common antenna with the ITT station which is a 40-foot cassegrain antenna. This test station (designated COMCON for communications control) is contained in two mobile trailers which are joined to form a single unit. Figure 8 gives an overall view of the Nutley site showing both COMCON and COMNUT. A separate antenna is used for the command and telemetry functions performed by the test stations. The other test station located in Mojave, Calif. (COMMOJ), is essentially identical to the Nutley site with the exception of the wideband test capability and the communication antenna. COMMOJ utilizes a 40-foot parabolic antenna on an XY mount. (See Fig. 9.) The antenna used for command and telemetry purposes at Mojave is identical to the one employed at Nutley.

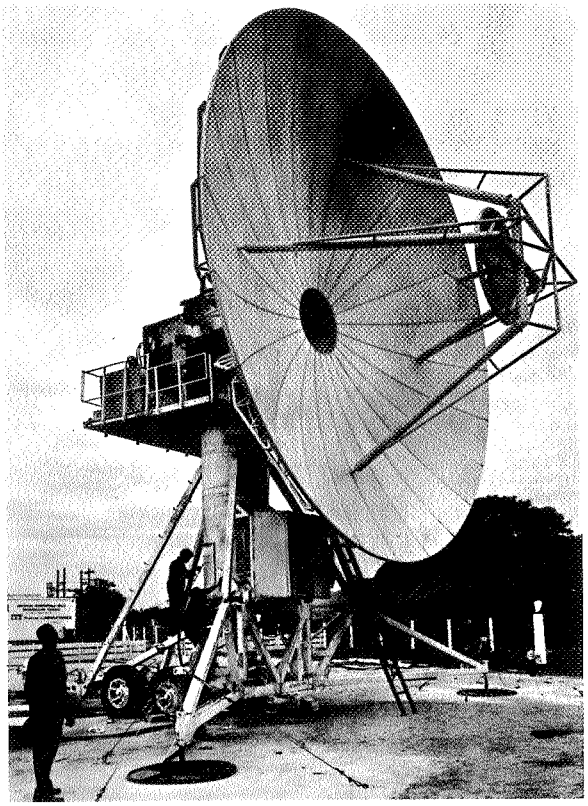

FIGURE 7.—Rio de Janeiro station.

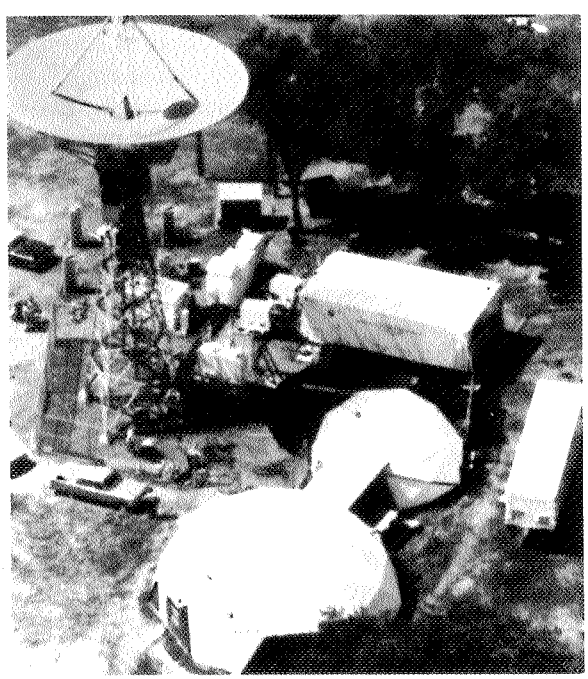

FIGURE 8.—Overall view of COMCON and COMNUT.

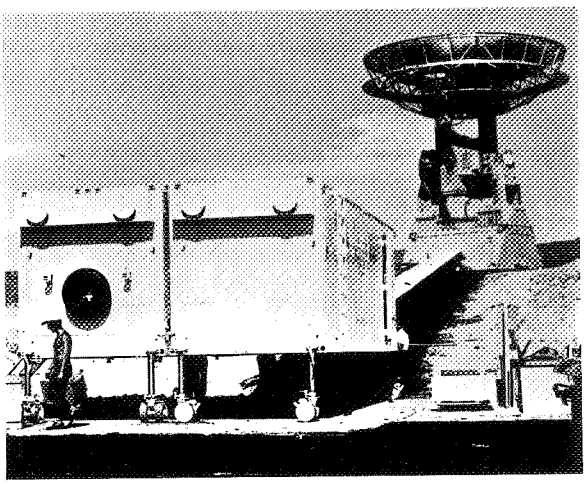

FIGURE 9.—View of COMMOJ.

The central point of the RELAY system is the operations control office at Goddard Space Flight Center. This office designated "COMSOC" for Communication Satellite Operations Center is used to direct all command and control of the satellite, evaluation of real-time data, and as the office through which all communications experiment scheduling and coordination is conducted. COMSOC issues all operation plans and experiment schedules and acts as a clearinghouse for orbital predictions and correlated data. Figure 10 is a typical view of COMSOC during an orbit operation. Figure 11 lists the specific functions performed by COMSOC.

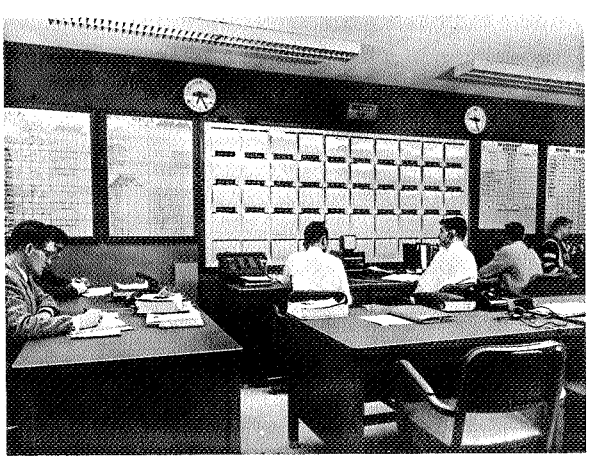

FIGURE 10.—Communication Satellite Operations Center.

FUNCTIONS OF COMSOC

a. Perform Day by Day Orbital Operations of Satellite
b. Issue all Commands to Test Stations to Control Satellite
c. Maintain Real Time Contact with Participating Stations During Operations to Ensure Effective Coordination of Experiment Including Cuing and Hot Switching
d. Analyze Class II Data Both in Real Time to Effect Satellite Control and Over Long Term Periods to Determine System Deterioration
e. Coordinate and Issue all Monthly, Weekly and Daily Operation Plans
f. Summarize All Station Operation Reports and Issue Daily Summaries to Include Spacecraft Performance and Correlated Data
g. Act as Clearing House to Ensure Issue of Orbital and Pointing Data to All Participating Stations

FIGURE 11.—Functions of COMSOC.

The RELAY satellite is operated daily on many successive orbit revolutions. Because of the practical size limitations on the power supply and since the wideband subsystem represents a severe electrical load, it is necessary to exercise precise control in order to realize maximum utilization of available power. This can only be effected through the means of reliable command capability and real-time telemetry data readout. These functions are performed by COMSOC utilizing the test station in a remote manner to provide the command and telemetry function at the direction of COMSOC. These functions become more critical when one considers the necessity for turning on the spacecraft at a prescheduled time in order that one or more communication stations can conduct experiments. The actual control of the satellite is performed by the COMSOC COMCON combination with direction being supplied by COMSOC.

Controlling the experimentation on RELAY is a continuous problem because each station has a diversified capability unique to itself. In addition, the variety of engineering communication experiments which were generated to be conducted are complex by their nature. These require adequate coordination so that the stations participating are assured of adequate test setup time. Of course, one aspect not to be neglected is that RELAY has the capability of supporting public demonstrations of television, teletype, facsimile and telephony. To make certain that these demonstration experiments are started at the precise time that the transponder is available, COMSOC has been used to cue the program network.

It is necessary to have full-period teletype and telephone hookup between COMSOC and most participants. This is required in order to transmit the operations plans and summaries and routine operational teletype traffic. Pointing data supplied to all stations is also teletyped over these same circuits. The full-period telephones are used for real-time coordination and cuing during the operational passes. Figure 12 gives a block diagram of the ground communication network with COMSOC.

Hot switching has been one other function possible with the use of COMSOC and the test station. This has enabled narrowband telephony tests between COMHIL and COMRIO followed by wideband television tests from COMAND, to COMBOD during the same 30-minute pass. Less than 10 seconds' switchover has been required. The transponder was commanded to the wideband mode at the prescheduled time with COMHIL and COMRIO instructed to cease transmission of carrier. At the same instant COMAND and COMBOD were instructed to commence television tests. These so-called Hot Switches were conducted several times between the communication station to illustrate a flexibility that allows

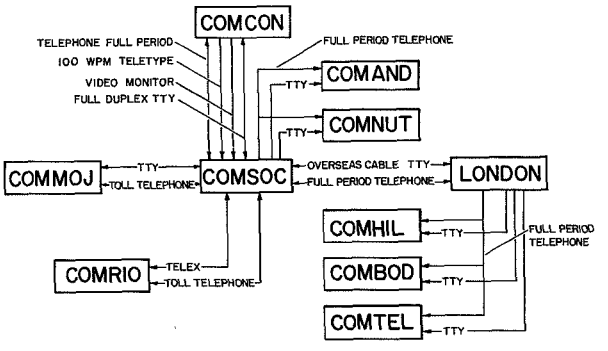

FIGURE 12.—Ground communications network.

maximum utilization of the available satellite visibility and transponder operation time.

The day-by-day operational planning and scheduling is performed at COMSOC in the following manner. An arbitrary assignment of operating days is made for each week by discussing the appropriate availability with each station. This leads to the generation of a monthly plan which assigns operational days to each station. The orbit is examined for this time period and the stations are scheduled by orbit pass number based upon adequate visibility between the participating station and COMCON. Since COMCON is used as the primary telemetry and command post, no passes are scheduled which are not in mutual visibility with COMCON. After assignment is made of particular orbit revolutions, the available spacecraft power, slant range, spacecraft look angles, and elevation angle constraints are considered and an approximate time period for the experiment is determined. This time is then further modified by the amount of telemetry data that is desired to be examined prior to and after the wideband operation. Coordination with participants is conducted both with teletype and full-period phone circuits until a detailed weekly plan can be generated. The resulting schedule is then teletyped to all participants to obtain their comments and inputs on RELAY experiments to be scheduled for the times indicated. A detailed daily operations plan, which incorporates all last-minute changes and recommendations, is finally teletyped to all participants by COMSOC and actual orbit pass is conducted in accordance with this schedule.

All orbit data on RELAY are generated by GSFC based on tracking data from the NASA minitrack stations and spatial orientation based on horizon scanner information from the satellite. This information takes the form of pointing data predictions in terms of azimuth and elevation angles and spacecraft look angles for each station. The pointing data are used by all stations for satellite acquisition and antenna steering. The look angle data are used in calculation of satellite antenna gain in analysis of communications experiments. COMSOC sends the look angle data to the stations on a continuous basis and makes certain that the pointing data are also sent.

One important consideration which has attributed to the success of COMSOC is the orbit data that is available. Printouts of slant range, elevation angle, azimuth angle, and spacecraft look angles for each station are maintained at COMSOC. These are listed for 1-minute intervals over the orbit revolutions for several weeks in advance. The high degree of accuracy of these data have allowed efficient scheduling of the experiments and has added much to controlling the operations.

As previously mentioned, COMCON provides the actual command function of the satellite. Further, the telemetry data are received and processed at COMCON for transmittal to CONSOC. In addition, it is necessary to perform loop tests with the wideband transponder independent of the formal communication experiments to determine if the wideband system is working as expected. These requirements dictate that the control and test station (COMCON) must have the capabilities listed in Figure 13.

TEST STATION CAPABILITIES

a) DETERMINING THE OPERATING CONDITION OF THE SPACECRAFT BY MEANS OF REAL-TIME TELEMETRY READOUT AND DISPLAY

b) OBTAINING QUICK-LOOK TELEMETRY FOR DAILY MONITORING OF THE SPACECRAFT CONDITION AND TRANSMITTING THESE DATA TO THE OPERATIONS CENTER BY TELETYPE

c) RAPIDLY TESTING THE PERFORMANCE OF THE SPACECRAFT WIDEBAND COMMUNICATION SUBSYSTEM

d) CONTROLLING THE SPACECRAFT BY RADIO COMMANDS AS REQUIRED BY THE EXPERIMENT TO BE PERFORMED

e) CONDUCTING WIDEBAND EXPERIMENTS WITH THE SPACECRAFT

FIGURE 13.—Test station capabilities.

The spacecraft's telemetry system consists of two telemetry transmitters which are redundant and a single encoder. The system is Pulse-Code-Modulated with 1,152 bits per second rate. Each telemetry word is comprised of 9 bits and this results in 128 main telemetry words. A large portion of these are used to telemeter information from radiation experiments. Only 10 of the main frame words are used for moni-

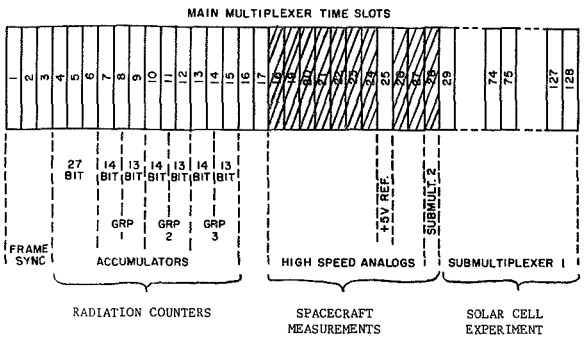

FIGURE 14.—Telemetry main frame word assignment

toring spacecraft performance. Figure 14 shows the assignment of the main frame words. One of the main frame words (28) is submultiplexed into 64 channels. In all, this provides 73 telemetry items for monitoring spacecraft subsystem performance.

Figure 15 shows the telemetry receivers at COMCON. The telemetry transmitters on the spacecraft transmit on 136.620 and 136.140 mc, respectively. COMCON is capable of receiving telemetry on either frequency.

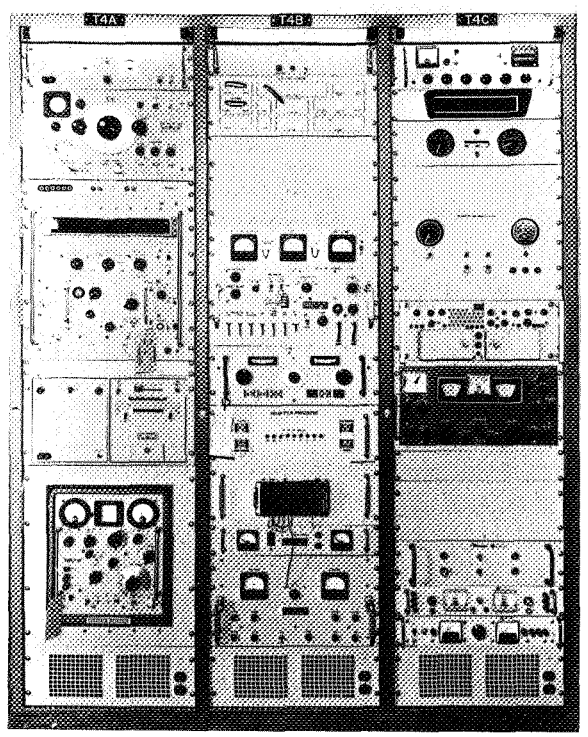

FIGURE 15.—Telemetry Receivers at COMCON.

The telemetry data have been separated into three categories: Class I, Class II, and Class III. The first of these, Class I, consists of 11 items which are decommutated at the test station and displayed on the strip chart recorder for real-time evaluation during an orbit pass. Six of these Class I items are further processed to provide signals through a limit checker which will give a green or red light indication at the test station to provide a rapid indication when these items are exceeding their expected limits.

The second category of data, Class II, consists of 39 spacecraft performance measurements, plus 8 radiation experiment measurements which are processed at the test station by a Packard Bell 250 computer. These reduced data are teletyped in real time to COMSOC by means of a 100-word-per-minute teletype circuit. Figure 16 shows the PB 250 computer which takes the raw telemetry bit stream, senses and corrects for the zero and 5-volt calibration, multiplies by the necessary linear calibration to reduce the raw data to final printout. This output is printed on plastic tape which is com-

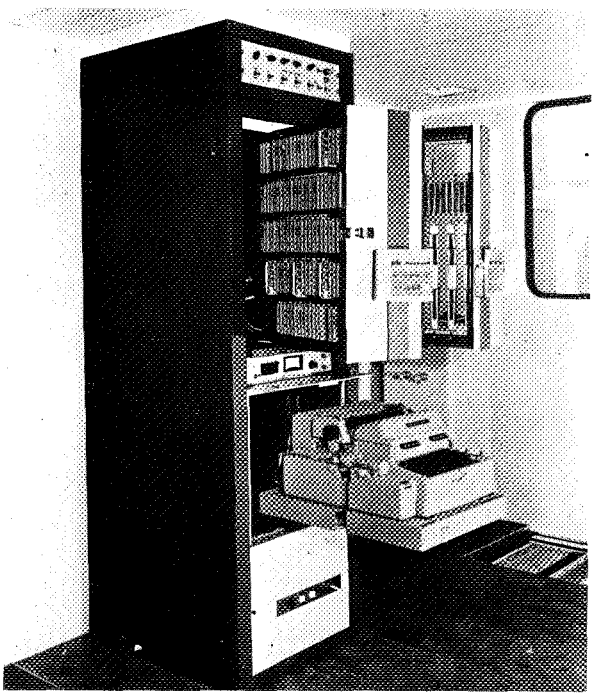

FIGURE 16.—Packard Bell 250 computer.

patible with the five digit code teletype format. A teletype tape distributor is located a few inches from the computer output tape. The tape distributor drives the 100-word-per-minute machine and provides the printout at COMSOC.

The remaining category of telemetry data actually consists of all of the received signals which is recorded as raw bit stream on magnetic tape for later processing and reduction by GSFC Data Processing Branch. Figure 17 shows the strip chart recorder for Class I and magnetic recorders for Class III data. Figure 18 gives block diagram of telemetry flow.

The Class I items have been selected because these represent the most critical measurements which indicate real time changes in the spacecraft condition. All the command verification voltages which are translated to command states of the spacecraft are also included. Figure 19 gives listing of the Class I items. Class I items can be decommutated and displayed independent of the Class II items. When difficulties with the computer are encountered making it impossible for Class II

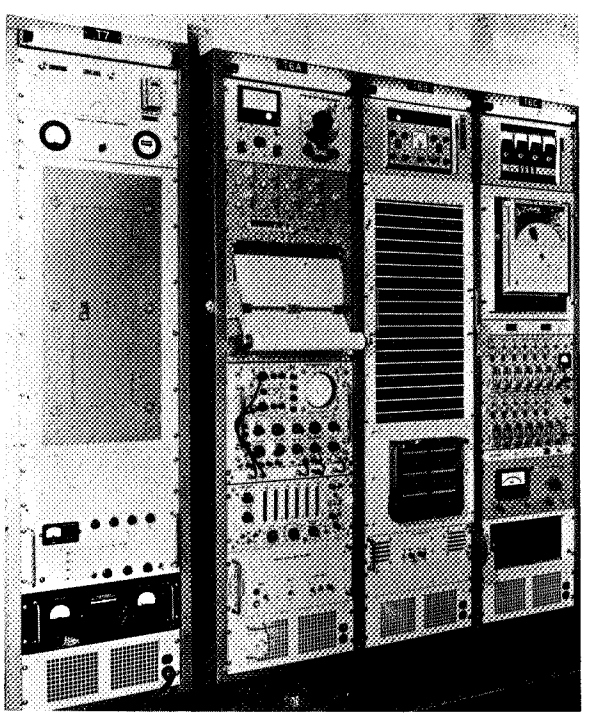

FIGURE 17.—Strip chart and magnetic tape recorder.

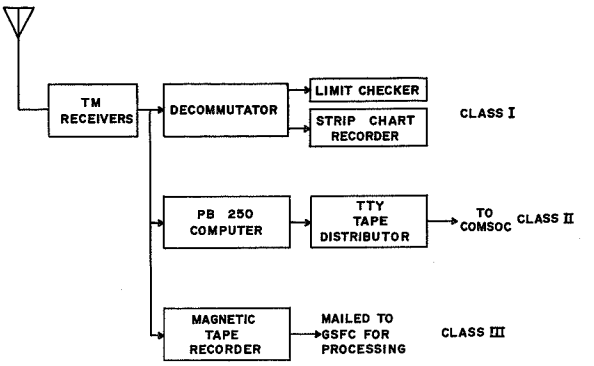

FIGURE 18.—Telemetry flow diagram.

CLASS I DATA

TELEMETRY WORD	ITEM	SAMPLE RATE
18	SOLAR CELL BUS VOLTAGE	1/SEC
20	TOTAL BATTERY CURRENT	1/SEC
21	COMMAND VERIFICATION JKL	1/SEC
24	*MAIN IF AGC VOLTAGE	1/SEC
28-11	*RADIATION EXPERIMENT REGULATED BUS	1/64 SEC
28-16	*TRANSPONDER REGULATED BUS	1/64 SEC
28-17	*BATTERY NO. 1 VOLTAGE	1/64 SEC
28-24	*TWT POWER OUTPUT	1/64 SEC
28-35	COMMAND VERIFICATION ABC	1/64 SEC
28-43	COMMAND VERIFICATION DEF	1/64 SEC
28-51	COMMAND VERIFICATION GHI	1/64 SEC
28-58	*BATTERY 3-2 TEMPERATURE	1/64 SEC

* ITEMS FURTHER PROCESSED THROUGH LIMIT CHECKER

FIGURE 19.—Class I data list.

CLASS II DATA

TM WORD	ITEM	TM WORD	ITEM
18	SOLAR CELL BUS VOLTAGE	28-24	TWT OUTPUT POWER
19	UNREGULATED BUS	28-25	BATTERY NO. 2 VOLTAGE
20	TOTAL BATTERY CURRENT	28-26	BATTERY #1-2 TEMPERATURE
21	COMMAND VERIFICATION JKL	28-27	TM XMTR #2 POWER OUTPUT
22	ACTIVE THERMAL CONTROLLER SENSOR TEMP	28-32	BEACON OUTPUT POWER
24	WB-AGC-MAIN IF	28-33	BATTERY NO. 3 VOLTAGE
26	NB SIGNAL PRESENT	28-34	BATTERY #2-1 TEMP
28- 2	SOLAR PANEL 4A-1 TEMP	28-35	COMMAND VERIFICATION ABC
28- 3	BATTERY PRESSURE, NOS. 1, 2, 3	28-41	SOLAR CELL BUS CURRENT
28- 4	VOLTAGE LIMITER CURRENT	28-42	BATTERY #2-2 TEMP
28- 5	TWT #1 POWER SUPPLY	28-43	COMMAND VERIFICATION DEF
28- 7	THERMISTOR NO. 4 TEMP	28-44	WIDEBAND BASEPLATE TEMP
28-10	SOLAR CELL PANEL 4A-2 TEMP	28-47	XMTR L.O. OUTPUT
28-11	RADIATION EXPT REGULATED BUS	28-50	BATTERY #3-1 TEMP
28-12	TWT COLLECTOR TEMP	28-51	COMMAND VERIFICATION GHI
28-13	PWR. SUPPLY #2 TEMPERATURE	28-55	TRANSMITTER INPUT SIGNAL POWER
28-16	REGULATED BUS VOLTAGE	28-58	BATTERY #3-2 TEMP
28-17	BATTERY NO. 1 VOLTAGE	28-59	COMMAND RECEIVER AGC
28-18	BATTERY #1-1 TEMPERATURE	4,5,6	RADIATION MONITOR "A"
28-19	TM XMTR NO. 1 POWER OUTPUT	16-17	SUN ASPECT INDICATOR
28-21	LOWER SURFACE TEMP	29-128-2-7	SOLAR CELLS S-1 TO S-6

FIGURE 20.—Class II data list.

data reduction and printout, and subsequent transmittal to COMSOC in real time, the passes have been conducted using Class I data exclusively.

The real-time reduction of many spacecraft performance measurements as are included in Class II (see Fig. 20 for listing of Class II data items) becomes the real significant operational tool for experimental satellites. Utilizing this capability has allowed us to accumulate per-

formance data in real time while critical functions were being conducted on the spacecraft. It has enabled real-time verification of the command states of the spacecraft which gives one the opportunity for correcting anomalous command states if they should occur. It also allows real-time verification that commands transmitted to the spacecraft were successfully received. Of course, the telemetry items themselves provide additional verification when subsystems are operating, thereby supplying proof that commands were received and acted upon successfully. The Class II data provide a printout of 39 spacecraft performance measurements which include the 4 command verification voltages and also the printout of 8 items from the radiation experiment package. Seven of the 39 items are main frame words and 6 of these are printed out every 16 seconds. The remaining 32 items are submultiplexed channels of main word 28 and are printed out each time they are sampled in the spacecraft or at a rate of every 64 seconds. Figure 21 shows the typical format of the Class II data printout.

If one considers a typical block starting with the symbol 02, this designator (02) is the channel number on the submultiplexer of word 28. The remainder of the first line includes subcom words 3, 4, 5, and 7. The next line contains the date time group printout with the main frame words. The letter N preceding the numbers refers to the station, in this case COMCON, where the data were received and reduced. In the same line, 63 is the year, 115 is the day of the year, 21 is the hour, 46 is the minute of the hour, and 35 the second within that minute. The word immediately following the date time group in the sample shown (Fig. 21) is main word 18, solar cell bus voltage which is reading 24.60 volts. The next word is the unregulated bus voltage main word 19 reading the same value. The remaining words in this line consist of main word 20 total battery current, main word 21, command verification voltage JKL, main word 22, active thermal control sensor temperature and main word 24 AGC main IF voltage which are reading 3.37 amps, 1.82 volts, 9.41°C and 2.57 volts, respectively. The last line of the sample given gives the output of six solar cells in the solar cell experiment, the proton total count of detector A of the radiation experiment package, the sun aspect indicator output and main word 26 which is the narrowband signal presence indication. The first three readings of this line beginning with 033, 031, and 031, are the output in millivolts of three solar cells which are identical to those used in the Relay main solar bus but which have no shielding. The item beginning with 094, 086, 091 are the output of three identical cells but with 30 mils of shielding. The proton counter detector A is reading 093022771 counts, and the sun aspect indicator output is 27 which is the decimal equivalent of a 6-digit binary output equivalent to a sun aspect of 10.2° from the equator of the satellite. The last reading, .78, is the narrowband signal presence indication main word 26. The symbol (/) in place of the decimal point indicates that the linear calibration data should be checked for precise interpretation of the number given.

```
02 19/0  03  /52  04 3.41  05 8/38  07  .01
  N63115214635 24.60 24.60  3/37 1.82 9/41 2.57
10 23/8  11 /10  12 11/9  13 11/8  16 22/8
17 24.9  18 3/91  19 -200/  21 -3/51  24 2.42
  N63115214651 24.51  24.51  3/28  1.82  9/35 2.57
25  4.56  26 8/67  27 241/  32 1.57
33  24.9  34 1/89  35  .73
  N63115214707 24.48  24.56  3/45 1.83  9/38 2.58
41  /96  42 3/55  43  .73  44 5/23  47 1.76
50 8/19  51 4.30  55  .20
  N63115214723 24.53 24.60  3/27 1.82  9/50 2.58
58 8/59  59 61/4
033 031 031 094 086 091 093022771 27  .78
```

CLASS II DATA FORMAT

FIGURE 21.—Class II data format.

There is approximately a 19-second delay between the time that these measurements are made in the spacecraft and printed out in COMSOC. This extremely short time delay makes the printout for all practical purposes in real time. This allows monitoring of battery discharge characteristics in real time, so one can command the transponder off should the spacecraft exceed lower acceptable voltage limits. It allows real time evaluation of the received signal strength from the ground stations in terms of the main IF AGC so it is readily discernible if a ground station is adequately transmitting

the proper power level or if troubles are being encountered in tracking the spacecraft. Monitoring of the radiation experiment and wideband transponder regulated bus voltage which are subcom words 11 and 16, respectively, gives real-time indication that these systems are either on or off and how well the regulated outputs are maintaining the required voltage level.

The RELAY command system uses the standard NASA command format with PCM/PDM/AM modulation which is compatible with all NASA Minitrack stations. However, as previously mentioned, command of the spacecraft is performed by the test stations to ensure real time control. Figure 22 shows the command encoder console at the test station. The transmitted commands sent to the spacecraft are verified by a printout on the two-channel chart recorder that can also be seen in Figure 22.

In addition to exercising command over the spacecraft and providing real-time telemetry for COMSOC, the test stations have the capability of transmitting and receiving communication data. Figure 23 is a picture of the wideband transmitter and is capable of transmitting

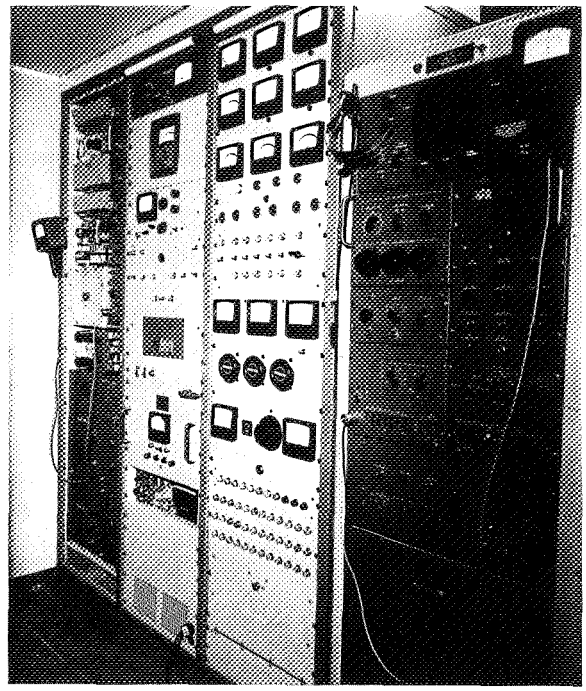

FIGURE 23.—Wideband transmitter.

a power of 10 kw. A variety of preselected test signals are transmitted to the spacecraft and received at COMCON for real-time subjective examination. Figure 24 shows the wideband test console which is used in the conduct of the experiments. Eighteen different tests signals can be transmitted, received, and analyzed. The console has the feature of a rapid switching

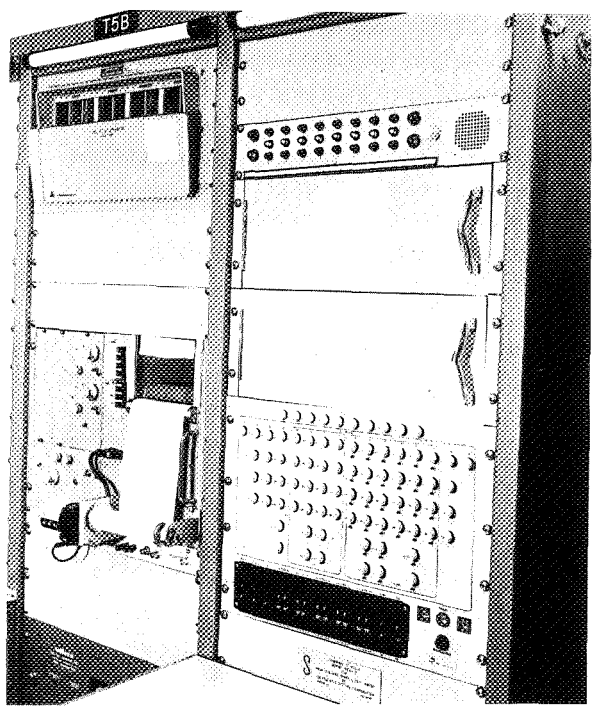

FIGURE 22.—Command encoder.

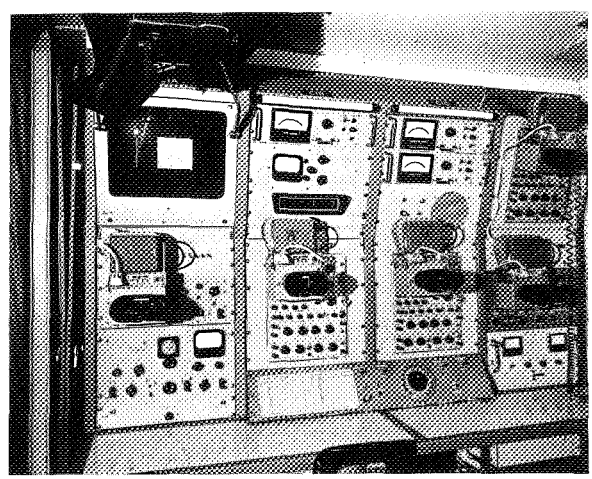

FIGURE 24.—Wideband test console.

capability which automatically switches the proper test channels in the console and displays results on the appropriate scopes and the TV monitor. This can be done in such a short period of time that a full sequence of 18 positions can be conducted during the course of a normal 30-minute wideband pass. This capability allows the test station to do real-time evaluation of the wideband transponder either prior to turning it over to a formal communication station for the conduct of an experiment or during a pass which is expressly scheduled for testing by COMCON. Further, during passes in which critical experiments are being conducted by other communication stations, the test station is capable of receiving these transmissions to monitor the performance of the wideband subsystem. A microwave link is used between COMCON and COMSOC to provide a display of the communications test being conducted so they may also be monitored as an aid to making the necessary decisions on whether experiments should be scrubbed because of poor conditions of the transponder. Continual examination of the transponder over a period of time will also lead to being able to detect deterioration of the system with respect to time; however, to date, after 4 months of operation, no apparent deterioration of the wideband system exists. The test positions and the experiments they represent are listed in Figure 25. Figure 26 shows a typical differential gain measurement test signal transmitted and received by COMCON. Figures 27 and 28 show some typical wideband demonstrations between Europe and the United States that were monitored by COMCON and COMSOC.

WIDEBAND TEST CAPABILITIES

Test Position	Experiment
1	Insertion Gain
2	Short-Time Distortion "T"
3	Short-Time Distortion "2T"
4	Continuous Random Noise
5	Television Slides
6	Field Time Distortion
7	Line-Time Non-Linearity
8	Stairstep
9	Bandpass Characteristics-Baseband
10	Envelope Delay Distortion
11	Synchronization Non-Linearity
12	Periodic Noise
13	Impulsive Noise
14	Fluctuation Noise
15	Fluctuation Noise
16	Fluctuation Noise
17	Fluctuation Noise
18	Multiburst Pattern

FIGURE 25.—Wideband test capabilities.

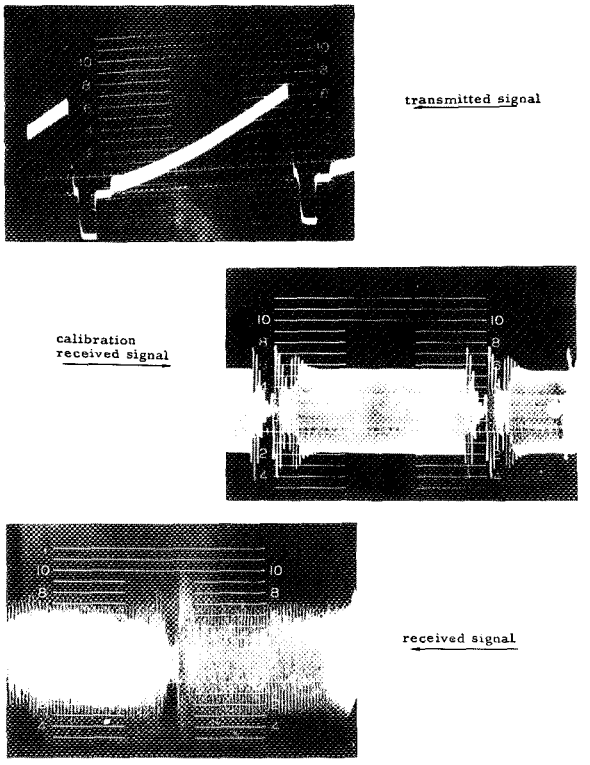

FIGURE 26.—Differential gain test transmission.

FIGURE 27.—Television demonstration monitor.

FIGURE 28.—Television demonstration monitor.

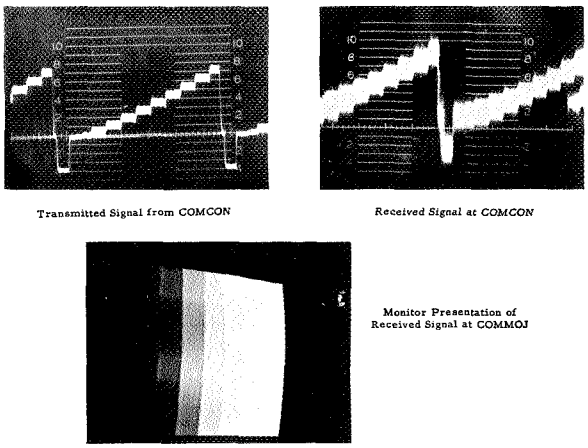

FIGURE 29.—Stairstep transmission received at COMMOJ

The test station at Mojave, COMMOJ, also has a wideband reception capability and this allows for communication experiment testing between the two test stations. When it is desirable to investigate specific areas in considerable detail and when participating stations are not available for experiments the test stations are used as the communication site. Figure 29 shows a stairstep test signal transmitted and received at COMCON and the resulting monitor presentation as received at COMMOJ. Figure 30 shows other COMCON test transmissions which were received at COMMOJ for subjective analysis.

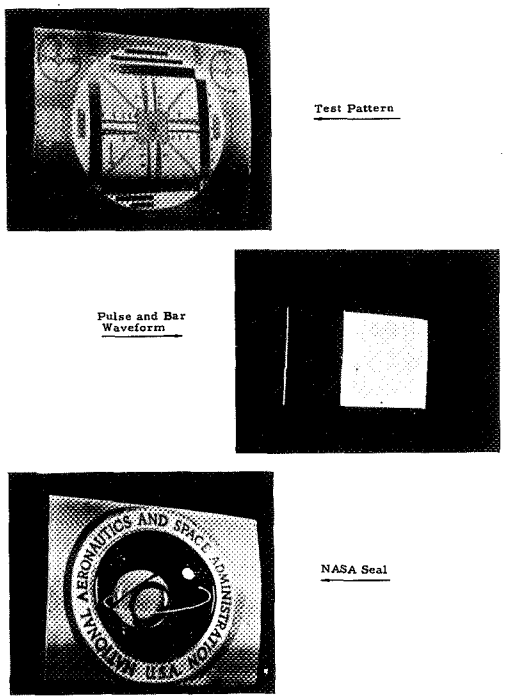

FIGURE 30.—Test pattern reception at COMMOJ.

ACKNOWLEDGMENTS

The successful conduct of the operations described in this paper represent the efforts of Mr. Wendell S. Sunderlin of Goddard Space Flight Center, responsible for Overall Operations on Project RELAY; Mr. John B. Flaherty of Goddard Space Flight Center, responsible for Ground Station Coordination; and Mr. Donald E. Kendall of Space Technology Laboratories, Inc., responsible for Operations Planning and the Day-by-Day Orbit Operations.

RELAY

SIDNEY METZGER
Communications Satellite Corp.

AND

ROBERT H. PICKARD
Goddard Space Flight Center

Relay I was launched into a nearly nominal orbit at 2330 GMT, December 13, 1962. As of Orbit 1826 on August 6, 1963, 189 hours of communications had been accumulated, and during this time 449 operations had been conducted. These were divided into 1,426 experiments and demonstrations of engineering and public interest.

This paper provides a general description of the subsystems of the spacecraft and their performance.

WIDEBAND COMMUNICATION EQUIPMENT

The purpose of this system is to provide an experimental repeater suitable for transmission of one TV signal (plus its sound channel) or 600 one-way voice channels; or of high-speed data, facsimile, or teletype traffic with bandwidths of up to 4 Mc. Two-way transmission tests through the repeater can be made, using 12 channels in each direction. This number is determined by the available ground-station equipment, rather than a limitation of the satellite repeater, which can handle several times this number.

Two completely independent wideband repeaters (except for the common antenna) are provided for increased reliability. Either one may be selected for operation by ground command.

The basic performance requirements of the satellite repeaters are similar to those used for conventional ground-based microwave links, so far as power output, bandwidth, gain, noise figure, and intermodulation are concerned. There are radical differences, however, in the size, weight, and power drain.

The system parameters were initially chosen to meet international (CCIR) standards (for a 2500-km reference circuit) between Europe and the United States. The sound channel is transmitted by frequency-modulating a 4.5-Mc subcarrier which is then added to the video signal, and the combination used to frequency-modulate the ground transmitter. The 10-kw klystron to be used for the ground-station transmitter has a bandwidth of only 10 Mc, requiring a frequency multiplier in the satellite so that the satellite-to-ground path will have an adequate signal-to-noise ratio.

The satellite transmitter output power of 10 w gives a margin of at least 6 db for TV transmission over a maximum slant range of 5000 n. mi.

The receiver is completely solid state, using separate crystal-controlled transistor oscillators and varactor multipliers for both the input and output oscillator sources. Incorporated in the receiver housing is a microwave beacon used for tracking by ground communications stations. The beacon is completely self-contained, with a crystal-controlled transistor oscillator and varactor multipliers. The receiver and beacon outputs are combined and fed to a traveling-wave tube (TWT) for amplification to 10 w power output. The microwave beacon signal at 4080 Mc as amplified by the TWT has a radiated power out of the antenna of more than 100 mw.

This TWT has been designed for long life, light weight, and high efficiency. A solid-state DC–DC converter is used to raise the 22.5 v regulated input to the high voltages needed by the tube.

The microwave antenna receives at 1725 Mc and transmits at 4170 Mc. It is contained in one mechanical assembly, consisting of a coaxial receiving antenna above a coaxial transmitting antenna. The whole assembly is located on top of the spacecraft, coincident with the spin axis. Both antennas are circularly polarized but of opposite sense. Vertical coverage extends from 40 to 115 deg (−1 db points).

TELEMETRY, TRACKING, AND COMMAND EQUIPMENT

The telemetry, tracking, and command subsystem provides three basic functions in the spacecraft:

1. A VHF CW signal, from which Minitrack stations give orbital data.
2. Telemetry of performance data from the communication system and the radiation experiments.
3. A command system, which receives and converts commands into a desired switching function.

The telemetry transmitters can be switched on and off by means of the command system. Operationally, one of the transmitters is on continuously to provide the tracking signal. The Minitrack ground stations utilize this signal to track the satellite and provide orbital measurements. The alternate transmitter is commanded ON when telemetry or horizon-scanner data is desired. A modulation switch selects the transmitters to be modulated and the source of modulation (telemetry encoder or horizon-scanner subcarrier oscillator). This switch is under control of the command system.

The transmitters are crystal-controlled, solid state, and phase-shift keyed by the modulating signals.

In the event of a failure of one transmitter, the other would provide both tracking and telemetry signals.

The command system consists of a redundant set of command receivers, subcarrier demodulators, and decoders. A pulse-modulated subcarrier is transmitted via a VHF carrier to the command receivers which demodulate the carrier and send the subcarrier to the subcarrier demodulators where the pulse code is reconstituted. The code output is then fed to both decoders through a cross-coupling network in such a fashion that either demodulator can activate either decoder. Thus, in the event of failure of receiver No. 1, subcarrier demodulator No. 1, and decoder No. 2, the command system will still function. The decoder uses a magnetic-core shift register to transform the pulse code into a command signal. The command signals from the two decoders are "paralleled" so that either or both decoders can activate the control function.

The VHF antenna consists of four monopoles extending out from the separation ring face of the spacecraft. For command reception, the anntennas are fed in phase to produce a dipole-like pattern. For telemetry and tracking transmission the monopoles are fed in phase quadrature to produce a circularly polarized wave in the plane perpendicular to the spin axis. A diplexer harness is used to couple the two receivers and two transmitters to the antennas.

POWER SUPPLY SUBSYSTEM

The power supply consists of a solar-cell array, hermetically sealed nickel-cadmium storage batteries, and charge-controlling electronics. The solar cells are boron-doped silicon cells, P/N, gridded and covered with 60-mil-thick fused silica sheets. Under typical operating conditions, the array is capable of generating an average power of 40 w. Battery capacity is 9 amp-hr.

STRUCTURE

The envelope of the spacecraft was dictated by the launch-vehicle low-drag fairing. This has resulted in an eight-sided prism with a maximum diameter of 29 inches and a height of 19 inches, topped by an eight-sided truncated pyramid 16 inches high. Figures 1 and 2 show a photo and cutaway drawing of the spacecraft.

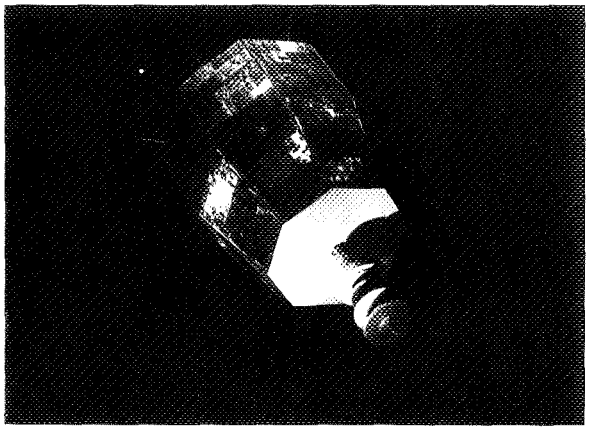

FIGURE 1.—Relay spacecraft.

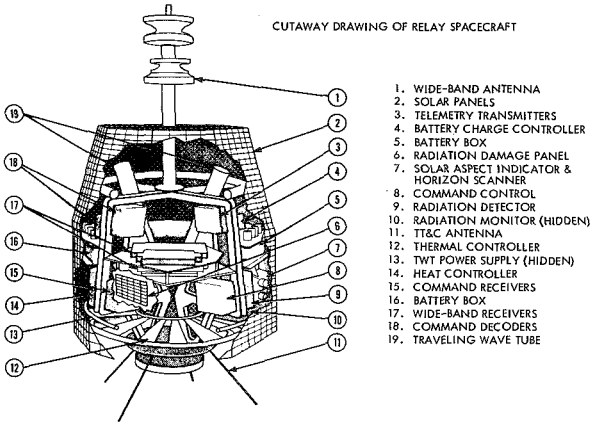

FIGURE 2.

The structure is fabricated of riveted sections of lightweight aluminum channels. Panels for support of the solar cells are epoxy-bonded, aluminum-honeycomb construction.

RADIATION EXPERIMENT

In addition to the communications repeaters, and other subsystems needed to support the principal mission of Relay, the spacecraft carries a group of components to obtain data on particle radiation in space. These consist of six radiation detectors, and a collection of isolated solar cells and semiconductor diodes. The latter are accumulated on a "radiation-damage-effects" panel.

The radiation detectors are included to monitor the proton and electron spectra by measuring the flux density in various domains of intensity levels. Two of them are scintillation counters and four are PN junctions. One of the detectors is omnidirectional; the others are restricted to a small solid angle and are gated by an onboard magnetometer to measure only the flux normal to the earth's magnetic field. Accumulators in the telemetry encoder count and store the detectors' outputs. Of the 128 telemetry channels, 100 are reserved for high-speed measurements of the outputs of the short-circuited cells. Thirty specially selected solar cells make up the radiation-damage panel. The effects of radiation are observed by measuring short-circuit current. The radiation-damage panel contains, in addition to the solar cells, six selected diodes used to measure minority-carrier lifetime as affected by radiation.

POWER-SUBSYSTEM PERFORMANCE

Figure 3 shows the variation of solar-cell array current (and the corresponding battery charge current) vs. time in orbit. It is seen that the output will be down to half its initial value about one year after launch. The two dips in the curves are due to passage of the satellite through eclipse. The effect of this decrease in output power of the solar cells due to radiation will be to decrease the permissible daily operation of the communication experiment. The graph also shows that, after one year of orbital

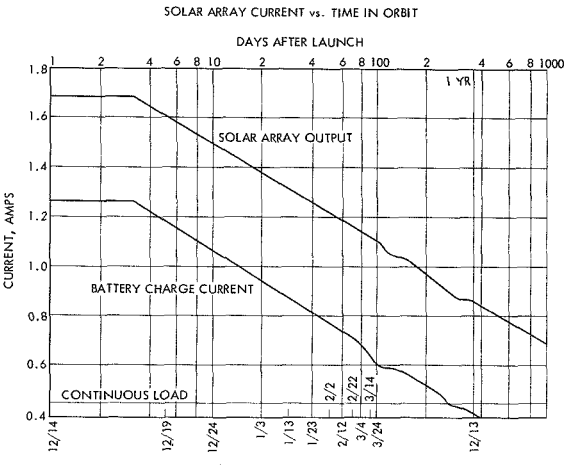

FIGURE 3.—Solar array current vs time in orbit.

lifetime, the solar array will be able to support some wideband operation. It is difficult to predict at this time what the duration of operation might be. Barring a major catastrophe, the functioning of the one-year timer will in all probability end the life of the spacecraft.

Battery performance was normal until Orbit 548, at which time it was noted that one of the three batteries could not be charged. Subsequent failure analysis has indicated a malfunctioning charge controller. The spacecraft has been operating on two batteries since then. These two battery packs are capable of supplying power for up to 100 min of wideband operation per day. The specification for operation is 120 min with a full battery complement. It is evident that this failure has not seriously hampered experimental operations.

SPACECRAFT TEMPERATURE

The temperature of the spacecraft is a function of available sunlight and the degree of battery overcharge permitted. When the batteries are subjected to extended overcharge, the electrical energy supplied by the solar array will be dissipated as heat, since chemical conversion is not possible once a fully charged state is reached.

Figure 4 shows the dependence of the average temperature on total time in sunlight. The fine grain variations in temperature are due to variations in the charge state of the battery pack.

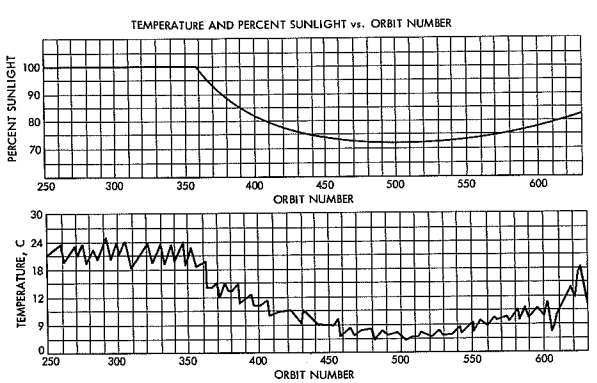

FIGURE 4.—Temperature and percent sunlight vs orbit number.

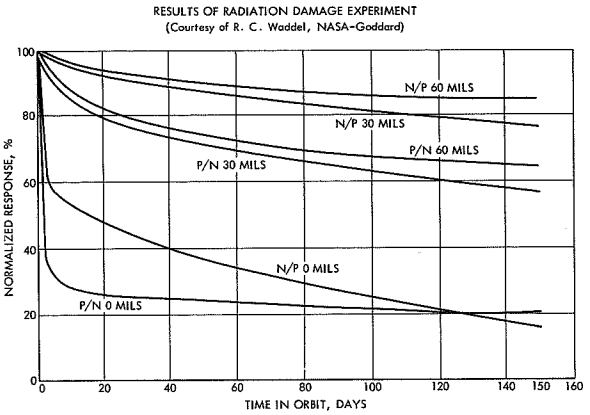

FIGURE 5.—Results of radiation damage experiment.

RADIATION EXPERIMENT RESULTS

Present data from the radiation damage experiment is consistent with a flux of about 5×10^{14} electrons/cm^2-day (1 mev equivalent). The output of the solar-cell experiment is summarized in Figure 5. The present output for these cells after 150 days in orbit are:

	Percent		*Percent*
N-P 60-mil shield	83	P-N 30-mil shield	57
N-P 30-mil shield	76	N-P 0-mil shield	15
P-N 60-mil shield	64	P-N 0-mil shield	19

TRANSMISSION TESTS

Various system performance experiments have been devised as objective tests to obtain quantitative and statistical data on the electrical parameters of the system by analyzing its response to carefully controlled excitations such as sine-squared pulses and white noise. From the resulting data, it is possible to determine performance degradation during the communications lifetime of the spacecraft, with particular emphasis on applying failure mode information to future designs.

System demonstration experiments emphasize quality television and telephony. They also include a variety of other data forms, including high bitrate digital data, facsimile, telephoto, and multichannel-teleprinter transmissions. The intent of these experiments is not only to demonstrate a system-transmission capability for a variety of signals, but also to

FIGURE 6.—Monitor at Goonhilly Downs, England, of picture material transmitted from United States via Andover, Maine, ground station.

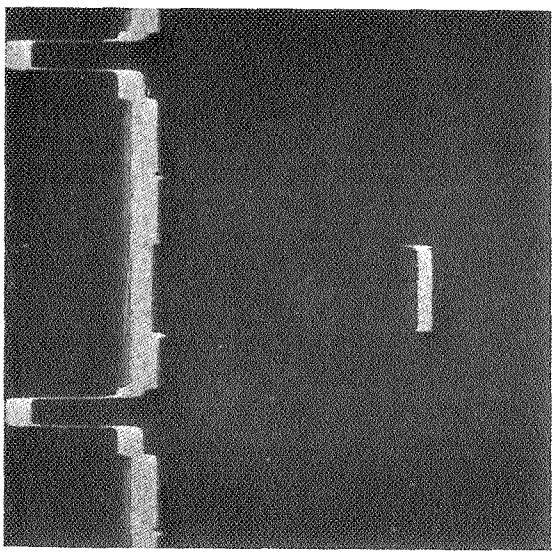

FIGURE 7.—Pulse and bar waveform received at Goonhilly Downs; 525-line standards, no preemphasis, 3.2-Mc bandwidth.

provide experimental data on the engineering aspects of these transmission forms.

Large numbers of television test patterns and picture material have been transmitted through the Relay system. Multiburst signals, EIA test patterns, bar and window patterns, and typical picture material all show excellent quality. Figure 6 is a photograph of a monitor at Goonhilly Downs, England, showing picture material transmitted from the United States via the Andover, Maine, Ground Station.

A number of measurements of field, line, and short-time distortions at Nutley, N.J., and Goonhilly have verified that the system objectives have been met. Line-time photographs, Figure 7, shows that overshoot, ringing, and tilt are within system objectives. The ringing is at a rate determined by a sharp cutoff 3.2-Mc lowpass filter in the ground

equipment which is used to remove the sound channel.

Multiple channel two-way telephone calls have been transmitted between the United States and Brazil, the United States and Europe and Europe and Brazil. In one experiment between the United States and Europe, a two-way telephone call was looped back and forth between the two stations several times until a time delay was accumulated equal to that which would be present in a synchronous communication satellite. The results indicated that echo problems are severe and can be intolerable without echo suppression.

Results of tracking the spacecraft with large-diameter narrow-beamwidth antennas have been highly encouraging. The Goonhilly station reports that prediction data provided at one-week intervals by NASA, have been sufficiently accurate to permit programmed steering of the 85-foot-diameter antenna.

In summary, the many successful experiments performed during Relay's seven months of operation have shown that satellite-borne microwave repeaters can provide high-quality wide-band communication service in a stable, predictable manner. The major problem to be faced for commercial application of communications satellites is attaining an operating lifetime in orbit of several years.

ACKNOWLEDGMENT

The authors wish to acknowledge the cooperation of Raymond Waddel, project scientist for Relay radiation experiments, in supplying the test results presented here.

RELAY I SPACECRAFT PERFORMANCE

ROBERT H. PICKARD
Goddard Space Flight Center

This paper describes RELAY I, an experimental communications spacecraft. RELAY is a part of the National Aeronautics and Space Administration's communications satellite program.

Factors leading to the design of an experimental communications satellite are considered. Limitations in the bandwidth of available klystrons for ground transmitters required the use of modulation index tripling in the spacecraft to obtain usable signal to noise ratios on the spacecraft to ground path. Simultaneous two-way telephony experiments required that two separate IF channels be provided to prevent signal suppression and to reduce cross modulation products.

It was necessary to provide 20 command channels and 128 multiplexed PCM telemetry channels to operate the spacecraft and evaluate its performance.

Prelaunch performance evaluation of the communications equipment consisted of measuring parameters such as S/N ratio, group delay, noise loading, bandwidth, crosstalk, frequency, and power output.

A summary of experimental results obtained from in-orbit operations indicates close correlation to prelaunch measurements. Illustrations of experimental results are given.

INTRODUCTION

Within the next 5 years, advances in space technology may create an operational communications satellite system that will vastly increase intercontinental telephone, telegraph, and data exchange channels and make possible transoceanic television. Contributing to progress toward this new communications era is NASA's RELAY satellite program.

RELAY is designed to carry out experiments in the intercontinental transmission of telephone, television, teleprint, facsimile, and other signals via a medium-altitude active repeater satellite. It is also equipped to telemeter the functioning of its equipment and radiation measurements in space.

RELAY I was launched into a nearly (see Fig. 1) nominal orbit at 2330 GMT, December 13, 1962. The satellite's perigee is 712 nautical miles, apogee is 4,200 nautical miles. The orbit inclination is 47.5°. Orbital period is 185 minutes.

As of orbit 1948 on August 21, 1963, 203 hours of communications had been accumulated, and during this time 499 operations had been conducted. These were divided into 1,555 experiments and demonstrations of engineering and public interest.

THE RELAY SPACECRAFT

Structure

The envelope of the spacecraft was dictated by the low drag nose fairing of the Delta launch vehicle. This has resulted in an eight-sided prism with a maximum diameter of 29 inches and a height of 19 inches, topped by an octagonal truncated pyramid 16 inches high. The 18-inch-long mastlike structure mounted on its narrow end is the transmitting and receiving antenna assembly for the microwave communications experiments. A photograph of the spacecraft and a cutaway drawing detailing the various subsystems are shown in Figures 2 and 3. The structure is fabricated of riveted sec-

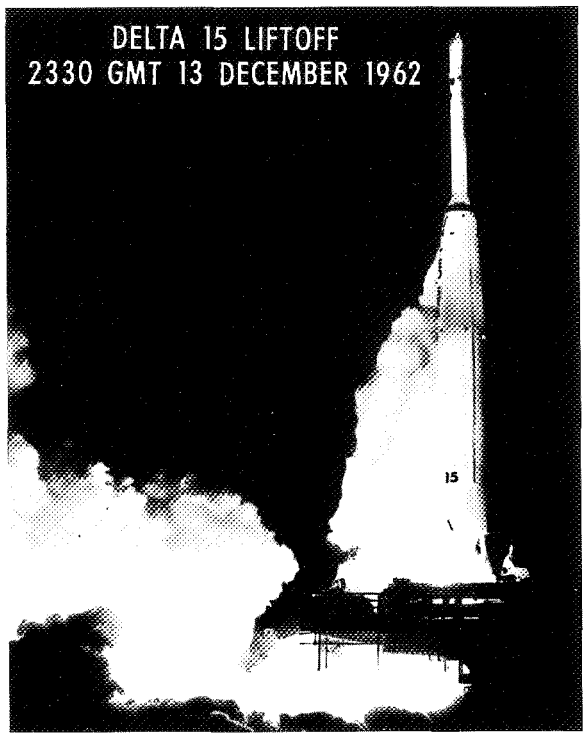

FIGURE 1.—Delta 15 launch.

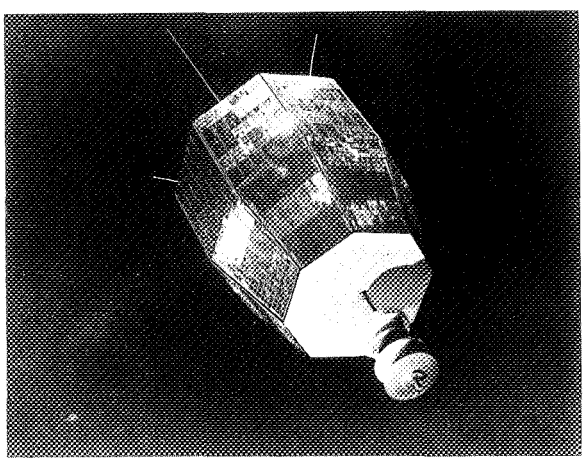

FIGURE 2.—The Relay spacecraft.

tions of lightweight aluminum channels. Panels for support of the solar cells are epoxy-bonded, aluminum-honeycomb construction. Attachment to the launch vehicle third stage is by means of a machined aluminum attachment ring.

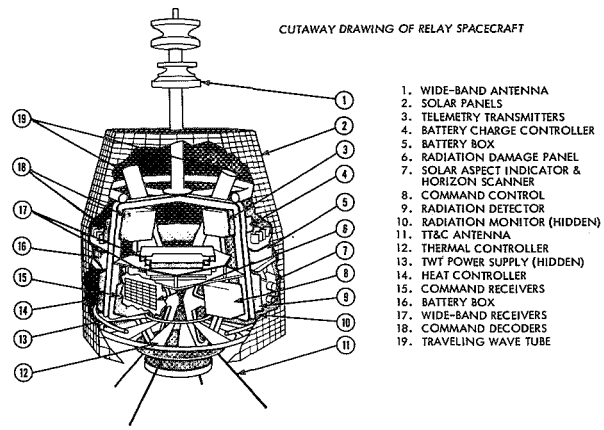

FIGURE 3.—Cutaway drawing of the Relay spacecraft.

Power Subsystem

The power supply consists of a solar cell array, hermetically sealed nickel-cadmium storage batteries, charge-controlling electronics, and a 1-year timing device. The solar cells are boron-doped silicon cells, P/N, gridded and covered with 60-mil-thick fused silica sheets. The cover sheets provide protection from energetic particles in space. Every possible square inch of the spacecraft exterior is covered with solar cells to provide the power necessary for operating the spacecraft. When the communications system is in operation, the power requirement is about 120 watts. Under typical operating conditions, the solar array is capable of generating an average power of 40 watts. The remaining power is provided by a 250-watt-hour storage battery. Battery depth of discharge is not permitted to exceed 50 percent except in special experiments with the spacecraft.

Telemetry, Tracking, and Command Equipment

The telemetry, tracking, and command subsystem provides three basic functions in the spacecraft:

1. A VHF CW signal, from which the Minitrack stations provide orbital data.
2. Telemetry of performance data from the communication system and the radiation experiments.
3. A command system, which receives the commands and converts them into a desired switching function.

The telemetry transmitters can be switched on and off by means of the command system. Operationally, one of the transmitters is on continuously to provide the tracking signal. The Minitrack ground stations utilize this signal to track the satellite and provide orbital measurements. The alternate transmitter is commanded on when telemetry or horizon scanner data are desired. A modulation switch selects the transmitters to be modulated and the source of modulation (telemetry encoder or horizon scanner subcarrier oscillator). This switch is under the control of the command system.

The transmitters are crystal controlled, solid state, and are phase shift keyed by the modulating signals. In the event of a failure of one transmitter, the other would provide both tracking and telemetry signals.

The telemetry encoder accepts digital, high- and low-level analog data inputs for conversion to a PCM format for transmission. The main commutator provides 128 channels which are sampled each second. Two subcommutators are provided, one, a 32-channel unit, and the other, a 64-channel subcommutator. Three of the main channels are used for frame synchronization.

The command system consists of a redundant set of command receivers, subcarrier demodulators, and decoders. A pulse-modulated subcarrier is transmitted via a VHF carrier to the command receivers which demodulate the carrier and send the subcarrier to the subcarrier demodulators where the pulse code is reconstituted. The code output is then fed to both decoders through a cross-coupling network in such a fashion that either demodulator can activate either decoder. Thus, in the event of failure of receiver No. 1, subcarrier demodulator No. 1, and decoder No. 2, the command systems will still function. The decoder uses a magnetic core shift register to transform the pulse code into a command signal. The command signals from the two decoders are "paralleled" so that either or both decoders can activate the control function. Twenty separate commands are provided to switch the spacecraft into its various modes of operation.

The VHF antenna consists of four monopoles extending out from the separation ring face of the spacecraft. For command reception the antennas are fed in phase to produce a dipole-like pattern. For telemetry and tracking transmission, the monopoles are fed in phase quadrature to produce a circularly polarized wave in the plane perpendicular to the spin axis. A diplexer harness is used to couple the two receivers and two transmitters to the antennas.

Microwave Communication Equipment

The purpose of this system is to provide an experimental repeater suitable for transmission of one TV signal (plus its sound channel) or 600 1-way voice channels; or of high-speed data, facsimile, or teletype traffic with bandwidths of up to 4 megacycles. Two-way transmission tests through the repeater can be made, using 12 channels in each direction. (This number is determined by the available ground-station equipment, rather than a limitation of the satellite repeater, which can handle several times this number.)

Two completely independent microwave, repeaters (except for the common antenna) are provided for increased reliability. Either one may be selected for operation by ground command.

The basic performance requirements of the satellite repeaters are similar to those used for conventional ground-based microwave links, so far as power output, bandwidth, gain, noise figure, and intermodulation are concerned. There are radical differences, however, in the size, weight, and power drain.

The system parameters were initially chosen to meet international (CCIR) standards (for a 2500-km reference circuit) between Europe and the United States. The sound channel is transmitted by frequency-modulating a 4.5-Mc subcarrier which is then added to the video signal, and the combination used to frequency-modulate the ground transmitter.

The satellite transmitter output power of 10 watts gives a margin of at least 6 db for TV transmission over a maximum slant range of 5,000 nautical miles.

The receiver is completely solid state using separate crystal-controlled transistor oscillators and varactor multipliers for both the input and output oscillator sources. Incorporated in the repeater is a microwave beacon which is used for tracking by the ground communications stations. The beacon is a completely self-contained unit with a crystal-controlled transistor oscillator and varactor multipliers. The receiver and beacon outputs are combined and fed to a traveling wave tube for amplification to 10-watts power output. The microwave beacon signal at 4080 megacycles as amplified by the traveling wave tube has a radiated power out of the antenna of more than 100 milliwatts.

This traveling wave tube has been designed for long life, light weight, and high efficiency. A solid-state DC-DC converter is used to raise the 22.5 volts regulated input to the high voltages needed by the traveling wave tube.

The microwave antenna receives at 1725 Mc and transmits at 4170 Mc. It is contained in one mechanical assembly, consisting of a coaxial receiving antenna above a coaxial transmitting antenna. The whole assembly is located on top of the spacecraft, coincident with the spin axis. Both antennas are circularly polarized but of opposite sense. Vertical coverage extends from 40 to 115 degrees (−1 db points).

Figure 4 shows the general configuration of the RELAY communications transponder. The incoming 1725-Mc/s signal is translated to a 70-Mc/s intermediate frequency where most of the amplification is accomplished, frequency tripled, and then translated up to 4170 Mc/s for power amplification and retransmission.

The reasons for tripling the signal are that with 10 watts RF/power output, the required bandwidth for the spacecraft-to-ground link is 25 Mc/s. Available high-power klystron amplifiers with 25-Mc/s bandwidths were not available for the ground-to-spacecraft link during the time schedule required for the RELAY Project. The required down-link deviation was divided by three, which yielded a 14-Mc/s bandwidth occupancy for the up-link signal. This was an achievable bandwidth for the state of the klystron art at that time.

Two modes of operation are available with the transponder. The first mode or wideband mode, as it is called, is utilized for one-way wideband communications such as television.

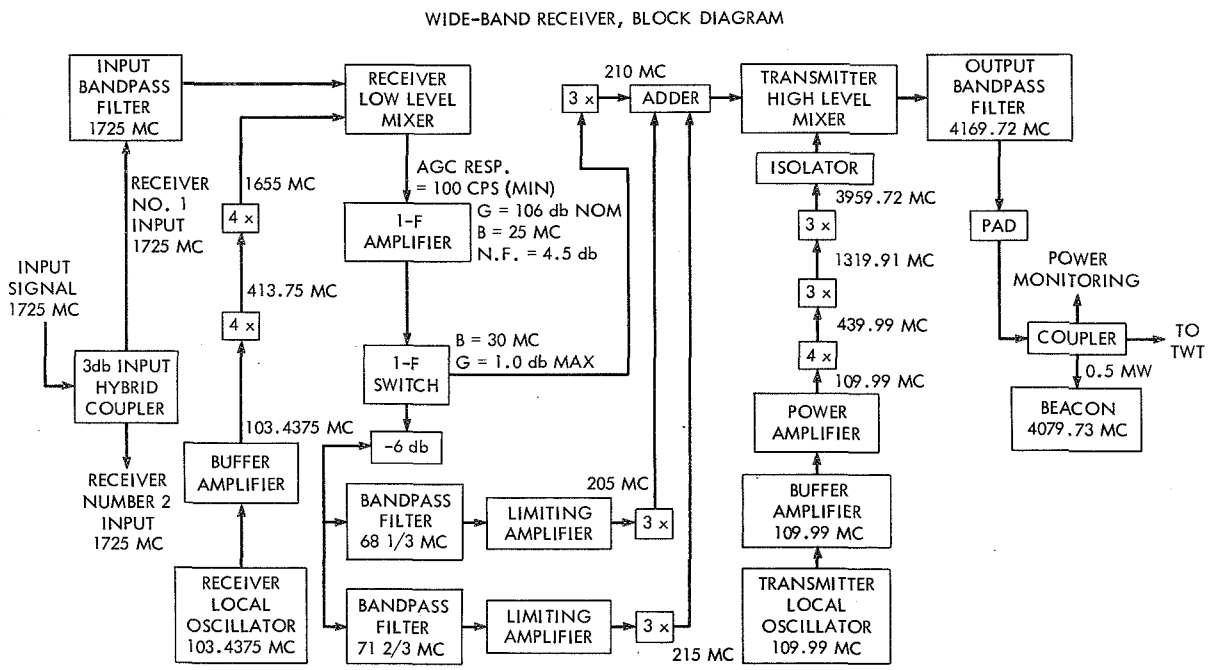

FIGURE 4.—Communications transponder block diagram.

The second mode available is called the narrowband mode. This is utilized for two-way narrowband communications such as 12-channel two-way telephony. In the narrowband mode, two ground stations communicate with each other, one transmitting on 1723.33 Mc/s, the other transmitting on 1726.67 Mc/s. The spacecraft transponder converts these frequencies to 4165 Mc/s and 4175 Mc/s, respectively.

In the two-way telephony mode, the incoming signals from the two communicating ground stations are separated after intermediate frequency amplification and then clipped to the same level by limiting. The deviation is tripled and the two signals enter the TWT at the same level, which prevents suppression of the weaker signal by the stronger one. This is especially important when the spacecraft is much closer to one of the ground stations than to the other and the antenna look angles to the two stations are sufficiently different that even controlling transmitted power from the ground stations will not equalize the power levels in the two directions. This feature of the transponder has been highly successful in operations conducted with RELAY I.

Two approaches were investigated for the tripler design, one using varactors, the other using transistors. The advantage of a varactor design, that no DC input power is required, was offset by the disadvantage of an extremely difficult tuning procedure, and that the units were not easily reproducible. The varactor design was used for a while during the prototype stage, but was then abandoned in favor of the transistor version which was much easier to tune and reproduce. The price paid was 1.5 watts of DC power.

The IF amplifier design proved to be more difficult than originally anticipated. The first design utilized triple-stagger-tuned stages which were necessary to achieve the required bandwidth. During electrical testing, however, it was found that the crosstalk for multichannel telephony was excessive. This was caused by AM to PM conversion on the passband skirts of the individual stages. The solution to this problem was to build a broadband video amplifier and then limit the bandwidth with a passive 70-Mc/s bandpass filter. The performance of this design was most satisfactory and it was selected for use.

The traveling wave tube development was well underway when short term (millisecond) fluctuations were noticed in the power output of some of the tubes when they were operated in vacuum. Also there was an occasional helix current runaway on a tube in vacuum. The tubes operated in a normal manner at atmospheric pressure. The vacuum anomalies were not repeatable. At first the power fluctuations were thought to be defective RF cables leading to the vacuum chamber. At times it appeared that tightening the connectors cured the problem. Helix current runaway was not always repeatable. At this point, a very serious design problem was evident: the TWT design would work at sea level conditions but not in the high vacuum of space. Innumerable design modifications were tried, some seemed to work for a while and then when the problems appeared to be solved, they reappeared. This caused delays in the launch schedule and it was finally decided to seal the TWT in a container pressurized at one atmosphere. The pressurized TWT models would be used in the first flight spacecraft and the problem would be further pursued in hopes of producing an unpressurized TWT for the remaining two spacecrafts. This was done and the presently orbiting RELAY spacecraft contains pressurized tubes. These are functioning normally and have shown no indication of instability.

The continuing design effort on the TWT has finally yielded a design that will perform just as well in vacuum as in air. Helix current runaway was found to be caused by insufficient thermal sinking of the helix. In air, there was enough convection cooling of the helix area of the bulb that runaway did not take place. The thermal design was modified to provide adequate removal of helix heat.

The solution of the power fluctuation problem was simple but took many months to perfect. The potential difference between the helix and collector is about 1,000 volts which creates a

region of high electrical field in this area of the bulb. Local outgassing was ionized by the field and would occasionally break down, momentarily reducing power output. The answer was to apply thin lines of silver paint directly on the exterior of the bulb between the area of the end of the helix and the beginning of the collector. The lines were electrically connected to the collector. They served to provide a low-impedance leakage path which eliminated the high field in this area. This design has performed very well in all tests and will be used in the next RELAY spacecraft.

Radiation Experiments

In addition to the communications repeaters, and other subsystems needed to support the principal mission of RELAY, the spacecraft carries a group of components to obtain data on particle radiation in space. These consist of six radiation detectors, and a collection of isolated solar cells and semiconductor diodes. The latter are accumulated on a "radiation damage effects" panel.

The radiation detectors are included to monitor the proton and electron spectra by measuring the flux density in various domains of intensity levels. Two of them are scintillation counters, four are PN junctions. One of the detectors is omnidirectional; the others are restricted to a small solid angle and are gated by an on-board magnetometer to measure only that flux normal to the earth's magnetic field. Accumulators in the telemetry encoder count and store the detectors' outputs. One hundred of the 128 telemetry channels are reserved for high-speed measurements of the outputs of the short-circuited cells. Thirty specially selected solar cells make up the radiation damage panel. The effects of radiation are observed by measuring short circuit current. The radiation damage panel contains in addition to the solar cells, six selected diodes, which are used to measure minority-carrier lifetime as affected by radiation.

Miscellaneous Equipment

In order to reduce the limits of temperature variation in the spacecraft, a thermally controlled radial vane assembly is located in the base of the spacecraft. It is operated by a temperature sensor connected to the battery assembly. When the batteries get hot, the vanes open; as the battery temperature decreases, the vanes close. In this manner the thermal radiation coupling to space is varied. This simple form of active temperature control reduces the mean spacecraft variation 5 centigrade degrees at each end of the range providing an operating variation of 0°C to +25°C.

Solar aspect and horizon transit time are measured by detectors located in the spacecraft. The data are telemetered and spacecraft spin axis attitude is computed on the ground. If necessary, commands can be sent to tilt the spin axis to a desired orientation by applying a current to the magnetic torquing coil.

RELAY Ground Facilities

RELAY ground facilities include stations for communications experiments; test stations for checking out the satellite in advance of communications experiments and turning its transponders on and off; and the NASA Minitrack network for tracking and acquiring data from the spacecraft.

The ground stations that conduct experiments in intercontinental and transoceanic communications are located at: Goonhilly Downs, England; Pleumeur-Bodou, Britanny, France; Fucino, Italy; Rio de Janeiro, Brazil; and in the United States at Andover, Maine, and Nutley, N.J.

The test stations check out the RELAY satellite, including operation of its communications transponder, prior to communications experiments. They set the transponder for the type of transmissions scheduled and shut it off when the experiment is concluded. If the satellite is out of range of the test station, an automatic timer will turn the equipment off 2 minutes after use to conserve the satellite's power supply. The test stations are located at Nutley, N.J., and Mojave, Calif.

NASA's worldwide Minitrack network is tracking the RELAY satellite and acquiring data on performance and condition of RELAY equipment and on radiation in space.

All stations transmit information for processing to NASA's Goddard Space Flight Center, Greenbelt, Md.

EXPERIMENTAL RESULTS

Power Subsystem Performance

The variation of solar cell array current (and the corresponding battery charge current) vs. time in orbit is shown in Figure 5. It is seen

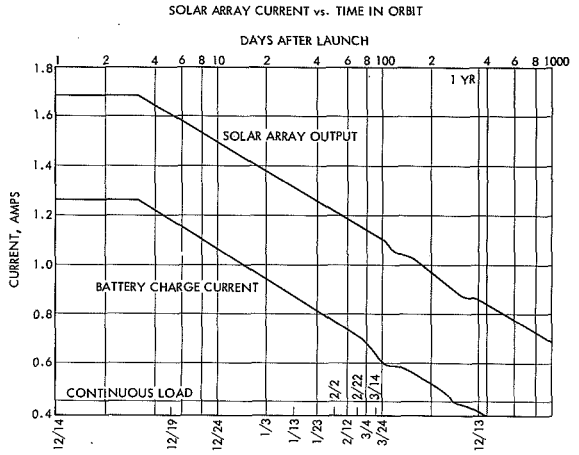

FIGURE 5.—Solar array current vs. time in orbit.

that the output will be down to half its initial value about 1 year after launch. The two dips in the curves are due to passage of the satellite through seasons of eclipse. The effect of this decrease in output power of the solar cells due to radiation will be to decrease the permissible daily operating of the communications experiment. Figure 5 also shows that after 1 year of orbital lifetime, the solar array will be able to support some wideband operation. It is difficult to predict at this time what the duration of operation might be. Barring any major catastrophe, the functioning of the 1-year timer will in all probability terminate the life of the spacecraft in December 1963.

Battery performance was normal until Orbit 548 at which time it was noted that one of the three batteries could not be charged. Subsequent failure analysis has indicated a malfunctioning charge controller. The spacecraft has been operating on two batteries since then. These two battery packs are capable of supplying power for up to 100 minutes of wideband operation per day. The specification for operation is 120 minutes with a full battery complement. It is evident that this failure has not seriously hampered experimental operations.

Spacecraft Temperatures

The temperature of the spacecraft is a function of available sunlight and the degree of battery overcharge that is permitted. When the batteries are subjected to extended overcharge, the electrical energy supplied by the solar array will be dissipated as heat since chemical conversion is not possible once a fully charged state is reached.

Examination of Figure 6 reveals the dependence of the average temperature on total time in sunlight. The fine grain variations in temperature are due to variations in the charge state of the battery pack.

Communications Performance

Shortly after the RELAY I spacecraft was launched, the No. 1 microwave transponder power regulator developed excessive current leakage. It was not possible to clear the leakage by ground command and it was believed at that time that the experiment was a failure. All stations were put on a standby basis for the next 2 weeks. On December 27, 1962, an attempt was made to interrogate the spacecraft and it was successful. The leakage

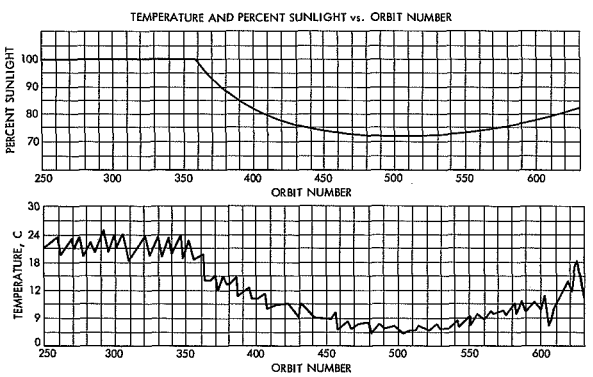

FIGURE 6.—Temperature and percent sunlight vs. orbit number.

had decreased to a tolerable value. It was found that the spacecraft would operate in a normal manner as long as the No. 2 microwave transponder was used for experiments.

Communications operations commenced on January 3, 1963. The RELAY spacecraft is still functioning, and as was previously mentioned, completed 1,555 experiments as of August 21, 1963. Of these, 95 were system demonstrations. The system demonstration experiments emphasize quality television and telephony, but they also include a variety of other data forms such as high bit-rate digital data, facsimile, telephoto, and multichannel teleprinter transmissions. The intent of these experiments is not only to demonstrate a system transmission capability for a variety of signals but also to provide experimental data on the engineering aspects of these transmission forms.

Prelaunch performance evaluation of the communications equipment consisted of measuring parameters such as S/N ratio, group delay, noise loading, bandwidth, crosstalk, frequency, and power output. The data derived from these measurements are being used as a criteria from which degradation of the communications system may be measured

Large numbers of television test patterns and picture material have been transmitted through the RELAY system. Multiburst signals, EIA test patterns, bar and window patterns, and typical program material all show excellent quality.

The important tests for determining quality telephony are group delay, noise loading, and crosstalk.

A small amplitude, high-frequency sinusoid is swept across the transponder bandwidth by a large amplitude sinusoid to measure group delay. Delay components of 30 ns parabolic, 45 ns linear, and 10 ns ripple have been measured at Andover, Maine.

Noise loading tests are performed to determine the level of intermodulation noise present in telephone channels during multiple-channel telephony tets. The Pleumeur-Bodou, France, station reported a maximum intermodulation noise level of 10,650 pw for 300-channel operation when using preemphasis. As expected with preemphasis, the noise peaks in the lowest channel. Additional tests at 600 channels indicated a 4-db increase in noise level over 300 channels.

Crosstalk measurements are performed to determine the amount of intelligible crosstalk transferred between two RF carriers passing through the spacecraft simultaneously. Intelligible crosstalk measurements have ranged

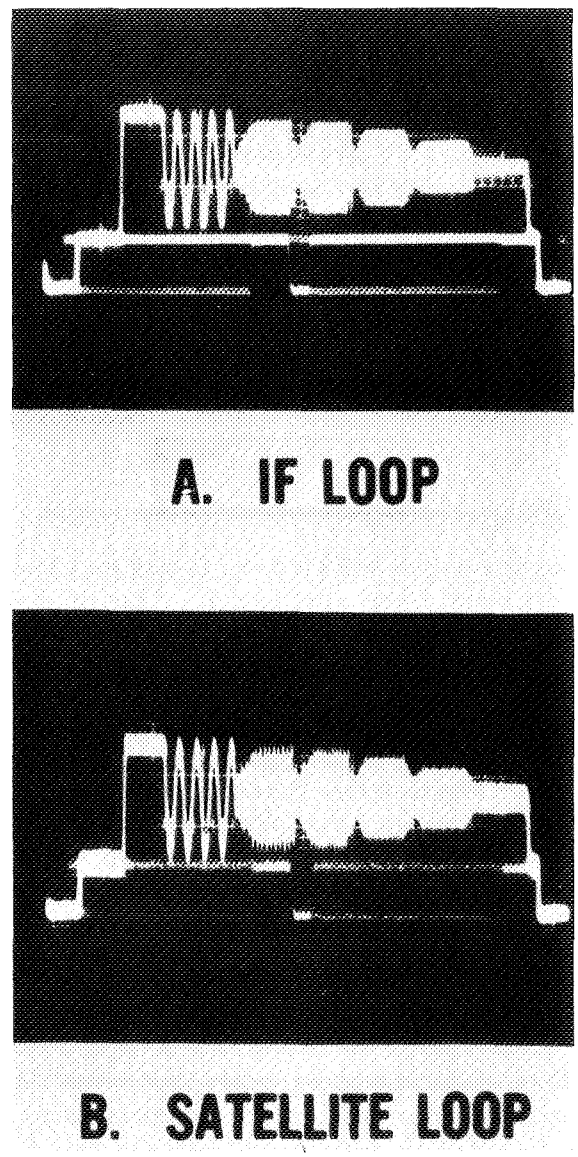

FIGURE 7.—Multiburst waveforms—Andover loop, March 3, 1963.

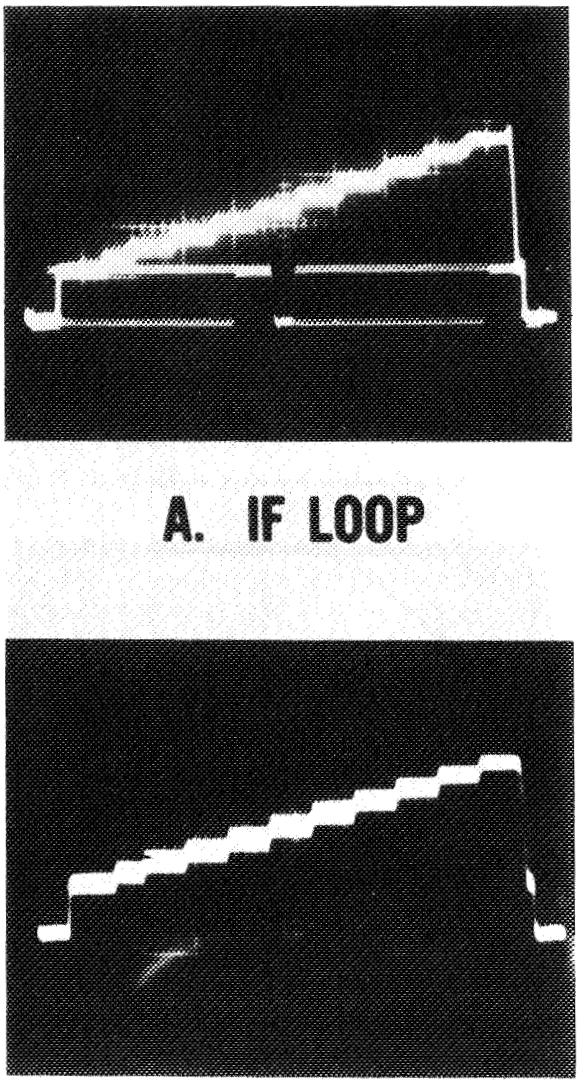

FIGURE 8.—Stairstep waveforms—Andover loop, March 3, 1963.

from −28 to −55 dbmO. The amplitude of the crosstalk has been shown to be nearly proportional to the modulating frequency (6 db per octave).

A special test simulating the delay of a synchronous communications satellite was performed at Goonhilly, England. The RELAY spacecraft was operated in the two-way mode and telephone channels were patched at baseband so that each side of the telephone conversation was looped through the spacecraft six times. A usable telephone link was established. There was a slight echo present which could have been reduced with echo suppressors. Initial results from SYNCON II, launched July 26, 1963, indicate that echo suppression is desirable.

Figures 7 and 8 show examples of multiburst and stairstep waveforms transmitted during loop tests at Andover, Maine. By comparing

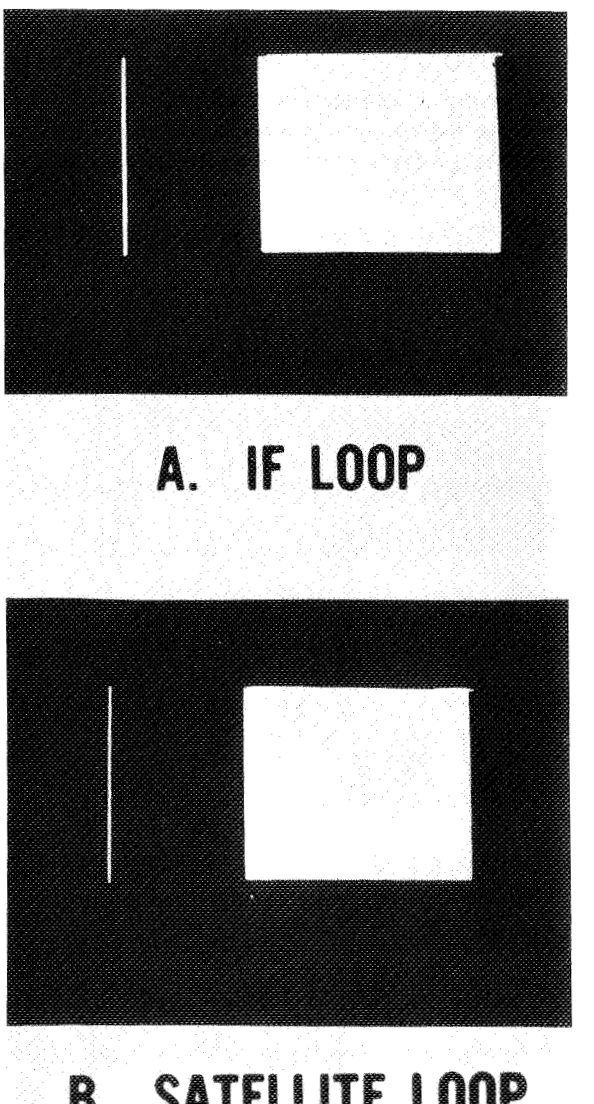

FIGURE 9.—Pulse and bar monitor presentation—Andover loop, March 3, 1963.

the results obtained with the IF loop (not including the RELAY spacecraft) to the results obtained with the satellite loop, it is evident that the RELAY spacecraft produces no visible effect on television transmissions. Evaluation of television picture quality at low signal to noise ratios is difficult. This can only be done on a subjective basis and as such is affected by the individual tastes of the viewer. Figures 9 through 14 are samples of telephoto and television material received at various ground stations. Figure 13 shows a slight ringing characteristic which is caused by a sharp cut-off 3.2-Mc/s low pass filter used in the ground equipment at Goonhilly, England.

Color television has been transmitted successfully via RELAY. The differential phase measured over a 7.0-Mc/s band for RELAY is 45°. Equalization is necessary to meet the CCIR objective for color transmission which is 5°.

FIGURE 10.—Telephoto received at Fucino, Italy.

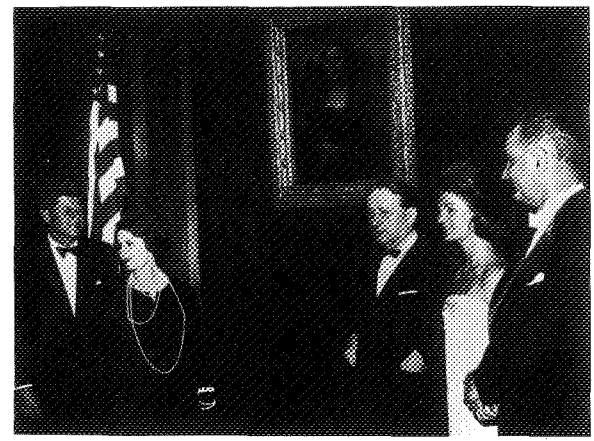

FIGURE 11.—Telephoto received at Pleumeur-Bodou, France.

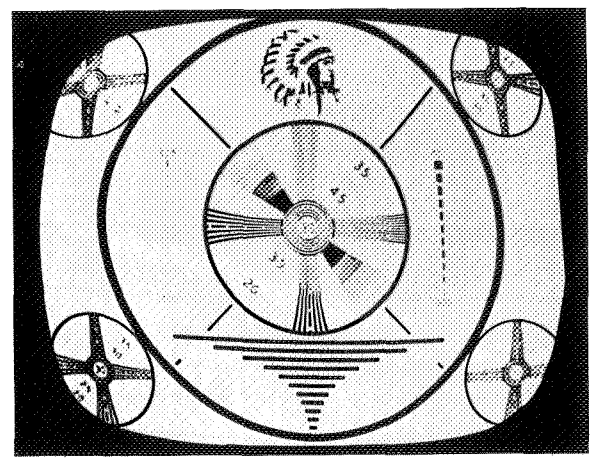

FIGURE 12.—Television test pattern received at Pleumeur-Bodou, France.

FIGURE 13.—Television program material received at Goonhilly, England.

FIGURE 14.—Color telephoto.

Results of tracking the spacecraft with large diameter narrow beamwidth antennas have been highly encouraging. The Goonhilly station reports that prediction data, provided at 1-week intervals by NASA, have been sufficiently accurate to permit programed steering of the 85-foot-diameter antenna.

CONCLUSIONS

RELAY I has met all of its experimental objectives. The spacecraft is presently operating satisfactorily and all indications are that the lifetime will be determined by the 1-year timer mechanism which is carried on board.

The experimental results obtained from in-orbit operations indicate close correlation to prelaunch measurements. The large number of experiments conducted have in general borne out the original system design philosophy and the choice of operating parameters.

RELAY, AN EXPERIMENTAL SATELLITE FOR TV AND MULTICHANNEL TELEPHONY COMMUNICATIONS

R. PICKARD, S. ROTH, J. KIESLING

Goddard Space Flight Center

HISTORY

The first technical publication of ideas relating to the improvement of long range communications in space was probably a 1955 paper "Orbital Radio Relays," prepared by Mr. J. R. Pierce of the Bell Telephone Laboratories. The feasibility of the communications satellite has since been demonstrated by the following projects:

1. *Project Score.*—The first communications satellite launched was Project Score. It was launched from the Atlantic Missile Range on December 18, 1958, by the Department of Defense (DOD). This satellite was the payload of an Atlas Intercontinental Ballistic Missile, the bulk of which was injected into orbit. The lifetime of the satellite was 33 days.
2. *Echo I.*—The first passive communications satellite, a 100-foot inflatable sphere of aluminized Mylar designated Echo I, was launched from the Atlantic Missile Range on August 12, 1960, by the National Aeronautics and Space Administration (NASA). Echo I was developed as a preliminary experiment to determine the feasibility of passive communications satellites. It was injected into orbit by a Delta vehicle and is still in orbit.
3. *Courier.*—The Courier satellite was launched from the Atlantic Missile Range on October 4, 1960, by the Department of Defense. Courier was primarily a sophisticated, delay-repeater satellite developed to investigate store-forward aspects and real-time capabilities. The satellite was injected into orbit by a Thor-Able-Star vehicle and, is still in orbit, although communications failed after 17 days from undetermined causes.
4. *Telstar.*—Telstar is a communications satellite built by A.T. & T., which is similar in performance to Relay. It was launched on July 10, 1962, and is still operating successfully at this date.

These four accomplishments represent the total experience in space communications to date.

INTRODUCTION

The capabilities of existing long-range communications facilities, already pressed by present demands, will be inadequate to accommodate anticipated traffic within the next decade. The greatest possibility for providing the needed increase in communications facilities is the satellite communications system. The communications satellite has the potential ability to provide long-distance communication at microwave frequencies, with bandwidths available to permit the transmission of television or, alternately, many simultaneous voice messages (600 2-way conversations per television channel). Thus, the communications satellite gives promise of new and reliable links in long-distance, transoceanic, telephone and telegraph communications, as well as new means for intercontinental radio and television transmission.

Project Relay has the following objectives: (1) to investigate wideband communications

between distant ground stations by means of a low-altitude orbiting satellite, and (2) to measure the effects of the space environment on such a satellite. The satellite will contain an active repeater to receive and retransmit communications signals between stations in the United States and Europe, and the United States and South America. Communications signals to be evaluated will be an assortment of television signals, multichannel telephony, and other communications that may be of interest. Two Relay satellites will be launched from the Atlantic Missile Range in calendar 1962.

The primary objective of Project Relay is to investigate the technological problems of wideband transmission and to develop operational experience in the use of a satellite communication system. As a major part of this project, a ground station network, consisting of six Relay ground stations located in the United States, South America, and Europe, is being developed to serve as the terminus of the communication links. Agencies currently participating in Project Relay, and their basic functions, are as follows:

A. Project management—National Aeronautics and Space Administration (NASA).
B. Assist in planning and coordination—STL.
C. Satellite design and fabrication—Radio Corp. of America.
D. Launch vehicle and launch operations:
   Douglas Aircraft Corp.
   NASA Field Projects Beaver.
E. Ground stations:
   Rumford, Maine: American Telephone & Telegraph Co.
   Nutley, N.J.: International Telephone & Telegraph Co.
   Rio de Janeiro, Brazil: Radio International de Brazil.
   Goonhilly, England: British Post Office.
   Pleumeur Bodou, France: National Center for Telecommunications.
   Weilheim, West Germany: West German Post Office.
   Mojave, Calif.: Goddard Space Flight Center.

Project Relay will also be used to perform experiments which will provide the following information: (1) a measurement of radiation damage to critical components such as solar cells and silicon diodes, and (2) the monitoring of radiation encountered at the orbital altitudes. The results of these experiments will be correlated with measurements of integrated flux and energy levels of protons and electrons to obtain experimental estimates of component lifetime.

Project Relay will be accomplished in three flight missions, identified as A–15, A–16, and A16a. All three flights will be launched from the Atlantic Missile Range, using the Delta launch vehicle. The pertinent operating parameters for Relay are listed in Table II–1.

TABLE II–1.—*Basic Operating Parameters for Project Relay*

Range (ground to spacecraft).	5,000 nautical miles.
Orbit	Elliptical: Perigee at 800 miles. Apogee at 3,000 miles.
Orbit inclination	50 degrees.
Stabilization	Spin stabilized at 150 rpm.
Attitude correction	Torquing coil in conjunction with horizon scanner and solar aspect indicator.
Power supply	Solar cells and storage batteries, approximately 100 watts during wideband transmission.

THE SPACECRAFT

Communications repeater satellites present special problems to the designers and users of these equipments. The satellite environment (including the launch environment), spacecraft acquisition by the ground station, the inaccessibility for repairs and routine maintenance, and thermal and power supply problems impose special constraints on the design. Most of these problems are relatively new and solutions for them are either not readily available or not proven by experience. These are the principle problems that require investigation and the experiments of Project Relay can provide the experience necessary to arrive at possible solutions to them.

Photographs of the satellite in various stages of assembly are shown in Figure 1. The

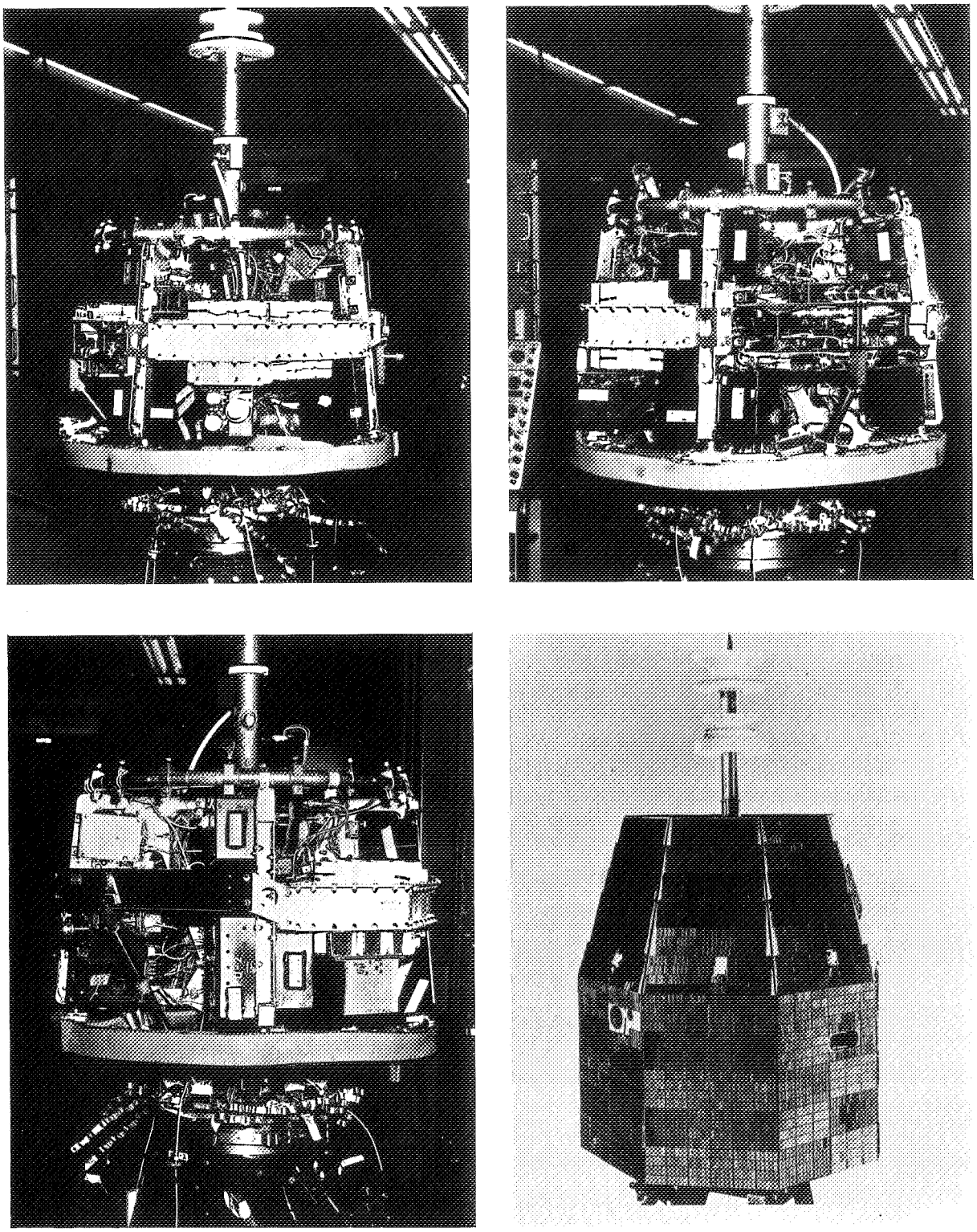

FIGURE 1.—Relay satellite in various stages of assembly.

envelope of the satellite is dictated by the launch vehicle low drag fairing. This has resulted in an eight-sided cylinder with a maximum diameter of 29 inches and a height of 19 inches, topped by an eight-sided, truncated pyramid 16 inches high. An artists conception of the satellite is shown in Figure 2.

The structure is fabricated of riveted sections of lightweight aluminum channels. The total structure weight is 18.8 pounds.

A breakdown of satellite system weights is given in Table III–1.

The Relay spacecraft weights 170 pounds and will be launched by a Delta vehicle from the

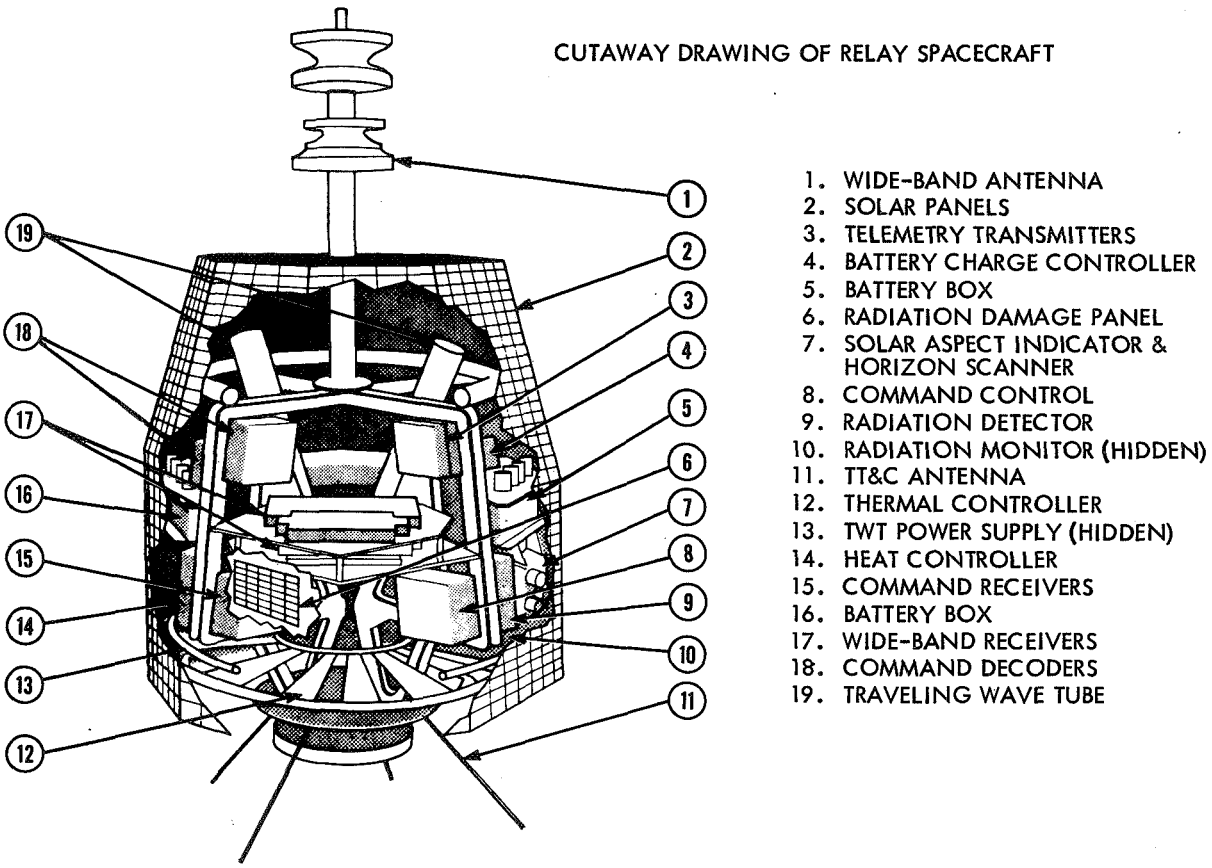

FIGURE 2.—Artist's conception of the Relay satellite mounted in the delta nose cone.

Atlantic Missile Range in late 1962. An eccentric orbit is planned having an agogee of 3,000 miles, perigee 800 miles, and an inclination of 50 degrees. The satellite will be spin stabilized. An overall view of satellite is shown in Figure 3.

The power supply consists of a solar cell array and hermitically sealed nickel cadmium storage batteries. The solar cells are boron-doped silicon cells, P on N, gridded and covered with 0.06 inch of fused silica. Under typical operating conditions they are capable of generating an average power approximately 40 watts. A block diagram of the power supply subsystem is shown in Figure 4. The satellite's internal temperature is maintanined between 0°C and 25°C by means of controlled thermal radiation through an active heat controller and by the satellite duty factor.

The attitude control system detects the satellite spin axis orientation in space. The attitude data is readout through the telemetry system and analyzed on the ground. Suitable commands can then be generated by the com-

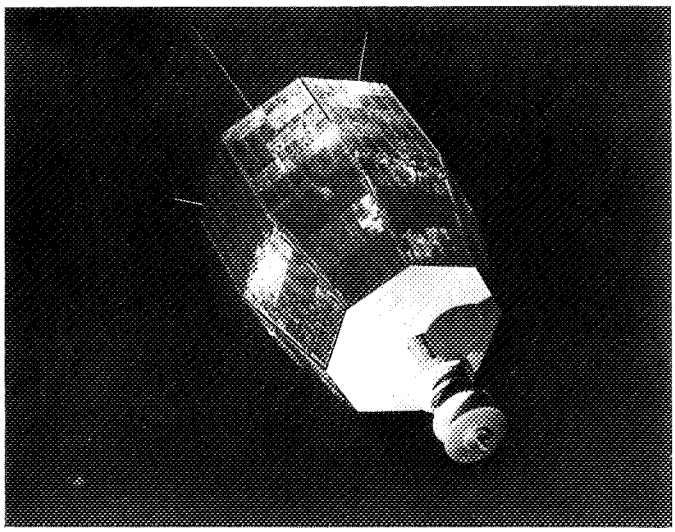

FIGURE 3.—Overall view of the satellite.

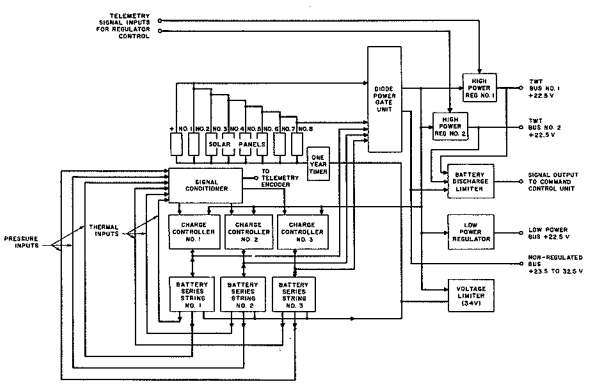

FIGURE 4.—Power supply subsystem block diagram.

mand system to tilt the spin axis to the desired orientation by applying a current to the torque coil.

In addition to the communications transponder, power supply, and attitude control systems, the spacecraft contains a VHF command and telemetry system for turning various equipments on and off and reading out telemetry data to monitor the overall performance of the spacecraft, its electronics systems, and the special radiation experiments. The latter consists of equipment to monitor the effects of nuclear radiation on such components as solar cells and silicon diodes.

A block diagram of the wideband communications repeater is shown in Figure 5. A completely redundant system is used in order to improve the overall reliability.

TABLE III–1.—*Satellite Weight Breakdown*

Power supply subsystem	66. 2
Attitude control subsystem	1. 4
Radiation equipment	13. 4
Structure	18. 8
Wideband subsystem	33. 7
T, T, and C subsystem	17. 7
Harness	6. 0
Miscellaneous	12. 8
Balance weights.	
Hardware.	
VF cables.	
Total	170. 0

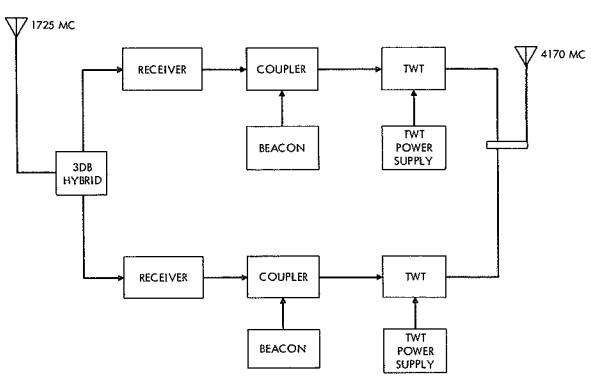

FIGURE 5.—Wideband communications repeater block diagram.

The two systems weigh 33.7 pounds, including the antennas and mounting hardware. Note that the beacon signal, generated by a separate transmitter, is fed through the TWT.

IV. RELAY COMMUNICATIONS SYSTEM

A *Objective*

The purpose of Project Relay is to provide a long-distance, high-quality, experimental communication link in order to study the various problems associated with relay communications circuits using a low-altitude (non synchronous) satellite.

Particular emphasis will be placed on evaluating performance degradation during the lifetime of the satellite with the object of applying the failure mode information to future designs. Failure and system degradation due to the high vacuum and nuclear environment are especially important to the future design of long-life satellite communications systems.

In all cases, high-quality performance, meeting the minimum requirements of CCIR (International Radio Consulting Committee), is expected. The satellite link was designed using the CCIR 1600-mile reference circuit with the two intermediate video points, as a model.

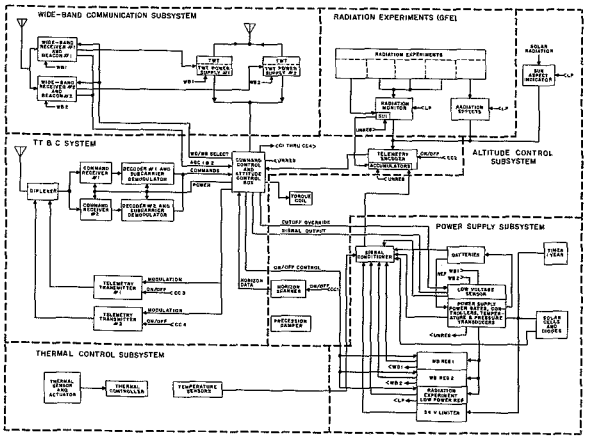

FIGURE 6.—Spacecraft electronics system block diagram.

Description

The communication system used in the Relay spacecraft is composed of three major subsystems; (1) wideband communications, (2) telemetry, and (3) command control. A block diagram of the spacecraft electronic systems is shown in Figure 6. Each active component of the communication subsystems is redundant, with the exception of the telemetry encoder. Weight limitations precluded redundancy for this unit.

The purpose of the wideband communications subsystem is to perform experiments on the following types of transmission; television, multichannel telephony, high bit-rate digital data, facsimile, telephoto, multichannel teleprinter transmissions, etc. Specifically, the subsystem will provide the following: (1) television transmission in either direction, between United States to European stations including the transmission of test signals and patterns, and a tie-in with television networks in the United States, England, France, and West Germany as both program sources and for the distribution of Relay programs; (2) multichannel, two-way telephone service of 12 channels each between the United States and Europe, and between the United States and Brazil; and (3) multichannel, record communications service and high-speed data transmission between the United States and European stations, and between the United States and Brazil.

In addition to communications over the link, a variety of television, telephony, and other communications techniques can be studied at a particular ground station by sending and receiving at that station. This will also allow a study to be made of the detailed link performance. A photograph of the wideband subsystem components is shown in Figure 7.

The telemetry system will provide remote monitoring of the critical electrical parameters of all subsystems carried on board the spacecraft. In addition, either telemetry transmitter can be operated without modulation to provide a 136-megacycle carrier for spacecraft tracking operations by the NASA Minitrack system.

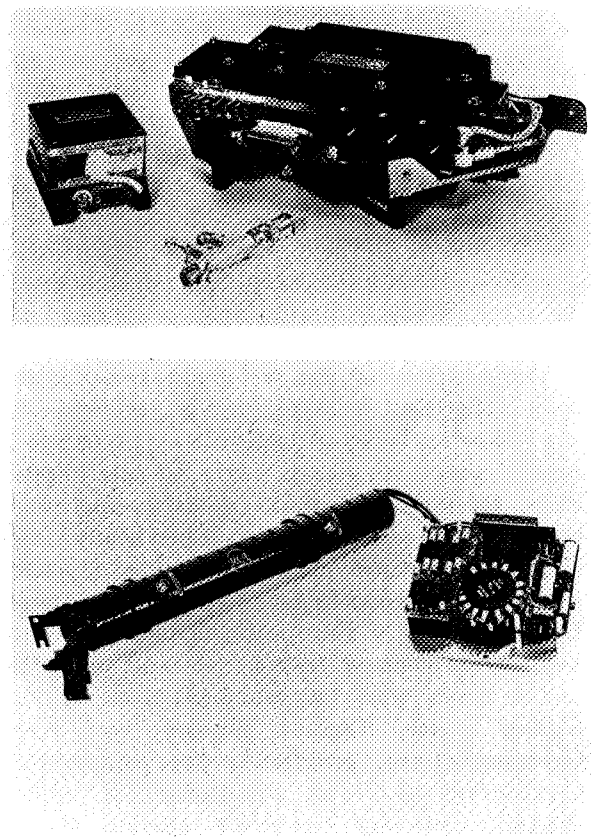

FIGURE 7.—Wideband subsystem components.

The command control system will permit radio remote control of all switched functions in the spacecraft.

The ground station transmitter for the television and 300-channel telephony circuits will use a frequency modulated 10-kw klystron with a spectrum bandwidth of 10 to 14 megacycles (Mc) per second. An 85-foot parabolic antenna or a 69-foot horn will be used depending on the particular ground station. The transmitted power to the satellite is sufficient so that the system threshold will be due almost entirely to the satellite to ground link. For the 12-channel 2-way telephone circuit, a 2-kw klystron with a 1-Mc-per-second bandwidth will be used with a 40-foot parabolic antenna. The ground transmitter frequency is 1725 Mc.

The ground receivers will use a variety of front ends consisting of a maser and parametric amplifiers. Typical link parameters are given in Table VI–1.

The satellite transponder performance is characterized by hard limiting and modulation index tripling. The tripling is required because of the limited bandwidth of the ground transmitter. The output power for television and 300-channel telephony is 10 watts at 4170 Mc. The output power for each of the two-way telephony channels is 4-watts. A 4080-Mc, 100-mw beacon signal is also provided as a tracking aid.

While the object of the experiments is to study the feasibility of satellite-type communications links, and considerable care has been exercised in the design of the links in order to achieve this objective, the link is not an operational system and the ability of various countries and organizations to participate in the program has been dictated by the availability of equipment and funds.

Components

A brief description of the salient features of the communications system components will be useful to indicate the system capability.

Antenna

The spacecraft communications antennas receive at 1725 Mc and transmit at 4170 Mc and are contained in one mechanical assembly, consisting of a coaxial receiving antenna inside the coaxial transmitting antenna. The whole assembly projects downward from the satellite. The antenna array for telemetry and command is mounted on the top of the spacecraft. Both antennas are circularly polarized but of opposite sense, and quasi-isotropic with a vertical coverage extending from 40 to 115 degrees (−1db points). The antennas consist of inclined slots around the periphery of the coaxial outer conductor. External plates convert the linear slot excitation into a circularly polarized wave. The receiving antenna is excited in the TEM mode. The transmitting antenna may be driven from either of two orthogonal ports which excite circularly polarized TEM modes of opposite rotation sense in the coaxial line. The two ports are thus isolated and the off TWT does not load the active TWT. The antenna weighs about 2¼ pounds. A picture of the antenna (mounted on the satellite) is

shown in Figure 8. Typical antenna radiation patterns are shown in Figure 9, sheets 1 through 3.

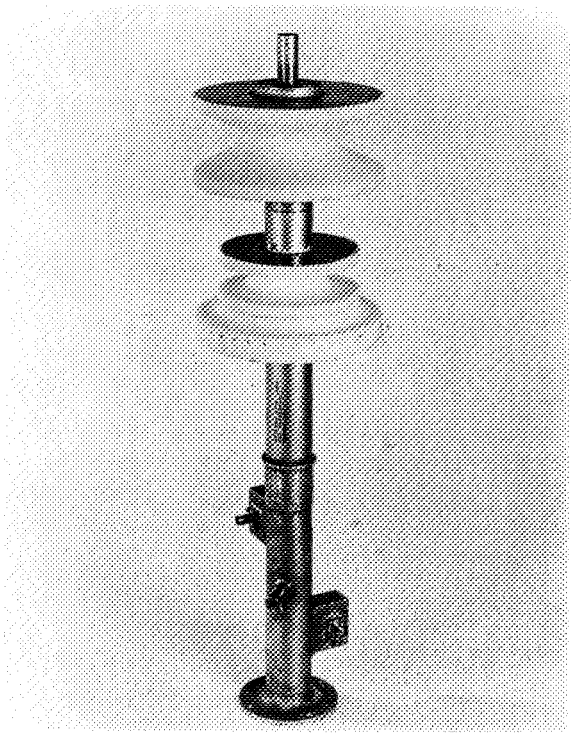

FIGURE 8.—Satellite antenna.

Receiver

A block diagram of the receiver is shown in Figure 10. The receiver is all solid state and conventional in design except for the varactor multipliers and the IF branching. The latter is required for two-way telephony because of the tripling. To accomplish this function, the later stages of the receiver IF amplifier are divided into three channels, switched by a voltage controlled silicon diode switch in the IF path. In the wideband mode, the diode switch completes the IF signal path through a broadband signal tripler stage, to the antenna, with a 1-db output bandwidth of 30 Mc. This channel is used for TV, one-way multichannel telephony, and other experimental wideband transmissions. For two-way transmission, the two ground transmitters are offset in frequency by plus and minus 5/3 megacycles. The ground receivers are offset in frequency by plus and minus 5 megacycles. In the satellite receiver the diode switch is in the alternate position, completing the IF through two parallel, narrowband channels displaced from the input center frequency by $\pm 5/4$ megacycles. Each narrowband channel consists of a narrowband filter, limiter-amplifier, signal tripler, and a linear adding circuit to complete the signal path to the antenna. Thus, the two-way signals are amplified together in the main IF, separated by filters, tripled in frequency, and recombined by a linear adding circuit. The receiver noise figure is 14 db, including 3-db loss in a branching hybrid, and the overall gain is 90 db. The receiver will operate at input levels from minus 80 dbm to minus 40 dbm.

Traveling Wave Tube (TWT)

The TWT amplifier is capable of a saturated output power of 11 watts at a gain of 36 db over the frequency range of 4050 Mc to 4250 Mc. The efficiency including heater power, is 21.5 percent. The tube is specially designed to operate in the vacuum environment of outer space. The tube is radiation and conduction cooled and is mounted inside a cylinder filled with a foam plastic to isolate the tube from the launch stresses and any other stresses that might be induced in the tube due to movement of the spacecraft structure.

Entire System

The entire system including the antennas has a typical unequalized group delay of 0.5-manosecond-per-megacycle linear component, and 10-manoseconds-per-Mc per Mc parabolic component over the temperature range yielding a total intermodulation noise of about 1500 picowatts for 300-channel telephony.

T, T, AND C SUBSYSTEM

The telemetry, tracking, and command subsystem provides three basic functions in the spacecraft:

1. A CW beacon signal, which the Minitrack stations track on;

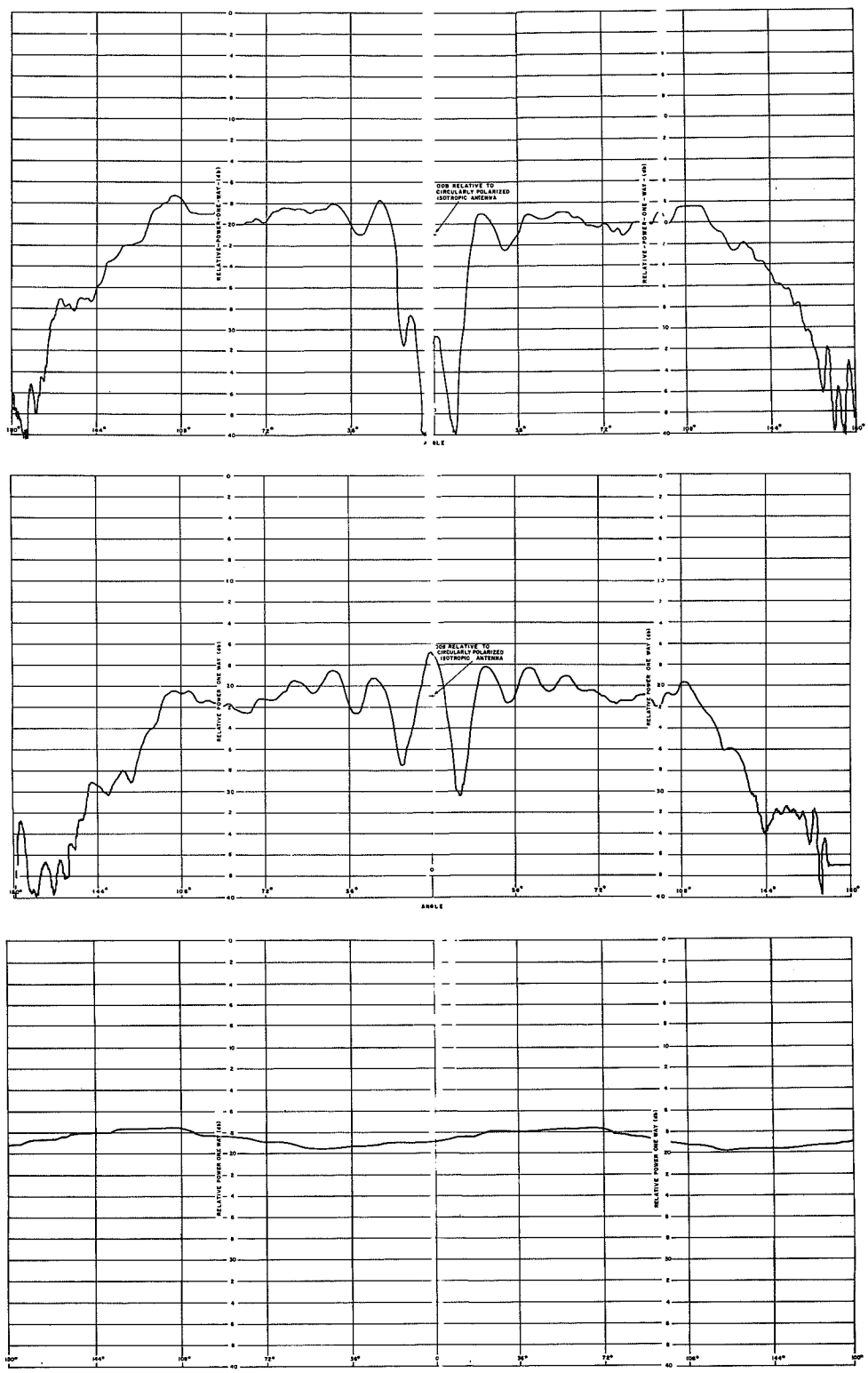

FIGURE 9.—Typical antenna radiation patterns.

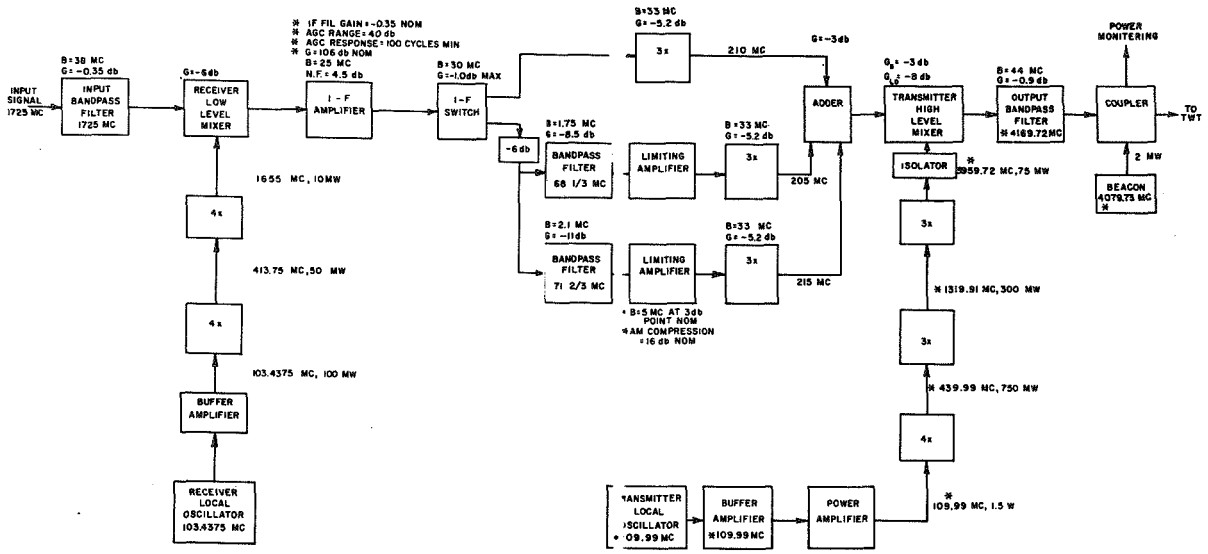

FIGURE 10.—Receiver block diagram.

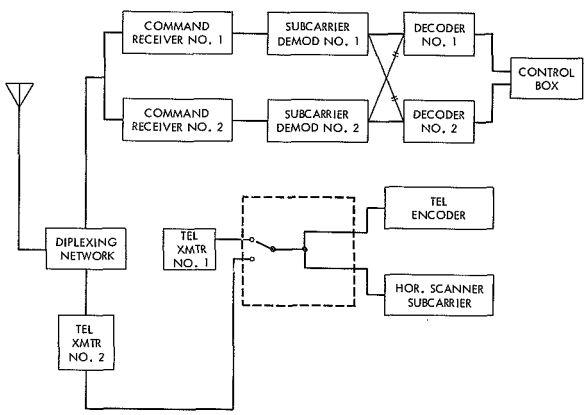

FIGURE 11.—TT and C system block diagram.

2. Telemetry, which transmits performance data from the communication system and the data gathered by the radiation experiments; and
3. A command system, which receives the commands and converts them into a desired switching function.

A block diagram of the T, T, and C system is shown in Figure 11. The telemetry transmitters can be switched on and off by means of the command system. Operationally, one of the transmitters would be on continuously to provide the tracking signal. The Minitrack ground station would utilize this signal to track the satellite and provide orbital measurements. The alternate transmitter would be commanded ON when telemetry or horizon scanner data are desired. The modulation switch, which is physically located in the control box, selects the transmitters to be modulated and the source of modulation (telemetry encoder or horizon scanner subcarrier oscillator). This switch is under the control of the command system.

On an operational pass, a typical sequence of events might be as follows:

1. Transmitter No. 1 would be on continuously.
2. The command to modulate transmitter No. 2 would be transmitted.
3. The command to energize transmitter No. 2 would be transmitted.
4. The command to energize the telemetry encoder would be transmitted.
5. The telemetry signals would be received and decommutated, and the proper functioning of the spacecraft would be ascertained. In addition, data from the radiation experiments would be accumulated.

6. The command to energize the horizon scanner would be transmitted. (This automatically turns off the telemetry encoder.)
7. Horizon scanner data will be accumulated in order to determine the attitude of the spacecraft.
8. The telemetry encoder will be commanded on again (automatically turning off the horizon scanner).
9. Spacecraft performance and radiation experiment data will again be collected.
10. The encoder will be commanded off.
11. Telemetry transmitter No. 2 will be commanded off.

This sequence of events pertains only to the T, T, and C subsystem. Other commands would be transmitted during an operational pass which would apply to the communication, attitude control, and power supply subsystems. These are covered in the discussion of the particular subsystems.

In the event of a failure of one transmitter, the other would provide both tracking and telemetry signals.

The command system consists of a redundant set of command receivers, subcarrier demodulators, and decoders. A pulse-code-modulated subcarrier is transmitted via a VHF carrier to the command receiver which demodulates the carrier and sends the subcarrier to the subcarrier demodulator where the pulse code is reconstituted. The code output is then fed to both decoders through a cross-coupling network in such a fashion that either demodulator can activate either decoder. Thus, in the event of failure of receiver No. 1 or subcarrier demodulator No. 1 and decoder No. 2, the command system will still function. The decoder uses a magnetic core shift register to transform the pulse code into a command signal. The command signals from the two decoders are "paralleled" so that either or both decoders can activate the control function. In the control box the command signal sets a bistable flip-flop multivibrator to the desired state. The flip-flop multivibrator provides the memory for the command, and also provides the bias signal for the switching transistors, in order to execute the desired command.

The pulse code word consists of series of bursts of audio tone (the subcarrier). A typical word is shown in Figure 12. The word is divided into eight time segments, the first two being used for word synchronization. The first segment is left blank and the second

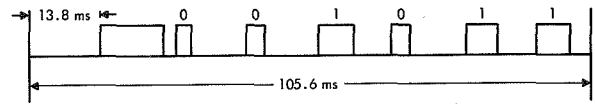

FIGURE 12.—Typical word pulse formation.

segment contains a subcarrier burst three-fourth segment in length. The next six segments contain the information bits. The information bits are constrained to a combination of three "zeros" and three "ones." This gives a capability of 20 commands (the combination of 6 things taken 3 at a time). The one of a "3 x 3" system provides for error detection. If the code received by the decoder contains any other combination, the code will be rejected. The probability of a proper code word being transformed into another proper code word due to noise (a one becoming a zero and a zero becoming a one) is very small indeed. The command word is transmitted five times in succession to insure its getting through. A "one" is represented by a tone burst one-half segment in length and a zero by a one-fourth segment. A description of each of the components of the T, T, and C system and its function in the system follows:

VHF Antenna

The VHF antenna consists of four monopoles extending out from the mounting ring face of the spacecraft. For command reception the antennas are fed in phase to produce a basically dipolelike pattern. For telemetry and tracking transmission, the monopole pairs are fed in phase quadrature to produce a circularly polarized wave in the plane perpendicular to the spin axis. In any plane parallel to the spin axis, the wave is linearly polarized. A diplexer harness is used to couple the two receivers and two transmitters to the antennas. A schematic of this harness is shown in Figure 13. The receivers are connected in parallel

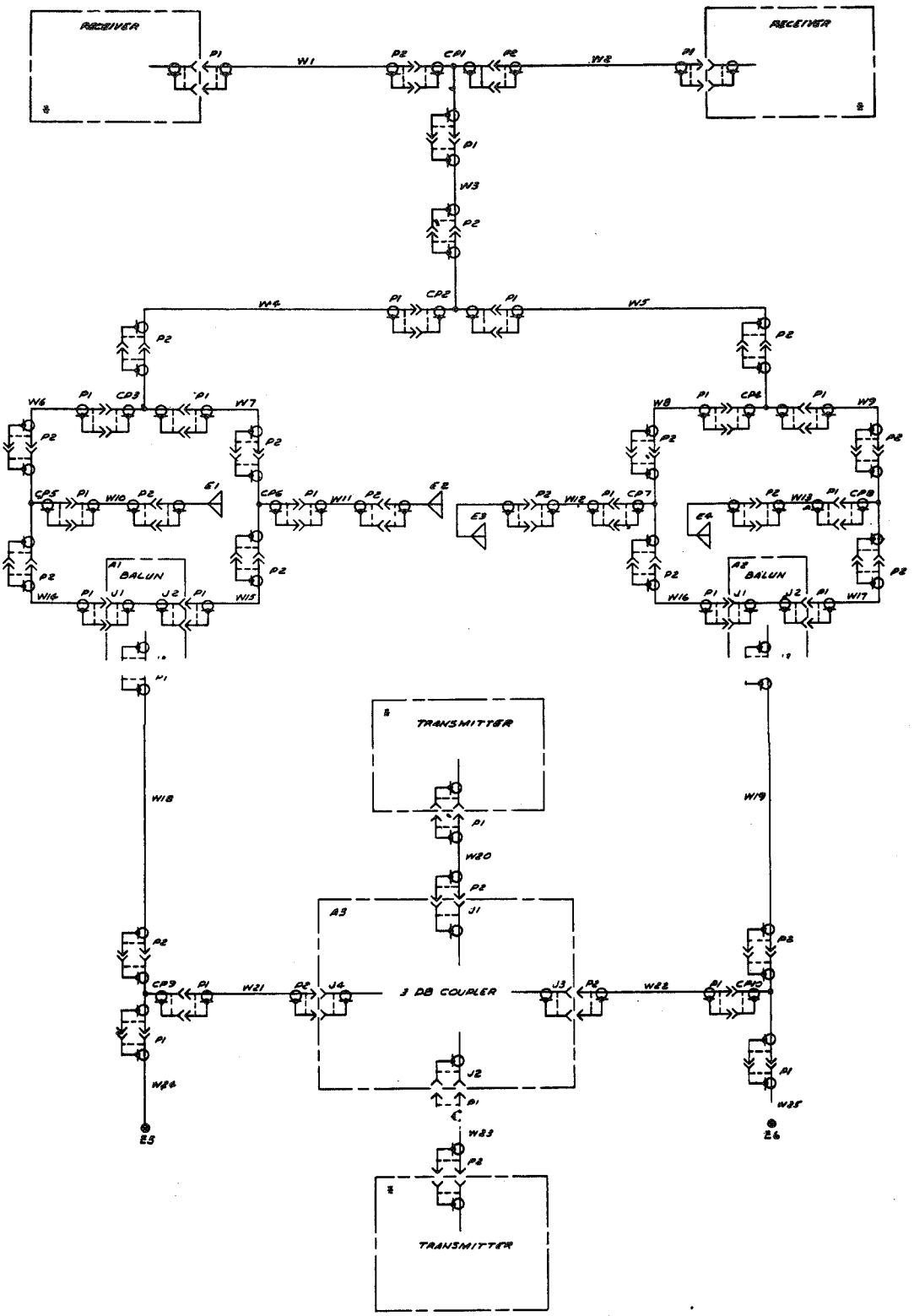

FIGURE 13.—Diplexer harness schematic.

through ⅛-wavelength cables, so that an open or short on one of the receivers will have a minimum effect on the other. The transmitters are coupled into the harness through a 3-db coupler providing a minimum of 20-db isolation between transmitters. The weight of the antenna assembly (monopoles and harness) is 1.25 pounds.

Telemetry Transmitter

The transmitter is an all-solid-state device using silicon transistors. The modulation is digital phase modulation with a nominal 130 degree peak-to-peak deviation. The oscillator is at 34 Mc and crystal controlled. The phase is varied by means of a variable capacitance diode. The signal is multiplied by a factor of four in the varactor stage and then amplified in a two-stage amplifier to obtain the quarter-watt output. The characteristics of the transmitter are summarized in Table V–1. A photograph of the transmitter is shown in Figure 14.

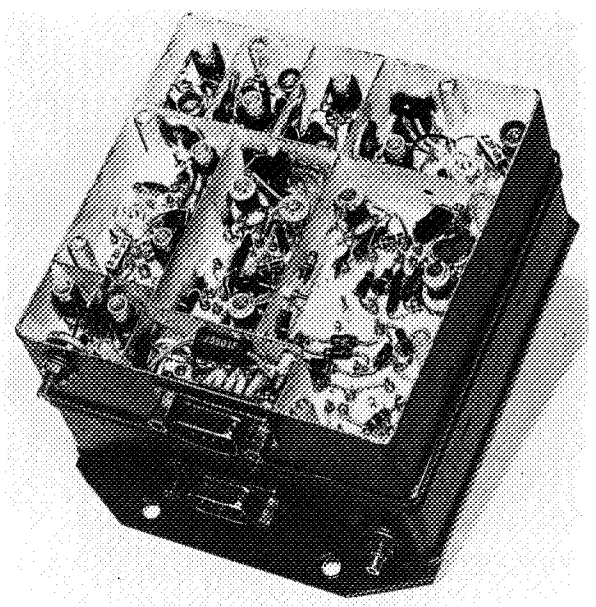

FIGURE 14.—Telemetry transmitter.

TABLE V–1.—*Telemetry Transmitter Characteristics*

Frequency	136 to 137 Mc crystal controlled.
Frequency stability	±0.003 percent for 24 to 33 volts 0 to 40 degrees C.
Modulation signal	1. Telemetry encoder signal rectangular pulses of either 0.4 or 0.8 millisecond. A space or "0" pulse will be from 0.0 to 0.5 volt and a mark or "1" pulse from 3.3 to 6 volts. 2. Horizon scanner signal square wave 1.3 kc subcarrier frequency modulated ±7½ degrees.
Modulation	Phase shift keyed 120 degree peak-to-peak phase.
Modulation sensitivity	Shift from "0" to "1."
Input power	2.0 watts at 28-volt input.
Weight (2 transmitters).	1.3 pounds.
Size (2 transmitters)	4 x 4 x 2.5 inches.

TABLE V–2.—*Encoder Characteristics*

Output code:	
Frame format	128 words per frame.
Word format	9 data bits per word.
Frame sync	3 9-bit words (27 bits), adaptable to various codes.
Frame rate	1 frame per second.
Bit rate	1,152 bits per second.
Output signal:	
Format	Serial split phase NRZ–PCM.
Output level	The output signal consists of 2 voltage levels defined as follows: Low voltage 0 to 0.5 V. High voltage +3.5 V to 4.5 V.
Output impedance	5,000 ohms.
Clock stability	0.01 percent.
System transfer accuracy:	
High-level input (0–5 V).	±0.5 percent overall.
Low-level input (0–200 mv).	±1.0 percent overall.
Main multiplexer:	
Total channels	128.
Sample rate	1 sample per second for each channel.
Analog inputs	0–5 volts.

TABLE V-2.—*Encoder Characteristics*—Continued

Main multiplexer—Continued	
Channel input impedance.	Analog: 1 megohm minimum. Digital: 100 kilohms minimum.
Back current during sample period.	0.25 microampere maximum.
Leakage current during nonsampling period.	0.0 microampere maximum.
Submultiplexer No. 1:	
Total channels	32.
Sampling rate	1 sample per 32 seconds for each channel.
Analog inputs	0 to 200 millivolts.
Channel input impedance.	100 kilohms minimum.
Back current during sample period.	0.25 microampere maximum.
Leakage current during nonsample period.	0.05 microampere maximum.
Submultiplexer No. 2:	
Total channel	64.
Sample rate	1 sample per 64 seconds for each channel.
Channel input impedance.	1 megohm minimum.
Back current during sample period.	0.25 microampere.
Leakage current during nonsample period.	0.05 microampere.
Input power	7.5 watts.
Mechanical characteristics:	
Weight	8 pounds.
Volume	170 cu. in. (approx.).

Telemetry Encoder

The telemetry encoder time division multiplexes the data from the communication and radiation experiments and converts it to PCM for transmission via the telemetry transmitter. Analog data are converted via an analog-to-digital converter and the digital data are entered directly into the output register. The encoder is made up of the following basic units.

1 128-channel main multiplex.
1 64-channel sub multiplex.
11 32-channel main multiplex.
7 accumulators — 108 bits total.
1 accumulator — 27 bits long.
3 accumulator — 14 bits long.
3 accumulator — 13 bits long.
1 amplifier (200 mv to 5 v).
1 analog to digital converter (9 bit).
One reference voltage source.
Logic and tuning circuitry.

The accumulators are used to monitor the outputs of the radiation detector. The 27-bit accumulator continuously monitor radiation flux, whereas the other accumulators are reset every 10 seconds. An information flow diagram for the encoder is shown in Figure 15, and the encoder characteristics are shown in Table V-2. A photograph of the unit is shown in Figure 16.

Command Receiver

The command receiver is a single superheterodyne AM receiver operating in the VHF band. It is all solid state and uses a crystal filter at the 20 Mc IF frequency to determine the IF bandpass. This receiver is identical to that used in the Tiros series of meteorological satellites. There are two redundant receivers packaged in a single case. Figure 17 shows a block diagram of the receiver and Figure 18 is a photograph of the unit. Table V-3 gives its characteristics.

TABLE V-3.—*Command Receiver Characteristics*

Input frequency	VHF.
Modulation	Amplitude.
Noise figure	8 db typical; 10 db max.
IF selectivity	40 kc at 6 db bandwidth. 100 kc at 60 db bandwidth.
Spurious rejection	50 db.
Voltage gain (without AGC) (−10°C to +60°C).	120±3db
Output voltage (90 percent modulated at 1 kc).	1 v rms.
Input impedance	50 ohms.
Output impedance	2000 ohms.
Local oscillator stability (−10°C to +60°C).	±0.005 percent.
Power supply (28 v)	330 mw/receiver.
Case dimensions	6 x 4 x 2.5 inches.
Weight (dual unit)	2.0 pounds.

Subcarrier Demodulator and Decoder

The subcarrier demodulator detects the PDM subcarrier tone burst from the command re-

764-173 O—65——10

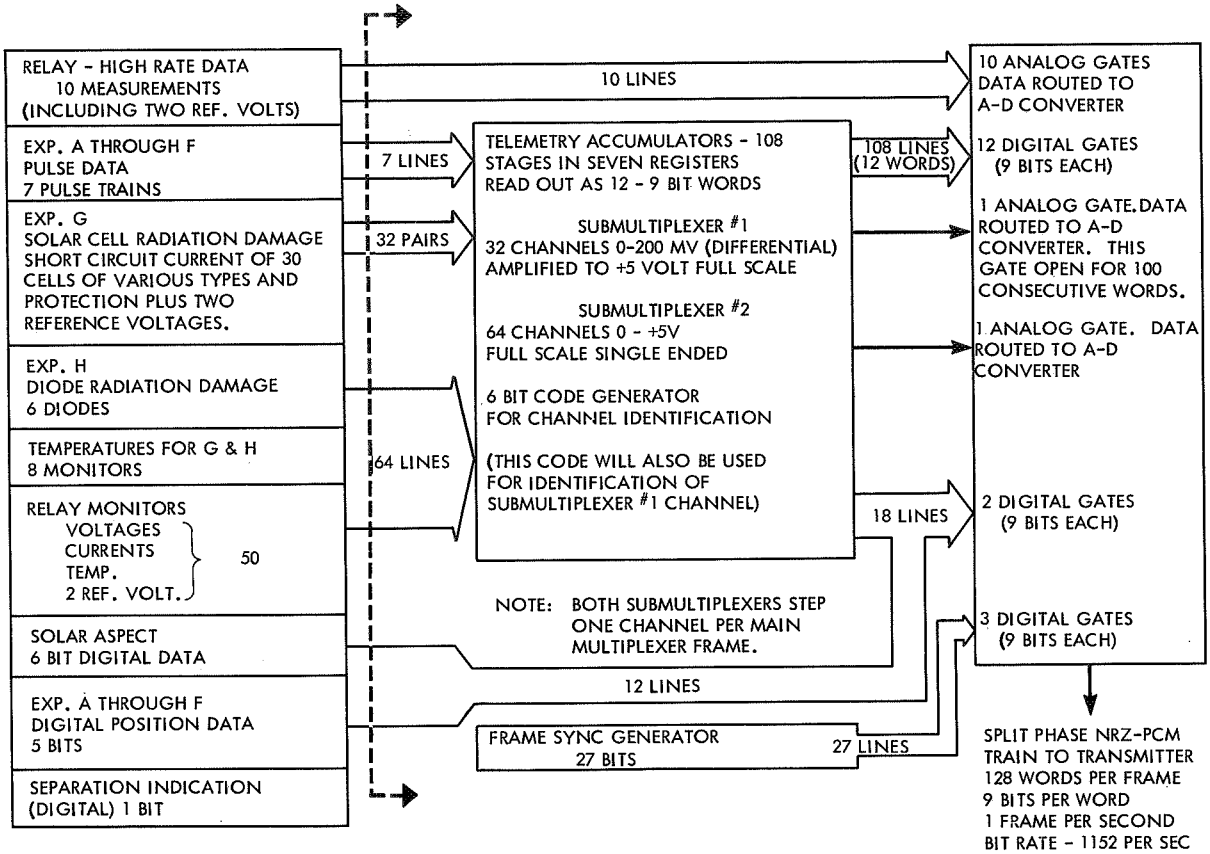

FIGURE 15.—Telemetry encoder information flow diagram.

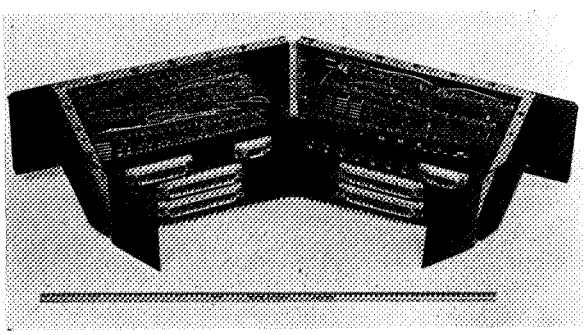

FIGURE 16.—Telemetry encoder.

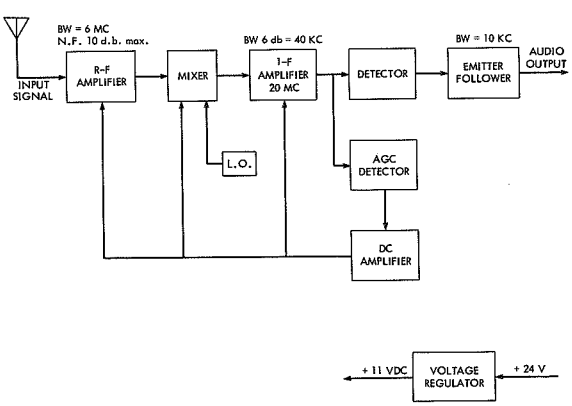

FIGURE 17.—Command receiver block diagram.

ceiver and regenerates the pulses for the decoder. The decoder checks the pulses for timing and duration; and accepts or rejects the command based on the error-detecting code. The PCM code conversion is accomplished by logic in a magnetic shift register, which eliminates the need for a diode matrix. The output of the decoder consists of 10 lines each capable of transmitting positive or negative pulses, thus providing 20 command pulses. A more complete description of the operation of this unit is given in the transactions of the IRE professional group on aerospace and navigational electronics

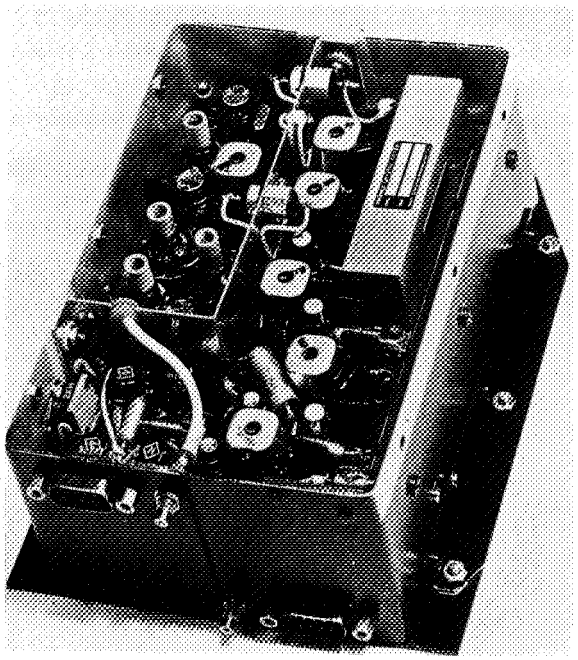

FIGURE 18.—Command receiver.

June 1962 in an article "Project Relay Digital Command System," by Roth and James.

A block diagram of the dimodulator dicoder is shown in Figure 19. Figure 20 is a photograph of the unit. Table V–4 gives the characteristics of the equipment.

Command Control Unit

The command control unit takes the command pulses from the decoder and performs the switching function command. The negative or positive pulses are combined in logic OR gates to control associated flip-flop switches. The flip-flops serve as memory units holding the command until the complementary command is sent. The state of the flip-flop is sensed in a level detector, which then actuates the proper transistor power switch for the commanded function. When a command has triggered a control flip-flop, a signal is sent to the telemetry encoder providing command verification. The

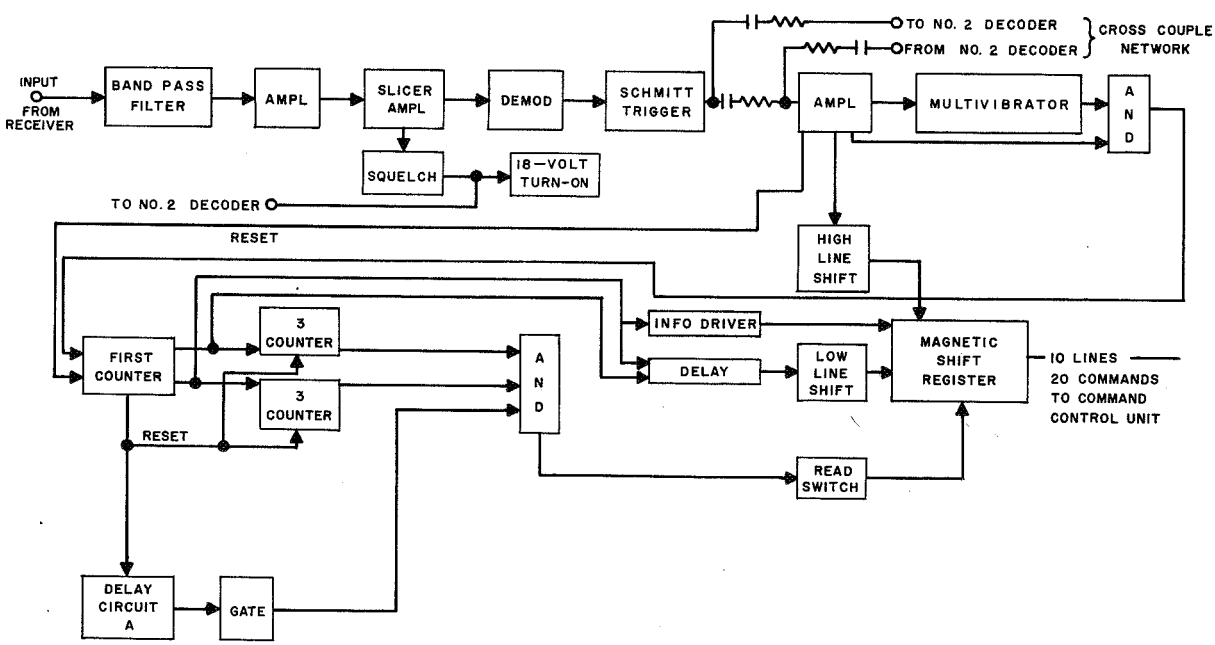

FIGURE 19.—Demodulator decoder block diagram.

control unit weighs 2 pounds and is 4 x 4 x 2.5 inches in size. A photograph of the unit is shown in Figure 21.

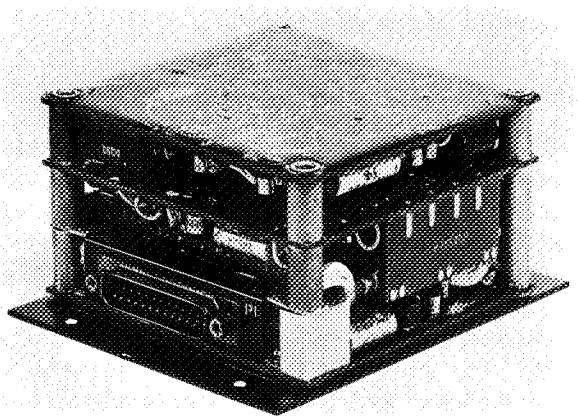

FIGURE 20.—Demodulator decoder.

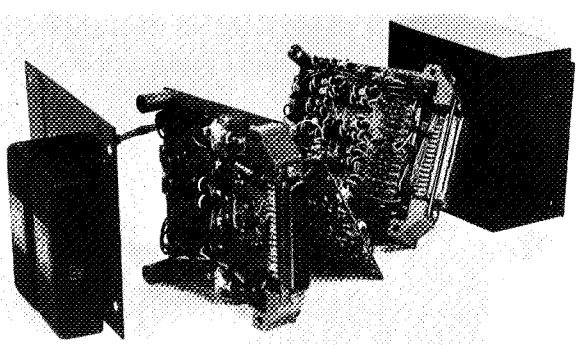

FIGURE 21.—Command control unit.

TABLE V-4.—*Subcarrier Demodulator and Decoder Characteristics*

Subcarrier demodulator:	
Input signal form	5451 cps tone, 100 percent amplitude-modulated by PDM coded signals.
Input signal level	1 vrm.
Input impedance	10 kilohms.
Decoder:	
Command message	40-segment PDM code consisting of and 8-sigment code repeated 5 times for each command. Each code word contains 6 information bits which are constrained to sequences consisting of 3 binary ones and 3 binary zeros, resulting in 20 different commands.
Bit structure	Binary ones, 6.60-millisecond duration. Binary zeros, 3.30-millisecond duration.
Bit rate	40 segments per 528.0 milliseconds. 1 word (8 segments) per 105.6 milliseconds. 1 segment per 13.2 milliseconds.
Word synchronization.	1st and 2d segment are identical for each work and are used for work identification, while the 3d through 8th segments are information bits. The 2d segment contains a pulse of 9.9-millisecond duration.
Output signal	5-volt pulse of either positive or negative polarity. Refer to Table 3.7.5.2.
Output impedance, uncommanded.	2200 pf in parallel with greater than 10 megohms.
Output impedance, commanded.	Less than 100 ohms.
Input power:	
Battery voltage	24 vdc to 28 vdc.
Idle	165 mw to 250 mw.
Operate	410 mw to 555 mw.
Size	4 x 4 x 2.5 in.
Weight	1.5 pounds.

EXPERIMENTAL PLAN

The operational sequence is accomplished in two steps. The satellite is first acquired by the NASA Test Site using the VHF (the VHF command system). The satellite's 136-Mc beacon signal is left on continuously for this purpose. Following acquisition, the spacecraft telemetry is read out and analyzed to determine the condition of the spacecraft. If the temperatures and condition of battery charge is satisfactory, the wideband repeater and microwave beacon are turned on for 3 minutes and the performance evaluated with test signals. The test site will then advise the Relay ground stations of the spacecraft condition. If the satellite is behaving satisfactorily, the test site will command the satellite on again, and permit the communications ground stations to proceed with experiments. The communication ground stations will then perform their experiments.

Telemetry will be continuously monitored by the test site.

The satellite is normally turned off by the test site. If peculiar conditions develop during the test, whereby the test site fails to turn off the spacecraft, a circuit sampling the AGC bus of the wideband repeater will detect a "no carrier" condition and deenergize the wideband system after 2 minutes.

The traffic test operation plan will be modified as information is accumulated by the experiments. In general, correlation will be made between the satellite and ground station performance so that the characteristics of the transmission medium can be explored, as well as the satellite performance degradation due to the space environment.

The transmission medium characteristics to be examined will be attenuation, attenuation stability, phase characteristics, interference, noise, time delay, and other characteristics that may be of interest.

The satellite receiver signal strength, telemetry data, and attitude will be correlated with ground stations performance (antenna elevation, pointing error, weather conditions, and doppler shift).

TABLE VI.—*Typical Link Performance*

	Andover (U.S.) to Goonhilly (England)		Nutley (U.S.) to Rio (Brazil)		Andover (U.S.) to Pleumeur Bodou (France)	
	Ground to spacecraft	Spacecraft to ground	Ground to spacecraft	Spacecraft to ground	Ground to spacecraft	Spacecraft to ground
Experiment	TV	TV	2-way telephony.	2-way telephony.	1-way telephony.	1-way telephony.
Frequency	1725 Mc/s	4170 Mc/s	1725 Mc/s	4170 Mc/s	1725 Mc/s	4170 Mc/s.
Modulation	FM	FM	FM	FM	FM	FM.
Deviation	4.6 Mc/s	13.7 Mc/s (peak to peak including sync).		462 kc, rms		2.08 Mc, rms.
Transmitter power	10 kw	10 w	2 kw	4 w	10 kw	10 w.
Receiver noise temperature	6960° K	175° K	6960° K	455° K	6960° K	51° K
Antenna gain (transmitter, circular polarization.	50.2 db	−1 db	42 db	−1 db	50.2 db	−1 db.
Antenna gain (receiver circular polarization).	−1 db	58.3 db	−1 db	51 db	−1 db	57.6 db.
Space loss	176 db	184 db	176 db	184 db	176 db	184 db.
Receiver noise bandwidth	23 Mc/s	23 Mc/s	23 Mc/s	600 kc/s	23 Mc/s	24.3 Mc/s.
Predetection signal/noise ratio.	27.6 db[3]	14.7 db	13.4 db	14.1 db	29.7 db	18.1 db.
Margin		7.0 db[1]		6.9 db		8.6 db.
Minimum baseband signal to noise (unweighted without preemphasis).		30.5 db[4]				
Baseband	3.5 Mc (video)[2] and 4.5 Mc aural subcarrier		12 channel		300 channel	

[1] Frequency following receiver.
[2] 525-line picture.
[3] Includes 1-db ellipticity loss and 1-db transmission line loss.
[4] Peak-to-peak signal to RMS noise.

As an aid in the data analysis, television signals will be examined for resolution, synch compression, streaking, smearing, ringing interference and the effects of preemphasis. The one-way multichannel telephony will be examined for intermodulation, distortion, intelligibility, interference. Two-way telephony will permit a study of echo and time delay phenomena. The digital data will be examined for error rate and waveform anomalies.

Performance dates for typical links is shown in Table VI–1. The parameters tabulated represents the expected performance based on data supplied by the various participants.* It may be observed that the system margins are small but adequate.

RADIATION EXPERIMENTS

The spacecraft carries experiments to determine the extent of radiation damage to various types of solar cells and silicon diodes, and particle detectors to measure the intensity, direction, and type of radiation encountered by the spacecraft. Correlation of the damage with the radiation measurements will be made in an attempt to permit future design of radiation tolerant solar cells and semiconductors for use in spacecraft systems.

The radiation damage experiment contains 30 specially calibrated solar cells of various types with shields of fused silica up to 0.060-inch thickness. The parameter to be measured is short circuit current, since this varies almost linearly with degradation. The minority carrier lifetime of six silicon diodes will be measured by passing a current through the diodes. The voltage output of this experiment will be proportional to the minority carrier lifetime. A solar aspect indicator will provide sun angle measurements to be used in analysis of the solar cell data.

In order to cover as wide an energy range of electrons and protons as possible, monitoring of the radiation will be performed by six detectors. This coordinated group of detectors will measure the proton spectrum in an energy range from 1.0 to 300 Mev and the electron spectrum from 0.25 to 1.2 Mev. The proton spectrum will be divided into 12 overlapping ranges and the electron spectrum into 5 ranges.

*See sec. II for participants.

TIROS OPERATIONS

ERNEST F. POWERS
Goddard Space Flight Center

Operational control for Tiros satellites, exercised by the Technical Control Center (TCC) at NASA Goddard Space Flight Center (GSFC), has grown as a technical challenge as the project evolved from its early R&D role in Tiros I to its present combined mission of furnishing operational meteorological data and supporting research and development in the study of the physics of the atmosphere.

Diagramed in Figure 1, TCC is responsible for the monitoring and operational evaluation of spacecraft and Command and Data Acquisition (CDA) station performance and for the direction and coordination of the operational phase of the Tiros mission. In accomplishing these tasks, TCC receives a variety of input data, derives the necessary courses of action, and provides the resultant data to the participating agencies and groups. Examples of the many types of input data include computed orbital information indicating minute-by-minute satellite position over the earth, solar illumination over the orbital track, and station acquisition predictions. TCC also provides a comprehensive summary of spacecraft spin-axis positions, both hindsight and predictive, for purposes of magnetic attitude steering, and the effects of these data on the spacecraft power supply and viewing angles of IR and TV camera sensors.

These data, plus requests from the U.S. Weather Bureau as to where on the orbit Tiros TV pictures are desired, enable TCC to program satellite data command and readout (Fig. 2). Once the spacecraft has been interrogated and the data received, a summary of all operations, including specific command times and responses as well as signal quality, strength, and duration, is reported to the control center.

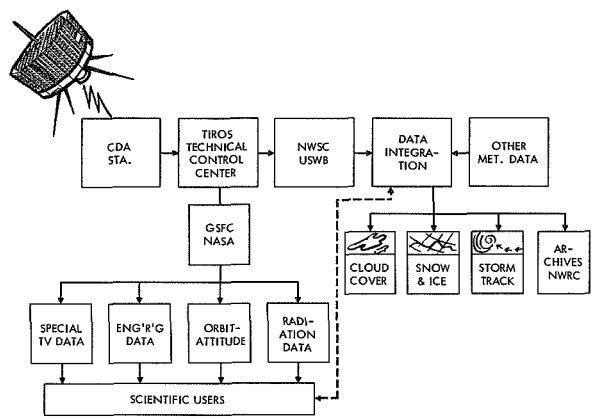

FIGURE 1.—Tiros data flow.

Selected parameters of the spacecraft telemetry (voltages, temperatures, etc.) are also forwarded after each orbital interrogation, along with the data from the Horizon Sensor and North (Sun Angle) Indicator Subsystems. The necessary computations are then performed immediately.

The next orbital interrogation is not undertaken until a summary analysis of these data has indicated an acceptable performance level of the spacecraft and the CDA station. Any unusual or abnormal response from the spacecraft is immediately analyzed and program changes, if needed, are made for the next interrogation.

The operational condition of the CDA stations is reported in summaries of orbital interrogation and data handling—for example, quality of antenna control, whether by automatic track or by slave to a special antenna programmer console; current capabilities for effective command and noise-free data readout; effective photo processing, attitude prediction and gridding; and meteorological analysis.

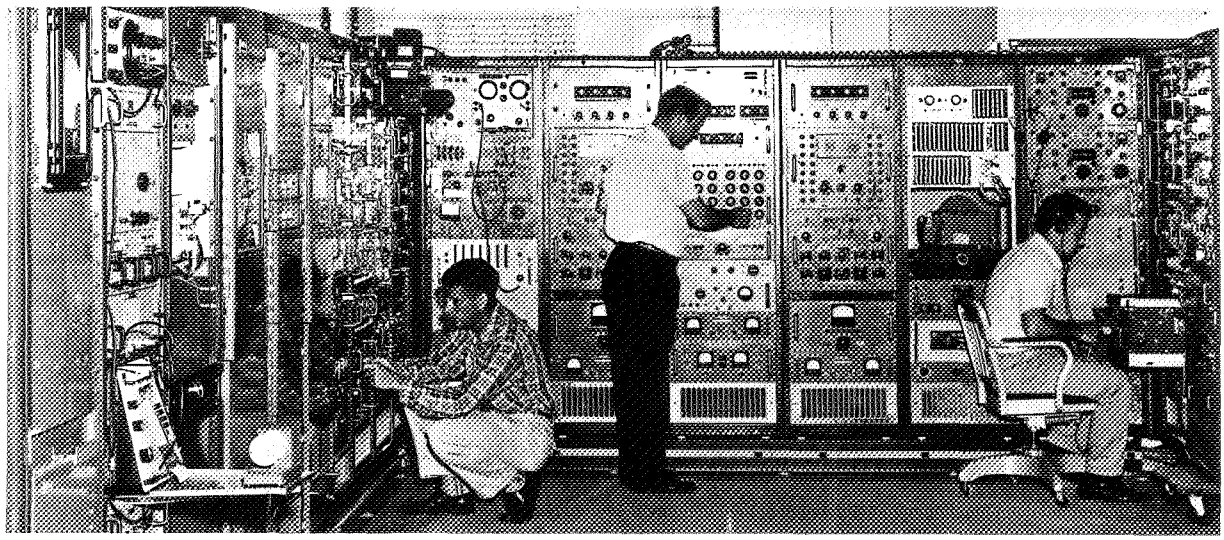

FIGURE 2.—CDA equipment at Wallops Station. Center: command-programing, antenna-control, and calibration devices. Right: receivers and recorders for horizon sensor and housekeeping telemetry. Left corner: equipment for reception, recording display, and photographic reproduction of 235-Mc TV data. Extreme left: 237.8-Mc IR equipment.

Special "hot" voice lines link TCC with each of the CDA stations to receive or relay these vital data.

Effective communications for command, control, and data dissemination have contributed much to the high performance level achieved with Tiros. Voice lines, photo facsimile, teletype, and data facsimile all play a part in the operation. Each represents an alternative method in the conveying of information from point to point, while maintaining a specific use.

Real-time analyses of the Tiros data as conducted by meteorologists at the CDA stations have presented a learning process since the early days of Tiros I. Progress from lengthy hand calculations and detailed map projections and analyses have given way to use of a digital computer and plotter requiring a variety of input data. Using special nomograms and ephemerides, the hand calculations are reduced where possible.

Research with Tiros TV data has been aided by producing a master 35-mm negative from which copies can be made for distribution. The Master negatives reside at the National Weather Records Center, Asheville, N.C. The production of this master negative demands rigid and accurate quality-control procedures from initial film derivation to the CDA stations. The establishment of exacting controls on ground-station TV kinescope settings and levels and darkroom development techniques has seen a major advance in only the past year. The large number of photographs requires automatic film processing and reproduction and a high degree degree of uniformity in the end product. This has recently been achieved with Trios data.

The motion of the spacecraft spin axis, which was originally thought to be relatively fixed in space, has been discussed in many technical reports. This axis has been found to have a regular precession of as much as 3–5° per day, due primarily to three torques acting upon the satellite (*1*, *2*). Angular motion of the axis arises from, first, a primary torque caused by the interaction of a magnetic dipole along the satellite spin axis with the earth's magnetic field; this magnetic dipole is caused by residual magnetism of the satellite's components along the spin axis and by closed current loops in the spacecraft instrumentation. Then, a secondary torque is caused by a differential in the earth's gravitational field, as related to the fact that the moment of inertia of Tiros about the spin axis being greater than the other principal moments of inertia, the orbital plane precession

of approximately 3.6° per day around the equator due to the oblateness of the earth, and the spin axis being normally out of the orbital plane. Therefore, whenever the spin axis is out of the orbital plane, a torque is exerted on the spacecraft due to this difference in moments of inertia. Third, a secondary torque arises from eddy currents caused by the satellite rotation about its axis in the earth's magnetic field (*2*). Continued research is being conducted at GSFC to examine the effects of this torquing plus effects of aerodynamic torquing on the spacecraft spin axis.

Concerning this work, a theoretical model has been constructed which gives the total torque acting on the satellite over one orbital period, and a GSFC computer program called MGAP (Magnetic Attitude Prediction) utilizes this theoretical model to predict the changes in satellite spin-axis attitude. Knowledge of these changes is extremely important for programming operation of the spacecraft systems in orbit, and for the effective utilization of the Tiros TV and IR data when received at CDA stations.

The need for constant knowledge of spin-axis position has led to two important changes in Tiros operations.

First, a variable-current closed circuit coil was installed on Tiros II and succeeding spacecraft. This coil allowed the creation of an additional calibrated dipole moment along the satellite spin axis. It can be energized by five variations of current of both positive and negative values as well as a zero value.

This coil actually allows *optimun magnetic steering* of the spacecraft spin axis. Motions of up to 10° per day can be added to the normal spin-axis precession rate or the precession motion can be retarded to a significant degree. Figure 3 shows a record of such action. Although the spin axis is still constrained to stay within the limits of the orbital plane, significant results using magnetic steering have been accomplished, that is, the sun-spin vector angle has been kept to within prescribed limits for proper illumination of the solar cells and the sunrays have been kept out of the field of view of IR sensors.

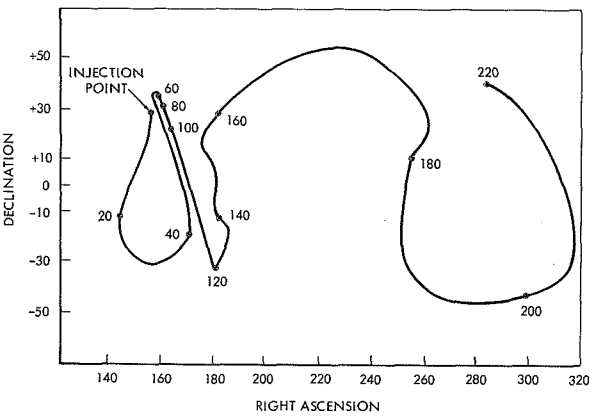

FIGURE 3.—Tiros V spin-axis attitude: As determined by CDA station teams for first 220 days in orbit.

Secondly, teams have been placed at the CDA stations to provide on-site daily determinations of satellite spin-axis attitude. Through the use of a small digital computer and special grid-plotting equipment, these teams first derive or or verify the attitude from the current orbit of Tiros data and then prepare the latitude and longitude grid overlays for the upcoming interrogation. The team at the Wallops CDA station collects and collates all data for determining the best spin-axis attitude for each orbit of the past day, and based upon these values predicts the attitude for the next 36 hr. GSFC makes long-range magnetic attitude predictions using the theoretical model previously mentioned. Excellent correlation exists ($\pm 1.5°$) between the observed attitude as computed by the CDA attitude-determination teams and the predicted values issued by GSFC.

An analysis of the many methods of Tiros attitude determination has shown that there is a great deal to be gained from the many sources of attitude derivation. The techniques and procedures used to determine the best attitude from Tiros include the horizon sensor, TV pictures (two types of analysis), and the output of Channel Two (8–12 micron) of the IR scanning radiometer. Although TV pictures continue to be the best source of attitude information, the other data plus predicted magnetic-steering information have given a high degree of confidence to the final attitude values, and hence picture interpretation and analysis.

Another change incorporated on Tiros II, based on experience with Tiros I, was the removal of the digitizing system for the horizon-sensor data from spacecraft to the ground readout sites. This was found to be desirable because the horizon sensor was subject to spurious responses from cloud elements. When read out as an analog signal on the ground, however, the spurious or unwanted responses could more easily be gated out or discarded before the digitization process. This has proven very successful.

Operational procedures for Tiros have evolved to achieve the best spacecraft and CDA station performance. Two changes of rather recent origin should increase the useful life of the Tiros spacecraft. The spacecraft are now interrogated for every orbit possible in order to consume power and prevent battery overcharging. And switching of the vidicons is held to a minimum.

The choice of launch dates and possible launch times for Tiros have been found to depend on many factors, besides availability of a flight-tested, accepted spacecraft. Launch dates are affected by the hemisphere's coverage desired from the television cameras, the orbit inclination, vehicle characteristics, direction of launch and season of the year, and the relationship of a planned orbital plane to the orbital plane of a spacecraft already in orbit.

For example, if Tiros is to be launched NE from Cape Canaveral on a Delta vehicle into a 58° inclination, 350-n. mi. orbit, the primary considerations for launch date are desired television coverage at some specific time, for example, hurricane coverage in mid-August and September, and the orbital-plane relationship with that of presently operating spacecraft. However, if Tiros is to be placed into a polar orbit, these same constraints plus such factors as the portion of the first verticality, the hemisphere (North or South) which is properly sunlit, and the precise type of polar orbit, for example, sun-synchronous, will demonstrably affect the eventual launch date.

Launch times (launch windows) are chosen so that the normal precession of the satellite spin axis for at least 7–10 days will not cause the sun-spin vector angle (Gamma) to shift beyond the accepted limits of 20°–70°, or will have allowed the sun's rays to enter the field of view of the IR scanning radiometer (39°–51° Gamma), and will provide proper solar illumination for TV pictures at the desired times for the selected period. It is the unusual occasion when all of the constraints of date and time are equally well satisfied, and some compromise must be made.

The programing of two satellites (Tiros V and VI) in orbit with orbital planes less than 15° apart introduced new areas of concern in the design of Tiros spacecraft and in the conduct of operations. The urgency for a different type of command system to enable selective interrogation was very evident. Operations procedures at TCC and at the CDA stations had to be adjusted so that, if the two spacecraft were to be interrogated within the time frame of the same orbital period, data readout from one spacecraft had to be completed in time to allow proper program setup time for the closely following interrogation. Then the data handling and processing had to be accomplished so that the final data were presented in time to be of value to the users. CDA equipment redundancy and duplicate communications facilities enabled these operations to be performed on a realistic basis. But there is need for a new or modified command system with selective address, and a modification has been designed for inclusion on future Tiros spacecraft.

Finally, experience in Tiros operations indicates that spacecraft interface requirements should never be assumed to be met merely by production of new units to supposedly identical specifications. Of course, any design changes which affect the spacecraft operation must see a complementary change in the CDA station equipment, but the CDA station must be prepared not only to optimize according to the individual spacecraft's calibration, but also must be prepared to make adjustments as new "calibrations" are received in orbit. It is at this point that flexibility and good engineering common sense have paid off in Tiros operations.

ACKNOWLEDGMENT

The author wishes to thank Herbert I. Butler, Associate Chief for Projects, GSFC Aeronomy and Meteorology Div., for his assistance and contributions.

REFERENCES

1. Bandeen, William R., and Manger, Warren P., "Angular Motion of the Spin Axis of the Tiros I Meteorological Satellite Due to Magnetic and Gravitational Torques," *Journal of Geophysical Research*, Vol. 65, No. 9, September 1960, pp. 2992–2995.
2. Mowlem, A. Robin, "Satellite Attitude Determination," paper presented at the Ninth East Coast Conference on Aerospace and Navigational Electronics, October 1962.

TIROS ACHIEVEMENTS

ROBERT M. RADOS
Goddard Space Flight Center

To assess properly the achievement of Tiros, one must keep in mind the system in its entirety—the spacecraft, the launch vehicle, the data-acquisition facilities, and the data-utilization areas. Each contributed much to the record of success summarized in the table here.

The first Tiros demonstrated the feasibility of providing and using cloud photographs. In addition, it demonstrated the utility of certain types of satellite dynamics and thermal control, the versatility of various electronic and mechanical components, and other capabilities of modern technology. The useful life of Tiros I ended with the burnout of a camera transmitter, caused by a failure of power turnoff relay, which affected the entire satellite system. Seventy-six days (approximately 185 active hours) of successful operation produced almost 23,000 pictures by both cameras, one with a wide-angle and one with a narrow-angle lens, both operating in remote and direct modes. Pictures stored on tape in the satellite and later played back were equally as satisfactory as the direct transmissions. The successful firing of the spin-up rockets was accomplished 57 days after launch and to the designed spin rate.

TABLE 1—*Launchings and performance*

Tiros	Launch date	Useful TV life (days)	Useful IR life (days)	Total pictures	Sensors	Special accomplishments
I	Apr. 1, 1960	77	--------	22, 952	Wide and narrow angle TV.	Proved feasibility of meteorological satellites.
II	Nov. 23, 1960	76	141	36, 156	Wide and narrow angle TV; 2 IR systems.	IR subsystem successful; magnetic attitude control successful; ice reconnaissance feasible.
III	July 12, 1961	145	81	35, 033	2 wide-angle TV; 3 IR systems.	Hurricanes, typhoons observed; photofacsimile pictures obtained routinely.
IV	Feb. 8, 1962	120	146	32, 593	Wide and medium angle TV; 3 IR systems.	Ice reconnaissance project established; supported Mercury, Ranger, Antarctic resupply, Joint Task Force 8.
V	June 19, 1962	[1] 240	--------	46, 634	Wide and medium angle TV.	Hurricane coverage.
VI	Sept. 18, 1962	[1] 149	--------	37, 389	Same as Tiros V	Do.

[1] Operational as of Feb. 14.

Remarks:

Tiros II:
Last TV pictures 301 days after launch.
Last IR data 525 days after launch.

Tiros III:
Last TV pictures 231 days after launch.
Last IR data 208 days after launch.

Tiros IV:
Last TV pictures 266 days after launch.
Last IR data 169 days after launch.

The analyses of the spin-axis motion of Tiros I resulted in the use of a controlled current loop (magnetic coil) in Tiros II to steer it, taking advantage of the effect of the earth's magnetic field.

Tiros II underscored the feasibility of obtaining and using satellite cloud pictures. More important, it demonstrated successful operation of the infrared experiment and the magnetic attitude-control systems. The former initiated extensive studies of the energies radiated and reflected by the earth and its atmosphere. And, of special engineering significance, its infrared subsystem was operated successfully 525 days after launch.

The quality of the pictures from Tiros II's wide-angle lens camera was reduced from that of Tiros I by a deposit on the lens from the exhaust gases of the third-stage rocket. Consequently, more attention was focused on the pictures from the narrow-angle lens system, and this led to valuable insight into the structural detail of both the type of cloud cover and the earth itself. The pictures from Tiros II proved the feasibility of using satellites to observe sea-ice conditions. Amid other accomplishments, Tiros II monitored the weather for the suborbital flight of Astronaut Alan Shepard and the launch of Ranger I.

Tiros III can be considered the first of the quasi-operational weather satellites. This satellite dramatically fulfilled its prime objective of providing hurricane surveillance by observing "Esther" 2 days before probable detection by conventional observations. On one day—September 11, 1961—Tiros III observed five hurricanes and typhoons on a global scale as well as several tropical and extratropical storms. Because of the large quantities of excellent data it delivered, hundreds of operational analyses were developed. The techniques for these analyses were developed through the availability of the data and the improvements in the ground-system communications and facilities afforded by experience from Tiros I and II. In addition to an infrared subsystem, Tiros II contained an omnidirectional radiation sensor designed to give additional insight into the earth's energy budget.

The launch of Tiros IV initiated the continuous meteorological satellite observations which have extended over one year. The Tiros IV established operationally the use of satellites for ice surveillance. It provided support for Astronaut John Glenn's orbital flight, Project Ranger, and the Antarctic resupply.

The accomplishments in the areas of design and development attributed to Tiros I–IV were repeated, and were augmented, by Tiros V and VI. Primarily intended to provide hurricane coverage for the 1962 season, these satellites increased coverage by virtue of orbits with 58° inclination, as compared with the 48° of their predecessors. Increasingly effective use of the attitude-control system, moreover, steered these satellites into a more extensive coverage of areas of vital concern. The use of a simple auxiliary command station in Chile, begun with Tiros IV, further extended the coverage of areas of interest. Tiros V demonstrated the excellence and thoroughness of the vehicle technologists when, through the secondary guidance system, despite random failure of the primary system, an acceptable orbit was achieved. On February 19, 1963, after 8 months for Tiros V and 5 months for Tiros VI, excellent data were being received and used.

Throughout the Tiros program, accomplishments in the data-utilization area have been significant and immediately applicable to the peaceful uses of space. A truly real-time use of Tiros data has been achieved. Meteorological analyses are made within 2–3 hours of data receipt, and the results transmitted not only to the forecast centers of the United States, but to those of foreign lands as well.

The continuous progress in the Tiros program can be attributed to the engineering and scientific accomplishments and thoroughness of many individuals from government and private industry, working together with a common aim and a will to succeed. Organizations that have contributed prominently to the program include NASA Goddard Space Flight Center, and Wallops Station; Department of Commerce, U.S. Weather Bureau; RCA Astro-Electronics Division; U.S. Navy, Pacific Missile Range; Allied Research, Inc., the U.S. Air Force; and

the U.S. Army Signal Research and Development Laboratories.

SUGGESTED ADDITIONAL READING

Besides articles in this special issue of *A/AE*, the following reports summarize Tiros performance:

NASA/GSFC Technical Report TR-R-131, "Final Report on the Tiros I Meteorological Satellite System," edited by L. Allison and E. Neil.

RCA/AED Report on "Final Operation Report, Tiros I Meteorological Satellite System," Oct. 1, 1960.

RCA/AED Report on "Post Launch Evaluation Report, Tiros II Meteorological Satellite System," May 31, 1962.

RCA/AED Report on "Post Launch Evaluation Report, Tiros III Meteorological Satellite System," Dec. 21, 1962.

THE ORBITING GEOPHYSICAL OBSERVATORIES

WILFRED E. SCULL

Goddard Space Flight Center

INTRODUCTION

The National Aeronautics and Space Administration is and has been engaged in a diversified research program to acquire geophysical data relative to phenomena in terrestrial and extraterrestrial space. Experimental data in these programs have been obtained from spacecraft launched by a series of increasingly powerful launch vehicles with the nature, scope, weight, number, and degree of integration of experiments limited largely by the payload capacity of the vehicles. These limitations of weight caused early spacecraft to be tightly integrated systems of experiments and basic spacecraft subsystems, with resultant difficulties in disassembly and repair or replacement of assemblies if discrepancies occurred during checkout or testing. These first generation spacecraft weighed 3 to 40 pounds and carried largely exploratory experiments that were integrated so closely with the spacecraft that it was difficult to distinguish experiment instrumentation and spacecraft subsystems. These early spacecraft included: Vanguards I and II; Explorers I, III, and IV; and Pioneers III and IV. (Vanguard I, and Explorers I, III, and IV were launched by other Government agencies.)

As launch vehicles became more powerful, heavier spacecraft carrying several to a dozen major experiments evolved. Experiments on these spacecraft were designed largely to investigate in more detail the phenomena crudely surveyed (in some cases discovered) by the experiments in earlier spacecraft. These spacecraft could be divided into subsystems, but a high degree of integration of experiments and spacecraft subsystems was still necessary to utilize all of the limited capability of launch vehicles. The spacecraft were basically systems for single missions in that considerable mechanical, electrical, and thermal redesign and rebuilding were necessary to fly a different set of experiments in a spacecraft of the same basic design. The second generation spacecraft include: Explorers VI, VII, VIII, X, XI, XII; Pioneers I, II, and V; and Vanguard III.

Both of these types of spacecraft will play a role in the space sciences program for a number of years by carrying small numbers of somewhat specialized experiments into orbits which precisely meet their requirements.

The Orbiting Geophysical Observatories, or OGO's, are third generation spacecraft. These spacecraft, which make possible the conduct of large numbers of experiments to investigate phenomena in still more detail, resulted from the concept of spacecraft as standardized carriers for experiments. With the observatories, more complex experiments could be designed to investigate independently the various parameters of a phenomenon, and to search for new phenomena that are more difficult to detect. In addition, because of the increasing capability of launch vehicles, experiments and subsystems of the spacecraft could be considered as separate portions of the same system, with the capability existing to integrate any of the subsystems into the entire system. From this background, the "observatory" concept developed.

The concept of an observatory allowed consideration of a standard spacecraft, standard

in incorporating flexibility for accommodating many types of experiments, and of operating up to a year in a wide range of orbits. It would not be necessary to design and develop a new spacecraft for each mission; spacecraft of the same design with only minor modifications could be used on successive missions to carry different combinations of experiments. Apparent inherent advantages in the concept of a standardized observatory include:

1. Capability of accommodating a large number of experiments per mission and of performing frequent missions. Frequent missions and large numbers of directly or indirectly related experiments would allow study and correlation of many phenomena at the same time and same point in space.
2. Convenience to the experimenter in designing his instrumentation by providing a well-defined interface between the spacecraft subsystems and the experiments, thereby allowing integration of each experiment with a minimum of effort.
3. Improved reliability through repeated use and stepwise improvement of a basic design of spacecraft in follow-on missions.
4. Considerations of the observatory in terms of well-defined and conservatively designed spacecraft subsystems for the experiments, thereby allowing extreme flexibility in their design.
5. Advantage of being able to handle a limited number of relatively "high risk" experiments late in the program. These experiments would represent a small percentage of the total experiments.
6. Improved operational efficiency through the continued evolution and use of a ground station network, operating procedures, and data-processing equipment and techniques.
7. Reduced cost of follow-on missions, on an experiment-pound basis, since development of a new spacecraft for each mission would be avoided.
8. Simplified data acquisition and data reduction, since tracking and data reduction equipment would be matched to fewer different designs of spacecraft.

PROGRAM OBJECTIVES

Primary objectives of the Orbiting Geophysical Observatories (OGO) program, a part of the national space sciences long-range program, is to conduct large numbers of significant, diversified experiments for making scientific and technological measurements within the earth's atmosphere, the magnetosphere, and cislunar space to obtain a better understanding of earth-sun relationships and the earth as a planet. A secondary objective is to design, develop, and have available for launching at regular intervals a standard-oriented spacecraft consisting of a basic system design that can be used repeatedly to carry large numbers of easily integrated experiments in a wide variety of orbits. A design objective for the standard spacecraft is reliable operation for a year in a wide variety of orbits from near earth circular to highly elliptical cislunar. During orbital operations, it is desired that portions of the spacecraft be oriented toward and away from the earth and the sun and forward and aft in the orbital plane.

The current OGO program consists of two different flight missions. For the first mission, the Eccentric Orbiting Geophysical Observatory (EGO), will be launched by an Atlas Agena B in the second quarter of 1964 from the Atlantic Missile Range into a highly eccentric orbit of approximately 31 degrees inclination. Its orbit will have a nominal perigee and apogee of 150 and 60,000 nautical miles, respectively. In this orbit, the observatory will traverse the radiation belts twice each orbital period and can make geophysical measurements from the region near earth to interplanetary space. Orbital period of EGO will be about 42.8 hours. A "backup" EGO is also scheduled in the event of a catastrophic or early failure of the first EGO.

The Polar Orbiting Geophysical Observatory (POGO) will be the second flight mission in the program. POGO will be launched into a polar

orbit in the fourth quarter of 1964. Launching will occur with a Thor Agena D from the Pacific Missile Range. The POGO orbit, with perigee and apogee of 140 and 500 nautical miles, respectively, will allow determination of the characteristics of the ionosphere over ranges in latitude and altitude and observation of many phenomena directly over the polar regions.

Overall weight of the observatories will be approximately 1,050 pounds, of which 150 pounds will be experiments.

Within the capacity of launch vehicles, future OGO's will be assigned to specific orbits required by the experiments. In addition, future OGO's may have increased weight-carrying capabilities or may be launched into higher orbits as the launch vehicles of increased capability are developed. The present OGO spacecraft is designed with the growth potential to be expanded into an observatory of 1,500 pounds, with most of the increase in weight available for experiments. Included in the growth potential may be the capability of carrying and separating in orbit a 300-pound pickaback satellite to perform experiments requiring an especially pure environment or experiments which need large separations between two of their parts.

SPACECRAFT

OGO, being developed for NASA by Space Technology Laboratories, Inc., of Redondo Beach, Calif., is shown in the orbital configuration in Figure 1. The observatory, or spacecraft plus experiments, is a rectangular parallelepiped main body approximately 33 inches square by 67 inches long, with two solar paddles and a number of appendages attached.

Electric power is furnished from silicon solar cells on the paddles. Experiments are mounted on the two horizontal surfaces (antigeocentric and geocentric), in packages at the ends of the solar paddles (solar and antisolar), in the Orbital Plane Experimental Package (OPEP), and at the ends of the booms, which are reserved for experiments which must be separated from the effects of the main body. In addition, antennas for command, tracking, and data transmission are located on the short booms.

Action of the control subsystem causes the spacecraft to pitch and roll to maintain the lower surface facing the earth, but at the same time to yaw so that the solar array which has a single degree of freedom relative to the body may be oriented normal to the sun. The OPEP, which requires orientation in the orbital plane, yaws relative to the body of the spacecraft.

Thermal louvers, on the sides of the spacecraft that do not face the sun, control body temperatures.

STRUCTURE

The main body of the spacecraft, shown in a nonorbital configuration in Figure 2, is fabricated of aluminum panels of a modified "sandwich" design and includes the "refrigerator door" concept. Experiments 8 inches in depth

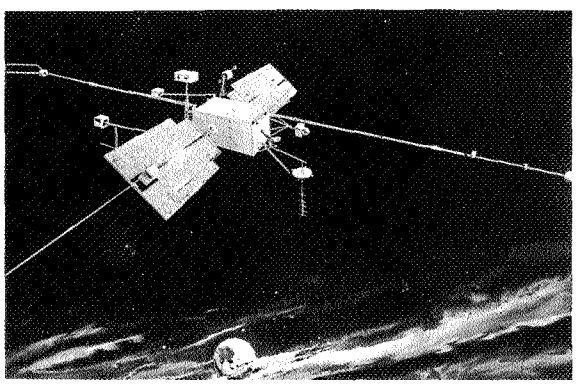

FIGURE 1.—OGO in orbital configuration.

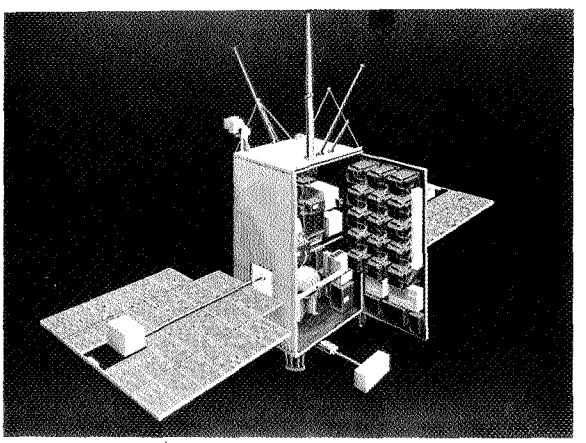

FIGURE 2.—OGO in nonorbital configuration.

764-173 O—65——11

may be mounted on the upper two-thirds of each door, which may be opened separately from the lower one-third that is reserved for spacecraft subsystems. In this manner, accessibility of experiments or subsystems is attained Other subsystem assemblies of the spacecraft are mounted in the central portion of the spacecraft. A completely open volume exists in the upper one-fourth of the spacecraft for a large experiment or experiments of depth greater than 8 inches.

The structure of the spacecraft, shown in the launch configuration in Figure 3, must fit within a 55-inch-diameter circle and must be designed to accommodate the growth version loads and loads which are 1½ times the anticipated loads imposed by launch vehicles. A truss-type interstage is used between the spacecraft and the Agena. A Marman clamp under tension around mating shoes joins the spacecraft to the interstage. Explosive release of the Marman clamp, plus separation springs mounted on pads between the spacecraft and the interstage, separate the spacecraft in orbit at a relative velocity of about 5 feet per second. Appendages and solar paddles, restrained in the launch configuration by pneumatically operated latches, are deployed sequentially by spring action after separation.

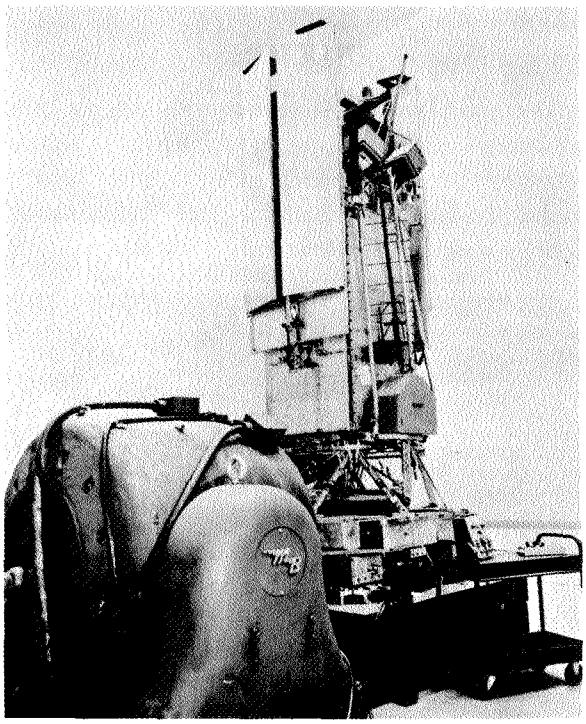

FIGURE 3.—S/C structure in launch configuration.

THERMAL CONTROL

Surfaces of the main body that may be exposed directly to the sun are insulated with aluminized Mylar. Thermal control louvers, actuated by bimetallic springs, are mounted on the sides, as shown in Figure 4, and one end of the spacecraft which do not see direct sunlight. Assemblies that dissipate large amounts of heat are mounted internally on radiating plates behind the louvers. The louvers, actuated by variations in temperature of the radiating plates behind them, control the amount of radiation from the spacecraft to maintain internal temperatures in orbit within 5° to 35° C. In addition, the system must operate during testing between −5° and +45° C.

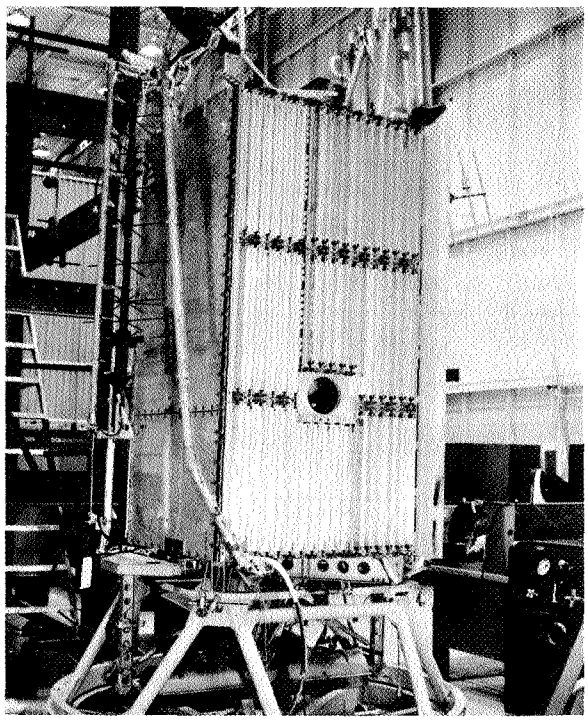

FIGURE 4.—Spacecraft showing thermal louvers.

Experiment packages on the appendages are controlled by combinations of insulation, radiating areas, and internal heaters. Low-power dissipation in these packages allows use of a combination of aluminized Mylar insulation and open radiating areas for maintaining the maximum temperatures below 40° C during sunlight, but requires use of heaters during eclipse to maintain temperatures above 0° C. In addition, during testing, appendage packages must operate at temperatures between −10° and +50° C.

POWER SUPPLY

The power supply subsystem consists of solar paddles, batteries, and charge regulating and distribution equipment. The solar paddles, one of which is shown in its handling fixture in Figure 5, carry a total of 32,256 silicon P on N cells of 10.5 percent space efficiency on beryllium substrates attached to a light aluminum truss frame. Beryllium substrates are used for low weight and the near compatibility of its thermal expansion coefficient with that of silicon. Area of the solar array is approximately 78 square feet, with a maximum initial design power of approximately 490 watts after allowances for losses due to the transmission, variations of the solar constant, orientation, cell matching, accuracy of measurement, etc. In EGO, power output at the end of 1 year is estimated to be reduced to approximately 300 watts due to damage from radiation and micrometeoroids. For POGO, radiation resistant N on P solar cells will be used in order to withstand the effects of the artificial radiation belt.

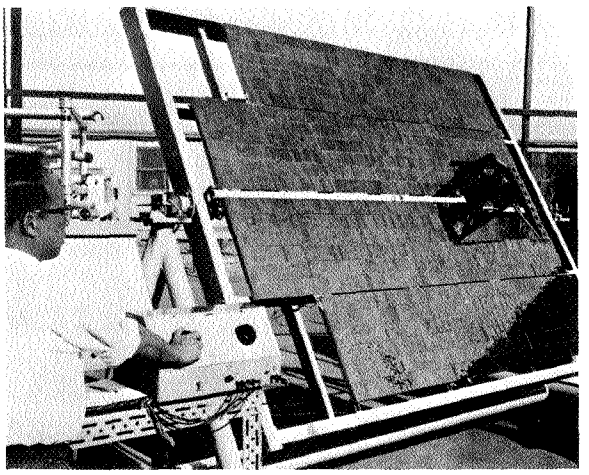

FIGURE 5.—Solar paddle in handling fixture.

Nickel-cadmium batteries, mounted on the radiating surfaces of the main body, are connected directly to the main 28-volt buss which has regulation of 23.5 to 33.5 volts and supplies power to the control subsystem, command receivers, and data-handling subsystems. There are no central line regulators, converters, or inverters; required regulators, converters, and one 400-cps inverter are included separately in various subsystems or in experiments. The two battery packs each weigh approximately 32 pounds and have 12 ampere-hours' capacity. Size of the batteries is determined by an allowable 75 percent depth of discharge during a maximum EGO eclipse (which will be limited to 2 hours). Depth of discharge on POGO during maximum eclipse will be approximately 25 percent.

Average power requirements of the OGO's are 250 watts, of which 50 watts are available for experiments. These 50 watts include 40 watts' continuous power, plus 40 additional watts peak on a 25-percent duty cycle.

Charge control of each battery is maintained by a current regulator which, at voltages that can be preset by ground command, shunts portions of the current from the arrays through power transistors mounted on heat sinks at the ends of the arrays. In this manner, the charge level can be selected to match readily predictable sunlight-eclipse conditions. Control sensors reduce the charge to a trickle charge when the battery is fully charged or if the battery temperature exceeds 95° F. If the battery temperature exceeds 125° F, a relay transfers operation to the other battery. In case of battery failure, the arrays are connected directly to the load buss.

An undervoltage relay, resettable by ground command, connects a secondary buss to the main buss. The secondary buss, which provides power to the remainder of the communication subsystem and experiments, is disconnected whenever voltage falls below 23.5 volts.

ATTITUDE CONTROL

OGO is controlled in attitude with five degrees of freedom to satisfy all orientation requirements of spacecraft and experiments. Desired pointing accuracies during orbital operation are as follows:

Geocentric, ±2°.

Solar ±5°; ±20° within 30° of the noon condition.

Orbital, ±5° (POGO); ±5° (EGO), when the orbital angular rates of EGO equal or exceed the rates of POGO.

A simplified functional diagram of the subsystem is shown in Figure 6.

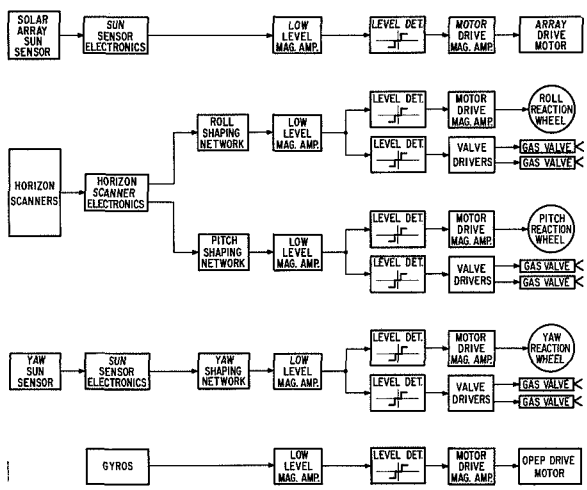

FIGURE 6.—Simplified functional block diagram OGO attitude control system normal control mode.

Sensing elements in the control subsystem consist of sun sensors, horizon scanners, and gyros. Torquing elements include wabble gear drives for the solar array and OPEP, reaction wheels, and gas jets.

Sun sensors mounted at the tips of the solar paddles provide error signals to the solar array drive, yaw reaction wheel, and gas jets in order to orient the array and the spacecraft for maximum production of power, while at the same time allowing thermal radiation from the sides of the main body. Two orthogonally mounted horizon scanners, each with two tracking heads, track the infrared gradient of the edge of the earth and provide error signals to the pitch and roll reaction wheels and gas jets.

Error signals form an integrating gyro (with a redundant unit) operating in a gyrocompassing mode actuate the OPEP wabble gear drive, which is identical to the array drive.

A rate gyro is also used during the acquisition phase to provide pitch error signals for controlling at a constant rate during the search for the sun and the earth.

Reaction wheels are used mainly to remove cyclic momentum disturbances. Since the wheels also absorb some noncyclic momenta such as separation transients, aerodynamic torques, and solar pressure, desaturation (dumping) of the wheels is necessary periodically. The yaw reaction wheel used to control the observatory during the yaw turn maneuvers twice per orbit is quite large (18 pounds) to compensate for the extremely large yaw moment of inertia. (Ninety percent of the yaw moment of inertia is in the appendages.) Since the yaw maneuver occurs in opposite directions during the orbit, the yaw wheel will not become saturated during the turns.

Argon, contained at 3,000 psi in a spherical titanium tank, is used in the gas system, since some experiments, especially on POGO, might be performing observations relative to gases of lighter molecular or atomic weight; e.g., nitrogen or oxygen. In addition, the combination of specific impulse and higher density of argon results in an efficient total weight of the pneumatic container and gas. The gas jets are mounted on the ends of short booms to improve the moment arms.

The solar array and OPEP are wired directly to the spacecraft body—slip rings are not used. As a result of this design, the spacecraft may require and execute a 180° turn twice per orbit, each time in opposite direction, to reverse direction of rotation of the array and OPEP drives and prevent wrapup of associated wiring harnesses.

Wabble gear drives for the solar array and the OPEP satisfy the requirement for a large overall reduction (23,839:1) between the drive motors and the driving elements to match low angular rates. The wabbling driving gear with 101 teeth is mounted on a sealed pair of metallic-convoluted bellows which flex to match the non-

rotating, wabbling movement. The driven gear, fastened to the array or OPEP shaft, has 100 teeth and advances 1 tooth each 360° wabbling cycle of the driver for a 100:1 reduction. A sealed-drive motor with a spur gear reduction of 240:1 provides the power to the wabbling drive gear.

COMMUNICATIONS AND DATA HANDLING

The communications and data-handling subsystem, shown in Figure 7, consists of a PCM wideband telemetry group, a special-purpose telemetry group, and an omnidirectional and a directional antenna. The complete subsystem must operate over a wide range of distances typified by the orbits of EGO and POGO.

The wideband telemetry system, which transmits the bulk of spacecraft and experimental data, is composed of two redundant equipment groups, each of which includes a digital data-handling assembly, an analog data-handling assembly, a tape recorder, and a wideband transmitter, and a low-frequency timing assembly. These groups can be used to transmit data in real time or into data storage from which it can be read out by ground command. Real-time bit rates of the system are 1,000; 8,000; and 64,000 bits/sec on EGO and 4,000; 16,000; and 64,000 bits/sec on POGO. The main frame of the basic telemetry format is composed of 128 words, each 9 bits in length. Of the 128 words, 116 words are available for experimental data, with the remaining words available for synchronization, accumulated time, mode of operation, and one 32-word and three 128-word subcommutators. Spacecraft data are included on 2 of the 128-word subcommutators, while experimental data are on the other 2.

One of the subcommutators carrying spacecraft data can be used in an accelerated mode to substitute spacecraft data in the main frame. This accelerated mode may be used during deployment of appendages or acquisition. The subcommutator with 32-word input can be substituted by command for the other commutators, and replaces the normal main frame with one of 32 different possible combinations of selected experiments. This mode, Flexible Format, can be used when a few experiments require high sampling rates for short periods of time.

The two tape recorders are each capable of storing 43.2×10^6 bits. Storage rate is 1,000 bits per second on EGO and 4,000 bits/second on POGO. Playback on EGO is 64,000 bits/sec and on POGO, 128,000 bits/sec. With this

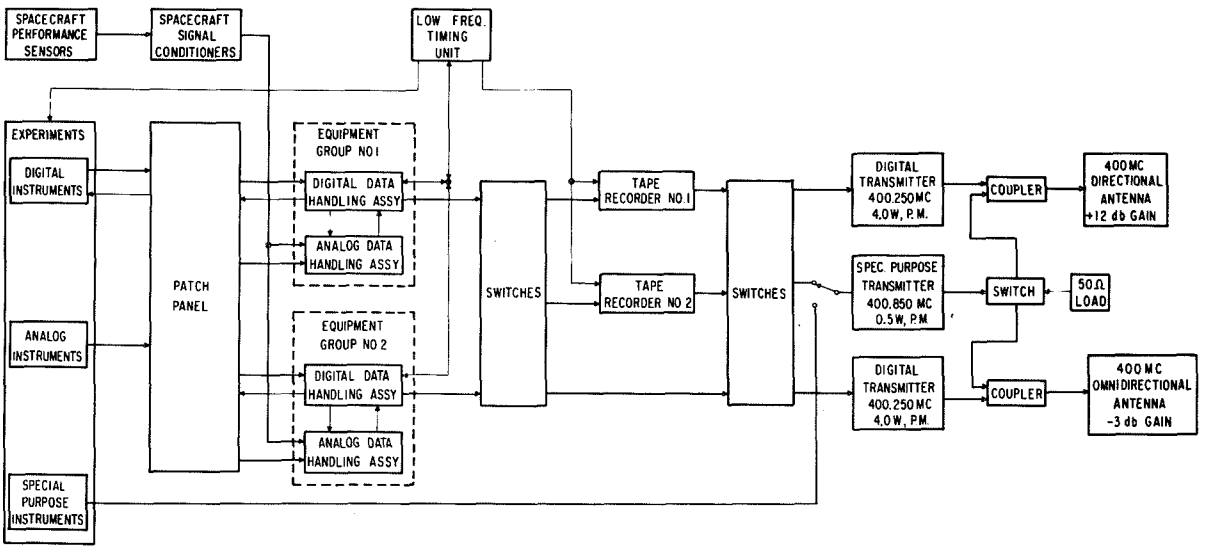

FIGURE 7.—Functional block diagram OGO data handling and data transmission subsystem.

data storage, 24 hours of data can be stored on EGO and 6 hours on POGO.

The low-frequency timing assembly, accurate to 1 in 10^6 for 1 hour and 1 in 10^5 for 1 year, furnishes timing signals to the spacecraft, including a 2,461-cps synchronization signal for converters and decimally related signals of 0.01 to 1,000 pulses/second for use by experimenters.

The wideband system accepts digital data through the digital data-handling assemblies. Analog data, with 0 to +5 volts input, are routed through the patch panel to the analog data-handling assembly where the analog signals are converted to digital output.

Two wideband 400-Mc/s transmitters with an output of 4 watts can be commanded to transmit over the omnidirectional or the directional antenna. The omnidirectional antenna will be used near earth. The directional antenna, with a gain of +12 db, will be used at apogee on EGO, but will be replaced with another omnidirectional antenna on POGO.

The special-purpose telemetry can be used by command to telemeter the outputs of up to five selected experiments or, in event of failure of both wideband transmitters, the output of the wideband telemetry. Signal inputs of selected experiments must lie within 300 cps to 100 kc/s and not exceed 5 volts peak to peak. This telemetry, which can accept frequency, phase, or amplitude modulated signals, is used for experiments whose outputs are incompatible with transmission by the wideband telemetry or which need to be transmitted in completely unprocessed form. Data from the special-purpose telemetry, which can be turned on or off by command, but is normally on continuously, do not go into data storage and are available only during real time. The ½-watt output of the special-purpose 400-Mc/s transmitter can be switched by command to either of the antennas. The special-purpose transmitter can transmit simultaneously with one wideband transmitter; however, simultaneous transmission of both wideband transmitters is not possible.

TRACKING AND COMMAND

The tracking and command subsystem, shown in Figure 8, uses the same omnidirectional antenna for tracking transmitters operating at 136 Mc/s and command receivers at approximately 120 Mc/s.

For POGO, two redundant 100-milliwatt tracking beacons, one of which is normally "on" continuously, are used for tracking the observatory. For EGO, a 10-watt beacon, which can be pulsed "on" for a period of 45 seconds by command, is also included for tracking near apogee. A timer automatically turns the 10-watt transmitter "off" after 45 seconds and turns the 100-milliwatt beacon "on" again.

A range and range rate (two-way Doppler) system is also included for more accurate and rapid determination of orbits.

Command for OGO is primarily digital, but "backup" sequential tones provide a limited number of commands for certain control of the communications and data-handling equipment as well as switching specific redundant equipments. Two redundant AM command receivers are cross-strapped to a single-tone decoder and redundant digital decoders. Failure detection features are included in each receiver to allow the gain of one receiver to be doubled should the other fail. Each digital decoder has a separate address, but the outputs are combined in parallel for redundance. Each digital

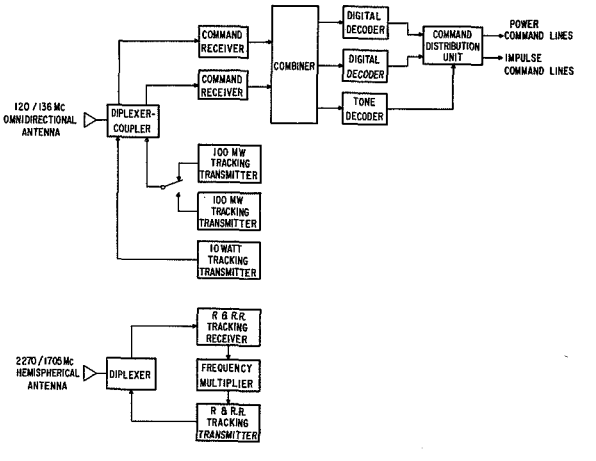

FIGURE 8.—OGO command and tracking systems.

decoder can receive and decode 254 commands, of which 150 are available for experiments in the form of 50 power "on" and "off" commands and 50 impulse commands. A command distribution unit processes the commands and controls the experiments or other subsystems of the spacecraft.

DATA ACQUISITION AND CONTROL

For purposes of data acquisition, tracking, and command of the observatories, facilities are located at a number of sites. These locations include Minitrack stations and two primary and three secondary sites. The Minitrack stations will be used only for tracking. The primary and secondary sites, which will be used for data acquisition, tracking, and command, will each have digital and tone command capability. The primary sites, Rosman, N.C., and Fairbanks, Alaska, will have 85-foot parabolic antennas. The secondary stations, Quito, Ecuador; Johannesburg, South Africa; and Carnarvon, Australia, will each have 40-foot dishes. PCM data-handling equipment will be located at the primary stations for limited decommutation and display of data for use in control of the spacecraft. The primary and secondary stations each will have capability of receiving data at maximum rates from both the wideband and special purpose telemetry.

Control of the spacecraft will be from Goddard: A microwave link to Rosman, which will "see" EGO approximately 75 percent of the time, allows practically full real-time coverage of EGO. In addition, a 48-kc/s line will connect Goddard with Fairbanks, Alaska, and will allow a pseudo-real-time control of POGO for the short periods of time it is in sight of this station. The primary and secondary sites together allow about 11 percent coverage of POGO, of which about 85 percent coverage is by Fairbanks.

For range and range rate, stations are located at Rosman, Johannesburg, and Carnarvon.

DATA PROCESSING

Data received from the OGO's will be processed at Goddard where individual computer tapes will be produced for each experimenter. Each experimenter will receive two tapes—one containing orbital and timing data, the other containing data from the spacecraft, including data from his own experiment, timing information, and necessary spacecraft housekeeping data (temperatures, voltages, etc.) and orbital data. Merging of the data and data analysis will be performed by the experimenters.

EXPERIMENTS

The experiments to be carried on EGO and POGO are shown in Tables I and II.

Experiments for the OGO's are selected by the Space Sciences Steering Committee, Office of Space Sciences, NASA Headquarters, Washington, D.C., following evaluation of written proposals, with an oral presentation, submitted by interested groups. Following selection of experiments, management responsibility for the experiments is delegated to Goddard.

In summary, the OGO's, the first of which are planned for launch within the next year, are oriented spacecraft designed to be capable of carrying many different, easily integrated experiments into a wide variety of orbits and transmitting to the earth a large amount of scientific data. The capabilities exist in the spacecraft without major changes to the spacecraft design between missions.

TABLE I.—*Experiments for EGO*

Experimenter	Experiment	Detector
K. A. Anderson, University of California.	Solar proton flux, 10–90 Mev, energy and variations.	Scint. counter.
J. H. Wolfe, Ames Research Center	Solar plasma flux, energy and direction.	Electrostatic analyzer.
H. J. Bridge, Massachusetts Inst. of Tech.	----do----------	Faraday cup.
T. L. Cline and E. W. Hones, Goddard Space Flight Center and Inst. for Defense Analysis.	Search for positrons and solar gamma ray flux and spectrum.	Scint. counters.
L. R. Davis, Goddard Space Flight Center.	Geomagnetically trapped electron and proton flux, energy and direction.	Phosphor scint. counter.
F. B. McDonald and G. H. Ludwig, Goddard Space Flight Center.	Galactic and solar cosmic ray flux, charge and energy.	dE/dx vs. E scint. telescope.
J. A. Simpson, University of Chicago.	----do----------	dE/dx vs. E and range detector.
J. A. Van Allen, State University of Iowa.	Geomagnetically trapped electron and proton flux and energy.	Omnidir. Geiger counters and solid state detector.
J. R. Winckler and R. L. Arnoldy, University of Minnesota.	Geomagnetically trapped electron energy and flux, and total ionization.	Magnetic electron spectrometer and ion chamber.
R. S. Lawrence, National Bureau of Standards.	Electron density by RF propagation, 40 and 360 Mc.	Radio transmitter.
R. Sagalyn, AF Cambridge Research Lab.	Thermal charged particle density, energy, and composition.	Spherical ion and electron trap.
E. C. Whipple, Goddard Space Flight Center.	----do----------	Planar ion and electron trap.
H. A. Taylor, Goddard Space Flight Center.	Atmospheric composition, 1–48 amu.	Bennett RF mass spectrometer.
J. P. Heppner, Goddard Space Flight Center.	Magnetic field strength and direction.	Rubidium-vapor and flux-gate magnetometer.
E. J. Smith, Jet Propulsion Lab.	Magnetic field low frequency variations, 0.01–1000 cps.	Triaxial search coil magnetometer.
W. M. Alexander, Goddard Space Flight Center.	Micron dust particle velocity and mass.	Time-of-flight and momentum det.
F. T. Haddock, University of Michigan.	Solar and Jovian radio-noise burst frequency spectrum, 2–4 Mc.	Radio receiver.
R. A. Helliwell, Stanford University.	VLF terrestrial noise, solar particle emissions, and cosmic noise frequency distribution and strength, 0.2–100 kc.	VLF receiver.
P. Mange, Naval Research Lab.	Geocoronal Lyman-alpha intensity and location of scattering layer.	Lyman-alpha ion chambers.
C. L. Wolff, K. L. Hallam, and S. P. Wyatt, Goddard Space Flight Center and University of Illinois.	Gegenschein intensity and location	Gegenschein scanning photometer.

TABLE II.—*Experiments for POGO*

Experimenter	Experiment	Detector
R. A. Hoffman, L. R. Davis, A. Konradi, J. M. Williamson, Goddard Space Flight Center.	Low-energy trapped radiations; electrons, 10–100 kev; protons, 100 kev–4.5 Mev.	Phosphor scint. counter.
H. V. Neher and H. Anderson, California Inst. of Tech. and Jet Propulsion Lab.	Total ionization over polar regions	Ionization chamber.
J. A. Simpson, University of Chicago	0.3–30 Mev nucleons	Scint. telescope.
J. A. Van Allen, University of Iowa	Net downflux of corpuscular radiation in auroral zones and over polar caps.	Geiger counters.
W. R. Webber, University of Minnesota.	Energy spectrum and charged-particle composition of galactic and solar cosmic rays.	Scint. Cerenkov det.
R. E. Bourdeau, Goddard Space Flight Center.	Ionospheric charged particles	Planar retarding potential analyzer.
L. M. Jones and E. J. Schaefer, University of Michigan.	Neutral-particle and ion measurements: 0–6 amu and 0–40 amu.	Paul massenfilter mass spectrometer.
G. P. Newton, Goddard Space Flight Center.	Neutral-particle density	Bayard-Alpert density gage.
H. A. Taylor and H. C. Brinton, Goddard Space Flight Center.	Atmospheric composition 1–45 amu	Bennett RF mass spectrometer.
W. M. Alexander, C. W. McCracken, O. E. Berg, L. Secretan, Goddard Space Flight Center.	Micrometeorites: mass, velocity, charge.	Time-of-flight and momentum det.
J. P. Heppner, H. R. Boroson, J. C. Cain, Goddard Space Flight Center.	World Magnetic Survey	Rubidium-vapor magnetometer.
R. E. Holzer and E. J. Smith, University of California at L.A. and Jet Propulsion Lab.	Magnetic field fluctuations, 1–1000 cps.	Triaxial search coil mangetometer.
F. T. Haddock, University of Michigan.	Radio-astronomy measurements of galactic emission at 2.5 and 3.0 Mc/s.	Radio receiver.
R. A. Helliewll, Stanford University	VLF measurements at 0.2–100 kc	VLF receiver.
M. G. Morgan and T. Laaspere, Dartmouth College.	VLF emissions and whistlers between 0.5 and 10 kc/s.	Do.
C. A. Barth, L. Wallace, Jet Propulsion Lab., Yerkes Observatory.	Measurements of airglow; 1100A to 3400A.	Ebert UV spectrometer.
J. Blamont, E. I. Reed, University of Paris, Goddard Space Flight Center.	Airglow in the UV and at 3914A, 5577A and 6300A.	Photometers.
H. E. Hinteregger	Solar emission in the 200–1600A region.	Scanning spectrometer.
R. W. Kreplin, T. A. Chubb, and H. Friedman, Naval Research Lab.	Solar X-ray emissions in the 0.5–3A, 2–8A, 8–16A, and 44–60A bands.	Ionization chambers.
P. M. Mange, T. A. Chubb, and H. Friedman, Naval Research Lab.	Lyman-alpha and far UV airglow between 1230A and 1350A.	Do.

ARIEL I, THE FIRST INTERNATIONAL SATELLITE

Goddard Space Flight Center

Introduction

PURPOSE OF DOCUMENT

The Ariel I (1962 ο 1) project summary document has been compiled to record the history of the first international satellite. Herein are described the events leading up to the conception of Ariel I, the technical and management plans used in the project development, the scientific and engineering considerations employed in the design of the satellite and support equipment, and the design details of these components. A list of related documentation containing design information and experimental results is also included.

LIST OF CONTRIBUTORS

This document is a collection of descriptions and reports authored prior to and after the launch of Ariel I (April 26, 1962). These contributions have been edited, revised, and updated to produce continuity. The following list includes the authors who have provided major contributions to this summary.

United Kingdom Contributors

Dr. P. J. Bowen, University College London
Prof. R. L. F. Boyd, University College London
Mr. A.C. Durny, Imperial College London
Prof. H. Elliot, Imperial College London
Dr. K. A. Pounds, Univesity of Leicester
Dr. J. J. Quenby, Imperial College London
Prof. J. Sayers, University of Birmingham
Mr. J. Wager, University of Birmingham
Dr. A. P. Willmore, University College London

United States Contributors

(National Aeronautics and Space Administration, Goddard Space Flight Center)

R. C. Baumann
R. E. Bourdeau
A. Buige
P. T. Cole
C. F. Fuechsel
W. H. Hord, Jr.
R. E. Kidwell
V. L. Krueger
T. J. Lynch
R. G. Martin
W. H. Meyer
M. Schach
J. C. Schaffert
J. T. Shea
J. M. Turkiewicz
C. L. Wagner, Jr.
H. D. White, Jr.
F. C. Yagerhofer

GENERAL INTRODUCTION

Ariel I, the first international satellite, was designed to contribute to man's knowledge of the ionosphere and its complex relation to the sun.

This project developed from proposals made in 1959 to NASA by the British National Committee on Space Research. These proposals were in response to a United States offer to the Committee on Space Research (COSPAR) of the International Council of Scientific Unions to launch scientific experiments or complete satellites prepared by scientists of other nations. The content of the program and the division of responsibility between NASA and the British Committee were agreed during discussions that took place in late 1959 and early 1960. Subsequently, the NASA Administrator assigned project responsibility for the United States to the Goddard Space Flight Center (GSFC).

This assignment included the design, fabrication, integration, and testing of the spacecraft structure, power supply telemetry, command receiver, thermal control, and data storage. GSFC supplied the vehicle, was responsible for launch, performs data acquisition via the worldwide Minitrack network, and provides data processing. The United Kingdom (U.K.) had the responsibility for the design, fabrication, and testing of all flight sensors and their associated electronics up the the telemetry encoder input. The U.K. also is responsible for data analysis and interpretation. The distribution of responsibilities is outlined in Figure 1–1.

A list of the experiments and electronic subsystems follows.

Experiments

Electron Temperature and Density—University College London

This experiment, based on Druyvesteyn's modification of the Langmuir probe, will determine the value of the electron density and temperature near the satellite.

Ion Mass Composition and Temperature—University College London

This experiment is, basically, the same as the electron temperature experiment. However, the method of measuring the temperature is different.

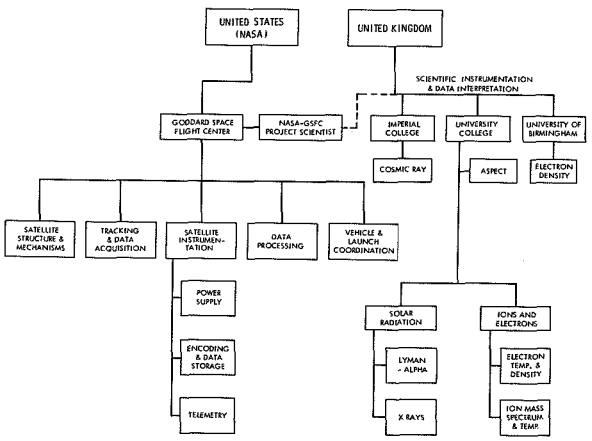

FIGURE 1–1.—Prime responsibilities for Ariel I.

Solar Lyman-Alpha Emission Measurement—University College London

Two parts of the solar spectrum were selected for measurement: the Lyman-alpha line of hydrogen, and the rather hard X-ray spectrum. The function of the two solar radiation measurements is to enable simultaneous and nearly continuous observations of the state of the ionosphere and of the solar atmosphere.

X-Ray Emission—University College London

This experiment provides an indication of solar conditions.

Solar Aspect Measurement—University College London

The solar aspect subsystem provides the latitude and longitude of the sun in the satellite coordinate system. Also, the subsystem provides the satellite spin rate.

Cosmic Ray Analyzer—Imperial College London

The purpose of this experiment is to make accurate measurements of the primary cosmic ray energy spectrum and the effects of interplanetary magnetic field modulation of this spectrum.

Ionosphere Electron Density Measurement—University of Birmingham

The measurement of electron density is performed by this experiment, and by the Langmuir probes of the University College London. However, the two methods of measurement are quite different and therefore complement one another.

Electronic Subsystems

Telemetry—Goddard Space Flight Center

Data Encoders—Goddard Space Flight Center

Tape Recorder—Goddard Space Flight Center

Power System—Goddard Space Flight Center

Spacecraft Parameters (Housekeeping) System—Goddard Space Flight Center

Spacecraft and orbital characteristics are detailed in the following list.

Scientific Instrumentation

Electron temperature and density sensors (2)
Ion mass sphere (1)
Solar radiation detectors, Lyman-alpha at 1216A (3)
Solar aspect meter (1)
Electron density sensors (1)
X-ray counters (1)

Spacecraft Characteristics

Size, basic structure—23 inches O.D. by 22 inches high
Weight—136 pounds
Spin rate—36 to 12 rpm throughout life
Lifetime—1 year
Power—p-on-n solar cells and nickel-cadmium batteries
Data Storage—100-minute tape recorder
Antenna—modified crossed dipole
Tracking and data frequency—136.408 Mc nominal

Orbit Parameters

Perigee—390 km (210 nautical miles)
Apogee—1212 km (654 nautical miles)
Inclination—53.86 degrees
Period—100.9 minutes
Eccentricity—0.057

Three complete payloads were constructed: one for prototype testing, a flight model, and a backup in case of malfunction in the first launch attempt. Provision was made for two launching vehicles, including one for backup. Ariel I was launched on April 26, 1962. A cutaway view of the satellite is shown in Figure 1–2.

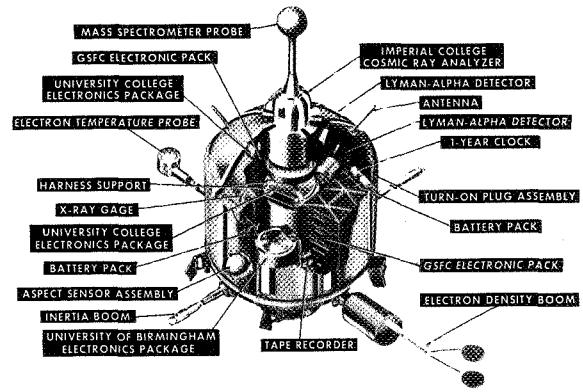

FIGURE 1–2.—Cutaway view of Ariel I.

RELATED WORK

Experiments relating to those in the Ariel I satellite have been performed in sounding rockets and satellites. Future plans include additional experiments in the following fields.

Ion and Electron Studies: Electron Density Measurements

Experiments similar to the ion mass spectrometer, the Langmuir probe, and the electron density experiments were flown successfully by Bourdeau and collaborators on the Explorer VIII satellite (1960 ζ1), which was launched on Nov. 3, 1960. Results have been published in the open literature (References 1 to 5). A spherical ion mass spectrometer was also flown on Sputnik III (1958 ζ2) by the USSR (Reference 6).

NASA plans to use similar experiments on the Atmospheric Structure Satellite and on the EGO and POGO satellites.

Cosmic Ray

The primary purpose of the Ariel I cosmic ray experiment is to carry out a satellite investigation of time variations of heavy nuclei in the primary cosmic radiation with a thin-walled omnidirectional Cerenkov counter. An experiment with a similar objective but using a completely different approach was carried out on Explorer VII (1959 ι1). In this case Pomerantz and Schwed used a thin-walled omnidirectional ionization detector. Again, the primary objective was the satellite investigation of time variation of heavy nuclei. During the eight months of operation of this detector on Explorer VII, significant changes in the spectrum of heavy nuclei were observed.

Detailed accounts of the findings of this satellite can be found in References 7, 8, and 9.

Solar Radiation

The purpose of the x-ray and ultraviolet measurements is to increase knowledge of the sun's ionizing radiations throughout the solar cycle. The measurements of solar radiation are similar to experiments previously performed in space vehicles.

Solar x rays were first quantitively measured in 1949, utilizing thin beryllium-window photocounters in a V–2 rocket flight (Reference 10). The Lyman-alpha line of hydrogen was first detected by Rense in 1952 (Reference 11). Since that time, there have been several dozen measurements of the solar x-ray and hydrogen Lyman-alpha intensities utilizing various rockets: Aerobee-Hi (with solar pointing controls), Nike-Deacon, and Nike-Asps. In addition, experiments have been flown on Explorer VII, the Naval Research Laboratory Greb satellites, and on the Orbiting Solar Observatory (1962 ξ1); these include radiation measurements of both the "quiet" and "active" sun. A survey of the results of measurements of the sun's ionizing radiations is given by Friedman in Reference 12.

The Orbiting Solar Observatory II (OSO II) satellite scheduled for 1963 will continue measurements of solar X-ray and ultraviolet radiations. This OSO series of satellites will make the most comprehensive coverage of the solar electromagnetic radiations ever attempted. For example, experiments will be flown to measure the 2500 to 3000A band, hydrogen Lyman-alpha line, 400 to 10A band (with 1A resolution), 1 to 8A region, 100 kev to 3 Mev gamma rays (100 kev to 1.5 Mev with 100 kev resolution), and 50 to 500 Mev gamma rays.*

RELATED DOCUMENTS

In addition to the specific reports referenced in the test, there are many reports relating to the design, development, and experimental measurements of Ariel I. The reference and bibliography list at the end of this summary report gives the specific reports referenced herein as well as an additional bibliography of related documents.

*For additional information, refer to the GSFC OSO II Project Development Plan.

Management Plan

APPROACH

The approach of the Ariel I project management utilized a concept of a joint United States–United Kingdom working group with various ad hoc committees named as required. The basic Ariel I working group membership was as follows:

United Kingdom

University of Birmingham	*Electron Density*
Prof. J. Sayers	Project Scientist
Imperial College London	*Cosmic Ray*
Dr. H. Elliot	Project Scientist
Dr. J. J. Quenby	Alternate
University College London	*All Other Experiments*
Dr. R. L. F. Boyd	Project Scientist
Dr. A. P. Willmore	Alternate
Mr. M. O. Robins	U.K. Project Manager
Dr. E. B. Dorling	U.K. Coordinator

United States

National Aeronautics and Space Administration

NASA Headquarters:	
Dr. J. E. Naugle	U.S. Project Officer
Mr. M. J. Aucremanne	U.S. Project Chief
Goddard Space Flight Center:	
Mr. R. C. Baumann	U.S. Project Manager
Mr. R. E. Bourdeau	Project Scientist
Mr. J. T. Shea	U.S. Coordinator
Mr. H. J. Peake	Telemetry RF
Dr. R. W. Rochelle	Telemetry coding
Mr. J. C. Schaffert	Sequence programming
Mr. P. T. Cole	Data storage
Mr. C. L. Wagner	Mechanical design
Mr. F. C. Yagerhofer	Power supply
Mr. M. Schach	Thermal design
Mr. W. H. Hord	Environmental testing
Mr. J. M. Turkiewicz	Electrical systems integration

Mr. C. H. Looney	Tracking systems
Mr. H. E. Carpenter	Tracking operations
Mr. C. J. Creveling	Data reduction
Mr. A. Buige	Operations control
Mr. C. P. Smith	Atlantic Missile Range, Vehicle Coordination
Mr. R. H. Gray	Atlantic Missile Range, Operations and Launch Director

ASSIGNMENTS

Management responsibility for the Ariel I project was assigned as follows.

Project Management

NASA's Goddard Space Flight Center was assigned project management responsibilities for the Ariel I project.

Experiments System Management

Experiments system management responsibilities were accepted by the U.K. Project manager and his staff, later to become the Space Research Management Unit, Office of the Minister of Science.

Spacecraft System Management

Goddard Space Flight Center was assigned system management responsibilities for the Ariel I spacecraft system.

Tracking and Data System Management

Goddard Space Flight Center was assigned system management responsibilities for the Ariel I tracking and data system. Acquired data are sent to the United Kingdom after processing (digitizing), and the U.K. is responsible for data reduction and analysis.

NASA Headquarters Direction

The Director, Office of Space Sciences, NASA Headquarters, is responsible for overall direction and evaluation of the performance of the Goddard Space Flight Center as the Ariel I Project Management Center and as the Systems Management Center for the spacecraft and the tracking and data systems.

The Director, Office of International Programs, NASA Headquarters, is responsible for defining and interpreting international agreements relating to the project and for providing the United States (NASA) coordination with the United Kingdom.

Each country has an Ariel I Project Manager, Project Coordinator, and Project Scientist. All working decisions are subject to the approval of the Project Managers. Responsibility for the coordination of the many aspects of the overall program is vested in the Project Coordinators. The Project Scientists are responsible for the ultimate compatibility and integration of the various experiments. Overall policy matters are decided by the NASA Administrator for the United States and by the Minister for Science for the United Kingdom, Scientific matters in the United Kingdom are decided by the British National committee for space research under the chairmanship of Sir Harrie Massey.

In the case of subsystems, the work (and contract monitoring) was the responsibility of the individual in charge of the subsystem.

SCHEDULE

The major phases planned and accomplished throughout the program are shown in Figures 2–1 and 2–2. Key milestones in the Ariel I project are reported in the Program Management Plan, described in the next section.

REPORTING PROCEDURES

Reports indicating progress in accomplishing the scheduled milestones and summarizing the project status were furnished by GSFC to NASA Headquarters on a biweekly basis as required by NASA Management Instruction G–2–3, "Program Management Plans." The U.S. Project Manager submitted to the Director, GSFC, each week a written report that described significant events occurring on the project, highlighted problem areas, and indicated any assistance that was required.

Periodic presentations on the Ariel I project

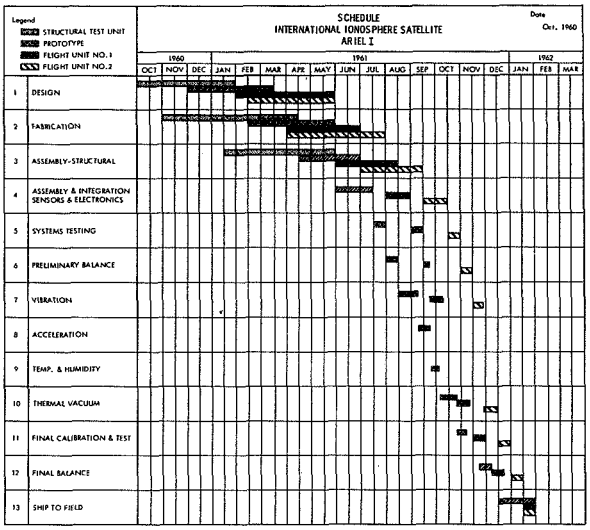

FIGURE 2–1.—Planned program schedule.

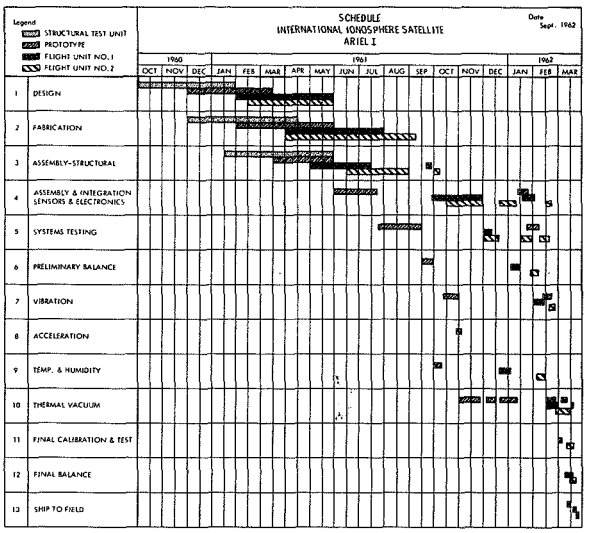

FIGURE 2–2.—Actual program schedule.

are made to the GSFC Executive Council. This group, chaired by the Director of GSFC, is composed of top management officials. The presentations cover all significant aspects, such as funding, procurement, etc. Emphasis is placed on defining problem areas and applying necessary measures to resolve them.

The U.S. Project Manager makes monthly submissions of data for the NASA Administrator's progress report. Such data include the progress made on Ariel I project objectives during the previous month, progress made during current month, and plans for the coming month.

The U.S. Project Manager is responsible for the preparation of semiannual budget reports on his project.

PROCUREMENT

All procurement in the U.S. was handled according to normal GSFC procedures. A singlepoint procurement contract system was used.

General Technical Plan

BACKGROUND AND PURPOSE

In determining the experiments to be carried out by Ariel I, every effort was made not to duplicate experiments already performed or underway by the United States and Russia. Simultaneously, experiments were selected to (1) take advantage of techniques developed in the U.K. as part of the Skylark sounding rocket program, and (2) provide an integrated assault on unknowns connected with the sun-ionosphere relation.

Of the *six* specific experiments carried on board, five are closely interrelated and provide concurrent measurement of two important types of solar emission and the resulting changing states of the ionosphere.

Of these *five*, the three ionospheric experiments measured electron density and temperature as well as the composition and temperature of positive ions. The remaining two experiments monitored the intensity of radiation from the sun in the ultraviolet (Lyman-alpha) and X-ray bands of the solar radiation spectrum. Lyman-alpha radiations originate in the sun's chromosphere (solar surface), while X-rays originate farther out in the area around the sun known as the corona. Previous work has shown that the Lyman-alpha radiation is rela-

tively constant but that X-ray emissions are quite variable with solar conditions.

The *sixth* experiment measured primary cosmic rays by means of a Cerenkov detector carried on board the Ariel I. Simultaneously, measurements of secondary cosmic rays were made by means of ground observations and by means of aircraft, balloons, etc.

ARIEL I CONFIGURATION

Figures 3–1, 3–2, and 3–3 provide essential major component outlines and relative positions for Ariel I. Its basic configuration, which must fit the envelope of the Delta vehicle's payload compartment, is that of a cylinder $10\frac{11}{16}$ inches long and 23 inches in diameter. The main element of each closure is a spherical section whose large (inboard) terminator circle is $8\frac{7}{16}$ inches in diameter. Each spherical section is $5\frac{1}{4}$ inches long and has an outer surface radius of curvature of $13\frac{1}{2}$ inches. To this basic 22-inch-high configuration are attached the various elements necessary for the support and conduct of the several experiments incorporated in the system.

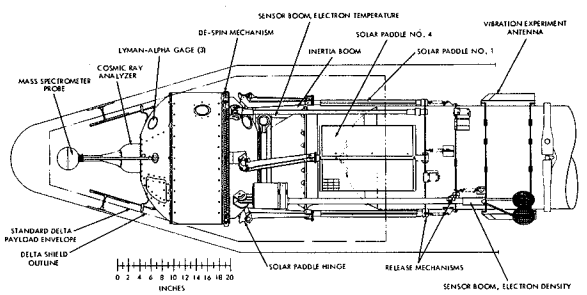

FIGURE 3–1.—Ariel I satellite-Delta vehicle compatibility, view 1.

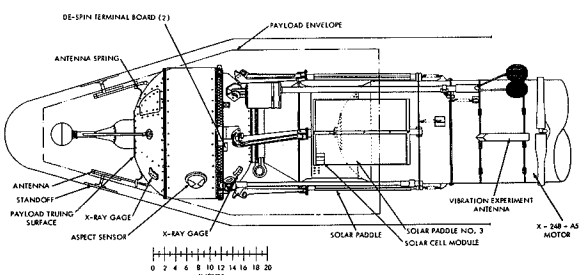

FIGURE 3–2.—Ariel I satellite-Delta vehicle compatibility, view 2.

The spin axis of the satellite is the central axis of the cylinder, which—for purposes of this description—is also considered as the vertical axis. At the bottom of the satellite is a $9\frac{3}{8}$-inch-diameter fourth-stage separation flange, within which is mounted the electron temperature gage and the tape recorder.

Extending out horizontally from about midway up the lower spherical section, at 90 degree intervals around the circumference of the satellite, are four solar paddles.

Offset 45 degrees circumferentially from the solar paddles, opposite and exactly counterbalancing one another, and extending radially in the same horizontal plane are two booms with nominal lengths of 4 feet. The end of one boom accommodates the two circular capacitor plates of the electron density sensor. Electronics associated with this experiment are housed in a $4\frac{1}{4}$-inch-diameter by $6\frac{1}{4}$-inch-long cylinder mounted on the boom close to the main body of the satellite. At the end of the other boom is a second electron temperature gage, whose electronics are located inside the satellite.

With the exception of a $3\frac{1}{2}$-inch-diameter hemispherical solar aspect sensor, the central cylindrical section is free of protuberances.

On top of the satellite, in line with the spin axis, is a 5-inch-diameter cylinder containing the cosmic ray Cerenkov detector. Above this, on an 8-inch-long conical and cylindrical section tapering from a 3-inch to 1-inch diameter, is a 4-inch-diameter ion mass sphere whose center of mass is located 14 inches above the forward face of the main body.

Four turnstile antennas, spaced circumferentially at 90 degrees and angling up at 45 degrees,

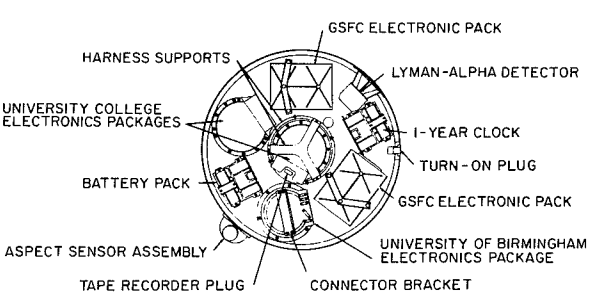

FIGURE 3–3.—Ariel I satellite mainshell, plan view.

are mounted on the top spherical section and are perpendicular to the sphere at the interfaces.

There are three flush-mounted solar radiation (Lyman-alpha) detectors on the satellite skin: two at 60 degrees (one up and one down) from the equator, and one on the Equator. All three are in the same vertical plane and in the same 180-degree sector. There are two proportional X-ray counters located 45 degrees up and down from the equator and directly opposite the Lyman-alpha gages.

ARIEL I CIRCUITRY

The electronic ciruitry is, in general, covered by the functional diagram of Figure 3–4 and produces the signals described in Figure 3–5. The United Kingdom supplied all equipment listed under the probes and conditioning circuits of Figure 3–4, while GSFC provided all other subsystems.

ARIEL I LAUNCH SEQUENCE

The sequence of events from nose cone ejection to satellite separation is:

1. Nose cone ejection
2. Second-stage burnout
3. Second and third-stage coast and yaw until peak of ascent path is reached and vehicle is aligned with its programmed attitude
4. Third-stage spin up to approximately 160 rpm and ignition
5. Second-stage separation and retrorockets fired
6. Burnout of third stage
7. Coast to allow outgassing (thrust) of the third stage to cease
8. De-spin of the third-stage—payload combination (first de-spin) to 76.5 rpm, by releasing "yo-yo" de-spin device
9. Release and erection of experiment booms (second de-spin) and de-spin to 52.4 rpm
10. Release and erection of the inertia booms and paddles, de-spin (third de-spin) to 36.6 rpm
11. Separation of the payload from the third stage at a differential velocity of 7 ft/sec
12. Final rate of spin at the end of 1 year should not be less than 12 rpm

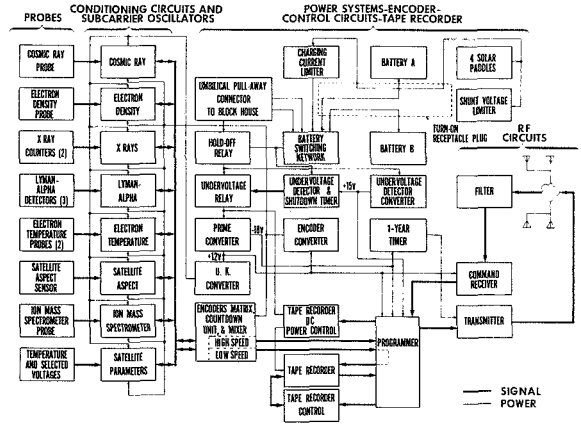

FIGURE 3–4.—Ariel I functional diagram.

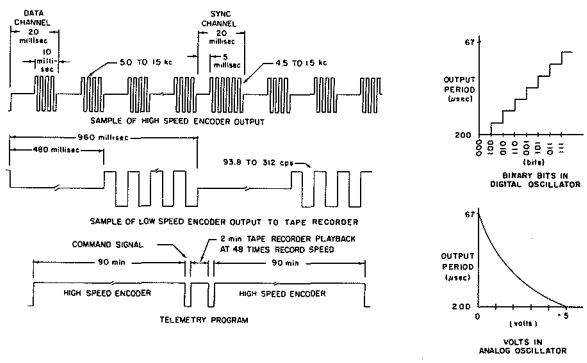

FIGURE 3–5.—Ariel I telemetry program.

UNITED KINGDOM EXPERIMENTS

LANGMUIR PROBE FOR MEASUREMENT OF ELECTRON TEMPERATURE AND DENSITY

Project Scientists

Dr. R. L. F. Boyd, University College London
Dr. A. P. Willmore, University College London

Project Engineers

Dr. P. J. Bowen, University College London
Mr. J. Blades, Pye Ltd., Cambridge
Mr. R. Nettalship, Pye Ltd., Cambridge

The Experiment

This experiment, based on Druyvesteyn's modification of the Langmuir probe, determines the local value of the electron density and temperature near the satellite. At heights well above the F–2 maximum, the ionization is probably in diffusive equilibrium, so that the variation of density with height can be related to the temperature and composition of the plasma. Moreover, it is very probable that temperature equilibrium is closely approximated between the electrons and the positive ions. Thus, the two measurements made in this experiment are related. When they are combined with those from the positive ion mass spectrometer probe—which enables the positive ion temperature and composition to be obtained, it should be possible to study in a comprehensive way the departures from thermal equilibrium and diffusive equilibrium in the atmosphere.

Since the probe is negative with respect to its local ambient atmosphere (potential of which, relative to the vehicle, will be called "space potential"), the density of the electrons is obtained by Boltzmann's relation as:

$$n_e = n_{e0} e^{-\frac{eV_p}{kT_e}},$$

where n_{e0} is the density far from the vehicle, V_p is the magnitude of the probe potential with respect to space, and T_e is the electron temperature.

Thus the current collected by the probe is:

$$i_p = i_0 e^{-\frac{eV_p}{kT_e}},$$

where $i_0 = (2nk/m)\ T_e n_{e0} A$ (A being the probe area).

In order to measure T_e and i_0, from which n_{e0} can also be calculated, a composite sweep wave form consisting of (1) a slow sawtooth wave, (2) a 500-cps sine wave whose amplitude is about kT_e/e, and (3) a 3.5-kc sine wave also of amplitude kT_e/e is applied to the probe.

Because the characteristic is exponential and nonlinear, the probe current contains not only 500-cps and 3.5-kc components, but also harmonics and cross-modulation terms. The cross-modulation component, which is a 3.5-kc wave modulated by 500 cps, is extracted by means of a tuned amplifier; and the carrier and the modulation are separated and measured by phase-sensitive rectifiers. The carrier component is used to derive an AGC feedback voltage that maintains the carrier amplitude at the detector constant. Then the control voltage is a nearly logarithmic function of the carrier amplitude in the probe current. Now it is easy to see that the carrier amplitude is a function of di_p/dV_p and that the rectified 500-cps voltage is a function of d^2i_p/d^2V_p divided by di_p/dV_p. The latter quantity depends on eV_1/kT_e, where V_1 is the amplitude of the 500-cps modulating voltage, while the former gives i_p (once T_e is known).

The function of the slow sweep, which has an amplitude of several volts, is simply to insure that the probe is sometimes a volt or so negative with respect to space. Space potential can be recognized as being very nearly the potential at which $d^2i_p/dV_p^2 = 0$; and thus the value of V_p corresponding to the measurement of i_p is known. This gives i_0 and hence n_{e0}.

A block diagram of the circuit is shown in Figure 4–1. The probe is a small disk, 2 centimeters in diameter, surrounded by a guard ring. This has the dual purpose of reducing edge effects arising from the fact that the satellite skin is not at probe potential and of reducing

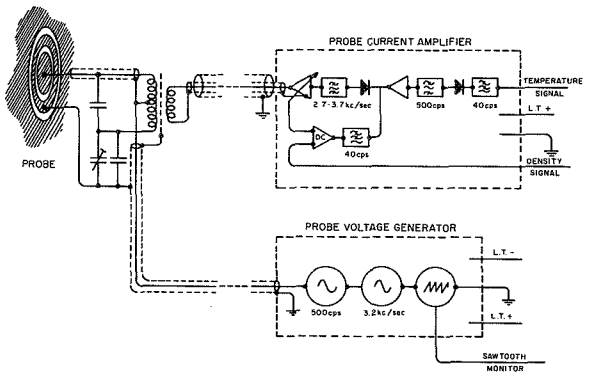

FIGURE 4–1 —Electron density and temperature probe, block diagram.

the stray capacitance from the probe to ground. (A similar probe constructed for Skylark is shown in Figure 4–2). The tuned input transformer of the amplifier is mounted behind the probe. The waveform generators and amplifiers are mounted on a 5½-inch card in the interior of the vehicle.

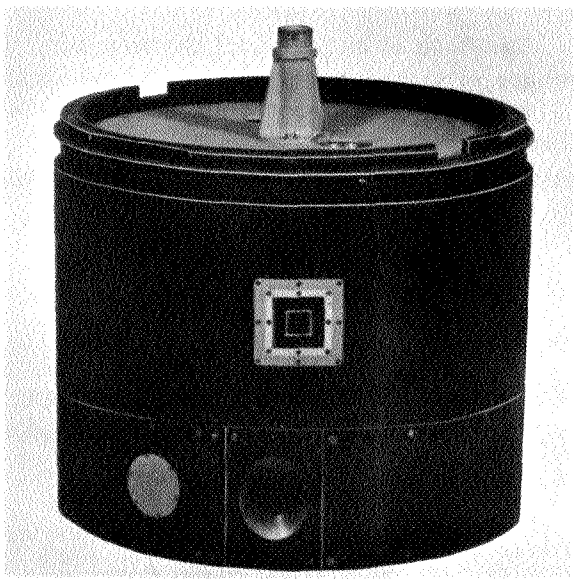

FIGURE 4–2.—Similar electron density probe constructed for Skylark rocket.

When direct transmission of telemetry data is being used, the modulation depth, carrier amplitude, and a sawtooth voltage are all transmitted over the complete probe curve, toge her with a monitor representing the amplitude V_1. In this case, the complete probe curve can be reconstructed, thus enabling a cross-check of electron temperature to be obtained. The low data rate of the tape store makes it impossible to record the probe curves in this way, so the curves are sampled at two points whose coordinates are recorded. The first chosen is the space potential point where $d^2i_p/dV_p^2=0$. A trigger circuit produces a sampling pulse as the sign of the second derivative reverses (and the phase of the 500-cps wave changes by 180 degrees), and a gate stores the value of the sawtooth and the carrier amplitude in capacitor stores. These values are read out by the telemeter. Then, when di_p/dV_p reaches a predetermined amplitude, which is set at the lowest value consistent with swamping amplifier noise, a second sampling pulse is generated; and the values of di_p/dV_p, V_p, and the modulation depth are all stored and in due course read out. Thus, there is recorded the space potential, modulation depth or electron temperature, and two points on the first derivative curve.

As there are in all four ionospheric sensors being swept in potential, the effects of mutual interference are being reduced by operating them synchronously. For this purpose, a trigger pulse is obtained from the encoder. The circuitry operates entirely from ± 6.5 volt lines, the total power dissipation being 75 milliwatts.

This experiment is duplicated in the satellite to check the validity of the assumption that the ambient electron density is not greatly affected by the motion of the vehicle. Both probes are mounted with the normal to the probe surface parallel to the spin axis so as to minimize spin modulation of the probe current. One sensor is located inside the separation ring, facing backward from the launch direction, and the other is on the end of the balance boom opposite to that carrying the dielectric experiment, facing forward.

SPHERICAL PROBE FOR MEASUREMENT OF ION MASS COMPOSITION AND TEMPERATURE

Project Scientists

Dr. R. L. F. Boyd, University College London
Dr. A. P. Willmore, University College London

Project Engineers

Dr. P. J. Bowen, University College London
Mr. J. Blades, Pye Ltd., Cambridge
Mr. R. Nettalship, Pye Ltd., Cambridge

The Experiment

The principle of this experiment is somewhat similar to the Langmuir probe. It can be shown that, if the current to a probe immersed in an isotropic plasma is i_p at potential V_p and the energy distribution function of the charged particles is $f(E)$, then

$$\frac{d^2 i_p}{dV_p^2} \alpha^e V_p^{-1/2} f(E).$$

Thus, by applying a slow sweep voltage V_p and by applying two sine waves of differing frequencies in the manner of the electron energy probe to obtain $d^2 i_p/dV_p^2$, the energy distribution function $f(E)$ can be constructed.

If V_p is positive, this distribution function will be that of the positive ions. However, the positive ion current is, in practice, swamped by the electron current; and the probe must be covered with a grid at a negative potential so that these are biased off. If a spherical probe is used, it is no longer necessary that the distribution function be isotropic. In this case it is easy to show from considerations of the conservation of energy and angular momentum that the presence of the grid will not affect the measurements. Thus, with such a probe the energy distribution of the positive ions can be determined.

If the temperature of the positive ions were very low, they would appear at the satellite as a homogeneous stream moving with the satellite speed v_s. Thus, they would have an energy $E=1/2mv_s^2$. Thus, the energy distribution function consists of peaks corresponding to the mass spectrum of the ions. In fact, the thermal velocities are not negligibly small; and, in consequence, the peaks are broadened to an easily measurable extent. The result is to degrade the mass resolution but to enable making a measurement of the ion temperature.

The basic problem of this experiment, then, is identical with that of the electron temperature measurement, namely, the determination of $d^2 i_p/dV_p^2$. The principal difference is in the construction of the probe, which is shown in Figure 4–3. The inner electrode is the probe proper, a sphere 9 centimeters in diameter. This is surrounded by a concentric spherical grid of nickel foil 0.1 millimeter in thickness, pierced with 0.5-millimeter holes. The diameter of the grid is 10 centimeters. The grid both serves to repel electrons and acts as an electrostatic shield for the inner electrode. Figure 4–4 is a photograph of this probe as flown on the Black Knight rocket. By making the sphere rather large in comparison with the Langmuir probe, it is possible to obtain probe currents that are not greatly different in the two cases; and in consequence the same circuitry serves for both with only slight modifications, the amplitudes of the sine waves and the input impedance of the tuned amplifier being different. The shape of the energy distribution curve is transmitted by direct telemetry but is not recorded.

The probe is mounted on the spin axis, to reduce spin modulation of the probe current. It is carried on a thin tubular support as far from the vehicle as possible—namely, some 10 centimeters in front of the cosmic ray package on which it is supported.

MEASUREMENT OF SOLAR LYMAN-ALPHA EMISSION

Project Scientists

Mr. J.A. Bowles, University College London
Dr. A. P. Willmore, University College London

The Experiment

The function of the two solar radiation experiments is to enable making simultaneous and nearly continuous observations of the state of the ionosphere and of the solar atmosphere, so as to investigate in detail this aspect of the solar-terrestrial relations. To this end, two parts of the solar spectrum have been selected: one where the radiation originates at a low altitude in the chromosphere, and the other in the corona. These are, respectively, the Lyman-alpha line of hydrogen and the rather

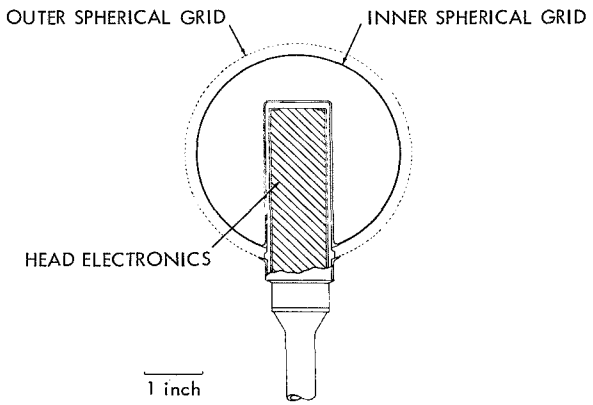

FIGURE 4–3.—Sectional view of mass spectrometer probe.

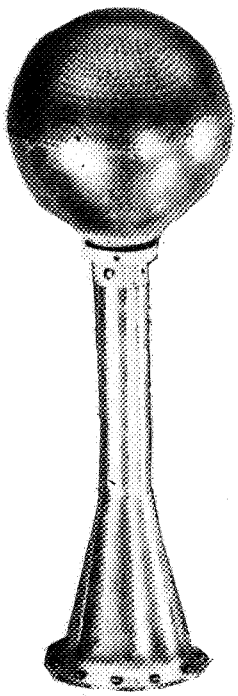

FIGURE 4–4.—Mass spectrometer probe as flown on Black Knight rocket.

hard x-ray spectrum. The latter radiation is also emitted from the high-temperature disturbed regions of the corona. The density measurement is made by means of the nitric oxide ionization chambers designed by Dr. H. Friedmann of the U.S. Naval Research Laboratory, Washington, D.C. These chambers are sensitive in the wavelength region 1100 to 1350A, where nearly all the energy in the solar spectrum is concentrated in the Lyman-alpha line. The chambers are mounted, as shown in Figure 4–5, on a molded nylon support cone

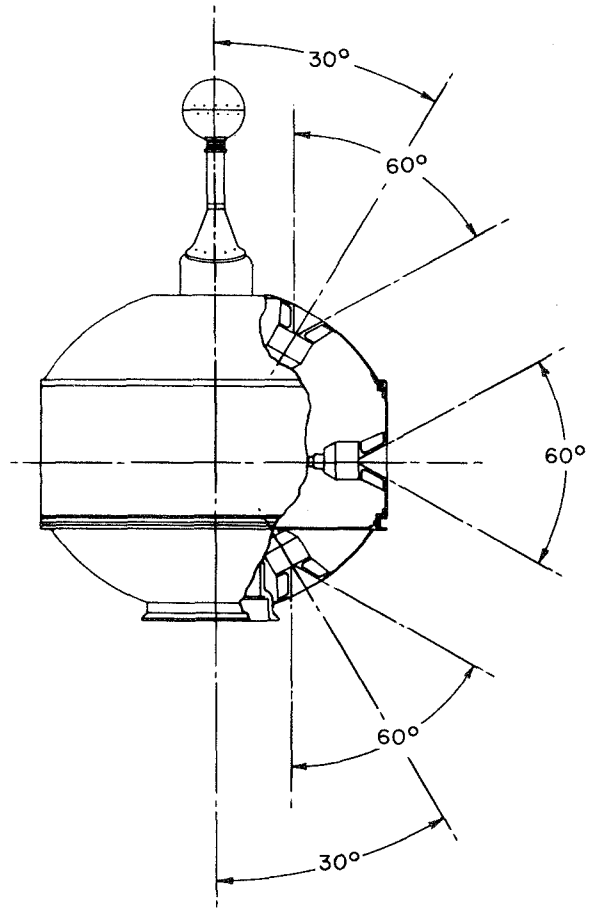

FIGURE 4–5.—Mounting of Lyman-alpha detectors.

that restricts the field of view to 60 degrees. Three such chambers are used, mounted at angles of 30, 90, and 150 degrees to the spin axis so that the array covers the whole sky—one in each revolution of the satellite, with nearly constant sensitivity.

The ionization current produced by solar radiation is approximately 5×10^{-8} ampere. This current is amplified by a transistor chopper amplifier, and the peak value of the current in each revolution is stored in a capacitor having a storage charge time constant of 200 seconds.

This store is sampled by both low and high speed encoders. The electronic module card shown in Figure 4–6 operates from —6.5 volts, 1.5 milliamperes, and a bias line of —14 volts.

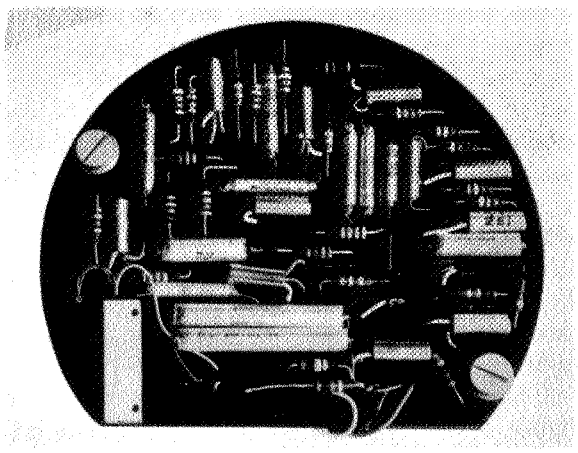

FIGURE 4–6.—Electronic card for Lyman-alpha emission experiment.

MEASUREMENT OF THE X-RAY EMISSION FROM THE SUN IN THE 3 TO 12A BAND

Project Scientists

Dr. R. L. F. Boyd, University College London
Dr. K. A. Pounds, University of Leicester
Dr. A. P. Willmore, University College London

Project Engineers

Mr. J. Ackroyd, Bristol Aircraft Company
Dr. P. J. Bowen, University College London
Mr. P. Walker, Bristol Aircraft Company.

The Experiment

The wavelength region selected for this observation is 3 to 12A, in which the solar emission is highly variable and is a sensitive indication of solar conditions. The circuitry has been designed, for this reason, to have a wide dynamic range. The radiation detectors are proportional counters, filled with argon and methane as a quenching gas, and using 25μ beryllium windows, which have a high quantum efficiency in the 3 to 12A region. Each counter has three windows, each 0.5 millimeter in diameter. The windows are spaced at 30 degree intervals round the circumference, giving the counter a field of view of 90 degrees in the plane normal to its axis, without the radiation angle of incidence exceeding 15 degrees. This condition of nearly normal incidence is necessary because, near the cutoff at 13A, the transmission of the window varies rapidly with angle of incidence. Two such counters are used, with matched characteristics, mounted at "latitudes" (reckoned as though the spin axis of the satellite were comparable with that of the earth) of ± 45 degrees, so that the whole sky is covered once in each revolution. Each counter is fitted with a mask that restricts the field of view in the longitudinal direction, so that the two counters together have a field of view which is a sector of 30-degree included angle.

A block diagram of the circuitry is shown in Figure 4–7. The counter is supplied from an extra high tension (EHT) generator, which is a dc to dc converter operating from —6.5 volts and producing 1600 volts; this is stabilized by a corona discharge tube. The counter pulses are fed by a gain-stabilized linear amplifier to a discriminator with a variable bias level. The discriminator output passes through a gate to a 15-stage binary counter capable of counting equally spaced pulses at 1 megacycle.

The gate circuit is operated by a 1-second pulse from the high speed encoder, so timed that the scaler read-out always occurs in the "off" period of the gate. Closing the gate also operates a staircase generator, which produces a waveform of five equal steps used to obtain the discriminator bias level. Thus, the discriminator automatically moves on at the end of each counting period to the next wavelength interval, until the range from 3 to 12A has been covered in five steps of equal quantum energy interval, after which the process is repeated.

In general, the sun is expected to be in the field of view for a time rather shorter than 1 second, so that the effective counting time is less than 1 second. The actual time will be determined from a spin rate measurement. Moreover, there is only a 1:12 chance that the sun will be in the field of view in any given gate period. Thus, the counters do not only observe

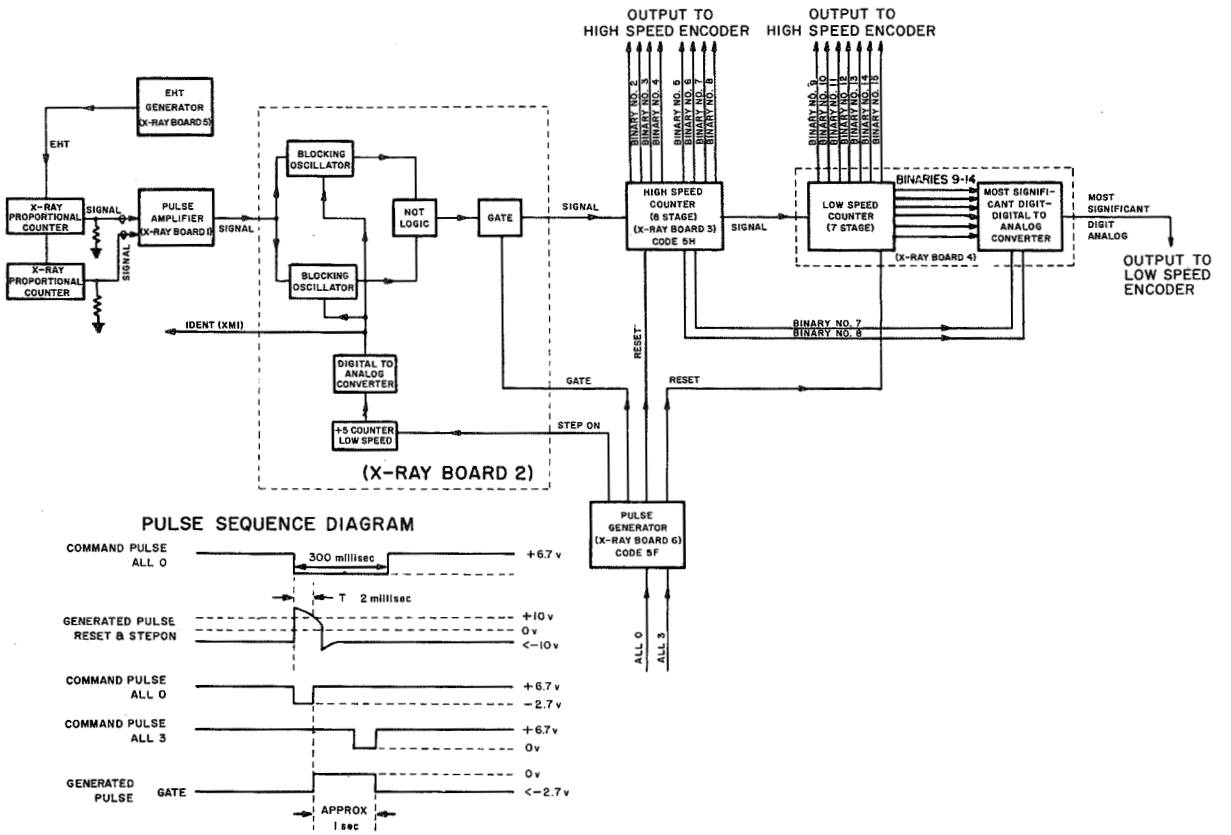

FIGURE 4–7.—Block diagram of X-ray spectrometer circuit.

the sun but also the background radiation from the rest of the sky. On an average, 5×12—or 60—telemeter periods of 5.12 seconds will be required to obtain a complete solar spectrum.

The high speed encoder is used to sample the binary outputs of all 15 scalers. For the low speed encoder the necessary information capacity is not available, so the outputs of the central eight scalers are combined to give an analog voltage representing the logarithm of the stored count to base 2, to one significant digit only, within the range covered by the scalers. In addition, the discriminator bias level is also telemetered and, on the high speed encoder only, an EHT monitor.

Figures 4–8 through 4–11 are photographs of the main electronic module elements. These

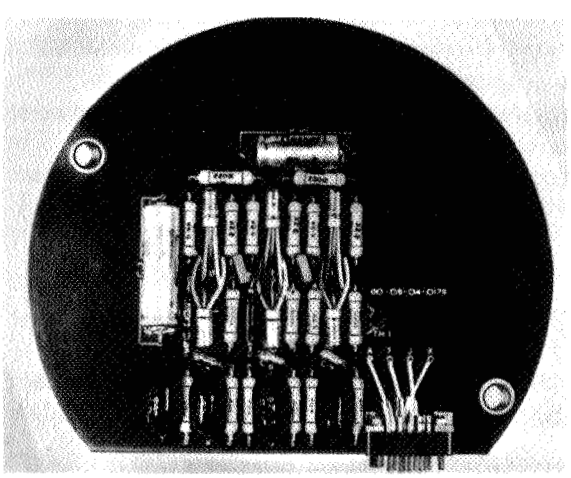

FIGURE 4–8.—X-ray linear amplifier.

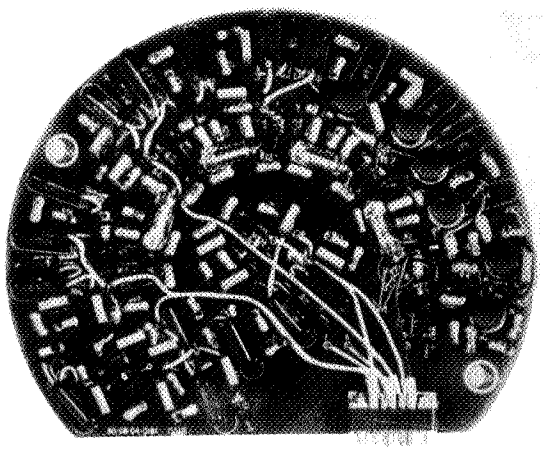

FIGURE 4–9.—X-ray high-speed counter.

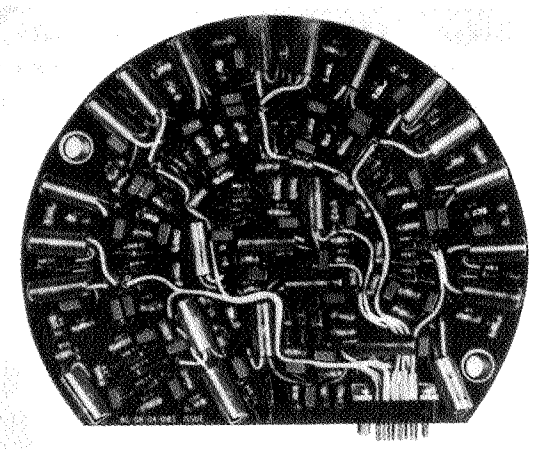

FIGURE 4–10.—X-ray low-speed counter.

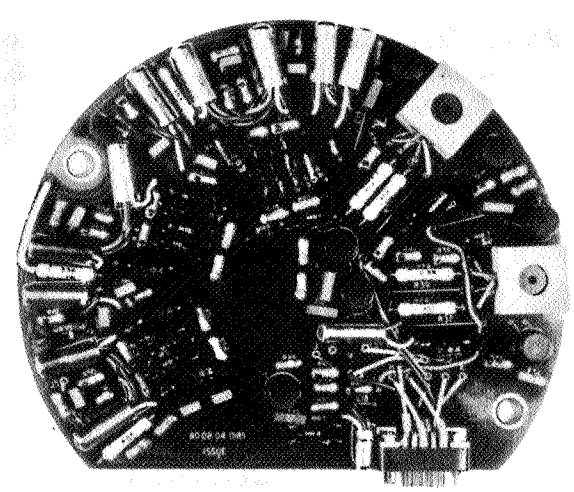

FIGURE 4–11.—X-ray discriminator circuit.

operate from +6.5 volt and −6.5 volt lines, with a power consumption of 130 milliwatts.

MEASUREMENT OF SOLAR ASPECT

Project Engineers

Mr. J. Alexander, University College London
Dr. P. J. Bowen, University College London

The Experiment

Both radiation experiments require information on the solar aspect, as their sensitivity is a function of aspect angle and spin rate; and it was considered that such information would also provide information on the spin rate and the stability of the spin axis which would also be valuable in the interpretation of the ionospheric experiments. In all, it was considered that the necessary information consisted of the solar aspect angle—that is, the latitude of the sun in the satellite system—and of the roll position of the sun or its longitude measured from a reference plane in the vehicle. In fact, the time intervals between telemetry samples of roll position are such as to make possible an ambiguity about the number of complete rolls occurring between measurements; so a spin rate indication has also been included.

The basic method of measurement utilizes a small pyramid of silicon solar cells at the center of a 9-centimeter-diameter hemisphere. The cells are illuminated by the sun through two slits whose shape is defined by the intersection with the hemisphere of a circular cylinder 4½ centimeters in diameter, the axis being parallel to the spin axis. The arrangement is shown in Figure 4–12. The cells are covered by an internal mask so that one cell on each side of the satellite equator is illuminated from one slit, and the outputs from the four cells are combined so that those from the two slits are of opposite polarity. The slit width and cell size are on the order of 1 degree, so that in each revolution of the vehicle one short positive pulse and one short negative pulse are produced. The time interval between positive pulses is then equal to the spin period; the actual time of their occurrence gives the roll position; and the ratio of the time interval between positive

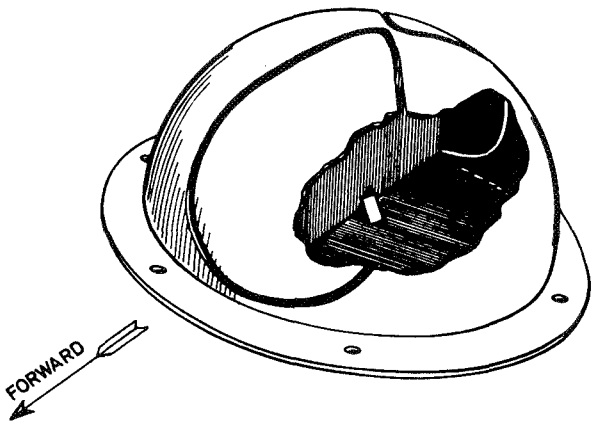

FIGURE 4–12.—Satellite aspect slit system.

and negative pulses to the interval between positive pulses is a linear function of the aspect angle.

The positive-going pulses are used to supply a simple pulse-rate circuit covering the range 180 rpm to 20 rpm. This will give an indication of the proper operation of the de-spin device and, at the same time, removes the roll position uncertainty. The positive pulses also operate a phase-locked sawtooth generator, which produces a triangular wave of constant anplitude whose commencement is always very close to that of the arrival of the pulse. Thus, this wave represents at any instant the roll position of the sun and is sampled by the telemeter. Finally, the positive pulses are used to turn *on*, and the negative pulses to turn *off*, a bi-stable circuit—thus producing a square wave of constant amplitude whose mean value is proportional to the solar aspect angle. The square wave is passed to a simple averaging circuit whose output is telemetered. The circuitry is supplied with 10 milliwatts from +6.5 volt and −6.5 volt lines.

COSMIC RAY ANALYZER

Project Scientists

Prof. H. Elliot, Imperial College, London
Dr. J. J. Quenby, Imperial College, London
Mr. A. C. Durney, Imperial College, London

Project Engineer

Mr. D. W. Mayne, McMichael Radio, Ltd.

The Experiment

Experimental Objectives

The main purpose of this experiment is to make accurate measurements of the primary cosmic ray energy spectrum and of the way in which this spectrum changes as a result of modulation by the interplanetary magnetic field. There are at present several alternative models of this field; and, to distinguish between the various possibilities, much more refined data are necessary than are now available from the observation of secondary cosmic ray intensity variations deep in the atmosphere and fragmentary information from balloon ascents.

In the present experiment it is proposed to investigate the cosmic ray spectrum by using a Cerenkov detector to measure the intensity of heavy nuclei ($Z \geq 6$) as a function of latitude. The energy spectrum can then be determined from the known values of the minimum energy that a particle must have in order to penetrate the earth's magnetic field at a given latitude. The advantages of measurements carried out in this way are: (1) It avoids the invalidation of cosmic ray measurements by inadvertent detection of Van Allen particles, and (2) it avoids the introduction of uncertainties by albedo particles scattered back from the atmosphere.

The detector will sweep through the cosmic ray energy spectrum four times on each orbit, giving a virtually continuous check on its variation with time. In addition, airplane surveys are to be carried out at the same time so that the intensity distribution in the atmosphere can be uniquely related to the primary spectrum. It is hoped by this means to obtain a sufficiently accurate relation so that the primary spectrum can be determined at any future time simply by an airplane survey.

A small Geiger counter will be included in the instrument package. On those parts of the orbit where the satellite is outside the Van Allen belts the large counter will give a measurement of the energy spectrum of the primary cosmic ray protons, and also bursts of solar protons, in the same way as the Cerenkov detector measures the heavy particle spectrum. Inside the Van Allen belts it will provide data on the time variations of the trapped radiation.

Operation of the Sensor

The Cerenkov detector consists of a hollow perspex sphere, 4 inches in diameter, together with an EMO 6097 photomultiplier 2 inches in diameter, which looks into a hole cut in the surface of the sphere. Cerenkov light flashes produced by cosmic rays in the wall of the sphere are detected by the photomultiplier. The pulse output of the tube is fed to a discriminator that only accepts pulses corresponding to primary nuclei of $Z \gg 6$ or $Z \gg 8$, rejecting smaller background pulses due to lighter nuclei and the Van Allen particles. Output from the discriminator is fed to a chain of eight binaries, and the contents of this store are sampled by both the data storage and direct telemetry encoders.

An electronic switch that controls the attenuation of the photomultiplier output pulses is coupled to the last binary. There are two levels of attenuation; and, each time the store is completely filled, a pulse is fed into the switch from the last binary, and the switch changes the attenuation to the other value. In this way, the two (effective) levels of the discriminator are obtained.

The complete instrument package is located on the spin axis at the forward end of the satellite, with the perspex sphere protruding outside the satellite surface and the photomultiplier and associated electronics just inside. Primary heavy nuclei can arrive at the sphere from the forward 2π solid angle, where the amount of shielding is in general less than 1 gm/cm^2, but are absorbed by the satellite structure in the backward 2π solid angle. It is advantageous to locate the Cerenkov detector on the spin axis, since the direction in which it sees cosmic rays changes only slowly in time with respect to the earth's surface and the geomagnetic field. The effect on the cosmic ray intensity of both absorption by the earth and deflection by the geomagnetic field must be taken into account in the analysis of the results.

The Geiger counter is placed in the instrument package with structure shielding on the order of 2 gm/cm^2 from the outside in the forward direction. The effective length and diameters of the counters are, respectively, 5 and 2 centimeters for the larger and 1 and 0.3 centimeters for the smaller. An additional 1 millimeter of lead is put around the small counter.

The counter feeds a chain of 13 binaries, and the contents of this store are read periodically by both the data storage and direct telemetry encoders.

Sensor Structure

A diagram of the sensor is shown in Figure 4–13. The perspex sphere is contained in an aluminium dome, 5 inches in diameter and 4$\frac{5}{16}$ inches high, protruding outside the satellite skin, to which the stalk of the University College probe is attached at the top. Eccofoam serves as a packing between the sphere land the aluminium container. The sphere temperaure must be kept below 70° C, the softening point of perspex. A light-tight air leak is provided between the interior of the sphere and the outside surroundings.

An aluminium cylinder 6½ inches in diameter and 5 inches deep is attached under the dome

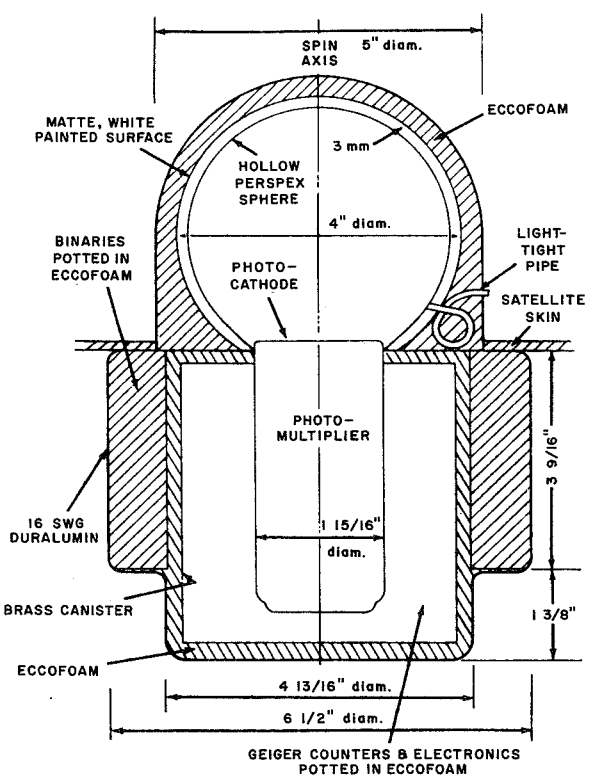

FIGURE 4–13.—Cosmic ray analyzer sensor diagram.

inside the satellite and contains the photomultiplier, Geiger counters, and electronics. The photomultiplier is placed along the spin axis and looks into a 2-inch-diameter hole cut into the wall of the sphere. Some of the electronics, together with the Geiger counter, are located in an annular space around the photomultiplier; and this whole is potted in Eccofoam and placed in a brass shielding canister. The canister is floated in a foam material to reduce the vibration acting on the photomultiplier. The remainder of the electronics is situated in a further ring surrounding the floating canister, and this also is potted in Eccofoam. Photographs of the sensor are shown in Figures 4–14 and 4–15.

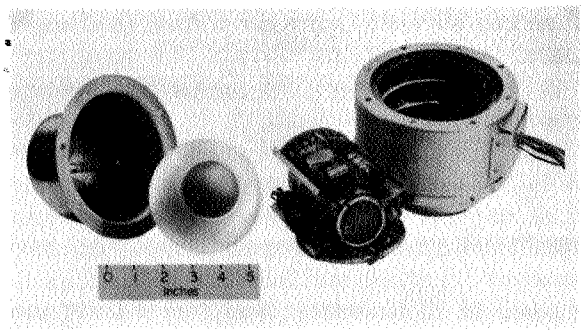

FIGURE 4–14.—Cosmic ray sensor and electronics.

The weight of the potted sensor, including the base of the University College London mass spectrometer, is 5.3 pounds. The center of gravity is on the spin axis, 3¼ inches up from the lowest surface on the base of the electronics cylinder. The moment of inertia about the spin axis is 0.2 lb ft²; and, about an axis through the center of gravity and perpendicular to the spin axis, the mass of inertia is 0.09 lb ft².

Sensor Electronics

A block diagram of the electronic circuitry is shown in Figure 4–16. Two input power suppy lines are required: 200 milliwatts at -9 ± 1 volts and 100 milliwatts at -6.5 ± 1 volts. The -9 volt line is fed to a dc converter, producing a very stable -6 volt line that is used to supply the EHT converter, the emitter follower, the discriminator, and the gate circuits.

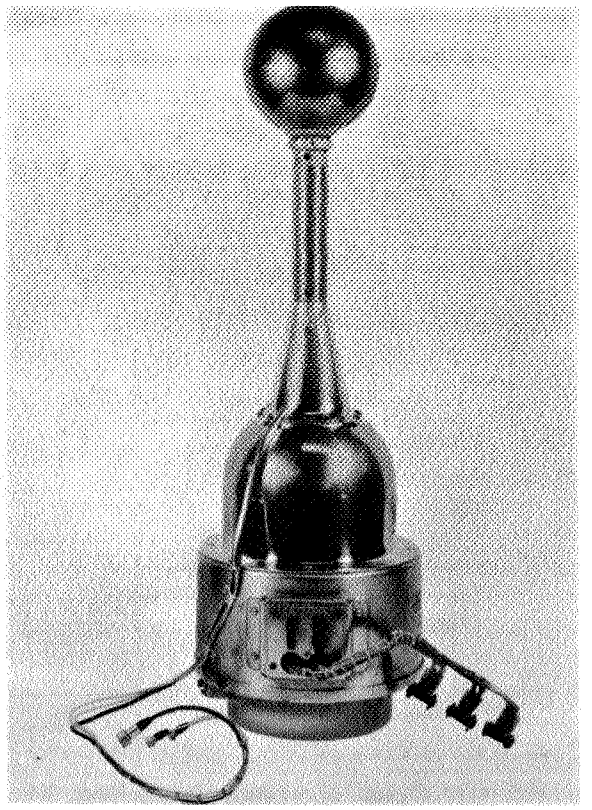

FIGURE 4–15.—Mass spectrometer probe and cosmic ray experiment assembly.

The dc converter incorporating a corona stabilizer supplies the 60-megohm dynode chain of the photomultiplier with -1000 volts, and this EHT voltage was designed to have a ±4 volt variation for a ±1 volt variation on the -9 volt input supply. The attenuator is switched to permit measurement of either the cosmic ray rate from $Z\gg6$ or from $Z\gg8$.

The discriminator output goes via a gate circuit to the chain of eight binaries. Figure 4–17 shows the circuit of a single binary, together with the size of the output wave form as a function of supply voltage. The outputs of the first six binaries are fed to the input gates of the high speed encoder, while the outputs of the last six binaries are fed to the input gates of the low speed encoder. When a particular information channel is to be sampled, the gate circuits feed three of the binary outputs to a digital oscillator that takes up one of eight different frequency levels,

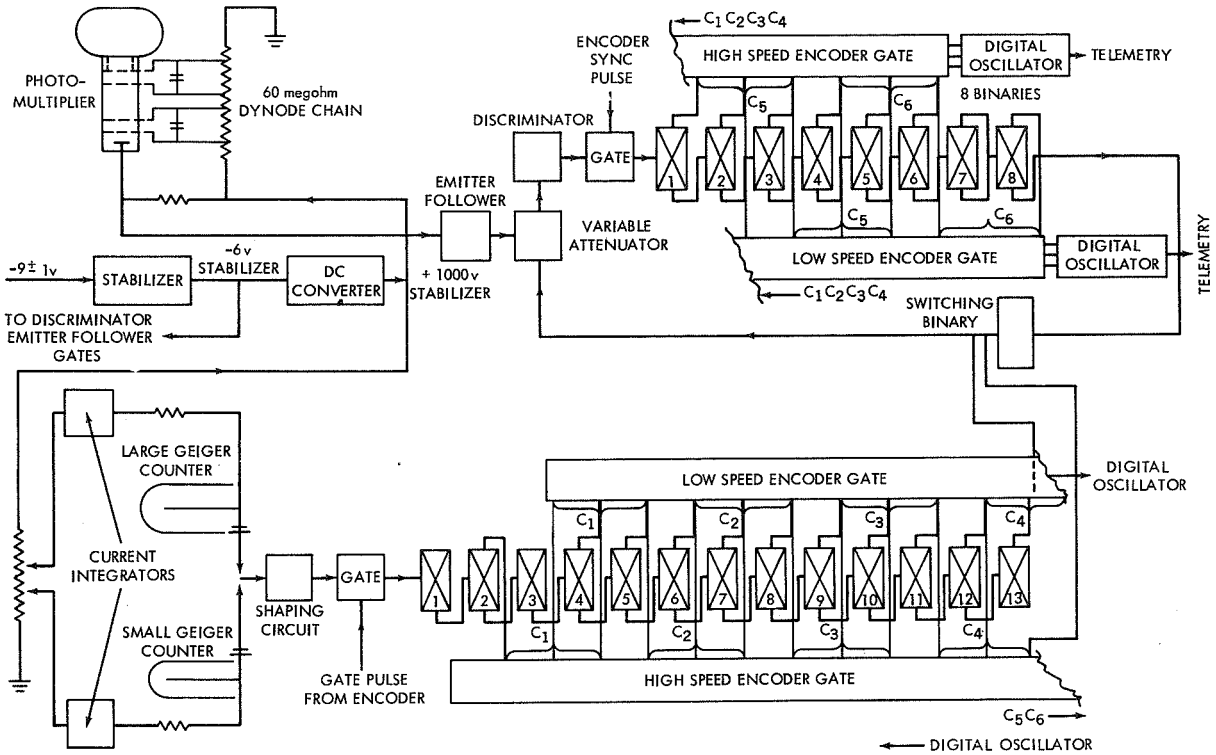

FIGURE 4–16.—Block diagram of cosmic ray analyzer circuit.

depending on the state of the three binaries. This frequency output is then put on the tape recorder in the case of the low speed encoder, and goes to modulate the telemetry transmitter in the case of the high speed encoder. Thus, to read the binary store, two channels are required on both the data storage and the direct telemetry systems.

While the low speed encoder is sampling the binary store, it is arranged that the gate circuit placed after the discriminator prevents any output reaching the first binary. This is done because the state of the binaries may change during the time taken to sample both binary sets. The gate circuit is driven by a pulse from the low speed encoder, which has a quiescent level of +6.7 volts and goes to −2.7 volts during the period when the state of the two sets of binaries is read by the digital oscillator. Zero current is drawn from the encoder at +6.7 volts, and 10μ amp at −2.7 volts.

An electronic switch working from the output of the last binary will change the value of the two-position attenuator and successively feed the two cosmic ray counting rates into the telemetry systems. When the binary store is filled, the flipover of the last binary changes the state of a switching binary, the output of which determines the value of the attenuation. To tell which attenuation value is being used, the switching binary output is also fed to both the low and high speed encoders as one of the three binary elements in information channel C4, the other two elements being taken from the Geiger counter store.

Appropriate voltages for the Geiger counter is tapped off the dynode chain. The anode-to-cathode voltage of the larger counter is made to fall below the working voltage at counting rates, in excess of that which the data encoder can handle. Pulse outputs from the two counters are mixed and fed via a gate circuit to a chain of 13 binaries. Numbers 2 to 12 are read by the high speed encoder, and numbers 3 to 13 are read by the low speed encoder. The design of the binaries and the method of sam-

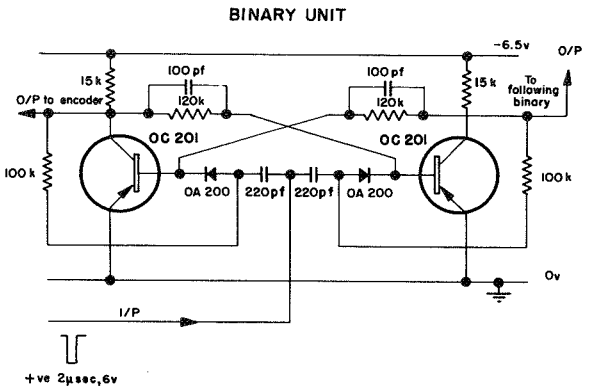

OUTPUT DETAILS

The output is a square wave of the following form:

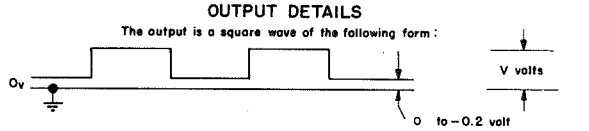

Output voltage V under various conditions,

SUPPLY VOLTS	OUTPUT with 100 k load *	OUTPUT with 50k load *
5	3.5	3.1
6	4.3	3.9
7	5.0	4.7

*Load resistor dc connected between output and earth.

*Recommended maximum dc or ac load - 50k

(Note: The binary units will be operated from the unstabilized - 6.5v (±1v) supply.)

FIGURE 4–17.—Circuit of a single binary unit with output details.

pling by the encoders are similar to the case of the Cerenkov channel. Thus, four channels of both the data storage and the direct telemetry systems are required. The gate circuit stops extra pulses being fed to the store, while the low speed encoder samples the four sets of binaries and works from similar pulses to the Cerenkov channel gate.

The digital oscillators and the associated input gate circuits for both encoders are located on a card held below the sensor by extensions to the bolts that locate the sensor on the satellite skin.

Plugs and Connections

About twenty-six leads are required between the gate and oscillator circuitry in the sensor and the encoder modules. Two power leads at −6.5 and −9 volts are also required. About eight further output leads are necessary if the sensor performance during environmental testing is to be monitored independently of the telemetry system.

Thermal Design

The following temperature restrictions are requested:

1. Perspex sphere, 70°C (this is the softening temperature of the plastic);
2. Electronics, 0° to 40°C;
3. Photomultiplier, 0° to 30°C (if possible).

Relevant information about materials:

1. The outer shell of the unit is made of 16 swg aluminium alloy (BS1470) and weights an estimated 16 ounces; it has a surface finish similar to duralumin.
2. The inner shielding canister is made of brass and weights about 16 ounces.
3. An estimated 23 ounces of Eccofoam is used in potting.
4. The remaining 2.3 pounds of sensor weight is made up of electronic components, circuit boards, photomultiplier, Geiger counters, etc.

PLASMA DIELECTRIC CONSTANT MEASUREMENT OF IONOSPHERIC ELECTRON DENSITY

Project Scientist

Prof. J. Sayers, University of Birmingham

Project Engineer

Mr. J. Wager, University of Birmingham

The Experiment

The measurement of electron density is performed both by this experiment and by the Langmuir probes of University College London. However, the two methods are quite different in principle and, being subject to different errors in general, therefore complement one another. Two circular disks of wire mesh, 3.5 inches in diameter and separated by 3.5 inches, form a parallel-plate capacitor (mesh is used in order to allow free passage of electrons into the capacitor). The capacitor is at the outer end of a boom 49.5 inches long, so that the electron density will not be greatly affected by the presence of the satellite.

The capacitor forms one arm of an RF capacitance bridge, operating at 10 megacycles. From a knowledge of the capacitance at 10 megacycles, and of the capacitance in vacuo, the dielectric constant k of the ionospheric

plasma can be found; this is related to the electron density by the expression

$$k=1-\frac{4\pi N_e e^2}{m\omega^2}$$

where N_e is the electron density, e and m are respectively the electronic charge and mass, and w is the angular frequency of operation of the bridge (here $2\pi\times10^{-7}$ rad/sec). However, N_e in the equation will be equal to the ambient electron density only if the potential of the capacitor plates is the same as the space potential. In general, there will be a potential difference between the satellite and space. To insure that at some times the capacitor plates are at space potential, a sawtooth wave with an amplitude of about 9 volts is applied to them; N_e is then taken to be the maximum value obtained during the sweep. Immediately before the start of each sweep a rather large negative potential (−5 volts) is applied to the plates to denude them of electrons and to provide a check on the in-vacuo capacitance.

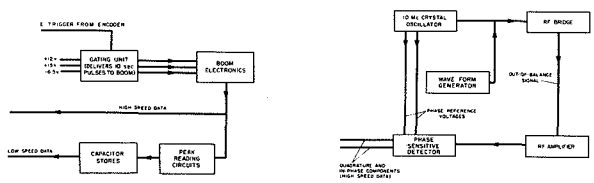

FIGURE 4–18.—Electron density circuit, block diagram.

Block diagrams of the circuitry are shown in Figure 4–18. To avoid a possible interaction with the University College London probe experiments, the experiment is turned on only for 10 seconds in each 61.42-second period. This is controlled by trigger pulses from the low speed encoder binary sequence. A gating unit then supplies power to the vf bridge circuitry and the bridge potential waveform generator—all of which are located at the hinge end of the boom—for this period. The output from the bridge is amplified, separated into in-phase and quadrative components (corresponding to the real and imaginary parts of the dielectric constant, respectively), and telemetered through the high speed encoder. Also, the maximum values in each sweep are selected by peak reading circuits and are stored in capacitors until they are read out by the low speed encoder.

The temperature of the boom electronics, the voltage supply levels, and the variable frequency (vf) amplitude are also measured and telemetered by both encoders.

DUTCHMAN EXPERIMENTS

Project Scientist

Dr. A. P. Willmore, University College London

Project Engineer

C. L. Wagner, Jr., Goddard Space Flight Center

The Experiment

The payload-supporting Dutchman contains two experiments directly connected with the spacecraft instrumentation. The first of these is designed to measure solar aspect and spin rate during the period before separation occurs, while the second is designed to detect contamination of the spacecraft thermal coatings and sensors as a result, for example, of evaporation from the nose fairing following aerodynamic heating. Each of these experiments receives power from the regulated +6 volt supply provided for the vibration experiment, and the signals from the two are combined for transmission over a single telemetry channel. In addition, and indication of the operation of a third-stage pressure switch is provided on this channel.

The aspect sensor is of the same pattern as that used in the spacecraft, but the aspect computer has been omitted. The pulse sequence from the solar cells is telemetered directly. The advantage of this procedure is that the rather long time delays associated with the aspect computer are eliminated, thus enabling third-stage spin and nutation to be calculated.

A diagram of the contamination experiment is shown in Figure 4–19. A small, focused lamp is used with a filter to produce an approximately parallel beam of suitably colored light. A small sample of this beam is obtained by reflection from an unsilvered glass surface, and its intensity is measured by means of a photodiode. The remainder of the light is incident on another glass slide, the intensity of the reflected light

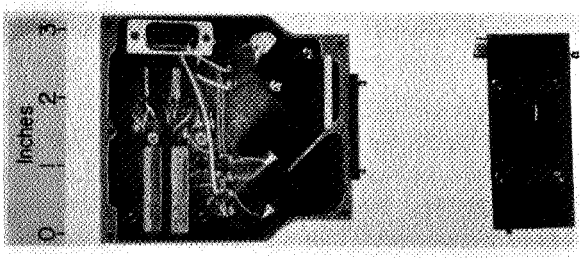

FIGURE 4–19.—Contamination experiment.

being monitored by means of a second photodiode. The second glass slide is exposed to contamination by the fairing, such contamination being revealed by the change in reflectivity of the glass.

A simple gating circuit is used to switch between the reference and sample slides at a rate of 1 cps. The output from the photodiodes is superimposed on the photocell pulses of the aspect sensor.

United States Satellite and Subsystems

STRUCTURE AND MECHANICAL DESIGN

Introduction

The Ariel I structure and mechanisms design encompasses two separate major areas of endeavor: (1) The satellite itself requires structure and mechanisms; and (2) just as important to the total payload is the development of a separation and release system interface structure and associated mechanisms.

The satellite itself relies heavily on the use of epoxy-bonded filaments of fiber glass for much of its structure, used in combination with machined wrought aluminum alloys. The ancillary interface system (Dutchman and separation structures) is largely composed of magnesium thin-wall castings.

Satellite Structure

General

The spacecraft structure should properly be divided into two main groups: the basic structure, and the appendages. The basic structure must then be further divided into the following subcomponents:

1. Upper dome,
2. Mid-skin,
3. Shelf and base assembly,
4. Lower dome.

The appendages are as follows:

1. Four solar paddles,
2. Two inertia booms,
3. Electron density experiment boom,
4. Electron temperature experiment boom,
5. Telemetry antennas.

Design Parameters

Several design considerations were paramount in the development of the structure:

The Scout 25.7-inch-diameter heat shield limited the payload size to 23 inches in diameter by 2 feet in length, not including certain experiments.

The aft appendages must be folded into the space described by a hollow cylinder 23 inch O.D. x 18 inch I.D. x 4 feet 8 inches long.

The structure should be manufactured of non-metals and/or nonmagnetic materials, so that the effects of magnetic spin damping are reduced to a degree that the half-life of the satellite's spin rate be 1 year.

The total satellite weight should not exceed 135 pounds.

The structure must withstand accelerations and vibrations of the launch vehicle. In this case the ABL–X248–A5 motor blast stage) governs.

Outer Structure

General: As a result of the above considerations the material chosen for the skin of the Ariel I was epoxy-bonded fiber glass. The domes were constructed from monofilament glass fibers cross-woven into cloth laminations that were molded into a spherical shell of 13½ inch radius by 5⅝ inches high. Shell Epon 828 with a CL hardener was used as the bonding agent. The top dome is $\frac{1}{16}$ inch thick, and the bottom dome—basically used only as a thermal shield—is $\frac{1}{32}$ inch thick. The mid-

skin was made from a cylinder of epon-bonded, monofilament-wound fiber glass $\frac{1}{16}$ inch thick x 23 inches in diameter x 10.7 inches long.

Upper Dome (Figure 5–1): Into the top of the upper dome skin was bonded and riveted an aluminum disk 8½ inches in diameter x 0.2 inch thick. Machined integrally with, and centrally located on, the disk is a 7-inch-I.D. thin-walled cylinder extending internally 3.7 inches. This hat-shaped structure supports the cosmic ray—ion mass sphere experiments and the eight radial fiber glass ribs, which are also attached to the dome skin—thus giving stiffness and strength to the dome. A machined aluminum ring was bonded and riveted to the base of the dome to allow the assembly to be bolted to the top of the 23-inch-diameter mid-skin. Holes were cut in the proper places of the dome to allow attachment of experiments and antenna mounts.

Mid-Skin (Figure 5–1a): The mid-skin fiber glass is bonded and riveted to two end flanges, machined from AISI 6061–T6 aluminum, which are shaped to provide nonshifting attachment to the upper structure and the shelf-base assembly. In detail, shear lips prevent radial movement, pins prevent rotational displacement, and machine screws tie the components together.

Lower Dome (Figure 5–1a): The lower dome is segmented and fitted with doublers for installation of sensors and the segments themsleves. Gold-plated aluminum machine screws hold these components in position.

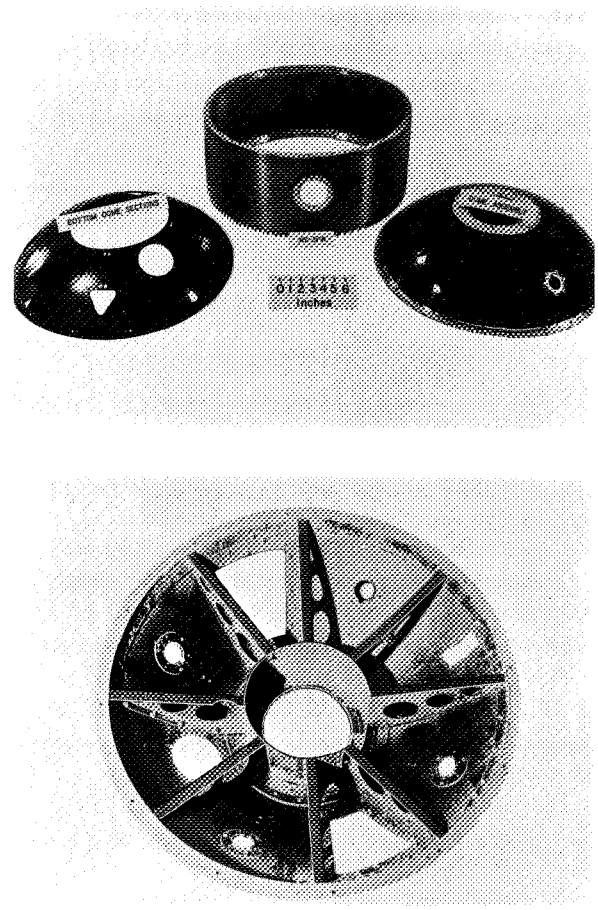

FIGURE 5–1.—Domes and midskin.

Shelf and Base Assembly (Figure 5–2)

General: The instrument shelf and base assembly is made from AISI 6061–T6 aluminum plates, bars, and billets machined into shape and semipermanently affixed into the assembly condition. The separate parts are as follows.

Shelf: The shelf is basically a 21-inch-diameter plate 0.08 inch thick with eight integral stiffening ribs leading radially from a 7½-inch-diameter integral cylinder to the outer periphery. This undercarriage of ribbing tapers from 0.7 inch at the cylinder to 0.3 inch at the 21-inch-diameter periphery. The top of the shelf at the 21-inch diameter is dished upwards 1 inch and then again extends radially until the shelf is 23 inches in diameter. This step is machined to supply room for the de-spin system and to provide a mating surface for the mid-skin.

Base: The base is a cylinder of 7 inches I.D. and fits into the 7½-inch-diameter short-shelf cylinder, extending aft 6½ inches. The aft 2 inches is machined to an 8½-inch I.D. to provide proper view angles for the spin-axis-mounted electron temperature sensor. The forward 7-inch-diameter x 4½-inch-long space is provided for containing the above sensor, the satellite's tape recorder, and the boom escapement mechanism. The outer diameter is machined to provide (1) a mounting surface for the separation adapter ring, (2) a mounting surface for the bottom dome segments, and (3) a key for six support struts.

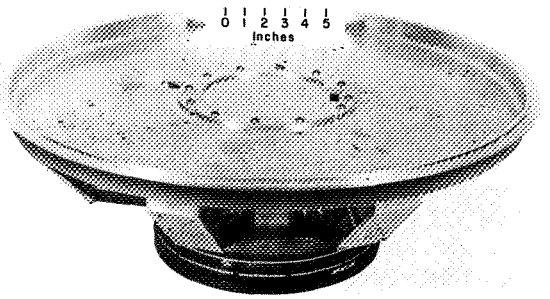

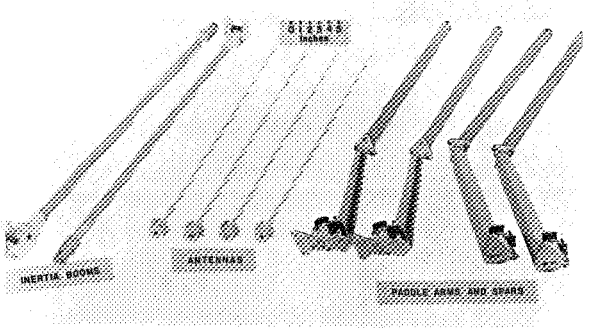

FIGURE 5–3.—Satellite appendages.

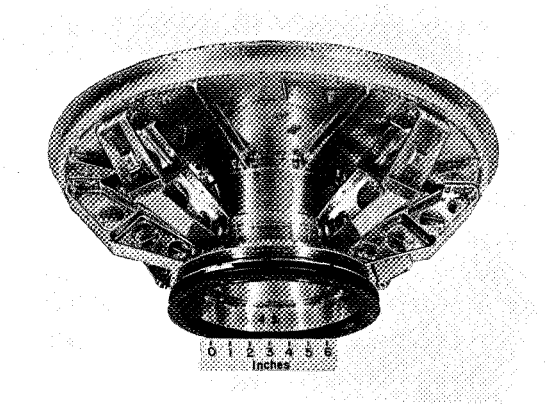

FIGURE 5–2.—Electronic shelf and base assembly.

Struts: The six struts are each machined from solid stock and take the shape of a modified "I" beam. Each strut serves to support the shelf and to supply the mount for a paddle arm or experiment boom hinge. The struts are keyed to the base and, after being fastened into position with machine screws, are keyed to the shelf by shrink-fit shear pins.

Appendages

General (*Figure 5–3*): The eight appendages should be considered in three separate groupings: paddle arms; inertia arms; and sensor, or experiment, booms.

Paddle Arms: The paddle arm and hinge design was suggested by that used on Explorer XII (1961) *v*1); however, space considerations dictated by the Scout heat shield and paddle location restrictions required by the experiments complicated the design considerably. The arms themselves are long slender channels machined from AISI 7075 aluminum. One pair of arms lead directly from their hinges to the paddle interface; but space and positional requirements for the other pair of solar paddles required a secondary folding hinge at the outboard end of each arm. From this secondary hinge extends the paddle interface of these two arms.

Inertia Booms: The inertia booms, when extended, provide a proper moment of inertia ratio so that the longitudinal axis remains the spin axis of the spacecraft. These booms are made of thin-walled tubes of epon-bonded fiber glass cloth, rolled into cylindrical shape. Each boom is attached to the shelf by a detent-locking, spring-loaded hinge; and at the outboard end of its 30 inches is a 0.7-pound steel weight that is 4 inches long. Both the inertia booms and the paddles are erected at 52.4 rpm, reducing spin to 36.6 rpm.

Experiment Booms: The sensor booms are made by the experimenters, but the method of erection is part of the structure's responsibility. The hinge valves are machined from solid stock and use a double detent lock and a torsion-spring positive force to assure opening in the event of no payload spin-up. (This consideration is true in all appendage extension.)

Escapement (Figure 5–4)

Boom erection rotation speed of the normal experiment is 76.5 rpm, which would produce large shocks to the experiments if these booms

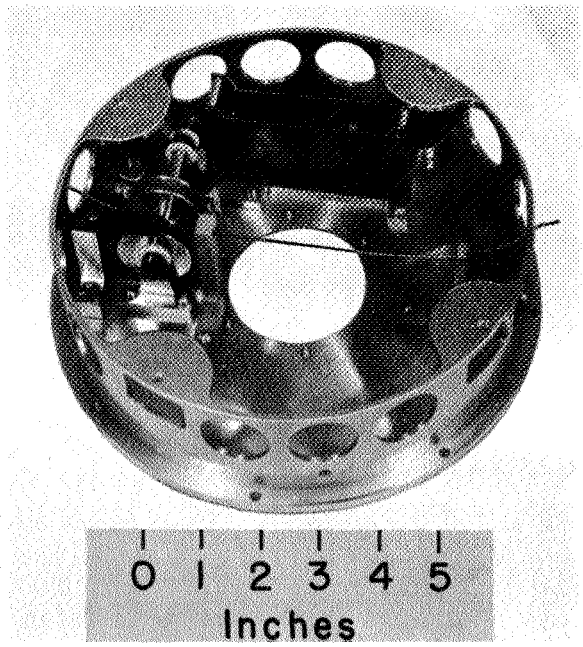

FIGURE 5-4.—Escapement mechanism.

were allowed to open without restraint. As a result, an escapement device was designed to reduce these forces by controlling erection speed.

The clock escapement principle is employed in the design of the timing mechanism. Since the primary interest in the application is to reduce shock—and not the accuracy or timing, the less sophisticated mechanism, called a "run-away-escapement," is used. It consists of a gear train coupled to an escape wheel, and a pallet fitted over the escape wheel to control its rotation rate. The two booms are required to be simultaneously controlled; thus a double pulley mounted on a common shaft is coupled to the free end of the gear train. A doubled nylon cord, with one end attached to the boom and the other end to the pulley, serves as the control links. The rotation rate of the escapement is a function of the satellite acting torque and the moment of inertia of the part. The pallet's moment of inertia is adjusted to allow the booms to erect in 2 to 3 seconds. This escapement will successfully control the boom erection when the satellite spin rate is between 60 and 90 rpm.

The booms are also tied together by this mechanism, so that they erect simultaneously and thus prevent any unbalance that would cause coning of the payload. (The other appendages open too quickly to create this problem.)

De-Spin Device

The de-spin system is built in a self-contained ring fitting in the space provided at the periphery of the shelf. It is of the "stretch yo-yo" design (Reference 13), which will de-spin a system having a ± 20 percent nominal spin rate error to ± 2 percent of the required final value. The basic components are a pair of equal weights attached to a matched pair of long tension springs wound one-half turn about the payload. The weights were released by pyrotechnique guillotine cutters, and the weight-spring combinations sunhook themselves when in a radical attitude from the spacecraft. By this system the payload is despun from 160 to 76.5 rpm.

Antennas (Figure 5-5)

The four turnstile-type antennas are of the double-fold design, so that they can fit into the heat shield. These antennas are located on the top dome equispaced 90 degrees apart, and in their erected position make an angle of 40 degrees with the spin axis. Upon ejection of the heat shield, the antennas are erected to their length of 21¾ inches.

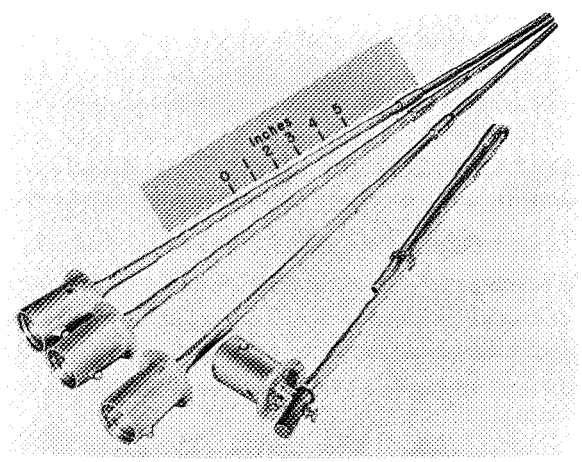

FIGURE 5-5.—Flight antennas.

Battery Containers

The two containers for the spacecraft battery power supply were designed to withstand the force of expanding gas generated internally in the sealed batteries, which could result from a partial power system malfunction. The container can withstand loadings of 50 pounds from each of two stacks of batteries without significant expansion—thus preventing rupture of the batteries and subsequent contamination of the payload. These containers are mounted on the instrument shelf and supply rigidity in the area of the inertia boom hinge.

Miscellany

The above-mentioned components plus a wealth of miscellaneous supports, adapters, and bracketry make up the structures and mechanisms of the orbiting spacecraft, accounting for 51.6 pounds of its weight.

Separation and Release Systems

Although not a part of the spacecraft, the separation and release system (Fig. 5–6) is responsible for programming proper de-spin of the system, erection of the appendages, and separation of the payload. The system was designed originally to adapt the spacecrafts directly to the fourth stage of the Scout vehicle. A thin-walled, machined magnesium casting in the shape of a hollow, truncated cone forms the basic transition unit from the satellite to the last stage. At the satellite interface is the separation spring, segmented marman clamp, and separation bolts. Here, too, are found the two 3-pin feed-through connectors that carry into the satellite the de-spin signal, battery charge, and turn-on, turn-off circuitry. The wide base of the cone fits over the forward shoulder of the vehicle interface and is bolted to studs protruding from that surface. Fastened to the cone itself are two 12-volt battery supplies and an electronic release sequencer. Bonded to the cylinder of the X–248 motor are brackets and supports holding the release cords and pin pullers—which, when retracted, release the cords and allow erection of the appendages. Total balanced weight of this system is 18.3 pounds.

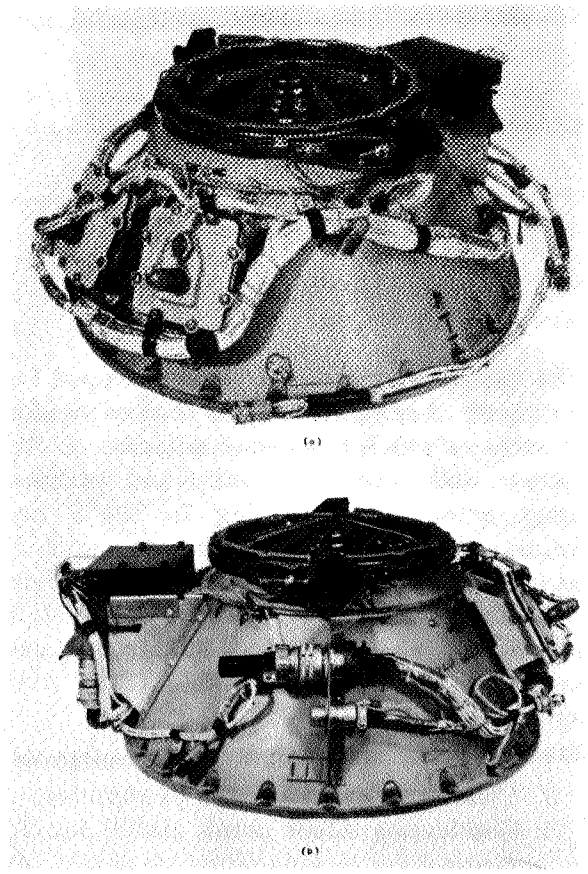

FIGURE 5–6.—Separation and release mechanism.

Delta Dutchman

When the Ariel I was transferred to the Thor-Delta vehicle, an adapter ring was required to move the folded payload forward some 12 inches so that the pedal-leaf second- to third-stage separation skirt would not damage the sensor booms during stage separation. This Dutchman (Fig. 5–7) is a fabrication of cast magnesium end rings separated by a 16-inch-diameter cylinder of rolled and welded 0.09-inch-thick magnesium sheet. The riveted fabrication is 13.0 inches long.

Since the Thor-Delta can carry a heavier payload than the Scout, the available space in the Dutchman cylinder is utilized to contain the electronics and sensors of a vibration and contamination experiment. The total weight of this composite is 17.0 pounds; the Dutchman accounts for 7.3 pounds of this total.

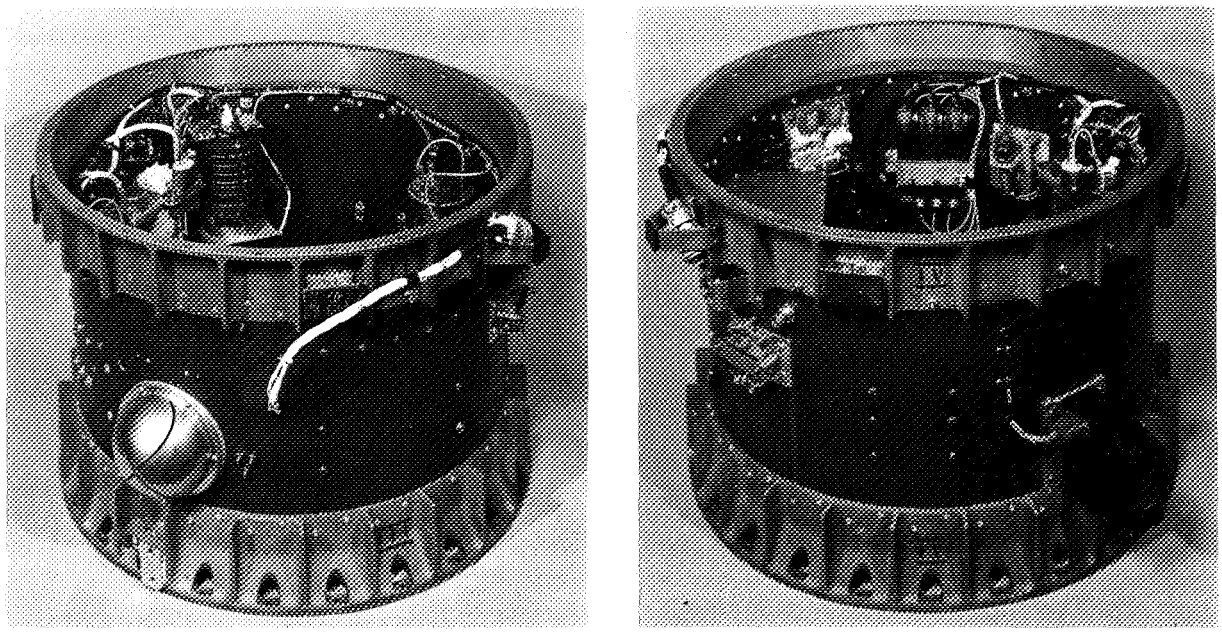

FIGURE 5–7.—Dutchman adapter cylinder and experiments.

Detailed Data on Structure and Mechanical Design

Physical measurements of the structures and mechanisms of the Ariel I payload are presented as Appendix A.

THERMAL DESIGN AND COATINGS

Thermal Design

For a given solar absorptance-thermal emittance (a/e) ratio, a variation in mean orbital temperature of 35° C can be expected in the main structure over a period of 1 year. This total variation may be subdivided as follows: (1) 0 to 6 watts internal power, 5° C; (2) 63 to 100 percent sunlight orbits, 20° C; and (3) variation in sun, spin-axis angle—including shading by paddles and booms, 10° C. A ±10 percent tolerance for achieving the design a/e would result in a tolerance of about ±7° C in mean orbital temperature for a given orbit, sun angle, and internal power. Skin temperature gradients can vary from about 20° to 60° C, depending on sun—spin-axis angle. The variation in mean orbital temperatures of the boom-mounted components due to sun—spin-axis angle changes will be somewhat greater than the corresponding temperature predictions for the main structure because of the nonspherical geometry and greater shading effects. Solar paddle temperatures should remain between +33° and −63° C, the temperatures corresponding to the hottest and coldest combinations of spin axis, orbital plane, and orbital position locations with respect to the sun.

Thermal Coatings

The thermal coatings are evaporated gold with not more than 25 percent of the total surface area covered with a combination of black and white paints. This represents a compromise of the experimenters' requirement for a conducting surface with a preference for gold or rhodium over other metals and a thermal requirement for maximizing the painted areas to minimize the tolerances on a/e ratio.

The following process has been developed for applying the thermal coatings so that mirrorlike gold surfaces which have good adhesion to the substrate and which can withstand without damage aerodynamic heating to 250°F are obtained. First, the surfaces are sanded,

cleaned, and baked at 310°F for 1 hour. Then layers of varnish, lacquer, paint, and metals are applied in the following sequence and are baked at the temperatures and for the time intervals indicated:

1. Sealing varnish, 300°F for 20 minutes,
2. Clear lacquer, 290°F for 30 minutes,
3. Conducting silver paint, 280°F for 18 hours,
4. Electroplated copper, 1.5 mil thickness,
5. Lacquer, 275°F for 30 minutes,
6. Evaporated gold, 0.00004 inch thick,
7. Four coats of black paint in eight longitudinal stripes, 250°F for 30 minutes.

Steps 3 and 4 are applied only to the cylindrical section and the forward dome to provide a ground plane for the antennas. The lacquer is the type used for providing a proper substrate for evaporative films. The combination of the varnish plus the repeated baking at decreasing temperatures with each successive step is used to protect the evaporated gold from damage by outgassing of the substrate. Final adjustment of a/e was made by the application of white paint over part of the black paint areas. The black and white paints are carbon black and zinc sulfide pigments, respectively, in a silicone vehicle.

DESCRIPTION OF ELECTRONIC SYSTEM

Electronic Subsystem

A typical electronic subsystem of the spacecraft is a printed circuit card, which is completely encapsulated in Eccofoam (Fig. 5–8).

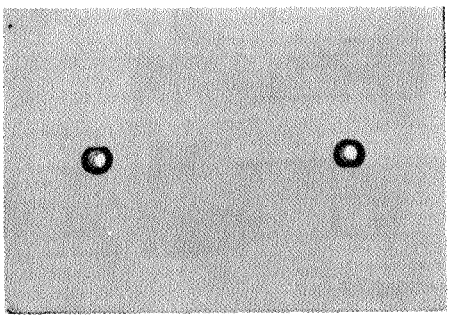

FIGURE 5–8.—Printed circuit card, completely encapsulated for space flight.

These printed circuit cards are of three types. One type of circuit card provides for mounting individual electronic components as shown in Figure 5–9. Medium component density is achieved by mounting the components vertically on the record type of printed circuit card shown in Figure 5–10. Maximum component density is achieved by mounting welded "cordwood" modules on the printed circuit cards as shown in Figures 5–11 and 5–12.

Block Diagram Discussion

A block diagram of the spacecraft's electronic system is given in Figure 5–13. Eight probes are shown with their data outputs processed by signal conditioning circuits. The outputs of the signal conditioning circuits are connected to subcarrier oscillators (analog and digital). The subcarrier oscillators convert analog and

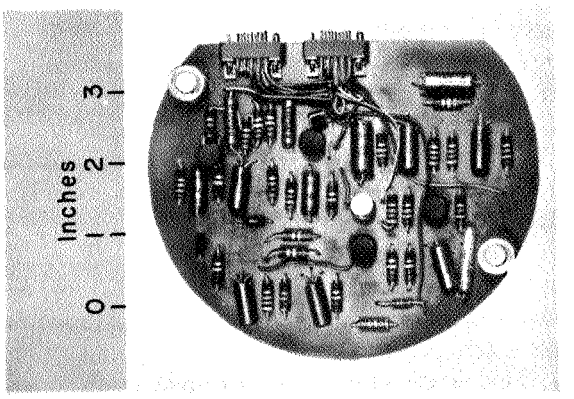

FIGURE 5–9.—Printed circuit card, mounting individual components.

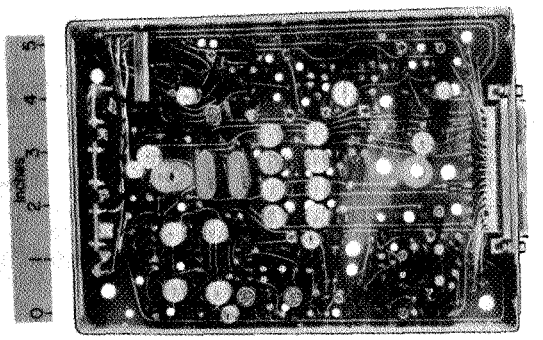

FIGURE 5–10.—Printed circuit card, mounting component of medium density.

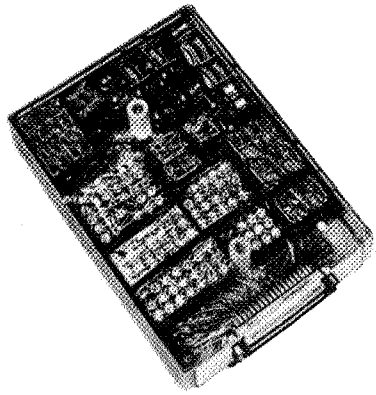

FIGURE 5–11.—Printed circuit card, mounting unencapsulated welded "cordwood" modules.

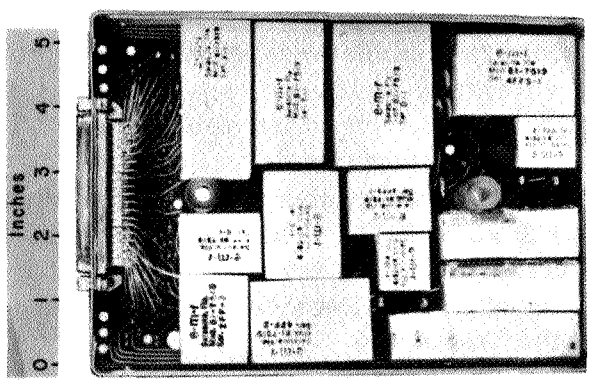

FIGURE 5–12.—Printed circuit card, mounting encapsulated welded "cordwood" modules.

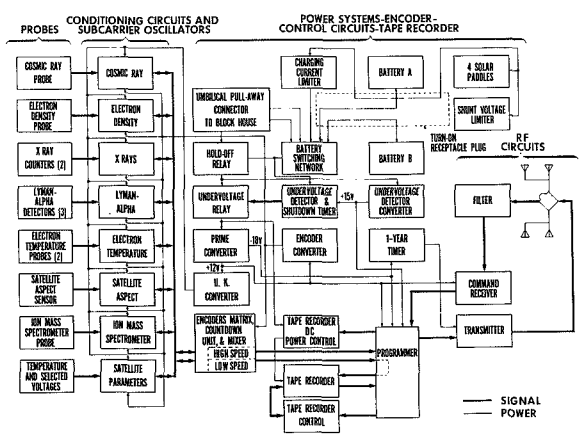

FIGURE 5–13.—Ariel I electronic function diagram.

digital data to representative ac signals. The frequencies of these signals are dependent on the value of the input analog voltage and/or digital data, Figure 5–14. The outputs from the subcarrier oscillators are sequentially gated as high speed (HS) or low speed (LS) data outputs by the respective encoder matrices. The encoder assignments of experimental data outputs are listed in Table 5–1.

The high speed encoder data are transmitted in real time, whereas the low speed encoder data are recorded on magnetic tape. There is a speed reduction between the two encoders of 48:1. By playing back the recorded data 48 times faster than it was recorded, the low speed data are transmitted at the same bandwidth as the high speed data.

Playback of the magnetic tape recorder is initiated by a ground station command to the Command Receiver in the spacecraft. The Command Receiver in turn commands the Programmer to switch the Tape Recorder from Record to Playback.

The output format of the high speed and low speed encoders is shown in Figure 5–14; also shown is the telemetry program for almost two complete orbits.

The power system for the spacecraft consists of solar paddles, two battery packs, shunt voltage limiter, battery charging current limiter, battery switching network, and undervoltage detector system.

The *four solar paddles* are mounted with silicon solar cells and together are capable of providing 0.5 to 2 amperes at 15 volts, depending on the spacecraft aspect to the sun. The

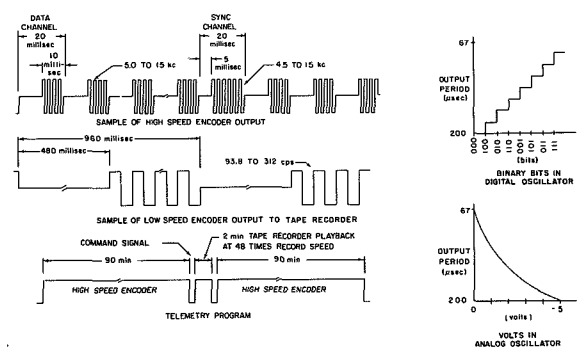

FIGURE 5–14.—Telemetry system.

shunt voltage limiter regulates the solar paddle output voltage to 14.5 volts. The *battery charging current limiter* regulates the battery charging current to a value not in excess of 0.5 ampere. The *battery switching network* selects the battery with the highest voltage to operate the spacecraft. The *undervoltage detector system* includes an undervoltage detector, converter, relay, and shutdown timer. Operation of this system turns off the entire spacecraft to provide maximum charging current to the batteries.

The hold-off relay is operated from the block house and is used to turn the power system *on* and *off* after the turn-on plug has been installed in the spacecraft.

The four converters are dc to dc converters that supply regulated voltages to the spacecraft's electronic subsystems.

Encoder

The encoder (Fig. 5–15) is operated by a crystal-controlled clock. The clock frequency is divided to produce a 50-cps signal for the high speed (HS) encoder data rate. The 50 cps is divided by 48 to produce the low speed (LS) encoder data rate of 50/48 cps.

The HS encoder format consists of 256 channels arranged in 16 frames (16 channels per frame). A complete set of 256 channels is referred to as a HS encoder sequence. The LS encoder format contains 2 frames, also with 16 channels per frame. A complete set of 32 channels is referred to as a LS encoder sequence. The channel allocation for both formats is given in Figures 5–16 and 5–17. These figures may be compared with the notations on Table 5–1 for identification of channels.

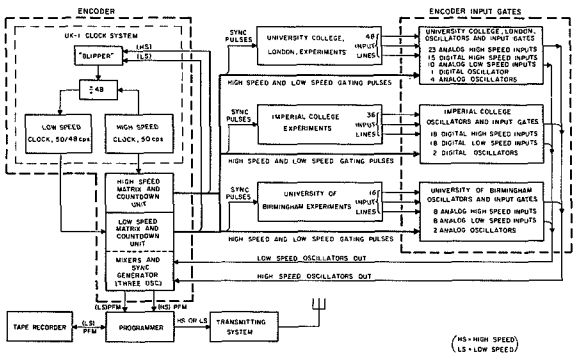

FIGURE 5–15.—Ariel I encoder function diagram.

Programer and Tape Recorder

The main function of the programer is to control the transmission of LS and HS encoder

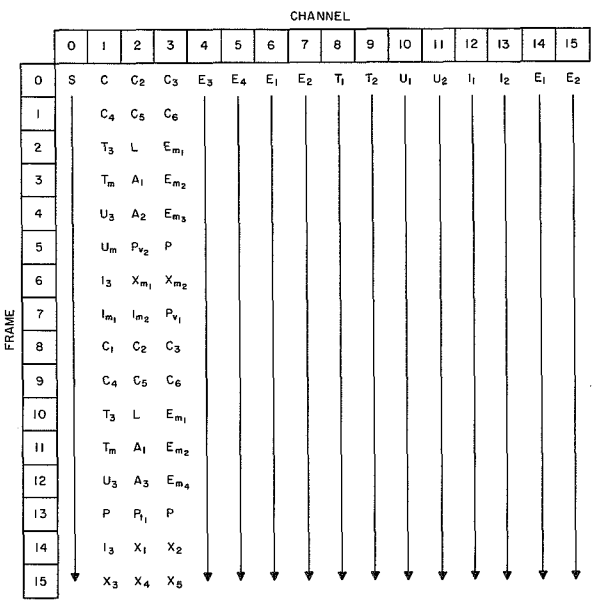

FIGURE 5–16.—High-speed encoder telemetry channel allocation.

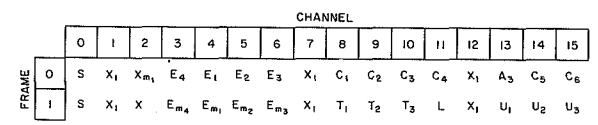

FIGURE 5–17.—Low-speed encoder telemetry channel allocation.

TABLE 5–1.—*Encoder Input Data*

Experiment	Nomenclature of Each Output
Electron temperature No. 1	U_1—HS U_2—HS U_3—HS U_m—HS U_1—LS U_2—LS U_3—LS
Electron temperature No. 2	T_1—HS T_2—HS T_3—HS T_m—HS T_1—LS T_2—LS T_3—LS
Mass spectrometer	I_1—HS I_2—HS I_3—HS I_{m1}—HS I_{m2}—HS
Lyman-alpha	L—HS L—HS
Aspect	A_1—HS A_2—HS A_3—HS A_3—LS
Performance parameters	P—HS PV_1—HS PV_2—HS Pt_1—HS
X-ray counter	X_1—HS X_2—HS X_3—HS
X-ray counter—Continued	X_4—HS X_5—HS X_{m1}—HS X_{m2}—HS X_1—LS X_{m1}—LS
Cosmic ray	C_1—HS C_2—HS C_3—HS C_4—HS C_5—GS C_6—HS C_1—LS C_2—LS C_3—LS C_4—LS C_5—LS C_6—LS
Electron density	E_1—HS E_2—HS E_3—HS E_4—HS E_{m1}—HS E_{m2}—HS E_{m3}—HS E_{m4}—HS E_1—LS E_2—LS E_3—LS E_4—LS E_{m1}—LS E_{m2}—LS E_{m3}—LS E_{m4}—LS

data to the ground station. A block diagram of the programer is shown in Figure 5–18.

To transmit the data stored by the tape recorder, an RF command is sent to the satellite from a ground station. The command receiver sends a pulse to the programer, at which time the programer (1) disconnects the HS encoder from the transmitter, (2) disconnects the tape recorder input from the LS encoder, and (3) gates a 320.83-cps signal for 2 seconds to the transmitter and tape recorder. The 2 seconds of 320.83 cps is thus transmitted and, at the same time, recorded on the tape recorder. The transmitted pulse signals receipt of the command, and the tape recorder playback follows immediately.

At the end of the 2 seconds of 320.83 cps the programer (1) switches the tape recorder from record to playback and simultaneously shifts the tape speed to 48 times its record

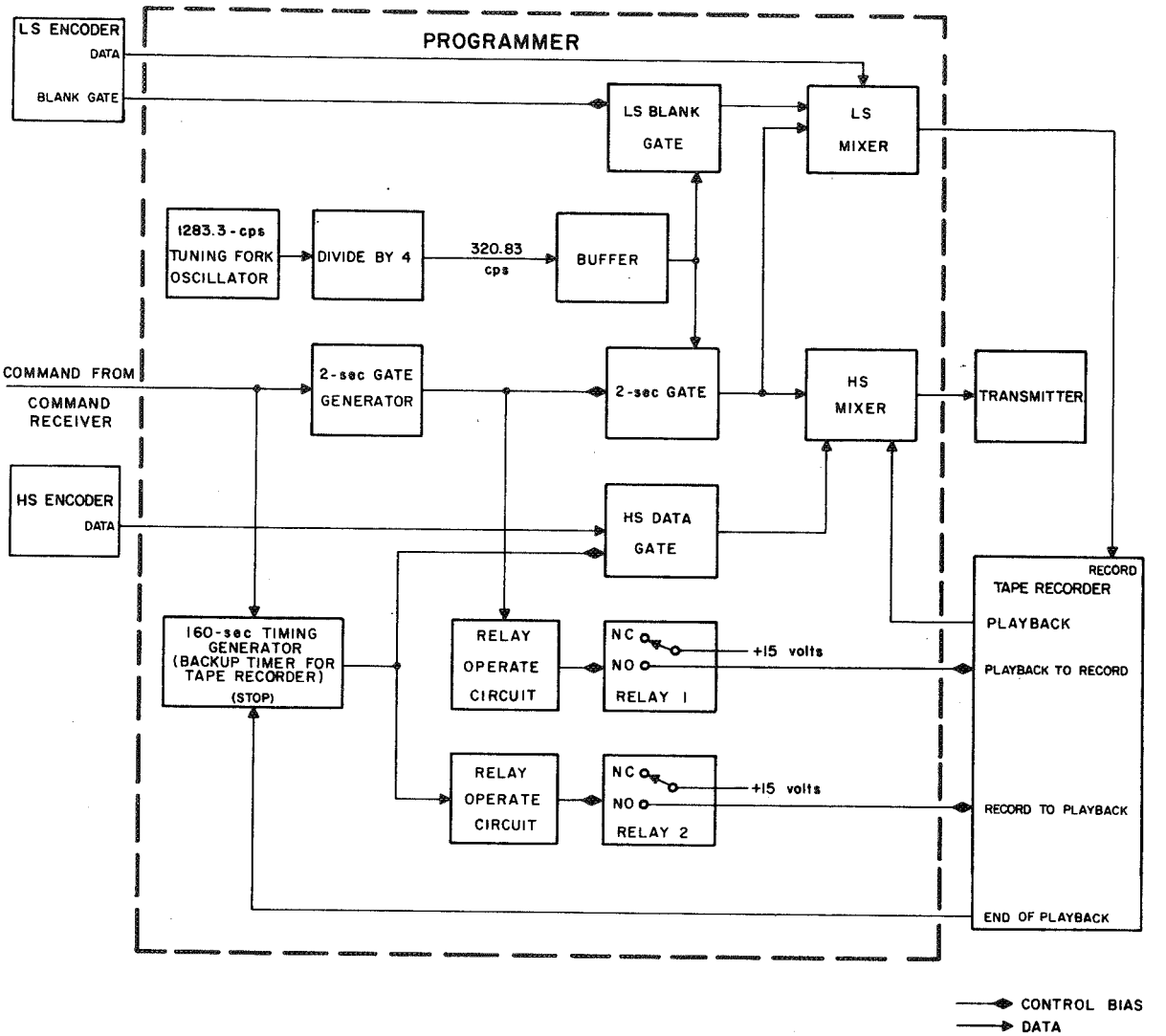

SEQUENCE OF EVENTS

1. Before command from Command Receiver:
   a. HS data applied through HS data gate and mixer to transmitter.
   b. LS data applied through LS mixer to record input of tape recorder.
   c. Blank gate from LS encoder causes a burst of 320.83 cps signal to be recorded.
2. Command from Command Receiver:
   a. Triggers 2-second gate generator and 160-second timing generator.
   b. Two-second gate generator output causes the 320.83 cps signal to be recorded on tape recorder, marking the end of HS data or the beginning of LS data.
   c. The end of the second gate generator output signal energizes relay 1, causing the tape recorder to switch from record to playback.
   d. Playback output of tape recorder is played back at 48 times record speed and is applied through HS mixer to transmitter.
   e. Output of 160-second timer inhibits the HS data gate, preventing the transmission of HS data while LS data are transmitted.
   f. The end of the 160-second timer signal opens the HS data gate and energizes relay 2.
   g. Output of relay 2 switches tape recorder from playback to record.
   h. The end-of-playback signal from the tape recorder inhibits the backup timer for the tape recorder only if the recorder switches automatically from playback to record.
3. End of playback cycle:
   a. Programmer is returned to the conditions outlined in 1 above.

FIGURE 5–18.—The programer function diagram and sequence.

speed, and (2) connects the transmitter to the tape recorder.

Transmission of tape recorder playback for a period of 125 to 134 seconds is controlled by a timer in the tape recorder. This period of time is sufficient to play back all stored data. This includes a 15.4-kc pulse, approximately 41 milliseconds long, which is the 2 seconds of the 320.83-cps signal recorded immediately prior to tape recorder playback. This pulse indicates the end of LS encoder data and also serves as a time reference for correcting data from both encoders.

The programer also generates a 140-second timing signal that is used to switch the tape recorder from playback to record. This signal is used by the recorder in the event that the tape recorder playback timer fails.

Figure 5–19 is a block diagram of the tape recorder. In the record mode, the tape speed is 0.25 inch/second; in the playback mode the tape speed is 12 inches/second; power consumption over a temperature range of −20° to +30° C in record mode is 0.5 watt, and 0.75 watt in the playback mode. Playback flutter is less than 1 percent p-p from dc to 200 cps; dynamic signal-to-noise ratio is a minimum of 30 decibels. The tape recorder is pictured in Figure 5–20.

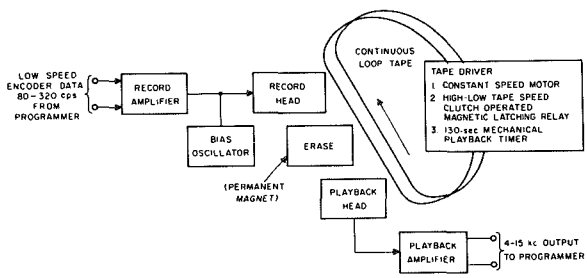

FIGURE 5–19.—Block diagram of tape recorder.

Power to the tape recorder drive motor is provided through a dc control circuit. A power overload greater than 300 milliamperes for 70 seconds causes power to be removed from the tape recorder motor. The dc control circuit receives a reset signal each time the programer switches the tape recorder from record to playback. This provides a means of testing whether the overload condition is continuous. (See Fig. 5–21.)

Command Receiver

The receiver is basically a double-superheterodyne unit with an amplitude-modulation detector (Fig. 5–22). A decoder, which follows the detector, contains a tone filter, a signal integrating circuit, and an output trigger circuit to signal the programer to switch the tape recorder from record to playback. The

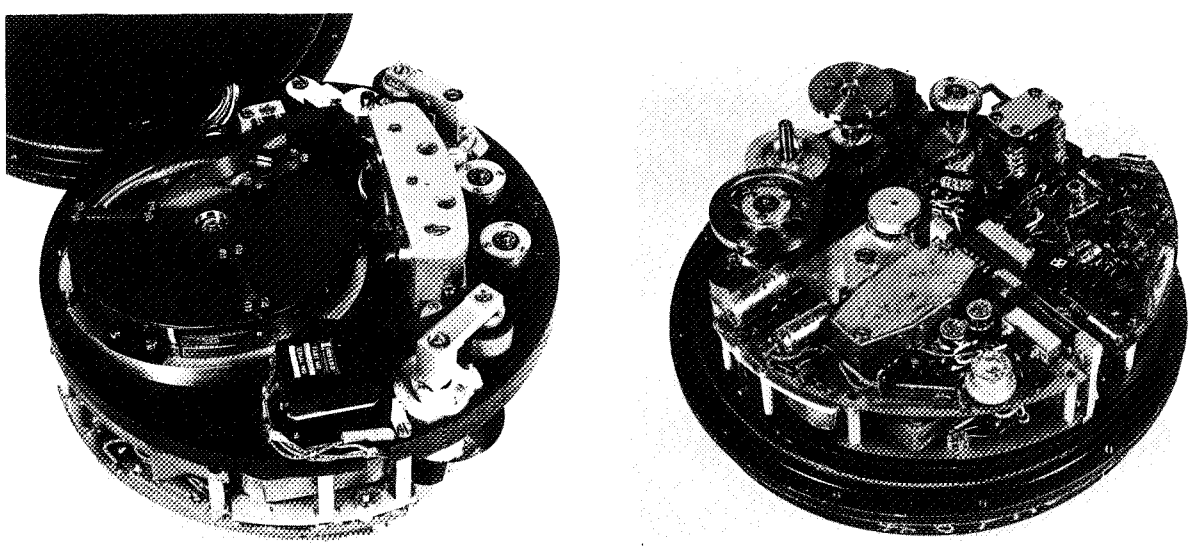

FIGURE 5–20.—The tape recorder, without its cover.

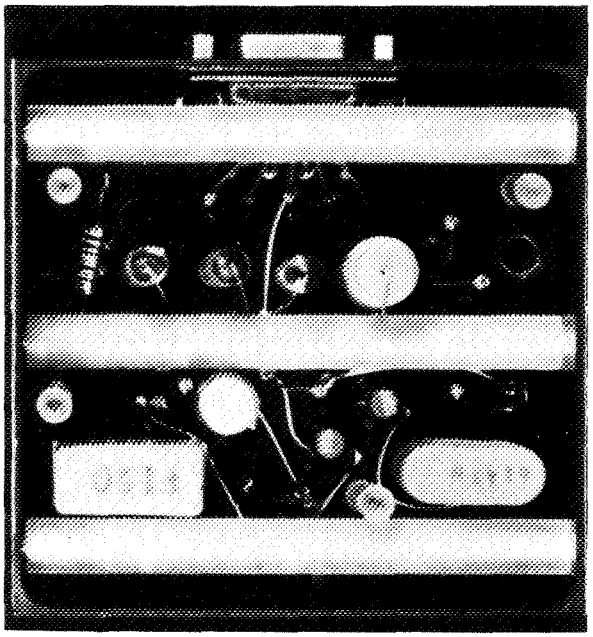

Figure 5–21.—Direct current control circuit.

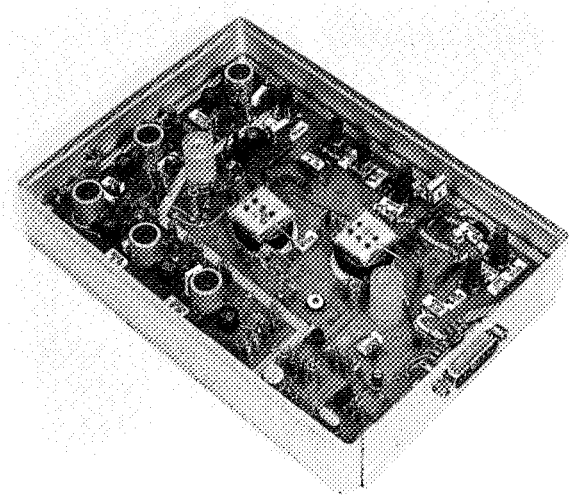

FIGURE 5–22.—The command receiver.

subcarrier tone that amplitude-modulates the received signal must be present for 0.1 second minimum, and the carrier must be modulated at least 30 percent before the decoder will command. The receiver is powered from the +12 volt line and requires 4.0 milliamperes of current. The receiver sensitivity is −100 dbm or greater.

Transmitter

The phase modulation transmitter is transistorized and delivers 260 milliwatts of power to the antenna system at a frequency of 136.410 megacycles. Frequency stability is ±0.002 percent or less over a temperature range of −20° to +60° C. Peak deviation from the square-wave modulation is +1 radian, with less than 2.5-cps incidental frequency modulation and less than 3-percent amplitude modulation. Harmonic frequencies are 60 decibels below the carrier power. Total power drain from the −18 volt power supply is about 900 milliwatts. The transmitter consists of a crystal-controlled oscillator operating at a frequency of 68.205 megacycles; a buffer stage to isolate the oscillator from the phase modulator; a phase modulator that employs voltage variable capacitors to shift the phase of the carrier (the instance phase excursions are controlled by the LS and HS encoder output data); a doubler stage that multiplies the output frequency of the modulator to 136.410 megacycles; a driver stage that amplifies the doubler output power to about 60 milliwatts; a final amplifier that delivers 250 milliwatts to an antenna load impedance of 50 ohms; and a harmonic filter to prevent radiation of unwanted harmonics of the carrier frequency. (See Figs. 5–23, 5–24, and 5–25.)

RF Antennas

The Ariel I spacecraft RF antenna system includes a coaxial hybrid power divider, coaxial phasing lines, and a canted turnstile antenna. The hybrid power divider and filter provides about 20-decibel isolation between the command receiver and the transmitter. The antennas are driven from the base, each pair acting as a dipole, with the dipole pairs in phase quadrature. Radiation in the plane of the turnstile is essentially linear, while circular polarization is obtained along the spin axis. The total power radiated varies with satellite aspect from +2 to −4 decibels relative to an isotropic radiator. Spacecraft commands are received through the same antenna system and have about the same pattern but see an additional 2-decibel loss because of mismatch at the command frequency.

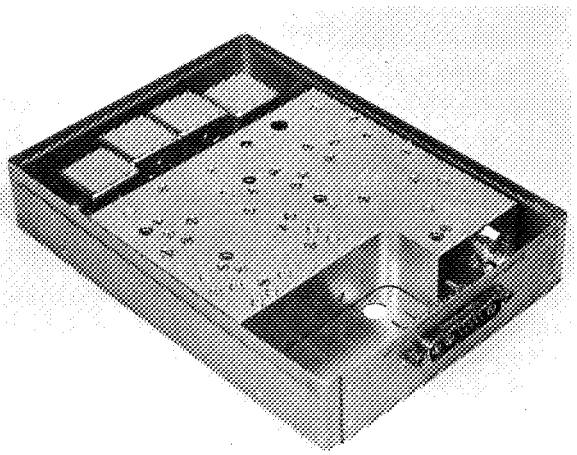

FIGURE 5–23.—Phase modulation transmitter prior to encapsulation.

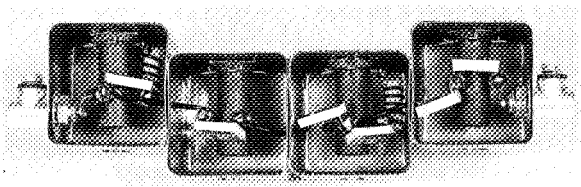

FIGURE 5–24.—Transmitter RF filter.

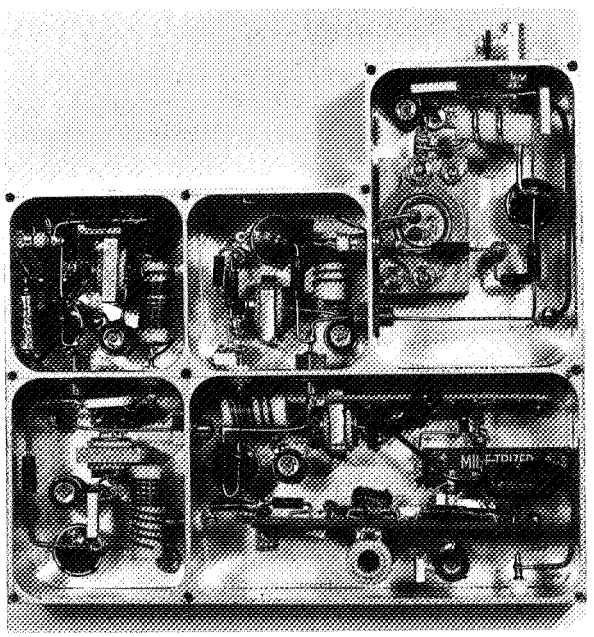

FIGURE 5–25.—Transmitter subassembly.

Power System

Power to the spacecraft electronics is provided by a solar cell array and two battery packs. Power control and regulator circuits include a shunt voltage limiter, a battery charging current limiter, a battery switching network, an undervoltage detector, a hold-off relay and turn-on plug, and several dc to dc converters.

Solar Cell Array

The solar cell array consists of four solar paddles (Fig. 5–26) arranged in a series-parallel matrix and furnishes 0.5 to 2 amperes at 15 volts, depending on the spacecraft aspect to the sun. The solar cells are p-n type silicon cells that perform as photoelectric converters. The cells are flat mounted, of gridded construction, and exhibit a high efficiency. While the

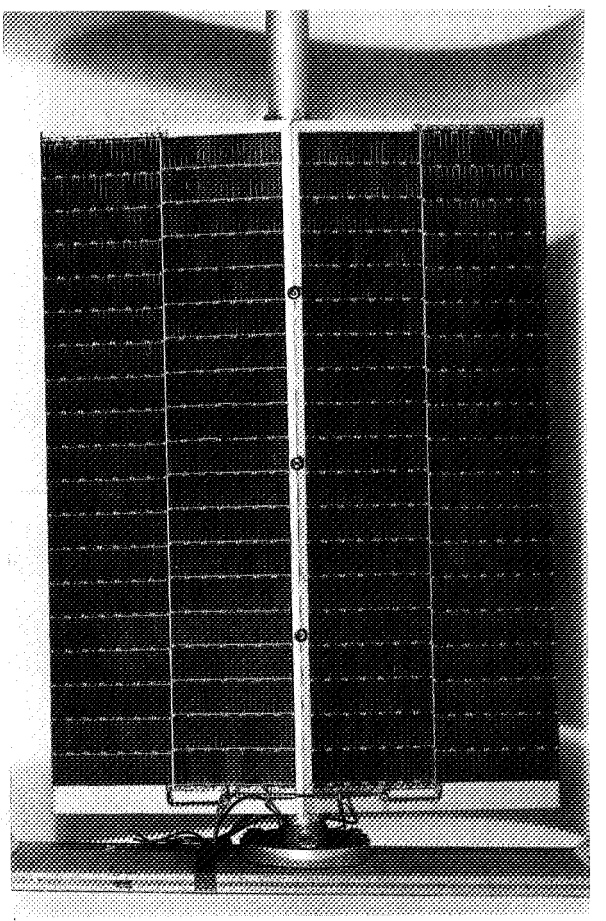

FIGURE 5–26.—Solar cell array.

spacecraft is orbiting in sunlight, the solar cells power all electronic subsystems on board the spacecraft and supply a charging current to the two battery packs.

Battery Packs

Each battery pack (Fig. 5–27) consists of ten individual cells connected in series. The cells are nickel-cadmium, sintered-plate type, hermetically sealed in a stainless-steel case. Each cell has a nominal potential of 1.3 volts. All ten cells have a nominal output of 13 volts.

Shunt Voltage Limiter

The shunt voltage limiter regulates the solar paddle output voltage to 14.5 volts. Excess power from the solar paddles is dumped through a pair of power resistors located on the arms that extend the solar paddles; the dumping is controlled by a pair of power control transistors.

Battery Charging Current Limiter

The battery charging current limiter (Fig. 5–28) regulates the battery charging current to a value not in excess of 0.5 ampere. This circuit prevents the generation of hydrogen in the batteries due to excessive charging currents.

Battery Switching Network

The battery switching network (Fig. 5–29) connects the battery with the highest voltage to operate the spacecraft. The other battery is connected to the solar cell array and receives a trickle charge from the array. When the voltage difference between the two batteries exceeds 1.2 volts, the standby battery is connected to operate the spacecraft.

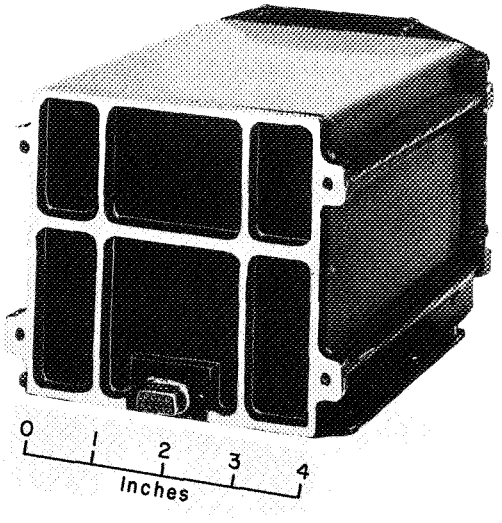

FIGURE 5–27.—Battery pack.

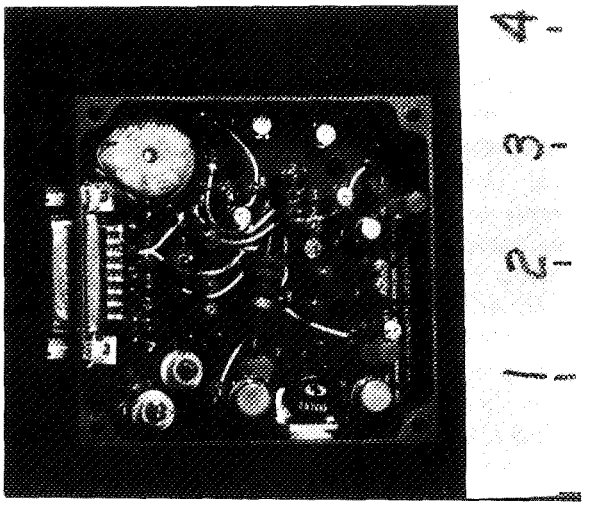

FIGURE 5–28.—Battery current regulator.

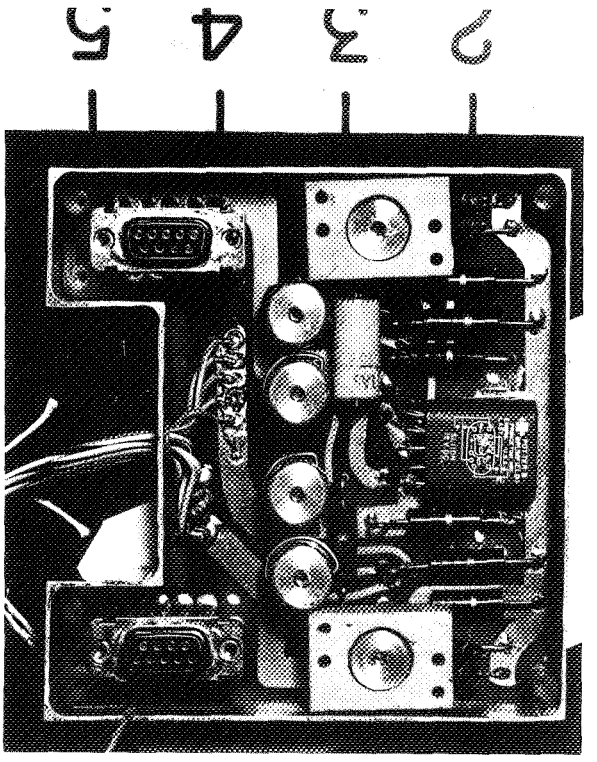

FIGURE 5–29.—Battery selector.

Undervoltage Detector

The undervoltage detector (Fig. 5–30) disconnects both battery packs from the spacecraft electronics when the output voltage of both batteries falls below the minimum acceptable level. The detector also activates a recycling timer which, after 18 hours, connects the battery output to the spacecraft electronics. During the 18 hours, the batteries are connected to the solar cell array and are charged. At the end of the 18-hour charging period, the batteries are connected to the spacecraft electronics. If, after this charging period, the batteries are still below the minimum acceptable level, the charging cycle is repeated.

Hold-Off Relay

The hold-off relay is controlled from the blockhouse and provides for turning the spacecraft power system *on* and *off* when the turn-on plug has been installed in the spacecraft. When the spacecraft is launched, the hold-off relay connects the battery to operate the spacecraft.

Dc to Dc Converters

The dc to dc converters supply the different dc voltage levels required to operate the spacecraft electronics. There are four converters in the power system: the prime converter, encoder converter, U.K. converter, and undervoltage detector converter.

The prime converter (Fig. 5–31) is connected to the main powerline at the output of the undervoltage relay. The outputs of this converter are +12 and −18 volts, regulated to ±11 percent at 80-percent efficiency. This converter supplies power to the transmitter, command receiver, programmer, encoder converter, and U.K. converter.

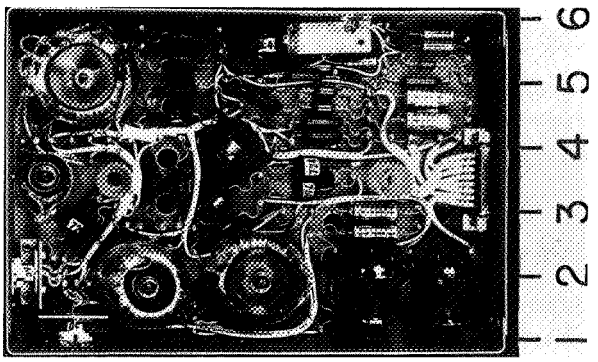

FIGURE 5–31.—Prime converter.

The encoder converter (Fig. 5–32) furnishes the +1.9, −4.0, −6.2, −2.7, and +6.7 volts to the encoder. The −2.7 volts is regulated to 0.25 percent; all the remaining voltages are regulated to ±5 percent. This converter has an efficiency of about 30 percent.

The U.K. converter (Fig. 5–33) supplies all power to the experiments. The output voltages are +6.5, +15, and −6.5 volts—all at ±5 percent; −9.0 volts at ±10 percent; 12 volts at −8 percent; −15 volts at ±7 percent; and 24 volts at ±8 percent. The overall efficiency is about 60 percent.

The undervoltage detector circuit converter (Fig. 5–34) is connected to the main powerline; this converter furnishes 15 and −18 volts, both at ±5 percent and at an efficiency of approximately 50 percent. This converter is disconnected from the batteries only when the hold-off relay is actuated.

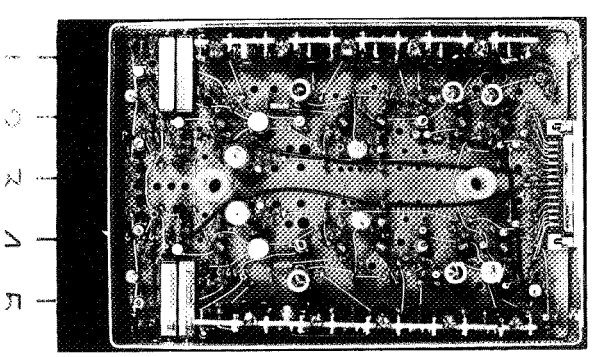

FIGURE 5–30.—Undervoltage detector.

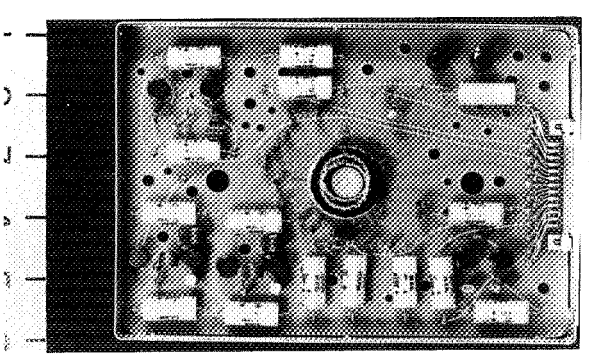

FIGURE 5–32.—Encoder converter

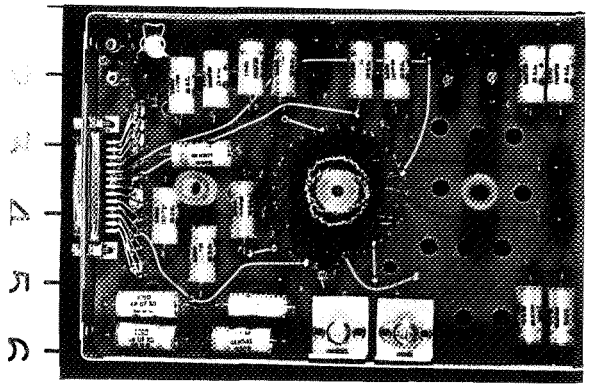

FIGURE 5–33.—U.K.–1 converter.

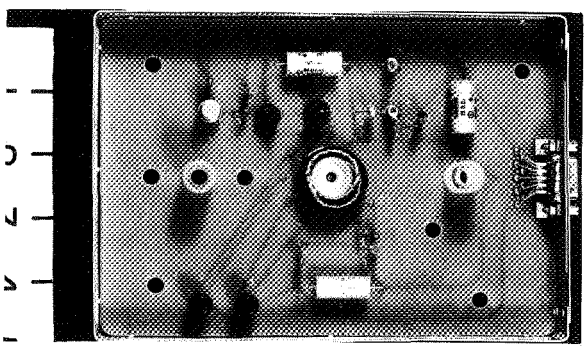

FIGURE 5–34.—Undervoltage detector circuit converter.

One-Year Timer

A 1-year timer (Fig. 5–35) incorporated in the spacecraft removes power from the transmitter at the end of 1 year. Two timers are used in a parallel redundant hookup. The timers employ an electrochemical de-plating process having a timing accuracy of ±10 percent.

Orbital Injection Programmer

The orbital injection programmer consists of a battery-operated electronic timing system. Its function is to program the events associated with the ignition and separation of the third stage. The orbital injection programmer is activated when the third-stage motor is ignited. At this time two pressure switches provide signals to start a 900-second timer. At the end of this timing period two pulses are applied to the silicon-controlled rectifier circuit, which in turn fires one pair of squibs. This time is designated t_1. The t_1 output from the 900-second timer starts a 60-second timer. At

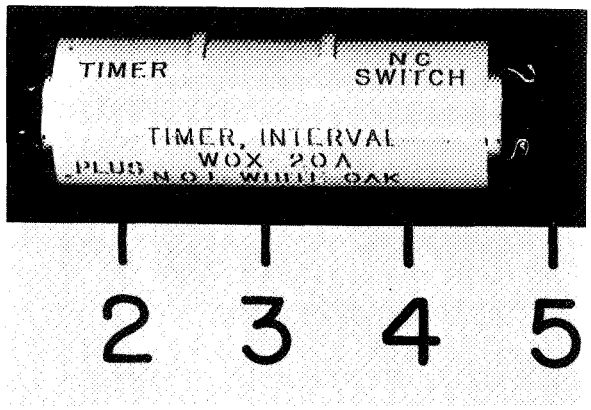

FIGURE 5–35.—One-year timer.

intervals of 60 seconds from time t_1, pulses are provided to the silicon-controlled rectifier circuit to fire three additional pairs of squibs. The times of these firings are designated t_2, t_3 and t_4. The orbital injection programmer is redundant throughout and is operated from two separate batteries. Failure of either programmer will not prevent the squib firing sequence from being completed. Accuracy of the timing cycles is 5 percent or better. The events at the squib firing times are: despin (t_1), boom release (t_2), paddle release (t_3), and separation (t_4). The three modules that make up this timer are shown in Figure 5–36.

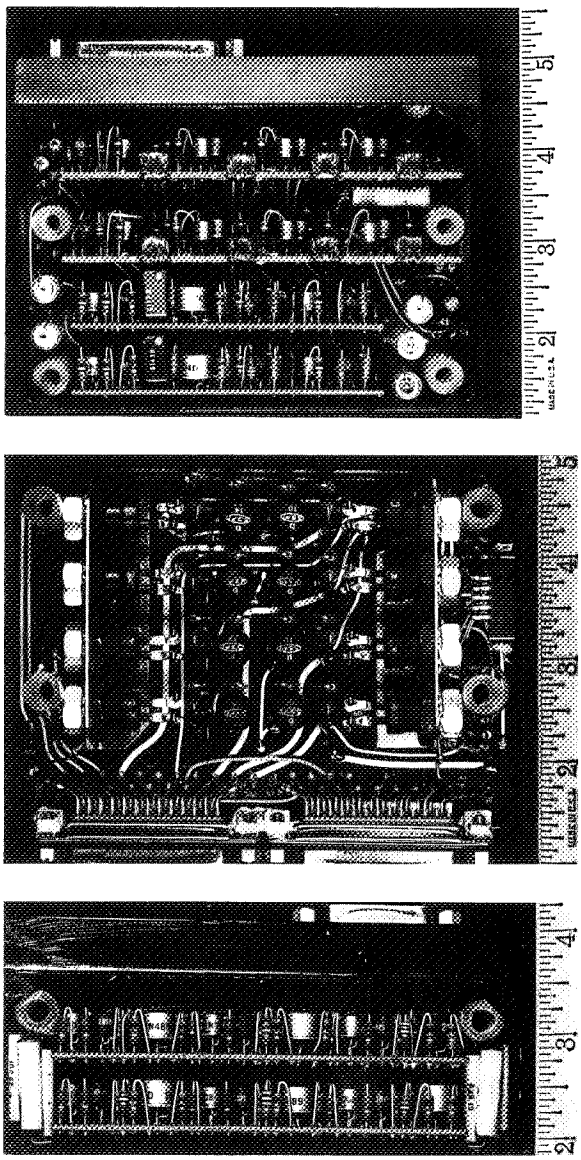

FIGURE 5–36.—Orbital injection programmer.

WIRE HARNESS

One of the early steps of the integration process was to plan the construction of the wire harness. The wire harness design was based on information from both the U.K. and the U.S. (GSFC) experimenters. This information included a wiring table listing the origin, function, and destination of each wire and the size, type, and color of each wire. All pin assignments were made by the individual experimenters and electronic subsystems designers.

Teflon-insulated wire was chosen for the harnesses on the basis that its outgassing properties were negligible. For all shielded leads, no. 22 shielded Teflon insulated wire was used. Test points were brought out to the turn-on plug to eliminate the need for separate test points. The number of test points brought out was limited to only those that were absolutely essential for checkout of the spacecraft. The solar paddle interconnections were facilitated by a mating 37-pin connector pair, with the common voltages bussed together on connectors at the solder-pot end of the contacts. This made it possible to remove the harness when the satellite was disassembled for inspection after tests. Also, the high voltage lines for the x-ray experiment were soldered and the joint encapsulated to eliminate the corona problem. To disassemble the x-ray detector from its associated printed circuit card, it was necessary to cut off the encapsulated solder joint in the high voltage (1600 volt) line.

Systems Integration

ELECTRONIC INTEGRATION TASK

Electronic integration of the subsystems was the responsibility of the Electronic Integration Group of NASA's Goddard Space Flight Center.

The task of integrating the subsystem included the molding of the subsystems into a compatible system, testing the system and evaluating the results, solving interface problems, and monitoring the spacecraft's signals until launch.

To successfully execute these tasks, the integration group had to (1) have a thorough knowledge of all subsystems (mechanical and

electronic), (2) design and fabricate a wiring harness, (3) design and fabricate a test stand for evaluating the performance of the spacecraft's electronics, and (4) originate test procedures for each electronic subsystem as well as for the integrated system.

ELECTRONIC INTEGRATION PLAN

Integration of the electronic subsystems required the cooperation and assistance of the experimenters in the United Kingdom and of many departments and branches at NASA's GSFC. Directly involved are the Project Managers (United Kingdom and United States), the U.K. experimenters, GSFC support subsystem designers, the GSFC Systems Integration Branch personnel, GSFC Data Systems personnel, the GSFC Environmental Test Facility personnel, and the vendors and suppliers.

The step-by-step plan for the integration of the Ariel I spacecraft subsystems was as follows:

1. To collect design and performance specifications for all electronic subsystems of the spacecraft.

2. To evaluate the subsystem specifications with the dual purpose of gaining knowledge of the subsystem operation and of designing a data processing system capable of monitoring the performance of all the electronic subsystems as an integrated electronic system within a reasonable time of 1 to 3 hours.

3. To obtain electronic subsystem wiring information for building a spacecraft wiring and test harness.

4. To build a power control panel to be used with the spacecraft wiring and test harness for integration and interference testing.

5. To design and build test panels for bench-testing the electronic subsystems as required.

6. To work out with the mechanical engineers, who assemble the spacecraft, any problems that may arise from wiring requirements (e.g., accessibility of connectors, holes in the spacecraft structure for routing of wires, supports, and tiedown fixtures for the wires).

7. To write a test procedure for the complete electronic system of the spacecraft from information and experience gained with electronic subsystems operated individually on the test bench.

8. To detect and assist in resolving problems due to electrical interference or incompatibilities between electronic subsystems as they are connected into the spacecraft.

9. To arrange with Test and Evaluation (T&E) Division, GSFC, to supply the exciters for the experiment sensors.

10. To arrange with T&E Division, GSFC, for the necessary wiring connections through the walls of the environmental test chambers.

11. To monitor the spacecraft performance as it undergoes all phases of integration testing, environmental testing, and launch site testing.

12. To report to the project coordinator and the subsystem designers all failures observed in an electronic subsystem during the three test phases specified in step 11.

PERFORMANCE EVALUATION

General

The task of the Ariel I Integration Group (GSFC) was to weld the electronic subsystems into an operational spacecraft. To accomplish this task, the Integration Group tested each subsystem to determine normal operating parameters, tested the integrated system for compatibility, and monitored the spacecraft performance during the environmental tests and launching.

For the convenience of presentation, the various test phases will be referred to as *integration* testing, *environmental* testing, and *launch site* testing.

Integration Testing

Integration testing consisted of developing bench test procedures for each subsystem, developing an overall system test procedure, connecting all subsystems to the wire harness and testing the spacecraft subsystems both individually and as an integrated operational spacecraft.

To develop and perform bench tests, the Ariel I Integration Group had to gather specifications information on operating char-

764-173 O—65——14

acteristics and input-output data for each subsystem. This was accomplished by using a wiring and test procedure checklist, which was distributed to the experimenters. The experimenters completed the checklists and returned them to the Integration Group. A bench test procedure for the cosmic ray experiment was developed from the data received from the experimenter. After approval by the experimenter, the procedure was circulated among all concerned as a guide for the development of the remaining bench test procedures.

Each subsystem, after proper bench testing, was installed in the spacecraft. Test points were incorporated in the wiring harness, and test cables connected these to a test stand. The test stand was used to check the compatibility of the integrated subsystems. Transients, power consumption, automatic controls, and operation of each subsystem were checked. If the results of any test were unsatisfactory, the Integration Group reported and sometimes recommended changes to correct the incompatibility. After much testing, redesign, and effort, the Integration Group developed a completely integrated electronic system. During this time the Integration Group developed the system test procedure.

Samples of spacecraft data sheets used during integration and environmental testing are shown in Figures 6–1 and 6–2.

Environmental Testing

The major objectives of the test program are twofold: (1) to determine the ability of the design to meet all performance requirements, and (2) to demonstrate the quality and dependability of the flight hardware. The first of these objectives is accomplished by qualification testing of prototype hardware. The reliability program and acceptance testing are directed toward the achievement of the second objective.

Qualification testing is conducted on the prototype spacecraft complete with simulated or prototype experiment, on the individual prototype experiments, and on prototype subassemblies. Qualification tests include environmental tests as well as tests that are entirely functional in nature. An environmental test has the following essential features: (1) preexposure examination and functional check, (2) exposure to environment, (3) functional check during or after exposure, and (4) postexposure examination.

Environments to which prototype items are subjected are sinusoidal and random vibration, acceleration, shock, static loading, humidity, temperature, and thermal vacuum. Hermetically sealed items are given a leak-detection test. The environments simulated by this series of tests are those expected to be imposed by storage, handling, transporation, prelaunch, boost, separation, and orbital flight.

In mechanical tests, the test levels are 1.5 times the maximum levels expected during transportation, handling, and launch.

In prototype temperature tests at atmospheric pressure and in thermal vacuum tests, temperatures above the maximum and below the minimum orbital operating temperatures are imposed on operating prototype items. In the thermal vacuum test, these temperature conditions are combined with space simulations at a vacuum of at least 1×10^{-5} mm Hg. Prototype items, while nonoperative, are exposed during the atmospheric temperature test to the maximum and minimum temperatures to which they could be subjected during storage and transportation. Humidity tests are performed as applicable. Equipment is designed to be operable between 0° and +50°C in orbital environment.

Acceptance testing, conducted on flight items, is limited to the environments of vibration, temperature, and thermal vacuum. The levels of test environment are no greater than the environments expected during launch and orbit.

Performance data developed throughout the course of the test program are used to the extent applicable for verification of reliability. Additional testing of components and subassemblies is conducted for the specific purpose of supporting the reliability program (References 14 through 17).

Launch Site Testing

Two complete ground stations, each consisting of two special telemeter radio receivers, were

TELEMETERED DATA OF EXPERIMENTS AND PARAMETERS

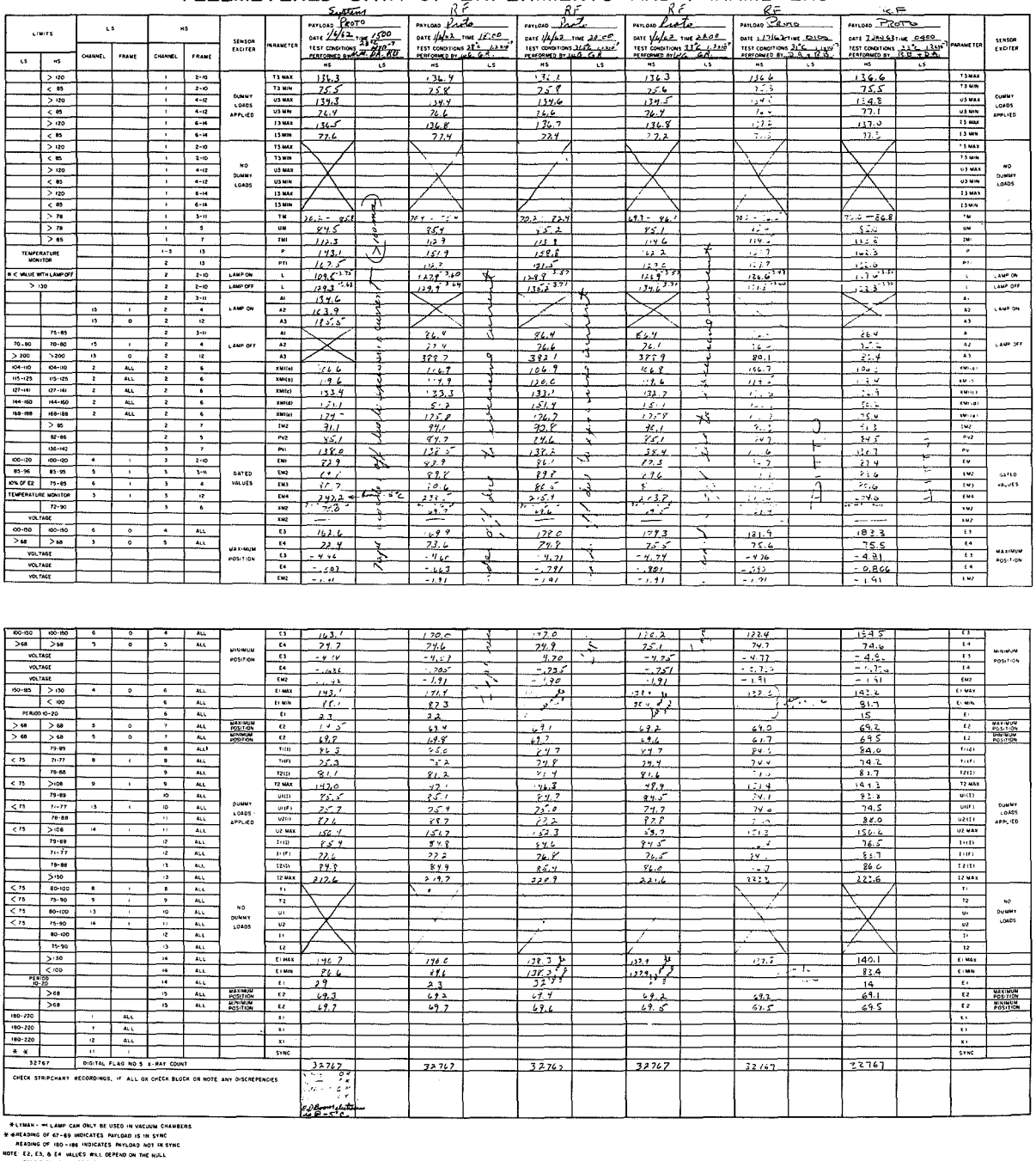

FIGURE 6-1.—Spacecraft data sheet used during integration and testing.

CONTINUOUS MONITOR OF GODDARD ELECTRONICS DURING TESTING

TEST				PAYLOAD ____ DATE ____ TIME ____ TEST CONDITIONS ____ PERFORMED BY ____	PAYLOAD ____ DATE ____ TIME ____ TEST CONDITIONS ____ PERFORMED BY ____	PAYLOAD ____ DATE ____ TIME ____ TEST CONDITIONS ____ PERFORMED BY ____	PAYLOAD ____ DATE ____ TIME ____ TEST CONDITIONS ____ PERFORMED BY ____	PAYLOAD ____ DATE ____ TIME ____ TEST CONDITIONS ____ PERFORMED BY ____	PAYLOAD ____ DATE ____ TIME ____ TEST CONDITIONS ____ PERFORMED BY ____
POWER SYSTEM CHECK	VOLTAGE	BATTERY A	CHARGE						
			DISCHARGE						
		BATTERY B	CHARGE						
			DISCHARGE						
	SYSTEM VOLTAGE (DUMPING RESISTORS)								
	CURRENT	BATTERY A	COMMAND						
			NON-COMMAND						
		BATTERY B	COMMAND						
			NON-COMMAND						
	POWER DRAIN ON BATTERIES		COMMAND						
			NON-COMMAND						
	VOLTAGES	U K CONVERTER	+6.5 V						
			-6.5 V						
			-9 V						
			+12 V						
			-15 V						
			+24 V						
		PRIME CONVERTER	+12 V						
			-18 V						
		PROGRAMMER CONVERTER	+15 V						
TRANSMITTER CHECK	TRANSMITTER POWER								
	TRANSMITTER FREQUENCY								
ENCODER CHECK	CHECK IF PAYLOAD IS IN SYNC								
	Ā - HS COUNT								
	Ō - LS COUNT								
	HS DIGITAL OSCILLATOR PERIODS CHANEL 0		FRAME 0 (1191.4 - 1976)						
			FRAME 1 (220.9 - 223.4)						
			FRAME 2 (175.6 - 181.6)						
			FRAME 3 (220.9 - 223.4)						
			FRAME 4 (157.8 - 163.6)						
			FRAME 5 (220.9 - 223.4)						
			FRAME 6 (140.9 - 146.7)						
			FRAME 7 (220.9 - 223.4)						
			FRAME 8 (122.2 - 127.4)						
			FRAME 9 (220.9 - 223.4)						
			FRAME 10 (105.6 - 110.6)						
			FRAME 11 (220.9 - 223.4)						
			FRAME 12 (86.7 - 92.1)						
			FRAME 13 (220.9 - 223.4)						
			FRAME 14 (68.5 - 72.9)						
			FRAME 15 (220.9 - 223.4)						
	LS DIGITAL OSCILLATOR PERIODS CHANEL 0		FRAME 0 (220.9 - 223.4)						
			FRAME 1						
			FRAME 0 (220.9 - 223.4)						
			FRAME 1						
BATTERY SWITCHING TEST	INITIAL VOLTAGE ON EXT POWER SUPPLY A								
	INITIAL VOLTAGE ON EXT POWER SUPPLY B								
	VOLTAGE ON A TO SWITCH TO B								
	VOLTAGE ON B TO SWITCH TO A								
	BATTERY SWITCHING DIFFERENTIAL (VOLTS)								
SHUNT REGULATOR TEST	VOLTAGE AT BATTERY TO CAUSE DUMPING								
	CURRENT IN RIGHT RESISTOR (ma)*								
	POWER DISSIPATION IN RIGHT RESISTOR (mw)								
	CURRENT IN LEFT RESISTOR (ma)*								
	POWER DISSIPATION IN LEFT RESISTOR (mw)								
	TOTAL CURRENT IN DUMPING CIRCUIT (ma)								
	TOTAL POWER DISSIPATED IN DUMPING CIRCUIT (mw)								
	TOTAL CURRENT INPUT TO SATELLITE (ma)								
TAPE RECORDER PLAYBACK	PROGRAMMER BACK UP TIMER COUNT								
	PLAYBACK BLANK PERIODS (63.8 - 65.3)								
UNDER VOLTAGE TEST	VOLTAGE AT BATTERY CAUSING UNDER VOLTAGE								
	UNDER VOLTAGE COUNT (SPEED UP)								
	UNDER VOLTAGE COUNT (NORMAL 18 HOURS)								

* RESISTOR VALUES ARE 10 OHMS

FIGURE 6–2.—Sample spacecraft data form.

used to monitor the spacecraft performance at the launch site. The main station was trailer-mounted, and the backup station was placed in hangar AE at the Atlantic Missile Range. The backup station was operated in parallel with the main station during testing.

The special telemeter radio receivers were fed by two 136-megacycle preamplifiers connected to a nine-element yagi antenna. A frequency counter and signal generator were used to measure the spacecraft transmitter frequency.

Launch site testing included a complete system test of the spacecraft in the trailer upon arrival at Cape Canaveral, Florida. All other tests were exclusively by RF link from the spin facility and launch pad gantry. Each test or checkout included a complete analysis of test data.

Several practice runs of the final pre-launch countdown were performed.

DESCRIPTION OF TEST STAND

The performance evaluation test stand is pictured in Figure 6–3 and is shown in block

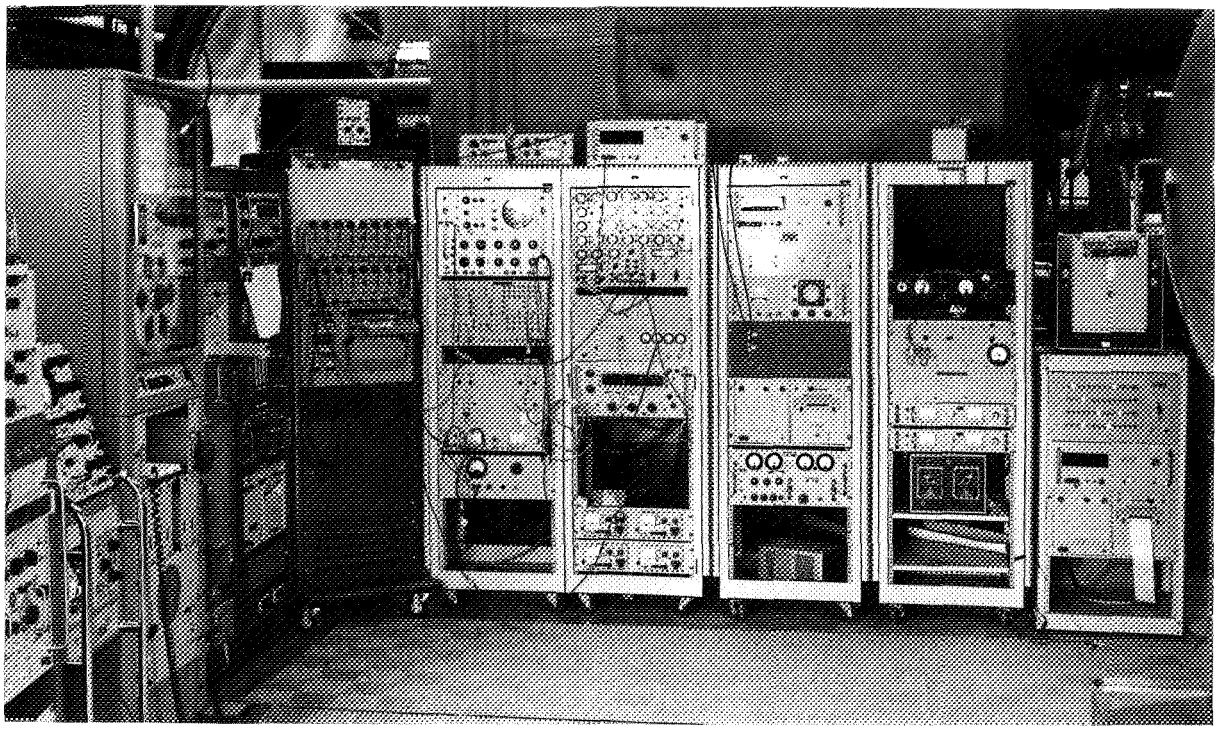

FIGURE 6–3.—Ariel I test stand, front view.

diagram form in Figure 6–4. This equipment can be classified into functional groups as follows: (1) power control system, (2) RF system, (3) sensor exciter panel, (4) data reduction system, and (5) data recorders.

Power Control System

This system simulates the power output, internal impediance of the solar array, and the sunlight/darkness cycling that the spacecraft will experience in orbit. The internal impedance and power output of the solar array is simulated by a 17.5-ohm resistor in series with a 30-volt power source, arranged as shown in Figure 6–5. The resistor and power supply form the Thevenin equivalent of the solar array and produce the same voltage and current as that of the array. The diode, connected between the resistor and the timer, prevents reverse current from flowing through the power supply from the spacecraft battery system should the power supply voltage accidentally fall below the battery voltage. Throughout the testing phase, the spacecraft was powered electrically by the solar array simulator.

The recycling timer is on for 60 minutes and off for 40 minutes; this simulates the least favorable sunlight-to-darkness ratio expected during the 100-minute orbit.

During the prototype tests a meter panel was used to measure the voltages and currents used by each subsystem (Figure 6–4). Each current meter is shunted by a shorting switch; this enables the operator to insert or remove the meter from the circuit. Individual current meters were used for each line that was monitored. A single voltmeter was switched to the voltage point to be measured. The voltage readings were normalized by placing a miniature potentiometer at each voltage test point, and the potentiometers were adjusted so that the voltmeter would show a midscale indication if the voltage was correct—which permits rapid voltage checking. Each power line to a subsystem was switch-controlled from the meter panel; this facilitated deactivation of individual subsystems. Also, each power converter was monitored at the input and switch-controlled at the output; this made it possible to remove any converter from its load and switch in external

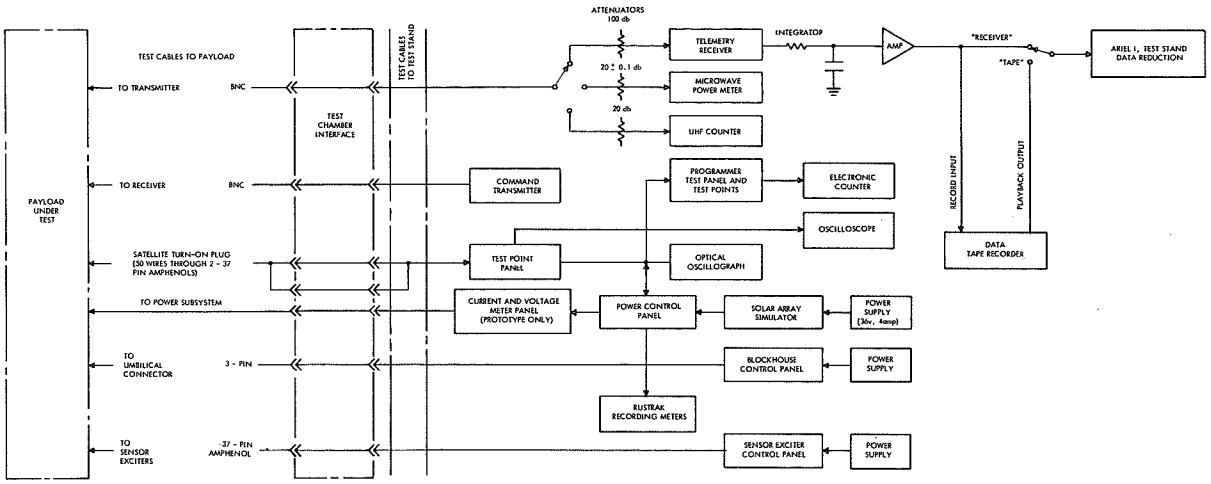

FIGURE 6–4.—Block diagram of test stand.

power. These switching arrangements greatly simplified many tests.

RF System

The RF system receives and demodulates the RF signal from the transmitter, measures transmitter power and frequency, and presents an RF load to the transmitter and the command receiver. The RF system consists of a simulated command transmitter, an RF power monitor, a UHF counter, and a special-purpose telemeter radio receiver. The simulated command transmitter consists of a crystal oscillator followed by an amplitude-modulated RF stage. The modulating signal is generated from an L–C audio oscillator, adjusted to the command subcarrier frequency. The total power output from the transmitter is about 80 milliwatts. At the launch site it was necessary to build a power amplifier (low decibel gain) to boost the power output, because the spacecraft was several miles from the test stand.

Sensor Excitor Panel

This panel provides artificial stimulation to the aspect sensor, the electron density sensor, and the Lyman-alpha sensors. The aspect stimulator is a transistor driver relay circuit that intermittently illuminates three flashlight bulbs. The flash rate and flash separation of the bulbs corresponds to a specific spin and

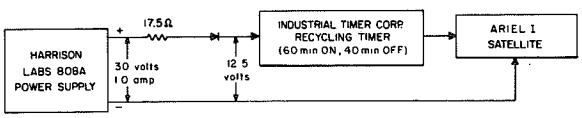

FIGURE 6–5.—Block diagram of solar cell array simulator.

aspect angle. The electron-density stimulato- consisted of an 8-inch plastic disk with a pier shaped piece of brass shim stock attached to it; this was mounted on the electron density boom and rotated by a 1-rpm synchronous motor. Two notches on the rim of the disk enabled a microswitch, with a roller-cam follower, to position the disk in one to two positions: (1), maximum proximity between brass and plates, and (2) minimum proximity between brass and plates. This is illustrated in Figure 6–6.

The Lyman-alpha sensor excitor consists of a hydrogen-discharge tube and a high-voltage power supply. The discharge tube was used in the vacuum chamber and illuminated one of the Lyman-alpha sensors. The Lyman-alpha line (for ultraviolet light) is readily absorbed in air by water vapor and can travel only a few millimeters.

The X-ray sensor, the cosmic ray sensor, and the electron temperature probes were not excited from the sensor excitor panel. A 50-millicurie source of iron (Fe55) was used to provide 5-kilovolt X-rays. A radioactive source was used to excite the cosmic ray experiment.

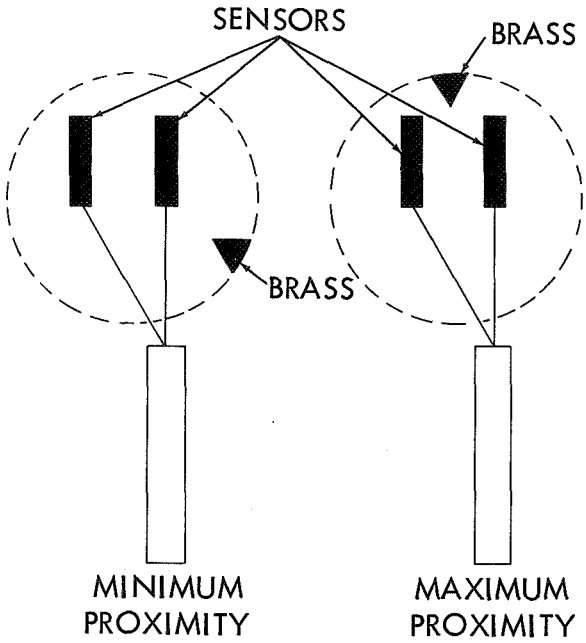

FIGURE 6–6.—Electron density boom excitor.

A diode-resistor dummy load was applied to the electron temperature probe sensors to simulate free electrons with a specific average energy.

Data Recorders

An instrumentation data magnetic tape recorder was used to record the complete demodulated RF from the spacecraft.

Printers in the Ariel I test stand data reduction system provided printed records of test stand data output.

TEST-STAND TELEMETER DATA REDUCTION SYSTEM

The Ariel I Integration Group (GSFC) performed a study on the decoding equipment requirements. The Data Systems Division of GSFC developed and supplied the system (Fig. 6–7). The requirements and development of this system are discussed herein.

The telemetered RF signal goes through a phase modulation receiver, a tracking filter, and into the PFM decoder, etc.

The input to the decoder is a series of pulses in the frequency range from 4.5 to 15.4 kilocycles. The length of the pulses is 10-milli-

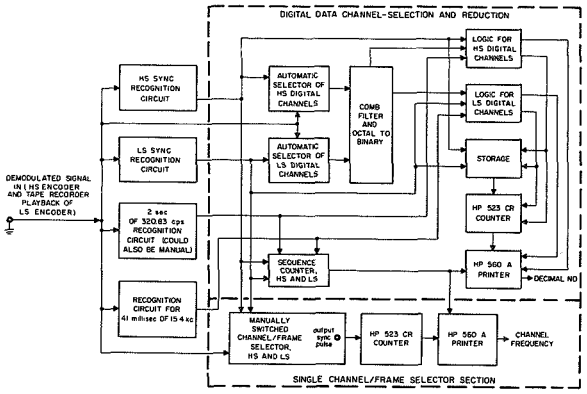

FIGURE 6–7.—Test-stand data reduction system.

second duration, and the pulses are separated by 10 milliseconds except for the frame sync pulses, which last for 15 milliseconds and are preceded by a space of 5 milliseconds. The frame sync pulses, in addition to being coded by an additional millisecond of pulse width, are also coded in frequency as listed in the following charts.

Channel zero in each frame for both HS and LS encoders is used for frame sync pulses. All

Frame Sync Pulses

High-speed encoder		Tape recorder playback of low-speed encoder	
Channel 0, frame	Frame sync pulse frequency (cps)	Channel 0, frame	Frame sync pulse frequency (cps)
0	4, 500	0	4, 500
1	5, 140	1	
2	4, 500		
3	5, 600		
4	4, 500		
5	6, 230		
6	4, 500		
7	6, 960		
8	4, 500		
9	8, 015		
10	4, 500		
11	9, 250		
12	4, 500		
13	11, 190		
14	4, 500		
15	14, 120		

the remaining channels are either digital data channels or analog data channels. The pulse frequency of the analog data channels varies from 5 to 15 kilocycles. The pulse frequency for the digital data channels will be one of the following eight values.

Digital Data Channel Pulses from HS Encoder and Tape Recorder Playback of LS Encoder

Binary bit input to digital oscillator	Frequency (cps)
0 0 0	5, 140
0 0 1	5, 600
0 1 0	6, 230
0 1 1	6, 960
1 0 0	8, 015
1 0 1	9, 250
1 1 0	11, 190
1 1 1	14, 120

General Requirements for Test-Stand Data Reduction Equipment

The HS and LS encoders are synchronized and the data from the two encoders are related. Since the data from the two encoders are transmitted at different times, it is necessary to reconstruct the time relation.

It was therefore required that, in addition to other requirements, the test-stand data reduction equipment have a four-place decimal counter to count each encoder sequence (HS or LS), independently of whether or not a data print-out occurred during the sequence.

Significance of Digital Data Channels and the Required Reduction and Presentation of Their Data

The cosmic ray and x-ray experiments have HS encoder digital data channels.

Cosmic Ray Experiment

The cosmic ray experiment has two separate binary counters. Binary counter no. 1 has HS encoder channels C_1(1–0) (1–8); C_2(2–0) (2–8); C_3(3–0) (3–8); and C_4(1–1) (1–9), which represent binary bits (2^1, 2^2, 2^3); (2^4, 2^5, 2^6); (2^7, 2^8, 2^9); and (2^{10}, 2^{11}) respectively. This is shown in Figure 6–8a.

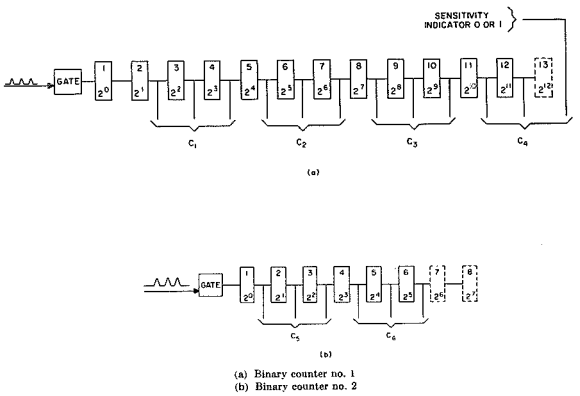

FIGURE 6–8.—HS encoder digital data channel connections.

In particular it should be noted that the most significant binary bit of C_4, called "Sensitivity Indicator 0 or 1," does not come from counter no. 1 and thus should be treated as a separate piece of data. In addition, the binary number stored in counter no. 1 is two times the number represented by C_1, C_2, C_3, and C_4 because binary 2^0 is not one of the digital data inputs.

Binary counter no. 2 has HS encoder channels C_5(2–1)(2–9) and C_6(3–1)(3–9), which represent binary bits (2^0, 2^1, 2^2) and (2^3, 2^4, 2^5) respectively. This is shown in Figure 6–8b.

In the experiment, "Sensitivity Indicator 0 or 1" indicates the sensitivity of the discriminator that sends pulses to counter no. 2, and so it is desirable to print "Sensitivity Indicator 0 or 1" and the number stored in counter no. 2 adjacent to each other.

Binary counter no. 1 also has LS encoder digital data channels C_1(8–0), C_2(9–0), C_3(10–0), and C_4(11–0), which represent binary bits (2^3, 2^4, 2^5); (2^6, 2^7, 2^8); (2^9, 2^{10}, 2^{11}); and (2^{12}, 2^{13}) respectively. This is shown in Figure 6–9a.

In particular it should again be noted that the most significant binary bit of C_4, called "Sensitivity Indicator 0 or 1," does not come from counter no. 1 and thus should be treated as a separate piece of data. In addition, the binary number stored in counter no. 1 is four times the

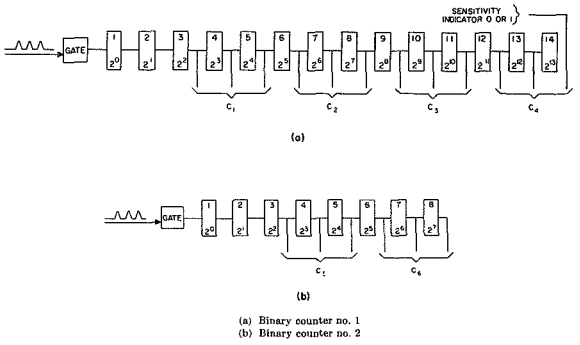

FIGURE 6–9.—LS encoder digital data channel connections.

number represented by C_1, C_2, C_3, and C_4 because binaries 2^0 and 2^1 are not used as digital data inputs.

Binary counter no. 2 has LS encoder channels $C_5(14–0)$ and $C_6(15–0)$, which represent binary bits $(2^3, 2^4, 2^5)$ and $(2^6, 2^7, 2^8)$ respectively. This is shown in Figure 6–9b.

In the experiment, "Sensitivity Indicator 0 or 1" indicates the sensitivity of the discriminator that sends pulses to counter no. 2, and so it is desirable to print "Sensitivity Indicator 0 or 1" and the number stored in counter no. 2 adjacent to each other.

X-Ray Experiment

The X-ray experiment has one 15-stage binary counter. HS encoder channels $X_1(2—14)$ $X_2(3—14)$, $X_3(1—15)$, $X_4(2—15)$, and $X_5(3—15)$ represent binary bits $(2^0, 2^1, 2^2)$, $(2^3, 2^4, 2^5)$, $(2^6, 2^7, 2^8)$, 2^9, 2^{10}, 2^{11}), and $(2^{12}, 2^{13}, 2^{14})$ respectively. This is shown below in Figure 6–10.

General Requirements

All numbers are to be converted to decimal before print out. Each decimal number is to be identified as to the experimental data it represents. It will be sufficient to print out the number stored in one counter of one experiment for each HS or LS encoder sequenec and to have a switch that will select which counter store will be printed. This means it would be sufficient to print $C_1(1—0)$, $C_2(2—0)$ $C_3(3—0)$, $C_4(1—1)$ as one number per HS encoder sequence; $C_5(2—1)$, $C_6(3—1)$, and "Sensitivity Indicator 0 or 1" of $C_4(1—1)$ as one number per HS encoder sequence; $C_5(2—9)$, $C_6(3—9)$, and "Sensitivity Indicator 0 or 1" of $C_4(1—9)$ as one number per HS encoder sequence; $X_1(2—14)$, $X_2(3—14)$, $X_3(1—15)$, $X_4(2—15)$, and $X_5(3—15)$ as one number per HS encoder sequence; and $C_1(8—0)$, $C_2(9—0)$, $C_3(10—0)$, and $C_4(11—0)$ as one number per LS encoder sequence. Each encoder sequence is to be counted and its number printed whenever a decimal number is printed from any of its channels.

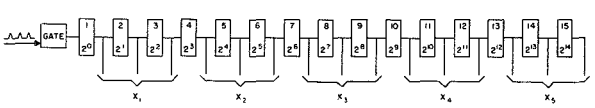

FIGURE 6–10.—X-ray binary counter.

Significance of HS and LS Encoder Analog Data Channels and the Required Reduction and Presentation of Their Data

Analog data channels are exactly what their name implies. The only reduction required for these channels is to count the frequency of the pulse. The presentation required is a print out of pulse frequency, data channel identification, and number of encoder sequence during which the frequency pulse occurred.

It would be sufficient if the selectivity of the "Single Channel/Frame Selector Section" were limited to selecting 1 of 16 channels to be printed once for every frame of the encoder sequence. The fact that this arrangement would print the pulse frequency of any digital data channels that happen to be in the column of selected channel "X" is not a drawback, since it will allow for checking the digital oscillator pulse frequency for any drift that might begin to occur. The same considerations apply equally well to frame sync channel 0.

For channels 1, 2, and 3 the channel of interest may occur only once per HS encoder sequence, and the rest of the printout is an inconvenience. However, for channels 0 and 4 through 15 the printout for each frame is a distinct advantage. In the case of the LS encoder data this type of selection is acceptable with no particular advantages or disadvantages.

It was also required that an "output sync pulse" be made available on one "Output Sync Pulse" terminal. It has one distinct output at the time of Channel 0, frame 0 (0—0) at the beginning of each encoder (HS or LS) sequence. It also has another distinct output that will occur during the time of telemetering of the channel selected for printout.

These pulses are for marking one channel of a strip chart recorder. Another channel of the strip chart recorder is connected by a wire to a test point in the satellite that monitors the voltage input to the encoder oscillator. The "Output Sync Pulses" will thus (1) identify the beginning of each encoder sequence and (2) mark that portion of the test point trace during which telemetering took place. Thus, the performance of the encoder oscillator may be checked at the same time that performance of an experiment parameter is being checked.

Correlation of HS Encoder Data with LS Encoder Data

If an auxiliary tape recorder is used to record the demodulated playback of the satellite tape recorder, the matter of correlation of HS and LS encoder data becomes a "straightforward" procedure. It consists of the following steps:

1. Operate the satellite for a little over 1½ hours while the HS encoder digital channel data on one printer and the selected channels "X" on the other printer are being recorded.

2. Arrange for the switch that initiates the RF command signal to the satellite to also put the auxiliary tape recorder into the record mode. Operate the switch, and record the 2 seconds of 320.83-cps signal and the full playback of the tape recorder, which must include the 41 milliseconds of 15.4-kilocycle time marker.

3. Rewind the auxiliary tape recorder and play it back while obtaining digital data on one printer and selected channel "X" data on the other printer. Repeat 16 times, once for each column of channels.

4. Correlate the data by counting back six sequences from the 320.83-cps time mark on the HS encoder data records for each sequence counted back from the 15.4-kilocycle time mark on the LS encoder data records.

Tracking and Data Acquisition

The Ariel I International Ionosphere Satellite was launched from Cape Canaveral, Florida by a Thor-Delta vehicle and was placed into a near-earth elliptical orbit having an apogee of 1214 kilometers (754 statute miles, 655 nautical miles), a perigee of 390 kilometers (242 statute miles, 210 nautical miles), an inclination of 55 degrees, and an anomalistic period of 99 minutes. (On board the satellite is a single PFM–PM telemeter with a power output of 250 milliwatts. This telemetry system is being used by the Minitrack network for tracking and data acquisition.)

Tracking

Tracking is the sole responsibility of the South Atlantic and Singapore Stations and the Minitrack network, during the active lifetime of the satellite, with the exception of the early orbit determination phase. A preliminary orbit was computed, based on nominal radius and velocity injection vectors; and an analysis of this orbit indicated that insufficient Minitrack tracking data would be obtained during the first 12 hours of operation to define the satellite's orbit. For this reason, outside tracking support was required.

The overall tracking picture is very good. An analysis of the first two weeks of operation for the Ariel I satellite has shown that sufficient tracking will be available to accurately compute and continually update the orbit. Ariel I is tracked by the following stations under GSFC control:

Antofagasta, Chile, S.A.
Blossom Point, La Plata, Md., U.S.A.
Lima, Peru, S.A.

Quito, Ecuador, S.A.
Santiago, Chile, S.A.
Johannesburg, South Africa
Woomera, Australia
Fort Myers, Fla., U.S.A.
St. Johns, Newfoundland
East Grand Forks, Minn., U.S.A.
Winkfield, England

In addition, the South Atlantic and Singapore stations track and record the satellite telemetry.

Data Acquisition

The Ariel I satellite utilized a PFM–PM telemetry system having a power output of 250 milliwatts. A signal-to-noise analysis of the telemetry system had shown that it could be adequately handled by the Minitrack Mod I Telemetry Acquisition System. Performance of the Mod I system with Ariel I has substantiated this investigation.

A block diagram illustrating the acquisition system is shown in Figure 7–1. The following system parameters were utilized:

1. Antenna polarization—linear
2. Dual channel preamplifiers—136.500 Mc
3. Mod I telemetry receivers
   Frequency:
   Receiver A—136.410 Mc
   Receiver B—136.410 Mc
   Inputs:
   Receiver A—output of vertically polarized antenna system
   Receiver B—output of horizontally polarized antenna system
   Operation—AGC mode

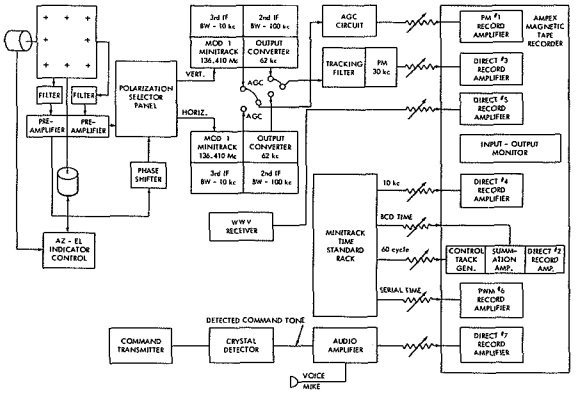

FIGURE 7–1.—Data acquisition system.

   Bandwidth (2nd IF)—100 kc
   Output converter—62-kc center frequency
   Output converter oscillator—3.312 Mc, ±20 cps
4. Tracking filter:
   Input—62-kc output of Mod I receiver having highest signal level
   AGC—fast
   Phase modulation output—detected 5 to 15 kc
   Phase modulation filter—30 kc
   Tracking loop bandwidth—Not less than 25 cps
5. Minitrack timing signals:
   Standard frequency—10 kc
   Time—Serial and binary coded time
   Precision clock drive—60 cps
6. Magnetic tape recorder track assignments—see table below

Track	Record amplifier	Source	Signal
1	FM	AGC circuit	AGC.
2	Direct	Control track generator and data input (Minitrack).	60 cps, 70% AM on 18.24-kc carrier; BCD time.
3	Direct	PM output of tracking filter	5 to 15 kc detected signal.
4	Direct	Minitrack	10 kc standard.
5	Direct	WWV receiver	WWV time.
6	PWM	Minitrack	Serial coded time.
7	Direct	Audio oscillator	Voice and command time.

7. Magnetic tape recorder tape speeds:
   FR–100—15 in./sec
   FR–600—7½ in./sec

The satellite telemetry acquisition requirements are such that real-time data are required as much as is possible and playback data are required once per orbit. There will be no problem in fulfilling the first of these requirements. The Spacecraft and Network Control Groups will schedule telemetry acquisition periods in accordance with the priority established for the Ariel I spacecraft, and real-time data will be obtained as often as is operationally possible.

The requirement that the satellite tape recorder be played back once per orbit may not be fulfilled 100 percent of the time. This is due primarily to the fact that each day there will be a 4- to 5-hour period during which no contact is available with the satellite. It is anticipated that these quiescent periods will be covered by the South Atlantic station but, since continuous contact with this station is not available, the effectiveness of this station's operation will not be known except on a post-facto basis. Another area of difficulty may be interference with other satellites. All efforts will be made to schedule interrogations on a noninterference basis, but there may be times when interference is unavoidable.

DATA HANDLING

General

Magnetic tapes of Ariel I telemetry data will be supplied the United Kingdom by the NASA Goddard Space Flight Center with the following general characteristics:

1. Two types of tapes will be supplied: high speed data tapes, and low speed data tapes.

2. Tapes will be digital and in standard IBM binary-coded decimal format.

3. Even parity and low density (200 characters/inch) will be used.

4. Each tape will have been checked for time consistency, and inconsistencies will be appropriately flagged on the tape. In addition, a print-out of the number of time inconsistencies and data word dropouts will be supplied with each tape.

5. Each tape will contain a number of files; the first record in each file will be an identification record.

The system that will be used for processing the data from Ariel I is shown in Figure 7–2. The equipment was designed to handle all telemetry formats of this general category (PFM). The elements of the system are the Tape Converter—Comb Filter, PFM Digitizer—Computer Format Control Buffer, High Speed Line Printer, and CDC–160 Data Processor. The output digital tapes will be used by the GSFC Computer Operations Branch personnel to merge the data with the orbital information in the IBM 7090 computer.

Tape Converter—Comb Filter

This portion of the system is designed to recover the telemetry signal in the presence of noise by utilizing the comb filter for signal-to-noise improvement and to recover the burst rate for use in synchronization. The comb filter has 120 filters equally spaced across the used frequency band with their response curves intersecting at the 3-decibel points. Integral logic permits determination of which filter is responding and allows electronic removal of all other filters. In this way sufficient resolution is obtained to permit the filter to function directly as the frequency measurement device. This design assumes that a single frequency exists in each burst. Some departure from this condition can be tolerated. However, experience on Explorer VIII shows that care must be taken to eliminate, or at least minimize, the switching transient effects on the oscillators in the payload encoder if the signal-to-noise improvement possible with the comb filter is to be utilized. This equipment will also provide a burst-blank envelope as well as a linearizing frequency and time code derived from the original telemetry tape.

PFM Digitizer—Computer Format Control Buffer

This equipment will utilize the outputs of the above equipment in such a manner as to establish synchronization, encode the 120 lines from

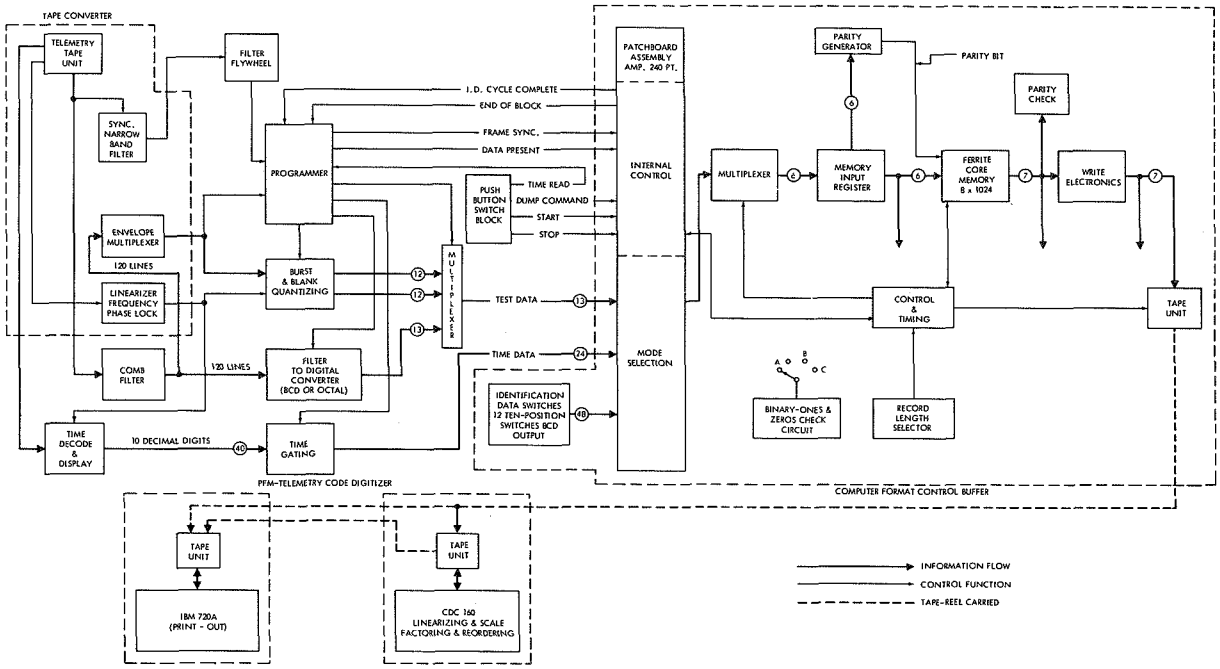

FIGURE 7-2.—PFM–PWM to tape conversion system.

the comb filter, and multiplex the frequency data with the time code. Time is stored from the time decoder when a frame sync occurs. The output of the Format Control Buffer is a digital magnetic tape in IBM binary-coded decimal format suitable for further processing by computer or off-line printer. The frequency data will appear as a number between 0 and 119 in the case of analog channels, and as a number between 0 and 7 in the case of digitally encoded channels. In the latter case this permits retention of the original bit configuration so that a full digital word can be accumulated visually on print-out or by the computer.

High-Speed Line Printer

The digital magnetic tapes prepared on the Format Control Buffer can be printed on this device. A full data print-out in terms of the telemetry and system units with 1 frame per line plus time of the sync pulse will result. Printing of selected sections of the full format can be provided after a simple operation in the off-line data processor.

CDC-160 Data Processor

The CDC-160 Data Processor is a small, transistorized, stored-program digital computer with magnetic tape and control equipment. The output magnetic tapes from the above equipment can be used as an input. Programs are available to decommutate, edit, accumulate, and record the data and provide digital magnetic tapes for further use as required.

DATA PROCESSING

Editing—Quick Look

The station telemetry tapes containing a 100-kilocycle standard frequency, Minitrack time code, telemetry signal, etc. will be received by the GSFC Data Systems Design Branch for editing and storage. Each tape will be reviewed for quality and quantity of usable data and will be checked against expected station performance. A summary of tapes by station will be maintained as a central input for station operation and as a guide for processing. It is anticipated that three categories of tapes will be stored: (1) unusable tapes resulting from

inadequate signal-to-noise ratio, interference, or operator error; (2) questionable tapes requiring extra handling to recover the data; and (3) good tapes of sufficient quality to warrant immediate machine processing. The first class of tapes will be retained for archival purposes and possible exploitation as the state of the art is advanced. The remaining two categories will be processed through the system described. The specific handling will depend on the quality of the recorded signal. The criterion will be the reliability of sync determination as the digital magnetic tapes are made.

Good Tape

These tapes are characterized by a good signal-to-noise ratio and consequently a high reliability of sync determination as mentioned above. This condition will permit preparing the digital format around the known sync location so that a full data print-out can be made immediately without calibration or linearization, data sequence correction or grouping, or error correction and removal. The frequency information will appear as previously described. Calibration information will be provided. This method will permit a quick look at the data. Further processing will be accomplished in the CDC–160 Data Processor. It will accept the magnetic tape prepared with time. The data will be placed on magnetic tape in a form suitable for printing on an IBM line printer. The output will be 1 frame per line, columnized by channels with one column for time. Identification data will be inserted as the first record of each digital magnetic tape. It will include day of the year, station number, experiment number, and analog tape number. This information will be printed at the top of each page. It is anticipated that only selected portions, not the bulk of data, will be printed.

Questionable Tapes

The extra handling is a direct result of poor signal-to-noise ratio. In this case, special processing and handling will be necessary. This is very time-consuming and hence costly, and should be avoided when possible. Adequate signal-to-noise is the best answer.

Digitizing and Format

Basic Format

Data on both types of tapes will be arranged (in order of decreasing length on tape) into files, records, frames, words, and characters.

1. *File.* A file will constitute data received from a single pass over a tracking station and will correspond to data taken from one analog tape recorded at the station. End-of-file records will be used to separate files, and these records will consist of a 3½- to 8-inch gap followed by a tape mark (0 0 0 1 1 1 1, for the track sequence C B A 8 4 2 1). The tape mark will be followed immediately by a longitudinal even-parity check character. The number of records in each file will vary depending on the length of the pass and the type of data: low speed, or high speed.

2. *Record:* A record will consist of a number of telemetry frames, where a frame is defined to be the interval between synchronization pulses. Identification records will also be used. The number of frames in each record will depend on the type of data (high or low speed), and is described in detail below. Immediately following the last character in a record the longitudinal even-parity check character will appear, followed by a ¾-inch inter-record gap.

3. *Frame:* The high speed frames will contain 16 data words corresponding to 16 bursts; the low speed frames will contain 32 data words corresponding to 16 bursts and 16 blanks. In both types of frames a time word will appear immediately following the first burst—the synchronization burst—of the frame. This time word can be used for computer synchronization. In addition, flag characters will be inserted at the end of each frame to indicate format inconsistencies.

4. *Word:* Data words will consist of 3 BCD characters; time words will consist of 12 BCD characters; flag words will be 1 character; and identification words will consist of 12 BCD characters. Data words will represent the burst frequency quantized by the filters in the comb filter bank. A conversion table will be supplied to relate the comb filter number (1 to 1963) to the actual frequency. Digital data

words will appear with numbers 0 through 7 in the first character, with the second two characters zero.

5. *Character:* All characters are the binary-coded decimal type. Numerics will be used for data and time characters. Special characters will be used for dropouts and time-inconsistency flags, and a list of these characters is given below.

Identification

Identification records will appear at the beginning of each file. These records will consist of a 12-character ID word repeated as many times as is necessary to fill up the record (the length of the record depending upon the type of data—low or high speed). Basic word format is as follows (in order of appearing characters):

1st	2nd	3rd	4th	5th	6th	7th	8th	9th	10th	11th	12th
X	X	X	X	X	X	X	X	X	X	X	X
Satellite		Yr		Day Count of Year			Station		Tape Number		

An end-of-file serves as a warning that the next usable record will be an ID record.

Time

Time insertions can contain up to a maximum of 12 characters. They will typically appear as follows:

1st Character	0001100 (CBA 8421 sequence)
2d Character	Blank
3d Character	Blank
4th Character	Ten of hours
5th Character	Units of hours
6th Character	Tens of minutes
7th Character	Units of minutes
8th Character	Tens of seconds
9th Character	Units of seconds
10th Character	Hundreds of milliseconds
11th Character	Tens of milliseconds
12th Character	Units of milliseconds

It is possible that the first three characters may be used for a day count of year. The U.K. will be notified if they are.

Time words will be inserted after the synchronization pulse in both types of data: high and low speed. The 0 0 0 1 1 0 0 character can be used as a sensing device for the time word.

High-Speed Data

A record of high speed data will include 16 frames of 976 characters. The number of characters is calculated as follows:

16 frames × 16 pulses/frame ×3 characters/pulse
+16 frames ×1 time word/frame × 12 characters/time word
+16 frames ×1 flag/frame ×1 character/flag
=976 characters/record.

Because of dropouts in data and occasional loss of synchronization, the first frame at the beginning of the record will not necessarily be the 0th frame of the 16-frame high speed cycle.

A high speed record that is completed by blank characters will indicate that an interruption in the high-speed data has occurred because of a playback of the low speed data from the satellite. The point of initiation of playback will correspond approximately to the beginning of the series of blank characters in the record.

Low-Speed Data

The low speed data records will consist of 8 frames of 872 characters. The number of characters is calculated as follows:

8 frames × 32 data words/frame ×3 characters/word
+8 frames × 1 time word/frame ×12 characters/time word
+8 frames ×1 flag/frame ×1 character/flag
=872 characters/record

As in the case of high-speed data, dropouts and loss of sync will make it impossible to insure that the first frame in each low-speed record is the 0th frame of the two-frame low-speed cycle.

The time inserted in the low-speed data is the ground time at the station at the time the low speed data was playing back on the on-board tape recorder. It is therefore to be used for relative time computations only. The absolute time of the low-speed data can be computed from the above relative time information and

the absolute time of the command signal, which will be inserted at the point of command.

Time Inconsistencies and Dropouts

The frame time advance will be checked, flagged if inconsistent, and these flags counted. The dropped-out data words will also be counted. Both counts will be accumulated and printed on a file basis.

1. *Inconsistent frame time advance:* The time of two successive frames will be differenced, and the difference compared to 320 ± 40 milliseconds. If the difference falls outside of this range, an asterisk (*) character willl be inserted at the end of the frame. The reference value (320) and the tolerance (± 40) may have to be changed in the case of the recorded data because of tape recorder speed fluctuations.

2. *Dropout count:* When a data word drops out, three dash characters will appear. These characters will be counted and a sum, based on 3 character words, will be accumulated for each file. This sum will be printed, along with the sum of time-interval inconsistency flags.

Special Characters

The following gives the characters other than numerics that will be used:

Purpose	Character	Print	Bit Sequence C B A 8 4 2 1
Data dropout	Dash	—	0 1 0 0 0 0 0
Improper time advance	Asterisk	*	0 1 0 1 1 0 0

Samples of Ariel I data are shown in Figures 7–3 and 7–4.

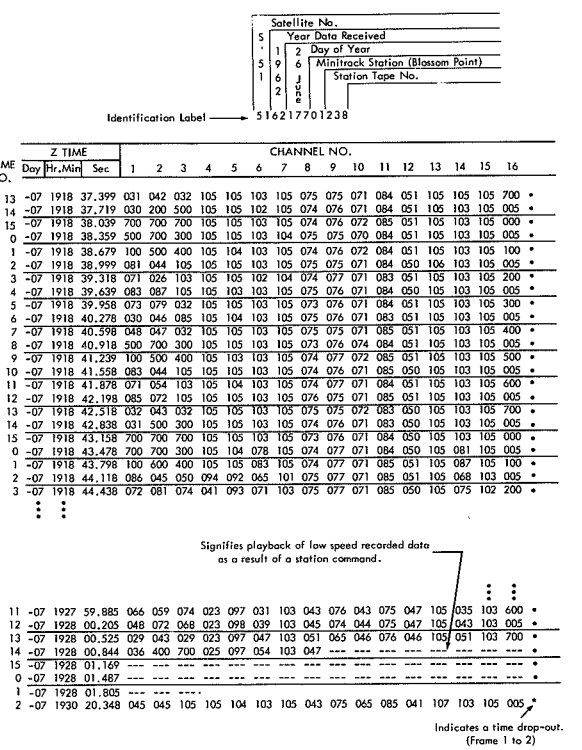

FIGURE 7–3.—Sample of high-speed (real-time) digitized data.

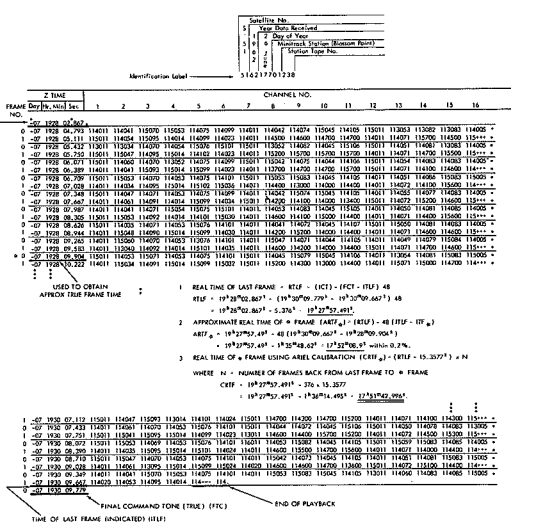

FIGURE 7–4.—Sample of low-speed digitized data (recorded 1/48th of high-speed data).

REFERENCES

1. BOURDEAU, R. E., DONLEY, J. L., SERBU, G. P., and WHIPPLE, E. C., Jr., "Measurements of Sheath Currents and Equilibrium Potential on the Explorer VIII Satellite," *J. Astronautical Sci.* 8(3) : 65–73, Fall 1961.
2. BOURDEAU, R. E., "Ionospheric Results with Sounding Rockets and the Explorer VIII Satellite," in *Space Research II : Proc. 2d Internat. Space Sci. Sympos., Florence (Italy), April 1961*, ed. by H. C. van de Hulst, C. de Jager, and A. F. Moore, Amsterdam : North-Holland Publ. Co., 1961, pp. 554–573.
3. SERBU, G. P., BOURDEAU, R. E., and DONLEY, J. L., "Electron Temperature Measurements on the Explorer VIII Satellite," *J. Geophys. Res.* 66(12) : 4313–4315, Dec. 1961.
4. BOURDEAU, R. E., WHIPPLE, E. C., JR., DONLEY, J. L., and BAUER, S. J., "Experimental Evidence for the Presence of Helium Ions Based on Explorer VIII Satellite Data," *J. Geophys. Res.* 67(2) : 467–475, February 1962.
5. BOURDEAU, R. E., and BAUER, S. J., "Structure of the Upper Atmosphere Deduced from Charged Particle Measurements on Rockets and the Explorer VIII Satellite," paper presented at 3rd Internat. Sci. Sympos., Washington, May 1962.
6. KRASSOVSKY, V. I., "Exploration of the Upper Atmosphere with the Help of the Third Soviet Sputnik," *Proc. IRE* 41(2) : 289–296, February 1959.
7. POMERANTZ, M. A., SCHWED, P., HANSON, H., and BENJAMIN, H., "Satellite-Borne Instrumentation for Observing Flux of Heavy Primary Cosmic Radiation," *J. Franklin Inst.* 271(275–291), Apr. 1, 1961.
8. POMERANTZ, M. A., AGARWAL, S. P., SCHWED, P., and HANSON, H., "Satellite Determination of Heavy Primary Cosmic-Ray Spectrum," *Phys. Rev. Letters* 6 : 7 (362), Apr. 1, 1961.
9. POMERANTZ, M. A., and WITTEN, L., "Satellite Investigation of Time Variations of Heavy Nuclei on the Primary Cosmic Radiation," *Proc. Internat. Conf. on Cosmic Rays and the Earth Storm, Kyoto (Japan), September 1961.* II Main Sessions, Tokyo: Physical Society of Japan, 1962.
10. FRIEDMAN, H., LICHTMAN, S. W., and BYRAM, E. T., "Photon Counter Measurements of Solar X-Rays and Ultra-Violet Light," *Phys. Rev* 83(5) : 1025 (1952).
11. RENSE, W. A., "Intensity of Lyman-Alpha Line in the Solar Spectrum," *Phys. Rev.* 91(2) : 299 (1953).
12. FRIEDMAN, H., "Solar Radiation," *Astronautics* 7(8) : 14, August 1962.
13. CORNILLE, H. J., Jr., "A Method of Accurately Reducing the Spin Rate of a Rotating Spacecraft," NASA TN D-1420, October 1962.
14. HORD, W. H., "General Environmental Test Specification and Test Procedures for Design Qualification & Flight Acceptance Testing of Delta Launched Satellite," NASA/GSFC/TE internal publication, September 1961.
15. HORD, W. H., "Environmental Test Specifications for Design Qualification and Flight Acceptance Tests of the International Satellite," NASA/GSFC/TE internal publication, December 6, 1961.
16. HORD, W. H., "Test Plan—Structural Test ETU S1 S-51 Satellite," NASA/GSFC/TE internal publication, April 1961.
17. HORD, W. H., "Environmental Exposures and Tests for Subassemblies of International Ionosphere Satellite S-51," NASA/GSFC/TE internal publication, February 1961.

ADDITIONAL BIBLIOGRAPHY

DESIGN AND DEVELOPMENT REPORTS

1. FEDOR, J. V., "Analytical Theory of the Stretch Yo-Yo for De-spin of Satellites," NASA Technical Note D–1676, April 1963.
2. ENG, T. L., "Energy Absorber for the Ariel I Instrument Booms," NASA Technical Note D–1857, 1963 (In press).
3. CONN, J. H., and SUTTON, J. F., "Report of Environmental Vibration Test—Structural Model No. 1, International Ionosphere Satellite, S–51," Goddard Space Flight Center 321.2(JC) S–51–11, June 1961.
4. FORSYTHE, R. W., "A Method for Simulating Zero Gravity Erection of Satellite Appendages," NASA Technical Note D–1852, 1963 (In press).
5. FORSYTHE, R. W., "Analysis of Dissimilar Satellite Appendages During Erection," NASA Technical Note D–1688, 1963 (In press).

PUBLICATION STATUS AS OF FEB. 1, 1963, FOR THE EXPERIMENTAL RESULTS OF MEASUREMENTS MADE BY ARIEL I

1. POUNDS, K., and WILLMORE, A. P., "X-Ray Measurements on the Ariel Satellite," *Proc. of the International Conference on the Ionosphere* (In press July 1962).
2. WILLMORE, A. P., BOYD, R. L. F., and BOWEN, P. J., "Some Preliminary Results of the Plasma Probe Experiments on the Ariel Satellite," *Proc. of the International Conference on the Ionosphere* (In press July 1962).
3. SAYERS, J. ROTHWELL, P., and WAGER, J. H., "Evidence for a Further Ionospheric Ledge Above the F_2 Region," Research Note No. 6210, University of Birmingham, Aug. 24, 1962; also published in *Nature Magazine*, Sept. 22, 1962.

764–173 O—65——15

Appendix A

PHYSICAL MEASUREMENTS OF ARIEL I

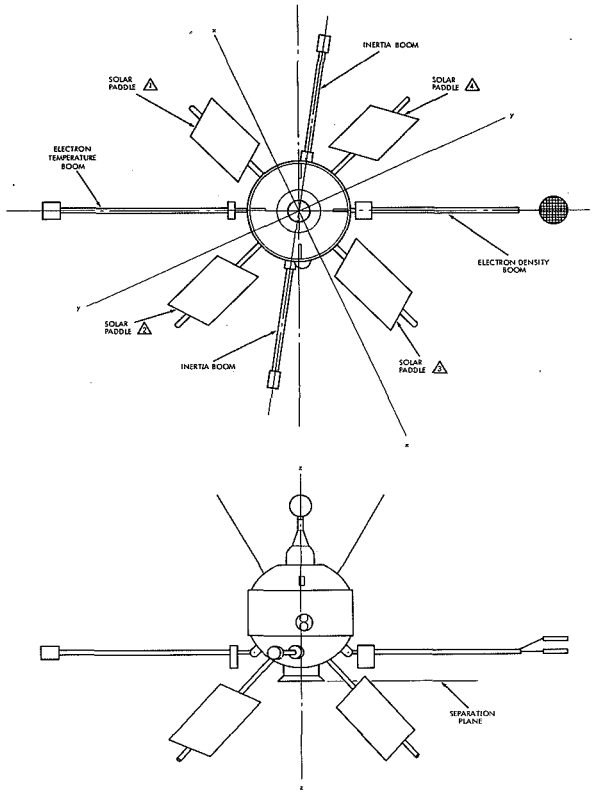

FIGURE A1.—Payload axes.

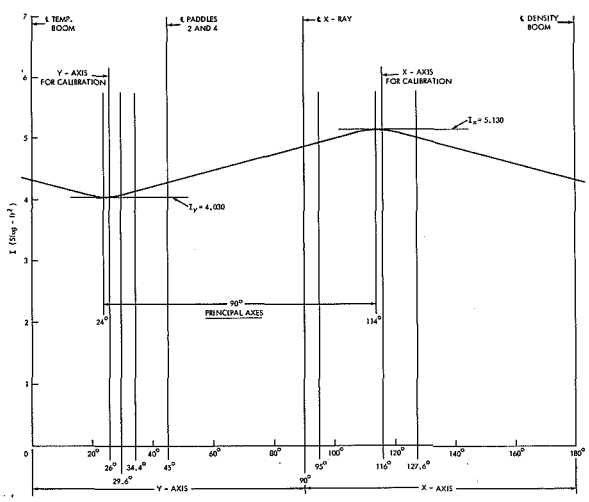

FIGURE A2.—Principal moments of inertia vs. payload axes, all components extended.

The weights, centers of gravity and moments of inertia are given in the following itemization:

SATELLITE ONLY*

Weight (lb)	135.82

All components folded

Center of gravity, forward of separation plane (in.)	5.961
Moment of inertia (slug-ft²):	
I_{xx}	5.25
I_{zz} (Roll axis)	1.99
I_{yy}	4.75

All components extended

Center of gravity, forward of separation plane (in.)	8.125
Moment of inertia (slug-ft²):	
x–x axis	5.130
Roll axis	5.484
y–y axis	4.030

FOLDED ARIEL I PAYLOAD†

Weight (lb):	
Orbiting satellite	133.8
De-spin weights	2.0
Separation and release system (with tiedowns)	21.3
Dutchman and vibration experiment‡	20.6
TOTAL payload weight not furnished by Delta vehicle	177.7
Center of gravity, forward of separation plane (in.)	1.42
Moment of inertia (slug-ft²):	
Pitch axis	9.277
Roll axis	2.610

SEPARATION UNIT AND DUTCHMAN†

Weight (lb)	35.56
Center of gravity, aft of separation plane (in.)	8.53

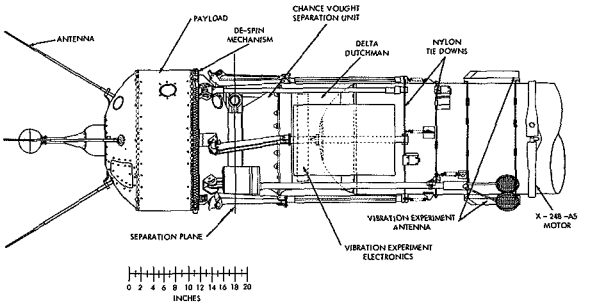

FIGURE A3.—Ariel I nomenclature diagram.

Moment of inertia (slug-ft²):

Pitch axis	0.294
Roll axis	0.451

ANTENNAS AND HARNESS (VIBRATION EXPERIMENT)†

Weight (lb)	3.58
Center of gravity, aft of separation plane (in.)	44.94
Moment of inertia (slug-ft²):	
Pitch axis	0.0705
Roll axis	0.0831

TIE DOWNS†

Weight (lb)	2.66
Center of gravity, aft of separation plane (in.)	32.30
Moment of inertia (slug-ft²):	
Pitch axis	0.010
Roll axis	0.086

*Refer to Figures A1 and A2.
†Refer to Figure A3.
‡Includes U.K.-designed contamination experiment and solar aspect sensor, and telemetering antennas.

TABLE A1.—*Detailed Weight Breakdown of Ariel I*

Item	Remarks	Weight (lb)
Upper dome	Includes thermal and RF coating.	6. 53
Mid-skin	Includes thermal and RF coating.	6. 80
Lower dome	Includes thermal grating only.	1. 52
Shelf and base assembly.	Shelf, struts, base, fasteners.	12. 63
Paddle arms and hinges (4).	Includes interface fasteners.	4. 36
Inertia booms and hinges (2).	Includes interface fasteners.	3. 85
Experiment boom hinges.	Includes interface fasteners.	. 87
Escapement assembly.	Includes nylon guides.	1. 54
De-spin housing	Includes guillotines	1. 76
De-spin weights, Spring antennas (4).	Excluded from orbit weight.	2. 00 . 80
Separation ring adapter.	Includes interface fasteners.	. 51
Battery containers	Includes spacers	3. 05
Dynamic balance		1. 93
Tape recorder and electron temperature supports.		1. 07
Turn-on plug and housing.		. 14
Harness bracketry	Includes clamps fasteners.	1. 34
Component bracketry.	Nonstructure components.	. 91
Internal thermal equalization.	Coatings and heat sinks.	. 97
University College London Experiments		
Lyman-alpha detectors (3).		1. 62
X-ray counters (2)		. 64
Solar aspect sensor		. 43
Ion mass spectrometer.	Includes 4-inch extension tube.	. 54
Electron temperature sensor.		. 37
Electron temperature boom.	Includes balance weights.	5. 50
UCL electronics container 1.	Includes 4 U.K. cards.	5. 67
UCL electronics container 2.	Includes 10 U.K. cards.	6. 76
Imperial College Experiment		
Cosmic ray analyzer	Includes electronics	5. 70
University of Birmingham Experiment		
Electron density boom.		5. 50
Electronics container		2. 79
GFSC Nonstructure Components		
Tape recorder		3. 66
Tape recorder dc control.		. 39
Encoder card UCL No. 1.	In UCL container 1	. 49
Encoder card UCL No. 2.	In UCL container 2	. 56
Cosmic ray encoder card.	Including container	. 96
Electronic pack A	2 encoder cards, encoder clock. 2 converter cards, lid.	5. 87
Electronic pack B	2 programer, 2 converter, 1 undervoltage detector, transmitter, and command receiver cards, lid.	6. 93
Battery selector		. 50
1-Year timers (2)		. 72
Solar paddles (4)	Including spars	8. 78
Battery packs (2)	Including potting	12. 08
Solar shunt regulator		. 24
Harness network	Top dome, main assemble below shelf assembly.	6. 54
TOTAL ARIEL I WEIGHT		135. 82

II. SPACECRAFT AND SUBSYSTEMS

Page intentionally left blank

SATELLITE ATTITUDE DETERMINATION: DIGITAL SENSING AND ON-BOARD PROCESSING

J. S. ALBUS AND D. H. SCHAEFER
Goddard Space Flight Center

The determination of the aspect or orientation of spin stabilized satellites is vital for the correct interpretation of scientific measurements made on these spacecraft. Aspect information is collected optically from the sun, moon and earth. Little channel capacity is generally available for telemetry of this information. Therefore, completely digital low power aspect sensing and on-board information processing systems have been built and flown on various satellites. Some interesting results of aspect measurements on Explorer XII showed an unexpected increase in spin rate due to solar pressure, and on Explorer XIV an erratic precession history.

INTRODUCTION

The problem of attitude determination is the problem of defining the angular relationships between two coordinate systems, one a coordinate system fixed in some reference space, the other a coordinate system fixed in the spacecraft There are of course six degrees of freedom of a spacecraft coordinate system with respect to a reference system. Three of these degrees of freedom concern the translational motion of the center of mass of the spacecraft. The problem of measuring this translational motion is an exercise in orbit or trajectory calculations. The remaining three degrees of freedom concern the rotational motion of the spacecraft about its center of mass. The measurement of this rotational motion is the problem of attitude or aspect determination. It is the aspect determination problem which will concern this paper and in particular the aspect determination problem for a rotating spacecraft using a digital aspect sensor.

DIGITAL ASPECT SENSOR

The digital aspect sensor consists of a number of photo-duo-diodes placed behind a light mask with slit openings as shown in Figure 1(a). Opaque separators are situated between the photo-duo-diodes so that each photo-diode "sees" only the portion of the light mask directly in front of it. The slits and photo-

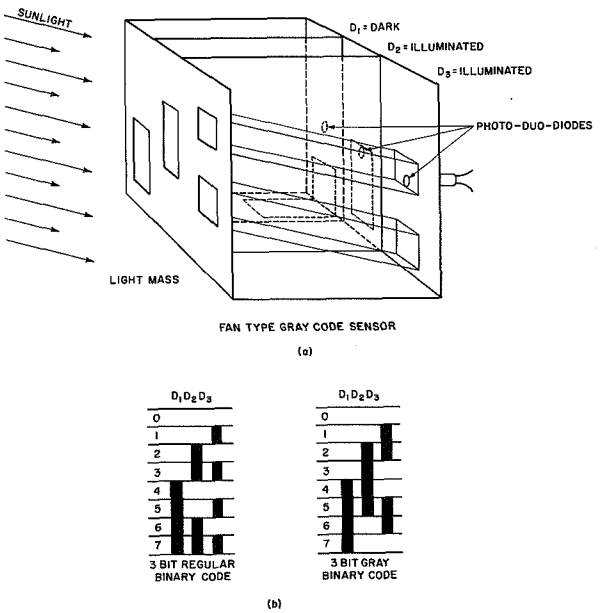

FIGURE 1.—Schematic representation of a digital solar aspect sensor and a Gray code light mask.

diodes are aligned in such a manner so that each photo-diode has a fan field of vision which lies in a plane parallel to the field of vision of the other photo-diodes. Since this sensor can be designed to detect either the sun or the moon, which are for all practical purposes point sources at infinity, these parallel planes can be assumed to be a single plane. If the sensor is rotated about a vertical axis which lies in this plane, the fan field of vision of the diodes will sweep out a solid angle. When the fan crosses the solar disc, the sensor presents a binary word to the output terminals in parallel readout. This word is the address of the particular fan segment which swept across the sun and hence gives a measure of the angle between the vehicle spin axis and the sun vector. The binary address word must then be encoded into a format suitable for transmission. The accuracy of this digital measurement depends, of course, on how many binary sensors are used. A fan field of view can be quantized into as many as 2^n-1 segments when there are N binary sensors. A Gray Code system [2] shown in Figure 1(b) is used instead of the regular binary code. This is because the Gray Code requires a decision from only one sensor for each transition between quantized segments. The regular binary code often requires simultaneous decisions from several diodes, making possible erroneous readings in the transition regions.

In a spinning satellite problem the exact time that the fan crosses the solar disc is also sometimes an important parameter. This time must be related to some known time standard and this relationship remembered, encoded, and presented to the transmitter. In various vehicles using various telemetry formats this problem naturally has different solutions.

Since there are three degrees of rotational freedom of a rigid body in a force-free field it would be expected that in addition to the sun angle and time of appearance, at least one other parameter would need to be measured in order to completely and uniquely solve the aspect problem. Indeed this is the case.

Since to the digital sun sensor the sun is for practical purposes a point source, the vector from the satellite to the sun is an axis of symmetry. This means that loci of the spin axis is a cone whose axis is the sun vector and whose half angle is the angle measured by the digital sun sensor, namely the angle between the spin axis and the sun vector. In order to complete an unambiguous calculation of the position of the satellite spin axis, a measurement must be made on another body which is not coincident with the satellite sun axis of symmetry. This may be done by measuring the direction to the earth or the moon. This measurement may be performed in various ways. Two methods described in this paper are the use of a narrow-beam horizon-detecting telescope, and the use of a wide-angle moon-detecting fan. These detectors, of course, must deal with such problems as phases of the moon, partial illumination of the earth disc, cloud cover, altitude variation, type of orbit, etc. The type of detector and the mounting arrangements must often be tailored to fit a particular set of circumstances.

A useful tool in visualizing the action of the digital sensor in the aspect determination problem is the concept of the celestial sphere shown in Figure 2. The digital fan can be

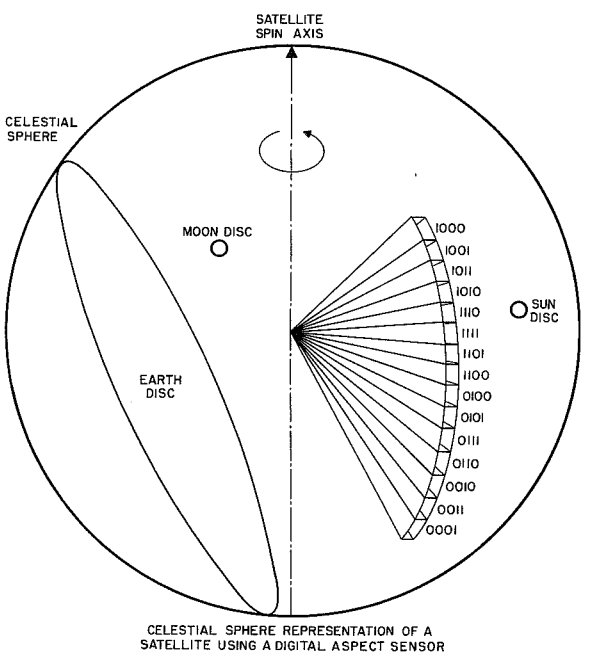

FIGURE 2.—Celestial sphere representation of the satellite attitude determination problem using a digital sensor.

visualized as a series of numbered light channels sweeping the sky. The celestial sphere is, of course, an inertial reference system. The sun is conceptualized as a 0.5° disc moving in the ecliptic on the celestial sphere approximately one degree per day. The moon is a 0.5° disc traversing its orbit once per month, and the earth a large disc covering a large part of the celestial sphere and moving completely around the sphere once per orbit of the satellite. The apparent size of the earth's disc is, of course, a function of the satellite altitude. At zero altitude the earth disc covers 2π sterradians or half the celestial sphere. At satellite altitudes the earth naturally appears somewhat smaller. The digital solar aspect fan sweeps across the celestial sphere producing a signal output whenever it crosses the sun disc. Digital sensors have also been designed which can detect the moon's disc at night when the earth disc covers the sun.

PROJECT RELAY

The specific satellite aspect systems to be discussed will be mentioned in order of increasing complexity. The most simple system is that used on the Relay communications satellite. It measures only one parameter, the angle between the spin axis and sun vector. This sensor system consists merely of a digital sun sensor combined with an additional slit sensor which is set so as to sweep across the sun about 10° of rotation before the digital field of view crosses the sun. A bistable flip-flop is connected to each of the digital sensor outputs. When the slit field of view sweeps the sun it resets all the bistable flip-flops to a "zero" state. When the digital sensor crosses the sun, it reads a binary word into the flip-flops. The outputs of these flip-flops are then sampled in parallel at a convenient rate by the telemetry system.

A sample of the data received from Relay is shown in Figure 3. The vertical bars refer to the width of the activated quantized fan segments. The change of the angle between the spin axis and the sun vector is due primarily to the apparent motion of the sun on the

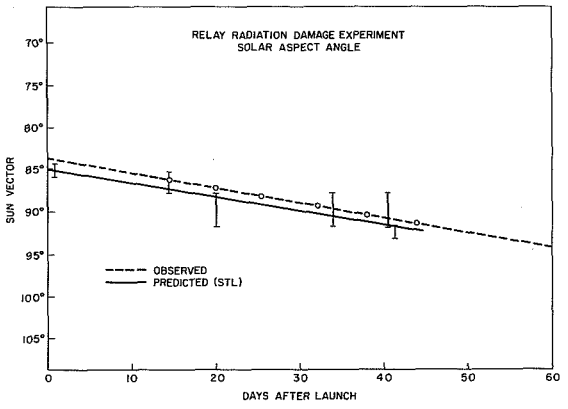

FIGURE 3.—Spin axis vector data from Relay satellite showing motion of sun accross sensor transitions.

celestial sphere. Note that a smooth curve can be drawn which lies within the quantized segments. Since the edges of the quantized segments are accurately calibrated, and data are plotted over many days, the angle between spin axis nd sun can be measured much more accurately than the nominal quantization accuracy.

THE S-3 SATELLITE SERIES

The attitude determination system used on the *S*-3 energetic particles satellite series is not complex. This series includes Explorer XII, XIV, XV.

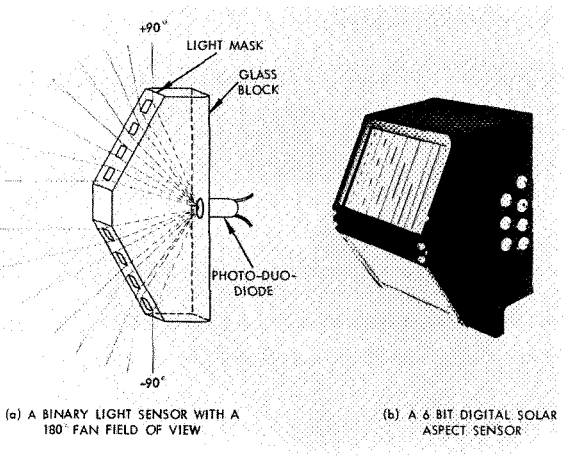

FIGURE 4.—S-3-type digital solar aspect sensor with a 180° fan field of view quantized into 63 parts. (a) A binary light sensor with a 180° fan field of view. (b) A 6-bit digital solar aspect sensor.

The *S*–3 series digital sun sensor is shown in Fig. 4(b). This sensor is made from six glass prisms similar to the ones shown in Fig. 4(a). Thus it has a 180° fan field of view. The sensor is then mounted so that as the satellite rotates the quantized fan field of view sweeps the entire sky.

On the *S*–3 satellite series the exact time the digital field crosses the solar disc is measured as well as the angle between the spin axis and the sun. A third parameter needed for a unique aspect solution is obtained from magnetic field sensors. On the *S*–3-type satellites the information rate is relatively slow; therefore the efficient use of telemetry bandwidth is important. For example, on Explorer XII the telemetry system samples the aspect system approximately five times per satellite revolution. In order to get more accurate rotation information the state of the telemetry sequencer at the time of occurrence of a sun appearance signal is remembered on three flip-flops while the angle information is stored on six magnetic cores. This information is then slowly fed to the PFM [3] telemetry system three bits at a time. The information on the magnetic cores is transferred to the three flip-flops as a part of the readout process. The flip-flops are connected directly to an eight-level PFM oscillator which is gated "On" once per telemetry frame.

A photograph of the signal conditioning circuitry is shown in Figure 5. Supermalloy cores are used as the magnetic memory elements. The cores are also used as synchronizing elements. Four complementry flip-flops are shown in the left-hand side of the picture. Three of these are tied to the telemetry system. The fourth is a switch to allow readout of the cores. This entire system including the digital sensor consumes less than 3 mw of power.

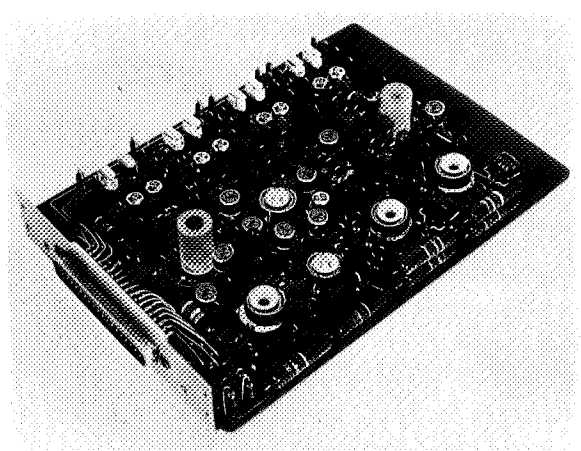

FIGURE 5.—Data processing circuitry for the S–3 satellite series.

Figure 6 shows data taken from Explorer XII

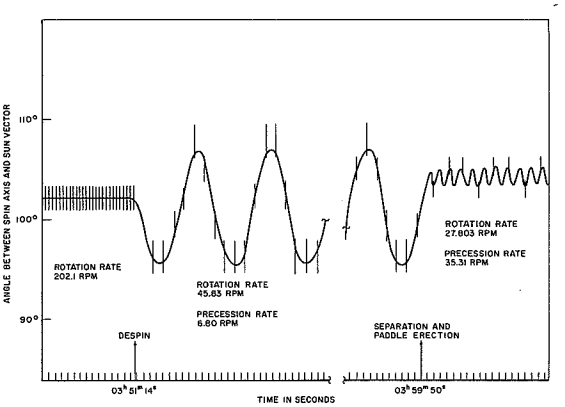

FIGURE 6.—Aspect data from Explorer XII during despin and separation.

during despin and separation. At $03^h\ 51^m\ 14.6^s$ the despin yo-yo's were released and the rotation rate dropped from 202.1 rpm to 45.83 rpm. Since the two yo-yo weights did not separate simultaneously, a precession coning of about 5.5° half angle was induced. This motion continued for approximately nine minutes until $03^h\ 59^m\ 50^s$. At this time separation of the satellite from the third stage rocket casing and erection of the solar paddles took place. The rotation period then dropped to 27.803 rpm and the precession coning decreased in amplitude to about 1° half angle. However, due to the change in inertia moments the precession rate increased from 6.8 rpm to 35.31 rpm. The precession amplitude damped out as expected in about 48 hours, but after several weeks a very unexpected phenomenon was observed. The rotation rate increased! This phenomenon was apparently not related to forces of terrestial origin since during an entire orbit the increase in rotation was observed to be independent of altitude. An explanation of this phenomenon

was found rather in solar radiation pressure acting on the solar paddles. The solar paddles were orientated unsymmetrically in propeller fashion. Sunlight falling on the paddles thus produced a net torque about the center of mass of the satellite in the proper direction and of sufficient magnitude to account for the observed effect.

Another interesting and rather surprising phenomenon was observed in Explorer XIV. On this satellite the rotation rate increased due to solar radiation pressure, as was by then expected, and in addition the amplitude of the precession coning after initially decreasing, began to increase sharply and unexpectedly. The history of the Explorer XIV precession

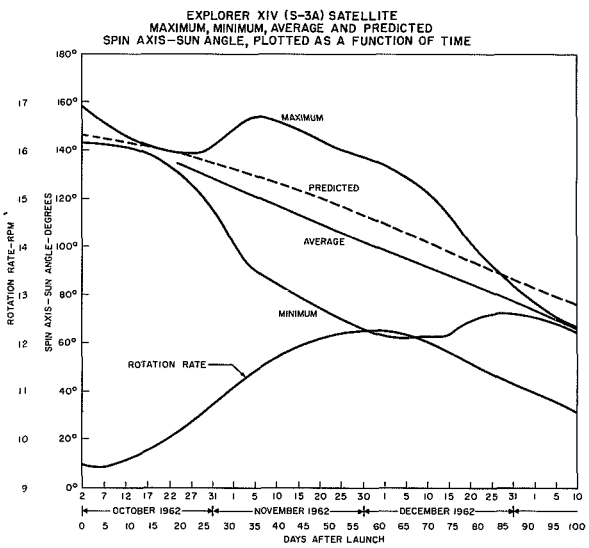

FIGURE 7.—Precession angle and spin rate history of Explorer XIV from launch to January 10, 1963.

coning is shown in Figure 7. This precession amplitude finally reached a plateau around November 5, and on December 5 began to decrease. This erratic behavior has been tentatively explained as caused by an interaction between the magnetic field of a pulse solenoid aboard the spacecraft and the magnetic field of the earth. The abrupt beginning and disappearance of this precession coning has not been fully analyzed as yet but is presumed to be caused by a resonance between the spacecraft rotation rate and the solenoid pulse repetition rate. The increase in the rotation rate early in the spacecraft life and subsequent decrease in rotation rate at a later date is easily explained by the solar pressure propeller theory. Early in flight the angle between the spin axis and the sun was larger than 90° such that the solar paddle propeller was of the proper sense to increase the rotation rate. At 90° between spin axis and sun the net torque was zero and the rotation rate held constant. At angles less than 90° the propeller sense was such that the rotation rate was decreased by radiation pressure.

This large angle of precession coning could have proved disastrous to many of the directional-sensitive experiments aboard Explorer XIV. However, the digital solar aspect sensor has the distinct advantage of producing data easily digested by automatic data processing systems. There is now operational at Goddard Space Flight Center an automatic aspect data reduction computer program which can reconstruct the complete history of the Explorer XIV precession and spin motions.

ATMOSPHERIC STRUCTURES SATELLITE—(EXPLORER XVII)

The Atmospheric Structures Satellite attitude determination system is called upon to provide a unique description of the satellite position relative to its orbital velocity-vector at any time day or night. This requires the use of infrared earth horizon detectors in conjunction with a digital sun sensor by day and a digital moon sensor by night.

The infrared horizon detectors shown in Figure 8 have pencil beam fields of view and are mounted so that one detector looks slightly forward at 68° from the spin axis and the other looks slightly aft at 112° from the spin axis. Both pencil beam fields of view lie in the same plane as the digital fan. The horizon detectors produce a pulse when the pencil field of view crosses into the horizon and another pulse when it crosses out. The digital sensor shown in Figure 9 has its light mask deposited on curved glass prisms which provide an optical light gathering amplification of approximately

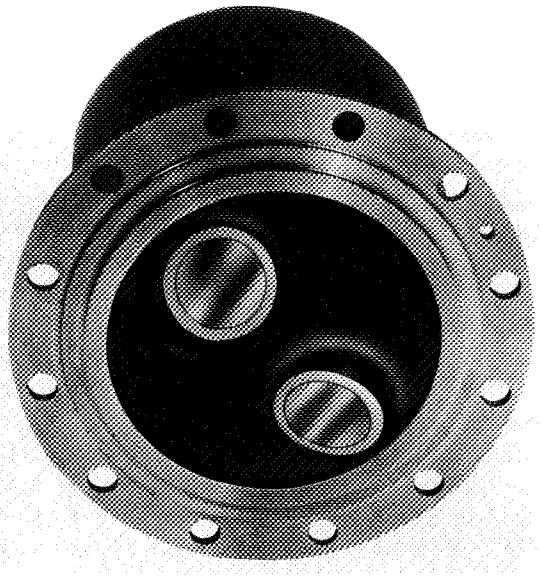

FIGURE 8.—Infrared horizon detectors for Atmospheric Structures Satellite.

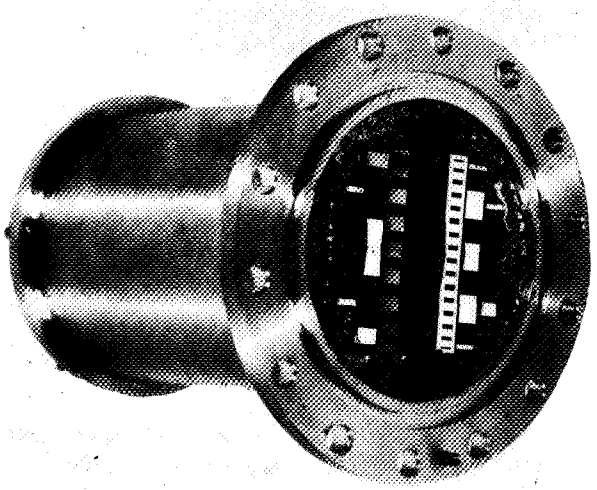

FIGURE 9.—Sun-moon digital sensor, sun-switch and sun-moon slit sensor for Atmospheric Structures Satellite.

ten over the *S*-3-type sensor. This sensor with sensitive amplifiers attached to the photodiodes thus has the capability of detecting the half moon. A separate sun sensor switches off the sensitive amplifiers for daytime operation. In addition there is another sensor located in the center of the digital sensor called the sun-moon slit whose field of view is a fan which is offset by a prism so that it trails the digital sensor field of view by 45° of rotation. This sun-moon slit is sensitive to the sun by day and the moon by night. Its function is to provide accurate time of appearance information for either sun or moon. The 45° offset of the slit field of vision prevents overloading of the available telemetry channel.

The telemetry system for the Atmoshperic Structures Satellite is a PCM system and transmits aspect information on a 9-bit binary word once every 20 msec.

Signal processing for this satellite consists of both a memory function and a priority system, incorporated to prevent overloading of the available channel. In the case of both sun slit and earth horizon sensor inputs appearing in a single frame the sun information is retained and the earth information rejected. There is also a similar priority setup between the two earth sensors.

Figure 10 is the logical diagram of the data processor on board this satellite. Table I shows the function of the various bits. The time indicators T_1 through T_4 give a binary number which indicates how many clock pulses lie between the time when the sensor of greatest priority had an input and the time of aspect word transmission. Priority is in the order of sun-moon slit, Earth I, and Earth II. The above is best clarified by examples. The transmitted word "01001000" means that earth sensor #1 had an output at time "1000" (i.e., 8 clock pulses before transmission) and no other sensor had output during the frame. "01111001" means that Earth I, Earth II and the slit provided outputs during the frame, and that the slit pulse arrived at time "1001." In this latter case no time information is given about the earth inputs. For a case when bit A is a "1" the word "11001000" means the spin-axis moon-angle is located in quantized fan segment "001000." Power dissipation in all circuitry required to perform this logic is less than five mw.

TABLE I

Bit	Indication	
A	"1" if digital sensor had an input since last aspect word transmission	
	If A *a* "O"	If A *a* "1"
B	"1" if earth sensor #1 had an input	"1" if moon amplifier on
C	"1" if slit had an input	"1" if least significant bit (D_1) of digital sensor had an input
D	"1" if earth sensor #2 had an input	"1" if D_2 had an input
E	Least significant time bit (T_1)	"1" if D_3 had an input
F	T_2	"1" if D_4 had an input
G	T_3	"1" if D_5 had an input
H	Most significant time bit (T_4)	"1" if D_6 (most significant digital sensor bit) had an input

EXPLORER X

Explorer X was launched into a highly elliptical orbit on March 25, 1961. Therefore, chronologically this is the oldest satellite discussed in this paper. Its mission was to measure magnetic fields and plasma. Explorer X attained a distance of 180 thousand miles from the earth during its intended lifetime of 50 hours. The attitude determination system in this satellite was designed to (1) measure the angle between spin axis and the sun vector by means of a 4-bit digital sun-sensor, (2) measure the time when the digitized field of view crossed the sun, (3) remove the ambiguity of the spin axis position, and (4) measure the height of the satellite above the surface of the moon. This latter ability was incorporated because during the planning of the project the possibility of a launch to the moon was present.

These measurements were made with a detector which uses a standard 4-bit digital sun sensor combined with a sun reset slit similar to the Relay sensor. There was also another slit sensor attached to a sensitive amplifier which was capable of sensing light from the moon or the earth. In addition there was a sun-switch sensor which opened a gate in the earth-moon amplifier output when the sensor was pointing toward the sun. The telemetry system used aboard Explorer X made available to the aspect system a five-second PFM burst once every two minutes. The PFM oscillator was quantized into 16 discrete frequencies. The reset slit set the subcarrier oscillator to its lowest frequency state. Twenty degrees of rotation later, the PFM oscillator was set and held at one of its 15 other discrete frequencies by the 4-bit digital solar sensor. After the satellite had rotated far enough so that the sun-switch was deactivated, control of the oscillator was transferred to the earth-moon amplifier. When the earth-moon fan slit was not illuminated the oscillator frequency remained unchanged. However, when the earth-moon sensor viewed a bright surface, the oscillator frequency was indexed upwards every 2.5 msec for as long as the bright object remained in the slit field of view. If the slit sensor still viewed the bright object when the oscillator reached its highest frequency, the next indexing pulse reset the oscillator to its lowest frequency and the indexing continued upward. The length of this counting sequence was a measure of the height of the satellite above the earth or moon. The relative position of the sun sensor reset-set sequence to the earth-moon sensor counting sequence removed the ambiguity of the spin axis position.

The length of time the earth or moon was seen could be determined to within ± 2.5 msec. by noting the difference between the frequency before and after stepping. This was most valuable at the moon distance as the signal-to-noise ratio was so poor that the stepping could not be seen. Filters, however, easily pulled out the before and after frequencies.

INTERPLANETARY MONITORING PLATFORM (IMP)

The Interplanetary Monitoring Platform is a fields and particles satellite which will have

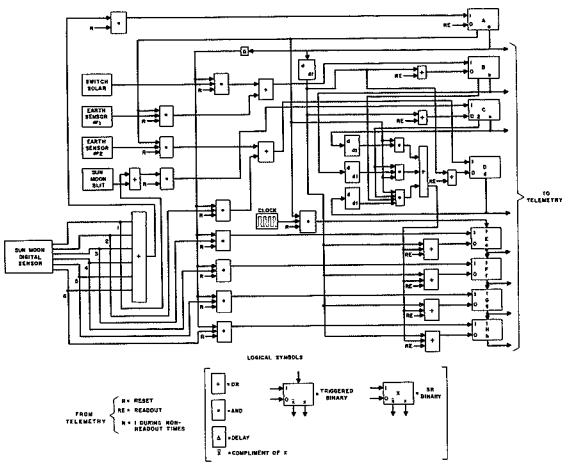

FIGURE 10.—Logical Diagram of Atmospheric Structures data processor.

a 150,000 nautical mile apogee. Its telemetry information rate is therefore quite low.

The IMP uses a digital sun sensor nearly identical to the *S*–3 series sun sensor. In addition it has an earth sensor sensitive to visible light with a pencil field of view mounted so as to scan 90° from the spin axis.

The data storage and readout system on this satellite is quite different from the previously discussed systems as there will be many revolutions of the satellite between readout times. The method used is to sample one of these revolutions and store all of the data collected during this revolution, a total of 45 bits of information. This collection of bits will then be telemetered once every 80 seconds.

The quantities to be telemetered are: (1) 10 bits of data defining the time between the sampling sync pulse and the first sun appearance in the sampling period; (2) six bits giving the angle between the spin-axis and the sun at this time; (3) 10 bits giving the length of time between the first and second sun appearance, (i.e., the spin period); (4) 10 bits defining the time at which the earth sensor pencil is pointed midway between horizon intersections on the earth disc; and (5) nine bits defining the azimuthal angle between the sun and the maximum magnetic field intensity as determined by a flux gate magnetometer sensor. This last quanity was included to facilitate reduction of magnetometer data. Near perigee, however, the situation can be reversed and magnetic data used as a parameter in aspect determination.

The data processing circuitry consists of a much greater number of memory units than any of the previously discussed systems. The data processor uses a clock running at a 200-cycle rate indirectly generated by a crystal that controls the satellite encoder. The logic in this circuitry controls the flow of information to the various memory elements. It turns counter chains on and off as determined by the input signals, while the binary digit sun angle memories are inhibited after receipt of one sun input.

The specific logic to determine the midpoint between the two horizon intersections may be of interest. Here the problem is to transmit information only about the midpoint between two pulses. The time of occurrence of the individual pulses is of no interest. Starting at the sync time a counter is indexed at 200 cps until the "horizon in" pulse occurs. It then is indexed at half this rate until the "horizon out" pulse occurs. The counter at this time contains the same number of counts as if it had been merely indexed at the original 200 cps rate from the sync time until midpoint between the two horizon pulses. The actual circuitry inserts a pre-stage on the counter chain at the time that the "horizon in" pulse

occurs and terminates all counting when the "horizon out" pulse occurs.

The complete data processing circuitry is

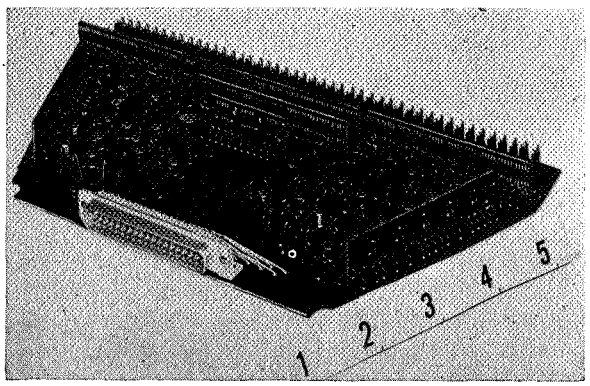

FIGURE 11.—IMP optical aspect data processor.

shown in Figure 11. The small upright devices are small printed circuit boards upon which have been mounted Texas Instruments integrated circuits. These small boards are in turn mounted on a larger board. The

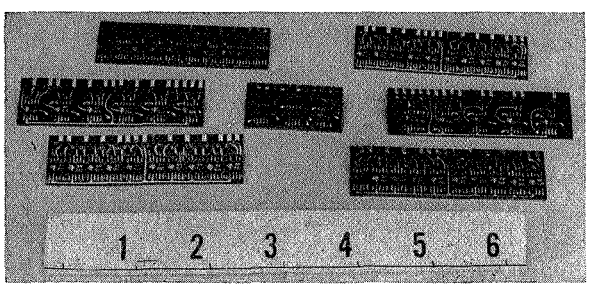

FIGURE 12.—Submodules on which integrated circuits are mounted.

small boards are shown unmounted in Figure 12. The use of integrated circuitry allowed this complete circuit to be mounted on one large printed circuit board. Three large boards would have been required if only conventional circuitry had been used. In Figure 12 the upper and lower two cards are 10 stage counters. The card with six solid circuits is the digital sensor memory. The three solid circuits on one board in the center is the logic for the sun inputs, while the board with the five solid circuits is the earth input circuitry.

The use of integrated circuits has been found quite satisfactory. The principal disadvantage over using conventional circuitry, is increased power usage. To overcome this the power to the precessor is turned off during the 80 percent of the time that no data is being collected.

ADVANCED SYSTEMS

In the data processing area it is obvious that for a stable spacecraft too much data is being transmitted. As spacecraft travel further from the earth, data transmission rates will be reduced and the transmission of data will become more and more costly. On future spacecraft experiments may be internally triggered or timed from sun or earth signals, so that the number of strictly aspect bits can be reduced an order of magnitude. For spacecraft well removed from the earth the use of stars as reference bodies appears to be the most practical approach, even for spin-stabilized spacecraft. Here even more extensive uses of onboard processing will be necessary to eliminate the transmission of superfluous information.

REFERENCES

1. J. S. Albus, "A Digital Solar Aspect Sensor," NASA, Washington, D.C., TN D–1062.
2. F. Gray, "Pulse Code Communications," U.S. Patent No. 2,632,058; Mar. 17, 1953.
3. R. W. Rochelle, "Pulse frequency modulation," *IRE Trans. on Space Electronics and Telemetry*, vol. SET–8, pp. 107–111; June, 1962. Also, for a description of the PFM digital oscillator see U. D. Desai, R. L. Van Allen, G. Porecca, "Explorer XII satellite instrumentation for the study of the energy spectrum of cosmic ray," *Proc. 1962 Nat'l Telemetering Conf.*, May 23–25, Washington, D.C., vol. 1, Sec. 7–5.

A SMALL MULTIPURPOSE ROCKET PAYLOAD FOR IONOSPHERIC STUDIES

S. J. BAUER AND J. E. JACKSON
Goddard Space Flight Center

A miniaturized version of the two-frequency CW propagation experiment has been developed for ionospheric measurements using small (15-cm diameter) sounding rockets. The choice of relatively high frequencies (24.5 and 73.6 Mc/s) for the propagation experiment permitted the use of a very simple configuration for the rocket antenna. The signals received on the ground at the two-frequencies were about 4 microvolts/meter for a slant range of about 180 km. About half of the payload space for a Nike-Cajun rocket is occupied by the CW propagation experiment, leaving the remaining space available for one or two secondary experiments. Two telemetry channels for these experiments are provided by modulation of the 73.6 Mc/s signal. A very high degree of frequency stability was provided in the two-frequency transmitter to permit Doppler radial velocity measurements at 73.6 Mc/s. A stability of one part in 10^8 has been achieved in ballistic flight, and about one part in 10^6 during the propulsion phase. If ranging errors during the propulsion phase can be overcome, the complete rocket trajectory can be calculated with an accuracy of 1 km from the Doppler data at a single receiving site.

The payload has been successfully flown on two Nike-Apache rockets, launched from Wallops Island, Va., late in 1962. The propagation experiment yielded electron density profiles from 85 km to 160 km, and the secondary experiment, a Langmuir probe, provided in situ measurements of ionospheric parameters. The paper discusses the payload design, the flight performance and the results of the ionospheric experiment. A new method for tracking using the CW propagation experiment is also outlined. The self-sufficient nature and relatively low cost of this payload should make it well suited for general use by the international scientific community.

INTRODUCTION

In the altitude region below about 250 km, a region inaccessible to satellites, sounding rockets represent one of the most important tools for basic geophysical studies. Although this altitude region is covered to some extent by ground-based techniques (e.g., ionosondes), there are still a number of problems which can best be solved by direct measurements. Furthermore, it is necessary for a detailed understanding of the physics of the ionosphere to measure *simultaneously* parameters affecting the structure of the ionosphere. Among the problems amenable to a solution by small sounding rockets are measurements of sporadic E, the equatorial electrojet, the extent of a possible valley between the E and F layers, the absorption of X and UV radiation responsible for the formation of the lower ionosphere, as well as the composition of neutral and ionic species. Typical problems presented by this region as well as the measurement techniques used are summarized in Figure 1.

For this reason, we have developed a small multiple-purpose payload which contains one experiment whose information is basic to all studies of the ionosphere; i.e., the electron density. This quantity is measured by the well-established CW propagation technique using the dispersive Doppler effect at two harmonically related frequencies. In addition, the higher frequency is also used for the telem-

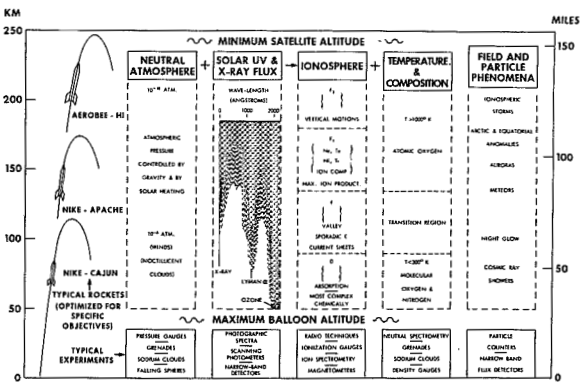

FIGURE 1.—Basic research requiring low altitude sounding rockets.

etry of two additional experiments, as well as to obtain trajectory information from the Doppler effect.

The two-frequency CW propagation, experiment, first introduced by Seddon (*1*) has been successfully used in the past in small sounding rockets before and during the IGY (*2, 3*) as well as in high altitude rockets in the 1960's (*4, 5*). In these experiments relatively low frequencies had been used with harmonic ratios of about 6; the higher frequency usually being 73.6 Mc/s. Use of low frequencies, however, requires more complicated antenna systems (e.g. erectable dipoles) to assure sufficient efficiency of radiation.

For the payload to be described in the following, it was found desirable to use a low frequency of 24.53 Mc/s, thus giving a harmonic factor of only 3, since at this frequency efficient, simple "shroud" antennas proved to be feasible (*6*). The loss in measurement-sensitivity by using a frequency of 24.53 Mc/s, however, can be offset largely by making use of a spinning rocket as shown later. Furthermore at this frequency a number of simplifications can be introduced in the data analysis.

GENERAL PRINCIPLES OF THE CW PROPAGATION EXPERIMENT

The rocket-borne CW propagation experiment introduced by Seddon (*1*) is based on the measurement of the dispersive Doppler effect at two harmonically related frequencies f and mf. This Doppler effect arises from the motion of a rocketborne transmitter within the ionosphere. Because of the splitting of the radio wave into an ordinary and extraordinary mode, each having a characteristic refractive index given by the Appleton-Hartree formula, the Doppler effect will be different for the two modes. The basic quantities measured at the ground are the best frequencies for each mode, which result from the difference between received high frequency (mf) and low frequency (f) signals. The latter is multiplied by m at the ground before the phase comparison process.

The beat frequencies for the two magnetoionic components, which are separated at the ground by virtue of their polarization can be expressed by

$$F_{o,x}=\frac{mf}{c}\left[(n^{(h)}_{o,x}-n^{(l)}_{o,x})\dot{R}_p+\int_0^R\frac{d}{dt}\,(n^{(h)}_{o,x}-n^{(l)}_{o,x})dR\right] \tag{1}$$

where $n^{(h)}$ is the refractive index at the high frequency (mf), $n^{(l)}$ is the refractive index at the low frequency (f) and the subscripts o and x refer to the ordinary and extraordinary mode, respectively; $\dot{R}_p$ is the velocity component in the propagation direction. The second term will, in general, be negligibly small compared to the first term representing the local refractive index (electron density) except at sunrise and during rapidly changing ionospheric conditions. In any event, the second term can be estimated from simultaneous, ionosonde measurements made during the rocket flight.

Equation (1) represents the beat frequency which would be observed if the rocket were not spinning. For reason of rocket stability, however, a certain spin rate ρ is required which modifies the observed beat frequency to

$$F'_{o,x}=F_{o,x}\pm(m-1)\rho. \tag{2}$$

At any given time, the roll contribution is added to one mode and subtracted from the other. Since the Doppler shift is of opposite sign during ascent and descent, the net effect upon the beat note frequencies depends upon both the direction of the rocket roll and the sign of the Doppler shift. Assuming the radial velocity component of the rocket with respect

to the ground station $\dot{R}$, to be a first approximation to $\dot{R}_p$, the velocity component in the propagation direction, we can rewrite the beat frequency

$$F_{o,x}=D(n_{o,x}^{(h)}-n_{o,x}^{(l)}), \tag{3}$$

where $D=\frac{mf}{c}\dot{R}$ is the free-space Doppler effect at the high frequency, a quantity which is directly obtainable from the experiment. It should be noted that in Equation (3), $F_{o,x}$ and D are experimentally determined quantities which are obtained during the rocket flight as a function of time (and hence altitude). Formula (3) therefore yields the difference between high and low frequency indices, which determines uniquely the electron density N. In the case when $F_{o,x}$ is relatively large, either as the result of high electron densities, or high rocket velocity or both, the (electronic) combination of ordinary and extraordinary beat frequencies $F'_o+F'_x=F_o+F_x=F_s$ can be used to simplify the data analysis, since this quantity according to Equation (1) is independent of the rocket spin (*4*). However, in the case of small dispersive Doppler effects which result from the use of $f=24.5$ Mc/s and small rockets with relatively low vehicle velocities, the use of F_s is not feasible, since it may correspond to only fractions of 1 c/s and the analysis of the resulting data with good height resolution is thus not possible. The details of the data analysis will be discussed in Section 6.

DESCRIPTION OF THE ROCKET PAYLOAD

The payload consists of two separate sections. The lower section is standard and it is used for the CW propagation experiment, the telemetry and the tracking. The upper section is used to do the additional experiments selected by the experimenter. A typical payload is illustrated by Figures 2 and 3 which show the rocket-borne instrumentation used for the first test of the overall system (Nike-Apache flight NASA 14.31). In this case the upper section of the payload was used to perform a Langmuir probe experiment. Space was also available in the upper section for an additional experiment; however, in NASA 14.31 this space was not utilized. The lower section contains the following components: A CW transmitter which provides two harmonically related signals at 24.53 and 73.60 Mc/s; a transmitter-to-antenna matching unit; a telemetry unit; and the flight batteries. The two harmonically related signals are radiated with shroud antennas which are held around the rocket body by means of mounting straps, as shown in Figure 4.

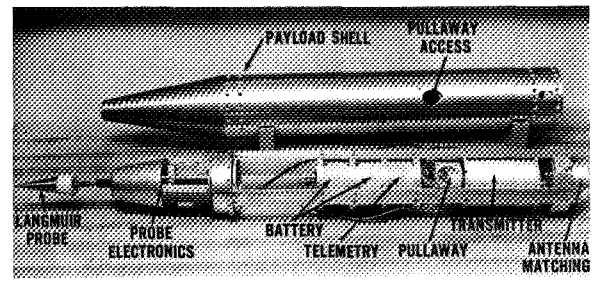

FIGURE 2.—Payload assembly.

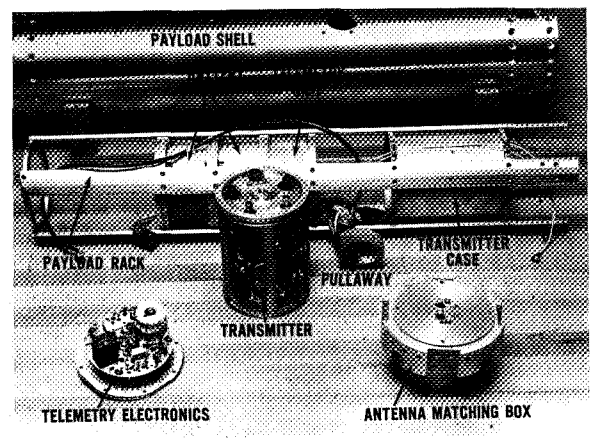

FIGURE 3.—Pay load components.

The transmitter is a transistorized unit built in a pressurized cylindrical case. It was originally designed and used for the P–21 program (*4*, *5*) in which the CW propagation experiment was performed at 12.26 and 73.60

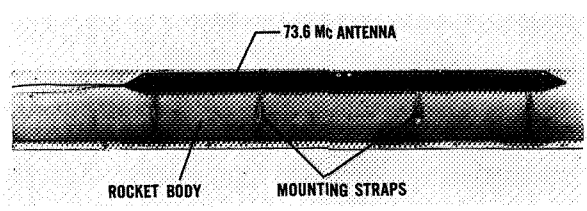

FIGURE 4.—Mounting of shroud antenna.

Mc/s using ARGO D–4 and Scout rockets. The same transmitter is used for the present program with one modification, namely the change of the low frequency from 12.26 to 24.53 Mc/s. A frequency stability of 1 part in 10^8 was achieved by enclosing the crystal and oscillator circuit in a proportional oven. The transmitter delivers 1.5 watts at 24.53 Mc/s and 0.5 watt at 73.6 Mc/s.

The shroud antennas used for the 24.53 and 73.60 Mc/s are modified versions of the antennas initially developed by the Ballistic Research Laboratory (Aberdeen, Md.). These antennas are mechanically very simple, they require no storage space inside the payload and with the modifications made at GSFC (*6*) an adequate efficiency can consistently be achieved. The antenna breakdown problem (*7*) usually encountered in the 60- to 100-km altitude range has been eliminated by operating the antennas at reduced voltage over this altitude range. Since reliable electron density profiles cannot be obtained at altitudes below 90 km, when antenna breakdown is present, the prevention of breakdown is a valuable feature if data are desired at altitudes between 60 and 90 km.

The telemetry is accomplished by modulating the 73.6-Mc/s signal a total of about 60 percent with two FM subcarriers having a center frequency of 7.35 kc/s and 10.5 kc/s, respectively, and a $\pm 7\frac{1}{2}$ percent deviation for a standard 0- to 5-volt dc input. The telemetry bandwidth is approximately 100 cycles. The battery consists of 26 nickel-cadmium cells which provide an output of 32 volts with a capacity of 1 ampere-hour. A dc-to-dc converter is also included to operate the telemetry subcarriers and to furnish any battery voltage required for the additional experiments. The pullaway cable provides a means for charging the batteries, for the preflight 1-hour warmup of the transmitter using external supplies, for monitoring the transmitter output voltages, and for the usual on-off controls of the entire payload. Some leads are also available for monitoring the additional experiments.

The payload dimensions as used for the Nike-Apache flight NASA 14.31 are shown in

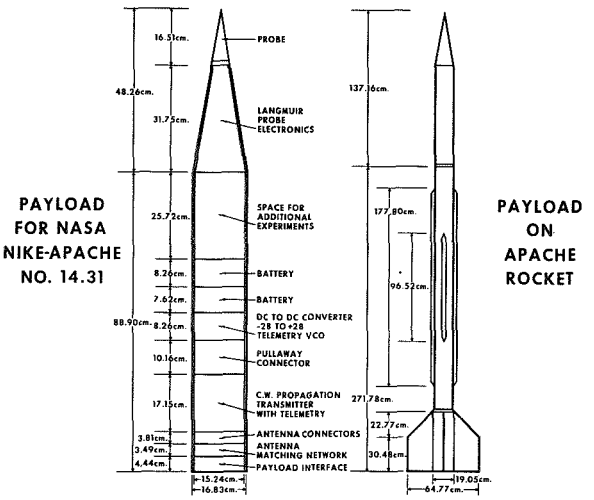

FIGURE 5.—Outline of a typical payload giving location of components and shroud antennas.

Figure 5. The total weight of the NASA 14.31 payload, including the additional Langmuir probe experiment, was 32 kg (70 lbs). No effort was made to reduce this weight, since the combined weight and length of the payload were close to optimum from the standpoint of the aerodynamic stability of the rocket. A peak altitude of 167 km was achieved with this payload, in spite of the additional drag introduced by the four shroud antennas.

DESCRIPTION OF THE GROUND STATION

The ground station is very similar to the receiving site used at Fort Churchill during the International Geophysical Year for the CW propagation experiments conducted by the Naval Research Laboratory (*8*). It consists basically of the subsystems shown by the block diagram of Figure 6. They include: the receiving antennas, the local oscillator, the 73.6-Mc/s receivers, the circuits used to derive the 73.6-Mc/s Doppler shift and the rocket roll, the 24.53-Mc/s receivers, the circuits used to derive the beat frequency signals $F'_{0,x}$, and the telemetry receiver. In addition, suitable equipment is required to record the experimental data.

The 73.6-Mc/s and the 24.53-Mc/s signals are each received with an antenna, which is essentially a circularly polarized Yagi. The 24.53-

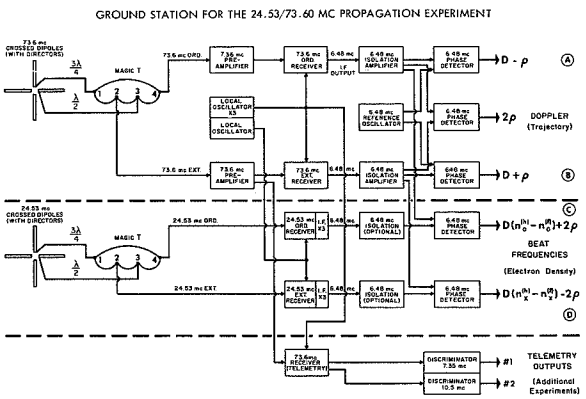

FIGURE 6.—Block diagram of the ground station.

Mc/s receiving antenna is fixed in position, and oriented to give maximum gain near the peak of the predicted trajectory. The smaller 73.6-Mc/s antenna is placed on a movable platform and its orientation is manually adjusted during flight according to the predicted look angle. A Magic T (*8*) is used with each antenna in order to detect both polarization modes. The ordinary and extraordinary modes are then fed to separate receiving systems.

In view of the unusual requirements placed upon the local oscillators, this function is performed by a separate unit. The local oscillator provides the first of the two reference signals used at the ground station for the Doppler measurement. An accurate Doppler measurement requires the local oscillator to maintain a stability of at least 1 part in 10^9 during the rocket flight. This stability is achieved with a crystal-controlled circuit which is enclosed in a well-regulated oven. A careful mechanical design also contributes to this stability. A high-quality capacitor is used to modify slightly the crystal frequency which makes it possible to adjust the Doppler signal to its initial prelaunch zero value. The amount of frequency-control available in this manner is about 0.002 percent. If the presence of radio interference requires some additional frequency shift, this is accomplished by replacing the crystals both in the transmitter and in the ground station local oscillator. The local unit provides outputs harmonically related in a 3-to-1 ratio. The low frequency outputs serve as local oscillators for the two 24.53-Mc/s signals and the high frequency outputs serve as local oscillators for the three 73.60 Mc/s receivers.

The two 73.6-Mc/s receivers used for Doppler measurement and for the CW propagation experiment convert the input signals to a 6.48-Mc/s IF frequency. The use of crystal filters in the IF amplifier yield a net receiver bandwidth of 2.5 kc/s which is more than adequate to accommodate the change in input signal frequency due to Doppler shift. This narrow bandwidth eliminates the telemetry subcarrier, and minimizes noise and radio interference. The receivers use automatic gain control; the AGC voltage is also recorded during flight to provide a measurement of signal strength. The output of each of these 73.6-Mc/s receivers is a CW signal at 6.48 Mc/s whose amplitude is maintained at approximately one volt by the combined action of the AGC and of a voltage limiter, for input signals to the 73.6-Mc/s preamplifier ranging from 0.1 to 1000 microvolts. This constant amplitude output is required for the proper operation of the subsequent phase comparison circuits. A preamplifier is used ahead of the 73.6-Mc/s receiver to provide additional gain. The preamplifier has a nominal 52-ohm input impedance, which can be adjusted resistively and reactively to provide precisely the impedance required for the optimum operation of the Magic T.

The 6.48-Mc/s outputs of the 73.6-Mc/s ordinary and extraordinary receivers have the following frequencies:

$$f_H - n_o^{(h)} D + \rho - f_o \tag{4}$$

and

$$f_H - n_x^{(h)} D - \rho - f_o \tag{5}$$

where

f_H=frequency of 73.6-Mc/s signal as transmitted from the rocket.

$n_o^{(h)} D$=73.6-Mc/s Doppler shift for the ordinary mode.

$n_x^{(h)} D$=73.6-Mc/s Doppler shift for the extraordinary mode.

ρ=rocket roll.

f_o=local oscillator frequency.

Direct comparison of the signals given by Equations (4) and (5) yield:

$$2\rho+D(n_o^{(h)}-n_x^{(h)})=2\rho$$
$$+\text{Faraday rotation at 73.6 Mc/s.}$$

For ionosphere experiments using small rockets the 73.6-Mc/s Faraday rotation is less than 0.1 c/s, whereas 2ρ is generally 10 c/s. Thus comparison of Equations (4) and (5) yields the rocket roll with an accuracy better than 1 percent.

Signals (4) and (5) are also individually compared to a 6.48-Mc/s reference oscillator whose frequency is actually f_H-f_o, and whose frequency stability is 1 part in 10^9. This yields the following difference frequencies:

$$n_o^{(h)}D-\rho\cong D-\rho \tag{6}$$

and

$$n_x^{(h)}D+\rho\cong D+\rho \tag{7}$$

Since the frequency of the Doppler signal is in general too high for direct reading from the record, commercial decade counters are used to divide the Doppler signals. Decade counters are also used to generate the timing signals, from the output of a timing oscillator.

Addition of Equations (6) and (7) yields the roll-free Doppler shift at 73.6 Mc/s:

$$D(n_o^{(h)}+n_x^{(h)})\cong 2D. \tag{8}$$

At 73.6 Mc/s the two indices are very nearly equal to each other, and for rocket flights below 180 km their values will range from 1.0 in free space to about 0.96 corresponding to a density of 5×10^5 el/cm^3. Thus, the sum of Equations (6) and (7) yield essentially the correct Doppler shift at altitudes below 100 km, and at higher altitudes a correction amounting to a few percent can be made for the ambient local electron density. This ambient density can be initially calculated with less than 5 percent error by using the approximation given in formula (8). This first calculation of electron density is adequate to determine D more accurately. If desired, the process can be repeated for additional accuracy, but this is usually not necessary.

The 24.53-Mc/s receivers are very similar to the high frequency receiver. In this case the impedance matching to the Magic T is accomplished at the input of the receiver (since a preamplifier is not used). The crystal filters used in the IF amplifier produce a net receiver bandwidth of 800 c/s. The outputs of IF amplifiers after frequency multiplication by a factor of 3 yield signals whose nominal frequency is 6.48 Mc/s. The actual frequency of the output signals are:

$$3\left[\frac{f_H}{3}-n_o^{(l)}\frac{D}{3}+\rho-\frac{f_o}{3}\right]=f_H-n_o^{(l)}D+3\rho-f_o \tag{9}$$

and

$$3\left[\frac{f_H}{3}-n_x^{(l)}\frac{D}{3}-\rho-\frac{f_o}{3}\right]=f_H-n_x^{(l)}D-3\rho-f_o. \tag{10}$$

These signals are compared to the corresponding ordinary and extraordinary outputs given by Equations (4) and (5) of the 73.6 Mc/s receivers and two difference signals are obtained having the frequencies

$$F_o'=D(n_o^{(h)}-n_o^{(l)})+2\rho$$

and

$$F_x'=D(n_x^{(h)}-n_x^{(l)})-2\rho$$

A third 73.6-Mc/s receiver is used for the telemetry. This receiver is identical to the two other 73.6-Mc/s receiver except for the fact that crystal filters are not used in the IF amplifier. This provides a 50-kc/s bandwidth which is adequate for the reception of the telemetry subcarrier.

A certain amount of test equipment is required to adjust the various components of the ground station and to check the overall operation. Some of the necessary equipment is available commercially such as impedance bridges and signal generators. A commercial frequency counter is also highly desirable. Special test equipment has been designed at GSFC to adjust and check the crystal filters used in the 24.53- and 73-6-Mc/s receivers. Since commercial signal generators are not sufficiently stable to simulate the input 24.53 and 73.6 Mc/s signals, special test generators have also been designed for this purpose.

USE OF DOPPLER DATA FOR TRAJECTORY DETERMINATION

If the ground station for the CW propagation experiment is located within 1 or 2 km from the launch site, the ground station Doppler data can be used to calculate small rocket trajectories (*9*) if the payload transmitter maintains a stability of the order of 1 part in 10^8. The rocketborne transmitter has a stability of 1 part in 10^9 in the laboratory and during ballistic flight its stability is at least 1 part in 10^8. During the propulsion period some difficulties have been experienced in maintaining the required 1 part in 10^8 stability. However it is anticipated that this can be achieved in the near future as a result of further refinements which are currently under investigation. The uncertainty of the trajectory determination (assuming a stability of at least 1 part in 10^8 in the Doppler data) is about ± 1 km in absolute altitude which is adequate for most purposes. The relative altitudes in a given region of interest are, of course, known with far greater accuracy and consequently profiles of the measured ionospheric parameters will not be appreciably distorted by the small uncertainty in the absolute altitude.

The method is based upon the following approximations which are valid for rockets such as the Nike-Cajun and the Nike-Apache which have peak altitudes less than 200 km:

1. Earth curvature and rotation can be neglected;
2. The trajectory is in a plane which contains the launch site;
3. If the ballistic portion of the trajectory is extended below the drag region, that is for altitudes below 70 km, the extension of the trajectory (assuming no drag) will intersect the ground within a few kilometers of the launch site and of the nearby ground station.

A more complete presentation of the technique, which includes a discussion of the errors introduced by the above assumptions and of the corrections which can be made if desired, is given (*9*).

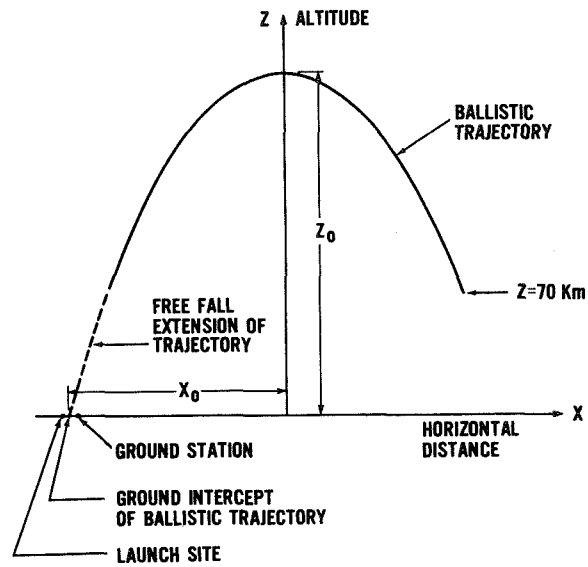

FIGURE 7.—Geometry of typical small rocket trajectory.

These assumptions are illustrated in Figure 7. Under these conditions the trajectory above 70 km is defined by the following equations, where the coordinate system is as shown in Figure 7:

$$X=X_o+\dot{X}t \qquad (\dot{X}=\text{constant}) \qquad (13)$$

$$Z=Z_o-g_o\frac{t^2}{2}[1+\alpha t^2] \qquad (14)$$

where

X=horizontal distance.
X_o=distance from launch to subpeak point (i.e.=horizontal distance at peak).
$\dot{X}$=horizontal velocity.
Z=altitude.
Z_o=peak altitude.
$\alpha=2.42\times10^{-7}/\text{sec}^2$ for typical small rocket trajectories.
$g_o=g_e\frac{R_e^2}{(R_e+Z_o)^2}$=value of g at peak.
g_e=value of g at the ground.
R_e=earth radius.

The term involving α takes into account the variation of the acceleration of gravity g with altitude. Since g_o is related to Z_o, the unknowns are actually X_o, $\dot{X}$, Z_o and the peak time (i.e., the number of seconds elapsed since rocket takeoff).

The fact that the extension of the ballistic trajectory is assumed to intercept the launcher leads to:

$$X_o=\dot{X}T$$

where

T is the total free fall time from Z_o to the ground, a quantity which is less than the peak time.

Since

$$Z_o=g_o\frac{T^2}{2}[1+\alpha T^2]$$

the following relationship holds between Z_o and X_o.

$$Z_o=g_o\frac{X_o^2}{2\dot{X}^2}\left[1+\alpha\frac{X_o^2}{\dot{X}^2}\right]. \qquad (15)$$

The Doppler measurement at 73.60 Mc/s yields the quantity $D=245.3\ \dot{R}$ c/s (where $\dot{R}$ is in km/sec) from which the radial velocity $\dot{R}$ and the radial distance R can be calculated.

These are related to X and Z in the following manner:

$$R^2=X^2+Z^2 \qquad (16)$$

$$R\dot{R}=X\dot{X}+Z\dot{Z}. \qquad (17)$$

The trajectory determination is based upon the relationships (15), (16) and (17). The calculation is done in two steps:

First the peak time is obtained by making use of the fact that the graph of $R\dot{R}$ versus time is symmetrical with respect to peak (*9*). A plot of $R\dot{R}$ versus time is shown in Figure 8 for the portion of the trajectory which is above 70 km. The value of $R\dot{R}$ at the peak of the trajectory is:

$$(R\dot{R})_o=\tfrac{1}{2}[(R\dot{R})_{\max}+(R\dot{R})_{\min}]$$

This yields the ordinate of point P on the graph, and having located point P, the corresponding abscissa is the peak time t_o. The value of t_o should be read to within 0.1 second, since the method yields the value of peak time to within a few tenths of a second in spite of the simplifying assumptions underlying the calculations. Knowing the peak time, we can readily obtain the corresponding radial distance R_o which

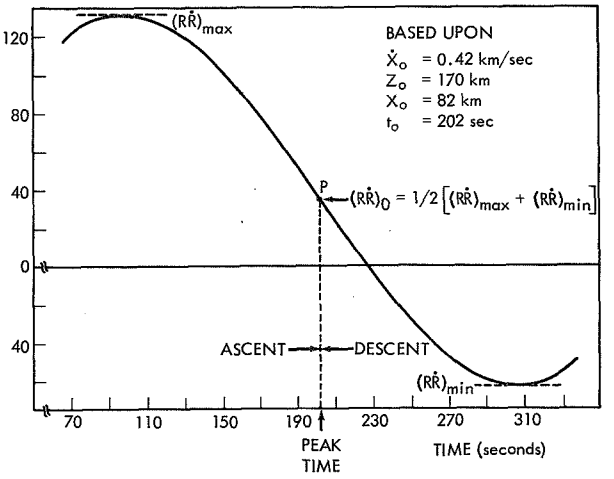

FIGURE 8.—The RR function for a typical Nike-Cajun trajectory.

gives the following equation between X_o and Z_o:

$$R_o^2=X_o^2+Z_o^2. \qquad (16)$$

Also at peak, Equation (17) reduces to the following:

$$(R\dot{R})_o=X_o\dot{X} \qquad (17)$$

The calculation of Z_0, X_0, and $\dot{X}$ can then be performed by solving simultaneously equations (15), (16′), and (17′). This system of equations can be solved analytically very rapidly (*9*) by a method which makes use of successive approximations to the correct value of g_0 and also makes use of one additional experimental value of the quantity $R\dot{R}$. A simpler method is to use a graph showing the value of Z_0 as a function of $(R\dot{R})_0$ and R_0. Such a graph is shown in fig. 9.

ANALYSIS OF CW PROPAGATION EXPERIMENT

For the data analysis of the present experiment, it has been found advantageous to make use of the normally unwanted rocket spin. Small rockets, of the Nike-Apache type usually require a spin of $\rho\approx 5$ c/s to insure proper rocket stability. Because of the relatively low vehicle velocity combined with the use of a relatively high frequency (24.53 Mc/s), the quantity F in equation (2) will usually be much smaller than 2ρ. The latter quantity is also

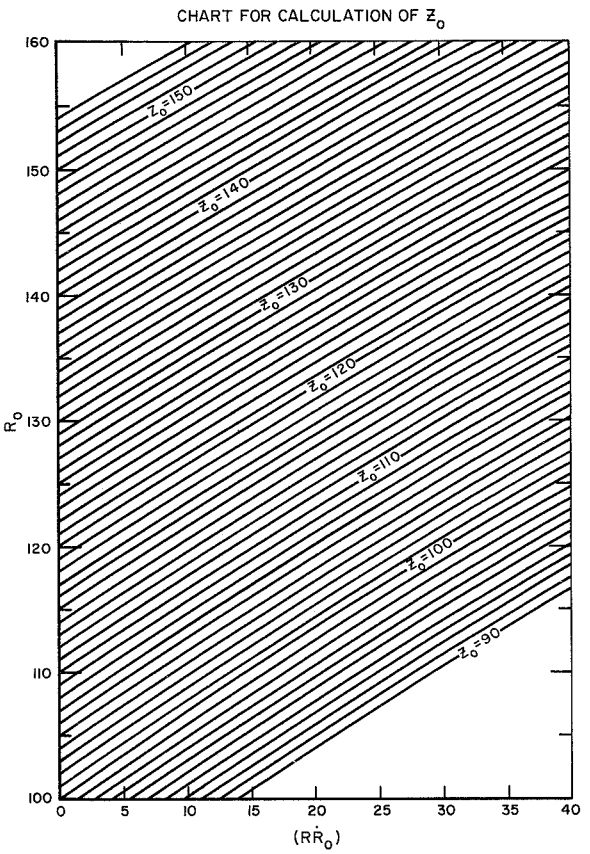

FIGURE 9.—Nomogram giving the peak altitude as a function of $(R\dot{R})_0$ and R_0.

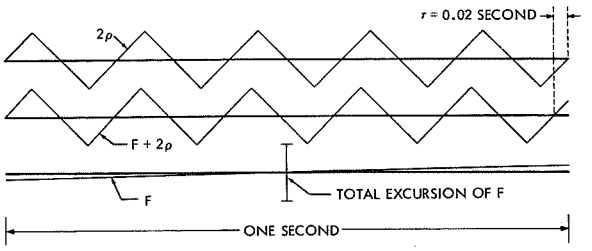

FREQUENCIES ASSUMED AS FOLLOWS: 2ρ = 5 CPS; F = 0.1 CPS
RESOLUTION IN MEASURING τ IS 0.001 SECOND

FIGURE 10.—Detection of very low frequency beats with the aid of rocket roll.

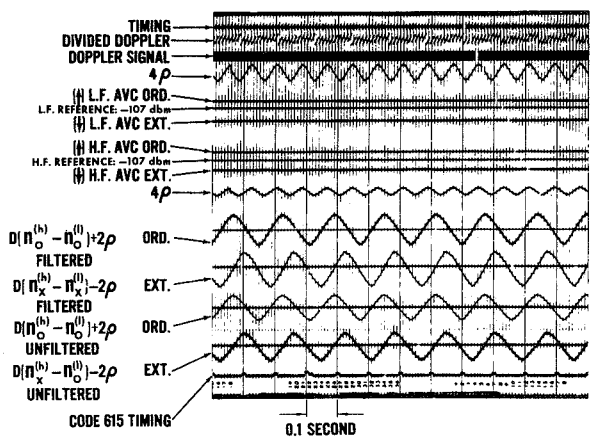

FIGURE 11.—Sample recording of CW propagation data.

obtained directly by comparing the ordinary and extraordinary propagation modes at 73.6 Mc/s. Since the accuracy in time measurements is of the order of 0.001 sec, a time difference as small as 0.01 sec can still be measured with a sufficiently high accuracy. For this reason the rather small quantity F can be measured by comparing the period of 2ρ with that of $F' = F \pm 2\rho$. The basic method of measuring the beat frequency F in this manner is illustrated in Figure 10, where the following assumptions were made:

$$F = 0.1 \text{ c/s and } 2\rho = 5 \text{ c/s}$$

The time difference in the periods of F' and 2ρ correspond in this case to 0.02 sec which can be measured with sufficiently high accuracy over a one second interval which is desirable for proper height resolution.

The actual case is somewhat different from the idealized case described above since the observed spin rate 2ρ is not uniform (*10*), but shows a modulation due to the changing aspect. It is therefore necessary to read data over complete roll periods or multiples to assure the same aspect and phase. Some actually recorded data of roll and beat frequency are shown in Figure 11, which corresponds to a flight where the rocket axis was very nearly pointed toward the ground station. Figure 12 shows data for the Nike-Apache flight NASA 14.32 illustrating the effect of poor aspect on the roll frequency. The interval A–B on the 4ρ signal corresponds to a full roll period and it is seen that it contains two fast and two slow cycles. The interval C–D corresponding to a higher altitude reveals a shift in the zero-crossings of F_0' and F_x' which is due to the total electron content

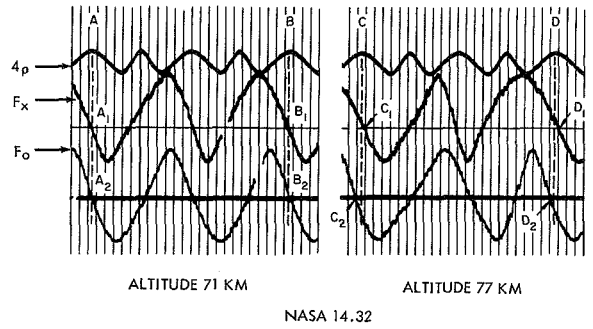

FIGURE 12.—Sample recording showing roll-modulated beat frequencies.

between the altitudes corresponding, respectively, to intervals A–B and C–D.

The determination of F from F' by comparing this quantity with 2ρ can obviously be made for both the ordinary and extraordinary mode, thus increasing the measurement accuracy. The sum beat frequency $F_s=F_o+F_x$ can also be obtained by combination of the periods T_0' and T_x' of F_0' and F_x' to give

$$F_s=\frac{T_o'+T_x'}{T_0'T_x'}.$$

Finally, for deriving the electron density N from the beat frequencies F_o, F_x, or F_s, it is convenient to represent the appropriate linear combination of refractive indices of high and low frequency which are individually computed from the complete Appleton-Hartree formula, graphically as a function of N with parametric values for the magnetic field H and the angle between the propagation direction and H. For the low altitude flights under consideration, an effective value of H can be assumed, since the magnetic field does not change significantly over the first 200-km altitude interval. By making use of the high accuracy in time measurements of the periods corresponding to the beat frequencies $F_{o,x}$, it is possible to obtain a resolution of about 500 el/cm^3 in the determination of electron density, using frequencies of 24.53 Mc/s and 73.6 Mc/s and a rocket of the Nike-Apache type.

From the viewpoint of easier data analysis, it is desirable to locate the ground station near the launch site. In this case the aspect of the rocket antennas will generally be good at least on the upward leg of the trajectory and for this portion of the trajectory the propagation path will fall essentially along the rocket trajectory.

As a first approximation to equation (1), it was assumed in equation (2) that the rocket velocity component in the propagation direction $\dot{R}_p$ is identical to the radial velocity component of the rocket, $\dot{R}$. At the relatively high frequencies used in this experiment, this is a reasonably good approximation for the lower part of the trajectory. However, with more oblique propagation paths in the uppermost portion of the trajectory and especially on the downleg, this ceases to be true and a correction for this effect is required. In essence, this correction is equivalent to a first-order refraction correction to account for the effect of the ionosphere, which causes the ray direction of the radio wave to depart from the radial direction of the rocket velocity component. Although the correction would essentially require a ray-tracing procedure, a simple first-order correction of the type outlined below has been found to be sufficiently accurate for low altitude rockets. If N' is the electron density derived from the beat frequency F, assuming $\dot{R}_p=\dot{R}$, the true electron density N taking into account the effect of obliquity (refraction) is given by (*4*)

$$N=N'+\frac{\epsilon}{1-\epsilon}(N'-\overline{N})$$

with $\epsilon=\frac{\dot{\theta}R\tan\theta}{\dot{R}}$, where θ is the zenith angle of the rocket position vector at the ground station, R is the radial distance between rocket and ground station and $\dot{R}$ is the radial velocity component, quantities which can be obtained from the trajectory data and where

$$\overline{N}=\frac{1}{R}\int_0^R NdR\cong\frac{1}{R}\int_0^R N'dR.$$

Inclusion of the above correction is equivalent to using the rocket velocity component $\dot{R}_p$ along the ray path as discussed by Kelso (*11*). The above analysis yields reliable electron

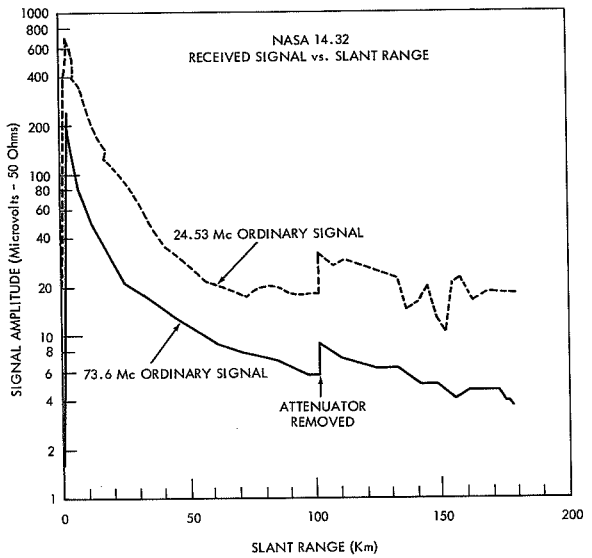

FIGURE 13.—Amplitude of received signals during a test flight.

density profiles up to an altitude within 5 to 10 km of apogee. Close to apogee altitudes a detailed ray-tracing analysis including a correction for the time variation in the ionosphere would be required, an effort which, in general, is not warranted for such a small height interval.

RESULTS

Two Nike-Apache flights (NASA 14.31 and 14.32) have been made from Wallops Island, Va., late in 1962 to test the operation of the described payload, both of which were completely percent obliquity correction $\left(\frac{N-N'}{N}\right)$ at 120 km, 140 km, and 160 km was 1, 7, and 17 percent for profile A, and 1, 3, and 7 percent for profile B, respectively. It should be noted that these two midday profiles at midlatitudes indicate once more the absence of a significant "valley" in the electron density distribution between the E and F regions as had been observed in earlier experiments (*12*).

In Figure 15 is shown a comparison of the electron density successful. In Figure 13 the CW signals received as a function of range are shown. It is obvious that the shroud antennas provided efficient radiation for performing the CW propagation experiment, the Doppler effect measurements as well as the telemetry mission. The field strength on the ground at the two frequencies were about 4 microvolts/meter for a maximum slant range of about 180 km.

Figure 14 shows the electron density profiles obtained from the CW propagation experiment for the two flights. The profile obtained with the CW propagation experiment with that obtained from a Langmuir Probe Experiment of L. G. Smith occupying some of the remaining payload space on NASA 14.31. This flight represented the first direct calibration of the asymmetric Langmuir Probe (*13*). In addition, electron densities obtained from a true-height analysis of the Wallops Island ionosonde observations at flight time are shown, indicating a departure from the rocket profiles at altitudes below 130 km, which is obviously the result of the lack of ionosonde measurements for the lowermost ionosphere.

CONCLUSION

The small payload for ionosphere studies described in this paper has been successfully tested on two Nike-Apache rockets. Its ver-

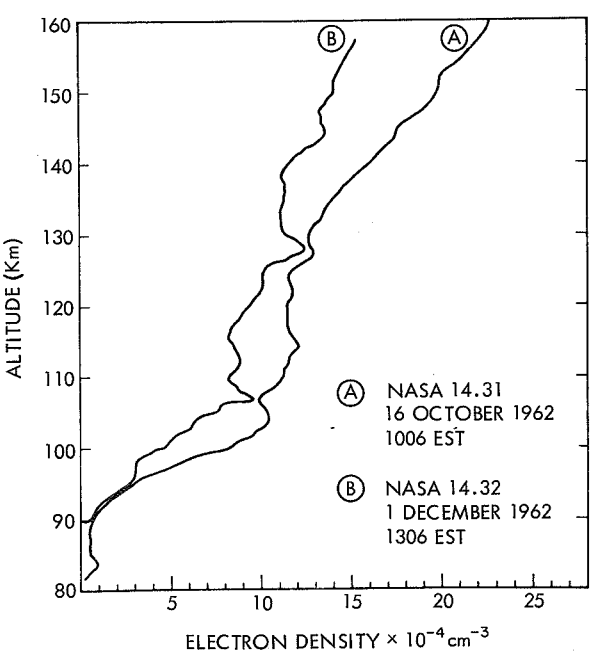

FIGURE 14.—Electron density profiles obtained during the two test flights.

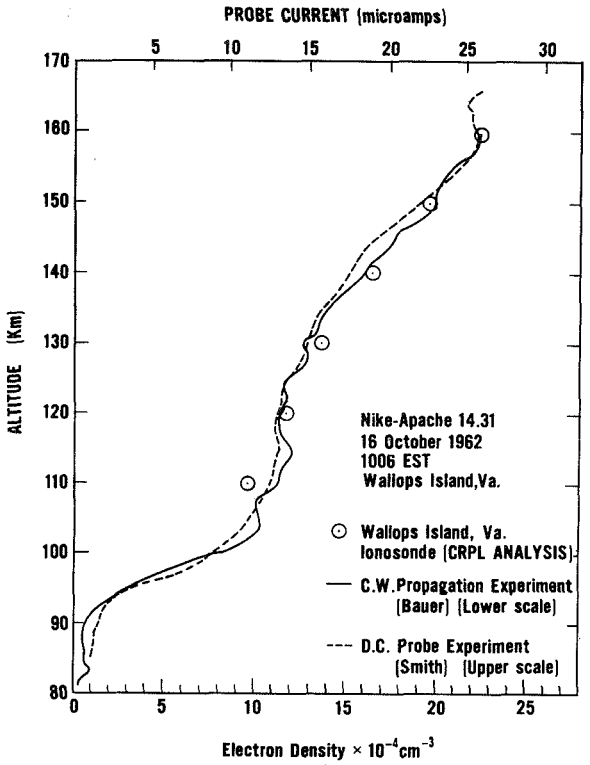

FIGURE 15.—Comparison between electron density profiles obtained simultaneously by two different techniques.

satility, simplicity and relatively low cost should make this payload an ideal tool for the investigation of many problems of the ionospheric E and F regions by the international scientific community, especially during the IQSY. Useful electron density measurements throughout the *D*-region appear also feasible as the results of the development of a 12-Mc/s shroud antenna which is presently under investigation. The details of the design of the payload and ground station will be made available to all interested experimenters upon request.

ACKNOWLEDGMENTS

Mr. G. H. Spaid and Mr. J. R. Hagemeyer have been responsible for the design of the payload and ground station as well as for the supervision of the field operations for the two rocket flights. Their suggestions and comments during the preparation of this paper are also gratefully acknowledged.

REFERENCES

1. J. C. SEDDON, "Propagation measurements in the ionosphere with the aid of rockets," *J. Geophys. Research*, 58 (1953), No. 3, pp. 323–335.
2. J. C. SEDDON and J. E. JACKSON, "Rocket arctic ionosphere measurements," Nat'l Acad of Sci. IGY Rocket Report No. 1 (1958), p. 140. Also published as: 3686—Pergamon—IGY—Vol. XI—180—7: 11.
3. J. A. KANE, "Arctic measurements of electron collision frequencies in the D-region of the ionosphere," *J. Geophys. Res.* 64 (1959), No. 2, pp. 133–139.
4. J. E. JACKSON and S. J. BAUER, "Rocket measurements of a daytime electron density profile up to 620 Km," *J. Geophys. Res.* 66 (1961), No. 9, pp. 3055–3057.
5. S. J. BAUER and J. E. JACKSON, "Rocket measurement of the electron density distribution in the topside ionosphere," *J. Geophys. Res.* 67 (1962), No. 4, pp. 1675–1677.
6. G. H. SPAID and R. J. HAGEMEYER, "Investigation of HF and VHF rocket-borne shroud antennas," to be published as a NASA/GSFC Report (1963).
7. J. E. JACKSON and J. A. KANE, "Breakdown and detuning of transmitting antennas in the ionosphere," NRL Report No. 5345, August 1959.
8. J. E. JACKSON and G. H. SPAID, "Ground stations for NRL rocket studies of the ionosphere," NRL Report No. 5342, August 1959.
9. J. E. JACKSON and S. M. RADICELLA, "Calculation of small rocket trajectories using only rocket-to-launcher radial velocity data," GSFC Rept. X–615–62–139, Aug. 15, 1962.
10. J. E. JACKSON, "Measurements in the E-layer with the Navy Viking rocket," *J. Geophys. Res.* 59 (1954), No. 3, pp. 377-390.
11. J. M. KELSO, "Doppler shifts and Faraday rotation of radio signals in a time-varying inhomogeneous ionosphere," Part I, J. Geophys. Res. 65 (1960), No. 12, pp. 3909–3914; Part II, J. Geophys. Res. 66 (1961), No. 4, pp. 1107–1115.
12. J. C. SEDDON and J. E. JACKSON, "Absence of bifurcation in the E-layer," *Phys. Rev.*, Vol. 97 (1955), pp. 1182–1183.
13. L. G. SMITH and S. J. BAUER, to be published in *J. Geophys. Res.* (1963).

TELEMETRY DATA PROCESSING FOR THE ECCENTRIC ORBITING GEOPHYSICAL OBSERVATORY SATELLITE

R. COATES, C. CREVELING, E. HABIB, M. MAHONEY, and C. STOUT

Goddard Space Flight Center

The Eccentric Orbiting Geophysical Observatory (EGO) is being designed to have PCM telemetry data rates of 1,000, 8,000, or 66,000 bits/second—selectable by ground command. This satellite will have on-board data storage for low speed data (1,000 bits/second), plus about 40 percent ground station coverage of each orbit for data acquisition at any of the bit rates. The program planned for the first EGO satellite anticipates receiving and average of 6,000 bits/second for a period of 6 months, or a total of about 10^{11} bits. The high-speed data-processing system for this high volume of data consists of two processing lines, plus a large-scale digital computer. The processing lines convert the analog recordings of the PCM telemetry signals to digital magnetic tapes in computer format. The computer then performs quality control and decommuntation of the data into separate digital tapes for each experimenter. The system will be described in detail.

INTRODUCTION

The Eccentric Orbiting Geophysical Observatory Satellite [1] (EGO) is the first of a series of large satellites designed to accommodate a variety of scientific space experiments. These satellites will be placed into orbit at regular intervals over the next several years. By their size and complexity, and by the number of experiments aboard (20 in the first EGO), these satellite projects have called for a fresh look at the problems of telemetering to earth vast quantities of data, and of processing this data into forms suitable for utilization by the experimenters. In order to appreciate these problems, a few statistics are in order.

The telemetry system of the EGO satellite provides many modes of operation in order to handle a variety of data types and provide sampling rate flexibility. The main telemetry system is a PCM system with a basic format of 128 9-bit words in the main frame. In the real-time mode, data can be telemetered at a rate of 1,000, 8,000, or 64,000 bits/sec as selected by command. This permits selection of the data rate which best matches the needs of the experiments at the particular time of observation. In addition to the choice of basic bit rate, provision is made for command selection of two special modes of operation to provide certain data at accelerated sampling rates.

In the first special mode, the normal main frame is replaced with one of 32 combinations of outputs from several specified experiments. This flexible format mode enables a subgroup of experiments to be operated when phenomena of special interest occur. In the second special mode, one of the spacecraft subcommutators may be substituted for experimental data in order to obtain more operating and functional data relating to the spacecraft itself.

Continuous on-board recording at a rate of 1,000 bits/sec is provided by two tape recorders with a capacity of 43.2 million bits each. The recorded data are played back on command at a rate of 64,000 bits/sec.

[1] W. E. Scull and G. H. Ludwig, "The Orbiting Geophysical Observatories," Proc. IRE, Vol. 50, pp. 2287–2296, November 1962.

In addition to the PCM system, a special-purpose FM/PM telemetry system is provided for transmission of continuous analog data which can not be time multiplexed into the PCM system.

The telemetry signal from the EGO satellite will be received at ground stations, demodulated, and recorded on magnetic tapes. These tapes will be mailed to the Goddard Space Flight Center's data processing facility for production processing. The amount of data to be acquired from EGO is estimated in Table 1.

In 6 months, a total of about 10^{11} bits of data will be acquired from this satellite. This large volume of data will be processed at the Goddard facility on data-processing systems consisting of signal conditioning and formatting units, plus a large-scale digital computer. These processing systems will extract the telemetry and ground station time signals from the station tapes, write this raw data on digital tape in computer format, fan out the data to produce a digital tape for each experiment (containing the data for the experiment plus supporting spacecraft data), generate an orbit-attitude digital tape, and convert spacecraft time to universal time.

PCM DATA PROCESSING

The telemetry tapes received from the data-acquisition stations will be logged and the contents of the tapes will be examined to determine their quality, whether or not the signals were recorded on the proper track, the presence of usable time signals, and whether there may be an equipment malfunction at the data-acquisition station. This tape evaluation provides feedback to the stations in addition to separating tapes which cannot be processed in the automatic system.

The processing of the PCM data on the acceptable station tapes can be described in four phases. Phase I will use specially designed processing equipment while Phases II, III, and IV will use a Univac 1107 digital computer.

The Phase I system (as outlined in Fig. 1) is

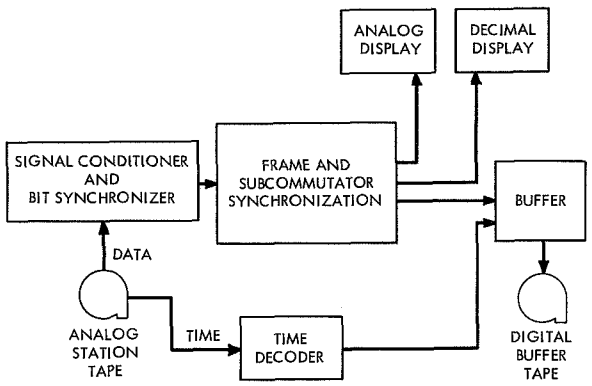

FIGURE 1.—Production data processor for EGO—phase I.

based upon the STARS (Satellite Telemetry Automatic Reduction System [2]) concept of initial digitization of the data to produce a digital tape in proper format for entry into a computer. The soundness of the STARS concept has been established by 2 years of processing

[2] C. J Creveling, C. Stout, A. Ferris, "Automatic Data Processing," IRE Trans. Vol. SET-8, No. 2, June 1962.

TABLE 1.—*Estimated Ego Data Acquisition*

[In percent]

	PCM			Special purpose
	64,000 b/s	8,000 b/s	1,000 b/s	
Normal:				
a. First month	10	30	[1] 100	40
b. Rest of EGO life	5	20	[1] 100	25
Alert: a. Entire EGO life	.5	6	----------	----------

[1] Using the on-board tape recorder.

of PFM data from numerous Goddard scientific satellites. These, however, utilized far lower data rates than EGO and similar "observatory" class satellites. The design of the EGO Phase I processing system contains many improved features for the faster and more efficient handling of the large volume of EGO data.

A pair of analog tape decks are used alternately for playback of the station tapes. The serial PCM signal (which will be very noisy when the satellite is at apogee) is routed to the signal conditioner, and the ground station time codes and reference frequencies are sent to the time decoder. The signal conditioner generates a "clock" signal synchronous with the incoming bit rate, decides whether each bit is a "one" or a "zero," and reconstructs a noise-free PCM signal with the same structure as the input PCM signal. The data from the signal conditioner is shifted into a 32-bit shift register via a code converter. This shift register is also used as a serial-to-parallel converter, from which the data is distributed in parallel form to appropriate units in the processor. The frame and subcommutator synchronization recognizers continuously check the incoming data for the presence of frame and subcommutator synchronization patterns respectively. Immediately upon recognition of the proper patterns, the frame and subcommutator sunchronization circuits are "locked" and the decommutation process is initiated. By having several decommutating units in the processor, decommutation of multiple subcommutation sequences randomly located in the main telemetry frame is made possible. The synchronization patterns are selectible by means of a patchpanel. For EGO, a 27-bit truncated autocorrelation code is used. The frame synchronization circuitry offers "flywheel" capability when frame synchronization is lost due to data dropout. It determines the number of errors in the frame synchronization pattern and remains in "lock" as long as the errors do not exceed a preset number (selectible between 0 and 5). When the number of errors is larger than the allowed number for several successive synchronization detections, data to the buffer is deleted and the circuit reverts to a "search" mode. This mode (also used during the initial period of processing a tape) looks for the synchronization pattern each "clock cycle," thus effectively determining the cross-correlation function of the signal with the stored frame synchronization pattern. When in synchronization, this function exceeds the amount preset in the "synchronization errors allowed" counter. After a few successive synchronization recognitions, the circuit proceeds to the "lock" mode and processing begins or continues. The actual error count in the frame synchronization word is provided to the buffer and interleaved with the data as an indication of data quality. The frame and subcommutation formats are selectible in order to handle the several classes of data that will be processed. For example, real-time data will be recorded at either 8 or 64 kilobits/sec in the standard or the special modes, and the data recorded on the spacecraft will be played back to the data-acquisition stations in reversed time sequence. Each of these classes require different frame and subcommutation format programs during the phase I processing, so that the buffer tape created as an end result of the Phase I operation will contain the data in a uniform format.

Decimal and analog displays are provided for a "quick look" at the incoming data and synchronization patterns. Information in particular frame locations can be read out directly to check the quality, validity, and proper decommutation of the acquired data before reduction in subsequent phases.

The synchronization information and the data are entered into the buffer memory and control circuitry where the data are merged with time readings and written on digital tape in high density IBM computer format (556 characters per inch).

The readings of the acquisition station time are provided to the buffer by the time decoder unit. The time decoder receives three signals from the station tape. The stations record the NASA binary coded decimal (BCD) time code [3] and the NASA serial decimal (SD) time

[3] Hewlett Packard Applications Note 52, pp. 1–6 January 1962

code from the station time standard plus a standard frequency. Since the tapes are played back at higher speeds in the processing operation than used in recording, the time decoder is designed to accept time signals with speedup ratios of 1, 2, 4, 8, and 16. A BCD code detector reads the BCD time code and a SD code detector reads the SD time code. Each decoded time is displayed for the operator. An internal 1-kc oscillator is phase locked to the incoming standard frequency through divider chains. The time, as decoded in either the SD or BCD decoders, is automatically set into the accumulating register at the beginning of each processing run or when the mode of operation changes. This register is updated by the 1 kc output from the internal oscillator. A comparison is made between the next BCD time reading, SD time reading, and the updated time in the accumulator. These will agree under normal circumstances, and a quality "flag" * indicating agreement will be presented to the buffer together with the time word from the accumulating register. If the BCD or SD times do not agree with the accumulator, this is also flagged. When the time readings disagree, the circuits automatically check themselves for malfunction. If there is no circuit malfunction, a determination is made as to whether or not the BCD circuit is in synchronism with the incoming BCD time code. If it is in synchronism, a new BCD time code is set in the accumulating register and updated. Thus, when there is a break in the data acquisition period, the time decoder automatically picks up the new time at the start of the new period. The time decoder will flywheel through momentary time signal dropouts or time code errors because the internal oscillator keeps updating the accumulator. If there is a BCD circuit malfunction or a loss of the signal, the BCD circuit is inhibited and the SD circuits provide the time reading. The reverse is true if the SD system fails. Thus, the decoder makes use of the redundancy of having both the BCD and SD time signals available for processing. If only one of these two signals is present, it automatically considers only that one. The "flags" included with each time reading sent to the buffer indicate the amount of confidence the experimenter can place on its accuracy.

The buffer tape produced as an output of Phase I will contain all the raw data, acquisition station time, and status information concerning time and the condition of bit, frame, or subcommutator sequence synchronization. The buffer tape format will be such that the raw data from each telemetry frame will have associated with it a time field and a status field, as shown in Figure 2.

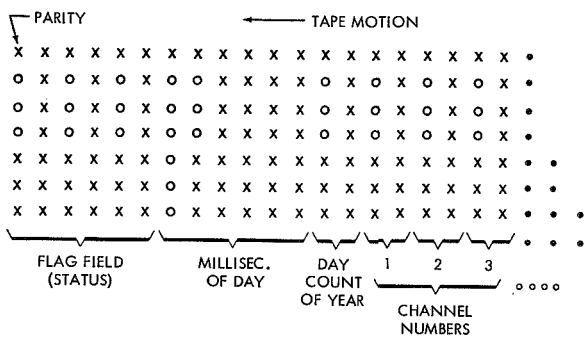

FIGURE 2.—EGO buffer tape format.

The status field contains six computer tape characters, the time-of-day field contains six characters, etc. Two 6-bit tape characters are used for each telemetry data word, but three of the bits in each character pair are left blank. The time indicated will be the time of occurrence of the first bit of the first word of the frame. In the case of on-board stored data, this acquisition station time will be of no interest to the experimenters because the station time will not be related in a simple manner to the time at which the data were recorded in the spacecraft. Consequently, station time will not be placed in the time field for the on-board recorded data during the Phase I processing.

Phase II (illustrated in Fig. 3) will be the processing of the buffer tapes to form the individual experimenter's tapes. This operation will use a Univac 1107 digital computer. Its ultimate outputs will be experimenter data tapes and an aspect housekeeping tape. The configuration of the computer is shown in

* The time quality flag consists of two characters.

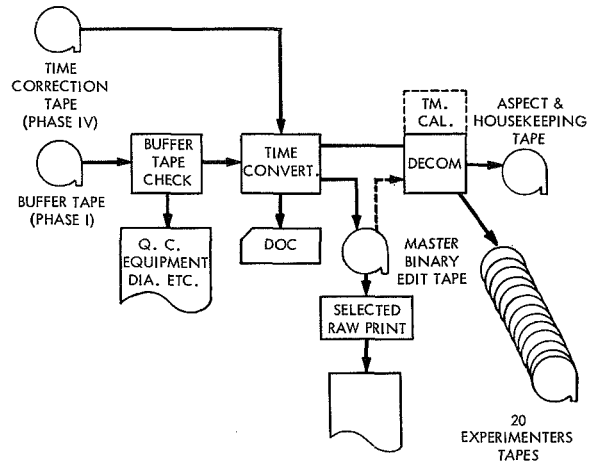

FIGURE 3.—Data processing—phase II.

Figure 4. It provides for simultaneous reading or writing on tape decks on the 3 channels, thereby providing a total tape handling capability of 28 tape units. A large random access drum storage system with a capacity for 1.5 million words provides for quick access of huge volumes of data. Other on-line peripheral equipment include a high-speed printer, a card reader/punch, paper tape reader/punch, and a console typewriter. The tape units and the peripheral equipment use a total of 8 input/output channels. The central processor has a 2-bank core storage with a total of 65,000 memory locations.

The basic word length for the 1107 computer is 36 bits. It has the additional feature of byte manipulation which permits handling of the data in bytes of 12 bits without time-consuming

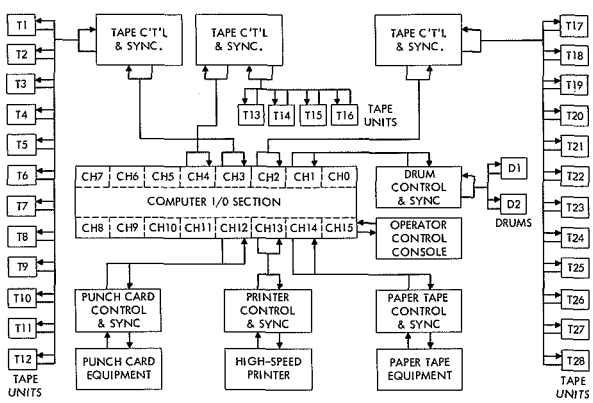

FIGURE 4.—Goddard-Univac 1107 computer configuration.

shift operations. This means a large saving in computer time when processing the short data words from EGO.

During the operation of Phase II the computer will check data quality as well as perform data decommutation. The computer will ascertain whether the data quality has deteriorated in the satellite or ground station telemetry links or in the Phase I operation. Multiple labels* in a file, record length, and frame length will be checked to verify the buffer tape format. Additional checks will involve the form of the data; the sync word will be checked for bit errors, the subcommutator count will be checked for proper sequencing, and data words will be checked to ensure that the first three bits of the 12-bit field are zero. A representative sampling of the analog channels will be checked to ensure that the first bit of the 9-bit field is zero. Additional checks will be made of certain channels in the frame which maintain at a nearly constant level.

This completes the buffer tape check portion of Phase II. The next step is the insertion of corrected universal time in the data format.

The task of correlating universal time with the data will be performed during the time-conversion portion of Phase II. A time-correction tape, generated in the Phase IV operation, will be used as one of the inputs to this operation. This tape will contain a lookup table which will list universal time as a function of the contents of the spacecraft-time word register (words 33, 34, and 35). In order to insert the time associated with a particular data frame, it will be necessary to examine the contents of words 33, 34, and 35, look up the corresponding universal time on the time-conversion tape, and insert this value in the time field. This scheme will provide an accuracy of about 11 milli-seconds for 1,000 b/s data. The time conversion process is discussed in Phase IV.

A master Binary Edit tape containing all data will be generated for further use by the processing personnel on an off-line basis.

*A buffer tape label contains the satellite number, station number, date of reception at ground station, and station tape number.

The decommutation routine is the next step of the Phase II operation. Figure 5 illustrates the manner in which the data will be treated in the computer. A data matrix will be formed in which "i" will denote the column and "j" will denote the row. Each row will consist of three flag elements, three corrected universal time elements derived from spacecraft time in the Phase IV process, one day count of the year element, and the 128 data words from the main frame (i=8 to i=135). The first row will include subcommutator words One. The j in the matrix denotes a subcommutator word number. A value (i, j) designates a *word* in the telemetry format; a row represents a main commutator cycle or *frame*; and the entire matrix represents a subcommutator *sequence*. The groundtime box in the 129th row of the figure is also part of the configuration for real-time data. It is the ground time at the data-acquisition station which was associated with the beginning of word One of the first frame in the matrix. The box will be all zero for spacecraft on-board recorded data.

Following the formation of each matrix in the computer memory, after receipt of data for each complete sequence the decommutation process will extract selected portions to form a number of data tapes equal to the number of experiments on the spacecraft. The experimenter's data tape will include the elements which the experimenter has selected from this matrix. The elements may be arranged within the matrix may be ordered as the experimenters' wish.

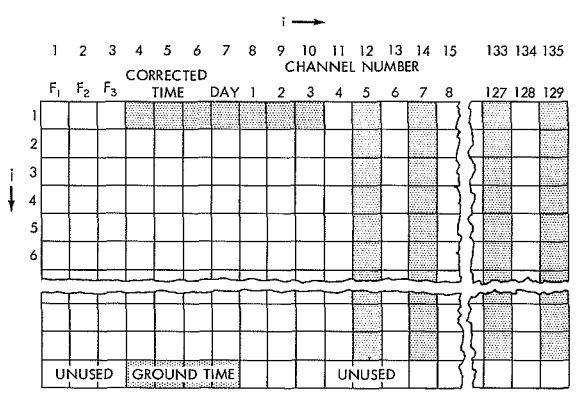

DECOM [(j = 1, 1, 1); (i = 4, 7, 1)*(j = 129, 129, 1); (i + 4, 7, 1)*(j = 1, 1, 1); (i = 8, 10, 1)* (j = 1, 128, 1); (i = 12, 14, 2)(i = 133, 135, 2)] ;

FIGURE 5.—EGO decommutation scheme.

A special feature of this phase is a program generator which uses a FORTRAN-type language to specify the elements of the matrix, and the order they are outputted onto experimenter tapes. An example of a source language statement required to generate a program which will output the cross hatched elements in Figure 5 is shown at the bottom of that illustration.

The generation of the orbit-attitude digital tapes takes place in Phase III. An orbit tape and an aspect housekeeping tape are used as inputs to the program, as shown in Figure 6.

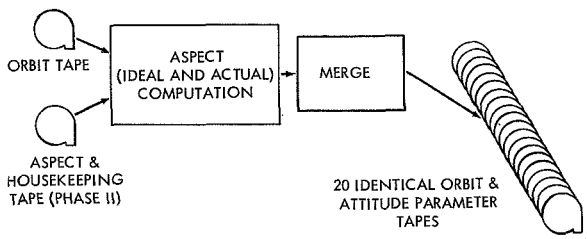

FIGURE 6.—EGO data processing—phase III.

The orbit-attitude tapes will contain the orbit and satellite attitude information in binary floating-point format, with 36 bits to a field. A label record will be located at the beginning of each tape file. The label record will contain the time coverd, the time interval between sets (normally one minute), the day of the year at the beginning of the present orbit, the orbit number, the orbital elements, the sun vector data, the time of the noon-turn, the times of entering and leaving eclispe, and other data. For each minute, the following set of information will be listed: time in milliseconds of the day; position and velocity in celestial inertial coordinates; geographic coordinates of sub-satellite point; height above the geoid; ideal and actual main body, solar array and OPEP orientations; and true anomaly.

The Phase IV operation shown in Figure 7 will result in the generation of a time-correction tape which will permit the conversion of spacecraft time to corrected universal time. On the real-time data tapes, the spacecraft time and the acquisition-station time will be compared

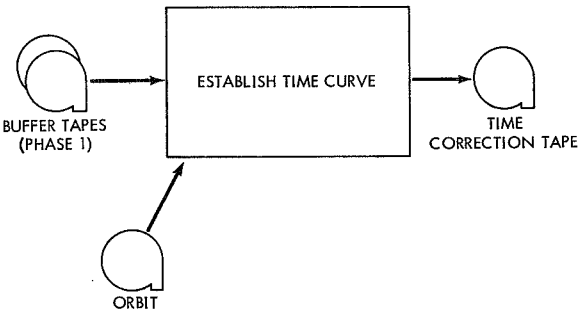

FIGURE 7.—EGO data processing—phase IV.

on a routine basis. Propagation delays in transmitting data from the satellite to the stations (about 0.4 sec at apogee) and of time from WWV (time standard station) to the receiving stations (0.058 sec for Woomera, Australia) will be taken into account, as well as any variations and discontinuities, if they exist, in the basic spacecraft clock system.

This time-correction tape will be used in the Phase II operation. Data time can easily be determined with an accuracy of 1 second if the available numbers are used and no additional computations are performed. Greater accuracy is possible. Figure 8 indicates the

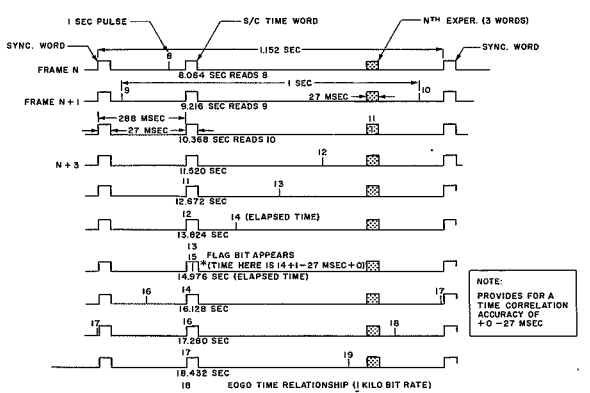

FIGURE 8.—Time insertion for EGO stored data.

manner in which the spacecraft clock and commutator format are phased when the data system is operating at the 1,000-bit-per-second rate. The 1-second pulses refer to the time at which one is added to the contents of the clock register. The contents of the clock register is telemetered once per main frame (words 33, 34, and 35). Sync words refer to the beginnings of the main frame. Each frame requires 1.152 seconds, while the clock period is 1.000 second. A marker "one" is included in the clock word whenever the 1-second pulse occurs while the time words are being telemetered. Whenever this marker "one" is seen the time being read at that instant (after the addition of 1 second) will be accurate to minus 27 milliseconds and plus zero.

Accuracy can be further improved by observing the phasing pattern. The number of frames between marker "ones" will follow a recurring 46, 46, 33, 46, 46, 33 . . . pattern. Whenever the marker "one" occurs after the 33-frame period, the time will be accurate at that time to minus 11 milliseconds, plus zero.

Although this discussion refers to the stored data mode, the same logic applies to the real-time 8, and 64-kilobit data, and similar operations will be performed on them to provide high-accuracy timing for the real-time data.

EGO SPECIAL-PURPOSE TELEMETRY DATA PROCESSOR

The special-purpose telemetry system on EGO will be used for the transmission of data from the Rubidium Vapor Magnetometer. The nature of this data is such that it is not well adapted to a PCM telemetry system in which it would have to be multiplexed with other signals. The signal is therefore transmitted separately on two of the five special-purpose telemetry channels. The magnetometer output signal is a noisy sine wave with a frequency proportional to the magnetic field intensity. The magnetometer frequency range is from about 10 cp/s for weak fields at apogee to frequencies about 100 Kc for the high fields near the earth at perigee. The response of the special purpose telemetry system is limited to 300 cp/s to 100 Kc, and so it is necessary to use two channels for the magnetometer signal. Channel No. 1 will be modulated by the signal taken directly from the magnetometer and will handle magnetometer frequencies between 300 cp/s and 100 Kc. Channel No. 2 will have a 40-kc subcarrier which will be phase modulated by the magnetometer signal for frequencies between 10 cp/s and 600 cp/s.

The special processor for the EGO magnetometer data is outlined in Figure 9. The recorded telemetry signal, the ground station time signal, and the station standard frequency are obtained from the reproduce analog tape deck. The station standard frequency will be either 1 Kc, 10 Kc, or 100 Kc. The tape deck can be made to reproduce the signals at either 1, 2, 4, 8, or 16 times the recorded speed, selectible by pushbutton control.

When processing the direct magnetometer signal (channel no. 1) the "A" phase lock tracking filter is locked to the noisy magnetometer telemetry signal, and the output of the tracking filter is a relatively clean signal which is phase locked to the magnetometer signal. The frequency of this clean signal is measured in the counter unit. The frequency is determined by measuring the number of cycles of the signal in a period of time, which can be selected by means of a set of switches on the control panel. The range of selection is 1 millisecond to 9.999 seconds. The standard frequency, extracted from the analog tape signal by the time decoder, is multiplied to 5 Mc/s to be used for the timing in the frequency measuring unit. By using this recorded standard frequency in this manner, compensation is obtained for effects of tape recorder wow and flutter. Specifically, a counter is started counting cycles of the multiplied standard frequency at a zero crossing of the tracking filter reproduction of the magnetometer signal. The counter is turned off at the second integral signal cycle after the preset time is reached. The number of signal cycles in this period is also counted. The ratio of these two counts gives the frequency of the magnetometer signal. At the shortest time

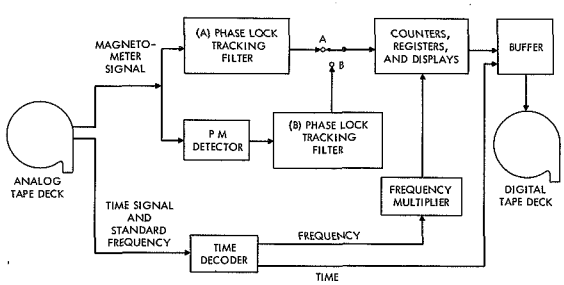

FIGURE 9.—Special data processor for EGO magnetometer.

period, the resolution is limited to one cycle of the 5-Mc/s timing waveform, or 1 part in 5,000. At the longest period the resolution is approximately 1 part in 5×10^7.

When processing the channel No. 2 signal consisting of the subcarrier modulated with the magnetometer signal, the subcarrier is demodulated in the phase-locked PM detector. The resulting noisy low frequency magnetometer signal is fed into the "B" phase lock tracking filter. The output of the tracking filter is sent to the frequency measuring counters through switch position B.

The magnetometer frequency data from the counter registers are put into the buffer where they are merged with ground station time from the time decoder and written on a digital tape in computer format. The time decoder, buffer and digital tape unit are identical to those in the EGO PCM data processor described earlier, and serve similar functions in the special magnetometer processor.

OPERATING TIME

The Table 1 estimate of the amount of data to be acquired from EGO has been used to predict the amount of PCM processor and 1107 computer time which will be required for EGO data processing. In establishing such predictions, many factors other than machine speed were considered such as operator efficiency, down time, tape deck loading time, etc.

During the first month the Phase I PCM processor time will average 18 hours per day, and for the rest of the EGO life the average processor time will be 12 hours per day. Two PCM processors have been built in order to provide the extra capacity for alert periods when the satellite is operated at the highest bit rate, and to provid sufficient redundancy to prevent equipment breakdown from slowing down the processing operations.

The 1107 computer time required for Phases II, III, and IV is predicted to be 22 hours per day for the first month and 14 hours per day for the remaining life of the satellite. It should be noted that Phase II, III, and IV do not include any true data reduction or analysis of the data. These data processing operations

produce a set of digital tapes for each experimenter. These tapes contain all of the experimenters' raw data plus the support data. Each experimenter will be responsible for the reduction and analysis of his data. Four of the EGO experimenters from the Goddard Space Flight Center have arranged for data analysis computations on the 1107 computer. It is estimated that these computations will require three additional hours of computer time per day.

MATHEMATICAL ANALYSIS FOR THE ORIENTATION AND CONTROL OF THE ORBITING ASTRONOMICAL OBSERVATORY SATELLITE

PAUL B. DAVENPORT
Goddard Space Flight Center

A mathematical model is developed by which the following satellite orientation and control problems may be resolved: (1) determining attitude for maximum area of solar cells in sunlight; (2) generating slewing commands for a change in attitude; (3) computing star tracker gimbal angles for maintaining proper orientation; and (4) determining when guide stars are occulted by the earth, sun, and moon.

INTRODUCTION

Sometime in 1964 the NASA expects to launch the first Orbiting Astronomical Observatory (OAO). The OAO, consisting of the spacecraft and the observatory (experimenter's package and equipment), is expected to have a lifetime of 1 year. The spacecraft, orbiting at an altitude of approximately 500 miles, will carry highly refined equipment to conduct astronomical experiments free from the disturbing influence of the earth's atmosphere.

The spacecraft will be capable of directing the experimenter's equipment anywhere in space and of maintaining this direction with a high degree of accuracy. This will be accomplished by a complex stabilization and control system whose major elements are: (1) sun sensors, rate gyros, and a jet system to initially orient and stabilize the spacecraft; (2) coarse inertia wheels to reorient the spacecraft, and fine inertia wheels to maintain the desired orientation; (3) a set of six star trackers to determine the orientation of the OAO; and (4) a magnetic unloading system to keep the momentum in the fine inertia wheels from building up excessively.

To place the OAO in the proper orientation in space, the precise slewing angles needed to accomplish this feat must be known, as well as the gimbal angles of the star trackers when they are locked on their respective guide stars. In addition to these problems various physical constraints such as star occulation by various bodies including the earth, sun, and moon must be considered. There are also many constraints due to the spacecraft itself, which include such things as obtaining maximum power by proper positioning of the solar paddles, keeping the optical axis away from the sun's damaging rays, and restricting the gimbal angles within their limits. This report describes the development of a mathematical model to aid in the solution of these problems.

COORDINATE SYSTEMS

The relative positions of the various bodies in space will be defined by giving their directions with respect to a fixed right-handed rectangular coordinate system with axes u, v, w and origin at the earth's center of gravity. The u–v plane will be the equatorial plane at some epoch T, the positive u axis pointed toward the vernal equinox and the positive w axis toward the true north pole at time T.

The position of a star will be denoted by its right ascension α and declination δ. In most applications the direction cosines a, b, c of the star will be needed; these are given by

$$a=\cos\delta\cos\alpha,$$
$$b=\cos\delta\sin\alpha,$$
$$c=\sin\delta.$$

Since the earth revolves about the sun, the position of the stars is not exactly fixed in this coordinate system; however, the maximum stellar parallax due to this motion is about 0.8 second of arc for the nearest star.

The positions of the sun, moon, and OAO will be given at any time t (measured from the epoch T) by their respective orbital elements, which are:

n=mean angular motion in the plane of the orbit
e=the eccentricity of the orbit
Ω=the right ascension of the ascending node; $0\leq\Omega<2\pi$
i=the inclination of orbital plane to the $u-v$ plane; $0\leq i\leq\pi$
ω=argument of perigee; $0\leq\omega\ 2\pi$
M_o=the mean anomaly at time T.

Since no orbit is truly Keplerian, first and higher derivatives of the various elements may be necessary according to the accuracy required. It may also be necessary to update these elements from time to time.

A secondary coordinate system with axes x, y, z is defined with respect to the OAO. The origin of the system is at the geometric center of the OAO with the optical axis coincident with the x axis. The positive slewing motions of yaw, pitch, and roll are defined to be clockwise rotations, as seen from the origin, about the positive z, y, and x axes, respectively.

The attitude of the OAO in space is described by specifying the right ascension α and declination δ of the x axis and the angle β, which is the angle the y axis makes with the $u-v$ plane measured in the $y-z$ plane (positive direction toward the positive z axis).

Because of the great distances involved, the angular coordinates of the stars and the sun will be considered to be the same whether the origin of the coordinate system is at the center of the earth or the spacecraft. In the case of the sun, placing the center at the OAO instead of the earth produces a maximum error of less than 10 seconds of arc because of parallax (for a 500-mile circular orbit). For the stars this error is completely negligible. However, for the moon the error can become as great as 1 degree.

For each star tracker on the OAO we define a coordinate system with axes x_i, y_i, z_i such that the outer gimbal angle σ is in the x_i-y_i plane (positive angle measured from positive x_i toward positive y_i) and the inner gimbal angle μ is the angle from the x_i-y_i plane (positive toward negative z_i). Thus the direction cosines of a star (with gimbal angles σ and μ) in this coordinate system are given by

$$a=\cos\mu\cos\sigma,$$
$$b=\cos\mu\sin\sigma,$$
$$c=-\sin\mu.$$

TRANSFORMATIONS

The mathematical approach here is based on the algebra of rotations (matrix algebra); but, since we are concerned only with directions, the rectangular coordinates of a vector will be identical to its direction cosines. Thus, from the preceding definitions, if the attitude of the OAO is given by α, δ, β and if (u_0, v_0, w_0) is any vector in the u, v, w system, then the coordinates x_0, y_0, z_0 of this vector in the OAO system are given by

$$\begin{pmatrix}x_0\\y_0\\z_0\end{pmatrix}=T_\beta T_\delta T_\alpha\begin{pmatrix}u_0\\v_0\\w_0\end{pmatrix},$$

where

$$T_\alpha=\begin{pmatrix}\cos\alpha & \sin\alpha & 0\\-\sin\alpha & \cos\alpha & 0\\0 & 0 & 1\end{pmatrix},$$

$$T_\delta=\begin{pmatrix}\cos\delta & 0 & \sin\delta\\0 & 1 & 0\\-\sin\delta & 0 & \cos\delta\end{pmatrix},$$

$$T_\beta=\begin{pmatrix}1 & 0 & 0\\0 & \cos\beta & \sin\beta\\0 & -\sin\beta & \cos\beta\end{pmatrix}.$$

In addition, if the spacecraft is yawed, pitched, or rolled by ψ, θ, or ϕ, respectively, the coordinates x_1, y_1, z_1 of the vector in this new coordinate system are given by

$$\begin{pmatrix} x_1 \\ y_1 \\ z_1 \end{pmatrix} = T_\psi \begin{pmatrix} x_0 \\ y_0 \\ z_0 \end{pmatrix}, \; T_\theta \begin{pmatrix} x_0 \\ y_0 \\ z_0 \end{pmatrix}, \text{ or } T_\phi \begin{pmatrix} x_0 \\ y_0 \\ z_0 \end{pmatrix},$$

where

$$T_\psi = \begin{pmatrix} \cos\psi & \sin\psi & 0 \\ -\sin\psi & \cos\psi & 0 \\ 0 & 0 & 1 \end{pmatrix},$$

$$T_\theta = \begin{pmatrix} \cos\theta & 0 & -\sin\theta \\ 0 & 1 & 0 \\ \sin\theta & 0 & \cos\theta \end{pmatrix},$$

$$T_\phi = \begin{pmatrix} 1 & 0 & 0 \\ 0 & \cos\phi & \sin\phi \\ 0 & -\sin\phi & \cos\phi \end{pmatrix}.$$

In order that all angles γ may be defined uniquely, we use the function

$$\gamma = \tan^{-1}(a/b) \tag{1}$$

with the understanding that the sign of a is the same as that of $\sin\gamma$ and the sign of b is the same as that of $\cos\gamma$. Thus the signs of a and b in Equation 1 determine the proper quadrant, and the inverse tangent of a divided by b determines the proper value. For all other inverse functions the principal value shall be taken. The range of all angles defined above is as follows:

Right ascension of x axis α	$0 \leq \alpha < 2\pi$
Declination of x axis δ	$-\pi/2 \leq \delta \leq \pi/2$
Roll of y axis β	$-\pi \leq \beta < \pi$
Yaw of OAO ψ	$-\pi \leq \psi < \pi$
Pitch of OAO θ	$-\pi \leq \theta < \pi$
Roll of OAO ϕ	$-\pi \leq \phi < \pi$

DETERMINATION OF FINAL ROLL

If α_2 and δ_2 are the right ascension and declination of a new target star S_2, then we wish to determine the roll β_2 which will orient the solar paddles such that they receive maximum sunlight when the optical axis points toward the star S_2. This will be the case when the angle γ between the sunline and a normal line of the paddle plane is a minimum. Let u_s, v_s, w_s be the direction cosines of the sunline in the u, v, w coordinate system. The direction cosines x_s, y_s, z_s of the sunline in the x, y, z system (optical axis pointing toward S_2) are then found as follows:

$$\begin{pmatrix} x_s \\ y_s \\ z_s \end{pmatrix} = T_{\delta_2} T_{\alpha_2} \begin{pmatrix} u_s \\ v_s \\ w_s \end{pmatrix}.$$

The direction cosines of the sunline in the x, y, z system after a roll of β are given by

$$x_s,$$
$$y_s \cos\beta + z_s \sin\beta,$$
$$z_s \cos\beta - y_s \sin\beta.$$

If x_p, y_p, z_p are the direction cosines of a directed normal from one side of the paddle plane, the cosine of the angle γ between this normal and the sunline is expressed by

$$\begin{aligned} f(\beta) &= \cos\gamma \\ &= x_p x_s + y_p(y_s \cos\beta + z_s \sin\beta) \\ &\quad + z_p(z_s \cos\beta - y_s \sin\beta). \end{aligned} \tag{2}$$

The requirement that γ be a minimum implies that $\cos\gamma$ be a maximum; that is,

$$\begin{aligned} \frac{df}{d\beta} &= -\sin\gamma \frac{d\gamma}{d\beta} \\ &= y_p(z_s \cos\beta - y_s \sin\beta) - z_p(z_s \sin\beta + y_s \cos\beta) \\ &= (y_p z_s - z_p y_s)\cos\beta - (y_p y_s + z_p z_s)\sin\beta \\ &= 0, \end{aligned}$$

or

$$\tan\beta = \frac{y_p z_s - z_p y_s}{y_p y_s + z_p z_s}. \tag{3}$$

There are two possible values of β that will satisfy Equation 3: β_0 and β_1. However, the value that maximizes Equation 2 is the desired value of β; denote this value by β_0.

The above analysis has considered only one side of the paddle plane, but the other side is

handled in exactly the same way with the normal whose direction cosines are $-x_p$, $-y_p$, $-z_p$. This requires that the negative of Equation 2 be a maximum, which again leads to Equation 3. The proper solution this time will be the other value of β to satisfy Equation 3, namely, β_1. Thus, to determine the best value of β, we evaluate $f(\beta_0)$ and $-f(\beta_1)$, and pick the value of β that gives the maximum of the two.

GENERATION OF SLEWING COMMANDS

If the OAO has an initial attitude of α_1, δ_1, β_1 and it is desired to reorient in order to obtain an attitude of α_2, δ_2, β_2, the slewing commands needed to accomplish this reorientation must be determined. Since the OAO may be rotated about any 1 of 3 axes, there are 12 possible slewing sequences. These slewing sequences are listed as follows:

yaw-pitch-roll	yaw-pitch-yaw
roll-pitch-yaw	roll-pitch-roll
yaw-roll-pitch	yaw-roll-yaw
pitch-roll-yaw	pitch-roll-pitch
pitch-yaw-roll	pitch-yaw-pitch
roll-yaw-pitch	roll-yaw-roll

The analysis for determining the amount of slewing required is similar regardless of the slewing sequence; therefore we shall refer to a general slewing sequence of i–j–k. The matrices of these i–j–k rotations will be denoted by T_i, T_j, and T_k, respectively.

If v is any vector with coordinates given in the OAO system with attitude α_1, δ_1, β_1, the matrix to find the coordinates of v in the OAO system with attitude α_2, δ_2, β_2 can be obtained as a product of six matrices:

$$T_{\beta_2}T_{\delta_2}T_{\alpha_2}T_{\alpha_1}^{-1}T_{\delta_1}^{-1}T_{\beta_1}^{-1},$$

where T^{-1} indicates the inverse of T. Likewise if a slewing sequence of i–j–k is given when the OAO has an attitude of α_1, δ_1, β_1, which causes the spacecraft to have a final attitude of α_2, δ_2, β_2 the matrix of the transformation from the initial attitude to the final is found from the matrix product $T_kT_jT_i$. Therefore T_i, T_j, and T_k must satisfy the matrix equation:

$$T_kT_jT_i=T_{\beta_2}T_{\delta_2}T_{\alpha_2}T_{\alpha_1}^{-1}T_{\delta_1}^{-1}T_{\beta_1}^{-1}.$$

The right-hand side of Equation 4 is a 3×3 matrix that can be determined from α_1, δ_1, β_1, α_2, δ_2, β_2. Therefore this matrix is independent of the slewing sequence. This right-hand matrix shall be denoted as C with elements C_{ij}. Thus for each slewing sequence the left-hand side of Equation 4 can be compared with the C matrix to determine the amount of slewing. Several examples are given below:

Sequence: Yaw-Pitch-Roll

$$T_\phi T_\theta T_\psi=\begin{pmatrix}\cos\theta\cos\psi, & \cos\theta\sin\psi, & -\sin\theta\\ \sin\phi\sin\theta\cos\psi-\cos\phi\sin\psi, & \sin\phi\sin\theta\sin\psi+\cos\phi\cos\psi, & \sin\phi\cos\theta\\ \cos\phi\sin\theta\cos\psi+\sin\phi\sin\psi, & \cos\phi\sin\theta\sin\psi-\sin\phi\cos\psi, & \cos\phi\cos\theta\end{pmatrix};$$

and comparing with the C matrix implies that

$$\sin\theta=-C_{13}, \qquad \sin\psi=C_{12}/\cos\theta, \qquad \sin\phi=C_{23}/\cos\theta,$$
$$\cos\theta=\pm\sqrt{C_{11}^2+C_{12}^2}=\pm\sqrt{C_{23}^2+C_{33}^2}, \qquad \cos\psi=C_{11}/\cos\theta, \qquad \cos\phi=C_{33}/\cos\theta.$$

Sequence: Roll-Yaw-Pitch

$$T_\theta T_\psi T_\phi=\begin{pmatrix}\cos\theta\cos\psi, & \cos\theta\sin\psi\cos\phi+\sin\theta\sin\phi, & \cos\theta\sin\psi\sin\phi-\sin\theta\cos\phi\\ -\sin\psi, & \cos\psi\cos\phi, & \cos\psi\sin\phi\\ \sin\theta\cos\psi, & \sin\theta\sin\psi\cos\phi-\cos\theta\sin\phi, & \sin\theta\sin\psi\sin\phi+\cos\theta\cos\phi\end{pmatrix};$$

and comparing this with the C matrix implies that

$$\sin\psi=-C_{21}, \qquad \sin\theta=C_{31}/\cos\psi, \quad \sin\phi=C_{23}/\cos\psi,$$
$$\cos\psi=\pm\sqrt{C_{11}^2+C_{31}^2}=\pm\sqrt{C_{22}^2+C_{23}^2}, \quad \cos\theta=C_{11}/\cos\psi, \quad \cos\phi=C_{22}/\cos\psi.$$

Sequence: Yaw-Pitch-Yaw

$$=\begin{pmatrix}\cos\psi_2\cos\theta\cos\psi_1-\sin\psi_1\sin\psi_2, & \cos\psi_2\cos\theta\sin\psi_1+\sin\psi_2\cos\psi_1, & -\cos\psi_2\sin\theta\\ -(\sin\psi_2\cos\theta\cos\psi_1+\sin\psi_1\cos\psi_2), & -\sin\psi_2\cos\theta\sin\psi_1+\cos\psi_2\cos\psi_1, & \sin\psi_2\sin\theta\\ \sin\theta\cos\psi_1, & \sin\theta\sin\psi_1, & \cos\theta\end{pmatrix};$$

and comparison to the C matrix gives

$$\sin\theta=\pm\sqrt{C_{31}^2+C_{32}^2}=\pm\sqrt{C_{13}^2+C_{23}^2}, \quad \sin\psi_1=C_{32}/\sin\theta, \quad \sin\psi_2=C_{23}/\sin\theta,$$
$$\cos\theta=C_{33}, \qquad \cos\psi_1=C_{31}/\sin\theta, \quad \cos\psi_2=-C_{13}/\sin\theta.$$

Thus for each slewing sequence we obtain two solutions corresponding to the plus and minus sign of the radical. Therefore there are actually 24 possible slewing commands.

We could continue the above process for all 12 combinations of the matrix $T_kT_jT_i$, compare each with the C matrix, and find that there is a definite pattern as to which elements of the C matrix to choose for a given slewing sequence. Let the numbers 1, 2, and 3 be used to represent roll, pitch, and yaw respectively (2–1–3 would indicate a pitch-roll-yaw sequence); then, for all sequences i–j–k where the same type of slew is not used more than once, we have the following relations:

$$\sigma_{123}=\sigma_{231}=\sigma_{312}=-\sigma_{132}=-\sigma_{213}=-\sigma_{321}=1,$$
$$\sin j=\sigma_{ijk}C_{ki},$$
$$\cos j=\pm\sqrt{C_{ii}^2+C_{ji}^2}=\pm\sqrt{C_{kj}^2+C_{kk}^2},$$
$$\sin i=-\sigma_{ijk}C_{kj}/\cos j, \quad \sin k=-\sigma_{ijk}C_{ji}/\cos j,$$
$$\cos i=C_{kk}/\cos j, \quad \cos k=C_{ii}/\cos j.$$

In the degenerate case where $C_{kj}=C_{kk}=C_{ii}=C_{ji}=0$, the value of j is either plus or minus 90 degrees. In this case i and k must satisfy the following:

$$\sin(k\pm\sigma_{ijk}i)=\sigma_{ijk}C_{ij},$$
$$\cos(k\pm\sigma_{ijk}i)=\mp\sigma_{ijk}C_{ik}.$$

The upper signs are taken when j is $+90$ degrees, and the lower sign when j is -90 degrees.

Example 1.—Assume the matrix C is given. Determine the slewing angles for a pitch-roll-yaw sequence.

By definition i is 2, j becomes 1, and k is 3. Here σ is -1; therefore,

$$\sin\phi=-C_{32},$$
$$\cos\phi=\pm\sqrt{C_{22}^2+C_{12}^2},$$
$$\sin\theta=C_{31}/\cos\phi, \quad \sin\psi=C_{12}/\cos\phi,$$
$$\cos\theta=C_{33}/\cos\phi, \quad \cos\psi=C_{22}/\cos\phi.$$

If the slewing sequence includes the same type of slew twice (of the form i_1–j–i_2), and k is the slew not used, then the slewing angles are defined by

$$\sin j=\pm\sqrt{C_{ij}^2+C_{ik}^2}=\pm\sqrt{C_{ji}^2+C_{ki}^2},$$
$$\cos j=C_{ii},$$
$$\sin i_1=C_{ij}/\sin j, \quad \sin i_2=C_{ji}/\sin j,$$
$$\cos i_1=\sigma_{ji}C_{ik}/\sin j, \quad \cos i_2=-\sigma_{ji}C_{ki}/\sin j,$$
$$\sigma_{12}=\sigma_{23}=\sigma_{31}=-\sigma_{13}=-\sigma_{21}=-\sigma_{32}=1.$$

When $C_{ij}=C_{ik}=C_{ji}=C_{ki}=0$, the angle j is either 0 or 180 degrees, depending on whether C_{ii} is plus or minus. In this case the angles i_1 and i_2 must satisfy the relations

$$\sin(i_2\pm i_1)=\sigma_{ji}C_{kj},$$
$$\cos(i_2\pm i_1)=\pm C_{kk},$$

where the plus sign is taken if C_{ii} is positive and the minus sign if C_{ii} is negative.

Example 2.—Determine the slewing angles for a yaw-pitch-yaw sequence.

In this case i becomes 3, j is 2, k equals 1, and σ is $+1$:

$$\sin\theta=\pm\sqrt{C_{32}^2+C_{31}^2}=\pm\sqrt{C_{23}^2+C_{13}^2},$$
$$\cos\theta=C_{33},$$
$$\sin\psi_1=C_{32}/\sin\theta,\ \sin\psi_2=C_{23}/\sin\theta,$$
$$\cos\psi_1=C_{31}/\sin\theta,\ \cos\psi_2=-C_{13}/\sin\theta.$$

DETERMINATION OF GIMBAL ANGLES

The determination of the star tracker gimbal angles will depend on the physical mounting of each star tracker with respect to the OAO's coordinate system. Let $T_i(i=1, \ldots, 6)$ be the transformation that determines the coordinates of a vector in the OAO system from the coordinates of the vector in the i^{th} star tracker system. Thus, if σ_i and μ_i are the outer and inner gimbal angles respectively of the i^{th} star tracker, the direction cosines in this star tracker system are given by $\cos\mu_i\cos\sigma_i$, $\cos\mu_i\sin\sigma_i$, $-\sin\mu_i$ and the direction cosines in the OAO system are obtained from the following relation:

$$T_i\begin{pmatrix}\cos\mu_i\cos\sigma_i\\ \cos\mu_i\sin\sigma_i\\ -\sin\mu_i\end{pmatrix}.$$

Thus, if the OAO has an attitude defined by α_2, δ_2, β_2 and the i^{th} star tracker is locked on a star with right ascension α_i and declination δ_i, the direction cosines x_i, y_i, z_i of the star with respect to this star tracker system can be determined from

$$\begin{pmatrix}x_i\\ y_i\\ z_i\end{pmatrix}=T_i^{-1}T_{\beta_2}T_{\delta_2}T_{\alpha_2}\begin{pmatrix}\cos\delta_i\cos\alpha_i\\ \cos\delta_i\sin\alpha_i\\ \sin\delta_i\end{pmatrix}.$$

The gimbal angles σ_i and μ_i are then found from the following expressions:

$$\sigma_i=\tan^{-1}(y_i/x_i),$$
$$\mu_i=\tan^{-1}(-z_i/\sqrt{x_i^2+y_i^2}).$$

If the OAO is slewed with a j–k–l slewing sequence and gimbal angles σ_{i_2}, μ_{i_2} after the slewing are desired as a function of the gimbal angles σ_{i_1}, μ_{i_1} before the slewing, the following formulas may be applied:

$$\begin{pmatrix}x_i\\ y_i\\ z_i\end{pmatrix}=T_i^{-1}T_lT_kT_jT_i\begin{pmatrix}\cos\mu_{i_1}\cos\sigma_{i_1}\\ \cos\mu_{i_1}\sin\sigma_{i_1}\\ -\sin\mu_{i_1}\end{pmatrix},$$
$$\sigma_{i_2}=\tan^{-1}(y_i/x_i),$$
$$\mu_{i_2}=\tan^{-1}(-z_i/\sqrt{x_i^2+y_i^2}).$$

SATELLITE CONSTRAINTS

Of the 24 possible slewing sequences there may be several that are not applicable because of restrictions imposed by the spacecraft itself. These restrictions may be investigated by the same techniques employed in the earlier sections.

One such restriction is that the sun shade may not protect the experimenter's equipment from the sun's rays if the optical x-axis is within 45 degrees of the sun. The first OAO also will have an experiment at the opposite end of the optical axis; thus in this case the minus x-axis must also be kept 45 degrees from the sun.

Although the sun shades are designed to shut if either experimental axis comes within the prohibited area of the sun, it is desirable to avoid a slewing sequence that would require such action. The avoidance of such slews will eliminate damage to the experimental equipment even if the sun shade fails to work properly.

Another satellite constraint is that at least two star trackers must not exceed their gimbal limits during the entire slewing sequence. If this is not possible, new star assignments must be made at intermediate slews.

To determine whether a target star with right ascension α and declination δ lies within the prohibited area of sun, we merely determine the angle from the star to the sun. The cosine of this angle γ is given by

$$\cos\gamma=x_s\cos\delta\cos\alpha+y_s\cos\delta\sin\alpha+z_s\sin\delta,$$

where x_s, y_s, z_s are the direction cosines of the sun. Thus, if γ is less than 45 degrees, this star may not be viewed. In the case of the

double-ended OAO, γ must lie between 45 and 135 degrees before viewing is permissible.

To check whether a slewing sequence will cause the optical axis to come within 45 degrees of the sun, the angle γ between the sun and optical axis can be written as a function of the slewing angle. From this functional relation determine the domain of the slewing angle that makes $\gamma=45$ degrees or less. If the desired slew lies within this domain, the slew is prohibited. If α_1, δ_1, β_1 define the attitude of the OAO before the slewing sequence begins and if u_s, v_s, w_s are the direction cosines of the sun in the inertial system, the direction cosines of the sun in the OAO system x_s, y_s, z_s are given by

$$\begin{pmatrix} x_s \\ y_s \\ z_s \end{pmatrix} = T_{\beta_1} T_{\delta_1} T_{\alpha_1} \begin{pmatrix} u_s \\ v_s \\ w_s \end{pmatrix}.$$

After a slew of λ, where λ may be either a yaw, pitch, or roll, the direction cosines of the sun x_s', y_s', z_s' after the slew are defined as

$$\begin{pmatrix} x_s' \\ y_s' \\ z_s' \end{pmatrix} = T_\lambda \begin{pmatrix} x_s \\ y_s \\ z_s \end{pmatrix}.$$

The cosine of the angle between the sun and optical axis as a function of λ is then

$$x_s \cos \lambda + b \sin \lambda,$$

where $b=y_s$ if λ indicates a yaw and $b=-z_s$ if λ is a pitch. A roll slew need not be considered, since a roll does not affect the angle between the sun and optical axis.

If λ_0 is the desired slew, the slew will be allowable if

$$x_s \cos \lambda + b \sin \lambda \leq \cos 45^\circ \qquad (5)$$

for all λ between 0 and λ_0. Equation 5 may be written as

$$\frac{x_s}{\sqrt{x_s^2+b^2}} \cos \lambda + \frac{b}{\sqrt{x_s^2+b^2}} \sin \lambda \leq \frac{\cos 45^\circ}{\sqrt{x_s^2+b^2}},$$

or

$$\cos \epsilon \cos \lambda + \sin \epsilon \sin \lambda = \cos (\epsilon - \lambda) \leq \frac{\cos 45^\circ}{\sqrt{x_s^2+b^2}},$$

where

$$\epsilon = \tan^{-1}(b/x_s), \qquad -\pi \leq \epsilon \leq \pi.$$

If

$$\left| \frac{\cos 45^\circ}{\sqrt{x_s^2+b^2}} \right| \geq 1,$$

the slew is always permissible. If

$$\left| \frac{\cos 45^\circ}{\sqrt{x_s^2+b^2}} \right| < 1,$$

the slew is permissible only if none of the following angles lie between 0 and λ_0:

$$\epsilon - \eta,$$
$$\epsilon + \eta,$$
$$\epsilon - \eta + 2\pi,$$
$$\epsilon + \eta - 2\pi,$$

where

$$\eta = \cos^{-1}\left(\frac{\cos 45^\circ}{\sqrt{x_s^2+b^2}} \right).$$

The next slew in the sequence may be checked in exactly the same way after replacing x_s, y_s, z_s by x_s', y_s', z_s'.

The gimbal angles after each slew of a sequence may be obtained in the same fashion that the final gimbal angles are determined. If σ_{i_0} and μ_{i_0} are the outer and inner gimbal angles of the i^{th} star tracker and a slewing sequence of l–m–n is to be performed, the gimbal angles after the j^{th} slew are given by

$$\left.\begin{aligned} \sigma_{ij} &= \tan^{-1}(y_{ij}/x_{ij}) \\ \mu_{ij} &= \tan^{-1}(-z_{ij}/\sqrt{x_{ij}^2+y_{ij}^2}) \end{aligned}\right\} j=1, 2, 3,$$

where

$$\begin{pmatrix} a_1 \\ b_1 \\ c_1 \end{pmatrix} = T_l T_i \begin{pmatrix} \cos \mu_{i_0} \cos \sigma_{i_0} \\ \cos \mu_{i_0} \sin \sigma_{i_0} \\ -\sin \mu_{i_0} \end{pmatrix},$$

$$\begin{pmatrix} x_{i_1} \\ y_{i_1} \\ z_{i_1} \end{pmatrix} = T_i^{-1} \begin{pmatrix} a_1 \\ b_1 \\ c_1 \end{pmatrix}, \begin{pmatrix} a_2 \\ b_2 \\ c_2 \end{pmatrix} = T_m \begin{pmatrix} a_1 \\ b_1 \\ c_1 \end{pmatrix},$$

$$\begin{pmatrix} x_{i_2} \\ y_{i_2} \\ z_{i_2} \end{pmatrix} = T_i^{-1} \begin{pmatrix} a_2 \\ b_2 \\ c_2 \end{pmatrix}, \begin{pmatrix} x_{i_3} \\ y_{i_3} \\ z_{i_3} \end{pmatrix} = T_i^{-1} T_n \begin{pmatrix} a_2 \\ b_2 \\ c_2 \end{pmatrix}.$$

OCCULTATION

The knowledge of stellar occultation is necessary for several important reasons: First, the attitude of the spacecraft cannot be maintained if less than two star trackers are tracking at any time; second, the occultation of the target star during an experiment would result in wasted time.

The three bodies that cause stellar occultation are the earth, sun, and moon. Occultation due to the sun and moon will be less frequent than that due to the earth. Because of this, the time of occultation due to the sun and moon can be determined in a similar manner. In both cases the origin of the coordinate system is assumed to be centered at the OAO. This introduces an error due to parallax of about 10 seconds of arc for the sun and about 1 degree for the moon.

Let i and Ω be the inclination and right ascension respectively of either the moon's or sun's orbit, and let α_i and δ_i be the right ascension and declination of the i^{th} star. The direction cosines a, b, c of this star in a coordinate system whose x–y plane is the plane of the orbit are given by

$$\begin{pmatrix} a \\ b \\ c \end{pmatrix} = \begin{pmatrix} 1 & 0 & 0 \\ 0 & \cos i & \sin i \\ 0 & -\sin i & \cos i \end{pmatrix} \begin{pmatrix} \cos\Omega & \sin\Omega & 0 \\ -\sin\Omega & \cos\Omega & 0 \\ 0 & 0 & 1 \end{pmatrix} \begin{pmatrix} \cos\delta_i & \cos\alpha_i \\ \cos\delta_i & \sin\alpha_i \\ \sin\delta_i & \end{pmatrix}.$$

The cosine of the angle γ between the star and the sun or moon is then

$$\cos\gamma = a\cos(\omega+\mu) + b\sin(\omega+\mu),$$

where ω is the argument of perigee and μ is the true anomaly. The general requirement is to determine when the angle γ will be less than some fixed angle λ (45 degrees for the sun, one-half the angle subtended by the moon plus errors for the moon). When γ just equals λ, the corresponding time t is the time of immersion or emersion for that star. This requirement of equality may be expressed as

$$a\cos(\omega+\mu) + b\sin(\omega+\mu) = \cos\lambda, \qquad (6)$$

or

$$\cos\epsilon\cos(\omega+\mu) + \sin\epsilon\sin(\omega+\mu) = \frac{\cos\lambda}{\sqrt{a^2+b^2}}, \qquad (7)$$

where

$$\epsilon = \tan^{-1}(b/a), \qquad 0 \le \epsilon < 2\pi.$$

Equation 7 may also be written as

$$\cos(\epsilon-\omega-\mu) = \frac{\cos\lambda}{\sqrt{a^2+b^2}}$$

so that

$$\mu = \epsilon - \omega - \eta,$$

where

$$\eta = \pm\left[\cos^{-1}\left(\frac{\cos\lambda}{\sqrt{a^2+b^2}}\right) + 2k\pi\right], \qquad k = 0, 1, 2, \ldots$$

Thus each value of η determines the value of μ at an immersion or emersion of the i^{th} star. This value of μ will correspond to an immersion if

$$\sin(\epsilon-\omega-\mu) > 0,$$

and to an emersion if

$$\sin(\epsilon-\omega-\mu) < 0.$$

Once μ is known, the corresponding value of time can be obtained by the following relations:

$$E = \tan^{-1}\left(\frac{\sqrt{1-e^2}\sin\mu}{e+\cos\mu}\right) + 2\pi\left[\frac{\mu}{2\pi}\right]^*$$

$$M = E - e\sin E$$

$$t = \frac{M-M_0}{n} \qquad (8)$$

where e is the eccentricity of the orbit, n the mean motion of the body in the plane of the orbit, M_0 the mean anomaly at epoch, and t the time from epoch.

Although occultation due to the earth is more frequent and troublesome than that due to the sun and moon, it can be handled in a similar manner. The angle λ (immersion or emersion occurs when the angle between OAO and the star equals λ) in this case is not a constant but a function of the OAO's range. Thus immersion and emersion can be determined analytically only when the spacecraft is in a circular orbit. For

*$[x]$ indicates the greatest integer less than or equal to x.

small eccentricity, however, the circular solution using the mean range should give sufficient accuracy.

Because of the great distances of the stars we may assume that the line from the origin to a star is parallel to the line from the OAO to the star. Then, with the additional assumption of a spherical earth, the cosine of λ (see sketch) may be determined by simple trigonometry.

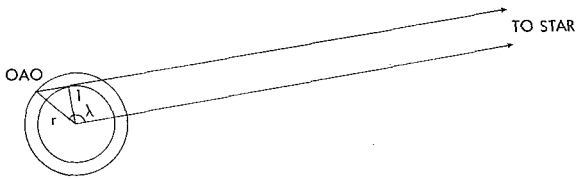

Thus

$$\cos \lambda = \frac{-\sqrt{r^2-1}}{r},$$

where the unit of distance is the earth's radius. Hence, if r is constant, occultation by the earth may be handled in the same manner as that of the sun and moon, that is, by Equations 6 through 8, where the elements are those of the OAO's and where the x–y plane of the coordinate system is the OAO's orbital plane. The test for immersion or emersion in this case is the reverse of that given for sun-moon occultation.

CONCLUDING REMARKS

The analysis and mathematical models contained in this report are intended to be quite general. In many cases the formulas may be simplified if accuracy requirements warrant it. In other cases a different coordinate system will simplify some models; for example, the ecliptic system would reduce any model involving the sun's coordinates. Thus the formulas contained herein are not dependent on any particular coordinate system, and simplifications may be made by simply omitting terms in various expressions.

A PRECISION ENDLESS-LOOP MAGNETIC TAPE RECORDER FOR SPACE APPLICATIONS

R. C. FALWELL, K. W. STARK, A. F. WHITE

Goddard Space Flight Center

The tape recorder developed for the Tiros satellite is a miniaturized, low power, two-speed recorder whose endless-loop tape cartridge stores 200 feet of ¼-inch lubricated magnetic tape. A two-phase 137.5-cps 14-vac hysteresis synchronous motor, requiring less than 0.300 watts drives the tape at 0.4 inch/second for recording. During playback, a 5,000-rpm motor requiring less than 1 watt drives the tape at 12 inches/second. A transistorized dc speed control unit maintains better than 1 percent regulation of this motor. Speed reduction from the motors to the capstan drive is obtained with reduction pulleys utilizing polyester film belts. Frictional drag from components not used during certain operating cycles is minimized by using spring clutches which prevent power drain on the motor. The record motor operates continuously, and spring clutches allow this motor to be overridden during the playback mode. Flutter and wow is maintained below 2.5 percent peak to peak from 0 to 1000 cps.

This exceptional performance is made possible by an extremely accurate gyro-type capstan assembly. The capstan has maximum runouts of 5×10^{-5} inch and the assembly uses the duplex bearing and integral race technique. The bearings in this assembly are preloaded by means of a fixed center distance. This recorder has survived sinusoidal vibration at 10 g from 0 to 2000 cps for ½ hour, and random vibration test at 20 g rms from 0 to 2000 cps for 4 minutes.

A time-sharing switch, operated from the record mode reduction system, time-divides the information to be recorded. A playback timing switch, operated through a 16,650-to-1 gear reduction from the playback motor, activates a microswitch that cuts off power to the motor and resets the record mode electronics after a playback cycle of 3.33 minutes.

This paper describes in detail the design of the particular components which combine to make this recorder a reliable, high performing, precision unit.

INTRODUCTION

Satellites are not always in an orbital position where their data can be immediately relayed to a receiving station on the earth. Therefore, some method of data storing must be used until the satellite is in a position to transmit information to a ground receiving station. When the Tiros program was conceived, magnetic tape recorders were the most practical answer to this problem. Existing tape recording methods required more power, weight, and space than could be afforded, and their performance capabilities were limited.

Project Vanguard was the beginning of a new concept in magnetic endless-loop tape storage systems.[1] The principal reasons for selecting the endless-loop cartridge are the following: The single reel provides compact storage; reversal mechanisms are not required for record and playback functions; the tape can drive beyond one pass without requiring safety cutoff devices for the motors; and tape storage makes momentum compensation simple when required.

During the Vanguard program many of the presently employed instrumentation techniques

[1] Hanel, R., Licht, J., Nordberg, W., Stampfl, R., and Stroud, W. G., "The Satellite Vanguard II: Cloud Cover Experiment," *IRE Trans. on Mil. Electronics*, MIL-4 (2 and 3): 245-247, April-July 1960.

were originated. The next program employing a recorder of this type was Project Score, the first communications satellite; the Vanguard recorder was so functionally reliable that no significant improvements were required for Project Score.

When the Tiros program was initiated, a rigid set of specifications was introduced to assure that the satellite would have the desired longevity and reliability. These specifications called for the development of a high-speed endless-loop tape recorder with a large data storage capacity. Initial attempts were made to use the techniques successfully employed in Projects Vanguard and Score. But these techniques were inadequate to achieve the required performance, reliability, and low flutter within the necessary weight and power limitations. Therefore, mechanical accuracy, low-tolerance machining, and assembly techniques had to be developed beyond the levels existing at that time.

The objective of this paper is to describe in detail the problems that arose and the solutions that were applied in the design and development of the Tiros satellite tape recorder. This recorder has been successfully flown in five Tiros satellites and its basic design will be used in future satellites.

OPERATIONAL DESCRIPTION

The Tiros IR tape recorder (Fig. 1) is a miniaturized, low power, two-speed recorder using an endless-loop tape cartridge. Its external overall dimensions without a time-sharing switch are: diameter, 6.25 inches; and height, 2.3 inches. The recorder weighs 4 pounds.

The operation of the recorder is divided into a record and a playback mode. For the record mode a two-phase hysteresis synchronous motor operates continuously and drives a capstan through two belt passes; a complete tape cycle requires 100 minutes. A servo-controlled dc motor operates the playback mode through one belt-reduction; a complete playback cycle requires 3.33 minutes. A spring clutch connecting the record motor pulley to the capstan shaft allows the playback motor to override the record motor during a 3.33 minute interrogation.

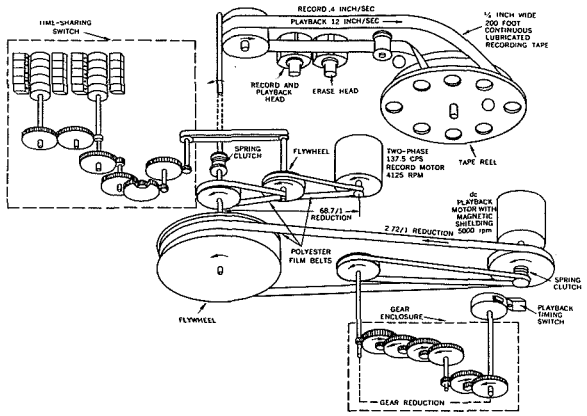

FIGURE 1.—Tiros tape recorder schematic.

Linear velocity is imparted to the tape from the rotating capstan by means of a pivoted spring-loaded rubber roller. Positive head-gap-to-tape contact and accurate tape guidance across the heads are obtained by the use of pressure pads and tape guides.

A time-sharing switch driven from the intermediate jack shaft of the record system permits data to be recorded in a preselected sequence. A gear box driven through a belt pass from the dc motor operates a microswitch which, by means of a relay, shuts off the playback mode and switches on the record mode electronics after one complete playback cycle.

MECHANICAL DESIGN

The mechanical design of the tape recorder had to meet the following requirements: (1) a 30-to-1 speed ratio, i.e., tape speeds of 0.4 inch per second on record and 12 inch per second on playback; (2) an increase of tape length from Vanguard's 75 feet to 200 feet; (3) the incorporation of a time-sharing switch; (4) an orbital life of 6 months; (5) an overall flutter of less than 2.5 percent peak to peak; (6) 0.750 watt power for the playback mode, and (7) 0.300 watt power for the record mode. These requirements led to many significant design advancements in miniature precision recorders.

Motors

Sufficient drive power was needed to drive the recorder under loads due to the 200-foot tape and associated tape cartridge, pressure pads, tape guides, guide roller brush, flywheels, etc. Therefore, to achieve the required low system power and low flutter, motors with high starting and running torques, high efficiencies, and better than 1 percent speed regulation were needed. The requirement for an orbital life of 6 months demanded motor development efforts. Properly preloaded bearings and proper sealing to eliminate dirt, yet not increase torque, were primary concerns.

A special two-phase hysteresis synchronous motor was developed for the record system. It weighs 4.28 ounces and requires a 0.300-watt input at 137.5 cps and 14 volts ac. Its efficiency is about 26 percent, with a running torque of 0.026 inch-ounce at a synchronous speed of 4125 rpm. It is 1.31 inches in diameter and 2 inches long. Because of the low starting torques, the system design allows the ac motor to run continuously. A transistorized power supply was built for this motor and is discussed later in this report.

The high-speed playback mode required a motor with a high starting torque for rapid acceleration of the tape from record speed to playback speed. The acceleration time is approximately 2 seconds. This requirement was satisfied by a 5000-rpm dc motor with a 0.750-watt input power rating at 15 volts dc, delivering about 0.1 inch-ounce of torque and weighing 1.94 ounces. This motor is 0.88 inch in diameter and 2.44 inches long. To compensate for the inherently poor speed regulation of the dc motor, an alternator (Fig. 2) is mounted on the rear shaft of the motor for the speed control. This dc speed control (described later) provided better than 1 percent regulation.

The ac motor is operated continuously to eliminate the possibility of its failure to start due to bearing damage; thus, the dc motor has to override the ac motor at certain times with minimum frictional torque loss. This was accomplished by the use of a spring clutch in the capstan assembly which permits the dc motor to rotate the capstan in the same direction as in the record mode without affecting the ac motor drive system. The frictional drag of this spring clutch reflected back to the dc motor is about 0.011 inch-ounce. Since both motors are interconnected through belts and pulleys to the common capstan shaft, an additional spring clutch (Fig. 2) is incorporated on the dc motor to prevent the ac motor from dragging the dc motor during the record mode. This results in a frictional drag torque reflected to the ac motor of about 0.0012 inch-ounce.

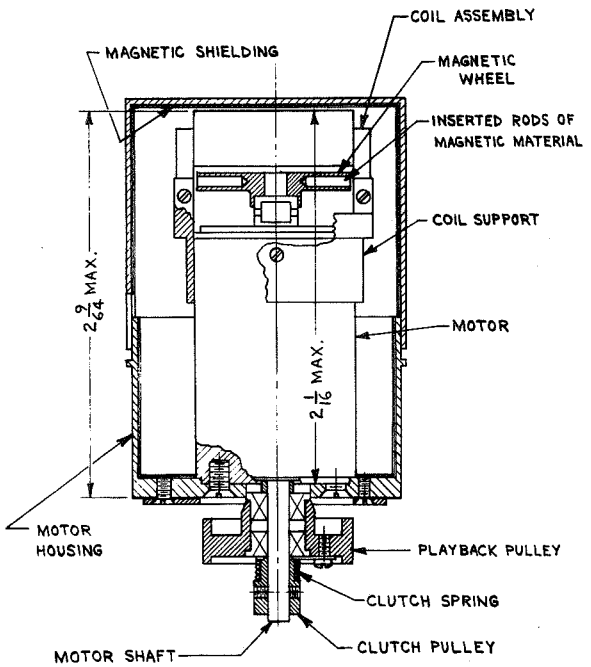

FIGURE 2.—Playback motor assembly.

Belt Drives

An efficient and accurate system of speed reduction and power transmission is provided by using endless-loop polyester film belts. Speed variations are minimized between the drive motors and the capstan because these belts are extremely uniform in thickness, are relatively stretch-free, and can handle transition from large to extremely small pulleys without showing bending fatigue or slippage. These belts were made by cutting a "donut" from a Mylar sheet 0.001 inch thick, stretching it into an endless-loop belt on two cone-shaped mandrels, and heat-treating them for stress relief.

Although the thickness and uniformity of the belt in belt drive systems [2] is frequently neglected, for extreme precision they must be taken into account. The use of 0.001-inch-thick Mylar belts which exhibit an average variation in thickness of only 0.0001 inch results in extremely small pitch line variations in the drive system. In addition, the minimum thickness results in very low alternating stress profiles over the pulley. The latter permits the use of extremely small pulley sizes where possible without affecting belt life radically; permits the use of small bearings for low power drain; and makes possible an extremely compact design. An example of the reliability of these belts is the Tiros II tape recorder, which has been operating in the record mode continuously since November 23, 1960.[3]

For additional control of speed variations, each pulley is machined to dimensional tolerances such that the speed variations due to the total accumulation of runouts will not exceed the required flutter values. There are three pulleys in the low-speed system and two in the high-speed system (Fig. 1). To achieve the desired tolerance on the ac motor pulley, a pulley blank is cemented onto the motor shaft and then turned in place as the motor shaft is rotated by an externally applied torque.

Capstan Assembly

An ideal approach to the design of the capstan assembly would have been to use a large diameter capstan; this would provide easy fabrication and facilitate a sufficient tape wrap around the capstan. However, a large capstan would cause more frictional drag and consequently require more power; this would subject the motors to torques beyond their design limits because of the increased tape tensions, larger bearings, and large pulley reduction ratios which could possibly present problems in belt slippage. Therefore, a 0.125-inch capstan diameter was selected.

During the initial phases of the program the design of the capstan unit was similar to the design of those used in the Vanguard and Score projects. However, it was realized that greater total indicated runout accuracies were required because of the flutter requirement. (Total indicated runouts of 5×10^{-5} inch were necessary on the capstan shaft.) Attempts to obtain centerless ground shafts to the specified tolerances and either press-fit or shrink-fit them into the capstan flywheel were unsuccessful: the final runouts were much too large. The problem was finally solved by grinding the shafts on centers and cementing them into the flywheels. In addition, to eliminate runouts due to the tolerance of the inner race of the bearing, it was decided to make the inner race part of the capstan shaft and to grind the raceway on the same centers of the shaft. Also, the use of duplexed bearings made it possible to assemble the capstan record-mode pulley on the shaft so that it would rotate in a plane perpendicular to the capstan axis with minimum runout.

An additional problem was the proper preloading of the bearings to insure their survival in a severe vibration environment. In previous designs, fixed preloads of capstan bearings had been used. However—because of inadequate measurement techniques—excessive preloads which could cause brinelling of balls and raceways, or insufficient preloads resulting in bearing damage during vibration, existed. Spring preloading met with little success. Bellville-type springs were displaced sufficiently during vibration to unload the bearings and cause damage. Therefore, in this design, the only adequate way of preloading was the bearing cap method. That method necessitated measuring the distance required between the two outer bearings for a specific preload. This dimension varied by a few thousandths of an inch for any given unit because of the accumulation of tolerances.

The entire capstan assembly is mounted in a basket which fastens to the upper plate of the recorder (Fig. 3). This feature eliminated the necessity of removing the capstan unit every time the bottom plate had to be removed, and thus minimized the chance of damaging a

[2] Licht, J., and White, A., "Polyester Film Belts," NASA Technical Note D–668, May 1961; also published in *Machine Design* 32(22): 137–143, Oct. 27, 1960.

[3] Interrogation of recorder was possible up to 18 months; however, a power failure in the satellite made it impossible to determine further operation.

764–173 O—65——18

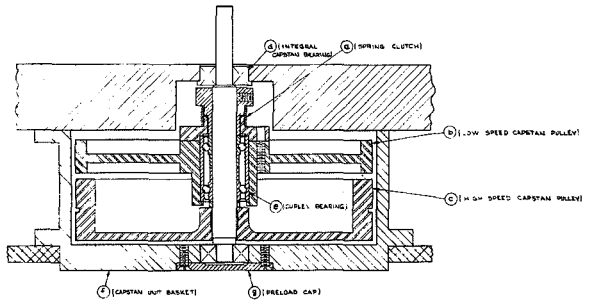

FIGURE 3.—Capstan assembly.

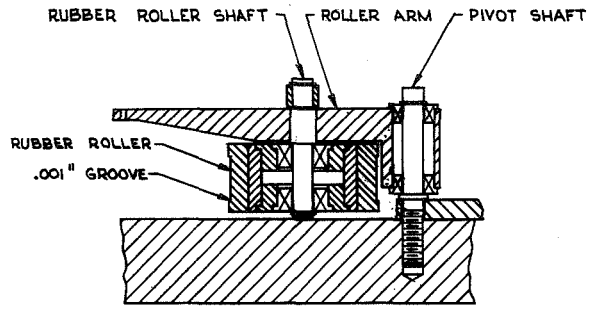

FIGURE 4.—Rubber roller assembly.

bearing or scratching the capstan shaft. The basket was was machined to fixed dimensions; therefore, the preload cap was the only part which had to be machined in order to determine the preload accurately. The amount of preload is determined from the load-deflection curves of the specific bearing used, and is based upon a load equal to 20 times the capstan weight; this takes into account all vibrations to which the unit is subjected. The final bearing was preloaded by machining the bearing cap so that interference amounting to 0.0004 inch introduced the required pressure on the outer race. Since the inception of this method of preload determination no bearing failure has occurred in the unit. The resulting configuration of the capstan unit appears in Figure 3. The capstan consists of the following components: (A) spring clutch; (B) low-speed capstan pulley; (C) high-speed capstan flywheel pulley; (D) outer capstan bearings—the top one having its inner race integral with the capstan shaft; (E) duplexed bearing pair; (F) capstan unit basket; and (G) preload cap.

Pressure Roller Assembly

Another recorder design problem involved the location of the pressure roller (Fig. 4) with respect to the capstan. In previous designs, the pressure rollers had been located a fixed distance from the capstan shaft with the major wrap of the tape around the roller. This resulted in a number of undesirable features: For example, the capstan caused an indentation in the roller whenever the recorder was idle; also, the roller acted more as a capstan than the capstan itself; i.e., its runouts actually influenced the flutter values. In the Tiros design, the tape wrap had to remain the same. If the major wrap were around the capstan, the amount of tape contact with the capstan would be small. In addition, the lubricated side of the tape would be in contact with the capstan; this tape path would have required excessive roller pressures to maintain tape speed without slippage, and thus would have caused higher transmitted torques and a possibility of bending the capstan. To alleviate these effects the rubber roller was ground to a diameter of 0.900 inch and mounted on a pivotal arm. The arm is spring loaded to 14 ounces to maintain constant tape speed. The spring is removable and when the recorder is not in use it is removed to minimize the amount of indentation. Another preventive measure against roller indentation was the selection of a rubber with a durometer rating between 50 and 60, which is hard enough to prevent indentation.

During vibration, with the tape driven in the record mode, the tape tends to ride up between the capstan and the rubber roller. This riding up was caused by fluctuations induced in the load spring at its resonant frequency which caused the roller periodically to leave contact with the capstan. The natural frequency of the roller system was determined, and a viscous damper was employed to critically damp the roller at this frequency. An additional precaution consisted of grinding a slot 0.25 inch wide by 0.001 inch deep into the roller to help guide the tape and prevent vertical motion.

Tape contact with the record-playback and erase heads is maintained by indenting the

heads 0.0313 inch into the tape path from the guide roller to the capstan. In addition, pressure pads (Fig. 5) are used for positive contact. A tape guide provides a mount for the pressure pads and also guides the tape across the heads. The record-playback head is adjustable for signal peaking purposes. A pressure arm, located on the guide roller (Fig. 6) where the tape emerges from the reel, maintains tape tension across the heads and damps any erratic motion of the tape emanating from the cartridge.

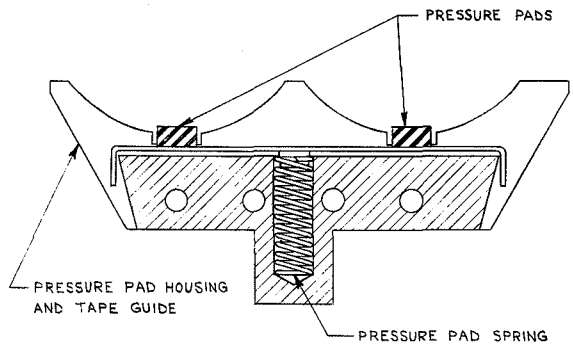

FIGURE 5.—Tape guide assembly.

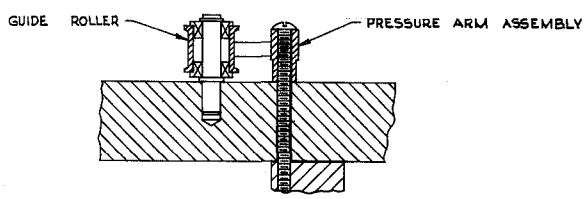

FIGURE 6.—Pressure roller assembly.

Tape Path

Figure 7 shows the upper plate of the recorder. The tape path starts at the inner diameter of the tape reel where the tape emerges through the upper plate, and passes along the guide roller and pressure arm through the tape guide and pressure pads in front of the record-playback and erase heads. It then passes between the capstan and rubber roller down through the top plate to rewind onto the outside wrap of tape on the tape reel.

The tape cartridge contains 200 feet of 0.0014-inch magnetic tape coated with a special lubricant on the side opposite the oxide. This cartridge operates by allowing the inner wrap of tape to be pulled by the capstan, the resultant force causing the cartridge to rotate. Because the tape moves at a specific velocity, the outer layer of tape moves at a speed lower than that of the reel. The resulting frictional drag rewinds the outer layer of tape on the periphery of the spool. Lubrication reduces the interlayer friction, thus reducing the flutter imparted to the tape and the amount of drive power required.

Playback Cutoff Switch

After one complete playback cycle, a mechanical switch shuts off the playback motor and resets the electronics to the record mode. Basically, a gear box is operated by a belt pass from the dc motor. Six gear passes (Fig. 8) using 200-pitch gears are incorporated to provide the necessary gear reduction. The entire gear reduction is enclosed in a magnesium case 3.4 inches long, 0.9 inch wide, and 0.45 inch thick. The pitch diameters of the gears vary from about 0.15 to about 0.6 inch and a total of twelve gears comprise the gear reduction. The total reduction is 16,650 to 1. The output shaft of the gear box is connected to a spring-operated disc. When this disc (Fig. 9) moves approximately ¾ revolution, the stop lever engages and stops the disc, causing the spring to be wound. When the entire revolution is completed, an arm on the output shaft releases the stop lever, permitting the disc lobe to actuate a microswitch. This results in a 15- to 25-millisecond pulse which initiates the aforementioned sequence of events.

Structure

The recorder supporting structure consists primarily of two plates, top and bottom, separated by standoffs. The structure is designed so that all parts are connected to the top plate, thus allowing the bottom plate to be removed without disturbing the alignment of any part. Initially, because of the weight consideration, both plates were made of 0.125-inch-thick magnesium. However, in testing the recorder for wow and flutter it was

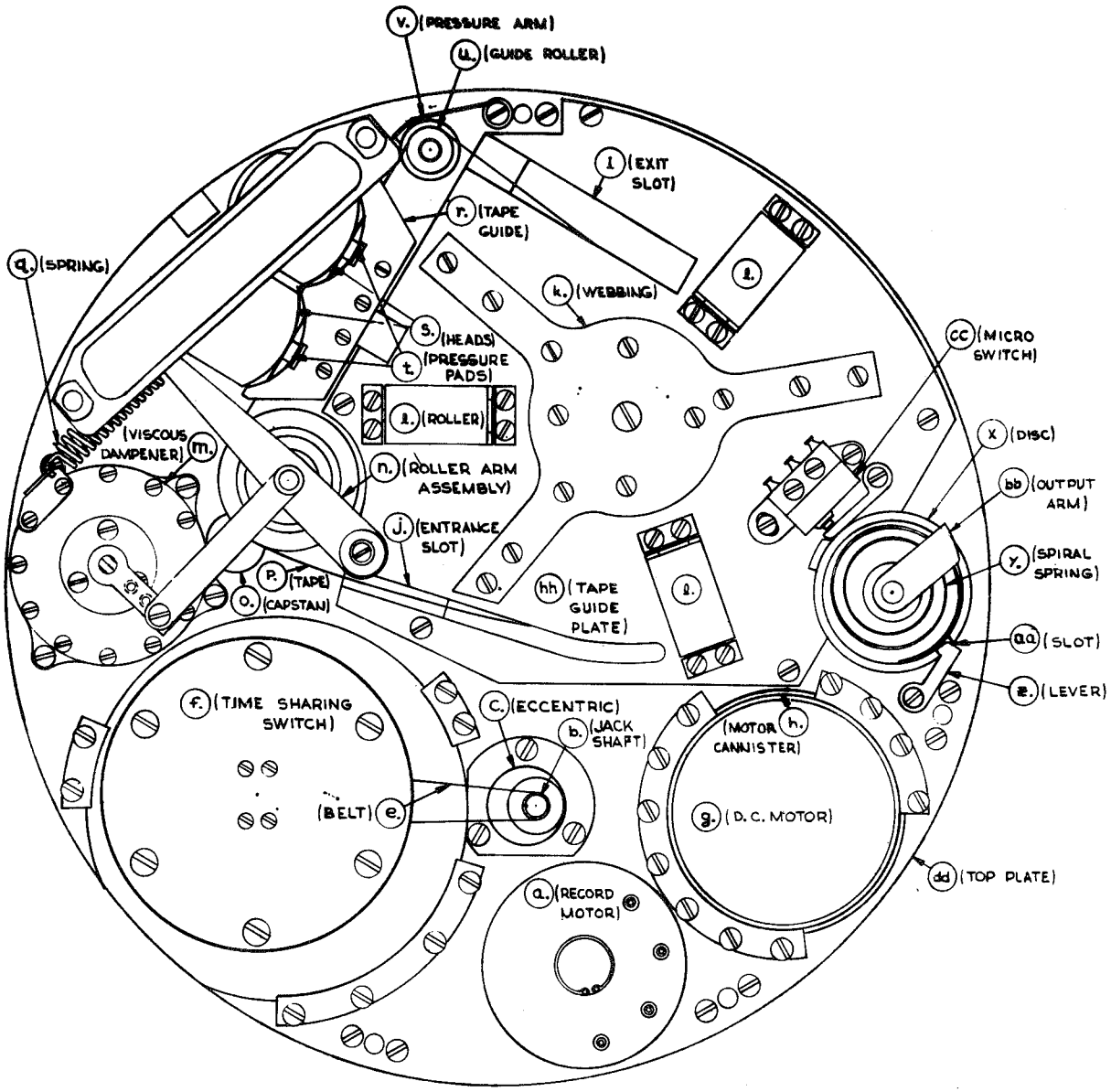

FIGURE 7.—Upper plate top view.

found that vibrations from the motors were being transmitted across the top plate to the record-playback head and affecting performance. It was then decided to use a material that would adequately damp any extraneous vibrations before they reached the heads. Investigation led to a special highly damped magnesium alloy called K–1A. A top plate 0.5 inch thick of this material eliminated the vibrational effects due to the motors.

Time-Sharing Switch

In the design of spacecraft telemetry systems it frequently is convenient to time-share items of data onto a single channel of a suitable storage or transmission medium. Electronic commutators are used for this purpose where features such as low signal levels, high data rates, and long life are required. Ordinary mechanical commutators are used where low data rates are

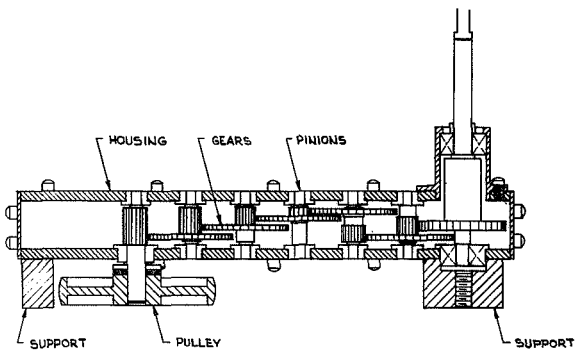

FIGURE 8.—Speed reduction for playback cutoff switch.

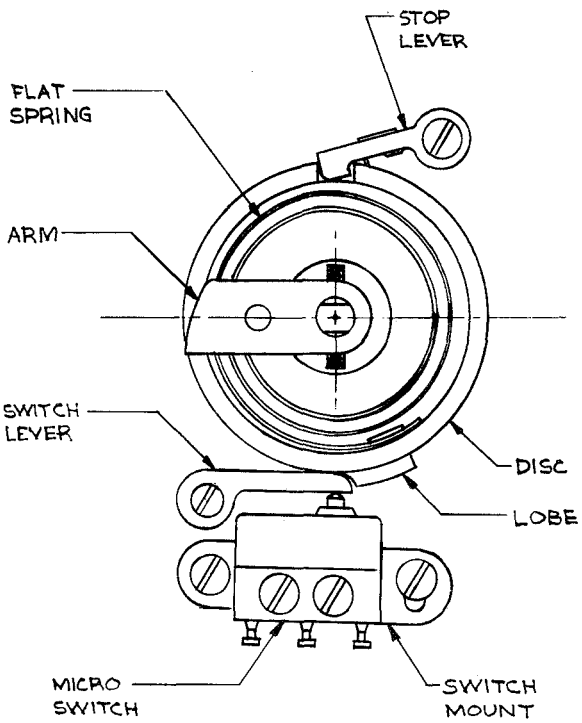

FIGURE 9.—Reset switch assembly.

required, but they are usually limited to applications involving medium signal levels. Furthermore, the lifetimes of ordinary mechanical commutators are usually limited. However, the time-sharing switch (TSS)[4] discussed in this paper operates reliably with low signal levels (about 20 microamperes, 0.05 microvolt, 450 cps) for long periods of time. In addition, this TSS rivals the ordinary mechanical commutator in low driving torque (0.0005 inch-ounce at 256 rpm), accurate timing, small size, and low weight.

The time-sharing sequence is obtained basically by stacking microswitches to face one or more cams. The cams are driven through a gear box located beneath the banks of switches, and levers are used to transform the rotary motion of the cams into a linear motion necessary to depress the microswitch plungers.

Successful operation of the TSS has been demonstrated in the Tiros II satellite's infrared instrumentation, where it was used to cycle data from twelve separate sensors onto a channel of the infrared tape recorder.

The TSS is composed of two assemblies: the lever-switch assembly and the transmission assembly. The lever-switch assembly includes the levers, microswitches, and supporting structure; the transmission assembly includes the input pulley, gear reduction and housing, and the cams. Figure 10 is a cutaway view of

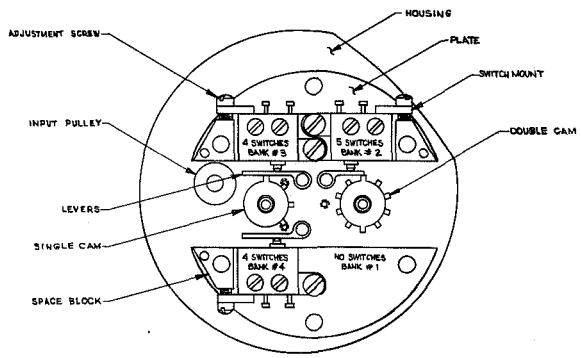

FIGURE 10.—Time-sharing switch assembly.

the entire assembly, showing the relative positions of the switches, levers, and cams.

The levers transform the rotational motion of the cams into a linear motion necessary to depress the switches. Figure 11 shows the switch stacking arrangement.

The input pulley, driven by a 1-mil Mylar belt 0.062 inch wide, is aluminum and operates at 256 rpm.

The gear reduction consists of six gears, five pinions, and the shafts, all made of type 303 stainless steel.

[4] Leavy, W. A., "A Time Sharing Switch for Spacecraft Telemetry Systems," NASA Technical Note D-1172, March 1962.

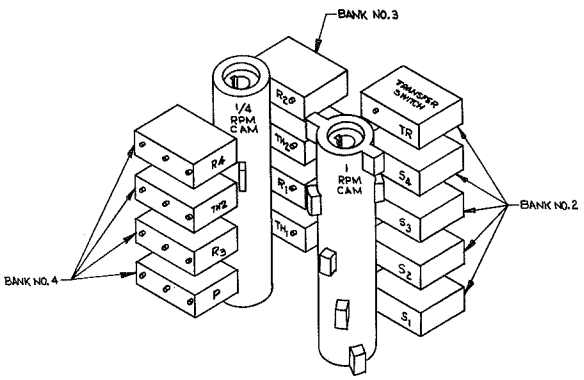

FIGURE 11.—Time-sharing switch stacking arrangement.

The magnesium housing of the gear train resembles a hat, being cylindrical in shape with a large flange on top. A round magnesium plate is screwed into the bottom of the housing to close it off. This plate and the top of the housing encompass the entire gear train.

The switch actuating cams are made of Kel-F plastic, and are fastened to the shafts by a key and snap ring. The cams are cylindrical as Figure 11 shows.

As is shown in Figure 12, switches S_1, S_2, S_3, and S_4 in bank 2 are wired individually, and the transfer switch is wired in series with all the switches in banks 3 and 4. This gives the following cycle of operation:

S_1, S_2, S_3, S_4, TH_1, S_1, S_2, S_3, S_4, R_1, S_1, S_2, S_3, S_4, TH_2, S_1, S_2, S_3, S_4, R_2, S_1, S_2, S_3, S_4, P, S_1, S_2, S_3, S_4, R_3, S_1, S_2, S_3, S_4, TH_2, S_1, S_2, S_3, S_4, R_4.

Each reading lasts approximately 6 seconds with an overlap of about ½ second between switching operations.

Environmental Testing

The prototype recorder has survived sinusoidal vibration test levels of 10 g from 0 to 2000 cps for 30 minutes total sweep time, and white noise random vibration of 20 g rms in a frequency bandwidth from 5 to 2000 cps for 4 minutes. It was subjected to temperature cycling from 0° to 60° C over extended periods with no degradation in performance. During the Tiros II and Tiros III testing programs, the flight acceptance units were subjected to flight

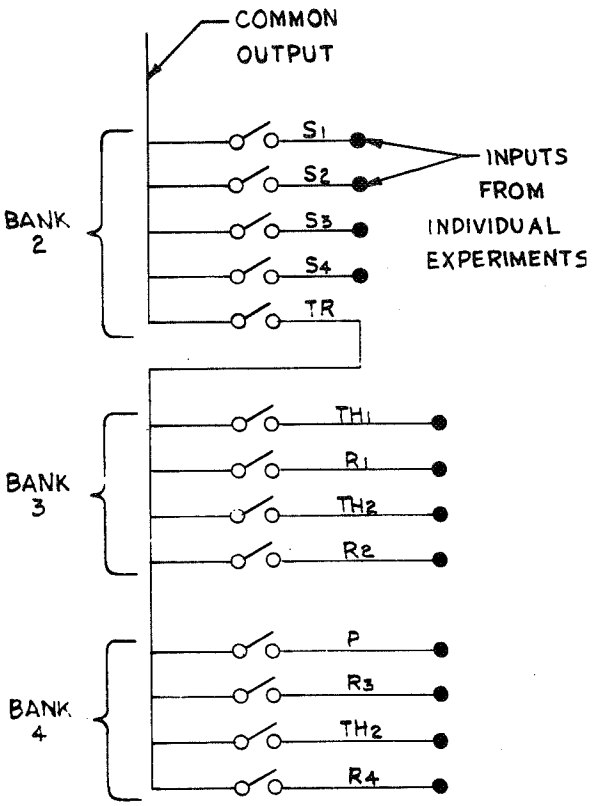

FIGURE 12.—Time-sharing switch circuit.

environmental testing levels, repeatedly demonstrating the high reliability achieved.

ELECTRICAL DESIGN

Record Motor Electronics

Because of the slow speed (0.4 inch/second) of the tape in the record mode, it was advantageous to use a synchronous motor. The motor is driven two-phase in preference to using a capacitor for the phase shift needed for the second motor winding; this gives a more constant torque pattern and thus less tape flutter. The supply voltage frequency is obtained by counting down a 550 cps tuning fork clock to 137.5 cps for the synchronous motor by the use of two bistable multivibrators. The 137.5 cps square wave is then fed to an amplifier tuned to 137.5 cps to obtain the fundamental sine wave. From this point the sine wave feeds two circuits: It feeds directly a class B push-pull amplifier to drive one winding of the motor; it also feeds a 90 degree phase shift

network which drives the other winding of the motor through a second class B amplifier.

Playback Motor Electronics

A synchronous motor was considered for use as the playback motor, but was found impractical for the following reasons:

1. Synchronous motors with the power rating required for playback were too large.
2. Synchronous motors are much less efficient than are dc motors. The playback motor requires appreciable power as compared to other components in the system; therefore, the maximum efficiency obtainable in the design area is important.
3. Since the playback duty cycle is quite short, the long-life advantage of a brushless motor was considered unnecessary.

A dc motor controlled by a servo loop was chosen. The use of mechanical governors was ruled out because of the inherent vibration problem and the interference caused by the constant making and breaking of contacts. Thus, an electronic means (Fig. 13) was devised to control the speed of the dc motor.

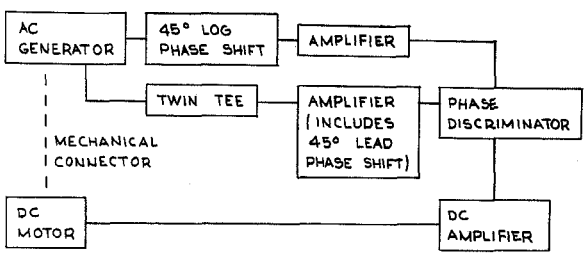

FIGURE 13.—Speed control block diagram.

The ac generator mounted on the motor shaft produces an output voltage whose frequency is proportional to the motor speed. The frequency, 583.3 cps, was selected for for mechanical design reasons. The ac generator consists of 14 magnetic poles (7 north and 7 south) alternately spaced around the circumference of a magnesium disc. The stator winding produces 583.3 cps output at the design motor speed of 5000 rpm. This signal is fed to a twin-tee network which is used as a frequency reference, and thence to a two-stage transformer-coupled amplifier including a 45-degree-lead phase shift at 583.3 cps and a phase detector. At the same time, the stator output is fed through a 45-degree-lag phase shift network (at 583.3 cps), through an amplifier, and back to the phase detector to be compared with the output of the amplified twin-tee signal. The phase characteristic of the twin-tee plus that of the 90 degree RC phase shift (45 degrees lead plus 45 degrees lag) add up as shown in Figure 14.

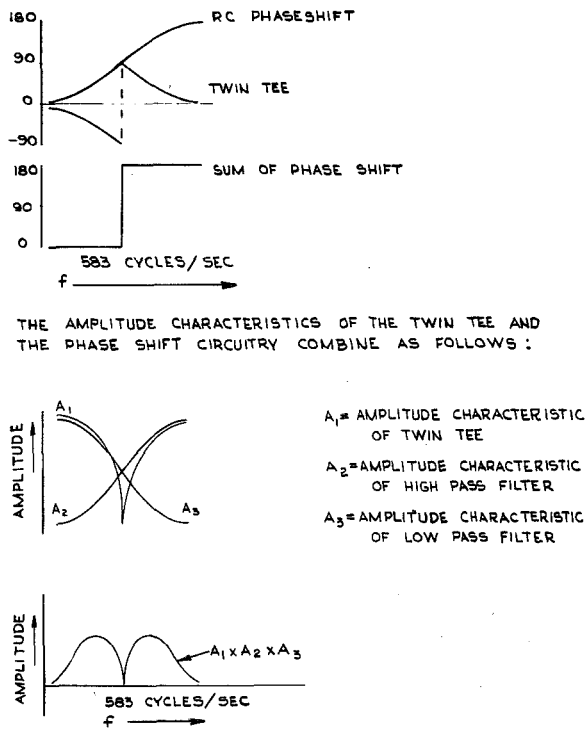

FIGURE 14.—Phase and amplitude characteristics of the twin-tee and 90° RC phase shift.

The phase detector circuit adds this amplitude characteristic to the 180 degree phase reversal, and the final output is as shown in Figure 15. The slope is about 1.5 volts/cps and the peaks are at ± 5 volts. The transformers are tuned to about 583 cps to improve the waveforms and maximize the loop gain at this point. The slope of the discriminator output is made as large as stability considerations

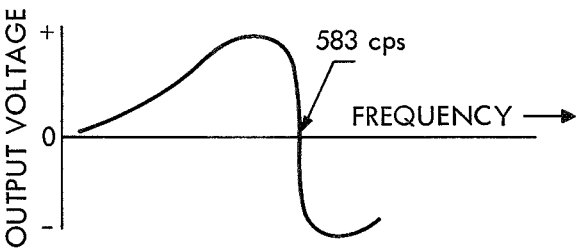

FIGURE 15.—Output voltage of dc motor speed control.

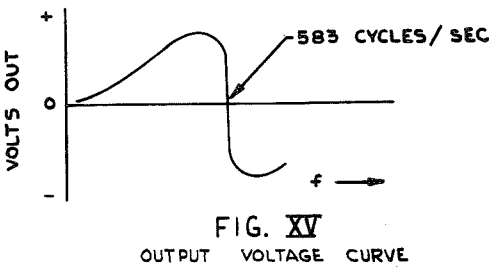

FIG. XV
OUTPUT VOLTAGE CURVE

will allow. Note also that the discriminator curve has a positive slope from zero motor speed up to the operating region; this insures positive, rapid starting.

The correction voltage is coupled to the motor by means of a dc amplifier which is designed to provide the nominal dc motor voltage for correct motor speed and to provide sufficient input impedance to prevent loading of the phase detector. The motor is series-controlled by means of a power transistor. A trim pot is included to afford easy compensation for mechanical torque variations in different tape recorders and electrical variations in the dc motors. Voltage feedback in the dc amplifier is essentially 100 percent; therefore, the error voltage is added directly to the motor voltage.

The degree of speed correction available depends on the loop gain; or, since the dc amplifier has unity gain, on the slope of the phase detector characteristic. By superimposing the motor speed versus voltage curve (for a given load) on the speed control motor voltage curve, the final speed regulation may easily be found as shown in Figure 16. The speed change produced by the increased load without the control system is ΔS. With the speed control operating, the speed change is reduced to ΔS_c. Measurements show that this system provides better than 1 percent speed regulation over a temperature range from 0° to 60° C.

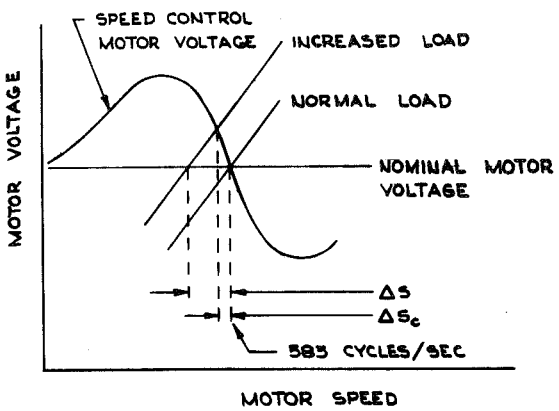

FIGURE 16.—Speed regulation of dc motor.

COMPONENT LAYOUT DESCRIPTION

Figures 7 and 17 show the assembled tape recorder. The record motor (A) is fastened to the top plate on an eccentric which allows the adjusting of belt tensions between the record motor and the intermediate jackshaft (B). This jackshaft is also mounted on an eccentric

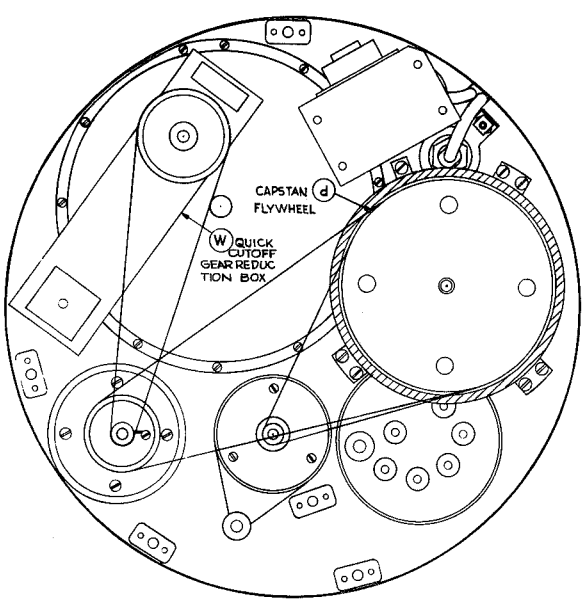

FIGURE 17.—Upper plate bottom view.

for the purpose of adjusting belt tension between itself and the low-speed capstan pulley (C). In addition to being a step pulley, the jackshaft is a flywheel which is necessary

because the large capstan flywheel (D) does not provide enough filtering at the low speed; 0.0015-inch polyester film belts are used for this reduction. From the jackshaft a belt (E) is connected to the time-sharing switch (F).

The playback system consists of the dc motor (G) potted in the lower half of a canister (H) to reduce vibration. The upper half of the cannister is lined with magnetic shielding to isolate the reproduce head from motor electrical noise. The canister itself is an eccentric to permit the adjusting of belt tension between the motor and the capstan flywheel pulley (D). The tape guide plate (HH) covers the tape cartridge, and slots cut into it at (I) and (J) allow the tape to leave and enter the cartridge. The webbing (K) stiffens the cover plate. The rollers (E) prevent the tape from rubbing on the inside of the cover plate. The viscous dampener (M) critically damps the roller arm assembly (N) to maintain rubber roller pressure on the capstan (O) and tape (P) under vibration. The spring (Q) provides the roller force required to prevent tape slippage.

The tape guide (R) guides the tape as it passes the heads (S), minimizing errors due to skew. The pressure pads (T) provide positive contact between the tape and the head gaps.

The guide roller (U) and pressure arm (V) provide tape tension and tend to damp any pulsations emanating from the cartridge.

A belt pass from the dc motor operates the quick cutoff gear reduction box (W). The output shaft of this box is connected to the disc (X) through a spiral ring (Y). The lever (Z) engages the slot in the disc (AA) when the cam has completed about ¾ revolution. When a revolution is completed, the output arm (BB) releases the lever, causing the dics to snap around actuating the microswitch (CC) shutting off the playback mode and setting the electronics into the record mode.

The top plate (DD) is made of K–1A magnesium to damp vibrations from the motors, which might otherwise affect the heads. All of the bulkier structural components are constructed of magnesium for weight economy.

CONCLUDING REMARKS

The Tiros recorder configuration has been adapted for use in the Nimbus meteorological satellite as a medium resolution infrared tape recorder. This modified Nimbus configuration is also being used in the later Tiros satellites. The basic tape cartridge and transport design have remained unchanged; however, some modifications were incorporated to satisfy the different interface problems and the modular design of the satellite components.

At present, work is proceeding toward the development of larger capacity endless-loop cartridges, and the related problems involved in the dynamics of these cartridges are under study. Special studies are being undertaken to develop tapes that will withstand high speeds and temperature without adverse effects on their magnetic performance.

ACKNOWLEDGMENTS

The authors wish to express their appreciation for the efforts of Mr. John H. Licht (now with Lockheed Electronics Corp.), who was responsible for leading the early development of the tape recorder. We would also like to thank our associates Messrs. William Leavy, William A. Kley, William Burton, Thomas Ashton, and Maxwell Strange for their major mechanical and electrical contributions leading toward the successful design and development of the tape recorder.

ANALYTICAL THEORY OF THE STRETCH YO-YO FOR DE-SPIN OF SATELLITES

JOSEPH V. FEDOR

Goddard Space Flight Center

An analysis of an advanced type of yo-yo for satellite de-spin is made. The analyzed stretch yo-yo consists of a weight, a spring, a wire, and end fittings, or simply a weight, a spring, and end fittings. Equations of motion are developed for the system but, because of the complex nature of the equations, they are not solved explicitly. By using a novel method of analysis, algebraic complexity is circumvented and simple design equations are derived. A straightforward step by step procedure is given for the design of the stretch yo-yo. The results calculated from the equations clearly indicate that the stretch yo-yo is less sensitive to satellite spin-up errors and uncertainty in the spin moment of inertia than is the conventional rigid yo-yo.

INTRODUCTION

In the early period of the U.S. space effort, common methods of spin reduction from the initial spin-up of the satellite or the satellite and last stage combination were: retro-rockets, increase of the spin moment of inertia, and, more recently, rigid yo-yo's (Reference 1 and 2). Invariably there are errors in initial spin-up. These errors can be quite large. For example, in the Explorer XII (1961 υ) satellite launching initial spin-up was about 30 percent greater than the desired spin-up value (189 rpm instead of 150 rpm). This error in spin-up is reflected in the final spin. With retro-rockets the *magnitude* of the error is reflected in the final spin (a 39-rpm increase in nominal initial spin would mean a 39 rpm increase in the final spin). With the change of moment of inertia device or the rigid yo-yo, the *percentage* of the error is reflected in the final spin (a 30-percent increase in nominal initial spin would mean a 30-percent increase in the final spin).

Another source of de-spin error is the uncertainty of the spin axis moment of inertia. Frequently the last rocket stage and the satellite are de-spun together. Because of fuel residue in the last-stage rocket the spin moment of inertia is not accurately known. This variation of inertia from the design value also causes an error in the final spin.

An appreciable error in the final de-spin value can have detrimental effects: Experiments and satellite appendages such as booms and paddles are designed to operate at a certain spin with a modest tolerance about this point. Hence, a large error in de-spin can compromise the experiment(s), and a large de-spin error could cause the satellite appendages not to function or damage them in functioning.

A device that greatly reduces spin-up errors and errors due to variations in spin moment of inertia is the stretch yo-yo (the stretch concept was first suggested by Henry Cornille of Goddard Space Flight Center (Reference 3)). It can consist of a weight, a spring, a wire, and end fittings (Fig. 1), or simply a weight, a spring, and end fittings (Fig. 2). The purpose of the spring is to compensate for errors in initial spin-up. For example, in a given stretch yo-yo application there will be a certain amount of stretching or elongation of the spring during normal operation. If the initial spin is greater

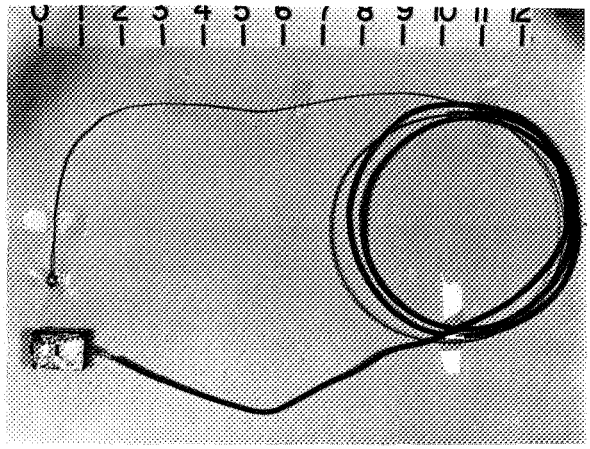

FIGURE 1.—Stretch yo-yo consisting of weight, spring, wire, and end fittings. (The scale is in inches.)

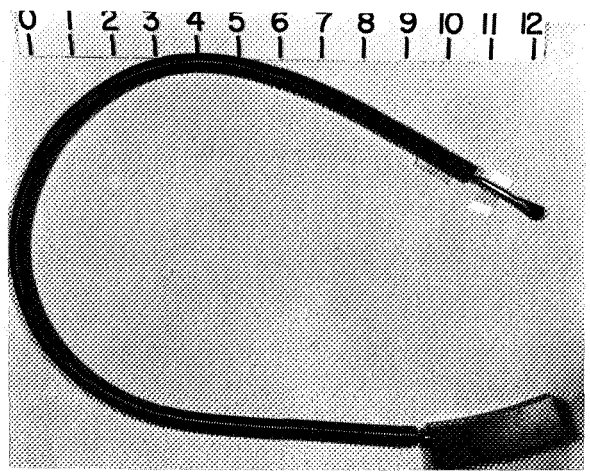

FIGURE 2.—A stretch yo-yo consisting of weight, spring, and end fittings. (The scale is in inches.)

than the nominal value, the spring will elongate more than normal during operation and reduce the spin to the desired value. If the initial spin is less than the nominal initial spin, the spring will elongate less than normal during functioning and correct for the under spin. The stretch yo-yo is a simple example of an adaptive control system: it senses the spin environment it is in and corrects accordingly. Also, it will be shown that the stretch yo-yo is relatively insensitive to variations (uncertainties) of the spin moment of inertia.

It should not be concluded that the stretch yo-yo will completely replace the rigid yo-yo for satellite spin reduction. It is believed that the rigid yo-yo still has an application: when de-spin requirements are not stringent, and ease and flexibility of operation are desired (for example, to permit large last minute changes in initial spin-up and spin moment of inertia).

DYNAMIC ANALYSIS

There are essentially two phases to the stretch yo-yo spin reduction process. In Phase 1 the spring changes in length and is tangent to the satellite. In Phase 2 the spring changes its position from tangent to perpendicular to it. At this point (perpendicular to the satellite) the yo-yo is released.

For a given set of satellite parameters and a given spin reduction, the design engineer wants to know the weight of the end mass, to know the proportions of the spring or spring wire, and to verify that there is adequate strength in the spring to insure linear operation of it. As may be expected, analysis of the stretch yo-yo is more complicated than that of the rigid yo-yo. Introducing a spring adds another degree of freedom. Equations of motion will first be developed for Phases 1 and 2, but they will not be solved explicitly because of the complicated nature of the equations. The conservation of momentum and energy equations and a force equation will be applied at the end of Phase 2 deployment, and a novel approach will be used to circumvent the algebraic difficulties encountered in solving these equations.

Phase 1

For analysis purposes, the satellite can be considered to be spinning about a fixed axis but otherwise stationary. A sketch of the Phase 1 coordinate system is shown in Figure 3. Only one spring and weight is shown, as the system is considered symmertical. Also, the system is considered torque-free; small torques due to the earth's magnetic or gravitational fields, the atmosphere, and the solar sun pressure are neglected. The Lagrangian method of dynamic description will be used to obtain the equations of motion. The total kinetic energy of the system is

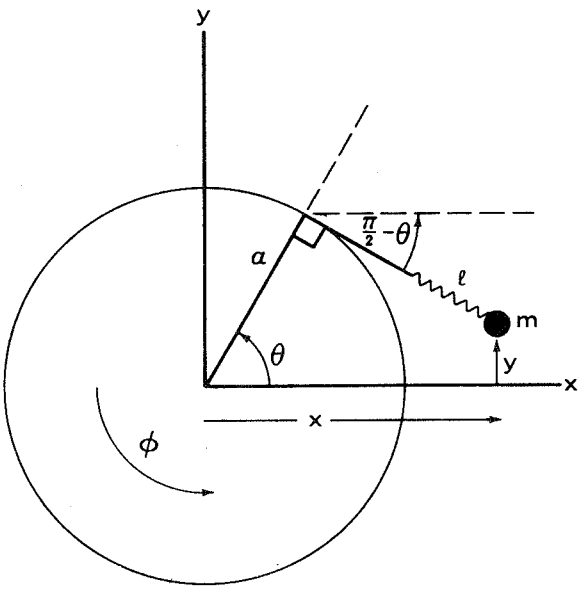

FIGURE 3.—Phase 1 coordinate system.

$$T=\frac{1}{2}I\dot{\phi}^2+\frac{1}{2}m(\dot{x}^2+\dot{y}^2), \tag{1}$$

where m is the total mass of both weights, I is the moment of inertia of the satellite about the spin axis, and $\dot{\phi}$, $\dot{x}$, and $\dot{y}$ are velocities. The weight of the springs is taken into account by the method developed in Reference 2. By using the transformation equations,

$$x=a\cos\theta+l\sin\theta, \tag{2}$$

$$y=a\sin\theta-l\cos\theta, \tag{3}$$

and

$$l=a(\theta-\phi)+\delta, \tag{4}$$

where a is the radius of the satellite or de-spin fixture, $a(\theta-\phi)$ is the amount of unwrapped yo-yo, and δ is the stretch of the spring, the kinetic energy function can be put into the form

$$T=\tfrac{1}{2}I\dot{\phi}^2+\tfrac{1}{2}m(l^2\dot{\theta}^2+a^2\dot{\phi}^2+\dot{\delta}^2-2a\dot{\phi}\dot{\delta}).^5 \tag{5}$$

The total potential energy of the system is $k\delta^2$ (two springs, where k is the spring constant).

[5] The dot indicates a derivative with respect to time and it is sometimes used with an actual time derivative for convenience of notation.

Thus the Lagrangian for the system is

$$L=\tfrac{1}{2}I\dot{\phi}^2+\tfrac{1}{2}m(l^2\dot{\theta}^2+a^2\dot{\phi}^2+\dot{\delta}^2-2a\dot{\phi}\dot{\delta})-k\delta^2. \tag{6}$$

The equations of motion, in Lagrangian notation, are:

$$\frac{d}{dt}\left(\frac{\partial L}{\partial\dot{\phi}}\right)-\frac{\partial L}{\partial\phi}=Q_\phi=0, \tag{7}$$

$$\frac{d}{dt}\left(\frac{\partial L}{\partial\dot{\theta}}\right)-\frac{\partial L}{\partial\theta}=Q_\theta=0, \tag{8}$$

$$\frac{d}{dt}\left(\frac{\partial L}{\partial\dot{\delta}}\right)-\frac{\partial L}{\partial\delta}=Q_\delta=0. \tag{9}$$

Explicitly writing out the equations of motion results in:

$$\lambda^2\frac{d\dot{\phi}}{dt}+al\dot{\theta}^2-a\frac{d^2\delta}{dt^2}=0, \tag{10}$$

$$\frac{d}{dt}(l^2\dot{\theta})-al\dot{\theta}^2=0, \tag{11}$$

and

$$\frac{d^2\delta}{dt^2}+\frac{2k}{m}\delta-a\frac{d\dot{\phi}}{dt}-l\dot{\theta}^2=0, \tag{12}$$

where $\lambda^2=I/m+a^2$. Equations 10, 11, and 12 are a formidable set of simultaneous nonlinear differential equations, and it is unlikely that they can be solved analytically to give the spin reduction or the length of spring as a function of time as was done in Reference 2 for the rigid yo-yo. (The equations have been solved on an analog computer without much difficulty.)

Phase 2

A sketch of the Phase 2 situation is shown in Figure 4. The Lagrangian in this phase is

$$L=\tfrac{1}{2}I\dot{\phi}^2+\tfrac{1}{2}m[a^2\dot{\phi}^2+l^2\dot{\gamma}^2+\dot{l}^2-2a\dot{l}\dot{\phi}\sin(\phi-\gamma)+2al\dot{\phi}\dot{\gamma}\cos(\phi-\gamma)]-k\delta^2, \tag{13}$$

and the equations of motion are:

$$\frac{d}{dt}[\lambda^2\dot{\phi}-a\dot{l}\sin(\phi-\gamma)+al\dot{\gamma}\cos(\phi-\gamma)]+a\dot{l}\dot{\phi}\cos(\phi-\gamma)+al\dot{\phi}\dot{\gamma}\sin(\phi-\gamma)=0, \tag{14}$$

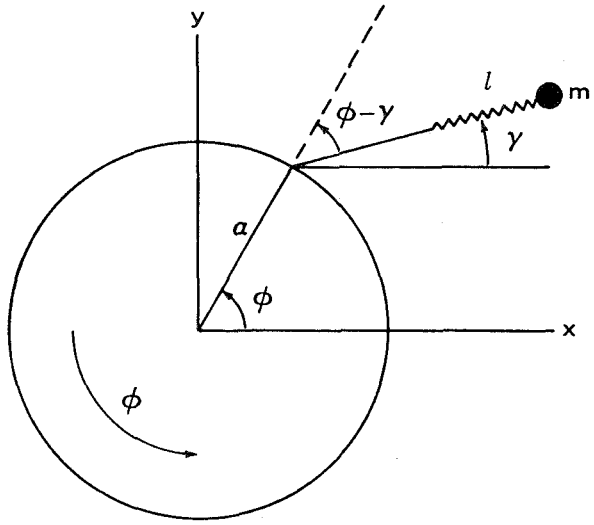

FIGURE 4.—Phase 2 coordinate system.

$$\frac{d}{dt}[l^2\dot{\gamma}+al\dot{\phi}\cos(\phi-\gamma)]-al\dot{\phi}\cos(\phi-\gamma)$$
$$-al\dot{\phi}\dot{\gamma}\sin(\phi-\gamma)=0, \quad (15)$$

$$\frac{d}{dt}[\dot{\delta}-a\dot{\phi}\sin(\phi-\gamma)]-l\dot{\gamma}^2-a\dot{\phi}\dot{\gamma}\cos(\phi-\gamma)$$
$$+\frac{2k\delta}{m}=0, \quad (16)$$

where $l=l_0+\delta$, l_0 being the unstretched length of the yo-yo. A brief glance at Equations 14, 15, and 16 shows that the equations of motion for Phase 2 are even more formidable than those for Phase 1.

SIMPLIFIED APPROACH TO THE STRETCH YO-YO DESIGN EQUATIONS

As was noted in earlier sections, the equations of motion for the stretch yo-yo are quite formidable and the direct equation of motion approach does not appear analytically fruitful. Equations for the conservation of momentum and energy, and a force equation will now be derived. A novel method of solution of these equations will then be applied. This will result in relatively simple design equations for the stretch yo-yo. Though they are not mathematically exact, analysis and tests have demonstrated that the equations are adequate for design and prediction of performance.

Combining Equations 14 and 15 of Phase 2 and integrating results in the equation for the conservation of momentum for Phase 2:

$$\lambda^2\dot{\phi}-al\sin(\phi-\gamma)+al\dot{\gamma}\cos(\phi-\gamma)+l^2\dot{\gamma}$$
$$+al\dot{\phi}\cos(\phi-\gamma)=\text{constant}. \quad (17)$$

At the release of the yo-yo ($\phi-\gamma=0$), Equation 17 reduces to

$$\frac{I}{m}\dot{\phi}_2+(l+a)(a\dot{\phi}_2+l\dot{\gamma})=\text{constant}, \quad (18)$$

where $\dot{\phi}_2$ is the final spin rate in radians/second. If we neglect the oscillatory motion of the spring ($\dot{\delta}$), the conservation of energy equation at release is

$$\frac{1}{2}I\dot{\phi}_2^2+\frac{1}{2}m(a\dot{\phi}_2+l\dot{\gamma})^2+k\delta^2=\text{constant}. \quad (19)$$

Equation 19 is essentially another integral of Equations 14, 15, and 16. A force equation can be obtained from Equation 16 by neglecting $\dot{\delta}$ and evaluating the equation at release; thus

$$k\delta=\frac{m}{2}(a\dot{\phi}_2^2+l\dot{\gamma}^2). \quad (20)$$

A straightforward approach to solving Equations 18, 19, and 20 (that is, to eliminate γ and solve for the stretch and the spin mass of the system in terms of the other parameters) leaves one in a quagmire of algebraic complexity. What is desired is a yo-yo system where the final spin is completely independent of the initial spin. Analytical attempts to develop equations along these lines did not meet with success. It is possible though to develop simple analytical equations where, for small variations in the spring length, the effect on the final spin is negligible. We start the development by taking a variation of Equations 18 and 19 and letting $\Delta\dot{\phi}_2=0$:

$$(a\dot{\phi}_2+l\dot{\gamma})\Delta\delta+(l+a\Delta(a\dot{\phi}_2+l\dot{\gamma})=0, \quad (21)$$

and

$$(a\dot{\phi}_2+l\dot{\gamma})\Delta(a\dot{\phi}_2+l\dot{\gamma})+\frac{2k\delta}{m}\Delta\delta=0. \quad (22)$$

Note that $\Delta l=\Delta\delta$. Dividing one equation by the other results in

$$(a\dot{\phi}_2+l\dot{\gamma})^2=2\frac{k\delta}{m}(l+a). \tag{23}$$

Substituting Equation 23 into the energy equation (constant taken to be approximately $(I/2)\ \dot{\phi}_0^2$ where $\dot{\phi}_0$ is the initial spin rate in radians/second) and solving for the spring stretch δ gives

$$\delta=\frac{-(l_0+a)+\sqrt{(l_0+a)^2+\frac{4I}{k}(\dot{\phi}_0^2-\dot{\phi}_2^2)}}{4}. \tag{24}$$

The positive sign is used in the quadratic formula since δ must be positive. By combining the momentum and energy equations and Equation 24 and using the approximation $\lambda^2\approx I/m$, the following simple relationship connecting the spin mass with the initial and final spins can be obtained:

$$\frac{I(l+a+\delta)}{m(l+a)^3}=\frac{\dot{\phi}_0+\dot{\phi}_2}{\dot{\phi}_0-\dot{\phi}_2}=\frac{1+r}{1-r}, \tag{25}$$

where $r=\dot{\phi}_2/\dot{\phi}_0$, the desired spin reduction Note that Equation 25 is analogous to Equation 22 of Reference 2 for the rigid yo-yo. In fact if δ is equal to zero in Equation 25 (rigid yo-yo), both equations are identical, as they should be.

To review the method briefly: essentially we had three simultaneous equations describing the stretch yo-yo system. What we did was to impose a physically desirable condition on two of the equations (conservation of energy and momentum) to replace the third equation. This enabled us to satisfy the conservation equations exactly and thus obtain an equation for the stretch of the yo-yo (spring) at its release without recourse to the additional equation. Also, an equation for the total spin mass was developed from the resulting equations. An estimate of how closely the third equation (force equation) is satisfied by this method is given in Appendix A.

The equations developed thus far do not put any restrictions on the spring constant k. We would like to use such a spring constant that for a variation in $\dot{\phi}_0$ and hence δ, the fina variation in $\dot{\phi}_2$ would be approximately zero A variation of Equation 24 gives

$$\Delta\delta=\frac{I\dot{\phi}_0\Delta\dot{\phi}_0}{k(l+a+3\delta)}. \tag{26}$$

A variation of Equation 25 gives

$$(\dot{\phi}_0^2-\dot{\phi}_2^2)\left[\frac{l+a+3\delta}{(l+a)(l+a+\delta)}\right]\Delta\delta=2\dot{\phi}_2\Delta\dot{\phi}_0. \tag{27}$$

Combining Equations 26 and 27 gives the op timum k for the stretch yo-yo at design con ditions,

$$k=\frac{\dot{\phi}_0^2(1-r^2)I}{2r(l+a)(l+a+\delta)}. \tag{28}$$

If the spring constant is the optimum one, the the stretch equation, Equation 24, reduces to

$$\delta=\frac{r(l_0+a)}{1-r}; \tag{29}$$

and, in turn, Equation 28 simplifies to

$$k=\frac{\dot{\phi}_0^2(1-r)^3I}{2r(l_0+a)^2}, \tag{30}$$

and the mass equation, Equation 25, reduces t

$$\frac{I}{m(l+a)^2}=\frac{1}{1-r}. \tag{31}$$

Thus for design conditions, the stretch yo-y equations are expressed in terms of readil known quantities. Note in Equation 30 tha if $r\to 0$, $k\to\infty$; that is, for zero final spin, th optimum stretch yo-yo becomes a rigid yo-yo It should be emphasized that Equations 29, 30 and 31 are used only at design conditions. T calculate the stretch at any other spin (erro computation for example) or k value, Equation 24 and 25 (or comparable preload equations) ar used.

In the practical world of fabrication, part (for example, the stretch yo-yo springs) are no made exactly the way equations specify Springs are not made precisely with a spring constant of say 12.5 lb/ft; there is a toleranc about this value. Also, springs can have a

preload which the derived equations do not take into account. By following a procedure similar to what has been outlined, a stretch equation taking preload into account can be derived:

$$\delta=\frac{-\left(l_0+a+\frac{3F_0}{k}\right)+\sqrt{\left(l_0+a+\frac{3F_0}{k}\right)^2+4\left[\frac{I}{k}(\dot{\phi}_0^2-\dot{\phi}_2^2)-\frac{2F_0}{k}(l_0+a)\right]}}{4}, \quad (32)$$

where F_0 is the spring preload. Also,a mass equation can be developed:

$$\frac{I\left(l+a+\delta+\frac{\delta F_0}{k\delta+F_0}\right)}{m(l+a)^3}=\frac{\dot{\phi}_0+\dot{\phi}_2}{\dot{\phi}_0-\dot{\phi}_2}=\frac{1+r}{1-r}. \quad (33)$$

These equations are used after hardware has been fabricated and a new mass weight must be calculated to correct for deviations from the optimum spring constant and preload. A desk calculator should be used in evaluating Equations 32 and 33 for accurate stretch yo-yo results. Calculations have indicated and tests have supported the fact that the preload of the spring is beneficial. That is, the spin error is less with preloaded springs. Full advantage cannot be taken of this because spring preload is an unpredictable thing.

An important element in the stretch yo-yo is the spring. Design procedures for the spring are developed in Appendix B.

APPLICATION OF DESIGN EQUATIONS AND DISCUSSION

We shall now apply the equations to a practical situation to illustrate how the equations are used and what precautions should be taken. The experimental verification of the stretch yo-yo equations will be covered in a future NASA Technical Note.

The following quantities are involved in establishing a stretch yo-yo design: I, a, $\dot{\phi}_0$, $\dot{\phi}_2$, l_0, δ, k, and m. The first four quantities are usually specified; l_0 is at the discretion of the designer; the last three quantities can be calculated from the developed equations. As an example, consider the design of a stretch yo-yo for a typical Goddard Space Flight Center satellite. Initial design parameters are tabulated below:

$I=2.885$ slug-ft^2,
$a=0.942$ ft,
$\dot{\phi}_0=160$ rpm$=16.755$ rad/sec,
$\dot{\phi}_2=73.9$ rpm$=7.735$ rad/sec.

Therefore $r=0.462$. The satellite structure is such that only about a half wrap of yo-yo will fit. Hence l_0 is chosen to be 2.365 ft. The design spin reduction stretch δ is calculated from Equation 29,

$$\delta=\frac{r(l_0+a)}{1-r}=2.841 \text{ ft.}$$

Thus, the total length of one yo-yo at release is $l=l_0+\delta=5.206$ ft. The optimum value for the spring constant is calculated from Equation 30,

$$k=\frac{\dot{\phi}_0^2(1-r)^3I}{2r(l_0+a)^2}=12.48 \text{ lb/ft.}$$

The force in the spring (wire) at design conditions is $k\delta=(12.48)\ 2.841=35.46$ pounds. The total spin weight (mass) of the system is obtained from Equation 31,

$$m=\frac{I(1-r)}{(l+a)^2}=0.0411 \text{ slugs}=600.5 \text{ gm.}$$

For the spring analysis, the procedure described in Appendix B is used. The quantities listed below were chosen (or were true for the selected spring material):

wire=NS355 spring steel,
ρ=weight density of the spring=0.282 lb/in.^{3},
G=shear modulus of elasticity=11.5 $\times 10^6$ lb/in.^{2},
l_s=length of spring=25 in.,
d=wire diameter=0.0625 in.

The following quantities were calculated according to the procedure in Appendix B:

R=mean helix radius=0.1875 in.,
Coil OD=0.4375 in.,
C=spring index=$\frac{2R}{d}$=6.0,
k_s=stress concentration factor for torsion and transverse shear=1.088,
$F_{max}=k\delta_{max}$=49 lb (25 percent overspin),
S_{max}=maximum torsional stress in the spring=208,500 lb/in.^{2},
m_s=weight of spring=0.4077 lb=185.1 gm.

Static tests of the spring showed that the 49-pound load was the maximum that the spring could maintain and still operate in the linear region.

Reference 2 shows that the mass of the wire in a rigid yo-yo can be approximately accounted for by adding ⅓ the mass of the wire to the spin mass. Full scale tests have verified that this method is also applicable to the stretch yo-yo. We thus define the total mass m_t of the yo-yo system in the following way:

$$m_t=2\left(m_0+\frac{m_s+m_w}{3}\right), \qquad (34)$$

where

m_0=mass of one spin weight,
m_s=mass of one spring,
m_w=mass of one wire (if there is any).

Once the weight of the spring has been established the weight of the end mass can be calculated from Equation 34:

$$m_0=\frac{m_t}{2}-\frac{m_s}{3}=238.6 \text{ gm}.$$

This completes the preliminary design calculations.

The error curve expected from this design is shown in Figure 5 (see Appendix C for the error calculation procedure). It will be noticed from Figure 5 that for ±20 percent error in initial spin, the final de-spin value is less than 5 percent from the desired spin. In contrast, for the rigid yo-yo, a 20 percent error in initial spin would result in a 20 percent error in the final spin. Note also in Figure 5 the flat portion of the error curve near zero percent spin-up error. This shows that the physically desired condition has been successfully imposed on the stretch yo-yo equations. That is, small spin-up errors have negligible effect on the final spin.

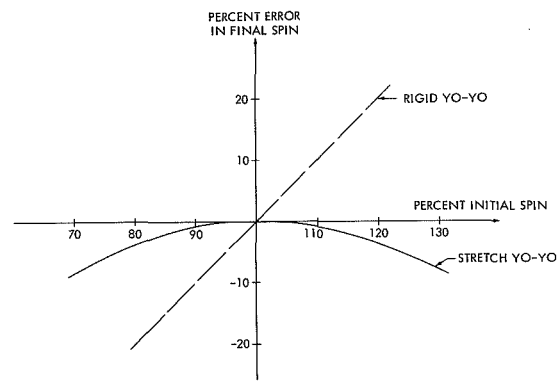

FIGURE 5.—Final spin error vs. spin-up error of a stretch yo-yo compared to that of a rigid yo-yo.

Figure 6 shows an error curve when the spin moment of inertia is varied ±20 percent. Superimposed is the error curve for a comparable rigid yo-yo. Except for the fortuitous conditions of a 20-percent increase in moment of inertia and a 20-percent decrease in initial spin-up (or vice versa), the stretch yo-yo is clearly less sensitive to variations in the spin moment of inertia. Physically, the error correction can be explained as follows: for design spin moment of inertia there is a certain amount of stretching of the spring during normal operation. If the spin moment of inertia is greater than the design value, the spin will be higher during early periods of the de-spin cycle (as com-

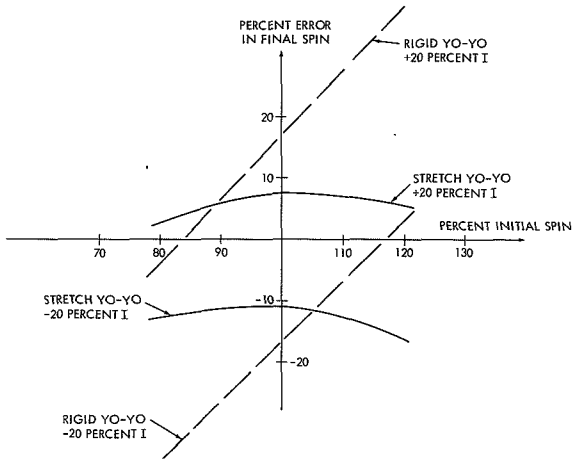

FIGURE 6.—Final spin error vs. spin-up error of a stretch yo-yo compared to that of a rigid yo-yo (spin moment of inertia varied ±20 percent).

pared to normal operation) because of the greater kinetic energy. This causes the stretch yo-yo to elongate more and thus compensate for the increased kinetic energy in the system. A similar explanation holds for a moment of inertia less than the design value. This type of action thus tends to reduce variations from the desired final spin.

As was pointed out in an earlier section, when the hardware is fabricated and accurate values of the spring constant, spring weight, and preload are known, Equations 32 and 33 must be used to calculate a precise value for the spin weight. It is also advantageous to have a plot of the spin moment of inertia versus the spin weight so that last minute changes due to increased satellite weight can be included. For convenience in making design calculations, a computation sheet is included in Appendix D.

During the writing of this technical note, a stretch yo-yo was used on Ariel I (1962 $o1$), April 1962.

RÉSUMÉ

The equations for an advanced type of yo-yo for satellite de-spin have been developed. As was noted, by using a variational method of analysis, simple design equations have been derived. A straightforward step by step procedure has been obtained for the design of the stretch yo-yo. The results calculated from the equations clearly indicate that the stretch yo-yo is less sensitive to satellite spin-up errors and uncertainty in the spin moment of inertia than the rigid yo-yo.

ACKNOWLEDGMENTS

The author is indebted to W. R. Mentzer, Jr., of Goddard Space Flight Center for checking the equations and developing Appendix B, and for the numerous calculations made prior to flying a stretch yo-yo.

REFERENCES

1. COUNTER, D. N., "Spin Reduction for Ion Probe Satellite S–30 (19D)." Marshall Space Flight Center document, Sept. 12, 1960.
2. FEDOR, J. V., "Theory and Design Curves for a Yo-Yo De-Spin Mechanism for Satellites," NASA Technical Note D–708, August 1961.
3. CORNILLE, H. J., Jr., "A Method of Accurately Reducing the Spin Rate of a Rotating Spacecraft " NASA Technical Note D–1420, October 1962.

Appendix A

ERROR ESTIMATE FOR THE FORCE EQUATION

In the variational approach, a physically desirable condition was imposed on the conservation of energy and momnetum equations. The resulting equation was used in place of the force equation to derive the stretch yo-yo properties. It is the purpose of this section to show what is neglected in the force equation when the variational method is used, and to give an indication of the accuracy of the derived equations.

The force equation (Equation 20 of the body of this report) is:

$$k\delta=\frac{m}{2}\,(a\dot{\phi}_2^2+l\dot{\gamma}^2). \tag{A1}$$

Multiplying Equation A1 by $l+a$ and rearranging gives

$$(l+a)\,k\delta=\frac{m}{2}\,(a^2\dot{\phi}_2^2+l^2\dot{\gamma}^2)+\frac{mal}{2}\,(\dot{\phi}_2^2+\dot{\gamma}^2). \tag{A2}$$

This can be put into the form,

$$(l+a)\,k\delta=\frac{m}{2}\,(a\dot{\phi}_2+l\dot{\gamma})^2+\frac{mal}{2}\,(\dot{\gamma}-\dot{\phi}_2)^2, \tag{A3}$$

by adding and subtracting $mal\dot{\phi}\dot{\gamma}$. From the energy equation (Equation 19 of the report proper) we have

$$\tfrac{1}{2}m\,(a\dot{\phi}_2+l\dot{\gamma})^2=\tfrac{1}{2}I\,(\dot{\phi}_0^2-\dot{\phi}_2^2)-2k\delta^2. \tag{A4}$$

Substituting Equation A4 into Equation A3 and rearranging gives

$$I\,(\dot{\phi}_0^2-\dot{\phi}_2^2)=2k\delta^2+2\,(l+a)\,k\delta-mal\,(\dot{\gamma}-\dot{\phi}_2)^2. \tag{A5}$$

Compare this with Equation 24 of the body of the report, which was obtained from the variational method and has been squared and arranged:

$$I\,(\dot{\phi}_0^2-\dot{\phi}_2^2)=2k\delta^2+2\,(l+a)\,k\delta. \tag{A6}$$

We see that $mal\,(\dot{\gamma}-\dot{\phi}_2)^2$ has been neglected in Equation A6. Hence, in the variational method of analysis we are neglecting $mal\,(\dot{\gamma}-\dot{\phi}_2)^2$ compared to $2(l+a)k\delta+2k\delta^2$ or $I(\dot{\phi}_0^2-\dot{\phi}_2^2)$. Defining the ratio of these as E, we have

$$E=\frac{mal\,(\dot{\gamma}-\dot{\phi}_2)^2}{I(\dot{\phi}_0^2-\dot{\phi}_2^2)}. \tag{A7}$$

An estimate of $\dot{\gamma}-\dot{\phi}_2$ must be made so that E can be evaluated. Letting $\dot{\gamma}-\dot{\phi}_2=\epsilon$, substituting this into the momentum equation (Equation 18 of the body of this report), and rearranging and comparing the result with Equation 25, we can conclude that $l/(l+a)\epsilon$ must be equal to

$$\frac{\dot{\phi}_0(l+a-\delta r)}{(l+a+\delta)},$$

for the two equations to be identical. Since $\delta=r(l+a)$, for design conditions, letting $l/(l+a)\approx 1$, we find

$$\epsilon=\dot{\phi}_0-\dot{\phi}_2. \tag{A8}$$

If we substitute Equations A8 and 31 into Equation A7, E can be expressed as

$$E=\frac{(1-r)^2al}{(l+a)^2(1+r)}. \tag{A9}$$

A calculation of E for the application mentioned in the discussion (see the body of the report) gives

$$E=\frac{(0.538)^2\,(0.942)\,(5.206)}{(6.148)^2\,(1.462)}=0.0256.$$

This indicates that the neglected term is approximately 1/40th of the retained terms. Since in general a square root is taken to determine δ,

the error in δ should be even less. Since the conservation of energy and momentum equations are satisfied exactly (within the approximation $I/m>>a^2$), the implication is that for engineering purposes the variational method gives essentially exact results. Of course in any design it is prudent to calculate E to verify that the neglected term is indeed small.

Appendix B

SPRING DESIGN

An important element in the stretch yo-yo is the spring. Conventional music wire can be used for the spring in some applications, but the most satisfactory spring material has been that manufactured by the National Standard Company of Niles, Mich. This material has an appreciably higher tensile strength than conventional music wire.

For predictable yo-yo performance, the spring should operate in the linear region. Hence the torsional stress level in the spring must be checked. Stress equations and spring design criteria given by Spotts may be used.[1] There are other methods that can be used, but the following seems to work well.

The maximum torsional stress in the spring is

$$S_{\max}=\frac{16}{\pi}F_{\max}k_s\frac{R}{d^3}, \tag{B1}$$

where

$F_{\max}=k\delta_{\max}$(lb),
k_s=stress concentration factor for torsion and transverse shear,
R=mean helix radius (in.),
d=wire diameter (in.).

$S_{\max}$ should be within the torsional yield stress prescribed by Spotts.[1] Thus

$$S_{yp\ \text{torsion}}=0.6S_{yp\ \text{tension}}. \tag{B2}$$

The other related spring equations are

$$\frac{R}{d^3}=\sqrt[3]{\frac{G}{64kl_sd^4}}, \tag{B3}$$

and

$$m_s=\frac{G\rho\pi^2}{128k\left(\frac{R}{d^3}\right)^2}, \tag{B4}$$

where

G=shear modulus of elasticity (lb/in.^{2}),
k=spring constant (lb/in.),
l_s=length of spring (close wound) (in.),
m_s=weight of spring (lb),
ρ=weight density of spring (lb/in.^{3}).

Spring design procedure:

1. Select a spring length, wire size, and type (l_s, d, G, ρ).
2. Compute R/d^3 from Equation B3; R can then be found.
3. Compute the spring index $C=2R/d$ and find the stress concentration factor k_s from Figure 4-4 of Spotts' book.[1] The value for k_s is usually between 1.0 and 1.2.
4. Compute $F_{\max}$ ($=k\delta$).
5. Compute $S_{\max}$ (Equation B1) and check if it is within the torsional stress limit of the material (Equation B2). If not, select a new wire diameter and repeat the above procedure.
6. If the stress level is satisfactory, compute the mass of the spring from Equation B4.

[1] Spotts, M. F., "Design of Machine Elements," Prentice-Hall Inc., Englewood Cliffs, N.J., 1960.

Appendix C

ERROR CURVE PROCEDURE

The error curve can be obtained in the following way. Choose a new spin-up value (for example, 20 percent over design spin-up); calculate the yo-yo stretch from Equation 24 assuming $\dot{\phi}_2$ is the design final spin. Check this assumption by calculating the final spin from Equation 25. This new value of $\dot{\phi}_2$ can be used in Equation 24 to calculate a new yo-yo stretch, etc. Calculations performed indicate that final spin does not change much and the first calculation for $\dot{\phi}_2$ is usually 99.9 percent of the second calculated value of $\dot{\phi}_2$.

Appendix D

STRETCH YO-YO DE-SPIN CALCULATION SHEET (RADIAL RELEASE AND DESIGN CONDITIONS ONLY)

Definitions of Symbols and Units:

I=moment of inertia about spin axis (slug-ft^2),
a=radius of de-spin fixture (ft),
l_0=unstretched length of one yo-yo (ft),
δ=stretch of one yo-yo at release (ft),
k=spring constant (lb/ft),
m_t=total mass of yo-yo system (slugs),
m_s=mass of one spring (slugs),
m_w=mass of one wire (slugs),
m_0=mass of one spin weight (slugs),
$\dot{\phi}_0$=initial spin rate (rad/sec),
$\dot{\phi}_2$=final spin rate (rad/sec).

Record:

I=_____ slug-ft^2,
a=_____ ft,
$\dot{\phi}_0$=_____ rad/sec,
$\dot{\phi}_2$=_____ rad/sec,
l_0=_____ ft,
m_s=_____ slugs.

Calculate:

$$r=\frac{\dot{\phi}_2}{\dot{\phi}_0}=\_\_\_\_\_=\_\_\_\_\_;$$

Stretch at release,

$$\delta=\frac{r(l_0+a)}{1-r}=\_\_\_\_\_=\_\_\_\_\_\text{ ft};$$

Optimum spring constant,

$$k=\frac{\dot{\phi}_0^2(1-r)^3 I}{2r(l_0+a)}=\_\_\_\_\_=\_\_\_\_\_\text{ lb/ft};$$

Force at release,

$$\text{force}=k\delta=\_\_\_\_\_=\_\_\_\_\_\text{ lb};$$

Total spin mass (weight) of yo-yo system,

$$m_t=\frac{I(1-r)}{(l_0+\delta+a)^2}=\_\_\_\_\_=\_\_\_\_\_\text{ slugs},$$
$$=\_\_\_\_\_\text{ gm};$$

Single spin mass [2]

$$m_0=\frac{m_t}{2}-\frac{(m_s+m_w)}{3}=\_\_\_\_\_=\_\_\_\_\_\text{ slugs},$$
$$=\_\_\_\_\_\text{ gm}.$$

[2] See Appendix B for calculation of the spring mass (m_s).

THE MRIR–PCM TELEMETRY SYSTEM: A PRACTICAL EXAMPLE OF MICROELECTRONIC LOGIC DESIGN

PAUL M. FEINBERG

Goddard Space Flight Center

Digital satellite systems containing microelectronic circuitry require the adaption of unique design techniques. This report describes the logic design for one such unit—the Medium Resolution Infrared-Pulse Dode Modulation (MRIR–PCM) telemetry system. In addition to a detailed logic analysis of the MRIR system, basic microelectronic design techniques are described.

INTRODUCTION

The Medium Resolution Infrared-Pulse Code Modulation (MRIR–PCM) logic system is a versatile telemetry unit originally intended for use as a subsystem in only the Nimbus satellite and later modified to be used in the TIROS satellite as well. In the MRIR system, voltages representing meteorological and experimental data are sampled in a formatted sequence, converted to digital form, stored on a digital tape recorder, and, upon interrogation, transmitted at a constant bit rate to a "readout" station on the ground.

Among the unique features in the logic system is circuitry which permits transmission of binary words of variable length—the word length being dependent on the amount of "wow and flutter" of the digital tape recorder. Because the effects of tape recorder "wow and flutter" are compensated for by providing variable word lengths, transmission errors introduced from tape recorder speed variations are eliminated.

To minimize system weight, size, and power dissipation, microelectronic circuitry has been used extensively in the implementation of the logic design. All microelectronics used in the MRIR system were produced under precise quality control programs to give improved reliability at the circuit level that could be translated directly into improved system performance and reliability.

NIMBUS AND TIROS MRIR–PCM SYSTEMS

General Description

In most respects the logic designs for the Nimbus and Tiros MRIR–PCM systems are identical; block-diagrams of these systems are shown in Figures 1 and 2. Inputs from a 100-cps two-phase clock and from a 200-kcps clock are shaped to provide all timing pulses required to operate either MRIR system. In the Nimbus as well as the Tiros system, analog meteorological data from 5 radiometer sensors is sequentially passed through analog gates to an analog-to-digital converter. Digitization of the analog data, whose range varies between 0 and −6.4 volts, is accomplished with a conversion accuracy of 1 part in 128. The total converter uncertainty over the operating temperature range is ±25 mv. (½ least significant bit) plus ±10 mv. (inaccuracy due to coder threshold variations). The output of the analog-to-digital converter is 7 bit parallel binary words with 1111111* representing the first level (0 volts) and 0000000* representing the 128th level (−6.4 volts).

*In the Nimbus and Tiros MRIR systems, (except where indicated), "1"=∇, "true" or zero volts; "0"=+, false or +3 volts.

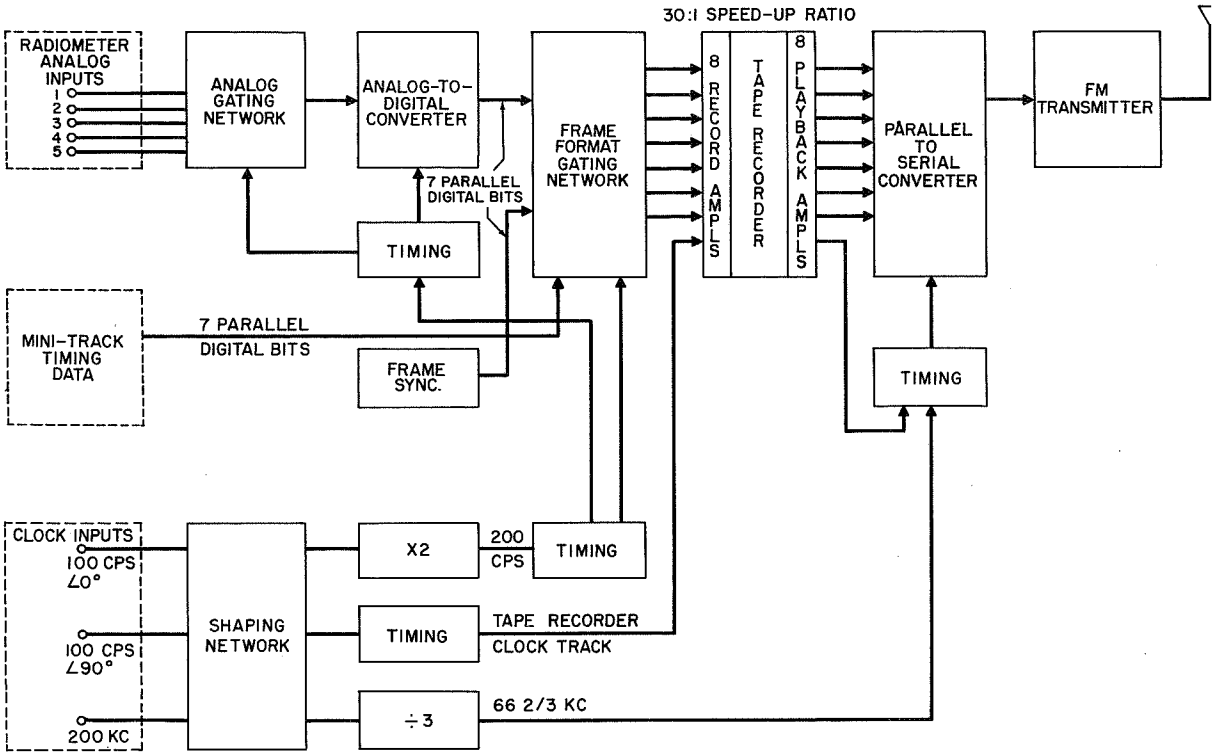

FIGURE 1.—Nimbus MRIR–PCM system block diagram.

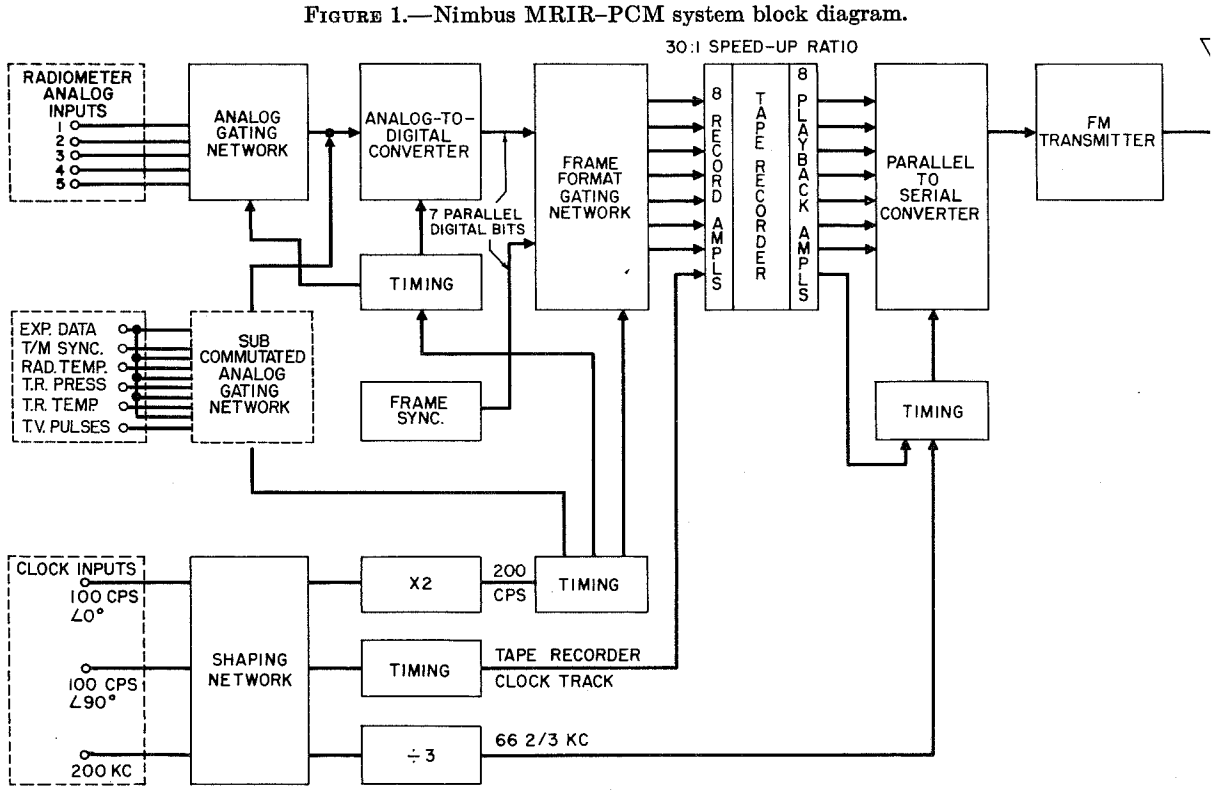

FIGURE 2.—Tiros MRIR–PCM system block diagram.

NIMBUS RECORD FORMAT

In Nimbus the 7-bit parallel radiometer data is formated with a 7-bit "Minitrack" timing data word and a 7-bit frame-synchronization word to produce a 60 ms Nimbus main frame (see Fig. 3). Each 7-bit word is stored in parallel on 7 tracks of an 8-track tape recorder; on the 8th track of the tape, a square wave "clock" which is out-of-phase with the data bits recorded on the 7 other tracks, is recorded.

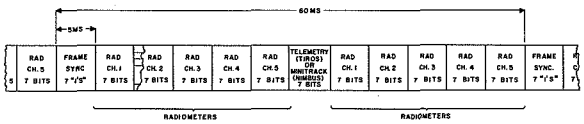

FIGURE 3.—Nimbus and Tiros digital main frame format.

TIROS RECORD FORMAT

In Tiros, due to different satellite requirements, the above Nimbus format is altered by the replacing of the Nimbus "Minitrack" circuitry with a "subcommutated telemetry" network. Sampled on this subcommutated channel for TIROS are TV picture pulses, radiometer temperature, tape recorder pressure, tape recorder temperature and subcommutated frame synchronization. A supersubcommutated experiment which alternates with the above telemetry data is also available in this frame position.

The Tiros subcommutated data is sequentially passed to the analog-to-digital converter and coded, exactly as if radiometer data, to a 7 bit parallel binary equivalent. Sampling of the Tiros subcommutated data channel occurs in the same time position as occurred the sampled Minitrack data in Nimbus (see Fig. 3), and as in Nimbus, the Tiros main frame length is 60 ms. The Tiros subcommutated frame length is 600 ms.

NIMBUS AND TIROS PLAYBACK FORMAT

The digital data stored on the tape is played back into identical Nimbus and Tiros logic systems at a 30:1 speedup ratio. The recorded out-of-phase clock track is used to develop a pulse to "load" the other 7-parallel-bit tracks into a shift-register parallel-to-serial converter. This register takes the 7-bit-parallel word, adds a word synchronization bit, and then serially shifts the data word into the modulation input of an FM transmitter. After a data word is shifted out of the parallel-to-serial converter, "1's" are transmitted until another "load" pulse presents the next 7-bit-parallel data word to the converter. The injected "1's" compensate for, and are therefore independent of, tape recorder wow and flutter; thus, errors introduced from tape recorder speed variations are eliminated.

MICROELECTRONIC DESIGN

Series 51 Solid Circuits

All microelectronic networks in the MRIR–PCM system, excluding the analog-to-digital converter and record and playback amplifiers, are Texas Instruments Series 51 Solid Circuits. This series of networks uses the RCTL (Resistor-Capacitor-Transistor-Logic) NOR/NAND configuration. RCTL logic is relatively insensitive to input noise and supply voltage variation. Although use is limited to relatively slow speeds (about 500 kcps maximum), the RCTL Series 51 networks are well suited to the maximum MRIR clock rate of 200 kcps. Module reliability was the prime factor in selecting TI networks over other types of microelectronic modules; low network power drain and flat packaging, affording optimum heat dissipation and packing density, were other important considerations. Schematic diagrams for each Series 51 solid circuit network are shown in Figure 4.

Fan-In and Fan-Out

All gate inputs, and the reset, set and present inputs of the flip-flops are considered DC loads; the DC fan-out of each network—the number of parallel loads that can be driven from one series 51 output node—is shown in Figure 4. AC loading occurs when any network drives the clock input of a flip-flop. An approximately 100 pf added capacitance per clock pulse input limits AC fan-out to 5.

Fan-in, that is the number of inputs that can be connected to a network gate, can be

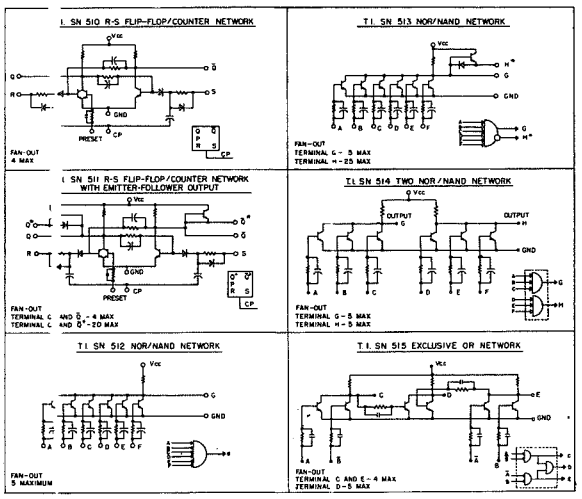

FIGURE 4.—Series 51 solid circuit networks.

increased by connecting together the output nodes of two gates while not connecting the supply voltage (V_{cc}) of one of the two gates.

Clock-Pulse Sources

The Series 51 flip-flop specifications call for a clock-pulse not to exceed the steered input voltage. If this is not followed, the excess charge on the clock-input capacitor can cause false clocking. Since in asynchronous systems any gate may have to be used as a clock pulse source, the logic design must insure that each clock-pulse does not exceed the steered input voltage. In the MRIR system, the clock-pulse voltages are kept lower than the steered input voltages by clamping the clock-pulse gate output with 2 silicon diodes. These diodes are clamped in the forward direction to approximately 1.2 volts.

A clock-pulse negative going edge (fall time) of 200 to 500 nsec. allows the greatest range of clock pulse voltage without effecting shift register operation. A fast clock negative going edge can be developed by connecting the SN513 "exclusive or" gate as a Schmitt trigger; "exclusive or" gates are used solely for this purpose in the MRIR system (See Figs. 5 and 6).

Emitter-Follower Outputs

If emitter-follower outputs of Series 51 networks are used, the emitter-follower output must be sufficiently "loaded" to fully turn on the gate. If a gate is not fully turned on, a threshold condition can develop in which a network cannot correctly distinguish between a "0" and a "1". To insure turnon of lightly loaded emitter-follower outputs, an external resistor of 5K ohms or more, depending on the load, should be attached from the emitter-follower output to zero volts.

Noise Susceptibility

To minimize Series 51 susceptibility to noise, gate inputs and flip-flop presents which are not used should be grounded. Also, if possible, each clock-pulse shiftline should be designed, to remain at a "false" level (+ volts) only at the shift time and remain at "true" level (zero volts) at all other times.

MRIR–PCM LOGIC CIRCUITRY

General

Complete circuit diagrams of the Nimbus and Tiros MRIR–PCM logic systems are shown in Figures 5 and 6, respectively; "timing" charts correlated to circuit points of Figures 5 and 6 are included as separate diagrams.

The numerous system clock-pulses generated from the $100\angle 0°$ cps and $100\angle 90°$ cps external sources are shown in Figure 7. The developed $200\angle 0°$ cps pulses ($\overline{A}_6$) are used to clock the main commutated "divide-by-six" ring-counter. Pulses from this counter are used to sequentially pass the analog meteorological data from each radiometer channel and to generate required frame formatting pulses. Each radiometer channel is sampled 33 times per second.

The passed analog radiometer data is sent to the system analog-to-digital converter, a low-power microelectronic unit engineered by CBS Laboratories. This converter encodes using the "successive approximation" or "bit-at-a-time" technique. Complete encoding occurs in 8 clock pulses or 320 μs. The developed system clock-pulses necessary to operate the analog-to-digital converter are shown in Figure 8. The converter encode pulse ($\overline{N}_4$) has been developed so that each pulse negative going

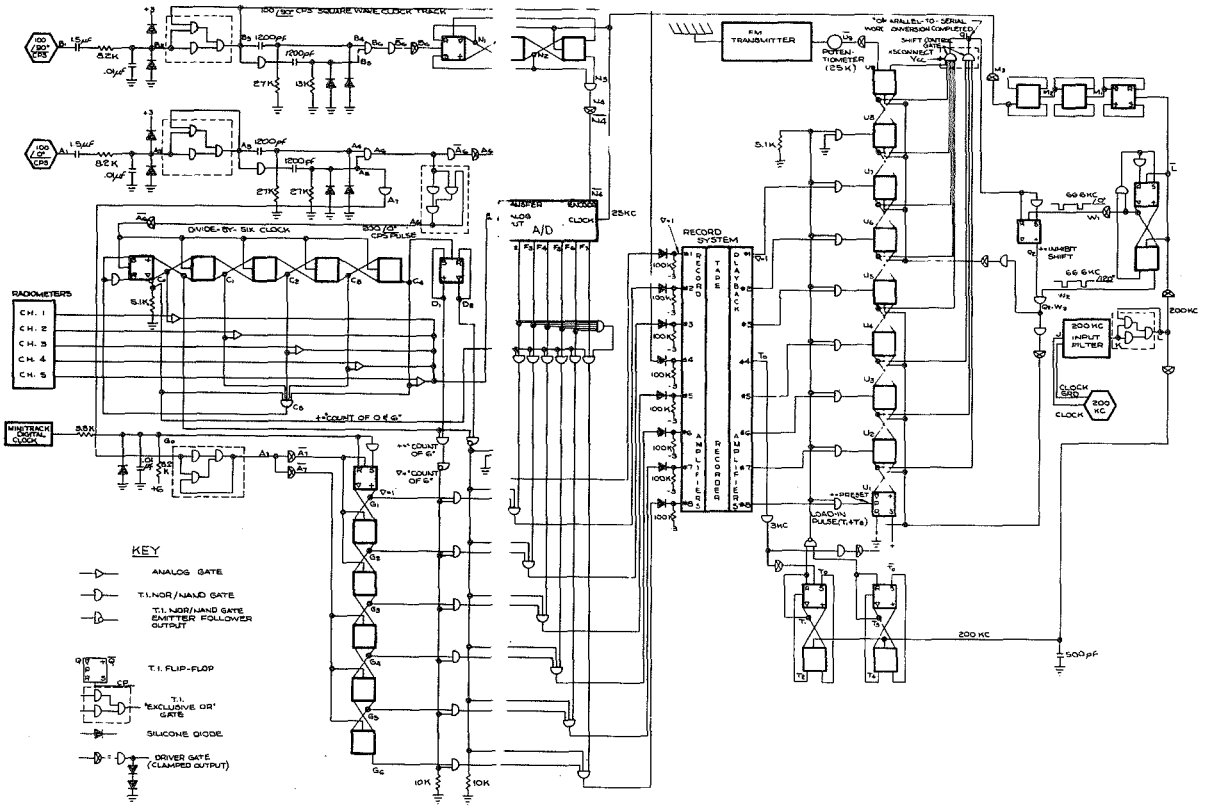

FIGURE 5.—Nimbus MRIR logic circuitry.

edge (fall time) is synchronous with a 25-kcps converter clock negative going edge; encoding is initiated at this synchronous edge time, occurring approximately at the center of each analog sample. After complete encoding, the 7 bit parallel binary data is held until a transfer pulse is received at the analog-to-digital converter. This transfer pulse allows read-out for 5 ms.

Nimbus Record Logic

The complete timing chart for the record portion of the Nimbus logic system is shown in Figure 9. During each Nimbus 60 ms frame, 2 samples of each radiometer channel are digitized and sent to the record amplifiers to be recorded on tape. Each of the 7 parallel bit outputs of the analog-to-digital converter is sent through 2 control gates which function as "inverters" when the converter digital bits are passed. The control gates pass the converter data throughout all frame "counts" [relative frame time positions] except the "counts of 0 and 6"; at the "counts of 0 and 6", the control gates inhibit the reading of the converter output and pass to the record amplifiers either frame synchronization (at the "count of 0") or Minitrack data (at the "count of 6"). Thus, at a given "count," control gates pass only one of either converter, frame-synchronization or Minitrack data, inhibiting the other two from being read into the tape recorder system. (See Fig. 9.)

The Nimbus minitrack clock generates real time in the form of an NRZ time code. The MRIR minitrack circuitry shapes the 100 ms per bit serial time-code, which is coherent with the $100\angle 90°$ cps external clock, and transfers the bits down a 6 bit shift register. During each frame "count of 6," parallel read-in of the Minitrack shift-register takes place.

The "count of 0" pulse, which is sent to control gates and passed to the record system, generates the unique system code word of

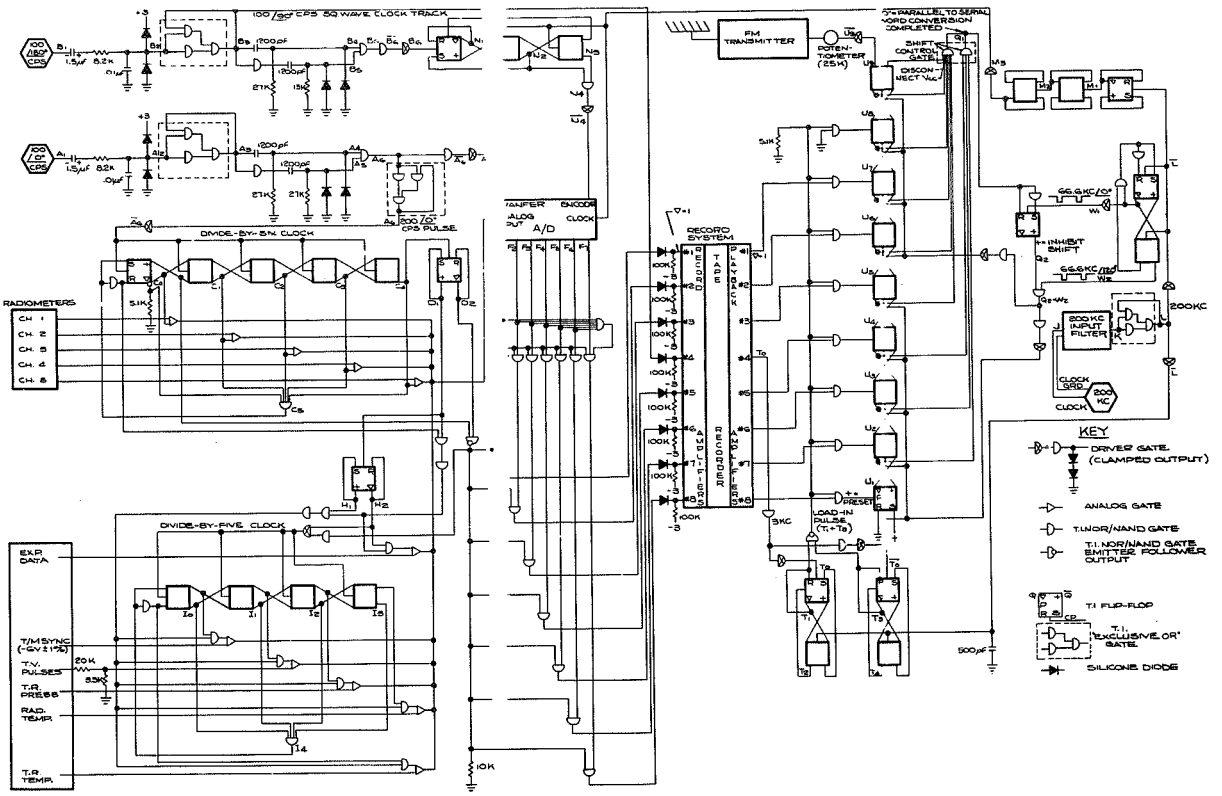

FIGURE 6.—Tiros MRIR logic circuitry.

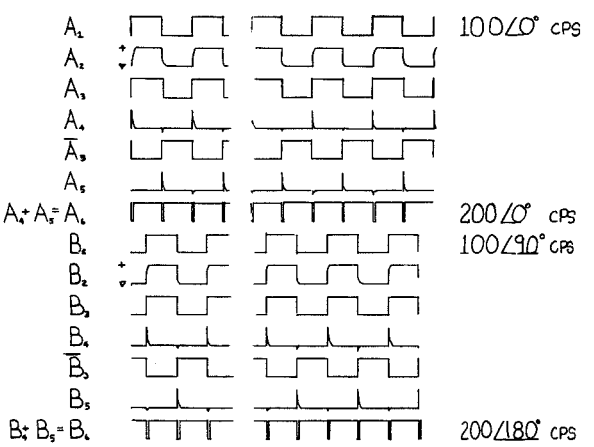

NOTE: ALL TIMING PULSES REFER TO POINTS ON FIGURES 5 AND 6

FIGURE 7.—Timing chart for MRIR system clocks.

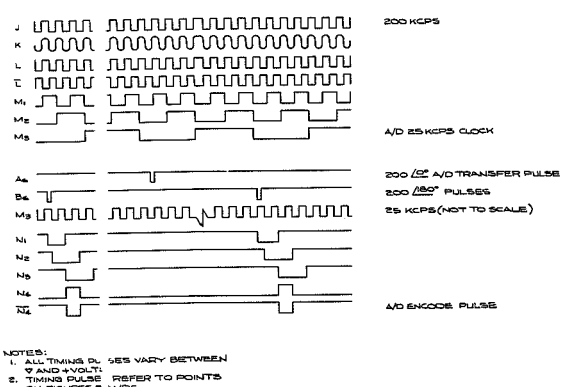

FIGURE 8.—Developed MRIR A/D converter clocks.

1111111; this unique code word is used for frame synchronization. When the code of 1111111 appears at the parallel output of the analog-to-digital converter, the 6-input gate with inputs from each of the 6 most significant converter bit outputs, inverts the converter least significant bit to prevent a 1111111 code from being passed during converter read-in. To prevent the frame synchronization code from appearing

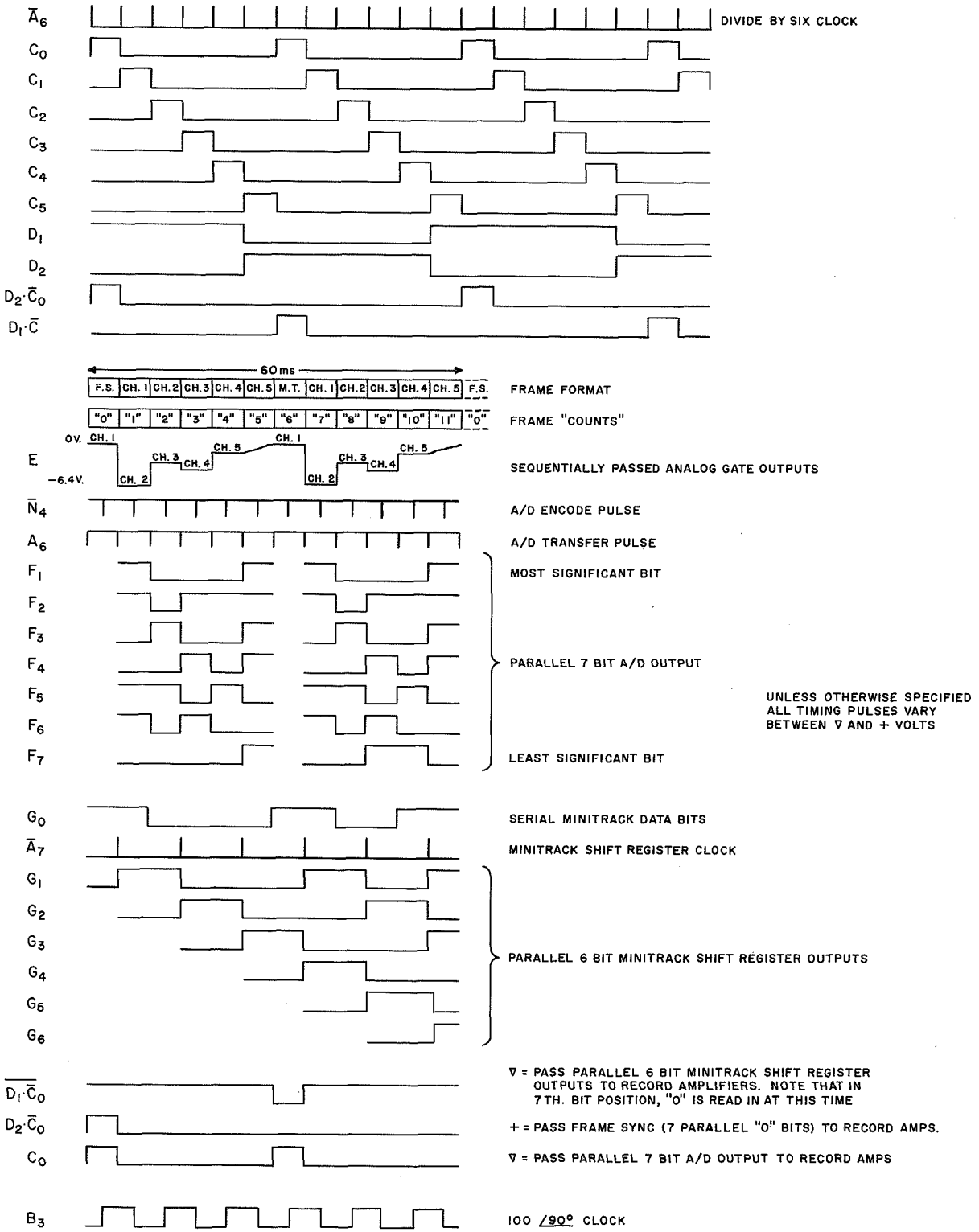

FIGURE 9.—Timing chart for Nimbus record logic.

during the 6 bit Minitrack read-in, an additional 7th bit position is continuously read in as a "0."

It should be noted that all data is "inverted" just before transmission; therefore, the frame synchronization word is actually transmitted as 0000000.

The diode-resistor network before each of the record amplifiers is used to transform the TI gate outputs to appropriate levels for the CBS microelectronic record amplifiers.

Tiros Record Logic

In the Tiros record logic system, the Nimbus Minitrack circuitry is replaced by a subcommutated telemetry network; complete timing for the Tiros record logic is shown in Figure 10. In the subcommutated network, TV picture pulse, radiometer temperature, tape recorder pressure, tape recorder temperature and subcommutated frame synchronization, all in analog form, are each sampled once every 600 ms and passed to the analog-to-digital converter. "Experimental Data" is alternated with each of the aforementioned datum and sampled once every 120 ms. When the Tiros frame data is decoded at the MRIR ground station, the subcommutated digital data will be separated from the radiometer data, converted back to analog levels, and then channeled to a visual readout unit.

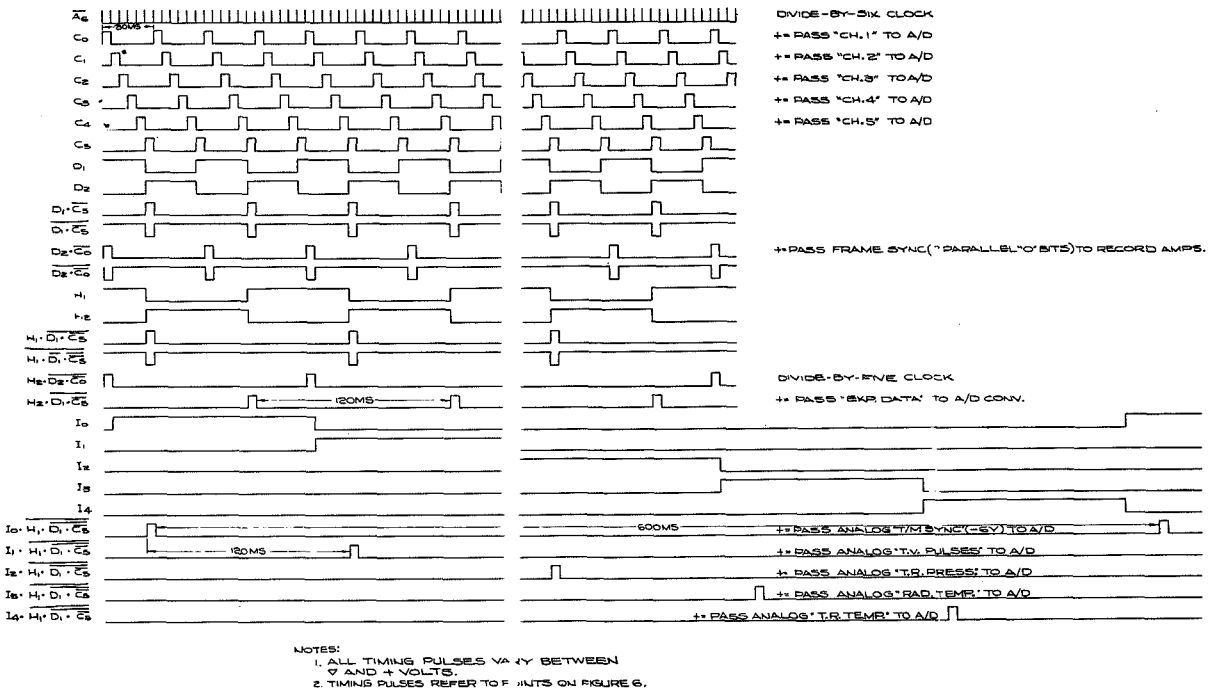

FIGURE 10.—Timing chart for Tiros MRIR record logic.

Nimbus and Tiros Playback Logic

Timing charts for the identical Nimbus and Tiros playback logic are shown in Figures 11 and 12. During playback the 7-bit parallel data words are stored or "loaded" into the parallel-to-serial converter by a pulse developed from each edge of the out-of-phase square wave clock track. Timing considerations, which will be subsequently discussed, make it necessary to "load" into the converter with a short duration pulse. A unique "synchronizer-frequency doubler" was therefore designed to develop the "load" pulses. (See Fig. 11.) Depending on the noncoherency of the 3 kcps and 200 kcps clocks of this circuit, the "load" pulses vary from approximately 0.5 to 6 μs in width: a resistor-capacitor frequency doubling network maintaining the same short pulse

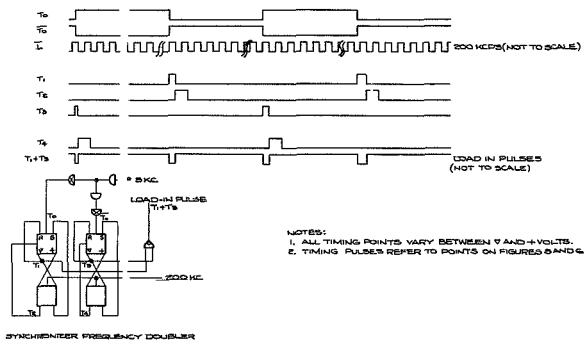

FIGURE 11.—Timing chart for synchronizer frequency doubler pulses.

widths over temperature was found to be physically impractical to implement.

The "load" pulse is not only used to store the parallel bits (1 data word) of playback data in the parallel-to-serial converter but also to logically force flip-flop output U_8 to the "0" state. This "0" is the system work synchronization bit used for ground station decommutation purposes.

The word synchronization bit is also used to logically indicate that a parallel data word has been stored in the converter and is seady to be serially transmitted. The stored data bits are then shifted out of the parallel-to-serial converter. To prevent concurrent converter "load-in" and shifting, a 10 to 25 μs delay is generated between "load-in" and the start of shifting. Shifting of the data bits continues until all "0's" remain at the "shift control gate" inputs. At this time the converter control circuitry inhibits further shifting, and not until another load pulse stores the next parallel data word will shifting resume. The "load" pulses would occur approximately 166 μs apart if "wow" and "flutter" were not present in the tape recorder. Tape recorder speed variations produce "load" pulses 166 ± 8 μs apart. Since a maximum time of 145 μs, representing 9 shift pulses plus control delay time is necessary to completely shift out any data word, at least 13 μs remain after a data word is shifted out until the next data word is stored in the converter. In the time interval between serial data words, the converter output $\overline{U}_9$, which goes to the transmitter to be deviated ± 20 KC, is at the "1" state.

The parallel-to-serial converter "load" pulses are not coherent with the converter shift clock; therefore, if the last converter flip-flop with output U_9 were not provided, word sync "0" bits narrower than the bit rate could be initially transmitted after each "load-in". This converter output flip-flop, which provides the transmitted bit rate, is independent of the "load-in" pulses and thus provides an unvarying transmission bit rate.

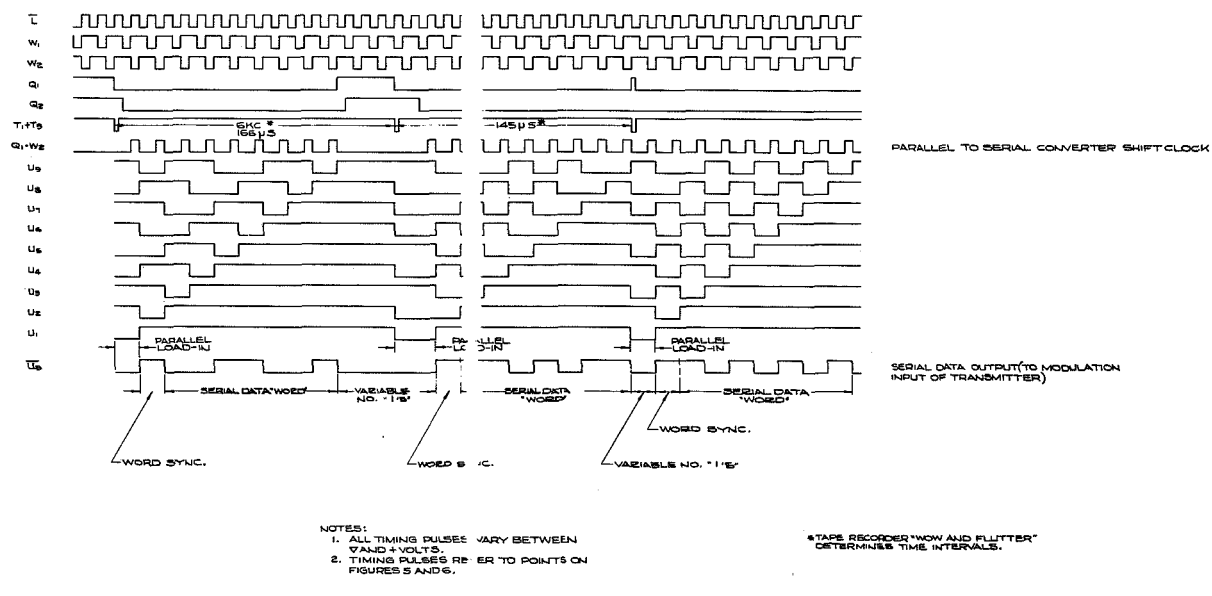

FIGURE 12.—Timing chart for Nimbus and Tiros MRIR playback logic.

In the ground station, after frame sync is established, "1's" will be sensed until a word sync "0" bit occurs. After word sync is sensed, a counter channels the next 7 data bits, and "1's" appear until the next word sync "0" bit. This cycle is continuously repeated throughout decommutation.

CONCLUDING REMARKS

The Nimbus and Tiros MRIR–PCM preprototype systems have been fabricatad and fully tested; prototype and flight model production has begun. The microelectronic circuitry employed in the MRIR–PCM systems have proven to be readily adaptable and ideally suited to present and future aerospace requirements.

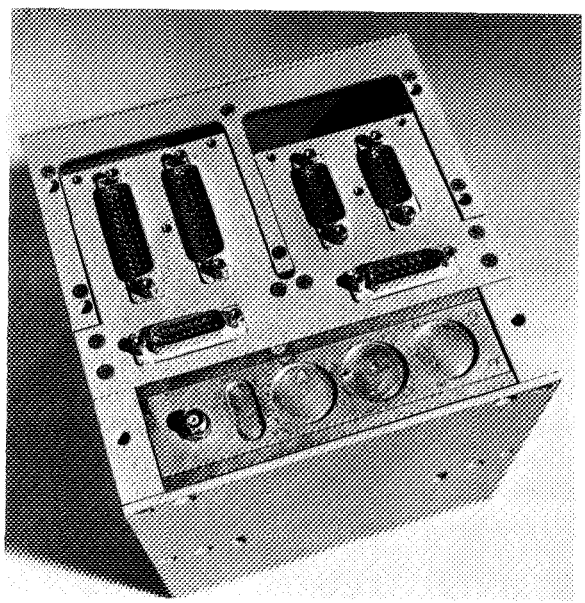

FIGURE 13.—MRIR preprototype.

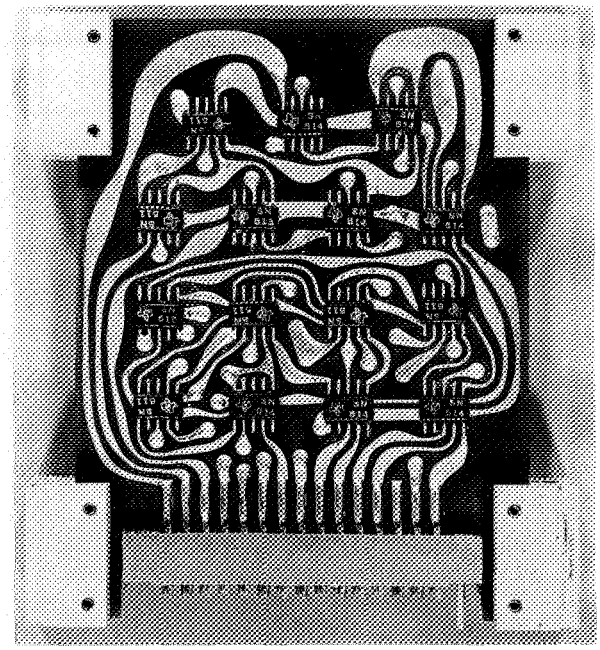

FIGURE 14.—MRIR preprototype logic module.

ACKNOWLEDGMENT

The author would like to express his appreciation to Mrs. Marjorie Townsend, Mr. John Lesko, and Mr. Marvin Maxwell for their assistance in the preparation of the MRIR logic design.

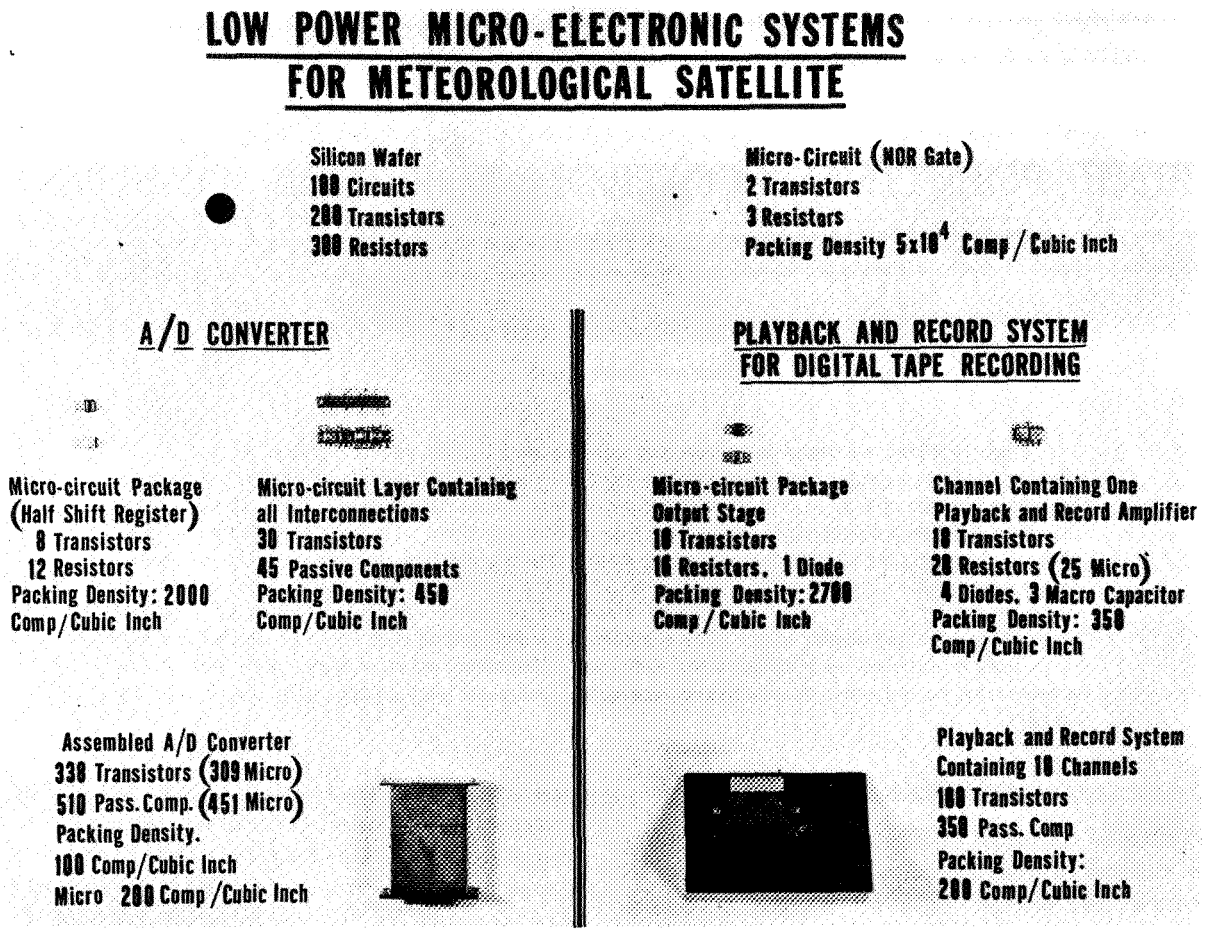

FIGURE 15.—MRIR A/D converter and record system microelectronics.

FINE POINTING CONTROL FOR THE ORBITING ASTRONOMICAL OBSERVATORY (OAO)

GORDON E. GRAHAM
Goddard Space Flight Center

High pointing accuracy requirements are imposed on the control system of the OAO. One tenth arcsec angular accuracy can be achieved in orbiting spacecraft using star references, long focal length optical systems, and relatively small torquing devices. Noise problems are introduced when a single error sensor is required to track stars with greatly different magnitudes. As star magnitude decreases, the compensating increase in the gain by the automatic gain control decreases the signal-to-noise ratio and degrades the pointing accuracy. A linear range of at least one arcmin will eliminate or reduce many restrictions on initial acquisition of a particular star. These restrictions are introduced by high initial satellite rates and/or unbalanced inertial wheel torques. Relatively small voltage rates out of the sensor may be detected by a suitably designed nonlinear lead circuit with low frequency corners.

INTRODUCTION

One of the most critical aspects in designing a control system accurate to 0.1 arcsec is, of course, the sensor. It must be able to detect motions of less than 0.1 arcsec and provide a linear output signal, without excessive noise, to some sort of actuator. These requirements alone would not be exceedingly difficult to meet; but unfortunately, for a satellite control system like the OAO, additional requirements are present. The sensor must have a field of view large enough to assure the desired star will be seen when the coarse control system, which may be misaligned, reaches its null position. In order for the control system to damp out large initial errors, the sensor must provide rate information to the loop. This is accomplished by designing the sensor with a linear range much larger than the ultimate accuracy limits. Thus, as the error decreases toward zero and the signal leaves the saturated region, the decreasing voltage can be detected by a suitably designed rate sensitive circuit. By summing the rate and position signals, zero crossing of the error can be predicted and the controller reversed in time to provide damping to the satellite motion. An additional requirement on the design is that it must be capable of withstanding a launch environment and thermal variations in orbit without becoming misaligned with respect to the experiment. Finally, in order to make the problem really interesting, the sensor system reliability must be sufficient to assure operation in orbit for one year.

CONTROL SYSTEM

Once the experimenter specified that 0.1 arcsec pointing accuracy control of the OAO was required for his experiment one of the first questions to be answered concerned a sensor and control system design. Inertia wheels were chosen as the controllers since they would provide small magnitude correction torques to the vehicle for an indefinite time (the power for the motors would be supplied through solar paddles and batteries). The size of the torque motor was chosen as soon as the expected disturbance torques on the satellite were defined. Since the gas jet momentum dumping system produces undesirable tran-

sients it is desirable not to dump the wheels during an experiment time. For this reason it was specified that the wheels be able to counteract the expected disturbance torques when running at 95 percent of maximum speed. This immediately defined the stall torque. From a predicted average disturbance torque of 2,000 dyne-cm. the OAO fine torque motor was chosen with a stall torque of 140,000 dyne-cm. (2 oz. in.). A logical question to be asked at this point is whether the torque resolution from the wheel is adequate to control the satellite to 0.1 arcsec. Being pessimistic and assuming the breakaway torque of 8 percent of stall to be the minimum increment of torque, resolution of satellite acceleration is 0.15 arcsec/sec^2. With solid state electronics controlling the acquired motor voltage, time response of the motor is sufficiently fast to keep the satellite velocity and hence pointing error within acceptable limits. Since the jets are not to be fired during experiment period, the wheels must be able to store the momentum generated by the disturbance torques for an orbit and a half. With the disturbance torque and experiment time known, the wheel inertia is uniquely determined once a maximum wheel speed is chosen. The wheel speed choice is based on windage losses and bearing wear and is 1000 rpm.

Combining the inertia wheel with the satellite and assuming a sensor with a linear range about null, it is possible to take a look at the form of the control loop. The open loop transfer function is defined as:

$$\frac{\Theta_S}{\Theta_R}=K_S\frac{K_mS}{(S\tau_m+1)}\left(\frac{1}{IS^2}\right)=\frac{K}{S(S\tau_m+1)}$$

Θ_S=satellite angle

Θ_R=reference angle

K_S=sensor gain, volts/rad

K_m=motor constant, $\frac{\text{motor volts}}{\text{sensor volt}}$

I=satellite inertia, lb sec^2 ft.

τ_m=motor time constant

$$K=\frac{K_SK_m}{I}$$

This is a type 1 servo or one which requires a steady state error to maintain the signal to the controller (torque motor). Since some error is required to maintain the inertia wheel spinning (no accelerations), the ultimate accuracy of the system immediately defines the sensor gain. Namely, 0.1 arcsec must generate full motor voltage. In this way the offset error necessary will not exceed the accuracy requirements even though the wheel may have accelerated to 95 percent of its maximum speed.

Using the information stated so far, one could calculate a Bode plot of the transfer function and observe that only a simple lead circuit would be required to stabilize the loop. However, additional requirements and limitations on the fine error sensor complicate the problem.

SENSOR DESIGN

When confronted with the problem of designing a 0.1 arcsec sensor, three questions immediately come to mind:

1. How can 0.1 arcsec be measured?
2. What is the required field of view?
3. What is the required linear range?

On the OAO, measurement or detection of angular motion of 0.1 arcsec is assisted by the 14 ft. focal lengths designed into the experiment optics. While 0.1 arcsec represents only 8 microns at 14 feet, it is about 16 percent of the image diameter at the focal point of the experiment optical system. This percent change in signal strength is not too difficult to detect with differencing techniques. The one experiment presently being built for 0.1 arcsec accuracy generates the error signal from a sensor which is an integral part of the experiment. Thus, even though launch environment or thermal shifts may cause misalignments bebetween the spacecraft and the experiment, star images will always be centered on the experiment. This is accomplished by the fact that the satellite control system receives its error signal from the experiment and drives the spacecraft to zero the error signal.

The minimum field of view of the sensor is determined from system specifications for accuracies and alignments of the various error

764-173 O—65——20

sensors—gimbaled star trackers, boresighted star tracker and fine error sensor. The gimbaled tracker system is required to orient the spacecraft axis to within 1 arcmin of the desired star. In order to provide sufficient overlap should the coarse pointing system not meet specification, the fine error sensor was required to have a minimum field of ± 2 arcmin.

The requirements for a minimum field of view (± 2 arcmin) and a high gain (0.1 arcsec generates full motor voltage) are incompatible in a practical hardware design. Since the maximum voltage out of the sensor is limited by the power supply, the sensor will saturate long before the error reaches the maximum field limits. The existence of this problem in itself is not serious since many systems operate very well with sensors which saturate for large errors. However, the minimum linear range desirable for the OAO fine pointing error sensor, as determined by computer studies, is about ± 1 arcmin. Existing engineering designs have encountered difficulties in obtaining even this linear range. For instance, the Goddard Experiment Package (GEP) with a system accuracy requirement of 1 arcsec has a fine sensor linear range of only 28–32 arcsec. The Princeton Experiment Package (PEP) with a system accuracy requirement of 0.1 arcsec has only a 15 to 20 arcsec linear range.

What does the decreased linear range mean to system performance? The most important effect is the limitation on allowable initial wheel speeds at the beginning of star acquisition. With a 30-percent wheel speed there will be about a 2-to-1 ratio in the two torque levels from the motor depending on whether the wheel is to be accelerated or decelerated.

Thus, if the initial error is such to require the wheel to decelerate, a high torque will act until the sensor comes out of saturation, near null. With the high rate signal near null, the lead circuit will reverse the applied motor voltage to decelerate the spacecraft. However, the momentum developed by the high torque may be too great to be counteracted by the low reverse torque before the satellite drifts beyond 2 arcmin from the star.

It can easily be seen that the wider the linear range, the sooner a high level torque will be reversed and the longer a low level torque can act. Thus, there is an inverse relationship between sensor linear range and allowable initial wheel speeds. Unfortunately, any initial satellite velocity toward null will aggravate the overshoot problem. The initial wheel speed limit is accordingly even lower than that determined for zero initial satellite rates. If there is a limit to the linear range available in a particular sensor, the only solutions are to increase the field of view or to command dump the inertia wheels to 5 percent before every star acquisition. The latter solution is undesirable since it is very wasteful of gas and the system would be very lightly damped for large errors. The problem with the Princeton error sensor, with its extremely short linear range, was solved by increasing the field of view to ± 4 arcmin.

PRINCETON FINE ERROR SENSOR

A very interesting problem was encountered stabilizing the control loop containing the PEP. At this point a short description of the PEP sensor is in order (*1*).

The Princeton Experiment has as its purpose the study of the far ultraviolet of many stars by using a grating spectrograph. The error signal for the control system is generated by determining the difference in the amount of the star image reflected from each side of the slit in front of the grating. The jaws which form the slit are highly polished and slightly inclined with respect to each other. A star image falling on either of the two jaws is reflected to either of two sectors of a rotating optical chopper and thence to a photo multiplier. The photomultiplier output is gated sequentially in correspondence with the chopper into four sample and hold networks. The outputs of the hold networks are then differenced to generate two axis error signals. When the star image is completely on one jaw, the error signal has a constant, saturated value. When the star image falls on the slit, the light reflected from each jaw generates voltage

levels which are subtracted to generate a linearly varying signal.

This approach to error detection has the advantage that it is relatively insensitive to mechanical misalignments due to launch environment or thermal expansion. It has the extreme disadvantage of having a linear range of only ±0.45 arcsec. In order to create a larger linear range, an optical coating is applied to the jaws extending from the slit out to 10 arcsec. This coating has a linearly varying reflectivity, ranging from 100 percent at 10 arcsec to 50 percent at the slit edge.

Thus, as the star image sweeps across the coating toward the slit, the decreasing light reflected to the photomultiplier will cause a diminishing output and a consequent linear range. This outer linear range, from 0.45 to 10 arcsec, will then have a much smaller slope than the central, 0 to 0.45 arcsec, section. It is this difference in slope which causes one of the compensation problems.

In order to stabilize the loop at null error, all that is necessary is a simple lead network. However, in the outer linear region the slope is smaller, and hence the loop gain is decreased. The lead network will not generate sufficient rate signals to reverse the motor torque when the error comes out of saturation.

A solution to this problem seems to be available by inserting a nonlinear lead circuit (*2*) with frequency corners much lower than the crossover frequency. The nonlinear lead circuit is simply a four terminal, bridged tee, rate-limiting, network with a capacitor and resistor in parallel with a second resistor shunted to ground across the output. By placing two Zener diodes back-to-back between ground and a point somewhere along the first resistance, the output voltage can be clamped at any given input value. This scheme offers the advantage of limiting the output voltage and thus reducing the rate required to bias the error signal to a negative or reversed value. It also affords some degree of adjustment to change the voltage rates required to reverse the circuit output.

Initial computer studies, not yet completed, indicate successful results can be obtained. The compensation will be accomplished by utilizing a nonlinear lead circuit with break corners about 1½ decades below the high gain corners of 16 and 80 rad/sec.

AGC AND NOISE

Still another problem in building a sensor is accommodating the large variation in incoming signal strength. The ratio of signal energies from second and tenth magnitude stars is about 1,500 to 1. To be able to generate suitable error signals from a single sensor, there must be an AGC (automatic gain control) in the sensor voltage supply. As the gain increases for the dimmer stars, the signal-to-noise ratio decreases and the pointing accuracy necessarily degrades. Thus, the 1 arcsec pointing accuracy quoted for the Goddard Experiment (*3*) is applicable to only second magnitude stars. For seventh-magnitude stars the requirements have been relaxed to ±5 arcsec accuracy, while for tenth-magnitude stars the limit is ±50 arcsec.

The requirement for an AGC rather aggravated the design problems already discussed for the Princeton fine error sensor. For large error signals all the star light is reflected from the polished slit jaws to the photomultiplier. At null, half the light is dumped down the slit to the experiment, while the half remaining is attenuated 50 percent by the optical coating before reaching the phototube. Thus, the gain about null is increased by a factor of four over what it is during acquisition. This only serves to accentuate the problem of the differences in slope of the inner and outer linear ranges. One improvement to the problem is gained by scraping the optical coating away from the slit jaws to a distance equivalent to 0.25 arcsec. This allows a gain change of only 2 instead of 4 due to the light lost down the slit.

ACKNOWLEDGMENTS

The author wishes to express his appreciation to Mr. W. D. Hibbard and Mr. H. Price for their helpful discussions and comments.

REFERENCES

1. *Fine Guidance Sensor for High Precision Control of the OAO.* Norman A. Gundersen, Sylvania Electronic Systems, Waltham, Mass. Paper No. 63–211, Summer Meeting AIAA, June 17–20, 1963.
2. *Results of Preliminary Investigation Into Compatibility of Proposed Perken-Elmer Fine Error Sensor and OAO Control System.* G. E. Graham, Stabilization and Control Branch Report No. 63. NASA-Goddard Space Flight Center, Jan. 31, 1963.
3. *System Response in the Fine Pointing Mode of the OAO Utilizing the Goddard Experiment Package.* G. E. Graham, Guidance and Control Section Report No. 50, NASA-Goddard Space Flight Center, Sept. 7, 1962.

ADVANCED EARTH SENSOR DESIGN CONSIDERATIONS

BARBARA K. LUNDE
Goddard Space Flight Center

Reliability must be improved by an order of magnitude before earth sensors can be of practical use in operational systems. This requires a new design which is thermal, rather than optical, and detectors which are extremely stable, rather than sensitive and fast. These elementary requirements have not been recognized by the industry.

Earth sensors for operational satellites [1] as well as other spacecraft infrared instruments have design requirements which differ from existing infrared systems.

Three requirements of advanced earth sensors—high reliability, thermal design, and stable detectors—will be considered here. These are rather elementary requirements, but, surprisingly, most of the 27 leading companies in the field completely ignored one or all of them in writing proposals to us. This leaves the field of infrared components for spacecraft open to other companies which are willing to recognize these important factors.

Figure 1 is an illustration of a typical simple earth sensor. It is a device which is used to tell a spacecraft which way is down.

The prime requirement is high reliability. The predicted mean time to failure for earth sensors or horizon scanners presently under development is 2.7 years (Fig. 2). Operational spacecraft systems require earth sensors with mean times to failure of about 29 years. Obviously, to achieve this improvement, a different type of design must be used.

The mean-time-to-failure estimate for the OGO (Orbiting Geophysical Observatory) scanner is based on an assumption of infinite life for the mechanical parts and the optics. Only the exponential distribution of failures of the electronic parts is taken into account. The failure rate of the detectors makes a minor contribution to this. A typical failure rate used in this computation is 0.025 percent per 1,000 hours for

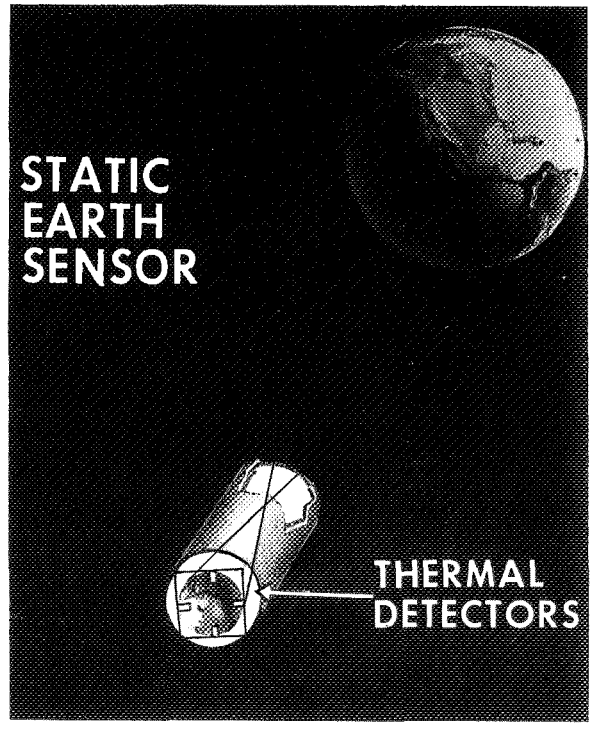

FIGURE 1.—Static earth sensor.

[1] "Specification for the Development and Test of a Reliable Earth Sensor," Procurement Control Number 19283, Stabilization and Control Branch, Goddard Space Flight Center, Greenbelt, Md. (Nov. 13, 1962).

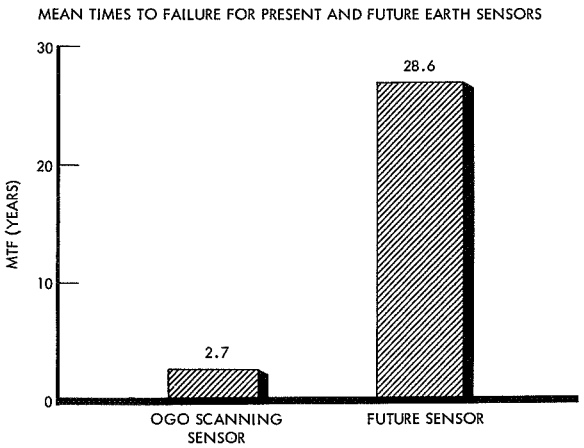

FIGURE 2.—Mean times to failure for present and future earth sensors.

silicon transistors. This is a very simplified method of computing reliability and is used only to compare systems. Undoubtedly the actual mean time to failure of the OGO scanner will be shorter than calculated by this method.

One method of approaching the desired reliability is to eliminate all moving parts and reduce the electronic parts to about 40 as shown in Figures 3 and 4. Figure 3 shows the number of moving parts in the two sensors. Figure 4 shows the number of electronic components.

To achieve this reliability, certain performance characteristics must be sacrificed, but the present equipment [2] has some characteristics which will not be necessary for some future missions, as shown in Table I, such as a wide range of working altitudes, one-third of a degree nominal accuracy (both short and long term), and fast response.

The importance of reliability cannot be overemphasized. A component of such an operational system as a network of weather or communication satellites must operate for a long period of time in order to be economically feasible. Desirable characteristics such as accuracy must be weighed against lifetime, and therefore cost of the entire system. In addition, earth sensors are competing with other orientation sensors and if earth sensors cannot be made reliable enough, they may not even be used in operational systems.

[2] E.g., the horizon scanners on Mercury, Orbiting Geophysical Observatory, and Nimbus.

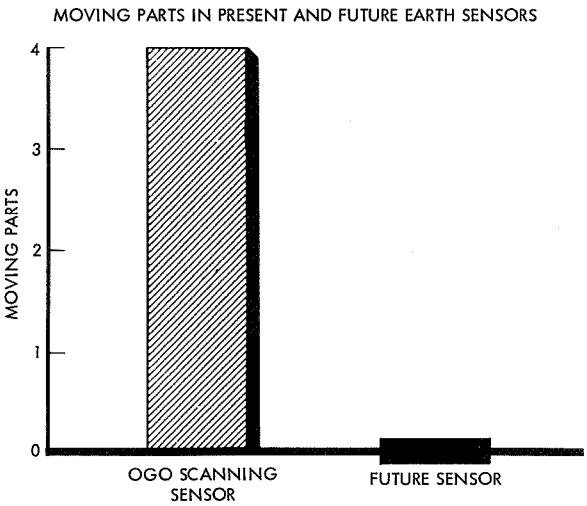

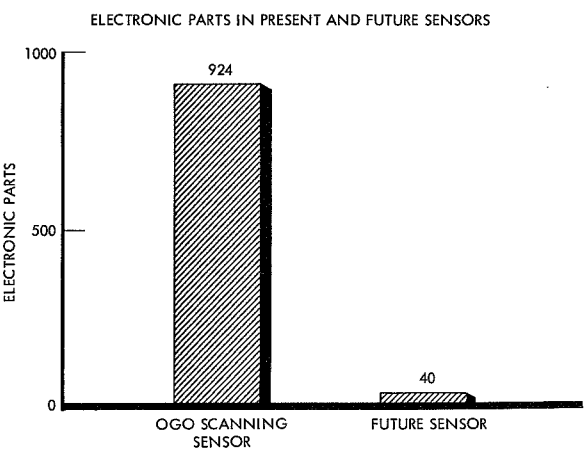

FIGURE 3. and FIGURE 4.—Moving parts (fig. 3) and electronic parts (fig. 4) in present and future earth sensors.

TABLE I.—*Earth Sensor Requirements*

	Present	Future (for reliable sensor)
Response time (seconds)	0. 07	1. 6
Accuracy (degrees)	. 3	3
Altitude range	120→60, 000 miles	5% of nominal altitude

The requirements of simplicity, no moving parts, and long life eliminate the possibility of a chopper and cooling and require the use of a nonchopped thermal detector. This requires emphasis on thermal design rather than on the optical design which has been used in previous sensors. This means that all forms of heat transfer in and around the sensor must be very carefully considered. Figure 5 shows the temperature difference or signal due to a 0.3° offset from vertical in a typical efficient earth sensor design and the temperature difference due to measured gradients over one-half inch in the OSO (Orbiting Solar Observatory) satellite in orbit. This measured gradient was caused by power dissipation in the satellite and power absorption from the sun and earth.

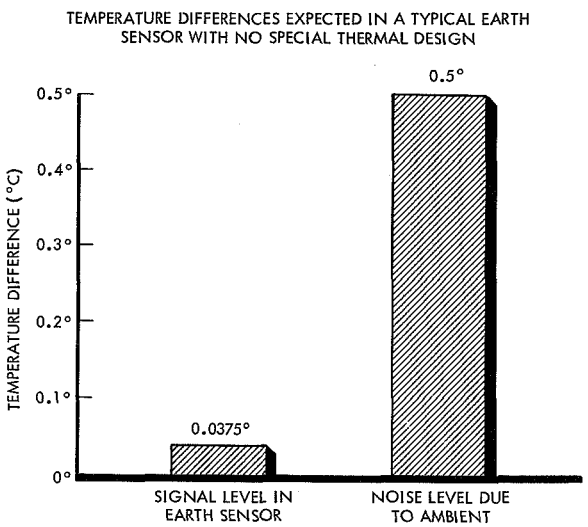

FIGURE 5.—Temperature differences expected in a typical earth sensor with no special thermal design.

It is clear from Figure 5 that unless extreme precautions in thermal design are taken, the "noise" will be many times the signal.

Another point may be made from Figure 5. The signal we are interested in is really a temperature difference, and a rather small one at that. To detect such a signal, we must have a temperature detector which is very stable. We would like a detector which will not have spurious outputs or drifts greater than 0.01° C.

Most existing infrared instruments use choppers, which are desirable for high sensitivity. In this case, we cannot use a chopper. In a chopped system the detector is compared with itself every few milliseconds. In the case of the reliable earth sensor, a detector must be compared with itself in perhaps 3 years, not a few milliseconds. So in advanced earth sensors, one must strive for a very stable, drift-free detector, rather than a supersensitive or fast one.

Finally, the three important design considerations in advanced earth sensors are high *reliability*, *thermal* design, and a *stable* detector. Reliability is the most important.

RELIABILITY VERSUS ACCURACY TRADEOFFS

BARBARA K. LUNDE

Goddard Space Flight Center

INTRODUCTION

Reliability has become a more important quantity since the advent of the space age, perhaps because of the finality of the launch. In the past, reliability has been improved by use of redundancy which increased power and weight. The functions of reliability versus power and weight have been approached qualitatively.

But when the nature of the mission is not such as requires maximum accuracy together with maximum reliability, it is worth considering whether reliability may be improved somewhat at the expense of accuracy. So this paper will deal with the functions of reliability versus accuracy rather than reliability versus power and weight.

I will suggest a general function for reliability vs. accuracy and give two examples—one for each case typical of the function.

An area where greatly increased reliability is necessary is in the area of long-term orbital missions such as the weather and communications satellites.

Here the spacecraft must remain in a fairly precise attitude with respect to the earth for a period of time far in excess of that which has been required previously. The spacecraft must be quite accurately oriented, but certain sacrifices in accuracy can be accommodated provided the attitude is maintained reliabily—that is, over a farily long period of time, counted in years rather than in days or weeks as has been the case in previous missions.

I should mention at this point that my specialty is in the area of earth sensors for spacecraft. These are the devices which, basically, tell the spacecraft which way is down. The sensors are used in stabilization and control systems and have, in the past, posed some serious reliability problems. There was an apparent earth sensor failure in one of the early Mercury shots, for example.

In the Orbiting Geophysical Observatory, the earth sensor is the least reliable component of the control system and the control system is the least reliable subsystem of the spacecraft, according to the reliability analysis.

On the Mariner voyage to Venus, the earth sensor malfunctioned during the first part of the journey and caused concern before it began to function correctly toward the end.

As I mentioned a moment ago, future missions for operational systems such as communications or weather satellite systems will require even greater reliability than is required, but not really delivered, now. In other words, the reliability of earth sensors will have to be drastically improved. Figure 1 shows the mean time to failure for two developed earth sensors, and the required mean time to failure for some future missions.

Reliability analysis is usually based on electronic parts count and consideration of mechanical parts. A study of available earth sensors led to the conclusion that although their reliability might be improved by mechanical improvements, improved circuit design, and use of more reliable components; it was not practical to improve their reliability as much as was necessary. There were a few reliability tradeoffs for accuracy that could have been made. Certain circuits were included to improve accuracy, which could have

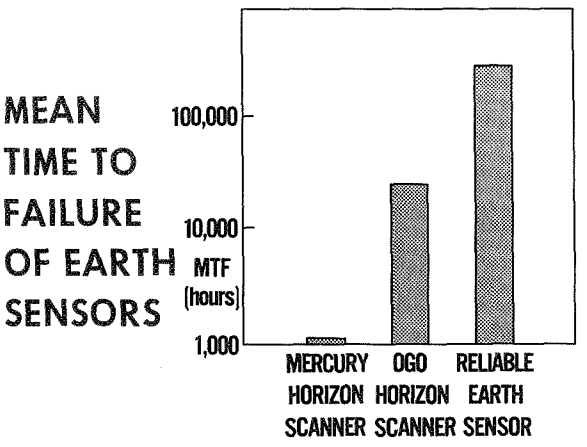

FIGURE 1.—Mean time to failure of earth sensors.

been eliminated, thus improving reliability; but these amounted to at most 10 percent of the components in the earth sensors, so this could not have led to the required improvement in reliability.

It appeared that we need to go to an entirely new design to get the reliability that was necessary. A design was proposed which appeared to lead to a sensor of much greater reliability and somewhat reduced accuracy, but it was not possible to assess the new design quantitatively until detail design and testing was done.

I would like to propose a statement on tradeoffs of accuracy for reliability for further discussion of the panel. I would propose that the reliability vs. accuracy function has small regions where a smooth curve can be drawn, or at least points may be found close together. Between these small regions will be large jumps to another short smooth section of curve. The short sections are due to particular designs and the various points on them represent modifications which could be made to a particular design. The various short sections are each due to a different basic design.

When some points of the reliability vs. accuracy curve are known, but one needs to move to a region on the graph far from any known points, it will probably be necessary to use a new basic design. One would then find a new short section of curve for that design. This additional part of the reliability vs. accuracy function can not be expressed qualitatively until a detail study and some testing is made of the new design. In other words, it is not certain what one can "buy" in reliability for a certain large sacrifice in accuracy unitl a detail study and testing of various design possibilities has been made. Therefore a typical graph of reliability versus accuracy will be a smooth, well defined curve over short regions, but will have quantum jumps as one goes from one basic design concept to another.

Figure 2 shows a particular reliability vs. accuracy function. Notice the segments of continuous curves. Each segment represents a different design concept. The function approaches zero reliability asymptotically, and is at zero accuracy beyond a certain reliability. There are regions of overlap, where one design is superior to another, and vacant regions, where, at present no design exists. The short, continuous streatches of the reliability vs. accuracy curve are not commonly determined for various components but they should be determined because they would be useful in system design.

I will now give you an example of a jump from one short curve to another or rather, one type of design to another.

As I have said before and illustrated in Figure 1, a vast reliability improvement in

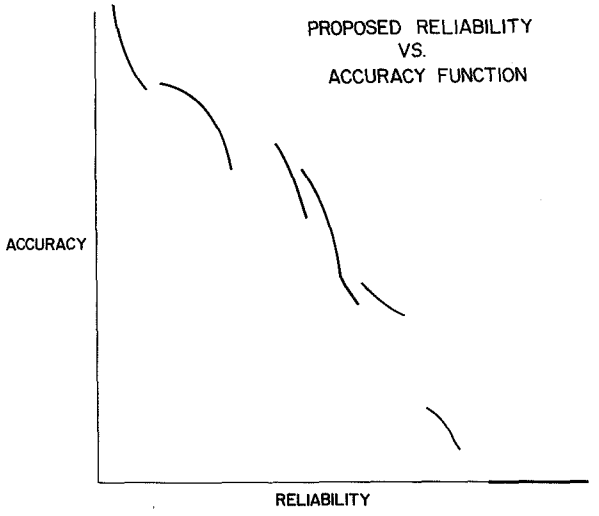

FIGURE 2.—Proposed reliability vs. accuracy function.

earth sensors was necessary. It did not appear possible to achieve the required reliability by an extension of known designs. The smooth curves for previous designs did not extend to the required reliability. A new design needed to be considered. Most earth sensors use the infrared radiation from the earth to locate it. Most such infrared systems use a mechanical infrared modulator or chopper. It is used for increased sensitivity and accuracy. It leads to several reliability problems, however, because it requires mechanical moving parts, drive circuitry and often a position pickoff. Pictures and other specifications of two typical earth sensors are shown in the next figures. They have somewhat complicated mechanical assemblies. A description of one type of sensor is that it sounds like a coffee grinder when working. Another had serious difficulty passing the required vibration tests. It appeared that

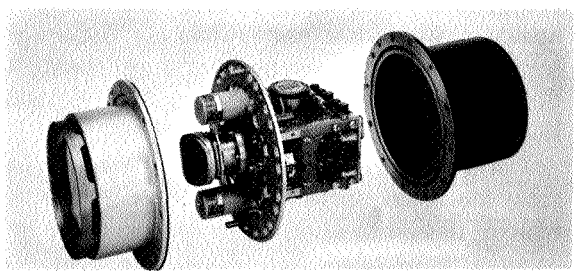

MERCURY EARTH SENSOR

ACCURACY : ± 0.5 ~ ± 1 RELIABILITY: 1008 HOURS MTF FOR COMPLETE SYSTEMS

FIGURE 3.—Mercury earth sensor.

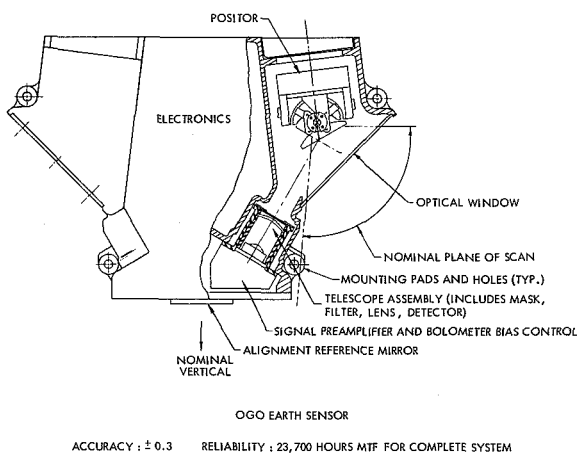

OGO EARTH SENSOR

ACCURACY : ± 0.3 RELIABILITY : 23,700 HOURS MTF FOR COMPLETE SYSTEM

FIGURE 4.—OGO earth sensor.

possibly a more reliable but less accurate earth sensor could be built if mechanical modulation were not used. This would reduce the accuracy of determination of the local vertical for at least three reasons.

The first reason is that in earth sensors with modulators, the output of one infrared detector is compared with itself from time to time. In this new design, two detectors will be used and their outputs will be compared. If the two detectors are not identical, there will be an error in the output.

The second source of error is inhomogeneities in the temperature of the earth. The next figures show the temperatures of the earth as observed by Tiros III, the weather satellite, on July 13, 1961. The new earth sensor design will image areas near the horizon on opposite sides of the earth on two detectors. If the temperature of the earth at the two places is the same and the earth sensor is pointed at the earth, there will be zero signal output. If the temperatures differ or the sensor is offset from the center of the earth there will be an output signal. A signal due to a temperature difference would be an error. Earth sensors with mechanical modulators are bothered by this problem in a different way, and can compensate for it.

Part of the globe in these pictures is blank because data for those areas was not available.

The third reason for the reduction in accuracy is that the electronic signal processing is different with a chopped system than without, and the electronic signal processing for a nonchopped system appeared to have greater errors than for a chopped system.

At the time this design was first considered, about 2 years ago, these errors could not be accurately estimated, but requirements for future sensors could be estimated. Errors greater than 3° would not be permissible.

Also, although it was obvious that elimination of a mechanical chopper would improve reliability. It was not possible to make an accurate reliability estimate of the new sensor.

Since then an extensive analysis of earth sensor with no mechanical chopper has been made, and the reliability and accuracy estimates

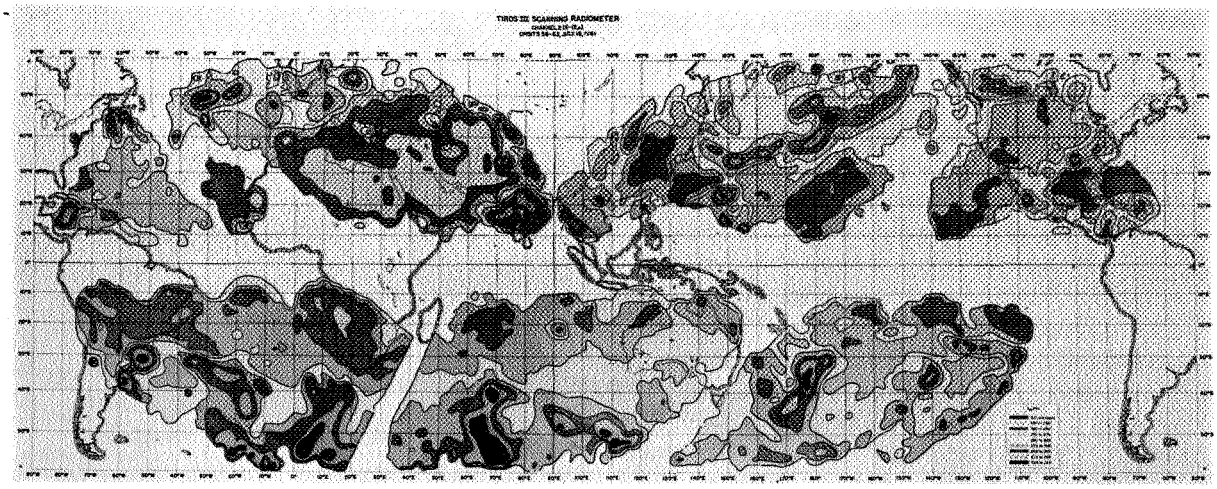

FIGURE 5.—Temperatures of the earth as observed by Tiros III, the weather satellite, on July 13, 1961.

are shown on the next figure. These will be confirmed only by more detailed design and testing.

The case of detailed tradeoff of accuracy for reliability came up in the development of the Reliable Earth Sensor. Because of the variability in the temperature of the earth it is desirable to have large fields of view for the detectors. If a small field of view were used, it would be possible for a detector to view only an extremely cold or an extremely hot area. You will note that the extreme areas are in general small. If a detector viewed only an extreme area, it would cause a large error in output.

Therefore, large fields of view are desirable. However, the largest fields of view possible cause much more cross coupling than certain smaller fields of view. The next figure shows cross coupling comparisons for two cases. Cross coupling is a source of error.

It is possible to reduce the cross coupling with the large fields of view by using electronic function generators, but this would reduce the reliability of the earth sensor. Two points on the detailed accuracy vs. reliability curve have been calculated for a particular choice of detector areas and a particular orbit. Without electronic compensation, the departure from linearity due to cross coupling would be ½°. The predicted reliability of the system without electronic compensation would be 268,000 hours mean time to failure.

The addition of electronic compensation to reduce the error due to cross coupling to ±⅓°

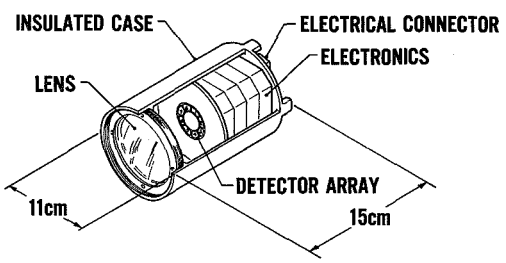

RELIABLE EARTH SENSOR ACCURACY 3% RELIABILITY 254,000 HOURS MTF FOR COMPLETE SYSTEM

FIGURE 6.—Reliable earth sensor.

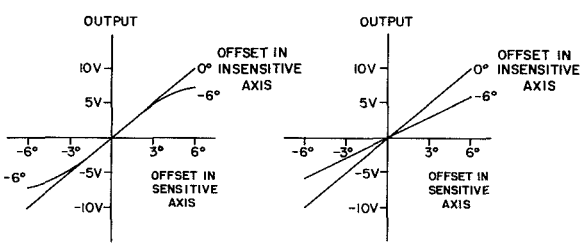

FIGURE 7.—Cross-coupling.

departure from linearity which meets the specifications in this regard, would reduce the mean time to failure to 173,000 hours.

The graphs for the two examples I have described are shown in the last figure. The two distinct design approaches are shown on the graph on the left. The points for them are widely separated. The two points derived for the slight modification in design are shown in the right. They are near together.

I have proposed an hypotheses for the general characteristics for the reliability vs. accuracy function and have described two examples to illustrate the two important aspects of the function. These are, one, short continuous curves corresponding to particular design and, two, jumps between the curves corresponding to changes of basic design.

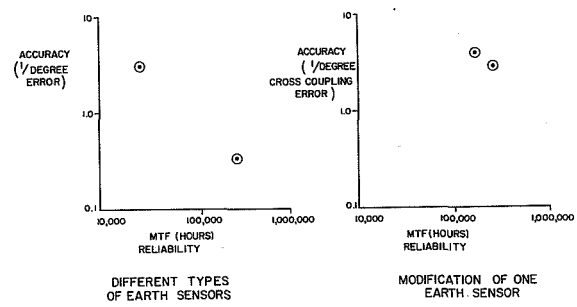

FIGURE 8.—Reliability vs. accuracy tradeoffs.

A RELIABLE EARTH SENSOR FOR ATTITUDE SENSING

BARBARA K. LUNDE

Goddard Space Flight Center

An infrared earth sensor that will be approximately 10 times as reliable as any previously developed is a current project of the Goddard Space Flight Center of NASA.

During the next few minutes I will present a little background on infrared earth sensors and then I will go into some of the details of the Reliable Earth Sensor program, the aim of which is to develop and test an earth sensor which will have these properties:

It will have a 90-percent probability of operation in space for 3 years without failure—or, to put it another way, it will have a mean time to failure of 29 years;

This long-term reliability will be required in order to make feasible the planned deployment in space of long-lived weather and communications satellites; and

This calculated mean time to failure of 29 years represents a radical improvement in reliability over the earth sensor for the Orbiting Geophysical Observatory which has a claculated mean time to failure of a little less than 3 years.

Now for the background. An earth sensor is simply a spacecraft orientation device. It tells the spacecraft which way is "down"—that is, it orients the spacecraft with relation to the earth.

Figure 1 shows an earth sensor of the type we are developing, working.

Earth sensors have been notorious for their lack of reliability. The earth sensor on the Orbiting Geophysical Observatory is considered that satellite's least reliable subsystem.

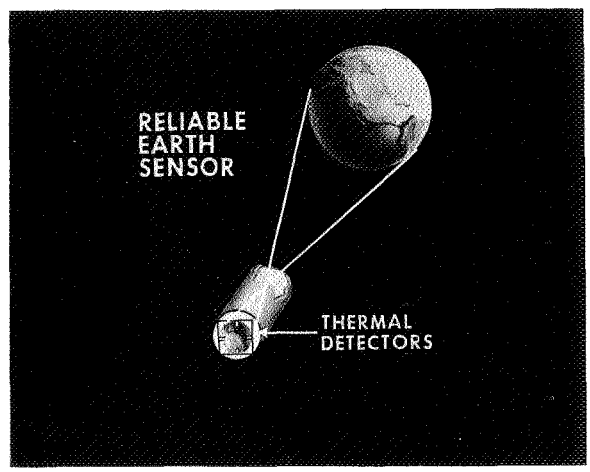

FIGURE 1.—A reliable earth sensor.

During the early part of the Mariner flight to Venus, it was an earth sensor which gave observers here some very anxious moments.

To go back even farther, the mean time to failure of the earth sensor used in Project Mercury was just a bit over 1,000 hours—a matter of days or weeks, which was sufficient for Mercury but hardly adequate for a satellite whose useful life will have to be measured in years if it is to achieve its mission. Earth sensors on Mercury missions had spurious outputs, causing problems with the control system.

Figure 2 illustrates graphically the great leap in reliability being sought in the Reliable Earth Sensor program. You will note that the graph starts off at a mean time to failure of 1,000 hours and that the midpoint of the graph is at 10,000,

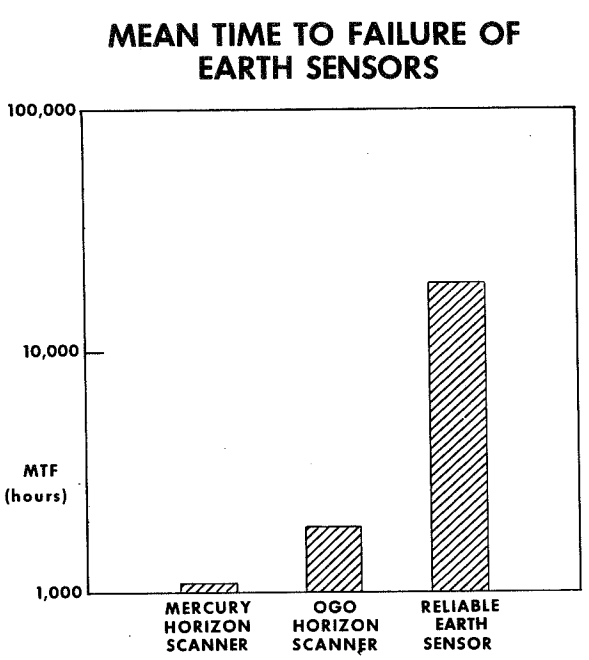

FIGURE 2.—Mean time to failure of earth sensors

with the upper portion of the graph marking another tenfold increase, to 100,000 hours. The increase in reliability being sought is in the order of magnitude of 10 times.

The previous earth sensors for stabilized spacecraft all have used mechanical devices to modulate the infrared radiation. Mechanical modulation requires moving parts and extra electronic components for controlling the movement. It achieves accuracy at the expense of reliability.

The Reliable Earth Sensor will not use mechanical modulation, and it will be somewhat less accurate than previous earth sensors. But its accuracy still will be sufficient to accomplish its mission, which may be described as that of orienting long-term operational satellites.

Table I shows the specifications for the Reliable Earth Sensor. You will note that it is being designed for circular orbits of periods between 6 and 12 hours. The figure in the published paper contained the proposed specifications, not those originally specified. There have been some changes to these figures in the intervening 3 months. I would now like to discuss the various design problems of the

TABLE 1.—*Specifications of the Reliable Earth Sensor*

Purpose	Measure the orientation of a spacecraft with respect to the earth in 2 axes.
Reliability	90 percent probability of operation after 1 year storage and launch and 90 percent probability of operation after 3 years operation under space conditions
Weight	1.8 kg.
Power	4 watts.
Size	15 cm- 15 cm- 15 cm
Accuracy	+ 3 inch. null shift + 0.15 inch resolution. Total 0.6 inch linearity and cross coupling. + 0.15 inch scale factor accuracy at 3° offset.
Linear range	+6.
Time constant	10 seconds.
Orbits	Circular orbits of 16,763 km to 42,240 km radius from center of earth.

Reliable Earth Sensor and the impact on the project of data gathered by means of the Tiros weather satellites. Figure 3 shows the physical layout of the sensor, which is quite simple.

Basically, the Reliable Earth Sensor consists of an infrared lens which images the earth and space surrounding it on a detector array. The detector array is an arrangement of heat detectors which measure the amount of infrared energy impinging upon them. The output of opposite detectors is compared and amplified in the electronics contained in the rear of the sensor.

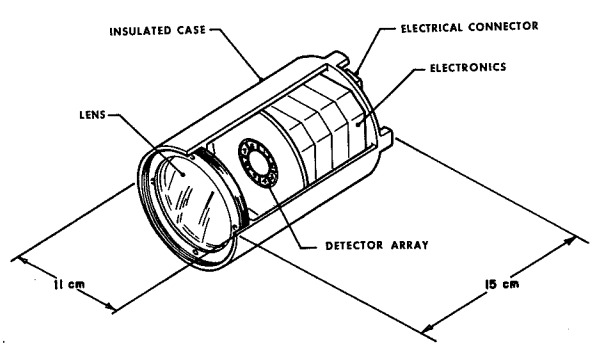

FIGURE 3.—Reliable earth sensor configuration.

First, I would like to discuss the optical system. The illustration shows a single lens. It will be made of germanium. The single lens appears to be adequate for those orbits which approach the higher limits specified, in the area of 42,000 kilometers, but for the low orbits, those toward about 17,000 kilometers, it may be necessary to use a two-element lens. The image quality required is not extreme. Resolution of 6 degrees at the edge of the field would be adequate, but still, this image quality may not be achieved if the lens used has spherical surfaces. The use of a lens with aspheric surfaces may solve the imaging problem, or it may be necessary to employ a two-element lens.

The optical system will include a filter that will determine the wavelengths which will reach the detectors and those which will be reflected or absorbed and thus not enter into the thermal balance of the sensor cavity, containing the lens and detector array. I will come back to this matter of wavelengths a little later when I discuss the impact of the Tiros data upon this project.

The detector array illustrated on this slide consists of eight infrared-sensitive detectors arranged in opposite pairs.

The detectors operate by absorbing infrared radiation, heating up, and indicating their temperature. To obtain the necessary accuracy, the two most important qualities for the detectors are stability of the radiation-absorbing surface and accuracy of temperature indication.

The contractor on the Reliable Earth Sensor, Space Technology Laboratories, is planning to use platinum resistance wire to indicate temperature. At the Goddard Space Flight Center, we are doing a parallel development of the Reliable Earth Sensor, and we are using thermopiles as temperature sensors. Figure 4 shows a laboratory test model of the Goddard version, complete with lens and detectors which are inside the sensor. The picture is not upside down. The sensor is correctly pointing toward the earth. The thermopile detector is not sensitive to temperature gradients across the sensor, while the simple resistance wire system

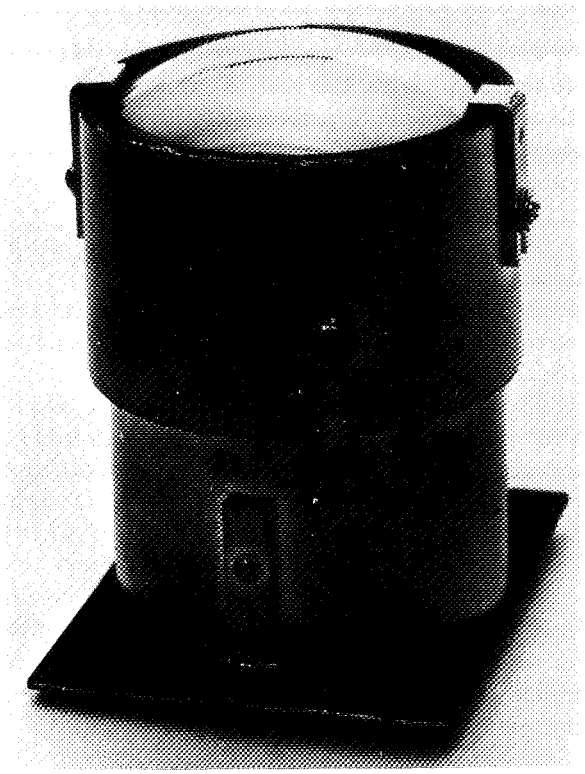

FIGURE 4.—Laboratory test model of Goddard reliable earth sensor.

cannot distinguish such gradients from an offset angle of the earth. Another difference is in the electronics. The thermopile system requires extremely low-noise DC amplifiers, while the resistance wire system can use ordinary AC electronics.

The shape of the detectors used poses a very important design problem, and I will return to this shortly, in connection with the Tiros data.

Next I would like to discuss thermal design, which is an important aspect of the Reliable Earth Sensor program. Both the absolute temperature and the temperature gradients must be closely controlled. For simple resistance wire elements, a temperature difference in detector elements of only three one-hundredths degree Kelvin would cause a spurious earth offset indication of six-tenths of an arc degree. Variations in the absolute temperature will cause the resistance of the detectors, and consequently the gain of the amplifier, to vary. To control these variations, an electric blanket

will be used on the lens and detector assembly to keep it at a constant temperature. It will be insulated from the rest of the sensor. The filter which will absorb some sunlight will be thermally connected to the spacecraft, so that variations in its temperature due to the angle of the sun will not affect the sensor.

But I want to return now to the Tiros data I mentioned earlier and to general problem of designing an earth sensor which utilizes the earth's infrared radiation to maintain satellite orientation.

The earth radiates as a black body of about 270° Kelvin and 99 percent of its radiation is of wavelengths longer than 5μ. A filter coating on the first optical surface of the sensor's optics will reflect or absorb the light of wavelengths shorter than 5μ. This will protect the sensor from the sun and make it insensitive to moon albedo. But a choice of wavelengths to be transmitted also has to be made, and this choice is somewhat difficult. This is because the earth is not actually of uniform temperature. Figure 5, made up from Tiros data, shows the temperature irregularity, which can have some serious effects on sensor accuracy.

Here we see the earth's temperature pattern as it appeared to the 8 to 12μ radiometer on the Tiros II satellite on July 16, 1961. The wavelengths of radiation to which this radiometer were sensitive, the 8μ to 12μ band, are radiation coming from the first solid or liquid level; that is, the tops of clouds or, if no clouds are present, the earth's surface. Each color represents a certain temperature range. The redder colors are hotter. The range of temperature observed was from above 300° K to below 225° K.

Figure 6 shows the pattern resulting from the 15μ CO_2 absorption band, detected by a radiometer on Tiros VII, also in July of this year. Radiation in this band originates high in the atmosphere, above weather patterns. Here we do not see the irregularities apparent at 8μ to 12μ, which are caused by weather patterns, but a more uniform variation from north to south, representing the seasonal difference. These data are taken from a letter to the editor of the Journal of Atmospheric Sciences by W. R. Bandeen, B. J. Conrath, and K. A. Hanel.

The Tiros data illustrated in these slides is being used to determine the desired spectral acceptance band for use on the Reliable Earth Sensor. The tentative choice is the area from 12μ to 20μ, but the wider band between 8μ and 20μ may be used. An extremely narrow band around 15μ might be optimum to reduce weather effects, but it is necessary to use a wider band so that enough energy is admitted in order to keep detector sensitivity and noise from being problems. The maximum error caused by the effect of weather on the earth and consequently the

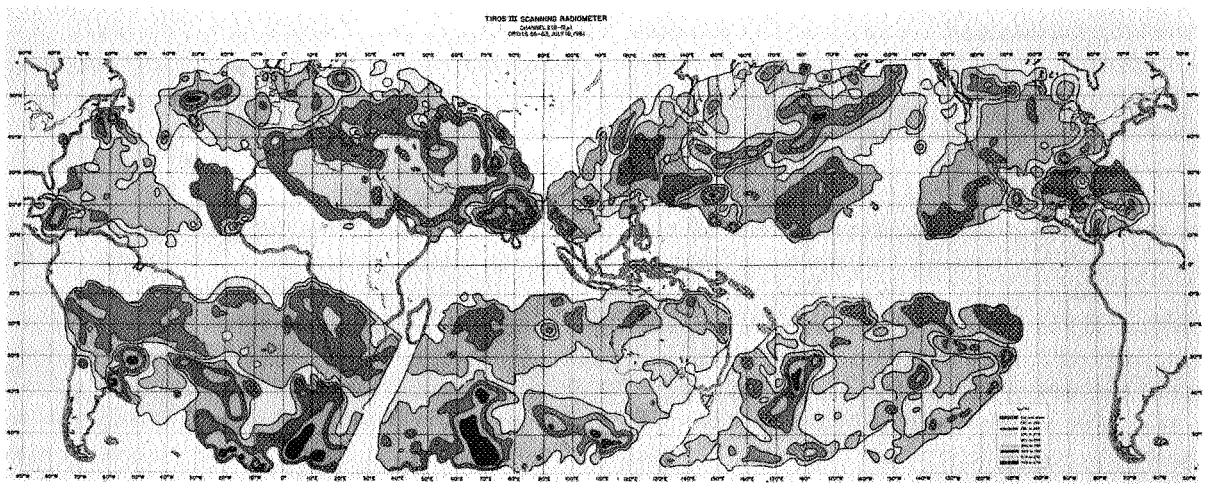

FIGURE 5.—Tiros III scanning radiometer, channel 2 (8–12μ), Orbits 56–63, July 16, 1961.

AVERAGE APPARENT BLACK BODY TEMPERATURE vs. SUBSATELLITE LATITUDE FOR 14.8 - 15.5μ RADIOMETER ON TIROS VII DURING JUNE, 1963.

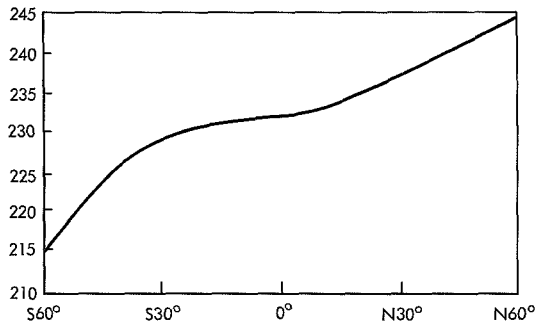

NOTE: THIS DATA TAKEN FROM A LETTER TO THE EDITOR OF THE J. OF ATM. SCI. TO BE PUBLISHED IN NOVEMBER, 1963, BY W.R. BANDEEN, B.J. CONRATH, & R.A. HANEL.

FIGURE 6.—Average apparent black body temperature vs. subsatellite latitude for 14.8–15.5μ radiometer on Tiros VII during June 1963.

radiation used by the earth sensor will be 1½ degrees.

The Tiros data also indicate another design consideration, that of the shape of the detectors which I mentioned earlier. As we have seen from the slides, the apparent temperature of the earth varies from place to place. Figure 9 shows the detector array chosen for the highest altitude orbit. For a detector of wide tangential extent and therefore field of view, only small variations in apparent temperature would appear because the detector would average the temperature over a large area of the earth. Correspondingly, a small detector would indicate a wider temperature range because its small field of view could be completely covered by a small area of extreme temperature on earth. But when radial extent is considered the opposite appears. The smallest possible detectors are desirable. Detector areas of overall radial extent greater than the 12° necessary for the linear range lead to offset indications due to temperature variability which would not exist with smaller array areas, since temperatures of adjacent areas of the earth are at best independent, and are probably on the same side of the average temperature.

The detector array illustrated on this slide consists of eight infrared-sensitive detectors arranged in opposite pairs. Now, only four

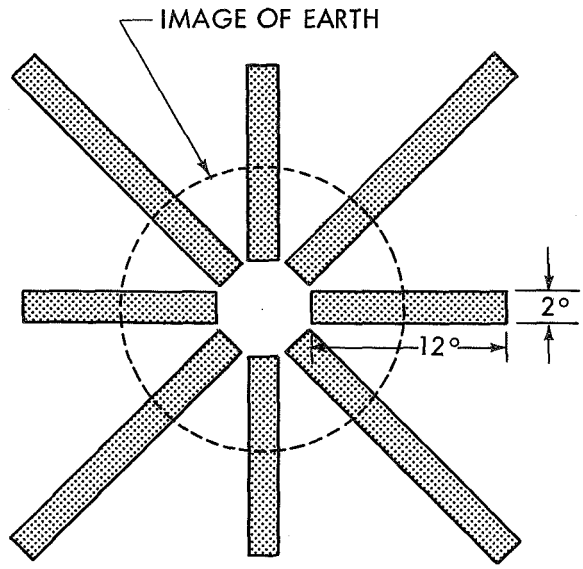

DETECTOR ARRAY CONFIGURATION FOR 42,000 Km ORBIT

FIGURE 7.—Detector array configuration for 42,000-Km orbit.

detectors arranged in two pairs would be necessary if it were not for the sun. As seen in this slide, the vertical pair would determine offset about the horizontal axis and the horizontal pair would determine offset about the vertical axis. However, if the sun would appear in the field of view of one of these detectors, a very large offset would be indicated where it did not actually exist. To avoid this large source of error caused by sun interference, a redundant set of detector elements is included. The slide of the earth sensor configuration shows an independant sun sensor. This is used to determine whether or not the sun is in the field of view of one set of four detectors. If the sun is present, the output of the other set of detectors is used to determine the output of the sensor.

The largest detector areas possible in this particular design would be 45° sections, with enough space between them so that the sun could not be focused on two detectors simultaneously. But if the detectors were in this shape there would be extreme cross-coupling of the outputs for the two axes; and a better design, to minimize cross-coupling, would be for

detectors to be shaped like long narrow bars lying on the axes.

The figure shows the detector array selected for the highest altitude orbits. When the off-axis array is used, the outputs are treated algebraically so that cross-coupling is eliminated. The time constant of the detectors determines the temperature difference versus offset coefficient. The specifications for the Reliable Earth Sensor call for a time constant of 10 seconds or less.

In the time remaining, I would like to talk briefly about the characteristics of the earth sensor's output signal.

Figure 8 illustrates the output of the earth sensor. The larger parallelogram shows the area on the graph containing all the possible positions of the output curve over the life of the satellite, movements over this area will be caused by changes of seasons and long term drifts of the detectors. The smaller parallelogram contains all the possible positions of the output curve over a short term. Variations in this area will be caused mainly by noise.

The program of development of the Reliable Earth Sensor calls for the delivery of four flight models to Goddard in December 1964. Two models will be for the maximum altitude orbit, and two for the minimum altitude orbit. One unit will have been qualification tested, and two others, one for each altitude, acceptance tested.

Besides probable use on many future satellites, the Reliable Earth Sensor has been recommended by a design study for the Synchronous Meteorological Satellite, and it will be flown on an experimental gravity gradient satellite.

In conclusion, let me mention again that reliability is the prime consideration here. As the work progresses, modifications of the design, having increased reliability as their objective, have been devised. For example, an AC excitation system was chosen from among three types of signal processing proposed for the sensor with resistance wire detectors, after a detailed study. The objective has been to achieve, within somewhat relaxed but fully adequate standards of accuracy, an operational earth sensor with a reliability ten times that of any previous earth sensor.

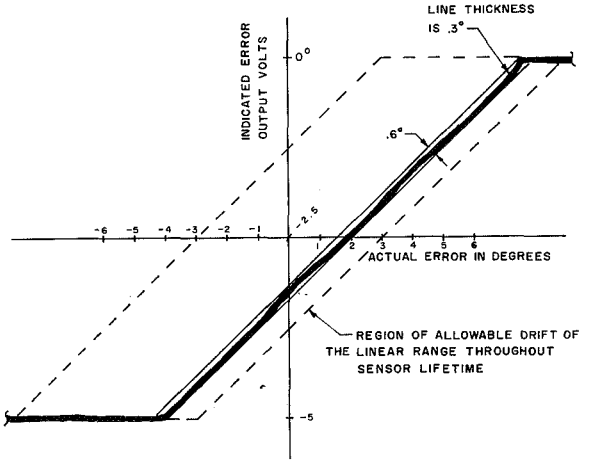

FIGURE 8.—Typical output of sensor.

ANALYSIS OF THE DYNAMIC TESTS OF THE STRETCH YO-YO DE-SPIN SYSTEM

WILLIAM R. MENTZER

Goddard Space Flight Center

Results of the stretch yo-yo feasibility and flight qualification tests are presented. These tests were conducted to prove the concept that the stretch yo-yo is a more accurate de-spin device than the rigid yo-yo, and to verify the analytical development of the stretch yo-yo properties. Variations in the design parameters and their effects on the final spin rate of the payload are noted in the analysis of the test results. The variables include initial spin rate, moment of inertia, and spring properties. A computer solution of the test payload equations of motion is included for comparison with the experimental results to confirm the mathematical analysis of the stretch yo-yo system. As a result of the successful flight qualification tests a stretch yo-yo was flown on Ariel I (1962 $o1$) in April 1962.

INTRODUCTION

The stretch yo-yo is a de-spin device that has the ability to compensate for errors in the initial spin rate and the moment of inertia of a payload. It is composed of an end mass, a helical spring, and, if necessary, a length of wire (Figs. 1 and 2). The spring elongates under a load, giving a variable yo-yo length. The square of the yo-yo length varies directly as the initial spin rate, and the ratio of final spin to initial spin varies inversely as the square of the yo-yo length. This produces an essentially constant final spin rate. The concept of the stretch yo-yo was suggested by H. J. Cornille (Reference 1). The analytical theory and design criterion were developed by Dr. J. V. Fedor (References 2 and 3).

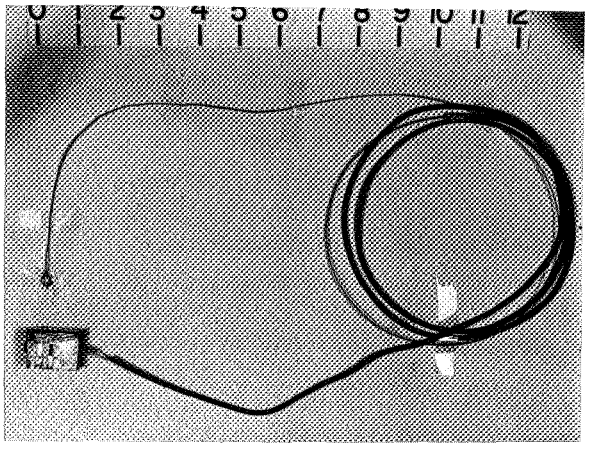

FIGURE 1.—Stretch yo-yo consisting of wire, spring, and end mass. (The scale is in inches.)

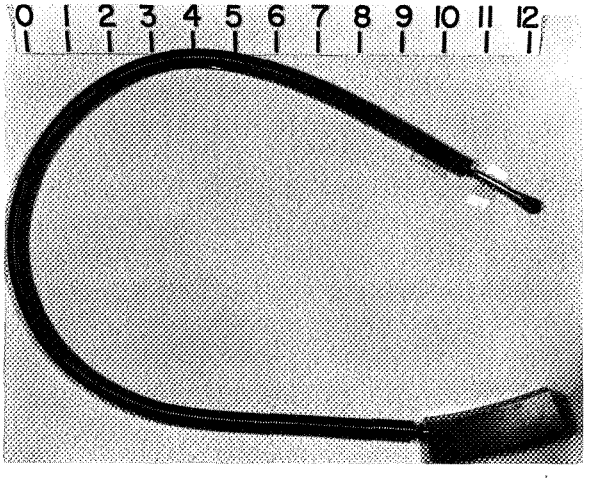

FIGURE 2.—Stretch yo-yo consisting of a spring and end mass. (The scale is in inches.)

Following dynamic analysis and development of design equations for the stretch yo-yo, the decision was made to fabricate and test stretch yo-yos on the Explorer XII (1961 $\sigma 1$) and Ariel I(1962 $\upsilon 1$) type payloads. Three

series of tests were conducted beginning with feasibility tests on the two payloads and concluding with flight qualification tests for the Ariel I payload. As a result of these tests, a stretch yo-yo was flown on the successful Ariel I spacecraft in April 1962.

In the record of the experimental results, the effects of the several variables involved in stretch yo-yo design can be readily noted. These variables include optimum spring constant, preload, initial spin rate, spin moment of inertia, and material strength.

OBJECTIVES OF THE TESTS

The stretch yo-yo tests had several objectives which overlapped the three series of tests. The first series of tests was intended to demonstrate the feasibility of the stretch yo-yo de-spin system in compensating for errors in initial spin rate. This series also was used to examine the characteristics of a helical spring operating as a yo-yo.

The second test series was planned as the flight qualification for the Ariel I stretch yo-yo made of National Standard Co.'s NS355 high-strength stainless steel. The yo-yos were to be tested for sensitivity to changes in spin moment of inertia, and for performance at overspin conditions when the yo-yos would be operating near the yield point of the material.

Because of an unexpected delay, the steel shipment did not arrive in time for the scheduled tests. Therefore, it was necessary to fabricate springs from conventional music wire. This change in spring material necessitated a change in the test series. The objects of the revised test series were to observe the effect of changes in moment of inertia, as originally planned, and to study the results of subjecting the spring to stresses greater than the yield point of the material.

When the NS355 steel was received and the Ariel I springs had been fabricated, the third, and last, test series was conducted. These tests qualified the stretch yo-yo as Ariel I flight hardware. The yo-yos were tested at overspin conditions to see if they could withstand the loading.

TEST APPARATUS

Tests on the stretch yo-yo were performed in the vacuum facilities at Langley Research Center, Hampton, Virginia. The vacuum tanks were spheres 41 and 60 feet in diameter. The test structures were the portions of the outer shells of the payloads (Explorer XII and Ariel I) on which the yo-yos were positioned and inertia plates for simulating the inertias of the complete payloads. A dc motor, sealed for vacuum operation, with an electromagnetic drive unit and an electromagnetic coupling and brake comprised the spin table drive system. The yo-yo firing signal was fed from an external manually operated circuit to the payload through a set of slip rings in the driven shaft of the spin table. Payload angular velocity was measured in the following manner. A disk with 32 equally spaced, radially protruding studs was mounted on the driven shaft; then, as the shaft turned, the study generated pulses in an adjacent magnetic pickup. The output signal from this circuit was fed into a recording oscillograph. In order to obtain a complete time record of the operation, the declutching signal, firing signal, and yo-yo release signal also were fed into the oscillograph.

The spin table and the mounting platform in the 60 foot vacuum chamber at Langley Research Center are shown in Figure 3. Figure 4 shows the Ariel I payload mounted on the spin table. The yo-yos can be seen in the picture. The details of the spin table with its drive mechanism and spin rate measuring device are shown in Figure 5.

TEST PROCEDURE

The original intent for the tests was to study only the ability of the stretch yo-yo to compensate for errors in the initial spin rate of the payload and errors in payload moment of inertia. But, as a result of yo-yo fabrication problems, the experimenters were forced to consider the effects on the final spin rate of preload in the yo-yos, of deviation from the optimum spring constsnt, and of spring loading in the region of the elastic limit of the material. Because of the increased complexity of the

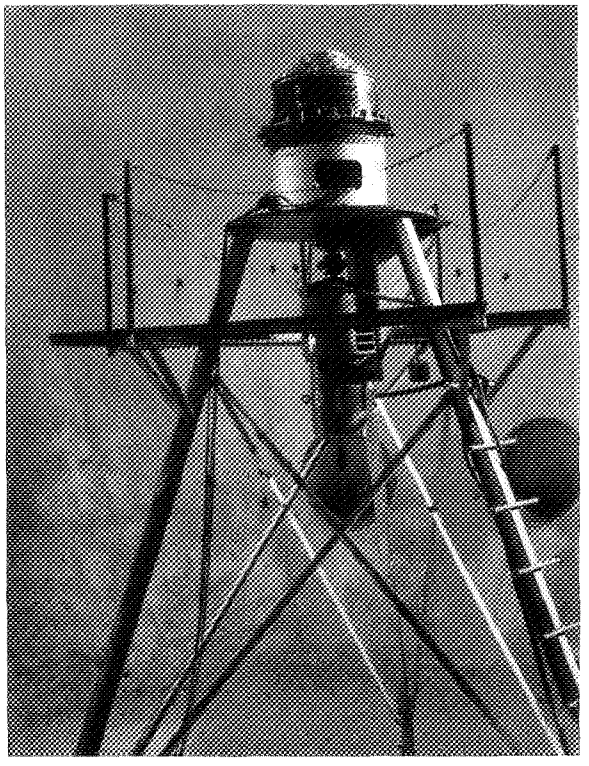

FIGURE 3.—The Ariel I payload mounted on the spin table in the 60-foot vacuum chamber.

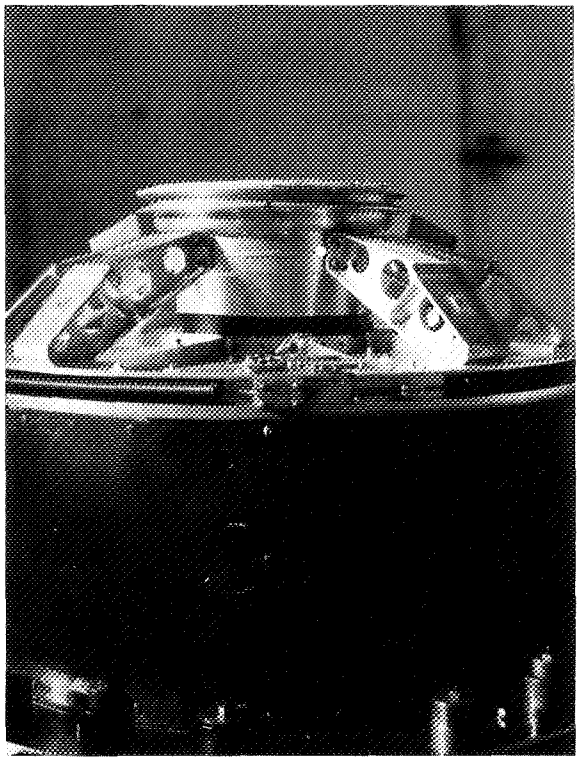

FIGURE 4.—Closeup of the Ariel I payload showing the yo-yos in place. Weights at the base of the structure are for simulating the entire payload moment of inertia.

program, it was necessary to be careful in pairing the springs for the test. The spring scale and the preload were determined for each spring to be tested. Heat treating and flexing were performed on the springs in an attempt to decrease the preloads. One spring from each group fabricated was statically loaded until permanent deformation occurred. This was done in order to obtain a strength limit to compare with the expected maximum yo-yo tension in the uncoming tests. With regard to the two factors affecting the tests, spring constant and preload, a deviation from the optimum spring constant was the variation most critical to the test results. In view of this fact, the springs with essentially equal spring constants were paired for testing. The pairs were then tested in the order of smallest to largest payload.

After the yo-yo springs were paired, the average values of spring scale and preload for a set were used to compute the end mass (Reference 2). The yo-yos were assembled so that both springs in each test were of the same length.

The tests were conducted at an absolute pressure of 10 mm Hg to minimize the atmospheric drag effects on the yo-yos. Payload spin rate was determined from the recording oscillograph records (Fig. 6). The oscillograph output consisted of a plot of pulses from the magnetic contact on a known time scale. Also included on the record were the declutching signal, the yo-yo firing signal, and the yo-yo release signal.

The spin table was constructed so that one pulse from the magnetic contact took $\frac{1}{32}$ of a revolution of the payload and that the time scale of the recorder chart τ was 1/100 of a second per division. The spin rate at the midpoint of the

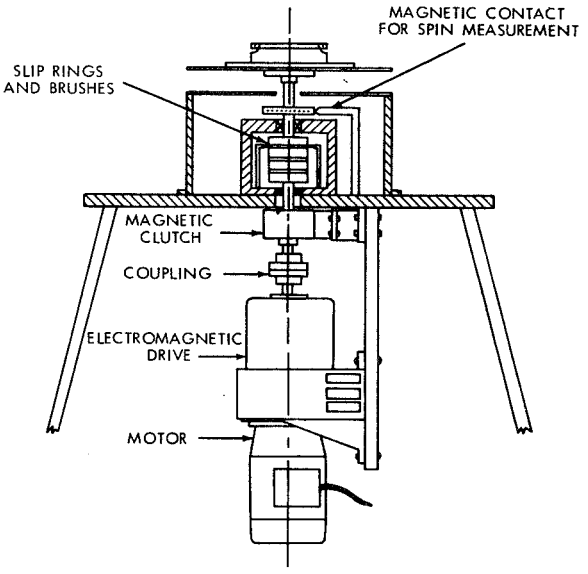

FIGURE 5.—Details of the spin table.

time interval between any two pulses was found from the relation

$$W=1.875\frac{N}{t},$$

where

W=spin rate in rpm,
N=number of pulses,
t=total time between pulses in seconds.

DISCUSSION OF TEST RESULTS

The stretch yo-yo tests were considered successful from several standpoints. The concept of the stretch yo-yo as a more accurate despin device than the rigid yo-yo was proven, and the analytically developed design criteria were verified (Reference 1). The difficulties of operating with a nonoptimum yo-yo system were evaluated. Finally, the yo-yo was qualified as flight hardware for Ariel I.

The results of the stretch yo-yo tests are recorded in Table 1. The tests are grouped by series and by payload and are numbered consecutively from the first successful test on each payload. System design parameters and actual test conditions have been tabulated in order that the effect on final spin rate of variations of test conditions from design values can be readily noted.

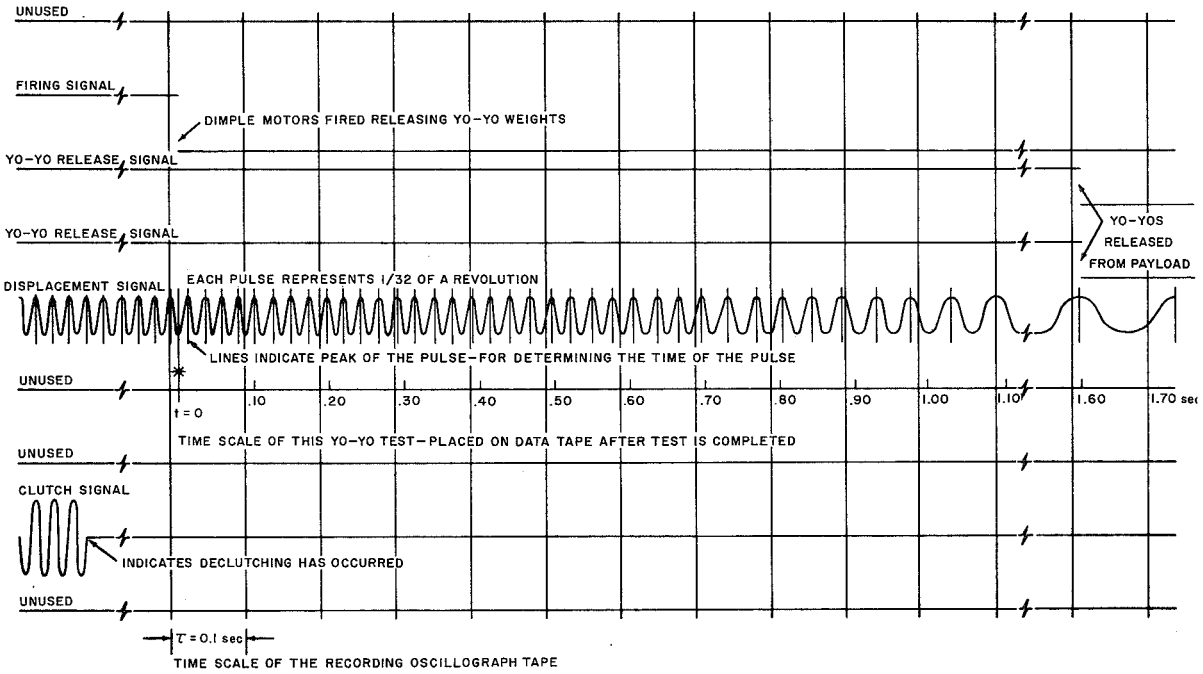

FIGURE 6.—A copy of the data tape used for the Explorer XII type stretch yo-yo, test IV, November 14, 1961

TABLE 1.—*Stretch Yo-Yo Test Summary*

Date	Payload	Test	Design parameters				Test conditions			Test spin data			
			Initial spin rate $\dot{\phi}_0$ (rpm)	Final spin rate $\dot{\phi}_f$ (rpm)	Spin moment of inertia I (slug-ft²)	Spring constant (optimum) k (lb_f/ft)	Spin moment of inertia I (slug-ft²)	Spring constant (average) k (lb_f/ft)	Preload (average) F_0 (lb_f)	Initial spin rate $\dot{\phi}_0$ (rpm)	Error in initial spin rate (percent)	Final spin rate $\dot{\phi}_f$ (rpm)	Error in final spin rate (percent)
Nov. 13–16, 1961	Explorer XII	II	103.0	14.48	2.135	7.88	2.135±0.1	7.745	0	101.81	−1.156	14.42	−0.415
		III	123.5					7.76	0	120.75	+17.23	14.48	0.0
		IV	82.5					7.66	0	82.50	−19.90	14.69	+1.45
		V	110.0	30.00				12.00	2.72	108.75	−2.028	26.79	−10.7
		VI	132.0					11.63	2.70	130.31	+17.40	27.50	−8.33
		VII	88.0					12.16	[1] 2.62	88.13	−20.60	20.46	−31.80
	Ariel I	II	160.0	74.80	2.774	11.00	2.774±0.1	10.85	9.325	162.56	+1.60	73.56	−1.658
		III	128.0					11.29	8.855	129.38	−19.14	73.75	−1.404
Jan. 22–24, 1962	Ariel I	IV	160.0	70.79	2.885	11.56	2.885±0.1	11.565	3.40	155.66	−2.712	71.20	+0.534
		V	184.0					11.53	3.35	184.42	+15.26	[2] 61.30	−13.44
		VI	136.0					11.58	3.50	138.89	−13.19	72.81	+2.807
		VII	160.0					11.605	3.675	157.90	−1.313	71.66	+1.183
		VIII	160.0	3.462			3.462±0.1	11.51	3.15	160.26	+.162	76.53	+8.06
		IX	128.0					11.64	3.20	131.25	−17.97	76.85	+8.512
		X	160.0	2.308			2.308±0.1	11.405	3.81	154.41	−3.494	66.96	−5.452
		XI	192.0					11.91	3.475	187.50	+17.19	[2] 57.25	−19.16
		XII	128.0					11.625	3.75	129.31	−19.18	64.21	−9.335
Feb. 7, 1962	Ariel I	XIII	160.0	73.90	2.885	12.48	2.885±0.1	11.93	1.90	160.71	+.444	77.16	+4.411
		XIV	184.0					11.915	2.175	182.96	+14.35	74.57	+.906
		XV	200.0					11.87	2.025	200.38	+25.54	72.58	−1.787

[1] 1 yo-yo had zero preload.
[2] Yielding occurred.

The Explorer XII type optimum spring scale tests clearly demonstrated the ability of the stretch yo-yo to compensate for errors in initial spin rate. In this series of tests, spin-up errors of ± 20 percent were reduced to within ± 1.5 percent of the design final spin rate. The fine performance was attributed to the fact that the yo-yo springs had the optimum spring constant and no preload. The yo-yos used in these tests were of the type shown in Figure 1.

The importance of the optimum spring constant in the proper functioning of the stretch yo-yo de-spin system was illustrated by the last three tests on the Explorer XII configuration. These tests were necessitated by the manufacturing of preloaded springs with incorrect spring constants. The tests were conducted at a higher spin level than tests II through IV because of apprehension concerning the functioning of a preloaded yo-yo. Spin limits were selected and calculations were made by using the measured values of preload and spring constant, which were nonoptimum for the spin rates used.

The percent error shown for these tests is large when referenced to the 30 rpm design final spin. If the results are referenced to test V, with a 26.8 rpm final spin rate, as design conditions, then the overspin error is $+2.7$ percent. The underspin error, -23.6 percent, is still large but is attributed to the fact that the test was made with yo-yos of unequal preloads, differing by 2.6 lb.

Ariel I yo-yo tests II and III proved the feasibility of the one-half wrap stretch yo-yo system (Fig. 1) and led to the use of the stretch yo-yo on this satellite. Tests IV and VII demonstrated the repeatability of the yo-yo results and, along with test VI, gave a picture of the system operating at the design moment of inertia.

The design final spin rate for these tests was computed from equations that included the effects of preload in the yo-yo springs. The value of the preload used in calculations was that of the springs used in test IV. Test results agreed closely with theoretically predicted final spin rates, the deviation resulting from the fact that the spring constants varied slightly from the optimum spring constant.

In tests V and XI the springs yielded because the load exceeded the yield point of the material. The yielding produced a spin rate that was much lower than theoretically predicted. This situation was permitted to occur since the springs being tested were of lower strength limits than flight hardware. The experimenters were afforded the opportunity to observe the behavior of the de-spin system when yielding occurred and the design equations no longer applied.

Tests VIII through XII verified the theoretical prediction that the stretch yo-yo would be relatively insensitive to variations in spin moment of inertia when compared with the behavior of the rigid yo-yo. Moment-of-inertia values of ± 20 percent of the design spin axis moment of inertia were used in the tests.

The stretch yo-yo tests were concluded with the Ariel I flight qualification tests, XIII through XV. In these tests, the NS355 high-strength stainless steel springs were used. The tests were conducted at design initial spin rate and then at $+15$ and $+20$ percent of design initial spin rate to determine whether the yo-yo could withstand the high loading at overspin conditions. Test XIII, with nominal initial spin rate, gave a final spin slightly higher than design final spin. In the overspin tests, the final spin rates were very close to design values. As a result of this test series, the stretch yo-yo of high-strength stainless steel was accepted as flight hardware for Ariel I which was launched successfully in April 1962.

An analytical method for determining the actual final spin rate of a satellite is given in Reference 2. The data necessary for performing the calculations include spring properties, design values of spin rate and inertia, and actual values of spin rate and inertia.

The equations of motion of the test payload were programmed for solution on an IBM 709C digital computer as a verification of the test results. Correspondence between this solution and the test results proved the validity of these equations of motion. The equations were developed for phase 1 of the yo-yo operation, when the yo-yo is unwinding and is tangential

to the payload. Spin table friction was included in the analysis. The development of the equations and the computer program is included as Appendix A.

A graph of the computer solution of phase 1 for one test is included with the plot of the entire de-spin test in Figure 7. The plot shows the angular displacement of the payload, in radians, versus time. The test data points are the pulses from the magnetic contact that were recorded by the recording oscillograph. Thirty-two successive points define one revolution of the payload. The end of phase 1 is determined by the computer program, and the end of phase 2 is indicated on data tape by the yo-yo release signal. At the end of phase 1 the computed angular displacement for test XIII of February 7, 1962, exceeded the recorded value by 2.42 percent.

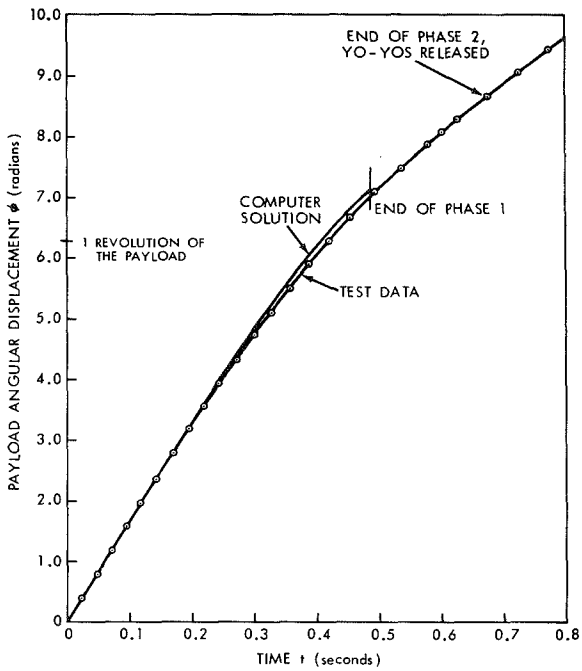

FIGURE 7.—Angular displacement vs. time for Ariel I test XIII, February 7, 1962.

Phase 2, when the yo-yo moves from a tangential to a radial position, was not analyzed because of algebraic complexity and similarity to phase 1 analysis. It was felt that the close agreement between the computer solution of the phase 1 analysis and the test results, combined with the similarity of the methods of solving phase 1 and 2 equations on a computer, justified the omission of the phase 2 analysis from this report.

REFERENCES

1. CORNILLE, H. J., JR., "A Method of Accurately Reducing the Spin Rate of a Rotating Spacecraft," NASA Technical Note D–1420, October 1962.
2. FEDOR, J. V., "Analytical Theory of the Stretch Yo-Yo for De-Spin of Satellites," NASA Technical Note D–1676, April 1963.
3. FEDOR, J. V., "Theory and Design Curves for a Yo-Yo De-Spin Mechanism for Satellites," NASA Technical Note D–708, August 1961.

Appendix A

COMPUTER SOLUTION OF PHASE 1 EQUATIONS OF MOTION

The theoretical development and the design criteria for the stretch yo-yo de-spin mechanism functioning on an orbiting spacecraft have been developed by J. V. Fedor.[1] The stretch yo-yo tests were performed to demonstrate the feasibility of the stretch yo-yo system and to verify the design parameters that had been developed. Since the observed final spin rates of the payloads corresponded to the theoretical predictions, the tests were considered successful.

The differential equations of motion of the test payload on the spin table were solved on an IBM 7090 computer for comparison with the experimental results to verify the analysis of the stretch yo-yo system. The equations were developed for phase 1 of the yo-yo operation when the yo-yo is unwinding and tangential to the payload (Fig. A1). In the analysis, the effects of gravity are considered negligible because of the short operating time of the yo-yo, 0.50 to 0.75 second, and because of the existence of a component of the tension in the yo-yo-spring which opposes the gravitational force. The validity of this assumption has been demonstrated in previous rigid yo-yo de-spin tests where test results agreed closely with theoretical calculations in which gravitational effects were neglected. Tests were conducted at a pressure of 10 mm Hg, which corresponded to an altitude of 100,000 feet and made the effect of atmospheric drag negligible.

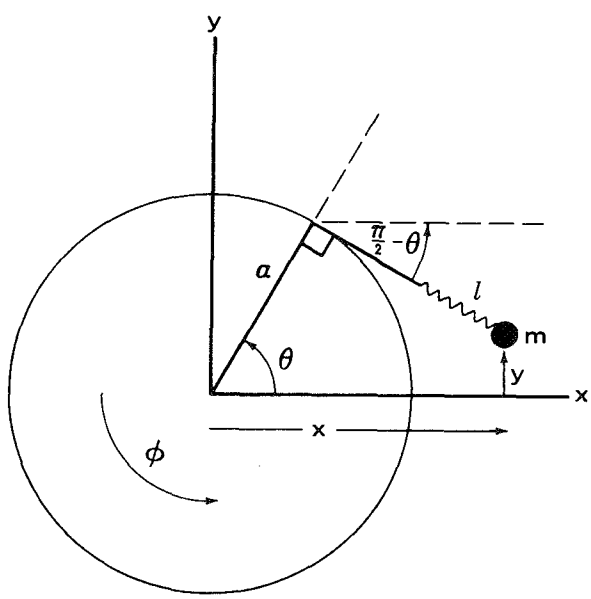

FIGURE A1.—Phase 1 coordinate system.

The coordinate system for phase 1 analysis is shown in Figure A1. Because of the symmetry of the system only one yo-yo is shown.

The stretch yo-yo de-spin system behaves as a rigid yo-yo until the preload is overcome by the force in the yo-yo. During this phase of operation the Lagrangian L, which is the kinetic energy of the system, is [2]

$$L=\tfrac{1}{2}I\dot{\phi}^2+\tfrac{1}{2}m(l^2\dot{\theta}^2+a^2\dot{\phi}^2), \qquad \text{(A1)}$$

where

I=spin moment of inertia less yo-yo masses,
$=\dot{\phi}$spin rate of payload,
θ=generalized coordinate,
m=mass of both yo-yos,
a=radius of yo-yo fixture,
l=length of yo-yo unwound.

The length of wire unwound at any time in rigid yo-yo operation is

$$l=a(\theta-\phi). \qquad \text{(A2)}$$

The mass of the yo-yo system, including the spring mass, is given by an approximate

[1] Fedor, J. V., "Analytical Theory of the Stretch Yo-Yo for De-Spin of Satellites," NASA Technical Note D-1676, April 1963.

[2] Fedor, J. V., "Theory and Design Curves for a Yo-Yo De-Spin Mechanism for Satellites," NASA Technical Note D-708, August 1961.

equation that accounts for the distributed spring weight,

$$m=m_0+\frac{\rho a}{3}(\theta-\phi), \tag{A3}$$

in which $(\rho a/3)(\theta-\phi)$ is the mass of yo-yo spring unwound for both yo-yos. The quantity ρ is twice the mass density of one helical spring and m_0 is the total end mass of the yo-yos. The equations of motion in terms of the Lagrangian are

$$\frac{d}{dt}\left(\frac{\partial L}{\partial \dot{\phi}}\right)-\frac{\partial L}{\partial \phi}=Q_\phi, \tag{A4}$$

$$\frac{d}{dt}\left(\frac{\partial L}{\partial \dot{\theta}}\right)-\frac{\partial L}{\partial \theta}=Q_\theta. \tag{A5}$$

Evaluation of these expressions, in which the generalized forces Q_ϕ and Q_θ consist only of the friction torque in the spin table, $Q_\phi=-sI$ and $Q\theta=0$, yields

$$\frac{d}{dt}[(I+ma^2)\dot{\phi}]+mal\dot{\theta}^2=-sI, \tag{A6}$$

$$\frac{d}{dt}(ml^2\dot{\theta})-mal\dot{\theta}^2=0, \tag{A7}$$

where s is the deceleration rate of the payload due to friction measured at $t=0$.

In order to obtain a difference equation for ϕ as a function of time, integrate Equation A6:

$$[(I+ma^2)\dot{\phi}]_k^{k+1}=-\int_k^{k+1}(sI+mal\dot{\theta}^2)dt.$$

Then

$$(I+m_{k+1}a^2)\dot{\phi}_{k+1}=(I+m_ka^2)\dot{\phi}_k-sI\Delta t-m_kal_k\dot{\theta}_k^2\Delta t. \tag{A8}$$

Represent $\dot{\phi}_{k+1}$ by a forward difference, $(\phi_{k+2}-\phi_{k+1})/\Delta t$, and then solve Equation A8 for ϕ_{k+2}:

$$\phi_{k+2}=\phi_{k+1}+\frac{\Delta t}{I+m_{k+1}a^2}[(I+m_ka^2)\dot{\phi}_k-sI\Delta t-m_kal_k\dot{\theta}_k^2\Delta t]. \tag{A9}$$

Performing the indicated differentiation of the second equation of motion yields

$$m\ddot{\theta}+\dot{m}\dot{\theta}=\frac{1}{l}(ma\dot{\theta}^2-2m\dot{l}\dot{\theta}), \tag{A10}$$

and the left-hand side of this expression is an exact differential which can be expressed as

$$\frac{d}{dt}(m\dot{\theta})=\frac{m\dot{\theta}}{l}(a\dot{\theta}-2\dot{l}). \tag{A11}$$

Integration of Equation A11, by the method of Equation A8, combined with the replacement of $\dot{\theta}_{k+1}$ by a forward difference, gives the relation for θ_{k+2}:

$$\theta_{k+2}=\theta_{k+1}+\dot{\theta}_k\Delta t\frac{m_k}{m_{k+1}}\left[1+(2a\dot{\phi}_k-a\dot{\theta}_k)\frac{\Delta t}{l_k}\right]. \tag{A12}$$

The computer solution is started by calculating the values of ϕ and θ for $t=0$. At $t=0$, $l=0$ and the right-hand side of Equation A12 becomes infinite; thus, an expression must be developed to evaluate θ_{k+2} at the time $t=0$.

From the expanded form of the second equation of motion, Equation A10, an expression for $\dot{\theta}_0$ is determined. Substitution of initial conditions into Equation A10 yields

$$\dot{\theta}_0=2\dot{\phi}_0. \tag{A13}$$

Application of L'Hospital's rule to the term $(2a\dot{\phi}_k-a\dot{\theta}_k)\Delta t/l_k$ from Equation A12 yields, at $t=0$,

$$(2\ddot{\phi}_0-\ddot{\theta}_0)\frac{\Delta t}{\dot{\phi}_0}.$$

From the differentiation in Equation A6 the general expression for the payload angular acceleration is

$$\ddot{\phi}_k=\frac{-\dot{m}_ka^2\dot{\phi}_k-m_kal_k\dot{\theta}_k^2-sI}{I+m_ka^2}, \tag{A14}$$

which can be evaluated at $t=0$:

$$\ddot{\phi}_0=\frac{-\frac{\rho a}{3}\dot{\phi}_0^2-sI}{I+m_0a^2}. \tag{A15}$$

Upon differentiating in Equation A7 and solving for $\ddot{\theta}$, it is found that this expression is undefined at $t=0$; and L'Hospital's rule must be applied again. The resulting expression for $\ddot{\theta}$ at $t=0$ is

$$\ddot{\theta}_0=\frac{-2\rho a\dot{\phi}_0^2}{9m_0}+\frac{4\ddot{\phi}_0}{3}. \tag{A16}$$

A combination of $(2\ddot{\phi}_0-\ddot{\theta}_0)\Delta t/\dot{\phi}_0$ with Equation

A12 yields an expression for θ_2 in terms of the initial conditions:

$$\theta_2=\theta_1+\left[1+\frac{\Delta t(2\ddot{\phi}_0-\ddot{\theta}_0)}{\dot{\phi}_0}\right]\frac{m_0}{m_1}\dot{\theta}_0\Delta t, \quad \text{(A17)}$$

where $\theta_1=\dot{\theta}_0\Delta t+\theta_0$.

The total force in the yo-yo system during the time when it performs essentially as a rigid yo-yo is given by

$$F_k=m_k(a\ddot{\phi}_k+l_k\dot{\theta}_k^2)+\dot{m}_k a\dot{\phi}_k. \quad \text{(A18)}$$

The rigid yo-yo operation is terminated when F becomes greater than $2F_0$, the total preload in the yo-yo springs.

After the tensile force in the yo-yo has exceeded the preload, the yo-yo functions as a stretch yo-yo. The Lagrangian for the stretch yo-yo in phase 1 of yo-yo operation is [3]

$$L=\tfrac{1}{2}I\dot{\phi}^2+\tfrac{1}{2}m(l^2\dot{\theta}^2+a^2\dot{\phi}^2+\dot{\delta}^2-2a\dot{\phi}\dot{\delta})-(k\delta^2+2F_0\delta), \quad \text{(A19)}$$

in which

δ=deflection of a spring,
k=spring constant,
F_0=preload in one spring.

The length of the stretch yo-yo at any time t is a function of the deflection and the amount of spring unwound; thus

$$l=a(\theta-\phi)+\delta; \quad \text{(A20)}$$

whereas the mass remains dependent only on the length of wire unwound,

$$m=m_0+\frac{\rho a}{3}(\theta-\phi).$$

Writing the equations of motion explicitly from the Lagrangian results in:

$$\frac{d}{dt}[(I+ma^2)\dot{\phi}-ma\dot{\delta}]+mal\dot{\theta}^2=-sI, \quad \text{(A21)}$$

$$\frac{d}{dt}(ml^2\dot{\theta})-mal\dot{\theta}^2=0, \quad \text{(A22)}$$

$$\frac{d}{dt}(m\dot{\delta}-ma\dot{\phi})-ml\dot{\theta}^2+2k\delta+2F_0=0. \quad \text{(A23)}$$

[3] Fedor, J. V., "Analytical Theory of the Stretch Yo-Yo for De-Spin of Satellites," NASA Technical Note D-1676, April 1963.

To determine ϕ as a function of time for stretch yo-yo operation, integrate Equations A21 and A23 in the manner of the preceding work to get

$$(I+m_{k+1}a^2)\dot{\phi}_{k+1}-m_{k+1}a\dot{\delta}_{k+1}-(I+m_ka^2)\dot{\phi}_k+m_ka\dot{\delta}_k=-m_kal_k\dot{\theta}_k^2\Delta t-sI\Delta t, \quad \text{(A24)}$$

$$m_{k+1}\dot{\delta}_{k+1}-m_{k+1}a\dot{\phi}_{k+1}-m_k\dot{\delta}_k+m_ka\dot{\phi}_k=m_kl_k\dot{\theta}_k^2\Delta t-2k\delta_k\Delta t-2F_0\Delta t. \quad \text{(A25)}$$

Solve Equation A25 for $m_{k+1}\dot{\delta}_{k+1}$ and substitute into Equation A24, simultaneously replacing $\dot{\phi}_{k+1}$ by a forward difference, $(\phi_{k+2}-\phi_{k+1})/\Delta t$, to get an expression for the angular coordinate of the payload:

$$\phi_{k+2}=\phi_{k+1}+\frac{\Delta t}{I}(I\dot{\phi}_k-sI\Delta t-2ak\delta_k\Delta t-2aF_0\Delta t). \quad \text{(A26)}$$

A treatment of Equation A22 by the same method of integration and substitution yields

$$\theta_{k+2}=\theta_{k+1}+\frac{\Delta t}{m_{k+1}l_{k+1}^2}(m_kal_k\dot{\theta}_k^2\Delta t+m_kl_k^2\dot{\theta}_k), \quad \text{(A27)}$$

where $\dot{\theta}_{k+1}=(\theta_{k+2}-\theta_{k+1})/\Delta t$ as above.

To determine the difference equation for δ, differentiate in Equation A23 as indicated and then simplify to the form:

$$\frac{d}{dt}(m\dot{\delta})=\dot{m}a\dot{\phi}+ma\ddot{\phi}+ml\dot{\theta}^2-2k\delta-2F_0. \quad \text{(A28)}$$

Integrate this expression and substitute a backward difference for $\dot{\delta}$ to get

$$\delta_{k+1}=\delta_k+\frac{\Delta t}{m_{k+1}}[m_k\dot{\delta}_k+(\dot{m}_ka\dot{\phi}_k+m_ka\ddot{\phi}_k+m_kl_k\dot{\theta}_k^2-2k\delta_k-2F_0)\Delta t]. \quad \text{(A29)}$$

This relationship is dependent upon $\ddot{\phi}$, which is determined by differentiating in Equation A21 as indicated and substituting from Equation A28:

$$\ddot{\phi}_k=-\frac{1}{I}(sI+2ka\delta_k+2F_0a). \quad \text{(A30)}$$

If there is no preload in the yo-yo springs the device will function as a stretch yo-yo from the start of the de-spin operation. For this reason it is necessary to be able to evaluate the expressions for ϕ, θ, δ, and $\ddot{\phi}$ at $t=0$. Dif-

ferentiation in Equation A22 gives

$$m\ddot{\theta}+\dot{m}\dot{\theta}=\frac{1}{l}\,(ma\dot{\theta}^2-2ml\dot{\theta}), \qquad \text{(A31)}$$

and substitution of initial conditions yields

$$\dot{\theta}_0=2\dot{\phi}_0,$$

which is also true for rigid yo-yo operation. At $t=0$, Equation A30 reduces to

$$\ddot{\phi}_0=-s, \qquad \text{(A32)}$$

which is compatible with the physics of the problem in that the payload is decelerating because of friction at $t=0$. The deflection equation becomes

$$\delta_1=\frac{\Delta t^2}{m_1}\,(\dot{m}_0a\dot{\phi}_0+m_0a\ddot{\phi}_0), \qquad \text{(A33)}$$

at $t=0$. Equation A26 for the payload angular coordinate takes the form:

$$\phi_2=\phi_1+\frac{\Delta t}{I}\,(I\dot{\phi}_0-sl\Delta t), \qquad \text{(A34)}$$

for $t=0$. Equation A27 for θ cannot be evaluated at $t=0$; thus, another formulation of the problem must be considered. Rewrite Equation A31:

$$\frac{d}{dt}\,(m\dot{\theta})=\frac{1}{l}\,(ma\dot{\theta}^2-2ml\dot{\theta}).$$

Then integrate and make a forward difference substitution for $\dot{\theta}$:

$$\theta_{k+2}=\theta_{k+1}+\dot{\theta}_k\Delta t\,\frac{m_k}{m_{k+1}}\left[1+(2a\dot{\phi}_k-a\dot{\theta}_k-2\dot{\delta}_k)\,\frac{\Delta t}{l_k}\right]. \qquad \text{(A35)}$$

This equation cannot be directly evaluated at $t=0$. Apply L'Hospital's rule and initial conditions to the quantity $(\Delta t/l_k)\,(2a\dot{\phi}_k-a\dot{\theta}_k-2\dot{\delta}_k)$ to get $(2\ddot{\phi}_0-\ddot{\theta}_0)\Delta t/\dot{\phi}_0$, where $\ddot{\theta}_0$ is found from Equation A31 by the same method used in deriving Equation A16:

$$\ddot{\theta}_0=\frac{-2\rho a\dot{\phi}_0^2}{9m_0}+\frac{4\ddot{\phi}_0}{3}. \qquad \text{(A36)}$$

And we have for Equation A35

$$\theta_2=\theta_1+\left[1+\frac{\Delta t}{\dot{\phi}_0}\,(2\ddot{\phi}_0-\ddot{\theta}_0)\right]\frac{m_0}{m_1}\,\dot{\theta}_0\Delta t, \qquad \text{(A37)}$$

with $\ddot{\phi}_0$ from Equation A32 and $\ddot{\theta}_0$ from Equation A36.

Phase 1 of the yo-yo operation is terminated when the entire yo-yo is unwound from the payload. The computer terminates the program when the relation

$$[B-a(\theta_k-\phi_k)]=0 \qquad \text{(A38)}$$

is satisfied, where B is the length of the yo-yo and $a(\theta_k-\phi_k)$ is the length of yo-yo unwound at time $t=t_k$.

An analysis of phase 2 of the yo-yo has been omitted from this report. Since the equations are similar to those for phase 1[4] and the computer solution of phase 1 was sufficiently close to the test data, it was felt that solution of the phase 2 equations would not add sufficient information to the report to warrant the additional effort involved.

The computer program is outlined on the following pages in the form of a block diagram, Figure A2, and a listing of the program in

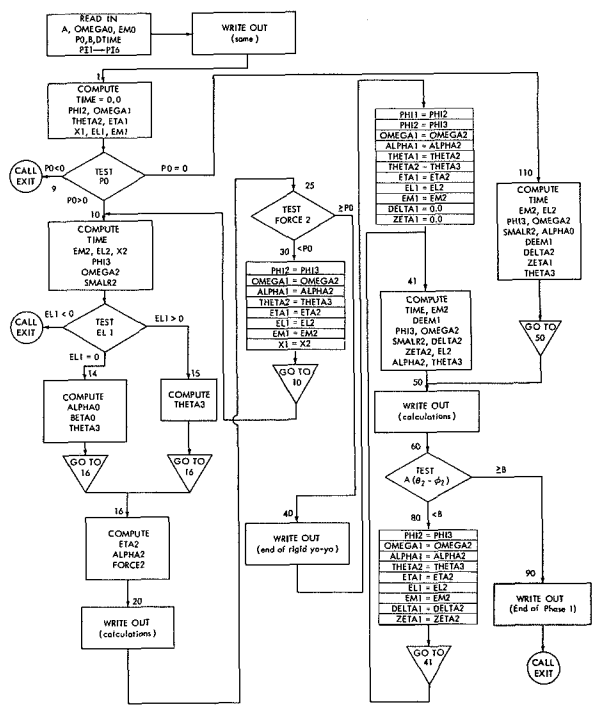

FIGURE A2.—Flow chart for the solution of the phase 1 equations of motion of the stretch yo-yo for the IBM 7090 digital computer.

[4] Fedor, J. V., "Analytical Theory of the Stretch Yo-Yo for De-Spin of Satellites," NASA Technical Note D-1676, April 1963.

Table A1

Fortran Computer Program for Phase 1.

```
*  W.R.MENTZER      MECHANICAL SYSTEMS BRANCH      G.S.F.C.
*      XEQ
*      CARDS COLUMN
*      LIST 8
C      STRETCH YO YO     PHASE 1
 1001 FORMAT(3XF6.4,2XF8.4,3XF8.6,3XF7.4,3XF7.4,3XF7.5,2XF6.3/4XF9.8,3XF
     C9.6,3XF10.8,3XF7.3,3XF6.3)
 1002 FORMAT(6X1HA,5X6HOMEGA0,6X3HEMO,9X2HP0,7X1HB,8X5HDTIME,6X3HPI1,6X3
     CHPI2,9X3HPI3,9X3HPI4,6X3HPI5,6X3HPI6/3XF6.4,2XF8.4,3XF8.6,3XF7.4,3
     CXF7.4,3XF7.5,2XF6.3,2XF9.8,3XF9.6,3XF10.8,3XF5.2,2XF6.3///)
 1003 FORMAT(1H1,20X51HPROGRAM FOR THE TEST OF THE STRETCH YO YO   PHASE
     C1 //5X4HTIME,4X10HSPIN RATIO,4X9HSPIN RATE,6X3HPHI,6X12HACCELERATI
     CON,5X5HTHETA,8X6HLENGTH,5X10HDEFLECTION,5X4HMASS,6X5HFORCE/5X5HISE
     CC),17X9H(RAD/SEC),5X5H(RAD),5X13H(RAD/SEC/SEC),4X5H(RAD),9X4H(FT),
     C9X4H(FT),7X7H(SLUGS),5X4H(LB)///)
 1004 FORMAT(3XF7.4,2XF11.8,3XF10.6,3XF10.7,3XF10.7,3XF10.7,3XF10.6,2XF1
     C1.8,3XF9.8,2XF7.4/)
 1005 FORMAT(///6X31HEND OF OPERATION AS RIGID YO YO )
 1006 FORMAT(3XF7.4,2XF11.8,3XF10.6,3XF10.7,3XF10.7,3XF10.7,3XF10.6,2XF1
     C1.8,3XF9.8/)'
 1007 FORMAT(///6X14HEND OF PHASE 1 )
 1008 FORMAT(6X12HNEGATIVE EL1)
      READ  INPUT  TAPE 2,100I,A,OMEGA0,EMO,P0,B,DTIME,PI1,PI2,PI3,PI4,P
     CI5,PI6
      WRITE OUTPUT TAPE 3,1002,A,OMEGA0,EMO,P0,B,DTIME,PI1,PI2,PI3,PI4,P
     CI5,PI6
      WRITE OUTPUT TAPE 3,1003
      J=1
    1 TIME=0.0
      FORCE1=0.0
      EM1=EMO
      EL1=0.0
      OMEGA1=OMEGA0
      PHI1=0.0
      PHI2=OMEGA1*DTIME
      ETA1= 2.0*OMEGA0
      THETA1=0.0
      THETA2=ETA1*DTIME
      X1=PI1+EM1*A**2
      IF (P0)      9,110,10
    9 CALL EXIT
  110 TIME=TIME+DTIME
      DELTA1=0.0
      ZETA1=0.0
      EM2=EMO+PI2*(THETA2-PHI2)
      EL2=A*(THETA2-PHI2)
      PHI3=PHI2+(DTIME/PI1)*(PI1*OMEGA1-PI4*DTIME)
      OMEGA2=(PHI3-PHI2)/DTIME
      SMALR2=OMEGA2/OMEGA0
      ALPHA1= -PI4/PI1
      DEEM1=(EM2-EM1)/DTIME
      DELTA2=(DTIME**2/EM2)*(DEEM1*A*OMEGA1+EM1*A*ALPHA1)
      ZETA2=(DELTA2-DELTA1)/DTIME
      BETA1=-(2.0*PI2*OMEGA1**2)/(3.0*EMO)+(4.0*ALPHA1)/3.0
      THETA3=THETA2+DTIME*ETA1*(EM1/EM2)*(1.0+(DTIME/OMEGA1)*(2.0*ALPHA1
     C-BETA1))
      ALPHA2=-(1.0/PI1)*(PI4+A*PI5*DELTA2+PI6*A)
      GO TO 50
   10 TIME=TIME+DTIME
      EM2=EMO+PI2*(THETA2-PHI2)
      EL2=A*(THETA2-PHI2)
      X2=PI1+EM2*A**2
      PHI3=PHI2+(DTIME/X2)*(X1*OMEGA1-PI4*DTIME-EM1*A*EL1*ETA1**2*DTIME)
      OMEGA2=(PHI3-PHI2)/DTIME
      SMALR2=OMEGA2/OMEGA0
      IF (EL1)      13,14,15
   13 WRITE OUTPUT TAPE 3,1008
      CALL EXIT
   14 ALPHA1=-(PI2*A**2*OMEGA1**2 +PI4)/X1
      BETA1=-(2.0*PI2*OMEGA1**2)/(3.0*EMO)+(4.0*ALPHA1)/3.0
      THETA3=THETA2+DTIME*ETA1*(EM1/EM2)*(1.0+(DTIME/OMEGA1)*(2.0*ALPHA1
     C -BETA1))
      GO TO 16
   15 THETA3=THETA2+DTIME*ETA1*(EM1/EM2)*(1.0+(2.0*A*OMEGA1-A*ETA1)*(DTI
     CME/EL1))
      GO TO 16
   16 ETA2=(THETA3-THETA2)/DTIME
      ALPHA2=-(PI2*A**2*OMEGA2*(ETA2-OMEGA2)+EM2*A*EL2*ETA2**2+PI4)/X2
      EM3=EMO+PI2*(THETA3-PHI3)
      DEEM2=(EM3-EM2)/DTIME
      FORCE2=EM2*(A*ALPHA2+EL2*ETA2**2)+A*DEEM2*OMEGA2
   20 IF(51 - J)      21,22,23
   21 CALL EXIT
   22 WRITE OUTPUT TAPE 3,1003
      WRITE OUTPUT TAPE 3,1004, TIME,SMALR2,OMEGA2,PHI2,ALPHA2,THETA2,FL
     C2,DELTA2,EM2,FORCE2
      J=1
      GO TO 25
   23 WRITE OUTPUT TAPE 3,1004, TIME,SMALR2,OMEGA2,PHI2,ALPHA2,THETA2,EL
     C2,DELTA2,EM2,FORCE2
      J=J+1
      GO TO 25
   25 IF(P0-FORCE2)  40,40,30
   30 PHI2=PHI3
      OMEGA1=OMEGA2
      ALPHA1=ALPHA2
      THETA2=THETA3
      ETA1=ETA2
      EL1=EL2
      EM1=EM2
      X1=X2
      GO TO 10
   40 WRITE OUTPUT TAPE 3,1005
      PHI1=PHI2
      PHI2=PHI3
      OMEGA1=OMEGA2
      ALPHA1=ALPHA2
      THETA1=THETA2
      THETA2=THETA3
      ETA1=ETA2
      EL1=EL2
      EM1=EM2
      DELTA1=0.0
      ZETA1=0.0
      WRITE OUTPUT TAPE 3,1003
      J=1
   41 TIME=TIME+DTIME
      EM2=EMO+PI2*(THETA2-PHI2)
      DEEM1=(EM2-EM1)/DTIME
      PHI3=PHI2+(DTIME/PI1)*(PI1*OMEGA1-PI4*DTIME-A*PI5*DELTA1*DTIME-PI6
     C*A*DTIME)
      OMEGA2=(PHI3-PHI2)/DTIME
      SMALR2=OMEGA2/OMEGA0
      DELTA2=DELTA1+(DTIME/EM2)*(EM1*ZETA1+(DEEM1*A*OMEGA1+EM1*A*ALPHA1+
     CEM1*EL1*ETA1**2-PI5*DELTA1-PI6)*DTIME)
      ZETA2=(DELTA2-DELTA1)/DTIME
      EL2=A*(THETA2-PHI2)+DELTA2
      ALPHA2= -(1.0/PI1)*(PI4+A*PI5*DELTA2+PI6*A)
      THETA3=THETA2+(DTIME/(EM2*EL2**2))*(EM1*A*EL1*ETA1**2*DTIME+EM1*EL
     C1**2*ETA1)
      ETA2=(THETA3-THETA2)/DTIME
   50 IF( 51 - J)      51,52,53
   51 CALL EXIT
   52 WRITE OUTPUT TAPE 3,1003
      WRITE OUTPUT TAPE 3,1006, TIME,SMALR2,OMEGA2,PHI2,ALPHA2,THETA2,EL
     C2,DELTA2,EM2
      J=1
      GO TO 60
   53 WRITE OUTPUT TAPE 3,1006, TIME,SMALR2,OMEGA2,PHI2,ALPHA2,THETA2,EL
     C2,DELTA2,EM2
      J=J+1
      GO TO 60
   60 IF(B-A*(THETA2-PHI2))  90,90,80
   80 PHI2=PHI3
      OMEGA1=OMEGA2
      ALPHA1=ALPHA2
      THETA2=THETA3
      ETA1=ETA2
      EL1=EL2
      EM1=EM2
      DELTA1=DELTA2
      ZETA1=ZETA2
      GO TO 41
   90 WRITE OUTPUT TAPE 3,1007
      CALL EXIT
      END
*     DATA


      THE DATA CARDS FOR THIS PROGRAM USING THE DATA FROM TEST III  OF
      FEB. 7 1962  ARE AS FOLLOWS

      A      OMEGA0       EMO          P0          B          DTIME       PI1
    .942     16.8300     .033850      3.8000      2.3650      .0002      2.885

         PI2           PI3           PI4          PI5          PI6
    .00336171     49.060077     .40181588     23.860       3.800
```

TABLE A1.—Fortran computer program for phase 1.

Fortran for the IBM 7090, Table A1. The nomenclature for the program is as follows:

ϕ=PHI,	$\dot{\phi}$=OMEGA,	$\ddot{\phi}$=ALPHA,
θ=THETA,	$\dot{\theta}$=ETA,	$\ddot{\theta}$=BETA,
δ=DELTA,	$\dot{\delta}$=ZETA,	
l=EL,		
m=EM,	$\dot{m}$=DEEM,	
F=FORCE,		
t=TIME,		

and in the input data:

a=A,	l_{SPRING}=B,	$(I+m_0a^2)\dot{\phi}_0$=PI3,
$\dot{\phi}_0$=OMEGAO,	Δt=DTIME,	sI=PI4,
m_0=EMO,	I=PI1,	$2k$=PI5,
$2F_0$=PO,	$\rho a/3$=PI2,	$2F_0$=PI6.

A METHOD TO OPTIMIZE THE SOLAR CELL POWER SUPPLY FOR INTERPLANETARY SPACECRAFT[1]

GRADY B. NICHOLS
Goddard Space Flight Center

The purpose of this paper is to present a generalized approach to the development of an optimized solar cell power supply. This method was developed for use on a spin-stabilized spacecraft requiring no control system or orientation mechanism for the solar panels. An optimized power supply is considered to be one that has the proper orientation of solar panels for maximum power output with minimum solar cell weight. In the method described here the area of each solar panel is expressed as a vector in general terms; the solar energy is also expressed as a vector. The power output at any instant is then merely the summation of the dot (inner) product of each area vector and the solar vector.

INTRODUCTION

The power supply for an interplanetary spacecraft warrants special consideration for two main reasons. First, and most important, the power supply must deliver the necessary power to operate the electrical components of the spacecraft throughout its expected lifetime. Second, the power supply constitutes a large portion of the available useful weight of the spacecraft.

The design of a power supply that will deliver the necessary power for a given trajectory is no great problem. However, there is no assurance that the required power has been delivered with a minimum weight of the solar panels. The expression for the power output at any point in the trajectory will contain two variables, panel area and panel angular orientation. These two variables are determined by the simultaneous evaluation of the expressions for the power output at the two points in the trajectory where the power minima occur.

For a class 1, type 1 trajectory the points of power minima generally occur at launch and at impact. If the points are at other places in the trajectory, reiterations will be necessary to determine the optimum power supply.

This report describes the calculations necessary to determine the minimum area and proper orientation of the solar collectors on a spin-stabilized spacecraft. A typical spacecraft and interplanetary trajectory are shown in Figures 1 and 2. In the calculations the area of an equivalent nonrotating solar collector is deter-

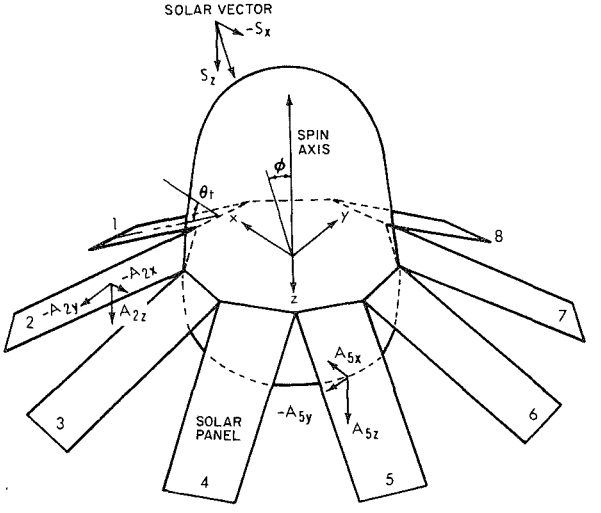

FIGURE 1.—Spacecraft with typical solar panel locations.

[1] A related discussion may be found in "Theoretical Considerations of a Solar Cell Generator on a Satellite," NASA Technical Note D-1904, By Bernard J. Saint-Jean.

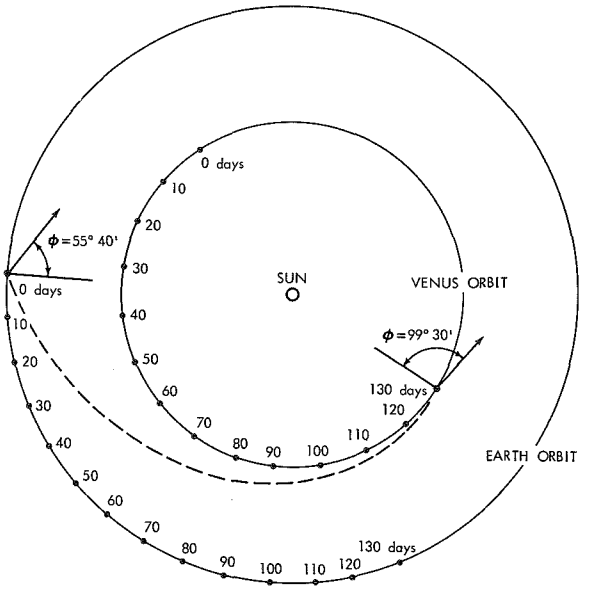

FIGURE 2.—Typical trajectory (type 1, class 1).

mined. (The individual area vectors are described in Appendix A.) This equivalent area is chosen to eliminate the necessity of considering the rotation of the spacecraft when the power equations are evaluated. The rotation of the spacecraft can be neglected because the response time of solar cells is very small when compared with the period of rotation of the spacecraft. A sample calculation for a 130 day flight to Venus is given in Appendix B. For this example a total solar panel area of 50.7 ft^2 is required to deliver 100 watts.

INITIAL CONSIDERATIONS

The following symbols are used in this report:

A_n=area vector normal to each panel $=A_{nx}i+A_{ny}j+A_{nz}k$.

d=degradation of solar cells due to temperature (0.6 percent for each degree above 25° C).

i, j, k=unit vectors in the x, y, z directions of the coordinate system.

P=power output from the solar cell power supply.

p=packing factor (negative value of the percentage of panel area containing active solar cells).

S=solar vector=$S_xi+S_yj+S_zk$.

η=solar cell conversion efficiency—watts (electrical)/watts (solar).

θ_t=angle between each solar panel and the x–y plane of the spacecraft's coordinate system.

ϕ=angle between the spin axis and the spacecraft-sun line.

Figure 3 shows A_n, S, θ_t, ϕ, and the coordinate system.

These assumptions are made:

1. The angle ϕ varies as a function of time throughout the trajectory.
2. The power output from a solar cell varies as the product of the solar constant and the cosine of the angle between the sun rays and the normal to the solar panel.
3. The spacecraft has n attachment points (n solar panels equally spaced around the circumference).
4. The solar panels must be folded and stored during launch, and deployed after injection.
5. The spacecraft trajectory is known. A sample trajectory, class 1, type 1, is shown in Figure 2:
   (a) For a type 1 trajectory the spacecraft travels less than half of an orbit around the sun, and for type 2 it travels more than half of an orbit.
   (b) For a class 1 trajectory the vehicle impacts the target on the first orbital intersection, and for class 2 it impacts on the second orbital intersection.

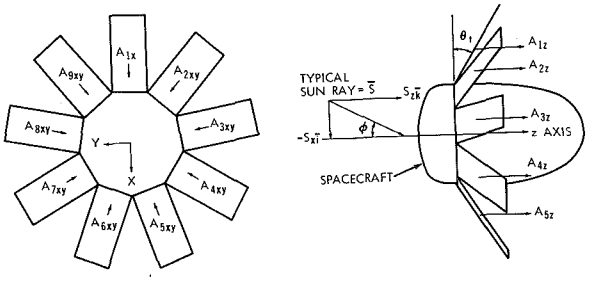

FIGURE 3.—Coordinate system and solar panel orientation.

THE POWER SUPPLY

The general orientation of the solar panels around the spacecraft (Fig. 1) was chosen because the power output from a single panel varies over a large range as the angle to the sun rays changes (cosine law). For any single panel, the power output varies from a maximum to zero as the angle of the sun with the normal to the panel varies from 0 to 90 degrees. If the variation of the sun angle is large several panels, each with a different orientation, must be used to insure that the required power is always delivered.

Since the power output from a solar panel is a function of the area of the panel, the solar constant, and the cosine of the angle between the sun and the normal to the panel, the power output readily lends itself to the use of vectors. If the area of each panel is expressed as a vector normal to the surface and the solar constant also is expressed as a vector, the total power output is the dot (inner) product of the area vectors and the solar constant or

$$P=\sum_{n=1}^{n_{\max}} S\cdot A_n.$$

CHOICE OF COORDINATE SYSTEM

When the trajectory of a spacecraft has been determined, the angle ϕ between the spin axis of the spacecraft and the spacecraft-sun line is known. This suggests a coordinate system centered on the spacecraft with the z axis coinciding with the spin axis. With this choice of a coordinate system, the angle ϕ determines the solar vector.

The x axis is chosen so that the solar vector always lies in the x–z plane (no y component). There is no loss of generality with this choice; it merely reduces the number of computations required. The y axis is chosen perpendicular to the x–z plane, generating a right-hand coordinate system.

SOLAR PANELS REPRESENTED AS VECTORS

With n solar panels spaced around the circumference of a spacecraft, n area vectors can be described. For a smooth power output as the spacecraft spins, the solar panels should be equally spaced around the spacecraft. Each area can be represented as a vector with the following components:

$$A_{nx}i+A_{ny}j+A_{nz}k.$$

Power output from the solar cell power supply varies as the spacecraft spins. The solar panels, spaced symmetrically about the z axis, maintain a constant area component in the z direction. The solar panels are not symmetric with respect to the x or to the y axis at all times. The x and y axes remain fixed in space, and the spacecraft spins in this coordinate system.

The area vectors spinning with the spacecraft in the stationary coordinate system could each be described as a vector rotating around the spin axis (z axis) with the spin rate of the spacecraft. But the response time of solar cells to solar energy is very short (1 millisecond). Therefore, it is equally valid to determine the variation in total effective area exposed to the solar energy as a function of the angular position of the spacecraft around the z axis, and consider the spacecraft to be stationary in the x–y plane at the position where a minimum area is exposed to solar energy.

The point where maximum or minimum effective area is exposed to solar energy can be determined by expressing the n area vectors as previously described with an arbitrary angular displacement ϵ. Then the first derivative of the expression for the total effective area

$$\sum_{n=1}^{n_{\max}} A_n$$

is taken and equated to zero, and the points of maximum and minimum effective area are determined. A sample calculation for the maximum and minimum areas for nine solar panels is included in Appendix A.

The area vectors contain the following information:

1. The area and orientation of each solar panel.
2. The solar cell conversion efficiency η.
3. The packing factor p.
4. The degradation due to temperature d.

The area vectors contain a constant A' such that

$$A' = A_n \eta p d;$$

η and p are known, and d can be determined once the temperature distribution is known.

DESCRIPTION OF THE METHOD

The output from the power supply at any time along the trajectory can be expressed as

$$P = \sum_{n=1}^{n_{max}} S \cdot A_n.$$

In evaluating this summation, all vectors that have a negative power contribution are neglected. The negative sign occurs because the panel is not illuminated by solar energy. Once the trajectory is known, the solar vector can readily be determined. This expression for power output contains two variables, θ_t and A_n. For evaluating these quantities, two equations are required. The equations should be evaluated at the two points where minimum power is delivered from the power supply. For a class 1, type 1 trajectory these points generally occur at launch and impact. Therefore, we will assume these points as the points at which to evaluate the power output in order to solve for the quantities A_n and θ_t. It is also necessary to assume the number of solar panels that are illuminated by solar energy.

By solving for A_n and θ_t, with the use of the original assumptions, a curve for power output as a function of flight time is generated. If the distribution curve confirms the original assumptions of minimum points and the number of active solar cells, the optimum power supply has been determined. If the original assumptions were not correct, the power equations are evaluated at the minimum points determined from the initial power distribution curve. Then it is necessary to again make an assumption on the number of active solar panels. The spin axis orientation at the two power minima and the general orientation of the solar panels must be kept in mind when these assumptions are made.

After the first iteration the assumption concerning the number of active panels is checked. If correct, the design is determined; if not, an additional iteration is required.

CONCLUDING REMARKS

This paper describes a systematic approach to the design of an optimum solar cell power supply. The method greatly reduces the work required to develop a power supply, compared with a conventional trial and error approach.

A more important factor to consider is that this method could be adapted readily to digital computer solutions. In programming the iteration process, the only input information necessary for determining a power supply for any space flight would be:

1. Trajectory.
2. Power requirement.
3. Injection angle.
4. Spacecraft spin axis reorientation, if required.

Further, for any launch window, a family of curves could be generated that would describe the optimum power supply as a function of the injection angle and the trajectory.

Appendix A

DETERMINATION OF THE MINIMUM AND MAXIMUM AREAS IN THE X DIRECTION

For this example assume 9 solar panels, $\eta=8.5$ percent, $p=90$ percent, and $d=51.2$ percent, Then

$$A'=A_n(0.085)(0.9)(0.512)=A_n(0.0392).$$

The area vectors can be expressed as follows (Figure 3):

$$A_1=A' \sin\theta_t i \quad +0j \quad +A' \cos\theta_t k,$$
$$A_2=A' \cos 40^\circ \sin\theta_t i + A' \sin 40^\circ \sin\theta_t j + A' \cos\theta_t k,$$
$$A_3=A' \cos 80^\circ \sin\theta_t i + A' \sin 80^\circ \sin\theta_t j + A' \cos\theta_t k,$$
$$A_4=A' \cos 120^\circ \sin\theta_t i + A' \sin 120^\circ \sin\theta_t j + A' \cos\theta_t k,$$
$$A_5=A' \cos 160^\circ \sin\theta_t i + A' \sin 160^\circ \sin\theta_t j + A' \cos\theta_t k,$$
$$A_6=A' \cos 200^\circ \sin\theta_t i + A' \sin 200^\circ \sin\theta_t j + A' \cos\theta_t k,$$
$$A_7=A' \cos 240^\circ \sin\theta_t i + A' \sin 240^\circ \sin\theta_t j + A' \cos\theta_t k,$$
$$A_8=A' \cos 280^\circ \sin\theta_t i + A' \sin 280^\circ \sin\theta_t j + A' \cos\theta_t k,$$
$$A_9=A' \cos 320^\circ \sin\theta_t i + A' \sin 320^\circ \sin\theta_t j + A' \cos\theta_t k.$$

The power output is directly proportional to the area of solar panels exposed to solar energy. Therefore, the maximum and minimum areas will be determined. The solar vector has only x and z components; the area in the z direction is constant because of symmetry.

For a power supply consisting of 9 panels, the maximum number of panels illuminated in the x direction is 5. Assume an arbitrary angular displacement between the number 1 panel and the x axis of ϵ. The total area exposed in the x direction is

$$A_T=\Sigma A_{nx}$$

where $n=1, 2, 3, 8,$ and 9;

$$A_{1x}=A' \cos(\epsilon+0) \sin\theta_t,$$
$$A_{2x}=A' \cos(\epsilon+40^\circ) \sin\theta_t,$$
$$A_{3x}=A' \cos(\epsilon+80^\circ) \sin\theta_t,$$
$$A_{8x}=A' \cos(\epsilon+280^\circ) \sin\theta_t,$$
$$A_{9x}=A' \cos(\epsilon+320^\circ) \sin\theta_t.$$

Expanding the expressions yields:

$$A_{1x}=A' \sin\theta_t (\cos\epsilon \cos 0 - \sin\epsilon \sin 0),$$
$$A_{2x}=A' \sin\theta_t (\cos\epsilon \cos 40^\circ - \sin\epsilon \sin 40^\circ),$$
$$A_{3x}=A' \sin\theta_t (\cos\epsilon \cos 80^\circ - \sin\epsilon \sin 80^\circ),$$
$$A_{8x}=A' \sin\theta_t (\cos\epsilon \cos 280^\circ - \sin\epsilon \sin 280^\circ),$$
$$A_{9x}=A' \sin\theta_t (\cos\epsilon \cos 320^\circ - \sin\epsilon \sin 320^\circ).$$

Therefore,

$$\begin{aligned}\Sigma A_{nx} &= A' \sin\theta_t [\cos\epsilon (\cos 0+\cos 40^\circ+\cos 80^\circ \\ &\quad +\cos 280^\circ+\cos 320^\circ) - \sin\epsilon (\sin 0 \\ &\quad +\sin 40^\circ+\sin 80^\circ+\sin 280^\circ \\ &\quad +\sin 320^\circ)] \\ &= A' \sin\theta_t (2.88 \cos\epsilon - 0 \sin\epsilon) \\ &= 2.88 A' \sin\theta_t \cos\epsilon;\end{aligned}$$

$$\frac{d\Sigma A_{nx}}{d\epsilon} = -2.88 A' \sin\theta_t \sin\epsilon,$$

$$\frac{d^2\Sigma A_{nx}}{d\epsilon^2} = -2.88 A' \sin\theta_t \cos\epsilon.$$

Setting $d\sum A_{nx}/d\epsilon=0$ and solving for ϵ yields

$$-2.88A' \sin \theta_t \sin \epsilon=0,$$

$$\epsilon=0°;\ 180°.$$

Since $d^2\sum A_{nx}/d\epsilon^2$ is negative the point $\epsilon=0$ is a maximum.

Because the entire area exposed $(A_x+A_y+A_z)$ is constant, and the area exposed in the z direction is also constant (symmetry), the area in the y direction is a minimum when that in the x direction is a maximum. Therefore, to determine the point where minimum area is exposed in the x direction, set $\epsilon=90°$. Because of the particular panel orientation the 90° rotation is equivalent to a 10° rotation.

The minimum area exposed in the x direction is

$$A_{\min}=\sum A_{nx};$$

$$A_{1x}=A' \cos 10° \sin \theta_t,$$

$$A_{2x}=A' \cos 50° \sin \theta_t,$$

$$A_{3x}=A' \cos 90° \sin \theta_t,$$

$$A_{8x}=A' \cos 290° \sin \theta_t,$$

$$A_{9x}=A' \cos 330° \sin \theta_t.$$

Then

$$A_{\min}=A' \sin \theta_t (\cos 10°+\cos 50°+\cos 90°+\cos 290°+\cos 330°)$$

$$=2.836A' \sin \theta_t;$$

also

$$A_{\max}=2.879A' \sin \theta_t.$$

Then the percentage of the variation in the area exposed is

$$\frac{A_{\max}-A_{\min}}{A_{\max}}=\frac{0.044}{2.879}=1.53 \text{ percent.}$$

For this small variation of 1.5 percent, the panel orientation is arbitrary.

Appendix B

SAMPLE CALCULATION

Consider a class 1, type 1 trajectory for a space flight to Venus continuously requiring 100 watts of power. The variation of the angle between the spin axis and the sun rays for a typical trajectory is shown in Table B1.

The following steps are required to determine the optimum power supply:

1. Assume two points in the trajectory where a minimum power output should occur.
2. Determine the number of active solar panels at each point.
3. Generate the expressions for the power output at these two points (this yields two equations, each with two unknowns); solve for A'.
4. Evaluate to see whether the assumption of item 2 holds. If it does, proceed; if not, correct and then recalculate A and θ_t.
5. With the correct values for A' and θ_t generate a curve for power output as a function of flight time (see Table B2 and Fig. B1).
6. From this power distribution curve evaluate to check item 1. If step 1 checks, the optimum power supply has been determined. If it does not check, evaluate step 3 using the points of power minimum indicated in step 5 and recalculate steps 4, 5, and 6. The optimum power supply has now been determined.
7. Generate the power distribution curve for the optimum power supply design (Table B3 and Fig. B1).

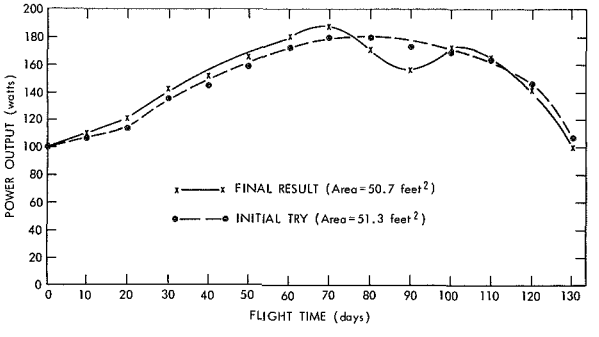

FIGURE B1.—Power output as a function of time (power required = 100 watts).

TABLE B1.—*Variation of the Solar Vector During the Flight*

Time (days)	ϕ	Solar constant (watt/cm²) [1]	Solar vector [1]
0	55°40′	0.135	$0.112i+0.077k$
10	47°	.137	$0.099i+0.092k$
20	38°	.140	$0.087i+0.110k$
30	28°40′	.147	$0.069i+0.130k$
40	19°10′	.150	$0.049i+0.140k$
50	9°10′	.157	$0.023i+0.153k$
60	1°30′	.167	$0\ \ i+0.167k$
70	12°40′	.178	$0.038i+0.174k$
80	24°30′	.192	$0.079i+0.174k$
90	37°30′	.207	$0.125i+0.163k$
100	51°20′	.224	$0.174i+0.140k$
110	66°10′	.241	$0.220i+0.097k$
120	82°30′	.256	$0.253i+0.033k$
130	99°30′	.267	$0.263i+0.043k$

[1] The solar constant varies as $1/R^2$, and the solar vector components vary because ϕ varies throughout the trajectory for a spin-stabilized spacecraft.

From the calculations, at launch the solar constant is a minimum and ϕ is large. This should be a minimum power point. The solar constant varies slowly with time throughout the trajectory. The solar constant is a maximum at the target planet and the angle ϕ is very large. Therefore this should be a minimum also.

Now that the points of minimum have been selected, estimate the number of active solar

TABLE B2.—*Values To Be Used in Determining the Power Distribution Curve*

Time (days)	Solar vector	P_x	P_z	Power output (watts)
0	$0.112i+0.077k$	55.5	44.5	100.0
10	$0.099i+0.092k$	32.1	74.2	106.3
20	$0.087i+0.110k$	28.2	88.2	116.4
30	$0.069i+0.130k$	−0.0	134.1	134.1
40	$0.049i+0.140k$	0	144.9	144.9
50	$0.023i+0.153k$	0	158.4	158.4
60	$0i+0.167k$	0	172.8	172.8
70	$0.038i+0.174k$	0	180.0	180.0
80	$0.079i+0.174k$	0	180.0	180.0
90	$0.125i+0.163k$	40.6	130.9	171.5
100	$0.174i+0.140k$	56.4	112.7	169.1
110	$0.220i+0.097k$	109.4	55.5	164.9
120	$0.253i+0.033k$	125.9	19.0	144.9
130	$0.263i+0.043k$	130.8	−24.5	106.3

panels at each point by examining the general configuration of the solar panels. Five should be active at launch, and three should be active at impact. Now generate the expression for P_L and P_I (power output at launch and impact):

$$P_L=\sum S\cdot A_n$$
$$=0.112(1+2\cos 40°+2\cos 80°)A'\sin\theta_t+0.077(5)A'\cos\theta_t$$
$$=(0.112)(2.88)A'\sin\theta_t+(0.077)(5)A'\cos\theta_t$$
$$=0.323A'\sin\theta_t+0.385A'\cos\theta_t$$
$$=100 \text{ watts}, \qquad \text{(B1)}$$

where $n=1, 2, 3, 8,$ and 9;

$$P_I=\sum S\cdot A_n$$
$$=0.263(1+2\cos 40°)A'\sin\theta_t-0.043(3)A'\cos\theta_t$$
$$=0.665A'\sin\theta_t-0.129A'\cos\theta_t$$
$$=100 \text{ watts}, \qquad \text{(B2)}$$

where $n=1, 2,$ and 9. From Equation B2

$$A'=\frac{100}{0.665\sin\theta_t-0.129\cos\theta_t}.$$

Substituting into Equation B1 yields:

TABLE B3.—*Power Distribution*

Time (days)	P_x	P_y	Power output (watts)
0	53.4	46.5	99.9
10	31.1	77.3	108.4
20	27.3	92.4	119.7
30	0	140.4	140.4
40	0	151.2	151.2
50	0	165.6	165.6
60	0	180.6	180.6
70	0	188.1	188.1
80	24.8	146.3	171.1
90	59.0	98.0	157.0
100	54.0	117.6	172.0
110	105.2	58.5	163.7
120	121.0	20.0	141.0
130	125.9	−26	99.9

$$(0.323)(100)\sin\theta_t+(0.385)(100)\cos\theta_t$$
$$=100(0.665\sin\theta_t-0.129\cos\theta_t);$$
$$34.2\sin\theta_t=51.4\cos\theta_t;$$
$$\tan\theta_t=\frac{51.4}{34.2}=1.5029;$$
$$\theta_t=56°22'.$$

Therefore $\sin\theta_t=0.8326$ and $\cos\theta_t=0.5539$. Solving for A' yields

$$A'=\frac{100}{0.665\sin\theta_t-0.129\cos\theta_t}$$
$$=\frac{100}{0.5536-0.0714}$$
$$=\frac{100}{0.4822}=207.4.$$

Then (from Appendix A)

$$A_n=\frac{A'}{0.0392}=\frac{207.2}{0.0392}=5290 \text{ cm}^2;$$

and

$$A_t=9A_n=47.610 \text{ cm}^2=51.3\text{ft}^2.$$

To check the assumptions, generate the dot product of the solar vector and the area vectors, neglecting the negative vector contributions:

$$P=\sum_{n=1}^{9} S\cdot A_n.$$

The curve for power output as a function of flight time for this condition, and the values used in determining it, are shown in Table B2 and Figure B1. The contributions from the area vectors (θ_t and A_n now known) at launch and impact are calculated from the following:

$$A_1=+172.7i+0j\quad+114.9k,$$

$$A_2=+132.3i+111.0j+114.9k,$$

$$A_3=+30.0i\ +170.1j+114.9k,$$

$$A_4=-86.4i\ +149.6j+114.9k,$$

$$A_5=-162.3i+59.1j\ +114.9k,$$

$$A_6=-162.3i+59.1j\ +114.9k,$$

$$A_7=-86.4i\ +149.6j+114.9k,$$

$$A_8=+30i\quad-170j\ +114.9k,$$

$$A_9=+132.3i-111.0j+114.9k,$$

$$S_L=0.112i+0j+0.077k,$$

$$S_I=0.263i+0j-0.043k.$$

The launch power contributions are:

$$A_1=19.3\quad+8.8=28.1,$$

$$A_2=14.8\quad+8.8=23.6,$$

$$A_3=3.3\quad+8.8=12.1,$$

$$A_4=-9.7\ +8.8=-0.9,$$

$$A_5=-18.2+8.8=-9.4,$$

$$A_6=-18.2+8.8=-9.4,$$

$$A_7=-9.7\ +8.8=-0.9,$$

$$A_8=+3.3\ +8.8=+12.1,$$

$$A_9=+14.8+8.8=+23.6.$$

The impact power contributions are:

$$A_1=45.4\quad-4.9=+40.5,$$

$$A_2=34.8\quad-4.9=+29.9,$$

$$A_3=7.9\quad-4.9=+3,$$

$$A_4=-22.7-4.9=-27.6,$$

$$A_5=-42.6-4.9=-47.5,$$

$$A_6=-42.6-4.9=-47.5,$$

$$A_7=-22.7-4.9=-27.6,$$

$$A_8=+7.9\ -4.9=+3,$$

$$A_9=+34.8-4.9=+29.9.$$

The power contributions from $A_{4,5,6,7}$ are neglected because the panels are in the shadows, as indicated by the negative sign. The total power contributions are then 99.5 watts in launch and 106.3 watts in impact.

Originally, it was assumed that only three area vectors contribute power at impact. However, calculating the dot products indicates five active panels. For all practical purposes the three active panels are correct because of the extremely small contribution from the other two paddles. However, for this example one reiteration will be performed. Entering the corrections into Equations B1 and B2 gives

$$0.323A' \sin\theta_t+0.385A' \cos\theta_t=100,$$

$$0.757A' \sin\theta_t-0.215A' \cos\theta_t=100.$$

Therefore,

$$A'=\frac{100}{0.757\sin\theta_t-0.215\cos\theta_t};$$

$$(0.323)(100)\sin\theta_t+(0.385)(100)\cos\theta_t$$

$$=(0.757)(100)\sin\theta_t-(0.215)(100)\cos\theta_t;$$

$$43.4\sin\theta_t=60.0\cos\theta_t;$$

$$\tan\theta_t=\frac{60.0}{43.4}=1.382;$$

$$\theta_t=54°7'.$$

Therefore $\sin\theta_t=0.8102$, $\cos\theta_t=0.5861$, and

$$A'=\frac{100}{0.757\sin\theta_t-0.215\cos\theta_t}$$

$$=\frac{100}{0.6133-0.1260}$$

$$=\frac{100}{0.4873}=205.2.$$

Also,

$$A_n=\frac{A'}{0.0392}=\frac{205.2}{0.0392}=5235 \text{ cm}^2;$$

$$A_T=9A_n=47{,}115 \text{ cm}^2=50.7 \text{ ft}^2$$

The area vectors become:

$$A_1= \quad 116.2i+0j \quad +120.2k,$$
$$A_2= \quad 127.3i+106.8j+120.2k,$$
$$A_3= \quad 28.9i+163.7j+120.2k,$$
$$A_4= -83.1i+143.9j+120.2k,$$
$$A_5=-157.1i+ \quad 56.8j+120.2k,$$
$$A_6=-157.1i+ \quad 56.8j+120.2k,$$
$$A_7= -83.1i-143.9j+120.2k,$$
$$A_8= \quad +28.9i-163.7j+120.2k,$$
$$A_9=+127.3i-106.8j+120.2k.$$

A comparison of the new values with the first ones shows

$\theta_{t_1}=56°22'$; θ_{t_2} $54°7'$; $A_{n_1}=$ 5290 cm^2; $A_{n_2}=5235$ cm^2.

The angle changed by $2°15'$ and the area per panel reduced by 55 cm^2 or 1.05 percent. In the example the change was very small, but the power of this approach has been demonstrated. The power output as a function of flight time is shown in Figure B1 and the values used are given in Table B3.

A MAGNETIC CORE VOLTAGE-TO-FREQUENCY CONVERTER

STEPHEN PAULL

Goddard Space Flight Center

In a Pulse Frequency Modulation (PFM) telemetering system, there is a need for a subcarrier oscillator with these characteristics: (1) operating frequency a linear function of a dc input control voltage, (2) high input impedance, (3) square wave output with constant amplitude over the entire frequency range, and (4) frequency stability within one cycle during gated *on-off* operation. This paper describes a method for controlling the frequency of a square-loop magnetic core oscillator by means of a dc voltage to give a voltage-to-frequency converter with the above characteristics. Various design considerations are discussed; and a voltage controlled oscillator that operates from 15 to 5 kc as the input control voltage varies from 0 to +5 volts is used as the design example.

INTRODUCTION

In a Pulse Frequency Modulation (PFM) telemetering system (References 1 and 2) there is a need for a subcarrier oscillator with the following characteristics:

1. Operating frequency a linear function of a dc input control voltage;
2. High input impedance looking toward the oscillator input terminals from the control voltage source;
3. Square wave output with constant amplitude over the entire frequency range; and
4. Frequency stability within one cycle during gated *on-off* operation.

This paper describes a method for controlling the frequency of a square-loop magnetic core oscillator by means of a dc voltage to give a voltage-to-frequency converter with the above characteristics. Design experience with this device has been chiefly in connection with Explorer VIII (1960 ζ), Explorer X (1961 κ), Explorer XII (1961 $\upsilon 1$), and the first International Satellite UK–1. The input control voltage range for all these applications was 0 to 5 volts. The frequency range was 8 to 24 kc on the Explorer VIII oscillators, 2 to 4 kc on the Explorer X oscillators, and 5 to 15 kc on the Explorer XII and UK–1 oscillators. The most recent design in the 5 to 15 kc range is an oscillator with the following characteristics:

1. Input impedance greater than 10 megohms;
2. Power consumption less than 12 milliwatts when the oscillator is *on*, negligible when *off;*
3. Linearity of the voltage-to-frequency characteristic, expressed as the percent deviation of incremental slope from the mean slope, not exceeding 6 percent;
4. Temperature compensation so that deviation from the frequency at +25° C does not exceed ±1 percent when the temperature varies between −10° and +60° C and
5. Frequency stability during gated *on-off* operation so that the period variation during an *on* burst is less than ±0.5 percent. This includes the first cycle in the burst.

VOLTAGE CONTROLLED OSCILLATOR CIRCUIT

Circuit Operation

The voltage controlled oscillator circuit, Figure 1, is a magnetic coupled multivibrator with switching transistors Q_1 and Q_2, and two square-loop magnetic toroids as frequency controlling elements. Magnetic coupling for oscillation is obtained from the feedback windings on core 1; hence the frequency is determined by the flux reversal rate in core 1. Each switching leg in the multivibrator circuit consists of a pair of series-connected windings, one winding of each pair on each core. These switching windings and their respective cores are designed so that the core 2 winding impedance exceeds the core 1 winding impedance when no loading is present on any of the core 2 windings. Two control transistors, Q_3 and Q_4, are connected to apply a load to the core 2 control windings, so that they act to limit each core 2 winding voltage and the core 2 flux reversal rate to a constant value during each half cycle. This limiting threshold is proportional to the input dc control voltage v_c. The normal operating range of v_c is from zero to some maximum value V (either positive or negative but not both), above which limiting action no longer occurs. The core 2 switching windings are designed with enough volt-seconds so that the core 2 flux never completely reverses for any frequency within the desired operating range. This results in constant voltages on the core 1 windings, in constant core 1 flux reversal rate during each half cycle, and in the oscillator frequency being controlled by the value of v_c.

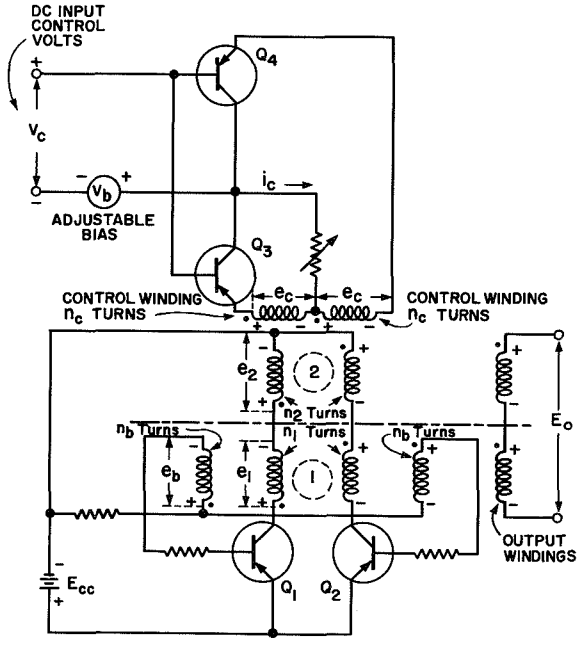

FIGURE 1.—Voltage controlled variable frequency oscillator.

Let us consider circuit operation during a half cycle when the switching transistor Q_1 and the control transistor Q_3 are conducting. The flux reversal rate in core 1 determines the oscillator frequency to be

$$f=\frac{e_1}{2n_1\chi_1} \text{ cps}, \tag{1}$$

where

e_1=the voltage across the core 1 switching winding, essentially constant during flux reversal;
n_1=the number of turns on each switching winding on core 1; and
χ_1=the total flux change in the core 1 switching from saturation in one direction to saturation in the opposite direction, in webers.

(All symbols used in this report are defined in Appendix A.)

To relate the frequency f to the core 2 winding voltages, consider the Q_1 collector circuit relation:

$$E=E_{cc}-v_s=e_1+e_2, \tag{2}$$

where

E_{cc}=collector supply voltage;
E=the effective voltage across the series-connected switching windings, essentially constant during flux reversal;
v_c=the voltage drop between the Q_1 collector and emitter plus the drop in the Q_1 collector circuit due to winding resistance; and
e_2=the voltage across the core 2 switching winding, essentially constant during flux reversal.

From Equations 1 and 2,

$$f=\frac{1}{2n_1\chi_1}(E-e_2). \tag{3}$$

Core 2 acts as a transformer and develops a voltage e_c across the control winding according to the relation

$$e_2=\frac{n_2}{n_c}e_c, \tag{4}$$

where

n_2 = the number of turns on each switching winding on core 2;
n_c = the number of turns on each control winding on core 2; and
e_c = the voltage developed across each core 2 control winding, essentially constant during flux reversal.

From Equations 3 and 4,

$$f=\frac{E}{2n_1\chi_1}-\frac{n_2}{2n_1n_c\chi_1}e_c. \tag{5}$$

This expression is simplified to a straight line equation in the slope-intercept form

$$f=f_h-me_c, \tag{6}$$

which shows f to be a linear function of the voltage e_c with a slope

$$|m|=\frac{n_2}{2n_1n_c\chi_1}\ \text{cps/volt} \tag{7}$$

and an intercept

$$f_h=\frac{E}{2n_1\chi_1}\ \text{cps}. \tag{8}$$

Operating Frequency Range

The highest possible frequency f_h is obtained when the core 2 control windings are shorted and $e_c=0$ (Equation 8). As e_c is allowed to increase, the voltage on the core 1 windings decreases, and the frequency becomes progressively lower (Equations 6 and 7). For proper operation, the core 1 feedback windings must be designed to develop a voltage e_b sufficient to maintain the nonconducting switching transistor at cutoff and to drive the conducting switching transistor into saturation at all frequencies in the desired operating range. The lowest possible frequency f_L is the frequency at which the core 2 flux completely reverses in each half cycle:

$$f_L=\frac{(e_2)_L}{2n_2\chi_2}=\frac{E-(e_1)_L}{2n_2\chi_2}, \tag{9}$$

where

$(e_1)_L$ = the voltage across the core 1 switching winding at the frequency f_L;
$(e_2)_L$ = the voltage across the core 2 switching winding at the frequency f_L; and
χ_2 = the total flux change in the core 2 switching from saturation in one direction to saturation in the opposite direction, in webers.

From Equations 1 and 8,

$$(e_1)_L=\frac{f_L}{f_h}E. \tag{10}$$

Substituting Equation 10 in Equation 9 and simplifying,

$$f_L=\frac{E}{2(n_1\chi_1+n_2\chi_2)}. \tag{11}$$

The voltage-to-frequency converter operates between a high frequency $f_0\leq f_h$ when the dc input control voltage $v_c=0$ and a lower frequency $f_v\geq f_L$ when the input control voltage $v_c=V$ greater than zero.

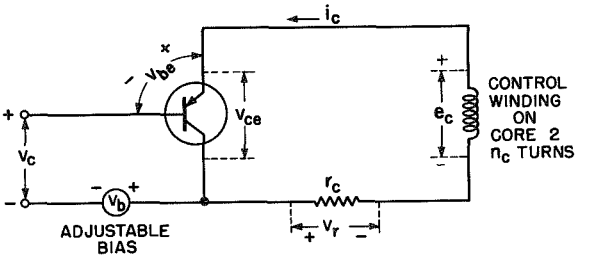

FIGURE 2.—Input control circuit analysis.

Input Control Circuit

The linear Equation 6 relates oscillator frequency to the voltage e_c across the core 2 control windings. To relate the frequency to the dc input control voltage v_c, it is necessary to consider the input control circuit in detail. Figure 2 is a schematic of the control circuit showing only the control transistor that is conducting and its associated control winding. It is assumed that silicon control transistors with negligible I_{co} are used. Voltages in the control circuit are the following:

v_c = the dc input control voltage, which can be set to any value in the range 0 to $+V$ (in case the control voltage varies between 0 and $-V$, an n-p-n control transistor must be used)

v_{be} = the control transistor base-to-emitter forward voltage drop, assumed to be constant over the entire operating range

v_{ce} = the control transistor collector-to-emitter voltage drop during the conducting half cycle

e_c = the effective voltage across the control winding during flux reversal

v_r = the voltage drop due to the control transistor collector current flowing through the resistive component r_c of the control transistor collector circuit

v_b = the net adjustable fixed bias in the control circuit input leg

In normal operation with limiting action in the control circuit, these voltages are essentially constant during each half cycle. In Figure 2,

$$v_c+v_{be}-v_{ce}-v_b=0,$$

and

$$v_{ce}+v_r-e_c=0.$$

From these two relations,

$$e_c=v_c+v_{be}+v_r-v_b. \tag{12}$$

The current i_c and the voltage v_r have been found experimentally to be decreasing linear functions of v_c. That is, v_r can be given by the expression

$$v_r=V_r-\frac{dv_r}{dv_c}v_c, \tag{13}$$

where V_r is the value of v_r when v_c is zero and $f=f_0$, and where $-dv_r/dv_c$ is the slope of the linear relation between v_c and v_r. Substituting Equation 13 in 12,

$$e_c=\left(1-\frac{dv_r}{dv_c}\right)v_c+v_{be}-v_b+V_r. \tag{14}$$

Substituting 14 in 6, the relation between control volts v_c and the oscillator frequency is

$$f=f_h-|m|(v_{be}-v_b+V_r)-|m|\left(1-\frac{dv_r}{dv_c}\right)v_c. \tag{15}$$

When the input control voltage $v_c=0$, the frequency is

$$f_0=f_h-|m|(v_{be}-v_b+V_r). \tag{16}$$

A simplification of Equation 15 expresses f as a function of v_c in the slope-intercept form of a straight line equation:

$$f=f_0-|p|v_c, \tag{17}$$

where

$$|p|=|m|\left(1-\frac{dv_r}{dv_c}\right) \tag{18}$$

is the slope of the v_c-to-f characteristic. Equation 18 shows the slope $|p|$ to be less than the slope $|m|$ of the e_c-to-f characteristic because of the presence of resistance in the control circuit. If this resistance is kept small, the slope $|p|$ is only slightly less than $|m|$. The effect of increasing the control circuit resistance is to reduce the value of $|p|$. This effect is used in circuit design as a slope adjustment for trimming the v_c-to-f characteristic.

From Equation 16 it is evident that the relation between f_0 and f_h depends on the biasing arrangement in the dc input control circuit. This can be adjusted for three possible cases:

Case 1, in which $v_{be}-v_b+V_r=0$: In this case $f_0=f_h$, and the oscillator operates at its highest possible frequency f_h when $v_c=0$, as illustrated by curve A, Figure 3.

Case 2, in which $v_{be}-v_b+V_r$ *is positive:* In this case $f_h>f_0$. When $v_c=0$, the oscillator operates at a frequency f_0 which is less than its highest possible frequency f_h, as illustrated by curve B, Figure 3.

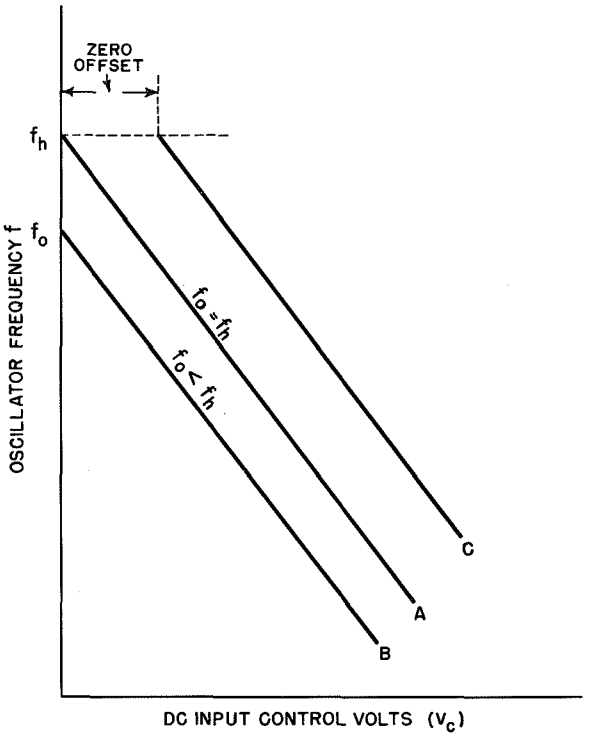

FIGURE 3.—Effect of control circuit biasing on the v_c-to-f characteristics.

Case 3, in which $v_{be}-v_b+V_r$ *is negative:* In this case the oscillator operates at its highest possible frequency f_h when $v_c>0$. This operation results in a zero offset in the dc voltage-to-frequency characteristic as illustrated by curve C, Figure 3.

DESIGN CONSIDERATIONS

Design of the voltage controlled oscillator for a specific requirement involves the parameter relations (Equations 1 through 18) that have been established on the basis of desired operation. Because of the fact that certain practical limitations such as winding capacitances, maximum number of turns possible on a given toroid, flux leakage, and power drain are not considered in these equations, it is to be expected that some modifications of results obtained may be necessary. Therefore the equations should be regarded mainly as a guide in circuit design.

Input Control Circuit and Transfer Characteristics

The starting point in a design problem is the v_c-to-f characteristic, as shown in Figure 4. This establishes a requirement for an oscillator to operate at frequencies from f_o to f_v as the input control voltage varies from 0 to V. The slope of this characteristic is

$$|p|=\frac{df}{dv_c}=\frac{f_0-f_v}{V}. \tag{19}$$

With this requirement given, the design problem begins with the proper selection of the end points for the e_c-to-f characteristic, also shown in Figure 4. This curve should be to the right of the v_c-to-f curve for two reasons: (1) f_h must exceed f_0 (as in curve B, Figure 3) to avoid having a zero offset in the v_c-to-f characteristic, and (2) e_c must exceed v_c throughout the operating frequency range so there is no reversal of current in the control circuit and consequent loss of input impedance.

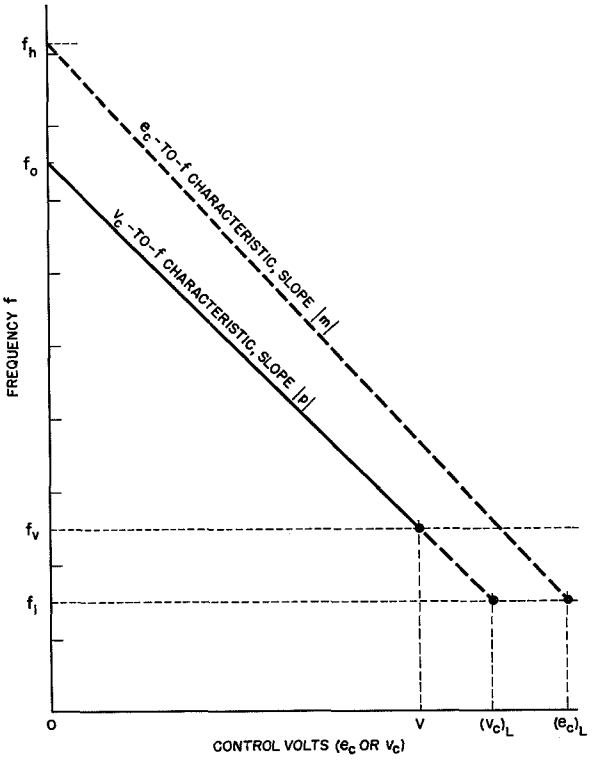

FIGURE 4.—Voltage-to-frequency characteristics for circuit design.

For stable operation over the required control voltage range 0 to V, the value of the control voltage necessary to produce oscillation at the low frequency extreme f_L should be substantially higher than V. When this voltage has been selected, it can be seen from Figure 4 that the low frequency extreme is

$$f_L=f_0-|p|(v_c)_L. \tag{20}$$

(The subscript L denotes the value of v_c when $f=f_L$.)

A choice of $(e_c)_L$, which is the value of e_c when $f=f_L$, depends on the control transistors being used. If $(e_c)_L$ is chosen to be equal to $(v_c)_L$, then the current in the control circuit is zero at f_L and is very low at the low frequency end of the desired operating range. This is usually undesirable because the lower transistor gain in the low current region results in a loss of input impedance. Design experience has shown that $(e_c)_L$ should be selected greater than $(v_c)_L$ to prevent loss of input impedance at the low frequency end of the operating range.

A choice of f_h at the other end of the e_c-to-f characteristic determines the slope $|m|$. From Figure 4,

$$f_h=f_L+|m|(e_c)_L. \tag{21}$$

In selecting f_h, it must be remembered that the slope $|m|$ must exceed $|p|$ by an amount sufficient to allow for control circuit resistance. If $|m|$ is not steep enough, the resulting slope $|p|$ will also be insufficient; and no amount of adjustment in the control circuit resistance will correct the slope. On the other hand, if $|m|$ is too steep, an excessive amount of resistance is necessary in the control circuit to correct the slope $|p|$; this results in other undesirable effects.

Cores and Windings

For minimum power drain and maximum input impedance, the core dimensions should be kept to a minumum consistent with winding requirements. The core 1 switching winding is determined from the relation of Equation 8:

$$n_1=\frac{E}{2f_h\chi_1}. \tag{22}$$

The core 2 switching winding is determined from the relationship in Equation 11:

$$n_2=\frac{E}{2f_L\chi_2}-\frac{\chi_1}{\chi_2}n_1; \tag{23}$$

and the core 2 control winding is determined from Equation 4:

$$n_c=\frac{e_c}{e_2}n_2. \tag{24}$$

At the frequency f_L,

$$e_c=(e_c)_L,$$

and

$$(e_2)_L=E-(e_1)_L=\left(\frac{f_h-f_L}{f_h}\right)E.$$

From Equation 8,

$$f_h=\frac{E}{2n_1\chi_1},$$

and therefore

$$(e_2)_L=2n_1\chi_1(f_h-f_L).$$

Substituting this in Equation 24,

$$n_c=\frac{(e_c)_L}{2n_1\chi_1(f_h-f_L)}n_2=\frac{n_2}{2n_1\chi_1|m|}. \tag{25}$$

The base feedback winding on core 1 must be designed so that the voltage e_b developed during flux change is sufficient to drive the conducting switching transistor into saturation and to keep the other switching transistor cut off. Because of transformer action in core 1, this winding develops a voltage

$$e_b=\frac{n_b}{n_1}e_1,$$

where n_b is the number of turns on the winding. Hence,

$$n_b=\frac{e_b}{e_1}n_1. \tag{26}$$

Now the voltage e_1 is a minimum at the frequency f_L.

$$(e_1)_L=\frac{f_L}{f_h}E. \tag{27}$$

Substituting Equation 27 in 26,

$$n_b=\frac{f_h e_b}{f_L E} n_1. \tag{28}$$

This expression gives the required number of turns n_b on the core 1 feedback windings in order to develop a voltage e_b at the frequency f_L. The e_b required for operation at f_L depends on the properties of the switching transistors.

The series-connected output windings are designed to give a constant output E_0 at all frequencies. For this requirement,

$$n_{0,1}=\frac{E_0}{E} n_1;\ n_{0,2}=\frac{E_0}{E} n_2. \tag{29}$$

DESIGN EXAMPLE

The following design example is a voltage controlled oscillator that operates from 15 to 5 kc as the input control voltage varies from 0 to +5 volts. The circuit, shown in Figure 5, has a pair of transistors on each leg of the control winding for added gain and high input impedance. These transistors are chosen according to the following specifications:

1. The product of h_{f_e} for the two transistors should be 100 or more, with the lowest h_{f_e} in the position nearest the winding. This is to minimize the leakage effects.
2. The reverse breakdown voltage, collector-to-emitter, base open, must exceed 6 volts.
3. The reverse breakdown voltage from the base of the first transistor to the emitter of the second transistor must exceed 12 volts.

Temperature compensation is obtained by means of forward-biased germanium diodes connected as part of the control circuit biasing network. The amount of compensation is adjusted as needed by the number of diodes included in the network.

Final trimming of the v_c-to-f characteristic is done by means of the *zero adjust* potentiometer and the *slope adjust* resistor. The setting of *zero adjust* determines the frequency f_0, and the setting of *slope adjust* determines the slope $|p|$. These adjustments are not entirely independent of one another; hence several trial values of each may be necessary to obtain the desired characteristic. The *slope adjust* should be kept as low as possible, preferably less than 1,000 ohms.

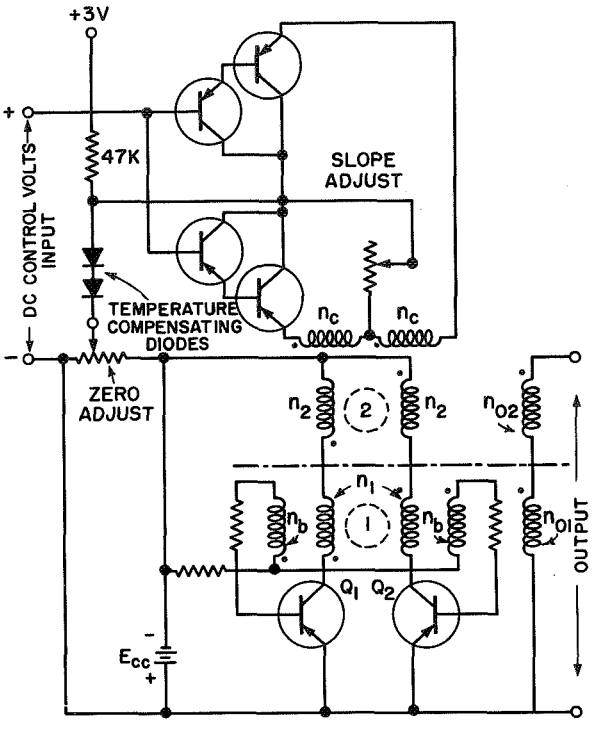

FIGURE 5.—Voltage controlled oscillator design example.

In this example, the general transfer characteristics shown in Figure 4 are assigned the following values:

$$f_0=15 \text{ kc}, f_v=5 \text{ kc}, V=+5 \text{ volts},$$

$$|p|=2 \text{ kc/volt};$$

$$f_h=18.050 \text{ kc}, f_L=f_6=3 \text{ kc},$$

$$(V_c)_L=6 \text{ volts}, (e_c)_L=7 \text{ volts},$$

$$|m|=2.150 \text{ kc/volt}.$$

The circuit is designed with p-n-p switching transistors operating from a collector supply $E_{cc}=-2.70$ volts. The resistive voltage drop in the switching transistor collector circuit is 0.10 volt (determined experimentally); hence the effective voltage applied across the series-

connected switching windings is $E=-2.60$ volts.

Core 1 is chosen from a batch of ⅛ inch by ¼ mil, 4–79 molybdenum permalloy bobbin cores with $\chi_1=28\times10^{-4}(\pm5\%)$ webers. The core 1 switching winding is designed so that $f_h=18.050$ kc with the largest core in the batch ($\chi_1=29.4\times10^{-4}$ webers), when the *slope adjust* is zero. Any other core with less flux and the same switching winding will give a higher f_h and a steeper slope $|m|$. The required slope $|p|$ can be obtained by adding the *slope adjust* resistance without the need for changing the number of turns on the winding. From Equation 22,

$$n_1=\frac{2.60}{2(18.05\times10^3)(29.4\times10^{-4})}=245 \text{ turns.}$$

Core 2 is chosen from a batch of ⅛ inch by 1 mil, 4–79 molybdenum permalloy bobbin cores with $\chi_2=128\times10^{-4}$ ($\pm5\%$) webers. The core 2 switching winding is designed so that $f_L=3.000$ kc with the smallest core in the batch ($\chi_2=121\times10^{-4}$ webers), when the *slope adjust* is zero. Any other core with more flux and the same switching winding will give a lower f_L and, again, a steeper slope $|m|$. From Equation 23,

$$n_2=\frac{2.60}{2(3\times10^3)(121\times10^{-4})}-\frac{29.4}{121}\times245=298 \text{ turns.}$$

From Equation 25,

$$n_c=\frac{298}{2\times245\times(29.4\times10^{-4})\times2150}=960 \text{ turns.}$$

The base feedback windings on core 1 must be designed to give adequate voltage at the lowest frequency f_L. If we assume that this is approximately 1 volt, Equation 28 gives

$$n_b=\frac{18050\times245}{3000\times2.60}=570 \text{ turns.}$$

REFERENCES

1. ROCHELLE, R. W., "Pulse Frequency Modulation," NASA Technical Note D–1421, 1962. Also published in: *IRE Transactions on Space Electronics and Telemetry* SET–8(2): 107, June 1962.
2. WHITE, H. D., JR., "On the Design of PFM Telemetry Encoders," NASA Technical Note D–1672, 1962. Also published in: *Proc. 1962 Nat. Telemetering Conf.*, Washington, May 1962, Vol. 1, Paper 3–4.

Appendix A

SYMBOLS

The symbols used in this report are defined as follows:

E	the effective voltage across the series-connected switching windings, essentially constant during flux reversal
E_{cc}	collector supply voltage
E_o	output square wave amplitude
e_b	the voltage across the core 1 feedback winding, essentially constant during flux reversal
e_c	the voltage developed across each core 2 control winding, essentially constant during flux reversal
$(e_c)_L$	the voltage across the core 2 control winding at the lowest possible frequency f_L
e_1	the voltage across the core 1 switching winding, essentially constant during flux reversal
$(e_1)_L$	the voltage across the core 1 switching winding at the lowest possible frequency f_L
e_2	the voltage across the core 2 switching winding, essentially constant during flux reversal
$(e_2)_L$	the voltage across the core 2 switching winding at the lowest possible frequency f_L
f	oscillator frequency, cps
f_h	highest possible frequency, cps
f_L	lowest possible frequency, cps
f_V	oscillator frequency when control volts$=V$
f_0	oscillator frequency when control volts$=0$
i_c	control transistor collector current
i_{co}	dc collector current when collector junction is reverse-biased and emitter is open-circuited.
$\|m\|$	the numerical value of the slope of the e_c-to-f characteristic, cps/volt
n_b	the number of turns on each core 1 feedback winding
n_c	the number of turns on each core 2 control winding
$n_{o,1}$	the number of turns on each core 1 output winding
$n_{o,2}$	the number of turns on each core 2 output winding
n_1	the number of turns on each core 1 switching winding
n_2	the number of turns on each core 2 switching winding
$\|p\|$	the numerical value of the slope of the $_{vc}$-to-f characteristic, cps/volt
r_c	resistive component of the control transistor collector circuit
V	the highest value of the dc input control voltage in the desired operating range
V_r	the value of v_r when v_c is zero and $f=f_0$
v_b	the net adjustable fixed bias in the control circuit input leg
v_{be}	the control transistor base-to-emitter forward voltage drop during the conducting half cycle
v_c	the dc input control voltage that can be set to any value between 0 and V
$(v_c)_L$	the value of the dc input control voltage when the oscillator is at its lowest possible frequency f_L
v_{ce}	the control transistor collector-to-emitter voltage drop during the conducting half cycle

v_r the voltage drop due to the control transistor collector current flowing through the resistive component r_c of the control transistor collector circuit

v_s the voltage drop between the Q_1 collector and emitter plus the drop in the Q_1 collector circuit due to winding resistance

χ_1 the total flux change in the core 1 switching from saturation in one direction to saturation in the opposite direction, in webers

χ_2 the total flux change in the core 2 switching from saturation in one direction to saturation in the opposite direction, in webers

CHARACTERISTICS OF PASSIVE COMMUNICATION SATELLITES WITH LAMBERTIAN SURFACES[1]

HERBERT P. RAABE

General Mills Electronics Division

Passive Communication Satellites with surfaces reflecting diffusely according to Lambert's law are particularly attractive since they afford a directional pattern well matched to the optimum pattern of satellites in lower orbits and since such surfaces are easily realized. The echo from diffuse reflectors varies statistically, and a combination diversity technique of frequency should be used to stabilize the signal. A spherical satellite is no longer required; and weight reduction and higher reliability can be gained from polyhedral structures. Compared with a rigidized specularly reflecting sphere, a Lambertian reflector affords a 7 db stronger echo for the same weight. Model tests of reflectivity agree well with the theory.

INTRODUCTION

The most attractive characteristic of passive communication satellites is their long lifetime. Other advantages are unlimited linearity and very broad bandwidth. Their major disadvantage, however, is their low ratio of radiant intensity to weight as compared with that of active satellites. The passive satellites must be very large to intercept sufficient electromagnetic radiation power for retransmission toward the earth, in contrast to active satellites which amplify the signal enormously. Actually, a very small amount of metal is required to intercept the electromagnetic energy over the cross section of a passive satellite. Most of its weight is required to provide strength and rigidity and to package and erect the satellite. The weight of Echo I (1960 ι) is about 1,000 times that of the theoretical minimum. This shows that there is a great need for improved satellite construction techniques.

To maximize the ratio of radiant intensity to weight—or the effectiveness of the passive satellite—not only should the intercepting cross section be increased or the weight decreased, but also the reflected power should be concentrated into the smallest solid angle consistent with the geometry of the desired propagation paths. Moreover, within this solid angle there is an optimum distribution of radiant intensity when various locations of terminals and their relations to the orbital position of the satellite are considered. Since a specularly reflecting sphere is an isotropic scatterer, the gain of a directional reflection or scattering pattern indicates the gain in radiant intensity over that of a perfect sphere having the same intercepting cross section as the modified satellite. Obviously, since the useful maximum gain is a function of orbital height, different approaches must be taken for synchronous satellites and for those in lower orbits. This paper discusses only satellites in the 2,000 to 5,000 km altitude range. The study of such satellites, partially supported by the U.S. Navy Contract Nonr (3545)(00)(X), showed that the theoretically achievable gain is not very high, so that parallel efforts to reduce the weight become more important. Attitude control of the satellites was, therefore, ruled out as an unacceptable complexity.

[1] Presented at the XIII International Astronautical Congress, Varna, Bulgaria, Sept. 28, 1962. This work was performed under contracts NAS 5-890 and NAS 5-1598 for the Goddard Space Flight Center.

Schemes utilizing refraction were also rejected because dielectric materials—even artificial ones—would be too heavy, and the problem of erection in space too difficult. Thus only one approach to a solution for the problem could be found, namely, an approximately spherical array of scatterers with more or less directive characteristics. As these scatterers reradiate waves of random phases, such a satellite becomes a diffuse reflector. Its scattering characteristic is always axially symmetric with respect to the direction of the transmitter.

THE OPTIMUM SCATTERING CHARACTERISTIC

Whenever the satellite is in a favorable position for communication between two terminals, the received power should exceed a maximized threshold. The received power is determined by

$$P_r=\frac{P_tG_t}{4\pi s_t^2}\frac{AG_\psi}{4\pi}\frac{G_r\lambda^2}{4\pi s_r^2}, \tag{1}$$

where

P_t=transmitted power,
G_t=gain of transmitting antenna,
G_r=gain of receiving antenna,
λ=wavelength,
A=intercepting area of the satellite,
G_ψ=gain of the satellite (pattern),
ψ=bistatic angle,
s_t=satellite distance from the transmitter,
s_r=satellite distance from the receiver.

The first term of Equation 1 defines the irradiance in the vicinity of the satellite, while the first two terms determine the radiant intensity of the satellite. As a comprehensive term we define the bistatic scatter cross section as

$$\sigma_\psi=AG_\psi. \tag{2}$$

Of particular interest is the factor

$$\alpha=\frac{\sigma_\psi}{s_t^2s_r^2}, \tag{3}$$

which consists of those parameters characteristic of the satellite and its orbital position. Figure 1 illustrates, in a general manner, the geometry of the triangle formed by the terminals and the satellite. The transmitter has been assumed to be at T and the receiver is at R. The satellite S may be found anywhere in the orbital shell, but it becomes operational as a communication link only during passage through the segment which is visible from both terminals. The ranges s_t and s_r and the bistatic angle ψ vary in a complicated manner, but one significant fact is obvious: larger angles are associated with shorter ranges.

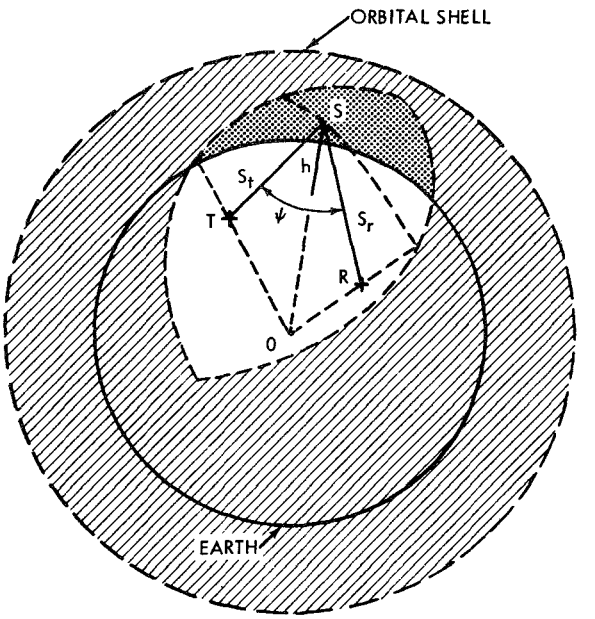

FIGURE 1.—Geometry of the propagation path.

For a realistic case, some characteristic ranges and angles have been determined as shown in Figure 2. The terminals are located

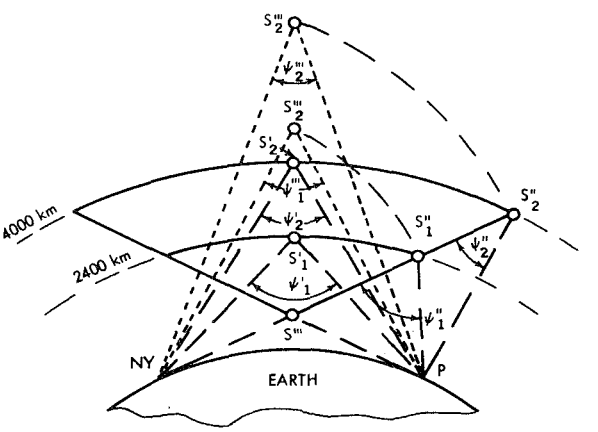

FIGURE 2.—Geometry of a satellite communication case.

at New York (NY) and Paris (P), while the satellite may be found in orbits between 2400 and 4000 km above the earth. Positions S_1 and S_2 correspond to the lowest and highest orbit respectively, while S' is in the center of the operational segment, S'' in the center of the arcs, and S''' at the intersection of the arcs. The true bistatic angles at S''' are illustrated in the "tilted-up" triangles. The correlation between angles and ranges is clearly indicated, so that the optimum pattern should be a broad lobe with a gradual dropoff toward larger angles.

THE SPHERICAL LAMBERTIAN SURFACE

Under certain conditions, a surface scatters incident electromagnetic radiation diffusely according to Lambert's cosine law. A spherical satellite with a Lambertian surface proved to be particularly useful because its scattering characteristic matches the optimum pattern rather closely, and Lambert's law applied to certain randomly distributed surfaces which greatly ease design specifications.

For a spherical Lambertian surface the bistatic scattering cross section can be derived as follows: A plane surface element whose normal is inclined toward the direction of the incident radiation at an angle β intercepts the power

$$dP_i = Hds \cos \beta \tag{4}$$

from the homogeneous radiation field of the irradiance H. If the albedo of this Lambertian surface element is a, the radiant intensity of the scattered radiation is described by

$$dJ_s = \frac{aHds}{\pi} \cos \beta \cos \phi, \tag{5}$$

where ϕ is the angle between the normal of this surface element and the observer. The term $\cos \phi$ is characteristic of Lambert's law, and means that the radiance of a plane surface is independent of the angle ϕ of the observer since the projected area in the direction of the observer also varies as $\cos \phi$.

If ds is a surface element on a Lambertian sphere of radius r, the radiant intensity can be derived by integration over the visible irradiated

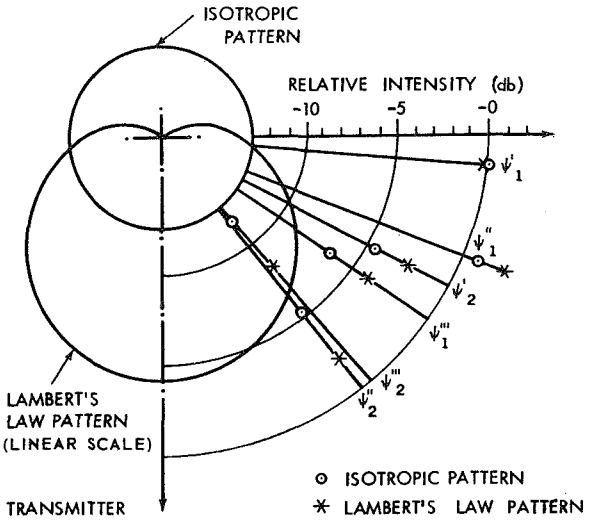

FIGURE 3.—Isotropic and Lambertian patterns and relative signal strengths for figure 2.

section of the surface:

$$J_s = aH \frac{2r^2}{3\pi} [\sin \psi + (\pi - \psi) \cos \psi]. \tag{6}$$

We can use Equation 3 to determine the bistatic scattering cross section of the Lambertian sphere and, with $a=1$, we obtain

$$\sigma_L = \frac{8r^2}{3} [\sin \psi + (\pi - \psi) \cos \psi]. \tag{7}$$

However, the isotropic scattering by a specularly reflecting sphere is simply

$$\sigma_s = r^2 \pi. \tag{8}$$

These two patterns are shown in Figure 3. The maximum gain of the diffuse sphere over the specular sphere is 2.67 (4.3 db) in the direction of the transmitter. The gain tapers off gradually and reaches zero at an angle of 83.7 degrees.

To prove the suitability of the Lambertian pattern for nonsynchronous satellites, the factor α (see Equation 3) was computed for the two patterns defined in Figure 2. The relative echo power level is plotted in Figure 3 for the bistatic angle designated. The Lambertian sphere is seen to afford a gain of 3 db to a system which must be designed to operate with the lowest level signal. Incidentally, at S_1' the diffuse

sphere is slightly less effective; but, because of the shorter ranges, the signal is still 8 db stronger than the least favorable position S_2''.

THE STATISTICAL PROPERTIES OF ECHO

Diffuse reflectors share one disadvantage with any scattering means of radio wave propagation. The echo does not appear to originate from a single phase center; it originates from a multitude of phase centers. Therefore, the power buildup is a statistical phenomenon, and the aforementioned scattering cross section is just the average of its statistical distribution. Moreover, the satellite is not stationary. As it revolves and travels along its orbit, the relative position (and hence the phase of the scatterers) changes. Consequently, a CW signal, or any spectral component of a signal, experiences a narrow-band noise modulation of phase and amplitude. Under the idealized assumption that the bistatic angle is zero and the satellite revolves about an axis which is perpendicular to the direction of the terminals, the situation illustrated in Figure 4 results. The lower half of the Lambertian sphere is illuminated and contributes to the echo. It is easy to show that the distribution of echo intensity with respect to the x axis is that of a parabola, as in the lower graph of Figure 4. Since the Doppler shift of the scattered radiation is proportional to x, the parabolic curve is also representative of the spectrum envelope.

The statistical distribution of a narrow-band noise voltage is Gaussian (Figure 5a). The envelope of the noise voltage follows the Rayleigh distribution. The intensity distribution of the noise signal (or the square-law rectified signal) follows the exponential curve shown in Figure 5b. These statistical variations can be very harmful to the transmitted signal. Special communication techniques can be applied, however, which result in very steady signals—a fact that is demonstrated by tropospheric scatter communication techniques. In principle, these techniques use a number of statistically independent samples for every bit of information. To get this independence, some diversity must be introduced. For example, if the satellite depolarizes the radiation completely, two independent samples can be derived from the two orthogonal polarization channels. After rectification, the signals are added and the distribution of the sum follows curve 2 (Fig. 5b).

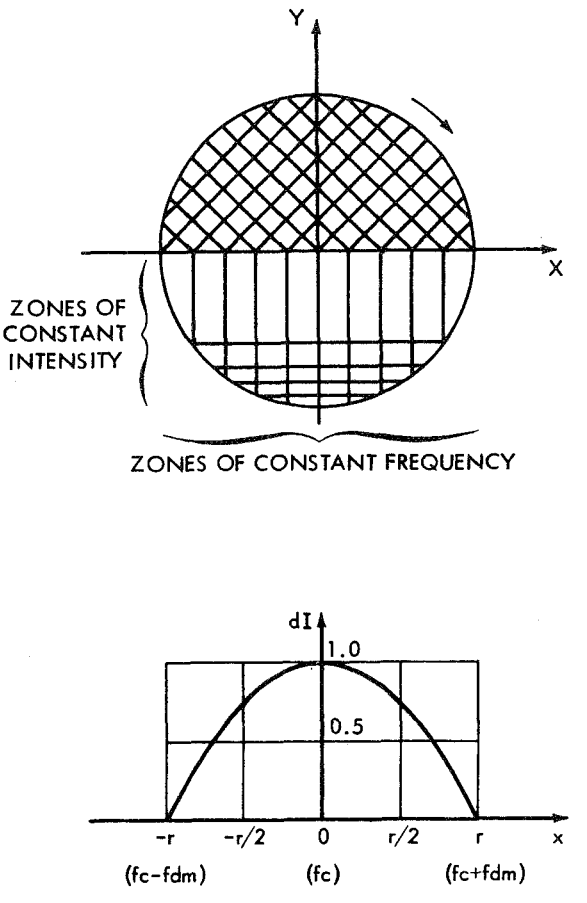

FIGURE 4.—Intensity distribution and spectrum of a Lambertian sphere.

The preferred technique for tropospheric scatter propagation is space diversity. Independent samples can thus be obtained with several receiving antennas placed side by side. This is not practical for satellite scatter propagation because the receiving antennas have to be spaced several kilometers apart, and the cost would become excessive. Time diversity is also unattractive because of the low sample rate which is dependent upon the rotational rate of the satellite. Furthermore, satellite spin is somewhat unpredictable and decreases

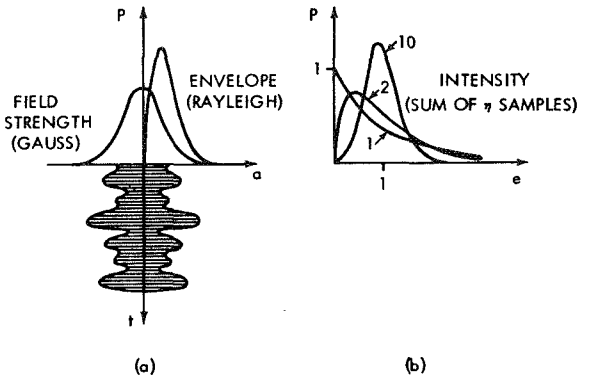

FIGURE 5.—Statistical distribution functions of Echo I.

with age. The most attractive diversity technique is frequency diversity.

Just as the rephasing of individual contributions of scattering centers causes signal fluctuation as the satellite revolves, rephasing due to a variation of the frequency also causes signal fluctuation, and one would like to know how much the frequency must be shifted to obtain a decorrelated amplitude. As a simplified model, we assume two equally strong scattering centers whose path-length difference is $2b$. Again, we assume that the two terminals are close together so that the separation in depth of the two scattering centers becomes b. Hence, a frequency can be chosen so that the contribution from both scatterers is in phase, resulting in a maximum amplitude. Then, a frequency shift to reduce the amplitude to zero would require the addition or subtraction of one-half wavelength within the delay path of $2b$. To get an approximate figure for the required phase shift for full-size satellites, we assume that the illuminated side is divided into a near and a distant zone of equal reflectivity and that both zones are represented by a single scattering center. From Figure 4 one can estimate that the separation in depth of these centers is at least ⅛ of the diameter. For a 200-foot-diameter satellite this separation is 25 feet (7.62 m) and the corresponding frequency shift is nearly 10 Mc/s. Thus, several statistically independent samples can be derived from carriers of sufficient frequency separation for each bit of information. They may be transmitted coincidentally or sequentially.

The most efficient form of diversity technique is combination diversity, first introduced by Kahn (Reference 1) and more generally investigated by Brennan (Reference 2). This technique adds the n independent samples after weighing them according to their individual signal-to-noise ratios p_i and results in an overall signal-to-noise ratio of

$$P=\sum_{i=1}^{n} p_i. \tag{9}$$

Thus, the combination diversity technique can provide the same signal-to-noise ratio for a noncoherent scatter communication path as the standard technique achieves for the coherent scatter communication path with no additional demand in levels of power or sizes of antennas.

REALIZATION OF LAMBERTIAN SURFACES

The mechanism of scattering from rough surfaces that obey Lambert's law is not well understood. Although an abundance of literature exists which theoretically treats the scattering of electromagnetic waves from rough surfaces, none was found where Lambert's law resulted. Most of the literature was generated with the intent of explaining scattering from the surface of the sea, which is not Lambertian. In this literature the surface is treated as a continuously illuminated or radiating boundary. Thus the effects of shadows and secondary scattering are not considered. Obviously, the sea never has a sufficiently rough surface to scatter radiation according to Lambert's law, so that simplifying assumptions are justified.

A rough surface may be treated as a random surface whose height over a smooth reference surface is defined as a continuous, single-valued statistical variable. The statistical parameters are constant over the entire reference surface. In application to satellites, this reference surface should be a sphere, but for general discussions it is assumed that the reference surface is a plane. As a further restriction only symmetrical, rough surfaces are considered, which means that the height of the surface has a symmetrical distribution about the first order mean; and for the sake of simplicity we assume that the reference surface

is defined in such a way that this first order mean becomes zero.

For complete definition of the rough surface, we must specify the second probability distribution of height or the spatial frequency spectrum. These functions determine the roughness; thus we must differentiate between theoretical and effective roughness. Theoretical roughness is independent of the linear scale of the surface. However, since the rough surface is probed by electromagnetic radiation of limited resolving power, the effective roughness must take wavelength into account.

It was found that effective roughness is the theoretical roughness of a surface which has been smoothed to such a degree that its structure can be resolved by the radiation. This means that, if a surface is rough enough to achieve Lambertian scattering at a given frequency, Lambertian scattering will be assured for any higher frequency. It also means that smooth surfaces to which geometric optics apply can yet be rough enough to assure Lambertian scattering. Smoothing of a rough surface causes suppression of the higher spatial frequencies. Two point scatterers must be positioned at least one-half wavelength of the probing radiation apart to allow resolution. This means that, for the purpose of determining effective roughness, all components of the spatial frequency spectrum whose wavelengths are shorter than one-half of the radiated wavelength should be suppressed.

In order to determine the degree of roughness required to achieve Lambertian scattering, an experiment was performed on paper in which the surface was assumed smooth enough to obey laws of geometric optics. It consisted of a layer of reflective spheres whose radius was large compared to the wavelength of the illuminating radiation. To form a random rough surface, the heights of these spheres were statistically distributed, and then the scattering angles were traced for each sphere. The distribution was Gaussian and was varied in three steps of increasing standard deviation. Statistical data were obtained by the Monte Carlo method. The sample surface consisted of 20 spheres; three spheres are shown in

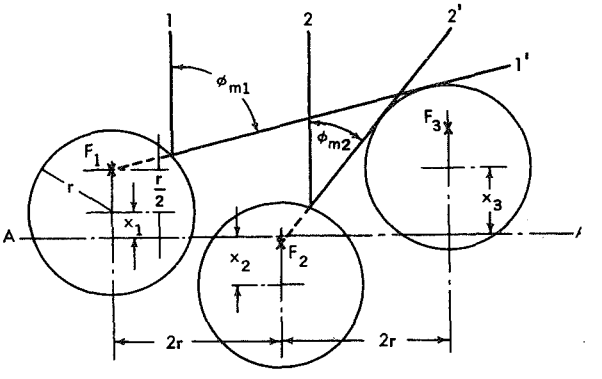

FIGURE 6.—Geometry of limiting rays for randomly distributed spheres.

Figure 6 to illustrate details of the ray tracing. The spheres were illuminated (normal to the reference plane) by a distant point source. The following simplifications and assumptions were considered justified: (1) The spheres are located in a vertical plane so that the problem can be treated as a two-dimensional one; (2) the image of the point source is in a fixed position halfway between the center and the surface of the sphere; and (3) only primary reflections were traced. The result of this experiment is shown in Figure 7, where the distribution functions of the limiting angles (ϕ) are plotted for the standard deviations of 0, 0.2 r, 0.5 r, and r, where r is the radius of the spheres. All distribution curves were based on the same set of random two-digit numbers. The approach to a Lambertian distribution is evident, although twenty samples are a relatively small number with which to establish a statistical distribution.

As a measure of roughness for the array of spheres, we can use the ratio of the average slant distance between adjacent scattering centers to the distance between the spheres of a smooth array, which equals the diameter of the spheres. For the roughest array ($\sigma=r$), this ratio was found to be 1.28. Hence, the conclusion appeared to be justified that a randomly wrinkled reflective sheet whose surface is larger than the reference plane by a linear factor of 1.28 should perform as well as the respective array of spheres, provided the wrinkles are coarse enough to be resolved by the radiated wavelength. This led to a simple technique of

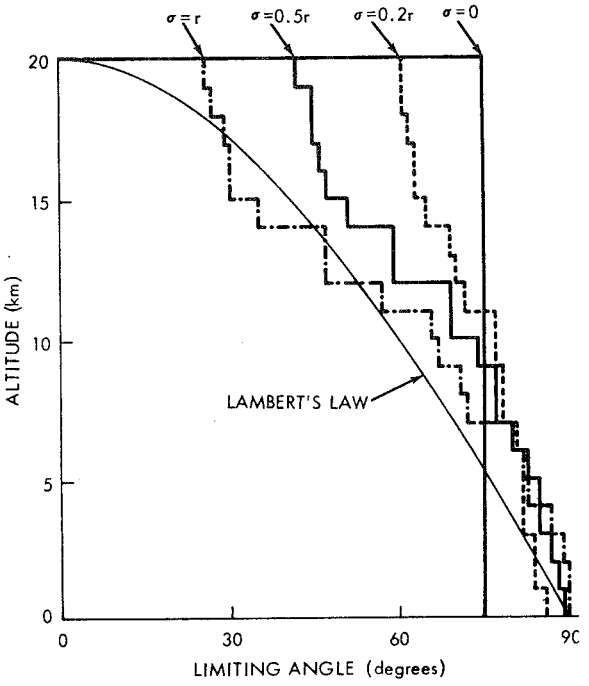

FIGURE 7.—Statistically derived scattering characteristics.

generating rough surfaces: A sheet of aluminum foil was crumpled and reexpanded until the desired ratio of linear surface dimensions was reached. The pressure applied to the crumpled package of foil determined the range of the spatial frequency spectrum, but an allowance was made for some unresolvable wrinkles; and it was found that a linear surface ratio of 1.3 offered good agreement with Lambert's law.

PROPOSED SATELLITE DESIGN

The overall shape of a satellite with Lambertian surface cannot be a sensitive factor in the scattering cross section. Therefore, an erection technique should be considered which does not require gas pressurization of the entire volume or a leakproof outer skin. Instead, only a framework of beams which form the edges of a polyhedron must be erected by gas pressure, and the skin can be lightened by using thinner, perforated sheets. With sufficiently small holes, no transparency or other losses will result up to microwave frequencies; however, the solar radiation pressure will be reduced.

Regular polyhedrons with parallel pairs of faces have an interesting property. If their surfaces obey Lambert's law, the monostatic scattering cross section becomes independent of the angular orientation, whereas the bistatic scattering cross section shows minor fluctuations which decrease as the number of faces increases. It is quite easy to derive this scattering cross section for the simplest polyhedron of this group, the cube. In Figure 8 the cube is shown in a special orientation, in which one pair of faces is parallel to the plane formed by the transmitter T, the receiver R, and the cube. The cube is rotated so that one face forms the angle ϕ with the direction of the transmitter. The bistatic angle is ψ and the side of the cube d. Hence, the powers intercepted by the two illuminated faces are

$$\left.\begin{aligned} P_1 &= Hd^2 \cos\phi \\ P_2 &= Hd^2 \sin\phi \end{aligned}\right\}. \qquad (10)$$

Lambertian scattering results in circular beam patterns; consequently, the peak values of the

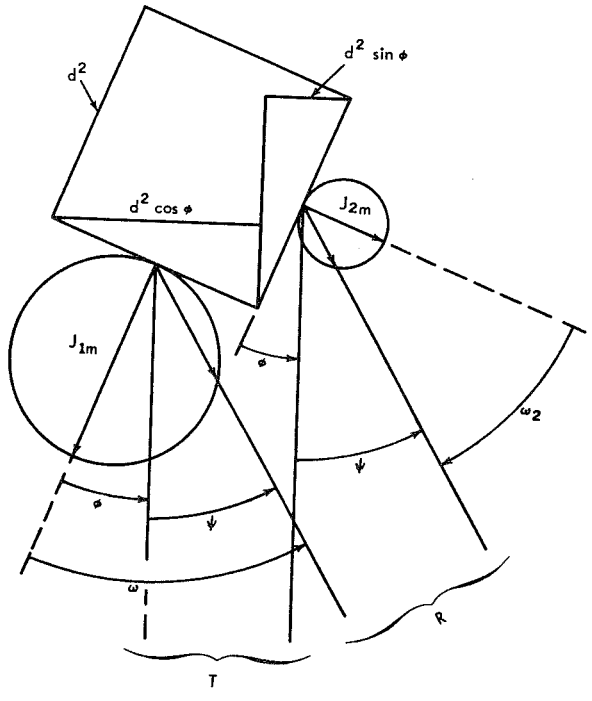

FIGURE 8.—Lambertian scattering from two faces of a cube.

radiant intensities become

$$\left.\begin{aligned} J_{1m}&=\frac{aP_1}{\pi}\\ J_{2m}&=\frac{aP_2}{\pi}\end{aligned}\right\}. \tag{11}$$

Thus, the intensity in the arbitrary direction ψ becomes

$$J_\psi=J_1+J_2=J_{1m}\cos\omega_1+J_{2m}\cos\omega_2. \tag{12}$$

From the expressions of Equations 10 and 11 and the angular relations of Figure 8, we derive

$$J_\psi=\frac{ad^2H}{\pi}\left[\cos\phi\cos(\phi+\psi)+\sin\phi\cos\left(\frac{\pi}{2}-\phi-\psi\right)\right],$$

$$J_\psi=\frac{ad^2H}{\pi}\cos\psi. \tag{13}$$

Equation 13 describes the Lambertian characteristic for a plane surface of the area d^2 normal to the incident radiation.

The rotation of the cube seems to have no effect. This, however, is not true because Lambert's law is restricted to a single lobe of the cosine pattern, which means that in Equation 12 ω_1 and ω_2 may only take values for which their cosines are positive. Consequently, the patterns take the forms of those shown (Fig. 9) for various angular orientations of the cube, and we can see that the monostatic cross section remains unaffected by rotation.

Since the pattern of a spherical satellite was shown to be particularly useful and since the frequency diversity technique requires scattering centers at various depths, a polyhedron with a large number of faces is preferable. A small model (1.83 m diameter) of the inscribed sphere was built and tested for the National Aeronautics and Space Administration.[2] A regular dodecahedron was chosen for the completed model (Fig. 10). The model was erected from a small, randomly compacted package by inflating the tubular framework; the skin, a perforated aluminum-polyester laminate, de-

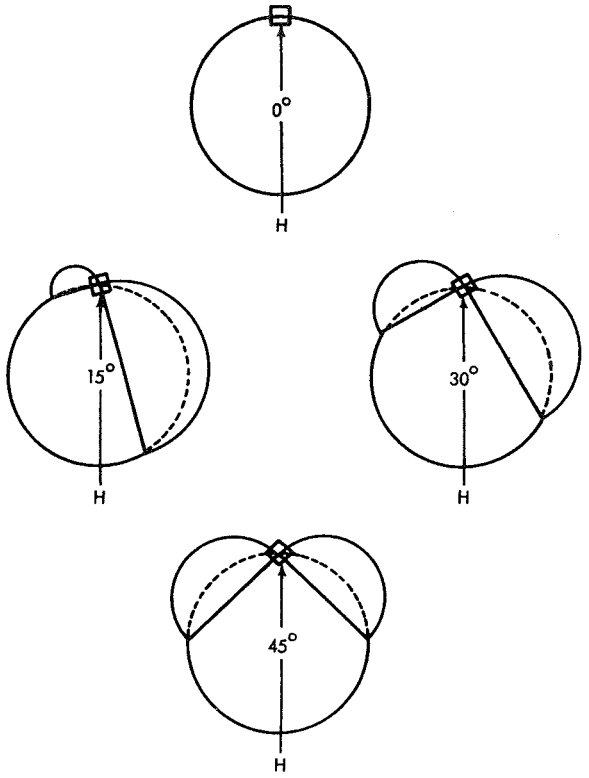

FIGURE 9.—Lambertian scattering patterns of a cube in various angular positions.

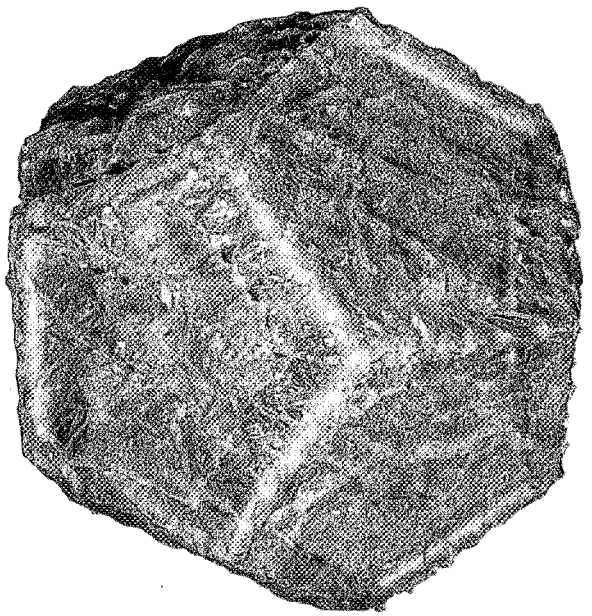

FIGURE 10.—Satellite model with Lambertian surface.

[2] Contracts NAS 5-890 and NAS 5-1598.

veloped wrinkles automatically. However, one of the pentagons was covered with unperforated, wrinkled aluminum foil. Seven adjacent pentagons were covered with a skin which was only 16.5 percent larger than the pentagon in linear dimensions, and five were covered with a 45-percent larger skin so that deeper wrinkles could form.

Designs and computations of full-size satellites have been prepared for the U.S. Navy by General Mills, Inc. (Reference 3). Of particular interest are the weight savings afforded by the diffusely scattering satellite over the specularly reflecting sphere. These savings increase with the size of the satellites. In other words, more signal strength per unit weight of the satellite can be obtained from diffusely reflecting satellites supported by a tubular framework. For example, a 200-lb, diffusely scattering sphere has a diameter of 165 feet, while the specularly reflecting sphere has a diameter of 105 feet, or even less. This means an increase of the intercepting cross section by a factor of 2.5, or 4 db. If we add the gain of 3 db due to the directivity of the scattered radiation from a diffuse satellite, the total gain becomes 7 db for the Lambertian satellite of near spherical shape.

Greater reliability and longer life can also be expected from the diffusely scattering satellite. The erection by inflation of the tubular framework can be controlled better than the inflation of a large balloon in space and a random surface within wide tolerances is easier achieved and maintained than a precise spherical surface.

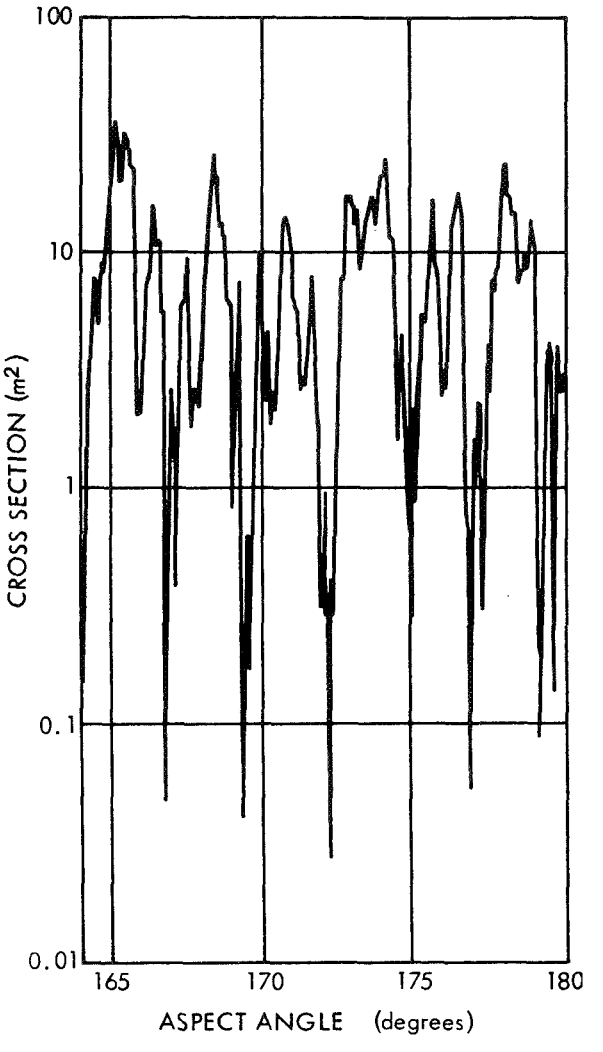

FIGURE 11.—Section of the recording of the monostatic scattering cross section.

ELECTROMAGNETIC TEST RESULTS

Measurements of monostatic and 90-degree bistatic scattering cross sections were performed by Radiation, Inc., on an outdoor range at a radio frequency of 10 Gc. The wavelength of 3 cm is about ten times too long to give realistic scaling with respect to the size of the model. However, if the cross section is at a level to confirm Lambertian scattering, it will stay that high for all higher frequencies, provided the perforation of the skin is small enough. During the tests, the model was rotated and tilted to give readings for all possible aspects. A typical recording of the cross section as the model revolved 16 degrees is presented in Figure 11. The recording is that of a stationary time series; therefore, statistical parameters were evaluated from the entire portion of the recording. Fluctuations extend over a wide range and, owing to the logarithmic scale, depressions are overemphasized. The probability distribution function and the probability density function derived by graphic means and shown in Figures 12 and 13 display good agreement with theoretical exponential distribution. The latter has been added to the figures with parameters chosen for the best fit. Since the probability density

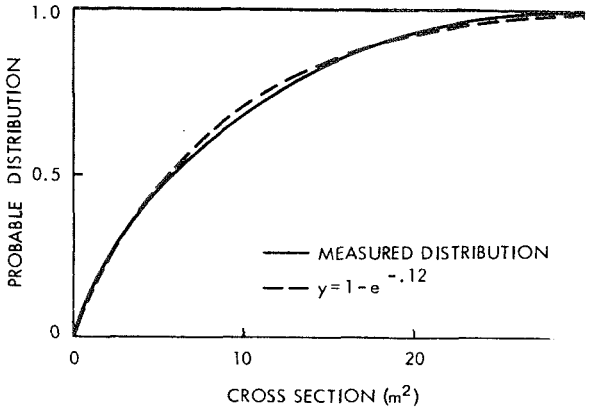

FIGURE 12.—Probability distribution function of the monostatic scattering cross section of the satellite model.

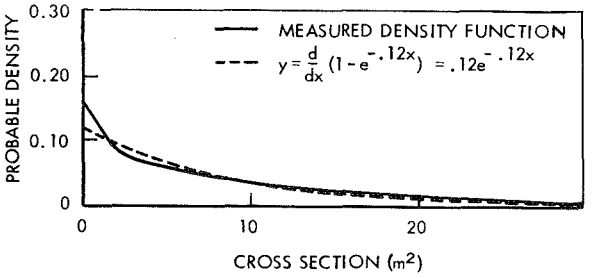

FIGURE 13.—Probability density function of the monostatic scattering cross section of the satellite model.

function as the derivative of the distribution function is very sensitive to errors in the evaluation process, some of the deviations of the density function from the experimental law may be discounted as errors.

The recording (Fig. 11) was calibrated by means of a flat disk of known cross section. Thus we obtained a median level of 7.1 m^2 and a mean of 10.2 m^2 and derived a monostatic gain of 4.8 db over the scattering cross section of a specularly reflecting sphere with the same physical cross section as that of the model. Theroretically, the gain of a Lambertian sphere would be 4.3 db.

The entire monostatic recording showed variations of statistical parameters. Evaluation of other portions which appeared stationary in time revealed many areas where the gain was higher, for example, 5 db over a 60-degree portion, 6.5 db over a 36-degree portion, and as much as 8.3 db over a 25-degree portion. Smaller portions showed less gain. The lowest gain was 1.9 db over a 20-degree portion. Some of these deviations could be explained: For example, the highest gain was noted when the lightly wrinkled aluminum foil face was in a position normal to the transmission path. It did not diffuse the radiation sufficiently and thus contributed to the lowest gain when the foil was tilted but still on the illuminated side of the model. When the deeply wrinkled faces were on the illuminated side, the return was so stationary that a periodicity due to symmetries of the model could not be observed.

The generally higher gain of the model than that of a Lambertian sphere is due to the polyhedral shape. For example, a cube (which deviates even more from a sphere) has a theoretical gain of 6 db. As a consequence, the bistatic scattering cross section was in average 4.5 db lower than that of a Lambertian sphere.

The fluctuation of the cross section shown in Figure 11 was the slowest recorded and agrees well with the expected rate because of the rotational rate, wavelength, and size of the model. Other portions of the recording showed considerably faster fluctuation. This fluctuation rate can be explained as a wind effect, since even the slight breeze observed caused the light and unsupported skin to wave. To test this explanation, the rotation of the model was stopped on one occasion; and, as the recorder continued, the distribution and fluctuation rate of the cross section remained unchanged.

Because of the wind, it was not possible to obtain the cross section-versus-frequency data necessary to determine the spacing for frequency diversity. The amount of depolarization was determined by rotating the polarization of the transmitting antenna 90 degrees. It was found that the crosspolarized echo was 6 db lower than the return of paralleled polarization.

CONCLUSION

A passive communication satellite consisting of a tubular framework and a randomly wrinkled, perforated, and reflective skin will scatter electromagnetic waves according to Lambert's law. Consequently, a scattering pattern of very suitable directivity can be

gained with a device which is lighter and more reliable than a specularly reflecting sphere. The Rayleigh distribution of the return requires the use of diversity techniques, whereby the frequency diversity is most attractive and can be realized with no additional power or antenna requirements.

REFERENCES

1. KAHN, L. R., "Ratio Squarer," *Proc. IRE* 42(11) : 1704, November 1954.
2. BRENNAN, D. G., "On the Maximum Signal-to-Noise Ratio Realizable from Several Noisy Signals," *Pro. IRE* 43(10) : 1530, October 1955.
3. "Large Passive Satellite Study," Vol. I and II Final report on Contract Nonr (3245)(00)(X).

DATA STORAGE FOR METEOROLOGICAL SATELLITES

M. I. SCHNEEBAUM AND R. A. STAMPFL

Goddard Space Flight Center

Huge quantities of data will be stored and readout from advanced weather satellites, such as Nimbus. Data storage thus becomes a critical feature of design. This paper discusses some of the advanced research being conducted by the Goddard Space Flight Center (GSFC) in the field of electronic and magnetic data storage of video information in meteorological satellites.

Electrostatic storage is the basis for two unique TV systems being developed by RCA for GSFC. Two basic processes characterize these systems:

1. An optical image is converted to an electrical charge pattern that can be stored for relatively long periods of time (writing process).
2. The transformation at will of this charge pattern into a video signal (reading process).

The storage vidicon is the heart of the Automatic Picture Transmission System (APTS) which will be flown on Nimbus. This system provides wide-angle cloud-cover pictures from a satellite and transmits them in real time on a narrow-band channel to a local ground station for recording on facsimile equipment.

The storage vidicon resembles a conventional vidicon except for the addition of a thin, high-resistance polystyrene storage layer on the photoconductive surface. A cutaway view of the front end of the vidicon is shown in Figure 1. The tube is operated by holding the target potential constant and raising or lowering the mesh potential with respect to the target during the prepare, expose and readout sequences. The vidicon photoconductor is optically exposed by means of a mechanical shutter, and is

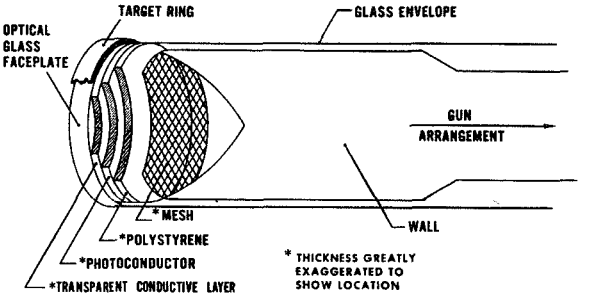

FIGURE 1.—Polystyrene Storage Vidicon.

then electronically "developed," that is, the charge image is transferred from the photoconductor layer to the polystyrene storage layer. The readout cycle follows for 200 sec, during which picture information is readout at the rate of 4 lines per sec.

Experimental evidence indicates that the polystyrene surface suffers radiation damage under prolonged electron bombardment, resulting in reduced lateral resistance and loss of storage capability. Research is being conducted to improve radiation resistance of the polystyrene by increasing the purity of the materials. The addition of a flood gun is being investigated to reduce the electron bombardment. In addition, other materials are being investigated.

On readout, the video signal amplitude modulates a 2400 cps subcarrier which in turn frequency modulates a 5-w transmitter as indicated in the block diagram in Figure 2. The requirement for the system to pass very low-frequency video signals was a difficult problem, solved by pulsing the cathode with a 4800 cps

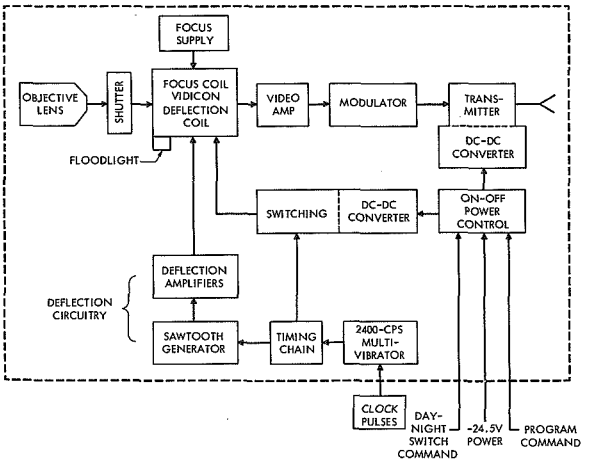

FIGURE 2.—APTS diagram for satellite.

subcarrier. This subcarrier signal causes the readout electron beam to be chopped at the 4800 cps rate. The charge pattern on the polystyrene storage layer amplitude modulates the subcarrier. The video modulated subcarrier is A.C. coupled to a bandpass amplifier and detector.

Video data is continuously transmitted during the daytime portion of the satellite orbit. The system has a linearity of 0.5 percent and a limiting resolution of 700 TV lines. System linearity was achieved through special yokes, vidicons, and digital sweep circuits. Highlight sensitivity is 0.7 foot-candle sec. Signal-to-noise ratio is 26 db, giving approximately 7 grey scales. A grey-scale calibration wedge, consisting of 11 known levels, is located at the top of each picture, parallel with the horizontal scan. A flash tube illuminates the wedge each time the shutter is activated, giving a calibrated scale on each picture. The angular coverage is 108 deg, which, for a 500-n. mi. altitude satellite, yields approximately 1150 by 1150-n. mi. ground coverage per picture.

The storage vidicon thus permits slow scan readout, and a narrow bandwidth permits use of simple ground-station equipment. The APTS ground station can be assembled from inexpensive, off-the-shelf commercial components. The ground station consists of a helix antenna and a preamplifier mounted on a pedestal, a narrow-band FM receiver, and a commercial facsimile recorder modified for automatic start and stop, employing the airborne subsystem control signals, and thus permitting any local weather station to obtain direct cloud-cover pictures of the immediate area whenever the satellite is in view.

With an investment for a ground station of approximately $30,000, meteorological groups throughout the world will receive local real-time cloud pictures at least once a day for immediate use.

A second television system under development for Nimbus which utilizes the electrostatic storage is the Dielectric Tape Camera. The storage medium is a thin flexible tape coated with suitable materials which permits storage of an electric-charge pattern on an outer insulating layer.

The writing process consists of exposure of the tape to an optical image through a lens system in a manner similar to photography. However, in this process, the tape is also exposed to a uniform electron beam that deposits an electric charge on each elemental area of the tape in proportion to the amount of light falling on that area. Optical and electrical exposures both occur from the insulating or dielectric side of the tape.

To convert this charge image to a video signal, the portion of tape on which the image is stored is moved to a location where it can be scanned by the electron beam that performs the readout process. In this process, the polystyrene surface is scanned by the read beam in much the same manner as an image orthicon target is scanned by the electron beam. The result is that in the scanning process, the return beam is modulated by the charge pattern on the insulation.

The tape itself is 35 mm wide and consists of three layers on a base material, as shown in Figure 3. The base material is optical quality nylon called "Cronar." These optical properties were important in early development, when the tape was exposed optically through the base material. Research into the basic process indicates that it may be advantageous to make the base from an opaque material since optical exposure can be performed directly on the

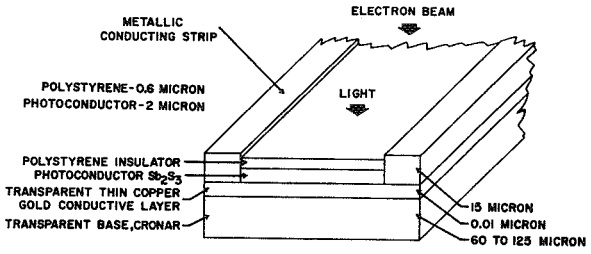

FIGURE 3.—Dielectric-tape construction.

dielectric material, rather than through the base.

Three layers are superimposed on this base in sequence using vacuum deposition techniques. These layers are deposited on a continuous basis, with the tape moving at a constant rate of speed. Lengths as long as 50 ft have been processed on this laboratory tape machine.

The first layer is a gold-and-copper combination approximately 0.01 micron thick which forms a transparent conducting coating that serves as the electrical connection to one side of the photoconductive layer.

The photoconductive layer is similar to the photosensitive layer of commerical vidicons, and the spectral response of the system is determined by this layer. The material used at present is arsenic trisulphide.

The final layer is an extremely thin uniform coating of polystyrene approximately 0.6 micron thick. This is the insulating layer that acts as a capacitor for holding the electric charges forming the charge pattern equivalent to the optical image.

A laboratory camera has been developed which has demonstrated the feasibility of utilizing the dielectric tape principles for observing the storing cloud-cover pictures from a satellite. The tape camera performs the combined function of observation and storage, replacing both the vidicon camera and the tape recorder. An advanced model is now under development which will closely approximate the flight configuration. This is shown in Figure 4. A number of problems remain to be solved, since the entire enclosure must be evacuated for proper operation.

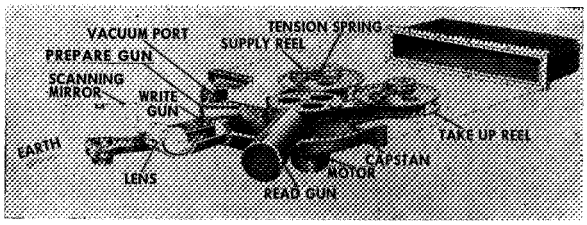

FIGURE 4.—Dielectric-tape camera.

The electrostatic camera possesses the following inherent capabilities:

1. Higher packing density per pound than the conventional camera/tape recorder configuration.
2. Limiting resolution comparable with the best image orthicons. 1200–1500 TV lines is currently achievable, with a target of 2500 TV lines in the foreseeable future.
3. Slit camera type operation, which permits wide angular coverage with low distortion.
4. Sensitivities comparable to currently available airborne vidicons, and low light sensitivities of the order of 0.01 ft-candle sec.
5. Variable resolution readout capability.

The present camera configuration can store on tape two complete orbits with horizon-to-horizon coverage with 0.2 mi. ground resolution.

The present Tiros and initial Nimbus spacecraft contain conventional vidicons with magnetic tape as the storage medium. The same is true of the infrared scanning system.

Simple calculations indicate that 10^7 infrared information bits and 5×10^8 TV informations in 96 pictures must be stored per orbit. These data are presented in analog or binary coded form. Data storage without mechanical movement is, of course, attractive. However, development of large memories with size, weight, and power comparable to magnetic tape recorders does not appear feasible within the next few years. For this reason, the improvement of magnetic-tape storage devices is constantly being investigated in-house at Goddard Space Flight Center.

A medium capacity endless-loop tape recorder has been successfully developed for satellite applications. The recorder utilizes 120 ft of ¼-in. tape, and records for 1½ hr. Playback is at 30 times the record speed. The recorder consumes 2 w of power on record and 10 w on playback.

Recorder development has emphasized flexibility so as to serve as many applications as possible. Momentum compensation has also been of prime importance. Stabilized spacecraft are controlled by small torques so that even the small unbalanced momentum generated by the recorders become major disturbances. Long-life applications require a sealed pressurized container; the lower section of the container houses drive-amplifiers for 100-cps synchronous motors, a pressure transducer, and auxiliary electronics. Inherent ruggedness of these units makes direct mounting on the container feasible with standard encapsulation employed.

An analog version of the recorder has the endless-loop cartridge in the center of the container, partly covered by plugs, and the record and playback motors in the form of two cyclinders to one side. A single capstan drives the tape across the head, held firm by a pressure pad. By single substitution, an eight-track digital head is mounted with the electronic record and playback amplifiers alongside.

Since the tape drive is a delicate mechanism, it must be mounted so as to survive the large range of vibration environments encountered in different structures. In general, resonance of these structures occurs at low frequencies, so the mount itself can be designed for resonance at higher frequencies. The tape drive is mounted between two plates tied to two shelves of the container by means of miniature dampers, and up to 20 g's rms of random noise vibration can be applied, or an equivalent sinusoidal sweep, without failure.

The record and playback amplifiers for analog units are inherently more reliable than the drive mechanism. Conventional analog amplifiers are being used. Digital amplifiers, however, lend themselves more readily to design by integrated circuits. The high reliability of these circuits when silicon planar transistors are used, and their small size, makes it practical to include an eight record/playback amplifer package in the recorder since it can be built with a volume equal to that of the recorder head. Such circuits can be operated at power levels of one microwatt per stage so that thermal dissipation of an assembly is negligible. Thus, these circuits run at low temperatures and are extremely reliable.

Each record amplifier consists of four transistors which can be mounted with its associated resistors in a standard transistor can. Conventional non-return-to-zero recording is used in which zeros and ones magnetize the tape in opposition. Separate erase is thus not needed. A microphotograph of the amplifier is shown in Figure 5. The small square is a field-effect transistor preamplifier; the next larger square a silicon crystal with load and coupling resistors etched on the surface which serves as the next transistor stage. The longest cyrstal contains two direct coupled transistors and associated circuitry.

Similarly, playback amplifiers have been developed where the head output is amplified

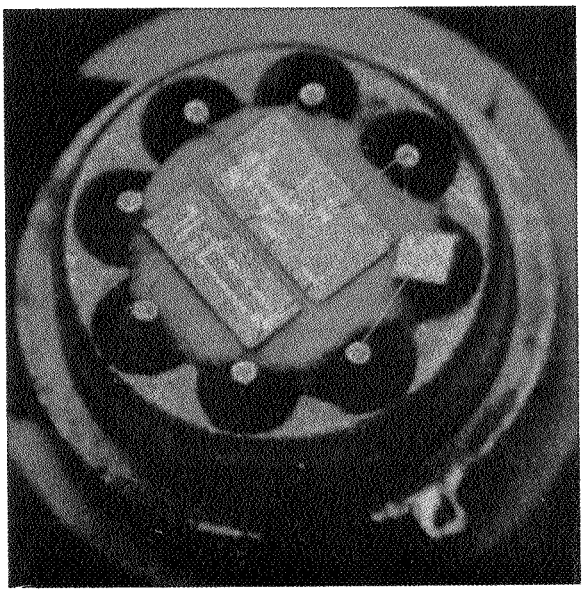

FIGURE 5.—Single digital record amplifier is shown in this microphotograph. Small square is a field-effect transistor; larger silicon crystals contain other circuitry.

and the wave-shape reconstructed by a multivibrator so that conventional or microminiature logic circuitry can process the pulse train. The power levels and small volume of these circuits permit selective redundance at small cost in terms of weight and volume.

Redundant logic circuitry can readily be designed to achieve long-life recorders. A contribution toward this end is the development of an analog-to-digital converter sufficiently small and of sufficiently low power that digital recorder techniques become comparable with analog.

Analog-to-digital converters can also be built according to any of the standard techniques using integrated circuits for the logic. The speed required for the conversion often determines the techniques used. A compromise between complexity and speed in an analog-to-digital converter leads to a design where the input signal is compared sequentially to a number of binarily related voltages, setting appropriate flip-flops. Readout can be serial or parallel as desired, since the flip-flops hold their positions until recycled. For most meteorological applications, seven bits or 128 levels is adequate. For infrared sensing, it is sufficient to operate this converter at a 40 microsec per bit rate, with total conversion requiring 280 microsec. Logic for such a converter has been microminiaturized and operates at less than 5 microwatts for this logic, with an additional 50 microwatts needed for the error amplifier and weighing network.

The requirement for large storage capacity led to the development of an endless-loop recorder having 1200 ft of ¼-in. tape. Playback speed is 30 ips, and record speed is either 30 cps or 3¾ cps. The unit will record analog video whose subcarrier is frequency modulated. Initially, infrared scanner signals will be recorded. Later models will record TV frames when a fast start and stop is perfected.

The advantages of endless-loop recorders over more conventional two-reel types lie in their convenient readout capability. Since the tape moves in the same direction for record and playback, no recycling time is lost and a complicated high-speed recycle mechanism is not needed. Readout can be commanded at arbitrary times and, since erase can be performed immediately prior to record, only the oldest information will be erased regardless of how many readouts are performed within a given time.

A view of a laboratory-model recorder and a cross-section of the tape cartridge are shown in Figure 6. Loops of a few hundred feet or shorter can be pulled without additional guide. The differential velocity between tape layers demands good tape lubrication, particularly in view of wide temperature requirements and attendant tension changes. These side effects became predominant when long loops were designed. Regular mylar magnetic tape cannot be used in untreated form. Preshrinkage at high temperatures creates good dimensional stability so that drive forces stay within tolerable limits. Tape lubrication has a direct

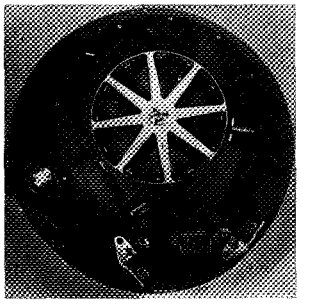

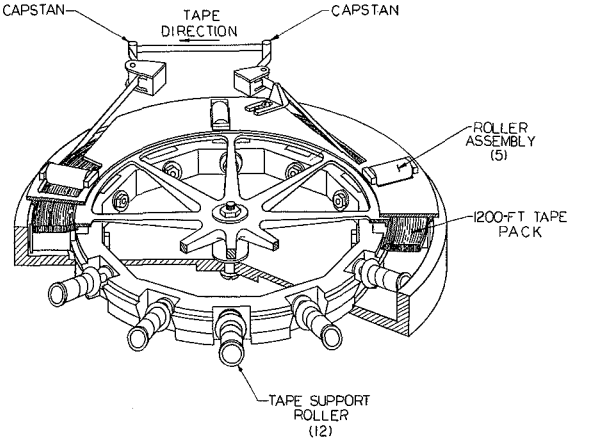

FIGURE 6.—1,200-ft-tape endless-loop recorder now looks as shown in the photo at top, a laboratory model. The drawing below shows details of its endless-loop cartridge.

influence on speed constancy, and the lubricant must be perfectly smooth. Low flutter and wow can only be achieved in long loops when tape support rollers are used, thus helping to overcome the velocity differential between the inner and outer radius.

Better performance has been achieved with long loops than with short ones with flutter and wow of 0.17 percent rms up to 1000 cps and 0.102 percent rms up to 300 cps measured on a laboratory model. The general layout of the tape drive is an outgrowth of the short loops. Around the spoked wheel, retained by rollers, is the tape loop which is driven by two capstans from the innermost portion of the tape to the outer. As in other recorders, Mylar belts are used for speed reductions and a clutch engages the capstans to the record or playback drive chain, respectively.

The same drive principle can be applied to multiple track ¼- and ½-in. tapes and to digital recorders, thereby generating a family of equipment for a variety of meteorological satellite requirements.

A MEDIUM-DATA-RATE DIGITAL TELEMETRY SYSTEM[1]

MARJORIE R. TOWNSEND, PAUL M. FEINBERG, AND JOHN G. LESKO, JR.
Goddard Space Flight Center

Earth-orbiting satellites require on-board data storage. A suitable medium-data-rate digital telemetry system with 10^7-bit storage is described. Since this storage is provided by a tape recorder, a unique technique for wow and flutter compensation has been developed. Hardware applicable to the radiation experiments on the Tiros and Nimbus meteorological satellites has been built and is currently being tested.

INTRODUCTION

In addition to television cameras for taking pictures of the earth's cloud cover, the Tiros series of meteorological satellites carries a radiation experiment.[2] The Nimbus series will carry a similar experiment. The earth's temperature is produced by self-emitted radiation and reflected solar radiation. Present medium resolution radiometers filter the combined radiations into five spectral regions. Their geometry is such that the signal has a $(\sin x)/x$ response, the first null occurring at 8 cps for Tiros and at 16 cps for Nimbus. The sampling rate required to reproduce this signal should therefore be greater than twice the maximum frequency response. In this system, each of the five radiometer channels is sampled 33⅓ times per second.

DATA STORAGE

In a circular earth orbit, data storage on board the satellite is a difficult problem. The most efficient storage system is a tape recorder. In the old FM telemetry system, the limiting factor in terms of signal-to-noise ratio was its wow and flutter. This limit was about 27 db. In the present system, where the data is digitized before it is recorded, it is anticipated that 40 db can be achieved; the limit will then be due to the radiometer itself. Error analyses, not theoretical but practical, which have been run in the laboratory show that the bit-error probability due to the transmission link will be less than 0.1×10^{-7}. This can be achieved even on a recorder having the equivalent of 2 months' operation in orbit.

A brief description of the digital storage system is in order. The tape recorder can store 10^7 bits of data, adequate for an orbit greater than 100 minutes. It measures 6 by 8 by 6½ in., weighs 10½ lb, and uses less than 2 watts in the record mode and about 12 watts in the playback mode. The two-speed recorder (0.45 ips and 11.7 ips) contains up to 250 ft of lubricated ¼-in. tape, in a continuous-loop cartridge driven across an 8-track staggered digital record-playback head. Saturation recording is used, the direction of the flux alternating for "ones" and "zeroes" with the bits conservatively packed at 500 per in.

Eight record and /eight playback amplifiers can require a considerable volume. In addition, head-lead length should be kept to a minimum to reduce noise pickup. This, then, seemed to be a critical area in which microelectronics could provide a considerable advantage. The result of a contract with CBS Laboratories to develop suitable amplifiers is a package 4 by

[1] This report supersedes Goddard Space Flight Center document X-650-63-194, September 1963.

[2] Davis, J. F., Hanel. R. A., et al., "Telemetering Infrared Data from the Tiros Meteorological Satellites," NASA Technical Note D-1293, June 1962.

1.359 by 1 in. (Fig. 1) containing ten record and ten playback amplifiers (two spares) which can be mounted directly on top of the tape recorder, accomplishing the triple purpose of minimizing weight, size, and head-lead length. Each head, which has a nominal impedance of 22 ohms, requires 3.5 ma of current. By deriving this from a constant current source, the power requirement is 10 mw per track during the record cycle.

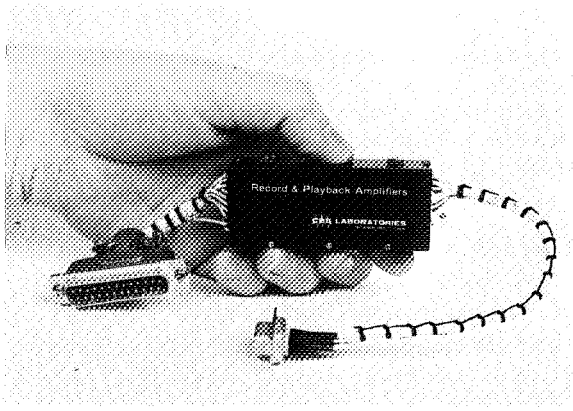

FIGURE 1.—Amplifier package.

SYSTEM DESIGN

The digital electronics package, which weighs about 8 lb, requires 1.5 watts in the record mode and 7.2 watts in the playback mode. This latter figure includes the power used by the transmitter. The total system power is 3.5 watts in record and about 20 watts for the 4 minute playback cycle. The way in which the data and synchronization signals are handled will be considered next. An eight track tape recorder lends itself well to a 7 bit signal recorded in parallel across the tape, the eighth track being used for a clock signal. Seven-bit digital conversion will provide an accuracy of 1 part in 128. The clock track, one of the middle tracks, will be recorded 90 degrees out of phase with the signals on the other seven tracks, so that its edges can be used to trigger the readout in the center of the other data bits.

The record rate chosen was 200 bits per sec on each of the eight tracks in nonreturn-to-zero (NRZ) format, each bit lasting 5 msec. The format (Fig. 2) as the signals go on tape is as

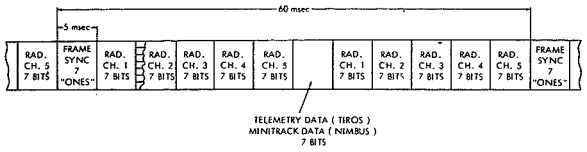

FIGURE 2.—Nimbus and Tiros digital main frame telemetry format.

follows: Frame sync, a signal composed of all "ones", is recorded laterally across the tape. This is followed by the 7-bit output of the analog-to-digital converter. The analog signal from the first of the five radiometer channels, varying between 0 and −6.4 volts, is converted with an accuracy of 1 part in 128. Similarly, the remaining four radiometer channels are converted sequentially to digital form and the resulting bits become words 3 through 6.

The seventh word will contain timing data for Nimbus or a subcommutated channel for Tiros. Coherent with the sampling rate, the Minitrack time code is generated in the Nimbus clock and presented to this system in NRZ format. This information is updated every second, each of its 100 sequential bits lasting 10 msec. Of these 100 bits, only 36 represent timing data. Hundreds of days, tens of days, units of days, tens of hours, units of hours, tens of minutes, units of minutes, tens of seconds, and units of seconds are each indicated by 4 bits. The remaining 64 bits are for synchronization and station identification data. During the 60-msec frame period, 6 of the Minitrack bits will be stored in a shift register. At the proper time for recording the timing word, a "zero" is added, and this plus the 6 Minitrack bits are recorded on tape. Obviously, the 6 bits do not maintain any specific pattern, but they can be unscrambled in a suitable demodulator.

In the Tiros system, the seventh word is reserved for housekeeping data and a low-data-rate experiment. With a data input channel in this slot every other frame, a piggyback experiment can be sampled 8 times per sec. Alternating with this is subframe sync, the temperature of the radiometer baseplate which is required for accurate data reduction, the temperature and pressure inside the digital tape recorder, and a signal which correlates the

radiation data with the TV pictures of the earth's cloud cover.

Words 8 through 12 are the next samples of the five radiometer channels in the same order as words 2 through 6. Thus, each radiometer channel is sampled once every 30 msec. This constitutes the frame, which is repeated over and over for the length of the orbit. The storage capability of the recorder is about 2 hours. Logic will prevent all "ones" from occurring at any time other than frame sync; i.e., 7 data "ones" (127) will never occur.

The Nimbus system block diagram in Figure 3 will help to clarify the system description. The frame format gating network selects 7 "ones" for frame sync, 7 binary bits in parallel from the analog-to-digital converter whose input is determined by the analog gating network, or the "zero" and 6 bits from the Minitrack storage shift register. The selected 7 pulses, each 5 msec long, either "ones" or "zeros," are applied to seven record amplifiers and recorded on the tape. On the clock track is recorded a 100-cps square wave, equivalent to alternating "ones" and "zeroes" at the 200 bit per sec rate. The change of state of these pulses is delayed by 2.5 msec (half a pulsewidth) in relation to that on the other seven tracks. The purpose of this, as described before, is to use the edges of the clock pulses to sample the data at the optimum time in the middle of the pulse. Figure 4 illustrates the similarities and differences between the Tiros and Nimbus systems. Feinberg gives a detailed description of the system design.[3]

DATA READOUT AND ACQUISITION

After each orbit which brings the satellite within range, it is interrogated as it passes over the data acquisition station. When the tape recorder is commanded into playback mode, it plays back the stored radiation data at 11.7 ips (a speedup ratio of 26:1) in about 4½ min. The record rate is 200 bits per sec, but the playback rate becomes 5,200 bits per sec. This 5.2-kc playback rate varies because of the wow

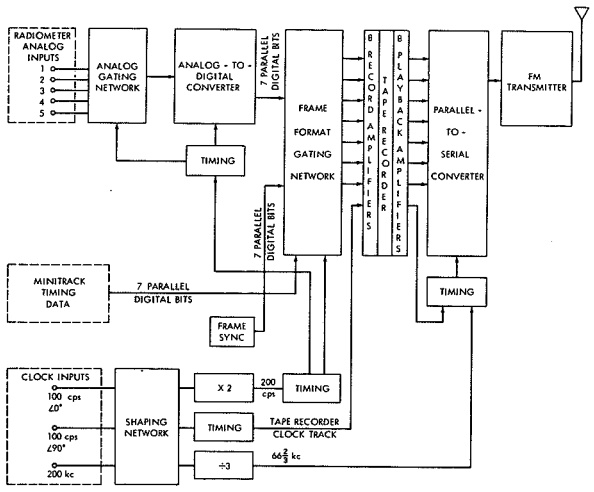

FIGURE 3.—Nimbus medium resolution infrared-pulse code modulation (MRIR–PCM) system.

and flutter inherent in the tape recorder. Several techniques are possible for reading out the data from the tape and converting it to serial form for transmission. A discriminator on the output of the clocking track may provide a voltage to control a voltage-controlled oscillator for clocking the parallel-to-serial converter at the output of the tape recorder. However, this would provide a varying transmission rate which would be difficult to synchronize on the ground, so a different technique has been chosen.

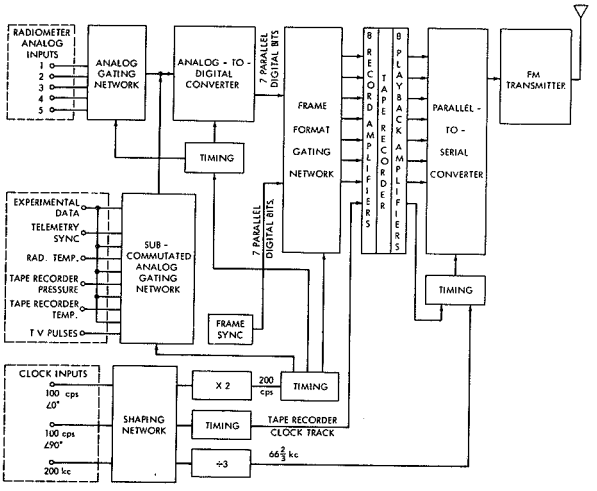

FIGURE 4.—Tiros MRIR–PCM system.

[3] Feinberg, P. M., "The MRIR–PCM Telemetry System—A Practical Example of Microelectronic Logic Design," NASA Technical Note, to be published.

Pulses developed from the clock track will trigger the readout of the other seven parallel tracks into storage flip-flops of a parallel-to-serial converter as described above. At this point the format of the frame is completed. A "one" for word sync is added to the beginning of each word in the parallel-to-serial converter as the data is strobed out of the storage flip-flops. A stable frequency from the Nimbus clock (66⅔ kc), or from a crystal-controlled oscillator for Tiros, is used for strobing these flip-flops so that the transmitted bit rate will be very stable. If no new data is in the storage flip-flops after one strobe is completed, the transmitter will transmit "zeroes" until new data is available. This will happen because the time required to strobe and transmit the seven tracks plus the added "one" will be less than the $\frac{5}{26}$ msec, 192 μsec, between words on the tape. Logic will prevent reading out of the tape while the output register is shifting. This system is designed to guarantee at least one "zero" to prevent the possible occurrence of 8 "ones" in a row at a time other than frame sync, and will average about 4 (4.82) "zeroes" or 12 (12.82) bits per word. This also guarantees a minimum bit rate of 5,000 bits per sec. Thus, the transmitted serial train of NRZ pulses contains words of varying length (9 to 15 bits per word) to compensate for the changes in speed of the tape recorder and any variations in the recording rate. The cost of keeping the transmitted bit rate stable is the need for a 50-percent wider video bandwidth. However, the advantage of the stable transmitted frequency and much less complex spacecraft system make the tradeoff worthwhile.

The serial train of pulses thus created frequency-shift-keys a 1.75-watt FM transmitter. Because of the system design, the frequency can vary only between 5,000 bits and 66⅔ kilobits per sec. The deviation selected was ± 25 kc, providing a minimum modulation index of 0.8. Table 1 gives the parameters for for a 600-mi. orbit. The results show a signal-to-noise ratio into the bit synchronizer of 28 db at the horizon, with 40 db when the satellite is at its zenith point. The use of the 60 ft dish for Tiros reduces these figures by 3 db if the same frequency is used, but the safety factor is adequate.

TABLE 1.—*Transmission Data*

Datum	Value
Range at horizon	2270 st. mi.
Orbital altitude	600 st. mi.
Path attentuation at horizon	147 db
Path attentuation at zenith	135 db
Satellite antenna gain	−3 db
Ground antenna (85-ft dish) gain	29 db
Antenna temperature	290° K
Cabling losses	−2 db
Transmitter frequency	136 Mc
Transmitter power	1.75 watts
Receiver bandwidth	100 kc
Receiver noise figure	5 db
Signal-to-noise ratio at horizon	28 db
Signal-to-noise ratio at zenith	40 db

GROUND DATA PROCESSING SYSTEM

After demodulation by the receivers (Fig. 5) the digital signal, still in serial form, is recorded at the ground station on an instrumentation tape recorder. Simultaneously, it is presented to a bit synchronizer whose output is recorded on another track of the same instrumentation tape recorder. A demodulator and digital-to-analog converters are used at the data acquisition station to judge the overall quality of the satellite data. Full-scale data processing must be handled by a computer because of the copious quantities of data.

Figure 6 illustrates the operation of the ground-station complex. After presentation

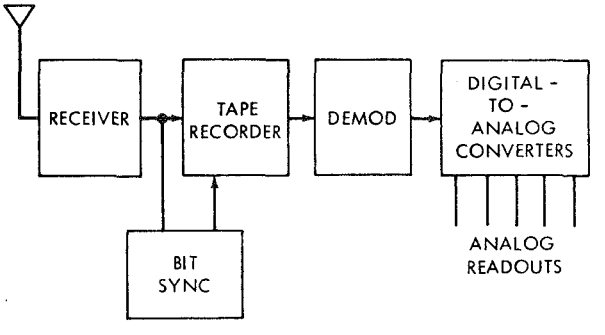

FIGURE 5.—Data acquisition station diagram.

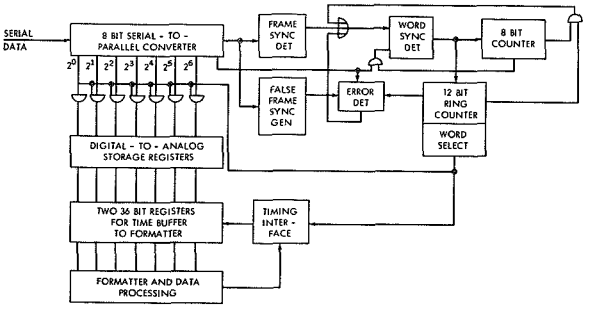

FIGURE 6.—Simplified ground station diagram.

to the bit synchronizer, the serial train of bits is converted to parallel format in an 8 bit shift register where a search is made for the unique frame sync word. When this is detected, a second search begins for the word sync bit which is used to direct the parallel output of the input shift register to the proper digital-to-analog converter flip-flop storage network. Eight bits are counted out for each word, if the "zero" bits which follow it are ignored, and 12 words are counted out between frames This procedure continues through the whole 12-word frame, after which the search for frame sync begins again.

If frame sync should fail to appear within a selected time tolerance, a false frame sync is generated in the Tiros ground stations, since the loss of data words could mean a loss in time correlation and thus an error in determining the correct orbital geometry. To provide a surer selection of true frame sync, three frame syncs must be detected, without error, before a frame sync error is locked out. Three errors in one frame will put the system back into the search mode again, looking for true frame sync. An error is defined as finding that the ninth bit after word sync is a "one" instead of a "zero," or that frame sync does not occur within the proper time interval.

An output signal will occur after 64 false frame syncs to flag the occurrence of the splice or serious losses of data. Almost that many can be expected each orbit at the tape splice. Sixty-four frames are equivalent to 3.84 sec of data, a small percentage from a 90-minute orbit, but important in terms of maintaining time.

The individual words can be directed to digital-to-analog converters, so that the signal levels for each channel may be analyzed by hand, or they may be directed to a formated where they are combined into standard 36-bit IBM words and transferred to a digital tape which can be handled automatically by a computer. The format will be the same as that now used for the Tiros radiation experiment data. However, the housekeeping data which appear on the subcommutated channel will appear periodically as a special word on the tape and will be decommutated by the computer. With this data the calibration of the radiometer data can be adjusted automatically to conform to the changing satellite temperature. The error-output signal described above will generate a special code word to tell the computer about the occurrence of unacceptable data.

For Nimbus, absolute time in the form of the Minitrack time code will appear on the computer tape as a single word, which is updated every real-time second. There will be about 33 data words between each timing word, which will be flagged to the computer by a special code word.

The normal five-channel data will be handled by shifting each 7-bit data word in parallel into a 36-bit shift register. After the register has 5 words or 35 bits, a "one" is added in the 36th bit and the IBM-formated word is shifted out in groups of 6 bits. While this shifting operation is occurring, the data words will be stored in a second identical 36-bit shift register which alternates with the first in accepting data and shifting them into a buffer. From the buffer the data are formated onto the digital tape.

HARDWARE

The hardware (Fig. 7) for this telemetry system has been designed and built with the Series 51 integrated circuits developed by Texas instruments. Flip-flops and different types of gates are fabricated in tiny individual modules from which the logic circuitry may be constructed. Using this type of circuitry should represent a significant advance in the reliability achieved in such a system. The record and

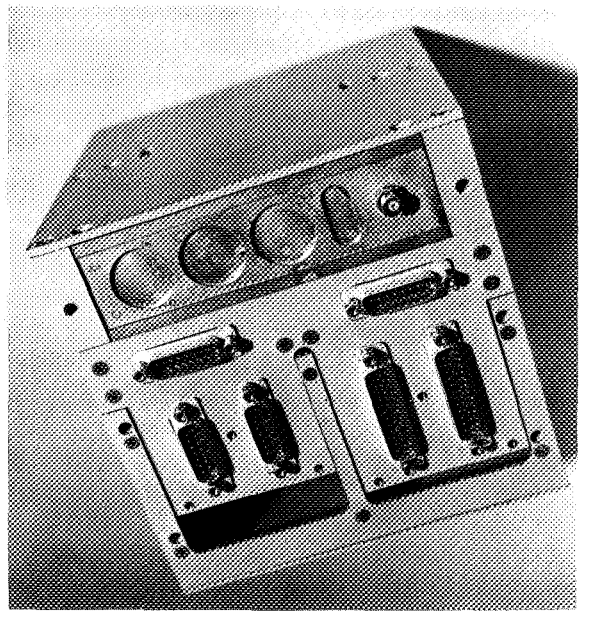

FIGURE 7.—Telemetry system.

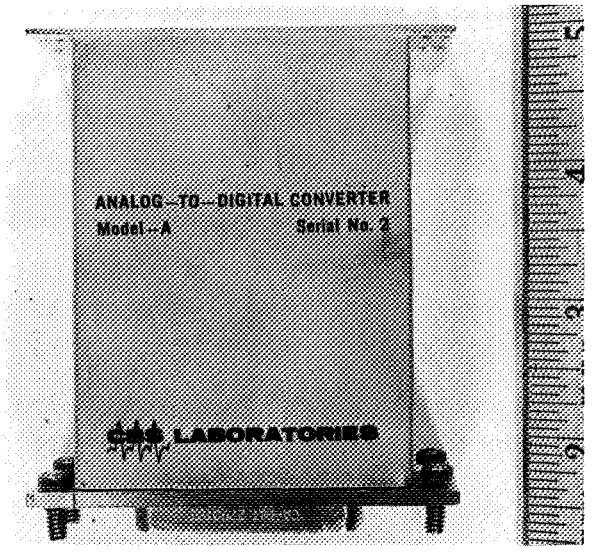

FIGURE 8.—Analog-to-digital converter.

playback amplifiers previously described and the logic for the analog-to-digital converter are being built in microelectronic form. Analog portions of the analog-to-digital converter and the analog gates are constructed from standard discrete components.

The converter (Fig. 8) encodes using the successive approximation technique; it completes the encoding process in 320 μ sec. The total conversion error over a temperature range of 0° to 60°C is $\pm$ 10 mv. The total accuracy is $\pm$ 25 mv, half the least significant bit of 50 mv. The converter is designed so that a simple change would make it an 8-bit converter; its inherent accuracy provides that capability. The power required to operate the converter is 170 mw; of this, only 12 mw is required for the micropower logic circuitry, the remaining power being used for the conventional solid-state circuits.

CONCLUSION

This digital method of treating the data from the medium resolution radiation experiments planned for future Tiros and Nimbus satellites is expected to result in a fivefold improvement in accuracy over the FM analog system previously used. The integrated circuits are versatile, reliable, and ideally suited for present and future aerospace requirements.

THE SOLAR POWER SUPPLY SYSTEM FOR THE ORBITING ASTRONOMICAL OBSERVATORIES

CARL J. WENZINGER
Goddard Space Flight Center
AND
HENRY CARLETON
Marshall Space Flight Center

INTRODUCTION

The Orbiting Astronomical Observatory (OAO) (see Fig. 1) is designed expressly for accomplishment of experiments that cannot be conducted from ground-based installations. This is intended to be an accurately stabilized general purpose or standardized satellite which will accommodate one or more astronomical observing systems. The principal dimensions of the satellite are shown on Figure 2. The proposed experiments are of such a nature as to include surveying the entire celestial sphere which dictates that the satellite have an orbital lifetime of at least 1 year (*1*). Hence, the design emphasizes reliability and longevity, and redundancy is used liberally throughout (*2*). The orbit will be approximately circular with the 3600-lb satellite capable of operating at altitudes of about 300 to 600 statute miles, inclined to the equator at an angle of 31 degrees. The period of the 500-mile orbit is 101 minutes. In the most unfavorable orbit (from a power viewpoint) there is a maximum of 65 minutes of sunlight and 36 minutes of eclipse. Detailed design and fabrication of the Spacecraft is under contract to the Grumman Aircraft Engineering Corp. of Bethpage, Long Island, N.Y.

The Power Subsystem of the Orbiting Astronomical Observatory is required to supply all electrical power for the Spacecraft equipment and for its experiments over a period of 1 year in orbit. The source of electrical power is solar radiation incident upon the Observatory which must be converted to useful electrical power by the Power Subsystem. Since the Observatory in orbit is alternately exposed to the periods of sunlight and eclipse, the system is required to store electrical energy for Spacecraft use during periods of eclipse. Included in the system is equipment required for regulation, conversion, inversion, distribution, and power protection.

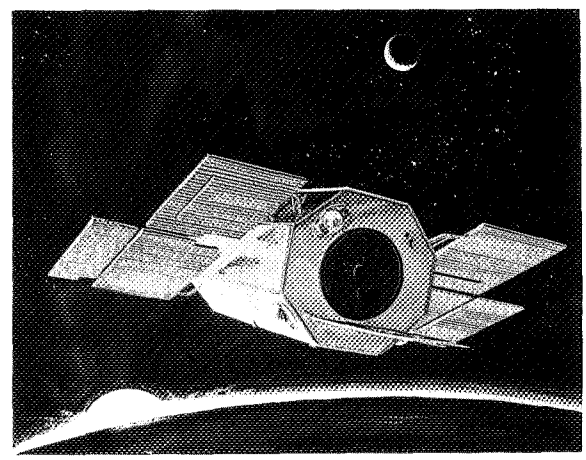

FIGURE 1.—Artist's concept of the Orbiting Astronomical Observatory.

POWER REQUIREMENTS

Block Diagrams

The various items of equipment in the OAO requiring electrical power are indicated in the block diagram of Figure 3. This equipment is included in various subsystems such as Stabiliza-

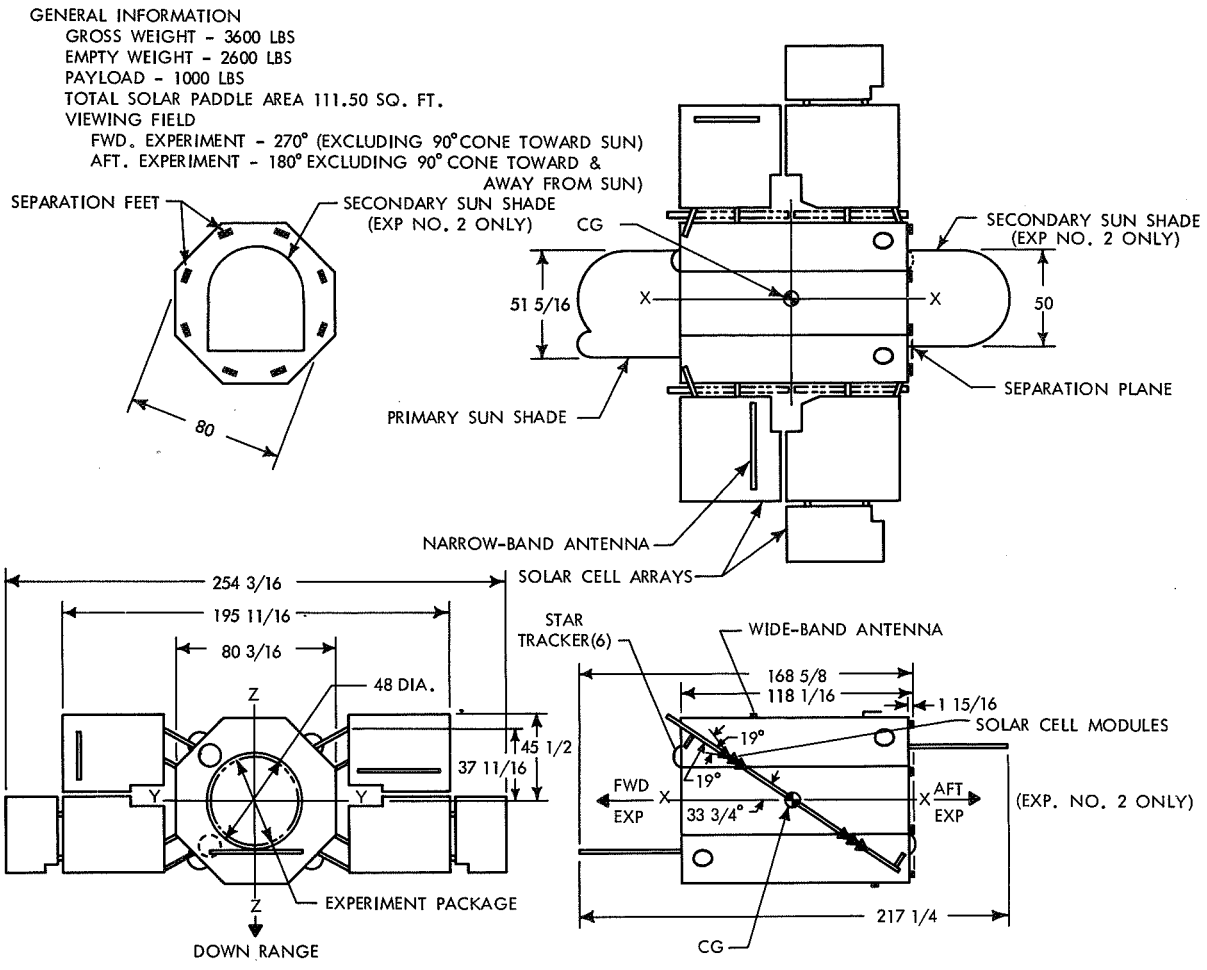

FIGURE 2.—General arrangement, OAO spacecraft.

tion and Control, Data Processing, Communications, Instrumentation, and the Experiments.

A block diagram of the Power Supply Subsystem is shown in Figure 4. The Solar Array, which is divided into six solar panels, supplies unregulated DC power to three regulators. Means are provided to select one charge regulator to operate at a time. The entire output from the solar array is controlled by the regulator and supplies power to a battery, and to the unregulated DC bus. The unregulated DC bus supplies DC power to a Regulator Converter, an Inverter, and other loads operated from this bus. The Regulator Converter supplies regulated DC power to all Spacecraft and Experiment loads that require such power.

Electrical Loads

The total electrical load requirements were determined from electrical load analyses based on duty cycles of the various OAO Subsystems. These duty cycles were calculated from studies of typical missions of some of the experiments presently in process for the OAO. The electrical load includes not only operating power for all Spacecraft equipment, but also the Astronomical Experiment power load. A typical load profile is shown in Figure 5.

Some basic conditions are presented as examples; these are Launch, Initial Stablization, Orbit and Restabilization. For each of these basic conditions, and considering the operating duty cycles, both maximum and

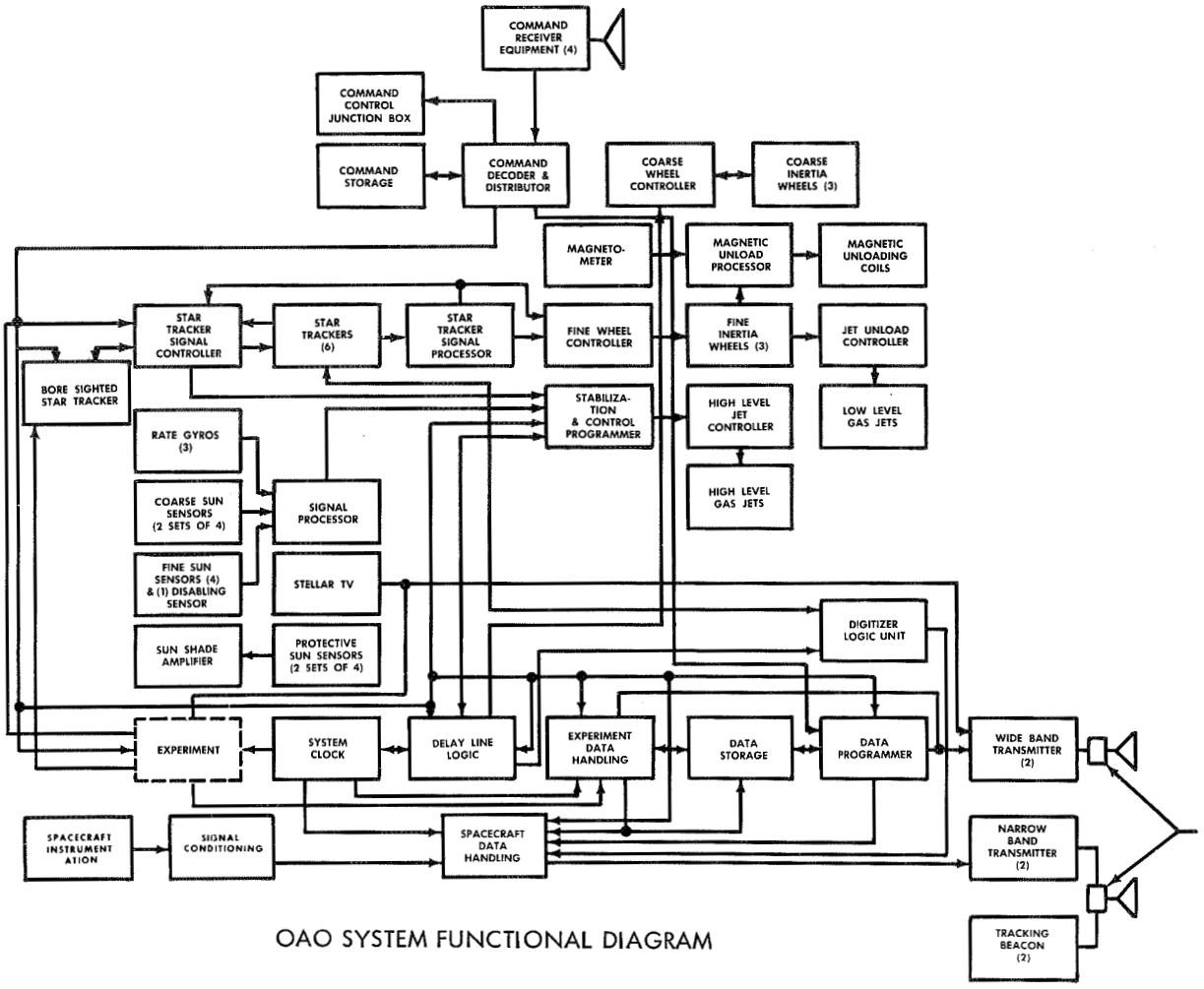

FIGURE 3.—OAO system functional diagram.

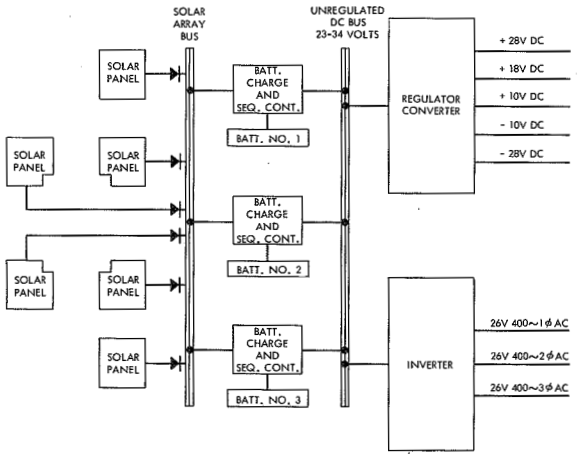

FIGURE 4.—Power supply subsystem.

average power requirements are considered. Table I lists the maximum and average watts of power required from the Unregulated DC bus, and also from the Solar Array bus. The latter values include the battery charge and regulator losses, plus wiring losses.

POWER SUBSYSTEM EQUIPMENT

Regulator Converter

The output and load characteristics specified for the Regulator Converter are listed in table II. These output voltages and loads are to be supplied for all input voltages between the limits of 23 and 34 volts DC. A Block Diagram of the Regulator Converter is shown in

TABLE I.—*OAO power demands*

OAO operation	From unregulated DC bus		From solar array bus	
	Maximum watts	Average watts	Maximum watts	Average watts
Launch (1.0 hr)	193. 5	137	X	X
Initial stabilization (4.5 hrs)	707. 9	339. 2	X	X
Complete orbit (101 min)	670. 5	323. 6	856	676
Restabilization (1.5 hrs)	931. 9	384. 6	X	X

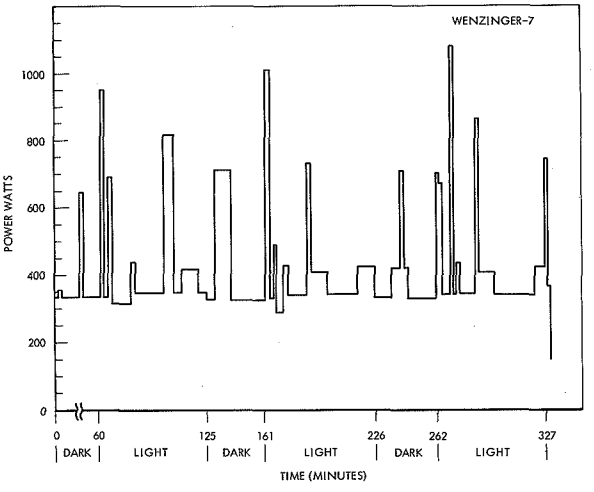

FIGURE 5.—Typical OAO load profile (launch and initial stabilization).

Figure 6. The operation of the Regulator Converter is as follows:

A master oscillator generates a frequency of 1500 cycles per second. The output excites the output transformer and the "A" Slave Oscillator. Outputs for the various voltages are fed through rectifiers and filters. Regulation is obtained by sampling the +18 DC voltage and comparing it to a reference voltage.

In the determination of the operation characteristics of the power system, it is important to know the transfer characteristic of every assembly in the system.

Since the efficiency of the Regulator Converter varies with the input voltage, it is also necessary to obtain the transfer characteristic of this device. Figure 7 shows the calculated transfer characteristics of the Regulator Converter.

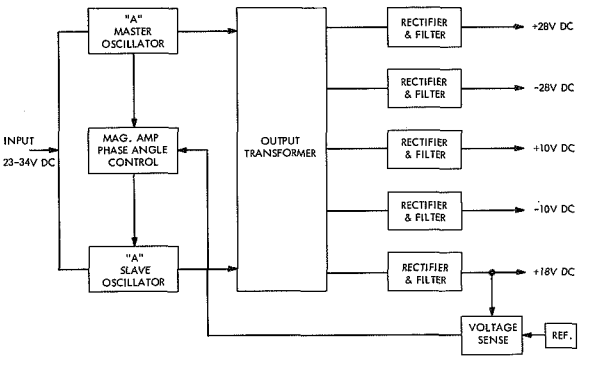

FIGURE 6.—Block diagram of the regulator converter.

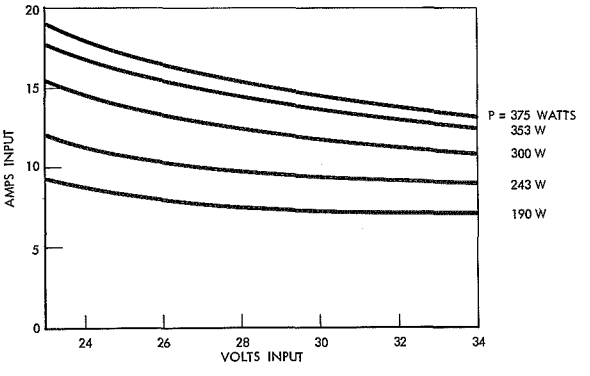

FIGURE 7.—Voltage regulator transfer characteristics.

Inverter

A Block Diagram of the inverter is shown in Figure 8. Regulated DC power is supplied to the inputs of three 400 cycle inverters. The DC regulator is pulse-width modulated to maintain a constant output on ØA, the voltage of which is sensed and fed to the regulator. Synchronizing signals are fed from ØA to ØB and from ØB to ØC. These synchronizing

TABLE II.—*Output voltage and load characteristics of the regulator converter. Output impedance shall be kept to a minimum for all values of frequency and shall be less than 1 ohm at DC*

Item	Nominal voltage [1] (volts)	Voltage regulation (percent)	Voltage ripple (peak-peak percent)	Voltage transient [2] (volts)	Peakload (watts)	Peakload duration (seconds)	Maximum load (watts)	Average load [3] (watts)	Minimum load [3] (watts)
1	+28	±2	0.1	3	273.6 267.8	0.020 1.0	258.8	135.7	131.9
2	−28	±2	.1	3	17.56	0.020	13.76	11.5	6.4
3	+10	±1	.1	1	51.9 51.7	0.020 2.0	49.7	48.7	47.0
4	−10	±1	.1	1	17.9	0.020	17.8	17.6	16.9
5	+18	±1	.1	2	119.8	10.0	92.3	81.0	81.0

[1] The preset tolerance on the nominal voltage shall be $^{+1\%}_{-0\%}$ for all outputs.

[2] Maximum voltage transient recovery time shall be 5 milliseconds for all outputs.

[3] Overall efficiency shall be 84% minimum at 28 volts input and average output load.

signals are phased so as to maintain proper phase relations of the output AC voltages. 2Ø is obtained by tapping ØB and ØC through a 2Ø transformer. A redundant inverter can be utilized by command. A motor driven switch transfers the DC input voltage from the first to the redundant inverter. The inverter has the calculated Input-Output characteristics as shown in Figure 9.

Unregulated Loads

Typical unregulated power transfer characteristics are shown in Figure 10.

Battery

The OAO uses three batteries in a redundant fashion, and the Power System can function on one battery in orbit. The battery uses 20 AH rectangular Nickel-Cadmium cells. (See Fig. 11.) There are 22 cells in each battery, and a total of 66 cells. The cells are arranged in 2 packs of 33 cells each. Eleven cells of each battery are in each pack. Figure 12 shows the mechanical arrangement of the battery pack. This arrangement provides a large heat sink for 11 cells of each battery, while the latter are undergoing charge or discharge. The cells are hermetically sealed and can operate in a vacuum. The expected operating temperature range of the batteries is from 40° F to 95° F. Under these conditions and at a 35-percent depth of discharge, a battery can be cycled for 1 year in the 101-minute orbit, and at the end of 1 year, should be able to deliver the energy required by the Observatory during eclipse. Some of the characteristics of the cells are presented in the following figures. Figure 13 shows some typical discharge curves of the 20 AH cells (*3*). It can be seen that when the voltage at the end of discharge reaches 1.15 volts, the capacity drops off very rapidly. The "C/1" curve represents a typical OAO condition. The maximum battery voltage above which the charger should not go due to temperature effects is shown in Figure 14. A voltage exceeding that shown will generate hydrogen in the cells. Hydrogen cannot be reabsorbed and

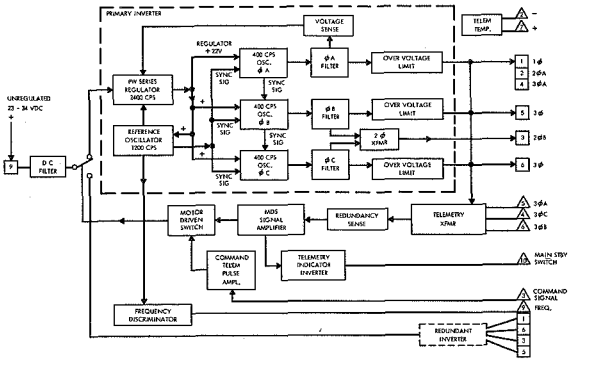

FIGURE 8.—DC to AC inverter block diagram.

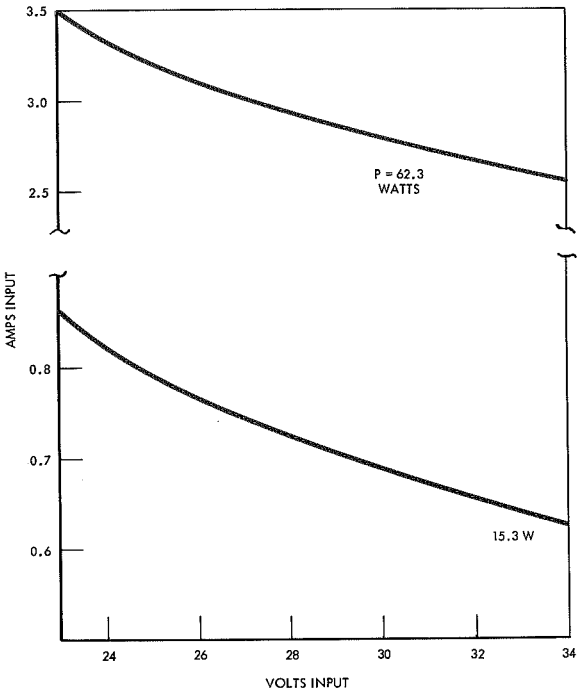

FIGURE 9.—Inverter transfer characteristics.

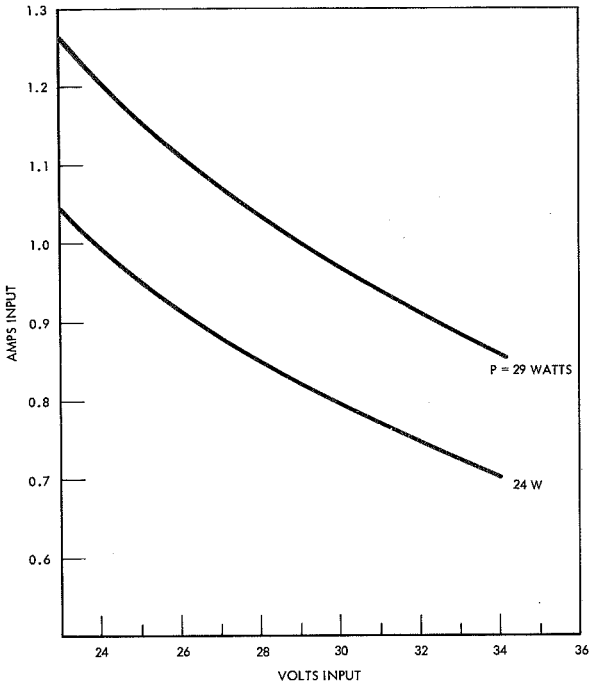

FIGURE 10.—Unregulated power transfer characteristics.

remains as a permanent increase in pressure within the cell.

Battery Charger and Sequence Controller

Figure 15 is a block diagram of the BCSC. During the entry of the Observatory into sunlight, the Solar Array is required to supply power to the unregulated bus and to recharge the batteries. It can be expected that under normal conditions, the battery which supplies power during eclipse will have depleted at least 35 percent of its capacity. Under these conditions, a built-in logic circuit will close a contact and bypass the power transistors, and supply power directly to the unregulated bus and battery. The battery will then commence to charge. When the battery reaches a predetermined voltage which represents a state of charge near the full state, a sequence control relay will switch the Solar Array to the next charge controller and battery. Since the voltage at which switching takes place is temperature dependent, a thermistor built in the battery compensates for temperature change. The previous Figure 14 shows the variation in end-

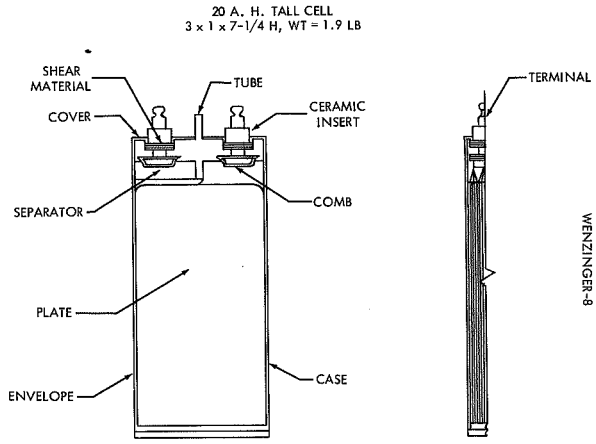

FIGURE 11.—Nickel-cadmium cell.

of-charge voltage versus battery temperature. The batteries can cycle six times in this fashion. A counter senses the number of times the sequencing takes place. After the sixth time, the regulator will be switched into the circuit. Regulation is accomplished by a pulse modulation technique. The width of the pulse is regulated to maintain the voltage on the battery within the acceptable limits, and at the same time supply the power required at the unregu-

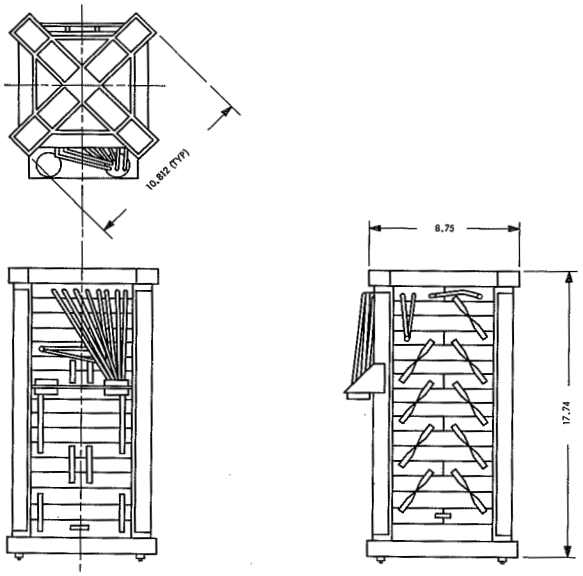

FIGURE 12.—Storage battery assembly.

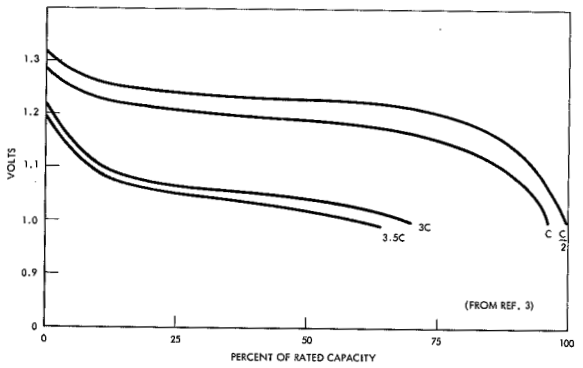

FIGURE 13.—Typical discharge curves of 20 AH cells.

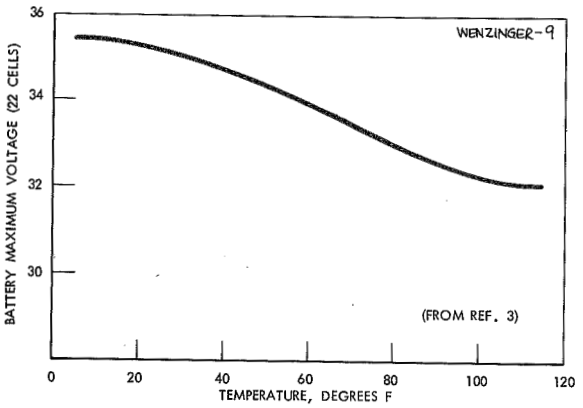

FIGURE 14.—Battery limiting charge voltage.

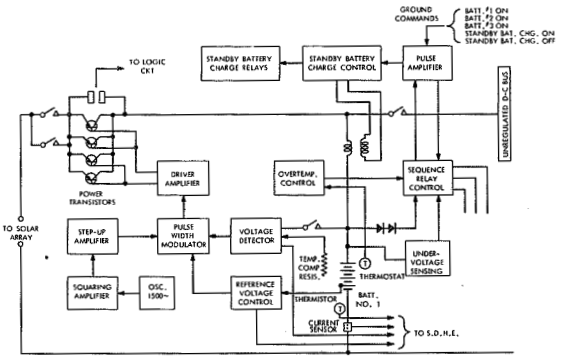

FIGURE 15.—Block diagram-battery charge and sequence controller (one channel shown).

lated bus. Other safeguards are included in the circuit. If the temperature of the battery exceeds 110° F, the Sequence Controller is activated to switch to the next battery. If on switching to another battery, a voltage sensor sees a battery voltage less than 23 volts, this battery is automatically bypassed. The latter may be an indication of a shorted cell in the battery pack. Upon entry into darkness, the Charge Regulator is shut off and retains this mode until entry into sunlight. The maximum power dissipation in the Charge Regulator is about 20 watts. A system is included to override the automatic features described. Any battery can be commanded "off" or "on" by ground command.

SOLAR POWER GENERATION

Solar Cells

The cells that were selected for the OAO are of the P on N type, i.e., they consist basically of an N-type silicon wafer onto which a P-type boron layer is diffused. Gridded cells of 1-cm x 2-cm size with 6-mil thick protective glass covers are used. An antireflective coating is deposited on the outside of the glass and an ultraviolet filter is placed on the underside. The latter is used to prevent browning of the adhesive used to attach the glass to the cell. The cells used have an efficiency of 13 percent (measured under tungsten light) which gives an estimated 11.5 percent efficiency in space.

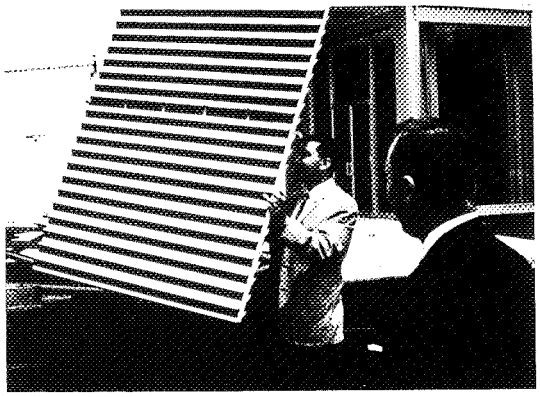

FIGURE 16.— Solar cell modules mounted on panel.

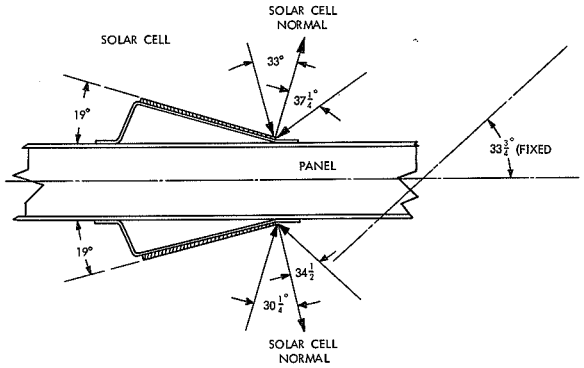

FIGURE 17.—Detail of solar cell mounting on panel.

Solar Array

The Solar Array has approximately 31,000 cells mounted on the front sides and a similar number on the rear sides of the solar panels. The mounting of cells on both sides of the solar panels is required in order to achieve the necessary maneuvers with the OAO during launch, stabilization, and orbital operation. The solar cells are mounted on angular modules as shown in Figure 16. A more detailed section of the cell mounting is shown in Figure 17. With the cells mounted in the Solar Array in the fashion indicated, the entire celestial sphere except for a 90° cone about the sun can be viewed with the cells not being required to operate at an angle of greater than about 37° with respect to the incident sunlight.

The Solar cell mounting arrangement on each solar cell module substrate consists of five cells (parallel connected, submodules) mounted transversely to the long dimension of the module, each submodule series connected to the next. Seventy-five submodules are connected in series to form a string. Each string is isolated by diodes. This arrangement of the 31,000 solar cells results in a Solar Array with some characteristics as shown in Figure 18.

A breakdown of weighs of various components of the Power Subsystem is given in Table III.

A typical power point on the output of the Solar Array may be calculated as follows:

Output of bare cell under 100 mw/cm² tungsten (2800° K)

$100 \times 0.13 \times 1.89$ cm²$=24.6$ milliwatts/cell

The following factors are used to convert from tungsten output to air mass zero ("space") output:

0.93	Assembly degradation factor (Diodes —wiring)
0.97	Filter loss
0.98	Filter derating factor to air mass 1
0.96	Spectral correction factor to air mass 1
0.99	Filter derating factor to air mass 0
0.91	Spectral correction factor to air mass 0
1.4	Increased output at air mass 0

Output of solar array$=30{,}960$ cells$\times 24.6 \times 0.93 \times 0.97 \times 0.98 \times 0.96 \times 0.99 \times 0.91 \times 1.4 = 815$ watts

Power System Analysis

A programed computer analysis has been performed to determine the performance and limitations of the Solar Array. The power

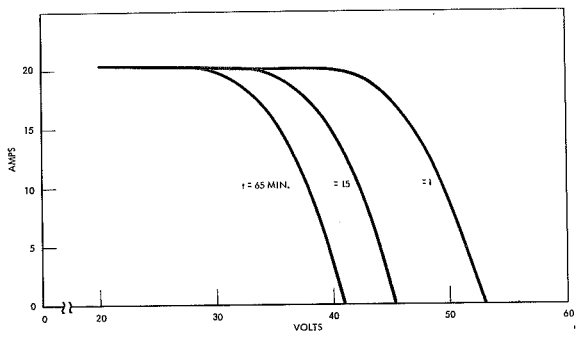

FIGURE 18.—Solar array characteristic, 65-min. sunlight orbit.

TABLE III.—*Component weights*

Component	Weight, lbs.
Paddle structure	92. 18
Paddle erection and locking mechanism	58. 58
Subtotal	150. 76
Solar cells, circuitry, diodes, filters, wiring	105. 74
Substrates	26. 50
	132. 24
Battery cells and case	153. 40
Battery charge and sequence controller	24. 00
Voltage regulator and converter	35. 80
Voltage inverter	34. 60
	70. 40
Cabling, plugs, etc., for power subsystem only	23. 62
Total	554. 42

Pi from the Solar Array required to satisfy the load P_L can be expressed as follows:

$$Pi=\frac{1}{65}\left(65\,P_L+\frac{36\,P_L}{0.70}\right)\text{ watts}$$

This formula assumes a dark period of 36 minutes, a light period of 65 minutes, and a battery charge efficiency of 0.70. In the case considered here a load P_L of 343 watts would require a Solar Array output $(Pi)=616$ watts. If a Solar Array would have a constant output and always operate at its maximum power point then the Solar Array could be sized from the value of Pi given above. However, the output of the Solar Array decreases with increasing temperature, and the operating point on the Solar Array output curve varies with changes in the output curve and power requirements of the Observatory. A Solar Array must therefore be chosen so that under all conditions of OAO orientation, temperature rise, and power demands, the Solar Array will be able to meet these demands and also recharge the batteries.

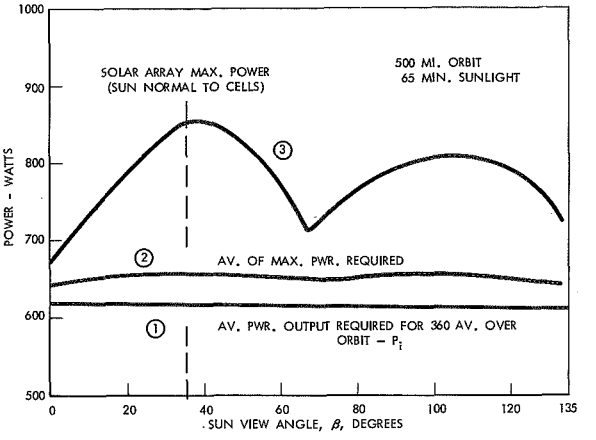

FIGURE 19.—OAO power system-power availability and requirements.

A computer analysis of the Solar Array was performed in which the latter was allowed to heat up after eclipse in a manner predicted by thermal analysis. The output was predicted on a minute-to-minute basis. The operating point on the Solar Array was arrived at by superimposing the load transfer functions and battery charging requirements on the Solar Array curves. It was found that the average of the maximum power output of the array was always higher than the averaged power required by the load. The relation

$$\frac{\text{Average of load}}{\text{Average of maximum output}}=\text{System utilization efficiency, }\eta$$

This value of η varies between 0.90 and 0.94, and holds for most conditions of operation of the OAO under normally expected loads.

Figure 19 shows a curve of OAO typical power requirements under various sun view angles. Curve ① shows the average power output required from the array at various angles in order to provide 360 watts average power over the 101 minute orbit. Curve ② indicates the average of the maximum power required of the Solar Array during the 65 minute daylight period. The power required, Pi, is related to Solar Array maximum output by the utilization factor η. Curve ③ shows the actual output of the OAO Solar Array. It can

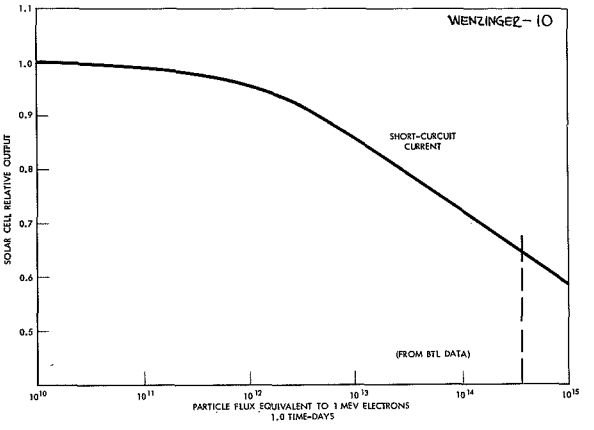

FIGURE 20.—Degradation of P/N solar cells.

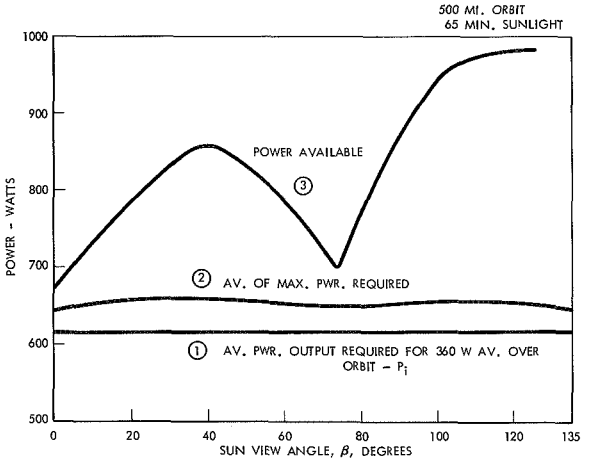

FIGURE 21.—OAO power system-modified solar array.

be seen that the latter exceeds the maximum required at all angles of sun viewing.

New Radiation Belt Considerations

Due to recently increased radiation in the region of the OAO orbit, reevaluation of these effects has become necessary relative to the OAO, particularly on the Solar Array components.

It is a characteristic of P/N Solar cells, that they begin to suffer a degradation in output when bombarded by 1×10^{12} electrons in the energy range of 1 mev. For the OAO 500-mile orbit, 1×10^{12} damaging electrons will probably cause degradation to begin in about 2 days. At this time the output of the Solar Array is estimated to degrade at about 18 percent per tenfold increase in the encountered electron flux. Figure 20 shows the estimated degradation of Solar Array power versus time and solar array flux.

The OAO could be operated in a restricted mode which would then require less power. It could operate in this mode up to 30 days. Since the OAO is required to operate up to 1 year in orbit, it will be necessary to increase the number of cells so that at the end of one year the power output will be sufficient to supply the required power. A study to increase the basic power has been made.

The investigation shows that if the number of solar cells is increased from about 31,000 to 41,000, the Solar Array will provide sufficient power to permit OAO operation up to 300 days. Based on the Experiment requirements and OAO orientations, it is necessary to add the extra 10,000 solar cells to only one side of the solar panels. This can be done by attaching these cells flat to the panel rather than at the 19° angle, so as to avoid any increase in the panel size. Figure 21 shows the calculated characteristics of the modified OAO Solar Arrays.

Possibilities other than the foregoing were also considered, such as lowering the OAO orbit, increasing solar cell cover glass thickness, use of different type cells, etc. However, due to the advanced stage of fabrication and assembly, together with schedule demands and project costs, the arrangement outlined was chosen for the first OAO.

REFERENCES

1. ZIEMER, ROBERT R., and KUPPERIAN, JAMES E., JR., "The Mission of the Orbiting Astronomical Observatory," AAS/AAAS/NASA Symposium on "Scientific Satellites," Philadelphia, Pa., Dec. 27 1962.
2. SCOTT, WALTER, "The Engineering Design of the Orbiting Astronomical Observatory," AAS/AAAS NASA Symposium on "Scientific Satellites," Philadelphia, Pa., Dec. 27, 1962.
3. SHAIR, R. C., and GRAY, W. "Hermetically Sealed Nickel-Cadmium Batteries for the Orbiting Astronomical Observatory Satellite," ARS Space Power Systems Conference, Santa Monica, Calif., Sept 25–28, 1962.

A LINEARIZED ANALYSIS AND DESIGN OF AN AUTOMATIC BALANCING SYSTEM FOR THE THREE-AXIS AIR BEARING TABLE

FELIX ZAJAC AND DAVID SMALL

Goddard Space Flight Center

INTRODUCTION

For the air bearing table to achieve its purpose of testing satellite attitude control systems, the extraneous torques on the table must be eliminated, if not totally, then to a value that will not affect the function of the attitude control system. When the design of the present attitude control system for the table was simulated on the analog computer, extraneous torques up to 10,000 dyne-cms around each axis were simulated with no apparent affect on the performance of the attitude control system. Most attitude control systems for satellites do not require a finer torquing control than that in the present table control system. Hence, elimination of extraneous (unbalanced) torques to within 10,000 dyne-cms is sufficient, not only for the present table control system, but for most attitude control systems that will be tested on this table in the future.

One of the many causes of unbalanced torques (temperature changes, air currents, static mass unbalance, magnetic fields, etc., static mass unbalance contributes substantially to the total unbalance. This report presents the analysis and design of an automatic control system to reduce this mass unbalance to 5000 dyne-cms or less.

To balance the table (eliminate the static mass unbalance) about three axes, the table is first balanced manually to within 200,000 dyne-cms of torque balance in the horizontal position. After this balancing the table should be pendulous, but with a period greater than 2.0 minutes. The table is then released from an appropriate initial position, and the automatic balancing system is activated. This system senses a positional error from the initial position, resulting from a torque unbalance, and corrects this unbalance by driving a weight along the appropriate axis.

Two different initial positions (balancing modes) of the table are needed to balance the table in three axes. In position 1 (fig.. I), the balancing system is in operation in the roll-and-yaw axes. Consequently, after the table is balanced in these axes, the center of gravity (c.g.) will lie on the pitch axis. In position 2 (fig. II), the table is rotated through 20° about the roll axis, where the pitch balancing mode is initiated and the movement of the pitch weight (Wp) brings the c.g. to coincide with the center of rotation (C.R.), completing the table balancing about all three axes. In the pitch balancing mode, an additional position sensor is used together with the yaw balancing controls to limit table movement relative to the axis "Y'." Finally, the table should be returned to the first position and the balancing procedure repeated in the roll and yaw axes. The following is the analysis and design of the complete balancing system.

DEFINITIONS

θ_R, θ_Y	angular position of table about the roll and yaw axes, respectively.	radians
ω_R, ω_Y	angular velocity of table about the roll and yaw axes, respectively.	radians/sec
d	dead zone of d.c. servomotor	d.c. volts
L	saturation voltage of d.c. servomotor	d.c. volts
K_M	gain of d.c. servomotor	rad/sec/d.c. volt
τ_M	time constant of d.c. servomotor	seconds
n	gear reduction	rad/rad
K_L	lead screw reduction	ft/rad
W_T	weight of table	lbs

R_R, R_Y	the perpendicular distance from the center of gravity (c.g.) to the roll and yaw axes (Fig. I).	ft
R_P	the distance from the c.g. to the center of rotation (C.R.) (Fig. II).	ft
ϕ_R	angle formed by the intersection of the line from the c.g. to the roll axis (R_R) and the roll-pitch plane (Fig. I).	rad
ϕ_Y	angle formed by the intersection of the line from the c.g. to the yaw axis (R_Y) and the yaw-pitch plane (Fig. I).	rad
ϕ_P	initial angular position of table about the roll axis when the pitch balancing mode is used (Fig. II).	rad
K_{SR}, K_{SP}	gain of position sensor in the roll axis control in the roll-yaw and pitch balancing modes, respectively.	a.c. volts/rad
K_{SY}	gain of position sensor in the yaw axis control in both balancing modes.	a.c. volts/rad
K_{DR}, K_{DP}	gain of demodulator in the roll axis control in the roll-yaw and pitch balancing modes, respectively.	d.c. volts/a.c. volts
K_{DY}	gain of demodulator in the yaw axis control in both balancing modes.	d.c. volts/a.c. volts
τ_{1R}, τ_{1P}	lead time constants of lead-lag networks in the roll axis control in the roll-yaw and pitch balancing modes, respectively.	seconds
τ_{1Y}	lead time constant of lead-lag network in the yaw axis control in both balancing modes.	seconds
τ_{2R}, τ_{2P}	lag time constants of lead-lag networks in the roll axis control in the roll-yaw and pitch balancing modes, respectively.	seconds
τ_{2Y}	lag time constant of lead-lag networks in the yaw axis control in both balancing modes.	seconds
τ_{3R}, τ_{3P}	time constants of filter networks in the roll axis control in the roll-yaw and pitch balancing modes, respectively.	seconds
τ_{3Y}	time constant of filter networks in the yaw axis control in both balancing modes.	seconds
κ_{AR}, κ_{AP}	gain of amplifier in the roll axis control in the roll-yaw and pitch balancing modes, respectively.	d.c. volts/d.c. volts
κ_{AY}	gain of amplifier in the yaw axis control in both balancing modes.	d.c. volts/d.c. volts
r_R, r_P	position of control weight in the roll axis control in the roll-yaw and pitch balancing modes, respectively.	ft
r_Y	position of control weight in the yaw axis control in both balancing modes.	ft
W_R, W_P	control weight in the roll axis control in the roll-yaw and pitch balancing modes, respectively.	lbs
W_Y	control weight in the yaw axis control in both balancing modes.	lbs
I_{RR}, I_{YY}, I_{PP}	moment of inertia of table about the roll, yaw, and pitch axes, respectively. $I_{RR}=50$ slug-ft^2, $I_{YY}=27$ slug-ft^2, $I_{PP}=50$ slug-ft^2.	
T_{WR}, T_{WP}	torque about roll axis due to moving weight when the balancing system operates in the roll-yaw and pitch balancing modes, respectively.	ft-lbs
T_{WY}	torque about yaw axis due to moving weight when the balancing system operates in both balancing modes.	ft-lbs
T'_{UR}, T'_{UP}	torque about roll axis due to initial static mass unbalance when balancing system operates in the roll-yaw and pitch balancing modes, respectively.	ft-lbs

T'_{UY}	torque about yaw axis due to initial static mass unbalance when balancing system operates in both balancing modes.	ft-lbs
T_{PR}, T_{PY}	incremental torque about roll and yaw axes, respectively, due to c.g. below the roll-yaw plane (pendulosity).	ft-lbs
T_{UR}, T_{UY}	total torque unbalance around the roll and yaw axes, respectively.	ft-lbs

ANALYSIS

Table Dynamics

Before the balancing system can be analyzed and designed, the table dynamics about each axis must be determined. The table dynamics about the roll and yaw axes, corresponding to position I (Fig. 1), will be analyzed first. Afterwards, the dynamics in the pitch balancing mode (Fig. 2) will be determined.

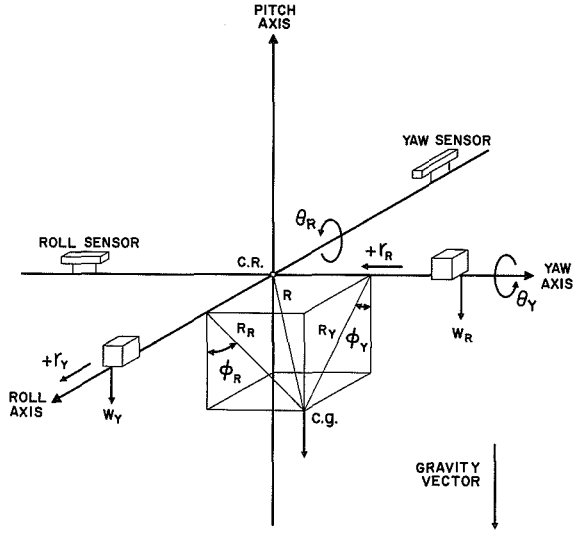

FIGURE 1.—Diagram of roll-yaw balancing mode.

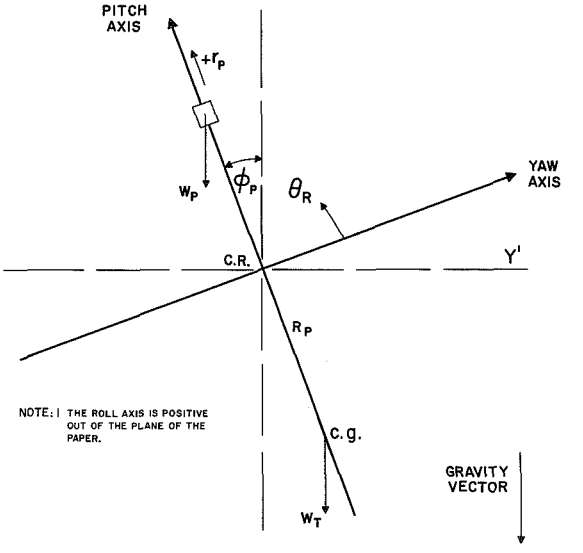

FIGURE 2.—Diagram of pitch balancing mode.

Position 1

Roll-Yaw Balancing Mode

Roll Axis

(1) $$\sum T_R = I_{RR}\ddot{\theta}_R.$$

(This is a linear approximation of the general equations of angular motion of a rigid body. Its validity will be shown later in this report.)

(2) $$\sum T_R = W_R r_R(t) \cos\theta_R - W_T R_R \sin(\phi_R+\theta_R) = I_{RR}\ddot{\theta}_R$$

(3) $$\sin(\phi_R+\theta_R) = \sin\phi_R \cos\theta_R + \sin\theta_R \cos\phi_R$$

for small variations of θ_R:

$$\sin(\phi_R+\theta_R) = \sin\phi_R + \theta_R \cos\phi_R$$

$$\cos\theta_R = 1$$

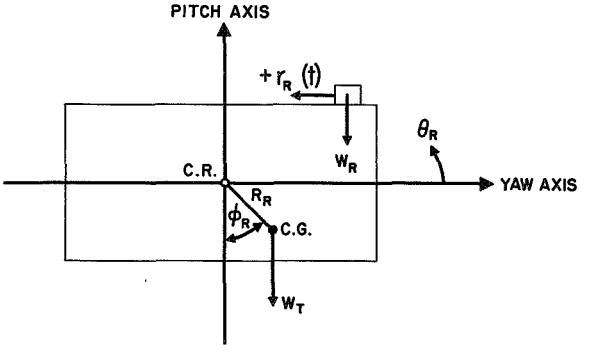

Hence: (4) $W_R r_R(t) - W_T R_R \sin\phi_R - W_T R_R \theta_R \cos\phi_R = I_{RR}\ddot{\theta}_R$.

With all initial conditions zero, the LaPlace transform yields:

(5) $W_R r_R(S) - \frac{W_T R_R}{S}\sin\phi_R = [I_{RR}S^2 + W_T R_R \cos\phi_R]\theta_R(S)$.

or (6) $\theta_R(S) = \frac{1}{I_{RR}S^2 + W_T R_R \cos\phi_R}\left[W_R r_R(S) - \frac{W_T R_R}{S}\sin\phi_R\right]$.

The corresponding servo block diagram is shown below:

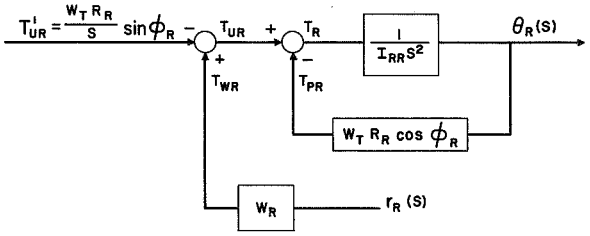

Of course, this block diagram will appear as part of the overall roll axis control loop, in the roll-yaw balancing mode.

Yaw Axis

The dynamics for the yaw axis can be obtained in the same manner, giving:

(7) $\theta_Y(S) = \frac{1}{I_{YY}S^2 + W_T R_Y \cos\phi_Y}\left[W_Y r_Y(S) - \frac{W_T R_Y}{S}\sin\phi_Y\right]$.

The corresponding servo block diagram for the yaw axis dynamics is shown below. This will form part of the overall yaw axis control loop, in the roll-yaw balancing mode.

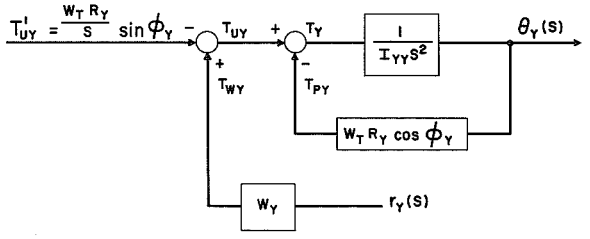

Position 2

Pitch Balancing Mode

Roll Axis

NOTE.—All roll angles and torques are positive in the counterclockwise direction.

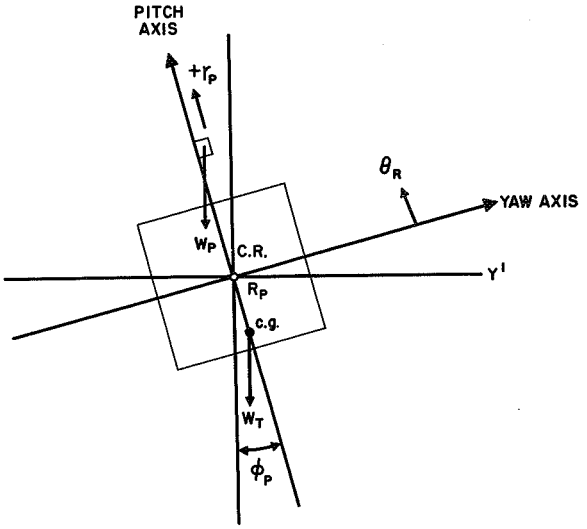

(8) $\sum T_R = I_{RR}\ddot{\theta}_R$

(9) $W_P r_P \sin(\phi_P+\theta_R) - W_T R_P \sin(\phi_P+\theta_R) = I_{RR}\ddot{\theta}_R$

(10) $\sin(\phi_P+\theta_R) = \sin\phi_P\cos\theta_R + \cos\phi_P\sin\theta_R$

for small variations of θ_R.

(11) $\sin(\phi_P+\theta_R) = \sin\phi_P + \cos\phi_P(\theta_R)$.

Hence:

(12) $W_P r_P[\sin\phi_P + (\cos\phi_P)\theta_R] - W_T R_P[\sin\phi_P + (\cos\phi_P)\theta_R] = I_{RR}\ddot{\theta}_R$.

Since $\phi_P >> \theta_R$, $\sin\phi_P >> (\cos\phi_P)\theta_R$. Therefore Equation (11) reduces to

(13) $W_P r_P[\sin\phi_P] - W_T R_P[\sin\phi_P] = I_{RR}\ddot{\theta}_R$.

With all initial conditions zero, the LaPlace transform yields:

(14) $W_P r_P(S)\sin\phi_P - \frac{W_T R_P}{S}\sin\phi_P = [I_{RR}S^2]\theta_R(S)$

or (15) $\theta_R(S) = \frac{1}{I_{RR}S^2}\left[W_P(\sin\phi_P)r_P(S) - \frac{W_T R_P}{S}\sin\phi_P\right]$

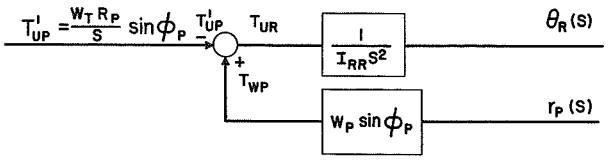

With the table dynamics linearized, a linear analysis and design of the balancing system can now be effected.

CONTROL SYSTEMS

Roll Axis Control (Roll-Yaw Balancing Mode)

The block diagram of this system is shown in Figure III. An explanation of the system and each component is described below.

The torque unbalance (T_{UR}') of the table causes a table position error (θ_R). The position sensor is an electrolytic potentiometer. When used in an a-c bridge circuit, it gives a proportional a-c signal up to $\pm\frac{3}{4}$ degrees of table tilt. The electronic demodulator produces a d-c signal whose polarity depends upon the phase of the a-c signal (i.e., the direction of tilt of the table). Due to excessive lag and instability, two lead-lag compensating networks are used to produce the necessary compensation. Any high frequency noise is attenuated via filter networks. (It is possible to utilize the motor armature inertia to obtain a lead effect. However the amount of this lead would be too small for the present system. See Appendix.)

Since the motor has a dead zone of ± 2 volts, an amplifier of gain ten is added so that in a steady-state condition the tilt of the table will be within $\pm 1\frac{1}{2}$ minutes of arc, the resolution of the sensor. Moreover, a limiting device set at ± 30 volts is used to protect the motor. The d-c motor with its gear reducer drives the control weight producing a compensatory torque (T_{WR}) on the table.

A Bode diagram of the uncompensated system ($G_{(UNC)R}(S)$) for $\phi_R = 90°$ (nonpendulous condition, which is the worst case) is plotted in Figure IV. The compensating networks were designed to give system unity gain crossover at 0.5 rad/sec., and 52 degrees of phase margin. The time constants of the lead-lag

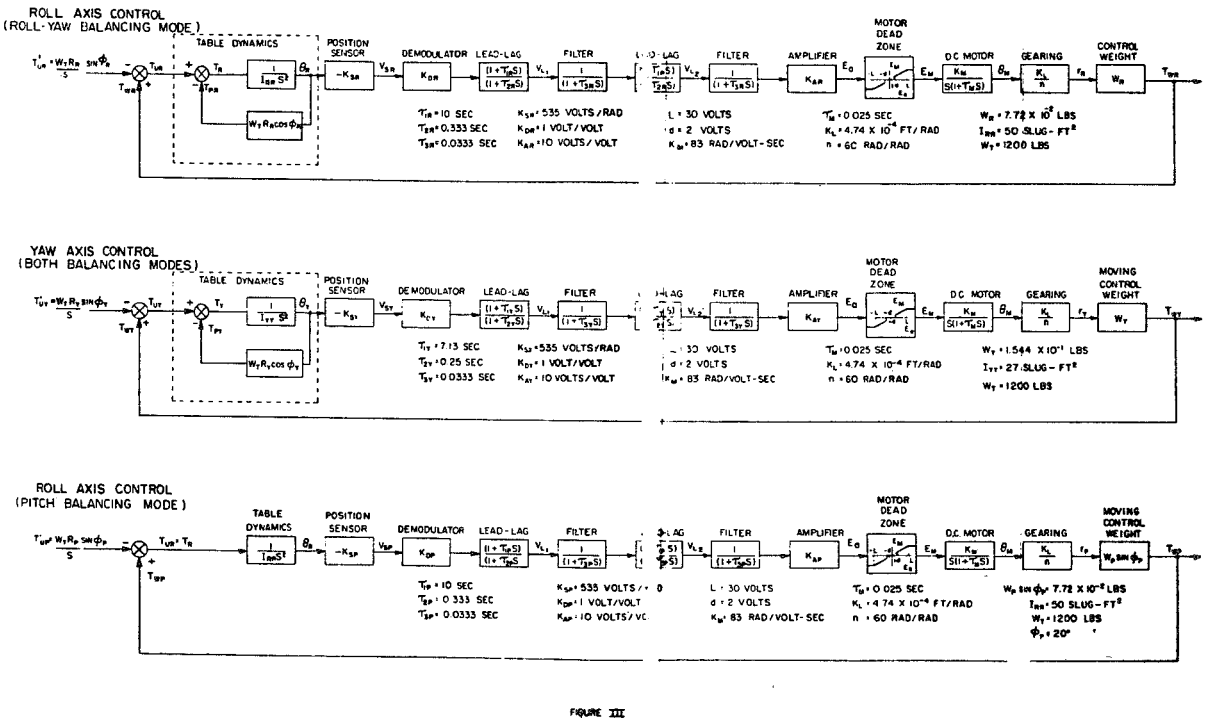

FIGURE III

FIGURE 3.—Servo block diagram of the balancing system.

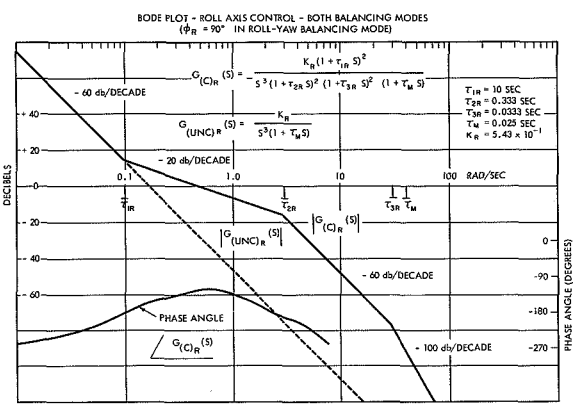

FIGURE 4.—Bode plot—roll axis control.

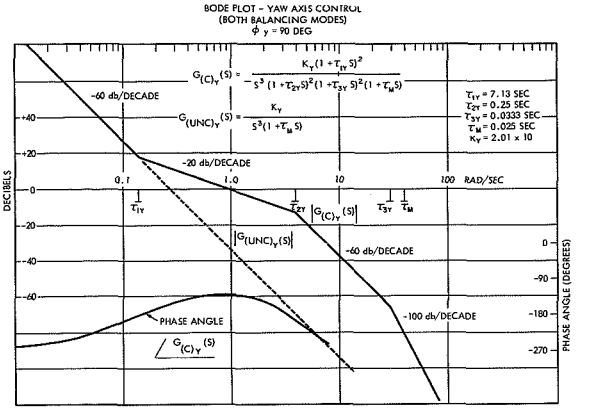

FIGURE 5.—Bode plot—yaw axis control.

networks are chosen to be $T_{1R}=10$ seconds, and $T_{2R}=0.333$ second while the time constant of the noise filters is set at 0.0333 seconds. The corresponding Bode diagram of the compensated system ($G_{(C)R}(S)$) is also shown in Figure IV. Notice that the gain may fluctuate as much as ± 14 db (a factor of 5 to a factor of 0.2) before the system goes unstable (i.e., the gain margins are ± 14 db).

Yaw Axis Control (Both Balancing Modes)

The block diagram of this system is shown in Figure III. Due to the similarity of this control system to the roll control system, a detailed explanation will not be made.

Since the moment of inertia of the yaw axis differs from the moment of inertia of the roll axis, the time constants of the lead-lag networks assume new values for near optimum response. These are $T_{1Y}=7.13$ seconds and $T_{2Y}=0.25$ second. The control weight is increased by a factor of two increasing the gain by two. The Bode diagrams of the uncompensated and compensated systems for $\phi_Y=90$ degrees are shown in Figure V. The resulting 0 db frequency crossover for the compensated system is 1.0 rad/sec and the phase margin is 48 degrees. The corresponding gain margins are $+12$ db and -18 db (a factor of 3.9 to a factor of 0.12).

Roll Axis Control (Pitch Balancing Mode)

The block diagram of this system is shown in Figure III. The only difference between this system and the roll control system in the roll-yaw balancing mode is the gain from the control weight to the torque on the table produced by this weight. In the roll-yaw balancing mode this gain is $W_R r_R(t)$ as compared to a gain in the pitch balancing mode of $W_P r_P(t)$ sin ϕ_P. Therefore, W_P sin ϕ_P is made to equal W_R, thus making the two systems identical as far as the analysis is concerned. Consequently, the Bode diagram, the unity gain crossover frequency, the phase margin, and the gain margins are identical to the roll axis control system in the roll-yaw balancing mode, which is shown in Figure IV.

COMPUTER RESULTS

Roll Axis (Roll-Yaw Balancing Mode)

The simulation on the analog computer of the roll axis control system (including the dead zone and limiting characteristics) verified the linear analysis. The natural frequency of the system corresponded to the unity gain crossover frequency and the gain margins were in agreement. A response of the system to an initial unbalance torque of 200,000 dyne-cms, with $\phi_R=90$ degrees, is shown in Figure VI. For variations in ϕ_R and torque (T_{UR}'), the form of the response is still the same. The chart in Figure VII shows the time for the total unbalance torques (T_{UR}) to reach 5,000 dyne-cms for varying input unbalance torques (T'_{UR}).

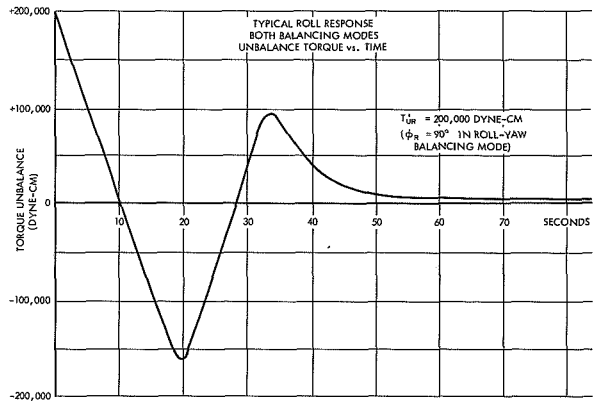

FIGURE 6.—Typical roll response—unbalance torque versus time.

Yaw Axis (Either Balancing Mode)

Again the analog computer results agreed with the linear analysis. The natural frequency of the system corresponded to the unity gain crossover frequency (1 rad/sec), and the gain margins were in agreement. A response of the system to an initial unbalance torque of 200,000 dyne-cms, with ϕ_Y=90 degrees, is shown in Figure VIII, and for variations in ϕ_Y and torque input (T'_{UY}), the form of the response is still the same. The chart in Figure IX shows the time for the total unbalance torques (T_{UY}) to reach 5,000 dyne-cms for varying input unbalance torques (T_{UY}').

Roll Axis (Pitch Balancing Mode)

First, the linearized control system was simulated on the computer, and of course the results were the same as the roll axis control in the roll-yaw balancing mode. Afterwards, the terms containing (cos ϕ_P) θ_R in equation (11), page 11, were added to see if they were negligible. No apparent change was found in the response.

A response of the system to an initial unbalance torque of 200,000 dyne-cms is shown in Figure VI. The chart in Figure VII shows the time for the total unbalance torques (T_{UP}) to reach 5,000 dyne-cms for varying input unbalance torques (T_{UP}'). These are the same responses for the roll axis control in the roll-yaw balancing mode.

ROLL AXIS CONTROL - BOTH BALANCING MODES
(ϕ_R = 90° in roll-yaw balancing mode)

Initial Unbalance Torque vs. Settling Time to 5,000 Dyne-Cms. Balance

Torque (Dyne-Cm.)	Time (seconds)
10,000	12
20,000	13
30,000	13
40,000	13
50,000	14
60,000	14
70,000	14
80,000	15
90,000	16
100,000	45
110,000	47
120,000	50
130,000	53
140,000	56
150,000	60
160,000	65
170,000	73
180,000	80
190,000	80
200,000	80

FIGURE 7.—Chart of initial unbalance torque versus settling time to 5,000-dyne-cm balance for the roll axis control.

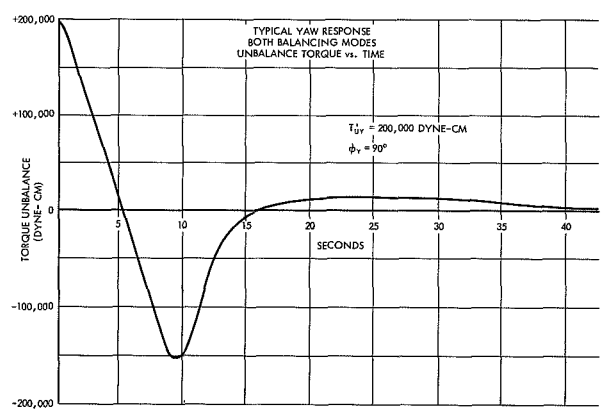

FIGURE 8.—Typical yaw response—unbalance torque versus time.

YAW AXIS CONTROL - BOTH BALANCING MODES
($\phi_Y = 90°$)

Initial Unbalance Torque vs. Settling Time to 5,000 Dyne-Cms. Balance

Torque (Dyne-Cm.)	Time (second)
10,000	2
20,000	4
30,000	5
40,000	6
50,000	8
60,000	8
70,000	9
80,000	9.5
90,000	10
100,000	11
110,000	11.5
120,000	12
130,000	13
140,000	33
150,000	34
160,000	35
170,000	35
180,000	36
190,000	37
200,000	38

FIGURE 9.—Chart of initial unbalance torque versus settling time to 5,000-dyne-cm balance for the yaw axis control.

INTER-AXIS CROSS-COUPLING

Below the general equations of angular motion of a rigid body are given from which the linear approximations

$$\sum T_R = I_{RR}\ddot{\theta};\ \sum T_Y = I_{YY}\ddot{\theta}_Y$$

result.

$$T_R = \dot{H}_R + \omega_Y H_P - \omega_P H_Y \tag{16}$$

$$T_Y = \dot{H}_Y + \omega_P H_R - \omega_R H_P \tag{17}$$

$$T_P = \dot{H}_P + \omega_R H_Y - \omega_Y H_R \tag{18}$$

where:

$$H_R = I_{RR}\omega_R - I_{RY}\omega_Y - I_{RP}\omega_P$$

$$H_Y = I_{YY}\omega_Y - I_{YR}\omega_R - I_{YP}\omega_P$$

$$H_P = I_{PP}\omega_P - I_{PR}\omega_R - I_{PY}\omega_Y.$$

Since the axes of the table are essentially the principal axes, the products of inertia will be much less than the moments of inertia, and therefore:

$$H_R \approx I_{RR}\omega_R;\ H_Y \approx I_{YY}\omega_Y;\ H_P \approx I_{PP}\omega_P$$

and

$$T_R = I_{RR}\dot{\omega}_R + I_{PP}\omega_Y\omega_P - I_{YY}\omega_P\omega_Y = I_{RR}\dot{\omega}_R - (I_{YY} - I_{PP})\omega_Y\omega_P \tag{19}$$

$$T_Y = I_{YY}\dot{\omega}_Y + I_{RR}\omega_R\omega_P - I_{PP}\omega_R\omega_P = I_{YY}\dot{\omega}_Y - (I_{PP} - I_{RR})\omega_P\omega_R \tag{20}$$

$$T_P = I_{PP}\dot{\omega}_P + I_{YY}\omega_Y\omega_R - I_{RR}\omega_Y\omega_R = I_{PP}\dot{\omega}_P - (I_{RR} - I_{YY})\omega_R\omega_Y. \tag{21}$$

The maximum rates of the table when the system was simulated on a single axis basis on the computer were:

$$\omega_{R_M} = 5\times10^{-4} \text{ rad/sec}$$

$$\omega_{Y_M} = 3\times10^{-4} \text{ rad/sec}$$

$$\omega_{P_M} = 0$$

Therefore, the only important cross-coupling term would be that in Equation (21), namely $(I_{RR} - I_{YY})W_R W_Y$. Since $I_{RR} - I_{YY} = 23$ slug-ft^2, the maximum value of this cross-coupling term would be as follows.

$$(I_{RR} - I_{YY})W_R W_Y = 46.5 \text{ dyne-cms, or } 3.45\times10^{-6} \text{ ft-lb}$$

This would produce a negligible maximum acceleration about the pitch axis as can be seen by substituting this value of maximum cross-coupling torque into Equation (21). The resulting $(\dot{\omega}_P)_{max}$ would be as follows.

$$(\dot{\omega}_P)_{max} = \frac{3.45\times10^{-6} \text{ ft-lb}}{50 \text{ slug-ft}^2} = 6.9\times10^{-8} \text{ rad/sec}^2.$$

Since the computer results show that the balancing system always stabilizes in less than 2 minutes, the resulting velocity about pitch must be less than 6.9×10^{-8} rad/sec$^2\times120$ sec or

8.3×10^{-6} rad/sec. This is two orders of magnitude less than the maximum rates in roll and yaw, and obviously causes no further cross-coupling effects.

Consequently, all cross-coupling terms in Equations (19) through (21) are negligible and can be dropped. The final equations of motion therefore reduce to the following.

$$T_R=I_{RR}\dot{\omega}_R=I_{RR}\ddot{\theta}_R \tag{22}$$

$$T_Y=I_{YY}\dot{\omega}_Y=I_{YY}\ddot{\theta}_Y \tag{23}$$

$$T_P=I_{PP}\dot{\omega}_P=I_{PP}\ddot{\theta}_P. \tag{24}$$

CONCLUSION

The analog computer results show the balancing systems to be stable, and the parameters of each system should be those stated in the block diagrams (Fig. III).

A balancing time of 2 minutes in each position should be a sufficient amount of time to allow the table to balance itself, and since three balancing procedures are necessary, the total time for fine balancing will be approximately 10 minutes.

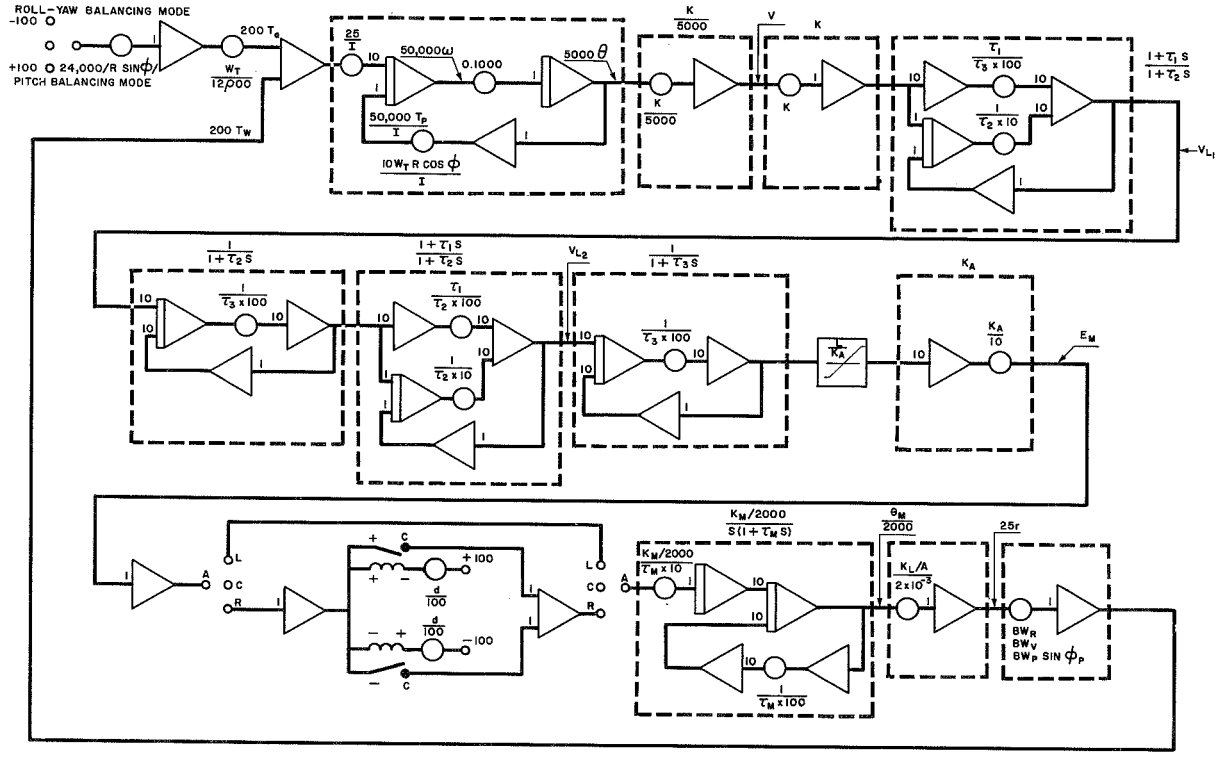

FIGURE 10.—Analog diagram of the balancing system.

APPENDIX

Since the possibility does exist to have the output shaft at right angles to the armature shaft of the motor, the torque caused by the moving armature may be used to help balance its own axis. In accordance, a very interesting result occurs. The equations of this phenomena are shown below:

$$\theta_M(S)=\frac{K_M}{S(\tau_M S+1)}\,E_M(S) \tag{25}$$

but

$$S^2\theta_M(S)=\alpha_M(S) \tag{26}$$

(since all initial conditions are zero) and

$$T_{AM}(S)=I_M\alpha_M(S) \tag{27}$$

therefore

$$\alpha_M(S)=\frac{SK_M}{(\tau_M S+1)}\,E_M(S) \tag{28}$$

and

$$T_{AM}(S)=\frac{I_M K_M S}{(\tau_M S+1)}\,E_M(S). \tag{29}$$

The block diagram from the input of the motor to the torque on the table is:

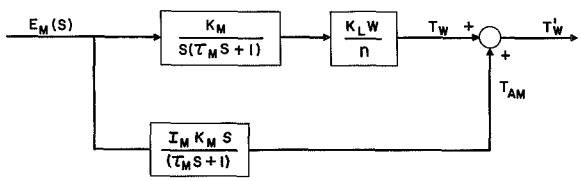

And simplifying this block diagram so that the motor, screw lead, and control weight may be represented by one block:

$$\frac{(T'_W(S)}{E_M(S)}=\frac{K_M K_L\frac{w}{n}}{S(\tau_M S+1)}+\frac{I_M K_M S}{(\tau_M S+1)} \tag{30}$$

$$=\frac{K_M K_L\frac{w}{n}+I_M K_M S^2}{S(\tau_M S+1)}$$

$$=\frac{K_M K_L\frac{w}{n}\left[1+\frac{I_M n}{K_L W}S^2\right]}{S(\tau_M S+1)}$$

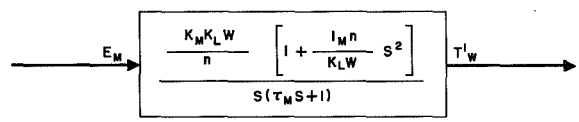

Notice that this transfer function has the lead term $(1+I_M n s^2/K_L W)$ in the numerator. If $I_M n/K_L W$ could be made large enough, the necessary phase lead would be obtained without any additional lead networks. However, in this system $I_M n/K_L W$ is approximately 0.2 (seconds)^2, producing no appreciable lead in the system in the region of interest. To increase $I_M n/K_L W$ without decreasing the gain of the system, only I_M can be increased. Preliminary investigations of a motor that satisfies all the necessary conditions (a high inertia, a low starting voltage, a low operating current, and a liner, high gain, speed-voltage characteristic) show this method to be impractical for this control system. But when all the above conditions do not have to be met, and when a great amount of phase lead is necessary, this type of compensation should be considered.

III. VEHICLE TECHNOLOGY

Page intentionally left blank

AN APPROXIMATION METHOD FOR DETERMINATION OF PROPULSION REQUIREMENTS ASSOCIATED WITH LOW THRUST COPLANAR ORBITAL TRANSFER IN A CENTRAL FORCE FIELD UNDER NEGLIGIBLE EXTERNAL PERTURBATIONS

KENNETH I. DUCK

Goddard Space Flight Center

This report presents a method for estimating propulsion system requirements associated with low thrust orbital transfer in a central force field under negligible external perturbations. It is intended to provide a useful analytical tool for sizing propellant storage requirements, estimating propulsion system weights, total impulse requirements, and transfer time. Equations are developed for transfer time and orbital eccentricity as functions of orbital elements, initial thrust to mass ratio, and propellant specific impulse. It is shown that this method is applicable for cases where initial thrust to mass ratios are equal to or less than 10^{-2} ft/sec^2 over a range of near circular orbital altitudes up to the twenty-four hour synchronous point. Comparison of the approximation method with numerical integration of the equations of motion using an IBM 7094 computer shows close agreement for selected cases reported herein. The results are presented in the form of parametric curves to enable the determination of propulsion requirements upon specific mission applications. The buildup of eccentricity was investigated and is shown to be relatively small for the cases studied.

DEFINITION OF TERMS

m=instantaneous satellite mass, slugs
m_0=initial satellite mass, slugs
$\dot{m}$=mass flow, slugs/sec
t=instantaneous time, seconds
τ=total transfer time, seconds
r=radial position of satellite at time (t) in the central force field, feet
$\dot{r}$=velocity component in the radial direction, ft/sec
$\ddot{r}$=acceleration component in the radial direction, ft/sec^2
ϕ=angle from perigee in the orbit plane, radians
$\dot{\phi}$=satellite angular velocity about the earth's center, radians/sec
$\ddot{\phi}$=satellite angular acceleration about the earth's center, radians/sec^2
F_r=radial component of thrust, pounds
F_ϕ=longitude component of thrust, pounds
I_{sp}=propellant specific impulse, seconds
I_t=total impulse, pound seconds
ΔV_t=total effective velocity increment, ft/sec
R_i=circular orbit radius (i=1, 2, 3, . . .), feet
C_i=defined constants (i=0, 1, 2, 3, . . .)
V_{ci}=circular orbit velocity at R_i, ft/sec
e=orbit eccentricity
v=instantaneous velocity, ft/sec
β_0=flight path angle, degrees
a_0=initial acceleration, C_0/m_0, ft/sec^2
g=acceleration of gravity, 32.146 ft/sec^2
μ=earth gravitational constant, 1.4076449×10^{16} ft^3/sec^2
W_0=initial satellite weight, pounds
W_p=propellant weight required for transfer, pounds

764-173 O—65——26

W_n=net payload weight delivered to final orbit, pounds

NOTE: All dot symbols above variables denote derivatives with respect to time, i.e.

$$\dot{r}=\frac{dr}{dt}$$

$$\ddot{r}=\frac{d^2r}{dt^2},$$

etc.

INTRODUCTION

This report is concerned with propulsion requirements for satellite orbital transfer under the assumptions of continuous, coplanar-tangential thrusting in a central force field neglecting external perturbations. Of special interest are propulsion systems of high specific impulse (>300 seconds). This generally eliminates conventional cold gas systems and the majority of monopropellant systems. Particularly promising applications lie in the use of various electric thrust devices (e.g., arcjet or resisto-jet), bipropellants, and heated high specific impulse gases.

The primary objectives of this study are: (1) to provide a method for rapid estimation of orbital transfer propulsion requirements; (2) to establish transfer time and total impulse as functions of the initial thrust to mass ratio, propellant specific impulse, and orbital elements; (3) to establish orbital eccentricity buildup for selected cases; and (4) to establish a range of validity for the approximate solution by comparison with numerical integration of the equations of motion using a digital computer.

ANALYSIS OF SATELLITE TRANSFER

Satellite motions in a plane can be described by a set of second order differential equations in polar coordinates in terms of r and ϕ. The following diagram illustrates the mathematical model of the system (Fig. 1).

Consider the initiation of transfer to occur in the instantaneous parking orbit shown in the above diagram. The thrust vector is assumed to lie always perpendicular to the instantaneous

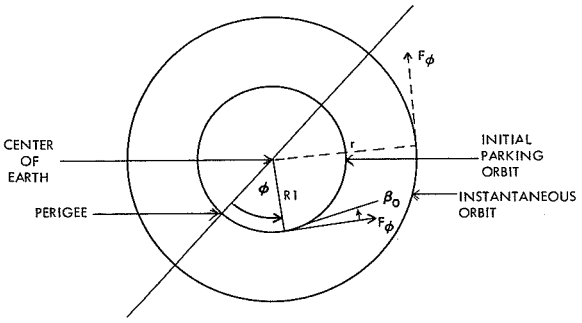

FIGURE 1

radius vector (r). The equations of motion are:

$$\frac{F_r}{m}=\ddot{r}-r\dot{\phi}^2+\frac{\mu}{r^2} \tag{1}$$

$$\frac{F_\phi}{m}=r\ddot{\phi}+2\dot{r}\dot{\phi} \tag{2}$$

Based upon the assumed conditions,

$$F_r=0,\ F_\phi=C_0. \tag{3}$$

Thus, Equation (1) becomes

$$r\dot{\phi}^2=\ddot{r}+\frac{\mu}{r^2}. \tag{4}$$

Solving Equation (4) for $\dot{\phi}$,

$$\dot{\phi}=\left[\frac{\ddot{r}}{r}+\frac{\mu}{r^3}\right]^{1/2}. \tag{5}$$

It is evident from Equation (4) that the radial acceleration is a function of the radial distance r and the angular velocity $\dot{\phi}$. The ensuing development is based upon the assumption that in Equation (5) the radial acceleration, $\ddot{r}$ does not contribute significantly to the angular velocity $\dot{\phi}$. Thus,

$$\frac{\ddot{r}}{r}<<\frac{\mu}{r^3}. \tag{6}$$

Rewriting Equation (6),

$$\frac{\ddot{r}r^2}{\mu}<<1. \tag{7}$$

Let,

$$\epsilon=\frac{\ddot{r}r^2}{\mu}. \tag{8}$$

Substituting Equation (8) into Equation (7) yields,

$$\epsilon << 1. \tag{9}$$

Using the above assumption Equation (5) reduces to,

$$r\dot{\phi}^2 \cong \frac{\mu}{r^2}. \tag{10}$$

Solving Equation (10) for $\dot{\phi}$ yields,

$$\dot{\phi} \cong \sqrt{\frac{\mu}{r^3}}. \tag{11}$$

Differentiating Equation (11),

$$\ddot{\phi} \cong -3/2\dot{r}\sqrt{\mu/r^5}. \tag{12}$$

Substituting Equations (3), (11), and (12) into Equation (2),

$$\frac{C_0}{m} \cong -3/2r\dot{r}\sqrt{\frac{\mu}{r^5}} + 2\dot{r}\sqrt{\frac{\mu}{r^3}}. \tag{13}$$

Equation (13) simplifies to

$$\frac{C_0}{m} \cong \frac{\dot{r}}{2}\sqrt{\frac{\mu}{r^3}}. \tag{14}$$

Mass flow is defined by (Ref. 1)

$$\dot{m} = \frac{C_0}{gI_{sp}}. \tag{15}$$

Substituting Equation (15) into Equation (14) and rearranging,

$$\frac{\dot{m}}{m} \cong \frac{\dot{r}}{2gI_{sp}}\sqrt{\mu/r^3}. \tag{16}$$

For continuous thrusting the instantaneous mass is related to the initial mass by,

$$m = m_0 - \dot{m}t. \tag{17}$$

Substituting Equation (17) into Equation (16) and separating the variables,

$$\int_0^\tau \frac{m\,dt}{(m_0 - \dot{m}t)} \cong \frac{\mu^{1/2}}{2gI_{sp}} \int_{R_1}^{R_2} \frac{dr}{r^{3/2}}. \tag{18}$$

Integrating this becomes,

$$ln\left(\frac{m_0}{m_0 - \dot{m}\tau}\right) \cong \frac{1}{gI_{sp}}\left[\sqrt{\frac{\mu}{R_1}} - \sqrt{\frac{\mu}{R_2}}\right]. \tag{19}$$

The total effective velocity is defined as

$$\Delta V_t = gI_{sp} ln\left(\frac{m_0}{m_0 - \dot{m}t}\right). \tag{20}$$

Thus,

$$\Delta V_t = \left[\sqrt{\frac{\mu}{R_1}} - \sqrt{\frac{\mu}{R_2}}\right] \tag{21}$$

which reduces to

$$\Delta V_t \cong V_{c1} - V_{c2} \tag{22}$$

where

$$V_{c1} = \sqrt{\mu/R_1} \tag{23a}$$

and

$$V_{c2} = \sqrt{\mu/R_2}. \tag{23b}$$

Substituting Equation (17) into Equation (14)

$$\frac{C_0}{(m_0 - \dot{m}t)} \cong \frac{\dot{r}}{2}\sqrt{\frac{\mu}{r^3}}. \tag{24}$$

Differentiating Equation (24) with respect to time,

$$\frac{d}{dt}\left[\frac{C_0}{(m_0 - \dot{m}t)}\right] \cong \frac{d}{dt}\left[\frac{\dot{r}}{2}\sqrt{\frac{\mu}{r^3}}\right] \tag{25}$$

$$\frac{C_0\dot{m}}{(m_0 - \dot{m}t)^2} \cong \sqrt{\frac{\mu}{4}}\left[-3/2\dot{r}^2 r^{-5/2} + \ddot{r}r^{-3/2}\right]. \tag{26}$$

Solving Equation (24) for $\dot{r}$ yields,

$$\dot{r} \cong \frac{2C_0 r}{(m_0 - \dot{m}t)}\sqrt{\frac{r}{\mu}}. \tag{27}$$

Substituting Equation (27) into Equation (26) and solving for $\ddot{r}$ yields,

$$\ddot{r} \cong 2\left[\frac{C_0\dot{m}r^{3/2}}{(m_0 - \dot{m}t)^2\mu} + \frac{3C_0^2 r^2}{(m_0 - \dot{m}t)^2\mu}\right]. \tag{28}$$

Substituting Equation (15) into Equation (20) and rearranging,

$$\frac{m_0}{\left(m_0 - \frac{C_0}{gI_{sp}}\tau\right)} = \exp\left(\frac{\Delta V_t}{gI_{sp}}\right). \tag{29}$$

Solving Equation (29) for τ,

$$\tau=\frac{m_0 g I_{sp}}{C_0}\left[1-\exp\left(-\frac{\Delta V_t}{g I_{sp}}\right)\right] \tag{30}$$

where τ is defined as the total transfer time. Equation (30) can be rewritten in the following form.

$$\tau=\frac{W_0 I_{sp}}{C_0}\left[1-\exp\left(-\frac{\Delta V_t}{g I_{sp}}\right)\right] \tag{31}$$

where W_0 is the initial satellite weight. In Equation (28) let $t=\tau$ and substituting Equations (15) and (30) into Equation (28) and rearranging yields,

$$\ddot{r}\cong\frac{2r}{g I_{sp}(\mu/r)^{1/2}}\left[\frac{C_0/m_0}{\exp-\left(\frac{\Delta V_t}{g I_{sp}}\right)}\right]^2\left[\frac{3g I_{sp}}{(\mu/r)^{1/2}}+1\right]. \tag{32}$$

In Equation (32) let $r=R_2$. Substituting Equation (32) into Equation (8) yields

$$\epsilon\cong\frac{2(R_2)^2}{g I_{sp}(\mu/R_2)^{3/2}}\left[\frac{C_0}{m_0}\exp\left(\frac{\Delta V_t}{g I_{sp}}\right)\right]^2\left[\frac{3g I_{sp}}{(\mu/R_2)^{1/2}}+1\right]. \tag{33}$$

For specified values of initial and final orbital radii and specific impulse, ϵ becomes a function of the thrust to initial mass ratio.

Since this analysis applies only to near circu lar orbits, it is desirable to derive an equation using the approximation method given here from which the orbit eccentricity buildup can be ascertained. From Reference (4) eccentricity is defined as

$$e^2=\left(\frac{rv^2}{\mu}-1\right)^2\cos^2\beta_0+\sin^2\beta_0 \tag{34}$$

and also from reference (4),

$$\cos\beta_0=\frac{r}{v}\dot{\phi}. \tag{35}$$

From elementary trigonometry

$$\sin^2\beta_0=1-\cos^2\beta_0. \tag{36}$$

Substituting Equations (35) and (36) into Equation (34) and simplifying yields,

$$e^2=\left(\frac{r\dot{\phi}}{v}\right)^2\left[\left(\frac{rv^2}{\mu}-1\right)^2-1\right]+1. \tag{37}$$

Substituting Equation (11) into Equation (37) and simplifying,

$$e^2\cong\frac{rv^2}{\mu}-1 \tag{38}$$

It is known from elementary kinematics that,

$$v^2=\dot{r}^2+(r\dot{\phi})^2 \tag{39}$$

and substituting Equation (27) into Equation (39) yields

$$v^2\cong\frac{4C_0^2r^4}{(m_0-\dot{m}t)\mu}+\frac{\mu}{r}. \tag{40}$$

Substituting Equation (40) into Equation (38) and simplifying,

$$e^2\cong\frac{4C_0^2r^4}{(m_0-\dot{m}t)^2\mu^2}. \tag{41}$$

Solving Equation (19) for R_2 yields,

$$R_2\cong\frac{\mu}{\left[\sqrt{\frac{\mu}{R_1}}+g I_{sp}ln\left(\frac{m_0-\dot{m}\tau}{m_0}\right)\right]^2}. \tag{42}$$

Let $r=R_2$ and $t=\tau$. Then substituting Equation (42) into Equation (41) and solving for e yields,

$$e\cong\frac{2C_0}{(m_0-\dot{m}\tau)}\left\{\frac{\mu}{\left[\sqrt{\frac{\mu}{R_1}}+g I_{sp}ln\left(\frac{m_0-\dot{m}\tau}{m_0}\right)\right]^4}\right\}. \tag{43}$$

One must remember in utilizing Equation (43) that it applies only to near circular orbits and it is an approximation.

It is known by definition that (Ref. 3)

$$I_t=\int_0^t F dt=C_0\tau. \tag{44}$$

From the given definition, $W_0=W_p+W_n$, and from Equation (15) one can write,

$$W_0=\frac{C_0\tau}{I_{sp}}+W_n. \tag{45}$$

Using Equation (30) one can rewrite Equation (44) as,

$$\frac{W_n}{W_0}=\exp\left(-\frac{\Delta V_t}{g I_{sp}}\right). \tag{46}$$

This provides an interesting fact that one can use Figures 5 and 6 to evaluate net payload weight fraction by directly reading the exponential function.

RESULTS OF STUDY

It is now necessary to examine the range over which the approximation method previously described is valid. Inspection of Equation (33) in conjunction with Equation (21) indicates that ϵ increases directly as R_2 increases. From the same relationship it can be seen that ϵ decreases with increasing propellant specific impulse. Table I presents ϵ as a function of the initial thrust to mass ratio where propellant specific impulse is 300 seconds for the case of orbital transfer from a 300 nautical mile near circular orbit to a near synchronous 24-hour orbit.

TABLE I

I_{sp}=300 seconds
R_1=3741.69 nautical miles
R_2=22,752.29 nautical miles

C_0/m_0	ϵ
1. 0	320. 6
0. 1	3. 206
0. 01	0. 03206
0. 001	0. 03206$\times 10^{-2}$
0. 0001	0. 03206$\times 10^{-4}$
0. 00001	0. 03206$\times 10^{-6}$
0. 000001	0. 03206$\times 10^{-8}$

Figure 2 is a plot of ϵ as a function of the initial thrust to mass ratio for the conditions that have been described above. The quantity ϵ exceeds unity for a thrust to mass ratio equal to 0.055 ft/sec^2. Table II presents a similar case with the exception that propellant specific impulse is 5,000 seconds.

It can also be seen in Figure 2 that for the latter case ϵ exceeds unity for an initial thrust to mass ratio of 0.27 ft/sec^2.

Since it is necessary to calculate the total effective velocity increment in evaluating many of the equations employed in this analysis, it would be especially useful to have graphs from which ΔV_t can be estimated. Figures 3 and 4 are such plots. On these two plots one can estimate the total ΔV_t required for transferring from a low or intermediate altitude to a higher altitude.

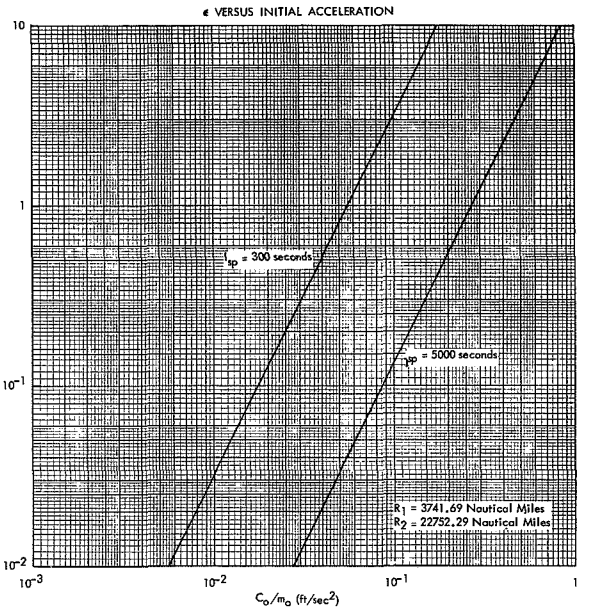

FIGURE 2.—ϵ versus initial acceleration.

It can be seen from the equations derived in this analysis that both the transfer time and ϵ require the evaluation of an exponential function. In Figures 5 and 6 the exponential of the ratio $-\Delta V_t/gI_{sp}$ is plotted as a function of the total effective velocity increment and for specific values of the propellant specific impulse.

TABLE II

I_{sp}=5,000 seconds
R_1=3741.69 nautical miles
R_2=22,752.29 nautical miles

C_0/m_0	ϵ
1. 0	13. 6
0. 1	0. 136
0. 01	0. 00136
0. 001	0. 00136$\times 10^{-2}$
0. 0001	0. 00136$\times 10^{-4}$
0. 00001	0. 00136$\times 10^{-6}$
0. 000001	0. 00136$\times 10^{-8}$

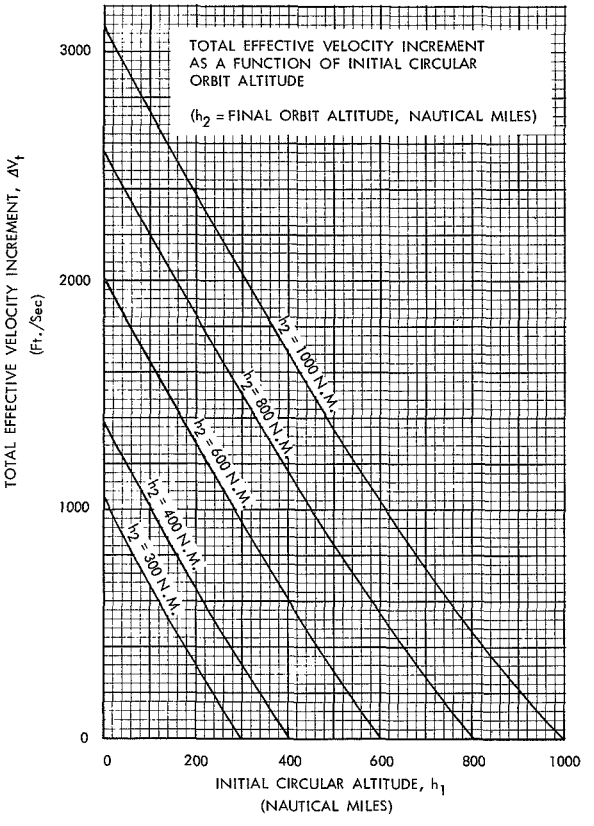

FIGURE 3.—Total effective velocity increment as a function of initial circular orbit altitude (h_2=final orbit altitude, nautical miles).

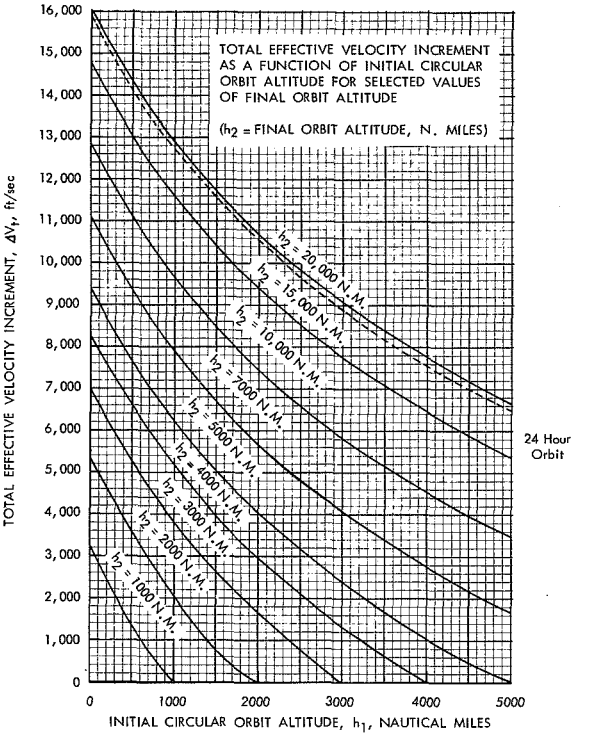

FIGURE 4.—Total effective velocity increment as a function of initial circular orbit altitude for selected values of final orbit altitude, (h_2=final orbit altitude, nautical miles).

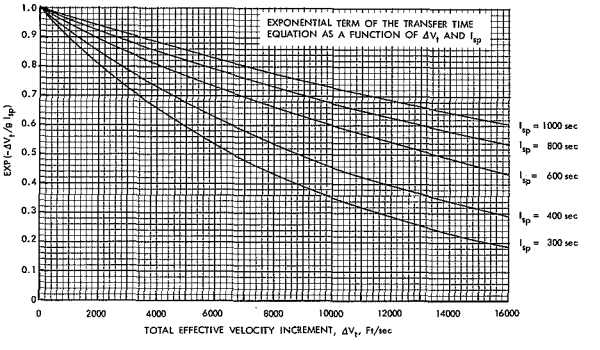

FIGURE 5.—Exponential term of the transfer time equation as a function of ΔV_t and I_{sp}.

Figures 7 and 8 present the quantity $m_0 g I_{sp}/C_0$, as a function of the initial acceleration, a_0, for specified values of propellant specific impulse. Figures 9 and 10 present total transfer time in days as a function of $m_0 g I_{sp}/C_0$ for specified values of a. One can employ Figures 3 through 10 in their respective order to establish transfer time, net payload weight fraction (equal numerically to a), final orbit altitude, velocity increment, or required specific impulse, providing other parameters are given for an application. Figures 11 and 12 plot total impulse required to transfer a satellite from a 300 nautical mile near-circular orbit to a 24-hour orbit altitude versus transfer time for selected values of thrust.

The final phase of investigation was directed toward an error analysis to establish a range of validity for the approximate method. Answers obtained from use of Figures 3 through 10, as well as equation (43) for eccentricity, were compared with results of numerical computations using the MASS program. The MASS program is a proven digital method originally developed by the General Electric Co. under NASA contract and later refined by GSFC. The dynamical equations are programed for use with the IBM 7094 and the numerical integration technique employed for this analysis is the Adams/Moulton

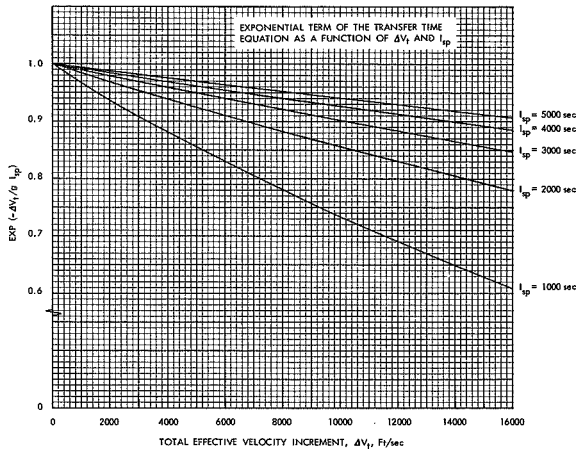

FIGURE 6.—Exponential term of the transfer time equation as a function of ΔV_t and I_{sp}.

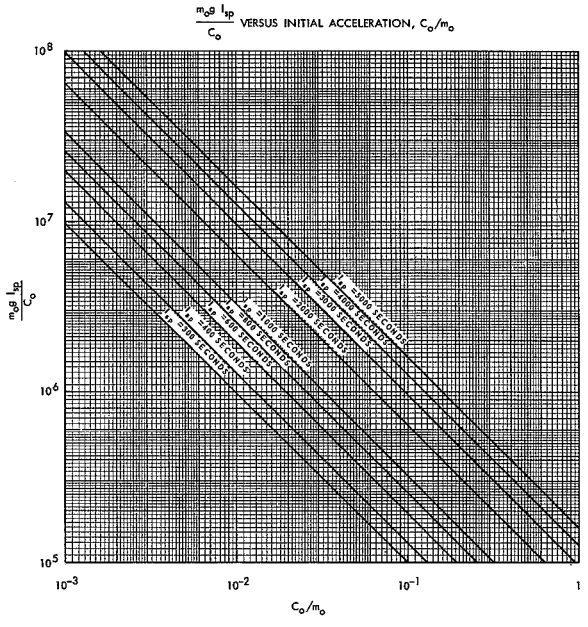

FIGURE 7.—$\frac{m_0 g I_{sp}}{C_0}$ versus initial acceleration, C_0/m_0.

method. From preliminary digital analysis it was found that computer time was excessive for cases of small a_0 as well as for the propellants having high values of specific impulse. Thus, the first series of comparisons was limited to satellite transfers between 300 and 400 nautical mile near-circular orbits. A specific impulse of 1,000 seconds was used in these cases. The

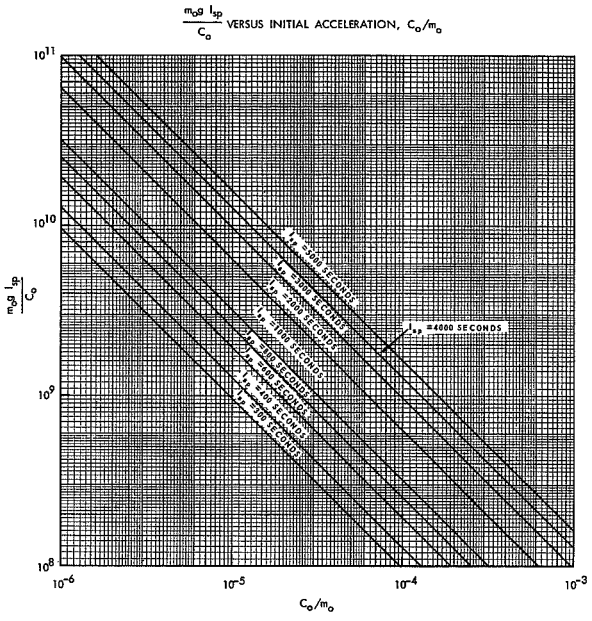

FIGURE 8.—$\frac{m_0 g I_{sp}}{C_0}$ versus initial acceleration, C_0/m_0.

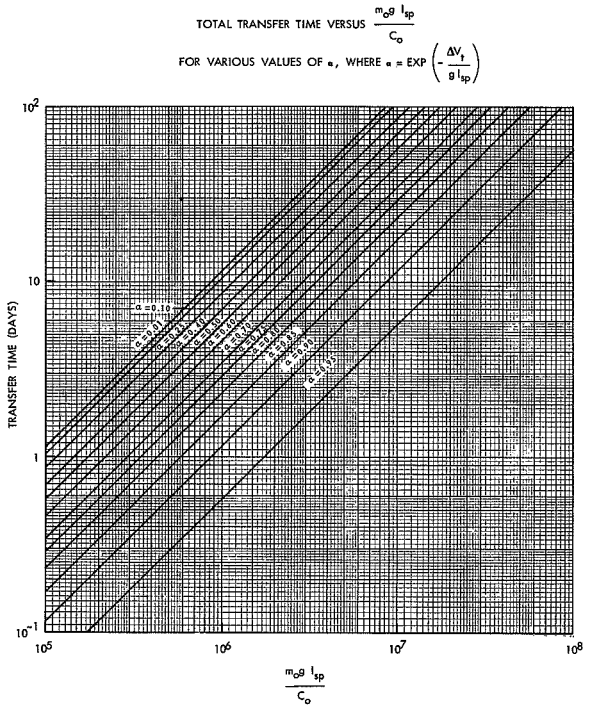

FIGURE 9.—Total transfer time versus $\frac{m_0 g I_{sp}}{C_0}$ for various values of a, where $a = \text{EXP}\left(-\frac{\Delta V_t}{g I_{sp}}\right)$.

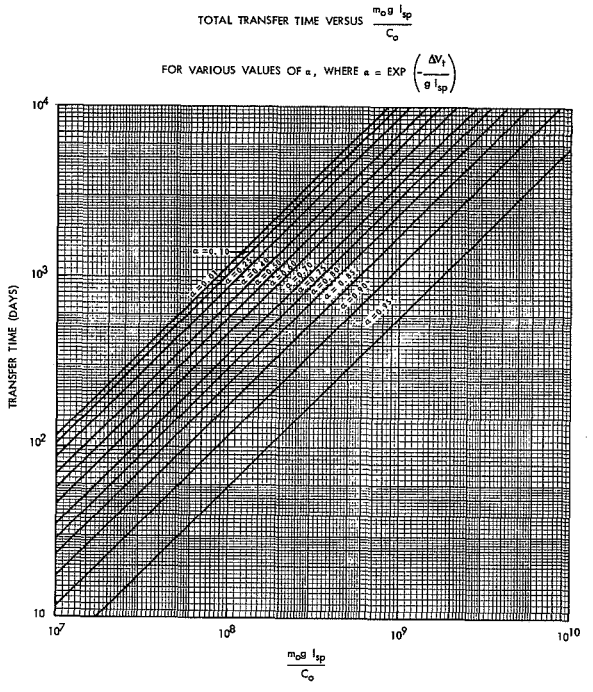

FIGURE 10.—Total transfer time versus $\frac{m_0 g I_{sp}}{C_0}$ for various values of a, where $a = \mathrm{EXP}\left(-\frac{\Delta V_t}{g I_{sp}}\right)$.

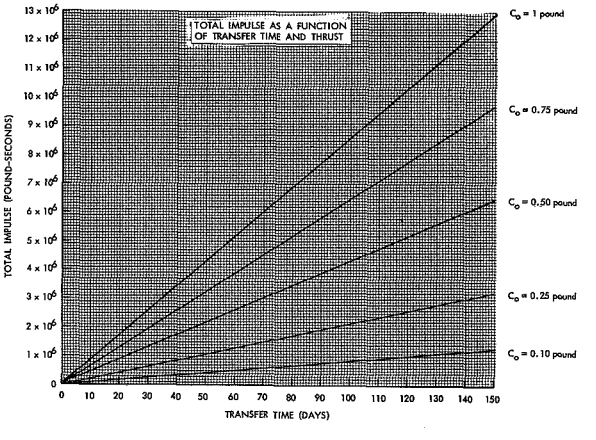

FIGURE 11.—Total impulse as a function of transfer time and thrust.

initial thrust to mass ratio was varied between 10^{-4} and 10^{-1} ft/sec^2 to establish the difference in altitude as found from the digital versus analytical solutions. The results are shown in Table III.[1]

TABLE III

a_0	Altitude difference, δh (n.m.)
10^{-4}	0. 01990
10^{-3}	. 16398
10^{-2}	2. 23701
10^{-1}	18. 65197

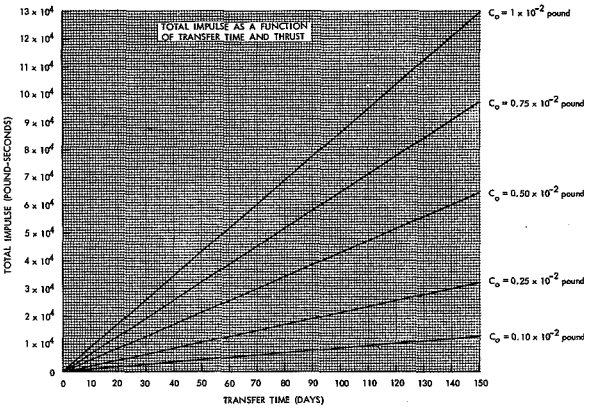

FIGURE 12.—Total impulse as a function of transfer time and thrust.

This series of comparisons was followed by a study of an assumed "worst case" which consisted of satellite transfer from a near-circular 300 nautical mile orbit to the 24-hour orbit altitude using a propellant specific impulse of 300 seconds and initial accelerations of 1, 10^{-1}, and 10^{-2} ft/sec^2, respectively. The reasons for these particular choices of propulsion system parameters was due to the fact that the accuracy of the approximation method decreases with increasing values of initial thrust to mass ratios and decreasing values of propellant specific impulse. In addition to the above cases a run was made for a 50-slug (1,607.3 pounds) satellite having propulsion system specifications of a heated hydrogen rocket (i.e., C_0=0.2 pound, I_{sp}=800 seconds). For this case at the 24-hour altitude the deviation in mission time between approximate and digital solutions was found to be 0.006 day, and smaller at lower altitudes. Figure 13 presents these results.

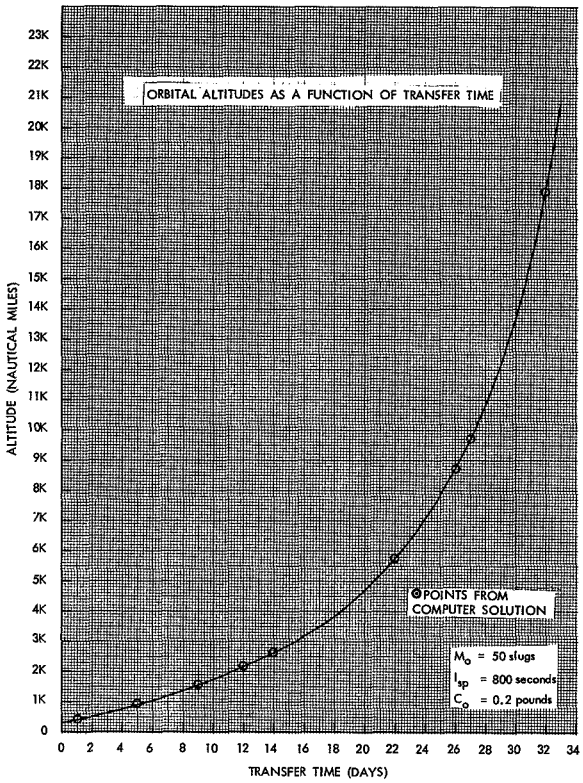

FIGURE 13.—Orbital altitudes as a function of transfer time.

For the same case, buildup in eccentricity was determined and compared with the approximate method. It was found that the initial eccentricity (following thrust application) had a value of 0.0003, whereas the final value increased to 0.019 at the 24-hour altitude. Figure 14 is a plot of this data. Using equation (43) for eccentricity determination, it was found that excellent agreement was obtained with the digital solution. The influence of propellant I_{sp} upon final orbit eccentricity is shown in Figure 15. These results were obtained directly by use of equation (43). Figure 16 presents the influence of I_{sp} upon transfer time. Here it is interesting to note that above 2,000 seconds the increase in transfer time is relatively small, meaning that high specific impulse rockets can deliver substantially more payload in essentially the same period of time. Of course, this does not take into account the high fixed weight of power supplies or related propulsion system hardware which would not be available as useful payload.

The final series of investigations are presented in Figures 17 and 18. Here, the objective has been to show that for initial accelerations greater than 10^{-2} ft/sec^2 that the deviation is

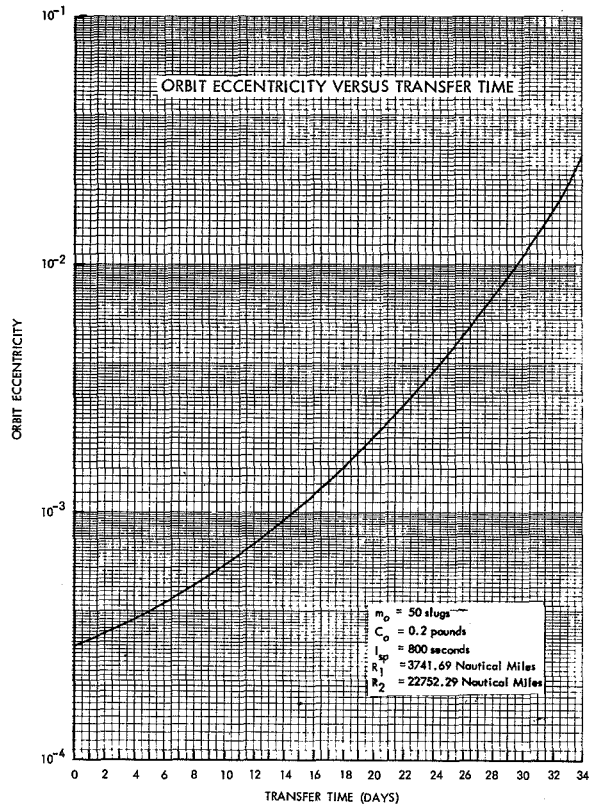

FIGURE 14.—Orbit eccentricity versus transfer time.

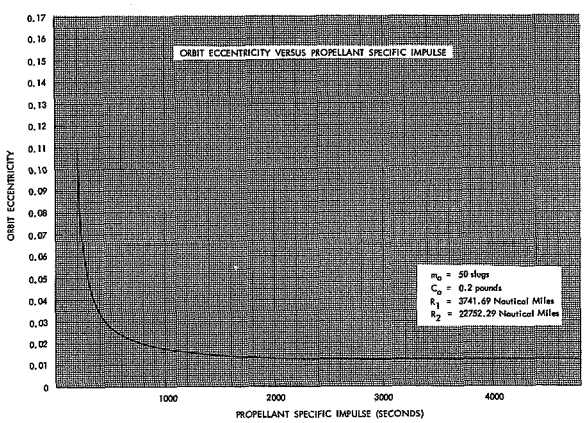

FIGURE 15.—Orbit eccentricity versus propellant specific impulse.

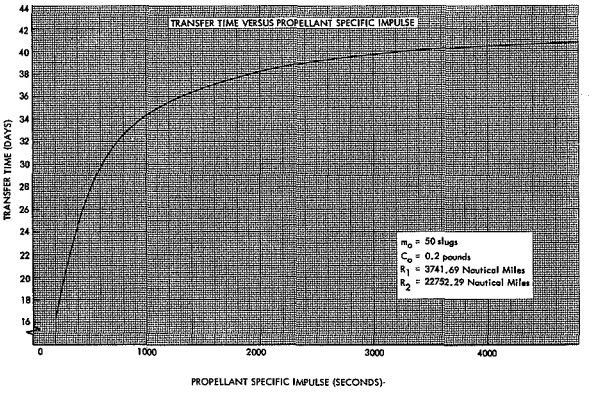

FIGURE 16.—Transfer time versus propellant specific impulse.

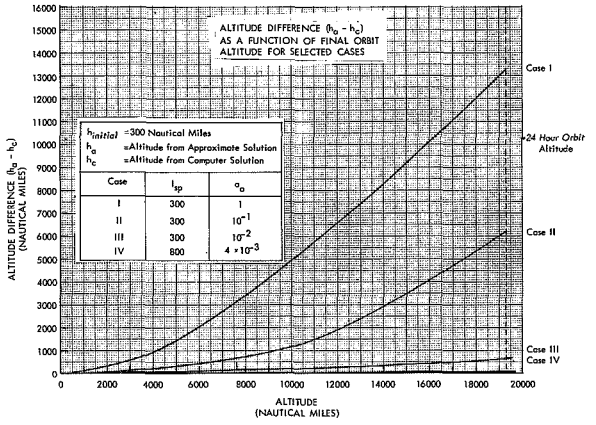

FIGURE 17.—Altitude difference ($h_a - h_c$) as a function of final orbit altitude for selected cases.

very large. It can be seen in Figure 17 for initial accelerations of 10^{-1} and 1 ft/sec^2 that the deviation at the 24-hour altitude is 6,000 and 13,000 nautical miles, respectively. For an initial acceleration less than 10^{-2} ft/sec^2 and a specific impulse greater than 300 seconds, one can expect the error in transfer time to lie within the shaded portion of Figure 18. This shaded region represents the maximum accepted transfer time difference between the approximate and computer solutions. The case of the 50-slug satellite is shown to lie well within the range of validity of this analysis. It might be added at this point that in order to develop an empirical equation in terms of orbital elements and propulsion system parameters from which a general error correlation

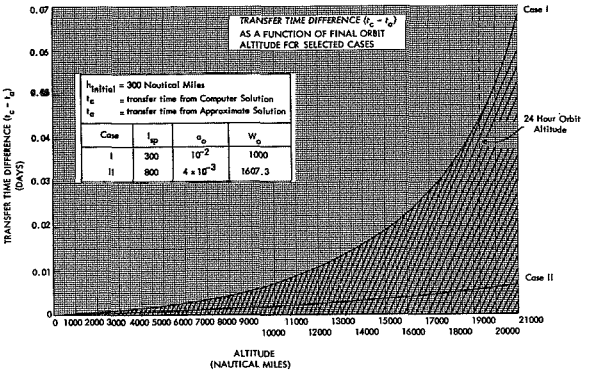

FIGURE 18.—Transfer time difference ($t_c - t_a$) as a function of final orbit altitude for selected cases.

could be obtained, one would have to conduct extensive computer runs.

CONCLUSIONS

It has been demonstrated that under certain specified conditions, satellite orbital transfer propulsion requirements can be approximated closely using simple analytical expressions. Three major considerations limit the general applicability of this study:

1. The thrust vector was assumed to lie 90° from the local vertical in a fixed plane throughout the transfer process. Obviously one can see that this is an idealization requiring perfect attitude control and zero external perturbations acting upon the satellite. Further investigation is necessary to establish increases in propulsion requirements resulting from a limit cycle characteristic for the thrust vector. The attitude control process is further complicated by various perturbational forces (e.g., solar pressure, gravitational harmonics, drag, etc.) leading to inclination changes and node regression. It is necessary to initiate another phase of study to determine the influence of such factors.
2. The initial parking orbit has been assumed to be perfectly circular. Injection errors, creating initial eccentricities, may substantially alter the range of validity expressed by this analysis. Further study is warranted

in this respect to establish the degree of "averaging out" which occurs in altitude during actual satellite transfer between elliptical orbits.

3. The influence of attitude control energy requirements and additional energy for compensation of solar pressure and aerodynamic drag is expected to increase transfer time and propellant weight somewhat.

The purpose of this paper has been to establish approximations for transfer time and total impulse as functions of the orbital elements, initial acceleration, and propellant requirements. It was necessary to determine the magnitude of any additional energy, if any, required to remove the orbit eccentricity. A range of validity for the approximate solution was established by comparing the analytical results with those obtained by numerical integration of the equations of motion using an IBM 7094 digital computer. Thus, the following conclusions can be stated.

1. Energy required to remove orbit eccentricity in transferring to a near-circular synchronous orbit from intermediate near-circular orbits is shown to be small under the assumption herein.
2. The approximate solution as described by this report holds with a very small error for a range in propellant specific inpulse between 300 and 5,000 seconds, respectively, and initial thrust to mass ratios equal to or less than 10^{-2} ft/sec.

ACKNOWLEDGMENTS

The author wishes to express appreciation to Mr. W. C. Isley, Mr. C. C. Barrett, and Mr. C. A. Wagner for their assistance in the derivations, computer studies, and proofreading the manuscript in the preparation of this paper.

REFERENCES

1. Huston, W. B., et al., "Notes on Space Technology," Compiled by the Flight Research Division, Langley Aeronautical Laboratory, Langley Field, Va., February–May 1958.
2. Isley, W. C., "A Summary of Constants Associated With Orbital Analysis of Earth Satellites, Including the Influence of Their Uncertainties Upon Gravitational Measurements for Synchronous Satelites": (GSFC–NASA Gray Cover Document X–623–62–169, 1962).
3. Stephanson, R. J., *Mechanics and Properties of Matter*, New York: John Wiley & Sons, 1960.
4. Thomson, W. T., *Introduction to Space Dynamics*, New York: John Wiley & Sons, 1961.

VEHICLE TECHNOLOGY CONSIDERATIONS FOR A SOLAR PROBE

JOHN A. FOSCHETTI
Goddard Space Flight Center

This report demonstrates that solar probes are feasible from the viewpoint of presently planned vehicle technology. For the early attempts the Saturn C–1 is considered to be the most likely vehicle to place the final stage or stages into a circular orbit. If two slightly modified but identical Centaur Jr. vehicles are used for the upper stages, then this four stage configuration will be capable of placing from 400 to 2,500 pounds at perihelion distances of 0.120 to 0.245 A.U. A more reliable three stage configuration, using one Centaur Jr. for the upper stage but requiring greater modification in the original design of the vehicle, would place payloads of 400 to 2,500 pounds at perihelion distances of 0.185 to 0.290 A.U.

Analysis of the upper stages was based on the payload value obtained for the Saturn vehicle by using the "Generalized Powered Flight Trajectory Program." At burnout there would be a payload of 24,612 pounds in a 100-nautical-mile parking orbit.

INTRODUCTION

This report continues the investigation and analysis of a possible solar probe attempt in this decade by extending the studies of References 1 and 2. Reference 1 includes temperature and solar radiation pressure considerations, and analytical and numerical trajectory studies. Reference 2 presents velocity requirements for achieving desired perihelion distances for both one- and two-impulse orbits, and concludes from time considerations that the one-impulse method is the more advantageous. Probe weight for various perihelion distances is given for two configurations, a Saturn C–1 plus H_2–F_2 stages and an Atlas-Centaur plus a solid stage.

Other vehicle configurations, using O_2–H_2 stages presently in existence or under consideration, which can place usable payloads of 400 to 2,500 pounds at perihelion distances of 0.1 to 0.3 A.U. are investigated in the current study. After considering the probe's trajectory and velocity requirements, we will use them to determine the number of stages necessary. This report also examines future vehicle payload capabilities and specific impulse demands for the upper stages. For the first attempt, the lightest structure considered—the Saturn C–1—appears to be the most likely vehicle to place the required payload in a circular orbit. The trajectory of the C–1 rocket was obtained from the IBM 7090 computer version of the "Generalized Powered Flight Trajectory Program" developed at the Jet Propulsion Laboratory and is included here.

For all upper stage designs, specific impulses of 420 seconds and thrusts of 15,00 pounds have been specified. The upper stage designs presented here emphasize: (1) payload optimization, achieved when each stage (two upper stages) acquires equal velocity increments; (2) design practicability, by having one design for each of two upper stages; (3) maximum reliability, by using, for example, a three stage rocket for less ambitious missions. Because of structural requirements payload optimization cannot be achieved, but the latter two aims can be, the more appropriate depending on a mission's goal and the payload specifications. The results of this report demonstrate that a solar probe is possible from the viewpoint of presently

planned vehicle technology and its purpose is to generate interest in the solar probe effort.

Experimental areas for solar probes include, as stated by Krafft A. Ehricke (Reference 3, pp. 107 and 108),

> the nature of the solar corona (ionization and excitation of coronal atoms); extension of coronal material into space; support and heating of coronal material; electron density in inner and outer corona; electric and magnetic fields in near-solar space; evaporation of protons and electrons from the corona and solar corpuscular radiation in general; solar cosmic radiation and extension of the solar atmosphere into interplanetary space.

Ehricke also mentions that "Another intriguing mission of the solar probe is the exploration of the zodiacal light. . . ." He points out that very little is known about the composition, mass, and motion of the huge disc-shaped cloud that causes this light. The entire scientific significance of solar probes cannot be appropriately assessed.

VEHICLE VELOCITY REQUIREMENT VS. PERIHELION DISTANCE [1]

The velocity v needed with respect to the earth, as a function of the desired perihelion distance r_π, is derived in this section. Let the orbital plane of the vehicle be in the plane of the ecliptic (Fig. 1), i.e.,

$$\frac{v_\infty \cdot U}{|v_\infty \cdot U|}=+1,$$

where U is the earth's orbital velocity, $v_\infty = U-V_1$, and V_1 is the heliocentric departure velocity; i.e., the aphelion velocity for the ellipse. If the departure is at the aphelion of the transfer ellipse, then

$$V_1=\sqrt{\frac{2K_\odot r_\pi}{r_A(r_\pi+r_A)}}, \qquad (1)$$

where $K_\odot$ is the gravitational constant for the sun, $r_\pi = mr_A$ is the perihelion distance, $0<m<1$, and r_A, the aphelion distance, is 1 A.U. The hyperbolic departure velocity with respect to the earth is

$$v=\sqrt{\frac{2K}{r}+v_\infty{}^2}, \qquad (2)$$

[1] The equations used in this section have been developed from Reference 4.

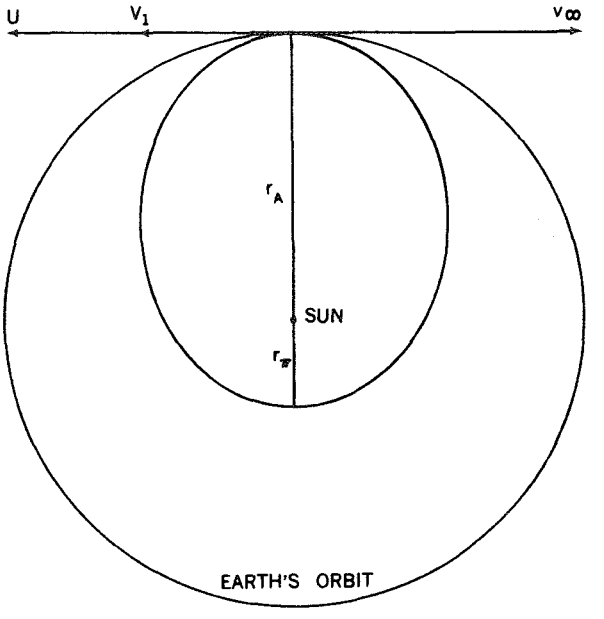

FIGURE 1.—Solar probe trajectory.

where K is the gravitational constant for the earth, r is the distance of the vehicle from the earth at the time of injection, and $2K/r$ is the escape velocity from the earth. By substituting $v_\infty = U-V_1$, $K_\odot/r_A = U^2$, $r_A=1$ A.U., and Equation 1 into Equation 2, we have

$$v=\sqrt{\frac{2K}{r}+U^2\left(1-\sqrt{\frac{2r_\pi}{1+r_\pi}}\right)^2}, \qquad (3)$$

where U is the earth's circular velocity about the sun and in astronomical units $0\leq r_\pi \leq 1$.

TRANSIT TIME

If P_E is the period for the earth's motion around the sun and P_v is the period for the vehicle's motion around the sun, then

$$\frac{P_v}{P_E}=\frac{a_v{}^{3/2}}{a_E{}^{3/2}}=\frac{\left(\frac{r_A+r_\pi}{2}\right)^{3/2}}{r_A{}^{3/2}},$$

where a_v is the semimajor axis of the transfer ellipse and a_E is the semimajor axis of the earth's orbit. By substituting $r_A=1$ A.U. and $P_E=365.25$ days we find

$$T=\frac{P_v}{2}=64.5677(1+r_\pi)^{3/2} \text{ days}, \qquad (4)$$

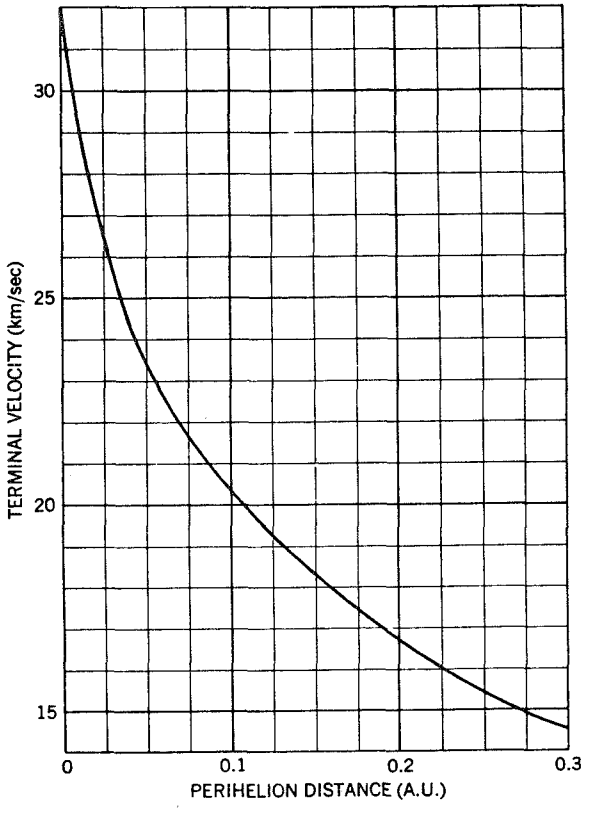

FIGURE 2.—Terminal velocity vs. perihelion distance.

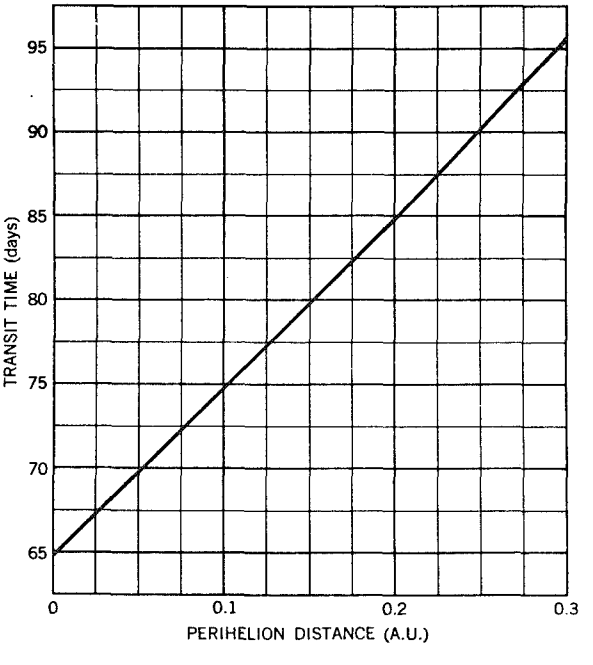

FIGURE 3.—Vehicle's transit time from earth to perihelion vs. perihelion distance.

the transit time of the vehicle from aphelion to perihelion. The expressions $v=f(r_\pi)$ for Equation 3 and $T=g(r_\pi)$ for Equation 4 are graphically presented in Figures 2 and 3, respectively, where $0 \geq r_\pi \geq 0.3$. In Figure 12 in Reference 1 both velocity and transit time vs. perihelion distance for the vehicle are shown with the earth at perihelion and at aphelion. Figures 2 and 3 in this report represent the same functions for the earth at 1 A.U., and they agree with the average of the two curves in Reference 1 to within 0.1 km/sec.

CHEMICAL ROCKET ANALYSIS

The well-known rocket equation is studied in considering such factors as:

1. The minimum number of stages necessary to attain the required velocity;
2. The velocity cutoff value which would optimize the final payload;
3. Possible vehicles for placing the upper stages into a parking orbit, from the viewpoints of present and future vehicle technology.

The rocket equation is:

$$\Delta v = g_0 I_s In \left(\frac{M_0}{M_f}\right), \tag{5}$$

where Δv is the increment of velocity from epoch to burnout, g_0 is the gravitational constant, I_s is the specific impulse, M_0 is the initial weight of the vehicle, and M_f is the weight at burnout. Let M_p be the propellant weight, M_s be the structural weight $(0.1M_p)$, M_l be the payload weight, and

$$x=\frac{\Delta v}{g_0 I_s};$$

then the ideal equation for chemical rockets becomes

$$e^x=\frac{M_p+M_s+M_l}{M_s+M_l}. \tag{6}$$

Substituting $M_s=0.1M_p$ and $M_0=M_p+M_s+M_l$ into Equation 6, we find

$$\frac{M_0}{M_l}=\frac{10e^x}{11-e^x}, \tag{7}$$

and we see that $M_l>0$ for $e^x<11$ or $x<2.4$. If the specific impulse is 422 seconds and $r_\pi=0.1$ A.U., then $v=20.33$ km, from Equation 3. We are here concerned with the velocity increment after circular orbit velocity is achieved; the total velocity increment for the upper stages is $\Delta v=v-v_a$, where v_a is the circular velocity, 7.8 km/sec. Substitution of the above values gives $\Delta v=(20.33-7.8)$ km/sec$=12.53$ km/sec, and from the definition of x,

$$x=\frac{12.53}{4.1356}=3.03>2.4.$$

Thus, we must have at least two stages after the vehicle is in a parking orbit in order that $\Delta v=12.53$ km/sec. Conversely, the minimum perihelion we can obtain with a single stage vehicle is 0.167 A.U. for $M_l=0$. The next problem is to determine the velocity cut-off of the first stage of the two stage rocket (after achieving the parking orbit) which would maximize the final payload. Let M_c be the weight in the parking orbit, M_i the weight of the last stage plus the payload, k the fractional part of Δv for the first stage, and c the fractional part of Δv for the second stage $(k+c=1)$. From Equation 7,

$$M_i=M_l\frac{10e^{cx}}{11-e^{cx}}, \tag{8}$$

$$M_c=M_i\frac{10e^{kx}}{11-e^{kx}}. \tag{9}$$

Substituting Equation 8 into Equation 9, we have

$$M_c=M_l\left(\frac{10e^{cx}}{11-e^{cx}}\right)\left(\frac{10e^{kx}}{11-e^{kx}}\right). \tag{10}$$

Replacing c by $1-k$ in Equation 10 and simplifying yields

$$\frac{M_c}{M_l}=\frac{100e^xe^{kx}}{121e^{kx}-11e^x-11e^{2kx}+e^xe^{kx}}. \tag{11}$$

We wish to differentiate Equation 11 with respect to k in order to find what value of k will give M_c/M_l its minimum value. Performing the differentiation and equating the result to zero,

$$\frac{d}{dk}\left(\frac{M_c}{M_l}\right)=0,$$

shows that M_c/M_l is a minimum when $k=1/2$. In this case $k=1/2=c$ and Equation 10 becomes

$$\frac{M_c}{M_l}=\left(\frac{10e^{x/2}}{11-e^{x/2}}\right)^2. \tag{12}$$

With

$$x=\frac{\Delta v}{g_0I_s}=\frac{12.53}{g_0I_s},$$

and $M_l=500$ pounds, a reasonable payload, the specified impulse was varied and the graph for $M_c=h(I_s)$ was derived as shown in Figure 4. The last problem mentioned at the beginning of

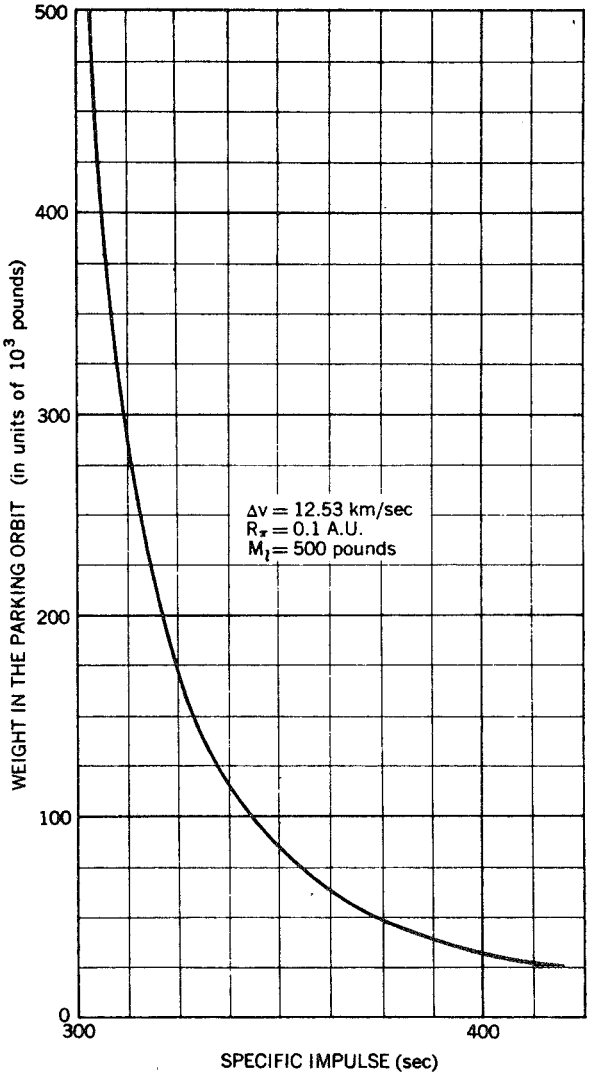

FIGURE 4.—Weight in a parking orbit vs. the specific impulse.

this section, selecting a vehicle which will place the upper stages into a circular orbit, is resolved by examining Figure 4 which shows that at least 25,000 pounds is required in a parking orbit for the maximum specific impulse being considered. Since the orbiting of payloads heavier than 25,000 pounds at present seems more distant than designing engines with specific impulses of 420 seconds, the C–1 vehicle has been chosen, its circular orbit payload capability being the required 25,000 pounds.

PAYLOAD IN A CIRCULAR ORBIT

The saturn C–1 vehicle was programmed for a 100 nautical mile circular orbit with the "Generalized Powered Flight Trajectory Program" developed by the Jet Propulsion Laboratory. For 15 seconds the vehicle followed a vertical path. It was then tilted at a rate of 0.7877 deg/sec for 15 seconds. The remainder of the first stage was programmed with zero lift. A pitch up control of 13 degrees above the local horizon was necessary during the second stage in order for the vehicle to enter into a circular orbit with zero flight path angle. The results for the trajectory are shown in the Figures 5–9. Payload weight in the circular orbit is 24,612 pounds.

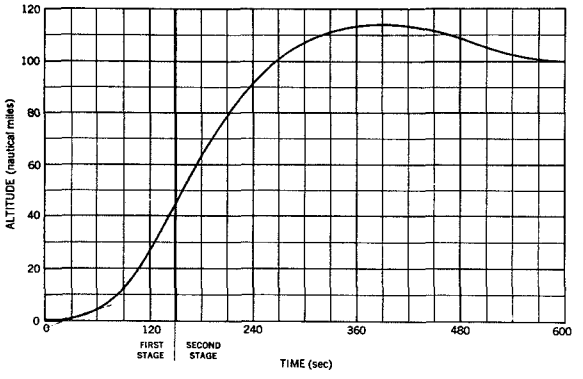

FIGURE 5.—Altitude vs. time for the Saturn C–1 trajectory for a 100-nautical-mile parking orbit.

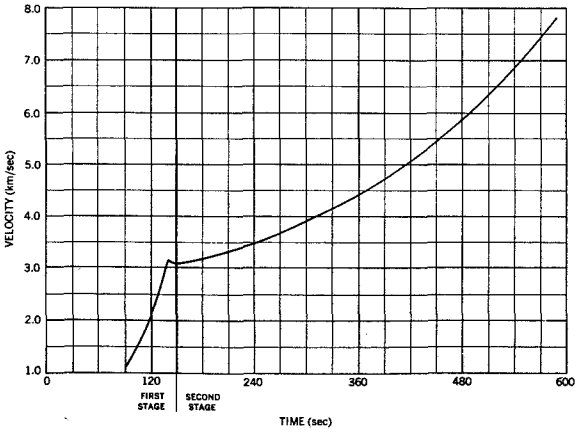

FIGURE 6.—Velocity vs. time for the Saturn C–1 trajectory for a 100-nautical-mile parking orbit.

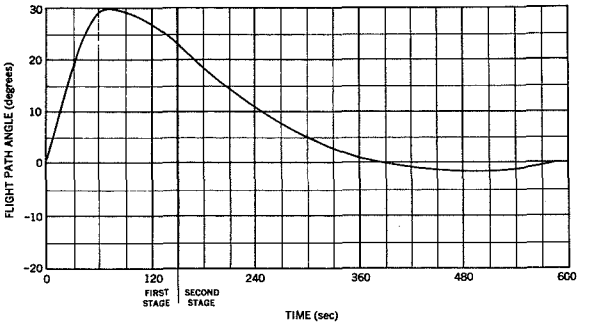

FIGURE 7.—Flight path angle vs. time for the Saturn C–1 trajectory for a 100-nautical-mile parking orbit.

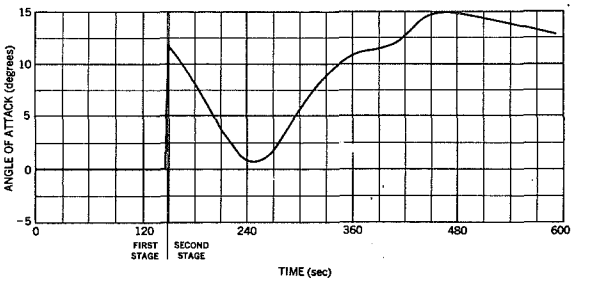

FIGURE 8.—Angle of attack vs. time for the Saturn C–1 trajectory for a 100-nautical-mile parking orbit.

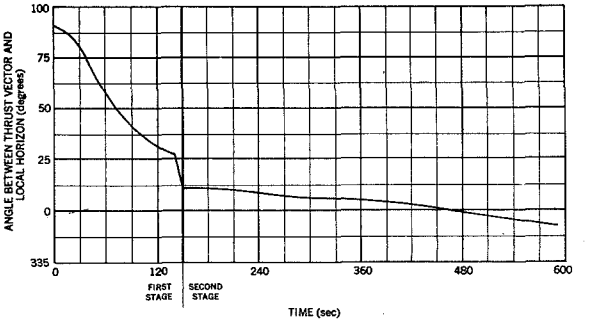

FIGURE 9.—Angle between thrust vector and local horizon vs. time for the Saturn C–1 trajectory for a 100-nautical-mile parking orbit.

UPPER STAGE DESIGNS

Three upper stage designs will be presented:

1. The design in which each stage aequires equal velocity increments. This design optimizes the payload, as discussed earlier.
2. One design for both upper stages, facilitating the engineering and lowering the cost of the project.
3. The design of a three stage rocket for less ambitious, more reliable missions.

Optimum Final Payload

For equal velocity increments in each stage let $k=1/2=c$. Since the total velocity is $\Delta v=\Delta v_1+\Delta v_2=12.53$ km/sec, then $\Delta v_1=6.265$ km/sec$=\Delta v_2$. From Equation 9, for $M_c=24{,}612$ pounds, $k=1/2$, and

$$x=\frac{\Delta v_1}{g_0 I_s},$$

where $I_s=422$ sec, we find that $M_i=3{,}445$ pounds. In Equation 8 substitute $M_i=3{,}445$, $c=1/2$, and

$$x=\frac{\Delta v_2}{g_0 I_s},$$

then $M_l=482$ pounds. Now $M_i=M_{p^4}+M_{s^4}+M_l$, where M_i is the total weight of the fourth stage, $M_{p^4}=10M_{s^4}$, and the number "4" indicates that the value applies to the fourth stage. Therefore $M_i=11M_{s^4}+M_l$, and the structural weight for the fourth stage is

$$M_{s^4}=\frac{M_i-M_l}{11}=270 \text{ pounds.}$$

The required structural weight of 270 pounds is not reasonable for the engine we are considering, a more reasonable estimate, taken from vehicle specifications, being 1,100 pounds. At 0.2 A.U., payload optimization is satisfied when the structural weight for the fourth stage is less than 445 pounds. Therefore it is necessary to deviate from the attempt of attaining equal velocities for each stage.

One Design for the Two Upper Stages

We will now investigate the possibility of using one design for two upper stages, each of which has a structural weight of 1,096 pounds, a reasonable figure for an engine such as the Centaur Jr. Let M_c be 24,612 pounds, M_s be 1,096 pounds, I_s be 420 seconds, M_{p^3} the propellant weight of the third stage$=10M_s=$ 10,960 pounds, and M_{p^4}, the propellant weight of the fourth stage$=11{,}460-M_l$. Substituting these values into the rocket equation yields

$$\exp\frac{\Delta v_1}{4.116}=\frac{M_c}{M_s+M_{p^4}+M_l}=\frac{24{,}612}{13{,}652}, \quad (13)$$

or

$$\Delta v_1=2.6943 \text{ km/sec.}$$

Since the circular orbit velocity is

$$v_c=7.795 \text{ km/sec,}$$

then

$$v_1=v_c+\Delta v_1=10.49 \text{ km/sec,}$$

where v_1 is the velocity at the end of the third stage. Also since the initial weight of the fourth stage is the burnout weight of the third stage less the structural weight, or $M_{t^4}=$ $13{,}652-1{,}096=12{,}556$, then

$$\exp\frac{\Delta v_2}{4.116}=\frac{12{,}556}{M_s+M_l} \quad (14)$$

and

$$v=10.49+4.116\ ln\left[\frac{12{,}556}{1{,}096+M_l}\right] \quad (15)$$

is the total velocity required for the two upper stages. The graph for

$$r_\pi[=f(v)=h(M_{p^4})]=g(M_l)$$

is shown in Figure 10. For $M_l=400$ pounds $r_\pi=0.120$ A.U., and for $M_l=2{,}500$ pounds $r_\pi=0.245$ A.U.

Payload and Velocity Capabilities for a Three Stage Vehicle (One Upper Stage)

The total weight of the payload (third stage now), M_c, is $M_p+M_l+M_s$. Since $M_p=10M_s$, $M_c=11M_s+M_l$ or

$$M_s=\frac{M_c-M_l}{11}=\frac{24{,}612-M_l}{11} \quad (16)$$

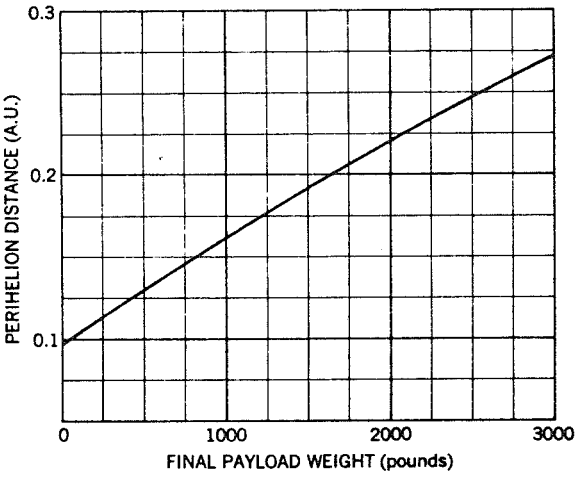

FIGURE 10.—Perihelion distance vs. final payload weight for the two-upper-stage configuration.

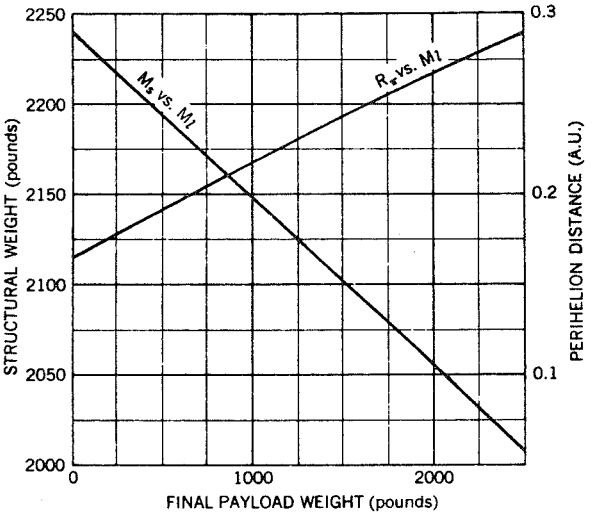

FIGURE 11.—Perihelion distance and structural weight vs. the final payload weight for the three-stage configuration.

and the rocket equation becomes

$$\exp \frac{\Delta v}{4.116}=\frac{24{,}612}{M_s+M_l}. \qquad (17)$$

Figure 11 is a graph of

$$M_s=\alpha(M_l)$$

from Equation 16 and

$$r_\pi[=f(v)]=\alpha(M_l)=h(M_s).$$

Here, for M_l=400 pounds r_π=0.185 A.U., and for M_l=2,500 pounds r_π=0.290 A.U.

CONCLUSION

Upon the completion and successful performance of the C–1 rocket and with slight modifications to the specifications of the Centaur Jr., a four stage configuration will be able to orbit payloads of 400 to 2,500 pounds at perihelion distances of 0.120 to 0.245 A.U. The minimum perihelion distance attainable for a 1 pound payload is 0.10 A.U.

A more reliable, three stage configuration, having the same specific impulse but requiring greater modifications in structural weight, will be able to deliver payloads of 400 to 2,500 pounds to perihelion distances of 0.185 to 0.290 A.U. Its minimum perihelion distance attainable for a 1 pound payload is 0.165 A.U. These figures demonstrate the feasibility of sending useful payloads to the sun.

ACKNOWLEDGMENTS

The author would like to acknowledge Samuel Pines, R. Kenneth Squires, and Ronald Kolenkiewicz for direction and advice in the preparation of this report.

REFERENCES

1. DUGAN, D. W., "A Preliminary Study of the Solar-Probe Mission," NASA Technical Note D–783, April 1961.
2. HALL, C. F., NOTHWANG, G. J., and HORNBY, H., "Solar Probes—A Feasibility Study," *Aerospace Engng.* 21(5): 22–30, May 1962.
3. EHRICKE, K. A., "Space Flight, Vol. 1: Environment and Celestrial Mechanics," Princeton, N.J.: Van Nostrand, 1960.
4. SEIFERT, H. S., ed., "Space Technology," New York: Wiley, 1959.

FLIGHT VIBRATION DATA FROM THE DELTA 9 LAUNCH VEHICLE

LLOYD A. WILLIAMS
Goddard Space Flight Center

Three channels of vibration data were obtained during the flight of the Delta 9 vehicle which was used to place the UK–1 satellite Ariel I (1962 σ1) into earth orbit on April 26, 1962, from Cape Canaveral.

Vibration data for the three principal axes of the payload support structure were obtained from liftoff through third-stage motor burnout. Maximum vibration levels during first- and second-stage burning occurred at liftoff, staging, and fairing jettison with low levels between events. The maximum composite vibration levels for first- and second-stage burning were 2.5 g peak and 1.9 g peak for the thrust and lateral axes, respectively and occurred at liftoff.

The third-stage motor exhibited the normal resonant burning characteristics for this type of motor, that is, the tangential and longitudinal modes caused by acoustical cavity resonances. However, since this phenomenon is already well documented, the primary purpose of this vibration experiment was to record low-frequency high-stress amplitude vibration. Consequently, the measuring systems were set up to measure low-level first- and second-stage modal vibrations. Most of the third-stage data are not realistic since the amplifiers were overloaded.

Shock transients occurred at times of premature despin. Despin of the third-stage motor and payload was scheduled to start 15 minutes after closure of the third-stage motor pressure switch; however, the first despin sequence started 1 minute and 40 seconds after the switch closed.

INTRODUCTION

A continuous long-term program which will increase confidence in laboratory environmental testing is in operation at Goddard Space Flight Center. Part of this program involves the acquisition of flight vibration data to give adequate definition to laboratory test criteria, since laboratory tests are required to demonstrate the ability of the payload to withstand the vibrations encountered during launch and flight.

Since measurements of vibrations at the thrust flange of a Thor-Delta vehicle's third-stage motor during flight are virtually nonexistent, and since space and weight were available on the Delta 9 vehicle which launched the UK–1 satellite Ariel I (1962 σ1) from Cape Canaveral on April 26, 1962, an experiment was placed aboard the Delta 9 to help provide data for future environmental simulation of this three-stage vehicle. This report presents the results of this in-flight experiment. The Delta 9 launch vehicle placed the Ariel I satellite in an elliptical orbit at a height ranging from 210.4 nautical miles at perigee to 655.4 nautical miles at apogee.

Located between the satellite's separation system and the Delta 9 third-stage motor was a cylindrical extension called "The Dutchman." The Dutchman housed the Goddard vibration experiment, the United Kingdom solar aspect sensor, and a United Kingdom contamination sensor.

The vibration experiment telemetered three channels of data from liftoff to beyond premature despin of the Delta 9 launch vehicle. The three channels measured the vibrations along three orthogonal axes of the vehicle

(longitudinal, lateral, and lateral plus 90 degrees). Telemetered data were received from Atlantic Missile Range stations Tel 2, Tel 3, Grand Bahama Island, Antigua, Whisky (downrange ship), and Hanger AE. First- and second-stage motor vibrations were monitored at Tel 2, Tel 3, Grand Bahama Island, and Hanger AE. Third-stage vibrations and premature despin transients were recorded at Antigua.

DESCRIPTION OF THE VEHICLE

Figure 1 shows the Delta 9 vehicle on its launch pad at Cape Canaveral. The description given here is extracted from Reference 1.

The first stage of the Delta 9 vehicle was a DM–18A Thor missile (320) modified to a DM–19 configuration by removal of the retro rockets, ACSP guidance system, one "engine control" pressure bottle, and nose cone. Further modifications consisted of the addition of: (1) a command destruction system, (2) an Azusa transponder tracking aid, (3) a PDM/-FM 30×30 telemeter, (4) special circuitry to accomplish a second-stage ignition, (5) a series-parallel arrangement of four fuel-injector-pressure switches to provide the main engine cutoff signal, (6) a pressure diaphragm, and (7) a Teflon exterior insulation applied to the leading edge of the fins. The main engine was an MB–3 Block I (S/N 4312) using RP–1 and liquid oxygen as propellants.

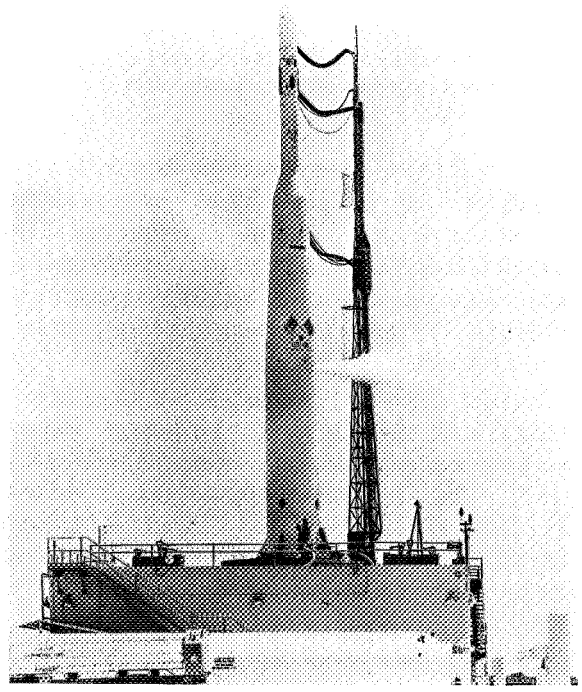

FIGURE 1.—The Delta 9 vehicle on its launch pad at Cape Canaveral.

The second stage consisted of an Aerojet-General liquid propellant propulsion system AJ10–118–009, equipment and guidance compartment, and the third-stage/payload spin table. The equipment and guidance compartment housed the Bell Telephone Laboratory guidance system, flight control system, electrical power system, flight termination system, and a PDM/FM telemeter. An externally mounted gaseous nitrogen retro system was employed to provide the required separation distance between the second and third stage at third-stage ignition. The oxidizer probes were provided as a backup engine cutoff source. Two 2KS–40 spin rockets and one 0.6KS–40 spin rocket were employed to attain the required spin rate. AC-band radar beacon was employed for vehicle tracking.

The third stage consisted of an ABL X248-A5DM (SV–186) solid propellant motor; the Dutchman; a separation system; and the UK–1 satellite. A low-drag fairing was used to protect the satellite from aerodynamic heating while flying through the sensible atmosphere. This fairing had thermal protection added to both its interior and exterior in the form of Armalon liner and Thermo-Lag, respectively. The pyrotechnic ignition of the third-stage motor was accomplished by a system employing a 15.5 ± 0.7 second delay. Because of the sensitivity of the Ariel I to contamination by motor outgassing, the dome and cylindrical portion of the third-stage motor were wrapped with aluminum foil.

INSTRUMENTATION

Three piezoelectric crystal accelerometers were secured to aluminum blocks which were bolted and cemented to the base flange of the Dutchman. The three accelerometer locations are shown on Figures 2, 3, and 4.

Signals from the accelerometers were conditioned using "charge" amplifiers and filter-clipper-bias units. The conditioned signals were then fed into an FM/FM telemeter and transmitted to ground stations via quadraloop antennas. Figure 5 is a block diagram of the instrumentation system and Figure 6 shows the instrumentation installed in the Dutchman.

The IRIG letter channels E, C, and A (15 percent deviation) were used in the FM/FM system. Thrust axis vibrations were measured on Channel E, the lateral axis vibrations were measured on Channel C, and the lateral plus 90-degree axis vibrations were measured on Channel A. These three channels had been broadbanded beyond IRIG specifications by filtering the charge amplifier outputs with low-rolloff RC low-pass filters. By this method, the frequency response of the channels was increased to 5 kc without causing an increase in intermodulation distortion on other channels.

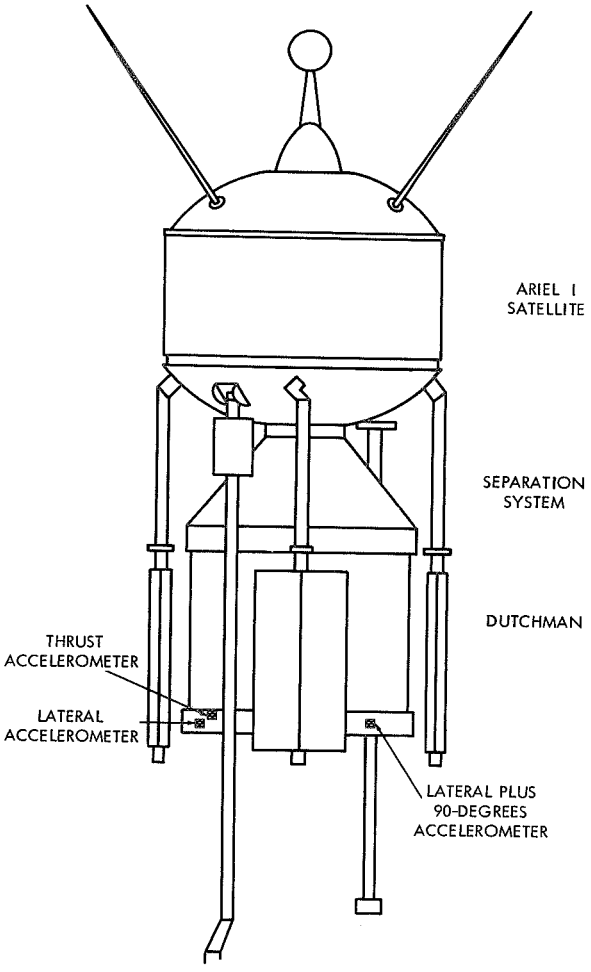

FIGURE 2.—Locations of the accelerometers on the Dutchman.

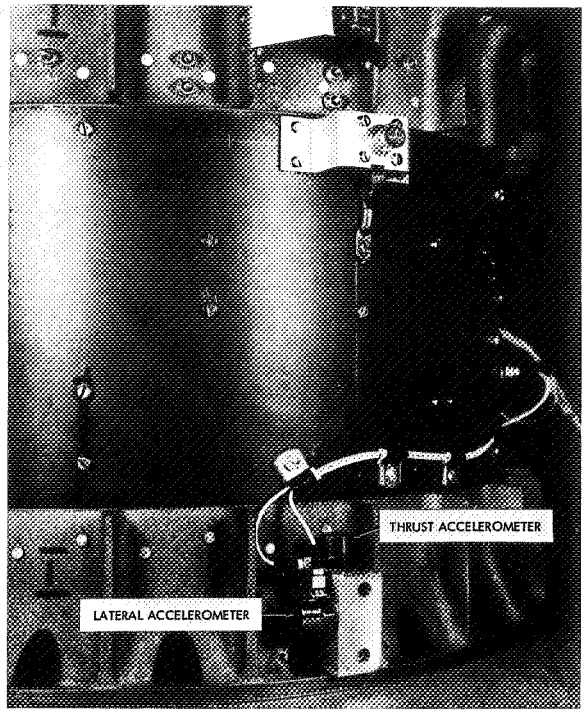

FIGURE 3.—Locations of the thrust and lateral accelerometers on the Dutchman.

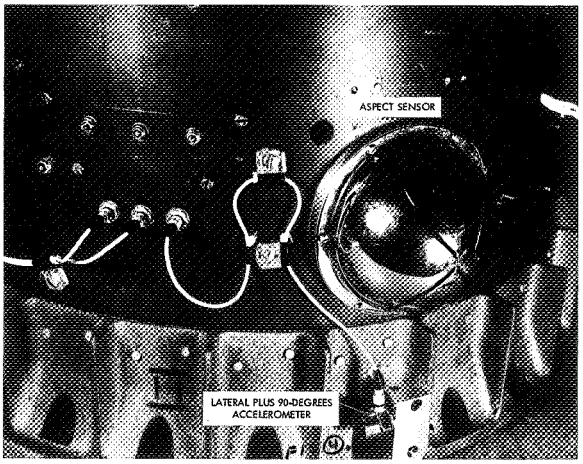

FIGURE 4.—Locations of the lateral plus 90-degrees accelerometer and the aspect sensor on the Dutchman.

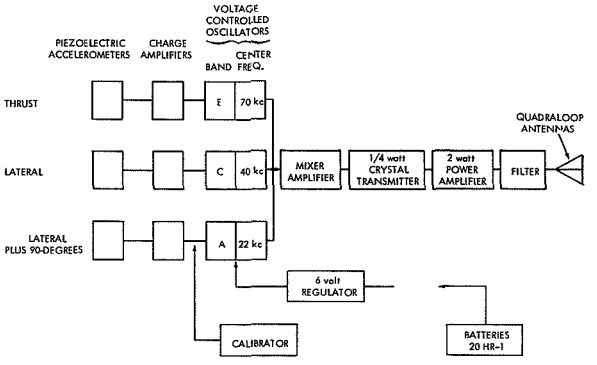

FIGURE 5.—Instrumentation system.

The frequency response of the vibration instrumentation is shown on Figure 7 for the three telemeter channels. The thrust accelerometer had a range of ±50 g, the lateral and lateral plus 90-degree accelerometers had ranges of ±20 g. It is possible to measure vibration levels greater than those mentioned above before clipping the signal due to the low-rolloff RC low-pass filters.

DATA REDUCTION

A block diagram of the data reduction system is shown in Figure 8. Data reduction consisted of various oscillograph records, rms vibration time plots, and ⅓-octave band analysis.

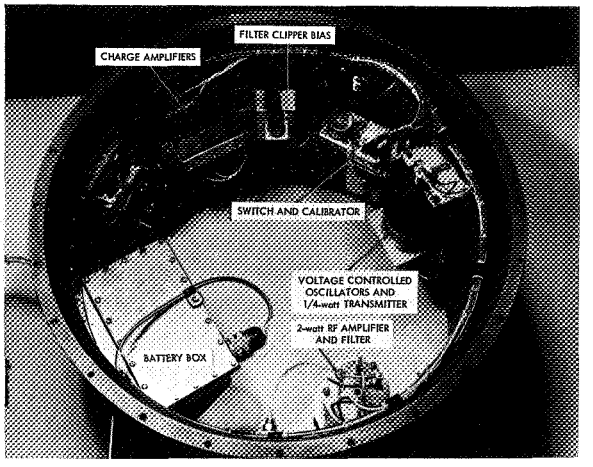

FIGURE 6.—Vibration telemetry package.

RESULTS

For ready reference and information, the vehicle trajectory parameters and event times are presented in Table 1. The trajectory of Delta 9 was considered nominal, and all flight events occurred approximately at the predicted

TABLE 1.—*Delta 9 Vehicle Trajectory Parameters and Event Times*

Event	Time (sec)	Greenwich Mean Time (Zulu)	Altitude (n. mi.)	Relative velocity (fps)
First-stage ignition	−3.5		0	
Liftoff	0	1800:16.9	0	0
Mach I	[1] 50	1801:06.9		1,100
Maximum Q	[1] 66	1801:32.9		2,000
1st-stage cutoff	159	1802:55.8	41.3	15,446
2d-stage ignition	163	1802:59.9	44.5	15,438
Fairing jettison	194	1803:29.3		
2d-stage cutoff	261	1804:37.9	103.8	20,619
Fire spin rockets	638	1810:55		
Blow separation bolts	640	1810:57		
3d-stage ignition	653	1811:10	213	19,638
3d-stage burnout	695	1811:52	212	24,955
Premature despin:				
1st	757	1812:54		
2d	767	1813:04		
3d	777	1813:14		
4th	837	1814:14		

[1] Calculated values, not actual flight data.

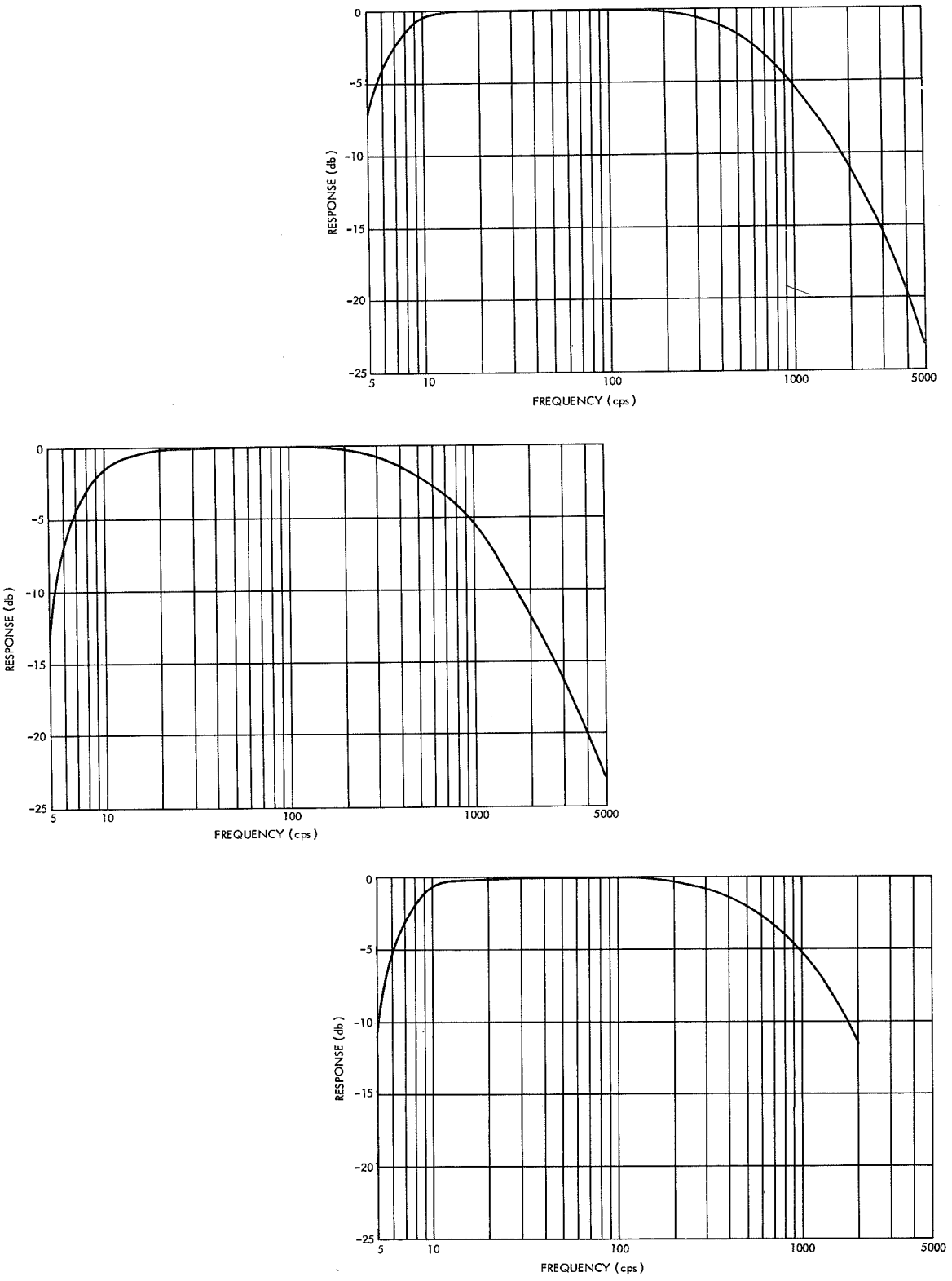

FIGURE 7.—Frequency response of the vibration experiment and playback instrumentation.

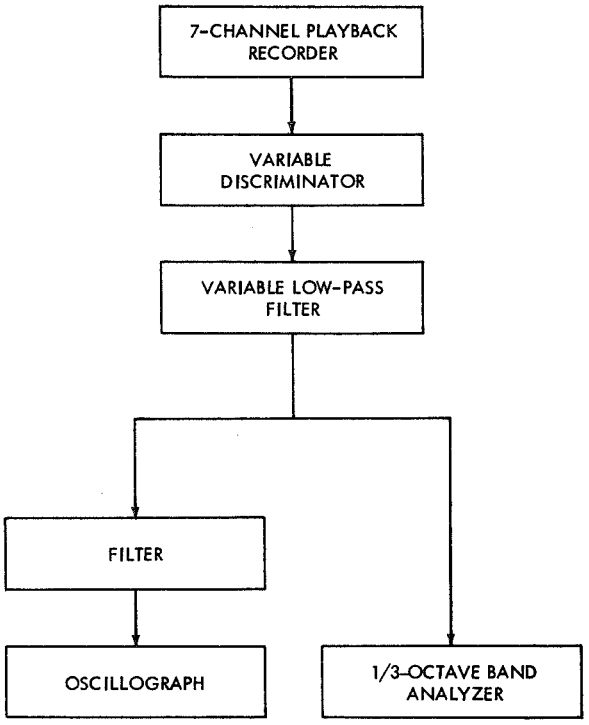

FIGURE 8.—The data reduction systems.

event time, except the time of the first despin sequence. Table 2 is a vibration data summary of the Delta 9 read from real-time oscillograph records.

TABLE 2.—*Vibration Data Summary of the Delta 9 Vehicle*

Event	Composite acceleration (peak g)		
	Thrust axis	Lateral axis	Lateral plus 90-degree axis
1st-stage ignition			
T–1	0. 5	0. 5	0. 3
Liftoff, T+0	2. 50	1. 9	. 9
Liftoff+1 second	0. 75	. 6	. 6
Main engine cutoff	2. 0	. 3	. 4
2d-stage ignition	(1)	(1)	(1)
Jettison fairing	0. 25	1. 0	1. 0
2d-engine cutoff	2. 25	. 3	. 3
Spinup		. 47	. 4
Blow 2d-3d-stage separation bolts		1. 57	. 4
3d-stage ignition	(2)	(2)	(2)

[1] RF signal dropout.

[2] See Table 4 and the discussion on pp. 416–417.

The rms vibration time histories for the three axes are shown on Figure 9 during first- and second-stage burning. Vibration transients occurred at liftoff and first-stage engine cutoff along the three axes. Second-stage ignition transients are obscured, because of RF dropout. Transients also occurred along the two lateral axes when the fairing was

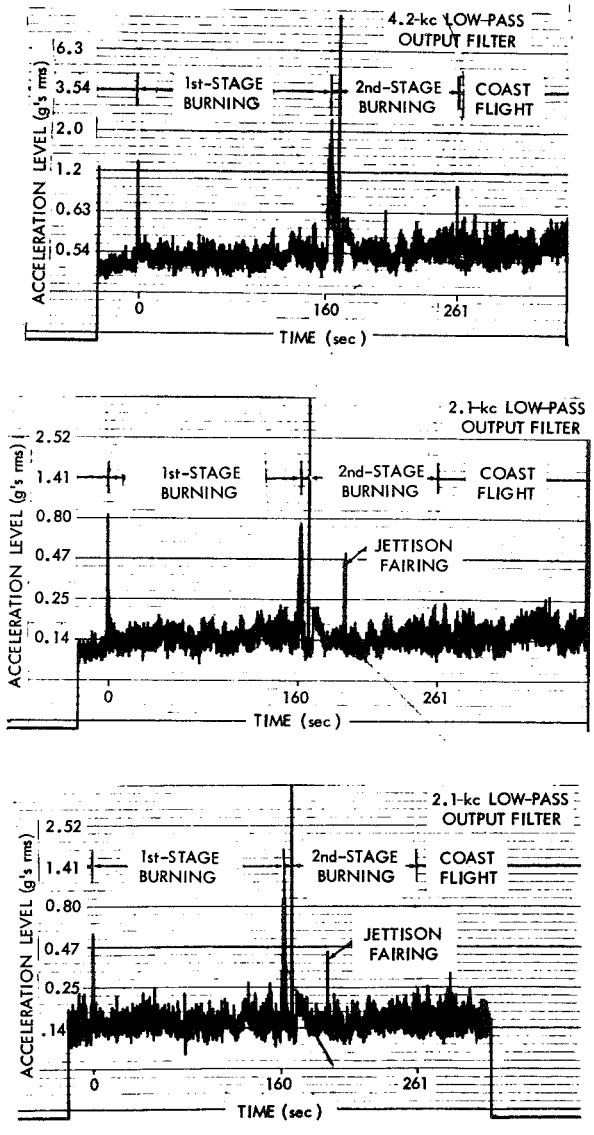

FIGURE 9.—Vibration time history, composite of all frequencies. Pen speed 160 mm/sec, paper speed 0.3 mm/sec.

jettisoned, and along all three axes at second-stage engine cutoff. Table 3 is a summary of the predominant frequencies and maximum levels of these transients. The vibration levels at times other than listed event times were less than 0.63 g rms and 0.25 g rms, in the thrust and lateral directions, respectively. There was no significant increase in vibration levels at either Mach 1 or Maximum Q.

Figure 10a displays the composite vibration along the thrust axis at liftoff of all frequencies below 1000 cps. The maximum peak level was 2.5 g. But, as shown on Figure 10b, the major vibration occurs at 16 cps. The maximum peak g level was 1.45. This level occurred at 0.25 sec after liftoff and decays to 0.3 g peak at T+2 sec. Figure 10c depicts the 46.5 cps component during liftoff. The maximum level at this frequency was 1.07 g peak but was a single cycle. An average over a six-cycle period was 0.55 g peak.

The lateral axis liftoff transient essentially consists of two frequencies; 10.5 cps and 40 cps with maximum levels of 0.7 g peak and 0.66 g peak, respectively (see Fig. 11). The lateral plus 90-degree axis liftoff transient (Fig. 12) consists of the same frequencies as the lateral axis with levels of 0.4 g peak and 0.58 g peak for 10.5 cps and 40 cps, respectively. The results of an experimental modal analysis performed on a Transit/Tiros vehicle, similar in configuration to the Delta 9, indicated a second bending mode at 10.7 cps (Ref. 2).

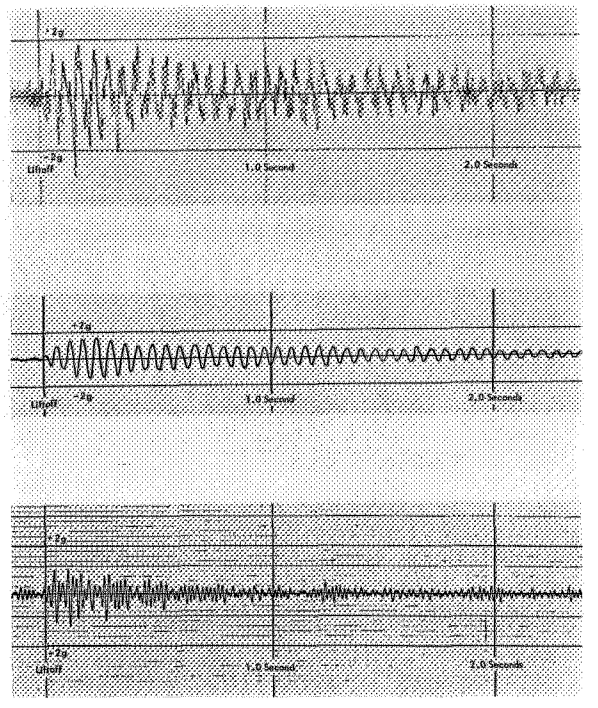

FIGURE 10.—Thrust axis vibration at liftoff; instantaneous acceleration versus time.

TABLE 3.—*Transient Component Analysis for the Delta 9 Vehicle: Predominant Frequencies and Maximum Levels*

Event	Thrust axis		Lateral axis		Lateral plus 90° axis	
	Peak acceleration (g)	Frequency (cps)	Peak acceleration (g)	Frequency (cps)	Peak acceleration (g)	Frequency (cps)
Liftoff	1.45	16	0.7	10.5	0.4	10.5
	1.07	46.5	.66	40	.58	40
1st-stage cutoff	1.47	[1] 26			.2	26
	.95	46.5				
Jettison fairing			.98	8	.57	8.9
					.31	60
2d-stage cutoff	1.25	44				
2d-3d-stage separation bolts			1.57	9.4		

[1] This frequency lasts for approximately 6 sec. The levels of all other frequencies decay to insignificant values within 3 sec.

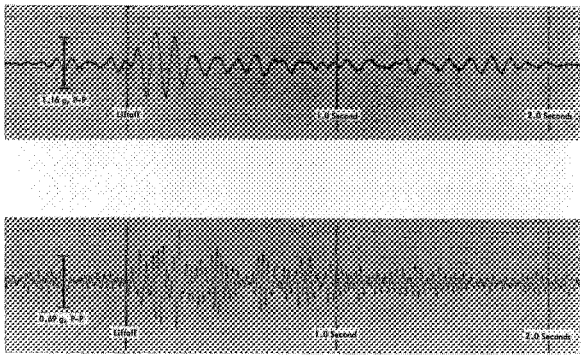

FIGURE 11.—Lateral axis vibration at liftoff; instantaneous acceleration versus time; signals filtered with a narrow-band filter.

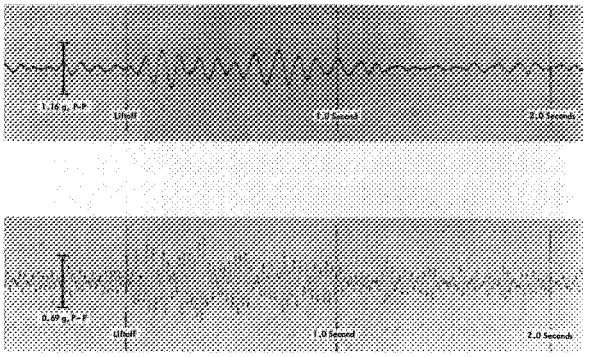

FIGURE 12.—Lateral plus 90° axis at liftoff; instantaneous acceleration versus time; signals filtered with a narrow-band filter.

The data exhibited on Figure 13 show the presence of a 26-cps thrust axis resonance associated with this Thor vehicle. The resonance starts at $T+155$ and lasts to main engine cutoff, that is, $T+159$, at which time elastic rebound is seen. This resonance dies out at $T+161$. The frequency of this resonance was 26 cps with a maximum acceleration level of 1.47 g peak. At $T+160.3$ the lateral plus 90-degree axis shows a level of 0.2 g peak at 26 cps. Figure 14 shows a 46.5 cps resonance in the thrust direction at main engine cutoff with an acceleration level of 0.95 g peak.

Figure 15a shows two transients that were measured along the lateral axis during fairing jettison. The two pulses occurred approximately 1 sec apart. The vibration level of the first transient was 0.88 g peak while the second transient's maximum level was 0.98 g peak at a frequency around 8 cps. Figure 15b depicts a component of the transient along the lateral plus 90-degree axis at approximately 9 cps with a level of 0.57 g peak. Figure 15c shows another component of the above transient at 60 cps with a level of 0.31 g peak.

Elastic rebound of the vehicle is noted at second-stage cutoff (Fig. 16). The major component of this transient was 44 cps with a maximum level of 1.25 g peak. This transient decays to an insignificant level in 0.2 sec.

Figure 17 depicts the major frequency component along the lateral axis of the transient that occurred during explosion of second- and third-stage separation bolts. The maximum level was 1.57 g peak at approximately 9.4 cps.

Figure 18 is an oscillograph record of uncorrected composite vibration levels during third-stage burning. A high percentage of the data shown on the record for the two lateral axes are erroneous.

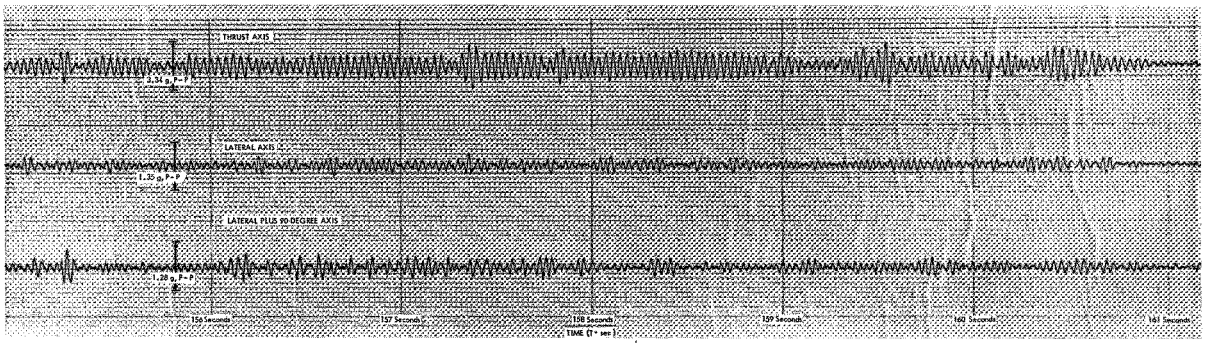

FIGURE 13.—Vibrations at first-stage engine cutoff; instantaneous acceleration versus time; signal filtered with a narrow-band filter. Signal of the 26-cps vibration.

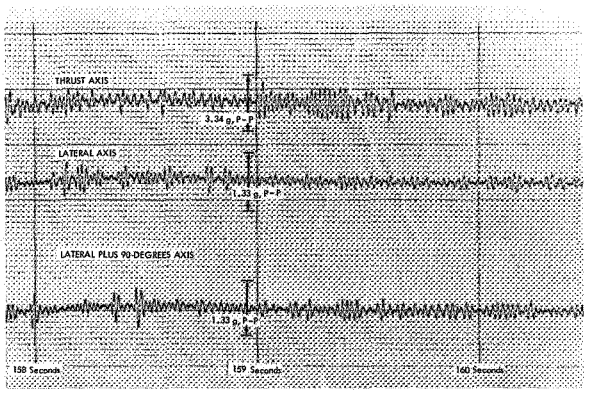

Figure 14.—Vibrations at first-stage engine cutoff; instantaneous acceleration versus time; signal filtered with a narrow-band filter. Signal of the 46.5-cps vibration.

The distorted shapes of the oscillograph traces are attributed to charge amplifier overload caused by high-level input signals. The accelerometer systems were set up to measure low-level first- and second-stage motor excitations. It was known that the electronic systems would probably be overloaded during third-

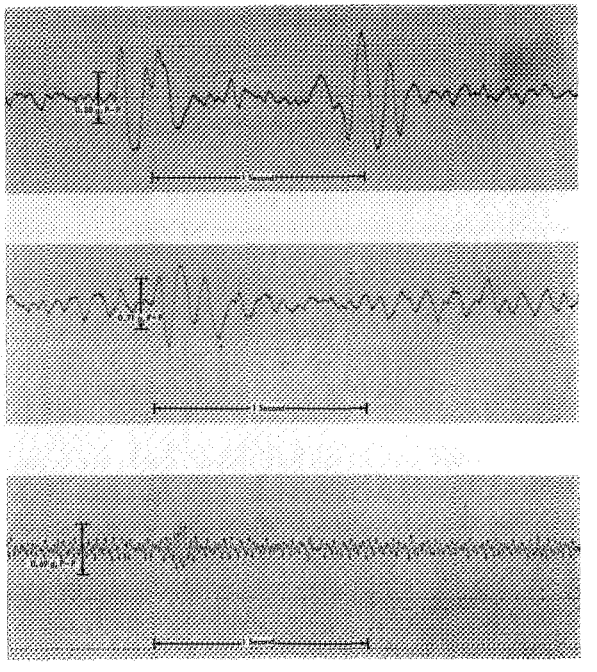

FIGURE 15.—Vibration at fairing jettison; instantaneous acceleration versus time; signals filtered with a narrow-band filter.

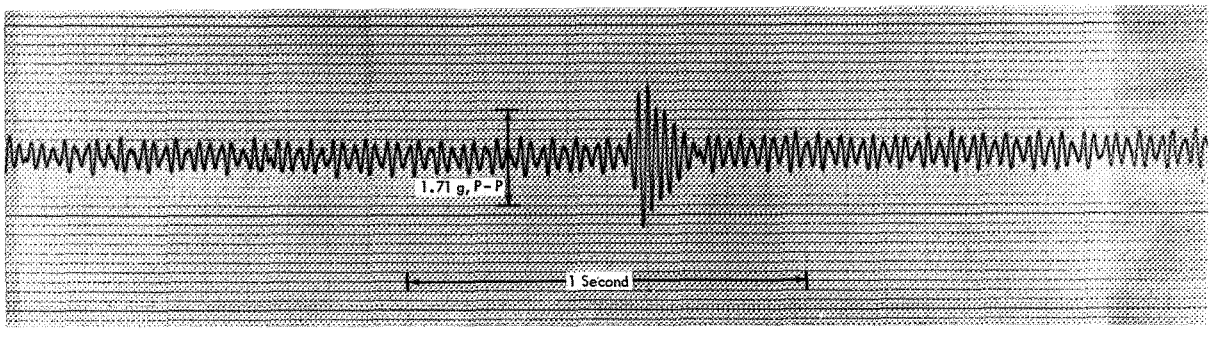

FIGURE 16.—Thrust axis vibration at second-stage engine cutoff; instantaneous acceleration versus time; signa filtered with a narrow-band filter. Signal of the 44-cps vibration.

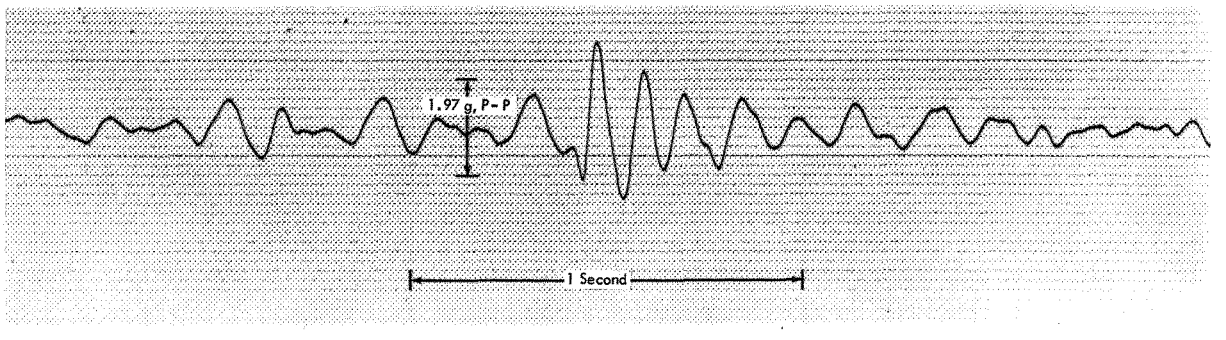

FIGURE 17.—Lateral axis vibration at second- and third-stage separation; instantaneous acceleration versus time; signal filtered with a narrow-band filter. Signal of the 9.4-cps vibration.

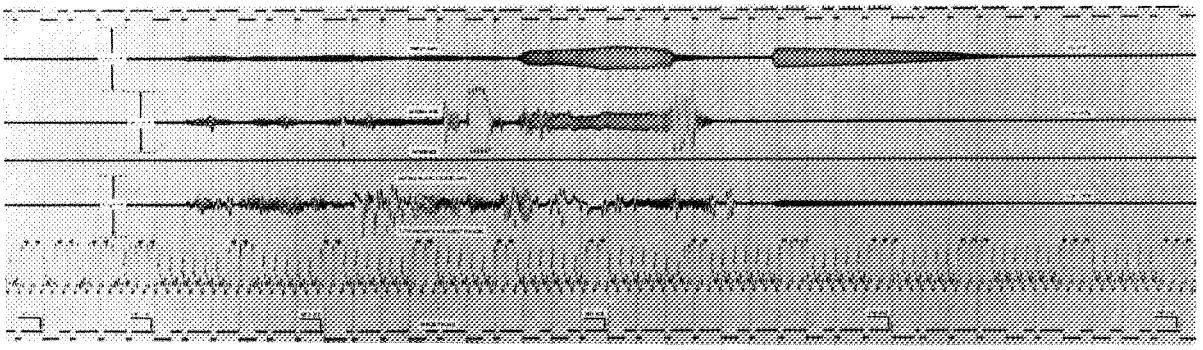

FIGURE 18.—Composite uncorrected vibration levels of the third-stage motor; instantaneous acceleration versus time

stage motor burning, but other data are available on this type of motor, that is, from Scout vehicle flights. However, some data for the thrust axis are valid. Since, at the present time, no tracking analyzer is available to lock onto the sliding tones that occurred during third-stage burning, a ⅓-octave band analysis was made on the thrust axis vibration. These tones slide at a rate of approximately 100 cps/sec. With two exceptions, vibration levels in the bands were corrected for system frequency response by applying the correction for the center frequency of that particular band as shown on Figure 7. The two exceptions are: the corrections in the center frequency (CF) bands 400 cps and 630 cps were taken at 450 cps and 580 cps, respectively, since these are constant frequency vibration. The results of the analysis are shown in Table 4.

A longitudinal resonant burning mode of the X–248 started 20 sec after motor ignition. The frequency of this oscillation was 577 cps. The vibratory level increased quickly to 13.4 g rms and in 10 sec had gradually decreased to 0.54 g rms. The level in the lateral plus 90° axis was 1.58 g rms at the start of this mode then gradually decreased with increased burn time.

The logitudinal vibrations (sliding tones) begin at ignition at frequencies in the 4-kc CF band and slide down to frequencies in the 2-kc CF band 17 sec later. These vibrations (sliding tones) reached a maximum level (56.1 g rms) 14 sec after ignition in the 2.5-kc CF band. This level is not realistic, since the charge amplifiers would be overloaded at this level. (See Table 4.)

Shock transients that occurred during premature dispin of the third-stage motor-payload combination are shown on Figure 19. The dispin sequence was scheduled to start 15 minutes after third-stage pressure switch closure. However, the first despin occurred 1 min and 40 sec after switch closure. At this time the rocket-payload despun from 158 ± 2 rpm to 122 ± 2 rpm in a few tenths of a second. Ten seconds later it despun to 103 ± 2 rpm and 20 sec after initial despin the spin rate dropped to 90 ± 2 rpm. There was no visible shock

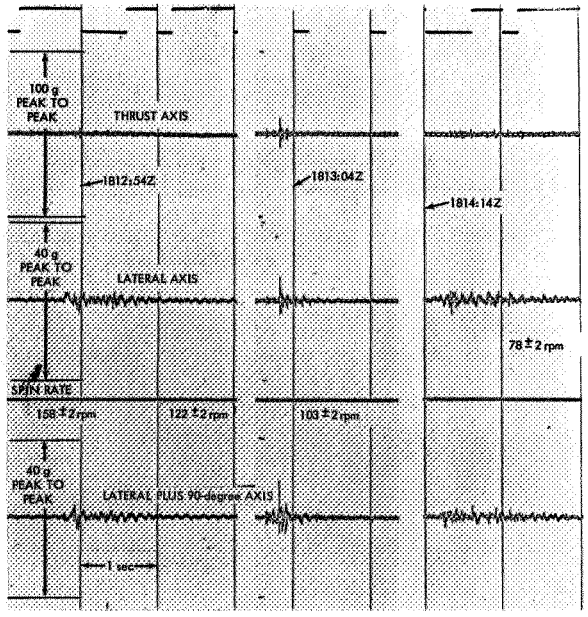

FIGURE 19.—Vibration levels at premature despin; instantaneous acceleration versus time.

transient on the oscilograph record at 90 rpm. Another minute later it again despun to 78 ± 2 rpm. The despins were caused by premature erection of booms and paddles.

DISCUSSION

No significant increase in vibration levels was noted during times of Mach 1 or Maximum Q. This is attributed to the streamlined design of the vehicle which greatly reduced buffeting, and to the mode of connection of the Delta 9 fairing. This vehicle used a low-drag fairing (bullet shaped) and not a bulbous one, and connects to the second-stage vehicle. All fairing vibration would be attenuated by the third-stage dynamics.

Three of the premature despin events of the third-stage vehicle were accompanied by short duration shocks which occurred when booms and paddles snapped into erected positions. The spin reduction was in these cases completed in about 0.5 sec, and it is clear from the records that the reduction was completed by the time that the shocks occurred. This is consistent with boom erection rather than the exertion of external impulses (as from motor "chuffing") where the despin accompanies the impulse. For the fourth despin there was no shock transient and the duration of the despin was slightly greater (A. P. Willmore, private communication).

REFERENCES

1. Flight Report for Vehicle 320/2019/3019, Delta Program—Mission No. 9 S–51 Spacecraft, Douglas Aircraft Co., Report SM–41911, June 1962.
2. Engineering Test Report—Model DM 1812–2, Vibration Test—Transit/Tiros Body Bending Modes, Douglas Aircraft Co., Tulsa Division Report TU–24534, June 16, 1960.

TABLE 4.—*Delta 9 3d-Stage Vibratory Acceleration Measured Along the Thrust Axis During 3d-Stage Burning ⅓-Octave Band Analysis. All Entries Corrected for Frequency Response; Paper Speed 10 mm/sec; Pen Writing Speed 160 mm/sec; Low-Pass Output Filter (4200 cps)*

Center Freq. (cps)	Ign $t=0$	Maximum acceleration (g rms) at time † (sec)																	
		$t=1$	2	3	4	5	6	7	8	9	10	11	12	13	14	15	16	17	18
40							0.4			0.13								0.2	
50						0.16	.22			.2			0.14						
63	0.18									.18									
80	.16									.18									
100	.16						.14	0.13		.16									
125	.18				0.16	.13			0.16	.18									
160	.16			0.16	.16		.16		.14	.22		0.22							0.13
200	.14		0.13	.16	.2		.25	.2	.18	.2	0.2	.16							.16
250	.16	0.16	.16	.16	.19	.26	.27	.2	.2	.30	.16	.16	.16	0.14	0.14	0.16	0.19	.19	.23
320	.30	.32	.40	.30	.30	.61	.54	.37	.34	.38	.25	.28	.28	.28	.30	.28	.29	.32	.43
400	.16	.20	.22	.20	.25	.25	.28	.22	.25	.25	.22	.20	.19	.16	.15	.16	2.08	2.08	.25
500	.22		.17		.22				.22	.27			.19				.68	.68	.22
630	.30	.30	.19	.19	.25		.25	.30	.26	.28	.22								.25
800	.35				.30	.24			.31	.33			.60						.31
1K	.32				.32	.57			.32	.33			.85				.24		.32
1250	.44				.40	.35			.40	.40	.38						.28	.40	.56
1600	.79				.50		.40		.56	.56	.44		1.12	.35	.40	.50	.71	.71	.56
2K	.71	.44	.44	.44	.71	.50	.56	.56	.71	.71	.79	.50	1.58	2.24	3.96	7.06	9.95	11.2	4.0
2.5K	2.5	.79	.79	.89	1.25	1.25	1.41	1.58	3.15	4.6	3.54	1.41	35.4	39.7	56.1	56.1	56.1	46.5	7.9
3.2K	2.5	3.5	5.0	7.9	17.7	21.8	21.8	12.5	12.5	12.5	11.0	11.0	8.8	7.9	5.6	5.6	4.4	3.5	3.5
4K	28.8	26.5	25.0	25.0	15.8	8.9	6.0	4.0	4.8	5.6	5.6	4.0	16.0	4.4	4.4	3.5	4.4	6.3	7.0
5K													←Overload→						

Center Freq. (cps)	Maximum acceleration (g rms) at time † (sec)																		
	19	20	21	22	23	24	25	26	27	28	29	30	31	32	33	34	35	36	37
40																			
50																			
63																			
80																			
100																			
125																			
160																		0. 14	
200														0. 14	0. 13				
250	0. 16	0. 16	0. 16	0. 18	0. 16	0. 18	0. 16	0. 16	0. 16	0. 17	0. 13	0. 14	0. 16	. 16	. 16	0. 13			
320	. 38	. 38	. 38	. 43	. 38	. 45	. 43	. 43	. 45	. 43	. 32	. 34	. 34	. 34	. 34	. 32	0. 30	. 38	0. 34
400	. 20	. 22	. 25	. 25	. 25	. 25	. 22	. 20	. 23	. 23	. 16	. 23	. 20	. 22	. 25	. 22	. 20	. 22	. 20
500		3. 9	3. 9	3. 9	3. 9	3. 9	3. 7	3. 0	2. 5	1. 3	. 49	. 49		. 24	. 43				
630		13. 4	13. 4	13. 4	12. 0	10. 7	9. 6	7. 6	5. 9	2. 5	1. 1	. 54	. 27	. 27	. 43				
800		. 54	. 54	. 54	. 52	. 48	. 39	. 31	. 26										
1K		. 24	. 24																
1250	. 28	. 71	. 79	. 63	. 50	. 44	. 35	. 32	. 32										
1600			. 40	. 40	. 44	. 44	. 44	. 40	. 40										
2K	. 50	. 56	. 56	. 50	. 44	. 56	. 56		. 56	. 50			. 56			. 44	. 44		
2.5K	. 89	1. 41	. 89	. 79	. 79	. 79	. 79	. 79	. 79	. 79	. 79	. 83	. 56	. 79	. 71	. 71	. 71		
3.2K	2. 0	3. 2	1. 8	1. 7	1. 6	1. 4	1. 4	1. 6	1. 4	1. 4	1. 4	1. 4	1. 4	1. 4	1. 4	1. 2			
4K	4. 0	4. 0	3. 5																
5K																			

Page intentionally left blank

IV: SOUNDING ROCKETS

764-173 O—65——28

Page intentionally left blank

ROCKET SOUNDINGS IN THE MESOSPHERE

WILLIAM NORDBERG

Goddard Space Flight Center

PHYSICS OF THE MESOSPHERE

The feature of a steadily declining temperature with altitude has been recognized as a distinct characteristic of the atmospheric region between 50 and 90 km long before the onset of systematic exploration of the upper atmosphere by means of sounding rockets. It was then proposed that this region be named "mesosphere."

The mesosphere is bounded by the "stratosphere" at the bottom and by the "thermosphere" at the top, both regions of generally positive temperature gradients with altitude. During recent years a variety of rocket-borne experiments have contributed to put the numerous characteristics of these regions into clearer focus. We have learned that there are consistent exceptions to the steadily declining temperature-altitude profile in the mesosphere (*1*) and that persistent, large-scale circulation systems which characterize the dynamics of the lower mesosphere change their behavior rather abruptly at the higher altitudes (*2*). These features are perhaps of equal or even greater significance than the existence of a temperature lapse rate. The eventual goal of the rocket experiments in the mesosphere is to explore these characteristics to the extent that the physical processes which determine the state of this region can be fully understood. Characteristics such as temperature profiles, wind fields and compositional structure are simply manifestation of the underlying physical processes.

The thermal structure of the mesosphere is thought to be determined mainly by the absorption of solar ultraviolet radiation by ozone and by the loss of energy through the emission of infrared radiation by ozone and carbon dioxide. Heating rates ranging from about 15° C per day near the summer pole at the bottom of the mesosphere to no heating near the winter pole at the top of the mesosphere have been computed (*3*). Computed cooling rates due to the emission of infrared radiation by carbon dioxide and ozone are of comparable magnitude but the distribution of these energy sinks with latitude and season is substantially different from the distribution of the heating sources (*3*). The global variation of this radiative energy balance profoundly affects the wind patterns which in turn relate to the convective exchange of energy.

On the basis of these physical processes the mesophere is unique in many respects. It is the highest region of the atmosphere where the existence of circulation systems in the meterorological sense have been observed; systems which change periodically with season and are primarily driven by latitudinal temperature gradients (*2*). At higher altitudes, above 70–90 km, the nature of the circulation changes abruptly probably due to the predominance of oscillatory forces such as tides and possibly due to interaction of the medium with electric and magnetic fields. Wind fields above 80 km have not exhibited any seasonal regularities. This boundary at 80 km also coincides roughly with the level where diffusive separation between the heavier and lighter constituents of the atmosphere begins to overcome the mixing processes which dominate below 80 km and which are responsible for keeping the gross composition of the atmosphere nearly constant from the ground up to about 80 km. Despite this constancy of gross moelcular weight, the thermal structure of the mesophere

is higly sensitive to minor variations in the concentration of photochemically active constituents such as atomic oxygen and ozone which take place in this region. Up to the 80-km level these constituents have no effect on the gross molecular weight. Above 80-km dissociation of molecular oxygen in addition to gravitational separation between lighter and heavier gases contributes to a rapid decrease in molecular weight.

The interactions between short term variations in solar radiation and the state of the atmosphere in the 50–90 km region are also of profound interest. At higher altitudes (200–300 km) such direct interactions have been positively identified (*4*), while in the stratosphere and troposphere they are not known to exist nor are they likely to occur. It is more likely that certain concurrent features may be found in circulation from the troposphere through the stratosphere well into the mesophere. If, on the other hand, we can also find a direct influence of fluctuations in the shortwave solar radiation on the structure of the mesosphere a link between such fluctuations and "weather" in the lower regions of the atmosphere may very well have been established.

Most of the rocket experiments conducted to date have been either too sparse of not adequately instrumented to permit a fundamental exploration of the physics of the mesosphere. This region is inaccessible to sounding balloons and indirect, ground based or satellite measurements have not been very successful yet in obtaining satisfactory measurements of the mesosphere. Therefore, the sounding rocket remains the only useful tool.

The fundamental physics of this region must then be derived from the results of a large number of rocket soundings which should take place at various key locations in the world and which should be conducted within the framework of a globally coordinated program. These soundings should consist of measurements of the typical structure parameters: temperature, pressure, density, wind and composition. Such measurements are well within the capability of existing instrumental techniques except perhaps for the measurement of composition. Measurements of the trace constituent composition in the mesosphere, through very important, has been grossly neglected during past years.

Finally with the advent of large spacecraft and manned spaceflight, the exploration of the mesosphere has taken on a new aspect. In many instances, launch vehicles as well as reentering spacecraft are expected to pass through critical phases of their flight in the 50–90 km region. In order to design appropriately for these conditions, engineers are keenly interested to obtain the best possible knowledge of the anticipated flight environment. Density and winds are the parameters of greatest importance for these purposes. This practical application, plus the fact that the basic physical processes which take place within the mesosphere still pose many, most challenging questions, clearly spell out the necessity for further experimental exploration. In the subsequent sections, therefore, the techniques employed in recent measurements, the various coordinated programs leading to a systematic exploration and the results of many typical soundings will be described.

EXPERIMENTAL TECHNIQUES

Launch Vehicles

Rocket vehicles used for upper atmosphere exploration can be generally classified into three categories. This classification applies to the aspect of cost, size and complexity, as well as to the capability of the rocket to carry a given weight to a given altitude. For the purposes of this discussion the three categories shall be defined as: small, medium, and large.

"Small" rockets generally carry payloads of about 1–5 kg and small diameters (less than 12 cm) to altitudes of 50–70 km. They are relatively inexpensive with the rocket and payload costing approximately $2,000. The entire launch operation can be performed with a minimum of complexity, generally requiring only a simple, easily transportable launching tube and crew of less than five. Simple sensors carried by these rockets perform temperature and wind measurements in the stratosphere and

wind measurements in the lower mesosphere. The rockets can be launched frequently and in fairly large numbers. This has made them useful as launch vehicles in synoptic soundings as part of the U.S. Meteorological Rocket Network (*5*). In the United States the "LOKI II" also called HASP and the "Arcas," are typical for such vehicles. These rockets and their associated instruments have been described in connection with the Meterological Rocket Network (*5*).

"Large" sounding rockets carry payloads of up to 100 kg and large diameters (30–40 cm) well into the thermosphere (200–300 km). They are relatively expensive (>$25,000) and require fairly complex launch installations with crews of more than ten. A typical example of a U.S. rocket of this category is the Aerobee (*6*). Because of the expense and complexity it is not practical to use such rockets in synoptic programs.

Rocket vehicles of "medium" category are the best suited for experiments in the mesosphere. They possess sufficient thrust to carry payloads of 30–40 kg and 15-20 cm diameters to altitudes of 100–200 km. The cost (about $10,000–$25,000 including payload) is such that "semisynoptic" programs at several sites with launchings at periodic intervals—though not continuous—are permissible. A crew of less than 10 can usually handle the launch operation from not a too complex rail launcher. In the United States, two stage rockets, using the "Nike" booster as a first stage, are most common. The "Cajun" rocket (*7*), which has been most commonly used as a second stage since the International Geophysical Year (IGY) has now been succeeded by the more powerful "Apache" (*8*). A typical Nike-Cajun rocket configuration is shown in Figure 1.

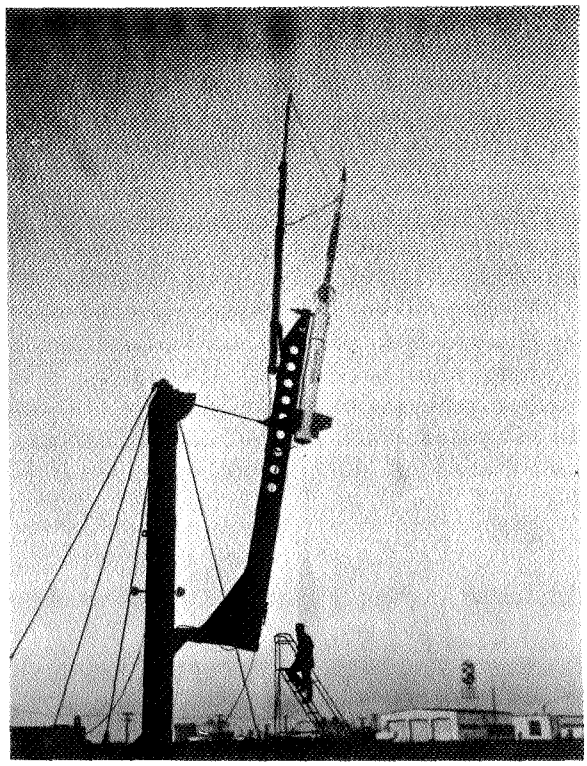

FIGURE 1.—Nike-Cajun rocket with grenade experiment ready for launch at Wallops Island.

Radar Tracking of Chaff

The only experiment which has been successfully performed in the mesosphere using "small" type rocket vehicles is the measurement of wind by means of dispersing chaff (*9*), whereby the drift of the chaff with the wind is tracked by radar on the ground as the chaff descends from altitudes of 80 km or below. In the upper part of the mesosphere, however, it is very difficult to measure wind by methods of dispersing solid materials such as chaff because the fall velocity of the chaff approaches free fall very rapidly with increasing altitude (*9*). Another disadvantage of the chaff method is the fact that the chaff, ejected from the rocket near apogee disperses rather rapidly (in many cases within about 20 km), as it falls through the atmosphere.

Sodium Vapor Ejection

Efforts have been made very early in the history of rocket soundings to measure winds by means of ejecting and tracking aerosole type particles or vapors from rockets. These payloads usually consist of smoke generators or vaporizors and require therefore, rockets of the "medium" category. The most successful of these techniques has been the method of injecting sodium vapor into the atmosphere between 70–200 km during twilight conditions.

Interaction of sunlight with the sodium vapor (resonance radiation) causes the sodium trails to be luminous, and with the proper ejection technique the sodium remains visible for periods up to 30 minutes at middle latitudes.

The trail moves instantly with the atmospheric wind field and its track is recorded by an array of cinetheodolite cameras which are spread over the ground on very long baselines (>50 km). The drift motion is determined by triangulation of significant features such as a sharp kink in the trail (Figure 2). This method was originated by Manring (*10*) and an estimated order of 50–100 soundings have been carried out at many locations of the globe. Figure 2 also shows how two different techniques; namely, the sodium release and acoustic grenade techniques (described below) were combined in one experiment. Flashes from the grenades can be seen in the center of Figure 2.

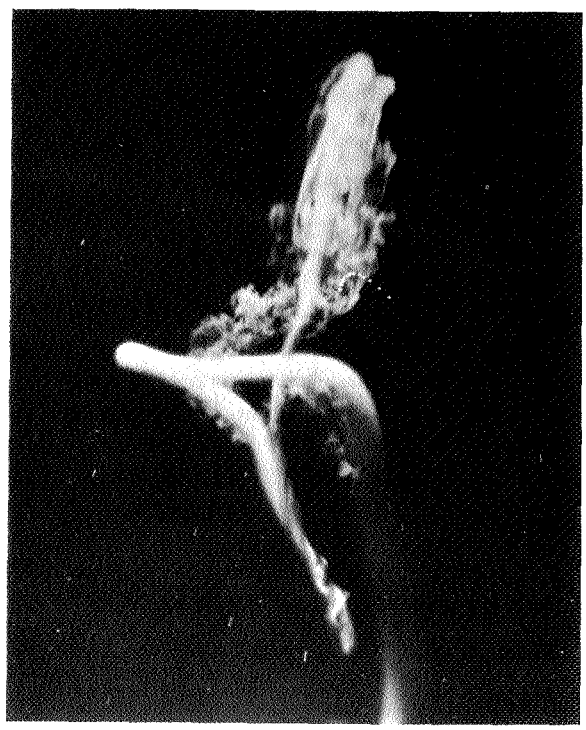

FIGURE 2.—Photograph of sodium trail exposed with simultaneous grenade experiment. Flashes from grenade explosions can be seen near center of photograph. Distinct features such as sharp bends in the trail which indicate extreme wind shears are used as identifying reference when triangulating the trail from various camera sites.

A disadvantage of the sodium technique is that it can only be carried out during a few minutes every 12 hours, during a time when the region above 70 km is illuminated by the sun, in order to produce the glow in the trail and when the cameras on the ground are in darkness, in order to permit proper exosure of the film. Also, the experiment must be carried out in clear skies.

Although this experiment functions only in the upper mesosphere—the resonance glow cannot be induced below 60–70 km because of the absorption of the incident sunlight by natural sodium in the atmosphere—it has produced valuable information on the tremendous wind shears in the transition region between the mesosphere and thermosphere. The great advantabe of this technique is that the continuous trail enables the observation of the fine structure of the wind with great detail. Research is progressing at this time on self-luminous vapors which glow for a sufficient time and with sufficient intensity to permit this type of wind measurement throughout the night.

Acoustic Grenades

The direct measurement of temperature which can be performed in the stratosphere by means of extremely small resistance thermometers (*5*) (thermistors) becomes questionable at altitudes above 50 km (*11*). In the mesosphere therefore, temperature must be measured by more complex, indirect methods. The method most commonly used in the Rocket-Grendade technique.

In this experiment grenades are ejected and exploded at altitudes up to 90 km at regular intervals during the ascent of the rocket. They are cylindrical in shape and are ejected forward through the nosecone of the rocket (Fig. 3) and contain high explosive, mainly TNT, which is detonated mechanically by means of a lanyard tied to the rocket. The explosives weigh between one and two pounds. Average temperatures and winds in the medium between two grenade explosions are determined

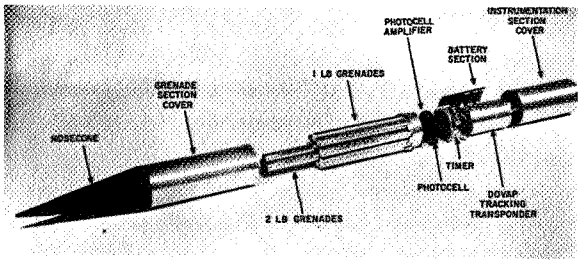

FIGURE 3.—Grenade experiment payload, exploded view.

by measuring exactly the time of explosion of each grenade, the time of arrival of each sound wave at various ground-based microphones, and the exact position of each grenade explosion. Thus the speed of sound in the layer between two explosions is measured and temperatures can be derived since the temperature is proportional to the square of the speed of sound. Molecular weight is contained in the proportionality factor. Wind speed and direction can be derived from the horizontal drift of the sound in the layer.

The grenade experiment requires a highly accurate tracking system. A network of ballistic cameras or Doppler tracking stations, or a high precision radar of the FPS–16 type are used to determine the coordinates of explosions. A schematic diagram of the essential components of the grenade experiment is shown in Figure 4. The highest altitude from which sound returns can be received with present explosive charges and existing sound ranging techniques is about 90 km. The greatest advantage of this experiment is that temperatures and winds can be measured simultaneously which is of great importance in describing the dynamics of the atmosphere and that the resulting measurements are very accurate. The drawbacks are that only average temperatures and winds in the layer between two grenades can be measured and that a fairly elaborate system of ground instruments for tracking and sound ranging is required. A detailed description of this experiment which has been successfully performed more than 50 times during the past decade is given in (*12*).

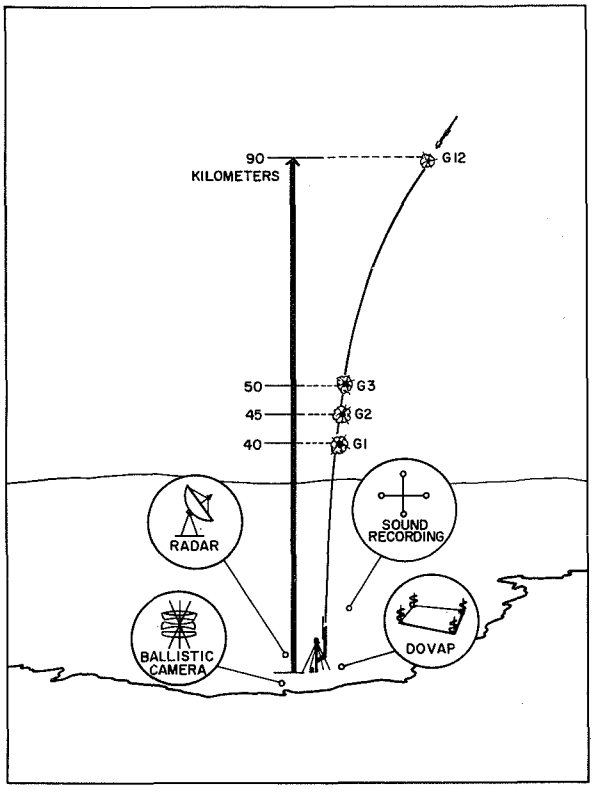

FIGURE 4.—Schematic diagram of grenade experiment system; radar, ballistic camera, and Dovap tracking systems are indicated. Each individual system or a combination thereof suffices for the experiment. Sound recording site is preferably located directly under trajectory of rocket. G–1 through G–12, indicate altitudes of grenade explosions.

Falling Sphere

In the altitude region concerned, pressure and density are more susceptible to measurement by in situ techniques than temperature. The simplest method in concept is the measurement of density by means of the falling sphere technique. This technique has been originally developed at the University of Michigan (*13*), and a large number of successful flights have been carried out since 1952.

In the sphere experiment the drag force (D) exerted on a perfect sphere dropped from a rocket at high altitude is measured and ambient density (ρ) is derived by means of the relationship:

$$mg+D=mh=\tfrac{1}{2}\rho h^2 C_D A+mg \qquad (1)$$

where h is the altitude of the sphere, A the cross sectional area and C_D the aerodynamic drag coefficient which is a function of Mach number and must be determined empirically; m is the mass of the sphere and h indicates the time derivative of h; g is the acceleration of gravity and depends on h.

Falling spheres have been used in many different combinations: as rigid shells (as shown in Figure 5) or as inflatable balloons; with built in accelerometers (active sphere), to measure h directly (Fig. 5), or with high precision radar tracking (passive sphere) to determine the drag acceleration from the second derivative of the altitude vs. time function given by radar track. Differentiation of the tracking data or integration of the measured accelerations, in case of the active sphere, leads to the velocity, h, required to solve equation (1) for $_{\rho}$.

The spheres are usually ejected from the rocket at an altitude of about 60 km and travel along a ballistic trajectory up to about 140 km. Acceleration is determined both along the upward and downward leg of the trajectory. Winds can be measured with inflatable spheres at altitudes below 50 km from the horizontal drift determined by radar. Density measurements with large (1–2 meters) passive inflatable spheres have been obtained up to 110 km (*14*). Results from smaller, rigid, active spheres have been reported by Jones (*15*).

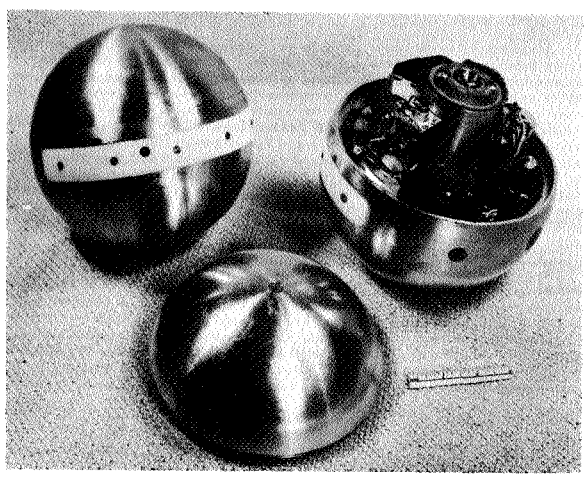

FIGURE 5.—Photographs of 7-inch diameter falling sphere (active, rigid). Left sphere, fully assembled, shows telemetering antenna slot. Open sphere on right shows built-in accelerometer.

Above the 120-km level the cross section over mass ratio of the sphere is too small to detect any deviations from free fall; at low altitudes there is usually a region where the velocity of the sphere approaches a Mach number regime in which C_D is not known accurately enough and where horizontal winds affect the fall of the inflatable sphere. This depends largely on the type of sphere used, but in general density data have been obtained down to 40 km with inflatable passive spheres and down to 20 km with rigid, active spheres.

The advantage of this technique is that for the active sphere the ground instrumentation is exceedingly simple (one telemetering receiver and recorder) and that, the flight instrumentation is quite compact although a high degree of perfection and engineering skill is required to manufacture the spheres and accelerometers. With the passive sphere the costs are greatly reduced, but the ejection and inflation mechanisms are of critical importance and high precision tracking radar must be available. Also, the fall velocity of the inflatable sphere is near the speed of sound in the vicinity of 70 km. Errors may be introduced at this altitude by insufficient knowledge of C_D which changes rapidly with fall velocity near $M=1$. The drag on the inflatable sphere could also be greatly affected by imperfect inflations and by strong horizontal winds. These problems, of course, do not exist with the active, rigid sphere.

Pitot Static Tube

A variety of techniques exist to perform in situ pressure measurements from rocket vehicles. These techniques are always based on the premise that ambient conditions of pressure, density or temperature can be derived from the direct pressure measurements carried out on board the vehicle by applying aerodynamic theories which relate the measured pressure to the ambient parameters. The accuracy of the derived ambient pressure, density and temperature thus depends not only on the precision of the pressure measurement itself, but also on

the validity and applicability of these aerodynamic theories. This applicability is generally ensured by keeping such rocket performance parameters as velocity and angle of attack within tolerable limits during the time of measurement. Effects on the pressure measurement by gases carried along with the sounding rocket must be carefully avoided.

In general, the pressure measurement is performed at least two aerodynamically different locations along the surface of a Pitot-static tube carried at the tip of the rocket (Fig. 6). Pressure sensors are usually placed in chambers which are exposed to the air flow by means of orifices in the skin of the rocket. In one chamber the stagnation pressure P_t at the tip of the Pitot tube is measured, and in a second chamber a measurement of static pressure P_s along the wall of the same tube is made, several calibers to the rear of the stagnation point. Aerodynamic tests of this configuration show that the pressure measured at this point is equal to ambient pressure. Additional chambers may be provided for redundancy. As a pressure sensor each chamber consists of a redioactive ionization source and a multi-range electrometer which measures the pressure sensitive ion current. The current, calibrated as a function of chamber pressure and susceptible to measurement in the altitude range of about 40–120 km, is telemetered to the ground. This technique which has been developed in its present state by J. J. Horvath et al. (*16*) is based on pressure measurements originally developed by Spencer (*17*) and LaGow (*18*). During various developmental stages, about

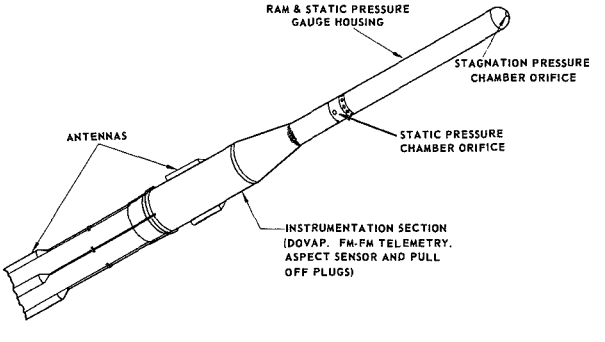

FIGURE 6.—Configuration of Pitot static tube experiment.

10–20 successful flights of this basic technique have been carried out since 1953 (*18,i19, 20*).

Ambient density ρ is derived from the interpretation of the basic Pitot static tube equation (Rayleigh equation) and from the equation of state:

$$\rho \sim \frac{P_t}{V^2}. \tag{2}$$

This proportionality holds essentially over a Mach number range of $3.5 < M < 7.5$; V being the tangential velocity of the rocket which must be determined by accurately tracking the rocket. This is usually done with a Doppler velocity tracking system.

The above proportionality relating impact pressure to ambient density as well as the ability to measure ambient pressure directly at the side of the Pitot tube hold only in the region of continuous flow where the mean free path between molecule collisions is small compared to the dimensions of the sensor. At higher altitudes, in the free molecular flow region, where the mean free path becomes larger than the sensor dimensions, these methods break down. The transition between continuous and free molecular flow occurs near the upper boundary of the mesosphere at about 90 km. Above that altitude the above proportion is replaced by the following expression, which relates the ambient density ρ to the impact pressure P_i in the region of continous flow:

$$\rho = \frac{P_i}{KV} \cos \alpha \tag{3}$$

where α is the angle of attack of the rocket and K is a function of the temperature in the chamber and of the molecular mass. With present techniques this type of density measurement can be performed up to 120 km. Ambient pressure can only be measured directly in the continuous flow region (up to 90 km).

Complete profiles of density (ρ), pressure (P) and temperature (T) can be derived from each one of the three experiments described above, although the primarily determined parameter is pressure in the Pitot tube experiment, density in the sphere experiment and temperature in the grenade experiment.

The three parameters are related through two well known relationships which are derived from the equation of state and from the hydrostatic equation:

$$-\frac{dP}{dh}=P(h)\,\frac{Mg(h)}{RT(h)}=\rho g(h) \qquad (4)$$

where g is the acceleration of gravity; M is the molecular mass (usually assumed constant up to 90 km) and R is the universal gas constant. Because these three parameters are so interrelated the need for a comparative measurement between the three experiments is obvious. A nearly simultaneous experiment involving the grenade, Pitot tube and falling sphere techniques was conducted on 6 June 1962, and the results are discussed below.

A summary of these four, most successful techniques for the measurement of temperature, pressure, density and wind with an indication of their altitude ranges is given in Figure 7.

In comparison to the number of pressure, density, temperature and wind soundings the number of rocket flights measuring composition of the mososphere has been very small. At higher altitudes, in the thermosphere, mass spectrometers have been sucecssfully used. These measurements, however, are not readily applicable at lower altitudes. Below 100 km two types of composition measurement are of greatest interest: the determination of the gross melecular mass; and of the concentration of trace constituents such as ozone, water vapor, and atomic oxygen important to the radiative equilibrium of this region. Water vapor measurements with balloons already become very difficult in the upper troposphere and in the stratosphere and at this time cannot be carried out at higher altitudes. Ozone content has been measured in occasional rocket flights by observing the increase in the intensity of solar radiation in the near ultraviolet with altitude. Originally this involved elaborate spectrographs carried aboard Aerobee rockets where the films had to be recovered (*21*). More recently attempts have been made to simplify this technique and adapting it to smaller rockets by measuring the absorption of sunlight by ozone in several narrow parts of the 2700–3300 A regions sensing the light intensities with phototubes. The phototube signals are telemetered to the ground, thus eliminating recovery (*22*). Ozone measurements in the upper stratosphere and mesosphere would be highly desirable during the polar night but, so far, all rocket-borne techniques are based on the absorption of sunlight. Research is presently directed toward the development of rocket-borne ozone sondes which are independent of sunlight.

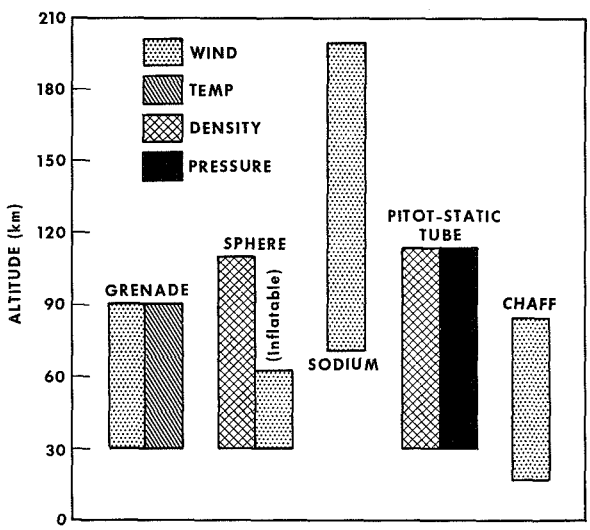

FIGURE 7.—Theoretical altitude range of experiments measuring winds, temperature, pressure and density in the mesosphere.

A technique for measuring composition of the atmospheric constituents in the 70–90 km is the collection of air samples by means of evacuated steel bottles. The sealed bottles are carried to the desired altitude, opened for about 5 seconds, and then sealed again. About six successful samplings were carried out in the United States (*23*) during 1953–56, and some in the Soviet Union (*24*). After recovery of the bottles the contents were chemically analyzed. Only the inert gases were susceptible to analysis; thus the ratios of helium, neon and argon to nitrogen were determined. This measurement permits the determination of the altitude level above which the gross molecular mass begins to decrease due to gravitational separation of the lighter constituents from the heavier ones.

A different technique has been used recently to obtain samples of particulate matter from the 70–90 km region (*25*). In this experiment, particles of sizes in the order of 0.1 micron were collected, recovered and analyzed to determine the nature and composition of noctilucent clouds, one of the most outstanding mesospheric phenomena at high latitudes.

PRESENT ROCKET SOUNDING PROGRAMS

Being geophysical measurements, atmospheric soundings should ideally be conducted as worldwide programs at all geographical locations and seasons. A concerted effort during the International Geophysical Year (IGY) brought about the first measurements from which geographical variations of the structure of the mesosphere could be derived. In fact, the four methods mentioned above: Sodium Release, Grenade, Pitot static tube and Falling Sphere reached their stage of full development during that period and their success during the IGY is the reason why the measurements of pressure, density, temperature and winds in the 50–90-km region still evolves around these four techniques.

Much progress has been made since IGY in extending the geographical coverage of the soundings. The world map (Fig. 8) indicates the sites at which rocket soundings employing the techniques described above were conducted during recent years. Many of these soundings were internationally coordinated as a first attempt toward a synoptic program. It is hoped that a further realization of synoptic soundings, as well as an increase in the number of launching sites will be accomplished during the forthcoming International Quiet Sun Year (IQSY).

In the United States, a program directed by the Goddard Space Flight Center of NASA has been in progress since 1959. This program is oriented toward the following objectives:

1. The exploration of the mesosphere during all seasons of the year over Wallops Island, Va. (38° N), a typical midlatitude site.
2. A direct comparison of the four techniques described above and a mutual "calibration" of these techniques by means of simultaneous soundings. Such a comparison was accomplished on June 6, 1962, at Wallops Island, Va.
3. The observation of continuous wind profiles throughout the lower atmosphere by combining radiosonde balloons, "small" meteorological rocket sondes, grenade and sodium experiments. On four occasions during 1961–63, this resulted in wind profiles from the ground up to above 150 km. The various circulation regimes in the various sections of the atmosphere were very well demonstrated in these experiments.
4. To conduct simultaneous soundings at midlatitudes (Wallops Island, 38° N), in the subarctic (Churchill, Canada, 59° N) and in the tropical Atlantic (7° S). Simultaneous launchings at Churchill and Wallops Island started in December 1962 and it is hoped a tropical site can be added by late 1963.

The program started with two sodium soundings each in August and November 1959 and in May and December 1960 at Wallops Island. One successful grenade sounding was conducted in June 1960 at the same site. Between 1961 and 1963 a total of 22 successful grenade experiments were launched at Wallops Island and five at Churchill during December 1962, February and March 1963. In the same period, 16 sodium releases were made at Wallops Island, 13 of which simultaneous with grenade experiments.

During November 1962 an international series of sodium releases coordinated with various sites around the world (Fig. 8) was conducted. On several other occasions coordinated sodium releases were made between Wallops Island and Italy and between Wallops Island, France and North Africa. One sphere experiment was conducted in 1961 and another simultaneously with grenade Pitot tube and sodium experiments at Wallops Island on June 6, 1962. On December 1, 1962, a simultaneous Pitot tube and grenade experiment was successfully launched at Wallops Island. Four grenade experiments were conducted during July and

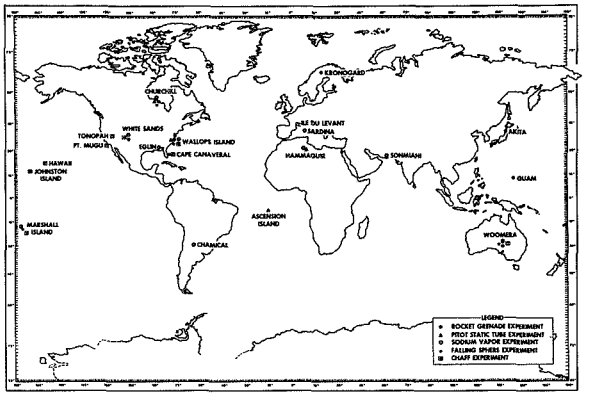

FIGURE 8.—Map of locations from which rocket soundings in the mesosphere have been conducted during and since IGY. The type of experiment performed is indicated at each station.

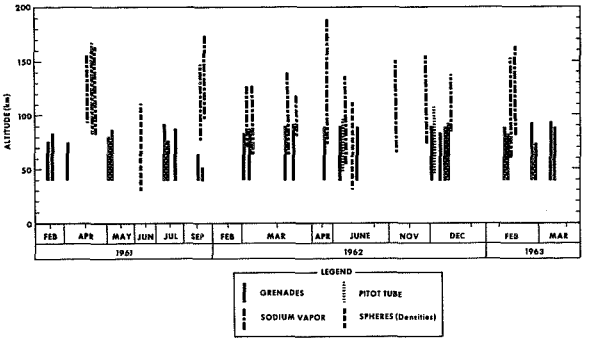

FIGURE 9.—Summary of mesosphere rocket soundings performed at Wallops Island, 1961 through 1963, showing time of launching, type of experiment and approximate range of actual data recovery for each sounding.

August 1963 in northern Sweden, two of them during the display of noctilucent clouds. These four experiments were carried out through the cooperation of the Swedish Space Committee and the NASA.

A summary of all firings at Wallops Island and their range of data recovery is shown in Figure 9.

RESULTS OF RECENT ROCKET SOUNDINGS

The following features of the mesosphere had been derived as a result of earlier sounding programs during IGY:

1. A large variation of the temperature profile in the 60–90-km region between high and low latitudes or between summer and winter at Churchill with large and multiple temperature maxima in the winter mesosphere at Churchill.
2. The existence of an extremely strong cyclonic circulation up to 80 km over the entire winter hemisphere, which extends, though greatly diminished, into the equatorial zone. This vortex is replaced by anticyclonic circulation of lesser intensity for the summer hemisphere, again reaching far into the tropics.
3. A breakdown of the wintertime circulation up to 70 km at Churchill where meridional circulation in the stratosphere and mesosphere preceded the occurrence of a typical explosive warming at lower levels.
4. A systematic seasonal variation of pressure, temperature, and density at high latitudes where variations by a factor of two in density were observed between summer and winter at 60 km.

Results from the recent soundings confirm the behavior of the temperature and wind structure previously derived from only 10 soundings at Churchill during IGY (*1*, *2*). This picture holds generally also for a typical midlatitude site such as Wallops Island (38° N). Average temperatures for summer and winter over Wallops Island and their variability from day to day are shown in Figure 10. The averages were derived from five soundings in June 1962 and July 1960 and 1961, and from nine soundings in December 1962, February 1961 and 1963, and March 1962 and 1963. Although the temperature difference between winter and summer above 60 km is not as large as previosly observed at Churchill, the temperatures at 38° N are still considerably higher during the winter months than during summer. The temperature variations between individual soundings are also much larger in winter than in summer. The maximum variation at 70 km during summer covers a range of about 23° K, while in winter the variation at the same altitude amounts to 39° K. At about 60 to 65 km summer and winter temperatures coinside; this has also

been observed at Churchill during IGY. At the 50-km level summer average temperatures at Wallops Island are about 15° K higher than winter temperatures. Individual temperature and wind profiles for the Wallops Island soundings up to June 1962 have been published previously (*26*). Results from four soundings in April and May indicate that temperatures during these transition months fall between the summer and winter profiles above 65 km but, that in the upper stratosphere, at the 50 km level and below, springtime temperatures are usually about 10° higher than summer temperatures.

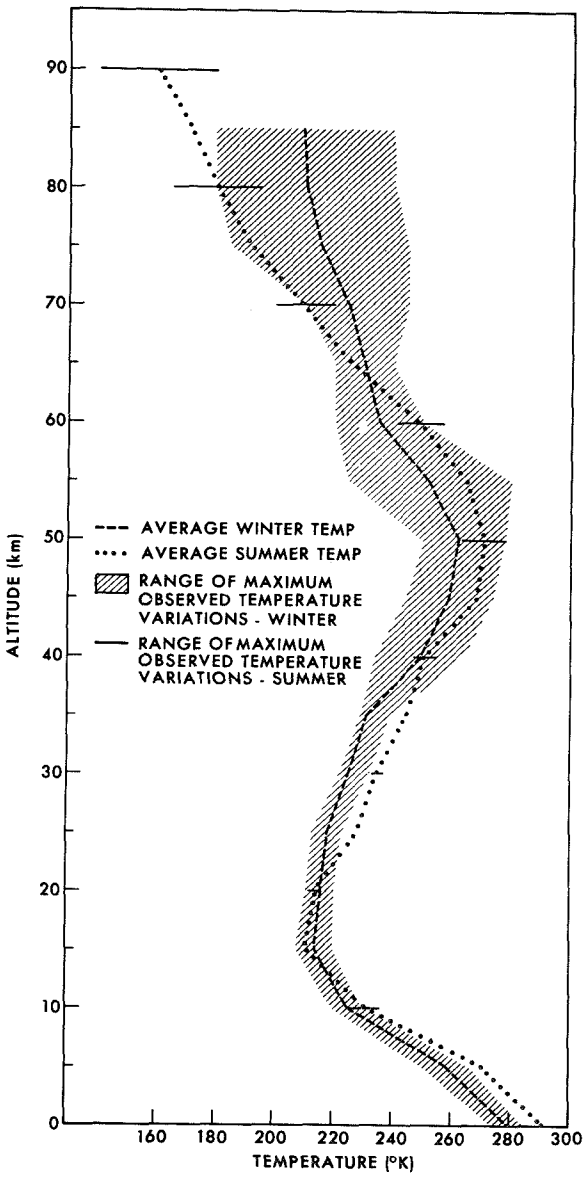

FIGURE 10.—Average profiles of temperature versus altitude for winter and summer over Wallops Island, Va. (38° N.). Summer average was obtained from 5 soundings 1961 through 1963, and winter average from 9 soundings 1961 through 1963. Maximum variation in temperature between soundings is indicated by shading for winter and by horizontal bars for summer soundings.

These temperature variations have a profound influence on the seasonal variations of density with altitude. Figures 11 and 12 show deviations of observed densities from the 1962 U.S. Standard Atmosphere (*27*) for each individual sounding as a function of altitude. The magnitude of this density variation at Wallops Island is not as large as previously observed at Chruchill (*28*), but winter densities throughout the 30–80-km region are still appreciably lower than summer densities. Maximum seasonal variation occurs between 60–80 km where winter densities are lower than summer densities by an average ratio of about 0.8 During IGY at Churchill, this ratio was about 0.5. Supplements to the United States Standard Atmosphere are now in preparation to reflect these seasonal and latitudinal changes (*29*). It is interesting to note that the two profiles for February 1961 are closer to a summer than winter condition. This is attributed to a very warm stratosphere which prevailed at that time at altitudes below 40 km. These high temperatures, at lower levels, cause the higher densities throughout the mesosphere.

The wind field again shows the same features as those found in IGY, namely easterly flow in summer and westerly in winter with strong meridional flow during the transitions in February and March. However, an additional feature stands out from the Wallops Island results (Figures 13 and 14). This feature, described as follows, is also obvious from the comparison between grenade and sodium winds in the 60–90 km region which can be made from Figure 15.

A sharp and remarkable boundary seems to separate the circulation below 80 km from

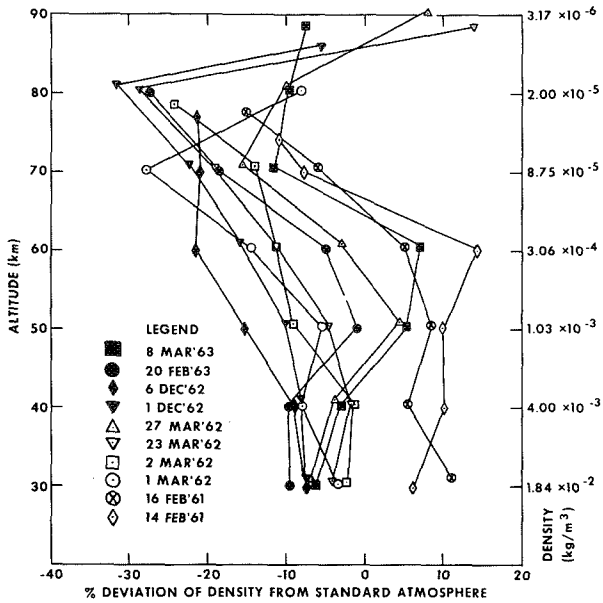

FIGURE 11.—Winter densities as a function of altitude derived from individual temperature soundings obtained with the rocket grenade experiment over Wallops Island, Va. (38° N.). Densities are shown as percent deviation from 1962 U.S. Standard Atmosphere (*27*).

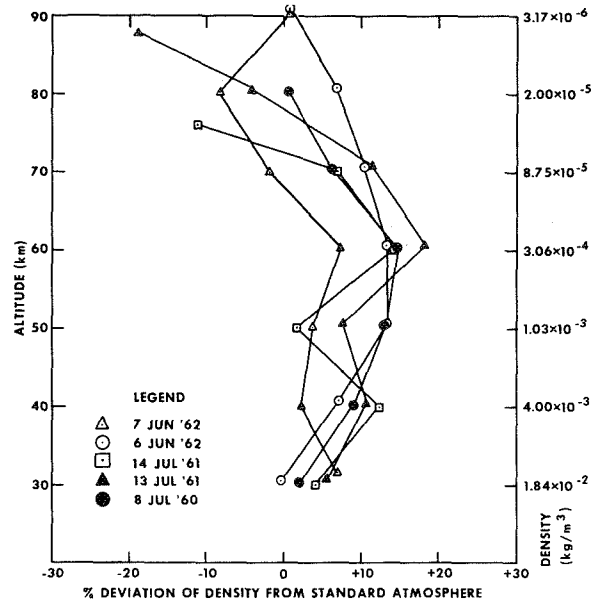

FIGURE 12.—Summer densities as a function of altitude derived from individual temperature soundings obtained with the rocket grenade experiment over Wallops Island, Va. (38° N.). Densities are shown as percent deviation from 1962 U.S. Standard Atmosphere (*27*).

the circulation in the regions where ionization of the atmosphere and dissosiation of oxygen sets in. This boundary lies near 80 km and seems to suggest that the physical causes which sustain the motions of the atmosphere are quite different in the two regions. As described above, the winds below 80 km conform to the pattern of uniform zonal flow, regularly reversing with season, interrupted only by occasional breakdowns during the spring transition. Above this altitude, however, the flow is no longer uniform and exhibits no regular seasonal pattern. Some features are common, nevertheless, to most of the wind profiles taken above 80 km; namely, the strong, but highly variable winds sandwiched between zones of relative calm resulting in extreme wind shears. Thus far, every sounding conducted has shown these wind shears between 90 and 110 km. Above 120 km greater uniformity seems to return but samples at these altitudes are too few to derive any definite circulation patterns.

A most interesting and important result of the sounding program at Wallops Island has been the direct comparison of various experiments at various altitude regions. We had previously reported (*26*) the rather discouraging disagreement between temperatures measured directly by the thermistor method used in the small meteorological rockets, and by the grenade method at the 50 km level. From recent results (Fig. 16, December 1962) it seems that this discrepancy has been greatly reduced and in the February and March 1963 comparisons (Fig. 17) has all but disappeared. This is attributed to a substantial improvement in the thermistor temperature sensor which is now flown in the HASP rocket at Wallops Island.

A comparison of wind measurements between the grenade method and the various methods used with small meteorological rockets in the 40 to 60 km region, in most cases, shows very good agreement.

Comparisons between the grenade technique which yields average winds in layers of few kilometers thickness and the sodium ex

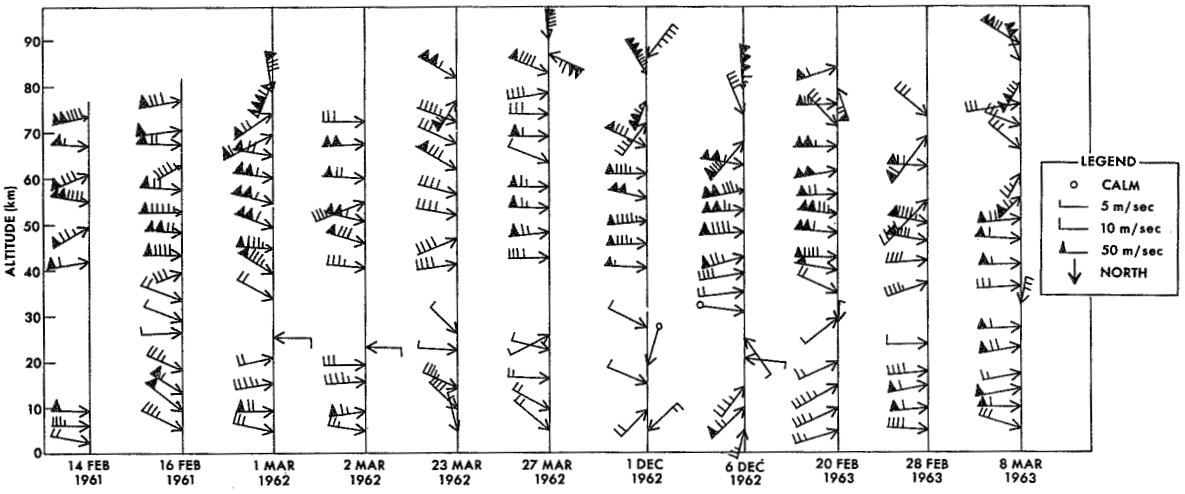

FIGURE 13.—Winter measurements of wind speed and direction versus altitude as measured by the grenade experiment over Wallops Island, Va. (38° N.).

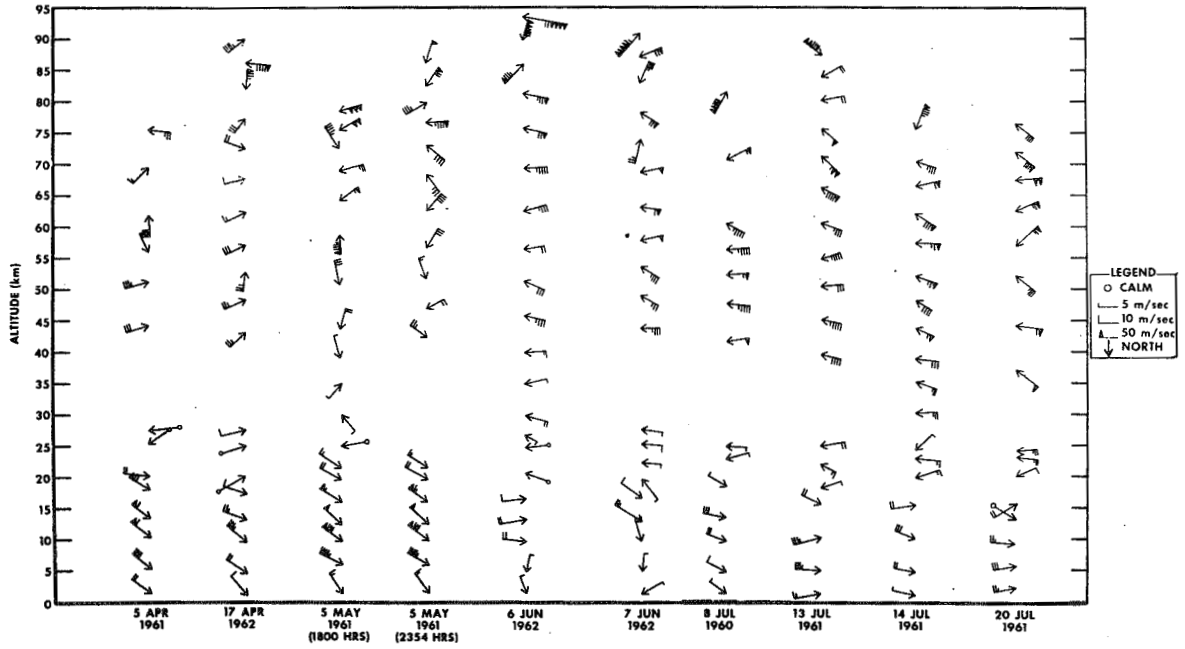

FIGURE 14.—Summer measurements of wind speeds and direction versus altitude as measured by the grenade experiment over Wallops Island, Va. (38° N.).

periment yielding a continuous wind profile with altitude show that there is fair agreement in many but not all cases where the flow pattern is still uniform (below 80 km) and where the violent wind shears usually observed at the higher altitudes do not exist. In the shear regions the agreement is generally very poor, obviously because the average winds obtained by the grenade method are not comparable to the rapidly changing instantaneous wind vectors determined by the sodium trails (Fig. 15).

A most interesting comparison was conducted between the sphere, grenade and Pitot tube experiments on June 6, 1962. A passive, inflatable falling sphere was carried on the same rocket as the grenade experiment (*14*) and a

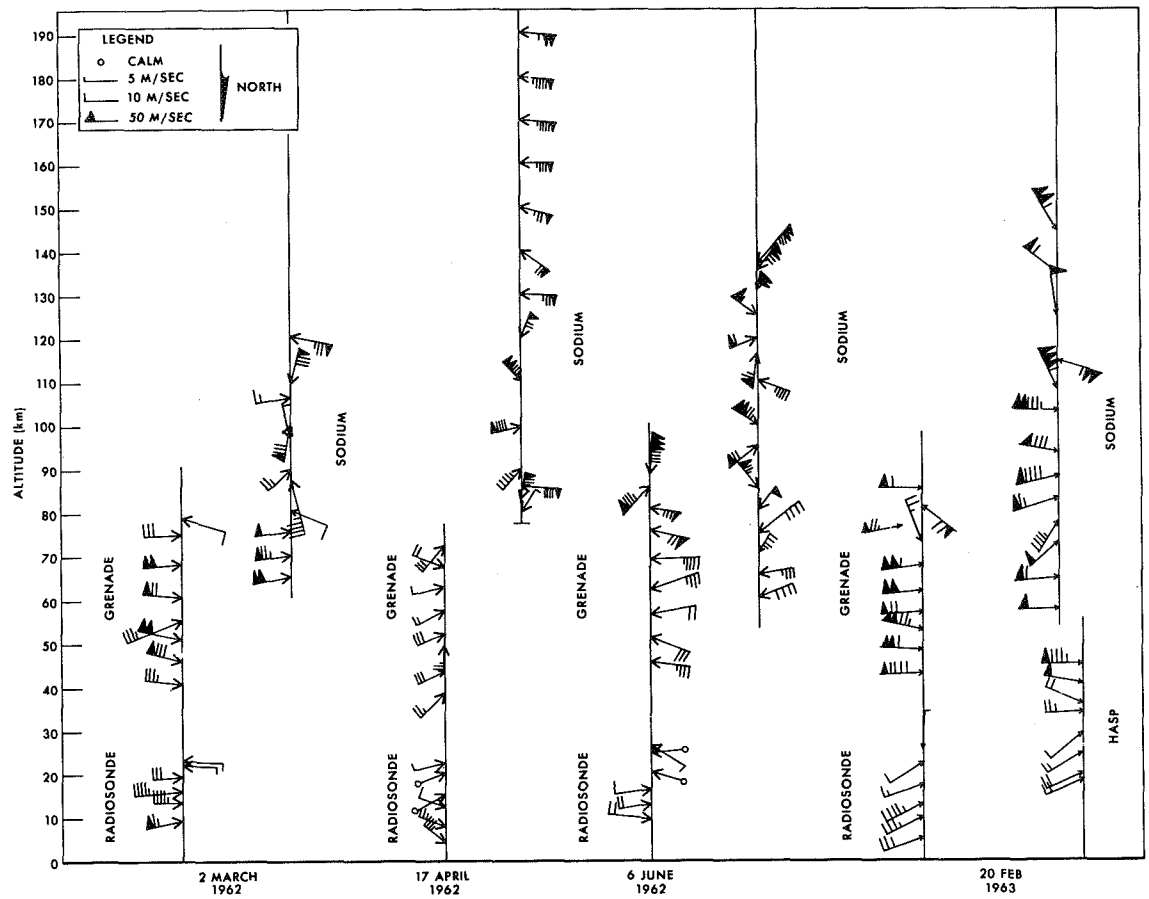

FIGURE 15.—Wind speed and direction versus altitude as obtained nearly simultaneously with balloon-radiosonde, grenade and sodium techniques over Wallops Island, Va. (38° N.) on March 2, April 17, and June 6, 1962 and with balloon-radiosonde, grenade, sodium and meteorological rocketsonde (HASP) techniques on February 20, 1963.

Pitot tube experiment was conducted within less than ½ hour. Density profiles resulting from each of the three techniques are shown in Figure 18.[1]

From 30–65 km and at 90 km the agreement between the Pitot tube and grenade techniques is quite good (better than 5 percent); this can be considered within the measurement errors of the two experiments. Between 65 and 85 km, the disagreement is considerably larger: 9 percent at 70 km and 13 percent at 80 km. The grenade and sphere methods are in fair agreement up to 75 km. Discrepancies there are less than 10 percent. From 65 to 75 km, grenade densities are about 5 percent lower than falling sphere densities and about 5 to 10 percent higher than Pitot-tube densities. Below 60 km falling sphere densities are generally lower than Pitot tube and grenade densities. Over the entire altitude range, the Pitot tube densities are always lower than the grenade densities indicating the possibility of a systematic error.

The largest discrepancies between falling sphere and grenade data (and Pitot tube) occur near 85 km, while at 90 km results from all three methods agree remarkably well.

[1] The Pitot static tube experiment was conducted by J. J. Horvath, the falling sphere experiment by J. W. Peterson, both of the University of Michigan, Ann Arbor, Mich. The grenade experiment was performed by Wendell S. Smith of NASA/Goddard Space Flight Center, Greenbelt, Md. The kind permission of these researchers to use their data for this comparison is gratefully acknowledged.

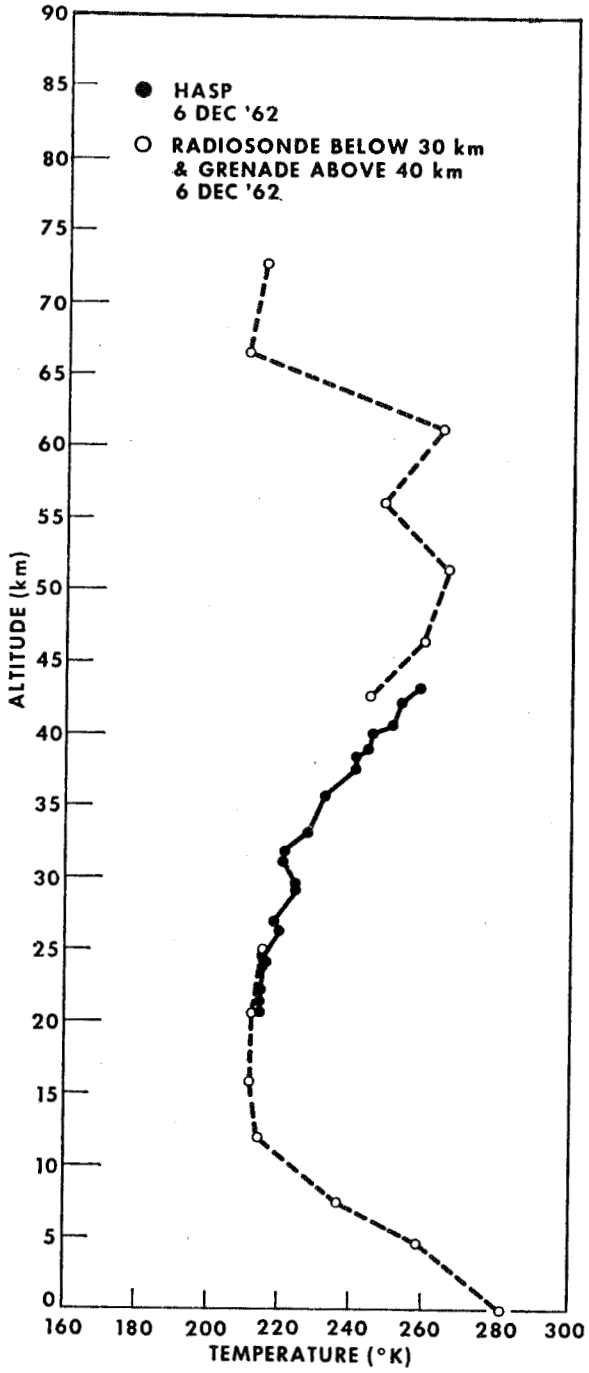

FIGURE 16.—Comparisons of nearly simultaneous temperature measurements obtained with grenade, meteorological rocketsonde (HASP), and radiosonde techniques over Wallops Island on December 6, 1962.

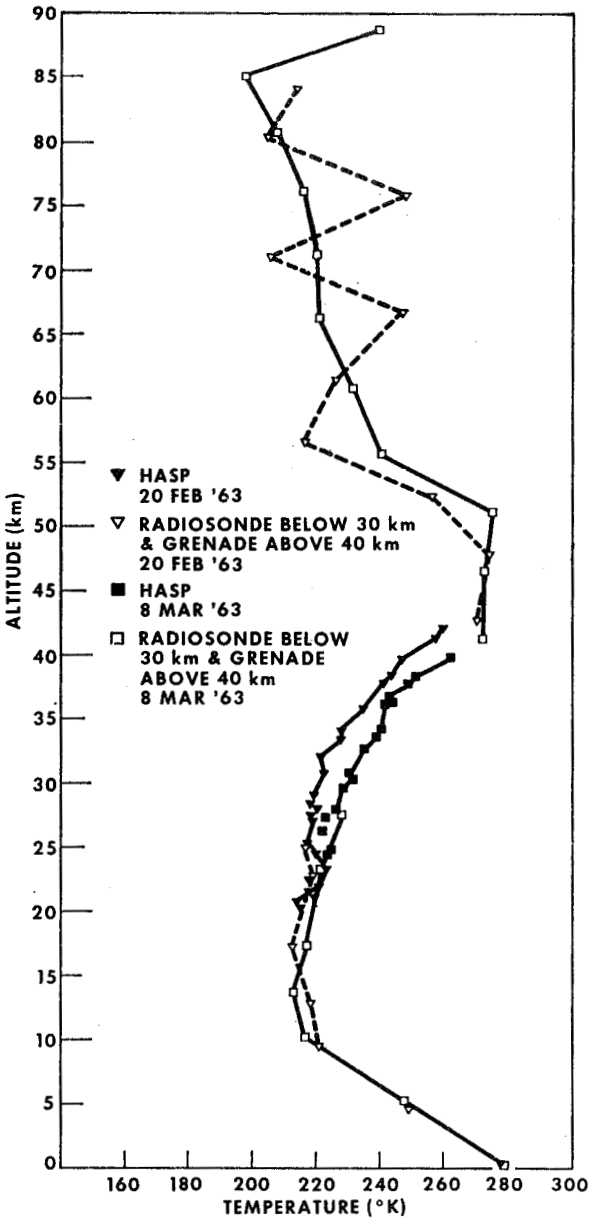

FIGURE 17.—Comparisons of nearly simultaneous temperature measurements obtained with grenade, meteorological rocketsondes (HASP) and radiosonde techniques over Wallops Island on February 20, 1963, and March 8, 1963.

It is possible that the fluctuation in the falling sphere data between 65 and 75 km could be explained by the fact that the sphere passes through the transonic velocity regime at this altitude range where the drag coefficient (C_D) changes rapidly. In fact, the Mach numbers

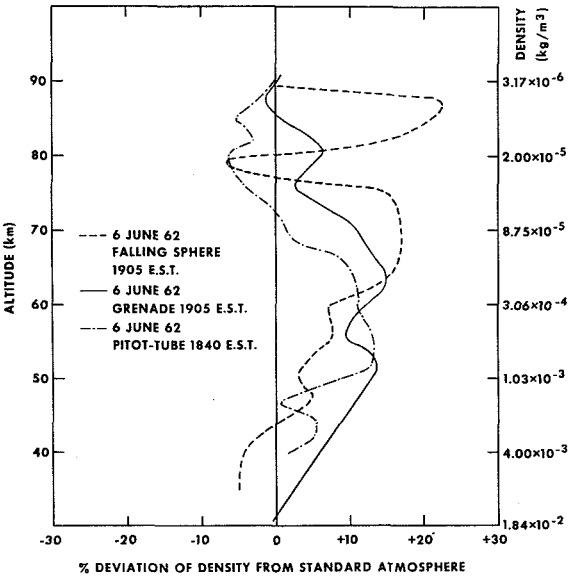

FIGURE 18.—Comparison of densities obtained nearly simultaneously with the falling sphere, rocket grenade, and Pitot tube techniques on June 6, 1962, over Wallops Island, Va. (38° N.). Densities are shown as deviations from 1962 U.S. Standard Atmosphere (*27*).

given for the sphere by Peterson (*14*) range from 1.46 at 75 km to 0.63 at 65 km and at 72 km $M=1$.

Since the passive, inflatable sphere is a relatively recent development, difficulties such as those mentioned on page 433 have not yet been fully evaluated. The conclusions which can be drawn from this comparison must therefore be considered highly preliminary.

A similar comparison was conducted between grenades and Pitot tube on December 1, 1962. Preliminary results indicate that the agreement is not as good as on June 6, 1962, but no final conclusions can be drawn until the data analysis is complete.

Finally, we were able to compare results from four simultaneous grenade soundings at Churchill and Wallops Island in December 1962 and February and March 1963. All four temperature profiles exhibit the same feature; one typical pair of soundings for March 8, 1963, is shown in Figure 19. At 90 km temperatures at the two sites nearly coincide. Temperatures at Churchill are higher by 10 to 20° K between 55 and 80 km. Around 55 km temperatures are

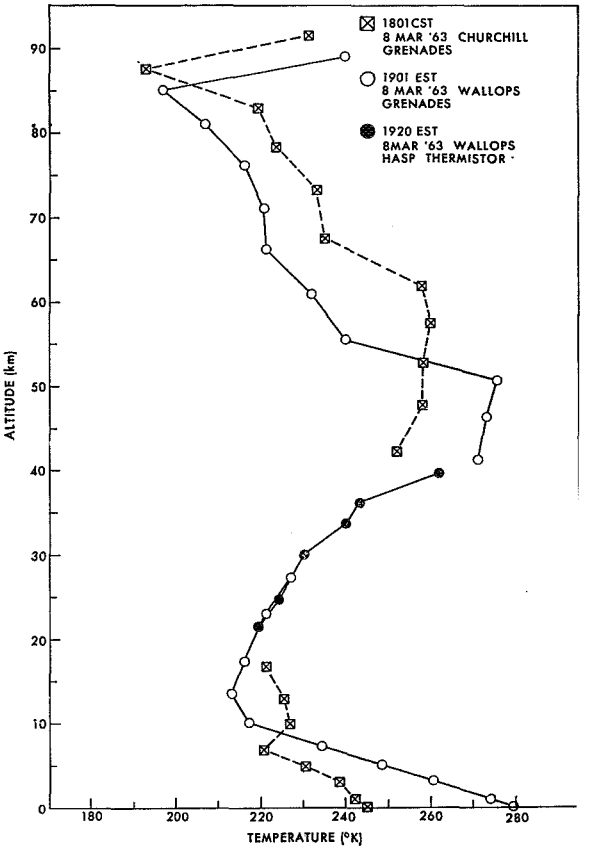

FIGURE 19.—Temperatures as a function of altitude as obtained by nearly simultaneous rocket grenade soundings over Wallops Island, Va. (38° N.) and Churchill, Canada (59° N.). Radiosonde temperatures at both sites and meteorological rocketsonde temperatures (HASP) for Wallops Island are also shown.

the same at the two locations and below 55 km Wallops temperatures are appreciably higher (10–20° K). It is assumed that this condition holds throughout the stratosphere although no meteorological rocket (thermistor) data exist for comparison at Churchill and stratospheric temperatures there must be inferred from interpolating between the balloon radiosondes at 20 km and the grenade data at 40 km.

There is, however a strong variation from day to day in the temperature profiles at each site that the above observation can only be made on individual pairs of simultaneously obtained profiles and does not hold for profiles averaged over several soundings. In general one may conclude that the temperature profile

between the ground and 90 km becomes more and more isothermal as one progresses from the tropics toward the winter pole.

OUTSTANDING PROBLEMS

The basic techniques used during IGY are still adequate for the measurement of temperature, density, pressure and wind. Because of their long history, their reliability is very high. However, the absolute accuracy of the measurements must be further tested and possibly improved through comparative "calibrations" of the various methods. Depending on the available facilities one or more of these techniques may be appropriately adopted to launching sites throughout the world. By far the greatest task is to increase the geographic coverage with these soundings by soliciting the cooperation of more individual launch sites all over the globe. For instance, lack of adequate launch facilities has made it impossible as yet to obtain structure measurements in the mesosphere during the polar night, which is of foremost importance in answering the question of heating in the mesosphere.

With respect to the physics of the mesosphere, the cause of the high temperatures and their great variability above 60 km during wintertime remains one of the biggest outstanding questions. The entire question of energy exchange between radiation and the potential energy stored in the atmosphere and between potential and kinetic energy should be investigated and more data both at more locations and at more frequent intervals are needed for that purpose.

More synoptic soundings throughout the atmosphere will also enable us to determine the interaction between various circulation regimes in the atmosphere and may possibly lead to a mechanism for the downward propagation of solar-terrestrial relationships.

It is imperative that the technology of composition measurements be improved. A technique must be found which permits the reliable measurement of ozone and atomic oxygen throughout the mesosphere even in the absence of solar illumination.

REFERENCES

1. Stroud, W. G., W. Nordberg, W. R. Bandeen, F. L. Bartman, and P. Titus, *J. Geophys. Res.*, 65 (August 1960).
2. Nordberg, W., and W. Smith, *Proceedings of the First International Symposium on Rocket and Satellite Meteorology*, Washington, D.C., 1962, Interscience Publishers, a division of John Wiley & Sons, Inc., New York, p. 119.
3. Murgatroyd, R. J., and R. M. Goody, *Quarterly Journal of the Royal Meteorological Society*, Vol. 84, No. 361, July 1958.
4. Harris, L., and W. Priester, *J. Geophys. Research*, Vol. 67, November 1962, No. 12.
5. Aufm Kampe, H. J., and M. Lowenthal, *Proceedings of the First International Symposium on Rocket and Satellite Meteorology*, Washington, D.C., 1962, Interscience Publishers, a division of John Wiley & Sons, Inc., New York, p. 15.
6. Annals of the International Geophysical Year, Vol. VI, Part 2, p. 76, Pergamon Press, New York, 1958.
7. Annals of the International Geophysical Year, Vol. VI, Part 2, p. 82, Pergamon Press, New York, 1958.
8. Jenkins, Reed, Nike-Apache Performance Handbook, NASA/Goddard Space Flight Center, Greenbelt, Md., Document No. X-616-62-103, July 1962.
9. Smith, L. B., *J. Meteorological Research*, Vol. 17, No. 3, p. 296–310, June 1960.
10. Manring, E., and J. Bedinger, Space Research—*Proceedings of the First International Space Sciences Symposium*, Nice 1960, H. K. Kallman Fijl, North Holland Publishing Co., Amsterdam, p. 154.
11. Wagner, N. K., Theoretical Accuracy of the Met. Rocket Sonde Thermister, 1 July 1963, Elec. Engrg. Res. Lab., Unvi. of Texas, Austin, Tex., Report No. 7–23.
12. Nordberg, W., and W. Smith, A Manual Describing the Rocket-Grenade Experiment, X-651-63-18 (1963), NASA/Goddard Space Flight Center, Greenbelt, Md.
13. Bartman, F. L., L. W. Chaney, L. M. Jones, and V. C. Liu, *J. App. Phys.*, 27, 7, 1956.
14. Peterson, J. W., and K. D. McWatters, The Measurement of Upper-Air Density and Temperature by Two Radar-Tracked Falling Spheres, University of Michigan, College of Engineering Technical Report 03598-13-T, May 1963, Ann Arbor, Mich.
15. Jones, L. M., J. W. Peterson, E. J. Schaefer, and H. F. Schulte, *J. Geophys. Res.*, 64, 12, 1959.

16. HORVATH, J. J., R. W. SIMMONS, and L. H. BRACE, Theory and Implementation of the Pitot-Static Technique for Upper Atmospheric Measurements, Technical Report 03554, 04673-1-5, University of Michigan, Ann Arbor, Mich.
17. SICINSKI, H. S., N. W. SPENCER, and W. G. DOW, *J. Appl. Phys.*, 25, 2, p. 161–168, February 1954.
18. LAGOW, H. E., and J. AINSWORTH, *J. Geophys. Res.*, 61, 1, March 1956.
19. AINSWORTH, J. E., D. F. FOX, and H. E. LaGow, *J. Geophys. Res.*, Vol. 66, 10, October 1961.
20. SPENCER, N. W., R. BOGGESS, and D. TAEUSCH, Seasonal Variation of Density and Temperature Over Churchill Canada During Solar Maximum (Submitted to J. Geophys. Res., September 1963).
21. JOHNSON, F. S., J. D. PURCELL, R. TOUSEY, and K. WATANABE, *J. Geophys. Res.*, 57, 157 (1952).
22. KRUEGER, A. J., The Arcas Ozone Sonde, IUGG/WMO, *Ozone Symposium Arosa*, August 1961.
23. WENZEL, E. A., L. T. LOH, M. H. NICHOLS, L. M. JONES, Annals of the International Geophysical Year, Vol. XII, Part I, p. 407, Pergamon Press New York, 1958.
24. MIRTOV, B. A., *Uspekhi Fiz. Nank*, Vol. 63, No. 1B, p. 181, 1957.
25. SOBERMAN, ROBERT K., *Scientific American*, June 1963, p. 51.
26. NORDBERG, W., and W. SMITH, *Proceedings of the International Symposium on Stratospheric and Mesospheric Circulation*, August 1962, Berlin, Germany, Edited by Richard Scherhag and Gunter Warnecke, Verlag Von Dietrich Reimer in Berlin.
27. U.S. Standard Atmosphere, 1962, U.S. Government Printing Office publication, Washington, D.C., December 1962.
28. NORDBERG, W., and W. G., STROUD, NASA Technical Note D-703, April 1961, NASA/Goddard Space Flight Center, Greenbelt, Md.
29. COURT, A., A. J. KANTOR, A. E. COLE, AFCRL-62-899, September 1962. Supplemental Atmospheres, Air Force Cambridge Research Laboratories, L. G. Hanscom Field, Mass.

THE ROCKET-GRENADE EXPERIMENT

W. NORDBERG AND W. SMITH
Goddard Space Flight Center

This manual describes the grenade technique which is employed to measure average ambient temperature and winds in horizontal layers between two successive grenade explosions. The technique is effective up to altitudes of ninety km. The method for deriving pressures and densities from the temperature information is discussed in detail. And finally, rocket-borne and ground-based instrumentation is delineated.

INTRODUCTION

The operation and performance of the rocket-grenade experiment is presented and intended to serve as a reference manual, reviewing the experiment techniques for the benefit of persons wishing to apply this experiment to their own needs. The purpose of the rocket-grenade experiment is to measure wind velocities and temperatures, and to derive densities and pressures, by detonating explosive charges (grenades) at predetermined height intervals during the ascent of the rocket to altitudes of approximately 90 km. The sound energy from the explosions is recorded by a microphone array on the ground. The time and direction of the arriving sound wave are calculated. The rocket position is accurately determined by a combination of radar, DOVAP (*Do*ppler *V*elocity *A*nd *P*osition), and optical-tracking systems. An analysis of these coordinates yields the direction and magnitude of the sound-velocity vector in the layer between two explosions; this vector is a measure of the temperature and wind in the layer.

The variations of atmospheric pressure, temperature, density, wind, and composition (humidity) with time and space are conventionally considered the parameters of greatest interest to the meteorologist, because they are presently best suited to describe the processes responsible for various weather conditions. In the past, meteorologists believed that knowledge of atmospheric conditions up to the altitude of the tropopause would be sufficient to describe and predict weather on the earth. However, as measurements at higher altitudes became available, researchers realized that many meteorological phenomena (especially those arising from the interaction between solar energy and the atmosphere) can be understood only by further exploration of the upper atmosphere.

Before World War II, scientists used kits and balloons to extend their knowledge of the atmosphere to higher altitudes. Balloon-borne radiotransmitting meteorological instruments (radiosondes) were introduced in the 1930's, and much valuable information still is accumulated by this method; however, these measurements are limited to altitudes below 30 km. After World War II, the German V–2 rockets were used to extend meteorological experimentation to higher altitudes. Present knowledge of the atmosphere between 30 and 100 km is derived almost entirely from rocket experiments; these experiments have shown that significant dynamic processes and meteorological variability in atmospheric conditions exist up to heights of 80 km.

During and just before the International Geophysical Year (IGY), rocket-grenade experiments were conducted to establish temperature and wind measurements in three typical areas of the globe, selected as best representing atmospheric behavior in the 30 to 90-km region.

These three areas were White Sands, New Mexico, in the continental subtropical region; Fort Churchill, Canada, in the subarctic; and Guam, Mariana Islands, in the Pacific equatorial region. A series of 12 Aerobee rockets was successfully fired at White Sands from 1950 to 1953, using ballistic cameras to provide the required tracking data. Ten Aerobee sounding rockets, which measured temperatures and winds up to 95 km, were fired at Fort Churchill, Canada, during November 1956; July, August, and December 1957; and January 1958. The windy, cloudy weather conditions of the Arctic required conversion of this experiment to an all-weather experiment by use of electronic tracking techniques (DOVAP) and of methods to reduce wind noise in the sound-ranging (Reference 1). With these changes, the only weather limitations were those imposed by the rocket ballistics. The results clearly indicated a seasonal and latitudinal temperature variation, with temperatures increasing toward the winter pole at 80 km and toward the summer pole at 50 km. Remarkable temperature inversions between 50 and 80 km with secondary peaks above 50 km were measured in all winter firings at Fort Churchill. In summer, prevailing winds were from the east, usually less than 50 m/sec; in winter, these winds were from the west, usually between 50 and 100 m/sec, but in many instances exceeding 100 m/sec.

Nine successful flights at Guam in November 1958 yielded new data in the near-equatorial region; these flights employed smaller, less expensive solid-propellant rocket vehicles. Since then, a smaller and more efficient payload was developed and flown with Nike-Cajun rockets from Wallops Island, Va. During 1960–61, about 10 such flights were successfully conducted with this "post-IGY" instrumentation.

INSTRUMENTATION

The rocket-grenade experiment system performs four essential tasks: (1) Places the payload in the desired trajectory; (2) produces explosions at desired points along this trajectory; (3) detects the arrival of the sound energy on the ground; (4) determines the position and time of each explosion. The description of the instrumentation needed to accomplish each of these tasks is divided into two sections, the first devoted to rocketborne instrumentation and the second to ground based. All prelaunch control (support) equipment, such as power switching, grenade-ejection timer checkout, and monitoring circuits, is contained in a blockhouse located near the rocket launcher to provide protection for personnel and equipment.

Rocketborne Instrumentation

The rocket presently used for the grenade experiment is the Nike-Cajun (Fig. 1). This two-stage combination of solid-fuel rockets is

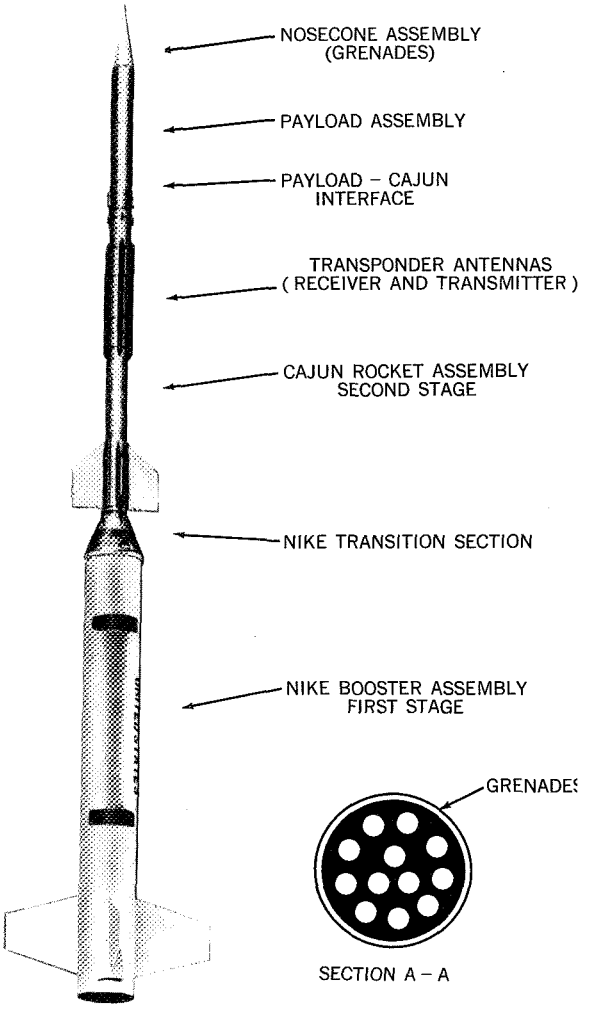

FIGURE 1.—Relation of payload to rocket vehicle.

TABLE 1.—*Grenade Experiment—Nike-Cajun Rocket Information*

Dimensions (inches)		Performance (60-lb payload)		Weights and aerodynamic characteristics	
Nosecone 18° inclination angle.	18. 8	Booster burnout velocity.	3,050 ft/sec	Total Nike-Cajun launch weight.	1,550 lbs
Total payload length	56. 0	Booster ignition time.	0.0 sec	Payload weight	60 lbs
Cajun length	107. 0	Booster burnout time.	3.5 sec	Payload center of gravity (CG) from nose tip.	36.5 in
2d-stage length	163. 0	Cajun ignition time.	17.0 sec	Cajun burnout weight (with 60-lb payload).	147 lbs
1st-stage length	151. 0	Cajun ignition altitude.	32,000 ft	Burnout CG (from nose tip).	92.5 in
Total length	314. 0	Cajun burnout time.	19.8 sec	Burnout Mach number (Cajun).	$M=5$
Payload diameter	6. 75	Cajun burnout velocity.	5,400 ft/sec	Burnout center of pressure (Cajun).	$C_p=105.5$
Cajun body diameter	6. 5	Cajun burnout altitude.	42,000 ft	Static stability margin (Cajun).	13.1 in=1.9 cal.
Cajun fin span	27. 3	Maximum acceleration.	58 G	Lift coefficient curve slope based on $d^2=45.5$ sq. in.), Cajun burnout.	$C_l=0.13$/deg
Nike body diameter	17. 0	Peak time	165 sec	Moment coefficient curve slope, Cajun burnout.	$C_m=-0.25$/deg
Nike fin span	54. 0	Peak altitude Impact time Impact range	365,000 ft 330 sec 228,000 ft	Moment curve slope at Cajun burnout.	$M=410\ \frac{\text{ft-lb}}{\text{degree}}$

easy to handle and can be launched from a modified transportable Nike launcher. When fired from a near-vertical position, the rocket is capable of carrying the present grenade-experiment payload to an altitude of 69 statute miles (105 km) above sea level. Present payload weight is 60 pounds; however, the drag created by the DOVAP antenna configuration is a greater factor in altitude determination than payload weight. In addition to the normal payload, a 90-pound lead weight was added to the Nike booster to increase stability and reduce lift forces at Nike burnout by reducing Nike burnout velocity; this additional weight, located in the Nike transition section, does not appreciably affect the peak altitude of the experiment because this section is discarded with the empty Nike booster. Additional Nike-Cajun characteristics are given in Table 1. Recovery of the rocket is not required because all results are recorded by ground instrumentation.

Figure 2 indicates the desired rocket trajectory. To produce nearly vertical sound propagation, the explosions should occur in the region above the microphones; this is sometimes difficult to achieve, as safety considerations related to booster and unignited or normal second, stage impact will require some intentional deviation from the optimum trajectory. For maximum accuracy in data reduction, it is also desirable that the rocket's trajectory give all grenades a nearly common line-of-sight when seen from the sound ranging site. In addition, the rocket's trajectory is affected by the wind it traverses, this effect being greatest at lower altitudes where the rocket's velocity is lowest (Table 2). Wind trajectory disturbances are determined and compensated for as follows:

1. Winds at low altitudes are measured at regular time intervals up to a short time before launching.

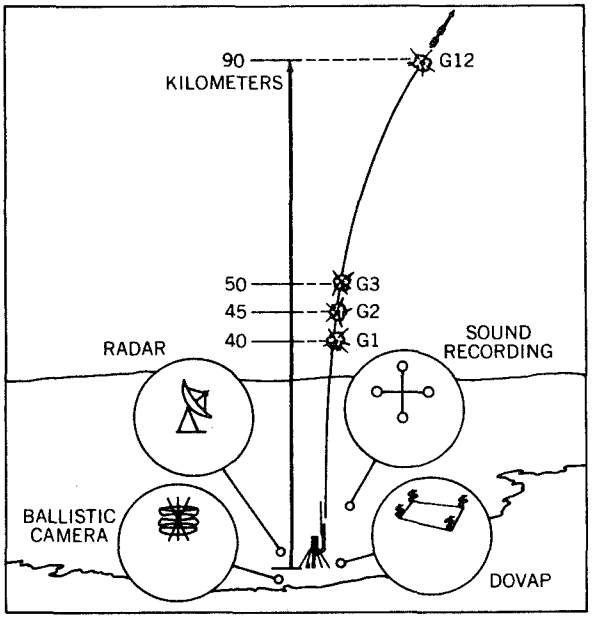

FIGURE 2.—Rocket-grenade experiment.

2. Winds at higher altitudes are measured a few hours before firing by means of standard radiosonde balloons.
3. The effect of the wind on the rocket is calculated, with the aid of analog or digital computers, by multiplying the measured wind speeds by a unit ballistic wind effect and wind-weighting factors which decrease with altitude. This computation yields a displacement of the impact point due to wind. It is applied to a computed "no-wind" impact point obtained from a launcher-tilt factor relating, generally in a linear fashion, to the launcher elevation angle and the horizontal range of the impact point. Unit wind effect, launcher-tilt factor, and a table of wind-weighting factors are usually predetermined by theoretical calculations and empirical adjustments. These factors are often stored in a computer, which facilitates the determination of launching settings; however, this determination can also be made by manual computations (References 2, 3, and 4).

Safety Considerations

Ignition of both the Nike and the Cajun propellant charges is accomplished by hot-wire squibs (Fig. 3). The Nike employs four instantaneous ignition squibs; the Cajun, two

TABLE 2.—*Wind-Weighting Factors Used for Nike-Cajun Grenade Shots from Wallops Island*

Weight table		Impact range and unit wind effect		
Altitude (feet)	Weight factor	θ (degrees down from vetical)	Impact range (n. mi.)	Unit wind effect (n. mi./fps)
50	0. 103	1	5. 15	0. 910
90	. 209	2	10. 30	. 910
150	. 310	4	20. 60	. 910
200	. 415	6	30. 90	. 910
400	. 515	8	41. 20	. 910
700	. 623	10	51. 50	. 910
1100	. 700	12	61. 80	. 910
2300	. 803	14	72. 10	. 910
5000	. 880	16	82. 40	. 910
10000	. 880	18	92. 70	. 910
20000	. 880	20	103. 00	. 910
30000	. 880			
32000	. 879			
34250	. 902			
36500	. 935			
38750	. 968			
41000	1. 000			

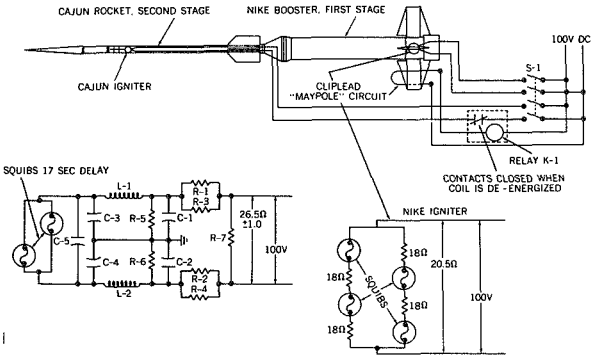

FIGURE 3.—Nike-Cajun rocket-ignition circuit.

17-second time-delay squibs. Power for ignition is available only through switch S–1 located in the blockhouse. Closing S–1 applies power to the Nike igniter; however, relay K–1 prevents the application of power to the Cajun igniters until liftoff from the laucher de-energizes the relay by severing the cliplead "maypole" circuit. This prevents Cajun ignition should the booster fail to fire. In addition, a RF filter (consisting of C–1—C–5, R–1—R–7, L–1, and L–2) connected between the power source and the Cajun igniter prevents firing by extraneous RF voltages.

Relation of Payload to Rocket

The rocket vehicle is composed of two distinct stages, shown in Figure 1. The first stage is the Nike booster which serves to lift the vehicle in the early moments of flight. Sitting on top of the Nike is the second-stage Cajun rocket. The Nike booster drag-separates from the Cajun rocket after first-stage burnout, leaving the Cajun to carry the payload to the desired altitudes. The payload itself is positioned forward of the Cajun up to and including the nosecone. Information on aerodynamic bending of Nike-Cajun rockets due to oversize payloads is given in Reference 5.

Payload

The payload provides the means for accomplishing the objectives of the experiment. The payload structure consists of three units (Fig. 4): Grenade section with nosecone; Timer and photocell assembly; and a DOVAP and battery section.

The nosecone, an 18° included-angle right circular cone, forms an integral unit with the cylindrical grenade section (Fig. 5) which is composed of 12 cylindrical tubes held in place by plastic resin. One-pound high-explosive grenades fit into a peripheral ring of nine cylindrical tubes, and 2-pound grenades fit in an inner ring of three tubes. The nosecone covering, a mixture of glue and asbestos through which each grenade breaks upon ejection, has the primary function of providing the proper

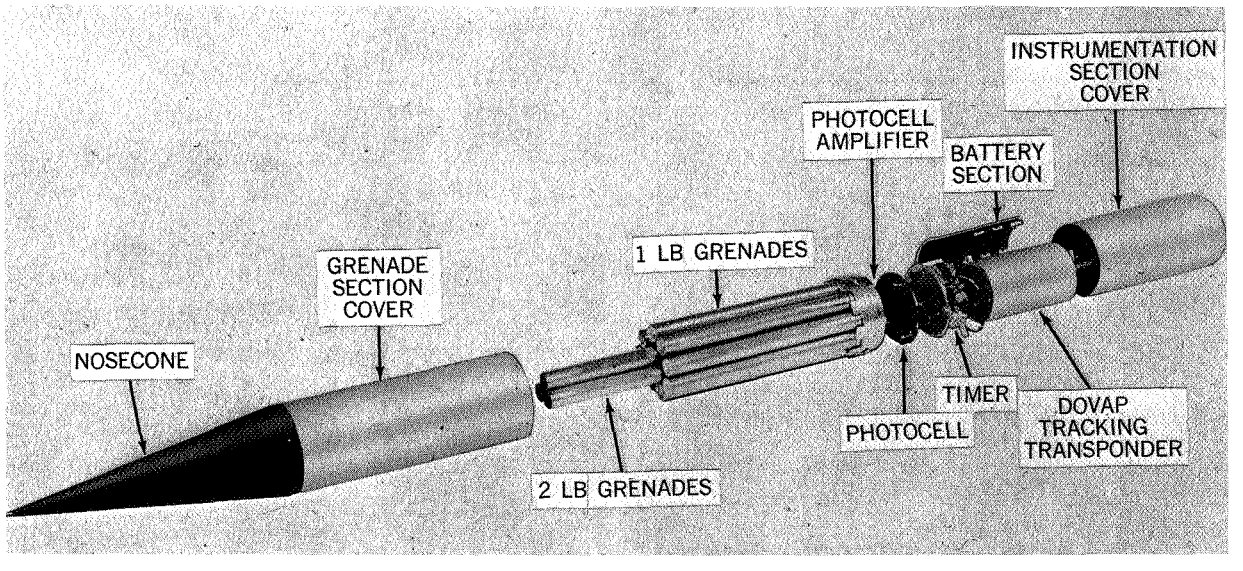

FIGURE 4.—Payload structure.

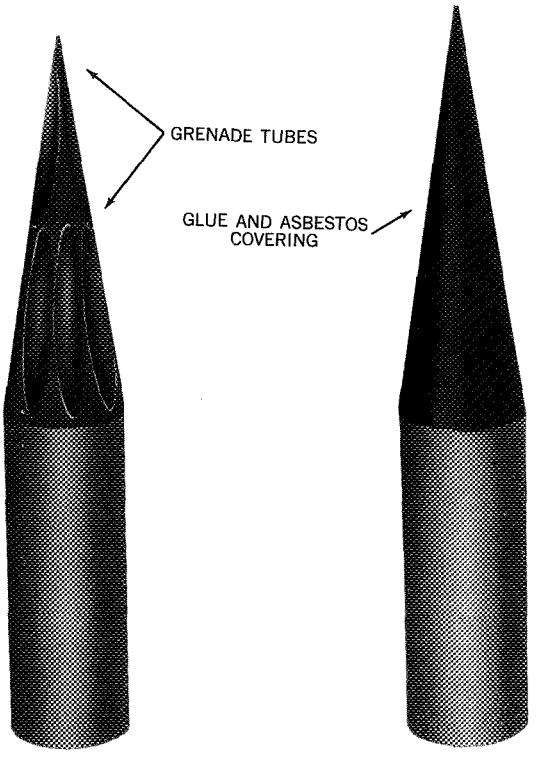

FIGURE 5.—Nosecone grenade assembly.

aerodynamic configuration during the high-drag portion of the flight.

The timer and photocell assembly contains three infrared-sensitive lead sulfide (PbS) photocells, a photocell amplifier, and an electromechanical timer to provide for grenade ejection. The function of the photocells is to detect the flash of the grenade explosions.

The DOVAP and battery section contains the batteries furnishing power to the photocell amplifier and the timer, and a transponder which receives and retransmits the tracking signals emitted from a DOVAP transmitter on the ground.

Grenades

The grenades are cylinders 1½ inches in diameter; the 1-pound grenade is 18 inches long, the 2-pound grenade is 28 inches long (Fig. 4). Construction of the grenades is shown in Figure 6. The design is intended to produce a minimum of shrapnel upon explosion, in order to avoid serious damage to the rocket

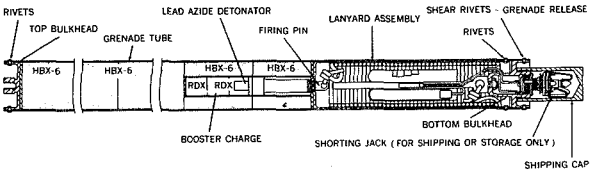

FIGURE 6.—Schematic diagram of grenade.

or instrumentation. Each grenade contains HBX–6 as the high explosive, an RDX booster charge, and a lead AZIDE detonator.

Grenade ejection is controlled by the timer described later in the text. Detonation is accomplished by a lanyard-operated device located in the bottom end of the grenade cylinder; the lanyard, 14 feet long, is attached to the firing pin at one end and the grenade-assembly bulkhead at the other. The grenade is ejected by electrically detonating two 3-gram black-powder charges contained in the lanyard end of the grenade. Two powder charges are used, although either charge should provide sufficient force for successful grenade ejection. The ejection force shears the four soft retaining rivets and ejects the genade through the nosecone covering. When the grenade has traveled 14 feet the lanyard pulls the firing pin which sets off the detonator, causing the RDX booster charge to explode; this in turn sets off the HBX–6 main explosive charge.

During 1960 and 1961, a number of grenade experiments failed because the whole payload exploded prematurely during early phase of the rocket flight. A laboratory study of the grenades to determine the cause of the detonations revealed that high vibration during burning of the Nike booster caused the RDX booster charge to pulverize at the surfaces of the pellets. The pulverized RDX sifted into the ejection cavity, where it could be detonated inside the payload as the black powder ignited. Steps were taken to reduce vibration and to increase the stability of the explosive, such as (1) bonding one explosive to the other to prevent chaffing; (2) introducing an O-ring to prevent dust from entering the ejection cavity.

Timer

The timer (Fig. 7), mounted on a ring located at the top of the DOVAP and battery section

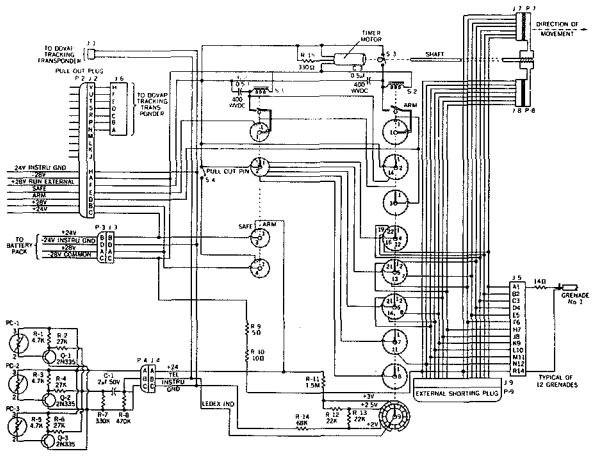

FIGURE 7.—Schematic diagram of timer and photocell amplifier.

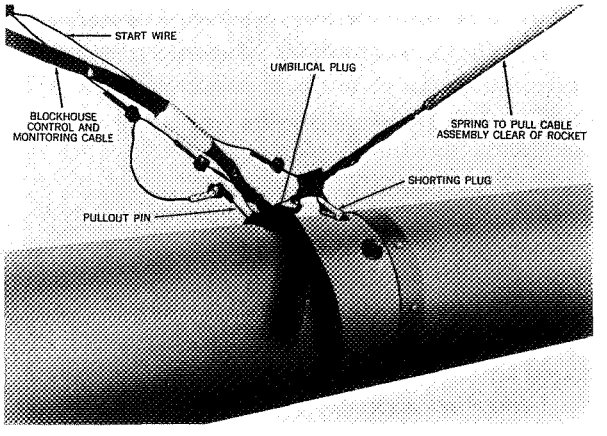

FIGURE 8.—Prelaunch rocket connections.

(Fig. 4), controls the sequence of grenade ejection. It consists primarily of a timer motor, two Ledex switches (S–1 and S–2), and appropriate monitoring and safety circuitry. S–1 is a 12-position Ledex switch; S–2 is a 24-position Ledex switch. Receptacle J–2 and mating plug P–2 provide the connections for external control and monitoring of the timer positions before launch. Internal battery power is furnished through receptacle J–3 and plug P–4.

Receptacles J–7, J–8, and J–9 and plugs P–7, P–8, and P–9 prevent premature grenade firing by shorting the plus side of each grenade terminal to a ground. Connectors J–7 and J–8 and plugs P–7 and P–8 are disengaged after launch by the timer-motor operation several seconds before the first grenade is scheduled to eject. External-shorting plug P–9 (Fig. 8), which serves as an additional safety short-circuit across the grenade terminals, is disengaged by pullout from J–9 during rocket launch. Receptacle J–5 and individual pin jacks provide electrical connections to the grenades. J–4—P–4 and J–1—J–6 provide electrical connections to the photocell amplifier and DOVAP tracking transponder, respectively.

As a third safety feature, accidental operation of the timer before launch is prevented by a pullout pin (Fig. 8) which holds microswitch S–4 in the open position. This pin, attached to a start wire on the launcher, is disengaged by liftoff of the rocket. In addition, to ensure safety during handling and loading, the timer has a "safe" position which prevents inadvertent application of power to the timer.

Before the grenades are installed, the timer operation is checked as follows: (1) Apply +28 volts to pin E of J–2 to advance Ledex switch S–1 clockwise to the "safe" position; (2) apply +28 volts to pin D of J–2 to advance S–1 to the "arm" position; and (3) apply +28 volts to pin F of J–2 to energize the timer motor, advancing S–2 clockwise at one increment per second. Deck 9 of S–2, in conjunction with voltage divider R–11, R–12, R–13 and R–14, provides a voltage-step function, via J–4, P–4 and J–1, to the 30-kc subcarrier, oscillator (SCO) located in the DOVAP tracking trasnsponder. This voltage modulates the telemetry output of the DOVAP, making it possible to monitor timer operation via the telemetered DOVAP signal; if the timer is functioning properly, the demodulated output should indicate a pulse train corresponding to Figure 9.

To prepare the timer for grenade installation, the following steps are required: (1) Apply +28 volts to pin E of J–2 to advance S–1 to the "safe" position; (2) apply +28 volts to pin D of J–2 to advance S–1 and S–2 to the "arm" position; at this time, deck 4 of S–1

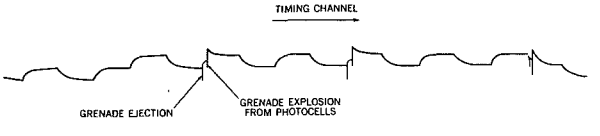

FIGURE 9.—Timer operation pulse train.

applies +28 volts through pin B of P–4 and J–4 to the photocell-amplifier filaments; and (3) apply +28 volts to pin E of J–2 to advance S–1 again to the "safe" position. (S–2 remains in the "arm" position.) Deck 4 of S–1 prevents application of power to the timer from either the remote source or the internal battery pack, making the timer safe for grenade loading. Two minutes before launch, power is again applied to pin D of J–2 to place both S–1 and S–2 in the "arm" position. Safety is maintained by the "start wire," the controlled switch S–4, and the grenade-terminal shorting plugs P–7, P–8, and P–9.

At lauch, the motion of the rocket will disengage the umbilical plug P–2 (Figure 8) and cause the start wire to remove the pullout pin from S–4. The closing of S–4 energizes the timer motor, which in turn drives a notched cam that opens and closes microswitch S–3. Voltage pulses produced by the action of S–3 rotate S–2 clockwise one step per second. At +14 seconds S–2, deck 2, provides a pulse to S–1, causing it to advance clockwise by one increment. (The time of 14 seconds was selected because the rocket is not under power at this time, and the vibration is less severe.) At approximately +30 seconds of motor operation, the rotation of the threaded motor-shaft actuator disengages grenade-terminal shorting plugs P–7 and P–8 from receptacles J–7 and J–8. At +38 seconds (14 seconds +24 seconds), S–1 is again advanced by a pulse from S–2, deck 2; in this position, S–1 completes the circuit to deck 4 of S–2. At +40 seconds, deck 4 contacts close the circuit to grenade No. 1, causing it to be ejected and detonated. S–1 and S–2 continue to advance through each position until all 12 grenades have been fired.

DOVAP Tracking Transponder

The DOVAP T–10A tracking transponder (Fig. 4) consists of a receiver, frequency-doubler, 2 watt transmitter, and 30-kc FM subcarrier-oscillator (Fig. 10). It operates on power supplied by the rechargeable battery pack. The transponder, part of the Doppler tracking system, operates in conjunction with the ground stations to provide accurate velocity measure-

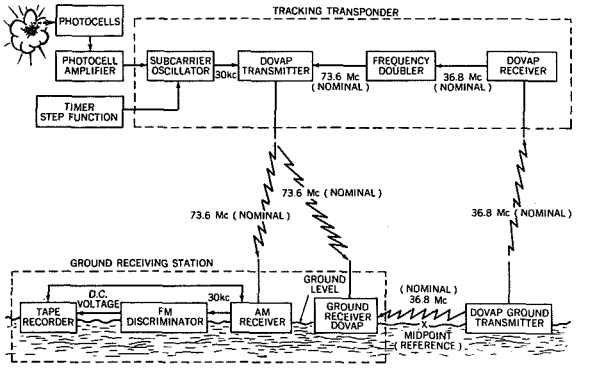

FIGURE 10.—DOVAP tracking transponder operation.

ments essential in determining the exact position of the grenade explosions.

A continuous-wave 36.8-Mc signal is beamed to the transponder receiver from the ground transmitter. The received signal is doubled (73.6 Mc) by the frequency-doubler and retransmitted to the ground receiver. If the frequency received from the rocket were exactly twice the frequency of the ground transmitter, no relative velocity would exist between the ground receiver/ground transmitter midpoint and the rocket; the amount by which these two frequencies deviate from an exact value of two is a measure of the relative velocity between the rocket and the ground station. The frequency difference between the two signals is recorded by the ground stations for analysis after the flight.

The DOVAP transponder contains a single-channel telemetry system, consisting of a 30-kc±15 percent FM subcarrier-oscillator used to amplitude-modulate the carrier. The frequency of the subcarrier-oscillator contains the telemetered information, consisting of amplified electrical signals caused by the response of the photocells on the rocket to the infrared light from the grenade explosions, plus a voltage-step function (Fig. 9) which monitors grenade-timer switch positions (Fig. 7).

Two pairs of antennas are used with the tracking transponder, one for transmitting and one for receiving. They are not included in the payload, but are attached to the propellant section of the second-stage rocket by means of steel straps (Fig. 1). Each antenna is approximately

33 inches long by 2 inches wide, and protrudes from the rocket approximately 1½ inches. Each antenna is covered by a molded glass-fiber housing to protect it from the flight environment.

Infrared Photocells and Telemetry Amplifier

Three infrared Kodak Ektron photocells (PC–1, PC–2, and PC–3) are located in three equally spaced ports 120 degrees apart on the side of the rocket, to detect the flashes of the grenade explosions. The photo cells are connected to transistors Q–1, Q–2, and Q–3 of the photocell amplifier (Fig. 7). The photocell amplifier operates on power supplied by a dry cell described later. The transistors offer a high-input impedance to the photocells, providing optimum coupling to prevent attenuation of the very small electrical signals generated by the grenade flashes. These flash signals are amplified and coupled through resistors R–2, R–4 and R–6 to a voltage-differentiating circuit composed of resistors R–7 and R–8 and capacitor C–1. A sharp differentiated pulse is applied to pin B of P–4 and fed to the SCO of the tracking transponder through receptacle J–1. The amplified signals modulate the 30-kc frequency of the SCO (Fig. 10). In addition, deck 9 of S–2 provides a voltage-step function that reflects timer advances and modulates the SCO, allowing for continuous monitoring of the timer operation. The modulated SCO frequency, in turn, amplitude-modulates the DOVAP carrier frequency, permitting the intelligence to be transmitted to a ground station.

Power Supply

Power requirements for the rocket-grenade experiment are furnished by three separate battery supplies. The timer and transponder equipment are powered by silver-zinc-alkaline batteries, the photocell amplifier by a dry-cell battery. A battery of five HR–3 silver-zinc cells located in the transponder section (Fig. 4) supplies the approximately 8 volts required for transponder operation. Nineteen HR–1 silver-zinc cells, mounted in a ring encircling the transponder, furnish the timer with approximately 28 volts (Fig. 4). One dry-cell battery provides approximately 24 volts for the photocell amplifier.

The silver-zinc-alkaline batteries are compact, lightweight, rechargeable Yardney HR–1 and HR–3 Silvercel [1] units (Fig. 11). These units are high-rate discharge cells having a life expectancy of approximately 10 to 20 charge-discharge cycles or an average wet life of 6 months. Silver (+) and zinc (−) are employed as electrodes, with a strong solution of potassium hydroxide (KOH) as the electrolyte.

As the Silvercel units may swell slightly perpendicular to the electrode face upon servicing, it is recommended that the units be assembled in the battery containers before servicing. Complete servicing, operation, and maintenance procedures are furnished with the batteries (Reference 6). Temperatures as low as −55° F will not permanently harm the units, although prolonged exposure to temperatures above 110° F is harmful. The units are relatively free from hydrogen explosion hazards when used in closed, non-ventilated areas. However, sufficient hydrogen to cause an explosion can be generated by defective or badly overcharged cell.

Flight Performance Instrumentation

During the initial phase of the experiment, flight-performance data were needed to assist in evaluating rocket problems. The performance instrumentation (Fig. 12) was installed in place of the three center grenades; the rack shown in the photograph houses sensors and associated circuitry to measure the flight environment of the payload. Electrical output of these sensors is transmitted by the single-channel DOVAP telemetry. Time-sharing of this telemetry is accomplished by a 24-segment commutator rotating at 10 revs/sec.

Parameters most frequently monitored during these tests were nosecone temperature, axial acceleration, vibration, and angle of attack. The resulting data were used to evaluate grenade-ejection problems, payload variations, and possible modifications.

[1] Proprietary name for Yardney Co. silver-zinc-alkaline power units.

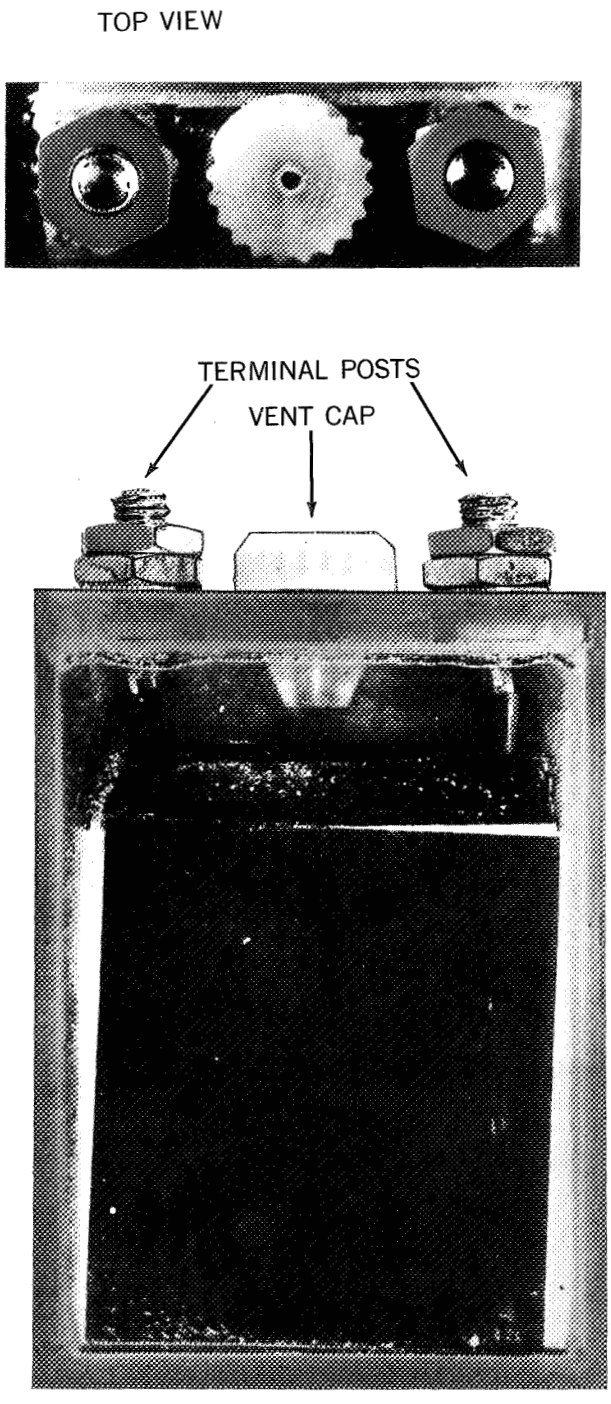

FIGURE 11.—Silvercel battery.

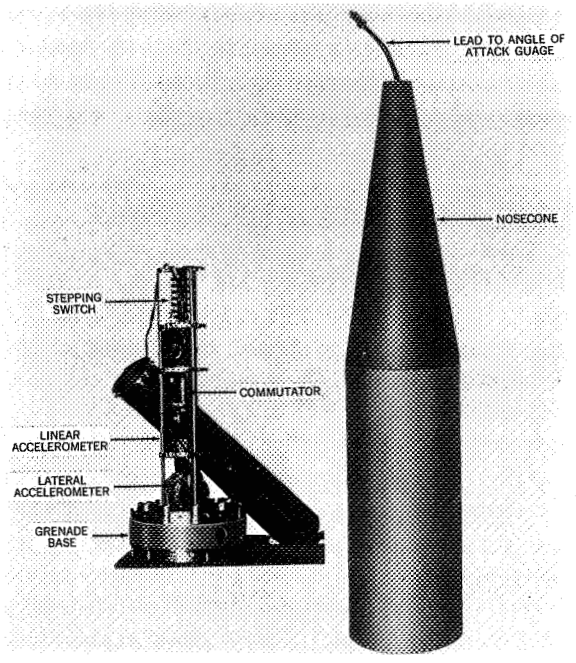

FIGURE 12.—Flight performance instrumentation.

Ground-Based Instrumentation

Sound-Ranging System

A block diagram of the sound-ranging system is shown in Figure 13. References 7 and 8 describe the instrumentation, installation, operation, and research activities required for a typical experimental sound-ranging system. The system consists of at least five microphones (arranged in a symmetrical pattern, as shown in Fig. 14), a recording oscillograph, a tape

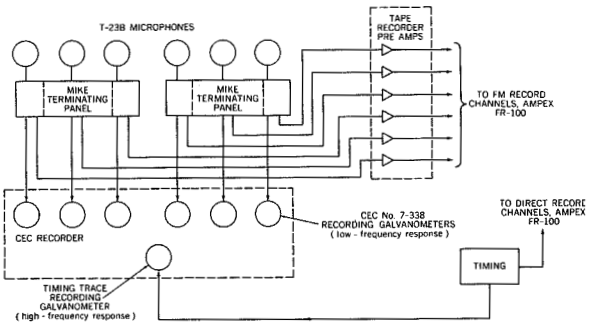

FIGURE 13.—Block diagram of sound-ranging system.

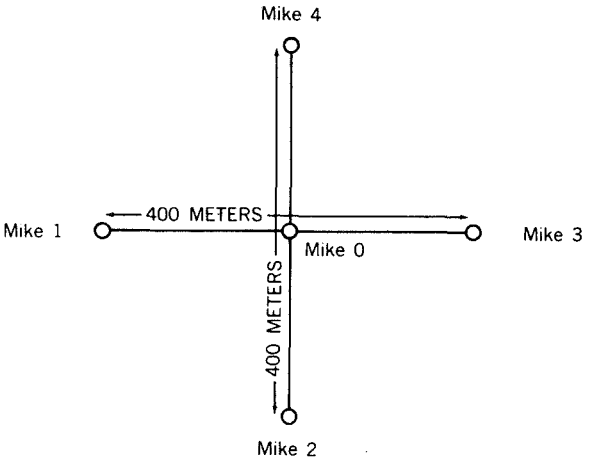

FIGURE 14.—Microphone array.

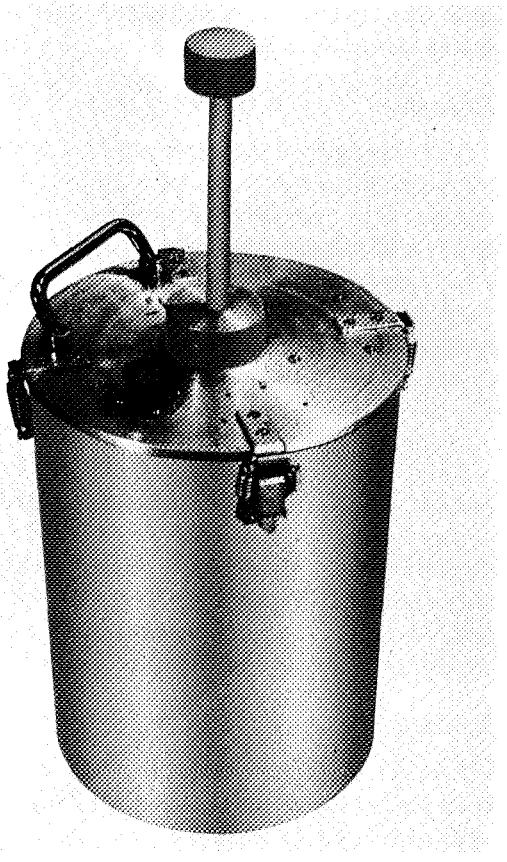

FIGURE 15.—T–23B microphone.

recorder, and appropriate amplification, timing, and interconnecting circuitry. The microphones are modified U.S. Army Signal Corps Type T–23B, a hot-wire suitable for sound-

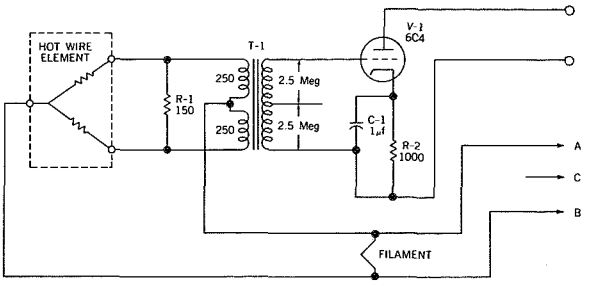

FIGURE 16.—Schematic diagram of modified T–23B microphone.

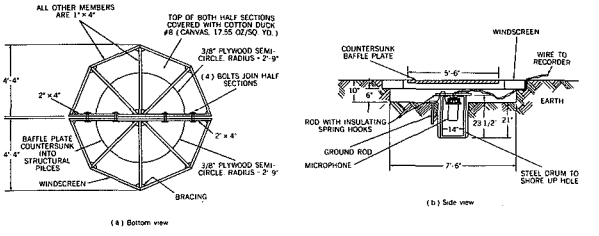

FIGURE 17.—Microphone ground installation.

ranging because of its sturdiness and low-frequency response. The microphones should be—as nearly as possible—in a horizontal plane; the distances between them should be nearly equal and approximately 400 m. Figure 15 shows the physical appearance of the microphone, and Figure 16 is a schematic diagram of the microphone as modified for this application. To reduce noise level due to wind and atmospheric pressure fluctuations, the microphones are mounted below ground level and covered by a large canvas screen and a wooden baffle plate. Figure 17 shows typical microphone-installation requirements. A terrain vegetated with underbrush or trees several feet high shielding the ground surface uniformly from the wind is best suited for this installation.

The oscillograph, a Consolidated Engineering Corp. 5–119, 36-trace mirror-galvanometer type, records by means of a light beam reflected on a moving strip of sensitized paper. It serves as a backup recorder and also provides an immediately available record of events. A typical record is shown in Figure 18. An Ampex FR–100 multichannel tape recorder is used as a primary recorder. The low-frequency (4–20 cps) output signals from the microphones are recorded by means of the

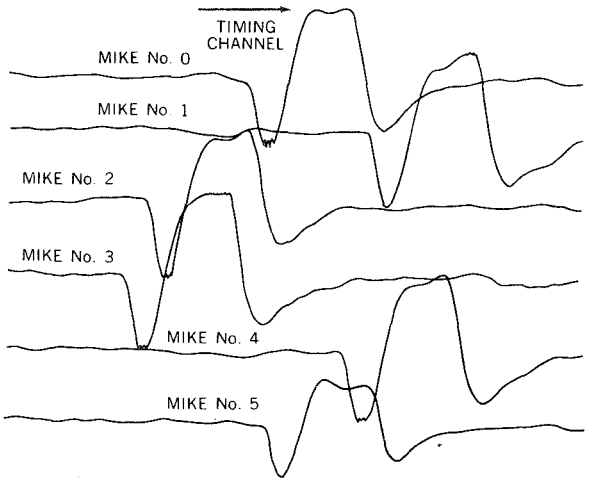

FIGURE 18.—Typical sound-ranging record.

tape recorder's FM record electronics. For exact analysis of the low signal-to-noise acoustic waves generated by the higher altitude grenade bursts (above 70 km), the tape records may be played back through a bandpass filter peaked at the optimum frequency (approximately 4 cps).

Accurate timing is provided by a Beckman/Berkley-type 7360 timer or other suitable means. Filament power is furnished by a pair of series-connected 12-volt automobile batteries; plate power for the microphone plate circuit is furnished by a Lambda Model 29 regulated power supply. A separate power supply is used for each microphone circuit to eliminate crosstalk.

The microphones are connected to two microphone terminating panels, three to each panel (Fig. 13). The terminating panel contains an array of dc amplifiers that provide impedance matching and input signals to the oscillograph and the tape-recorder preamplifiers; the dc amplifiers match the microphone impedance to a regulated 28 ohms, providing a balanced line to the recorders. The output of each microphone is recorded as a separate trace on the photographic paper. The dc amplifiers also decouple the B+ voltage from the galvanometer circuit.

Ground Flash Detector

A ground flash detector, consisting of a lead sulfide photocell mounted behind a germanium filter at the focal point of a parabolic mirror, is capable of detecting the grenade bursts even in daylight. The mirror axis is pointed in the direction of the anticipated grenade explosions to permit the photocell to detect the emitted infrared radiation. Since the instrument encompasses a field-of-view of approximately $20°\times20°$, it can detect all explosions without change of orientation. The output of the photocell is recorded along with a timing trace to constitute an accurate record of the time of each grenade explosion. The disadvantage of this system, as with any optical or sight system, is that a clear sky is required in the vicinity of the rocket's trajectory. In the present series of grenade experiments, therfore, it is used only as a backup to the rocketborne flash-detector system described previously.

Telemetry

The telemetry data is received on the ground by recording the demodulated Doppler tracking signal. The telemetry ground station consists of an AM receiver, an FM discriminator, and a tape recorder. The single-channel telemetry data containing grenade-flash times and timer-performance information is received in the form of an amplitude-modulated 73.6-Mc DOVAP signal. The AM receiver detects the frequency-modulated 30-kc intelligence from the 73.6-Mc carrier, transmitted by the DOVAP transponder, and feeds the 30-kc ±15 percent subcarrier signal to the discriminator where it is demodulated. This results in the voltage signals shown in Figure 9. The voltage signals are recorded by oscillogram, and the 30-kc subcarrier wave is recorded on magnetic tape.

Tracking

The DOVAP System, a continuous-wave tracking system utilizing the Doppler-frequency shift, provides a highly accurate method of determining the position of each grenade explosion by integrating the velocity of the rocket over the whole flight path. The rocket-grenade experiment can use DOVAP tracking in any of three combinations:

1. Three or more DOVAP receiving stations (Reference 9).

2. Single-station DOVAP (SSD) receiver with interferometer antenna array (Reference 10); or
3. Single-station DOVAP receiver using conventional antenna in conjunction with a ballistic camera (Reference 11).

In each instance, a continuous-wave transmitter of approximately 1 kw power is also required.

The following paragraphs describe the various DOVAP tracking systems; References 12, 13, 14 and 15 describe DOVAP data-reduction methods.

The Multistation DOVAP System consists of a transmitting station and at least three receiving stations. Each receiver uses the Doppler shift to define an ellipsoid surface through the rocket vehicle. The intersection of these three surfaces determines the vehicle position. At each DOVAP ground receiver, continuous comparison is made between two radio signals from the ground transmitter; one signal is transmitted directly to the receiver, the other is transmitted to the receiver via the rocket. Figure 19 shows a typical transmitter-rocket-receiver path for these systems. A nominal 36.8-Mc signal is sent to the rocket, its frequency is doubled (73.6 Mc) and retransmitted to a receiving station. The station has two receivers, one receiving the doubled-frequency signal from the rocket; the other receives the signal directly from the ground transmitter and doubles the frequency *after* reception. The signals are heterodyned, and the difference-frequency is obtained. The signal sent via the rocket generally experiences a Doppler shift due to the rocket's motion; thus, the difference in frequency obtained between the two receivers at the receiving stations is proportional to the time-rate of change of the transmitter-rocket-receiver path length. The known transmitter-receiver distance remains constant. Integration of the difference-frequency over the time of flight determines radial distance to the rocket.

A block diagram of a typical ground station is shown in Figure 20. An operational ground station generally uses two receivers to receive the 73.6-Mc signal from the rocket; one receiver operates through a lefthand circularly polarized helical antenna, the other through a righthand one. Each of the signals is independently heterodyned with the ground-transmitter signal, in order to obtain a measure of the component of the Doppler shift introduced by the roll of the rocket. The difference frequencies (resulting from heterodyning the signals from each helical antenna with the origi-

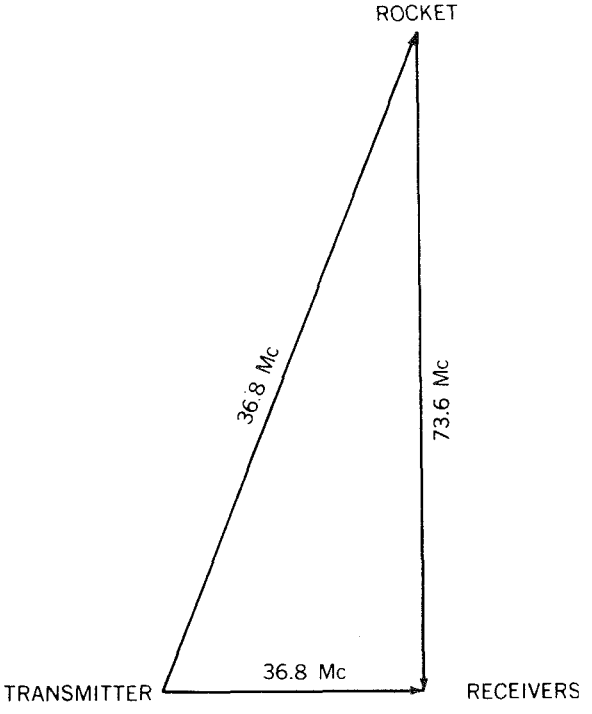

FIGURE 19.—Typical transmitter/rocket receiver path.

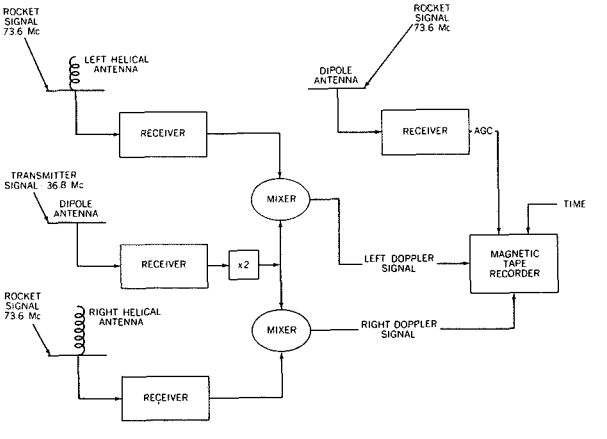

FIGURE 20.—Four-station DOVAP instrumentation.

nal signal) are recorded on magnetic tape along with a timing signal.

The difference frequencies are integrated over time for each receiver; by comparing the results produced by the lefthand and righthand polarized antenna at one station, the rocket's position can be defined as the surface of an ellipsoid of revolution whose foci are located at the receiving and transmitting stations respectively. If this integration is performed manually, it requires accurate counting of about 80,000 cycles for each receiver up to the peak altitude of the rocket—in the case of a 4-station experiment, 640,000 cycles. Three receiving stations (the intersection of three ellipsoids) theoretically will provide information sufficient to pinpoint the position of the rocket at any time; operationally, however, at least four stations are used, to statistically improve the accuracy of the solution. The accuracy of a four-station system is generally better than ± 15 meters with the rocket at an altitude of 90 km. Disadvantages of this system are the long baselines required between receivers (20–30 km) and the large number of cycles to be counted.

The DOVAP system yields the position of the center of the transponder antennas rather than of the grenade explosion. The grenade is designed so that the explosion occurs within less than 5 meters from the rocket, a negligible distance, and the location of the transponder antenna at the time of the grenade explosion can therefore be taken as the position of the explosion. In addition, roll rate of the rocket can be measured from the periodic fading of the signal received through a simple dipole antenna.

The Single-Station DOVAP (SSD) rocket-tracking system uses the Doppler effect measured at one receiving station to define one ellipsoidal surface, and a square array of antennas to define the direction cosines to the rocket by means of interferometer techniques. The Doppler frequency is obtained by the method described previously. The receiving station automatically compares the phase of the signals received at each antenna, and the direction cosines as well as the roll correction are thus determined electronically without resort to manual techniques. The SSD therefore eliminates the disadvantages of the multistation DOVAP mentioned above.

Figure 21 illustrates the instrumentation plan of the single Doppler-receiver station. A single circularly polarized turnstile antenna, instead of the lefthand and righthand helical antennas of the multistation DOVAP, is used to receive both the lefthand and righthand signals; the resulting signal is heterodyned with the doubled transmitter signal to produce twice the Dopler frequency, which is recorded on magnetic tape. In order to obtain a "quick look" at the range component of the trajectory, the signal is also fed through a tracking filter into an automatic cycle-counter that produces lists of cycle counts and time on paper tape.

The SSD system uses two continuous-phase interferometers, each of which measures and records a phase difference in the arrival of the signal from the rocket at two ground-receiver antennas. The instrumentation of the interferometer is shown in Figure 22. Two ground-receiver antennas located 214 feet apart in the north-south direction and two receiver antennas located 214 feet apart in the east-west direction (all located in a horizontal plane) form the interferometer antenna array. The SSD receiver is located in the center of the array (Fig. 23).

The signal from the rocket is considered to be a plane wave; the normals to the wavefront

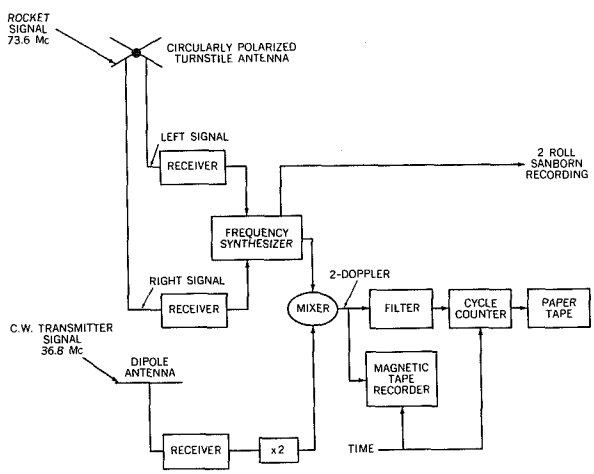

FIGURE 21.—Single-station DOVAP (SSD) instrumentation.

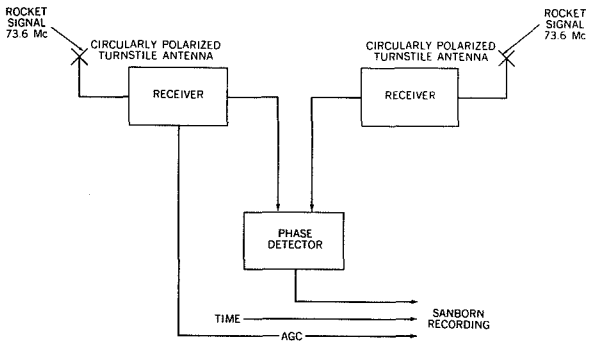

FIGURE 22.—Continuous-phase interferometer instrumentation.

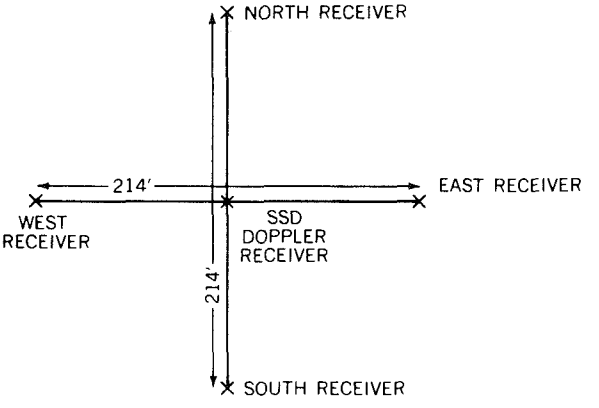

FIGURE 23.—Single-station DOVAP antenna array.

through the receivers can be considered as ray paths along which the signal has a sinusoidal variation. The ray paths from the rocket are parallel as they arrive at each pair of receivers. The signal is received at each receiver antenna, amplified, and combined in a phase detector which measures the difference in electrical phase of the two received signals. A recording is made of the phase difference between the output of each pair of receivers. The phase differences are a direct measure of the direction cosine of the wavefront. The accuracy of this system is comparable in the radial component to the accuracy of the multistation system, but is less in the direction cosines.

The Single-Station Doppler Ballistic Camera system consists of a single receiver station with one lefthand and one righthand circularly polarized helical antenna, and a ballistic camera. The light from grenade bursts is recorded on the photographic plate of the ballistic camera. This system can be used only at night when the sky is clear; its use is therefore limited by severe time restrictions on the conduct of the experiment.

The ballistic camera, a fixed-plate camera with a field-of-view of about 60°, is mounted with its optical axis pointed in the direction of the expected grenade explosions. Time exposures of f/8 or f/11 on infrared-sensitive plates (Kodak F–103) are generally used. Immediately before and after a rocket flight, an image of the star background obtained with a series of precisely timed exposures (within 0.1 sec sidereal) is taken on the same plate with the camera positioned precisely as for the rocket flight. The star trails with known celestial coordinates serve to determine the direction of the optical axis of the camera. Direction cosines for the grenade explosions can be derived by measuring the positions of the grenade-flash images relative to the star trails; the direction cosines from the ballistic camera for each flash of light define a straight line passing from the camera location to each flash. The range sum derived from the Doppler-cycle count at each flash time defines an ellipsoid of revolution, with foci at the transmitter and receiver and with the major axis equal to the range sum obtained from the cycle count, the flash position being located on the surface of the ellipsoid. Each flash position is obtained by solving for the intersection of the ellipsoid and the given straight line, the solution representing the space positions of the light flashes (Reference 16).

Ballistic-Camera Tracking. A minimum of two ballistic cameras will provide an accurate and sufficient method of determining grenade-explosion positions in experiments that do not employ electronic-tracking systems. Grenade-explosion positions are determined by locating two or more ballistic cameras along a baseline exceeding 20 miles (Fig. 24); each camera is positioned to photograph the grenade bursts against a known star background. Grenade-burst coordinates are obtained by determining direction cosines to the grenade explosions at each camera site and intersecting the lines-of-view. Although only two cameras are necessary, an array of four is generally used to

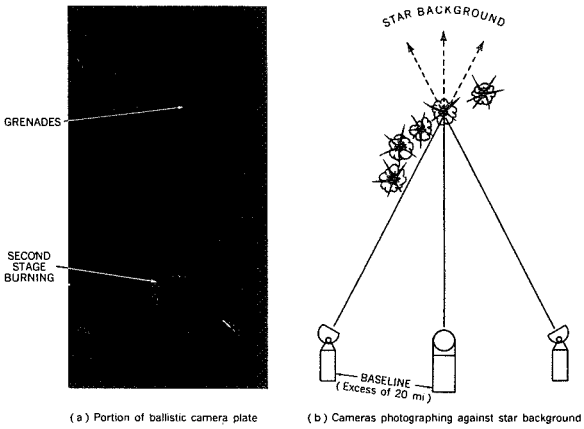

FIGURE 24.—Ballistic camera tracking.

(a) Portion of ballistic camera plate.
(b) Cameras photographing against star background.

improve the statistical accuracy of the solution. Disadvantages of this method of determination are the requirements for night operation, the need for clear weather, and the baseline length required between cameras for accurate measurements.

Radar Tracking, an alternate means of obtaining rocket trajectory, is ordinarily used in conjunction with, and as a supplement to, other tracking systems; however, if sufficiently accurate, it may be used to determine grenade-explosion coordinates. Several radar data-acquisition systems are used to perform various functions in the rocket-grenade experiments. These systems include: permanently installed (modified) SCR–584 radar; mobile (van-mounted) SCR–584 radar; Mod II SCR–584 radar (extensively modified); AN/FPS–16 radar; and long-range S-band radar (SPANDAR). In addition to the data-acquisition radar systems, an AN/FPS-12 medium-range surveillance radar is used for range-safety clearance (sea and air traffic). Functions and principal characteristics of the various data-acquisition radar systems are described in the following paragraphs; additional details may be found in Reference 17.

The SCR–584 radar systems are essentially World War II gun-laying S-band radar systems modified for missile tracking. The permanently installed SCR–584 modifications include automatic range tracking, increased output power, a larger antenna reflector, a data-recording system, a boresight camera, and a master-slave range system. The system operates over a frequency range of 2,800 to 2,900 Mc with a normal peak power output of 400 kw. The maximum beacon-tracking range (using an active radar beacon on the rocket) is 384,000 yards; the maximum skin-track range (no active radar beacon) is 62,000 yards (for a 1 m^2 target).

The mobile SCR–584 is essentially standard, the only modification being a change in the range system to include automatic range-tracking at a maximum range of 96,000 yards. These radar systems are used to obtain backup data during early portions of rocket flight. Their main purpose is to provide acquisition data and designation for other higher precision radars.

The Mod II SCR–584 is extensively modified and rehabilitated to perform automatic angle- and range-tracking. Mod II improvements include dual local oscillators for skin and beacon track, A-scope range presentation, intermediate servosystem for smoothing purposes, tunable S-band magnetron, output-power attenuation, multipulse and coding capability, vertical or horizontal polarization, and pulse-repetition frequency selection. The Mod II operates over a frequency range of 2,700 to 2,950 Mc with a normal peak power output of 250 kw. Maximum beacon-track range is 768,000 yards; skin-track range is 14,000 yards.

This radar provides recorded data as follows:

1. Synchro voltages: representing slant range, azimuth, and elevation angles
2. Potentiometer voltages: representing slant range, and sine and cosine functions of azimuth and elevation angles
3. Precision digital data: representing slant range, azimuth, and elevation angles.

The Mod II provides real-time position data for range safety, and acquisition data for other equipment. Like the SCR–584, its accuracy is not sufficient for position determination of the grenade explosions.

The AN/FPS–16 radar is a high-precision C-band monopulse tracking radar designed and built for missile-range instrumentation. The AN/FPS–16 is the only radar described here

that is sufficiently accurate to determine grenade-explosion coordinates. The AN/FPS–16 has a frequency range of 5,400 to 5,700 Mc with a tunable magnetron, and a fixed frequency of 5,500 Mc with a fixed magnetron. Normal power output, using the tunable magnetron, is 250 kw, or 1 megawatt with a fixed magnetron. The system has a maximum beacon-tracking range of 1,000 km and a skin-track range of 260 km (with a 1 m^2 target).

The AN/FPS–16 radar, in addition to synchro and potentiometer voltages and precision digital data, provides real-time present-position analog data for use in range safety.

The long-range S-band radar (*SPANDAR*) is a high-power conical scan-tracking radar employing a 60-foot parabolic reflector. The system has a frequency range of 2,700 to 2,900 Mc with a peak power output of 5 megawatts. The beacon-tracking range is 8,000 km, and the estimated skin-tracking range (for a 1 m^2 target) is 1,000 km.

The system includes a parametric amplifier in the receiving system and digital-data system. As a backup, it is used in conjunction with other tracking equipment in the rocket-grenade experiment.

METHOD

General

In the rocket-grenade experiment, average atmospheric temperatures and winds for the interval between two high-altitude grenade explosions are determined by measuring exactly the time when each grenade explodes the time when each soundwave arrives at various ground-based microphones, and the position of each grenade explosion. The method can be expanded to n—1 data points for n explosions: thus, the greater the number of grenades carried aloft by the rocket, the greater the number of data points for determining temperatures and winds.

Besides the initial parameters—angles of arrival of the sound wavefront at the center of the ground-microphone array; the times of explosion of the "upper" and "lower" grenades; and the position coordinates of these grenades—certain additional data must be available to facilitate the computation of temperatures and winds. These are: a measurement of temperature (within $\pm 0.25°$ C) at the ground in the vicinity of the microphones; the surface-wind vector in the same area (within ± 2.5 m/sec); as well as standard radiosonde observations of temperature in the general area of the experiment, up to about the altitude of the lowest grenade. If, in addition to this, a measurement is available of pressure or density at the surface, profiles of pressure and density may be calculated up to the altitude of the highest grenade explosion. An exact geodetic survey of all ground-station locations is also required.

The location of each microphone in relation to all others must be known within ± 0.2 meter. The precision of the survey for the other (non-acoustic) ground system varies with the tracking system used, but generally the relative location of each element of each tracking system (for example, DOVAP antennas) must be known within ± 0.5 meter. As the DOVAP tracking system in particular operates on the principle of tracing the rocket's trajectory back to its origin (the launcher), the rocket launcher must be included in this survey.

If a ballistic-camera system is used, an absolute survey is required in addition to the relative one mentioned above; the position of each camera must be known within about 30 seconds of latitude and longtiude. An absolute time measure must also be provided (within ± 0.1 sec) during exposure of the star trails. For all other systems, relative timing must be provided at all recording stations, with a precision of 0.005 sec over the period from launch to the time of soundwave arrival (usually 500 sec), and with a precision of 0.0005 sec at the sound-ranging station only during the period of each soundwave arrival at the microphone array (usually 1 sec).

Determination of Initial Parameters

Times and Positions of Explosions

The times of grenade explosions are read directly off the records of the rocketborne or ground flash-detector outputs. Once these times are known, the grenade coordinates may be read off or interpolated from trajectory tables

produced by the various tracking systems. If FPS–16 radar tracking is used, the trajectory can be obtained in the form of punched cards or digital magnetic tape; for all other tracking systems, more or less laborious manual steps (such as reading ballistic-camera plates or integrating DOVAP cycles) will be necessary to produce a trajectory (refer to section on tracking).

Angles of Arrival of Soundwaves

Direction cosines of the sound wavefront are mathematically derived from the times of arrival at each microphone. These times are read off the sound-ranging records. Since the position of each microphone is known, a plane or spherical wavefront is analytically fitted through the set of spacetime microphone coordinates.

A least-square solution for a plane wave may be derived from the arrival times and coordinates of more than 3 microphones. An array is shown with the wavefront at time $t=0$ passing through the microphones in Figure 25. Microphone 0 is chosen as the origin of the righthand Cartesian coordinate system. All coordinates and times are referenced to microphone 0, and it is assumed that the time of passage of the wavefront through microphone 0 is measured precisely. The distance r_i from microphone i to the wavefront should thus be: $r_i=c_0t_i$ where t_i is the observed time of arrival of the soundwave at microphone i and c_0 is the speed of sound on the ground. The direction cosines for the wave normal can be obtained from a least-square bit of the wavefront tangent to all spheres r_i.

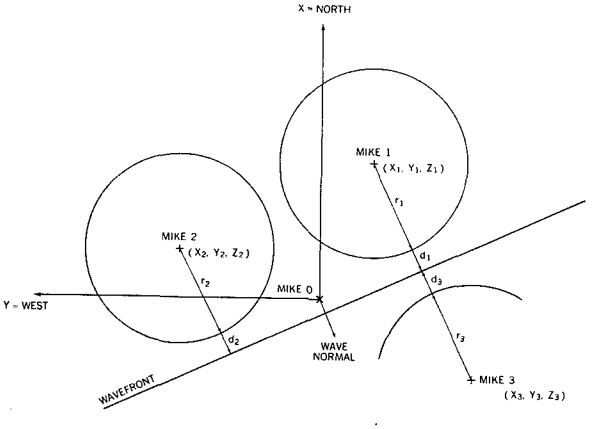

FIGURE 25.—Pictorial representation for fitting the wavefront.

The normal equations of the least-square solution are obtained from the following analytic expression for the distance d_i between the plane wavefront and the surface of a sphere of radius r_i around microphone i with the coordinates $(X_iY_iZ_i)$; d_i is measured along the direction of the normal to the plane:

$$d_i=X_i\alpha+Y_i\beta+Z_i\gamma-r_i, \tag{1}$$

where ($i=1, 2, \ldots, 5$) and α, β, γ are the direction cosines of the wave normal. The best fit for the plane wave is obtained when the sum of the squares of the distances d_i is a minimum; i.e.,

$$\frac{\partial\sum d_i^2}{\partial a}=\frac{\partial\sum d_i^2}{\partial\beta}=0. \tag{2}$$

Since

$$\alpha^2+\beta^2+\gamma^2=1, \tag{3}$$

d_i in Equation 1 becomes a function of α, β and the known coordinates X_i, Y_i, Z_i, and r_i only. Using Equation 1 and summing up for all microphones ($i=1, 2, 3, \ldots$), solutions are obtained for the two unknowns α and β from the two equations (Equation 2), and the solution for γ from Equation 3.

By solving these equations for the direction cosines, the plane wave through microphone 0 is uniquely determined, considering that the wave must travel in a downward direction. The wavefront may be more conventionally expressed in terms of elevation and azimuth angles, rather than in terms of direction cosines:

$$\phi=\frac{\beta}{\alpha},\quad e=\pi-\arccos\alpha,$$

where e is the elevation angle of the sound source and ϕ the azimuth angle counted counterclockwise from north to the direction from which the sound arrives. As a further refinement, a spherical wavefront may be fitted to the microphone coordinates X_i, Y_i, Z_i, r_i; this method is described in Reference 18.

The fitting of the wavefront is a lengthy manual computation because the number of

microphones is always greater than four and the number of explosions in any firing is greater than 10. The procedure has therefore been programed on a small digital computer (LGP–30) which can compute the wavefront for one explosion in less than 1 minute.

Computation of Temperatures and Winds

The method of calculating average temperatures and winds in a horizontal layer between the explosions G_1 and G_2, as illustrated in Figure 2, is described briefly below. It can be extended to the calculation of $n-1$ temperature and wind values between n explosions.

The soundwave traveling from grenade G_1 to the microphone is displaced by the horizontal wind blowing between the level of grenade G_1 and the ground. This displacement (the vector quantity $\bar{v}_1$) is proportional to the time t_1 that the wave spends in the medium between the grenade and the ground. The same consideration holds for the soundwave from grenade G_2, where the displacement $\bar{v}_2$ is composed of a term $\bar{w}\tau$ (the product of $\bar{w}$, the average horizontal-wind vector in the layer between G_2 and G_1, and τ, the time the soundwave spends in this layer) and a term $\bar{v}^*$ (the displacement of the wave from G_2 due to winds below G_1):

$$\bar{v}_2=\bar{w}\tau+\bar{v}^*. \tag{1}$$

The time t_2 elapsing between the explosion of G_2 and the arrival of the sound from G_2 at the ground may be written as

$$t_2=\tau+t^*, \tag{2}$$

where t^* is the time the soundwave from G_2 spends in the medium below the altitude of G_1.

Generally, the approximation

$$t^* \sin e_2=t_1 \sin e_1 \tag{3}$$

will hold, where e_1 and e_2 are the average elevation angles along the soundpath from G_1 and G_2, respectively. Because of the proportional relationship between the $\bar{v}$'s and t's,

$$\bar{v}^* \sin e_2=\bar{v}_1 \sin e_1. \tag{4}$$

The terms t_1 and t_2 are measured quantities, and $\bar{v}_1$ and $\bar{v}_2$ can be calculated from the exact coordinates of the grenade explosions, the temperature and wind field below G_1, and the angles at which the soundwaves arrive at the microphone array. These parameters are measured. Thus, the unknowns $\bar{v}^*$, t^*, τ, and $\bar{w}$ can be calculated from Equations 1–4, and the average wind in the layer between G_1 and G_2 is determined.

After determining the wind in the layer, Snell's law may be used to compute c, the speed of sound in the layer between G_1 and G_2:

$$c \csc e_1+\bar{w}_\phi=c_0 \csc e_2, \tag{5}$$

where c_0 is the speed of sound at the microphone array, and $\bar{w}_\phi$ is that component of the wind in the layer which acts within the plane of the soundpath trajectory from G_2. At the surface of the earth, the wind is assumed to be zero; e_1 is the average zenith angle of the soundpath from G_2 within the layer between G_1 and G_2, expressed by:

$$\cos e_1=\frac{H}{c\tau}, \tag{6}$$

where H is the difference in height between G_1 and G_2. Hence, c can be calculated from Equations 5 and 6. The temperature T in the layer is related to c by the equation

$$c=\left(\frac{C_p}{C_v}\frac{RT}{M}\right)^{1/2} \tag{7}$$

where R=universal gas constant, C_p/C_v= ratio of specific heats of the medium between G_1 and G_2, M=mean molecular weight of the medium. These parameters should be available from independent measurements, so that T can be calculated from Equation 7.

An error analysis (Reference 19) indicates that temperature errors generally are less than 1° K, and that the wind error is about 1 m/sec, if the error in determining the coordinates of the grenade explosions is less than 5 meters. The accuracy of determining the temperatures and winds is limited by the random errors inherent in measuring the arrival times of the low-frequency soundwaves at the microphones.

For explosions below 75 km, a time error of 2–3 milliseconds is probable, which will result in an uncertainty of the soundwave angle of about 0.1 degree. The resulting error for temperatures in this case will generally be less than $\pm 3°$ K; for wind speed and direction, the errors are about ± 5 m/sec and $\pm 15°$, respectively. For explosions at higher altitudes, sound arrivals at the ground may be so weak that arrival-time errors in some cases may be as large as 5–10 milliseconds. The resulting temperature errors may increase to about $\pm 10°$ K, while a wind-speed error of about 15 m/sec may be expected. The existence of vertical winds in the layer between G_1 and G_2 is not considered in these calculations, as the speeds of such winds are known to be negligible compared with the velocity of sound.

For grenade explosions at altitudes higher than 50 or 60 km, the calculations must allow for the fact that acoustic energy at these levels propagates as a shockwave rather than a soundwave over a substantial portion of its path (finite-amplitude effect). This correction is small and is described in Reference 20.

The highest altitude from which sound returns can be received, with present explosive charges and existing sound-ranging techniques, is about 90 km. The LGP–30 computer is used to derive temperatures and winds from the coordinates, arrival times, and explosion times. Computationally, the largest effort lies in the determination of $\bar{v}_1$ and $\bar{v}_2$, which is done by ray-tracing the soundwave up to G_1 and G_2, respectively. For error estimates, it is desirable to compute one data point several times under varying input conditions; here a high-speed computer is particularly useful. (A detailed description of this method of analysis is found in Reference 20.)

Derivation of Pressures and Densities

The analysis described in the preceding section yields an altitude profile of temperatures and winds as a direct result of the grenade-experiment measurements. The temperature profile—consisting of discrete points, each representing an average value for an altitude layer between grenade explosions—is used to obtain density and pressure profiles, provided the pressure or density is known at a given level at the bottom of the temperature profile. Pressure is calculated by means of the following relation, derived by combining the hydrostatic equation with the ideal gas law:

$$ln p_i = ln p_{i-1} + \frac{g(h_i - h_{i-1})}{R(T_i - T_{i-1})} ln \frac{T_i}{T_{i-1}} \qquad (8)$$

where R is the universal gas constant, g is the gravitational constant which is assumed to vary inversely with the square of the altitude, and p_i the pressure at the altitude h_i at which the temperature T_i has been measured. The levels i can be chosen to represent the midpoint altitudes of each grenade-explosion layer.

The density ρ_i at the level i may then be derived simply from the pressure by using

$$\rho_i = \frac{p_i}{RT_i}. \qquad (9)$$

It is more accurate to derive density or pressure from a measured temperature profile, than to derive temperature from a measured density or pressure profile. The reason for this is that, in deriving densities and pressures, an integration must be performed over the temperature profile, which can be done with far more precision than the differentiation involved in the later process.

REFERENCES

1. Bandeen, W. R., and Kaschek, G. R., "A Wind Noise Reduction Installation for Sound-Ranging Microphones," U.S. Army Signal Research and Development Lab. Tech. Memo. 1864, Fort Monmouth, N.J., 1957.
2. Thomas, E. S., "Dispersion Analysis for Nike-Cajun Sounding Rocket," Aerojet General Corp. Rept. No. 1628, Azusa, Calif., June 29, 1959.
3. Lewis, J. V., "Effect of Wind and Rotation of Earth on Unguided Rockets," Ballistic Research Labs. Rept. No. 685, Aberdeen, Md., March 1949.
4. Daw, Harold A., "A Wind-Weighting Theory for Sounding Rockets Derivable From the Rocket Equations of Motion," New Mexico State Univ., Physical Science Lab., Univ. Park, N. Mex., Nov. 5, 1958.
5. Barr, W. C., Burt, J. W., and Nordberg, W., "A Study of Structural Problems Concerning Nike-Cajun Rockets," U.S. Army Signal Research

and Development Lab., Fort Monmouth, N.J., Jan. 15, 1959.
6. "Servicing and Operation Instructions for the Yardney Silvercel Battery," Yardney Electric Corp., N.Y., June 1961.
7. DEAN, E. A., "A Sound-Ranging System for the Rocket-Grenade Experiment at Wallops Island, Virginia," Schellenger Research Lab., Texas Western College, El Paso, Tex., September 1960.
8. "Ground Support and Data Analysis and Associated Research and Development for the Rocket-Grenade Experiment, July 16, 1960–September 15, 1962," Schellenger Research Lab., Texas Western College, El Paso, Tex., Final Rept., September 19 2.
9. ZANCANATA, H. W., "Ballistic Instrumentation and Summary of Instrumentation Results for the IGY Rocket Project at Fort Churchill," Ballistic Research Labs., Aberdeen, Md., Rept. No. 1091, January 1960.
10. SEDDON, C. J., "Preliminary Report on the Single-Station Doppler Interferometer Rocket Tracking Technique," NASA Technical Note D-1344, January 1963.
11. ALLEN, H., et al., Univ. of Mich., Dept. of Aeronautical and Astronautical Eng. Rept. No. 2387–51–P, Ann Arbor, Mich., March 1959.
12. HINES, P. B., "DOVAP Systems and Data-Reduction Methods," New Mexico State Univ., Physical Science Lab., Univ. Park, N. Mex., Jan. 31, 1962.
13. HINES, P. B., "A Simplified Data-Reduction Method for the Single-Station DOVAP System," New Mexico State Univ., Physical Science Lab., Univ. Park, N. Mex., July 31, 1962.
14. HINES, P. B., "A Data-Reduction Method for a Total Power Interferometer Mode Single-Station DOVAP," New Mexico State Univ., Physical Science Lab., Univ. Park, N. Mex., Oct. 1, 1962.
15. HINES, P. B., "Error Study," New Mexico State Univ., Physical Science Lab., Univ. Park, N. Mex., Oct. 1, 1962.
16. WHYBRA, M. G., Univ. of Mich., Dept. of Aeronautical and Astronautical Eng. Rept. No. 2387–57–T, Ann Arbor, Mich.
17. "Wallops Station Handbook, Volume II, Flight Test and Support Service Facilities," Wallops Island, Va., Sept. 15, 1961.
18. DEAN, A. E., "A Least Squares Solution to the Spherical Wave Sound-Ranging Problem," Schellenger Research Lab., Texas Western College, Interim Rept. NAS5–556, El Paso, Tex., November 1961.
19. NORDBERG, W., "A Method of Analysis for the Rocket-Grenade Experiment," U.S. Army Research and Development Lab. Tech. Memo. M–1856, Fort Monmouth, N.J., 1957.
20. BANDEEN, W. R., and OTTERMAN, J., "Temperature Correction in the Rocket-Grenade Experiment Due to the Finite-Amplitude Propagation Effect," J. Geophys. Res., 65(3), March 1960.

BIBLIOGRAPHY

BANDEEN, W. R., GRIFFITH, R. M., NORDBERG, W., STROUD, W. G., "The Measurement of Temperatures, Densities, Pressures, and Winds over Fort Churchill, Canada, by Means of Rocket-Grenade Experiments," U.S. Army Signal Research and Development Lab. Tech. Rept. 2076, Fort Monmouth, N.J., 1959.

NORDBERG, W., "Upper Atmosphere Soundings on the Island of Guam," U.S. Army Signal Research and Development Lab. Tech. Rept. 2078, Fort Monmouth, N.J., 1959.

STROUD, W. G., TERHUNE, E. A., VENNER, J. H., WALSH, J. R., WEILAND, S., "Instrumentation of the Rocket-Grenade Experiment for Measuring Atmospheric Temperatures and Winds," *Rev. Sci. Inst.* 26: 427–432, 1955.

WEBB, W. L., and MCPIKE, A. L., "Sound-Ranging Techniques for Determining the Trajectory of Supersonic Missiles," White Sands Signal Corps Agency Progress Rept. No. 1, White Sands Missile Range, N. Mex.

INVESTIGATION OF HF AND VHF ROCKET-BORNE SHROUD ANTENNAS

G. H. SPAID AND J. R. HAGERMEYER
Goddard Space Flight Center

The rocket-borne shroud antenna system originally developed by the Ballistic Research Laboratory for their 38 Mc/75 Mc DOVAP tracking system, has been modified at GSFC to meet the requirements of ionospheric experiments in which 24.5 and 73.6 Mc CW signals are transmitted from a rocket to the ground. These modifications were accompanied by significant improvements in matching and in pre-flight antenna adjustment techniques. In addition, it was found that shroud antennas could be used quite satisfactorily at frequencies lower than those used in the DOVAP system. Experimental results from two rocket flights showed that the antenna performance was in good agreement with theoretical predictions.

INTRODUCTION

The antennas to be discussed are currently a part of the instrumentation used by GSFC for the measurement of electron densities in the ionosphere. The rocket-borne propagation technique (*1*) used for this purpose is based upon the measurement of the dispersive Doppler effect of two harmonically related frequencies. The antenna used to radiate the lower of the two frequencies presents the more difficult problem. Experiments conducted in the past using various choices of the lower frequency (4.27 Mc, 7.75 Mc, and 12.27) have indicated that the quality of the ionospheric measurements does not deteriorate when the low frequency was raised from 4.27 Mc to 12.27 Mc. Furthermore, raising the low frequency leads to significant simplifications in both the antenna design and the data analysis.

Various types of extendable antennas (*2*, *3*) have previously been used successfully in the program. Although these antennas were electrically very satisfactory, the required extension introduced mechanical complications which resulted in reduced reliability. Another serious drawback in small payloads was the storage space required for these antennas. In view of the changes in operating frequencies for the CW propagation experiment to 24.53 Mc and 73.6 Mc, it appeared feasible to use modified versions of the DOVAP shroud antennas which require no extension and no payload storage space. The investigation of this problem led to improvements in the basic design of the antenna networks and the entire system was successfully tested in two rocket flights. The present report discusses in detail the modified antenna design and the results of the rocket tests. The modification included the use of a switched attenuator to prevent antenna breakdown (*2*) in the 60 to 100 km altitude range.

DISCUSSION OF THE STANDARD 76 MC DOVAP SHROUD ANTENNA

Mechanical Design

The 76 Mc shroud antennas (*4*) were designed and developed by the Ballistic Research Laboratories at the Aberdeen Proving Ground, Md., as a part of their DOVAP instrumentation for determining rocket trajectories during the IGY launchings at Fort Churchill, Canada. These antennas are normally mounted and phased to approximate a one turn rectangular

loop with the rocket axis in the plane of the loop and parallel to two sides of the loop. The loop is made of two shrouds clamped on opposite sides of the rocket. A flat copper foil conductor that has been formed into a semicircular shape is molded between two layers of a heat resistant fiberglas-plastic laminate. These shrouds are illustrated by Figures 1 and 2. The 76 Mc shroud is about

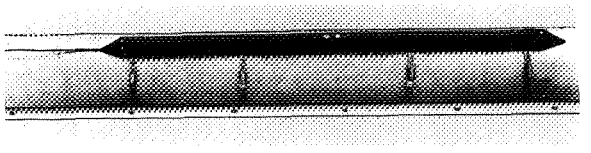

FIGURE 1.—73.6-Mc shroud mounted on a ground plane.

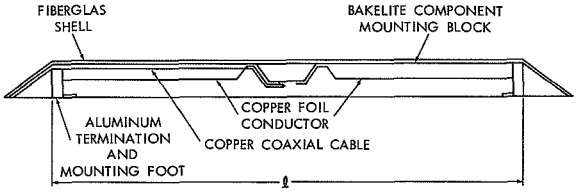

FIGURE 2.—Side view of shroud (cutaway).

38 inches long, the width is 1½ inches and it extends 1¼ inches from the rocket. The copper foil conductor is broken in the middle of the shroud to form two terminals. The ends are electrically connected to the rocket at each end of the shroud when the antennas are mounted on the rocket. A small solid copper shielded coaxial cable is mounted near and connected in several places to the inner surface of the copper foil from one end to the center of the shroud. Thus, in operation the cable shield is excited to the same potential as the conductor to which it is attached. A schematic of a shroud is shown in Figure 3.

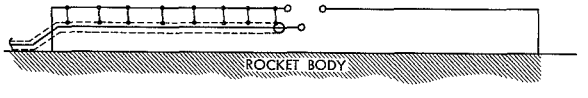

FIGURE 3.—Schematic of shroud.

A block of bakelite is provided at the center of the shroud to serve as a mounting for the components used to match the shroud terminal impedance to the coaxial cable.

Theory of Operation

For loop antennas in which the dimensions are small compared with a wavelength, the current is usually assumed to be constant throughout the loop and the radiation pattern is practically independent of the shape of the loop. The field strength is given by (*5*)

$$E=\frac{120\pi^2}{d}N(A/\lambda^2)I\cos\theta$$

where

E=field strength, volts per meter
d=distance, meters
N=number of loop turns
A=area of loop, square meters
λ=wavelength, meters
A/λ^2=area of loop, wavelengths squared
I=loop current, amperes
θ=angle with respect to the plane of the loop.

The shrouds on opposite sides of the rocket are oppositely phased so that the current flows in the same direction around the loop. For purposes of calculating field strength the effective area A of the antenna is taken to be the total area between the antenna and the rocket body or

$$A=2ld$$

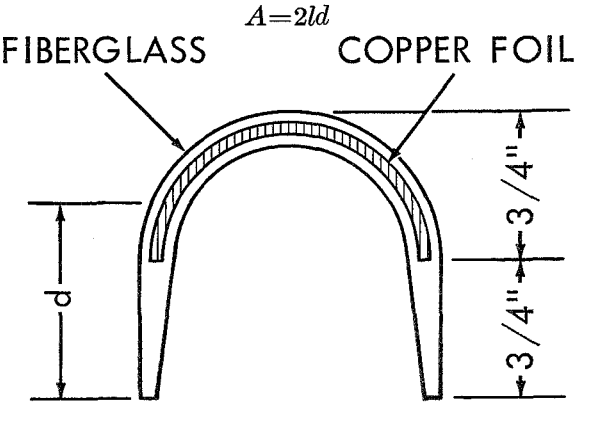

FIGURE 4.—Shroud antenna cross section.

where l is shown in Figure 2 and d is shown in Figure 4. For the 76-Mc shrouds l=83 cm and d=2.54 cm. Since the loop dimensions are small compared to one wavelength, the impedance of the shroud antenna can be represented by a small resistance in series with a large inductive reactance.

Matching Techniques

The 76-Mc shroud antennas are usually matched with a transformer whose secondary is in series with a capacitor across the terminals of the shroud; the transformer input winding is connected to the coaxial cable that terminates at the center of the shroud. Equal lengths of cable from each shroud transformer are connected in parallel at an L-matching network which matches the parallel impedance presented by the shrouds to a cable connected to a transmitter or receiver in the payload. The phase inversion required between the two shrouds is accomplished by reversing the transformer leads connected to the coaxial cable on one shroud of each set.

The standard method of adjusting the matching networks is accomplished after the complete antenna system has been mounted on a rocket. A test oscillator or transmitter with a power output of about 1 or 2 watts is first connected to each shroud through a directional coupler. Each shroud matching network is adjusted individually for a lowest standing-wave ratio. The shrouds are then fed in parallel and readjusted to compensate for the coupling between them. Finally, using a field strength meter as an indicator of phasing, the networks are readjusted for minimum VSWR and 180° phase difference.

This method of adjustment does not take advantage of the symmetry of the shrouds to eliminate the problem of coupling between them while making individual tuning and matching adjustments; the adjustments are not independent of each other. The use of test equipment that measures VSWR does not indicate what specific adjustment should be made to improve the match. In general, a trial adjustment is made and the test equipment is then used to indicate whether or not an improvement in adjustment has been obtained. Proximity of surrounding objects influence the accuracy of adjustment that can be obtained. The accuracy of the resulting adjustment obtained by this method can vary greatly, depending upon the skill and judgment of the technician.

Since the adjustments are often made on a loaded rocket there is a danger that the radio frequency power used (1 to 2 watts) will ignite the rocket propellant. Finally, when all adjustments are completed, there is considerable uncertainty as to the matching efficiency which has been achieved.

REDESIGN OF THE VHF SHROUD ANTENNA SYSTEM

In an effort to simplify the above adjustment procedures, the authors were led to consider the use of ground plane techniques which take advantage of the antenna symmetry. It was also found necessary to improve the circuit design since the original tuning controls were very difficult to adjust to the required accuracy. The first step in redesigning the antenna systems was to measure accurately the terminal impedance of the shroud antennas. The terminal impedance was found to be $8.61+j191$ ohms at 73.6 megacycles, which lends itself very well to matching with an L section network (7). The arrangement used to match the shroud to the cable is shown in Figure 5.

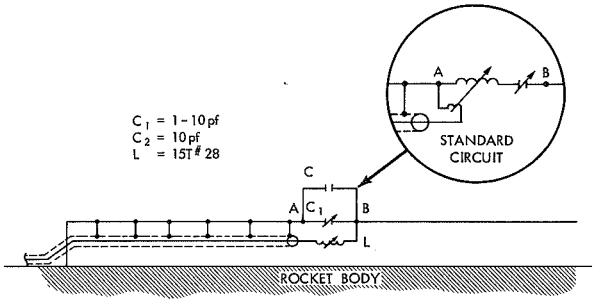

FIGURE 5.—Schematic of 73.6-Mc shroud.

Since the L section required to match the impedance corresponds to a loaded Q of only nine, the efficiency can be made high and adjustments are not critical. Since the redesigned matching network does not provide an easy method of inverting the phase at one of the shrouds, the phase shift is accomplished with a half-wave cable included in the matching network (Fig. 6) located between the two shroud cables and the transmitter cable.

Several measurements were made to determine the effects of removing and remounting

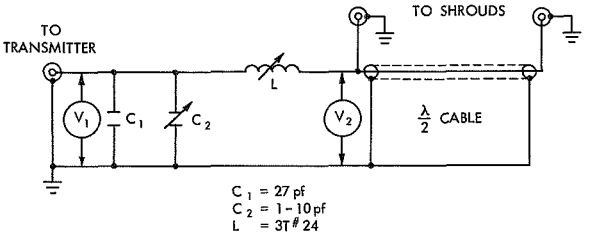

FIGURE 6.—73.6-Mc matching and phase inverting network.

the shrouds on the half-racket. In the worst cases the change in the value of the antenna terminal impedance was only about 5 percent. No variable is introduced by the matching network and half-wave cable shown in Figure 6 since they are adjusted with dummy loads. It is therefore practical to preadjust the entire antenna system before it is taken to the field and installed on the rocket. Built-in diode monitors reading voltages V_1 and V_2 (Fig. 6) are observed during the preflight check to insure that the final installation has been correctly done. A further advantage of the new design is in the elimination of the antenna matching transformer which leads to somewhat lower RF voltages near the antenna terminals, and helps overcome the problems of RF breakdown in the critical pressure range.

DESIGN OF THE 24.53 MC SHROUD ANTENNA SYSTEM.

Shroud antennas having the same physical cross section as the 73.6 Mc shrouds and an overall length of 70 inches were used at 24.53 Mc (Fig. 7). The terminal impedance measured on the ground plane was $1.24+j105$ ohms. These antennas were matched with two series capacitors (C_1 and C_2 of Fig. 8) adjusted to match the shroud impedance to the cable at the terminal common to both capacitors.

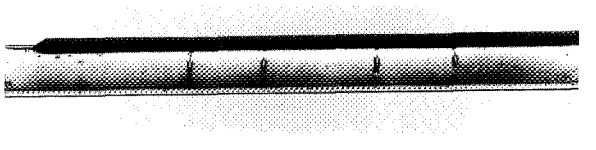

FIGURE 7.—24.53-Mc shroud mounted on a ground plane.

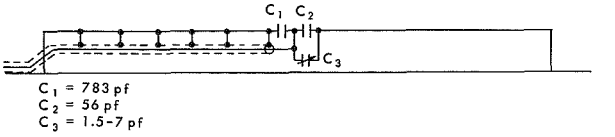

FIGURE 8.—Schematic of 24.53-Mc shroud.

The principal advantage of this design is the high efficiency of the matching network. The network also has the advantages of being simple and stable. The capacitor C in parallel with the cable is not extremely critical and is selected (or trimmed) rather than adjusted. Since the individual shroud-matching network does not provide for the 180° phase difference that is required, the phase reversal is accomplished in the matching box (Fig. 9) located between the two shroud cables and the transmitter cable. The 24.53-Mc antenna system is preadjusted, installed on the rocket and checked in a manner similar to that described for the 73.6-Mc antenna system.

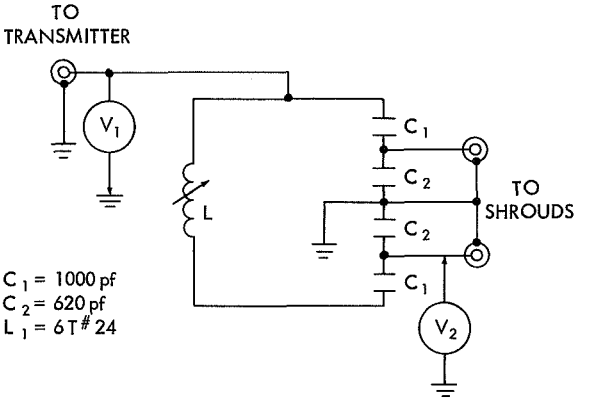

FIGURE 9.—24.53-Mc matching and phase inverting network.

PERFORMANCE OF ANTENNAS DURING THE ROCKET FLIGHTS

Nike-Apache 14.31

The graphs of received signal amplitude versus slant range for Nike-Apache 14.31 are given for both frequencies in Figures 10 and 11. Tests conducted in a vacuum chamber before the 14.31 flight had indicated that breakdown would not occur. However, breakdown did

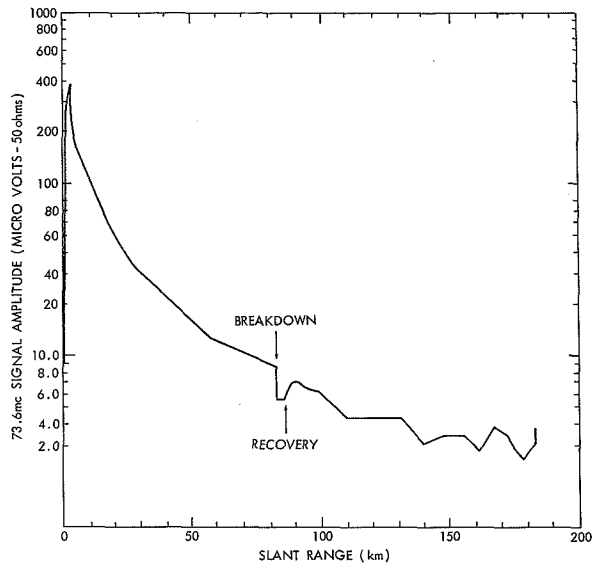

FIGURE 10.—73.6-Mc received signal amplitude for Nike Apache 14.31.

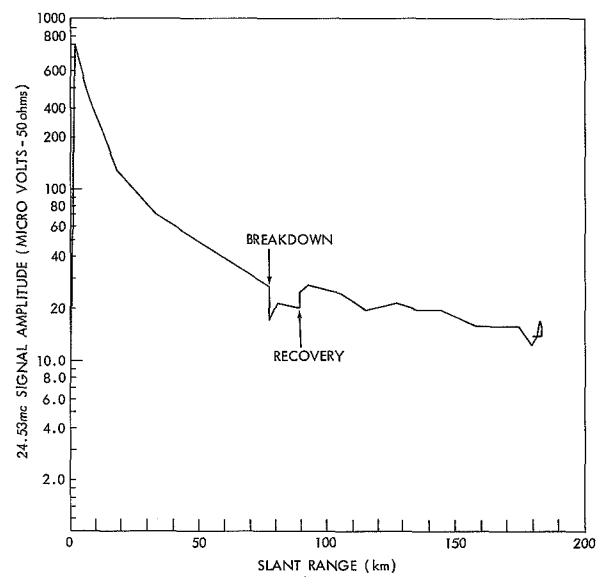

FIGURE 11.—24.53-Mc received signal amplitude for Nike Apache 14.31.

occur at both frequencies during the Apache 14.31 flight as indicated on the signal amplitude graphs. Richard (*8*) who had a similar experience at the Ballistic Research Laboratory suggested that an ionization source in the chamber would help initiate the discharge and make the test more realistic.

The rectangular notch beginning at 77 km and ending at 89 km slant range (74 km and 85 km altitude) on the 24.53-Mc graph is due to breakdown. The 73.6-Mc signal amplitude indicates breakdown began at 82 km and ended at 87-km slant range (78.5 km and 83 km altitude). Since the potential required for breakdown is a function of frequency and pressure (*2*), different ranges of breakdown as a function of altitude are expected for the two radio frequencies.

With the exception of breakdown, the antennas used on Nike-Apache 14.31 performed very successfully as predicted. The 24.53-Mc shroud antennas provided a field strength 14.3 db below a dipole driven at the same power level. Since this is the first time that shrouds have been used at 24.53 Mc there were no other independent measurements that could be used for comparison.

The 73.6-Mc shroud antenna provided a field strength 13.9 db below a dipole. This value was computed by assuming that the actual power delivered to the measured value of the shroud impedance was supplied to a dipole on the rocket. The field strength actually obtained from the shrouds was computed from the measured characteristics of the receiving antenna and the observed signal levels obtained. This value is in excellent agreement with the best flight results of standard 73.6 Mc shroud antennas used for SSD tracking (*9*) at Wallops Island, Va. However, this value disagrees with 76-Mc data on similar shroud antennas reported by Richard (*4*) of the Ballistic Research Laboratories, Aberdeen, Md.

Nike-Apache 14.32

The graphs of received signal amplitude versus slant range for Nike-Apache 14.32 are shown in Figures 12 and 13. To avoid breakdown, as observed in the Nike-Apache 14.31 (Figs. 10 and 11) approximately 5 db of attenuation was placed between each transmitter and its antenna system. A timer was provided to remove the attenuation after the rocket passed through the breakdown region. The resulting increase in signal amplitude is shown by the abrupt change at 102-km slant range.

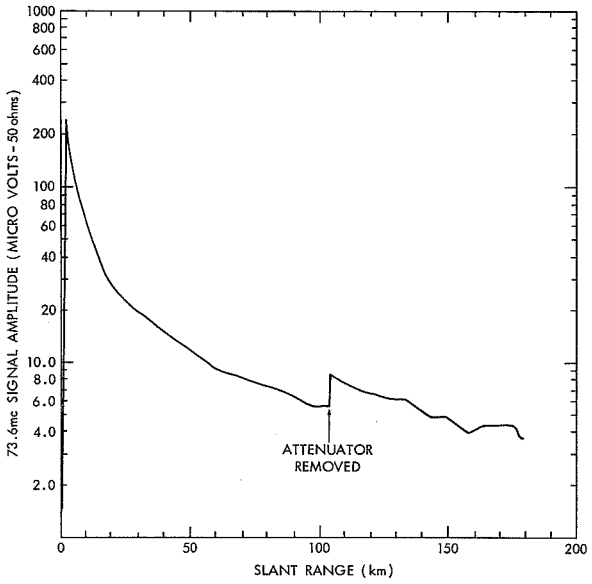

FIGURE 12.—Mc received signal amplitude for Nike Apache 14.32.

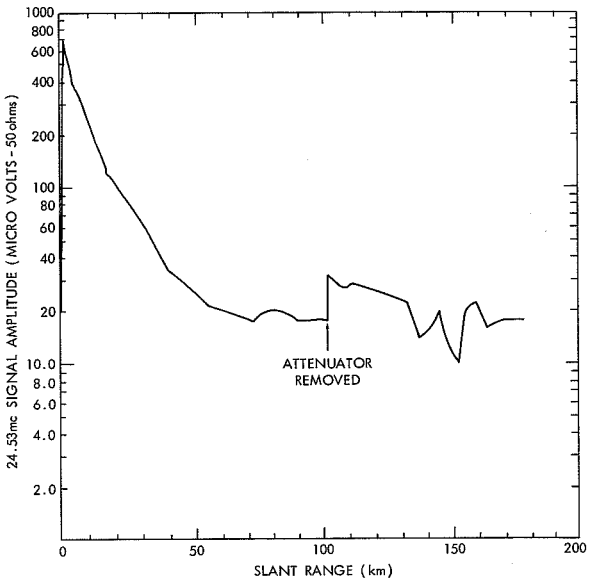

FIGURE 13.—24.53 Mc received signal amplitude for Nike Apache 14.32.

Computations, using the power-input to the shroud antennas in flight and the measured characteristics of the receiving antennas on the ground, indicated that the 24.53-Mc shroud antennas gave a field strength 14.8 db below a dipole. Similar computations indicated that the 73.6 Mc shrouds were 13.6 db below a dipole during this flight. These values are in close agreement with the values obtained for the Nike-Apache 14.31. The power level applied to the 73.6-Mc shroud antennas, after removal of the attenuation was about 3 db less than for 14.31 but a more directive receiving antenna was used on the ground.

CONCLUSIONS

The present investigation of the application of shroud antennas to the rocket-borne propagation technique resulted in these major accomplishments:

1. The operating frequency-range of the shroud antennas has been extended into the HF region. By doubling the physical length of the 73.6-Mc shrouds, the radiating efficiency obtained at 24.53 Mc was comparable with that obtained at the higher frequency. The longer antennas apparently did not affect the rocket performance, due probably to the fact that the frontal area, contributing to the rocket drag, remained the same.
2. Computations indicate that suitable changes in the geometry of the shrouds would result in antennas with the same efficiency for frequencies as low as approximately 10 Mc without appreciably increasing rocket drag.
3. Matching techniques have been developed that provide efficient performance and predictable signal levels.
4. A simple method has been successfully used to prevent RF breakdown at critical pressures.
5. Agreement between predicted and observed signal strength indicate that the terminal impedance of the shrouds have been adequately measured on a ground plane.
6. It was found that the performance of the shroud antennas can be predicted satisfactorily by small loop-antenna theory.
7. It was demonstrated that shroud antenna matching networks can be adjusted prior to installation on the rocket, and that only a simple built-in monitoring is required to insure proper adjustments at the time of the launching.

ACKNOWLEDGMENTS

The authors are indebted to Mr. J. E. Jackson and Dr. S. J. Bauer for many helpful suggestions during the preparation of this report. We wish to thank Mr. Billy Gammill of the New Mexico State University for helpful information supplied.

We also acknowledge several helpful discussions with Mr. Victor W. Richard of the Ballistic Research Laboratory.

REFERENCES

1. SEDDON, J. C., "Propagation Measurements in the Ionosphere with the Aid of Rockets." *J. Geophis. Res.* 58(3): 323–335, September 1953.
2. JACKSON, J. E., and KANE, J. A., "Breakdown and Detuning of Transmitting Antennas in the Ionosphere." Upper Atmosphere Research Report No. XXXVI, NRL Report 5345.
3. BAUER, S. J., and JACKSON, J. E., "Rocket Measurements of the Upper Ionosphere by a Radio Propagation Technique." NASA Technical Note D–1123.
4. RICHARD, V. W., "The Shroud Antenna." Ballistic Research Laboratory Memorandum Report No. 1283, June 1960.
5. TERMAN, F. E., Radio Engineer's Handbook, p. 813, McGraw-Hill Book Co., Inc.
6. TERMAN, F. E., Radio Engineer's Handbook, p. 774, McGraw-Hill Book Co., Inc.
7. BRUENE, W. B., "How to Design R–F Coupling Circuits," Electronics, Volume 25, No. 5, May 1952.
8. RICHARD, V. W., private communication.
9. GAMMILL, B., private communication.

Appendix

THE MEASUREMENT OF THE TERMINAL IMPEDANCE OF THE SHROUD ANTENNA

To measure the terminal impedance of the shroud antenna, advantage was taken of the symmetry of the set of shrouds. By mounting a shroud on a suitable mockup (half-rocket) which was placed on a ground plane (an aluminum sheet about 15 ft. square appears to be adequate for small rockets) the terminal impedance of an individual shroud with its electrical image can be adequately simulated.

If space is available under the ground-plane for an impedance bridge to be used, the measurements can be made near the shroud without disturbing the field of the antenna. Although it would be possible to measure the impedance through an arbitrary length of cable it is generally more convenient to use a half-wave length. An additional piece of cable was connected in series between the cable normally supplied with the shroud and the impedance bridge. The additional cable had the same characteristic impedance as the shroud cable. The length of the added cable was adjusted until the impedance bridge indicated that the electrical length of the whole cable was precisely one-half wavelength at the operating frequency. This was done by leaving the end of the cable open and adjusting the cable length for a high impedance and zero reactance at the bridge end of the cable. This procedure includes the electrical length of the bridge terminals in the half-wave length.

After the cable had been adjusted to a half-wave length it was connected to the shroud terminals. The impedance presented by the cable connected to the antenna was measured on the bridge. Since the values obtained indicated that the antenna impedance was higher than the unterminated cable impedance, special care had to be taken in determining the shroud impedance. The bridge used for these measurements indicated the parallel components of the impedance. It was assumed that the resistive component of the antenna impedance was in parallel with the resistive component of the half-wave cable as measured with the cable unterminated. The assumption was also made that the reactive component of the antenna would be essentially the same as that measured through the cable. A dummy antenna load as computed using the above assumptions was built and substituted for the antenna. When the dummy antenna was measured through the half-wave cable the impedance read at the bridge was the same as when the actual antenna was connected at the end of the half-wave cable.

The value obtained by this substitution technique for the 73.6 Mc shroud was 4220 ohms in parallel with 191 ohms inductive reactance, which is equivalent to an $8.6+j191$ ohms series impedance.

764–173 O—65——31

Page intentionally left blank

V. SENSORS

Page intentionally left blank

A POSSIBLE METHOD OF CORRECTING LOW FREQUENCY RADIO OBSERVATIONS FOR IONOSPHERIC ABSORPTION

LARRY W. BROWN
Goddard Space Flight Center

Low frequency radio observations of cosmic radio sources are very important for understanding the nature of nonthermal radio sources and determining the thermal absorption in the interstellar medium. However, the earth's ionosphere limits such information since any extraterrestrial radio noise at a frequency below the critical frequency of the ionosphere cannot be propagated through the medium, and just above the critical frequency the cosmic noise suffers heavy absorption in the ionospheric region. Most low frequency observations are corrected for absorption by semi-empirical methods relying on ionospheric sounding stations which are many miles from the observatory.

Herein is described a possible on-site method of observationally arriving at the absorption correction by using a simple two-antenna interferometer operating in the swept-lobe mode.

If such measurements can be made, one can obtain more accurate low frequency spectral data and thus learn more about the interstellar medium. The interstellar HII regions will absorb the non-thermal radiation of the galactic background and of the discrete sources as one observes at lower frequencies (Fig. 1). Such measurements may also provide a possible distance scale for the galactic HII regions (Komesaroff 1961).

THEORY

Consider a radio telescope in a vacuum. The telescope will receive a certain intensity of radiation, $I(\nu)$, from the extraterrestrial

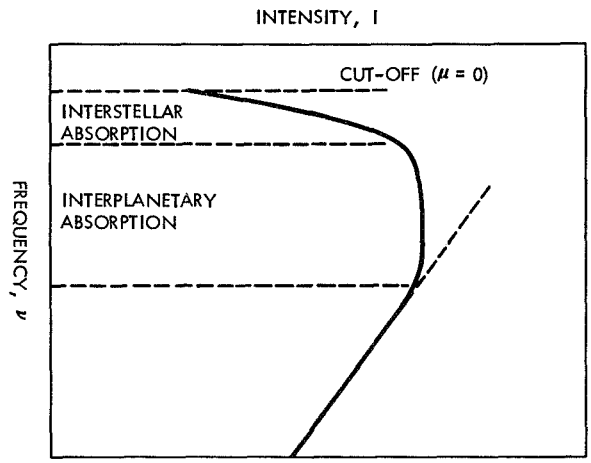

FIGURE 1.—Absorption of cosmic radio waves.

radio sources. The intensity will be equal to the energy passing through a unit area subtending a unit solid angle per unit of time over a unit frequency interval.

$I(\nu)$ = watts meter^{-2} (cycle per second)$^{-1}$ steradian^{-1}.

The spectral flux density is then the intensity integrated over the angular extent of the source.

$S(\nu)$ = watts meter^{-2} (cycle per second)$^{-1}$

or,

$$S(\nu) = \int I(\nu) d\omega. \quad (1)$$

The power available to the radio telescope depends on the collecting area, $A(\theta, \phi)$, of

the antenna.

$$P_R=1/2S(\nu)A(\theta,\phi)\Delta\nu \tag{2}$$

where,

1/2 arises from the linear polarization of the antenna.

$\Delta\nu$ is the bandwidth of the receiver which is assumed to have square response.

The power actually used by the receiver is less than that which is available to the antenna.

$$P_u=\eta P_R \tag{3}$$

where, η depends on the losses in the telescope system and must be less than unity. Then,

$$P_u=1/2\eta S(\nu)A(\theta,\phi)\Delta\nu. \tag{4}$$

Consider two discrete radio sources of small angular extent whose flux is measured in the vacuum of space.

First Source:

$$(P_u)_1=1/2\eta_1 S_1(\nu)A_1(\theta,\phi)\Delta\nu_1. \tag{5a}$$

Second Source:

$$(P_u)_2=1/2\eta_2 S_2(\nu)A_2(\theta,\phi)\Delta\nu_2. \tag{5b}$$

If a relative measurement of the two sources is made, the ratio of the received power is

$$\left(\frac{P_1}{P_2}\right)_u=\frac{S_1(\nu)}{S_2(\nu)}\frac{\eta_1\Delta\nu_1}{\eta_2\Delta\nu_2}\frac{A_1(\theta,\phi)}{A_2(\theta,\phi)}. \tag{6}$$

Since the same antenna is used for both measurements $\eta\Delta\nu$ will be the same for each observation, although $A(\theta,\phi)$ is not necessarily the same. One can define an antenna pattern $f(\theta,\phi)$ so that

$$A(\theta,\phi)=Af(\theta,\phi) \tag{7}$$

where, A is the antenna collecting area in the forward direction.

This antenna pattern will be affected by the presence of the earth's surface in its field due to reflection and side lobes. Any change in the antenna elevation will change the ground effect and thus change the antenna pattern. There are two methods of eliminating this effect.

1. Both sources could be measured at approximately the same zenith angle.
2. The antenna could carry its own ground screen which would be always oriented the same with respect to the antenna for all zenith angles.

By eliminating this area effect, the ratio of the received power is then just the ratio of the fluxes of the two sources.

$$\left(\frac{P_1}{P_2}\right)=\frac{S_1(\nu)}{S_2(\nu)} \tag{8}$$

An absorbing atmosphere can be introduced into the path of the radio wave. The atmosphere is assumed to be composed of many absorbing layers with a vertical thickness dh.

Assuming that Lambert's Law of Absorption holds, then an incident plane wave will lose a certain fraction of its intensity in traversing an atmospheric layer which is proportional to the path length dx through the layer.

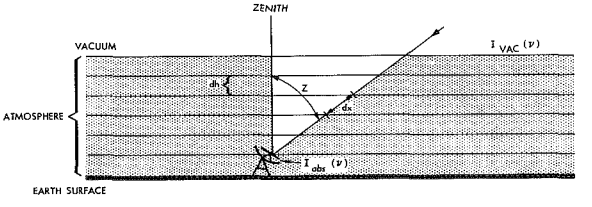

FIGURE A

$$\frac{dI}{I}=-k(\nu,h)\,dx \tag{9}$$

where, $k(\nu,h)$ is the absorption coefficient which depends on the frequency (ν) of the observation and on the vertical path length (h) through the absorbing medium.

For a plane parallel atmosphere, the thickness of a layer along the line of sight is simply related to the vertical thickness of the layer (dh) provided the absorption is uniformly parallel to the surface.

$$dx=\sec Z\,dh \tag{10}$$

where, Z is the zenith distance of the source. Such an assumption is true for small zenith

distances, but in general, the atmosphere is not plane parallel but curved so that at large zenith angles the relationship is more complicated and can be represented by $F(z)$.

$$dx=F(z)dh. \tag{11}$$

Thus, equation (9) becomes

$$\frac{dI}{I}=-k(\nu)F(z)dh. \tag{12}$$

Integrating,

$$I(\nu)_{\text{obs}}=I(\nu)_{\text{vac}}\exp\left[-\int K(\nu, h)F(z)dh\right] \tag{13}$$

where,

the integral is over the vertical path length,
$I(\nu)_{\text{vac}}$ is the intensity incident on top of the atmosphere,
$I(\nu)_{\text{obs}}$ is the intensity measured by the radio telescope.

Since in radio astronomy, it is difficult to make absolute intensity measurements, relative measurements between two sources can be made.

First Source:

$$I_1(\nu)_{\text{obs}}=I_1(\nu)_{\text{vac}}\exp\left[-\int K_1(\nu, h)F_1(z)dh\right]. \tag{14a}$$

Second Source:

$$I_2(\nu)_{\text{obs}}=I_2^{(\nu)}{}_{\text{vac}}\exp\left[-\int K_2(\nu, h)F_2(z)dh\right]. \tag{14b}$$

The relative measurement:

$$\left(\frac{I_1(\nu)}{I_2(\nu)}\right)_{\text{obs}}=\left(\frac{I_1(\nu)}{I_2(\nu)}\right)_{\text{vac}}\exp\left[\int F_2(z)K_2(\nu, h)dh-\int F_1(z)K_1(\nu, h)dh\right]$$

or,

$$ln\left(\frac{I_1(\nu)}{I_2(\nu)}\right)_{\text{obs}}=ln\left(\frac{I_1(\nu)}{I_2(\nu)}\right)_{\text{vac}}+\int F_2(z)K_2(\nu, h)dh-\int F_1(z)K_1(\nu, h)dh. \tag{15}$$

A general extinction coefficient exists which gives the total absorption experienced by the radiation, incident vertically ($F(z)=1$).

$$A(\nu)=\int k(\nu, h)dh. \tag{16}$$

Equation (15) becomes

$$ln\left(\frac{I_1(\nu)}{I_2(\nu)}\right)_{\text{obs}}=ln\left(\frac{I_1(\nu)}{I_2(\nu)}\right)_{\text{vac}}+F_2(z)A_2(\nu)-F_1(z)A_1(\nu). \tag{17}$$

If the observations required by Equation (17) are taken at approximately the same time or over an interval of time which is short compared to the relaxation time of the atmosphere, then for uniform absorption perpendicular to h,

$$A_1(\nu)\approx A_2(\nu) \tag{18}$$

with,

$$ln\left(\frac{I_1(\nu)}{I_2(\nu)}\right)_{\text{obs}}=ln\left(\frac{I_1(\nu)}{I_2(\nu)}\right)_{\text{vac}}+A(\nu)[F_2(z)-F_1(z)]. \tag{19}$$

Plotting this equation will yield a straight line whose slope is the extinction coefficient.

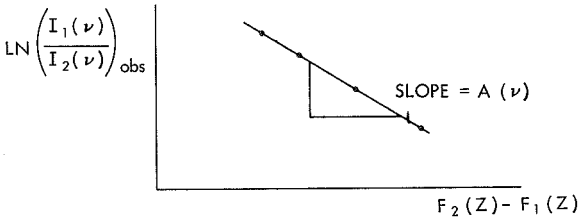

FIGURE B

OBSERVATIONAL METHOD

There are two observational methods available for the solution of Equation (19).

Single Source

A single source may be observed at many zenith distances to obtain the extinction coefficient. Since

$$I_1(\nu)_{\text{vac}}=I_2(\nu)_{\text{vac}} \tag{20}$$

TABLE I
Latitude, $\phi=40°$
$\Delta Z=Z_{\text{transit}-Z}$
Δt, hours

Source	ΔZ	$Z_T-60°$		$Z_T-50°$		$Z_T-40°$	
	Z_T	Δ sec Z	Δt	Δ sec Z	Δt	Δ sec Z	Δt
Cas A	18°5	0.945	6.5	0.501	5.1	0.250	3.8
Cyg A	0°6	1.000	5.5	.556	4.5	.305	3.6
Tau A	18°0	.949	4.6	.505	3.7	.245	2.8
Vir A	27°3	.874	4.1	.430	3.2	.179	2.2

Source	$Z_T-30°$		$Z_T-20°$		$Z_T-10°$	
	Δ sec Z	Δt	Δ sec Z	Δt	Δ sec Z	Δt
Cas A	0.100	2.5	0.009	0.8	----------	----------
Cyg A	.155	2.6	.064	1.7	0.015	0.8
Tau A	.104	1.9	.013	.7	----------	----------
Vir A	.029	1.0	----------	----------	----------	----------

at any two zenith distances, then,

$$ln\left(\frac{I_1(\nu)}{I_2(\nu)}\right)_{obs}=\bar{A}(\nu)[\sec z_2-\sec z_1] \quad (21)$$

for a plane-parallel atmosphere. The extinction coefficient obtained in this manner is the average value over the time between measurements. Such a time interval must be long in order to obtain the accuracy needed. Table I shows some typical time intervals and the dependence of accuracy on the difference in zenith distance for a plane-parallel atmosphere for the four brightest discrete sources. Within the time interval of the observations the probability of change in the absorbing properties is very high; therefore, the method gives the average extinction over a time interval of several hours. The instantaneous extinction will greatly differ from the average.

Two Sources

Examination of Equation (19) shows that if two sources are measured at the same zenith distance and time, the observed ratio of intensities is just the ratio of the intensities of the radiation incident on the atmosphere.

$$F_2(\nu)=F_1(\nu) \quad (22)$$

then,

$$\left(\frac{I_1(\nu)}{I_2(\nu)}\right)_{obs}=\left(\frac{I_1(\nu)}{I_2(\nu)}\right)^{vac} \quad (23)$$

Observations can be taken as the sources approach and recede from the same zenith distance to determine the extinction coefficient and its change over a short period of time. Using several sets of sources as in Figure 2, the extinction coefficient and its change can be monitored throughout the day. The instantaneous extinction coefficient is the slope of the straight line connecting each point of observation.

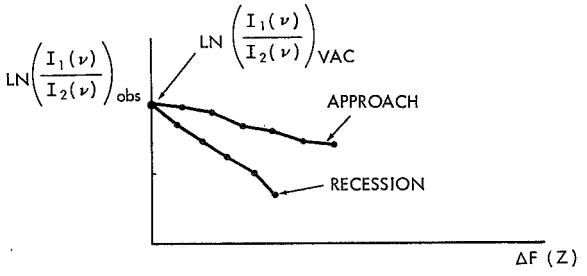

FIGURE C

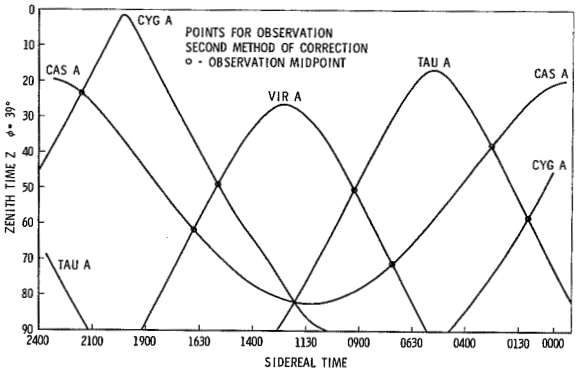

FIGURE 2

Such a method will require an equatorially mounted telescope, which is steerable in both hour angle and declination. If the sensitivity of the receiver, $\zeta(\nu)$, is defined as the number of detected quanta per unit input energy, then the response of the measuring system or the number of measurable quanta per second is

$$R=\zeta(\nu)P_u \tag{24}$$

or, from Equation (4)

$$R=\zeta(\nu)C_\nu S(\nu). \tag{25}$$

If the sensitivity is uniform over the bandwidth

$$R=C_\nu S(\nu). \tag{26}$$

The observed response is

$$lnR=lnC_\nu+lnS(\nu)_{\text{obs}}. \tag{27}$$

From Equation (14a)

$$lnS(\nu)_{\text{obs}}=ln\int I(\nu)_{\text{obs}}d\omega \tag{28}$$

or,

$$lnS(\nu)_{\text{obs}}=lnS(\nu)_{\text{vac}}-F(z)A(\nu). \tag{29}$$

Then the response is

$$lnR=lnC_\nu+lnS(\nu)_{\text{vac}}-F(z)A(\nu) \tag{30}$$

This equation suggests that the measurements be made in the following manner.

1. Measurement of standard source (noise diode)

$$lnR_{ss1}=lnC_\nu+lnS(\nu)_{ss}. \tag{31a}$$

2. Measurement of first source

$$lnR_1=lnC_\nu+lnS(\nu)_1-F_1(z)A(\nu). \tag{31b}$$

3. Measurement of second source

$$lnR_{ss2}=lnC_\nu+lnS(\nu)_2-F_2(z)A(\nu). \tag{31c}$$

4. Measurement of standard source (same as 1)

$$lnR_{ss2}=lnC_\nu+lnS(\nu)_{ss}. \tag{31d}$$

Combining measurements

$$ln\left(\frac{R_1}{R_2}\right)\left(\frac{R_{ss2}}{R_{ss1}}\right)=ln\left(\frac{S(\nu)_1}{S(\nu)_2}\right)_{\text{vac}}+A(\nu)[F_2(z)-F_1(z)]. \tag{32}$$

Then, providing that the receiver system is truly *linear* the response need only be considered as the deflection of the recorder. Then, the extinction coefficient is

$$A(\nu)=\frac{ln\left(\frac{R_1}{R_2}\right)\left(\frac{R_{ss2}}{R_{ss1}}\right)-ln\left(\frac{S(\nu)_1}{S(\nu)_2}\right)_{\text{vac}}}{F_2(z)-F_1(z)}. \tag{33}$$

For a plane-parallel atmosphere

$$F_2(z)-F_1(z)=\sec Z_2-\sec Z_1. \tag{34}$$

The assumption of uniform layers of atmosphere is not exactly true since there is a curvature associated with earth's atmosphere. The function $F(z)$, the dependence on zenith distance, will not be

$$F(z)=\sec Z$$

but will be

$$F'(z)=\sec\Theta$$

where, Θ is an angle less than Z due to the curvature.

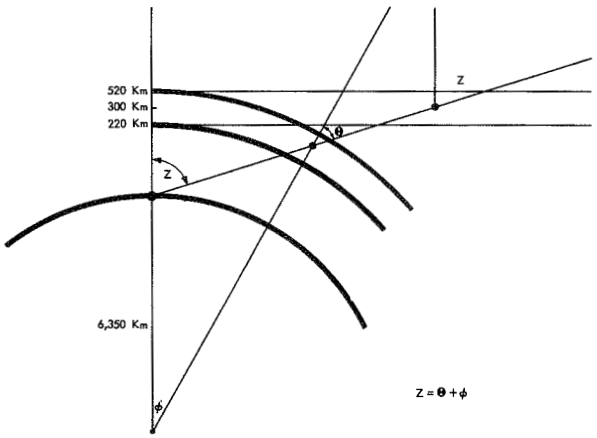

FIGURE D

At low frequencies, the extraterrestrial radio noise suffers absorption mainly due to the ionosphere. The absorption takes place in a thin shell with half-width 300 km with the maximum absorption occurring at a height of 300 km. Employing this model for the absorption, the above diagram can be used to calculate

$$F(z) = \sec Z$$
$$F'(z) = \sec \text{Ⓗ}$$

TABLE II

Z	ϕ	Θ	$F(z)$		$\frac{\Delta F(z)}{F(z)} \times 100$	$\Phi = \frac{\sec \Theta}{\sec Z}$
			sec Z	sec Θ		
					Percent	
0°	0°00	0°00	1.0000	1.0000	0.00	1.000
5°	0°22	4°78	1.0038	1.0035	.03	1.000
10°	0°47	9°53	1.0154	1.0140	.14	.999
15°	0°69	14°31	1.0353	1.0321	.31	.997
20°	0°94	19°06	1.0642	1.0580	.59	.994
25°	1°18	23°82	1.1034	1.0931	.94	.991
30°	1°42	28°58	1.1549	1.1388	1.41	.986
35°	1°65	33°35	1.2208	1.1971	1.98	.981
40°	1°89	38°11	1.3054	1.2710	2.72	.974
45°	2°12	42°88	1.4142	1.3647	3.63	.965
50°	2°36	47°64	1.5557	1.4840	4.83	.954
55°	2°60	52°40	1.7434	1.6390	6.37	.940
60°	2°83	57°17	2.0000	1.8443	8.44	.922
65°	3°07	61°93	2.3662	2.1254	11.3	.898
70°	3°30	66°70	2.9238	2.5282	15.6	.864
75°	3°54	71°46	3.8637	3.1461	22.8	.814
80°	3°78	76°22	5.7588	4.1973	37.2	.729
85°	4°01	80°99	11.474	6.3807	79.8	.556
90°	4°25	85°75	∞	13.494	----------	----------

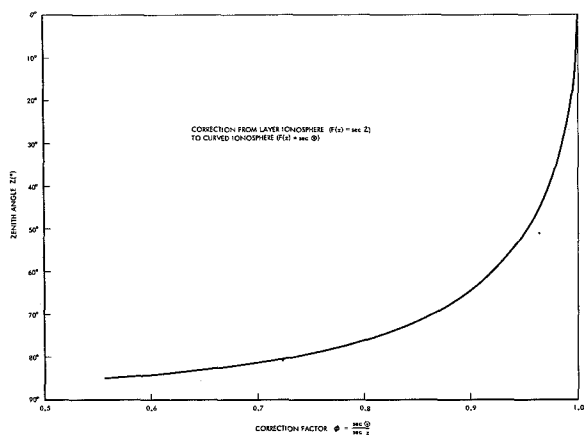

FIGURE 3

Figure 3 gives a plot of the correction factor as a function of zenith angle.

INSTRUMENTATION

One must now construct a radio telescope which will observe several of the stronger discrete sources at various zenith angles. A possible, simple arrangement would be an interferometer mounted in equatorial coordinates. An acceptable type is either the total power or swept-lobe interferometer.

One can now determine the antenna and receiver characteristics which should be used. The minimum detectable antenna temperature

for a receiver is given by

$$\Delta T_A = T_i(\Delta\nu \cdot \tau)^{-\frac{1}{2}} \tag{35}$$

where,

$T_i = T_b + T_R$, for a total power interferometer

with,

T_b is the background galactic radiation
T_R is the receiver input noise temperature

but,

$T_i = T_R$, for a lobe-switched interferometer.

The minimum detectable antenna temperature determines the effective area required to see a source of a particular flux density.

$$k\Delta T_A = 1/2 S(\nu) A \tag{36}$$

where, the antenna is linearly polarized.

The effective area of the antenna is related to the gain of the antenna by

$$A(m^2) = \frac{G}{4\pi}\left(\frac{300}{\nu(\text{Mc/s})}\right)^2 \tag{37a}$$

Then,

$$G = 1.39\times10^{-4} A(m^2)\ \nu(\text{Mc/s})^2 \tag{37b}$$

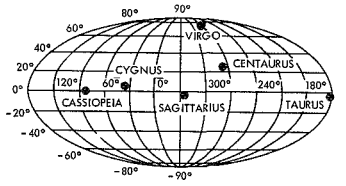

POSITIONS OF THE BRIGHTEST DISCRETE RADIO SOURCES (GALACTIC CO-ORDINATES)

RADIO SOURCE	POSITION (EPOCH 1950) RIGHT ASCENSION	POSITION (EPOCH 1950) DECLINATION	FLUX DENSITY AT 100 Mc/SEC	APPROXIMATE ANGULAR EXTENT AT 100 Mc/SEC	OPTICAL IDENTIFICATION	EMISSION
CASSIOPEIA A	$23^h\ 21^m$	58° 32' N	200 X 10^{-24} (WATTS/M^2/CPS)	3'	PECULIAR GALACTIC NEBULOSITY	NON-THERMAL
CYGNUS A	$19^h\ 58^m$	40° 36'N	125 X 10^{-24}	1.1'	PAIR OF COLLIDING GALAXIES OR PECULIAR BINARY SYSTEM	NON-THERMAL
CENTAURUS A	$13^h\ 22^m$	42° 46' S	18.5 X 10^{-24}	25'	PECULIAR GALAXY NGC 5128	NON-THERMAL
TAURUS A	$05^h\ 31^m$	22° 00' N	18.5 X 10^{-24}	4'	CRAB NEBULA	NON-THERMAL
VIRGO A	$12^h\ 28^m$	12° 40' N	12.5 X 10^{-24}	5'	PECULIAR GALAXY NGC 4486	NON-THERMAL

BRIGHTEST DISCRETE SOURCES

FIGURE 4

and from Equation (36)

$$G = 3.84\times10^{-27}\frac{\Delta T_a\,\nu(\text{Mc/s})^2}{S(\nu)} \tag{38}$$

Also the angular resolution of the antenna can be approximated by

$$\Theta \approx 1.82\times10^2 G^{-\frac{1}{2}} \tag{39}$$

with an antenna efficiency of 90 percent.

Consider the four brightest discrete sources (Table III):

TABLE III
(Whitfield 1957)

Source	ν(Mc/s)	$S(\nu)$ $(wm^{-2}\ c/s^{-1})$ $\times10^{-25}$
Cas A	100	1900
	40. 6	3800
	20. 0	5000
Cyg A	100	1200
	40. 6	2100
	20. 0	2600
Tau A	100	170
	40. 6	220
	20. 0	270
Vir A	100	180
	40. 6	300
	20. 0	360

See figure 4.

In order to be sure that these sources will be visible one can assume a ficticious source such that

$$S(\nu) = 1\times10^{-23}\ wm^{-2}\ c/s^{-1}$$

Then the sources are visible by a factor of 2 at least.

A total power interferometer measures both the flux from the discrete source and the galactic background; therefore, in order to calculate the radio telescope characteristics needed to observe the discrete source, the input noise must be the sum of the receiver noise plus galactic background (Table IV). The interferometer characteristics are given in Table V.

TABLE IV.—*Galactic Background*

ν(Mc/s)	$S(\nu)$ ($wm^{-2}c/s^{-1}$)		T_b(°K)	
	Maximum	Minimum	Maximum	Minimum
100	9.4×10^{-20}	1.9×10^{-20}	5.4×10^{3}	1.5×10^{3}
40. 6	18.0	4.0	5.4×10^{4}	2.3×10^{4}
20. 0	27.0	9.5	1.7×10^{5}	8.0×10^{4}

(Ellis 1962, Turtle et al. 1962)

Telescope characteristics for a total power interferometer:

Typical receiver:
- Input noise temperature___T_R=800 °K
- Receiver bandwidth_____$\Delta\nu$=1 to 100 Kc/s
- Integration time constant__τ=1 to 10 sec

At low frequencies, the resolution of the interferometer can be improved by operating in the swept-lobe mode (Ryle 1952). A discrete source passing through the lobe pattern

TABLE V

ν(Mc/s)	T_b(°K)	T_R(°K)	T_i(°K)	τ(sec)	$\Delta\nu$(cps)	ΔT_a(°K)	G	Θ
20. 0	1.7×10^{5}	8×10^{2}	1.7×10^{5}	1	10^{3}	5400	830	6°.3
					10^{4}	1700	260	11°
					10^{5}	540	83	20°
				2	10^{3}	3800	580	7°.6
					10^{4}	1200	180	14°
					10^{5}	380	58	24°
				5	10^{3}	2400	370	9°.5
					10^{4}	760	120	17°
					10^{5}	240	37	30°
				10	10^{3}	1700	260	11°
					10^{4}	540	83	20°
					10^{5}	170	26	36°
40. 6	5.4×10^{4}	8×10^{2}	5.5×10^{4}	1	10^{3}	1700	1000	5°.8
					10^{4}	550	340	9°.9
					10^{5}	170	100	18°
				2	10^{3}	1200	740	6°.7
					10^{4}	390	240	12°
					10^{5}	120	74	21°
				5	10^{3}	780	480	8°.3
					10^{4}	250	150	15°
					10^{5}	78	48	26°
				10	10^{3}	550	340	9°.9
					10^{4}	170	100	18°
					10^{5}	55	34	31°
100	5.4×10^{3}	8×10^{2}	6.2×10^{3}	1	10^{3}	200	770	6°.6
					10^{4}	62	240	12°
					10^{5}	20	77	21°
				2	10^{3}	140	540	7°.9
					10^{4}	44	170	14°
					10^{5}	14	54	25°
				5	10^{3}	88	340	9°.9
					10^{4}	28	110	17°
					10^{5}	8. 8	34	31°
				10	10^{3}	62	240	12°
					10^{4}	20	77	21°
					10^{5}	6. 2	24	37°

See Figures 5, 6, and 7.

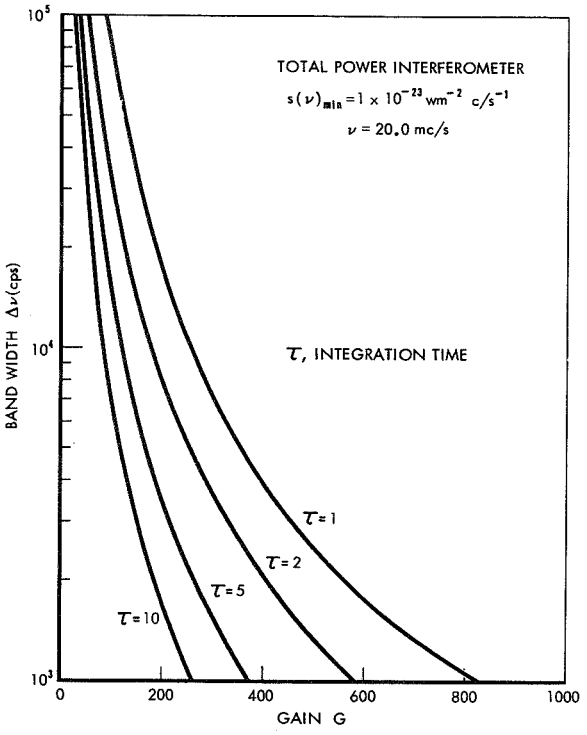

FIGURE 5.—Gain of antenna for given minimum flux density.

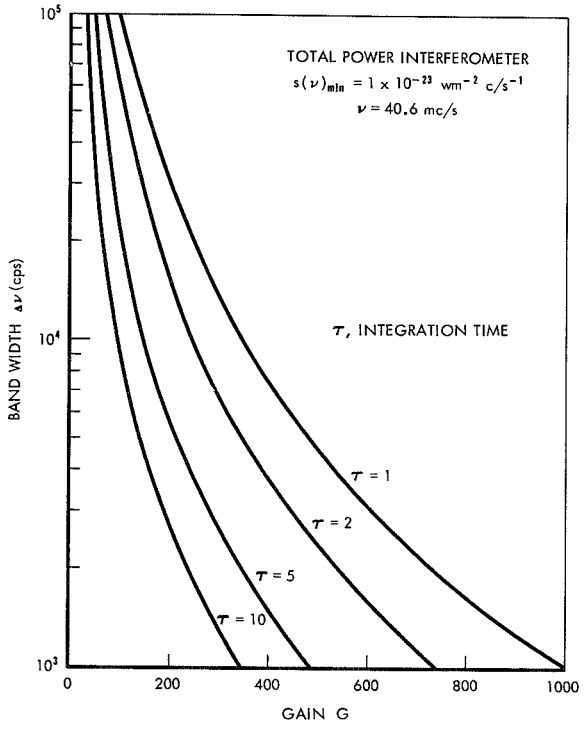

FIGURE 6.—Gain of antenna for given minimum flux density.

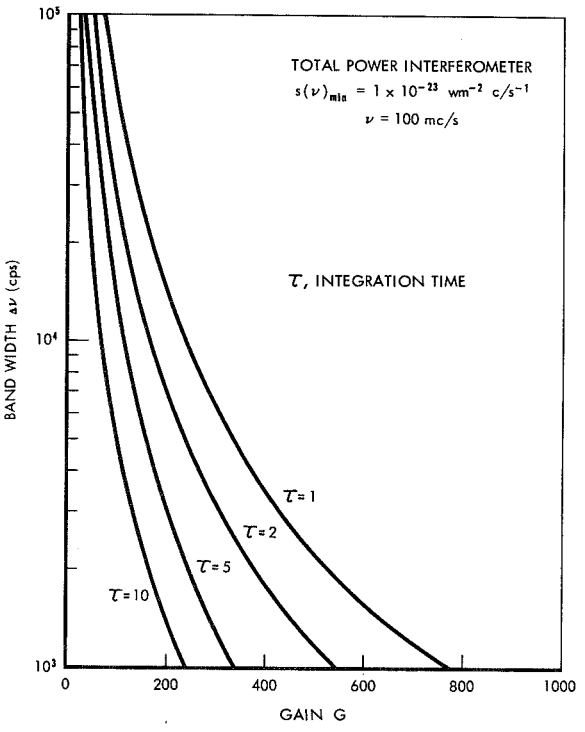

FIGURE 7.—Gain of antenna for given minimum flux density.

of the interferometer produces a modulation of the input signal. Since the galactic background is smooth, it will cause no modulation in the signal. The swept-lobe interferometer then measures only the modulated signal, so that a discrete source must only produce a modulated signal which is distinguishable above the geometrical mean of the input noise of the receiver. Table VI gives the radio telescope parameters needed for such measurements.

Telescope characteristics for a swept-lobe interferometer: Typical receiver (as above):

TABLE VI

ν(Mc/s)	T_i(°K)	τ(sec)	$\Delta\nu$(cps)	ΔT_a(°K)	$s(\nu)=1\times10^{-23}$		$s(\nu)=1\times10^{-24}$	
					G	θ	G	θ
100	8×10^2	1	10^3	25	96	19°	960	5°.9
			10^4	8.0	31	33°	310	10°
			10^5	2.5	9.6	59°	96	19°
		2	10^3	18	69	22°	690	6°.9
			10^4	5.7	22	39°	220	12°
			10^5	1.8	6.9	70°	69	22°
		5	10^3	11	42	28°	420	8°.9
			10^4	3.6	14	49°	140	15°
			10^5	1.1	4.2	89°	42	28°
		10	10^3	8.0	31	33°	310	10°
			10^4	2.5	9.6	59°	96	19°
			10^5	.8	3.1	100°	31	33°
40.6	8×10^2	1	10^3	25	15	47°	150	15°
			10^4	8.0	4.9	82°	49	26°
			10^5	2.5	1.5	115°	15	47°
		2	10^3	18	11	55°	110	17°
			10^4	5.7	3.5	97°	35	31°
			10^5	1.8	1.1	170°	11	55°
		5	10^3	11	6.7	72°	67	22°
			10^4	3.6	2.2	120°	22	39°
			10^5	1.1	.7	220°	6.7	72°
		10	10^3	8.0	4.9	82°	49	26°
			10^4	2.5	1.5	115°	15	47°
			10^5	.8	.5	260°	4.9	83°
20.0	8×10^2	1	10^3	25	3.8	93°	38	30°
			10^4	8.0	1.2	170°	12	53°
			10^5	2.5	.4	290°	3.8	93°
		2	10^3	18	2.8	110°	28	34°
			10^4	5.7	.9	190°	9	61°
			10^5	1.8	.3	330°	2.8	110°
		5	10^3	11	1.7	140°	17	44°
			10^4	3.6	.6	230°	6.0	74°
			10^5	1.1	.2	410°	1.7	140°
		10	10^3	8.0	.2	170°	12	53°
			10^4	2.5	.4	290°	3.8	93°
			10^5	.8	.1	580°	1.2	170°

See figures 8, 9 and 10.

One can now reverse the problem by assuming known antenna and receiver characteristics and calculating the minimum observable flux density.

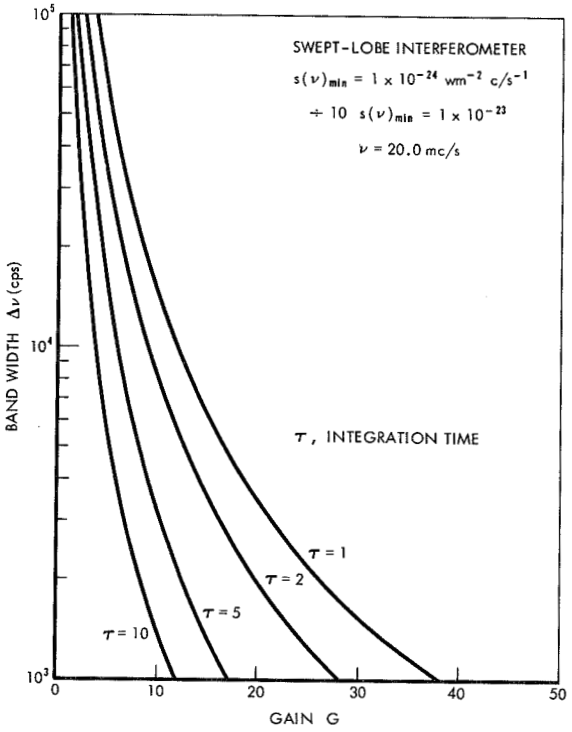

FIGURE 8.—Gain of antenna for given minimum flux density.

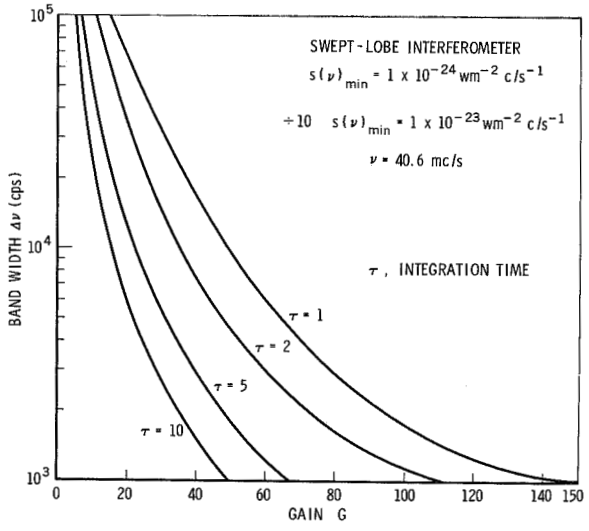

FIGURE 9.—Gain of antenna for given minimum flux density.

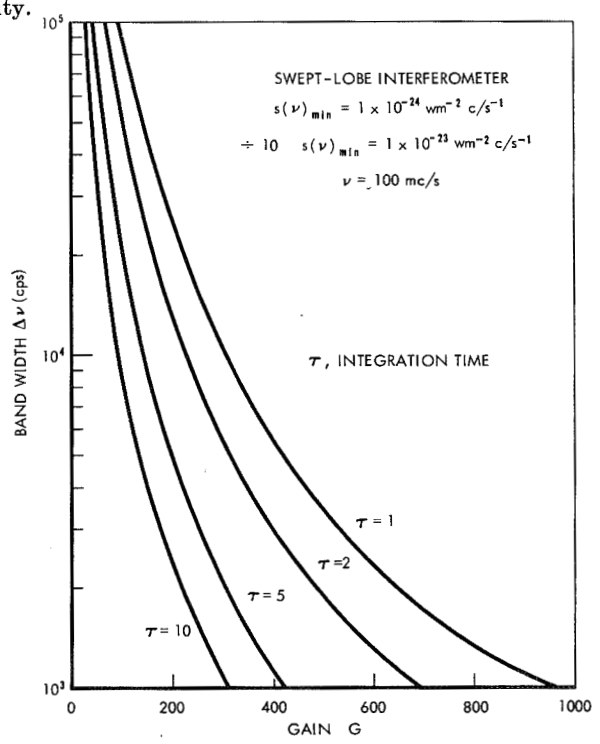

FIGURE 10.—Gain of antenna for given minimum flux density.

From Equation (38),

$$s(\nu)=3.84\times10^{-27}\Delta T_a\nu \text{ (Mc/s)}^2 \ G^{-1} \quad (40)$$

TABLE VII

ν(Mc/s)	T_i(°K)	τ(sec)	$\Delta\nu$(cps)	ΔT_a(°K)	$G=50$	100	150
						$s(\nu)$	
20.0	8×10^2	1	10^3	25	77×10^{-26}	39×10^{-26}	26×10^{-26}
			10^4	8.0	25	12	8.2
			10^5	2.5	7.7	3.9	2.6
		2	10^3	18	55	28	19
			10^4	5.7	18	8.8	5.9
			10^5	1.8	5.5	2.8	1.9
		5	10^3	11	34	17	11
			10^4	3.6	11	5.5	3.7
			10^5	1.1	3.4	1.7	1.1
		10	10^3	8.0	25	12	8.2
			10^4	2.5	7.7	3.9	2.6
			10^5	.8	2.5	1.2	.8
40.0	8×10^2	1	10^3	25	310×10^{-26}	15×10^{-26}	100×10^{-26}
			10^4	8.0	98	49	33
			10^5	2.5	31	15	10
		2	10^3	18	220	110	74
			10^4	5.7	70	35	23
			10^5	1.8	22	11	7.4
		5	10^3	11	140	68	45
			10^4	3.6	44	22	15
			10^5	1.1	14	6.8	4.5
		10	10^3	8.0	98	49	33
			10^4	2.5	31	15	10
			10^5	.8	9.8	4.9	3.3

See figures 11, 12 and 13.

For $\nu=20$ Mc/s and 40 Mc/s the four brightest discrete sources will be greater than the minimum detectable antenna temperature by an order of magnitude (interferometer provides factor of 2) for gains greater than 50.

The fringe width of the interferometer pattern greatly determines the ability to detect source positions. The angular extent of the fringes for a two antenna interferometer is given by

$$\Delta\Theta=\lambda d^{-1} \quad (41)$$

where d is the separation of antennas. If one assumes that the antennas used are Yagi arrays which are 70 percent efficient with symmetrical antenna patterns, then the angular resolution of one antenna is

$$\Theta=1.60\times10^2G^{-1/2} \quad (42)$$

TABLE VIII

G	Ⓗ
50	22°.6
100	16°.0
150	13°.1

One can now calculate the separation of the antennas provided the number of fringes are assumed.

TABLE IX

μ(Mc/s)	G	Number fringes	$\Delta\textcircled{H}$	d		
20	50	8	2°8	20λ	300 meter	980 feet
		10	2°3	25	380	1200
		12	1°9	30	450	1500
		14	1°6	36	540	1800
		16	1°4	42	630	2100
	100	8	2°0	29	440	1400
		10	1°6	36	540	1800
		12	1°3	43	650	2100
		14	1°1	50	750	2500
		16	1°0	59	890	2900
	150	8	1°6	36	540	1800
		10	1°3	43	650	2100
		12	1°1	53	800	2600
		14	0°9	63	950	3100
		16	0°8	71	1100	3600
40.6	50	8	2°8	20	150	490
		10	2°3	25	190	620
		12	1°9	30	220	720
		14	1°6	36	270	890
		16	1°4	42	310	1000
	100	8	2°0	29	210	690
		10	1°6	36	270	890
		12	1°3	43	330	1100
		14	1°1	50	370	1200
		16	1°0	59	440	1400
	150	8	1°6	36	270	890
		10	1°3	43	330	1100
		12	1°1	53	390	1300
		14	0°9	63	470	1500
		16	0°8	71	530	1700

See figure 12.

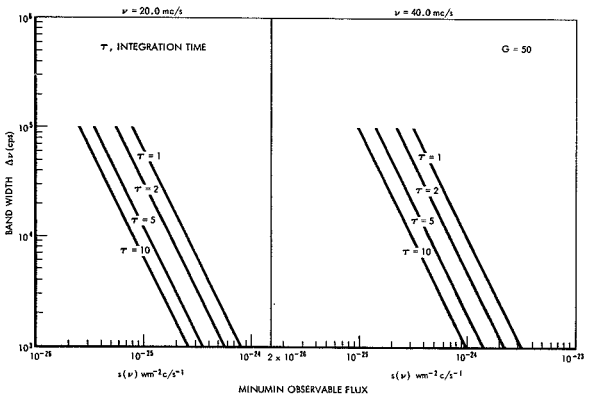

FIGURE 11.—Minimum observable flux for given antenna gain.

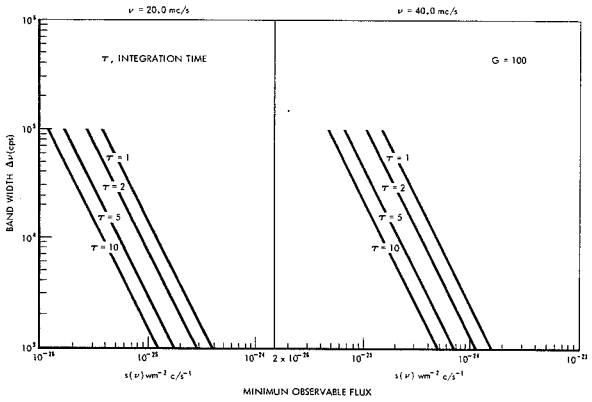

FIGURE 12.—Minimum observable flux for given antenna gain.

TABLE X.—*Zenith Angles*

	t	Cos Z		Z	
		ϕ=39°00′	35°20′	ϕ=39°00′	35°20′
Cas A	0h00m	0. 94234	0. 91913	19°33′	23°12′
α=23h21m	0h40m	. 93618	. 91266	20°35′	24°08′
δ=+58°32′	1h20m	. 91789	. 89345	23°23′	26°41′
	2h00m	. 88800	. 86208	27°23′	30°27′
	2h40m	. 84744	. 81950	32°04′	34°58′
	3h20m	. 79744	. 76702	37°07′	39°55′
	4h00m	. 73951	. 70621	42°19′	45°04′
	4h40m	67539	. 63894	47°31′	50°17′
	5h20m	. 60712	. 56724	52°37′	55°27′
	6h00m	. 53668	. 49329	57°33′	60°27′
	6h40m	. 46624	. 41934	62°13′	65°12′
	7h20m	. 39797	. 34764	66°33′	69°39′
	8h00m	. 33385	. 28037	70°30′	73°43′
	8h40m	. 27592	. 21956	73°59′	77°19′
	9h20m	. 22592	. 16708	76°57′	80°23′
	10h00m	. 18536	. 12450	79°19′	82°51′
	10h40m	. 15547	. 09313	81°03′	84°39′
	11h20m	. 13718	. 07392	82°07′	85°46′
	12h00m	. 13102	. 06745	82°28′	86°08′
Vir A	0h00m	. 89583	. 92241	26°23′	22°43′
α=12h28m	0h40m	. 88431	. 91031	27°50′	24°27′
δ=+12°37′	1h20m	. 85009	. 87441	31°47′	29°02′
	2h00m	. 79423	. 81576	37°25′	35°20′
	2h40m	. 71840	. 73616	44°05′	42°36′
	3h20m	. 62494	. 63804	51°19′	50°21′
	4h00m	. 51664	. 52438	58°54′	58°22′
	4h40m	. 39684	. 39861	66°37′	66°31′
	5h20m	. 26915	. 26457	74°23′	74°39′
	6h00m	. 13746	. 12633	82°06′	82°45′
	6h40m	. 00577	----------	89°40′	----------
	6h42m	. 00000	----------	90°00′	----------
	6h37m	----------	. 00000	----------	90°00′
Cyg A	0h00m	. 99961	. 99581	1°36′	5°15′
α=19h58m	0h40m	. 99064	. 98640	7°51′	9°28′
δ=40°35′	1h20m	. 96403	. 95845	15°25′	16°35′
	2h00m	. 92054	. 91280	23°00′	24°06′
	2h40m	. 86153	. 85085	30°31′	31°42′
	3h20m	. 78878	. 77449	37°56′	39°14′
	4h00m	. 70451	. 68603	45°13′	46°41′
	4h40m	. 61126	. 58814	52°19′	53°59′
	5h20m	. 49081	. 48383	60°36′	61°04′
	6h00m	. 40940	. 37624	65°50′	67°54′
	6h40m	. 32799	. 26865	70°51′	74°25′
	7h20m	. 20754	. 16434	78°01′	80°32′
	8h00m	. 11429	. 06645	83°26′	86°11′
	8h40m	. 03002	----------	88°17′	----------
	8h56m	. 00000	----------	90°00′	----------
	8h30m	----------	. 00000	----------	90°00′

TABLE X.—*Zenith Angles*—Continued

	t	Cos Z		Z	
		ϕ=39°00′	35°20′	ϕ=390°0′	35°20′
Tau A	0^{h}00^m	.95664	.97332	16°56′	13°16′
α=05^{h}31^m	0^{h}40^m	.94565	.96182	18°59′	15°53′
δ=22°04′	1^{h}20^m	.91320	.92772	24°03′	21°55′
	2^{h}00^m	.86013	.87201	30°40′	29°18′
	2^{h}40^m	78813	.79642	37°59′	37°13′
	3^{h}20^m	.69936	.70324	45°37′	45°19′
	4^{h}00^m	.59653	.59529	53°23′	53°28′
	4^{h}40^m	.48275	.47585	61°08′	61°35′
	5^{h}20^m	.36148	.34856	68°49′	69°36′
	6^{h}00^m	.23642	.21727	76°19′	77°27′
	6^{h}40^m	.11136	.08598	83°36′	85°04′
	7^{h}17^m	.00000	----------	90°00′	----------
	7^{h}07^m	----------	.00000	----------	90°00′

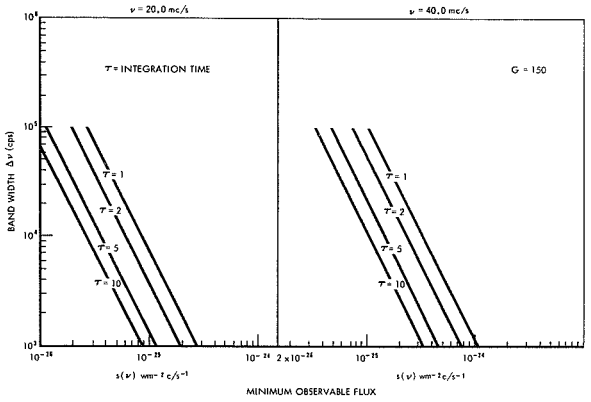

FIGURE 13.—Minimum observable flux for given antenna gain.

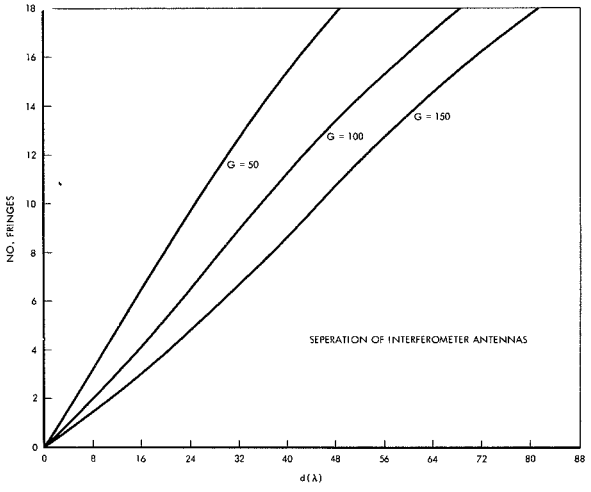

FIGURE 14

SUMMARY

An on-site method of observationally correcting radio astronomical measurements for ionospheric absorption has been discussed. The method consists of observing two discrete radio sources as they approach and recede from a common zenith distance (in both time and angle).

The observation requires an equatorially driven radio telescope with a resolution capable of observing several bright radio sources scattered over the sky. It is suggested that a swept-lobe interferometer be used at frequencies near 20 Mc/s and 40 Mc/s. Each antenna should have a gain of approximately 17 db and a separation of 1,500 feet. The noise figure of the receiver should be less than 4.

The above experiment should be able to determine accurate ionospheric absorption corrections for low frequency radio astronomy. Some questions of performance which cannot be answered before attempting the experiment are

1. Time interval over which the measurement may be performed.
2. Functional dependence of absorption on zenith angle.
3. Effect of ionospheric irregularities.
4. Catalogue of sources needed for continuous observation.

The accuracy of the experiment will depend on these questions, but should be high, especially if the two source method is used.

REFERENCES

ELLIS, G. R. A., WATERWORTH, M. D., and BESSELL, M., *Nature, 196*, 1079, 1962.

KOMESAROFF, M. M., *Aust. J. Phys. 14*, 515, 1961.

RYLE, M., *Proc. Royal Society A211*, 351, 1952.

TURTLE, A. J., PUGH, J. F., KENERDINE, S., and PAULINY-TOTH, I. K. K., M.N. *124*, 1962.

WHITFIELD, G. R., M.N. *117*, 680, 1957.

A SCINTILLATION COUNTER TELESCOPE FOR CHARGE AND MASS IDENTIFICATION OF PRIMARY COSMIC RAYS

D. A. BRYANT, [1]

G. H. LUDWIG, AND F. B. McDONALD

Goddard Space Flight Center

Two major objectives of the experiment employing the scintillation counter telescope described here are the determination of: (1) the amount of interstellar material through which primary cosmic rays pass between their source and the earth's vicinity; and (2) the rigidity dependence of the modulation mechanism of hydrogen and helium nuclei. The telescope is a combination of scintillators (CsI crystals) giving both the energy E of the charged particle and its rate of energy loss dE/dx. The method is sensitive to particles whose energy is sufficient to penetrate the dE/dx scintillator, yet too low to pass through the E one. In satellite applications, both the dE/dx and E signals will be analyzed and sorted digitally into 256 channels. Two ranges of sensitivity will be required to detect heavy particles as well as protons and alpha particles. Data from a series of cosmic ray balloon flights made with a prototype of this detector are presented.

INTRODUCTION

A cosmic ray telescope has been developed to study the charge and energy spectra of primary cosmic radiation. The two major objectives of this program are:

(1) To determine the amount of interstellar material through which primary cosmic rays have passed between their source and the vicinity of the earth (this amount can be deduced from the shape of the low-energy spectra of the primary nuclei, from helium to oxygen, measured at solar minimum); and

(2) To study the rigidity dependence of the various forms of H and He nuclei modulations.

A secondary objective is to study the charge and energy spectra of cosmic rays produced by the sun.

The telescope described herein is a combination of scintillators giving both the energy of a charged particle and its rate of energy loss dE/dx. This technique has been used extensively in medium-energy nuclear physics and in the study of the charge spectra of light fission fragments. A prototype detector was flown in balloons for a series of cosmic ray measurements in July 1961. Excellent charge and energy resolutions were obtained for electrons, protons and alpha particles late in the large cosmic ray event of July 1961. It is planned to fly a satellite version of the instrument on the first NASA Orbiting Geophysical Observatory. This report covers both the data obtained from balloon flights and the proposed satellite instrumentation.

COSMIC RAY MEASUREMENTS AT THE PREVIOUS SOLAR MINIMUM

During the last period of solar minimum, the charge and energy spectra of primary cosmic radiation were measured at balloon altitudes by the Cerenkov detector-scintillation counter technique (Reference 1). The experiment yielded the energy spectra of H and He nuclei for energies above 150 Mev/nucleon, and the

[1] NAS–NASA Post doctoral research associate.

rigidity dependence of the various forms of cosmic ray modulations. Similar results were obtained for Be through O at energies above 450 Mev/nucleon, with a better charge resolution than is generally achieved in nuclear emulsion work. The results are interpreted as placing an upper limit of 4 gm/cm^2 on the amount of interstellar hydrogen traversed by the C, N and O nuclei.

During the coming period of solar minimum, it appears vital to extend these observations to the lower energies that are accessible by the dE/dx and E technique, in order to obtain greater sensitivity in the measurements of both modulation mechanisms and the shapes of the energy spectra of heavy particles.

THE dE/dx AND E TECHNIQUE

Figure 1 shows the scintillator assembly.

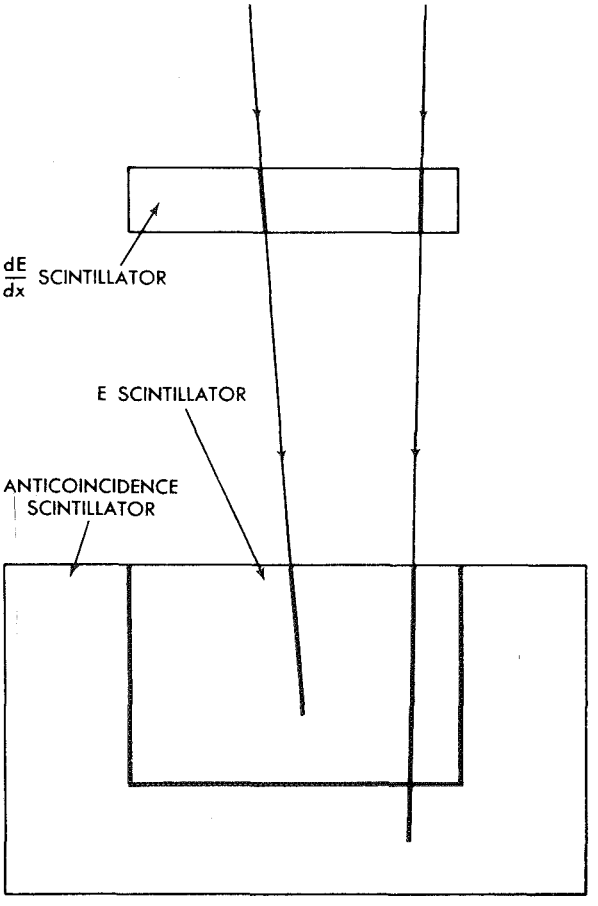

FIGURE 1.—Schematic of scintillator assembly.

There are three scintillators; two measure energy loss, and one acts as a guard counter. A signal is received from both energy loss scintillators when a coincidence occurs, unless the guard scintillator shows that a particle has entered it as well. The top scintillator is made as thin as is consistent with a reasonable light output, so that a charged particle passing through it will be little changed in energy. The light output of this scintillator is then a measure of the particle's rate of energy loss. If the particle is stopped by the lower scintillator, the light output from this scintillator is a measure of the energy of the particle. If the particle completely traverses the E scintillator, an anticoincidence signal from the guard scintillator indicates that the particle has lost only part of its energy in the E scintillator, and the energy measurements are discarded. The particle's energy and its rate of energy loss, together with the theoretical relation between these quantities, identifies the particle. This detector is sensitive to those particles with enough energy to penetrate the dE/dx scintillator, yet little enough to be stopped in the E scintillator.

DETECTOR ASSEMBLY

A diagram of the detector is shown in Figure 2. The dE/dx scintillator, a CsI crystal 0.15 gm/cm^2 thick and 5 cm in diameter, is viewed by the upper left photomultiplier in the Figure. The E scintillator, a CsI crystal 10 gm/cm^2 thick and 5 cm in diameter, is viewed by the center photomultiplier. An aluminum alloy

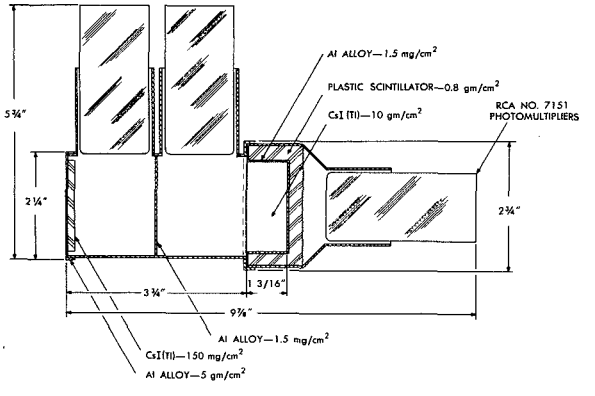

FIGURE 2.—Detector configuration.

foil 0.001 gm/cm ^{2} thick optically divides the space between the scintillators. It is essential, of course, that the material in this space be kept to a minimum. The anticoincidence scintillator, a cupshaped plastic scintillator surrounding the sides and bottom of the E scintillator, is viewed by a third photomultiplier shown at the right. A block diagram of the electronic assembly is shown in Figure 3.

RANGE AND SENSITIVITY

In practice it is impossible to measure dE/dx without changing the energy of the particle at the same time, and instead of obtaining dE/dx and E we obtain $\Delta E/\Delta x$ and E–ΔE. This distinction will be made in the text, however, only where necessary.

The calculated relations between the ΔE and E–ΔE signals are shown in Figure 4 for various particles, including the isotopes of H and He. Note that the energy range for protons and alpha particles, for example, is from 6 Mev/nucleon to 76 Mev/nucleon. Figure 5 shows the calculated relations between the light outputs of the crystals when allowance is made for the experimentally measured non-linearity between light output and energy loss in CsI (Reference 2, 3, and 4). The dashed lines show for comparison ΔE plotted against E–ΔE for protons and O.

In the satellite, both the dE/dx and E signals will be analyzed and sorted digitally into 256 channels each. To accommodate heavy particles as well as protons and alpha particles, two ranges of sensitivity are required; the are shown by the open blocks in Figure 5. The proton and alpha-particle dE/dx signals are covered by 256 channels at 0.1 Mev/channel, and their E signals, by 256 channels at 1.0 Mev/channel. The heavier particles need 0.5 Mev/channel and 10 Mev/channel for the dE/dx and E measurements respectively.

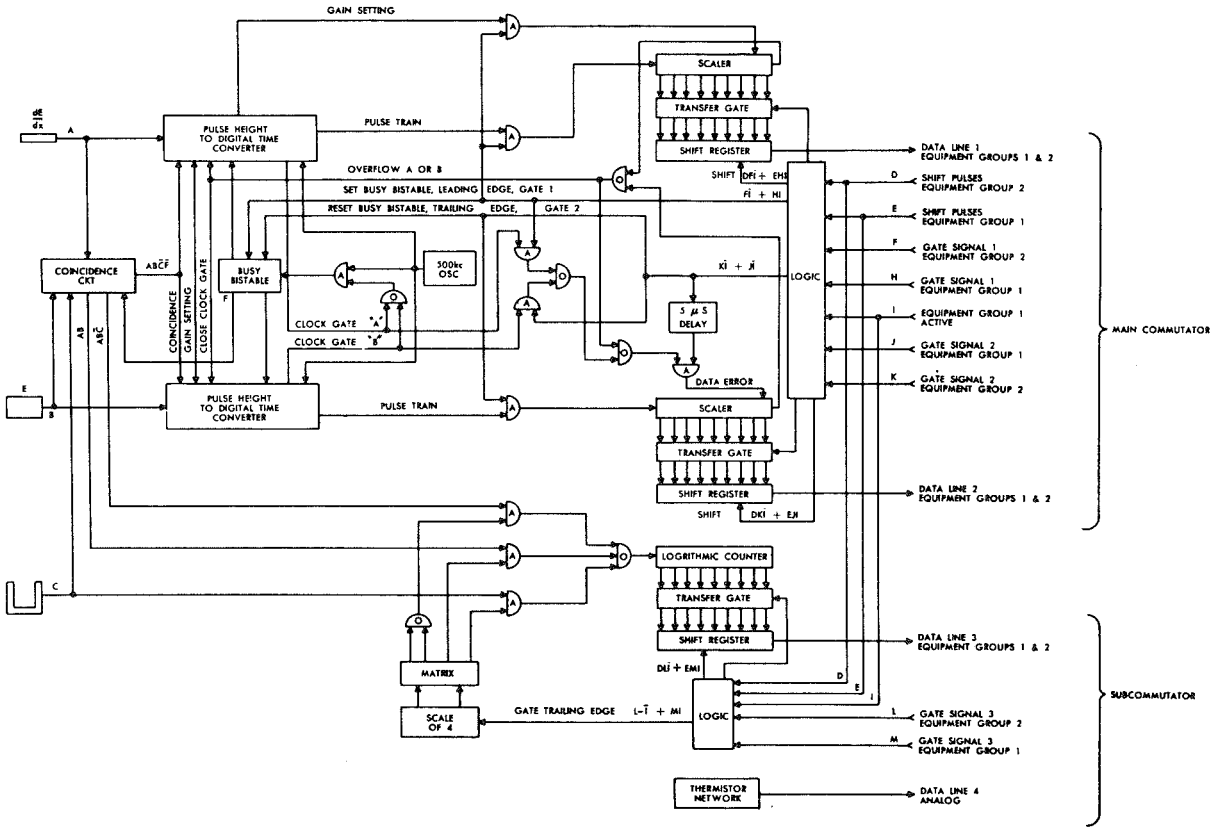

FIGURE 3.—Block diagram of electronic assembly.

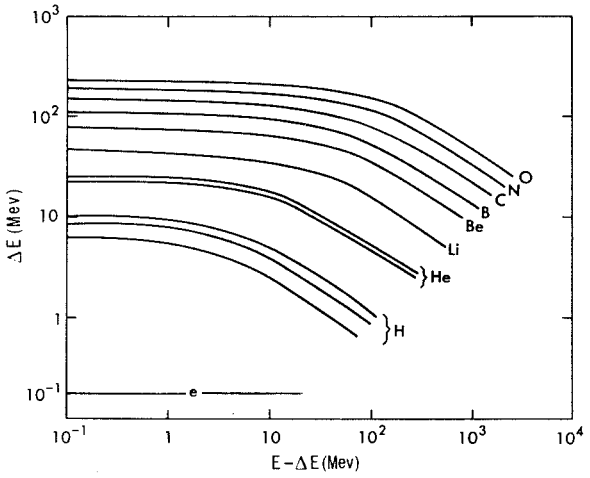

FIGURE 4.—Energy relations for various particles.

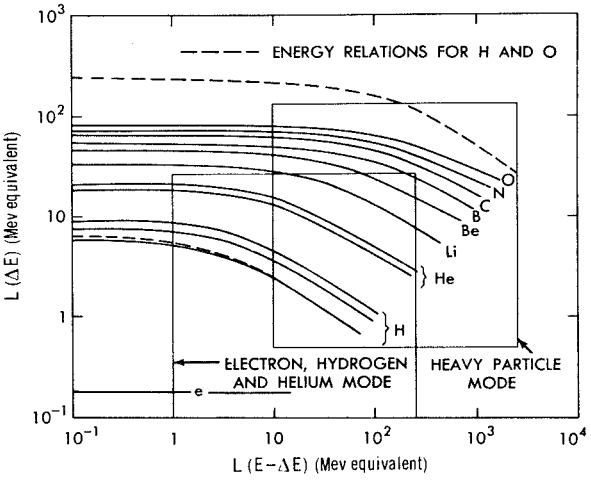

FIGURE 5.—Light output relations for various particles.

The analyzers will normally operate in the proton and alpha-particle mode, and switch over to the heavy-particle mode only when a heavy particle is detected. The expected rates of the various particles are such that less than 20 percent of the heavy particles will be missed by this method, while in the proton and alpha-particle mode, the apparatus will be almost continuously sensitive to intensity modulations.

REPORT OF COSMIC RAY MEASUREMENTS MADE BY THE dE/dx AND E TECHNIQUE

A series of balloons were flown carrying apparatus very similar to that shown in Figure 2, except that the E scintillator consisted of 9 gm/cm^2 of CsI and the dE/dx scintillator consisted of 0.4 gm/cm^2 of plastic (the latter material being readily available at the time). For this purpose, a plastic scintillator is inferior to a CsI crystal since it exhibits a marked nonlinearity between energy loss and light output (References 5 and 6). For the balloon flights, the dE/dx and E signals were each recorded on 128-channel analyzers, and standard analog-to-digital conversion cards from Nuclear Data Corporation of Madison, Wisconsin, were used. For each event, two seven-bit words representing dE/dx and E, together with anticoincidence signals from the third scintillator and timing information, were recorded on a miniature 16-channel tape recorder in the balloon gondola.

Figure 6 illustrates the resolution of the detector by showing the frequency distribution of signals from the dE/dx scintillator due to cosmic ray mu-mesons at sea level. The spread in the signal is seen to be only slightly greater than the inherent Landau spread due to statistical fluctuations in energy loss (about 15 percent for relativistic mu-mesons in a thin absorber). This shows that the spread introduced by geometrical factors and nonuniformity of light collection is of the same order or less.

Figure 7 shows how the dE/dx and E measurements made at 125,000 feet (an atmospheric depth of 4 gm/cm^2) permit identification of cosmic ray particles. It should be pointed out that these results are preliminary and represent

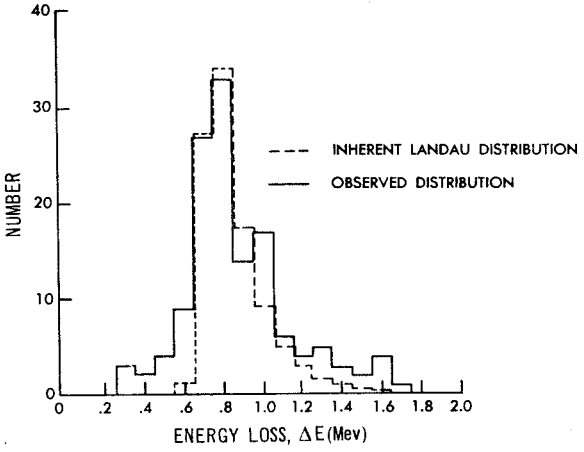

FIGURE 6.—Frequency distribution of sea level μ-mesons ΔE in scintillator.

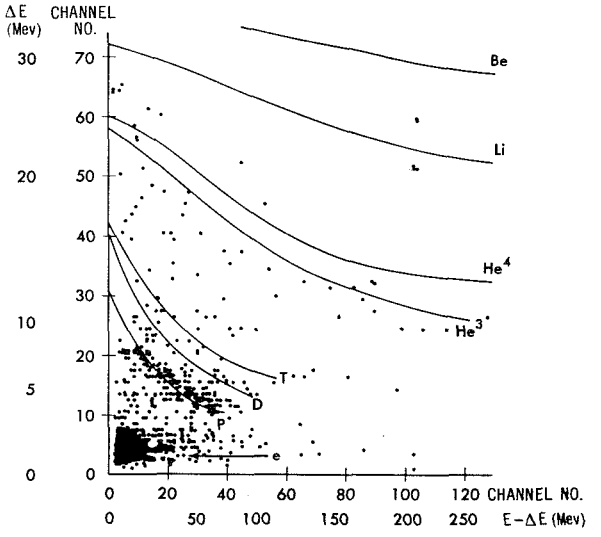

FIGURE 7.—Measurements of ΔE and $E-\Delta E$ at 125,000 feet (4gm/cm²).

only about one third of the data from a 12-hour flight. The experimental points are superimposed on the theoretical relations for various particles in which allowance has been made for the nonlinearity of the plastic and CsI scintillators (References 2–6).

There is a very clear proton distribution lying close about the predicted curve. It has a spread of about 10 percent, as expected, from the sea-level mu-meson distribution. The spread of the electron group is larger than can be explained by statistical fluctuations alone, and is probably due to the familiar range straggling and the results of electron showers produced in the few gm/cm² of atmosphere above the detector. About 40 points can be identified as He nuclei, with the separation of the He³ and He⁴ predicted curves being very close to the limit of the equipment's resolution. Thus, until the density of points is increased threefold by analysis of data from the rest of the flight, the relative numbers of He³ and He⁴ nuclei cannot be determined. The same considerations apply to deuterons and tritons. The relative numbers of He nuclei and protons are roughly 1:7, as was expected. In the present data only a few points represent particles heavier than alpha particles. The background of points may probably be accounted for by more than one particle at a time entering the dE/dx and E scintillators as a result of nuclear interactions in the atmosphere above the detector and in the detector material itself.

Figure 8 shows a cross-section, parallel to the ΔE axis, of the proton and He grouped points near the predicted curves. From the proton cross-section in Figure 8a, we see that most of the points lie within 10 percent of the predicted value. A point lying halfway between the He³ and He⁴ predicted curves would fall at 1.0 on the scale of Figure 8b; therefore, He³ particles should fall below 1.0, and He⁴ should fall above. It is thus far impossible to distinguish two humps in the distribution at this stage, but as was mentioned before, analysis of the remainder of the data should make it possible to determine the relative intensities of these two components.

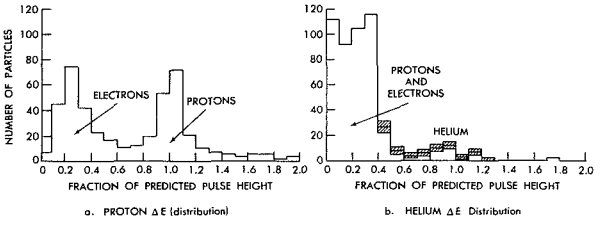

FIGURE 8.—Cross sections of Proton and Helium ΔE distributions; the shading indicates statistical uncertainty.

ACKNOWLEDGMENTS

The authors are most grateful to Mr. C. A. Cancro for the design and integration of the balloon electronic circuitry, and to Mr. F. M. Clese and Mr. D. I. Wright for their assistance with the maintenance of the balloon equipment.

REFERENCES

1. McDONALD, F. B., and WEBBER, W. R., "A Study of the Rigidity and Charge Dependence of Primary Cosmic Ray Temporal Variations" In: *Proc. Internat. Conf. on Cosmic Rays and the Earth Storm*, Kyoto, Sept. 1961, II: 428–435, Main Session Tokyo, Physical Society of Japan, 1962.

2. BIRKS, J. B., "Scintillations from Organic Crystals: Specific Fluorescence and Relative Response to Different Radiations" *Proc. Phys. Soc. (London)* 64A(10): 874–877, Oct. 1, 1951.

3. HALBERT, M. L., "Fluorescent Response of CsI(T1) to Energetic Nitrogen Ions" *Phys. Rev.* 107(3): 647–649, Aug. 1, 1957.
4. QUINTON, A. R., ANDERSON, C. E., and KNOX, W. J., "Fluorescent Response of Cesium Iodide Crystals to Heavy Ions" *Phys. Rev.* 115(4): 886–887, Aug. 15, 1959.
5. EVANS, H. C., and BELLAMY, E. H., "The Response of Plastic Scintillators to Protons" *Proc. Phys. Soc. (London)* 74(4): 483–485, Oct. 1, 1959.
6. GOODING, T. J., and PUGH, H. G., "The Response of Plastic Scintillators to High-Energy Particles" *Nuclear Instr. and Methods* 7(2): 189–192, May 1960.

FINE SUN TRACKER FOR ADVANCED ORBITING SOLAR OBSERVATORY

CLARENCE CANTOR

Goddard Space Flight Center

The analysis and design of a fine sun tracker for the Advanced Orbiting Solar Observatory are discussed. The tracker provides accurate pointing information in pitch and yaw, permitting precise static and dynamic orientation of the observatory with respect to the sun's apparent disc, in accordance with ground commands. The tracker uses a servo driven optical slab in each axis to offset the optical null by the required amount. The error signal thus developed in a pair of matched silicon photo-voltaic cells is fed to the observatory control system, to produce the desired orientation in that axis. The essential features of the tracker design are incorporated in a breadboard model. The performance of this model verifies the inherent capability of the design to achieve a 2 arc-second r.m.s. pointing accuracy.

INTRODUCTION

This report describes the basic analysis and design of a fine sun tracker for the Advanced Orbiting Solar Observatory (AOSO). One of the prime requirements of the AOSO, as well as the most critical, is the need for precise static and dynamic attitude orientation of the observatory with respect to the sun's apparent disc, in accordance with ground commands. This requires the use of a precision sun tracker to provide accurate pointing information for the AOSO control system, which can then produce the commanded attitude orientation in pitch and yaw. A separate inertial reference is used for the required AOSO roll control during this pitch and yaw orientation.

There are two basic fine attitude orientation modes required of the AOSO. One is offset pointing of the observatory to any point within a 10 degree square field of view centered on the sun. The second mode is raster scanning of the spacecraft in either a 5 arc-minute or 40 arc-minute square field of view, at the rate of 0.06 deg/sec or less. The 5 arc-minute raster is always within a 40 arc-minute square centered on the sun, while the 40 arc-minute raster can be located anywhere within the 10 degree square field of view. The required overall control system accuracies are ± 5 arc-seconds in each axis when either pointing or raster scanning within a 40 arc-minute square field centered on the sun, and ± 1 arc-minute for pointing outside of this region. The fine tracking modes and accuracies are summarized in Figure 1.

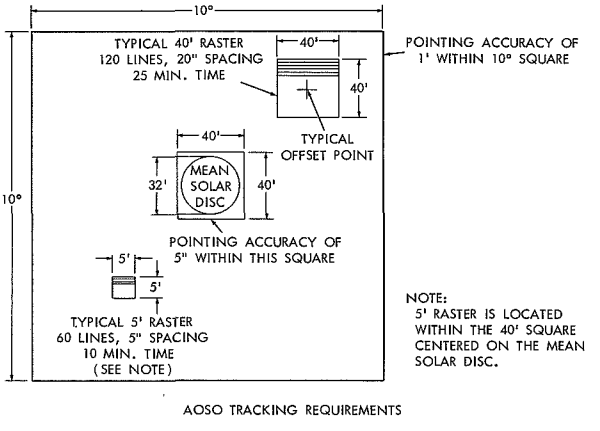

FIGURE 1.—AOSO tracking requirements.

In order for the overall control system to obtain a ± 5 arc-second accuracy in each axis within the 40 arc-minute square centered on the sun, it is necessary for the sun tracker to provide pointing information that is accurate to within 2 arc-seconds in this region. Hence the design goal for the fine sun tracker is an accuracy of 2 arc-seconds. In the region outside of the 40 arc-minute square centered on the sun, the tracker accuracy can be less, but must still be within ± 1 arc-minute. The proposed sun tracker can meet these requirements.

GENERAL DESCRIPTION

Figure 2 is a block diagram of the sun tracker system. The digital command system in the tracker converts the ground command into an optical positional reference for the AOSO, by means of the tracker servo drive. This commanded rotation of the optics then produces a positional error signal via the optics and photo-detector. This error signal is amplified and fed to the AOSO control system. The latter drives the observatory until the photo-detector signal is nulled. At this point, the observatory position will correspond with the commanded rotation of the optics and hence, with the ground command as well.

Offset pointing is accomplished by transmitting the appropriate ground command number in each axis to the digital command system in the tracker. This system develops an appropriate analog error signal that causes the servo drive to rotate the optics to a reference position corresponding to the ground command number. A 16 bit digital encoder, directly coupled to the optics, provides the optical position information to accomplish the above. The rotation of the optics produces an observatory error signal via the optics and photo-detector. This signal is fed to the observatory control system which drives the observatory to a position corresponding to the commanded rotation of the optics, and hence to the ground command number. In order to prevent large overshoots of the observatory control system, as well as to permit the use of a relatively small instantaneous field of view for the photo-detector (± 1 deg), the digital command system in the tracker incorporates rate limiting at a value that the observatory fine control system is designed to follow (± 0.06 deg/sec).

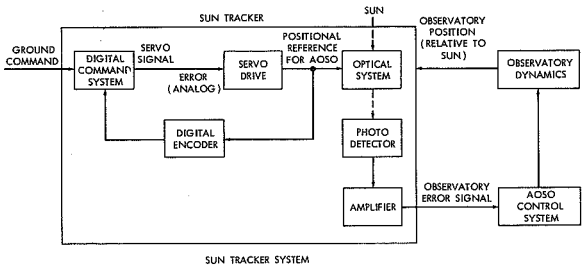

FIGURE 2.—Sun tracker system.

Raster scanning utilizes the same basic principles as those described above. When the observatory has stabilized at some offset point, the appropriate raster scan ground command will cause the following to take place. In yaw, the tracker digital command system will generate a triangular function of time having a quantization of approximately 1.3 arc-seconds referred to the observatory position (sun angle). The consequent rotation of the yaw optics will cause the observatory to oscillate back and forth in yaw, corresponding to the triangular command function. The slope of this command function is such that the observatory yaw rate will be 0.06 deg/sec. The peak-to-peak value of the command function is such as to produce a 5 arc-minute or 40 arc-minute observatory scan, depending on the ground command. Meanwhile, the pitch digital command system is generating a series of small unidirectional, step functions which occur each time the yaw rate reverses. The combination of these yaw and pitch command functions produces the desired observatory raster scanning (either 5 arc-minute or 40 arc-minute field of view). The command system automatically stops the scanning after one raster scan is completed.

OPTICAL SYSTEM

Figure 3 is a schematic diagram of the sun tracker optical system for each of the pitch and yaw axes. An optical slab of thickness d and index of refraction n is located midway between the photo-detector and the slit at the front of the tracker, where the sun's rays

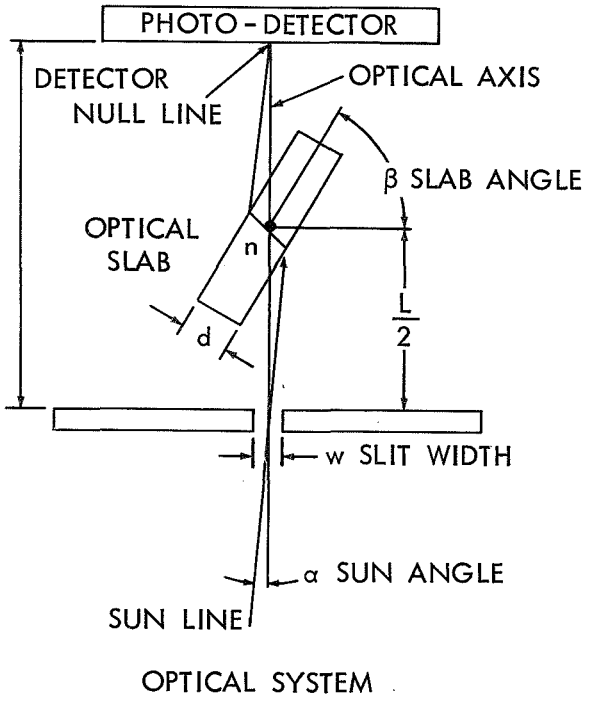

FIGURE 3.—Optical system.

are admitted. The slab is rotated through an angle B, corresponding to the command signal, by means of the tracker servo drive.

The rays of the sun are refracted through the slab and form a narrow beam on the photo-detector surface. When the center of this beam is off the null line of the detector, an error signal is generated which is amplified and fed to the observatory control system. The latter then drives the observatory until the observatory position (sun angle α) is such as to cause a null at the photo-detector. Under this condition, the sun angle α is a precise function of slab angle B, and hence of the ground command as well.

This function of B vs. α is shown in Figure 4 for a few values of L/d and index of refraction n. It can be seen that the optical gain (ratio of slab angle to sun angle) is greater for the larger value of L/d. However, the practical limit of 75 to 80 degrees of slab rotation, combined with the AOSO requirement of tracking up to sun angles of ± 5 degrees, results in a maximum practical value of 10 for L/d. Hence, $L/d=10$ is the selected value of optical gain for the sun tracker.

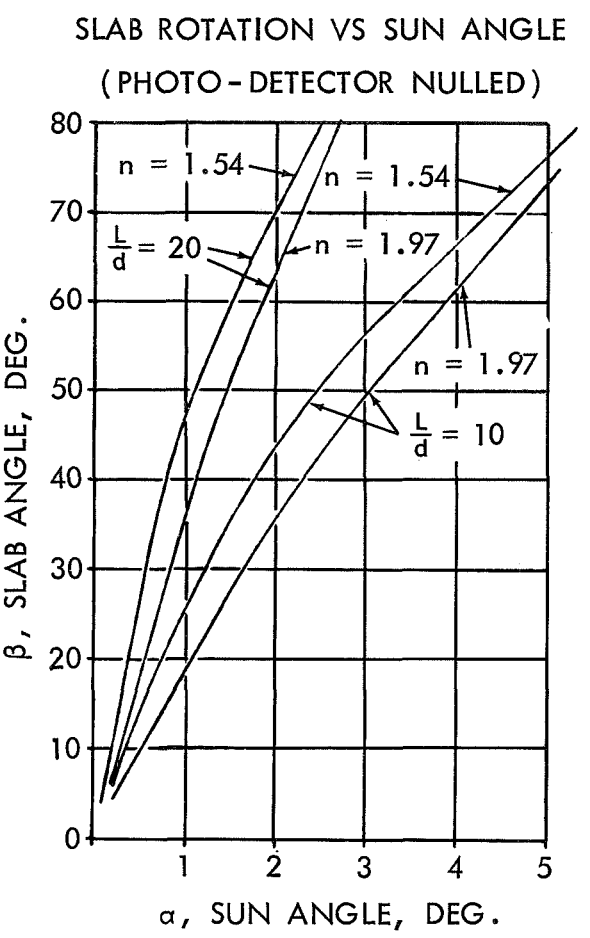

FIGURE 4.—Slab rotation vs. sun angle.

Slab angle β is measured by a 16 bit digital encoder, directly coupled to the slab. The tracker servo drive causes the slab to be driven to an angle β such that the output number of the encoder corresponds to the command number. Because of the non-linear β vs. α curves, as shown in Figure 4, the commanded sun angle α would not be proportional to the command number, if the encoder output is linear with angle. It is highly desirable, for simplifying the digital logic, that the sun angle α be proportional to the command number. This can be accomplished by specifying a non-linear encoder output characteristic that is exactly the same as $\alpha=F(\beta)$ for the particular optical gain curve. Baldwin Electronics has indicated that such non-linearization of the encoder output is practical. Hence, this non-linearization

of encoder output is selected for the tracker design.

There still remains the selection of the index of refraction n. The value $n=1.54$ corresponds to ordinary crown glass, while $n=1.97$ corresponds to heaviest flint glass. The lower value of n results in higher optical gain for small sun angles, and hence a greater accuracy in sun angle for any given resolution in commanded slab angle β. However this advantage is offset by several other factors. One is the fact that the required non-linearization of the 16 bit encoder results in a constant sun angle resolution (1.3 arc-second) associated with the least significant bit, regardless of sun angle. This is a direct consequence of linearizing commanded sun angle as a function of command number. Secondly, the large curvature of the β vs. α curve for $n=1.54$, combined with the associated non-linearization of the encoder, results in large variations in tracker servo loop gain as well as higher tracking velocity following errors at small sun angles. Finally, the lower value of n results in slightly higher inter-axis cross coupling errors. For these reasons, the value of $n=1.97$ (heaviest flint glass) is recommended for the tracker design.

A cross coupling error arises whenever the sun line is out of the sensitive plane of the detector (plane normal to slab axis of rotation). For the critical accuracy region of ± 20 arc-minutes centered on the sun, the calculated cross coupling error is less than 0.2 arc-seconds. The maximum error, over the entire ± 5 degree range, is calculated to be 21 arc-seconds, which is well within the allowable 1 arc-minute accuracy for this region. Hence, it is not necessary to correct for cross coupling error, even though it is predictable.

The remaining optical parameters that must be finalized are optical length L, slit width w, and slit length h. Since the finalization of these parameters is influenced by the photo-detector scheme, it will be discussed under that section.

PHOTO-DETECTOR

Tests conducted to date have shown that a matched pair of silicon photovoltaic cells can serve as a stable null detector for the sun tracker. Therefore, this scheme is utilized as the photo-detector. The photo-cell arrangement is as shown in Figure 5.

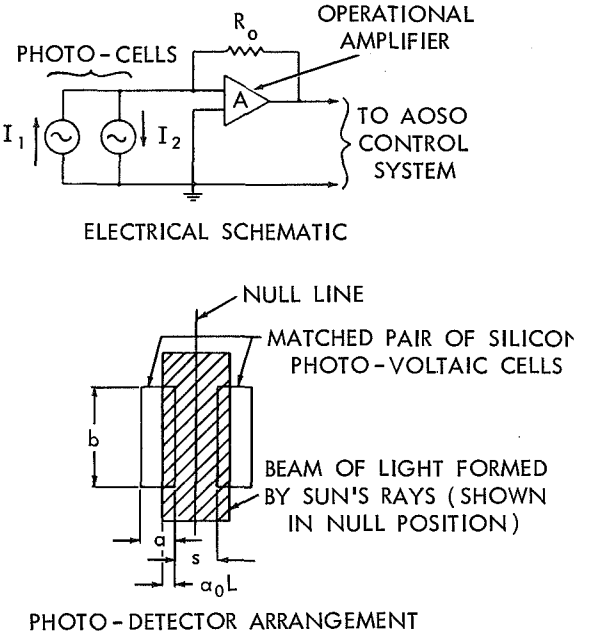

FIGURE 5.—Electrical schematic and photo-detector arrangements.

The photo-cells are used as current sources in the short circuit mode since silicon photocells have a relatively stable, repeatible characteristic when used in this mode. The difference in short circuit current of the two cells is measured and amplified via a d.c. operational amplifier as shown in the electrical schematic of Figure 5. Since the short circuit current of each cell is proportional to the light flux falling on the cell, an error signal will be developed at the amplifier output whenever the center of the beam of light is off the null line. This error signal is fed to the observatory control system which drives the observatory such as to reduce this error to zero.

At null, the beam of light slightly overlaps both cells. This is necessary in order to obtain satisfactory error signal linearity and gain, as well as to allow for the change in beam width at different times of the year due to the changing distance from the sun. The beam width

variation requires a nominal overlap angle of at least 1.6×10^{-4} radians on each cell. However, linearity considerations require that the overlap angle α_0 be increased to 0.002 radian. This places each photo-cell edge in the straight line portion of the calculated light intensity distribution curve, resulting in a linear error signal near null.

It can be shown that for a straight line light intensity distribution curve, the angular error $\Delta\alpha$ at null caused by a fractional gain variation p between the photo-cells is given by the following: $\Delta\alpha=\frac{1}{4}\,p\alpha_0$.

For an expected 1% differential gain change and $\alpha_0=0.002$ radian, this null shift would be 1.0 arc-seconds, which is satisfactory.

A consideration of such factors as tracker size and weight, detector sensitivity, desired detector field of view (±1 degree), constancy of detector gain in the linear region, detector saturation characteristic, and errors due to amplifier current and voltage drift, has resulted in the selection of the following values for the remaining key parameters:

(a) Focal length $L=5$ in. ($d=0.5$ in.)
(b) Slit width $w=0.025$ in.
(c) Photo-cell length $a=0.05$ in.
(d) Photo-cell width $b=0.20$ in.
(e) Photo-cell spacing $s=0.05$ in.
(f) Amplifier saturation at $\Delta\alpha=\alpha_0=0.002$ radian

The above values result in a linear detector range equal to ±0.002 radian (±7 arc-minutes) and a saturated range from 0.002 radians to 0.020 radian (±70 arc-min.). The gain in the linear region is fairly constant, varying by no more than 30 percent from the gain at null. The detector sensitivity is calculated to be about 0.20 μ a/arc-sec. This, together with an estimated 0.1 μ a current drift of the operational amplifier, results in an error component of 0.5 arc-seconds. Another angular error component equal to about 0.5 arc-seconds results from the expected voltage drift of the amplifier combined with the internal shunt resistance of the photocells. Thus the photodetector design meets the objectives for field of view, linearity, and accuracy.

DIGITAL COMMAND SYSTEM

The digital system generates a series of command numbers in each axis in accordance with the transmitted ground command. The output of the 16 bit digital encoder is compared with the existing value of the generated command number. The difference is converted to an analog error signal which is fed to the servo system controlling the rotation of the optical slab. Thus, the slab is driven to an angle β such that the encoder output matches the generated command number. As explained previously, the photo-detector error signal will drive the AOSO to a sun angle α that is a precise function of the commanded slab angle β. Hence the final sun angle α is directly related to the generated command number. This relation (α vs. command number) is perfectly linear since the encoder output characteristic is tailored to the B vs. α curve of the optical slab. The overall gain is such that one count of the 16 bit digital system corresponds to 1.32 arc-seconds of sun angle.

In offset pointing, the ground command (offset Pointing) number in each axis is stored in the command generator. The latter then causes a command register to be counted up or down from its last value until it equals the offset pointing number. The counting rate is limited to 164 counts/sec, or 0.06°/sec of sun angle. The encoder output is compared with the present number in the command register by means of a serial subtractor. The difference is converted to an analog signal, by means of a D/A converter. This error signal causes the optical slab to be driven to a position corresponding to the present number in the command register. Hence the AOSO will be driven to the sun angle corresponding to this number. Since the command register number is changing at the rate of 164 counts/sec the AOSO will be driven at 0.06°/sec. The spacecraft will stabilize about the desired offset point when the command register number reaches and stops at the ground command number.

Raster scanning about any offset point can begin once the AOSO has stabilized about the offset point. The appropriate ground com-

mand will than cause the following to take place. The number in the yaw command register will be increased at the rate of 164 counts/sec, or 0.06°/sec. When the command register number has been increased by the equivalent of 5 arc-minutes or 40 arc-minutes, depending on the desired raster scan, the command generator will cause a smooth reversal in the command register counting rate. After about 3.6 seconds, this reversal will be completed and the command register number will be counting down at the rate of 164 counts/sec. When the command register number reaches its original value, another smooth reversal occurs, and the process is repeated. Concurrently, the pitch command register is counted down by 15 counts (20 arc-seconds) during every yaw reversal. The net result is that the spacecraft is commanded to perform raster scanning of the desired width at the rate of 0.06 deg/sec. The pitch and yaw command registers automatically stop counting after one complete raster scan. This occurs after 15 lines for the 5 arc-minute command and after 120 lines for the 40 arc-minute command.

SERVO DRIVE SYSTEM

The servo drive system positions the optical slab in accordance with the command number generated by the digital command system. This is accomplished by comparing the slab angle position (encoder number) with the command number, converting the difference to an analog signal via the D/A converter, and feeding this signal to the servo drive system. The latter then drives the slab so as to reduce this difference to zero.

The basic design criteria for the servo system are a bandwidth of approximately 40 rad/sec, in order that it be fast compared to the AOSO control system, and a total random servo following error of less than 1 arc-second referred to the spacecraft. On this basis, two different servo systems have been designed. One is a geared drive which utilizes an inertially damped servomotor to drive the optical slab, via anti-backlash gearing. This design was selected initially because of its simplicity and the relative ease in predicting its servo performance. A breadboard model of this drive has been constructed and successfully operated. The second design is a direct drive which utilizes a d-c torquer motor and d-c tachometer, both of which are directly coupled to the optical slab. This design has been investigated via analog simulation. The latter design, though it contains more components, appears preferable because of its greater mechanical reliability compared to the geared servo drive. For this reason, the direct servo drive is recommended for the sun tracker.

A block diagram of the direct servo drive is shown in Figure 6. The D/A converter output is amplified and fed to a d-c torquer motor which is directly coupled to the optical slab. Also directly coupled to the slab is a d-c tachometer. The tachometer signal is amplified, fed through a high-pass filter, and then subtracted from the D/A converter output, in order to provide the necessary servo system stabilization. At servo equilibrium, the slab angle β, and hence the commanded sun angle α, correspond to the digital command.

A d-c torquer motor suitable for this application is an Inland Corp. Type T–2136–13. The gain of this motor is $K_v=8.33$ rad/sec/volt. The time constant of the motor is 0.033 second. However, the additional load inertia increases this to $T_1=0.3$ second. The total stiction of the motor and load is equivalent to about 1.3 volts of motor voltage. In order to limit the resulting static error to about 0.5 arc-second of sun angle, it is necessary to have a major loop gain of about 225,000, i.e., $K_eK_dK_aK_t=225{,}000$. Obviously, the resulting servo characteristic would be unstable without suitable compensation.

Tachometer feedback through a high-pass filter can provide the necessary compensation. It is important, for stability reasons, that the closed minor loop response be equivalent to $1/K_TS$ in a broad frequency range centered about 40 rad/sec, the desired major loop crossover frequency. Then, in order to realize this major loop crossover frequency, it is necessary for the following to be true:

$$K_eK_d\frac{1}{K_tS}=\frac{40}{S}.$$

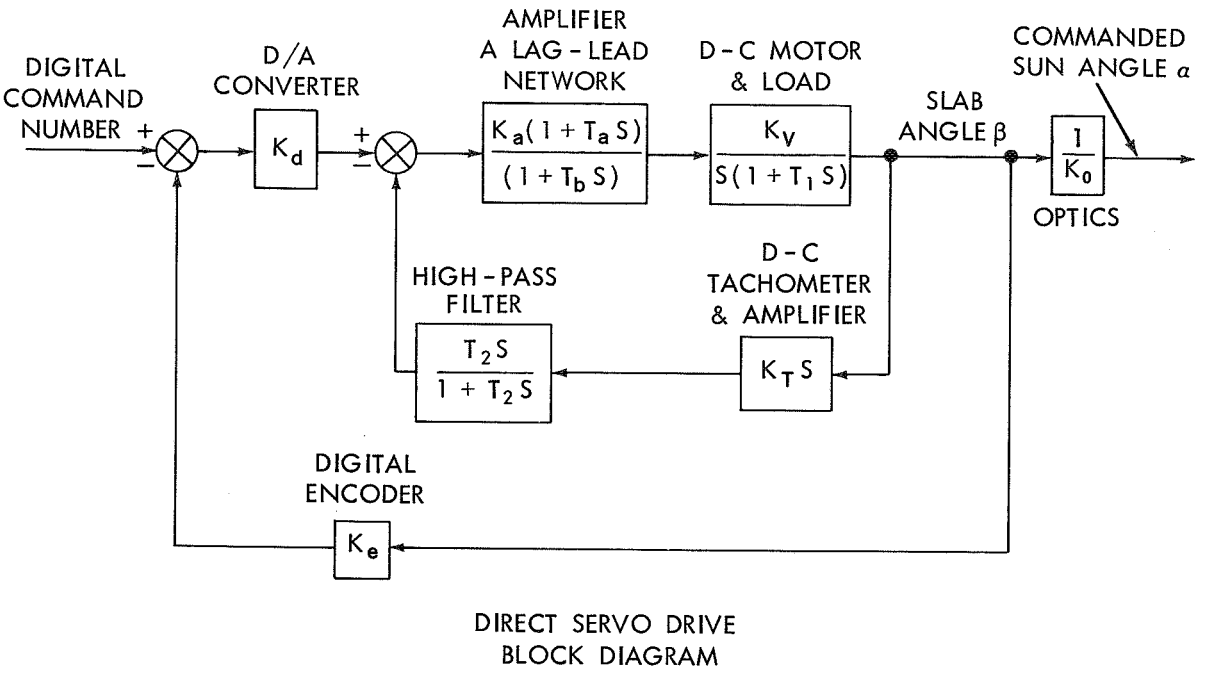

FIGURE 6.—Direct servodrive block diagram.

However, $K_eK_dK_aK_v$ has been selected to be 225,000 based on static error considerations. Hence, $K_tK_aK_v=5,626$. This defines the necessary minor loop gain.

In order to preserve the $1/K_TS$ behavior of the closed minor loop over a wide frequency range near 40 rad/sec, it is necessary for the high-pass filter time constant T_2 to be considerably larger than 1/40 sec. A value of $T_2=0.3$ second accomplishes the above purpose.

The lag-lead network in the minor loop forward path is introduced in order to limit the minor loop bandwidth, without affecting the compensated major loop characteristic in the frequency range of interest. Otherwise, an excessive minor loop bandwidth, together with the usual higher order time constants, would make the system unfeasible. The selected values for the lag-lead network are $T_a=0.0025$ sec and $T_b=0.125$ sec.

An analog simulation of the system has been performed, including stiction. The results indicate good servo performance, in both the offset pointing and raster scanning modes of the sun tracker. The occasional limit cycle that occurs has an amplitude, referred to the spacecraft, only slightly higher than the 0.5 arc-seconds necessary to overcome stiction.

ERROR ANALYSIS

The following is a listing of spacecraft attitude errors caused by the sun tracker inaccuracies discussed previously. The magnitudes of these error components are those associated with small sun angles (up to ±20 arc-minutes). While a few of the error components increase in magnitude for the larger sun angles, this is not critical because of the much larger value of allowable tracker error (1 arc-minute) outside of the fine accuracy region.

Error Source	*Magnitude of Error (arc-seconds)*
Digital system resolution (1 count)	1. 32
Photo-detector null shift	1. 0
Detector amplifier current drift	. 5
Detector amplifier voltage drift	. 5
Inter-axis cross coupling	. 2
Index of refraction variation	. 4
Random servo error	1. 0

Assuming these errors to be uncorrelated, the rms value of the total error would be as follows:

$$e_{rms}=\sqrt{(1.32)^2+(1.0)^2+(0.5)^2+(0.5)^2+(0.2)^2+(0.4)^2+(1.0)^2}$$

or

$e_{rms}=2.1$ arc-seconds.

Hence, the predicted sun tracker accuracy essentially meets the design goal of 2 arc-seconds rms for sun angles up to ± 20 arc-minutes.

For sun angles up to ± 5 degrees, the maximum error is always less than 0.5 arc-minute, which is well within the allowable accuracy of ± 1 arc-minute. The largest error component in the region is that due to cross coupling, reaching a maximum of 21 arc-seconds.

BREADBOARD SUN TRACKER

About half-way through the design study, a breadboard model of the sun tracker was constructed in order to verify several key factors in the design. These factors included the optical slab concept, the use of a matched pair of silicon photo-voltaic cells as the photo-detector, and the feasibility of a servo drive system capable of positioning the slab with an accuracy of less than 1 arc-second referred to the spacecraft. None of these areas were optimized since the basic intent of the breadboard model was to demonstrate the feasibility of the design concepts. Thus, for expediency, a 1 inch thick slab of ordinary crown glass ($n=1.54$) was used rather than the final recommended ½ inch slab of 1.97 index of refraction. Similarly, ordinary solar cells were used instead of the smaller, precision photo-voltaic cells in the recommended design. Finally, a geared servo drive was constructed instead of the preferred direct drive, because of time limitations as well as servo design considerations. The digital command system, though important, was not considered critical in the tracker design because it did not entail advances in the state-of-the-art. Hence, a more readily available analog command system was utilized in the breadboard sun tracker.

The breadboard tracker servo drive receives its command signal from a 25 speed 400 cycle control transmitter (25 pair of poles) having an absolute accuracy of 20 arc-seconds (about 1 arc-second referred to the spacecraft). The control transformer, directly coupled to the optical slab, develops an error signal proportional to the difference between slab angle β and the command angle. At servo equilibrium, a photo-detector error signal is generated by a pair of solar cells, as indicated by a sensitive voltmeter. The operator, simulating the AOSO control system, turns the Leitz Head, on which the sun tracker is mounted, until the photo-detector signal is zero. The angle through which the sun tracker is turned is the spacecraft sun angle α, which in turn corresponds to the command angle β.

The breadboard tracker focal length is 10 inches. Thus, with the one inch thick slab of crown glass ($n=1.54$), the recommended value of $L/d=10$ is maintained. In order to obtain a light beam at the detector of comparable width and intensity to that attainable in sunlight, a comparatively large slit is used in conjunction with a collimated light source.

The tracker optical characteristics were checked by determining the sun angle α, as measured by the Leitz Head, for various values of command angle β up to 75 degrees. The latter was measured via a circular scale on the control transmitter. The resultant curve of β vs α corresponds, within measurement accuracies, to the theoretically derived curve in Figure 4. This demonstrated the validity of the optical slab concept and the associated theoretical calculations.

In order to determine the resolution and accuracy of the servo drive, in the critical accuracy region ($|\alpha|<20$ arc-minutes), a precision method for measuring command angle β was followed. This consisted of directing a sharply defined beam from a collimated light source to a mirror attached to the control transmitter shaft, and thence onto a wall about 20 feet from the mirror. The measurement accuracy obtained in this manner was equivalent to a fraction of 1 arc-second re-

ferred to the Leitz Head (spacecraft). A given command angle β could thus be repeated many times with considerable accuracy. The total spread in the readings of the corresponding sun angle α, over a short time period, was always less than ± 1 arc-second. This proved that the servo system introduced a static error less than 1 arc-second referred to the spacecraft.

The accuracy of the photo-detector was checked by repeating the above measurements over a longer time interval (8 Hours) as well as by separate measurements of the photo-detector alone. Both sets of measurements indicated an 8 hour drift of approximately 5 arc-seconds, nearly all of which could be attributed to temperature changes at the solar cell.

The above results were very encouraging for the following reasons: The solar cells, though "matched", were far from the precision match that can be obtained with photo-voltaic cells. Secondly, for expediency, the solar cells were operated essentially in the open circuit mode rather than the recommended short circuit mode. This resulted in a greater change in cell output with temperature. Thirdly, no attempt was made to minimize temperature variations between the cells through the use of an appropriate heat sink. Finally, in order to obtain a high detector sensitivity at null, the light beam overlap on each cell at null was much larger than the 0.002 radian in the recommended design. This magnified the drift caused by solar cell temperature variations. It is believed that an optimization of these factors, as previously discussed, will result in an order of magnitude improvement in accuracy. Hence, a 1 arc-second detector accuracy, over a $\pm 20°$ C ambient temperature variation, is not unreasonable to expect from an optimized design.

In summary, the test results of the breadboard tracker system verified the optical slab concept and calculations; demonstrated the feasibility of designing a servo drive system that contributes less than 1 arc-second of error to the spacecraft attitude orientation; and confirmed the inherent accuracy of the photo-detector scheme.

RECOMMENDED DESIGN CONFIGURATION

Based on the preceding analysis and design, a recommended design configuration has been evolved, which is shown in Figure 7. This configuration represents one axis only. The complete sun tracker would consist of two such units mounted orthogonally on the spacecraft. The tracker dimensions, per axis, are approximately 5½ in. x 5½ in. x 11¾ in. The estimated weight and average power, per axis, are 8½ lbs. and 12 watts respectively.

The tracker design is simple and reliable. It is mechanically rugged and should have little difficulty in withstanding the AOSO launch environment. The design can meet the required accuracy of 2 arc-seconds.

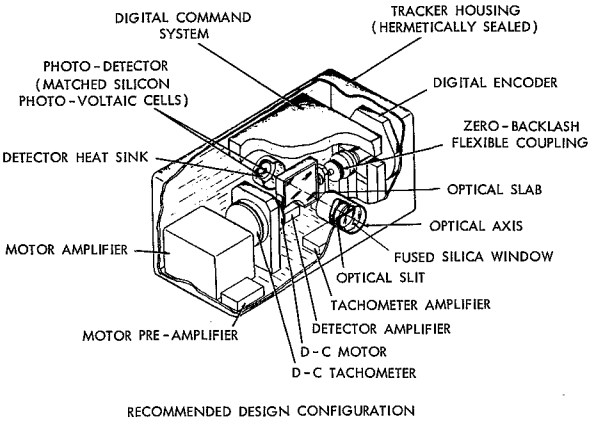

FIGURE 7.—Recommended design configuration.

ACKNOWLEDGMENTS

The analysis and design of the sun tracker represent the effort of many people in the Stabilization & Control Branch at Goddard Space Flight Center. In particular, the author wishes to acknowledge the work of Mr. B. Zimmerman and Mr. F. Volpe in the optical design and analysis, the breadboard tracker design performed by Mr. J. Kelly, the detector light intensity analysis by Mr. C. Barton, the servo analysis and design performed by Mr. L. Draper, and the digital design by Mr. T. Colburn.

REFERENCES

1. Goddard Space Flight Center Report No. X–622–63–80, April 25, 1963, "Fine Sun Tracker for Advanced Orbiting Solar Observatory," by C. Cantor.

DELINEATION OF TRACKS OF HEAVY COSMIC RAYS AND NUCLEAR PROCESSES WITHIN LARGE SILVER CHLORIDE CRYSTALS[1]

CHARLES B. CHILDS[2]
University of North Carolina
AND
Goddard Space Flight Center
AND
LAWRENCE M. SLIFKIN
University of North Carolina

Tracks of energetic charged particles, such as heavy primary cosmic rays and the products of nuclear collisions, have been made visible within the interior of large, transparent crystals of silver chloride. The tracks are delineated by photoelectric formation of metallic silver along them. This technique may be useful as a convenient and distortion-free method for the study of heavy primaries and fission fragments.

INTRODUCTION

The study of cosmic ray particles by means of photographic emulsions has been reviewed by Powell, Fowler, and Perkins (Reference 1). Photographic emulsions, while representing a very powerful and useful technique of study, do have disadvantages such as high sensitivity to the exact processing conditions and distortion of tracks resulting from swelling and drying of the gelatine. Thus, exploration for other recording methods seems worthwhile.

This paper describes the development of one such alternative technique—the delineation of tracks throughout the interior of single crystals of silver chloride. Crystals as large as about $1.5 \times 1.0 \times 0.5$ cm have been employed; and the use of larger crystals would also be feasible. Preliminary reports have been published elsewhere (References 2 and 3). The tracks are made visible by "decoration" with print-out silver, and have been reproduced without distortion.

It is perhaps of interest to briefly review the photographic process as normally employed, and compare it with the physical processes involved in the formation of print-out silver within a large crystal. In an emulsion, the cosmic ray particle registers its passage through the silver halide microcrystal by the liberation of electrons which ultimately combine with silver ions to form metallic specks on the surface of the microcrystal (References 4 and 5). During subsequent chemical development, these specks catalyze the reduction of the entire crystal to metallic silver. In the interior of a large crystal, however, the decomposition products (silver and a halogen) have little chance of reaching the surface before recombination; moreover, any silver specks formed in the interior cannot interact with a chemical developer applied to the surface. The registration and magnification of the trajectories of particles through large crystals must therefore rely upon other phenomena.

The passage of a charged particle through matter produces local vibrational and elec-

[1] This work was supported in part by the Office of Scientific Research, U.S. Air Force; and the Army Research Office; and was published in substantially the same form in *Rev. Sci. Instr.* 34(1): 101–104, January 1963.

[2] Presently at University of Illinois, Urbana, Ill.

tronic excitation, resulting in intense heating of a cylindrical region about the track (see Reference 6). In a crystal as plastic as silver chloride the expansion of this hot region deforms the surrounding material, and the cylinder is in turn deformed as it is rapidly quenched (within about 10^{-11} second) to room temperature (see References 7 and 8). The track of a charged particle is thus surrounded by a cylindrical region of severely deformed matter. It should be possible to decorate this track by applying the techniques already developed for the study of dislocations in crystals.

During the past decade there has been an extensive development of methods for making dislocations visible by the deposition of matter of some sort on them. The technique of precipitation of a solute from a supersaturated solid solution (see Reference 9) presumably could not be applied to cosmic ray track delineation, because annealing the crystal would probably decrease the damage in the track. Hedges and Mitchell (Reference 10), however, were able to decorate dislocations in Ag Br at room temperature by photolyzing the regions near the crystal surface. Moreover, Haynes and Shockley (Reference 11) showed that with pulsed photoresponse techniques it is possible to sweep photoelectrons many millimeters through AgCl. Each electron trapped in the interior then gives rise to an atom of metallic silver, by virtue of the ability of interstitial silver ions to migrate to the trapping sites. A combination of these two techniques has been shown to be capable of delineating imperfections throughout large crystals (see Reference 12), and it is this process that has been employed in the present work.

EXPERIMENTATION

The specimens employed in this work were in the form of slabs, cut from Harshaw Chemical Company AgCl single crystal discs. It was found that only those specimens for which the polyvalent metal impurity content was less than six parts per million (as gauged from the ionic conductivity) gave good decoration. The careful removal (by means of polishing papers and cloths moistened with 3 percent KCN solution) of 2 to 3 mm from one of the broad surfaces was necessary to produce a relatively strain-free surface through which the photoelectrons could subsequently be driven. The crystals were annealed in air on finely powdered silica for 14 hours at 425°C, and returned to room temperature at a rate of no more than 12°C/hour. They were again etched with KCN solution.

The crystals were mounted in plexiglass holders which also carried nuclear photographic emulsions. The strain-free face of each crystal was parallel to an emulsion slab, and separated from it by only a ¼-mil sheet of Mylar. The positioning of the emulsion and crystal was well defined, so that after separation of the two it would be possible to transform from coordinates based on the emulsion to those based on the crystal.

These holders, wrapped in Mylar and in black plastic tape to produce a light-tight package, were flown in a balloon for 9 hours at an altitude of 108,000 feet. The orientation of the package during the flight was such that the emulsion slab was above the crystal, and both were inclined 30 degrees to the horizontal.

Some 3 months after the flight, the specimens were subjected to the internal decoration procedure; photoelectrons created at the strain-free surface by an ultraviolet mercury lamp were swept into the crystal by an electric field. Although AgCl is an ionic conductor at room temperature, the relaxation time of an internal electric field in AgCl is hundreds of microseconds as compared with a photoelectron lifetime on the order of microseconds. Thus, if the ultraviolet radiation is applied in pulses a few microseconds in length, and spaced at about one millisecond, and if the sweeping field is pulsed synchronously with the light flashes; the photoelectrons may be displaced before the ionic conductivity can produce appreciable relaxation. Various mechanical and electronic arrangements to provide these synchronous pulses have been described by Haynes and Shockley; Webb; Hamilton, Hamm, and Brady; and Süptitz (References 11, 13, 14, and 15). The apparatus employed in this work (Reference 16) applies a potential difference of

2 kv across the crystal, and obtains the ultraviolet flashes from a General Electric BH–6 lamp at a repetition rate of 1000 per second. Approximately 10^9 photoelectrons per cm^2 of crystal surface are produced in each flash.

In a crystal several millimeters thick, most of the photoelectrons are usually trapped within the crystal at the sites of imperfections or impurities. Mobile interstitial silver ions with jump frequencies of almost 10^{11}/sec (Reference 17) migrate to trapped electrons to form metallic silver atoms. Repeated electron trapping and neutralization result in the formation of specks of silver about one micron in size. At the intensity and pulse repetition rate used in this work, an exposure of two hours is sufficient to form a colloidal distribution within the crystal. A typical crystal, as seen by scattered light, is shown in Figure 1. Observation under a conventional microscope shows that (if the material is sufficiently pure) the Ag specks delineate dislocations and the tracks of energetic charged particles.

OBSERVATIONS

A one-to-one correspondence between the tracks of heavy (carbon and above) primary cosmic rays in the emulsions and in the crystals was established. Every heavy particle track in an emulsion was also observed in the corresponding crystal, at the expected location and orientation. Moreover, there was a correspondence between track widths in the emulsions and widths of the same tracks in the crystals. Figure 2 shows one such track inside a crystal, and Figure 3 shows a portion of another track in the emulsion along with its continuation in the crystal. No tracks attributable to protons, alphas, or light primaries have been found in the crystals; apparently the density of energy released by particles of low charge and high velocity is too small to produce much thermal strain in the crystals. Control experiments were performed on many crystals which were not flown at high altitudes, and no patterns attributable to cosmic ray tracks were ever observed in these.

It was always possible to follow the tracks of the heavy primaries completely throughout the 5-mm thickness of the crystals, as shown in Figure 4. The apparent increase in track width in the photographs of track segments below about 3000μ is due to the scattering of light within the crystal. This was demonstrated by viewing the same track through the opposite surface of the crystal.

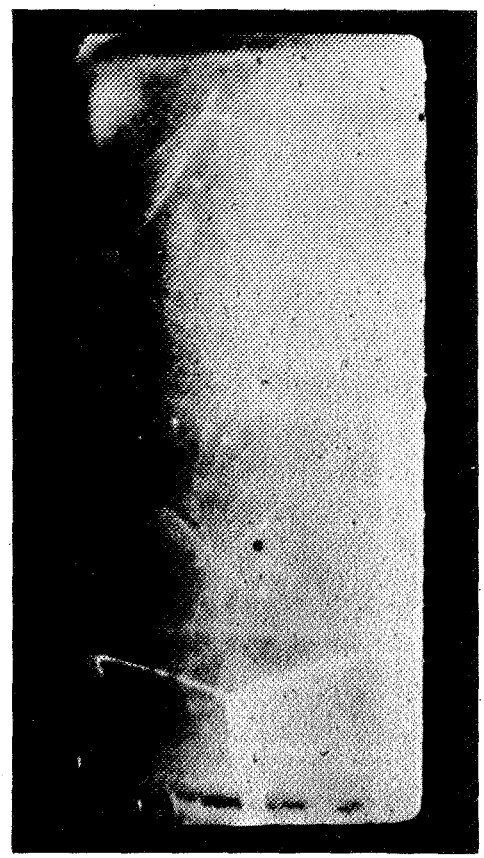

FIGURE 1.—Dark field photograph of silver chloride crystal after exposure to synchronous electric field and ultraviolet light. The crystal is 4.8 mm high and 10 mm wide. The lines visible in the photograph are grain boundaries.

Only one primary track was found which ended within the crystal; a large increase in track density was apparent near the end of its range.

In addition to the straight tracks of the primary radiation, 12 events with 2 or more secondary particles were found. Examples of these are given in Figures 5 through 9. They were apparently induced by fast light primaries,

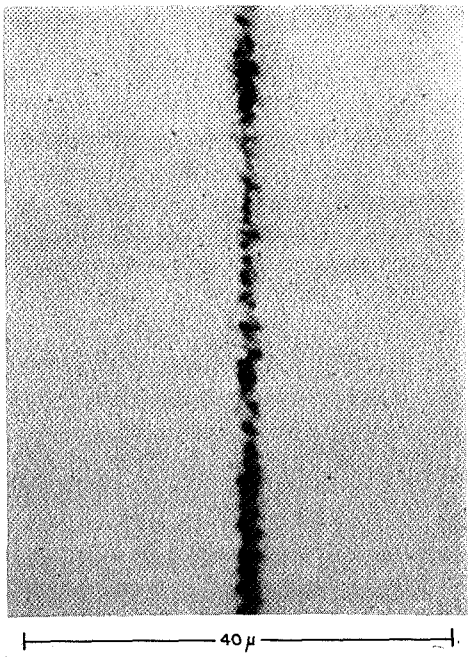

FIGURE 2.—Heavy cosmic ray particle track inside the crystal of figure 1.

since the tracks of the incoming particles are not visible.

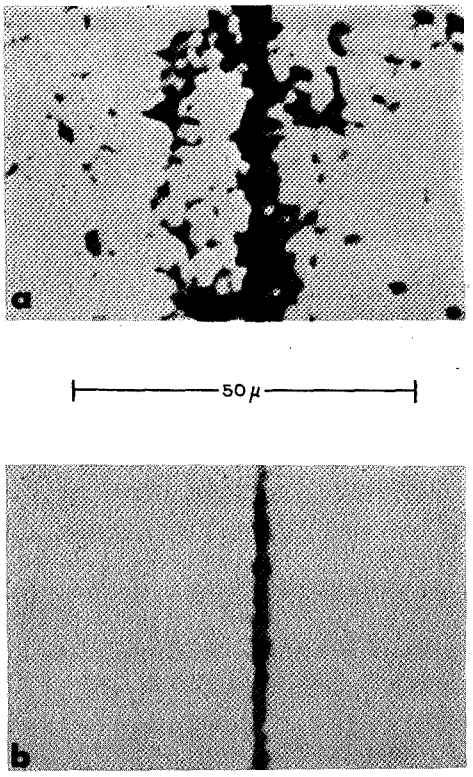

FIGURE 3.—Tracks of the same cosmic ray particle (a) in the adjacent emulsion and (b) 72μ below the crystal surface.

CONCLUSION

It is thus established that the internal printout technique is capable of recording the tracks of energetic charged particles, provided that the energy loss density is great enough. Therefore, at relativistic speeds, only highly charged particles are seen; aplha particles are recorded if they move slowly enough to release sufficient energy to damage the crystal thermally. For example, this technique has been used to detect nuclear disintegrations produced by 1.55 Bev protons, in which more than 12 secondary particles had ranges greater than 1800μ which is equivalent to about 3½ mm of emulsion (Reference 15).

Further experiments will be necessary in order to evaluate the potential utility of this technique. The question of whether the track width in the crystal is a reliable measure of energy loss rate—and hence, of the charge of relativistic particles—must be settled. Extensive comparison of tracks in crystals and emulsions would then permit a calibration of the method. The effects of crystal purity and the possible use of AgBr as well as AgCl should be investigated. Finally, elimination of the dislocation background by the recrystallization method of Bartlett and Mitchell (Reference 19) seems promising. These investigations are currently in progress.

If the method does indeed prove to be reliable, several specialized applications suggest themselves. The collection of statistics on heavy primaries by means of prolonged exposures from recoverable satellites would now be simplified, and without the fogging normally produced by the high incidence of lighter particles. Heavy particles in solar flares could similarly be studied. Moreover, in any collision recorded in the crystal, angles could be measured rather accurately, since the development process does not distort the medium. Finally, this technique seems well-suited to the

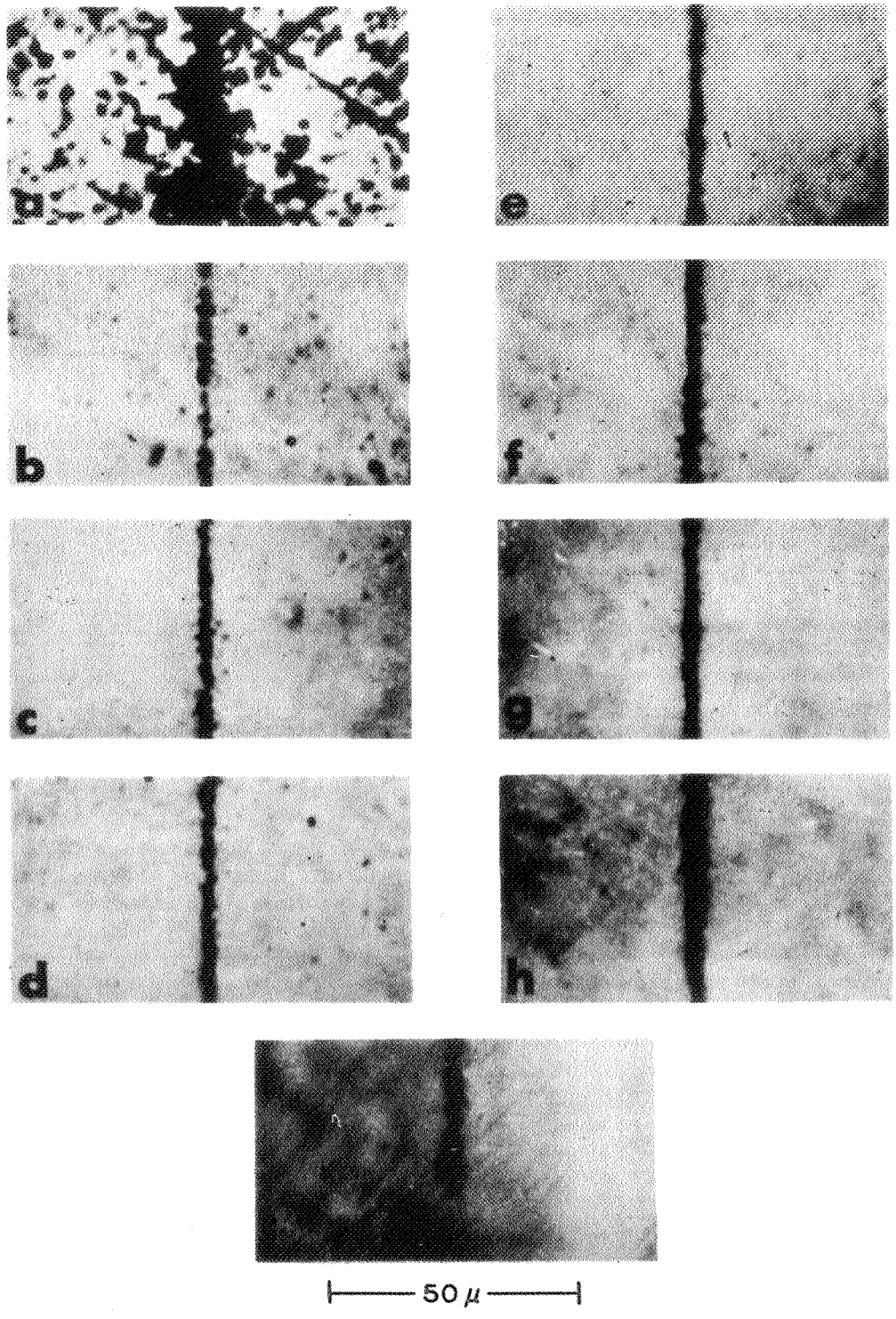

FIGURE 4.—Cosmic ray particle track (a) in the emulsion, and within the crystal at depths of (b) 500μ; (c) 1000μ; (d) 1500μ; (e) 2000μ; (f) 2500μ; (g) 3000μ; (h) 3500μ; (i) bottom surface, 4860μ. The apparent increase in track diffuseness below about 3000μ is due to scattering of light in the crystal.

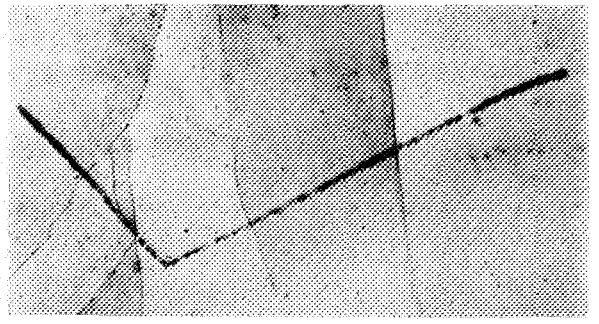

FIGURE 5.—Two secondary particles produced in a collision at a depth of 1560μ below crystal surface. Note the increase in the track densities near the ends of the ranges. This figure and those following are composites of several photographs taken at different depths. The faint, irregular lines in the figures are the edges of the individual photographs.

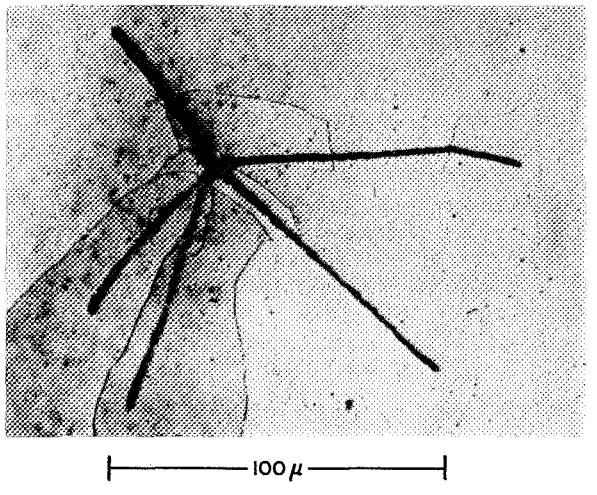

FIGURE 6.—A five-prong star produced 1440μ below the crystal surface.

study of fission fragments, either by exposure of pure crystals to particles from high-energy accelerators (References 18 and 19), or by exposure to slow neutrons of crystals doped with fissionable material.

ACKNOWLEDGMENTS

One of the authors (L. S.) derived much benefit from early discussions with Drs. E. Ney, P. Freier, and J. Naugle at the University of Minnesota. Also, the authors sincerely appreciate the generous assistance of Drs. E. Ney,

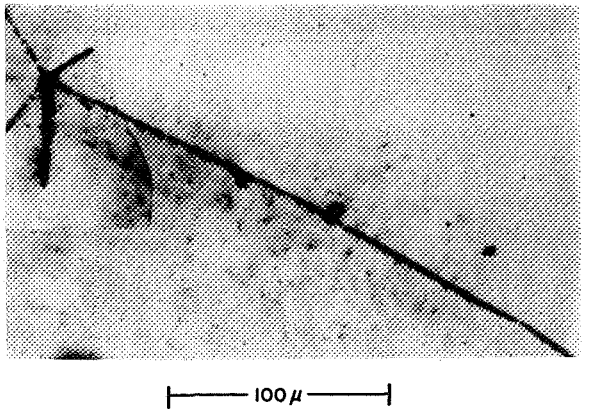

FIGURE 7.—A star with eight prongs, two of which are only lightly decorated, produced 1500μ below the crystal surface.

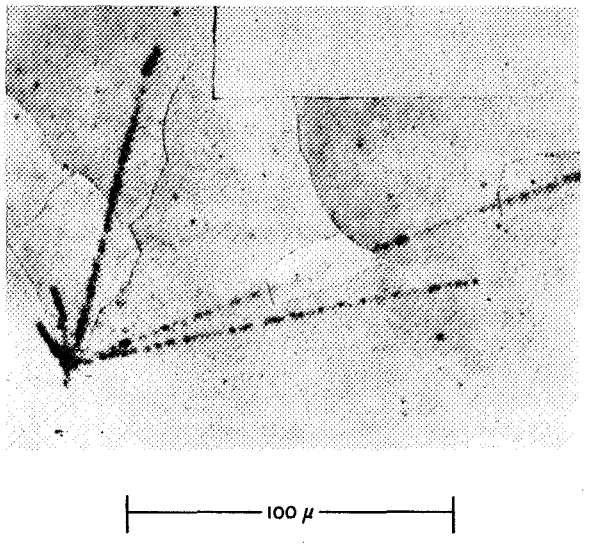

FIGURE 8.—A six-prong star observed at a depth of 1500μ below crystal surface.

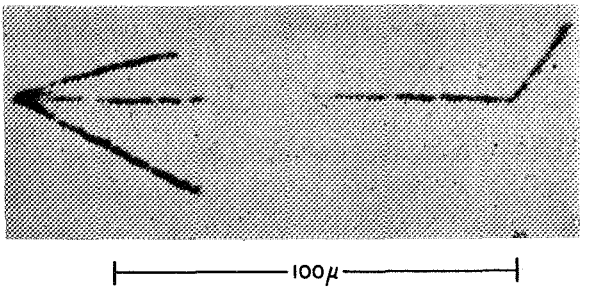

FIGURE 9.—A three-prong star produced at 1740μ below the crystal surface. A poorly decorated segment, such as that seen in the center of the long track of this figure, is quite uncommon; the reason for this lack of decoration is not understood at present.

M. W. Friedlander (Washington University), and C. Fichtel (Goddard Space Flight Center) in flying crystals and processing emulsions.

REFERENCES

1. Powell, C. F., Fowler, P. H., and Perkins, D. H., "The Study of Elementary Particles by the Photographic Method," New York: Pergamon Press, 1959.
2. Childs, C. B., and Slifkin, L. M., "Detection of Primary Cosmic-Ray Particles in Large Silver Chloride Single Crystals," *Bull. Am. Phys. Soc.* Series II, 6(1): 52–53, Feb. 1, 1961.
3. Childs, C. B., and Slifkin, L. M., "A New Technique for Recording Heavy Primary Cosmic Radiation and Nuclear Processes in Silver Chloride Single Crystals," *I.R.E. Trans. Nuclear Sci.* NS-9(3): 413–414, June 1962.
4. Mitchell, J. W., "Photographic Sensitivity," *Repts. on Prog. in Phys.* 20: 433–515, 1957.
5. Mitchell, J. W., "The Nature of Photographic Sensitivity," *J. Photogr. Sci.* 5: 49–70, 1957.
6. Seitz, F., and Koehler, J. S., "Displacement of Atoms During Irradiation," *Solid State Physics.* Vol. 2. New York: Academic Press, Inc., 1956.
7. J. A. Brinkman, "On the Nature of Radiation Damage in Metals," *J. Appl. Phys.* 25(8): 961–970, August 1954.
8. Harrison, W. A., and Seitz, F., "On the Theory of Radiation Damage," *Phys. Rev.* 98: 1530, 1955.
9. Amelinckx, S., "The Direct Observation of Dislocation Nets in Rock Salt SIngle Crystals," *Phil. Mag.* Series 8, 1(3): 269–290, March 1956.
10. Hedges, J. M., and Mitchell, J. W., "The Observation of Polyhedral Sub-Structures in Crystals of Silver Bromide," *Phil. Mag.* Series 7, 44(349): 223–224, February 1953.
11. Haynes, J. R., and Shockley, W., "Mobility of Electrons in Silver Chloride," *Phys. Rev.* 82(6): 935–943, June 15, 1951.
12. Childs, C., and Slifkin, L., "Room-Temperature Dislocation Decoration Inside Large Crystals," *Phys. Rev. Letters* 5(11): 502–503, Dec. 1, 1960.
13. Webb, J. H., "Ultrashort Light and Voltage Pulses Applied to Silver Halide Crystals by Turbine-Driven Mirror and Spark-Gap Switch," *J. Appl. Phys.* 26(11): 1309–1314, November 1955.
14. Hamilton, J. F., Hamm, F. A., and Brady, L. E., "Motion of Electrons and Holes in Photographic Emulsion Grains," *J. Appl. Phys.* 27(8): 874–885, August 1956.
15. Süptitz, P., "Die Eigenschaften von Photoelektronen in Silberchlorid bei Zimmertemperatur," *Z. Physik* 153(2): 174–185, 1958.
16. Childs, C. Master's Theses, University of North Carolina, 1959.
17. Seitz, F., "Speculations on the Properties of the Silver Halide Crystals," *Revs. Modern Phys.* 23(4): 328–352, October 1951.
18. Childs, C., and Slifkin, L., "Detection of Nuclear Disintegrations Produced by 1.55-Bev Protons in Silver Chloride Single Crystals," *Phys. Rev. Letters* 9(8): 354–355, Oct. 15, 1962.
19. Bartlett, J. T., and Mitchell, J. W., "The Generation of Dislocation Loops at the Surfaces of Crystals of Silver Bromide," *Phil. Mag.* Series 8, 5(53): 445–459, May 1960.
20. Baker, E. W., and Katcoff, S., "Fission of Ag and Br in Nuclear Emulsion by 1.0–3.0 Bev Protons," *Phys. Rev.* 126(2): 729–734, Apr. 15, 1962.

SPECTRALLY SELECTIVE PHOTODETECTORS FOR THE MIDDLE AND VACUUM ULTRAVIOLET[1]

LAWRENCE DUNKELMAN, WALTER B. FOWLER, AND JOHN P. HENNES

Goddard Space Flight Center

A number of "solar blind" photodetectors have been developed in recent years. Measurements made on several phototubes with photocathodes of rubidium-tellurium, cesium-tellurium, cesium-iodine and copper-iodine are described. Cathode quantum efficiencies for semitransparent cathodes of rubidium-tellurium or cesium-tellurium range from 10^{-1} to 10^{-2} photoelectrons/quantum in the middle and vacuum ultraviolet, with long wavelength responses of less than 10^{-4} photoelectrons/quantum beyond about 3500A. By combining solar blind cathodes with windows of LiF, CaF_2, or fused silica, detectors with relatively flat quantum efficiencies can be produced, marked by high sensitivities in specific ultraviolet spectral regions and by very low sensitivities at all longer wavelengths.

INTRODUCTION

The need for photodetectors that are efficient in the middle and vacuum ultraviolet but relatively insensitive in the near ultraviolet and visible has led, in recent years, to the development of a variety of spectrally selective ultraviolet photodetectors (References 1 and 2). The photoemissive surfaces in these devices have been described as "solar blind" (Reference 3). This term refers to the fact that these detectors are relatively insensitive to wavelengths greater than about 3000A and thus quite unresponsive to solar radiation viewed through the earth's atmosphere. Photocathodes with these solar blind responses are very useful for astrophysical and geophysical experiments in the ultraviolet, as well as for laboratory ultraviolet spectroscopy or radiometry wherever the amount of long wavelength stray light is undesirably large. The "middle" ultraviolet is considered to extend from 3000A to 2000A, with the "far" or "vacuum" ultraviolet extending downward from 2000A. This report describes the recent program of Goddard Space Flight Center in developing solar blind photodetectors. Future improvements in ultraviolet detectors and answers to questions concerning the physics of high-work function cathodes and their use in phototubes may be anticipated.

Spectrally selective ultraviolet photoemitting surfaces may be of two types: pure metal cathodes such as nickel, tungsten, gold, etc., or composite surfaces such as the well known cesium-antimony (Cs-Sb) or the selective alkali-tellurium surfaces. Pure metal photosurfaces, selective for the middle ultraviolet, have been reported in the literature since the 1920's and an excellent review of these researches in photoelectric emission from solids, emphasizing the vacuum ultraviolet, is contained in a chapter by Weissler in Reference 4. A recent study of gold cathode photomultipliers was made by Childs (Reference 5). Pure metal photosurfaces are characterized by low quantum efficiencies in the middle ultraviolet (10^{-3} to 10^{-5} photoelectrons/quantum), although the yield of some metals, such as tungsten, may rise to as much as 10^{-1} photoelectrons/quantum at shorter wavelengths in the vacuum ultraviolet (References 4, 5, and 6). Two examples of metal photoemitters will

[1] Presented at the Los Angeles meeting of the Optical Society of America, October 1961. Published in *Applied Optics*, 1(6): 695–700, November 1962.

be discussed shortly, in connection with Figure 5.

Composite photosurfaces of Cs-Sb, Na-K-Cs-Sb, Cs-Sb-O, and Rb-Ag-O have been in use in commercial phototubes for many years (References 7 and 8). The high-yield ultraviolet selective photocathodes of cesium-tellurium (Cs-Te) and rubidium-tellurium (Rb-Te) were reported in 1953 by Taft and Apker (Reference 9) and were further described in 1956 by Harper and Choyke (Reference 10). Since then others have prepared alkali-tellurium opaque and semitransparent photosurfaces (References 11 through 14 and private communications from J. E. Roderick, G. G. Kretschmar, S. Essig, H. L. Sowers, B. Linden, A. H. Sommer, and J. P. Causse). The photoemissive properties of some of these cathodes were studied at the Naval Research Laboratory in the 1950's, and of others, more recently, at Goddard Space Flight Center.

PHOTODETECTOR RESPONSES

Figure 1 gives the spectral response (quantum efficiency) from 3500A to 1000A of several phototubes containing a variety of representative photocathode materials. The curve marked 1P21 shows the short wavelength portion of the response of this well known Cs-Sb photomultiplier. This tube has a glass envelope and is used primarily in the visible region. The 1P28 photomultiplier, introduced some 15 years ago, has an envelope of Corning 9741 ultraviolet transmitting glass which extends the Cs-Sb range by over 1000A, putting it into the beginning of the vacuum ultraviolet as shown. By using a quartz envelope Cs-Sb photosurface, which was described by Dunkelman and Lock (Reference 15), the range is extended to approximately 1600A. A photomultiplier using these materials became commercially available several years ago as type 7200. Recently a photosurface of Cs-Sb with a CaF_2 window was examined at Goddard Space Flight Center. Figure 1 shows the further extension of the comparatively flat, high quantum efficiency of Cs-Sb down to 1225A with this phototube.

In cases where high efficiencies and solar blindness are desired, one of the alkali-tellurium photosurfaces such as Rb-Te is required. If it is important to limit the response of a photodetector to the vacuum ultraviolet, then a material such as cesium-iodine (Cs-I) with a window of LiF is necessary. Cesium-iodine rejects even more of the middle and near ultraviolet as well as the visible wavelengths. Both of those photocathode materials will be discussed here.

Finally, in Figure 1 there are shown for comparison two dashed lines (ethyl sulfide gas in a chamber with a BaF_2 window and ethylene oxide gas in an ion chamber with a LiF window) representing examples of relatively narrow response photodetectors which operate not by photoelectric emission from a solid photocathode, as in the above materials, but by photoionization of a gas chamber (Reference 16). Photoionization chambers, with their very narrow vacuum ultraviolet response bands and high quantum efficiencies, have proved useful in vacuum ultraviolet spectroscopy and stellar astronomy from rockets (References 17 and 18).

Figures 2, 3 and 4 give details of the spectral

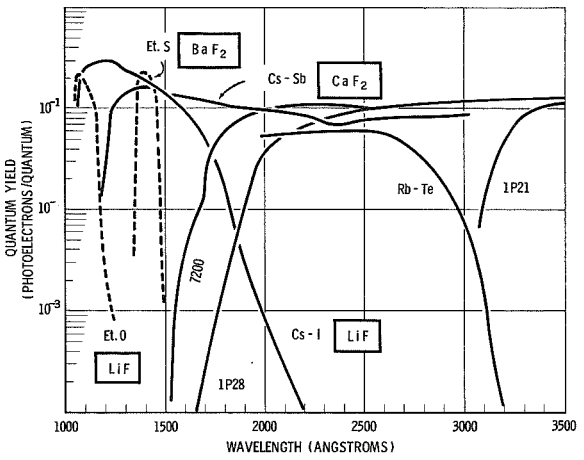

FIGURE 1.—Spectral response curves for representative ultraviolet photodetectors. Boxed symbols refer to the phototube window materials. The 1P21, 1P28, and 7200 curves show the short wavelength portions of photomultipliers with Cs-Sb cathodes and envelopes of glass, Corning 9741 and fused silica, respectively (Reference 15). For comparison, the two dashed curves represent the narrow responses of photoionization chambers containing ethyl sulfide and ethylene oxide (Reference 16).

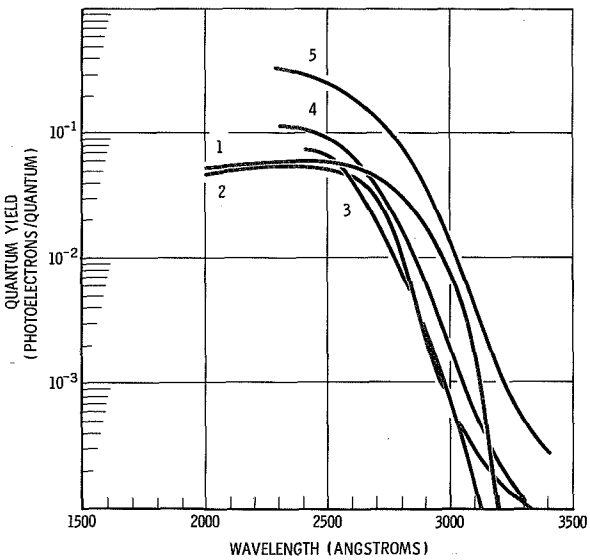

FIGURE 2.—Spectral response curves of Rb-Te opaque-cathode photodiodes showing various degrees of solar blindness and quantum efficiency. Curves 1, 2, and 3 refer to Kretschmar's diodes 16, 4, and 59 (Reference 11 and private communication). Curves 4 and 5 represent Roderick's diodes 21 and 14 (private communication).

response of several types of spectrally selective solar blind photocathodes. In Figure 2 the responses of several Rb-Te opaque-cathode phototubes are shown. Curves 4 and 5 represent the average of the extremes of many tubes prepared by Roderick (private communication). These curves with their high efficiencies below 2500A may be compared with curves 1 and 2 which show the response of two photodiodes prepared by Kretschmar (private communications and Reference 11). Although exhibiting lower efficiencies, the latter phototubes provide higher selectivity. Curve 1, for example, refers to a photodiode having a quantum efficiency of 7×10^{-2} photoelectrons/quantum at the 2537A mercury line and a rejection ratio of 1000 over the wavelength interval 2900A to 3300A. Curve 3, although representing another photodiode by Kretschmar, is similar to curves 4 and 5 and indicates the variability found in these experimental tubes.

It should be mentioned that no major differences between Rb-Te and Cs-Te cathodes with respect to either quantum efficiency or rejection ratios have been found. Even though some problems are caused by a reaction of the cesium with AgCl seals, most manufacturers have preferred to work with Cs-Te rather than Rb-Te. This choice is evidently based on the desirability of being able to cesiate photomultiplier dynodes to a limited extent, on the ready availability of pure cesium compounds, and on prior familiarity with evaporation of cesium compounds.

In Figure 3 there are compared a variety of Cs-Te cathodes. The curves marked XCD–12 and FW 140–12 show the spectral response of sapphire windowed opaque photoiodes made at the ITT Federal Laboratories,[2] while the curve marked FW 157–1 refers to an ITT photodiode with fused silica windows. The curve marked S.883 refers to the opaque cathode of a 13-

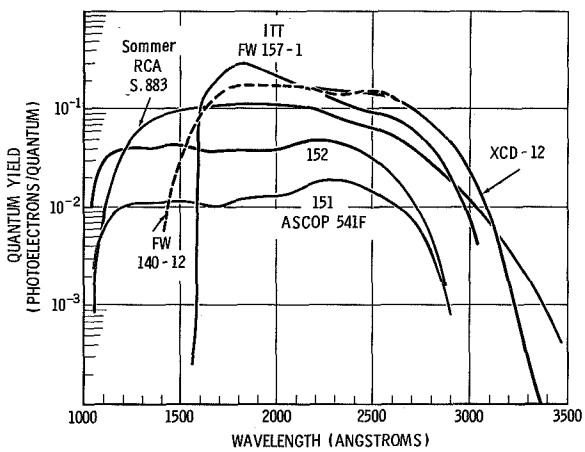

FIGURE 3.—Spectral response curves of Cs-Te phototubes. Note the variation in long wavelength responses as well as the differences in quantum efficiency between opaque and semitransparent cathodes. The FW 140–12 and XCD–12 curves refer to opaque-cathode photodiodes made by the ITT Federal Laboratories with sapphire windows; the FW 157–1 curve is the response of an ITT opaque-cathode diode with a fused silica window; the S.883 curve is the response of a 13-stage photomultiplier with an opaque cathode and LiF window made by Sommer (Reference 13). The 151 and 152 curves represent the responses of 14-stage semitransparent-cathode photomultipliers with LiF windows made at ASCOP (Causse, private communication).

[2] International Telephone and Telegraph Federal Laboratories.

[3] ASCOP Division of Electro-Mechanical Research, Inc.

stage photomultiplier with LiF window made by Sommer (Reference 13). Note that a quantum efficiency of better than 10^{-1} photoelectrons/quantum is achieved with these opaque cathodes; the yields are considerably lower on the two lower curves marked 151 and 152, which refer to the response of semitransparent photocathodes in a 14-stage ASCOP [3] photomultiplier (Causse, private communication). It is not clear with the limited data on hand whether this is due to a transmission loss in the metallic conducting substrate or to incomplete escape of photoelectrons from a thick transmission photocathode. A semitransparent cathode just behind the front window does result in far better optical coupling than is possible in recessed opaque cathodes. This is frequently an important consideration in application.

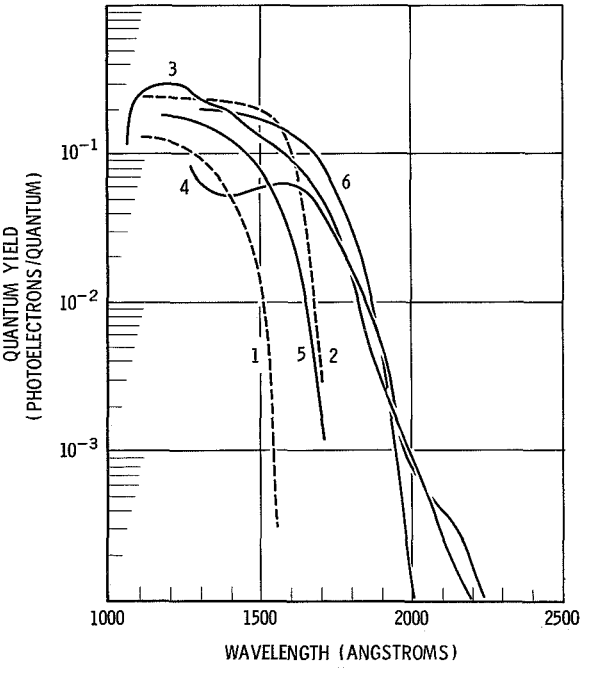

FIGURE 4.—Spectral response curves of several high-work function cathodes. Curve 1, K-Br; curve 2, Cs-Br; and curve 5, Rb-1 are taken from the work of Taft and Philipp (Reference 20). Curve 3 is the response of a diode with a semitransparent cathode of Cs-1 behind a LiF window in a tube made by Sommer (Reference 13). Curve 4 is the response of Cu-1 estimated from the work of Shuba and Smirnova (Reference 12). Curve 6, the response of Cs-1, is from the paper of Philipp and Taft (Reference 19).

Figure 4 displays the spectral responses of several high-work function photocathodes. Curve 6 refers to the response of a Cs-I surface from the work of Philipp and Taft (Reference 19) who studied various iodine compounds evaporated on opaque metallic discs. Curve 3 represents recent measurements of the spectral distribution of efficiency from a Cs-I surface prepared by Sommer and studied at Goddard Space Flight Center. Here the photocathode is deposited on a conducting substrate of thin tungsten immediately behind the LiF window which makes possible, again, convenient end-on coupling. Curves 1, 2, and 5 (K-Br, Cs-Br, and Rb-I) are taken from the work of Taft and Philipp (Reference 20) and are shown here for comparison and for a suggestion of surfaces which should be considered if shorter wavelength cutoffs are of interest. The copper-iodine (Cu-I) curve, curve 4, is taken from the work by Shuba and Smirnova (Reference 21) and will be discussed in connection with Figure 5.

The long wavelength response of some of these photocathodes is displayed in Figure 5,

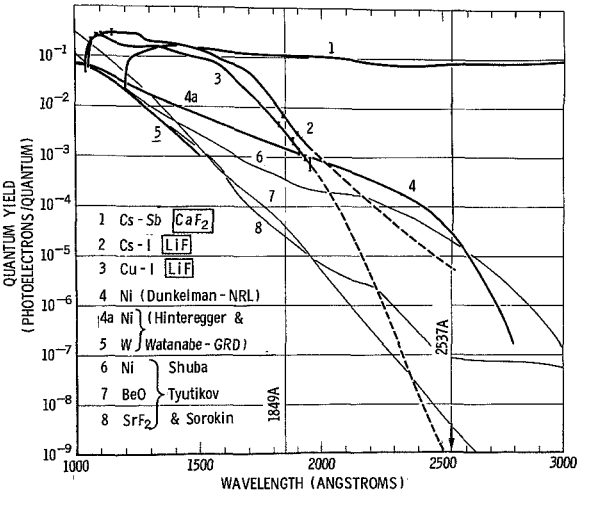

FIGURE 5.—Spectral response curves of various photosurfaces showing their long wavelength response. Boxed symbols refer to the phototube window materials. Excellent rejection ratios and high sensitivity can be seen in the iodine compounds. Curves 1, 2, and 3 are measurements made at GSFC (see text). Curve 4 is from Reference 1; curves 4a and 5 from Reference 6. Curves 6, 7, and 8, shown for further comparison, are taken from Reference 23.

where 9 orders of magnitude of quantum efficiency are shown. Curve 1 is the familiar Cs-Sb photosurface discussed in Figure 1. Curve 2 is the Sommer Cs-I surface discussed in Figure 4, but in this figure it can be seen that at 2537A the absolute quantum efficiency is only 7×10^{-6} photoelectrons/quantum; this was measured with a calibrated low-pressure mercury arc. Curve 3 is a result of some recent measurements at Goddard Space Flight Center of a Cu-I semitransparent surface on a tungsten substrate in a photodiode made by Sommer. This response is similar to that of his Cs-I tube (curve 2), except for the much improved long wavelength rejection ratio which is at least 7 orders of magnitude between 1849A and 2537A. The upper limit of yield at the latter wavelength was determined to be less than 10^{-9} photoelectrons/quantum. In both curves 2 and 3 the response has been measured at many wavelengths from about 2000A down to 1050A and also at the intense mercury 2537A line.[4] Between 2000A and 2537A an estimated curve has been drawn. These measurements can be compared with the results reported in 1960 by Shuba and Smirnova and mentioned in connection with Figure 4. They have estimated a quantum efficiency of 10^{-1} photoelectrons/quantum at the short wavelengths but a rejection ratio of only 6 orders of magnitude. The absolute quantum efficiency of their photosurface has been estimated from their paper, and curve 4 (Fig. 4) is for comparison purposes only. Since their article was published, other yield curves of vacuum ultraviolet photoemitters have appeared by Tyutikov and Shuba (Reference 22), and Shuba, Tyutikov and Sorokin (Reference 23). In 1957, D. W. Turner of Imperial College reported (Reference 24) a Cu-I photoemitter with a "cutoff" at 2300A and a peak efficiency somewhere between 10^{-2} and 1 photoelectrons/quantum; however, he does not define "cutoff."

[4]The large quantum efficiencies shown for these tubes represents an early and preliminary measurement. Subsequent measurements of Cs-I and Cu-I cathodes show that in general a peak quantum efficiency of 10 to 20 percent is more typical with Cs-I being 3 to 5 times more sensitive than Cu-I at the Lyman-alpha wavelength (1216A).

Copper-iodine, it can be seen from Figures 4 and 5, makes a useful detector for spectroscopic studies in the vacuum ultraviolet, not only because of high quantum efficiency but also because it makes negligible the effect of scattered light. This scattered light comes primarily from the longer wavelength emission of the hydrogen or other gaseous discharge tubes generally used with vacuum monochromators. It is also interesting to compare the alkali-iodine surfaces with some of the pure metal photosurfaces. Curves 4 and 4a of Figure 5 show a nickel cathode response which was obtained by combining middle and vacuum ultraviolet measurements made in 1953 as shown in the figure (Reference 6). Copper-iodine appears to be more advantageous at these wavelengths than nickel and other metal photocathodes which have been the only readily available vacuum ultraviolet photoemitters. Finally, we can compare the Cu-I efficiency with that of tungsten, curve 5.

For measurements below the LiF cutoff (1050A) it is necessary to use an open window photomultiplier, such as the Bendix magnetic strip multiplier with a tungsten cathode developed by Goodrich and Wiley (Reference 25) and first used by Heroux and Hinteregger (Reference 26) in the late 1950's. Subsequent experiments with this detector have been reported by Hinteregger (Reference 27) and recently by Behring, Neupert, and Nichols (Reference 28) of Goddard Space Flight Center. Current measurements indicate that Cu-I will also prove useful in windowless phototubes as a far ultraviolet photosurface of high quantum efficiency.

PHOTODETECTOR TECHNIQUES

It should be kept in mind that the spectral response being measured is a combination of the phototube window transmission, the conducting substrate transmission, and the photoemissive response of the cathode material. At the long wavelength end of the response curve, the degree of solar blindness is essentially determined by the amount of cesium or rubidium introduced in excess of the stoichiometric ratio. The greater the excess the more pronounced is

the long wavelength tail in the response. A great deal of care must be exercised in tube processing to keep the excess alkali metal to a minimum (References 9 and 14). The rigid restrictions on the amount of cesium present in a tube rule out, of course, the use of highly cesiated high-gain dynodes. Most frequently used in their place have been dynodes of silver-magnesium (Ag-Mg) or copper-beryllium (Cu-Be).

At the short wavelength end the transmission cutoff characteristic of the phototube window is the principal determinant of the shape of the response curve. Figure 6 is a summary of measurements made during the past year on currently available window and cutoff filter materials. The two curves numbered 5, showing two different sapphire windows, indicate the transmittance variation sometimes found in commercial crystals. The materials represented by curves 7, 8 and 9 are useful in subtractive filter photometry. The other materials are useful as detector windows or as supplementary windows to narrow the photodetector spectral band. Windows of fused silica and sapphire are readily sealed to various glass photodiode and photomultiplier shells by conventional methods, but it is much more difficult

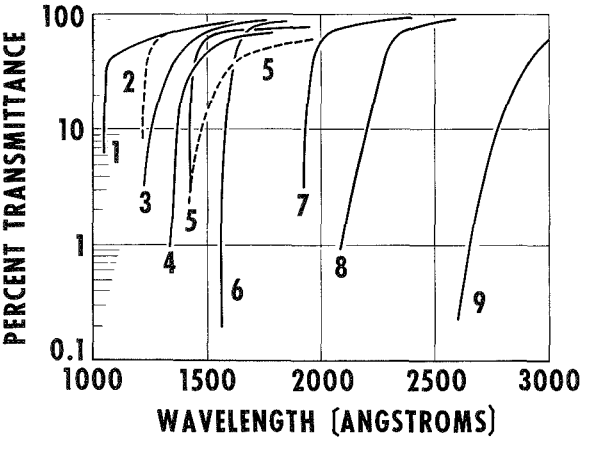

FIGURE 6.—Transmittance characteristics of materials useful in the ultraviolet, uncorrected for surface reflectance: curve 1, LiF (1 mm); curve 2, CaF_2 (1 mm); curve 3, NaF (1 mm); curve 4, BaF_2 (1 mm); curve 5, Sapphire (1 mm); curve 6, Fused silica (1 mm); curve 7, $NiSO_4$ $(H_2O)_6$ (3 mm); curve 8, Corning 9–54 (7910); curve 9, Corning 9700 (2 mm).

to make good seals with windows of cleaved or polished LiF and CaF_2 crystals. The large expansion coefficients of these crystals have made necessary special sealing techniques—employing silver chloride, silver, and epoxies—which have been only partially described in the literature (References 13, 29, 30, and 31).

At wavelengths greater than 1400A the slightly lower yield of the photosurfaces shown in these figures might be attributed to a transmittance loss in the conducting substrate. The highly resistive alkali-tellurium and alkali-halide surfaces require that the photoemissive material be deposited on a substrate of some material which is both transparent to the wavelengths of interest and electrically conductive. Very thin deposits (approximately 80 to 90 percent transmittance) of tungsten, nickel, and platinum have proved effective in satisfying both of these requirements.

Figure 7 pictures a variety of photodiodes with sapphire and LiF windows. These diodes are quite small and inherently rugged. The type of ITT diode shown in the figure (second from left) has been flown in recent Aerobee-Hi sounding rockets as part of a solar ultraviolet flux photometric experiment. Kretschmar diodes have proved to be very useful in laboratory radiometry. It is important to minimize electrical leakage so that full advantage can be taken of the intrinsically small dark currents from the low thermionic emission of the high work function cathodes described in this paper.

Figure 8 shows some of the photomultipliers mentioned in the previous section. These phototubes have been developed to meet certain requirements for detectors for use in ultraviolet space or laboratory research. These requirements are: (1) suitable cathode sensitivity, (2) suitable solar blindness, (3) suitable windows and window seals, (4) adequate gain and dark current characteristics and, for space environments, (5) ruggedness and small size.

Relative curves of the distribution of photoelectric quantum efficiencies of the various surfaces were obtained by using a McPherson 1-meter grating monochromator and the double monochromator of the Cary spectrophotometer.

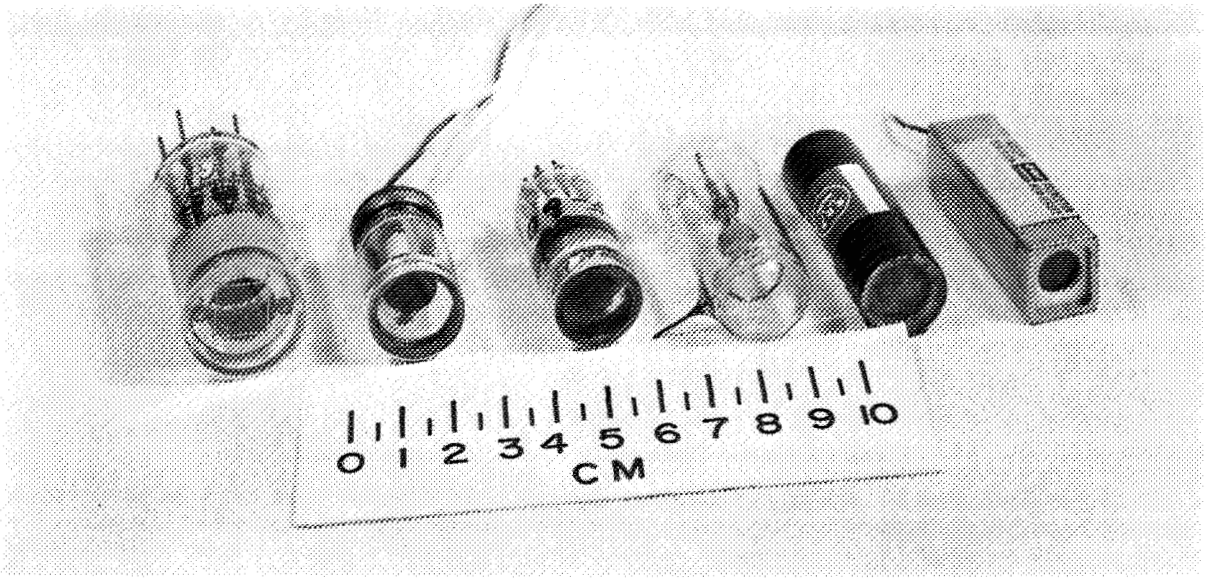

FIGURE 7.—Some of the photodiodes examined at Goddard Space Flight Center. Left to right: CBS CL1051, opaque Cs-Sb cathode, sapphire window; ITT FW156, opaque Cs-Te cathodes, LiF window; RCA, semitransparent Cs-Te cathode, LiF window; Kretschmar, NOLC, opaque Rb-Te cathode, 9741 glass window; Westinghouse, semitransparent Cs-1 cathode, LiF window; ASCOP 540F, semitransparent Cs-Te cathode, LiF window.

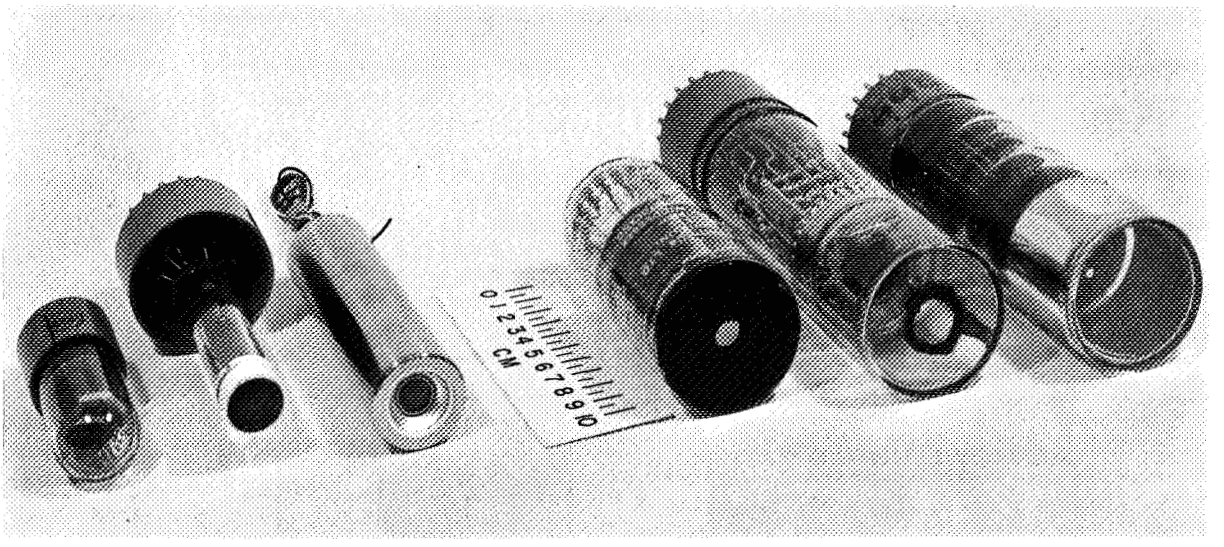

FIGURE 8.—Some of the photomultipliers examined at Goddard Space Flight Center. Left to right: RCA 1P28, Cs-Sb cathode, 9741 glass envelope; RCA C70128 (in test base), semitransparent Cs-Te cathode, LiF window; ASCOP 541F08, semitransparent Cs-Te cathode, LiF window (potted with registor chain in place); EMI 6256B, semitransparent Cs-Sb cathode, fused silica window; RCA (A. H. Sommer experimental tube), semitransparent Cu-I cathode, LiF window; CBS CL1067, semitransparent Cs-Te cathode, sapphire window.

The photocathode response is compared with the fluorescence response of sodium salicylate to obtain a relative response curve. Within the accuracy of these measurements the response of sodium salicylate is taken to have a relatively constant quantum efficiency over the wavelength region studied. At wavelengths greater than 3000A a comparison photocathode, which had been calibrated against a thermopile, was used as a reference surface. The relative response curves thus obtained were put on an absolute basis by measurements using either a calibrated mercury arc line at 2537A (Reference 32) or a calibrated ion chamber at the 1216A hydrogen Lyman-alpha line. Use was also made of intense lines of other discharges such as the mercury 1849A line.

As a guide for application, the photosurfaces described herein are summarized in Table 1 which shows the wide variety of spectral responses available by combining various windows and cathodes.

TABLE 1.—*Typical Photodetector Spectral Response Regions*

The upper figure given for each window material represents typical wavelengths at which the photocathode response is 50 percent of the maximum response; the lower figure, the wavelength at 1 percent of maximum. For cathode materials the spectral region between the short wavelength cutoff and the long wavelength cutoff is a region of 10^{-2} to 10^{-1} photoelectrons/quantum. Some of the values given are averaged from the phototubes reported in this paper. The window cutoff values are taken from Figure 6. The Cs-Sb long wavelength cutoff is estimated from RCA tube handbook data. Those categories for which actual tubes were not yet available were estimated by combining typical window transmittances with typical cathode responses.

Window materials	Short wavelength cutoff (A)	Cathode materials long wavelength cutoff (A)		
		Cu-I	Cs-Te	Cs-Sb
Glass	3220	----------	----------	4600
	3050	----------	----------	7000
Corning 9741	2160	----------	2700	4600
	1780	----------	3100	7000
Fused silica	1620	1750	2700	4600
	1550	1950	3050	7000
Sapphire	1460	1640	2780	4600
	1420	1960	3200	7000
CaF_2	1300	1420	2700	4600
	1220	1880	3100	7000
LiF	1120	1420	2600	4600
	1050	1880	2900	7000

ACKNOWLEDGMENTS

The authors wish to thank the laboratories of the industrial and governmental centers referred to in this paper who have cooperated in supplying these photodetectors. We also wish to thank Charles B. Childs, Richard L. Hartman, Roger P. Main, and Alan I. Penn of Goddard Space Flight Center for some of the measurements made on the photocathode and window materials.

REFERENCES

1. DUNKELMAN, L., "Spectrally Selective Middle Ultraviolet Photodetectors (Solar-Blind Detectors)," *J. Opt. Soc. Amer.* 47(11): 1048, November 1957 (Abstract).
2. DUNKELMAN, L., "Spectrally Selective Ultraviolet Detectors—Their Characteristics and Applications," in: *Collection of Preprints of Papers Presented to 5th Conf. of the Internat. Commission for Optics, Stockholm, August, 1959* (Conference on Modern Systems for Detecting and Evaluating Optical Radiation) Unpublished.

3. DUNKELMAN, L., "Solar-Blind Ultraviolet Multiplier Phototubes," *J. Opt. Soc. Amer.* 45(2): 134–135, February 1955.
4. WEISSLER, G. L., "Photoionization in Gases and Photoelectric Emission from Solids," in: *Handbuch der Physik*, ed. by S. Flügge, Berlin: Springer-Verlag, 1956, vol. 21, pp. 304–382.
5. CHILDS, C. B., "Broad-Band Ultraviolet Filters," *J. Opt. Soc. Amer.* 51(8): 895–897, August 1961.
6. HINTEREGGER, H. E., and WATANABE, K., "Photoelectric Cells for the Vacuum Ultraviolet," *J. Opt. Soc. Amer.* 43(7): 604–608, July 1953.
7. SPICER, W. E., "Photoemissive, Photoconductive, and Optical Absorption Studies of Alkali-Antimony Compounds," *Phys. Rev.* 112(1): 114–122, Oct. 1, 1958.
8. ENGSTROM, R. W., "Absolute Spectral Response Characteristics of Photosensitive Devices," *RCA Rev.* 21(2): 184–190, June 1960.
9. TAFT, E., and APKER, L., "Photoemission from Cesium and Rubidium Tellurides," *J. Opt. Soc. Amer.* 43(2): 81–83, February 1953.
10. HARPER, W. J., and CHOYKE, W. J., "Semitransparent Photocathodes at Low Temperatures," *Rev. Sci. Instr.* 27(11): 966, November 1956.
11. KRETSCHMAR, G. G., "A Solar-Blind Photodiode Having Maximum Sensitivity in the Middle Ultraviolet," Naval Ordnance Lab. Corona NOLC Rept.
12. SOWERS, H. L., MCBRIDE, W. R., and OGAN, L., "High Quantum Efficiency Solar Blind Photometers," *J. Opt. Soc. Amer.* 51(12): 1460, December 1961 (Abstract).
13. SOMMER, A. H., "Spectrally Selective (Solar Blind) UV Photomultipliers with Flouride Windows," *Rev. Sci. Instr.* 32(3): 356, March 1961.
14. CAUSSE, J. P., DUNKELMAN, L., and HENNES, J. P., "Far UV 'Solar Blind' Photomultipliers," *J. Opt. Soc. Amer.* 51(12): 1461, December 1961 (Abstract).
15. DUNKELMAN, L., and LOCK, C., "Ultraviolet Spectral Sensitivity Characteristics of Photomultipliers Having Quartz and Glass Envelopes," *J. Opt. Soc. Amer.* 41(11): 802–804, November 1951.
16. HENNES, J. P., SCOLNIK, R., and STOBER, A. K., "Characteristics of a Photoionization Chamber for the Vacuum Ultraviolet," *J. Opt. Soc. Amer.* 51(12): 1461, December 1961 (Abstract).
17. FRIEDMAN, H., "The Sun's Ionizing Radiations," in: *Physics of the Upper Atmosphere*, ed. by J. A. Ratcliffe, New York: Academic Press, 1960, pp. 133–218.
18. BOGGESS, A., III, "Ultraviolet Astronomical Photometry from Rockets," in: *Space Astrophysics* ed. by W. Liller, New York: McGraw-Hill, 1961, pp. 121–132.
19. PHILIPP, H. R., and TAFT, E. A., "Photoelectric Emission from the Valence Band of Cesium Iodide," *Phys. Chem. Solids* 1(3): 159–163, 1956.
20. TAFT, E. A., and PHILIPP, H. R., "Photoelectric Emission from the Valence Band of Some Alkali Halides," *Phys. Chem. Solids* 3(½): 1–6, 1957.
21. SHUBA, YU. A., and SMIRNOVA, I. V., "Photoemission of Electrons by Copper and Silver Iodides," *Fizika Tverdogo Tela* 2(6): 1321–1322, June 1960 (In Russian); Translation in *Soviet Physics Solid State* 2(6): 1201–1202, December 1960.
22. TYUTIKOV, A. M., and SHUBA, YU. A., "Measurement of Small Photocurrents in the Study of Photoelectric Emission," *Optika i Spektroskopiya* 9(5): 631–634, November 1960 (In Russian); Translation in *Optics and Spectroscopy* 9(5): 332–334, November 1960.
23. SHUBA, YU. A., TYUTIKOV, A. M., and SOROKIN, O. M., "Photocathodes for Investigations of the Sun's Short-Wave Emission," *Iskusstvennye Sputniki Zemli* 10: 55–60, 1961 (In Russian): Translation in *Planet. Space Sci.* 9: 869–874, 1962.
24. TURNER, D. W., "A Photon Counter of High Sensitivity for the Vacuum Ultra-violet Region," *Nature* 179(4568): 1022–1023, May 18, 1957.
25. GOODRICH, G. W., and WILEY, W. C., "Resistance Strip Magnetic Electron Multiplier," *Rev. Sci. Instr.* 32(7): 846–849, July 1961.
26. HEROUX, L., and HINTEREGGER, H. E., Resistance Strip Magnetic Photomultiplier for the Extreme Ultraviolet," *Rev. Sci. Instr.* 31(3): 280–286, March 1960.
27. HINTEREGGER, H. E., "Telemetering Monochromator Measurements of Extreme Ultraviolet Radiation. Part I: Introduction and Technology," in: *Space Astrophysics*, ed. by W. Liller, New York: McGraw-Hill, 1961, pp. 34–73.
28. BEHRING, W. E., NEUPERT, W. M., and NICHOLS, W. A., "Far Ultraviolet Spectrometer for Solar Observations," *J. Opt. Soc. Amer.* 52(5): 597, May 1962 (Abstract).
29. FRANK, R., and STOW, R. L., "Securing Rocksalt Windows to Sealed-Off Vacuum Tubes," *Rev. Sci. Instr.* 25(5): 514–515, May 1954.
30. VOGL, T. P., MCINTOSH, R. O., and GARBUNY, M., "Vacuum-Tight Windows," Patent No. 2966592, Issued Dec. 27, 1960.
31. GREENBLATT, M. H., "Sealing a Calcium Fluoride Window to Glass," *Rev. Sci. Instr.* 29(8): 738, August 1958.
32. CHILDS, C. B., "Low Pressure Mercury Arc for Ultraviolet Calibration," *Applied Optics* 1(6): 711–716, November 1962.

ULTRAVIOLET PHOTODETECTORS

LAWRENCE DUNKELMAN
Goddard Space Flight Center

The need for detectors in spectroscopic research in both the laboratory and in space has led in recent years to the development of a variety of spectrally selective detectors which may be put into three broad categories: (1) photoionization chambers having relatively narrow passbands within the region from 1050A to approximately 1500A; (2) multiplier phototubes having high-work-function photocathodes and ultraviolet transmitting windows: and (3) multiplier phototubes having high-work-function cathodes and no windows. This report reviews the characteristics of vacuum ultraviolet ion chambers having fill gases such as nitric oxide, acetone, carbon disulfide, or ethylene oxide with windows of lithium fluoride, cadmium fluoride, or barium fluoride. Their quantum efficiencies range from approximately 0.10 to 0.50 photoelectron/quantum, and the chambers may be operated in a gas multiplication mode with gains of 10^3 at 600 to 800 volts. The characteristics of photomultipliers and phototubes having alkali-tellurium, copper-iodine, or other cathodes with lithium flouride, sapphire, quartz, or no windows are described. Some of the photomultipliers studied have quantum efficiencies as high as 0.20 photoelectron/quantum and exhibit long-wavelength rejection ratios of many orders of magnitude over only several hundred angstroms.

INTRODUCTION

A substantial part of the space sciences consists of measurements of astrophysical or geophysical quantities made by means of detectors sensitive to various portions of the ultraviolet wavelength region. The development of observational programs has required considerable extension of the variety of ultraviolet detectors available for scientific use. At the Stockholm meeting of the International Commission for Optics in 1959, characteristics of middle ultraviolet detectors (3000A to 2000A) investigated during the preceding 10 years were presented. Spectral response curves of typical examples of these detectors are given in Figure 1 which is taken from Reference 1. Additional information on the techniques of middle ultraviolet detection is given by Dunkelman, Fowler, and Hennes (Reference 6).

In the past 3 years the continuing need for detectors in observational programs in astrophysics and planetary optics has necessitated increased efforts in the development of ultraviolet detectors.

These spectrally selective detectors may be put in three broad categories; (1) photoionization chambers having relatively narrow passbands within the region from 1050A to approximately 1500A; (2) multiplier phototubes having high-work-function photocathodes and ultraviolet transmitting windows; and (3) multiplier phototubes having high-work-function cathodes and no windows. Both the measurements and the detectors described in the first category have been made primarily at GSFC. The measurements described in the second category have been made at GSFC on detectors prepared for GSFC by industrial or governmental research and development laboratories. The measurements described in the third cateogry have been made partly at GSFC and partly at other governmental or industrial laboratories.

PHOTOIONIZATION DETECTORS

Photoionization chambers can be filled with gases whose ionization potential is of interest for use in a variety of applications in the space

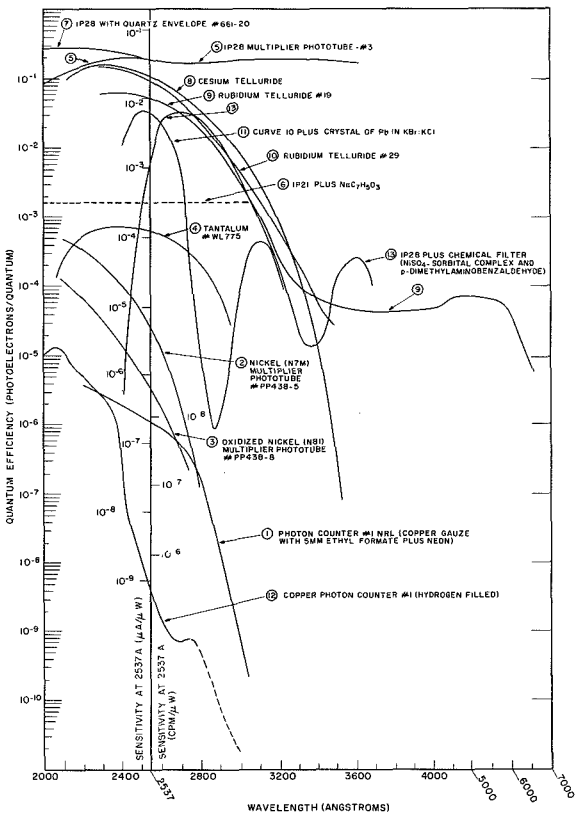

FIGURE 1.—Spectral response curves (quantum efficiencies) for some typical middle ultraviolet detectors. Curves 1, 9, 10, 11, and 12 are unpublished measurements by L. Dunkelman while at the Naval Research Laboratory, Washington, D.C. Curves 2 and 3 are from Reference 2, curve 4 from a Westinghouse Specification, and 5 and 7 from Reference 3. Curve 6 is shown for comparison of the typical overall quantum efficiency of sodium salicylate coated on a 1P21 photomultiplier. This yield is small; however, by using a high-yield end-window Cs-Sb type photomultiplier and optimizing coating thickness, overall efficiencies of about 5×10^{-2} photoelectrons/quantum may be obtained. Curve 8 is from Reference 4. Curves 9 and 10 were obtained with an opaque cathode in a phototube of 9741 Corning glass; curve 9 shows the long-wavelength sensitivity of a phototube having excess rubidium. Curve 13 gives the response of the Cs-Sb surface of the 1P28 photomultiplier modified by a combination chemical filter to produce a convenient passband (see also Reference 5).

sciences. In the papers on Photon-Gas Cross Sections of the First International Conference on Vacuum Ultraviolet Radiation Physics, the subject was reviewed by Ditchburn (Reference 7), Watanabe (Reference 8), Weissler (Reference 9), and Vodar (Reference 10).

The effort at GSFC has been a continuation of the investigation and development of ion chambers first used in a series of rocket measurements at the Naval Research Laboratory in the last decade and described by Chubb and Friedman (Reference 11) Byram, Chubb, et al. (Reference 12), and Friedman (Reference 13).

From the experience gained with these early detectors a somewhat newer design was developed at GSFC and reported by Stober (Reference 14) and Stober, Scolnik, and Hennes (Reference 15). This type of ion chamber (Fig. 2) consists of a small ceramic shell, gold plated on the inside, fitted with a central collecting wire electrode and employing a window of suitable transmittance characteristics to limit the short wavelength response. A completed crystal-window chamber is shown in the center of the figure. At the right is a chamber in which a thin metal window, such as aluminum or beryllium, is used, with the supporting grids, for ion chamber detection in the soft X-ray region.

The most desirable features of these ion chambers are: (1) extremely high spectral selectivity, (2) high quantum efficiency, (3) ruggedness and compactness, (4) low electrical leakage, and (5) good vacuum seal properties. Figure 3 shows a section of the ion chamber. The shell of alumina ceramic was made for GSFC

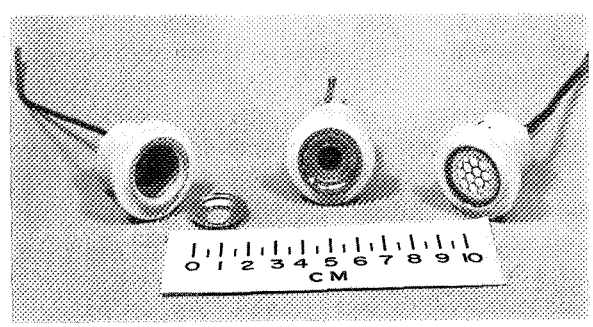

FIGURE 2.—Three NASA ceramic ion chambers. Left, an unfinished chamber with a LiF crystal window and a gold plated window flange lying in front of the ceramic shell. Center, a completed ion chamber. Right, a chamber with an aluminum window, for use in the soft X-ray region.

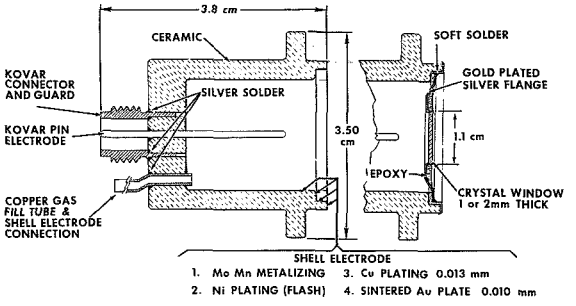

FIGURE 3.—Cross section of an alumina ceramic metal-coated ion chamber.

by the Coors Porcelain Co.;[1] its interior has several layers of metallic deposits, the outermost (surface) layer being a gold plating. Around the central pin collector electrode where it passes through the shell is an electrical guard ring which is normally kept at ground potential. The window is held onto a gold plated silver flange by several coats of one of the Hysol epoxies. The flange is in turn fastened to the metal plated ceramic shell by soft solder. Window materials of LiF, CaF_2, and BaF_2 cleaved crystals have been used, as well as the thin beryllium and aluminum foils mentioned. An extensive collection of the transmission properties of a number of solid and gaseous materials has been published by Bryam, Chubb, et al. (Reference 12).

Figure 4 shows the measured yields of five of the filling gas and window material combinations which have been used recently in several series of rocket experiments. Smoothed curves are shown which obscure, in some cases, fine structure in the gas ionization yield curves. Note the high quantum efficiency and narrow response region of, for example, acetone with a CaF^2 window. In measurements of solar flux, or in other situations where there are high fluxes, the ion chambers are used in a nongas-gain condition. A flat plateau region for ion-collection exists when the applied voltage is in the range of 20 to 60 volts. However, in many cases the incident flux is so small—as for example, with stellar fluxes—that the ion chambers are operated at gas gains of the order of 1000.

[1] Coors Porcelain Company, Golden, Colorado.

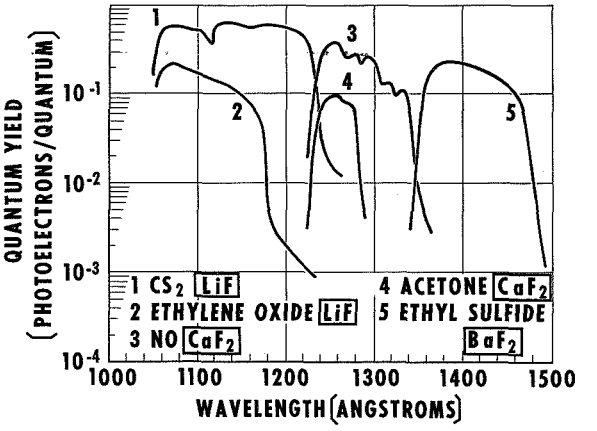

FIGURE 4.—Spectral responses of several ion chambers for the region from 1000A to 1500A. Boxed symbols refer to the phototube window materials. Smoother curves are shown, although a certain amount of fine structure is obscured in this way. Note the high quantum efficiencies and narrow response regions of some of these detectors.

This gain requires 600 to 800 volts, although the steep gain curve makes the response quite sensitive to voltage fluctuations. Table 1 summarizes the most pertinent features of these ion chambers.

PHOTOEMISSIVE DETECTORS

The second category of detector development described in this report is the photoemissive detector. In this area GSFC has worked rather closely with industrial research and development laboratories which have prepared a variety of high-work function photocathodes, both opaque and semitransparent. The intention has been to develop cathode preparation techniques which lead to laboratory and eventually flight photodiodes, photomultipliers, and image tubes. Until recently the only spectrally selective ultraviolet detectors have been of the pure metal type resulting from the early work of Rentschler, Henry, and Smith (Reference 16), and others who studied tantalum, cadmium, nickel, and other metals in the 2000A to 3000A region. Quantum efficiencies in the middle ultraviolet are at best 10^{-3} but more generally 10^{-5} photoelectrons/quantum.

Typical of these pure metals is gold, whose distribution of quantum efficiency has been

TABLE 1.—*NASA Ion Chamber Features*

Gas Filling	Chemical Formula	Window Material	Spectral Response (A)	Quantum Efficiency [1] (photoelectrons/quantum)
Ethylene oxide	$(CH_2)_2O$	LiF	1050–1180	0. 10–0. 20
Carbon disulfide	CS_2	LiF	1050–1240	0. 50–0. 60
Acetone	$(CH_3)_2CO$	CaF_2	1230–1290	0. 08–0. 10
Nitric oxide	NO	CaF_2	1230–1350	0. 10–0. 30
Nitric oxide	NO	LiF	1050–1350	0. 10–0. 50
Diethyl sulfide	$(C_2H_5)_2S$	BaF_2	1350–1480	0. 10–0. 25

[1] Based on a value of 0.81 photoelectrons/quantum for NO at the Lyman-alpha wavelength (1216A).

measured by Childs (Reference 17) and others. Childs found that the quantum efficiency of one photomultiplier at 2000A was approximately 10^{-3} photoelectrons/quantum. A comparison of his data with Figure 1 of this report shows that the spectral response characteristic of gold is similar to that of nickel except that the gold has a better rejection at the longer wavelengths. Extensive studies of the quantum efficiencies of metals in the far ultraviolet were made in the early 1950's by Hinteregger and Watanabe (Reference 18) and by Walker, Wainfan, and Weissler (References 19 and 20), and were reviewed later by Weissler (Reference 21).

Also useful has been the well known composite surface, cesium-antimony (Cs-Sb), discovered and studied in 1936 by Görlich (Reference 22), which has enjoyed a deserved reputation as a very efficient visible and near ultraviolet photoemitter. A comprehensive study of the photoelectric effect in alkali-antimony has been made by Spicer (Reference 3). Cesium-antimony has been well developed but the extension of its usefulness towards and into the vacuum ultraviolet has been slow.

Figure 5 includes the spectral distribution of the quantum efficiencies of several photocathode materials in the vacuum and middle ultraviolet regions. The extreme right curve shows the short wavelength portion of the response of the 1P21, a Cs-Sb photomultiplier which has a glass envelope and is used primarily in the visible region or with phosphors in the vacuum ultraviolet. Another photomultiplier, the 1P28, introduced some 15 years ago, extends the Cs–Sb range just into the beginning of the vacuum ultraviolet by employing an ultraviolet transmitting glass. By using a quartz envelope (Reference 2) with a Cs-Sb photosurface in photomultiplier designated as 7200, the range is extended to approximately 1600A. Dunkelman, Fowler, and Hennes (Reference 23) reported on the results obtained with several ultraviolet photodetectors—among them a Cs-Sb photomultiplier having a CaF_2 window. Figure 5 shows the resulting comparatively flat, high quantum efficiency down to 1225A. Windows of LiF have further extended the sensitivity to 1050A. It is of interest to note that in 1952 a photocell with a LiF window was prepared by Hinteregger and Watanabe (Reference 18), but it was not until 1957 that a LiF windowed multiplier was reported. At that time Garton, Webb, and Wildy (Reference 24), used such a photomultiplier having a tungsten cathode.

A most significant advance in selective ultraviolet detection occurred when Taft and Apker (Reference 4) and their colleagues about 10 years ago reported on the distribution of the photoelectric yield of several alkali-tellurium surfaces. Since then Harper and Choyke (Reference 25), Roderick (General Electric Co., private communication), Behring (Reference 26), Kretschmar (private communication and Reference 27), Sowers (Armour Research Foundation, private communication), Sowers, McBride, and Ogan (Reference 28), Linden (CBS Laboratories, private communication), Essig (ITT Laboratories, private communication),

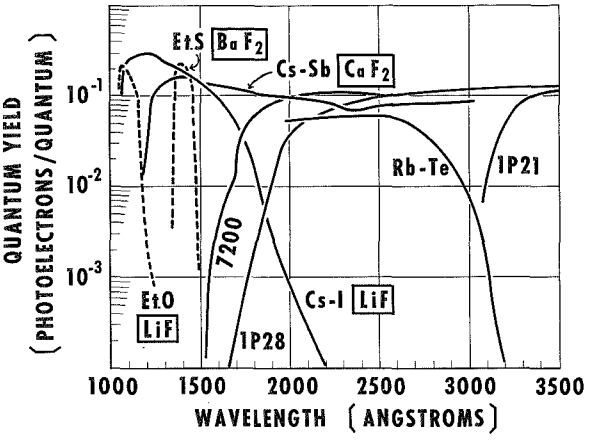

FIGURE 5.—Spectral responses of several photodetectors in the vacuum and middle ultraviolet regions. Boxed symbols refer to the phototube window materials. The 1P21, 1P28, and 7200 curves indicate the responses of a few of many photomultiplier types with Cs-Sb cathodes and envelopes of glass, of Corning 9741, and of fused silica, respectively. The Cs-Sb $\boxed{CaF_2}$ curve gives the measured response of a photomultiplier with a Cs-Sb photocathode and also a CaF_2 window that extends its response down to 1250A. The Rb-Te curve is a typical response of a "solar blind" photocathode. This term refers to the fact that the high-work function photosurface is relatively insensitive to all visible and near ultraviolet wavelengths and therefore to the sun's light as seen through the earth's atmosphere. The Cs–I $\boxed{LiF}$ curve gives the response of a photosurface which rejects a good deal of the middle and near ultraviolet as well as the visible wavelengths. The $(C_2H_5)_2S$ $\boxed{BaF_2}$ and $(CH_3)_2O$ $\boxed{LiF}$ curves show, for comparison, the responses of two photoionization chambers also shown in figure 4.

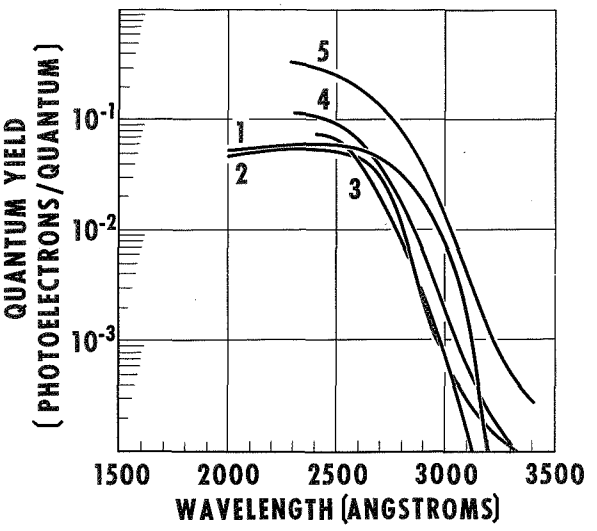

FIGURE 6.—Spectral response curves of Rb-Te opaque-cathode photodiodes showing various degrees of spectral selectivity and quantum efficiency. Curves 1 and 2 refer to diodes made by Kretschmar at the Naval Ordnance Laboratory, Corona, Calif. (Reference 27); and curve 3 refers to the diode made by Kretschmar at the Naval Ordnance Test Station, China Lake, Calif. (private communication). Curves 4 and 5 represent diodes made by Roderick at the General Electric Co. (private communication).

Sommer (Reference 29), Causse (Reference 30) and Causse, Dunkelman, and Hennes (Reference 31) have prepared alkali telluride opaque and semitransparent surfaces. In Figure 6 there are shown two groupings of the spectral responses of phototubes with rubidium-tellurium (Rb-Te) opaque cathodes. The curves numbered 4 and 5 represent the average of the extreme of many tubes prepared by Roderick which were examined several years ago. Note the high efficiencies of these opaque cathodes at 2500A. The opaque surfaces prepared by Kretschmar (curves 1, 2, and 3), while exhibiting lower yields provide higher selectivity. This may be due to little or no excess rubidium, and thus appears to be consistent with the early work of Taft and Apker who found that excess cesium produced the impurity-type yield at low photon energies, causing a response tail to extend beyond 3200A. Figure 7 shows a comparison of spectral response curves of a variety of phototubes containing cesium-tellurium (Cs-Te) photocathodes. No major differences between Rb-Te and Cs-Te with respect to either quantum efficiencies or rejection ratios have been found. The curves marked FW 157–1 and FW 140–12 show the spectral response of photodiodes with opaque cathodes and sapphire windows. The curve marked S.883 refers to the response of a 13-stage experimental photomultiplier with an opaque cathode and a LiF window made by Sommers at RCA (Reference 29). A quantum efficiency of better than 10 percent is achieved with these opaque cathodes, whereas in the case of semitransparent cathodes (curves marked 151 and 152) the efficiencies are appreciably lower. However, a semitransparent cathode

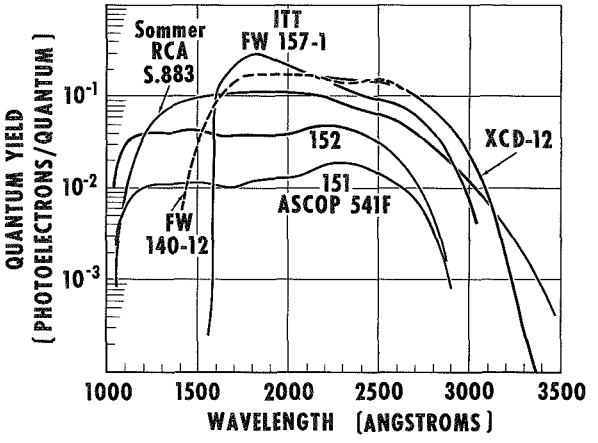

FIGURE 7.—Spectral response curves of Cs-Te phototubes. The 151 and 152 curves refer to 14-stage photomultipliers with semitransparent photocathodes and LiF windows manufactured by ASCOP Division of Electro-Mechanical Research, Inc. The S.883 curve refers to a 13-stage experimental photomultiplier with an opaque cathode and a LiF window made by Sommer at RCA. The other curves refer to opaque-cathode photodiodes made by ITT Laboratories: FW 140–12 and XCD–12, with sapphire windows; and 157–1, with a fused silica window.

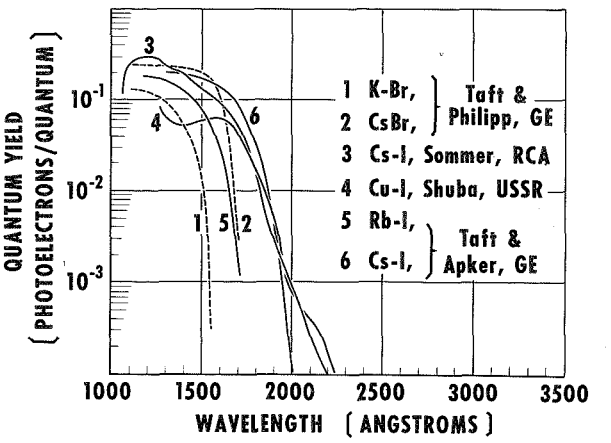

FIGURE 8.—Spectral response curves of several high-work function photocathodes. The K-Br, Cs-Br, and Rb-1 curves are taken from Reference 33, the Cs-1 curve from Reference 23. The Cu-1 is estimated from work presented in Reference 34. The Cs-1 curve, given for comparison, is from the work of Reference 32.

just behind the front window results in far better optical coupling than is possible in recessed opaque cathodes. This is frequently an important consideration in application.

Two developments in photoemissive photodetectors have been reviewed thus far. One is the extension of available photocathodes in the ultraviolet merely by the use of appropriate windows which serve to broaden the inherent useful response. This wider spectral response may be very desirable in some applications, especially with dispersive optics. The second development, the use of photoemitters spectrally selective to the ultraviolet, such as the high-work function alkali tellurides, is useful in applications where discrimination against the longer wavelengths is an overriding consideration. Figure 8 is a compilation of the yields of some still higher work function materials which are, in general, spectrally selective to the vacuum ultraviolet region. Curve 6 is taken from the early work by Philipp and Taft (Reference 32) who studied cesium-iodine (Cs-I). Curve 3 represents our recent measurements (Reference 23) of the spectral distribution of the quantum efficiency from a phototube with a Cs-I cathode prepared by Sommer of RCA. Here the photocathode is deposited on a conducting substrate of thin tungsten immediately behind the LiF window; this makes possible, again, convenient end-on coupling. Curves 3 and 6 are quite similar. The slightly lower yield (curve 3) at wavelengths greater than 1400A might be attributable to a transmittance loss in the tungsten conducting substrate, or to excessive thickness of Cs-I. Curves 1, 2, and 5 [potassium-bromide (K-Br), cesium-bromine (Cs-Br), and rubidium-iodine (Rb-I), respectively], from Reference 33, are shown here for comparison and for suggestions of surfaces which should be considered if shorter wavelength cutoffs are of interest. Curve 4, copper-iodine (Cu-I) is discussed along with the curves of Figure 9.

In Figure 9, the scales have been changed in order that 9 orders of magnitude may be displayed. Curve 1 is the familiar Cs-Sb surface. Curve 2 is the Cs-I surface already discussed (curve 3 of Figure 8). Here it can be seen that at 2537A the absolute yield of the Cs-I surface is only 7×10^{-6}. This, as well as the quantum efficiency at 2537A of other cathodes investigated at GSFC, was measured in a calibrated

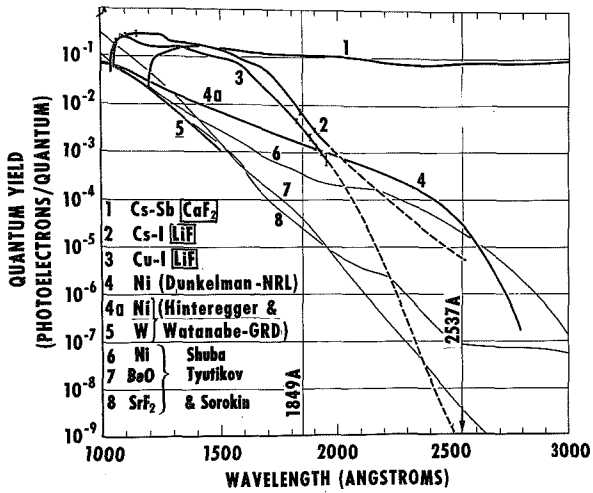

FIGURE 9.—Spectral responses of various photocathodes showing the high sensitivity and excellent long wavelength rejection possible with the high work function materials. Curves 1, 2, and 3 are measurements reported in Reference 23; curve 4 is from Reference 37; and curves 4a and 5 are from Reference 18. Curves 6, 7, and 8, shown for comparison, are from Reference 38.

low-pressure mercury arc described by Childs (Reference 35). Curve 3 is a result of recent GSFC measurements of a Cu-I semitransparent surface on tungsten deposited on a LiF window in a phototube which was prepared by Sommer of RCA. This response is similar to that of his Cs-I tube, curve 2, except for the much improved long wave length rejection ratio which is at least 7 orders of magnitude between 1849A and 2537A. The upper limit of the quantum efficiency at the latter wavelength is less than 10^{-9}. The quantum efficiencies at short wavelengths displayed in curves 2 and 3 represent preliminary measurements made at GSFC. In general a peak efficiency of about 0.20 photoelectrons/quantum Lyman alpha (1216A) can be expected for Cs-I with the efficiency of Cu-I being 3 to 5 times less. The dashed portions represent estimated yields interpolated between the measured values at 2000A and 2537A. We can compare these measurements with the results reported in 1960 by Shuba and Smirnova (Reference 34) who established a quantum efficiency of 10^{-1} at the short wavelengths but only a 6 order of magnitude rejection ratio. In 1957, Turner of Imperial College reported (Reference 36) a Cu-I photoemitter with a cutoff at 2300A (although he did not define cutoff) and a peak yield somewhere between 10^{-2} and unity. Additional surfaces of Cu-I recently prepared by Sommer of RCA and Stober at GSFC have been found to remain fairly stable after exposure to air.

WINDOWLESS DETECTORS

The investigation of Cu-I at wavelengths below 1100A is being made with the aid of a Bendix-resistance-strip magnetic photomultiplier, developed by Goodrich and Wiley (Reference 39) and first used by Heroux and Hinteregger (Reference 40) in the late 1950's. Soon after NASA was established it was apparent that smaller versions of the resistance-strip photomultiplier would be needed for the continued observation from rockets and satellites of solar emission in the very extreme ultraviolet. Work was initiated and the middle-sized detector (type M306) shown in Figure 10 was developed. This photomultiplier was reported by Goodrich and Wiley (private communication) to be very quiet, with a dark current, referred to a tungsten cathode, as low as of the order of 1 electron/minute. The multiplier has been successfully employed in the soft x-ray spectrometer to study the solar spectrum in the 10A to 400A region. The instrument was first used in an Aerobee rocket launched on September 30, 1961, as described

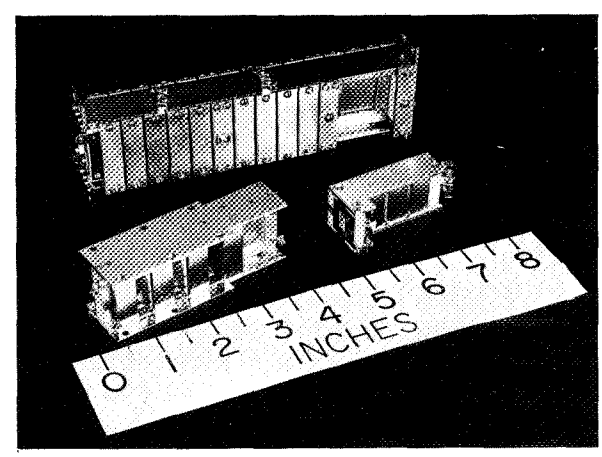

FIGURE 10.—Bendix-resistance-strip magnetic phtomultipliers.

by Behring, Neupert, and Nichols (Reference 41) and then used in the Orbiting Solar Observatory launched March 7, 1962, as described by Behring, Neupert, and Lindsay (Reference 42). Some results and a preliminary interpretation of the solar observations taken with this soft x-ray spectrometer are given by Neupert and Behring in Reference 43. Other investigators have been working with the windlowless electron multiplier developed and investigated by Allen (References 44 and 45).

Another significant design in windowless and small multiplier phototubes is the continuous channel multiplier developed by Goodrich and Wiley (Reference 46) and shown in Figure 11. Briefly, this Bendix channel multiplier is in the form of a hollow glass tube with a highly resistive inner surface. It has an internal bore diameter of several tenths of a millimeter and has a length to bore diameter ratio (l/d) of approximately 50. A potential difference of 1000 to 2000 volts is maintained between the ends, causing a current on the inner surface; thus, a uniform axial electric field is established down the length of the tube. An initial electron is generated from the inner surface near the open input end. This first electron may be a photoelectron caused by an ultraviolet photon striking the surface, by a photoelectron emitted from the external photocathode, or by any other particle with sufficient energy to cause secondary emission. The emitted electrons cascade down the length of the tube, producing gains of 10^5 or more.

FIGURE 11.—Bendix channel photomultiplier.

The channel multiplier has been further developed in cooperation with GSFC because of its potential for both laboratory and space applications. Hunter (Reference 47) has recently investigated the channel multiplier and determined that its spectral response is similar to that of tungsten, although the highly resistive inner surface (which is also the photoemitting surface) on the inside of the tube is not tungsten. This type of multiplier will be used in a forthcoming Naval Research Laboratory experiment as described by Angel, Copper, et al. (Reference 48) on the next Orbiting Solar Observatory to study the solar disk at several extreme ultraviolet wavelengths. This type of multiplier has also been under study for other applications such as in an array whose photocathode end is aligned to conform with the exit slit of a spectrometer. Consideration has also been given to employing this detector in an image intensifier which would be useful in nuclear track imaging as well as in other fields.

CONCLUDING REMARKS

In conclusion it should be pointed out that, in this short review, the discussion has been mostly confined to work that has been done either at GSFC or in association with it and which has appeared fruitful for astrophysical and geophysical programs. No attempt has been made here to review the many other areas of photodetector investigation. It is hoped that current researches, such as those described by Hartman (Reference 49) and Walker and Weissler (Reference 50) will soon lead to further advances in photodetection techniques.

ACKNOWLEDGMENTS

It is a pleasure to acknowledge the work of my colleagues, J. P. Hennes, W. B. Fowler, R. Main, and R. Scolnik, who have participated in making many of the measurements reported here.

REFERENCES

1. DUNKELMAN, L., "Spectrally Selective Ultraviolet Detectors—Their Characteristics and Applications," in: *Collection of Preprints of Papers*, presented to *5th Conf. of the Internat. Commission for Optics, Stockholm, August 24–30, 1959* (Conference on Modern Systems for Detecting and Evaluating Optical Radiation), Unpublished.
2. DUNKELMAN, L., and LOCK, C., "Ultraviolet Spectral Sensitivity Characteristics of Photomultipliers Having Quartz and Glass Envelopes," *J. Opt. Soc. Amer.* 41(11): 802–804, November 1951.
3. SPICER, W. E., "Photoemissive, Photoconductive, and Optical Absorption Studies of Alkali-Antimony Compounds," *Phys. Rev.* 112(1): 114–122, Oct. 1, 1958.

4. TAFT, E., and APKER, L., Photoemission from Cesium and Rubidium Tellurides," *J. Opt. Soc. Amer.* 43(2): 81–83, February 1953.

5. CHILDS, C. B., "Broad-Band Ultraviolet Filters," *J. Opt. Soc. Amer.* 51(8): 895–897, August 1961.

6. DUNKELMAN, L., FOWLER, W. B., and HENNES, J. P., "Middle Ultraviolet Photoelectric Detection Techniques," in: *Space Research III: Proc. 3rd Internat. Space Sci. Sympos., Washington, May 1962*, North-Holland Publ. Co., Amsterdam (To be published).

7. DITCHBURN, R. W., "Absorption Cross sections for Photoionization", presented at the 1st Internat. Conf. on Vacuum Ultraviolet Radiation Physics, U. of Southern California, April 16–19, 1962; published in *J. Quant. Spectr. and Radiative Transfer* 2: 361–368, October/December, 1962.

8. WATANABE, K., NAKAYAMA, T., and MOTTL, J. R., "Ionization Potentials of Some Molecules", presented at the 1st Internat. Conf. on Vacuum Ultraviolet Radiation Physics, U. of Southern California, April 16–19, 1962; published in *J. Quant. Spectr. and Radiotive Transfer* 2: 369–382, October/December, 1962.

9. WEISSLER, G. L., "Cross Section Measurements for some Photo-Gas Interaction Processes", presented at the 1st Internat. Conf. on Vacuum Ultraviolet Radiation Physics, U. of Southern California, April 16–19, published in the *J. of Quant. Spectr. and Radiative Transfer* 2: 383–392, October/December, 1962.

10. VODAR, B., "Cross Section and Absorption Spectra in Gases, Reflection and Absorption of Solids", presented at the 1st Internat. Conf. on Vacuum Ultraviolet Radiation Physics, U. of Southern California, April 16–19 published in the *J. of Quant. Spectr. and Radiative Transfer* 2: 393–412, October/December 1962.

11. CHUBB, T. A., and FRIEDMAN, H., "Photon Counters for the Far Ultraviolet", *Rev. Sci. Instr.* 26(5): 493–498, May 1955.

12. BYRAM, E. T., CHUBB, T. A., et al., "Observations of the Intensity of Solar Lyman-Alpha Emission," *Astropkys. J.* 124(2): 480–482, September 1956.

13. FRIEDMAN, H., "The Sun's Ionizing Radiations," in: *Physics of the Upper Atmosphere*, ed. by J. A. Ratcliffe, New York: Academic Press, 1960, Section 4.2.2.

14. STOBER, A. K., "Ceramic Vacuum Ultraviolet Ion Chambers," NASA Technical Note D–1180, March 1962.

15. STOBER, A. K., SCOLNIK, R., and HENNES, J. P., "Characteristics of a Photoionization Chamber for the Vacuum Ultraviolet," *J. Opt. Soc. Amer.* 51(12): 1461, December 1961 (Abstract).

16. RENTSCHLER, H. C., HENRY, D. E., and SMITH, K. O., "Photoelectric Emission from Different Metals," *Rev. Sci. Instr.* 3(12): 794–802, December 1932.

17. CHILDS, C. B., "Quantum Yield of Gold-Cathode Photomultipliers," *J. Opt. Soc. Amer.* 51(5): 583, May 1961.

18. HINTEREGGER, H. E., and WATANABE, K., "Photoelectric Cells for the Vacuum Ultraviolet," *J. Opt. Soc. Amer.* 43(7): 604–608, July 1953.

19. WAINFAN, N., WALKER, W. C., and WEISSLER, G. L., "Preliminary Results on Photoelectric Yields of Pt and Ta and on Photoionization in O_2 and N_2 in the Vacuum Ultraviolet," *J. Appl. Phys. 24*(10): 1318–1321, October 1953.

20. WALKER, W. C., WAINFAN, N., and WEISSLER, G. L., "Photoelectric Yields in the Vacuum Ultraviolet," *J. Appl. Phys.* 26(11): 1366–1371, November 1955.

21. WEISSLER, G. L., "Photoionization in Gases and Photoelectric Emission from Solids," in *Handbuch der Physik*, ed. by S. Flügge Berlin: Springer-Verlag, 1956, Vol. 21, pp. 304–382.

22. GÖRLICH, P., "Über Zusammengesetzte, Durchsichtige Photokathoden," *Zeitschrift für Physik* 101(5/6): 335–342, 1936.

23. DUNKELMAN, L., FOWLER, W. B., and HENNES J. P., "Spectrally Selective Photodetectors for the Middle and Vacuum Ultraviolet," *Applied Optics*, 1(6): 695–700, November 1962.

24. GARTON, W. R. S., WEBB, M.S.W., and WILDY, P. C., "The Application of Vacuum Ultra-Violet Techniques to the Continuous Monitoring of Trace Concentrations of Water in Several Gases," *J. Sci. Instr.* 34(12): 496–500, December 1957.

25. HARPER, W. J., and CHOYKE, W. J., "Semitransparent Photocathodes at Low Temperatures," *Rev. Sci. Instr.* 27(11): 966, November 1956.

26. BEHRING, W. E., "Photoemission from Potassium Telluride," Ph.D. Thesis, University of Colorado, August 1959.

27. KRETSCHMAR, G. G., "A Solar-Blind Photodiode Having Maximum Sensitivity in the Middle Ultraviolet," Naval Ordnance Lab., Corona Rept. 554, October 15, 1961.

28. SOWERS, H. L., MCBRIDE, W. R., and OGAN, L., "High Quantum Efficiency Solar Blind Photometers," *J. Opt. Soc. Amer.* 51(12): 1460, December 1961 (Abstract).

29. SOMMER, A. H., "Spectrally Selective (Solar Blind) UV Photomultipliers with Fluoride Windows," *Rev. Sci. Instr.* 32(3): 356, March 1961.

30. CAUSSE, J. P., "Status Report on the Development of the ASCOP Photomultiplier," *IRE Trans. Nuclear Science* NS–9(3): 90–96, June 1962.

31. CAUSSE, J. P., DUNKELMAN, L., and HENNES, J. P., "Far UV Solar Blind Photomultipliers, *J. Opt. Soc. Amer.* 51(12): 1461, December 1961 (Abstract).

32. PHILIPP, H. R., and TAFT, E. A., "Photoelectric Emission from the Valence Band of Cesium Iodide," *Phys. Chem. of Solids* 1(3): 159–163, November 1956.
33. TAFT, E. A., and PHILIPP, H. R., "Photoelectric Emission from the Valence Band of Some Alkali Halides," *Phys. Chem. of Solids* 3(1/2): 1–6, 1957.
34. SHUBA, YU. A., and SMIRNOVA, I. V., "Photoemission of Electrons by Copper and Silver Iodides," *Fizika Tverdogo Tela* 2(6): 1321–1322, June 1960 (In Russian); Translation in *Soviet Physics—Solid State* 2(6): 1201–1202, December 1960.
35. CHILDS, C. B., "Low-Pressure Mercury Arc for Ultraviolet Calibration," *Applied Optics*, 1(6): 711–716, November 1962.
36. TURNER, D. W., "A Photon Counter of High Sensitivity for the Vacuum Ultra-Violet Region," *Nature* 179(4568): 1022–1023, May 18, 1957.
37. DUNKELMAN, L., "Spectrally Selective Middle Ultraviolet Photodetectors (Solar-Blind Detectors)," *J. Opt. Soc. Amer.* 47(11): 1048, November 1957 (Abstract).
38. SHUBA, YU. A., TYUTIKOV, A. M., and SOROKIN, O. M., "Photocathodes for Solar Short-Wave Radiation Investigation," *Iskusstvennye Sputniki Zemli* 10:55–60, 1961 (In Russian); Translation in *Artificial Earth Satellites* 9–10: 191–196, July 1962.
39. GOODRICH, G. W., and WILEY, W. C., "Resistance Strip Magnetic Electron Multiplier," *Rev. Sci. Instr.* 32(7): 846–849, July 1691.
40. HEROUX, L., and HINTEREGGER, H. E., "Resistance Strip Magnetic Photomultiplier for the Extreme Ultraviolet," *Rev. Sci. Instr.* 31(3): 280–286, March 1960.
41. BEHRING, W. E., NEUPERT, W. M., and NICHOLS, W. A., "Far Ultraviolet Spectrometer for Solar Observations," *J. Opt. Soc. Amer.* 52(5): 597, May 1962 (Abstract).
42. BEHRING, W. E., NEUPERT, W. M., and LINDSAY, J. C., "Preliminary Solar Flare Observations with a Soft X-Ray Spectrometer on the Orbiting Solar Observatory," in: *Space Research III: Proc. 3rd Internat. Space Sci. Sympos., Washington, May 1962*, North-Holland Publ. Co. (To be published.)
43. NEUPERT, W. M., and BEHRING, W. E., "Solar Observations with a Soft X-Ray Spectrometer", presented at the 1st Internat. Conf. on Vacuum Ultraviolet Radiation Physics, U. of Southern California, April 16–19, 1962; published in *J. of Quant. Spectr. and Radiative Transfer* 2: 527–532, October/December, 1962.
44. ALLEN, J. S., "The Detection of Single Positive Ions, Electrons and Photons by a Secondary Electron Multiplier," *Phys. Rev.* 55(10): 966–971, May 15, 1939.
45. ALLEN, J. S., "An Improved Electron Multiplier Particle Counter," *Rev. Sci. Instr.* 18(10): 739–749, October 1947.
46. GOODRICH, G. W., and WILEY, W. C., "Experiments with the Bendix Continuous-Channel Multiplier," in: *Proc. Image Intensifier Sympos., Fort Belvoir, Virginia, October 1961*, NASA SP–2 1962, pp. 211–213.
47. HUNTER, W. R., "Extreme Ultraviolet Detection with the Bendix Channel Multiplier," in: *Space Research III: Proc. 3rd Internat. Space Sci. Sympos. Washington, May 1962*, Amsterdam: North-Holland Publ. Co. (To be published).
48. ANGEL, D. W., COOPER, H. W., et al., "Extreme Ultraviolet Detection with the Bendix Single-Channel Photomultiplier," in: *Proc. Image Intensifier Sympos., Fort Belvoir, Virginia, October 1961*, NASA SP–2, 1962, pp. 215–219.
49. HARTMAN, P. L., "Investigations on Some Alkali Halides in the Vacuum Ultraviolet", presented at the 1st Internat. Conf. on Vacuum Ultaviolet Radiation Physics, U. of Southern California, April 16–19, 1962: published in the *J. Quant. Spectr. and Radiative Transfer* 2:579–587, October/December, 1962.
50. WALKER, W. C., and WEISSLER, G. L., "Vacuum Ultraviolet Optical and Photoelectric Effects in Solids", presented at the 1st Internat. Conf. on Vacuum Ultraviolet Radiation Physics, U. of Southern California, Apr. 16–19, 1962: published in *J. Quant. Spectr. and Radiative Transfer* 2: 613–620, October/December 1962.

MIDDLE ULTRAVIOLET PHOTOELECTRIC DETECTION TECHNIQUES

LAWRENCE DUNKELMAN, JOHN P. HENNES and WALTER B. FOWLER
Goddard Space Flight Center

Astronomical and geophysical observations from rockets in the ultraviolet region of the spectrum have been either spectral studies with dispersive optical systems or broad-band photometric measurements at particular wavelength regions of interest. In this paper nondispersive optical techniques are described for the middle (3000–2000A) ultraviolet. Bandpass (200–300A) and cutoff filters which may be used with conventional cesium-antimony photodetectors are described. When near ultraviolet and longer wavelength radiation must be rejected to a greater degree, "solar blind" photocathodes, with higher work functions, such as the alkali tellurides, can be used. These photodetectors, their calibration, and their applications are discussed.

INTRODUCTION

Optical measurements from rockets by Goddard Space Flight Center have placed new emphasis on regions of the ultraviolet spectrum that cannot be observed from the ground because of absorption by the ozone layer at about 25 km altitude. This and other absorbing layers block geophysical and astrophysical measurements at wavelengths shorter than 3000A. Measurements from rockets in the region below 3000A have been restricted to certain spectral passbands by the limited development of filters and detectors. These ultraviolet wavelengths of interest may be divided into two regions: the middle and vacuum ultraviolet. In round numbers, the middle ultraviolet is from 3000 to 2000A, while the vacuum ultraviolet extends below 2000A. This paper is primarily concerned with techniques of nondispersive optics in the middle ultraviolet.

FILTERS

The variety of optical materials used in the visible part of the spectrum is not available in the middle ultraviolet. Those materials which are useful can be put into three classes: longwave pass filters which transmit all wavelengths longer than a short wavelength absorption edge; bandpass filters which transmit moderately well over broad regions of the middle ultraviolet; and absorption edge filters which have strong absorption over small wavelength intervals and are useful for producing sharp transmission cutoffs.

The first category of filter is used in photodetector envelopes, windows, or trimmers to produce the short wavelength cutoff in spectral response; Figure 1 shows the transmittance curves for various materials which are available for such use. Corning 9700 glass, with a transmittance of less than 0.05 percent at 2537A, is useful for subtractive filter photometry, for example, with a low pressure mercury arc source. Corning 7910 (9–54), which is 96 percent silica, is also useful for subtractive photometry techniques and can be compared with pure fused silica. The nickel sulfate hexahydrate, $NiSO_4$ $(H_2O)_6$, crystal* is not strictly a cutoff filter, since it has an absorption region from 3500 to 4500A. However, its absorption edge at 1900 makes it a very useful solid for separating the middle from the vacuum

*Supplied by Dr. W. R. McBride of the Naval Ordnance Test Station, China Lake, California.

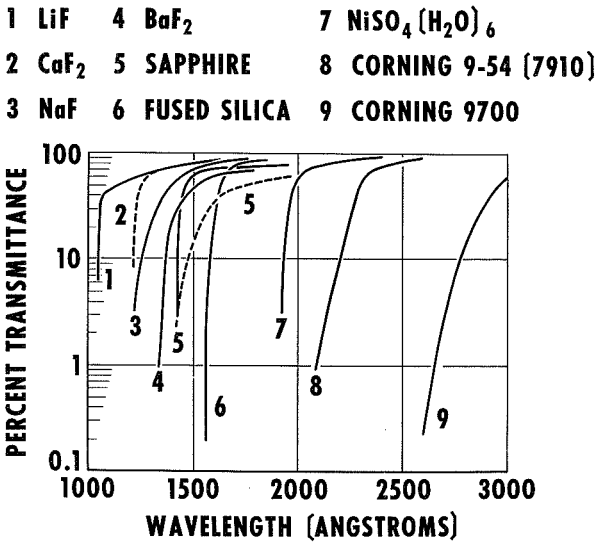

FIGURE 1.—Window transmittance cutoffs in the ultraviolet region. Curve 1 is LiF (1 mm); curve 2 is CaF_2 (1 mm); curve 3 is NaF (1 mm); curve 4 is BaF_2 (1 mm); curve 5 is sapphire (1 mm); curve 6 is fused silica (1 mm); curve 7 is $NiSO_4(H_2O)_6$ (3 mm); curve 8 is Corning 7910 glass (9–54); curve 9 is Corning 9700 glass (2 mm). The two curves numbered "5" indicate the variation in ultraviolet transmission qualities of commercial sapphire.

ultraviolet, and it is included here for comparison.

In Figure 1, the two curves marked "5" show different samples of commercial sapphire. The wide variation in ultraviolet transmittance shows the problem that faces users of this material. The similar variations in transmittance found in the vacuum ultraviolet materials such as LiF, CaF_2, NaF, BaF_2, etc.—are not found in the fused silica and other materials whose transmittances are shown in curves 6 to 9. In choosing between fused silica (or cultured quartz) and sapphire as a phototube window, the advantages in transmission properties must be weighed against those of sealing properties. For example, with fused silica a long-graded seal is required while sapphire is readily sealed to glass without a graded seal.

Some of the curves in Figure 2 illustrate the second category of filter materials, those which transmit within a limited band of wavelengths. The $NiSO_4$ $(H_2O)_6$ curve mentioned above is seen here to have two large transmission

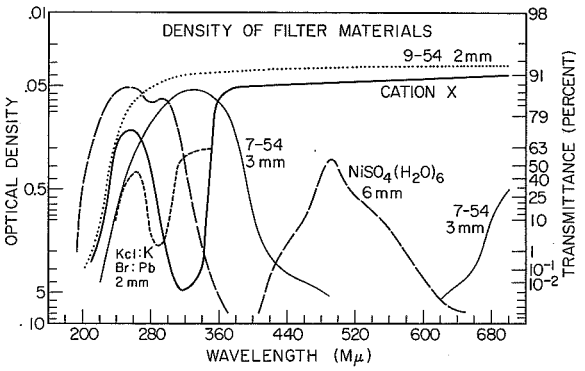

FIGURE 2.—Optical densities of typical samples of $NiSO_4(H_2O)_6$ crystal, KCL:KBr:Pb crystal, cation-X, and Corning filters 9–54 and 7–54.

regions: one covering the middle ultraviolet, the other in the blue-green.

The dashed curve representing the optical density of a crystal of KCl: KBr doped with 0.05 percent lead is an example of an absorption edge filter and is shown in more detail in Figure 3. The very sharp absorption edges of these alkali halide crystals can be used to produce equally sharp edges in transmission filter responses when they are combined with other materials. A useful variation in the wavelength of this edge can be achieved by varying the amounts of KBr and KCl in the crystal.

The narrow-band multilayer dielectric interference filters widely used for the visible and infrared regions have not been generally available in the ultraviolet. In the last 5 years, however, rocket measurements have been made with several broadband ultraviolet filters. One of these is the chemical filter described by Dunkelman and Field in 1955 (Reference 1). The transmission of this filter, which was developed to replace the liquid "chemical" filters described by Kasha (Reference 2), can be inferred from a comparison of curves 13 and 5 in Figure 6. The quantum efficiencies of a variety of photosurfaces discussed in the next section are also shown in this figure. This chemical filter, however, is unstable in direct sunlight and its use has been restricted to measurements of the night airglow and stellar fluxes.

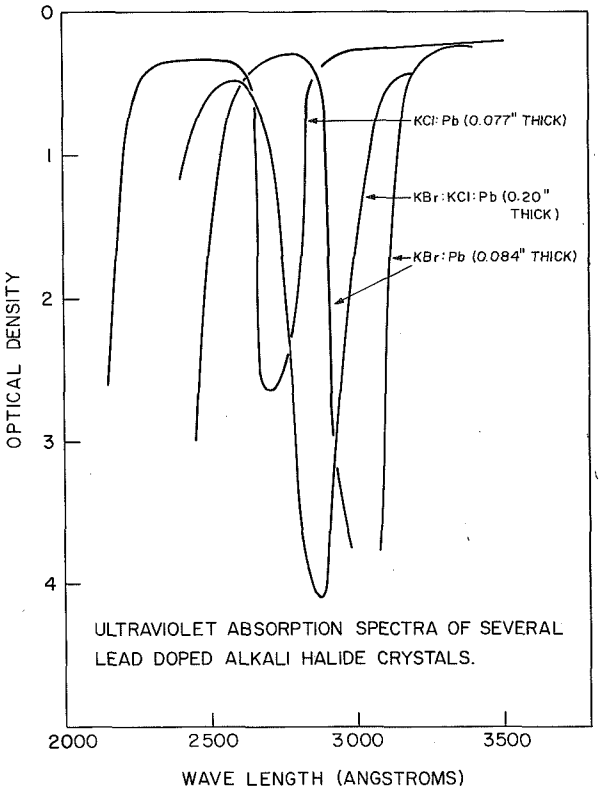

FIGURE 3.—Ultraviolet absorption curves of several lead-doped alkali halide crystals. The absorption edge may be shifted between 2650 and 2900A by varying the amounts of KBr or KCl in the crystal.

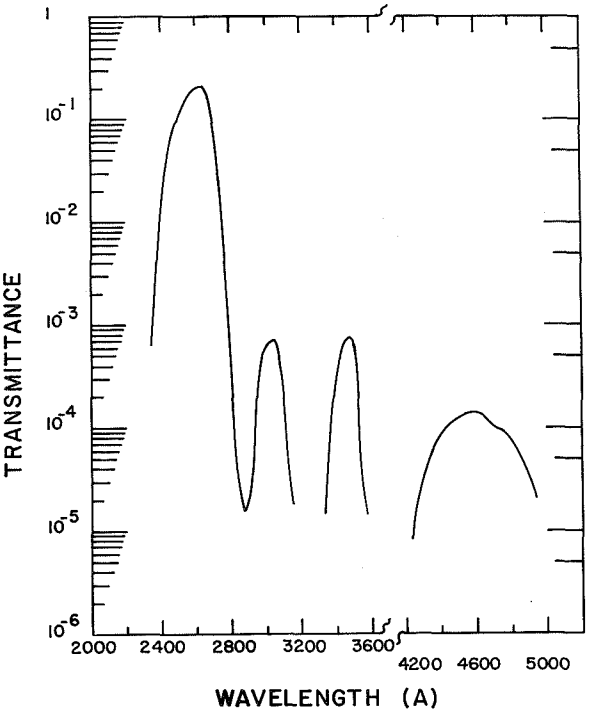

FIGURE 4.—Transmittance curve of a 2600A filter made up of lead-doped KCl:KBr, cation-X, $NiSO_4(H_2O)_6$, a Corning 7–54 filter, and a Corning 9–54 filter.

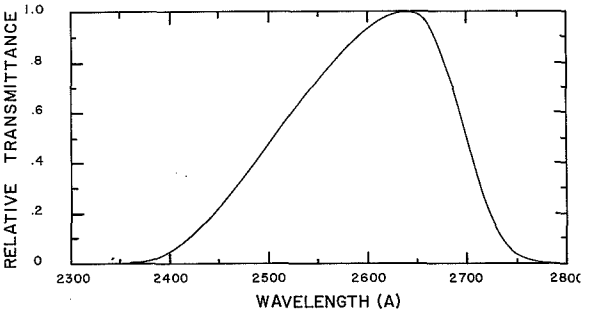

FIGURE 5.—Passband portion of the 2600A filter transmittance curve shown in figure 4, here normalized and put on a linear scale.

In 1960, several filters were assembled at Goddard Space Flight Center which were quite stable and that have been used for measurements of both solar and stellar fluxes. These filters, described in a recent paper by Childs (Reference 3), are made up of the solid glasses and crystals whose characteristics are shown in Figures 1 through 3. The transmittance characteristics of a typical filter are shown in Figures 4 and 5.

Figure 4 shows the transmittance of a 2600A filter made up of lead-doped KCl:KBr, a sheet of cation-X, a 3 mm crystal of $NiSO_4(H_2O)_6$, a Corning 7–54 filter, and a Corning 9–54 filter. This filter has an effective bandwidth of 200A and a peak transmittance of 23 percent. Figure 5 shows the passband portion of the same curve normalized on a linear scale. The long wavelength and relatively minor "leaks" in these filters at longer wave-lengths can be greatly reduced if necesssry by using them with "solar blind" cathodes; the latter will be described below.

Broadband interference filters for the middle ultraviolet can now be obtained commercially for wavelengths longer than 2100A. These are of the Fabry-Perot MDM type (metal-dielectric-metal). They have a 15 to 20 percent peak transmittance with a 300A bandwidth

at half peak. A somewhat narrower bandwidth can be obtained with lower peak transmission. For solar flux measurements, selected optical materials described above have been added to these interference filters for further trimming. Research on improved Fabry-Perot filters of the MDMDM type—where M represents aluminum and D a low-index dielectric such as MgF or chiolite (2 $NaF \cdot AlF_3$)—is being carried out by A. F. Turner (private communication) at Bausch and Lomb and by D. J. Schroeder (private communication) at the University of Wisconsin.

Notable advances in multilayer interference filters have been reported abroad. Sokolova and Krylova (Reference 4) report an excellent transmission filter of ThO_2 and SiO_2 at wavelengths as short as 2200A. Sebire, Cojan, and Giacome (Reference 5) report a 2595A multilayer dielectric filter with 28 percent peak transmission and a 12A passband at half peak. The multilayers are of PbF_2, and cryolite (Na_3AlF_6).

CATHODES

Photocathodes can be divided into three spectral types: those sensitive to both visible and ultraviolet wavelengths, those sensitive only to ultraviolet wavelengths below 3500A, and those sensitive only to vacuum ultraviolet wavelengths.

Typical of the first category is the 1P28 photomultiplier which contains a cesium-antimony (Cs-Sb) cathode and a Corning 9741 glass envelope. The long wavelength response, which extends into the red (Figure 6, curve 5), is a property of the Cs-Sb photoemitter. The short wavelength response is limited by the glass envelope to 1800A. With a quartz envelope, as described by Dunkelman and Lock (Reference 6) in 1950, the short wavelength response is extended to below 1600A. Recently the spectral range has been further extended by means of a CaF_2, window. Such tubes have been studied at Goddard Space Flight Center (Reference 7), and the response was found to be comparatively flat down to 1225A, the window cutoff.

A spectral response with a more constant quantum efficiency can be obtained by coating

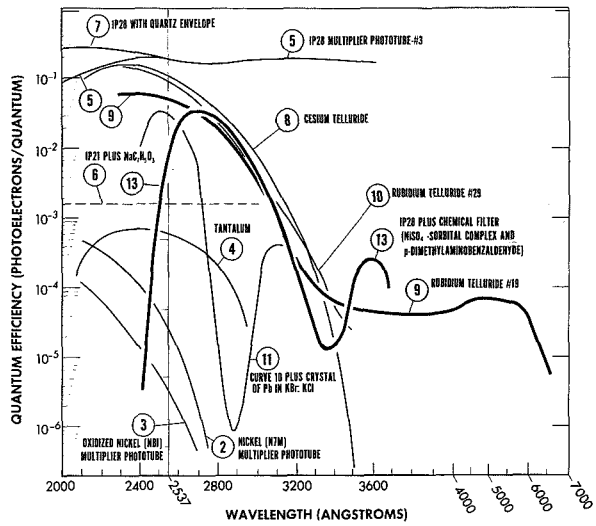

FIGURE 6.—Quantum efficiency of various photocathodes. Curves 11 and 13 represent responses which include optical filters to improve selectivity. Note that the wavelength scale changes at 4000A. Curve 6, sodium salicylate, represents the expected flat response but is not a measured spectral yield.

the front face of a glass-enveloped multiplier, for example, the 1P21, with a layer of sodium salicylate ($NaC_7H_5O_3$). Sodium salicylate has been shown by Watanabe (Reference 8) to have a nearly constant quantum efficiency of fluorescence for excitation wavelengths from below 1000A to beyond 3000A; emission is in the blue-green. Curve 6 in Figure 6 shows a typical quantum efficiency of a 1P21 coated with sodium salicylate. By using a high-yield end-window photomultiplier and optimizing the coating thickness, overall quantum efficiencies of up to 5 percent have been obtained. The use of reflectors to collect some of the forward-emitted fluorescent light can increase this figure somewhat.

For many applications there is a need for cathodes responsive to middle ultraviolet but insensitive to wavelengths longer than about 3500A. These cathodes have been described as "solar blind" because they are insensitive to sunlight at the earth's surface. They are, of course, responsive to sunlight above the ozone layer.

The most useful of the solar blind photosurfaces known to date are the alkali tellurides.

Cesium-tellurium (Cs-Te) and rubidium-tellurium (Rb-Te) offer high quantum efficiencies with good solar blindness (curves 8, 9 and 10 in Fig. 6). These responses were first reported by Taft and Apker in 1953 (Reference 9). For the middle ultraviolet, Cs-Te and Rb-Te cathodes have shown no significant difference in response. The long wavelength tail of curve 9 is produced by an excess of rubidium above the stoichiometric ratio of two rubidium atoms to one tellurium atom. By varying the cesium or rubidium content of the cathode, the manufacturer has some control over both the shape of the response curve in the 3000A region and the peak quantum yield. Increased proportions of cesium generally cause both slightly higher quantum yield at short wavelengths and increased sensitivity at long wavelengths. With a LiF window the response of the Cs-Te continues approximately uniformly into the vacuum ultraviolet. Tubes using Cs-Te cathodes and quartz, sapphire, or LiF windows are now commercially available and make possible a number of interesting measurements that must be made in the presence of a strong long-wavelength background, such as that from the sun.

Even more solar blind but much less sensitive are the pure metal photocathodes (Reference 10). Figure 6 shows responses of cathodes of nickel, curve 2; tantalum, curve 4; and oxidized nickel, curve 3. In each case here, and with other metals not shown, the quantum yields are down by two or three decades from those of the alkali halide photosurfaces.

Applications using the second category of photocathodes described above often depend on selection of phototubes for solar blindness as well as quantum yield. One criterion for determining their merit is their sensitivity to wavelengths below 2900A as compared with this small but measurable response to sunlight. One such figure of merit, arbitrarily taken, is the irradiance at 2537A necessary to produce an anode current equal to that produced by full sunlight with skylight excluded. This "equivalent sunlight input" is admittedly not a precise measurement since the intensity of short wavelength sunlight, to which the phototube is relatively most sensitive, depends on the angular altitude of the sun, the clarity of the sky, and the amount of atmospheric ozone. Nevertheless, "equivalent sunlight input" has proved useful in comparing a wide variety of photodevices. Values for a number of cathodes are listed in Table 1. The measurements were taken with the sun above 30 degrees altitude in a cloudless sky. The quantum efficiency at

TABLE 1.—*Solar Blindness of Various Cathodes*

Photocathode	Equivalent sunlight input [1] at 2537A $\left(\frac{\text{watts}}{\text{cm}^2}\right)$	Quantum efficiency at 2537A $\left(\frac{\text{photoelectrons}}{\text{quantum}}\right)$	Remarks
Cesium-Tellurium	1.7×10^{-5}	5×10^{-2}	Semitransparent cathode in a photodiode.
Cesium-Tellurium	1.2×10^{-5}	2.7×10^{-2}	Semitransparent cathode in a 14-stage photomultiplier.
Cesium-Tellurium	8.5×10^{-6}	13×10^{-2}	Opaque cathode in a photodiode.
Cesium-Tellurium	6.7×10^{-6}	1.4×10^{-2}	Semitransparent cathode in a 14-stage photomultiplier.
Tantalium	8×10^{-9}	6.5×10^{-4}	Opaque cathode in a photodiode.
Oxidized Nickel	6×10^{-9}	3.5×10^{-4}	Opaque cathode in a 9-stage photomultiplier.
Silver	3×10^{-9}	1.5×10^{-5}	Opaque cathode in a 9-stage photomultiplier.
Nickel	1×10^{-9}	5×10^{-6}	Opaque cathode in a 9-stage photomultiplier.
Copper Gauze	2×10^{-11}	2.8×10^{-7}	Photon counter.

[1] Watts/cm² of 2537A radiation required to produce a detector signal equal to that produced by full sunlight (less sky background).

2537A is also listed. Both the quantum efficiency and solar blindness should be considered, particularly when available flux in the middle ultraviolet is low and considerable long-wavelength background is present.

The curves of Figure 7 include the third category—vacuum ultraviolet photodetectors. Phototubes made by Sommer at RCA with cathodes of copper iodine (Cu–I), curve 3, and cesium iodine (Cs–I), curve 2 have a very strong rejection of all middle and near ultraviolet wavelengths but a large response at the short wavelengths around 1200A.[1] Also shown for comparison are two metal cathode responses (nickel and tungsten), and the flat response of Cs–Sb in the phototube with the CaF_2 window mentioned above.

Figure 8 shows some of the photomultipliers examined at GSFC. The ASCOP [2] tube (third from the left) with the LiF window, and the CBS [3] tube (at the far right) with the sapphire window, are both commercially available solar blind photomultipliers using Cs-Te photocathodes.

Additional data on specific phototubes are included in Table 2. A recent paper (Reference 11) describes the properties of spectrally selective photocathodes in more detail.

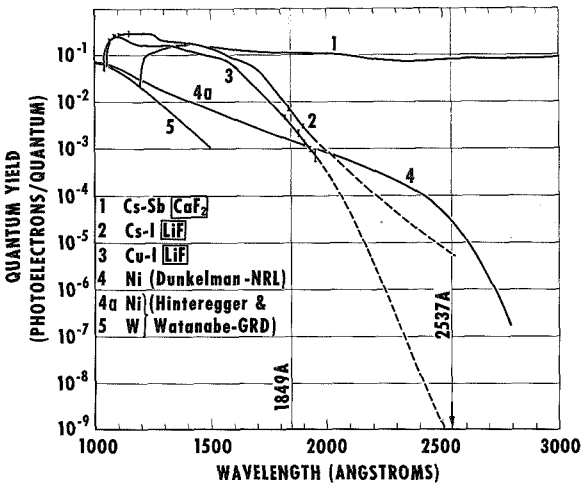

FIGURE 7.—Spectral response curves of a variety of photocathodes showing the high rejection of some of the iodide compounds at longer wavelengths. The advantage of the relatively high yield composite photo surface over the lower yield pure metal is also evident. The dashed portions represent estimated yields interpolated between the measured values at 2000A and 2537A.

CALIBRATION

Calibration of the photocathodes has been divided into two phases. In the first phase, the relative cathode spectral response is determined from measurements taken at the exit beam of the Cary 14 double monochromator and the 1 meter McPherson vacuum monochromator. A hydrogen arc light source is used with both instruments. The quantum yield of sodium salicylate fluorescence is taken to be constant throughout the wavelength region from above 3300A down to below 1000A. For this reason the relative spectral response of the unknown photocathode, in terms of quantum yield, can be obtained by comparing the photocathode response to the monochromator beam with the fluorescent response of sodium salicylate to the same beam.

In the second phase, the relative quantum yield is put on an absolute basis by optical bench measurements. In general, use is made of a calibrated 2537A line of the mercury arc. On some occasions, the 2138A line of a zinc arc and the 1849A line of the mercury arc are also employed.

The mercury arc used is a small pencil-like septum lamp described by Childs (Reference 12). This lamp has a flux at one meter of about 2 $\mu w/cm^2$ for a specified axial position and is relatively insensitive to ordinary changes in line voltage or room temperature. The mercury arc 2537A line calibration is based on the use of three calibrated ultraviolet intensity meters, each consisting of a cadmium photocell and simple electrometer amplifier. These intensity meters were manufactured by the Lamp

[1] The large quantum yields shown for these tubes represent an early and preliminary measurement. Subsequent measurements of Cs–I and Cu–I cathodes show that in general a peak quantum efficiency of 10 to 20 percent is more typical with Cs–I being 3 to 5 times more sensitive than Cu–I at the Lyman Alpha wavelength (1216A).

[2] ASCOP Division of Electro-Mechanical Research Inc.

[3] CBS Laboratories, a Division of Columbia Broadcasting System, Inc.

TABLE 2.—*Commercial Photomultipliers and Photodiodes Examined at Goddard Space Flight Center*

Tube	Cathode	Window	Cathode diameter (mm)	Tube diameter (cm)	Tube length (cm)	Quoted dark currents [1] at gains of 10^6 (amperes)
Photomultipliers						
EMI [2]						
6256B	CsSbO	Quartz	10	5.1	10.7	10^{-9}
6255S	"S"	Quartz	42	5.1	12.0	6×10^{-9}
CBS [3]						
CL1050	Cesium-antimony	Sapphire	19	5.1	16.8	3×10^{-9}
CL1067	Cesium-tellurium	Sapphire	42	5.1	15.0	Not available
RCA [4]						
1P28	Cesium-antimony	9741	[5] 8×23	3.3	8.0	5×10^{-8}
C70128	Cesium-tellurium	LiF	12	1.9	8.9	Not available
ASCOP [6 7]						
541FO8	Cesium-tellurium	LiF	10	3.2	12.7	2×10^{-11}
541FO5M	Cesium-tellurium	Sapphire	25	3.2	11.4	1×10^{-10}
Photodiodes						
CBS CL1051	Cesium-antimony	Sapphire	[5] 12	2.5	7.0	
RCA c70126 [8]	Cesium-tellurium	LiF	11	1.9	4.4	
ITT FW 156 [9]	Cesium-tellurium	LiF	[5] 11	1.9	3.8	
ASCOP 540F	Cesium-tellurium	LiF	8	1.9	6.3	
Westinghouse	Cesium-Iodine	LiF	12	1.9	6.3	

[1] Much lower dark currents have been measured at GSFC for all of these tubes. A dark current of 2.5×10^{-12} ampere at a gain of 10^6 has been observed for a Cs-Te photomultiplier.

[2] Electrical Musical Instruments/United States.

[3] CBS Laboratories, a Division of Columbia Broadcasting System, Inc.

[4] Radio Corporation of America Laboratories.

[5] Opaque cathode deposited on a metal substrate.

[6] ASCOP Division of Electro-Mechanical Research, Inc.

[7] Tubes potted with resistor chain in place.

[8] Radio Corporation of America Electron Tube Division.

[9] International Telephone and Telegraph Laboratories.

Development Laboratory of the General Electric Co. They were calibrated by the GE Co. and are frequently compared against each other at GSFC. Their accuracy is estimated to be within 5 percent. These meters are used as a laboratory calibration reference and are employed each time a photosurface yield is measured against a mercury arc lamp. Thus, reliance is placed on photosurfaces rather than on discharge sources. The calibration of these meters has been checked by comparison with National Bureau of Standards (NBS) sources: first with an NBS mercury source by means of an NBS tantalum cell; then at GSFC with an NBS standard carbon filament lamp by means of a gold-black Golay cell.

GEOPHYSICAL AND ASTRONOMICAL APPLICATIONS

To date, middle ultraviolet astronomy (Reference 13) has been limited to preliminary surveys of the sky from unguided rockets. Most of these sky-survey type measurements have been made from White Sands, N. Mex. (Reference 14), and Wallops Island, Va., with American Aerobee vehicles. More recently, southern sky measurements have been made from Woomera, Australia, with United Kingdom Skylark rockets. Although filter limitations have allowed only broadband photometry in certain spectral regions, these surveys are nevertheless of considerable value for com-

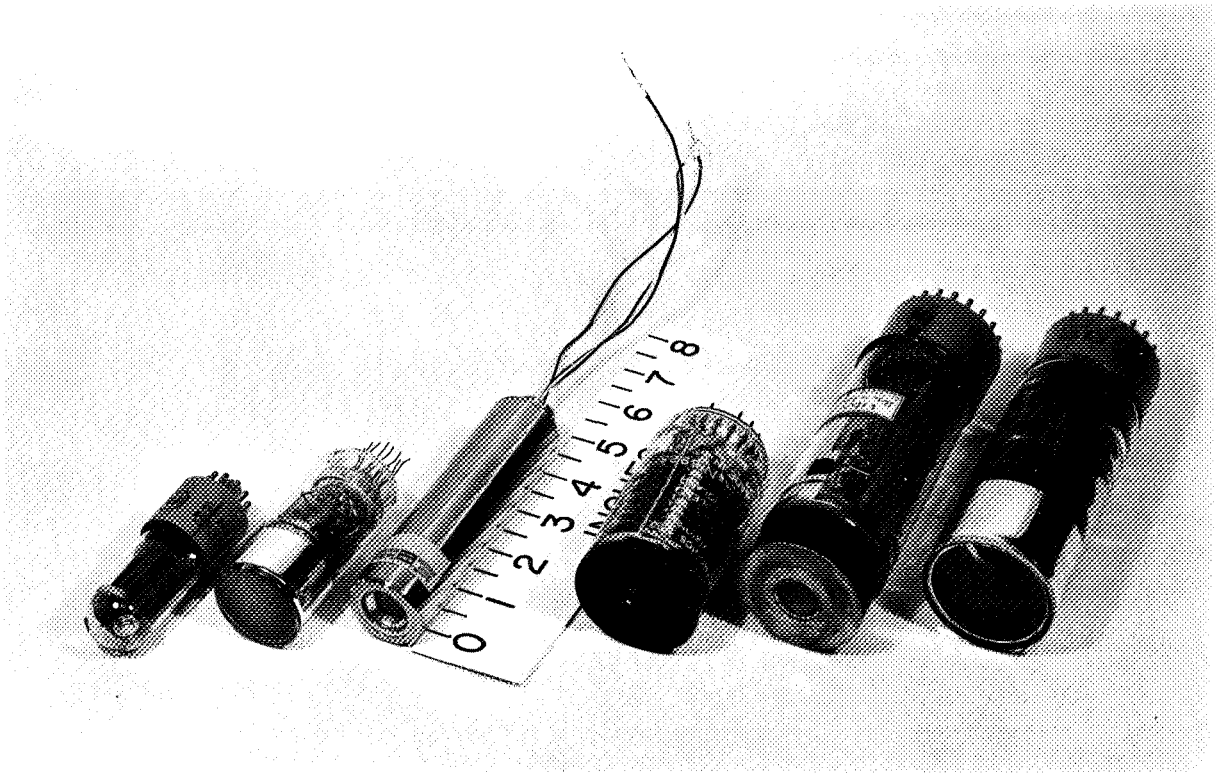

FIGURE 8.—Some of the photomultipliers examined at the Goddard laboratory. Left to right: RCA 1P28, Cs-Sb cathode, 9741, glass envelope; RCA 7151c (ruggedized version of 6199 tube); ASCOP 541F, semitransparent Cs-Te cathode, LiF window (potted with resistor chain in place); EMI 6256B, semitransparent Cs-Sb cathode, fused silica window; RCA (A. H. Sommer experimental tube), Cs-Te cathode, LiF window; CBS CL 1067, semitransparent Cs-Te cathode, sapphire window.

parison with predicted ultraviolet intensities and for intelligent planning of more sophisticatd experiments.

A typical photometer is shown in Figure 9. These photometers may be mounted in pairs, triplets, etc., with parallel optical axes. With each photometer sensitive to a different band, multicolor observations can be taken. The orientation is such that during observation the combined precession and rotation of the rocket causes the photometers to scan a large portion of the sky. To increase the sky area coverage, sets of photometers may be pointed at several angles with respect to the rocket axis. On recent flights instruments have been mounted 105, 90, and 75 degrees from the longitudinal axis of the rocket.

Figure 10 shows, as an example, selected portions of a telemeter record for one photometer and demonstrates the heretofore unavailable data which may be obtained from simple middle ultraviolet techniques. In this case, the photometer optical axis was inclined 75 degrees from the rocket axis. During the portion of the flight represented by the upper trace the rocket was rising out of the airglow layer, and the stars may be seen superimposed on a decreasing airglow signal. In the lower traces the rocket was above the emitting layer, and the strong saturated signal at the edges of the trace is due to the bright airglow "horizon."

The ultraviolet airglow is of interest in its own right. Broida and Gayden (Reference 15) found that the Herzberg bands of molecular oxygen were the dominant feature in laboratory-produced air afterglow between 2500 and 3000A. Rocket measurements have shown this layer to

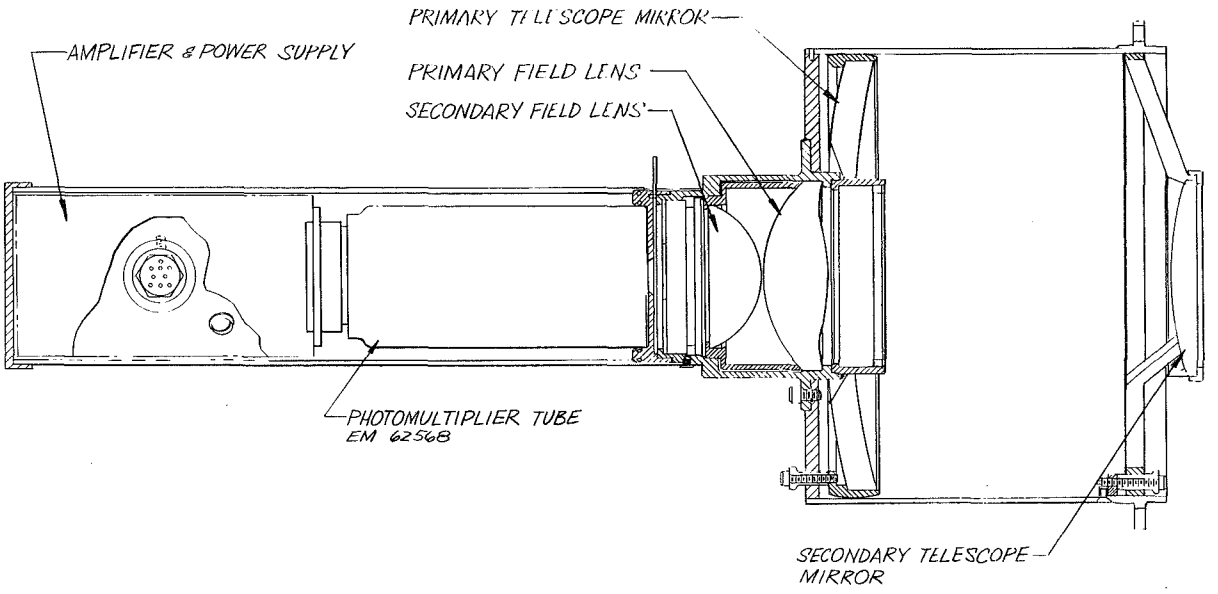

FIGURE 9.—Photometer used for recent stellar measurements at Woomera, Australia. The objective mirrors are a modified Cassegrainian arrangement with a concave parabolic primary and a spherical secondary. The field lenses are quartz. In the filter cavity, filter pieces with diameters from 2.8 to 4.2 mm are centered over the entrance aperture.

be between 85 and 120 km, with ozone absorption evident up to 50 km.

The solar blind photocathodes described earlier may be used in photomultipliers for many conventional applications. In addition, work has begun on image converter tubes which will be selective to the middle and vacuum ultraviolet. Using such devices in a monocular or binocular system, an astronaut might survey for astrophysical or geophysical effects.

REFERENCES

1. DUNKELMAN, L., and FIELD, D. E., "A Middle Ultraviolet Transmission Filter," U.S. Naval Res. Lab. Rept. 4647, November 1955.
2. KASHA, M., "Transmission Filters for the Ultraviolet," *J. Opt. Soc. Amer.* 38(11): 929–934, November 1948.
3. CHILDS, C. B., "Broad-Band Ultraviolet Filters," NASA Technical Note D-697, April 1961; also published in *J. Opt. Soc. Amer.* 51(8): 895–897, August 1961.
4. SOKOLOVA, R. S., and KRYLOVA, T. N., "Interference Filters for the Ultraviolet Region of the Spectrum," *Optics and Spectroscopy* 6(6): 513–515, June 1959. (English translation of: *Optika i Spektroskopiya* 6(6): 788–791, June 1959.)
5. SEBIRE, N., COJAN, J. L., and GIACOMO, P., "Filtres Interferentiels Multi-Dielectriques pour l'Ultraviolet vers $\lambda \equiv 2500$A," *Comptes Rendus Sciences* (Paris) 254(3): 448–449, Jan. 15, 1962.
6. DUNKELMAN, L., and LOCK, C., "Ultraviolet Spectral Sensitivity Characteristics of Photomultipliers having Quartz and Glass Envelopes," *J. Opt. Soc. Amer.* 41(11): 802–804, November 1951.
7. CAUSSE, J. P., "Status Report on the Development of the ASCOP Multipliers," *IRE Trans. on Nuclear Science* NS-9(3): 90–96, June 1962.
8. WATANABE, K., and INN, E. C. Y., "Intensity Measurements in the Vacuum Ultraviolet," *J. Opt. Soc. Amer.* 43(1): 32–35, January 1953.
9. TAFT, E., and APKER, L., "Photoemission from Cesium and Rubidium Tellurides," *J. Opt. Soc. Amer.* 43(2): 81–83, February 1953.

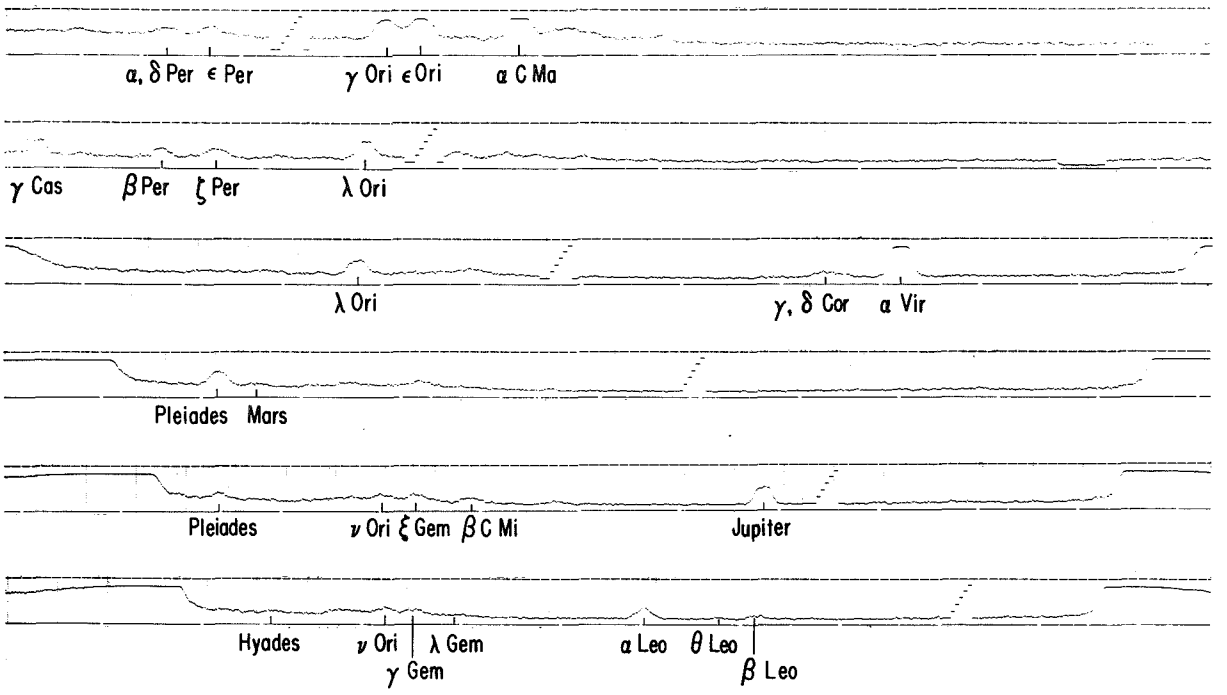

TELEMETER SIGNALS FROM ROCKET BORNE 2700 Å PHOTOMETER

FIGURE 10.—Telemeter record of 2700A rocket borne photometer. Saturated signals at the ends of the trace are due to the airglow horizon. Each trace is 12 seconds in duration. Telemeter calibrations indicate 1 volt steps.

10. DUNKELMAN, L., "Solar-Blind Ultraviolet Multiplier Phototubes," *J. Opt. Soc. Amer.* 45(2:) 134–135, February 1955.
11. DUNKELMAN, L., FOWLER, W. B., and HENNES, J. P., "Spectrally Selective Photodetectors for the Middle and Vacuum Ultraviolet," *J. Opt. Soc. Amer.* 51(12): 1461, December 1961 (Abstract); also to be published in *Appl. Optics*, November 1962.
12. CHILDS, C. B., "Low Pressure Mercury Arc for Ultraviolet Calibration," to be published in *Appl. Optics* November 1962.
13. BOGGESS, A., III, "Ultraviolet Astronomical Photometry from Rockets," NASA Technical Note D–673, June 1962. Also included *Space Astrophysics* ed. by W. Liller, New York: McGraw-Hill Book Co., 1961, pp. 121–132.
14. BOGGESS, A., III, and DUNKELMAN, L., "Stellar Flux Measurements at 2700Å," *Astronom. J.* 63(1262): 303, September 1958 (Abstract).
15. BROIDA, H. P., and GAYDON, A. G., "The Herzberg Bands of 0_2 in an Oxygen Afterglow and in the Night-Sky Spectrum," *Proc. Royal Soc.* London 222A(1149): 181–195, March 9, 1954.

FAILURE PROBLEM WITH A RHENIUM MASS SPECTROMETER FILAMENT AND ITS SOLUTION

A. G. EUBANKS AND H. E. FRANKEL
Goddard Space Flight Center

Rhenium mass-spectrometer filaments to be used in an atmospheric structure satellite failed when prototype spectrometer models were subjected to shock and vibration testing. Laboratory analysis showed that the failures were due to cold-working of the filament wire in a critical area. A redesign of the filament was carried out to alleviate this problem and subsequent testing showed that the new design was successful in that no additional failures occurred.

INTRODUCTION

Rhenium is a relatively scarce metal, its concentration in the earth's crust being about the same as that of most of the platinum group metals. It is presently produced only in small quantities, the total current production in the United States being on the order of 200 pounds per year. Some typical properties of rhenium are given in Table I.

Because of its limited availability and high cost, no extensive use of rhenium in large structural applications is likely. However, certain of its properties make it especially suitable for use in electron tube applications (Reference 1). It has also been found to be a good material for mass spectrometer filaments and was selected for use in this capacity in a small double-focusing magnetic-sector mass spectrometer for incorporation in an Atmospheric Structure Satellite. When pre-flight spectrometer units were subjected to shock and vibration testing, however, failures occurred in 80 percent of the filaments. Laboratory analysis disclosed the failure mechanism involved and a redesign of the filament based on this information was carried out. The success of this redesign was demonstrated when five spectrometer units were subsequently tested without failure.

TABLE I.—*Physical and Mechanical Properties of Rhenium*

Property	*Values*
Melting point, °C	3180
Boiling point, °C	5900
Recrystallization temperature, °C	1200 to 1500°C (1 hr)
Crystal structure	HCP
Density, gm/cm³	21.0
Electrical resistivity at 20°C, micohm-cm.	19.3
Temperature coef. of resistivity at 20°C, per °C.	0.0039
Electrical conductivity, percent IACS.	9.3
Thermal conductivity, 0°–100°C Cal/cm²/cm/sec/°C.	0.17
Coef. of thermal expansion, 20° to 500°C, $\times 10^{-6}$.	6.7
Thermionic work function, eV	4.8
Ultimate tensile strength, psi, $\times 10^3$	
20°C, 15 percent wrought	340
20°C, annealed	170
2000°C	20

DESCRIPTION OF FILAMENT

A spectrographic analysis of the 0.007 in diam rhenium wire from which the filaments were fabricated showed the metal to be of relatively high purity. The elements detected and their concentrations were as follows: 0.0001–0.001 percent Ca, 0.0001 percent Cu, 0.001–0.01 percent Fe, 0.01–0.1 percent Mo,

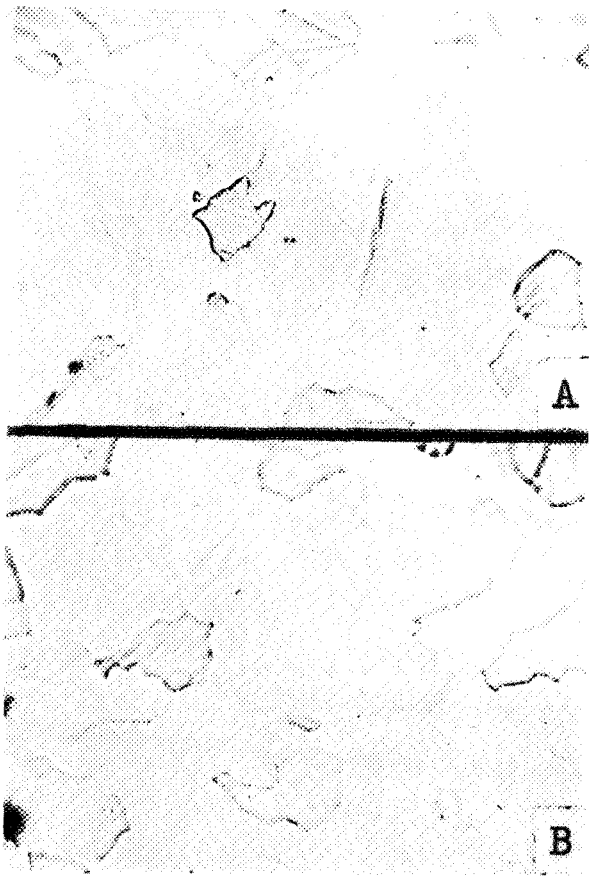

FIGURE 1.—Diagram of rhenium filament and supports.

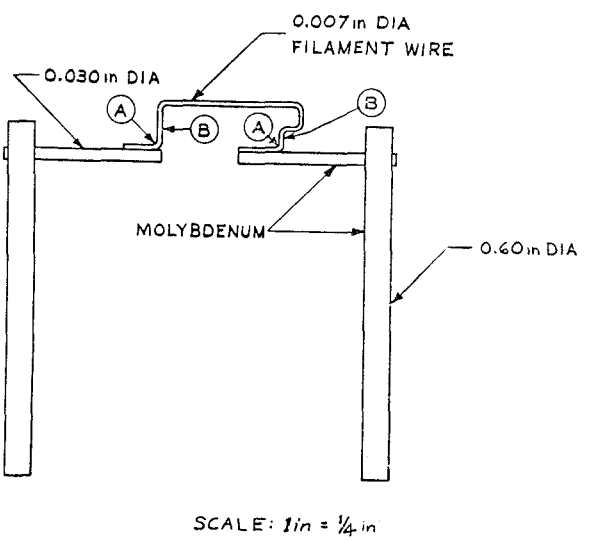

FIGURE 2.—Micrographs of rhenium wire prior to fabrication into a filament. (A) perpendicular to wire axis, (B) parallel to wire axis. × 500

and 0.001–0.01 Si. A micrograph of this wire prior to fabrication is shown in Figure 1. A sketch of the filament and its molybdenum supports as originally designed is shown in Figure 2.

Preparation of the filament consisted simply of bending the wire, in the annealed condition, into shape and spot-welding the ends to the supports. The radius of the bends was approximately $\frac{1}{32}$ in. Tungsten electrodes were used for the spot-welding and thin platinum foil was placed between the filament and support to promote bonding at the weld. Rhenium has the highest cold-working rate of any known metal. In the recrystallized condition, however, rhenium wire can be bent around a mandrel of its own diameter. Careful microscopic examination of mounted and polished sections of the filaments, especially at the bends, showed that no cracking of the wire had occurred during forming. Consequently, it was not considered necessary to carry out intermediate anneals during the forming operation.

TESTING PROCEDURE

After fabrication, the filament with its supports was installed in the mass spectrometer. Five filaments were operated successfully for approximately 40 hours "on-time" each. During the testing period each filament was turned on and off approximately 50 times. The operating temperature of the filaments was 2000°C as measured with an optical pyrometer. Several complete spectrometer units were then subjected to standard launch level shock and vibration tests for the particular launch vehicle (Thor-Delta) to be used with the satellite. The filaments were not heated during these tests. Four of the five filaments failed during the shock and vibration tests. All of the failures occurred at one or the other of the bends nearest the filament supports.

LABORATORY ANALYSIS

Portions of failed filaments taken from areas A and B in Figure 1 were mounted and polished for microscopic examination. Figure 3, from one of the areas marked A, when compared with

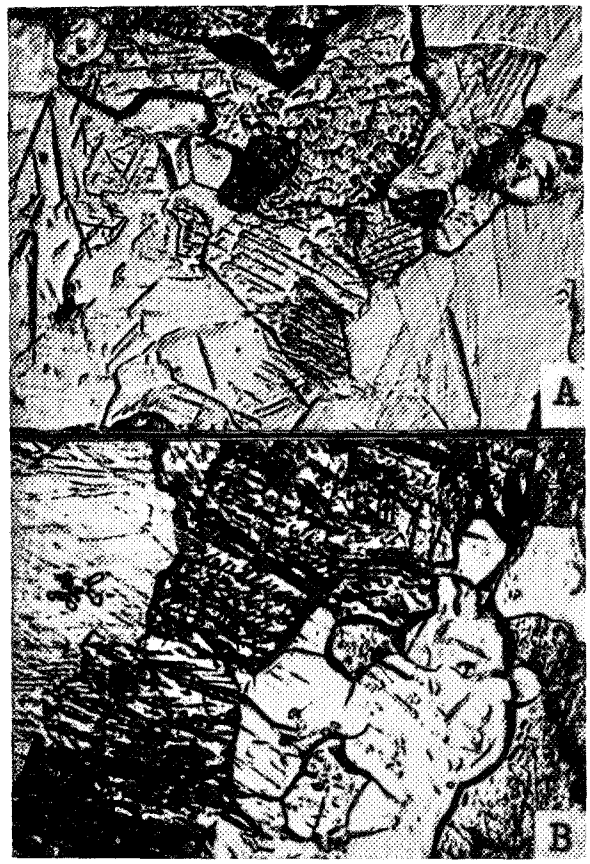

FIGURE 3.—Micrograph from area A (see fig. 1) in bend near filament support. (A) perpendicular to wire axis, (B) parallel to wire axis. × 500

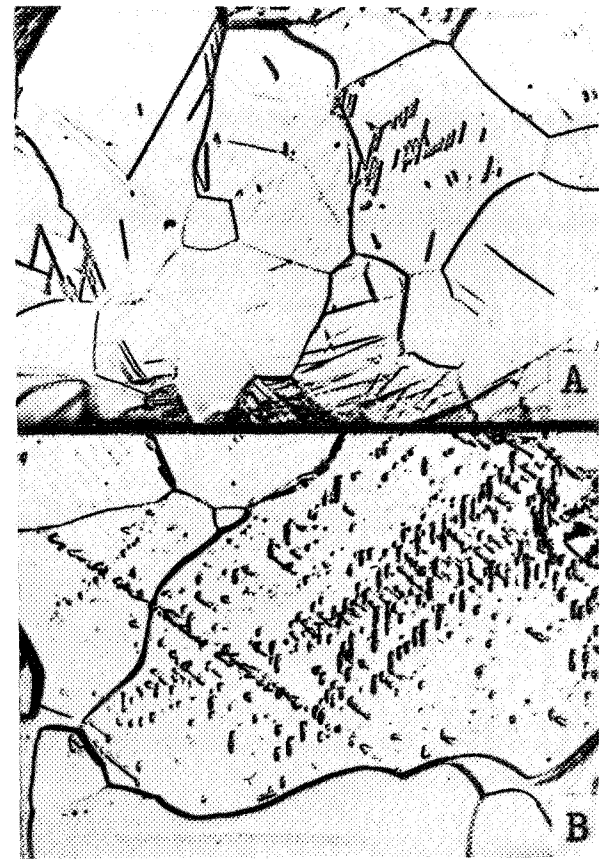

FIGURE 4.—Micrograph from area B (see fig. 1) above bend. (A) perpendicular to wire axis, (B) parallel to wire axis. × 500

Figure 2 showing the original wire, indicates that grain growth in the bends near the filament supports was insignificant and that considerable plastic straining had occurred. It is believed that the heavy molybdenum supports acted as heat sinks to keep the filament wire cool in this area. On the other hand, Figure 4, taken from one of the areas marked B, shows that grain growth had occurred in the wire above the bends. These observations are taken to indicate that the wire above the bends was heated to a significantly higher temperature than that in the bends.

DISCUSSION

The expansion and contraction of the filament during heating and cooling caused a flexing of the wire at the bends. In those areas where the wire was not heated sufficiently hot to bring about stress relief, the continued cold-working caused embrittlement which eventually led to failure during the shock and vibration tests. Accordingly, a redesign of the filament and supports was carried out to assure that the bends near the supports were heated sufficiently hot to bring about stress relief in the bends. This was done by shortening the left-hand (Fig. 1 orientation) filament support cross piece so that the bend was at least 0.010 in. beyond the end of the support. Also, the minimum distance between the last of the spot-welds and the bends was set at 0.020 in. These steps were taken to reduce the heat transfer from the filament to the supports and thus increase the filament temperature at the critical points.

In addition, the radius of the bends in the filament wire near the supports was increased to $\frac{3}{32}$ in. to reduce the magnitude of the flexural stresses occurring at any given point in the bend. Incorporation of the new filament design and subsequent testing indicated that the redesign was successful inasmuch as five filaments were operated and vibration tested without any failures.

ACKNOWLEDGMENT

The micrographs were prepared by P. D. Sarmiento of the Goddard staff.

REFERENCES

1. Anon, The Role of Rhenium in Electronics, Electronics, *34* (14), 98 (Apr. 7, 1961).

AN ATTITUDE CONTROL SYSTEM FOR THE ADVANCED ORBITING SOLAR OBSERVATORY

PAUL G. FAHLSTROM

Goddard Space Flight Center

The scientific objectives of solar research require ever increasing accuracy requirements for orbiting observatories. To speak of "seconds of arc" is now quite common among engineers designing control systems for scientific spacecraft. One such spacecraft is the Advanced Orbiting Solar Observatory (AOSO). The attitude control subsystem for the AOSO must meet a number of stringent performance requirements. For instance, it must have a pointing accuracy of ± five seconds of arc to observe the smallest sun spots, and it must also have the capability of raster scanning to map phenomena emanating from the sun's surface. (Fig. one indicates the pointing and scan pattern requirements for AOSO.)

The AOSO control subsystem needs to be considerably more accurate than the over-all observatory requirements, because of possible misalignment of experiments. The key component affecting its accuracy is the fine sun sensor. This device has been the subject of great concern and study for the past year. Innumerable concepts, from industry and government, have been discussed, studied, dissected, praised and damned. "No moving parts" was a characteristic hard sought after. A number of concepts using a mosaic of detectors were investigated and rejected because of high power requirements and developmental problems. It became apparent that there would be moving parts in the AOSO fine sun sensor. Several workable designs, meeting most of the control subsystem requirements, came to the surface. The sensor that will be used for AOSO was conceived by the combined efforts of Minneapolis-Honeywell and Republic Aviation Corporation. Conceptually, this sun sensor deviates the line-of-sight by a series of rotating quartz wedges which can accurately position and control the line-of-sight to one second accuracies. The quartz wedges deviate the entering sunlight in response to digital pointing or scanning commands. The wedges are positively controlled by an optical readout, and fed back to the digital logic electronics. After controlled deviation by the wedges, the sunlight enters the detector prism. This prism has its exit faces cut to the critical reflective-refractive angle for the particular material, and registers tracking deviations on a solar detector. Operating in a servo loop closed through the observatory, the system seeks a null to keep constant the apparent position of the sun, as seen by the critical angle prism. (Fig. two A and B show a block diagram of the fine sun sensor signal

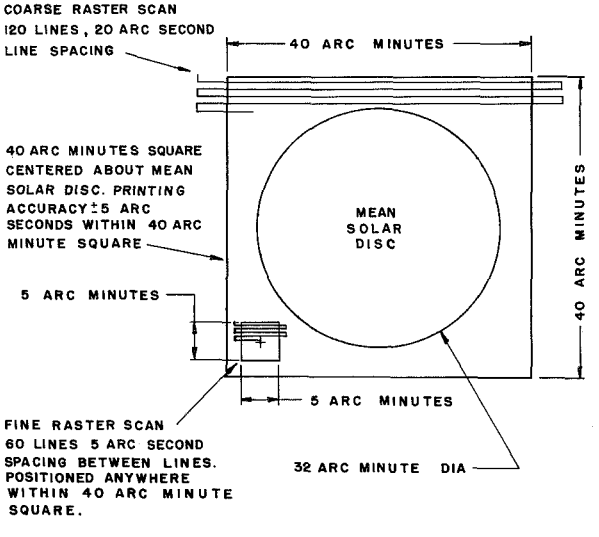

FIGURE 1.—AOSO tracking requirements.

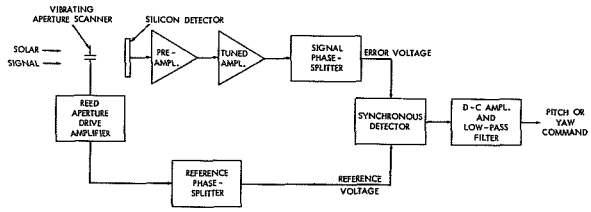

FIGURE 2(a).—Sun sensor signal processing electronics

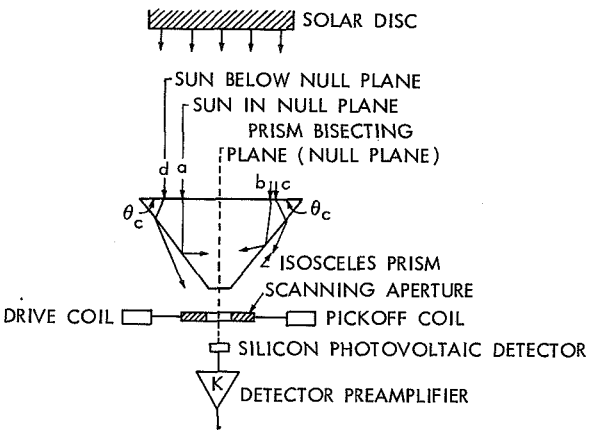

FIGURE 2(b).—Prism and detector arrangement.

processing electronics and prism detector arrangement.)

A different type of fine sun sensor was devised by the Goddard Space Flight Center. In this sensor, a digital command system converts a ground command into an optical slab positional reference for the observatory by means of the sensor servo drive. This commanded rotation of the optics produces a positional error signal from a photodetector and is fed to the control system. The latter drives the observatory until the photodetector is nulled. At this time, the observatory position will correspond to the commanded rotation of the optics. This type of mechanization results in a very simple but accurate sensor. (Fig. three is a schematic of the Goddard sun sensor.)

Closely related to the raster scanning requirements of the observatory are the control actuators. Control actuator selection is based on the required lifetime of the observatory and demonstrated dependability. One year required life eliminates a pneumatic system, and demonstrated dependability suggests a flywheel driven by electric motors (reaction wheels). Many ingenious devices such as control moment gyros, momentum flippers, and radar antenna drive systems were considered, to take advantage of the "conserved energy" nature of raster scanning, but were rejected. Mechanical complications and heavy weight were the main reasons for their rejection, but familiarity and successful experience with reaction wheel systems were also a factor in their selection. Reaction wheels, essentially, absorb momentum imparted to the observatory from internal and external disturbance torques or from control torques required to raster scan. Constant external disturbance torques will result in an increasing wheel speed and a loss in actuator torque capability. The point is soon reached where raster scanning is adversely effected, i.e.,

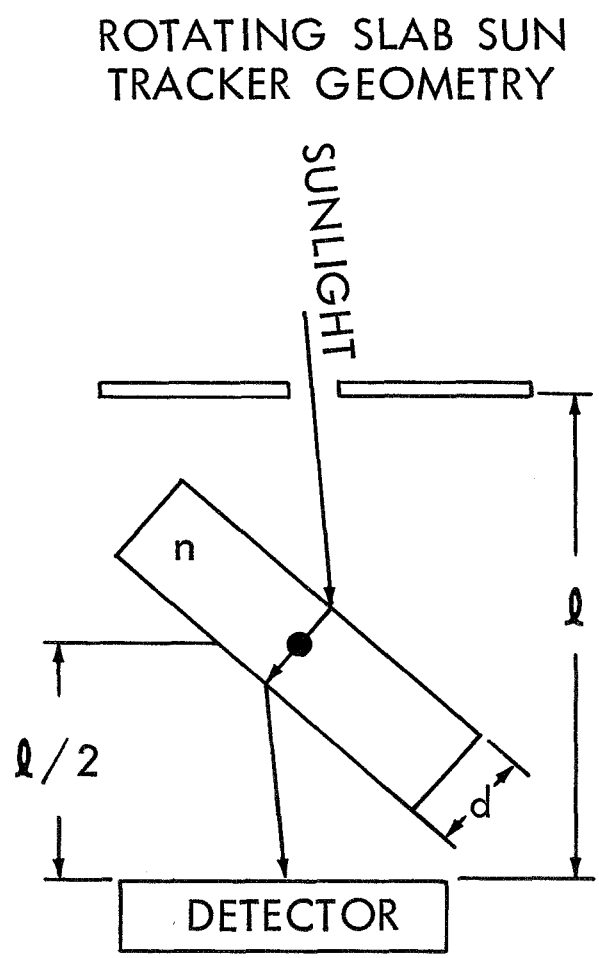

FIGURE 3.—Rotating slab sun tracker geometry.

the torque capability is reduced such that direction reversal in the raster is sluggish or impossible. Stored momentum in the reaction wheel can be reduced by applying an external torque to the observatory in the proper direction. Pneumatic systems appear to be in favor at the present time for momentum unloading, however, systems which react with the earth's magnetic field (magnetic torque generators) have advantages, especially for low-altitude long-life observatories. Intuitively, one might think that the pneumatic system would be more reliable than a magnetic torque generator. When considering leaks and dirt, some reliability analyses show up in favor of the magnetic system. For a one year observatory of the AOSO type, weight considerations give the nod to magnetic systems even though a pneumatic system must be used for initial stabilization and acquisition. A rule of thumb is that the gas storage tankage is equal to the weight of gas stored. It is the tankage weight that really hurts with observatories whose life is of one year or more. For the AOSO control subsystem a magnetic torque generator is desirable because the raster scan would not be disturbed when the reaction wheel momentum is being reduced. A pneumatic system with a healthy torque capability (required for rapid acquisition) would create transients in the scan lines when actuated.

Roll orientation of the spacecraft must be maintained if the raster scan is to have a meaningful pattern. The fine sun sensor controls pitch and yaw leaving the observatory free to roll. A logical sensing instrument to control roll is a star tracker. A desirable star to track would be one 90 degrees from the observatory-sun line. Unfortunately acceptable stars for roll control are occulted by the earth once every orbit. Two attractive alternatives show feasibility. A combination of a star tracker and rate integrating gyro or a pair of star trackers to alternately track an acceptable star in either the northern or southern celestial hemisphere. In either case the tracker need be only a single axis device, allowing the observatory to maintain a roll angle in place of the second gimbal. The continuous use of a gyro for time periods of one year or more has been argued long, loud, and hard. No doubt only a gas bearing gyro is feasible at this time. With proper redundancy and good quality hardware, a star tracker gyro combination is practical. The use of multiple star trackers is attractive because of the availability of hardware and the absence of a wear-out problem. Recent developments have indicated problems of reflected light from the earth saturating detectors. Even though proper shading can eliminate this problem it detracts from the advisability of using star trackers alone.

In closing, a word must be said about reliability. The control subsystem of an observatory, by its very nature, must be one of the most reliable subsystems onboard. It is also, in most cases, the most complicated. In the past, component redundancy has been heavily relied upon. With AOSO there will be a newer means of increasing reliability, integrated circuits in addition to redundancy. Digital logic circuits will utilize semiconductor integrated circuits and control electronics will use thin-film circuits. The AOSO control subsystem will be unique in its class because of its specialized performance requirements as well as its utilization of advanced electronic hardware and precision sensors.

EXPERIMENTS FROM A SMALL PROBE WHICH ENTERS THE ATMOSPHERE OF MARS

R. A. HANEL, L. E. RICHTMYER, R. A. STAMPFL, AND W. G. STROUD

Goddard Space Flight Center

In the long-range national space program for this decade, Mars and Venus unmanned landing missions are planned with the purpose of exploring the physical and biological properties of these near-Earth planets. The capsule entering the Martian or Cytherean atmosphere will provide unparalleled opportunity for "in situ" experimentation. This paper addresses itself to the design of a Mars capsule capable of a safe entry and landing on Mars. Quite simple sensors of pressure, temperature, density, molecular weight, and gross composition of the atmosphere can yield significant physical and ecological data. The safe landing will permit the execution of significant biological experiments for the detection of life.

Data transmitted at a rate of 1 bit/second during the capsule descent and following the landing are best handled by a direct planet-to-Earth communication link. The significance of the experiments and the techniques required are discussed.

INTRODUCTION

Instrumented entry capsules capable of making measurements both during descent through the Martian atmosphere and after landing on the surface will be essential in man's approach to a detailed study of Mars. Present knowledge derives mainly from observations and measurements made by instruments mounted on a spinning *fly-by* platform, the planet Earth; the miss distance in this case is about 10^8 km. Artificial spacecraft, on a much closer fly-by trajectory, will necessarily sacrifice complexity and refinement of instruments in exchange for the increased angular size presented by the planet and for the freedom from interference of the Earth's atmosphere. This trade-off of instrument complexity to gain proximity to the target is a favorable one, and much can be learned from a vehicle that passes very close to a planet. The recent success of the Mariner II (1962 $A\rho 1$) Venus fly-by demonstrates this well, and fly-by experiments should also be performed on Mars. However, even closer approaches are desirable: Altitude profiles of pressure, temperature, and composition can be determined more accurately from a probe that actually penetrates the planetary atmosphere. Proof of the existence or nonexistence of living organisms on Mars requires the landing of instruments on the planetary surface. Television pictures from a fly-by spacecraft will not lead to conclusions about life on Mars. This is illustrated by a TIROS television picture (Fig. 1) which, even at the achieved 2-km resolution, does not reveal the presence of life on Earth in the geographic area shown, even though this area has been occupied by man for many thousands of years.

For an entry probe, the necessary sacrifice in experimental "elegance" is even more severe than for a fly-by, but the reward is direct contact with the planetary atmosphere and surface. This paper describes a set of relatively simple experiments that could be performed, and shows how the few points of data provided by these experiments could yield much new and hitherto unattainable information.

DELIVERY SYSTEM

The delivery system and the overall mission profile will not be discussed in detail; however, a few comments are appropriate.

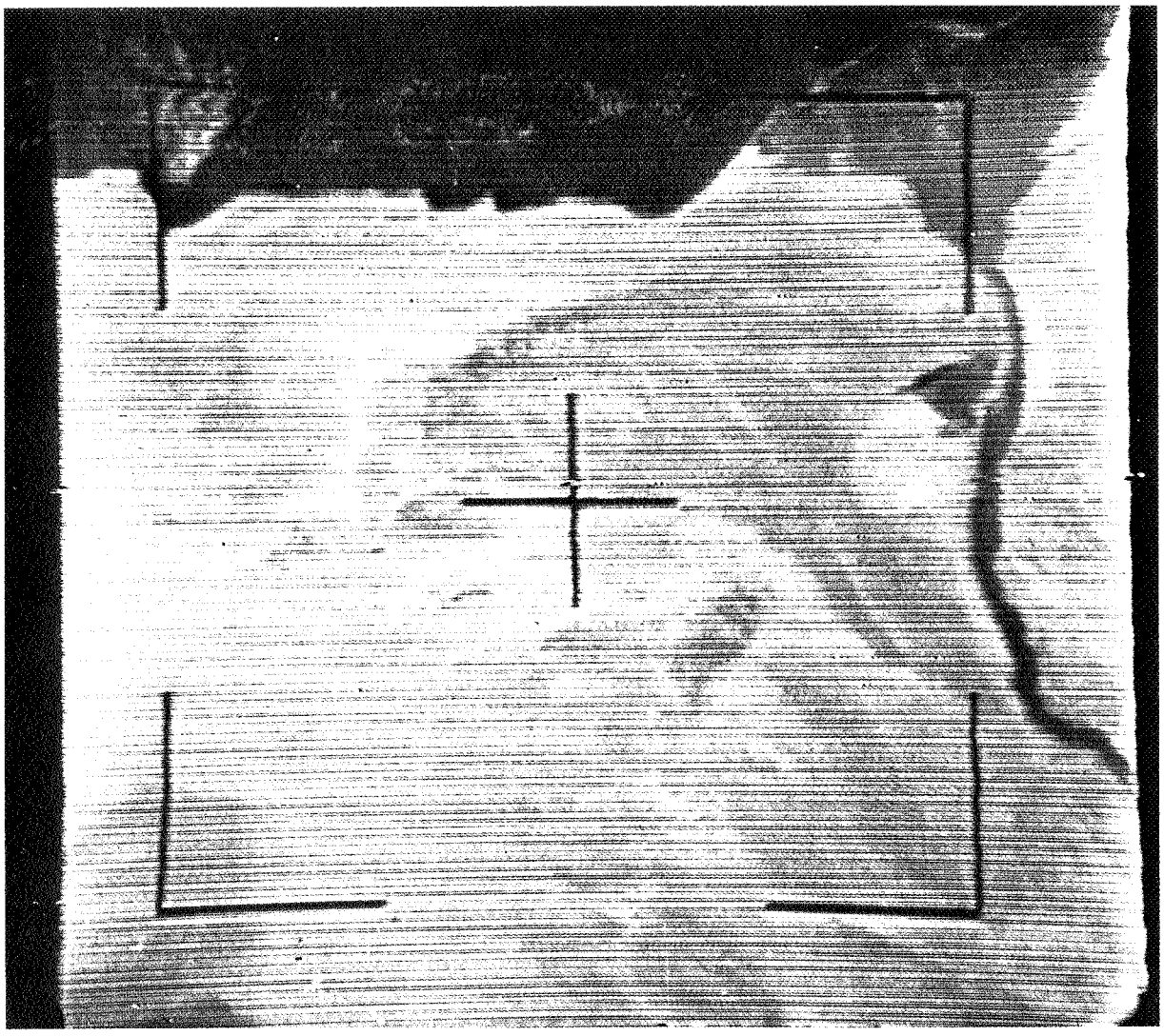

FIGURE 1.—TIROS picture of the Nile Delta and surroundings.

Current spacecraft propulsion and guidance technology can achieve Earth-to-Mars transfers of payloads in the 100-pound class by taking advantage of the relatively close approaches made by Mars as it goes through its oppositions each 26 months. Both the transfer time from Earth-launch to Mars-encounter and the communication distance from Earth to Mars on the date of encounter are variable from one opportunity to the next; typical values are 6 months travel time and 200×10^6 km separation at encounter. Capsule-to-planet approach velocity cannot be controlled; that is, spacecraft weight limitations preclude propulsive (retrorocket) braking. Thus the actual atmospheric entry velocity, representing the combined effects of orbital approach velocity and Mars' gravitational attraction, will be in the neighborhood of 7 km/sec.

The deceleration and heating that a planetary capsule experiences during atmospheric entry at these velocities will require special attention. Fortunately, the technique of high-speed entry has been advanced extensively in the last year or two. Theoretical investigation, shock tube tests, and actual flight experience—such as in

the NERV program and the military programs—demonstrate that survival of a small capsule entering the Martian atmosphere is well within present capabilities. The importance of the problem should not, however, be minimized; on the contrary, the entry is recognized as a critical link in the chain of events necessary for a successful landing mission.

All events not absolutely necessary should be removed from in-line positions. Interplanetary experiments, for example, should not be attempted if their functioning or failure could interfere in any way with the primary objective of making planetary entry and landing experiments.

The principle of minimizing the number of in-line events leads to the preference of a direct communication link between capsule and Earth rather than an indirect link that would relay the signal by way of the spacecraft bus.

Hybrid missions that would land a capsule and, at the same time, attempt to use the delivery bus as a fly-by are more complex and might be avoided—at least for the early Mars attempts—in the interest of maintaining simplicity and therefore inherent high reliability.

We shall assume that spacecraft and capsule both follow an impact trajectory, the capsule being separated a day or so before impact; the spacecraft, now without further function, is allowed to enter and disintegrate in the Mars atmosphere. This of course will require the spacecraft, as well as the capsule itself, to be fully sterilized to avoid the danger of contaminating Mars with Earth-type life forms.

The capsule, having the familiar hemisphere-cone shape and including heat shield and parachute, will weigh approximately 125 pounds. When the shielded capsule has entered the Martian atmosphere, a parachute is deployed. capsule shielding is dropped, and the periodic measurements of atmospheric pressure, temperature, composition, and scattering of light are transmitted from the capsule directly to Earth until the capsule touches the Martian surface (see Fig. 2). These readings can be stored in a memory for subsequent retransmission to Earth.

After landing is completed and the capsule has come to rest in an upright position, measurements of these same quantities are resumed and a biochemical growth experiment is initiated to search for Martian life forms. The measurements are made and transmitted to Earth at regular intervals until sunset on Mars. Sufficient battery energy remains to maintain the capsule temperature at a satisfactory value throughout the Martian night and to permit several transmissions on the following day.

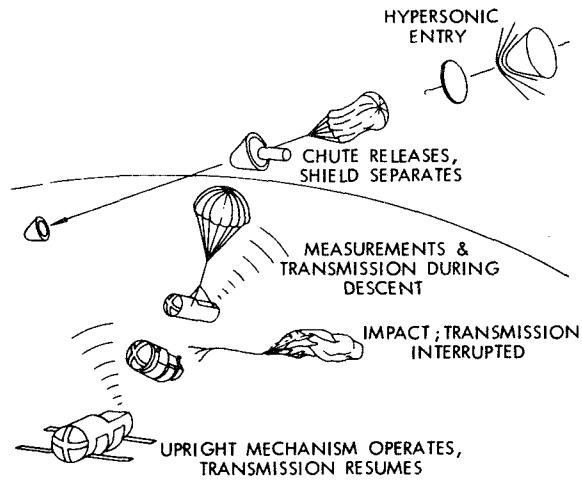

FIGURE 2.—Mars probe entry profile.

EXPERIMENTS

It is appropriate to mention that the purpose here is to describe a set of experiments which might be suitable for Mars entry capsules and that this paper is not addressed to any particular mission or program. The descriptions, although presented in the *indicative mood* for ease of expression, should not be interpreted as representing a final selection of experiments for a specific Mars mission.

The measurements during parachute descent through the Martian atmosphere will determine: (1) the atmospheric temperature, pressure, and density altitude profiles of the Martian atmosphere; (2) altitude profiles of the attenuation and of the scattering of sunlight in the blue, ultraviolet, and near-infrared regions by haze, dust, and clouds; (3) the daylight altitude profiles of the CO_2, H_2O, O_3, N_2, and A content of the atmosphere; and (4) the mean-molecular-mass altitude profile of the atmosphere. The

maximum altitude of all profiles will be somewhere in the region of 2.5 to 26 km, depending on the Martian atmosphere's density altitude profile, which in turn will control the function height of the automatic mechanism deploying the parachute and initiating the experiments. On the surface of Mars, measurements will continue throughout the Martian day to determine: (5) atmospheric pressure and temperature; (6) the amounts of blue, ultraviolet, and infrared radiation arriving at the surface directly from the Sun; (7) the amounts of scattering in the blue, ultraviolet, and infrared regions produced by molecules and suspended particles; (8) the attenuation of incoming radiation in absorption bands associated with CO_2, H_2O, and O_3 for varying optical thicknesses of the atmosphere; and (9) the amount of CO_2 metabolically generated by micro-organisms that may have been collected into the incubation chamber of the biological experiment.

Some of these determinations (e.g., temperature and pressure) will be made by direct measurements obtained from appropriate sensors; others (e.g., mean molecular mass) will be derived from sensors that measure related quantities, such as velocity of sound and acoustic impedance. Additional sensors are provided to make the engineering and housekeeping measurements (e.g., solar aspect and various instrument temperatures) that are needed for proper calibration and interpretation of the basic experiments. A complete list of the sensors, and the symbols used to represent their outputs, is presented as Table 1. Discussion of the experiments and descriptions of the sensors follow, in the order given in the table.

TABLE 1.—*Sensors and Symbols*

Sensor	Symbol
1. Atmospheric pressure, 0–65 mb	P_1
2. Atmospheric pressure, 0–200 mb	P_2
3. Atmospheric temperature, 180°–300°K	T_1
4. Atmospheric temperature, 150°–320°K	T_2
5. Local velocity of sound	c
6. Acoustical impedance of Martian air	z
7. Ultraviolet extinction in an O_3 band (2π ster).	UV_1
8. Ultraviolet extinction in a reference window (2π ster).	UV_2
9. Direct solar radiation in the reference window (collimated sun only).	UV_3
10. Infrared extinction in a CO_2 band (2π ster).	IR_1
11. Infrared extinction in an H_2O band (2π ster).	IR_2
12. Infrared extinction in a reference window (2π ster).	IR_3
13. Direct solar radiation in the reference window (collimated sun only).	IR_4
14. Solar zenith angle with respect to the capsule (along logitudinal axis of capsule).	S_x
15. Solar zenith angle with respect to the capsule (along lateral axis of capsule).	S_y
16. Probe inclination after landing (along longitudinal axis of capsule).	I_x
17. Probe inclination after landing (along lateral axis of capsule).	I_y
18. Temperature of the acoustic instrument (47°C).	T_3
19. Temperature of the infrared detectors (27°C).	T_4
20. Background count rate, biochemical experiment.	L_0
21. Count rate, biochemical experiment	L_1
22. Temperature of biochemical instrument and batteries.	T_5
23. Battery voltage, and biochemical experiment confirmation.	E

Pressure

The two pressure sensors are absolute-pressure aneroid potentiometer gages with full-scale ranges of 65 and 200 mb. The gage openings are on the side of the cylindrical instrumentation capsule.

Temperature

Air temperature will be measured over two different ranges by essentially duplicate instruments. The temperature sensors consist of platinum resistance elements mounted on the side of the cylindrical capsule. Ranges from 180° to 300°K and 150° to 320°K are planned.

Molecular Mass, Density, and Specific Heat Ratio

The mean molecular mass $\overline{M}$, the density ρ, and the mean specific heat ratio $\overline{\gamma}=C_p/C_v$ will be determined by acoustical means. The velocity of sound c in a gas is given by

$$c^2=\frac{\overline{\gamma}RT}{\overline{M}},$$

where R is the gas constant. This well-known relation has been used in the past in various instrumental techniques to measure the temperature of the Earth's atmosphere by determining c, where $\overline{M}$ and $\overline{\gamma}$ are well known. It is proposed here to reverse this method and to bring a volume of the Martian atmosphere into a thermostatically controlled tube and then to measure $\overline{M}/\overline{\gamma}$ by determining c, where the temperature is well known. Simultaneously, the acoustical impedance $z=\rho_1 c$ of the gas will be measured in the tube, which yields the density ρ_1 of the gas in the tube. From ρ_1 the density of the ambient gas ρ is obtained by the equation

$$\rho=\frac{\rho_1 T_3}{T_1},$$

where T_3 denotes the absolute temperature of the thermostatically controlled tube and T_1 the ambient air temperature measured by the resistance thermometer.

Knowing the ambient air density and temperatures, we arrive at the mean molecular mass by applying the gas law:

$$\overline{M}=\frac{\rho RT}{P}=\frac{zT_3R}{cP}.$$

Since $\overline{M}/\overline{\gamma}$ has been obtained by the velocity measure, $\overline{\gamma}$ can now be determined.

Figure 3 shows $\overline{M}$ versus $\overline{\gamma}$ for a mixture of the three gases N_2, CO_2, and A. It is generally accepted today that these gases are the major constituents of the Martian atmosphere. The $\overline{M}/\overline{\gamma}$ point of an arbitrary mixture of these gases must fall within the triangle shown. Only the lower part of the triangle need be considered here, since the amounts of CO_2 and A probably will be relatively small compared with the amount of N_2. According to present estimates, the amounts of water vapor, O_2, and O_3 are too small to contribute appreciably to $\overline{M}$; however, a refined analysis will incorporate these components also. Curves of constant c^2 are straight lines through the origin (because c^2 is proportional to γ/M at constant temperature). The relative abundances of the respective components in the three-gas mixture can thus be completely determined by a c and an $\overline{M}$

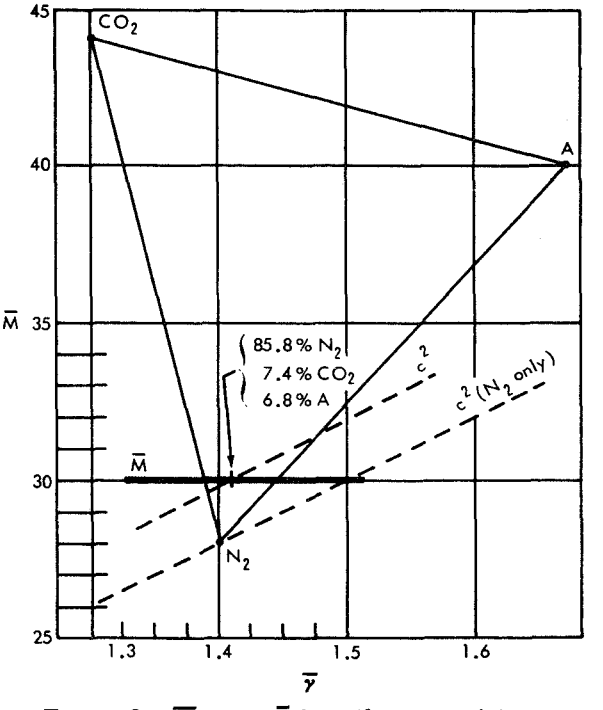

FIGURE 3.—$\overline{M}$ versus $\overline{\gamma}$ for a three-gas mixture.

measurement. The CO_2 concentration found by the acoustical method, although not as accurate as the one derived by the optical means described below, is a most desirable and independent check. Also, the acoustical measurement works equally well in the presence of clouds. In conjunction with a successful optical CO_2 determination, the acoustical experiment will provide a conclusive test of the hypothesis that the Martian atmosphere consists mainly of nitrogen, carbon dioxide, and argon.

The proposed technique, as shown in Figure 4, measures the velocity of sound of a sample of the Martian atmosphere contained in a tube wound in spiral form of about 1 meter in length and 0.5 cm diameter. For ease in illustration, however, Figure 4 shows a linear arrangement of this tube. At one end of the tube, a generator drives a small sonic transducer at a frequency of about 4 kc. Two identical condenser microphones are separated by approximately nine wavelengths. Both microphones form part of the tube wall. The acoustic tube is extended beyond the second microphone and is terminated by damping

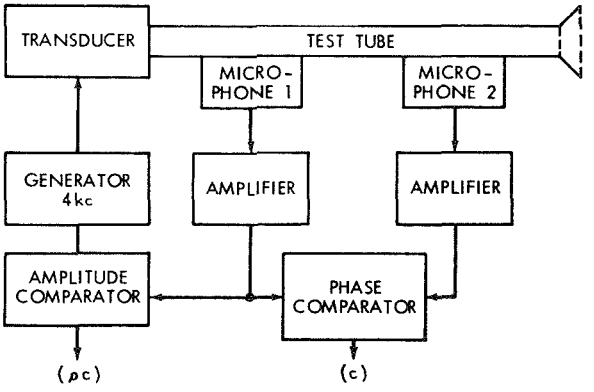

FIGURE 4.—Acoustic experiment.

material which, in conjunction with rough wall surfaces, avoids acoustic reflections and standing waves in the tube. The phase shift, measured by the phase comparator, is determined soley by the wavelength of sound in the tube and, since the generator frequency is constant, by the propagation velocity.

In addition to determining the speed of sound, the instrument is capable of measuring the density of the gas in the tube. The mechanical and the electrical impedances of the sound generator are chosen so that the velocity of the diaphragm is practically independent of the acoustic radiati on impedance of the tube. Under these conditions, the sound pressure developed in the contained gas is proportional to the acoustical impedance. Since the microphones respond to sound pressure, their electrical signals will be proportional to the acoustical impedance of the gaseous medium. The constant of proportionality, which also depends on the transducer sensitivity, is easily determined by calibration in an N_2 atmosphere over the expected pressure range of 20 to 150 mm Hg.

The accuracy requirements imposed on the speed of sound determination can be judged by considering values shown in Table 2. Values are calculated for a gas temperature of 320° K. The first and last rows of gases represent what are presently considered to be the boundaries for the probable composition of the Martian atmosphere. The instrument is designed to cover the range from about 347 to 365 m/sec. The two microphones, nine wavelengths apart, register phase differences between 0 and 180 degrees over the 18 m/sec change in sound velocity. A ± 1 percent error in the phase measurements yields the velocity of sound to ± 0.2 m/sec, or an overall error of ± 0.05 percent.

Calculation of the velocity of sound in Table 2 was based on the ideal gas law. It would be more accurate so use Van der Waal's equation, but it can be shown that a change occurs only in the fourth significant figure. Also, the specific heat of gases shows a frequency dependence in the vicinity of molecular relaxation frequencies. This condition is especially true for CO_2 at low pressures and is one of the reasons why a relatively low operating frequency was chosen for the experiment. Because of these conditions, direct calibration is preferred and will be performed by placing the instrument in artificial atmospheres at low pressure for a number of $N_2:CO_2:A$ ratios. An experimental version of the instrument is shown in Figure 5.

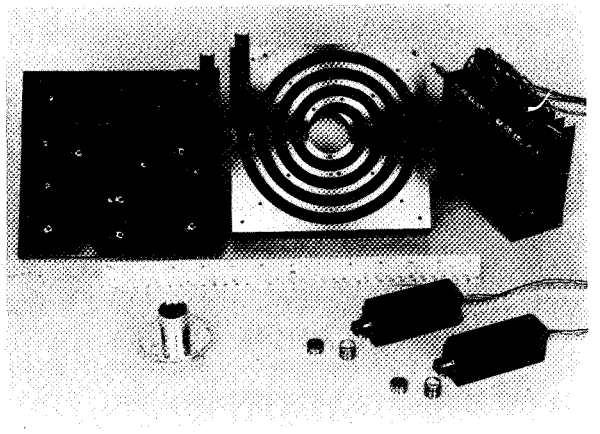

FIGURE 5.—Acoustic experiment hardware.

Atmospheric Composition by Optical Means

The physical basis for the determination of the atmospheric composition by optical means is provided by the extinction of sunlight as it passes through the Martian atmosphere. Quantitatively, the extinction is expressed by

$$I_\lambda = I_{0\lambda} \exp(-\tau_\lambda),$$

where $I_{0\lambda}$ is the intensity of radiation at wave-

length λ incident on a column of gas and I_λ the intensity emerging from the gas at the optical thickness τ, where τ is given by:

$$\tau_\lambda = \int_x^0 n(x)\delta_\lambda dx.$$

TABLE 2.—*Velocity of Sound for Various Atmospheric Compositions*

Gas	Velocity of sound (m/sec)
100% N_2	364
95% N_2+5% A	362
95% N_2+5% CO_2	358
90% N_2+5% CO_2+5% A	356
80% N_2+10% CO_2+10% A	349

The path length traversed in the gas, given by x is the product of the concentration of the particles producing the absorption and their extinction cross section. If the rate I/I_0 is measured, and if x and δ_λ are known, then the concentration of particles $n(x)$ may be computed.

The total absorption produced by the individual constituents may be computed for various conditions (pressure and temperature) in selected wavelength regions with experimentally determined extinction coefficients.

The O_3 measurement can be best performed in the ultraviolet portion of the spectrum, while the CO_2 and H_2O measurements are better suited to the near-infrared spectral region. The proposed instrumentation will be described under the separate headings of ultraviolet and infrared experiments because of the difference in the required instrumentation for the respective spectral regions.

Ultraviolet Experiments

Extinction Experiments

The ozone content is studied in terms of absorption of solar radiation in the Hartley band region. A 200A bandwidth at about 2800A serves the purpose well.

If Johnson's data (Reference 1) for the solar spectral irradiance in these regions are converted from Earth distance to Mars distance, and conservative estimates of energy losses through the optical system are made, a sufficient amount of energy is found to be available so that standard, readily available photomultipliers and filters may be used for the measurements. Hence, with the Sun as the source, a small (1.5-cm radius) opalescent diffusing hemisphere with a field of view of 2π steradians will collect the solar energy flux and uniformly illuminate (regardless of solar elevation) a small aperture at the center of its base, where a filter will transmit only the energy in the desired spectral region to the photomultiplier. The arrangement is depicted schematically in Figure 6.

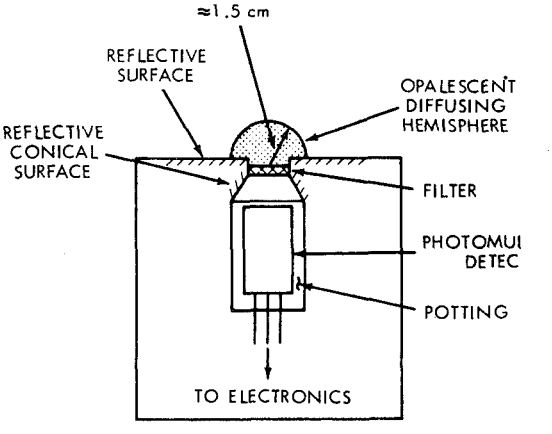

FIGURE 6.—Ultraviolet detector.

Regarding the detector response, only a small reduction in solar radiation is expected in the transmission window at the reference wavelength (3500A) because of extinction in a clear atmosphere, so that a linear response is preferred for the reference channel. A logarithmic response is used for the ozone channel, where large changes in intensity may be anticipated because of the large absorption coefficients.

Ultraviolet Scattering Measurements

Observed clouds and haze are important factors in the Martian atmosphere, especially in the ultraviolet. The existence of the blue haze, for example, will modify the O_3 estimates and must be taken into account. In itself, the alti-

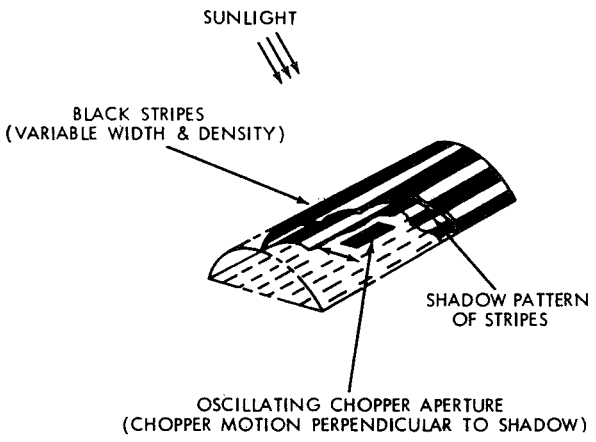

FIGURE 7.—Scattering sensor.

tude determination of the blue haze (if present at the time) will be a valuable experiment.

Direct solar radiation and scattered skylight are measured by a simple *space chopping* technique. The essential part of the instrument is a transparent shell in the form of a half-cylinder painted in a zebra-like fashion with black stripes parallel to the longitudinal axis (see Fig. 7). In direct sunlight, the black stripes cast a sharp shadow pattern on the horizontal plane through the cylinder axis. However, if a portion of the incident sunlight has been scattered by molecules, haze, or dust, the shadows are not completely black. An oscillating aperture, vibrating perpendicularly to the shadow pattern, channels the radiation signal to the detector. If there is no atmospheric scattering the output of the detector has a peak-to-peak amplitude proportional to the intensity of the direct sunlight appearing between the shadows. Large detector output is thus obtained when there is primarily direct sunlight and little scattering, and hence high pattern contrast. But, when there is only scattered light incident on the cylinder, the shadow pattern is completely destroyed, and no output signal will be developed. The output of the detector is thus proportional to the amount of unscattered sunlight. This measurement is made at 3500A, and a comparison of the results with the UV_3 measurement of the total amount (2π ster) of light in the 3500A reference channel enables us to determine the total scattering produced by the atmosphere in this spectral region.

Infrared Experiments

Extinction Measurements

The measurements in the near-infrared region of the spectrum are similar in principle to those described for the ultraviolet region. Calculations show that the CO_2 content can be inferred from attenuation in its 1.6-micron absorption band. The H_2O content is somewhat more difficult because of the blending of its bands with certain CO_2 bands. However, a several hundred angstrom bandwidth near 1.87 microns (avoiding the strong 2.0-micron band of CO_2) is adequate. Both the H_2O extinction and the CO_2 extinction will be measured with respect to the attenuation in a reference window near 1.7 microns.

Figure 8 shows the total absorption produced by CO_2 and H_2O in the near-infrared region, using present estimates of these constituents and Howard's data (Reference 2) referring to an atmospheric pressure of 42 mb. As with the ultraviolet experiments, the detectors will not require alignment to the Sun, because they are provided with a 2π steradian field of view. Since the expected total amount of absorption is small, it is preferable to measure directly the

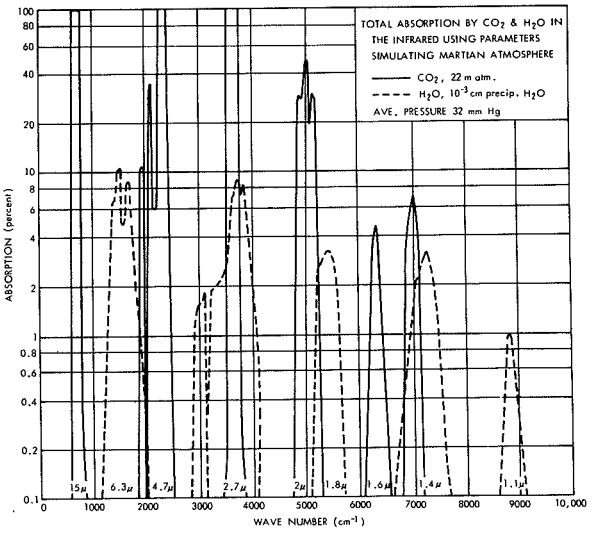

FIGURE 8.—Atmospheric infrared absorption.

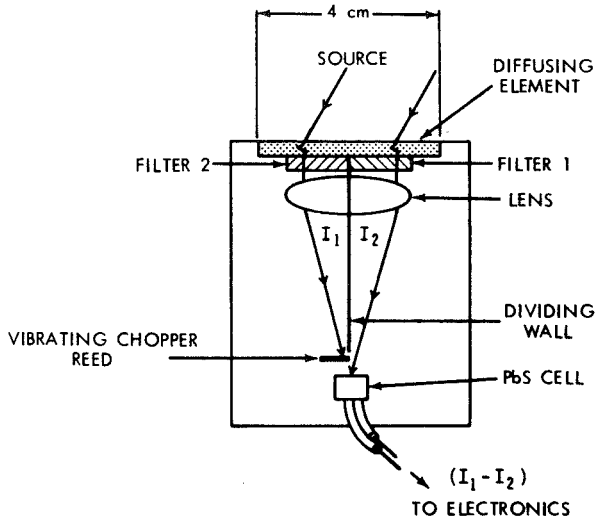

FIGURE 9.—Infrared detector.

intensity difference between the reference channel and each of the spectral bands chosen for the extinction measurements. The instrumentation is outlined schematically in Figure 9.

As shown in Figure 9, the vibrating chopper alternately exposes the detector to the intensities I_1 and I_2, where I_1 is the intensity in the reference window and I_2 the intensity in a spectral band of CO_2 or H_2O. Hence, the intensity difference I_1-I_2 will be measured for both CO_2 and H_2O; and, in addition, the reference window intensity I_1 will itself be measured using the same configuration, simply by blocking out I_2. Lead sulfide is best suited as the detector for this spectral region, although its temperature must be controlled if optimum reliability and stability are to be achieved.

Infrared Scattering Measurements

An experiment to determine the scattering power of the Martian atmosphere in the near-infrared region will also be included. By combining these data with the information obtained from the scattering results in the ultraviolet portion of the spectrum, considerable insight can be gained concerning the nature of the scattering processes and the sizes of haze, dust, and cloud particles. The infrared detector (PbS) and the ultraviolet detector will be housed together, using the same light collector and chopper shown in Figure 7. Two filters will transmit the spectral regions of interest to the respective detectors.

Biological Experiment

Basic Concept

The concentration of water vapor, oxygen, and the amount of ultraviolet radiation at the surface of Mars are important in considering the environment which living organisms might have to face; but knowledge of these environmental conditions will not suffice to answer the question of the existence of life on Mars. To provide a conclusive answer to this question, a life detection experiment has been incorporated into the proposed capsule design. (It is recognized, of course, that only a positive experimental result would be conclusive.) The particular biological experiment, which has been suggested by Mr. G. Levin of Resources Research, Inc., (Reference 3), already exists in breadboard form and will adapt easily to the proposed capsule.

The Experiment

The experiment depends on measurements to detect metabolically generated CO_2 derived from a nutrient medium mixed with a sample of Martian soil under the assumptions that, if life does exist on Mars, almost any soil sample will contain micro-organisms and that the metabolic process of these micro-organisms results in the generation of CO_2.

The medium (broth) is carried with the instrument to Mars, where a soil sample is obtained by shooting out sticky strings to which soil particles adhere as the strings are wound back into the culture chamber in the instrument. The medium is tagged with C^{14}; and hence any micro-organisms using the medium in their metabolic processes will generate a small amount of $C^{14}O_2$, which can be detected by radioactive methods.

The gases leaving the liquid medium will be collected on a thin absorbent-impregnated window above the culture chamber. Immediately behind this window is a solid-state detector that will be used to make periodic counts of the evolved radioactivity. The experiment will show radioactivity and, hence, gas evolved as

a function of time. A resultant curve showing an initial lag period followed by the characteristic exponential growth phase and population plateau would constitute evidence for the presence of life. Confirmation of the metabolic origin of the evolved gas would be accomplished by the injection of an anti-metabolite into the culture and the observance of a consequent diminution or cessation in the evolution of gas.

Supplementary Measurements

The solar zenith angle must be known at the time of the extinction measurements to interpret the data properly. This measurement will also help to determine the latitude and longitude of the capsule landing site, for which two instruments are necessary. The first is an inclinometer to determine the probe's attitude with respect to the local vertical. The second instrument determines the solar angle with respect to the probe's fixed coordinate system. By determining the solar zenith angle at regular time intervals, and combining these data with measurements of the solar azimuth, the position of the probe can be determined in terms of Martian latitude and longitude.

The aspect of the Sun will be determined by a passive device employing gray coded light masks and photocells to yield a digital indication of the solar aspect. The sensor is made up of two identical rectangular glass recticles perpendicular to each other. Each recticle contains a thin slit on the top and a 7-bit gray coded pattern on the underside. Seven corresponding photoconductive strips are located under the gray coded masks.

The inclinometer is essentially a set of two pendulums placed at right angles to each other. The shaft of each pendulum positions the slider of a low-friction potentiometer, which in turn generates the desired signal voltage proportional to the position angle of the pendulum. The small unit is hermetically sealed and is designed to operate within the limits of ± 60 degrees from the vertical with an accuracy of ± 2 degrees.

Altitude Measurement

Two methods are used to measure the altitude of the instrument during parachute descent. The first one is based on integration of the hydrostatic equation:

$$dp = -\rho g\, dh,$$

and consequently

$$h = -\int_{p_0}^{p} \frac{dp}{\rho g}.$$

The second method for obtaining capsule altitude is based on the known terminal velocity, which can be determined in terms of the "weight" and the coefficient of drag of the capsule and parachute. Integrating over the terminal velocity region yields

$$h = \int_{t_0}^{t} \left[\frac{2mg}{\rho C_D A}\right]^{1/2} dt.$$

The change in g with altitude, small to begin with, may be handled by an iteration process. The computation of altitude does not require capsule survival, but surface impact time must be known to establish the zero level of the altitude scale.

TELEMETRY

Data transmission from planetary distances requires high efficiency in the transmitting system and low noise in the receiving system in order to minimize payload weight and battery power requirements. The capsule transmitter will operate in the space telemetry band at 2300 Mc, where low system noise temperatures (50°K) are achieved in receiving installations. The relatively few measurements to be transmitted in the available time leads us to trade bandwidth against time; however, the problem of building physical equipment with the required properties indicates practical lower limits of information bandwidth below which no favorable trade-off is achieved. Doppler frequency shift interferes with the acquiring and frequency tracking of extremely narrow bandwidth signals. The major source of Doppler shift will be the relative motion between Earth and Mars, and it can be predicted quite accurately; however, the Doppler shift associated with Mars' axial rotation depends on the location of the landing

site. This location will be unknown at the time when the signal is to be acquired; and, as a consequence, a residual frequency uncertainty of approximately 1500 cps will remain. Also affecting the bandwidth versus time trade-off is the achievable crystal stability. Granting this effect the same band uncertainty as the Doppler shift, a crystal stability of 5 parts in 10^7 is needed. Fortunately, once the signal has been acquired, the rate of frequency tracking achievable in such narrow-band receivers is compatible with the maximum rate of Doppler change due to Martian spin (0.06 cps/sec).

As may be seen from the discussion of the measurements, 1 bit/sec is entirely adequate for the transmission of data. With Pulse Code Modulation non-return-to-zero, only a 2.5-cps bandwidth would be necessary for processing this signal; on the other hand, since the loop bandwidth of the receivers is much wider, the use of a subcarrier is indicated. Normally, a strong carrier is needed for locking the loop in the receiver; this forces the designer to compromise in his desire to modulate as much power as he can in the information-carrying side band, and only the necessary minimum in the carrier itself. This minimum is given by the 8 to 9 db locking threshold of present-day receivers. The double-side-band suppressed carrier modulation suggested by Costas (Reference 4), combined with phase-locked loop techniques, eliminates this disadvantage. Costas' technique reconstructs the carrier by making use of the coherence in the two side bands. When such a detector is part of a phase-locked loop, locking is achieved at the reconstructed carrier. Phase modulation in the transmitter can easily be adjusted so that essentially all power lies in the side bands and virtually none in the carrier; thus a receiver as described will lock above threshold and produce an output. If we choose a subcarrier coherent with both the main carrier and the bit generator, the output of the first demodulator is known in its frequency—regardless of Doppler shift—and can be filtered optimally. Table 3 shows a set of calculated system parameters.

The calculation assumes a capsule antenna pattern such that 0-db gain can be achieved at all resting positions on the Martian ground and for all polarization. Obviously, a null must exist tangentially to the surface, and a design objective of linear polarization at 50 degrees from the vertical is more realistic. The capsule antenna will transmit circularly with a gain of approximately 7 db at the vertical. A slight possibility of an unfavorable resting position of the capsule remains, but the chance appears to be no greater than that of failure in the uprighting mechanism itself.

TABLE 3.—*Data Transmission Link Information*

Parameter	Value
Distance	220×10^6 km
Path attenuation at 2280 Mc	−266.2 db
System noise temperature	50°K
Noise power (bandwidth, 1 cps).	−211.6 dbw
Receiving antenna gain (210-in. diameter).	+61.1 db
1st demodulator noise (bandwidth, 8 cps).	−9.0 db
Bit rate	1 bps
Transmitter mismatch	−1.5 db
Transmitter output	+18.5 dbw (70 watts)
Vehicle antenna gain	0 db
Margin	−5 db
Loss due to spectral power distribution.	−1.1 db
S/N at input of subcarrier PCM demodulator in 8 cps.	+9.5 db—acquisition and locking threshold.
2nd demodulator (PCM) (bandwidth, 2.5 cps).	+5 db
S/N of PCM output	14.5 db
Single-bit error probability	$<10^{-3}$

PCM encoded transmissions, where every single measurement is of importance in the sense that interpolations are virtually impossible to make, need error detection bits in their structure to enhance confidence in the measurement taken. Only small additional redundancy is needed for single-bit error correction and dual-bit error detection in a matrix. This is accomplished by the provision of horizontal and vertical parity checks. A frame consists of 10 words, each of which contains 7 measurement bits plus 1 parity bit. The frames are generated at a 1 bit/sec rate and are organized as

follows: Word number 1 is the frame tag; bit positions 1 and 2 specify the type of frame, and the remaining 5 data bits specify the number of the frame. The parity bit in position 8 is 1 or 0 so as to make the total number of 1's in the 8 bits odd. Words number 2 through 9 contain the data; the parity bit is made 1 or 0 so as to make the total number of 1's in the word odd or even in a specifically chosen pattern. Word number 10 is the vertical parity checkword, and each bit is made a 1 or 0 so as to make the total number of 1's in its vertical column either even or odd following a similarly prearranged pattern. Synchronism is established by checking for the uniqueness of the parity pattern. Once word and frame synchronization have been established, this structure provides single-bit error correction and dual-bit error detection. The data are transmitted serially by increasing bit number in each word and by ascending word number.

There are three types of frames: *A*, *B*, and *C*. Frame *A* contains pressure, temperature, and acoustical data and thus is used to provide information during descent—whether by day or night—and after landing. Frame *B* contains data from the optical experiments and gathers information during descent—if by day—and after landing. Frame *C* contains data from the biological experiment and from the attitude sensors, and is used only after landing.

The uncertainties involved in communication over planetary distances warrant inclusion of a storage capability in the capsule so that certain transmissions can be repeated. The storage also can be used for recording data taken between data transmission times.

Selected frames of data acquired during descent will be stored and later re-transmitted, along with data taken after landing. If descent occurs during daylight, the data that are simultaneously transmitted and selectively stored in a magnetic core memory will consist of alternate frames of types *A* and *B*. If descent occurs during the Martian night, frame *A* data only will be stored. About 15 minutes after landing, one frame of type *C* will be acquired and stored. Transmissions will then occur every 2 hours after landing until sunset, and they will be interrupted until 2 hours after sunrise. The batteries provide sufficient energy to power a maximum descent-time transmission, four transmissions of 20 minutes each, the necessary electronics for 24 hours of operation, and heaters needed to survive the low temperatures of the Martian night.

Because of the lack of accurate knowledge of the Martian atmosphere, the descent time can vary widely; and the storage and re-transmission of data must be adjusted so as to assure measurements from at least a few different altitudes. Depending on the density of the Martian atmosphere and entry velocity, the descent time may vary from a minimum of 4 minutes or 3 frames to a maximum of 57 minutes or 42 frames.

During descent, *A* and *B* frames are transmitted and stored in four slots of a storage matrix. When the descent time is long enough, the oldest frame is erased and replaced by a new one; this will occur after the fourth frame. The first, however, is stored permanently. To accommodate very long descent times, the tenth frame is stored permanently, and the two remaining slots are filled with the two most recent measurements. The transmission sequence after landing for three different descent times is then:

For minimum descent—4 minutes, 3 frames acquired:

C–0, B–0, A–0, C–1, A–1, B–1, A–1, B–1, A–2, B–1, C–0, A–0, B–0

For nominal descent—30 minutes, 22 frames acquired:

C–0, *B*–0, *A*–0, *C*–1, *A*–1, *B*–1, *A*–10, *B*–10, *A*–9, *B*–9, *A*–11, *B*–11, *C*–0, *A*–0, *B*–0

For maximum descent—57 minutes, 42 frames acquired:

C–0, *B*–0, *A*–0, *C*–1, *A*–1, *B*–1, *A*–10, *B*–10, *A*–20, *B*–20, *A*–21, *B*–21, *C*–0, *B*–0, *A*–0

If descent occurs in the dark, only *A* frames are stored.

The proposed power profile requires approximately 800 watt-hours of energy to accomplish the capsule mission. About 23 pounds of individually potted silver-zinc cells providing 40 watt-hours/pound will be used in

the pressurized battery package. The battery temperature will be maintained at, or just below, +10°C during the flight aboard the bus. At this temperature, the loss of capacity is less than 0.2 percent per month, and the need for trickle charging is thus eliminated.

The optimum operating temperature for silver-zinc cells is about 25°C. It is anticipated that entry heating will raise the battery temperature no more than a few degrees above the 10°C storage temperature. Hence a good operating temperature, in the neighborhood of 15°C, may be expected at the start of the parachute descent phase when the capsule measurements and transmissions are initiated.

INTERPRETATION OF RESULTS

Each individual sensor will provide valuable information, but the scientific significance of the overall mission lies in the interrelation of the results, shown in Figure 10. Each sensor contributes information to one or more of blocks representing the important physical properties; these in turn serve as stepping stones to formulate a consistent and detailed picture of the Martian atmosphere. Conclusions that would exceed our present knowledge markedly can be drawn about the general circulation, heat balance, composition of clouds, and even geological history. The block diagram presented here is far from complete. Earth-bound observations, for example, would show up as a third dimension to this network of conclusions. It is important to note that then network is overdetermined—that is, that some parameters, such as the molecular weight, are derived from different sensors independently. This provides both a convenient check of consistency and a form of redundancy. The failure of one or another sensor, therefore, would not be of fatal consequence in interpreting the results, and the determination of various parameters by essentially independent methods will confirm, and even improve, the overall accuracy of the experiments.

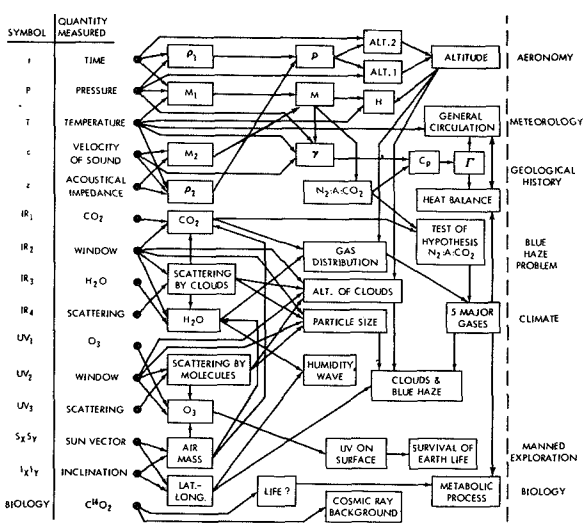

FIGURE 10.—Mars probe, flow diagram of conclusions.

CONCLUSIONS

A program to deliver instrumented entry capsules into the atmosphere and thence to the Martian surface to telemeter back a few points of fundamental data is seen as an essential part of man's future approach to a detailed study of Mars: Observations from Earth and from "fly-by" spacecraft—both extremely useful—suffer from the absence of direct contact; entry capsules, although necessarily limited at present to "simple-minded" experiments, can make up for this deficiency.

Current technology can deliver a 125-pound capsule containing the necessary heat shield, parachute, and telemetry for 15 pounds of "experiments." A set of interrelated experiments based on obtaining a few data points from each of several sensing devices can provide data on altitude profiles of pressure, temperature, and density; on atmospheric composition and structure through optical scattering and absorption measurements; and on the presence or absence of life forms through a simple test for metabolism in a mixture of a nutrient medium and Martian soil.

Telemetry at 1 bit/second, achievable with a 70-watt capsule transmitter and a 210-foot receiving antenna, will allow real-time transmission during parachute descent and for brief periods subsequent to landing. Storage for delayed transmission will permit a few night-time measurements when the capsule is out of sight from both Sun and Earth. The com-

munication link will transmit both *scientific* information and the supporting *engineering* information (e.g., temperature of sensors, attitude of the instrument package, and location of its landing site).

Mission design stresses *reliability through simplicity*. Only a few basic quantities are measured, but they are selected so that each of several important properties—e.g., composition, nature and altitude of clouds, and habitability to various life forms—can be inferred from more than one combination of the basic measurements. This will afford effective cross-checking and a form of redundancy in that none of these important properties is completely dependent on a single sensor for its determination. Similarly, the important properties to be determined are themselves selected so that they can be combined in various ways to yield broad conclusions in the general fields of aeronomy, climatology, geological history, biology, and manned exploration.

Just as the individual data points and the properties inferred from them may be seen as a network of interrelated information leading to a set of general conclusions, so also would a series of Mars entry capsule missions become part of a much larger network contributing to man's knowledge of the universe around him.

ACKNOWLEDGMENTS

The authors wish to acknowledge the contribution of many members of the Goddard Space Flight Center, expecially Mr. J. Ainsworth for his contribution to the pressure and temperature experiments, Mr. F. Bartko and Dr. D. Harris for calculations regarding the absorption and scattering experiments, Mr. J. Cressey for valuable calculations concerning the communication link, and Mr. M. Maxwell for specific work on the proposed storage and synchronous techniques.

REFERENCES

1. JOHNSON, F. S., "The Solar Constant," *J. Meteorology* 11(6): 431–439, December 1954.
2. HOWARD, J. N., BURCH, D. E., and WILLIAMS, D., "Near-Infrared Transmission Through Synthetic Atmospheres," U.S. Air Force, Cambridge Res. Ctr., Geophysical Res. Paper No. 40 (AFCRC–TR–55–213) November 1955; also issued as: Ohio State Univ., Res. Found., Scientific Rept. No. 1, Contract AF 19(604)–516, December 1954.
3. LEVIN, G. V., HEIM, A. H., et al., " 'Gulliver'—A Quest for Life on Mars," *Science* 138(3537): 114–121, Oct. 12, 1962.
4. COSTAS, J. P., "Synchronous Communications," *Proc. IRE* 44(12): 1713–1718, December 1956.

PHYSICAL MEASUREMENTS FROM METEOROLOGICAL SATELLITES

R. A. HANEL
Goddard Space Flight Center
AND D. Q. WARK
National Weather Satellite Center

Extensive discussions of the meteorological observations successfully obtained from artificial satellites, including the photographs taken by the Tiros series and the radiometric measurements by Tiros and by Explorer VII, have been given elsewhere. The forthcoming Nimbus series of meteorological satellites will carry similar television and radiometric instruments. In addition, other experiments are being planned and further experiments of meteorological importance are under study.

One of these experiments involves indirect determination of the atmospheric temperature. The radiance of the atmosphere to space in the infrared depends on the transmittance and the temperature, by the well-known principles of radiative transfer. The transmittance of an atmospheric gas depends mainly on its vertical distribution and if, as in the case of carbon dioxide, one can assume a uniform mixture, the transmittance is known as a function of the pressure. From measurements of radiance at several wavelengths with different transmittances, one should be able to deduce the temperature of the atmosphere as a function of pressure.

In 1959, L. Kaplan suggested that the temperature structure of the atmosphere could be deduced from radiance measurements from a satellite in several narrow intervals of the 15-micron carbon dioxide band. (*1*) At a conference to discuss infrared satellite experiments, it was suggested that the most feasible instrument at the present time for carrying out the suggested measurements would be an infrared grating spectrometer with multiple detectors.

The Weather Bureau and NASA have proceeded with the development of an instrument of suitable bandwidth and radiometric accuracy. The first "breadboard" model has been produced and tested. The spectrometer, with its specially designed wedge-immersed thermistor detectors, has been described in detail elsewhere. (*2*) Figure 1 shows the spectrometer and gives a view of the grating and the detectors. Figures 2 and 3 show the layout. An *f*/5 Ebert-

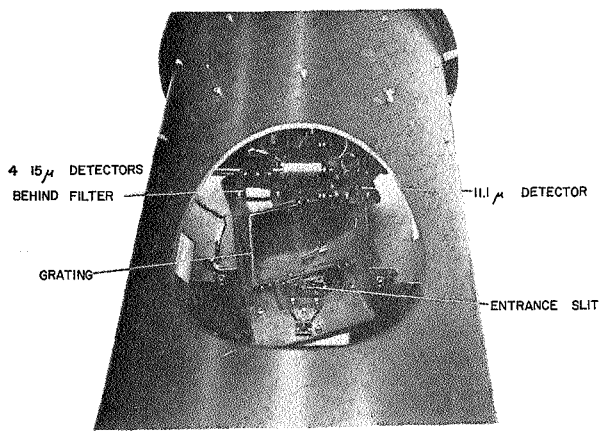

FIGURE 1.—"Breadboard" Spectrometer photo above shows entrance slit, grating, detectors, and parts of viewing ports. The diagram on the opposite page shows side view of the spectrometer. The signal is the view out of the paper ("space") chopped against the view into the paper ("earth") as reflected off the mirror at the left, which here appears rotated to view a calibration black body.

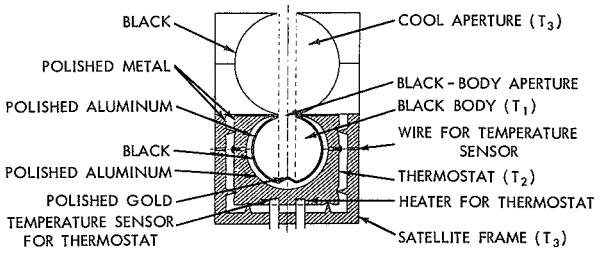

FIGURE 2.—Detector Assembly.

type spectrometer of the "under and over" sort, it employs a grating 5 in. square that has a dispersion of about 1.4 cm^{-1} per mm at 15 microns. Exit slits are about 5 cm^{-1} wide, with the detector lenses situated behind the slits. In addition to four intervals in the 15-micron band, there is a fifth detector 7 cm^{-1} wide located in the 11.1-micron "window" whose purpose is to measure the temperature of the surface or cloud tops. A chopper wheel allows alternate views through "space" and "earth" ports.

This breadboard instrument has been used to conduct experiments from the ground, and has been found to perform approximately to the required radiometric accuracy. A report on its performance will be published in the near future. Currently under construction are instruments containing most of the design elements required for a satellite-borne instrument. These will first be tested in high-altitude balloons.

The spectrometer, however, is bulky (16 by 32 in.), heavy (55 lb, exclusive of electronics except the preamplifiers), and a heavy drain on power (10 w). Aboard a satellite, an interferometer would be more satisfactory from every standpoint. Although interferometer development is now considerably behind that of grating spectrometers, there is every promise that they will eventually achieve the spectral resolution and radiometric accuracy needed for indirect temperature soundings.

In the microwave region, the 5-mm band of oxygen might be employed for the same purpose, as suggested by Lilley and Meeks. (*3*) Discussions of some problems with indirect soundings will be found elsewhere. (*4–7*)

Microwave radiometry is another area of interest. The infrared region from 3–40 microns is presently the domain of many meteorological satellite experiments. The presence of atmospheric absorption bands of H_2O, CO_2, and O_3 make this region well suited

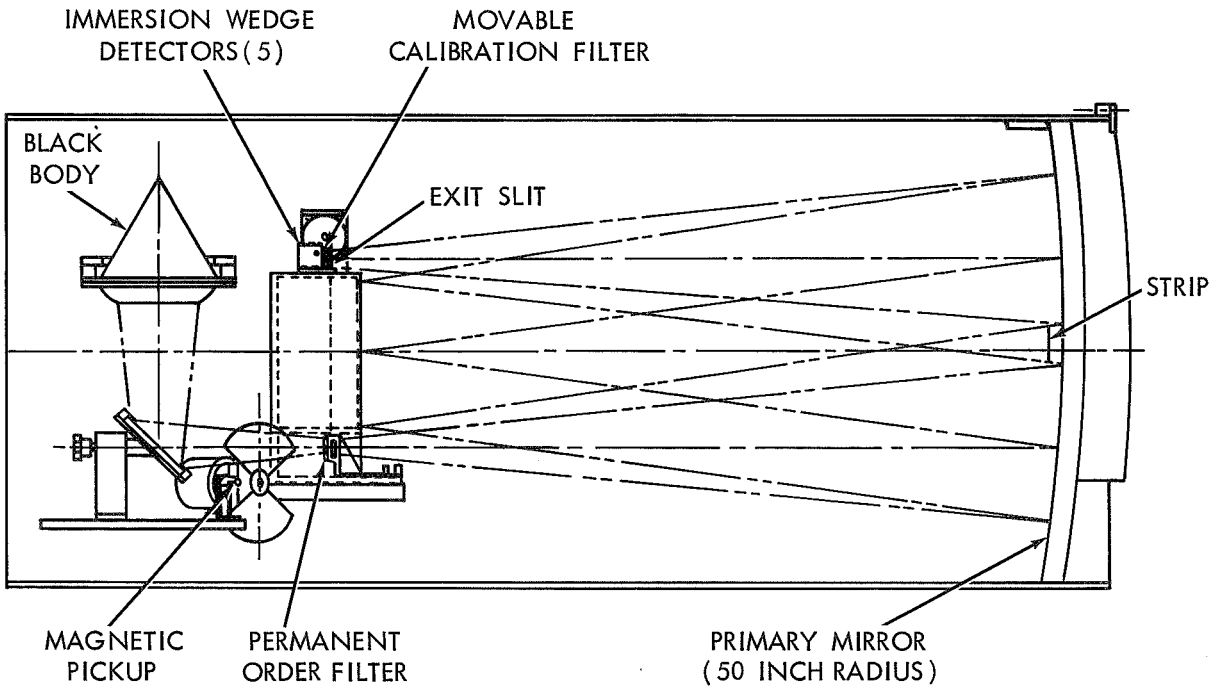

FIGURE 3

for a variety of investigations. Furthermore, detectors are readily available and instrumental techniques fairly well established. But thermal emission at much longer wavelengths, in the regime of microwaves, also deserves attention. Some atmospheric constituents show a number of rotational lines there. Oxygen, for example, has a strong line at 2.5 mm and a band of 36 lines at 5 mm, while water absorbs at 0.85 and 13.5 mm.

The microwave range differs from the infrared by a factor of about 100 in the wavelengths. Theoretical concepts for experiments in the region of thermal emission are applicable to both infrared and microwave wavelength regions. However, the physical phenomena, and especially the instrumental techniques used, in both wavelengths make them distinctly different in many respects.

The longer microwaves penetrate clouds much easier than infrared rays. Only Rayleigh scattering must be considered for microwaves, since cloud droplets are very small compared to the wavelength. This is not necessarily so for larger rain drops, so that a method to detect precipitation in clouds may be based on this phenomenon. Furthermore, the high resolving power of microwave receivers and the existence of individual strong lines fairly isolated from others, removes some of the difficulties inherent in interpretation of infrared bands that consist of many overlapping lines of different strength.

These apparent advantages must be contrasted to certain drawbacks. In the infrared the radiant emittance of a source, say at 250K, is very sensitive to small temperature changes. The emittance in a narrower band near the 6.3μ water band, for example, is approximately proportional to the 10th power of the temperature. The same source shows a third power relation between emittance and temperature at 20μ. For microwaves, the signal strength is only linearly proportional to temperature.

The available emittance over useful ranges is orders of magnitudes lower at microwaves than at normally useful ranges in the infrared. This particular shortcoming, however, is compensated by the different operating concept of microwave receivers.

In the far infrared, the thermal detectors in use today register the radiation by means of the heating they undergo in absorbing the radiation. They are, however, affected by noise fluctuations which are the ultimate limitations on their sensitivity. In most instances, the noise is entirely unaffected by narrowband optical filters placed in front of them.

In contrast to this, the tuned circuit (cavity) of the microwave receiver (and other methods which restrict the effective bandwidth) short-circuits all frequencies not within its passband. This very effective reduction in noise makes possible microwave intensity measurements to an accuracy equivalent to a fraction of a degree centigrade.

Before useful meteorological experiments can be performed in this spectral range, many physical parameters must be considered. Absorption coefficients of atmospheric gases, extinction cross-sections of water droplets and ice crystals, the transmissivity of clouds and the emissivity of various types of terrain, plus state of the art of low-noise receivers, are important design criteria.

In much the same way that temperature structure can be obtained from a satellite, the distribution of ozone might also be found from measurements in the strong Hartley band in the ultraviolet. Because the transmittance of ozone is known, measurements of scattered sunlight at several wavelengths or of the occultation of direct sunlight by the atmosphere, at a series of positions of the satellite, can be used for the deduction of ozone distribution. Originally suggested by Singer (*8*), this topic has been discussed in more detail by Singer and Wentworth (*9*), Twomey (*10*), and others.

Frith (*11*), of the British Meteorological Office, suggested the occultation method; his instrument is to be carried in a satellite in the near future. Another instrument has been flown briefly in a polar orbiting satellite (*12*). Each of these instruments employs a filter which admits a rather broad band in the ozone band below 3000 A. They are basically broad-beam receptors, in contrast with vertically viewing spectrometers considered for ozone and temperature experiments.

A wavelength scan for vertical viewing of scattered sunlight would require a spectrometer (or interferometer) with a resolution of a few angstroms and a field of view of not more than about 0.04 steradian. Such instruments have been considered, but have not yet been implemented by the Weather Bureau of NASA.

In another area, measurements of reflected sunlight by a satellite instrument can indicate the presence of a cloud, but meteorologists also require a knowledge of the height of cloud tops. Infrared radiometric measurements can be used to determine cloud-top temperatures, but the relation between height (or pressure) and temperature in the atmosphere is highly variable. Another method, largely independent of the temperature variations is available to us.

If a gas has a known mixture in the atmosphere, the transmittance of sunlight from the top of the atmosphere down to a cloud, and back to a satellite, will depend (aside from a slight temperature term) upon the optical path, given by the pressure at the cloud top and the angles of incidence and view. The only unknown is the pressure at the cloud top, which can be deduced from transmittance as measured from the relative radiance in the band and in the nearby continuum.

This experiment was proposed by Hanel, (*13*) who suggested using the 2-micron band of carbon dioxide. Yamamoto and Wark (*14*) suggested that the 0.76-micron band of oxygen would be better. While the 1.8-micron band of water vapor overlaps the 2-micron band rather seriously, the oxygen band does not suffer from blending of other atmospheric bands. For high clouds or for low water-vapor content, the situation for the 2-micron band is more favorable, although high spectral resolution would be necessary to take advantage of this band.

The detail of the 0.76-micron band is shown in Figure 4. In the upper part is the R branch which contains the band head (left), the band center, and 5 lines of the P branch. Below is an additional part of the P branch. This spectrum was obtained with the 150-ft tower telescope at Mt. Wilson. Many details can be seen, including the lines due to the O^{17} and O^{18} isotopes. Using this and other spectra, a study is being conducted to determine all the necessary physical parameters of the band and to calculate transmittance under the range of optical path found in the atmosphere.

The illustration shows that the *R* branch can become nearly totally absorbing, and therefore the transmittance becomes insensitive to optical path. In the *P* branch, there remain regions of rather great absorption, but, at the longer wavelengths, there is a region of significant but not overwhelming absorption where sensitive measurements of transmittance might be made. Where the optical path is short (vertical incidence off high clouds), the *P*

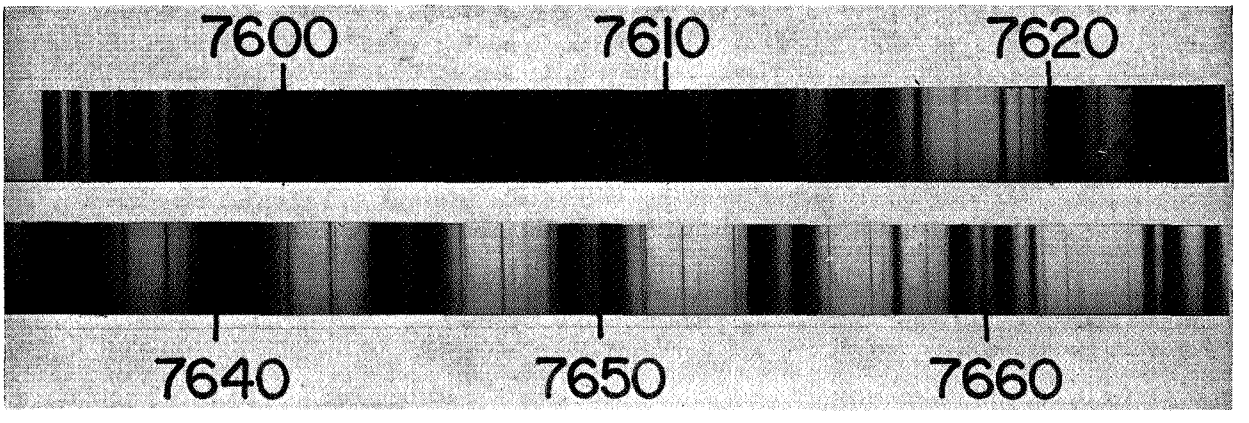

FIGURE 4.—Spectrum of 0.76-Micron Oxygen Band, obtained with the 150-ft tower telescope at Mount Wilson. In the upper part is the band head (left); the R branch lies between the band head and the band center; five lines of the P branch can be seen to the right of the band center. In the lower part are lines farther out in the P branch. The very narrow lines throughout are from the isotopic molecules $O^{16}O^{17}$ and $O^{16}O^{18}$. There are also some solar lines.

ranch may become too weak to allow good transmittance measurements, and the R branch could be the preferable region. Thus it would probably be better to monitor several regions of the spectrum to cover all ranges of transmittance to be encountered with changing cloud heights, sun angle and viewing angle. Because filters do not cut off sharply, this experiment might require a spectrometer of low spectral resolution.

There is as yet no active effort to build an instrument to carry out this experiment from a satellite. The study of the band must first be completed in order to set forth the instrumental requirements.

Another interesting experiment would deal with the solar constant.(*15*) The fraction of solar energy absorbed by the earth and its atmosphere is of great importance for the understanding of meteorological processes. Absorbed sunlight heats the atmosphere and surface, and provides the energy source for evaporation of water and atmospheric circulation. The amount of radiation absorbed by the earth can be determined from a satellite by measuring the incident and the reflected components of the solar flux.

So far, only the reflected component has been measured from meteorological satellites, but refinements in these measurements will soon reach the point where uncertainties in the incident radiation become appreciable, and both components (the incident and reflected flux) must be determined. This holds for certain narrow spectral regions of special interest, such as the strong absorption bands of ozone in the ultraviolet (2200–2800A), as well as for total solar energy flux integrated from the ultraviolet to far infrared part of the spectrum.

The latter quantity, per unit area, and at the mean distance of the earth from the sun is the "solar constant." A numerical value of 1.94 cal min^{-1} cm^{-2}, or 1350 watt m^{-2}, is generally accepted today, (*16–18*) although a more recent survey indicates that 2 cal min^{-1} cm^{-2} is a better estimate.(*19*) These values were derived from measurements made in recent decades from the earth's surface. Atmospheric extinction, however, necessitates considerable correction of experimental results. The atmosphere is completely opaque to large portions of the ultraviolet and infrared spectrum.

Satellites now present the opportunity to determine the solar constant directly, without the interference of the atmosphere.

The method chosen for a future experiment exposes a black body to the sun, registers the equilibrium temperature of the body, and telemeters the data back to earth. In equilibrium, the incoming solar flux balances the black-body flux from the cavity which is well defined by Stefan-Boltzmann's law. The measurement of energy flux can thereby be reduced to a temperature measurement.

Certain precautions must be taken, concerning mainly the blackness of the body, the degree of isolation achieved, and the accuracy of the temperature sensing devices.

The principle of the instrumentation is shown on page 564. The black cavity is thermally insulated from its surrounding as much as possible. In addition, the net flux between the cavity and its mounting is made negligible by thermostating the housing to approximately the operating temperature of the black body.

One final experiment that might be mentioned involves the measurement of "sferics," or the RF emissions by lightning (from "atmospherics"). The detection and mapping of sferics could be an important contribution to meteorology by indicating areas of strong vertical motion related to tropical storm development and to other violent phenomena bearing on strong winds, heavy rainfall, and turbulence.

Following a discussion among experts to determine the necessity of satellite measurements of sferics (*20*), and the instrumental requirements for such an experiment, the Weather Bureau has sought to establish a more firm design requirement. Although there are no commitments at present on an instrument of this sort, it has been suggested that a simple receiver of fairly broad bandpass (probably in the vicinity of 100 mc/s), and with an antenna

pattern encompassing the entire visible earth, would be the proper initial experiment.

The experiments discussed here are part of a possible future effort in meteorological observations from satellites. They may eventually be flown as space becomes available, and other experiments, not discussed here, may also be carried on satellites. However, instruments for such experiments must be conceived well in advance of possible flights because of the long lead-time involved.

Some of the Tiros experiments and those planned for Nimbus will be continued on an operational basis. Others may have only limited observational requirements, and can be discontinued after objectives have been achieved. These can then be replaced by others, so that the vital requirements for flexibility in scientific investigation can be realized, and new ideas and concepts continually tested.

REFERENCES

1. KAPLAN, L. D. (1959), "Inference of Atmospheric Structure from Remote Radiation Measurements," *J. of Opt. Soc. of Am.*, Vol. 49, pp. 1004–1007.
2. DREYFUS, M. G., and D. T. HILLEARY (1962), "Satellite Infrared Spectrometer—Design and Development," *Aerospace Engineering*, Vol. 21, No. 2, pp. 42–45.
3. LILLEY, A. E., and M. L. MEEKS (1962), "Atmospheric Radiation at Wavelengths Near Five Millimeters," paper presented at 43rd annual A.G.U. meeting, Washington, D.C., June 1962.
4. KAPLAN, L. D. (1960), "The Spectroscope as a Tool for Atmospheric Sounding by Satellites," Instrument Society of America Conference, September, 1960.
5. KING, J. I. F. (1959), "Deduction of Vertical Thermal Structure of a Planetary Atmosphere from a Satellite," Aerosciences Lab, General Electric Co., *Tech. Info. Ser. R59SD477*, December 1959.
6. YAMAMOTO, G. (1961), "Numerical Method for Estimating the Stratospheric Temperature Distribution from Satellite Measurements in the CO_2 Band," *J. of Meteorol.*, Vol. 18, pp. 581–588.
7. WARK, D. Q. (1961), "On Indirect Soundings of the Stratosphere from Satellites, *J. of Geophys. Res.*, Vol. 66, pp. 77–82.
8. SINGER, S. F. (1956), "Geophysical Research with Artificial Earth Satellites," "Advances in Geophysics," Vol. 3, pp. 301–367, Edited by H. E. Landsberg (Academic Press, N.Y., N.Y.).
9. (1957), "A Method for the Determination of the Vertical Ozone Distribution from a Satellite," *J. of Geophys. Res.*, Vol. 62, pp. 299–308.
10. TWOMEY, S. (1961), "On the Deduction of the Vertical Distribution of Ozone by Ultraviolet Spectral Measurements from a Satellite," *J. of Geophys. Res.*, Vol. 66, pp. 2153–2162.
11. FRITH, R. (1961), "Meteorological Satellites," *Weather*, Vol. 16, pp. 364–370.
12. MAYFIELD, E. (1962), private communication.
13. HANEL, R. A. (1961), "Determination of Cloud Altitude from a Satellite," *J. of Geophys. Res.*, Vol. 66, p. 1300.
14. YAMAMOTO, G., WARK, D. Q. (1961), "Discussion of the Letter by R. A. Hanel, 'Determination of Cloud Altitude from a Satellite,' " *J. of Geophys. Res.*, Vol. 66, p. 3596.
15. HANEL, R. A., "An Instrument to Measure the Solar Constant from a Satellite," *NASA Technical Note TND-674.*
16. Smithsonian Institution, "Smithsonian Meteorological Tables," *Smithsonian Miscellaneous Collections*, Vol. 114, 6th ed., Washington, D.C., 1951.
17. MINNEART, M. (1953), "The Photosphere," Ch. 3 of "The Sun" ed. by G. P. Kuiper, (Univ. of Chicago Press), pp. 88–185.
18. ALLEN, C. W., et al. (1953), "Empirical Problems and Equipment," Ch. 9 of "The Sun" ed. by G. P. Kuiper, (Univ. of Chicago Press), pp. 592–721.
19. JOHNSON, F. S. (1954), "The Solar Constant," *J. of Meteorol.*, Vol. 11, pp. 431–439.
20. SOULES, S. D. (ed.) (1962), Conference of Sferics Measurements from Satellites, Meteorological Satellite Laboratory Report No. 13 (U.S. Weather Bureau, Washington).

IMAGE CONSTRUCTION FOR CONCAVE GRATINGS AT GRAZING INCIDENCE, BY RAY TRACING

S. O. KASTNER AND W. M. NEUPERT

Goddard Space Flight Center

The images formed by a concave grating used at grazing incidence are constructed by a ray-tracing method. The method, equivalent to a recently developed procedure of Spencer and Murty, can be used for any configuration of grating and object. The results are compared with a third-order approximate theory for the case of rays parallel to the Rowland plane.

INTRODUCTION

Recently, the imaging properties of diffraction gratings have been discussed from several points of view. Namioka [1,2] has studied the aberrations of concave gratings, using Fermat's principle. Spencer and Murty [3] have developed a general ray-tracing procedure which includes gratings as elements of complete optical systems.

In the present work a ray-tracing method equivalent to that of Spencer and Murty is used to obtain the images formed by a concave grating used at grazing incidence, a configuration which is very important in space spectroscopy.

The results are compared with computations using an equation derived by Behring [4] from Fermat's principle for the special case of light rays initially parallel to the Rowland plane.

LIST OF SYMBOLS

$A(X, Y, Z)$—object point

$B(x, y, z)$—image point

$P(x_1, y_1, z_1)$—point on grating

$C(R, 0, 0)$—center of curvature of grating

$\mathbf{D}$—vector with direction cosines as components

$p=[z_1^2+(R-x_1)^2]^{-1/2}$

$q=[(R-x_1)^2+y_1^2+z_1^2]^{-1/2}$

$\mathbf{\Lambda}$=matrix of transformation between (x, y, z) and (x', y', z') systems

$\boldsymbol{A}$=matrix of quadric coefficients

DESCRIPTION OF METHOD

From any specified object point (X, Y, Z) (which need not be on the Rowland cylinder) a ray is constructed which impinges on the grating at the point $(x_1y_1z_1)$. The elemental part of the grating centered on $(x_1y_1z_1)$ is considered to be a plane grating whose plane is that of the tangent plane to the spherical surface (Fig. 1); the rulings on this elemental plane grating are the projection of the actual rulings on to the tangent plane. The direction of the resulting diffracted ray is then determined by the diffraction equation [5]

$$m\lambda/\sigma=(\sin\alpha+\sin\beta)\cos\delta, \qquad (1)$$

in which the parameters α,β,δ are computed relative to the elemental plane grating, as illustrated in Figure. 2.

The intersection of the diffracted ray with any desired surface is then obtained and is the image point corresponding to the given incident ray. This imaging surface is usually the Rowland cylinder, or a cylinder centered on the grating in the case of an exit slit whose plane is normal to the grating pole-slit line.

[1] T. Namioka, J. Opt. Soc. Am. 49, 446 (1959).

[2] T. Namioka, J. Opt. Soc. Am. 49, 460 (1959).

[3] G. H. Spencer and M. V. R. K. Murty, J. Opt. Soc. Am. 52, 672 (1962).

[4] W. E. Behring (private communication).

[5] C. S. Rupert, J. Opt. Soc. Am. 42, 779 (1952).

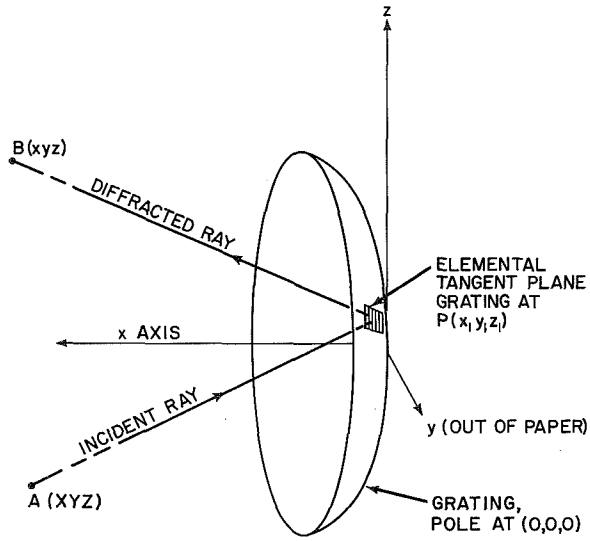

FIGURE 1.—Concave grating and coordinate system, illustrating also an elemental tangent plane grating.

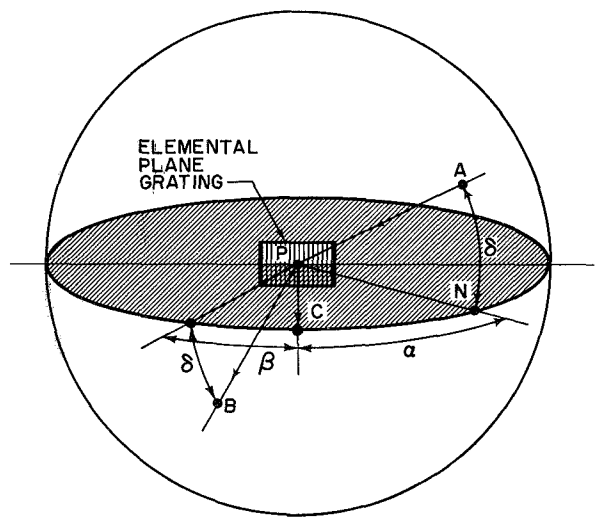

FIGURE 2.—Angles of diffraction equation (1), referred to an elemental plane grating.

In this way, by having incident rays from one object point impinge on a net of points on the grating, and repeating this process for a desired net of object points, the image distribution is obtained.

DETAILS OF CALCULATION

Derivation of Elemental Grating

In the following, each point such as $A(X,Y,Z)$ is considered to have vector **A** associated with it, the components of **A** being (X, Y, Z).

Let the object point be $A(X, Y, Z)$: the incident ray from it to an arbitrary point $P(x_1y_1z_1)$ on the grating has the parametric line equation

$$\mathbf{x}=\mathbf{P}+\frac{s(\mathbf{A}-\mathbf{P})}{[(X-x_1)^2+(Y-y_1)^2+(Z-z_1)^2]^{1/2}}, \quad (2)$$

where s is the distance of point $\mathbf{x}(x, y, z)$ from P.

If $C(R, 0, 0)$ is the center of curvature of the grating, then the normal at P has the equation:

$$\mathbf{x}=\mathbf{P}+\frac{s(\mathbf{C}-\mathbf{P})}{[(R-x_1)^2+y_1^2+z_1^2]^{1/2}}, \quad (3)$$

where s is the distance of point $\mathbf{x}(x, y, z)$ from P along the normal.

Since the grating sphere equation is

$$(x-R)^2+y^2+z^2=R^2, \quad (4)$$

the equation of the tangent plane at $P(x_1y_1z_1)$ is

$$(x_1-R)(x-R)+y_1y+z_1z=R^2. \quad (5)$$

The equation of the projection of the ruling at $P(x_1y_1z_1)$ onto this tangent plane results from the intersection of the plane $y=y_1$ with this tangent plane, being therefore

$$(x_1-R)(x-R)+y_1^2+z_1z=R^2. \quad (6)$$

Application of Grating Equation

The tangent plane, with projected rulings on it is the elemental plane diffraction grating mentioned earlier. The incident ray at $P(x_1y_1z_1)$ produces a diffracted ray leaving this elemental grating according to the equation

$$m\lambda/\sigma_e=(\sin\alpha+\sin\beta)\cos\delta, \quad (7a)$$

where

$$\sigma_e=\sigma/[1-(y_1/R)^2]^{1/2}, \quad (7b)$$

σ_e being a slowly varying function of y_1 because the actual ruling does not have a constant separation in the assumed type of grating. The reference plane in which α and β are measured is the plane through $P(x_1y_1z)$ which is normal to the line (6). This plane is now considered to be the x', y' plane of a new coordinate system $(x'y'z')$, whose x' axis is the grating normal at P, and whose z' axis is the projected line (6).

Thus the new z' axis has the direction cosine vector

$$\mathbf{D}^{z'}=\frac{1}{[z_1^2+(R-x_1)^2]^{1/2}}\begin{vmatrix} z_1 \\ 0 \\ R-x_1 \end{vmatrix}\equiv p\begin{vmatrix} z_1 \\ 0 \\ R-x_1 \end{vmatrix}; \quad (8)$$

the new x' axis has the direction cosine vector

$$\mathbf{D}^{x'}=\frac{1}{[(R-x_1)^2+y_1^2+z_1^2]^{1/2}}\begin{vmatrix} R-x_1 \\ -y_1 \\ -z_1 \end{vmatrix}\equiv q\begin{vmatrix} R-x_1 \\ -y_1 \\ -z_1 \end{vmatrix}. \quad (9)$$

The direction cosine vector of the new y' axis is obtained as the cross product of those above:

$$\mathbf{D}^{y'}=\mathbf{D}^{z'}\times\mathbf{D}^{x'}$$
$$=pq\{\mathbf{i}[y_1(R-x_1)]+\mathbf{j}[z_1^2+(R-x_1)^2]+\mathbf{k}[-y_1z_1]\}. \quad (10)$$

The equation of the $x'y'$ plane in the original coordinates, it should be mentioned, is found to be

$$z_1x+(R-x_1)z-z_1R=0. \quad (11)$$

We now can find the angle α for the incident ray AP, defined as the angle between its projection on the $x'y'$ plane and the x' axis. This projected line is most easily obtained by finding the projection N of point A onto the $x'y'$ plane and then forming the equation of line PN. The equation is found to be.

$$\mathbf{x}'=\mathbf{P}+\frac{s}{\{(X-Uz_1-x_1)^2+(Y-y_1)^2+[Z-U(R-x_1)-z_1]^2\}^{1/2}}\begin{vmatrix} X-Uz_1-x_1 \\ Y-y_1 \\ Z-U(R-x_1)-z_1 \end{vmatrix}, \quad (12)$$

in which

$$U=\frac{z_1X+(R-x_1)Z-z_1R}{z_1^2+(R-x_1)^2}. \quad (13)$$

The angle α of the diffraction formula (7a) is the angle between this line (12) and the normal (x' axis):

$$\cos\alpha=Vq\{[X-Uz_1-x_1][R-x_1]+[Y-y_1][-y_1]+[Z-U(R-x_1)-z_1][-z_1]\}, \quad (14a)$$

in which

$$V=\{[X-Uz_1-x_1]^2+[Y-y_1]^2+[Z-U(R-x_1)-z_1]^2\}^{-\frac{1}{2}}. \quad (14b)$$

Similarly, the angle δ of the diffraction formula is the angle between PA and PN and is therefore given by

$$\cos\delta=VW\{[X-Uz_1-x_1][X-x_1]+[Y-y_1]^2+[Z-U(R-x_1)-z_1][Z-z_1]\}, \quad (15a)$$

in which

$$W=[(X-x_1)^2+(Y-y_1)^2+(Z-z_1)^2]^{-\frac{1}{2}}. \quad (15b)$$

The diffraction angle β, in the new coordinate system ($x'y'z'$), can now be obtained as

$$\sin\beta=(m\lambda/\sigma_e\cos\delta)-\sin\alpha. \quad (16)$$

To get the direction of the diffracted ray in the ($x'y'z'$) system, then, we must rotate some point initially on the x' axis through an angle β in the PCN plane, and then perform a second rotation on the point to bring it out of the plane by the angle δ, both rotations being performed in appropriate directions. The situation is illustrated in Figure 2. This is the usual transformation in spherical polar coordinates (r, θ, ϕ):

$$y=r\sin\theta\cos\phi,$$
$$y=r\sin\theta\sin\phi,$$
$$z=r\cos\theta, \quad (17)$$

except that here $\delta=(\pi/2)-\theta$, $\beta=\phi$, so that

$$x'=\cos\delta\cos\beta,$$
$$y'=\cos\delta\sin\beta,$$
$$z'=\sin\delta, \quad (18)$$

taking (1, 0, 0) as the original point on the x' axis. It should be noted that the sign of δ must always be taken opposite to that of the z' coordinate of the object point A.

Now, (x', y', z') are the coordinates of a point x_D' on the diffracted ray, in the new system. To obtain this point's coordinates in the original system we must transform these coordinates by the matrix

$$\Lambda=\begin{vmatrix} D_x^{x'} & D_x^{y'} & D_x^{z'} \\ D_y^{x'} & D_y^{y'} & D_y^{z'} \\ D_z^{x'} & D_z^{y'} & D_z^{z'} \end{vmatrix}. \tag{19}$$

Thus, the coordinates of this point in the (x, y, z) system are

$$\mathbf{x}_D=\begin{vmatrix} D_x^{x'}\cos\delta\cos\beta+D_x^{y'}\cos\delta\sin\beta+D_x^{z'}\sin\delta \\ D_y^{x'}\cos\delta\cos\beta+D_x^{y'}\cos\delta\sin\beta+D_x^{z'}\sin\delta \\ D_z^{x'}\cos\delta\cos\beta+D_z^{y'}\cos\delta\sin\beta+D_z^{z'}\sin\delta \end{vmatrix}+\begin{vmatrix} x^1 \\ x^1 \\ y^1 \end{vmatrix}, \tag{20}$$

remembering that the origin of the $(x'y'z')$ system is the point $P(x_1y_1z_1)$.

The equation of the diffracted ray is now written down as

$$x=\mathbf{P}+s(x_D-\mathbf{P})T, \tag{21}$$

where T is a normalizing factor.

IMAGE POINTS

To find the intersection of this diffracted ray with the Rowland cylinder ,we can conveniently use the matrix method described by Heading [6] as follows. If the line equation is $\mathbf{w}=\mathbf{sh}$, and the quadric equation is $\mathbf{w}z\mathbf{A}\mathbf{w}=0$, where $\mathbf{w}_1$ does not lie on the quadric, then the intersection values of s are given by

$$(w_1{}^T+sh^T)A(w_1+sh)=0 \tag{21a}$$

or- expanding,

$$w_1{}^TAw_1+s(h^TAw_1+w_1{}^TAh)+s^2h^TAh=0 \tag{21b}$$

in which

$$T=(H^2+J^2+K^2)^{-\frac{1}{2}}. \tag{25b}$$

If the intersection of the diffracted ray with a grating-centered cylinder of radius r is desired, $\mathbf{A}$ is given instead by

[6] J. Heading, *Matrix Theory for Physicists* (Longmans Green and Company, Inc., New York, 1958), Chap. III.

In the notation of the present problem, this equation is:

$$\mathbf{P}^TA\mathbf{P}+2s\mathbf{L}^TA\mathbf{P}+s^2\mathbf{L}^TA\mathbf{L}=0, \tag{22}$$

where:

$$\mathbf{P}=\begin{vmatrix} x_1 \\ y_1 \\ z_1 \\ 1 \end{vmatrix}, \tag{23}$$

$\mathbf{A}$ for the Rowland cylinder is

$$A=\begin{vmatrix} 1 & 0 & 0 & -R/2 \\ 0 & 1 & 0 & 0 \\ 0 & 0 & 0 & 0 \\ -R/2 & 0 & 0 & 0 \end{vmatrix},$$

and the componets of $\mathbf{L}$ are

in which

If the intersection of the diffracted ray with a grating-centered cylinder of radius r is described $\mathbf{L}$ is given instead by

$$\begin{aligned} \mathbf{L}_x&=T[q(R-x_1e\cos\delta\cos\beta+pqy_1(R-x^1)\cos\delta\sin\beta+pz_1\sin\delta] &&\equiv TH, \\ \mathbf{L}_y&=T\{q(-y_1)\cos\delta\cos\beta+pq[z_1{}^2+(R-x_1)^2]\cos\delta\sin\beta\} &&\equiv TJ, \\ \mathbf{L}_z&=T[q(-z_1)\cos\delta\cos\beta+pq(-y_1z_1)\cos\delta\sin\beta+p(R-x_1)\sin\delta] &&\equiv TK, \end{aligned} \tag{25a}$$

$$A=\begin{vmatrix} 1 & 0 & 0 & 0 \\ 0 & 1 & 0 & 0 \\ 0 & 0 & 0 & 0 \\ 0 & 0 & 0 & -r^2 \end{vmatrix} \tag{26}$$

The algebraically larger value of s is used in all cases.

COMPUTER USE OF THE EQUATIONS

For a given angle of incidence, a single central ray is calculated; i.e., the incident ray lying in the Rowland plane and impinging on the pole (0,0,0) of the grating. The intersection of the diffracted ray with the Rowland cylinder is found. This gives the radius r_c of the grating-centered cylinder upon which the image is to be formed, assuming that we want the image in a surface normal to the line from the image to the grating pole. A multiple run can then be made using a net of i object points, and a net of j grating points for each object point. Thus $i \cdot j$ image points are obtained.

APPLICATION TO A SPECTROMETER

The procedure developed in the foregoing sections has been applied to the problem of image formation in a grazing incidence spectrometer designed for observation of the solar extreme ultraviolet spectrum from the first orbiting solar observatory. This case corresponds to observation of an extended source at a very great distance from the entrance slit. Under such circumstances a beam of nearly parallel radiation from each element of the source illuminates the entire entrance slit so that the direction cosines for the incident rays from a specified element of the source can be taken as the same for every point on the grating which is illuminated through the (infinitely narrow) entrance slit. For ease of comparison with an approximate (third-order) theory, it is assumed that the beam of radiation is parallel to the Rowland plane. This is justified only because in the case being considered (observation of the sun), the maximum deviation from this plane is only 0.005 rad.

TABLE I.—*Values of β_0, the central ray diffraction angles, corresponding to angles of incidence α_0 and wavelength λ used for the curves of Figure 3* (m=+1).

$\alpha_0 \backslash \lambda$	50 Å	100 Å	300 Å
88°	85° 12.7	83° 31.8	79° 8.8
86°	85° 5.4	82° 40.0	78° 36.2

Rays satisfying the above assumptions were selected from a more general machine ray tracing computation for angles of incidence of 88° and 86°. The results are given in Figure 3 for several different values of the angle of diffraction β_0. In each case a 5×5 net of grating points was used corresponding to values of $y_1/R=0, \pm 0.005, \pm 0.01$, where y_1 is the horizontal distance of the illuminated grating point from the pole of the grating and R is the radius of curvature of the grating. The distances of the grating points from the Rowland plane were taken as 0, ±0.5, and ±1.0 cm. For $\sigma=0.00017361$ cm, $R=100$ cm the wavelengths corresponding to values of β_0 specified in Figure 3 are given in Table I. Values of $\Delta\beta \cos \beta$ are directly convertible into $\Delta\lambda$ using the differentiated grating equation. The values of $y_1/R=\pm 0.005$ correspond to images formed by those portions of the solar limb lying in the Rowland plane and represent the maximum deviations from the image formed by the central ray from the center of the sun.

It should be pointed out that these images are obtained for the specified values of α and β in any grating system for values of y_1/R equal to 0.01 and 0.005. The values of wavelength for which the results apply are found using the grating equation.

An inspection of the figures reveals the improvement in image quality obtained either by reducing the angle of incidence α or the value y_1/R. They show also how the curves based on third-order theory depart from the exact ray-traced results as the angle of incidence increases.

CONCLUSIONS

The ray-tracing method developed for a concave grating enables one to obtain image shapes for all configurations in which a concave grating may be used; it can be used equally well at near normal incidence or at grazing incidence. It serves therefore as a standard of comparison against which approximate theories can be tested.

Because of the "closed" nature of the calculation, making its use in a computer program

convenient, it is possible to generate quickly as many images as may be required for spectrometer design purposes. A few such images have been presented above for the OSO extreme ultraviolet spectrometer.

ACKNOWLEDGMENTS

The authors thank W. E. Behring for valuable discussions and C. Wade for writing the computer program.

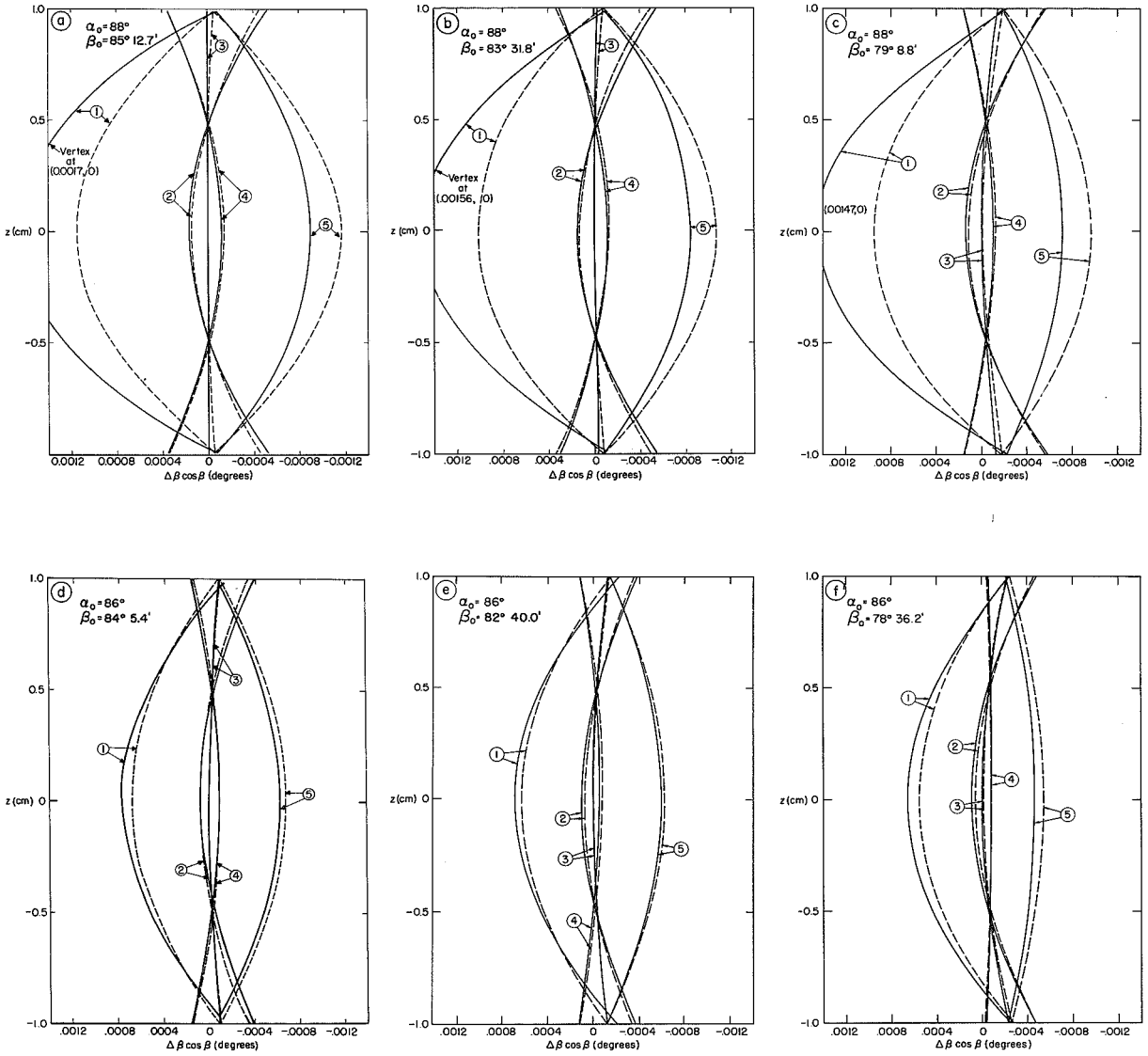

FIGURE 3.—Images (solid line) obtained by ray-tracing method compared with images (dashed line) obtained from third-order theory (diffraction order $m=+1$). Curves are illustrated for values of y_1/R of: (1) −0.01, (2) −0.005, (3) 0.0, (4) 0.005, (5) 0.01.

A DETECTOR-ANALYZER FOR STUDYING THE INTERPLANETARY PLASMA

K. W. OGILVIE, N. McILWRAITH, AND H. J. ZWALLY
Goddard Space Flight Center

T. D. WILKERSON
Institute for Fluid Dynamics and Applied Mathematics
University of Maryland

The energy distributions of protons and other species of ions in interplanetary space as well as at satellite altitudes will be studied by using a new detection technique. Observations will be made as a function of time, direction, and position, over an energy range of at least 10 ev to 10 kev, with a maximum sensitivity of 10^{-18} A and with the capability of detecting single ions. Previous studies of the "solar wind" suggest many important measurements of its state, its interactions with planets, and its wave phenomena. The present instrument, $10\times30\times20$ (cm^3) in size, contains an electrostatic energy analyzer, a secondary-electron-scintillation detector, high voltage supplies, and signal conditioning circuits. Laboratory work demonstrates constant response for protons having energies from 30 ev to 3 kev and a minimum detectable current corresponding to about 10 particles per second. Progress is reported on the development of a velocity selector for separating ionic species. Hopefully this will lead to the solution of an important problem in solar wind studies, the determination of the relative abundances of protons and alpha particles.

INTRODUCTION

Ample evidence now exists for significant particle and energy density in what used to be thought of as "empty space" in the solar system. Even during quiet periods the solar atmosphere extends to the earth's orbit and beyond in the form of a tenuous, streaming plasma having roughly these properties: a number density of 20 per cm^3, a mean velocity of 5×10^7 cm/sec, a temperature between 10^5 and 10^6 °K. This "solar wind" was first proposed by Biermann (References 1–3) and was the subject of subsequent calculations by Parker (References 4–6). Satellite observations by Gringauz, et al., Bridge, et al., and Neugebauer and Snyder (References 7–11) confirm the existence of such a plasma outside the earth's magnetosphere, and as far away from the earth as the orbit of Venus.

Many properties of the solar wind are not well defined. A satellite instrument is now being developed to study some of them, such as the flow-direction and temperature of the plasma. The ionic composition of the solar wind will also be studied for the first time. Because of high sensitivity, it should be possible to scan the particle energy distributions at various angles with respect to the satellite-sun line and thereby search for anisotropies such as different temperatures parallel and perpendicular to the interplanetary magnetic field. Nonthermal distributions and large changes in plasma composition may be observed following the passage of magnetic storm-fronts.

Previous experiments have enabled some inferences to be made on these subjects, but the evidence is still incomplete in many respects. This shows the difficulties inherent in (and in many cases peculiar to) space probe experimentation. The experimenter must strike a balance between the exhaustive measurements he wants to make and the capacity of the vehicle's telemetry system. Such a system can impart information only so rapidly, particularly

when several experiments go on simultaneously. On long distance flights, such as the Mariner trajectory, information can only be transmitted at a rate of a few bits per second. There are weight and power limitations upon the extent to which data can be stored and processed on-board. Several years of successively refined experimentation will be necessary before such complex objects as the interplanetary plasma become well understood. The present work is a step along the way; extensions of the instrument for future work are also being developed.

PRINCIPLES OF THE PLASMA ANALYZER AND DETECTOR

The analyzer-detector is actually a low energy ion detector, in which mass and energy discrimination are combined to give differential energy spectra for ions with a given value of m/Z. None of the individual components are original in concept; rather it represents the combination of them into a system which has advantages for operation in space.

Figure 1 is a diagram of the system. The ions enter through the slit and are selected differentially in terms of energy per unit charge by the electrostatic analyzer. The analyzer's acceptance cone can be varied over wide limits from say ± 1 to ± 20 degrees. Energy resolution can be varied from a low value to approximately 15 percent. The 127-degree deflection configuration is used (References 12 and 13) even

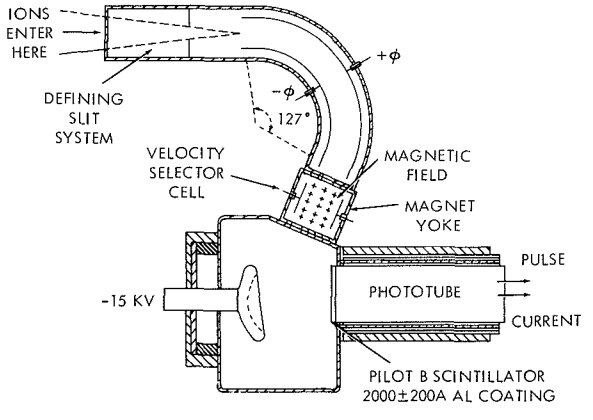

FIGURE 1.—The energy-per-unit-charge and mass analysis instrument. The velocity selector is inserted between the analyzer and the detector box.

though we do not need resolution better than 10 percent at present, both so that the resolution can be increased at any time, and also because it gives a convenient physical arrangement. Equal negative and positive potentials V are applied to these plates, and they can either be stepped or driven slowly through a range. In round numbers, not allowing for fringing effects,

$$\frac{E}{Z}=\frac{R}{d}\times V,$$

to the first order in d/R, where R is the plate radius and d is the plate separation. The maximum usable value of R/d is of the order of 10. At the same time V/d must be kept below about 10^4 in order to avoid certain problems connected with field emission. Thus the maximum practicable value of proton energy which can be measured by this method is approximately 100 kev, a few times greater than the minimum energy which can be detected by a conventional scintillation counter. The two methods are therefore complementary.

Figure 2 shows the result of the analysis of approximately monoenergetic beams of protons. The extractor potential of the ion source is shown for each curve, and it will be seen that the resolution of the analyzer is close to the predicted value. The arrows on the abscissa show the potentials which should be required to detect protons with the nominal potentials shown. The differences between the positions of these arrows and the positions of the peaks of current represent the usual difference between the extraction potential of the ion source and the energy of the resulting ions.

After leaving the analyzer the ions enter a conventional velocity selector of the $E\times B$ type. The potential applied to the electrostatic deflection plates in this device is fixed for a given m/Z and magnetic field B. In the space application the magnetic field is kept fixed and the deflection cell must be surrounded by a well-designed yoke to prevent stray fields from interfering with other experiments on the same satellite. An example of the program of po-

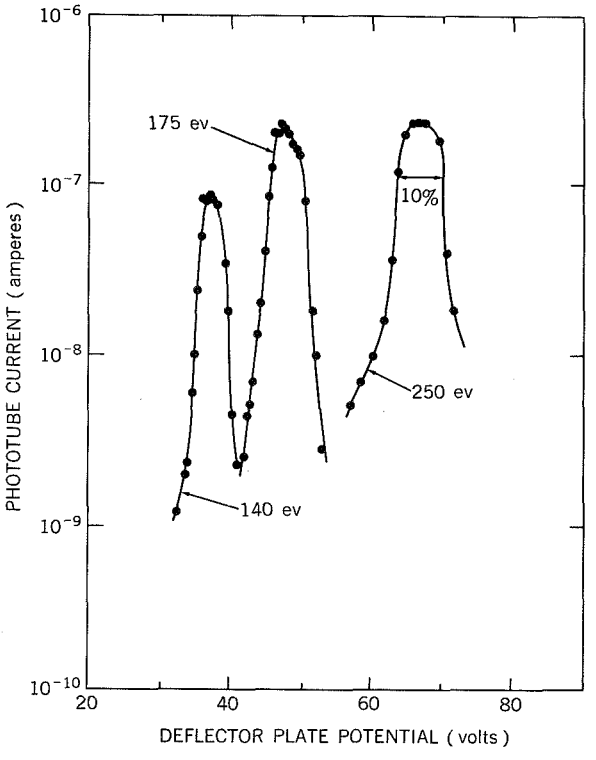

FIGURE 2.—The result of analysis of approximately monoenergetic beams of protons. The figures attached to each curve show the extractor potential applied to the ion source. The deflector plate potential for selecting a proton of energy E is E/4 volts.

tentials applied to the various electrodes in a specific experiment is given below.

The ions, now belonging to a few species with fixed m/Z and energy, enter the detecting chamber where they are attracted to a high voltage electrode. This emission knob, made of highly polished aluminum, emits several (approximately 3) secondary electrons for each incident ion when maintained at −15 kv (Reference 14). These secondaries are accelerated by the same high potential and detected by a plastic scintillator-photomultiplier detector. The scintillator is covered by a thin (2000A) film of Al which does the double duty of grounding the plastic and keeping visible light from the phototube.

Thus, for each incident ion, on the average 3 electrons are actually detected, each with 15 kev energy. These arrive at the scintillator in a time short compared with the resolving time of the output circuit of the tube. The detection efficiency for each 15 kev electron after it has passed through the Al film is of the order of 50 percent, and together these electrons give a pulse which is several times higher than the average dark current pulse of the tube. Assuming that 50 ev is required for each photon produced in the plastic scintillator and that 5 kev is lost in the Al layer, if the light collection efficiency is 50 percent and the quantum efficiency at the photocathode is 10 percent then we see that the average pulse contains

$$G\times\frac{10^4}{50\times2}\times0.1=10G \text{ electrons},$$

where G is the gain of the tube. The efficiency of detecting at least 1 of 3 such electrons can be made greater than 80 percent. The detector thus counts single ions with a high efficiency. Such systems were independently developed by Schutze and Bernhard, Daly, and Afrosimov, et al. (References 15–19). Eubank and Wilkerson (Reference 20) have used the overall analysis and detection system for measuring plasma ion distributions in the laboratory, and Lincke and Wilkerson (Reference 21) have used the detector part alone for vacuum ultraviolet spectroscopy.

Figure 3 shows 3 pulse height analyses for the detector operating in the pulse mode. The ordinate scale is logarithmic and the abscissa represents 256 channels. Note two important points:

1. One of the difficulties encountered is reducing the background counting rate in the absence of ions entering the slit. The rate to be expected due to cosmic rays is of the order of 5 per second, but to realize this in practice requires extreme care. The surfaces of the high voltage electrode and the interior of the detecting chamber must be free from dust, since field emission from points can take place when the average field is of the order of 10^4 v/cm (Reference 22). If field emission occurs it makes itself felt by the presence of a mumber of pulses at least as large as pulses due to ions. These are seen in the second picture.

2. The third picture, which represents only $\frac{1}{10}$ of the counting time of the first two, shows

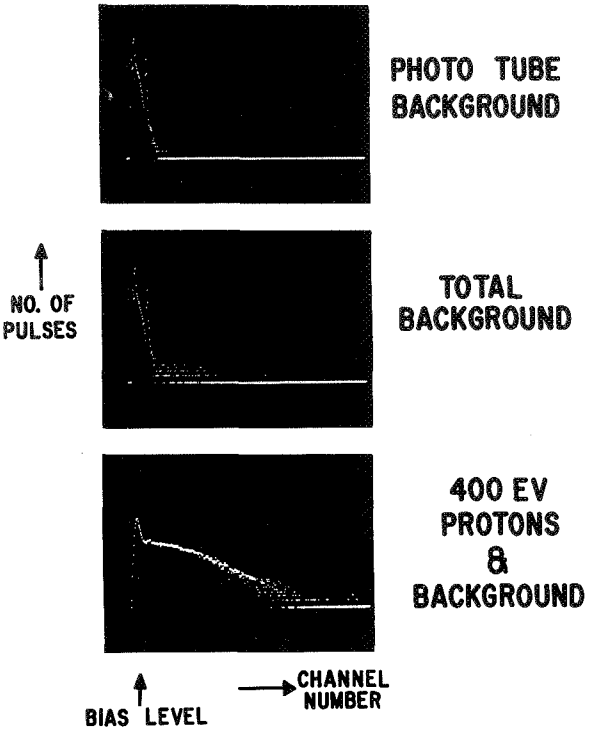

FIGURE 3.—Pulse height analyses for the detector The ordinate is logarithmic and the abscissa is 256 channels.

the position of the bias level which is set to reduce background. The lack of a distinct peak in the pulse height distribution is due to scattering in the coating covering the plastic scintillator. Although, as noted above, the average pulse at the cathode consists of approximately 10 photoelectrons, the spread is very wide.

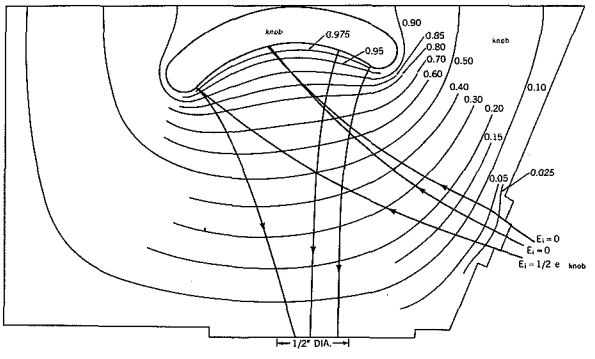

FIGURE 4.—Equipotentials and trajectories for ions and electrons.

Some refinements have been introduced in the analyzer-detector for space application. Figure 4 is a plot of ion and electron trajectories obtained by the conducting-paper technique (Reference 23) for motion in two dimensions. The electrode shape shown allows all ions over a wide range of incident energies to strike the knob and the resulting electrons to reach the scintillator. A direct check of this point has been made by measuring the current gain of the detector as a function of incident proton energy, and it was found to be constant from 30 ev to 3 kev.

In order to provide a very wide dynamic range of detectable current we proceed as follows. From 0 to 10^5 pulses per second the pulse-counting mode is used. For higher incident currents an electrometer is connected to measure the current from the eighth dynode of the phototube. The dark current to this electrode is of the order of 3×10^{-10} A, and with an overall gain of the order of 10^5 some overlap exists between the two modes of operation. The maximum current which can be recorded in this way is approximately 10^{-4} A, corresponding to an imput current of 10^{-9} A. Such a wide range is necessary for studying relative abundances in the solar plasma.

Figures 5 and 6 show photographs of a prototype of this device which was flown on an Argo D–4 rocket, NASA 8–18, to an altitude of about 1000 km from Wallops Island, Va., on September 28, 1963, with the intention both to

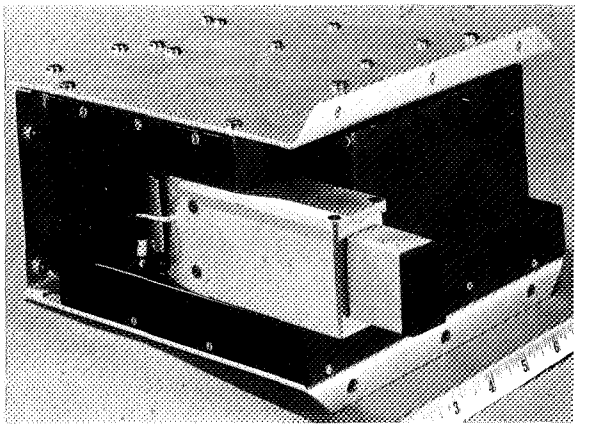

FIGURE 5.—Prototype energy-per-unit-charge analyzer for the rocket flight test.

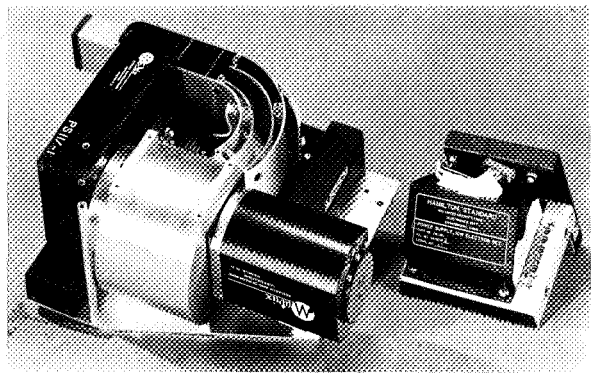

FIGURE 6.—Partially assembled view of the rocket instrument.

test its characteristics for space flight and to obtain some information about the ionic constituents of the upper atmosphere (Reference 24). During flight the high voltage (15 kv) was turned on 10 sec after ejection of the nose-cone. This turned out to be too short a time and glow discharge occurred in the detector box. This effect is partially due to outgassing of other parts of the payload, and will be avoided in subsequent flights by the provision of a large pipe between the detector box and analyzer, leading outside the payload. This unfortunate circumstance prevented us from getting any useful geophysical data, but evidence from telemetry indicates that all parts of the instrument otherwise functioned perfectly.

For this flight, only energy per unit charge was selected, ten steps between 2 and 1000 ev being provided. The various parts of the apparatus are indicated in Figure 5. Figure 6 shows a partially assembled view of the detector system, which weighs 7.4 lb when complete and consumes approximately 1½ watt at 28 volts dc. For satellite use the weight must be reduced, but this should not present an insuperable problem.

The solar plasma comes almost radially from the sun (Reference 10) and thus we are interested in counting ions when the entrance angle of the detector includes the radius vector between the sun and the satellite. Neither visible light nor ultraviolet radiation should produce counts. This problem has not been completely solved, but some precautions are shown in Figure 6. Visible light presents a great difficulty because of the very great flux of visible photons. Thus, as much as possible of the visible light must be prevented from entering the detection chamber, and that which does enter must then be prevented from entering the phototube. The thickness of the Al layer on the scintillator is fixed, since 5 kev is the maximum acceptable mean energy loss for electrons passing through it. The purpose of the horn-type light absorber (Reference 25) is to prevent light passing through the metal gauze window in the outer plate from re-entering the box around the analyzer. The principle variable is the degree to which light scattered from the metal gauze can penetrate to the box. Undesirable effects due to visible light can be prevented, but work in progress has shown that the counting rate due to the sun's ultraviolet radiation may limit the minimum detectable intensity of ions when the device looks directly at the sun. This limitation has been estimated to be about 1 order of magnitude above the normal background, which under the most pessimistic assumptions is about 100 counts per sec. Thus the background when facing away from the sun is about 100 sec^{-1}, and when facing the sun about 1000 sec^{-1}. There is considerable difficulty in determining the effect of solar ultraviolet radiation since the most usual and easily set up sources are monochromatic and are difficult to calibrate in absolute terms.

The development and testing of the dectetor has been carried out using a vacuum system with an RF ion source. By introducing hydrogen through a palladium leak, a beam consisting principally of protons is produced. By separating the detector a distance of the order of 1–2 meters from the source a uniform beam of particles may be obtained which is large enough to fill the slit of the analyzer. Current measurements are carried out using Faraday cups, and current division can be carried out to a fair degree of accuracy by such cups with a small hole in the bottom, if stops are introduced at the correct places in the ion beam. By substituting suitable guns for the

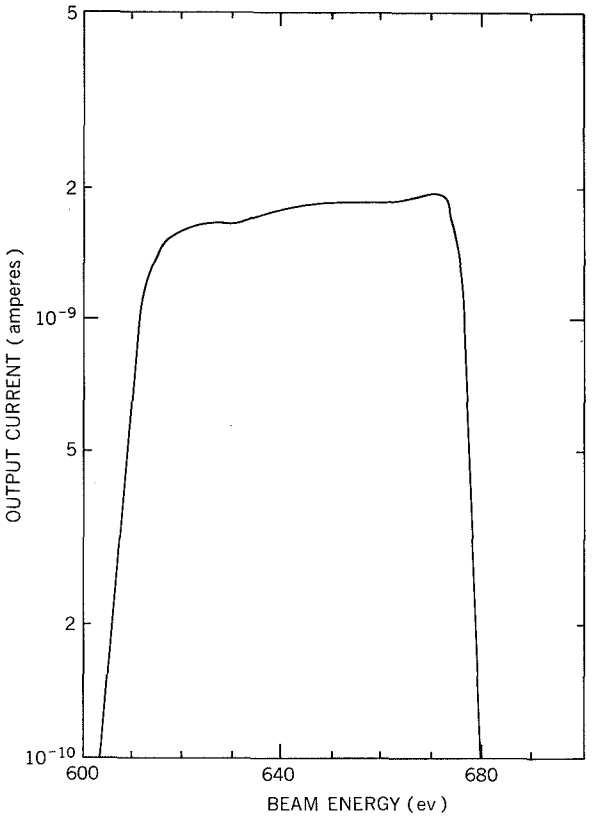

FIGURE 7.—The energy profile of the analyzer, measured by using electrons.

ion source, it is possible to use electrons for which the energy is accurately known. These were used to obtain the energy profile shown in Figure 7 for the energy-per-unit-charge analyzer. The detector is mounted inside the vacuum on a system of motor-driven tables, allowing both rotation about the axis of the defining slit and translation across the beam axis. This is used to check the solid angle of acceptance of the system, at present approximately 6×6 degrees.

A SPECIFIC SATELLITE EXPERIMENT

For the first experiments it is proposed to select $m/z=1$ and $m/z=2$, for a range of E/z. It is important to choose the values of E/z and the resolution in such a way that a peak in the spectrum of the solar plasma is unlikely to fall between values. As an example of this suppose the resolution chosen is ±15 percent. Then a suitable set of center values of E/z is given below:

E/z for protons

0, 300, 450, 600, 850, 1200, 1700, 2400.

These values and the resolution obtained are shown in Figure 8.

There are two classes of satellites, those which are spin stabilized and those in which a surface or surfaces face fixed directions. The latter usually incorporate a surface oriented toward the sun, on which the instrument can be mounted. The values of E/z and m/z are then stepped through cyclically. For a spinning satellite, however, the acceptance cone of the instrument sweeps through the solar direction, and the signal becomes a pulse lasting for a time of the order of 0.1 sec. The response time of the electrometer must thus be short compared with this, and the category of E/z and m/z must be changed in synchronism with the rotation of the vehicle.

Clearly, high resolution will someday be required in view of the many constituents likely to be present in the interplanetary plasma. The work of Nier illustrates the developments in this field (Reference 26). The presently proposed lower resolution experiment is considered a necessary first step to assess the degree to which the mass spectrum may vary with the range of particle energy considered.

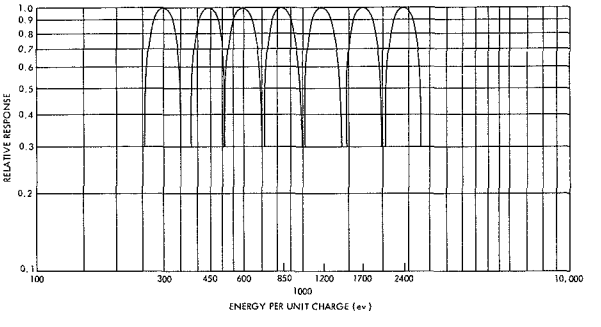

FIGURE 8.—This figure shows the relative response of an analyzer having 15 percent resolution for the choice of valves given here.

OTHER EXPERIMENTS

Apart from the sounding rocket and satellite measurements discussed, many other experiments are possible with this apparatus, depending on the satellite orbit. The most important appears to be the study of the structure of the sun-ward boundary between the earth's magnetic field and the solar wind. A satellite such as the Eccentric Orbiting Geophysical Observatory (EGO) would be appropriate for this study since its orbit is designed for repetitive transits into and out of the magnetosphere.

Orbits of greater eccentricity than that of the EGO may provide an opportunity for study of the "standing shock" which some theoreticians believe to be the result of interaction between gas reflected from the magnetosphere and the incoming solar wind (Reference 27). By picking out the proton component, for example, and recording energy distributions as a function of position and angle, we would find density and temperature profiles in the plasma over some depth in the interface region.

ACKNOWLEDGMENTS

We wish to thank R. E. Bourdeau for support and encouragement. We are grateful for the advice and help of H. P. Eubank and F. B. McDonald, who independently suggested the analyzer-detector combination. We also wish to thank L. A. Terry for his valuable technical assistance.

REFERENCES

1. Biermann, L., "Kometenschweife und solare Korpuskularstrahlung," *Z. Astrophys.* 29(3): 274–286, September 1951.
2. Biermann, L., "The Tail of Halley's Comet in 1910," *Z. Naturforsch.* 7a: 127–136, January 1952 (in German).
3. Biermann, L., Solar Corpuscular Radiation and the Interplanetary Gas," *Observatory*, 77(898): 109–110, June 1957.
4. Parker, E. N., "Dynamics of the Interplanetary Gas and Magnetic Fields," *Astrophys. J.* 128(3): 664–676, November 1958.
5. Parker, E. N., "The Hydrodynamic Treatment of the Expanding Solar Corona," *Astrophys. J.* 132(1): 171–183, July 1960.
6. Parker, E. N., "The Hydrodynamic Theory of Solar Corpuscular Radiation and Stellar Winds," *Astrophys. J.* 132(3): 821–826, November 1960.
7. Gringauz, K. I., Bezrukikh, V. V., et al., "A Study of the Interplanetary Ionized Gas, High-Energy Electrons, and Corpuscular Radiation of the Sun by means of Three-Electrode Trap for Charged Particles in the Second Soviet Cosmic Rocket," *Dokl. Acad. Nauk SSSR*, 131(6): 1301–1304, Apr. 21, 1960, translation in *Sov. Phys.-Dokl.*, 5(2): 361–364, September–October 1960.
8. Gringauz, K. I., et al., "Ionized Gas and High Energy Electrons in the Vicinity of the Earth and in the Interplanetary Space," *Dokl. Acad. Nauk SSSR*, 132(5): 1062–1065, June 1960 (in Russian).
9. Gringauz, K. I., and Rytov, S. M., "Relationship Between the Results of Measurements by Charged-Particle Traps on the Soviet Cosmic Rockets and Magnetic-Field Measurements on the American Satellite 'Explorer VI' and Rocket 'Pioneer V,' " *Dokl. Akad. Nauk SSSR*, 135(1): 48–51, November 1, 1960, translation in *Sov. Phys.-Dokl.*, 5(6): 1225–1228, May–June 1961.
10. Bridge, H. S., Dilworth, C., et al., "Direct Observations of the Interplanetary Plasma," Proc. of the Internat. Conf. on Cosmic Rays and the Earth Storm, publ. in *J. Phys. Soc. Japan*, vol. 17, supplement A–II, January 1962, pp. 553–562.
11. Neugebauer, M., and Snyder, C. W., Jet Propulsion Lab. Tech. Memo 33–111, 1962.
12. Hughes, A. L., and Rojansky, V., "Analysis of Electronic Velocities by Electrostatic Means," *Phys. Rev.* 34(2): 284–290, July 15, 1929.
13. Hughes, A. L., and McMillen, J. H., "Re-Focussing of Electron Paths in a Radial Electrostatic Field," *Phys. Rev.* 34(2): 291–295, July 15, 1929.
14. Bourne, H. C., Jr., Cloud, R. W., and Trump, J. G., "Role of Positive Ions in High-Voltage Breakdown in Vacuum," *J. Appl. Phys.* 26(5): 596–599, May 1955.
15. Schütze, W., and Bernhard, F., "A New Method of Measuring Very Small Ion Currents in High Vacuum," *Zeits. für Phys.* 145(1): 44–47, 1956 (in German).
16. Daly, N. R., "Scintillation Type Mass Spectrometer Ion Detector," *Rev. Sci. Instrum.* 31(3): 264–267, March 1960.
17. Daly, N. R., "High Sensitivity Mass Spectrometer Leak Detector," *Rev. Sci. Instrum.* 31(7): 720–723, July 1960.
18. Afrosimov, V. V., Gladkovskii, I. P., et al., "Method of Investigation of the Flux of Atoms Emitted by a Plasma," *Zh. Tekh. Fiz.* (*USSR*) 30(12): 1456–1468, December 1960, translation in *Sov. Phys.-Tech. Phys.* 5(12): 1378–1388, June 1961.

19. Afrosimov, V. V., Gladkovskii, I. P., et al., "Investigation of the Stream of Neutral Atomic Particles Emitted by the 'Alpha' Plasma," *Zh. Tekh. Fiz.* (*USSR*) 30(12): 1469–1484, December 1960, translation in *Sov. Phys.-Tech. Phys.* 5(12): 1389–1402, June 1961.
20. Eubank, H. P., and Wilkerson, T. D., "An Ion Energy Analyzer for Plasma Measurements," Princeton Univ. Plasma Phys. Lab. Rept. Matt 121, 1962.
21. Lincke, R., and Wilkerson, T. D., "New Detector for the Vacuum Ultraviolet," *Rev. Sci. Instrum.* 33(9): 911–913, September 1962.
22. Llewelyn-Jones, F., and Nicholas, D. N., "The Theory and Design of an Analyser for Investigating the Electron Emission Characteristics of Surfaces in Gases," *Brit. J. Appl. Phys.* 13(10): 514–520, October 1962.
23. Selgin, P. J., "Plotting Electron Paths," *Electronics*, 21(9): 124, September 1948.
24. Bauer, S. J., "Helium Ion Belt in the Upper Atmosphere," *Nature*, 197(4862): 36–37, January 5, 1963.
25. Wood, R. W., "Physical Optics," 3rd ed., New York: Macmillan Company, 1936.
26. Nier, A. O., "Small General Purpose Double Focusing Mass Spectrometer," *Rev. Sci. Instrum.* 31(10): 1127–1132, October 1960.
27. Axford, W. I., "The Interaction Between the Solar Wind and the Earth's Magnetosphere," *J. Geophys. Res.* 67(10): 3791–3796, September 1962.

ATMOSPHERIC SAMPLING INSTRUMENTATION

NELSON W. SPENCER
Goddard Space Flight Center

Man has, for centuries, deduced probable properties of both the planets and their atmospheres, primarily on the basis of radiation received from the planets. Astronomers today continue increasingly in this manner to expand further our knowledge of the Solar System. In addition, we now have the opportunity to work toward the making of direct measurements, which will enable confirmation of our present beliefs. Thus, we can look forward to verification that the surface of Venus is very hot, or, as some researchers suggest, it is obscured by a very dense ionosphere. Also, direct measurements can tell us whether or not there is some small concentration of oxygen and water vapor in the Martian atmosphere permitting us to conclude whether or not life as we know it is possible. In addition, we now appear to be close to making direct measurements of, for example, the Moon's "vacuum" atmosphere, which will give us more insight into lunar properties and Solar System history.

Although we now have access to many direct measurement techniques that will permit acquisition of new knowledge, or confirmation of old as suggested above, plans for specific space missions, such as Ranger, Mariner, Surveyor, and others, indicate to the experimenter the constraints he must accept when considering possible experimentation. The primary handicaps are, clearly, limited weight, power, volume, data transmission rate, as well as the obvious requirement that experimental equipment will not deteriorate during the unavoidably long transit period.

One naturally turns to his experience gained while determining properties of the Earth's atmosphere, to borrow techniques which can be applied to planetary atmosphere exploration. These methods common to data gathered by balloon and seemingly directly applicable to measurements in other atmospheres employ sensors such as thermistors for temperature measurement, aneroid devices for pressure measurement, and hydrometers for water vapor content evaluation. Rocket exploration of the Earth's higher atmosphere to altitudes of several hundred kilometers has provided a variety of techniques, generally of a much more complex nature than those employed with balloon measurements. Some of the techniques developed use companion ground equipment, a requirement that is probably not feasible for planetary work, at least at this time. Instruments resulting from this work include a variety of sensors, such as pressure gauges which respond to many orders of magnitude of pressure change, and a limited number of mass spectrometers which can help define the detailed composition of an atmosphere, provided a representative sample of the atmosphere is made available. Other measurement techniques, such as the grenade experiment that has been developed for air temperature and wind measurements, and the falling-sphere experiment that has been developed for air density measurements, have special characteristics which may make them particularly valuable.

Finally, there are the basically observational techniques such as employed in the Tiros satellite system, which observe infrared and visual radiations from a distance; the spectacular sodium release flights which enable wind velocity and direction determination from observations of vapor trail movement; and the spectrographic methods where absorption of

764-173 O—65——38

solar radiation by gaseous constituents provides information about atmospheric content.

In considering application of these techniques to the making of measurements in the Martian atmosphere, for example, one comes face to face with several problems that are basically different from those encountered in measurements in the terrestrial atmosphere. Several of these are consequences of our seemingly limited capability to "get there" with adequately extensive equipment.

In contrast to probing the Earth's atmosphere, we find, for example, such basic differences as the need to measure from the "top" of the planetary atmosphere down, rather than from the planet's surface up. Related to this is the problem of determining an instrument's altitude in the planetary atmosphere, in the absence of "ground" based techniques as employed in terrestrial atmospheric exploration.

The present relatively limited weight capability imposes restraints primarily because it restricts the available power and data-link capacity. As a consequence of these restraints one considers performing the more elementary experiments in preference to those employing relatively sophisticated devices. The need for very high reliability arising from the generally long transit time, and, in some cases, from the hostile environment (for example, the atmosphere of Venus) are consistent with the approach of employing elementary experiments. Many of these intriguing special problems have been solved, and others will certainly be solved; thus, it is reasonable to expect that meaningful measurements will be made before many years have passed, and will be best made initially by an elementary approach.

The lunar atmosphere provides a challenging measurement problem because its apparent density is very low. Sensors which are capable of detecting the estimated values (the expected pressure is of the order of 10^{-13} mm Hg) are still in the development stage and their operation is not well understood. Simulation of such density values in the laboratory for calibration and testing purposes is possible, but is not readily achieved.

The development of an experiment for the measurement of the pressure of the lunar atmosphere is underway by the Goddard Space Flight Center and the University of Michigan at this time, for the Surveyor mission. A "Redhead" cold-cathode ionization gauge has been adopted as the sensor. It is one of only two or three devices in existence known to be capable of detecting such low pressures. Special problems anticipated in use of this equipment on the lunar surface arise from the presence of possible surface-derived dust, contaminating gas from the vehicle control jets, undesirable gases from other experiments which will be relatively insensitive to such gaseous contamination, and from the gas cloud, due to the spacecraft itself, which is expected to be present for an unknown time period after landing.

Studies have been made in regard to the design of instrumentation that would be suitable for first measurements in the Martian atmosphere. The approach taken in these studies has considered reliability as a primary requirement for a first measurement attempt, and thus has included the concept of employing relatively unsophisticated experiments, to be consistent with the adopted reliability standards and other constraints.

It has been concluded in these studies relative to Martian atmosphere measurements, that the use of a capsule as an instrument carrier, to be dropped into the atmosphere for descent by parachute, would optimize the resources of typical available vehicle systems, and would most readily accommodate the instruments chosen for the desired measurements.

Figure 1 illustrates a representative capsule design, showing the heat shield and the basic instrument package. Capsule entry into the atmosphere will slow the capsule from its high (order of 7 km/sec) initial velocity. After the velocity is greatly reduced by drag and the shielded capsule base pressure increases to about 10 mm Hg, a timer is started that will initiate the heat shield release seconds later, and will then, somewhat later, effect parachute deployment. This sequence should be complete at an altitude of about 25 km, this esti-

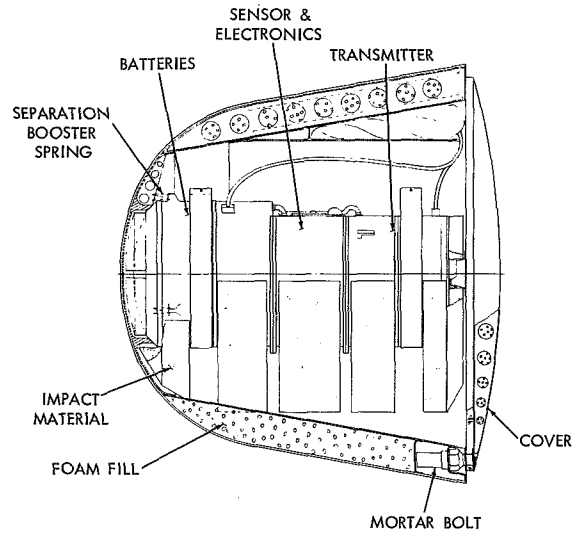

FIGURE 1.—Representative capsule design.

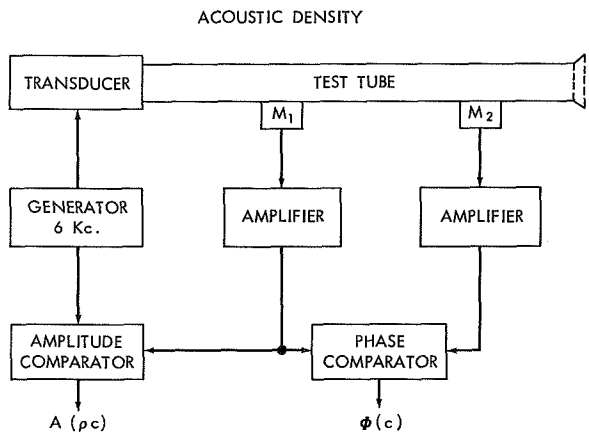

FIGURE 2.—Schematic of possible acoustical device.

mate being based on the average atmosphere that one may expect.

During the subsequent descent to the surface, antennae are deployed and measurements are are made and telemetered directly to Earth.

The measurements to be made and the instruments considered appropriate thereto, in accord with the general philosophy discussed earlier, are as follows:

Atmospheric Temperature, Pressure: The air temperature altitude-profile can be measured by a thermistor mounted atop the capsule, and the pressure profile can be determined somewhat redundantly by two aneroid-potentiometer gauges of full scale ranges typically 40 and 120 mm Hg. The temperature of the gauges, necessary to pressure evaluation, can either be controlled or can be measured each time a pressure measurement is made. It should be noted that the devices employed would be rocket-proven, off-the-shelf components.

Mean Molecular Mass Divided by γ, the ratio of specific heats, and, secondly, the "air" density: An acoustical device as illustrated in Figure 2 can be employed for determination of these quantities. Since the equation $V^2=\frac{\gamma RT}{M}$ relates the sonic velocity (V), the temperature (T), the mean molecular weight (M), and the ratio of specific heats (γ), a measurement of V and T can yield M/γ. Our present information is that the atmosphere contains N_2, CO_2, and A, with N_2 greatly predominant. With this assumption and a knowledge of the CO_2 content from another experiment to be discussed, one can determine the ratio of Argon to Nitrogen.

The instrument illustrated schematically in Figure 2 enables a determination of the sonic velocity V through at direct phase-angle measurement of a sonic wave passing down the tube. It also permits a measurement of gas density (ρ) by reference to the ratio of amplitudes of the microphone signals, the ratio depending on the product ρV. A knowledge of the velocity V determined as discussed above then permits computation of the density (ρ).

Composition: Optical means can be used to measure the total amounts of CO_2, H_2O and O_3 between a sensor and the Sun. Figure 3 illustrates the scheme of the measurement, which enables determination of the relative absorption of a particular infrared band by a particular atmospheric gas, in comparison with a "band" which is not absorbed significantly. In the instrument, a single detector observes both radiations and provides an output signal magnitude which is proportional to their intensity ratio. For the three gases noted, three detector systems are required. Proper choice of filters enables one to select reference emanations which lie in windows of the infrared spectrum for comparison with absorbed frequencies. Independent measurements of the magnitude of the

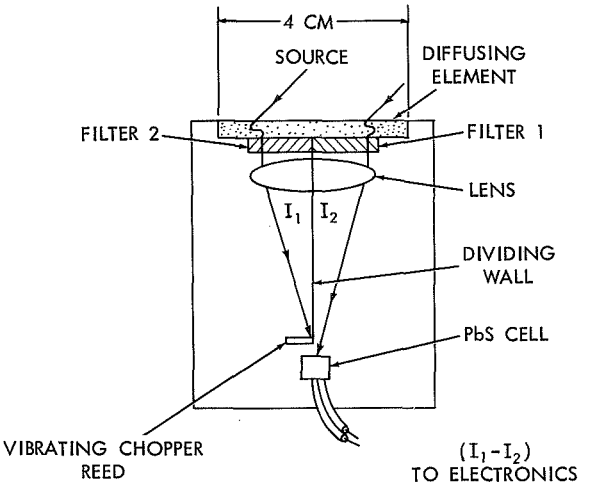

FIGURE 3.—Sketch of representative infrared detector.

reference components permits determination of the total attenuation due to haze, dust and/or clouds, for example.

The above detectors are capable of providing a very large amount of information about the Martian atmosphere, and have the common attribute of being almost completely passive instruments. With these, it appears to be possible to determine the pressure, temperature, density, and gross composition profile of the atmosphere. Use of more complex instruments, for example a mass spectrometer, which would require provision of an adequately low density sample of the low altitude atmospheric gas, would seem to the author to pose problems of much greater complexity, that could be solved more easily when the techniques of planetary exploration are more extensively developed.

This paper has been restricted to consideration of measurement of properties of the neutral atmosphere, as these appear to be of primary interest. It is clear, however, that a similar approach of determining properties of charged particles could be employed.

An atmospheric constituent whose measurement has not been considered in this paper is O_2, whose quantitative determination would naturally be very interesting and significant. Unfortunately, its direct detection is very difficult with elementary instruments. Although a mass spectrometer technique could give a relative altitude profile, quantitative determination with confidence is not state-of-the-art, even in the Earth's atmosphere. An approach which would provide detection of specific ultraviolet wavelengths offers some promise, but again is not state-of-the-art.

In conclusion, techniques such as those discussed in this paper appear to the author and colleagues at the Goddard Space Flight Center to offer the greatest promise of obtaining direct, quantitative measurements of properties of atmospheres such as that of Mars. Extension of these techniques to the Venus atmosphere will be possible when the much higher temperatures expected can be accommodated.

A MASS SPECTROMETER FOR AN AERONOMY SATELLITE

N. W. SPENCER AND C. A. REBER
Goddard Space Flight Center

A double-focusing mass spectrometer designed for the quantitative measurement of atmospheric H_e, N, O, H_2O, N_2, and O_2 is described. The instrument will detect particle densities of approximately 10^5 per cc, and has weight and power requirements appropriate to satellite use.

INTRODUCTION

The determination of the absolute composition of the neutral particle atmosphere at high altitudes poses challenging and interesting technological problems. Ideally, one would like to analyze an atmospheric sample to determine precisely the total neutral particle number density and the number densitites of the constituent gases. At present, however, our technological progress makes possible the determination of approximate values by inference only. Satellite orbit decay data permit only gross estimates of the composition, taking into account probable temperatures. Ion composition measurements yield data in which we probably have the most confidence. Direct measurement, however, will provide better information and it is for this reason that much effort has been devoted to developing appropriate instruments and making such direct measurements.

This paper describes an instrument designed (*1*, *2*) to make possible the determination of absolute values, the details of the design having been established as a consequence of experience gained in earlier attempts at composition measurement.

THE BASIS OF THE DESIGN

Several parameters of the atmosphere can be estimated from theoretical and practical considerations to provide primary guide lines in the design of a satellite-borne mass spectrometer. In addition to fundamental considerations of expected gases and their approximate concentrations, there are secondary considerations of charged particle content and particle temperature.

Any measurement which involves the sampling of particles of thermal or near-thermal energies by a satellite instrument involves an experimental situation wherein the measuring instrument disturbs the environment. It then becomes the task of the investigator to interpret the data he obtains, as modified by the presence of the instrument, in terms of the ambient conditions. This task is particularly difficult in the case of mass spectrometer measurements, and the general problem has not been solved. Data obtained have usually been expressed in terms of measured currents and, occasionally, in terms of upper bounds.

In the design of the subject mass spectrometer, particular attention has been paid to design aspects which, if properly satisfied, would simplify data interpretation. Thus, a design was chosen to (a) minimize surface contacts of gases to reduce possible dissociation or recombination, (b) provide a relatively inaccessible hot filament to minimize reaction effects of active gases with a hot surface, (c) provide for focusing of relatively high energy (as compared with thermal) ions to minimize the effects of satellite velocity, and (d) provide an "external"

ion source geometry to reduce problems due to consideration of gas flow into a sampling chamber. Other design considerations, relatively independent of data interpretation but essential to satellite use include: adequate sensitivity and electrical response, reasonably low weight and volume, capability of surviving substantial environmental stress both mechanical and thermal, and constancy of electrical characteristics with time.

DESCRIPTION OF THE MASS SPECTROMETER SYSTEM

The major elements of the system, shown in Figure 1, are: the mass spectrometer tube, the electrometer amplifier system, the logic which directs the operating sequence, an ionization electron beam current regulator, and associated power supplies (battery energy source in satellite). The most interesting element and the primary subject of this paper is the spectrometer tube shown in cross-section in Figure 2.

To simplify problems involving flow into a sampling chamber, the instrument has been designed so that the ion source projects outside the satellite surface. Thus, in Figure 2, the satellite surface location is shown about ⅛ the distance from the right side of the sketch.

One can trace the ion paths from their origin to their terminus as follows: the point of ion generation is shown as a small dotted rectangle just to the left of the "repeller," the dotted lines representing possible ion paths pass to the left through the ion lens assembly and converge

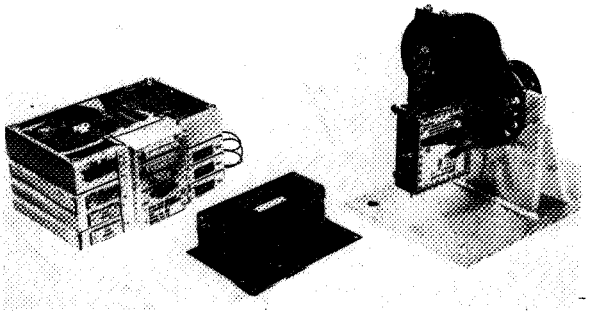

FIGURE 1.—Major Mass Spectrometer System units, including electronics package, emission regulator and mass spectrometer/electrometer.

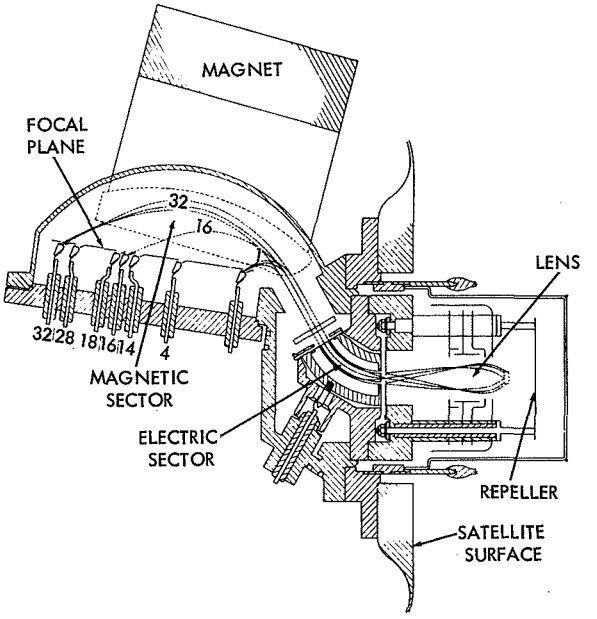

FIGURE 2.—Schematic line drawing of mass spectrometer tube showing major elements and representative ion paths.

on the "slit" just inside the satellite surface. The ions are then deflected by the electric sector and sorted in terms of mass in the magnetic sector, for collection at the various collectors (mass-number designated on the figure). Due to the double-focusing resulting from the electric and magnetic field action the ion current reaching the collectors is independent of first and second order energy variation and first order ion source entry-angle variation. It is this property of the system which is expected to simplify data interpretation. As an example of the effect of side energy the dotted paths shown in Figure 2 have been computed for a particle side energy of approximately 12 eV.

Secondary aspects of the design to be noted are (a) the total ion beam current will be measured periodically at the electric sector to provide a measure of the sum of the individual ion currents, (b) the ground potential element (screen) shown in Figure 2 as the external element of the ion source shields the repeller and ion source to prevent ionosphere electron flow to the repeller, (c) the entire ion source is covered by a vacuum-tight cap (and the previously baked spectrometer evacuated) until

orbit is achieved, at which time the cap is to be ejected.

Attached directly to the ion collector flange is the system electrometer amplifier (shown in Fig. 1) whose sensitivity will permit determination of a minimum useful signal of approximately 10^{-15} amperes. A single electrometer (tube) is sequentially switched from collector to collector, dwelling for 8 seconds on each collector as directed by the system logic. While on a given collector, the electrometer input resistance is switched from 10^{13} to 10^{10} Ohms providing high and low sensitivity positions. The linear electrometer system is followed by a logarithmic amplifier. Telemetery of both the electrometer and log-amplifier outputs provide an overall collector current range of better than 10^6 with redundant overlap. The total current (at the electric sector), and a zero current point are also sampled. Periodic calibration of the electrometer/amplifier system (less input resistor) is provided by a staircase generator voltage in the electrometer feedback loop.

SENSITIVITY AND OTHER SYSTEM CHARACTERISTICS

A discussion of the use and interpretive aspects of a system such as described here will be presented in a subsequent publication, with data that is expected to be obtained. In general, however, the system sensitivity will permit the detection of partial pressure levels of 10^{-11} mm Hg at the ion source. The relationship between the density at this point and the ambient is a variable, dependent upon several factors including the ion source geometry, the satellite velocity, and the orientation of the instrument with respect to the satellite velocity vector. As has been pointed out, the design of this instrument has been guided so as to minimize the influence of such variables. System calibration is affected utilizing a specially constructed laboratory system, using gases having only thermal energy.

SUMMARY

In summary, the mass spectrometer described briefly in this paper exhibits the following features.

(a) fixed tuned to AMU 4, 14, 16, 18, 28, 32;
(b) sensitivity approximately 10^{-11} mm Hg (electrometer, 5×10^{-16} amperes);
(c) double focusing;
(d) baked and sealed prior to exposure in orbit;
(e) weight 12 pounds;
(f) power 20 watts.

These characteristics denote an instrument that is believed to be suitable for measurements from an Earth satellite with an apogee of 700–1000 km. Although the preparation of complete spectrometer systems and their testing and qualification for flight use have demonstrated the apparent soundness of the basic design, as with other instruments used in atomospheric investigations only ultimate use and the generation of scientific data will confirm the competence of the design and its implementation.

REFERENCES

1. L. G. Hall, P. F. Howden, and T. F. Iwasaki, Design of a Mass Spectrometer For Use In A Satellite, 8th Annual Meeting of ASTM Committee E–14 on Mass Spectrometry, Altantic City, June 26–July 1, 1960
2. E. B. Meadows, Design Requirements of a Mass Spectroemter For Satellite Use, 8th Annual Meeting of ASTM Committee E–14 on Mass Spectrometry, Atlantic City, June 26–July 1, 1960

THE AUTOMATIC PICTURE TRANSMISSION (APT) TV CAMERA SYSTEM FOR METEOROLOGICAL SATELLITES [1]

RUDOLF A. STAMPFL AND WILLIAM G. STROUD

Goddard Space Flight Center

Nimbus, the second generation meteorological satellite which is the successor to TIROS, is a stabilized platform designed for global coverage of the earth's cloud cover and for future atmospheric research. A three camera TV system operating during daylight and an infrared scanner operating during the night store the cloud data on magnetic tape for later command readout.

This paper describes an additional camera system, designed for automatic and continuous real-time picture transmission during daylight. Although it is planned for trial on a TIROS satellite in a time-restricted mode, its operation on Nimbus will be continuous during daylight.

The camera uses an electrostatic storage vidicon which is exposed for 40 milliseconds, and read-out during the succeeding 200 seconds. The 800 line resolution and the 0.25 second scanning time per line are compatible with standard 240 rpm facsimile equipment which can be used for ground display. Full compatibility is achieved by amplitude modulation of a 2400 cps subcarrier and by transmission of a turn-on and phasing signal during the 8 seconds preceding actual picture transmission. The subsystem is independent of the spacecraft except for power and a frequency reference. A 5 watt transmitter broadcasts the signal in the 136 Mc space telemetry band. FM is used and this makes a large variety of standard mobile communication equipment readily adaptable.

The value of the system lies in its simplicity both in the spacecraft and on the ground. Neither command links nor storage are required. On the ground a manually tracked or even a fixed 10 db helix antenna, with a commercially available receiver and facsimile, is the only equipment required.

INTRODUCTION

This paper describes a television system developed for the Nimbus meteorological satellite that takes pictures of the cloud cover over 1000 mile square areas and transmits the information directly to simple, inexpensive ground stations within sight of the spacecraft. The development of this equipment is a response to the local weather forecaster's need for current (real-time) data on the distribution of atmospheric parameters within his station's meteorological environment. It reflects a fundamental advantage of the weather satellite, i.e., its ability to collect atmospheric data *and* deliver it to the user on a global, regional, or local basis.

Nimbus is a second generation meteorological satellite following the less sophisticated, experimental, and quasi operational TIROS. In contrast to the spin-stabilized TIROS, it has been designed as a stabilized platform tailored to carry sensors for the measurement of a wide range of atmospheric phenomena. Primarily, the first Nimbus will provide global coverage of the earth's daytime cloud cover by using a three camera television subsystem which stores up to two orbits of sets of three frame pictures. The nighttime cloud cover will be obtained

[1] This report supersedes Goddard Space Flight Center Document X-650-63-77, published under the same title.

with an IR scanner sensitive in the 4 micron atmospheric window.

The value of cloud cover measurements has been demonstrated by the TIROS satellites, which have delivered pictures of daytime cloud cover when the camera geometry was favorable. Pictures have been analyzed routinely, nephanalyses prepared, and the results made available to the world meteorological network. The tracking of storms, such as the hurricanes and typhoons in 1961 and 1962, has been performed many times and a multitude of corrections have been applied to daily weather maps.

SPACECRAFT CONFIGURATION

The Nimbus spacecraft (Fig. 1) is earth-oriented and stabilized in all three axes so that one area continuously faces the earth and has a fixed azimuth with respect to the spacecraft velocity vector. It consists of two rigidly interconnected structures. The upper, smaller structure contains the IR horizon sensors, gyros, pneumatics, inertia wheels, computer, inverters, and voltage and temperature regulators used to control the attitude of the satellite and keep it pointed to the local vertical. The solar array is attached to the control subsystem

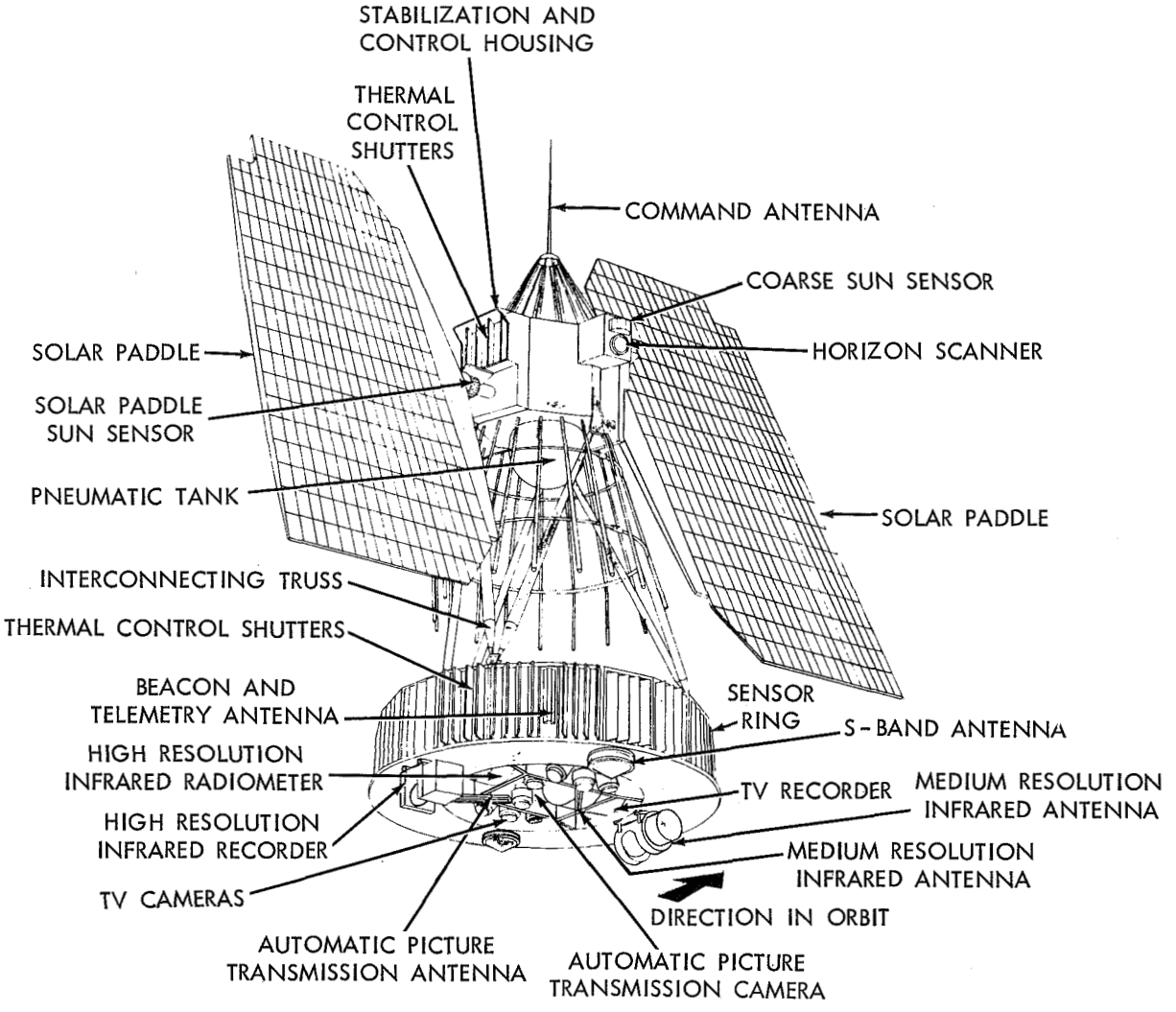

FIGURE 1.—Nimbus spacecraft.

and is stabilized normal to the sun while in orbit. Launching the satellite into an 80 degree inclination retrograde orbit will cause the orbital plane to drift at the same rate as the earth moves around the sun thereby maintaining constant sun attitude for the entire spacecraft life. As a consequence, the solar power collectors need only rotate once per orbit around a single axis. The control system will stabilize to ± 3 degrees in yaw and roll, and to about ± 2 degrees in the pitch axis. Angular rates are less than 0.05 degree per second.

The low, larger structure houses the meteorological sensors. Full picture coverage of the daytime cloud cover of the entire earth will be obtained from a three camera vidicon TV system. This system, however, requires tape recorder storage, major ground station facilities to receive the wideband transmitted picture data, and wide-band microwave links to relay the data from the command and data acquisition sites to the users. The lower structure also contains clocks, transmitters, and the telemetry, data storage, programming, command, and other electrical, electronic, and mechanical components required for the functioning of the meteorological subsystems.

THE AUTOMATIC PICTURE TRANSMISSION SYSTEM (APT)

Figure 2 is a block diagram of the APT system, both spacecraft-borne and ground

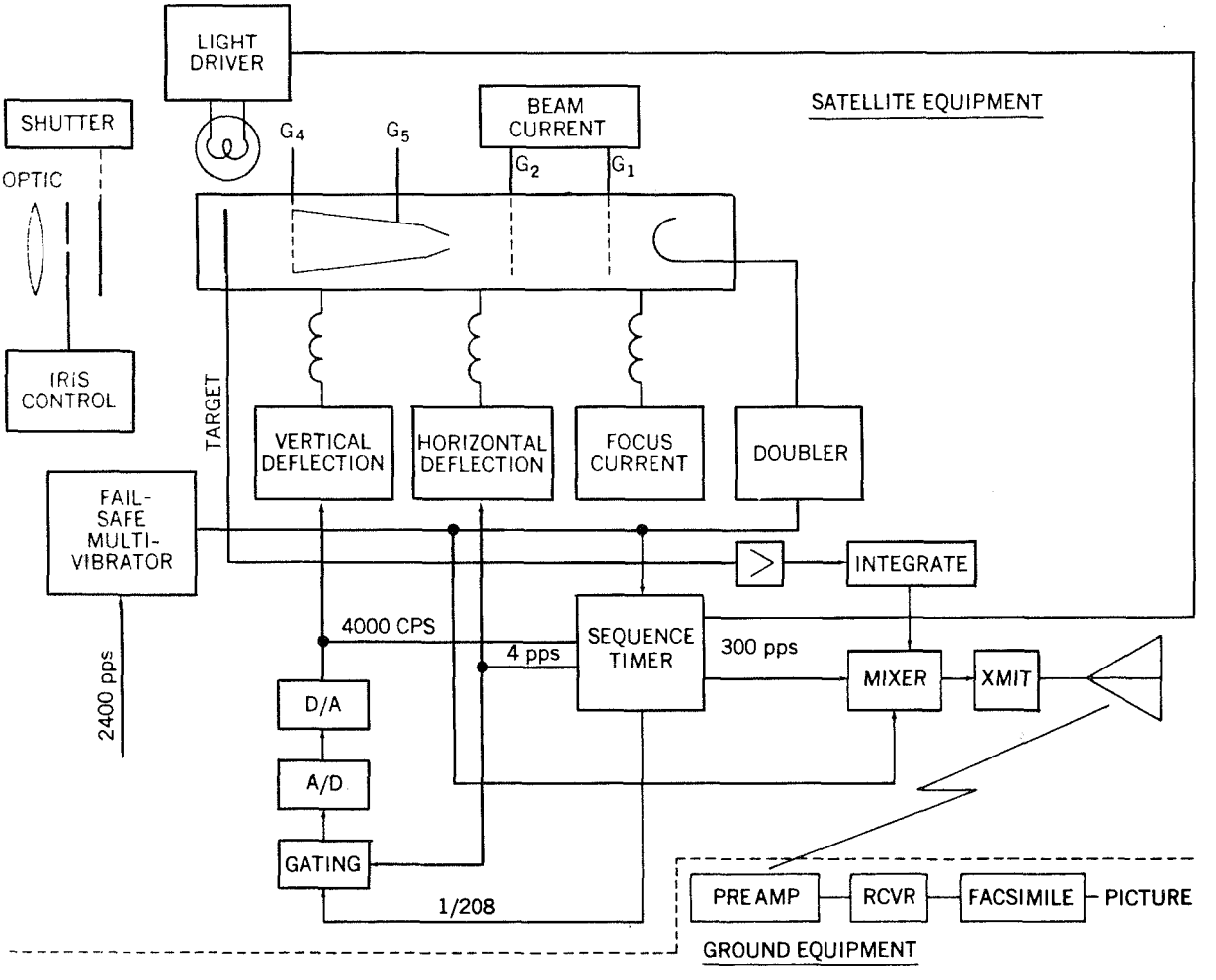

FIGURE 2.—Block diagram of the APT system.

components. In the spacecraft, appropriate optics focus the cloud map below the satellite on the face of a storage vidicon. This image is converted to an electric signal by electron beam readout; a subcarrier is modulated which in turn modulates the VHF transmitter. The signal passes through the antenna and receiver on the ground and the image is re-created directly on a facsimile unit in real time.

SYSTEM PARAMETERS

It is desirable, from the point of view of global cloud coverage, to provide users at least one cloud cover picture per day of their local areas. A compromise between satellite altitude, available lenses, and vidicon format resulted in the selection of a Kinoptic "Tegea" lens with the following characteristics:

1. Focal length—5.7 mm
2. F-number—1.8
3. Field of view—107 degrees
4. Illumination at F/18 at 50 degrees—a half angle of 22 percent

This lens, used in an APT camera in a 900 km altitude circular orbit, produces a picture width of 1720 km on each side. Higher orbits may be used in later flights and a 1300 km altitude, for example, could yield a 2485 km picture width. Center-of-the-picture resolutions for an 800 line vidicon are 2.3 and 3 km, respectively, for the two altitudes. Picture overlap in the direction of flight will vary with altitude. Since Nimbus transverses approximately one picture width during the 208 seconds between pictures, overlap is small. The geometry is illustrated in Figure 3.

Computations show that longitude coverage at points on the equator is incomplete. The area of gap is 1140 km at 900 km altitude and 600 km at 1300 km. Farther to the north or south, this gap decreases; it disappears at a latitude of 50 degrees. Optical exposure time is 40 milliseconds which is sufficiently small to avoid smear due to orbital velocity and residual angular velocities of the spacecraft (0.1 degree/sec). The smear is less than 10 percent of one picture element. A vidicon frame scanning time of 200 seconds was selected as compatible

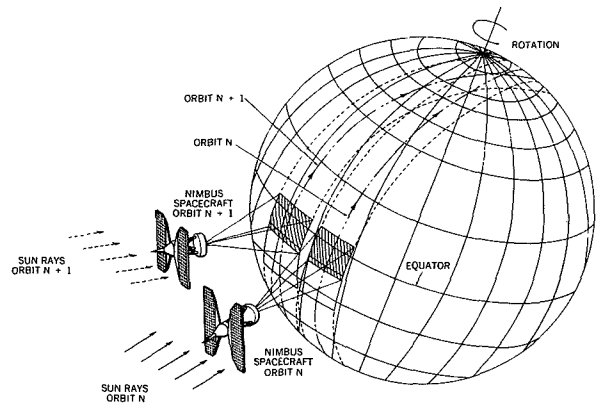

FIGURE 3.—APT picture coverage.

with the standard 240 rpm facsimile record speed, avoiding the need to develop special display equipment. In order to be compatible with facsimile transmission standards, the 2400 cps subcarrier is amplitude modulated and serves as the clock to drive the vidicon deflection circuitry. The subcarrier is modulated to the 80 percent level with white being maximum amplitude (positive modulation). A 3 second start tone followed by a 5 second phasing signal precedes readout.

The subcarrier modulates the frequency of a 136 Mc, 5 watt transmitter, deviating it by ± 10 kc so that receivers with 30 kc IF bandwidth can be used. These receivers then drive standard facsimile equipment for display purposes. Full tonal reproduction can be achieved by a display medium which can resolve 800 elements per line with an aspect ratio of 1:1. Detailed considerations of the RF link will show that a 10 db gain receiving antenna and a receiver having a noise figure better than 7 db provide good quality pictures.

THE PREPARE, EXPOSE, AND DEVELOP CYCLE OF THE STORAGE VIDICON

The operation of the camera can best be explained by describing the operation of the storage vidicon itself. The APT vidicon is a conventional vidicon in which a polystyrene layer has been evaporated on the photoconductive layer. The high resistivity of the polystyrene permits an image to be stored as a distribution of electrostatic charges for a

period of months. The tube therefore performs both the imaging function and the storage function. The charge distribution is created by exposure of the faceplate to light and flooding of the surface with electrons.

Operation of the camera requires the vidicon faceplate to follow an electrical sequence called the prepare, expose, and develop cycle, prior to readout. An equivalent circuit of a small faceplate element is given in Figure 4. As the figure shows, the photoconductor can be represented as an $R_p - C_p$ network. The insulator capacitance C_I and the load R_I are in series with it.

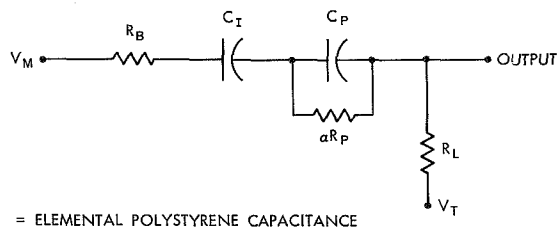

C_I = ELEMENTAL POLYSTYRENE CAPACITANCE
C_P = ELEMENTAL PHOTOCONDUCTOR CAPACITANCE
R_B = BEAM IMPEDANCE
R_L = LOAD RESISTANCE
R_P = PHOTOCONDUCTOR IMPEDANCE
V_M = MESH VOLTAGE
V_T = TARGET VOLTAGE
a = FACTOR INDICATING VARIATION OF ELEMENTAL ILLUMINATION ON PHOTOCONDUCTOR $0 < a < 1$

FIGURE 4.—Equivalent network, APT vidicon faceplate.

The prepare operation is used to change the gunside of the polystyrene to a uniform potential in order to prepare the surface to receive image information. It also erases any residual charge from the preceding picture. During this operation the electron beam and floodlights mounted around the faceplate are turned on and a rapid vertical sweep and normal horizontal sweep are in process. The floodlights are used to raise the conductivity of the photoconductor to a high value. The beam strikes the polystyrene surface ejecting secondary electrons which are attracted to the mesh (G_4—see Fig. 2) until the potential of the mesh and polystyrene are equal. The vertical scan assures that the beam strikes all parts of the polystyrene surface. At the completion of this operation, C_I still retains a net charge across the insulating layer. The floodlight is then turned off, so that R_p assumes a very high value. It is now necessary to transfer the charge from C_I to C_p and this is accomplished by changing electrode voltages appropriately.

During the expose operation the shutter opens and the photoconductor acquires a resistance corresponding to the illumination it receives. In order to maintain a very constant potential the electron beam remains on, and scan is active in both directions. The voltage across the photoconductor capacitance depends on the intensity of illumination at that point.

During the develop operation, the electron beam is off and the floodlights are again turned on. With the electron beam off, the polystyrene voltage cannot change; however, the photoconductor is driven to a low value. Simultaneously, grid potentials are chosen so that the charge pattern is transferred to the polystyrene layer (C_I). It is this charge pattern which is discharged through R_L by the beam during the readout process converting the image to a video signal.

PICTURE QUALITY

C_I and C_P are in the order of picofarads; consequently, the electrical charge is very small. The discharge current, of course, varies inversely with the dwell-time of the electron beam on the target. Since these small variations in beam current are the signal for readout, the beam must be very constant and the discharge time should be chosen as short as possible. These considerations led to pulsed operation of the beam. Conversely, the shorter the pulses, the wider the bandwidth requirement of the preamplifier with an increase in noise power. Empirically it was found that 25 microsecond pulses applied every 208 microseconds (4800 pps rate) to the cathode yield optimum results.

A low noise preamplifier amplifies the pulses and feeds a hold circuit which restores the video signal. Since 800 elements are scanned in 250 milliseconds, a 1600 cps video band is required. The preamplifier, however, must be designed to pass the 25 microsecond pulses and therefore is designed for a 25 kc bandpass. Peak signal

to rms noise ratios of 20 db have been measured on an actual camera. A start code consisting of a 300 cps modulation of the subcarrier (100 percent amplitude) is sent for 3 seconds. Phasing pulses are then sent for 5 seconds at the regular line rate. A black pulse (12.5 milliseconds long) is sent at the beginning of each line. A measure of picture quality is contained in the number of gray levels which the eye can distinguish. This figure of merit depends on both noise and linearity of the system and is expressed as the dynamic range. Although this range exceeds 15 steps in very small areas of the picture and has been achieved in conventional vidicons, the storage vidicons produced so far show large variation over the entire picture area. This property makes brightness calibration of the picture impractical and judgment of relative brightness variations must be exercised. In general, six levels can be distinguished. Figures 2, 5, and 6 show a block diagram of the system and photographs of the camera and transmitter.

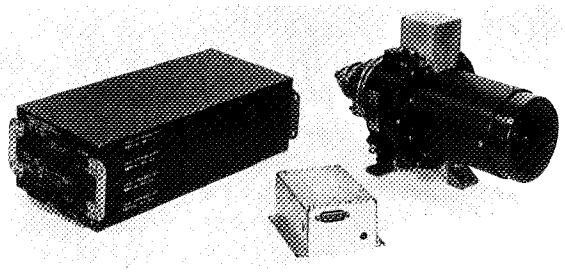

FIGURE 5.—APT camera and electronics.

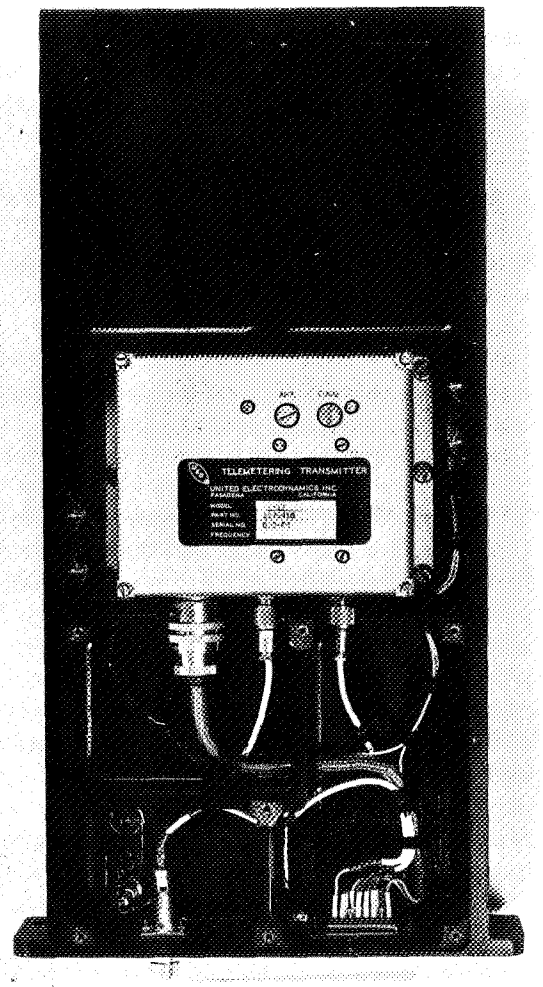

FIGURE 6.—APT transmitter.

COMMUNICATIONS

The APT picture is communicated to an earth station in the space research band of 136–137 Mc. The video output, the turn-on, and the phasing code drive a modulator which amplitude modulates the 2400 cps subcarrier, thus requiring 4000 cps maximum frequency capability. The subcarrier is derived from the Nimbus master clock which is stable to 1 part per million. This stability is more than adequate for conventional facsimile receivers. The VHF carrier is deviated ± 10 kc, and with a 30 kc predetection bandwidth 5 watts must be transmitted from the spacecraft. The transmitter is a standard commercial unit which uses a 128 Mc fifth-overtone crystal oscillator. Modulation is applied to a 9 Mc voltage-controlled oscillator using a capacitor (varicap) as the variable element. A transistor mixer generates the upper sideband which is filtered and amplified in subsequent stages. An output stage designed with two TA2084 transistors operating in parallel develops more than 5 watts. Stability over the operating temperature of the transmitter is better than 0.01 percent and, since pre-aged crystals are employed, it is expected to stay within those limits over its projected lifetime of 6 months. The transmitter radiates through a small quadraloop antenna mounted on the base area of the space-

craft. The antennas have the appearance of a dielectric-loaded, shorted transmission line. Towards the open end of the line a tuning capacitor permits fine tuning. The feedpoint is removed from the shorted end for impedance match. The antennas radiate in a pattern similar to that on a dipole. Since the antennas are mounted on the base area, only small gain can be realized because the spacecraft acts as a reflector influenced by the position of the solar paddles. Figure 7 shows samples of the many patterns measured. Two mutually perpendicular components have been plotted demonstrating that the design objective of a gain larger than 1 was realized with a ± 61 degree cone as measured from the spacecraft symmetry axis. This angular requirement stems from the fact that the horizon-to-horizon angle as viewed from the spacecraft is 122 degrees for a 1000 km altitude. Polarization components range from circular to linear and are dependent on the position of the solar panels. For the worst case of receiving station design, the best assumption is that the spacecraft antenna has a gain of 1 and emits a linearly polarized wave. Circular components emitted have right-handed polarization. In most cases ground reception below horizon angles of 10 degrees will not be practical. However, for design purposes the horizon distances of 4260 and 3480 km for the two altitudes mentioned should be considered. Path losses up to 148 and 146.2 db, respectively, are encountered. A ground receiving antenna having a gain of 10 db would receive -134 and -132 dbw for the two ranges.

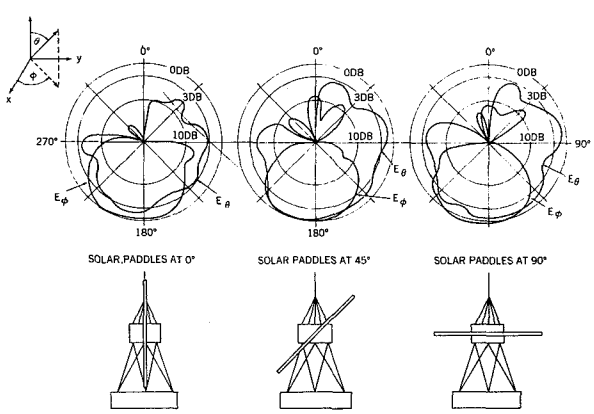

FIGURE 7.—Antenna pattern.

RECEIVING EQUIPMENT

The remaining parameters which determine the quality of the received picture depend heavily on the equipment chosen by an individual user. A set of ground equipment which is actually being used in various combinations at different locations is discussed here. In general, a helical receiving antenna yields good circularity with 10 db gain or better. The wide receiving angle avoids the necessity for autotrack. However, an azimuth and elevation pointing capability is necessary for effective use of the available transmission time.

Sky temperature at 136 Mc varies greatly, but is averaged over the wide antenna beam. A sky temperature of 1000 °K can be expected around a wide angle centered approximately at the celestial equator.[2] However, users with more favorable celestial geometry can use receivers with higher noise figures. For the overall system a temperature of 1400 °K can be assumed when a high quality preamplifier is employed. Preamps are available with noise figures of 3 to 6 db. The resulting carrier to noise ratio exclusive of the vidicon would be approximately 20 db. It is clear that this signal is at the threshold and postdetection signal-to-noise ratios of 30 db can be obtained from a variety of equipment. Mobile communication receiver equipment can be adapted for this application with only minor modifications. Noise properties of this type of equipment are higher than can be achieved, but operation can be satisfactory. As mentioned before, receiver output must be fed to a suitable facsimile recorder. Photographic and wet electrolytic papers are available on a variety of equipment. The four types in use at the present time will be described briefly.

FACSIMILE EQUIPMENT

The Westrex Model 3030 TP is a photographic-type recorder designed for automatic turn-on and phasing. It remains synchronized over the duration of a frame through the use of a stable tuning fork oscillator. Polaroid

[2] Ko, H.C., "The Distribution of Cosmic Radio Background Radiation," *Proc. IRE* 46(1): 208–215, January 1958.

film or paper can be exposed and both are available for immediate use. The use of appropriate paper permits a 70 mm picture to be inspected within 10 seconds. The light transducer is an R–1168 readout tube which illuminates an oscillating mirror for line scan. The scanning voltage driving this mirror is coherent with the paper or film advance drive moving the medium continuously.

The Muirhead D700S is a photographic-type facsimile recorder. Eight inch film is wound around a drum which has a scanning speed of 240 rpm. The light transducer and optic are driven across the film at a synchronous speed providing the line advance. Automatic turn-on and phasing are provided and can be monitored.

Electrolytic paper recorders are less critical and more rugged in their operation, simpler in maintenance and less costly. On the other hand the quality of the picture presentation is poorer than in the photographic units. The moist paper is driven by and pressed against a rotating cylinder. The cylinder contains a metallic, single turn, helical bar which provides one point contact between paper and cylinder. By turning the cylinder and advancing the paper, successive lines can be drawn on the paper. The electrolyte blackens in proportion to the current sent through it (actually in proportion to the current density for a small constant picture element), so that the moist paper and the cylinder alone are part of the video output circuit. Approximately 10 gray scales can be achieved with these machines. The Muirhead D900S and Fairchild Scan-a-fax are in use at the present time, the latter being used in APT ground stations now being installed throughout the world. A small modification of both is needed to obtain an aspect ratio of 1.

Figure 8 shows a comparison of picture quality. The original photograph, a photographic presentation reproduced by the Muirhead D700S, and a paper reproduction from the Fairchild Scan-a-fax are shown. Figure 9 pictures the manually controlled APT ground station and Figure 10 the antenna. Both of these were built for the NASA by the Fairchild Stratos Corp.

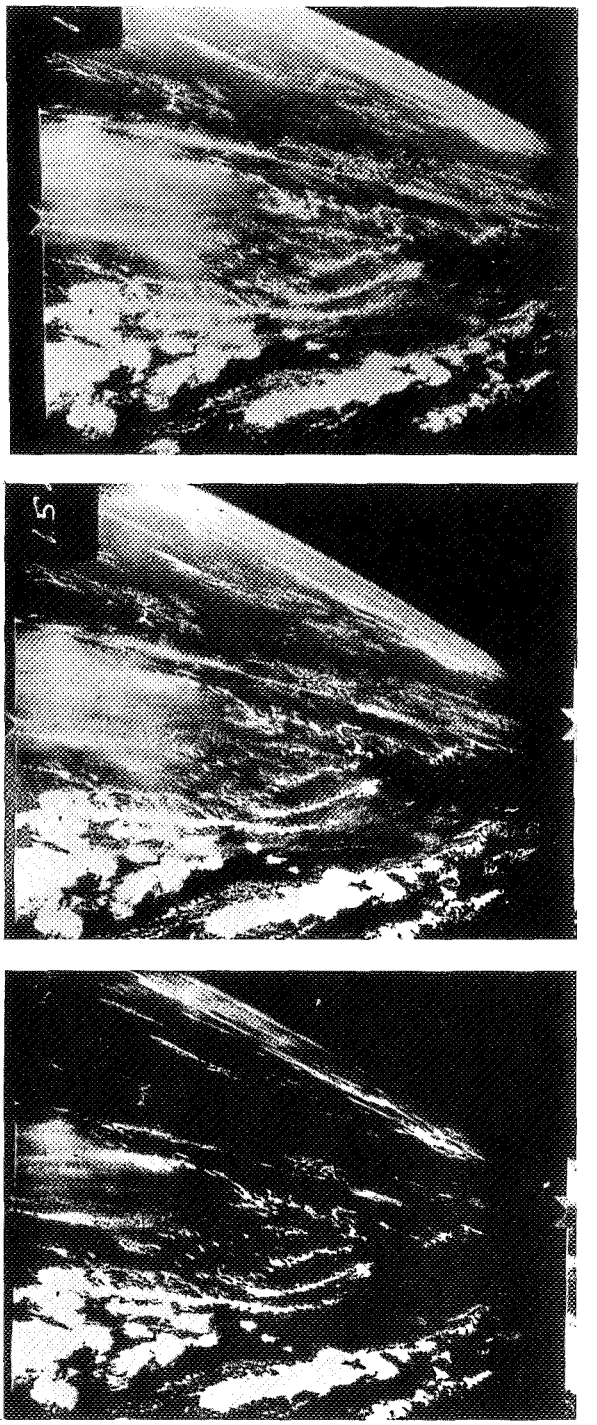

FIGURE 8.—An original cloud photograph taken from a high altitude rocket and reproductions from the Muirhead D700S and Fairchild Scan-a-Fax.
(a) Original Cloud Photograph
(b) Muirhead D700S
(c) Fairchild Scan-a-Fax

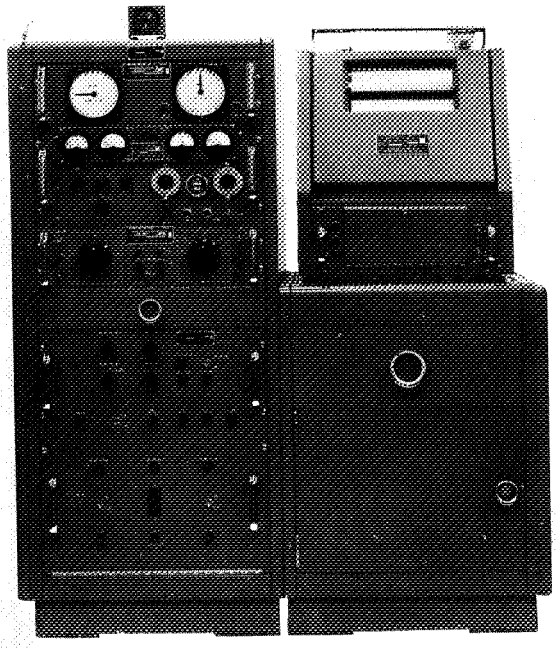

FIGURE 9.—Photograph of the APT ground station showing antenna position indicators, receiver, antenna controls, facsimile calibrator, and power supply on left; facsimile is on right.

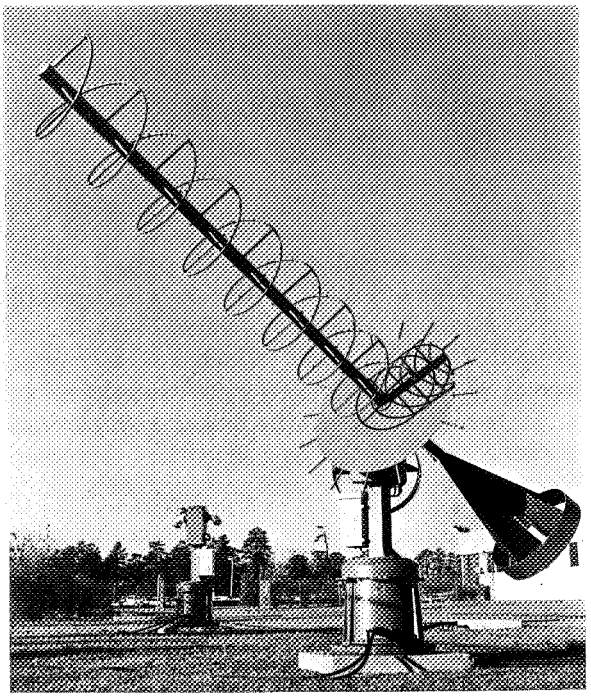

FIGURE 10.—The APT antenna.

A VACUUM ULTRAVIOLET PHOTOIONIZATION DETECTOR

A. K. STOBER, R. SCOLNIK, AND J. P. HENNES
Goddard Space Flight Center

A small ceramic ion chamber has been developed for a rocket astronomy program in the vacuum ultraviolet. The chamber consists of a small metal-plated ceramic shell incorporating a window of LiF, CaF_2, or BaF_2 and containing a filling gas of nitric oxide, acetone, carbon disulfide, or others. Typical quantum yields range from 8–10 percent for acetone with CaF_2 window to 50–60 percent for carbon disulfide with LiF window. Details of the chamber construction are given, and some recent applications of the detector are described.

INTRODUCTION

As part of a continuing program of observations of astrophysical and geophysical quantities in the vacuum ultraviolet wavelength region a small ceramic photionization chamber has been developed at the Goddard Space Flight Center. These ion chambers, intended primarily for photodetection in the 1500 Å to 1050 Å wavelength region, have proved useful in a space science program which has included rocket- and satellite-borne experiments designed to measure both solar and stellar fluxes, as well as upper atmospheric emissions.

Ion chambers and photon counters were first used in a series of rocket experiments carried on at the Naval Research Laboratory in the 1950's. The literature contains several accounts of these vacuum ultraviolet detectors(*1,2*), and the experimental results obtained from their use(*2–5*). When the space science program at Goddard Space Flight Center was established in 1959 the experience gained from use of these earlier photoionization detectors was employed to design the present chamber. A brief description of the NASA ion chamber appears in a review of current ultraviolet photodetector developments by Dunkelman(*6*).

DESIGN DETAILS

Gas ionization photodetectors have the useful properties of high spectral selectivity and relatively high quantum efficiencies. They can also be made very rugged and very compact. If meticulous attention is given to a number of fabrication details(*7*), the NASA ionization chamber has the capability of having a long "shelf life," and of having the low noise and the stability needed for measuring very small incident photon fluxes (100–1000 photons/sec). Specifically electrical leakage between electrodes must be minimized—a 10^{15} Ω path is easily achieved; photoelectric emission from the chamber walls must be reduced; recontamination of the filing gas after purification must be avoided; and window and connector seals must hold a high vacuum—better than 1×10^{-6} torr. The NASA ion chamber, Figures 1 and 2, was designed to satisfy these requirements.

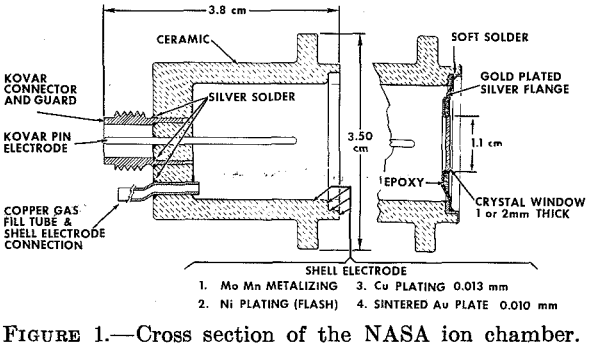

FIGURE 1.—Cross section of the NASA ion chamber. The inside diameter of the chamber is 1.9 cm and length 2.3 cm. Window materials are generally of LiF, CaF_2, or BaF_2 crystals.

764–173 O—65——39

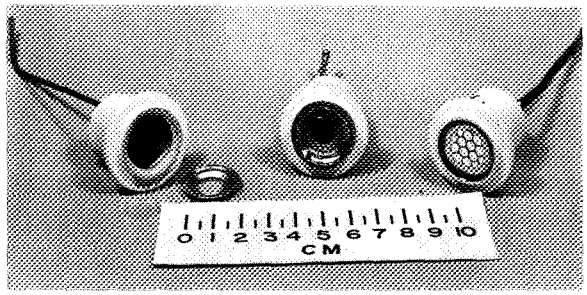

FIGURE 2.—Three of the ceramic ion chambers. At left is an unfinished chamber with window and flange. In the center is a completed tube. At right is a tube with a thin aluminum window for X-ray use.

The chamber consists of a ceramic shell, gold-plated on the inside, fitted with a highly polished central collecting wire electrode and incorporating a window of suitable transmission properties. The shell, which has an external lip to provide a surface for making an O-ring seal into either the exit port of a vacuum monochromator or the skin of a rocket or satellite package, is usually fitted with an 11-mm diam crystal window and has an inside diameter of 1.9 cm and an inside length of 2.3 cm.[1]

The ceramic shell[2] itself is of a high density alumina and is plated on the inside with several layers of metallic coatings, finishing with a gold plate on the surface, to form one of the electrodes. Brazed into the unplated rare face of the tube are a kovar central pin electrode, a guard-ring and connector and a 10-cm long, copper, gas-filling tube which also provides the electrical connection to the metal-plated shell electrode.

The ion chamber window, usually consisting of 1- or 2-mm thick cleaved crystals of LiF, CaF_2, or BaF_2, is fastened to a thin gold-plated silver flange by an epoxy layer. The flange, whose 9.5-mm diam defines the aperture of the chamber, is soft-soldered onto the metalized ceramic shell prior to forming the window seal. The sealed tube is baked at 100°C for several hours. The assembled chamber is evacuated through the copper, gas-fill tube, while being heated to 100°C, until a pressure of 1×10^{-6} torr or less is reached. The filling gas, which has previously been distilled from a supply of commercial "pure" gas, is admitted through the tube, and the chamber sealed by pinching the copper tube closed and dipping the tube end in solder.

The choice of the ceramic chamber ensures the ruggedness and low-electrical leakage desired and provides a surface which is resistant to contamination. The gold plating on the chamber walls provides both a conducting surface with low-photoelectric emission and a high work function (*8*), and one that will not react with any of the chemicals used as filling gases. In addition, by keeping the entrance window small and leaving the rear wall of unplated ceramic (except for the center pin, guard ring, and gas-filling tube), the amount of photoemissive surface exposed to the incident flux is kept to a minimum. The epoxy, soft-solder window seal has proved very tight and, since high-temperature baking is not required, quite stable over long periods of time. The general success of these design features can be demonstrated by the almost zero rejection rate which has been achieved in assembly of chambers and by the existence in our laboratory of ion chambers assembled almost 2 years ago which still maintain their quantum yields. A single exception appears to be a diethyl sulfide ion chamber with barium fluoride window. These chambers have a spectral bandpass from 1350 to 1480 Å and an efficiency approaching 20 percent, but the few detectors made have had a shelf life of little more than one month. The investigation of gas purification and anti-recontamination is in the early stages of attempting to increase the "shelf life" of this detector.

The short wavelength limit of the spectral response of these chambers is usually determined by the transmission cutoff of the window materials. In addition to the LiF, CaF_2, and BaF_2 crystals mentioned above, windows of NaF or sapphire may also prove useful. The transmittance curves of these materials are

[1] Ceramic ion chambers of this design are now commercially available from the Geophysics Corp. of America, Bedford, Mass., and Melpar, Inc., Falls Church, Va.

[2] Manufactured by the Coors Porcelain Co., Golden, Colo.

included in a paper by Dunkelman et al. (*9*). Also used with these ceramic ion chambers have been windows of thin (0.03–0.2 mm) foils of aluminum and beryllium. When used with a filling gas such as xenon these ion chambers become useful X-ray detectors in the 2–8 Å region. Window materials and filling gases for use in either the vacuum ultraviolet or X-ray region have been tabulated by Friedman (*2*).

Pictured in Figure 2 are some of the chambers discussed herein. At the left is an unfinished shell with a window flange and LiF window. In the center is a completed ion chamber and at the right one of the X-ray chambers mentioned above.

DETECTOR CHARACTERISTICS

In normal use the ceramic ion chamber is operated with the guard ring at ground potential and the shell electrode at −45 to −90 V, depending on the gas filling. When is is necessary to suppress photoelectric emission from the walls completely, the shell electrode is operated at a positive potential. In many applications, however, the available flux is so exceedingly small that is necessary to operate these tubes as gas-gain detectors. If the collecting voltage is raised past the low-voltage plateau region the output current increases in an exponential fashion. Gains of 1000 are generally attainable with voltages of 600 to 800 V. The shell electrode carries the negative high voltage in this case.

A variety of filling gases have been used with these tubes. The choice of the gases is determined by the spectral region of experimental interest and, of course, it fixes the long wavelength cutoff. The stability of the gas when incorporated in an ion chamber determines whether any specific gas can make a useful detector. Figure 3 shows the spectral response of five of the gas-window combinations which have been used in ion chambers in rocket-borne experiments by Goddard Space Flight Center. The curves represent smoothed values of quantum-yield as measured on a McPherson 1-m vacuum monochromator operating with a resolution of 3–4 Å. Some of the fine structure of nitric oxide is shown in curve 3 but most of the details do not appear (*10–12*). Of particular interest are the relatively narrow response bands and the fairly high, quantum-yields. The measured quantum-yield of any given chamber is a combination of the actual photoionization yield of the gas, the transmittance of the window, the absorption efficiency, and ion collection efficiency of the chamber.

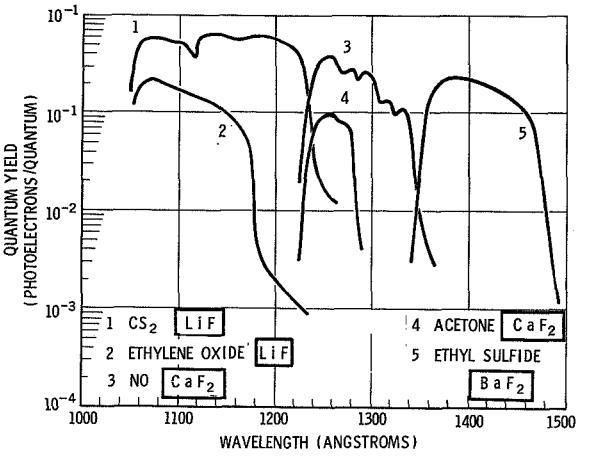

FIGURE 3.—Typical ion chamber spectral response curves for several gas and window combinations. Smoothed curves are shown although a certain amount of fine structure is obscured in so doing: 1. Carbon disulfide with LiF window; 2. ethylene oxide with LiF window; 3. nitric oxide with CaF_2 window; 4. acetone with CaF_2 window; 5. diethyl sulfide with BaF_2 window.

Table I lists some of the gas and window combinations used in our space science program and gives some of the most pertinent features of these ion chambers.

CALIBRATION

The shape of the spectral response curves are determined by a comparison of the ion chamber response to a hydrogen arc lamp with the response of a sodium-salicylated detector to the same lamp. The fluorescence yield of sodium salicylate is assumed to be fairly constant over this wavelength region from 1500 Å to 1000 Å (*13*). Measurements were made at the exit slit of the 1-m vacuum monochromator mentioned above. Absolute quantum-yield values were determined by a direct comparison of the signal from the ion chamber

TABLE I.—*Typical NASA Ion Chamber Characteristics*

Gas filling	Chemical formula	Gas pressure (torr)	Window material	Window thickness (mm)	Spectral response region (Å)	Typical quantum yields [1] (photoelectrons/photon)
Diethyl sulfide	$(C_2H_5)_2S$	5	BaF_2	1	1350–1480	0. 10–0. 2
Nitric oxide	NO	20	CaF_2	1	1230–1350	0. 20–0. 3
Nitric oxide	NO	20	LiF	1	1050–1350	0. 30–0. 4
Acetone	CH_3COCH_3	4. 5	CaF_2	1	1230–1290	0. 08–0. 1
Carbon disulfide	CS_2	15	LiF	1	1050–1240	0. 50–0. 6
Ethylene oxide	$(CH_2)_2O$	4. 5	LiF	1	1050–1180	0. 10–0. 2
Xenon	Xe	775	Be	0. 13	2–8	Not measure

[1] Based on an absolute photoionization yield of 0.81 ion pairs/photon for NO at Lyman-alpha.

in question, when exposed to Lyman-alpha (1216 Å) radiation, with the signal from a reference "standard" ion chamber (*7*) exposed to the same beam. The reference ion chamber is a large volume, windowless, glass cylinder containing large, flat, plane-parallel collecting electrodes for both efficient absorption of the incident flux and efficient collection of the ion-pairs produced. The electrodes are rigidly mounted to avoid vibration pickup.

Calibration of the ion chamber quantum-yields are based on the absolute photoionization-yield of nitric oxide (NO) at the Lyman-alpha wavelength (1216 Å). From the work of Watanabe (*14*) this yield is taken to be 0.81 ion-pairs/photon. The flat sodium salicylate response is used to transfer the quantum-yield measurements from Lyman-alpha to other wavelengths when the efficiency of the gas being measured is required for wavelengths other than Lyman-alpha.

APPLICATIONS

The NASA ceramic ion chambers were first used successfully in the spring of 1960 in a series of Aerobee-Hi rocket experiments designed to survey the northern night sky (*15*). Ion chambers containing nitric oxide, acetone, or carbon disulfide were positioned at the foci of 10-cm diam collecting mirrors which scanned the sky as the rocket rolled and precessed. Because of the weak signals expected from stellar sources the ion chambers were operated with gas gains of about 200. The signals observed were on the order of 10^{-12} A with this system, indicating a flux of abou 10^{-7} ergs/sec cm^2.

In August–November 1961 a similar surve of the southern hemisphere night sky wa obtained from a series of Skylark rocket firing from Woomera, Australia (*16*). A single rocke carried four ion chamber telescopes, eac consisting of two chambers located alongsid one another at the focus of a 15-cm dian mirror. Useful signals were obtained fron about 60 stars with the ion chambers operatin at gains of 300–500.

Figure 4 shows three seconds of a typica telemetry record from this flight. The to and bottom channels represent middle ultra violet photomultiplier photometers. The mid dle channel gives the signal from an io chamber telescope. The difference in nois level of the two types of detector is evident The three double-peaked ion chamber signal represent the sweep of the ion chamber tele scope across three stars as the rocket slowl turned. The asymmetry of the right and lef parts of each double-peak is produced by th off-axis location of the ion chambers, whic causes the effective mirror aperature to chang as the star moves across the field of view The double-peak itself is a function of the posi tion of the highly convergent beam in the io chamber cavity. When the ion chamber i operated in a collimated beam the angula response to a point source is more or less flat topped. When the chamber is operated in highly focused beam the central region of th telescope angular response signal may be de

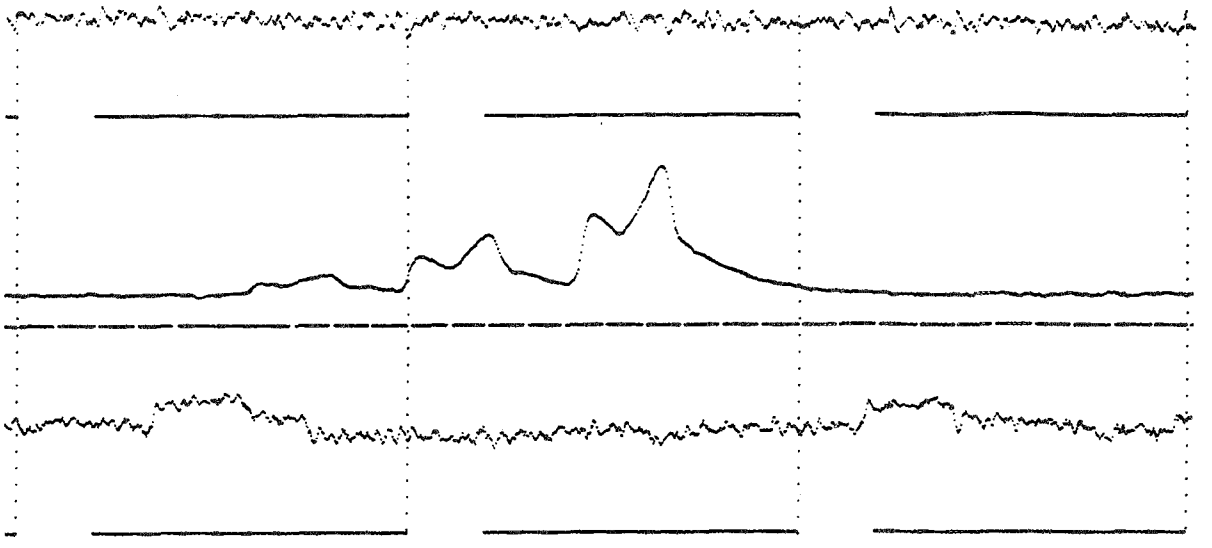

'IGURE 4.—Telemetry record showing a 3-sec portion of several detector signals; the top and bottom channels are signals from photomultiplier photometers; the middle channel is the signal from an ion chamber telescope. The difference in detector noise levels is evident. Three double-peaked ion chamber star signals are shown. The unsymmetrical shape of these star signals in levels is evident. Three double-peaked ion chamber star signals are shown. The unsymmetrical shape of these star signals is caused by telescope geometry (see text).

ıressed by as much as 75 percent. The choice f focus conditions presents different problems /hich the experimenter must resolve for himself.

More recently these ion chambers have been sed in the Orbiting Solar Observatory, ıunched in March 1962, to observe the sun in wo wavelength regions. One ion chamber, of itric oxide with a LiF window, periodically bserved the solar Lyman-alpha emission :om behind an aperture of about 0.4-mm diam. 'wo others, operated in parallel with 0.13-mm hick beryllium windows and xenon gas, con- ınuously measured the sun's X-ray emission ı the 2 Å to 8 Å region. Other current uses ıclude a rocket-borne ion chamber for meas- rement of the Lyman-alpha radiation emitted :om the top of the earth's atmosphere and a yman-alpha detector in an ionosphere probe ɔ measure the rate of photoionization in the) region.

Perhaps the most important use for these etectors is as stable vacuum ultraviolet photo- etectors for laboratory purposes. By com- ining the simple physical principles of gas ɔnization with a vacuum-tight and stable hamber a very useful reference standard for ıboratory spectroscopy can be obtained.

The basic ion chamber design was suggested by J. E. Kupperian, Jr., the use of a ceramic shell was suggested by E. V. Serra, the choice of an epoxy was suggested by W. A. Gallo, Jr., and E. V. Serra assisted in the development of the epoxy window sealing technique.

REFERENCES

1. Chubb, T. A. and Friedman, H., Rev. Sci. Instr. 26, 493 (1955).
2. Friedman, H., in *Physics of the Upper Atmosphere*, J. A. Ratcliffe, ed. (Academic Press, New York, 1960), Chap 4.
3. Byram, E. T., Chubb, T. A., Friedman, H., and Kupperian, Jr., J. E., in *Threshold of Space*, M. Zelikoff, ed. (Pergamon Press, London, 1957), pp. 203–210.
4. Kupperian, Jr., J. E., Boggess III, A., and Milligan, J. E., Astrophys. J. 128, 453 (1958).
5. Byram, E. T., Chubb, T. A., Friedman, H., Kupperian, Jr., J. E., and Kreplin, R. W., Astrophys. J. 128, 738 (1958).
6. Dunkelman, L., Quant. J. Spectry. & Radiative Transfer 2, 533 (1962).
7. Stober, A. K., "Ceramic Vacuum Ultraviolet Ion Chambers," NASA Tech. Note TN D–1180 (March 1962).
8. Childs, C. B., J. Opt. Soc. Am. 51, 583 (1961).
9. Dunkelman, L., Fowler, W. B., and Hennes, J. P., Appl. Opt. 1, 695 (1962).

10. WATANABE, K., MARMO, F. F., and INN, E. C. Y., Phys. Rev. 91, 1155 (1953).
11. MARMO, F. F., J. Opt. Soc. Am. 43, 1186 (1953).
12. WATANABE, K., J. Chem. Phys. 22, 1564 (1954).
13. WATANABE, K., and INN, E. C. Y., J. Opt. Soc. Am. 43, 32 (1953).
14. WATANABE, K., revision of earlier value of 0.85 ion-pairs/photon (private communication).
15. BOGGESS, III, A., in *Space Astrophysics*, W. Liller, ed. (McGraw-Hill, New York, 1961), Chap. 7; BOGGESS, III, A., MILLIGAN, J. E., and STECHER, T. P. (private communication).
16. BOGGESS, III, A., SCOLNIK, R., and WINDSOR, R. M., (private communication); also R. M. WINDSOR, "The Southern Sky Survey Payload," NASA Technical Note D-1719 (February 1963).

ULTRAVIOLET OPTICAL PROPERTIES OF DIAMOND[1]

W. C. WALKER[2] AND J. OSANTOWSKI
University of California

The absolute reflection spectrum of type IIa diamond was measured at room temperature from 4 to 30 eV and analyzed by dispersion techniques to obtain the optical parameters. Structure observed in the dielectric constant near 7, 12, 16, 20, and 24 eV was attributed to interband transitions at critical points in the joint density-of-states function. The new high-energy structure near 16, 20, and 24 eV was assigned to transitions near the L point of the Brillouin zone. Experimental interband transition energies are compared to band theory calculations.

INTRODUCTION

Considerable progress has been made recently in our understanding of the detailed physics of tetrahedrally coordinated solids through the comparison of band structure calculations[3] and experimental ultraviolet optical properties.[4] These studies have shown in some detail the similarity in band structure of Ge, Si, and the group III–V compound semiconductors. To a lesser extent this similarity has been shown to extend to certain of the group II–VI compounds. Diamond, the simplest of all tetrahedrally coordinate solids because of its extremely small core composed only the completed $1S$ shell has, however, not received the attention necessary to place it on the same basis as the others of its class in spite of the fact that extensive band calculations were carried out several years ago by Herman[5] using the orthogonalized plane-wave method. Herman's calculations were subsequently shown to be nearly self-consistent by Kleinman and Phillips.[6]

With the exception of a single recent paper by Philipp and Taft,[7] no experimental verification of these calculations has been made for energies greater than that corresponding to the lowest lying transition. In view of the fundamental role of diamond in solid-state physics and the recent interest in its semiconducting form, such verification is desirable.

The present paper reports measurements of the absolute reflection spectrum of a polished, type IIa diamond for the region 4 to 30 eV. Dispersion relation analysis of the reflectivity was used to obtain the complex dielectric constant as well as the optical constants n and k. The improved purity of the diamond specimen employed and increased resolution for energies above 12 eV have lead to significant new high-energy results.

MEASUREMENTS AND ANALYSIS

The absolute reflection spectrum, between 4 and 30 eV of a polished specimen of type IIa diamond[8] was measured at room temperature

[1] Work supported by the National Aeronautics and Space Administration.

[2] Currently at Goddard Space Flight Center under a NASA Post-Doctoral Fellowship (on leave from the Physics Department, University of California, Santa Barbara, Calif.).

[3] J. C. Phillips, Phys. Rev. 125, 1931 (1962).

[4] H. Ehrenreich, H. R. Philipp, and J. C. Phillips, Phys. Rev. Letters 8, 59 (1962).

[5] F. Herman, Phys. Rev. 93, 1214 (1954).

[6] L. Kleinman and J. C. Phillips, Phys. Rev. 116, 880 (1959); *ibid.* 125, 819 (1962).

[7] H. R. Philipp and E. A. Taft, Phys. Rev. 127, 159 (1962).

[8] The type-IIa diamond, a rectangular parallelipiped measuring $1.09\times2.98\times4.96$ mm and weighing 0.28 carat was graciously supplied by Dr. F. A. Raal of the Diamond Research Laboratory, Crown Mines, Johannesburg, South Africa.

and at a fixed angle of incidence of 20°. The absolute accuracy of the reflectivity was determined mainly by the experimental scatter which amounted at most to 5 percent in the region between 12 and 20 eV. Both below and above this region the absolute accuracy of the data was about 3 percent and the relative accuracy somewhat better. Averaging of several independent measurements allowed structure amounting to 1 or 2 percent to be determined.

A Jarrell-Ash one-half meter Seya monochromator was used with a bandpass ranging from 3 to 6 Å giving an energy resolution between 0.005 and 0.1 eV depending on the spectral region involved. In the important region between 12 and 20 eV the maximum spacing between source emission lines was 0.7 eV and was more typically of the order of 0.2 eV or less. Reflectivities were determined at approximately 130 points.

A dc discharge in hydrogen at a pressure of a few tenths Torr, operated at 100 V and 350 mA provided a usable continuum extending through the near ultraviolet to 7 eV and a many-lined molecular spectrum from 8 to 12 eV. A Weissler [9] spark source in argon operated at a repetition rate of 60 pulses/sec and at 8 kV provided a sufficiently constant and dense spectrum between 12 and 30 eV to enable the measurements to be performed. Emission lines of multi-ionized oxygen, nitrogen and argon constituted the bulk of the usable radiation in this region. The intensity of the spark source varied between 1 and 5 percent depending on the emission line used and for many points it was necessary to rely on averages of incident intensities, bracketing a reflection spectrum, to achieve the desired accuracy.

Reflection measurements were made with a vacuum reflectometer which utilized a fixed photomultiplier and a rotatable, fluorescent sensitized light pipe to monitor the incident and reflected beams. Care was taken to keep the optical path of the incident and reflected light identical and to eliminate scattered radiation. The phosphor-light pipe combination discriminates strongly against scattered light and is an excellent detector for reflection and transmission studies.

A dispersion relation analysis was performed on the final reflection spectrum using the Western Data Processing Center's IBM–7094 and a modified version of a program originally written by Nodvik and Greenstreet. To increase the accuracy of the data below 5.5 eV for this analysis, the reflection data were matched to values calculated from published indices of refraction near 3.1 and 5.5 eV.[10] Beyond 27.7 eV the reflection data were extrapolated to 100 eV at 0.2-eV intervals by matching the measured values to a decaying power-law function. The numerical integration for the phase angle of the reflected amplitude was cut off at 100 eV and an extrapolated reflectivity of the order of 0.1 percent.

RESULTS

Reflectivity data averaged from several separate measurements are shown in Figure 1.

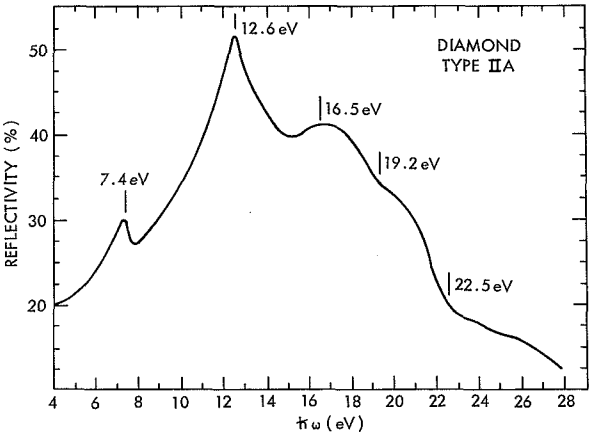

FIGURE 1.—Reflection spectrum of diamond.

Peaks are observed at 7.4, 12.6, and 16.5 eV and inflection points leading to shoulders are seen at 19.2 and 22.5 eV. Comparison to the only other spectrum measured over this region, that

[9] N. Wainfan, W. C. Walker, and G. L. Weissler, J. Appl. Phys. 24, 1318 (1953).

[10] *Handbook of Chemistry and Physics* (Chemical Rubber Publishing Company, Cleveland, Ohio, 1960), 42nd ed.

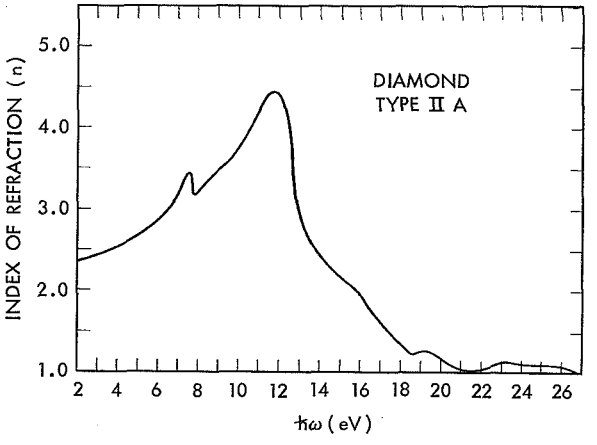

FIGURE 2.—Spectral dependence of the index of refraction (n) of diamond.

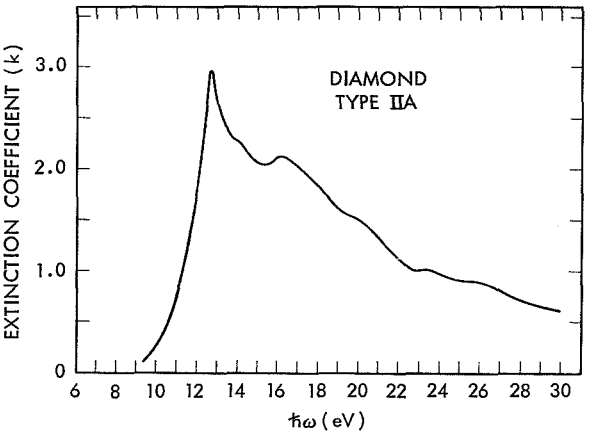

FIGURE 3.—Spectral dependence of the extinction coefficient (k) of diamond.

of Philipp and Taft,[5] shows agreement below 12 eV. At higher energies the present results display more structure. The lack of agreement above 12 eV may be explained by the higher purity of the specimen used in the present work (type IIa rather than type I) and the increased resolution resulting from the more dense emission spectrum employed. Typical type I diamonds are known to have a high concentration (10^{20} atoms/cm^3) of dissolved nitrogen.[11] Absorption of this substitutional atomic nitrogen, particularly in the ionization continuum beginning at 14.5 eV,[12] could perhaps account for some of the difference. The maximum reflectivity value of 52 percent at 12.6 eV is below the 61 percent value at 12.5 eV observed by Philipp and Taft. Reflectivity values below 5.6 eV were calculated from published values of n. This procedure was necessary since the measured reflection curve showed a sudden jump at 5.6 eV due to reflections from the rear surface of the crystal. This indicates that the onset of the indirect transition $\Gamma_{25}' \rightarrow \Delta_1$ occurs at 5.6 eV in agreement with previous results.[5]

Values for the index of refraction n and the extinction coefficient k obtained from a dispersion analysis of the data of Figure 1 are shown in Figures 2 and 3, respectively. Both n and k differ somewhat from those obtained by Philipp and Taft, as would be expected from the differences in the high-energy reflection data. The most significant differences are the smaller values for k below 12 eV and the large peak in n at 12.6 eV in the present work. Both of these differences may be attributed to the increased purity of the type-IIa specimen used in the present study over the type-I specimen studied by Philipp and Taft. It is well known, for instance, that type I diamonds display a broadened and enhanced absorption between 5 and 6 eV. Even though the substitutional nitrogen impurity of type I diamonds may amount to 4×10^{20} atoms/cc, the additional absorption due to the impurity is insufficient to account directly for the differences noted except in the immediate vicinity of the first absorption edge. It seems more likely that the present differences are due rather to the distortion of the lattice produced by this high concentration of impurities. In this regard Kaiser and Bond[9] report a relative change in lattice constant of up to 10^{-4} between type-I and type-II specimens.

It will be noted that the structure in the reflectivity curve near 7 eV shows up as a peak in n but is absent in k. This can be explained by the fact that the magnitudes of the k values in this region are of the order of 0.2 or less. Such small values are not accurately given by

[11] W. Kaiser and W. L. Bond, Phys. Rev. 115, 857 (1959).

[12] A. W. Ehler and G. L. Weissler, J. Opt. Soc. Am. 45, 1035 (1955).

the dispersion analysis. The k values are proportional to the sine of the imaginary part θ of the reflected amplitude. Thus as θ approaches zero, small errors accumulated in the dispersion inversion become magnified and may even cause meaningless negative values of k to appear. This situation does not occur in the calculation of the index so that accurate values of n can be obtained at small energies. It was found that the k values near the first absorption band were very sensitive to the extrapolation technique employed. For the reason mentioned above it was not practical to adjust the extrapolation to yield accurate k values for small energies. Instead the extrapolation was chosen in such a way that the n values agreed with published values near 2 eV and so that the calculated values of n and k were internally consistent.

The correlation of the reflection peaks with basic mechanisms is shown more directly by the real (ϵ_1) and imaginary (ϵ_2) parts of the dielectric constant. These parameters derived from well-known relations connecting them to n and k are shown in Figure 4. As is the case with n and k the values of ϵ_1 and ϵ_2 differ somewhat from those of Philipp and Taft.[5] It can be shown that the energy loss per unit volume of the radiation passing through the solid is proportional to $\epsilon_2\omega$. Thus, peaks in ϵ_2 correspond directly to the positions of interband transitions. The present results show three definite transitions at 12.6, 16.0, and 20.0 eV together with an indication of an additonal one near 24 eV. The 7.4-eV reflection peak, although due to a direct interband transition, fails to show up strongly in ϵ_2 for the reason mentioned earlier in the description of the curve for k. It is clear from Figure 4 that the reflection peak at 7.4 eV is associated with a maximum in ϵ_1, that at 12.6 eV is due to simultaneous maxima in ϵ_1 and ϵ_2, and the higher peaks are due almost entirely to structure in ϵ_2.

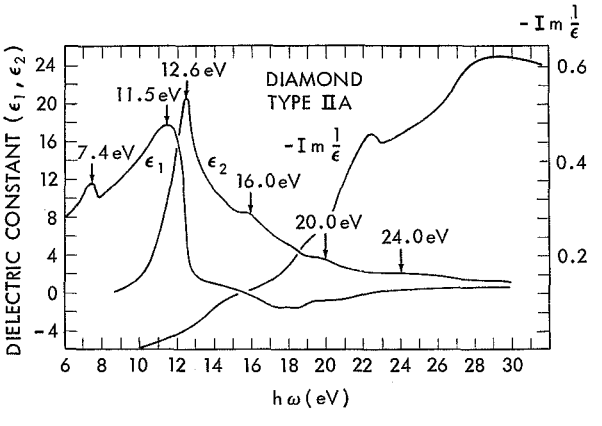

FIGURE 4.—Spectral dependence of the real part (ϵ_1) and the imaginary part (ϵ_2) of the dielectric constant of diamond.

The energy loss function—Im $1/\epsilon$ is shown also in Figure 4. Although insufficient electron energy loss data for diamond exists to justify a detailed comparison, certain features of this curve are of interest. The broad peak near 30 eV, while it cannot be taken too seriously due to the sensitivity of the dispersion analysis at energies above 27 eV to the arbitrary extrapolation employed, at least indicates an electron-plasma frequency of this magnitude. This should be compared to the free-electron plasma frequency $\omega_p \simeq 31$ eV calculated on the basis of four free electrons per atom. It is also interesting that a prominent energy loss in carbon at 22 eV coincides with the 22.5-eV peak in the energy loss function.

DISCUSSION

In view of the special status of diamond among the covalent bonded solids it is of interest to compare the results of the preceding section with the general behavior of the optical properties of Si, Ge, and the III–V compounds. In a recent paper, Philipp and Ehrenreich [13] show that tetrahedrally bonded semiconductors have quite similar optical behavior. They point out that the spectral dependence of the dielectric constant divides naturally into a region governed by valence to conduction-band transitions and a region governed by the electron plasma oscillation. In those materials possessing d electrons a third region involving transitions originating in the d band occurs. The dielectric constant reflects these regions by displaying a strongly structured behavior with peaks and shoulders

[13] H. R. Philipp and H. Ehrenreich, Phys. Rev. **129**, 1550 (1963).

corresponding to the various interband transitions followed by a significant decrease as the interband oscillator strengths become saturated. The dielectric constant then begins to behave much like that for an ideal plasma given by $\epsilon_1 \simeq 1-(\omega_p/\omega)^2$, ($\omega_p$ is the plasma frequency) until d-band transitions force it to peak once more. Figure 4 shows that a similar situation occurs in diamond. Because the plasma frequency of diamond is large (30 eV) and the $1S$ core electrons are very strongly bound, the optical properties of diamond are governed solely by valence band transitions. Thus, the peaks in ϵ_1 at 7.4 and 11.5 eV and in ϵ_2 at 12.6, 16.0, 20.0, and 24 eV correspond to interband transitions between bands displaying critical points in the joint density of states function as described by Brust, Phillips, and Bassani.[14] The evidence for a 9-eV transition derived by Philipp[5] by considering the 12.6-eV transition as due to an ideal oscillator appears from the present work no longer valid.

By using as guides, estimates of oscillator strengths for various transitions, the "insensitivity" [3 15] of certain transitions to shifts in the core energy and certain crystal selection rules it is possible to make a tentative identification of the above transitions. Thus, in agreement with Philipp and Taft,[7] we can assign the 7.4-eV transition to $\Gamma_{25}' \rightarrow \Gamma_{15}$ at the center of the Brillouin zone and that at 12.6 eV to the two transitions $X_4 \rightarrow X_1$ at $k=(2\pi/a)$ (100) and $\Sigma_4 \rightarrow \Sigma_1$ at $k=(2\pi/a)$ (0.61, 0.61, 0). This assignment can be made with some confidence on the basis of the results of Reference 12 which show that for a broad range of band structures obtained by varying chemical shifts or crystal potential parameters certain features of the band structure retain the same shape. The pairing of $X_4 \rightarrow X_1$ and $\Sigma_4 \rightarrow \Sigma_1$ was shown to be one such feature. An interpretation of the remaining structure may be made by considerations based on oscillator strengths and selection rules. Kleinman and Phillips[6] have shown that the largest part of the oscillator strength comes from the smooth part of the wave function outside the core. This is particularly true in diamond because of the small extent of the core. The oscillator strength for those portions of the wave function outside the core are large between levels which are degenerate in the nearly free-electron approximation. This criterion leads to the consideration of transitions between the states Γ_{25}', Γ_{15}', and Γ_2' at the center of the Brillouin zone, L_3', L_1, L_3, and L_2' at the L point and X_4 and X_1 at the X point. In addition, since the group of the k vector at L contains the inversion operator we need consider transitions only between states of opposite parity. Using these criteria, the broad, strong peak at 16.3 eV may be assigned to $L_3' \rightarrow L_1$. The hint of structure in the curve for k near 14 eV is probably due to $L_3' \rightarrow L_3$. Assignment of the 20.0 and 24.0 eV transitions is more tentative but they may be at or near $L_3' \rightarrow L_2'$. Although this transition cannot occur precisely at L because of the parity selection rule, transitions near this point may proceed with relatively large oscillator strengths.

TABLE I.—*Comparison of Experimental and Band Theory Interband Transitions of Diamond*

Transition	Experimental gap E_{exp} (eV)	Theoretical gap E_{th} (eV)	ΔE(eV)
$\Gamma_{25}' \rightarrow \Gamma_{15}$	7.4	6.1	1.3
$X_4 \rightarrow X_1$	12.6	13.8	1.2
$L_3' \rightarrow L_1$	16.3	13.6	2.7
	Unresolved, near.		
$L_3' \rightarrow L_3$	14.0	13.6	~0.5
$L_3' \rightarrow L_2'$	24.0	25.6	1.6

The experimental energy gaps and their assigned transitions are summarized in Table I and compared with the theoretical values for these transitions tabulated by Kleinman and Phillips[6] from calculations based on Herman's crystal potential. These calculated values are essentially the same as those originally obtained by Herman[5] and are felt to be the most accurate yet available. It is clear that the insensi-

[14] D. Brust, J. C. Phillips, and F. Bassani, Phys. Rev. Letters **9**, 92 (1962).

[15] F. Herman and S. Skillman, *Proceedings of the International Conference on Semiconductor Physics, Prague, 1960* (Czechoslovakian Academy of Sciences Publishing House, Prague, 1961), p. 20.

tive gaps, as expected, agree better with theoretical results than does the sensitive gap $L_3' \rightarrow L_1$. Even for this transition, however, the agreement is remarkably good. Assuming that the insensitive level L_3' is correctly given by the calculated value, the present assignment would require a shift of the L_1 level upward by 2.7 eV thus separating the nearly coincident L_3 and L_1 levels. The consistency of the agreement between the experimental and theoretical values for the several transitions identified indicates that the absolute accuracy of the band calculation is within 2 eV. It would be extremely interesting to see if a re-evaluation of the band structure of diamond using improved techniques would better the agreement with the sensitive $L_3' \rightarrow L_1$ transition

The location of each of these transitions coul be improved by low-temperature reflection an fluorescence measurements which may partiall resolve the spin-orbit splitting of the L_3 an L_3' levels as well as separate the $L_3' \rightarrow L$ transition from the 12.6-eV peak.

ACKNOWLEDGMENTS

The authors are grateful to Dr. J. C. Phillip of the University of Chicago for supplyin much of the information concerning the detaile assignment of the various interband transition and to Dr. J. Nodvik of the University o Southern California for his help with the origina dispersion analysis program.

THE ULTRAVIOLET REFLECTION SPECTRUM OF CADMIUM SULFIDE*

W. C. WALKER† AND J. OSANTOWSKI
University of California

Spectroscopy of solids in the ultraviolet has recently been recognized as a powerful technique for the detailed study of band structure (*1*). Structure observed, for example, in reflection spectra can be, in many cases, identified with specific interband transitions and directly compared to band calculations. Such a program has been carried out by several investigators for diamond (*2*), Cu, Si, Ge, the majority of the III–V compounds (*1*) and several of the II–VI compounds (*3*).

The present note reports the near normal incidence reflection spectrum of freshly cleaved CdS for photon energies from 4 to 28 eV. Measurements were made at room temperature on a single crystal obtained from the Eagle-Picher Co. of Cleveland, Ohio. The crystal was cleaved immediately before mounting in the vacuum reflectometer which was maintained at 10^{-5} torr. during the measurements. Slit widths of 100μ were used with a one-half meter Seya Namioka monochromator giving a bandpass with a half width of approximately 2Å. The average energy resolution was thus better than 0.1 eV over most of the spectrum.

The reflection spectrum obtained by averaging several sets of data is shown in Figure 1. Peaks associated with valence to conduction band transitions were observed at 5.6, 7.1, 7.9, 9.3 and 9.7 eV. Higher energy peaks observed at 14.4, 16.1, and 17.4 eV are believed due to

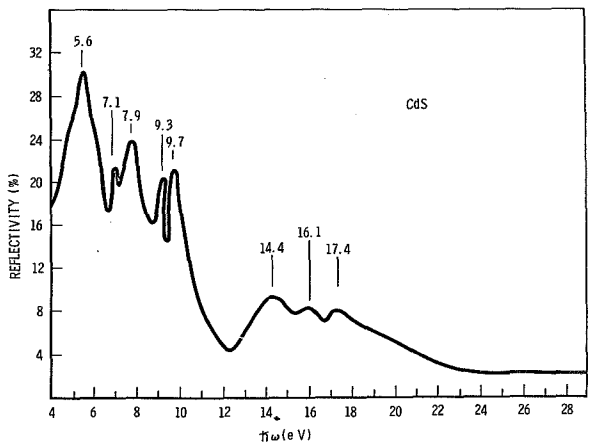

FIGURE 1.—Ultraviolet reflection spectrum of cadmium sulfide.

transitions from a mixed band composed essentially of the 4d electrons of cadmium and the 3s electrons of sulphur. Similar structure has been obtained by Cardona (*4*) up to 9.5 eV. From measurements on vapor phase grown platelets, he reported a broad peak near 5 eV having a satellite peak at 6.1 eV, a weakly resolved doublet at (7.1, 8.0) eV, and a single peak at 9.5 eV. In the present work the (7.1, 7.9) eV doublet was clearly resolved and in addition a doublet at (9.3, 9.7) eV was observed. A study of polarization effects at low temperature in the broad 5.6 eV peak recently carried out by Cardona (*5*) has shown that this peak is composite being composed of a doublet at (4.95, 5.03 eV together with a single peak at 5.58 eV. On the basis of the relationship between the zincblende and wurtzite structures proposed by Birman (*6*, Cardona attributes the (4.95, 5.03) eV doublet to the spin orbit doublet

* Work supported by the National Aeronautics and Space Administration.

† Currently at Goddard Space Flight Center under a NASA Post Doctoral Fellowship (on leave from the Physics Department, University of California Santa Barbara).

$(\Delta_5, \Delta_6) \rightarrow (\Delta_1, \Delta_3)$ and the 5.58 eV peak to a transition analogous to $I_3' \rightarrow L_3$ of zincblende with the degeneracy removed by the hexagonal crystal field. The new doublet at (9.3, 9.7) eV found in the present work is tentatively assigned to the spin-orbit doublet $(\Gamma_7, \Gamma_9) \rightarrow \Gamma_7$ derived from a degenerate $\Gamma_5 \rightarrow \Gamma_1$ transition of the wurtzite structure. Granted this assignment the spin-orbit splitting would be 0.4 eV. This value is so large compared to the value of 0.02 eV adopted by Birman (*7*) for the lowest energy $(\Gamma_7, \Gamma_9) \rightarrow \Gamma_7$ doublet that some other additional source of splitting such as "crystal field" must be involved to account for the data. The triplet structure in the high energy peak at 14.4, 16.1 and 17.4 eV is exceedingly interesting but difficult to assign at present. It is undoubtedly due to structure in the joint density of states for the cadmium 4d, sulphur 3s and conduction bands. If the 3s–4d electron interaction is sufficiently large to widen the mixed band to 6 eV, the structure could be a true property of the joint density of states for these bands. If, however, as is the case for many materials, the d band is relatively narrow, 3 eV or less, the structure would be associated primarily with the conduction band states in a way directly analogous to soft X-ray transitions. A detailed assignment of this high energy structure should be extremely important in testing the limits of conventional band theory.

REFERENCES

1. PHILIPP, H. R., and EHRENREICH, H., Phys. Rev. 129, 1550 (1963). See the extensive list of references contained in this paper.
2. WALKER, W. C., and OSANTOWSKI, J., to be published in Physical Review.
3. CARDONA, M., and GREENWAY, D. L., *Phys. Rev. 131*, 98 (1963).
4. CARDONA, M. *Phys. Rev. 129*, 1068 (1963).
5. ——— private communication, to be published.
6. BIRMAN, J. L., *Phys. Rev. 115*, 1493 (1959).
7. ——— *Phys. Rev. 114*, 1490 (1959).

THE IMPEDANCE OF AN ELECTRICALLY SHORT ANTENNA IN THE IONOSPHERE[1]

H. A. WHALE[2]
Goddard Space Flight Center

Measurements from rocket flights are used to show that the impedance of a short antenna operating above the local plasma frequency can be predicted if the following factors are considered:

1. The formation of an ion sheath around the antenna and the vehicle,
2. The enhancement of this sheath when large RF voltages are applied to the antenna, and
3. The loading that apparently arises from electroacoustic waves excited in the medium by the RF field close to the antenna.

Sufficient design data are included to calculate the effect of the ionosphere on both the resistive and reactive parts of the impedance of a short antenna.

INTRODUCTION

An investigation on the use of RF impedance probes for measuring ionospheric electron densities has disclosed several important factors affecting the impedance of an antenna immersed in the ionosphere. If the ratio of the operating frequency to the electron gyrofrequency is sufficiently high that magnetic field effects may be neglected, then these factors are the following:

1. The capacitive part of the antenna impedance is affected as though the antenna were immersed in a medium with a dielectric constant given by

$$K=1-\frac{\omega_p^2}{\omega^2} \qquad (1)$$

(where ω_p and ω are the plasma and operating frequencies), except that there is a sheath region around the antenna where the electron density is usually less than ambient because of the negative potential acquired by the vehicle If the sheath's dimensions are known, a correction can be made for this effect.

2. Unless the RF voltage applied to the antenna is small, the ionospheric electrons tend to leave the vicinity of the antenna; this creates an enhanced ion sheath, which may be many times the size of that present with no RF field. Computations of the size of the sheath formed in this way agree with experimental observations.

3. The resistive part of the antenna impedance contains at least two terms: The first, arising from the electromagnetic radiation, varies approximately as $\sqrt{K}$; while the second, which can be quantitatively explained as arising from an electroacoustic type of radiation, varies approximately as $(1-K)/\sqrt{K}$.

EXPERIMENTAL REACTANCE MEASUREMENTS

The most important of the measurements used as a basis for this paper are those made on Naval Research Laboratory (Reference 1) rocket flight NN 3.08 F and on NASA rocket flight 4.07 (Reference 2). The type of data obtained is exemplified in Figure 1, where the

[1] Presented at The Institute of Physics and The Physical Society Conference on "The Ionosphere," London, England, July 1962.

[2] On leave from the University of Auckland, New Zealand, with NASA Post-Doctoral Research Associateship from the National Academy of Science.

apparent electron density was derived from Equation 1 in the form

$$K'=1-\frac{Ne^2}{\epsilon_0 m\omega^2}, \qquad (2)$$

where

K'=apparent dielectric constant of the medium,
N=density in electrons per cubic meter,
e=the electronic charge,
m=the electronic mass, and
$\epsilon_0=\frac{1}{36\pi}\times 10^{-9}$ farad/meter

Since the antennas were electrically short, the value of K' was obtained from

$$K'C_0=C, \qquad (3)$$

where C is the measured antenna capacity in the ionosphere, and C_0 the free space antenna capacity.

A more general treatment indicates that the dielectric constant of the medium in a direction ψ with respect to the earth's magnetic field is given by

$$K=1-\frac{X}{1-Y^2}+\frac{XY^2}{1-Y^2}\cos^2\psi, \qquad (3a)$$

where

$X=\omega_p^2/\omega^2$,
$Y=\omega_H/\omega$, and
ω_H=the electron gyrofrequency.

Equation 3a indicates that the effective dielectric constant of the medium, when investigated with a capacitor of any geometry, should appear to be of the form (Reference 2)

$$K=1-\frac{X}{1-Y^2}+\frac{XY^2}{1-Y^2}G, \qquad (3b)$$

where G is a factor which depends on the geometry and orientation of the capacitor and is less than unity. Under the conditions of the NASA 4.07 experiment, the difference in electron density obtained by using Equation 3b instead of the simplified expression, Equation 1, would be less than 4 percent.

The comparison curve showing the true electron density (Fig. 1) was obtained by a CW propagation method (Ref. 3) which, under the conditions chosen for this experiment, yielded very accurate results for the major portion of the ascending trajectory.

If the ion sheath that formed around the antennas on the NASA 4.07 flight is assumed to have been cylindrical, the two results shown in Figure 1 can be reconciled. It is difficult to assign an exact value to the sheath radius, and a comparison of the results obtained by different methods is shown in Figure 2. Here, the dots are the values of sheath radius (in meters) calculated from the difference between the

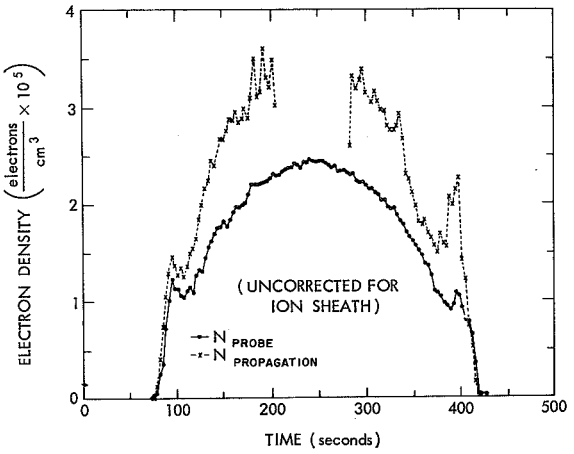

FIGURE 1.—Curves of electron density versus flight time for the RF probe and CW propagation methods (NASA Rocket 4.07, Churchill, Canada, 1128 CST, September 14, 1959).

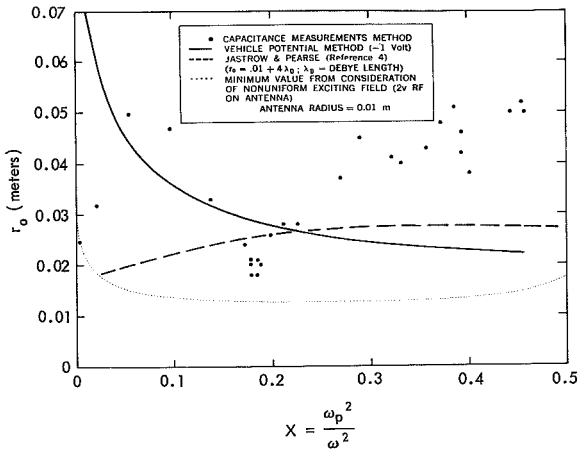

FIGURE 2.—Sheath radius obtained by different methods.

apparent and true dielectric constant of the ionosphere. The solid line is obtained from a measurement of the vehicle potential (measured as approximately −1 volt with respect to the plasma potential), while the dashed line is derived from Jastrow and Pearse's (Ref. 4) theoretical treatment of the problem. Some error in the measured results was inevitable in this particular experiment because of the complicated geometrical configuration near the base of the antenna.

It should be noted that, with the 2-volt peak RF voltage used on the antenna in these measurements, the sheath radius was of the order of 2 to 5 centimeters. In two other experiments, when the apparent dielectric constant was obtained with a 200-volt peak on the antenna, much larger sheaths, generally of the order of 15 centimeters, were obtained. The mechanism responsible for these large sheath distances is described in the following section.

SHEATH FORMATION BY LARGE RF VOLTAGES

At distances from the cylindrical antenna that are small compared with the antenna length, the RF is essentially perpendicular to the antenna axis and is inversely proportional to the distance from the axis. The electron motion will be along the field lines but, because of the field gradient, will not be simply sinusoidal. The net effect of this nonlinearity is that the electrons tend to move away from the antenna, and leave an electron-deficient region, or sheath, near the antenna.

The differential equation describing the motion of the electrons near the sheath edge is of the form

$$\ddot{r}=-\frac{\omega_p^2}{2}\,\mathrm{r}+\frac{eE_0}{mr}\cos\omega t, \qquad (4)$$

where r is the instantaneous distance of the electron from the antenna axis. Solution of this nonlinear differential equation by numerical methods gives the mean radius of the sheath for various values of ω_p (plasma frequency of the medium) and E_0 (peak radial field strength from the antenna axis). The results of this analysis are plotted in Figure 3, where $\bar{r}_0$ is the average sheath radius (i.e., time-averaged over one RF cycle) and X is the normalized electron density. The quantity B is given by

$$B=\frac{eE_0}{m\omega^2} \qquad (5)$$

and is numerically equivalent to the amplitude of vibration that a single electron would have in an RF field of peak field strength E_0 at a frequency $\omega/2\pi$. For easy computation,

$$B=\frac{E_0}{224.3f^2}\ \text{meters}, \qquad (6)$$

where f is the operating frequency in Mc.

Comparison of the computed effective sheath radius with experimental measurements is shown in Figure 4, where all the results have been normalized to $B=10^{-2}$. Of the two sets of results shown, the NN 3.08 F data are more accurate, since the method of measurement

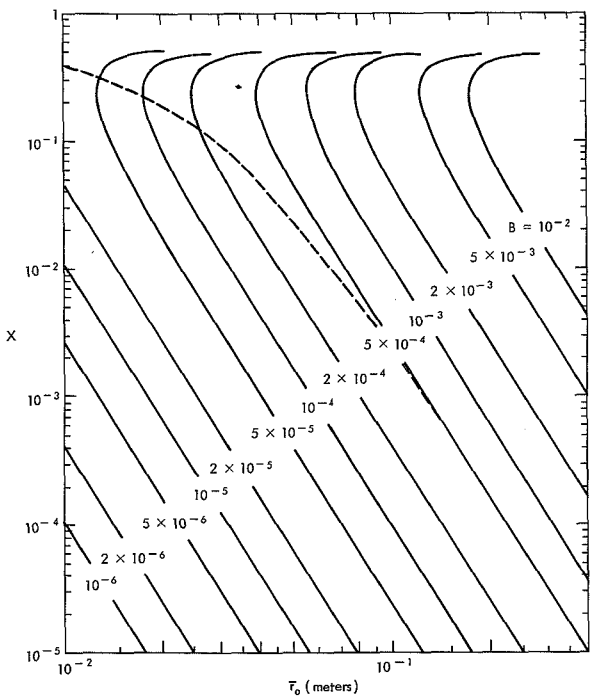

FIGURE 3.—Effective sheath radius $\bar{r}_0$ as a function of $X=\omega_p^2/\omega^2$ for various values of the parameter B. (Dashed line shows the closest distance from the antenna for electrons vibrating about the mean position $\bar{r}_0$ for $B=5\times10^{-4}$.)

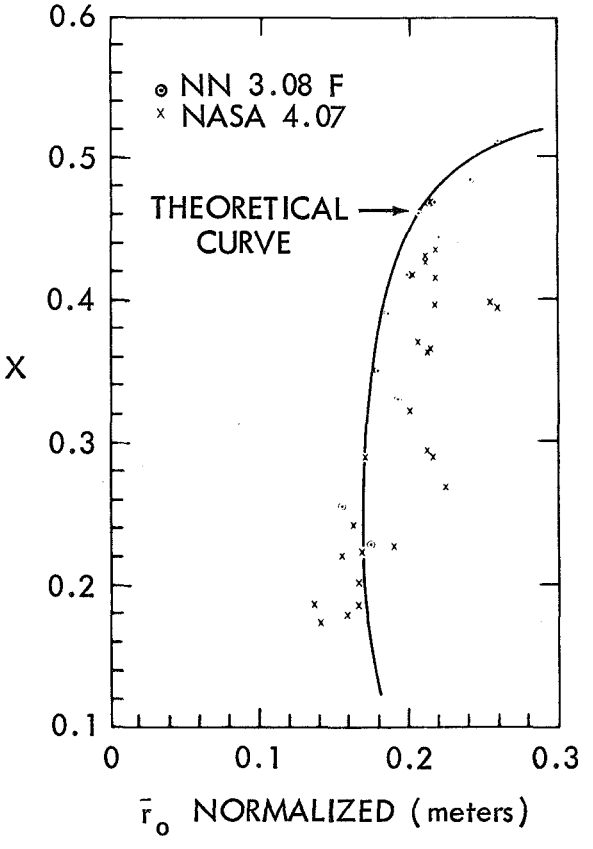

FIGURE 4.—Experimental measurements of sheath radius normalized to B=10^{-2}.

permitted allowance for the changes in the resistive component of the antenna impedance. In the NASA 4.07 measurements at high RF voltages, the data were obtained from the variation of the antenna voltage (i.e., detuning from resonance) only.

It is to be noted that, since the controlling parameter B is inversely proportional to the frequency squared, the effect of sheath formation by the applied RF voltage is very marked at low frequencies.

RESISTIVE COMPONENT OF ANTENNA IMPEDANCE

The radiation resistance for the electromagnetic radiation of a small dipole of constant dipole moment, when immersed in a dielectric medium of dielectric constant K, is proportional to $\sqrt{K}$. Under the conditions of the NASA 4.07 experiment, the relative amplitude of the peak obtained as the output circuit is tuned through resonance should then be as shown in the two upper curves in Figure 5. The parameter r_0, referring to the sheath radius, appears in the upper curves, since it affects the impedance of the antenna and hence the current flowing in it. With the two collinear 3-meter antennas operating at 7.75 Mc, the power P radiated as electromagnetic radiation is calculated as

$$P=1.4\times10^{-5}K'^2\sqrt{K}V^2 \text{ watts}, \qquad (7)$$

where

K'=apparent dielectric constant obtained by the antenna reactance measurement,
K=ambient dielectric constant of the medium,
V=½ the peak RF voltage applied between the antenna terminals.

The actual measured relative amplitude of the resonance peak is shown by the data points in Figure 5. There is apparently some mechanism in addition to electromagnetic radiation operating in absorbing power from the antenna.

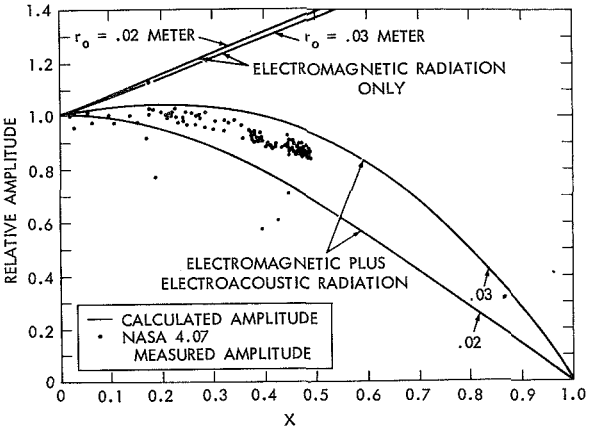

FIGURE 5.—Comparison of the calculated variation of the amplitude of the resonance peak as a function of X with the observed data points. The curves are computed for values of ion sheath radius, 0.02 and 0.03 meter.

On the assumption that this power is radiated as an electron-pressure (electroacoustic) wave excited in the medium by the RF field close to the antenna, computation gives, for this additional power Q,

$$Q=\frac{(1-K)v}{4\pi\epsilon_0 r_0\sqrt{K}}B^2(kr_0)V^2C^2 \text{ watts}, \quad (8)$$

where

$v=\sqrt{\gamma\kappa T}/m$, a velocity corresponding to the sound wave phase velocity in a neutral gas; γ is the ratio of specific heats, κ the Boltzmann constant, T the electron temperature, and m the electron mass;

$B(kr_0)$ = a factor accounting for the simultaneous excitation of all the electrons in the vicinity of the antenna, with

k = the propagation constant of the longitudinal electron pressure wave and

r_0 = the effective radius of the ion sheath boundary;

C = capacity of the antenna per unit length (farads/meter); and

$\epsilon_0=\frac{1}{36\pi}\times10^{-9}$ farad/meter.

The total power radiated (with 1-volt antenna voltage) for the conditions of the NASA 4.07 experiment is then given by

$$P+Q=1.4\times10^{-5}K'^2\sqrt{K}+3.6\times10^{-6}\frac{1-K}{\sqrt{K}}\frac{B^2(kr_0)}{r_0} \text{ watts}. \quad (9)$$

By this formula, the calculated relative amplitude of the resonance peaks would then be as shown in the two lower curves in Figure 5. It is apparent that the assumption of an electroacoustic effect, calculated for a sheath radius of 0.025 meter, gives excellent agreement with the actual measurements.

CONCLUSIONS

In considering the impedance of an antenna in the ionosphere, due allowance must be made for the ion sheath that forms around the surface. An estimate of the size of the sheath can be made if the electron density and electron temperature are known or if the vehicle's potential with respect to the ionospheric plasma is known.

When a large RF voltage is applied to the antenna, an enhanced sheath may be formed—an effect particularly noticeable at high RF voltages and low frequencies. Since it arises from a nonlinear process, the reciprocal relations between transmitting and receiving antennas are no longer valid for antennas immersed in the ionosphere.

The resistive component of the antenna impedance contains terms arising from the radiation of power both as electromagnetic waves and as longitudinal electron-pressure (electroacoustic) waves. The two effects (P and Q, Equations 7 and 8) become of comparable magnitude when the dielectric constant of the medium drops to about 0.9; an important consequence of the electroacoustic mechanism is that the antenna should become very heavily damped at the plasma resonance frequency. Thus receiving antennas in the ionosphere may receive energy arising from the electron thermal motions via the electroacoustic wave with an efficiency considerably exceeding that with which they receive electromagnetic waves.

There is little evidence as to how well these electroacoustic waves propagate in the ionosphere. If the attenuation is not too high, they may be a very useful tool for investigating the temperature and structure of an ionized medium.

REFERENCES

1. Jackson, J. E., and Pickar, A. D., "Performance of of a Rocket-Borne 7.75-Mc Transmitting Antenna in the Ionosphere," Naval Research Laboratory Rept. 4940, May 1957
2. Kane, J. A., Jackson, J. E., and Whale, H. A., "The Simultaneous Measurement of Ionospheric Electron Densities by CW Propagation and RF Impedance Probe Techniques," NASA Technical Note D-1098, January 1962
3. Seddon, J. C., "Propagation Measurements in the Ionosphere with the Aid of Rockets," *J. Geophys. Res.* 58(3): 323–335, September 1953
4. Jastrow, R., and Pearse, C. A., "Atmospheric Drag on the Satellite," *J. Geophys. Res.* 62(3): 413–423, September 1957

ION SHEATH EFFECTS NEAR ANTENNAS RADIATING WITHIN THE IONOSPHERE

H. A. WHALE [1]
Goddard Space Flight Center

A theoretical treatment of the electron displacement in the vicinity of a linear cylindrical antenna immersed in the ionosphere has been developed. This treatment explains the surprisingly thick ion sheaths observed experimentally when large RF voltages are applied to the antenna. The force that displaces the electrons is obtained from numerical solutions to the nonlinear differential equation describing their motion, and the results are consistent with the observations.

INTRODUCTION

Early observations of changes in the impedance of an electrically short antenna in the ionosphere (References 1 and 2) led to the method of determining the dielectric constant—and hence the electron density—of the ionosphere from measurements of a linear antenna's capacity (References 3, 4, and 5).

It is well known that an ion sheath a few centimeters thick normally forms spontaneously around a body immersed in the ionosphere; and it has been shown (Reference 5) that, provided the RF voltage applied to the antenna is small (less than 2 volts at 7.75 Mc), the sheath thickness observed agrees approximately with that predicted by Jastrow and Pearse (Reference 6). However, when large RF voltages are applied to the antenna (e.g., 200 volts at 7.75 Mc), the ion sheath appears to be very much larger. The redistribution of the electrons under the influence of RF fields is investigated in the present paper, and a relatively simple analysis yields values of sheath diameter in good agreement with the experimental results.

[1] On leave from the University of Auckland, New Zealand, with NASA Post-Doctoral Research Associateship from The National Academy of Sciences.

ION SHEATH ARISING FROM VEHICLE POTENTIAL

The Jastrow and Pearse treatment of the sheath problem proceeds in two steps: First, the vehicle potential is computed from a knowledge of the electron temperature and density of the ionosphere. Second, this calculated potential is used to derive the sheath thickness. In practice, thermal- and photo-emission effects change the actual potential of the vehicle in a way difficult to predict, so that an actual measurement of the potential is necessary. Such measurements have indicated that the vehicle potential is generally in the range 0 to -1 volt with respect to the ambient medium (References 5 and 7). The size of the sheath that forms around a long cylindrical surface for different values of electron density and vehicle potential may then be found from the following simplified calculation.

Assume that the ion sheath is a sharply bounded cylindrical region around the antenna and that there are no electrons within this region. The transition region from sheath to plasma will actually be smoothed out because of the thermal motions of the electrons, but we will assume that there is an equivalent sharp boundary or sheath edge. This sheath edge is assumed to be at zero (plasma) potential.

The capacity of the antenna to this surface is

$$C=\frac{2\pi\epsilon_0}{\log (R/R_0)} \text{ farads/meter} \quad (1)$$

where

R=the sheath radius,
R_0=antenna radius,
$\epsilon_0=\frac{1}{36\pi}\times 10^{-9}$ farad/meter.

Thus the charge Q on the antenna is

$$Q=\frac{2\pi\epsilon_0 V}{\log (R/R_0)} \text{ coulombs/meter,}$$

where V is the antenna potential in volts; and the field E_1 at the sheath boundary is

$$E_1=\frac{V}{R\log (R/R_0)} \text{ volts/meter.} \quad (2)$$

Inasmuch as the effect of the sheath is to shield the ambient medium from the effects of any charge on the antenna, we can also equate this field from the antenna with that arising from the electron density deficiency. The polarization field arising from the electron deficiency is

$$E_2=\frac{(R^2-R_0^2)Ne}{2R\epsilon_0} \text{ volts/meter,} \quad (3)$$

where N is the ambient density in electrons/cubic meter, and e is the electronic charge in coulombs. By equating Equations 2 and 3 to obtain the equilibrium condition, the value of R can be found from

$$2\epsilon_0 V=Ne(R^2-R_0^2)\log (R/R_0). \quad (4)$$

The solution to this equation is plotted in a convenient form in Figure 1, from which the ratio R/R_0 is readily obtained from different values of V/N at various values of R_0 (meters). The usual simplifying assumption of negligible magnetic field effects is made in the above treatment.

The sheath size can be increased if the antenna is biased negatively with respect to the vehicle. This has the effect of decreasing the influence of the ionosphere on the antenna reactance, and is helpful when an approximately constant antenna impedance is desired.

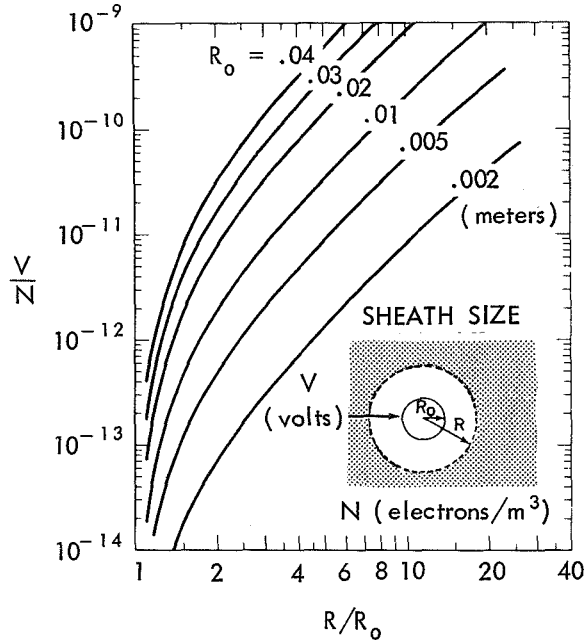

FIGURE 1.—Effective sheath size as a function of antenna potential (in volts) and electron density (per cubic meter).

If the antenna voltage varies sufficiently slowly, the sheath thickness will also vary—the maximum frequency at which the sheath can follow the voltage changes being close to the electron plasma frequency (Ref. 8). This does not mean that the electrons remain stationary when the applied frequency is greater than the plasma frequency but rather that they cannot rearrange themselves quickly enough to shield out the applied RF field. In the following treatment we are concerned with motions of the electrons at frequencies above the plasma frequency, so that it is their time-averaged positions that are affected by any sheath effects.

MOTION OF A SINGLE ELECTRON

At distances from a long cylindrical antenna that are small compared with the antenna length, the field is essentially perpendicular to the antenna axis. If effects arising from any magnetic field or from collisions or other losses are neglected, the electron motions will be along the field lines. The strength of the cylindrically radial field (i.e., perpendicular to the antenna axis) is inversely proportional to the

distance from the axis. The motion of a single electron is thus described by the nonlinear differential equation

$$m\ddot{r}=\frac{eE_0}{r}\cos\omega t, \tag{5}$$

where

e=the electronic charge,
m=the electronic mass,
r=the distance of the electron from the antenna axis in meters,
E_0=the peak field strength at a distance of 1 meter from the axis, and is found from
$E_0=V_0C/2\pi\epsilon_0$ volts/meter,
$V_0\cos\omega t$=the antenna voltage at any point measured with respect to the medium,
C=antenna capacity per unit length,
$\epsilon_0=\frac{1}{36\pi}\times10^{-9}$ farad/meter,
ω=operating frequency$\times2\pi$.

Equation 5 may be solved by approximate methods or by numerical computation of electron trajectories.

Although the exciting voltage is sinusoidal, the fact that the electron experiences forces that are no longer sinusoidal (because of the inverse distance term) introduces an average force that accelerates an individual electron toward the lower field-strength region. This same phenomenon occurs when there are many electrons present, provided the frequency is above the plasma frequency, as is shown in the next section

MOTION OF ELECTRONS IN AN IONIZED MEDIUM

When the antenna is immersed in an ionized medium, all the electrons will oscillate in the RF field and will also tend to move away from the antenna; but, since this motion produces a polarization of the medium, an equilibrium condition is attained. The situation then is that, with an RF field applied, a sheath appears—the sheath radius increasing with the field strength. The sheath edge, together with the electrons in the medium, vibrates at the applied frequency. To solve this problem, we require steady state solutions to a modified form of Equation 5, which should include the terms arising from the restoring forces. The deficit of negative charge in a cylindrical space of radius r free of electrons around the antenna is

$$Q=\pi r^2Ne \text{ per meter},$$

where it has been assumed that the space occupied by the antenna itself is negligible compared with the space free of electrons. The surface field at the sheath edge arising from this charge is

$$F=\frac{Q}{2\pi r\epsilon_0}=\frac{Ner}{2\epsilon_0} \text{ volts/meter}, \tag{6}$$

which is the same as Equation 3 with $R_0=0$.

The equation of motion for an electron at the sheath edge thus becomes

$$m\ddot{r}=-Fe+\frac{eE_0}{r}\cos\omega t$$

$$=-\frac{Ne^2r}{2\epsilon_0}+\frac{eE_0}{r}\cos\omega t. \tag{7}$$

Thus

$$\ddot{r}=-\frac{\omega_p{}^2r}{2}+\frac{eE_0}{mr}\cos\omega t, \tag{8}$$

where ω_p=plasma frequency$\times2\pi=(Ne^2/m\epsilon_0)^{1/2}$.

Equation 8 may be written in the following form, where the differentiations are with respect to a new variable $\tau(\tau=\omega t)$ and where the notation y represents $r(\tau)$ and $\ddot{y}$ represents $d^2r/d\tau^2$:

$$\ddot{y}=-\frac{\omega_p{}^2y}{2\omega^2}+\frac{eE_0}{m\omega^2y}\cos\tau,$$

where τ is in radians. This leads to the simplified expression:

$$\ddot{y}=-Ay+\frac{B}{y}\cos\tau; \tag{9}$$

where

$A=X/2$ $(X=\omega_p{}^2/\omega^2)$,

$B=\frac{eE_0}{m\omega^2}$=the oscillation amplitude of an isolated single electron in a uniform field of strength E_0.

Equation 9 may be regarded as specifying the trajectory of an electron under specified values

of B (which depends on the antenna voltage and the frequency) and A (which depends on the electron density and frequency) for particular initial conditions. In general, the solution will describe an electron vibrating at about the applied frequency, with its center of motion oscillating at a frequency close to $\omega_p/2\sqrt{2\pi}$. This latter oscillation may, in some cases, carry the electron on to the antenna or completely out of the field. Our interest is in the steady state solution (i.e., the condition in which each cycle of the oscillation at the applied frequency is a repeat of previous cycles). To find these solutions, values of B and the initial radial distance y (when $\dot{y}=0$) were chosen, and A was varied in a systematic manner until a repetitive (steady state) solution was obtained. The physical interpretation is as follows: The term Ay in Equation 9 may be written

$$Ay=A\bar{y}+A\delta y, \qquad (10)$$

where $\bar{y}$ is the time-averaged value of y and δy is the instantaneous displacement of the electron from $\bar{y}$.

The term $A\delta y$ in Equation 10 then represents the effect of the polarization in returning the electron to its stable position at $\bar{y}$. Thus $A\bar{y}$ is a measure of the steady polarization required to balance the mechanical force tending to move the electron away from the antenna. For a given B, the steady state trajectories for a series of initial y's may be found, each yielding a value for A and thus X (since $A=X/2$). The magnitude of $\bar{y}$ may be found from the calculated trajectory and thus a plot prepared in which $\bar{y}$ is shown as a function of X for various values of the parameter B. A series of such solutions is drawn in Figure 2.

The calculated value of $\bar{y}$ may be taken as the effective average sheath radius, since electrons closer to the antenna will experience—on the average—larger repelling forces and will tend to move out to this position. The more distant electrons in the medium will also oscillate in the RF field and will experience two forces tending to displace them from their mean positions. These two forces are:

1. The field that arises from the electron deficiency near the antenna and that varies as $1/r$, tending to move the electrons towards the antenna;

2. The average force that tends to move the electrons into the region of low RF field strength.

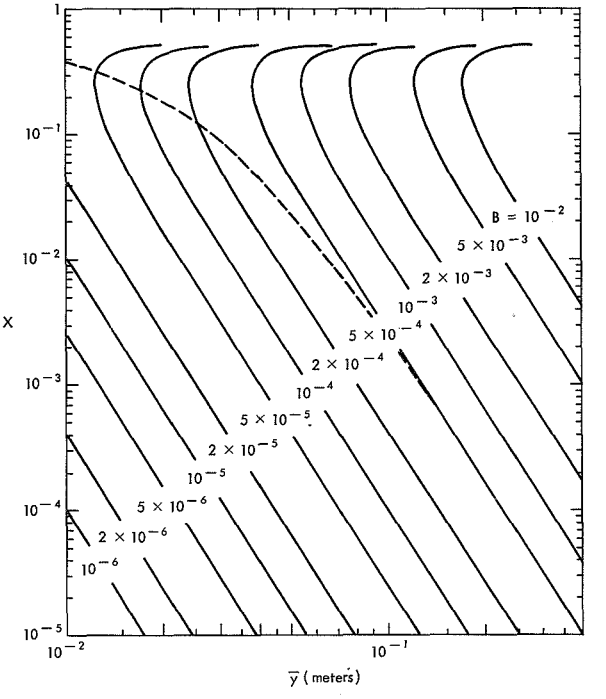

FIGURE 2.—Effective sheath radius $\bar{y}$ as a function of $X(=\omega_p^2/\omega^2)$ for various values of the parameter B. (Dashed line shows the closest distance from the antenna for electrons vibrating about the mean position $\bar{y}$ for $B=5\times10^{-4}$.

The resulting motion of an electron at $z(z>y)$ is then described by the differential equation

$$\ddot{z}=C-A\frac{y^2}{z}+\frac{B}{z}\cos\tau,$$

where y satisfies

$$\ddot{y}=-Ay+\frac{B}{y}\cos\tau$$

and C is a constant that can be adjusted to obtain a stable solution. Solution of these equations yields small positive values of C and indicates that the electrons in the medium drift towards the antenna. This is to be expected, since the field from the electron-deficient region near the antenna decreases as $1/r$ while the force arising from the movement of the electrons de-

creases as $1/r^4$ approximately (as in the approximate analysis in the next section leading to Equation 15).

This effect may lead to some local increase in the electron density just outside the sheath region (i.e., a moderate electron sheath forms outside the positive ion sheath). In practice, it is probable that this boundary region, which has been assumed to be a step function for the purposes of the above analysis, will merge into a relatively smooth transition region.

APPROXIMATE SOLUTIONS

Approximate solution to Equation 9 may be obtained by using certain simplifying assumptions. Assume that the motion of the electrons is sinusoidal, so that we may write

$$y=\bar{y}+a\cos\tau. \tag{11}$$

Then,

$$\ddot{y}=-a\cos\tau.$$

Substituting in Equation 9, neglecting the second harmonic terms that appear, and equating the steady and the oscillatory terms in the resulting equation, we obtain

$$a=\frac{B}{(2A-1)}\bar{y}$$

$$=-\frac{B}{(1-X)}\bar{y} \tag{12}$$

and

$$a^2=\frac{2A\bar{y}^2}{1-A}$$

$$=\frac{2X\bar{y}^2}{2-X}. \tag{13}$$

Eliminating a, we find that

$$\bar{y}^4=\frac{(2-X)B^2}{2X(1-X)^2}$$

$$\approx\frac{B^2}{X}, \text{ for small } X; \tag{14}$$

and thus,

$$A=\frac{X}{2}\approx\frac{B^2}{2\bar{y}^4}. \tag{15}$$

Further harmonic terms could be added, assuming a series for y in Equation 11. This leads to a more accurate solution but becomes progressively more complicated, so that it is much simpler to use the computed curves than to attempt to increase the accuracy of these approximate solutions by including more harmonic terms.

DISCUSSION

It is seen from Equation 15 that, for small values of X, the mean distance $\bar{y}$ of the electrons from the antenna axis decreases as X increases, in agreement with the computed curves in Figure 2. With large X, $\bar{y}$ increases again. Some resonance effect would be expected from Equation 8 since, if the driving voltage E_0 is removed, the equation becomes

$$\ddot{r}=-\frac{\omega_p^2 r}{2}$$

$$=\text{constant}-\frac{\omega_p^2}{2}\delta r,$$

where δr is the excursion of the sheath edge from its average position, with the oscillatory solution

$$\omega^2=\frac{\omega_p^2}{2}.$$

Note that, for the particular geometry studied here, the simplified approach indicates that this resonance is not exactly at the plasma frequency but at

$$\omega=\frac{\omega_p}{\sqrt{2}}.$$

If the sheath is very small, it is not permissible to take $r_0 \ll r$, as was assumed in Equation 6. With $r_0 \approx r$, Equation 8 becomes (with $E_0=0$)

$$\ddot{r}=-\omega_p^2\frac{r^2-r_0^2}{2r}$$

$$\approx-\omega_p^2(r-r_0)$$

$$=\text{constant}-\omega_p^2\delta r.$$

In this case, the resonance occurs more nearly at the plasma frequency. The nonlinear motion of the electrons complicates the resonance phenomenon, and a more detailed investigation than is attempted in this particular paper is required.

In interpreting these results, remember that there generally is also a dc sheath formed around any antenna immersed in the ionosphere. This arises from the charge acquired by the vehicle from electron capture. The dc sheath thickness (i.e., in the absence of any RF fields applied to the antenna) is commonly of the order of 1 or 2 centimeters so that, although this dc effect may be negligible compared with the effects arising from the RF field at high voltages, it will be the controlling influence when the RF field is very small.

NUMERICAL EXAMPLE

Let us consider a typical situation, taking the following conditions:

Antenna radius (m)	0.01
Antenna capacity ($\mu\mu f/fm$)	16
Peak RF voltage (v)	200
Frequency (Mc)	7.75

Then,

$$E_0=\frac{V_0C}{2\pi\epsilon_0}$$

$$=57.6 \text{ volts/meter;}$$

so that

$$B=\frac{eE_0}{m\omega^2}$$

$$=\frac{E_0}{224.3f^2} \text{ meters } (f \text{ in Mc})$$

$$=4.3\times10^{-3} \text{ meter.}$$

From Figure 2, as X increases, the mean distance of the inner layer of electrons from the antenna axis decreases from 0.22 meter at $X=0.01$ to 0.125 meter at $X=0.1$, with a minimum of 0.105 meter at about $X=0.3$.

The minimum distance from the antenna axis attained by the nearest electrons to the antenna during their oscillations is also known. It is the initial value of y (for $\dot{y}=0$) that was used in computing the solution of the differential equation.[2] This distance is shown, for example, as the dashed curve in Figure 2 for the conditions of $B=5\times10^{-4}$. It is seen that, in this latter case, neglecting the effects of any dc bias on the antenna, electrons will strike the antenna (of radius 0.01 meter) when the electron density becomes greater than the value corresponding to $X=0.4$.

EXPERIMENTAL OBSERVATIONS

The equation from which Figure 2 was derived is

$$\ddot{y}=-Ay+\frac{B}{y}\cos\tau.$$

If the scale of y is changed by a factor n, we may write

$$n\ddot{y}=-Any+\frac{n^2B}{ny}\cos\tau$$

or

$$\ddot{Y}=-AY+\frac{B'}{Y}\cos\tau,$$

where $Y=ny$ and $B'=n^2B$.

It is thus possible to draw all the curves in Figure 2 as a single curve with suitable normalizing factors. This type of curve is shown in Figure 3, in which the computed results are normalized to $B=10^{-2}$ with only the portion of the curve for $X>0.1$ shown.

In Figure 3, a few experimental results normalized to $B=10^{-2}$ are also plotted. These values were obtained during two rocket firings: NN 3.08 F (Reference 3), and NASA 4.07 (Reference 5).

In the NN 3.08 F experiment, the antenna impedance was obtained from measures of the voltages on the input and output sides of the antenna matching network. From these two measurements, both the resistive and reactive components of the antenna impedance can be derived (Reference 3). In the NASA 4.07 experiment, the approximate reactance was deduced only from a measurement at the output side of the antenna matching network—the matching circuit being fixed-tuned to resonate in free space so that the output voltage was a measure of the detuning. Since no allowance for any resistive changes could be made in the latter measurement, the results obtained cannot be considered as accurate as those obtained from NN 3.08 F.

[2] The differential equation was solved by a Runge Kutta method on the Goddard Space Flight Center IBM 7090 computer.

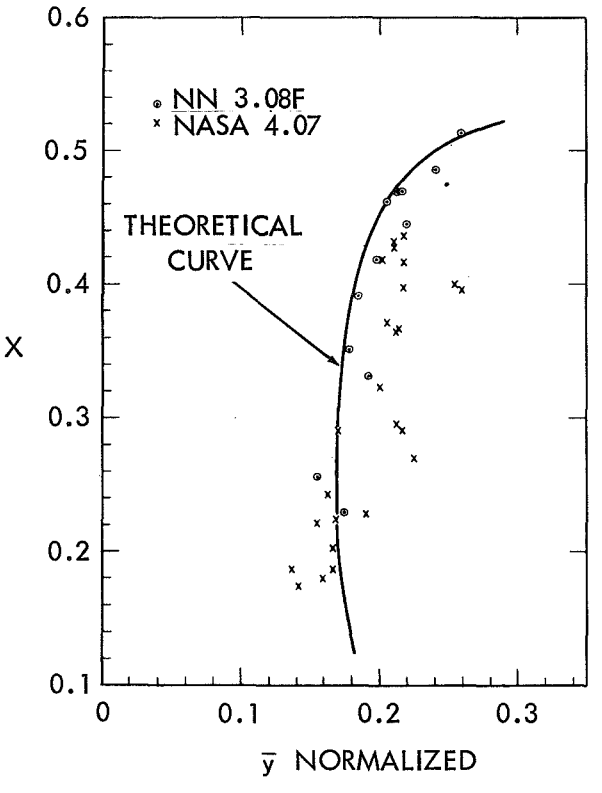

FIGURE 3.—Experimental measurements of sheath radius normalized to B=10^{-2}.

In both these flights the antennas were electrically short so that their impedances were primarily capacitive. The reactance measurements then yielded the apparent dielectric constant $K'(=1-X')$ of the medium from the relation

$$C'=K'C_0,$$

where C' is the measured capacitance and C_0 is the free space capacitance.

From this experimental value of X' and a knowledge of the true value (obtained from a two-frequency propagation experiment), the size of a cylindrical region free of electrons around the antenna, which would give the measured effective capacity, was calculated in the manner indicated below.

Since the antenna is long enough as compared with the sheath radius to be considered to be infinitely long, the effect of the sheath may be calculated by considering the sheath edge as one plate of a cylindrical capacitor around the antenna. Then it is found that

$$X'=\frac{C_s-C}{C_s-XC}X, \tag{16}$$

where C_s is the capacity of antenna to sheath per unit length and C is the free space capacity of antenna per unit length.

In the experimental measurements, the values of X and X' are obtained. The value of C can be deduced from free space measurements of the antenna impedance (in these cases, C was about $16\mu\mu f/m$ for the NASA 4.07 rocket and about $19\mu\mu f/m$ for the NN 3.08 rocket), so that C_s can be obtained from Equation 16. The sheath radius is calculated from the capacity of this cylindrical condenser by Equation 1. This radius was used (after normalizing to $B=10^{-2}$) for the abscissa $\bar{y}$ in plotting the experimental results in Figure 3.

In the above treatment we have assumed that the sheath radius is constant along the length of the antenna, so that this approach is only applicable to electrically short antennas as used on NN 3.08F and NASA 4.07, in which the voltage is nearly constant along the length. Although the value of C (the free space capacitance of the antenna per unit length) is also variable since it depends on the spacing between the two halves of a dipole antenna, the values quoted for C may be regarded as effective average values.

For very long antennas, the sheath radius is greatest at the voltage antinodes; these points are also the places where capacitance changes have the most effect on the input impedance of the antenna. It has been found that applying Equation 16 to a long antenna gives results in good agreement with experimentally measured impedances.

Under the conditions of the NN 3.08 F rocket measurements, Table 1 is obtained for the ratio of the measured X' to the true X; this is compared to the ratio obtained from Equation 16 using the theoretical value of C_s (obtained from $\bar{y}$) and using $C=19\mu\mu f/m$.

It is of interest that the theoretical value of the sheath radius for NN 3.08F (corresponding to $B=5\times10^{-3}$) is about 13 cm, in good agreement with the value of about 6 inches (15.2 cm)

TABLE 1.—*Comparison of Measured* X′/X *and Calculated* X′/X

Height (km)	Apparent X'	True X	Measured X'/X	Calculated X'/X
120	0.067	0.229	0.29	0.31
130	.089	.256	.35	.32
140	.104	.331	.31	.34
150	.124	.351	.35	.35
160	.140	.391	.36	.35
170	.147	.418	.35	.36
180	.147	.445	.33	.35
190	.155	.452	.34	.35
200	.155	.459	.34	.35
210	.155	.459	.34	.35
220	.162	.486	.33	.33
230	.166	.513	.32	.25

published by Jackson and Kane (Reference 3). The column in Table 1 labeled *Measured* X'/X can also be interpreted as N'/N, where N' is the apparent electron density and N is the true electron density. This ratio (or discrepancy) could not be explained previously, since the sheath thickness required appeared to be unreasonably large.

CONCLUSION

At frequencies above the plasma frequency, under conditions such that collisions and magnetic field effects may be neglected, it is possible to deduce—from the relatively simple analysis given above—the way in which an RF voltage applied to a cylindrical antenna affects the mean position of electrons close to the antenna. The results obtained are, within the limits of the accuracy of the measurements, in good agreement with observations. The theory accounts for the discrepancies observed between true and apparent electron densities when a large RF voltage is applied to an RF impedance probe.

REFERENCES

1. JACKSON, J. E., "Rocket-Borne Instrumentation for Ionosphere Propagation Experiments," Naval Res. Lab. Rept. 3909, January 1952.
2. JACKSON, J. E., and PICKAR, A. D., "Performance of a Rocket-Borne 7.75-Mc Transmitting Antenna in the Ionosphere," Naval Res. Lab. Rept. 4940, May 1957.
3. JACKSON, J. E., and KANE, J. A., "Breakdown and Detuning of Transmitting Antennas in the Ionosphere," Naval Res. Lab. Rept. 5345, August 1959.
4. JACKSON, J. E., and KANE, J. A., "Performance of an RF Impedance Probe in the Ionosphere," *J. Geophys. Res.* 65(7): 2209–2210, July 1960.
5. KANE, J. A., JACKSON J. E., and WHALE, H. A., "The Simultaneous Measurement of Ionospheric Electron Densities by Cw Propagation and Rf Impedance Probe Techniques," NASA Technical Note D–1098, January 1962. Also published in: *Jour. Research of Nat'l Bureau of Standards* 66D: 641–648, November–December 1962, with title "RF Impedance Probe Measurements of Ionospheric Electron Densities."
6. JASTROW, R., and PEARSE, C. A., "Atmospheric Drag on the Satellite," *J. Geophys. Res.* 62(3): 413–423, September 1957.
7. BOURDEAU, R. E., JACKSON, J. E., et al., "Ionospheric Measurements Using Environmental Sampling Techniques", in: *Space Research: Proc. 1st Internat. Space Sci. Sympos., Nice, January 1960*, ed. by H. K. Bijl, Amsterdam, North-Holland Publ. Co., 1960, pp. 328–339.
8. ROSE, D. J., and CLARK, M., JR., "Plasmas and Controlled Fusion," Cambridge, Mass.: M.I.T. Press; New York: Wiley, 1961, p. 195.

THE SOUTHERN SKY SURVEY PAYLOAD

RICHARD M. WINDSOR
Goddard Space Flight Center

Four Skylark rockets were fired from Woomera Missile Range, Australia, to measure stellar fluxes and nebulosities at energy bands between 1050 and 2800A. The payloads contained two basic types of detector systems: photomultipliers for the spectral region between 1900 and 2800A, and ionization chambers for the 1050 to 1500A range. Data acquisition was optimized by a spin control gas jet system. Also described are the vehicle, field operations, and performance.

INTRODUCTION

During the past several years a number of measurements have been made from rockets of the ultraviolet fluxes of stars and nebulosities visible in the northern hemisphere. The presence in southern skies of features such as the Magellanic Clouds and the more pronounced structure of the Milky Way suggested that such flux measurements might profitably be extended into the Southern Hemisphere. Accordingly, four identical payloads were constructed to be flown in Australia from the Woomera range, using the British-manufactured Skylark rocket.

Each payload contained 10 telescopes: 6 with electron multiplier phototube detectors filtered for sensitivity to energy bands at 2600 and 2100A; and 4 with ionization chamber detectors, 2 per telescope, responsive to selected energy ranges between 1050 and 1500A. Since the scanning of the sky was determined by the motion of the rocket, a spin control system was used to optimize data acquisition.

VEHICLE

Skylark is a high altitude research rocket (Reference 1)—see Figure 1—designed to carry a payload of 250 pounds to altitudes up to 100 miles when used as a single-stage vehicle and to 140 miles when boosted. It is powered by the Raven solid propellant motor and is

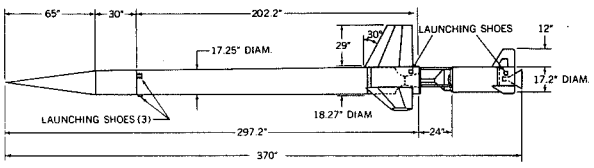

FIGURE 1.—The Skylark rocket with Cuckoo booster.

dart-stabilized by three fixed fins; it has no other form of control.

The Raven II motor with Cuckoo booster selected for these firings performs as illustrated in Figures 2 and 3. The motor burns for about 40 seconds and provides a thrust of 12,000 pounds. Its longitudinal acceleration is less than 10g, and the fin-induced roll is less than 0.5 rps in either direction. The diameter of the motor is 17 inches, and its length is 17 feet 2 inches. A quick-release manacle ring clamps the payload to the motor assembly.

PAYLOAD STRUCTURE

The payload (Fig. 4) consisted of an unpressurized cylindrical section containing the telescopes and a pressurized nose ogive containing support instrumentation. The structural member in the unpressurized section was a hexagonal magnesium casting with mounting and access holes in each face. The telescopes were mounted in alternate faces 120 degrees apart. One face supported two photomultiplier and two ion chamber telescopes, and the other two

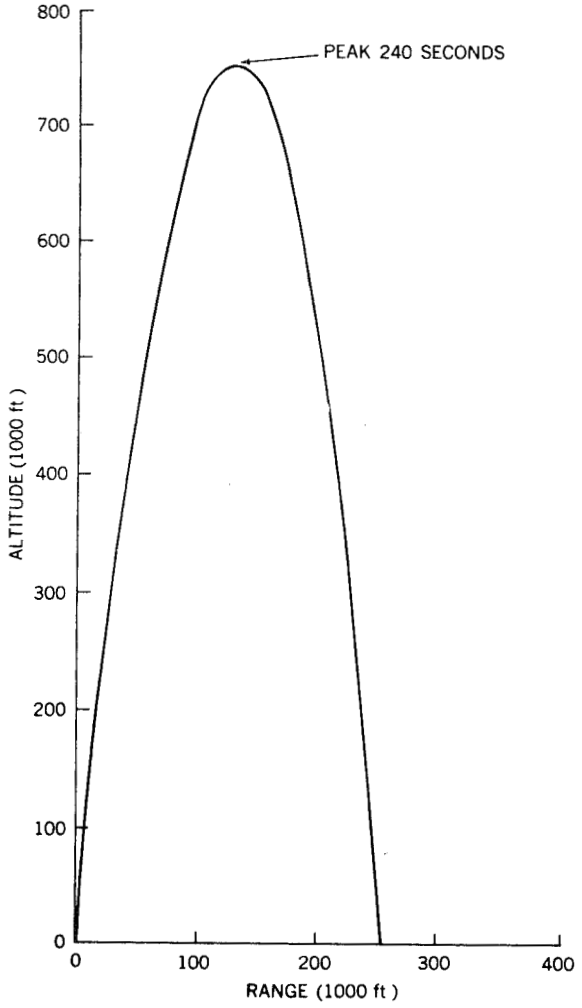

FIGURE 2.—Skylark trajectory using Raven II motor and Cuckoo booster.

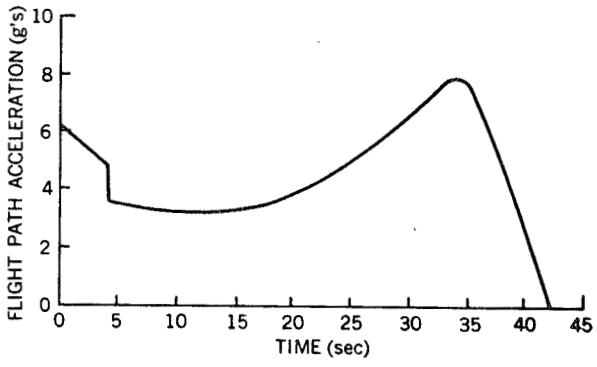

FIGURE 3.—Skylark acceleration profile: Raven II motor and Cuckoo booster.

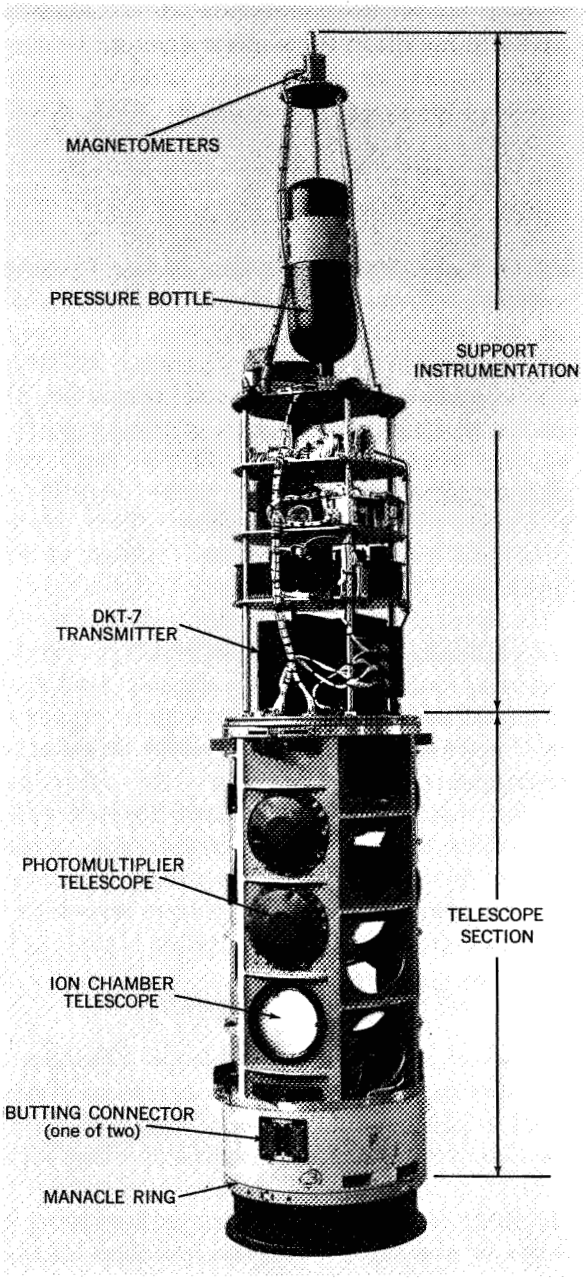

FIGURE 4.—Southern Sky Survey payload. Nose ogive and skin panels are removed; protective dust covers are mounted over telescope apertures.

faces each supported two photomultiplier telescopes and one ion chamber telescope. All mounting holes on all four rockets and the mounting flanges on all the telescopes had accurately machined surfaces so that the tele-

scopes could be completely interchangeable and still maintain the angular relation between optical axes to within ±3 minutes of arc. Three 120-degree panels were fitted around the casting to provide an aerodynamic fairing during boost. In addition, the panels protected the telescopes from contamination on the ground and in early flight, and permitted an in-flight dark calibration of the telescope systems. These spring-loaded panels were held on at top and bottom by two steel straps. Squib-powered pin pullers separated the straps 70 seconds after takeoff and permitted the panels to eject. At the base of the magnesium casting were mounted amplifiers, high voltage supplies, and battery packs directly associated with the telescopes. Two 48-pin umbilical connectors were also located at this position.

In the nose ogive, the support instrumentation was mounted on aluminum plates suspended between four longitudinally stressed steel rods. A tripod mount above the top plate supported two magnetometers as far away from other instrumentation as possible. An ogive was chosen instead of the standard Skylark right-cone nose not only to provide more usable volume but also to furnish a nearly cylindrical section near the base of the nose on which a quadraloop telemetry antenna could be mounted.

TELESCOPES

The photomultiplier telescope (Figures 5 and 6) was a 6-inch f/3.5 Cassegrainian system with a paraboloidal primary and a spherical secondary, and a 2-degree field of view. The secondary was ground to a sphere instead of the more conventional hyperboloid in order to degrade the image quality. Image quality was not a primary factor, provided all the incident flux from a star within the field reached the cathode of the photomultiplier. However, a perfectly imaging system would impose a square wave input on the amplifier, producing overshoot and a tendency to cathode fatigue with the logarithmic circuitry used. Therefore the image quality was intentionally reduced so that the shapes of the leading and trailing edges of the light pulse would approximate the shape of the amplifier response curve. A two-element quartz field lens in the focal plane imaged the primary mirror on the photocathode to eliminate nonuniformities in cathode response. The detectors for these telescopes were EMI 6256N photomultipliers.

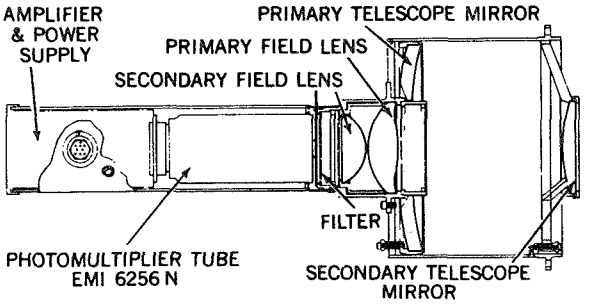

FIGURE 5.—Photomultiplier telescope assembly.

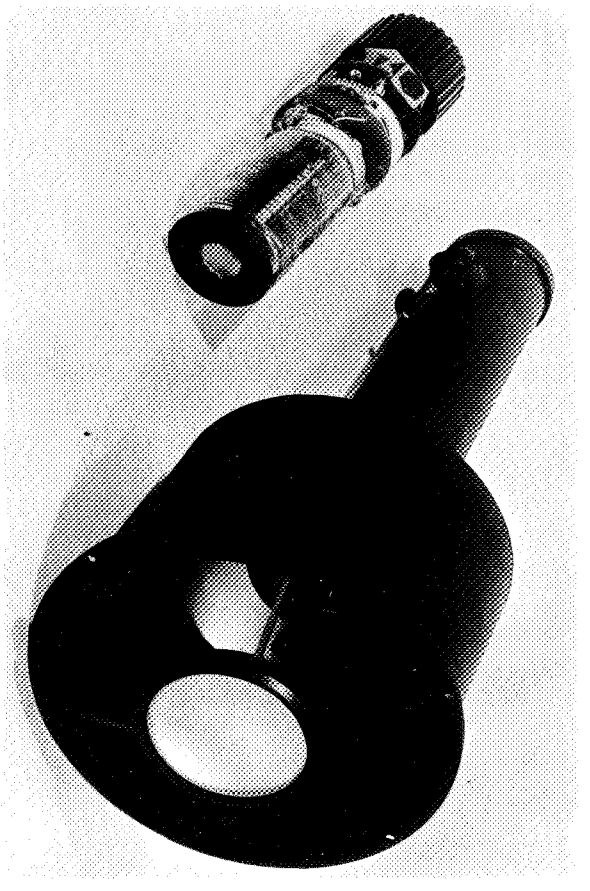

FIGURE 6.—Photomultiplier telescope. The detector-amplifier assembly is shown removed from its pressurized housing.

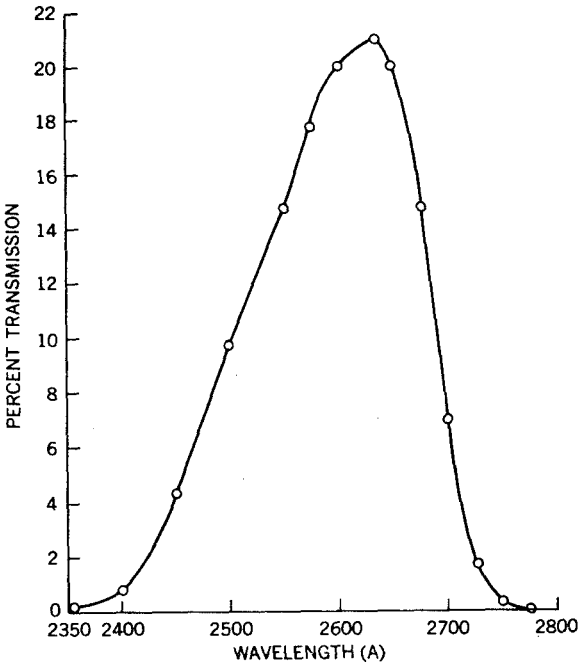

FIGURE 7.—Transmission of 2600A filter.

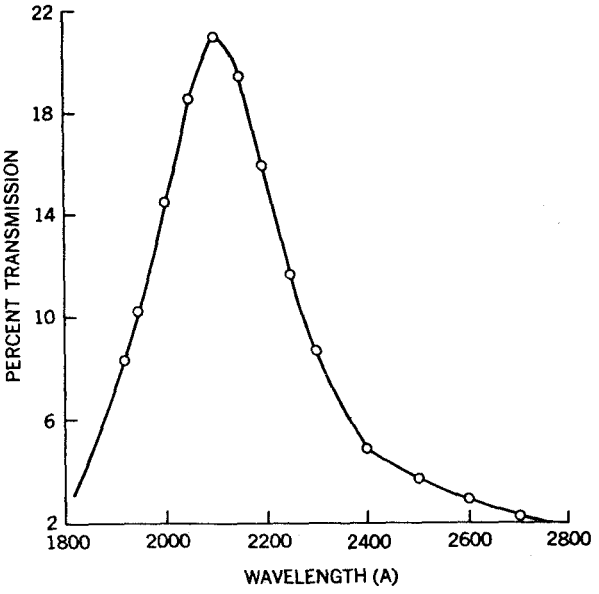

FIGURE 8.—Transmission of 2100A filter.

The Sweet type logarithmic amplifier circuit (Reference 2) was modified [1] for use at the required low energy levels. Each photomultiplier, with its amplifier and high voltage supply, was mounted in a pressurized housing to eliminate corona during depressurization of the rocket. As a result, each telescope-detector assembly was an integrated unit interchangeable with other units. This interchangeability considerably reduced field maintenance problems.

A filter was mounted in each telescope to provide spectral discrimination. Two types of filters were used. The first was a crystal and glass sandwich (Reference 3) with a 180A bandpass centered at 2600A (Fig. 7). The mount for this filter was directly in front of the photomultiplier, where the light formed an f/1 converging beam approximately 1 inch in diameter. The second type of filter was an interference filter peaking at 2100A (Fig. 8). In order to avoid the highly convergent beam between the photomultiplier and field lens, this filter was made 2 inches in diameter and was mounted in front of the field lens. In this f/3.5 beam the filter had an effective bandwidth of 230A. The *spectral* sensitivity of each telescope unit was computed from the measured transmission curves of the filter and field lenses and from the measured spectral sensitivity of the photocathode. A relative calibration curve of each photomultiplier-amplifier system was obtained by comparison with a reference photomultiplier and linear amplifier. The *absolute* sensitivity of the assembled telescope was measured at 2537A with a standard mercury arc source. This measurement was made at three distances to check the shape of the relative calibration curve. A secondary standard lamp was carried to the field, and the inverse square law calibration was repeated a few days before flight as a final check.

The six photomultiplier telescopes in each rocket were mounted in pairs having parallel optical axes. One telescope of a pair contained a 2600A filter, while the other contained a 2100A filter; this permitted simultaneous two-color observations of stars at these wavelengths.

Each ion chamber telescope (Figs. 9 and 10) consisted of a 6-inch spherical mirror with two

[1] Unpublished data obtained by Gerald R. Baker; to be published as a NASA Technical Note with title "A Sensitive Logarithmic Photometer for Rocket Astronomy."

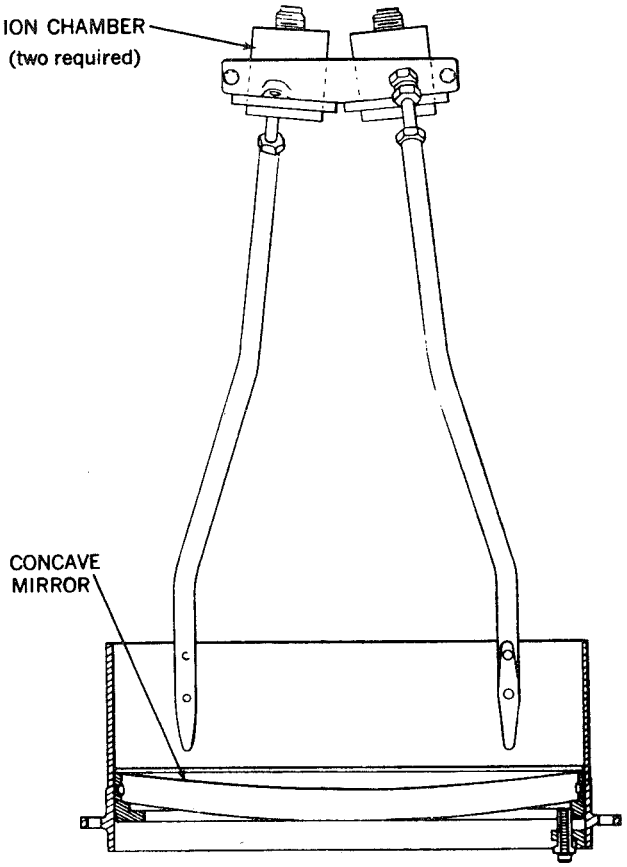

FIGURE 9.—Ion chamber telescope assembly.

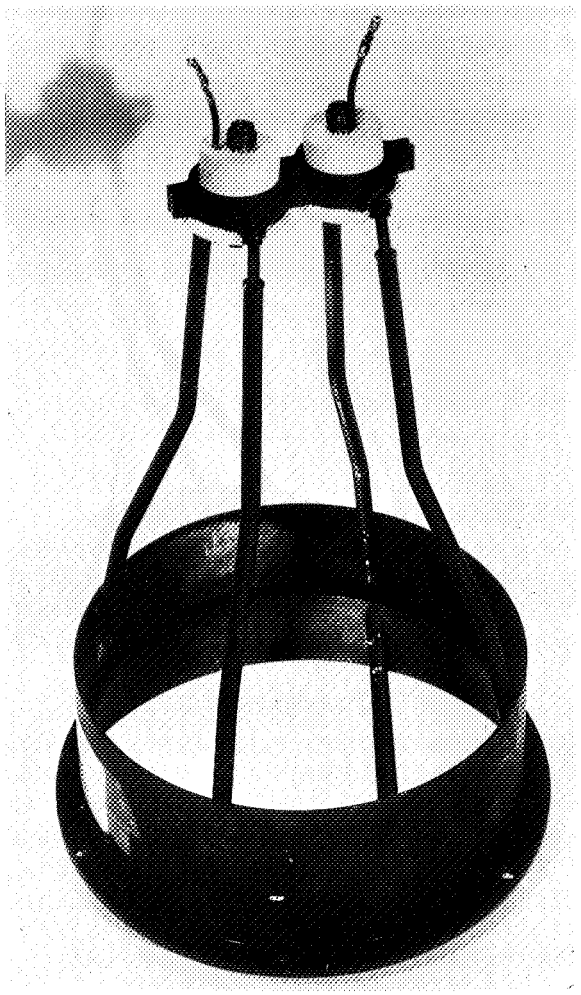

FIGURE 10.—Ion chamber telescope.

ion chambers mounted on the focal surface. The ion chambers had 2-degree fields of view and were mounted in the roll plane of the rocket so that a star would be seen first by one chamber and then by the other as the rocket spun. The mirror was aluminum-coated with an overcoat of magnesium fluoride to enhance the reflectance in the vacuum ultraviolet (Reference 4). The mirror was mounted in the rocket so that it looked across the rocket diameter. A 6.25-inch hole on the opposite side of the rocket casting provided an entrance stop to improve the off-axis imagery of the spherical mirror. The combined vignetting from the stop and the ion chamber support brackets was essentially constant over the 2-degree field of each detector. The measured effective aperture of the system was 4.8 inches.

The ion chambers used were the ceramic type developed at the Goddard Space Flight Center (Reference 5); see Figure 11. The fill gases, window materials, and resulting spectral sensitivities are summarized in Table 1. The ionization efficiency of nitric oxide at Lyman-α (Reference 6) was used as the fundamental calibration standard. The calibration was extended to other wavelengths by means of a sodium salicylated photomultiplier, which is assumed to have a uniform response over this wavelength region. The spectral response curve of each flight chamber was determined by comparison with the sodium salicylated multiplier. Each ion chamber had a linear electrometer amplifier of the type developed by Praglin and Nichols (Reference 7) with a sensitivity of 10^{-12} ampere per telemetered volt. The system

TABLE 1.—*Spectral Responses of Flight Ion Chambers*

Gas	Gas cutoff (A)	Window cutoff (A)	Window material
Ethylene oxide	1150	1050	Lithium fluoride.
Nitric oxide	1350	1225	Calcium fluoride.
Carbon disulfide	1240	1050	Lithium fluoride.
Acetone	1280	1225	Calcium fluoride.
Ethyl sulfide [1]	1500	1350	Barium fluoride.

[1] These chambers had just been developed in an attempt to extend the spectral range beyond 1350A. They were found to have a very short shelf life. After one month in the field, all had deteriorated to a point where they were no longer usable. Only one of this type of chamber was flown, and that was in the first rocket.

sensitivity was adjusted to the desired value by varying the negative high voltage on the ion chamber and thus changing the gas gain of the detector. The overall sensitivity was computed from the effective aperture and reflectance of the mirror, together with the quantum efficiency and operating gain of the ion chamber.

It was not practical to carry a vacuum monochromator into the field to check ion chamber calibrations before flight. As an alternative, a small fixture was built to hold an ion chamber a fixed distance from a hydrogen lamp while the intervening path was flushed with nitrogen. Immediately after calibration in the laboratory, each ion chamber was placed in this fixture to record an output current. In the field, this procedure was repeated before flight to determine whether the chamber sensitivity had significantly changed. While this technique was not as satisfactory as a laboratory calibration, sensitivity changes greater than 15 percent could be detected. No changes of this magnitude were found in any but the ethyl sulfide chambers (see footnote to Table 1). Unlike the photomultipliers, the ion chamber telescopes could not remain pressurized throughout flight. Therefore, high voltage was not applied to the chamber shells until 70 seconds after takeoff, when the telescope volume had evacuated enough to prevent corona.

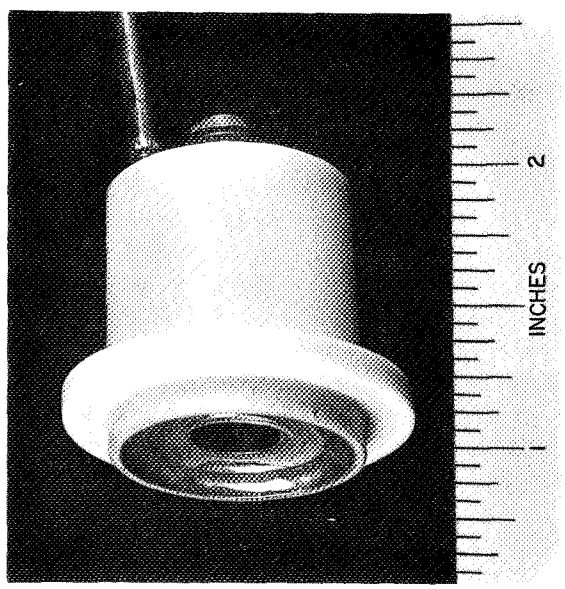

FIGURE 11.—Ceramic ion chamber.

SUPPORT INSTRUMENTATION

To obtain a reliable measurement of stellar flux levels, it was desirable that a star remain in the 2-degree field of view of each telescope for at least 0.1 second, corresponding to a spin rate of 0.05 rps. Because of manufacturing tolerances in the fins, the Skylark may achieve spin rates as high as 0.5 rps. Accordingly a spin control device capable of sensing both magnitude and direction of spin and adjusting the rate to the desired value was necessary. A nitrogen bottle was placed in the nose with parallel plumbing leading to two opposed pairs of roll jets, each with its own normally closed valve, mounted near the rocket's center of gravity. A rate gyro sensed the rate and direction of spin and controlled

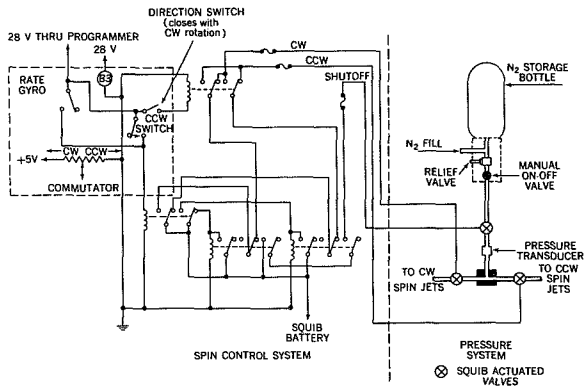

FIGURE 12.—Spin control logic and pressure system.

a relay system (Fig. 12) that established an electrical path to the appropriate valve. This valve was opened by the timer 78 seconds after takeoff. When the preset rate was achieved, the rate gyro closed a normally open valve in the line to stop the spin control action. A pressure gauge monitored the line pressure aft of the normally open valve. When spin control action was requested, there was a drop in the line pressure; and, at completion, the pressure dropped to zero—giving positive indication of the operation of the spin control system.

The remaining nose instrumentation consisted of two Schoenstedt RAM–3 magnetometers (one parallel and one perpendicular to the rocket axis) for preliminary aspect information, an accelerometer to monitor rocket performance during boost, battery packs, and the telemeter transmitter. A motor-driven timer switched a full time telemeter channel from the accelerometer to telescope data after burnout, turned on ion chamber high voltage, ejected skin panels, and initiated the spin control system.

The PPM DKT–7 transmitter was used for these flights. The standard DKT–7 calibrator was modified to provide a voltage calibration of each channel once every 60 seconds. Fourteen of the channels were used for the six photomultipliers and eight ion chambers, and the 15th channel was subcommutated to preset magnetometer data and to preset monitors of power supplies, spin control system, and door ejection. A telemetry receiving van was equipped in the United States and shipped to Australia for these firings.

Pre-flight checkout of each rocket was accomplished with an external control console (Fig. 13). This console permitted rocket checkout on either external or internal power, independent operation of each rocket subsystem, and read-out of each data channel on the panel meter. A *stop action* button was installed on the panel to interrupt the firing circuits in case of a last minute malfunction; fortunately this button was never used. The control console was connected to the rocket through land lines terminating in two 48-pin connectors at the base of the payload. Disconnect occurred 15 seconds before firing. In addition, a 4-pin "snatch plug" was attached to the rocket and pulled out by a lanyard at takeoff. When this plug was pulled, shorts were removed from the pyrotechnic devices, the timer was started, and all rocket systems were turned on—regardless of the condition of the control panel at disconnect.

FIELD OPERATIONS

The rocket preparation was done at the Weapons Research Establishment (WRE) in Salisbury, about 20 miles north of Adelaide, south Australia. The Aerodynamics Division of WRE provided a test area 25 by 40 feet with work benches and 220 volt, 50 cycle power; a machine shop and parts stores were made available.

At Salisbury each subsystem was checked out, and a full simulated flight check was performed with all systems functioning, but with a set of non-flight telescopes. Then a selected set of flight photomultiplier telescopes was installed and checked for performance in the payload. Finally, the payload and all the equipment necessary for testing, checkout, and the actual firing was packed for shipment to the Woomera missile range. For the first firing, personnel and equipment were transported to Woomera via a commercial airline under contract to provide shuttle service between Adelaide and Woomera. However, transportation procedures required that shipments of this size be released to the shipper at least 10 days prior to expected delivery at Woomera. After

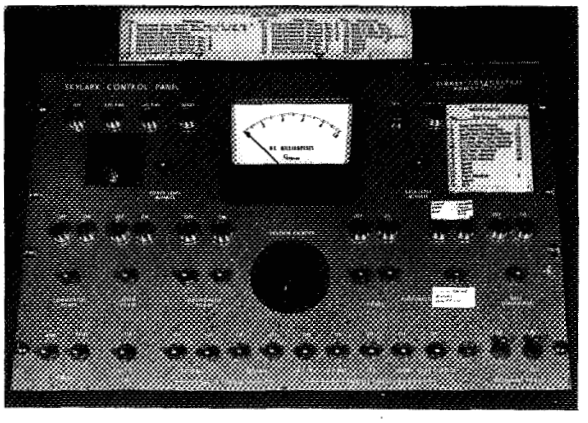

FIGURE 13.—Skylark control panel.

the first firing this delay was reduced to 1 day by sending the equipment via truck, with the personnel following via air.

The missile ranges operated by WRE are based at Woomera, some 300 miles northwest of Adelaide. (The town of Woomera—population about 4000—is located 5 miles from Pimba, on the Trans-Australian Railway, and is served by a spur line. The country is semidesert with a mean rainfall of about 7 inches per year.) A number of ranges are used at Woomera for special purposes. The principal missile range, however, is based at Koolymilka, about 25 miles from town. It provides a number of independent launching aprons, so that work can proceed on several projects at the same time. A range of approximately 1250 miles over practically uninhabited land is available. A "Homestead Warning System" has been developed to control stock and other movements in the range areas during trial periods.

At the range a test shop is available for the test and checkout of Skylark payloads. Here the payload was checked for damage in transit. Final settings were made for all detector sensitivities and amplifier zeros, and high voltage levels were set for the ion chambers. All flight chambers were then installed in the payload, high voltage leads were soldered to the copper fill stems, and the stems were completely epoxied to prevent corona from the stem to the signal ground shell less than 2 mm away.

A final pre-tower checkout was held with all systems complete and functioning: All detectors were activated, all channels were positively identified, every de-spin situation was simulated by vertical suspension of the payload from the ceiling, door blowoffs were simulated, and all monitor voltages were checked. All telescope protective covers and tapes were removed, and the skin farings were placed in position for the final time. The payload was then transported by truck to the Skylark launching pad for erection into the tower.

The tower is a 100-foot open structure made up primarily of three army Bailey bridges. Depending on whether or not a booster is used, two different working levels are provided. A removable rail permits access to the payload. Attached to the launcher is a pneumatically operated system for extracting the umbilical connectors. The land lines run from these connectors to the Equipment Center some 500 feet away.

Upon arrival at the launcher, the payload was hoisted to the appropriate level and mounted in the firing position on a temporary plate set between the rails. The final pre-flight check was then made. After this check the payload was swung clear of the rails, and the launcher was released to the launcher officer for installation of the motor and booster. The motor was backed up to the tower base on a railed dolly, and the dolly was pivoted into the tower. The motor was then hoist-held about 10 feet up in the tower while its dolly was removed and a second dolly holding the booster was erected into the tower. (The booster dolly is part of the tower structure during launch.) The motor was lowered onto the booster, and mating was completed. Finally, the payload was swung back in line and permanently bolted to the forward skirt of the motor. A removable service plate at the forward end of the motor permits access for connection of the ignition lines. After the motor is placed in the tower, range safety regulations require that no voltage sources (i.e., ohmmeters) be on the tower and that no personnel remain on the tower after 8 hours of duty in any 24-hour period.

The Skylark launch procedure requires automatic programming of the firing sequence during the last 2 minutes of the countdown. If

desired, the automatic sequencer is able to control the final 6 minutes. Prior to this, the count is conducted informally. For the NASA payloads the support instrumentation was turned on at T–6 minutes; but, in order to provide optimum zero settings, the detector amplifiers were turned on as early as T–45 minutes. At T–2 minutes the automatic sequencer took control to close firing lines, extract umbilicals, start the tracking cameras, and close the firing switch.

FLIGHT PERFORMANCE

Skylark 9.01 was fired at 1215UT on September 18, 1961. Two of the six photomultiplier telescopes performed perfectly throughout the flight. Corona in the photomultiplier high voltage circuitry of the remaining four units, implying a break in the pressure tightness of the unit, caused full scale noise on the associated telemetry channels. The noise induced into the ion chamber amplifiers through the 28-volt supply line caused the latter to show off-scale readings during part of the flight. Compounding these difficulties, the *stop* spin control valve closed the pressure line before spin control action was called for. Thus, no spin control occurred and the missile attained a coasting spin of about 0.08 rps—still slow enough to obtain useful data. Finally the protective skin panels were late in ejecting, which was attributed to the mechanical assembly rather than to the electrical or pyrotechnical system.

Skylark 9.01 came in streamlined and, while the motor was found beside a hole in the desert, no part that could convincingly be identified as payload was ever found. In order to simplify post-flight analysis, the remaining payloads were modified to separate the instrument head from the Skylark body at 375 seconds so that the payload could be recovered and inspected. The de-spin control checkout procedure was modified to include a more rigorous checkout, and no further difficulty was experienced in controlling the spin of the final three Skylarks. Additional care was given the pressure-tight sealing of the photomultiplier telescope electronics to prevent corona. Finally, the bands holding the protective skin panels were eased in tension; it had been concluded that aerodynamic heating had increased the band tension so that the pin pullers could not operate.

Skylark 9.02 was fired at 1119UT on October 4, 1961. The photomultiplier detectors and associated circuitry performed satisfactorily throughout the flight. A few brief periods of saturation in the ion chamber amplifiers were attributed to interaction caused by the use of a single converter to supply all the ion chamber high voltages. Again, the skin panels ejected late and at different times. These factors, coupled with the recovery of a panel and adjacent pieces of the casting, led to the unmistakable conclusion that design calculations for heat expansion of the panels could not have been correct. Heating of the panels early in the flight had wedged them against the retaining limits of the casting and prevented them from being ejected. As the heat was dissipated differently around the missile, each panel sprung loose at different times. Fortunately, the last door was ejected by 140 seconds. A reduction in the length of the panels cured this problem for the remaining two Skylarks.

Skylark 9.03 was fired at 1756UT on November 1, 1961. Not a single multiplier telescope maintained pressure tightness through takeoff, and all high voltage units went into corona. In addition, the ion chamber data were seriously affected because of the electrical coupling previously described in 9.01.

In spite of the success of the multiplier telescopes in 9.02, it was now apparent that the mechanical design involving their pressure tightness was basically faulty. A complete redesign at this stage of the firings was out of the question. Because of this and because the ion chamber data were considered more important, the last payload was converted to an all-ion-chamber experiment with only two multiplier telescopes retained to yield rocket attitude. The two multiplier units were epoxy-flooded in order to improve pressure tightness.

Skylark 9.04 was fired at 1804UT on November 20, 1961. The multiplier telescopes performed perfectly, and the ion chambers yielded

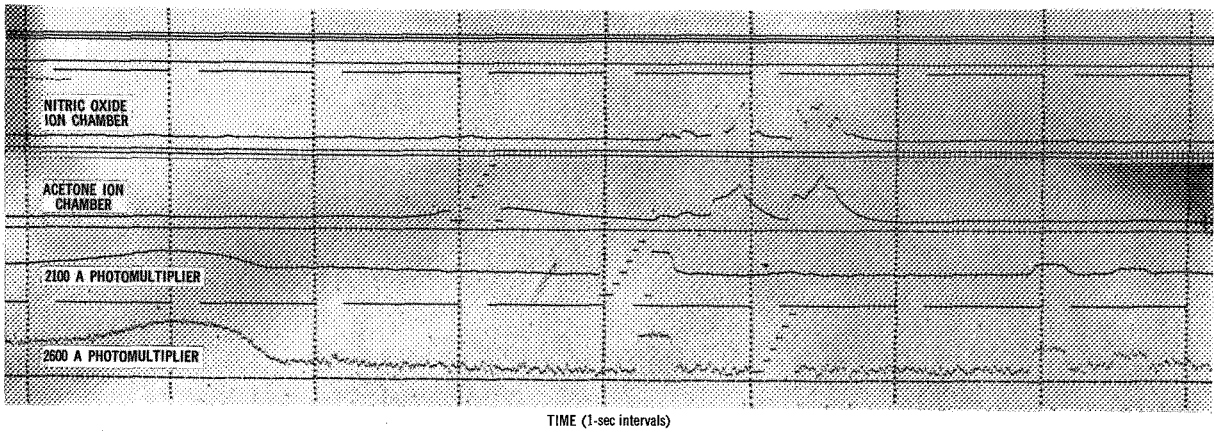

FIGURE 14.—Sample telemetry from Skylark 9.02. Channel identifications from top to bottom are: nitric oxide ion chamber, acetone ion chamber, 2100A photomultiplier, and 2600A photomultiplier. The extended source to the left on the photomultiplier channels is night airglow. All other signals are stellar. Vertical timing marks represent 1-second intervals.

good data from both stars and extended sources. There were still some brief periods of ion chamber amplifier saturation; the cause is not yet determined.

CONCLUSIONS

A telemetry sample from 9.02 is shown in Figure 14. These data are now in the process of being reduced. It is already evident that the project produced a great deal of significant data. The data received by the photomultipliers in the 2100 and 2600A bands and the nitric oxide ion chamber in the 1300A band will be of great value in supplementing existing information from the northern hemisphere at similar wavelengths. In addition, data on stellar fluxes in the 1225 to 1280A region were obtained with the acetone ion chambers; and weak stellar signals were recorded at wavelengths below Lyman-α.

ACKNOWLEDGMENTS

This work could not have been accomplished without the complete cooperation and support of a number of people under the direction of Dr. Albert Boggess III. Among those are Mr. Edward Bissell, for the preparation of the telemetry system and the operation and preparation of the ground station at Woomera; and Messrs. Baker, Fiorelli, and Scolnik for the preparation of the payload. The author also wishes to thank Mr. Ralph Cartwright, Principal Officer of the Research Vehicles Group, and his entire group at the Weapons Research Establishment for their complete cooperation in support of the preparation and firing of the rockets in Australia.

REFERENCES

1. DORLING, E. B., "The First Six Skylark Firings," Royal Aircraft Establishment, Farnborough, England, Technical Note No. G.W. 530, October 1959.
2. SWEET, M. H., "Logarithmic Photometer," *Electronics* 19: 105–109, November 1946.
3. CHILDS, C. B., "Broad-Band Ultraviolet Filters," *J. Opt. Soc. Amer.* 51(8): 895–897, August 1961.
4. HASS G., and TOUSEY, R., "Reflecting Coatings for the Extreme Ultraviolet," *J. Opt. Soc. Amer.* 49(6): 593–602, June 1959.
5. STOBER, A. K., "Ceramic Vacuum Ultraviolet Ion Chambers," NASA Technical Note D–1180, March 1962.
6. WATANABE, K., "Photoionization and Total Absorption Cross Section of Gases. I—Ionization Potentials of Several Molecules. Cross Sections of NH_3 and NO," *J. Chem. Phys.* 22(9): 1564–1570, September 1954.
7. PRAGLIN, J., and NICHOLS, W. A., "High-Speed Electrometers for Rocket and Satellite Experiments," *Proc. I.R.E.* 48(4): 771–779, April 1960.

Page intentionally left blank

VI. ENVIRONMENTAL TESTING

Page intentionally left blank

SINUSOIDAL VIBRATION TESTING OF NONLINEAR SPACECRAFT STRUCTURES

WILLIAM F. BANGS

Goddard Space Flight Center

The vibration testing of large spacecraft structures in accordance with procedures similar to those developed for military equipment during the 1940's has numerous shortcomings, particularly if the testing process is considered to be a duplication of an equipment's in-service vibration. The purpose of this technical note is to discuss some of the shortcomings associated with the familiar sinusoidal sweep test.

Waveform distortion, being one of the more obvious problems, is discussed. An analytical model of a simplified structure undergoing vibration testing was studied with the aid of an analog computer. Solutions for a nonlinear model demonstrate distortion of the armature acceleration even though the applied force is sinusoidal. Filtering the control signal to eliminate distortion may unduly penalize the specimen, although this technique is acceptable where the distortion is the "random" type caused by the banging of parts.

The current trend toward larger spacecraft structures will undoubtedly continue, and the problems we now face will be small in comparison to those of the future unless some revisions are made in today's philosophy.

INTRODUCTION

The sinusoidal sweep vibration test is required by Goddard Space Flight Center (GSFC) for the qualification of spacecraft structures and subassemblies. Although it is generally agreed that random vibration testing more closely simulates the actual flight environment, sinusoidal tests will continue to be specified either as a supplement to the random test or, in some cases, as the sole vibration requirement. The reason for this policy is that the sinusoidal test offers certain advantages over the random test:

1. The sinusoidal test is superior as a diagnostic tool. Since excitation is applied at a single frequency, resonant frequencies and modes can be accurately described. Because random excitation produces the simultaneous response of many modes, the behavior of each mode is obscured. Performed in the development stage, the sinusoidal test invariably points out design deficiencies that can be corrected early in the test program.

2. Sinusoidal vibration can be applied in the frequency ranges not included in typical random tests. Most important is the frequency range of 5 to 20 cps, in which stress levels are likely to be high and interaction of a spacecraft and a vehicle, in its low frequency modes, is likely to occur. Many of the larger spacecraft now being developed have resonances below 20 cps.

3. Sinusoidal testing is relatively inexpensive, and equipment is readily available. For this reason, testing at the subassembly level is often accomplished by using only sinusoidal excitation. Sine wave tests are usually specified in terms of motion (acceleration, velocity, or displacement) at the normal mounting point of the equipment under test.[1] One of the major problems occurring in sinusoidal vibration testing of structures that are heavy

[1] One exception is the specification for the NASA Scout and Delta payloads, in which there is an option allowing simulation of the solid rocket motor vibration by controlling the force imparted to the payloads.

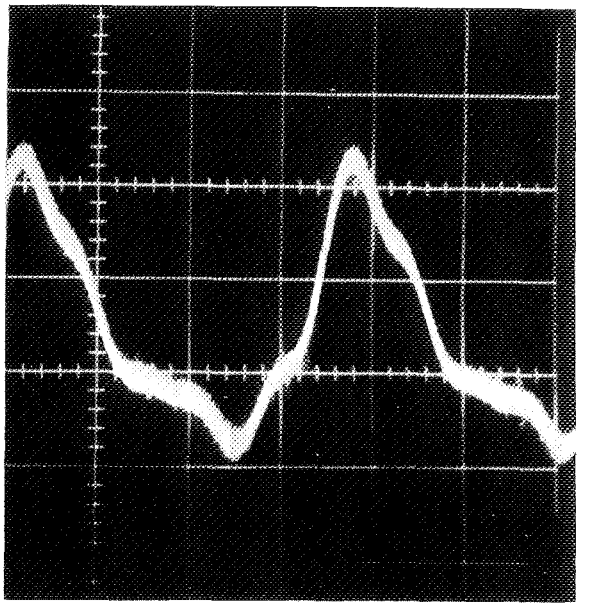

FIGURE 1.—Harmonic distortion of "input."

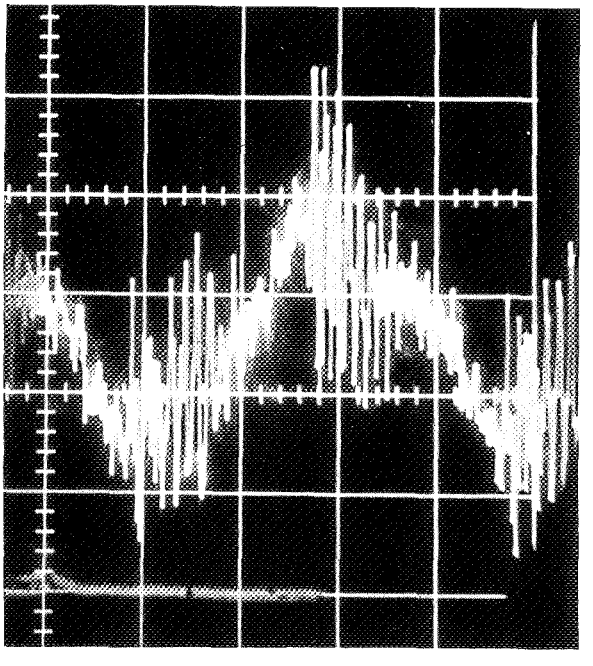

FIGURE 2.—Aperiodic distortion of "input."

compared with the shaker armature is waveform distortion in the motion of the mounting point.

Since the "input," or specification level, is normally monitored at the mounting point, waveform distortion here raises questions about the adequacy of the test. Figures 1 and 2 show examples of distorted waveforms that were observed during the vibration testing of the Orbiting Solar Observatory I satellite (1962 ζ 1) structural model.[2]

The purpose of this report is to review some possible sources of waveform distortion, present the results of an analog study of a nonlinear system that exhibited distortion, and discuss the effects of distortion on vibration testing.

SOURCES OF DISTORTION

The problem of distortion in sinusoidal vibration testing is not a new one. However, its magnitude has increased in recent years until it can no longer be ignored as it has in most cases in the past. In some recent tests,[3] the harmonic components have exceeded the fundamental, so that determination of the source of the distortion has became imperative.

Wrisley (Reference 1) suggests that in some cases the equipment can be at fault. If a small amount of harmonic distortion is present in the output of the vibrator's power supply, we can expect a condition in which the frequency of a harmonic is coincident with that of a lightly damped resonance in either the structure being tested or the armature. The resonant structure could then be excited at a level great enough to produce a significant amount of harmonic motion at the "input" transducer location.

Although waveform distortion in the electrical input can certainly be a cause of "input" motion distortion, the type of distortion plaguing the engineer in spacecraft testing is that resulting from structural nonlinearities. The following symptoms support this theory:

1. The frequency of the harmonic usually does not correspond to a resonant frequency of the structure.

2. The apparent resonant frequency varies

[2] Kirchman, E. J., and Hartenstein, R., "Evaluation of Vibration Test Data from the S-16 Structural Model Tests," NASA Report 321-1 (RH) S-16-09, Goddard Space Flight Center, May 1961.

[3] For example, Shockey, E. F., "S-51 Dutchman-Separation Mechanism Vibration Tests," NASA/GSFC Memorandum Report 621-7, December 16, 1961.

with the amplitude of excitation. This is a well-known characteristic of nonlinear structures.

3. The "random" distortion (as shown in Fig. 2) couldn't very well be attributed to electrical wave distortion.

Structures exhibiting nonlinear stiffness properties can be broadly classified as either continuous or discontinuous. An example of a *discontinuous* structure is one in which there is small clearance or looseness between parts. If, during the vibration excitation, parts collide, many modes of the parts will be excited at high accelerations. Figure 2 shows the effect of this phenomenon on the "input" acceleration.

Structures that are *continuously* nonlinear influence the shaker motion by adding harmonics to the waveform. Figure 1 is an example of this. To further understand the effects of nonlinear structures undergoing vibration, a simplified shaker and a single-degree-of-freedom specimen with a cubic hardening spring were studied by means of an analog simulation.

ANALOG SIMULATION

The mathematical model is based on the following assumptions:

1. The vibrator's armature, the test fixture, and the part of the test specimen not resonating act as a rigid mass.

2. The part of the specimen in resonance can be represented as a mass with a nonlinear connecting spring.

3. The force acting on the vibrator's armature coil is sinusoidal regardless of the motion of the armature.

The system is shown in Figure 3. Summing the forces on each mass yields the equations of motion:

$$M\ddot{x}+C\dot{x}+D(\dot{x}-\dot{y})+Kx+f[x-y]=F\sin\omega t, \quad (1)$$

$$m\ddot{y}+D(\dot{y}-\dot{x})+f[y-x]=0, \quad (2)$$

where $f[\ ]$ is the nonlinear spring force, a function of the spring extension $(y-x)$ or compression $(x-y)$, and the notation for masses, spring constant, damping coefficients, and coordinates is indicated in Figure 3.

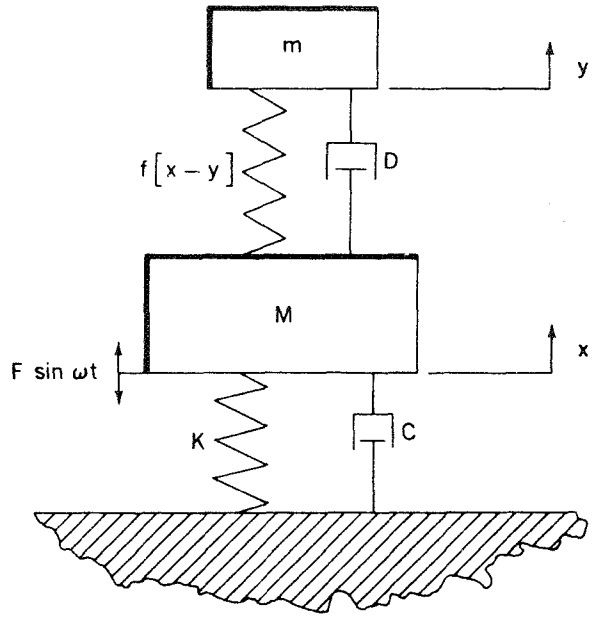

FIGURE 3.—Mathematical model of vibration exciter and nonlinear specimen.

Structures often have a tendency to become stiffer or to "harden" with deflection. Thin panels are known to behave in this manner (Ref. 2). The Duffing spring, represented by a linear plus a cubic term in the force deflection expression, has been used to represent the structural stiffness. Thus, $f[x-y]$ in Equation 1 has been taken as

$$\left.\begin{aligned} f[x-y]&=k(x-y)+\beta(x-y)^3 \\ f[y-x]&=-f[x-y] \end{aligned}\right\}. \quad (3)$$

Equations 1 and 2 can be expressed in dimensionless form by making use of Equation 3 and the following identities:

$$\tau=\omega_0 t,\ \omega_0^2=\frac{k}{m},\ \Omega^2=\frac{K}{M},\ \frac{C}{C_c}=\frac{C}{2\Omega M},\ \frac{D}{D_c}=\frac{D}{2\omega_0 m};$$

$$x=\left(\frac{g}{\omega_0^2}\right)\phi,\ y=\left(\frac{g}{\omega_0^2}\right)\psi,$$

$$\dot{x}=\left(\frac{g}{\omega_0}\right)\frac{d\phi}{d\tau},\ \dot{y}=\left(\frac{g}{\omega_0}\right)\frac{d\psi}{d\tau},$$

$$\ddot{x}=g\frac{d^2\phi}{d\tau^2},\ \ddot{y}=g\frac{d^2\psi}{d\tau^2};$$

where g is the acceleration of gravity.

By substitution, Equations 1 and 2 become

$$\frac{d^2\phi}{d\tau^2}+2\frac{\Omega}{\omega_0}\frac{C}{C_c}\frac{d\phi}{d\tau}+2\frac{m}{M}\frac{D}{D_c}\frac{d}{d\tau}(\phi-\psi)+\frac{\Omega^2}{\omega_0^2}\phi$$

$$+\frac{m}{M}(\phi-\psi)+\frac{m}{M}\frac{\beta}{k}\frac{g^2}{\omega_0^4}(\phi-\psi)^3=\frac{F}{Mg}\sin\frac{\omega}{\omega_0}\tau, \tag{4}$$

$$\frac{d^2\psi}{d\tau^2}+2\frac{D}{D_c}\frac{d}{d\tau}(\psi-\phi)+(\psi-\phi)+\frac{\beta g^2}{k\omega_0^4}(\psi-\phi)^3=0. \tag{5}$$

Most of the dimensionless coefficients in Equations 4 and 5 are simple ratios that need no explanation. The significance of the term $\beta_g{}^2/k\omega_0{}^4$, however, isn't immediately obvious. If the substitution for the static deflection δ of a mass resting on a linear spring (of rate k) is made,

$$\frac{\beta g^2}{k\omega_0{}^4}=\frac{\beta}{k}\delta^2=\frac{\beta\delta^3}{k\delta}.$$

Thus, $\beta g^2/k\omega_0{}^4$ is the ratio of the nonlinear force component to the linear force at the deflection δ. Figure 4, which shows the force deflection curves for the linear and the Duffing springs, better illustrates the significance of the parameter. It should be emphasized that the deflection δ is the static deflection for a linear spring (i.e., mg/k) and not the actual deflection for the Duffing spring.

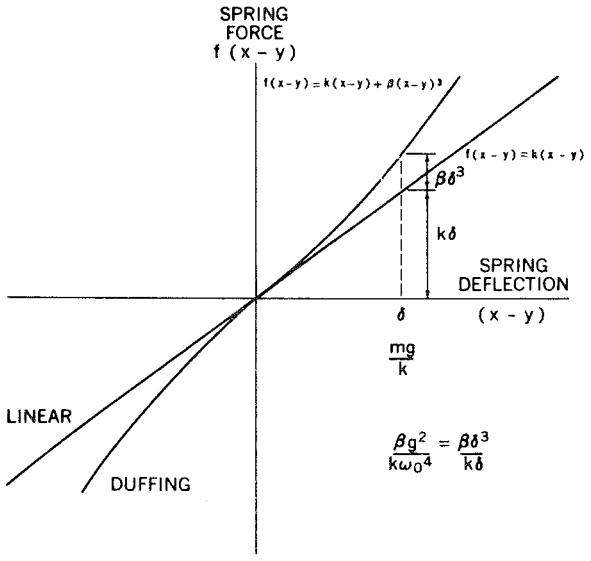

FIGURE 4.—Force deflection curves for the linear and the Duffing springs.

An analog computer was used to obtain some solutions to Equations 4 and 5. The Duffing spring characteristic was obtained with a diode function generator. Seven connected straight line segments approximated the force deflection curve for the spring. Thus the accuracy of the solutions, for very low amplitudes, leaves something to be desired. Where $\phi-\psi$ is not small, several line segments are being utilized and the approximation is adequate.

To obtain a solution to Equations 4 and 5, specific numerical values had to be selected for the coefficients. The following values were selected as possibly representing an actual system:

$$\frac{C}{C_c}=0.05,\ \frac{m}{M}=0.50,$$

$$\frac{D}{D_c}=0.05,\ \frac{\beta g^2}{k\omega_0{}^4}=0.10,$$

$$\frac{\Omega}{\omega_0}=0.20.$$

With these parameters set into the computer, a sinusoidal input $\frac{F(\omega)}{Mg}\sin\frac{\omega}{\omega_0}\tau$ was applied such that the peak nondimensional acceleration $d^2\phi/d\tau^2$ was approximately constant for the forcing frequency range of ω/ω_0, varying from 0.7 to 1.38. Some resulting waveforms are shown in Figure 5 for the three values of zero to peak acceleration: 0.25, 0.50, and 0.75.

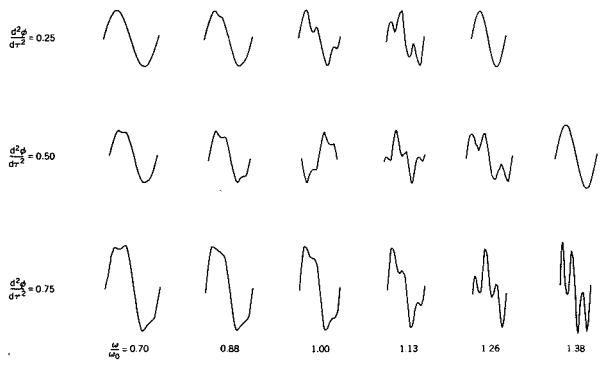

FIGURE 5.—Wave shapes for $d^2\phi/d\tau^2$ (peak) = 0.25, 0.50, 0.75.

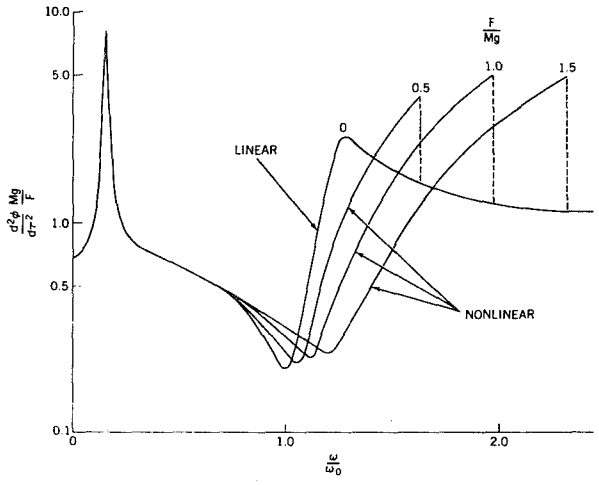

FIGURE 6.—Vibration acceleration for a constant force input $\frac{d^2\phi}{d\tau^2}\frac{Mg}{F}$ vs. $\frac{\omega}{\omega_0}$.

It is also interesting to note how the charcateristics of the model vibrator change when the usually assumed linear load is replaced with a nonlinear load. Here, the sinusoidal force amplitude was held constant as frequency was varied. The armature acceleration $d^2\phi/d\tau^2$ was monitored, and the response curves for four forcing amplitudes are presented in Figure 6. The zero to peak values of $d^2\phi/d\tau^2$ were plotted after dividing by F/Mg to normalize the curves. The curve for the near-zero force corresponds to the well-known linear solution in which the resonant specimen influences the vibrator's characteristics by the insertion of a notch and peak in the response curve. The distortion of the frequency response curve for the nonlinear case is clearly shown in Figure 6. The waveform of $d^2\phi/d\tau^2$ is a distorted sine wave for all of the nonlinear curves. As the driving frequency is increased, a point is reached where the system response abruptly changes. The deflections of the nonlinear spring become small, and the system behaves very nearly as a linear system.

DISCUSSION

The analysis has explained one of the causes of distortion that occurs during a sinusoidal test. Experience with large spacecraft structures has shown that the nonlinear structural phenomenon is the most important one, namely because it appears at the major structural resonances where large excursions and high stress levels are likely to cause structural failure. On smaller packages the effect of nonlinear stiffness of the package isn't too important because the major resonances occur at higher frequencies with lower stress levels and also because the harmonic forces generated within the small structure are not capable of driving the relatively large mass of the shaker armature and fixture at significant amplitudes.

The usefulness of the analysis ends here since, by the nature of nonlinear problems, a solution for a given set of parameters cannot readily be extended to another problem. Also, the nonlinear parameters for a real structure are extremely difficult to define.

The question that naturally follows an explanation of the source of a problem is what to do about it. Suggestions from literature on the subject are summarized below:

1. Wrisley (Reference 1) attributes most distortion to harmonics in the amplifier output that may be multiplied when one of the harmonics corresponds to the armature or some other structural resonant frequency. He points out the errors in trying to measure and control peak acceleration by using an averaging meter for varying percentages and phase of third harmonic distortion. Wrisley concludes that vibration facilities should be equipped to use feedback proportional to the peak acceleration and a true peak reading meter to monitor acceleration.

2. Schafer (Reference 3) points out that vibration amplitudes may be in error by ±90 percent because of distorted acceleration waves. He feels that the insertion of a filter on the output of the control accelerometer, to eliminate all but the driving frequency component of acceleration waveform, would result in a test that comes closer to carrying out the intent of the specification.

Apparently these authors disagree, since Wrisley proposes that the instrumentation be such that the actual peak is sensed and used for control—regardless of the frequency com-

ponents contributing to the peak, whereas Schafer feels that everything but the fundamental should be disregarded.

When a specification requires a given acceleration in the sinusoidal test schedule, it seems reasonable to assume that this level applies to the fundamental forcing frequency even if the motion cannot be maintained sinusoidal. Schafer's approach, then, is the obvious choice if the test is to be carried out in strict accordance with the specification.

There are cases, especially when testing large structures, where presently available vibration equipment is being driven at maximum force output and still not meeting the specified acceleration levels, even including harmonics. In general, this situation arises at the major resonances of the structure where distortion is most likely to occur. If the recommendation given by Schafer is followed, the deficiency of available force will be even greater. Likewise, the percentage of harmonic content will increase since it is generated by nonlinear phenomena.

Specifications can be satisfied if substantial changes are made in the basic vibrator design. First of all, force output could be increased to the 100,000-pound range. Armature weight, presently kept to a minimum, could be increased substantially, and thereby increase the mechanical impedance of the shaker table and reduce the effect of harmonic forces on "input" motion.

The thought of applying a vibratory force of even 30,000 pounds (today's limit) to a rocket-borne payload structure should raise a question regarding the soundness of the philosophy behind such requirements: What are the requirements dictating that a structure be qualified by the following procedure?

1. Attaching it to another structure that is unspecified and drastically different from the launch vehicle,
2. Exciting it by a force that is generally unknown and that is controlled only by the response of a point where the spacecraft structure and vibrator structure are joined, and
3. Limiting the input force to the maximum force capability of the vibrator.

The answer to this question probably lies in the evolution of vibration testing. The philosophy in the early days was to "drive" a relatively small article with a high impedance device: either a mechanical shaker, or the electrodynamic machines availabe at the time. Here, the assumptions were simply that the environment could be simulated by duplicating motion because of the high impedance of the equipment's normal mounting structure as well as the shaker.

Today there is no technical justification for motion-controlled testing; it exists only because of its history. The reference to the shaker's acceleration as an "input" demonstrates the need for revision in our thinking. In large test specimens, the shaker table's motion is no more an "input" than is the motion of the end of the structure. In some cases, it's likely to be a node; in others, an antinode. The major resonances observed during the test are usually nonexistent when the spacecraft is mated with its vehicle.

The problem of waveform distortion presents a dilemma that has to be resolved by the originator of the specification rather than the vibration equipment manufacturer. It is he who has failed to recognize the fact that, in testing real structures, nonlinearities exist and deviations from the required test are natural occurrences. This problem, which is one of many associated with vibration simulation, can be resolved only through a revision of present requirements.

CONCLUDING REMARKS

Test concepts for the future should include considerations for monitoring force as well as motion; for the effect of the impedance of the body being tested, the launch vehicle, and the vibrator; for control of the vibrator's impedance, if feasible; for reliance on vehicle/spacecraft analyses for loads and mode shapes that cannot be duplicated but certainly should be considered in the laboratory. The possibility of eliminating shaker-driven vibration testing above 200 cps, for example, and reliance on acoustic testing in the high frequency range should also be considered where applicable. Testing with

the structure cantilevered from a solid foundation, for more controlled testing and the acquisition of structural dynamic properties not distorted by shaker and slip table characteristics, might more closely simulate in-flight load distributions.

A few procedures that are recommended by GSFC for the testing of large spacecraft structures might be useful to those presently facing the problem with similar structures:

1. Waveform should be closely monitored so that we can at least know what happened during the test—right or wrong. This, by necessity, requires that data be stored on magnetic tape and spectrum-analyzed at critical frequencies.
2. The signal from the control transducer should not be filtered unless it has been established that the distortion is that resulting from looseness or banging of parts. On a satellite structure recently tested at GSFC, the second harmonic of the table acceleration was 3.8 times that of the forcing frequency.* In this case, filtering and driving the fundamental to the specified level would surely have destroyed the structure.
3. Since motion control can result in unreasonably high loads, fixtures should be equipped with force transducers to monitor bending moment and axial load. These loads should not be allowed to exceed the design limit during the vibration test.

*See footnote re Shockey report, p. 640.

ACKNOWLEDGMENTS

The author wishes to thank Dr. J. E. Greenspon, J. G. Engineering Research Associates; Messrs. E. J. Kirchman, W. R. Forlifer, and R. G. Hartenstein, GSFC, for their assistance in this study.

REFERENCES

1. Wrisley, D. L., "Some Effects of Acceleration Waveform Distortion in Sinusoidal Vibration Testing," *Test Engineering* 5(2): 16–18, February 1961.
2. Kirchman, E. J., and Greenspon, J. E., "Nonlinear Response of Aircraft Panels in Acoustic Noise," *J. Acoust. Soc. Amer.* 29(7): 854–857, July 1957.
3. Schafer, C. T., "Uniform Input Control—a Must for Accurate, Repeatable Tests," *Vibration Note book*, published by MB Electronics, 7(4), October 1961.

THE PURPOSES OF ENVIRONMENTAL TESTING FOR SCIENTIFIC SATELLITES

JOHN H. BOECKEL
Goddard Space Flight Center

The economic necessity of high reliability dictates a major role for environmental testing in the exploration of space. High reliability in spacecraft can be achieved only through extensive environmental testing. Successful testing depends on a comprehensive test plan that is formulated from the requirements of specific programs. Successful satellites and space probes can be achieved most economically by full use of such test programs and by the timely application of object lessons learned from previous programs.

INTRODUCTION

Reliability is an attribute of a device that cannot be directly measured. In treating reliability numerically, the concepts of probability are introduced; and reliability can be defined as:

> The probability of a successful operation of the device in the manner intended and under the conditions of intended customer use.

This definition (Reference 1, p. 20)—and many similar ones—leads to a large number of questions concerning, chiefly, the determining of the required level of "probability" and the defining of criteria for "success."

The required level for the reliability of a satellite is a function of its mission. This paper will discuss the reliability and environmental testing problems that apply to *scientific* satellites as distinguished from spacecraft used for manned space flight or for military purposes. In general, the manned and military missions require a considerably higher degree of reliability than does the scientific one. Unreliability in a scientific satellite implies loss of data; in a manned satellite, loss of life; and, in a military satellite, risk to the nation's defense posture. On the other hand, the scientific satellite is usually more complex, is developed in a short period of time, and carries instrumentation at the highest levels of the state-of-the-art. The problems of reliability assessment are therefore of comparable difficulty for all three categories but are approached from slightly differing points of view.

The objective of the scientific satellite is to make fundamental measurements that cannot be made from the earth. In some cases, these measurements must be made in situ; in others, the instruments must be raised above the distorting effects of the earth's atmosphere, magnetic field, and ionosphere. A given satellite usually carries a set of experiments intended to make *simultaneous* measurements of interest in a given discipline: thus, Explorer VIII (1960 ζ1) makes direct measurements of the ionosphere, Explorer XI (1961 ν1) orbits a gamma ray telescope, Explorer XII (1961 υ1) measures energetic particles, and the Orbiting Solar Observatory I (1962 δ1) measures electromagnetic radiation from the sun. A list of satellites and space probes launched by the Goddard Space Flight Center (GSFC) as of December 1962 is attached as Appendix A.

In broader terms, Dr. Robert Jastrow (Reference 2) has summarized the intent of NASA's scientific investigations in space as follows:

> Although they involve many questions in physical science, nonetheless most of

the matters under investigation by space flight vehicles may be grouped around a relatively small number of central problems:

First, problems relating to the structures of stars and galaxies: stellar evolution, nucleosynthesis, the cosmic abundances of the elements.

Second, the origin and evolution of the solar system, the formation of the sun and planets, and the subsequent history of planetary bodies.

Third, the control exercised by the sun over the atmosphere of the earth, the structure of the upper atmosphere, and the causes of weather activity in the lower atmosphere.

The level of reliability that should be required of a satellite whose purpose is to gather data applicable to these fundamental problems is difficult to set. In terms of the usual time scale for evolving new scientific theory from basic data, the scientist is not particularly interested in whether the data come from today's launching or from the launching of the backup flight unit a few months hence. (Favorable planetary orbital conjunctions are an obvious restriction on this freedom in time. However, the "launch window" is often sufficiently long to provide for a second launching.) The circumstance of a backup unit, then, gives the impression that the only requirement is a reasonably high probability that at least one of the two units should be successful.

Another problem arises when the question of what constitutes success is considered. Since perhaps five experiments may be flown on even a small satell te, not all experiments are required to work perfectly before the shot is called a success. Furthermore, the required duration for acceptable operation should be defined. For some satellites, transmission of data for a few orbits might suffice. For others, from which we hope to determine expected ranges of the measured parameters, months may be needed.

On the basis of scientific considerations alone, assignment of reliability requirements is impossible. Reliability is fundamentally a ratio; it is used to weigh risk against investment. Traditionally, scientific investigation has been concerned with the gathering of accurate data, subjecting it to rigorous analysis, fitting it to theoretical hypotheses, and subsequently gathering further independent data for verification of the results. Employing satellites as a scientific tool has changed one factor in this process markedly: the *cost* of making the experiment. Expensive tools have been used before (e.g., the cyclotron); however, the "one-shot" nature of the satellite experiment is probably paralleled only by the investigations of the effects of atomic explosions.

With the introduction of cost considerations, we have a basis for stating the satellite reliability problem: A level of performance must be obtained to balance the high cost of an individual firing against the need for obtaining timely, accurate data with a package of minimum weight containing exotic instrumentation.

TABLE 1.—*Scientific Satellite Costs* [1]

Satellite	Vehicle	Cost (10^6 dollars)	
		Spacecraft	Vehicle
International II	Scout	1.3	1.0
Explorer XII	Delta	2.7	2.5
POGO	Thor-Agena	11.5	6.5
Advanced OSO	Atlas-Agena	17.0	8.3

[1] These numerical values are estimates and must not be taken as authoritative.

Typical scientific satellite costs are given in Table 1.

By taking the total dollars budgeted and the total weight of satellites in orbit, an estimate of $50,000 per pound may be derived for all efforts to date (Reference 3). It is clear, then, that we cannot be promiscuous in launching unproven designs.

A TYPICAL SCIENTIFIC SATELLITE—EXPLORER XII

Before proceeding further with a discussion of reliability, a brief exposition of a typical satellite's makeup is in order. Explorer XII,

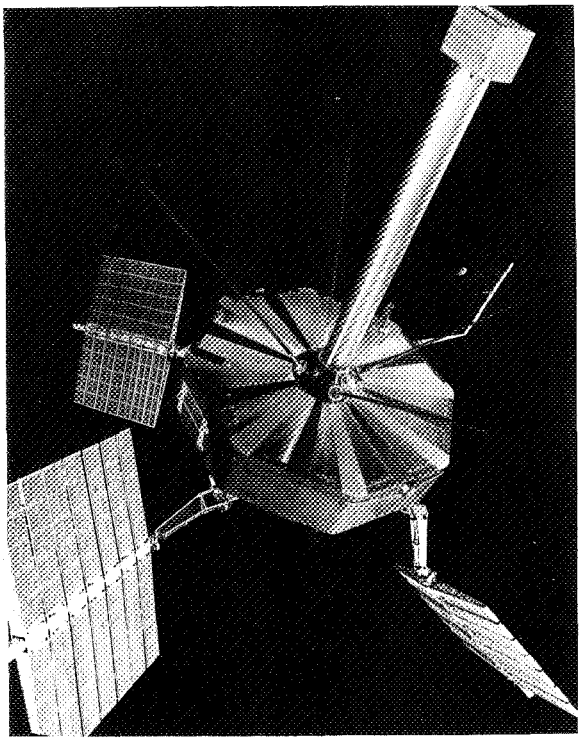

FIGURE 1.—Explorer XII.

TABLE 2.—*Weight Breakdown by Function*

Function	Weight (lb)	Percent of total weight
Structure	22.5	27.0
Telemetry	5.5	6.6
Power supply	21.7	26.0
Interface hardware	6.0	7.2
Experiments	27.5	33.0
Total	83.2	99.8

launched on August 15, 1961,[1] carried some five experiments and provided 2568 hours of real-time data before it ceased transmitting.

Figure 1 is a picture of Explorer XII. Figure 2 shows a block diagram of the system. A weight breakdown by function is given in Table 2.

This basic satellite with different experiments was also successfully flown as Explorers XIV and XV (1962 Bγ1 and 1962 Bλ1).

[1] See Appendix A description.

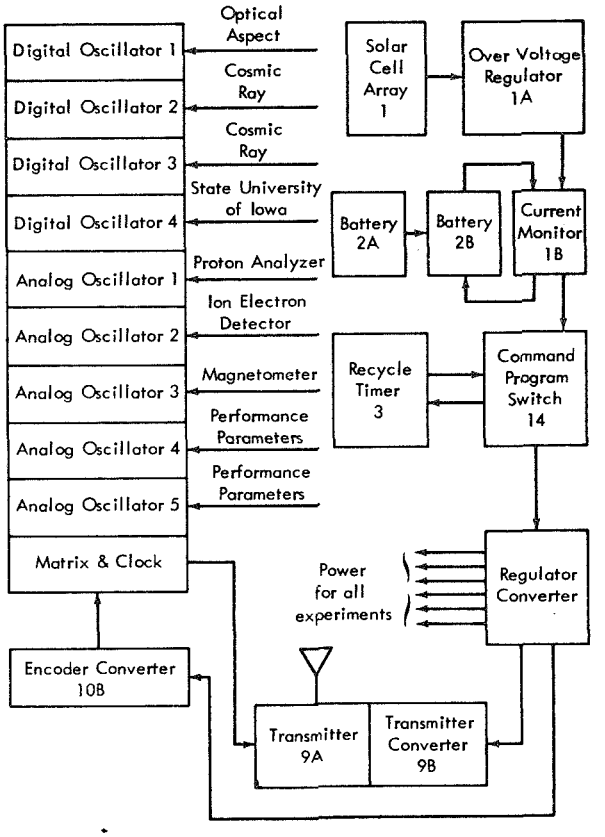

FIGURE 2.—Explorer XII system.

From a reliability point of view, there is nothing striking thus far. There is an electronics package weighing little more than a typical television set. However, a closer look reveals an impressive number of electronic parts (Table 3). It may be taken for granted that

TABLE 3.—*Electronic Parts*

Part	Quantity
Capacitors (fixed)	1,121
Capacitors (variable)	9
Diodes	813
Resistors (fixed)	2,633
Resistors (variable)	11
Transistors	1,063
Connectors	70
Inductors	93
Transformers	43
Crystals	2
Switches	10
Solar cells	6,144
Total	12,002

these parts are taxed as heavily as the designers dare in an effort both to minimize weight and to perform sophisticated tasks.

MATHEMATICAL MODELS

Lloyd and Lipow (Reference 1, ch. 9) discuss the establishment of mathematical models of physical systems wherein the reliability of each function of the system can be estimated for a point in time. This type of model can be extended to cover the probability of successful operation as a function of time. The reliability assessment of the Mariner spacecraft by the Planning Research Corp. is a good example of this technique (Reference 4).

After the model is established, empirical data for the expected performance of the individual parts (under predicted electrical and environmental stresses) are inserted. These data are almost always in terms of failure rates as defined for an exponential distribution (Reference 1, p. 137). By suitable combination of these rates, we may derive the expected *mean time between failures* for the complete system. Table 4 gives such predictions for the Explorer XII spacecraft.

TABLE 4.—*Expected Mean Time Between Failures*

Satellite subassembly	Mean time between failures (10^6 hr)
Overvoltage regulator	0.085
Current monitor	.16
Batteries A and B	2.5
Recycle timer	.051
Command program switch (essential components)	.12
Command program switch (all components)	.061
Regulator converter	.012
Encoder converter	.044
Digital oscillator 1 (optical aspect)	.030
Digital oscillator 2 (cosmic ray)	.033
Digital oscillator 3 (cosmic ray)	.022
Digital oscillator 4 (SUI)	.031
Analog oscillator 1 (Ames)	.046
Analog oscillaotr 2 (I and E)	.045
Analog oscillator 3 (magnetometer)	.046
Analog oscillator 4 (performance parameters)	.020
Analog oscillator 5 (performance parameters)	.016
Transmitter	.030

There is a fundamental difficulty in employing the output of a satellite's mathematical model: the applicability of the empirical data used. Because the pace of electronic-parts development has been so rapid, the large sample sizes, uniform populations, and statistical product quality control that must form the basis for the prediction of parts performance do not apply. Or, as was stated recently, "The model is good; if only we had some decent parts data." NASA is now trying to assemble a "preferred parts list" for space applications. However, it is very difficult to tell the designer that he must wait months for qualification testing when a supplier markets a new high-performance device.

At present, then, the mathematical prediction is only indicative. The intent in setting up a model of a satellite system is to highlight those elements of the assembly having the greatest impact on system performance rather than to make accurate quantitative predictions.

TESTING PHILOSOPHY

Satellites not only are *one-shot* but are virtually *one of a kind.* Usually a prototype, a flight unit, and a backup flight unit are the only complete assemblies that are made. Thus, the variations between individual elements and the unpredictable interactions and dependencies that are the curse of accurate mathematical analysis tend to dominate the problem. Therefore, flight unit performance cannot be predicted statistically from the previous test results, and rigorous testing of *the actual flight units* becomes a necessity.

The purpose of environmental testing in a satellite program is to establish the suitability for flight of a given flight unit. Hereafter, we will speak almost entirely of systems tests. Subassembly testing under environmental stresses more severe than those expected in actual use is presupposed. It must be noted here that the difficulty of conducting adequate subassembly tests of complicated new devices on the time scale of the typical satellite development program is frequently overwhelming. This results

in the presence in early systems tests of subsystems that may never have experienced environmental exposures. This fact is particularly true of the experiments themselves.

The emphasis on systems testing is sound on a statistical basis, as pointed out by Lloyd and Lipow in their discussion of experimentation and testing (Reference 1, pp. 350 and 371). There is one point, however, that these authors do not discuss: the fact that, in tests of a complete system, no information is generated as to the input and output sensitivities of individual subassemblies. A marginal condition may exist and remain undetected. Subassembly testing must cover this problem.

SYSTEMS TEST OBJECTIVES

The systems test program for a satellite has six goals:

1. Verification that novel or unproven designs meet performance requirements and have a satisfactory life expectancy.
2. Verification that particular samples of previously employed hardware are suitable in a new application.
3. Elimination of defects in design, material, or workmanship (i.e., finding the weak links in the chain).
4. Discovery of unexpected interactions between subassemblies when the system is exposed to environmental stress.
5. Training of personnel who will be responsible for the satellite at the launching site and who will be responsible for data reduction and analysis.
6. Generation of information that will serve as a guide in making new designs and in assessing their reliability.

(It should be noted that we do not pretend in any way to *measure* the reliability of the satellite.)

In attempting to reach these goals, despite the limitations, a model of the failure pattern that we might expect to encounter must be formulated. The test philosophy is then based on this concept. Our somewhat limited experience suggests that satellite failures fall into four categories:

1. Early failures caused by a major design weakness.
2. Early failures resulting from defects in material or workmanship.
3. Random failures whose frequency of occurrence is a function of design and quality control.
4. Wear-out failures.

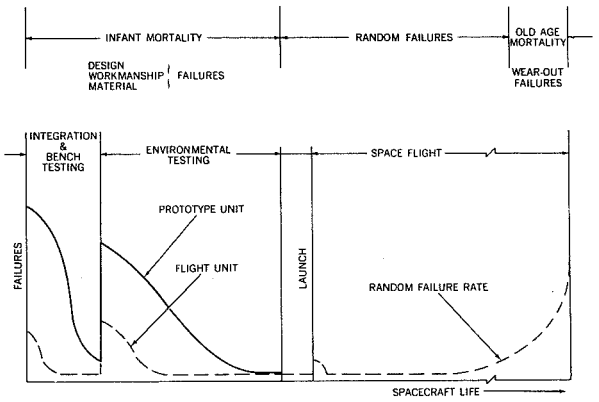

FIGURE 3.—Failure pattern.

Figure 3 illustrates this failure pattern, which is also discussed by Lloyd and Lipow (Reference 1, p. 416) as being applicable to rocket engines.[2]

The systems test program is directed chiefly at eliminating those failures that arise from the first two causes. Although some insight is gained during the program into the pattern of random failure to be expected, the mathematical reliability analysis (despite its weaknesses) is probably the best guide, after infant mortality has been accounted for, to expected performance. Wear-out caused by exposure to mechanical environments is often covered in the test program. Wear-out caused by other factors—such as surface deterioration under high vacuum—is usually best attacked at a materials, component, or subassembly level because of the extreme cost of conducting extended systems tests.

[2] It should be noted that this failure pattern has been attacked as unsupported by data by many authors (e.g., Cuthill, R. W., "The Reliability Concept and Its Relationship to Performance," American Management Association Report).

DESIGN QUALIFICATION (PROTOTYPE) TESTS

In a given satellite development program there may or may not be an electronic breadboard of the complete system. In any case, the *prototype* is almost invariably the first unit in which the subassemblies appear together in their-near final configuration, packaged in their proper relation in the final structure. As Figure 3 indicates, many problems may be expected in integrating the subassemblies into the prototype before a "working" satellite is produced. At some point in the integration of the prototype, the pursuit of perfection in "bench" performance must be discarded in favor of the study of the design's performance in the environmental rigors to be encountered in the prelaunch, launch, and space flight phases of its life. This is a conscious decision on the part of the project manager.

Tests of the prototype system are directed toward the *qualification* of a design. It is in this series of tests that failures in the first category (major design weakness) should be eliminated. In attempting design-qualification with one sample, we must break with many traditional environmental test concepts. Overtesting is a necessity but, because of weight limitations, designs cannot be expected to have too great a margin.[3] Test-to-failure in several environments becomes nearly impossible in the time scale of a typical program. In the face of these problems, prototype test levels are usually established at what might be considered the 99 percent probability level—that is, there should be no more than one chance in a hundred that the flight unit will experience an environment more severe than that employed in prototype testing. The difficulties in setting a 99 percent level in a field as new as space flight are self-evident: Adequate data usually do not exist.

[3] We must also be aware of another trap in over-specifying environments. For example: A design temperature set arbitrarily high may force the use of low-gain silicon transistors when one-half as many germanium transistors might have done the job. Here, reliability may have been *decreased* rather than enhanced.

FLIGHT UNIT TESTING

Tests of the flight units are directed toward the *acceptance* of a particular system for flight. Because only one prototype has been qualified, virtually no information is available on the variation to be expected between units of the same design. Flight unit testing is intended, then, to discover failures in the second category: Defects in material or workmanship. The exposure of flight hardware to severe environments is often attacked as tending to shorten its useful life; but the purpose of the tests is valid, and they must be run. The key to the problem lies in the *duration* of the prototype tests: They must be long enough to give reasonable assurance that flight units can survive the environments imposed both in acceptance testing and in actual launching and flight. In the Pioneer V (1960α) program, for example, the prototype was subjected to its vibration schedule ten times to gain such assurance. Test levels for the flight units are usually set at the 95 percent probability level; that is, there is 1 chance in 20 that they will be exceeded when the actual launching takes place.

TEST LEVELS

Severity of applied environments has been set at the 99 percent level for *qualification* testing and the 95 percent level for *acceptance* testing. In view of the paucity of available data, we can hardly justify thinking of these levels in statistical terms with carefully computed standard deviations and levels of confidence. Instead, the 95 percent level is usually taken to imply a condition that is supported by the most severe valid data obtained. The 99 percent level is then set at an assumed mean value plus 1.5 times the difference between the mean and the 95 percent level. This procedure is approximately correct mathematically for a normally distributed variable.[4]

THE TEST PLAN

Environmental testing of a satellite system is an integral part of the development cycle.

[4] The 95 percent point of a cumulative normal is at 1.65 σ. Then $1.5 \times 1.65\ \sigma = 2.47\ \sigma$; this is the 99.3 percent point.

As such, it must be carefully preplanned to assure that all factors of importance in a given program will be given proper consideration. Because environmental tests come just before launch, the time available for them inevitably shrinks as unexpected problems delay the development program, while launching schedules remain inflexible. In this situation, a valid and comprehensive test plan, approved and directed by management, is needed to prevent errors and omissions during the drive to get acceptable flight units. Corners will be cut unless a clearly defined program has been established previously.

A test plan must first include the procedures by which the system's performance under test is to be evaluated. In practice, there are usually three levels of such a checkout. First, there is what might be termed an *in-line systems check*. (In-line systems are rigorously defined as those whose individual failure would cause failures of the whole system. In practice, the term is usually applied to the power supply, encoding, telemetry, and command receiver systems.) Such a checkout procedure might be used, for example, during a vibration exposure. While survival of vibration is frequently all that is required, anomalies in performance as indicated by an in-line check made during vibration may indicate marginal conditions. Second, there is the *experiment exercise check*. This procedure not only checks the in-line systems but also requires that the experiments be excited in some manner to cause their indicated output to leave the base line. This check might be used at some intermediate point in a vibration test during one of the many changes in setup usually involved. Third, there is the *integrated systems test*, during which experiments are not only exercised but also calibrated. This check is required before and after all major environmental conditionings.

The bulk of a test plan is an exposition of the detailed procedures for applying environmental conditioning to the particular satellite. While general specifications serve as a guide, they cannot be applied indiscriminately.[5] For example, acceleration levels depend on the weight of the satellite; and the manner of simulating the thermal environment in space depends on the detailed techniques employed in the satellite for temperature control. In establishing the proper procedures for environmental testing, a thorough knowledge of the satellite, the environment, and the capabilities of the test equipment must be available. Improper test technique can lead either to the acceptance of an unsuitable system or to the overdesign of the system to pass an unrealistic test.

A final portion of the test plan is devoted to the criteria for "passing" a test, what procedures are to be followed in the event of certain classes of failures, and the manner in which failures are to be reported. The failure report system is usually part of a policy that transcends the particular test program. However, the test plan must assure that this procedure is followed to permit the use, in the design of future satellites, of object lessons painfully learned today.

ENVIRONMENTAL EXPOSURES

The selection of the environmental exposures to be applied to a particular satellite during its test program must be made on the basis of an intimate knowledge of its purpose, functioning, and life cycle. Many exposures, levels, and procedures that are meaningful in one application do not apply in others. Many tests included in an environmental test program are operation checks (e.g., a de-spin test) or are in the nature of property determinations (e.g., a moment-of-inertia measurement) rather than environmental exposures. These are included because of the complexity of the facilities involved.

The environments to be considered in planning a satellite test program are illustrated in Figure 4. Assurance of the spacecraft's ability to withstand all *applicable* environments in a given case must be gained. Some aspects may be covered by engineering calculation (e.g., radiation shielding). Other problems are treated on a subassembly basis (e.g., operation of bearings in ultrahigh vacuum). Systems tests are directed toward those areas

[5] E.g., "General Environmental Test Specification for Delta Launched Spacecraft," Goddard Space Flight Center, Preliminary Draft, November 1962.

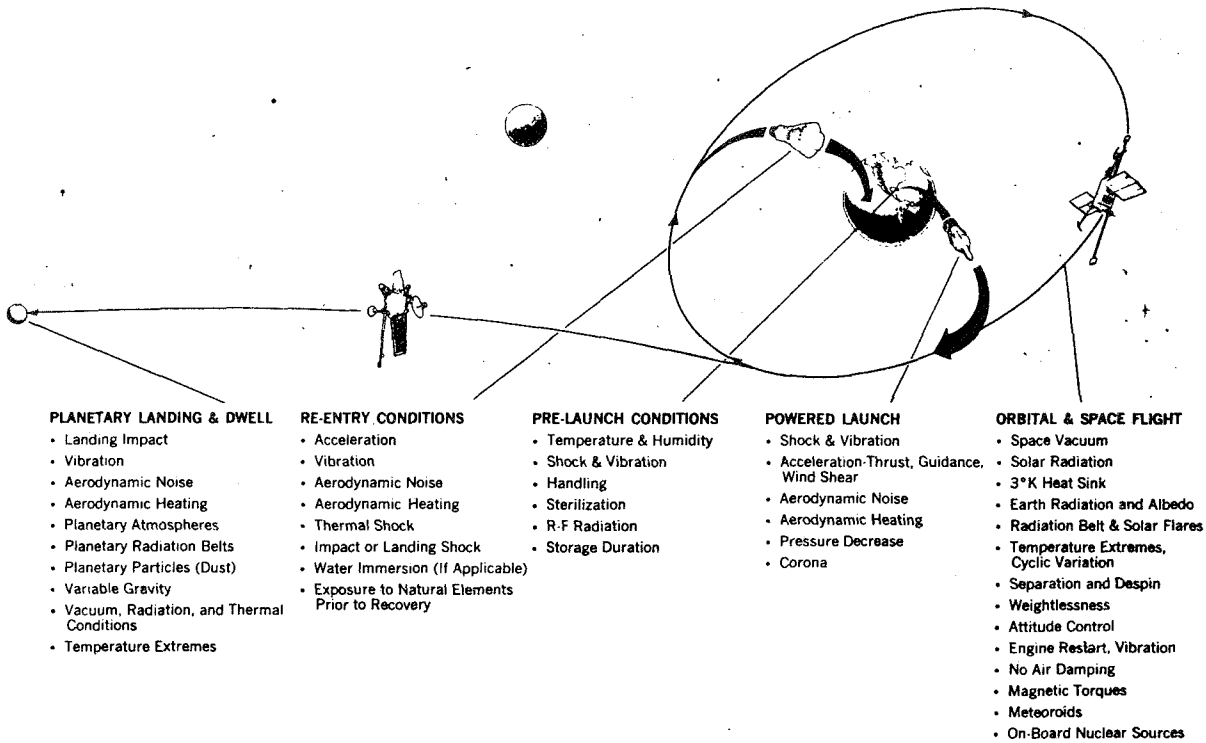

FIGURE 4.—Environmental conditions experienced by space systems.

in which the interactions of subassemblies will be strongly felt. The following discussion will cover the environmental tests that are most often employed and are believed to be of the greatest significance.

Since qualification testing of the prototype is directed toward verifying the soundness of the system design, this portion of the test program is relatively broad in scope. Typically, the following exposures are included: dynamic balancing and spin (if applicable), acceleration, vibration, shock, temperature, humidity, and thermal-vacuum. On the other hand, acceptance testing of the flight units is intended to uncover significant deviations of these samples from the qualified prototype design—chiefly in the areas of material and workmanship—and to verify that the particular unit is suitable for launching. Usually vibration, thermal-vacuum, and final balancing are the only exposures employed.

Balance and Spin

Dynamic balancing of a spinning satellite is required to assure stability of the spin axis. Even for a stabilized satellite, measurement of its inertial properties and trim-balancing may be required to assure proper performance of the control system. A spin test (for a spinning satellite) is a natural adjunct to balancing, since both tests usually are conducted on the same machine. While we think of satellites as operating in a zero-g environment, at 600 rpm the centripetal acceleration amounts to 10 g/inch away from the center of rotation.

Acceleration

Acceleration tests are quite "straightforward" when the maximum acceleration imparted by the vehicle to a satellite of a given weight is known. A major problem is raised by the fact that most satellites are relatively long compared with the radius of available centrifuges. We must then consider the significance of the acceleration gradient existing in the satellite under test. A more subtle problem arises from the various possible combinations of axial and lateral accelerations that may exist simultaneously.

Vibration

Vibration testing is a compromise of many factors. First, our machines apply vibration in only one direction at a time, in contrast to the actual flight condition; this results in extended test durations. Second, the vehicles currently in use inject both random and quasi-sinusoidal inputs to the satellite; separate tests are frequently required. Third, the final rocket stage and satellite mounting may exhibit a mechanical impedance comparable with that of the satellite; test levels are then conditioned by the properties of the particular satellite. Fourth, the applicability of existing data has been seriously questioned from many quarters. A careful in-flight measurement program for vibration has been undertaken by GSFC in conjunction with its scientific satellite launching.

Shock

There are two sources of shock for a satellite system: handling, and rocket staging. Neither of these is especially severe in most cases. Normally, a satellite is packaged with reasonable care to mitigate handling shock. Rocket staging rarely results in a pulse representing a velocity change of more than a very few feet per second. Typically, a drop test is used to verify resistance to shock.

Temperature

A temperature test is conducted on the prototype for two reasons. First, we must assure that the system will not be damaged by the temperatures to be encountered in handling, storage, or transit. If a controlled environment is provided by exotic packaging, this must be considered. Second, tests in a temperature chamber provide a first look at performance under expected space conditions. The presence of rapidly moving air, of course, depresses the temperatures to be attained by power-dissipating elements. Nevertheless, experience has shown the test to be very valuable.

Humidity

Satellites are usually subjected to a relatively mild (compared with military specifications) humidity exposure: 95 percent RH at 30°C for 24 hours. The test is used to assure that no permanent damage will be inflicted and to obtain an estimate of the "drying" time that may be involved when the satellite is returned to controlled conditions after exposure to high humidity. Damage to the satellite or excessive recovery times resulting from this test may dictate that the satellite be protected from high humidity at all times.

Thermal-Vacuum

Thermal-vacuum tests attempt to simulate the temperature and pressure environment the satellite will encounter in space. Chamber pressures below 10^{-4} mm Hg are usually considered acceptable, since air conduction is essentially negligible at this level. The study of surface effects that occur at much lower pressures (below 10^{-8} mm Hg) is not a suitable objective for most overall systems tests.

Simulation of the thermal environment is a much more complicated matter. Techniques range from controlling the temperature of the vacuum vessel's wall (soak tests), through predicted temperature contour reproduction and heat flux simulation, to full solar simulation. In choosing the technique for a given test, a detailed knowledge of the thermal control system is required. Further, the distinction between a performance test and a thermal design verification must always be kept clearly in mind.

EXPERIENCE WITH EVALUATION PROGRAMS

The Goddard Space Flight Center has been responsible for the launching of some twenty-six satellites and space probes, as described in Appendix A. These have ranged from the 79-pound Explorer X (1961κ) to the 458-pound Orbiting Solar Observatory I. Eight of these satellites have been tested in-house; the remainder has been tested by the prime contractor under GSFC supervision. These programs have molded much of the philosophy discussed herein.

In general, these satellites have been highly successful. They range from six successful

TIROS satellites in six attempts to the highly publicized failure of one-half the Relay Communications Satelite (redundancy paid off).

The question now arises as to the contribution of the environmental testing program to these successes. In discussing the reasons for Goddard's success, Dr. J. W. Townsend, Assistant Director for Space Science and Satellite Applications, said: [6]

The principal cornerstone of our development philosophy has been our belief and reliance in a strong testing program.

(a) GSFC believes in the FULL SYSTEMS test approach. Every reasonable attempt should be made to test the *entire system* under as realistic conditions as possible and as early in the development cycle as feasible.
(b) GSFC believes in 100 percent flight acceptance testing at expected average flight levels plus 2 σ (95 percent level).
(c) GSFC believes in testing a flight unit, designated to prototype, at approximately 150 percent of the flight acceptance tests.
(d) After the testing program, the system should remain intact and last minute changes avoided like the plague (firing jitters problem).

A review of our weekly reports for a 1-year period revealed references to some 266 malfunctions during the testing phase on a dozen satellites and probes. All of these would, of course, not result in outright failure of the mission. It is (very crudely) estimated that 25 percent would have been in this "disaster" category.

Table 5 gives a compilation of the data for five particular cases. The high incidence of pretest checkout failures indicates the pace of a satellite development program and the need to enter systems testing as quickly as possible. The failures under test follow the pattern expected.

From another point of view, we have always had much more difficulty with prototype qualification than was expected. However, there has been much less trouble with the flight units than was feared after the prototype experience.

[6] Internal GSFC memorandum dated Jan. 21, 1963.

TABLE 5.—*Failures During Systems Test (Summary for Five Spacecraft)*

Test condition	Type of failure		
	Electrical	Mechanical	Total
Checkout	12	6	18
Vibration	20	14	34
Temperature	3		3
Vacuum	5		5
Thermal-vacuum	51	3	54
Total	91	23	114

ADEQUACY OF TEST LEVELS

Vibration

As discussed earlier, there is considerable uneasiness over the proper levels of vibration to be applied to a given satellite. In-flight success has indicated that they are probably sufficiently high. The failures in flight of one non-in-line subassembly which, having failed to qualify in vibration, was flown anyway suggests that the levels are not excessive. It is believed that the data gathered by our in-flight measurements program will verify these conclusions. The results so far tentatively indicate that the test levels are somewhat low at low frequencies where vehicle structural modes are found and somewhat high at intermediate frequencies.

An unexpected failure of one experiment, probably during the powered-flight phase of the Ariel I (1962σ) launching, suggests that the testing did not cover adequately the combined effects of acceleration and vibration. This area of combined environmental testing appear to be somewhat weak.

Thermal-Vacuum

Problems exist in both level and duration of thermal-vacuum testing. Recent experience, particularly with Explorer XIV, had indicated

TABLE 6.—*Solar-Powered Satellite Lifetime*

Satellite*	Date Launched	Silent	Life (months)	Remarks
Vanguard I	Mar. 17, 1958	Active	57+	Oldest active satellite; first use of solar cell (weight, 3 lb; two experiments)
Explorer VI	Aug. 7, 1959	Oct. 6, 1959	2	Decayed from orbit July 1961 (weight, 143 lb; eight experiments)
Explorer VII	Oct. 13, 1959	Aug. 24, 1961	26	Tracking beacon ceased on silent date; 20-Mc transmitter still active; clock failed on launch(?) (weight, 92 lb; six experiments)
Explorer XI	Apr. 27, 1961	Dec. 6, 1961	7	All experiments working until silent date; tape recorder never functioned (weight, 82 lb; six experiments)
Explorer XII	Aug. 15, 1961	Dec. 6, 1961	4	Abrupt stop in transmission (weight, 83 lb; 10 experiments)
Explorer XIV	Oct. 2, 1962	Jan. 11, 1963	3+	Encoder started malfunctioning Jan. 11, 1963; good data until then (weight, 89 lb; six experiments)
Explorer XV	Oct. 27, 1962	Active	2+	Good data being received on artificial radiation belt (weight, 100 lb; seven experiments)
Ariel I	Apr. 26, 1962	Active	4+	Showed undervoltage problems in Aug. 1962; encoder malfunctioned at times; some data still being received (weight, 132 lb; seven experiments)
Alouette	Sept. 29, 1962	Active	3+	Good data being received; solar cell output diminished by radiation effect (weight, 320 lb; three experiments)
OSO I	Mar. 7, 1962	Active	10+	Data still being received; some problem in positioning control (weight, 458 lb; 13 experiments)

*The satellite designations for Explorers XI, XII, XIV, XV and for Ariel I have been given with previous text mention; the designations for Vanguard I, Explorers VI and VII, and Alouette are, respectively: 1958 $\beta 2$, 1959 $\delta 1$, 1959 $\iota 1$, and 1962 B $\alpha 1$.

that our ability to predict temperatures on the basis of engineering calculation is not particularly good for complicated satellite geometries.[7] This strongly suggests solar simulation as the desired test method. However, here the test equipment is marginal at best.

In the matter of test duration, there is the quandary of when to stop testing. This is mentioned by Lloyd and Lipow (Reference 1, p. 416 and ch. 16) in their discussion of the development of a test program for a liquid rocket engine. In their case, they were able to project desirable test duration and make reliability estimates on the basis of many tests (approx. 100) of suitably similar devices having the same design. In our case, we have had one similar device: the prototype.

Experience with the more sophisticated satellites now being flown indicates that the 1-year life nominally felt to be desirable is not being achieved. Table 6 shows typical performance. We are attacking this problem on both the design and testing levels. (It might also be noted that timers are being included in many satellites to shut them off after 1 year, to clear the communications channels.)

From the testing viewpoint, there is another duration problem. It will be recalled that our failure model proposes initial testing be long enough to eliminate "infant" faults. Figure 5 (Reference 5) shows experience on three satel-

[7] The Jet Propulsion Laboratory encountered a similar problem in their Mariner II (1962 Aρ1) Venus fly-by.

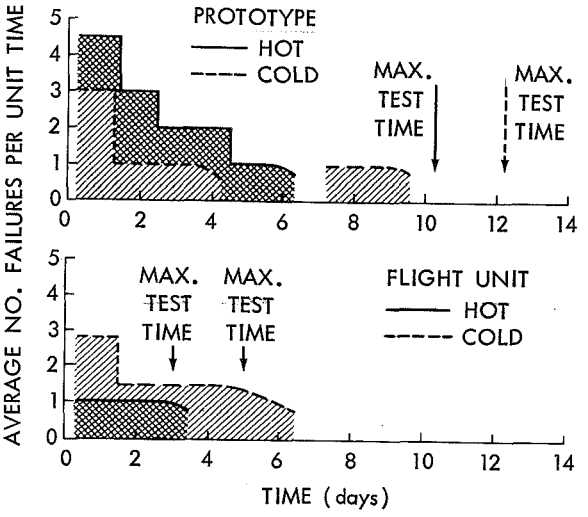

FIGURE 5.—Experience in thermal-vacuum testing.

lites. These data indicate that failures are still occurring at a significant rate as the test ends. Extending the required duration of thermal-vacuum tests is under serious consideration.

UTILIZATION OF EXPERIENCE

Currently, utilization on the next program of experience gained in the development and evaluation of a previous satellite is a significant problem. The difficulty is caused largely by the fact that the state-of-the-art is progressing so rapidly that only the most recent experience has application. The problems in instant acquisition, digestion, and dissemination of such information are obviously manifold. We can only say that constant effort is being made to improve the procedures and mechanisms used for this purpose.

CONCLUDING REMARKS

In the foregoing, an attempt has been made to follow the rational used in establishing an environmental test program and to fit this program into the overall satellite reliability picture. Perhaps the most distinctive feature of a satellite test program is that stringent environmental tests of the actual flight units are conducted. The success of the approach is demonstrated by highly successful satellites in orbit.

REFERENCES

1. LLOYD, D. K., and LIPOW, M., "Reliability: Management, Methods, and Mathematics," Englewood Cliffs, New Jersey: Prentice-Hall, 1952.
2. JASTROW, R., "Developing Special Skills for Research in the Space Sciences," *Proceedings of the NASA-University Conference on the Science and Technology of Space Exploration, November 1–3, 1962*, Chicago, Ill., Vol. I, pp. 41–45.
3. NEW, J. C., "Achieving Satellite Reliability Through Environmental Tests," NASA Technical Note D–1853, 1963. Also to be published in: *Proceedings of the Institute of Environmental Sciences, April 1963.*
4. Planning Research Corporation, "Reliability Assessment of the Mariner Spacecraft," PRC R–293, Dec. 17, 1962.
5. TIMMINS, A. R., and ROSETTE, K. L., "Experience in Thermal-Vacuum Testing Earth Satellites at Goddard Space Flight Center," NASA Technical Note D-1748, 1963. Also to be published in: *Proceedings of the Institute of Environmental Sciences, April 1963.*

Page intentionally left blank

Appendix A

SATELLITE AND SPACE PROBE SUMMARY

Goddard Space Flight Center Satellites and

Designation	Date		Launch vehicle and site	Objectives	Instrumentation	Period (minutes)
	Launch	Silent				
EXPLORER VI 1959 Delta I (S–2)	Aug. 7, 1959	Oct. 6, 1959	Thor-Able AMR	To measure three specific radiation levels of Earth's radiation belts; test scanning for Earth's cloud cover; map Earth's magnetic field; measure micrometeorites; study behavior of radiowaves.	Equipment to measure radiation levels; TV-type scanner; micrometeorite detector; two types of magnetometer and devices for space communication experiments.	12½ hours
VANGUARD III 1959 Eta	Sept. 18, 1959	Dec. 12, 1959	Vanguard AMR	To measure the Earth's magnetic field, x-radiation from the sun, and several aspects of the space environment through which the satellite travels.	Proton precisional magnetometer, ionization chambers for solar X-rays, micrometeor detectors, and thermistors.	130

Space Probe Projects as of December 1962

Orbital elements (statute miles)		Project manager and project scientist	Experiment	Experimenter	Affiliation	Remarks
Perigee	Apogee					
156	26,357	Dr. John C. Lindsay	Triple coincidence telescopes.	J. A. Simpson C. Y. Fan P. Meyer	U. of Chicago	Orbit achieved. All experiments performed. First complete televised cloud-cover picture was obtained. Detected large ring of electrical current circling Earth; complete map of Van Allen radiation belt obtained. Weight: 142 lb Power: Solar Life: 2 months
		Dr. John C. Lindsay	Scintillation counter.	T. A. Farley Allen Rosen C. P. Sonnett	Space Technology Laboratories	
			Ionization chamber Geiger counter.	J. Winckler	U. of Minnesota	
			Spin-coil magnetometer.	E. J. Smith D. L. Judge	STL	
			Fluxgate magnetometer.	P. J. Coleman	STL	
			Aspect sensor	----------	STL	
			Image-scanning television system.	----------	STL	
			Micrometeorite detector.	----------	Cambridge Research/ STL	
319	2329	----------	Magnetometer	J. P. Heppner	GSFC	Orbit achieved. Provided comprehensive survey of earth magnetic field over area covered; surveyed location of lower edge of Van Allen Radiation Belt. Accurate count of micrometeorite impacts. Weight: 100 lb including attached 3rd stage. Power: Battery Life: 85 days
			Ionization chambers.	H. Friedman	NRL	
			Environmental Measurements.	H. E. LaGow	GSFC	

Goddard Space Flight Center Satellites and Space

Designation	Date		Launch vehicle and site	Objectives	Instrumentation	Period (minutes)
	Launch	Silent				
EXPLORER VII (S-1a)	Oct. 13, 1959	Aug. 24, 1961	Juno II AMR	Variety of experiments, including solar ultraviolet; X-ray; cosmic ray, Earth radiation and micrometeor experiments.	Sensors for measurements of Earth-Sun heat balance; Lyman-alpha and X-ray solar radiation detectors; micrometeor detectors, Geiger-Mueller tubes for cosmic-ray count; ionization chamber for heavy cosmic rays.	101.33
PIONEER V 1960 Alpha	Mar. 11 1960	June 26, 1960	Thor-Able AMR	Investigate interplanetary space between orbits of Earth and Venus, test extreme long range communications, study methods for measuring astronomical distances.	High intensity radiation counter, ionization chamber Geiger-Mueller tube to measure plasmas, cosmic radiation, and charged solar particles. Magnetometer and micrometeorite temperature measurements.	311.6 days

Probe Projects as of December 1962—Continued

Orbital elements (statute miles)		Project manager and project scientist	Experiment	Experimenter	Affiliation	Remarks
Perigee	Apogee					
342	680	H. LaGow	Thermal radiation balance.	V. Suomi	U of Wisconsin	Orbit achieved. Provided significant geophysical information on radiation and magnetic storms; demonstrated method of controlling internal temperatures; first micrometeorite penetration of a sensor in flight. Weight: 91.5 lb Power: Solar Life: 26 months
			Solar X-ray and Lyman-alpha.	H. Friedman R. W. Kreplin T. Chubb	NRL	
			Heavy cosmic radiation.	G. Groetzinger P. Schwed	Martin Co.	
				M. Pomerantz	Bartrol Research	
			Radiation and solar-proton observation.	J. Van Allen G. Ludwig H. Whelpley	St. U. of Iowa	
			Ground-based ionospheric observations.	G. Swenson Dr. C. Little G. Reid O. Villard, Jr. W. Ross W. Dyke	U. of Illinois Nat. Bu. of Stand. U. of Alaska Stanford U. Penn State U. Linfield Res. Inst.	
			Micrometeorite penetration experiment.	H. LaGow	GSFC	
Perihelion 74.9 million from sun	Aphelion 92.3 million from sun	Dr. John C. Lindsay Dr. John C. Lindsay	Triple coincidence, proportional counter, cosmic ray telescope.	J. Simpson	U. of Chicago	Highly successful exploration of interplanetary space between orbits of Earth and Venus; established communication record of 22.5 million miles on 6/26/60; made measurements of solar flare effects, particle energies and distribution, and magnetic field phenomena in interplanetary space. Weight: 94.8 lb Power: Solar Life: 3 months
			Search-coil magnetometer and photo electric cell aspect indicator.	D. Judge	STL	
			Ionization chamber and G–M tube.	J. Winckler	U. of Minnesota	
			Micrometeorite counter.	E. Manring	AFCRC	

Goddard Space Flight Center Satellites and Space

Designation	Date		Launch vehicle and site	Objectives	Instrumentation	Period (minutes)
	Launch	Silent				
TIROS I Beta 1960 (A–1)	April 1, 1960	June 12, 1960	Thor-Able AMR	Test of experimental television techniques leading to eventual worldwide meteorological information system.	One wide and one narrow angle camera, each with tape recorder for remote operation. Picture data can be stored on tape or transmitted directly to ground stations.	99.1
ECHO I 1960 Iota	Aug. 12, 1960	Still in Orbit	Thor-Delta AMR	Place 100-foot inflatable sphere into orbit.	Two Minitrack tracking beacons on sphere.	118.3
EXPLORER VIII 1960 Xi (S–30)	Nov. 3, 1960	Dec. 28, 1960	Juno II AMR	Investigation of the ionosphere by direct measurement of positive ion and electron composition; collect data on the frequency momentum and energy of micrometeorites impacts; establish attitude of the base of the exosphere.	RF impedance probe using a 20-foot dipole sensor; single grid ion trap; four multiple-grid ion traps; Langmuir probe experiment; rotating shutter electric field meter; micro plier; micrometeorite microphone; thermistors for reading internal and surface temperatures of the space craft; and despin mechanisms to reduce spin from 450 to 30 rpm.	112.7

Probe Projects as of December 1962—Continued

Orbital elements (statute miles)		Project manager and project scientist	Experiment	Experimenter	Affiliation	Remarks
Perigee	Apogee					
428.7	465.9	W. G. Stroud (GSFC) H. Butler (Army)	TV camera systems (2).	----------	----------	Provided 1st global cloud-cover photographs (22,952 total) from near circular orbit. Weight: 270 lb Power: Solar Life: 72 days
945	1049	Robert J. Mackey	----------	----------	----------	Demonstrated use of radio reflector for global communications, numerous successful transmissions. Visible to the naked eye. Weight: 132 lb (including inflation powder). Power: Passive Life: Still in orbit
258	1423	Robert E. Bourdeau Robert E. Bourdeau	RF impedance Ion traps Langmuir probe Rating-shutter electric field meter. Micrometeorite photomultiplier. Micrometeorite microphone.	J. Cain R. Bourdeau G. Serbu E. Whipple J. Donnelly R. Bourdeau G. Serbu E. Whipple J. Donnelly J. Donnelly M. Alexander K. McCracken O. Berg M. Alexander K. McCracken	GSFC GSFC GSFC GSFC GSFC GSFC	Measured the electron density, temperature, ion density and composition, and charge on the satellite in the upper ionosphere. The micrometeorite influx rate was measured. Weight: 90.14 lb Power: Battery Life: 55 days

Goddard Space Flight Center Satellites and Space

Designation	Date		Launch vehicle and site	Objectives	Instrumentation	Period (minutes)
	Launch	Silent				
TIROS II 1960 Pi I (A–2)	Nov. 23, 1960	Feb. 7, 1961	Delta AMR	Test of experimental television techniques and infrared equipment leading to eventual worldwide meteorological information system.	Includes one wide and one narrow angle camera, each with tape recorder for remote operation; infrared sensors to map radiation in various spectral bands; attitude sensors; experimental magnetic orientation control.	98.2
EXPLORER IX 1961 Delta I (S–56a)	Feb. 16, 1961	Passive Satellite.	Scout Wallops Island	To study performance, structural integrity and environmental conditions of Scout research vehicle and guidance controls system. Inject inflatable sphere into Earth orbit to determine density of atmosphere.	Radio beacon on balloon and in fourth stage.	118.3
EXPLORER X 1961 Kappa (P–14)	Mar. 25, 1961	Mar. 27, 1961	Thor-Delta AMR	Gather definite information on earth and interplanetary magnetic fields and the way these fields affect and are affected by solar plasma.	Includes rubidium vapor magnetometer, two flux-gate magnetometers, a plasma probe, and an optical aspect sensor.	112 hours

Probe Projects as of December 1962—Continued

Orbital elements (statute miles)		Project manager and project scientist	Experiment	Experimenter	Affiliation	Remarks
Perigee	Apogee					
406	431	Dr. R. Stampfl	TV camera system (2). Widefield radiameter experiment. Scanning radiometer exment.	----------	----------	Orbit achieved. Narrow-angle camera and IR instrumentation sent good data. Transmitted 36,156 pictures. Still operative. Weight: 277 lb Power: Solar Life: 76 days
395	1605	----------	----------	----------	----------	Vehicle functioned as planned. Balloon and fourth stage achieved orbit. Transmitter on balloon failed to function properly requiring optical tracking of balloon. Weight: 80 lb Power: Passive Life:
100	186,000	Dr. J. P. Heppner Dr. J. P. Heppner	Rubidium vapor magnetometer and fluxgate magnetometers Plasma probe Spacecraft attitude experiment.	J. P. Heppner T. L. Skillman C. S. Scearce H. Bridge F. Scherb B. Rossi J. Albus	GSFC MIT GSFC	Probe transmitted valuable data continuously for 52 hours as planned. Demonstrated the existence of a geomagnetic cavity in the solar wind and the existence of solar proton streams transporting solar interplanetary magnetic fields past the earth's orbit. Weight: 79 lb Power: Battery Life: 52 hr.

Goddard Space Flight Center Satellites and Space

Designation	Date		Launch vehicle and site	Objectives	Instrumentation	Period (minutes)
	Launch	Silent				
EXPLORER XI 1961 Nu I (S–15)	Apr. 27, 1961	Dec. 6, 1961	Juno II AMR	Orbit a gamma ray astronomy telescope satellite to detect high energy gamma rays from cosmic sources and map their distribution in the sky.	Gamma ray telescope consisting of a plastic scintillator, crystal layers, and a Cerenkov detector; sun and earth sensors; micrometeorite shields; temperature sensor; damping mechanism.	108.1
TIROS III 1961 Rho I (A–3)	July 12, 1961	Dec. 4, 1961	Thor-Delta AMR	Develop satellite weather observation system; obtain photos of Earth's cloud cover for weather analysis; determine amount of solar energy absorbed, reflected and emitted by the Earth.	Two wide-angle cameras, two tape recorders and electronic clocks; infrared sensors, five transmitters, attitude sensors, magnetic attitude coil.	100.4
EXPLORER XII 1961 Upsilon I (S–3)	Aug. 15, 1961	Dec. 6, 1961	Thor-Delta AMR	Investigate solar wind, interplanetary magnetic fields, distant portions of Earth's magnetic field, energetic particles in interplanetary space and in the Van Allen Belts.	Ten particle detection systems for measurement of protons and electrons and three orthogonally mounted fluxgate sensors for correlation with the magnetic fields, optical aspect sensor, and one transmitter. Telemetry is PFM and transmits continuously.	26.45 hours

Probe Projects as of December 1962—Continued

Orbital elements (statute miles)		Project manager and project scientist	Experiment	Experimenter	Affiliation	Remarks
Perigee	Apogee					
304	1113.2	Dr. J. Kupperian, Jr. Dr. J. Kupperian, Jr.	Gamma ray telescope.	W. Kraushaar G. Clark	MIT	Orbit achieved. Detected first gamma rays from space. Directional flux obtained. Disproved one part of "steady state" evolution theory. Weight: 82 lb Power: Solar Life: 7 months
461.02	506.44	R. Rados	Omnidirectional radiometer Widefield radiometer experiment, scanning radiometer experiment TV cameras (2).	V. Suomi	U. of Wisconsin.	Orbit achieved. Cameras and IR instrumentation transmitted good data. Transmitted 35,033 pictures. First hurricane covering international program. Weight: 285 lb Power: Solar Life: 145 days
180	47,800	P. Butler Dr. F. McDonald	Proton analyzer Magnetometer Cosmic ray Ion-electron detector. Solar cell	M. Bader L. Cahill B. O'Brien F. B. McDonald L. Davis G. Longanecker	Ames Research Center. U. of New Hampshire. St. U. of Iowa GSFC. GSFC GSFC	Orbit achieved; all instrumentation operated normally. Ceased transmitting on Dec. 6, 1961, after sending 2568 hours of realtime data. Provided significant geophysical data on radiation and magnetic fields. Weight: 83 lb Power: Solar Life: 4 months

Goddard Space Flight Center Satellites and Space

Designation	Date		Launch vehicle and site	Objectives	Instrumentation	Period (minutes)
	Launch	Silent				
EXPLORER XIII 1961 Chi	Aug. 25, 1961	Aug. 27, 1961	Scout Wallops Island.	Testing performance of the vehicle and guidance; investigation, nature and effects on space flight of micrometeoroids.	Micrometeoroids impact, detectors, transmitters.	97.5
P21 ELECTRON DENSITY PROFILE PROBE. (P–21)	Oct. 19, 1961	Oct. 19, 1961	Scout Wallops Island.	To measure electron densities and to investigate radio propagation at 12.3 and 73.6 Mc under daytime conditions.	Continuous wave propagation experiment for the ascent portion of the trajectory, and an RF probe technique for the descent.	
TIROS IV 1962 Beta (A–9)	Feb. 8, 1962	June 19, 1962	Delta AMR	Develop principles of weather satellite system; obtain cloud and radiation data for use in meteorology.	Two TV camera systems with clocks and recorders for remote pictures, infrared sensors, heat budget sensors, magnetic orientation control horizon sensor, north indicator.	100.4

Probe Projects as of December 1962—Continued

Orbital elements (statute miles)		Project manager and project scientist	Experiment	Experimenter	Affiliation	Remarks
Perigee	Apogee					
74	722	C. T. D'Aiutolo	A cadmium sulfate photoconductor experiment. A wire grid experiment.	M. W. Alexander L. Secretan	GSFC	Orbit was lower than planned. Reentered August 27, 1961. Weight: 187 lb including 50-lb 4th stage and 12-lb transition section. Power: Solar Life: 2 days
N/A	N/A 4261	John E. Jackson Dr. S. J. Bauer	RF probe	H. Whale	GSFC	Probe achieved altitube of 4261 miles and transmitted good data. Electron density was obtained to about 1500 miles, making the first time such measurements have been taken at this altitude. Weight: 94 lb Power: Battery Life: Hours
471	525	R. Rados	Omni-directional radiometer. Wide-field radiometer experiment. Scanning radiometer experiment. TV camera systems (2).	V. Suomi	U. of Wisconsin.	Orbit achieved. All systems transmitting good. Tegea Kinoptic lens used on one camera. Elgeet lens on the other. Support to Project Mercury. Weight: 285 lb Power: Solar Life: 131 days

Goddard Space Flight Center Satellites and Space

Designation	Date		Launch vehicle and site	Objectives	Instrumentation	Period (minutes)
	Launch	Silent				
ORBITING SOLAR OBSERVATORY OSO–1. 1962 Zeta (S–16)	Mar. 7, 1962	Active	Delta AMR	Placed satellite in Earth orbit to measure solar electromagnetic radiation in the ultra-violet, X-ray, and gamma ray regions; investigated effect of dust particles on surfaces of spacecraft.	Devices to conduct 13 different experiments for study of solar electromagnetic radiation; investigate dust particles in space and thermo radiation characteristics of spacecraft surface materials.	96.15

Probe Projects as of December 1962—Continued

Orbital elements (statute miles)		Project manager and project scientist	Experiment	Experimenter	Affiliation	Remarks
Perigee	Apogee					
343.5	369	Dr. John C. Lindsay	X-ray spectrometer.	W. Behring W. Neupert	GSFC	Orbit achieved. Experiments transmitting as programmed. Weight: 548 lb Power: Solar Life: Active
		Dr. John C. Lindsay	0.510 Mev gamma ray monitoring; 20–100 kev X-ray monitoring; 1–8A X-ray monitoring.	K. Frost W. White	GSFC	
			Dust particle experiment.	M. Alexander C. McCracken	GSFC	
			Solar radiation experiment, solar ultraviolet.	W. White K. Hallam		
			Solar gamma rays, high energy distribution.	W. White K. Frost	GSFC	
			Solar gamma rays, low energy distribution.	J. R. Winkler L. Peterson	U. of Minnesota.	
			Solar gamma rays, high energy distribution.	M. Savedoff G. Fazio	U. of Rochester.	
			Neutron monitor experiment.	W. Hess	U. of California.	
			Lower Van Allen belt.	S. Bloom	U. of California.	
			Emissivity stability of surfaces in a vacuum environment.	G. Robinson	Ames Research Center.	

Goddard Space Flight Center Satellites and Space

Designation	Date		Launch vehicle and site	Objectives	Instrumentation	Period (minutes)
	Launch	Silent				
P21A ELECTRON DENSITY PROFILE PROBE. (P-21A)	Mar. 29, 1962	Mar. 29, 1962	Scout Wallops Island.	To measure electron density profile, ion density, and type of ions in the atmosphere.	A continuous wave propagation experiment to determine electron density and associated parameters of ionosphere. A swept frequency probe for direct measurements of electron density and a positive ion experiment to determine ion concentration under nighttime conditions.	
ARIEL INTERNATIONAL SATELLITE. (UK 1) (S-51)	Apr. 26, 1962	Active	Delta AMR	To study ionosphere and cosmic rays relation.	Electron density sensor, electron temperature gage, solar aspect sensor, cosmic ray detector, ion mass sphere, Lyman-alpha gages, tape recorder, X-ray sensors.	100.9

Probe Projects as of December 1962—Continued

Orbital elements (statute miles)		Project manager and project scientist	Experiment	Experimenter	Affiliation	Remarks
Perigee	Apogee					
N/A	N/A 3910	John E. Jackson Dr. S. J. Bauer	CW propagation. RF probe Ion traps	S. Bauer H. Whale R. Bordeau E. Whipple J. Donnelly G. Serbu	GSFC GSFC GSFC	Afforded nighttime observations. Characteristics of the ionosphere differ drastically from daytime state when the temperature of the ionosphere is much cooler. See P–21. Weight: 94 lb Power: Battery Life: Hours
242.1	754.2	R. C. Baumann Robert E. Bourdeau	Electron density sensor. Electron temperature gage. Solar aspect sensor. Cosmic ray detector. Ion mass sphere Lyman-alpha gage.			Orbit achieved. All experiments except Lyman-alpha transmitting as programmed. First international satellite. Contains six British experiments, launched by American Delta vehicle. Weight: 150 lb Power: Solar Life: Active

Goddard Space Flight Center Satellites and Space

Designation	Date		Launch vehicle and site	Objectives	Instrumentation	Period (minutes)
	Launch	Silent				
TIROS V 1962 Alpha Alpha One. (A–50)	June 19, 1962	Active	Delta AMR	Develop principles of weather satellite system; obtain cloud-cover data and radiation data for use in meteorology.	Two TV camera systems with tape recorders for recording remote picture areas, infrared sensors, magnetic orientation control, horizon sensor, north indicator.	100.5
TELSTAR I	July 10, 1962	Active	Delta AMR	Joint A.T. & T. investigation of wide-band communications.	The system provides for TV, radio, telephone, and data transmission via a satellite repeater system.	157.8

Probe Projects as of December 1962—Continued

Orbital elements (statute miles)		Project manager and project scientist	Experiment	Experimenter	Affiliation	Remarks
Perigee	Apogee					
367	604	R. Rados	TV camera systems (2).	----------	----------	Launched at a higher inclination (58°) than previous TIROS satellites to provide greater coverage. Time of launch chosen to include normal hurricane season for South Atlantic. IR sensor inoperative, all other systems transmitting good. Weight: 285 lb. Power: Solar Life: Active
592.6	3503.2	C. P. Smith, Jr.	----------	----------	----------	Orbit achieved. Television and voice transmissions were made with complete success. Bell Telephone Laboratories provide spacecraft and ground stations facilities. Government to be reimbursed for cost incurred. Weight: 175 lb Power: Solar Life: Active

Goddard Space Flight Center Satellites and Space

Designation	Date		Launch vehicle and site	Objectives	Instrumentation	Period (minutes)
	Launch	Silent				
ALOUETTE SWEPT FREQUENCY TOPSIDE SOUNDER. (S-27)	Sept. 29, 1962	Active	Thor Agena. PMR	To measure the electron density distribution in the ionosphere at altitudes between 180 miles and 620 miles. To study for a period of a year the variations of electron density distribution with time of day and with latitude, under varying magnetic and auroral conditions; and with particular emphasis on high latitude effects. To determine electron densities in the vicinity of the satellite by means of galactic noise measurements, and to make observations of related physical phenomena; such as the flux of energetic particles.	A swept frequency pulsed sounder covering the frequency range 1.6 to 11.5 Mc.	105.4
TIROS VI (A-51)	Sept. 18, 1962	Active	Delta AMR	To study cloud cover and earth heat balance; measurement of radiation in selected spectral regions as part of a program to develop meteorological satellite systems.	Two TV camera systems (78° and 104° lens), clocks and tape recorders for remote operation, infrared and attitude sensors, magnetic attitude coil.	98.73

Probe Projects as of December 1962—Continued

Orbital elements (statute miles)		Project manager and project scientist	Experiment	Experimenter	Affiliation	Remarks
Perigee	Apogee					
620	638	John E. Jackson.	Diurnal hour to hour change. Electron density. Ionization. Whistler experiment.	----------	----------	The Alouette satellite is a project of the Canadian Defense Research Board. The project is part of NASA's Topside Sounder Program. This will be NASA's first satellite to be launched from the Pacific Missile Range. 80.84 inclination. Alouette is the first spacecraft designed and built by any other country than the U.S. and U.S.S.R. Weight: 320 lb Power: Solar Life: Active
425	442	R. Rados	Medium angle camera failed Dec. 1, 1962 after taking 1074 pictures.	----------	----------	Inclination 58.3°, velocity perigee 16,822, apogee 16,756. Weight: 300 lb Power: Solar Life: Active

Goddard Space Flight Center Satellites and Space

Designation	Date		Launch vehicle and site	Objectives	Instrumentation	Period (minutes)
	Launch	Silent				
ENERGETIC PARTICLES SATELLITE EXPLORER XIV (S–3a)	Oct. 2, 1962	Active	Delta AMR	To describe the trapped corpuscular radiation, solar particles, cosmic radiation, and the solar winds, and to correlate the particle phenomena with the magnetic field observations.	An actagon-walled platform, fabricated from nylon honeycomb and fiber glass, houses most of the instruments, experiments, and electronics. The transmitter is located in the base of the spacecraft. A magnetometer package containing three orthogonally mounted magnetometers and calibration coils is located on a boom forward of the platform. Telemetry is PFM and transmits continuously.	37 hours (2185 minutes).
EXPLORER XV (S 3–b)	Oct. 27, 1962	Active	Delta AMR	To study new artificial radiation belt created by nuclear explosions.	Similar to Explorer XII.	5 hours (C. 315 min.)

Probe Projects as of December 1962—Continued

Orbital elements (statute miles)		Project manager and project scientist	Experiment	Experimenter	Affiliation	Remarks
Perigee	Apogee					
175	61,226	Paul G. Marcotte Dr. Frank B. McDonald	Cosmic ray experiment. Ion detector experiment. Solar cell experiment. Probe analyses Trapped radiation experiment. Magnetometer experiment.	F. McDonald L. Davis G. Longanecker. M. Boder B. O'Brien L. Cahill	GSFC GSFC GSFC Ames State U. of Iowa U. of New Hampshire	Velocity of apogee 1507 mph, perigee 23,734 mph. Inclination to Equator 33°. Weight: 86 lb Power: Solar Life: Active
195	10.950	Dr. John W. Townsend Dr. Wilmot Hess	Electron energy distribution. Omnidirectional detector. Angular distributor. Directional detector. Ion-electron detector. Magnetic field experiment. Solar cell gage	W. Brown V. Desai C. McIlwain W. Brown C. McIlwain L. Davis L. Cahill H. K. Gummel	Bell Telephone Laboratories U. of California Bell Telephone Laboratories U. of California GSFC U. of New Hampshire Bell Telephone Laboratories	Good data received on artificial radiabelt. Weight: 100 lb Power: Solar Life: Active

Goddard Space Flight Center Satellites and Space

Designation	Date		Launch vehicle and site	Objectives	Instrumentation	Period (minutes)
	Launch	Silent				
RELAY (A–16)	Dec. 13, 1962	Active	Delta AMR	To investigate wide-band communications between ground stations by means of low-altitude orbiting spacecraft. Communications signal to be evaluated will be an assortment of television signals, multichannel telephony and other communications.	The spacecraft will contain an active communications repeater to receive and retransmit communications between the U.S. and Europe, and an experiment to assess radiation damage to solar cells.	185.09

Probe Projects as of December 1962—Continued

Orbital elements (statute miles)		Project manager and project scientist	Experiment	Experimenter	Affiliation	Remarks
Perigee	Apogee					
819. 64	4612.18	Joseph Berliner Dr. R. C. Waddel	First TV transmission U.S. to France, Jan. 9, 1963.	----------	----------	Wide-band Stations: Rumford, Maine; Pleumeur-Bodou, France; Goonhilly, England; Weilhelm, W. Germany. Narrowband stations: Nutley, N.J.; Rio de Janeiro, Brazil. Inclination 47.47°. Weight: 185 lb Power: Solar Life: Active

ENVIRONMENTAL TENSILE TESTING OF NYLON PARACHUTE MATERIALS

JOSEPH A. FARKAS

Goddard Space Flight Center

Tensile tests have been performed to investigate the possible degradation in strength of textile parachute components at −190°C after sterilization by exposure to 135°C in air or nitrogen, and to an ethylene oxide gas mixture of 12 percent concentration by weight. Materials utilized in the parachute canopy, suspension, and reinforcing were selected for consideration. All were composed of nylon, except one of the experimental fiber, HT1. After each phase of sterilization, specimens were tested at room temperature and at −190°C.

Break load and strain measurements indicated that heating in air produced various degrees of degradation to the load limit while heating in nitrogen and exposure to ethylene oxide had no apparent effect. The immediate cold temperature environment appeared to effect only the strain, which was severely restricted.

INTRODUCTION

A primary requirement for landing a capsule on Mars is the sterilization of all materials that would impact the planet. Currently, effective sterilizing procedures involve both heating to at least 120°C and exposure to ethylene oxide, in a nonflammable mixture concentrated 12 percent by weight.

Another subject of concern is the extreme cold which might be encountered in the atmosphere of Mars. It has been suggested shat the temperature could reach −190°C.

Among the problems arising from these considerations is the possible decrease in strength of the parachute textiles. In order to assess the suitability of contemporary materials for a Mars landing mission in regard to sterilization and an extremely cold stress environment, a test program has been carried out and is the subject of this report.

TEST PROCEDURE

The test specifications were defined by the most severe conditions that the parachute might experience. Somewhat arbitrary were the temperature for heating, and the time element in both facets of sterilization. Selected for testing were several canopy fabrics, and principal webbings and tapes. Investigation of effects to their strength took form in the following series of tensile tests, conducted on each variety of material whenever the supply permitted.

Material condition	*Test condition*
normal	Room temperature
heated in air, 24 hrs., 135°C	Room temperature
heated in N_2, 24 hrs., 135C°	Room temperature
heated in air, 24 hrs., 135°C; ethylene oxide, 5 days.	Room temperature and −190°C
heated in N_2, 24 hrs., 135°C; ethylene oxide, 5 days.	Room temperature and −190°C

Additional tests were made when it seemed advisable.

The program was devised so that the effect of each of the four material conditions of interest, namely, heated in air, heated in nitrogen, exposure to ethylene oxide, and cold temperature, could be studied invividually or in a combined fashion as they would be encountered in an actual mission. Furthermore, the program accounted for the effect of each condition in at least two tests on every variety of material. As a measure of strength, fracture

load and strain were recorded. Because of the unreliability inherent in such tests, the results did not have significance in themselves, but by comparison among the results of related tests, any consistent degradation in strength was revealed.

Comparison among the results of the various tests necessitated a standard specimen. An effort was therefore made to retain an approximate five inch free-length which denotes the original length of material between the grips of the testing apparatus, and which is the initial length used in break strain calculations.

APPARATUS

The machine used for tensile testing was a Tinius-Olsen Tension-Compression Machine, having a load capacity of 60,000 pounds, set at a head separation rate of 0.5 ipm. The grips holding the specimen were of the split cylinder type, recommended by the Tinius-Olsen Corp., and by Wright Patterson AFB. Wedge clamps, used in preliminary tests, were difficult to operate and produced inaccurate readings. The split cylinder clamps eliminated shear to a satisfactory extent as the material was held largely by tangential frictional forces, and, although stress tended to concentrate at the free edge of the grip, load readings proved to be more reliable than those obtained using the wedge clamps.

From preliminary tests it was found that closely surrounding the specimen by a copper chamber of constantly evaporating liquid nitrogen provided the necessary tensile test environment of −190°C. Satisfactory production of any cold temperature effect required that a large portion of the stressed material be cooled. Because of the way in which the grips operated, strain resulted in a movement of the free-length away from the grips and its original position. In order that a majority of the free-length, the portion of material under concern, be kept at −190°C, its downward movement had to be followed by the cooling chamber. In addition, the apparatus had to provide access for placement of the specimens in the clamps. A chamber was designed such that its four inch length and means of travel made it possible to maintain approximately a 3¼-inch length of material at −190°C. The chamber interior opened to the front and was closed by an aluminum door to complete the cooling surface and reduce the flow of air through the cooling area. To determine when the temperature had reached −190°C, a thermocouple was placed halfway in the cooling area, not touching the surface of the chamber, and near to the front, expected to be the warmest portion. (The apparatus described thus far is pictured in Figs. 1 and 2.)

The specimens to be tested were subjected to sterilizing heat in both air and nitrogen in an oven which maintained 135°C±3°. The problem of heating in a nitrogen atmosphere was handled in the following manner. Once the materials were placed in the oven, it was evacuated to a reasonable extent. Dry nitrogen was then fed to the oven until the pressure rose just above atmospheric, where it was retained to compensate for any leaks through which air might otherwise enter. Connected

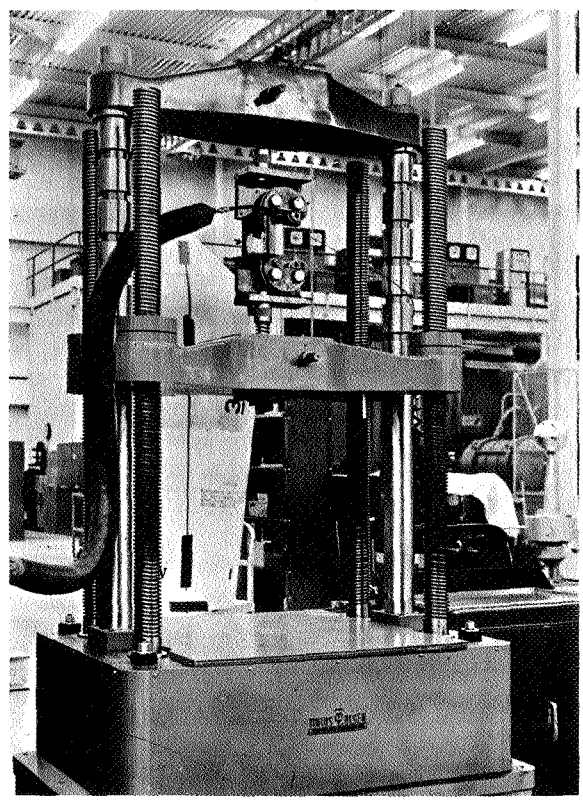

FIGURE 1.—Tensile Test Machinery.

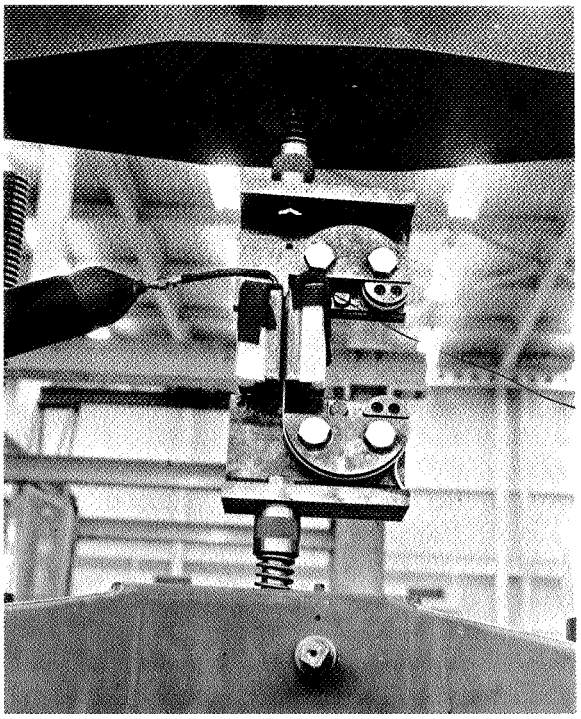

FIGURE 2.—Grips and Cooling Chamber.

to the nitrogen feed line was a U-tube manometer, which was oppositely open to the atmosphere. A small column of mercury not only revealed whether the nitrogen inside the oven was above atmospheric pressure, but also served as a regulator to prohibit the pressure from rising much higher.

Ethylene oxide exposure was accomplished in a hermetically sealed container, which, in preparation, was flushed with dry nitrogen and evacuated. Ethylene oxide in the appropriate mixture with Freon-12 was fed into the chamber from a commercially available bottle. When the pressure reached 12 psig, the chamber was closed, and the pressure retained.

OPERATION

Conducting the test program was merely the straightforward operation of the apparatus just described. Several details do, however, deserve mention.

Previous elongation measurements taken automatically by a Tinius-Olsen device appeared untrustworthy; furthermore, the use of the instrument was hindered by the new grips. In this series of tests, measurements were taken manually.

In cold temperature tests, no stress was applied to the specimen until the cooling area had definitely reached −190°C. A copper-constantan thermocouple was used to read temperature, and temperature-emf. conversion tables for this combination terminated at −190°C. Therefore, in recording test conditions it could only be stated that −190°C had been reached, although potentiometer readings indicated that the temperature was appreciably lower during all testing.

ACCURACY DISCUSSION

As mentioned above, elongation readings were taken manually; the strain data is therefore subject to a tolerance of 2 percent. It had been suggested that the tensile testing machine, designed for the measurement of relatively large loads, would be unsuitable for testing the weak canopy materials. The data, nevertheless, did prove to be reliable enough for the comparative purposes of these tests.

No consistency rating of the tensile testing process was performed before the tests began. The results, themselves, indicated the degree to which individual tests could be trusted, and it became evident that only through consideration of all related tests could a responsible conclusion be reached.

DISCUSSION OF RESULTS

The tests are denoted by the material and the conditions to which it was subjected. A number designates each material variety; the subscripts distinguish different supplies which were expected to vary slightly in strength. In all cases the supplies of each material belonged to the same military specification category and, except for #3, satisfied identical load requirements. (The materials are pictured and described in Fig. 3 and Table 1.)

The data (Tables 2–9), with few exceptions, was consistent throughout the test program and followed predictions. There was no interaction among the various conditions to produce a

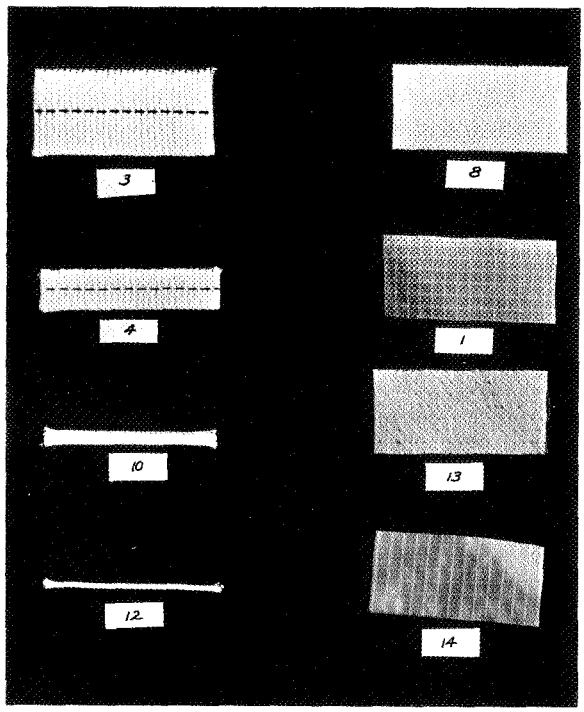

FIGURE 3.—Test Materials.

separate effect, so each condition can be considered individually.

In all varieties of material, the specimens heated in air displayed various degrees of degradation. In no case did the "heat, air" break load reading exceed that of the normal material. The #3a tests showed a large difference in strength between the samples heated in air and in nitrogen but the "heat, N_2" reading was extraordinarily high, judging from the military specification for the material and the "heat, N_2, ethylene oxide" reading. With this in mind, heating in air had its smallest effect on #3 and #13, the canopy fabric of high temperature resistent HT1, while its effect was greatest in #12a and canopy materials #1 and #14. Very generally, in reference to the nylon materials, the amount of degradation increased as the bulk of the material decreased. The effect can be explained by oxidation of the individual fibers and, in turn, the extent of fibers oxidized.

In contrast, heating in nitrogen seemed to have no effect on the strength. This was apparent since in several instances the "heat, N_2" load reading exceeded that of the normal sample. Exposure to ethylene oxide also appeared to have no degrading effect. The results of ethylene oxide exposure were not, however, as unequivocal as those of heating in air or heating in nitrogen. On the whole, "heat, ethylene oxide" tests at room temperature compared equally with "heat" tests. Among those materials heated in air there were two exceptions, #8a, and #8b. The corresponding test of #8a at −190° C., however, gave a confirmative reading. There were also discrepant results in the "heat, N_2, ethylene oxide" tests of #4b and #8a, but a second test of #4b at room temperature yielded a favorable load reading, and the cold temperature test of #8a was substantiating.

Up to the stage of testing at −190°C., strain had not been influenced noticeably, but elongation of the cold material was extremely limited In many instances strain was reduced to one-half its room temperature value. From visual observation, the material appeared to freeze rigid, but it did not seem brittle. In actuality, the strain measurements were much higher than they would have been if the entire sample had been cooled. As mentioned earlier, the standard free-length was approximately 5 inches, while the cooling chamber was 4 inches in height. And, as the material was strained, more of the free-length passed outside the chamber. All of the materials were poor conductors of heat, and the air surrounding the chamber was not cooled appreciably, therefore the portion of the specimen outside the chamber was relatively close to room temperature and subject to conventional strain.

On the other hand, the break load did not appear to be effected by the cold temperature. A number of readings taken at −190° C., on samples #10, #12, #1, #13, and #14, seemed to indicate a decrease in strength, but because the materials in question were those of low strength, there are several explanations. The cold temperature apparatus was quite rugged and any stress produced by movement of the chamber, or by contraction or expansion of the liquid nitrogen inlet line would have an effect on the load reading, most probably to the

extent of five, or less, pounds. Furthermore, movement of the chamber, although it did not effect the stress on the specimen, produced a temporary increase in reading of the machine, which might have altered its zero balance. Realizing the above, on tests of the weak canopy materials the chamber was held stationary, made possible by the low break loads and strains. Finally, the condensation of water vapor on the cold nylon material may have caused a loss in strength. Actually, the above arguments were disregarded. The most substantiating evidence for the noneffect of cold temperature was the fact that in no case did the specimen break inside the chamber. Visual observation and strain measurements indicated that the portion of the sample inside the chamber was at very low temperature, while the portions just outside the chamber were not cooled appreciably. The lack of heat conductivity assured that the material inside the chamber was at or near the temperature of the air, −190° C.

In summary, tensile characteristics of all the materials were influenced to varying degrees by heating in air and to a consistently large extent by the cold temperature environment, while the other conditions produced no apparent effect. Specifically, in regard to the canopy materials, the decrease in strength due to heating in air was much less noticeable in the high temperature, HT1 fabric than in the ordinary nylon cloths.

ACKNOWLEDGMENTS

Appreciation is extended to those persons who supplied equipment and assistance in the test program, especially to Mr. Wilson Simms, Physics Branch, for his help with the oven, to Mr. Edward Rich, Instrumentation Branch, who performed the ethylene oxide exposure, and to Mr. Lloyd Davis and other members of the Mechanical Test Section, Structural Dynamics Branch, for their complete support by providing the tensile test apparatus and aiding in its operation.

TABLE 1.—*Test Materials*

3 a, b	Webbing, nylon, tubular; main suspension; Mil-W-5625, 1″; 3a—3000 lbs. 3b—4000 lbs.
4 a, b, c	Webbing, nylon, tubular; gore seams; Mil-W-5626, ½″; 1000 lbs.
8 a, b	Tape, nylon, reinforcing; bag; Mil-T-5038, type IV, 1″; 1000 lbs.
10 a, b	Cord, nylon; secondary suspension; Mil-C-5040, type III, core thread removed; 250 lbs.
12 a	Cord, nylon; secondary suspension; Mil-C-5040, type I; 100 lbs.
1	Cloth, nylon, acrylic coated; canopy; Mil-C-7020, type I; 42 lbs. (1 inch width).
13	Cloth, HT1 [1]; canopy; Mil-C-7020, type I; 42 lbs. (1 inch width).
14	Cloth, nylon, acrylic coated; canopy; Mil-C-7020, type I; 42 lbs. (1 inch width).

[1] Developed by E. I. du Pont de Nemours & Co.

TABLE 2.—*Test data*

Specimen-condition	Test condition	Fracture load		Fracture strain	Comments
		Test	Specification		
		Pounds	*Pounds*	*Percent*	
3a—heat, air	Room temp	3080	3000	29	Pre-stressed.
3a—heat, N_2	Room temp	3760	3000	33	Load seems unusually high.
3a—heat, air eth. ox	Room temp	3300	3000	30	
3a—heat, N_2 eth. ox	Room temp	3360	3000	32	
3a—normal	Room temp	3190	3000		Comparable prior test; strain reading not trusted.
3b—normal	Room temp	3990	4000	30	
3b—heat, air	Room temp	3910	4000	33	
3b—heat, N_2	Room temp	4030	4000	33	
3b—heat, air eth. ox	Room temp	3920	4000	33	
3b—heat, N_2 eth. ox	Room temp	3970	4000	32	
3b—heat, N_2 eth. ox	−190°C	4100	4000	20	Broke in uncooled portion.

TABLE 3.—*Test data*

Specimen-condition	Test condition	Fracture load		Fracture strain	Comments
		Test	Specification		
		Pounds	*Pounds*	*Percent*	
4a—heat, air	Room temp	1148	1000	20	
4a—heat, air eth. ox	Room temp	1178	1000	22	
4a—normal	Room temp	1272	1000		Comparable prior test; strain reading not trusted.
4b—normal	Room temp	1309	1000	18	
4b—heat, N_2	Room temp	1318	1000	25	
4b—heat, N_2 eth. ox	Room temp	1218	1000	24	Judging from other data, load reading seems too low.
4b—heat, N_2 eth. ox	Room temp	1370	1000	24	
4c—normal	Room temp	1465	1000	22	
4c—heat, N_2	Room temp	1425	1000	23	
4c—heat, air eth. ox	Room temp	1358	1000	23	
4c—heat, N_2 eth. ox	−190°C start; −90°C finish.	1406	1000		Broke in uncooled portion; cooling chamber had been damaged, temp. dropped; visually, strain severely limited.
4c—heat, N_2 eth. ox	−190°C	1454	1000	14	Broke in uncooled portion.

TABLE 4.—*Test data*

Specimen-condition	Test condition	Fracture load		Fracture strain	Comments
		Test	Specification		
		Pounds	*Pounds*	*Percent*	
8a—heat, air	Room temp	1054	1000	29	
8a—heat, N_2	Room temp	1141	1000	29	
8a—heat, air eth. ox	Room temp	924	1000	26	Judging from other data, load reading seems too low.
8a—heat, N_2 eth. ox	Room temp	1052	1000	25	Judging from other data, load reading seems too low.
8a—heat, air eth. ox	−190°C	1024	1000	15	Broke in uncooled portion.
8a—heat, N_2 eth. ox	−190°C	1115	1000	14	Broke in uncooled portion.
8a—normal	Room temp	1158	1000		Comparable prior test; strain reading not trusted.
8b—normal	Room temp	1120	1000	20	
8b—heat, N_2 eth. ox	Room temp	1088	1000	24	
8b—heat, air eth. ox	Room temp	950	1000	23	

TABLE 5.—*Test Data*

Specimen-condition	Test condition	Fracture load		Fracture strain	Comments
		Test	Specification		
		Pounds	*Pounds*	*Percent*	
10a—normal	Room temp	270	250	37	
10a—heat, air	Room temp	247	250	21	Pre-stressed.
10a—heat, air	Room temp	264	250	39	
10a—heat, air eth. ox	Room temp	236	250	37	
10a—heat, air eth. ox	−190° C	250	250	19	Broke in uncooled portion.
10a—normal	Room temp	268	250		Comparable prior test; strain reading not trusted.
10b—normal	Room temp	286	250	35	
10b—heat, air	Room temp	265	250	37	
10b—heat, N_2	Room temp	289	250	35	
10b—heat, N_2 eth. ox	Room temp	280	250	35	
10b—heat, N_2 eth. ox	−190° C	261	250	20.5	Broke in uncooled portion of material.

TABLE 6.—*Test Data*

Specimen-condition	Test condition	Fracture load		Fracture strain	Comments
		Test	Specification		
		Pounds	*Pounds*	*Percent*	
12a—normal	Room temp	110	100	22	
12a—heat, air	Room temp	74. 5	100	19	
12a—heat, N_2	Room temp	109	100	24	
12a—heat, air eth. ox	Room temp	82	100	20	
12a—heat, N_2 eth. ox	Room temp	124	100	26	
12a—heat, air eth. ox	−190° C	53	100	7. 2	Broke in uncooled portion.
12a—heat, N_2 eth. ox	−190° C	102	100	12. 5	Broke in uncooled portion.

TABLE 7.—*Test data*

Specimen-condition	Test condition	Fracture load		Fracture strain	Comments
		Test	Specification		
		Pounds	*Pounds*	*Percent*	
1—normal	Room temp	30. 5	42	12	
1—normal	Room temp	35	42	13	
1—heat, air	Room temp	20. 5	42	9. 8	
1—heat, N_2	Room temp	32	42	12	
1—heat, air eth. ox	Room temp	24	42	13	
1—heat, N_2 eth. ox	Room temp	35	42	13	
1—heat, air eth. ox	−190° C	24	42	5. 1	Broke in uncooled portion.
1—heat, N_2 eth. ox	−190° C	28	42	4. 5	Broke in uncooled portion.

TABLE 8.—*Test Data*

Specimen-condition	Test condition	Fracture load		Fracture strain	Comments
		Test	Specification		
		Pounds	*Pounds*	*Percent*	
13—normal	Room temp	35	42	11	
13—normal	Room temp	33. 5	42	10	
13—heat, air	Room temp	29	42	8. 3	
13—heat, N_2	Room temp	31	42	9. 3	
13—heat, air eth. ox	Room temp	33	42	10	
13—heat, N_2 eth. ox	Room temp	34	42	11	
13—heat, air eth. ox	−190°C	36	42	7	Broke in uncooled portion.
13—heat, N_2 eth. ox	−190°C	29	42	4. 5	Broke in uncooled portion.
13—normal	−190°C	37	42		Broke in uncooled portion.

TABLE 9.—*Test Data*

Specimen-condition	Test condition	Fracture load		Fracture strain	Comments
		Test	Specification		
		Pounds	*Pounds*	*Percent*	
14—normal	Room temp	45	42	16	
14—normal	Room temp	43	42	16	
14—heat, air	Room temp	27	42	10	
14—heat, N_2	Room temp	47. 5	42	18	
14—heat, air eth. ox	Room temp	26. 5	42	11	
14—heat, air eth. ox	−190°C	27	42	4. 5	Broke in uncooled portion.
14—heat, N_2 eth. ox	−190°C	40	42	9. 5	Broke in uncooled portion.
14—heat, N_2 eth. ox	−190°C	42	42		Broke in uncooled portion.
14—normal	−190°C	38. 5	42	5. 6	

MECHANICAL IMPEDANCE STUDY OF THE X–259 ROCKET MOTOR

RAYMOND G. HARTENSTEIN AND WILLIAM G. ELSEN
Goddard Space Flight Center

The impedance analysis of the X–259 rocket motor and roll-rig firing assembly presented in this report indicates that the roll rig gives a soft spring effect to the rocket motor which, if unaccounted for, could lead to the misinterpretation of vibration levels especially in the higher frequency range. The mechanical impedance concept has proved to be a straightforward and plausible method of analyzing this phenomenon and, at the same time, increases the general usefulness of static firing data.

To define the static firing arrangement completely, a study of the thrust cell mounted against the firing bay wall was also made. This study revealed the dynamic character of the thrust cell and provided excellent correlation with the design parameters of the device.

INTRODUCTION

To achieve a realistic laboratory simulation of in-flight vibration levels, an exact knowledge of the dynamic behavior of both rocket and payload is needed. The mechanical impedance concept offers this knowledge in a very useful form. Another dimension, force, is added to the dynamic picture by this concept, which allows a kinetic investigation that is more thorough than the limited kinematic approach used in the past. Mechanical impedance is a measure of the mechanical system's response (motion) to an applied excitation (force). It is in fact exactly equal to the ratio of the applied force to the resulting velocity at a point (or what may be assumed to be a point) in a structure. Instrumentation systems have been developed sufficiently so that impedance data are now being gathered on the upper-stage solid rocket motors—namely, the X–259 and X–248 manufactured by Allegany Ballistics Laboratory, Cumberland, Md., used as third and fourth stages of NASA Scout Vehicles. These data, in conjunction with subsequent payload impedance data measured in the laboratory, will permit the determination of more accurate environmental test levels.

This report sets forth the data and findings of an initial study, conducted January 20, 1962, of the X–259 rocket motor (Serial No. HPC–7) mounted in a special static firing fixture called a "roll rig," the purpose of which is to allow the measurement of motor roll torques during firing.

THRUST CELL—FIRING BAY WALL COMBINATION

The thrust cell, essentially a very stiff spring placed between the nose of the rocket bottle and the bay wall (test bay No. 2 at ABL), is designed to measure the thrust of the rocket motor during burning. (The thrust cell used was a 20,000-pound Baldwin L–H cell SR–4, Type TXX, Serial No. Z1009.) This cell is of considerable interest, since the impedance it presents to the rocket bottle affects to a large extent the dynamic motion, and hence acceleration, of the rocket bottle during burning (Refer to Appendix A.)

The impedance tests on the thrust cell were expected not only to provide information on the spring constant of the thrust cell but also to give a picture of any idiosyncrasies present over the frequency range of interest.

The curve given in Figure 1 for impedance versus frequency of the thrust cell shows clearly its springlike characteristic, which holds well until 2 kc. Above 2 kc the device approaches its major resonance, which is clearly established at 3 kc. Beyond 3 kc for a small region the curve tends to approach the mass line represented by the armature (see Fig. 3).

The very minor dip in the impedance curve at 1500 cps is of little significance not only because it represents a small magnitude variation but, more importantly, because it is not accompanied by any great phase change, as may be seen in the Figure 2 curve of the impedance phase angle versus frequency. Inasmuch as this dip is at half the frequency of the major resonance, it probably is a subharmonic.

The major resonance at 3.0 kc checks well with a theoretical value of 3.1 kc if the cell consists basically of the arrangement shown in Figure 3.

A thorough study of the thrust cell data revealed that it functions very nearly as expected. The equivalent circuit shown in Figure 3, with mass and spring constant values as indicated, will accurately simulate the thrust cell response up to 3 kc. The region above 3 kc is, presently at least, of little interest; this is fortunate, since both the magnitude and angle of impedance begin to

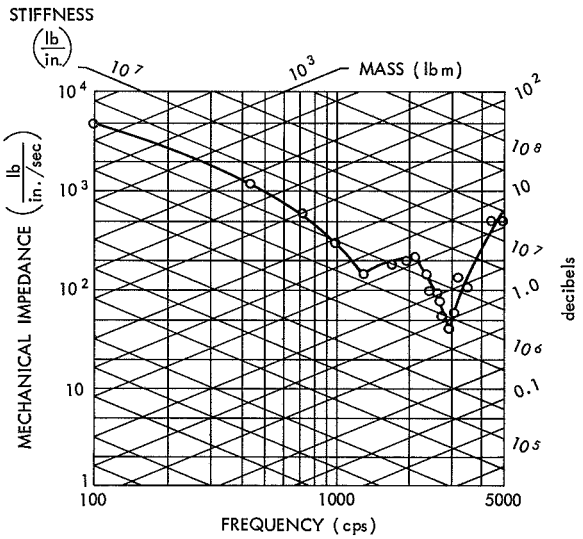

FIGURE 1.—Impedance vs. frequency for the Baldwin L–H thrust cell.

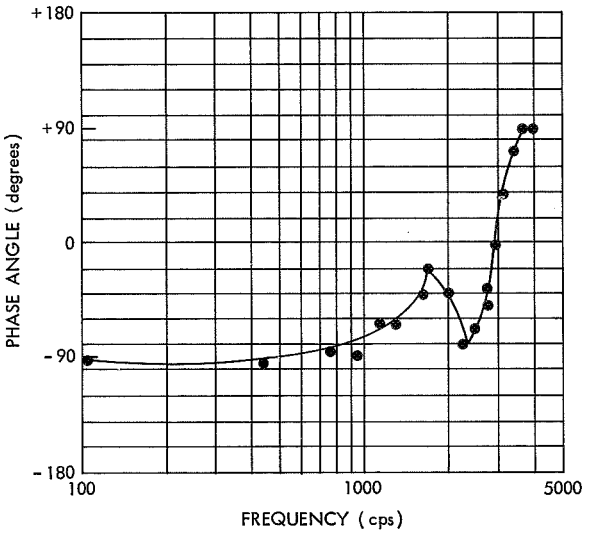

FIGURE 2.—Phase angle vs. frequency for the Baldwin L–H thrust cell.

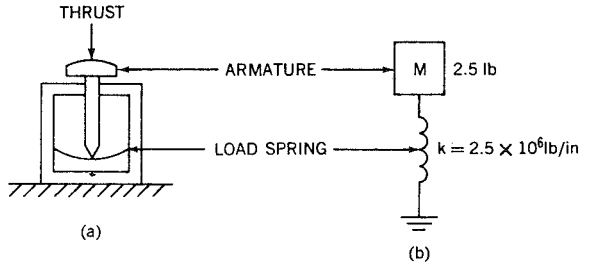

FIGURE 3.—Thrust cell: (a) Functional schematic; (b) Mechanical equivalent circuit.

perform in an extremely irrational manner above 3 kc. Some of the variation above 3 kc may, of course, be due to high frequency nonuniformities of the intstrumentation system itself.

Thus we can write the thrust cell impedance for the region below 3 kc as

$$Z=\frac{k}{j\omega}\left[1-\left(\frac{\omega}{\omega_n}\right)^2\right],$$

where k=the spring constant in lb/in. and, for a 20,000 lb thrust cell, $\omega_n=2\pi\times 3kc=19\times 10^3$ rad/sec.

The damping of this system may be read directly from the impedance curve. The damping, probably due to friction, is of some significance, being equal to 40 lb/in./sec, and is read from the impedance curve in Figure 1 as the

magnitude of impedance at resonance (3 kc). It can, however, be neglected for most engineering calculations (certainly below 1 kc).

The damping is included for correctness of the present analysis, and the impedance function takes the form

$$Z=D-\frac{jk}{\omega}\left[1-\left(\frac{\omega}{\omega_n}\right)^2\right].$$

The above equation then is an adequate representation of the thrust cell impedance between 0 and 3 kc, and will be used in general to simulate dynamically the static firing restraint system.

X-259 ROCKET MOTOR

The X–259 rocket motor was mounted in a roll-rig fixture constructed by the NASA Langley Research Center for special rocket firing studies (see Fig. 4). The system was kept intact; and, immediately after the rocket was fired, these impedance measurements were taken. The rocket motor was backed away from the thrust cell to allow installation of the instrumentation and force exciter as shown in Figure 5.

The point of contact chosen was the bearing surface which, during firing, was in direct contact with the thrust cell previously discussed. The impedance plot for this system is shown in Figure 6.

The impedance plot as a whole tends to follow a rather soft spring constant line, as indicated. The cause for this can only be postulated but is suspected to be the oil bearing surface of the roll rig. This tendency is unfortunate in a sense, since the soft spring likeness "swamps out" to a large degree modes and resonances of the bottle that are also of interest. However, the primary purpose of this test was to define the impedance characteristics of the entire system as presented to the force generated in the rocket.

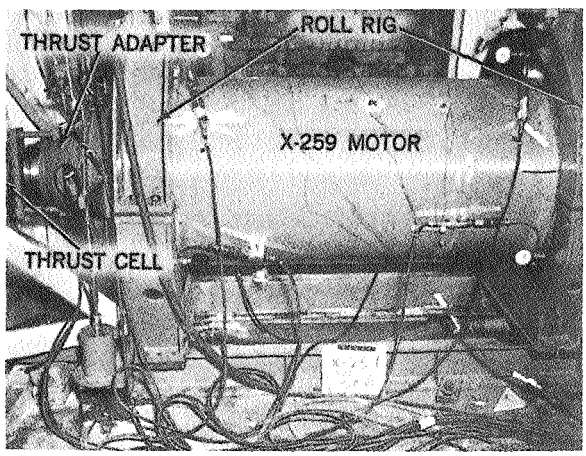

FIGURE 4.—X–259 motor and roll-rig assembly.

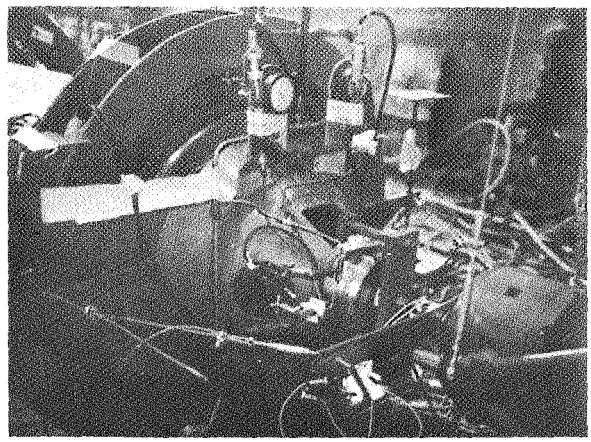

FIGURE 5.—Impedance test arrangement.

A study of the impedance plot of Figure 6 indicates five departures from the springlike characteristic. Of these, only three are significant: numbers 2, 4, and 5. The notches at 150 cps and 350 cps represent either minor structural resonances or, possibly, weak acoustical modes in the motor cavity; neither is accompanied by an appreciable phase shift, as seen in Figure 7.

Regions 2, 3, 4, and 5 of Figure 6 all represent previously identified [1] resonant burning modes of the X–254 motor.[2] Regions 2, 4, and 5 are accompanied by large phase shifts about zero degrees.

[1] "Information and Preliminary Data on the Scout ST–2 Launching, Sections A&H," NASA Langley Research Center letter to Chance Vought, June 26, 1961.

"Preliminary Flight Test Results of Scout ST–4," NASA Langley Research Center, Mar. 8, 1961.

[2] The X–254 motor is identical to the X–259 mechanically with the exception of fuel type and configuration. Since we are considering an empty bottle, they are equivalent.

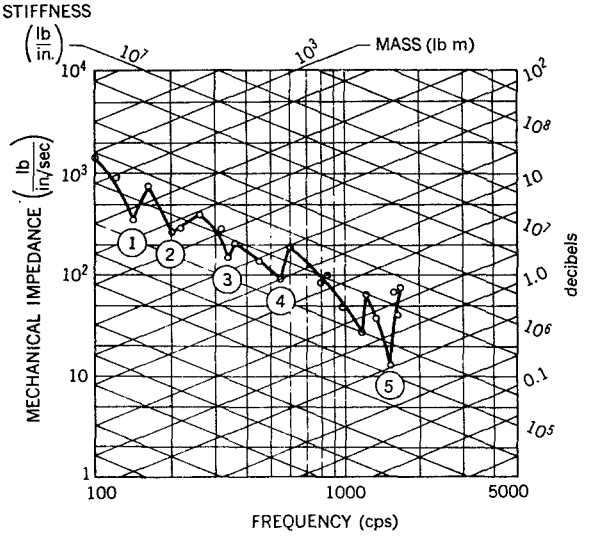

FIGURE 6.—Impedance vs. frequency for the X–259 mounted in roll rig.

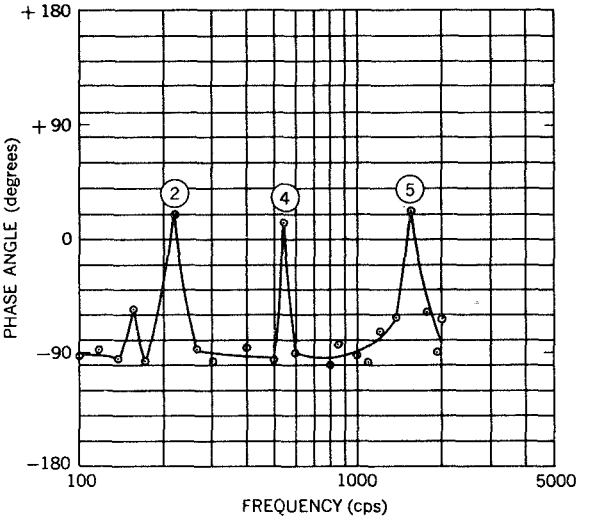

FIGURE 7.—Phase angle vs. frequency for the X–259 and roll rig.

The notches (resonances) that always precede the peaks (antiresonances) are in each case preceded by a phase shift through zero degrees with a positive slope. Likewise, the peaks, or antiresonances, are always accompanied by the negative-going angle through zero degrees, which substantiates theory very well. The phase angle remains, as would be expected, at very nearly −90 degrees all other times and thus verifies the overall soft spring characteristic of the impedance plot in Figure 6.

In order to present an impedance equivalent for this sytem, the importance of the three departures from the springlike characteristic must be considered. Certainly, for random vibration levels, these three regions are sufficiently narrow to be given little attention. However, for considering sinusoidal levels, there may be sufficient reason for their inclusion, particularly when resonant burning conditions are to be simulated.

If we choose to neglect all but the dominant feature of these data, the impedance of the X–259 rocket motor and roll-rig combination may be established as that of a spring, or

$$Z=\frac{k}{j\omega};$$

and the equivalent impedance circuit for the entire device is as shown in Figure 8.

STATIC FIRING EQUIVALENT IMPEDANCE

To establish completely the dynamic relation between rocket motor, roll rig, and thrust cell, it is necessary simply to combine the previously found equivalent impedance for these systems. Connecting these impedance circuits of Figures 3 and 8 gives the Figure 9 circuit.

The terminating or load impedance (labeled point 1 in Fig. 9) as seen by the forward collar of the rocket has a great effect on the motion at this point. This effect is directly proportional to frequency because of the springlike character of the X–259 roll-rig assembly. It must be noted that the high frequency limit placed on this circuit is 1500 cps because of the radical departure beyond this point of the impedance of the roll-rig assembly. Further studies must be made before a clear definition of the region above 1500 cps can be established.

Solving for the impedance at point 1 of Figure 9 gives

$$Z_\sigma=\frac{k_1}{j\omega}\left(\frac{k_2-\omega^2M}{k_1+k_2-\omega^2M}\right),$$

which below 2 kc may be closely approximated as

$$Z_\sigma=\frac{1}{j\omega}\left(\frac{k_1k_2}{k_1+k_2}\right); \qquad (1)$$

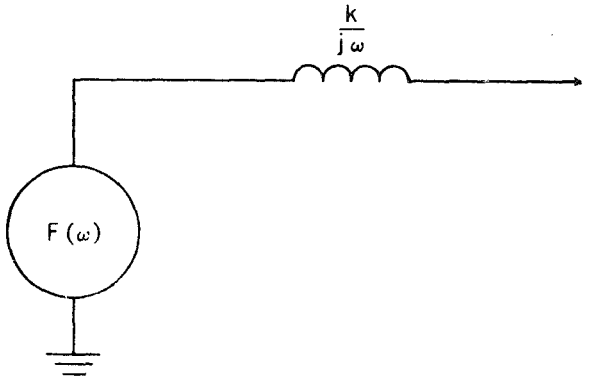

FIGURE 8.—Impedance equivalent of the X–259 and roll rig.

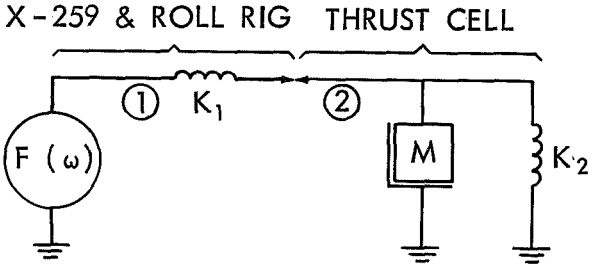

FIGURE 9.—Impedance equivalent of the X–259 static firing assembly.

or the net effect of the entire system at point 1 is that of a spring of stiffness

$$K_{eff}=\frac{k_1k_2}{k_1+k_2}.$$

Equation 1 may then be written

$$Z_\sigma=\frac{K_{eff}}{j\omega}. \tag{1a}$$

The impedance Z_σ is that presented to the force generator shown in Figure 9. The point of connection between the force generator and Z_σ (point 1) can be assumed to exist physically at the forward collar of the X–259 motor, according to our previous approximations.

It would be extremely desirable to know the function $F(\omega)$ because it represents a property that, together with the motor impedance, describes wholly the dynamic behavior of the X–259 rocket motor. This function may be found analytically as follows:

By definition,

$$F(\omega)=V(\omega)\times Z_\sigma(\omega);$$

and also, in order to use acceleration data, since

$$V(\omega)=\frac{A(\omega)}{j\omega},$$

$F(\omega)$ may be written as

$$F(\omega)=\frac{A(\omega)}{j\omega}\times Z_\sigma(\omega).$$

Assuming the frequency dependence is obvious,

$$F=\frac{AZ_\sigma}{j\omega}, \tag{2}$$

and substituting Equation 1a into 2 gives

$$F=\frac{AK_{eff}}{-\omega^2}. \tag{3}$$

With the aid of Equation 3 and acceleration data from static firings, the forcing function F, or $F(\omega)$, may be established. The function $F(\omega)$ is, as indicated, dependent on frequency and to some degree will be time-dependent as well. The time dependency results from the steady decrease of fuel mass during burning, along with a corresponding increase in chamber dimensions. This function can be measured and accounted for quite readily.

After the forcing function $F(\omega)$ and the static firing arrangement impedances have been established, the acceleration levels for other terminating impedances may be determined by analyzing the circuit of Figure 10.

It is assumed here that the payload—rocket motor configurations do not appreciably affect

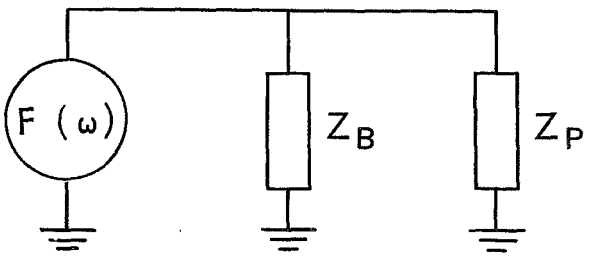

FIGURE 10.—Equivalent impedance circuit for the rocket and payload combination.

the forcing function $F(\omega)$ as previously found by Equation 3. The impedance of the rocket motor Z_B and the impedance of the payload Z_P will need to be firmly established. The X–259 and X–248 rocket motors are presently being studied by NASA and others.[3]

Since the payload configurations vary considerably, the impedance Z_P in each instance must be determined. The summation of the complex impedances Z_B+Z_P can be accomplished efficiently on an analog computer with curve-following plotters.

The predicted flight level accelerations could then be established, since

$$A=j\omega\frac{F}{Z_{eq}}, \tag{4}$$

where

$$Z_{eq}=Z_B+Z_B.$$

Flight levels can then be compared with those derived from Equation 4, and regions of error can be established to increase the accuracy of subsequent predictions.

INSTRUMENTATION AND ANALYSIS

The impedance tests all were run at Allegany Ballistics Laboratory, Ridgely, W. Va., on January 20, 1962. The equipment needed for these tests was mounted in a mobile trailer that also provided a work area. The data recording schematic is shown in Figure 11. The tape recorder provided permanent records that were returned to Goddard Space Flight Center for thorough analysis. In order to make a preliminary analysis, an oscillograph recording of a slow sine sweep was made; and from this the areas of interest (peaks and valleys) could be quickly verified. Many points were taken in these areas during the discrete frequency tests to define fully each peak or valley. The force and acceleration signals from the impedance head were carried through 100 feet of driven shield triax cable into the instrumentation van, where they were amplified, monitored, and

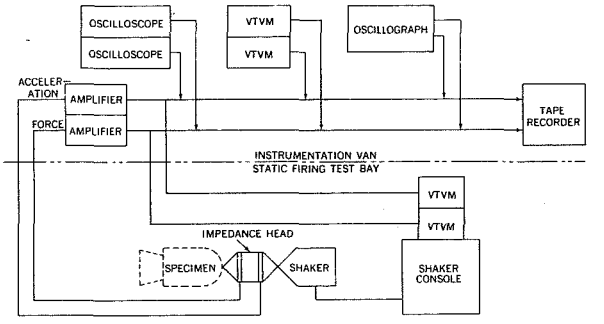

FIGURE 11.—Instrumentation diagram for impedance measurements.

recorded. After amplification these signals were returned to the test bay so that the control console operator also could monitor them conveniently.

The structures were excited through the impedance head by means of an electrodynamic shaker system suspended from an overhead crane, as shown in Figure 12.

This shaker system is capable of approximately 150 pounds force but was operated at a force level of 20 pounds for the thrust cell study and 70 pounds for the motor tests. The lower force level for the thrust cell tests was necessary to avoid extreme acceleration levels at resonance and yet provide a constant force level that would simplify analysis procedures.

Minor noise and pickup problems that existed in the instrumentation system were traced to faulty input connectors on the high input impedance signal conditioners used. This, however, presented only slight analysis difficulties because the signals had to be filtered in any case, to eliminate extraneous structural noises.

The impedance data analysis consisted of playing back the tape recordings through the instrumentation shown in Figure 13.

The rms voltmeter readings of the filtered, force and acceleration signals were recorded and quotients were taken to provide magnitude values of the apparent weight function as discussed in Appendix A. The phase angle values necessary to describe fully the apparent weight vector were found from the phase meter reading of the filtered signals. (These filters were compared with each other for filter-induced phase shift, and no difference was found

[3] Belsheim, R. O., and Harris, J. J., "Apparent-Weight Measurements of Rocket Payload and Test Structures," Naval Research Laboratory Memorandum Report 1099, December 1960.

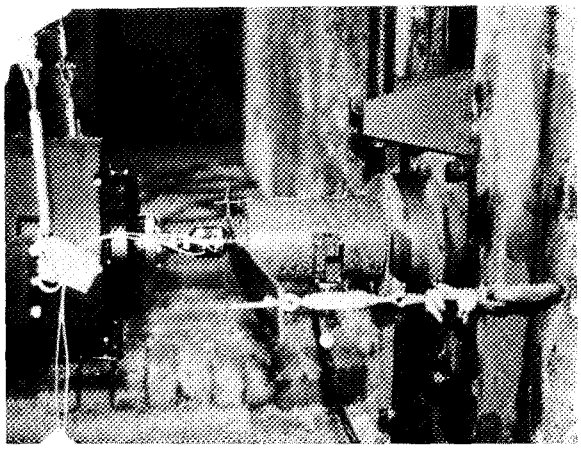

FIGURE 12.—Test configuration for thrust cell measurements.

between them.) The apparent weight data could then be plotted on the special impedance graph paper from which either impedance or apparent weight could be read. To plot the impedance phase angle, it was necessary simply to add 90 degrees to the apparent weight values, since impedance is a function of velocity rather than acceleration (discussed in Appendix A).

CONCLUSIONS

From this initial study of the static firing arrangement, at least two points should be noted:

1. The thrust cell acts as a stiff spring below resonance, encouraging acceleration in the higher frequencies while subduing those in the lower frequencies. This tendency exists whenever a thrust cell is used.
2. The X–259 roll-rig assembly contributes an exceedingly soft spring constant that is not completely defined but that must exist at or near the normal point of thrust cell attachment where an oil bearing surface is known to exist.

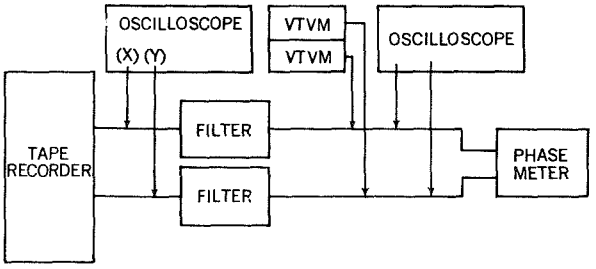

FIGURE 13.—Instrumentation diagram for data analysis.

The resonance of the unloaded thrust cell at 3 kc is not in itself significant, but the possibility and almost certain existence of a lower natural frequency under load must be fully recognized. A mass load of only 150 lb would bring this resonant frequency down into the 500 cps region, which can be extremely critical when resonant burning problems exist. Tentative evidence already points to a correlation between propellant mass decrease versus time and the time after ignition at which certain resonant burning conditions are initiated.

For roll-rig firings, the soft-spring-constant characteristic introduces a very low impedance to the motor and tends to reinforce the higher frequencies to an even greater degree than the thrust cell; however, the large mass of the thrust adapter and oil bearing guides may considerably diminish this effect.

Since this preliminary study has been most encouraging, a more intensive study of the X–259 and X–248 rocket motors is presently in progress and a continuing investigation with constant improvement in instrumentation and techniques is planned.

ACKNOWLEDGMENT

The wholehearted cooperation of Allegany Ballistics Laboratories, in particular the generous assistance of Mr. Claude Rutherford, in the performance of the field tests is gratefully acknowledged.

Appendix A

AN INTRODUCTION TO MECHANICAL IMPEDANCE AND APPARENT WEIGHT CONCEPTS

INTRODUCTION

Impedance is by definition a measure of the responsiveness of an element to some external excitation. *Mechanical Impedance* is a measure of the mechanical system's response (motion) to an applied excitation (force). It is exactly equal to the ratio of the applied force to the resulting velocity at a point (or what may be assumed to be a point) in a structure.[1] Thus a system (or element), to have a high impedance, requires large forces to set it in motion, that is, to give it a velocity; and, to have a low impedance, a system requires only small forces to achieve high velocities. In dynamics remember that we are primarily concerned with sinusoidal functions of force and velocity and that in mechanical impedance studies the further limitation of having only steady-state sinusoids is often assumed in order that we may work in the frequency domain rather than in the time domain.[2]

Another dynamic relation follows from the definition of impedance (since we assumed only that a ratio of excitation to motion was required); this is the *Apparent Mass* relation, equal to force divided by acceleration. Since acceleration in dynamics is most often used in terms of g's, this term is commonly referred to as the *Apparent Weight*, so called because the apparent weight presented by a mass at low frequencies is equal to its weight. The apparent weight concept seems the most natural of the two and, in most cases, is the simplest to acquire with laboratory instruments. Fortunately these two phenomena are related simply, as will be seen, and either may be used to derive the other as the situation demands.

The mechanical impedance or apparent weight concepts, then, define the dynamic behavior at a point in a system or element that meets certain requirements, the most important of which is that the device be composed of linear, bilateral element(s) that can be considered to act in a straight line.[3]

SYMBOLS AND MECHANICAL ELEMENTS

The symbols and mechanical elements used herein are defined as follows:

A	acceleration (g's) [4]
D	viscous damping (lb/in./sec), units mt^{-1}
F	force (lb),[4] mlt^{-2}
f_n	natural frequency (cps), t^{-1}
g	gravitational constant equal to 32.2 ft/sec^2, lt^{-2}
j	indicates an angular advancement of +90 degrees
k	spring constant (lb/in.), mt^{-2}
M	mass (lb mass), mlt^{-2}
V	velocity (ft/sec),[4] lt^{-1}
W_a	apparent weight (lb),[4] mlt^{-2}
$\angle W_a$	phase angle of the vector or angle by which F leads A
Z	mechanical impedance,[4] mt^{-1}
$\angle Z$	phase angle of the vector or angle by which F leads V
ω	angular frequency (radians/sec), t^{-1}

damper D
spring k
mass M

[1] Assuming of course that proper units of length l, mass m, and time t are chosen; and keeping in mind that all variables will be assumed to be rotating vectors, i.e., contain both a real and an imaginary part.

[2] This limitation is being applied for the present discussion, and is in no sense required by the impedance concept.

[3] For a discussion of these limitations, refer to the literature recommended at the end of the Discussion section.

[4] Unless otherwise stated, a vector quantity.

force generator $F(t)$
fixed reference plane (the earth)

DISCUSSION

Of the many mechanical elements available, three of the most important are discussed here: damping (viscous), mass, and spring.

Damping.—The viscous damper D is normally rated in pounds per foot per second and hence is a constant impedance:

$$Z=\frac{F}{V}=D. \tag{A1}$$

Mass.—The relation between force and motion for a mass $F=MA$ allows the determination of the ratio of F/V by the following procedure:

Let

$$F(t)=F_0e^{j\omega t}.$$

Then

$$A(t)=\frac{F_0e^{j\omega t}}{M},$$

and

$$V(t)=\frac{1}{M}\int F_0e^{j\omega t}dt;$$

or

$$V(t)=\frac{F_0}{j\omega M}e^{j\omega t},$$

and finally,

$$Z=\frac{F}{V}=j\omega M. \tag{A2}$$

Spring.—In a similar manner the impedance of the spring is

$$Z=\frac{k}{j\omega}. \tag{A3}$$

With the establishment of the above three equations, we need only to set up the ground rules whereby the combination of elements in systems may be reduced by mathematical manipulations to determine the magnitude and phase of Z.

There are basically only two types of circuits or interconnections to consider: the series, and the parallel. The series circuit is indicated whenever two elements are so arranged that the forces acting on each of them must be identical (as illustrated by Example 2, which follows this discussion). The parallel circuit is simply the inverse of this and is evidenced by the fact that the forces need not be equal; however, the velocity drops [5] across the elements (as seen in Example 1) will be equal. The rules for combining elemental impedances for these two conditions are as follows:

I—Elements in series present an impedance Z as:

$$\frac{1}{Z_{\text{total}}}=\frac{1}{Z_1}+\frac{1}{Z_2}+\frac{1}{Z_3}+\ \ldots\ +\frac{1}{Z_n}.$$

II—Elements in parallel present an impedance Z as:

$$Z_{\text{total}}=Z_1+Z_2+Z_3+\ \ldots\ +Z_n.$$

Since any combination of impedance, regardless of complexity, may be viewed step by step as either a series of parallel combination of two or more elements, any circuit may be reduced by the above rules to a single impedance consisting of a real component (if damping is present) and an imaginary component.

The relation between Z and W_a may be derived by using the known relation between velocity and acceleration:

$$A=j\omega V,$$

and

$$W_a=\frac{F}{A}=\frac{F}{j\omega V};$$

then

$$W_a=\frac{Z}{j\omega}.$$

In order to emphasize the foregoing rules and conclusions, three solutions to simple mechanical circuits are illustrated and analyzed on the following pages. The literature cited below is recommended for a more thorough discussion of this subject.

A1. Firestone, Floyd A., "American Institute of Physics Handbook," New York: McGraw Hill Book Co., 1957.

A2. Olson, Harry F., "Dynamical Analogies," New York: D. Van Nostrand, 1943.

[5] The velocity drop across an element is simply the force acting on the element divided by the impedance, or $V=F/Z$.

A3. Mason, W. P., "Electromechanical Transducers and Wave Filters," Princeton, N.J.: D. Van Nostrand, 1948.

A4. Bradley, Wilson, Jr., "Mechanical Impedance Testing," in *Proc. Institute of Environmental Sciences National Meeting April 1960*, p. 535.

Example 1

The first example to be considered is a spring-mass combination (see Fig. A1) with one side of the spring rigidly mounted to a fixed plane. The point at which the spring is attached to the mass is also the point of force application. However, it is to be noted that this excitation may be applied to any part of the mass as long as our previous assumption of linear motion holds, since the mass element may be considered dimensionless physically [Fig. A1(a)]. The circuit is analyzed with and without damping to illustrate this effect. Since the velocity of all masses is referred to ground, all masses will have a connection similar to that of Figure A1(b), where the viscous damper could be applied across either the mass or the spring with the same resulting effect.

The impedance may be solved by using Equations A1, A2, and A3 and the rule for parallel combination:

A. Without damping,

$$Z=j\omega M-\frac{jk}{\omega}.$$

B. With damping,

$$Z=D+j\omega M-\frac{jk}{\omega}.$$

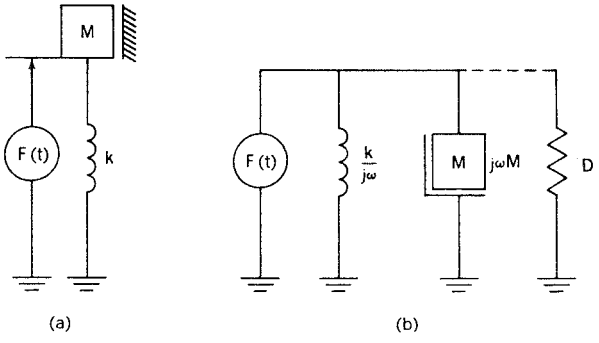

FIGURE A1.—Spring-mass system (a) Mechanical circuit (b) Impedance circuit.

It is often of interest to know the low and high frequency tendencies of a system, and these may be readily found by letting ω approach zero or infinity in the above equations.

Using case B, with damping, gives

$$\underset{f\to 0}{Z}=D-\frac{jk}{\omega}, \tag{A4}$$

$$\underset{f\to\infty}{Z}=D+j\omega M. \tag{A5}$$

At resonance the reactive terms cancel, and

$$\underset{f=f_n}{Z}=D. \tag{A6}$$

Using the previously found relation,

$$W_a=\frac{Z}{j\omega},$$

W_a may be directly written as

$$\underset{f\to 0}{W_a}=\frac{D}{j\omega}-\frac{k}{\omega^2}, \tag{A4a}$$

$$\underset{f\to\infty}{W_a}=\frac{D}{j\omega}+M, \tag{A5a}$$

and

$$\underset{f=f_n}{W_a}=\frac{D}{j\omega}. \tag{A6a}$$

With these asymptotic forms of the impedance function and specially designed graph paper, both Z and W_a may be plotted as one curve and read directly from the graph in Figure A2.

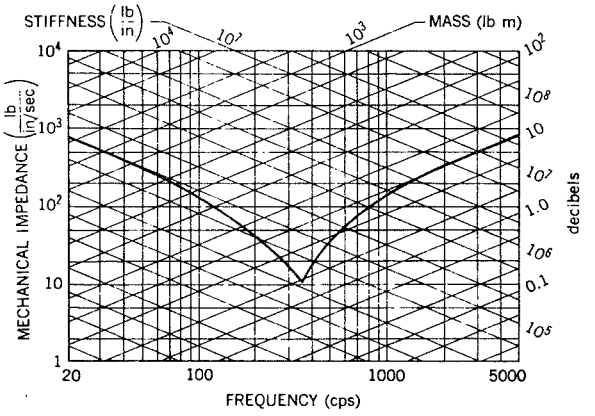

FIGURE A2.—Impedance and apparent weight (figure A1) vs. frequency.

As Equations A4, A5, and A6 indicate, the impedance function follows a spring constant line below resonance and a constant mass (or apparent weight) above resonance. The region near resonance is influenced by the Q of the circuit, defined as

$$Q=\frac{2\pi E}{\Delta E},$$

where E is the energy stored and ΔE is the energy dissipated per cycle.

At resonance the impedance value is exactly equal to the damping D.

The phase angles of Z and W_a may also be sketched to give a more complete picture of the response. In the curves below (Fig. A3) it can be seen that the only time Z has a significant real part is at resonance or $f=f_n$, while W_a has a very large real part (phase angle equal to zero) for all frequencies significantly above f_n. This indicates that the mechanical system appears masslike at high frequencies because of the spring's ineffectiveness.

Example 2

Another configuration of interest is the antiresonant arrangement of Figure A4 below.

The impedance of this circuit may be solved by again using Equations A1, A2, and A3 and the rules for series and parallel combination:

C. Without damping,

$$Z=\frac{j\omega Mk}{k-\omega^2 M}.$$

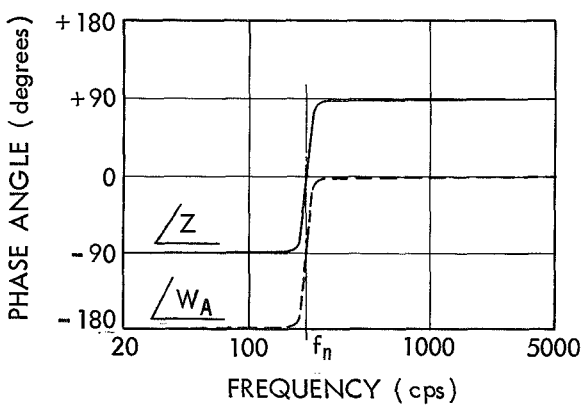

FIGURE A3.—Phase angle of Z and W_a vs. frequency.

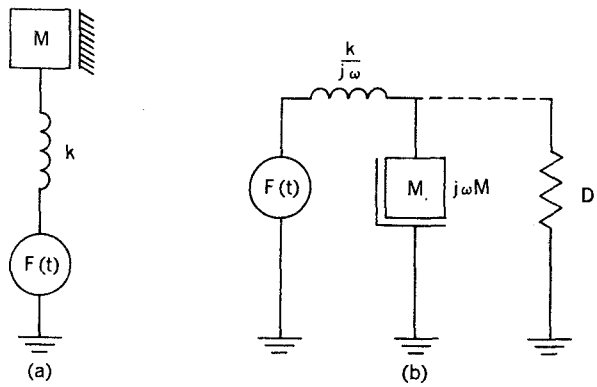

FIGURE A4.—A driven spring-mass system (a) Mechanical circuit, (b) Impedance circuit.

D. With damping,

$$Z=\frac{Dk^2}{k^2-\omega^2(2Mk-D^2)+\omega^4M^2}+j\omega\frac{Mk(k-\omega^2M)-D^2k}{k^2-\omega^2(2Mk-D^2)+\omega^4M^2}.$$

The frequency spectrum of Z and W_a may again be found by studying the high and low frequency asymptotes of Z and the antiresonant conditions for cases C and D.

Using case D, which includes damping, gives

$$\underset{f\to 0}{Z}=D+j\omega M \tag{A7}$$

$$\underset{f\to\infty}{Z}=\frac{k}{j\omega}+\frac{Dk}{M}, \tag{A8}$$

and

$$\underset{f=f_n}{Z}\cong\frac{Mk}{D}. \tag{A9}$$

The apparent weight relations can again be written from Equations A7, A8, and A9 as

$$\underset{f\to 0}{W_a}=M+\frac{D}{j\omega},$$

$$\underset{\to\infty}{W_a}=\frac{Dk}{j\omega M}-\frac{k}{\omega^2},$$

$$\underset{f=f_n}{W_a}=\frac{Mk}{j\omega D}.$$

The magnitude of both Z and W_a peak up at antiresonance as expected (Fig. A5).

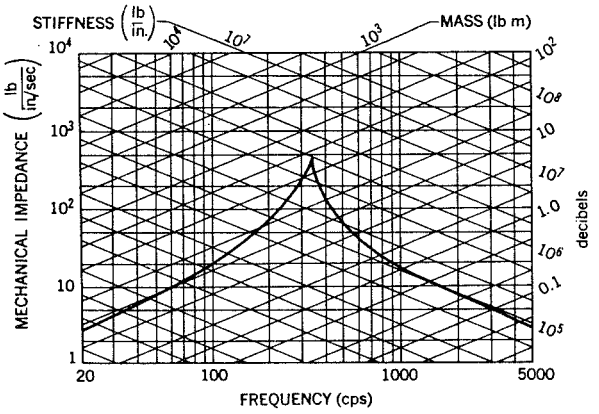

FIGURE A5.—Impedance and apparent weight vs. frequency.

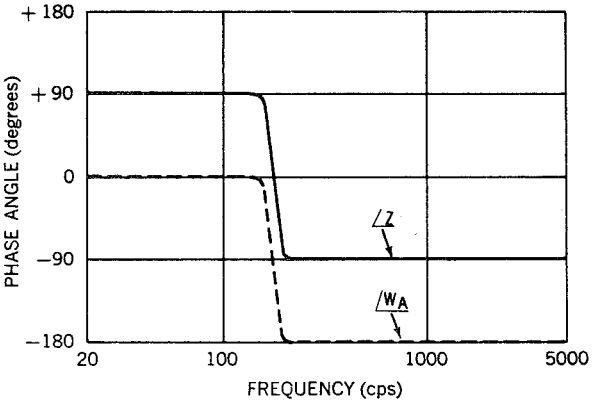

FIGURE A6.—Phase angles of Z and W_a vs. frequency.

The phase angles also may be of interest and may be approximated from the impedance equations. The degree of approximation is dependent on the degree of damping, but of course these equations may be solved very easily for any desired degree of accuracy.

The Figure A6 plot shows the phase shift passing through antiresonance but, most importantly, note that the phase angles at antiresonance are identical for both Z and W_a, as they were for resonance (see Fig. A3).

Example 3

The final circuit to be considered, Figure A7, contains properties similar to both of the preceding circuits and shows important aspects of both resonance and antiresonance not strictly deduceable from the previous two illustrations.

The circuit consists of two masses separated by a spring, with the forcing function $F(t)$ acting on one of the masses.

For this problem we will discuss only the impedance function Z, since by now the transformation to W_a is obvious.

$$Z=D+j\omega M_2+\frac{j\omega M_1\times\frac{k}{j\omega}}{\frac{k}{j\omega}+j\omega M_1},$$

which reduces to

$$Z=D+j\omega\,\frac{kM_1+kM_2-\omega^2M_1M_2}{k-\omega^2M_1}.$$

When the impedance function is written in the above form, the frequency characteristics

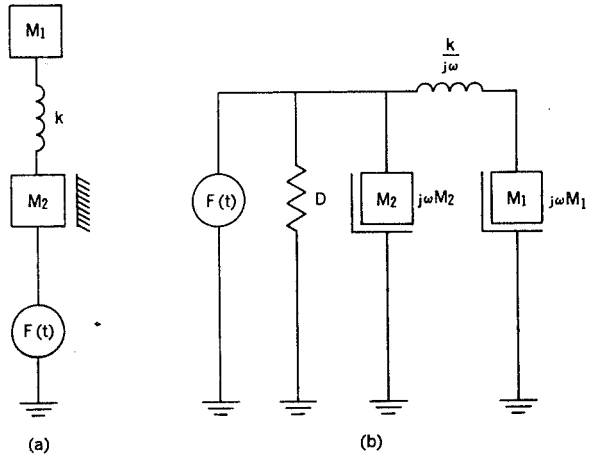

FIGURE A7.—Complex mechanical system (a) Mechanical circuit (b) Impedance circuit.

often may be derived simply by contemplating this equation in the following steps:

(1) At low frequency the ω factor in the numerator will tend to zero, or

$$\underset{f\to 0}{Z}\approx D+j\omega(M_1+M_2).$$

(2) At high frequency the D certainly will become insignificant, and the ω^2 terms will dominate; hence,

$$\underset{f\to\infty}{Z}\approx j\omega M_2.$$

(3) A zero (or minimum) can readily be seen in the numerator by looking at the term

$$(kM_1+kM_2-\omega^2M_1M_2);$$

this must go to zero when

$$k(M_1+M_2)=\omega^2M_1M_2,$$

which gives us a zero, minimum, when

$$f=f_0=\frac{1}{2\pi}\sqrt{\frac{k(M_1+M_2)}{M_1M_2}}.$$

(4) Also, then, looking at the denominator we see that it is similar to case C of our second illustration and must give a pole (maximum) of impedance when

$$f=f_x=\frac{1}{2\pi}\sqrt{\frac{k}{M_1}}.$$

The magnitude and phase of Z may then be sketched as before (Fig. A8).

The peak-notch effect is clearly present in Figure A8(a). It is caused essentially by the fact that a series resonance between k and M_1 is present, as well as a possible parallel antiresonance between k and M_2. The relation between f_x and f_0 may be found as follows:

$$f_0=\frac{1}{2\pi}\sqrt{\frac{k}{M_1}+\frac{k}{M_2}}.$$

From this last expression it follows that, for $M_2>>M_1$, f_0 approaches f_x and the peak-notch effect becomes extremely sharp and, for $M_2\cong M_1$, $f_0=\sqrt{2}f_x$. Also, for $M_2<<M_1$, $f_0\to\infty$.

In Figure A8(b) it is important to note that, as the frequency varies through both f_0 and f_x, the phase angle of Z passes through 0 degrees. It is significant that the phase angle between f_0 and f_x need not reach -90 degrees but, for our considerations, it *must* pass through zero.

Some very important facts can be drawn from the foregoing data and curves, namely:

1. When the phase angle of the apparent weight W_a is near zero degrees, the system is masslike; that is,

$$W_a\approx M.$$

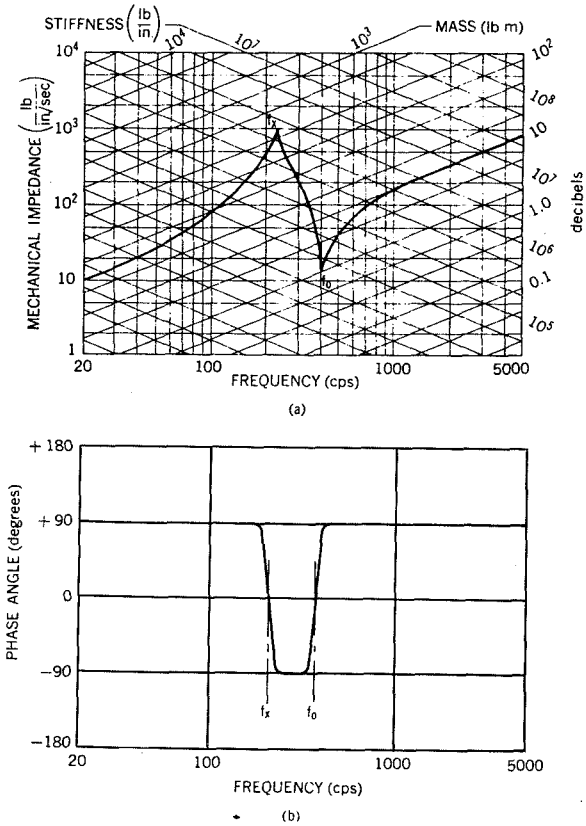

FIGURE A8.—Typical frequency response of Figure A7 (a) Impedance vs. frequency (b) Phase angle of Z vs. frequency.

2. When the phase angle of W_a is near 180 degrees, the system is springlike; or

$$W_a\approx-\frac{k}{\omega^2}.$$

3. When the phase angle of W_a is -90 degrees, the system is at resonance if $d\angle W_a/df$ is positive, and is at antiresonance if $d\angle W_a/df$ is negative.
4. If the system does not depart from our previous assumptions of linearity, etc., the $\angle W_a$ must lie in quadrants 3 and 4 only.

These rules of thumb are extremely valuable in the interpretation of impedance and apparent weight data.

A SURVEY OF LARGE SPACE CHAMBERS

R. T. HOLLINGSWORTH
Goddard Space Flight Center

Construction has been authorized for a number of large thermal-vacuum chambers to simulate orbital altitudes in the environmental testing of complete spacecraft. The proposed facilities shall be capable of simulating the low temperatures, solar and earth radiation, and vacuum of outer space.

We have outlined in this report the individual specifications and capabilities of each of the proposed space simulation facilities. Since the field of space simulation is growing rapidly, it is recognized that this survey will be out of date upon issue.

The need for ground-test facilities which simulate environments encountered at orbital altitudes has caused the government and private industry to authorize and construct large thermal-vacuum chambers for testing complete spacecraft in many combined environments.

Since the major portion of a spacecraft's operational life is spent in a vacuum, high reliability must be assured by ground testing in a similar environment prior to launching. Some of the principal space environment factors are: the low temperatures, solar and earth radiation, ionizating radiation, meteoritic impacts, and zero gravity. Current technological limitations preclude the simulation of the last three factors in large space chambers. The remaining factors are chiefly concerned with the thermal cycles, heat balance, and temperature extremes experienced by the spacecraft.

While scientific theory and analytical procedures permit design calculations, the many simplifying assumptions must be verified by testing of the final complex structure. It is often necessary to control the spacecraft temperature within a few degrees centigrade for proper operation of scientific instruments and experiments; this is achieved by regulation and ejection of the heat generated by internal power sources. The complexity of this problem with large spacecraft is so great that experimental verification must be made under test conditions simulating outer space.

The current thermal-vacuum techniques employed at the Goddard Space Flight Center include the following:

1. Uniform soak temperature.—For spinning satellites of simple geometric configuration, with very low power dissipation, a uniform soak test may be sufficient. Even for complex systems, it is felt that a soak test is required as a preliminary test to provide a well defined datum plane.

2. Predicted temperature contour reproduction.—This method involves using a combination of cold walls and lamps to reproduce the temperatures predicted (by the thermal design) in several important regions of the spacecraft. Usually the spacecraft is brought to "power-off" temperatures, and the inputs are held constant when the power is turned on. This technique was employed with Explorer XII. In this test, realistic temperature gradients are produced to verify performance.

The following will briefly illustrate the above: The solar aspect for Explorer XII was 150 degrees in September 1961. The solar aspect for March 1962 (shown in position 2 on Fig. 1) was 30 degrees. Figure 2 shows the positioning of the lamps for the thermal-vacuum testing of Explorer XII. The two aspect tests were

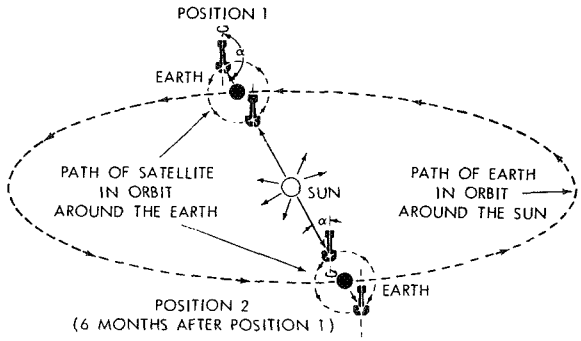

FIGURE 1.—Relative positions of sun and satellite at different times of year.

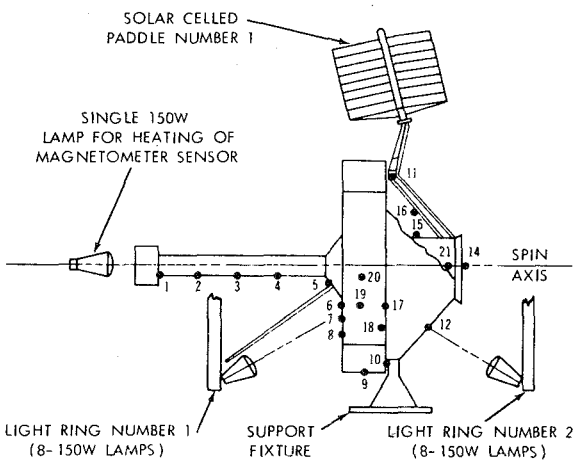

FIGURE 2.—Thermal-vacuum aspect tests. Numbers designate thermocouple stations.

chosen because the main instrumentation compartment is located in the octagon, while the transmitter section is near the base of the spacecraft. Since these two locations will alternately "see" the direct solar radiance and the cold of space, the thermal-vacuum test was designed to observe the thermal gradients through the spacecraft and their effect, if any, on the subsystems.

As spacecraft become more sophisticated, more accurate simulation of the expected environment will be required. Thus, many facilities now planned or under construction will include solar simulation and cryogenic wall temperatures.

In light of the foregoing, it is interesting to review the facilities under consideration for the spacecraft of the future. The following pages present illustrations and tabular summaries of a number of such facilities.

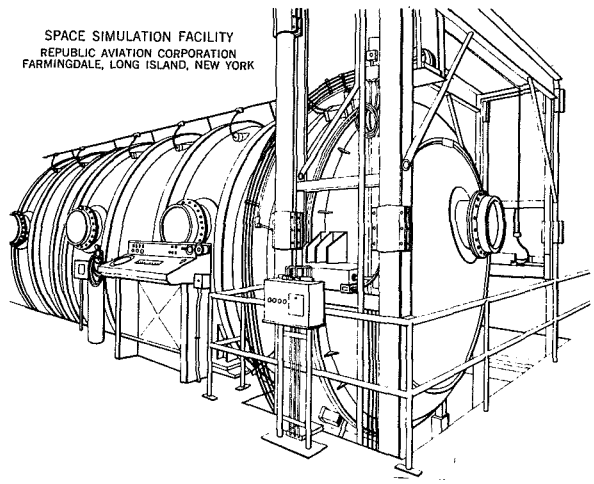

Construction:
- Overall dimensions: 13 ft diameter x 30 ft long.
- Construction material:
  - Shell: 304 stainless steel.
- Work space dimensions:
  - Entry lock: 13 ft diameter x 8 ft long.
  - Operating lock: 13 ft diameter x 18 ft long.

Pressure:
- Ultimate pressure: 8.8×10^{-7} mm-Hg.
- Time to achieve ultimate pressure: 3 hours.
- Pumping system: Electronic gettering and blower system.

Temperature:
- Temperature range: Under evaluation.
- Thermal system: Under evaluation.

Cryogenics:
- LN_2 panel area: Under evaluation.
- He panel area: Under evaluation.

Solar Simulation:
- Area illuminated: 10 ft diameter.
- Maximum intensity: 250 watts/ft^2.
- System type: Xe lamps.

Other Environment Capabilities:
- A sinusoidal vibration system with a 30,000-pound force output is being installed.

Systems Contractor:
- Design: Tenney Engineering, Inc.
- Fabrication: Tenney Engineering, Inc.

Operational Date:
- September 1961 (vacuum).

LOCKHEED AIRCRAFT CORP.
SUNNYVALE, CALIFORNIA

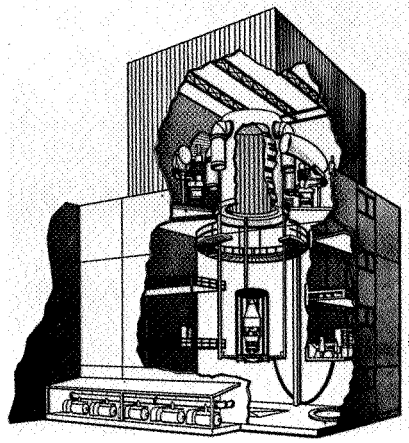

Construction:
- Overall dimensions: 18 ft inside diameter x 20 ft high.
- Construction materials:
  - Shell: 304 stainless steel.
  - Shroud: extruded aluminum.
- Work space dimensions:
  - Initial configuration for 5 ft diameter x 15 ft vertically mounted vehicle.

Pressure:
- Ultimate pressure: 1×10^{-8} mm-Hg.
- Time to achieve ultimate pressure: 4 hours.
- Pumping system: Twenty-two 32-inch oil diffusion pumps backed by diffusion ejector and mechanical pumps.

Temperature:
- Temperature range: Shell −273°F, ambient to +375°F.
- Thermal system: Circulating Dowtherm-A.

Cryogenics:
- LN_2 panel area: 5800 square feet.

Heat Flux:
- Present configuration: 5 ft diameter x 15 ft with 1000 Btu/hr/ft².
- System type: Quartz lamps backed by alum. reflectors, computer programmed for simulated orbital motion.

Systems Contractor:
- Design: Consolidated Vacuum Corp.
- Fabrication: Consolidated Vacuum Corp. (prime).

Operational Date:
- February 1, 1962.

RADIO CORPORATION OF AMERICA
Princeton, New Jersey

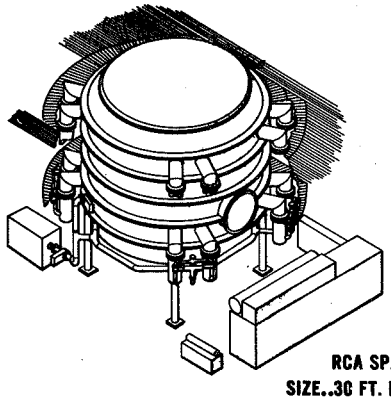

Construction:
- Overall dimensions: 30 ft diameter x 34 ft high.
- Construction materials:
  - Shell: 304 stainless steel.
- Work space dimensions: 24 ft diameter x 20 ft.

Pressure:
- Ultimate pressure: 10^{-7} or better, 5×10^{-6} mm-Hg with test vehicle.
- Time to achieve ultimate pressure: 24 hours.
- Pumping system: Sixteen 32-inch oil diffusion pumps backed by booster and mechanical pumps.

Temperature:
- Temperature range: −100°F to +250°F.
- Thermal system: Cascade Freon 13 brine system and immersion electric heaters.

Cryogenics:
- Forecasted for 1962: Operational LN_2 open cycle.

Solar Simulation:
- Forecasted for 1963.

Other environment capabilities of this chamber:
- 28,000 vibration potential.

Systems Contractor:
- Design: RCA Major Systems Division.
- Fabrication: Chicago Bridge and Iron Co.

Operational Date:
- November 1961.

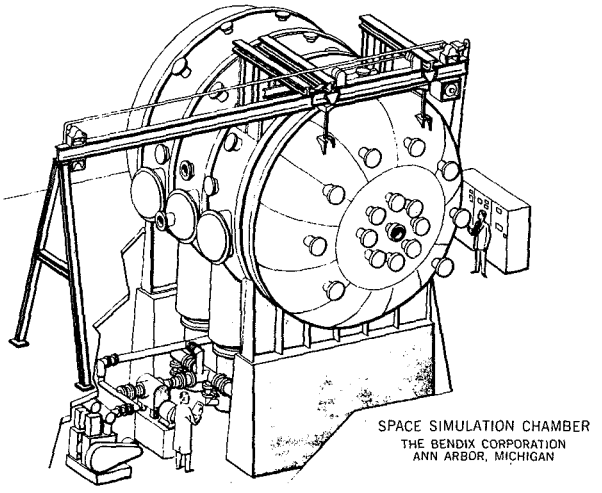

SPACE SIMULATION CHAMBER
THE BENDIX CORPORATION
ANN ARBOR, MICHIGAN

Construction:
- Overall dimensions: 20 ft diameter x 27 ft long.
- Construction materials:
  - Shell: 304 stainless steel.
  - Shroud: 304 stainless steel.
- Work space dimensions: 18 ft diameter x 20 ft long.

Pressure:
- Ultimate pressure: 4.8×10^{-8} mm-Hg with cold wall.
- Time to achieve ultimate pressure: 11–12 hours.
- Pumping system: Six 32-inch oil diffusion pumps backed by blower pumps and rotary gas pumps.

Temperature:
- Temperature range: −300°F to +2000°F.
- Thermal system: Quartz lamps and nitrogen curtain wall.

Cryogenics:
- LN_2 panel area: 1600 square feet.

Solar Simulation:
- Area illuminated: 7 ft diameter.
- Maximum intensity: 140 watts/ft^2.
- System type: Carbon arc.

Other Environment Capabilities:
- Structural loading, shock and vibration provisions.

Systems Contractor:
- Design: Bendix Systems Division.
- Fabrication: Chicago Bridge and Iron Co.

Operational Date:
- Vacuum: November 1961.
- Complete system: January 1962.

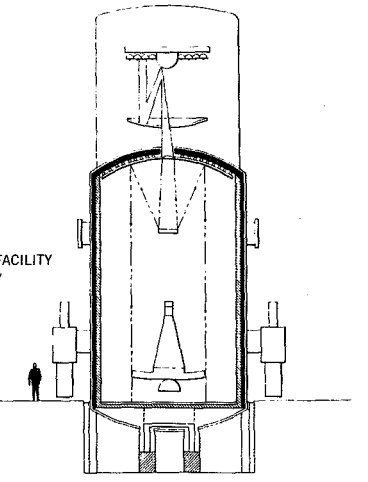

25−FOOT SPACE ENVIRONMENT FACILITY
JET PROPULSION LABORATORY
PASADENA, CALIFORNIA

Construction:
- Overall dimensions: 27 ft diameter x 80 ft high.
- Construction materials:
  - Shell: 304 stainless steel.
  - Shroud: Aluminum.
- Work space dimensions: 25 ft diameter x 25 ft high.

Pressure:
- Ultimate pressure: 1×10^{-6} mm-Hg.
- Time to achieve ultimate pressure: 3¼ hours.
- Pumping system: Ten 36-inch oil diffusion pumps backed by blowers and the wind tunnel compressors.

Temperature:
- Temperature range: −320°F to ambient (possible).
- Thermal system: LN_2 panels and solar simulation.

Cryogenics:
- LN_2 panel area: 4200 square feet.

Solar Simulation:
- Area illuminated: 11 ft diameter.
- Maximum intensity: 75 watts/ft^2 (or 5 ft diameter 130 watts/ft, future 15 ft diameter 275 watts/ft^2).
- System type: Hg-Xe lamps.

Other Environment Capabilities:
- Provision is made to use electrodynamic shakers in the chamber with force ratings up to approximately 30,000 pounds.

Systems Contractor (Prime):
- Design: Consolidated Vacuum Corp.
- Fabrication: Consolidated Vacuum Corp.

Operational Date:
- December 1962.

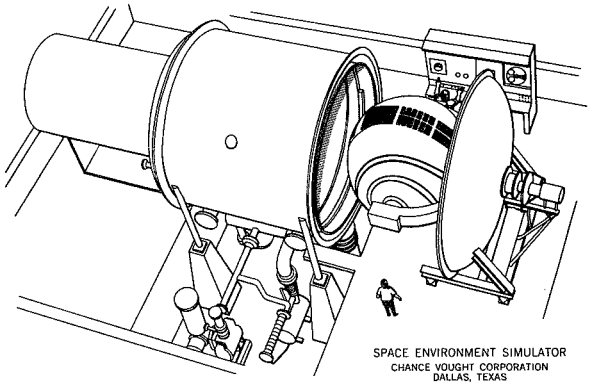

SPACE ENVIRONMENT SIMULATOR
CHANCE VOUGHT CORPORATION
DALLAS, TEXAS

Construction:
- Overall dimensions: 12 ft diameter x 15 ft long.
- Construction materials:
  - Shell: 304 stainless steel.
  - Shroud: Finned aluminum tubing.
- Work space dimensions: 10 ft diameter x 10 ft.

Pressure:
- Ultimate pressure: 1×10^{-7} mm-Hg.
- Time to achieve ultimate pressure: 2½ hours.

Pumping system: Three 32-inch oil diffusion pumps backed by a booster and mechanical pump.

Temperature:
- Temperature range: −320°F to ambient.
- Thermal system: LN_2 heat sink and solar simulation.

Cyrogenics:
- LN_2 panel area: 460 square feet.

Solar Simulation:
- Area illuminated: 6 ft diameter.
- Maximum intensity: 130 watts/ft^2.
- System type: Hg-Xe lamps with external elliptical reflectors.

Other Environmental Capabilities:
- Two-axis orbital rotation of specimen of 1000-pound maximum weight. Maximum envelope of 8-foot diameter sphere. Slip rings on motion gimbal for power in/data out.

Systems Contractor:
- Design: Tenney Engineering, Inc.
- Fabrication: Tenney Engineering, Inc. (prime).

Operational Date:
- December 1961 (partial operation).

SPACE SIMULATION SYSTEM
GRUMMAN AIRCRAFT ENGINEERING CORPORATION
BETHPAGE, LONG ISLAND, NEW YORK

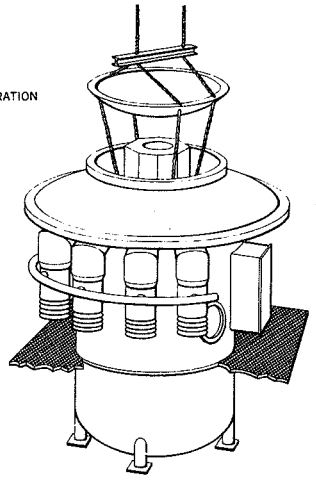

Construction:
- Overall dimensions: 19 ft diameter (30 ft at bustle) x 28 ft high.
- Construction materials:
  - Shell: 304 stainless steel.
  - Shroud: stainless steel.
- Work space dimensions: 15 ft diameter x 20 ft high.

Pressure:
- Ultimate pressure: 5×10^{-9} mm-Hg with cryo.
- Time to achieve ultimate pressure: 6 hours.
- Pumping system: Eight 32-inch oil diffusion pumps backed by roughing system.

Temperature:
- Temperature range: −320°F to +300°F.
- Thermal system: Liquid or gaseous N in shroud.

Cryogenics:
- LN_2 panel area: 2200 square feet.

Solar Simulation:
- Provisions made for heat flux simulation tailored to specific project.

Other Environment Capabilities of this Chamber:
- Backfilling with N_2 gas 1 to 3 tor.

Systems Contractor (Prime):
- Design: Chicago Bridge and Iron Co.
- Fabrication: Chicago Bridge and Iron Co.

Operational Date:
- March 1, 1962.

GENERAL ELECTRIC CO.
VALLEY FORGE, PENNA.

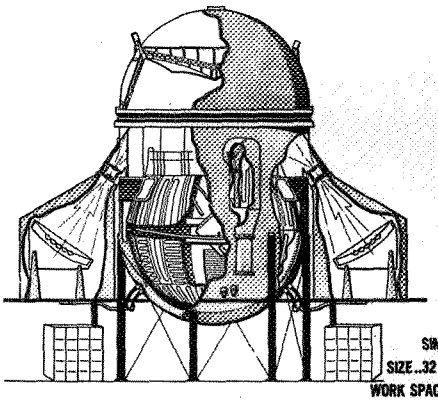

Construction:
- Overall dimensions: 32 ft diameter x 54 ft high.
- Construction materials:
  - Shell: 304 stainless steel.
  - Shroud: Aluminum.
- Work space dimensions: 20-ft diameter sphere.

Pressure:
- Ultimate pressure: 1×10^{-9} mm-Hg.
- Time to achieve ultimate pressure: 6 hours.
- Pumping system: Cryogenic pumping and two 32-inch oil diffusion pumps backed by booster and mechanical pumps.

Temperature:
- Temperature range: Function of experiment design.
- Thermal system: Solar simulation and 100°K walls.

Cyrogenics:
- LN panel area: 5400 square feet.
- He panel area: 725 square feet.

Solar Simulation:
- Area illuminated: 20 ft diameter.
- Maximum intensity: 140 watts/ft².
- System type: Off axis parabolic collimating reflector with xenon arc-lamp source.

Other Environment Capabilities:
- Provision for future addition of vibration facilities.

Systems Contractor:
- Design: General Electric Co.
- Fabrication: General Electric Co. (prime).

Operational Date:
- March 1962.
- November 1962 for solar.

SPACE TECHNOLOGY LABORATORIES, INC.
Los Angeles, California

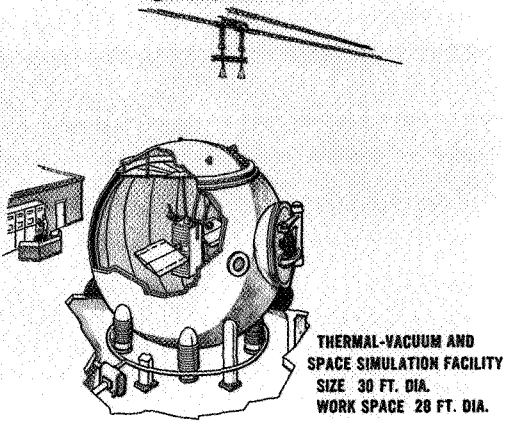

Construction:
- Overall dimensions: 30-ft diameter sphere.
- Construction materials:
  - Shell: 304 stainless steel.
  - Shroud: Aluminum.
- Work space dimensions: 28-ft diameter sphere.

Pressure:
- Ultimate pressure: 3×10^{-7} mm-Hg.
- Time to achieve ultimate pressure: 12 hours.
- Pumping system: Four 32-inch oil diffusion pumps backed by blower and mechanical pumps.

Temperature:
- Temperature range: −320°F to +275°F.
- Thermal system: Gaseous N within shroud.

Cryogenics:
- LN_2 panel area: 2450 square feet.

Solar simulation:
- Area illuminated: 7 ft x 4 ft expandable to 11 ft x 11 ft.
- Maximum intensity: 260 watts/ft², current system 130 watts/ft².
- System type: Carbon arc source.

Systems Contractor:
- Design: Chicago Bridge and Iron Co.
- Fabrication: Chicago Bridge and Iron Co.

Operational Date:
- November 1962; with solar January 1, 1963.

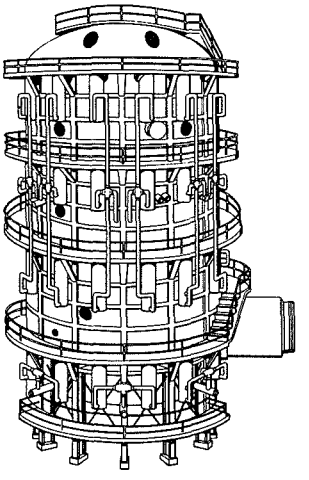

MARK I AEROSPACE SIMULATOR
ARNOLD ENGINEERING DEVELOPMENT STATION
ARNOLD AIR FORCE STATION, TENNESSEE

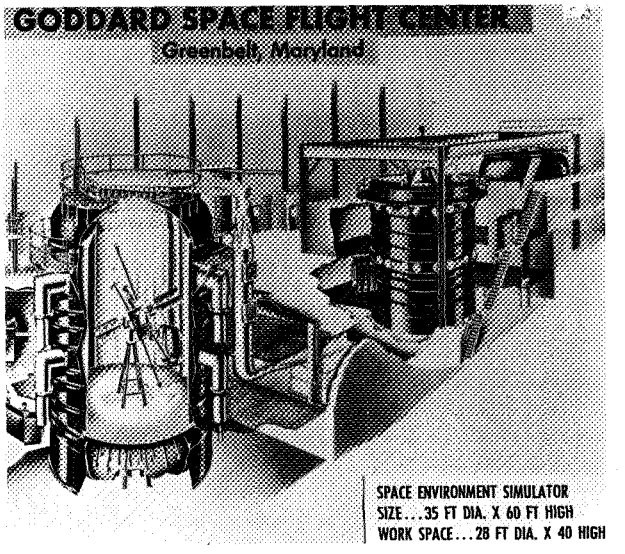

Construction
- Overall dimensions: 42 ft diameter x 82 ft high.
- Construction materials:
  - Shell: 304 stainless steel.
  - Shroud: Copper.
- Work space dimensions: 35 ft diameter x 65 ft.

Pressure:
- Ultimate pressure: 1×10^{-8} mm-Hg.
- Time to achieve ultimate pressure: 24 hours.
- Pumping system: Forty-eight 32-inch oil diffusion pumps and a 20°K cryogenic system backed by roughing pumps and wind tunnel facilities.

Temperature:
- Thermal system: Solar simulation and LN_2 panels.

Cryogenics:
- LN_2 panel area: 13,376 square feet.
- He panel area: 8160 square feet.

Solar Simulation:
- Area illuminated: 5 ft x 32 ft.
- Maximum intensity: 130 watts/ft.^{2}
- System type: Carbon arc lamps in optical system.

Other Enviornment Capabilities:
- Vibration:
  - Up to 200,000-pound force from 10 to 600 cps.
  - Up to 5,000-pound force from 600 to 2000 cps.
- Ascent simulation: Sea level to 80,000 feet in 90 seconds.

Systems Contractor:
- Design: Radio Corporation of America.
- Fabrication: Compudyne Corp.

Operational Date:
- August 1963.

Construction:
- Overall dimensions: 35 ft diameter x 60 ft high.
- Construction materials:
  - Shell: 304 stainless steel.
  - Shroud: Aluminum.
- Work space dimensions: 28 ft diameter x 40 ft.

Pressure:
- Ultimate pressure: 2×10^{-9} mm-Hg.
- Time to achieve ultimate pressure: 24 hours.
- Pumping system: Cryogenic and seventeen 32-inch oil diffusion pumps backed by mechanical booster pumps.

Temperature:
- Temperature range: -320°F to $+215$°F.
- Thermal system: Liquid and gaseous N.

Cryogenics:
- LN_2 panel area: 8000 square feet.
- He panel area: 2000 square feet.

Solar Simulation:
- Area illuminated: 20 ft diameter.
- Maximum intensity: 275 watts/ft.^{2}
- System type: Multimodular, He-Xe lamps.

Systems Contractor:
- Design:
  - Minneapolis-Honeywell Regulator Co. (Prime).
  - F. J. Stokes Corp.—vacuum and cryogenics.
- Fabrication:
  - Minneapolis-Honeywell Regulator Co. (prime).
  - F. J. Stokes Corp.—vacuum and cryogenics.

Operational Date:
- December 1962.
- Solar simulation—early 1963.

POWER TRANSISTOR COOLING IN A SPACE ENVIRONMENT [1]

JAMES E. A. JOHN AND JOHN J. HILLIARD [2]
Goddard Space Flight Center

The cooling of power transistors was investigated in a space environment, where the only available mode of heat transfer is conduction to a heat sink and radiation from the heat sink to space. An attempt was made to minimize the thermal resistance between the transistor case and the heat sink, so that the transistor would dissipate as much power as possible while maintaining its temperature within the maximum tolerable level to prevent thermal runaway. Further, it was necessary to electrically insulate the transistor from the heat sink. Beryllium oxide washers provided electrical insulation and added very little to the thermal resistance between case and sink, the BeO being a good heat conductor. However the problem of contact thermal resistance at each interface arose, especially in vacuum; this contact resistance provided practically all the termal resistance between case and sink. The effect on the contact resistance of surface pressure, insertion of foil, and soldering was examined. It was concluded that, for the most efficient cooling, indium foil should be inserted at each interface, the indium foil having the effect of reducing the contact resistance in vacuum by a factor of 8.

INTRODUCTION

The problem of maintaining the junction temperature of a transistor within certain limits to prevent runaway and failure is well known. The work performed to date has been concerned with transistor cooling in an atmospheric environment, by either free or forced convection. Typical of the work in this area is that performed by Abel (Reference 1) and others (Reference 2). The investigation performed here, however, had the purpose of extending present knowledge to cover transistor cooling in a space environment.

The only mode of heat transfer available in space is radiation, either directly from the transistor or from a heat sink to which the transistor is thermally coupled. Calculations show that the surface area of the transistor is too small to provide more than a few milliwatts of direct radiactive heat dissipation, whereas several watts may have to be dissipated. Therefore the problem resolves itself into an investigation of the thermal path between the transistor junction and the heat sink, with the goal of making the thermal conductance as high as possible.

Figures 1 and 2 show how a typical power transistor is mounted on a heat sink. Two thermal paths are available: one from the case, through the top washer, to the heat sink; and the other from the case, through the stud and nut, through the bottom washer, to the heat sink. Essentially, the thermal resistances are in parallel.

The net thermal resistance desirably should be as low as possible. However it is often necessary that the transistor be *electrically* insulated from the sink. This means that some sort of device, such as a washer, must be used to provide good thermal conductivity while serving as an electrical insulator. Further, if

---

[1] Work was performed by the authors for the NASA Goddard Space Flight Center Summer Workshop Program 1962.

[2] Mr. John is an instructor in the Department of Mechanical Engineering, University of Maryland. Mr. Hilliard is a graduate student in the Department of Electrical Engineering, Catholic University.

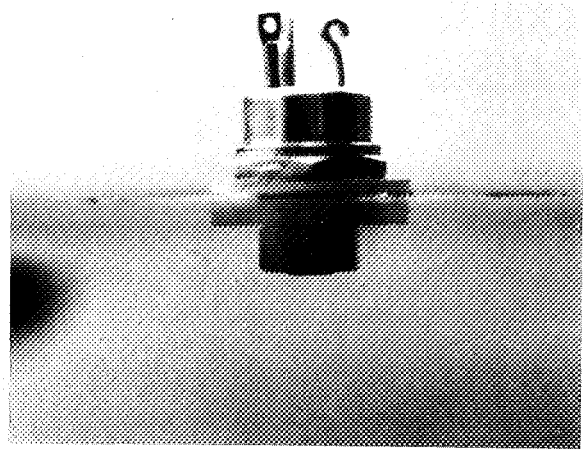

FIGURE 1.—Mounting of 2N1724 transistor on anodized aluminum heat sink, using two BeO washers.

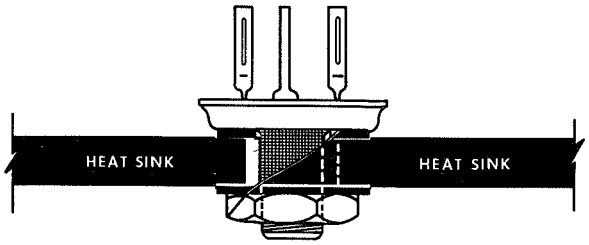

FIGURE 2.—Mounting of a typical power transistor.

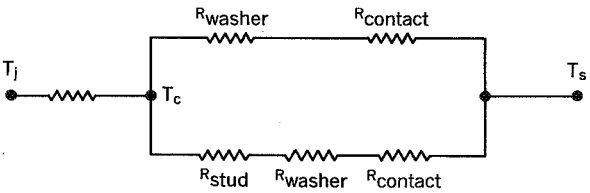

FIGURE 3.—Thermal network.

washers are to be used, they must have good mechanical properties to resist cracking when the nut on the transistor is tightened during mounting. Materials satisfying these specifications, to a greater or lesser degree, are beryllium oxide (Reference 3), mica, and aluminum oxide.

Figure 3 shows the thermal network. All quantities are readily determinable with the exception of contact resistance (the thermal resistance at the inferface of two different materials).

Contact resistance is due to improper thermal contact between the two materials. Since no surfaces are perfectly smooth, they touch only at a limited number of points—the remainder of the space being filled with a nonconducting vacuum. Variables affecting the contact resistance include the pressure between the two surfaces, the smoothness of the surfaces, the materials themselves, and the possible addition of greases, solders, or some soft material to fill the empty regions between the surfaces.

Several theoretical and experimental investigations have been made in the general area of thermal contact resistance. Theoretical considerations must necessarily assume an idealized shape of contact point and a distribution of contact points. An analysis carried out by Fenech and Rohsenow (Reference 4) attempted to predict, with some degree of success, the thermal conductance of metallic surfaces in contact. It is felt, however, that an analysis of this type can be at the best only a fair approximation and that experimental values should be determined. Several investigators have done experimental work (References 5, 6, and 7); their results are not considered applicable to this problem because the data were obtained in air, not in vacuum. Also, their data necessarily depended on the configurations of the surfaces they employed, which were somewhat different from the ones dealt with herein.

Tests were run to determine the thermal resistance from transistor case to heat sink as a function of the previously mentioned variables. It was hoped to minimize this thermal resistance so as to provide a practical means of cooling in a space environment.

EXPERIMENTAL APPARATUS AND PROCEDURE

In this experiment the junction temperature, case temperature, heat sink temperature, and energy dissipated per unit time were measured for each test. Variations in contact resistance were introduced by applying different

torques on the transistor nut with a torque wrench and by employing various interface materials such as foils and solders. Variation in surface smoothness was not undertaken be cause of the difficulty of measuring and controlling this parameter; in any case, it was felt that this could offer only limited improvement.

Case and heat sink temperatures were measured with copper-constantan thermocouples and a potentiometer. The thermocouples were fastened to the surfaces with aluminum tape, as shown in Figure 4. Two thermocouples were used on the heat sink, one at the base of the transistor, and the other at the extreme edge of the heat sink; and a third thermocouple was used on the case.

Because the collector junction was inaccessible to a thermocouple, its temperature had to be measured indirectly. Junction temperature T_j was determined by measuring the forward voltage drop V_{CBO} from collector to base with emitter open, since this voltage is directly dependent on junction temperature. Appendix A explains the technique employed and gives a schematic of the circuit used to make this measurement.

Figure 1 shows a typical power transistor (2N1724, used for all tests) mounted on a $10\times10\times1/16$-inch black anodized aluminum plate, which served as a heat sink. In this configuration, beryllium oxide (BeO) washers were placed between the transistor case and the aluminum plate, and between the nut and the bottom of the plate. The transistor stud was 1/4 inch in diameter, and the hole through the plate was 5/16 inch. The transistor base diameter was 3/4 inch. All the BeO washers were 1/16 inch thick.

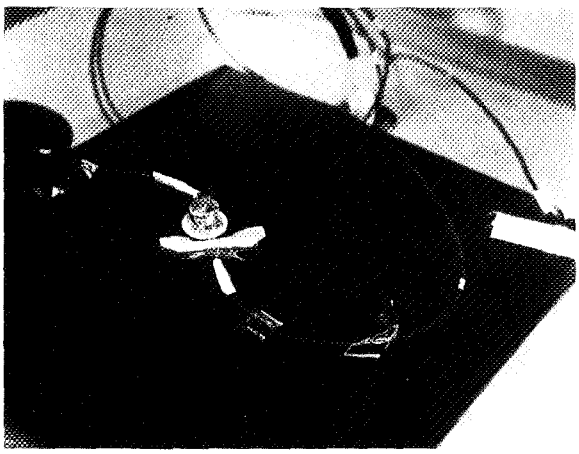

FIGURE 4.—Location of thermocouples on anodized aluminum heat sink.

An environmental pressure of approximately 2×10^{-5} mm Hg was obtained with a bell-jar vacuum system employing a mechanical fore pump and an oil diffusion pump. In the tests made under both atmospheric and vaccum conditions, the measuring procedure was the same. Power was applied to the transistor from a constant-voltage power supply, and all temperatures were allowed to stabilize for approximately 30 minutes. The junction, case, and heat sink temperatures were then measured; and the temperature difference between the case and the sink was calculated. The thermal resistance was obrained by dividing the temperature difference by the input power. The input power was set at several different levels, and the procedure was repeated at each level.

RESULTS

Table 1 is a compilation of the experimental data obtained in this investigation, both in air and in vacuum.

Early in the program it became apparent that the thermal resistance of the BeO washer ($R=L/Ak=0.02$°C/watt [3]) was much lower than the thermal contact resistances. Hence, instead of testing the effects of different washer materials, it was decided to use BeO exclusively since little improvement over BeO could be expected.

Effect of Environment

Figure 5 illustrates the increase in thermal resistance between the transistor case and the heat sink in a vacuum as compared with the resistance in air. In a vacuum the only mode of heat flow between the surfaces in conduction through the few discrete contact points; in air there is also the possibility of heat convection between the surfaces or heat conduction across

[3] Where L is the heat path length, A is the cross-sectional area normal to the heat flow path, and k is the thermal conductivity of the material.

TABLE 1.—*Experimental Data Obtained in Air and in Vacuum*

Configuration	Vacuum or air	Torque (in.-lb)	θ_{c-s} (°C/watt)
2 BeO washers	Vaccum	6	4.79
	Air	6	1.19
2 BeO washers + 3 indium foil washers	Vacuum	6	0.61
	Air	6	0.50
2 BeO washers + 3 aluminum foil washers	Vacuum	6	1.59
	Air	6	0.81
2 BeO washers + 3 copper foil washers	Vacuum	6	3.15
	Air	6	1.04
2 BeO metallized washers + 3 indium foil	Vacuum	3	0.71
	Air	3	0.54
	Vacuum	6	0.66
	Air	6	0.50
	Vacuum	9	0.61
	Air	9	0.43
	Vacuum	12	0.55
	Air	12	0.42
2 BeO metallized washers	Vacuum	6	4.40
	Air	6	1.12
2 BeO metallized washers + 2 indium foil + transitor soldered to washer (indium solder)	Vacuum	6	0.49
	Air	6	0.40
Transistor soldered to metallized washer (indium solder), washer soldered to plate; 1 BeO washer + indium foil on bottom	Vaccum	6	0.56
	Air	6	0.43
1 BeO washer + 2 indium foil; stud insulated	Vacuum	6	0.70
	Air	6	0.49
2 BeO washers + 2 indium foil + Apiezon grease on threads	Vacuum	6	0.57
	Air	6	0.47
No washers	Vacuum	6	5.16
	Air	6	1.36

Washer dimensions: O.D.—0.90″; I.D.—0.26″.

the narrow air layer. The presence of a vacuum thus tends to amplify the cooling problem.

Use of Foils

Figure 6 illustrates the effect of using foils along the interfaces of the BeO washers in a vacuum environment. In each case, a foil washer with the same surface dimensions as the BeO washer was placed between the transistor case and the top washer, between the top washer and the heat sink, and between the bottom washer and the heat sink. The graph shows that the use of any of the three interface materials lowered the thermal resistance from

case to heat sink. Indium foil, however, proved most effective and lowered the thermal resistance to 0.61 °C/watt, approximately ⅛ of its value without interface material.

The foil's effect is to fill the void between the surfaces with heat-conducting material. The softness of the foil seems very critical in determining its effectiveness. Indium, by far the softest of the foils, in most cases was found to adhere to the contact surfaces because of the penetration of contact points into the foil.

Surface Pressure

The effect of surface pressure on thermal resistance is shown in Figure 7. The transistor was mounted with two BeO washers and three indium washers as interface material, and the torque on the nut was varied from 3 to 12 in.-lb in 3 in.-lb steps. As the graph illustrates,

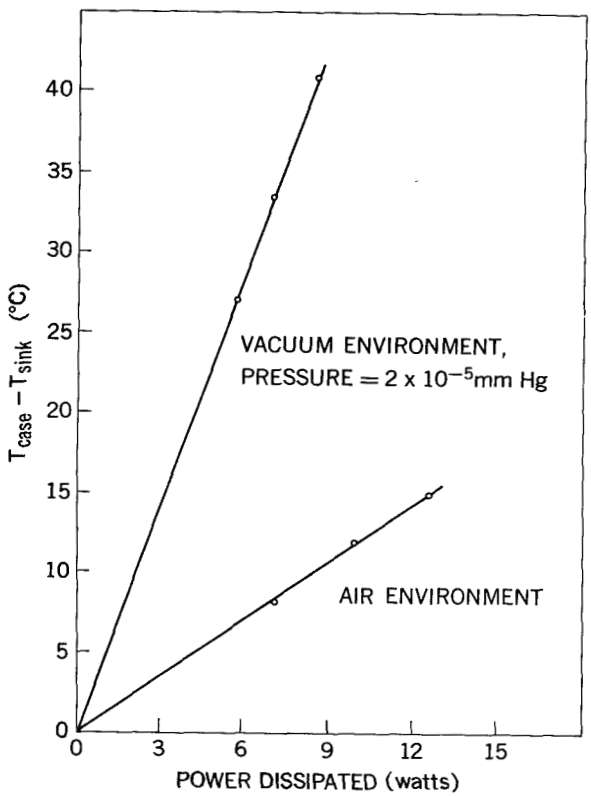

FIGURE 5.—Effect of environment on thermal resistance. 2N1724 transistor mounted on anodized aluminum heat sink; 6 in.-lb torque on nut; 2 BeO washers, no foils.

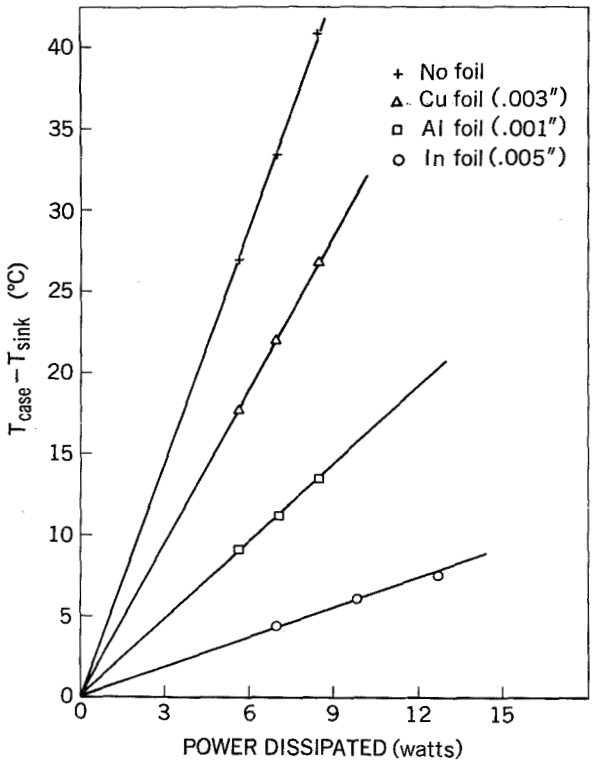

FIGURE 6.—Effect of interface foil on thermal resistance in a vacuum environment. 2N1724 transistor mounted on anodized aluminum heat sink; 6 in.-lb torque on nut; 2 BeO washers; environmental pressure = 2×10^{-5} mm Hg.

thermal resistance decreases linearly with an increase in surface pressure. Greater pressures probably would result in a still smaller thermal resistance; however the cracking of the washer limited further tightening of the nut.

This increase in conductivity is believed to be due to further penetration of the indium into the voids as the surfaces are further compressed.

Effect of Soldering on Contact Resistance

One way of reducing thermal contact resistance is to solder the surfaces together: in this case, soldering transistor to washer, and then washer to heat sink. As the ceramic washer material cannot be directly soldered, the beryllium oxide must be metallized and then copper- or silver-plated. The metallizing was accomplished by depositing on the washer surface a molybdenum manganese compound, a process carried out by the National Beryllia Corpora-

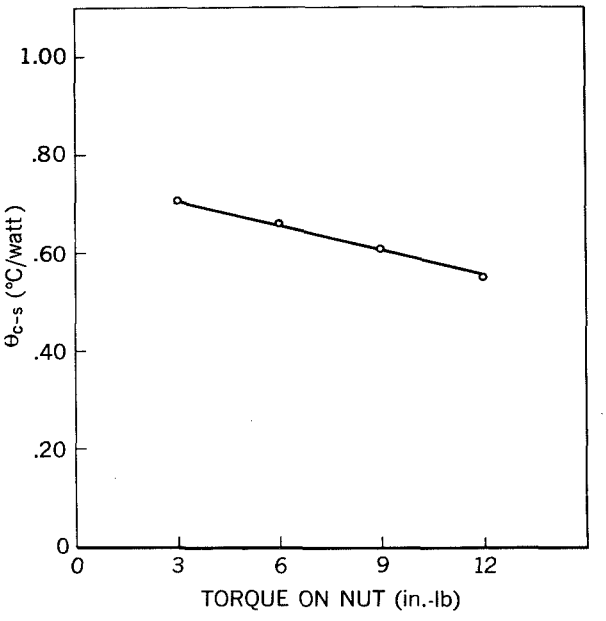

FIGURE 7.—Effect of surface pressure on thermal contact resistance from case to sink, O_{c-s}' in a vacuum environment. 2N1724 transistor mounted on anodized aluminum heat sink; 2 BeO washers with indium foil used at all interfaces; environmental pressure $= 2 \times 10^{-5}$ mmHg.

tion or the Brush Beryllium Co. The first tests made were for the purpose of investigating any change in thermal contact resistance due to the use of plated rather than unplated washers. With the same configurations, plated and unplated washers gave about the same value for contact resistance. Next, the plated washer was soldered to the transistor and also soldered to the aluminum heat sink, the heat sink being nickel-plated to hold the solder more easily. A low melting point, indium-alloy solder was used on the transistor to avoid any possible damage to it. Results showed that the soldering reduced the thermal resistance to roughly the same level as that achieved using indium foil in the interfaces.

To determine the magnitude of heat conduction through the stud, nut, and bottom washer in relation to that path through the top washer, the stud was insulated with Teflon and paper; and conduction was allowed only through the upper path. The change in thermal resistance was so small that the lower path might almost be neglected when a good conductive configuration such as the indium-BeO washer method is used for the upper path. The high resistance of the lower path is thought to be caused mostly by ineffective contact between the screw threads and the nut, and between the nut and the BeO washer. An attempt was made to improve thermal conduction through the lower path by applying a film of Apiezon vacuum grease along the threads and putting indium between the nut and the BeO washer; however this made no appreciable change in overall thermal resistance.

Several power transistor manufacturers have attempted to combine the necessary thermal conduction and electrical insulation by insulating the collector from the transistor case internally, as in the 2N1724/I (identical to the 2N1724 except for this modification); this transistor therefore may be mounted directly on the heat sink. A test run in vacuum showed that direct contact between the two metal surfaces still gave a high thermal resistance, 5.16°C/watt; this could be lowered considerably by the addition of indium foil to the interface. However measurements made with the 2N1724/I transistor showed it to have a thermal resistance from collector juuction to case of 1.17°C/watt, while that of the 2N1724 transistor was 0.36°C/watt. If the latter transistor is provided with the indium-BeO washer method, the total resistance from junction to the heat sink is 0.98°C/watt, which is less than the junction-to-case resistance alone of the modified 2N1724/I transistor.

CONCLUSIONS

In summarizing, several facts stand out as important in the problem of cooling a power transistor in a space environment by conduction to a heat sink. The use of a soft interface foil is highly effective. Indium foil, used as an interface material, reduces interface resistance to almost 1/8 of its normal value; and the ease with which it may be shaped to the required geometry makes it very desirable. The use of aluminum and copper foils, which offer some reduction in interface resistance, depends on the amount of thermal conductivity desired.

The effect of surface pressure, although critical when no interface material is used, is not of too much importance when indium foil is employed. At very high pressures the effect probably could be made appreciable; however cracking of the BeO washers prevents this. If might be noted that the use of indium along the faces of the washers allows a sizeable increase in the amount of torque that may be applied to the transistor nut before the washers crack.

The process of soldering the transistor to the BeO washer and the washer to the heat sink provided effective cooling. The indium eutectic solder used between the case and washer proved very satisfactory, not only because of its conductive properties but also because of its low melting point, which decreases the danger of harming the transistor during soldering.

RECOMMENDATIONS

As a result of this investigation, recommendations can be made concerning the most efficient methods of cooling a power transistor in a vacuum. First, the insertion of indium foil at the interface between the BeO washer and the heat sink and between the BeO washer and the transistor base is sufficient to reduce the thermal resistance between case and heat sink to a very low level. Thus the indium foil aids in maintaining the junction temperature within its maximum permissible value while the transistor is able to dissipate a fairly large amount of power. The use of indium in space will necessarily depend on its rate of sublimation and consequent deterioration. Reference 8, however, indicates that, even at a temperature of 400°C, the rate of sublimation of indium in space is only 10^{-5} centimeters per year, which is less than that of lead or zinc. Since the temperature encountered by the indium in this application is less than 100°C, it is felt that sublimation will be no problem.

A second recommended procedure for cooling in a vacuum is to metallize the BeO washer and to solder the transistor to washer and the washer to the case. This method provided roughly the same thermal resistance from case to heat sink as the previous method involving indium foil.

The first procedure recommended, the indium foil, appears more advantageous because of its ease in assembly and adaptability. Once the joints have been soldered, it would be impossible to remove the transistor from the heat sink easily. Further, it is felt that the former method gives a more reliable joint, which would better tolerate vibration and shock.

REFERENCES

1. Abel, A. D., "Power Transistor Cooling," Honeywell Semiconductor Products Div., Application Lab. Rept. ALR-3, Mar. 3, 1961.
2. "Thermal Resistance as Applied to Transistors," Tung-Sol Electric Inc., Semiconductor Div., Application Note 2-62, July 5, 1952.
3. McPhee, K. H., "Cooling Transistors with Beryllia Heat Sinks," *Electronics* 34(18): 76-78, May 5, 1961.
4. Fenech, H., and Rohsenow, W. M., "Prediction of Thermal Conductance of Metallic Surfaces in Contact," ASME Paper No. 62-HT-32 (Presented at ASME-AICHE Conference, Houston, Tex., August 1962).
5. Weills, N. D., and Ryder, E. A., "Thermal Resistance Measurements of Joints Formed Between Stationary Metals Surfaces," *Trans. ASME* 71(3): 259-267, April 1949.
6. Barzelay, M. E., Tong, K. N., and Holloway, G. F., "Thermal Conductance of Contacts in Aircraft Joints," NACA Technical Note 3167, March 1954.
7. Barzelay, M. E., Tong, K. N., and Holloway, G. F., "Effect of Pressure on Thermal Conductance of Contact Joints," NACA Technical Note 3295, May 1955.
8. Jaffee, L. D., and Rittenhouse, J. B., "Evaporation Effects on Materials in Space," Calif. Inst. of Tech., Jet Propulsion Lab. Technical Rept. No. 32-161, Oct. 30, 1961.
9. Laffin, J. P., "Evaluation of IERC U-P Type Transistor Heat Dissipators," International Electronic Research Corp., IERC Test Rept. No. 172A, July 31, 1961.

Appendix A

MEASUREMENT OF THE JUNCTION TEMPERATURES

The transistor junction temperature T_j can be determined by measuring electrical parameters of the transistors that are functions of T_j. The parameter used in this experiment was the forward voltage drop V_{CBO} from collector to base with emitter open. A schematic of the circuit used to make this measurement is included as Figure A–1 (also, see Reference 9).

To determine the relation between V_{CBO} and T_j for each transistor, the transistor—in a nonoperating condition—was placed in an oven and heated to temperatures in the transistor's operating region (between room temperature and 100° C). At each temperature the transistor was allowed to reach a constant temperature throughout its structure. The switch (S–1 of Figure A–1) was then closed, so that the relay D–1 energized momentarily at set intervals and permitted V_{CBO} to be measured on the oscilloscope and the calibration curve to be plotted (Fig. A–2).

In the actual tests the transistor first was mounted on a metallic plate serving as a heat sink and then was placed in a bell jar, which was evacuated to a vacuum of 10^{-5} mm Hg (Fig. 1–3). Electrical connection was provided between the transistor and the circuit of Figure 3. Power into the transistor was varied by means of the rheostat in the base lead of the transistor; the emitter-to-collector voltage V_{EC} was kept constant at 14 volts while the emitter current I_E was varied. At each power level, the transistor temperature was allowed to stabilize,

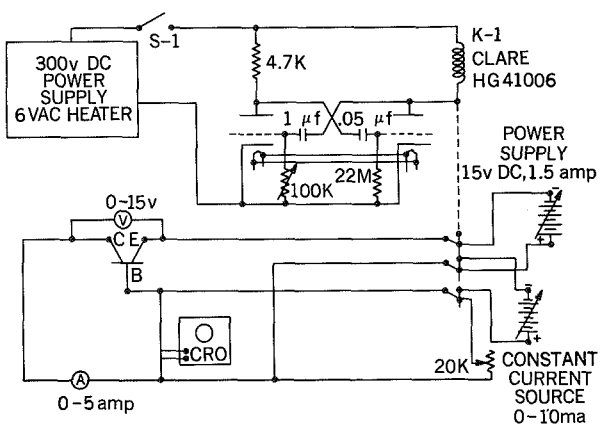

FIGURE A1.—Circuit for measuring heat dissipation and V_{CBO} of a transistor.

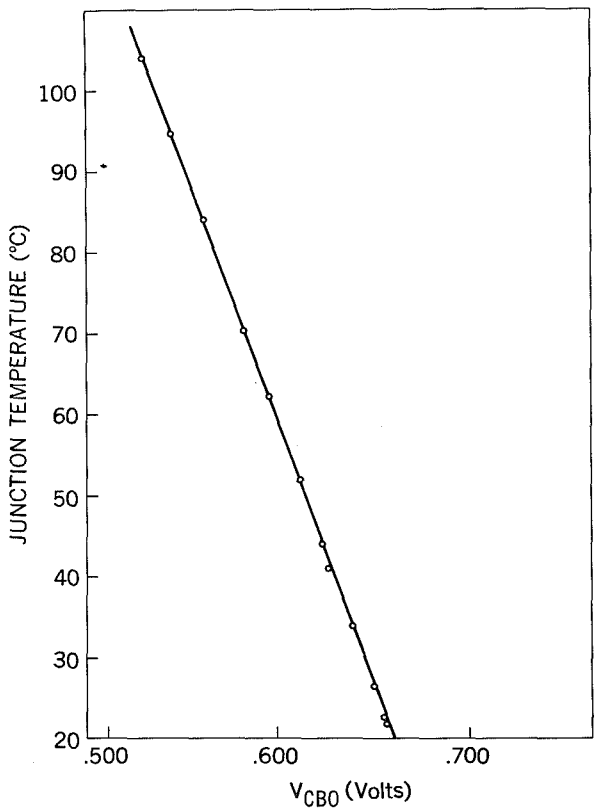

FIGURE A2.—Junction temperature vs. V_{CBO}, 2N1724 transistor.

with the assumption that the input power would be equal to the heat dissipated per unit time. For each configuration three or four different power levels were used. Switch S–1 was then closed, activating the multivibrator; subsequently power was switched from the power circuit to the V_{CBO} measuring circuit and back. The transistor remained in an operating condition for intervals of 2.25 seconds and was in the measuring circuit for 100 milliseconds. Since the switching time was in the order of 2 milliseconds, it was possible to read V_{CBO} before the junction temperature had decreased from its operating value. The value V_{CBO} was then measured, converted to degrees centigrade, and recorded.

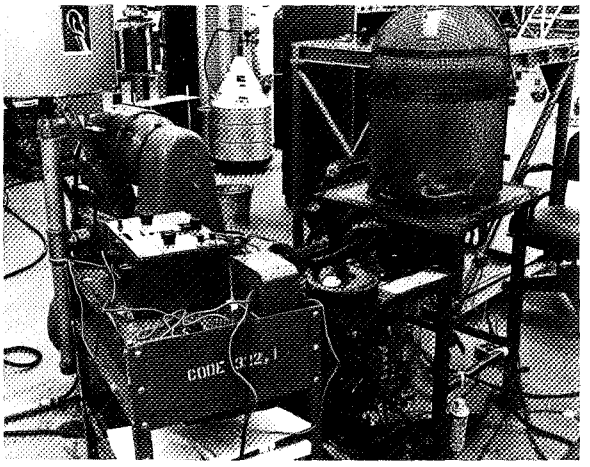

FIGURE A3.—Experimental equipment.

ACHIEVING SATELLITE RELIABILITY THROUGH ENVIRONMENTAL TESTS

JOHN C. NEW
Goddard Space Flight Center

The principles, policies, and procedures used by NASA in achieving satellite reliability by exploiting environmental testing techniques are described. The formalized environmental test plan for a typical satellite program is reviewed to illustrate these objectives. A discussion that highlights the reliability objectives of space missions as contrasted with military or industrial missions is given. Actual experience gained by utlization of this program is shown by results obtained with several scientific satellites that have been successfully orbited.

INTRODUCTION

Perhaps no venture in history has so completely captured the attention and resources of the peoples of the world as the series of events now unfolding as the *Space Age*. Also, there is probably no age in history—the supersonic age, the jet age, or the automatic age not withstanding—that ultimately could be as important to each of us, either as individuals or as nations.

The *Space Age* was ushered in October 4, 1957, with the dramatic announcement by the U.S.S.R. of the successful orbit of Sputnik I (1957 α 2). Since that date, 150 space systems—including Vanguards, Explorers, Cosmos, Pioneers, Luniks, Vostoks, Discoverers, Mercurys, Mariners, Tiros—have been successfully launched. The U.S. program has placed an estimated 167,000 pounds in orbit, in contrast with the 250,000 pounds estimated for the U.S.S.R. program. A summary of space activity is presented in Table 1.

The echo passive satellite has been sighted by millions; television programs have been relayed across the Atlantic by Telstar; astronauts of the Mercury program have seen six sunsets in less than a day; Mariner has probed the Venus atmosphere and established a communication distance record in excess of 50 million miles; and Tiros has faithfully produced weather pictures that have saved countless lives and millions of dollars by timely warnings of hurricanes alone.

These achievements don't belong to any single group. They are a product resulting from the industrial, governmental, and academic communities working together as partners in a gigantic technological race. Great im-

TABLE 1.—*Space Activity Summary (as of Dec. 31, 1962)*

Spacecraft orbited	Earth satellites	Manned spacecraft	Lunar probe	Interplanetary probe	Total
U.S.	115	3	1	5	124
U.S.S.R.	18	4	1	3	26
Total	133	7	2	8	150

petus was given to this program when President Kennedy set forth the national goal of landing a man on the moon and returning him safely *within this decade.* By authority of the Space Act of 1958, the resources of this nation have been organized under the direction of the National Aeronautics and Space Administration (NASA) to implement the space program for the peaceful benefit of mankind. Total expenditure for this space effort through calendar year 1962 is estimated at $8 billion. The cost of space activities during 1963 will approach nearly 1 percent of the gross national product. While it is difficult to assess costs in a research and development program, dollar economy must never be overlooked. For example, the cost of a typical 200-pound scientific satellite in orbit, when launched by a Thor-Delta vehicle, is about $10 million. Thus, the cost per pound is about $50,000.[1]

SPACE SYSTEM DEFINED

Before proceeding, it is desirable to define just what is being discussed. In the unmanned exploration of space, three systems are usable: the sounding rocket, the earth satellite, and the space probe (identified in Fig. 1). A space system is composed of a launch vehicle or booster that lifts the payload—spacecraft or satellite—to the desired altitude. At this point the spacecraft or probe is injected into an earth or sun orbit by means of a final stage that imparts the necessary kinetic energy to maintain the orbital or escape velocity. The

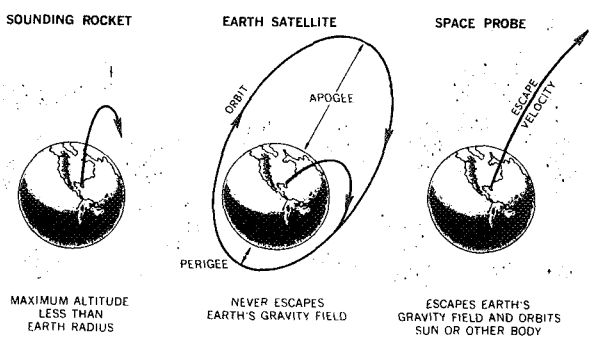

FIGURE 1.—Space exploration.

[1] Earlier estimates, Reference 1, had cited this figure at $67,000 per pound.

main functions occurring during this trajectory are shown in Figure 2. The spacecraft, which has shed its protective shroud after leaving the atmosphere, is composed of a structure, power supply, telemetry system, interface hardware (such as cabling, connectors, junction boxes, etc.), and the prime payload—the scientific experiments; these elements are shown in Figure 3. The distribution of weight is shown for five different satellites in Table 2. A satellite typical of the second generation observatory class is shown in Figure 4.

A spacecraft or satellite is a very complex system. It is primarily electronic in nature, since all actions must be effected through radio commands. A scientific satellite might include 1000 transistors, 1500 diodes, 5000 passive components (resistors, capacitors), and 8000 solar cells. It must be capable of "unfolding" in space large antennas, solar paddles, and remote positioning booms. The structures might

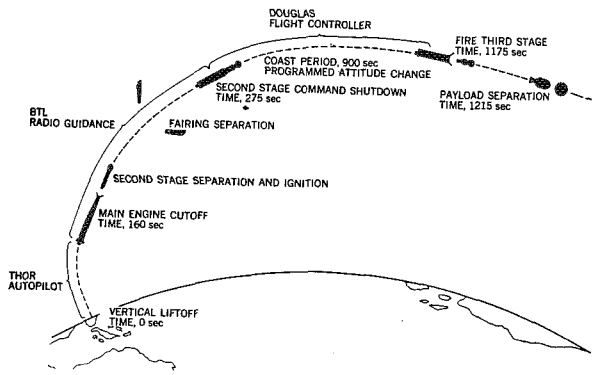

FIGURE 2.—Typical launch sequence for Thor-Delta vehicle.

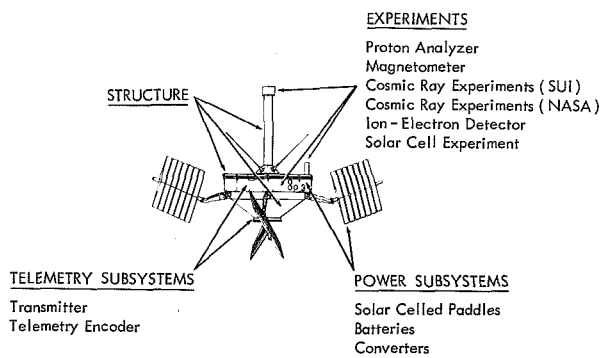

FIGURE 3.—Elements of a spacecraft.

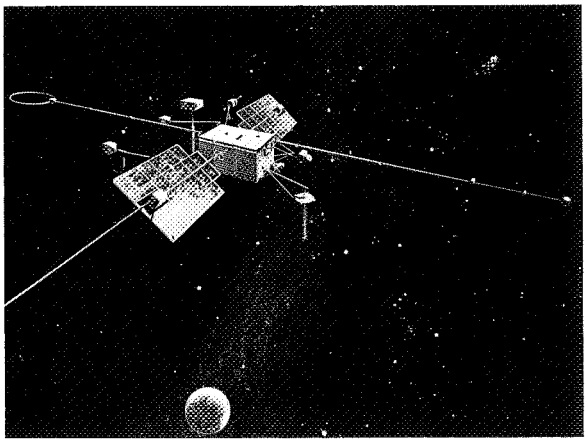

FIGURE 4.—Orbiting Geophysical Observatory.

TABLE 2.—*Weight Distribution in Percent for Spacecraft*

Item	Spacecraft weight (lb)				
	97	125	145	275	1000
Structure	28	20	28	22	20
Telemetry	3	3	11	7	13
Power supply	33	35	23	35	20
Interface hardware	20	14	7	19	17
Experiments	16	28	31	17	17
Guidance and control	----	----	----	----	13

extend from a few feet to several hundred feet. In addition, there are precise and exacting "laboratory type" instruments—Geiger counters, photomultipliers, mass spectrometers, precision optics—all of which must operate without benefit of human hands.

Perhaps we now have a basis to consider the extreme importance of satellite reliability and the complexity of the quality assurance problem. Factors that vitally affect this effort are:

The high unit cost of each launch
The small quantities involved—no mass production
Impact on national prestige
Complexity of spacecraft
Consequences of launch blowup
Lack of environmental knowledge
Use of unproven hardware in a new design application
Flight readiness at specific periods for orbital, rendezvous, or planetary operations

The achievement of high reliability with such diverse factors requires an intensive effort and demands near-perfection in materials, design, management, manufacture, assembly, test, and launch. And *PEOPLE* must produce this perfection.

THE RELIABILITY PROBLEM DEFINED

The reliability problem is easy to cite. But just what is it? Is it a fad, a figure, or a fancy way of saying something else? The accepted definition for reliability of a given system is:

The PROBABILITY of performing the REQUIRED FUNCTIONS under DEFINED CONDITIONS for a specified PERIOD OF TIME

The four key elements of this definition are probability, success, environment, and time. We will examine the meaning of each element as it applies to the space program.

Probability

This element cites the degree of success desired, or the number of failures permitted—or the mean time between failures. It describes how well the system must work, or it is a measure of one's confidence in a system's performing as designed. This probability is more of a goal than an established fact. Specific values depend on missions as well as systems. For example, a higher reliability is demanded of a manned mission to the moon than for a Venus fly-by or for an unmanned Orbiting Solar Observatory. Specific probabilities for space space missions are difficult to assign. A goal of 0.95 is commonly used or, stated differently, the risk of failure should not be greater than 1 in 20.

It is interesting to compare the requirements for a military missile weapon system and the orbiting of an unmanned spacecraft: In both systems the reliability of the launch vehicle should be as high as possible. The required function of the missile system is the detonation of a warhead in a defined target area; the

required function of the spacecraft is the transmission by radiotelemetry of encoded scientific data. The overall success of the missile system (target-kill) can be enhanced by multiple launchings; in contrast, failures in the spacecraft simply mean loss of the scientific data. The weapon system must be capable of being launched on demand; the spacecraft, within limits, can wait "favorable conditions" and can be protected from adverse climatic conditions—it generally can be given the "white-kid-glove" treatment.

Required Functions

The operation of a scientific satellite after it is injected into orbit depends on the mission requirements. In a general way, the required functions consist of sensing some space characteristic (e.g., electron density, energetic particle, solar radiation, or micrometeorite), converting the characteristic to an electrical signal, encoding several such signals, and telemetering the encoded signal to Earth. In addition there are requirements for temperature regulation, spin-up attitude sensing, and perhaps pointing control. It is not an easy task to define these required functions in terms of success or failure; they seldom are either black or white. The recovery of the information signal from the noise is a challenging task requiring a complex of electronic computers.

Environmental Conditions

The general environmental categories that a satellite encounters may be categorized as: (1) prelaunch, (2) launch, (3) orbit, (4) planetary dwell, and (5) atmospheric entry.

A significant design factor for a satellite is that careful control of the environment can be exercised under category (1), but beyond that category the full range of conditions must be considered. As would be expected, the general configuration of the spacecraft may be different for each of the categories cited. The several environments to be encountered are shown in Figure 5. Some quantitative values for the cislunar space environments are shown in Figure 6.

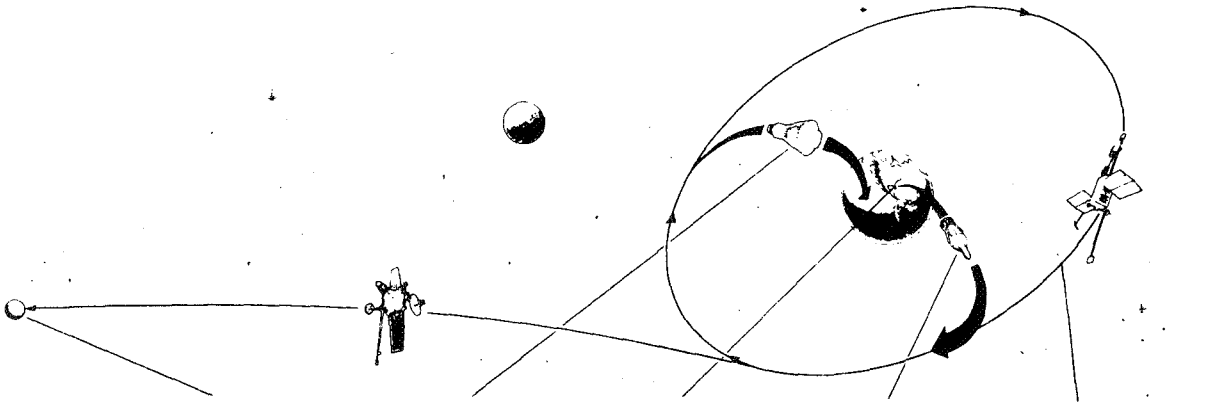

FIGURE 5.—Environmental conditions experienced by space systems.

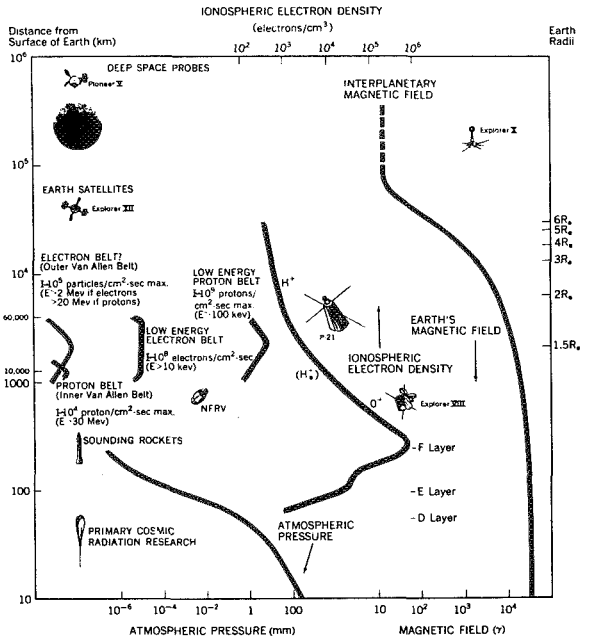

FIGURE 6.—Properties of cislunar space.

Lifetime

The effective life of a satellite with a perigee of better than 150 miles is often dictated by its power supply and duty cycle. Where chemical batteries alone are used, the satellite life has averaged about 3 months. When a solar-cell rechargeable battery system is used, lifetimes of 1 year or more have been achieved with the average closer to 6 months. The most damaging effect is that of the enhanced radiation belt. Some details on selected satellite lifetimes are presented in Appendix A. It is noteworthy that the solar-powered transmitter of Vanguard 1 (1958 β 2) is still operating after nearly 5 years.

A TEST PHILOSOPHY

Reliability is an attribute of a system that must be designed into it. Testing can be used to test and evaluate the efficiency of a design. To some extent, testing can be used as a design tool to eliminate "weak links" in a system and thereby upgrade its quality. It can also be used to discover failure modes. Some of the popular concepts of testing are given in Table 3.

TABLE 3.—*Testing Concepts*

Type tests	Purpose
Failure test	Design margin, failure mode.
Life test	Fatigue limit, time-to-failure.
Specification test	Qualification, production, acceptance.
Special test	Investigate special conditions.
Environmental test	Performance under environmental stress.

Achieving confidence in the successful performance of a spacecraft poses a new type of reliability problem. The mathematical model so successfully employed in missile systems, while useful in highlighting critical system elements, provides little assurance for space systems. Spacecraft are one-of-a-kind, virtually hand-built systems. At most a prototype and two flight units are available. There are no "experience data" or failure mode information. The spacecraft as a system is very complex, utilizing thousands of components, and extends the state-of-the-technology both in design and fabrication. The sage advice of the statistician can be heard: "When you have only one sample, why try to predict its strength?—Just test it." Thus an *Environmental Test Philosophy* for spacecraft has been developed at the Goddard Space Flight Center (GSFC) for the purpose of determining the suitability for launch of a flight spacecraft (Reference 2).

THE ENVIRONMENTAL TEST PROGRAM

The ETP consists of a realistic series of environmental exposures that simulate the mission profile applied to both prototype and flight spacecraft in a configuration and mounting arrangement that duplicate space flight conditions as nearly as possible. The performance of the spacecraft is monitored either by the on-board telemetry or by means of special instrumentation. The performance of the spacecraft is continuously evaluated as calibrated stimuli are applied to the scientific experiments. Failures are diagnosed and corrected as they occur, thereby eliminating the "weak links" and continuously upgrading the

TABLE 4.—*Test and Evaluation Objectives*

Military system	Space system
1. Performance tests: To demonstrate system operability under environmental conditions.	1. Performance tests: To demonstrate system operability under environmental conditions.
2. Evaluation of design disclosure documents (dwgs., spec., manuals).	2. Evaluation of interface problems between actual subsystems.
3. Evaluation of mass producibility and production lot characteristics.	3. Evaluation of single sample with continuous upgrading.
4. Classification of defects.	4. Redesign, repair, or replacement of defective hardware.
5. Evaluation of performance data to establish statistical limits for user.	5. Training of launch team and data acquitition group in individual characteristics of system.
6. System evaluation for feedback into future designs.	6. Systems evaluation for feedback into future designs.

quality level of the system. Upon completion of the expected life exposure or after accumulation of sufficient exposure to reduce the failure rate to a random level, the spacecraft is considered qualified. The foregoing process might be summarized by stating that the spacecraft is *launched* and *orbited* in the laboratory by means of an integrated series of environment simulation tests.

It is significant to note the fundamental difference in the test and evaluation process as it is commonly applied to a mass-produced military weapon system and to a one-of-a-kind space system. A comparison is shown in Table 4.

One element contributing to the success of the ETP in spacecraft development has been the establishment of the environmental specification *early* in the project development cycle. This can generally be accomplished after the mission and the vehicle have been selected.[2] This specification gives the designer a specific and tangible goal to work toward; he knows when he has "cleared the hurdle" and thus places a finite end to the development cycle. However, this also means that the environmental test must be valid and based on an intelligent and realistic interpretation of measured data. In the GSFC program an attempt is made to measure new environmental data with each launch to provide a basis for updating and providing timely test specifications.

Establishment of environmental test levels for a system yet to be designed and for a mission into space is very vexing. We must be conservative to cover the unexpected and unknown, and yet be realistic so that the design and development can be accomplished within the restraints of the schedule, budget, and state-of-the-art. For *prototype systems* in which qualification of a design is the main objective, test levels have been set at 1½ times the worst conditions expected in flight. *Flight systems* are tested for acceptance at the worst conditions expected, compatible with the mission profile. This philosophy recognizes that some of the flight system's useful life is used by these ground tests, but reduced longevity is considered a prudent tradeoff to insure against infant mortality. Added confidence in the design and assurance that fatigue failures will not be critical are achieved by running the prototype system tests for twice the duration of flight unit tests. Sometimes the prototype unit is cycled through the test series for a number of cycles to establish failure modes and time-to-failure history.

The practical and specific application of the foregoing philosophy might be illustrative. For vibration tests the expected measured frequency range is covered for both prototype and flight units. The amplitude (g's) is set at the average $+2\sigma$ (95 percent point) value where

[2] "General Environmental Test Specifications for Delta Launched Spacecraft." NASA Goddard Space Flight Center, System Evaluation Branch Specification No. G–2–000.

several measurements are available; otherwise, the worst case projected from similar vehicles is assumed for the flight unit. This amplitude value is increased 50 percent for prototype units; and the duration is twice the flight unit value, which is based on approximate flight time or a sweep rate that will allow a resonant condition to achieve at least 95 percent of its peak amplitude.

While the application of this philosophy to the launch environments is fairly "straightforward," there are some difficulties with the orbital environments, such as space vacuum, solar simulation, and the 4°K heat sink of space. Likewise, it is impractical to test for the expected satellite lifetime. This has led to the formulation of a failure model as shown in Figure 7. The principal factor in this model is the reduction of failures under environmental tests until some random rate is reached. Also, the curves suggest that the failure rate is more severe for the prototype than for the flight unit, as would be expected from the more severe environmental stress levels used. It is current practice to expose the spacecraft to a test that permits thermal balance of a predetermined part of the system under the best attainable vacuum conditions, which must be 1×10^{-5} torr or better. This thermal-vacuum test is conducted for both the "hot" and "cold" calculated orbital temperature extremes. This temperature is arbitrarily raised and lowered 10°C for the prototype units. The length of the test

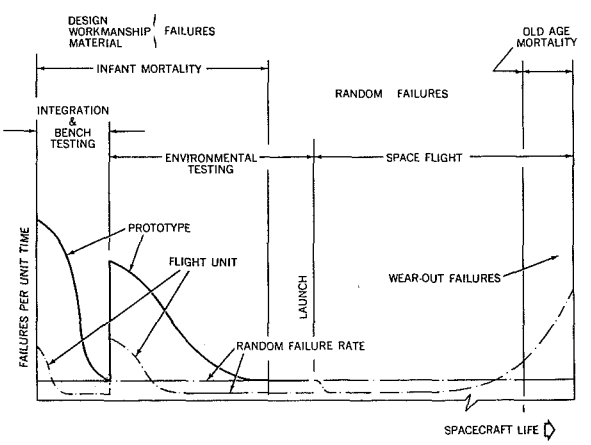

FIGURE 7.—Failure patterns.

should be consistent with the failure model, and has often been set as 3 days hot and 2 days cold, or a total of 5 days. The prototype is often tested for 7 days or more. Sufficient experience to evaluate the appropriateness of these choices is just now being accumulated. Reference 3 treats this problem in detail and suggests that this type test should be lengthened to 4 days hot and 4 days cold.

The space environments of meteorites and energetic particles are known to be particularly damaging; however, facility limitations have precluded their use in environmental test programs. In general these effects have been treated and allowed for on an analytical basis or by extrapolation of test results on materials and components. For example, it has been quite common to shield solar cells from radiation damage by means of glass covers of varying thickness up to 60 mils.

TYPICAL TEST PROGRAM

A typical environmental test program for a spacecraft includes background information about the mission requirements, the launch vehicle, the spacecraft and its functions, and the data handling systems. Detailed information is given on the environmental tests, the spacecraft checkout procedures, the test schedule, and the data collection procedures for both the on-board telemetry and special instrumentation.

The environmental exposures are normally applied in a sequence consistent with major events in the mission profile, such as prelaunch operations, launch, separation and injection, and orbital flight. A typical sequence is shown as Table 5.

In addition, there may be several tests of a specialized nature dependent on the particular spacecraft or mission. Tests of this type could include sterilization, radiation damage, life tests, ordnance safety tests, structural tests, atmospheric heating tests, shroud fit, ejection and contamination test, guidance and control tests, and pressurization tests.

One of the really challenging tasks of the *Space Age* is completing the environmental test program for a spacecraft on a schedule

TABLE 5.—*Typical Environmental Test Sequence*

1. Pyrotechnic RF hazard
2. Leak test for hermetically sealed units
3. Static and dynamic balance
4. Mass property determinations (wt, c.g., $M=1$)
5. Spin and paddle boom or antenna deployment
6. Temperature and humidity
7. Shock
8. Vibration and acoustic
9. Steady state acceleration
10. Thermal-vacuum and corona check
11. Solar simulation and/or solar power check
12. Magnetic check
13. Antenna pattern and RF spectrum check

that allows it to be joined to the launch vehicle and successfully launched. Normally this process may have up to 6 months allocated to it (Fig. 8); however, since this is the last major function before launch site checkout, it often must be accomplished in 6 weeks or less. This places a premium on a properly planned program: It means that the required facilities must be available and thoroughly checked out. It means that each participant in the program must be thoroughly trained in his job and know the lines of authorities and responsibilities.

It is difficult to generalize the manpower and dollar costs of such programs. In fact the necessary data whereby a meaningful analysis can be made are just being accumulated. As a point of reference, manpower requirements for the environmental test program range between 15 and 25 percent of the total for the project development. On a recent satellite project in the 100 to 150 pound class the manpower requirements totaled 15 direct man-years of effort. To date, the dollar cost of the spacecraft environmental test programs has been less than 10 percent of the irrecoverable cost of the spacecraft launch. It is estimated that the in-orbit cost of a Thor-Delta launched spacecraft is $10 million. Included in the 10 percent figure cited is the prorated cost of spacecraft test facilities distributed over about 20 launches and 10 years of time.

It is very essential that a modern, well-equipped environmental test laboratory be available to carry out the type of program discussed. The Goddard Space Flight Center has just completed such a laboratory, which has a capitalized cost of about $15 million. It makes available nearly 3 acres of air-conditioned, dust-free working area including office space. It has been designed to handle spacecraft weighing up to 4000 pounds with a maximum dimension of 10 feet in diameter by 15 feet in length. Centralized data handling facilities including digital computers are available for rapid processing of spacecraft data. Some typical views of this laboratory are shown in Figures 9, 10, and 11.

SPACECRAFT FAILURE DISTRIBUTION

A review of scientific satellite failures that have been detected by means of environmental

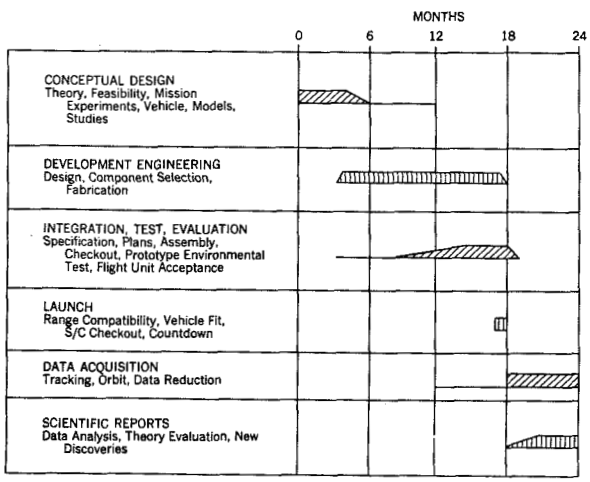

FIGURE 8.—Scientific satellite development cycle.

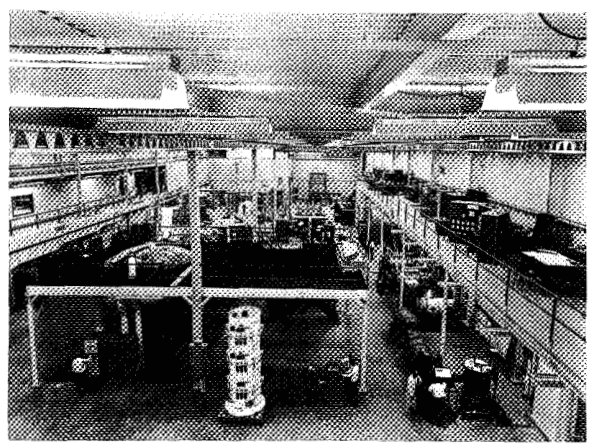

FIGURE 9.—Spacecraft test facility at GSFC.

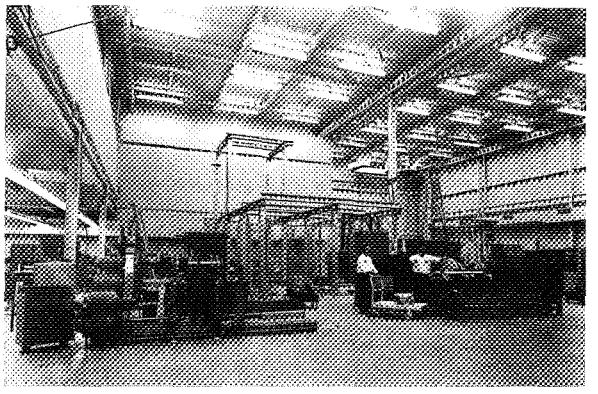

FIGURE 10.—Mechanical test area.

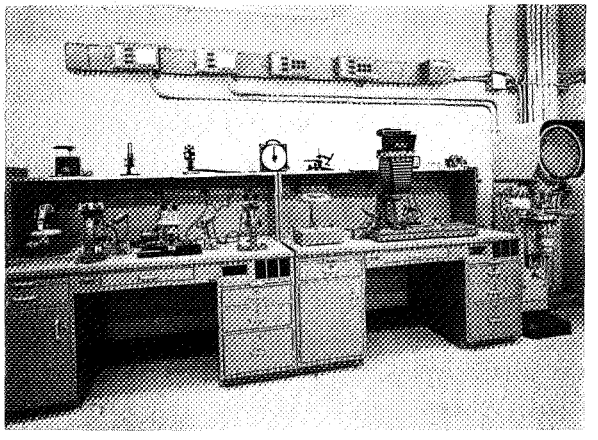

FIGURE 11.—Failure analysis laboratory.

test programs has been made for the calendar year 1962. This review of 114 failures, while not exahaustive, is believed to be representative of results that can be achieved. Five satellites were chosen for this review, all of which were launched and successfully performed in space during 1962. These satellites were chosen to represent several factors that might influence their complexity. For example, weights varied from less than 100 to over 300 pounds; three launch vehicles were represented; the scientific disciplines represented by the onboard experiments covered electron density; galactic noise; corpuscular, solar, and cosmic radiation; magnetic fields; ionospheric relations; and communication experiments. The telemetry systems were typically PFM, although one system included traveling wave tubes. Only one of the systems used batteries exclusively; the other four included solar cells for power. The satellites reviewed include those developed by NASA, by industry, and through international cooperation. They all, however, were tested under the same philosophy expressed in this paper.

Detailed statistics will be found in Tables 6 and 7 (also see Figure 12). Some salient observations are that the ratio of electrical to mechanical failures is 4:1 (80 percent vs. 20 percent). The mechanical problems were chiefly concerned with antenna design, subsystem mounting, and local resonances. Stronger and stiffer designs, together with damping (often by potting), were general solutions to these problems. Electrical problems were often erratic and spurious, requiring much troubleshooting. Solid state components were often found to be faulty. Local overheating was often corrected by providing improved heat sinks and heat conduction paths. The failure distribution seems reasonably consistent among the satellites. While not evident from the information presented, there appears to be a general relation pointing toward increasing failures with satellite complexity and development group inexperience. This result would be expected.

Nearly one-half of all the failures reviewed occured during the thermal-vacuum test, which simulated space conditions. However, nearly one-sixth of the failures occurred during checkout, and about one-third during vibration. One observation to be made from these data is the importance of completing the entire system and checking it out early in the project life. One-sixth of the errors noted here are primarily indicative of the interaction of subsystems and the many interface problems. Cabling and connectors are particular offenders at this stage of checkout. The primary item to note again is that each of these failures was detected, corrected, tested, and evaluated. The final result in space was a successful satellite. One unanswered question is whether there is some other, or more effective, mechanism whereby these failures can be detected earlier in the project life.

TABLE 6.—*Failure Distribution by Spacecraft*

Spacecraft	Weight (lb)	Vehicle	Failure during test					
			Electrical		Mechanical		Total	
			Number	Percent	Number	Percent	Number	Percent
A	94	Scout	10	71	4	29	14	12
B	170	Delta	15	83	3	17	18	16
C	86	Delta	18	78	5	22	23	20
D	150	Delta	42	86	7	14	49	43
E	310	Thor-Agena	6	60	4	40	10	9
Total			91	80	23	20	114	100

TABLE 7.—*Failure Distribution by Test Condition*

Failure category	Failure during test [1]														
	Electrical							Mechanical						Total	
	A	B	C	D	E	Total		A	B	C	D	E	Total		
						Number	Percent						Number	Percent	Number	Percent
Checkout	----	2	3	5	2	12	13	----	----	1	4	1	6	26	18	16
Vibration	7	5	3	4	1	20	22	4	3	3	1	3	14	61	34	30
Temperature	----	1	1	----	1	3	3	----	----	----	----	----	----	----	3	3
Vacuum	----	1	3	1	----	5	5	----	----	----	----	----	----	----	5	4
Thermal-vacuum	3	6	8	32	2	51	56	----	----	1	2	----	3	13	54	47
Total	10	15	18	42	6	91	100	4	3	5	7	4	23	100	114	100

[1] Test conditions for spacecraft A, B, C, D, and E.

OBSERVATIONS AND CONCLUSIONS

The most important element in achieving satellite reliability is the quality of the *project people* and their proper motivation. Most failures can ultimately be traced to some individual who failed to appreciate the importance of details. Seldom has it been found that there was a basic material deficiency. Personal attitudes, work habits, training, and management policies are all vitally important. However, written directives are poor substitutes for technical competence. A few axioms, developed from the GSFC space experience, might prove helpful in the experience feedback cycle:

PEOPLE are the most important product.

There is no substitute for firsthand knowledge.

Retain responsibility from concept through completion.

Be a little suspicious.

Even the best designs have "weak links."

Be pessimistic about success until achieved.

Mistakes are disastrous in one-of-a-kind programs.

Reliability and complexity abhor each other.

A single failure should not defeat a mission.

Minimize the required number of sequential events.

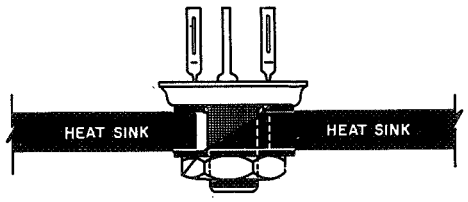

TYPICAL ELECTRICAL FAILURE (THERMAL RUNAWAY) REVEALED DURING THERMAL-VACUUM TESTS AND INADEQUATE HEAT SINK OR POOR THERMAL CONTACT ARE COMMON FAILURE CAUSES

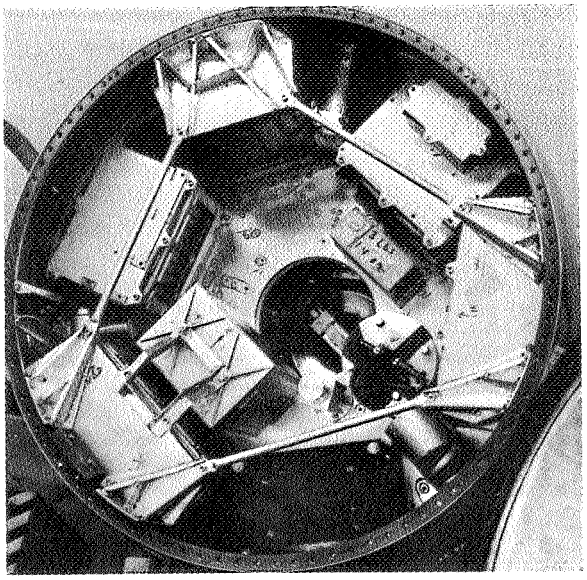

INTERNAL BRACING AND STIFFENERS REDUCING RESONANT AMPLITUDE BY FACTOR OF 10

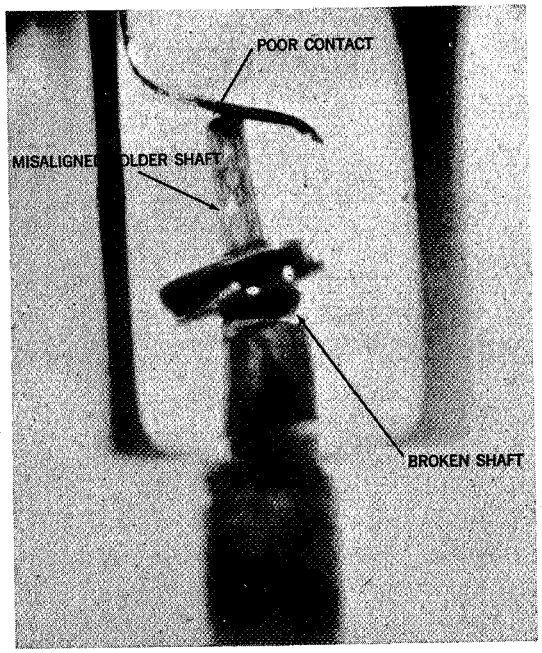

DIODE WORKMANSHIP FAILURE REVEALED DURING TEMPERATURE TEST

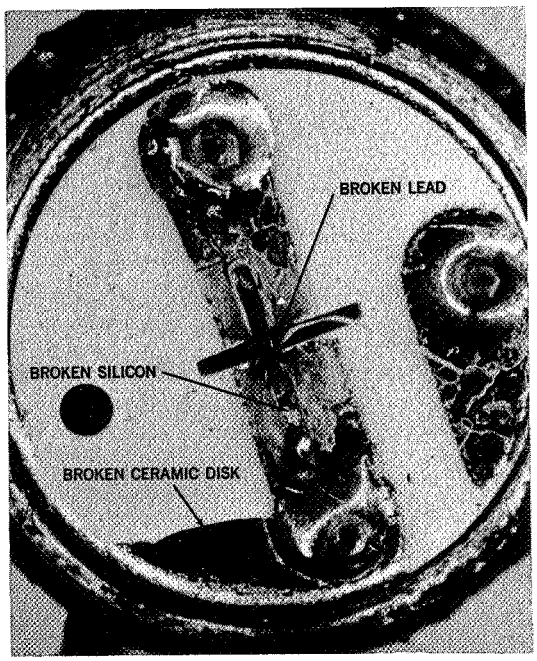

MECHANICAL FAILURE OF TRANSISTOR DURING VIBRATION

FIGURE 12.—Failures in spacecraft.

Do not launch mistakes; prove corrective actions by ground tests.

Last-minute "improvements" have a 100 percent failure rate.

Qualify all flight units by full system tests.

A qualified flight system is held inviolate to change or modification.

The success of the environmental test program at GSFC is attributed to the high quality of the people conducting the program; the excellent facilities available; and the favorable, responsive, and encouraging attitude of NASA management. The importance of having competent, professional environmental engineers—not machine operators—plan and conduct this program cannot be overstressed.

The benefits derived from an environmental test program conducted on a full system include the verification of novel or unproven hardware, elimination of weak links, discovery of unexpected interactions, qualification of the flight system, training of launch personnel, and development of future design guidance.

The large cost and national importance of the space program has set the goals of high reliability and successful performance for each launch in the space program. These goals have been achieved for scientific satellites by means of a comprehensive test program duplicating operational and space environment conditions on each flight system prior to launch.

REFERENCES

1. New, J. C., "Scientific Satellites and the Space Environment," NASA Technical Note D-1340, June 1962.
2. Boeckel, J. H., "The Purposes of Environmental Testing for Scientific Satellites, "NASA Technical Note D-1900, 1963.
3. Timmins, A. R., and Rosette, K. L., "Experience in Thermal-Vacuum Testing Earth Satellites at Goddard Space Flight Center," NASA Technical Note D-1748, 1963.

Page intentionally left blank

Appendix A

SATELLITE HISTORY

Goddard Space Flight Center Satellites and

Designation	Date		Launch vehicle and site	Objectives	Instrumentation	Period minutes
	Launch	Silent				
EXPLORER VI 1959 Delta I (S–2)	Aug. 7, 1959	Oct. 6, 1959	Thor-Able AMR	To measure three specific radiation levels of Earth's radiation belts; test scanning for Earth's cloud cover; map Earth's magnetic field; measure micrometeorites; study behavior of radiowaves.	Equipment to measure radiation levels; TV-type scanner; micrometeorite detector; two types of magnetometer and devices for space communication experiments.	12½ hours
VANGUARD III 1959 Eta	Spet. 18, 1959	Dec. 12, 1959	Vanguard AMR	To measure the Earth's magnetic field, x-radiation from the sun, and several aspects of the space environment through which the satellite travels.	Proton precisional magnetometer, ionization chambers for for solar xrays, micrometeor detectors, and thermistors.	130

Space Probe Projects as of December 1962

Orbital elements (statute miles)		Project manager and project scientist	Experiment	Experimenter	Affiliation	Remarks
Perigee	Apogee					
156	26,357	Dr. John C. Lindsay. Dr. John C. Lindsay.	Triple coincidence telescopes. Scintillation counter. Ionization chamber Geiger counter. Spin-coil magnetometer. Fluxgate magnetometer. Aspect sensor Image-scanning television system. Micrometeorite detector.	J. A. Simpson. C. Y. Fan P. Meyer T. A. Farley. Allen Rosen. C. P. Sonnett. J. Winckler E. J. Smith D. L. Judge P. J. Coleman.	U. of Chicago Space Technology Laboratories. U. of Minn. STL STL STL STL Cambridge Research/ STL.	Orbit achieved. All experiments performed. First complete televised cloud-cover picture was obtained. Detected large ring of electrical current circling Earth; complete map of Van Allen Radiation Belt obtained. Weight: 142 lb. Power: Solar. Life: 2 months.
319	2329	----------	Magnetometer Ionization Chambers. Environmental measurements.	J. P. Heppner. H. Friedman. H. E. LaGow.	GSFC NRL GSFC	Orbit achieved. Provided comprehensive survey of earth magnetic field over area covered; surveyed location of lower edge of Van Allen Radiation Belt. Accurate count of micrometeorite impacts. Weight: 100 lb including attached 3rd stage. Power: Battery. Life: 85 days.

Goddard Space Flight Center Satellites and Space

Designation	Date		Launch vehicle and site	Objectives	Instrumentation	Period minutes
	Launch	Silent				
EXPLORER VII (S–1a)	Oct. 13, 1959	Aug. 24, 1961	Juno II AMR	Variety of experiments, including solar ultraviolet; x-ray; cosmic ray, Earth radiation and micrometeor experiments.	Sensors for measurements of Earth-Sun heat balance; Lyman-alpha and x-ray solar radiation detectors; micrometeor detectors, Geiger-Mueller tubes for cosmic-ray count; ionization chamber for heavy cosmic rays.	101.33

Probe Projects as of December 1962—Continued

Orbital elements (statute miles)		Project manager and project scientist	Experiment	Experimenter	Affiliation	Remarks
Perigee	Apogee					
342	680	H. LaGow	Thermal radiation balance.	V. Suomi	U. of Wisconsin.	Orbit achieved. Provided significant geophysical information on radiation and magnetic storms; demonstrated method of controlling internal temperatures; first micrometeorite penetration of a sensor in flight. Weight: 91.5 lb. Power: Solar. Life: 26 months.
			Solar x-ray and Lyman-alpha.	H. Friedman.	NRL	
				R. W. Kreplin.		
				T. Chubb		
			Heavy cosmic radiation.	G. Groetzinger.	Martin Co.	
				P. Schwed		
				M. Pomerantz.	Bartrol Research.	
			Radiation and solar-proton observation.	J. Van Allen.	State U. of Iowa.	
				G. Ludwig		
				H. Whelpley.		
			Ground-based ionospheric observations.	G. Swenson	U. of Illinois	
				Dr. C. Little.	Nat. Bu. of Stand.	
				G. Reid	U. of Alaska	
				O. Villard, Jr.	Stanford U.	
				W. Ross	Penn State U.	
				W. Dyke	Linfield Res. Inst.	
			Micrometeorite penetration experiment.	H. LaGow	GSFC	

Goddard Space Flight Center Satellites and Space

Designation	Date		Launch vehicle and site	Objectives	Instrumentation	Period minutes
	Launch	Silent				
PIONEER V 1960 Alpha	Mar. 11, 1960	June 26, 1960	Thor-Able AMR	Investigate interplanetary space between orbits of Earth and Venus, test extreme long range communications, study methods for measuring astronomical distances.	High intensity radiation counter, ionization chamber Geiger-Mueller tube to measure plasmas, cosmic radiation, and charged solar particles. Magnetometer and micrometeorite temperature measurements.	311.6 days
TIROS I Beta 1960 (A–1)	Apr. 1, 1960	June 12, 1960	Thor-Able ARM	Test of experimental television techniques leading to eventual worldwide meteorological information system.	One wide and one narrow angle camera, each with tape recorder for remote operation. Picture data can be stored on tape or transmitted directly to ground stations.	99.1
ECHO I 1960 Iota	Aug. 12, 1960	Still in Orbit.	Thor-Delta AMR	Place 100-foot inflatable sphere into orbit.	Two minitrack tracking Beacons on sphere.	118.3

Probe Projects as of December 1962—Continued

Orbital elements (statute miles)		Project manager and project scientist	Experiment	Experimenter	Affiliation	Remarks
Perigee	Apogee					
Perihelion 74.9 million from Sun.	Aphelion 92.3 million from Sun.	Dr. John C. Lindsay. Dr. John C. Lindsay.	Triple coincidence, proportional counter, cosmic ray telescope. Search-coil magnetometer and photo electric cell aspects indicator. Ionization chamber and G–M tube. Micrometeorite counter.	J. Simpson D. Judge J. Winckler E. Manring	U. of Chicago STL U. of Minnesota. AFCRC	Highly successful exploration of interplanetary space between orbits of Earth and Venus; established communication record of 22.5 million miles on June 26, 1960; made measurements of solar flare effects, particle energies and distribution, and magnetic field phenomena in interplanetary space. Weight: 94.8 lb. Power: Solar Life: 3 months.
428.7	465.9	W. G. Stroud (GSFC) H. Butler (Army).	TV camera systems (2).	----------	----------	Provided 1st global cloud-cover photographs (22,952 total) from near circular orbit. Weight: 270 lb. Power: Solar. Life: 72 days.
945	1049	Robert J. Mackey.	----------	----------	----------	Demonstrated use of radio reflector for global communications, numerous successful transmissions. Visible to the naked eye. Weight: 132 lb (including inflation powder). Power: Passive. Life: Still in Orbit.

Goddard Space Flight Center Satellites and Space

Designation	Date		Launch vehicle and site	Objectives	Instrumentation	Period minutes
	Launch	Silent				
EXPLORER VIII 1960 Xi (S–30)	Nov. 3, 1960	Dec. 28, 1960	Juno II AMR	Investigation of the ionosphere by direct measurement of positive ion and electron composition; collect data on the frequency momentum and energy of micrometeorites impacts; establish attitude of the base of the exosphere.	RF impedance probe using a 20-foot dipole sensor; single grid ion trap; four multiple-grid ion traps; Langmuir probe experiment; rotating shutter electric field meteor; micro plier; micrometeorite microphone; thermistors for reading internal and surface temperatures of the space craft; and despin mechanisms to reduce spin from 450 to 30 rpm.	112.7
TIROS II 1960 Pi I (A–2)	Nov. 23, 1960	Feb. 7, 1961	Delta AMR	Test of experimental television techniques and infrared equipment leading to eventual worldwide meteorological information system.	Includes one wide and one narrow angle camera, each with tape recorder for remote operation; infrared sensors to map radiation in various spectral bands; attitude sensors; experimental magnetic orientation control.	98.2

Probe Projects as of December 1962—Continued

Orbital elements (statute miles)		Project manager and project scientist	Experiment	Experimenter	Affiliation	Remarks
Perigee	Apogee					
258	1423	Robert E. Bourdeau.	RF impedance	J. Cain	GSFC	Measured the electron density, temperature, ion density and composition, and charge on the satellite in the upper ionosphere. The micrometeorite influx rate was measured. Weight: 90.14 lb. Power: Battery. Life: 55 days.
		Robert E. Bourdeau.	Ion traps	R. Bourdeau. G. Serbu E. Whipple J. Donnelly.	GSFC	
			Langmuir probe	R. Bourdeau. G. Serbu E. Whipple J. Donnelly	GSFC	
			Rotating-shutter electric field meter.	J. Donnelly.	GSFC	
			Micrometeorite photomultiplier.	M. Alexander. K. McCracken. O. Berg	GSFC	
			Micrometeorite microphone.	M. Alexander. K. McCracken.	GSFC	
406	431	Dr. R. Stampfl	TV camera system (2). Widefield rad ometer experiment. Scanning radiometer experiment.	----------	----------	Orbit achieved. Narrow-angle camera and R instrumentation sent good data. Transmitted 36,156 pictures. Still operative. Weight: 277 lb Power: Solar Life: 76 days

Goddard Space Flight Center Satellites and Space

Designation	Date		Launch vehicle and site	Objectives	Instrumentation	Period minutes
	Launch	Silent				
EXPLORER IX 1961 Delta I (S–56a)	Feb. 16, 1961	Passive Satellite	Scout Wallops Island	To study performance, structural integrity and environmental conditions of Scout research vehicle and guidance controls system. Inject inflatable sphere into Earth orbit to determine density of atmosphere.	Radio beacon on balloon and in fourth stage.	118.3
EXPLORER X 1961 Kappa (P–14)	Mar. 25, 1961	Mar. 27, 1961	Thor-Delta AMR	Gather definite information on earth and interplanetary magnetic fields and the way these fields affect and are affected by solar plasma.	Includes rubidium vapor magnetometer, two fluxgate magnetometers, a plasma probe, and an optical aspect sensor.	112 hours
EXPLORER XI 1961 Nu I (S–15)	Apr. 27, 1961	Dec. 6, 1961	Juno II AMR	Orbit a gamma ray astronomy telescope satellite to detect high energy gamma rays from cosmic sources and map their distribution in the sky.	Gamma ray telescope consisting of a plastic scintillator, crystal layers, and a Cerenkov detector; sun and earth sensors; micrometeorite shields; temperature sensor; damping mechanism.	108.1

Probe Projects as of December 1962—Continued

Orbital elements (statute miles)		Project manager and project scientist	Experiment	Experimenter	Affiliation	Remarks
Perigee	Apogee					
395	1605					Vehicle functioned as planned. Balloon and fourth-stage achieved orbit. Transmitter on balloon failed to function properly requiring optical tracking of balloon. Weight: 80 lb Power: Passive Life:
100	186,000	Dr. J. P. Heppner	Rubidium vapor magnetometer & fluxgate magnetometers.	J. P. Heppner T. L. Skillman C. S. Scearce	GSFC	Probe transmitted valuable data continuously for 52 hours as planned. Demonstrated the existence of a geomagnetic cavity in the solar wind and the existence of solar proton streams transporting solar interplanetary magnetic fields past the earth's orbit. Weight: 79 lb Power: Battery Life: 52 hr.
		Dr. J. P. Heppner	Plasma probe	H. Bridge F. Scherb B. Rossi	MIT	
			Spacecraft attitude experiment.	J. Albus	GSFC	
304	1113.2	Dr. J. Kupperian, Jr. Dr. J. Kupperian, Jr.	Gamma ray telescope.	W. Kraushaar G. Clark	MIT	Orbit achieved. Detected first gamma rays from space. Directional flux obtained. Disproved one part of "steady state" evolution theory. Weight: 82 lb Power: Solar Life: 7 months

Goddard Space Flight Center Satellites and Space

Designation	Date		Launch vehicle and site	Objectives	Instrumentation	Period minutes
	Launch	Silent				
TIROS III 1961 Rho I (A-3)	July 12, 1961	Dec. 4, 1961	Thor-Delta AMR	Develop satellite weather observation system; obtain photos of Earth's cloud cover for weather analysis; determine amount of solar energy absorbed, reflected and emitted by the Earth.	Two wide-angle cameras, two tape recorders and electronic clocks; infrared sensors, five transmitters, attitude sensors, magnetic attitude coil.	100.4
EXPLORER XII 1961 Upsilon I (S-3)	Aug. 15, 1961	Dec. 6, 1961	Thor-Delta AMR	Investigate solar wind, interplanetary magnetic fields, distant portions of Earth's magnetic field, energetic particles in interplanetary space and in the Van Allen Belts.	Ten particle detection systems for measurement of protons and electrons and three orthogonally mounted fluxgate sensors for correlation with the magnetic fields, optical aspect sensor, and one transmitter. Telemetry is PFM and transmits continuously.	26.45 hours
EXPLORER XIII 1961 Chi	Aug. 25 1961	Aug. 27, 1961	Scout Wallops Island	Testing performance of the vehicle and guidance; investigation, nature and effects on space flight of micrometeoroids.	Micrometeoroids impact, detectors, transmitters.	97.5

Probe Projects as of December 1962—Continued

Orbital elements (statute miles)		Project manager and project scientist	Experiment	Experimenter	Affiliation	Remarks
Perigee	Apogee					
461.02	506.44	R. Rados	Omnidirectional radiometer. Widefield radiometer experiment, scanning radiometer experiment TV cameras (2).	V. Suomi	U. of Wisconsin	Orbit achieved. Cameras and IR instrumentation transmitted good data. Transmitted 35,033 pictures. First hurricane covering international program. Weight: 285 lb Power: Solar Life: 145 days
180	47,800	P. Butler	Proton analyzer	Mr. Bader	Ames Research Center	Orbit achieved; all instrumentation operated normally. Ceased transmitting on Dec. 6, 1961, after sending 2568 hours of real-time data. Provided significant geophysical data on radiation and magnetic fields. Weight: 83 lb Power: Solar Life: 4 months
		Dr. F. McDonald	Magnetometer	L. Cahill	U. of New Hampshire	
			Cosmic ray	B. O'Brien F. B. McDonald	State U. of Iowa GSFC	
			Ion-electron detector.	L. Davis	GSFC	
			Solar cell	G. Loganecker	GSFC	
74	722	C. T. D'Aiutolo	A cadmium sulfate photoconductor experiment. A wire grid experiment.	M. W. Alexander L. Secretan	GSFC	Orbit was lower than planned. Reentered Aug. 27, 1961. Weight: 187 lb including 50-lb 4th stage and 12-lb transition section. Power: Solar Life: 2 days

Goddard Space Flight Center Satellites and Space

Designation	Date		Launch vehicle and site	Objectives	Instrumentation	Period minutes
	Launch	Silent				
P21---------- ELECTRON DENSITY PROFILE PROBE (P–21)	Oct. 19, 1961	Oct. 19, 1961	Scout------ Wallops Island	To measure electron densities and to investigate radio propagation at 12.3 and 73.6 Mc under daytime conditions.	Continuous wave propagation experiment for the ascent portion of the trajectory, and an RF probe technique for the descent.	----------
TIROS IV-------- 1962 Beta (A–9)	Feb. 8, 1962	June 19, 1962	Delta------ AMR	Develop principles of weather satellite system; obtain cloud and radiation data for use in meteorology.	Two TV camera systems with clocks and recorders for remote pictures, infrared sensors, heat budget sensors, magnetic orientation control horizon sensor, north indicator.	100.4------

Probe Projects as of December 1962—Continued

Orbital elements (statute miles)		Project manager and project scientist	Experiment	Experimenter	Affiliation	Remarks
Perigee	Apogee					
N/A	N/A 4261	John E. Jackson Dr. S. J. Bauer	RF probe	H. Whale	GSFC	Probe achieved altitude of 4261 miles and transmitted good data. Electron density was obtained to about 1500 miles, making the first time such measurements have been taken at this altitude. Weight: 94 lb Power: Battery Life: Hours
471	525	R. Rados	Omni-directional radiometer. Widefield radiometer experiment. Scanning radiometer experiment. TV camera systems (2)	V. Suomi	U. of Wisconsin	Orbit achieved. All systems transmitting good. Tegea Kinoptic lens used on one camera. Elgeet lens on the other. Support to Project Mercury. Weight: 285 lb Power: Solar Life: 131 days

Goddard Space Flight Center Satellites and Space

Designation	Date		Launch vehicle and site	Objectives	Instrumentation	Period minutes
	Launch	Silent				
ORBITING SOLAR OBSERVATORY OSO–1 1962 Zeta (S–16)	Mar. 7, 1962	Active	Delta AMR	Placed satellite in Earth orbit to measure solar electromagnetic radiation in the ultra-violet x-ray, and gamma ray regions; investigated effect of dust particles on surfaces of spacecraft.	Devices to conduct 13 different experiments for study of solar electromagnetic radiation; investigate dust particles in space and thermo radiation characteristics of spacecraft surface materials.	96.15

Probe Projects as of December 1962—Continued

Orbital elements (statute miles)		Project manager and project scientist	Experiment	Experimenter	Affiliation	Remarks
Perigee	Apogee					
343.5	369	Dr. John C. Lindsay	X-ray spectrometer	W. Behring W. Neupert	GSFC	Orbit achieved. Experiments transmitting as programmed. Weight: 458 lb. Power: Solar. Life: Active.
		Dr. John C. Lindsay	0.510 Mev gamma ray monitoring; 20–100 kev X-ray monitoring; 1–8A X-ray monitoring	K. Frost W. White	GSFC	
			Dust particle experiment	M. Alexander C. McCracken	GSFC	
			Solar radiation experiment, solar ultraviolet	W. White K. Hallam		
			Solar gamma rays, high energy distribution	W. White K. Frost	GSFC	
			Solar gamma rays, low energy distribution	J. R. Winkler L. Peterson	U. of Minnesota	
			Solar gamma rays, high energy distribution	M. Savedoff G. Fazio	U. of Rochester	
			Neutron monitor experiment	W. Hess	U. of California	
			Lower Van Allen belt	S. Bloom	U. of California	
			Emissivity stability of surfaces in a vacuum environment	G. Robinson	Ames Research Center	

Goddard Space Flight Center Satellites and Space

Designation	Date		Launch vehicle and site	Objectives	Instrumentation	Period minutes
	Launch	Silent				
P21A ELECTRON DENSITY PROFILE PROBE (P-21A)	Mar. 29, 1962	Mar. 29, 1962	Scout Wallops Island	To measure electron density profile, ion density, and type of ions in the atmosphere.	A continuous wave propagation experiment to determine electron density and associated parameters of ionosphere. A swept frequency probe for direct measurements of electron density and a positive ion experiment to determine ion concentration under nighttime conditions.	
ARIEL INTERNATIONAL SATELLITE (UK 1) (S-51)	Apr. 26, 1962	Active	Delta AMR	To study ionosphere and cosmic rays relation.	Electron density sensor, electron temperature gage, solar aspect sensor, cosmic ray detector, ion mass sphere, Lyman-alpha gages, tape recorder, x-ray sensors.	100.9

Probe Projects as of December 1962—Continued

Orbital elements (statute miles)		Project manager and project scientist	Experiment	Experimenter	Affiliation	Remarks
Perigee	Apogee					
N/A	N/A 3910	John E. Jackson Dr. S. J. Bauer	CW propagation RF probe Ion traps.	S. Bauer H. Whale R. Bordeau E. Whipple J. Donnelly G. Serbu	GSFC GSFC GSFC	Afforded night-time observations. Characteristics of the ionosphere differ drastically from daytime state when the temperature of the ionosphere is much cooler. See P–21. Weight: 94 lb. Power: Battery. Life: Hours.
242.1	754.2	R. C. Baumann Robert E. Bourdeau	Electron density sensor. Electron temperature gage. Solar aspect sensor. Cosmic ray detector. Ion mass sphere. Lyman-alpha gage.	----------	----------	Orbit achieved. All experiments except Lyman-alpha transmitting as programmed. First international satellite. Contains six British experiments, launched by American Delta vehicle. Weight: 150 lb. Power: Solar. Life: Active.

Goddard Space Flight Center Satellites and Space

Designation	Date		Launch vehicle and site	Objectives	Instrumentation	Period minutes
	Launch	Silent				
TIROS V 1962 Alpha Alpha One (A–50)	June 19, 1962	Active	Delta AMR	Develop principles of weather satellite system; obtain cloud-cover data and radiation data for use in meteorology.	Two TV camera systems with tape recorders for recording remote picture areas, infrared sensors, magnetic orientation control, horizon sensor, north indicator.	100.5
TELSTAR I	July 10, 1962	Active	Delta AMR	Joint AT & T investigation of wide-band communications.	The system provides for TV, radio, telephone, and data transmission via a satellite repeater system.	157.8

Probe Projects as of December 1962—Continued

Orbital elements (statute miles)		Project manager and project scientist	Experiment	Experimenter	Affiliation	Remarks
Perigee	Apogee					
367	604	R. Rados	TV camera systems (2).	----------	----------	Launched at a higher inclination (58°) than previous TIROS satellites to provide greater coverage. Time of launch chosen to include normal hurricane season for South Atlantic. IR sensor inoperative, all other systems transmitting good. Weight: 285 lb. Power: Solar. Life: Active.
592.6	3503.2	C. P. Smith, Jr.	----------	----------	----------	Orbit achieved. Television and voice transmissions were made with complete success. Bell Telephone Laboratories provide spacecraft and ground stations facilities. Government to be reimbursed for cost incurred. Weight: 175 lb. Power: Solar. Life: Active.

Goddard Space Flight Center Satellites and Space

Designation	Date		Launch vehicle and site	Objectives	Instrumentation	Period minutes
	Launch	Silent				
ALOUETTE SWEPT FREQUENCY TOPSIDE SOUNDER (S–27)	Sept. 29, 1962	Active	Thor Agena PMR	To measure the electron density distribution in the ionosphere at altitudes between 180 miles and 620 miles. To study for a period of a year the variations of electron density distribution with time of day and with latitude, under varying magnetic and auroral conditions; and with particular emphasis on high latitude effects. To determine electron densities in the vicinity of the satellite by means of galactic noise measurements, and to make observations of related physcal phenomeina; such as the flux of energetic particles.	A swept frequency pulsed sounder covering the frequency range 1.6 to 11.5 Mc.	105.4

Probe Projects as of December 1962—Continued

Orbital elements (statute miles)		Project manager and project scientist	Experiment	Experimenter	Affiliation	Remarks
Perigee	Apogee					
620	638	John E. Jackson	Diurnal hour to hour change. Electron density. Ionization. Whistler experiment.	----------	----------	The Alouette satellite is a project of the Canadian Defense Research Board. The project is part of NASA's Topside Sounder Program. This will be NASA's first satellite to be launched from the Pacific Missile Range. 80.84 inclination Alouette is not spacecraft designed and built by any other country than the U.S. and USSR. Weight: 320 lb. Power: Solar. Life: Active.

Goddard Space Flight Center Satellites and Space

Designation	Date		Launch vehicle and site	Objectives	Instrumentation	Period minutes
	Launch	Silent				
TIROS VI (A-51)	Sept. 18, 1962	Active	Delta AMR	To study cloud cover and earth heat balance; measurement of radiation in selected spectral regions as part of a program to develop meteorological satellite systems.	Two TV camera systems (78° and 104° lens), clocks and tape recorders for remote operation, infrared and attitude sensors, magnetic attitude coil.	98.73
ENERGETIC PARTICLES SATELLITE EXPLORER XIV (S-3a)	Oct. 2, 1962	Active	Delta AMR	To describe the trapped corpuscular radiation, solar particles, cosmic radiation, and the solar winds, and to correlate the particle phenomena with the magnetic field observations.	An octagon-walled platform, fabricated from nylon honeycomb and fiber glass, houses most of the instruments, experiments, and electronics. The transmitter is located in the base of the spacecraft. A magnetometer package containing three orthogonally mounted magnetometers and calibration coils is located on a boom forward of the platform. Telemetry is PFM and transmits continuously.	37 hours (2185 minutes)

Probe Projects as of December 1962—Continued

Orbital elements (statute miles)		Project manager and project scientist	Experiment	Experimenter	Affiliation	Remarks
Perigee	Apogee					
425	442	R. Rados	Medium angle camera failed Dec. 1, 1962 after taking 1074 pictures.	----------	----------	Inclination 58.3°, velocity perigee 16,822, apogee 16,756. Weight: 300 lb. Power: Solar. Life: Active.
175	61,226	Paul G. Marcotte Dr. Frank B. McDonald.	Cosmic ray experiment. Ion detector experiment. Solar cell experiment. Probe analyses. Trapped radiation experiment. Magnetometer experiment.	F. McDonald L. Davis G. Longanecker M. Boder B. O'Brien L. Cahill	GSFC GSFC GSFC Ames St. U. of Iowa. U. of New Hampshire	Velocity of apogee 1,507 mph, perigee 23,734 mph. Inclination to Equator 33°. Weight: 86 lb. Power: Solar. Life: Active.

Goddard Space Flight Center Satellites and Space

Designation	Date		Launch vehicle and site	Objectives	Instrumentation	Period minutes
	Launch	Silent				
EXPLORER XV (S 3-b)	Oct. 27, 1962	Active	Delta AMR	To study new artificial radiation belt created by nuclear explosions.	Similar to Explorer XII.	5 hours (C. 315 min)
RELAY (A-16)	Dec. 13, 1962	Active	Delta AMR	To investigate wide-band communications between ground stations by means of low-altitude orbiting spacecraft. Communications signal to be evaluated will be an assortment of television signals, multichannel telephony and other communications.	The spacecraft will contain an active communications repeater to receive and retransmit communications between the U.S. and Europe, and an experiment to assess radiation damage to solar cells.	185.09

Probe Projects as of December 1962—Continued

Orbital elements (statute miles)		Project manager an project scientist	Experiment	Experimenter	Affiliation	Remarks
Perigee	Apogee					
195	10,950	Dr. John W. Townsend Dr. Wilmot Hess	Electron energy distribution. Omnidirectional detector. Angular distributor. Directional detector. Ion-electron detector. Magnetic field experiment. Solar cell gage.	W. Brown V. Desai C. McIlwain W. Brown C. McIlwain L. Davis L. Cahill H. K. Gummel	Bell Telephone Laboratories U. of California. Bell Telephone Laboratories. U. of California GSFC U. of New Hampshire Bell Telephone Laboratories	Good data received on artificial radiation belt. Weight: 100 lb. Power: Solar. Life: Active.
819.64	4612.18	Joseph Berliner Dr. R. C. Waddel	First TV transmission U.S. to France, Jan. 9, 1963.	----------	----------	Wide-band Stations: Rumford, Maine; Pleumeur-Bodou, France; Goonhilly, England; Weilhelm, W. Germany. Narrow-band stations: Nutley, N.J.; Rio de Janeiro, Brazil. Inclination 47.47°. Weight: 185 lb. Power: Solar. Life: Active.

A THEORETICAL BASIS FOR MECHANICAL IMPEDANCE SIMULATION IN SHOCK AND VIBRATION TESTING OF ONE-DIMENSIONAL SYSTEMS

F. J. ON AND R. O. BELSHEIM [1]

Goddard Space Flight Center

The feasibility of mechanical impedance control and simulation in environmental shock and vibration testing of mechanical structures was investigated theoretically. Fundamental and useful mathematical expressions for impedance are given for the analysis, control, and simulation in mechanical structures that can be considered as one-dimensional linear-passive systems. The validation of these expressions in the application to impedance control and simulation is approached primarily from analytical considerations. General theories of application are summarized, along with a few simple examples of specific cases. The overall results of the investigation, as well as certain conclusions that may be drawn, are discussed. Several recommendations are made in connection with the information obtained from this study.

INTRODUCTION

One of the most vexing problems confronting the environmental test engineer today is the problem of how to achieve a more realistic simulation of the shock and vibration environment in the test laboratory. The shock and vibration environmental testing of today attempts to incorporate a certain degree of conservatism in its techniques and procedures for defining a qualification test. It is necessary for the test engineer to consider the problem of how to minimize such conservatism so that a higher degree of *optimum* design criteria can be approached. The intent of this paper is to present methods, based on the concepts of mechanical impedance, whereby simulation in environmental testing techniques and procedures may be optimized.

It is well known that the analysis of structures under dynamic loadings requires that the dynamic characteristics of the structures be known in addition to the characteristics of the excitations. Based on usage it is less well known that the *simulated* dynamic environmental test in the laboratory should depend similarly on these requirements. A useful method of specifying these requirements, for structures that can be considered as linear elastic systems, is in terms of mechanical impedance. The concepts of mechanical impedance are directly analogous to the concepts of electrical impedance, and many of the same theorems and operational methods apply (Reference 1). Although the concepts of mechanical impedance have been employed for many years in the analysis of dynamic responses of structures (References 2, 3, and 4), little contribution has been made toward a solution of the *simulation* and *control* of pertinent structural dynamic characteristics in the test laboratory. The importance of attempting such a solution cannot be overemphasized. As the problem of achieving optimum structural design criteria becomes increasingly important, particularly in the areas of aerospace applications, the need for a solution is readily evident.

[1] Dr. Belsheim, Head of the Structures Branch, Mechanics Division, Naval Research Laboratory, Washington 25, D.C., served as a consultant to Goddard Space Flight Center for the study reported herein.

IMPEDANCE ANALYSES OF ONE-DIMENSIONAL SYSTEMS

Continuous mechanical systems that can be considered as linear systems often can be evaluated by applying the concepts of mechanical impedance. The adequacy of such an approach is generally dependent on the exactness of the assumption that the system is linear and *passive*.[2] Consequently, in the analyses that follow, this assumption is tacitly made. Furthermore, for convenience in presentation the following analyses are referred to aerospace-vehicle—payload and testing-machine—payload systems, which are considered the most significant system combinations because weight is so important.

Theoretical Relations

An assumption that any realistic aerospace structure behaves as a one-dimensional system is unquestionably an oversimplification. The prevalence of modes of vibration due to bending, shear, and rotary inertia forces is frequently observed in the field. However, to a first approximation, significant information can often be obtained from a one-dimensional consideration; and this can be of great advantage to the design, analysis, and qualification of the structure.

A general representation of a vehicle-payload system, which is identified by V_a and P_b for the vehicle and payload respectively, is depicted in Figure 1. For the sake of analysis, the configuration of the vehicle-payload has been approximated by the method of lumped parameters. By the application of the force-current analogy for dynamical systems, the vehicle-payload representation of Figure 1 is further simplified by its equivalent mechanical network, as shown in Figure 2. The application of the mechanical network theory (Norton's theorem) further reduces the network of Figure 2 to that of Figure 3. In Figure 3, $Q^b_{V_a}(s)$ is termed the transform of the force $F(t)$ measured at terminal a when that terminal is blocked so that no motion occurs (hereafter, $Q^b_{V_a}(s)$ shall be termed *blocked force*); the impedances $Z_{V_a}(s)$ and $Z_{P_b}(s)$ are the transform mechanical impedance of the vehicle and payload looking back from terminal a, respectively. The quantity $\dot{q}_{V_a 0}(s)$ (hereafter termed *free velocity*) is the transform of the velocity $\dot{x}(t)$ measured at terminal a when that terminal is unrestrained. In general, these transform quantities are complex.

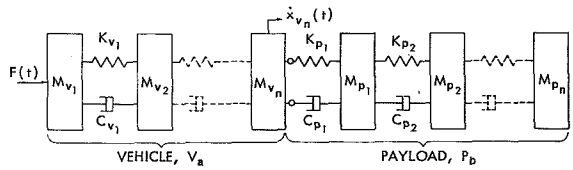

FIGURE 1.—Lumped parameter representation of one-dimensional vehicle-payload system.

Steady-State Vibrations

In the case of steady-state sinusoidal vibrations, the transform velocity at terminal a in

[2] *Passive* systems as defined here are systems that do not possess any type of internal energy sources.

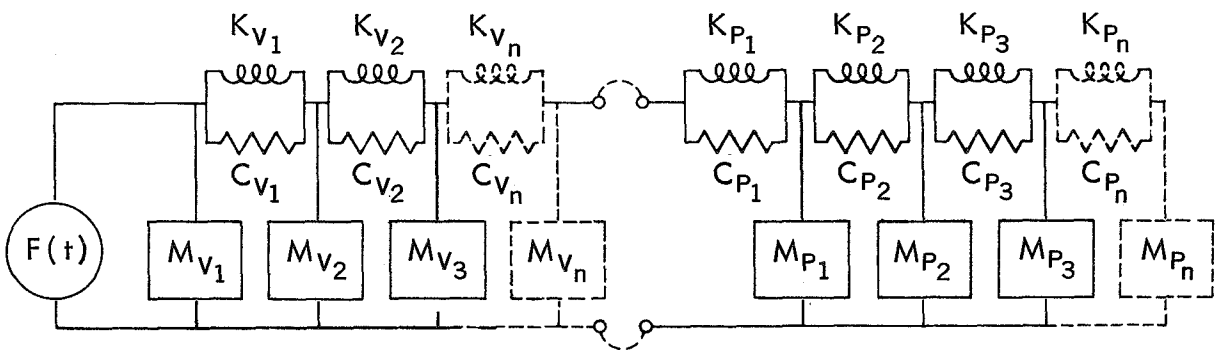

FIGURE 2.—Mechanical network equivalent of Figure 1.

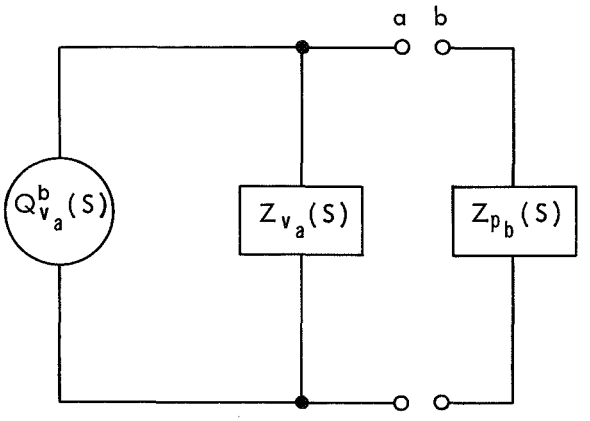

FIGURE 3.—Simplified mechanical network equivalent of a vehicle-payload system by use of Norton's theorem.

Figure 3 prior to the connection of the payload impedance $Z_{P_b}(a)$ is given by

$$\dot{q}_{V_{a0}}(s)=Z_{V_a}^{-1}(s)Q^b_{V_a}(s). \quad (1)$$

(All symbols are defined in Appendix A.) With the mechanical impedance $Z_{P_b}(s)$ of the payload connected to terminal a, the resultant mechanical impedance is

$$Z_{V_{ab}}(s)=Z_{V_a}(s)+Z_{P_b}(s) \quad (2)$$

and the transform velocity at the joining terminal of a and b becomes

$$\dot{q}_{V_{ab}}(s)=H_1(s)Q^b_{V_a}(s), \quad (3)$$

where

$$H_1(s)=[Z_{V_a}(s)+Z_{P_b}(s)]^{-1} \quad (4)$$

may be considered as some frequency response function. Since Equation 1 shows that

$$Q^b_{V_a}(s)=Z_{V_a}(s)\dot{q}_{V_{a0}}(s), \quad (5)$$

then Equation 3, in terms of *free velocity* $\dot{q}_{V_{a0}}(s)$, becomes

$$\dot{q}_{V_{ab}}(s)=H_2(s)\dot{q}_{V_{a0}}(s), \quad (6)$$

where

$$H_2(s)=Z_{V_a}(s)[Z_{V_a}(s)+Z_{P_b}(s)]^{-1} \quad (7)$$

may be considered as another frequency response function.

With $H_1(s)$ and $H_2(s)$ predetermined, Equation 3 or 6 may be used to predict the resulting velocity characteristic at the terminal joining the vehicle V_a and payload P_b.

In cases whereby either V_a or P_b is replaced by another V_k or P_r, new velocity characteristics may be predicted. Suppose that the velocity characteristic corresponding to a new payload P_r on the same vehicle V_a is desired; then, using Equations 3 and 6, the new velocity is

$$\dot{q}_{V_{ar}}(s)=H_3(s)\dot{q}_{V_{ab}}(s), \quad (8)$$

where

$$H_3(s)=[Z_{V_a}(s)+Z_{P_b}(s)][Z_{V_a}(s)+Z_{P_r}(s)]^{-1} \quad (9)$$

and $Z_{P_r}(s)$ is the transform mechanical impedance of the new payload P_r.

Similarly, for the same payload P_b on a new vehicle V_k, the new velocity may be predicted by [3]

$$\dot{q}_{V_{kb}}(s)=H_4(s)\dot{q}_{V_{ab}}(s), \quad (10)$$

where

$$H_4(s)=[\dot{q}_{V_{k0}}(s)][\dot{q}_{V_{a0}}(s)]^{-1}\left[\frac{Z_{V_a}(s)+Z_{P_b}(s)}{Z_{V_a}(s)}\right]\times\left[\frac{Z_{V_k}(s)+Z_{P_b}(s)}{Z_{V_k}(s)}\right]^{-1}; \quad (11)$$

or by

$$\dot{q}_{V_{kb}}(s)=H_5(s)\dot{q}_{V_{ab}}(s), \quad (12)$$

in which

$$H_5(s)=[Q^b_{V_k}(s)][Q^b_{V_a}(s)]^{-1}[Z_{V_a}(s)+Z_{P_b}(s)]\times[Z_{V_k}(s)+Z_{P_b}(s)]^{-1}. \quad (13)$$

It follows that other variations of Equations 3 and 6 may be accomplished. One that seems most significant is the case of a payload P_b designed to ride on a vehicle V_a, but to be vibration-tested on a machine of dynamic characteristic $Zs_m(s)$. To provide a realistic test, the dynamic characteristic of V_a should be simulated by the test machine. By the

[3] This prediction, based on Equations 10 to 13, is only of academic interest, since all terms in Equations 3 to 7 are required; it may be done with the simpler equations.

method of lumped parameters, the simplified vehicle-payload and machine-payload systems may be represented by Figures 3 and 4, respectively. From Equations 3 and 6, we may obtain (with appropriate subscripts) the following:

$$\dot{q}_{V_{ab}}(s)=H_2(s)\dot{q}_{V_{a0}}(s), \tag{14}$$

$$\dot{q}_{S_{mb}}(s)=H_6(s)\dot{q}_{S_{m0}}(s), \tag{15}$$

where

$$H_6(s)=Z_{S_m}(s)[Z_{S_m}(s)+Z_{P_b}(s)]^{-1}; \tag{16}$$

or, in terms of *blocked force*,

$$\dot{q}_{V_{ab}}(s)=H_1(s)Q^b_{V_a}(s), \tag{17}$$

$$\dot{q}_{S_{mb}}(s)=H_7(s)Q^b_{S_m}(s), \tag{18}$$

where

$$[H_7(s)=[Z_{S_m}(s)+Z_{P_b}(s)]^{-1}. \tag{19}$$

For the condition of simulation

$$\dot{q}_{S_{mb}}(s)=\dot{q}_{V_{ab}}(s); \tag{20}$$

and this requires that

$$\dot{q}_{S_{m0}}(s)=E_{2,6}(s)\dot{q}_{V_{a0}}(s), \tag{21}$$

where

$$E_{2,6}(s)=H_2(s)H_6^{-1}(s); \tag{22}$$

or, in terms of *blocked force*,

$$\dot{q}_{S_{m0}}(s)=E_{1,6}(s)Q^b_{V_a}(s), \tag{23}$$

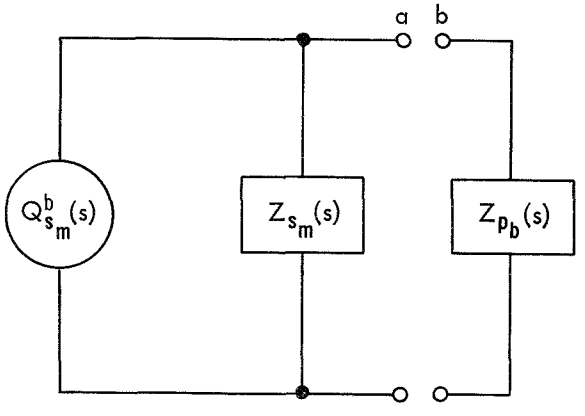

FIGURE 4.—Simplified mechanical network equivalent of a test-machine—payload system by use of Norton's theorem.

where

$$E_{1,6}(s)=H_1(s)H_6^{-1}(s). \tag{24}$$

With $\dot{q}_{S_{m0}}(s)$ from Equation 21 or 23, the dynamic characteristic of the vehicle-payload system of Figure 3 is simulated in the system of Figure 4, in which a test machine has replaced the vehicle; that is,

$$\dot{q}_{S_{mb}}(s)\rightarrow\dot{q}_{V_{ab}}(s)=H_2(s)\dot{q}_{V_{a0}}(s), \tag{25}$$

or

$$\dot{q}_{S_{mb}}(s)\rightarrow\dot{q}_{V_{ab}}(s)=H_1(s)Q^b_{V_a}(s). \tag{26}$$

Equations 21 and 23 yield relations between the *free velocity* characteristics of the machine and the *free velocity* or *blocked force* characteristics at the terminal of the vehicle. As a consequence of Equations 21 and 23, Equations 25 and 26 are obtained. These are statements of simulation for one-dimensional systems that are linear and passive.

So far, the steady-state case in which the forcing function is a harmonic function of time has been considered. If the forcing function is given by a series of harmonic functions, the response can be obtained by superposition of the elementary solutions. The principle of superposition can be applied to all cases in which the effect of simultaneous superposed actions is the sum of the effects of each individual action. Thus, in the general case of steady-state vibrations, the principle of superposition yields for any periodic excitation the equations analogous to Equations 1 to 26.

If it is assumed that the *blocked force* is given by a series of the form

$$F^b(t)=\sum_{N=1}^{M}F_N{}^b e^{iN\omega t} \tag{27}$$

and the *free velocity* by

$$\dot{x}_0(t)=\sum_{N=1}^{M}\dot{x}_{0,N}e^{iN\omega t}\qquad(M=1,\,2,\,\ldots), \tag{28}$$

then the equations analogous to Equations 3 and 6 are respectively:

$$\dot{x}_{V_{ab}}(t)=\sum_{N=1}^{M}H_1(iN\omega)F^b_{V_a,N}e^{iN\omega t}\qquad(M=1,2,\ldots), \tag{29}$$

where

$$H_1(iN\omega)=H_1(s)|_{s=iN\omega}; \quad (30)$$

and

$$\dot{x}_{V_{ab}}(t)=\sum_{N=1}^{M} H_2(iN\omega)\dot{x}_{V_{a0,N}}e^{iN\omega t}, \quad (31)$$

where

$$H_2(iN\omega)=H_2(s)|_{s=iN\omega}. \quad (32)$$

Analogous to Equation 8,

$$\dot{x}_{V_{ar}}(t)=\sum_{N=1}^{M} H_3(iN\omega)\dot{x}_{V_{ab,N}}e^{iN\omega t}, \quad (33)$$

where

$$H_3(iN\omega)=H_3(s)|_{s=iN\omega}. \quad (34)$$

Analogous to Equations 10 and 12 respectively:

$$\dot{x}_{V_{kb}}(t)=\sum_{N=1}^{M} H_4(iN\omega)\dot{x}_{V_{ab,N}}e^{iN\omega t}, \quad (35)$$

where

$$H_4(iN\omega)=H_4(s)|_{s=iN\omega}; \quad (36)$$

and

$$\dot{x}_{V_{kb}}(t)=\sum_{N=1}^{M} H_5(iN\omega)\dot{x}_{V_{ab,N}}e^{iN\omega t}, \quad (37)$$

where

$$H_5(iN\omega)=H_5(s)|_{s=iN\omega}. \quad (38)$$

Analogous to Equations 21 and 23, respectively:

$$\dot{x}_{S_{m0}}(t)=\sum_{N=1}^{M} E_{2,6}(iN\omega)\dot{x}_{V_{a0,N}}e^{iN\omega t}, \quad (39)$$

where

$$E_{2,6}(iN\omega)=E_{2,6}(s)|_{s=iN\omega}; \quad (40)$$

and

$$\dot{x}_{S_{m0}}(t)=\sum_{N=1}^{M} E_{1,6}(iN\omega)F^{b}_{V_{a},N}e^{iN\omega t}, \quad (41)$$

where

$$E_{1,6}(iN\omega)=E_{1,6}(s)|_{s=iN\omega}. \quad (42)$$

As a consequence of Equations 39 and 41, the statements of simulation for the general case of periodic excitations, which are analogous to Equations 25 and 26, are respectively

$$\dot{x}_{S_{mb}}(t)\rightarrow\dot{x}_{V_{ab}}(t)=\sum_{N=1}^{M} H_2(iN\omega)\dot{x}_{V_{a0,N}}e^{iN\omega t} \quad (43)$$

and

$$\dot{x}_{S_{mb}}(t)\rightarrow\dot{x}_{V_{ab}}(t)=\sum_{N=1}^{M} H_1(iN\omega)F^{b}_{V_{a},N}e^{iN\omega t}. \quad (44)$$

Transient Motions

From the literature (Reference 2) transient force $F(t)$ and velocity $\dot{x}(t)$ may be expressed by the Fourier integral, while the inverse relation also holds. The response $\dot{x}(t)$ to the transient force $F(t)$ is related to the mechanical impedance $Z(i\omega)$ of the system, and the Fourier spectrum $G_F(i\omega)$ of the transient force $F(t)$. The Fourier spectrum of $\dot{x}(t)$ is

$$G_{\dot{x}}(i\omega)=Z^{-1}(i\omega)G_F(i\omega) \quad (45)$$

and the response itself is

$$\dot{x}(t)=\int_{\omega=-\infty}^{+\infty} Z^{-1}(i\omega)G_F(i\omega)e^{i\omega t}d\omega. \quad (46)$$

From Equation 45, mechanical impedance may be expressed by

$$Z(i\omega)=G_{\dot{x}}^{-1}(i\omega)G_F(i\omega). \quad (47)$$

It follows from Equation 45, denoting with appropriate subscripts, that the equations for transient motions corresponding to the steady-state Equations 3 and 6 are respectively

$$G_{\dot{x}_{V_{ab}}}(i\omega)=H_1(i\omega)\,G_{F^{b}_{V_a}}(i\omega) \quad (48)$$

and

$$G_{\dot{x}_{V_{ab}}}(i\omega)=H_2(i\omega)\,G_{\dot{x}_{V_{a0}}}(i\omega); \quad (49)$$

and the response itself is

$$\dot{x}_{V_{ab}}(t)=\int_{\omega=-\infty}^{+\infty} H_1(i\omega)\,G_{F^{b}_{V_a}}(i\omega)\,e^{i\omega t}d\omega \quad (50)$$

or

$$\dot{x}_{V_{ab}}(t)=\int_{\omega=-\infty}^{+\infty} H_2(i\omega)\,G_{\dot{x}_{V_{a0}}}(i\omega)\,e^{i\omega t}d\omega. \quad (51)$$

In a similar manner the equations for the transient motions that are analogous to the equations for the steady state are obtained:

From Equation 8,

$$\dot{x}_{V_{ar}}(t)=\int_{\omega=-\infty}^{+\infty} H_3(i\omega)\,G_{\dot{x}_{V_{ab}}}(i\omega)\,e^{i\omega t}d\omega. \quad (52)$$

From Equations 10 and 12,

$$\dot{x}_{V_{kb}}(t)=\int_{\omega=-\infty}^{+\infty}\left[E_{8,2}(i\omega)\,G^{-1}_{\dot{x}_{V_{a0}}}(i\omega)G_{\dot{x}_{V_{k0}}}(i\omega)\right] G_{\dot{x}_{V_{ab}}}(i\omega)\,e^{i\omega t}d\omega, \quad (53)$$

where

$$E_{8,2}(i\omega)=H_2^{-1}(i\omega)\,H_8(i\omega); \tag{54}$$

or

$$\dot{x}_{V_{kb}}(t)=\int_{\omega=-\infty}^{+\infty}\left[E_{9,1}(i\omega)\,G^{-1}_{F^b_{V_a}}(i\omega)\,G_{F^b_{V_k}}(i\omega)\right] G_{\dot{x}_{V_{ab}}}(i\omega)\,e^{i\omega t}d\omega, \tag{55}$$

in which

$$E_{9,1}(i\omega)=H_1^{-1}(i\omega)H_9(i\omega). \tag{56}$$

From Equations 21 and 23,

$$\dot{x}_{S_{m0}}(t)=\int_{\omega=-\infty}^{+\infty}E_{2,6}(i\omega)G_{\dot{x}_{V_{a0}}}(i\omega)e^{i\omega t}d\omega \tag{57}$$

or

$$\dot{x}_{S_{m0}}(t)=\int_{\omega=-\infty}^{+\infty}E_{1,6}(i\omega)G_{F^b_{V_a}}(i\omega)e^{i\omega t}d\omega. \tag{58}$$

From Equations 25 and 26,

$$\dot{x}_{S_{mb}}(t)\rightarrow\dot{x}_{V_{ab}}(t)=\int_{\omega=-\infty}^{+\infty}H_2(i\omega)G_{\dot{x}_{V_{a0}}}(i\omega)e^{i\omega t}d\omega \tag{59}$$

or

$$\dot{x}_{S_{mb}}(t)\rightarrow\dot{x}_{V_{ab}}(t)=\int_{\omega=-\infty}^{+\infty}H_1(i\omega)G_{F^b_{V_a}}(i\omega)e^{i\omega t}d\omega. \tag{60}$$

Equations 48 to 60 may be used for predicting responses due to transient excitations in one-dimensional systems that are linear and passive.

Random Vibrations

In the case of random vibrations (Ref. 5), if $S_F(\omega)$ is the spectral density of a *stationary ergodic* [4] random force (with a Gaussian probability distribution) applied at a point, the spectral density of the response at the same point is

$$S_{\dot{x}}(\omega)=|Z^{-1}(i\omega)|^2S_F(\omega), \tag{61}$$

where $|Z^{-1}(i\omega)|^2$ is the square of the absolute value of either the reciprocal complex impedance function or the mobility (inverse of impedance). The root-mean-square (rms) value of the motion is

$$\dot{x}\ (\text{rms})=\left[\frac{1}{2\pi}\int_0^\infty|Z^{-1}(i\omega)|^2S_F(\omega)d\omega\right]^{1/2}. \tag{62}$$

It follows from the fundamental relation, Equation 61 (after denoting with appropriate subscripts), that the equations for random vibrations which are analogous to those of the steady-state vibrations may be obtained.

With Equation 61, the equations for random vibrations corresponding to the steady-state Equations 3 and 6 are, respectively,

$$S_{\dot{x}_{V_{ab}}}(\omega)=|H_1(i\omega)|^2S_{F^b_{V_a}}(\omega), \tag{63}$$

$$S_{\dot{x}_{V_{ab}}}(\omega)=|H_2(i\omega)|^2S_{\dot{x}_{V_{a0}}}(\omega). \tag{64}$$

The rms value of $\dot{x}_{V_{ab}}$ may be obtained from Equations 63 or 64:

$$\dot{x}_{V_{ab}}\ (\text{rms})=\left[\frac{1}{2\pi}\int_0^\infty|H_1(i\omega)|^2S_{F^b_{V_a}}(\omega)d\omega\right]^{1/2} \tag{65}$$

or

$$\dot{x}_{V_{ab}}\ (\text{rms})=\left[\frac{1}{2\pi}\int_0^\infty|H_2(i\omega)|^2S_{\dot{x}_{V_{a0}}}(\omega)d\omega\right]^{1/2}. \tag{66}$$

Likewise, analogous to the steady-state Equation 8,

$$S_{\dot{x}_{V_{ar}}}(\omega)=|H_3(i\omega)|^2S_{\dot{x}_{V_{ab}}}(\omega), \tag{67}$$

$$\dot{x}_{V_{ar}}\ (\text{rms})=\left[\frac{1}{2\pi}\int_0^\infty|H_3(i\omega)|^2S_{\dot{x}_{V_{ab}}}(\omega)d\omega\right]^{1/2}. \tag{68}$$

Analogous to Equations 10 and 12, respectively,

$$S_{\dot{x}V_{kb}}(\omega)=|E_{8,2}(i\omega)|^2S^{-1}_{\dot{x}V_{a0}}(\omega)S_{x_{V_k}}S_{\dot{x}_{V_{ab}}}(\omega), \tag{69}$$

$$S_{\dot{x}_{V_{kb}}}(\omega)=|E_{9,1}(i\omega)|^2S^{-1}_{F_{V_a}}(\omega)S_{F^b_{V_k}}(\omega)\,S_{\dot{x}_{V_{ab}}}(\omega); \tag{70}$$

[4] A *stationary* random variable may be crudely defined as one whose source does not change character. An *ergodic* variable is one that obeys the "ergodic hypothesis" of statistical mechanics; this hypothesis permits consideration of an event that occurs some percentage of total time as an event with a corresponding probability of occurrence.

and their rms values are

$$\dot{x}_{V_{kb}}(\text{rms})=\left[\frac{1}{2\pi}\int_0^\infty |E_{8,2}(i\omega)|^2 S^{-1}_{\dot{x}_{V_{a0}}} \times(\omega)S_{\dot{x}_{V_{k0}}}(\omega)S_{\dot{x}_{V_{ab}}}(\omega)d\omega\right]^{1/2}, \quad (71)$$

$$\dot{x}_{V_{kb}}(\text{rms})=\left[\frac{1}{2\pi}\int_0^\infty |E_{9,1}(i\omega)|^2 S^{-1}_{F_{V_a^b}} \times(\omega)S_{F_{V_k^b}}(\omega)S_{\dot{x}_{V_{ab}}}(\omega)d\omega\right]^{1/2}. \quad (72)$$

Analogous to Equations 21 and 23, respectively,

$$S_{\dot{x}_{S_{m0}}}(\omega)=|E_{2,6}(i\omega)|^2 S_{\dot{x}_{V_{ao}}}(\omega), \quad (73)$$

$$S_{\dot{x}_{S_{mo}}}(\omega)=|E_{1,6}(i\omega)|^2 S_{F_{V_a^b}}(\omega); \quad (74)$$

and their rms values are

$$\dot{x}_{S_{mo}}(\text{rms})=\left[\frac{1}{2\pi}\int_0^\infty |E_{2,6}(i\omega)|^2 S_{\dot{x}_{V_{ao}}}(\omega)d\omega\right]^{1/2}, \quad (75)$$

$$\dot{x}_{S_{mo}}(\text{rms})=\left[\frac{1}{2\pi}\int_0^\infty |E_{1,6}(i\omega)|^2 S_{F_{V_a^b}}(\omega)d\omega\right]^{1/2}. \quad (76)$$

Analogous to Equations 25 and 26, respectively,

$$S_{\dot{x}_{S_{mb}}}(\omega)\rightarrow S_{\dot{x}_{V_{ab}}}(\omega)=|H_2(i\omega)|^2 S_{\dot{x}_{V_{ao}}}(\omega), \quad (77)$$

$$S_{\dot{x}_{S_{mb}}}(\omega)\rightarrow S_{\dot{x}_{V_{ab}}}(\omega)=|H_1(i\omega)|^2 S_{F_{V_a^b}}(\omega); \quad (78)$$

and their rms values are

$$\dot{x}_{S_{mb}}(\text{rms})\rightarrow\dot{x}_{V_{ab}}(\text{rms})=\left[\frac{1}{2\pi}\int_0^\infty |H_2 \times(i\omega)|^2 S_{\dot{x}_{V_{ao}}}(\omega)d\omega\right]^{1/2}, \quad (79)$$

$$\dot{x}_{S_{mb}}(\text{rms})\rightarrow\dot{x}_{V_{ab}}(\text{rms})=\left[\frac{1}{2\pi}\int_0^\infty |H_1 \times(i\omega)|^2 S_{F_{V_a^b}}(\omega)d\omega\right]^{1/2}. \quad (80)$$

Equations 63 to 80 may be used for predicting responses due to random excitations in one-dimensional systems that are linear and passive.

THEORIES OF APPLICATION

The equations of the preceding section show how the effects of mechanical impedance variations on motion may be determined. Although these determinations are generally quite involved, it is recommended that some applications (calculations or measurements) of this type be made on actual systems before their dynamic environments are firmly specified. With the dynamic environment defined for one set of systems, the dynamic environment for another set may be predicted by using the appropriate equations obtained in the last section. After the dynamic environment is defined, the next obvious step is to attempt to simulate it in the testing environment. In the following sections, various methods of application that may be useful in achieving some degree of "simulation" are presented.

Development of Specifications

The development of realistic shock and vibration specifications has been hindered largely by the fact that the true dynamic environmental conditions have not been known until the system actually has undergone service environments. Consequently, attempts to consider new dynamic environments often result in merely modifying existing specifications into new specifications to be used for testing *prior* to subjecting the system to service. Unless specifications are changed and are developed on a sound basis, they may be much in error. It is evident from the relations previously given that the dynamic characteristics of the system components should be considered. These equations thus provide a set of relations by use of which realistic specifications may be rectified or formulated. Simple examples illustrating the application of the relations are given in the following examples.

Examples of Application

Simple examples illustrating the application of Equations 3, 29, 50, and 63 are given in the following discussion.

Measurement Approach

Consider a block representation of a foundation-equipment system as depicted in Figure 5. In Figure 5b, let $F_b(t)=0$. We wish to predict the velocity at terminal b resulting from the application of $F_a(t)$ at terminal a, after connecting an equipment of mechanical impedance Z_e to the terminal b.

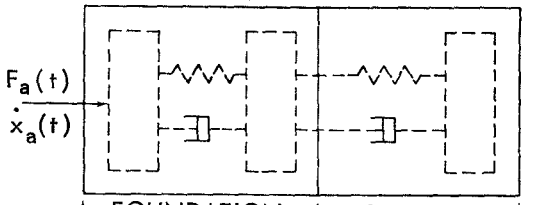

a. One-dimensional foundation — equipment system

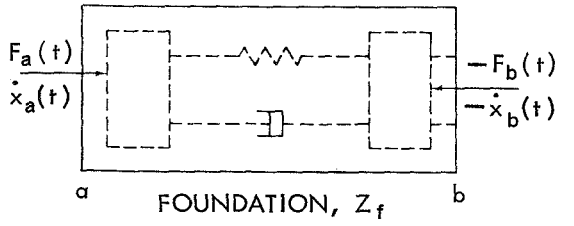

b. Foundation system before connection to equipment system

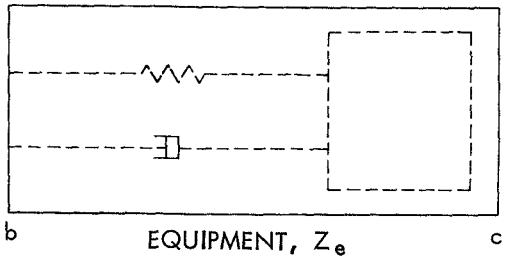

c. Equipment system before connection to foundation system

FIGURE 5.—Block diagrams of foundation and equipment systems.

First, block the terminal b and measure the blocked force $F_b{}^b(t)$ exerted at that terminal; the quantity $F_a(t)$ is the normal exciting forcing function acting. Its nature—that is, whether it is steady-state, transient, or random—determines which cases below must be used. Replace all force generators with impedances equal to their internal impedances; then measure the mechanical impedance Z_f looking back into the foundation from the terminal b, and the mechanical impedance Z_e looking into the equipment from the terminal b.

1. *Steady-state case:*

From Equation 3, the velocity *phasor*[5] $\dot{q}_b$ corresponding to the velocity $\dot{x}_b(t)$ at the terminal b after connecting Z_e is

$$\dot{q}_b=[Z_f+Z_e]^{-1}Q_b{}^b, \qquad \text{(a)}$$

where $Q_b{}^b$ is the force phasor corresponding to the blocked force $F_b{}^b(t)$.

2. *Transient case:*

From Equation 50, the response $\dot{x}_b(t)$ at the terminal b after connecting Z_e is

$$\dot{x}_b(t)=\int_{-\infty}^{+\infty}[Z_f(i\omega)+Z_e(i\omega)]^{-1}G_{F_b{}^b}(i\omega)e^{i\omega t}d\omega, \qquad \text{(b)}$$

where $G_{F_b{}^b}(i\omega)$ is the Fourier spectrum of the blocked force $F_b{}^b(t)$.

3. *Random case:*

From Equation 63, the spectral density $S_{\dot{x}_b}(\omega)$ of the response $x_b(t)$ at the terminal b after connecting Z_e is

$$S_{\dot{x}b}(\omega)=|Z_f(i\omega)+Z_e(i\omega)|^{-2}S_{F_b{}^b}(\omega), \qquad \text{(c)}$$

where $S_{F_b b}(\omega)$ is the spectral density of the blocked force $F_b{}^b(t)$.

Analytical Approach

Consider a lumped parameter representation of a foundation-equipment system as depicted in Figure 6. Replace this representation by its equivalent mechanical network shown in Figure 7.

[5] The term *phasor* as used here implies magnitude and phase of a quantity.

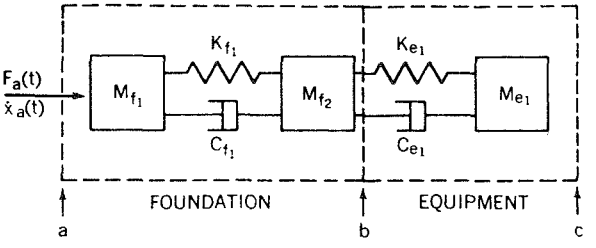

FIGURE 6.—Lumped parameter representation of a one-dimensional foundation-equipment system.

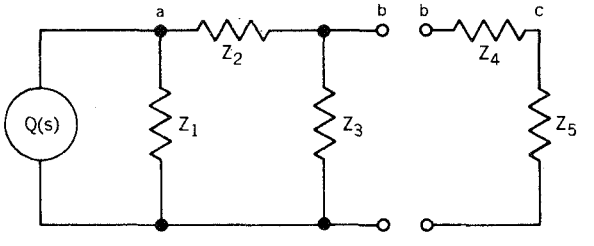

FIGURE 7.—Mechanical network equivalent of Figure 6.

In Figure 7,

$$\left.\begin{aligned} Z_1&=sM_{f_1}\\ Z_2&=\frac{K_{f_1}}{s}+C_{f_1}\\ Z_3&=sM_{f_2}\\ Z_4&=\frac{K_{e_1}}{s}+C_{e_1}\\ Z_5&=sM_{e_1} \end{aligned}\right\} \quad (d)$$

Block terminal b and determine the transform blocked force $Q_b{}^b$ corresponding to the blocked force $F_b{}^b(t)$ exerted at that terminal. Assuming the excitation

$$F_a(t)=F_0 \sin \omega t \quad (e)$$

and letting $Q(s)$ be the Laplace transform of $F_a(t)$, the transform $Q_b{}^b$ is

$$Q_b{}^b(s)=[1+Z_1Z_2^{-1}]^{-1}Q(s). \quad (f)$$

(For other excitations, the appropriate expressions must be written.) Assuming that the impedance of the force generator is low (≈ 0), the impedance looking back into the foundation from the terminal b is

$$Z_f(s)=Z_1Z_2(Z_1+Z_2)^{-1}+Z_3; \quad (g)$$

and the impedance looking forward into the equipment is

$$Z_e(s)=Z_4Z_5(Z_4+Z_5)^{-1}. \quad (h)$$

1. *Steady-state case:*

Using Equation 3 and letting

$$H_1(s)=[Z_f(s)+Z_e(s)]^{-1}, \quad (i)$$

the transform velocity $\dot{q}_b$ corresponding to the velocity $\dot{x}_b(t)$ at the terminal b after connecting Z_e is

$$\dot{q}_b(s)=H_1(s)[1+Z_1Z_2^{-1}]^{-1}Q(s). \quad (j)$$

2. *Transient case:*

Determining the Fourier spectrum $G_{F_b{}^b}(i\omega)$ of the blocked force $F_b{}^b(t)$ from

$$G_{F_b{}^b}(i\omega)=\frac{1}{2\pi}\int_{-\infty}^{+\infty} F_b{}^b(t)e^{-i\omega t}dt, \quad (k)$$

where

$$F_b{}^b(t)=\int_{\omega=-\infty}^{+\infty} G_{F_a}(i\omega)\,[1+Z_1(i\omega)Z_2^{-1}(i\omega)]^{-1}e^{i\omega t}d\omega, \quad (l)$$

and using Equation 50, the response $\dot{x}_b(t)$ at the terminal b after connecting Z_e is

$$\dot{x}_b(t)=\int_{\omega=-\infty}^{\infty} H_1(i\omega)G_{F_b{}^b}(i\omega)e^{i\omega t}d\omega, \quad (m)$$

where

$$H_1(i\omega)=H_1(s)|_{s=i\omega}. \quad (n)$$

3. *Random case:*

Determining the spectral density $S_{F_b{}^b}(\omega)$ of the blocked force $F_b{}^b(t)$ from

$$S_{F_b{}^b}(\omega)=|1+Z_1(i\omega)Z_2^{-1}(i\omega)|^{-2}S_{F_a}(\omega), \quad (o)$$

where $S_{F_a}(\omega)$ is the spectral density of the excitation ($F_a(t)$), and using Equation 63, the spectral density $S_{\dot{x}_b}(\omega)$ of the response $\dot{x}_b(t)$ at the terminal b after connecting Z_e is

$$S_{\dot{x}_b}(\omega)=|H_1(i\omega)|^2|1+Z_1(i\omega)Z_2^{-1}(i\omega)|^{-2}S_{F_a}(\omega). \quad (p)$$

The examples that would illustrate the application of the other equations of the section, "Impedance Analyses of One-Dimensional Systems," would be similar to the preceding examples.

Reshaping of Frequency Response Characteristic of Test Machines

The method as proposed here involves the control of test-machine bare-table frequency response characteristics, so that appropriate mechanical impedance compensations are introduced: This results in dynamic characteristics at the table that are simulations of the vehicles' terminal characteristics. In some instances this control may be accomplished by various spectrum-shaping techniques employing present-day machine system equalization methods. It is the purpose here to present some general ideas behind such an approach.

In the section on impedance analyses, it was shown that the *free velocity* (bare-table velocity) of a test machine may be related to the *free velocity* or *blocked force*—as the case may be—of a vehicle. (Refer to Equations 21, 23, 57, 58, 75, and 76.) For this discussion, the steady-state case only shall be used, as the general idea is equally valid for the cases of other types of excitations. It can be shown from test-machine technology that the *blocked force* $Q_{s_{m^b}}(s)$ at the bare table may be related to the armature current $I_a(s)$ by an expression of the form

$$Q_{s_{m^b}}(s)=B_1(s)I_a(s), \tag{81}$$

where $B_1(s)$ is a transfer function. As the consequence of Equation 81, the *free velocity* of the test machine $q_{s_{m^0}}(s)$ may be related by an expression in a similar form:

$$\dot{q}_{s_{m^0}}(s)=B_2(s)I_a(s), \tag{82}$$

where $B_2(s)$ may be considered as another transfer function. With the assumption that the above relations are practical, the nature of the control will be studied.

Let us suppose that an uncontrolled frequency response function is defined by

$$\log\left|\frac{\dot{q}_{s_{m^0}}(i\omega)}{I_a(i\omega)}\right|=\log|B_2(i\omega)|. \tag{83}$$

For simulation the *free velocity*, Equation 21, may be expressed by

$$\dot{q}_{s_{m^0}}(i\omega)\rightarrow\dot{q}'_{s_{m^0}}(i\omega)=K(i\omega)\dot{q}_{s_{m^0}}(i\omega) \tag{84}$$

and the new armature current by

$$I'_d(i\omega)=C(i\omega)I_d(i\omega), \tag{85}$$

where $K(i\omega)$ and $C(i\omega)$ may be considered as correction factors.

The substitution of Equations 84 and 85 in 83 yields

$$\log\left|\frac{\dot{q}'_{s_{m^0}}(i\omega)}{I'_d(i\omega)}\right|=\log|B_2(i\omega)|+\log|R(i\omega)|, \tag{86}$$

where $R(i\omega)=K(i\omega)/C(i\omega)$.

It is seen that the controlled frequency response function of the test machine is given by Equation 86; the last term on the right of the equation may be considered the correction to be made. This correction may be attempted by either mechanical or electrical means. Mechanically, it would involve mechanical fixture designs; and, electrically, it probably would involve spectrum-shaping techniques.

Electronic Computer Applications

Advances made in servo control theory and problem simulation with electronic computers offer some hope that methods of mechanical impedance simulation could revolve around the use of electronic computer techniques. In view of the multitude of physical applications employing computers for real-time servo control and as problem simulators for analysis, these approaches offer some promise. The general ideas behind these approaches may be summarized as follows.

In servo control applications the electronic computer forms a part of a larger system. It receives impedance and velocity information from other parts of the system and from the outside, processes this information, and—as a result—furnishes instructions to other parts. Since the timing of the computer operations is tied in with that of the system, the computer works in real time. The type of computer (analog or digital) to be used depends on the natural advantages to be derived. The role of the computer is to perform mathematical computations so as to convert stored information supplied from outside into velocity magnitudes to be used as variable inputs (level sets) to the servo control system.

For use as problem simulators for analysis, special-purpose computers may be built. For

instance, if a mechanical system is defined by the appropriate impedances, the computer can simulate the reaction of the components of the system. If true dynamic inputs are employed, the computer outputs would yield realistic dynamic responses of the system.

The details of these approaches have not been investigaed, but the authors believe that such approaches are possible and warrant further study.

DISCUSSION

The objective of this paper was not to investigate in detail the many existing problems in employing the concepts of mechanical impedance to dynamic environmental simulation but rather to provide guidelines based on theoretical considerations, by which certain aspects of simulation possibly may be achieved.

The equations governing the nature of simulation for one-dimensional structural systems have been derived and are summarized in the section on impedance analyses. Study of these equations shows the potential errors resulting from neglect of mechanical impedance effects during measurements, testing, and design of a system. Too frequently the tacit assumption that shock and vibration testing machines possess dynamic characteristics much like those of the actual equipment foundation is not true. Likewise, the tacit assumption that foundation impedance is large in comparison with equipment impedance is often wrong and may result in large errors in design and subsequent qualification testing of the system.

The possible magnitude of the bad effects in neglecting mechanical impedance should stimulate a desire to understand further the mechanisms by which the dynamic characteristics of system components alter the behavior of combined system dynamic environments. Theoretically, the effect of impedance variations on the motional parameter at any joining terminal of system components is related both to the influence of the backward and forward impedance at the terminal and to the nature of the type of excitations. This point is illustrated by the equations summarized in the impedance analyses section.

In the opinion of the authors, some amount of structural impedance consideration in design and qualification procedures is highly necessary to prove the suitability and efficiency of any new type of structural design or to improve existing designs.

The application of mechanical impedance simulation to systems of more than one dimension is an exceedingly complex problem and requires much more study. However, some practices now used yield such large errors that even one-dimensional analysis (which often will be approximate) should yield significant improvement.

CONCLUSIONS

Several main conclusions may be drawn from this study:

1. The study, and possibly the control, of pertinent structural dynamic characteristics for one-dimensional structures that are linear-passive in nature is theoretically feasible, by use of mechanical impedance.
2. The usefulness of these mechanical impedance relations is of three kinds: (1) as a means of expressing dynamic characteristics of component structures in a manner that concisely tells the experienced engineer what he needs to know about the structures; (2) as a description of integral parts of structures, since it can be used together with a comparable description of the dynamic inputs to specify the response at any desired terminal; and (3) if dynamic responses are known for a particular integrated structure, the modified responses when integral parts of the structure are altered can be determined provided impedance information for the new and old integrated structures are known.
3. The practical applications of the mechanical impedance relations covered in the foregoing theory cannot be stated accurately because of the restrictive assumptions underlying this work. However, the proper extent of their

application may be determined by suitable experiments.

RECOMMENDATIONS

Several recommendations result from this investigation:

1. Experimental studies should be undertaken to validate (or refute) the usefulness of the theoretical relations summarized in this paper and to define limits of applicability and validity for each type of excitation.
2. Effort should be directed toward the development of sensors for measurement and the development of data reduction equipment and methods for analysis of the parameters that have been discussed.
3. The validity of the approaches presented to improve test control or simulation should be investigated in further studies.
4. As most structures are not ideal one-dimensional systems, effort should be expended toward developing theoretical relations for multi-dimensional systems.

ACKNOWLEDGMENTS

The authors wish to express their sincere appreciation to Mr. William Forlifer and to Mr. Neal Granick of the Structural Dynamics Branch, Test and Evaluation Division, Goddard Space Flight Center, for their most helpful suggestions during the preparation of the manuscript.

REFERENCES

1. Olson, H. F., "Dynamical Analogies," 2d Ed., Princeton, N.J.: Van Nostrand, 1958.
2. von Kármán, T., and Biot, M. A., "Mathematical Methods in Engineering," New York: McGraw-Hill, 1940, pp. 365–409.
3. Blake, R. E., and Belsheim, R. O., "The Significance of Impedance in Shock and Vibration," in: *Colloquium on Mechanical Impedance Methods for Mechanical Vibrations*, ed. by R. Plunkett, New York: American Society of Mechanical Engineers, 1958, pp. 101–107.
4. Firestone, F. A., "The Mobility and Classical Impedance Analogies," in: *American Institute of Physics Handbook*, New York: McGraw-Hill, 1957, Section 3, pp. 140–177.
5. Lawson, J. L., and Uhlenbeck, G. E., "Threshold Signals," New York: McGraw-Hill, 1950.

Appendix A

Symbols

GENERAL

a, k sub-subscripts for specific vehicle

ab, ar, kb, mb denote respectively the joining terminal of V_a-P_b, V_a-P_r, V_k-P_b, and S_m-P_b

b, r sub-subscripts for specific payload

m sub-subscript for specific test machine

N denotes Nth harmonic component

P subscript for payload

S subscript for test machine

s Laplace variable

t time variable

V subscript for vehicle

ω circular frequency

$\rightarrow$ denotes simulating a quantity

VELOCITIES

$\dot{q}(s)$ transform velocity

$\dot{q}_{V_a0}(s)$ transform *free velocity* of V_a at terminal a

$\dot{q}_{V_k0}(s)$ transform *free velocity* of V_k at terminal a

$\dot{q}_{S_m0}(s)$ transform *free velocity* of S_m at terminal a

$\dot{q}_{V_{ab}}(s)$ transform velocity at joining terminal of V_a-P_b

$\dot{q}_{V_{ar}}(s)$ transform velocity at joining terminal of V_a-P_r

$\dot{q}_{V_{kb}}(s)$ transform velocity at joining terminal of V_k-P_b

$\dot{q}_{S_{mb}}(s)$ transform velocity at joining terminal of S_m-P_b

$G_{\dot{x}}(i\omega)$ Fourier spectrum of a transient velocity $\dot{x}(t)$

$S_{\dot{x}}(\omega)$ spectral density of a random velocity $\dot{x}(t)$

$\dot{x}(t)$ time-dependent velocity

FORCES

F_N^b amplitude of Nth harmonic component *blocked force*

$G_F(i\omega)$ Fourier spectrum of a transient force $F(t)$

$Q(s)$ transform force

$Q_{V_a}^b(s)$ transform *blocked force* of V_a at terminal a

$Q_{V_k}^b(s)$ transform *blocked force* of V_k at terminal a

$S_F(\omega)$ spectral density of a random force $F(t)$

IMPEDANCES

$Z(s)=Q(s)/\dot{q}(s)$, definition of transform mechanical impedance

$Z(i\omega)=Z(s)|_{s=i\omega}$

$Z_{P_b}(s)$ mechanical impedance of P_b looking forward from terminal a

$Z_{P_r}(s)$ mechanical impedance of P_r looking forward from terminal a

$Z_{S_m}(s)$ mechanical impedance of S_m looking back from terminal a

$Z_{V_a}(s)$ mechanical impedance of V_a looking back from terminal a

$Z_{V_{ab}}(s)$ point mechanical impedance at joining terminal of V_a-P_b

FREQUENCY RESPONSE FUNCTIONS

$E_{1,6}(s)=H_1(s)H_6^{-1}(s)$

$E_{2,6}(s)=H_2(s)H_6^{-1}(s)$

$E_{8,2}(i\omega)=H_8(i\omega)H_2^{-1}(i\omega)$

$E_{9,1}(i\omega)=H_9(i\omega)H_1^{-1}(i\omega)$

$E(i\omega)=E(s)|_{s=i\omega}$

$H(i\omega)=H(s)|_{s=i\omega}$

$|H(i\omega)|$=absolute value of $H(s)|_{s=i\omega}$

$$H(iN\omega)=H(s)|_{s=iN\omega}$$

$$H_1(s)=[Z_{V_a}(s)+Z_{P_b}(s)]^{-1}$$

$$H_2(s)=Z_{V_a}(s)[Z_{V_a}(s)+Z_{P_b}(s)]^{-1}$$

$$H_3(s)=[Z_{V_a}(s)+Z_{P_b}(s)][Z_{V_a}(s)+Z_{P_r}(s)]^{-1}$$

$$H_4(s)=[\dot{q}_{V_{k^0}}(s)][\dot{q}_{V_{a^0}}(s)]^{-1}[1+Z_{P_b}(s)Z_{V_a}^{-1}(s)]\times[1+Z_{P_b}(s)Z_{V_k}{}^{-1}(s)]^{-1}$$

$$H_5(s)=[Q_{V_k}^b(s)][Q_{V_a}^b(s)]^{-1}[Z_{V_a}(s)+Z_{P_b}(s)]\times[Z_{V_k}^{-1}(s)+Z_{P_b}(s)]^{-1}$$

$$H_6(s)=Z_{S_m}(s)[Z_{S_m}(s)+Z_{P_b}(s)]^{-1}$$

$$H_7(s)=[Z_{S_m}(s)+Z_{P_b}(s)]^{-1}$$

$$H_8(s)=Z_{V_k}(s)[Z_{V_k}(s)+Z_{P_b}(s)]^{-1}$$

$$H_9(s)=[Z_{V_k}(s)+Z_{P_b}(s)]^{-1}$$

FLIGHT SHOCK AND VIBRATION DATA OF THE ECHO A–12 APPLICATION VERTICAL TESTS [AVT–1 AND AVT–2]

W. B. TERENIAK
Goddard Space Flight Center
AND
S. A. CLEVENSON
Langley Research Center

This paper presents shock and vibration data measured at the base of the spacecraft adapter during the flights of Echo A–12 Application Vertical Tests numbers 1 and 2 (AVT–1 and AVT–2). A modified Thor missile was employed as the launch vehicle for each flight. Also included are data obtained from a vibration survey performed on the AVT–2 spacecraft equipment compartment prior to flight. The two sets of flight data, the vibration flight acceptance test specification, and the results of the vibration survey are compared.

It was found that levels and frequencies measured during the two flights were comparable and that the frequencies measured during flight were similar to those measured during the vibration survey. The previously written vibration flight acceptance test specification was determined to be adequate and not overly severe.

INTRODUCTION

One of the many obstacles that a spacecraft must overcome in order to operate successfully in space is the severe environment imposed during the launch and powered flight phases. To assure that the spacecraft is capable of surviving such environments, it is subjected to extensive environmental testing. In order to establish adequate environment simulation criteria, flight data must be obtained. Two of these environments, shock and vibration, were measured during the Echo A–12 Application Vertical Tests numbers 1 and 2 (AVT–1 and AVT–2). Prior to AVT–1 neither flight shock nor vibration data had been measured at the Thor interface. A limited amount of flight vibration data had been measured in the Thor forward compartment, and has been published. However, it was felt that vibration data measurements at the Thor interface, which could be used to determine Thor vibration inputs to the adjoining spacecraft or rocket motor, would be of great value in establishing environmental test criteria for spacecraft or flight hardware located above the Thor booster.

Consequently, vibration measurements were made during the flights of AVT–1 and AVT–2 with three vibration accelerometers at the base of the spacecraft adapter, oriented to measure vibrations in three mutually perpendicular axes: (1) along the longitudinal axis, (2) along the pitch axis, and (3) along the yaw axis.

Both flights were launched from Cape Canaveral, Florida, the AVT–1 on January 15, 1962, and the AVT–2 on July 17, 1962. The *primary* objective of these tests was to study and observe the deployment and inflation characteristics of the 135-foot space inflatable rigidized sphere and to determine its stability for orbital launch. One of the *secondary* objectives was to measure the shock and vibration environment to which the spacecraft would be subjected during these tests.

The purpose of this paper is to present the flight shock and vibration data measured during the flights of AVT–1 and AVT–2 and to indicate the adequacy of the previously determined shock and vibration environmental test specifications. The flight data will be compared (1) with the vibration response data obtained from the ground vibration survey of the spacecraft equipment compartment of the AVT–2 launch vehicle, and (2) with the environmental test specification. These data are presented in the forms of overall accelerations as a function of flight time; relative vibratory levels as a function of frequency at various times of interest, such as liftoff, fairing separation, and spacecraft separation; power spectral density as a function of frequency; and probability density curves. In addition the vehicle is described, and typical time histories of flight performance are given.

DESCRIPTION OF SPACECRAFT AND LAUNCH VEHICLE

A photograph showing the AVT–2 vehicle on its launch pad at Cape Canaveral prior to liftoff is given in Figure 1. Figure 2 shows the spacecraft, containing the 135-foot inflatable sphere and the spacecraft mounting adapter. The general arrangement of the vehicle is given in Figure 3. The configurations of the launch vehicles were identical to the extent that their differences would not influence their dynamic characteristics. The main booster employed was the modified Douglas Aircraft Company (DAC) Model DM–21 Thor missile with its Bell Telephone Laboratory guidance system located in the Thor forward compartment.

Mounted above the Thor forward compartment was the spacecraft equipment compartment, which housed the coast attitude control system; television camera system; recoverable data capsule and its separation mechanism; and electrical power, signal distribution, and sequence command systems. The spacecraft adapter was bolted to the top of the spacecraft equipment compartment. The spacecraft in turn was secured to the adapter with a marman clamp held together with explosive bolts. The spacecraft was housed in an oblate spheroid

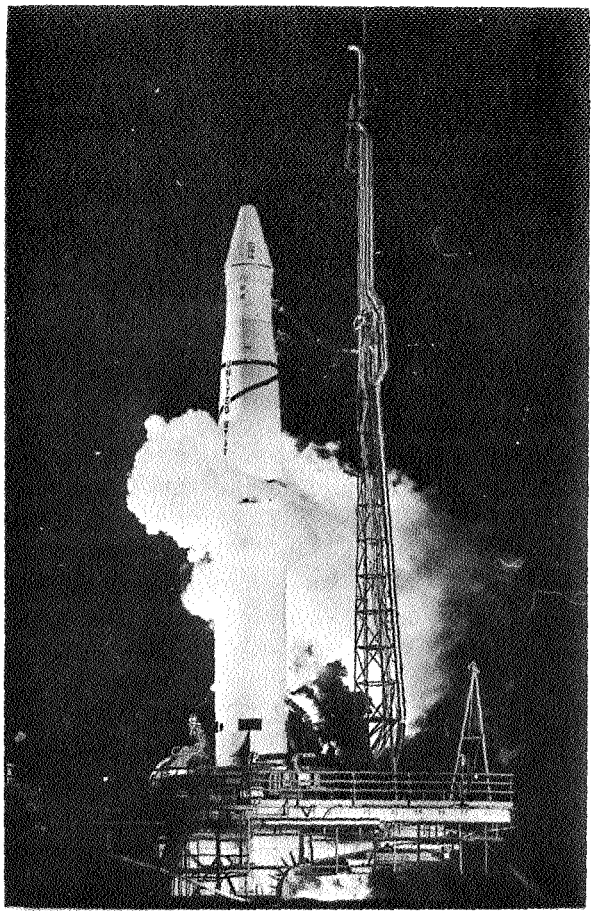

FIGURE 1.—AVT vehicle on launch pad at Atlantic Missile Range.

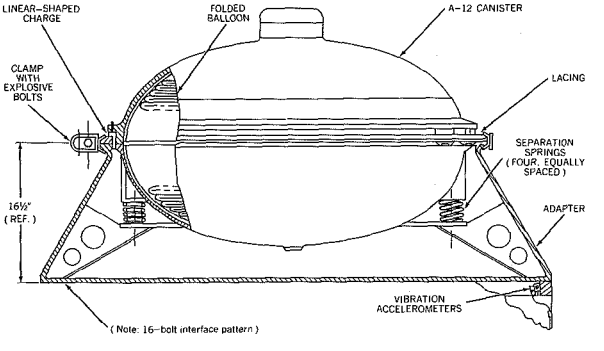

FIGURE 2.—AVT spacecraft and adapter.

canister, and used a linear-shaped charge to separate its halves and allow inflation of the 135-foot sphere.

Inflation of the sphere in space was accomplished by utilizing a subliming powder inside

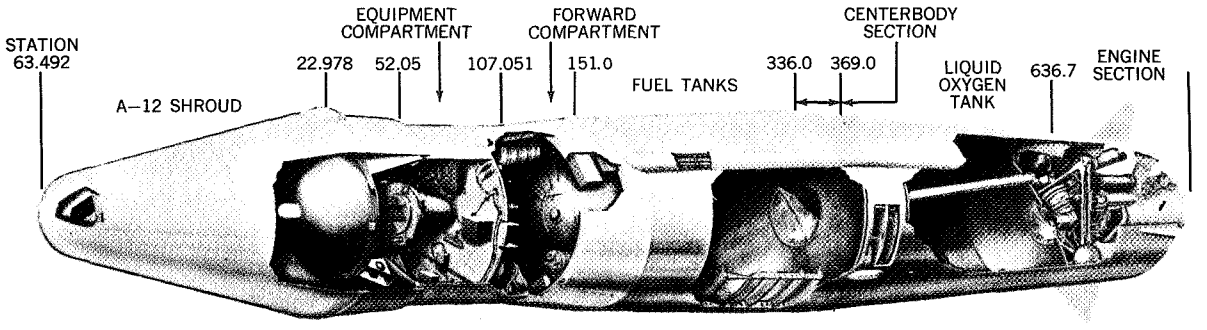

FIGURE 3.—Cutaway view of vehicle.

the balloon. Fifty-two pounds of acetamide provided the pressure for inflating the AVT–1 sphere, while 52 pounds of benzoic acid was used for the AVT–2 sphere. Also inside the balloons was 10 pounds of red dye to be used as an easily distinguishable visual indicator of balloon rupture or leakage.

INSTRUMENTATION AND DATA REDUCTION

The AVT vehicles were instrumented, at Langley Research Center's request, with three vibration transducers located at the base of the spacecraft adapter and oriented to measure vibrations in the three principal axes. The selection and installation of the three-channel measuring system, and performance of all system calibration tests, were accomplished by the Douglas Aircraft Co.

Three piezoelectric vibration accelerometers were mounted at vehicle station 52.05 on the yaw left axis at the top of the spacecraft equipment compartment, as shown in Figure 4. Accelerometer signals were conditioned by "charge" amplifiers located on the main shelf of the equipment compartment. The output of each amplifier was filtered by a low pass filter before passing into its respective voltage controlled oscillator (VCO). The vibration measuring systems for both flights are considered to be identical except for maximum signal capability. A block diagram of the flight vibration measuring system and a table summarizing the characteristics of the two flight systems are shown in Figure 5.

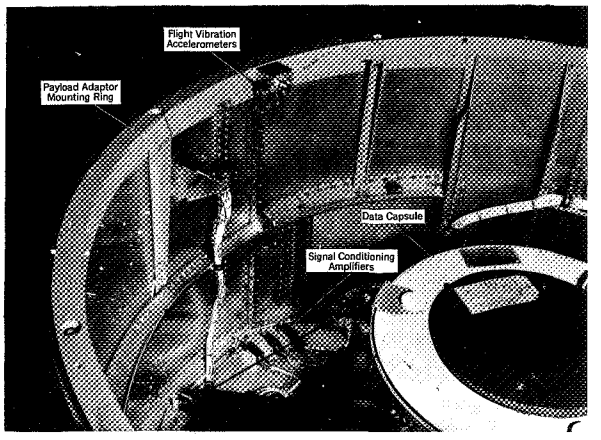

FIGURE 4.—AVT flight accelerometer locations.

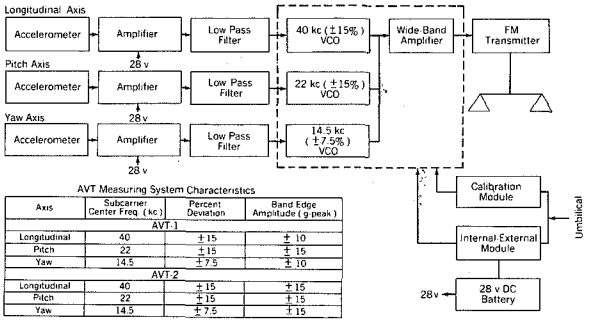

AVT Measuring System Characteristics

Axis	Subcarrier Center Freq. (kc)	Percent Deviation	Band Edge Amplitude (g-peak)
AVT-1			
Longitudinal	40	±15	±10
Pitch	22	±15	±15
Yaw	14.5	±7.5	±10
AVT-2			
Longitudinal	40	±15	±15
Pitch	22	±15	±15
Yaw	14.5	±7.5	±15

FIGURE 5.—AVT flight shock and vibration measuring system.

Figure 6 gives the frequency response curves for both flight systems. The vibration data were transmitted via the vehicle performance telemeter, located in the Thor centerbody section. This telemeter was a Pulse Duration Modulation/Frequency Modulation/Frequency

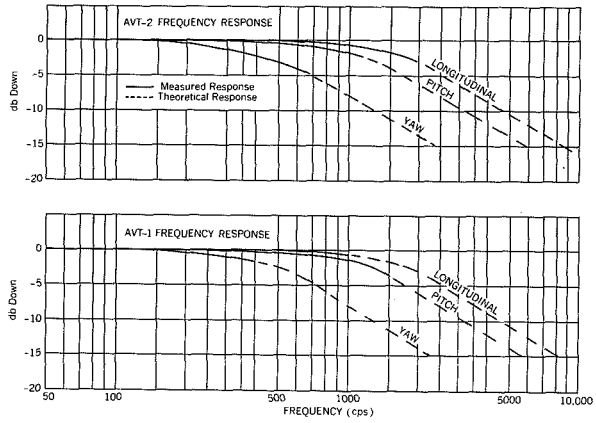

FIGURE 6.—AVT measuring system frequency response curves.

Modulation (PDM/FM/FM) system, with nine continuous data subcarrier channels available. The vibration system incorporated channels 13, A, and C for the yaw, pitch, and longitudinal axis accelerometers, respectively. Composite FM data were received and recorded by both Douglas Aircraft Company and Goddard Space Flight Center (GSFC). A magnetic tape record of the composite FM data, obtained from the GSFC Telemeter 2 Ground Station, was consequently reduced.

The data were reduced, using the system given in Figure 7, by GSFC. The composite FM data were played into discriminators to restore the data to the analog form. Discriminator outputs were then filtered with low pass filters having 3 db down points of 2100 cps for subcarrier channels A and C and 1200 cps for channel 13. From this point the vibratory acceleration data were played into an oscillograph for composite level and narrow-band level versus time records, and into a root-mean-square (rms) level recorder for rms level versus time displays. Power spectral density (PSD) and probability density records were obtained by first re-recording a 2-second time-sample continuous tape loop of the composite FM data at the point of interest. The loop data were then discriminated and filtered, as above, and paralleled into a PSD analyzer and a probability density analyzer. The results of the PSD analysis were corrected for the frequency response of the measuring systems by multi-

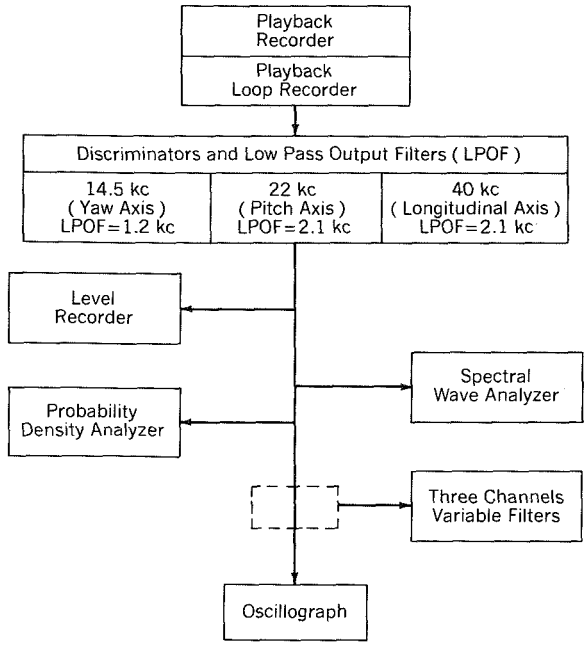

FIGURE 7.—AVT data reduction system.

plying the indicated level at each frequency by twice the inverse of the attenuation given in Figure 6. However, corrections for the frequency response have not been applied to the other types of analyses—that is, rms, composite, etc.

Analysis of the transient shock data during liftoff, fairing separation, and payload ejection was accomplished by making a continuous tape loop including the transient data and directing the tape output into a spectral wave analyzer. The wave analyzer plot indicated the predominate amplitudes and frequencies of the complex wave caused by the transient vibration.

FLIGHT TIME HISTORY

It is appropriate to mention the flight time history of AVT–1 and AVT–2 as a reference for the flight vibration data. Typical time histories of longitudinal steady-state acceleration, velocity, and altitude are shown in Figure 8.

Table 1 lists the sequence of events and their predicted time of occurrence. At T+144.3 seconds, main engine cutoff (MECO) occurs; and, at T+146.3 seconds, the nose fairing is

TABLE 1.—*Typical Sequence of Events and Predicted Event Times for the AVT Vehicles*

Time (seconds)	Event
T+0	(1) Start flight control programmer (2) Uncage gyros
T+2	Start roll program (−0.71086 deg/sec)
T+9	Stop roll program
T+10	Start first pitch command (−0.569 deg/sec)
T+50	Start second pitch command (−0.433 deg/sec)
T+65	Start third pitch command (−0.302 deg/sec)
T+80	First control system gain change
T+90	Second control system gain change
T+93	Start fourth pitch command (+1.4423 deg/sec)
T+134	Start fifth pitch command (−5.86 deg/sec)
T+139	Stop pitch program
T+140	Retrorocket cover ejection Enable MECO circuitry
T+144.3	MECO
T+144.3	Start sequence command programmer
T+146.3	Fairing ejection
T+149.3	F/C timer stop
T+153.3	(1) VECO (Vernier Engine Cutoff) (2) Transfer control to coast attitude system
T+159.3	Start motion picture camera
T+164.3	Separate payload
T+165.3	Ignite retrorocket
T+1344.3	Arm data capsule
T+1349.3	Cut data capsule wires
T+1355.1	Eject data capsule
T+1364.3	Motor reverse

ejected. At T+164.3 seconds, the payload canister is ejected with a forward velocity differential of 5.5 feet/second; and, at T+165.3 seconds, the retrorockets on the booster are ignited to cause an additional velocity differential of −8 feet/second between the booster and the payload canister. At T+185 seconds a linear-shaped charge is ignited to blow the halves of the payload canister apart at a relative velocity of about 50 feet/second to allow the 135-foot rigidized sphere to inflate. The inflation is observed by real-time television and is recorded on a camera that is ejected at T+1355 seconds and is later recovered.

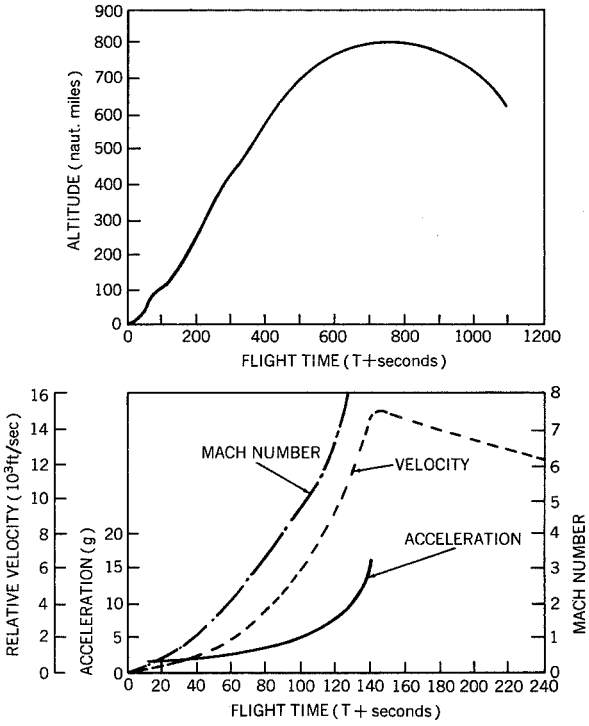

FIGURE 8.—Typical AVT flight parameters

RESULTS AND DISCUSSION

Overall Vibration Levels

Real-time oscillograph records of the composite vibratory accelerations for the longitudinal, pitch, and yaw axes measured during the flight of AVT–1 are given in Figure 9. AVT–2 real-time composite levels are given in Figure 10. Maximum levels, excluding transients, were found to occur at T+39 seconds for both flights. These relatively high levels are attributed to aerodynamic buffeting at transonic

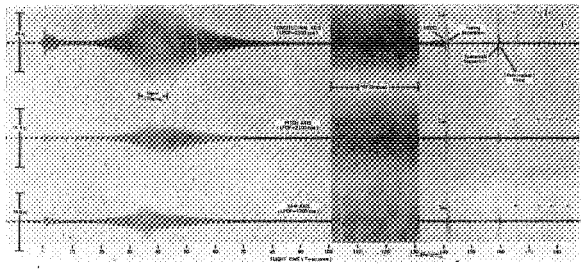

FIGURE 9.—AVT–1 composite levels vs. flight time. (Paper speed, 0.1 in./sec.)

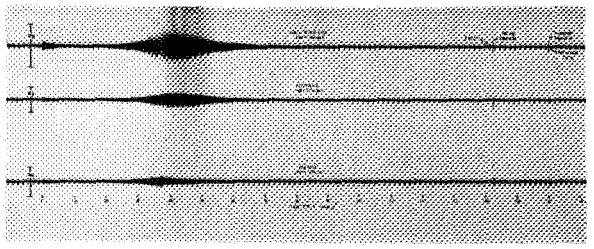

FIGURE 10.—AVT–2 composite levels vs. flight time. (Paper speed, 0.1 in./sec.)

speeds and maximum dynamic pressure. The accuracy of these high longitudinal levels cannot be determined, as they are beyond the calibrated range and probably in the nonlinear range of the system. The optimum range for the AVT–2 longitudinal axis was ±15 g-peak; however, levels of 24.7 g-peak were read, with linearity assumed above this range. These signals were not clipped, and therefore the rms analysis for AVT–2 is considered valid except for the possibility of nonlinearity (linearity not established above 16 g-peak). In the case of AVT–1 the longitudinal channel was clipped from T+35 to T+50 seconds. The optimum range for this channel was ±10 g-peak; however, clipping occurred at approximately 18 g-peak as indicated in Figure 9.

Figure 11 indicates how closely the overall rms vibratory levels measured on AVT–2 compare with those measured on AVT–1. The levels for the accelerations measured on AVT–1 and AVT–2 are given as one curve for the pitch axis and one curve for the yaw axis, since there was less than 10 percent difference in level between the two flights. The accelerations in the longitudinal direction closely agree except for the clipped region of AVT–1. During the AVT–1 flight there were two periods of radio frequency signal dropout where no data were received; AVT–2 experienced no such dropouts. It is significant that at AVT–2 liftoff (T+2 seconds) the value of acceleration measured on the longitudinal axis was 2.2 g-rms, whereas at approximately Mach 1 (T+39 seconds) the acceleration level was 9.4 g-rms. The measured vibration level of 9.4 g-rms is somewhat greater than that indicated by previous measurements made in the forward compartment during flights of the Thor booster. A comparison of AVT–1, AVT–2, and previous Thor flight data—at the main event times—is given in Table 2.

Differences in flight-measured vibratory levels between AVT and previous Thor flights may be accounted for by differences in transducer location, mass loading, and stiffness of the mounting structure and by differences in the thrust output of the Thor booster (AVT–1 and AVT–2 had 10 percent greater thrust than previous Thor boosters). In general, the previous low measurements were obtained from transducers located on the central bulkhead in the Thor forward compartment, whereas on AVT–1 and AVT–2 the transducers were located on the inner circumference of the structural attach ring at the top of the spacecraft equipment compartment (see Fig. 3).

"Transient" Vibrations

The composite vibratory records (Figs. 9 and 10) clearly indicate the vibrations excited by liftoff, MECO, fairing separation, and spacecraft separation. These vibrations are short in duration and relatively high in level. Overall levels measured during fairing separation and spacecraft separation are beyond the optimum signal range of the measuring channels. These signals are in the nonlinear range of the system and may have been "clipped" by the limiter circuit in the charge amplifier. However, it was felt that a spectral analysis of these data would be enlightening.

A tabulation of the results of the qualitative analysis performed on the vibrations excited

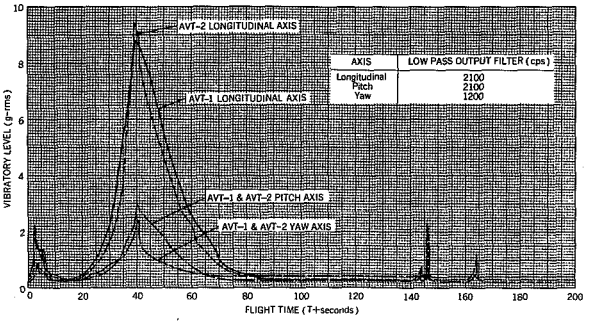

FIGURE 11.—AVT–1 and AVT–2 rms levels vs. flight time.

TABLE 2.—*Comparison of AVT–1, AVT–2, and Thor Flight Data at Main Event Times*
[Vibration Level, g-rms]

Event	AVT–1 [1]			AVT–2 [1]			Previous Thor data		
	Longitudinal axis	Pitch axis	Yaw axis	Longitudinal axis	Pitch axis	Yaw axis	Longitudinal axis	Pitch axis	Yaw axis
Main engine ignition	1.8	0.93	0.63	2.2	0.8	0.8	1.7	3.7	Not reported
Mach 1	[2] 8.8	3.2	2.5	9.4	3.0	2.4	--------	------	↓
Maximum dynamic pressure	3.5	1.6	.62	4.7	1.6	.84	1.7	3.2	
Main engine cutoff	.35	.45	.1	.95	.47	.54	--------	.5	

[1] AVT low pass output filters at 2.1, 2.1, and 1.2 kc for longitudinal, pitch, and yaw axes respectively.
[2] Signal clipped, and level not considered valid.

by the above mentioned events of both flights is given in Table 3. The data were reduced by re-recording a continuous 1-second loop that included the transient vibration, and were then played back into a spectral wave analyzer that employed a 20-cps bandwidth filter. The levels presented are relative, since the time duration of the vibration signal was considerably shorter than the analyzer RC averaging time (1 second) used. The tables summarizing the predominant frequencies indicate that as a result of shocklike excitation certain resonant frequencies are excited. At liftoff these frequencies are excited by both shocklike and acoustic excitations. It is noteworthy that the frequencies are similar in value for these events. This similarity indicates that these high frequencies (greater than 200 cps) are due to a more localized response—that is, from the Thor spacecraft equipment compartment—and are not indicative of the response of the entire vehicle. The previous statement is based on the fact that the mass varies during powered flight and, in turn, varies the vibratory modes of the vehicle.

Figure 12 gives three of the low frequencies excited during AVT–2 liftoff; 17 cps is seen on the longitudinal axis, 8 cps on the pitch axis, and 11 cps on the yaw axis. Figure 13 gives the 45-cps signal, for the three principal axes, excited during liftoff of AVT–2. A tabular summary of the low frequency data obtained during liftoff and MECO of AVT–1 and AVT–2 is given in Table 4. The accuracy of the low frequency (<50 cps) vibratory levels is questionable, since the frequency response of the measuring system below 50 cps was not measured.

Random Vibrations

As shown in Figure 11, the overall rms vibratory level begins to build up again at about T+20 seconds and reaches a point of inflection at T+39 seconds, at a level of 9.4 g-rms for AVT–2. This buildup in level, which occurs in the transonic region of flight, is attributed to the random excitation caused by aerodynamic buffeting.

Power spectral density (PSD) plots are given in Figures 14 through 16 for the three axes measured during the flights of AVT–1 and AVT–2. The data sample loops for both flights were made at maximum rms level (about T+38 to T+40 seconds). AVT–1 longitudinal axis data are an exception since signal

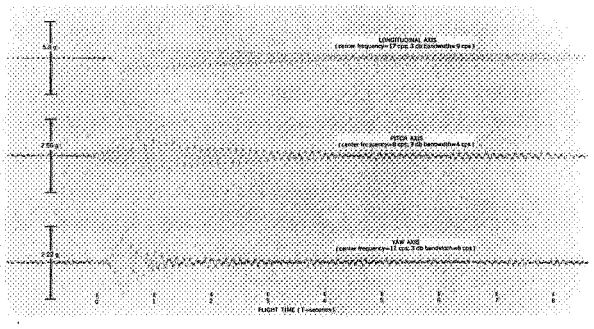

FIGURE 12.—AVT–2 discrete frequencies measured at liftoff. (Paper speed, 1.6 in./sec.)

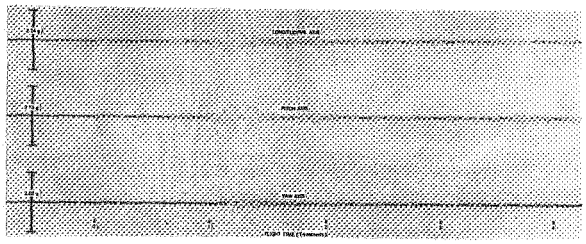

FIGURE 13.—AVT–2 discrete frequencies measured at liftoff. (Paper speed, 4 in./sec; center frequency, 45 cps; 3 db bandwidth, 24 cps.)

"clipping" occurred during this time; because of clipping, the loop was obtained at T+31 to T+33 seconds. The PSD plots show that the spectra are discrete in nature with peak values at frequencies closely associated to those measured during the events of liftoff, MECO, etc. Table 5 compares the predominant frequencies of the PSD plots of the longitudinal axes of AVT–1 and AVT–2 along with the frequencies obtained during liftoff of AVT–2, and indicates the similarity of the frequencies measured. It is significant to point out the high PSD level (0.488 g^2/cps) measured at 1030 cps along the longitudinal axis of AVT–2 at T+39 seconds. The equivalent g-rms level in the region 940 cps to 1120 cps (see Fig. 14b) is 6.62 g-rms, whereas the overall level at this time was 9.4 g-rms. PSD levels of AVT–1 given in Table 5 are not comparable to AVT–2 levels. AVT–1 data were not obtained at the same time, since the maximum level was clipped by the measuring system.

TABLE 3.—*Summary of Predominate "High" Frequencies and Relative Vibratory Levels Measured on the AVT–1 an d AVT–2 Principal axes* [1]

Liftoff				Main engine cutoff				Fairing separation				Spacecraft separation			
AVT–1		AVT–2		AVT–1		AVT–2		AVT–1		AVT–2		AVT–1		AVT–2	
Freq. (cps)	Level	Freq. (cps)	Level	Freq. (cps)	Level	Freq. (cps)	Level	Freq. (cps)	Level	Freq. (cps)	Level	Freq. (cps)	Level	Freq. (cps)	Level
Longitudinal axis															
130	0. 05	130	0. 09	170	0. 02	140	0. 13	------	------	------	------	------	------	------	------
------	------	------	------	230	. 02	280	. 04	225	0. 04	230	0. 15	------	------	------	------
300	. 05	330	. 09	330	. 02	340	. 04	------	------	350	. 19	------	------	350	0. 10
430	. 08	430	. 32	380	. 04	400	. 03	420	. 04	420	. 24	410	0. 08	440	. 12
510	. 12	------	------	480	. 01	500	. 02	------	------	480	. 30	------	------	520	. 12
585	. 15	580	. 49	570	. 01	------	------	575	. 11	570	. 58	580	. 08	580	. 11
------	------	640	. 60	620	. 02	------	------	------	------	650	. 33	------	------	670	. 48
------	------	680	. 51	700	. 02	------	------	------	------	------	------	710	. 13	------	------
760	. 10	780	. 41	750	. 01	------	------	770	. 08	780	. 43	790	. 23	------	------
------	------	------	------	800	. 03	800	. 01	------	------	------	------	------	------	800	. 36
------	------	830	. 35	850	. 02	------	------	------	------	850	. 52	840	. 25	850	. 48
890	. 15	------	------	920	. 02	------	------	910	. 05	------	------	------	------	------	------
970	. 11	960	. 43	990	. 01	950	. 01	------	------	960	. 86	------	------	------	------
1070	. 19	1030	. 57	------	------	1040	. 01	1060	. 09	1020	. 24	1060	. 26	1010	. 55
1200	. 11	1160	. 31	1190	. 40	------	------	1170	. 04	1120	. 29	------	------	------	------
------	------	1260	. 25	------	------	1240	. 01	1270	. 04	------	------	1280	. 09	1220	. 26
1320	. 09	1340	. 16	1350	. 01	------	------	------	------	------	------	1310	. 09	1340	. 21
1420	. 08	------	------	------	------	------	------	1400	. 08	1450	. 22	1420	. 09	------	------
------	------	1490	. 27	------	------	------	------	1510	. 05	------	------	1500	. 09	1490	. 14
1580	. 07	1600	. 05	------	------	------	------	------	------	------	------	------	------	------	------
1710	. 04	1700	. 05	------	------	------	------	------	------	1700	. 11	------	------	------	------
------	------	1780	. 10	------	------	------	------	1800	. 02	------	------	1770	. 06	1800	. 07

[1] All levels are relative; analysis filter bandwidth, 20 cps.

TABLE 3.—*Summary of Predominate "High" Frequencies and Relative Vibratory Levels Measured on the AVT–1 and AVT–2 Principle axes*[1]—Continued

Liftoff				Main engine cutoff				Fairing separation				Spacecraft separation			
AVT–1		AVT–2		AVT–1		AVT–2		AVT–1		AVT–2		AVT–1		AVT–2	
Freq. (cps)	Level	Freq. (cps)	Level	Freq. (cps)	Level	Freq. (cps)	Level	Freq. (cps)	Level	Freq. (cps)	Level	Freq. (cps)	Level	Freq. (cps)	Level
Pitch axis															
------	-----	------	------	------	------	110	0. 08	------	------	------	------	133	0. 12	110	0. 12
------	-----	------	------	180	0. 05	150	. 07	------	------	------	------	------	------	170	. 11
200	0. 06	210	0. 08	------	------	210	. 05	220	0. 20	220	0. 22	210	. 11	------	------
240	. 09	260	. 16	------	------	280	. 03	------	------	260	. 28	------	------	260	. 08
310	. 06	340	. 10	330	. 04	330	. 07	340	. 08	------	------	------	------	310	. 09
------	-----	------	------	380	. 03	------	------	390	. 10	360	. 14	------	------	------	------
460	. 09	470	. 12	470	. 02	------	------	440	. 13	440	. 10	440	. 07	440	. 09
------	-----	540	. 11	------	------	500	. 02	550	. 08	------	------	------	------	520	. 05
------	-----	------	------	580	. 02	------	------	------	------	600	. 17	------	------	620	. 09
650	. 06	640	. 04	------	------	------	------	------	------	650	. 15	650	. 08	650	. 07
------	-----	700	. 09	------	------	680	. 01	------	------	------	------	------	------	------	------
------	-----	------	------	740	. 03	------	------	------	------	------	------	------	------	740	. 04
------	-----	790	. 04	------	------	800	. 01	780	. 10	780	. 14	810	. 08	820	. 11
830	. 05	860	. 10	860	. 03	------	------	------	------	------	------	------	------	------	------
900	. 05	------	------	------	------	------	------	920	. 09	------	------	------	------	------	------
980	. 04	970	. 08	960	. 04	------	------	------	------	------	------	990	. 07	1000	. 05
1050	. 04	1030	. 07	1030	. 04	------	------	1060	. 08	1030	. 01	1060	. 07	------	------
1100	. 03	------	------	1080	. 04	1100	. 01	------	------	1100	. 23	------	------	1100	. 10
------	-----	1160	. 07	1170	. 09	------	------	------	------	------	------	------	------	------	------
------	-----	------	------	1210	. 05	------	------	------	------	------	------	------	------	1220	. 06
1290	. 04	1260	. 07	1205	------	------	------	1260	. 07	------	------	------	------	------	------
------	-----	------	------	1205	------	------	------	1340	. 08	1370	. 19	1350	. 07	1340	. 06
1440	. 03	------	------	------	------	1470	. 02	1500	. 06	------	------	1480	. 05	1460	. 05
1650	. 03	------	------	------	------	------	------	1680	. 06	1650	. 12	1640	. 06	1650	. 06
------	-----	1810	. 04	------	------	1880	. 02	1800	. 05	1850	. 06	1830	. 05	1850	. 04
Yaw axis															
------	-----	130	0. 05	------	------	140	0. 04	170	0. 17	------	------	140	0. 12	130	0. 18
220	0. 12	------	------	180	0. 09	200	. 03	210	. 39	------	------	200	. 12	------	------
260	. 10	230	. 13	------	------	------	------	------	------	250	0. 04	250	. 07	250	. 18
------	-----	300	. 14	------	------	270	. 02	280	. 08	------	------	280	. 07	------	------
------	-----	350	. 18	330	. 11	330	. 05	320	. 09	340	. 03	320	. 05	340	. 24
------	-----	------	------	------	------	------	------	420	. 14	420	. 03	410	. 04	430	. 12
440	. 09	------	------	450	. 06	------	------	450	. 08	460	. 02	------	------	------	------
490	. 07	480	. 12	500	. 08	------	------	------	------	530	. 02	520	. 04	------	------
------	-----	600	. 10	620	. 09	600	. 01	560	. 05	600	. 02	------	------	620	. 09
650	. 05	------	------	680	. 09	------	------	------	------	670	. 02	650	. 04	670	. 10
780	. 05	770	. 07	750	. 10	------	------	770	. 06	------	------	------	------	780	. 06
820	. 05	------	------	------	------	800	. 01	------	------	800	. 01	810	. 03	------	------
------	-----	840	. 07	850	. 12	------	------	830	. 05	850	. 02	850	. 03	------	------
980	. 04	------	------	950	. 12	------	------	------	------	------	------	------	------	------	------
------	-----	1000	. 04	1000	. 10	------	------	------	------	------	------	------	------	------	------
1040	. 03	1080	. 03	------	------	1070	. 01	------	------	1030	. 01	------	------	1030	. 04
------	-----	------	------	1120	. 10	------	------	------	------	------	------	------	------	------	------
------	-----	------	------	1160	. 19	------	------	------	------	------	------	------	------	------	------
------	-----	1270	. 02	1280	. 08	------	------	------	------	------	------	------	------	1280	. 02
------	-----	1380	. 01	1390	. 07	------	------	------	------	------	------	------	------	------	------
------	-----	1740	. 01	------	------	------	------	------	------	------	------	------	------	------	------

[1] All levels are relative; analysis filter bandwidth, 20 cps.

TABLE 4.—*Summary of AVT Low Frequencies at Their Maximum Level*

Longitudinal axis				Pitch axis				Yaw axis [1]			
AVT–1		AVT–2		AVT–1		AVT–2		AVT–1		AVT–2	
Freq. (cps)	Level (g-pk)	Freq. (cps)	Level (g-pk)	Freq. (cps)	Level (g-pk)	Freq. (cps)	Level (g-pk)	Freq. (cps)	Level (g-pk)	Freq. (cps)	Level (g-pk)
Liftoff											
17	1. 8	17	1. 0	8	0. 70	8	0. 5	11	1. 4	11	1. 1
22	2. 0					9	. 80	22	. 70		
33	1. 6					11	1. 0	33	. 50		
44	1. 3	45	1. 0	22	. 40					45	. 30
57	1. 8			33	. 40			57	. 70		
						45	. 90				
				57	. 80						
Main engine cutoff											
		32	0. 76			52	0. 3				
		42	. 65			58	1. 1				
55	0. 4	55	. 65	87	0. 69						
95	. 2			116	. 87						
122	. 91										
		137	2. 8								

[1] Yaw axis has no significant levels in the 5–150 cps range during main engine cutoff.

Figure 17 presents the probability density curves of the data loops used for the PSD analyses and compares them to a Gaussian distribution. Figure 18 gives a distribution curve obtained from data measured along the longitudinal axis of AVT–1 during time T+37 to T+39 seconds. The curve clearly illustrates "clipping" at -1.90σ and $+2.20\sigma$. Although the plots show that the probability distribution of the data are non-Gaussian, the deviation is slight.

Comparison of AVT Data

The vibration data obtained from Echo A–12 application vertical tests include data measured during the flights of AVT–1 and AVT–2 and data measured during a vibration survey performed on the AVT–2 equipment compartment. The vibration survey was performed on the fully assembled AVT–2 vehicle on its launch pad at Cape Canaveral. Low-level sinusoidal vibration inputs (15 to 2000 cps) into the equipment compartment were accomplished by attaching two 25-pound electromagnetic shakers to the nose fairing dummy explosive bolts located 180 degrees apart at station 52.05. Response to sinusoidal excitations was measured by the flight transducers and by transducers mounted at various external locations on the equipment compartment. Figure 19 shows a physical arrangement of the test setup. In addition to the sinusoidal test, the equipment compartment natural frequencies were excited by striking the vehicle at various locations and directions at station 52.05 with a rubber mallet. A comparison of the AVT–2 flight data, vibration survey data, and the AVT payload vibration flight-acceptance-test specification levels is given in Table 6. The comparison indicates that resonant frequencies excited manually by mallet and those excited by the electromagnetic shakers were the predominant frequencies de-

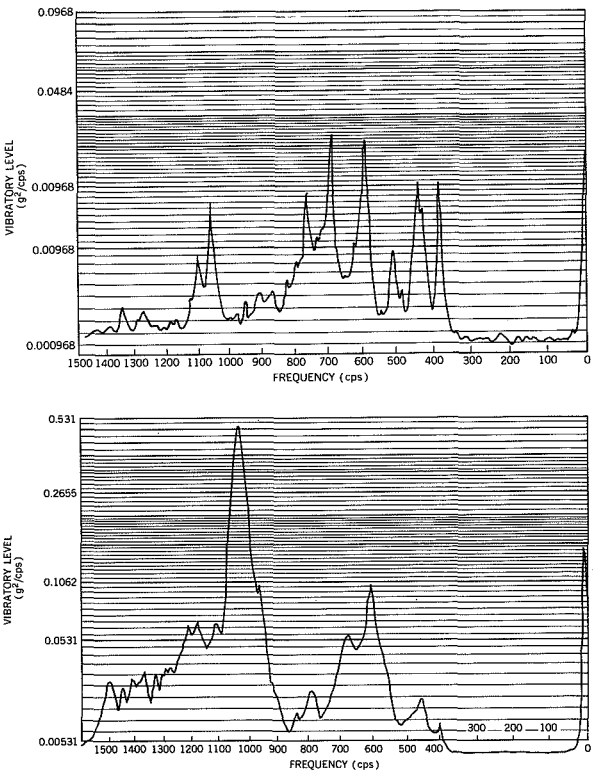

FIGURE 14.—PSD plot, longitudinal axis. Filter bandwidth, 20 cps; RC averaging time, 1 sec; sample length, 2 sec.
(a) AVT–1, T+31 to T+33 seconds.
(b) AVT–2, T+38 to T+40 seconds.

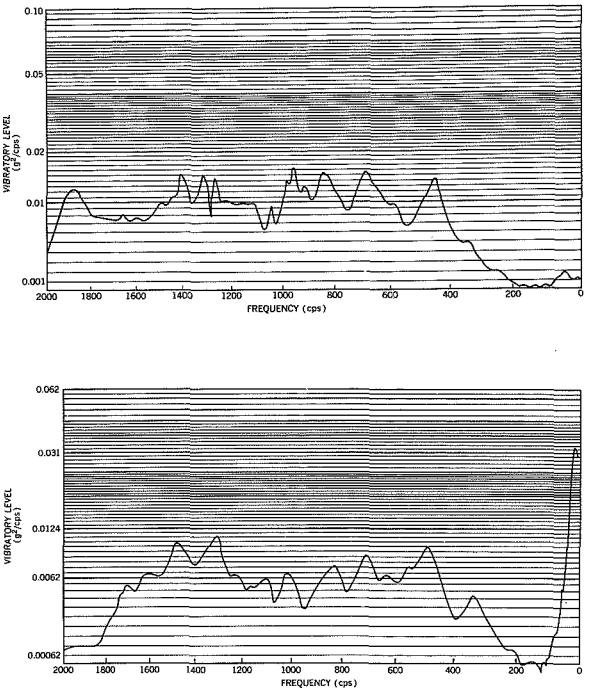

FIGURE 15.—PSD plot, pitch axis. Filter bandwidth, 50 cps; RC averaging time, 1 sec; sample length, 2 sec.
(a) AVT–1, T+37 to T+39 seconds.
(b) AVT–2, T+38 to T+40 seconds.

termined from the PSD analyses of the flight vibration data. It may be remembered that similar predominant frequencies occurred during liftoff, MECO, fairing separation, and spacecraft separation (Table 3).

One of the effects of buffeting is the acoustical excitation of random vibrations in the vehicle and payload structures. Buffeting is usually defined as the result of unstable flow over the body and generally occurs as the vehicle approaches transonic speeds. The flow instability is independent of body motion but is directly related to the vehicle nose shape. References 1, 2, and 3 report recent studies of buffeting forces on certain types of vehicle nose shapes. Figure 20 shows the nose shapes of three vehicles used to launch the S–51 (Thor-Delta), Transit BI (Thor-Able-Star), and AVT (Thor); from this comparison, it might be expected that the highest vibratory levels due to buffeting would be measured on the Thor-Able-Star vehicle and the lowest on the Thor-Delta vehicle. Figure 21, which compares the overall rms flight vibratory levels for these three vehicles,[1] confirms that the vibratory levels at transonic speeds were highest on the Thor-Able-Star and lowest on the Thor-Delta.

A comparison of the flight-measured values with the flight test specification (Table 6) indicates that the previously written test specification is both adequate and not overly severe. The flight-measured overall level of 9.4 g-rms, at transonic speeds, is slightly below the test specification of 9.5 g-rms random excitation.

[1] Thor-Able-Star data were obtained from Reference 4, and Thor-Delta data from unpublished results by L. A. Williams of GSFC.

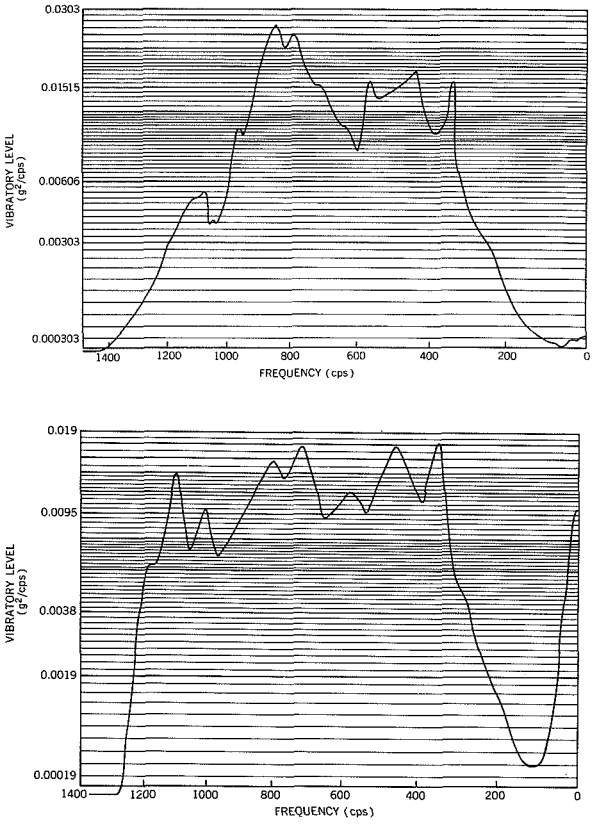

FIGURE 16.—PSD plot, yaw axis. Filter bandwidth, 50 cps; RC averaging time, 1 sec; sample length, 2 sec.

(a) AVT–1, T+37 to T+39 seconds.
(b) AVT–2, T+38 to T+40 seconds.

However, since the predominant excitation occurred in the frequency band of 940 to 1120 cps with an overall excitation level of 6.62 g-rms over this bandwidth (corresponds to a PSD of 0.488 g^2/cps), it is felt that the sinusoidal sweep at the level of 6 g-rms adequately simulates the flight vibration environment.

CONCLUDING REMARKS

The flight data presented in this report indicate that (1) the major vibration levels measured during the AVT flights occurred during liftoff, Mach 1, fairing separation, and payload separation; (2) the composite levels of both flights measured during these occurrences are in close agreement; (3) the spectra (level and frequency) are similar for comparative time

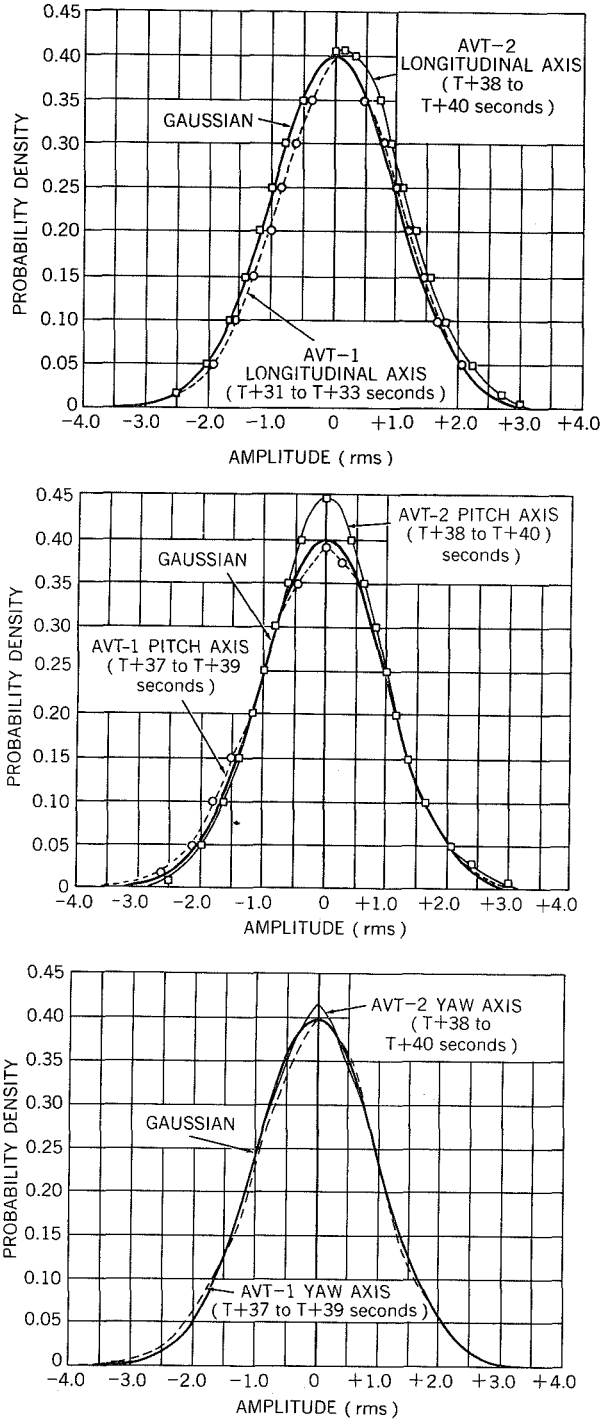

FIGURE 17.—AVT–1 and AVT–2 probability density curves. Gaussian distribution, $Y=\frac{1}{\sqrt{2\pi}}-e^{x^2/2}$

(a) Longitudinal axis.
(b) Pitch axis.
(c) Yaw axis.

TABLE 5.—*Comparison of Predominant Frequencies Measured Along the Longitudinal Axis of AVT–1 and AVT–2* [1]

AVT–1 (T+31 to T+33) PSD analysis		AVT–2 (T+38 to T+40) PSD analysis		AVT–2 (T+1 to T+2) Spectral analysis	
Freq. (cps)	Level (g^2/cps)	Freq. (cps)	Level (g^2/cps)	Freq. (cps)	Relative Level
				130	0.09
380	0.0198			330	.09
420	.0202			430	.32
480	.0046	470	0.02		
510	.0091				
580	.035	600	.102	580	.49
620	.0078			640	.60
680	.0321	660	.058	680	.51
700	.0096			720	.38
750	.0181				
810	.006	790	.024	780	.41
860	.005	840	.014	830	.35
		900	.028		
		950	.102	960	.43
1020	.0163	1020	.488	1030	.51
1100	.0085	1120	.066		
		1180	.069	1160	.31
		1220	.065		
1280	.0038	1280	.035	1260	.25
1340	.0039	1320	.032	1340	.16
		1380	.033		
		1440	.026		
		1500	.029	1490	.27
				1700	.05
				1780	.10

[1] Filter bandwidth, 20 cps.

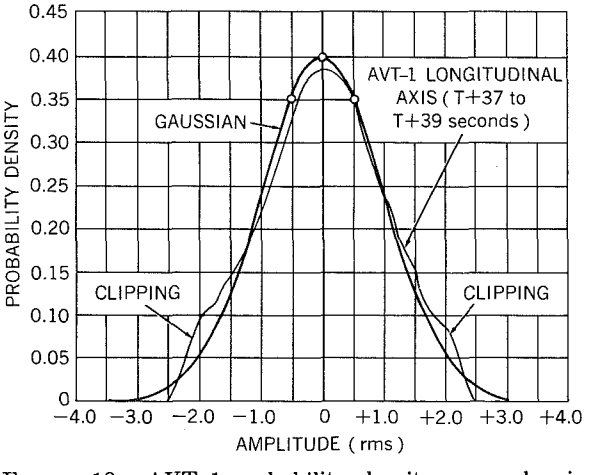

FIGURE 18.—AVT–1 probability density curve, longitudinal axis. Gaussian distribution, $Y=\frac{1}{\sqrt{2\pi}}-e^{x^2/2}$

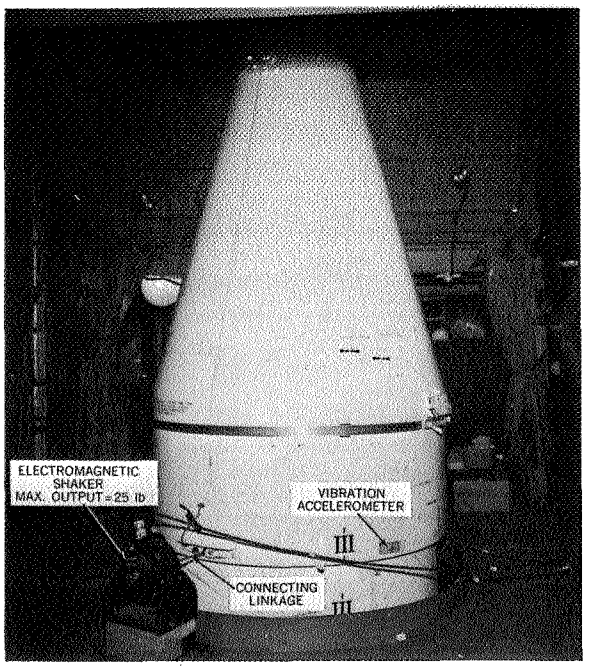

FIGURE 19.—AVT–2 ground vibration survey test setup.

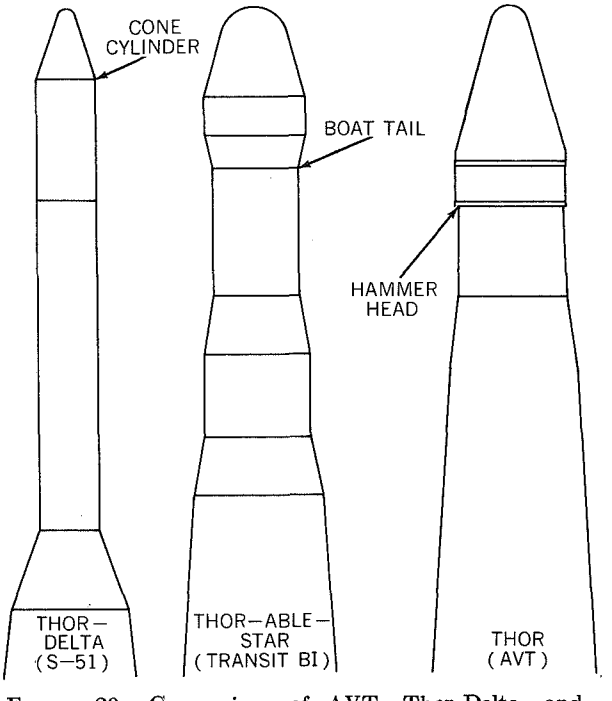

FIGURE 20.—Comparison of AVT, Thor-Delta, and Thor-Able-Star nose shapes.

TABLE 6.—*Comparison of Flight Vibration Data With Ground Vibration Survey Frequencies and Test Specification Levels*[1]

Ground vibration data, thrust			AVT-2 flight vibration data, power spectral density[1]				Flight test levels, sinusoidal	
Tapping	Forced vibration							
Freq. (cps)	Freq. (cps)	Response (±g)	Freq. (cps)	Yaw (g^2/cps[2])	Pitch (g^2/cps[3])	Thrust (g^2/cps[4])	Freq. range (cps)	Level
210	----------	----------	----------	----------	----------	----------	5–14	¼ inch D.A.
400	390	3.3	340	0.0171	0.0071	----------		
435	490	5.8	470	.0169	.0098	0.02	14–400	4 g-rms
----------	585	4.6	575–625	.0114	.0065	.102	400–2000	6 g-rms
----------	----------	----------	675–710	.0168	.0088	.058		
----------	795	5.3	775–825	.0148	.0076	.024		
915	915	8.3	900	----------	----------	.028		
----------	970	8.8	950	----------	----------	.102		
----------	1040	10	1030	.0098	.0066	.488		
1100	1120	7.4	1100	.0133	.0062	.066		
1180	----------	----------	1180	----------	----------	.069		
1250	1200	6.4	1220	.0060	.0063	.065		
----------	----------	----------	1280	----------	----------	.035		
----------	----------	----------	1320	----------	.0012	.032		
----------	----------	----------	1380	----------	----------	.033		
----------	----------	----------	1440	----------	----------	.026		
1570	1550	5.7	1500	----------	.014	.029		
----------	----------	----------	1630	----------	.0067	----------	Gaussian random	
							15–2000 cps	0.045 g^2/cps (9.5 g-rms)

[1] Data sample measured at maximum flight vibration level, T+38 to T+40 seconds.
[2] Filter bandwidth, 50 cps.
[3] Filter bandwidth, 50 cps.
[4] Filter bandwidth, 20 cps.

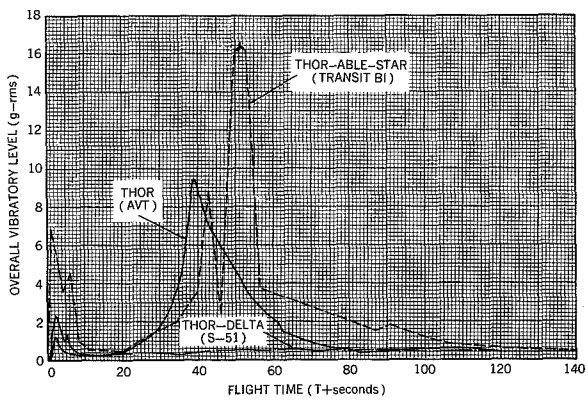

FIGURE 21.—Longitudinal vibration-time history comparison of AVT, Thor-Delta, and Thor-Able-Star flights.

data samples; and (4) the frequencies measured during flight were similar to those measured during the ground vibration survey.

Payload vibration data measured during a recent Thor-Delta flight show that no increase in level was measured during Mach 1 or maximum dynamic pressure; in contrast, high vibration levels were measured on the AVT flights. Also, high vibration levels were measured at Mach 1 and maximum dynamic pressure during flights of the Thor-Able-Star. The differences in the vibratory levels of these vehicles measured at transonic speeds are attributed mainly to the vehicle nose shape.

A comparison of the flight-measured vibration levels with the environmental flight acceptance test specification indicates that the previously written test specification is both adequate and not overly severe.

REFERENCES

1. Woods, P., and Ericsson, L. E., "Aeroelastic Considerations in a Slender, Blunt-Nose, Multistage Rocket," *Aerospace Eng.* 21(5): 42–51, May 1962.
2. Coe, C. F., "Steady and Fluctuating Pressures at Transonic Speeds on Two Space-Vehicle Payload Shapes," NASA TM X–503, March 1961.
3. Coe, C. F., "The Effects of Some Variations in Launch-Vehicle Nose Shape on Steady and Fluctuating Pressures at Transonic Speeds," NASA TM X–646, March 1962.
4. Douglas, D. G., "Measurement and Analysis of Missile Vibration, Shock, and Noise Environments," *Proc. Instrum. Soc. Amer.* 17(2): Paper No. 38.1.62, 1962.

THE MERCURY-XENON ARC AND THE CARBON ARC AS SOURCES OF SOLAR SIMULATION

M. P. THEKAEKARA

Goddard Space Flight Center

A critical analysis has been made of the problems of solar simulation in testing thermal balance of spacecraft. In particular, the spectral energy distributions of the mercury-xenon arc and the carbon arc have been compared to that of solar radiation in outer space. The results of previous investigators have been analyzed. A technique has been developed for precision measurement of intensity, using a high dispersion Jarrell-Ash grating spectrograph, and also two compact prism spectrograghs, a Leiss and a Perkin-Elmer. The variability of both total energy and spectral distribution with discharge conditions has been investigated experimentally and theoretically.

INTRODUCTION

One of the major problems concerning solar simulation is the spectral energy distribution of the sources which one uses for simulating the radiation of outer space. The Test and Evaluation Division of the Goddard Space Flight Center is vitally interested in solar simulation. In the simulator will be placed the different types of spacecraft prior to their being launched into orbit. The spacecraft will be exposed to a collimated beam of radiant energy. The irradiation will be essentially similar to that of outer space in spectral characteristics and total energy. Temperatures at different points on the surface and in the interior of the spacecraft will be continually monitored to see whether at any time during the test runs the temperatures exceed the maximum and minimum limits which the components of the different experiments within the payload can withstand. These tests are being made on the assumption that the temperatures attained by the spacecraft during the test run can be correlated to those which the same spacecraft will attain while in orbit. If the test runs show that the thermal balance is inadequate at some of the spots within the spacecraft, suitable adjustments will be made in the geometry of the spacecraft, thermal insulation of the materials, ratio of absorption to emission coefficients of the surface coating and other adjustable parameters, so that a thermal balance that meets the specifications of the experimenters can be safely predicted for the satellite in orbit. This in brief is the basic philosophy of solar simulation for thermal balance. The cost of a satellite being what it is, it is essential that every precaution be taken before the satellite is launched to ensure the smooth functioning of all the experiments aboard when the satellite will be in orbit.

ANALYSIS OF EARLIER DATA

The source of radiant energy for simulating solar radiation will be a battery of 127 mercury-xenon lamps for the large simulator under construction and individual mercury-xenon lamps or carbon arc lamps for the smaller simulators already in operation. We need to know whether the spectral energy distribution of these lamps is a close enough match to that of solar radiation in outer space.

Data have been presented by the manufacturers of these high-energy sources; other data have been compiled by different observers. A comparison between the data presented by

764-173 O—65——51

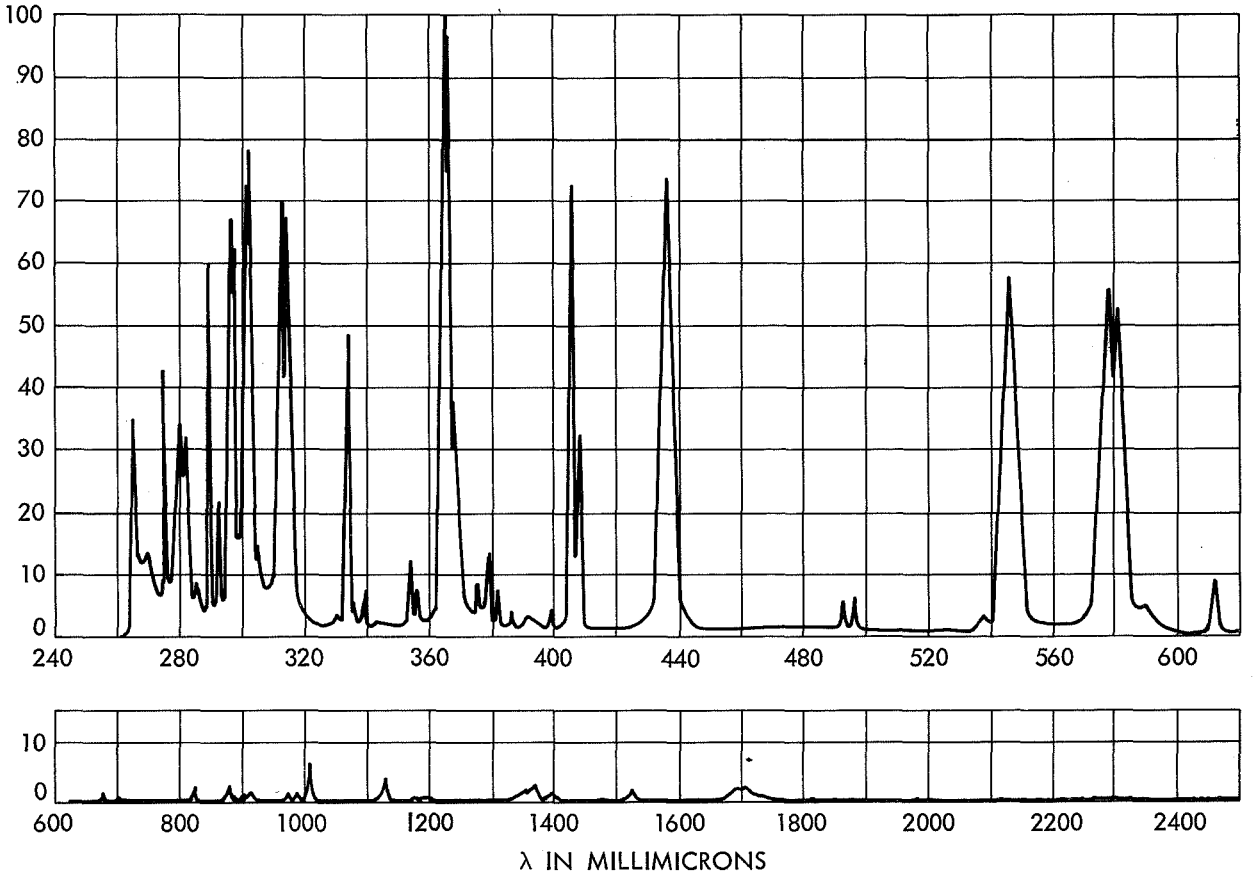

FIGURE 1.—Spectral Distribution of the Mercury-Xenon Compact Arc Lamp.

different observers on the same type of lamp shows very large divergences. We are interested in particular in the mercury-xenon lamp, since it plays an important role in the effectiveness of our large Solar Environment Simulator. The general features of the spectral energy distribution of the mercury-xenon lamp are shown in Figure 1. The wavelength in millimicrons is shown on the x-axis, and the monochromatic irradiance (in arbitrary units) is shown on the y-axis. There are several strong emission lines of mercury and xenon in the visible and near infrared regions of the spectrum and hence the energy integrated over fairly wide spectral ranges is a close enough spectral match to the solar radiation. How close is this spectral match will be a major point to be discussed in this paper.

A comparison between the spectral energy distribution of the mercury-xenon lamp and that of solar radiation of zero air mass is shown in Figure 2. The x-axis is wavelength in microns, and the y-axis is the energy emitted by the lamp in all directions in watts per 100A wavelength range. The thin line continuous curve is based on data supplied by the manufacturers on a Westinghouse 2500 watt lamp. The total output is 1729 watts. The dotted curve is based on data supplied, also by the manufacturers, on a Hanovia 1000 watt lamp. The values are supplied on a percentage basis for each 100A range. The total value of the energy when multiplied by 2.5 agrees closely with that of the Westinghouse data.

One observes that the peaks of the Hanovia lamp are considerably higher, especially in the

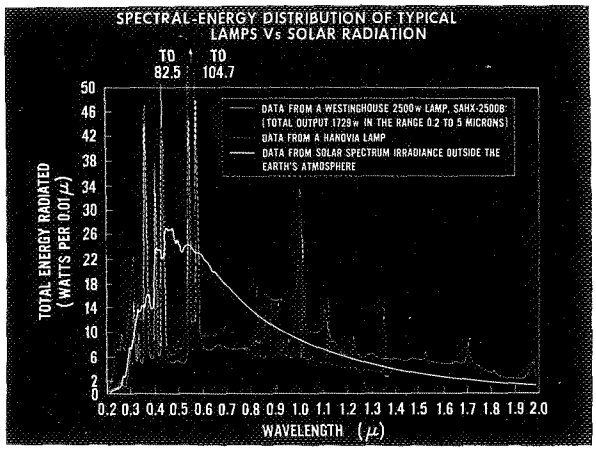

FIGURE 2.—Spectral Distribution of Typical Hg-Xe Lamps vs. Solar Radiation.

range below 0.7 micron. The continua in the longer wavelength range are correspondingly lower. On the same graph is drawn the spectral energy distribution of solar radiation in outer space based on the well-known Johnson data. The solar radiation in outer space is very close to Planckian black body radiation at 6000°K. The various dips one observes in the curve are due to absorption in the reversing layer of the sun. The spectral mismatch between the solar radiation and the mercury-xenon lamp is most pronounced in the range 0.3 to 0.8 micron; but on the other hand in this same range there are the very strong emission lines of mercury. The energy in these emission lines is sufficiently great so that an absorbing surface which has a constant absorption coefficient over a wide range will presumably receive on the test floor a total energy equal to what it will receive in outer space. Before examining this statement any further it is worth while to look more closely at the data concerning mercury-xenon lamps available from other sources.

An independent set of data is available in a paper published by Mann and Dubey (Reference 1). The authors give the energy distribution for each 500A band. Minneapolis-Honeywell performed a series of tests on three Hanovia lamps of 2.5 kilowatt rating. A fifth set of data is available from a series of four tests on 2.5 kilowatt Westinghouse lamps, made also by Minneapolis-Honeywell. The information from all five sets of data have been normalized to the same total energy output and to 500A bands. These five sets of data along with the Johnson data are presented in Figure 3. A more complete discussion of these data and of the method of normalization which we adopted in presenting the data are given in Reference 2. The differences between data presented by different observers which we saw earlier in Figure 2 are even more pronounced here. There is a certain amount of agreement in that all five sets of data give relatively low value for the spectral radiation in the range 0.45 to 0.50 micron and relatively high value in the range 0.55 to 0.6 micron. The dip in the spectrum of the mercury-xenon lamp occurs precisely at the maximum of the solar radiation curve. In the infrared range beyond 1 micron all data are relatively closer but in the ultraviolet and the visible range, in the region where the solar radiation is the strongest, the differences between data of various observers are as high as 200 percent.

A comparative study of this type between data of different observers raises a question of major importance. In an age when techniques for intensity measurement have been developed to a high degree of precision, the information available on one of the strongest

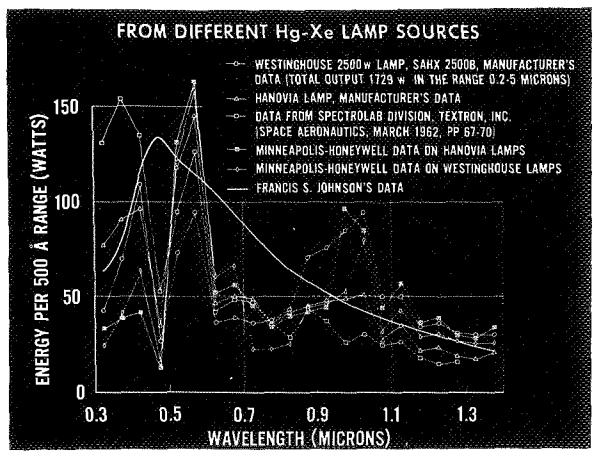

FIGURE 3.—Comparison of Spectral Distribution Data from Different Hg-Xe Lamp Sources

sources of radiant energy leaves a great deal to be desired. Is the mercury-xenon lamp one that changes its color every time one looks at it? Or are these differences due merely to experimental errors? This obviously is difficult to admit. Techniques of intensity measurement are not that imperfect to permit a 200 percent error. That prism spectrographs of relatively low resolving power were used in these studies may perhaps be a source of error. Also one would concede that in the ultraviolet range below 0.4 micron, the ratio of intensity of the mercury-xenon lamp to that of the standard of comparison, the tungsten filament lamp, varies from 50 at 6000A to 5000 at 3500A and at the peaks of the mercury lines. This large ratio puts a heavy strain on the linearity of response of the amplifier electronics. That different observers averaged their results over widely varying wavelength ranges also renders difficult a meaningful comparison between their data.

On the other hand for those who are going to use these lamps for solar simulation, a reliable set of data on the spectral energy distribution is of the utmost importance. We want these lamps to simulate the total radiation of the sun. We want them to simulate also, within limits, the spectral energy distribution of the sun. The energy E absorbed by the surface on the test floor is an integral of the monochromatic radiant energy E_λ, the absorption coefficient a_λ, and the differential wavelength range.

$$E=\int_o^\infty E\lambda a\lambda d\lambda \qquad (1)$$

If the monochromatic absorption coefficient a_λ is constant throughout the spectral range, this factor can be taken outside the integral and spectral match is of no consequence. One would be interested solely in the total energy on the test floor being equal to the solar constant of 130 watts per square foot. However, no surface coating of spacecraft has an absorption coefficient independent of wavelength. Hence, we should attempt a certain degree of spectral match and should have accurate information on the spectral distribution.

RESULTS OF CURRENT INVESTIGATIONS

We attempted at Goddard Space Flight Center an accurate measurement of the spectral distribution of the mercury-xenon lamp. A high resolution grating spectrograph was used for this purpose. The experimental arrangement is shown in Figure 4. The wavelength resolution is about 0.4A. The standard of comparison was a tungsten ribbon lamp calibrated by the National Bureau of Standards. The same optical arrangement, distance of the source, width of the slit, condensing system, etc. were used for both the mercury-xenon lamp and the standard tungsten lamp. Since the signal due to the mercury-xenon lamp was considerably higher, neutral filters of known transmission coefficient were used to bring the signal within range for the recorder. At the peaks of the emission lines the filters reduced the intensity by a factor of 100, and at the continua by a factor of 10. The results have been tabulated from different series of measurements and are given in reference 2.

One or two salient points concerning our observations may be briefly summarized here. For a given lamp under identical operating conditions one can obtain reproducible results. Of the total radiant energy of 463 watts (adopting the same normalization procedure as previously) in the range 0.36 to 0.65 micron, 68 percent is concentrated in five short wave-

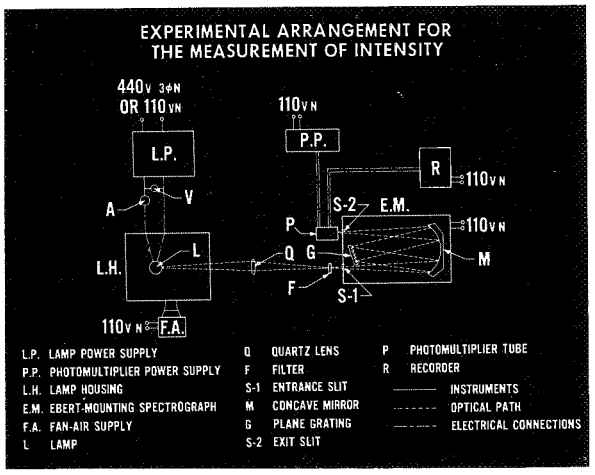

FIGURE 4.—Experimental Arrangement for the Measurement of Intensity

length ranges each of about 10A. These wavelength ranges correspond to the strong emission lines of mercury. The line profiles in these ranges are shown in Figure 5. Comparing the output with the solar energy, one observes that over most of this wavelength range, 3600 to 6500A, the energy from the mercury-xenon lamp is one-fifth that of the solar energy, and in the short wavelength ranges around the peaks of the emission lines the energy from the mercury-xenon lamp is 25 times greater than that of solar energy. This result is somewhat at variance from what had been presented in earlier data.

Another interesting feature about these strong emission lines is that most of them show a strong self-reversal effect. In a low density mercury arc operated at a pressure of about 1 to 10 mm of mercury, these strong lines have a half-width of 1/100th of an angstrom. In a high pressure arc, of pressure about 25 atmospheres, the lines broaden out to a half-width of 10 angstroms. The line profile is asymmetrical, and as is to be expected, the profile is intermediate between the totally asymmetric profile or Holtsmark profile of statistical broadening and the totally symmetric profile or Lorentz profile of collision broadening. The peak of the broadened line is a fraction of an angstrom to the red side of the low pressure unperturbed line. Another interesting feature about the line profile is that for all the strongest lines one observes a sharp dip of about two angstrom width just where the peak ought to be present. This also is readily explained as due to the self-absorption of the line emitted from the high-temperature plasma near the electrodes and absorbed by the relatively cooler low temperature mercury vapor between the electrodes and the quartz envelope of the bulb. But for this self-absorption, the energy at the peaks would have been many times greater.

Lamps were studied under widely different operating conditions, some with normal cooling and others with overcooling. Different series of runs were made under both sets of conditions. There is fairly good consistency between the signals of any one set of readings but comparing

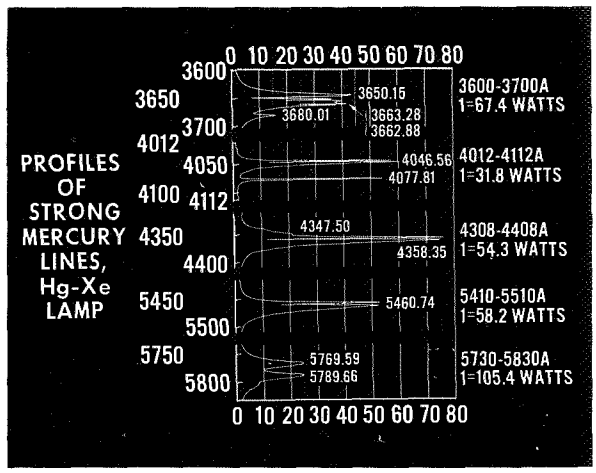

FIGURE 5.—Profiles of Strong Mercury Lines, Hg-Xe Lamp.

two sets of readings under different conditions one observes that there is clear evidence of the shifting of the energy from one spectral range to another. Thus in the 3000A range, for one set of readings the energy output for both the continua and the peaks is about one-half that of the other set of readings, while in the longer 6000A range the energy output is nearly double. Thus by changing the operating conditions a complete change in the spectral characteristics of the arc is produced. This poses a major problem for solar simulation and at the same time explains why there are such wide divergences between the results of various observers.

The same phenomenon has been observed also in a series of measurements made with a carbon arc. Two different instruments were used in the course of these studies, a double prism Leiss monochromator with both quartz and flint glass prisms, with three detectors, 1P28, lead sulfide and thermocouple, and a Perkin-Elmer single prism monochromator also with the three detectors. Every precaution was taken to ensure that the readings could be expressed in absolute units. Two tungsten ribbon lamps calibrated recently by the National Bureau of Standards were used as the standard of comparison. The intensity values for the different sources in the wavelength range 3000A to 23,000A are available in a series of tables. We do not intend to present these

tables here, partly because two later papers in this symposium will be dealing with the same topic more in detail (References 3 and 4).

Both the mercury-xenon arc and the carbon arc are being used for solar simulation. Neither gives a perfect spectral match; on the other hand, no laboratory source can be expected to give a perfect spectral match to the solar radiation. The continuum of the carbon arc is almost equal to that of the sun in the visible range, but considerably weaker in the ultraviolet. The carbon arc shows a large number of emission lines which are due to the rare earth elements which are embedded in the carbon rods. One major advantage of the mercury-xenon arc is that it can be operated for very long intervals of time without trouble and with fairly constant energy output. The carbon arc entails periodic shut-downs for changing the rods.

THEORETICAL DISCUSSION OF THE RESULTS

A point that requires closer examination is the shifting of the energy from one wavelength range to another for different operating conditions. This leads us to examine the mechanism of spectral radiation in a high energy source like the mercury-xenon arc and the carbon arc as compared to that of the sun.

A solar spectrum is very nearly that of a black body at 6000°K, a smooth Planckian curve with a few dips due to the solar atmosphere. The black body radiation density at a given temperature and wavelength range is given by the average energy per degree of freedom for that temperature multiplied by the total number of degrees of freedom in that wavelength range.

$$\psi_\lambda d\lambda = \frac{8\pi}{\lambda 4}\, d\lambda\, \frac{hc/\lambda}{e^{hc/\lambda kT}-1} \qquad (2)$$

This simple formula is strictly applicable when the atoms of the radiating body are very closely packed together as happens in solids and liquids and there are no discrete energy levels as in gaseous atoms. The continuous spectrum of the Planckian theory is one extreme case of the emission of radiant energy.

The other extreme case is the spectrum of a gaseous discharge at low pressures, 1 mm of Hg or lower. Each excited atom is at relatively large distance from all other atoms and ions; the valence electrons are in the central force field of the respective atoms. The half-width of an energy level on the frequency scale is according to the Heisenberg principle the reciprocal of the half-life of the atom at the given level. Thus, for a half-life of 10^{-8} sec, the half-width of an emission line at 5000A is about one milliangstrom. The spectrum in this case consists of sharp emission lines of which the energy is predictable from discharge conditions. The energy in the continuum is practically zero.

The ideal source for solar simulation, a black body at 6000°K is impossible to achieve in a laboratory. The melting point of the most refractory metal, tungsten, is about 3400° and the Wein displacement law shows that the peak of the black body spectrum at this temperature is 8500A. The energy in the visible range is far too little. On the other hand the strong emission lines of most elements lie in the visible range. Hence, one would inquire whether it is possible to broaden the emission lines, increase their number, and to coalesce them to form a continuum.

Increasing the pressure and temperature of a gaseous discharge produces a broadening of the spectral lines. The causes are relatively simple. The doppler broadening is due to the velocity of the atoms in the line of sight. The collision broadening is due to interruptions in the wave train. Both these causes give a symmetric profile. The strong electric fields due to the ions in the plasma cause a more significant effect; the energy levels and hence also the lines are broadened and shifted, the shift being for most of the lines toward the red and by a fraction of an angstrom. The line profile is highly assymmetric. Raising the temperature also increases the relative population of the higher energy levels, as shown by the Boltzman equation or the Saha ionization equation. Thus many of the lines which are practically absent in a low temperature discharge, the higher members of the Rydberg-

Ritz series, appear in a high temperature discharge. These large number of lines, all broadened and coalescing into each other, make a major contribution to the continuum.

Another contributing factor may be readily seen from a study of any of the series in the hydrogen spectrum. In a discharge which brings out strongly the higher members of the Balmer Series, one observes also a strong Balmer continuum. It is due to the transitions of electrons from positive energy states, the parabolic orbits, to the state of principal quantum number two. In a complex spectrum like that of mercury or xenon there are many more series than in hydrogen, each obeying the Rydberg-Ritz combination principle. Each of these shows a strong continuum at high temperatures. These continua, like the discrete spectral lines, are also in the visible range of the spectrum.

A third contribution to the continuum comes from the wings of the strong resonance lines. The peaks of these lines stand well above the continuum. The lines have half-widths of 10 to 20 angstroms. The asymmetric profile is sufficient proof that the statistical approximation of the Holtzmark theory modified by the Lorentz collision theory is applicable. The spectral lines according to this theory have a

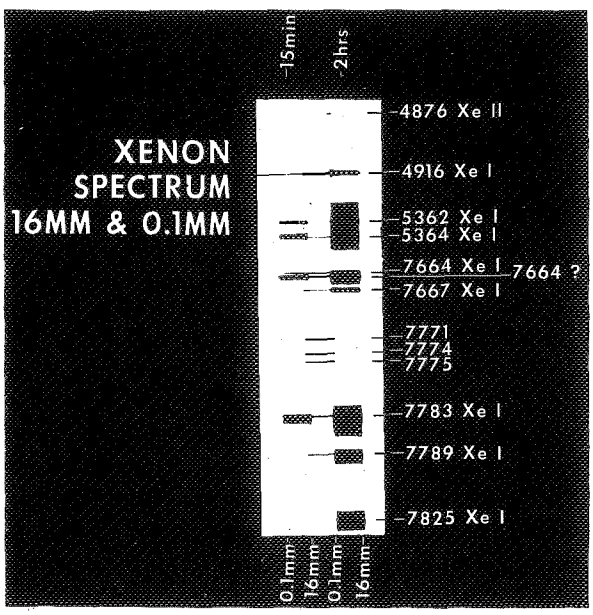

FIGURE 6.—Xenon Spectrum, 16mm and 0.1mm.

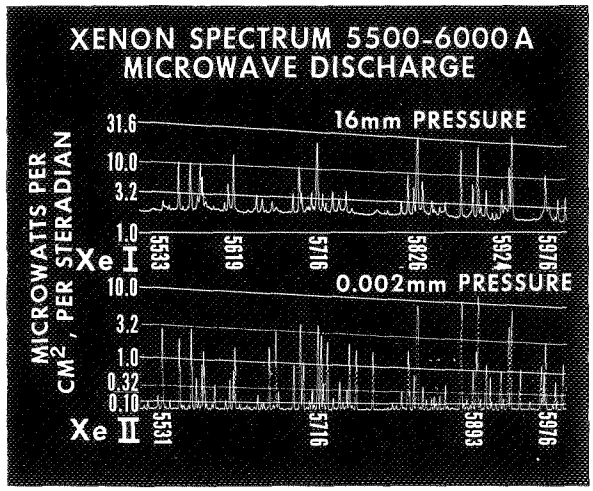

FIGURE 7.—Xenon Spectrum 5500–6000A, Microwave Discharge.

narrow high intensity peak and wide low intensity wings on either side.

Figures 6 and 7 serve to illustrate the effects described in this section. They show how spectral lines change with the pressure of the gaseous discharge. The spectrum on which these studies are based is that of xenon. In Figure 6 are shown the photographs of selected small spectral ranges, taken with a grating instrument of dispersion 0.6A per mm of plate. By increasing the pressure certain lines disappear, while others are enhanced and broadened, and a continuum begins to appear in certain regions. In Figure 7 is shown a spectrophotometric chart of the xenon spectrum over a 500A range for two pressure conditions. A more complete discussion of these phenomena is given in Reference 5.

We conclude that the continuum in a high pressure discharge depends on a large variety of factors. Among the more significant parameters are partial pressures of the gases and vapours in the arc, the temperatures of the plasma and the reversing layer, the voltage and current supplied to the arc, the ion density, the air flow around the arc. Each of these affects the relative intensities and half-widths of the lines and the Rydberg-Ritz continua.

In any facility for solar simulation we attempt a compromise between spectral match and other factors such as collimation, uniformity

of energy input over the test floor, size of the test floor, constant output over long intervals of time and overall cost of the facility. That the energy integrated over wide spectral ranges is close to that of solar radiation will be adequate for most cases of solar simulation. But it is of the utmost importance for tests on thermal balance that both the total energy and the spectral distribution incident on the test floor be accurately known.

EXPERIENCE IN THERMAL-VACUUM TESTING EARTH SATELLITES AT GODDARD SPACE FLIGHT CENTER [1]

A. R. TIMMINS AND K. L. ROSETTE
Goddard Space Flight Center

The philosophy used for conducting thermal-vacuum tests of unmanned earth satellites is presented. The application of the philosophy is examined through the results of the thermal-vacuum tests of three unmanned spacecraft. These results are summarized and discussed with respect to prototype and flight unit spacecraft, hot and cold environments, and kinds and frequency of failures. Brief commentaries on the space performance of the spacecraft are included.

INTRODUCTION

High system reliability is a prime requirement for an effective space program. This requirement is underscored by the high cost of the launch vehicles and spacecraft. Early estimates indicate that the average cost *per pound* of material in orbit results in an investment of about $67,000 (Reference 1). Furthermore since launch opportunity for certain space studies is dependent on interplanetary relations, success on the first launch attempt is necessary in order to effect timely acquisition of needed space data. Thus, assurance of success must be enhanced by every possible means. One of the most effective techniques for enhancing the reliability of our space systems has been the application of laboratory tests that simulate, insofar as practical, the many environmental conditions actually encountered by the spacecraft. Environmental tests must be applied in a well-defined test program that gives proper attention to the test levels, test duration, sequence of application, and appropriate evaluation of results. The specifications for such tests involve consideration of ground handling, launch, injection, and orbital environs.

At the start of the space program, evaluation experience with space hardware was limited to that obtained from research sounding rockets, weapons systems, and missile testing. While this experience provided a foundation for environmental specifications covering ground handling and launch, little foundation was available for the orbital space environs. Facility limitations prevented duplication of the effects of the more exotic space environs (such as micrometeorites and energetic particles) on a complete satellite. These environments were more properly evaluated on a material or subsystem basis. For the complete spacecraft, thermal-vacuum tests were used to evaluate the performance under simulated space conditions. These tests gave information on the performance at expected orbital temperature extremes, on the adequacy of the thermal design, and on the failure rate versus time.

A number of scientific earth satellites have been tested and launched by the Goddard Space Flight Center. A review of the specifications, laboratory test results, and orbital performance of the spacecraft should be profitable in determining the adequacy of some aspects of the specifications used. This report

[1] Presented at the Institute of Environmental Sciences, Los Angeles, April 17, 1963; to be published in Proceedings.

will be restricted to the thermal-vacuum test experience and analysis related to three scientific satellite projects. The choice of parameters, the philosophy used, and the experience gained by the Test and Evaluation Division of the Goddard Space Flight Center will be discussed.

TEST PHILOSOPHY

The test philosophy (Reference 2) employed has been the use of environmental tests to gain information from which the suitability of a spacecraft for flight can be assessed. To this end, the systems test program for a satellite has six goals:

1. Verification that novel or unproven designs meet performance requirements and have a satisfactory life expectancy.
2. Verification that particular samples of previously employed hardware are suitable in a new application.
3. Elimination of defects in design, material, or workmanship (i.e., finding the *weak links* in the chain).
4. Discovery of unexpected interactions between subassemblies when the system is exposed to environmental stress.
5. Training of personnel to be responsible for the satellite at the launching site and for the data reduction and analysis.
6. Generation of information that will serve as a guide in making new designs and in assessing their reliability.

The degree to which these goals may be attained is strongly conditioned by the fact that, in typical programs, only one prototype and two flight spacecraft are available for test.

In attempting to reach these goals, despite limitations, we must (a) formulate a model of the failure pattern that we might expect to encounter, and (b) base the test philosophy on this concept. Our somewhat limited experience suggests that satellite failures fall into four categories:

1. Early failures cased by a major design weakness.
2. Early failures resulting from defects in material or workmanship.
3. Random failures whose frequency of occurrence is a function of design and quality control.
4. Wear-out failures.

Figure 1 illustrates this model pattern. If the failure pattern is applicable, progressive improvement in the dependability of the system should occur during the test program. As the *weak links* in the subsystem chain are found and strengthened, the curve should approach the random failure rate level. The length of time necessary to reach this level is vital and elusive. Consistent with locating weaknesses is the practice of providing a margin of safety over expected extremes of operation. To this point, prototype spacecraft are subjected to more severe environmental stress than flight models. In the thermal-vacuum tests, prototype model spacecraft are subjected to temperature extremes 10°C in excess of those predicted for orbit. Flight models are subjected to thermal-vacuum tests at predicted orbital temperature extremes.

For this philosophy to be workable, an extensive program of parts qualification on the basis of tests or previous successful utilization must be presupposed. Similarly, subassembly testing under environments more severe than those expected in actual use is a near necessity. (It should be noted that the difficulty of conducting adequate subassembly tests of complicated new devices on the time scale of the typical satellite development program is frequently overwhelming. If not accomplished, however

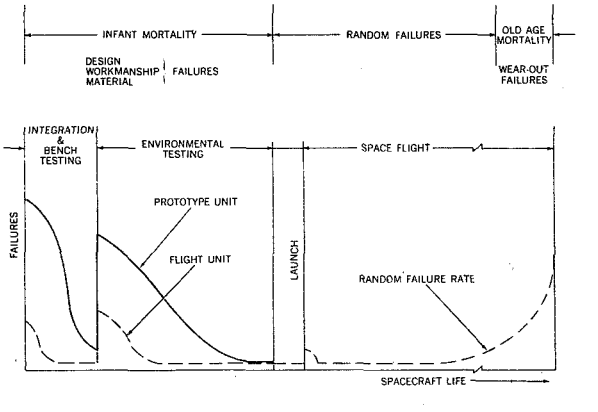

FIGURE 1.—Failure pattern.

a risk is incurred that the system test may be unnecessarily interrupted or extended by the subassembly failure.)

SPACECRAFT TESTED

The data developed in this report are based on the experience gained in testing three spacecraft: (1) Explorer X (1961 κ), the Interplanetary Probe (one prototype and three flight models); (2) Explorer XII (1961 $\upsilon 1$), the Energetic Particles Satellite (one prototype and two flight units); and (3) Ariel I (1962 $\sigma 1$), the International Ionosphere Satellite (one prototype and two flight units). Figures 2, 3, and 4 show these spacecraft.

DESCRIPTION OF TESTS CONDUCTED

The tests conducted were accomplished in thermal-vacuum chambers having a vacuum capability of 1×10^{-5} mm Hg or better. The thermal control in most cases was accomplished by control of the chamber walls. Additional thermal gradient tests were conducted with tungsten lamps used to control local temperatures of a sector of the spacecraft while the chamber was used to control the temperature of other portions of the spacecraft (at a different temperature). These tests were conducted to determine whether any weaknesses existed when high thermal gradients existed within the spacecraft, corresponding to a particular orientation of the spacecraft with respect to the sun.

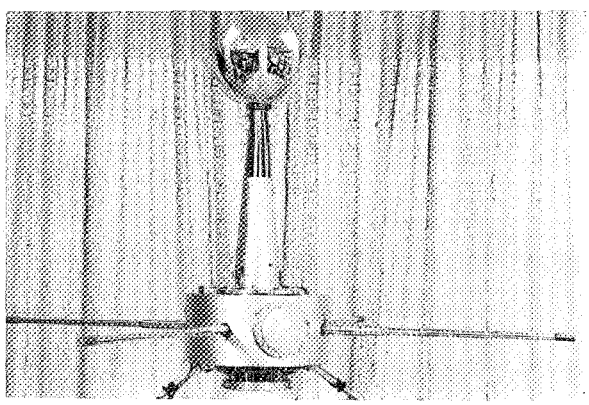

FIGURE 2.—Explorer X, the Interplanetary Probe.

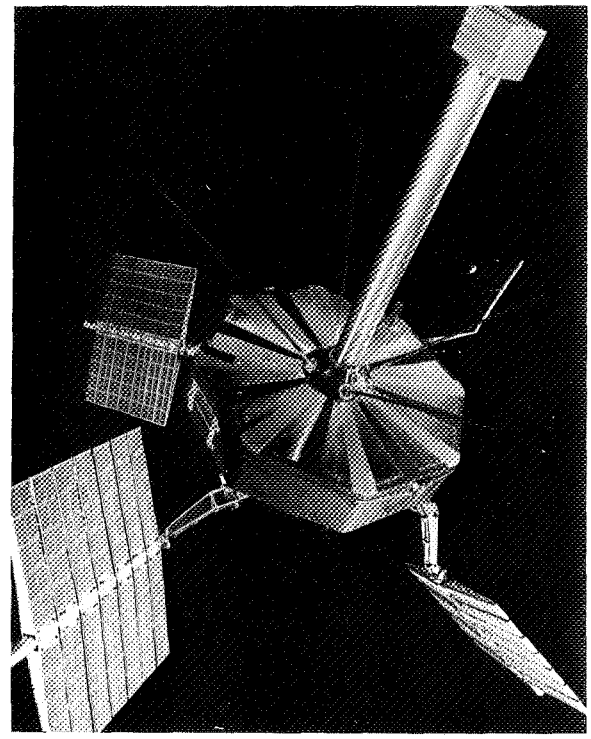

FIGURE 3.—Explorer XII, the Energetic Particles Satellite.

The temperature capabilities of the chambers were −65°C to +100°C. Solar simulation was not available for any of the tests reported herein. The three types of tests used were: cold soak test, hot soak test, and temperature gradient test. Table 1 shows the scheduled test duration for each spacecraft.

TABLE 1.—*Scheduled Test Times (days)*

Spacecraft	Hot	Cold	Gradient	Total
Explorer X:				
Prototype	[1] 1. 25	[1] 1. 25		2. 5
Flight units	1	1		2
Explorer XII:				
Prototype	2	2	4	8
Flight units		1	4	5
Ariel 1:				
Prototype	3	2	2	7
Flight units	3	2		5

[1] Half of battery life.

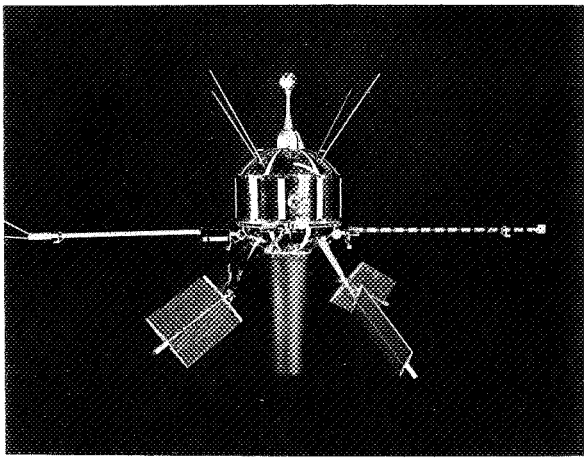

FIGURE 4.—Ariel I, the International Ionosphere Satellite.

LABORATORY TEST RESULTS

The data presented in this report have been arranged to examine essentially two aspects of failures encountered in the conduct of the thermal-vacuum tests: (1) effects of high versus low temperature, and (2) the failure rate for both the high and low temperature levels. A word of explanation is necessary on what constituted a failure. A severe criterion was used—that is, any malfunction that caused substandard performance or loss of data was classed as a failure. This, of course, is not synonymous with satellite, or even experiment, failure.

The data are organized in accordance with the following criteria. Examination of the test results must be made with these rules in mind:

1. Time to failure is satellite (or subsystem) operating time under vacuum (conditioning time under vacuum was not counted).
2. Time to failure for any subsystem that did not have a continuous duty cycle was the operating time of that subsystem.
3. Time to failure for any hot test does not include any time under the cold test environment and, similarly, time to failure for any cold test does not include any hot test time.
4. Time to failure for any subsystem that was retested was the total operating time of the subsystem *except* for the case where the same component failed.
5. Failures that occurred during chamber evacuation on retests were counted as early failures. (For example, if a corona type of failure occurred on a retest of the spacecraft, the time to failure did not include the duration of the original test.)
6. The operating time of the spacecraft in the thermal gradient type of test is included in the failure rate curves. The failures are identified as hot or cold, depending on conditions at time of failure.

Table 2 summarizes the failures for both prototype and flight unit spacecraft with respect to the thermal environment. Table 3 presents the same information, but segregated according to the type of failure. Table 4 gives additional detail on failures that occurred after 4 days of testing. Table 5 lists the temperature levels used for the testing of the three spacecraft.

Figure 5 depicts failures versus time information. Failures of prototype and flight spacecraft tests are presented separately and, in each case, show the influence of the hot and cold environments.

TABLE 2.—*Summary of Failures in Thermal-Vacuum Tests*

Spacecraft	Type of test				Totals [1]
	Hot		Cold		
Prototype:					
Explorer X	4		0		
Explorer XII	6	24	4	15	39
Ariel I	14		11		
Flight units:					
Explorer X	2		6		
Explorer XII	0	5	11	28	33
Ariel I	3		11		
Totals [1]	29		43		72

[1] Totals do not include setup, corona, or operator failures.

TABLE 3.—*Summary of Types of Failures* [1]

Type system	Test	Mechanical [2]	Component	Design [3]	Thermal [4]	Totals
Prototype	Cold	2	7	3	3	15
	Hot	6	9	2	7	24
Flight	Cold	4	10	9	5	28
	Hot	0	1	2	2	5
Total	Cold	6	17	12	8	43
	Hot	6	10	4	9	29
Grand total		12	27	16	17	72

[1] Does not include setup, corona, or operator failures.
[2] Mechanical failures include cold solder joints, connectors, sheared screws, and broken leads.
[3] Design failures include underrated components and unbalanced circuits.
[4] Thermal failures include inadequate heat sinks, poor thermal contacts, and temperature sensitivity.

TABLE 4.—*Table of Long-Term* [1] *Failures*

Spacecraft	Item	Exposure time (days) [2]	Kind of failure [3]	Defect
Ariel I, Flight Unit	Solar array protective circuit	C–4	R	Circuit would not operate
Ariel I, Prototype	Electron density	C–6	R	Temperature-sensitive
	Solar array shunt regulator	C–7	N	1 Mc sine wave present when circuit operating
	Optical aspect	C–9	N	Voltage spikes
	Tape recorder	C–11	R	Tape recorder did not play back on command
	Tape recorder	H–5	R	Excessive current for tape recorder
	Recycle timer	H–6	N	Spacecraft did not turn on after under voltage test

[1] Long term defined as 4 days or greater.
[2] C=cold test; H=hot test.
[3] Kind of failure: N=new failure; R=repeat failure.

DISCUSSION

High vs. Low Temperature Failures

The terms *high* and *low* temperatures have been used in a general sense. Table 5 lists the actual temperatures used in testing the spacecraft. It shows that *high* temperatures ranged from 20° to 55°C while *low* temperatures ranged from 0°C to −15°C. Table 2 shows that the high temperature level produced more failures on the prototype spacecraft than the low temperatures. With these failures corrected

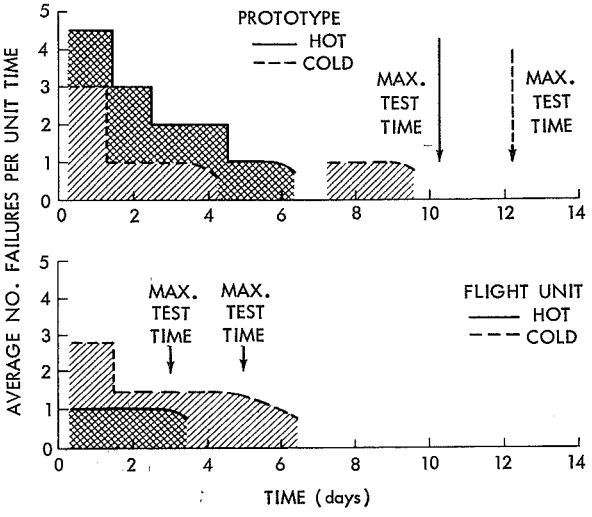

FIGURE 5.—Summary of spacecraft failures vs. Time in thermal vacuum tests.

(and with a slightly lower temperature level used), the total number of high temperature failures on all the flight unit spacecraft was reduced to 5. This was expected, and is consistent with the philosophy of testing used.

The data on low temperature tests show more failures on flight spacecraft than on prototype spacecraft. These results were *not* expected. Examination of the failures results indicates that approximately 40 percent of the failures were repeat failures—that is, the same item had caused a failure before. This trend indicates that prototype failures should be examined carefully for other potential failures and that a repaired item should be completely requalified before reentering the system. Another 40 percent, which could not be related to previous failures, were evident in less than

TABLE 5.—*Summary of Thermal-Vacuum Test Parameters for Three Spacecraft*

Spacecraft	Temperature (°C)		Solar aspect (°C)	
	High	Low		
Explorer X:				
Prototype	35° and [1] 43°	0° and [1] 25°	(This type of test did not apply.)	
Flight Units 1 and 2	20° and [1] 40°	0° and [1] 30°		
Explorer XII: [2]			45° Aspect	135° Aspect
Prototype	35°	−10°	+45°(1) −20°(2)	+35°(2) −20°(4)
Flight Units 1 and 2	(see 45° aspect)	−10°	+32°(3) −20°(2)	+35°(2) −10°(4)
Ariel I: [3]			30° Aspect	135° Aspect
Prototype:				
(1)	55°	−10°		
(2)	47°	−10°	+30°(4)	+10°(4)
(3)	42°	−15°		
Flight Units 1 and 2	37°	−8°	(This type of test was not conducted.)	

[1] Stabilized temperature of bias sphere.
[2] (1) Top cover; (2) transmitter; (3) battery; (4) magnetometer.
[3] (1) Test no. 1; (2) test no. 2; (3) test no. 3; (4) UCL Electronics Stack 2.

24 hours of testing. The remaining 20 percent were new type failures and appeared after 2 to 9 days of exposure to the cold environment.

Types of Failures

Table 3 summarizes the types of failures. Component (resistor, capacitor, transistor, etc.) failures account for 35 percent of the total. Mechanical, design, and thermal categories are the other major types of failures. This table gives further detail on the excessive number of cold failures on flight spacecraft; it shows that 65 percent of these failures were in the component and design categories.

Long-Term Failures

During laboratory tests, one prototype spacecraft had several problem areas that required retests of the entire spacecraft. The test time amounted to 12 days at low remperatures and 10 days at high temperatures. This gave an opportunity to disclose failures that might occur if testing time was increased beyond the present 8 to 10 days for prototype spacecraft (7 at high temperature, and 3 days at low tenperature).

Table 4 shows that 55 percent of the long-term failures were repeat failures—that is, the same item had shown trouble previously in the test. The results verify the need for full-time testing after repair of an item. There is always a temptation to shorten the time for a retest, but this temptation should be resisted.

The failures listed as new failures in Table 4 must be examined carefully. These are data that may be helpful in affirming or revising the test duration specified for thermal-vacuum tests of prototype and flight spacecraft. Two of the failures, one at 7 days and one at 9 days. occurred during a cold test on a prototype spacecraft. Although listed as failures, there was no malfunction or loss of data; in each case, it was interference in the signal output. Another failure, after 6 days of operating time, occurred in a hot test on a prototype spacecraft. This failure was important, since it would have resulted in a satellite failure at the time the recycle timer was required to work. (It should be noted, however, that the recycle timer does not operate continuously but only at times when the battery supply voltage decreases to a predetermined level. The cause for this failure could have been influenced more by the number of times the unit was actuated than by the time under vacuum.)

Most of the failures listed in Table 4 may be analyzed as to importance or effect on spacecraft performance. Such an analysis shows that no in-line subsystems are involved and that total spacecraft operation is not jeopardized. However, it is interesting to note that all of the reported long-term failures were from three models of spacecraft out of a total of 10 tested for the three projects. The test duration for the other spacecraft tested was 3 days or less, at the high or the low temperature level. It would appear that additional long-term testing of both prototype and flight unit spacecraft is needed to gain additional data on this subject.

FLIGHT PERFORMANCE

Brief commentaries on the flight performance of each of the three spacecraft are given below. The scientific findings and the detailed performance reports are covered in other publications.

The Interplanetary Probe (Explorer X) was launched on March 25, 1961. Its transmitters functioned for the expected life of the spacecraft (60 hours). One failure was encountered. Temperature measurements inside the sphere housing the rubidium vapor magnetometer showed a continuous rise for several hours after satellite injection. When the temperature rose above 55°C after 2 hours, the rubidium vapor magnetometer operation became intermittent. Postflight tests demonstrated that, during launch, out-gassing of the hot nose cone surface adjacent to the sphere caused deposition of a film on the sphere that greatly increased the absorptivity of the surface. This caused the temperature to be higher than predicted.

The Energetic Particles Satellite (Explorer XII) was launched from Cape Canaveral on August 15, 1961. Operation of the satellite ceased abruptly at 1:12 e.s.t. on December 6, 1961, after 112 days of operation. All experiments functioned perfectly during its orbital

life. The exact cause of the failure has not been determined.

The International Ionosphere Satellite (Ariel I) was launched from Cape Canaveral on April 26, 1962. The Lyman-alpha experiment failed on launch. Otherwise, operation of the spacecraft was perfect until July 12, 1962, at which time the system began to go into 18-hour periods of undervoltage. As of December 1962, Ariel I had a total equivlaent operating time of 127 days. The spacecraft was continuing to send good scientific data approximately one-third of the time. The intermittent operation was attributed to degradation of the solar array and other damage caused by the enhanced radiation belt that resulted from the high-altitude nuclear detonation which occurred on July 9, 1962.

FAILURE RATE—LABORATORY TEST AND FLIGHT

The model curve shown in Figure 1 indicates that the number of failures during laboratory tests should decrease with time until some random failure rate is reached. The curve also postulates different failure rates for prototype and flight unit spacecraft. It does not deal with the effect of temperature level on the failure rate.

It is of interest to see how the laboratory test data reported herein compare with the model curve. The data did not permit generation of a curve to predict the time at which a random failure rate is attained. However, the limited data were used to prepare Figure 5. This figure, although restricted to thermal-vacuum tests, can be examined with respect to the environmental testing part of the model curve. The difference in failure rate between the prototype and flight units for the high temperature test is in agreement with that postulated by the model curve. The low temperature test results (failure rate for prototype versus flight units) are not in agreement with those postulated from the model curve. Figure 5 also presents information on the effect of temperature level on failure rate. The figure shows both the high and low temperature tests starting simultaneously at zero time. This is not possible, of course, but is presented in this manner to have some basis of comparability for the three satellites (the satellites had different test duration, different amounts of retest, etc.). The results, especially for the prototype spacecraft, indicate that the two temperature extremes should be considered as separate failure rate curves.

The curves in Figure 5 may be useful in judging the performance of a spacecraft during thermal-vacuum testing. The curves are considered a best estimate of failures versus time for a typical satellite. Performance better than the levels shown would be encouraging for predicting successful space performance. Performance worse than the levels shown would be reason for concern and for extending test time.

The flight performance of the three spacecraft has, in general, been quite satisfactory. Failures in two of the spacecraft (Explorer X and Ariel I) were of a type not covered in the thermal-vacuum tests. The Explorer XII failure, after approximately 4 months, might have been detected if longer term and more severe thermal-vacuum tests had been conducted.

The laboratory and flight data presented are insufficient to form any firm test times. However, some useful estimates can be made, such as:

Recommended time to test *prototype* spacecraft: (hot) 6 days; (cold) 4 days.

Recommended time to test *flight unit* spacecraft: (hot) 4 days; (cold) 4 days.

The above estimates discount the failures shown at 7 to 9 days on prototype spacecraft. This point requires clarification by additional data. The above estimates compare, respectively, with presently used test durations of 7, 3, 3, and 2 days.

LIMITATIONS OF DATA

An important point with respect to interpreting the failure data is the lack of complete subassembly testing and the use of unproved components. These programs were often forced by firm launch dates to use partially proven components and/or subsystems. Principal difficulties in trying to use the laboratory failure

rate data from system tests to predict long-term satellite orbital performance is that conventional statistical methods require tests on many samples in order that distribution curves may be generated and used in establishing probability levels. At present, there are insufficient performance data and hence no satisfactory method for determining conclusive probability figures.

The data reported herein do not justify, at the present time, the use of an exponential decrease in failure rate as a basis for mathematically determining a reliability figure with statistical confidence. Cooperative effort now being applied throughout the space industry will, in time, establish conclusive data on mean time between failures for components operating in the space environment. These data, coupled with failure data from the system tests, will permit more accurate prediction of the probability of the spacecraft's successful performance for its specified design life.

CONCLUSIONS

The data presented are not sufficient to indicate more than a trend, which may be useful in establishing test parameters and time durations for the conduct of thermal-vacuum testing of earth satellites. Also, these data do not include any experience in which solar simulation tests were conducted. With these limitations recognized, the following points are offered.

1. The philosophy and test programs carried out on three earth satellites have been helpful in attaining generally successful performance in space.
2. The cause of the premature failure (3 to 4 months operation instead of 1 year) of one spacecraft is not fully known.
3. Although the data reported show some similarity to a model exponential decrease in failure rate with time under thermal-vacuum test, the results are neither consistent nor extensive enough to justify using an exponential curve as a basis for computing performance probability.
4. Susceptibility of spacecraft to failure from high versus low temperature environments varies between spacecraft, but experience to date indicates that additional time should be considered for the low temperature environmental phase of the test.
5. Duration of prototype thermal-vacuum tests should be extended to at least 10 days (operating time); 6 days at the maximum temperature level and 4 days at the minimum temperature level are recommended.
6. Duration of flight unit thermal-vacuum tests should be extended to at least 8 days; 4 days at the maximum temperature level and 4 days at the minimum temperature are recommended.
7. The $\pm 10°C$ margin used for prototype spacecraft testing should be continued.

REFERENCES

1. NEW, J. C., "Scientific Satellites and the Space Environment," NASA Technical Note D–1340, June 1962.
2. BOECKEL, J. H., "The Purposes of Environmental Testing for Scientific Satellites," NASA Technical Note D–1900, 1963. Also published internally as GSFC X–320–63–26, February 1963.

764–173 O—65——52

Page intentionally left blank

VII. TRACKING SYSTEMS

Page intentionally left blank

MINITRACK CALIBRATION SYSTEM

J. H. BERBERT, J. D. OOSTERHOUT, P. D. ENGELS, AND E. J. HABIB
Goddard Space Flight Center

The calibration cameras and associated equipment employed in the airplane calibrations of the Minitrack satellite tracking stations are described. The methods for dealing with the various optical and electrical system errors and the results obtained with this system over the past five years are also given.

The Minitrack optical calibration system was developed to provide highly accurate reference angular positions for calibrating the worldwide network of Minitrack satellite tracking stations. These stations are radio interferometers with East-West and North-South baselines and a design accuracy of 20 sec of arc. To fully realize the Minitrack capability, the optical calibration system was designed to have an order of magnitude higher accuracy, or 2 sec of arc. This report describes the optical calibration system including the equipment, the data reduction, and the results.

CALIBRATION PROCEDURE

A high-flying aircraft is flown through the Minitrack antenna beams, simulating a satellite radiating on a 108.0 and/or 136.5-Mc tracking frequency and simultaneously flashing a light located at the center of the radiating antenna, in a coded time sequence (Fig. 1).

The Minitrack system tracks the radio beacon vs. time, and the optical system records the time-coded sequence of flashing-light images on a photographic plate against a star background. The angular coordinates of the light flashes are determined from the known star co-ordinates and are the same as the radio source co-ordinates since the light is coincident with the radio source. The optically determined source angular co-ordinates are then compared with the Minitrack-measured angular co-ordinates to determine the calibration corrections to the Minitrack system for different parts of the antenna beam pattern.

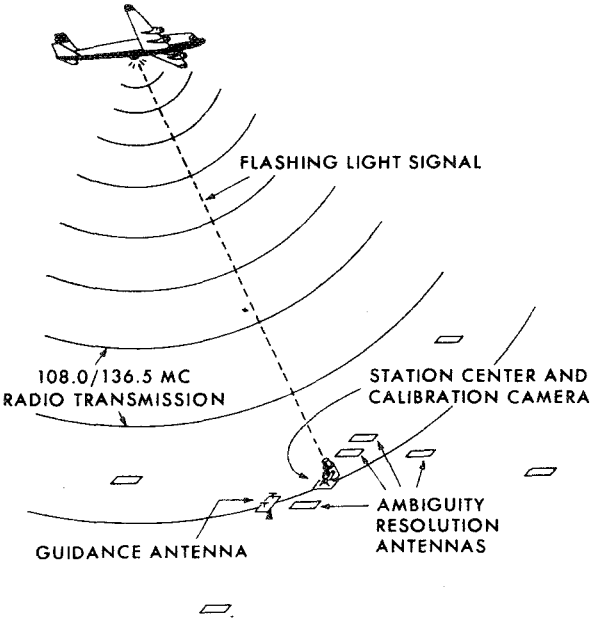

FIGURE 1.—Minitrack calibration method using an airplane radiating on the satellite tracking frequency and flashing a light.

CALIBRATION EQUIPMENT

Figure 2 indicates the flow of information and the kinds of equipment utilized in the calibration system. The ground equipment is housed in a shelter at the center of the Minitrack antenna layout. The roof of the shelter is slid back during a calibration allowing

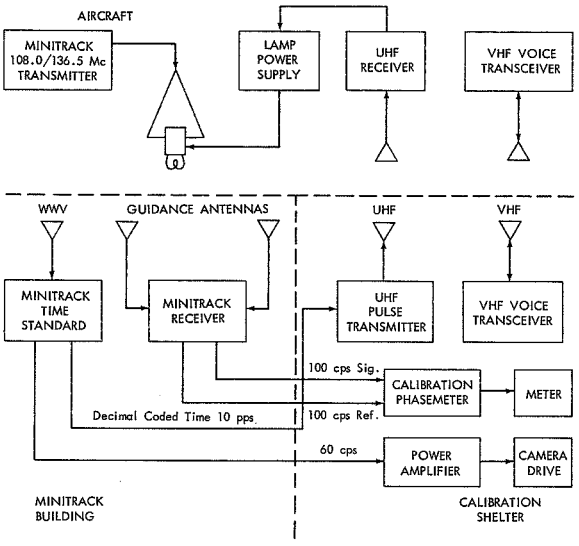

FIGURE 2.—Calibration system.

an unobstructed view down to about 30° above the horizon. Inside the shelter is a calibration camera on an equatorial mount. There is also a rack of equipment containing camera shutter and motor drive controls, a 60 cps power amplifier for energizing the camera drive motor, and a phasemeter for measuring and displaying phase information from an airplane guidance Minitrack baseline. A VHF radio link is used for voice communications between ground and aircraft, and a UHF transmitter sends the coded time pulses to a receiver in the aircraft in order to flash the light. Besides the UHF receiver, the aircraft carries a demodulator and lamp power supply for flashing the lamp. Each time-code pulse from the ground triggers a gas tube in the power supply causing a 20,000-v pulse to ionize the gas in the flash lamp. The flash lamp is connected across a 10-μf capacitor charged to 1000 v; when the gas in the lamp becomes ionized, it becomes a good conductor, discharging the capacitor and producing a brilliant flash of light lasting about 50 μsec. The total delay involved in transmitting and receiving each time-code pulse until the end of the light flash is less than 200 μsec, during which time the aircraft moves less than 1 sec of arc.

The flashing lamp is mounted at the center of the beacon radio antenna, which is a flat spiral antenna fed by both a 108.0-Mc transmitter and a 136.5-Mc transmitter through a diplexor so it can radiate on either frequency or both at the same time. The radio signals are received by the regular Minitrack antenna pairs and also by an additional pair, spaced one wavelength apart, and used for guiding the aircraft. The signals from the guidance antennas are received and processed like those from any of the other Minitrack interferometer pairs, deriving a pair of 100 cps signals whose phase difference corresponds to the original phase difference between the satellite signals at the two antennas. These 100 cps signals are sent to the phasemeter in the calibration shelter which is adjusted so the meter needle points to the center of the scale when the phase difference of the signals received at the two antennas is zero, i.e. when the aircraft lies in the plane which perpendicularly bisects the baseline joining the two antennas. If the aircraft is off to one side of this plane, the meter needle moves a proportionate distance off from center scale and the aircraft is requested to alter course to bring the needle back to center scale. The guidance antenna pair is mounted on a rotatable, tiltable baseline so the center scale meter reading conforms to any desired straight-line path in the sky depending on the orientation of the guidance baseline.

If a photograph is desired in a particular part of the Minitrack beam, both the camera and the perpendicular to the guidance antenna ground screens are pointed in the chosen direction. Then an observer on the ground directs the aircraft through that part of the sky by watching the phasemeter needle. This guidance method is particularly effective when the calibration must be obtained through clear patches in the clouds and the aircraft is hidden by clouds on its approach run. If the skies are perfectly clear, a skilled observer can guide the aircraft through the camera field of view by sighting along the barrel of the camera. Besides aiding in the aircraft guidance signal processing, the Minitrack system provides the calibration system with the decimal coded time pulses for flashing the light on the aircraft

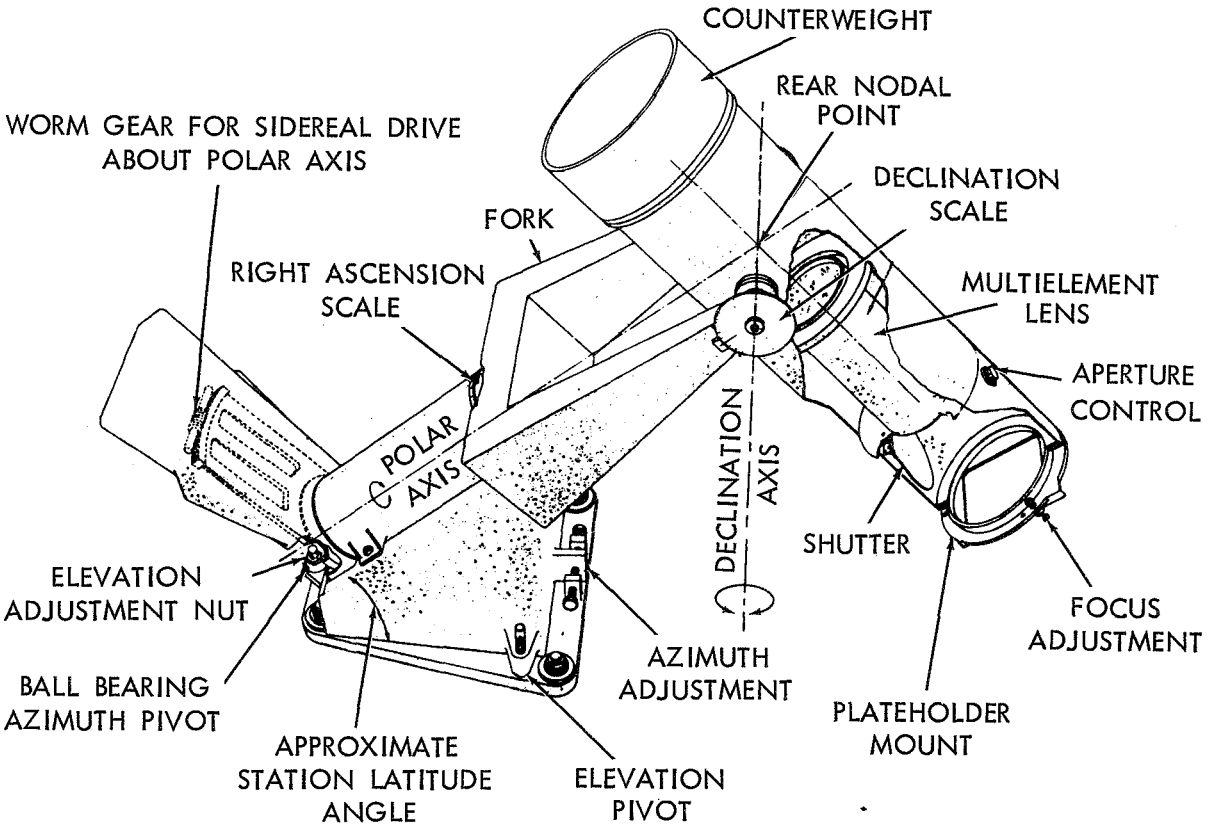

FIGURE 3.—Calibration camera.

and a 60 cps signal for the camera-drive power amplifier.

The calibration camera uses an 8-element, 40-in. focal length, 8-in.-aperture lens, which was originally built by the Perkin-Elmer Co. for the Air Force for obtaining high-quality aerial reconnaissance photographs.

For the calibration photographs a yellow filter is used with red-sensitive Type 103a-F, 8 x 10-in. glass spectroscopic plates to minimize chromatic aberration, and the aperture is closed down to 5 in. to produce the sharpest star images.

An equatorial mount was designed for this lens (Fig. 3), such that the right ascension axis intersects the declination axis at the rear nodal point of the lens. As the camera is pointed in various directions within the antenna beam, the rear nodal point remains stationary. This nodal point is also located at the station center, i.e. at the midpoint of the East-West and North-South baselines and at the height of the antenna ground screens. Thus, both the optical and the radio angular position measurements are referenced to the same point on the ground, avoiding the need for parallax corrections.

The camera is driven at a sidereal rate about its polar axis to track the stars. The axes are aligned with the adjusting screws shown in Figure 3, so that a 30-min exposure, with sidereal drive on, produces no detectable residual trailing of the star images. Normally, the calibration exposures are limited to 1 min, which is long enough to register 11th magnitude stars and to allow the aircraft plenty of time to fly through the 11° x 14° field of view determined by the 8 x 10-in. plate size.

The Minitrack station crystal clock is stable to about 0.5 msec per day and is synchronized with station WWV once per day, giving the

time with an accuracy of about 1 msec when WWV propagation time corrections are included. This clock provides the coded time pulses for flashing the lamp on the aircraft. Since the time of each light flash is known to about 1 msec, there is no need for an accurately timed mechanical shutter on the camera. A simple hinged shutter controlled by a timer accurate to 1 sec is more than adequate. For the calibration exposure conditions outlined above, eighth and ninth magnitude stars provide the best star images for measurement purposes, having image diameters of only 70 to 90 μ.

DATA REDUCTION

The photographic plate reductions, wherein the flashing-light image and star positions on the plates are measured and used to determine the apparent right ascensions and declinations of all the flashing-light images, are performed by the very capable staff of the Physical Science Laboratory of the New Mexico State University. The plate-reduction procedures are described in a report by a representative of that laboratory.[1] The techniques were originally those recommended by Paul Herget of the University of Cincinnati Observatory at the beginning of the International Geophysical Year. Since then, the use of a larger and faster computer has permitted more complete automation of the data-reduction procedures so that much more data can be reduced in less time. The accuracy with which a star's co-ordinates can be determined in these plate reductions is better than 1 sec of arc. The accuracy with which the flashing-light image co-ordinates are determined is deteriorated slightly by scintillation and refraction. A refraction correction is necessary because the airplane is submerged within the atmosphere and rays from the flashing light do not undergo full atmospheric refraction as do the stars. The catalogued star positions are already corrected for refraction, so the uncorrected position of the light derived from the plate reduction would equal the corrected position of a star occulted by the light. This light position is corrected by increasing its elevation angle from the refraction-corrected, occulted star elevation angle to the elevation angle of the straight-line path to the airplane. Herget originally derived the optical refraction corrections to use in this case. More recently, Vonbun [2] derived an analytical solution which takes into account the height of the tracking station. His analysis shows that at the two highest Minitrack stations at Quito and Johannesburg the effect of station height changes the previous refraction correction by 4 sec of arc for a 30° zenith angle. Also, seasonal fluctuations in the atmosphere may introduce an error of 3 sec of arc for a 30° zenith angle.

The flashing-light image right ascensions and declinations are converted in the computer to direction cosines and then to expected Minitrack phase readings so they can be compared easily with the measured Minitrack phase readings. The measured Minitrack phase readings obtained at the times of the light flashes are read into the computer where they are modified by the following equations:

$$a_0 = a_r - K_c + (K_{s2} - K_{s1}) + \dot{a}_r(K_f - 0.010a) \quad (1)$$

where

a_0 = Modified Minitrack data corrected for principal calibration constant and for predictable system phase shifts.

a_r = Raw Minitrack data lumping together positional phase difference plus system phase difference.

K_c = Average system phase difference at calibration, including differential shifts in antennas, cables, and receivers.

K_{s1} = System shift at calibration due to receivers only.

K_{s2} = System shift at satellite pass due to receivers only.

$(K_{s2} - K_{s1})$ = Drift in K_c due to receivers.

[1] Emily W. Good, J. H. Berbert, and J. D. Oosterhout, *Phot. Sci. Eng.*, 6: 324 (1962).

[2] F. O. Vonbun, *Correction for Atmospheric Refraction at the NASA Minitrack Stations*, NASA Technical Note D-1448.

$K_c+(K_{s1}-K_{s1})$=System phase difference corrected for receiver drift.

a_r=Rate of change of a_r.

K_f=Small phase shift in narrow band post detection filter due to change in frequency of detected signal caused by time rate of change of phase when source moves.

0.010=Time in sec for one full period of 100 cps reference signal with which phase of 100 cps detected signal is compared.

a=Decimal phase reading—determines time error made due to finite time required to obtain a phase measurement.

A value for K_c is derived for every flashing-light image by subtracting the optically determined phase difference a_c from a_r, thus,

$$K_c=a_r-a_c.$$

Since the value of K_c is not always exactly the same for all the flashing lights in different parts of the antenna field, the average value is calculated and used in Eq. (1). A polynomial error function is fitted to the less important but still significant residual variations of K_c, as will be seen later in this report.

The effect of the atmosphere on the two radio paths from the source to the antennas is to increase the radio path lengths by an amount equal to the vacuum path lengths multiplied by the average index of refraction along the two paths, as experimentally verified.[3] Therefore, the modified phase-difference data, which is equal to the difference in the two radio path lengths, will be too large by the same factor. The appropriate correction is to divide the modified phase difference by this factor, i.e., by the average index of refraction between source and antennas.

[3] E. J. Habib, J. H. Berbert, and J. D. Oosterhout, *Two Path Refraction for Nonparallel Rays*, Project Vanguard Tracking and Guidance Branch Memorandum, 29 November 1956.

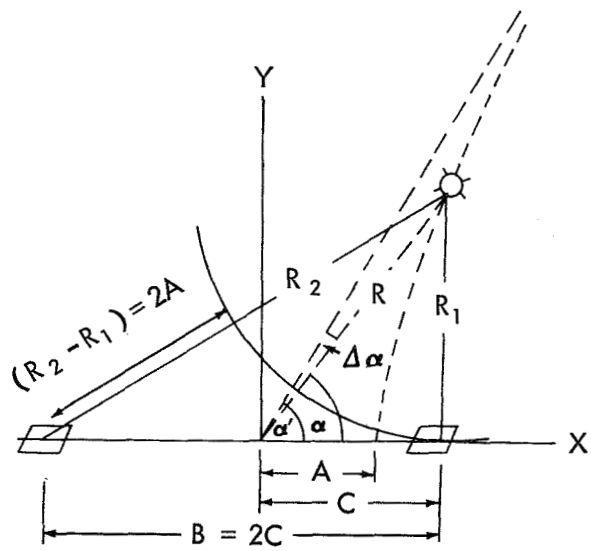

FIGURE 4.—Geometry of interferometer measurements.

Another correction to the modified Minitrack phase readings arises due to the geometry of interferometer measurements. A particular phase reading defines a hyperbolic surface on which the source must lie. For satellite passes the direction cosines of the source are obtained from the Minitrack modified phase data by means of the following equation (see Fig. 4).

$$\cos\alpha=a_0/n=A/C$$

where

α=angle of source with respect to Minitrack baseline.

a_0=modified Minitrack phase reading.

n=number of 108.0 or 136.5-Mc wave lengths in the baseline.

Actually, α is not the angle to the source on the hyperboloid defined by a_0, but it is the angle measured from the center of the baseline to the asymptotic cone of that hyperboloid. For satellite ranges the difference is insignificant. For the calibration aircraft flying at a height of 25,000 ft the difference is small but is corrected as follows:

The equation of the hyperbola

$$(x^2/A^2)-y^2/(C^2-A^2)=1.$$

In polar form

$$(R^2 \cos^2 \alpha)/A^2-(R^2 \sin^2 \alpha)/(C^2-A^2)=1.$$

Solving for $\cos \alpha$

$$\cos \alpha=\frac{A}{C}\left\{1+\left(\frac{C}{R}\right)^2\left[1-\left(\frac{A}{C}\right)^2\right]\right\}^{1/2}$$

$$=\cos \alpha' \left\{1+\left(\frac{C}{R}\right)^2 \sin^2 \alpha'\right\}^{1/2}.$$

Expanding

$$\cos \alpha=\cos\ (\alpha'-\Delta\alpha)\cong\cos \alpha'+\Delta\alpha \sin \alpha'$$

$$\cong\cos \alpha'[1+(C^2 \sin^2 \alpha')/2R^2].$$

Solving for $\Delta\alpha$

$$\Delta\alpha=(C^2/2R^2) \cos \alpha' \sin \alpha'=(C^2 \sin 2\alpha')/4R^2.$$

The hyperbola correction angle $\Delta\alpha$ is a maximum at α' equal to 45°, but even there it is less than 2 sec of arc for the longest Minitrack baseline when the range is greater than 40,000 ft.

Ideally, the modified Minitrack phase measurement, corrected for the atmosphere and the hyperbola error, would be the same as the optical phase measurement, corrected for optical refraction, as computed for the time of each light flash. In reality, these two measures differ slightly and the differences represent the residual calibration corrections, referred to earlier, which should be applied to the Minitrack data in that part of the beam in which they were obtained. To calibrate all of the Minitrack antenna beam, the normal procedure is to take 10 photographs spaced 10° apart, providing a trail of flashing-light data points every 10° in the Minitrack 10° by 100° beam. The modified Minitrack phase measurements obtained at the times of the flashes on all the calibration photographs are included in a least-squares polynomial fit to the optically measured and calculated phase measurements for each of the Minitrack baselines. The East-West baseline polynomial for a North-South fan beam has the form:

$$a_c=c_0+c_1a_0+c_2b_0+c_3a_0b_0+c_4a_0^2+c_5b_0^2+c_6b_0^3$$
$$+c_7 \sin'' a_0''+c_8 \cos'' a_0''.$$

There is a similar North-South baseline polynomial for b_c where

a_c, b_c=optical camera data to which modified Minitrack data is fitted.

a_0, b_0=Minitrack data modified by corrections for principal calibration constant, system errors, atmosphere, and hyperbola errors.

$c_0, \ldots c_8$=polynomial coefficients determined from calibration data.

"a_0," "b_0"=decimal parts of a_0, b_0 used with sine and cosine terms to correct for small periodic error due to cross talk between signals from either end of a baseline.

For Minitrack stations having an East-West fan beam the cubic term in the polynomials is changed to $c_6a_0^3$ instead of $c_6b_0^3$.

CALIBRATION RESULTS

The stability of the antenna-field correction functions from one calibration to the next, and hence the degree to which they contribute to the accuracy of the Minitrack system is discussed in another report.[4] However, the stability of the main calibration constant K_c from one calibration to the next is shown in Table I for both the 108 and the 136-Mc calibrations for the period September, 1957, to January, 1962. These results verify that, on the average, the error due to unmonitored drift in Kc in the individual Minitrack station calibration is about 15 sec of arc for the 108-Mc system and 11 sec of arc for the 136-Mc system. The residual uncorrected ionospheric effects for an average pass within the 30° zenith angle acceptance limits may deteriorate this accuracy to 30 sec of arc for 136 Mc, and perhaps 40 sec of arc for 108 Mc. The orbital accuracies now approach these figures very closely, being about 1 min of arc over a week's data. Normally a week's observations, consisting of 30 to 100 data messages from the whole network are used in a differential correction scheme to update the orbital elements from the previous

[4] J. H. Berbert and J. D. Oosterhout, *Calibration of Minitrack*, NASA Technical Note in preparation.

TABLE 1.—*Summary of Calibration Results Showing Stability of Principal Calibration Constant* K_o *Between Calibrations.*

Freq. (Mc)	Fan beam	No. of calibrations	Avg. time between calibrations (months)	Baseline	Avg. error due to drift between calibrations (sec of arc)
108.0	NS	86	5.4	EW	17
				NS	13
136.5	NS	35	4.3	EW	10
				NS	10
136.5	EW	19	4.3	EW	14
				NS	10

week. The updated orbital elements are used to compute the direction cosines at the time of each of the reported observations. The average difference between the measured and the calculated cosines is zero, and the standard deviation of these differences averages about 1 min of arc.

Besides providing the necessary calibration data, the optical calibration system is useful in diagnosing difficulties when they occur. Occasionally, parameter changes in the antennas or cables due to oxidation of connector contacts or to other effects will affect the phase measurements so gradually and by such a small amount that the first indication of trouble comes from the calibration data, where certain types of irregularities can be recognized as characteristic of certain types of trouble in the Minitrack system.

ACKNOWLEDGMENT

Mr. James Bradford of the U.S. Naval Research Laboratory and Mr. William Jennings of the National Aeronautics and Space Administration, as original members of the team which developed the Minitrack Optical Calibration System, contributed heavily in all areas to its success. Mr. Robert Chaimson, also of the U.S. Naval Research Laboratory, is responsible for the excellent mechanical design of the camera mount and drive system.

REAL-TIME AUTOMATIC DIGITAL OPTICAL TRACKER

W. J. CARRION
Goddard Space Flight Center

The exploration and the development of space technology have placed new demands on tracking. The real-time automatic digital optical tracker (radot) will provide research instrumentation for the development and field evaluation of future laser tracking and communications techniques; it will permit the tracking of passive satellites both day and night, will provide the large communications antennas with pointing information, and will increase the number of optical-tracking data points per orbit. Radot is a transportable optical tracker which will give real-time angle information to an accuracy of better than ± 5 seconds of arc, for early trajectory determination from the point of injection of a spacecraft into intermediate or final orbit, for midcourse corrections of lunar trajectories, or for evaluation of rocket performance.

In tracking satellites and spacecraft, whether for data acquisition or for trajectory information, the prime portion of the orbit is at zenith. The demands on the servodrive for the x–y antenna configuration at zenith are far less than for the conventional altazimuth mount. The altazimuth mount has an azimuth error at zenith of 90 degrees for the slightest collimation error of its optical axis (or RF axis, in the case of radio antennas); the x–y mount has the same problems as the altazimuth mount, but the error occurs at the horizon when the system has to track around the pole of the mount. The region of the horizon is less appealing to both optical and radio tracking and data acquisition; most optical tracking is done above an elevation angle of 15 degrees.

The x–y configuration is the same as an equatorial mount at zero latitude. The two axes are mounted orthogonally to one another; the x–x axis (north-south) is oriented parallel to the meridian and level to the local gravity of the station, and the y–y axis (east-west) is perpendicular to the x–x axis. This configuration allows full sky coverage from east-west, and only a small keyhole or lockup zone of approximately 10 degrees at the pole of the north-south axis. With both axes in level position, the telescope is pointing to zenith (see Fig. XIV–1) for zero readout.

The x–x axis is a box-constructed gimbal made of stainless steel fabricated and welded together. The weldment type of fabrication was chosen because it is most economical and

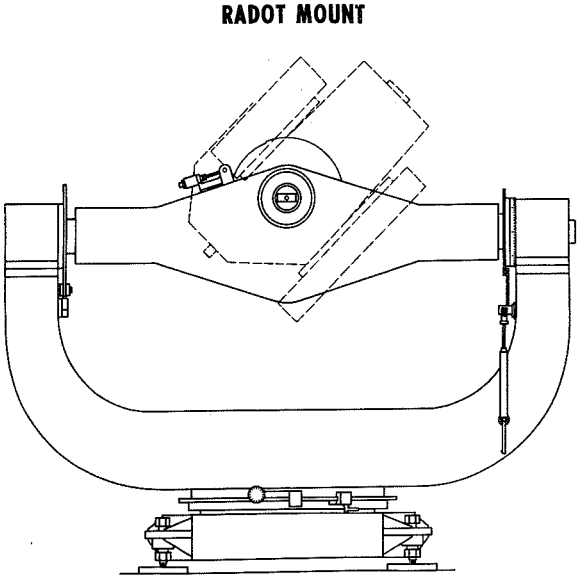

FIGURE XIV–1.—Radot mount.

has the advantage that section thickness can be controlled more easily than in a casting, which is subject to core shifting and uneven wall thicknesses. With good control of the section thickness, the symmetry of design can be maintained, thereby decreasing the effects of thermal expansion and deflection on the accuracy of the mount. The yoke, also a weldment, supports the gimbal in a horizontal plane. Both the yoke and the gimbal are mounted on a turntable so that the x–x axis can be precisely aligned to the meridian and levelled. The y–y axis is made orthogonal to the x–x during assembly by scraping and by using tapered shims in conjunction with autocollimating measuring techniques.

Of the factors affecting the accuracy of the mount, one of the hardest to control is temperature. A 10°F temperature gradient in one side of the gimbal or yoke of the mount will cause an error of 9.5 seconds of arc. In addition to ordinary environmental control, the cooling air for the image orthicon tube will be circulated through the gimbal ring; this filtered air will help stabilize the mount temperature, and at the same time will pressurize the bearing from the inside. A double-labyrinth frictionless seal is employed, and together with the air pressure will prevent dust from entering the bearing.

To maintain a high degree of accuracy and still be able to rotate the gimbal through 180 degrees, the double-row angular contact bearing was selected. Because the bearings must support both radial and reverse thrust loads, and because a high shaft-rotational accuracy with minimum deflection is required, the DB mounting has been used. The DB double-row angular contact bearing, designed with a fixed preload, offers the greatest resistance to misalignment of the shaft under combined load conditions. This rigid bearing configuration imposes severe tolerances on the shafts and bearing housings for both in-line bores and parallel bores. The tolerances will be carefully controlled in fabrication and assembly, where each part is checked by optical tooling techniques.

An analysis of the servodrive system shows the tracking accuracy to be 6.5 sec of arc at acceleration rates of 0.25 degrees per sec/per sec. The system will correct for any tracking error within 2 sec of arc of being on the target. (The 6.5 sec of arc error is not the real-time error of the system, because the computer corrects the tracking error for $\Delta x \Delta y$, keeping the shaft-angle readout accuracy within the ± 5 sec of arc.) Inland torque morros are used, eliminating gear problems. The gimbal will be driven by two motors, one on each end of the shaft, to keep torsional twist in the shaft at a minimum. The y axis has only one motor because calculations of torsional twist effect shows the error to be negligible. The system will track up to a velocity of 5 degrees per sec.

The telescope is a 12-inch Dahl-Kirkham system designed to give a blur circle of 0.003 inch which matches two TV scan lines. Figure XIV–2 shows the radot optical system, with the image orthicon mounted on top of the main tube and the laser transmitter on the bottom. The field-of-view is 1.4 degrees in the acquisition mode; the relay system converts the 28.6-inch prime focal length to 400 inches, giving a field-of-view of 0.1° degree in the autotrack mode. The narrow field improves the signal-to-noise ratio, especially for daylight and ninth magnitude at night. Good image quality is maintained because the error signal developed

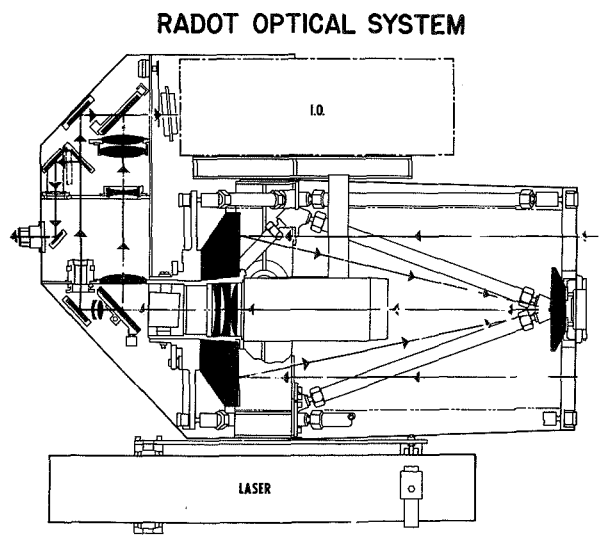

FIGURE XIV–2.—Radot optical system.

for the servodrive is referenced to the centroid of the image, and energy density is decreased by various optical aberrations such as coma, astigmatism, and field curvature.

The optics are mounted in Invar cells; the tube configuration is an A-frame parallelogram designed to maintain alignment of the optical elements regardless of deflection of the tube. The front section of the tube is made of Invar rods, but the A-frames supporting the primary mirror are made of steel. Although the deflections have been computed to be equal for both the primary and secondary mirror ends of the tube, final compensation can be made, if necessary, by changing the wall thickness of the supporting rods.

Figure XIV–3 is a block diagram of the system. The telescope focuses the image directly on the image orthicon; the IO chain is a modified Bendix BX7 chain using the Westinghouse WX4323 tube, sequential scan, 560 lines, and 15 frames per second. Two reticles are used; one reticle, viewed through a reflex viewer for

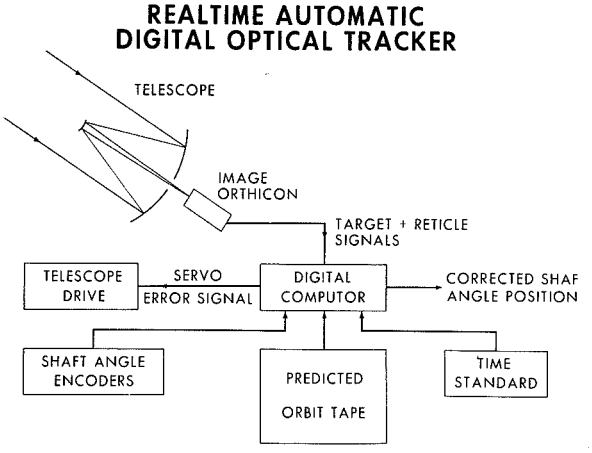

FIGURE XIV–3.—Real-time automatic digital optical tracker, block diagram.

aligning the optical axis to the mechanical axis, is not used during operation. The second reticle is projected across the top of the raster and down the left side. This area is blanked out of the field-of-view. As the IO raster is scanned, the sweep produces a zero signal until the lighted reticle is detected, at which time an ordinate counter is started and all succeeding sweeps are counted. Each horizontal sweep initiates an abscissa counter referenced to the vertical line of the reticle on the side of the frame.

The target is detected in the 1.4-degree mode by the operator, who tracks the target, establishing a tracking rate for the system. When the target is within 0.1 degree, the operator switches to the track mode, changing the focal length to 400 inches and the field-of-view to 0.1 degree and at the same time reducing the sensitivity of the control stick by a factor of 14. The image-orthicon scan information is fed into the computer, which determines the position of image in the field by storing and comparing the information for consecutive scans. If more than one target is in the field, the computer can select the desired satellite, unless the second target has the same angular rate as the desired target. When locked on the target, the computer will determine the tracking error with reference to the center of the field and will generate two error signals (x and y) which control the servo-drive system.

The shaft-angle readout system employs Norden Microgon encoders which have been checked using the autocollimation and pollygon technique, verifying the accuracy of 2.47 sec of arc. The shaft-angle readout is fed into the computer and corrected in real time for the system tracking error. Therefore, the real-time data is more accurate than the servo-tracking accuracy.

NASA PRECISION MULTI-MODE MOUNT

WALTER J. CARRION
Goddard Space Flight Center

EDGAR Y. LEE
Nortronics

The exploration and the development of space technology has placed new demands on tracking instrumentation. The Optical Systems Branch of the Goddard Space Flight Center is developing new techniques applicable to space tracking and communication systems. Instrumentation is being developed to give real-time angle information to an accuracy of better than ± 5 seconds of arc for early trajectory determination from the point of injection of a spacecraft into intermediate and/or final orbit, for mid-course correction of lunar trajectories and to provide daylight optical tracking capabilities.

The Research and Development Program of the Optical Systems Branch includes such tasks as: Development of digital TV readout techniques, satellite attitude determination, precision servo drive systems, image orthicon development, laser developments and laser application to long range tracking and communication. In order to support the R&D program both in conducting field investigations and system evaluation, an instrument is required to provide precision real-time readout data with precise pointing accuracy and rotate with optimum smoothness. A design study conducted at Goddard showed the need and feasibility of designing a Precision Multi-Mode Mount.

In tracking satellites and spacecrafts, whether it be for data acquisition, trajectory information or system evaluation of newly developed techniques, the prime portion of the orbit is at zenith. The demands on the servo drive for the X–Y configuration at zenith are far less than the conventional altazimuth mount. The altazimuth mount has an asimuth error at zenith of 90° for the slightest collimation error of its optical axis. The X–Y mount has the same problems as the altazimuth mount but it occurs when the system has to track around the pole of the mount which is on the horizon. This region is less appealing to optical (and radio) tracking and most of the tracking is done above an elevation angle of 15°, therefore, an X–Y configuration would fulfill many of our needs.

In addition a large portion of our program is directed to the development of a 24 hour real-time optical tracking capability. The heavens provide us with a wide range of various magnitude targets. Therefore, a precision equatorial telescope would be a very useful research tool in our observatory.

In June 1962, the Goddard Space Flight Center awarded a contract to Nortronics, a division of Northrop Corporation, for the design and fabrication of a large precision multi-mode mount to support a 3500 lb. telescope system. The telescope will be a 24″ C.A. Catadioptric System which is interchangeable from a Newtonian, to Reflector-Corrector, to a Cassegrainian System with focal length variable from 132″ to 2500″. The mount can operate either in the X–Y mode or the equatorial mode with axis rotation maintained to ± 2 seconds of arc. Figure 1 shows the yoke and gimbal of the mount. To meet these requirements, extreme care was taken in the design to size all structural members for maximum rigidity. This was especially true in the case of moving

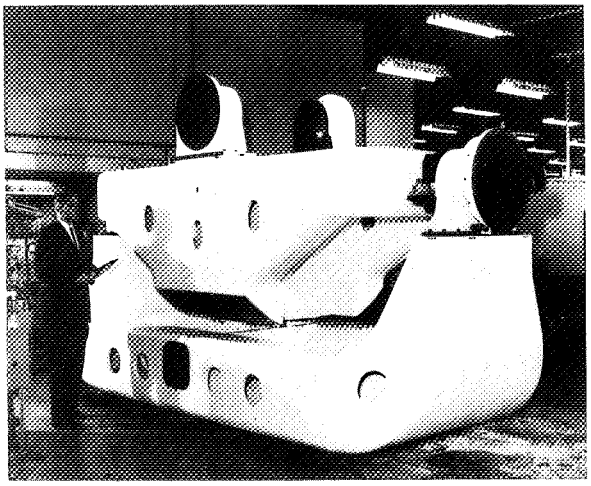

FIGURE 1.

members. Proper design of the gimbal for example depended to a great extent upon proper distribution of its physical mass about the X axis of rotation so as to produce a satisfactory isoelastic structure. The long term dimensional stability exhibited by cast meehanite, properly heat treated, led logically to its choice as the primary material for construction of the mount's structural elements.

In designing the tracking mount, the requirement of high degree of precision and broad range of control clearly indicated the need for use of the best available techniques for design and construction of the mount's main elements. These can be generally described in terms of the structure, support bearings, and the servo drive and control system.

The tracking mount structure weighs 25 tons and consists of three basic elements: the two axis gimbals, the support yoke, and the base. The use of massive symmetrically shaped Meehanite castings minimizes the effect of thermal changes, deflections in the structure and the stability of the material insures that the accuracy of alignment can be maintained over long periods of time.

The gimbal supports trunnion bearings, which permit rotation of the optical system about the Y-axis, and also the counterweights which serve to provide a balanced load for rotation of the gimbal and optical system about the X-axis. The gimbal casting is a 146 inch by 68 inch box with an 18 inch by 12 inch C-channel cross section, one inch in thickness. Webbed trunnion mounts support the Y-axis bearings at a distance of 33 inches above the X-axis, while the counterweights are underhung about 40 inches below this same axis. The total weight of the gimbal, including parts which are rigidly attached to it, is eight tons. The degree of anisoelasticity about the X-axis exhibited by the gimbal has been shown in actual tests to be much less than one arc second.

The yoke carries a second set of trunnion bearings which serve to permit rotation of the gimbal and optical system about the X-axis, and has been designed to support this load without significant physical distortion of its own structure. The yoke casting has a C-channel cross section two inches thick, 68 inches wide by 18 inches at the base, and tapering to 28 inches wide by 12 inches at the X-axis bearing supports. This yoke structure weighs nine tons, including all parts which are rigidly attached to it.

Figure 2. The base carries a third set of trunnion bearings which permit the entire yoke, gimbal, and optical system assembly to be rotated and thereby tilted from the X–Y (horizontal) mode to an equatorial mode, and

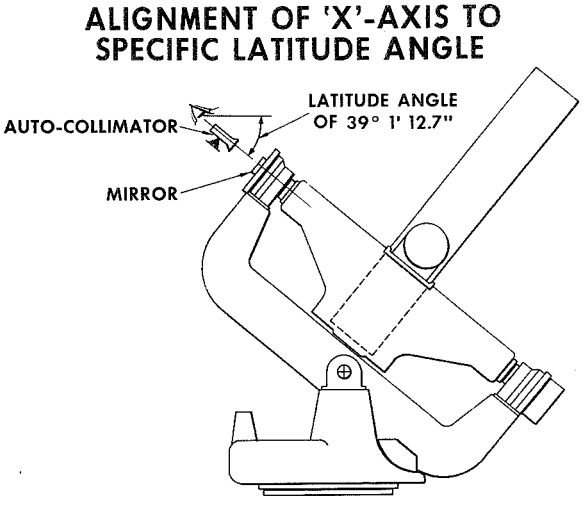

FIGURE 2.

vice versa. The driving mechanism employed for this purpose is a manually controlled hydraulic actuator. Rotational limits are precisely established by the combined use of spacer blocks for coarse adjustment, and matched wedge elements for fine adjustment. Similar adjustment devices are employed at the tilt axis bearings to facilitate initial alignment of the mount or for later realignment and calibration whenever required. The base is secured to the foundation structure by means of tie-down bolts fastened into a metal ring which is embedded in the concrete pier. There are provisions on the underside of the base for installing bearings and drive elements, if at some future date it is desired to add an azimuth drive unit to the tracking system.

Hydrostatic bearings are used to obtain the highest degree of positional stability of the mount's rotational axes, and for optimum smoothness in the rotational movements which take place about these same axes. Smooth and stable rotations are necessary to motion stabilize optical images which will be recorded by photo-optical detectors attached to the optical system, since these allow the use of long integration times when tracking faint targets.

The degree of precision which has been built into the mount will be matched by servo drives employing integrating gyro rate control with direct drive torque motors to provide high resolution for position and rate control. These drives incorporated in position control loops using high accuracy digital encoders are fully capable of meeting the angular positioning and pointing accuracy requirements. The inherent smoothness, rigidity and friction-free characteristics of hydrostatic bearings, permits the development of a precise pointing instrument to direct laser transmitters and receivers to distant spacecraft. An immediate application of this instrumentation will be the S–66 satellite laser experiment. The S–66 satellite will place a laser target in a polar circular orbit at 1000 km. This target will be used primarily for laser research and requires a precise programmable mount to enable experimenters to develop 24-hour optical tracking and communication systems with narrower and narrower beam widths. The mount can be operated in a manual, autotrack and programmed mode.

HYDROSTATIC BEARINGS

The principal design requirements for these bearings are: ability to support the load both radially and axially, maximum resistance to deflection under load, and minimum breakaway and dynamic friction. While the loads involved are not identical at the X and Y axes, physically identical pairs of bearings are used for support at both axes, thereby simplifying operation and routine maintenance. Three classes of bearings were originally considered for this application: oil hydrostatic bearings, air lubricated bearings, and conventional precision rolling-contact bearings. For each class, the design concept was based on the support of the structural element on one end by a thrust and radial bearing and held on the other end by a radial bearing only Fig. *3*.

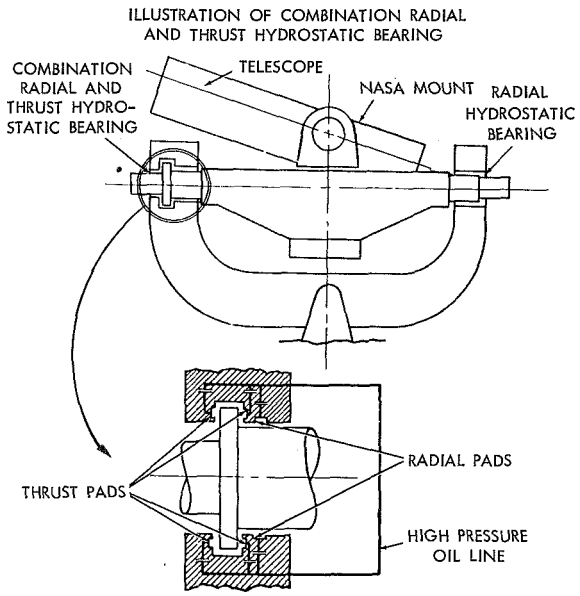

FIGURE 3.

The superior operational characteristics of oil hydrostatic bearings in this instance is clearly indicated by the tabulated comparison of bearings characteristics, which follows:

Characteristic	Hydrostatic	Air	Rolling contact bearing
Working load—lbs:			
Radial	10, 000	10, 000	10, 740
Axial	10, 000	10, 000	10, 740
Stiffness—lb/in	5×10^6	10×10^6	1.8×10^6
Fluid flow	1.03 gal/min	5.28 lbs/min	Not applicable
Supply pressure psi	353	108	Not applicable
Power required hp	0. 2	13. 1 [1]	Not applicable
Breakaway torque—in.-lb	0	0	130
Running torque [2] in.-lb	0. 93	0. 05	120

[1] Almost 70 Time Hydrostatic.
[2] Note—at 10 degrees/sec rotational speed.

The primary advantages inherent in the use of oil hydrostatic bearings are in the extremely low friction torques and high stiffness values.

By contrast, the rolling element bearings introduce a level of static and dynamic friction that makes attainment of the requisite drive performance impossible.

The air bearings, while possessing desirably low friction, are excessively large and consume excessive power.

The hydrostatic bearings can be expected to operate indefinitely without wear or excessive maintenance as long as they are provided with a supply of clean oil. Since dissimilar materials are used at the bearing surfaces, the bearings will suffer no ill effects from relative motion between these surfaces, whenever the supply system is shut down. Therefore, the reliability of the bearing system virtually corresponds to the reliability of the hydraulic supply system itself. This supply system consists of mainly a pump, reservoir, filters, pressure regulators, and orifices. The bearings are protected by a filter in the pump outlet line and by individual filters on the orifice flow restrictors. Periodic routine replacement of the system filter is required. However, as long as this simple maintenance routine is carried out, the bearings will function with complete reliability. Individual orifice filters further prevent any escaping particles from entering the bearing.

TRACKING MOUNT ALIGNMENT

The mount will be housed in the Goddard Optical Research Facility. A complete static and dynamic evaluation of the mount performance will be conducted by both Nortronics and Goddard personnel.

The accuracy specifications are as follows:

(1) In either modes (X–Y or equatorial) the X-axis of rotation is parallel to the meridian plane to within ±2 arc seconds.
(2) In the X–Y mode, the X-axis of rotation is horizontal to within ±2 arc seconds.
(3) In the equatorial mode, the X-axis of rotation is at an angle elevated horizontal by 39 degrees, one minute, and 12.7 seconds.
(4) The orthogonality between X and Y axes and shaft wobble is equal to or less than ±2 arc seconds.

Preliminary alignment tests conducted at the Nortronics facility in Needham Heights, Mass., have shown the orthogonality and shaft wobble conditions to be less than 2 arc seconds. The measurements were made with simulated telescope load and bearings operating for several hours.

Provisions have been made for mounting a mirror on the end of shafts and a polygon in the center of the gimbal for checking the accuracy of mount and for aligning the mount in the equatorial and X–Y modes.

Ground reference points have been established by a first order survey at the site. The mount will be levelled and the "X" axis will be aligned to the meridian using an auto-collimating theodolite and the ground reference marks. The final alignment will be made by star observations (Ref. Figure 2). The shaft rotation accuracy is determined by measuring the mirror tilt with an auto-collimator (Figs. 4 and 5). With the auto-collimator established parallel to the "X" axis, the mirror is removed and a polygon is placed in the center of the gimbal in the plane of the "Y" axis and adjusted to the auto-collimator on the "X" axis. Provisions have been made to view the 90° faces

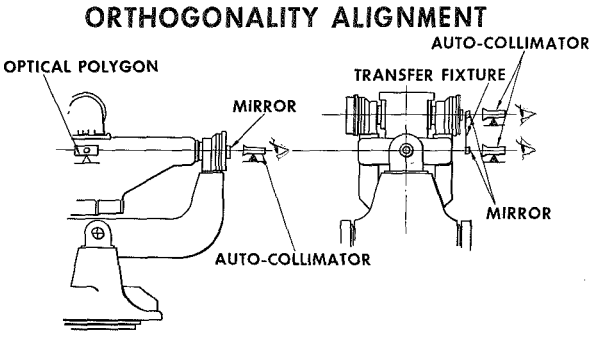

FIGURE 4.

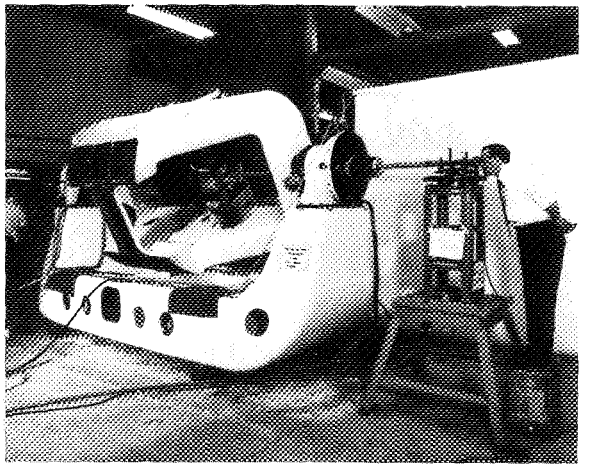

FIGURE 5.

with a second auto-collimator or theodolite to check the orthogonality of "Y" axis to the "X" axis. Since the "Y" axis is offset approximately 2 ft, a transfer fixture or theodolite is used to establish the "Y" bearing axis. (Fig. 4.) By placing a mirror on the "Y" shaft, the bearing runout and orthogonality can be determined.

The mount structure is complete and soon will be aligned in the Goddard Optical Research Facility to the surveyed field markers. The servo drive and optical system are being developed.

The instrument will be ready for Optical Research and Development experiments by June 1964.

DIGITAL TELEVISION SCANNING SYSTEM

L. O. CAUDILL
Goddard Space Flight Center

INTRODUCTION

The digital scanning of cathode-ray image-tube sensors has several advantages over conventional analog-scanning techniques: (1) flexibility, (2) adaptability, and (3) precision. A very flexible scan system is required for the image-tube pickup to accommodate the wide range of conditions of target visibility and target motion, background illumination, star population, and star magnitudes which must be accepted in a versatile long-range detection and tracking system. The system must be quickly adjustable for optimum performance in any situation. With digitally controlled scan circuitry, parameters such as frame-scanning time, frame-repetition rate, interlace ratio, number of lines per frame, and number of resolution elements per line can be varied over a wide range. Because of the digital control, this flexibility can be obtained with no sacrifice in linearity or accuracy of the sweep.

By adaptability is meant the ability of a digital scan system to perform nonroutine tasks on command. At least two adaptive techniques are available in digital scanning. One is the ability to stop at any significant scan position to perform an operation such as position readout or video encoding, and then resume scanning from that position. A second example of an adaptive technique is to perform scanning subroutines, such as small localized scans, at various positions, the particular subroutine being determined by the video signal in these positions.

Scan precision may be defined as the ability of the scanning device to identify each scan position to some order of accuracy. Digital scan is limited in its precision only by the stability of the power supplies used in the digital-to-analog decoders.

The ability of the digital-scanning system to present the image information in discrete elements makes it especially useful in preparing data for recording and computer processing. A continuous, accurate digital register of the scanning-beam position is maintained for reading out the X–Y coordinates of the image signal.

This paper will cover briefly the digital TV system being developed by the Space Guidance Center of IBM to enable the Optical Systems Branch of GSFC to carry on its program of real-time optical tracking.

After a technical description of the system, a brief outline will be given of the in-house program of experimental studies.

SYSTEM DESCRIPTION

The equipment supplied by IBM provides a flexible digital format for the readout of data presented to the image-orthicon target from the telescope by way of the image-orthicon photocathode. The digital format is a matrix of scanning-beam positions, with a maximum matrix of 1024 positions horizontally by 1024 positions vertically, and with a minimum matrix of 100 positions horizontally and 100 positions vertically. The basic matrix-scanning sequence is left to right for each horizontal line, and top to bottom for each frame.

System timing is provided by a maximum clock-pulse rate of 1 megacycle, which dictates a minimum position-to-position time of 1 microsecond. Under the maximum scan matrix of 1024 by 1024 and position-to-position rate of 1 microsecond, line rate is 1.024 milliseconds and

frame rate is approximately 1.05 seconds (excluding flyback time). Under the minimum scan matrix of 100 by 100 and position-to-position rate of one microsecond, line rate is 0.1 millisecond and frame rate is 10 milliseconds (excluding flyback time). Flexibility of system design will allow for any frame rate between the two mentioned above if it satisfies the following equation:

$$\text{Frame rate} = \frac{fcp}{VXH} \qquad \frac{1}{V\delta}$$

where

fcp is clock-pulse frequency (DC to 1 mc)
H is number of horizontal line positions (100 to 1024) range
V is number of vertical line positions (100 to 1024)
δ is flyback delay ($\approx$ 40 μsec)

Video information from the image orthicons will necessarily have the same format as the scan matrix and will be received and amplified by Goddard and presented to the IBM equipment. The IBM system provides the necessary controls to stop the main deflection at any matrix position containing video above a chosen reference level. The stopping of the main deflection allows the horizontal and vertical beam position to be read out in decimal form to an accuracy of one matrix position. Deflection restart is then automatic or manual, at the operator's discretion.

The system contains the capability of choosing photocathode exposure time and number of frame readouts per exposure. Exposure-time resolution is one frame time, with the capability to choose any number of frame times from 1 to 16. The selection of the number of readout frames is similarly provided for.

Fiducial markers for telescope alignment are provided on the front panel.

EQUIPMENT

The bulk of the electronic circuitry for the digital TV scanning system is housed in a rollaway cube approximately 29 inches wide, 30 inches deep, and 31 inches high (Fig. XXIV–1). Two monitors are attached to this cube: one, a conventional 14-inch monitor, and the other an 8-inch monitor containing a special

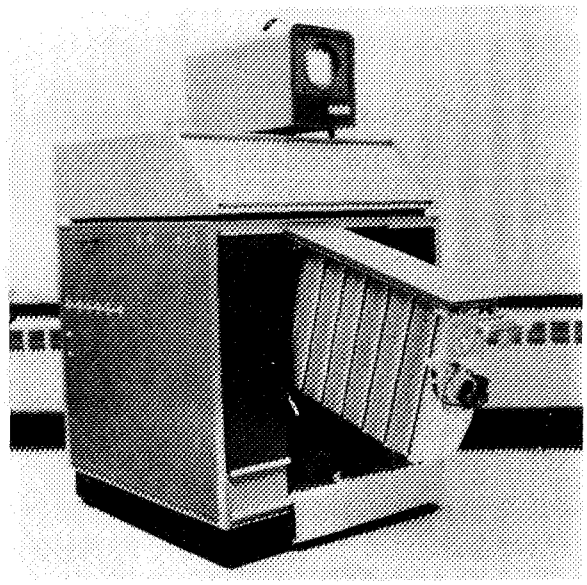

FIGURE XXIV–1.—Digital TV scanning system, electronic circuitry housing.

flatfaced cathode-ray tube. Also attached to the module by a minimum of 30 feet of cable are two small electronic packages containing the two image-orthicon yokes and the power stages of the deflection amplifiers.

Provisions are made for either monitor to be operated next to either image orthicon as well as at the cube.

Both monitors were purchased commercially and reworked to be compatible with the system. Except for small variations, the video amplifier and low- and high-voltage supplies are unchanged. The CRT's unblanking circuitry and yokes have been replaced or modified.

The two electronic packages contain the deflection amplifiers and yokes for each of the two image-orthicon tubes. Blanking and unblanking waveforms are also provided at the mounting area.

Electronic parameters of the deflection amplifiers are discussed in the next section.

The electronics cube, besides housing most of the system circuitry, has a control panel for the operator's use (Fig. XXIV–2) and a programmable plugboard (Fig. XXIV–3) for flexibility of experiment format. The control panel contains the system controls most commonly

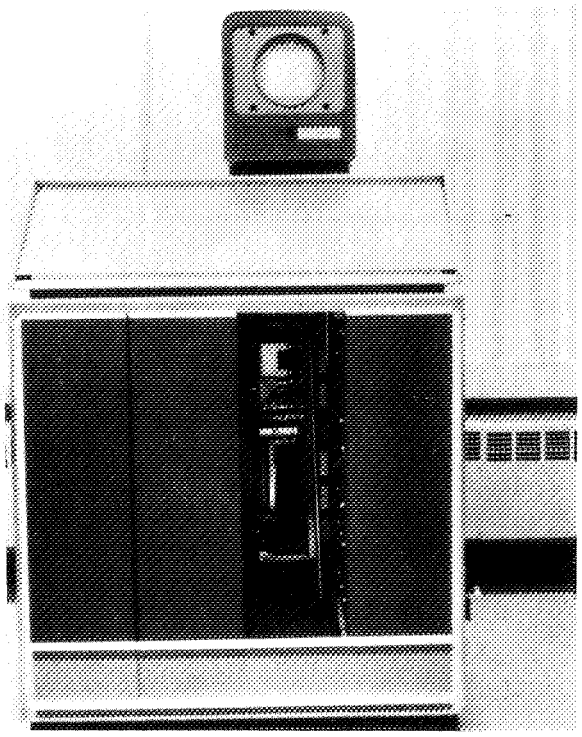

FIGURE XXIV–2.—Control panel for electronic circuitry.

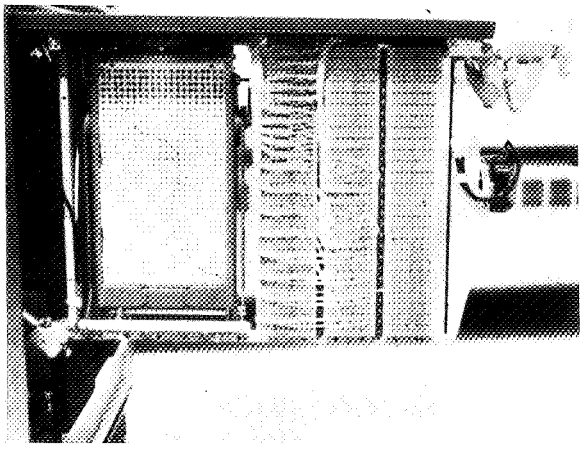

FIGURE XXIV–3.—Programmable plugboard for electronic circuitry.

used in an experiment, and the plugboard provides the controls less frequently used.

The cube circuitry is contained in eight gate positions. The gates containing the logic and deflection circuitry and the gate containing the miniwatt power supplies (Figs. XXIV–4 and XXIV–5) are swing-out gates to allow for ease of maintenance and trouble shooting, as the gates can be serviced by removal of a side panel. The fixed gate positions contain some fixed power supplies and some deflection alignment circuitry.

The four front gates will contain the logic and deflection circuitry, one gate being completely assembled with blank receptacles to provide ready expansion capabilities. The four back gates will house the power supplies. Each gate position has its own cooling fan and cover assemblies to direct the air flow; the cover assemblies are easily removable to provide access to the gate circuitry.

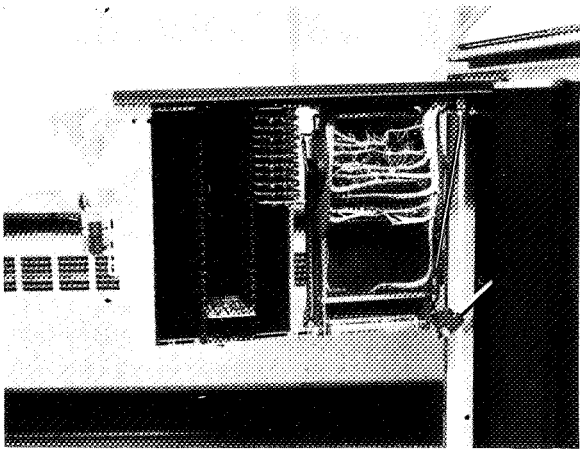

FIGURE XXIV–4.—Gate containing logic and deflection circuitry.

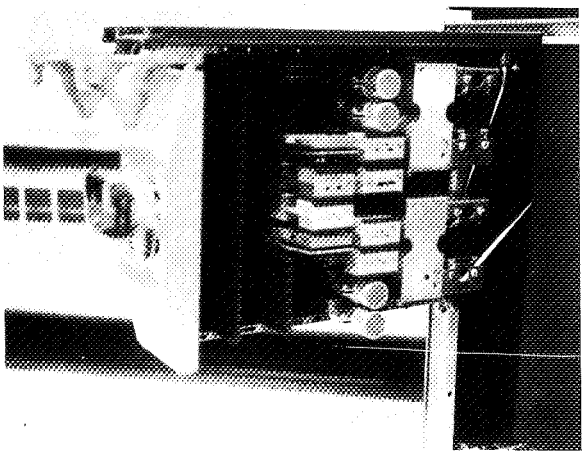

FIGURE XXIV–5.—Gate containing miniwatt power supplies.

TECHNICAL DESCRIPTION

The technical description of the Digital TV Scanning System (Fig. XXIV–6) is presented in a sequential signal flow manner.

System timing is accomplished in two ways. IBM furnishes an SMS oscillator card of 1 Mc which may be divided by two through plugboard connections; this defines two basic system timing rates, 500 kc and 1 Mc, readily selectable by the operator. Following the oscillator card is an SMS sample pulse generator (SPG) which shapes the incoming sinewaves into stable clock pulses (cp). The plugboard also provides an input jack through which a wider range of frequencies may be fed to the SPG. Any frequency (either sinewave, squarewave or pulse) below 1 Mc may be an input to this circuit as long as it meets the amplitude requirements.

The SPG puts out clock pulses used for system timing and signal generation. The clock pulses are fed through a driver stage to provide the necessary driving capability; the output of this driver is a positive pulse varying between 0 and −6 volts.

The SPG can be gated ON and OFF under control of the "OR" circuit in Figure XXIV–6. Normally, the SPG is gated ON, allowing clock pulses to pass through. The clock pulses then drive the horizontal counter, consisting of ten bistable multivibrators or flip-flops connected through the plugboard in binary fashion. This arrangement allows a maximum count of 1024,

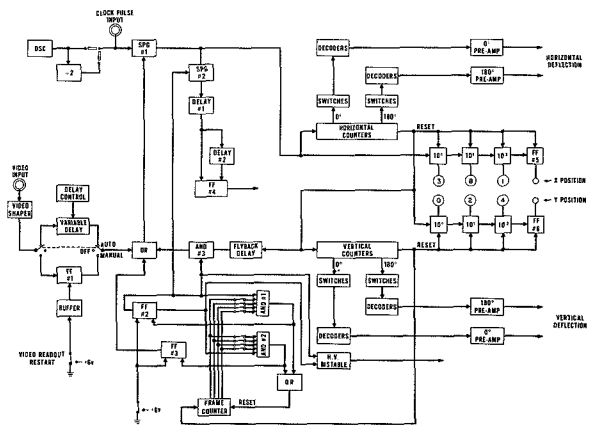

FIGURE XXIV–6.—Digital TV scanning system, schematic diagram.

after which the counters are zeroed, thereby generating one horizontal line. Since deflection is push-pull, both collector outputs of all ten flip-flops are decoded through electronic switches and summed in the deflection preamplifiers to yield two deflection outputs: one an increasing staircase waveform, and the other a decreasing staircase waveform.

The vertical counter is simply an extension of the horizontal chain, being driven by the output of the last horizontal flip-flop and having the same count capability (1024). An accumulation of 1024 horizontal outputs will constitute one frame. Deflection waveforms for the vertical channel are obtained in exactly the same manner as the horizontal waveforms, the only difference being the time base (i.e., there are 1024 horizontal staircase waveforms for each vertical staircase).

Commercial display counters are provided in parallel with the horizontal and vertical counters to provide a decimal readout of beam position whenever the counters are stopped. The horizontal system counters reset and synchronize the horizontal display counters each line, while the vertical system counters reset and synchronize the vertical display counters each frame.

The display counters complete only a count of 1000 before rezeroing, but the main horizontal and vertical system counters return to zero on counts of 1024. To resolve the 24-count difference between the display and system counters, a flip-flop driving a neon indicator is provided to indicate the display-counter rollover at 1000, thereby allowing the system counters to complete a count to 1024 before resetting to zero.

The last flip-flop of the horizontal counter also drives a flyback delay circuit that allows the beam to position itself at the beginning of a new line after scanning the preceding line. The output of the flyback delay circuit is one input to the SPG "OR" circuit, the output of which inhibits the clock pulses to prevent them from entering the "X" counter. This action provides some deadtime in the scanning sequence which allows the deflection yokes to recover from a maximum flux condition to a

minimum flux condition. At the self-timed termination (approximately 40 μs of the flyback delay monostable), the AND gate in the SPG is closed and clock pulses once again pass into the "X" counter. This means that every line is delayed approximately 40 μs before starting, thus increasing frame time by a maximum of 1024 x 40 μs or 40 milliseconds.

The flyback delay circuitry is enabled through an AND circuit which is under control of the exposed counters which are discussed in a later section. The AND circuit removes the 40-μs delay when shuttering times are being measured.

Because the deflection yokes are inductive, they cannot follow the rapid changes in current from position to position in synchronism with the rise time from current step to current step. It is necessary, therefore, to provide beam blanking and unblanking signals which allow the yokes to settle out in a new condition before the beam is turned on. This blanking circuitry, composed of an SPG, a flip-flop, 2 delay lines and associated drivers, operates as follows:

The beam is normally blanked. The SPG feeding the first delay, operating as an AND gate in this case, is used to inhibit unblanking during the expose time. The clock pulse from the SPG is delayed for a chosen length of time by delay #1 and then turns the beam on by setting a flip-flop. The ON time of the flip-flop is determined by delay #2 which is fed by the output of delay #1; the output of the delay #2 sets the flip-flop to its original condition. For a 1-Mc clock rate, both delays are 0.5 μs. Two 0.8-μs delay lines are also provided to allow variation in settling time and unblanking time when the system is operating at lower clock rates.

The frame counters for timing both photocathode-exposure time and video-readout time will accumulate the output pulses from the last vertical counter. These pulses are frame-rate pulses, one to a frame. Frame-counter operation is automatic and sequential in that there is a cycle of operation. This cycle, initiated by the cycle restart microswitch, operates as follows: With reference to Figure XXIV–6, assume that flip-flops #2 and #3 are set up so that (1) the clock pulses are gated off (thereby blanking the beam); (2) the high-voltage bistable is off; (3) AND gate #2 is open. Under these conditions, the system is quiescent, sitting at rest with no deflection, photocathode off, and all counters at their zero positions.

Pushing the cycle restart microswitch initiates the following actions:

1. Flip-flop #3 changes state, enabling clock pulses to pass into the horizontal counters.
2. Flip-flop #2 changes state and performs four functions:
   a. It inhibits SPG #2 from passing pulses into the unblanking circuitry.
   b. It opens AND gate #1, and closes AND gate #2.
   c. It disables the flyback delay through the operation of AND gate #3.
   d. It sets the high-voltage bistable in the state in which it allows the image section of the image orthicon to be operative.

Under these conditions, the frame counter will accumulate frame pulses to a predetermined value. When this value is reached, a pulse is generated which changes the state of flip-flop #2, and resets to frame counter. This action negates the conditions listed under (2) above. That is:

   a. SPG #2 is enabled to pass pulses into the unblanking circuitry, thereby allowing video to be read from the IO target.
   b. AND gate #1 closes, and AND gate #2 opens. This reprograms the accumulation of pulses in the frame counter, causing an output pulse for FF #3 and reset to be generated at a different frame count.
   c. It enables the flyback delay, thus instrumenting the logic to operate properly with the deflection system during video readout.
   d. It resets the high-voltage bistable, thus disabling the image section of the image orthicon. This action prevents further accumulation at image charge on the IO target during this cycle.

With this circuit logic in this condition, the scanning system will operate in its conventional manner, generating a readout matrix with 1024 x 1024 positions. This readout cycle continues until the frame counters accumulate

a predetermined number of vertical rollover pulses. At this time, when the system has read out a desired number of frames of the information stored on the IO target, a pulse is generated by the frame counter which resets flip-flop #3. When this occurs, clock pulses are inhibited from passing through SPG #1, ending the cycle as the system returns to its original state.

At the operator's discretion, the readout portion of the cycle may be interrupted by the occurrence of the video signal which exceeds a predetermined level. The interruption of the scan occurs when either the monostable or the flip-flop in the video stop-count circuitry are triggered by a video shaper pulse. The video shaper generates pulses only for those input video pulses which exceed the predetermined level. The level assumed by the monostable or by the flip-flop passes through the OR circuit to SPG #1; this condition inhibits clock pulses from the main counters and from the display counters. The termination of this operation occurs in the automatic mode when the monostable assumes its stable state, and in the manual mode by the manual operation of the video readout restart switch. During the time when the main counters and the display counters are stationary because of lack of input pulses, it is possible for the opeatorr to read the coordinates of the video pulse from the display counters.

Selection of the count to be accumulated in the frame-rate counters is made possible through an array of eight switches on the control panel which allows the operator to rapidly change expose and readout conditions. The frame count logic may be removed from the system by an SMS connector card so that the system can be operated in a continuous mode when shuttering is not desired.

PROGRAMS

The two important criteria for evaluating the performance of a tracking system are tracking range and tracking accuracy. We feel that optical systems are superior to all other passive tracking systems in both of these criteria, and as a result of our laser program we hope to show capability in the field of active tracking as well. To achieve the full superiority of optical systems, however, it is important to adjust their parameters of operation carefully. The sensitivity and resolution of an optical tracking system which makes use of electronic imaging devices is a function of many parameters:

1. Telescope resolution and transmission.
2. Background intensity and background clutter.
3. Image-tube scanning rates.
4. Image-tube resolution.
5. Image-tube storage time.
6. Video amplifier noise level.
7. Video amplifier frequency response.
8. Image-tube spectral response.
9. Image-tube response to short-duration light sources.

Present and future programs utilizing the IBM digital TV system will include investigation of each of these parameters, as well as many others which are significant, to determine their influence on the performance of a tracking system. Several types of image tubes, as well as different scan techniques and video amplifying techniques, will be evaluated.

Techniques for increasing system performance, such as image-tube storage, frame adding, and signal-shaping and background-clipping in the video amplifiers, will be investigated. In addition, several problem areas which prevent the attainment of the ultimate performance will be studied and attempts will be made to provide solutions. These problem areas include loss of sensitivity and resolution in the camera tube, due to saturation or fogging when bright objects appear in its field of view, and the difficulty of recognizing and keeping track of dimly reflecting space vehicles at long ranges in the face of the background clutter of sky noise and the multitudes of stars and other celestial objects.

It is felt that the IBM digital TV system described here, used in conjunction with a telescope mounted in a precision X–Y mount, will provide a capability that does not presently exist and will enable the Optical Systems Branch at Goddard Space Flight Center to make valuable contributions to the field of real-time optical tracking. The Optical Systems Branch wishes to acknowledge the support of Jim Ross, IBM Space Guidance Laboratory, Owego, N.Y., for his assistance with this technical description.

DEVELOPMENT OF A RANGE AND RANGE RATE SPACECRAFT TRACKING SYSTEM

E. J. HABIB, G. C. KRONMILLER, JR., P. D. ENGELS, AND H. J. FRANKS, JR.

Goddard Space Flight Center

A spacecraft tracking system is described which will measure range and range rate for distances varying from 150 to 400,000 km with a resolution of ± 15 m in range and ± 0.1 m/sec in range rate. This system will provide an order of magnitude increase in tracking accuracy and will use less power at lunar distances than present tracking methods. In addition this system is simple, transportable, and economically feasible.

A preliminary portion of the system, with capability for measuring range only, has been constructed and tested by tracking an aircraft flying over the Blossom Point, Maryland, Minitrack facility; and an analysis of the results shows that the quoted accuracies and performance are feasible. Finally, several system configurations are given as they would apply to specific satellite programs.

INTRODUCTION

With the advent of the artificial satellite as a tool for furthering research in space, the need for precise position determination and prediction on a world-wide basis became a pressing problem. Prior to that time, this need had existed mainly in two fields: The military required knowledge of the position and velocity of an attacking aircraft in order to take effective countermeasures; and the missile age required more exact determinations in order to guide a missile and to evaluate its performance. These situations had in common two salient factors: The distance involved was not too great (in comparison with interplanetary distances), and power for transmitting radio carriers was fairly abundant, although never enough in the case of radar reflection.

Early satellite tracking was characterized by one dominant factor: a lack of sufficient electrical power, first to carry out the intended experiment, and second to provide an adequate communication channel for the data as well as a signal by which the satellite might be tracked. The earliest satellites launched in the United States provided 10 to 20 mw of radiated power for tracking purposes and 0.1 to 0.5 w for the data channel.

Of course, optical tracking provided enough accuracy to satisfy the most strigent requirements; but this was hampered both by insufficient light, either generated or reflected by the satellite, and by the vagaries of the earth's weather. Even so, an optical tracking net was constructed and has operated very successfully.

Successful radio frequency tracking demanded new concepts in the measurement method, and several have evolved. The most successful to date is the application of the interferometer principle to measure the angle between the observer's reference plane and a line connecting the observer and the satellite. *Minitrack* is such a system.

Given a sufficient number of these measurements made at different points along the satellite's orbit, a well designed computer program can produce elements which describe the satellite's past position and velocity with accuracies limited mainly by tracking station abilities, and predict its future positions with accuracies further limited by knowledge of the satellite's environment. Present day abilities can produce

satellite angular positions with respect to nearly any position in the world, 24 hours in advance, to accuracies slightly better than 0.05 degree. The need for higher accuracies has not been great until very recently, although it has always existed with respect to orbital mechanics theory, in which higher accuracies are needed to improve knowledge of the earth's gravitational field and the magnitudes of extraterrestrial influence.

To determine which system would best serve the majority of requirements, an appraisal must be made of both the present day systems and those realizable in the near future. A system should be chosen that would: (1) provide an order-of-magnitude increase in tracking accuracy; (2) demand a minimum of carrier power from vehicles as distant as the moon, and further if possible; (3) share the data communication channel; (4) be simple and transportable so that elements of the system could be relocated as needs changed; and (5) be economically feasible.

Tracking systems measure some or all of six basic elements: the three spatial coordinates of a vehicle and the three coordinate rates. Some systems measure pseudo-coordinates. For example, an interferometer measures the x, y, z position of a satellite, but normalized to the range; the rates are inferred by observing the change in x, y, z over a small time interval. A Doppler system measures range rate directly and the second derivative can be inferred.

Two classes of measuring systems exist: those requiring only the emanation of a radio frequency from a satellite, and those requiring responses from the satellite when it is interrogated by a ground-emanated signal. Angle measurements can make use of only the satellite-emanated signal, and the spatial coordinates are determined by combining angle measurements made at several different locations. With prior knowledge of the exact radio frequency, Doppler measurements can be made; and again by combining measurements made at several locations the spatial coordinates may be determined. A range measurement can be made only by measuring the phase delay of a signal or the time of transit of a recognizable modulation of the carrier. This usually requires that the signal originate in the ground station and be transponded back by the satellite. If a signal could be generated on board at a precisely predictable earth time and modulated on a carrier, one-way transmission would suffice for range measurements.

Of these several methods, the Doppler and range techniques are the most easily instrumented; they can yield accuracies limited only by knowledge of the propagating medium and of the velocity of the wave. The interferometer technique, in addition to being hampered by instrumental and environmental conditions, would require frequencies so high that only steerable antennas would provide sufficient sensitivities; and since more antennas would be needed than in a range or Doppler technique, this is ruled out for economic reasons.

Of the range and Doppler techniques many variations are possible. The next section describes what would appear to be a readily obtainable system that will meet all the presently imposed requirements. Parts of this system have been constructed and tested at the Minitrack site at Blossom Point, Maryland, proving the feasibility of the approach taken. A prototype system, to be used mainly for concept evaluation, is now being produced by the Goddard Space Flight Center. Also, ADCOM Inc. is under contract to NASA to provide both a theoretical and experimental basis for choosing many of the system parameters. Of especially great importance is the choice of the modulation method for the ranging portion of the system. Finally, specifications for an operational Range and Range Rate System have been written.

A preliminary analysis of the system sensitivity shows, for example, that with an 85-foot-diameter antenna on the ground and a 5-foot-diameter vehicle antenna in the vicinity of the moon, a transmitter output of only 10 mw is required, and an accuracy (limited only by knowledge of the velocity of light) of 0.4 km is achieved. Replacing the 5-foot-diameter spacecraft antenna with an omnidirectional antenna raises the transmitter power output requirement to 1 watt.

A background on the fundamental principles involved and the ultimate accuracies obtainable by measuring range and range rate will be found in Appendix A.

SYSTEM DESCRIPTION

General

The system described here can measure the distance to a satellite from a ground station with a resolution of 15 m and with an accuracy limited only by this resolution, unknowns of the propagating medium, and knowledge of the velocity of light. It can also measure directly the range rate with a resolution of 0.1 m/sec and an accuracy limited only by the aforementioned factors. An ambiguity in range occurs every 937 km; however, this distance can be extended very easily by adding additional lower frequency tones (see Table 1).

TABLE 1.—*Wavelengths for Various Frequencies* $\left(\lambda=\frac{299{,}792.5\pm.4 \text{ km/sec}}{f}\right)$.

Frequency	Half wavelength λ/2		
	(Km)	(Statute mi)	(Ft)
1 Mc	0.1498963	0.093	492
0.5 Mc	.2997925	.186	984
100 kc	1.498963	.931	4,918
20 kc	7.494813	4.657	24,589
4 kc	37.47406	23.285	122,946
800 cps	187.3703	116.42	614,731
160 cps	936.8516	582.13	3,073,654
32 cps	4,684.258	2,910.6	15,368,270
16 cps	9,368.516	5,821.0	30,736,540
10 cps	14,989.63	9,314.0	49,178,460
8 cps	18,736.90	11,642.5	61,472,640

The system measures range on the principle that any wave propagated at a given velocity undergoes a delay that depends upon the distance traversed by the wave. It measures velocity on the Doppler principle.

Figure 1 shows the entire block diagram of the range and the range rate system. The system operates as follows: The ground station produces a reference carrier plus sideband pairs obtained by frequency modulating the carrier with several harmonically related lower frequencies. (The lowest of these latter is further divided down to provide both a range and a Doppler reference signal at 10 pulses per second, which is synchronized to WWV and initiates counting of 10 Mc by the Time Interval Units.)

Through digital techniques, the phase delay of the highest frequency signal (100 kc) in going to the satellite and back is measured to an accuracy of 1 percent (15 m) and the remaining lower frequencies (for which one wavelength is greater than the measured range) are used to resolve the ambiguity of how many whole cycle delays have occurred; the combined data constitute the range measurement.

The transmitter carrier is used in performing the range rate measurement; it is derived from the same ultrastable oscillator that provides the sidetone for the range measurement.

The carrier frequency plus sidebands are received in the satellite unit, whose bandwidth can simultaneously handle three ground stations separated approximately by 1 Mc. The transponder unit translates the received signal to a different position in the radio spectrum and acts as a booster amplifier; it has nearly enough total gain to make up for the attenuation of the path from ground to satellite.

On the ground, the translated carrier and sidebands are received in the *range and range rate (RRR) receiver*. Initial mixing with the ground-transmitted reference carrier and phase locking of the receiver to the latter produces a difference frequency that equals the airborne local oscillator's frequency plus its drift and one-way Doppler shift plus the two-way Doppler shift of the carrier. Simultaneously the airborne local oscillator's frequency plus its drift and one-way Doppler shift are received in the *Frequency Translation (FT) Receiver*, where appropriate frequency conversion by means of phase locked oscillators results in an output that is these same frequencies plus a bias frequency. Mixing this output with that of the RRR Receiver removes all local oscillator effects and produces a detected output that is the bias frequency plus the two-way Doppler shift of the carrier.

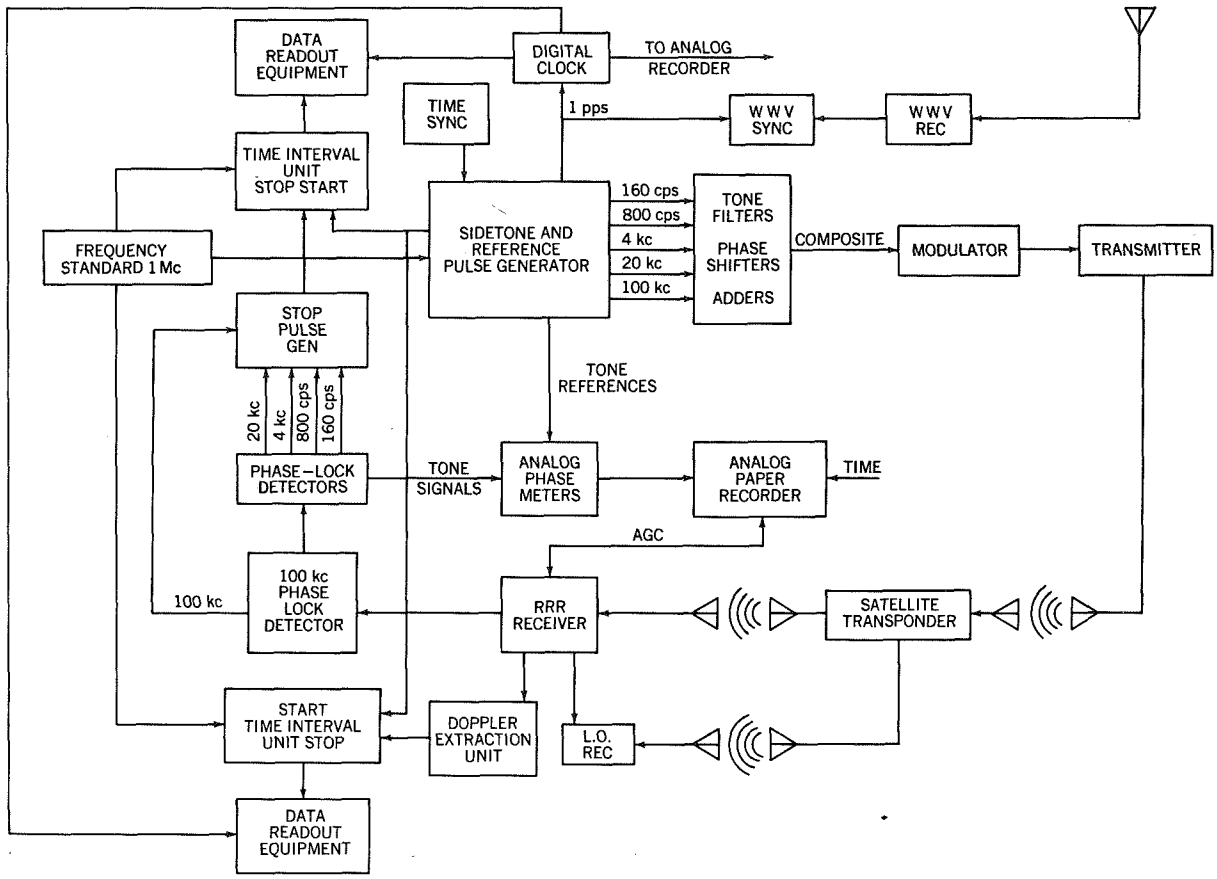

FIGURE 1.—Overall range and range rate system diagram.

This detected output is sent to the Range Extraction Unit, which uses narrow band phase-locked loops to separate the ranging frequencies and improve their signal-to-noise ratios. In addition, the outputs are fed to analog phase meters, whose outputs are recorded by an analog paper recorder as a backup.

The 200-kc-biased Doppler is fed to the Doppler Extraction Unit which is set to count 10 Mc in a second Time Interval Unit for a period equal to 6400 periods of the 200 kc ±Doppler frequency. At 1700 Mc, the maximum Doppler expected is ±120 kc. Counting 0.1-μ sec units for 6400 periods of 200 kc ±Doppler frequency produces a nonlinear measure of Doppler with an accuracy varying from approximately 0.25 to 1.0 cps for two-way Doppler, or a nonlinear measure of range rate to an accuracy of approximately 2.2 to 9 cm/sec. The 6400 period counter is gated ON by the 10 pps from the Reference Pulse Generator, thus synchronizing the Doppler Extraction Unit to WWV. The digital outputs from both the Range and the Doppler Time Interval Units are multiplexed with the output from the Digital Clock and punched on two separate teletype punch units, producing data at 10 readings per second in teletype code.

Figure 2 shows a typical trailer layout housing all the necessary equipment for the system. Figure 3 is a typical ground station layout showing the approximate area required and the arrangement of auxiliary equipment for the system.

Sidetone and Reference Pulse Generator

It can be seen in Figure 1 that the heart of the system is the ultrastable (5 parts in 10^{10}) oscillator. As Figure 4 shows, the output of

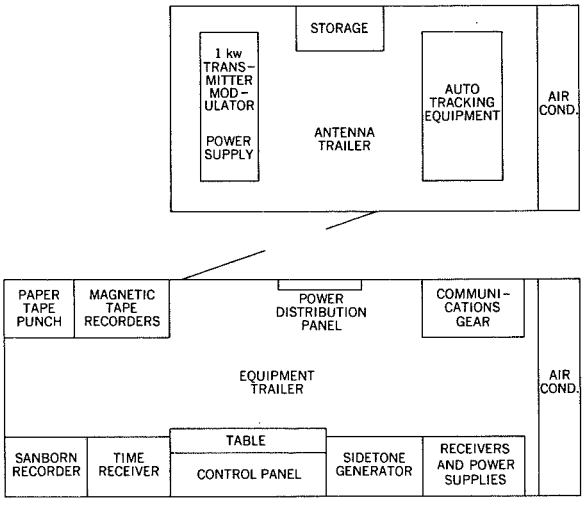

FIGURE 2.—Typical trailer layout.

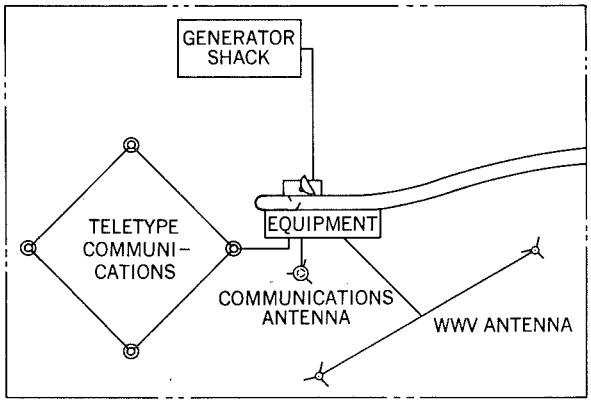

FIGURE 3.—Typical ground station layout.

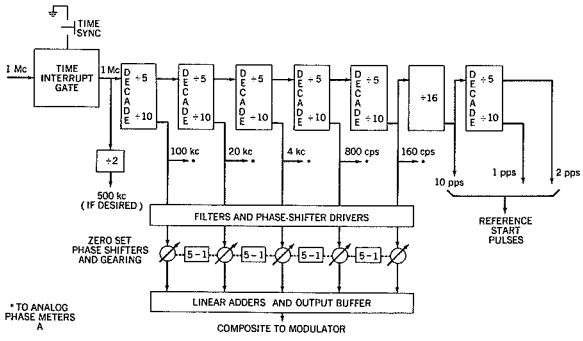

FIGURE 4.—Sidetone and reference pulse generator, tone filters, phase shifters and adders (see Fig. 1).

this oscillator feeds the Sidetone and Reference Pulse Generator. The latter, through a digital countdown from the 1 Mc oscillator, produces five harmonically related sidetones: 100 kc, 20 kc, 4 kc, 800 cps and 160 cps. The countdown is continued to form 10 cps as reference start pulses for both the Range and Doppler Time Interval Units (Figure 1) and 1 cps for the Digital Clock. The countdown logic outputs are square waves, so filter and buffer networks are necessary to produce sine waves that can be used in the electro-mechanical phase shifters and for modulating the carrier frequency. The 1 cps sidetone, synchronized to WWV, is used by the Digital Clock to produce days, hours, minutes, and seconds in Greenwich Mean Time for the station.

The phase shifters are used to cancel out any differential or fixed phase shifts that may be present in the various electronic paths. A mechanical linkage with a ratio of 5:1 connects the phase-shifters so that zero-setting of the entire system can be easily accomplished. From the phase shifters, the tones feed the Linear Adders and Output Buffer (Fig. 5). This section has a switching arrangement that allows for sending any or all tones with individual amplitude control. Provision is also made for mixing the tones with 100 kc to produce the complementary tones 80, 96, 99.2, and 99.84 kc. This is done in order to gather the FM spectrum so that no

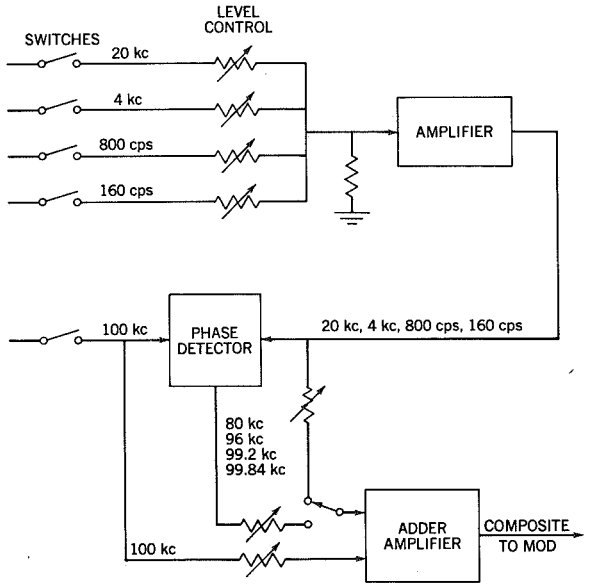

FIGURE 5.—Linear adders and output buffer.

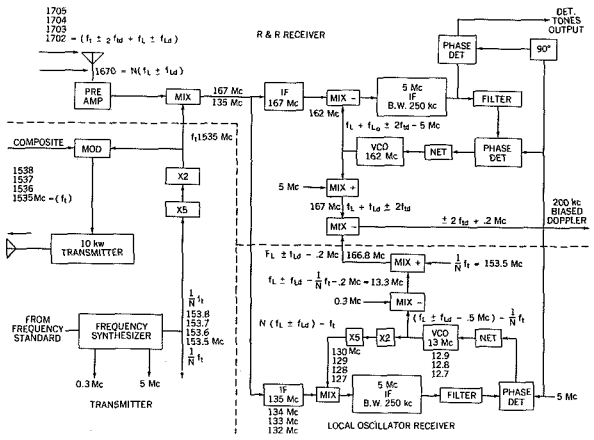

FIGURE 6.—RF ground systems: modulator-transmitter, range and range rate receiver, local oscillator receiver.

components lie too close to the carrier. The composite signal from the Output Buffer then is fed to the FM Modulator and Transmitter (Fig. 6). To preserve coherence and to minimize short-term instabilities, the transmitter frequency is derived from the ultrastable oscillator.

Transponder

The satellite borne Transponder (Fig. 7) receives the frequency-modulated carrier signal from the ground and mixes the spectrum with a frequency which is $(N-1)$ times the Transponder's basic local oscillator frequency.

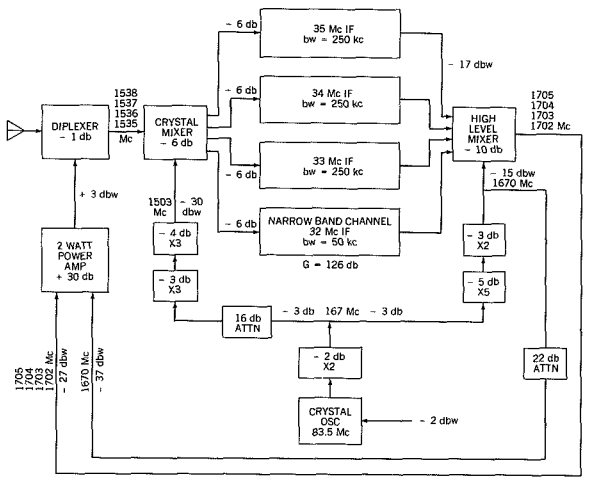

FIGURE 7.—Satellite transponder.

The relatively low difference frequencies (32, 33, 34 or 35 Mc) are extracted and fed to high-gain limiting IF amplifiers. The resulting amplified signal is then converted to a new carrier frequency by mixing with N times the local oscillator frequency. Thus, the received and transmitted carriers differ by exactly the local oscillator frequency. The desired transmitter power is obtained in the power amplifier. In order that the system be coherent, the local oscillator frequency must be available on the ground; thus, N times that frequency is also fed to the power amplifier and transmitted.

Provision is made for three ground stations to operate simultaneously through the transponder, and each receives a coherent translation of its own carrier frequency. It is worthwhile to note that the only other way that coherent transponding could have been accomplished would be to provide each ground station with its own complete transponder in the satellite. A further feature of the transponder is the added 50 kc bandwidth *IF* strip, for use at extreme ranges where the 100 kc sidetone is not required.

The transponder input contains a diplexer to isolate the transmitted and received signals. The received signals are then jointly mixed in a wide-band crystal mixer with a noise figure of 11 db. The mixing signal is $(N-1)$ times the local oscillator output; thus the mixer output consists of $f_t \pm f_{td} - (N-1)f_L$. Any one of the four IF strips is then selected, depending on f_t. When the output of the IF strip is mixed with N times f_L in a high level mixer, the resulting final output frequency is $f_t \pm f_{td} - (N-1)f_L + Nf_L$, or $f_t \pm f_{td} + f_L$, which is then amplified by the power amplifier and retransmitted. At the same time, the local oscillator frequency is multiplied by N to produce Nf_L, which is also transmitted to the ground station.

Ground Receiver and Signal Detection

The transponded signal is received by the range and range rate receiver shown in Figure 6. After preamplification in a low-noise-figure preamplifier, the signals are mixed with the ground transmitter frequency and converted to the

first IF frequency. Two IF's are necessary: one for the sidetone signals and one for the transponder local oscillator frequency. Synchronous detection is used to regain the sidetones, and the transponder local oscillator frequency is used to remove the effects of its own Doppler and drift. An offset frequency of 200 kc is introduced to facilitate the Doppler counting by preventing it from passing through zero.

Referring again to Figure 6, it is noted that one of the received frequencies, "A", nominally 1702 Mc, can be thought of as the transmitted frequency (f_t) $\pm$ twice its Doppler shift ($2f_{td}$) + the transponder local oscillator frequency (f_L) $\pm$ its Doppler shift (f_{Ld}). The other, "B", nominally 1670 Mc, can be thought of as N ($f_L \pm f_{Ld}$). The frequency of the first local oscillator of the receiver, f_t, is nominally 1535 Mc. Thus, from A we obtain

$$f_t \pm 2f_{td} + f_L \pm f_{Ld} - f_t = \pm 2f_{td} + f_L \pm f_{Ld},$$
$$= 1702 - 1535 = 167 \text{ Mc}$$

which we call A'. From B we obtain

$$N(f_L \pm f_{Ld}) - f_t$$

or

$$f_t - N(f_L \pm f_{Ld}) = 1670 - 1535 = 135 \text{ Mc } (N=10).$$

Let this equal B'. The frequencies A' and B' are the first IF frequencies. Since these frequencies are very high, the first IF frequencies need only enough gain to offset the loss from mixing and to feed the second mixer. In the second mixer A' is mixed with a frequency from a phase-locked oscillator that differs from A' by 5 Mc. The result is

$$f_L \pm f_{Ld} \pm 2f_{td} - (f_L \pm f_{Ld} \pm 2f_{td} - 5 \text{ Mc}) = 5 \text{ Mc},$$

which is the second IF frequency. A second phase detector is used to separate the sidetones from the 5 Mc IF.

Frequency B' is also mixed with a frequency from a phase-locked oscillator that differs from it by 5 Mc. Thus we have (for $N=10$)

$$-f_t + Nf_L \pm f_{Ld} - N\left(f_L \pm f_{Ld} - 0.5 \text{ Mc} - \frac{1}{N} f_t\right) = 5 \text{ Mc}$$

since in this voltage controlled oscillator $f_L \pm f_{Ld} - 0.5$ Mc $- f_t/N$ was also generated.

To obtain the Doppler information, we take $f_L \pm f_{Ld} - 0.5$ Mc $- f_t/N$ and mix it with 0.3 Mc instead of 0.5 Mc to provide the 200 kc bias frequency and then mix with f_t/N to obtain $f_L \pm f_{Ld} - 0.2$ Mc.

In section A of the receiver we mix 5 Mc with $\pm f_{Ld} + f_L \pm 2f_{td} - 5$ Mc to form $\pm f_{Ld} + f_L \pm 2f_{td}$. Next this is mixed with $f_L \pm f_{Ld} - 0.2$ Mc to obtain $\pm 2f_{td} + 0.2$ Mc, which is then fed to the Doppler extraction unit.

Range and Doppler Extraction Units

The tones from the receiver may be either complemented or uncomplemented; therefore in the Range Extraction Unit (Fig. 8) an additional phase detector may be necessary, for the complemented case, to retrieve the original sidetones. The tones are separated by bandpass filters and stable voltage-controlled oscillators are locked to them, thus making possible the use of very narrow loop bandwidths.

The tones, when properly phased, are ready for the stop pulse generator. The proper phasing is shown in Figure 9 along with the action of the flip-flop circuits. The positive-going edge of the 160 cps tone turns flip-flop B_1 "on", allowing the next positive rise of 800 cps to turn it "off" and thus send an "on" pulse to B_2. This operation continues through the higher frequencies until the 20 kc wave selects the proper 100 kc wave and a stop pulse is sent to the counter. This method of ambiguity resolving allows for up to ± 10 percent phase noise on each tone before ambiguities cannot be resolved. The output of this logic is a single pulse at a repetition rate equal to the lowest frequency (160 cps), and a rise time definition of ½ percent of the period of the highest frequency (100 kc). The proper phasing of the tones is accomplished by rotating the individual phase-shifters, and the delay between start time and stop time for zero range is removed by employing a simulated transponder to rotate the phase-shifters as a unit. The actual range measurement is made in the Range Time Interval Unit which is started by the 10 pps start pulse and counts at a 10 Mc rate until stopped by the stop pulse.

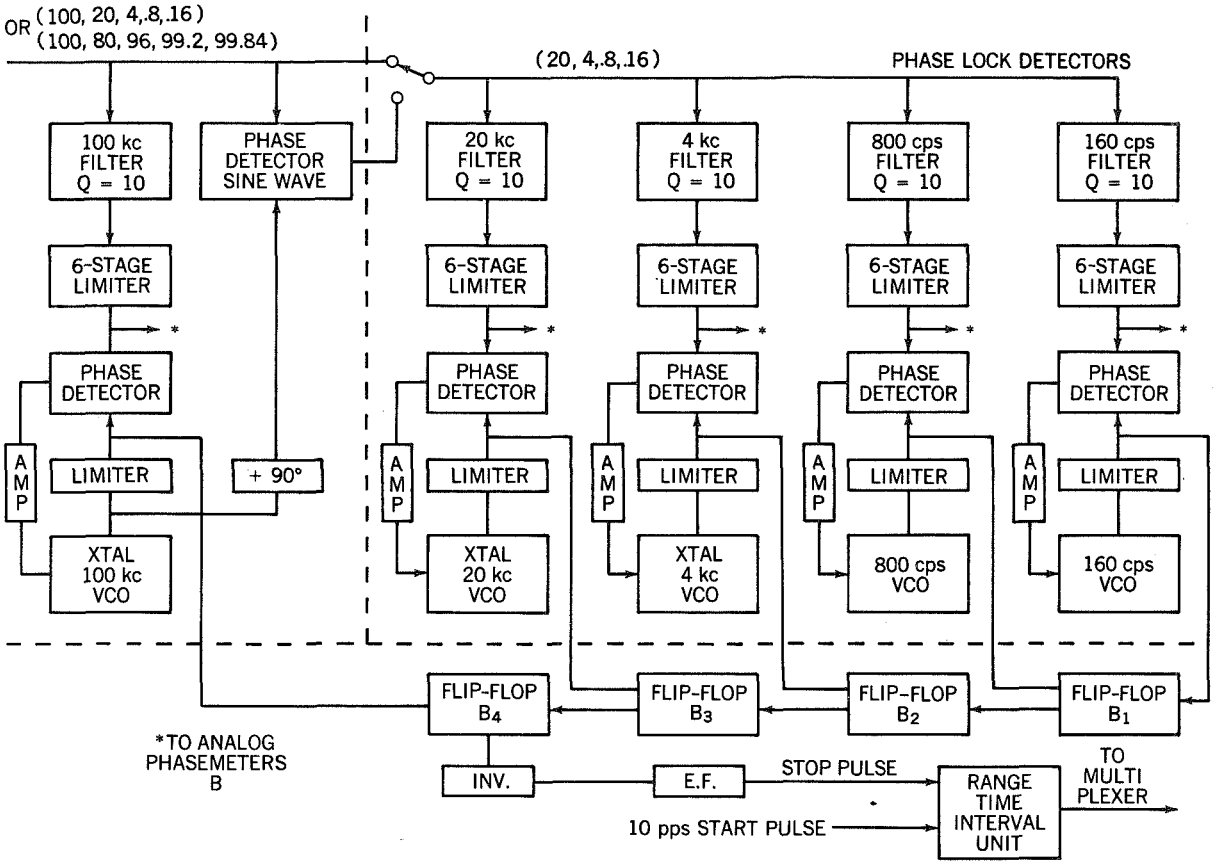

FIGURE 8.—Range extraction unit.

As an auxiliary measure, analog phasemeters and analog recording are provided as shown in Figure 10. Reference tones are obtained from the tone generator and signal tones from the Range Extraction Unit. Receiver AGC and time signals are also displayed on the recorder.

Doppler information is obtained from the Doppler Extraction Unit (Fig. 11). The Doppler signal with its 200 kc offset is gated by the 10 pps start pulse and fed to a preset counter which starts and stops the time interval unit. The time interval unit counts at a 10 Mc rate.

The range and Doppler information, together with time from the Digital Clock, is sent to the multiplexer and buffer storage for printout on paper tape punches as in Figure 12. The

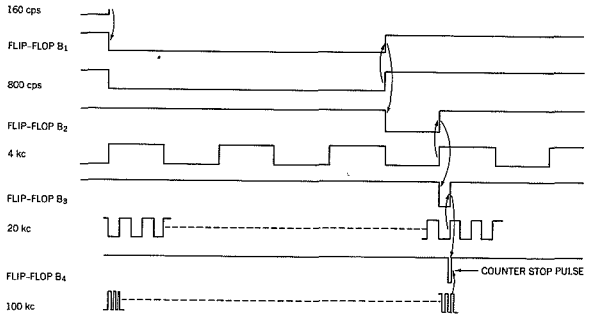

FIGURE 9.—Sidetone phasing diagram.

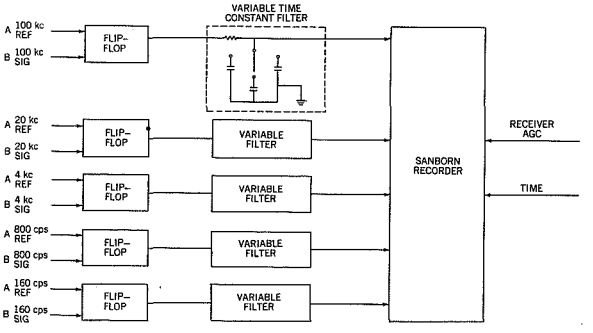

FIGURE 10.—Analog phasemeters.

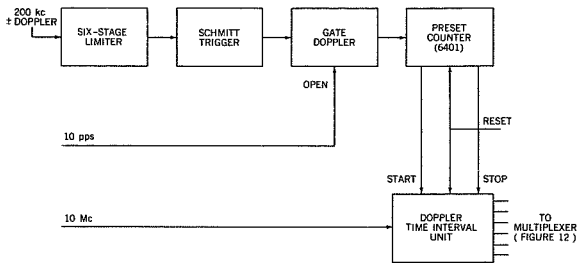

FIGURE 11.—Doppler extraction unit and time interval unit (see Fig. 1).

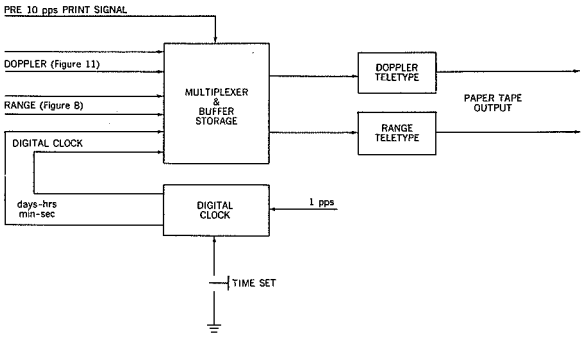

FIGURE 12.—Data readout equipment and digital clock (see Fig. 1).

punches then present the information ready for teletype relay to the computing center.

Antennas

The choice of antennas for the ranging system is essentially determined by two categories of operation. The first is for satellite altitudes below 10000 km and the second for altitudes beyond 10000 km. To track satellites up to 10000 km, high tracking rates will be required; and since the system will be used to produce either guiding or predicting information for very narrow beamwidth antennas (less than 1 degree) a beamwidth of at least 3 degrees will be required. Because this is still a very narrow beamwidth, autotracking is required.

With these considerations in mind, a 14 ft diameter dish antenna with a gain of 35 db at 1600 Mc, or its equivalent, has been chosen. On the basis of this antenna and a range of 10000 km, the minimum system is calculated as shown in Tables 2 and 3.

When the range is beyond 10000 km, the higher sidetones are not necessary and a reduction in transponder bandwidth can be realized. Thus, for a range of 100,000 km, the minimum system calculation is as shown in Tables 4 and 5.

These calculations represent the minimum satellite transmitter power required. They are very conservative as no satellite antenna gain is assumed, the ground receiver noise figure of 3 db can be bettered and the required signal-to-noise ratios have a 6 db margin included. Also, very conservative receiver and sidetone bandwidths are assumed. They may be bettered by approximately 10 db.

TABLE 2.—*Characteristics of the Minimum System for Transmission-to-Satellite at 10,000 km*

System parameter	Value
1535 Mc ground transmitter power	+60 dbm
Ground antenna gain	+35 db
Polarization loss	−3 db
Path loss (1535 Mc)	−176.5 db
Vehicle antenna gain	0 db
Received total power (satellite)	−84.5 dbm
Receiver noise power at 250 kc bandwidth and noise figure of 11 db.	−109 dbm
Total signal-to-noise ratio in vehicle	+24.5 db

TABLE 3.—*Characteristics of the Minimum System for Transmission to Ground at 10,000 km*

System parameter	Value
Vehicle antenna gain	0 db
Ground antenna gain	+35 db
Polarization losses	−3 db
Path loss (1705 Mc)	−177.3 db
Total losses	−145 db
Receiver noise power at 100 cps bandwidth and noise figure of +3 db.	−152 dbm
Required carrier power for carrier-to-noise ratio of +20 db.	−132 dbm
Required transmitter carrier power	+13 dbm
Required minimum total transmitter power for remaining 5 sidetones at 10 cps bandwidth each and S/N= +30 db (each sidetone requires −132 dbm) add 7 db.	+20 dbm
Local oscillator leak power	+13 dbm
Total transmission power (13 dbm+ 7 db+3 db) 200 milliwatts.	+23 dbm

TABLE 4.—*Characteristics of the Minimum System for Transmission to Satellite at 100,000 km.*

System parameter	Value
Transmitter power increase 1 kw to 10 kw.	+70 dbm
Ground antenna gain	+35 db
Polarization loss	−3 db
Path loss (1535 Mc)	−196.5 db
Vehicle antenna gain	0 db
Received total power	−94.5 dbm
Receiver noise power with a bw of 40 kc and a noise figure of 11 db.	−117 dbm
Total signal-to-noise ratio in vehicle	+22.5 db
Additional ground antenna gain by using 85-foot diameter antenna (total gain=50 db).	+15 db
Total signal-to-noise ratio in vehicle	+37.5 db

TABLE 5.—*Characteristics of the Minimum System for Transmission to Ground at 100,000 km*

System parameter	Value
Vehicle antenna gain	0 db
Ground antenna gain	+35 db
Polarization losses	−3 db
Path loss (1705 Mc)	−197 db
Total loss	−165 db
Receiver noise power at 30 cps bandwidth and a noise figure of 3 db.	−156 dbm
Required carrier power for carrier-to-noise ratio of +20 db.	−136 dbm
Required minimum carrier power	+29 dbm
Required power for sidetones	+7 dbm
Required power for local oscillator	+3 dbm
Total transmitter power (minimum)	+39 dbm (10 watts)
85 ft diameter antenna gain	+50 db
Total transmitter power required	+24 dbm (250 milliwatts)

For transmission to the moon (400,000 km) a vehicle antenna gain of 25 db is assumed and an 85 ft diameter ground antenna is mandatory.

The distance is about four times (12 db) greater than the 100,000 km case; therefore, the net gain is +13 db (Tables 6 and 7).

TABLE 6.—*Received Signal to Noise Ratio for Transmission to Satellite at 400,000 km*

Vehicle antenna gain (db)	Received signal-to-noise ratio (db)
+25	+50. 5
+7	+32. 5

TABLE 7.—*Required Transmitter Power for Transmission to Ground at 400,000 km*

Vehicle antenna gain (db)	Required transmitter power
+25	+11 dbm (+12 milliwatts)
+7	+28 dbm (0.63 watt)

RANGING SYSTEM APPLICATIONS

At present it is contemplated that the ranging system will be required on the Relay I, the Synchronous Communications (SYNCOM) and the Eccentric Orbiting Geophysical Observatory (EGO) satellites and for Atlas Agena injection tracking.

Relay I Satellite

The Relay I communications satellite has a planned eccentric orbit with an apogee of 4000 km. Because the satellite's flight equipment had been established, the only system which could be used with this satellite was one that employed the existing electronic equipment on board. This limitation made it impossible to incorporate both a Range and a Range Rate System. A Range Only System, however, could be used without modification of the existing on-board transponder, and by using only a part of the ground based ranging equipment. Figure 13 shows the block diagram of the equipment provided. The existing Relay I receivers, transmitters, antennas, and transponder were used on a time-share basis with the communication experiments which constitute the satellite's mission.

Fortunately, the Relay I transponder has two extra channels with narrower bandwidths (2 Mc) than the main experiment channel. These channels were provided for duplex voice

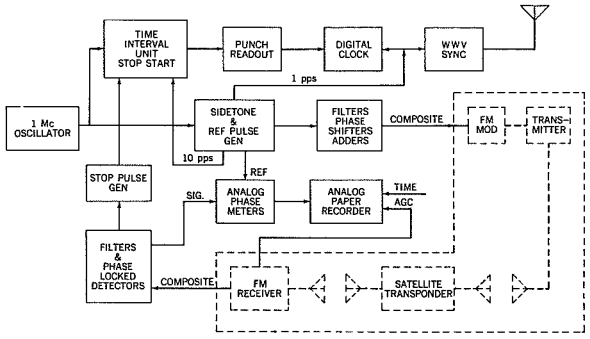

FIGURE 13.—Relay I system block diagram.

communication and can be operated when the main channel is turned off. With these two channels, simultaneous ranging can be performed by two stations. Three systems were originally planned, for use at sites in England, Washington, D.C., area, and Goldstone, Calif. (Fig. 14). The calculations for the Sidetone Range Only System for Relay I at 10,000 km are shown in Tables 8 and 9.

Synchronous Communications Satellite [SYNCOM]

SYNCOM is the second of a series of communication satellites in the NASA communications experiment program. Initially it will be a fairly light satellite with moderate communication abilities and will be placed in a 24-hour (synchronous) orbit. Perliminary planning calls for the satellite to be placed in orblt with a 33 degree inclination angle approximately centered on the 30 degree meridian. The

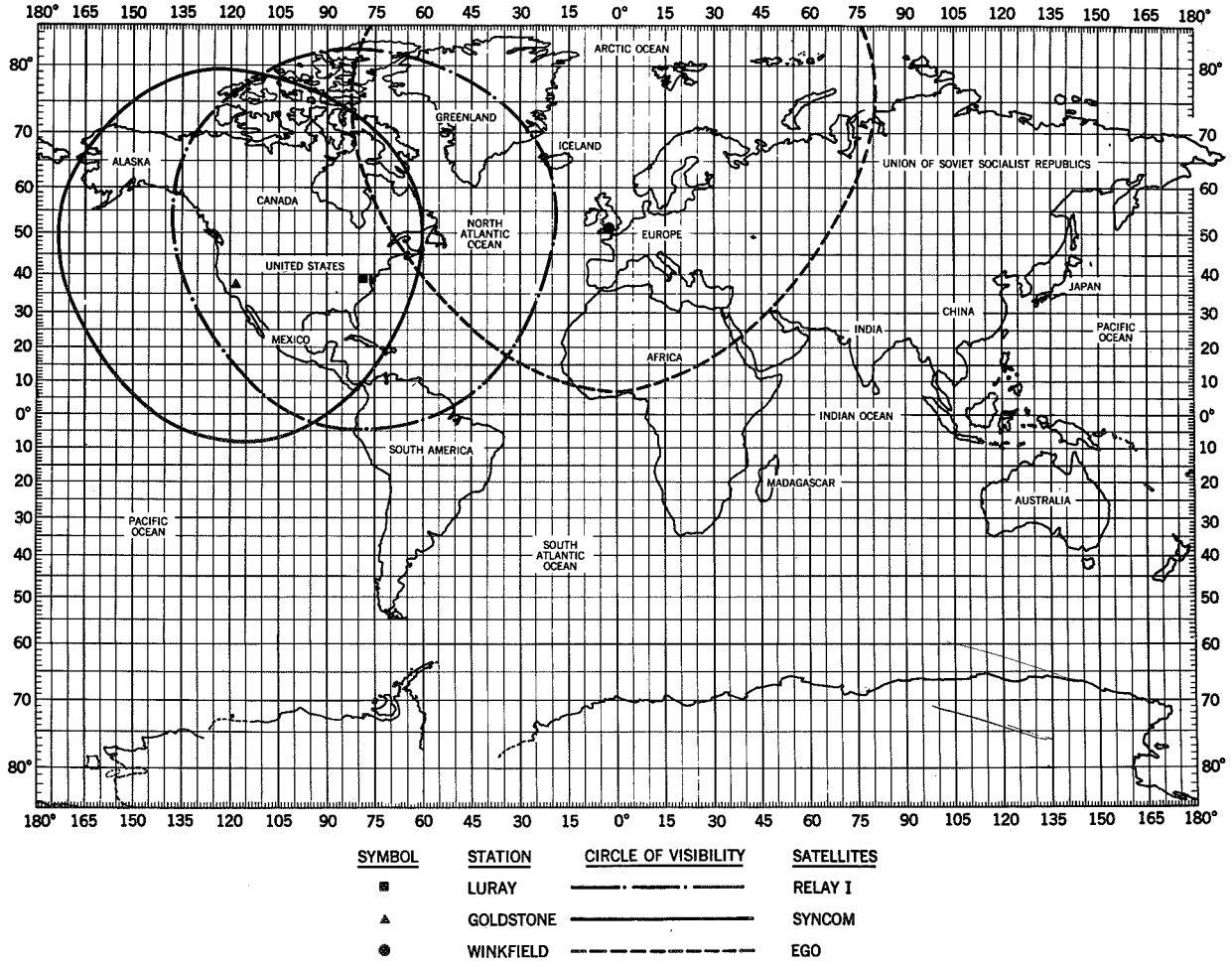

FIGURE 14.—Radio horizon coverage for Relay I station (1500 mi altitude).

TABLE 8.—*Characteristics of the Relay I System for Transmission to Satellite at 10,000 km* [1]

System parameter	Value
Transmission power, 10 kw	+70 dbm
Satellite antenna gain	0 db
Losses	−3 db
Ground antenna gain 40 ft diameter antenna at 1700 Mc	+44 db
Path loss for 10^4 km at 1700 Mc	−177 db
Received signal power	−66 dbm
Receiver noise figure	11 db
Receiver noise power at 2 Mc bw	−100 dbm
Received signal-to-noise ratio (FM, M.I.=2)	+34 db

[1] Synchronous detection of the FM carrier is assumed only for the ranging system.

TABLE 9.—*Characteristics of the Relay I System for Transmission to Ground at 10,000 km* [1]

System parameter	Value
Transmission power, 10 watts	+40 dbm
Satellite antenna gain	0 db
Losses	−3 db
Ground antenna gain 40 ft diameter antenna at 4 Gc	+51 db
Path loss for 10^4 km at 4 Gc	−184 db
Received signal power	−96 dbm
Receiver noise power density at 290°K	−174 dbm
Receiver noise power at 100 cps bw	−154 dbm
Received carrier-to-noise ratio	+58 db
Sidetone signal-to-noise ratio 10 cps bw assuming 10 percent total power available in sidetone	+58 db

[1] Synchronous detection of the FM carrier is assumed only for the ranging system.

transponder will receive on approximttely 7 Gc and transmit on 1.8 Gc with a power output of 2 watts. Two channels are provided with 500-kc bandwidth. The design of the transponder is so similar to that required for a coherent range rate tracking system that the program manager has agreed to incorporate coherent translation from 7 Gc to 1.8 Gc and also to transmit a multiple of the satellite local oscillator frequency.

The location of the synchronous orbit is such that tracking performed by the Minitrack network will be marginal. Although the accuracies

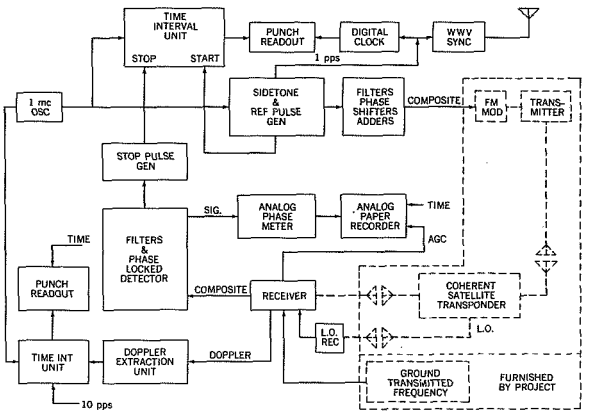

FIGURE 15.—Syncom block diagram.

required are not very great—since tracking is mainly needed for station-keeping—range and range rate measurements are still necessary.

It is planned to incorporate the Range and Range Rate System at three SYNCOM ground stations, using the available SYNCOM modulators, transmitters and antennas (Fig. 15).

With the two channels available, simultaneous tracking can be performed by two ground stations, time-sharing the satellite with the communications experiment. Thus, accurate angle measurements can be made by triangulation, as well as by the range and range rate data, and complete position information can be obtained.

An example of the calculated system parameters is given in Tables 10 and 11.

TABLE 10.—*Characteristics of the SYNCOM System for Transmission to Satellite at 40,000 km* [1]

System parameter	Value
Ground transmission power, 2 kw	+63 dbm
Satellite antenna gain	0 db
Losses	−3 db
Ground antenna gain 30 ft diameter at 7 Gc	+54 db
Path loss for 4×10^4 km at 7 Gc	−202 db
Receiver signal power	−88 dbm
Receiver noise figure	12 db
Receiver noise power at 250 kc bw	−108 dbm
Received signal-to-noise ratio	+20 db

[1] Synchronous detection of the FM carrier is assumed only for the ranging system.

TABLE 11.—*Characteristics of the SYNCOM System for Transmission to Ground at 40,000 km* [1]

System parameter	Value
Satellite transmission power, 2 watts	+33 dbm
Satelitte antenna gain	0 db
Losses	−3 db
Ground antenna gain 30 ft diameter antenna at 1,800 Gc	+42 db
Path loss	−190 db
Received signal power	−118 dbm
Receiver noise power density at 290°K	−174 dbm
Receiver noise power at 100 cps bw	−154 dbm
Received carrier-to-noise ratio	+36 db
Sidetone signal-to-noise ratio at 10 cps bw assuming 10 percent of total power available in sidetone	+36 db

[1] Synchronous detection of the FM carrier is assumed only for the ranging system.

Eccentric Orbiting Geophysical Observatory [EGO]

The Eccentric Orbiting Geophysical Observatory (EGO) satellite will be launched into a highly eccentric orbit with an apogee of 100,000 km and an inclination of 33 degrees. This high an apogee is not conducive to tracking by the Minitrack network. It is felt that the Range and Range Rate System can augment the Minitrack network so that accurate postion information required by the experimenters can be obtained. Three complete Range and Range Rate stations, and an appropriate transponder are planned for this satellite. The stations will be located to obtain a maximum of data when the satellite is near apogee.

For system sensitivity calculations, refer to the antenna section of this report (page 840).

Agena-B Injection Tracking

It has been suggested that it would be desirable to obtain very precise information on position and velocity during the orbit injection period for the Agena-B vehicle series. Both EGO and the Orbiting Astronomical Observatory (OAO) use an Agena-B, and injection occurs over northern Australia, four Range and Range Rate Systems are proposed with a simplified ground antenna system. The suggested station locations are shown in

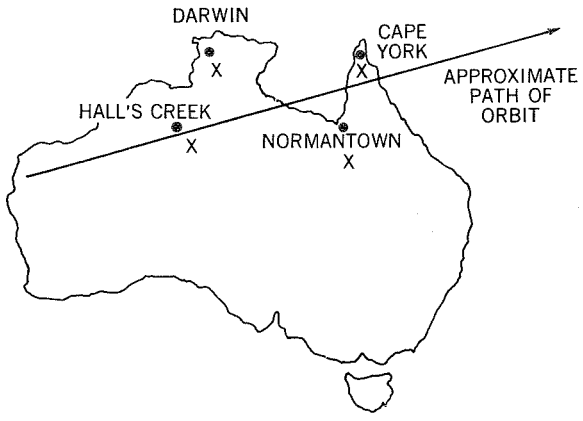

FIGURE 16.—Typical arrangement in Australia for Agena injection tracking.

Figure 16. The system sensitivity calculations are given in Tables 12 and 13 for a 2-foot diameter antenna with a beamwidth of 20 degrees. The greatly simplified antenna system will reduce the cost of the overall system considerably; however, if immediate access to final position information is required, a small, general purpose digital computer will be included at one station.

TABLE 12.—*Characteristics of AGENA Injection for Transmission to Satellite at 1000 km* [1]

System parameter	Value
Ground transmission power, 1 kw	+60 dbm
Satellite antenna gain	−8 db
Losses	−3 db
Ground antenna gain 2 ft diameter at 1535 Mc	+17 db
Path loss 1000 km at 1535 Mc	−156 db
Received signal level	−90 dbm
Receiver noise figure	11 db
Receiver noise power at 250 kc bw	−109 dbm
Received signal-to-noise ratio	+19 db

[1] Satellite antenna gain of −8 db is assumed because shroud may still be on satellite.

PRELIMINARY SYSTEM TEST

General

While the concepts for the Range and Range Rate System are still being formulated, a concurrent program for preliminary testing is

TABLE 13.—*Characteristics of AGENA Injection for Transmission to Ground at 1000 km* [1]

System parameter	Value
Satellite transmission power, 0.2 watt	+23 dbm
Satellite antenna gain	−8 db
Losses	−3 db
Ground antenna gain 2 ft diameter at 1.7 Gc	+18 db
Path loss 1000 km at 1.7 Gc	−157 db
Received signal level	−127 dbm
Receiver noise power density at 290°K	−174 dbm
Receiver noise power at 100 cps bw	−154 dbm
Received carrier-to-noise ratio	+27 db
Received sidetone signal-to-noise ratio at 10 cps bw assuming 10 percent total power available in sidetone	+27 db

[1] Satellite antenna gain of −8 db is assumed because shroud may still be on satellite.

being carried out by the Goddard Space Flight Center.

A complete Range Only System was designed and constructed to check out the system's capability of automatic ambiguity resolution, to determine its sensitivities for the communication links used, and to verify that the resolution of 15 meters was realizable. The Doppler portion has not been instrumented to date but special receivers for this system testing are expected very shortly. As soon as they are incorporated into a system configuration, that portion will also be tested.

The configuration chosen is the one at Blossom Point, Md. (Fig. 17). It consisted of a range tone generator consisting of a 1 Mc oscillator stabilized to 5 parts in 10^{10} feeding

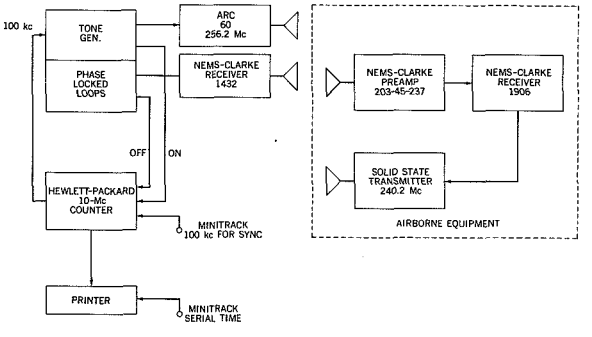

FIGURE 17.—Blossom Point test block diagram.

a system of Packard-Bell transistorized modules; a modified commercial version of an ARC–60 AM transmitter; a Nems-Clarke AM receiver with a 300 kc bandwidth; a 2-watt phase-modulated solid-state transmitter from Vector Telemetry Corp.; an FM Nems-Clarke receiver modified to produce PM synchronous detection operating at 500 kc bandwidth, an H.P. 524C frequency counter used as time interval unit; an H.P. 561A printer.

The range tone generator produced four sidetone frequencies: 100 kc, 20 kc, 4 kc, and 800 cps. A frequency of 160 cps was contemplated, but was not used for two reasons. First, the transmitter on hand could not be modulated properly at this frequency, and secondly, the airplane range was not expected to exceed 100 mi so there was no need for the finer (580 mile) ambiguity resolution provided by the 160 cps. The tone generator outputs fed the amplitude modulated transmitter which was transmitting 1 watt at 256.5 Mc. A 10-element TACO yagi array provided 10 db of gain. The signal was received by the airborne equipment in the plane. A preamplifier was used to reduce the noise figure to 3 db in the Nems-Clarke receiver. A phase-modulated, solid-state, transmitter transmitting 2 watts at 240.2 Mc was used to retransmit the received signal back to the ground station. The second Nems-Clarke receiver on the ground was used to receive the retransmitted signal. It was preceded by another yagi, with 10 db antenna gain. This receiver was normally a phase-locked FM receiver with a 500 kc bandwidth, but was modified so that the phase-locked loop was narrowed in frequency to about 200 cycles bandwidth, effectively providing PM synchronous detection.

The modulation indices for the transmitter were adjusted on the ground from the transmission end so that the received signals at the four frequencies were all equal in amplitude when detected by the ground receiver. Each signal was fed through individual active tuned filters and then fed to phase-locked oscillators, as shown in Figure 8.

The remaining system is standard, using a H.P. frequency counter for the 10 Mc time

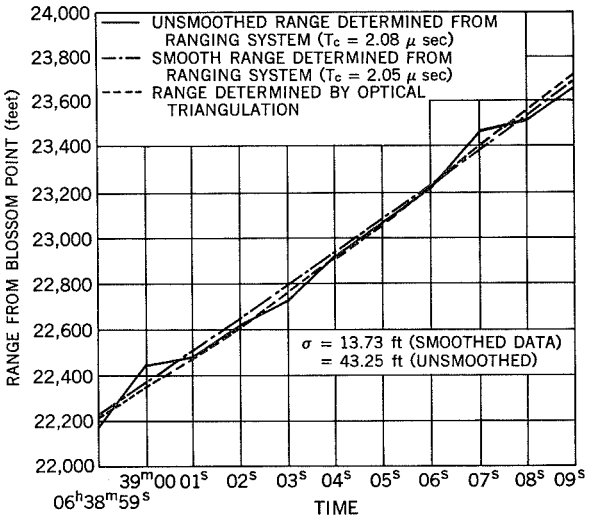

FIGURE 18.—Graph of residuals.

interval unit, a frequency standard, and a H.P. digital printer which printed at a rate of four readings per second. This data was compared to the optical tracking data and results from one run are shown in Figure 18.

In addition to the automatically ambiguity resolved digital print out, four analog phasemeters were included, consisting of essentially 4 flip-flops and four simple R–C network filters with time constants of 0.1 sec. The phase-lock loops at 100 kc, 20 kc, 4 kc, and 800 cps had corresponding loop bandwidths of 30 cps, 20 cps, 10 cps, and 3 cps. The outputs from the analog phasemeters were recorded on an eight-channel Sanborn recorder along with timing and AGC from the receiver.

Because multivibrators were used for the voltage controlled oscillators at the three lower frequencies, and because the power supply system tended to drift, there were instabilities in the VCO's. Apart from this, the system operated very satisfactorily. Various amounts of attenuation were inserted alternately and simultaneously in both the ground transmitter end and the airborne transmitter end, and again the system behaved as was expected. Spurious outputs from the ambiguity-resolving logic were noted when the received signal levels approached 120 dbm—this would be expected from an AM system operating at such a wide bandwidth. It should be pointed out that the antennas used on board the aircraft were standard commercial UHF stub antennas with probable gains of −5 to −10 db.

Calibration and Data Analysis

To provide a standard by which to calibrate the ranging system, two sidereally driven astrographic cameras located at Blossom Point and Blossom Point Annex were used to determine the airplane's position optically. The camera at Blossom Point Annex is located approximately 6 miles due east of the camera at Blossom Point. A second order survey was performed to locate the position of the camera at the Annex with respect to the camera at Blossom Point to an accuracy of within 6 inches.

The cameras are identical, each consisting of an Air Force aerial reconnaissance lens on a sidereal mount. Each camera has an *f*5, 40-inch focal length lens, and each covers an angular field of about 11 by 14 degrees. The image is recorded on an 8 x 10-inch glass photographic plate in a holder at the bottom end of the camera tube.

The sidereal mount allows the cameras to rotate about two perpendicular axes which intersect at the nodal point of the lens. The polar axis is aligned parallel to the earth's axis of rotation. The cameras may be rotated about the declination axis and clamped in the desired angular position.

The calibration was performed by flying an airplane on a West-to-East course between the two stations at night (Fig. 19). The airplane contained a flashing light (triggered by the Minitrack time code) and the ranging transponder. As the airplane passed over the Blossom Point area the two cameras simultaneously photographed the trail of flashing light images against a star background. These photographic plates were then reduced by the standard techniques developed for Minitrack calibrations. In this manner the direction cosine of the flashing light in the airplane was determined from both cameras, and the range of the light from the Blossom Point transmitter and receiver was accurately determined through triangulation. The airplane was flown at an

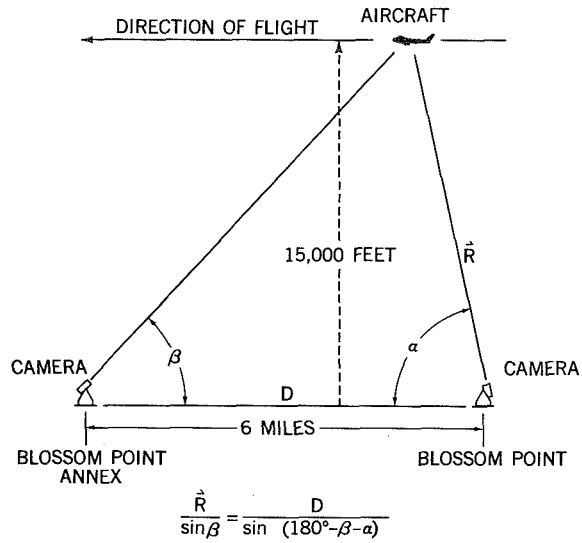

FIGURE 19.—The ground setup at Blossom Point, Md.

altitude of 15,000 ft so that the resulting triangle approximated an isosceles triangle. In this configuration the computed range is the least sensitive to small random errors within the direction cosines from the cameras to the flashing light.

Ideally the two vectors defined by the set of direction cosines from the two cameras should exactly meet at the flashing light. However, because of small errors in the measurement and reduction of the optical data, that ideal is seldom attained. In such cases the computer solves for the shortest line connecting the two vectors and locates the flashing light at the mid-point of this line. A measure of the accuracy of the optical range determination can be deduced from the length of this connecting line.

The range of the airplane from the Blossom Point ranging transmitter and receiver can be found by the formula

$$r=49.1679\,(N-T_c)$$

where r is the range in feet, N is the raw reading of the range counter, and T_c is the electronic time delay within the ranging system measured in units of 10^{-7} sec.

Second and possibly third order time correction terms would have to be included if the system were being used to track a fast moving satellite at a great distance. However, an analysis has shown that this formula is entirely sufficient for the case of an airplane calibration run.

It is the purpose of the calibration to determine the values of T_c such that the parallax corrected range as computed from the optical calculations and the ranging system shall agree as closely as possible. The calibration time constant derived on the basis of a single observation is given by

$$T_c=\frac{49.1679N-R}{49.1679}$$

where R is the computed range determined by optical triangulation.

The T_c adapted as a result of this calibration is the simple average of T_c's determined for each observation.

The H. P. printer used to record the time and counter (N) readings was not functioning perfectly at the time of calibration, and some jitter was observed in the recording of the least significant digit the counter reading. For the

TABLE 14.—*Tabulation of Ranging Data*
[$T_c=20.8\times10^{-7}$ sec]

Time	N	$\overline{N}$	r (ft)	R (ft)	r (ft)	ΔR (ft)
06h38m59s	472	472.650	22,219	22,204	−15	20.0
39m00s	477	475.442	22,352	22,342	−10	20.2
01s	478	478.278	22,494	22,480	−14	1.8
02s	481	481.158	22,637	22,623	−14	2.3
03s	483	484.082	22,779	22,769	−10	1.7
04s	487	487.051	22,927	22,918	−9	2.0
05s	490	490.064	23,074	23,072	−2	21.6
06s	493	493.122	23,222	23,225	+3	0.1
07s	498	496.223	23,374	23,386	+12	1.5
08s	499	499.369	23,532	23,549	+17	1.5
09s	502	502.559	23,689	23,716	+27	1.3

N= Uncorrected 10 Mc counter reading.
$\overline{N}$= Smoothed counter reading (2d degree least squares pit).
r= Computed range from ranging system using $T_c=20.8$.
R= Computed range from optical triangulation.
r= Range residual (R-r).
ΔR= Miss distance in optical triangulation.

reason, as well as the fact that the ranging system has a resolution only to ± 50 ft, a second order polynomial was fitted to the raw integral one-second counter readings by the least squares method and the range was determined from the smoothed data.

A calibration time constant of 20.8×10^{-7} sec was computed for the ranging system. Table 14 shows some of the computed results of the ranging calibration. The probable error derived from the smoothed data was found to be 13.73 ft.

ACKNOWLEDGMENTS

The authors wish to thank Dr. F. O. Vonbun for establishing the accuracy needed for such a system, Mr. V. R. Simas for suggesting the method of coherent transponding described in this report, and Dr. Elie Baghdady of ADCOM Inc. for the many consultations provided by him and other members of his company.

REFERENCES

1. BAGHDADY, E. J. (Ed.), "Lectures on Communication System Theory," New York: McGraw-Hill, 1961.
2. NICHOLS, M. H., and RAUCH, L. L., "Radio Telemetry," 2d Ed., New York: John Wiley and Sons, 1956.
3. "Final Report Project Relay Active Communication Satellite System Study," Contract NAS 5-825, 2 Vol., Space Technology Labs. 8949-0004-RU-000, Apr. 19, 1961.
4. VONBUN, F. O., "Analysis of the 'Range and Range Rate' Tracking System," NASA Technical Note D-1178, February 1962.

Appendix A

HIGH-ACCURACY SATELLITE TRACKING SYSTEMS

INTRODUCTION

The need for greater reliability and accuracy in measuring the range, range rate, direction cosines and angle rates of distant missiles and satellites has recently intensified the need for new radio tracking systems, or for extension of the capabilities of existing ones. New or improved communication techniques are needed to yield these measurements within tight tolerances despite various limiting factors. Several promising approaches are under study by ADCOM, Inc., of Cambridge, Mass., under NASA contract No. NAS5–1187, in close coordination with and in direct support of activities of the Goddard Space Flight Center. The main objectives are to provide information needed for designing distance, velocity, and angle measuring radio systems that meet both immediate and future NASA requirements.

This discussion constitutes the first Quarterly Progress Report and the "Task I Report" specified in the contract, and it presents the results of investigations carried out at ADCOM, Inc., between April 20 and June 30, 1961.

FUNDAMENTAL CONSIDERATIONS

Radio techniques for measuring ranges, velocities, and relative positions of distant objects make use of three basic properties of wave propagation:

1. Electromagnetic waves travel with a finite and known speed.
2. The instantaneous phase of a traveling wave (with respect to a standard reference) changes linearly with the distance traveled.
3. The frequency f_{rec} received by an observer moving with velocity v *toward* a source which is emitting a note of frequency f_{trans} is given by

$$f_{\text{rec}}=\sqrt{\frac{c+v}{c-v}}f_{\text{trans}}$$

where c is the velocity of wave propagation in the intervening medium.

Property 1 is the basis for radar-type pulsing distance-and-velocity measurement systems. Such systems may or may not use a vehicle-borne transponder, although a system capable of repeating signals to a ground station is generally preferable.

Property 2 can be used in a number of ways to extract tracking data. For example, the direction cosines of a beacon-carrying missile can be determined from the instantaneous phase difference between a signal from the missile as received simultaneously by two antenna pairs equally spaced on short, mutually perpendicular, accurately measured baselines. Similarly, in the sidetone ranging technique, the instantaneous phase shift acquired by tones modulating an RF carrier, after transmission from the ground station, amplification and retransmission (or reflection) at the missile, and final reception back at the ground station can (after correction for spurious phase shifts for the Doppler effect) be used to determine the total distance to and from the missile.

Property 3, the Doppler effect, is the basis for measuring the rate at which a radiating source approaches, or recedes from an observer. If the transmitter frequency is known the preceding equation can be solved for the relative velocity. The Doppler frequency shift ($f_{\text{trans}}-f_{\text{rec}}$) experienced by a narrow-band signal in a receiver that moves with vector velocity V_{missile} and receives a wave traveling in vector direction $\vec{n}_T$ from a stationary transmitter is approximated by

$$\frac{(\vec{V}_{\text{missile}}\cdot\vec{n}_T)\,f_{\text{trans}}}{c+\vec{V}_{\text{missile}}\cdot\vec{n}_T}$$

for small values of V. If the signal is re-radiated in a new vector direction $\vec{n}_R$ and is re-received by a stationary receiver, the narrow-band sig-

nal will experience an additional Doppler shift of

$$\frac{\vec{V}_{\text{missile}} \cdot \vec{n}_R}{c+\vec{V}_{\text{missile}} \cdot \vec{n}_R}\left(1-\frac{\vec{V}_{\text{missile}} \cdot \vec{n}_T}{c+\vec{V}_{\text{missile}} \cdot \vec{n}_T}\right) f_{\text{trans}}.$$

These elementary properties of traveling waves can be applied in a variety of ways to measure the range, velocity, and direction cosines of a missile. Systems using missile-borne transponders capable of repeating signals to a ground station would seem to provide increased flexibility, simplicity, and reliability in ground reception at the cost of missile-borne power and payload weight. Severe limitations on the weight and volume of missile-borne equipment are imposed by considerations of available thrust and total impulse. An appropriate choice of modulation and signal-processing techniques may greatly increase the reliability and accuracy attainable with a given amount of transponder power.

Spacecraft communications and tracking are handicapped also by the uncertainties of propagation. Foreknowledge of the nature of the perturbations imposed on the signal in transit aids the choice of modulating waveforms most easily distinguished from, and most immune to, fluctuations in transmission. Even in the absence of sufficient data on this subject, however, it is possible to anticipate the likely difficulties and select modulation waveforms that can be isolated from disturbances with a minimum of error in identifying the information-bearing characteristics.

There are also important uncertainties in our knowledge of the speed of light: the most refined measured value known today fixes it at $c=299792.5\pm0.4$ km/sec. Since the speed of light enters vitally into all the basic propagation computations, the inaccuracy in the value of c ultimately limits the accuracy of all radio tracking measurements. For example, in the measurement of range, if we ignore the contributions of all other potential sources of error, the range error ΔR caused by the uncertainty ±0.4 km/sec in c is approximately $1.33\times10^{-6}R$. If $R=250{,}000$ mi, then $\Delta R\approx\pm\frac{1}{3}$ mi.

Finally, there is the inevitable problem of circuit stability and reliability, especially where reference oscillators form an essential part of the system.

SURVEY OF RADIO TRACKING SYSTEMS

Angle Measurement

The basic method of angle tracking requires the measurement of the phase difference between the carrier signals as received simultaneously at separate antennas from a single remote source. The carrier frequency and antenna separation (baseline length) are design parameters; the measured variable is the carrier phase difference. Provided that the baseline is very short compared to the distance to the object being tracked (so that the arriving rays are essentially parallel), the cosine of the angle included between the line of sight and the baseline may be calculated as follows:

$$\cos\theta=\phi_d c\omega_c D,$$

where ϕ_d=phase difference between received signals (radians), $c=299792.5\pm0.4$ km/sec, ω_c=carrier frequency (radians/sec), D=baseline length (km). There are practical limits to the precision of direct measurement of small phase shifts. Long baselines and high carrier frequencies are therefore indicated, in order to provide increased differential carrier phase shift.

The Minitrack system measures the ratio ϕ_d/ω_c in the equation above. This ratio represents the time delay between the reception of corresponding phases of the carrier wave at the separate antennas. Because of practical limits on the resolution of small time delays, use is made of the heterodyne principle, which provides that relative phase shifts may be preserved while translating signals in frequency. The Minitrack system translates the incoming 108 Mc signals to 500 cps signals for phase comparison. Because of the preservation of phase shifts, the differential time delay of reception is magnified by the ratio $108\times10^6/500=2.16\times10^5$ prior to the time delay measurement. The digital phasemeter counts the pulses from a standard 500 kc source during the delay interval measured; hence, it has a delay time resolution of 2 μ sec. Referring this resolution

limit to the 108-Mc signal reduces the differential delay resolution at the antennas to $2\times10^{-6}/2.16\times10^{5}=9.25\times10^{-12}$ sec. Differential time delay resolution may be translated directly into differential range resolution as follows:

$$\Delta R=c\Delta t=9.83\times10^{8}\times9.25\times10^{-12}$$
$$=9.1\times10^{-3}\text{ foot.}$$

For the 500-foot baseline employed, the resolution of direction cosines becomes $9.1\times10^{-3}/500=1.82\times10^{-5}$. For angles near the zenith, the resolution then becomes 3.7 seconds of arc.

The AZUSA tracking system similarly employs the heterodyne principle to preserve differential carrier phase shift at a frequency of 2 kc for fine angle measurement. In addition, the phase shift is magnified by frequency multiplication of the 2-kc signal to 320 kc. The phase shift at 320 kc thus becomes 160 times as great as the original carrier phase shift. It is necessary to resolve the phase shift at 320 kc only to the nearest ½ cycle. This is equivalent to resolving the 5-Gc carrier phase shift to 1/320 cycle. In terms of range difference, resolution is thereby provided to about 0.0003 ft.

A baseline of about 164 feet is employed by AZUSA for the fine angle measurement. Hence the fine direction cosine resolution becomes $0.0003/164\pm2\times10^{-6}$.

The MISTRAM system uses a 10,000-foot baseline together with an 8-Gc carrier to provide a range difference accuracy of 0.03 ft. The technique employed for phase measurement has not been disclosed in available documents.

To obtain accuracies of angle measurement commensurate with the available resolution, it is necessary to maintain stable carrier frequencies and baseline lengths. Short baselines may be stabilized through choice of materials of construction for waveguides, temperature control, and protection of guides from mechanical stress. MISTRAM, because of its long baselines, employs in addition a correction technique whereby the two-way phase shift of waveguides is continuously measured and used to correct for changes in one-way phase shifts.

Range Measurement

The basic principle employed for range measurement is that the two-way phase shift of an RF carrier or a modulation of the carrier is proportional to the range. AZUSA and MISTRAM measure carrier phase shifts for high-resolution range and range rate determination, and modulation phase shifts for ambiguity resolution. AZUSA employs three harmonically related waves to modulate the carrier frequency: 98.3 kc, 3.93 kc, and 157 cps. The measured phase shift of the received 98.3-kc component can provide unambiguous range data, except during temporary signal loss. The two lower frequencies are used only as needed to resolve coarse and intermediate range ambiguities. A ranging system under development by the Goddard Space Flight Center proposes the use of 5 or 6 harmonically related waves (500 kc, 100 kc, 20 kc, 4 kc, 800 cps, 160 cps) to provide a single-sideband modulation of the carrier. Here, again, the measured phase shift of the highest component, 500 kc or 100 kc, provides unambiguous range information, with the provision that the lower-frequency terms may be employed to resolve ambiguities resulting from signal loss or lack of initial data.

The MISTRAM system for unambiguous ranging uses a ramp function to sweep the carrier from 7.884 Gc to 7.892 Gc. During the sweep modulation, the cycles of phase difference between the transmitted and received carriers are counted. Since the maximum frequency deviation is known to be precisely 8 Mc, the average range during the sweep may be determined from $R=Nc/(4\pi\times8\times10^{6})$, where N is the number of cycles counted and c is the velocity of propagation. Note here that if only *whole* cycles are counted, the resolution of range ambiguity is limited to 9.77 ft. To provide for the published system range accuracy of 0.4 ft, some means not presently apparent must be employed to refine the measurements of carrier phase shift.

The Minitrack system provides no ranging data, since no communication exists from the ground to the satellite.

The importance of preserving carrier phase information in the transponder is recognized in

both the AZUSA and MISTRAM systems, where phase-locked loops provide for retransmission of coherent carriers having constant frequency offsets from incoming signals. In addition, the AZUSA transponder plays a part in an overall system automatic-frequency-and-phase-control loop. By this system, the ground-received carrier is maintained at 5 Gc, whereas the ground-transmitted carrier contains the Doppler information. An apparent advantage is that angle measurements may be referred to a constant carrier wavelength.

The transponder proposed for the Goddard Space Flight Center single-sideband ranging system must handle simultaneously the signals from three ground stations. It is necessary to preserve the phase relationships between each carrier and its associated ranging sidetones. However, it is not necessary to maintain carrier phase information, since range measurements will be made only with the modulation frequencies.

THE SIGNALING PROBLEM IN SIDETONE RANGING

Having briefly surveyed the fundamental physical principles employed in radio tracking, and the approach taken in well-known systems to the application of the fundamental principles, we now consider the technique of *sidetone ranging* and examine the signal design problem involved. The ultimate signal that will be transmitted to and from the satellite is here considered to have an RF spectrum derived in some reversible manner from the sum of a number of discrete tones. In application to radio tracking systems, the signal design problem may therefore be concerned with:

1. The choice of the individual frequencies, the relationships among the frequencies, the initial relative phases, and the amplitude weightings of the baseband tones; and
2. The modulation technique to be employed in generating the radio-frequency spectrum from the sum of the baseband tones.

We shall begin with an examination of the modulation problem first, assuming that a specific choice of sidetones has been made, and lead up to the considerations that should govern the choice of the sidetones. For convenience we might start by posing the following question: "If the baseband time function is made up of K discrete tones of equal amplitudes, and if the desired information is carried in the phases of the tones, what is the best modulation technique to employ in transmitting these tones to and from the satellite?"

The important considerations in evaluating the alternative modulation methods are:

1. Efficiency of utilization of available (transponder) power in conveying the tones,
2. simplicity of system implementation,
3. signal bandwidth requirements,
4. peak factor of the signal, and
5. the effect of the associated demodulation process upon the spectral distribution of the noise power.

Let us justify briefly each of these points:

The question of the efficiency utilization of available power arises from the fact that a limited amount of power is available in the transponder for investment in the structure of the signal.

The emphasis on simplicity of system implementation is motivated by the desire to minimize the amount of signal processing necessary to extract the desired information, and hence to minimize the potential sources of error and distortion in the circuitry.

The interest in the signal bandwidth requirements is based upon the desirability of minimizing the noise bandwidth, especially in the transponder, and of avoiding dependence on wide-band transmission filters with their relatively greater possibilities of drifting phase characteristics.

The peak factor (i.e., the ratio of the peak value to the rms value) of the signal is important because the ultimate performance of a communication system is usually determined by the average signal power, while the peak power is often a limiting factor in transmitter design.

As for the effect of the demodulation process upon the power spectral density of the ambient noise, it is important to remember that the

demodulation process in some systems (e.g., FM) will alter the noise power spectral density in such a way as to favor certain frequencies over others.

Linear Modulation Systems

Amplitude modulation makes inefficient use of available power because a major fraction of the signal power resides in the carrier, and half of the remainder resides in a redundant sideband. This inefficiency secures advantages that are either not exploited (e.g., simplicity of the detector for high signal to noise ratios) or are not sufficiently important in radio tracking systems. The value of these advantages actually vanishes under severe noise conditions, and AM becomes especially undesirable. If the desired sidetones are extracted directly from the IF spectrum by product demodulation and phase-locked oscillator means, then a considerable amount of potential signal power will not be utilized. Other linear-modulation systems are superior to AM in this regard.

Therefore, since it is either comparable with DSB and SSB or is inferior to them, AM is ruled out.

In general, double-sideband (DSB) suppressed-carrier operation may have an advantage over single-sideband (SSB) operation from the standpoint of the peak factor of the signal with peak-power-limited transmitters (as well as a potential 3 db advantage against random noise resulting from the redundant sideband). But this possible advantage may be negated with appropriate initial phasing of the baseband tones. On the other hand, SSB operation uses the minimum permissible bandwidth, avoiding the detrimental effects (likely in DSB) of unsymmetrical phase shifts of corresponding upper and lower sideband components by concentrating the available signal power in one sideband.

With regard to the other considerations, SSB is either equivalent to DSB or superior to it.

With or without a residual carrier component, the SSB system is the most commendable among the linear modulation systems. However, a potentially serious disadvantage of SSB, as opposed to the exponential modulation systems discussed next, lies in the limitation on the system's noise performance imposed by an undersirable signal peak factor in a peak-power-limited transmitter. For a signal described by

$$s(t)=\sum_k A_k \cos\left[(\omega_c+k\omega_m)t+\phi_k\right]$$

the peak factor is given by

$$PF=\sqrt{\frac{\left[A_0+\sum_{k=0} A_k \cos(\phi_k-\phi_0)\right]^2+\left[\sum_k A_k \sin(\phi_k-\phi_0)\right]^2}{\sum_k \frac{A_k^2}{2}}}$$

where the initial phases ϕ_k of the components have been chosen so that the envelope of $s(t)$ attains an absolute maximum at $t=0$. It is clear that the peak factor can be reduced by an appropriate adjustment of the relative phases $(\phi_k-\phi_0)$ and/or the amplitude factors A_k.[1] But if the initial relative phases are adjusted for a minimum peak factor for the signal radiated to the transponder the phases, of the sidetones extracted from the transponder-reradiated signal should be *readjusted* to correspond to the phase relationships that ensure the greatest simplicity and reliability of the final ranging-information extraction and calibration operations. This readjustment is greatly facilitated by the fact that ground transmitter and receiver are usually located next to each other.

[1] Contrary to initial suspicions, a choice of $\phi_k-\phi_0$ and of A_k that corresponds to what would obtain in the spectrum of a baseband square wave is very disadvantageous for SSB operation, especially when compared with DSB operation.

Exponential-Modulation Systems

Viewed as a sinusoid that moves back and forth on the frequency scale (in accordance with

the instantaneous value of the resultant of the baseband tones for FM, or its derivative for PM), an exponential-modulation signal can be readily seen as an effective carrier of tracking information because its detectability in the presence of random-fluctuation noise is ultimately limited by the noise power spectral density, not the total noise. Although wasteful of frequency space when compared with SSB, exponential modulation offers the following advantages over SSB:

1. The satellite repeater design is simplified because the signal can be amplitude limited; hence, no peak-factor problem.
2. Class C radio-frequency power amplification can be used in the transponder as well as on the ground; this improves the efficiency of available power use.
3. The exponential modulation signal offers a degree of flexibility in the delivery of tracking information which is not available in SSB. This will be explained presently.
4. An interesting by-product of the flexibility just cited is that the desired FM tracking signal can be generated more easily than the corresponding SSB signal.

In the present application, the desired baseband sidetones can be extracted from the exponent-modulation signal in at least two ways:

1. by some exponential-demodulation means followed by appropriate phase-locked oscillator isolation of the desired tones; or
2. by direct operation on the IF signal spectrum in a manner similar to that used with SSB.

With high signal-to-noise ratios, the use of exponential-demodulation techniques prior to isolating the desired tones can be very advantageous. If a phase demodulator is involved in the operation, the baseband noise spectrum varies with frequency exactly in the same manner as the IF noise spectrum varies with frequency deviation from the instantaneous signal frequency. For example, white noise plus a carrier at the demodulator input leads to white noise at the demodulator output. But with a frequency demodulator the output noise power spectral density is given by the IF noise spectral density as a function of the frequency deviation from the signal's instantaneous frequency, weighted by the square of this frequency deviation. Thus, white noise plus a carrier at the FM demodulator input leads to baseband noise having a parabolically rising power spectral density with increasing frequency.

These output noise characteristics of FM and PM demodulators in the case of high input signal-to-noise ratios must be seriously considered in selecting the amplitudes of the baseband sidetones before the modulation process. First, since the higher-frequency sidetones are used for deriving more detailed range information than are the ambiguity-resolving components, it is logical to favor these tones, whose higher fraction of the signal power will better enable them to override the noise. Thus, even in the case of SSB and PM output white noise, it is advantageous to invest more power in the higher-frequency sidetones than in the ambiguity-resolving sidetones. The desirability of this type of intensity distribution among the sidetones is even more strikingly ovbious in the case of FM demodulation.

The baseband sidetone amplitudes should, therefore, be chosen *not equal*. Rather, these amplitudes should rise with frequency in accord with (1) the accuracy required in identification of the sidetone's phase, and (2) the expected post-demodulation ambient noise spectral density in the vicinity of the desired sidetone frequency. However, when operation in the vicinity of the demodulator's noise threshold is expected, the foregoing recommendation should be reconsidered in a new light: Increasing the amplitudes of the higher-frequency sidetones widens the bandwidth occupancy of the FM or PM signal. This in turn calls for wider IF filter bandwidths, and hence increased noise threshold.

An interesting way to avoid the "parabolic" spectral density of the FM post-demodulation noise in the case of high signal-to-noise ratios

would be to frequency modulate at the transmitter with a set of sidetones whose initial phases are set 180 degrees away from the desired reference phases, phase demodulate the FM signal back at the ground receiver, and then use phase-locked oscillators to isolate the desired sidetones. The phase-locked oscillations with a zero static phase error would bear a 90 degree relative phase relationship with the tones at the phase demodulator output, and hence should be immediately suitable (without further phase changes) for phase-comparison operations leading to extraction of the desired ranging information.

The desired ranging tones can also be extracted from the *spectrum* of the exponent-modulated signal directly and without using an exponential-demodulator, in exactly the same manner as in SSB. This manner of baseband-tone extraction may be desirable for several reasons:

1. When the signal-to-noise ratio is well below the demodulator threshold, the action of an FM demodulator (for example) upon the sum of signal and noise leads to a substantial suppression of the signal and of the signal modulation. Consequently, even though the desired tones may be present in the demodulator output deep in the noise, they can be expected to be less favorable to work with than the spectral components in the IF signal.
2. An exponential-modulation signal that is suitable for sidetone ranging can be generated from one basic tone (or, if desired, two harmonically related tones) which frequency- or phase-modulates the desired carrier. Such an approach both permits amplitude limiting and class C power amplification in the transponder, and significantly simplifies the signal-generation problem in the ground transmitter. As will be shown shortly, such a signal can be designed to have a set of spectral components whose initial relative phases and amplitude distribution make them particularly suitable for use in ranging measurements. Moreover, the spectrum will be rich in components spaced sufficiently far from the carrier frequency to be suitable for more and more accurate ranging when the signal-to-noise ratio is high (as is fortunately the case for ranging below 3000 mi or so).

But the proper extraction of desired ranging tones from a signal of the type described here must be made directly from the IF spectrum.

The price for the advantages of this approach is of course bandwidth and inefficient utilization of available signal power. A 3-db improvement in performance against random noise may be achieved by using both the upper and the lower sideband components as in DSB. Care must be taken not to choose a modulating frequency (or frequencies) that results in an overcrowded spectrum for the resulting signal and thus complicates the problem of isolating the desired tones.

In order to substantiate some of the foregoing statements about the use of a single-tone or a double-tone exponential-modulation signal, let us review briefly the spectral properties of such a signal. First, recall that for the single-tone case,

$$e_{\exp}(t)=A_c \cos [\omega_c t+\phi_c+\delta \sin (\omega_m t+\phi_m)]$$

$$=A_c \sum_{n=-\infty}^{\infty} J_n(\delta) \cos [(\omega_c+n\omega_m)t+\phi_c+n\phi_m].$$

The important properties of this spectrum are:

(1) $J_{-n}(\delta)=(-1)^n J_n(\delta)$.
(2) The initial phase $\phi_c+n\phi_m$ offers a potentially useful control over the relative phasing of the components.
(3) $J_n(\delta)$ as a function of n undulates (assuming positive as well as negative values) with gradually increasing amplitude all the way from $n=0$ to the last maximum (which is absolute) just to the left of $n=\delta$, and then decays quickly toward zero.

Additional flexibility in the properties of the spectrum can be gained by using two tones instead of only one, but a detailed treatment of this matter will not be undertaken here.

764-173 O—65——55

Pseudo-Random Waveforms

The use of pseudo-random waveforms or binary sequences in signaling for communication and/or tracking purposes is of particular interest as a potentially effective technique whenever one or a combination of the following goals is a requirement:

1. Maximum immunity to deliberate or accidental jamming.
2. Maximum security from interception by an agency seeking to determine, for example, the most effective countermeasures against the system.
3. Combatting some special propagation (multiplicative) and/or additive noise disturbances.

The price for resorting to pseudo-random signaling techniques can be quite heavy with regard to equipment complexity, but this is not necessarily true of the transponder. The fact that the ultimate ground transmitter and receiver are usually side-by-side (in the applications contemplated in the present program) allows substantial simplifications in instrumenting such a system. But no real and compelling justification is presently apparent for resorting to pseudo-random signaling as opposed to "harmonic" signaling of the type under discussion. However, pseudo-random signaling will not be excluded from further consideration in the present program, especially as more information is gathered on the anomalies of propagation.

Total Versus Incremental Tracking

In the preceding sections we have examined methods for implementing a relatively fixed scheme of range determination. In the present section we shall look at the entire measurement problem from a broader viewpoint. In general, it is possible to distinguish between two basic tracking techniques: In one technique, which we might call "total tracking", the measuring system provides complete tracking data (up to some maximum range) *at each reading*, making use of no previously gathered information. Such a system could follow an object which "jump around" (makes large, random changes in range between measurements). In the other tracking technique, which we might call "incremental tracking," the measuring system capitalized upon the fact that the tracked object can be expected to follow a smooth trajectory and therefore *only the changes in that trajectory* need be measured. Such a system might start from previously acquired data and thereafter it accumulates the incrementally gathered data. A "mixed" system would make occasional ambiguity resolving measurements to maintain accurate reference for the tracking data.

Evidently, when objects move smoothly an "incremental tracking" system should be more efficient, as the following computation indicates. Suppose that a ranging system is to measure and determine, 10 times per second, within which 10-foot interval of range an object lies, for ranges from zero to 30,000 miles. Suppose also that the rate of change of the object's range will never exceed 10 miles per second. A "total-tracking" system (which cannot use velocity information) will require an information rate of about 240 bits per second. (There are about 2^{24} 10-foot intervals in 30,000 miles, and this 24-bit information is sent ten times per second.) In a comparable "incremental tracking" system, we would send tracking data 10 times per second, giving information only about changes in position. If in addition, to be conservative, we send complete range information once per second, the information rate is now only about 114 bits per second. (We send 24 bits of range data once per second and realize that in 0.1 second the position can change by at most ± 1 mile or a total of about 2^9 10-foot intervals, so that each "tracking" measurement requires only 10 bits.) If constraints on acceleration can be efficiently incorporated into the "incremental" system, a much greater saving in channel capacity can be achieved.

A "total tracking" system, though less efficient, is likely to be simpler to instrument than an "incremental" system. Continuous sidetones would seem to perform as well as any other type of signal in such a system. To increase efficiency, the coarse ranging (lower-frequency) sidetones should be reduced in amplitude and performance regained by averaging over longer periods the phase shifts of

these tones. However, efficiency will be lower than for an "incremental" system, and if the power in the coarse sidetones is made too small, system reliability will suffer.

An example of a particularly interesting "mixed" system is the use of switched-sidetone ranging, also called "frequency hopping," with coarse-ranging sidetones switched in for ambiguity resolution only as the occasion demands. This system appears to have the greatest efficiency among the systems considered here and, for very deep space probe applications, represents the most effective way to use the available transponder power. Ideally, only one tone would be sent at a time, and reference would be obtained from a bank of local phase-locked oscillators in the ground receiver whose phase behaviors extrapolate (on the basis of behavior noted while a sidetone is on) the slowly changing phases of corresponding tones while a tone is cut off. Corresponding sharp filters in the transponder (ideally, phase-locked loops whose outputs are interrupted in the absence of input tones) minimize the amount of noise fed to the power amplifier.

Additional representative examples of "mixed" systems are AZUSA and MISTRAM, both of which derive incremental data from measurements of the carrier phase shift. The AZUSA system employs FM sidetones for determination of "total" ranging data, when required. "Total" ranging by the MISTRAM system is accomplished by periodically offsetting the carrier frequency.

TRANSPONDER DESIGN

The major (and interrelated) criteria for transponder design and operation have been assumed to be simplicity and reliability. We must also always bear in mind the existence of power and weight limitations. These criteria and limitations suggest that the transponder be little more than a simple, wide-band linear repeater. One additional feature, automatic gain control, probably should be incorporated so that the output power capabilities of the transponder are fully used regardless of input signal level. While it might also seem desirable to conserve power by shutting off the transmitter when no useful input is detected by the receiver, the advantage of such a scheme must be weighed against a possible decrease in system reliability and increase in transponder weight and power consumption.

Now let us consider the problem of noise received in addition to signal at the transponder input. The amount of this noise which is amplified along with the signal and appears in the transponder output will evidently depend on the bandwidth of the circuitry. In particular, it is reasonable to assume that for linear circuitry, the noise power (with no limiting or no automatic gain control) appearing in the transponder output is directly proportional to the bandwidth. For example, suppose that a simple wide-band transponder has a noise bandwidth of ½ Mc. The reduction in noise power (no agc) that could be achieved by narrowing the effective noise bandwidth to 5 cps (say, by using phase-locked oscillators as tracking filters) would then amount to 50 db. This improvement would scarcely be noticeable for high signal-to-noise ratio transponder inputs, but at low signal-to-noise ratios and with agc much of the 50 db would appear as an increase in useful signal power (contrasted to noise) at the transponder output.

Even assuming that such an improvement as that described above would be very useful, it is necessary to consider the effect of more complicated signal processing upon system reliability. In the above example, a faulty phase-locked oscillator could make the system completely unuseable. To show how system realiability might be at least partially restored, the transponder could have two modes of operation. One, the "normal" mode (in which the transponder always operates, in the absence of other information) is a simple, side-band repeater mode. To this circuitry may also be attached tracking filters (e.g., phase-locked oscillators) which normally sweep a localized frequency band, searching for a signal carrier and/or sidetones. If these filters find a signal and lock onto it, decision circuits could determine that the filters were both operating and

not sweeping, and the transponder could then be switched to a narrow-band mode. Any failure or loss of lock would cause a return to the wide-band mode, so that the system should not break down completely because of failure in the additional signal-processing circuitry.

Another possible modification of simple transponder design is the introduction of nonlinearities into the signal-processing circuitry. The particular example we wish to discuss is the employment of class C amplifiers in the transponder transmitter. The power efficiency of class C stages does exceed that of linear stages by a relatively small amount; however, such an efficiency gain may be more than outweighed by a degradation in system performance, especially with linear-modulation (e.g., SSB) signals, but the same is not true for exponential-modulation signals, as we shall now explain.

Suppose that some type of exponential modulation (say, FM) signaling is employed. Then class C amplification provides limiting action and a certain degree of automatic gain control. The limiting action can suppress noise relative to signal if the received signal-to-noise ratio is high; it is also very possible for the noise to suppress the signal (but to a negligible extent) at very low received signal-to-noise ratios. Hence, in FM signaling systems, class C amplification is more desirable from the viewpoint of transmitter power efficiency than it is objectionable from the viewpoint of noise.

In the case of linear-modulation signaling systems (e.g., SSB), however, the situation is clearly unfavorable to class C amplification. At low noise levels, the resultant limiting action can produce spurious sidetone components that may interfere with phase-comparison measurements to a very objectionable extent. To a less consequential extent, it is also probable that limiting will alter the relative amplitudes of carrier and sidetone signal components. At high noise levels there exists the additional possibility of relative signal suppression by noise, much as in the preceding discussion of FM.

In view of the preceding remarks, we recommend that class C amplification be employed in the transponder in exponential-modulation (FM, PM) operation, but *not* in SSB operation.

IMPLEMENTATION OF SIDETONE RANGING

The range information to be derived from a SSB sidetone ranging signal is contained in the differential phase shifts of the sideband components relative to the carrier phase shift. Three problems are immediately apparent with regard to reliable recovery of range data: (1) obtaining precision in the measure of phase shifts, (2) resolving ambiguities, and (3) reducing the uncertainties of extraneous phase shifts.

A straightforward approach to the attainment of precision is through the use of digital techniques. It is proposed, therefore, to express phase shift of the demodulated sidetones as time delays and to make the smallest digital increment of time as short as possible. Representative of such a subsystem for measurement of time intervals is the HP5275A counter, operating in conjunction with an HP101A frequency standard. The minimum time increment that may be resolved by typical equipment is 10 nanoseconds. The equivalent resolution of range is 4.92 ft, independent of the frequencies of the sidetones employed.

Selection of the number of sidetones to be employed and the frequencies of these tones should be made with regard to accuracy of ranging, including the resolution of ambiguities. The choice of 160 cps for the lowest frequency term will provide for unambiguous ranging up to 508 n. mi. If it were presently possible to measure the phase shift of 160 cps with high accuracy, this single tone would suffice for our ranging requirements. However, the following example will indicate the need for other ranging tones as well. Let the system ranging accuracy be specified as ± 10 ft. Because of the uncertainty of 4.92 ft allotted to the time measurement, there would remain a maximum allowable uncertainty of about 5 ft ascribed to the measurement of 160-cps phase shift. Referred to the digital time delay measurement above, the tolerance becomes about ± 10 nanoseconds. The allowable phase error then becomes

$$\Delta\phi = \pm 360 \times 160 \times 10^{-8} \text{ degrees}$$
$$= \pm 5.76 \times 10^{-4} \text{ degrees.}$$

It is not expected that drifts in the parameters of circuits which handle the 160-cps information could be maintained within these limits. The allowable phase error increases directly with the sidetone frequency. For example, a 500-kc tone could have a maximum of ± 1.8 degrees of phase error. Provided that circuit developments can insure such performance, the specified ranging precision is attainable.

Accuracy requirements imply also that ambiguous data must be eliminated. A technique by which this may be accomplished requires that the phase shift tolerance on each of the lower frequency sidetones be sufficient for identifying a whole cycle of the next higher tone employed. The proposed system would employ successive tones with 5 :1 frequency ratios. With a tolerance of about ± 1.8 degrees on the phase error of the 500-kc tone, the phase tolerance for 100 kc would be slightly less than 36 degrees, and for the other lower tones would be about 30 degrees.

The process of extracting the demodulated sidetones for obtaining ranging precision and resolution of ambiguities requires tone filter. Phase-locked oscillators have been suggested for their properties of narrowband filtering combined with frequency tracking. It appears that such filters as presently conceived may function adequately for extraction of the lower sidetones. However, considerable improvements in stability and in reduction of static phase errors are needed in order to enable such filters to function with the highest frequency tone.

It may prove more satisfactory to avoid or simplify, rather than to solve directly, some of the problems caused by the need to measure small phase shifts between sinusoidal signals. In particular, if errors in phase-shift measurement are primarily due to random noise, it will generally be advantageous to increase the range-signal frequency up to a point where there need only be about three distinguishable phases per cycle, instead of the 200 required for a 500-kc highest-frequency sidetone. An argument supporting this statement follows:

Suppose that the range-signal frequency is multiplied by n. Then the number of distinguishable phases per cycle of shift need only be $1/n$ as great as before to attain the same range precision. Assuming that the signal power is unchanged, we are then effectively multiplying lengths of the phase message by n, or increasing the phase-message power by n^2. Other things being equal, the system bandwidth, hence also the noise power, must increase by n. But this means that the effective message-to-noise power ratio of the system is increased by n, which would either increase system reliability or permit a reduction in transmitter power by n to achieve the same reliability. Thus the ranging-signal frequency should be made as high as possible, at least to the point where the number of distinguishable phases per cycle is quite small, perhaps as small as three. With only two it would be impossible to tell, without Doppler measurement, whether relative phase was increasing or decreasing. Our major assumption in the foregoing argument is that the system is not marginal, that is, that the noise peaks seldom if ever are large enough to cause the phase to jump a cycle.

ANGLE MEASUREMENT

Although major effort is being directed to the development of a precise ranging system, it is of interest to investigate the measurement of angular position for several reasons. Ultimately the angular position of the satellite being tracked will be derived from the range information collected by a number of ranging stations. It would be instructive to investigate the measurement of angular position at a single station if only for comparison with the method presently under consideration at Goddard Space Flight Center. However, there is another consideration which enters the problem of position measurement. If some form of repeating satellite is to be interrogated by a ground station, it may be necessary to use a highly directional transmitting antenna which must be given up-to-date information on the angular position of the satellite in order to allow it to be directed toward the vehicle. This information can be derived in three ways:

1. A prediction can be made of the satellite's orbit and the antenna directing

mechanism can then be programmed to track the satellite; or

2. Angular position can be computed in real time at a data collecting station which uses the range information from the system of ranging stations and feeds back to these stations angular-position information; or
3. Each station can generate its own angular-position data by using a local short-baseline angle-measuring system.

The method of tracking with a predicted program is undesirable from the standpoint of accuracy, and it requires considerable intital information. It could not be used reliably for tracking objects while they are being placed in orbit because of uncertainties in launching.

The second alternative—remote real-time data processing—requires reliable long-range communication links. The additional system complexity is located in the data-reduction equipment, and all stations are dependent on the control center and are partially slaved to it.

The third method allows each station to operate independently but makes the individual stations more complex. Since it appears that real-time angular measurements must be made to facilitate tracking, it is necessary to compare short baseline and ultra-long baseline systems.

The ranging system under consideration by Goddard Space Flight Center at present is an ultra-long baseline system in which pairs of ranging stations define baselines that are not necessarily perpendicular or coplanar and bear no particular relation to each other in length. Even though these baselines may not be considered explicitly in signal processing, the system possesses the advantages and the disadvantages of a long baseline system. If ranging stations are separated by some hundreds of miles, making the baselines of the same order of magnitude as the altitude of an orbiting satellite, then the position of the satellite can be located accurately by simultaneous but independent range measurements. In this case, the method of location is that of triangulation, and the uncertainty in position will be that of the individual range measurements, provided that the timing of range measurements can be related to within some figure significantly less than 0.4 msec (which is the ratio of range resolution to velocity for 10-ft accuracy and a velocity of 25,000 ft/sec).

However, when vehicles are being tracked at lunar distances the character of the system changes. The system has perforce become a short-baseline system. As presently envisioned, the system would continue making independent range measurements. The differences between ranges from pairs of stations would define angles, but angular accuracy could be reduced. A range difference would be the difference between two large numbers whose uncertainties increase with range, although it will not be noted that a part of these uncertainties could be made to cancel.

In order to compare the angular resolution of a short baseline system with that of an ultra-long baseline system, consider the change in angle corresponding to a change in range or range difference that equals the uncertainty in range measurement. Consider horizontal baselines, denoting the angle from the vertical by θ. Thus, from

$$\sin\theta=\frac{l}{d}$$

we have

$$\Delta\sin\theta=\frac{\Delta l_1}{d_1}=\frac{\Delta l_2}{d_2},$$

where d_1=length of short baseline system (=500 ft), d_2=length of long baseline system, Δl_1=uncertainty of range-difference measurement in the short baseline system, and $\Delta l_2=\sqrt{2}$ times the uncertainty of a single range measurement in the long baseline system assuming completely random relative behavior of errors. If f=400 Mc and if the measurable phase difference $\Delta\phi$=2 degrees (which is the accuracy of the present Minitrack system), then

$$\Delta\phi=\frac{2\pi d_1}{\lambda}\Delta\sin\theta=\frac{2\pi d_1}{\lambda}\cdot\frac{\Delta l_2}{d_2},$$

whence

$$\frac{d_2}{\Delta l_2}=\frac{2\pi d_1}{\lambda\Delta\phi}=\frac{2\pi\times500\times4\times10^8\times180}{9.821\times10^8\times2\times\pi}=36{,}540.$$

If range can be measured to ±10 ft then $\Delta l_2=10\sqrt{2}$ ft and d_2=517,000 ft$\approx$100 miles.

A baseline of 100 miles will provide the same angular resolution from simultaneous range measurements as will a 500 ft baseline system that measures phase to 2 degrees. The angular resolution considered here is 0.03 mrad near the vertical. An angular resolution of 0.01 mrad (10 ft at 200 mi) is desirable and would require a 300-mi baseline. It should be noted that these baselines will give the required precision only if range can be measured to ± 10 ft and if the baselines are laid out with negligible error. At extreme ranges where range accuracy is limited by knowledge of the velocity of propagation, range can be measured only to 1 part in 10^6. Thus at lunar distances (250,000 mi), range might be measured to 0.25 mi accuracy, but if the precision of the measurements is maintained at ± 10 ft the propagation velocity uncertainty will affect each range measurement proportionately and will essentially cancel when the difference is taken. In this case the angular resolution will remain at 0.01 mrad for a 300 mi baseline.

The precision of a short-baseline system that measures range difference directly is independent of range. Thus, it appears that once the satellite range becomes large enough to permit the assumption that plane waves are being received from a distant source, a measuring system that makes independent range measurements at each end of a baseline and computes their difference is inferior to one that measures the difference directly.

If some form of short-baseline system is to be used to gain angular precision at long ranges, consideration must also be given to the resolution of ambiguities. Systems such as Minitrack use a series of baselines of decreasing length to resolve angular ambiguities, in effect fixing frequency and varying the baseline. Ambiguities could also be resolved by keeping the baseline fixed and varying the frequency. This could be accomplished by transmitting a carrier and sidetones. The highest-frequency sidetones might be used for angular ambiguity resolution as well as for ranging precision. If a baseline of 2000 ft were used in conjunction with a 400 Mc carrier and a 500 kc upper sidetone, unambiguous angle measurement could be made if phase could be measured to 1 percent and if there were one effective sidetone at 10 or 12 Mc. This effective sidetone might be the difference frequency between the carrier and a multiple of the satellite transponder local oscillator.

It is of interest to investigate the sensitivity to angular change and to frequency change of a short-baseline angle measuring system. Let

$\Delta\phi$ = phase difference between signals at two antennas (horizontal baseline),
θ = angle from the vertical
λ = wavelength of signal from vehicle.

Then

$$\Delta\phi = \frac{2\pi d}{\lambda} \sin\theta,$$

and the sensitivity to angular change is given by

$$\frac{\partial(\Delta\phi)}{\partial\theta} = \frac{2\pi d}{\lambda} \cos\theta.$$

Thus, the sensitivity is highest near the vertical where signal strength is also greatest.

Now let

$\delta\phi$ = minimum detectable phase change,
$\delta\theta$ = required angular resolution,
$\frac{\delta\phi}{\delta\theta}$ = sensitivity $= \frac{2\pi d}{\lambda} \cos\theta.$

Then, sensitivity to frequency shift or drift is given by

$$\frac{\partial(\Delta\phi)}{\partial f} = \frac{2\pi d}{c} \sin\theta.$$

Thus, with δf the frequency shift,

$$\frac{\delta\phi}{\delta f} = \text{sensitivity} = \frac{2\pi d}{c} \sin\theta,$$

from which

$$\delta f = \frac{\delta\phi \cdot c}{2\pi d \sin\theta} = \frac{2\pi d f}{c} \delta\theta \frac{c}{2\pi d \sin\theta} \cos\theta = f\delta\theta \cot\theta,$$

and required frequency precision is

$$\frac{\delta f}{f} = \delta\theta \cot\theta.$$

As an example, let $\theta=60$ degrees and $\delta\theta=10^{-5}$ rad. Then $\delta f/f=5.77\times10^{-6}$, and for the conditions specified a frequency shift or drift greater than 5 parts in 10^6 would appear as a measurable error. For satellite orbits, Doppler shifts of 5 parts in 10^5 are expected; this requires that these shifts be allowed for in the phase comparator.

Some investigation has also been made of angle measuring techniques as used by radio astronomers. They have applied the interferometer antenna principle to a variety of methods of making angle measurements. Their techniques invariably result in a measurement of received power variations as the received signals at two antennas alternately cancel and reinforce. The very nature of this power measurement promises crude results as compared with the precise phase measurement of a Minitrack-type system. The precision of angle measurements attainable by this power-measurement practice is considerably less than present satellite tracking system requirements.

Although many of the radio astronomy methods are not immediately applicable to satellite tracking, some techniques may prove useful for tracking lunar probes. One interesting system for orbiting satellites is the "post-detection correlation" interferometer. This technique is intended for use with long baselines, and requires high signal-to-noise ratios. It uses a separate receiver and detector at each antenna of the interferometer. If several frequencies from the same source are received by each antenna, amplified, and detected in a square-law detector, the output of each detector will be the difference frequencies between the signal components, and the relative phases between corresponding difference frequencies at each antenna will give a measure of the path difference to the two antennas. The proponents of this system claim that the two signals will now be of such a low frequency that additional phase shifts introduced by passage through slightly unequal lengths of cable to a common processing area will be negligible. That this claim is fallacious can be seen from the following computation.

Let Δl be the uncertainty in the equality of cable lengths between the antenna positions and the common processing point. This uncertainty may result from originally inaccurate measurement of cable lengths, or from unequal length variations caused by environmental conditions. It will be a fixed error (and hence its electrical effects may be zeroed out in advance for extended periods) only if care is taken to ensure uniform environmental conditions for the cable.

A phase error $\epsilon_1=k_1f_0\Delta l$ will arise from the unequal cable lengths if a single frequency f_0 if received and the phases of the received signals are compared. If f_0 is received with phase ϕ_0 at one antenna and $\phi_0+\delta$ at the other, the ratio

$$E_1=\frac{\epsilon_1}{\delta}=\frac{k_1f_0\Delta_l}{\delta}$$

will represent a fractional measurement error.

Now let two frequencies, f_0 and (f_0+f_1), be received and post-detection correlation be employed. If f_0 and (f_0+f_1) are from a common source and originate in phase at some time, and if the first antenna receives f_0 with phase ϕ_0, then it will receive (f_0+f_1) with phase $\theta_0(1+f_1/f_0)$. The second antenna will receive f_0 at $(\phi_0+\delta)$ and (f_0+f_1) at $(\phi_0+\delta)\ (1+f_1/f_2)$. The output of detector 1 will be f_1 at ϕ_0f_1/f_0 and that of detector 2 will be f_1 at $(\phi_0+\delta)f_1/f_0$. Now, when the signals are sent to the processing area, the unequal cable lengths will contribute phase error $\epsilon_2=k_1f_1\Delta l$. If $f_1<<f_0$, the phase error ϵ_2 will be $<<\epsilon_1$. Note, however, that the fractional measurement error $E_2=E_1$, that is

$$E_2=\frac{\epsilon_2}{\delta f_1/f_0}=\frac{k_1f\Delta_l}{\delta f_1/f_0}=\frac{k_1f_0\Delta_l}{\delta}=E_1.$$

The percent measurement errors are the same in each case, indicating the fallacy of the claim cited above for the "post-detection correlation" interferometer.

PHASE-LOCKED LOOPS

Generally, a phase-locked loop excited by a signal plus noise can simulate a very narrow-band filter. It actually performs a cross-correlation between the incoming signal plus noise, and a locally generated semblance of the signal. Input noise components whose fre-

quency differences from the incoming signal frequency exceed a small multiple of the nominal bandwidth of the low-pass filter in the loop do not affect the locked oscillation. This statement applies regardless of the nature of these noise components as long as the oscillation is locked to the incoming signal frequency to within a small static phase deviation from orthogonality with the desired input sinusoid. In thinking of the loop as a narrow-band filter, the output noise bandwidth can be shown to be a function of the loop filter bandwidth modified by the input signal level. The modification factor ranges between one and approximately two. The wider bandwidth occurs for large input signals. Therefore, the bandwidth could be made roughly proportional to input signal-to-noise ratio if the rms noise is constant.

Phase-locked oscillators are particularly suited to the function of isolating a desired sinusoid in the presence of other sinusoids whose frequencies, as just noted, differ from the frequency of the desired sinusoid by more than a small multiple of the low-pass loop-filter nominal bandwidth. If the frequency of the incoming sinsusoid is exactly equal to the free-running oscillator frequency, then the oscillation will lock to the incoming sinusoid and maintain a 90 degree phase difference with it. Any difference in frequency between the input sinusoid and the free-running oscillator frequency will give rise to a nonzero phase deviation from the 90 degree phase difference. In application to the isolation of the desired sidetones, it is important that no variant and intolerable phase deviations from the ideal 90 degree phase lock exist. Such errors would reduce the potential accuracy of the time measurements that are used in ranging. Sources of such errors in the phase-locked oscillators are either in voltage-controlled oscillator instabilities or in inadequate phase detector circuits or both. In the present application to the isolation of sidetones, phase-detector circuits are not critical because only a small portion of their phase detection characteristics is used. It is of interest here to discuss some of the problems associated with the design of phase-locked loops.

Phase Detectors

Basically, there are two types of phase detectors: the gating type and the diode bridge type. The first type uses the zero crossing of one signal to turn on a current, and the zero crossing of the other to turn off that current. The output is then integrated to give a voltage proportional to the phase difference. If both signals are thought of as square waves, the use of a logical AND, or coincidence, circuit produces an output only when both signals are, say, positive. When integrated, the output is triangular rising from 0 at phase opposition to a maximum value when in phase. Since the circuit gates a current, the output contains a dc component (the mean value of the wave).

If the square waves are differentiated, and the positive pulses from one signal gate on a current, while the positive pulses of the other signal gate off the current, a linear phase progression produces a linear output from 0 to 360 degrees; but here also, a dc component is present in the output wave.

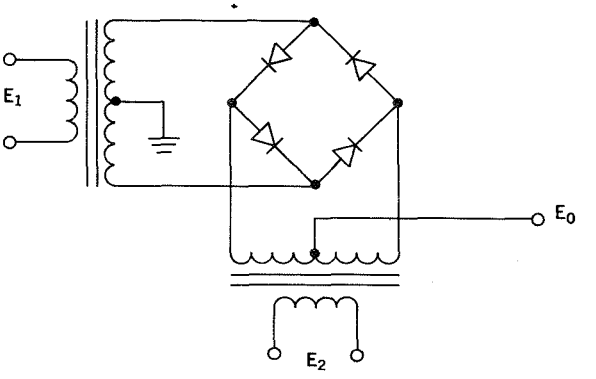

FIGURE A1.—Diode bridge phase detector.

The balanced diode bridge (Fig. A1), or product detector, will produce excellent results as a phase detector. Its operation is similar to that of the logical AND circuit but, usually, sine waves are used for input signals. In this case, the linear phase progression produces a *zero-mean* sine wave output with zero crossings at 90 degrees and 270 degrees phase difference. If square waves are used for input, the output is a zero-mean triangular wave with zero cross-

ings at 90 degrees and 270 degrees input phase difference.

A major point in favor of the use of diode-bridge type phase detectors is the fact that the output has a zero mean that does not vary with signal level or noise bandwidth. With sine wave inputs, however, the slope at zero crossing will change with a change in signal level.

Since the intended use of the phase-locked loop requires very small phase errors, the use of the diode-bridge type detector is not only desirable, but nearly mandatory. The errors in phase shift through the detector must be much smaller than 1 percent and, therefore, the operating point will be within 3.6 degrees of 90 degrees. Since this is such a small angle, the sinusoidal output of the diode bridge phase detector is very nearly linear over the required range.

Voltage-Controlled Oscillators

The width of the spectrum of the output of a free-running oscillator is a measure of the coherence of the oscillation. Slow drifts in the frequency location of this spectrum are readily corrected for in a phase-locked loop. But the disturbances represented by the spectral components that are displaced more than (nearly) the nominal bandwidth of the open loop frequency characteristic from the center of the oscillation spectrum cannot be compensated for by the action of the loop. (This action simulates a high-pass response to internal variations.) Unfortunately, an oscillation whose spectrum is extremely narrow does not yield easily to voltage control over a wide range. Therefore, some sacrifice of oscillator coherence (spectral narrowness or short-term stability) must be made in order to achieve the desired control over the center frequency of the oscillation. The usual approach is to use a crystal oscillator whose short-term stability is very good, and use some variable reactance (which tends to degrade this stability) to control the frequency of oscillation. It is doubtful if the multivibrator-type VCO would be stable enough to produce a satisfactorily usable system, because of the inherent voltage sensitivity of the circuit using semiconductors.

Loop Filter

A considerable amount of work has been done and published on loop filters. In a noisy environment, a phase-locked loop will work best with an optimized lag network. Since this will give us the minimum mean square error in the output signal, it is the type that should be used for this system.

Zero Phase Error

Since an error voltage from the phase detector is necessary to make the VCO oscillate at a frequency other than its free-running frequency, a phase error must occur in the steady-state condition. The only time zero error voltage is fed back is when the input signal is at the natural oscillating frequency of the VCO.

In the system required to provide range information, the phase error must be small to stay within the required range accuracy. There are two ways to make the error voltage come out zero, one is to use an infinite gain amplifier in the error loop, and the other is to provide a method of making the error voltage accumulate and be self-zeroing. Since the error must accumulate, a time constant is necessarily involved and zero error can occur only after infinite time. It would seem that the time lag would provide a better solution than the high gain.

Zero-Error Extraction of a 100-kc Sidetone

The system illustrated in Figure A2 is proposed here for extracting a 100-kc sidetone with

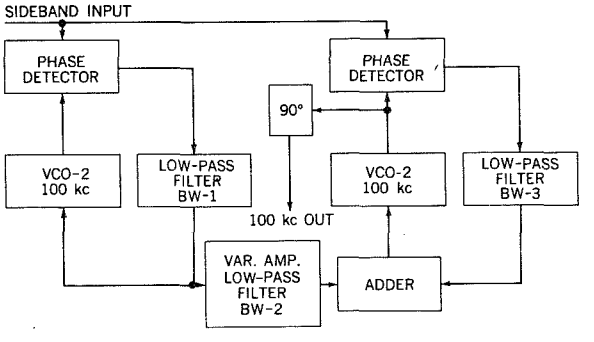

FIGURE A2.—Zero phase error extraction of a 100 kc sidetone.

a zero phase error. The operation may be explained as follows. Loop 1 is a simple phase-locked loop, and as the 100 kc moves an amount δ from VCO–1 natural frequency, the loop error pulls off zero to make VCO–1 fall exactly on the frequency of the 100 kc$+\delta$ input in the steady state. This voltage is proportional (by the VCO–1 transfer characteristic) to the frequency offset of the 100 kc$+\delta$ input. We may make use of this voltage to move another identical VCO–2 to the frequency of the incoming 100 kc signal.

In the steady state, VCO–2 and VCO–1 will both have exactly the same frequency as the 100 kc$+\delta$ input signal even though loop 2 is not closed. If we close that loop temporarily, the loop will pull VCO–2 directly 90° out of phase with the 100 kc$+\delta$ input, and the error meter will decay to zero as $t\rightarrow\infty$.

The above will be true under the following conditions:

(1) Steady state ($t\rightarrow\infty$), and

(2) VCO–1 transfer characteristic identical to VCO–2 transfer characteristic.

The system is essentially an open loop correction on the VCO–2 frequency, and the error may be adjusted, by the gain balance, from positive through zero, to negative.

There are many methods to instrument this type of a system. One is to obtain the Doppler information from the tracking receiver VCO in the manner illustrated in Figure A3. With reference to this figure, we note that ϕ_e will go to zero throughout the operating range if:

(1) The VCO–1, zero-error point has been moved to the Doppler zero point;

(2) The matching between the VCO–2 transfer characteristic and the VCO–1 transfer characteristic holds over the operating range;

(3) The phase shift in the detection loop is exactly 90 degrees;

(4) The antenna and RF stage are phase linear around 400 Mc$\pm$10 kc;

(5) The IF strip is phase linear around 4.9 Mc$\pm$2.5 cps.

Another application of the same technique is shown in Figure A4. An investigation of this system shows that with no signal input, the

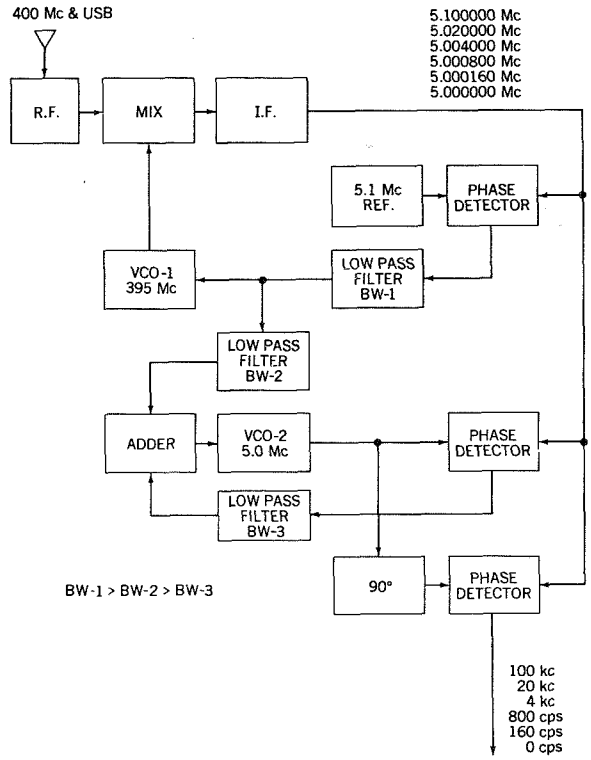

FIGURE A3.—Small phase error sidetone extraction receiver.

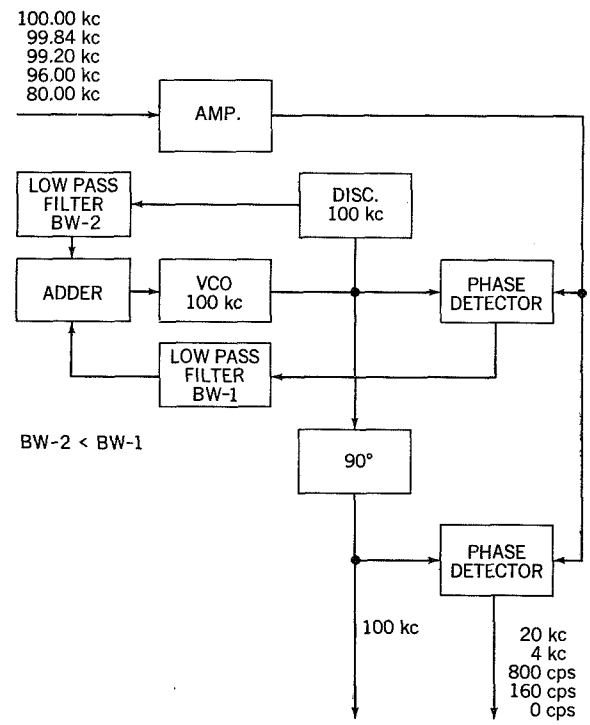

FIGURE A4.—Small phase error phase-locked loop.

VCO will search for a signal within limits provided by the discriminator when the discriminator loop gain is greater than unity, will lock on a signal when one comes in, and will have a steady-state phase error of very nearly zero. In order to make the conditions such that sweep search can take place, the discriminator loop gain must be greater than unity (open loop), and, therefore, any phase error present will be negative, but arbitrarily small.

Critique of a System Under Consideration by Goddard Space Flight Center

The system still under consideration by GSFC at this writing provides a 100 kc synchronous detector as illustrated in Figure A5.

As stated earlier, a diode-bridge type phase detector would be superior to the coincidence type phase detector used by GSFC.

Again in the light of our introductory remarks on phase-locked loops, the 100 kc filter that precedes the phase-locked loop is superfluous if it is only intended to eliminate the other sidetones. A phase-locked oscillator whose low-pass loop bandwidth is of the order of a few cycles will, if tuned to the desired input sidetone, extract this sidetone within the desired phase accuracy as long as the nearest sidetone to it is a few tens of cycles or more away, assuming that the background noise can be ignored. If the total background noise is very strong, the same conclusion should hold as long as the free-running oscillator frequency coincides with the frequency of the desired input tone. Otherwise widening the noise bandwidth before the phase-locked loop by a large factor may cause a large rise in the locking threshold. Amplitude limiting before the phase-locked loop is dsirable in combatting random-fluctuation noise, but it is not basically important to the isolation of the desired sidetone from among the other sidetones as long as the various frequency differences are sufficiently high in comparison with the loop bandwidth.

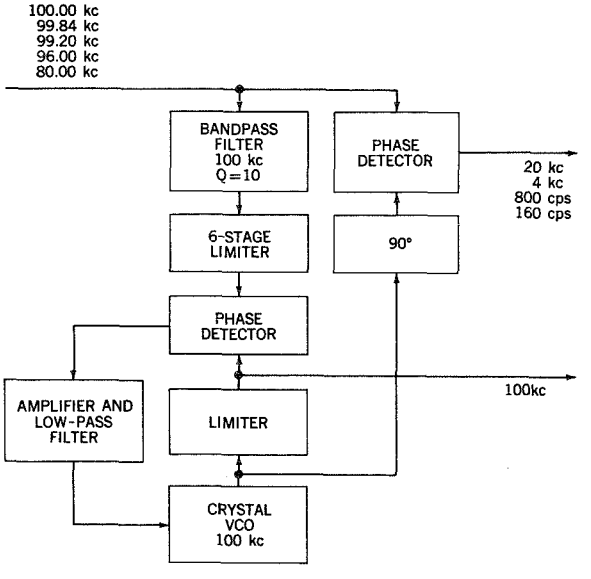

FIGURE A5.—Original phase-locked loop.

TASK I RECOMMENDATIONS

Signaling

In the light of the investigations carried out thus far at ADCOM, five methods of signaling stand out among the many possibilities as possessing, to varying but reasonable degrees, the merits of simplicity, efficiency, capability to yield satisfactory accuracy, and potentiality for high immunity to many important varieties of noise and disturbances. These are:

(1) SSB modulation of a carrier by a set of appropriately chosen sidetones. The high-frequency sidetones should be favored with the high amplitudes, and the phases of the returned lower-frequency sidetones should be favored with the longer integration times.

(2) Frequency modulation of a carrier by a set of appropriately chosen sidetones, phase demodulation of the FM signal returned by the transponder, followed by isolation of the desired tones by means of phase-locked loops whose oscillations are then used directly (without any further phase shifting) for phase comparison operations leading to the extraction of the desired ranging information. The sidetone amplitudes fed to the ground FM modulator must be so pre-emphasized that after two integrations they emerge with the higher-frequency sidetones still more heavily favored than the lower-frequency sidetones. Again the longer integration times should be used in

processing the phases of the lower-frequency components.

(3) Frequency or phase modulate a carrier by one or at most two appropriately chosen sidetones, and isolate a set of desired sidetones directly from the spectrum of the returned signal (without a prior use of an exponent demodulator) by means of phase-locked oscillators.

(4) A combined technique that employs one of the above signaling methods until the tracked object becomes so distant that the returned signal falls to some pre-specified design level, then the signaling tactic is switched to a frequency-hopping mode with one or perhaps no more than two tones being transmitted at a time.

(5) Use a single carrier with rounded-envelope phase-reversal keying according to some carefully planned binary coding scheme that embodies a combined ambiguity-resolving as well as high-accuracy ranging code groupings. A closely related alternate might use two phase-reversal keyed carriers—one intended for coarse resolution, the other for fine measurement. The "baud" length of the coarse-resolution carrier is varied in a discrete manner according to current data on the range so that it will automatically continue to provide the necessary "coarse" resolution as the object recedes deeper and deeper into space.

The only merit that can be cited for SSB over the others is its bandwidth economy. For tracking under adequately favorable signal-to-noise ratios, a more desirable alternative is a combination of techniques (2) and (3) in which the ground transmitter uses a few tones (intended principally for coarse ranging) to frequency modulate a carrier with a moderate deviation ratio, and the ground receiver operates on the returned signal with a phase demodulator followed by phase-locked oscillators in order to extract the "coarse-ranging" tones, and in addition operates directly upon the i–f spectrum with phase-locked oscillators to extract high-frequency tones for "finer-ranging" measurements.

Techniques (4) and (5) are particularly suited for deep-space-probe ranging because of the more efficient manner in which they utilize available signal power. Frequency hopping may well prove to be the most desirable signaling for deep-space ranging. However, phase-extrapolating locked-oscillators must be developed for frequency hopping, and requisite coding strategies remain to be devised for phase-reversal keying.

Transponder Design

With FM and unrounded-envelope phase signaling, design an amplitude-limiting class C power-amplifying repeater which translates the incoming spectrum from the neighborhood of one frequency to the neighborhood of another in such a way that transponder-oscillator drifts are automatically subtracted out.

If SSB signal or if rounded-envelope phase-reversal keying is used, a linear repeater must be used with class B power amplification.

A transponder design with "narrow-band" and "wide-band" modes of operation as explained earlier merits serious consideration, especially for deep-space probes.

Phase-Locked Oscillators

It is recommended that crystal oscillators be employed because of their characteristic stability in the absence of external control. The importance of stability stems from the desire to use these oscillators in the simulation of very narrow tone-isolating filters. Internal instabilities may cause phase errors that are not compensated for automatically by action of the loop.

Further improvements of phase-locked oscillators by means of higher order loop corrections are needed to reduce static phase errors that result from small (Doppler) frequency shifts of incoming tones.

A diode-bridge type of phase detector is also recommended for use in phase-locked loops becuase it appears to be more capable of producing a stable null operation at center frequency than other alternatives.

PROGRAM FOR NEXT INTERVAL

The following program is planned for the next interval.

Theoretical Investigations

1. Further study and evaluation of the application of exponential modulation techniques to side tone ranging.

2. Study of available information on the anomalies of propagation within 250,000 miles of the earth's surface and consideration of pseudo-random signaling techniques as well as frequency hopping and phase-reversal keying in combatting the random effects of propagation and of additive random-fluctuation noise.

3. Implementation of frequency hopping, phase-reversal keying, and other exponential modulation techniques for ranging.

4. Further study of angle and angle rate measurement techniques.

5. Study of Doppler effects upon range and angle measurements and their application to range rate and angle rate measurements.

6. Study of sources of phase errors caused by spurious components in output of envelope detectors, class C amplifiers and amplitude limiters.

Experimental Investigations

1. Studies of stability and maintenance of zero-phase errors in phase-locked loops, in particular, breadboarding of 100-kc zero-error phase-looked loops of the type illustrated in Figures A2, A3, and A4 for the purpose of determining the long-term and short-term stabilities as well as the degree of improved performance resulting from the use of such systems.

2. Comparative study of various types of phase detectors used in phase-locked loops.

3. Development of phase-locked oscillators that are capable of extrapolating the smooth phase behavior of signals of the type used in sidetone ranging, on the basis of observed behavior during some preceding time interval of specified duration.

MOTS—THE MINITRACK OPTICAL TRACKING SYSTEM

D. W. HARRIS, J. H. BERBERT, E. J. HABIB, AND B. W. McKENDREE

Goddard Space Flight Center

The Minitrack Optical Tracking System (MOTS) is an outgrowth of the Minitrack calibration technique. It employs the same camera used in the calibration. When tracking the brighter satellites, a modification is connected by which the plate is moved laterally in a time-coded sequence temporarily displacing the trail. This replaces the need of using a shutter to "chop" the trail. Positional accuracies of less than 5 sec of arc are realized for satellites brighter than sixth magnitude.

In May 1960 the astrographic cameras available at all National Aeronautics and Space Administration Minitrack sites were modified for the purpose of optically tracking the brighter satellites. By 12 August 1960, the launch date of the Echo Balloon satellite (1960 Iota), this new system called MOTS (Minitrack Optical Tracking System) was ready to provide useful data on the positions of the satellite. Since then, over 1000 photographs of the Echo satellite have been obtained.

GENERAL DESCRIPTION

The camera is an equatorially mounted calibration camera employing a special, ultralinear, *f*/5.0, 40-in. focal length lens (Fig. 1). It accepts 8 x 10-in. photographic plates affording an 11° x 14° field of view. Being equatorially mounted, the camera has the ability to tract the star field at the sidereal rate, permitting stars as faint as 11th magnitude to be photographed with an exposure time of 1 min. A yellow filter is placed in the camera and, in combination with the red-sensitive Kodak 103a–F spectroscopic plates, tends to reduce chromatic aberration in the star images.

The camera was originally placed at the center of each Minitrack site for the sole purpose of calibrating the station. To adapt the camera for optical tracking, a solenoid assembly was attached to it, and a special plateholder was designed to allow lateral motion of the plate when pushed by the solenoid (Fig. 2). By

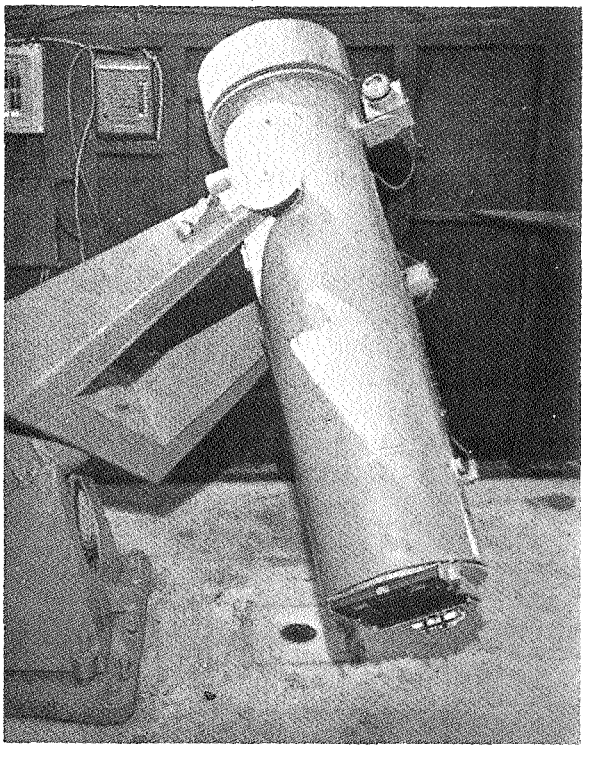

FIGURE 1.—Calibration camera.

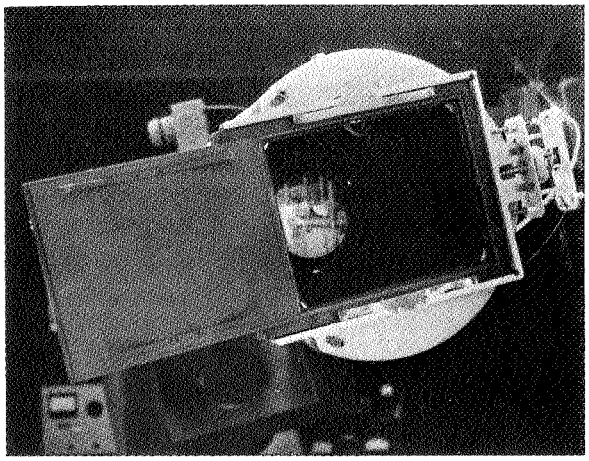

FIGURE 2.—Solenoid assembly and plateholder.

means of an electronic chassis (the heart of which is a one-shot multivibrator) a time-coded pulse is taken from the Minitrack digital clock, activating the solenoid and moving the spring-loaded photographic plate approximately ½ mm for the duration of the pulse. The time code is thus inscribed as identifying breaks in the trail of the passing source. By maintaining the solenoid pulse duration to be 30 percent or less of the timing interval between successive pulses, two images of each star are formed which are easily identifiable. By measurement of the positions of the breaks in the trail with respect to the star background, the position of the source at the time of each break in its trail can be determined. Star and trail-break measurements are determined to an accuracy of several microns by means of a comparison engine manufactured by David W. Mann, Inc.[1] An overall accuracy of determination of the position of the breaks is estimated to be better than 5 sec of arc. This corresponds to a timing accuracy of 5 msec for a nominal angular rate of 1 sec of arc/msec of time. The timing accuracy is limited by how well the time delay in the solenoid can be measured. This time delay is about 12 msec and is measured with an accuracy of about 2 msec. Because of the uncertainty in the propagation time the accuracy with which the Minitrack digital clock can be linked to station WWV is limited to 1 msec. With the yellow filter removed MOTS has successfully photographed the Polka Dot 12-ft Balloon (1961 Delta), which has a visual magnitude of approximately +5. The limiting magnitude of the MOTS system with the yellow filter removed and with 103a–F plates for a satellite in a circular orbit with a height of 1000 miles is +6. With Kodak 103–F plates, under the same circumstances, the limiting magnitude is +6.7.

FAST-METHOD STATION REDUCTION

For the first few days after the launching of a new satellite, and throughout its entire lifetime in the case where its orbital elements are rapidly changing, the speed with which the stations can report its position is very important. A method has been devised whereby four positions of the satellite from any plate are reported to the Goddard Space Flight Center within 2 hr after the plate has been exposed, yielding quick-look data having a probable error of about 1 min of arc. These data have been extremely important in keeping the predictions current for 1960 Iota because of its orbit changes due to radiation pressure and atmospheric drag. In reducing the quick-look data the plate is developed and rinsed for 30 min. Then a transparent Bonner Durchmusterung or Cordoba Durchmusterung star chart on which the scale has been reduced to that determined by a 40-in. focal length lens is placed on top of the plate. Therefore, every star on the plate with a visual magnitude of nine

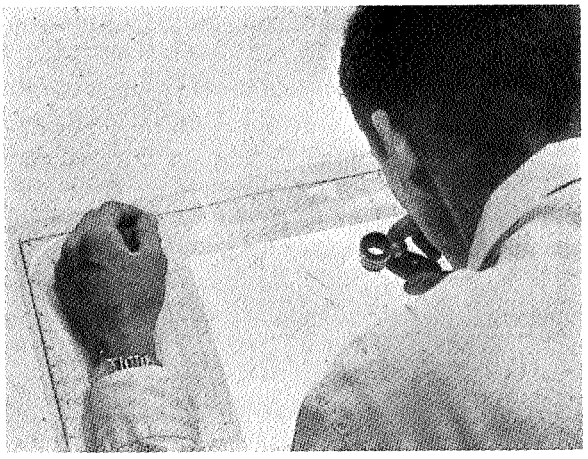

FIGURE 3.—Station reduction of a MOTS plate.

[1] Lincoln, Mass.

or brighter should line up with a corresponding star on the chart (see Fig. 3). The trail-break positions are then obtained by using the co-ordinate system available on the star chart. Trail-break times are determined by reading the time code. The data are teletyped to the Goddard Space Flight Center where the positions are updated from the epoch of the chart to the day the photograph was taken, using the annual precession and secular variation terms to obtain the mean places of the stars for the date of the plate. The aberration and mutation terms are ignored since their values are less than the probable error obtained in the reading of the positions from the chart. These updated satellite co-ordinates are then used for orbital computations.

REFINED PLATE-REDUCTION PROCEDURE

After the plates are received from the Minitrack site they are reduced by a more rigorous plate-reduction technique similar to that used for the Minitrack System calibration plates. By identifying various stars on the plate and knowing their right ascensions and declinations from star catalogues, a coordinate system is developed for the plate from which right ascensions and declinations of the trail breaks are determined.

Approximately 32 stars are chosen from the plate, of which 22 are in a narrow band along the satellite trail and the other 10 are spread uniformly over the plate. These stars are identified from the transparent star charts, and their positions as of the epoch 1950.0 are taken from the star catalogues. These positions are then updated to the date the plate was taken by using the annual precession and secular variation terms to obtain the mean places of the stars for any particular year, and the Besselian Day Numbers to obtain the apparent places of the stars for the date of the plate. The plate is then placed on the comparison engine and x, y coordinates of the chosen stars, trail breaks, and plate center are read. The standard coordinates ξ and η are described by Smart.[2] Briefly, the center or origin of the standard coordinate system is the point at which the true optical axis of the camera intersects the sphere of the stars. Taking the plane that is tangent to the celestial sphere at the origin, the η axis is the line determined by projecting the meridian circle passing through the origin onto the plane. The ξ axis is perpendicular to the η axis at the point of tangency and is therefore parallel to the celestial equator. The camera lens images this projection of the celestial sphere directly on the photographic plate. The coordinates of the star images may then be thought of as rectangular coordinates and can be calculated from the stars' known right ascensions and declinations by the following equations:

$$\begin{aligned}
\xi &= [\cos\delta(*)\sin\Delta\alpha]/D \\
\eta &= [\sin\Delta\alpha - \sin\delta(c)\cos\delta(*)\cos(\Delta\alpha-1)]/D \\
D &= \cos\Delta\delta + \cos\delta(c)\cos\delta(*)\cos(\Delta\alpha-1) \\
\Delta\alpha &= \alpha(*) - \alpha(c) \\
\Delta\delta &= \delta(*) - \delta(c)
\end{aligned} \tag{1}$$

and $\alpha(c)$ and $\delta(c)$ are the estimated right ascension and declination of the plate center.

The standard coordinates are related to the measured coordinates by the following equations, the higher order terms of which were recommended by Herget [3] after a great deal of experience with similar plates:

$$\begin{aligned}
\xi &= a + bx + cy + dxy + ex^2 + fx(x^2+y^2) \\
\eta &= a' + b'x + c'y + d'xy + e'y^2 + f'y(x^2+y^2)
\end{aligned} \tag{2}$$

where x and y are the measured coordinates of the stars and the coefficients a, b, c, d, e, and f *and* a', b', c', d', e', and f' are the 12 plate constants, six in each of the two equations. The solution of each set requires six equations, employing six different values of ξ or η and of x and y. For this purpose data from only six stars would be sufficient. However, it is desired that the plate constants be more representative of the entire plate, and so the data for all 32 of the measured stars are used. The resulting 32 equations are reduced to the sufficient six, preserving the weighting value of each star, by means of a least-square method.

[2] W. M. Smart, *Spherical Astronomy*, Cambridge University Press, Cambridge, England, 1956, p. 284.

[3] P. Herget, *Project MX-1593 Guidance System on the Accuracy of Azusa Calibration by Stars.* Work completed under Purchase Order 174330 SD, Contract AF 33(038)-19956, September-November 1953.

764-173 O—65——56

Once the plate constants have been determined, the measured x, y coordinates of any point on the plate may be substituted into the polynomials, Eq. (2), and its standard coordinates calculated. Then, by inverting and rearranging the parts of Eq. (1), relating the standard coordinates to α and δ and obtaining the following equations:

$$\tan \Delta\alpha = \frac{\xi}{\cos \delta(c) - \eta \sin \delta(c)} \qquad (3)$$

$$\alpha = \Delta\alpha + \alpha(c)$$

$$\tan \delta = \left(\frac{\sin \delta(c) + \eta \cos \delta(c)}{\cos \delta(c) - \eta \sin \delta(c)}\right) \cos \Delta\alpha$$

the right ascension and declination of the point may be computed. In this manner, before computing the positions of the trail breaks, a check is made on the accuracy of the plate reduction by using the measured x and y coordinates of each of the 32 stars to determine the positions of these stars. The difference between the right ascensions and declinations thus computed and the apparent positions derived from the catalogues represent the accuracy of the plate reduction. If for any reason residuals of larger than 3 sec of arc in declination or 3 sec of arc times the secant of the declination in right ascension are present, these stars are omitted and a new least-squares solution is run for the plate constants. At no time are less than 22 stars run in a solution. If

TABLE I.—*Positions of Echo I from a MOTS Plate Reduction*

Apparent satellite positions in celestial co-ordinates, in azimuth and elevation, and in direction cosines

Fort Myers, Plate 03–44, 1960 Iota observed 8/23/60

UT hr min sec	RA hr min sec	Dec deg min sec	AZ radians	EL radians	Cos N	Cos E	Cos Z
74955. 013	108. 204	560818. 540	6. 148228600	1. 046998600	0. 495624410	0. 067296877−	0. 865925930
74956. 013	223. 542	560149. 680	6. 153356000	1. 049479800	. 493829870	. 064486425−	. 867164230
74957. 013	337. 430	555521. 620	6. 158410500	1. 051923900	. 492046170	. 061715525−	. 868378880
74958. 013	452. 071	554841. 880	6. 163606300	1. 054408800	. 490216270	. 058900527−	. 896608430
74959. 013	605. 857	554206. 490	6. 168824800	1. 056845000	. 488410800	. 056099645−	. 870808740
75000. 013	719. 709	553521. 410	6. 174115600	1. 059306400	. 486568670	. 053281312−	. 872016170
75001. 013	832. 666	552837. 710	6. 179419800	1. 061733100	. 484738350	. 050480389=	. 873201380
75002. 013	945. 840	552148. 090	6. 184817700	1. 064167400	. 482886890	. 047654168−	. 874385190
75003. 013	1058. 812	551456. 630	6. 190282500	1. 066586700	. 481032400	. 044818227−	. 875556550
75004. 013	1211. 148	550800. 480	6. 195773400	1. 069002000	. 479163250	. 041991543−	. 876720880
75005. 013	1323. 412	550104. 420	6. 201345500	1. 071393200	. 477298900	. 039149440−	. 877868540
75006. 013	1435. 359	545400. 830	6. 206968900	1. 073795600	. 475407310	. 036304117−	. 879016510
75007. 013	1546. 833	544656. 200	6. 212638400	1. 076177000	. 473516120	. 033460357−	. 880149440
75008. 013	1657. 883	543951. 190	6. 218360000	1. 078534400	. 471627910	. 030616298−	. 881266070
75009. 013	1809. 021	543240. 080	6. 224072300	1. 080897300	. 469717870	. 027751656−	. 882380360
75010. 013	1920. 095	542523. 640	6. 230064900	1. 083260900	. 467789400	. 024872514−	. 883490040
75011. 013	2030. 431	541808. 860	6. 235984300	1. 085588600	. 465872930	. 022005982−	. 884578060
75012. 013	2140. 473	541047. 750	6. 241963500	1. 087920800	. 463933600	. 019134989−	. 885663370
75013. 013	2250. 736	540323. 830	6. 248054000	1. 090241300	. 461986420	. 016236824−	. 886738470
75014. 013	2400. 087	535558. 840	6. 254152700	1. 092538800	. 460039240	. 013359861−	. 887798200
75015. 013	2509. 817	534828. 650	6. 260378200	1. 094835600	. 458073670	. 010449125−	. 888852930
75016. 013	2618. 340	534057. 880	6. 266584300	1. 097106700	. 456110250	. 007572555−	. 889891230
75017. 013	2727. 394	533321. 520	6. 272933700	1. 099378000	. 454126640	. 004655659−	. 890925050
75018. 013	2835. 718	532541. 430	6. 279308500	1. 101639600	. 452131240	. 001752810−	. 891949860
75019. 013	2943. 795	531801. 270	. 002570291	1. 103873300	. 450139550	. 001156992	. 892957580
75020. 013	3051. 507	531017. 640	. 009078270	1. 106095700	. 448136980	. 004068418	. 893955750
75021. 013	3159. 081	530231. 970	. 015669653	1. 108299400	. 446129550	. 006991264	. 894941180
75022. 013	3306. 420	525442. 220	. 022336029	1. 110493900	. 444108500	. 009921265	. 895918170
75023. 013	3413. 098	524649. 600	. 029035681	1. 112673900	. 442078810	. 012839659	. 896884450

the case arises where more than ten stars yield high residuals, it is an indication of faulty catalogue or comparison engine data, and the plate is reread with some new stars chosen for the solution.

By introducing the x,y co-ordinates of the trail breaks into Eqs. (2) and (3), right ascension and declination positions for these points are obtained, and their values are used in determining new orbital elements. Table I shows the positions for 1960 Iota, derived from the reduction of a Fort Myers plate of 23 August 1960, and using the measured positions of the stars shown in Table II.

ACCURACY

The accuracy with which the position of a break in the trail may be stated is indicated to some degree by the accuracy with which the positions of each of the 32 reference stars are fitted by the polynomials derived in the plate reduction. This is obtained by reading the residual between the positions of the stars computed from their x,y co-ordinates by means of the polynomials and their updated apparent positions from the star catalogues as described in the previous section. Table II is the plate-reduction print-out with 28 apparent star positions, showing their residuals.

TABLE II.—*Stars Used in a MOTS Plate Reduction and Their Residuals*

Fort Myers, Plate 03–44, 1960 Iota observed 8/23/60

Star number	Apparent star positions		Plate measurement residuals	
	RA min sec	Dec ° ′ ″	RA ″	Dec ″
108230344	532. 027	522618. 567	1. 501	0. 406
208230344	1608. 361	521136. 509	. 882	. 633
308230344	1213. 621	525026. 907	1. 314−	1. 512−
408230344	2043. 133	525820. 524	4. 177	1. 675
508230344	2923. 530	525137. 745	. 314	. 089
608230344	1559. 353	533626. 109	1. 322−	1. 483−
708230344	731. 976	540750. 089	2. 329−	1. 966−
808230344	1003. 049	544807. 250	. 647−	1. 559
908230344	3635. 001	542007. 588	1. 182	. 384
1008230344	3330. 761	550525. 711	. 347	1. 640−
1108230344	2446. 201	543706. 995	1. 112	1. 638
1208230344	1605. 391	551235. 338	2. 634	1. 693−
1308230344	1047. 601	561518. 586	3. 712−	. 710
1408230344	1934. 402	555940. 095	1. 233−	2. 902
1508230344	2937. 910	555746. 544	1. 283−	. 241−
1608230344	3944. 319	555100. 657	3. 494−	. 856−
1708230344	3530. 440	570641. 467	2. 224−	. 132
1808230344	2603. 312	564212. 449	1. 966	. 804
1908230344	1744. 795	572621. 397	1. 865	. 371−
2008230344	548. 774	565741. 319	1. 230	. 633
2108230344	1348. 802	508633. 251	5. 238−	2. 207
2208230344	2928. 555	575526. 479	2. 176−	. 289−
2308230344	4742. 338	583325. 891	3. 344	. 103
2408230344	3524. 167	585702. 889	5. 392−	2. 826−
2508230344	3046. 439	600854. 628	5. 860	2. 310
2608230344	2414. 155	585743. 791	1. 392−	1. 299
2708230344	1309. 346	593328. 883	3. 201	1. 877−
2808230344	812. 440	594817. 410	2. 235	1. 073−

Choosing five older plates from the more than 1000 MOTS plates of 1960 Iota now available, the star residuals in both right ascension and declination have an average of the absolute values of less than 2 sec of arc. When a station calibration is performed, a plane carrying a flashing light, which is commanded by the ground station, passes through the Minitrack beam. In this case the solenoid assembly remains inactive and the plate remains stationary, yielding star residuals having an absolute average of less than 0.8 sec of arc in both co-ordinates. This is also true when a satellite will actively flash at discrete times rather than simply reflect sunlight.

Using the five plates selected, right ascensions and declinations of the trail-break points from each were then fitted to a third power polynomial of the form $a+bt+ct^2+dt^3$ to determine the value of the random component of the residuals over the length of the satellite trail. In all cases the average of the absolute values of this "noise" was less than 5 sec of arc in right ascension and 2 sec of arc in declination. Figures 4 and 5 graphically present the residuals of right ascension and declination, respectively, after the satellite positions were applied to second and third power polynomials. The smaller amounts of noise found in the declination co-ordinate is explained by the fact that the plate is moved by the solenoid primarily in the right ascension direction, and the plate probably does not return to precisely the same rest position after each displacement.

Table III shows a comparison of one position per plate between the results obtained by the fast-method station reduction and the refined plate-reduction procedure. Station reductions are quoted with a probable error of 1 min of arc while the refined reduction has a quoted

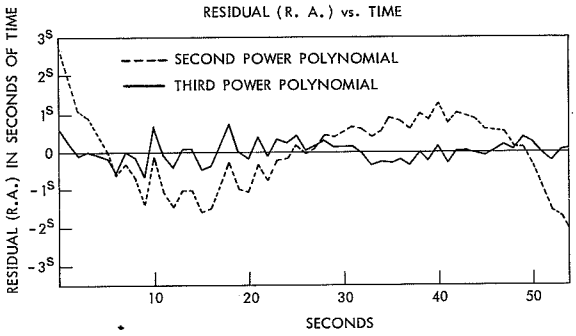

FIGURE 4.—"Noise" in right ascension.

TABLE III.—*Comparison Between Station and Refined Reductions*

Station and date	Universal time			Station reduction α_S			Refined reduction α_R			$\Delta\alpha$ $\alpha_S-\alpha_R$	Station reduction δ_S		Refined reduction δ_R			$\Delta\delta$ $\delta_S-\delta_R$	
	h	m	s	h	m	s	h	m	s		°	′	°	′	″	′	″
Fort Myers, Fla., Aug. 21, 1960.	08	34	44.012	01	05	54	01	05	56.0	−2ˢ.0 (−21.″5)	44	18	44	18	25	−0	25
Fort Myers, Fla., Aug. 22, 1960.	08	12	32.012	00	47	42	00	47	41.8	+0ˢ.2 (+1.″9)	49	00	48	58	45	+1	15
Fort Myers, Fla., Aug. 23, 1960.	07	50	19.013	00	29	42	00	29	43.8	−1ˢ.8 (−16.″1)	53	18	53	18	04	−0	04
Johannesburg, S.A., Sept. 2, 1960.	02	45	21.013	03	23	18	03	23	15.0	+3ˢ.0 (+23.″0)	−59	13	−59	13	12	+0	12
Woomera, Australia, Sept. 26, 1960.	19	38	35.015	04	57	21	04	57	21.4	−0ˢ.4 (−4.″1)	−46	42	−46	42	13	+0	13

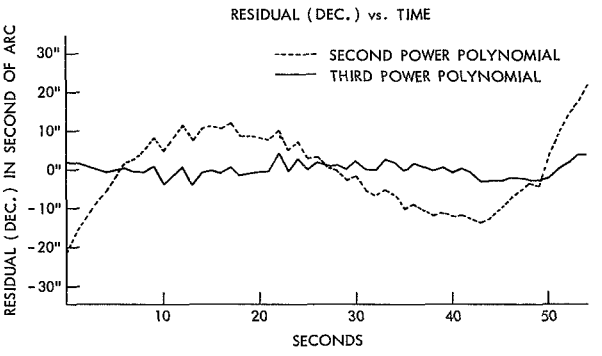

FIGURE 5.—"Noise" in declination.

probable error of 5 sec of arc in right ascension and 2 sec of arc in declination. The values of $\Delta\alpha$ are given in seconds of time and seconds of arc, where $\Delta\alpha'' = 15 \cos \delta(\Delta\alpha^s)$.

CALIBRATING MINITRACK BY MOTS

The present method of calibrating the Minitrack sites involves the use of an airplane carrying a Minitrack transmitter and a light that flashes in a time-coded sequence replacing the need to move the plate by means of the solenoid. The airplane flies at an altitude of 25,000 ft, well under the major portion of the atmosphere and the entire ionosphere. In this respect the calibration is to a small degree limited. However, using the MOTS technique on a satellite having a magnitude brighter than +4.0 and also having a strong radio signal, this limitation would be alleviated. 1960 Iota, in the early days after launch, was used for this purpose, and the results seem quite satisfactory. By this method any station can be calibrated as often as is felt necessary without waiting to schedule an airplane calibration flight, provided the ionosphere effect can be independently determined.

MOTS has already proven its usefulness as a secondary tracking system to the Minitrack network by supplying important positional data for Echo I about the period of the 3+ solar flare of November 12, 1960. During that period Minitrack data alone were insufficient to show the orbital changes over short periods due to solar radiation pressure. Experimental usage of Kodak Royal X-Pan emulsion on the 8 x 10-in. plates is anticipated in the near future for fainter satellites.

ACKNOWLEDGMENT

The authors would like to thank the members of the Systems Evaluation Branch of the Goddard Space Flight Center, especially Mr. J. D. Oosterhout, for their patient help. We would also like to express our appreciation to the personnel at all the Minitrack sites for their services rendered in gathering the data.

REFERENCES

E. J. HABIB, B. W. MCKENDREE, and D. W. HARRIS, *Instructional Manual for Minitrack Optical Tracking System*, National Aeronautics and Space Administration, Washington, D.C., 1960.

Minitrack System Training Manual, rev. ed., National Aeronautics and Space Administration, Washington, D.C., September, 1958.

PULSED-LASER RANGING

T. S. JOHNSON

Goddard Space Flight Center

The introduction of sophisticated optical tracking systems, such as radot mentioned previously, makes it desirable to increase the capability of such systems to track 24 hours a day. An obvious application of the laser is its use as a searchlight to illuminate satellites equipped with the necessary reflectors. When a laser is used in such an application, range information and, ultimately, range rate can be added to the precise angle information available from optical tracking systems.

Typical radio or radar ranging systems measure phase difference or Doppler shift in a modulated carrier introduced by a given range and range rate. These techniques are also applicable to laser ranging systems, but they require ambiguity resolution.

Pulsed ranging systems have a basic advantage over modulated CW systems because no requirement exists for ambiguity resolution. Solid-state lasers are suitable for integrating into such a system because of the ease with which fast rise-time short-duration pulses of high peak power can be generated.

A pulsed-laser ranging system measures distance by measuring the time-of-flight of a short-duration pulse, and converting time to range by the relationship $S=ct$. The basic error in calculating distance from time-of-flight measurements results from the inaccuracies in the knowledge of the velocity of light and the resolution of the system in measuring relative time. The resolution of a pulsed system, then, is dependent on time measurement, and the absolute accuracy is dependent on the time measurement plus the accuracy in the known value of the velocity of light.

Ranging systems utilizing the normal output of a ruby laser suffer in resolution because it is not possible to determine when, during the pulse duration, the measurement is made. The resolution of this type of system depends upon the total pulse duration and the integrating time constant of the measuring system. Systems employing the hairtrigger mode of operation are also dependent on pulse duration because the output of the hair-trigger-operated laser is a multispiked pulse. Systems capable of greater resolution should therefore use a single short-duration, fast rise-time pulse such as that from a Q-switched laser. Ranging systems using Q-switched lasers are limited in resolution by the duration of the single pulse if the total energy is used, or by the rise time of the pulse if narrow bandpass-measuring systems are used. As the rise time of a pulse is shorter than the duration of the pulse, it is obvious that a system with the greatest resolution should make this type of measurement.

Two systems will be used to measure range in the S–66 laser tracking experiment. The first system, illustrated in Figure XV–1, is analog in nature and uses a delayed- or normal-sweep oscilloscope as the time-measuring system. This type of system, advantageous because of its simplicity, is limited in operation to either stationary or slowly moving targets in delayed-sweep operation, or is limited in time resolution in normal-sweep operation. Furthermore, permanent time records cannot be obtained without photographing the oscilloscope trace, which of course eliminates the possibility of real-time readout. An advantage of this system is the possible reproduction of pulse shape, which would provide the ability

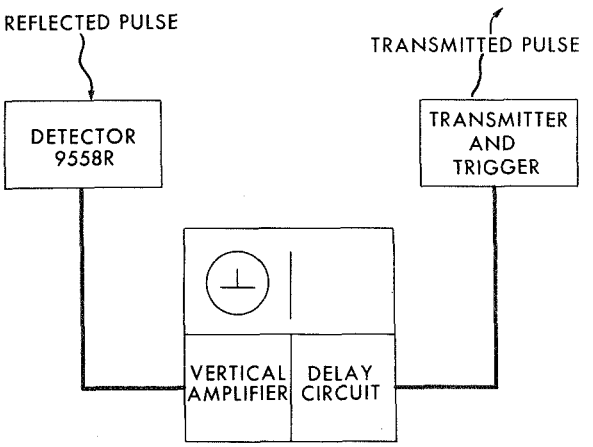

FIGURE XV–1.—Delayed-sweep CRO ranging system.

to correlate measurement points on the transmitted and received pulse if both are displayed, as would be possible with a dual-beam oscilloscope.

The second system, shown in Figure XV–2, is digital in nature and uses a high-resolution time-interval unit. The digital time-measuring system, operationally more convenient and operating in real time, is more subject to false measurements because it distinguishes pulse shape only through the operation of the input electronics.

To develop a ranging system for the S–66 tracking experiment, tests have been conducted at the Goddard Optical Facility site here at Goddard and at the Wallops Island Test Center. To date, the tests have been concerned with determining under actual field conditions the problem areas in the design of a field-operational ranging system.

The test range at the Goddard observatory site consists of four 6-cm-diameter corner reflectors mounted on a water tower at a distance of approximately 4.5 kilometers. These corner reflectors present a target area of approximately 80 cm^2, or about half that expected from the satellite. The receiving telescope used is a tracking cine-theodolite with a clear aperture area of approximately 275 cm^2, as opposed to 1050 cm^2 aperture area of the IGOR telescope to be used in the initial phase of the actual experiment on the satellite; this is a reduction of about 0.3 in collecting area. Taking into account the difference in range and in these two factors, any signal detected from a beam transmitted over the test range will be larger by a factor of 10^9 than what would be expected from S–66. For satisfactory simulation of the signal expected from the satellite, it was necessary to install attenuating filters in the laser transmitter.

The laser transmitter used in the tests, shown in Figure XV–3, has already been described by Dr. H. Plotkin. The attenuating filters were installed between the positive objective lens and the negative lens, and the cine-theodolite was modified by removing the 35-mm camera normally at the focal plane and replacing it with the detector to be used for S–66.

To operate at the Goddard site, the laser transmitter is first boresighted on the target by installing a collimating unit in front of the transmitter, removing the attenuating filters and firing the laser. Firing the laser blows a hole in a piece of recording paper placed in the focal plane of the collimator. The boresight eyepiece is then moved into place and the crosshairs adjusted to coincide with the center of the hole in the paper. The collimator is then removed and the laser is aimed at the target by looking through its optics and adjusting the tripod on which the laser is mounted until the crosshairs cover the target. At night, the target is located by illuminating it with a flashlight. Eight filters were installed with an average transmission of 13 percent per filter at 6943 A.

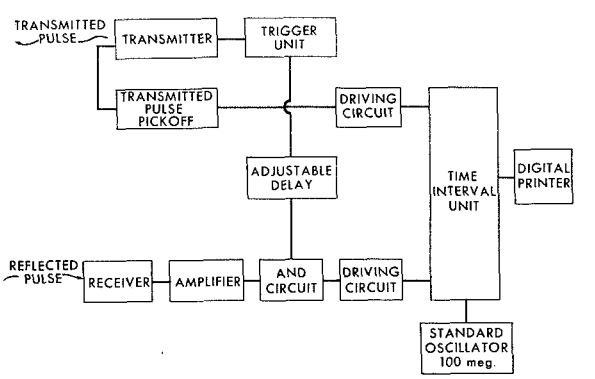

FIGURE XV–2.—Digital range-readout system.

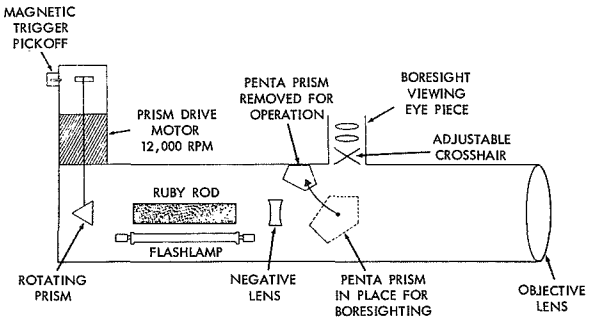

FIGURE XV–3.—Block diagram, laser transmitter.

Tests using a delayed-sweep operation oscilloscope have been conducted at the site. A CB–1 photodiode sampling the transmitted beam is used to trigger the delayed sweep. Results using sweep speeds to 0.1 μs/cm have given time-of-flight measurements of 29.7 μs on the range to our water tower. The receiver used in all tests to date has been the one which will be used in the initial tests with the S–66. The tests have been performed both at night and in daytime, with easily detectable signals obtained with up to seven attenuating filters in the transmitter beam and three 10 A bandpass filters in front of the 9558R photomultiplier tube. The output of the transmitter has been on the order of ½ joule during these tests, and the beam divergence has been adjusted to about 2 milliradians before the filters are installed. Each filter increases the divergence by about ½ milliradian, but, because of the difficulty of measuring the divergence with the filters in place, no attempt has been made to readjust the optical system for minimum divergence.

A week of operational tracking tests has just been concluded at the Wallops test center, using the IGOR telescope which will be used in the initial phase of the S–66 experiment. The purpose of the tests at Wallops Island was to determine if there were integration problems between the IGOR telescope and the equipment to be mounted on it, and to find out what operational problems existed. Both methods of measuring time-of-flight were checked at Wallops and the problems in the use of each determined. Initial tests at Wallops used an array of cube corners mounted on a tower 200 feet above the ground and about 22 km from the IGOR. Operational flight tests were conducted with an array of seven corner reflectors mounted on the Minitrack calibration plane. In the dynamic tests, the airplane flew a course either directly towards the telescope or away from it.

The results of the Wallops test have not yet been completely evaluated but certain problem areas have been defined. The analog measuring system, using the oscilloscope in delayed-sweep operation as previously described, was found impossible to operate because of the rapid changes in the length of delay required. However, in normal-sweep operation, the oscilloscope was useful as a gross monitoring system. The digital system, consisting of a 10-Mc counter with a time-interval unit and a digital clock and printout unit, worked quite well; however, it was found that with as few as four filters attenuating the beam, backscatter would usually trigger the stop input.

The time indicated on the counter when it was stopped by backscatter coincided with a distance of about 600 meters, or that distance at which the laser beam just entered the telescope and detector field-of-view.

The tests conducted so far at Wallops Island, at our site, and here in the laboratory, indicate that a more stable and operationally convenient laser transmitter is necessary. The greatest problem encountered in the present transmitter is the shift in the output-pulse energy and shape as the ruby crystal warms up. To counter this problem, and to eliminate the bulky, noisy, and inconvenient air blower presently used, a new liquid-cooled laser is being fabricated in which the cooling medium will be changed to purified water. Both the ruby and the flashlamp will be contained as before in glass tubes, through which water at the desired operating temperature will be circulated. Initial tests have shown that the flashlamp operates satisfactorily when immersed in water if the dc resistance measured between anode and cathode is greater than about 100 K ohms. Higher pulse rates are expected to be obtained

with this laser, the upper limit probably being determined by the rate at which the flashlamp can be pulsed.

Not all pulsed-laser ranging systems need to be of the type being built for the S–66 experiment. The most efficient operation of a pulsed laser with systems such as radot would need energy outputs higher than are presently obtainable with the Q-switched lasers necessary for good ranging resolution. A normally operated (not Q-switched) high-energy ruby laser can be used with a detector such as an image orthicon, if an additional point detector and suitable correlation techniques are employed.

THE S–66 LASER TRACKING EXPERIMENT

H. H. PLOTKIN
Goddard Space Flight Center

INTRODUCTION

The optical-tracking experiment planned for the S–66 experiment is embarrassing in its simplicity. As seen in Figure XIII–1, we will illuminate a special reflector with a pulse from a laser, receive the reflected light, measure time of flight for range, and—if we have an angle sensor—try to autotrack on the reflected pulse to obtain angle coordinates as well.

The future importance of lasers for tracking, navigation, and communications in space has become increasingly evident. When the opportunity arose to instrument a forthcoming satellite in this way, there seemed to be no reason not to get started as soon as possible, even though the technology of the lasers themselves did not seem all that we might want. We would, at least, get a target into space that would serve as a useful reflector for many years to come. It would be available for testing new pulsed transmitters and cw lasers as they developed; we could perform experiments to determine the effects of the entire atmosphere upon the intensity and coherence of optical beams; and we could learn about the most difficult of problems confronting lasers in space: How to aim accurately and steadily at an unseen target in order to make effective use of its high degree of collimation. Not incidentally, the accurate range and angle tracking that this technique may make possible, both day and night, would permit measuring the orbit of S–66 to sufficient accuracy to add to our knowledge of gravitational harmonics. Over long periods of many years, the precision may even be high enough to uncover some predicted secular changes in the universal gravitational constant.

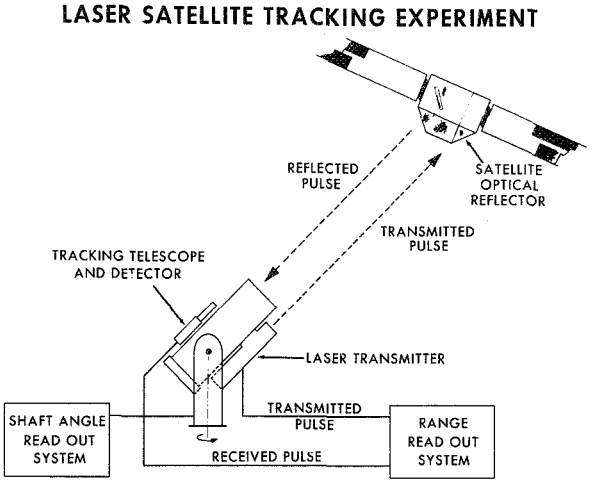

FIGURE XIII–1.—Laser Satellite-Tracking Experiment.

SATELLITE DESCRIPTION

The primary mission of S–66 is as a polar ionosphere beacon radiating a number of harmonically related tones. By receiving these tones on the ground and comparing phases, a value can be derived for the integrated electron density over the radiation path. As measurements of this sort will be carried out by observers throughout the world, the project should result in a grand overall profile of the earth's ionosphere and its variations with solar events and season.

Our concern here is for the satellite as a platform for our reflector. Figure XIII–2 illustrates that S–66 will travel in an approximately circular polar orbit at an altitude of about 1000 km. The satellite will be magnetically stabilized so that one end of its symmetry axis will always point in the north-seeking direction

S-66 ORBIT AND STABILIZATION

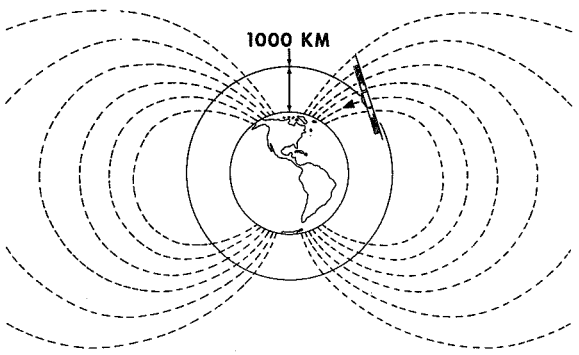

FIGURE XIII–2.—S–66 Orbit and Stabilization.

along the magnetic lines of force; it might slowly rotate about this axis. An array of cube-corner reflectors will be placed on the face which points generally toward the earth when the satellite is in the northern hemisphere.

Figure XIII–3 is a cutaway view of the satellite. The distance across flats on the octagonal face is 18 inches. Most of the instrumentation does not concern us; note, however, that there are many beacons radiating at different frequencies simultaneously. Among these

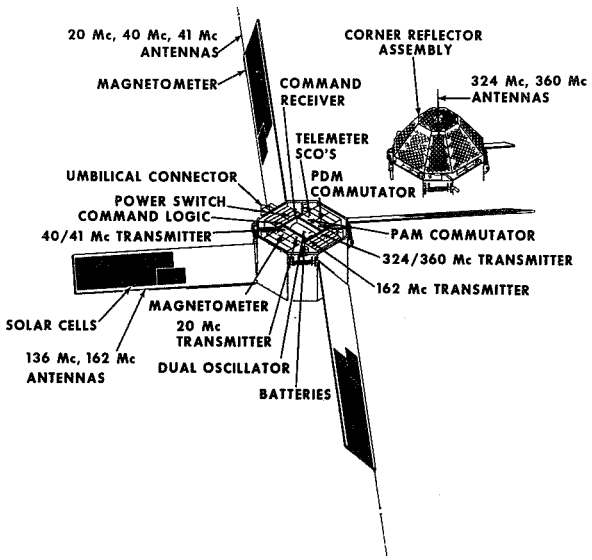

FIGURE XIII–3.—S–66 Spacecraft, Cutaway View.

are the frequencies of the Minitrack network and the Transit tracking network. This should ensure good orbital predictions throughout the active lifetime of S–66, or make it possible for an autotrack antenna to lock on to it. The top lid, free of external instruments, is fortunately available for our optical reflector.

Figure XIII–4 is an artist's rendition of the essential features of the reflector assembly, executed from the design drawings. The reflector has now been completed and is at the Applied Physics Laboratories of Johns Hopkins University for environmental testing and integration with the spacecraft. Built by General Electric's Missiles and Space Division, it is composed of a mosaic of fused silica cube-corners each about 1 inch across. The back surfaces are aluminized, epoxy-cemented to aluminum brackets which in turn are cemented to the aluminum-honeycomb structure panels. The assembly weighs just 10 pounds, compared to the satellite's total weight of about 120 pounds.

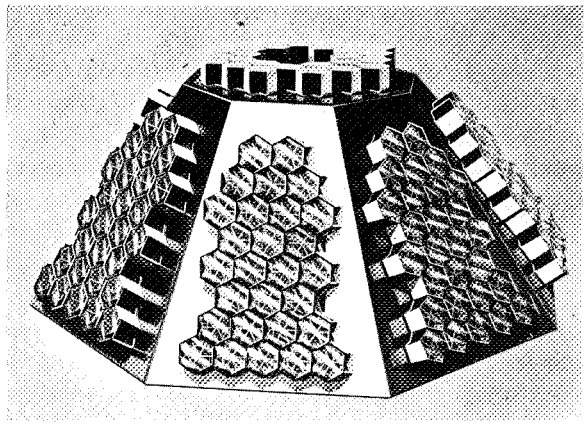

FIGURE XIII–4.—S–66 Reflector Assembly.

VELOCITY ABERRATION EFFECT

To justify the use of a mosaic of small retroreflectors rather than fewer but larger ones, let us briefly consider the velocity aberration effect demonstrated in Figure XIII–5. If the corner reflector behaved properly, light entering along the solid line would be reflected back to its source along the solid line. However, S–66 will be moving at a velocity of about

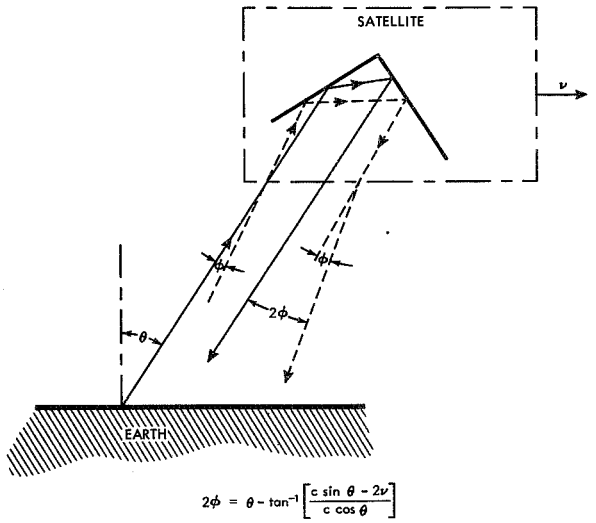

FIGURE XIII–5.—Nonrelativistic Velocity Aberration.

7.4 km/sec; it will, therefore, transform the direction of the incoming ray into its own reference frame, consider the ray incident along the dotted line, and reflect back along the dotted line. When we transform back again to a stationary earth, we find that the ray has been deflected by an angle as great as 2 v/c.

The geometry of our experiment would displace the reflected beam on the ground as much as 70 meters. If the spot were small, as would result from a large, high-quality cube-corner, the transmitter and receiver would need to be displaced according to the velocity and direction expected for each pass; in addition, the displacement would be changing within a pass. This would have been a serious operational burden, and we had to resign ourselves to sacrificing reflected intensity for convenience in this first experiment. With the present arrangement, the transmitter always lies within the reflector's divergence cone, so the receiver can be put on the same mount.

PLANS FOR EARLY TRANSMITTER

As a basis for some specific numerical calculations, we will describe the pulsed-ruby laser NASA will use in its experiments during S–66's early life. Figure XIII–6 is a schematic of the Q-switched laser which has been used in conducting field experiments. There are no really novel features: ruby rod ⅜ by 6 inches; total internal-reflection roof prism rotating at 12,000 rpm as a Q-switch; collimating optics, and boresighting optics. The beam divergence can be controlled down to 10^{-3} radians angular diameter. Figure XIII–7 is an exploded view of the laser without collimating optics. Using air cooling at dry-ice temperatures, the laser has been able to operate indefinitely at one pulse per second. Each pulse has an energy of somewhat less than 1 joule, and a duration of about 0.2 microsecond. The timing of the flash within a rotation cycle of the prism is extremely critical in avoiding multiple pulses, but once the laser has been adjusted and warmed up, it is stable.

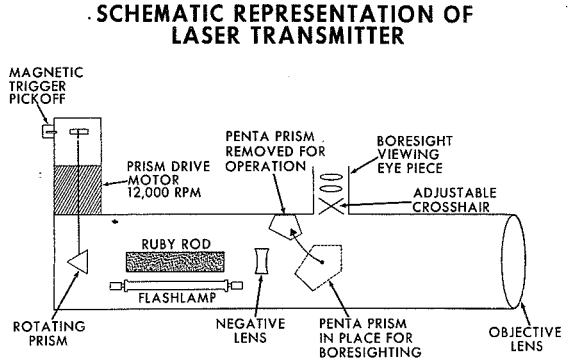

FIGURE XIII–6.—Schematic Representation, Laser Transmitter.

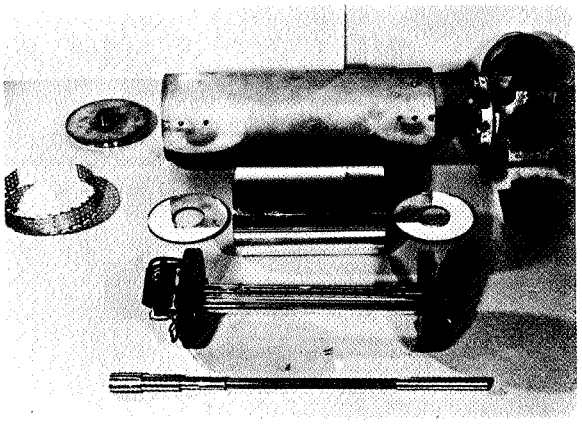

FIGURE XIII–7.—Exploded View of Laser (Without Collimating Optics).

NUMERICAL ESTIMATE

Figure XIII–8 will give an idea of signals to be expected in a typical situation. In this case we are assuming that a pulse of 1 joule from a ruby laser, which is diverging in a cone of 10^{-3} radians, attenuated to 0.8 in each passage through the atmosphere, is reflected by an array having an effective area of 200 cm², at a range of 1500 km, the reflected rays being contained uniformly within a cone of 10^{-4} radian diameter, and received in a telescope with aperture area of about 500 cm². This is a modest 10-inch telescope but the number of photons collected is not inconsiderable.

What can be done with these? If they were focused to an image of 30-micron diameter on sensitive astrographic film, we would just begin to get photographic impressions. Of course, we need not Q-switch a laser for photography, so that we can gain an order of magnitude in intensity by running the laser in a normal fashion. Thus, precise photographs of S–66 in relation to the fixed stars could be obtained on a wide-field astronomical plate.

As for photoelectric ranging, one would, of course, use a narrow filter about the ruby wavelength in order to discriminate against background. With a 10A filter, a 0.2-microsecond pulse duration, and the parameters quoted above, we would expect a postdetection signal-to-noise ratio of better than 10 to 1 against a clear daylight sky. (The detection time constant would be made to match the pulse duration for optimum signal-to-noise.)

NUMBER OF PHOTONS ENTERING TELESCOPE:

$$N = \frac{16\, E\, \lambda\, \Delta^2\, \alpha\, A_S\, A_R}{\pi^2\, h\, c\, \theta_t^2\, \theta_S^2\, R^4} = 3.62 \times 10^4 \text{ PHOTONS}$$

ASSUMED PARAMETERS

- E = TOTAL PULSE ENERGY = 1 JOULE
- λ = RUBY LASER WAVELENGTH = 6943Å
- Δ = ONE-WAY ATMOSPHERE TRANSMISSION = 0.8
- α = REFLECTOR EFFICIENCY = 0.5
- A_S = REFLECTOR PROJECTED AREA = 200 cm²
- A_R = TELESCOPE APERTURE AREA = 506 cm²
- θ_t = TRANSMITTER DIVERGENCE = 10^{-3} radian
- θ_S = REFLECTOR BEAM DIVERGENCE = 10^{-4} radian
- R = RANGE = 1500 km

FIGURE XIII–8.—Signals Encountered in a Typical Situation.

EARLY RECEIVER PLANS

Again, in order to make the discussion specific, the equipment to be used shortly after S–66 is launched will be described. Figure XIII–9 is the mount for a 9558 photomultiplier tube, with provisions for up to 3 interference filters and reflex optics for boresighting. The iris which allows adjustment on the field-of-view is placed in the focal plane of the telescope shown in Figure XIII–10. It happens to be a tracking telescope which was available at the Wallops test station; the detector in the previous figure merely slips into the fittings that ordinarily hold the recording camera. The laser is mounted under the instrument and carefully boresighted to it. Fly-by tests which have already been conducted will be discussed in one of the following papers.

During operation, we would have a prediction as to when and where the satellite is expected to be as it comes over the horizon, accurate to about ±¼ degree. Two operators, one for azimuth, one for elevation, look through viewing scopes and detect it in their viewing field illuminated by the sun against the dark sky (we expect it to be equivalent to an apparent eighth-magnitude star.). They then track to keep S–66 at the center of their fields. This tracking can be good to 1 or 2 minutes of arc.

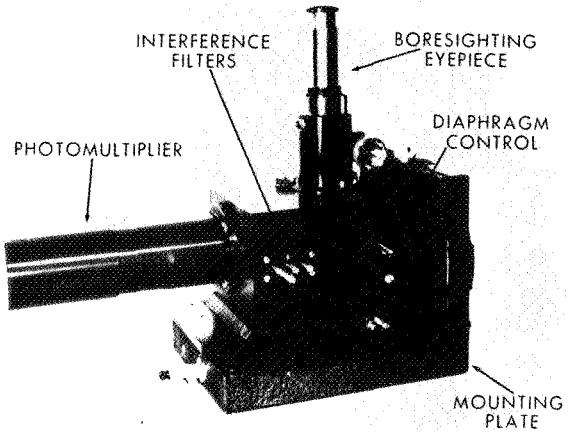

FIGURE XIII–9.—Mount for a 9558 Photomultiplier Tube.

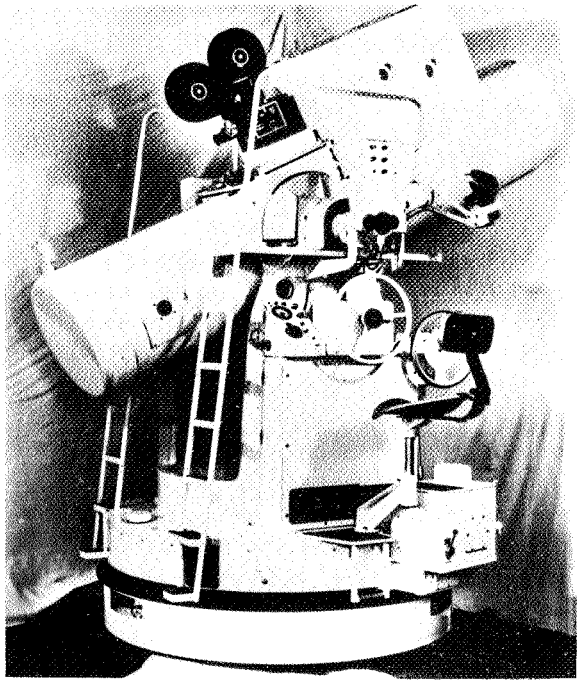

FIGURE XIII-10.—Tracking Telescope.

We track across the sky in this way, taking range data if desired once per second, using the range display equipment shown in Figure XIII-11. This is nothing but a very elementary radar setup. An optical signal from the

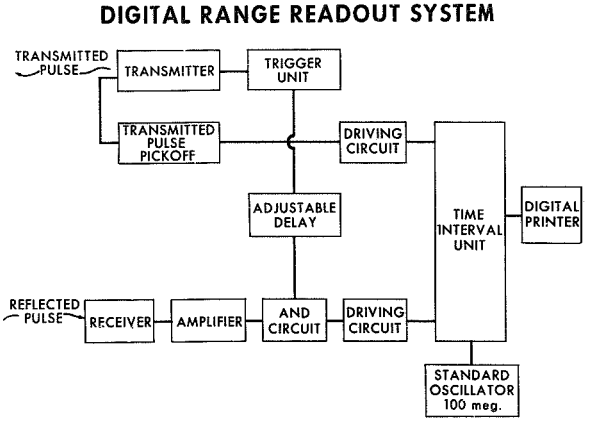

FIGURE XIII-11.—Digital Range-Readout System.

transmitted beam starts a counter operating at 100 Mc and the reflected pulse then stops the counter. The time printed out will thus have a resolution of $\pm 10^{-8}$ sec or ± 3 meters in range.

This arrangement is certainly not satisfactory. Although this is intrinsically an optical-tracking system which should be suitable during the day or in the shadow of the earth, it is again limited as before to the twilight condition: sunlit satellite and dark sky. Using radot as the transmitter mount and receiver should greatly expand the useful operating conditions: it will be described in the next paper.

CHARACTERISTICS OF THE X-Y ANTENNA MOUNT FOR DATA ACQUISITION[1]

ANDREW J. ROLINSKI, DONALD J. CARLSON AND ROBERT J. COATES
Goddard Space Flight Center

Scientific satellite programs demand optimum performance from automatic tracking antenna systems. Certain criteria, such as maximum drive shaft rates and best satellite data transmission conditions, are considered in the design of the antenna mount. In this paper, maximum shaft rates of two-axis mounts are compared under similar satellite pass conditions and the advantages of using an X–Y antenna mount for data acquisition and satellite tracking functions are discussed. Some general design considerations for servo control systems, and a discussion relating the error constants to the satellite rates, are given. A few salient features illustrating the advantages of the X–Y mount from the servo drive system designer's viewpoint are also presented. The paper concludes with a brief description of NASA's 85-foot parabolic X–Y antenna at the Data Acquisition Facility at Gilmore Creek (Fairbanks), Alaska.

INTRODUCTION

Most previous configurations for tracking antennas were developed as parts of radar systems. Since the latter were, for the most part, designed for low-elevation tracking of land vehicles, ships, and distant aircraft, elevation-over-azimuth mounts were developed and have been used almost exclusively for this application.

The first antennas used for satellite tracking and data acquisition employed radar-type elevation-over-azimuth mounts because this was the most common type available commercially. The serious deficiencies of the elevation-over-azimuth mount for satellite tracking immediately became apparent and showed the necessity of using antenna mounts that are optimum for tracking satellites. The development of a new antenna mount configuration was initiated at the Goddard Space Flight Center.

[1] A preliminary version of this paper under the title "The X–Y Antenna Mount for Data Acquisition from Satellites" was published in the *IRE Trans. on Space Electronics and Telemetry*, SET-8(2): 159–163, June 1962.

REQUIREMENTS FOR SATELLITE TRACKING

Satellites are put into orbit to gather scientific data; consequently, the usual prime objective of a satellite tracking antenna is to receive telemetered data from the satellites. Data are generally transmitted by the satellite during most of a pass, and it is desirable that all the data be received; this means that the data acquisition antenna must track the satellite for the maximum length of time. The ideal situation would be to acquire the satellite on the horizon and track it continuously to the other horizon. However, in practice good reception is not possible at very low-elevation angles because of multipath propagation and the higher level of received interference. Antenna sites selected for low interference are usually valleys surrounded by hills, which shield the antenna from man-made interference but prevent data acquisition near the horizon.

Over a period of time, satellites may be observed in all parts of the sky at many of the data acquisition stations. Therefore, a data acquisition antenna must be able to track a

satellite at any position in the sky above a few degrees elevation.

The best quality of data reception occurs when the telemetry signal is strongest, i.e., when the satellite is closest to the ground station. The range to a satellite is a minimum when the perigee point of the orbit is directly over the station, that is, in the zenith direction from the ground antenna. Thus, it is most important that a data acquisition antenna be capable of continuous, good tracking through and near the local zenith in order to assure quality reception of the telemetered data.

COORDINATE SYSTEMS

The position of a satellite, as measured from a tracking station, can be described in terms of various systems of coordinates, some of which are illustrated in Figure 1. For example, the position can be described in terms of the direction angles α, β, and γ and the slant range; more commonly, the position is described in terms of the cosines of those angles and the slant range. The position can also be described in terms of the east, north, and vertical components of the slant range; it is anticipated that this system will be used in the future for transmitting predicted positions to various NASA tracking stations. The position is often described in terms of the azimuth angle A, the elevation angle E, and the slant range; but it can also be described in terms of the X angle, the Y angle, and the slant range, as shown in Figure 1.

In the X–Y angle and slant range system adopted by the Goddard Space Flight Center, the X axis is oriented north-south and is parallel to the surface of the earth. The X angle is taken to be zero when the east component of range is zero; limits of ± 90 degrees are set on the value of this angle, and the sign of the angle is taken to be the same as the sign of the east component. The Y angle is taken to be zero when the north component of range is zero; limits of ± 90 degrees are set on the value of the angle, and its sign is taken to be the same as the sign of the north component Thus, for the case illustrated in Figure 1, the X angle has a positive value and the Y angle has a negative value.

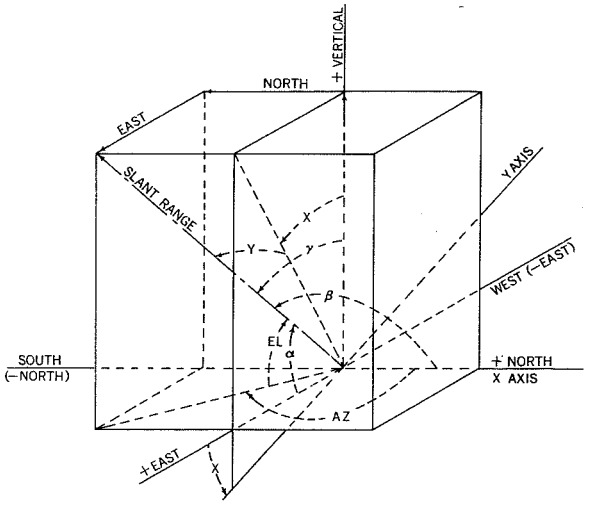

FIGURE 1.—Coordinate systems.

The familiar arrangement of the primary (azimuth) and secondary (elevation) axes of an elevation-over-azimuth mount is shown in Figure 2. The arrangement of the primary X and secondary Y axes of an X–Y mount[2] is shown in Figure 3.

SATELLITE TRACKING WITH AN ELEVATION-OVER-AZIMUTH MOUNT

To bring certain tracking considerations into sharp focus, let us examine the elevation-over-azimuth mount from the standpoint of its tracking characteristics.

Passes of three orbits, all having the same perigee height and speed, are shown in Figure 4. Let it be assumed that each satellite is at perigee at the time of its closest approach to the station—the time of meridian crossing for the orbits shown. The maximum azimuth shaft speed for each pass, then, is

$$A_{\max}=\frac{\sec E_1}{S_1} V_p, \qquad (1)$$

[2] This arrangement of axes has been described as "Cross-Elevation over Elevation" instead of "X–Y" in Cady, W. M., Karelitz, M. B., and Turner, L. A., "Radar Scanners and Radomes," vol. 26 of the Radiation Laboratory Series, New York: McGraw-Hill, 1948, Figure 4.1(c), p. 104.

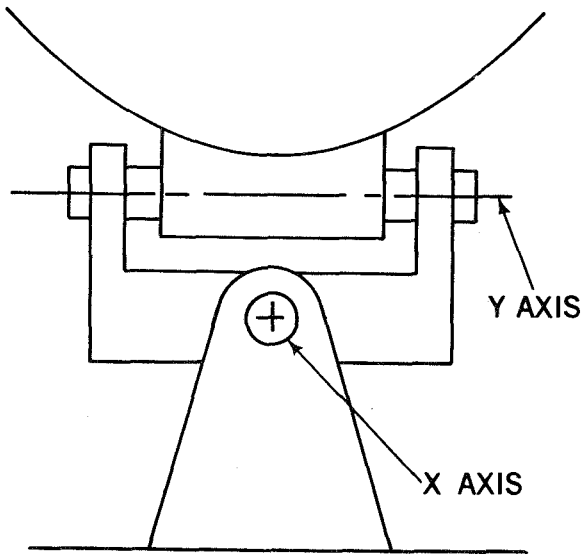

FIGURE 2.—Elevation-over-azimuth mount.

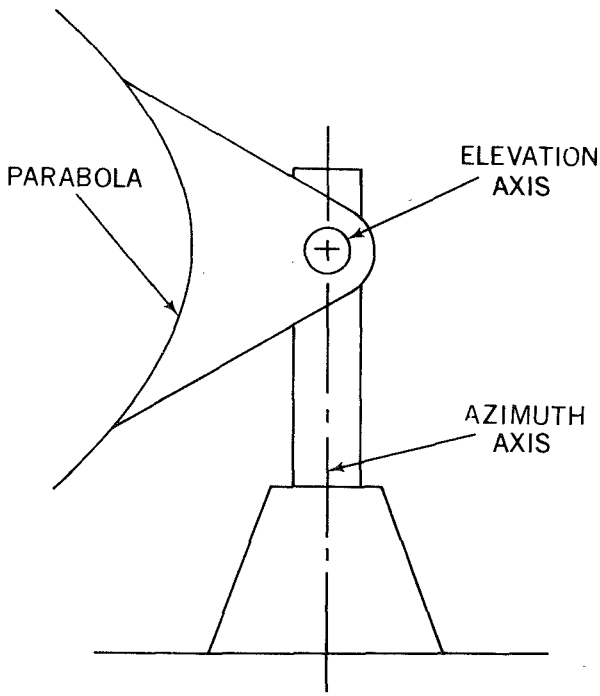

FIGURE 3.—X–Y mount.

where E_1 is the elevation angle at the time of closest approach, S_1 is the slant range at that time, and V_p is the perigee speed of the satellite. For orbit A, crossing the meridian at a low elevation angle, sec E_1 is close to unity and S_1 is large, so the maximum azimuth shaft speed is relatively low. But for orbits B and C, crossing the meridian at successively higher elevation angles, sec E_1 becomes successively larger and S_1 becomes successively smaller. As a result, the maximum azimuth shaft speed increases rapidly as a function of meridian elevation angle, going to infinity at 90 degrees elevation. The azimuth drive, being a physical system, can drive the antenna only at speeds below a certain maximum. Consequently, for any elevation-over-azimuth mount, there is always an area of the sky around zenith in which it is impossible for the mount to follow a satellite because the required azimuth shaft speed exceeds the limiting speed of the drive system. This shortcoming makes the elevation-over-azimuth mount a poor choice for a satellite data acquisition antenna.

THE *X–Y* MOUNT CONCEPT

A "brute force" solution to the problem of tracking through the zenith is to add a third axis [3] to an elevation-over-azimuth mount, but the increased complexity of the servo and drive system for a three-axis mount makes this solution unattractive. It appears more desirable to use a two-axis mount which is better

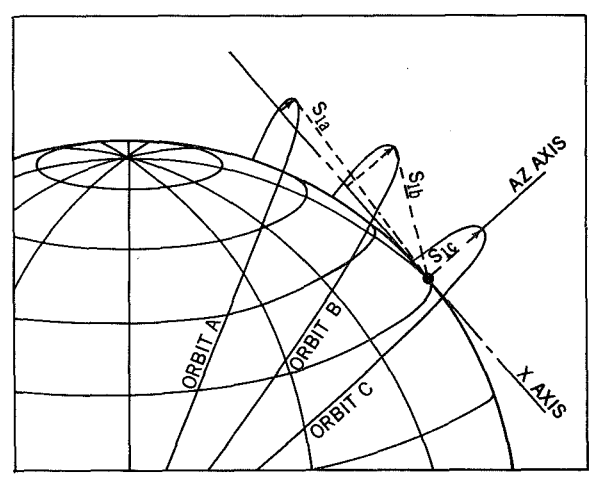

FIGURE 4.—East-west satellite passes with meridian elevation angles of 5°, 30°, and 90°.

[3] Victor, W. K., "Ground Equipment for Satellite Communication," Jet Propulsion Lab. Tech. Report 32–137, August 1, 1961, p. 54.

suited to satellite tracking, since a two-axis mount with orthogonal axes is the simplest configuration capable of pointing an antenna at any position in the sky.

The gimbal lock, or inability to track at zenith, for an elevation-over-azimuth mount illustrates a characteristic of all two-axis configurations. Any two-axis antenna mount has a gimbal-lock zone in the direction of the primary axis. Satellite tracking requires the absence of gimbal-lock zones above elevation angles of a few degrees. A possible solution is, therefore, to place the gimbal-lock positions on the horizon—in other words, to place the primary axis horizontally, as is done with the *X–Y* mount. Full sky coverage is obtained by orienting the secondary axis orthogonal to the primary axis so that the secondary axis is horizontal when the antenna is pointed at the zenith.

SATELLITE TRACKING WITH AN *X–Y* MOUNT

The worst-case pass with respect to an X axis is a pass on which the satellite, at perigee, crosses the meridian plane in an east-west direction, as illustrated in Figure 4. The maximum X axis speed during such a pass is

$$\dot{X}_{\max}=\frac{\csc E_1}{S_1}V_p. \qquad (2)$$

For a pass through the zenith (orbit C) an X–Y mount has the lowest possible primary axis speed of any two-axis mount. For east-west passes at successively lower meridian elevation angles, csc E_1 becomes greater, but S_1 also becomes greater and partially cancels the increase in csc E_1; the net result is that $\dot{X}_{\max}$ does not become great until the meridian elevation angle is quite small. But as mentioned previously, it is not possible to get good telemetry reception at low elevation angles; consequently, tracking at these angles is of little interest.

COMPARISON OF TRACKING RATES FOR *AZ–EL* AND *X–Y* MOUNTS

Equation 1 may be rewritten in the form

$$\dot{A}_{\max}=\frac{\csc \gamma_1}{S_1}V_p, \qquad (3)$$

where $\gamma_1=90°-E_1$. The angle γ_1 is measured from the primary axis of an *AZ–EL* mount, just as the angle E_1 in Equation 2 is measured from the primary axis of an *X–Y* mount; γ_1 and E_1 can each be described as an "angle off axis." In Figure 5, $\dot{A}_{\max}$ is plotted as a function of γ_1 and $\dot{X}_{\max}$ as a function of E_1, for satellites in circular orbits at various heights above the earth.[4] For a given small angle off axis, it is evident that the maximum azimuth speed is much greater than the maximum X axis speed. In other words, for a given maximum shaft speed capability, an *X–Y* mount can track a satellite at a much smaller angle off the primary axis.

It is shown in Appendix A that the maximum primary-axis acceleration during a worst-case pass is very nearly proportional to the square of the maximum shaft speed. Consequently, for a pass at a given small angle off axis, the maximum azimuth acceleration would be much greater than the maximum X axis acceleration.

The worst-case pass with respect to a secondary axis (either elevation or Y) is one on which the satellite travels through the zenith in a direction normal to a vertical plane containing the secondary axis. If we ignore the rotation of the earth, the shaft rates of the secondary axis during such a pass would be identical to the shaft rates of the X axis during orbit C of Figure 4; the maximum speed of the secondary axis would be equal to $\dot{X}_{\max}$ at $E_1=90$ degrees, as plotted in Figure 5.

SERVO SYSTEM CONSIDERATIONS

Servo Control System

In the design of the servo control system, consideration should be given to such factors as: system response and stability, dynamic

[4] The shaft speeds in Figure 5 were calculated for a non-rotating spherical earth of radius equal to the actual equatorial radius. More exact calculations for a particular station would take into account (1) the increase in slant range due to flattening of the earth at the latitude of the station, (2) the surface speed of the earth at that latitude, and (3) the direction of the orbit (direct or retrograde). At 60 degrees latitude, these factors could affect the shaft speeds for a 100-nautical-mile satellite by as much as 12 percent.

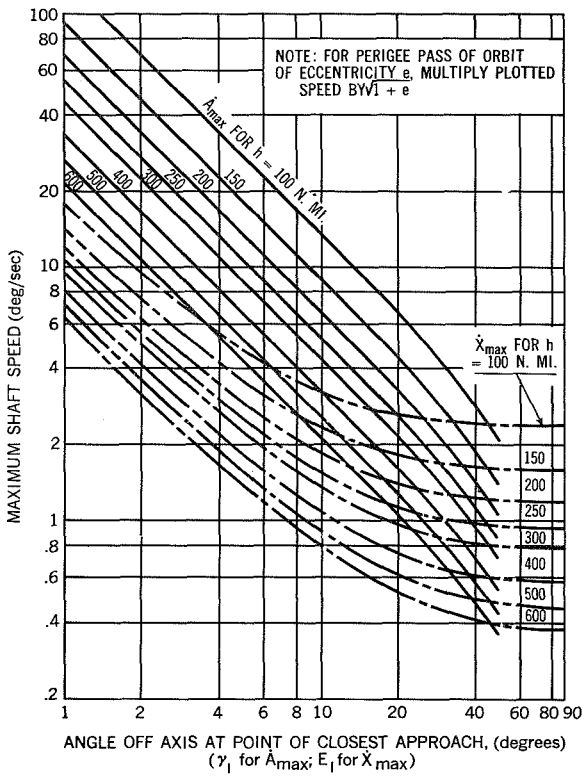

FIGURE 5.—Maximum shaft speeds on worst-case passes of circular orbits.

behavior at no-load and full-load conditions, and oscillation due to random load disturbances applied to the output shaft. Other factors which influence the design approach are large steady-state wind-induced torques and transient wind gusts. Within the framework of these factors, it is not possible to employ a standard or fixed method of synthesizing the optimum control system design, particularly since no previous knowledge of the X–Y system is available. Hence an intuitive, heuristic approach was pursued in the design of the servo control system for the first X–Y mount. Design parameters such as the velocity constant K_v and/or the acceleration constant K_a control the manner in which the system design is carried out. The constants K_v and K_a can be specified in terms of tracking servo bandwidth and maximum tracking rates. If, in the region of interest, the same tracking accuracy is specified for an X–Y system as for an equivalent *AZ–EL* system, the lower X shaft rate requirements for near-zenith tracking allow lower error coefficients values to be selected for the X–Y system; hence, the design limits on the system can be relaxed. The mathematical relationship equating the X axis lag error to the time derivatives of the input variable, satellite motion, can be expressed as follows:

$$e_x(t)=\frac{\dot{x}}{K_v}+\frac{\ddot{x}}{K_a}+\cdots\cdots$$

The actuating signal $e_x(t)$ is the lag error in the control system loop and X is the input variable, that is, the description of the satellite's motion. From the above equation, it can be inferred that if the error coefficients are not changed, lower shaft rates decrease the lag in the system.

Servo Drive System

Because the total power required to move the antenna is a function of its maximum acceleration and velocity, it is of primary importance not only to select a power element with an adequate power rating, but also to choose an antenna configuration that requires lower shaft rates. On the basis of the foregoing discussion, X–Y mounts seem to possess the characteristics which lend themselves most appropriately to the specified conditions.

Such factors as antenna inertia, friction load, unbalanced mass load, and wind load, as well as the maximum velocity and acceleration, control the selection of the drive element. Consequently, the lower shaft rates allow the choice of a drive element with a lower power rating. The last assumption is based on the premise that the duty cycle—the factor which establishes the heat dissipation property of the drive element—is not affected by other considerations.

It was mentioned earlier that the singularity or the gimbal-lock condition in the X–Y case exists about the X axis. This singularity is best described as a "keyhole" interference contour about the X axis on the horizon. In the data acquisition function, one of the operational conditions is the demand for maximum sky coverage where the best tracking conditions exist; in the region of interest, the X–Y mount provides maximum usable sky coverage at lower shaft rates.

DISCUSSION

The elevation-over-azimuth mount cannot continuously track satellites which reach high elevation angles; since it is here that the telemetry data are of the highest quality, this type of mount is therefore undesirable for satellite data acquisition antennas.

On the other hand, the tracking characteristics of an X–Y mount meet the requirements for satellite tracking. The zone of minimum primary-axis speed matches the zone of best-quality data transmission. Zones of excessive shaft speed occur near the horizon around the ends of the X axis, but the data quality in these zones is poor, and the desirable sites for data acquisition antennas are those with natural horizon shielding from man-made interference. The X–Y mount will track satellites through nearly the entire sky with moderate shaft speeds and accelerations. Thus, efficient tracking can be accomplished with moderate drive and servo systems.

The X–Y mount has another advantage. It is not necessary to use slip rings, rotary RF joints, or extensive cable-wrap systems to bring out the RF and power lines. Each axis travels only ± 90 degrees; thus, a simple, flexible section of cable is all that is needed to go across either axis. With the requirement for high receiver sensitivity for satellite data acquisition, this becomes a worthwhile advantage by eliminating a source of possible RF interference.

The Goddard Space Flight Center has sponsored the development of two types of X–Y antenna mounts for data acquisition from satellites; one of these was for an 85-foot-diameter parabolic antenna. This antenna (Fig. 6) was constructed to GSFC specifications by the Blaw-Knox Co. at a site in the Gilmore Creek Valley 12 miles north of Fairbanks, Alaska. The site is located in a small valley and the surrounding hills provide RF shielding from outside sources. The Gilmore Creek Valley has a horizon 9 degrees in the north and 8 degrees in the south; and the horizon decreases to about 2½ degrees in the west and 5 degrees in the east. The antenna is a paraboloid of revolution with a focal length of 36 feet. Its surface consists of doubly curved aluminum sheet panels. The X–Y mount was designed to provide optimum satellite tracking without requiring excessive shaft velocities from the antenna drive system. The antenna is capable of tracking at shaft speeds from 0 to 3 deg/sec with shaft accelerations of up to 3 deg/sec^2; this is sufficient for acquisition and tracking of 150-nautical-mile satellites throughout the sky above the local horizon. The antenna has six operational modes; it will automatically track on a satellite signal, it can be driven by a teletype tape input, it can be manually directed, it can be slaved to another antenna, or it can be operated in either of two search modes for initial acquisition.

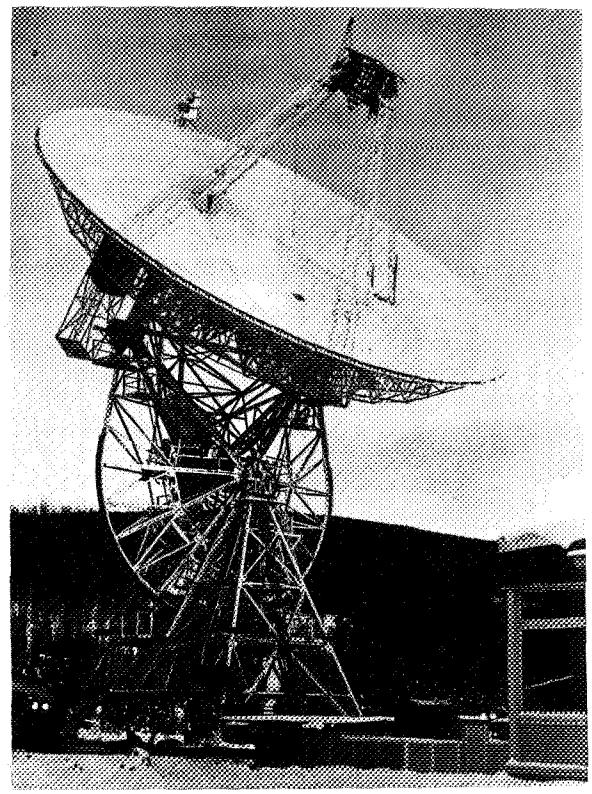

FIGURE 6.—X–Y mounted 85-foot antenna at the NASA data acquisition facility, Fairbanks, Alaska.

ACKNOWLEDGMENTS

The authors wish to acknowledge the many contributions of Mr. C. H. Looney, Jr., Mr. P. A. Lantz, and Mr. V. R. Simas to the development of the X–Y mount.

Appendix A

APPROXIMATE EXPRESSIONS FOR SHAFT SPEED AND ACCELERATION

Figure A–1 depicts an approximation to a satellite's motion relative to a tracking station. An azimuth axis and an X axis (on separate antennas) are located at the station. At time t_1 the satellite lies in the meridian plane (the plane of the front view) and is traveling directly eastward at a velocity V.

Let it be assumed that the earth does not rotate. Also, let it be assumed that the satellite continues to travel directly eastward at the constant velocity V; in other words, let it be assumed that the north and vertical components of slant range, as measured from the station, are constant during the pass.

At time t_1 the azimuth axis speed is at its maximum value for the pass, namely,

$$\dot{A}_{\max}=\frac{V}{S_1 \sin \gamma_1}. \qquad \text{(A–1)}$$

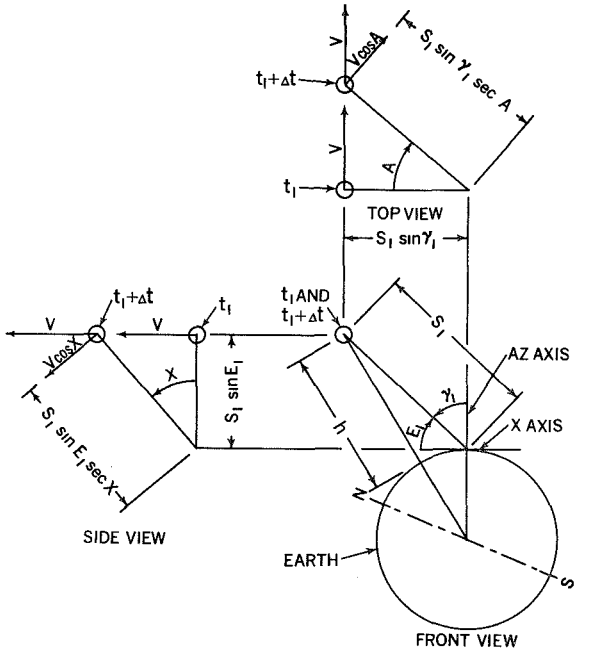

FIGURE A1.—Approximation to motion of a satellite.

At time $t_1+\Delta t$, the satellite reaches a point defined by the angle A in the top view. This azimuth shaft angle is

$$A=\tan^{-1}\frac{V\Delta t}{S_1 \sin \gamma_1}=\tan^{-1}[(\dot{A}_{max})\Delta t]. \qquad \text{(A–2)}$$

At this time, the azimuth speed is

$$\dot{A}=\frac{V \cos A}{S_1 \sin \gamma_1 \sec A}=\dot{A}_{\max} \cos^2 A \qquad \text{(A–3)}$$

and the azimuth acceleration is

$$\ddot{A}=-2(\dot{A}_{\max})^2 \cos^3 A \sin A. \qquad \text{(A–4)}$$

By setting the derivative of $\ddot{A}$ with respect to A equal to zero, it is found that the absolute value of $\ddot{A}$ reaches a maximum at $A=\pm 30$ degrees, and hence

$$|\ddot{A}|_{\max}=\frac{3\sqrt{3}}{8}(\dot{A}_{\max})^2 \text{ rad/sec}^2,$$

where $\dot{A}_{max}$ is expressed in rad/sec. In more convenient units,

$$|\ddot{A}|_{\max}=\frac{\pi\sqrt{3}}{480}(\dot{A}_{\max})^2 \text{ deg/sec}^2, \qquad \text{(A–5)}$$

where $\dot{A}_{\max}$ is expressed in deg/sec.

In a similar fashion, it can be shown that

$$\dot{X}_{\max}=\frac{V}{S_1 \sin E_1}, \qquad \text{(A=6)}$$

$$X=\tan^{-1}[(\dot{X}_{\max})\Delta t], \qquad \text{(A–7)}$$

$$\dot{X}=\dot{X}_{\max} \cos^2 \dot{X}, \qquad \text{(A–8)}$$

$$\ddot{X}=-2(\dot{X}_{\max})^2 \cos^3 X \sin X \qquad \text{(A–9)}$$

where $\dot{X}_{\max}$ is expressed in rad/sec, and

$$|\ddot{X}|_{\max}=\frac{\pi\sqrt{3}}{480}(\dot{X}_{\max})^2 \text{ deg/sec}^2, \qquad \text{(A–10)}$$

where $\dot{X}_{\max}$ is expressed in deg/sec.

Values of maximum shaft accelerations calculated from Equations A–5 and A–10 have been compared with values of maximum acceleration calculated in Goddard Space Flight Center's IBM 7090 orbital prediction programs, for certain passes of circular orbits at heights of 100 and 600 nautical miles. The passes were all "worst-case" in the sense that the satellite velocity was, in each instance, normal to the meridian plane at the time of meridian crossing.

For passes at $\gamma_1=10$ degrees, the approximate value of $\ddot{A}_{max}$ exceeded the IBM 7090 value by less than 0.5 percent, for both orbits. For passes at $E_1=10$ degrees, the approximate value of $\ddot{X}_{max}$ exceeded the IBM 7090 values by 2.3 percent for the 100-mile orbit and by 7 percent for the 600-mile orbit. At equal angles off axis, the approximation is better for $\ddot{A}$ than for $\ddot{X}$ because the time interval between the instant of maximum speed and the instant of maximum acceleration (at a shaft position approximately 30 degrees away) is smaller for the azimuth axis case than for the X axis case. As this time interval becomes smaller, the satellite moves a shorter distance along its curved orbital path and the earth rotates through a smaller angle about its spin axis; hence, the actual motion of the satellite during the interval more nearly approaches the type of motion depicted in Figure A1. Consequently, the approximations for shaft acceleration are relatively good for passes at small angles off axis, for low perigee heights, and for high perigee velocities.

For meridian crossings at large angles off axis, it was found that the approximations were not terribly bad, especially for low perigee heights. At $\gamma_1=85$ degrees, the approximate value of $\ddot{A}_{max}$ was about 1 percent greater than the IBM 7090 value for the 100-mile circular orbit, and about 8 percent greater for the 600-mile circular orbit. At $E_1=85$ degrees, the approximate value of $\ddot{X}_{max}$ was about 3.5 percent greater than the IBM 7090 value for the 100-mile circular orbit, and about 17.5 percent greater for the 600-mile circular orbit. At $E_1=88$ degrees, the approximate value for $\ddot{X}_{max}$ for a perigee pass of the highly elliptical EGO orbit, at a height of 150 nautical miles, exceeded the IBM 7090 value by only 2.3 percent.

For all of the passes calculated on the IBM 7090, with meridian crossings at both small and large angles off axis, the maximum shaft accelerations occurred at shaft angles very close to ± 30 degrees.

It is believed that the foregoing approximate expressions for shaft speed and acceleration are sufficiently accurate for purposes of designing servo control and drive systems for most tracking and data acquisition antennas.

PRELIMINARY REPORT ON THE SINGLE STATION DOPPLER-INTERFEROMETER ROCKET TRACKING TECHNIQUE

J. CARL SEDDON

Goddard Space Flight Center

A portable trailer-housed system is described that provides range timing, range safety, telemetry and rocket tracking services where normal rocket range facilities may not be available. Various methods of operating the station and preliminary results are presented with approximate cost estimates. This report discusses the general theory involved and the procedures used at the present time. Further development is in progress and will be described in a later report. Upon completion of the development, a detailed report will include electronic computer programming and a machine method of data-reading instead of the slower desk-computer technique described here to illustrate the data reduction theory.

INTRODUCTION

During the International Geophysical Year, the very large volume of rocket firings frequently resulted in long delays in obtaining rocket trajectory information. This difficulty prevailed to such an extent that the scientific data obtained in the rocket firings often had to be shelved until the trajectory data were made available. Frequent troubles with the radar beacon or the radar itself sometimes caused the final trajectory to be incomplete. In addition, the highly accurate DOVAP[1] method required so much time consuming labor that these trajectories were completed only to an altitude of 100 km; this forced the experimental scientists to make a free-fall computation to determine the remainder of the trajectory. In addition, some experiments, such as the Seddon two-frequency ionosphere propagation experiment (Reference 1), require the radial velocity of the rocket which must be calculated from the position data. In order to eliminate much of the computational labor and to speed up the determination of the rocket's trajectory, a Single Station Doppler (SSD) technique was devised. Crude tests made on this system at Churchill, Canada indicated that a reasonably accurate trajectory could be determiued in a relatively short time. Since the equipment required cost a very small fraction of the cost of a radar system, and since it readily could be made portable, it was decided to develop the system further to determine its capabilities, especially for synoptic rocket soundings where normal rocket range facilities might not be available.

Synoptic rocket firings at various places on the earth's surface can provide a wealth of information concerning the upper atmosphere. Often, geophysical considerations require that the firing take place in remote areas where rocket range facilities are nonexistent. From the safety standpoint, it is very desirable that there be no densely populated areas in the vicinity. The SSD system provides a reasonably economical and transportable means for supplying the needed services for such operations, i.e., range timing, rocket tracking, range safety, and telemetry. For tracking with moderate accuracy, the equipment can be housed in one

[1] Doppler Velocity And Position.

trailer. If electrical power is not available, another trailer with a motor-generator may be required. For tracking with the highest-accuracy, an additional trailer is required for a high powered transmitter. The system can be simplified somewhat, but usually at the sacrifice of other features, such as real-time read-out or increased effort in the reduction of the data obtained.

The SSD system uses the Doppler effect to obtain the radial velocity of the rocket with respect to the ground station and measures the direction cosines of the radius vector by means of a two-axis radio interferometer. Integration of the radial velocity provides the radial distance. With these data it is possible to compute the position of the rocket with respect to the ground station. For a moderately accurate trajectory (about ½ percent in altitude on ascent), a very stable frequency of 73.6 Mc is radiated from the rocket to the ground station. For experimenters requiring higher accuracy, a 2 kw transmitter on the ground (in the vicinity of the SSD station) radiates half this frequency to the rocket which carries a transponder that doubles the frequency and transmits the result back to the ground station. The antennas and transponder used are the same as those employed in the usual DOVAP system.

This preliminary report describes the theory involved and the SSD station set up at Wallops Island, Va. Advantages and disadvantages of various ways of operating the station are pointed out, and cost figures are also given.

CONTINUOUS PHASE INTERFEROMETER

Most of the SSD experiments conducted thus far have made use of a continuous phase interferometer (CPI). A system such as that utilized by the Minitrack network (Reference 2) was rejected for a number of reasons: (1) the receivers required are not receivers in the usual sense because of the rather complicated circuitry required in the "front end," which makes the receiver unsuitable for both Doppler and telemetry reception; (2) it is very difficult to utilize such a technique and at the same time have a range safety system; and (3) a very large number of antennas are required. Other CPI systems were rejected because of the labor involved in reducing the data and the large number of recording channels required. Figure 1 is a block diagram of the system currently employed.

The circularly-polarized antennas employed in the SSD system are manufactured to be as nearly identical as possible. The four interferometer antennas located on a circle of 8λ radius, are carefully surveyed so that they lie on a true North-South or true East-West line. The radio frequency cables from these antennas are brought into a trailer located at the center of this circle (Fig. 2). The cables, laid in wooden troughs to prevent damage, are carefully cut to equal lengths which are an integral multiple (electrically) of a half wavelength. These cables are connected to line stretchers having the same characteristic impedance so that the electrical lengths of the cables can be adjusted. A crossed-dipole turnstile antenna on the roof of the trailer is used for measuring the Doppler effect.

Since the interferometer receivers have a common local oscillator, their 6.48–Mc IF outputs have the same phase relationships as do their input signals, provided that the two receivers have identical phase characteristics. A 90-degree phase shifter shifts the phase of one receiver output so that it may be applied to a phase detector. Under these circumstances, equal phase conditions at the antennas will provide a zero voltage from the detector. A difference in phase between the signals will

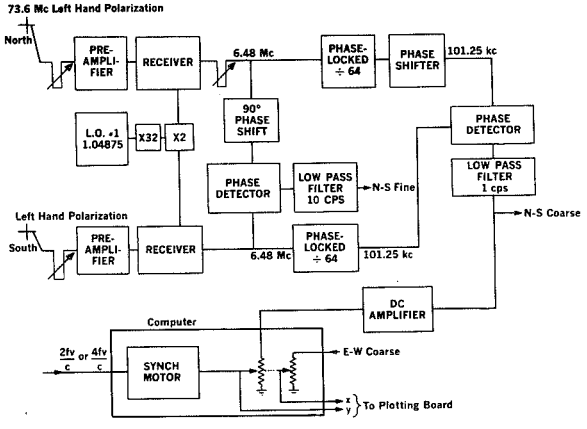

FIGURE 1.—Continuous phase interferometer and flight safety system.

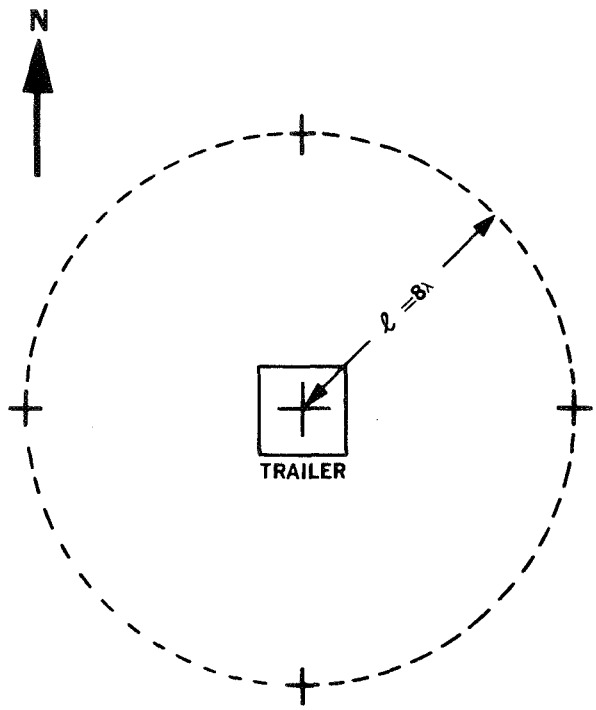

FIGURE 2.—Station layout.

provide a voltage output either positive or negative, at the detector. The sense of the phase shift may be determined by adding a very short cable in series with one of the line stretchers. The phase detector output, almost linear with phase, is put through a low pass filter and is recorded on a Sanborn recorder. The antennas on each axis are separated by 16 wavelengths, and the phase detector output maximizes at ± 90 degrees; thus there are 64 different interpretations for any reading of the phase difference between the input signals. It is necessary to remove this ambiguity.

The IF outputs to the receivers are fed to phase-locked dividers wherein the frequency is divided by 64. After a 90-degree phase shift on one channel, these 101.25 kc signals are applied to a phase detector. After filtering, the output of this phase detector is also recorded on a Sanborn recorder. The difference in phase of the signals arriving at the antennas from the launcher can be computed, because the direction of the launcher from the SSD station is known. This result is divided by 64 to provide the phase difference at 101.25 kc. Calibration of the phase detector therefore determines, except for sign, what voltage the phase detector should have. The sign is readily determined from the geometry.

A signal is radiated from the rocket on the launch pad to the ground station and the phase detector is set to the proper voltage by repeatedly pressing a microswitch on the phase-locked dividers until this voltage is obtained as closely as possible. The switch-pushing merely causes the dividers to slip 360 degrees at the 6.48 Mc frequency. Owing to the fact that the transmission is close to the ground where some re-radiation effects can occur, the voltage cannot be set exactly, but this is not harmful, since the dividers are locked on the proper cycle. This procedure has been called lobe-setting. Tests conducted thus far indicate that the ground, launcher, and neighboring buildings do not affect the phase difference at the 73.6 Mc frequency by more than about 90 degrees. Therefore, the coarse phase detector can be set to within about 1½ degrees. This error will disappear as soon as the rocket is away from the ground. The approximate direction cosine for this axis is obtained from the relation

$$\cos\theta=\frac{64\lambda\delta_n}{360L}=0.0111\delta_n, \qquad (1)$$

where L is the distance between the antennas and δ_n the phase difference, in electrical degrees, indicated by the calibration of the phase detector. The direction cosine for the other axis is determined in a similar manner.

COMPUTER FOR RANGE SAFETY

To provide a plot of the subrocket point on a horizontal plane through the SSD station, a simple computer is used. The outputs of the two coarse phase detectors are applied to ten-turn ganged helipots. The variable contacts of these helipots are driven by a synchronous motor which in turn is driven by the Doppler voltage obtained from the antenna on the roof of the trailer as will be explained shortly. Therefore this motor integrates the rocket's radial distance, and since the coarse phase detector outputs are proportional to the direction cosines, the computer outputs are a product of

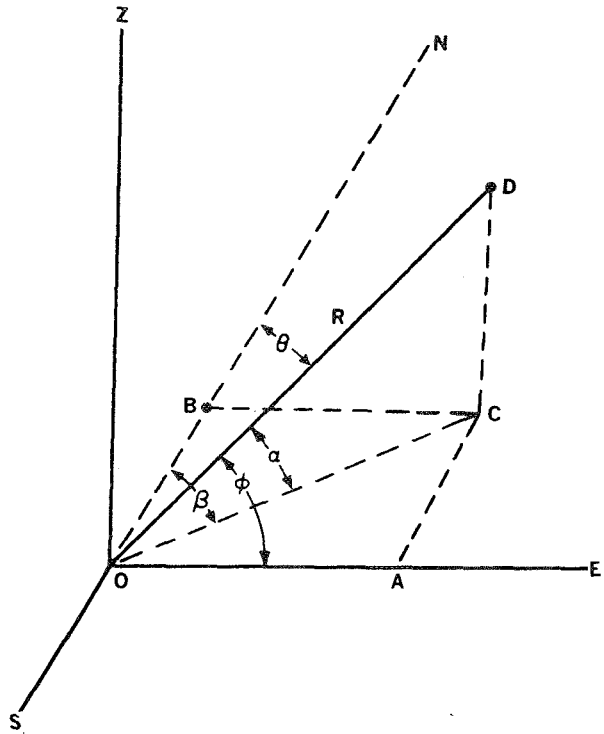

FIGURE 3.—Vector diagram of the rocket and the SSD station.

these factors. This output may be applied to an X–Y recorder, which will plot out the sub-rocket position. In the geometrical representation (Fig. 3) the rocket is at D and the SSD station at 0; the radial distance is indicated by R and the angles with respect to the axes are θ and ϕ; C is the position of the sub-rocket point. Before flight, the synchronous motor is rotated by an audio oscillator until a counter geared to the motor reads the correct radial distance in meters from the SSD station to the launcher.

DOPPLER MEASUREMENT

The One-Frequency Method

In the one-frequency method of Doppler measurement, the signal received by the crossed dipoles on the trailer's roof is separated into left and right hand components by means of a $\lambda/4$ delay line in one antenna cable and a cable-type magic-T (Fig. 4). These two components were selected to permit the elimination of the effects of the rocket's roll, and also to double the sensitivity of the system.

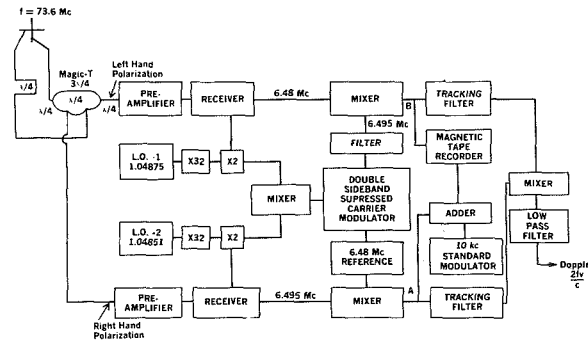

FIGURE 4.—The one-frequency method of radial velocity measurement.

The left hand polarization (lhp) signal is fed into a receiver which employs the same local oscillator as is used for the interferometer receivers. The receiver used for the rhp signal, however, has an oscillator that results in an IF frequency 15 kc higher than that of the lhp signal. This frequency difference is used to double-sideband-modulate a 6.48 Mc standard reference oscillator with the carrier suppressed. The filter is used to select the higher frequency for mixing with the IF of one receiver, whereas the reference oscillator signal is mixed with the IF of the other receiver. The outputs of these mixers have frequencies, respectively, of 15 kc plus the Doppler plus the rocket roll rate, and 15 kc minus the Doppler plus the rocket roll rate. Phase-locked tracking filters provide an improvement in the signal to noise ratio; and after mixing, a Doppler frequency of $2vf/c$ is obtained. The magnetic tape recorder preserves the data in case the tracking filter should lose lock, and also makes possible an improvement in the accuracy of the final results (see p. 902). As there are only two channels on the magnetic recorder, timing is added to one of the Doppler channels by an adder circuit.

The Two-Frequency Method

Because the rocket's rough treatment of the transmitter may change its frequency slightly and thereby introduce some error into the

measurements, the two-frequency method of Doppler measurement is more accurate, although it introduces additional technical problems. A 36.8 Mc signal is radiated at a power level of 2 kw from a right-hand circularly polarized antenna near the SSD station. By means of a short wire aerial, the SSD station will receive enough of this signal for use as a comparison frequency, injecting it into the mixer as shown in Figure 5. This frequency is quite constant; but even if it did change slightly, it would have very little effect on the final results. The transponder in the rocket receives this signal shifted by the Doppler effect, doubles it in frequency, and transmits the resulting signal which is again shifted by the Doppler effect. Owing to the high signal level at 36.8 Mc, a double-stub trap is placed in the antenna cables ahead of the receivers.

Since the rocket roll rate changes the received signal frequency, and since this is doubled in the transponder, and since the transmitted frequency is also affected by roll, the frequency of the signals received on the ground are shifted by 3 times the roll rate (3ρ) for one polarization and 1 times the roll rate (ρ) for the other polarization. In other words, the upward transmission of the 36.8 Mc signal is polarized right-handed; therefore the received lhp signal contains a 1ρ term, and the rhp signal contains a 3ρ term. To eliminate the roll, the lhp signal is frequency-multiplied by 3 in a tripler stage. The transmitted 36.8 Mc frequency is mixed with half the local oscillator frequency, and the result is frequency multiplied by 4 before mixing with the output of the tripler. The result is a 6.48 Mc signal with Doppler and a 3ρ term, the latter having the same sign as that obtained from the rhp signal. These frequencies are combined in a mixer which provides a frequency of 15 kc with a Doppler shift of $4fv/c$. This frequency is applied to the tracking filter, and then to a phase detector along with the 15 kc difference frequency between the local oscillators. The result is a roll-free Doppler frequency of $4fv/c$. Thus the sensitivity of this system is twice as great as for the single frequency system; but this advantage is partially offset by the slight ionospheric effect at the lower frequency, which introduces some error.

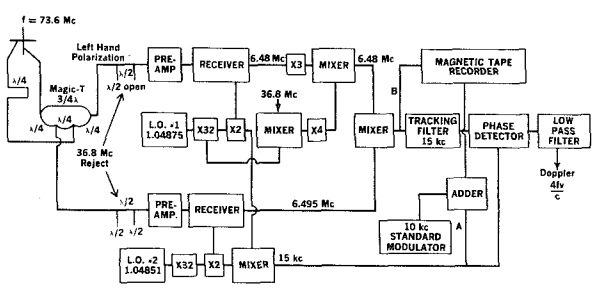

FIGURE 5.—The two-frequency method of radial velocity measurement.

REAL-TIME READ-OUT, RECORDING AND RANGE TIMING

The block diagram of the real-time read-out, recording and range timing is shown in Figure 6. The Doppler frequency, applied to a frequency meter, gives a continuous reading of the rocket's radial velocity during the flight. For the two-frequency system, $4f/c$ is very close to unity if c is in km/sec. Therefore a frequency meter set on the "kilocycles" scale will read directly the radial velocity in km/sec. For the one-frequency system, the reading must be doubled. To obtain total radial distance, the integration of this Doppler frequency is performed in the following manner:

The distance from the SSD station to the launcher is determined in km and the hp 521C industrial counter is set for the integral number of km. The remaining fractional km is converted into Doppler cycles and the resulting number is set on the dual preset counter (see

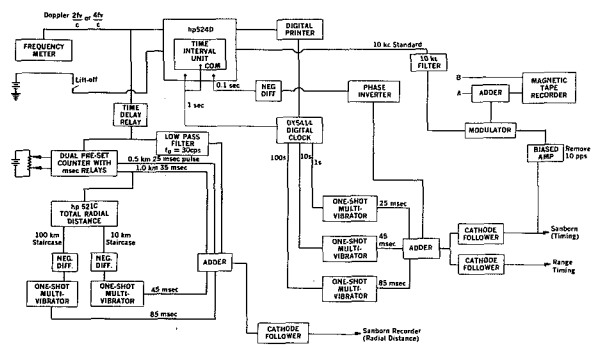

FIGURE 6.—Real-time read-out, recording and range timing.

Appendix A). The time delay relay is open so that these settings remain fixed. The lift-off switch is held open by the weight of the rocket on the launching stand. As soon as the rocket lifts off the switch, this contact is closed and the battery voltage is transmitted by land-line to the SSD station, where it activates the time delay relay. The purpose of this relay, usually set for an interval between 0.5 and 1.5 seconds depending on the circumstances, is to prevent erroneous results due to takeoff noise. In general, the change in radial distance during this short time is small enough to be neglected, but it may be computed, if desired, from predicted rocket performance data (Appendix A).

By the closure of the time delay relay, the Doppler frequency is applied to the dual preset counter with millisecond relays. The two potentiometers provide the relays with slightly different voltages; the smaller is applied to relay A. For the one-frequency system, relay A is preset at 245 and relay B at 246, so that 1-kilometer marks occur every 491 cycles. For the 2-frequency system, relay A is set at 491 and relay B at 491. Thus relay B provides a pulse every 1.0 km and relay A a pulse halfway between. The application of the 1 km pulses to the hp 521C counter provides a real-time read-out of the total radial distance in kilometers.

For recording, the 10 km and 100 km staircase voltages are each brought out to a differentiation circuit and to a one-shot multivibrator with 45 and 85 millisecond widths, respectively. The ½, 1, 10, and 100 km pulses are applied to an adder which drives a Sanborn recorder. The resultant pulse shapes (Fig. 7) illustrate how the differing amplitudes and shapes of the resulting pulses provide identification. In addition, the adder is supplied with the voltage obtained from a low pass filter with a 30 cps cutoff. Thus, a sinusoidal voltage is superimposed whenever the Doppler frequency is less than 30 cps; this is necessary for an accurate determination of the maximum slant range. Just before the maximum slant range occurs, a ½ or a 1 km pulse will appear "riding" on top of the sinusoidal voltage. The number of cycles from the latter pulse are counted until the frequency becomes zero, at which time the phase of the sinusoidal voltage reverses; at this time the slant range is maximum. To obtain the slant range during rocket descent, this maximum range must be subtracted from the indicated distances.

The timing and a digital print-out of the radial velocity are obtained in the following manner: Before launch, the phantastrons in the counter are disabled by means of a relay in the plate circuit, with the gate circuit open. In this state, the counter will continuously add up any noise coming from the Doppler circuitry. By means of an internal connection, the one-per-second gating pulses are connected to a digital clock and to the "common" connection of the time interval unit. There will be no pulses at this time because the phantastrons are inoperative.

When the rocket is launched, the lift-off switch energizes a relay (not shown) which closes the phantastron circuit, thereby providing a 1-second pulse to operate the time interval unit and the digital clock. The clock has been preset at its highest reading (239999) so that the first pulse from the counter causes it to read all zeros. This first pulse occurs 15 milliseconds after closure of the lift-off switch. Succeeding pulses alternately open and close the counter gate so that the digital printer prints the number of cycles occurring in the intervals 0 to 1, 2 to 3, 4 to 5 seconds, etc. The time recorded (in even seconds) by the digital clock is printed on the first five units of the digital printer. Thus, a print-out of 100 cycles

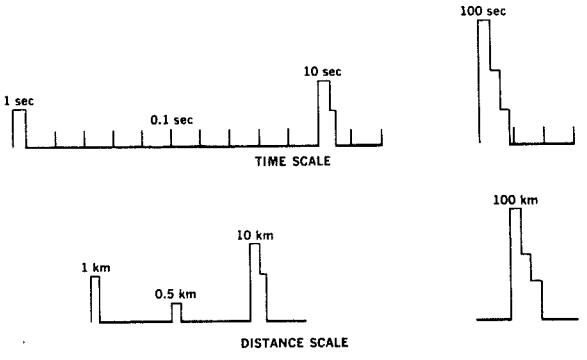

FIGURE 7.—Pulse shapes recorded by the Sanborn recorder.

at a printed time of two seconds indicates that 100 cycles were recorded during the interval 2 to 3 seconds and that the average velocity was 100 cycles/sec at 2.5 seconds.

Short, sharp pulses are obtainable from the digital clock at the rate of 1 each second, one every 10 seconds, and one every 100 seconds. These pulses are applied to an adder circuit along with very narrow sharp pulses having a frequency of 10/sec, which are obtained by differentiation of a staircase voltage in the electronic counter. The output wave forms are like those of Figure 7. This timing is recorded with the interferometer and radial distance channels on a Sanborn recorder. Additional cathode followers are also supplied so that the timing may be transmitted over land-lines to the launcher or to other trailers containing the equipment used by the research groups. An additional sinusoidal frequency of 100 cps (not shown in Fig. 6) is also available for any research groups requiring such a frequency synchronized to the timing signals. A 10 kc standard frequency can also be made available. If extreme accuracy of the standard frequency is required, the electronic counter can be operated from a one-Mc standard frequency source.

The timing signal, in addition to being recorded on the Sanborn recorder, is also recorded on a magnetic tape recorder but with the low-amplitude 10 cps spikes removed by a biased amplifier. This same amplifier drives a modulator which modulates the 10 kc standard voltage upward, and the result is added to one of the 15 kc channels recorded. A four-channel head for the magnetic tape recorder would obviate this undesirable mixing, and this head is presently being developed. The plans are to record separately the two 15 kc channels with Doppler and roll; the 15 kc difference between the local oscillators; and the modulated 10 kc frequency. These modifications will simplify the playback circuitry.

STATION CALIBRATION

One hour before scheduled launch time, the interferometer antenna cables are disconnected and their electrical lengths checked by means of an R-X bridge. The line stretcher is used to adjust each cable to an exact multiple of a half-wavelength. Then the antennas are reconnected and their impedances checked; and the four interferometer receiver input impedances are adjusted to the characteristic impedance of the cable. Next, a signal generator connected to a tee applies equal phase signals simultaneously to the North and South receivers at the point where the antenna cables are normally connected.

The gain on the Sanborn amplifiers is checked by substituting a separate local oscillator for one of the receivers. This oscillator's frequency differs from that of the other by about 1 cps. The gain should be such that the amplitude of the 1-cps voltage nearly fills the channel. This signal is recorded on the Sanborn recorder and provides the necessary calibrations, since the phase variation is proportional to the chart speed. The amplitude of the coarse detector output is also checked and recorded in this fashion with the local oscillator frequency differing by about 64 cps. Then the original local oscillator is reconnected, and the line stretcher in the IF circuit is adjusted to make the output of the fine phase detector bring the Sanborn pen exactly to the middle of the chart paper. Next, the switch on the phase-locked divider is pressed repeatedly until the coarse channel is 16 steps from maximum channel deflection. A final adjustment to exact center is made by the phase shifter. The East-West receivers are similarly adjusted. If it is desired to make corrections to the phase because of possible low signal level, an AGC calibration of phase is also made. This is done at 0 degrees in 10 db steps, after which the one-cycle calibrations are made at these same levels.

The Doppler circuitry is then checked for proper amplitude by throwing a switch on local oscillator No. 1, thus changing its frequency and thereby simulating a Doppler signal. If the two-frequency system is being used, the high-powered transmitter must be turned on for this test. The operation of the counters and printer are checked. The oscillator is then returned to its original frequency; and the 15 kc difference frequency between the

two oscillators is checked. A slight adjustment of local oscillator No. 2, which does not affect the Doppler frequency, may be necessary. The magnetic tape recorder is checked by a test recording played back on an oscilloscope to insure that the amplitudes are appropriate, especially the modulated 10 kc standard. The timing is then recorded on the Sanborn recorder to insure that this is operating properly. The lift-off circuitry and the time delay relay are also checked.

The X–Y plotter is adjusted in the following manner. With equal-amplitude equal-phase signals into the E–W receivers, the switch on the divider is pressed repeatedly until the X reading is 8 steps from either maximum or center. At this 8th lobe, $\phi=60$ degrees and $\cos\ \phi=0.5$. The gain of the X amplifier is adjusted to provide the deflection desired for one-half the distance reading on the counter connected to the synchronous motor. The Y scale is adjusted similarly, using the N–S receivers. The zero lobes (16 steps from maximum) for both axes are made coincident at the point representing the SSD station on the graph. Next, a protractor and ruler are used to mark the location of the launcher (the direction and distance are known).

By means of a simulated low frequency Doppler signal, the hp 521C is set at the proper value, usually either 0 or 1 km. The dual preset counter is also set at the proper number of cycles to account for the number of cycles in the remaining fractional km distance from the SSD station to the launcher. The "Operate" switch is turned off when the setting is correct, and remains in this position until shortly before rocket launch. The relay in the phantastron circuit of the electronic counter is then opened, at a time when the gate is open, and will not close again until the lift-off switch operates at the launcher. The digital clock is set at 239999.

By the time, the launch should be imminent. If a long "hold" occurs, the calibration should be repeated. If no long hold occurs, the transponder (or the transmitter) in the rocket is energized about 5 minutes before launch. The switches on the dividers are pushed a sufficient number of times to set the pen of the X–Y plotter as nearly as possible on the position of the launcher on the chart.

In the one-frequency system, a very low Doppler frequency will be present; this is adjusted to zero frequency by very slightly varying the frequency of either the reference oscillator or local oscillator No. 1 with the radial distance channel on the Sanborn recorder under observation. The time delay relay switch is opended and the preset counter switch set to "Operate". The tracking filters are then locked on the signal. The station is in readiness for launch.

Thirty seconds before launch, the recording equipments are turned on. One man's position is at the X-Y plotter, and the other two in front of the tracking filters. The latter employ earphones to permit manual lock-on of the tracking filters should they lose lock. Additional circuitry has been incorporated into the standard tracking filters so that a panel meter indicates the amount and direction of the pulling voltage applied to the variable controlled oscillator (VCO) in the tracking filter. At takeoff, this meter reading changes from zero to some value dependent upon the acceleration of the rocket. The operator manually adjusts the VCO voltage for a meter reading of approximately zero, but slightly in the direction in which it is forced by the rocket's acceleration. This assists the tracking filter in maintaining lock, especially with high-acceleration rockets.

Shortly after last stage burnout, the acceleration is only -1g due to gravity; thus the tracking filters will require only occasional attention. When the Doppler frequency becomes so low that it appears on the Sanborn record, it is monitored until the frequency becomes zero and reverses phase. At this time the reading of the digital clock is noted and also the reading of the industrial counter (which is reading the maximum slant range in km). This information is telephoned to the blockhouse for it provides a fair indication of whether the rocket is performing as predicted. On descent, it is sometimes necessary to watch the tracking filters very closely, because the rocket's

rotation may cause signal nulls with attendant rapid phase variations severe enough to unlock the tracking filters. On signal cessation at impact, the equipment is turned off and a recalibration of the station is made.

DATA REDUCTION

Manual reduction of the data will be discussed, although a more refined and rapid technique suitable for data readers and electronic computers has been developed. Part of the latter technique is discussed in a recent unpublished report (Reference 3).

The theory involved is illustrated by describing the method that was used originally with a desk calculator. The pre-flight and post-flight calibrations of the phase detectors are examined to insure that no changes occurred during the flight. From the 1-cps calibrations, two scales can be prepared showing the amplitude at about 5 or 10 degree intervals over a 360-degree range. These scales are made for both fine channels and over a ± 90 degree range for the coarse channels. An approximate value for the direction cosine can be obtained by using this scale to determine the phase reading of the coarse channel in degrees and multiplying this by the factor 0.0111 (see Equation 1).

If the lobe number vertically overhead is assumed to be 0, the lobe number n (an integer) may be determined by means of the relation

$$n=\frac{64\delta_c}{360}=0.1778\delta_c, \tag{2}$$

where the decimal portion is neglected. The fine interferometer channel is read for the same time and if this reading is called δ_f, then the total number of electrical degrees δ of phase difference between the 73.6 Mc signals at the two antennas is

$$\delta=360n+\delta_f. \tag{3}$$

This number of degrees, multiplied by the factor $\lambda/360L=0.00017349$, provides the direction cosine with high accuracy. The other direction cosine may be determined in the same fashion at the same time. The slant range R is read from the record, and the altitude may be computed by the relation (see Fig. 3):

$$h=R\sqrt{1-(\cos^2\theta+\cos^2\phi)}. \tag{4}$$

The horizontal range d from the SSD station is given by

$$d=R\sqrt{(\cos^2\theta+\cos^2\phi)}. \tag{5}$$

The coordinates of the sub-rocket point in the horizontal plane through the launcher are obtained from $R\cos\theta$ and $R\cos\phi$; and the angle β is given by

$$\beta=\tan^{-1}\frac{\cos\phi}{\cos\theta}. \tag{6}$$

To compute the azimuth it is necessary merely to know in which quadrant the rocket is flying. For example, if the outputs of the coarse phase detectors are positive, they are represented by a + for an easterly direction, $\oplus$ for a north direction and similarly for negative values, then the quadrant can be determined by the following chart:

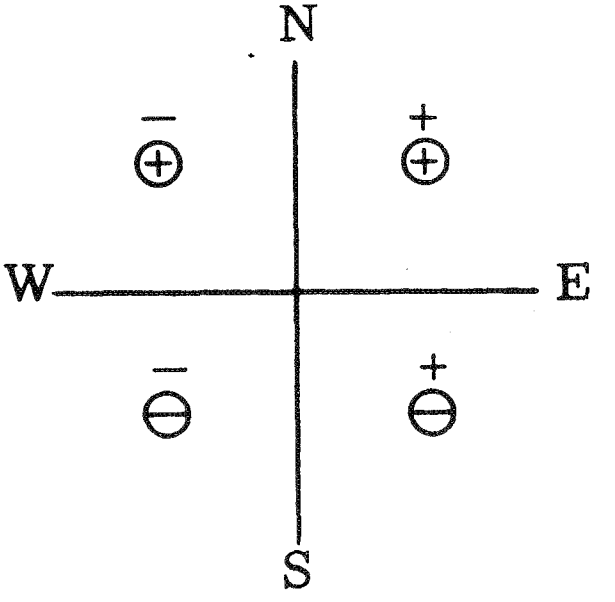

The foregoing discussion has assumed that all of the data were properly taken. In the event that the tracking filter lost lock, or if a more exact value for R is desired than that read from the Sanborn record, the data from the magnetic tape must be played back (as described on page 15). If the dividers should lose

lock, as sometimes occurs when the transmitter momentarily malfunctions, or if the radio propagation conditions are badly disturbed—such as by the explosion of a grenade in the vicinity of the rocket—the direction cosines must be computed, in the following manner, from the fine interferometer data.

From a previous calculation, the lobe number of the launcher for a given axis is n_1, and the lobe numbers are decreased at rocket takeoff by one unit for every 360 degree change on the fine interferometer record. However, if a phase reversal occurs on the record, then the next lobe number is taken to be the same as the last one and succeeding lobe numbers are one larger. This procedure is quite satisfactory except in rare instances when the phase reversal may occur within 3 or 4 degrees of ± 90 degrees, in which case it may be difficult to ascertain that the phase did reverse. If the phase reversal is not noted, answers are obtained which are obviously ridiculous and the point of phase reversal must be found. This process is described later.

DATA PLAYBACK

Figure 8 is a block diagram of a method for obtaining digital values of the radial velocity at one-second intervals by playback of the magnetic tape record. The digital clock is set at 239999 and, if it is desired to obtain the same data as was obtained during the flight, the electronic counter gate should be open. Usually it is desirable to obtain the data during the odd-numbered seconds which were not obtained during the flight, so the gate is closed initially. The magnetic tape recorder is started, and at the time corresponding to lift-off the 10 kc standard frequency appears, moving the digital clock to zero. The tracking filters are manned in the usual fashion until the end of the record. By summing the odd-second and even-second tapes and adding in the number of cycles equal to the distance from the SSD station to the launcher, the radial distance R is obtained as a function of time.

If the summation of the one-second intervals is regarded as too tedious, a longer time interval can be summed by means of a slight change in the circuitry. For example, the one-shot multivibrator may be utilized to start the time interval unit, and the 10-second signal from the digital clock may be used to stop it. Thus, this digital tape with give a nine-second count and the additional first second count may be added from the one-second tape. This process can be extended to 99 seconds if desired.

A method for determining the accurate time of occurrence of each integral km of radial distance is given in Figure 9. The counter gate is closed and the digital printer is set at 239999. The dual preset counter scales for the two-frequency system are set at 1 and 981 (1;981) and for the one frequency system is set at 1;490. The counter is started by the one-second pulses and is stopped at the end of 1 km at which time the printer prints. For example if the printer reads 00028009172, then the time for that integral km is 28.9172 seconds. The fifth digit from the right must be ignored. This system will not function during any

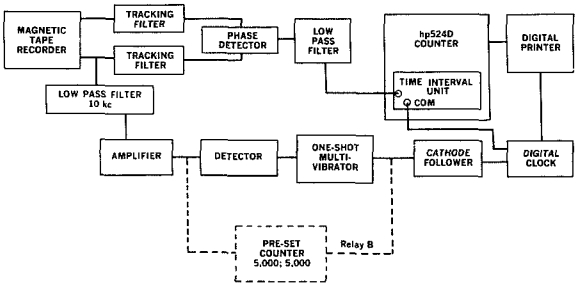

FIGURE 8.—Data playback (1 second intervals). Dashed lines indicate alternative method.

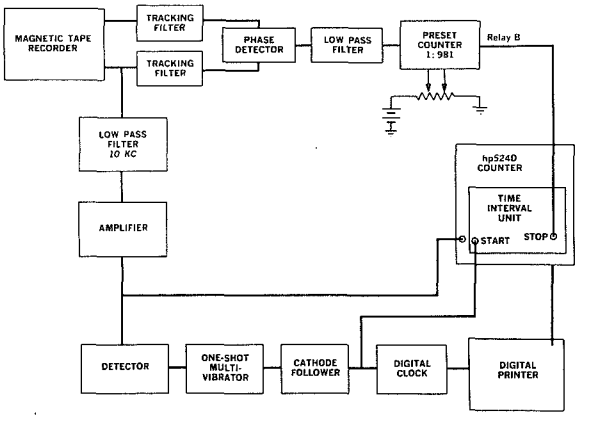

FIGURE 9.—Method of obtaining accurate time of occurrence of each integral km of radial distance.

interval of time when the radial velocity exceeds 1 km/sec. In this case, however, the times of the integral km are printed correctly for the portion of time when the radial velocity is less than 1 km/sec. A few exceptions may be found, in which the time may be in error by exactly 1 second or the print-out may be blurred. The 1-second error usually can be spotted easily, but the blurred reading cannot be remedied. The portion of the record in which the rocket velocity exceeds 1 km/sec may be re-run, using 2 km intervals with the preset counter changed to 1;1963 for the two-frequency system or 1;981 for the one-frequency system.

Except near times of ignition or burnout of a rocket stage, when the radial velocity does not vary approximately linearly with time, a more accurate value of the radial velocity can be obtained by means of equations such as the following:

$$\overline{V}_{m+1/2}=\frac{V_{m-1}+V_m+V_{m+1}}{3},$$

or

$$\overline{V}_{m+1/2}=\frac{V_{m-2}+V_{m-1}+V_m+V_{m+1}+V_{m+2}}{5}, \quad (7)$$

where m is the printed time. This improvement in accuracy results from the ± 1 cycle possible error in one individual counter reading.

UNUSUAL PROBLEMS

It has been found that, on a few occasions, the tracking filters obviously did not remain locked during a small portion of the first 3 to 5 seconds of flight. Investigation indicated that, in the case of very high acceleration rockets, very rough burning of the propellant may result in a 10g drag due to air resistance immediately followed by a very high acceleration of 25g or more. Under such circumstances the tracking filter sometimes fails to remain locked. In some cases a playback of the record will provide the required data, but in a few instances even this has failed. Thus far, the only solution found is to play back the tape, recording the Doppler frequency on an oscillograph and hand-counting the first few seconds.

The SSD station should be located on a flat area with no high towers or buildings in the vicinity, since re-radiation from such structures can introduce some difficulties, in particular, second-harmonic interference from the high-powered transmitter. This is apparently due to slight rectification and re-radiation from the metal structures. Also, considerable work was necessary on the transmitter itself in order to avoid second harmonic interference. However, a special filter in the transmitter and careful shielding have solved this problem. The trailer housing the transmitter and its antenna are now being operated approximately 300 feet from the SSD trailer.

Before this second harmonic problem was solved, a temporary solution was found by removing the transmitting antenna to a more distant location—about 2 km away. However, this introduced the problem of receiving a sufficient 36.8 Mc signal, free of fading effects, at the trailer; and also greatly increased the computational difficulties for obtaining the correct trajectory. Also, under such conditions, the first 10 seconds or so of data obtained by the X–Y plotter may be in error by several degrees with regard to the azimuth from the launcher. The azimuth from the SSD station will still be correct, however. It is better, of course, to have the transmitter close to the station; and in this case the fixed distance from the launcher to the station for the two-frequency system is taken to be the distance from the launcher to the mid-point between the transmitting antenna and the Doppler antenna at the SSD site.

Owing to momentary transponder failure or to the effects of an exploding grenade, there have been instances where the determination of the radial velocity has been impossible during a given second of time. This problem can be surmounted if the particular interval does not include the ignition or burnout of a rocket stage. In the latter case, a graphical plot of the velocity data can give an approximate value; but, in general, this is not necessary and the data can be handled as follows:

If v_L is the number of cycles in the distance from the SSD station to the launcher, the radial distance in cycles can be found by the summation

$$v_L+v_1+v_2+v_3+v_4+v_5, \text{ etc.}$$

Now for example, if v_3 is obviously incorrect, the summation may be made in the following manner:

$$v_L+v_1+1.5\,v_2+1.5\,v_4+v_5, \text{ etc.}$$

In other words, the preceding coefficient and the following coefficient are increased by one-half. The subscripts are the times as read by the printer, and the distance obtained is to the end of the final second. In the example given above, where v_5 is the last term, the total distance obtained is the distance at 6.0 seconds.

RECEIVER ADJUSTMENTS

The 73.6 Mc receivers, as delivered, do not contain a necessary special crystal filter circuit (Reference 4). These crystal circuits must be installed in shield cans with octal plugs to fit the sockets provided in six of the receivers. The crystal filters can be dispensed with only if (1) no telemetry signals are to be used on the carrier; (2) there is no radio interference in a range of about ± 100 kc; and (3) the improved signal to noise ratio is not considered necessary.

The north, east, and two Doppler receivers are supplied with these crystal circuits and aligned to give the proper center frequency with a bandwidth of about 4 to 5 kc, an essentially flat response over a range of 3 kc, and a 60-to-6 db bandwidth ratio of 5. The south and west receivers are then matched with the north and east receivers, respectively, so that the phase versus frequency variation over approximately a 3 kc band is less than ± 1 degree. This procedure involves an unpublished technique similar to an impedance bridge balancing technique and will be described in a later report.

The differential phase variation between the north and south receivers with equal input signals varying from 0.1 microvolt to 500 microvolts, is measured. If this differential phase variation is not satisfactory, the values of small degenerative resistors in the cathode circuits of the IF amplifiers must be changed to minimize this undesirable effect. The present SSD receivers have very little phase variation with input signal from 500 down to about 50 microvolts; but at lower signal levels it has been difficult to obtain completely satisfactory results. For signals larger than about 1 microvolt, however, the total phase change is approximately 4 degrees. In general, this phase variation can be neglected in data reduction except for very low signal levels, to which a correction can be applied. The calibration must be done before or immediately after the flight by recording the one-cycle fine interferometer output as a function of various weak signals.

The present receivers will provide direction cosine information down to -105 dbm. By using a calibration chart, this may be extended to as low as -117 dbm. The Doppler receivers utilizing the tracking filters can stay locked to the signal down to -135 dbm.

TOTAL POWER INTERFEROMETER

The continuous phase interferometer described above has the very desirable feature of providing continuous data. However, great care must be exercised by the SSD crew to avoid the introduction of phase errors. For example, the air must be circulating at almost constant temperature through the racks containing the interferometer receivers. Thermostatic control of the trailer air temperature is absolutely necessary; therefore air-conditioning and controllable heat are required. Heat shields are required around the receivers which must be checked frequently to insure that their differential phase characteristics with respect to signal input amplitude have not changed. The total power interferometer (TPI) eliminates these differential phase problems, but is subject to other disadvantages; mainly: (1) the X–Y plotter for range safety purposes cannot be used; and (2) the data reduction is more laborious. The block diagram is shown in Figure 10. This circuitry has been constructed and 30 db nulls are quite easy to obtain; moreover, this value can probably be improved. The nulls in one receiver occur exactly at an integral lobe number and if the other receiver is used, these nulls occur halfway in between the lobes. It is planned to test this system on a rocket flight in the near future.

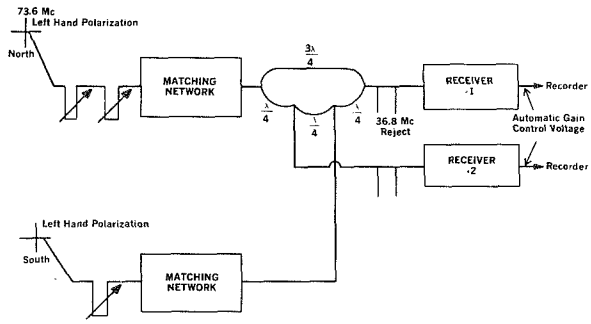

FIGURE 10.—Total power interferometer.

With the CPI, the input impedances of the receivers are adjusted to insure that the antennas see exactly equal impedances. However, with a magic-T the impedances cannot be made exactly equal and a matching network is required. The cable lengths are made equal and the line stretcher is adjusted in the same manner as for the CPI, except that the second line stretcher is adjusted to obtain a minimum AGC voltage on receiver No. 1.

The nulls will occur very frequently as the rocket takes off and if it behaves in its predicted fashion, the lobe numbers can be computed, although it is a rather tedious process. If the rocket does not follow the expected trajectory, however, the lobe numbers must be determined in a different fashion. Near motor burnout, and for a very large portion of the rocket's ascent, very few nulls will be observed. Also, a null may appear if the rocket antenna points at the ground station as a result of yaw and roll. The latter case can usually be detected by the lack of sharpness of the null if the roll rate is not high, and also by its simultaneous occurrence on both the E–W and N–S channels. In order that the data be reducible, the nulls must be recorded during the rocket's free-fall period, i.e., while it is above about 55 km. Thus the interferometer must be capable of tracking the rocket well beyond peak altitude. This is not a requirement for the CPI.

The method suggested for reducing the data is first to determine the lobe numbers for each of the nulls and then to compute X and Y as analytical functions of time. Since the lobe number at launch is known and these lobe numbers usually decrease for a time thereafter, the approximate lobe numbers during the early portion of the flight are known. These lobe numbers are tentatively assigned to the various nulls. A graph of $R \cos \Theta$ as a function of time is then prepared. The first value selected is the first null which occurs for R greater than about 60 km. The value of R at this particular time is determined and, on the assumption of the known value of the lobe number, $\cos \Theta$ is determined from the relation

$$\cos \Theta = 00.625n \tag{8}$$

The product $R \cos \theta$ is computed and plotted on the graph at this time. It is also advisable to calculate $R \cos \theta$ for lobes $n+1$ and $n-1$. If two receivers are in use, the half-lobe numbers may also be plotted. A plot determined from a theoretical trajectory is shown in Figure 11 where the use of only one receiver was assumed so that all lobe numbers would be integers. As $R \cos \theta$ represents the coordinate of the sub-rocket point plotted on a horizontal plane through the SSD station, this function must be very close to a straight line, since Coriolis effects are very small. It is found that only one straight line can be drawn through the various points obtained when the lobe numbers vary in sequence. The straight line in Figure 11 is therefore the proper solution; it can be seen that the lobe numbers changed their direction between 60 and 260 seconds. (The

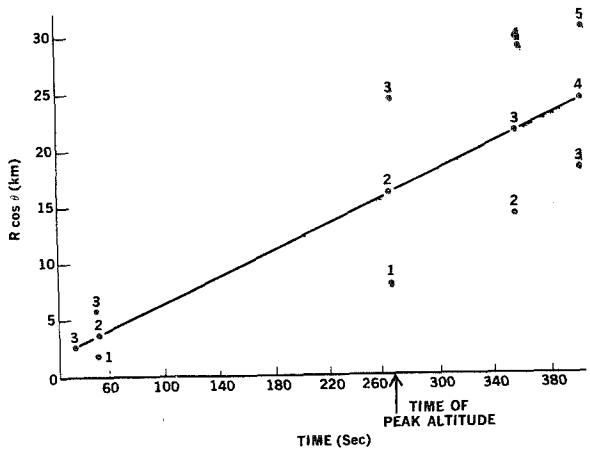

FIGURE 11.—Method of determining lobe numbers.

curve would have been easier to draw if the half-lobe points had also been used.) This straight line can then be expressed as an analytical function of time:

$$Y=Y_1+\dot{Y}(t-t_1). \tag{9}$$

A similar procedure is also performed for $X=R\cos\phi$. However, if there is a large east or west component, the Coriolis effect may be sufficient to cause the straight line to become slightly curved. The curvature is not usually enough to cause confusion in selecting the lobe numbers, but the X function is not quite linear with time. It may be determined as an analytical function of time in the following manner.

A point on the graph of X is selected so that R is greater than about 60 km, thereby insuring that the rocket is in free fall. The earliest value meeting this requirement is read from the graph at the time a null occurred on either receiver—this value is X_1. Another point is selected at a later time, the later the better, but before the rocket's peak altitude is attained, this is X_2. The approximate average E–W velocity is calculated from

$$\bar{\dot{X}}_2=\frac{X_2-X_1}{t_2-t_1}. \tag{10}$$

Y_2 is calculated for $t=t_2$ (Equation 11) and the altitude is:

$$h_2=\sqrt{R_2^2-X_2^2-Y_2^2}. \tag{11}$$

The elevation angle α is computed from

$$\alpha=\tan^{-1}\sqrt{\frac{1-(\cos^2\theta+\cos^2\phi)}{(\cos^2\theta+\cos^2\phi)}}. \tag{12}$$

Next, the radial velocity near time t_2 is determined from the printer tape and Equation 7 to determine R_2 at time t_2 as accurately as possible:

$$R_2=V_2\sin\alpha+\sqrt{X_2^2+Y^2}\cos\alpha, \tag{13}$$

from which the vertical component of velocity V_2 may be computed. The Coriolis effect on the vertical acceleration is given by

$$\Delta g=2\omega\bar{\dot{X}}_2\cos\gamma, \tag{14}$$

where Δg is positive if X_2 is toward the west, ω is the earth's angular velocity and γ is the latitude. The gravitational acceleration at an altitude h_2 can be determined by

$$g_2=g_0\frac{R_e^2}{(R_e+h_2)^2}, \tag{15}$$

where R_e is the radius of the earth and g_0 is the acceleration of gravity at the surface of the earth.[2] The actual acceleration is $g_2+\Delta g$ at the altitude h_2 with E–W velocity $\dot{X}_2$. To calculate the approximate peak altitude, let

$$h_p=h_2+\frac{V_2^2(R_e+h_2)}{2R_e\bar{a}-V_2^2}, \tag{16}$$

where

$$\bar{a}=\sqrt{g_2+\Delta g}\,\sqrt{g_0+\Delta g}.$$

Let g_p be the value of gravity at the peak altitude at time t_p; then

$$t_p=\frac{\mu\sqrt{h_p-h_2}}{\sqrt{g_p+\Delta g}}, \tag{17}$$

where

$$\mu=\sqrt{2}(1-0.167k-0.030k^2)$$

and

$$k=\frac{h_p-h_2}{R_e+h_p} \tag{18}$$

The term in parentheses in Equation 17 provides an approximate correction for the variation of gravity with altitude. Therefore, the E–W velocity $\dot{X}_1$ at time t_1 can be computed with much better accuracy from the relation:

$$X_2=X_1+\dot{X}_1(t_2-t_1)-2\omega\cos\gamma\left[(h_p-h_1)(t_2-t_1)-\frac{1}{6}\bar{g}\,(t_2-t_p)^3-\frac{1}{6}\bar{g}\,(t_p-t_1)^3\right] \tag{19}$$

where $\bar{g}$ is an average acceleration between h_1 and h_p:

$$\bar{g}=\left[1+\frac{1}{6}\left(\frac{g_1+\Delta g}{g_p+\Delta g}-1\right)\right]g_p. \tag{20}$$

The expression for X as a function of t becomes

[2] Includes the centrifugal acceleration $(\omega^2\cos^2\gamma)R_e$.

$$X=X_1+\dot{X}_1(t-t_1)-2\omega\cos\gamma\left[(h_p-h_1)(t-t_1)\right.$$
$$\left.-\frac{1}{6}g(t_p-t_1)^3-\frac{1}{6}\bar{g}(t-t_p)^3\right] \quad (21)$$

Other values of X obtained with the interferometer may be checked with this equation, which is valid beyond the peak until the rocket descends into the air drag region at approximately 55 km.

The altitude for any other time may be computed from Equation 11 with the subscripts changed to the new times used. The peak altitude previously obtained from Equation 16 can be checked but a modest error does not greatly affect Equation 21. This technique was satisfactorily tested on one Nike-Cajun flight by using only the integral lobe numbers obtained from the CPI, i.e., when the fine interferometer read 0 degrees; this is equivalent to using only one receiver in a TPI.

COST REDUCTION

The TPI System

The CPI listed in Appendix B can be reduced by one 6.4 Mc phase detector, two frequency dividers, one X-Y plotter, two receivers and the range safety equipment. This reduces the cost by $32,900.00, bringing the cost of the TPI system to $100,100.00. If the items marked with an asterisk are omitted, the cost reduces to $79,415.00.

Airbone Equipment

The present cost of the rocket antennas is $300.00 per frequency. Both the two-frequency transponder and the one-frequency transmitter cost $1,500.00 each. The transponder weighs 5 pounds, is 5½ inches in diameter and 5¾ inches high telemetry included. The transmitter weighs 6 pounds, is 5½ inches in diameter and 7 inches high. The transmitter does not contain telemetry, but room has been left on the panel for a small plug so that an external telemetry modulator can be connected. The telemetry modulator would be easy to design but this has not yet been done.

ADDITIONAL SYSTEM ADVANTAGES

The spare receiver in the station is very useful in the event of any receiver failure, although its use has not yet been necessary. By the simple expedient of removing the four crystal plug-in units from this receiver, the bandwidth is increased to about 60 kc without appreciable change in gain or AGC characteristics. The final tube in the receiver is removed and a plug-in unit built on a minature tube socket plug changes its limiter to an amplitude-modulated detector with a considerably larger voltage output. This output is applied to the FM discriminator to provide the telemetry signal. The cost estimates (Appendix B) include these items but do not include a suitable recorder for the telemetry.

By connecting an additional 6.48 Mc phase detector to both IF outputs of the Doppler receivers and connecting the output to another 15 kc phase detector with the fixed 15 kc frequency, a frequency is obtained that is exactly twice the roll frequency of the rocket; this can be recorded on a separate Sanborn recorder if desired.

The frequency meter employed in the Doppler circuitry contains a discriminator which provides a voltage proportional to the Doppler frequency. This voltage can be recorded during the flight, or by playback after the flight, to obtain an analog plot of the radial velocity as a function of time. Thus information is immediately provided that normally takes an appreciable time to acquire, such as the time of ignition and burnout of various stages of the rocket, and the approximate acceleration obtained from the various stages. More accurate values of the acceleration can be obtained by analysis of the digital tape record.

ACCURACY

The two frequency SSD system has been the one most used thus far; but the results have been analyzed completely for only a few early flights made when many of the sources of phase variation had not yet been located and eliminated. Data from a few more recent flights have been partially reduced by means of a new program written for an electronic

computer. These flights were performed with the low frequency high-powered transmitter at a distance of 2 km from the SSD station, and that circumstance complicated the data analysis. The second harmonic problem having been eliminated, the transmitter is again close to the SSD station for the next flights.

Preliminary results on these more recent flights indicate agreement with the FPS–16 radar data within approximately 50 meters, except at the very highest altitudes where the small rocket was giving too small a return to the radar receiver. The radar has sometimes been unable to track the rocket all the way to peak altitude, whereas the SSD station has tracked each rocket all the way to re-entry. The descent data, however, have not as yet been reduced.

The angular accuracy of the interferometer is of the order of ± 3 degrees, corresponding to roughly ± 2 minutes of arc, although this was attained only recently after considerable effort had been expended on the equipment. Examination of the FPS–16 radar data indicates angular tracking errors up to 6 minutes in elevation and distance errors up to about 30 meters (Reference 5).

Previously, one single-frequency trajectory was reduced at Churchill with less refined equipment, but no radar data were available for comparison. The individual altitudes computed were all within 70 meters of a calculated free-fall trajectory curve where 70 meters was the smallest difference that could be observed.

No attempts have as yet been made to correct for the ionospheric effect, since not all of the two-frequency rockets tracked have reached sufficient altitude to introduce an appreciable error from this effect. One rocket penetrated the ionosphere to very high altitudes using the one-frequency system in which this error (about ½ km) was small enough to be neglected. Corrections could be made by rough methods involving an ionospheric sounder located nearby if the additional accuracy were considered worth the effort. Under the worst conditions, such as midday near a sunspot maximum, the error at an altitude of about 300 km is about 1¼ km for the two frequency system. For the single frequency method, the error would be about ¼ km.

The X–Y plotter presently used has a 3 x 3 foot chart. The results obtained show that if the dividers remain locked, the plotted azimuth from the launcher is accurate to $\pm$½ degree. Trouble has been experienced, however, at rocket takeoff when the phase-locked dividers would sometimes slip one cycle. This difficulty is thought to be greatly aggravated by the unavoidable shadowing of two of the interferometer antennas by the huge enclosed Aerobee launching tower. Signal levels at the various antennas differ markedly until about 1 second after launch. The error in azimuth introduced by one cycle slippage is about 6 degrees with respect to the SSD station; and much larger with respect to the launcher, in some cases as much as 20 degrees. A different circuit is now being tested which seems to hold lock more securely. This new circuit will be tried on the next flights in the hope that the lobe-slipping problem will be solved.

ACKNOWLEDGMENTS

The SSD system was conceived by the author while employed at the U.S. Naval Research Laboratory, Washington, D.C., which initiated the development of an SSD station under contract with the New Mexico State University. This contract was transferred to and renewed by the Goddard Space Flight Center. The system checks have been conducted at the NASA Wallops Island Station, Virginia.

The special equipment was designed and assembled under the supervision of Messrs. Wesley L. Joosten and Robert J. Sabin, NMSU project engineers. Flight testing at Wallops Island has been under the direction of Mr. Billy Gammill, also of NMSU. All three have made helpful contributions to the instrumentation.

REFERENCES

1. Seddon, J. C., "Propagation Measurements in the Ionosphere with the Aid of Rockets," J. Geophys. Res. 58(3): 323–335, September 1953.
2. Mengel, J. T., "Tracking the Earth Satellite, and Data Transmission, by Radio," Proc. IRE 44(6): 755–760, June 1956.

3. HINES, P. B., "DOVAP Systems and Data Reduction Methods," New Mexico State University, Physical Science Laboratory, Report on Contract NASA 5–1032, Jan. 31, 1962.
4. SEDDON, J. C., "Stable Crystal Filter is Parallel Resonant," Electronics 31(11): 155–157, Mar. 14, 1958.
5. CARVER, A. C., "An Examination of Errors in FPS-16 Radar Data," Part I, New Mexico State University, Physical Science Laboratory, Radar Investigation Report IA, Contract NASA 5–1032, Feb. 8, 1962.

Appendix A

SDD INITIAL CONDITION COMPUTATION ROUTINE

SINGLE PATH
DOUBLE PATH

Missile Name and No._____
Firing Range_____
Date_____

	N-S	E-W
0. Transmitter Coordinates feet	_____	_____
1. Launcher Coordinates feet	_____	_____
2. SSD Coordinates feet	_____	_____
3. Line 1–Line 2 N-S	_____ ft.	
4. Line 1–Line 2 E-W		_____ ft.
5. $R_0 = \sqrt{(\text{Line } 3)^2 + (\text{Line } 4)^2}$	_____ ft.	
6. h=Missile Altitude (Feet) at Lift Off Delay Relay Closure	_____ ft. at	_____ sec.
7. $R_0^1 = R_0 + \frac{\frac{1}{2}h^2}{R_0}$	_____ ft.	

PLOTTING BOARD

8. $R_0 = \frac{\text{Line } 5}{3.281} =$ _____ Mtrs

9. N-S Lobe Number $= \frac{16 \text{ Line } 3 - 0.5 \text{ Line } 4}{\text{Line } 5}$, $\delta_{\text{N-S}} =$ _____ +North, −South

10. E-W Lobe Number $= \frac{16 \text{ Line } 4 + 0.5 \text{ Line } 3}{\text{Line } 5}$, $\delta_{\text{E-W}} =$ _____ +East, −West

PRESET AND Km COUNTER

11. N_0^1=Initial Cycles $= \frac{\text{Line } 7}{6.68} =$ _____ cycles

12. If $N_0^1 \leqq 245$, Preset Counter A With N_0^1_____
13. If $245 < N_0^1 \leqq 491$, Preset Counter B With $N_0^1 - 245$._____
14. If $491 < N_0^1 \leqq 736$, Preset Counter A With $N_0^1 - 491$,_____
    Km Counter With 1, etc.

NOTES:

Line 6 must be determined from past or theoretical performance.

Lines 9 and 10 contain an approximate correction due to Wallops Island grid coordinates being different from true coordinates.

For a remotely located trasmitter the plotting board data at Wallops Island will be elongated from 0 to 300 feet along a line connecting SSD and the missile subpoint.

Appendix B

STATION COSTS

The cost of establishing the SSD system, exclusive of land, electrical power and surveying cost is summarized below. An asterisk preceding an item indicates that the item is not commercially available and must be constructed from schematic diagrams. A cost figure followed by an asterisk indicates that it may be possible to omit the item or to substitute another piece of equipment that might be available in the laboratory, although the substitution or deletion requires additional labor.

Installation:	
Trailer (with air conditioning)	$21,500.00
Power cables	200.00
Racks	1,900.00
Chassis slides	500.00
Power cabinet	75.00
Power plugs (R and X)	100.00
Tools	400.00
Filing cabinet	40.00
Work benches	600.00
Desk and chair	190.00
Water cooler	400.00*
Installation labor	8,000.00
	$33,905.00
Timing-frequency standard	3,400.00*
*Timing mixer chassis	900.00
Dymec clock 5414	1,200.00
	$5,500.00
Doppler Equipment:	
Electronic counter hp 524D	2,300.00
Printer hp 560A	1,400.00
Industrial counter hp 521C	650.00
Time interval unit for 524D, hp 526B	175.00
Counter, dual pre-set	$825.00
Tracking filter, interstate mod. IV (2)	13,500.00
Tape recorder, modified	1,000.00
Pre-amplifiers, Ceco or equivalent (2)	600.00
Local oscillators (2)	3,000.00
Receivers (2)	5,000.00
Reference oscillator (6.48 Mc)	600.00
*Crossed dipole, with magic-T	150.00
Phase detector, 15 kc	200.00
Phase detector, 6.48 Mc to 15 kc	300.00
*Frequency synthesizer chassis	500.00
Pre-amplifier, 36.8 Mc	300.00
	$30,500.00
Interferometer	
Sanborn 6 channel recorder	4,700.00
Constant Z line stretchers (7)	600.00
Antenna cables, connectors	150.00
Local oscillators	1,500.00
Receivers (4)	10,000.00
*Phase detectors, 6.48 Mc (2)	600.00
*Phase detectors, 101.25 kc (2)	600.00
Antennas, ground planes (4)	1,200.00
Pre-amps Ceco or equivalent (4)	1,200.00
*Phase-locked frequency dividers (2)	2,000.00

Interferometer—Continued	
Crystals	$200.00
	$22,750.00
Telemetry and/or Spares	
Receiver	2,500.00*
Pre-amp (Ceco or equivalent)	300.00*
*Discriminator	500.00*
*Antenna, ground plane	300.00*
	$3,600.00
Range Safety	
*Delay line chassis (AD–YU 521C)	500.00
*Computer chassis	800.00
*Computer control	500.00
*Frequency divider (2)	1,500.00
	$3,300.00
High power 36.8 Mc Gates transmitter:	
Transmitter	12,000.00*
Plotting Board:	
Prices vary (approximately)	20,000.00
Test and Peripheral Equipment:	
AC line regulator	$700.00
Oscilloscope (Tektronix) 541	1,200.00
Oscilloscope plug-in unit CA	250.00
Receiver, Collins 51J4 (range communications, WWV)	1,000.00*
Signal generator hp 608D	1,100.00
Frequency meter	285.00
hp 525A mixer plug-in unit	250.00
R–X meter 250–A	1,600.00
Audio generator	300.00
hp Attenuators 355 A and B (2)	250.00
Sierra power meter (for adjusting rocket antennas)	375.00
Vacuum tube voltmeter hp 410B	245.00
Sweep generators, for rec. alignment	500.00
	8,055.00
Overall total	$139,610.00
Total of items with*	$20,685.00

It has been shown that the above cost can be reduced appreciably at the expense of convenience without losing the necessary features.

THE RANGE AND RANGE RATE SYSTEM AND DATA ANALYSIS FOR SYNCOM I (1963 4A)

H. W. SHAFFER, W. D. KAHN, W. J. BODIN, JR.,
G. C. KRONMILLER, P. D. ENGELS, AND E. J. HABIB
Goddard Space Flight Center

A range and range rate system similar to the Goddard Range and Range Rate System was used to track the Syncom I through the transfer ellipse until the apogee kick motor fired. This report discusses the Syncom Range and Range Rate System operation and the data processing. The standard deviations achieved were 15.49 m in range and 0.05 m/sec in range rate with respect to the calculated orbital elements. Analysis of the data over short continuous intervals shows the data to have an accuracy better than 20 m in range, with either the 100 or 20 kc ranging tone, and a range rate accuracy within 0.05 m/sec.

INTRODUCTION

The Syncom Range and Range Rate System, which is similar to the Goddard Range and Range Rate System (Reference 1), was developed to track the Syncom I satellite, launched on February 14, 1963, during the transfer ellipse and while it was in the synchronous orbit. Equipment was developed which utilized the existing communications transmitter, 30 foot parabolic antenna, spacecraft communication transponder, and ground preamplifier (Fig. 1). Because of weight limitations, a range and range rate transponder could not be placed on the spacecraft, therefore all measurements had to be made with the spacecraft's communication transponder. This required the up link frequencies to be 7361.275 Mc for channel I and 7363.00 Mc for channel II. The down link frequencies were 1814.069 Mc for channel I and 1815.794 Mc for channel II. Also, a beacon frequency of 1820.177 Mc was transmitted from the spacecraft.

The two field installations for tracking were Lakehurst, New Jersey, for the synchronous orbit, and a ship located in the harbor of Lagos, Nigeria, for the transfer ellipse, the injection into the synchronous orbit, and the synchronous orbit. Data were to be taken during two 15 minute segments, one when the satellite was between 10,000 and 15,000 km, the other when the satellite was between 30,000 and 35,000 km. The data in this report were acquired by the tracking ship, but only during the transfer ellipse (because of the failure of spacecraft communications after the apogee motor fired).

This report presents the computed standard deviations with respect to the calculated orbital elements and an analysis of the data for continuous functions of time over short intervals.

DESCRIPTION OF THE SYNCOM RANGE AND RANGE RATE SYSTEM

Range measurements are accomplished by utilizing the principle that any wave or group of waves propagated at a given velocity experiences a delay which depends upon the distance traversed. Range rate measurements utilize the principle that a wave emanating from an object which is in motion relative to an observer arrives at the observer at a different frequency than that at which it emanated.

Figure 1 shows the block diagram of the Syncom Range and Range Rate System. The tracking station generates a carrier plus side-

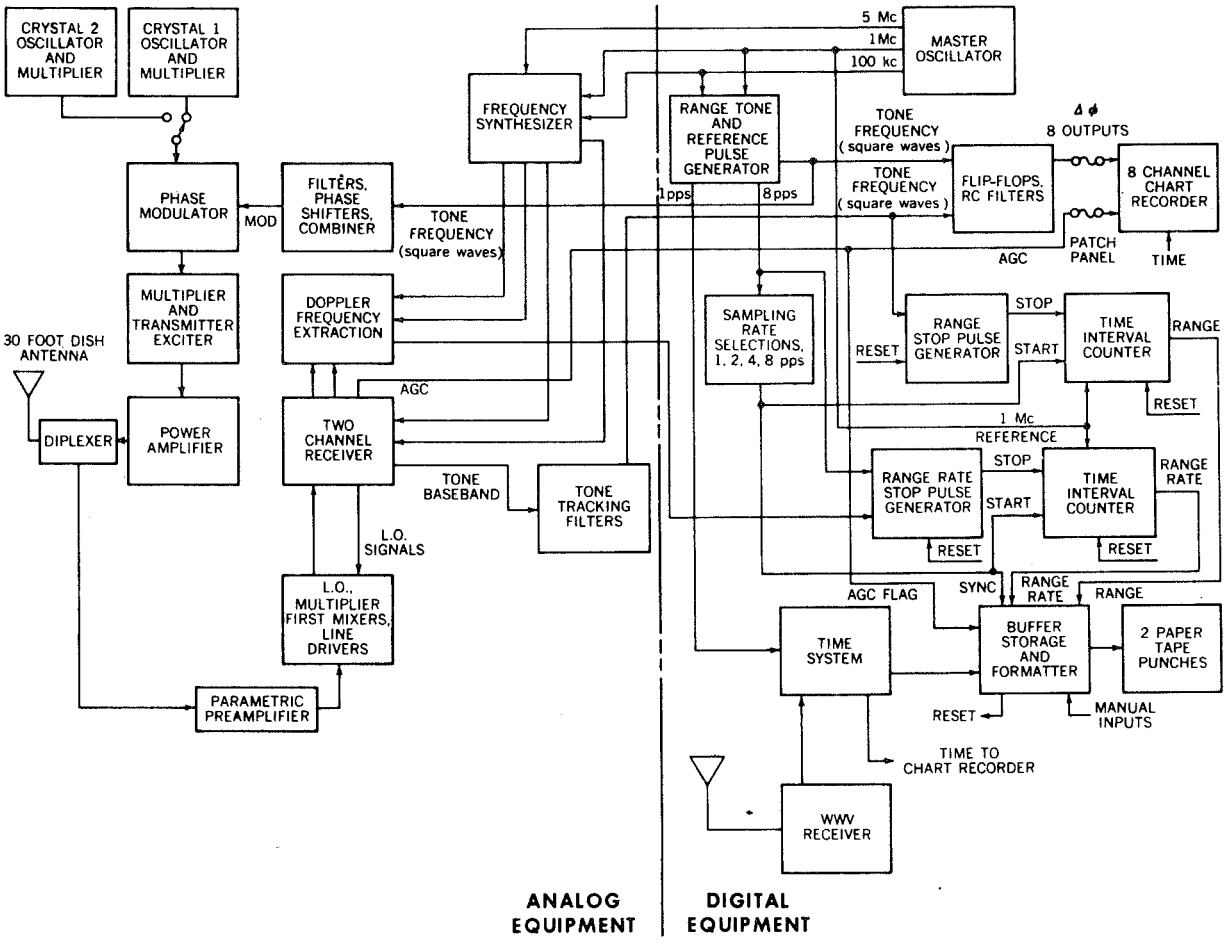

FIGURE 1.—Block diagram of the Syncom Range and Range Rate System.

band pairs obtained by phase modulating the carrier with the ranging tones of 100, 20, 4.800, 4.160, 4.032, 4.008, and 4 kc (Fig. 2). The 800, 160, 32, and 8 cps range tones are complemented on the high side of 4 kc to assure that the carrier will be absolutely free of modulation products for range rate or Doppler measurements.

A reference data rate of 8, 4, 2, or 1 cps, synchronized to WWV, initiates the counting of 10 Mc by the time interval units, which measure the phase delay of the ranging tones and the time necessary for counting 81924 cycles of Doppler frequency plus bias frequency.

The 100 kc sidetone phase delay to the spacecraft and return is measured to an accuracy of 1 percent by controlling the 100 kc phase-locked loop so that the deviation of the phase of the 100 kc signal and the phase-locked loop frequency is less than 3.6 degrees. This equals 1 count of 10 Mc which in turn is equivalent to a resolution of ± 15 meters. The lower range tones of 20 kc, 4 kc, 800 cps, 160 cps 32 cps, and 8 cps are controlled so that their individual phases do not vary more than ± 36

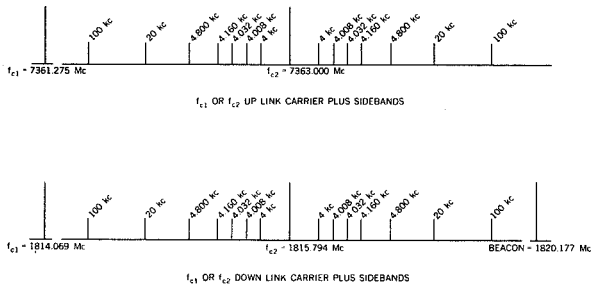

FIGURE 2.—Spectra.

degrees, which resolves the ambiguity of the next higher tone to the whole cycle.

The carrier of the ground transmitter is used in the mixer operations for the range rate measurements. It is derived from one of two ultra-stable oscillators, the one used depending on frequency selection. The carrier and the ranging sidetones are received at the spacecraft transponder, which acts as a booster amplifier and translates the spectrum down to either 1814.069 or 1815.794 Mc from 7361.275 or 7363.000 Mc, respectively (Figs. 2 and 3).

The receivers at the tracking station receive the transmitted carrier frequency from the ground transmitter minus 192 times the satellite local oscillator frequency for the range tone frequency. For the beacon frequency they receive 63 times the satellite local oscillator frequency. The receivers provide initial mixing and phase locking to the transmitted carrier frequency and beacon frequency. This produces a difference frequency equal to the sum of the following:

1. The satellite local oscillator frequency.
2. The one-way Doppler shift of the carrier in the 7.3 Gc range.
3. The one-way Doppler shift of the ground-transmitted carrier frequency minus 192 times the satellite local oscillator frequency.
4. The one-way Doppler shift of 63 times the satellite local oscillator frequency.
5. The satellite local oscillator drift.
6. The Doppler frequency (Fig. 4).

The ranging frequency (ground-transmitted carrier frequency minus 192 times the satellite local oscillator frequency) is converted by utilizing phase-locked oscillators for carrier and range tone detection.

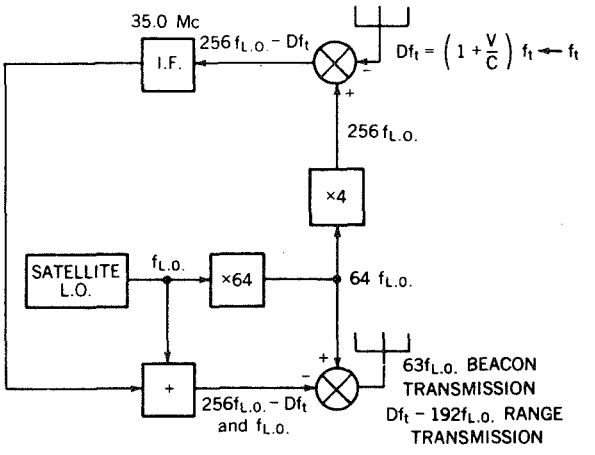

FIGURE 3.—Spacecraft transponder.

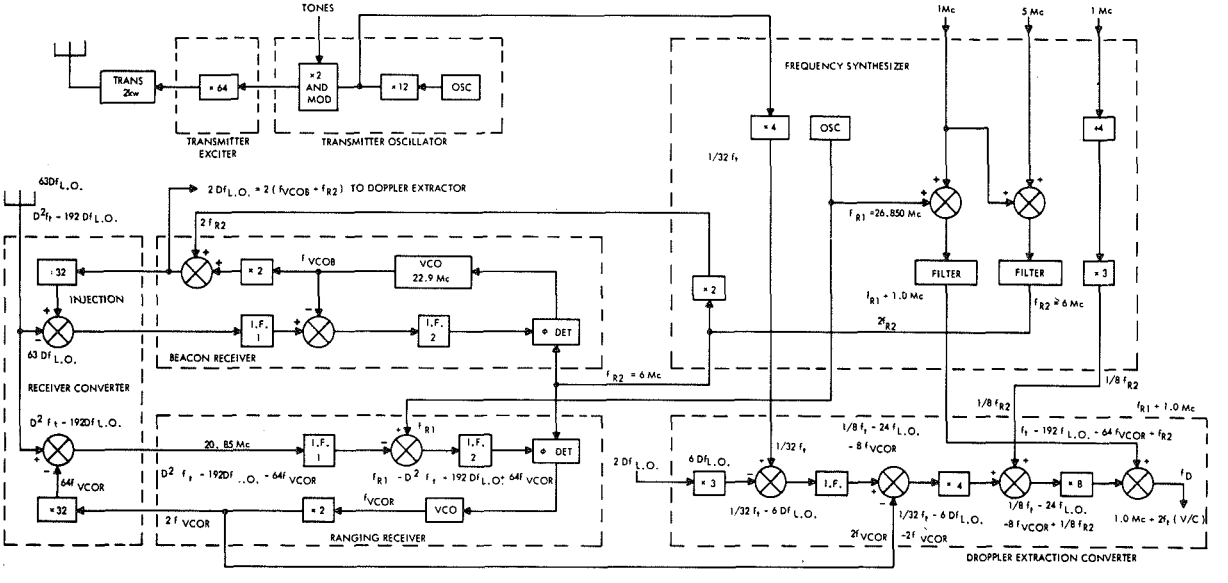

FIGURE 4.—Receivers and doppler extraction process f_{VCOR} is the frequency of the VCO in the ranging receiver and f_{VCOB} is the frequency of the VCO in the beacon receiver.

The Doppler extractor mixes the outputs of both receivers to remove all satellite local oscillator drifts and produces the two-way Doppler shift of the transmitted carrier impressed on a bias frequency of 1 Mc (Fig. 4). The range tones from the ranging receiver are actually demodulated in the range extractor, which uses narrow-band phase-locked loops for separating and improving the signal-to-noise ratios of the individual range tones. The 1-Mc-biased Doppler is fed to a digital unit of the Doppler extractor which counts at a 10 Mc rate in a second time interval unit for a period of 81924 counts of the 1-Mc-biased frequency $\pm$ the Doppler frequency. Ranging data may be extracted at the rate of 8, 4, 2, or 1 time per second. The 8, 4, 2, and 1 cps are synchronized to WWV and used as start pulses to start the 10 Mc range time interval unit counting. During calibration the tones are aligned alternately positive and negative with the 100 kc tone going positive. All ranging tones have the same phasing characteristics at 8, 4, 2, and 1 times per second. The time interval between the start and stop pulses, with respect to the speed of light, is the range to and from the spacecraft.

The digital outputs from both range and range rate (Doppler) time interval units are multiplexed with the output of the antenna azimuth and elevation and the output of the digital clock. They are punched on two separate teletype punch units which produce data at the reference rate in teletype code for transmission to Goddard Space Flight Center.

Functions of Subsystems

Master Oscillator

This oscillator, with its associated distribution amplifier and stand-by power supply, provides a stable frequency source of 5 parts in 10^{-10} per second and 5 parts in 10^{-10} per day at 5 Mc, 1 Mc, and 100 kc for the frequency synthesizer, time interval counters, digital clock, and range tone and reference pulse generator.

Range Tone and Reference Pulse Generator

The range tone and reference pulse generator produces, through a digital countdown from the 1 Mc of the master oscillator, eight harmonically related sidetones: 500 kc, 100 kc, 20 kc, 4 kc, 800 cps, 160 cps, 32 cps, and 8 cps. The countdown is continued from 8 cps for the 8, 4, 2, and 1 cps reference pulses or data rates. The countdown unit is clocked so that as much jitter as possible may be eliminated.

Filters, Phase Shifters, and Combiner

The countdown outputs for the range tones are square waves, therefore requiring low Q filters to provide sine waves that can be used in the electromechanical phase shifters. The tones are fed to individual phase shifters which adjust their phase and remove any differential phase delay throughout the system, including the transmitter, spacecraft communication transponder, and receivers. The individual phase shifters have a mechanical linkage ratio equal to the transmitter range tone ratio. The combiner simply adds all range tones to form a single complex wave for phase modulating the carrier frequency.

Transmitting Section

The transmitting section consists of two basic crystal oscillators at different frequencies to derive the two transmitting frequencies. The two frequencies correspond to the two channels of the satellite transponder, and the channel selection is a ground function of choosing one of the two crystal oscillators, the nominal being 4.79 Mc. The chosen oscillator output is processed through several multipliers which multiply the basic frequency by 12 to approximately 57.6 Mc. This is used in the frequency synthesizers (for Doppler extraction) and is also used as the input to the phase modulator. It is phase modulated by the complex wave representing the summation of the ranging tones in the phase modulator. The phase-modulated 57.6 Mc is multiplied by 2 and sent to the transmitter exciter which multiplies the 115.2 Mc to approximately 7.3 Gc. Then the 7.3 Gc is amplified to 20 kw and transmitted to the satellite.

Beacon Receiver (Doppler)

The beacon receiver operates in either search or track mode. During the search mode the voltage-controlled oscillator (VCO) is not in the locked condition and is operating at a crystal-controlled frequency of approximately 22.9 Mc. The VCO frequency is repeatedly scanned through a frequency spectrum which includes the satellite beacon transmission signal. In the locked mode the VCO follows the phase of the input signal.

Twice the VCO frequency is heterodyned with twice the reference frequency, f_{R2} (=6 Mc). In the receiver converter the thirty-second harmonic of the above mixer is heterodyned with the satellite beacon transmission frequency (Fig. 4).

The output of IF amplifier 2 is 6 Mc $\pm$ the Doppler frequency; this is fed into the loop phase detector which compares this frequency with f_{R2} (6 Mc). If the signals are not of the same frequency, the output of the phase detector will be a sinusoidal error signal, with a beat frequency equal to the frequency difference of the two inputs. If the signals are of the same frequency, which occurs first in acquisition, the output then will be a dc error voltage equal in magnitude and polarity to the phase difference of the two input signals. The output of the phase detector controls the frequency and phase of the VCO so that they equal the frequency and phase of the input signal. The VCO is a crystal-controlled oscillator which has a normal resting frequency of approximately 22.9 Mc, but the frequency and phase of the VCO are controlled by a dc voltage. The output of the VCO multiplied by $2+2\ f_{R2}$ ($2\ f_{R2}$=12 Mc) is used in the Doppler extractor.

Both receivers have a threshold of −154 dbm.

Ranging Receiver

The operation of the ranging receiver is similar to that of the beacon receiver. The sixty-fourth harmonic of the VCO frequency is heterodyned with the satellite-range-transmitted frequency, and the difference, 20.85 Mc, is fed to the first IF. The 20.85 Mc is then mixed with f_{R1} (26.85 Mc) from the frequency synthesizer; this produces a 6 Mc$\pm$Doppler frequency output. One of the outputs of the second IF is fed to a modulation phase detector which extracts the range tones. The other output is fed to the VCO.

During the search mode the AGC, which is in the ranging receiver only, is not activated. During the locked mode, the same operations as those of the beacon receiver are performed, the VCO follows the phase of the input signal, and the AGC is in operation.

Doppler Extractor

The Doppler extractor consists of mixers, multipliers, and amplifiers. The beacon frequency, $2Df_{L.O.}$. (D is the Doppler-shifted frequency), is multiplied by 3 in the first multiplier (Fig. 4) to produce 6 $Df_{L.O.}$, which is mixed with $(\frac{1}{32})f_t$ to yield $(\frac{1}{32})f_t-6Df_{L.O.}$. The output is mixed with $2\ f_{VCOR}$ (f_{VCOR} is the frequency of the VCO in the ranging receiver) to produce $(\frac{1}{32})f_t-6Df_{L.O.}-2f_{VCOR}$ which is then multiplied by 4 to give the output at the times 4 multiplier of $(\frac{1}{8})f_t-24f_{L.O.}-8f_{VCOR}$. This is mixed with $(\frac{1}{8})f_{R2}$(750 kc) to produce $(\frac{1}{8})f_t-24f_{L.O.}-8f_{VCOR}+\frac{1}{8}f_{R2}$. this is subtracted from $f_{R1}+1$ Mc (f_{R1}=27.85 Mc) which is equal to 1.0 Mc$\pm 2f[1\pm(v/c)]$.

The 1.0 Mc$\pm 2f_D$ is counted by an "N" counter which counts a set number of 81924, synchronized with the data rate. The second pulse of the 81924 pulses starts the counting of the range rate time interval unit at 10 Mc. The pulse following the 81924 count, pulse 81925, stops the time interval unit. This allows the interval to vary about 819240 microseconds, depending upon the magnitude of the Doppler and whether it is positive or negative Doppler. The time interval is multiplexed with other data and punched on paper tape.

Range Extractor

One of the outputs of the second IF in the ranging receiver is fed to a modulation phase detector which feeds the range tones to the high and low range tone filters (Fig. 5).

High Range Tone Filter.—The input portion of the high range tone filter contains a predetection band separation filter. This filter consists of 100 and 20 kc band-pass amplifiers,

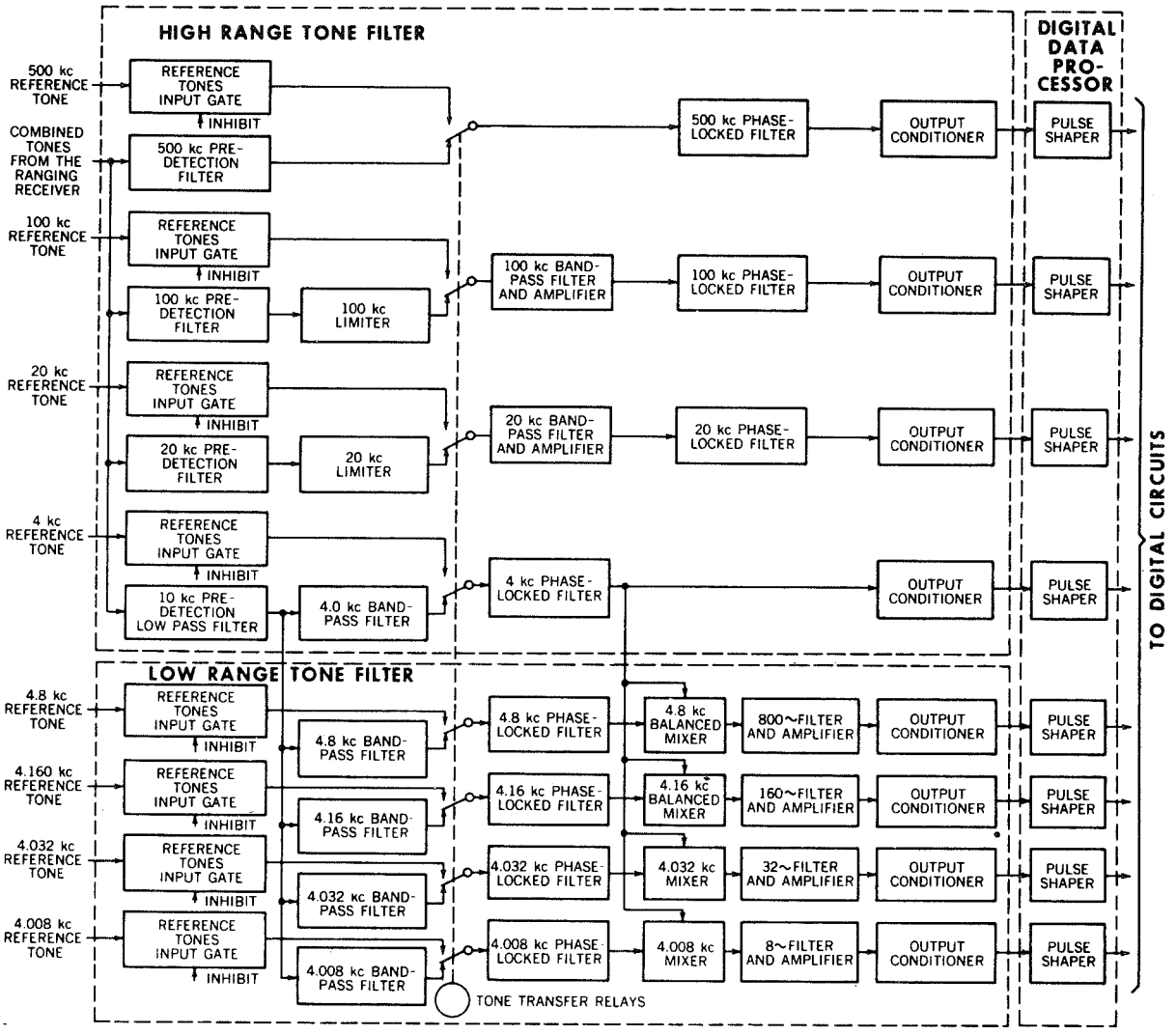

FIGURE 5.—High and low range tone filters.

and a 10 kc low pass RC filter and amplifier. The 500 kc band-pass amplifier output is connected directly to the tone transfer relay. The 100 and 20 kc band-pass amplifier outputs are connected to limiters which maintain the signal-to-noise power at a constant level. The outputs of the limiters are connected to the tone transfer relays. The 10 kc low pass amplifier delivers signals to a 4 kc band-pass filter and to the low range tone filter. The output from the 4 kc band-pass filter is connected to the 4 kc tone transfer relay.

The reference tones input to the high range tone filter are connected to the tone transfer relay via the reference tones input gate. The reference tones are always present until the signal is detected. This enables the phase lock loops to rest at the exact range tone frequency transmitted, and the loop has to shift by the amount of Doppler that is present on the signals.

The 100 and 20 kc channels contain additional band-pass amplifiers to remove the harmonic components generated by the limiters. The phase-locked filter output signals are accurate reproductions of the input signals except that

they are shifted exactly 90 degrees in phase and the noise and distortion are removed. The resulting sine waves from the high range phase-locked filters are converted to pulses and fed to a stop pulse generator. The pulse shaper output signals are pulses with maximum rise times of less than 10 nanoseconds occurring at the same rate as the input tones.

Low Range Tone Filter.—The input to the low range tone filter is received from the 10 kc low pass predetection filter in the high range tone filter. The output signal from the predetection filter is connected to the 4.8, 4.16, 4.032, and 4.008 kc band-pass amplifier stages. These filters separate the individual tones from the composite signal. The outputs of the filters are connected to one side of the tone transfer relays and the reference tones are connected to the other. The relays perform the same function as described for the high range tone filter.

The outputs of the relays are fed to the phase-locked loops. The output signals from each phase-locked loop are fed to a balanced mixer. The second mixer input is the output of the 4 kc phase-locked loop and the mixer output is the difference frequency. The outputs of the mixers are passed through filter amplifiers only for more filtering effect. The outputs of the filters are converted to pulses and fed to a stop pulse generator.

Range Stop Pulse Generator.—The negative going pulses, corresponding to the negative going zero crossings of the delayed range tones from the high and low range tone filters, are individually fed to the set inputs of individual flip-flops (Fig. 6). The 8 cps return pulse sets the 8 cps flip-flop which in turn enables the 32 cps flip-flop. In a similar manner each subsequent flip-flop is enabled by the set condition of the previous flip-flop. Since the phase relation of the 8 tones had previously been adjusted during calibration, the 8 flip-flops are reset in sequence from the lowest tone chosen. When the highest tone chosen has reset its respective flip-flop, a pulse is generated which is used as the stop pulse for the time interval unit.

A choice of tones is available. Either 8, 32, or 160 cps is available for the lowest tone used

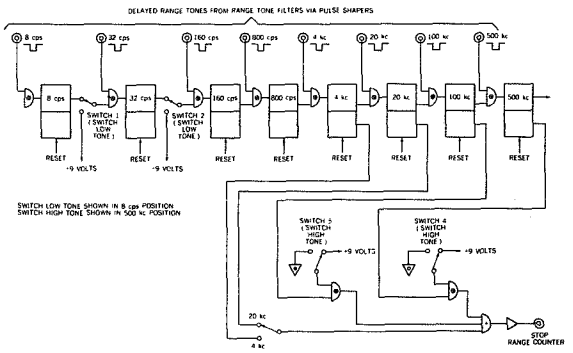

FIGURE 6.—Range stop pulse generator.

and the choice is usually dependent on the altitude of the spacecraft; 100, 20, or 4 kc may be chosen for the higher sidetones, by eliminating frequencies from the highest, in sequence.

Satellite Communication Transponder

The range and range rate measurements are made by utilizing the satellite communication transponder (Fig. 3), which has a wide bandwidth and essentially no time delay for the ranging tones. It is a booster amplifier and shifts the spectrum from 7.3 to 1.8 Gc. Fundamentally, range and range rate measurements were made with zero added weight and used very little spacecraft power.

Antenna

The Syncom tracking stations at Lakehurst, New Jersey, and on the USNS *Kingsport* (tracking ship) utilize a 30 foot parabolic antenna for transmitting and receiving. The antenna uses the conical scan principle and has approximately a 1.8 degree beamwidth at 1.8 Gc. The data output of azimuth and elevation has an accuracy of 0.1 degree.

Parametric and Power Amplifiers

The parametric amplifier is a 3 stage device which has 40 db gain and a noise figure of approximately 2.7 db.

The Syncom Range and Range Rate System supplies the actual transmitting frequency to the power amplifier which serves to amplify the signal to 20 kw for transmission.

Calibration of the System

Calibration eliminates any differential phase delay in the system and any bias errors which may be present. The system is operated as a closed loop through a transponder at a known distance from the antenna. After the receiver and range tone phase-locked loops are locked to the signal, the individual range tones are set positive and negative, alternately with each other, by the phase resolvers. All the resolvers are then rotated simultaneously, which in effect rotates the stop pulse, until the range time interval unit reads the time required for the range tones to traverse the known distance to and from the calibration transponder.

The range, range rate, antenna pointing angle, time, and station data are multiplexed and punched on paper tape for transmission to Goddard Flight Center.

DATA DESCRIPTION AND HANDLING

Syncom I was launched from Cape Canaveral, Florida, on February 14, 1963. The transfer ellipse phase of the trajectory was south of Lagos, Nigeria, and southeast of Maligasy. After this phase the altitude was approximately 35,000 km. A rocket motor was fired at apogee to place the satellite into a synchronous orbit.

The tracking data presented in this report were acquired by the tracking ship in the harbor of Lagos, Nigeria. They consist of two 15 minute segments, separated by approximately 2 hours and 19 minutes. The first segment was acquired when the satellite height was between 10,000 and 15,000 km. The highest range tone used for making range measurements was 100 kc.

During the second segment of data, the satellite altitude above the earth was between 30,000 and 35,000 km. For the first 5 minutes of this segment the 4 kc tone was used, because of communication problems. The 100 and 20 kc tones were turned off. This provided more power in the lower tones in order to receive ranging data; though the range accuracy was degraded to ± 500 m with the 4 kc tone. The power in the 4 kc tone could not be increased to decrease the phase jitter which is due to the 4.008 kc phase-locked loop locking on the 4 kc tone. After approximately 5 minutes, the 20 kc tone was turned on and the modulation index increased, increasing the power in the 20 kc tone, which decreased the phase jitter of this tone. This tone was used as the highest ranging tone for the rest of this interval. The deviation in range with the 20 kc tone was less than ± 20 m.

During the two tracking intervals 1052 measurements of range data and 945 measurements of range rate data were recorded. At the Goddard Space Flight Center the 1052 points of range data, including the 4 kc data, were smoothed to 68 points of which 55 points were used for final orbital calculations. If the measurements using the 4 kc tone are excluded, only 5 smoothed points were eliminated from the calculations. The 945 points of range rate data received were smoothed to 71 points and all 71 were used in the final orbital calculations.

The data from the system is punched on paper tape for transmission to the Goddard Space Flight Center in the format shown in Figure 7. The received data is processed in a two-computer operation. The reproduced teletype tape with the data is first processed in the CDC–160 computer which performs the following operations:

1. Computes range in meters from the time of propagation or phase delay of the ranging tones to the spacecraft and return.
2. Computes range rate in m/sec from the time interval required to count "N" cycles of a standard frequency $\pm$ the Doppler frequency of the carrier.
3. Reproduces the 30 foot communications antenna angle readout which the system measures to 0.1 degree.
4. Makes the necessary adjustments to time for the propagation time of the ranging tones to and from the spacecraft, and for the difference in time between the sampling of the time register and the range and range rate registers.

The raw data from the CDC–160 is reproduced on punched cards and magnetic tape for

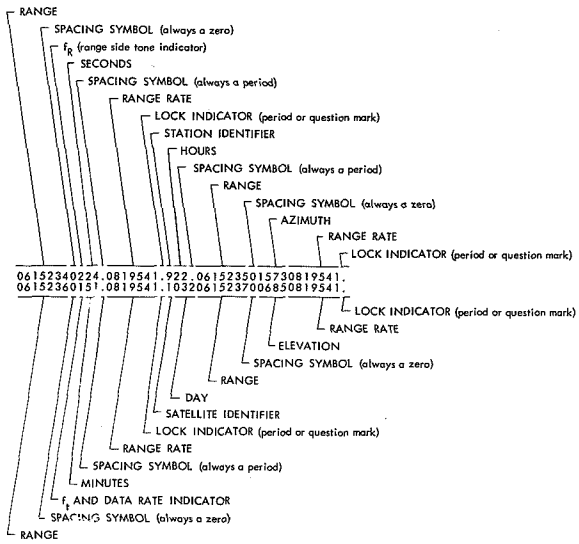

FIGURE 7.—Data format.

processing by the IBM 7090 or 7094 computer, which uses the punched cards and magnetic tape for an input program. The data is then smoothed by fitting a quadratic or higher degree polynomial to it in the least squares sense. After smoothing, a differential correction program is applied to the data by using either the Brouwer or MCOI orbit generators for calculating the orbital elements and standard deviations.

DATA ANALYSIS

Computer Results for Standard Deviations

The MCOI orbit generator was used for the Syncom I satellite. It is a numerical integration program that applies a Runge-Kutta Gill Integration Technique (Reference 2) to the solution of the equations of motion, by assuming a spheroidal earth. The integrated equations of motion include effects due to the principal term and second, third, fourth, and fifth harmonics of the earth's potential, as well as lunar and solar perturbations, drag, and solar radiation. For lunar and solar perturbations the program requires as input, ephemerides' tapes for the sun and moon. Drag effects are computed by assuming an exponential atmosphere with a constant temperature gradient. The standard output is an ephemeris tape giving the position and velocity vectors of the satellite at a given interval of time. The differential correction program uses the position and velocity vectors to calculate the orbital elements and their standard deviations. The standard deviation for Syncom I was 15.49 m in range and 0.05 m/sec in range rate.

The calculated orbital elements used range and range rate data and angular data from the Johannesburg Minitrack station. The range data had a weighting factor of 40, the range rate data had a weighting factor of 24, and the Minitrack data had a weighting factor of 1. Therefore the orbital elements were heavily influenced by the range and range rate data.

The Minitrack data agreed with the calculated orbital elements to 0.12 milliradian or about 25 seconds of arc, which proves that the range, range rate, and Minitrack data agree with the calculated orbital elements.

Analysis of Range and Range Rate Data Over Short Continuous Intervals

For analysis of the range and range rate data over short continuous intervals a polynomial fit was made to the data. It was found that a second degree polynomial best fit the data in all the cases considered. That is

$$g_k=a_0+a_1k+a_2k^2, \tag{1}$$

where

$g_k=g(t_k)$, the value of the function at time t_k, the function being either range or range rate,

$k=\dfrac{t_k-t_o}{\Delta t}$ $(k=0, 1, 2, \cdots, n-1)$;

t_k=the time corresponding to the k^{th} observation,

t_o=the time corresponding to the initial observation,

Δt=the time interval between successive observations.

The total interval over which the data is time continuous is defined by

$$T=t_{n-1}-t_o.$$

Application of the method of least squares (Ref. 3) gives the coefficients (a_0, a_1, a_2) and the standard deviation of fit of the polynomial to the data. That is, the normal equations are:

$$\begin{bmatrix} \sum_{k=0}^{n-1} g_k \\ \sum_{k=0}^{n-1} k g_k \\ \sum_{k=0}^{n-1} k^2 g_k \end{bmatrix}_{(3\times1)} = \begin{bmatrix} n & \sum_{k=0}^{n-1} k & \sum_{k=0}^{n-1} k^2 \\ \sum_{k=0}^{n-1} k & \sum_{k=0}^{n-1} k^2 & \sum_{k=0}^{n-1} k^3 \\ \sum_{k=0}^{n-1} k^2 & \sum_{k=0}^{n-1} k^3 & \sum_{k=0}^{n-1} k^4 \end{bmatrix}_{(3\times3)} \begin{bmatrix} a_0 \\ a_1 \\ a_2 \end{bmatrix}_{(3\times1)} . \quad (2)$$

In abbreviated matrix form Equation 1 is:

$$G_{(k\times1)} = T_{(k\times3)} A_{(3\times1)}, \quad (3)$$

where $k>3$. The resultant normal equations given by Equation 2, in abbreviated form, are

$$[T^T_{(3\times k)} G_{(k\times1)}]_{(3\times1)} = [T^T_{(3\times k)} T_{(k\times3)}]_{(3\times3)} A_{(3\times1)}. \quad (4)$$

The solution of Equation 4 is given by

$$A_{(3\times1)} = [T^T T]^{-1}_{(3\times3)} [T^T G]_{(3\times1)}. \quad (5)$$

From this least squares solution the measure of how well the data fits the assumed polynomial is given by the value of σ. The meaning of σ is that the probability will be 68.3 percent that all the data fitted to the polynomial will lie in the region bounded by $+\sigma$ and $-\sigma$.

For evaluating σ, use is made of the solution to Equation 2 or 4 as follows:

$$\sigma = \pm \frac{1}{n-3} \left[\sum_{k=0}^{n-1} g_k^2 - a_0 \sum_{k=0}^{n-1} g_k - a_1 \sum_{k=0}^{n-1} k g_k - a_2 \sum_{k=0}^{n-1} g_k k^2 \right]^{1/2}, \quad (6)$$

where $n>3$. In matrix form

$$\sigma = \pm \left\{ \frac{1}{n-3} [(G^T G) - A^T (T^T G)] \right\}^{1/2}. \quad (7)$$

And it is from this point of view that the analysis of range and range rate data is considered here.

Figures 8 and 9 are plots of the residuals in the region where the satellite height was between 10,000 and 15,000 km. The highest range tone used in this region was 100 kc. The residuals represent deviations of the raw data from the second degree polynomial fitted to the data in the least squares sense.

Corresponding to Figures 8 and 9, the polynomials fitted to the data in the 10,000 to 15,000 km region are:

1. For range (R) data

$T=t_{n-1}-t_o=206$ sec,

$\Delta t=2$ sec,

$k=\frac{t_k-t_o}{\Delta t}=0, 1, 2, \ldots, 103,$

$R_k=13408663.406+8937.701k-1.6413k^2$ (in meters),

$\sigma_R=\pm 14.0$ m (see Equation 6 or 7). (8)

2. For range rate ($\dot{R}$) data

$T=206$ sec,

$\Delta t=2$ sec,

$k=\frac{t_k-t_o}{\Delta t}=0, 1, 2, \ldots, 103,$

$\dot{R}_k=4467.7189-1.6428k+0.0004k^2$ (in meters/sec),

$\sigma_{\dot{R}}=\pm 0.031$ m/sec. (9)

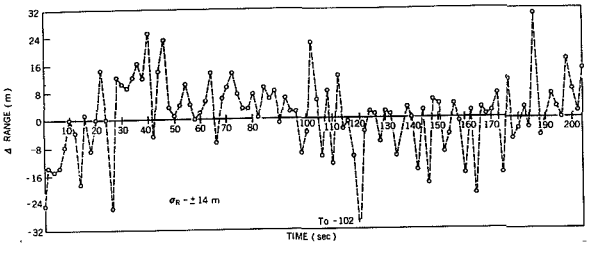

FIGURE 8.—Data at 10,000–15,000 km (100 kc tone range).

In the 10,000 to 15,000 km region, second degree polynomial fits to the range and range rate data over smaller values of T were also made. For all those intervals of T containing more than 15 data points, the second degree polynomial fitted the data best.

Range data in the region between 30,000 and 35,000 km must be divided into two classes:

1. Data extracted from a 4 kc ranging tone.
2. Data immediately following the above, which was extracted from a 20 kc ranging tone.

The plots of the residuals of the class 1 data are given in Figures 10 and 11 and those of class 2 data are given in Figures 12 and 13. Corresponding to the residual plots, the polynomials fitted to these data are:

1. For class 1 range data

$$T=62 \text{ sec},$$

$$\Delta t=2 \text{ sec},$$

$$k=\frac{t_k-t_o}{\Delta t}=0, 1, 2, \ldots, 31,$$

$$R_k=34902312.641+1825.673k$$
$$-3.7109k^2 \text{ (in meters)},$$
$$\sigma_R=\pm 496.0 \text{ m}. \qquad (10)$$

2. For class 1 range rate data

$$T=62 \text{ sec},$$

$$\Delta t=2 \text{ sec},$$

$$k=\frac{t_k-t_o}{\Delta t}=0, 1, 2, \ldots, 31,$$

$$\dot{R}_k=906.5779-0.4128k$$
$$-0.0002k^2 \text{ (in meters/sec)},$$
$$\sigma_{\dot{R}}=\pm 0.0445 \text{ m/sec}. \qquad (11)$$

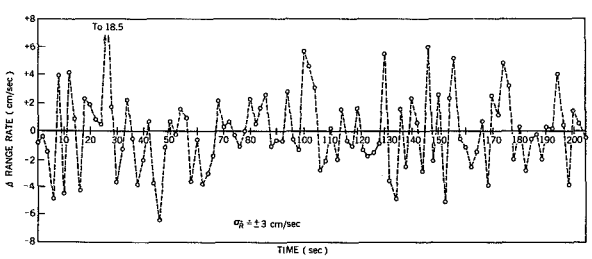

FIGURE 9.—Data at 10,000–15,000 km (range rate).

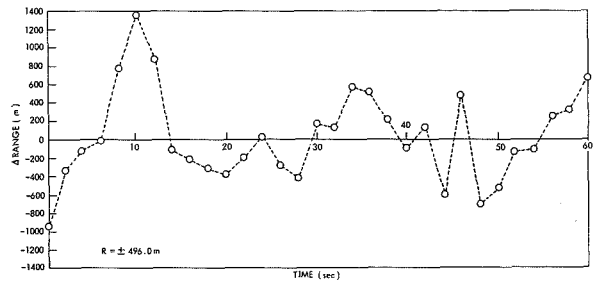

FIGURE 10.—Data at 30,000–35,000 km (4 kc tone range, class 1).

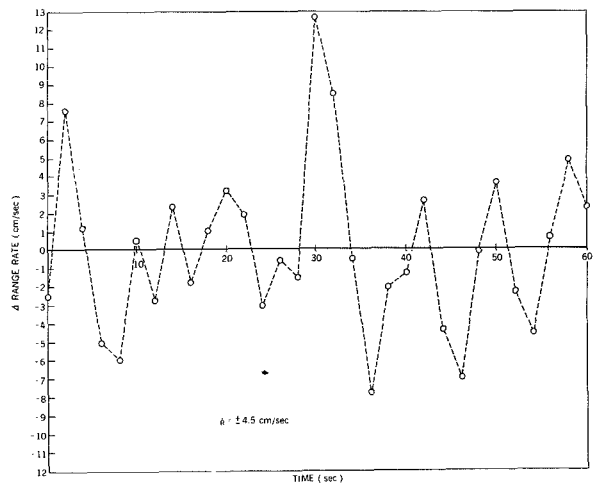

FIGURE 11.—Data at 30,000–35,000 km (range rate, class 1).

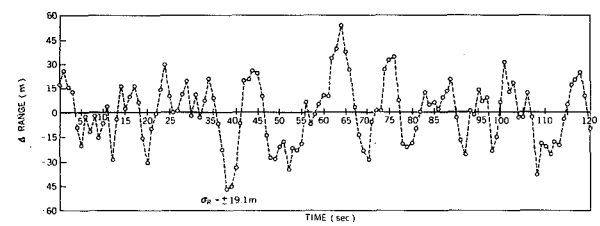

FIGURE 12.—Data at 30,000–35,000 km (20 kc tone range, class 2).

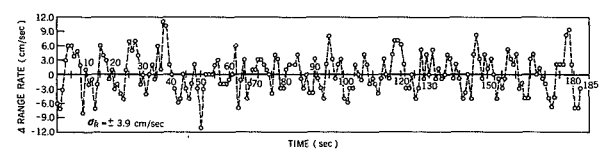

FIGURE 13.—Data at 30,000–35,000 km (range rate, class 2).

3. For class 2 range data

$$T=120 \text{ sec},$$

$$\Delta t=1 \text{ sec},$$

$$k=\frac{t_k-t_o}{\Delta t}=0, 1, 2, \ldots, 120,$$

$$R_k=35647734.938+724.109k - 0.0992k^2 \text{ (in meters)},$$

$$\sigma_R=\pm 19.1 \text{ m}. \quad (12)$$

4. For class 2 range rate data

$$T=182 \text{ sec},$$

$$\Delta t=1 \text{ sec},$$

$$k=\frac{t_k-t_o}{\Delta t}=0, 1, 2, \ldots, 182,$$

$$\dot{R}_k=725.674-0.1964k+0.00001k^2 \text{ (in meters/sec)},$$

$$\sigma_{\dot{R}}=\pm 0.039 \text{ m/sec}. \quad (13)$$

CONCLUSION

It should be noted that, from the standpoint of only the 100 or 20 kc highest range tone data, the precision of a signal measurement is better than ±20 m in range and better than ±0.05 m/sec in range rate for satellite heights between 10,000 and 35,000 km.

Although range measurements were not made with the 100 kc sidetone, the data proves the system's ability to make accurate (±20 m) range measurements using the 20 kc sidetone.

ACKNOWLEDGMENTS

The authors wish to express their appreciation for the efforts of the members of the Systems Analysis and Program Design Section, the Advanced Orbital Programming Branch, and the Theory and Analysis Office of the Goddard Space Flight Center. And, we are particularly grateful to Edward Hayes, Paul Wren, and Frank Wrigley.

REFERENCES

1. "Goddard Range and Range Rate System Design Evaluation Report," prepared by Motorola Inc. Military Electronics Division, Scottsdale, Arizona, under Contract NAS 5-1926, Report W2719-2-1, Revision 1, November 1962.
2. Gill, S., "A Process for the Step-by-Step Integration of Differential Equations in an Automatic Digital Computing Machine," *Proc. Cambridge Philos. Soc.* 47(1): 96-108, January 1951.
3. Vonbun, F. O., and Kahn, W. D., "Tracking Systems, Their Mathematical Models and Their Errors, Part 1—Theory," NASA Technical Note D-1471, October 1962.

A SYSTEM FOR RE-ENTRY TRACKING OF THE APOLLO SPACECRAFT

V. SIMAS

Goddard Space Flight Cente

The re-entry of the Apollo spacecraft can be considered to be one of the more crucial phases of the mission. The problems associated with the control of the spacecraft through the narrow re-entry corridor, in addition to the radio blackout and various trajectory anomalies, suggest that consideration be given toward the development of ground tracking systems having characteristics specifically suited to the problem. Although narrow beam antennas are required during the predominate portion of the lunar mission, tracking systems exhibiting nearly omnidirectional characteristics are considered to be most appropriate at close ranges where the received signal level is high. Such a tracking system has significant advantages, the foremost of which is its operational reliability, achieved through its simplicity. In addition, it is a relatively low cost system and will be entirely self-contained and semi-portable, resulting in the need for little logistic support. Application of particular tracking stations to a variety of missions and programs at various locations is also a possibility.

In order to point out the applicability of the proposed system it might be well to review, in brief, the characteristics of the re-entry phase of the Apollo spacecraft. Re-entry includes that part of the flight beginning with the first contact with the atmosphere and ending when the spacecraft descends by parachute to the landing site. The tracking system described herein is concerned only with the final portion of the re-entry phase, which is designated here as the glide phase. The glide phase begins at the end of the ballistic or pitch-up phase of the flight. During the glide phase of the flight the spacecraft is generally at an altitude of less than 80 Km and traveling at velocities up to 8 Km/sec. Uncertainty in the lateral and vertical position of the spacecraft during the glide phase can be quite large. In view of the presently conceived Texas landing site the glide corridor will extend roughly to the coast of southern California providing an opportunity for continuous glide path tracking coverage by a string of land-based tracking stations.

These tracking stations can be either narrow beam Radar Beacon trackers (FPS 16, FPQ 6, etc.) or wide beam radio interferometer systems equipped with Ranging capability. Both tracking systems provide the same data which completely determine the spacecraft's location and movement—orthogonal direction angles (a and b), Range (R), and their differentials. System accuracy is not really a question since only about 0.1 space degree and 50 meters in Range are required for the circumstance surrounding glide path trajectory. Each type of system is capable of vastly greater accuracy.

There is, however, a very significant fundamental difference between the two types of trackers; the Radio Interferometer system with its wide beam antennas has *virtually no signal acquisition operational problem* (*1*) while the Radar tracker must either be provided with very accurate trajectory prediction data or must search manually for the spacecraft.

In view of the perturbations in the trajectory caused by minute variations in the re-entry angle of attack, in addition to the radio blackout period and the high angular velocities (about 5 deg/sec), a very high probability of lock-up by radar trackers is difficult to guaran-

tee. On the other hand, the realization that the radio interferometer system is completely passive, i.e., requires no manual operation (except possibly for a minor phase lock-up), would appear to be a most comforting situation during the periods of duress associated with operations of this importance.

THE TRACKING STATION

A complete mobile tracking station is shown in Figure 1. Atop one van, arbitrarily designated the interferometer van, is a complete, horizontal-baseline interferometer antenna array, including elements for ambiguity resolution.

Inside the van is the interferometer instrumentation, a simple analog angular data reduction computer, a small computer which reduces range data from a range and range rate system in the second van, and an X–Y plotter. Driven by the angle and range computers, the X–Y plotter produces a complete real-time angle and range plot of spacecraft position. A radio system in the van, for communication with a central network control facility located, probably, at the landing site, utilizes the ground-plane antenna to the left of the vans.

The second van contains the ranging transmitter and receiver gear, telemetry receiving and recording instrumentation, a ground-to-spacecraft communication system and, possibly, an auxiliary autotrack system to aim the two dishes atop the van

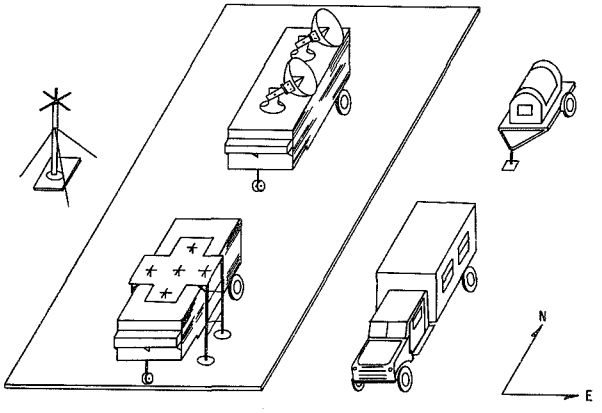

FIG. 1 MOBILE INTERFEROMETER AND RANGE TRACKING STATION

FIGURE 1.—Mobile interferometer and range tracking station.

One of these two small (5-ft-diameter) dishes serves as a transmitting antenna for the voice and ranging signals to the spacecraft, while the second dish serves as the receiving antenna for voice, telemetry and ranging signals from the spacecraft. The dishes are slaved together and aimed by X–Y antenna position commands obtained from the angular data reduction computer in the interferometer van. Although not essential for application in glide phase tracking, a monopulse autotrack system could also be provided for antenna steering, independent of the interferometer. This will be considered in more detail later in this report.

A personnel transport and facilities truck and a trailer-mounted power generator complete the station equipment, making it completely self-sustaining for short periods of time. Long operating periods are possible with a relatively small amount of basic logistical support.

Fortunately the relatively high, (2 Kmc), transmission signal frequency, together with the required angular resolution (0.1 degree), permits the complete interferometer antenna array to be sufficiently small for mounting atop one of the trailers. This feature has several advantages, among which are: (1) completely factory wired, integrated antenna and receiving system requiring no on-site tailoring of RF transmission cables, (2) practically no on-site system installation time and manpower requirement except for the installation of the concrete pad and the array stilts, (which isolate the array from movements of the trailer), (3) the array height, which permits free movement of men and equipment about the station with relatively little effect on the interferometric operation. It is conceivable, using this array mounting scheme, that the interferometer system could be calibrated at the factory since the ground plane will be supplied with split-bubble coincidence levels capable of resolution at least an order of magnitude better than that required to avoid deterioration of the 0.1 degree system accuracy.

THE INTERFEROMETER SYSTEM

The entire interferometer system is diagrammed in figure 2. A representation of the antenna field is shown on the left, with orthogonal baselines oriented arbitrarily N-S and E-W. Antenna baseline-pairs are fed to four individual receiver/phase-meter channels to develop a N-S phase measurement and an E-W phase measurement, and an ambiguity resolution measurement for each. The E-W fine and E-W ambiguity data is sent to a computing device which directly generates direction cosine angle a and angular rate $\dot{a}$, in real time. Similarly both b and $\dot{b}$ are also developed, in a separate but identical computing device. The two angles a and b could then, if necessary, be applied to a third computing device to develop the third direction angle r and its angular rate $\dot{r}$.

The reduced angular outputs can take several forms, including command signals for steerable narrow-beam antenna aiming, X–Y plotter control voltages, chart recorder voltages or tape recorder inputs for permanent flight log recording. The utility and effectiveness of the entire system hinges largely upon exploitation of the available outputs, as demonstrated by innovations adopted by the Time Measurement Branch of the Tracking Systems Division in data recording, reduction and display. Later solidification of both operational and data requirements will better define this area of consideration.

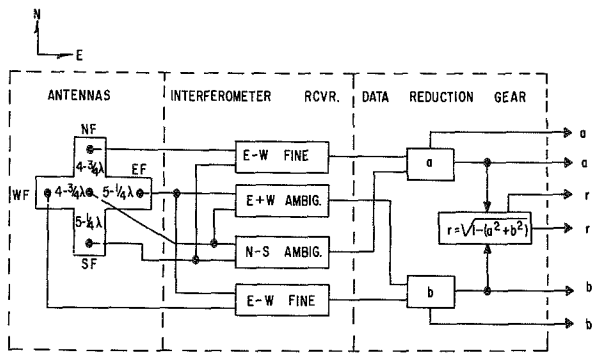

FIGURE 2.—Interferometer system.

INTERFEROMETER CHARACTERISTICS

The antenna array in figure 2 is based on fundamental interferometer considerations as presently embodied in the existing NASA Minitrack tracking systems (*2*).

When the range between receiver and transmitter is very much greater than the antenna separation, the received wave at the antennas can be considered to be planar, as shown in figure 3. To determine the angle to

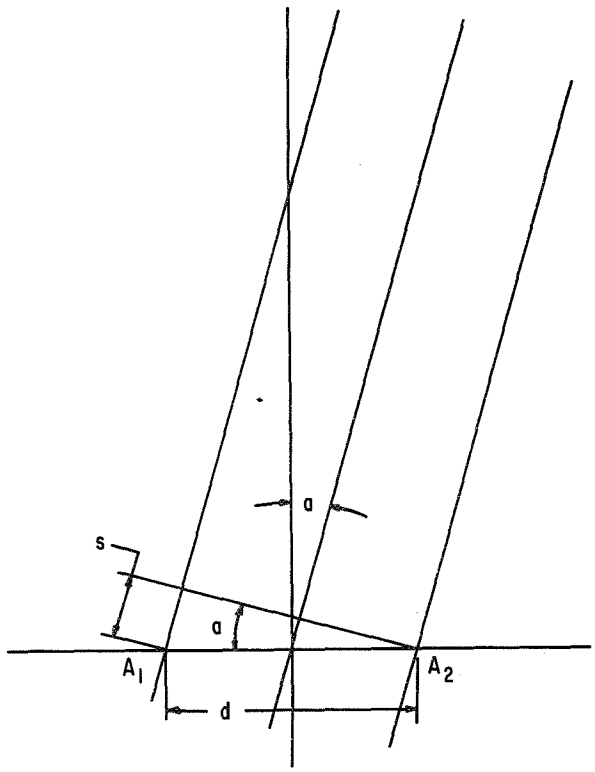

FIGURE 3.—Fundamental interferometer relationships.

the distant emitter, the phase distance, s, is measured by the interferometer system according to the relationship $s=\phi$, where ϕ is the antenna phase difference in cycles (exactly equivalent to wavelengths at a frequency f). The angle a can then be calculated by:

$$a=\sin^{-1}\left(\frac{s}{d}\right)$$

where d is the known antenna separation in wavelengths at frequency f. Expressing this more directly:

$$\sin a = \frac{s}{d}$$

thus:

$$s = d \sin a.$$

The simple relationship between space angle and antenna phase difference is thus seen to be:

$$\phi = d \sin a. \quad (1)$$

From equation (1), the sensitivity of the interferometer system as a function of the angle to the distant emitter is:

$$\frac{d\phi}{da} = d \cos a. \quad (2)$$

SYSTEM RESOLUTION

The requirements of the first program in which this system will be used define a space angle resolution of 0.1°. It is felt that this resolution will be quite adequate for similar future missions as well. Completely hemispherical coverage is impractical because of the effects of ground reflections from the surrounding terrain, and the natural RF shielding from trees and hills at low elevation angles. In addition, antenna sensitivity decreases sharply at low angles (as per equation 2). These factors specify satisfactory tracking above an elevation angle of about 10°, with undetermined operational characteristics at lower angles.

In conjunction with the required angular resolution, a system phase measurement resolution of 1 electrical degree is considered appropriate. Inserting this figure and the required 0.1° space angle resolution at 10° elevation into Equation (2), the required baseline length is found to be:

$$\frac{d\phi}{da} = \frac{1/360 \text{ phase cycles}}{.1/57 \text{ space radians}} = d \cos 80°.$$

Thus, $d = 9.12$ phase cycles, or about 10 wavelengths.

At the system operating frequency, about 2 Gc, one wavelength is nearly 0.5 ft so that there will be a baseline separation of about 5 ft between the antenna pairs.

AMBIGUITY RESOLUTION

With an antenna separation of 10λ, the maximum phase length of s is 9.85λ at 10° elevation. This requires auxiliary ambiguity resolving antennas spaced to provide an ultimate, unambiguous baseline length of ½λ. The most elementary method for achieving this is to construct additional antenna pairs with progressively shorter baselines until a half-wavelength or less is achieved. This can be accomplished for both the N–S and E–W baselines by simply adding a third antenna spaced 4¾λ from one of the existing antennas and 5¼λ from the other, as shown in Figure 2.

Only the phase difference between the 5¼λ baseline ambiguity antenna pair is actually measured by the interferometer; the phase difference between the 4¾λ baseline antenna pair is then derived by subtracting the 5¼λ baseline data from the 10λ baseline data. With data corresponding to both ambiguity baselines determined, a second subtraction 5¼λ −4¾λ=½λ, derives the completely unambiguous interferometer data. This technique is used for ambiguity resolution of present Minitrack tracking data.

The resolution step of approximately 2:1, from 10λ to 5¼λ and 4¾λ, is quite small and presents no problems. The final step of 9.5:1, from 4¾λ to ½λ, is considered entirely practical, and is compatible with the resolution capability that will be established in the system.

SPACECRAFT DIRECTION DETERMINATION

Two mutually perpendicular antenna baselines, as shown in Figure 2, completely describe the direction vector to the spacecraft. Each baseline measures a separate direction angle, as shown in Figure 4. From the geometric relation;

$$\cos^2 a + \cos^2 b + \cos^2 r = 1$$

the angle r, (angle measured from zenith), can be easily derived.

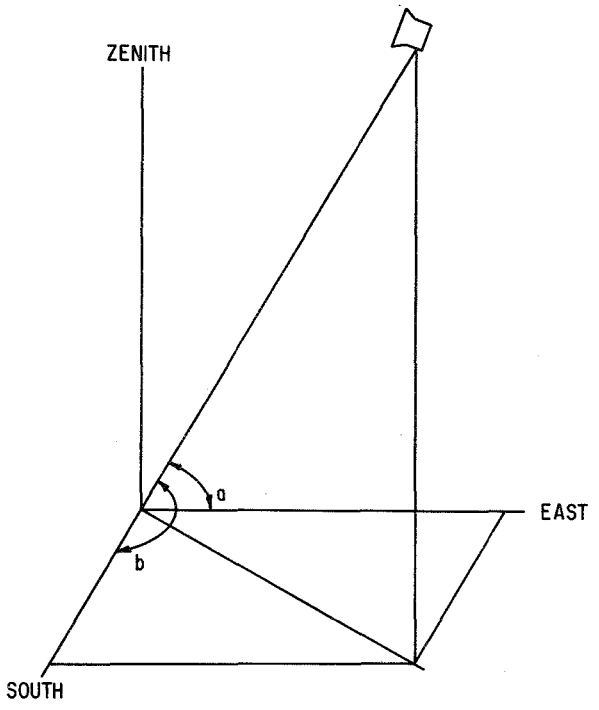

FIGURE 4.—Direction angles a and b.

ANTENNA CHARACTERISTICS

The required antenna characteristics are roughly as follows: No less than -3 *db* gain at 10 degrees elevation angle (overhead can be down about 6 *db*), circularly polarized elements (assuming spacecraft radiates a linearly polarized signal), and side lobes about 40 *db* down, (received ground reflected waves interfere with interferometric operation). A theoretical E-plane antenna pattern for a 0.4λ spacing between the dipole and the ground plane is shown in Figure 5. (*3*) The pattern exhibits 0 *db* gain at 10° elevation, $+6$ *db* at 40° and $+1.6$ *db* at zenith. It is realized that the design and development of an array having these characteristics is somewhat formidable; however, in the estimate of local antenna experts they can in general be achieved. Flyover calibration may be necessary to calibrate out the residual effects of ground reflections.

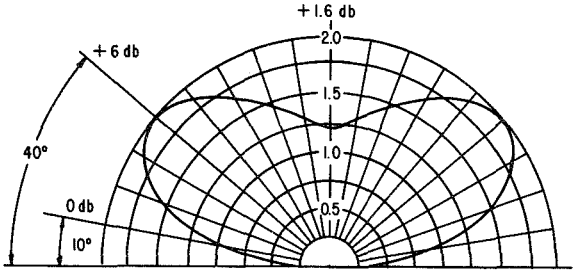

FIGURE 5.—E-plane antenna pattern for horizontal dipole with 0.4λ spacing above ground plane.

THE INTERFEROMETER RECEIVER

The interferometer receiver is shown in simplified form in the center portion of Figure 2. Each of the four channels is entirely separate in function; all channels are identical and are supplied by common local conversion oscillators to enhance differential phase stability between channels. Experience with similar Minitrack receivers has shown that receivers of this general configuration are quite practical and reliable.

Figure 6 shows the block diagram of a single interferometer channel. As in the present Minitrack system, a special local oscillator having two outputs slightly offset in frequency, (about 500 cps), is employed so that, immediately after the first conversion, the two IF signals of an interferometer antenna pair can be combined and amplified by a common IF amplifier. Since the predominant portion of the amplification and filtering of the received signals occurs after combining, the phase and amplitude relationship between the two signals is largely preserved.

The IF output can be detected by a conventional envelope detector or coherently, employing phase lock techniques. (*4*) Coherent amplitude demodulation avoids deterioration of the detected SNR at predetected SNR below unity. The detected signal, which is the beat note between the combined IF signals, bears the same phase relationship to the double local

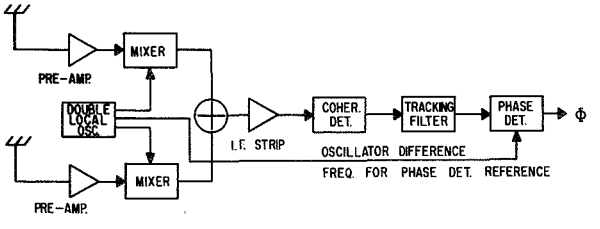

FIGURE 6.—Functional diagram of interferometer channel.

oscillator reference signal as exists between the received signals at the receiver input terminals.

Because information rates associated with radio interferometers suitable for glide path tracking are only a few cycles per second, the post detection bandwidth is vastly narrower than the predetection bandwidth. The predetection bandwidth must, of course, be about 200 Kc wide to accommodate the doppler.

In Receiver operation, wide predetection pass bands and narrow post detection pass bands generally lead to deterioration of the signal to noise ratio by the detector unless coherent detection is the method employed. In coherent detection a narrow band tracking filter phase locks onto one of the IF signal components, thereby supplying a clean reference to the detector and effectively removing the SNR deterioration.

SYSTEM NOISE CONSIDERATIONS

Figure 7 shows the relationship between the received signal level and the phase noise at the output of the phase measuring equipment. The straight lines represent the coherent demodulation case while the envelope or diode detection method results in the curved portion, the difference between the two relationships being the deterioration.

Although the procedure required to establish the phase lock-up is rather elementary and takes only a few seconds, it violates, somewhat, the principal attribute of the interferometer—no required operator thinking or manipulations. Thus, to obtain practically complete automation, this system will operate with an envelope detector until lock-up is established. After lock-up, the coherent detector output will override the other.

The curves in Figure 7 are the graphical representation of the Minitrack equation: (5)

$$\phi=\left(\frac{N1}{Pr}\right)^{1/2}\left(2+\left(\frac{N2}{Pr}\right)^{1/2}\right.$$

where

ϕ is the output phase noise in radians rms

$N1$ = Noise in the postdetection pass band

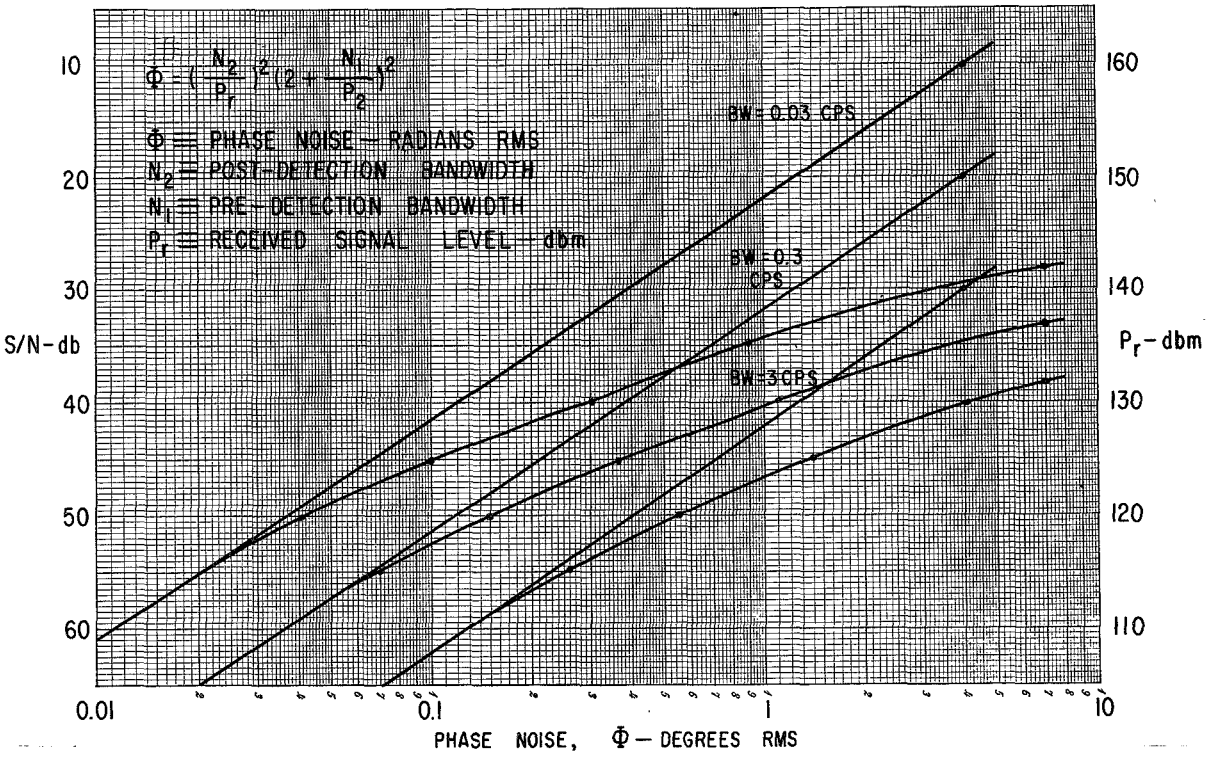

FIGURE 7.—Phase noise vs received signal level.

Pr=Received signal level in watts
$=KTeB_1$ where K=Boltzmann's constant
$Te=T$ sky$+T$ antenna
$+T$ receiver
$=10°K+50°K+240°K$
$=300°K$
B=0.03, 0.3, or 3 cps
$N2$=Noise in the predetection pass band
$=KTeB2$ where, $B2=200Kc$.

Coherent detection essentially removes the predetection noise factor so that the equation for coherent detection simplifies to:

$$\phi=\left(2\frac{N1}{Pr}\right)^{1/2}.$$

The postdetection pass band is established by a tracking filter adjustable to three bandwidths; 0.03 cps, 0.3 cps, and 3 cps. Because of the slow change in frequency of the signal at this point, lock-up is automatic, requiring no operational effort. It is interesting to note that in spite of the relatively rapid variations in the received output frequency, the postdetection tracking filter, under most conditions, could operate at exceedingly narrow tracking bandwidths.

However, the price for this greatly enhanced system sensitivity is the time required for the mechanism to reach its quiescent state, i.e., not only to lock-up but to integrate out transient phase errors. In view of the fact that it requires 100 seconds at 0.03 cps, 10 seconds at 0.3 cps, and 1 second at 3 cps to establish the proper relationship, only the 3 cps and possibly the 0.3 cps setting will be utilized for glide path tracking.

TRANSMITTER POWER REQUIRED

If the received wave at the interferometer antennas is planar with a power flow per unit area of Po, the available signal power Pr at the output terminals of the receiving antenna is:

$$Pr=ArPo,$$

where Ar is the effective area of the receiving antenna. The power flow per unit area decreases inversely as the square of both the distance R from the radiating antenna and the wavelength λ. Thus:

$$Po=\frac{AtPt}{R^2\lambda^2},$$

where At is the effective area of the transmitting antenna. Then:

$$\frac{Pr}{Pt}=\frac{AtAr}{R^2\lambda^2}.$$

Characteristics of antennas are normally better known in terms of their gain, G, rather than effective area, and:

$$G=\frac{4\pi}{\lambda^2}A,$$

so that:

$$\frac{Pr}{Pt}=\frac{\lambda^2}{(4\pi)^2}\frac{GrGt}{R^2}.$$

The required transmitted power then is:

$$Pt=\frac{(4\pi)^2R^2}{\lambda^2GrGt}Pr.$$

Taking the maximum slant range as 300 Km., and assuming that the spacecraft antenna and the receiving antenna provide zero gain (i.e., isotropic where $Gr=Gt=0$ *db*), the required transmitting power becomes;

$Pt=-128+22+120-0+0-(-6)$
$=148-128=20$ *db* or 100 milliwatts

Transmitted power on board the re-entering spacecraft in the forthcoming program will be 20 watts. Approximately 20 percent of this power is assumed to be in the carrier component of the complex, phase modulated spectrum. This is 7 *db* down, or an equivalent power of 4 watts in the carrier component. As can be seen from the foregoing calculations, this is 16 *db* above the required radiated power Pr.

There are, however, possible losses in the system that have not been revealed as yet. It should be indicated that, to achieve a satisfactory antenna pattern with 160°, nearly hemispherical coverage, 10° above the horizon, and perhaps circular polarization, the 10° points could be approximately 3 *db* down from

the assumed 0 *db* antenna gain. In addition, the spacecraft antenna pattern and polarization scheme may exhibit characteristics which will cause considerable additional losses, possibly 10 *db*, so that the 16 *db* safety factor is not exorbitant.

RANGE AND RANGE RATE SYSTEM

As indicated in the foregoing discussion, a Range and Range Rate system, (*6*) with possibly some modifications, is proposed as a part of the complete tracking station. While the omnidirectional interferometer system supplies continuous direction cosine information, the ranging system will supply range and radial velocity information. The composite output from the two systems will directly define spacecraft position, eliminating the need for derivation or approximation of any spacecraft position parameter. This is necessary, of course, to satisfy the requirement for accurate real-time positional data-relay back to the spacecraft.

Although simple dipole ground receiving antennas provide adequate gain for the interferometer system, operating on the carrier component of the unified S-Band signal from the Apollo spacecraft (*7*), substantial antenna gain is still necessary for the receiver system which accommodates voice, telemetry and ranging modulation on the unified S-Band signal. The simplest method of determining the required ground antenna gain, so that the same or better quality signals are received during re-entry as at lunar ranges, is to examine the normal antenna gains during the mission. The eighty-five foot ground dishes and a five foot spacecraft dish required at lunar ranges provide antenna gains of 52 *db* and 27 *db* respectively. On the other hand, the range has decreased from about 4×10^5 km to 4×10^2 km, or an equivalent of 60 *db* in terms of transmission loss. Thus, the required antenna gain during glide path operation is 52 *db*+27 *db*−60 *db*=19 *db*. Since the spacecraft is considered to have a nominal transmitting antenna gain of 0 *db* during the re-entry phase, the ground antenna must have at least 19 *db*.

Although it now appears that there will be an acquisition problem since a somewhat directional antenna is to be used, this antenna, in fact, can be driven completely automatically, including the acquisition phase. The answer simply results from the completely unambiguous angle data from the interferometer, which can easily drive a small 5-foot dish adequate for the collection of the spacecraft telemetry, voice and ranging signals.

To lend versatility to the composite ground station, an independent monopulse autotrack system could be supplied to drive the antenna after acquisition. Necessary acquisition aiming data would be supplied by the interferometer. While this represents duplication of antenna steering instrumentation, the gain of the dish would render the monopulse autotrack system approximately 19 *db* more sensitive than the interferometer system. In future projects, where severe fading at increased slant ranges might be a consideration, a monopulse system for aiming the antenna could prove quite beneficial. For the forthcoming re-entry program, the independent autotrack system would not be an absolute requirement, but might be considered for use as a ranging system back-up, and for phases of the program other than re-entry.

DATA DISPLAY AND TRANSMISSION

Presentation of the interferometer and range tracking data at the ground station will be quite useful to the station operators during both calibration and operation. More important, however, would be the use of a data display at the ground station in a proposed scheme in which voice navigational information only is relayed to the spacecraft. The data could be examined by a trained communicator, at each station, who would direct an astronaut on board the spacecraft to manually correct his path as required. With this arrangement, spacecraft control would be relayed from station to station as the spacecraft passes over the network.

The SPAAC (servo-phasemeter and analog computer) equipment, now in the final stages of development by the Time Measurement Branch, will be capable of controlling a conventional X–Y plotter to produce fully auto-

matic real-time sub-positional plots of the spacecraft on a map or appropriate grid structure, without ambiguity, from raw interferometer output data. A separate plot of range and radial velocity, or altitude, derived from the ranging data, would complete the data display.

A very promising concept of a complete sub-positional/altitude plot involves a vertical, 30′ x 30′ X–Y, EM plotter. Such a unit would be especially adaptable to space limitations inside the interferometer instrumentation van. The SPAAC computer system would drive an arm along as east-west grid, and a pen on the arm along a north-south grid, to produce a plot of sub-spacecraft track across a chart or map. The proposed ground track would be traced on the chart in advance. Correction of the actual track could then be accomplished, quite directly, to make it coincide with the proposed track.

A second pen, attached to the east-west arm, could be driven independently by command voltages from an auxiliary computing device receiving data from the ranging system. The second pen would thereby produce a plot of altitude vs. ground track position. The altitude plot would be displaced from the ground track plot on the chart or map, and would be compared to a proposed altitude vs. position plot. Spacecraft altitude corrections could then be made in a direct fashion similar to ground track corrections. A time index could be provided at the edge of the chart.

This scheme would probably require the least amount of unique computing and plotting instrumentation. In addition, the SPAAC equipment is now being implemented with X–Y antenna aiming outputs which could be applied directly to the range system's steerable antenna drive mechanisms to provide an autotrack mode, commanded by the interferometer angular data.

A second scheme for providing spacecraft guidance control would involve no control originating from the ground station. Instead, the tracking data from each station would be relayed, via the radio communication link, to the central landing control facility. At the central facility, this data would be coordinated to provide one composite tracking read-out over the entire glide phase, as the spacecraft passes from station to station. Navigational control would be supplied by relaying either the reduced tracking data or voice commands from the central facility to all the tracking stations. An automatic relay at the stations would then beam this information to the spacecraft via the ground-to-spacecraft radio communication link.

This approach would lend considerable continuity to the guidance scheme and would relieve the individual stations of a somewhat critical operational responsibility. It should be noted that a data display scheme at the central control facility will be a necessity, regardless of the guidance scheme employed. A display of the type discussed earlier, using an X–Y plotter, might be considered for this application.

DEVELOPMENTAL CONSIDERATIONS

Development of the antenna array and the electronics for the interferometer will be the primary effort in fabrication of the complete glide phase re-entry tracking station. All other systems will be either direct purchases, with minor modifications, or adaptations of existing systems.

The interferometer antenna array should be relatively simple in construction. Baseline orientation and leveling hardware will be provided through essentially off-the-shelf procurement and should present no problems. Some effort will be required, however, in design of the antennas and ground screen to obtain the required antenna pattern. This seems to be the major area of difficulty. Antenna support structure design will involve a study of both rigidity and thermal stability but will involve no unproved techniques.

Development of the interferometer electronics will be based primarily on principles and techniques now in use for satellite tracking. Differential phase stability, incorporation of post-detection tracking filters, double local oscillator conversion and suitable phase measuring techniques are all familiar areas in which the Tracking Systems Division at GSFC has had wide experience. It should be noted, however, that development of the phase-stable low-noise pre-

amplifiers at 2 Gc will require a somewhat substantial amount of attention and effort. However, developments at GSFC demonstrate that the requirements on the preamplifiers can be met.

In conclusion, it must be stated that this discussion is the result of preliminary study and suffers from lack of available information regarding many facets of the problem, including more defined spacecraft trajectory and reentry characteristics, spacecraft RF propagation characteristics, the nature of the desired output data forms, etc. On the other hand, the basic station concepts, as discussed throughout, appear most sound and the development of the required instrumentation can be regarded as entirely feasible.

REFERENCES

1. VONBUN, F. O., "Parking Orbits and Tracking for Lunar Transfers," GSFC X-520-62-83, Fig. 10, June 7, 1962.
2. MENGEL, J. T., "Minitrack System Design Criteria," Elec. Engr., Vol. 76, No. 8; August, 1957, p. 666.
3. Henney, Radio Engineering Handbook, Fifth Edition, pp. 20-42.
4. WOODMAN, R. F., "A Phase Locked Phase Filter for the Minitrack System," GSFC Technical Note TND-1419, September, 1962.
5. Reference to Viking Rocket Report, by Dr. Freeman, NRL, in Appendix of: J. T. MENGEL, R. L. EASTON, and C. A. SCHROEDER, "Application of Radio Phase-Comparison Techniques to the Study of Atmospheric and Rocket-Flame Refraction," NRL Report 4598, 1955.
6. HABIB, E. J., ET AL, "Goddard Range and Range Rate Tracking System," NASA Technical Note, to be published.

   "Range and Range Rate System Design Evaluation Report," Report No. W2719-2-1, Contr. No. NAS 5-1962 (GSFC), March 16, 1962.

   VONBUN, F. O., "Analysis of the 'Range and Range Rate' Tracking System," NASA Technical Note D-1178, Feb. 1962.

   ESTERLING, MAHLON, "A Long-Range Precision Ranging System," JPL Technical Report 32-80, July 10, 1961.

   RECHTIN, EBERHARDT, ET AL, "JPL Range and Doppler System," Technical Memorandum No. 33-13, Sept. 22, 1961.

   BAUGH, H. W., "Mod II Ranging Equipment," JPL Technical Report No. 32-337, Sept. 15, 1962.
7. "A Ground Instrumentation Support Plan for the Near-Earth Phases of Apollo Missions," GSFC No. X-520-62-211, Nov. 23, 1962.

   "Interim Report Apollo Modulation Technical Study, Cislunar Communication," North American Aviation, Inc., SID 62-1039, Aug. 28, 1962.

   "Apollo Modulation Techniques and Circuit Margins," North American Aviation, Inc., AP-63-10, Jan. 1963.

VIII. GENERAL

764-173 O—65——60

Page intentionally left blank

EARTH REFLECTED SOLAR RADIATION INCIDENT UPON AN ARBITRARILY ORIENTED SPINNING FLAT PLATE

FRED G. CUNNINGHAM

Goddard Space Flight Center

A general derivation is given for the earth reflected solar radiation input to a flat plate—a solar cell paddle, for example—which is spinning about an axis coincident with the axis of symmetry of the satellite to which it is affixed. The resulting equations are written for the general case so that arbitrary orientations of the spin axis with respect to the earth-satellite line and arbitrary orientations of the normal to the plate with respect to the spin axis can be treated.

No attempt is made to perform the resulting integrations because of the complexity of the equations; nor is there any attempt to delineate the integration limits for the general case. However, the equations governing these limits are given. The appendixes contain: the results, in graphical form, of two representative examples; the general computer program for the calculation is given in Fortran notation; and the results of a calculation of the distribution of albedo energy on the proposed Echo II satellite. The value of the mean solar constant used is 1.395×10^6 erg/cm^2-sec; the mean albedo of the earth is assumed to be 0.34; and the earth is assumed to be a diffuse reflector.

INTRODUCTION

In a recent series of papers (References 1 through 5) an attempt has been made to derive and present in a clear, useful manner the methods and results by which some of the power inputs to an orbiting earth satellite can be determined (this is necessary before a thermal analysis can be undertaken). The intention has been to treat the problems by assuming models which would provide the most useful and accurate information for the design engineer, and which would be soluble within the scope of the limited mathematics used in this paper and throughout the previous work. The approach used in this work assumes that (1) any latitudinal fluctuations and variations in the surface radiation and reflection properties of the earth, including the effect of the atmosphere, can be overlooked; and (2) that the net effect on the satellite can be predicted, to within useful limits, by assuming an average, uniform distribution of these properties over the surface of the earth. The advantage of this type of treatment is that these mean properties enter into the problem simply as multiplicative factors and, hence, the results already obtained can be brought up to date (as new values of the mean parameters become available) by a simple multiplication. It is apparent that a detailed analysis of the spectral distribution, intensity, variation with altitude, variation with latitude, etc., of earth radiation and earth reflected solar radiation is certainly necessary for any study pertaining to the physics of the atmosphere and the radiation balance of the earth, from which more accurate values of these "mean" parameters can be determined.

The previous papers (References 1 through 5) have not considered the problems which allow for easy calculation (for example, the earth radiation to a sphere reduces to a trivial problem once the model for the earth has been chosen) nor do they contain approximations for

satellite geometries which are so complicated that even an attempt at a description of the problem would be excessively complicated and tedious. The analyses have been limited to spheres and to flat plates, both stationary and spinning. It is hoped that all these results can be applied usefully to the bulk of satellites which do approximate spherical shapes or which are composed of a group of planes or flat plates. In addition, this analysis lends itself to the solution of the unshaded solar cell paddle problem.

The present paper extends the results of the previous work to the problem of determining the earth reflected solar radiation (the albedo) incident upon a spinning flat plate. This flat plate is, presumably, the best representation of a typical solar cell paddle commonly in use today.

The following assumptions are made:

(1) The earth can be represented by a uniform sphere whose radius is equal to its mean radius, 6367.5 km (Ref. 6);
(2) The albedo of the earth is latitude and longitude independent and can best be represented by its mean value, 0.34 (Ref. 7);
(3) The earth is a diffuse reflector of solar radiation;
(4) The solar constant can be replaced by its mean value, 1.395×10^6 erg/cm^2= sec (Ref. 8);
(5) The axis of spin of the satellite is coincident with its axis of symmetry (Ref. 4).

Save for these assumptions, the paper contains no further approximations. In fact, the paper is perfectly general, and in it an attempt has been made to treat every possible orientational configuration regardless of the geometrical complexity. Of course, this means that it is impossible to define all of the possibilities separately and list the limits of integration for each case. However, the rules for determining these limits are clearly listed just as they were written into the computer program.

In Appendixes F and G, there are presented in graphical form the results of two calculations. Appendix F treats what is hoped to be a suitable representative example of the case where the spin axis of the plate (satellite) is coincident with the radius vector from the satellite to the earth's center. Appendix G treats a representative example from the general case where the spin axis makes an arbitrary angle with the radius vector. In Appendix H, there is presented a general Fortran program for the computation. Since an elemental area of any satellite—whatever its configuration—can be considered a flat plate and its normal defined, the method developed in this paper lends itself to the determination of the albedo energy distribution on the satellite, albeit a tedious process for the general case. However, for a spherical satellite the problem is quite simple. Consequently, in Appendix I there are presented curves showing the distribution of albedo energy on the proposed Echo II satellite. This example is included to illustrate the use of the method for determining the energy distribution on unshielded portions of a satellite.

ANALYTICAL TREATMENT

The geometrical situation and the relevant parameters are depicted in Figure 1. The associated definitions are:

$\mathcal{S}$ = the mean solar constant;
$\boldsymbol{S}$ = the solar vector;
α = the mean albedo of the earth;
$d\Sigma$ = the element of terrestrial surface area;
$\boldsymbol{r}$ = the vector between the plate and the earth's center;
$\boldsymbol{\rho}$ = the vector between the plate and $d\Sigma$;
$\boldsymbol{A}$ = the normal to the plate;
β = the angle between the negative of the solar vector and $d\Sigma$;
θ_s = the angle between the solar vector and $\boldsymbol{r}$;
θ = the colatitudinal coordinate of $d\Sigma$;
λ = the angle between $\boldsymbol{A}$ and $\boldsymbol{r}$;
η = the angle between $\boldsymbol{A}$ and $\boldsymbol{\rho}$;
ϕ = the azimuthal coordinate of $d\Sigma$;
r_o = the radial coordinate of $d\Sigma$, r_o is equal to 1 by definition;
ξ = the angle between $d\Sigma$ and $-\boldsymbol{\rho}$; and
σ = the angle between $\boldsymbol{r}$ and $\boldsymbol{\rho}$.

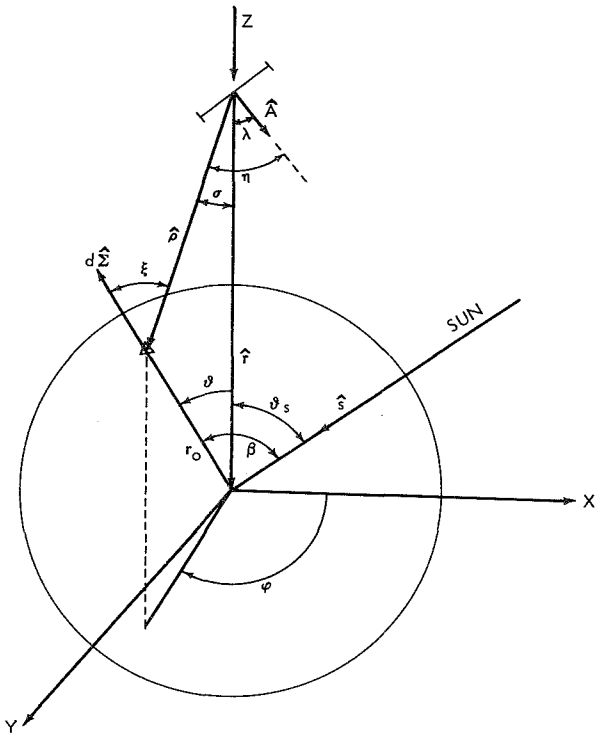

FIGURE 1.—Geometry of the problem.

The general expression for the reflected solar radiation incident upon a flat plate of unit area is

$$P=\int_{\Sigma} \frac{\mathcal{S}\alpha \cos\beta}{\pi} \cos\xi \frac{\cos\eta}{\rho^2} d\Sigma. \qquad (1)$$

In this expression it is not necessary to refer to the vector properties of the parameters because the angular dependence is already indicated. In Equation 1, $S\alpha \cos\beta d\Sigma$ gives the amount of incident solar energy reflected by $d\Sigma$. This quantity multiplied by $(\cos\xi)/\pi$ gives the amount of energy reflected by $d\Sigma$ in the direction of the plate per unit solid angle. The factor $(\cos\eta)/\rho^2$ gives the solid angle subtended at $d\Sigma$ by the plate of unit area; and $d\Sigma$ is the relevant terrestrial surface area over which the function is integrated.

As is shown in Reference 2 and Appendix A, Equation 1 becomes

$$P=\frac{\mathcal{S}\alpha}{\pi}\int_{\theta}\int_{\phi} \frac{\left[(r\cos\theta-1)(\cos\theta\cos\theta_s+\sin\theta \atop \sin\theta_s\cos\phi)\cos\eta\sin\theta\, d\theta d\phi\right]}{(r^2+1-2n\cos\theta)^{3/2}}, \qquad (2)$$

where r is in mean earth radii. A method for determining all of the relevant geometrical quantities using simple vector analysis is presented in the Appendixes. In Appendix A the derivation for $\cos\xi$ is given.

The expression for $\cos\eta$ in Equation 2 has not yet been determined. Before this can be done another angle, ζ, must be introduced, which will help define the position of A more precisely (see Fig. 2). It is obvious that even though the angle λ remains constant, the value of the angle η is not invariant for rotation of A about r. The angle ζ introduced above will define this angle of rotation of A about r. In fact, the case mentioned here is just a special case of a more general rotation, or spin, about an arbitrary axis, which shall be considered. Clearly, we must define a system reference from which all quantities will be measured. The obvious one is the combination of the solar vector S, and the plane of S and r, that is, the Sr plane. The Z axis is chosen to lie along r and the X axis lies perpendicular to r in the Sr plane. The azimuthal angle ϕ, as well as ζ, is measured from the X axis in the XY plane. The angle ζ is taken equal to zero when A lies in the positive XZ plane, as shown in Figure 1. Following the right-hand rule, the motion is then in the positive Y direction.

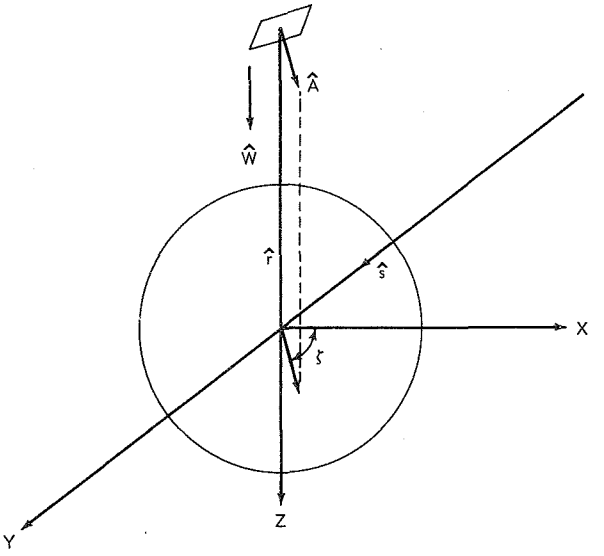

FIGURE 2.—Definition of the angle ζ.

The first and simplest case we shall consider, then, is the situation represented by the plate spinning about an axis coincident with the vector $\boldsymbol{r}$. This axis of spin will be denoted henceforth by ω. We shall then extend this to the most general case, where the spin axis makes an arbitrary angle with the vector $\boldsymbol{r}$.

Part I: The Spin Axis ω Is Coincident With r

In this section the case for which the spin axis ω is coincident with r is considered.

From Appendix B we have

$$\cos\eta=\frac{\sin\lambda\sin\theta(\sin\zeta\sin\phi+\cos\zeta\cos\phi)}{(r^2+1-2r\cos\theta)^{1/2}}+\frac{(r-\cos\theta)\cos\lambda}{(r^2+1-2r\cos\theta)^{1/2}}. \quad (3)$$

Inserting Equation 3 into Equation 2 we have

$$P=\frac{\mathcal{S}\alpha}{\pi}\int_\theta\int_\phi\frac{\left[(r\cos\theta-1)(\cos\theta\cos\theta_s+\sin\theta\sin\theta_s\cos\phi)\right]}{(r^2+1-2r\cos\theta)^2}[(r-\cos\theta)\cos\lambda+\sin\lambda\sin\theta(\sin\zeta\sin\phi+\cos\zeta\cos\phi)]\sin\theta\,d\theta d\phi. \quad (4)$$

We now consider Equation 1 from which some qualitative statements can be made concerning the limits of the θ and ϕ integration.

The upper limit θ_m of the θ integration is determined from the value of ξ for which the terrestrial surface element $d\Sigma$ is no longer visible from the plate, that is, $\xi=\pi/2$. Then, $\theta_m=\cos^{-1}(1/r)$. Because the upper limit of the ϕ integration is determined by the fact that the side of the plate in question no longer receives any reflected solar radiation from that particular element $d\Sigma$, one of whose coordinates is ϕ, the upper limit ϕ_m of the ϕ integration can be determined in two ways.

The two quantities which determine ϕ_m are the source function $\mathcal{S}\alpha\cos\beta\,d\Sigma$ and the solid angle factor $(\cos\eta)/\rho^2$. In the first instance the the source function becomes 0 when $\beta=(\pi/2)$. Then $\cos\beta=0$, from which

$$\phi_m=\cos^{-1}(-\cot\theta\cot\theta_s). \quad (5)$$

For $\beta>(\pi/2)$, the source function, of course, remains 0. For many values of θ and θ_s the argument of the $\cos^{-1}$ in Equation 5 is less than -1, for which the upper limit of the ϕ integration is π (if we take advantage of the symmetry and multiply by 2). For other values of θ and θ_s the argument will be greater than $+1$, for which the source function is always 0.

In the second case where the upper limit of the ϕ integration is determined by the solid angle dependence we see that the incident energy from any element $d\Sigma$ is 0 when $\eta\geq\pi/2$. The geometrical representation for this case is shown very clearly in Reference 1. A symmetry condition cannot be used here because the source function is symmetric only about the $\boldsymbol{rS}$ plane and this symmetry condition is applicable only to the case where $\zeta=0$. Hence, we must consider the situation presented for a given value of ζ as the value of ϕ is varied. For many values of the parameters, the value of $\cos\eta$ will never become 0 for any value of ϕ. However, for other values of the parameters, the side of the plate in question ceases to be visible from the elements of area $d\Sigma$ (denoted by some specific values of the parameter ϕ) and $\eta\geq\pi/2$. Then, for values of ϕ the plate will once again become visible from $d\Sigma$. From Reference 1 it is clear that the symmetry plane for this situation is the $\boldsymbol{rA}$ plane. Therefore, we consider the biquadrant $\zeta\leq\phi\leq(\zeta+\pi)$. If the value of $\cos\eta$ because 0 at all, it will do so somewhere in this range of ϕ. Because of the symmetry with respect to the $\boldsymbol{rA}$ plane, the value of ϕ somewhere in this range for which $\cos\eta=0$, call it ϕ', is mirrored in the plane. In other words, the angle ϕ'' at which the plate again becomes visible in the range $\zeta+\pi\leq\phi\leq\zeta+2\pi$ is given by $\zeta+\pi-\phi'=\phi''-(\zeta+\pi)$ or $\phi''=2(\zeta+\pi)-\phi'$. In order to determine ϕ' we equate Equation 3 to 0 from which we obtain

$$-\frac{(r-\cos\theta)\cos\lambda}{\sin\lambda\sin\theta}=\sin\zeta\sin\phi+\cos\zeta\cos\phi.$$

Transferring the second term on the right-hand side to the left-hand side and squaring gives

$$\cos^2\phi+\frac{2(r-\cos\theta)\cos\lambda\cos\zeta}{\sin\lambda\sin\theta}\cos\phi+\frac{(r-\cos\theta)^2\cos^2\lambda}{\sin^2\lambda\sin^2\theta}-\sin^2\zeta=0. \quad (6)$$

The solution of Equation 6 for ϕ will yield, when applicable, two solutions, one each in the ranges $\zeta \leq \phi \leq \zeta+\pi$ and $\zeta+\pi \leq \phi \leq \zeta+2\pi$ symmetric about $\phi=\zeta+\pi$. The solution of Equation 6 is

$$\cos\phi = \frac{-(r-\cos\theta)\cos\lambda\cos\zeta}{\sin\lambda\sin\theta} \pm \sin\zeta\sqrt{1-\frac{(r-\cos\theta)^2\cos^2\lambda}{\sin^2\lambda\sin^2\theta}}, \quad (7)$$

where the double roots are given by the plus and minus signs. Obviously, when ζ is equal to 0 or π, Equation 7 yields only one result, because of the multivaluedness of the cosine function. This follows quite clearly from the symmetry condition. For these cases, the roots will always lie in the second and third or first and fourth quadrants, with the limiting case $\phi=\pi/2$ and $3\pi/2$; one root will never be found in the first quadrant and the other in third, for example.

If the absolute value of the argument in Equation 7 is greater than 1, then the roots do not exist and either the entire spherical cap of the earth lying within the cone defined by θ is visible from the plate for all ζ or it is never visible. The former case occurs when

$$0 \leq \lambda < \sin^{-1}\frac{(r-\cos\theta)}{(r^2+1-2r\cos\theta)^{1/2}}$$

(first quadrant), and the second when

$$\lambda \geq \sin^{-1}\frac{(r-\cos\theta)}{(r^2+1-2r\cos\theta)^{1/2}}$$

(second quadrant). An even more useful range of the parameter λ is $0 \leq \lambda \leq \theta_m$ for which the entire spherical cap of the earth (that portion lying within the tangent cone delineated by θ_m) is visible. For this case the problem is greatly simplified.

Until this point we have discussed only the determination of the upper limit of the ϕ integration by using the conditions considered above. However, from the considerations of Equation 7 we have actually obtained both the lower and upper limit. For those cases where $\lambda > \theta_m$, Equation 7 is applicable and the limits are given by the two roots already stated. This does not mean that the region of integration contains the origin necessarily. For example, considering the situation presented by $\zeta=\pi$ and $\lambda=\pi/2$, we see that the roots given by Equation 7 are $\phi=\pi/2$ and $3\pi/2$. However, the geometry of the situation clearly shows that the range of integration is from $\pi/2$ to $3\pi/2$. Therefore, the criterion which determines the way of proceeding from limit to limit is that the range must always contain the angle ζ.

Since Equations 5 and 7 must both be consulted in order to determine the relevant range of the variable ϕ, it is not practical to attempt to write down Equation 4 as a sum of terms each with the proper limits of integration clearly shown. A complicating feature is that the limit on the θ integration is dependent upon the limits of the ϕ integration; that is, if for a particular case the upper limit of the ϕ integration is equal to π for certain values of θ where $0 \leq \theta \leq \theta' < \theta_m$ and is given by Equation 5 for $\theta' < \theta \leq \theta_m$, then the appropriate range of the variable θ must be coupled with corresponding values of the limits of the ϕ integration.

For any given value of the parameter ζ the computer program is written so that Equations 5 and 7 are solved for their respective ranges of the variable ϕ for which the input to the plate is not 0. The overlapping portions of the regions determined in the above manner, then, represent the cogent ranges of ϕ over which the function in Equation 4 must be integrated.

Thus far, all discussions of Equation 4 and the limits of integration of θ and ϕ have been based on the assumption that the value of ζ is fixed. Since this is not in general the case, it is necessary to average the results of Equation 4 over a spin period. This problem was discussed extensively in Reference 4 and the relevant expressions for various ranges of the parameter ζ were written. In Equation 7, the values of the range of the ϕ integration are clearly seen to be dependent upon ζ as is the function itself given by Equation 4. The average over a spin period is given by

$$\langle P \rangle = \frac{1}{2\pi}\int_0^{2\pi} P(\zeta)\,d\zeta. \quad (8)$$

Clearly, the integrals of Equation 4 could be given explicitly, after much labor, as a function of the parameters and as a function of the upper limits of ϕ. However, it is doubtful whether Equation 8 could be integrated explicitly except for a few special cases. Consequently, Equation 8 is integrated by the computer and the results thereby obtained are the spin averages. Of course, in order to perform the integration over ζ the integration over θ and ϕ for every ζ ($\Delta\zeta$ apart) must be performed. If in a specific application results should be required for any of these intermediate values of ζ, a very simple modification of the program will suffice. These, however, do not constitute by themselves spin averages.

Thus far, the only case considered has been that in which the spin axis is coincident with r. Variation of the angle λ has been sufficient to describe all the degrees of freedom here allowed; that is, the variation of the angle between the normal to the plate and the spin axis.

Part II: The Spin Axis ω Makes an Arbitrary Angle χ With r

In this section the case for which the spin axis ω makes an angle χ with r is considered. Figure 3 shows the geometry of this new situation. We introduce a new angle ϵ which defines the angle between the normal to the plate A and the axis of symmetry of the satellite ω (the spin axis for our problem). The quantity ϵ is generally fixed for a given satellite. In addition, we must introduce another angle κ, the azimuthal angle of ω from the rS plane (an angle similar to ϕ).

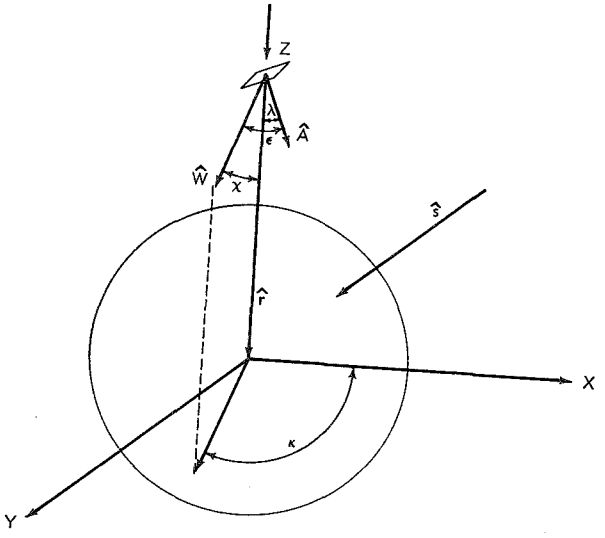

FIGURE 3.—Definitions of the parameters defining the general orientation of the flat plate.

For this case it becomes necessary to take the zero point of ζ as the point when A lies in the $r\omega$ plane and the motion is in the direction of the X' axis (see Appendix C, Fig. C5). From Appendix C we have

$$\cos\eta=\frac{(r-\cos\theta)}{(r^2+1-2r\cos\theta)^{1/2}}(\cos\chi\cos\epsilon-\sin\chi\sin\epsilon\cos\zeta)+\frac{\sin\theta}{(r^2+1-2r\cos\theta)^{1/2}}[\cos\phi\cos\kappa\cos\epsilon\sin\chi+\sin\phi\sin\kappa\cos\epsilon\sin\chi+\cos\phi\cos\kappa\sin\epsilon\cos\chi\cos\zeta+\sin\phi\sin\kappa\sin\epsilon\cos\chi\cos\zeta+\sin\phi\cos\kappa\sin\epsilon\sin\zeta-\cos\phi\sin\kappa\sin\epsilon\sin\zeta]. \quad (9)$$

Equation 9 substituted into Equation 2 now gives the albedo input.

To determine the range of the ϕ integration, equate Equation 9 to 0 making the following substitutions for convenience:

$$F=\frac{(r-\cos\theta)}{\sin\theta}(\cos\chi\cos\epsilon-\sin\chi\sin\epsilon\cos\zeta),$$

$$G=(\cos\kappa\cos\epsilon\sin\chi+\cos\kappa\sin\epsilon\cos\chi\cos\zeta-\sin\kappa\sin\epsilon\cos\zeta),$$

$$H=(\sin\kappa\cos\epsilon\sin\chi+\sin\kappa\sin\epsilon\cos\chi\cos\zeta+\cos\kappa\sin\epsilon\sin\zeta).$$

Then,

$$-F=G\cos\phi+H\sin\phi. \quad (10)$$

Transferring the first term on the right-hand side to the left-hand side and squaring we have

$$F^2+2FG\cos\phi+G^2\cos^2\phi=H^2\sin^2\phi=H^2(1-\cos^2\phi),$$

from which

$$(G^2+H^2)\cos^2\phi+2FG\cos\phi+F^2-H^2=0. \quad (11)$$

Solving Equation 11 for $\cos\phi$ we have

$$\cos\phi=\frac{-FG\pm H\sqrt{G^2+H^2-F^2}}{(G^2+H^2)}. \quad (12)$$

When $\kappa=0$ and $\zeta=0$, the problem is symmetric in ϕ as before and $H=0$. Therefore, it is necessary to remember that the solution of Equation 12 for these conditions includes two roots, one each in the first and fourth quadrants or one each in the second and third quadrants. The situation is much more complicated for the general case because there the angle η is symmetric about the rA plane, which is not, in general, coincident with the rS plane which defines the angle ϕ. If, for example, we consider the case presented by $\kappa=\pi/2$ and $\zeta=0$, or π (where the rA plane makes an angle κ with the rS plane), the solution of Equation 12 reduces to

$$\cos\phi=\pm\frac{1}{H}\sqrt{H^2-F^2}. \quad (13)$$

Now, we know that if $\eta\geq\pi/2$ at all, one root ϕ' say, of Equation 13 must lie in the range $0\leq(\phi-\pi/2)\leq\pi$ and from this we obtain $\pi/2\leq\phi\leq3\pi/2$ (for the general case when $\zeta=0$, or π and $\kappa\leq\phi\leq\pi+\kappa$); the other corresponding value ϕ'' is given by $(3\pi/2-\phi')\equiv(\phi''-3\pi/2)$.

Equation 13 has two roots, one given by the minus sign and the other given by the plus sign. From the geometry we know that one root must lie in the range $\pi/2\leq\phi\leq3\pi/2$, a solution corresponding to the minus sign. However, $\cos\phi<0$ for both quadrants given in the range $\pi/2\leq\phi\leq3\pi/2$, so another criterion is needed by which the computer can select the proper value of ϕ in such cases. Since the only ϕ values of interest here are those in the range for which $\eta\leq\pi/2$, the value of $\cos\eta$ given by Equation 9 must be positive in all such cases. If it is desired to determine the range of ϕ for any particular values of the set of parameters, and if such a case as the above should occur, the only course open is to calculate the value of $\cos\eta$ for both possible values of ϕ and thereby directly determine the one corresponding to $\eta=\pi/2$. If this value of ϕ is the larger value, the smaller ϕ value will automatically meet all criteria. However, a slightly different approach can be used when the computer program is written. We must integrate over the relevant range of ϕ for a given value of the set of parameters, κ, χ, ϵ, and ζ (whether or not we ultimately want the average overall values of ζ). Since the computer does this in arithmetic steps, changing the value of ϕ by $\Delta\phi$ each time, it may as well start at the value of ϕ representing the symmetry of the given condition. The plane of symmetry for this part of the problem is the rA plane. If we can determine the value of ϕ for this case, the computer can be programmed to start here and go in the plus and minus directions relative to ϕ, and continue the computation until $\cos\eta$ (which must be calculated at each step anyway)$=0$. If $\cos\eta$ does not become 0 at all, the integration is terminated at $\pm\pi$ radians from the starting point. If at the starting point $\eta\geq\pi/2$, no further consideration is necessary. Proceeding thus, we need only correlate with the apposite range of ϕ dictated by the source function which is symmetric about the rS plane. This restriction is given by Equation 5. The starting point ϕ_0 of ϕ as developed in Appendix D is given by $\phi_0=(\kappa+\gamma)$, for $0\leq\zeta\leq\pi$ and $\phi_0=(\kappa-\gamma)$ for $\pi\leq\zeta\leq2\pi$, where

$$\cos\gamma=\frac{\cos\epsilon\sin\chi+\sin\epsilon\cos\chi\cos\zeta}{[1-(\cos\chi\cos\epsilon-\sin\epsilon\sin\chi\cos\zeta)^2]^{1/2}}, \quad (14)$$

and where γ is the angle between the projection of A and ω onto the XY plane. It will be helpful to remember that $\gamma\leq\epsilon$, the equal sign holding only when $\chi=\pi/2$ and $\zeta=3\pi/2$ or $\pi/2$. The appropriate sign from the square root can then be readily determined. When $\chi=0$ the equation has no meaning.

RECAPITULATION

The development is now complete for all the equations necessary to determine the albedo input to a spinning flat plate in the most general orientation, under the condition, of course, that the plate is not shielded at any time by other members of the satellite. However, the equation for this input has been developed for a "stationary" satellite, that is, a satellite at a fixed altitude and whose satellite-earth line

makes an angle θ_s with the solar vector. Appendix E gives the development for expressions for r and θ_s in terms of general orbital parameters so that transformations may be made with facility from one set of parameters to the other.

The equation giving the albedo input is

$$P=\frac{\mathcal{S}\alpha}{\pi}\int_\theta\int_\phi \frac{(r\cos\theta-1)(\cos\theta\cos\theta_s+\sin\theta\sin\theta_s\cos\phi)\cos\eta\sin\theta d\theta d\phi}{(r^2+1-2r\cos\theta)^{3/2}}. \quad (2)$$

The value of $\cos\eta$ is given by:

$$\cos\eta=\frac{\sin\lambda\sin\theta(\sin\zeta\sin\phi+\cos\zeta\cos\phi)}{(r^2+1-2r\cos\theta)^{1/2}}+\frac{(r-\cos\theta)\cos\lambda}{(r^2+1-2r\cos\theta)^{1/2}}; \quad (3)$$

when the spin axis ω is coincident with r (Part I) and

$$\cos\eta=\frac{(r-\cos\theta)}{(r^2+1-2r\cos\theta)^{1/2}}(\cos\chi\cos\epsilon-\sin\chi\sin\epsilon\cos\zeta)+\frac{\sin\theta}{(r^2+1-2r\cos\theta)^{1/2}}[\cos\phi\cos\kappa\cos\epsilon\sin\chi$$
$$+\sin\phi\sin\kappa\cos\epsilon\sin\chi+\cos\phi\cos\kappa\sin\epsilon\cos\chi\cos\zeta+\sin\phi\sin\kappa\sin\epsilon\cos\chi\cos\zeta$$
$$+\sin\phi\cos\kappa\sin\epsilon\sin\zeta-\cos\phi\sin\kappa\sin\epsilon\sin\zeta]. \quad (9)$$

when the spin axis ω makes an arbitrary angle χ with r (Part II). The range of the θ integration is $0\leq\theta\leq\theta_m$ where $\theta_m=\cos^{-1}(1/r)$. The limits of the ϕ integration are given by those values of ϕ which simultaneously satisfy two conditions. For the case considered in Part I (ω coincident with r) the two conditions given by (a) and (b):

(a) $0\leq\phi\leq\phi_m$, where $\phi_m=\cos^{-1}(-\cot\theta\cot\theta_s)$
$(2\pi-\phi_m)\leq\phi\leq 2\pi$ note: $\phi_m\leq\pi$, (5)

and

(b) $\phi_1\leq\phi\leq\phi_2$ where ϕ_1 and ϕ_2 are given by the solution of the equation

$$\cos\phi=\frac{-(r-\cos\theta)\cos\lambda\cos\zeta}{\sin\lambda\sin\theta}\pm\sin\zeta\sqrt{1-\frac{(r-\cos\theta)^2\cos^2\lambda}{\sin^2\lambda\sin^2\theta}}, \quad (7)$$

with the condition that $\phi_1\leq\zeta\leq\phi_2$, where we mean only to imply that the angle ζ lies between the limiting values of ϕ, thereby excluding the path from ϕ_1 to ϕ_2 that does not include the angle ζ. For the case considered in Part II (ω makes an angle χ with r) the two conditions given by (c) and (d):

(c) $0\leq\phi<\phi_m$, where $\phi_m=\cos^{-1}(-\cos\theta\cot\theta_s)$
$(2\pi-\phi_m)\leq\phi\leq 2\pi$ note: $\phi_m\leq\pi$,

and

(d) $\phi_1'\leq\phi\leq\phi_2'$ where the roots ϕ_1' and ϕ_2' are given by the solutions to

$$\cos\phi=\frac{-FG\pm H\sqrt{G^2+H^2-F^2}}{(G^2+H^2)}, \quad (12)$$

where

$$F=\frac{r-\cos\theta}{\sin\theta}(\cos\chi\cos\epsilon-\sin\chi\sin\epsilon\cos\zeta),$$
$$G=(\cos\kappa\cos\epsilon\sin\chi+\cos\kappa\sin\epsilon\cos\chi\cos\zeta-\sin\kappa\sin\epsilon\sin\zeta),$$
$$H=(\sin\kappa\cos\epsilon\sin\chi+\sin\kappa\sin\epsilon\cos\chi\cos\zeta+\cos\kappa\sin\epsilon\sin\zeta),$$

with the condition that the path from ϕ_1' to ϕ_2' must contain the angle $(\kappa+\gamma)$, for $0\leq\zeta\leq\pi$, and $(\kappa-\gamma)$ for $\pi\leq\zeta\leq 2\pi$, where

$$\cos\gamma=\frac{\cos\epsilon\sin\chi+\sin\epsilon\cos\chi\cos\zeta}{[1-(\cos\chi\cos\epsilon-\sin\epsilon\sin\chi\cos\zeta)^2]^{1/2}}. \quad (14)$$

In fact the angles $(\kappa+\gamma)$ or $(\kappa-\gamma)$—depending upon the value of ζ in question—lie exactly midway between the angles ϕ_1' and ϕ_2'.

This equation has no meaning when $\chi=0$.

In addition, as is pointed out in Appendix C, we need only consider the following ranges of the parameters κ, χ, and ϵ for the general case: $0\leq\chi\leq\pi$, $0\leq\epsilon\leq\pi/2$, and $0\leq\kappa\leq\pi$. For any

value of $\epsilon > (\pi/2)$ the same physical picture is obtained if χ is replaced by $(\pi-\chi)$, ϵ by $(\pi-\epsilon)$, and κ by $(\pi+\kappa)$. Any value of $\kappa > \pi$ can be replaced by its equivalent value $(2\pi-\kappa)$. Therefore, the incident power (averaged over ζ) obtained, for example, for $\chi=150°$, $\epsilon=110°$ and $\kappa=30°$, is identical to the result obtained for $\chi=30°$, $\epsilon=70°$ and $\kappa=150°$.

CONCLUDING REMARKS

It should be quite clear from the foregoing that the equation for the reflected solar power input to the spinning plate—even though it has not been solved explicitly—is an exact expression only for the geometric aspects of the problem. The assumption that the earth is perfectly spherical diffuse reflector is necessary if the equation is not to be a much more complicated expression than it already is. However, these assumptions are not as serious (the error introduced by them is probably negligible in a first approximation even if enough were known to treat them analytically) as the assumption that the reflectivity is latitude and longitude independent. Undoubtedly there is a variation in this parameter with position on the earth and also a variation with time. If this θ and ϕ dependence were known in some explicit form it could easily be introduced into the equations. However, since information of this kind is not now available, the use of a hemispherical average would seem justified. It is also obvious that the figure of 0.34 used for the magnitude of the albedo, being a yearly hemispherical average [1] is not correct for many atmospheric conditions, in particular extreme cloud cover. Assuming that these conditions can always be represented reasonably well by an average value it still follows that the albedo might increase or decrease at any given time by a factor of 2 or more. However, by taking the mean value we introduce this parameter as a multiplicative factor. Consequently, the results of this paper can easily be modified at any time.

Appendix F and G contain in graphical form the results of two example calculations; Appendix H contains a Fortran program for the general problem; and Appendix I contains curves showing the distribution of albedo energy on the proposed Echo II satellite, thereby illustrating the utility of a flat plate analysis for the purpose of determining energy distributions.

[1] Obtained from unpublished studies of atmospheric radiation, Department of Meteorology, Massachusetts Institute of Technology, Cambridge, Mass., 1952.

ACKNOWLEDGMENT

The IBM 7090 computations included in this report were performed by Mr. E. Monasterski of Goddard Space Flight Center.

REFERENCES

1. CUNNINGHAM, F. G., "Power Input to a Small Flat from a Diffusely Radiating Sphere, with Application to Earth Satellites," NASA Technical Note D-710, July 1961.
2. CUNNINGHAM, F. G., "Earth Reflected Solar Radiation Input to Spherical Satellites," NASA Technical Note D-1099, October 1961; Also *ARS J.* 32(7): 1033–1036, July 1962.
3. CUNNINGHAM, F. G., "Calculation of the Eclipse Factor for Elliptical Satellite Orbits," NASA Technical Note D-1347, June 1962; Also *ARS J.* 32(9): 1399–1400, September 1962.
4. CUNNINGHAM, F. G., "Power Input to a Small Flat Plate from a Diffusely Radiating Sphere with Application to Earth Satellites: The Spinning Plate." NASA Technical Note D-1545, February 1963.
5. CUNNINGHAM, F. G., "Earth-Reflected Solar Radiation Incidence upon Spherical Satellites in General Elliptical Orbits," NASA Technical Note D-1472, February 1963.
6. EHRICKE, K. A., "Space Flight. Vol. 1. Environment and Celestial Mechanics," Princeton, N.J.: Van Nostrand, 1960, p. 154.
7. JOHNSON, J. C., "Physical Meteorology," New York: Wiley, 1954, p. 171.
8. JOHNSON, F. S., "The Solar Constant," *J. Meteorol.* 11(6): 431–439, December 1954.

Appendix A

THE CALCULATION OF THE ANGLES β AND ξ

From Figure 1 we have the two angles β and ξ to calculate. The angle β is the angle between $d\Sigma$ and $-S$. The coordinates in the X, Y, Z frame of reference are:

$$\left.\begin{aligned} -S_X &= \mathcal{S}\sin\theta_s & d\Sigma_X &= d\Sigma\sin\theta\cos\phi \\ -S_Y &= 0 & d\Sigma_Y &= d\Sigma\sin\theta\sin\phi \\ -S_Z &= -\mathcal{S}\cos\theta_s & d\Sigma_Z &= -d\Sigma\cos\theta \end{aligned}\right\}\cdot \quad \text{A(1)}$$

Therefore,

$$\cos\beta = \cos\theta\cos\theta_s + \sin\theta\sin\theta_s\cos\phi. \quad \text{(A2)}$$

The angle ξ is the angle between $d\Sigma$ and $-\rho$. We need only determine the coordinates of $-\rho$ in the X, Y, Z frame which are,

$$\left.\begin{aligned} -\rho_X &= -\rho\sin\sigma\cos\phi \\ -\rho_Y &= -\rho\sin\sigma\sin\phi \\ -\rho_Z &= -\rho\cos\sigma \end{aligned}\right\}\cdot \quad \text{(A3)}$$

Therefore,

$$\cos\xi = \cos\sigma\cos\theta - \sin\sigma\sin\theta. \quad \text{(A4)}$$

In terms of the angle of integration θ the expression for $\cos\xi$ becomes,

$$\cos\xi = \frac{r\cos\theta - 1}{(r^2+1-2r\cos\theta)^{1/2}}. \quad \text{(A5)}$$

Appendix B

THE CALCULATION OF COS η WHEN ω IS COINCIDENT WITH r

To determine the value of cos η for the case when ω is coincident with r consider Figure B1. The angle σ is the angle between r and ρ. The X axis lies in the Sr plane normal to r, or the Z axis. The spin ω of the satellite is determined from the right-hand rule. The azimuthal angle of spin ζ delineates the position of A as it spins about ω. Since the vector A will lie in the XZ plane for two values of the angle ζ, π radians apart, the zero value of ζ is defined to occur when A lies in the XZ plane and when the motion at that time is in the positive Y direction. This zero value of ζ is shown in Figure B1. In the general case, the symbol ϵ represents the angle between A and ω, but in the present case this is synonymous with λ so we shall use the latter notation.

The components of the vectors A and ρ are given by

$$\left.\begin{aligned} \rho_X &= \sin\rho\cos\phi & A_X &= A\sin\lambda\cos\zeta \\ \rho_Y &= \sin\rho\sin\phi & A_Y &= A\sin\lambda\sin\zeta \\ \rho_Z &= \cos\rho & A_Z &= A\cos\lambda \end{aligned}\right\}. \quad \text{(B1)}$$

Therefore,

$$\cos\eta = \frac{A\cdot\rho}{A\rho} = \sin\sigma\cos\phi\sin\lambda\cos\zeta + \cos\sigma\cos\lambda + \sin\sigma\sin\phi\sin\lambda\sin\zeta. \quad \text{(B2)}$$

In terms of θ, the angle used in the integration, we have,

$$\cos\eta = \frac{(r-\cos\theta)\cos\lambda}{(r^2+1-2r\cos\theta)^{1/2}} + \frac{\sin\theta\sin\lambda}{(r^2+1-2r\cos\theta)^{1/2}} (\cos\phi\cos\zeta + \sin\phi\sin\zeta). \quad \text{(B3)}$$

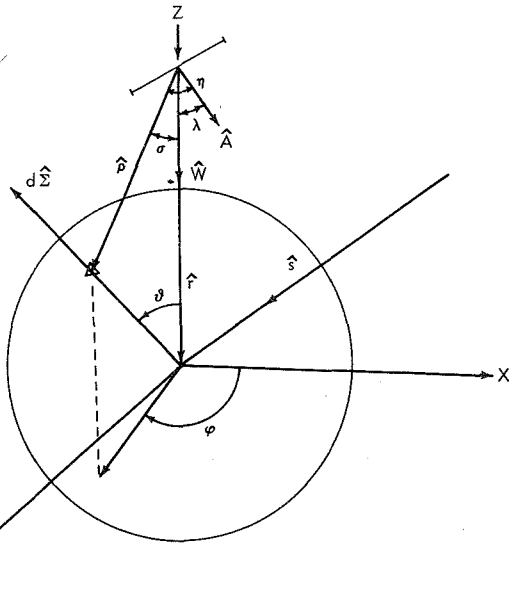

FIGURE B1.—Geometry for determining cos η when ω is coincident with r.

Appendix C

THE CALCULATION OF COS η WHEN ω MAKES AN ANGLE χ WITH r

Figure C1 shows the general case. In order to determine cos η we introduce a new coordinate system, the primed system. The projection of ω onto the XY plane is defined as the X' axis. The X' axis makes an angle κ with the X axis. Therefore, the primed coordinate system is obtained by a rotation of angle κ about the Z axis. The ωr plane, by definition the $X'Z'$ plane, is now the plane from which the angle ζ is measured.

As before $\zeta \equiv 0$ when A lies in the $X'Z'$ plane and the motion is in the positive Y' direction. In Figure C1, the top position of A shows the $\zeta=0$ position.

We now introduce the direction cosines cos μ, cos ν, and cos λ where μ, ν, and λ are the angles between A and X', Y', and Z', respectively.

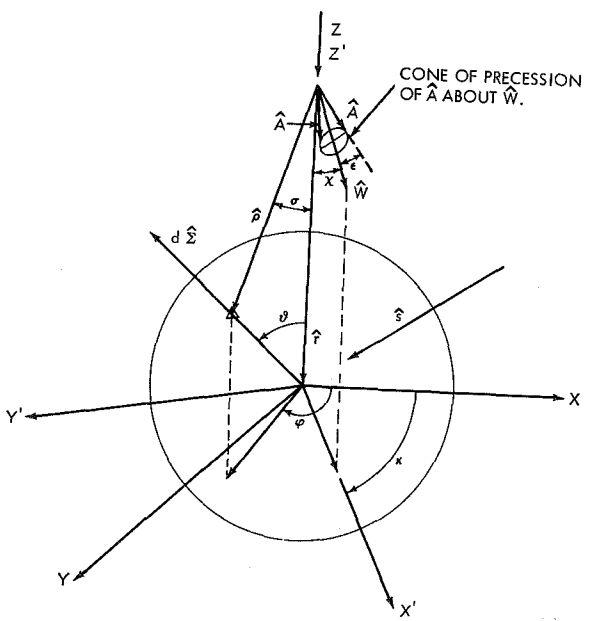

FIGURE C1.—Geometry for determining cos η when ω makes an angle x with r'.

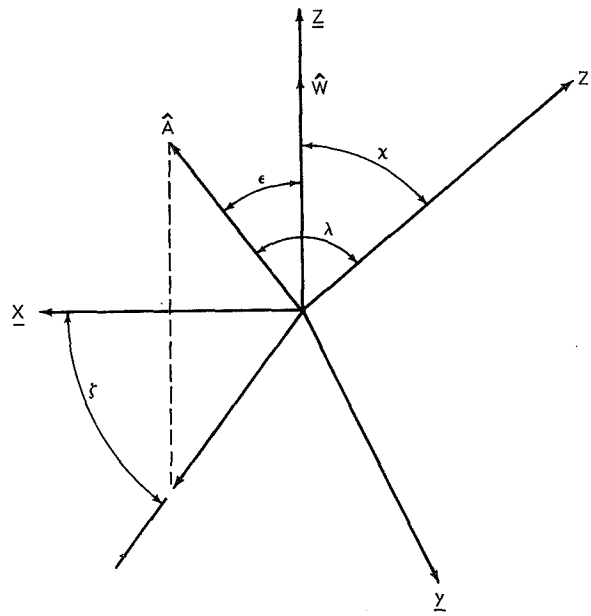

FIGURE C2.—Illustration of the "barred" coordinate system.

The components of the vectors A and ρ are now:

$$\left.\begin{aligned} A_{X'} &= A\cos\mu & \rho_{X'} &= \rho\sin\sigma\cos(\phi-\kappa) \\ A_{Y'} &= A\cos\nu & \rho_{Y'} &= \rho\sin\sigma\sin(\phi-\kappa) \\ A_{Z'} &= A\cos\lambda & \rho_{Z'} &= \rho\cos\sigma \end{aligned}\right\} \cdot \quad \text{(C1)}$$

However, before calculating cos η, we must determine cos μ, cos ν, and cos λ. In Figure C2 we depict the coordinate system $\underline{X}$, $\underline{Y}$, and $\underline{Z}$, used for determining cos λ. The $\underline{Z}$ axis lies along ω; the $\underline{X}$ axis is normal to ω in the $Z'\omega$ plane and the $\underline{Y}$ axis lies along Y'. The $\underline{X}$, $\underline{Y}$, $\underline{Z}$ coordinate system is obtained by a simple rotation of the primed system an angle χ about Y'. When $\zeta=0$, the motion of A is in the positive $\underline{Y}$ direction. This coordinate system meets the specifications as shown in Figure C1: that is,

$$\zeta=0, \quad \lambda=\chi+\epsilon$$
$$\zeta=\pi, \quad \lambda=\chi-\epsilon \text{ for } \epsilon<\chi$$
$$\lambda=\epsilon-\chi \text{ for } \epsilon>\chi.$$

The coordinates of A and Z' are:

$$\left.\begin{aligned} A_{\underline{X}}&=A\sin\epsilon\cos\zeta & Z'_{\underline{X}}&=-Z'\sin\chi \\ A_{\underline{Y}}&=A\sin\epsilon\sin\zeta & Z'_{\underline{Y}}&=0 \\ A_{\underline{Z}}&=A\cos\epsilon & Z'_{\underline{Z}}&=Z'\cos\chi \end{aligned}\right\}. \quad \text{(C2)}$$

Therefore,

$$\cos\lambda=\frac{\boldsymbol{A}\cdot\boldsymbol{Z'}}{AZ'}=\cos\epsilon\cos\chi-\sin\epsilon\sin\chi\cos\zeta. \quad \text{(C3)}$$

In Figure C3 we depict the geometry from which we can determine the angle μ. The coordinate system used is the $\underline{X}$, $\underline{Y}$, $\underline{Z}$ system defined in Figure C2. The coordinates of A and $\boldsymbol{X'}$ are:

$$\left.\begin{aligned} A_{\underline{X}}&=A\sin\epsilon\cos\zeta & X'_{\underline{X}}&=X'\sin\left(\frac{\pi}{2}-\chi\right) \\ A_{\underline{Y}}&=A\sin\epsilon\sin\zeta & X'_{\underline{Y}}&=0 \\ A_{\underline{Z}}&=A\cos\epsilon & X'_{\underline{Z}}&=X'\cos\left(\frac{\pi}{2}-\chi\right) \end{aligned}\right\}. \quad \text{(C4)}$$

Therefore,

$$\cos\mu=\frac{\boldsymbol{A}\cdot\boldsymbol{X'}}{AX'}=\cos\epsilon\sin\chi+\sin\epsilon\cos\chi\cos\zeta. \quad \text{(C5)}$$

Using the condition that the sum of the squares of the direction cosines is equal to unity, we have

$$\cos^2\nu=1-(\cos\epsilon\cos\chi-\sin\epsilon\sin\chi\cos\zeta)^2 -(\cos\epsilon\sin\chi+\sin\epsilon\cos\chi\cos\zeta)^2. \quad \text{(C6)}$$

Squaring and reducing Equation C6 we have

$$\cos\nu=\sin\epsilon\sin\zeta. \quad \text{(C7)}$$

Now, from Equations C3, C5, and C7 we have

$$\cos\eta=\sin\sigma\cos(\phi-\kappa)\cos\mu+\sin\sigma\sin(\phi-\kappa)\cos\nu+\cos\sigma\cos\lambda. \quad \text{(C8)}$$

Expanding Equation C8 we have

$$\begin{aligned}\cos\eta=&\sin\sigma\,(\cos\phi\cos\kappa+\sin\phi\sin\kappa)(\cos\epsilon\sin\chi \\ &+\sin\epsilon\cos\chi\cos\zeta)+\sin\sigma\,(\sin\phi\cos\kappa \\ &-\cos\phi\sin\kappa)\sin\epsilon\sin\zeta \\ &+\cos\sigma\,(\cos\chi\cos\epsilon \\ &-\sin\chi\sin\epsilon\cos\zeta). \end{aligned} \quad \text{(C9)}$$

And in terms of the angle of integration θ we have finally

$$\begin{aligned}\cos\eta=&\frac{\sin\theta}{(r^2+1-2r\cos\theta)^{1/2}}[\cos\phi\cos\kappa\cos\epsilon\sin\chi \\ &+\sin\phi\sin\kappa\cos\epsilon\sin\chi \\ &+\cos\phi\cos\kappa\sin\epsilon\cos\chi\cos\zeta \\ &+\sin\phi\sin\kappa\sin\epsilon\cos\chi\cos\zeta \\ &+\sin\phi\cos\kappa\sin\epsilon\sin\zeta \\ &-\cos\phi\sin\kappa\sin\epsilon\sin\zeta \\ &+\frac{(r-\cos\theta)}{(r^2+1-2r\cos\theta)^{1/2}} \\ &[\cos\epsilon\cos\chi-\sin\epsilon\sin\chi\cos\zeta]. \end{aligned} \quad \text{(C10)}$$

It might be well to point out here that identical results will be obtained by a reflection of the vectors ω and A in a plane normal to ω. It then follows that for any given values of k, χ, and ϵ an entirely equivalent physical picture,

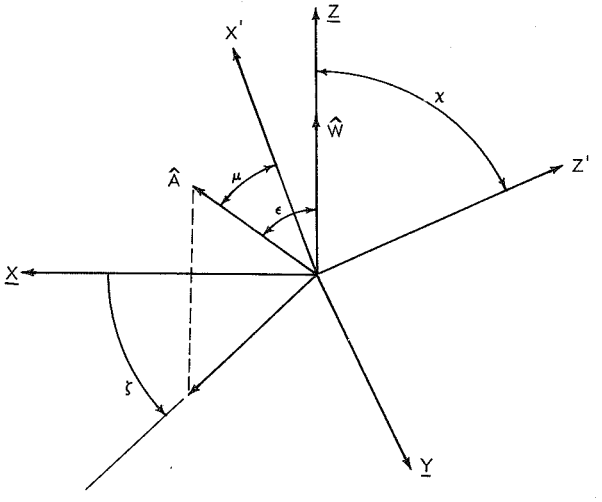

FIGURE C3.—Geometry for determining the angle μ.

is obtained if we replace these values by $(\kappa+\pi)$, $(\pi-\chi)$, and $(\pi-\epsilon)$, respectively. However, this reflection causes the rotation of A about ω to be in the opposite sense from what it was before. The zero point and positive direction of ζ remain the same, but the coordinate system is rotated, so the consequences of the reflection of ω is that the geometrical configuration that was presented at $\zeta=\pi/2$ before reflection is presented at $\zeta=3\pi/2$ after reflection. Consequently, the total number of calculations required to cover the entire range of the parameters χ and ϵ is reduced by a factor of 2. In addition, geometrical changes given by the parameter κ are symmetric about the ***Sr*** plane so that we need not consider any values of κ other than $0\leq\kappa\leq\pi$.

Appendix D

THE CALCULATION OF THE ANGLE γ

To determine the angle γ between the Ar plane and the $r\omega$ plane consider Figure D1. From Appendixes B and C we can write

$$A \sin \lambda \cos \gamma = A \cos \mu. \tag{D1}$$

Here, γ is the angle between the projection of A onto the $X'Y'$ plane and the X' axis (the angle between the Ar and $r\omega$ planes. Obviously, $\phi=(\kappa+\gamma)$ for $0<\zeta<\pi$, and $\phi=(\kappa-\gamma)$ for $\pi<\zeta<2\pi$. Then

$$\cos \gamma = \frac{\cos \epsilon \sin \chi + \sin \epsilon \cos \chi \cos \zeta}{[1-(\cos \chi \cos \epsilon - \sin \chi \sin \epsilon \cos \zeta)^2]^{1/2}}. \tag{D2}$$

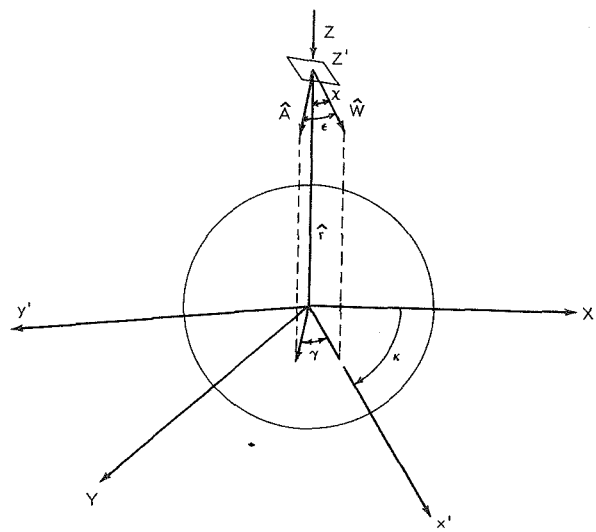

FIGURE D1.—Geometry for determining the angle γ.

764-173 O—65——61

Appendix E

DETERMINATION OF THE PARAMETERS USED IN THIS REPORT IN TERMS OF THE GENERAL ORBITAL PARAMETERS

If we assume the gravitational field to be spherical (that is, to have a $1/r$ potential), then the orbit on an artificial satellite will be an ellipse with the earth at a focus. Such an orbit represented in polar coordinates is

$$r=\frac{a(1-e^2)}{1+e\cos(\psi-B)}, \tag{E1}$$

where

r=the radius vector from the earth's center to the satellite,
a=the semimajor axis of the orbit,
e=the eccentricity of the orbit,
ψ=the azimuthal position of the satellite in orbit measured from some fixed direction in space,
B=the angle between the projection of the solar vector (taken this time to be positive from the earth to the sun) onto the orbital plane and r_p where r_p is the radius vector at perigee.

The angle B, then, serves as one of the angles which determines the orientation of the satellite orbit. The remaining angle δ, which determines the orientation, is defined as the angle between the orbital plane and the solar vector. The zero point of the angle ψ is measured from the projection of the solar vector onto the orbital plane and the positive direction is taken as the direction of motion of the satellite. Hence, the value of r at perigee, r_p, is given by Equation E1 when $(\psi-B)=0$; and likewise the value of r at apogee r_a is given when $(\psi-B)=\pi$.

Since for many purposes the satellite orbit is specified in normal apogee and perigee values we have

$$a=\frac{r_a+r_p}{2}$$

and

$$e=\frac{r_a-r_p}{r_a+r_p}.$$

Figure E1 shows the geometry of the general case. In it the azimuthal angle ψ and the angle δ are clearly shown. The vector $\boldsymbol{r}$ corresponding to $\psi=0$ is called $\boldsymbol{r}'$. The α axis lies in the plane of the orbit along $\boldsymbol{r}'$. The β axis lies in the plane of the orbit normal to $\boldsymbol{r}'$, and the γ axis lies in the $\boldsymbol{Sr}'$ plane normal to $\boldsymbol{r}'$. Then

$$r_\alpha=r\cos\psi \qquad S_\alpha=S\cos\delta,$$
$$r_\beta=r\sin\psi \qquad S_\beta=0,$$
$$r_\gamma=0 \qquad S_\gamma=S\sin\delta,$$

from which we have

$$\cos\theta_s=\cos\psi\cos\delta. \tag{E2}$$

Throughout the body of this report we have made use of a set of parameters defining the orientation of the satellite and its spin axis with respect to a coordinate system whose origin lies in the earth. And, the results of sample calculations for specific values of these parameters are presented in Appendixes F and G. In the following discussions the type of problem presented in Appendix G is used as it represents the most general case.

The values of the parameters there chosen represent only a possible set of the instantaneous values an actual satellite will encounter. A satellite in orbit, whether it is "free" so that its angular momentum vector is constant—apart from external perturbations—or whether its angular momentum is fixed with respect to the earth or fixed with respect to the sun (the latter two conditions being accomplished by

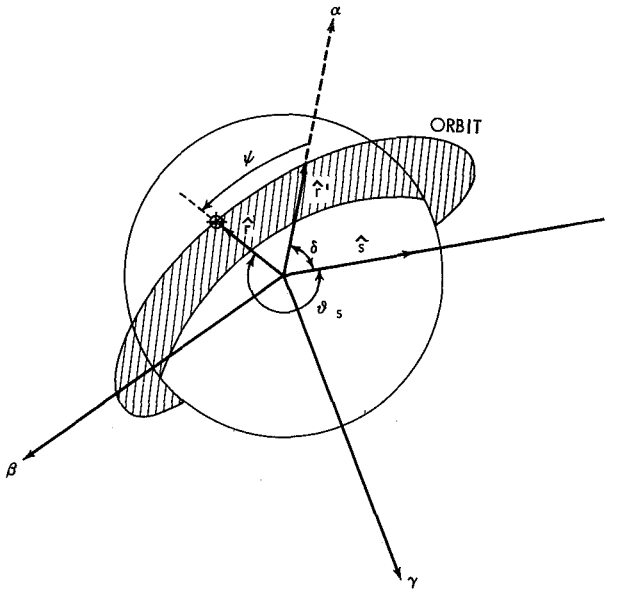

FIGURE E1.—A pictorial representation of the α, γ, β, coordinate system and the satellite orbital parameters.

internal orientational correction mechanisms) will experience instantaneously changing values of the parameters θ_s, χ, and κ. In order to determine these values for any given time, it is necessary to know not only the orientation of the orbit and its parameters but also the angle between the solar vector (now defined to be positive from the satellite to the sun) and the spin axis Γ, and the variation of this angle with time.

Of course, there is nothing sacred about this particular angle insofar as the contents of this paper are concerned. However, the satellite is, after all, only a means of placing scientific instruments in the space environment: For any meaningful interpretation of data it is necessary that the orientation of the satellite be known, and the most readily available and usable reference system is the sun. Consequently, this angle Γ will always be continuously made available as part of the data from the satellite itself. This is not so for some of the parameters used in this work. Since no unique set of parameters exists with which to treat the problem it can always be argued that a rather unfortunate choice was made. However, since this is predominantly a matter of taste the author deems it essential to retain parameters pertaining to the satellite-earth system—the only problem under consideration—in order to minimize the difficulty of the required integrations. And since a solution in closed form may not exist, at least in any form which could be termed reasonable, the usefulness of retaining a parameter (the angle Γ) the functional dependence of which is required but cannot be determined explicitly, is doubtful. It can also be argued that the methods derived herein will be useful not for the purpose of determining the incident energy at every instant (which would scarcely be of interest) but will be useful for determining the upper and lower limits that any particular satellite component can be expected to experience.

As alluded to above, we have three situations with which to deal. The simplest of these from the present point of view is the case of fixed orientation of the spin axis with respect to the satellite-earth line. If $\chi=0$, which for the case under consideration will probably be most often the situation, the problem reduces to the least complicated form. A knowledge of Γ here (though necessary to insure the constancy of χ) is not essential for the solution of our problem. If, however, $\chi\neq 0$ but is constant, the problem is only slightly more complicated because now κ is free to change unless the spin axis is also fixed with respect to the Sr plane (see Fig. C1). This complication is rather trivial, however, and if κ is not fixed, all values will probably be experienced and the maximum and minimum power inputs can be readily determined. The consideration of this point will be left to the reader (a knowledge of Γ may be helpful here).

A more complicated problem presented by an equally likely number of satellites is that for which the spin axis orientation is constant with respect to the sun. Here we need only a functional relation between Γ and χ for various values of the position of the satellite in orbit.

The third situation is the one for which the angular momentum vector is fixed in space (a quite common state of affairs apart from perturbations) and it requires, in addition to the functional relation just mentioned, a func-

tional relation giving the variation of Γ with time of year; and this in turn requires a knowledge of the value of Γ at injection.

We will now derive the most important of these functional relations.

Figure E2 shows the satellite orbit geometry and defines a new coordinate system, the X'', Y'', Z'' system. The X'' axis is coincident with the radius vector r and the Y'' axis lies normal to r in the plane of the orbit. The Z'' axis is normal to the orbital plane and its sense is determined by the direction of motion of the satellite in orbit (normal to the page and toward the reader in Fig. E2). The positive or negative direction of δ is determined by whether S lies above or below the orbital plane (that is, its projection along Z'' is positive if above the orbital plane, or negative if below). In addition, the absolute value of δ need never be taken greater than $\pi/2$.

To determine the relation between Γ and χ we need only determine the components of S and ω (not shown) in the X'', Y'', Z'' system. Using the angle δ as previously defined, we have the components of S:

$$\begin{aligned} S_{X''} &= S \cos\delta \cos\psi, \\ S_{Y''} &= -S \cos\delta \sin\psi, \\ S_{Z''} &= S \sin\delta. \end{aligned} \tag{E3}$$

To determine the components of ω we need to know the angle Δ between ω and the orbital plane and the angle Ω between r and the projection of ω onto the orbital plane. For the case of constant angular momentum, the angle Δ will be constant and equal to its value at injection Δ_0. This does not take into consideration its change due to environmental perturbing effects, but such changes are made available from satellite data. Its value is also taken plus or minus in the same sense as the angle δ. For the possible case where the spin axis is constantly oriented to coincide with the solar vector—either in a plus or minus sense—the angle Δ is equal to $\pm\delta$. In the former instance (when ω is constant in space) the angle Ω is given by

$$\Omega = \Omega_0 - (\psi - B'), \tag{E4}$$

where B' is the value of ψ at injection. If the satellite is injected at perigee $B' \equiv B$. The value Ω_0 of the angle between $\omega \cos\Delta$ and r_0 (where r_0 is the radius vector at injection) is taken positive in the direction of ψ, and Ω is positive in the direction of motion of the satellite: that is, if $\omega \cos\Delta$ is normal to r_0 at injection (tangent to the orbital plane) and in the direction of motion, then $\Omega_0 = \pi/2$; and if $\omega \cos\Delta$ is tangent to r_0 but in the direction opposite to the motion, then $\Omega_0 = 3\pi/2$. In Equation E4, the resulting value of Ω will sometimes be negative but will always correspond to the proper value of Ω measured positive as defined for Ω_0. The angles Δ_0 and Ω_0 defined here are commonly referred to as the angles of yaw and pitch at injection, respectively. Therefore, the components of ω are:

$$\left.\begin{aligned} \omega_{X''} &= \omega \cos\Delta \cos\Omega \\ \omega_{Y''} &= \omega \cos\Delta \sin\Omega \\ \omega_{Z''} &= \omega \sin\Delta \end{aligned}\right\}. \tag{E5}$$

We can now write

$$\begin{aligned} \cos\Gamma = &\cos\delta \cos\psi \cos\Delta \cos\Omega \\ &-\cos\delta \sin\psi \cos\Delta \sin\Omega + \sin\Delta \sin\delta. \end{aligned} \tag{E6}$$

As yet we have not derived an explicit functional relation between Γ and χ. In fact, it should be obvious that since we can determine the X''

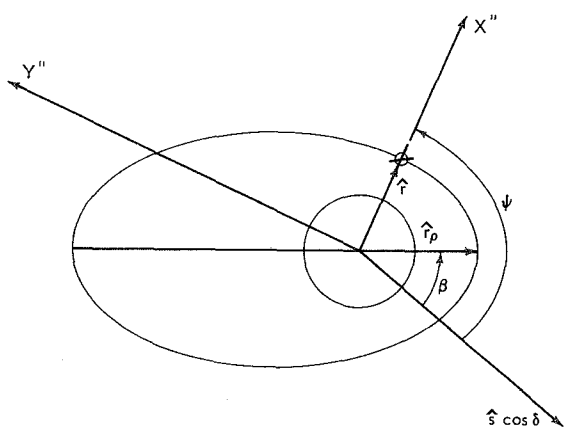

FIGURE E2.—A pictorial representation of satellite orbit and definition of the double primed ('') coordinate system.

component of ω we automatically have the angle between ω and r. From Equation E5 we have

$$\cos \chi' = \cos \Delta \cos \Omega, \tag{E7}$$

where χ' is the angle between ω and r. Remembering that the r used in this appendix is in the opposite sense from the r used in the actual problem (see Fig. E2) we have $\chi = (\pi - \chi')$. The solution of χ' from Equation E7 lies in the range $0 \leq \chi' \leq \pi$. The expression given in Equation E6, then, is not necessary to determine the value of χ. However, in the event that the value of Δ or Ω has changed so that one or the other cannot readily be determined, Equation E6 provides a method for determining the unknown one from a knowledge of Γ which is normally made available.

The value of the angle κ (the angle between the projection of both ω and S onto the plane normal to r, the $Y''Z''$ plane) is now given by

$$\cos \kappa = \frac{(S \sin \theta_s) \cdot (\omega \sin \chi)}{S\omega \sin \theta_s \sin \chi},$$

where $S \sin \theta_s$ and $\omega \sin \chi$ are for the present considered as vectors.

Clearly the Y'' and Z'' components of these vectors are identical to the Y'' and Z'' components of S and ω determined in a different manner above, that is, Equations E3 and E5,

$$(S \sin \theta_s)_{Y''} = -S \cos \delta \sin \psi,$$

$$(S \sin \theta_s)_{Z''} = S \sin \delta,$$

and

$$(\omega \sin \chi)_{Y''} = \omega \cos \Delta \sin \Omega,$$

$$(\omega \sin \chi)_{Z''} = \omega \sin \Delta,$$

so that

$$\cos \kappa = \frac{\sin \delta \sin \Delta - \cos \delta \cos \Delta \sin \Omega \sin \psi}{\sin \theta_s \sin \chi}. \tag{E8}$$

Because of the great length required to discuss the variation of δ, Δ, and Ω as a function of time of year, these considerations will not be included here.

Appendix F

GRAPHIC RESULTS GIVING THE INCIDENT POWER AS A FUNCTION OF THE PARAMETERS r, θ_s, AND λ FOR A REPRESENTATIVE SAMPLE OF THE CASE FOR WHICH ω IS COINCIDENT WITH r

The graphs that follow present the incident energy to a spinning flat plate for the case in which the spin axis is coincident with the satellite-earth line. The results have been calculated to an altitude of 200 km. Each of the four graphs has been calculated for a different value of the parameter θ_s: These values are: $\theta_s=0$, 30, 60, and 90 degrees. On each graph, various curves generated by the parameter λ are given.

Thus far, we have only spoken about the case for which χ, the angle between ω and $\boldsymbol{r}$, is zero. We need not go to the more complicated general case to treat the case given by $\chi=\pi$. The results presented herein are applicable for this latter situation. However, before the values can be found from the graphs, it is necessary to first determine the appropriate values of the parameter λ. To determine the value of λ to which any of the given curves corresponds when $\chi=\pi$, merely subtract the value of λ given on the curve from 180 degrees. Hence, the curve drawn for $\chi=0$ degrees, $\lambda=40$ degrees corresponds to the situation given by $\chi=180$ degrees, $\lambda=140$ degrees. And conversely, to determine the given curve to use for a chosen value of λ and for $\chi=\pi$, merely subtract the desired value of λ from 180 degrees. Hence, the curve to use for $\chi=180$ degrees, $\lambda=80$ degrees is the given curve for $\chi=0$ degrees, $\lambda=100$ degrees.

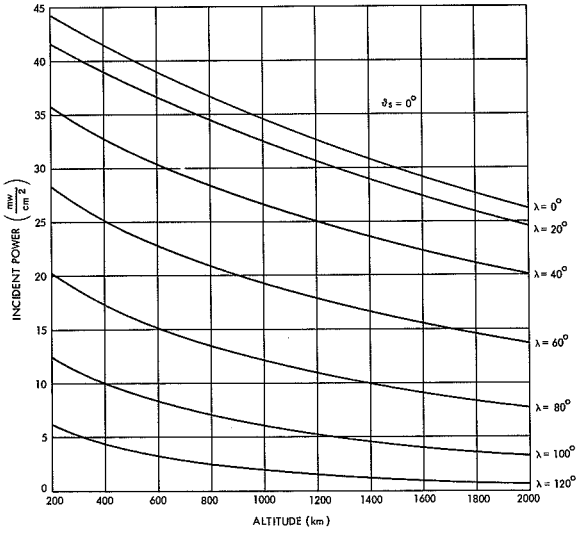

FIGURE F1.—Incident power versus altitude for $\theta_s=0°$.

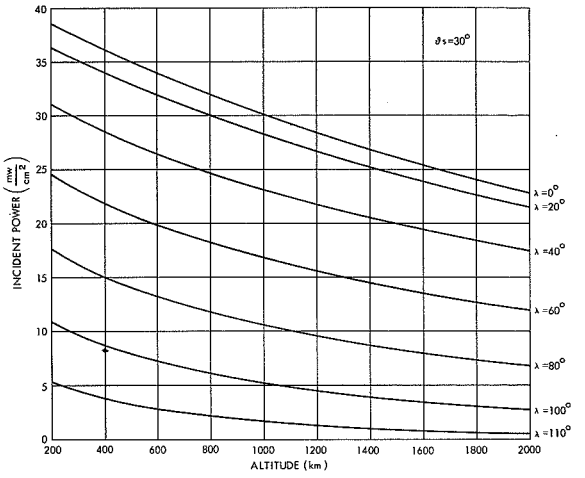

FIGURE F2.—Incident power versus altitude for $\theta_s=30°$.

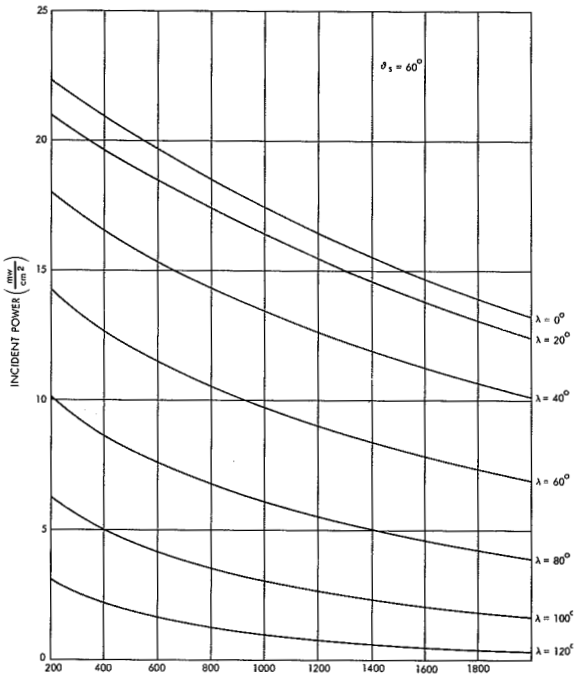

FIGURE F3.—Incident power versus altitude for $\theta_s = 60°$.

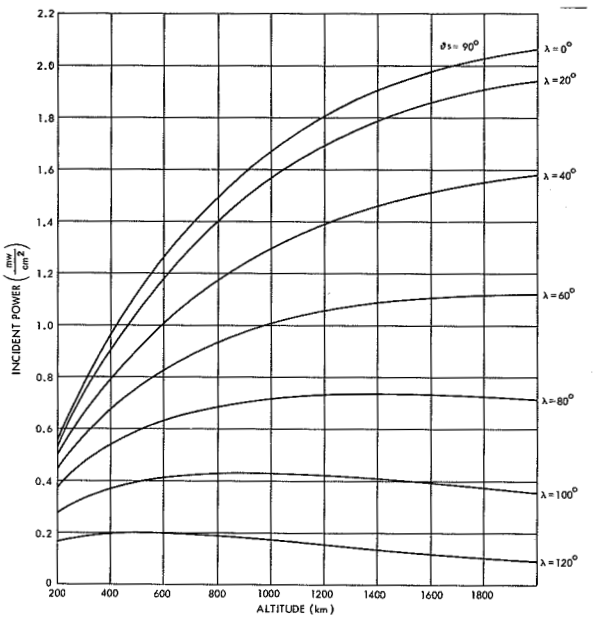

FIGURE F4.—Incident power versus altitude for $\theta_s = 90°$.

Appendix G

GRAPHIC RESULTS GIVING THE INCIDENT POWER AS A FUNCTION OF THE PARAMETERS r, θ_s, κ, , χ AND ϵ FOR A REPRESENTATIVE SAMPLE FOR THE GENERAL CASE

The graph (Fig. G1) contained in this appendix presents the results of an example calculation. The values of the parameters used are: $\chi=60$ degrees, $\theta_s=30$ degrees; $\kappa=0$ degrees and 180 degrees; and $\epsilon=30$ and 60 degrees. The average incident power is plotted as a function of altitude out to 2000 km. This example is included only as an illustration of the method presented in this paper.

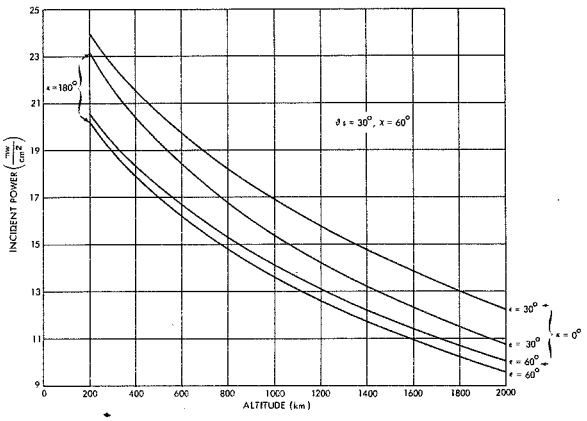

FIGURE G1.—Incident power versus altitude for $\theta_s=30°$, $\chi=60°$.

Appendix H

FORTRAN PROGRAM FOR THE GENERAL CASE

This appendix gives the program (in Fortran notation) for the general case. In addition, the results of a sample problem are given so that the readout format can be seen.

For the evaluation of the double integral, Equation 4 (which give P), and to obtain the average (Equation 8), the following data must be put into the program. All angles are expressed in degrees.

The Fortran listings of the program are given first; the subroutine used by the program is given next. Sample data cards are also listed.

TABLE H1.—*Correspondence of Computer Notation to Analytical Notation*

Computer Notation	Analytic Notation
GL1	κ
THS1	θ_s that is, the first θ_s
THMX	Last θ_s
DTHS	The increment by which the θ_s's are augmented.
THS1	$\theta_s, \theta_s + {}^{\circ}\theta_{s'} \ldots\ldots \theta_{s'} + j\theta_{s'} = \text{THMX}$
S2	$\mathcal{S}$
ALF	α
DX1	The increment of δ
DPHI	The increment by which ϕ is measured
CHI1	χ
EI1	ϵ

FORTRAN IBM 7090 PROGRAM FOR CALCULATIONS OF THE GENERAL CASE

```
 EARTH REFLECTED SOLAR RADIATION FALLING ON SPINNING FLAT PLATE

     DIMENSION P(1000),T(1000),XS(1000),SX(1000),CX(1000),CP(1000),
    1 SP(1000),CTH(1000),STH(1000)
   3 FORMAT (0PF7.4,1P7E15.4)
   4 FORMAT (7E10.5)
   5 FORMAT (1P6E19.7)
1300 FORMAT (1H0,13X,5HKAPPA,16X,3HCHI,12X,7HEPSILON,18X,1HR,12X,7HTHET
    1A S,12X,7HAVERAGE)
1301 FORMAT (1H1,39X,20HKAPPA.....,1PE15.7/40X,20HINITIAL THE
    1TA-S.....,1PE15.7/40X,20HMAX. THETA-S.....,1PE15.7/40X,20HTHETA
    2-S INCREMENT...,1PE15.7/40X,20HS.....,1PE15.7/40X,20
    3HALPHA.....,1PE15.7/4CX,20HDZETA INCREMENT.....,1PE15.7/
    44CX,20HPHI INCREMENT.....,1PE15.7/4CX,20HCHI.....,1P
    5E15.7/4CX,20HEPSILON.....,1PE15.7//)
1302 FORMAT (1H0,3X,I4,43H VALUES OF DOUBLE INTEGRAL FOR GIVEN DZETAS)
     DTR= 1.74532925E-02
     RTD= 1.0/DTR
     PI=3.1415926
     TUPI=PI+PI
     PI2=0.5*PI
     PI4=0.25*PI
   6 READ INPUT TAPE 2,4,GL1,THS1,THMX,DTHS,SZ,ALF,DX1,DPHI,CHI1,EI1
     WRITEOUTPUTTAPE3,1301,GL1,THS1,THMX,DTHS,SZ,ALF,DX1,DPHI,CHI1,EI1
     SAP=ALF*SZ/PI
     THS1=DTR*THS1
     THMX=DTR*THMX
     DTHS=DTR*DTHS
     PGL=GL1
     PCHIL=CHI1
     PEIL=EI1
     CHI1=DTR*CHI1
     EI1=DTR*EI1
     GL1=DTR*GL1
     GLMX=DTR*GLMX
     DGL=DTR*DGL
     DPHI=DTR*DPHI
     DX1=DTR*DX1
     I=0
     X=-DX1
     TUPE=TUPI - DX1
  11 X= X+DX1
     IF (X-TUPE) 12,12,13
  12 I=I+1
     CX(I)=COSF(X)
     SX(I)=SINF(X)
     GO TO 11
  13 IM=I
     FIM=FLOATF(IM)
     I=0
     PHI=-DPHI
  14 PHI=PHI+DPHI
     IF(PHI-TUPI)15,15,16
  15 I=I+1
     CP(I)=COSF(PHI)
     SP(I)=SINF(PHI)
     GO TO 14
```

EARTH REFLECTED SOLAR RADIATION FALLING ON SPINNING FLAT PLATE

```
 16 KM=I
 10 READ INPUT TAPE 2,4,R
    IF (R) 6,6,111
111 GRA= 1.0/R
    R21=R**2+1.0
    THM=ATANF(SQRTF(1.0-GRA**2)/GRA)
    IF (THM) 112,100,100
112 THM=THM + PI
100 IF (THM-PI4) 50,50,51
 50 DTH=THM/26.0
    GO TO 52
 51 DTH=THM/50.0
 52 GL=GL1
    CHIL=CHI1
    EIL=EI1
    I=0
    TH=-DTH
 17 TH=TH+DTH
    IF(TH-THM)18,18,20
 18 I=I+1
    CTH(I)=COSF(TH)
    STH(I)=SINF(TH)
    GO TO 17
 20 JM=I
 31 CL=COSF(GL)
    SL=SINF(GL)
    CCHIL=COSF(CHIL)
    SCHIL=SINF(CHIL)
    CEIL=COSF(EIL)
    SEIL=SINF(EIL)
    THS=THS1
    GO TO 36
 35 THS=THS+DTHS
    IF(THS-THMX)36,36,10
 36 CSTS=COSF(THS)
    SNTS=SINF(THS)
    PTHS=RTD*THS
    DO 1250 I=1,IM
    DO 1100 J=1,JM
    RCTH=R*CTH(J)
    RCTHM1=RCTH-1.0
    R21R=R21-2.0*RCTH
    FAC=STH(J)*RCTHM1/(R21R*R21R)
    CTTHS=CTH(J)*CSTS
    STTHS=STH(J)*SNTS
    SLST=SL*STH(J)
    RMCTHL=R-CTH(J)
    DO 1007 K=1,KM
    CB=CTTHS+STTHS*CP(K)
    IF(CB)1003,1003,1004
1003 P(K)=0.0
    GO TO 1007
1004 CETA=RMCTHL*(CCHIL*CEIL-SCHIL*SEIL*CX(I))+STH(J)*(CP(K)*CL*CEIL*SC
    1HIL + SP(K)*SL*CEIL*SCHIL + CP(K)*CL*SEIL*CCHIL*CX(I) + SP(K)*SL*S
    2EIL*CCHIL*CX(I) + SP(K)*CL*SEIL*SX(I) - CP(K)*SL*SEIL*SX(I))
    IF(CETA)1005,1005,1006
```

EARTH REFLECTED SOLAR RADIATION FALLING ON SPINNING FLAT PLATE

```
1005 P(K)=0.0
     GO TO 1007
1006 P(K)=CB*CETA
1007 CONTINUE
1010 CALL SIMP(P,KM,ANS)
1100 T(J)=ANS*FAC
1200 CALL SIMP(T,JM,ANS)
1250 XS(I)=SAP*ANS*DPHI*DTH/9.0
     TOUT=0.0
     DO 1251 IX=1,IM
1251 TOUT=TOUT+XS(IX)
     AVE=TOUT/FIM
     WRITE OUTPUT TAPE 3,1300
     WRITE OUTPUT TAPE 3,5, PGL,PCHIL,PEIL,R,PTHS,AVE
     WRITE OUTPUT TAPE 3,1302,IM
     WRITE OUTPUT TAPE 3,5, (XS(I2),I2=1,IM)
     GO TO 35
     END(0,0,0,1,0,0,1,0,0,0,0,0,0,0,0)
```

```
     SUBROUTINE SIMP(P,K,ANS)

     SUBROUTINE SIMP(P,K,ANS)
     DIMENSION P(1000)
1010 IEND=K-1
     SUM=0.0
     DO 1011 IX=2,IEND,2
1011 SUM=SUM+P(IX)
     IEND=IEND-1
     SUM2=0.0
     DO 1012 IX=3,IEND,2
1012 SUM2=SUM2+P(IX)
     ANS=P(1)+P(K)+4.0*SUM+2.0*SUM2
     RETURN
     END(0,0,0,1,0,0,1,0,0,0,0,0,0,0,0)
```

Kappa	1.8000000E 02
Initial theta—*S*	3.0000000E 01
Max. theta—*S*	3.0010000E 01
Theta—*S* increment	3.0000000E 01
S	1.3950000E 02
Alpha	3.4000000E−01
Dzeta increment	1.0000000E 01
Phi increment	1.0000000E 00
Chi	5.9999999E 01
Epsilon	3.0000000E 01

Kappa	*Chi*	*Epsilon*	R	*Theta* S	*Average*
1.8000000E 02	5.9999999E 01	3.0000000E 01	1.0314000E 00	2.9999999E 01	2.3202087E 01

36 Values of double integral for given dzetas

1.3761604E 01	1.3888321E 01	1.4266056E 01	1.4886069E 01	1.5734338E 01	1.6792933E 01
1.8043202E 01	1.9480528E 01	2.1106825E 01	2.2781268E 01	2.4476020E 01	2.6184151E 01
2.7816340E 01	2.9400020E 01	3.0794582E 01	3.1967988E 01	3.2874174E 01	3.3444360E 01
3.3639385E 01	3.3444357E 01	3.2874168E 01	3.1967979E 01	3.0794570E 01	2.9400007E 01
2.7816328E 01	2.6184139E 01	2.4476009E 01	2.2781258E 01	2.1106816E 01	1.9480520E 01
1.8043196E 01	1.6792928E 01	1.5734336E 01	1.4886067E 01	1.4266054E 01	1.3888320E 01

SAMPLE PROBLEM AND RESULT FORMAT

Appendix I

ENERGY DISTRIBUTION PREDICTED FOR THE PROPOSED ECHO II SATELLITE

This appendix presents a graph (Figure I1) showing the distribution of albedo energy on the proposed Echo II satellite. The satellite is assumed stationary at an altitude of 700 nautical miles. In this case, the angle λ designates the angle between the normal to the surface area of the sphere and the satellite-earth line. The azimuthal average input to a zone lying between λ and $(\lambda+d\lambda)$, is identical to the average input to a flat plate of elemental area spinning about the satellite-earth line at an angle λ. The average incident power is plotted as a function of λ for various values of the parameter θ_s.

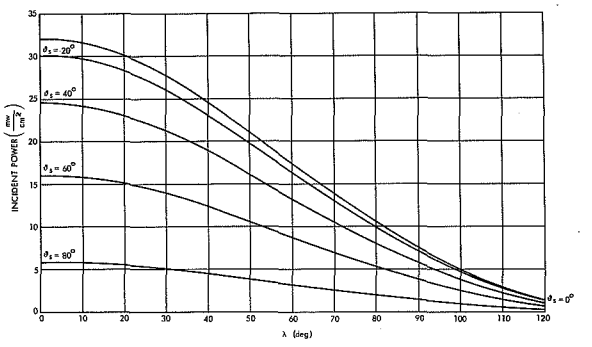

FIGURE I1.—Prediction of the distribution of incident albedo energy on the Echo II ($R=700$ nautical miles) satellite for various values of θ_s.

POWER INPUT TO A SMALL FLAT PLATE FROM A DIFFUSELY RADIATING SPHERE WITH APPLICATION TO EARTH SATELLITES: THE SPINNING PLATE

FRED G. CUNNINGHAM

Goddard Space Flight Center

A general derivation is presented for the radiation from a uniformly radiating sphere incident on a small flat plate, spinning about an axis not coincident with its normal. The results are presented as a function of the separation of the bodies, the orientation of the plate, and the orientation of the spin axis. In addition, a series of curves is given which represents the power input from earth radiation to one side of a spinning flat plate (averaged over a spin period) for a range of altitude from 200 to 32000 km. These curves are based upon the assumption that the earth is a uniform diffuse emitter radiating as a blackbody at a temperature of 250°K.

INTRODUCTION

In a previous paper[1] (Part I) the power input to a stationary flat plate was calculated. The present paper will apply these results to the problem of the spinning plate in order to determine the instantaneous earth-radiated power incident upon the solar cell paddles associated with the various satellites. This analysis does not consider any shielding of the paddles by other paddles or by the body of the satellite itself.

In the previous paper we defined three cases for which the limits of integration were easily determinable. These were dependent upon the value of the angle between the normal to the plate and the earth-satellite line. For a spinning plate, however, this simplification is not possible since a spinning plate whose axis of spin is not coincident with the normal to the plate defines a varying angle between the normal and the earth-satellite line.

In general, a free rigid body whose axis of spin does not coincide with a principal axis exhibits, to an external observer, a precession of the spin axis about the angular momentum vector and a precession of the axis of symmetry (in this case the normal) about the spin axis, so that both the axis of symmetry and the axis of spin appear to precess about the angular momentum vector. However, since we are considering plates attached to larger satellite bodies which usually spin about their axis of symmetry (also a principal axis), the spin axis coincides with the angular momentum vector and the net result is simply a precession of the normal about the spin axis. The main assumption here is that the satellite's spin axis deviates no more than slightly from its axis of symmetry and hence, possesses a negligible amount of precessional motion.

From the aforementioned paper, we can write the general expression for the instantaneous power input to a stationary flat plate as

$$P=\frac{2\Lambda\epsilon\alpha A}{\pi}\int_{\phi}\int_{\psi}(\cos\lambda\cos\phi + \sin\lambda\sin\phi\cos\psi)\sin\phi d\phi d\psi \quad (1)$$

[1] Cunningham, F. G., "Power Input to a Small Flat Plate from a Diffusely Radiating Sphere with Application to Earth Satellites", NASA Technical Note D-710 (Corrected copy), August 1961.

where:

Λ=the generalized emittance of the surface (or $\sigma\tau^4$ for thermal radiation);
ϵ=the emissivity of the surface of the radiating sphere;
α=the absorptivity of the plate;
$\boldsymbol{A}$=the elemental vector area of the plate;
ϕ=the angle defining the position from the earth-satellite line of the radiating element ds on the disk replacing the sphere;
ψ=the azimuthal designation of the element ds; and
λ=the angle between the normal to the plate and the earth-satellite line.

The upper limit of the ϕ integration is given by $\phi_m=\sin^{-1}(1/H)$ where $\boldsymbol{H}$ is the earth-satellite vector, and H is given in units of mean earth radii. The upper limit of the ψ integration is determined by the conditions governing the three previously mentioned cases:

$$(1)\ 0\leq\lambda\leq(\pi/2-\phi_m)$$

$$(2)\ (\pi/2-\phi_m)<\lambda\leq\pi/2$$

$$(3)\ \pi/2<\lambda\leq(\pi/2+\phi_m).$$

In the first case the upper limit of ψ is π for all ϕ, and in the second case the upper limit is π for $0\leq\phi\leq(\pi/2-\lambda)$. For the remaining portion of the second case and for all of the third case the upper limit of ψ is given by

$$\cos\psi_m=\frac{-\cos\lambda\cos\phi}{\sin\lambda\sin\phi}. \qquad (2)$$

EXTENSION OF THE METHOD TO A SPINNING PLATE

The flat plate whose spin axis ω passes through the center of mass but is not coincident with the normal $\boldsymbol{A}$ is shown in Figure 1, where

$\boldsymbol{H}$=the earth-satellite vector;
a=the angle between $\boldsymbol{A}$ and $\boldsymbol{\omega}$;
b=the angle between $\boldsymbol{H}$ and $\boldsymbol{\omega}$.

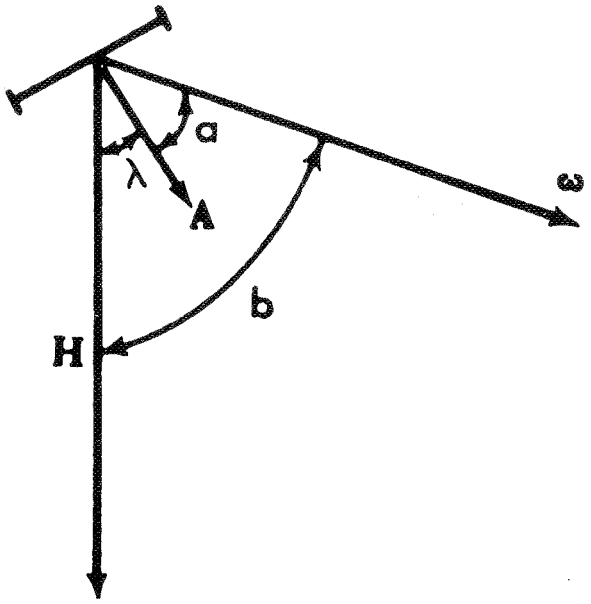

FIGURE 1.—Geometry showing the orientation of the spin axis and normal to the plate.

We now define a new angle ζ as the aximuthal angle of spin of the plate about ω; i.e., $\omega=d\zeta/dt$. Figure 1 shows the zero value of the spin angle ζ for the values of a and b shown. In general the zero value of ζ is defined when $\boldsymbol{A}$ lies in the $\boldsymbol{H}$, $\boldsymbol{\omega}$ plane and λ is a minimum. Because of symmetry we need not consider ζ outside the range $0\leq\zeta\leq\pi$. In addition, $\boldsymbol{\omega}$ is assumed to be constant and of sufficient magnitude so that we need not consider a time weighted average over the angle ζ to determine the average power input over the spin period, which is our ultimate goal.

We shall consider the vectors $\boldsymbol{\omega}$, $\boldsymbol{H}$ and $\boldsymbol{A}$ as unit vectors. Figure 2 shows the general orientation of the spinning plate, where the ends of the vectors $\boldsymbol{\omega}$, $\boldsymbol{H}$ and $\boldsymbol{A}$ lie on the surface of a unit sphere. With the above definitions, we can employ spherical trigonometry to determine λ. Clearly,

$$\cos\lambda=\cos a\cos b+\sin a\sin b\cos\zeta. \qquad (3)$$

By inserting Equation 3 into Equation 1, we have

$$P=\frac{2\Lambda\epsilon\alpha A}{\pi}\int_\phi\int_\psi(\cos a\cos b+\sin a\sin b\cos\zeta)\sin\phi\cos\phi d\phi d\psi$$

$$+\frac{2\Lambda\epsilon\alpha A}{\pi}\int_\phi\int_\psi[1-(\cos a\cos b+\sin a\sin b\cos\zeta)^2]^{1/2}\cos\psi\sin^2\phi d\phi d\psi. \quad (4)$$

The upper limit of the ψ integration as given by Equation 2 becomes

$$\cos\psi_m=\frac{-(\cos a\cos b+\sin a\sin b\cos\zeta)\cos\phi}{[1-(\cos a\cos b+\sin a\sin b\cos\zeta)^2]^{1/2}\sin\phi} \quad (5)$$

and

$$\sin\psi_m=\left\{\frac{\sin^2\phi-(\cos a\cos b+\sin a\sin b\cos\zeta)^2}{[1-(\cos a\cos b+\sin a\sin b\cos\zeta)^2]\sin^2\phi}\right\}^{1/2}. \quad (6)$$

However, as pointed out in the earlier paper, there are values of ϕ for which the argument of Equation 5 is greater than unity although λ lies within the proper bounds; for this situation $\psi_m=\pi$. The values of ϕ in question are listed on page 2. A complete discussion of the values of ϕ and λ for which Equations 5 and 6 are applicable will be presented subsequently.

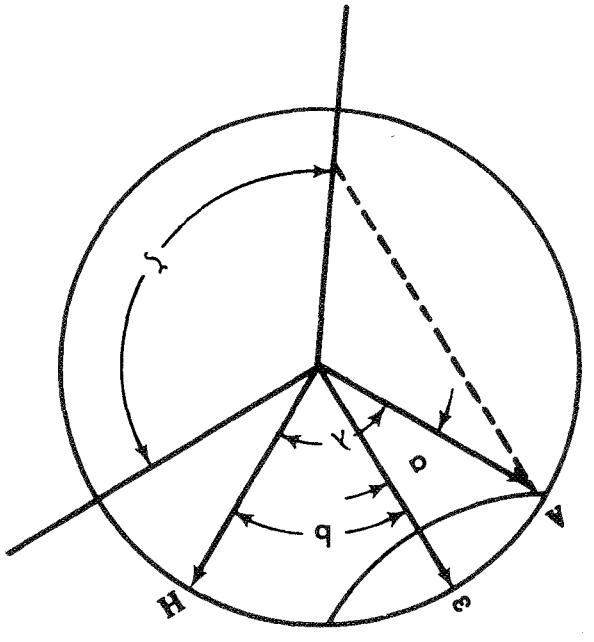

FIGURE 2.—Unit sphere from which the angle λ can be calculated.

Performing the ψ integration of Equation 4 we have:

$$P=\frac{2\Lambda\epsilon\alpha A}{\pi}\int_0^{\phi_m}(\cos a\cos b+\sin a\sin b\cos\zeta)\psi_m\sin\phi\cos\phi d\phi$$

$$+\frac{2\Lambda\epsilon\alpha A}{\pi}\int_0^{\phi_m}[1-\cos a\cos b+\sin a\sin b\cos\zeta)^2]^{1/2}\sin\psi_m\sin^2\phi d\phi. \quad (7)$$

In the regions where Equations 5 and 6 apply we have,

$$P=\frac{2\Lambda\epsilon\alpha A}{\pi}\int_0^{\phi_m}(\cos a\cos b+\sin a\sin b\cos\zeta)\cos^{-1}$$

$$\left\{\frac{-(\cos a\cos b+\sin a\sin b\cos\zeta)\cos\phi}{[1-(\cos a\cos b+\sin a\sin b\cos\zeta)^2]^{1/2}\sin\phi}\right\}$$

$$\sin\phi\cos\phi d\phi+\frac{2\Lambda\epsilon\alpha A}{\pi}\int_0^{\phi_m}[\sin^2\phi-(\cos a$$

$$\cos b+\sin a\sin b\cos\zeta)^2]^{1/2}\sin\phi d\phi. \quad (8)$$

The values of λ which define the upper bounds of the regions of interest are $\lambda=\pi/2-\phi_m$, $\pi/2$, $\pi/2+\phi_m$, for which the corresponding ζ (for a given a and b) can be determined. These ζ are defined as follows:

$$\cos\zeta_1=\frac{\sin\phi_m-\cos a\cos b}{\sin a\sin b}, \text{ for } \lambda=\pi/2-\phi_m; \quad (9a)$$

$$\cos\zeta'=\frac{-\cos a\cos b}{\sin a\sin b}, \text{ for } \lambda=\pi/2; \quad (9b)$$

$$\cos \zeta_2 = \frac{-(\sin \phi_m + \cos a \cos b)}{\sin a \sin b}, \text{ for } \lambda = \pi/2 + \phi_m. \tag{9c}$$

Equation 8 gives the instantaneous power on a spinning flat plate as a function of the altitude (from the upper limit of the ϕ integration), the angle between the instantaneous spin axis and the normal to the plate a, the angle between the instantaneous spin axis and the earth-satellite line b, and the azimuthal angle of spin ζ about the spin axis ω. In the equation the arc cosine factor in the first term and the square root factor in the second term arise from the ψ integration; the first corresponds to ψ_m and the second to sin ψ_m. The arguments of these two factors contain functions of ϕ, and functions of a, b, and ζ. These latter factors arise from the value of cos λ given by Equation 3. In the previous paper the value of λ was assumed to be constant and calculations were made in the appropriate range for various values of λ. In that case it was shown that for certain values of λ the range of integration over ϕ had to be divided into two subdivisions, for the first $\psi_m = \pi$ and the absolute value of the argument of the arc cosine factor is greater than unity, and for the second, ψ_m is less than π and the correct value is given by the arc cosine factor. In fact, since λ was held constant, it was possible to define the limiting value of the ϕ integration which depended upon λ, and hence, to break the integral into its parts—only one of which contained the arc cosine factor as an upper limit. However, in the present discussion we are considering the plate as it spins about an arbitrarily oriented axis. Consequently, it follows from Equation 3 that λ is no longer constant in time but varies with ζ for the constant angles a and b. Then, in order to define the limiting values of the ϕ integration we must make use of the dependence of λ upon ζ where the corresponding limiting values of ζ are given by Equation 9.

As mentioned previously, a plate spinning about an axis not coincident with its normal (which is a principal axis) exhibits a wobbly motion as the axis of symmetry (the normal) precesses about the axis of spin. Before, we were able to hold λ within the range for which the power is incident upon the side of the plate in question. The upper limit of this range is given by Equation 9c. When the combination of the angles a, b, and ζ is such that λ, as given by Equation 3, is greater than $\pi/2 + \phi_m$ then the side of the plate under consideration is not visible from the earth, and the incident power is zero.

Clearly we can define three distinct combinations of the angles a and b:

$$(1)\ \lambda \leq (\pi/2 - \phi_m) \text{ for } 0 \leq \zeta \leq \pi; \tag{10a}$$

$$(2)\ 0 \leq \lambda \leq (\pi/2 + \phi_m) \text{ for } 0 \leq \zeta \leq \zeta_2; \tag{10b}$$

$$(3)\ \lambda > (\pi/2 + \phi_m) \text{ for } 0 \leq \zeta \leq \pi. \tag{10c}$$

Equation 10c defines the situation with no radiation incident on the side of the plate in question; and is of no further interest here. The condition defined in Equation 10a is the least complicated expression, integrable over ζ, for the power because the upper limit of the ψ integration is π for all values of ϕ in the range $0 \leq \phi \leq \phi_m$. The general case is represented by Equation 10b where we intend to imply that, over the range of ζ from 0 to π, the value of λ might be less than $\pi/2 - \phi_m$ for certain values of ζ, greater than $\pi/2 - \phi_m$ but less than $\pi/2 + \phi_m$ for other values of ζ, and greater than $\pi/2 + \phi_m$ for still other values of ζ, or any other variation on the theme.

Equation 8 is the expression which must be integrated over ϕ. It is identical to the equation in Part I except that the corresponding expressions involving a, b, and ζ for cos λ and sin λ are included. Before attempting to calculate a given problem we must first examine the range of values of λ (given by Equation 3) to determine the ranges of ζ which are of interest. After the ϕ integration it then becomes necessary to average over ζ, being careful to keep the appropriate range of ζ coupled to the proper expression.

For the case where Equation 10a applies, Equation 8 integrates to

$$P = 2\Lambda\epsilon\alpha A \int_0^{\sin^{-1}(1/H)} (\cos a \cos b + \sin a \sin b \cos \zeta) \sin \phi \cos \phi d\phi, \tag{11}$$

which becomes

$$P=\frac{\Lambda\epsilon\alpha A}{H^2}(\cos a\cos b+\sin a\sin b\cos\zeta). \quad (12)$$

Equation 12 is identical to the expression given as P_1 in Part I. We indicate the average over ζ by $\langle P\rangle_\zeta$ which is

$$\langle P\rangle_\zeta=\frac{\Lambda\epsilon\alpha A}{H^2}\left(\cos a\cos b+\frac{\sin a\sin b}{\pi}\int_0^\pi\cos\zeta d\zeta\right) \quad (13)$$

$$=\frac{\Lambda\epsilon\alpha A}{H^2}\cos a\cos b. \quad (14)$$

The most general integral expression for the case of Equation 10b is:

$$P=2\Lambda\epsilon\alpha A\int_0^{\sin^{-1}(1/H)}(\cos a\cos b+\sin a\sin b\cos\zeta)\sin\phi\cos\phi d\phi$$

$$\left\{0\le\zeta\le\cos^{-1}\left[\frac{\frac{1}{H}-\cos a\cos b}{\sin a\sin b}\right]\right\}$$

$$+2\Lambda\epsilon\alpha A\int_0^{\pi/2-\cos^{-1}(\cos a\cos b+\sin a\sin b\cos\zeta)}(\cos a\cos b+\sin a\sin b\cos\zeta)\sin\phi\cos\phi d\phi$$

$$+\frac{2\Lambda\epsilon\alpha A}{\pi}\int_{\pi/2-[\cos^{-1}(\cos a\cos b+\sin a\sin b\cos\zeta)]}^{\sin^{-1}(1/H)}(\cos a\cos b+\sin a\sin b\cos\zeta)$$

$$\cos^{-1}\left\{\frac{-(\cos a\cos b+\sin a\sin b\cos\zeta)\cos\phi}{[1-(\cos a\cos b+\sin a\sin b\cos\zeta)^2]^{1/2}\sin\phi}\right\}\sin\phi\cos\phi d\phi$$

$$\left\{\cos^{-1}\left[\frac{-\cos a\cos b+\frac{1}{H}}{\sin a\sin b}\right]<\zeta\le\cos^{-1}\left(\frac{-\cos a\cos b}{\sin a\sin b}\right)\right\}$$

$$+\frac{2\Lambda\epsilon\alpha A}{\pi}\int_{\pi/2-[\cos^{-1}(\cos a\cos b+\sin a\sin b\cos\zeta)]}^{\sin^{-1}(1/H)}[\sin^2\phi-(\cos a\cos b+\sin a\sin b\cos\zeta)^2]^{1/2}\sin\phi d\phi$$

$$+\frac{2\Lambda\epsilon\alpha A}{\pi}\int_{\cos^{-1}(\cos a\cos b+\sin a\sin b\cos\zeta)-\pi/2}^{\sin^{-1}(1/H)}(\cos a\cos b+\sin a\sin b\cos\zeta)$$

$$\cos^{-1}\left\{\frac{-(\cos a\cos b+\sin a\sin b\cos\zeta)\cos\phi}{[1-(\cos a\cos b+\sin a\sin b\cos\zeta)^2]^{1/2}\sin\phi}\right\}\sin\phi\cos\phi d\phi$$

$$\left\{\cos^{-1}\left(\frac{-\cos a\cos b}{\sin a\sin b}\right)<\zeta\le\cos^{-1}\left[\frac{-\cos a\cos b-\frac{1}{H}}{\sin a\sin b}\right]\right\}$$

$$+\frac{2\Lambda\epsilon\alpha A}{\pi}\int_{\cos^{-1}(\cos a\cos b+\sin a\sin b\cos\zeta)-\pi/2}^{\sin^{-1}(1/H)}[\sin^2\phi-(\cos a\cos b+\sin a\sin b\cos\zeta)^2]^{1/2}\sin\phi d\phi. \quad (15)$$

Equation 15 integrates out exactly as Equations 21 and 35 of Part I except that we have replaced the cosine λ and sine λ factors by their equivalents in terms of a, b, and ζ. We now have:

$$P=\frac{\Lambda\epsilon\alpha A}{H^2}(\cos a\cos b+\sin a\sin b\cos\zeta)\qquad\{0\leq\zeta\leq\zeta_1\}$$

$$+\frac{\Lambda\epsilon\alpha A}{\pi}\left[\frac{\pi}{2}-\sin^{-1}\left\{\frac{(H^2-1)^{1/2}}{H[1-(\cos a\cos b+\sin a\sin b\cos\zeta)^2]^{1/2}}\right\}\right.$$

$$+\frac{1}{H^2}\Big((\cos a\cos b+\sin a\sin b\cos\zeta)\cos^{-1}\left\{\frac{-(H^2-1)^{1/2}(\cos a\cos b+\sin a\sin b\cos\zeta)}{[-(\cos a\cos b+\sin a\sin b\cos\zeta)^2]^{1/2}}\right\}$$

$$\left.-(H^2-1)^{1/2}[1-H^2(\cos a\cos b+\sin a\sin b\cos\zeta)^2]^{1/2}\Big)\right]\qquad\{\zeta_1<\zeta\leq\zeta'\}$$

$$+\frac{\Lambda\epsilon\alpha A}{\pi}\left[\frac{\pi}{2}-\sin^{-1}\left\{\frac{(H^2-1)^{1/2}}{H[1-(\cos a\cos b+\sin a\sin b\cos\zeta)^2]^{1/2}}\right\}\right.$$

$$+\frac{1}{H^2}\Big(-(H^2-1)^{1/2}[1-H^2(\cos a\cos b+\sin a\sin b\cos\zeta)^2]^{1/2}$$

$$+(\cos a\cos b+\sin a\sin b\cos\zeta)$$

$$\left.\cos^{-1}\left\{\frac{-(H^2-1)^{1/2}(\cos a\cos b+\sin a\sin b\cos\zeta)}{[1-(\cos a\cos b+\sin a\sin b\cos\zeta)^2]^{1/2}}\right\}\Big)\right].\qquad\{\zeta'<\zeta\leq\zeta_2\}\quad(16)$$

where the expression in parentheses following certain terms in Equations 15 and 16 indicates the range of ζ over which the preceding terms are applicable. Because of the complexity of some of the terms in Equation 16 the average over ζ cannot be easily calculated in closed form so that this portion of the problem will be left to the digital computer.

Equation 16 applies in its entirety only to the situation for which λ does, indeed, have values within all three regions defined by $0\leq\lambda\leq(\pi/2-\phi_m)$, $(\pi/2-\phi_m)<\lambda\leq\pi/2$, and $\pi/2<\lambda\leq(\pi/2+\phi_m)$ each of which corresponds to a particular range of values of ζ as ζ goes from 0 to π. If λ does not take on values in all the regions for the entire range of ζ certain modifications of Equation 16 must be made which are pointed out subsequently. To determine which parts of Equation 16 to use and the corresponding limits for any case, we must examine the range of λ for that case by checking its extremes. Since A precesses about ω at a constant angle a, the extremes can be determined by considering the cases when A lies in the H, ω plane; i.e., when $\zeta=0$, π. The only additional requirement is that $\lambda\leq\pi$. In defining values of a and b it suffices that if we let b lie in the range $0\leq b\leq\pi$, we need only consider a in the range $0\leq a\leq\pi/2$. For example, the situation represented by $a=100°$, $b=10°$ is identically represented by the situation $b=170°$, $a=80°$. The direction of ω, and consequently the value of b, is always determined by the right-hand rule. It also follows that interchanging the values of a and b does not alter the problem. In addition, if we wish to determine the input to the other side of the plate (called side β) after having determined it for one side (called side α), by the methods outlined above, the extremes of the range of λ for side β can be easily calculated by subtracting the limits for side α from 180 degrees. Then, once the extremes of λ_β are known, it is quite easy to construct the corresponding values of a and b which, used in conjunction with Equation 3, will allow for the determination of all the parameters of the new problem. For example, if $a=80°$, $b=170°$, for side α, we have that $90°\leq\lambda\leq110°$; whereas $70°\leq\lambda\leq90°$ for side β. The latter set corresponds to $b=10°$, $a=80°$ or $a=10°$, $b=80°$.

We now outline the various possibilities of the general case represented by Equation 10b. But first we shall make the following definitions for simplicity:

$$A=\frac{\Lambda\epsilon\alpha A}{H^2}\,[\cos a\cos b+\sin a\sin b\cos\zeta], \tag{17a}$$

and

$$B=\frac{\Lambda\epsilon\alpha A}{\pi}\left[\frac{\pi}{2}-\sin^{-1}\left\{\frac{(H^2-1)^{1/2}}{H[1-(\cos a\cos b+\sin a\sin b\cos\zeta)^2]^{1/2}}\right\}\right.$$
$$+\frac{1}{H^2}\left((\cos a\cos b+\sin a\sin b\cos\zeta)\cos^{-1}\left\{\frac{-(H^2-1)^{1/2}(\cos a\cos b+\sin a\sin b\cos\zeta)}{[1-(\cos a\cos b+\sin a\sin b\cos\zeta)^2]^{1/2}}\right\}\right.$$
$$\left.\left.-(H^2-1)^{1/2}[1-H^2(\cos a\cos b+\sin a\sin b\cos\zeta)^2]^{1/2}\right)\right]. \tag{17b}$$

Equation 16 can now be written in symbolic form:

$$P=A(0\leq\zeta\leq\zeta_1)+B(\zeta_1<\zeta\leq\zeta')+B(\zeta'<\zeta\leq\zeta_2). \tag{18}$$

The first step in any problem is to determine the range of λ. We shall define three cases:

$$\lambda\leq\pi/2 \text{ for all } \zeta; \tag{19a}$$

$$\lambda\gtrless\pi/2 \text{ for suitable values of } \zeta \text{ in the range } 0\leq\zeta\leq\pi; \tag{19b}$$

$$\lambda>\pi/2 \text{ for all } \zeta. \tag{19c}$$

In 19a the only value of ζ of concern is that for which $\lambda=\pi/2-\phi_m$ or $\zeta=\zeta_1$ as given by Equation 9a. If for a given value of H the argument of the arc cosine in 9a is greater than $+1$ then $\lambda>(\pi/2-\phi_m)$ for all ζ and Equation 16 reduces to

$$P=B(0\leq\zeta\leq\pi). \tag{20}$$

If, for a given value of H, the argument of the arc cosine in Equation 9a is greater than or equal to -1 but less than or equal to $+1$, so that Equation 9a defines the value of ζ at which $\lambda=(\pi/2-\phi_m)$, then Equation 16 becomes

$$P=A(0\leq\zeta\leq\zeta_1)+B(\zeta_1<\zeta\leq\pi). \tag{21}$$

However, if for a given value of H the argument of the arc cosine term in 9a is less than -1, then $\lambda<(\pi/2-\phi_m)$ for all ζ and Equation 16 becomes

$$P=A(0\leq\zeta\leq\pi), \tag{22}$$

which, when averaged over ζ, yields Equation 14 once again.

From 19b it immediately follows that λ can never be less than $(\pi/2-\phi_m)$ or greater than $(\pi/2+\phi_m)$ for all ζ. Equations 9a and 9c define the limits of ζ in question. In the preceding statement, the fact that the value of the argument of the arc cosine in 9a can never be less than -1 and that the value of the argument of the arc cosine in 9c can never be greater than $+1$ can easily be shown for any problem satisfying the conditions of 19b. If the argument of the arc cosine in 9a is greater than or equal to -1 but less than or equal to $+1$ and the argument of the arc cosine in 9c is less than -1, Equation 16 reduces to

$$P=A(0\leq\zeta\leq\zeta_1)+B(\zeta_1\leq\zeta\leq\pi). \tag{23}$$

If both the arguments of the arc cosines in 9a and 9c lie between $+1$ and -1 we then have Equation 16. If the argument of the arc cosine in 9a is greater than $+1$ while the argument of the arc cosine of 9c lies between $+1$ and -1, Equation 16 becomes

$$P=B(0\leq\zeta\leq\zeta_2). \tag{24}$$

Finally, if the argument of the arc cosine in 9a is greater than $+1$ while the argument of the arc cosine in 9c is less than -1, Equation 16 reduces to

$$P=B(0\leq\zeta\leq\pi). \tag{25}$$

In 19c the only value of ζ of concern is that for which $\lambda=\pi/2+\phi_m$ or $\zeta=\zeta_2$ as given by Equation 9c. If the argument of the arc cosine in 9c is less than -1, $\lambda<(\pi/2+\phi_m)$ for all ζ and Equation 16 becomes

$$P=B(0\leq\zeta\leq\pi). \tag{26}$$

If the argument of the arc cosine of 9c lies between $+1$ and -1, the value of ζ_2 is defined and Equation 16 is

$$P=B(0\leq\zeta\leq\zeta_2). \tag{27}$$

If the argument of the arc cosine of 9c is greater than $+1$ then $\lambda>(\pi/2+\phi_m)$ for all ζ, and the corresponding power input is zero.

DISCUSSION

Equation 16 is general and applies to any sort of diffusely radiating sphere. However, in the following calculations we are considering the diffusely radiating sphere to be the earth which radiates as a blackbody at a temperature approximately equal to 250°K. Thus

$$A\epsilon=\sigma T_0^4, \tag{28}$$

where ϵ equals unity because of the equivalent blackbody approximation and α is taken equal to unity in order to give the energy incident upon the plate. In addition, Equation 16 can be modified to give directly the incident power to the plate as a function of the orbital position of the satellite by giving H as a function of the orbital parameters and the azimuthal position of the satellite in orbit. This can be done by utilizing the polar equation of an ellipse,

$$H=\frac{\alpha(1-e^2)}{1+e\cos\eta}, \tag{29}$$

where η is the angle giving the azimuthal position of the satellite from perigee, α is the semi-major axis and e is the eccentricity. However, in the subsequent evaluations of Equation 16 this additional information will not be included besause the presence of the arc cosine factor in the equation renders it almost impossible to write, in terms of the orbital parameters, the equation in closed form (after averaging over ζ) so that not a great deal is to be gained unless we wish the computer to print out the value for each orbital position.

So far we have only considered the case where the spin axis passed through the center of the plate. However, it is easy to see that the dependence of λ on ζ remains identical to that given by Equation 3 for the case where a and b are defined as usual but the axis of spin is displaced from the center of the plate. As long as this lateral displacement (usually half the width of a satellite) is small in comparison to the distance of the plate from the surface of the sphere (which always obtains for earth satellites) the previous analysis remains applicable.

RESULTS

In the graphs that follow, the average incident power to the flat plate per spin period is plotted as a function of altitude above the surface of the earth for various values of the angles a and b. The situation occurring when b equals 0 or π results in $\lambda=a$ for all ζ so that these values are not considered, since the incident power for $\lambda=$constant is readily available in Part I. This situation also applies for $a=0$ for which $\lambda=b=$constant. The first 16 graphs apply for H in the range $200\leq H\leq 3200$ km (Appendix A), while the remaining graphs apply to the entire range $200\leq H\leq 32000$ km (Appendix B).

ACKNOWLEDGMENT

The author wishes to thank Mr. E. Monasterski, Goddard Space Flight Center, for the IBM 7090 computations.

Appendix A

THE AVERAGE INCIDENT POWER TO A FLAT PLATE PER SPIN PERIOD FOR VARIOUS ANGLES a AND b AS A FUNCTION OF ALTITUDE FOR THE RANGE 200 $\leq H \leq$ 3200 KM

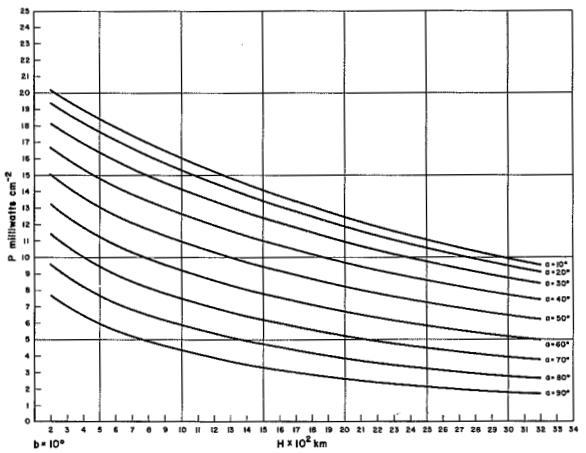

FIGURE A1.—$b=10°$.

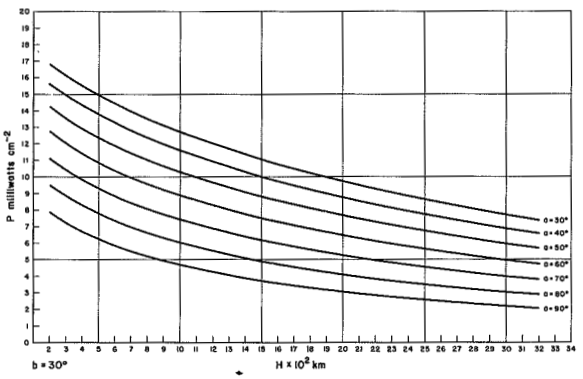

FIGURE A3.—$b=30°$.

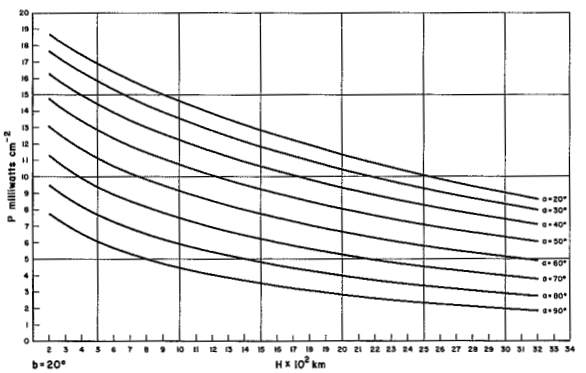

FIGURE A2.—$b=20°$.

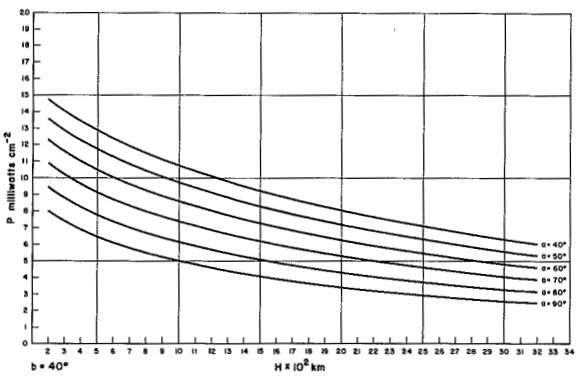

FIGURE A4.—$b=40°$.

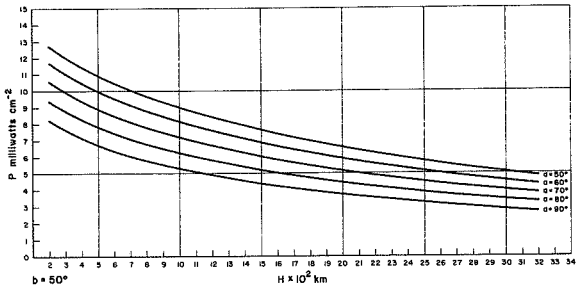

FIGURE A5.—$b=50°$.

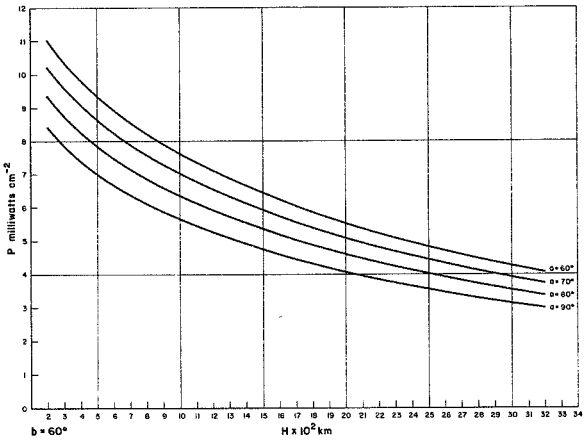

FIGURE A6.—$b=60°$.

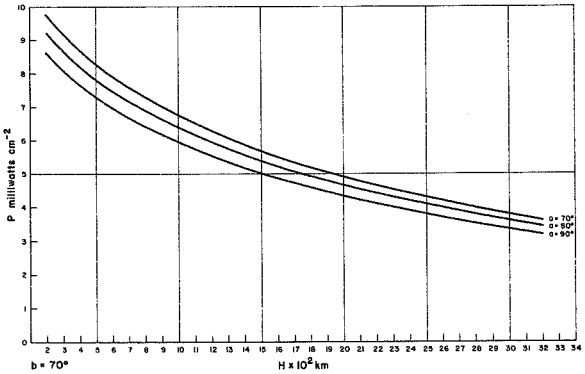

FIGURE A7.—$b=70°$.

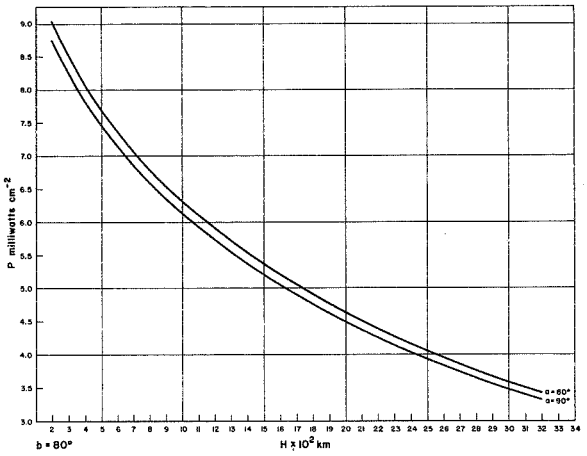

FIGURE A8.—$b=80°$.

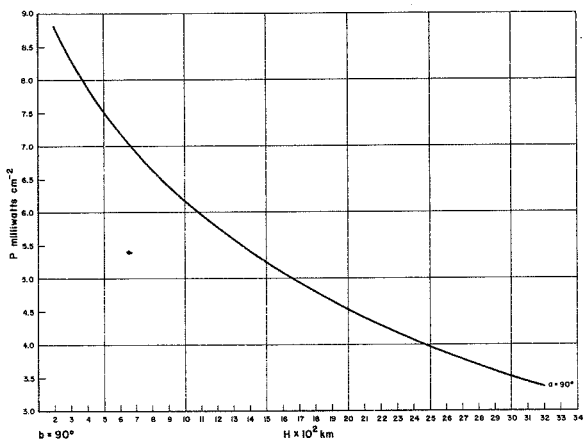

FIGURE A9.—$b=90°$.

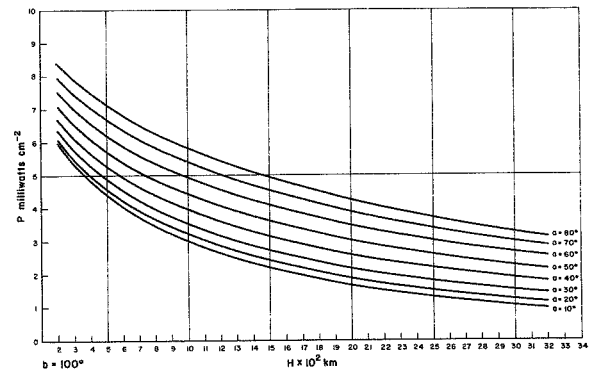

FIGURE A10.—$b=100°$.

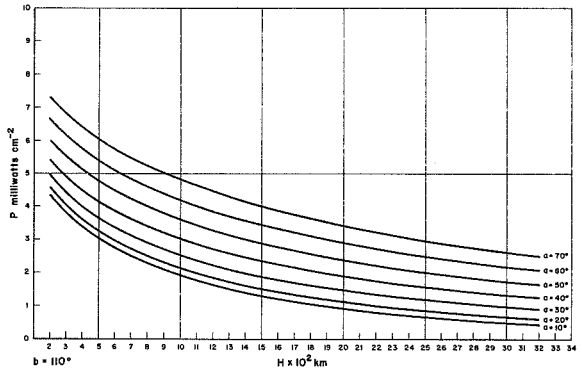

FIGURE A11.—$b=110°$.

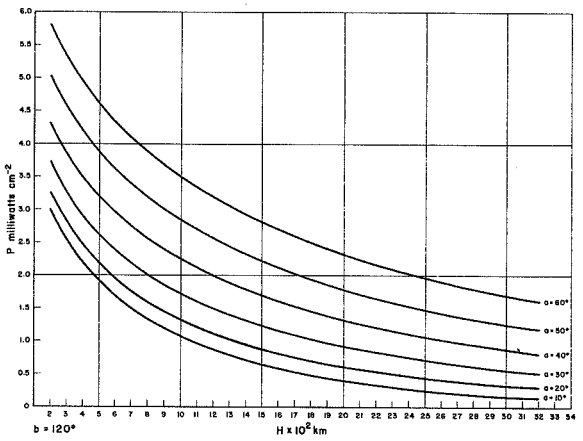

FIGURE A12.—$b=120°$.

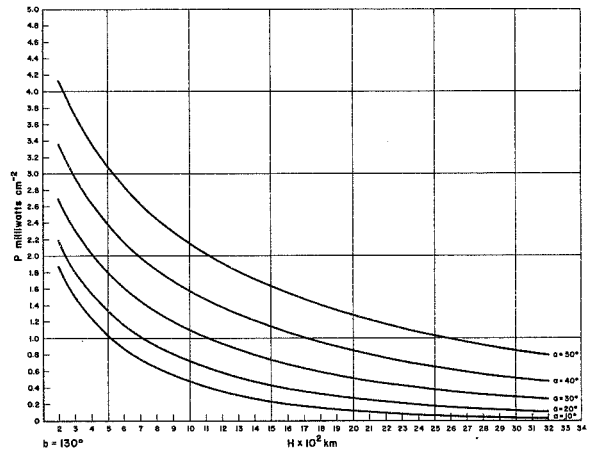

FIGURE A13.—$b=130°$.

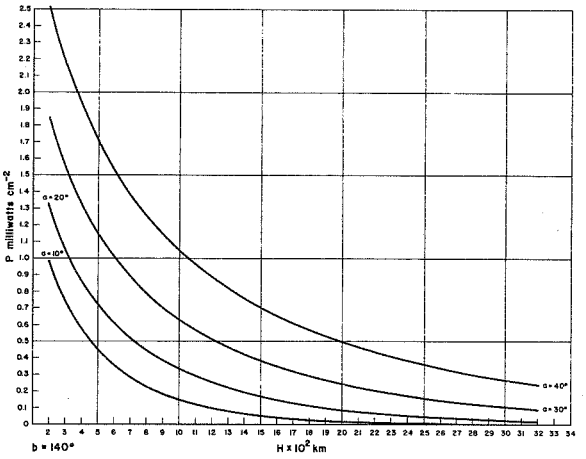

FIGURE A14.—$b=140°$.

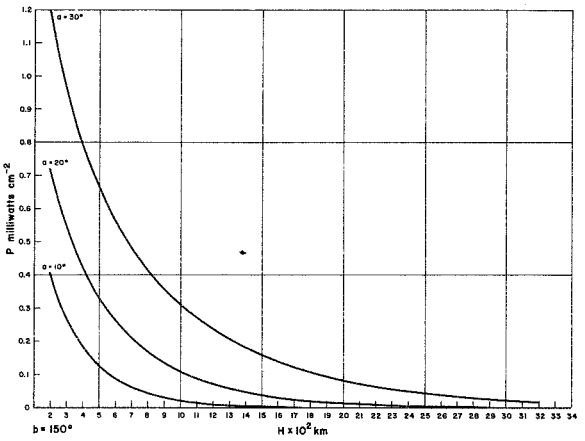

FIGURE A15.—$b=150°$.

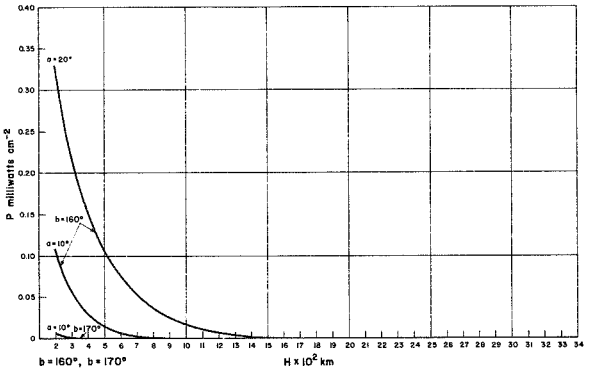

FIGURE A16.—$b=160°$, 170°.

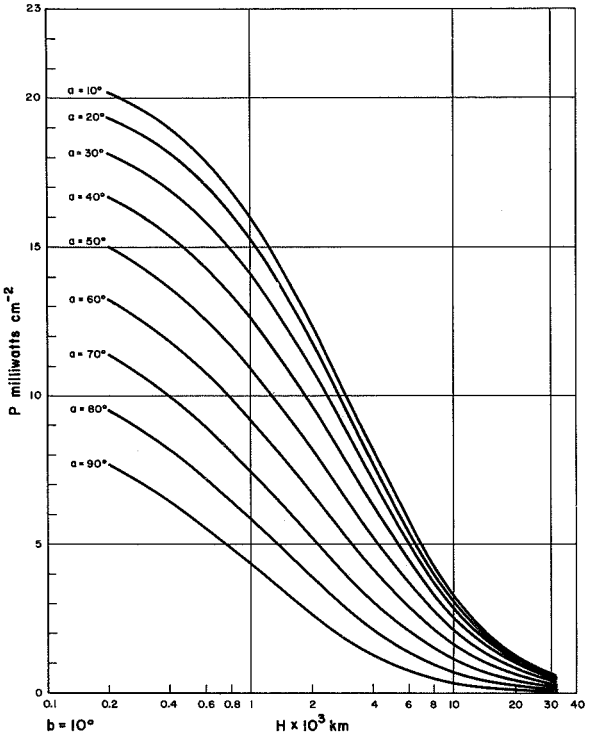

FIGURE B1.—$b=10°$.

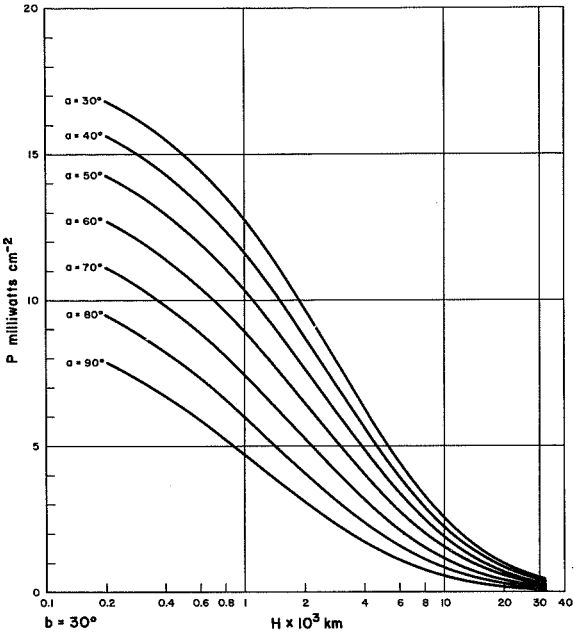

FIGURE B3.—$b=30°$.

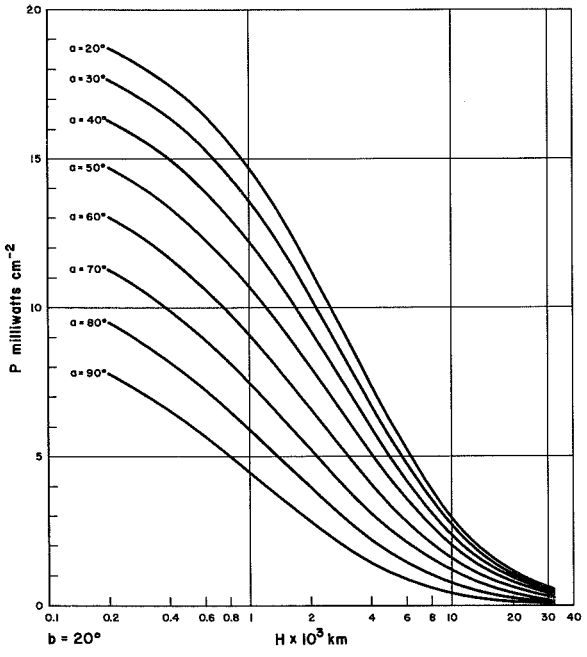

FIGURE B2.—$b=20°$.

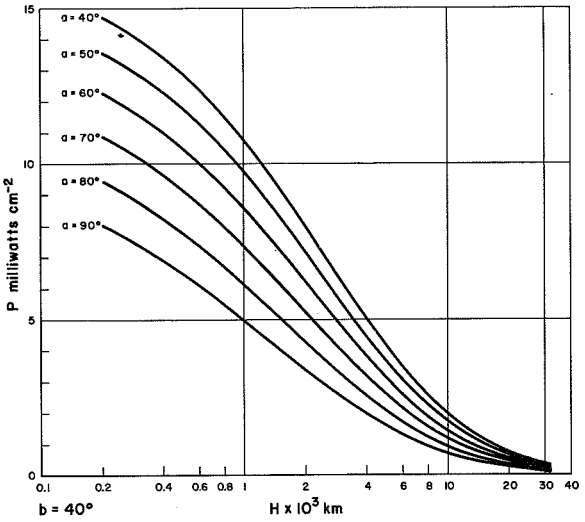

FIGURE B4.—$b=40°$.

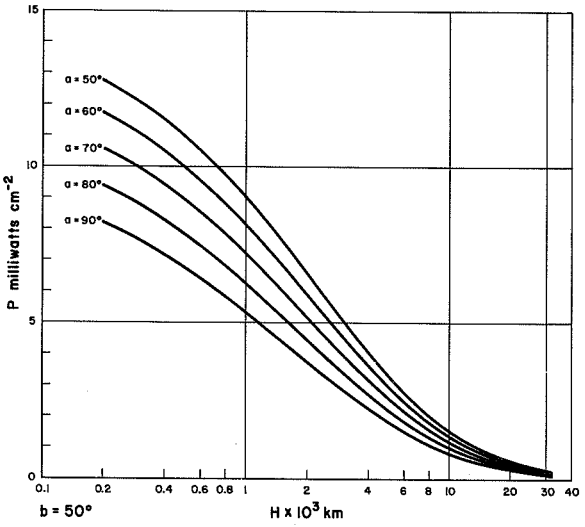

FIGURE B5.—$b=50°$.

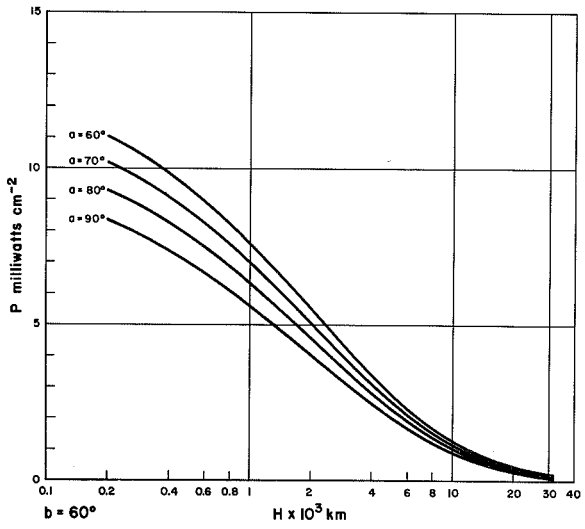

FIGURE B6.—$b=60°$.

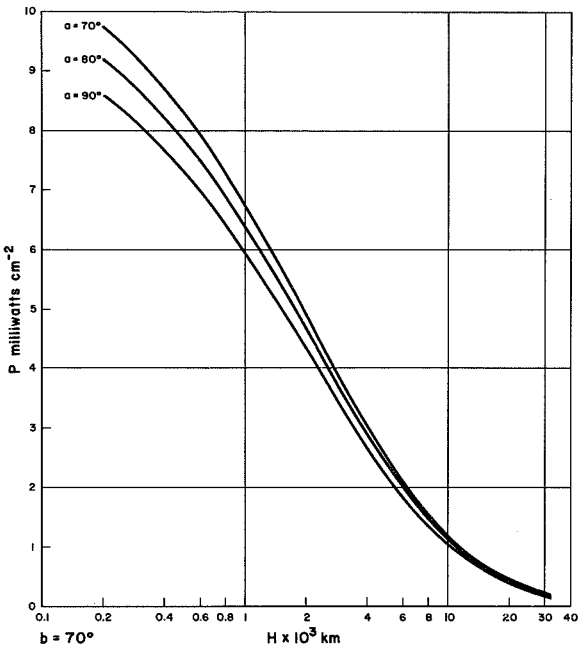

FIGURE B7.—$b=70°$.

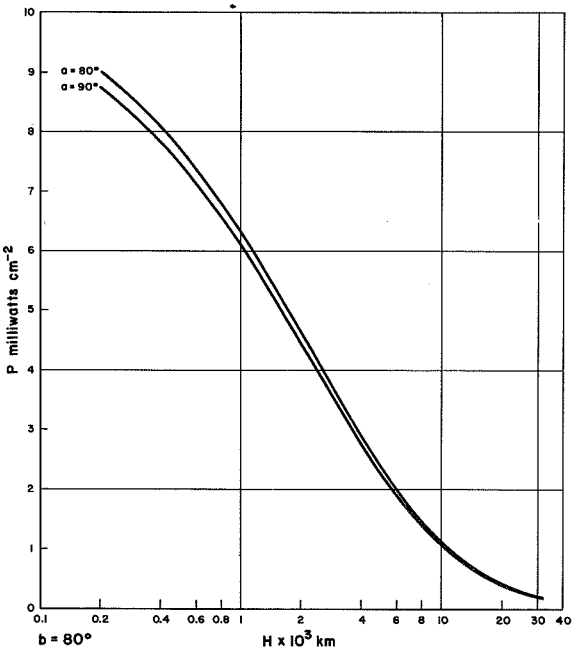

FIGURE B8.—$b=80°$.

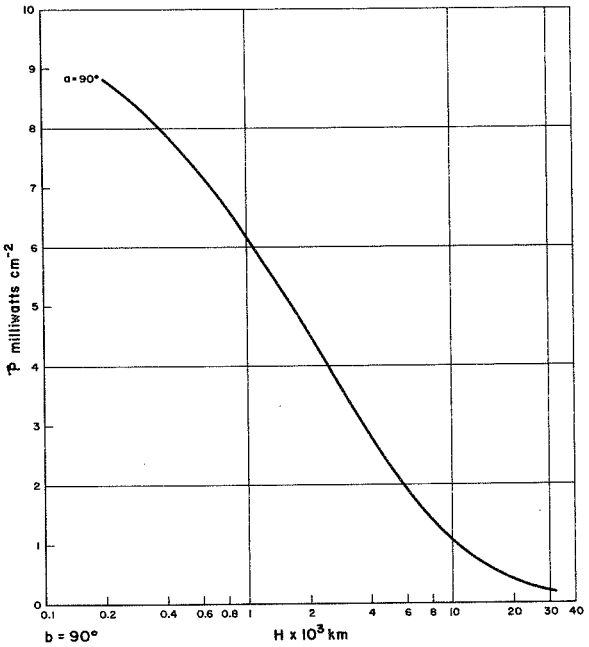

FIGURE B9.—$b=90°$.

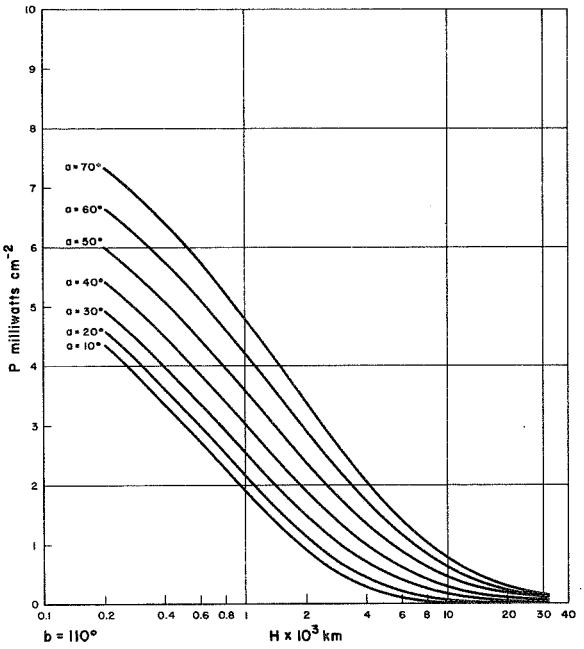

FIGURE B11.—$b=110°$.

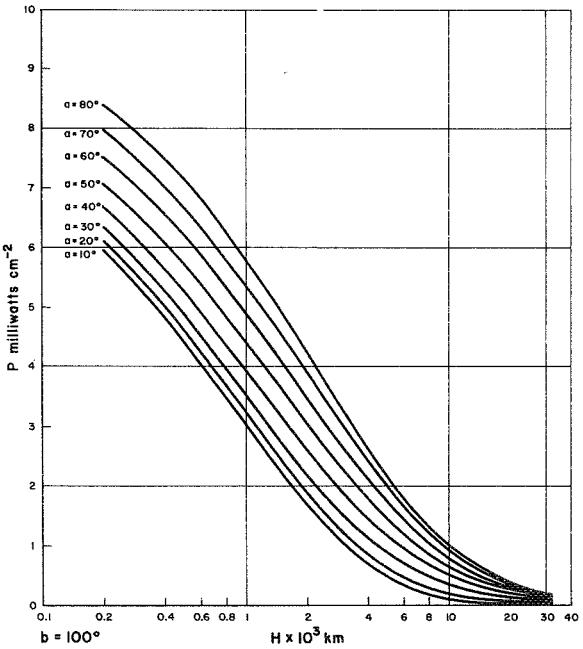

FIGURE B10.—$b=100°$.

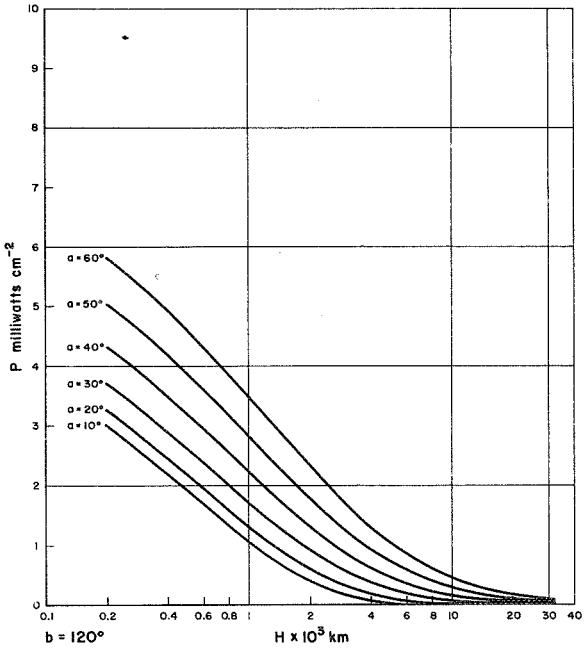

FIGURE B12.—$b=120°$.

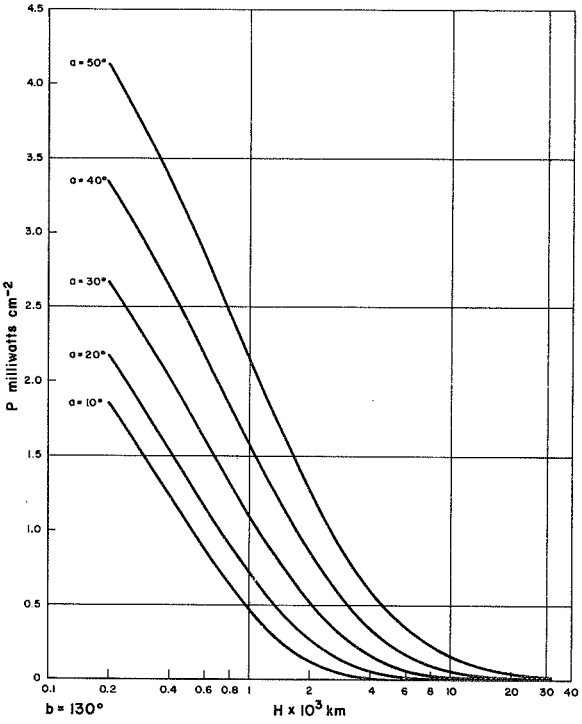

FIGURE B13.—$b=130°$.

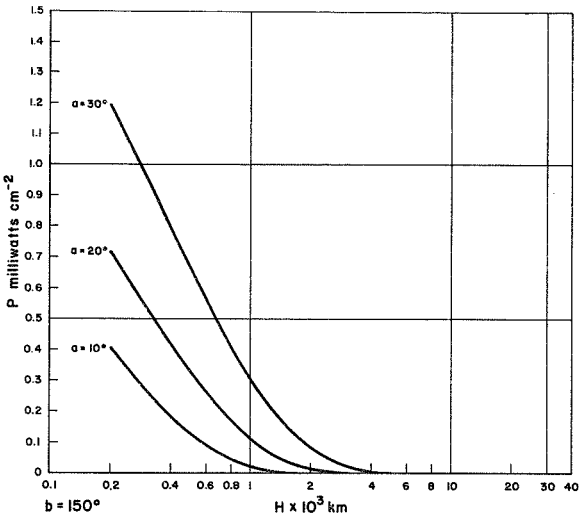

FIGURE B15.—$b=150°$.

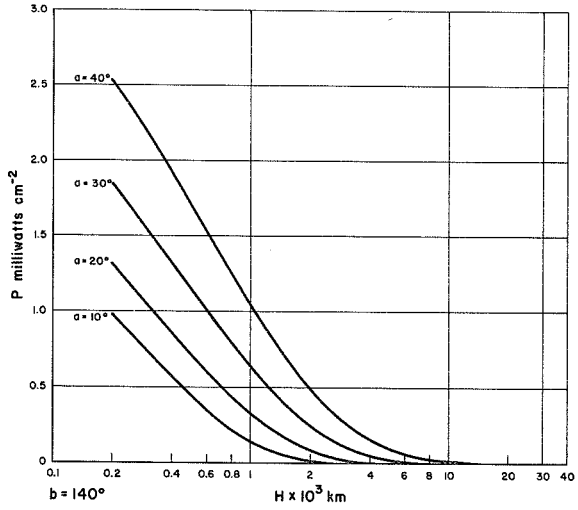

FIGURE B14.—$b=140°$.

ON THE TEMPERATURE DEPENDENCE OF THE BREAKDOWN FIELD OF $BaTiO_3$

By P. H. FANG

Goddard Space Flight Center

In the recent work of Ueda, Takiuchi, Ikegami and Sata[1], and of Bogdanov[2], experimental results of the temperature dependence of the breakdown field of ceramic BaTiO were reported. These authors found some result which are different from the observations made by Fang and Brower[3]. In this note, we propose to explain the differences.

The results of Ueda et al., and of Bogdanov show that the breakdown field of $BaTiO_3$ is essentially independent of the temperature in a large temperature region, and has a slight maximum in the region of tetragonal-cubic phase transformation temperature. On the other hand, the results of Fang and Brower show a minimum at each of the three regions of the temperature where the rhombohedral-orthorhombic, orthorhombic-tetragonal, and tetragonal-cubic transitions occur.

We note that the geometrical shape of the specimens used by Ueda et al. and Bogdanov have essentially a spherical cavity and the breakdown measurement is conducted in a region of a small volume for a thickness of 0.01 to 0.035 cm., surrounded by the same $BaTiO_3$ with a thickness of 0.2 to 0.3 cm. In such a configuration, when one applies a voltage, the electric field strength is the highest, therefore, heat generated by the electric conduction is largest, in this small volume. This heat is efficiently conducted away by the surrounding massive medium. The result is a minimization of any thermal breakdown process.

The specimen used by Fang and Brower is in the form of a planar disk with a thickness of 0.1 to 0.15 (cm) and a diameter of 0.95 or 1.5 cm. The specimen is immersed in a silicone insulation liquid. Such a configuration would not conduct the heat as effectively as the spherical cavity configuration. Therefore, one could observe a thermal breakdown process.

Bogdanov also pointed out that the planar configuration would not prevent a breakdown along the edge. First, if there is indeed an edge breakdown, there is no reason to assume this breakdown will be prominent near the phase transformation temperature of $BaTiO_3$. Second, one can actually observe visually the breakdown path after this breakdown has occurred. In no case in our experiment, was breakdown along the edge observed.

From the above consideration, we conclude that the differences in the specimen configuration contribute to the differences in the experimental results. The gradual decrease of the breakdown strength with the temperature observed by Fang and Brower points to the preponderance of the thermal breakdown in their experimental arrangement. The minimum of the breakdown strength near the transition temperatures emphasizes the contribution of the electric conduction current due to the polarization: in the ceramic in difference from a single crystal, there is a maximum polarization at each of the transition temperatures.[6] We also would like to point out that in the work of Fang and Brower, breakdown was measured on the pure B_2TiO_3 specimen[4], as well as "commercial" $BaTiO_3$. The "commercial" $BaTiO_3$ presumably has different impurities from the "commercial" materials used by Ueda et al., and by Bogdanov. The large difference in the behavior of the pure specimen indicated a profound influence of the impurities on the

temperature dependence of the breakdown field. Therefore, it would seem to have little physical significance to make an experiment on the breakdown of $BaTiO_3$ with impurities, unless one is interested in the particular aspect of the impurity effect.

The effect of the electrode material used, which was presumably also different in the three experiments under discussion, according to the recent results of Branwood et al.,[5] would not affect the value of the breakdown field.

The author is indebted to Dr. H. Jaffe, of Clevite Corporation, for his suggestions and comments.

REFERENCES

1. I. Ueda, M. Takiuchi, S. Ikegami and H. Sato; J. Phys. Soc. Japan 17 (1962) 1679.
2. S. V. Bogdanov; Fiz. Tverdogo Tela (USSR) 4 (1962) 2179 (Translation, Soviet Phys. Solid State Phys. 4 (1963) 1596).
3. P. H. Fang and W. S. Brower; Phys. Rev. 113 (1959) 456.
4. The major impurity in these specimens was Sr, which was between 0.01 and 0.10 percent, and all other impurities totaled not more than 0.01 percent.
5. A. Branwood, J. D. Hurd and R. H. Tredgold; Brit. J. Appl. Phys. 13 (1962) 528.
6. G. Mesnard and L. Eyrand; J. Phys. Radium 17 suppl. (1956) 62A.

THE EFFECT OF SOLAR RADIATION PRESSURE ON THE SPIN OF EXPLORER XII

J. V. FEDOR

Goddard Space Flight Center

An equation of motion about a satellite spin axis is derived that includes solar radiation torques produced by a solar paddle array. The equation is applied to the Explorer XII and solved to explain the observed increase in the satellite spin. Also, an approximate equation is developed which permits rapid calculation of the effect of solar torques on satellite spin.

INTRODUCTION

Recent Goddard Space Flight Center satellites have had relatively large solar cell paddles to obtain power from the sun. An interesting effect of this has been the marked change of satellite spin. For the Explorer XII (launched Aug. 16, 1961), the spin increased approximately 20 percent from its initial value in four months. It is the purpose of this note to report an analysis which shows that the increase of the Explorer XII spin can be attributed to solar radiation pressure.

ANALYSIS

It is a well established fact that sunlight is electro-magnetic energy. From Einstein's equation $E=mc^2$, where E is energy, m is mass, and c is the velocity of light, a mass and thus a momentum can be associated with sunlight. Whenever light impinges on a surface (for example, solar paddles on a satellite) there is a change of momentum and hence a force (torque) developed which in the case of spinning satellite may effect the rotation. Although this torque is usually small, it can under certain conditions produce significant results.

In the interest of reducing algebraic complexity, improving clarity, and to develop equations for engineering application, a restricted point of view will be taken in the subsequent analysis. That is, motion and torques only about the satellite spin axis will be considered. For the Explorer XII, this is found to be adequate to describe spin changes. A more general and abstract approach to solar torques acting on a satellite is given in Reference 1 and 2.

Once the satellite is injected into orbit and any nutation angle has been damped out due to energy dissipation, the satellite can essentially be considered as a one degree of freedom system (a favorable moment of inertia ratio is assumed). The effect of forces other than around the spin axis usually can be neglected if satellite spin is relatively high (20 to 30 rpm with a spin moment of inertia of about 3 to 4 slug feet^2). Moments tending to affect the spin axis are mainly magnetic, solar radiation, and aerodynamic. Because of the highly eccentric orbit of the Explorer XII and relatively high perigee (after one month in orbit: apogee 77, 199 km, perigee 448 km), the aerodynamic moments are small and can be neglected. The Explorer XII was also designed to minimize magnetic torques and the high apogee tends to reduce magnetic effects even further. Hence, magnetic torques will also be neglected. Thus, only solar radiation torques are left to be considered.

Figure 1 shows the general configuration of the satellite. Only direct radiation torques produced by the solar paddles will be considered; radiation torques produced by the

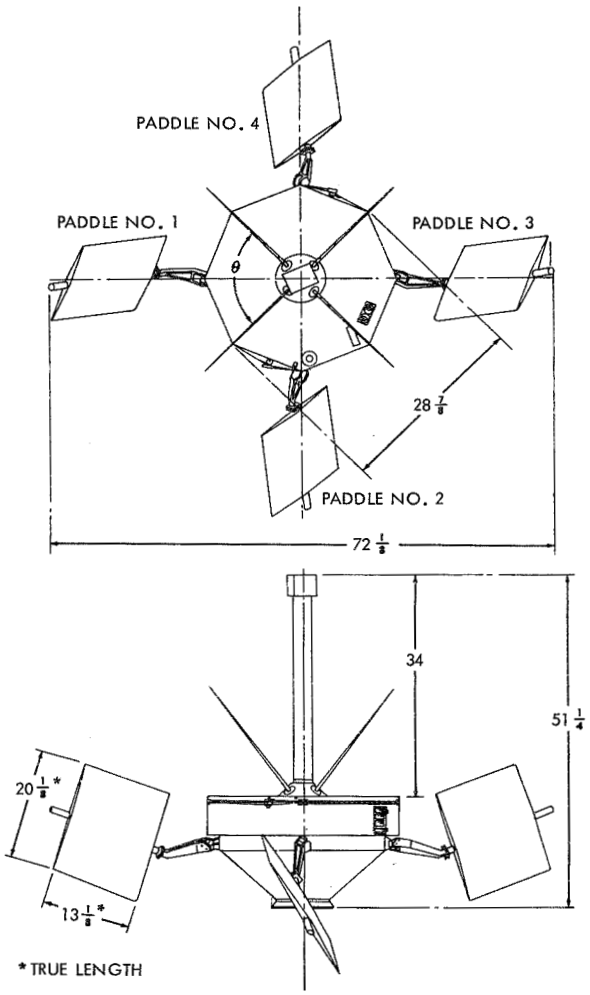

FIGURE 1.—Explorer XII Energetic Particle Satellite.

main satellite body geometry about the spin axis are considered negligible. The equation of motion around the spin axis is simply

$$\sum \text{torques} = I \frac{d\omega}{dt} \qquad (1)$$

where $\omega = d\theta/dt$, θ is the angular coordinate around the spin axis, and I is the spin axis moment of inertia.

In developing the moment expression it will be assumed that there are two distinct pairs of paddles. The force acting on a paddle is the product of the radiation pressure factor, P (lbs/ft^2), and the projected area perpendicular to the sun's rays, A (ft^2):

$$\text{Incident light force} = PA.$$

For the reflected light, a reflectivity coefficient, ρ, must be included

$$\text{Reflected light force} = \rho PA.$$

In general P varies with the earth-sun distance and this is discussed later. The reflected light from a solar paddle is a rather complicated phenomenon, being dependent upon the optical properties of the reflecting surface and the impinging light. It is assumed here that the reflection is spectral, that is, angle of incidence equals angle of reflection and that the reflectivity is independent of the incident angle. Figure 2 shows the geometry for the torque

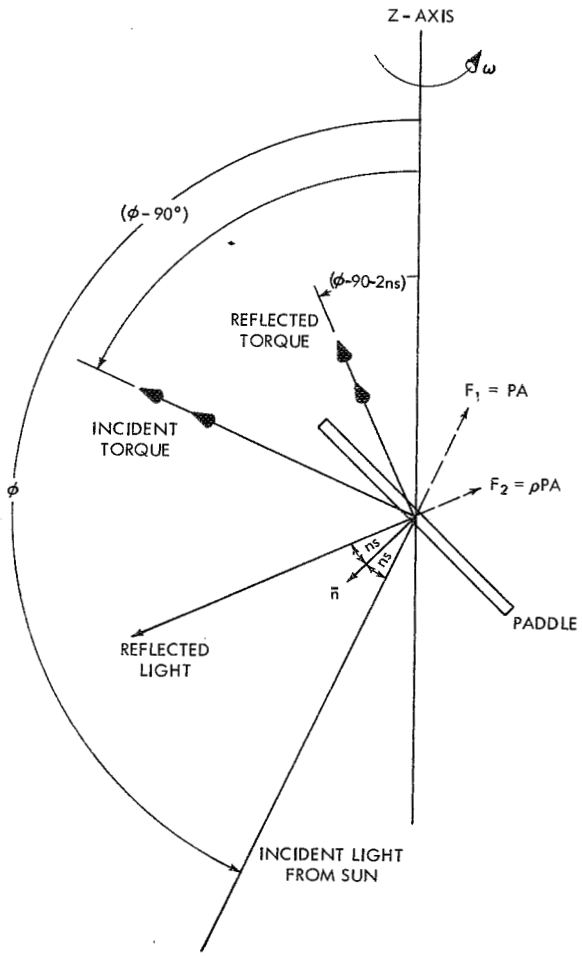

FIGURE 2.—Geometry for solar radiation torques produced by a solar paddle.

equation. The partial component of torque about the spin axis for the incident light is

$$PAh\,|\cos\theta|\,\sin\phi,$$

where h is the distance from the spin axis to the centroid of the paddle, and ϕ is the sunline-spin axis angle. For the reflected light it is

$$\rho PA|h\,\cos\theta|\,\sin(\phi-2ns),$$

where ns is the angle between the normal to the paddle and the direction of the sun. Absolute signs are used on the cosine term since the moment arm is always positive. Summing the torques for each paddle and considering counterclockwise positive, we obtain

$$\begin{aligned}\Sigma\text{torques}=&-PA_1h_1|\cos\theta|\,(\sin\phi\\&+\rho\,\sin(\phi-2ns_1))+PA_2h_2|\sin\theta|\,(\sin\phi\\&+\rho\,\sin(\phi-2ns_2))+PA_3h_1|\cos\theta|\,(\sin\phi\\&+\rho\,\sin(\phi-2ns_3))-PA_4h_2|\sin\theta|\,(\sin\phi\\&+\rho\,\sin(\phi-2ns_4)).\end{aligned}\quad(2)$$

Equation 2 is the basic torque expression for direct solar radiation effects about the spin axis due to the solar paddles.

The projected area of a paddle as a function of ϕ, θ, and the geometry of the paddle is developed in Appendix A. Using the basic projected area equation, the projected area of the four paddles can be expressed in the following way

$$\left.\begin{aligned}A_1&=A_0\,|\cos\theta\,\sin nz_1\,\sin\phi+\cos nz_1\,\cos\phi\,|\\A_2&=A_0\,|-\sin\theta\,\sin nz_2\,\sin\phi+\cos nz_2\,\cos\phi\,|\\A_3&=A_0\,|-\cos\theta\,\sin nz_1\,\sin\phi+\cos nz_1\,\cos\phi\,|\\A_4&=A_0\,|\sin\theta\,\sin nz_2\,\sin\phi+\cos nz_2\,\cos\phi\,|\end{aligned}\right\},\quad(3)$$

where nz_1, nz_2 are the angles from the normal to the paddle to the spin axis and A_0 is the geometric area of the paddle. Absolute signs are used since a minus area means that the back side of a paddle is illuminated. Substituting Equation 3 into 2, Equation 2 into 1, and making the abbreviation

$$M=\sin nz\,\sin\phi,$$
$$N=\cos nz\,\cos\phi,$$

the equation of motion becomes

$$\begin{aligned}I\frac{d\omega}{dt}=PA_0K(\phi,\theta)\Big\{&-\Big|M_1|\cos\theta|+N_1\Big|h_1|\cos\theta|\\&(\sin\phi+\rho\sin(\phi-2ns_1))+\Big|-M_2|\sin\theta\\&|+N_2\Big|h_2|\sin\theta|\,(\sin\phi+\rho\sin(\phi-2ns_2))\\&+\Big|-M_1|\cos\theta|+N_1\Big|h_1|\cos\theta|\,(\sin\phi\\&+\rho\sin(\phi-2ns_3))-|M_2\Big|\sin\theta|+N_2\Big|h_2\\&|\sin\theta|\,(\sin\phi+\rho\sin(\phi-2ns_4))\Big\}.\end{aligned}\quad(4)$$

Again absolute signs are used inside the parentheses because there is 180 degree symmetry with the two paddles. That is, one paddle presents the same area as the other paddle 180 degrees later. A shadow factor $K(\phi,\theta)$ is included to account for paddle on paddle shadowing and shadowing by the satellite structure.

Strictly speaking Equation 4 should contain a torque term due to albedo radiation from the earth. Because of the complicated mathematical description and the fact that it contributes very little in this application (it decreases as $1/\sigma_2$ where σ is the ratio of the satellite distance to earth radius, Ref. 3), the albedo radiation term will be neglected.

As was noted earlier, the solar radiation factor, P, in Equation 4 is variable; it varies inversely as the square of the earth-sun distance. By considering the earth's orbit around the sun as a perturbed circular orbit, it can be shown that the distance between the sun and the earth a sa fnnction of time can be expressed as

$$r(t)=r_0(1+e\,\cos 2\pi t/T)^2,\quad(5)$$

where

e=eccentricity of the earth's orbit=.01674,
T=365 days,
r_0=mean earth-sun distances.

Time zero is at the maximum earth-sun distance of approximately June 21st. P can then be expressed as

$$P(t)=\frac{p_0}{(1+e\,\cos 2\pi t/T)^2}\quad(6)$$

where p_0 is the mean solar constant at the mean solar-earth distance. $P(t)$ is considered zero when the satellite is eclipsed by the earth.

The change of satellite spin is obtained by integrating Equation 4; this is indicated symbolically in two ways below:

$$\omega-\omega_0=\frac{A_0}{I}\int_0^t P(t)K(\phi,\theta)\{\ \}dt, \qquad (7)$$

or

$$\omega^2-\omega_0^2=\frac{2A_0}{I}\int_0^\theta P(t)K(\phi,\theta)\{\ \}d\theta, \qquad (8)$$

where the ns angles are obtained from the following equations

$$\begin{aligned}
\cos ns_1&=\left|M_1|\cos\theta|+N_1\right|\\
\cos ns_2&=\left|-M_2|\sin\theta|+N_2\right|\\
\cos ns_3&=\left|-M_1|\cos\theta|+N_1\right|\\
\cos ns_4&=\left|M_2|\sin\theta|+N_2\right|
\end{aligned} \qquad (8a)$$

and the quantity inside the brace is the same as that given in Equation 4. To carry out the integration indicated by Equation 7 or 8 is impossible by analytical means and very messy and tedious to do numerically; a digital computer solution is required. This has been done and the results are discussed below. It is of value though to develop an approximate equation (and solution) so that "ball park" answers can be determined readily. Within certain limits, it has been found that the approximate solution gives answers comparable to the digital solution.

APPROXIMATE METHODS

An approximate expression will now be developed for the torque equation. Directing attention to Equation 4 and noting that if ns, ns_2, ns_3, and ns_4 are replaced by an average angle, $\langle ns\rangle$, Equation 4 can be put into the following form:

$$\begin{aligned}
I\frac{d\omega}{dt}=PA_0K(\phi,\theta)\Big\{&\Big(\left|-M_1|\cos|\theta\right.\\
&\left.+N_1\right|-\left|M_1|\cos\theta|+N_1\right|\Big)h_1|\cos\theta|\\
&+\Big(\left|-M_2|\sin\theta|+N_2\right|-|M_2|\sin\theta|\\
&\left.+N_2\right|\Big)h_2|\sin\theta|\Big\}(\sin\phi\\
&+\rho\sin(\phi-2\langle ns\rangle)).
\end{aligned} \qquad (9)$$

For θ near zero and $M>N$ (this restricts ϕ around 90°), the quantity in the brace in Equation 9 has the approximate value

$$-2N_1h_1|\cos\theta|.$$

and for θ near $\pi/2$ the brace has the approximate value

$$-2N_2h_2|\sin\theta|$$

For an approximate solution, it does not seem unreasonable to replace the complicated expression inside the brace by the sum of these two quantities

$$-2N_1h_1|\cos\theta|-2N_2h_2|\sin\theta|$$

throughout the paddle array rotation. Therefore, the following approximation can be made to Equation 7.

$$\begin{aligned}
\omega-\omega_0=-2\frac{A_0}{I}\int_0^t P(t)K(\phi,\theta)\Big\{&\cos nz_1h_1|\cos\theta|\\
&+\cos nz_2h_2|\sin\theta|\Big\}(\sin\phi\\
&+\rho\sin(\phi-2\langle ns\rangle))\cos\phi dt.
\end{aligned} \qquad (10)$$

The same result can be obtained by squaring a typical quantity $|M\cos\theta+N|$, neglecting N^2, then taking the square root, expand in a power series and retain the first two terms.

The average angle $\langle ns\rangle$ must now be evaluated. In an approximate equation it is desirable to have the equation as simple as possible and still retain the essence of the phenomena it is to describe. An expression can be developed for the average angle but it is complicated and unwieldy. The simplest value for $\langle ns\rangle$ would be zero. At first glance, this may appear to be an unwarranted simplification. Subsequent comparison of numerical results from the theoretically correct equation will show that this is justified. Essentially, when $\langle ns\rangle$ is given a value of zero, it ist acitly assumed that the reflected light reinforces the direct light effect.

Using the method of Kryloff and Bogoliuboff (Ref. 4), that is, averaging over a cycle while considering $d\omega/dt$ constant during the averaging period, Equation 10 can be simplified to

$$\omega-\omega_0=-\beta\int_0^t R(t)K(\phi)\sin 2\phi dt, \qquad (11)$$

where

$$R(t)=\frac{1}{(1+e\cos 2\pi t/T)^2}$$

$$\beta=2(1+\rho)\frac{A_0 p_0}{\pi I}(h_1\cos nz_1+h_2\cos nz_2).$$

Equation 11 still cannot be integrated analytically since $K(\phi)$ and ϕ are usually known only graphically. Using the trapezoidal rule, the integration can be replaced by a finite summation

$$\omega_N-\omega_0=-\beta\sum_{i=0}^{N}\delta_i R(t_i)K(\phi_i)\sin 2\phi_i\Delta t, \quad (12)$$

where $\delta_0=\delta_N=\frac{1}{2}$, and the other δ's are equal to 1. If ϕ is known day by day, the increment of integration, Δt, can be a day without any appreciable loss of accuracy. For a quick estimate of solar radiation effect on the spin, $K(\phi)$ can be set equal to unity.

DISCUSSION

The exact spin equation (Equation 8) was applied to the Explorer XII satellite with the following parameters:

$$A_0=1.75\ \text{ft}^2,$$
$$h_1=h_2=2.35\ \text{ft},$$
$$nz_1=nz_2=59°47',$$
$$M_1=M_2,\ N_1=N_2,$$
$$I=3.53\ \text{slug ft}^2,$$
$$p_0=9.50\times10^{-8}\ \text{lb/ft}^2,$$
$$\rho\approx0.10.$$

The reflectivity coefficient for a solar paddle is a rather uncertain quantity; the above value for ρ was estimated from tests conducted on plain solar cells. A plot of the telemetry optical aspect sunline-spin axis angle used in the calculations is shown in Figure 3. The shadowing factor, K vs ϕ, is shown in Figure 4. Since Explorer XII was in the sunlight more than 98 percent of the time, no eclipse factor was used. Equation 8 was solved on a 7090 digital computer in an iterative procedure by calculating the change of spin over one rotation and considering this change of spin applied for 200 revolutions. The elapsed time was calculated and the sunline-spin axis angle was changed accordingly; the calculation was then repeated. The above method resulted in reasonable computer times and still gave, it was felt, accurate results. Computer results are compared with actual satellite spin data in Figure 5. Calculations were started two days after launch to allow the nutation angle to dampen out since after yo-yo operation (a spin reduction device), Explorer XII had a five degree half cone angle nutation. The optical aspect sensor indicated that after the initial coning angle damped out, there was virtually no nutation angle during the active life of the satellite. It will be noticed from the figure that there is good agreement between the theoretical curve and actual spin data. Maximum deviation from the theoretical

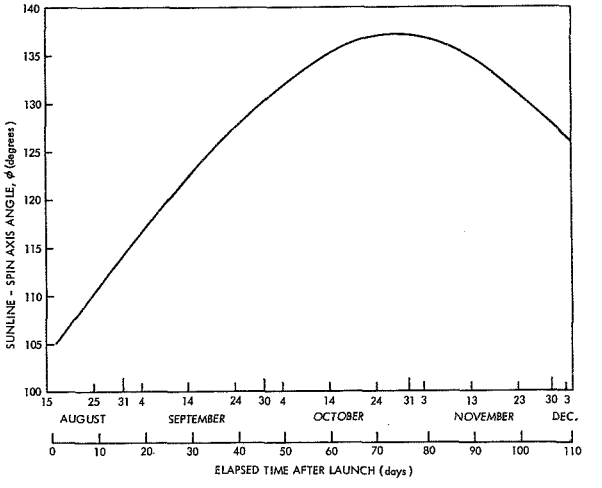

FIGURE 3.—Sunline-spin axis angle vs. time.

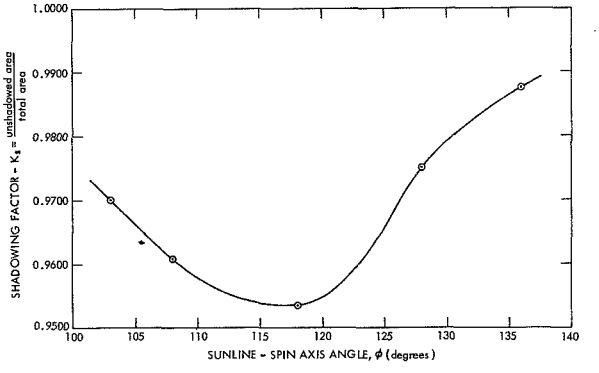

FIGURE 4.—Shadowing factor vs. sunline-spin axis angle.

curve is about one percent. Considering the uncertainty of the reflectivity coefficient and the small but finite perturbations of the albedo, magnetic, and aerodynamic torques, the agreement is satisfactory.

The approximate equation given by Equation 12 was also applied with the Explorer XII parameters (Δt was taken to be one day) and results are compared with the computer solution. This is shown in Figure 6. It will be noted that there is very little difference between the computer solution and the approximate solution. For most practical purposes the curves are essentially the same. Because of the good agreement it is inferred that the approximate equation gives satisfactory results for ϕ between 45° and 135° and cos nz $<\frac{1}{2}$.

It is of value to note that in general solar radiation torques about the spin axis occur because of the different tilt (projected area) of the paddles. This is clearly seen in Equation 2; if the projected areas are equal, (ns angles are also equal) there are no solar torques about the spin axis. For small reflectivities, it can also be stated that if the sun shines from below the equator of the satellite ($\phi>90°$), the satellite will spin up; if the sun shines from above the equator ($\phi<90°$), the satellite will spin down. This is easily seen from the approximate Equations 10 or 11. This effect has been observed in satellites launched after Explorer XII. It is interesting to note that the maximum value of the solar torque around the spin axis is about 2×10^{-7} ft. lbs. This is a very small torque, indeed. As was noted though, a small but persistent torque acting on a satellite for a long period of time does have an appreciable effect.

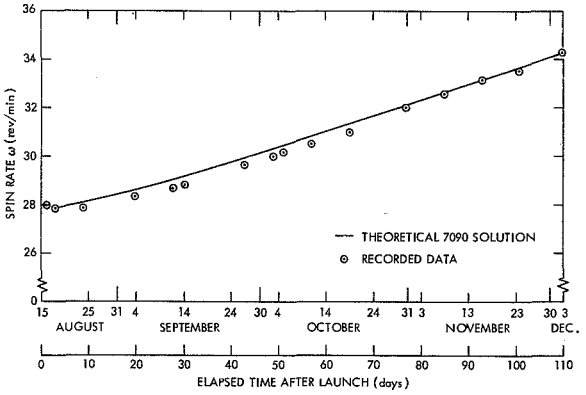

FIGURE 5.—Spin rate of Explorer XII vs. time.

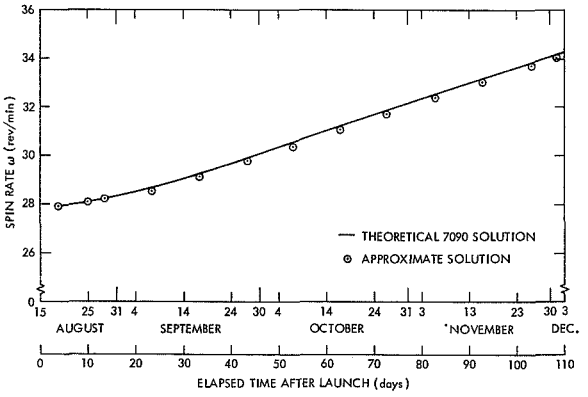

FIGURE 6.—Explorer XII spin rate vs. time: comparison of computer calculation with approximate solution (Equation 12).

RÉSUMÉ

An equation of motion about a satellite spin axis has been developed that includes spectral solar radiation torques. The equation was applied to the Explorer XII to account for the observed increase in spin. Calculated spin values agree within about one percent of the observed satellite spin values. It is concluded from the analysis and calculations that Explorer XII spin-up was due to solar radiation torques. Also, an approximate spin equation was developed which permits rapid calculations of the effect of solar radiation on satellite spin.

ACKNOWLEDGMENT

The author is indebted to W. R. Mentzer of GSFC for performing the hand calculations, drawing the curves and figures and programming the equations on the IBM 7090 Computer.

REFERENCES

1. MCELVAIN, R. J., "Effects of Solar Radiation Pressure upon Satellite Attitude Control," in: Progress in Astronautics and Rocketry edited by Roberson, R. E., and Farrior, J. S., New York: Academic Press, 1962.

2. CLANCY, T. F., and MITCHELL, T. P., "Effects of Radiation Forces upon the Attitude of an Artificial Earth Satellite," Center for Radiophysics and Space Research Report #129, September 1962, Cornell University, Ithaca, N.Y.
3. LEVIN, E., "Reflected Radiation Received by an Earth Satellite", ARS Journal 32(9): 1328–1331, September 1962.
4. KRYLOFF, N., and BOGOLIUBOFF, N., "Introduction to Non-Linear Mechanics" (translation), Princeton: Princeton University Press, 1947, chapters 10–12.
5. CURTISS, D. R., and MOULTON, E. J., "Essentials of Trigonometry", New York: D. C. Heath and Co., 1942.

Appendix A

PROJECTED AREAS OF A SOLAR PADDLE

The effective projected area of a solar paddle will now be determined. We wish to derive an expression involving the angle between the spin axis of the satellite and the sunline, ϕ, the rotation angle θ, and geometrical properties of the solar paddles. Initially the paddle will be considered stationary and any shadowing by the satellite will be neglected.

Let $\bar{n}$ be the unit normal to the paddle and $\bar{s}$ the unit vector in the direction of the sun (Fig. A1). The projected area perpendicular to $\bar{s}$ is

$$A_p = A_0 \cos ns, \tag{A1}$$

where

A_p=effective paddle area,
A_0=geometric paddle area,
ns=angle between vector $\bar{n}$ and $\bar{s}$.

Now cos ns can be obtained from the vector dot product

$$\cos ns = \bar{n} \cdot \bar{s}. \tag{A2}$$

If we choose the coordinate system shown in Figure A2, where i, j, k are unit vectors, the $\bar{n}$ and $\bar{s}$ vectors have the following components:

$\bar{n}$ components—cos nx, cos ny, cos nz,
$\bar{s}$ components—sin ϕ, 0, cos ϕ.

Carrying out the dot product results in

$$\bar{n} \cdot \bar{s} = \cos nx \sin \phi + \cos nz \cos \phi. \tag{A3}$$

Hence, Equation A1 can be written as

$$A_p = A_0 (\cos nx \sin \phi + \cos nz \cos \phi). \tag{A4}$$

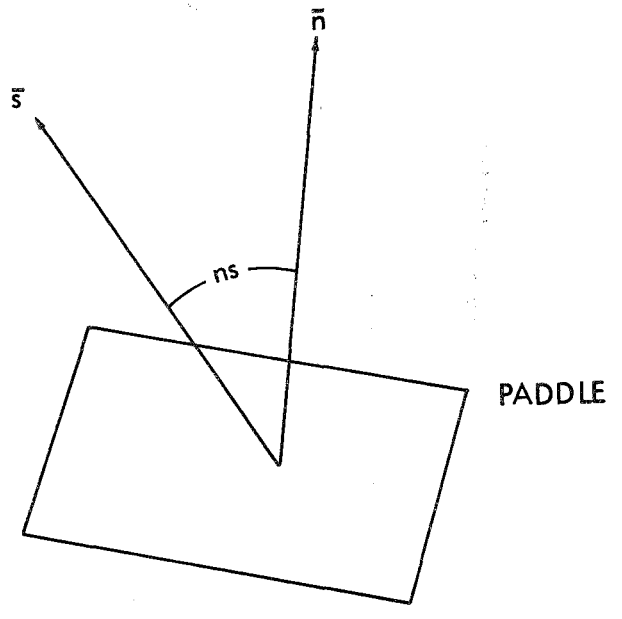

FIGURE A1

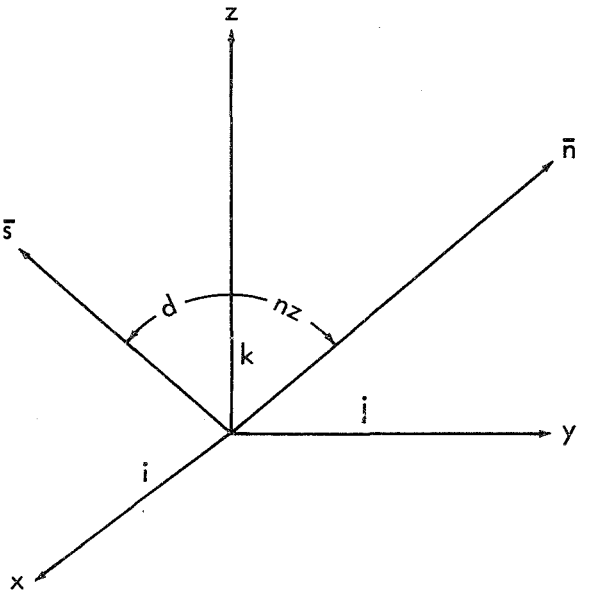

FIGURE A2

Equation A4 is for the static case (no spin). When spin is present we have the situation shown in Figure A3. Though $\bar{s}$ is not shown in the figure for clarity, it is still pointing in the direction of the sun. The z axis is considered to be the spin axis and therefore the angle nx will vary with time (see Eq. A4). From solid trigonometry we can write the following formula (Ref. 5, pp. 112–113)

$$\cos nx = \cos\theta \cos(\pi/2 - nz) = \cos\theta \sin nz. \quad \text{(A5)}$$

Substituting Equation A5 into Equation A4 results in

$$A_p = A_0 |\sin nz \sin\phi \cos\theta + \cos nz \cos\phi|. \quad \text{(A6)}$$

Absolute signs are used since a negative area means that the back side of a paddle is illuminated. Equation A6 is the basic equation for the projected area of a solar paddle.

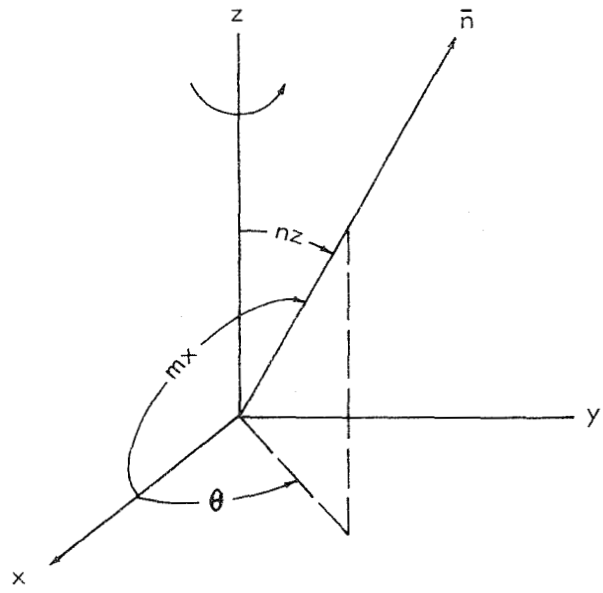

FIGURE A3

CONSERVATIVE TORQUES AND MOMENTS OF INERTIA INVOLVED IN THE DESIGN OF A LABORATORY MODEL SOLAR ARRAY WITH VARIABLE PADDLE-ARM ORIENTATION

S. G. McCARRON

Goddard Space Flight Center

In an effort to provide design data for the construction of an electromechanical system with the two degrees of freedom required for solar paddle orientation, the following expressions were determined: (1) the total conservative torque acting at the paddle-arm-rotation axis as a function of geometry and paddle-arm angle, and (2) the moment of inertia about the paddle-arm-rotation axis for a rectangular solar paddle as a function of geometry and pitch angle. The appendices include examples of determining the paddle-arm angles at which equilibrium and maximum conservative torques occur, data tables, and curves of the derived expressions for a specific geometry.

INTRODUCTION

To date, spin-stabilized satellites powered by solar paddles generally have stationary paddles. As a spin-stabilized satellite travels around the sun, the angle between the spin axis and sun line continually changes (except for the special case where the sun line is always normal to the spin axis) because the spin axis is fixed in space. In addition, torques resulting from atmospheric drag, magnetic-field gradient, solar pressure, etc., cause the sun-line spin-axis angle to undergo changes after launching. For a particular satellite, shadowing occurs in a specific part of the sun-line spin-axis range of angle. That is, the body of the satellite shades the solar paddles or the solar paddles shadow one another. In order to improve a particular solar-paddle aspect ratio when shadowing occurs, a system was devised in which two nonadjacent solar paddles (out of a total of four) are allowed two degrees of freedom. Two ideal degrees of freedom would be: (1) movement about the paddle-arm-rotation axis, and (2) movement about the longitudinal axis of the paddle. The orientation system of the model satellite being built within the Space Power Technology Branch is to eventually incorporate those degrees of freedom, and to have the adjustable paddle arms move in a 180-degree out-of-phase fashion when shadowing occurs. A further development of such a system could be variable solar-paddle aspect ratio at any sun-line spin-axis angle; this could maintain the charging rate as solar cell degradation occurs, or decrease the charging rate as the battery system becomes charged. The present system under construction is an intermittent duty one, whereas future systems will be continuous duty.

CONSERVATIVE TORQUES

The total conservative torque acting at the fulcrum of a solar-paddle arm (on a model satellite) is composed of centrifugal and gravitational components. The centrifugal torque results from the spin of the satellite and the fact that the center of mass of the paddle does not lie at the paddle-arm-rotation axis. The gravitational torque arises from the fact that gravity acts near the geometrical center of the paddle, which lies off the paddle-arm-rotation axis. The nonconservative torques which arise from frictional forces are neglected in the calculations.

Figure 1 shows an IMP-type satellite with two of the four rectangular solar paddles movable. The geometry of the satellite is labeled as follows: (1) R is the radius of the satellite, (2) λ is the length of a paddle arm, (3) a is the width of a paddle, (4) b is the length of a paddle, (5) c is the thickness of a paddle, (6) θ is the subtended paddle-arm angle, (7) p is the paddle-pitch angle, and (8) ω_z is the angular velocity [1] about the spin axis of the figure. Figure 2 shows a schematic diagram of the conservative torques acting at the paddle-arm-rotation axis. The total conservative torque acting at the fulcrum of the paddle arm at an angle θ to the vertical is given by

$$\sum_{i=1}^{2} M_i = F_c\left(\lambda+\frac{b}{2}\right)\cos\theta - W\left(\lambda+\frac{b}{2}\right)\sin\theta \quad (1)$$

where F_c is the centrifugal force given by

$$F_c = m\left[R+\left(\lambda+\frac{b}{2}\right)\sin\theta\right]\omega_z^2 = \frac{W}{g}\left[R+\left(\lambda+\frac{b}{2}\right)\sin\theta\right]\omega_z^2 \quad (2)$$

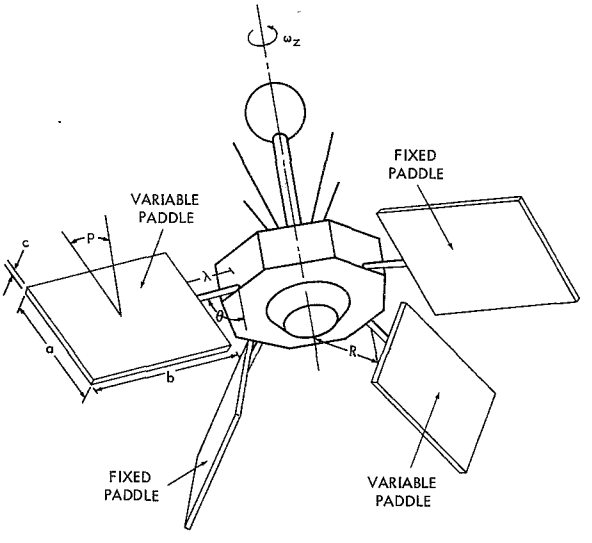

FIGURE 1.—An IMP type satellite, whose configuration was used in designing the laboratory satellite, is shown with the variable rectangular solar paddles.

[1] The model is being driven by a constant speed motor, thus making ω_z constant.

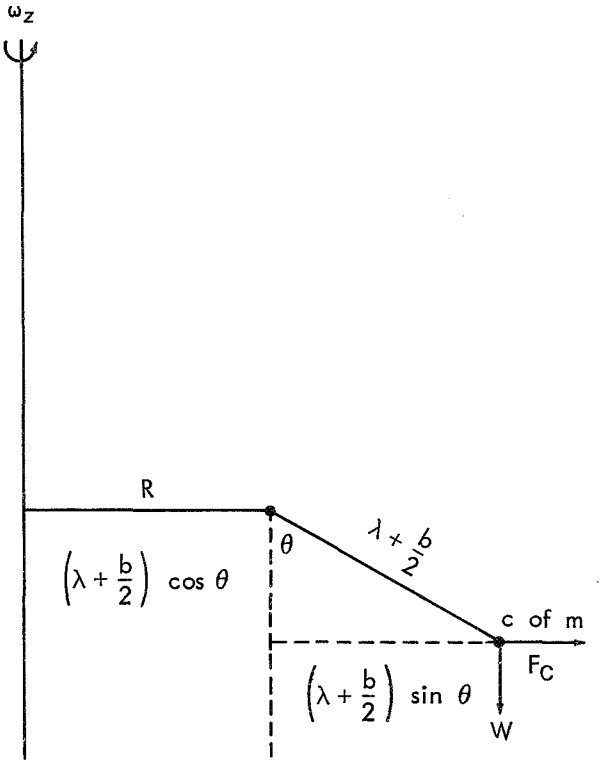

FIGURE 2.—A schematic diagram of the conservative torques acting at the paddle-arm-rotation axis of the laboratory model.

and W is the weight given by

$$W = mg \quad (3)$$

where m is the mass of the paddle and g is the acceleration due to gravity. Substituting Equations (2) and (3) into Equation (1) gives

$$\sum_{i=1}^{2} M_i = W\left(\lambda+\frac{b}{2}\right)\left\{\frac{\omega_z^2}{g}\left[R\cos\theta + \left(\lambda+\frac{b}{2}\right)\frac{\sin 2\theta}{2}\right] - \sin\theta\right\}. \quad (4)$$

The equilibrium condition is given by

$$\sum_{i=1}^{2} M_i = 0;\ \frac{\omega_z^2}{g}\left[R\cos\theta+\left(\lambda+\frac{b}{2}\right)\frac{\sin 2\theta}{2}\right] - \sin\theta = 0. \quad (5)$$

Reducing equation (5) to terms containing

powers of sin θ gives

$$\left(\lambda+\frac{b}{2}\right)^2 \omega_z^4 \sin^4\theta+2R\left(\lambda+\frac{b}{2}\right)\omega_z^4\sin^3\theta$$
$$+\left[R^2\omega_z^4-\left(\lambda+\frac{b}{2}\right)^2\omega_z^4+g^2\right]\sin^2\theta$$
$$-2R\left(\lambda+\frac{b}{2}\right)\omega_z^4\sin\theta-R^2\omega_z^4=0. \quad (6)$$

Appendix I gives a solution of Equation (6) for the case of the model satellite under development. Horner's method is used to approximate the desired root of Equation (6) with the determined coefficients.

The derivative of Equation (4) gives

$$\frac{d}{d\theta}\left[\sum_{i=1}^{2} M_i\right]=W\left(\lambda+\frac{b}{2}\right)\left\{\frac{\omega_z^2}{g}\left[-R\sin\theta+\left(\lambda+\frac{b}{2}\right)\cos 2\theta\right]-\cos\theta\right\}. \quad (7)$$

Maxima and minima are obtained from the equation

$$\frac{d}{d\theta}\left[\sum_{i=1}^{2} M_i\right]=0. \quad (8)$$

Reducing Equation (8) to terms containing powers of sin θ gives

$$4\omega_z^4\left(\lambda+\frac{b}{2}\right)^2\sin^4\theta+4R\omega_z^4\left(\lambda+\frac{b}{2}\right)\sin^3\theta$$
$$+\left[\omega_z^4R^2-4\omega_z^4\left(\lambda+\frac{b}{2}\right)^2+g^2\right]\sin^2\theta$$
$$-2R\omega_z^4\left(\lambda+\frac{b}{2}\right)\sin\theta$$
$$+\omega_z^4\left(\lambda+\frac{b}{2}\right)^2-g^2=0. \quad (9)$$

Appendix II gives a solution of Equation (9) for the case of the model satellite under development. Again Horner's method is used to approximate the desired root.

The general torque equation is normalized by rearranging the terms of Equation (4)

$$\frac{\sum M_i}{W\left(\lambda+\frac{b}{2}\right)}=R\omega_z^2\left[\frac{\cos\theta}{g}\right]+\left(\lambda+\frac{b}{2}\right)\omega_z^2\left[\frac{\sin 2\theta}{2g}\right]+[-\sin\theta]. \quad (10)$$

Let

$$f_1=R\omega_z^2\left[\frac{\cos\theta}{g}\right] \quad (11a)$$

$$f_2=\left(\lambda+\frac{b}{2}\right)\omega_z^2\left[\frac{\sin 2\theta}{2g}\right] \quad (11b)$$

$$f_3=[-\sin\theta] \quad (11c)$$

Normalizing equations (11) with respect to the geometrical parameters and spin rate gives

$$\frac{f_1}{R\omega_z^2}=\left[\frac{\cos\theta}{g}\right] \quad (12a)$$

$$\frac{f_2}{\left(\lambda+\frac{b}{2}\right)\omega_z^2}=\left[\frac{\sin 2\theta}{2g}\right] \quad (12b)$$

$$f_3=[-\sin\theta]. \quad (12c)$$

Each right-hand side of Equations (12) is plotted in Figure 3. The value of f_3 and the normalized values of f_1 and f_2 are determined from the

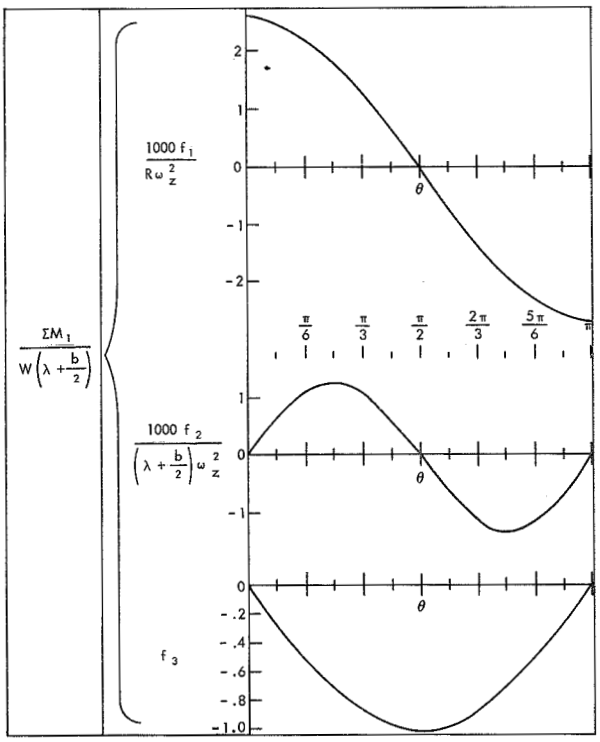

FIGURE 3.—A graph of the normalized components of the general torque equation versus paddle-arm angle.

curves for each particular θ. Denormalizing each amplitude factor and algebraically adding them gives the total normalized torque. Denormalizing again gives the total torque for a particular value of θ. A specific example for the model satellite is given in Appendix III. Figure 6 in Appendix III shows a plot of the total torque as a function of θ, for the model satellite.

MOMENT OF INERTIA

Figure 4 shows an isolated solar paddle drawn with respect to the paddle-arm uv-rotation plane. The geometry of the paddle, as labeled, refers to the translated-rotated $u'v'w'$ coordinate system. Coordinates in the $u'v'w'$ system are related to the coordinates in the $u'v'w'$ system by the following transformations:

$$\left.\begin{aligned} u' &= w'' \sin p + u'' \cos p \\ v' &= v'' \\ w' &= w'' \cos p - u'' \sin p \end{aligned}\right\} \tag{13}$$

where p is the pitch angle of the paddle. The moment of inertia about the w'-axis of the

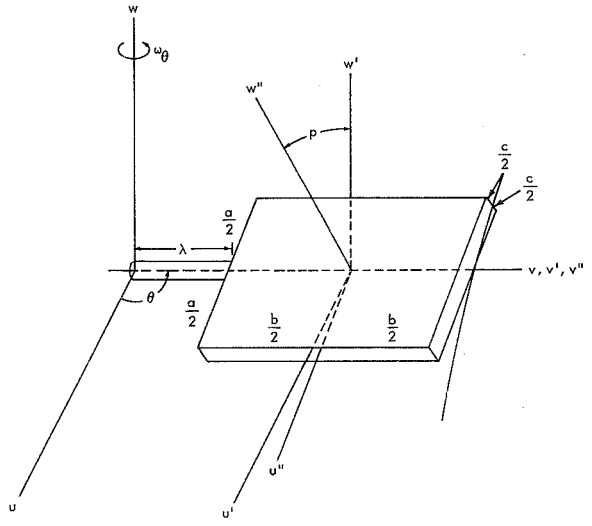

FIGURE 4.—An isolated solar paddle drawn with respect to the paddle-arm uv-rotation plane.

$u'v'w'$ coordinate system is by definition

$$I_{w'w'} = \int_m (u'^2 + v'^2)\, dm. \tag{14}$$

Using the transformation Equations (13), the above equation becomes

$$I_{w'w'} = \int_m (\sin^2 pw''^2 + \cos^2 pu''^2 + \sin 2pu''w'' + v''^2)\, dm \tag{15}$$

or

$$I_{w'w'} = \rho \int_{-\frac{c}{2}}^{\frac{c}{2}} \int_{-\frac{b}{2}}^{\frac{b}{2}} \int_{-\frac{a}{2}}^{\frac{a}{2}} (\sin^2 pw''^2 + \cos^2 pu''^2 + \sin 2pu''w'' + v''^2)\, du''dv''dw'' \tag{16}$$

where

$$dm = \rho du''dv''dw''. \tag{17}$$

Integrating over w'' gives

$$I_{w'w'} = \rho \int_{-\frac{b}{2}}^{\frac{b}{2}} \int_{-\frac{a}{2}}^{\frac{a}{2}} \left(\frac{c^3}{12} \sin^2 p + c \cos^2 pu''^2 + cv''^2\right) du''dv''. \tag{18}$$

Integrating over u'' gives

$$I_{w'w'} = \rho \int_{-\frac{b}{2}}^{\frac{b}{2}} \left(\frac{ac^3}{12} \sin^2 p + \frac{a^3c}{12} \cos^2 p + acv''^2\right) dv''. \tag{19}$$

Integrating over v'' gives

$$I_{w'w'} = m\left(\frac{a^2}{12} \cos^2 p + \frac{b^2}{12} + \frac{c^2}{12} \sin^2 p\right) \tag{20}$$

where

$$m = \rho abc. \tag{21}$$

Coordinates in the uvw system are related to the coordinates in the $u'v'w'$ system by the following transformations:

$$\left.\begin{aligned} u &= u' \\ v &= v' + \left(\lambda + \frac{b}{2}\right) \\ w &= w' \end{aligned}\right\} \tag{22}$$

where λ is the length of the paddle arm. The moment of inertia about the w-axis of the uvw coordinate system is by definition

$$I_{ww}=\int_m (u^2+v^2)\,dm \tag{23}$$

substituting Equations (22) in Equation (23) gives

$$I_{ww}=\int_m (u'^2+v'^2)\,dm + \left(\lambda+\frac{b}{2}\right)^2\int_m dm+2\left(\lambda+\frac{b}{2}\right)\int_m v'\,dm \tag{24}$$

Integrating the above expression, the third term reduces to zero because of symmetry and the result is

$$I_{ww}=I_{w'w'}+\left(\lambda+\frac{b}{2}\right)^2 m \tag{25}$$

or

$$I=I_{ww}=m\left[\frac{a^2}{12}\cos^2 p+\frac{b^2}{12}+\frac{c^2}{12}\sin^2 p+\left(\lambda+\frac{b}{2}\right)^2\right]. \tag{26}$$

The moment of inertia equation is normalized by writing it in the following form:

$$\frac{I}{m}=\frac{(a^2-c^2)}{12}[\cos^2 p]+\left[\frac{b^2}{12}+\frac{c^2}{12}+\left(\lambda+\frac{b}{2}\right)^2\right]. \tag{27}$$

Let

$$f_4=\left(\frac{a^2-c^2}{12}\right)[\cos^2 p] \tag{28a}$$

$$f_5=\frac{b^2}{12}+\frac{c^2}{12}+\left(\lambda+\frac{b}{2}\right)^2. \tag{28b}$$

Normalizing Equations (28) with respect to the geometrical parameters gives

$$\frac{f_4}{\frac{(a^2-c^2)}{12}}=[\cos^2 p] \tag{29a}$$

$$\frac{f_5}{\frac{b^2}{12}+\frac{c^2}{12}+\left(\lambda+\frac{b}{2}\right)^2}=[1]. \tag{29b}$$

Each right side of Equations (29) is plotted in Figure 5. The normalized values of f_4 and f_5 are determined from the curves for each particular p. Denormalizing each amplitude factor and algebraically adding them gives the total normalized moment of inertia for a particular paddle-pitch angle. Denormalizing again gives the moment of inertia. A specific example for one of the model's paddles is given in Appendix IV. Figure 7 in Appendix IV shows a plot of the data obtained from Figure 5 for the particular paddle.

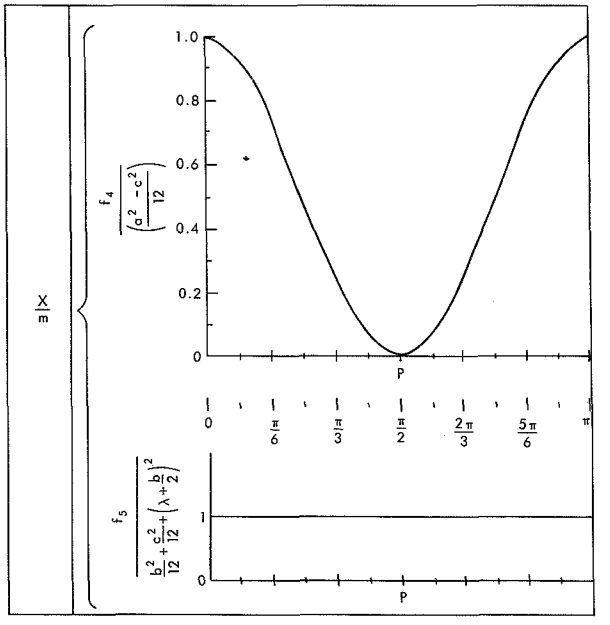

FIGURE 5.—A graph of the normalized components of the paddle moment of inertia versus the paddle-pitch angle.

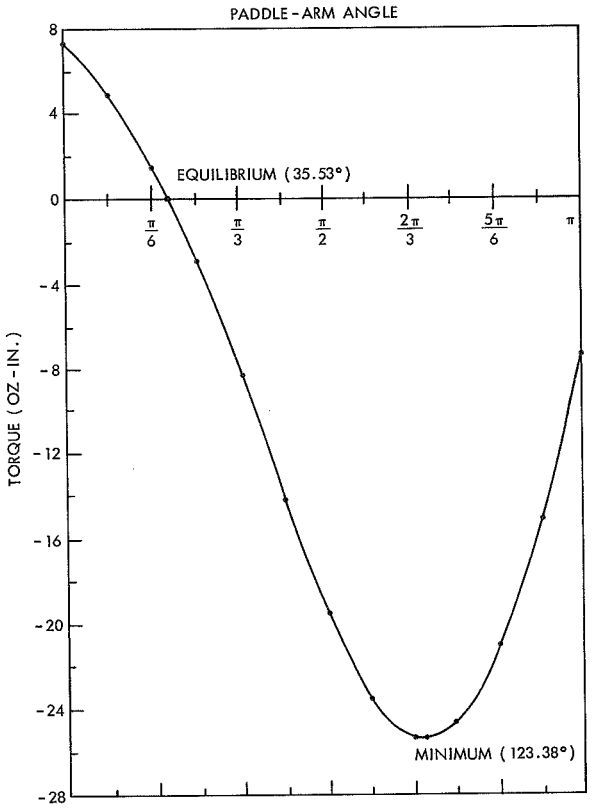

FIGURE 6.—A plot of conservative torque versus paddle-arm angle for the model satellite..

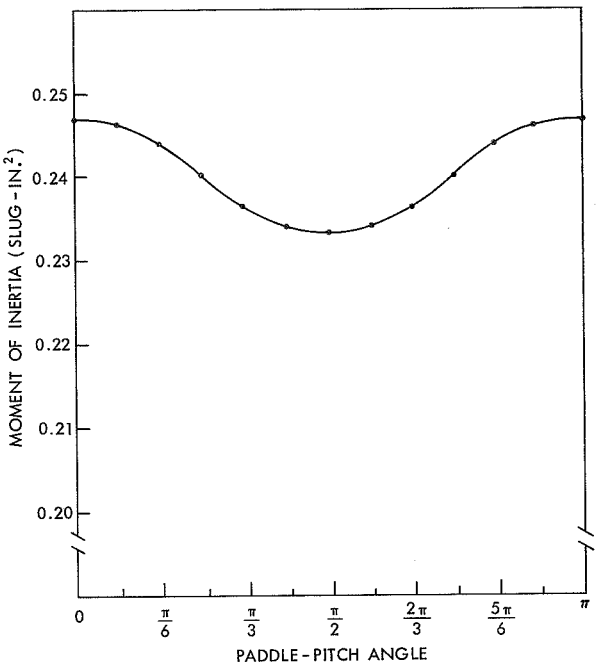

FIGURE 7.—A plot of the moment of inertia versus pitch angle for the model paddle.

Appendix I

$a=5.00$ in. $\quad \lambda=2.25$ in. $\quad \omega_z=2\pi$ rad-sec^{-1}

$b=6.50$ in. $\quad R=3.75$ in. $\quad g=384$ in.-sec^{-2}

$$\left(\lambda+\frac{b}{2}\right)^2 \omega_z^4 \sin^4\theta+2R\left(\lambda+\frac{b}{2}\right)\omega_z^4 \sin^3\theta$$
$$+\left[R^2\omega-_z^4\left(\lambda+\frac{b}{2}\right)^2 \omega_z^4+g^2\right]\sin^2\theta$$
$$-2R\left(\lambda+\frac{b}{2}\right)^2 \omega_z^4 \sin\theta-R^2\omega_z^4=0. \quad (6)$$

Evaluating the coefficients in the above equation gives

$$\left(\lambda+\frac{b}{2}\right)^2 \omega_z^4=0.472\times10^{-5} \text{ in.}^2\text{-sec}^{-4}$$

$$2R\left(\lambda+\frac{b}{2}\right)\omega_z^4=0.643\times10^{-5} \text{ in.}^2\text{-sec}^{-4}$$

$$R^2\omega_z^4-\left(\lambda+\frac{b}{2}\right)^2 \omega_z^4+g^2=1.22\times10^{-5} \text{ in.}^2\text{-sec}^{-4}$$

$$2R\left(\lambda+\frac{b}{2}\right)\omega_z^4=0.643\times10^{-5} \text{ in.}^2\text{-sec}^{-4}$$

$$R^2\omega_z^4=0.219\times10^{-5} \text{ in.}^2\text{-sec}^{-4}.$$

Substitution of calculated coefficients in quartic gives

$$\sin^4\theta+1.36\sin^3\theta+2.58\sin^2\theta$$
$$-1.36\sin\theta-0.464=0$$

Horner's Method gives

1	1.36	2.58	−1.36	−0.464	0.5
	0.5	0.93	1.76	0.200	
1	1.86	3.51	0.40	−0.264	
	0.5	1.18	2.34		
1	2.36	4.69	2.74		
	0.5	1.43			
1	2.86	6.12			
	0.5				
1	3.36	6.12	2.74	−0.264	0.08
	0.08	0.27	0.51	0.260	
1	3.44	6.39	3.25	−0.004	
	0.08	0.28	0.53		
1	3.52	6.67	3.78		
	0.08	0.29			
1	3.60	6.96			
	0.08				
1	3.68	6.96	3.78	−0.004	0.001
	0.001	0.004	0.007	0.0038	
1	3.681	6.964	3.787	−0.0002	

$$\therefore \sin\theta=0.5+0.08+0.001+\cdots=0.581^+$$
$$\theta=\text{arc sin } (0.581)$$
$$\theta=35.53°$$

This is the angle at which equilibrium occurs.

Appendix II

$a=5.00$ in. $\quad \lambda=2.25$ in. $\quad \omega_z=2\pi$ rad-sec^{-1}

$b=6.50$ in. $\quad R=3.75$ in. $\quad g=384$ in.-sec^{-2}

$$4\omega_z^4\left(\lambda+\frac{b}{2}\right)^2\sin^4\theta+4R\omega_z^4\left(\lambda+\frac{b}{2}\right)\sin^3\theta$$
$$+\left[\omega_z^4R^2-4\omega_z^4\left(\lambda+\frac{b}{2}\right)^2+g^2\right]\sin^2\theta$$
$$-2R\omega_z^4\left(\lambda+\frac{b}{2}\right)\sin\theta+\omega_z^4\left(\lambda+\frac{b}{2}\right)^2-g^2=0. \quad (6)$$

Evaluating the coefficients in the above equation gives

$$4\omega_z^4\left(\lambda+\frac{b}{2}\right)^2=1.89\times10^{-5}\text{ in.}^2\text{-sec}^{-4}$$

$$4R\omega_z^4\left(\lambda+\frac{b}{2}\right)=1.29\times10^{-5}\text{ in.}^2\text{-sec}^{-4}$$

$$\omega_z^4R^2-4\omega_z^4\left(\lambda+\frac{b}{2}\right)^2+g^2=-0.193\times10^{-5}\text{ in.}^2\text{-sec}^{-4}$$

$$2R\omega_z^4\left(\lambda+\frac{b}{2}\right)=0.643\times10^{-5}\text{ in.}^2\text{-sec}^{-4}$$

$$\omega_z^4\left(\lambda+\frac{b}{2}\right)^2-g^2=-1.00\times10^{-5}\text{ in.}^2\text{-sec}^{-4}.$$

Substitution of calculated coefficients in quartic gives

$$\sin^4\theta+0.682\sin^3\theta-0.102\sin^2\theta$$
$$-0.340\sin\theta-0.529=0$$

Horner's Method gives

1	0.682	−0.102	−0.340	−0.529	0.8
	0.8	1.186	0.867	0.422	
1	1.482	1.084	0.527	−0.107	
	0.8	1.826	2.328		
1	2.282	2.910	2.855		
	0.8	2.466			
1	3.082	5.376			
	0.8				
1	3.882	5.376	2.855	−0.107	0.03
	0.03	0.117	0.165	0.091	
1	3.912	5.493	3.020	−0.016	
	0.03	0.118	0.168		
1	3.942	5.611	3.188		
	0.03	0.119			
1	3.972	5.730			
	0.03				
1	4.002	5.730	3.188	−0.016	0.005
	0.005	0.020	0.029	0.0161	
1	4.007	5.750	3.217	+0.0001	

$$\therefore \sin\theta=0.8+0.03+0.005-\cdots=0.835-$$
$$\theta=\text{arc sin }(0.835)$$
$$\theta=123.38°.$$

This is the angle at which maximum torque occurs.

Appendix III

$a=5.00$ in.

$b=6.50$ in.

$\lambda=2.25$ in.

$R=3.75$ in.

$\omega_z=2\pi$ rad-sec^{-1}

$W=100$ gm-wt$=3.53$ oz

$\lambda+\frac{b}{2}=5.50$ in.

$W\left(\lambda+\frac{b}{2}\right)=19.4$ oz-in.

$\frac{R\omega_z^2}{1000}=0.148$ in.-sec^{-2}

$\frac{\left(\lambda+\frac{b}{2}\right)\omega_z^2}{1000}=0.217$ in.-sec^{-2}

θ	$\frac{1000\,f_1}{R\omega_z^2}$	f_1	$\frac{1000\,f_2}{\left(\lambda+\frac{b}{2}\right)\omega_z^2}$	f_2	f_3	$f_1+f_2+f_3$	$W\left(\lambda+\frac{b}{2}\right)(f_1+f_2+f_3)$
0°	2. 60	0. 385	0. 00	0. 000	0. 000	0. 385	7. 47
15°	2. 51	. 371	. 65	. 141	−. 259	. 253	4. 91
30°	2. 25	. 333	1. 13	. 245	−. 500	. 078	1. 51
45°	1. 84	. 272	1. 30	. 282	−. 707	−. 153	−2. 97
60°	1. 30	. 192	1. 13	. 245	−. 866	−. 429	−8. 32
75°	. 67	. 099	. 65	. 141	−. 966	−. 726	−14. 1
90°	. 00	. 000	. 00	. 000	−1. 000	−1. 000	−19. 4
105°	−. 67	−. 099	−. 65	−. 141	−. 966	−1. 21	−23. 4
120°	−1. 30	−. 192	−1. 13	−. 245	−. 866	−1. 30	−25. 3
135°	−1. 84	−. 272	−1. 30	−. 282	−. 707	−1. 26	−24. 5
150°	−2. 25	−. 333	−1. 13	−. 245	−. 500	−1. 08	−20. 9
165°	−2. 51	−. 371	−. 65	−. 141	−. 259	−. 771	−15. 0
180°	−2. 60	−. 385	. 00	. 000	. 000	−. 385	−7. 47

764-173 O—65——64

Appendix IV

$a=5.00$ in.
$b=6.50$ in.
$c=0.375$ in.

$m=6.89\times10^{-3}$ slugs

$\lambda+\frac{b}{2}=5.50$ in.

$\frac{a^2-c^2}{12}=2.07$ in.^{2}

$\frac{b^2}{12}+\frac{c^2}{12}+\left(\lambda+\frac{b}{2}\right)^2=33.8$ in.^{2}

p	$\frac{f_4}{\frac{(a^2-c^2)}{12}}$	f_4	f_4+f_5	$m(f_4+f_5)$
0°	1.000	2.07	35.9	0.247
15°	.933	1.93	35.7	.246
30°	.750	1.55	35.4	.244
45°	.500	1.04	34.8	.240
60°	.250	.518	34.3	.236
75°	.067	.139	33.9	.234
90°	.000	.000	33.8	.233
105°	.067	.139	33.9	.234
120°	.250	.518	34.3	.236
135°	.500	1.04	34.8	.240
150°	.750	1.55	35.4	.244
165°	.933	1.93	35.7	.246
180°	1.000	2.07	35.9	.247

A FINITE DIFFERENCE SOLUTION FOR THE TRANSVERSE VIBRATION OF A RECTANGULAR PLATE WITH INTERNAL VISCOUS DAMPING SUPPORTED AT A FINITE NUMBER OF POINTS UNDER GENERAL BOUNDARY CONDITIONS

C. A. WAGNER
Goddard Space Flight Center

INTRODUCTION AND SUMMARY

The design of solar panels for spacecraft involves consideration of critical support vibration during the launch-burnout phase. The panels themselves, during this phase are often attached to the body of the spacecraft at three or more points or along an entire edge and at a single additional point. It is felt that the complexity of the actual time dependent boundary conditions is critical to the design of the panels and warrants a finite difference analysis where *all* the differential equations describing the deflection of the plate are approximated and the resulting equations solved exactly at a finite number of points on the plate. In this manner, a great number of boundary conditions may be handled by a single analysis without difficulty or special consideration.

In this report, all the necessary finite difference equations of equilibrium, boundary restraint, and initial conditions have been written for the general case of the transversely loaded vibrating thin plate. Once the viscous response parameter of the real plate is known or assumed, as well as a number of other material constants, and parameters specifying the boundary and initial conditions, the vibratory and the state of stress history at a finite number of points on the plate may be calculated in a simple step by step fashion to any desired length of time by following the procedure detailed in Part 13. This step by step solution is ideally suited for digital programming. No actual solutions are calculated. The report details a simply executed analytic tool for investigating the complex state of stress and vibration in a plate whose boundaries may be supported in an arbitrary way, subject to mathematical definition and the laws of linear small deflection elasticity. Specific examples of the specification of input parameters for all simple and all free edge supports, are included.

The model employed is a thin homogeneous and isotropic elastic plate (with linear internal viscous damping) unstressed in the middle plane and having negligible deflection due to shear. The analysis may be modified without essential difficulty to cover sandwich-type plates. It is proposed that the natural modes of vibration be determined for quite general fixed or free boundaries from the solutions to a high order algebraic equation. The most rapid period of natural vibration so determined serves as the basis for fixing the time step in continuing the finite difference solution for the forced vibration of the plate. The viscous response of an actual plate may be evaluated by causing the plate to vibrate in a simple natural mode, and measuring the Log. to the base "e" of the decrement of the amplitude over a number of cycles.

NOMENCLATURE

i, j	Space mesh indices corresponding to the x, y or x_1, y_1 dimensionless space axes of the plate.
k	Time index corresponding to the t (real time) or T (dimensionless time) axes.
W	Lateral displacement of the plate. (units: length)
h	Thickness of the plate. (units: length)
a	Longest side of the plate. (units: length)
b	Shortest side of the plate. (units: length)
r_1, r_2	Number of divisions of sides a and b of the plate respectively.
q	Load on the plate. (units: force/length^2)
D	Plate rigidity. (units: force·length)
E	Elastic modulus of the plate. (units: force/length^2)
γ	Poisson's ratio of the plate. (units: dimensionless)
M	Mass density of the plate. (units: mass/length^2)
μ	Viscosity of the plate. (units: force · time/length)
S_v	Lateral displacement of the plate in a natural mode v. (units: length)
M_x or M_y	Bending moment per unit length along x or y faces.
M_{xy}	Twisting moment per unit length on x faces.
$M_{yx}(=-M_{xy})$	Twisting moment per unit length on y faces.
Q_x or Q_y	Shear force per unit length along x or y faces.
h_1, h_2	Mesh spacing along the x and y axes respectively.
h_1^1, h_2^1	Mesh spacing along the x_1 and y_1 dimensionless space axes respectively.
$(x, y), (x_1, y_1)$	Real and dimensionless space axes respectively.
$\cdot$ (dots)	Derivatives with respect to real time, t.
t, T	Real and dimensionless time respectively.
ΔT	Mesh spacing along the T dimensionless time axis.
t_0	The "characteristic time" of vibration of the plate. (units: time)
α^2	A plate inertia constant. (units: accel · length^3·)
q_1	The acceleration load on the plate. (units: acceleration)
B	A plate viscous-density constant. (units: force/vel · mass)
v	One of n natural modes of vibration for the plate.
$(A_{i,j}), (B_{i,j})$	Matrix coefficients of the system of equations defining the natural modes of vibration of the plate.
x_v	The characteristic frequency of the plate in the natural mode of vibration v. (units: dimensionless)
p_v	The undamped frequency of natural vibration in mode v. (units: time^{-1})
n_v	The damped frequency of natural vibration in mode v. (units: time^{-1})
T_v	The time variation of the natural mode v of the plate. (units: dimensionless)
A_v	Amplitude of a natural mode of vibration v. (units: . . . dimensionless)
ϕ_v	Phase angle of the vibration of the plate in a natural mode v. (units: dimensionless)
a_l	Boundary condition constants.
c	Initial displacement constants. (units: length)
d	Initial displacement rate con stants. (units: velocity)
$W_{i,j,k}, S_{i,j,k}$	Displacement of the plate at grid point i, j, k. (units: length)

$+$	Plus.
Δ_t	Mesh spacing along the t real time axis.
k_0	Time axis index to which the vibratory behavior is desired.

THE PROBLEM (see figure 1)

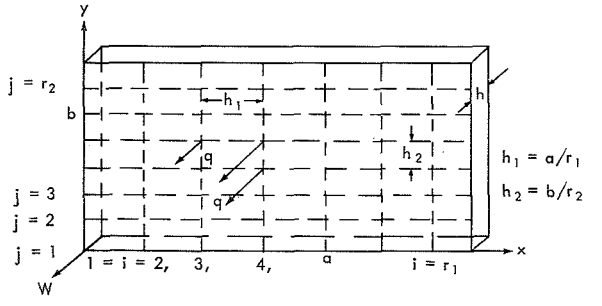

FIGURE 1.—The plate with space grid mesh (i, j).

A rectangular plate is given of sides a and b and supported at any of three or more points on the boundaries: $j=1$; $i=1, 2 \ldots r_1+1$: $i=r_1+1; j=2, 3 \ldots r_2+1$: $j=r_2+1; i=2, 3 \ldots r_1$: $i=1$; $j=2, 3 \ldots r_2+1$.

Small h_1 is the uniform mesh spacing along the x axis and h_2 is the uniform mesh spacing along the y axis. Small h is the thickness of the plate. It is assumed that ordinary thin plate theory holds. In particular, the shear in the plate is assumed to make negligible contribution to the transverse deflection W, and the stress in the middle plane of the plate is assumed to be of minor consequence on W also. These limitations of the analysis are not severe as far as real plates are concerned. The general validity of thin plate theory is amply discussed in Reference 2.

A viscous damping force of $-\mu\dot{W}$ is assumed to act at every point within the boundary of the vibrating plate. (See Fig. 2.) The density of the plate is M in units of Mass/Area. The elastic modulus is E. Poisson's ratio is γ and the plate rigidity is $D=Eh^3/12(1-\gamma)$, in Force·Length units. Small q is the load on the plate in units of Force/Area. The problem is to determine the natural modes of vibration of the plate and its response to an arbitrary transverse motion of the support points.

THE ANALYSIS (see figure 2)

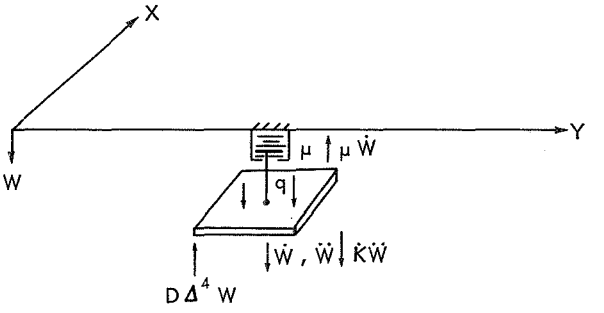

FIGURE 2.—Loading diagram with model of viscous response.

The differential equation of transverse motion of the plate is given as a dynamic equilibrium (D'Alembert) equation:

$$D\nabla^4 W+\mu\dot{W}+M\ddot{W}-q=0. \qquad (1)$$

(See Fig. 2 and Refs. 2 and 4.)

Dividing (1) by M yields:

$$(D/M)\nabla^4 W+(\mu/M)\dot{W}+\ddot{W}=q/M. \qquad (2)$$

checking the dimensions of (2):

$$\nabla^4 W=\frac{\partial^4 W}{\partial x^4}+\frac{2\partial^4 W}{\partial x^2\partial y^2}+\frac{\partial^4 W}{\partial y^4}\text{: Units-Length}^{-3}$$

$$D/M\text{: Units}-\frac{\text{Force}\cdot\text{Length}}{\text{Mass}/(\text{Length})^2}$$
$$=\text{Acceleration}\cdot\text{Length}^3.$$

Therefore,

$$(D/M)\nabla^4 W\text{: Units}-\text{Acceleration}$$

$$\mu\text{: Units}-\text{Force/Length}^2\cdot\text{Velocity}$$

$$\frac{\mu\dot{W}}{M}\text{: Units}$$

$$-\frac{\text{Force}}{\text{Length}^2\cdot\text{Velocity}}\cdot\frac{\text{Velocity}}{\text{Force/Accel}\cdot\text{Length}^2}$$
$$=\text{Acceleration}.$$

TRANSFORMING TO DIMENSIONLESS COORDINATES

Let T, x_1 and y_1 be dimensionless coordinates such that:

$$x_1=x/a$$

$$y_1=y/b$$

$$T=t/t_0.$$

Small b is the shortest side of the plate. Small t_0 is a characteristic vibration time to be determined later. With the above new variables:

$$\frac{\partial}{\partial x}=\frac{\partial}{a\partial x_1},\ \frac{\partial^2}{\partial x^2}=\frac{\partial^2}{a^2\partial {x_1}^2}\ \text{etc.}$$

$$\frac{\partial}{\partial t}=\frac{\partial}{t_0\partial T},\ \frac{\partial^2}{\partial t^2}=\frac{\partial^2}{t_0^2\partial T^2}.$$

Also let:

$\alpha^2=D/M$ (Units—Accel · Length^3)

$q_1=q/M$ Units—(Force/Area)/(Mass/Area) =Acceleration)

$B=\mu M$ (Units—Force/Velocity · Mass.)

With these new variables and constants, (2) becomes:

$$\alpha^2\left\{\frac{\partial^4 W}{a^4\partial {x_1}^4}+\frac{2\partial^4 W}{a^2b^2\partial {x_1}^2\partial {y_1}^2}+\frac{\partial^4 W}{b^4\partial {y_1}^4}\right\}+\frac{B}{t_0}\frac{\partial W}{\partial T}+\frac{1}{t_0^2}\frac{\partial^2 W}{\partial T^2}=q_1(v_1, y_1, T). \quad (3)$$

DETERMINING THE NATURAL MODES OF VIBRATION

In (3), let:

$$W_v=W=[S_v(x_1, y_1)][T_v(t)],$$

when $q_1\equiv 0$. The W_v are the natural vibrations of mode v. With the natural modes so defined, (3) becomes;

$$\alpha^2\left[\frac{S_v^{x_1^4}T_v}{a^4}+\frac{2S_v^{x_1^2y_1^2}T_v}{a^2b^2}+\frac{S_v^{y_1^4}T_v}{b^4}\right]+BS_v\dot{T}_v+S_v\ddot{T}_v=0. \quad (4)$$

In (4):

$$S_v^{x_1^4}=\frac{\partial^4 S_v(x_1, y_1)}{\partial x_1^4},\ \text{etc.}$$

$$\dot{T}_v=\frac{\partial T_v(t)}{\partial t},\ \text{etc.}$$

Dividing (4) by T_vS_v and rearranging:

$$\frac{\alpha^2}{S_v}\left[\frac{S_v^{x_1^4}}{a^4}+\frac{2S_v^{x_1^2y_1^2}}{a^2b^2}+\frac{S_v^{y_1^4}}{b^4}\right]=-(B\dot{T}_v+\ddot{T}_v)/T_v=+p_v^2. \quad (5)$$

Small p_v^2 is a constant since the left side of (5) is a function of (x_1,y_1) only and the right is a function of t only. Solving the right side of (5) for the time variation, (5) *rt.* becomes:

$$\ddot{T}_v+B\dot{T}_v+p_v^2T_v=0. \quad (6)$$

A solution of (6) is taken in the form:

$$T_v(t)=A_ve^{-k_vt}\cos(n_vt+\phi_v). \quad (7)$$

Substituting (7) into (6) implies:

$$e^{-k_vt}\cos(n_vt+\phi_v)[p_v^2-Bk_v+k_v^2-n_v^2]+e^{-k_vt}\sin(n_vt+\phi_v)[-Bn_v+2n_vk_v]=0. \quad (8)$$

In order for (8) to hold for all time, the following identities must be satisfied:

$$p_v^2-Bk_v+k_v^2-n_v^2\equiv 0 \quad (9)$$

$$-Bn_v+2n_vk_v\equiv 0. \quad (10)$$

From (10), for $n_v\neq 0$, it follows that:

$$k_v=B/2. \quad (11)$$

With these results in (9), it follows that:

$$p_v^2-(B^2/2)+(B^2/4)-n_v^2=0.$$

Solving for n_v:

$$n_v=\tfrac{1}{2}(4p_v^2-B^2)^{1/2}. \quad (12)$$

It may be seen that the solution $n_v=0$ also implies that $k_v=B/2$. This condition (called critical damping) can only come about when the essential parameters of the vibrating plate, p_v, the undamped natural mode frequency, and B, the damping coefficient, are so adjusted that

$4p_v^2=B^2$, as may be verified in (12). When $n_v=0$, (9) shows that $k_v=(B/2)\pm\frac{1}{2}(B^2-4p_v^2)^{1/2}$. But since $4p_v^2=B^2$ at critical damping, $k_v=B/2$ there also.

The general solution of (7) thus becomes:

$$T_v(t)=A_v e^{-Bt/2}\cos\left[\tfrac{1}{2}(4p_v^2-B^2)^{1/2}t+\phi_v\right]. \quad (13)$$

In (13), A_v and ϕ_v are constants to be determined from the initial conditions, and p_v is found for each mode v from the solution of the left side of (5).

BOUNDARY CONDITIONS

The general boundary condition equation, two of which must be satisfied at each mesh point, is written as:

$$a_1W+a_2\frac{\partial W}{\partial x}+a_3\frac{\partial W}{\partial y}+a_4\frac{\partial^2 W}{\partial x^2}+a_5\frac{\partial^2 W}{\partial y^2}+a_6\frac{\partial^2 W}{\partial x\partial y}+a_7\frac{\partial^3 W}{\partial x^3}+a_8\frac{\partial^3 W}{\partial y^3}+\ldots+a_9\frac{\partial^3 W}{\partial x^2\partial y}+a_{10}\frac{\partial^3 W}{\partial y\partial x^2}+a_{11}=0. \quad (14)$$

In (14), the a's take on assigned values depending on the particular edge conditions at the mesh point.

DETERMINING THE VISCOUS RESPONSE (μ) OF THE PLATE

We assume that the viscous response in each mode v is the same. Therefor, $W=\sum_v S_vT_v=e^{-Bt/2}\sum_v S_v\cos[\frac{1}{2}(4p_v^2-B^2)^{1/2}t+\phi_v]$. The series $\sum_v$ may or may not be periodic at all times over the naturally vibrating surface of the plate, depending on the initial conditions imposed. However, if the plate is placed initially in a mode close to S_v, the other modes, after a short time, will affect the vibration to a negligible degree due to the damping. In this way, a periodicity of motion (period$=2\pi/p_v$) is assured for the entire plate after a reasonable length of time.

In the case of initial oscillation in or close to mode v, let

$$T_v'=4\pi/(4p_v^2-B^2)^{1/2}. \quad (15)$$

Then, if the maximum amplitude at the m oscillation is A_m, the amplitude at the $m+1$ oscillation is A_{m+1}. It may be shown that if $4p_v^2>>B^2$, then

$$A_i/A_{m+1}\doteq\frac{e^{-Bt_m/2}}{e^{-(B/2)(t_m+T_v)}}=\ldots e^{BT_v'/2}$$

$$=\text{a constant for all } m. \quad (16)$$

From (16), it follows that:

$$\ln(A_m/A_{m+1})\doteq BT_v'/2, \quad (17)$$

as long as the damping is far from critical. Therefore, from measurements of a series of nearly equal time spaced maximum amplitudes of the plate in modal oscillation, average values of $\ln(A_m/A_{m+1})$ may be evaluated from which B may be calculated from (17) on eliminating T_v' from (15) at the known p_v of the oscillation. μ is then computed as:

$$\mu=BM. \quad (18)$$

In the general case, once periodicity of the motion has been established at any point on the plate, (16) may be assumed to hold where T_v' is computed as the period of a complex oscillation and μ computed from (17) and (18) as in the case for a simple oscillation of a single mode.

DETERMINING THE MODE SHAPES AND FREQUENCIES OF FREE-NATURAL VIBRATIONS BY FINITE DIFFERENCE METHODS

Equation (5) becomes on rearranging:

$$S_{v_1}^{x_1^4}+2(a/b)^2S_{v_1}^{x_1^2y_1^2}+(a/b)^4S_{v_1}^{y_1^4}=(P_va^2/\alpha)^2S_v. \quad (19)$$

We approximate (19) by the following central difference equation:

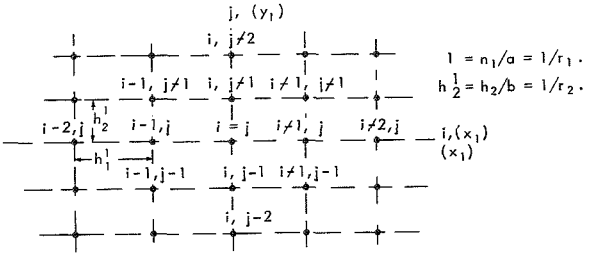

FIGURE 3.—Central difference grid (i, j).

$$S_{i,j}[8(a/b)^2r_1^2r_2^2+6\{(a/b)^4r_2^4+r_1^4\}-(P_va^2/\alpha)^2]+S_{i+1,j}[\ \ldots -4\{(a/b)^2r_1^2r_2^2+r_1^4\}]$$
$$+S_{i-1,j}[-4\{(a/b)^2r_1^2r_2^2+r_1^4\}]+S_{i,j+1}[\ \ldots -4\{(a/b)^2r_1^2r_2^2+(a/b)^4r_2^4\}]$$
$$+S_{i,j-1}[-4\{(a/b)^2r_1^2r_2^2+(a/b)^4r_2^4\}]\ \ldots +S_{i+1,j+1}[2(a/b)^2r_1^2r_2^2]+S_{i-1,j+1}[2(a/b)^2r_1^2r_2^2]$$
$$+S_{i-1,j-1}[\ \ldots 2(a/b)^2r_1^2r_2^2]+S_{i+1,j-1}[2(a/b)^2r_1^2r_2^2]+S_{i+2,j}[r_1^4]+S_{i-2,j}[r_1^4]$$
$$+\ \ldots +S_{i,j+2}[(a/b)^4r_2^4]+S_{i,j-2}[(a/b)^4r_2^4]=0. \quad (20)$$

The boundary Equations (14) are written in the nondimensional coordinate form:

$$a_1W+(a_2/a)\left(\frac{\partial W}{\partial x_1}\right)+(a_3/b)\left(\frac{\partial W}{\partial y_1}\right)+(a_4/a)\left(\frac{\partial^2 W}{\partial x_1^2}\right)+(a_5/b^2)\left(\frac{\partial^2 W}{\partial y_1^2}\right)+\ \ldots +(a_6/ab)\left(\frac{\partial^3 W}{\partial x_1\partial y_1}\right)$$
$$+(a_7/a^3)\left(\frac{\partial^3 W}{\partial x_1^3}\right)+(a_8/b^3)\left(\frac{\partial^3 W}{\partial y_1^3}\right)+(a_9/a^2b)\left(\frac{\partial^3 W}{\partial x_1^2\partial y_1}\right)\ldots +(a_{10}/b^2a)\left(\frac{\partial^3 W}{\partial x_1\partial y_1^2}\right)+a_{11}=0. \quad (21)$$

Small a_1, a_2/a, a_3/b, etc., are dimensionless except a_{11} which has the dimensions of length.

(21) written in finite difference form is:

For the $i=1$ and $j=1$ boundaries

$$W_{i,j}\left[(a_1)_{i,j}-\frac{2(a_4)_{i,j}(r_1)^2}{a^2}-\frac{2(a_5)_{i,j}r(r_2)^2}{b^2}-\frac{5(a_7)_{i,j}(r_1)^3}{2a^3}+\ \ldots -\frac{5(a_8)_{i,j}(r_2)^3}{2b^3}\right]$$
$$+W_{i+1,j}\left[\frac{(a_2)_{i,j}(r_1)}{2a}+\frac{(a_4)_{i,j}(r_1)^2}{a^2}+\ \ldots +\frac{9(a_7)_{i,j}(r_1)^3}{a^3}-\frac{(a_{10})_{i,j}(r_1)(r_2)^2}{b^2a}\right]+W_{i+2,j}\left[-\frac{12(a_7)_{i,j}(r_1)^3}{a^3}\right.$$
$$\left.+\ \ldots +W_{i+3,j}\frac{7(a_7)_{i,j}(r_1)^3}{a^3}\right]+W_{i+4,j}\left[-\frac{3(a_7)_{i,j}(r_1)^3}{2a^3}\right]+W_{i-1,j}\left[\ \ldots -\frac{(a_2)_{i,j}(r_1)}{2a}+\frac{(a^4)_{i,j}(r_1)^2}{a^2}\right.$$
$$\left.+\frac{(a_{10})_{i,j}(r_1)(r_2)^2}{b^2a}\right]+W_{i,j+1}\left[\ \ldots +\frac{(a_3)_{i,j}(r_2)}{2b}+\frac{(a_5)_{i,j}(r_2)^2}{b^2}-\frac{3(a_6)_{i,j}(r_1)(r_2)}{4ab}+\frac{9(a_8)_{i,j}(r_2)^3}{b^3}+\ \ldots\right.$$
$$\left.-\frac{(a_9)_{i,j}(r_1)^2(r_2)}{2a^2b}\right]+W_{i,j+2}\left[-\frac{12(a_8)_{i,j}(r_2)^3}{b^3}\right]+W_{i,j+3}\left[\ \ldots +\frac{7(a_8)_{i,j}(r_2)^3}{b^3}\right]+W_{i,j+4}\left[-\frac{3(a_8)_{i,j}(r_2)^3}{2b^3}\right]$$
$$+W_{i,j-1}\left[\frac{3(a_6)_{i,j}(r_1)(r_2)}{4ab}\ \ldots -\frac{(a_3)_{i,j}(r_2)}{2b}+\frac{(a_5)_{i,j}(r_2)^2}{b^2}+\frac{(a_9)_{i,j}(r_1)^2(r_2)}{a^2b}\right]$$
$$+W_{i+1,j+1}\left[\ \ldots +\frac{(a_6)_{i,j}(r_1)(r_2)}{ab}+\frac{(a_{10})_{i,j}(r_1)(r_2)^2}{2ab^2}+\frac{(a_9)_{i,j}(r_1)^2(r_2)}{2a^2b}\right]+\ \ldots$$

$$+W_{i+1,j-1}\left[-\frac{(a_6)_{i,j}(r_1)(r_2)}{ab}+\frac{(a_{10})_{i,j}(r_1)(r_2)^2}{2ab^2}+\ldots-\frac{(a_9)_{i,j}(r_1)^2(r_2)}{2a^2b}\right]+W_{i+2,j+1}\left[-\frac{(a_6)_{i,j}(r_1)(r_2)}{4ab}\right]$$

$$+W_{i-1,j-1}\left[\ldots-\frac{(a_{10})_{i,j}(r_1)(r_2)^2}{2ab^2}-\frac{(a_9)_{i,j}(r_1)^2(r_2)}{2a^2b}\right]+W_{i+2,j-1}\left[\frac{(a_6)_{i,j}(r_1)(r_2)}{4ab}\right]\ldots$$

$$+W_{i-1,j+1}\left[-\frac{(a_{10})_{i,j}(r_1)(r_2)^2}{2ab^2}+\frac{(a_9)_{i,j}(r_1)^2(r_2)}{2a^2b}\right]+(a_{11})_{i,j}=0. \quad (22\text{–A})$$

And for the $i=r_1+1$ and $j=r_2+1$ boundaries

$$W_{i,j}\left[(a_1)_{i,j}-\frac{2(a_4)_{i,j}(r_1)^2}{a^2}-\frac{2(a_5)_{i,j}(r_2)^2}{b^2}+\frac{5(a_7)_{i,j}(r_1)^3}{2a^3}+\ldots+\frac{5(a_8)_{i,j}(r_2)^3}{2b^3}\right]$$

$$+W_{i+1,j}\left[\frac{(a_2)_{i,j}(r_1)}{2a}+\frac{(a_4)_{i,j}(r_1)^2}{a^2}\right]+W_{i-2,j}\left[\ldots+\frac{12(a_7)_{i,j}(r_1)^3}{a^3}\right]+W_{i-3,j}\left[-\frac{7(a_7)_{i,j}(r_1)^3}{a^3}\right]$$

$$+W_{i-4,j}\left[\frac{3(a_7)_{i,j}(r_1)^3}{2a^3}\right]\ldots+W_{i-1,j}\left[-\frac{(a_2)_{i,j}(r_1)}{2a}+\frac{(a_4)_{i,j}(r_1)^2}{a^2}+\frac{(a_{10})_{i,j}(r_1)(r_2)^2}{ab^2}+\ldots-\frac{9(a_7)_{i,j}(r_1)^3}{a^3}\right]$$

$$+W_{i,j+1}\left[\frac{(a_3)_{i,j}(r_2)}{2b}+\frac{3(a_6)_{i,j}(r_1)(r_2)}{4ab}+\ldots+\frac{(a_5)_{i,j}(r_2)^2}{b^2}-\frac{(a_9)_{i,j}(r_1)^2(r_2)}{2ba^2}\right]$$

$$+W_{i,j-2}\left[\frac{12(a_8)_{i,j}(r_2)^3}{b^3}\right]+\ldots+W_{i,j-3}\left[-\frac{7(a_8)_{i,j}(r_2)^3}{b^3}\right]+W_{i,j-4}\left[\frac{3(a_8)_{i,j}(r_2)^3}{2b^3}\right]+W_{i,j-1}\left[\ldots\right.$$

$$\left.-\frac{(a_3)_{i,j}(r_2)}{2b}+\frac{(a_5)_{i,j}(r_2)^2}{b^2}+\frac{(a_9)_{i,j}(r_1)^2(r_2)}{a^2b}-\frac{9(a_8)_{i,j}(r_2)^3}{b^3}\ldots-\frac{3(a_6)_{i,j}(r_1)(r_2)}{4ab}\right]+W_{i-2,j+1}\left[\frac{(a_6)_{i,j}(r_1)(r_2)}{4ab}\right]$$

$$+W_{i+1,j+1}\left[\ldots\frac{(a_{10})_{i,j}(r_1)(r_2)^2}{2ab^2}+\frac{(a_9)_{i,j}(r_1)^2(r_2)}{2a^2b}\right]+W_{i-1,j-1}\left[\frac{(a_6)_{i,j}(r_1)(r_2)}{ab}-\frac{(a_{10})_{i,j}(r_1)(r_2)^2}{2ab^2}\right.$$

$$\left.-\frac{(a_9)_{i,j}(r_1)^2(r_2)}{2a^2b}\right]+W_{i-1,j+1}\left[\ldots-\frac{(a_6)_{i,j}(r_1)(r_2)}{ab}-\frac{(a_{10})_{i,j}(r_1)(r_2)^2}{2ab^2}+\frac{(a_9)_{i,j}(r_1)^2(r_2)}{2ba^2}\right]+\ldots$$

$$+W_{i-2,j-1}\left[-\frac{(a_6)_{i,j}(r_1)(r_2)}{4ab}\right]+W_{i+1,j-1}\left[\frac{(a_{10})_{i,j}(r_1)(r_2)^2}{2ab^2}+\ldots-\frac{(a_9)_{i,j}(r_1)^2(r_2)}{2ba^2}\right]+(a_{11})_{i,j}=0. \quad (22\text{–B})$$

TYPICAL BOUNDARY CONDITIONS (NOT TIME DEPENDENT)

The specification of $(a_l)_{i,j}$ for $l=1, 2, 3 \ldots 11$, overall boundary i, j, defines the coefficients in (22–A) and (22–B), and thus defines the boundary equations for a particular configuration and mesh size.

(A) Simple support on all sides (continuous)

The conditions on y_1=constant faces are:

$$W=0 \text{ and } W_{y_1y_1}=0.$$

The conditions on x_1=constant faces are:

$$W=0 \text{ and } W_{x_1x_1}=0.$$

Note that at the corner, one of the $W=0$ conditions is redundant and three conditions only remain to be specified. The analogy with the boundary specifications for problems in plane stress elasticity is instructive. There, the solution of a 4th order biharmonic equation on the Airy stress function serves to define the state of stress in a body in which only two direct and one shear component of the stress

traction exists. For rectangular bodies in plane stress, the boundary traction necessary and sufficient to give uniquely the state of stress within is evidently the specification of one direct stress and the shear at every point on each boundary face. Thus at the corners, the natural conditions are the specification of two direct stresses and the single complementary shear stress-three enforced conditions.

The assignment of $(a_l)_{i,j}$ for all simple supports and a mesh size r_1, r_2 is as follows:

For one writing of (22–A) around the boundary:

$$(a_1)_{i,j}=1;\ (a_l)_{i,j}=0, \qquad l=2,\ 3,\ \ldots\ 11,$$

and write (22–A) for:

$$j=1,\ i=1,\ 2,\ \ldots\ r_1+1$$

$$i=r_1+1,\ j=2,\ 3,\ \ldots\ r_2+1$$

$$j=r_2+1,\ i=2,\ 3,\ \ldots\ r_1$$

$$i=1,\ j=2,\ 3,\ \ldots\ r_2+1.$$

For one writing of (22–A) along the y_1= *constant boundaries:*

$$(a_5)_{i,j}=1;\ (a_l)_{i,j}=0, \qquad l=2,\ 3,\ 4,\ 6,\ 7,\ \ldots\ 11,$$

and write (22–A) for:

$$j=1,\ i=1,\ 2,\ 3,\ \ldots\ r_1+1$$

$$j=r_2+1,\ i=1,\ 2,\ 3,\ \ldots\ r_1+1.$$

Foe one writing of (22–A) along the x_1= *constant boundaries:*

$$(a_4)_{i,j}=1;\ (a_l)_{i,j}=0, \qquad l=2,\ 3,\ 5,\ 6,\ \ldots\ 11,$$

and write (22–A) for:

$$i=1,\ j=1,\ 2,\ 3,\ \ldots\ r_2+1$$

$$i=r_1+1,\ j=1,\ 2,\ 3,\ \ldots\ r_2+1.$$

(B) The Unsupported Plate

The conditions on the y_1=constant boundaries are (see ref. 2)

$$W_{yy}+W_{xx}=0$$

$$W_{yyy}+(2-\gamma)W_{xxy}=0.$$

The conditions on the x_1=constant boundaries are:

$$W_{xx}+W_{yy}=0$$

$$W_{xxx}+(2-\gamma)W_{yyx}=0.$$

At the corners, three conditions will be enforced:

$$W_{xx}=0$$

$$W_{yy}=0$$

$$W_{xy}=0.$$

The first two conditions at the corners stem from enforcing zero moment on the complementary corner faces. Thus:

$M_x=0$ implies:

$$W_{xx}+\gamma W_{yy}=0,$$

and $M_y=0$ implies:

$$W_{yy}+\gamma W_{xx}=0$$

at the corners. Thus, in order for *both* relations to hold at a corner

$$W_{xx}\equiv W_{yy}\equiv 0$$

there unless:

$$\begin{vmatrix}1 & \gamma\\ \gamma & 1\end{vmatrix}=0=1-\gamma^2;\ \text{or}\ \gamma=\pm 1.$$

$\gamma=1$ is impossible for an elastic material since it would imply a negative bulk modulus. $\gamma=-1$ implies an infinite shear modulus for a material with a finite elastic modulus. While it is true that the equilibrium Equation (1) is strictly true only for a plate with an infinite shear modulus, in practice, the influence of shear on deflection is small for thin plates with finite shear moduli and (1) approximates the behavior well for these plates. Poisson's ratio for a real elastic solid has the range: $-1<\gamma\leq\frac{1}{2}$. The last deflection condition at the free corner stems from enforcing a zero twisting moment there. Twisting moment at the corner of a plate can exist only in the presence of an externally supplied reaction. (See Ref. 2.)

The assignment of the $(a_l)_{i,j}$ for the free plate with mesh size r_1, r_2 is as follows:

For one writing of (22–A) along the j=1 *and* j=r_2+1 *faces:*

$(a_5)_{i,j}=1$; $(a_4)_{i,j}=1$; $(a_l)_{i,j}=0$

for $l=1, 2, 3, 6, 7, \ldots 11$

at:

$j=1$; $i=1, 2, 3, \ldots r_1+1$

$j=r_2+1$, $i=1, 2, 3, \ldots r_1+1$.

For one writing of (22–A) along the j=1 *face:*

$(a_8)_{i,j}=1$; $(a_9)_{i,j}=(2-\gamma)$; $(a_l)_{i,j}=0$

for $l=1, 2, \ldots 6, 7, 10, 11$

at:

$j=1$, $i=2, 3, \ldots r_1$.

For one writing of (22–B) along the j=r_2+1 *face:*

$(a_8)_{i,j}=1$; $(a_9)_{i,j}=(2-\gamma)$; $(a_l)_{i,j}=0$

for $l=1, 2, \ldots 6, 7, 10, 11$

at:

$j=r_2+1$, $i=2, 3, \ldots r_1$.

For one writing of (22–A) along the i=*1 and* i=r_1+*1 faces:*

$(a_5)_{i,j}=\gamma$; $(a_4)_{i,j}=1$; $(a_l)_{i,j}=0$

for $l=1, 2, 3, 6, 7, \ldots 11$

at:

$i=1$; $j=1, 2, 3, \ldots r_2+1$

$i=r_1+1$; $j=1, 2, 3, \ldots r_2+1$.

For one writing of (22–A) along the i=*1 face:*

$(a_7)_{i,j}=1$; $(a_{10})_{i,j}=(2-\gamma)$; $(a_l)_{i,j}=0$

for $l=1, 2, \ldots 5, 6, 8, 9, 11$

at:

$i=1$; $j=2, 3, \ldots r_2$.

For one writing of (22–B) along the i=r_1+*1 face:*

$(a_7)_{i,j}=1$; $(a_{10})_{i,j}=(2-\gamma)$; $(a_l)_{i,j}=0$

for $l=1, 2, \ldots 5, 6, 8, 9, 11$

at:

$i=r_1+1$; $j=2, 3, \ldots r_2$.

For one writing of (22–A) at two corners:

$(a_6)_{i,j}=1$; $(a_l)_{i,j}=0$

for $l=1, 2, \ldots 4, 5, 7, 8 \ldots 11$

at:

$i=1$; $j=1, r_2+1$.

For one writing of (22–B) at two corners:

$(a_6)_{i,j}=1$; $(a_l)_{i,j}=0$

for $l=1, 2, \ldots 4, 5, 7, 8, \ldots 11$

at:

$i=r_1+1$; $j=1, r_2+1$.

TO DETERMINE THE NATURAL FREQUENCIES AND MODE SHAPES OF VIBRATION

A. Choose a low (r_2, r_1) mesh size compatible with the complexity of the boundary conditions.

B. Write (20) for each interior mesh point.

C. Write (22–A) or (22–B) with the appropriate assignment of the $(a_l)_{i,j}$ for each boundary mesh point. (Replacing $W_{i,j}$ by $S_{i,j}$ for consistent notation . . . also see D. below.)

D. Since the time dependence of the solution has been separated out in this free vibration; $W=S$, and the matrix of equations in B. and C. above, is square of order n (say) in $S_{i,j}$. Let $(p_v a^2/\alpha)^2=x_v$.

E. Solve $|A_{i,j}|_n=0$, for all the real roots of x_v; where $A_{i,j}$ is the matrix of coefficients of the equations in $S_{i,j}$ of B. and C.

The matrix equation from B. and C. is:

$$(A_{i,j})(S_{i,j})=0.$$

Small n is the order of the square matrix.

$$n=r_1r_2+3(r_1+r_2)+7. \qquad (23)$$

Small n is also the number of real roots x_v of the determinantal equation in E. for the characteristic frequencies of natural vibration.

F. In any of the n equations of $(A_{i,j})(S_{i,j})=0$, set the $S_{i,j}$ with the smallest coefficient equal to 1. Then set this particular $S_{i,j}$ equal to 1. in all n equations and solve the reduced matrix equation of order $n-1$: $(A_{i,j})(S_{i,j})=B_{i,j}$; for the relative deflection $(S_{i,j})_v$

in the mode v which has the undamped frequency:

$$p_v=\frac{\alpha}{a^2}(x_v)^{1/2}\cdot(\text{units—Time}^{-1}). \qquad (24)$$

From (12), the damped frequency is:

$$n_v=\tfrac{1}{2}(4p_v^2-B^2)$$

TO DETERMINE THE GENERAL RESPONSE OF A PLATE UNDER ARBITRARY TIME DEPENDENT LOADS AND BOUNDARY CONDITIONS

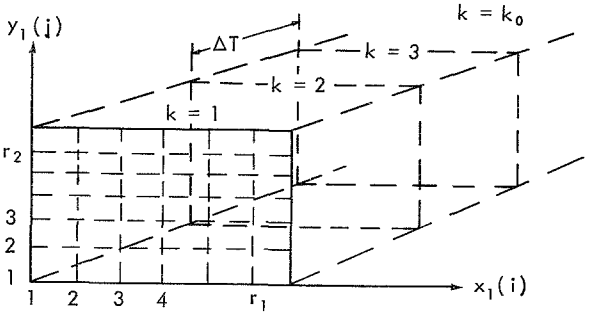

FIGURE 4.—The plate with space-time grid mesh (i, j, k).

The mathematical boundary value problem defining the vibratory response of the plate is as follows: $W=W(x, y, t)$.

Differential Equation:

$$D\nabla^4W+\mu\dot{W}+M\ddot{W}=q:t>0$$

x, y everywhere inside the boundary. (25)

Boundary Conditions:

$$a_1W+a_2\frac{\partial W}{\partial x}+a_3\frac{\partial W}{\partial y}+a_4\frac{\partial^2W}{\partial x^2}+a_5\frac{\partial^2W}{\partial y^2}+a_6\frac{\partial^2W}{\partial x\partial y}+a_7\frac{\partial^3W}{\partial x^3}+a_8\frac{\partial^3W}{\partial y^3}+\ldots+a_9\frac{\partial^3W}{\partial x^2\partial y}+a_{10}\frac{\partial^3W}{\partial y\partial x^2}+a_{11}=0, \qquad (26)$$

for: $a_l=a_l(x, y, t)$; $t\geq 0$; x, y everywhere on the boundary.

Initial Conditions:

$$W=c(x, y, t)$$
$$W=d(x, y, t) \qquad (27)$$

for; $t=0$; x, y everywhere inside the boundary.

Equation (3) is the dimensionless (in the independent variables) form of (25). Multiplying (3) through by a^4/α^2 transforms it to:

$$\frac{\partial^4W}{\partial x_1^4}+2(a/b)^2\frac{\partial^4W}{\partial x_1^2\partial y_1^2}+(a/b)^4\frac{\partial^4W}{\partial y_1^4}+\frac{Ba^4}{t_0\alpha^2}\frac{\partial W}{\partial T}+\frac{a^4}{t_0^2\alpha^2}\frac{\partial^2W}{\partial T^2}=\frac{q_1a^4}{\alpha^2}. \qquad (28)$$

(28) written as a finite difference equation is:

$$W_{i,j,k}\left[6r_1^4+8(a/b)^2r_1^2r_2^2+6(a/b)^4r_2^4-\frac{2a^4}{t_0^2\alpha^2(T)^2}\right]-\frac{(q_1)_{i,j,k}a^4}{\alpha^2}+\ldots+W_{i+1,j,k}[-4r_1^4-4(a/b)^2r_1^2r_2^2]+W_{i+2,j,k}[r_1^4]+W_{i,j+1,k}[\ldots-4(a/b)^2r_1^2r_2^2-4(a/b)^4r_2^4]+W_{i,j+2,k}[(a/b)^4r_2^4]+W_{i-1,j,k}[\ldots-4r_1^4-4(a/b)^2r_1^2r_2^2]+W_{i-2,j,k}[r_1^4]+W_{i,j-1,k}[-4(a/b)^2r_1^2r_2^2+\ldots-4(a/b)^4r_2^4]+W_{i,j-2,k}[(a/b)^4r_2^4]+W_{i,j,k-1}\left[-\frac{Ba^4}{t_0\alpha^2(\Delta T)}+\frac{a^4}{t_0^2\alpha^2(\Delta T)^2}\right]+\ldots+W_{i,j,k+1}\left[\frac{Ba^4}{t_0\alpha^2(\Delta T)}+\frac{a^4}{t_0^2\alpha^2(\Delta T)^2}\right]=0; \qquad (29)$$

for all i, j inside the boundary and $k>1$.

The characteristic time t_o may be taken as the period of the most rapid natural vibration previously calculated in part 9. Δt may be arbitrarily set at $t_o/4(\Delta T=\frac{1}{4})$ to insure convergence of the numerical solution to the actual solution for all t. (See Ref. 1, p. 124.) It is evident that for forced vibrations, if the forcing function (load or support movements) cannot be well described by a series of modes whose smallest period is greater than t_o, the general solution from (29) is likely to be a poor description of the actual solution at all times.

A decrease in the space mesh size (increase in r_1, r_2) is called for in these cases. Since t_o is equal to the smallest period of natural vibration, a finer mesh will result in a smaller t_o corresponding to a higher highest natural frequency for the finer mesh.

THE TREATMENT OF THE INITIAL CONDITIONS

Initial difference conditions of displacement and velocity will be specified at each mesh point inside the boundary on the $k=1$ face in accordance with (27).

$$W_{i,j,1}=c_{i,j,1}, \text{ at every } i \text{ not equal to 1 or } r_1+1 \text{ and every } j \text{ not equal to 1 or } r_2+1. \quad (30)$$

$$W_{i,j,2}\left[\frac{1}{2(\Delta T)}\right]+W_{i,j,1}\left[\frac{-1}{2(\Delta T)}\right]=t_o d_{i,j,1}, \quad (31)$$

at the same mesh points of (30).

THE TREATMENT OF THE BOUNDARY CONDITIONS

Equations (22–A) and (22–B) will be satisfied at all boundary points for $k\geq 1$.

THE STEP BY STEP PROCEDURE FOR THE GENERAL NUMERICAL SOLUTION

The solution proceeds in a step by step fashion as follows:

A. Write (30), (22–A) and (22–B) for all relevant i, j at $k=1$.

B. Solve this initial matrix for all $W_{i,j,1}$.

C. Write (31) for all relevant i, j at $K=1$.

D. Solve the diagonal matrix of C. above for all interior $W_{i,j,2}$.

E. Write (22–A) and (22–B) for the boundary of $k=2$.

F. Solve the matrix of E. above for $W_{i,j,2}$ on the boundary at $k=2$.

G. Write (29) for all interior points at $k=2$.

H. Solve the diagonal matrix of G. above for all interior $W_{i,j,3}$.

I. Increment k and repeat E. through H. above, etc.

After the deflection has been determined to a desired time $(k_o-1)\Delta T$ by A.–I. above, the following stresses may be found.

$$M_x=-D\left[\frac{\partial^2 W}{\partial x^2}+\gamma\frac{\partial^2 W}{\partial y^2}\right]$$

· (bending moment per unit length on x faces) (32)

$$M_y=-D\left[\frac{\partial^2 W}{\partial y^2}+\gamma\frac{\partial^2 W}{\partial x^2}\right]$$

· (bending moment per unit length on y faces) (33)

$$M_{xy}=D(1-\gamma)\frac{\partial^2 W}{\partial x\partial y}$$

· (twisting moment per unit length) (34)

$$Q_x=-D\left[\frac{\partial^3 W}{\partial x^3}+\frac{\partial^3 W}{\partial x\partial y^2}\right]$$

· (shear force per unit length on x faces) (35)

$$Q_y=-D\left[\frac{\partial^3 W}{\partial y^3}+\frac{\partial^3 W}{\partial y\partial x^2}\right]$$

·(shear force per unit length on y faces) (36)

These stresses may be calculated at all the mesh points to the boundary, by solving (22–A) or (22–B) for a_{11}=stress (M_x, M_y, etc.):

where ↓ Stress	: when ↓
$=M_x$	: $a_4=D\gamma$, and $a_5=D$, all other a's$=0$.
" $=M_y$	: $a_4=D\gamma$, and $a_5=D$, "
" $=M_{xy}$	: $a_6=-D(1-\gamma)$, all other a's $=0$.
" $=Q_x$	: $a_7=D$, $a_{10}=D$, "
" $=Q_y$	: $a_8=D$, $a_9=D$, " (37)

THE CONVERGENCE OF THE FINITE DIFFERENCE SOLUTION TO THE ACTUAL SOLUTION

The convergence criteria stated in part 10: that the time step be always made ¼ of the smallest period of natural vibration for the space mesh (r_1, r_2), may not actually insure uniform convergence through all time, of the finite difference solution to the actual solution, as $(r_1, r_2)\to\infty$. It may not even insure boundedness of the solution for a fixed mesh (r_1, r_2, ΔT) as $t\to\infty$. In general, for explicit formulations of difference problems equivalent to time dependent differential problems of a

quasi-parabolic type, a convergence and stability criteria of form $0<\frac{\Delta t_1{}^n}{h^m}\leq\lambda$ (dimensionless) exists. A quasi-parabolic type problem may be a combination of initial value problem of hyperbolic type and a boundary value problem of elliptic type. Small h in the stability-convergence criteria above is the space step and Δt_1 is a certain time step in the same units as $h^{m/n}$. For the one dimensional vibration problem analogous to this plate problem, $\lambda=\frac{1}{2}$ probably is the criteria for convergence. (See Ref. 3, p. 133) where $n=2$ and $m=4$ in the convergence criteria above. But in the extension of the one dimensional heat equation to two space dimensions, the stability criteria is found to be reduced from $\lambda=\frac{1}{2}$ (see Ref. 3, p. 92), to $\lambda=\frac{1}{4}$ [see Ref. 1, p. 218; where (Δt_1) above is $tk/\delta c$] with $n=1$ and $m=2$ in the stability criteria above. In the case of the heat equation, the criteria in each case is such as to make the coefficient of the dependent variable at $i, j, k\geq 0$. In the case of the vibration equation, it is seen from Ref. 3, p. 132, that for $\lambda\leq\frac{1}{2}$, the coefficient of the analogous $(i, j, k-1)$ term $\leq$ the coefficient of the analogous (i, j, k) term. Stated otherwise: $(i, j, k)-(i, j, k-1)\geq 0$. We will tentatively apply this criteria to (29) under the assumption that:

$a=b$, $r_1=r_2$, $B=0$. Applying it to the homogeneous equation: $q=0$ (free vibrations); setting $(i, j, k)=(i, j, k-1)$ in (29) implies:

$$6r_1{}^4+8r_1{}^4+6r_1{}^4-\frac{2a^4}{(t_0\Delta T)^2\alpha^2}=\frac{a^4}{(t_0\Delta T)^2\alpha^2}. \quad (38)$$

The space-time coupled convergence criteria for this problem as derived from (38) is tentatively proposed as:

$$3/20=\frac{(t_o\Delta T\alpha)^2}{(a/r_1)^4}=\frac{(\Delta t_1)^2}{h^4}=\lambda, \text{ in the notation of the general criteria formulation.} \quad (39)$$

The procedure for determining ΔT from the chosen mesh (r_1, r_2) is as follows:

A. Calculate t_o as the minimum period of natural vibration for (r_1, r_2).

B. Then:

$$\Delta T=\begin{cases}\frac{1}{4}\\ \dfrac{0.387(a/r_1)^2}{\alpha t_o}\end{cases} \text{ whichever is least.} \quad (40)$$

In this way, we retain the reasonable $\frac{1}{4}t_o$ criteria as an upper bound for the time step. A more complex convergence criteria than (40) is being developed based on the intuition that stability of the difference solution for large t will be assured if the propagation in time ΔT of a single error ϵ at any mesh point in (r_1, r_2) is not likely to be greater than $|\epsilon|$.

REFERENCES

1. Salvadori and Baron: Numerical Methods in Engineering. (Prentice-Hall; 1952, 4th printing.)
2. Timoshenko and Goodier: Theory of Plates and Shells.
3. Forsythe and Wasow: Finite Difference Methods for Partial Differential Equations. (Wiley—1960.)
4. Harris and Crede: Shock and Vibration Handbook. (McGraw-Hill; 1961, vols. 1 and 3.)

Appendix A

THE METHOD OF FINITE DIFFERENCES APPLIED TO THE PLATE VIBRATION PROBLEM

The method of finite differences used to develop the difference equations in this report may be thought of as solving exactly at a specified number of points, for the vibrations of a plate which deflects into a surface algebraic in space and time, closely approximating the true deflection contour.

Consider the true deflection contour in the x_1 direction at time t. (Fig. A–1.) Since initially we wish to solve for the deflection at only the mesh points on the plate, it is natural to replace the true surface, whose derivatives may be complicated functions of space and time, with an approximating algebraic surface passing through the mesh points. The derivatives at the mesh points on this approximating surface are simple linear functions of the mesh point deflections themselves.

For example, consider an algebraic surface through the actual deflections w_0, w_1, w_2 (Fig. A–2) such that the intersection of this surface with the $w-x_1$ plane is given by the parabola:

$$w=w_0+(w_2-2w_1+w_0)x_1^2/2(h^1)^2 + (-3w_0+4w_1-w_2)x_1/2h^1$$

The slope in the x_1 direction, of the approximate surface at $i=1$ may be shown to be simply: $(W_2-W_0)/2h^1$. If h^1 is sufficiently small, the parabolic surface fits the actual one more and more closely. Therefore, in the neighborhood

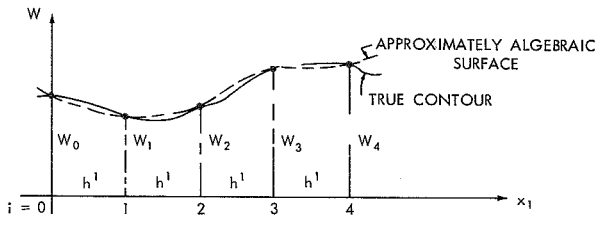

FIGURE A–1.—True and approximate deflection contours of the vibrating plate.

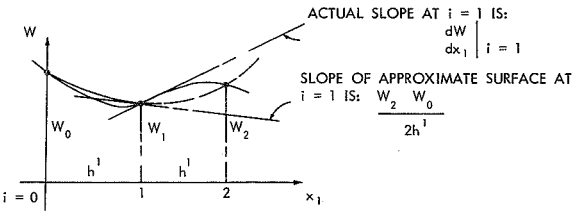

FIGURE A–2.—True and parabolic approximation of the contour of the vibrating plate.

of $i=1$, if the actual surface is reasonably well behaved there, we may write:

$$\left.\frac{dW}{dx_1}\right|_{i=1} \doteq (W_2-W_0)/2h^1, \qquad \text{(A–1)}$$

for h^1 sufficiently small. $(W_2-W_0)/2$ is called the averaged first central difference of W at $i=1$. In like manner, the higher derivatives may be approximated as simple linear functions of the deflection at neighboring mesh points. If we ignore the small errors implicit in these approximations, we can replace the differential equations describing the vibration at every point on the plate by so-called "difference equations" involving simple linear combinations of the unknown deflections themselves. The difference equations, of course, only apply at the mesh points on the plate. Each such difference equation is inexact to the extent that the piece of algebraic surface only approximates the real surface over the mesh of its application. Therefore, when the unknown deflections of the set of difference equations are found, they will be in error from the true deflections by the order of this approximation, for each such set of difference equations solved. However, if the mesh proportions in space and time are carefully chosen, the successive solutions in time of the systems of finite difference equations should converge to the actual solution as the mesh is refined and the pieced approximate algebraic

solution surfaces fit more and more smoothly with the actual surface. Such convergent behavior in time of finite difference systems is known as "stability."

Consider the three dimensional mesh (i, j, k) with equally spaced k in the time direction and (i, j) a square space mesh (Fig. A–3).

It may be shown (see Ref. 1, ch. 2.7 and p. 69) that with reference to this mesh, the derivatives of the vibration surface $W(x_1, y_1, T)$ can be approximated to the same order of smallness $(h^1)^2$ as:

$$\left.\frac{\partial W}{\partial x_1}\right|_{i,j,k} \doteq (W_{i+1,j,k}-W_{i-1,j,k})/2h^1 \quad \text{(A–2)}$$

$$\left.\frac{\partial W}{\partial y_1}\right|_{i,j,k} \doteq (W_{i,j+1,k}-W_{i,j-1,k})/2h^1 \quad \text{(A–3)}$$

$$\left.\frac{\partial^2 W}{\partial x_1^2}\right|_{i,j,k} \doteq (W_{i+1,j,k}-2W_{i,j,k}+W_{i-1,j,k})/(h^1)^2 \quad \text{(A–4)}$$

$$\left.\frac{\partial^2 W}{\partial y_1^2}\right|_{i,j,k} \doteq (W_{i,j+1,k}-2W_{i,j,k}+W_{i,j-1,k})/(h^1)^2 \quad \text{(A–5)}$$

$$\left.\frac{\partial W}{\partial T}\right|_{i,j,k} \doteq (W_{i,j,k+1}-W_{i,j,k-1})/(2\Delta T) \quad \text{(A–6)}$$

$$\left.\frac{\partial^2 W}{\partial T^2}\right|_{i,j,k} \doteq (W_{i,j,k+1}-2W_{i,j,k}+W_{i,j,k-1})/(\Delta T)^2. \quad \text{(A–7)}$$

Combining (A–4) and (A–5) as operational equations:

$$\left.\frac{\partial^4 W}{\partial x_1^2 \partial y_1^2}\right|_{i,j,k} \doteq (4W_{i,j,k}-2W_{i-1,j,k} -2W_{i+1,j,k}-2W_{i,j+1,k}-2W_{i,j-1,k}+\cdots +W_{i+1,j+1,k}+W_{i-1,j-1,k}+W_{i-1,j+1,k} +W_{i+1,j-1,k})/(h^1)^4 \quad \text{(A–8)}$$

$$\left.\frac{\partial^4 W}{\partial x_1^4}\right|_{i,j,k} \doteq (6W_{i,j,k}-4W_{i+1,j,k}-4W_{i-1,j,k} +W_{i+2,j,k}+W_{i-2,j,k})/(h^1)^4 \quad \text{(A–9)}$$

$$\left.\frac{\partial^4 W}{\partial y_1^4}\right|_{i,j,k} \doteq (6W_{i,j,k}-4W_{i,j+1,k}-4W_{i,j-1,k} +W_{i,j+2,k}+W_{i,j-2,k})/(h^1)^4. \quad \text{(A–10)}$$

To illustrate the use of these finite difference

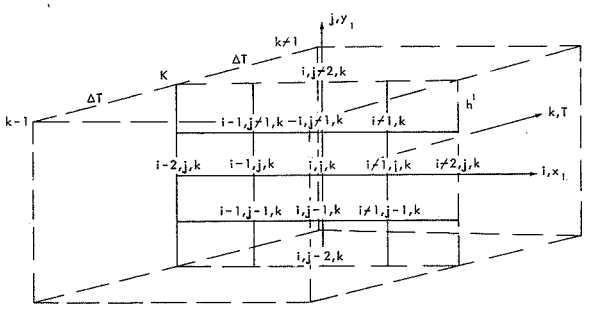

FIGURE A–3.—The space-time finite difference mesh for the vibrating plate.

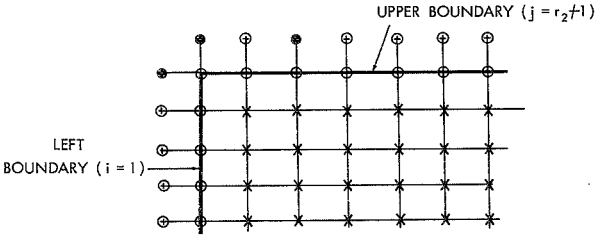

FIGURE A–4.—Interior, exterior, and boundary space mesh points of the vibrating plate solution.

approximations, the differential Equation (28) is transformed to the difference Equation (29) by use of the central difference operators (A–6), (A–7), (A–8), (A–9) and (A–10) above; for the case where $h^1=1/r_1=1/r_2=$the non-dimensional interval of the square mesh (r_1, r_2).

The other approximate difference equations in this report are derived in a similar manner using linear difference operators appropriate to specific regions of the mesh to insure that square solution matrices will result. Thus, in the transformation of the general boundary differential Equation (21) to the difference Equations (22), the mixed and third derivatives of (21) are approximated with the use of so-called "forward" or "backward" difference operators depending on the orientation of the boundary.

Consider a set of finite difference equations used to solve (19) for the natural modes of vibration P_v. (See Fig. A–4.)

Writing the central difference Equation (20) at all the x interior mesh points introduces unknown W's at all boundary and adjacent mesh points 0. For all boundary points except the

corners, two boundary conditions of the form of (21) must be satisfied for a properly posed problem. It is clear that unless noncentral approximations for the third derivatives in (21) are used, the solution matrix, with the boundary equations included, will not be square.

For the left and lower boundary points, the critical derivatives in this regard are:

$$\left.\frac{\partial^3 W}{\partial x_1^3}\right|_{i,j,k} \doteq (-5W_{i,j,k}+18W_{i+1,j,k}-24W_{i+2,j,k} +14W_{i+3,j,k}-3W_{i+4,j,k})/2(h^1)^3 \quad \text{(A–11)}$$

$$\left.\frac{\partial^3 W}{\partial y_1^3}\right|_{i,j,k} \doteq (-5W_{i,j,k}+18W_{i,j+1,k}-24W_{i,j+2,k} +14W_{i,j+3,k}-3W_{i,j+4,k})/2(h^1)^3. \quad \text{(A–12)}$$

For the upper and right boundary points, the critical derivatives are:

$$\left.\frac{\partial^3 W}{\partial x_1^3}\right|_{i,j,k} \doteq (5W_{i,j,k}-18W_{i-1,j,k}+24W_{i-2,j,k} -14W_{i-3,j,k}+3W_{i-4,j,k})/2(h^1)^3 \quad \text{(A–13)}$$

$$\left.\frac{\partial^3 W}{\partial y_1^3}\right|_{i,j,k} \doteq (5W_{i,j,k}-18W_{i,j-1,k}+24W_{i,j-2,k} -14W_{i,j-3,k}+3W_{i,j-4,k})/2(h^1)^3. \quad \text{(A–14)}$$

With these forms used, satisfying boundary conditions which include the third derivatives will not introduce additional unknown w's beyond those already introduced by the central difference Equation (20) at the interior points.

Thus, satisfying two boundary difference equations will, with the above discriminations, produce a square solution matrix leaving the three corner unknowns unsatisfied. These may be satisfied by writing the three boundary equations there which are necessary and sufficient for a properly posed problem.

To avoid introducing a fourth corner unknown, the mixed derivatives must utilize forward or backward difference forms, as mentioned previously.

With these considerations in mind, the general boundary difference Equations (22–A) and (22–B) have been derived from (21) to produce a set of equations equal in number to the unknown w's at the mesh points indicated by implication in Figure (A–4). In the solution for the modes of vibration P_v, this set of linear equations in the mesh point w's will be homogeneous. Thus, nonzero solutions for the w's (the natural mode contours) can only result if the determinant of the coefficients of this "square solution matrix" is zero. This determinantal equation will be algebraic in P_v^2 to a power equal to the number of interior mesh points$=(r-1)^2$, for $r=r_1=r_2$.

Similarly, in the solution for the vibrating plate outlined in part 13, the application of the appropriate difference equations across the mesh at each stage of the solution is just sufficient to produce square solution matrices in the w's at that particular step in time. The solution is said to be stepped off in time, as is typical for an initial value problem. (See Figs. A–5 to A–7.)

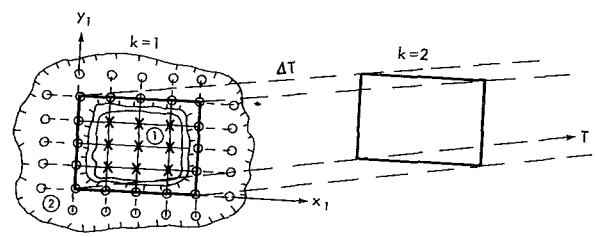

FIGURE A–5.—Initial regions of solution for the vibrating plate in the space-time mesh.

Thus, step 13.B solves for the W's in region ① by Equation (30) and in region ② by Equations (22–A) and (22–B) applied at $k=1$.

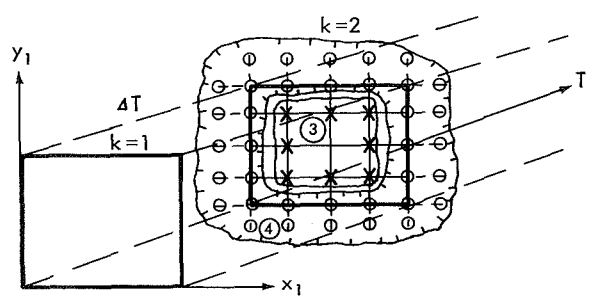

FIGURE A–6.—The second region of solution for the vibrating plate in the space-time mesh.

Step 13.D solves for the W's in region ③ by Equation (31) with the W's of region ① known from step 13.B.

The boundary W's in region ④ of $k=2$ are solved for in step 13.F by Equations (22–A) and (22–B) applied at $k=2$.

The interior W's in region ⑤ are solved for in step 13.H by Equation (29) applied to region ③ at $k=2$, since all W's in regions ①, ③ and ④ have been previously determined. In this manner, alternating solutions of the boundary equations and the dynamic equilibrium equation, the time history of the vibration is resolved.

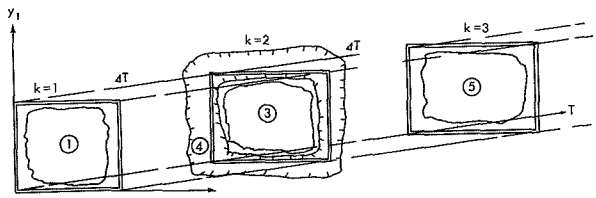

FIGURE A–7.—The first three regions of vibration solution in the space-time mesh.

Appendix B

TO DETERMINE THE MODES AND FREQUENCIES OF LATERAL VIBRATION FOR A TYPICAL HONEYCOMB SANDWICH SOLAR PANEL, PROPOSED FOR THE ADVANCED OSO SPACECRAFT

1. JUSTIFICATION FOR THE NEGLECT OF SHEAR DISPLACEMENT

In Reference 4, Equation (15) gives the frequency of lateral vibration in mode nm for a simply supported sandwich plate including the effect of shear displacement. The formula is:

$$f_{nm}=\frac{a_{nm}}{2(a_{nm}\bar{M}/U+\bar{M}/D)^{1/2}}, \qquad \text{(B–1)}$$

where

$a_{nm}=(n^2/a^2+m^2/b^2)$,

$n=1, 2, 3 \ldots, m=1, 2, 3 \ldots$

and

$$D\doteq E_f(fc^2)/2(1-\gamma^2), \qquad \text{(B–2)}$$

for a sandwich plate of equal facing thickness f, core thickness (inner) c, where $f/c<<1$, and where the flexural rigidity of the core is negligible (see Ref. 4). γ is Poisson's ratio for the facing material. U is the transverse shear stiffness and is equal to G (core) $\times$ Unit Length. The theory assumes that the shear stress is uniform over the depth c at a typical section of the plate.

The specifications for the advanced OSO solar panel sandwich are as follows:

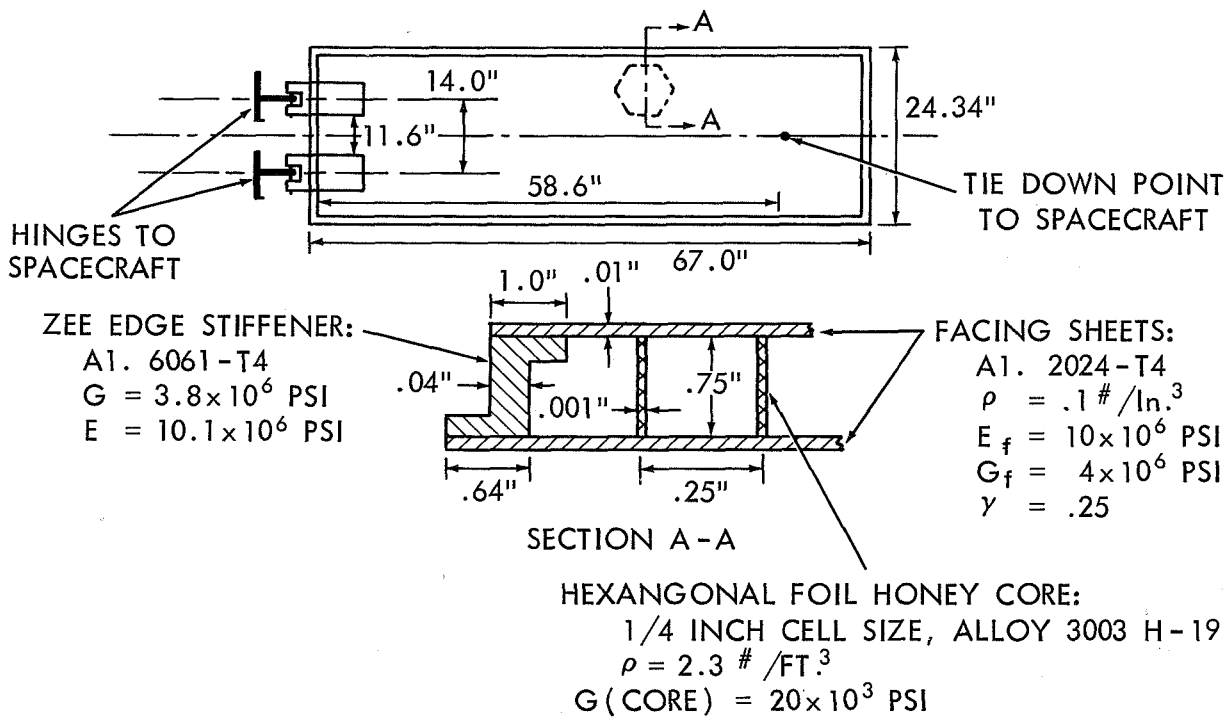

FIGURE B–1.—Specifications and layout of the advanced OSO solar panel.

For this configuration,

$$D=\frac{10\times10^6\times.01\times.75^2}{2(1\frac{1}{16})}=44.4\times10^3\#\text{-in.}$$

$$1/D=22.1\times10^{-6}\ 1/\#\text{-in.}$$

For the lowest harmonic, $n=m=1$, ($a=67$ in., $b=24.3$ in.);

$$a_{11}=9.86(1/4490+1/590)=18.93\times10^{-3}\text{ in.}^{-2}$$

$$U=20\times10^3\#/\text{in.}$$

Therefore, $a_{11}/U=18.93\times10^{-3}/20.0\times10^3=.946\times10^{-6}$ 1/#-in. Thus the shear term is sufficiently small compared to the flexure term, that for harmonics lower than the 3d or 4th, the effect of shear stiffness on the frequency is small.

The solar panel, when it is attached to the spacecraft, is in the configuration of Figure B–2.

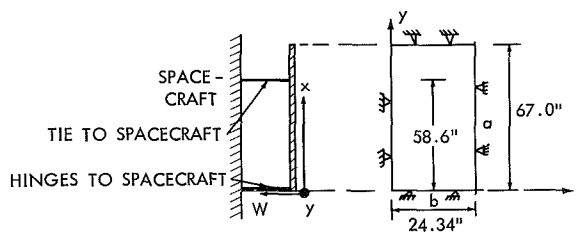

FIGURE B–2.—Simplified mechanical configuration of the advanced OSO solar panel during launch.

It is assumed that the free vibration modes of the panel have zero relative displacement at the tie down point and around the stiffened edge which may be taken as a simply supported edge. At the tie down point, the force free equilibrium Equation (4) does not hold, so that in place of satisfying (20) there, the equation to be satisfied is:

$$W\text{ (tie down point)}=0. \qquad \text{(B–3)}$$

But since the tie down point will not fall on a mesh point, in general, the satisfaction of (B–3) exactly will be replaced by an approximate condition which assumes that the actual deflection surface in the neighborhood of the tie down point is a certain 4th degree algebraic surface. This assumption will lead to a condition equation relating a linear combination of the 9 mesh point W's which form the closest rectangular net around the tie down point. Consider below, a rectangle of 9 mesh points in the x, y plane with W displacements attached to them. The tie down point is point T. It can be verified that if the polynomial:

$$W(u,v)=A+Bu+Cv+Duv+Eu^2+Fv^2+Gu^2v+Huv^2+Iu^2v^2, \qquad \text{(B–4)}$$

is passed through the 9 mesh point W's below, the coefficients are uniquely determined so that:

$$W(u,v)=\sum_{v=-1}^{v=+1}\sum_{u=-1}^{u=+1}A_uA_vW_{i+u,j+v}, \qquad \text{(B–5)}$$

where, for A_s:

$A_1=s(s+1)/2 : A_0=-(s-1)$

$(s+1) : A_{-1}=s(s-1)/2$

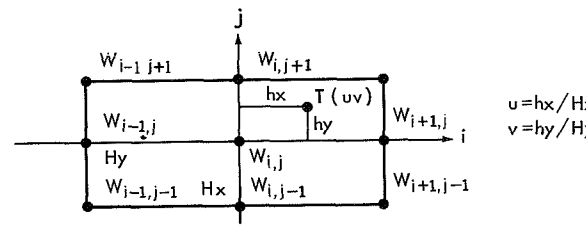

FIGURE B–3.—A 3 point mesh on which an approximate quadratic vibrating surface is built.

Therefore, the general polynomial approximate deflection surface above the 9 mesh points is given as:

$$\begin{aligned}W(u,v)=&W_{i,j}[(u-1)(u+1)(v-1)(v+1)]\\&+W_{i+1,j}[-u(u+1)(v-1)(v+1)/2]\\&+W_{i-1,j}[\ldots-u(u-1)(v-1)(v+1)/2]\\&+W_{i,j-1}[-u(u-1)(u+1)(v-1)v/2]\\&+W_{i+1,j-1}[u(u+1)(v-1)v/4]\ldots\\&+W_{i-1,j-1}[u(u-1)v(v-1)/4]\\&+W_{i,j+1}[-(u-1)(u+1)v(v+1)/2]\\&+W_{i+1,j+1}u[u\ldots u(u+1)v(v+1)/4]\\&+W_{i-1,j+1}[u(u-1)v(v+1)/4]. \qquad \text{(B–6)}\end{aligned}$$

In solving for the approximate vibration modes and frequencies, we consider a 4 x 2 space mesh: $r_1=4$, $r_2=2$ (see Fig. B–4).

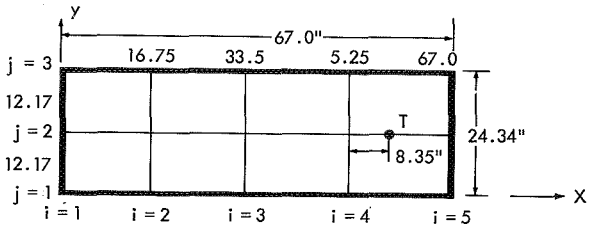

FIGURE B–4.—Advanced OSO solar panel spacel mesh points for the first approximation of the fundamental mode of vibration.

The spacing in the x direction is: $h_1=67.0/4=16.75$ in.

The spacing in the y direction is: $h_2=24.34/2=12.17$ in.

Therefore, the u and v of the tie down point T, with respect to the mesh point (4, 2) is: $u(T)=8.35/16.75=0.499$, $v(T)=0$.

The condition that at the tie down point, the deflection is zero, is evaluated by the approximate polynomial surface of (B–6) at $i=4$, $j=2$ as:

$$W_T(0.499.0)=0=W_{4,2}(0.750)+W_{5,2}(0.374)+W_{3,2}(-0.125). \quad \text{(B–7)}$$

At the other two interior points ($j=2$, $i=2, 3$) Equation (20) is written since, for the lowest mode, the shear deflection can be neglected. Evaluating the plate parameters of that equation:

$$a/b=67.0/24.34=2.755;$$

$$(a/b)^2=7.590;\ (a/b)^4=57.5,$$

$$r_2/r_1=0.50;\ (r_2/r_1)^2=0.25;\ (r_2/r_1)^4=0.0625.$$

The distributed inside weight of the solar panel is calculated as:

$$\begin{aligned} & & 11.50\#\ \text{(Solar cell weight)} \\ &+0.1\times2\times0.01\times67.0\times24.34 &= 3.26\#\ \text{(Aluminum facing weight)} \\ &+2.3\times67.0\times24.34\times0.75/1728 &= 1.63\#\ \text{(Core weight)} \\ & & \overline{16.39\#\ \text{(Total interior panel weight)}} \end{aligned}$$

Therefore, $M=16.39\times144/32.15\times67.0\times24.34=0.0451\#-\text{sec}^2/\text{ft}^3$, and $D=44.4/12=3.70\#-\text{ft}$. Therefore, $\alpha^2=D/M=3.70/0.0451=82.0\ \text{ft}^4/\text{sec}^2$. Therefore, $a^4/r_1^4\alpha^2=(67.0/12)^4/256\times82.0=0.04625\ \text{sec}^2$.

With this evaluation of the plate parameters, (20) becomes:

$$\begin{aligned} &W_{i,j}(42.70-0.04625P_v^2)+W_{i+1,j}(-11.57)+W_{i-1,j}(-11.57)+W_{i,j+1}(-21.95) \\ &\quad+W_{i,j-1}(-21.95)+W_{i+1,j+1}(3.79)+W_{i-1,j+1}(3.79)+W_{i-1,j-1}(3.79) \\ &\quad+W_{i+1,j-1}(3.79)+W_{i+2,j}(1.0)+W_{i-2,j}(1.0)+W_{i,j+2}(3.595)+W_{i,j-2}(3.595)=0. \quad \text{(B–8)} \end{aligned}$$

(B-8) is written for $j=2$, $i=2$, 3 giving 2 equations. The outer boundary is simply supported so that following the specification on page 10, there are 28 boundary equations:

$$W_{i,j}=0;\ \text{for } j=1, 3;\ i=1, 2, 3, 4, 5 \text{ and } i=1, 5;\ j=2 \text{ (12 equations)}, \quad \text{(B–9)}$$

$$W_{i,j}(-2.0)+W_{i,j+1}(1.0)+W_{i,j-1}(1.0)=0;\ \text{for } j=1, 3;\ i=1, 2, 3, 4, 5 \text{ (10 equations)}, \quad \text{(B–10)}$$

$$W_{i,j}(-2.0)+W_{i+1,j}(1.0)+W_{i-1,j}(1.0)=0;\ \text{for } i=1, 5;\ j=1, 2, 3 \text{ (6 equations)}. \quad \text{(B–11)}$$

It will be seen that we have generated a set of 31 equations, linear and homogeneous in the mesh point deflections of Figure B–5 below.

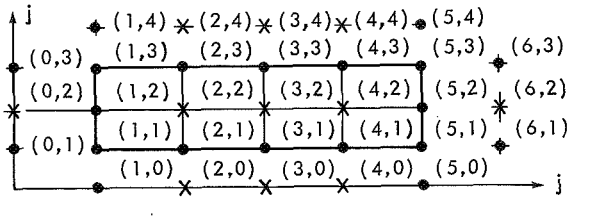

FIGURE B–5.—Full mesh layout in the approximation of the fundamental mode of vibration for the advanced OSO solar panel.

(B–9) substituted into (B–7), (B–8), (B–10) and (B–11) reduces the basic set of 31 equations in the mode deflections $W_{i,j}(P_v^2)$ to 19 equations. But then (B–10) and (B–11) applied at the four corners determines the 8 exterior corner deflections to be zero. The relevant set is further reduced to 8 equations in 8 unknowns by consideration of the symmetry about the $j=2$ axis. Thus, it is evident that:

$$W_{2,0}=W_{2,4}\,:\,W_{3,0}=W_{3,4}\,:\,W_{4,0}=W_{4,4}.$$

Among the unknowns $W_{0,2}$, $W_{2,2}$, $W_{3,2}$, $W_{4,2}$, $W_{6,2}$, $W_{2,0}$, $W_{3,0}$, $W_{4,0}$, the reduced solution set is:

From Eqs. (B–7) through (B–11) at mesh point i, j

$$(\text{B–7})_{4,2}\ldots -0.125W_{3,2}+0.750W_{4,2}=0. \tag{B–12}$$

$$(\text{B–8})_{2,2}\ldots 1.0W_{0,2}+W_{2,2}(42.70-0.04625P_v^2)+1.0W_{4,2}+-11.57W_{3,2}+7.190W_{2,0}=0. \tag{B–13}$$

$$(\text{B–8})_{3,2}\ldots -11.57W_{2,2}+W_{3,2}(42.70-.04625P_v^2)+7.190W_{3,0}-11.57W_{4,2}=0 \tag{B–14}$$

$$(\text{B–10})_{2,1}\ldots 1.0W_{2,2}+1.0W_{2,0}=0 \tag{B–15}$$

$$(\text{B–10})_{3,1}\ldots 1.0W_{3,2}+1.0W_{3,0}=0 \tag{B–16}$$

$$(\text{B–10})_{4,1}\ldots 1.0W_{4,2}+1.0W_{4,0}=0 \tag{B–17}$$

$$(\text{B–11})_{1,2}\ldots 1.0W_{0,2}+1.0W_{2,2}=0 \tag{B–18}$$

$$(\text{B–11})_{5,2}\ldots 1.0W_{4,2}+1.0W_{6,2}=0. \tag{B–19}$$

Eliminating $W_{0,2}$, $W_{2,0}$ and $W_{3,0}$ from (B–18), (B–15) and (B–16), (B–12)–(B–14) becomes:

$$-0.125W_{3,2}+0.750W_{4,2}=0\cdot \tag{B–20}$$

$$W_{2,2}(34.51-0.04625P_v^2)+1.0W_{4,2}-11.57W_{3,2}=0 \tag{B–21}$$

$$-11.57W_{2,2}+W_{3,2}(35.51-0.04625P_v^2)-11.57W_{4,2}=0. \tag{B–22}$$

Substituting $W_{4,2}$ from (B–20) into (B–21) and (B–22) gives the two relevant homogeneous equations as:

$$W_{2,2}(34.34-0.04625P_v^2)-11.40W_{3,2}=0 \tag{B–23}$$

$$W_{2,2}(-11.57)+(33.58-0.04625P_v^2)W_{3,2}=0. \tag{B–24}$$

Thus, in order for (B–23) and (B–24) to hold for nonzero $W_{2,2}$ and $W_{3,2}$, the determinant of the coefficients of this set of equations must be zero, or:

$$(34.34-0.04625P_v^2)(33.58-0.04625P_v^2)=131.9. \tag{B–25}$$

(B–25) has solutions:

$$P_v^2=734\pm 251\ 1/\text{sec}^2.$$

Thus, P (fundamental) $=(483)^{1/2}=21.95$ 1/sec and,

$$f\ (\text{fundamental})=21.95/6.28=3.50\ \text{cycles per second} \tag{B–26}$$

As a check on the accuracy of this result and in order to make a closer estimate of the fundamental frequency with the coarse mesh alone, we can calculate from the numerical procedure, what the fundamental frequency would be if the panel were simply supported without the tie rod. We can then compare this result with the exact fundamental frequency for a simply supported sandwich plate evaluated from (B–1).

In the numerical procedure without the tie

rod for the 4 x 2 mesh, in place of Equation (B–12), we apply (B–8) at (4, 2) which gives:

$$W_{4,2}(42.70-0.04625P_v^2)+W_{3,2}(-11.57)+W_{6,2}(1.0)+W_{2,2}(1.0)+W_{4,4}(3.595)+W_{4,0}(3.595)=0. \quad \text{(B–27)}$$

From symmetry:

$$W_{4,4}=W_{4,0}:W_{4,2}=W_{2,2}.$$

From (B–17) and (B–19):

$$W_{4,0}=-W_{4,2}:W_{6,2}=-W_{4,2}.$$

Therefore (B–27) becomes:

$$W_{4,2}(35.51-0.04625P_v^2)+W_{3,2}(-11.57)=0. \quad \text{(B–28)}$$

(B–21) becomes:

$$W_{4,2}(-23.14)+W_{3,2}(35.51-0.04625P_v^2)=0. \quad \text{(B–29)}$$

(B–22) is now redundant with (B–28) so that (B–28) and (B–29) is the essential homogeneous set for the 4 x 2 mesh with only simple supports. Setting the determinant of the coefficients of (B–28) and (B–29) to zero, we have the frequency equation as:

$$(35.51-0.04625P_v^2)=267.5. \quad \text{(B–30)}$$

From (B–30),

$$P_v^2=766\pm343\ 1/\text{sec}^2.$$

Therefore,

f (fundamental $\doteq(423)^{1/2}/6.28$

$\doteq 3.31$ cycles per second (simple supports).

From (B–1), neglecting the shear term which is small for the fundamental mode, the exact fundamental frequency for the simply supported solar panel is:

$$f(\text{fundamental})=f_{11}=\frac{18.93\times10^{-3}\ \text{in.}^{-2}\times144\ (\text{in.}^2/\text{ft}^2)\times(82.0\ \text{ft}^4/\text{sec}^2)^{1/2}}{6.28\ (1/\text{cycles})}$$

Thus, f (fundamental) = 3.93 cycles per second (simple supports –exact).

The numerical approximation of 3.31 cycles per second is in error from the exact frequency by –16 percent for the simply supported panel. This error is typical for a coarse mesh in the method of finite differences. Judging the error in the tied simply supported plate fundamental frequency to be of the same order of magnitude, and sign, we arrive at a better estimate of the fundamental frequency of the tied solar panel in lateral vibration as:

f (fundamental, tied down solar panel) $\doteq 3.93$

$\times 3.50/3.31 \doteq 4.2$ cycles/sec. (B–31)

For the deflection along the $j=2$ axis of the panel in the fundamental mode, consider the approximate fundamental frequency of 3.50 cycles/sec. This frequency reduces (B–23) and (B–24) to a single independent equation: say (B–23)

$$W_{2,2}(34.34-0.04625\times483)-11.40W_{3,2}=0,$$

or

$$11.99W_{2,2}-11.40W_{3,2}=0. \quad \text{(B–32)}$$

Thus, let $W_{2,2}$ (fundamental) = 1.0. Then from (B–32),

$$W_{3,2}\ (\text{fundamental} \doteq) 11.99/11.40 \doteq 1.04,$$

and from (B–20),

$$W_{4,2} \doteq 0.167W_{3,2} \doteq 0.167\times1.04 \doteq 0.173.$$

Therefore, to a first approximation, the fundamental mode shape is as shown in Figure B–6.

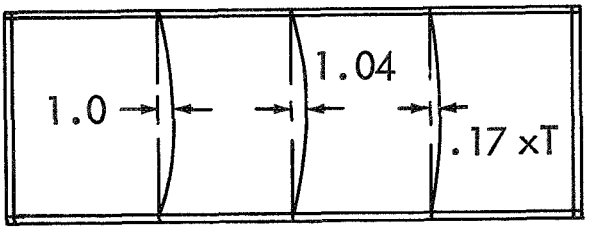

FIGURE B–6.—First approximation of the fundamental mode of vibration for the advanced OSO solar panel during launch.

Appendix C

THE EFFECT OF SHEAR DEFORMATION ON THE VIBRATORY BEHAVIOR OF THE THIN PLATE

Equation (13) of Reference 4 shows that the finite shear stiffness of the plate can be accounted for by adding an additional "shear compliance" inertial term,

$$\frac{-DMV^2\ddot{W}}{U},$$

to the dynamic equilibrium Equation (1) of this report, under the same assumption as was made in developing that equation: that the core is, on average, isotropic in the plane of the plate. Furthermore, it is assumed that the transverse shear is uniformly distributed across the core of the plate. While this assumption is not strictly true, the error made does not materially affect the resultant behavior. With the shear compliance term added, Equation (1) becomes:

$$D^4W+\mu\dot{W}+M\ddot{W}-\frac{DM\nabla^2\ddot{W}}{U}-q=0. \quad \text{(C–1)}$$

In dimensionless coordinates (x_1, y_1, T) (C–1) becomes:

$$\alpha^2\left[\frac{\partial^4W}{a^4\partial x_1^4}+\frac{2\partial^4W}{a^2b^2\partial x_1^2\partial y_1^2}+\frac{\partial^4W}{b^4\partial y^4}\right]+\frac{B}{t_0}\frac{\partial W}{\partial T}+\frac{1}{t_0^2}\frac{\partial^2W}{\partial T^2}$$
$$-B^2\left[\frac{\partial^4W}{t_0^2a^2\partial x_1^2\partial T^2}+\ldots+\frac{\partial^4W}{t_0^2b^2\partial y_1^2\partial T^2}\right]$$
$$=q_1(x_1,y_1,T) \quad \text{(C–2)}$$

where $B^2=D/U$.
multiplying (C–2) by a^4/α^2 gives:

$$\frac{\partial^4W}{\partial x_1^4}+\frac{2(a/b)^2\partial^4W}{\partial x_1^2\partial y_1^2}+\frac{(a/b)^4\partial^4W}{\partial y_1^4}+\frac{Ba^4\partial W}{t_0\alpha^2\partial T}+\frac{a^4\partial^2W}{t_0^2\alpha^2\partial T^2}$$
$$-\frac{B_1^2a^2\partial^4W}{t_0^2\partial x_1^2\partial T^2}-\frac{B_1^2a^2(a/b)^2\partial^4W}{t_0^2\partial y_1^2\partial T^2}=q_1a^4/\alpha^2 \quad \text{(C–3)}$$

where $B_1^2=M/U$.

(C–3) replaces (28) with the effect of shear displacement considered in generating the time history of a forced vibration.

Considering the natural force free modes of vibration, it may be verified that, for $q=0$, (C–1) is not generally separable into time and space product functions unless B–0 or the damping is negligible. It may be said that the damping of the shear mode is incompatible, in general, with the damping of the flexural mode. The incompatibility of in phase harmonic vibrations over the shear plate can be seen by the following argument.

Assume such in phase vibrations:

$$W_v=S_ve^{-k_vt}\cos(n_vt+\phi_v). \quad \text{(C–4)}$$

If (C–4) is to satisfy the force free (C–1) for all time, then it can be shown that the following two linear constant coefficient differential equations in the space variation S_v must be satisfied for every point on the plate:

$$D\nabla^4S_v+S_v^2[M(k_v-n_v^2)-\mu k_v]$$
$$-\frac{DM}{U}(k_v^2-n_v^2)^2\nabla S_v=0 \quad \text{(C–5)}$$

$$S_v(-n_v\mu+2Mn_vk_v)-\frac{2DM}{U}k_vn_v\nabla^2S_v=0. \quad \text{(C–6)}$$

Only the fourth order equation (C–5), together with the boundary equations, serve to define a properly posed problem for the plate's space deflection in the natural mode v. (C-5) can never be made to imply (C–6) as well, as long as the plate has shear rigidity. As an independent condition, (C–6) can only be satisfied for k_v constant over the deflected plate when $-2DM/U=0$. This is the case under the assumption of infinite shear rigidity where $k_v=\mu/2M$.

To emphasize and clarify this argument, consider (C–5) as the frequency equation rewritten as:

$$D\nabla^4S_v+r_{1v}S_v+r_{2v}\nabla^2S_v=0. \quad \text{(C–7)}$$

(C–7) must hold at all points on the plate for there to be an harmonic vibration of the entire plate. It is assumed that a constant damping k_v exists for the mode v across the plate. r_{1v} and r_{2v} are the two (interrelated) characteristic constants of the mode v. They will only depend on the boundary conditions for a given plate. Equating coefficients of (C–5) and (C–7):

$$r_{1v}=M(k_v^2-n_v^2)-\mu k_v$$

$$r_{2v}=\frac{-DM}{U}(k_v^2-n_v^2). \qquad \text{(C–8)}$$

Let the frequency in mode v of the undamped plate be n_{vo}. From (C–6) for $\mu=0$, $k_{vo}=0$ for $n_v\neq 0$ (a nontrivial solution). The characteristic constants from (C–8) are, for this case, evaluated as:

$$r_{1v}=Mn_{vo}^2,$$

$$r_{2v}=\frac{DMn_{vo}^2}{U}. \qquad \text{(C–9)}$$

Thus, for the general damped case, from (C–8), we have:

$$n_v^2=\frac{U}{DM}(r_{2v})+k_v^2=n_{vo}^2+k_v^2, \qquad \text{(C–10A)}$$

and also,

$$n_v^2=\frac{r_{1v}-\mu k_v+Mk_v^2}{M}=n_{vo}^2-\frac{\mu k_v}{M}+k_v^2. \qquad \text{(C–10B)}$$

It is evident that the set (C–10) is only compatible for $k_v=0$. But in this case, (C–6) is always left with the small residual:

$$S_v(-n_v\mu).$$

As a first approximation to determining the damping characteristic of the lightly damped sandwich solar panel, we can assume that for the lowest modes, flexural action dominates and the damping is given as:

$$k_v=\mu/2M=B/2. \qquad \text{(C–11)}$$

The mode shape and frequency may then be approximated by the procedure of section 9 for pure flexural vibrations. A test oscillation in one of these low modes can be initiated and the decrement of amplitude measured from which μ may be determined as in section 6. If μ is sufficiently small, both the set (C–10) and (C–6) can be almost satisfied for $k_v\doteq\mu/2M$, so that for a certain length of time, a near modal vibration for the damped shear-flexure plate may be observed. These modal frequencies may be approximated by solving the characteristic boundary value problem outlined in section 9 with a finite difference approximation to (C–5) used in place of (20). The computation is simplified if the solution (n_{vo}) for $k_v=0$ is first obtained. Then from (C–10B), for $k_v\doteq\mu/2M$:

$$n_v\doteq(n_{vo}-\mu^2/4M^2)^{\frac{1}{2}}, \qquad \text{(C–12)}$$

as in the flexural case.

To convert (C–5) for $k_v=0$ to the finite difference form of (20) requires adding $\frac{a^4M}{U}n_v^2\nabla^2S_v$ in the nondimensional form of (20) to that equation.

$$\nabla^2S_v=\frac{\partial^2S_v}{\partial x^2}+\frac{\partial^2S_v}{\partial y^2}=\frac{1}{a^2}\frac{\partial^2S_v}{\partial x_1^2}+\frac{1}{b^2}\frac{\partial^2S_v}{\partial y_1^2}.$$

We use the central finite difference approximations:

$$\frac{\partial^2S_v}{\partial x_1^2}\doteq\frac{1}{1/r_1^2}(S_{v_{i-1,j,k}}-2S_{v_{i,j,k}}+S_{v_{i+1,j,k}}) \qquad \text{(C–13)}$$

$$\frac{\partial^2S_v}{\partial y_1^2}\doteq\frac{1}{1/r_2^2}(S_{v_{i,j-1,k}}-2S_{v_{i,j,k}}+S_{v_{i,j+1,k}}). \qquad \text{(C–14)}$$

Thus Equation (20) is modified for the shear-flexure plate by adding:

$$S_{i,j,k}[-2(B_1a)^2\{r_1^2+(a/b)^2r_2^2\}p_v^2]$$
$$+S_{i-1,j}[(B_1ar_1)^2P_v^2]+S_{i+1,j}[(B_1ar_1)^2p_v^2]$$
$$+S_{i,j-1}[(B_1ar_2)^2(a/b)^2p_v^2]$$
$$+S_{i,j+1}[(B_1ar_2)^2(a/b)^2p_v^2]$$

to the left side of (20).

With this modification, the procedure of part 9 solves for the undamped frequencies of vibration of the shear-flexure sandwich plate.

To complete the set of equations necessary to define the history of forced vibration of a damped shear-flexure sandwich plate, the last

term on the left of (C–2) must be converted to finite difference form and added to (29).

We use the central difference approximations:

$$\frac{\partial^4 W}{\partial x_1^2 \partial T^2} \doteq \frac{1}{(1/r_1^2)\Delta T^2}\,(4W_{i,j,k} - 2W_{i-1,j,k} - 2W_{i+1,j,k} - 2W_{i,j,k+1} - 2W_{i,j,k-1} + W_{i+1,j,k+1} + W_{i+1,j,k-1} + W_{i-1,j,k+1} + W_{i-1,j,k-1}).$$

A similar approximation is used for $\partial^4 W/\partial y_1^2 \partial T^2$. Thus (29) is modified for the shear-flexure sandwich plate by adding to its left side the following terms:

$$W_{i,j,k}\left[\frac{-4B^2 r_1^2 a^2}{\Delta T^2 \alpha^2 t_o^2} - \frac{4B^2 r_2^2 a^2 (a/b)^2}{\Delta T^2 \alpha^2 t_o^2}\right] + W_{i-1,j,k}\left[\frac{-2B^2 r_1^2 a^2}{\Delta T^2 \alpha^2 t_o^2}\right] + W_{i+1,j,k}\left[\frac{-2B^2 r_1^2 a^2}{\Delta T^2 \alpha^2 t_o^2}\right]$$

$$+ W_{i,j,k+1}\left[\frac{-2(Ba)^2}{\Delta T^2 \alpha^2 t_o^2} - (r_1^2 + r_2^2 (a/b)^2)\right] + W_{i,j,k-1}[-2(Ba/\Delta T \alpha t_o)^2 \ldots (r_1^2 + r_2^2 (a/b)^2)]$$

$$+ W_{i+1,j,k+1}[(Br_1 a/\Delta T \alpha t_o)^2] + W_{i+1,j,k-1}[(Br_1 a/\Delta T \alpha t_o)^2] + W_{i-1,j,k+1}[(Br_1 a/\Delta T \alpha t_o)^2]$$

$$+ W_{i-1,j,k-1}[(Br_1 a/\Delta T \alpha t_o)^2] + W_{i,j-1,k}[-2(Ba/\Delta T \alpha t_o)^2 \ldots (r_2 a/b)^2] + W_{i,j+1,k}$$

$$[-2(Ba/\Delta T \alpha t_o)^2 (r_2 a/b)^2] + W_{i,j+1,k+1}[(Ba/\Delta T \alpha t_o)^2 (r_2 a/b)^2] + W_{i,j+1,k-1}[(Ba/\Delta T \alpha t_o)^2 (r_2 a/b)^2]$$

$$+ W_{i,j-1,k+1}[(Ba/\Delta T \alpha t_o)^2 (r_2 a/b)^2] + W_{i,j-1,k-1}[\ \ldots\ (Ba/\Delta T \alpha t_o)^2 (r_2 a/b)^2].$$

It is evident that in the vibration history solution of part 13, step H no longer gives a diagonal matrix in the interior displacements at $k=3$. In the modified procedure, step H is eliminated and step I reads:

Increment k and repeat steps E through G.

In this modified procedure for the shear flexure plate, the interior solution at each time level is sensitive to the boundary conditions at *that* level.

ACKNOWLEDGMENTS OF NON-NASA PUBLICATIONS

The following is a listing of the non-NASA sources from which the various articles reprinted in this book have been taken.

American Institute of Aeronautics and Astronautics Journal

ROCKET SOUNDINGS IN THE MESOSPHERE, *by* W. NORDBERG

Applied Optics

A VACUUM ULTRAVIOLET PHOTOIONIZATION DETECTOR, *by* A. K. STOBER, R. SCOLNIK, *and* J. P. HENNES

Astronautics and Aerospace Engineering

PHYSICAL MEASUREMENTS FROM METEOROLOGICAL SATELLITES, *by* R. A. HANEL, *and* D. Q. WARK
RELAY, *by* S. METZGER, *and* R. H. PICKARD
TIROS OPERATIONS, *by* E. F. POWERS
TIROS ACHIEVEMENTS, *by* R. M. RADOS
DATA STORAGE FOR METEOROLOGICAL SATELLITES, *by* M. I. SCHNEEBAUM *and* R. A. STAMPFL

East Coast Conference on Aerospace and Navigational Electronics, 10th Baltimore, October 1963

FINE SUN TRACKER FOR ADVANCED ORBITING SOLAR OBSERVATORY, *by* C. CANTOR
AN ATTITUDE CONTROL SYSTEM FOR THE ADVANCED ORBITING SOLAR OBSERVATORY, *by* P. G. FAHLSTROM
A RELIABLE EARTH SENSOR FOR ATTITUDE SENSING, *by* B. K. LUNDE

IEEE Proceedings

THE S-66 LASER TRACKING EXPERIMENT, *by* H. H. PLOTKIN

IEEE Transactions on Space Electronics and Telemetry

SATELLITE ATTITUDE DETERMINATION: DIGITAL SENSING AND ON-BOARD PROCESSING, *by* J. S. ALBUS *and* D. H. SCHAEFER

International Astronautical Congress, 12th, Washington, 1961

ATMOSPHERIC SAMPLING INSTRUMENTATION, *by* N. W. SPENCER

Journal of the Optical Sciences

IMAGE CONSTRUCTION FOR CONCAVE GRATINGS AT GRAZING INCIDENCE, BY RAY TRACING, *by* S. O. KASTNER *and* W. M. NEUPERT

Journal of the Physical Society of Japan

ON THE TEMPERATURE DEPENDENCE OF THE BREAKDOWN FIELD OF $BaTiO_3$, *by* P. H. FANG

Photographic Science and Engineering

MINITRACK CALIBRATION SYSTEM, *by* J. H. BERBERT, J. D. OOSTERHOUT, P. D. ENGELS, *and* E. J. HABIB

MOTS—THE MINITRACK OPTICAL TRACKING SYSTEM, *by* D. W. HARRIS, J. H. BERBERT, E. J. HABIB, *and* B. W. MCKENDREE

The Physical Review

ULTRAVIOLET OPTICAL PROPERTIES OF DIAMOND, *by* W. C. WALKER *and* J. OSANTOWSKI

Space Science Reviews

THE ORBITING GEOPHYSICAL OBSERVATORIES, *by* G. H. LUDWIG

AUTHOR INDEX

Albus, J. S., 221
Bangs, W. F., 639
Bartoe, O. E., 16
Bauer, S. J., 230
Belsheim, R. O., 762
Berbert, J. H., 811, 869
Blumle, L. J., 1
Bodin, W. J., Jr., 913
Boeckel, J. H., 646
Brown, L. W., 475
Bryant, D. A., 491
Cantor, C., 497
Carleton, H., 369
Carlson, D. J., 885
Carrion, W. J., 818, 821
Caudill, L. O., 826
Childs, C. B., 506
Clevenson, S. A., 776
Coates, R. J., 242, 885
Cooper, H. W., 32
Creveling, C., 242
Cunningham, F. G., 937, 965
Davenport, P. B., 251
Dolder, F. P., 16
Duck, K. I., 391
Dunkelman, L., 513, 522, 532
Elsen, W. G., 693
Engels, P. D., 811, 832, 913
Eubanks, A. G., 542
Fahlstrom, P. G., 546
Falwell, R. C., 260
Fang, P. H., 980
Farkas, J. A., 684
Fedor, J. V., 272, 282
Feinberg, P. M., 283, 363
Ferris, A. G., 32
Fitzenreiter, R. J., 1
Foschetti, J. A., 402
Fowler, W. B., 513, 532
Frankel, H. E., 542
Franks, H. J., Jr., 832
Gablehouse, R. H., 16
Genatt, S. H., 22
Graham, G. E., 294
Habib, E. J., 32, 242, 811, 832, 869, 913
Hagemeyer, J. R., 464
Hanel, R. A., 48, 549, 563
Harris, D. W., 869
Hartenstein, R. G., 693
Hennes, J. P., 513, 532, 599
Hilliard, J. J., 713
Hollingsworth, R. T., 706
Jackson, J. E., 1, 230
John, J. E. A., 713
Johnson, T. S., 876
Kahn, W. D., 913
Kastner, S. O., 569
Kiesling, J., 122
Kronmiller, G. C., Jr., 832, 913
Lee, E. Y., 821
Lesko, J. G., Jr., 363
Lindsay, J. C., 16
Ludwig, G. H., 62, 491
Lunde, B. K., 299, 302, 307
Mahoney, M., 242
Mazur, D. G., 93
McCarron, S. G., 991
McConaughy, R. L., 32
McDonald, F. B. 491
McIlwraith, N., 575
McKendree, B. W., 869
Mentzer, W. R., 313
Mercure, R. C., Jr., 16
Metzger, S., 105
Neupert, W. M., 569
New, J. C., 722
Nichols, G. B., 326
Nordberg, W., 425, 443
Ogilvie, K. W., 575
On, F. J., 762
Oosterhout, J. D., 811
Osantowski, J., 605, 611
Paull, S., 336
Pickard, R. H., 105, 111, 122
Plotkin, H. H., 880
Powers, E. F., 141
Raabe, H. P., 346
Rados, R. M., 146
Reber, C. A., 587
Richtmyer, L. E., 549
Rolinski, A. J., 885
Rosette, K. L., 799
Roth, S., 122
Schaefer, D. H., 221
Schneebaum, M. I., 357
Scolnik, R., 599
Scull, W. E., 149
Seddon, J. C., 893
Shaffer, H. W., 913
Simas, V., 925

SLIFKIN, L. M., 506
SMALL, D., 379
SMITH, W., 443
SPAID, G. H., 464
SPENCER, N. W., 583, 587
STAMPFL, R. A., 357, 549, 590
STARK, K. W., 260
STOBER, A. K., 599
STOUT, C., 242
STROUD, W. G., 549, 590
TERENIAK, W. B., 776
THEKAEKARA, M. P., 791
TIMMINS, A. R., 799
TOWNSEND, M. R., 363
WAGNER, C. A., 1001
WALKER, W. C., 605, 611
WARK, D. Q., 563
WENZINGER, C. J., 369
WHALE, H. A., 613, 618
WHITE, A. F., 260
WILKERSON, T. D., 575
WILLIAMS, L. A., 409
WINDSOR, R. M., 626
ZAJAC, F., 379
ZWALLY, H. J., 575

U. S. GOVERNMENT PRINTING OFFICE: 1965 O - 764-173